к научному докладу на соискание ученой степени

доктора химических наук

СКОРБ ЕКАТЕРИНА ВЛАДИМИРОВНА

По теме:

РЕАКЦИОННО-ДИФФУЗИОННЫЕ ХИМИЧЕСКИЕ ПРОЦЕССЫ НА ГРАНИЦЕ МЕТАЛЛОВ ИЛИ ПОЛУПРОВОДНИКОВ С ПОЛИМЕРНЫМИ НАНОСЛОЯМИ

Специальность 1.4.4 - физическая химия

Санкт-Петербург – 2022

Recent Progress of Layer-by-layer Assembly, Free-Standing Film and Hydrogel Based on Polyelectrolytes

Artemii S. Ivanov, Lyubov V. Pershina, Konstantin G. Nikolaev, and Ekaterina V. Skorb*

Nowadays, polyelectrolytes play an essential role in the development of new materials. Their use allows creating new properties of materials and surfaces and vary them in a wide range. Basically, modern methods are divided into three areas—the process of layer-by-layer deposition, free-standing films, and hydrogels based on polyelectrolytes. Layer-by-layer assembly of polyelectrolytes on various surfaces is a powerful technique. It allows giving surfaces new properties, for example, protect them from corrosion. Free-standing films are essential tools for the design of membranes and sensors. Hydrogels based on polyelectrolytes have recently shown their applicability in electrical and materials science. The creation of new materials and components with controlled properties can be achieved using polyelectrolytes. This review focuses on new technologies that have been developed with polyelectrolytes over the last five years.

1. Introduction

The development of materials science has now allowed it to go beyond purely technical boundaries. The main development takes place in the interdisciplinary plane, that is, at the junction of different sciences. Materials are thus increasingly considered not only from the point of view of physics and engineering. The chemical and biological approach to the development of materials is becoming very popular and important.

However, these approaches require unique materials with specific properties. They should be represented by a broad class of molecules with various properties. Equally important is the ability to combine these properties, supplement them with new ones and manage them. Polyelectrolytes have become such a class of substances. Their diversity and properties, various application techniques have become key to the development of materials science and engineering over the past few decades.

However, despite such a relatively long-term study and use of polyelectrolytes, they do not lose their relevance. The emergence of new approaches, techniques, and materials in physics, biology, and chemistry expands the possibilities of using polyelectrolytes. Nowadays, they are starting to be used in completely new

A. S. Ivanov, L. V. Pershina, Dr. K. G. Nikolaev, Prof. E. V. Skorb
Infochemistry Scientific Center of ITMO University
Lomonosova str. 9, Saint Petersburg 191002, Russia
E-mail: skorb@itmo.ru

fields. They are capable of modifying surfaces for corrosion protection, local control and pH variation, and improved biocompatibility. Polyelectrolytes are used in film membranes, filters, and sensors, increasing their selectivity. They are also capable of forming hydrogels with programmable mechanical, electrical, and other properties. Despite a good number of review articles on polyelectrolyte biochemical applications, only a few reviews have focused on the correlation between the molecular structures and their mechanical and physicochemical properties.[1–4] At the same time, there is an increasing trend for the design of self-organized supramolecular structures with the inclusion of polyelectrolytes.[5] The study of the processes occurring between macromolecules makes it possible to create more complex systems.[6] On the other hand, the use of hybrid composites based on polyelectrolytes and inorganic nanostructures makes it possible to study their mutual influence on the properties of the obtained materials.[7,8] Thus, the properties of the composite materials directly depend on the method of interaction of polyelectrolytes with biomolecules or inorganic nanostructures.

In our review, we describe the last articles dedicated to the main areas of the polyelectrolytes approach—layer-by-layer, free-standing films, and hydrogels (**Figure 1**). Based on these applications, the use of these molecules is based on three methods—layering, films without substrates, and hydrogels. Each of these methods opens up exceptional special opportunities for the creation and functionalization of materials. The most relevant are the studies and works on the use of polyelectrolytes, written over the past five years.

2. Layer-by-Layer Approach

The layering method is based on the alternate attachment of oppositely charged polyelectrolytes. The first is applied to a charged or uncharged substrate or particle and is attached to it by Coulomb attraction or physical adsorption forces, respectively. The next polyelectrolyte is attached to the first and is held by the opposite charge. Thus, by recharging the surface, it is possible to create multi-layer coatings. Measurement of charge exchange can be carried out by evaluating the zeta potential between the surface's cation and anion potential.

Due to the large contact area of the polymer with the substrate, it assemblies on any surfaces. The sorption process itself, in this
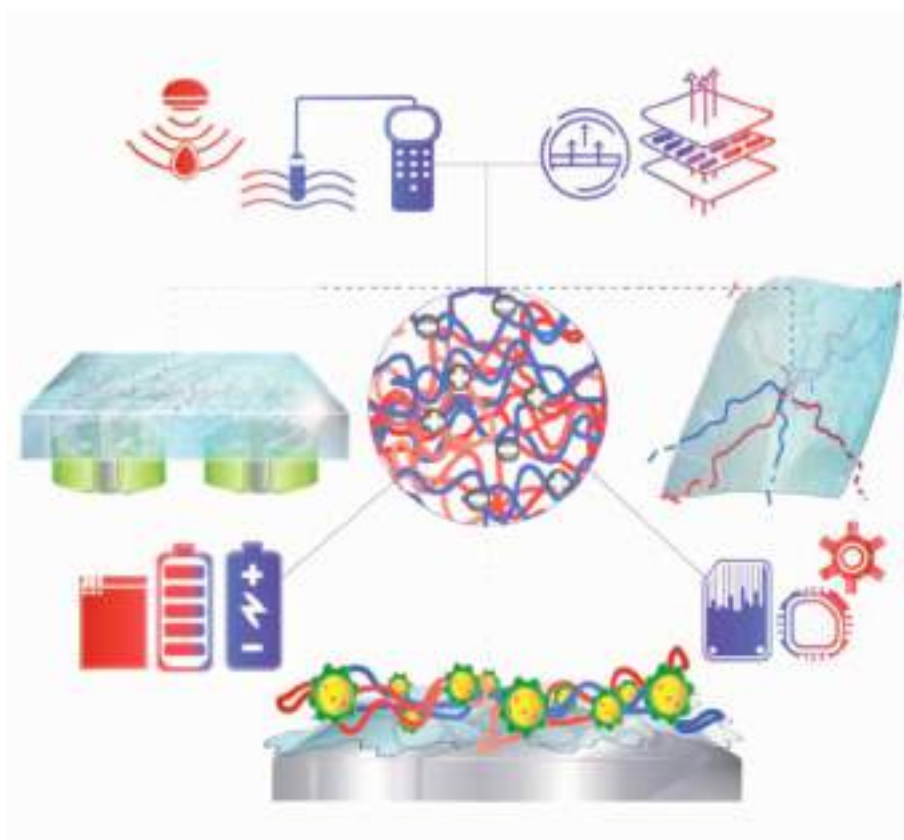
Figure 1. Free-standing films, hydrogels, and layer-by-layer assembly are powerful techniques for polyelectrolytes and last five year progress of area development with specific examples (2016–2021) is discussed in the review.

case, is limited only by the rate of diffusion of molecules from the solution to the surface. When the polyelectrolyte accumulates on the surface, the charge changes, and the next layer's attachment with the same charge does not occur.

There is still no theoretical model for layering processes. However, some patterns have already been established. Thus, the kinetics of layer growth depends significantly on the charge density of the polyelectrolytes used. With their low charge density, the exponential growth of layers is observed, with a high one, linear growth. Thus, the build-up processes can be controlled by selecting the required polyelectrolyte. Its structure is equally important. Linear or branched polyelectrolytes form layers of different uniformity and configuration. So linear polyelectrolytes form more uniform layers, in contrast to branched ones. Surface rinsing with water has also been successfully used to obtain monolayers. This removes excess adhered molecules and achieves an even layer. Polyelectrolyte layers allow the formation of hydrogels at various levels of organization. For example, the swelling of the layers poly-(L-lysine) (PLL), poly-(L-glutamic acid), and hyaluronan has been shown.[9]

It can also be controlled by varying the ionic strength and the solution's nature from which the application occurs. Solvent selection is one of the key conditions in layering. The interaction of solvent molecules with polyelectrolytes determines their conformation. This conformation has a significant impact on the formation of layers. Depending on the solvent, the polymer can coagu-

late into globules. This unfavorable conformation will prevent it from being applied to a substrate. It is necessary to select a solvent that cannot screen the charges in the polyelectrolyte's repeating chains. This will allow it to take on more linear conformation due to the electrostatic repulsion of functional groups.

Similarly, the polyelectrolyte conformation can be controlled by the concentration of the salt in the solution. High concentrations of dissolved salt promote the twisting of polyelectrolytes into globules. A small number of ions, in turn, are not capable of screening the charge of functional groups. Due to this, the polyelectrolyte takes on a linear conformation.

Modification of various 2D and 3D surfaces by layers of polyelectrolytes allows a significant development of their functional applications. This chapter focuses specifically on layering applications related to biology, health care, and medical sensors. It is for these rapidly developing areas that this technique is extremely important.

2.1. Biomimetics and Drug Delivery

An important challenge for biomimetics is creating surfaces and instruments for the delivery and controlled release of various drugs[10] and proteins.[11] This allows you to target damage to the body. A widely used biocompatible surface for this application is titanium dioxide. The modification of titanium dioxide by
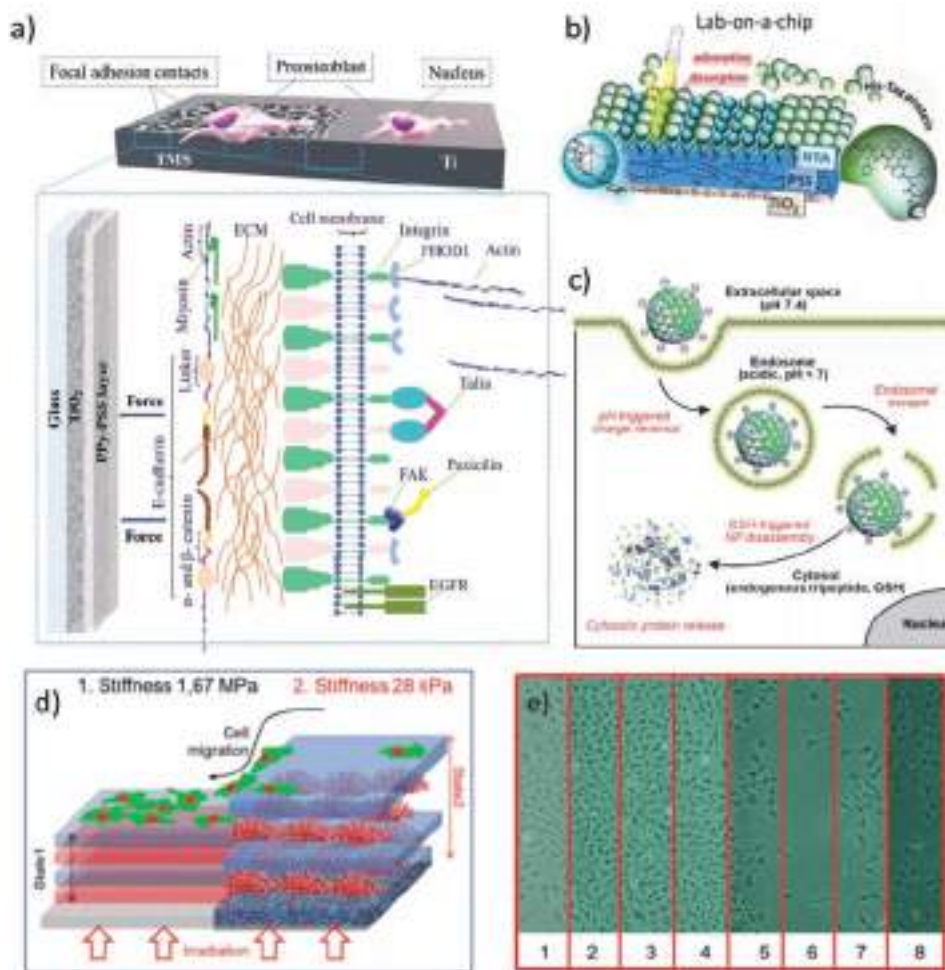
**ADVANCED
SCIENCE NEWS**
www.advancedsciencenews.com

acro-
olecular
Bioscience
www.mbs-journal.de

Figure 2. a) The schematic illustration of MC3T3-E1 behavior during their formation of focal adhesion contacts on different topography of mesoporous and smooth titanium surface. The model of direct mechanotransduction identifying the direct link between an extracellular matrix (ECM) and cell membrane. Membranes serve as an interface between the cell and its environment. Cell adhesion molecules embedded in the membrane, such as integrin or E-cadherin, allow interactions with the ECM and neighboring cells, respectively. Abbreviations: TiO_2—ultrasonically generated titanium dioxide mesoporous surface, PPy—polypyrrole, PSS—polysodiumstyrenesulfonate, FHOD1—FH1/FH2 domain-containing protein 1, FAK—focal adhesion kinase, EGFR—epidermal growth factor receptor. Reproduced with permission.[14] Copyright 2020, Wiley-VCH. b) TiO_2 surface decorated with a layer-by-layer assembly of polystyrenesulfonate (PSS) and nickel−nitrilotriacetic acid (NTA) to bind (poly) histidine-tagged (His-Tag) proteins. Spatially resolved protein desorption is regulated by irradiation with light, causing a local pH shift that affects the pH-sensitive NTA/protein complex but not the PSS/NTA assembly. Reproduced with permission.[112] Copyright 2019, American Chemical Society. c) Scheme depicting intracellular protein delivery from a protein−polyphenol nanoparticles. Reproduced with permission.[15] Copyright 2020, American Chemical Society. d) Schematic of cell reorganization over the surface after irradiation. e) Cell density zone relevant calculation after irradiation of the surface after 30 min of cell migration. Reproduced with permission.[16] Copyright 2016, Wiley-VCH.

layer-by-layer deposition of polyelectrolytes is a powerful tool for the development of biomimetics.[12,13]

In particular, Ulasevich et al. presents the use of polypyrrole (PPy) and polyethyleneimine (PEI) polyelectrolyte layers for the controlled and targeted release of bone morphogenic protein (BMP).[14] For this, BMP was applied to the surface of mesoporous titanium oxide, and then PPy-PEI was applied layer by layer. Due to the photothermal properties of PPy, a controlled release of BMP was achieved under the influence of light. This was demonstrated by the growth of prostate cells that responded to the amount of BMP released (**Figure 2**a). Such a hybrid TiO_2-PPy-PEI system is very promising for lab-on-a-chip applications (Figure 2b).

Also, the layering method can be used to form nanoparticles and nanocapsules for drug and protein delivery.[15] In this work, the use of sacrificial mesoporous silicon nanoparticles is proposed. They are coated with layers of protein and tannic acid. This structure allows the clusters to change the surface charge from negative to positive, depending on the pH of the medium. This enables them to avoid capture by endosomes. Once inside the cell, competitive interactions (mainly with glutathione) lead to structural stratification and protein release (Figure 2c). This principle has promising results for intracellular drug and protein delivery.

Another example of the use of TiO_2-based substrates can be the control of cell movement. This article describes the behav-

**ADVANCED
SCIENCE NEWS**
www.advancedsciencenews.com

[M]acro-
molecular
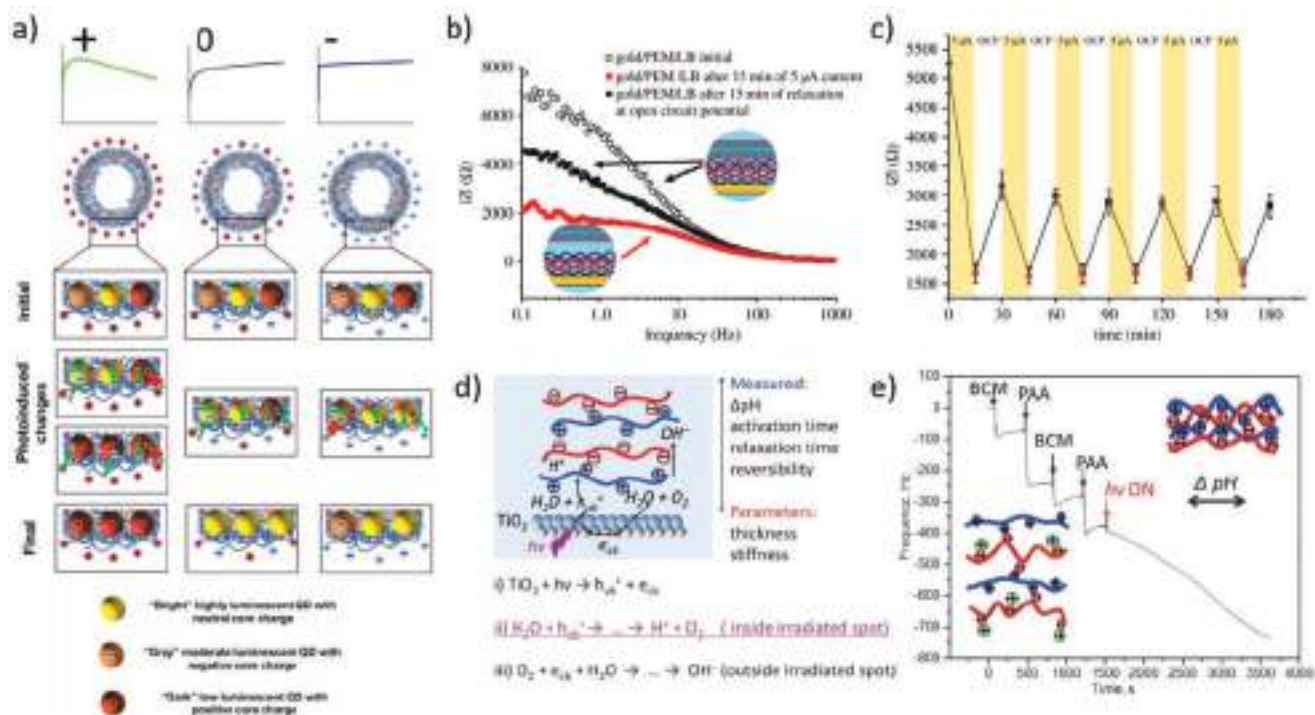Bioscience
www.mbs-journal.de

Figure 3. a) Scheme of charge-transfer processes in positively, neutrally, and negatively charged nanoparticle-doped polyelectrolyte microcapsules. Reproduced with permission.[27] Copyright 2020, American Chemical Society. b) Impedance curves of both plots of impedance spectra for the gold/PEM/LB composite before passing 5 µA current, after 15 min of current passing, and after 15 min of relaxation. c) Cycles of passing current and relaxation at open circuit potential associated with impedance oscillations at 1 Hz of gold/PEM/LB composite due to LB repulsion in acidified media via hydroquinone oxidation. Reproduced with permission.[29] Copyright 2019, The Royal Society. d) Surface decoration and photoinitiated light–pH reactions. Primary and secondary photocatalytic reactions on TiO_2 resulting in a local change of pH. e) Light activation and relaxation of a high-amplitude switchable pH-sensitive layer-by-layer assembly on a low-photoactivity TiO_2 layer. Reproduced with permission.[30] Copyright 2016, Wiley-VCH.

ior of cells on surfaces with varying surface stiffness.[16] It has been shown that preosteoblast cells predominantly migrate to areas with greater surface rigidity. Surfaces with controlled hardness were obtained by TiO_2 substrate modification with block copolymer micelles (BCM) and poly-(acrylic acid) (PAA). Due to the photosensitivity of the titanium oxide surface, local pH changes are possible. This, in turn, changes the self-assembly stiffness. Thus, the light-controlled behavior of bacteria is shown (Figure 2d,e).

Biocompatible multilayer coatings have also been produced based on heparin and PEI.[17] The stability of these coatings has been further enhanced with catechols.[18] Their introduction also made it possible to incorporate copper particles through a coordination bond. In this way, coatings were obtained to gradually release heparin and nitrogen oxide (NO). This effect allows achieving a high anti-thrombogenic effect.[19]

Research shows the possibility of the successful application of polyelectrolytes to create biocompatible surfaces and materials. They allow for targeted delivery of proteins and drugs, as well as their controlled release.

2.2. Stimuli-Responsive Cover Shells

Layer-by-layer deposition of polyelectrolytes has been successfully used to coat magnetic, fluorescent, and plasmonic nanoparticles.[20,21] The most important principles and mechanisms for the formation of stimuli effects in polyelectrolyte systems are explained by Delcea et al.[22] These principles allow to create systems that respond to various stimuli.[23] Such systems are essential for the controlled delivery and release of drugs even deep into tissues.[24] However, such coatings can change the response signal.[25,26] The most revealing example is the change in the photoluminescence of quantum dots covered with a polyelectrolyte shell. Thus, the study of the phenomenon of charge transfer in polyelectrolyte layers is an important task. This article analyzed the change in fluorescence associated with different thicknesses and charges of the capsules. Nifontova et al. determined that the thickness of the layers has little effect on the change in fluorescence.[27] The decisive condition is the charge of the capsule surface (**Figure 3**a). The recharging processes of quantum dots and their surrounding capsules are of decisive importance for fluorescence stability.

Also of considerable interest is the development of polyelectrolyte coatings with incorporated photodegradable esters. The photolysis of ethers under the action of light leads to the disclosure of these shells, which leads to the release of substances imprisoned inside.

A number of works are devoted to the use of self-assembly layering to create stimulating, responsive interfaces. Modification with hybrid coatings based on polyelectrolytes and silicon nanoparticles improves the sensitivity by increasing the adsorption area and, thus, allows the determination of lower

ADVANCED
SCIENCE NEWS

www.advancedsciencenews.com

[M]acro-
molecular
Bioscience

www.mbs-journal.de

concentrations of volatile organic compounds.[28] Interfaces, using photochemical or electrochemical stimuli, can change the pH locally. Such pH-sensitive layers can be successfully used to obtain freestanding films. This paper describes a layer-by-layer PEI/poly(sodium 4-styrene sulfonate) (PSS) self-assembly on which a lipid bilayer is applied. The production of such layers is very important for bio-applications.[29] Using electrochemical oxidation of hydroquinone, the pH of the environment was reduced from 7 to 3–4. In this case, the protonation of the phosphate groups of the lipid bilayer took place. As a result, the distance between the protonated lipid bilayer and the positively charged PEI increased. This made it possible to obtain a freestanding lipid bilayer. Oscillations of impedance associated with the acidification process of the medium are shown in Figure 3b,c.

A change in pH can also be induced by irradiating the titanium dioxide surface.[30] During this process, water splits, which leads to a decrease in pH. This change causes a rearrangement of bonds in polyelectrolytes. This can lead to a local change in the mechanical and other properties of such surfaces modified with polyelectrolytes (Figure 3d,e).

Equally important is the protective application of layer-by-layer self-assemblies. They are used to protect particles from corrosion and photocorrosion.[31] Thus, polyelectrolyte coatings can significantly improve nanoparticles and quantum dots' properties and stabilize them in various media.

2.3. Electrode Modification

Recently, many assembly methods have been developed for chemical and physicochemical modification of surfaces, including in the sensing field. The special attention is focused on the method of layer-by-layer application of modifiers for nanostructuring the working part of sensors and creating coatings with a wide range of functionality. For the nanostructuring of electrodes surface in sensor devices, various types of layer-by-layer modifications are known, depending on the substrates' nature and the modifiers themselves. Various options for modifying the working surface of sensor devices are shown in the **Table 1**.

It's known the layer-by-layer assembly in biosensing for the creation of biosensitive elements based on bacterial and yeast strains,[32] binding protein,[33] and aptamers.[34] The most commonly used layer-by-layer assembly based on electrostatic interactions using polyelectrolytes,[35–38] silver nanowires with oppositely charged part,[39] quantum dots,[40] carbon nanotubes,[41,42] and nanoparticles Bi/graphene oxide.[43] Described is the production through layer-by-layer electrodeposition of polyethylene and organometallic frameworks[44] and Au nanoparticles and polyelectrolytes.[45] A modification of the electrochemical sensor with the inclusion of an electroactive dye molecule is also proposed.[46]

The use of layer-by-layer deposition of polyelectrolytes for modifying electrodes makes it possible to significantly increase the sensitivity and accuracy of sensor systems.

3. Freestanding Films

Freestanding films based on polyelectrolytes have become an important area of research associated with the interest in creating the production of packaging and consumables following the principles of green chemistry.[47] The polyelectrolyte film synthesis process does not require toxic reagents, solvents, and extractants and occurs at ambient temperature and pressure.[48] Products made from polyelectrolyte films are biodegradable and easily recyclable.[49] Freestanding polyelectrolyte films with excellent processability can be customized easily into arbitrary shapes as actually needed and is suitable for mass production to meet low-cost requirements.[50] Despite this, the creation of such films is based on complex physicochemical processes that make it possible to create films with desired properties and use them as model systems for studying biological macromolecular interactions.[51,52]

3.1. Membranes

Membrane separation methods are widely used for various purposes: environmental cleaning,[53,54] selective ion concentration,[54,55] and water desalination.[56,57] The principle of forming a freestanding film is based on the formation of a polyelectrolyte complex (PEC).[58] The complexation process includes compensating the charge of the polyelectrolyte with the oppositely charged polyelectrolyte. This process is influenced by factors such as ionic strength, pH, and dissociation constant. A characteristic feature of PECs is their ability to carry out ionic transport under polymer dynamics control.[59] Different dynamics of ions caused by differences in local hydration levels into PEC. Thus, the processes of ion transfer in polyelectrolyte membranes depend on the thermodynamics of macromolecules. The pH of the medium also affects membranes' properties, as it changes the pore size in the membrane. For example, for a membrane with a PEI/PSS composition, changes in the pore size are observed with varying pH in the range from 3.6 to 5.0.[60] In this case, the pore size grows with an increase in pH from 60 to 650 nm. A change in the pore diameter can be achieved by changing the pH values if one of the polyelectrolytes is a "weak" acid or base. To impart functional properties to PEC membranes, they are modified with various materials with desired properties. The use of such 2D materials as graphene oxide affects the properties of PEC.[55]

The number of competing processes increases as one more charged particle appears in the system—graphene oxide. In this regard, a more complex redistribution of charges occurs with competing for polyelectrolyte-graphene processes (**Figure 4**a). The course of competing processes in the membrane with a change in the type of mobile ion can be determined using X-ray diffraction (Figure 4b). Polyamines as positively charged polyelectrolytes interact with graphene oxide, which compensates for the charge of the polyelectrolyte. When mobile ions migrate into the membrane, a competing charge compensation process occurs. This competing process makes it possible to increase the membrane's selectivity concerning a specific type of ions in the series K^+, Na^+, Cs^+, and Li^+. It should be considered that each process of charge compensation in the polyelectrolyte is accompanied by a rearrangement of the hydrated shell of both the ion and the macromolecule.

Membranes can also be modified with semiconductor structures (Figure 4c). Silicon dioxide, which can be co-precipitated electrochemically with polyvinyl alcohol, as well as coated with

Table 1. Layer-by-layer modification of sensor electrodes.

Substrate	Composition of layers	Sensor design	Details of modification	Application	Reference
Hydrogel of PVA modified with *N*-vinylpyrrolidone	Bacterial microorganisms *Paracoccus yeei*, *Pseudomonas veronii*, and *Bacillus proteolyticus*; yeast cells of *Ogataea angusta*, *Blastobotrys adeninivoran*s, and *Debaryomyces hansenii*	Bioreceptor element fixed to the surface of the Clarke electrode with a nylon mesh	Biosensitive elements based on bacterial and yeast strains are created via the layer-by-layer immobilization of microorganisms in a PVA hydrogel modified with *N*-vinylpyrrolidone to formation of three layers of the cell containing gel	Biosensors for determination the biochemical oxygen demand	[32]
Screen-printed electrodes	OBP of *Drosophila melanogaster*	Polyethyleneglycol terephthalate is substrate of the electrodes, conductive graphite paste, rGO, and AuNPs, OBPs	Through one-step reduction, AuNPs and rGO are deposited on the screen-printed electrodes for improving the electrochemical properties of electrodes. After the electrodes are immobilized with OBPs	The biosensor for the determination of bitter taste	[33]
GCE	PTCA, rGO, and TBA	APTES-modified GCE with PTCA-rGO composite film	The APTES-modified GCE electrode is immersed in GO solution. The GCE/rGO electrode is immersed in a PTCA aqueous solution to form a PTCA layer on the electrode and dried in N_2. The electrode is designated as the GCE/rGO/PTCA electrode	Biosensing in clinical diagnosis (thrombin determination)	[34]
PGE	PDPA, PMA, and Pt particles	The PGE surface modified with a mixture of chitosan and MWCNT followed by deposition (Pt/PMA/PDPA)n	The multilayer film (Pt/PMA/PDPA)n on the chitosan MWCNTs/PGE surface is obtained by consistent deposition on the electrode surface of a layer oxidized PDPA as a cationic layer by electropolymerization, the anionic layer PMA on the cationic layer of PDPA via electrostatic forces and Pt particles	As an anode material in direct methanol fuel cells	[35]
GCE	MWCNT, NGr, and PEDOT:PSS	GCE modified by MWCNT-NGr/PEDOT:PSS multilayer thin film	The PEDOT:PSS is drop-coated on the surface of the clean GCE, and placed under an infrared lamp until dry. After that the MWCNT-NGr dispersion is dropped on the GCE surface and dried again	A supercapacitor as the electrochemical energy storage	[36]
Glass substrate	MoS_2/PDDA	Microfluidic chip based on glass substrate with ITO coated modified by MoS_2/PDDA hybrid film	The WE is soaked in the as-prepared carboxyl-functionalized MoS_2 nanosheet solution and PDDA solution alternately. MoS_2/PDDA multilayer film is assembled through electrostatic binding	Clinical diagnosis (immunosensing of alpha-fetoprotein)	[37]
SPCEs	CB and polyelectrolytes (PAA or PEI)	SPCEs is modified with CB-polyelectrolyte films	The electrodes modified with 2, 3, and 4 bilayers of CB-PEI and CB-PAA using the drop casting approach	Immunosensor for the determination of cancer antigen biomarker CA19-9	[38]
Glass substrate	AgNW-NH_2 and AgNW-COOH	The conductive electrode based on glass substrate with (AgNW-COOH/AgNW-NH_2)n multilayers	The glass substrate is immersed into AgNW-COOH and AgNW-NH_2 alternately to form desired number of bilayers is reached	Optoelectronic devices	[39]
Quartz substrates	CdSe/ZnS-COOH QDs (negatively charged) and CdSe/ZnS-NH_2 (positively charged)	Luminescence temperature sensor based on ordered all-QD multilayers.	The substrates are immersed into CdSe/ZnS-NH_2 QDs solution and then rinsed with deionized water. Next, the substrates are immersed into the CdSe/ZnS-COOH QDs solution to synthesize and assemble a periodic multilayer of CdSe/ZnS samples	Applications requiring sensors for optical thermometry	[40]

(Continued)

ADVANCED
SCIENCE NEWS

www.advancedsciencenews.com

acro-
olecular
Bioscience

www.mbs-journal.de

Table 1. Continued.

Substrate	Composition of layers	Sensor design	Details of modification	Application	Reference
ITO-coated glass substrates	ZnONPs complexed with PAH and MWNTs	ITO-coated glass substrates is modified with PAH-ZnO/MWNT LbL films	The films are fabricated by alternated immersion of the ITO substrate into a PAH-ZnO solution and MWNT dispersion	Supercapacitors electrodes for energy storage applications	[41]
Cotton fabrics	Poly(ethylenimine), ammonium polyphosphate and CNTs, followed by post-treatment with PDMS.	The conductive cotton fabric with (bPEI/CNTs)10/APP/PDMS-coated	Cotton fabric is immersed into bPEI solution, then rinsed with deionized water and dried; then the bPEI-coated fabric is immersed into CNTs dispersion for and dried. This process is repeated to obtain multilayer of (bPEI/CNTs)n-coated fabric	Wearable electronics as multifunctional smart textiles	[42]
GCE	Bi-BTC and rGO	GCE modified by [Bi-BTC/rGO]$_2$ conductive film	Bi-MOFs suspension is cast on the GCE surface and dried. After that GO solution is dripped on Bi-MOFs/GCE to form one Bi-MOFs/GO layer on the GCE. The same way is used to obtain the second layer. Finally, [Bi-MOFs/GO]$_2$/GCE is reduced to [Bi-MOFs/rGO]$_2$/GCE by an electrochemical method	Assay of Pb^{2+} in real water samples	[43]
LIG substrate	PANI and the metal-organic frameworks MOFs crystals	The LIG with deposition of multilayer films of PANI and MOF via an electrochemical method, and assembly of LIG-PANI-ZIF-67 into microsupercapacitors	The deposition of multilayer films of PANI and MOF via an electrochemical method	The power supply for the small and wearable devices	[44]
ITO and GCE	PEDOT/PEDOT-SH/Au	Multilayered PEDOT/PEDOT-SH/Au nanocomposite on GCE and ITO	Sequential deposition of layers PEDOT and PEDOT-SH; electrodeposition of Au NPs to form (PEDOT/PEDOT-SH/Au) nanocomposite on glassy carbon electrode surface	Detection of nitrite in tap water and milk samples	[45]
ITO coated PET substrates	LbL assembled Alizarin red S and LDHs (ARS/LDHs)n	Solid state sensor indium tin oxide coated PET (ITO/PET) LbL assembled (ARS/LDHs)n	Alternate immersion of the electrode surface in aqueous ARS solution and LDH dispersion with optimal pH values to obtain multilayer films of (ARS/LDHs)n	Flexible electrochemical sensor to detect Al^{3+} ion accurately	[46]

Abbreviations: PVA—poly(vinyl alcohol); OBP—odorant-binding protein; AuNPs—gold nanoparticles; GCE—glassy carbon electrode; PGE—pencil graphite electrode; rGO—reduced graphene oxide; PTCA—3,4,9,10-perylenetetracarboxylic acid; TBA—thrombin aptamer; APTES—3-aminopropyltriethoxy silane; PDPA poly(diphenylamine); PMA—phosphomolybdic acid; MWCNT—multiwalled carbon nanotubes; NGr—N-doped graphene; PEDOT:PSS—poly(3,4-ethylenedioxy-thiophene):poly(styrenesulfonate); PDDA—poly(diallyldimethylammonium chloride); ITO—indium-tin oxide; WE—working electrode; SPCEs—screen-printed carbon electrodes; CB—carbon black; AgNW—silver nanowires; QD—quantum dot; ZnONPs—ZnO nanoparticles; PAH—polyallylamine hydrochloride; PDMS—poly(dimethylsiloxane); bPEI—branched poly (ethyleneimine); LIG—laser-induced graphene; PANI—porous polyaniline; MOFs—metal-organic frameworks; PET—polyethylene terephthalate; LDHs—layered double hydroxides.

polystyrene-block-poly (2-vinyl pyridine), allows varying the degree of membrane swelling (Figure 4d).[61] In this case, competing processes are also observed that take place inside the membrane. The swelling rates of polyelectrolytes and silicon dioxide are different, which leads to a competing hydration process between them (Figure 4e). Varying the solvent also affects the degree of swelling of the composite membrane. All this leads to a predetermined change in the pore diameter.[61] Modification of polyelectrolyte membranes with semiconductor particles makes it possible to switch their hydrophobicity/hydrophilicity. PSS and poly(diallydimethyl-ammoniumchloride) (PDDA)

membrane containing TiO$_2$ demonstrate switchable hydrophobicity/hydrophilicity. The counterion exchange influences this switching process. Counterions Cl$^-$, SCN$^-$, PF$_6^-$, and perfluorooctanoate result in additional charge compensation into the membrane. Modification of PEC with various nanostructures makes it possible to chemically control their properties and parameters.

The use of modified membranes makes it possible to use them in industry and the environment and study biomimetic processes and the possibility of programming the properties of materials with their help.
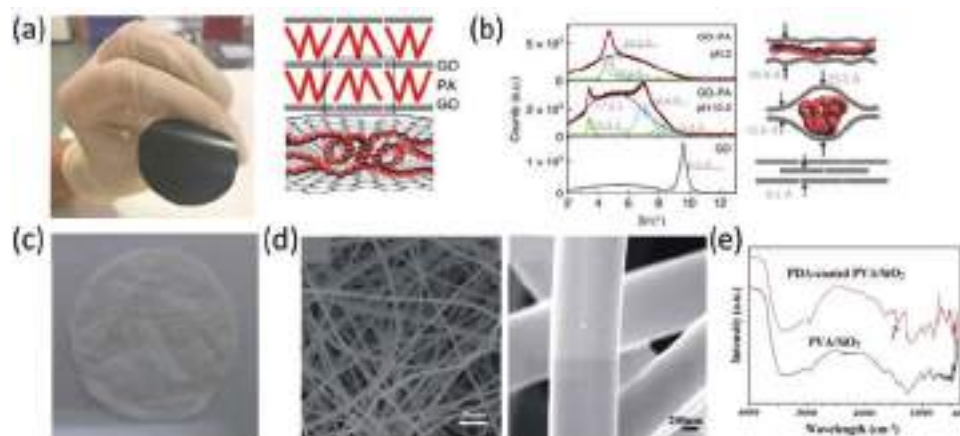
Figure 4. a) Photograph of a 1-μm-thick freestanding GO–PA 25 kDa membrane. b) Schematic illustration of the sandwiched architecture of our membranes. Grey lines, GO layers; red zigzag lines, polyamine molecules. The bottom half of the panel shows the magnified structure, with the chains and hexagonal planes representing polyamine molecules and GO layers, respectively. Schematic illustrations for the membranes' structure depending on pH of the solution during assembly based on the X-ray diffraction data. Reproduced with permission.[55] Copyright 2021, Nature Publishing Group. c) Optical photo of the as-prepared PVA/SiO$_2$ fibrous membrane. d) SEM images of the as-prepared PVA/SiO$_2$ fibrous membrane at a different level of magnification. e) ATR-FTIR spectra of as-prepared PVA/SiO$_2$ fibrous membrane before and after PDA coating. Reproduced with permission.[61] Copyright 2017, Royal Society of Chemistry.

3.2. Chemical Sensing

PEC is used in chemical sensing to create various devices. The possibility of incorporating selective reagents into films makes it possible to create technologically simple solutions. PEC can also act as a buffering agent for unstable reagents over time or when exposed to air. The most apparent application of PEC films is their ability to be stimuli-responsive for such external factors as pH value, chemical ions, media, temperature, etc.[62,63] The simplest way to detect changes in the morphology of PEC films is photodetection over a pre-structured film surface.[64] An example of such a film is the PAA and poly-(allylamine hydrochloride) complex, which, when structuring the microarray, allows detecting external environmental changes.[65] These changes are minor or are invisible to the human eye are magnified and transformed in real-time into diffraction patterns that can be perceived and visualized, even with the naked eye, on the laser scattering patterns. The ability to observe changes on the surface or in the PEC film's thickness determines the most preferred method of instrumental detection. These methods include many spectral analysis methods such as IR spectroscopy,[66] Raman spectrometry,[67] UV–vis spectroscopy,[68] and others.

PEC property of absorbing water is widely used to determine the humidity.[69] Due to its high molecular weight, PEC allows the adsorption of a large amount of water which can be detected using a QCM sensor.[69] The combination of a dual detection method—by the morphology of the film and UV–vis—improves moisture determination accuracy. For this, PEC film patterning and its modification with hygroscopic substances are used. One such example is a poly (diallyldimethylammonium chloride)/heparin film modified with cobalt chloride (**Figure 5**a).[70] Nikolaev et al.[70] showed that even in such a simple system, complex, competitive thermodynamically favorable molecular hydration reactions proceed. The incorporation of redox molecules, such as ferrocene, into

the polystyrene sulfonic acid matrix, allows nitric oxide redox detection.[71]

PEC films can also be used as a surface-enhanced Raman scattering (SERS) background. Films make it possible to grow nanostructures for SERS in situ.[72] Also, the application of the gradient structure formation based on the Liesegang rings formation process allows the formation of multifunctional complex films (Figure 5b). The ordered structure of silver nanoparticles in a film of agarose and pectin demonstrates a selective response to benzenethiol, which is a calibration standard for the determination of pesticides (Figure 5c).[72]

Separately, it should be noted the mechanism of inclusion of biomolecule films into the PEC composition. Since most biomolecules themselves are "weak" polyelectrolytes, they can interact with the PEC matrix. Such interaction can lead to the preservation of the activity of the bio-recognizing element of the chemical sensor. For example, the inclusion of the enzymes glucose oxidase and horseradish peroxidase into the PEI film makes it possible to create flexible electrochemical sensor platforms.[73] The development of freestanding films based on PEC opens up opportunities for creating health monitoring devices and emerging energy and bioelectronics applications.

3.3. Antibacterial and Cell-Support PEC Films

PEC films based on biopolymers are biocompatible and biodegradable. These facts make it possible to use them in biomedicine and tissue engineering applications. Based on polyelectrolyte membranes and titanate/graphene nanostructures, freestanding films possess a good antibacterial activity[74] (**Figure 6**a,b). Alginate, chitosan, and gelatin are used for the tissue engineering substrates. These polyelectrolytes serve as cell scaffolds for 2D and 3D cell cultures. Natural polysaccharides such as chitosan and gellan gum are appropriate precursors for polyelectrolyte complexation. Chitosan is a linear cationic polyelectrolyte
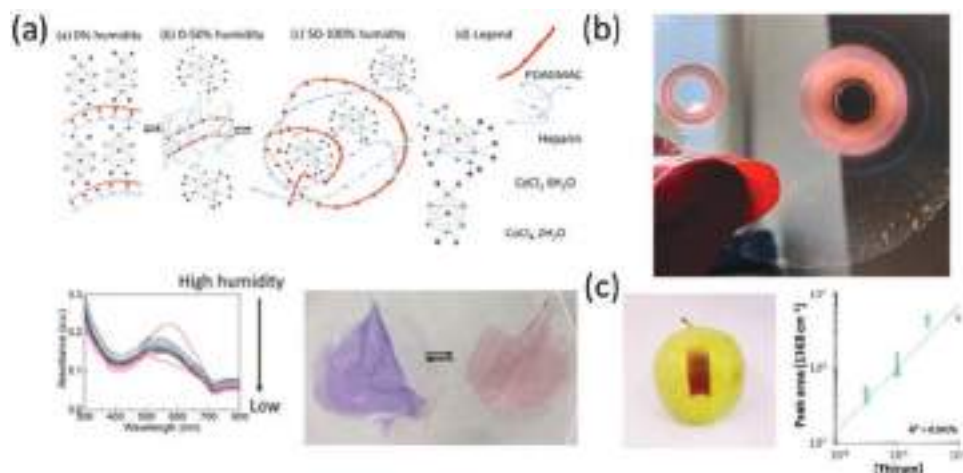
ADVANCED
SCIENCE NEWS

www.advancedsciencenews.com

Macro-
molecular
Bioscience

www.mbs-journal.de

Figure 5. a) Proposed mechanism of PDADMAC/heparin/CoCl$_2$ film swelling during humidity measurements: from the dried film with salt crystals (i) to reptation model for the PE complex melt (ii), blob formation at high humidity (iii), and legend for schematics (iv), UV–vis calibration curve for the peak area dependence on humidity. The optical image of PDADMAC/heparin/CoCl$_2$ film color transition depends on humidity. Reproduced with permission.[70] Copyright 2020, American Chemical Society. b) Photo of silver melamine thin film as flexible platform 2 wt% (upper pattern) 0.2 wt% (below the pattern), correspondingly. c) Transfer the pesticide from the apple surface to the film by spraying ethanol. Correlation of the peak area of the CS stretching with the thiram concentration. Reproduced with permission.[72] Copyright 2021, The Royal Society of Chemistry.

derived from chitin, one of the richest polysaccharides appearing in nature. Gellan gum is a linear anionic polysaccharide formed by Sphingomonas elodea bacteria.[75] PEC fibers obtained with chitosan and gellan gum exhibit high mechanical strength, which is an important factor in interactions with living cells (Figure 6c). The antibacterial activity of the film is shown when the PEC film was modified with the antibiotic levofloxacin (Figure 6d). In addition, when the same PEC was modified with semiconductor TiO$_2$ nanostructures, it was possible to initiate fibroblast cells' growth (Figure 6e).[76] The chitosan/levofloxacin freestanding film is another example of a biocompatible PEC biopolymer, a self-coacervated silk-like protein.[77] The PEC is formed based on liquid–liquid phase separation. This interaction is somewhat complicated since there is an interaction of two "weak" polyelectrolytes. Nevertheless, it is of great interest both from the point of view of biomedicine and from the point of view of biotechnology. Protein-based PECs are thermodynamically metastable but deformable and low-interfacial energy assemblies (Figure 6f). Protein PECs can be strong adhesive assembly between cellulosic surfaces.

Poly(4-styrenesulfonic acid), poly(diallyldimethylammonium chloride) (PDADMAC) based films exhibit antibacterial activity (Figure 6g–i).[78] PEC film is the robust, transparent, and ultralow bacterial-fouling film synthesized via spin-coating of complex coacervates. Poly(4-styrenesulfonic acid), PDADMAC PEC film demonstrates the safety and biocompatibility necessary for implementing antifouling coatings.

Freestanding films based on biopolyelectrolytes and biocompatible polyelectrolytes will find application in biomedicine and make it possible to create complex programmable, biomimetic systems. Freestanding films have a significant advantage over other methods of creating polyelectrolyte interfaces since their use does not depend on the substrate material. This makes freestanding films the most promising material for applied and fundamental research.

4. Hydrogels

Polymer gels are networks of polymer chains cross-linked by covalent bonds. Due to swelling with solvent molecules, they have a significant volume. A high water-absorption capacity is also characteristic of polyelectrolyte gels.[79] During dissociation, charged units are formed in the polymer chains. Due to the same charge, the chains begin to repel each other and stretch. Thus, the gel increases significantly in size. In addition, the contribution is made by the electrostatic repulsion of counterions formed during dissociation. They create osmotic pressure, which also increases the volume of the hydrogel.

Changes in external conditions can change the distribution of bonds in gels, due to which their collapse is possible. Hydrophobic interactions and hydrogen bonds can significantly reduce the volume of the gel. Sensitive gels can be divided into thermo-, photo-, and pH-sensitive depending on the effect of collapse.[80,81] In addition, a change in bonds within gels formed by different polyelectrolytes can significantly change their mechanical properties.[82] This makes polyelectrolyte-based hydrogels an attractive material for the design of stimulating responsive materials, flexible electrical components.[9,83,84]

4.1. Flexible Electronics

New requirements for electronic devices lead to the fact that they must have more and more specific properties. In particular, electronic components for biomedicine and wearable electronics should have special properties.[85,86] In addition to optimum electrical properties, they must have special mechanical properties.[87] Flexibility, extensibility, deformability—these are just some of the properties required for new generation electronics.[88–90] The creation of a class of electronic components based on soft materials will pave the way for the design of artificial organs, bioprostheses, etc.[91]
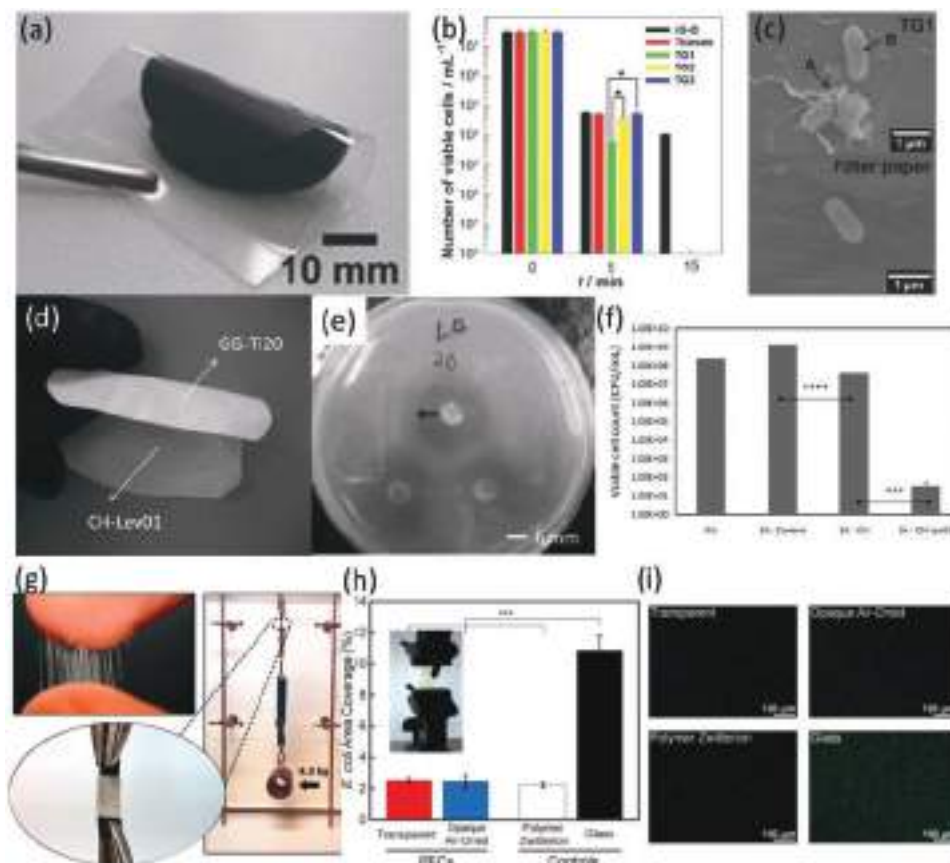
Figure 6. a) Side-view photoimages of layered titanate/graphene PEC freestanding film, b) Time-dependent variation of the number of viable *E. coli* cells dropped on titanate/graphene PEC freestanding film, c) FE-SEM images of *E. coli* cells on the titanate/graphene PEC freestanding film after exposure for 15 min. Reproduced with permission.[74] Copyright 2013, Wiley-VCH. d) Photograph of atypical dual-layer material and e) photograph of qualitative antimicrobial test of chitosan/levofloxacin film against *E. coli*., the inhibition zone is indicated by the arrow, f) Effectiveness against *E. coli* expressed inviable colony counts (CFU/mL) for chitosan/levofloxacin, chitosan, and control (inoculum without film) against *E. coli* after 1 h. "0 h" indicates the number of colonies in the inoculum. Error bars indicate 1 standard deviation (*n* ¼ 3). Reproduced with permission.[76] Copyright 2011, Wiley-VCH. g) Illustrating the adhesive strength of the protein-based PECs by hanging a 4.5 kg weight from two pieces of glued bacterial cellulose mat. Reproduced with permission.[77] Copyright 2018, American Chemical Society. h) PSS/PDADMAC film with 1.6 M KBr and spin-coated at 2000 rpm. i) Representative micrographs of transparent and opaque poly(4-styrenesulfonic acid), poly(diallyldimethylammonium chloride) films as well as polymer zwitterion and glass controls after a 24 h incubation with *E. coli*. Reproduced with permission.[78] Copyright 2019, American Chemical Society.

Hydrogels are one of the most promising soft materials for creating flexible electrical systems.[92,93] Doping hydrogels with polyelectrolytes allows their electrical characteristics to be optimized using ion currents.

Much research work focuses on obtaining individual components. Some of these components are capacitors and supercapacitors. A number of works show that hydrogels are good materials for producing supercapacitors.[94] One of the promising techniques is the use of double crosslinks. This binding has been used to prepare a hydrogel based on hydrophobic association and ionic complexation. Acrylamide with an amphiphilic monomer was bound by hydrophobic interaction, acrylic acid with Fe^{3+} cations—by ionic complexation. The use of such a crosslinking made it possible to obtain a hydrogel with high strength and impact strength. The addition of $LiClO_4$, as well as the presence of carboxy, amino, and ethoxy groups, provides a high ionic conductivity and capacity of such a gel.

In another work, the authors propose the use of hydrogels based on polyvinyl alcohol.[95] The researchers recognize its poor

mechanical properties and therefore propose the addition of vinyl hybrid silica particles. Their addition makes it possible to crosslink polyacrylamide gels to obtain supercapacitors with very high extensibility and compressibility.

Another approach to the creation of organic polyelectrolyte capacitors is to combine electronic and ionic charge transfer.[96] Such a capacitor is a device consisting of two electrolyte ionic conductors (PEDOT/PSS) interconnected by an electronically conductive barrier.

Despite the favorable properties of hydrogel capacitors, their use is still significantly limited.[97] Although they are capable of deformation, their electrical characteristics are not sufficiently stable. When twisted, compressed, or stretched, the conductivity and capacity of such materials can drop significantly. This circumstance can be leveled if the hydrogel has the property of self-healing. In particular, this work proposes the use of physically crosslinked polyvinyl alcohol with polyaniline built up around it. Such a polymer supercapacitor demonstrates not only significant capacity but also the ability to self-repair. This is due to the
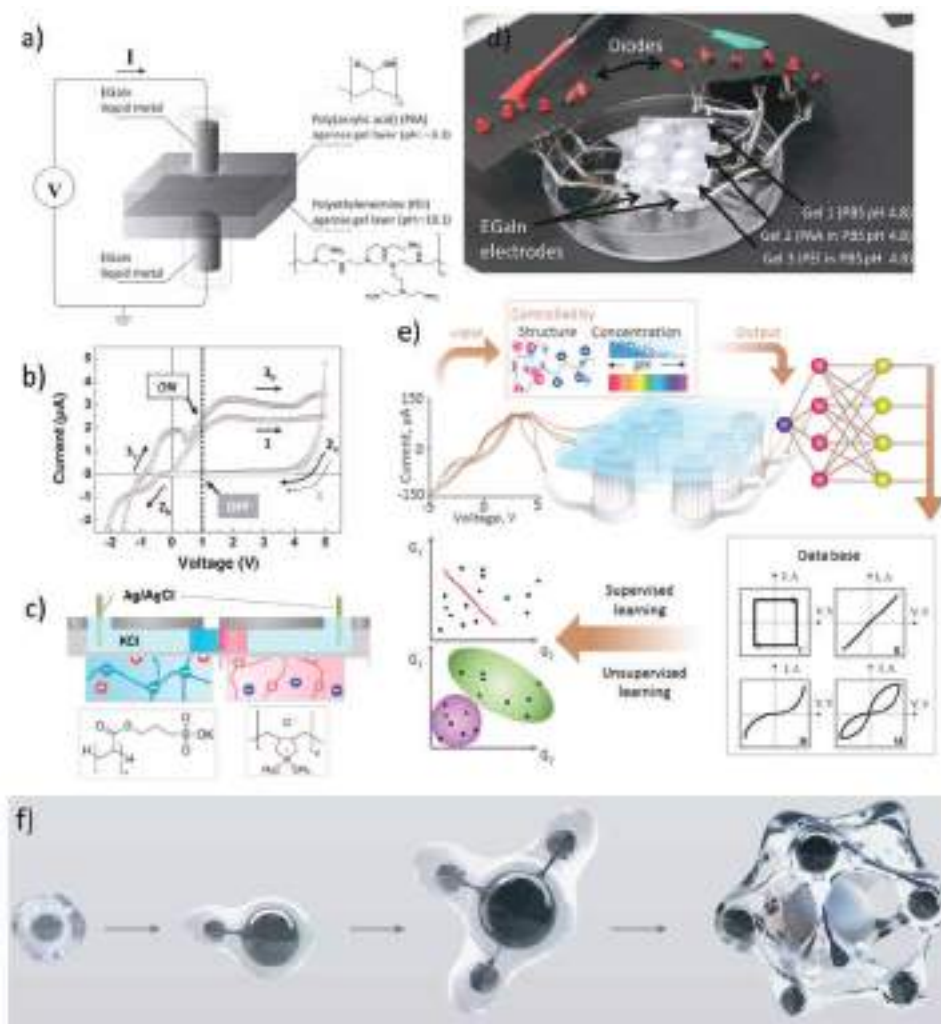
ADVANCED SCIENCE NEWS

www.advancedsciencenews.com

[M]acro-
molecular
Bioscience

www.mbs-journal.de

Figure 7. a) A schematic depiction of the memristive device. Two polyelectrolytes entrapped in a matrix of agarose/H_2O dictate the pH values of each hydrogel layer. b) I–V traces of the device with ±5 V sweeps. The numbers and the arrows represent the order and the direction of the bias sweeps, respectively. The hysteresis of the I–V curves is a characteristic feature of memristors. Reproduced with permission.[99] Copyright 2011, Wiley-VCH. c) Schematic diagram of the PEDOT:PSS/TX OECT with 0.1 M NaCl electrolyte. Reproduced with permission.[111] Copyright 2019, United States National Academy of Sciences. d) Photograph of electrochemical multielectronic component system. e) An input signal in the form of an electric current passes through two hidden layers and converts into an output signal. The hidden layers are eGaIn electrodes connected by hydrogels of various compositions. Reproduced with permission.[110] Copyright 2021, American Chemical Society. f) Possible prototypes of further devices based on liquid metals and polyelectrolytes.

possibility of a dynamic rearrangement of the hydrogen bond within the chains that form the hydrogel. This allows a high capacity to be maintained even after a large number of recharge cycles.

In addition to capacitors, hydrogels are also used to create soft diode devices. For this, hydrogels doped with differently charged polyelectrolytes are often used. This leads to the appearance of a rectification current. Earlier work presented the use of cationic and anionic cellulose nanocrystals for doping agarose gels.[86] Such gels can subsequently be used as diode devices.

Another approach consists of doping agarose gels with PAA and PEI. In addition to the hydrogels, liquid electrodes made of an indium-gallium eutectic alloy were connected.[98] Thus, a completely liquid and flexible diode was assembled. In this design,

the rectifying current can be controlled by forming an oxide film at the hydrogel/liquid metal interface. The use of different pH values within the hydrogel also aids in conductivity control.

In addition to a diode, such a system, when an oxide film of sufficient thickness is grown, can lead to the appearance of memristive behavior.[99] Such a system can be a flexible replacement for solid-state titanium oxide-based memristors (**Figure 7**a–c).

In previous works, attention was mainly paid to cationic and anionic polyelectrolyte hydrogels. However, the use of zwitterionic polymers can significantly improve the quality of organic electronic components. This study presents a comparative study of ionic conductivity characteristics for cationic, anionic, and zwitterionic polyelectrolytes.[100] It has been shown that zwitterionic hydrogels are more suitable for an electronic application.
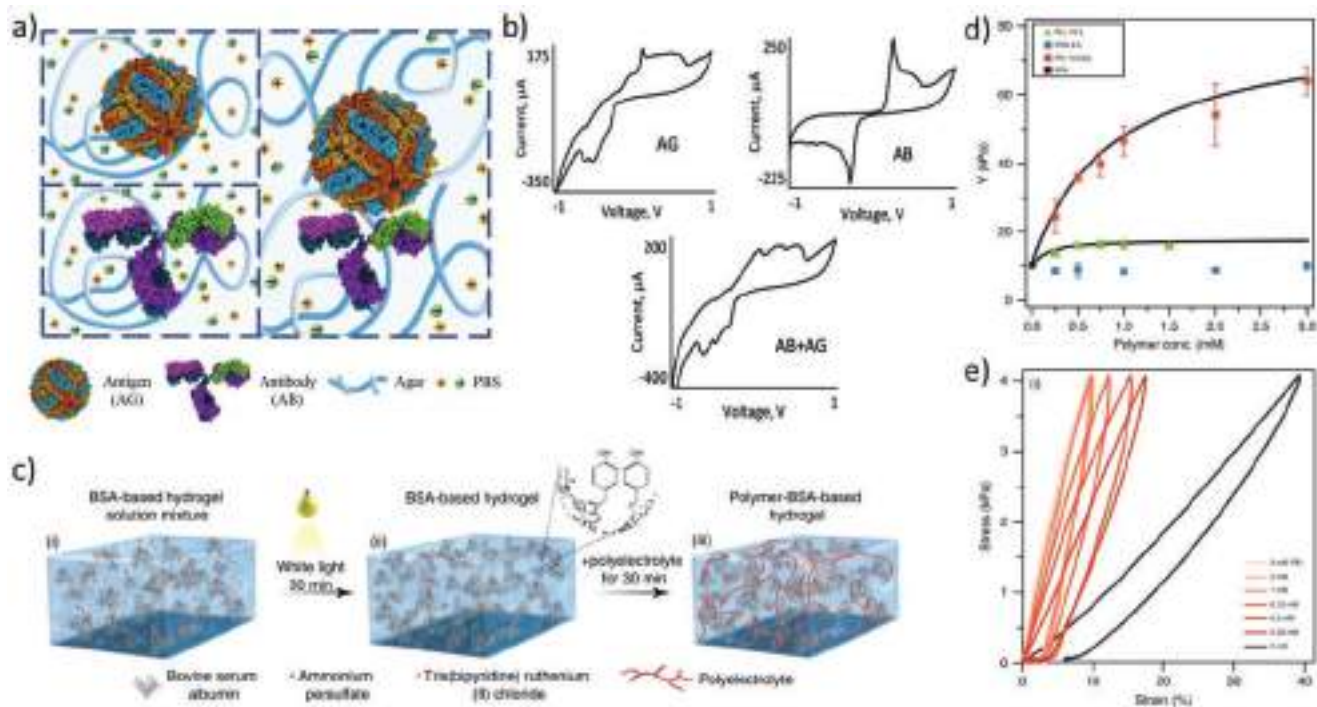
Figure 8. a) Antigen, antibody, and antibody–antigen complex in the media of agar and PBS. b) Characteristic $I-V$ curves with 200 points per cycle for different gels with antigen, antibody, and antibody–antigen complex in a voltage range of −1 to 1 V. Reproduced with permission.[105] Copyright 2020, American Chemical Society. c) Strengthening process of BSA-based hydrogel using polymer–protein interaction: i) BSA, ammonium persulfate (APS), and tris(bipyridine) ruthenium (II) chloride ([(Ru(bpy)$_3$]$^{2+}$) are mixed together; ii) the hydrogel mixture is exposed to white light for 30 min at room temperature (RT), which leads to covalent crosslinking between BSA domains via adjacent exposed tyrosines amino acids (inset); afterward, the hydrogel is extruded into the TRIS solution; iii) the hydrogel is treated with one of three polymer solutions for 30 min: PEI, PLL, or PEG, all dissolved in TRIS buffer. Thereafter, the hydrogel is moved back to TRIS solution, to remove any unbounded polymer molecules. d) Stress–strain curves of native-BSA and incubated with various concentrations of PEI ranging from 0 to 3 mM. e) Average Young's moduli calculated from stress–strain curves of native-BSA, and incubated with PEG (blue), PLL (green), and PEI (red) as a function of the polymer concentrations. Fits represent a Langmuir-like behavior, with equilibrium constants of $K_{PLL} = 1.1$ and $K_{PEI} = 5.3$ mM^{-1}. Reproduced with permission.[107] Copyright 2019, Nature Publishing Group.

This is due to their better conductivity. However, they swell weakly and generally have low mechanical characteristics. Simultaneously, cationic and anionic hydrogels have better mechanical characteristics, with weaker conductivity and capacity. This is due to the influence of side chains of polyelectrolytes, which repel polyelectrolyte chains and better attach water molecules.

Apart from the gel systems that work as individual components, the possibility of designing a system with a programmable electrical response was also shown. Such a programmable component is based on phosphate-buffered hydrogels doped with PAA and PEI. Liquid indium-gallium alloy is used as electrodes. An insoluble mixed layer of phosphates and oxides is formed on the flow of current at the interface. The system response depends on the thickness of this layer. With a small thickness, a capacitor or resistor is formed, with a film growth, a diode or memristor is formed (Figure 7d,e). Moreover, it is possible to switch between these behaviors. A single application of high voltage allows part of the layer to dissolve. Controlling film growth is also possible by varying the pH and polyelectrolyte in the system. Thus, it was shown the possibility of transition from one component to another in real-time.

Despite the fact that hydrogels cannot be used in electronics without additional materials (such as liquid metals), their use for the development of flexible electrical components is very promis-

ing. It is especially important to note that not only conductive polyelectrolytes have potential, but also non-conductive ones. The further development of flexible electronics based on hydrogels opens up interesting opportunities for the development of technology (Figure 7f).

4.2. Programmable Materials

Hydrogels can be widely used in neuromorphic and programmable systems. The necessity to create such systems is associated with the spread of hydrogels' applicability in various fields—from biomimetics to soft robotics.[101,102] In all these areas, the need to modify and program the system's response and behavior is very important. For hydrogels, it is possible to vary a wide range of properties—from mechanical to electrical.[103 104]

Hydrogels with adjustable mechanical properties are currently the most promising. Changes in elasticity, extensibility, and compressibility are most often achieved by changing the internal structure of polyelectrolyte chains and their structure. Changing properties (like electrical) can be used for detection. In this work, the electrochemical detection of antigens, antibodies, and their complex in hydrogels was carried out (**Figure 8**a,b).[105] Under various conditions, the chains can curl up into balls or unfold. A

number of studies devoted to the change in mechanical properties by varying pH are based on this property.[106]

Another work used the property of proteins to change their structure to change the rigidity of the hydrogel. For this, a hydrogel-based on bovine serum albumin was prepared with the addition of PEI and PLL.[107] The use of different PEI concentrations makes it possible to vary the hardness of the gel and increase it up to six times. This control is achieved by chemical denaturation of the protein (Figure 8c–e).

For biomimetic use, hydrogels for imitation and modeling of body parts and organs are of great importance. In particular, this work proposes the use of bovine serum albumin and PEI hydrogels to simulate cartilage. In this case, an imitation of the lubricating mechanism of the cartilage interface is proposed. Several layers of the hydrogel are responsible for the recognition and regulation of characteristics. The layer with one of the polyelectrolytes is responsible for thermal regulation; the other layer is responsible for changing the configuration and mechanical properties and changing the lubricity.[108]

Also, systems with more complex programmable behavior, capable of memorizing various states, have been demonstrated. The proposed agarose hydrogels are doped with gold nanoparticles and photosensitive acid.[109] When exposed to light, the acid dissociates, and the pH changes, which entails a change in the photoresponse.

The development of programmable materials requires new approaches. The use of hydrogels capable of changing their structure under the influence of external factors makes it possible to use them to simulate biosystems' behavior. Such hydrogels can be used to create artificial skin and cartilage.

5. Conclusions

In conclusion, it should be noted that the development of the use of polyelectrolytes is an extremely important task. Currently existing methods of application—layering, films without substrates and hydrogels—have ample opportunities for use in modern technologies. The most important and rapidly developing at the moment are biomimetics, medical technologies, and materials science. In each of these areas, the use of polyelectrolyte assemblies is a powerful tool. They have broad capabilities for drug delivery and release, and the creation of biocompatible surfaces. Membrane and filtration technologies also use polyelectrolytes. Moreover, the creation of programmable materials, flexible electrical components can also be achieved through the stimulation of responsive polymers. All this makes polyelectrolyte technologies extremely interesting for further study.

Acknowledgements

Conflict of Interest

The authors declare no conflict of interest.

Keywords

[1] K. Achazi, R. Haag, M. Ballauff, J. Dernedde, J. N. Kizhakkedathu, D. Maysinger, G. Multhaup, *Angew. Chem., Int. Ed.* **2021**, *60*, 3882.
[2] D. Alkekhia, P. T. Hammond, A. Shukla, *Annu. Rev. Biomed. Eng.* **2020**, *22*, 1.
[3] L. Séon, P. Lavalle, P. Schaaf, F. Boulmedais, *Langmuir* **2015**, *31*, 12856.
[4] A. S. Timin, M. M. Litvak, D. A. Gorin, E. N. Atochina-Vasserman, D. N. Atochin, G. B. Sukhorukov, *Adv. Healthcare Mater.* **2018**, *7*, 1700818.
[5] M. Criado-Gonzalez, D. Wagner, M. H. Iqbal, A. Ontani, A. Carvalho, M. Schmutz, J. B. Schlenoff, P. Schaaf, L. Jierry, F. Boulmedais, *J. Colloid Interface Sci.* **2021**, *588*, 580.
[6] V. Kudryavtseva, S. Boi, J. Read, D. Gould, P. K. Szewczyk, U. Stachewicz, M. V. Kiryukhin, L. Pastorino, G. B. Sukhorukov, *Mater. Des.* **2021**, *202*, 109527.
[7] M. N. Zharkov, E. P. Brodovskaya, O. A. Kulikov, E. V. Gromova, V. P. Ageev, A. V. Atanova, Z. V. Kozyreva, A. M. Tishin, A. P. Pyatakov, N. A. Pyataev, G. B. Sukhorukov, *Colloids Surf., B* **2021**, *199*, 111548.
[8] R. L. Abbett, R. A. Tigaa, S. L. Sonawane, G. F. Strouse, J. B. Schlenoff, *ACS Appl. Polym. Mater.* **2021**, *3*, 691.
[9] P. Lavalle, C. Picart, J. Mutterer, C. Gergely, H. Reiss, J.-C. Voegel, B. Senger, P. Schaaf, *J. Phys. Chem. B* **2004**, *108*, 635.
[10] D. Yılmaz Aykut, Ö. Yolaçan, H. Deligöz, *Colloids Surf. A* **2020**, *602*, 125113.
[11] R. A. Bataglioli, J. B. M. Rocha Neto, B. S. Leão, L. G. L. Germiniani, T. B. Taketa, M. M. Beppu, *Langmuir* **2020**, *36*, 12532.
[12] X. Guan, Y. Yong, Q. Wu, X. Zhang, X. Guo, C. Li, J. Xu, *Energy Technol.* **2020**, *8*, 2000278.
[13] X. Li, T. Wang, Y. Luo, A. M. Asiri, S. Chen, X. Sun, *ChemBioChem* **2020**, *21*, 801.
[14] S. Ulasevich, N. V. Ryzhkov, D. V. Andreeva, D. S. Ozden, E. Piskin, E. V. Skorb, *Adv. Mater. Interfaces* **2020**, *7*, 2000980.
[15] Y. Han, J. Zhou, Y. Hu, Z. Lin, Y. Ma, J. J. Richardson, F. Caruso, *ACS Nano* **2020**, *14*, 12972.
[16] S. A. Ulasevich, N. Brezhneva, Y. Zhukova, H. Möhwald, P. Fratzl, F. H. Schacher, D. V. Sviridov, D. V. Andreeva, E. V. Skorb, *Macromol. Biosci.* **2016**, *16*, 1422.
[17] L. Yang, L. Li, H. Wu, B. Zhang, R. Luo, Y. Wang, *J. Controlled Release* **2020**, *321*, 59.
[18] A. C. Almeida, A. C. Vale, R. A. Pires, R. L. Reis, N. M. Alves, *J. Biomed. Mater. Res., Part B* **2020**, *108*, 1412.
[19] A. Seimei, D. Saeki, H. Matsuyama, *J. Colloid Interface Sci.* **2020**, *569*, 211.
[20] M. Motay, D. Martel, B. Vileno, C. Soraru, L. Ploux, M. G. Méndez-Medrano, C. Colbeau-Justin, G. Decher, N. Keller, *ACS Appl. Mater. Interfaces* **2020**, *12*, 55766.
[21] E. Palo, H. Zhang, M. Lastusaari, M. Salomäki, *ACS Appl. Nano Mater.* **2020**, *3*, 6892.
[22] M. Delcea, H. Möhwald, A. G. Skirtach, *Adv. Drug Delivery Rev.* **2011**, *63*, 730.
[23] J. K. J. Yong, G. W. Stevens, F. Caruso, S. E. Kentish, *J. Membr. Sci.* **2016**, *514*, 556.
[24] M. J. Feeney, S. W. Thomas, *Langmuir* **2019**, *35*, 13791.

[25] P. Borgul, K. Rudnicki, L. Chu, A. Leniart, S. Skrzypek, E. J. R. Sud-hölter, L. Poltorak, *Electrochim. Acta* **2020**, *363*, 137215.

[26] E. V. Lengert, S. I. Koltsov, J. Li, A. V. Ermakov, B. V. Parakhonskiy, E. V. Skorb, A. G. Skirtach, *Coatings* **2020**, *10*, 1131.

[27] G. Nifontova, V. Krivenkov, M. Zvaigzne, P. Samokhvalov, A. E. Efimov, O. I. Agapova, I. I. Agapov, E. Korostylev, S. Zarubin, A. Karaulov, I. Nabiev, A. Sukhanova, *ACS Appl. Mater. Interfaces* **2020**, *12*, 35882.

[28] D. Al Husseini, Y. Karanth, J. Zhou, D. Willhelm, X. Qian, R. Gutierrez-Osuna, G. Coté, P. Lin, S. Sukhishvili, *Coatings* **2021**, *11*, 118.

[29] N. V. Ryzhkov, N. A. Mamchik, E. V. Skorb, *J. R. Soc., Interface* **2019**, *16*, 20180626.

[30] S. A. Ulasevich, G. Brezesinski, H. Möhwald, P. Fratzl, F. H. Schacher, S. K. Poznyak, D. V. Andreeva, E. V. Skorb, *Angew. Chem., Int. Ed.* **2016**, *55*, 13001.

[31] D. V. Andreeva, A. Kollath, N. Brezhneva, D. V. Sviridov, B. J. Cafferty, H. Möhwald, E. V. Skorb, *Phys. Chem. Chem. Phys.* **2017**, *19*, 23843.

[32] V. A. Arlyapov, N. Y. Yudina, A. V. Machulin, V. A. Alferov, O. N. Ponamoreva, A. N. Reshetilov, *Appl. Biochem. Microbiol.* **2021**, *57*, 133.

[33] Z. Chen, Q. Zhang, J. Shan, Y. Lu, Q. Liu, *ACS Omega* **2020**, *5*, 27536.

[34] H. Wu, K. Xi, S. Xiao, S. Ngai, C. Zhou, M. He, K. Shi, Y. Yu, Y. Yang, G. Chen, K. Ding, *Surf. Coat. Technol.* **2020**, *402*, 126491.

[35] F. Amouzad, K. Zarei, *J. Electron. Mater.* **2020**, *49*, 3583.

[36] T. Xue, P. Liu, J. Zhang, J. Xu, G. Zhang, P. Zhou, Y. Li, Y. Zhu, X. Lu, Y. Wen, *ACS Omega* **2020**, *5*, 28452.

[37] T. Hu, M. Zhang, Z. Wang, K. Chen, X. Li, Z. Ni, *Microchem. J.* **2020**, *158*, 105209.

[38] G. Ibáñez-Redín, E. M. Materon, R. H. M. Furuta, D. Wilson, G. F. Do Nascimento, M. E. Melendez, A. L. Carvalho, R. M. Reis, O. N. Oliveira, D. Gonçalves, *Microchim. Acta* **2020**, *187*, 417.

[39] F. Oytun, V. Kara, O. Alpturk, F. Basarir, *Thin Solid Films* **2017**, *636*, 40.

[40] N. Liu, S. Li, L. Chen, W. Zheng, *Opt. Mater.* **2020**, *108*, 110460.

[41] V. O. Fávero, D. A. Oliveira, J. L. Lutkenhaus, J. R. Siqueira, *J. Mater. Sci.* **2018**, *53*, 6719.

[42] C.-H. Xue, C. Wu, X.-J. Guo, B.-Y. Liu, H.-D. Wang, S.-T. Jia, *Cellulose* **2020**, *27*, 3455.

[43] J. Zou, W. Zhong, F. Gao, X. Tu, S. Chen, X. Huang, X. Wang, L. Lu, Y. Yu, *Microchim. Acta* **2020**, *187*, 603.

[44] M. Wang, Y. Ma, J. Ye, *J. Power Sources* **2020**, *474*, 228681.

[45] Y. Ge, R. Jamal, R. Zhang, W. Zhang, Z. Yu, Y. Yan, Y. Liu, T. Abdiryim, *Microchim. Acta* **2020**, *187*, 248.

[46] S. Lajevardi Esfahani, S. Rouhani, Z. Ranjbar, *Nanoscale Res. Lett.* **2020**, *15*, 210.

[47] C. Jiang, V. V. Tsukruk, *Adv. Mater.* **2006**, *18*, 829.

[48] A. Francesko, K. Ivanova, J. Hoyo, S. Pérez-Rafael, P. Petkova, M. M. Fernandes, T. Heinze, E. Mendoza, T. Tzanov, *Biomacromolecules* **2018**, *19*, 3628.

[49] J. M. Silva, S. G. Caridade, R. L. Reis, J. F. Mano, *Soft Matter* **2016**, *12*, 1200.

[50] H. Zhang, M. Fujii, Y. Okamura, L. Zhang, S. Takeoka, *ACS Appl. Mater. Interfaces* **2016**, *8*, 16296.

[51] B. Le Ouay, S. Guldin, Z. Luo, S. Allegri, F. Stellacci, *Adv. Mater. Interfaces* **2016**, *3*, 1600191.

[52] M. Gauvin, J. Grisolia, T. Alnasser, B. Viallet, S. Xie, J. Brugger, L. Ressier, *Nanoscale* **2016**, *8*, 11363.

[53] X. You, K. Xiao, Q. Yu, H. Wu, J. Yuan, R. Zhang, Y. Ma, Y. Li, T. Huang, Z. Jiang, *Chem. Eng. J.* **2021**, *416*, 129139.

[54] X. Pei, L. Gan, Z. Tong, H. Gao, S. Meng, W. Zhang, P. Wang, Y. Chen, *J. Hazard. Mater.* **2021**, *406*, 124746.

[55] D. V. Andreeva, M. Trushin, A. Nikitina, M. C. F. Costa, P. V. Cherepanov, M. Holwill, S. Chen, K. Yang, S. W. Chee, U. Mirsaidov, A. H. Castro Neto, K. S. Novoselov, *Nat. Nanotechnol.* **2021**, *16*, 174.

[56] M. Mohammadifakhr, J. De Grooth, K. Trzaskus, H. D. W. Roesink, A. J. B. Kemperman, *Sep. Purif. Technol.* **2021**, *264*, 118430.

[57] B. Meng, G. Liu, Y. Mao, F. Liang, G. Liu, W. Jin, *J. Membr. Sci.* **2021**, *623*, 119076.

[58] W. Ouyang, M. Müller, *Macromol. Biosci.* **2006**, *6*, 929.

[59] S. A. Shaheen, M. Yang, B. Chen, J. B. Schlenoff, *Chem. Mater.* **2020**, *32*, 5994.

[60] M. I. Baig, P. P. I. Sari, J. Li, J. D. Willott, W. M. De Vos, *J. Membr. Sci.* **2021**, *625*, 119114.

[61] M. Zhou, Y.-N. Wu, P. Luo, J. Lyu, D. Mu, A. Li, F. Li, G. Li, *RSC Adv.* **2017**, *7*, 49568.

[62] M. Nolte, I. Dönch, A. Fery, *ChemPhysChem* **2006**, *7*, 1985.

[63] Z. Liu, Z. Yin, J. Wang, Q. Zheng, *Adv. Funct. Mater.* **2019**, *29*, 1806092.

[64] V. Rengarajan, J. Geng, Y. Huang, *Micromachines* **2020**, *11*, 903.

[65] J. Zhang, M. Gai, A. V. Ignatov, S. A. Dyakov, J. Wang, N. A. Gippius, J. Frueh, G. B. Sukhorukov, *ACS Appl. Mater. Interfaces* **2020**, *12*, 19080.

[66] B. Čalija, S. Savić, D. Krajišnik, R. Daniels, S. Vučen, B. Marković, J. Milić, *J. Appl. Polym. Sci.* **2015**, *132*, 42583.

[67] M. Park, K. S. Shin, J. W. Lee, K. Kim, *Bull. Korean Chem. Soc.* **2015**, *36*, 743.

[68] Y.-J. Kim, S.-Y. Park, *ACS Appl. Mater. Interfaces* **2020**, *12*, 47342.

[69] J. Dai, H. Zhao, X. Lin, S. Liu, T. Fei, T. Zhang, *Adv. Electron. Mater.* **2020**, *6*, 1900846.

[70] K. G. Nikolaev, S. A. Ulasevich, O. Luneva, O. Y. Orlova, D. Vasileva, S. Vasilev, A. S. Novikov, E. V. Skorb, *ACS Appl. Polym. Mater.* **2020**, *2*, 105.

[71] S. Mathi, P. K. Gupta, R. Kumar, R. K. Nagarale, A. Sharma, *ChemistrySelect* **2019**, *4*, 3833.

[72] A. Nenashkina, S. Koltsov, O. Y. Orlova, A. A. Nikitina, D. A. Kirilenko, D. V. Andreeva, M. Blanco-Formoso, N. Pazos-Perez, R. Alvarez-Puebla, E. V. Skorb, *Nanoscale* **2021**, *13*, 7375.

[73] S.-W. Lee, T.-H. Kang, S. K. Lee, K.-Y. Lee, H. Yi, *ACS Appl. Mater. Interfaces* **2018**, *10*, 36267.

[74] I. Y. Kim, S. Park, H. Kim, S. Park, R. S. Ruoff, S.-J. Hwang, *Adv. Funct. Mater.* **2014**, *24*, 2288.

[75] K. Amin, M. In Het Panhuis, *Fibers* **2013**, *1*, 47.

[76] K. A. Mat Amin, K. J. Gilmore, J. Matic, S. Poon, M. J. Walker, M. R. Wilson, M. in het Panhuis, *Macromol. Biosci.* **2012**, *12*, 374.

[77] P. Mohammadi, G. Beaune, B. T. Stokke, J. V. I. Timonen, M. B. Linder, *ACS Macro Lett.* **2018**, *7*, 1120.

[78] I. S. Kurtz, S. Sui, X. Hao, M. Huang, S. L. Perry, J. D. Schiffman, *ACS Appl. Bio Mater.* **2019**, *2*, 3926.

[79] R. A. Batista, P. J. P. Espitia, D. M. C. Vergne, A. A. Vicente, P. A. C. Pereira, M. A. Cerqueira, J. A. Teixeira, J. Jovanovic, P. Severino, E. B. Souto, J. C. Cardoso, *Polymers* **2020**, *12*, 2173.

[80] S. Srivastava, A. E. Levi, D. J. Goldfeld, M. V. Tirrell, *Macromolecules* **2020**, *53*, 5763.

[81] H. Fan, J. P. Gong, *Macromolecules* **2020**, *53*, 2769.

[82] C. Qian, T.-A. Asoh, H. Uyama, *Macromol. Rapid Commun.* **2020**, *41*, 2000406.

[83] A. Adak, G. Das, S. Barman, S. Mohapatra, D. Bhunia, B. Jana, S. Ghosh, *ACS Appl. Mater. Interfaces* **2017**, *9*, 5067.

[84] X. Zhang, C. L. Pint, M. H. Lee, B. E. Schubert, A. Jamshidi, K. Takei, H. Ko, A. Gillies, R. Bardhan, J. J. Urban, M. Wu, R. Fearing, A. Javey, *Nano Lett.* **2011**, *11*, 3239.

[85] G. Qin, M. Wang, L. Fan, X. Fang, D. Zhang, J. Liu, J. Qin, J. Shi, J. Yang, Q. Chen, *J. Power Sources* **2020**, *474*, 228602.

[86] K. Nyamayaro, P. Keyvani, F. D'acierno, J. Poisson, Z. M. Hudson, C. A. Michal, J. D. W. Madden, S. G. Hatzikiriakos, P. Mehrkhodavandi, *ACS Appl. Mater. Interfaces* **2020**, *12*, 52182.

[87] S. Lin, H. Yuk, T. Zhang, G. A. Parada, H. Koo, C. Yu, X. Zhao, *Adv. Mater.* **2016**, *28*, 4497.

[88] X. Jing, H. Li, H.-Y. Mi, P.-Y. Feng, X. Tao, Y. Liu, C. Liu, C. Shen, *ACS Appl. Mater. Interfaces* **2020**, *12*, 23474.

[89] P. Chakraborty, B. Das, P. Pal, S. Datta, S. Bera, P. Dastidar, *Chem. Commun.* **2020**, *56*, 5251.

[90] S. Zhao, P. Tseng, J. Grasman, Y. Wang, W. Li, B. Napier, B. Yavuz, Y. Chen, L. Howell, J. Rincon, F. G. Omenetto, D. L. Kaplan, *Adv. Mater.* **2018**, *30*, 1800598.

[91] Y. Zhou, C. M. Duque, C. D. Santangelo, R. C. Hayward, *Adv. Funct. Mater.* **2019**, *29*, 1905273.

[92] Y. Wang, H. Huang, J. Wu, L. Han, Z. Yang, Z. Jiang, R. Wang, Z. Huang, M. Xu, *ACS Sustainable Chem. Eng.* **2020**, *8*, 18506.

[93] J. Ko, X. Wu, A. Surendran, B. T. Muhammad, W. L. Leong, *ACS Appl. Mater. Interfaces* **2020**, *12*, 33979.

[94] Y. Huang, M. Zhong, F. Shi, X. Liu, Z. Tang, Y. Wang, Y. Huang, H. Hou, X. Xie, C. Zhi, *Angew. Chem., Int. Ed.* **2017**, *56*, 9141.

[95] W. Li, X. Li, X. Zhang, J. Wu, X. Tian, M.-J. Zeng, J. Qu, Z.-Z. Yu, *ACS Appl. Energy Mater.* **2020**, *3*, 9408.

[96] P. Janson, E. O. Gabrielsson, K. J. Lee, M. Berggren, D. T. Simon, *Adv. Mater. Technol.* **2019**, *4*, 1800494.

[97] W. G. Moon, G.-P. Kim, M. Lee, H. D. Song, J. Yi, *ACS Appl. Mater. Interfaces* **2015**, *7*, 3503.

[98] J.-H. So, H.-J. Koo, M. D. Dickey, O. D. Velev, *Adv. Funct. Mater.* **2012**, *22*, 625.

[99] H.-J. Koo, J.-H. So, M. D. Dickey, O. D. Velev, *Adv. Mater.* **2011**, *23*, 3559.

[100] C.-J. Lee, H. Wu, Y. Hu, M. Young, H. Wang, D. Lynch, F. Xu, H. Cong, G. Cheng, *ACS Appl. Mater. Interfaces* **2018**, *10*, 5845.

[101] S. Y. Zheng, C. Y. Li, M. Du, J. Yin, J. Qian, Z. L. Wu, Q. Zheng, *ACS Appl. Mater. Interfaces* **2020**, *12*, 57497.

[102] M. Vahdati, F. J. Cedano-Serrano, C. Creton, D. Hourdet, *ACS Appl. Polym. Mater.* **2020**, *2*, 3397.

[103] H. C. Yu, S. Y. Zheng, L. Fang, Z. Ying, M. Du, J. Wang, K.-F. Ren, Z. L. Wu, Q. Zheng, *Adv. Mater.* **2020**, *32*, 2005171.

[104] C. Y. Li, X. P. Hao, S. Y. Zheng, W. Hong, Q. Zheng, Z. L. Wu, *Adv. Intell. Syst.* **2019**, *1*, 1900055.

[105] A. S. Ivanov, K. G. Nikolaev, A. A. Stekolshchikova, W. T. Tesfatsion, S. O. Yurchenko, K. S. Novoselov, D. V. Andreeva, M. Y. Rubtsova, M. F. Vorovitch, A. A. Ishmukhametov, A. M. Egorov, E. V. Skorb, *ACS Appl. Bio Mater.* **2020**, *3*, 7352.

[106] G. Lalevée, L. David, A. Montembault, K. Blanchard, J. Meadows, S. Malaise, A. Crépet, I. Grillo, I. Morfin, T. Delair, G. Sudre, *Soft Matter* **2017**, *13*, 6594.

[107] L. R. Khoury, I. Popa, *Nat. Commun.* **2019**, *10*, 5439.

[108] H. Liu, X. Zhao, Y. Zhang, S. Ma, Z. Ma, X. Pei, M. Cai, F. Zhou, *ACS Appl. Mater. Interfaces* **2020**, *12*, 51114.

[109] H. Zhang, H. Zeng, A. Priimagi, O. Ikkala, *Nat. Commun.* **2019**, *10*, 3267.

[110] A. S. Ivanov, K. G. Nikolaev, A. S. Novikov, S. O. Yurchenko, K. S. Novoselov, D. V. Andreeva, E. V. Skorb, *J. Phys. Chem. Lett.* **2021**, *12*, 2017.

[111] S.-M. Lim, H. Yoo, M.-A. Oh, S. H. Han, H.-R. Lee, T. D. Chung, Y.-C. Joo, J.-Y. Sun, *PNAS* **2019**, *116*, 13807.

[112] N. V. Ryzhkov, D. V. Andreeva, E. V. Skorb, *Langmuir* **2019**, *35*, 8543.

Artemii S. Ivanov is starting his PhD program at National University of Singapore now. He was a MSc student at ITMO University with Prof. Ekaterina Skorb. In 2021 he was fellow at the at the Ilmenau University of Technology with Prof. Thomas Hannappel. Currently, motivated by needs for flexible electronics, surface science, and development of chemical perceptron.

Liubov V. Pershina is a MSc student at Infochemistry Scientific Center of ITMO University in Saint Petersburg, Russia, and fellow at Jülich Research Center (2021). She graduated with BSc degree in chemistry from the department of analytical chemistry and chemical expertise, Saratov State University. Currently, motivated by needs for point-of-care diagnostics, surface science, and electrochemistry.

Konstantin G. Nikolaev is a group leader at Infochemistry Scientific Center of ITMO University in Saint Petersburg, Russia. He has received his M.Sci. (2013) and Ph.D. (2017) in analytical chemistry from the Institute of Chemistry, Saint Petersburg State University. His current work focuses on an interdisciplinary approach to solving fundamental physical chemistry problems and integrating electrochemical sensors with machine learning methods and algorithms to explain complex systems' physicochemical principles.

Ekaterina V. Skorb is full professor at ITMO University and director of Infochemistry Scientific Center in Saint Petersburg, Russia. She received her PhD in physical chemistry (2008). Subsequently, she was postdoc and AvH fellow at the Max Planck Institute of Colloids and Interfaces (MPIKG) with Prof. Helmuth Möhwald. From 2013, she has been working with Prof. Peter Fratzl (MPIKG) as a group leader. She was a Visiting Scholar in Harvard in Prof. George Whitesides group (2016–2017). Her current research interests are spatiotemporal control of ion concentration gradients for soft matter actuation, biosensing, and development of alternative pathways of chemical computing, e.g. chemical perceptron.

Annual Review of Chemical and Biomolecular Engineering

Infochemistry and the Future of Chemical Information Processing

Nikolay V. Ryzhkov, Konstantin G. Nikolaev, Artemii S. Ivanov, and Ekaterina V. Skorb

Infochemistry Scientific Center of ITMO University, 191002 Saint Petersburg, Russia;
email: ryzhkov@itmo.ru, kgnikolaev@itmo.ru, art_ivanov@scamt-itmo.ru, skorb@itmo.ru

Keywords

infochemistry, molecular logic gates, iontronics, nonlinear oscillators, self-assembly, sensors

Abstract

Nowadays, information processing is based on semiconductor (e.g., silicon) devices. Unfortunately, the performance of such devices has natural limitations owing to the physics of semiconductors. Therefore, the problem of finding new strategies for storing and processing an ever-increasing amount of diverse data is very urgent. To solve this problem, scientists have found inspiration in nature, because living organisms have developed uniquely productive and efficient mechanisms for processing and storing information. We address several biological aspects of information and artificial models mimicking corresponding bioprocesses. For instance, we review the formation of synchronization patterns and the emergence of order out of chaos in model chemical systems. We also consider molecular logic and ion fluxes as information carriers. Finally, we consider recent progress in infochemistry, a new direction at the interface of chemistry, biology, and computer science, considering unconventional methods of information processing.

1. INTRODUCTION

In the digital era in which we now live, information technology plays a crucial role in the economic development of societies. The advent of transistor technologies laid the foundation for this stage of human development (1). Improved computing performance is the driving force behind social evolution (2, 3). Modern electronic devices perform calculations through use of semiconductor-based integrated circuits (4). The boundaries of silicon-based electronics have been designated repeatedly (5). Meanwhile, living organisms demonstrate fundamentally different approaches to storing, transferring, and processing information (6, 7).

Storage and transmission of information about an organism's structure and vital functions are based on self-replicating DNA macromolecules. Biological computing can be significantly inferior in speed to classical semiconductor computers. However, the amount of information humans process daily is comparable to all information stored in the world on printed media. This has inspired scientists to explore DNA's potential in applied computing and information storage (8, 9).

In addition, an important feature of living organisms is their ability to think, remember, and respond to external stimuli, in other words, to work with information. These processes are implemented in neuronal cells, or neurons. The nerve cell axon membrane contains voltage-gated ion channels (10). Thus, axons can transmit electrical signals along the body, which in practice is realized by the transport of sodium, potassium, calcium, or chloride ions. Thanks to this, the human (and animal) brain can implement many computational processes simultaneously. This underlies the ability to recognize patterns and learn. At the same time, these tasks are considered extremely difficult for computers (2, 11).

Many algorithms have been developed based on the principles of information processing in nature, among them, the cellular automaton (12), swarm intelligence (13), neural networks (14), and evolutionary algorithms (15). These have given a big boost to enhancing computing power and the ability to solve complex problems. At the same time, we believe that not only the principles but also the methods of practically implementing biological computing could give a new stimulus to the development of information technologies. Broadly, infochemistry is a fundamental experimental area of chemistry that deals with information storage and processing on the molecular level (16). The term infochemistry was originally introduced to describe communication between primitive organisms. Compounds such as pheromones and quorum-sensing agents were respectively designated as infochemicals (17). Later, George M. Whitesides introduced the term infochemistry in a new context, combining artificial and bioinspired ways of processing information. According to Whitesides, realization of an infochemical strategy for information processing requires energy release from chemical reactions, not electricity supply, encoding information using orthogonal chemical and physical properties, integration of chemical sensing, and the possibility to operate in environments such as the human body. Infofuses, droplet shutters, droplet lasers, and oscillating flames were considered infochemical computers (18, 19).

In this review, we describe how information theory concepts are being introduced into chemical research. We focus on recent advances in the development of nature-inspired computational tools at the interface of chemistry, biology, and information theory, forming a new research area: infochemistry.

2. CHEMISTRY AND INFORMATION

2.1. From Chemical Logic Gates to Chemical Computers

Logic gates are the basic elements of logical calculations that underlie information processing. These elements convert input logic signals to output following the logic laid down in the element.

For example, NOT, AND, OR, and XOR logic gates calculate the values, respectively, of the functions of negation, conjunction, disjunction, and strict disjunction from the incoming arguments. In this case, both the arguments and values of the functions are logical values, either 0 or 1. Chemical logic gates by definition operate via Boolean logic (the basis of artificial computers) and, therefore, represent perhaps the first attempt to consider molecular processes from the point of view of information theory (20). By and large, chemical logic gates are a kind of spin-off from the study of various sensors and responsive materials (21).

Stimuli-responsive (or intelligent, or smart) materials behave in a particular and preset way in response to changes in external conditions. Smart materials can be easily attributed to piezoelectric (22), thermoelectric (23), and photovoltaic (24) materials and shape memory alloys (25). However, multiresponsive systems are required to organize complex logic calculations. Among materials that are simultaneously sensitive to several simple stimuli, such as light, temperature, and chemical concentrations, are polymer vesicles (26, 27) and brushes (28, 29), polymer-decorated nanoparticles (30, 31), hydrogels (32, 33), and layer-by-layer capsules and films (34, 35). Describing multiresponsive materials in terms of information theory promotes the idea of chemical computing (20, 36). Such materials are also interesting because their constituent molecules are similar to or are themselves biomolecules. This fact opens great opportunity for smart material implementation in biomedicine, development of human–computer interfaces, and novel bioinspired approaches to information storage and processing.

pH is perhaps the most important chemical parameter influencing the outcome of various physicochemical processes and causing changes in supramolecular assemblies (37). Thus, materials undergoing hydrolytic cleavage or conformational change with protonation are implemented in smart materials. Among such materials are acid-degradable block-copolymer micelles (38), copolypeptide hydrogels (39), and charge-shifting and amphiphilic polyelectrolytes (40). Herewith, several ways to regulate pH in bulk and locally and therefore transmit the input signal are developed.

Thermosensitive materials are represented, for example, by polymer mixtures and block-copolymers characterizing critical solution temperatures (41) at which aggregation and disaggregation occur. With such a transition, material hydrophobicity (42) or, for example, cell-attractive and cell-repellent states (43) can switch.

Light-sensitive materials have attracted much attention recently. Electromagnetic irradiation can be localized in space easily, and such a stimulus provides high-speed on–off switching and also allows instant parameter changes (intensity and wavelength of radiation, for example). Azobenzene derivatives are among the most well-studied photo-switchable systems (44, 45). Reversible sol-gel (46) and solid-to-liquid (47) transitions were demonstrated for polymer systems containing azobenzene moieties. Light–pH coupling can endow light sensitivity to systems sensitive to changes in environmental acidity (48, 49).

Such materials are used for a variety of applications, such as drug delivery, tissue engineering, biosensors, smart coatings, and composite materials. But fundamentally, such systems are molecular computers converting chemical, biochemical, and physical input signals into responses. Information theory sees any stimuli-responsive material as a simple Buffer logic gate: Positive input leads to positive output, and vice versa. By combining different sensitive moieties, simultaneous sensitivity to various inputs can be achieved. This can be exploited to perform simple logic operations. Different types of logic gates [AND (50–52), OR (53, 54), NOR (55), NAND (56, 57)] have been assembled from multiresponsive molecules. Ryzhkov et al. (58) demonstrated the concept of basic logic operations using ion fluxes as input/output signals. Microelectrode arrays immersed in water solutions provide one example of simple logic calculations. By polarizing the electrodes in a certain way, it is possible to obtain a pattern of the acidity distribution in solution. Simple AND

a

AB

AND

A   B

A	B	AB
0	0	0
1	0	0
0	1	0
1	1	1

b

Input 1 (A)   Input 2 (B)

Output

A 0V = '0'   B +V = '1'   pH > 5.5 '0'

A 0V = '0'   B 0V = '0'   pH > 5.5 '0'

A +V = '1'   B +V = '1'   pH < 5.5 '1'

pH
6.0
5.8
5.6
5.2
4.8
4.4
4.0

100 μm

c

365 nm   405 nm

XOR

OR

Programming potential

Ti/TiO$_2$

Programming input	Input A (365 nm)	Input B (405 nm)	Output	Logic
−300 mV	0	0	0	XOR
	1	0	1	
	0	1	1	
	1	1	0	
300 mV	0	0	0	OR
	1	0	1	
	0	1	1	
	1	1	1	

d

A = 0 A = 0 A = 0 A = 1 A = 0 A = 1
B = 0 B = 1 B = 0 B = 0 B = 0 B = 1

Output = 1
Output = 0
Output = 1

e

A = 0 A = 1 A = 0 A = 0 A = 0 A = 1
B = 0 B = 0 B = 0 B = 1 B = 0 B = 1

Output = 1
Output = 0
Output = 1

Figure 1

(*a*) An AND logic gate and corresponding truth table. (*b*) A system of two working electrode arrays embedded in an epoxy holder and pH maps over two input electrodes in hydroquinone solution during polarization of electrodes in different regimes and interpretation in terms of logic gates: positive polarization +V is determined as input 1, no polarization 0V as input 0, pH > 5.0 as output 0, and pH < 5.0 as output 1 (adapted with permission from Reference 58). (*c*) A reconfigurable logic system based on nanostructured Ti/TiO$_2$ and corresponding truth table; inputs are light sources with different wavelengths (1, illumination ON; 0, illumination OFF; photocurrent is considered as output, photocurrent value other than zero was taken as 1 output), and the choice between XOR and OR function is determined by programming input of potential bias. (*d*) XOR logic realized on nanostructured Ti/TiO$_2$. (*e*) OR logic realized on nanostructured Ti/TiO$_2$ (adapted with permission from Reference 64; copyright 2020 Royal Society of Chemistry).

logic operations have been demonstrated (**Figure 1*a***). The electrodes may be designated as inputs and the acidity of the space between the electrodes as outputs in terms of logic gates (**Figure 1*b***).

Unconventional photonic computing has been demonstrated through use of TiO$_2$ nanocrystalline photoelectrodes. Following modification with cyanoferrate (59, 60) and ruthenium (61) complexes, thiamine and folic (62) and carminic (62) acid demonstrated photoelectrochemical photocurrent switching behavior (63); i.e., under appropriate external polarization or/and

illumination by light with appropriate photon energy, switching between anodic and cathodic photocurrent can be observed. Ryzhkov et al. (64) demonstrated this effect recently using bare and unmodified photoelectrodes made of nanostructured TiO_2. Switching between XOR and OR logic gates has also been performed via polarization change under ultraviolet or blue illumination (**Figure 1c**). The light is considered as the input signal, illumination as input 1, and no illumination as input 0. The photocurrent is read as an output signal, which is taken as 1 if it differs from 0. Depending on the photoelectrode polarization, either anodic or cathodic photocurrents arise under different illuminations. If both light sources give a photocurrent of the same sign, the logic gate OR is implemented under simultaneous irradiation; if photocurrents are of different signs, XOR is implemented (**Figure 1d**).

Along with chemical logic systems, biological logic networks are also of interest. Information processing via complex metabolic systems of living organisms could be used to successfully design next-generation unconventional computing approaches. Li et al. (65) demonstrated a bacteria (*Pseudomonas aeruginosa*)–based AND logic gate; in this study, two quorum-sensing molecules were considered as the input signals, and electrochemical signals of living bacteria were registered as outputs.

The next step toward full-fledged complex chemical calculations is simple logic elements concatenation. For example, Guliyev et al. (66) demonstrated the concept of independently functioning chemical logic gates concatenation based on the inner filter effect (approach 1) and intramolecular energy transfer (approach 2). Guliyev et al. (62) performed an experiment to illustrate the first approach. In this experiment, the first AND gate was represented by a thionine molecule, which becomes transparent to 560-nm light (give 1 output) only when photochemically reduced. The second independent AND gate was a styryl-bodipy derivative with a dipicolylamine group tethered at the meso-(8) position. Intensive fluorescence (output 1) appeared at 560 nm and in the presence of Zn^{2+} ions. When these gates were combined, the output of the first AND gate (560 nm) served as the input for the second gate, and the two gates were integrated.

Approach 2 was demonstrated by clicking together a tyryl-bodipy derivative with a dipicolylamine group tethered from the previous example and monostyryl derivative with azathiacrown moiety attached through its amine nitrogen atom. This system performed AND logic with photonic (580 nm) and ionic (Hg^{2+}) inputs and red (660 nm) emission as output. Combination of these gates demonstrated output 1 (intense 660-nm fluorescence) only when 3 inputs (560 nm, Zn^{2+}, and Hg^{2+}) were present.

The key advantage of molecular logic gates is their molecular scale, which enables their employment in living cells and tissues. DNA and RNA are thus attracting particular attention. In these molecules, nature has gracefully implemented a coding system and syntax. Along with this, DNA is characterized by an astonishing density of information, and DNA computations inherent in living organisms are characterized by parallelism and remarkable energy efficiency. However, in vitro DNA computations are still in their infancy. Theoretically, in a test tube with DNA it is possible to solve surprisingly complex combinatorial problems by synthesizing all solutions simultaneously and then enzymatically decomposing the unsuitable ones. Unfortunately, practical implementation is faced with the need to carry out an extremely time-consuming series of reactions under close supervision. In addition, the problem of scaling often requires nontrivial solutions.

Several recent reports have used nucleic acids to solve classical combinatorial problems. For instance, Braich (67) used a DNA computer to solve the 20-variable 3-satisfiability problem (the Boolean satisfiability problem of determining whether the variables of a given Boolean formula can be replaced by the values 1 and 0 in such a way that the formula evaluates to 1). Braich performed calculations for a 20-variable, 24-clause, 3-conjunctive normal-form formula. This problem has more than a million possible solutions (2^{20}), and the DNA computer allows us to obtain

all of these solutions in a reasonable time and then choose those that satisfy the condition (in this problem, there was only one such a solution). Solving any problem with a DNA computer begins with synthesizing a library of solutions. For each of the 20 variables in the equation, 2 different sequences of 15 nitrogenous bases are developed, one representing true and one representing false. Each of the 2^{20} truth assignments is represented by a library sequence of 300 bases, consisting of an ordered concatenation of one sequence of values for each variable. A solution is then selected that satisfies the condition of the problem. In this case, the DNA computer is implemented in the form of an electrophoresis box with two chambers. The first hot chamber is filled with polyacrylamide gel containing a full solutions library and the second cold chamber with polyacrylamide gel–containing probes designed to capture library strands satisfying the logic equation. Polyacrylamide melts in the hot chamber and migrates to the capturing layer in the cold chamber. Consequently, library strands satisfying the equation are captured, and the rest are passed by. The captured answer is then extracted, amplified by polymerase chain reaction, and read.

A different approach to finding the right solutions among the set of all possible is via use of repeated cycles of mark, destroy, and unmark operations (68). First, DNA strands representing all possible solutions are synthesized. At the mark stage, DNA strands corresponding to solutions satisfying the conditions of the problem are hybridized to complement strands. Then, an enzyme that destroys nonhybridized oligonucleotides is added. Hybridized complements are then removed at the unmark stage. Several conditions can be checked in repetitive cycles. Ultimately, only strands that are problem solutions remain.

DNA computers are thus especially effective for solving problems that cannot be solved other than by enumerating all possible solutions. Such tasks are especially difficult for classical computers because at a sufficiently large scale these tasks require colossal memory resources. A classic example of such a task is a Hamiltonian path problem, e.g., the traveling salesman problem (to find the most profitable route passing through the indicated cities at least once with a subsequent return to the original city) (69). It has been estimated that even with relatively few cities, no theoretically conceivable computer could solve this problem via enumerating options in less than several billion years (66 and others). Ouyang et al. (70) used a DNA computer to solve a model Hamiltonian path problem. Similarly, Faulhammer et al. (71) used an RNA solution to solve the classic 3×3 knight problem in chess (to determine which configurations of knights one can place on an $n \times n$ chessboard such that no knight is attacking any other knight on the board). In addition to solving combinatorial problems with the help of DNA computers, which is nevertheless presented in some theoretical exercises, the principles of DNA computers can also find practical applications, for example, in controlling biological processes (72) and programming conditional gene expression (73).

Scientists' searches are not limited to nucleic acid molecules. Pattern-generating molecules provide another interesting example (74). Such molecules can perceive several chemical input signals, and the output signal also depends on signals' order of appearance and concentrations. Such systems could be used as molecular keypad locks (75). Rout et al. (76) used selective enzyme–substrate interactions as complementary molecules for information storage and cryptography. Message encryption was also demonstrated in a 3D photonic crystal with functionalized surfaces. Ratner et al. (77) proposed a memory device capable of performing arithmetic operations based on organic molecules and their ^{1}H NMR analysis, thus obtaining complex 3D wettability patterns that were used to encode messages.

2.2. Self-Assembly

Infochemistry is also used to explore supramolecular self-organization. The design of self-organizing systems implies that the components of the supramolecular assembly carry information

about other components and ways of assembling into supramolecular structures. Controlling self-organization at various scales opens up prospects for the development of a new design method to preprogram spatial and temporal features of assembling matter.

Nenashkina et al. (78) presented a novel way of using Liesegang pattern formation for information recording, protection, and transmittance. Under certain conditions, periodic precipitation occurs in a gel containing a diluted solution of reactants. As a result, periodic patterns occur whereby information can be barcoded. In one experiment, silver nanoparticles were embedded in each self-assembling Liesegang ring (**Figure 2a**), enabling reading of the encoded information via surface plasmon resonance (78).
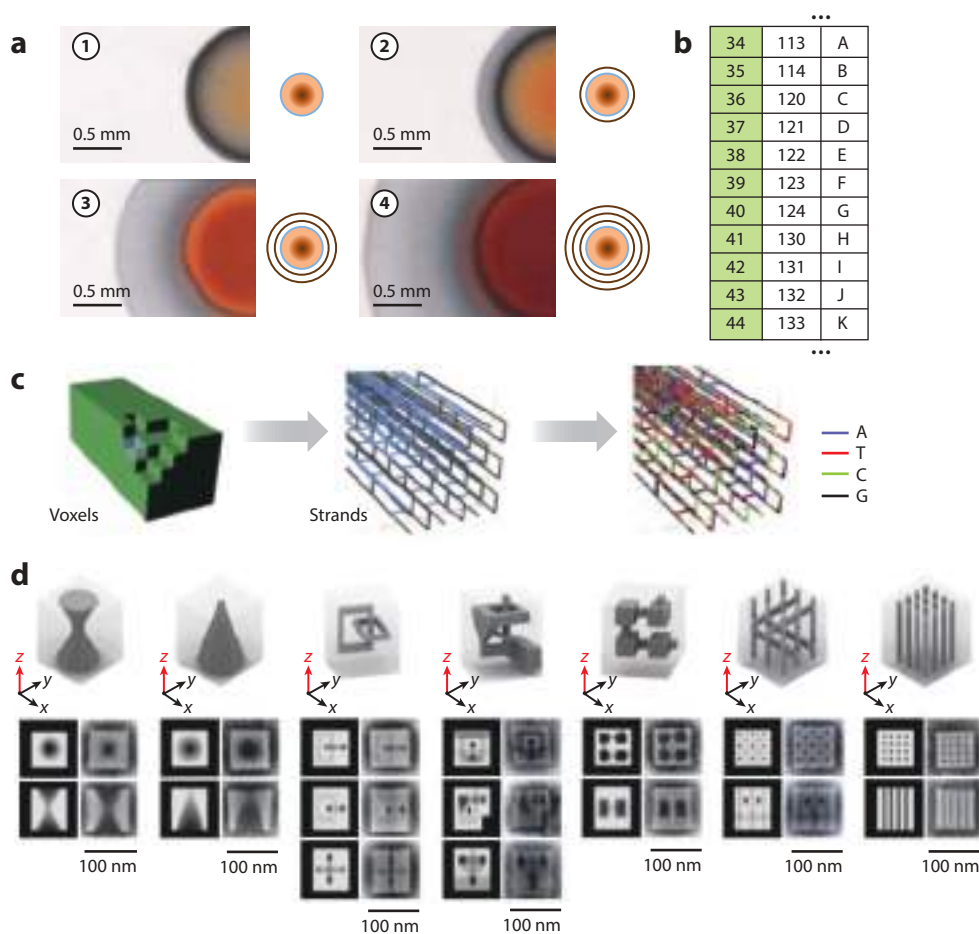
Figure 2

(*a*) Liesegang rings with various concentrations of $AgNO_3$ and corresponding numbers in program code. (*b*) An alphabet-encoded table (adapted with permission from Reference 78; copyright 2020 American Chemical Society). (*c*) A procedure for obtaining complex DNA structures: (*left to right*) design of a desired shape by editing voxels through a 3D interface, translation to strands, and translation to assigned sequences. (*d*) Various cavity shapes: 3D models of the designed shapes and averaged transmission electron microscopy images from different projections (adapted with permission from Reference 84; copyright 2017 American Chemical Society).

Rogers et al. (79) used DNA-modified nanoparticles to program their assembly. Interparticle interactions arising from DNA hybridization provide preprogrammed self-assembly of particles (79). In another example, Kanaras et al. (80) demonstrated nanostructure manipulation using DNA-coated gold particles, assembly of which was controlled via selective cleavage and ligation by DNA-processing enzymes. Assembly of various similar structures has been demonstrated (81–83). Ong et al. (84) recently reported the assembly of a 3D structure containing 30,000 building blocks (**Figure 2***b*). User-predetermined assembly enables creation of complex shapes such as letters.

In addition to the DNA molecules described above, many exclusively artificial systems also undergo self-organization. Many self-organization processes are based on molecular recognition. Peptides endowed by host–guest recognition moieties demonstrate controlled self-organization (85). A system containing aromatic amino acids, a C3-symmetric compound, and bipyridine demonstrated three assembly pathways, the choice between which was programmed by substituents at the α-position of amino acids (86). Dynamic superstructures made of coengineered recombinant proteins and nanoparticles have been demonstrated (87).

Another popular object for constructing self-organizing assemblies is anisotropically patterned patchy particles. Their highly interactive surfaces promote colloidal crystal assembly from particles. Taniguchi et al. (88) demonstrated self-assembly of branch-shaped semiconductor particles into tetrapods and octapods. With the help of computer modeling, Morphew et al. (89) proposed rules for programming the organization of assemblies from colloidal particles.

Self-assembly is thus a perspective bottom-up technique to design adaptive materials. This phenomenon provides a strategy for creating hierarchical materials at multiscale levels. This research is interesting not only from the point of view of the programmed assembly of macro-objects (a new method of construction) but also fundamentally, because self-organization is the driving force behind the origin and evolution of living matter. Therefore, artificial self-assembling systems provide a convenient model for studying adaptation processes and self-regulation.

An important class of self-organizing assemblies is pH-sensitive materials. Such materials include peptides, charge-shifting polyelectrolytes, and various copolymers balancing between hydrophobic, electrostatic, hydrogen-bonding, and steric forces. pH-responsive matter combined with pH clock reaction enables time-programmed self-assembly (90). Reversible pH-controlled assembly and disassembly is possible (**Figure 3***a*), as exemplified by ligand-modified poly(ethylene glycol), dibutylamines, and pyrrolidinamines on the surface of gold nanoparticles. Reversible shielding/deshielding of the targeting ligands at various pHs leads to reversible self-assembly of particles. Zhang et al. (91) reported on lithocholic acid tube self-assembly. Reversible transformation into a spiral and further into spiral shape can take place in various pH conditions. Liu et al. (92) demonstrated the assembly of star terpolymers into different aggregates at varying pH.

Various self-assembling systems that undergo morphological transitions in response to environmental conditions (e.g., pH) require fine-tuning and control. For instance, self-assembling peptides assemble and transit from molecules or spherical micelles into nanofibers in a narrow range of pH from 7.4 to 6.6 (93). Several techniques have been developed to visualize ion fluxes and gradients and in particular proton fluxes and pH, gradients triggering self-assembly in solutions. Although fluorescent dyes can be added in systems (94), additional components may alter it. Therefore, methods of potentiometric microelectrode detection, e.g., the scanning ion-selective electrode technique, are popular and hold potential for logic operation and infochemistry (48, 95) (**Figure 3***b,c*).

2.3. Synchronization

Propagating waves are an important feature of living matter. Potential propagation in nervous system (96) and electrical activity of heart tissue (97) could be considered in this context. Ensembles
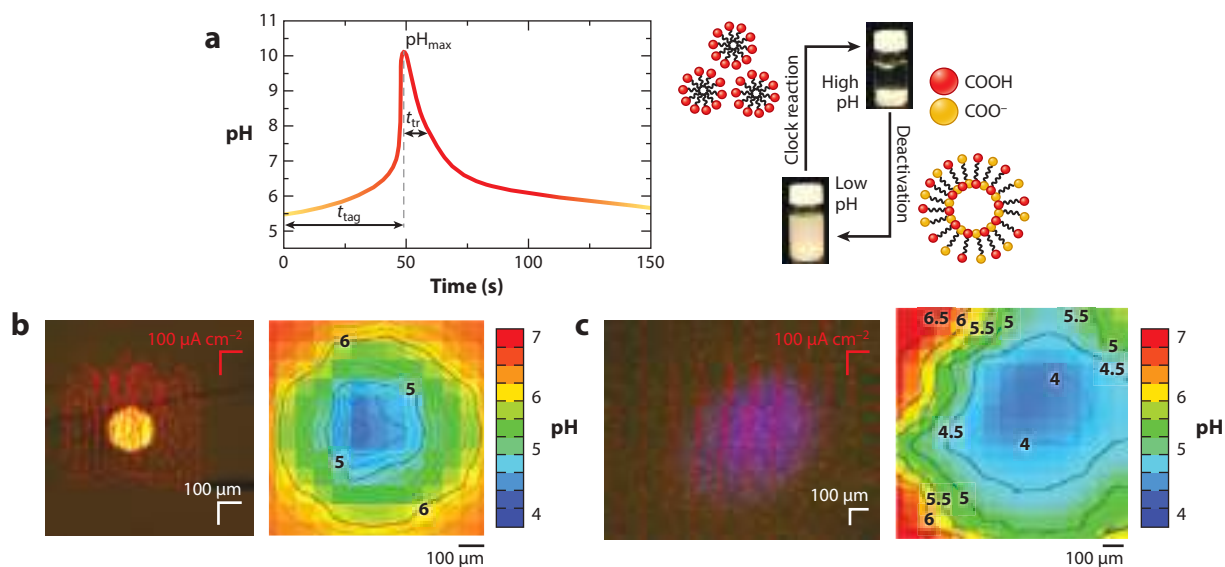
Figure 3

(*a*) A methylene glycol–sulfite clock reaction with a delayed fast pH spike and reversible vesicle–micelle transformation of oleic acid molecules (adapted with permission from Reference 90; copyright 2017 Royal Society of Chemistry). (*b*, *left*) Top view of a gold microelectrode embedded in an epoxy holder; red arrows represent anodic activity. (*right*) A pH map obtained via the scanning ion-selective electrode technique (SIET) over a polarized microelectrode (adapted with permission from Reference 95). (*c*, *left*) An ultraviolet-illuminated spot on the surface of nanostructured anodized TiO_2. (*right*) A pH map obtained via SIET over the irradiated region of a TiO_2 photoelectrode (adapted with permission from Reference 48).

of nonlinear oscillators of various natures are a good model for study of wave propagation and synchronization regimes. In particular, chimeric states, characterized by the coexistence of groups of coherent and incoherent elements in networks of coupled oscillators, are of interest owing to the observation in real systems of states whose properties correspond to chimeras (98). Biological and chemical objects are often considered as such systems. For example, chimera states are realized in mammalian brains when some areas remain active during sleep. The functional behavior of various living systems arises from coupling and synchronization of activity, for instance, neurons and heart cells or quorum-sensing phenomena in bacterial communities. Hankins et al. (99) thus showed that electrical interaction in an anode array–single cathode system can be described similarly to quorum sensing. In other words, the system can sense the number of anodes and change its behavior accordingly.

To study phenomena in coupled oscillators, several model artificial systems are widely used, including electrochemical oscillators. Electrochemical oscillator coupling can be studied via the classic three-electrode configuration of electrochemical cells, in which the working electrode is the electrode array (**Figure 4a**). Various synchronization patterns were observed in such systems coupled under different network topologies. Electrodissolution of nickel in sulfuric acid revealed oscillations coupled through capacitance and resistance. Antiphase collective synchronization can be implemented between two groups of oscillators with strong internal coupling, provided that external coupling is weak and interactions are delayed by the capacitance (100). Rotating wave synchronization patterns have been obtained in dissolving nickel electrode systems (101–103). In this case, 20 oscillators interact through resistance coupling and demonstrate in-phase synchronization. Additional connections and application of negative feedback provide rotational
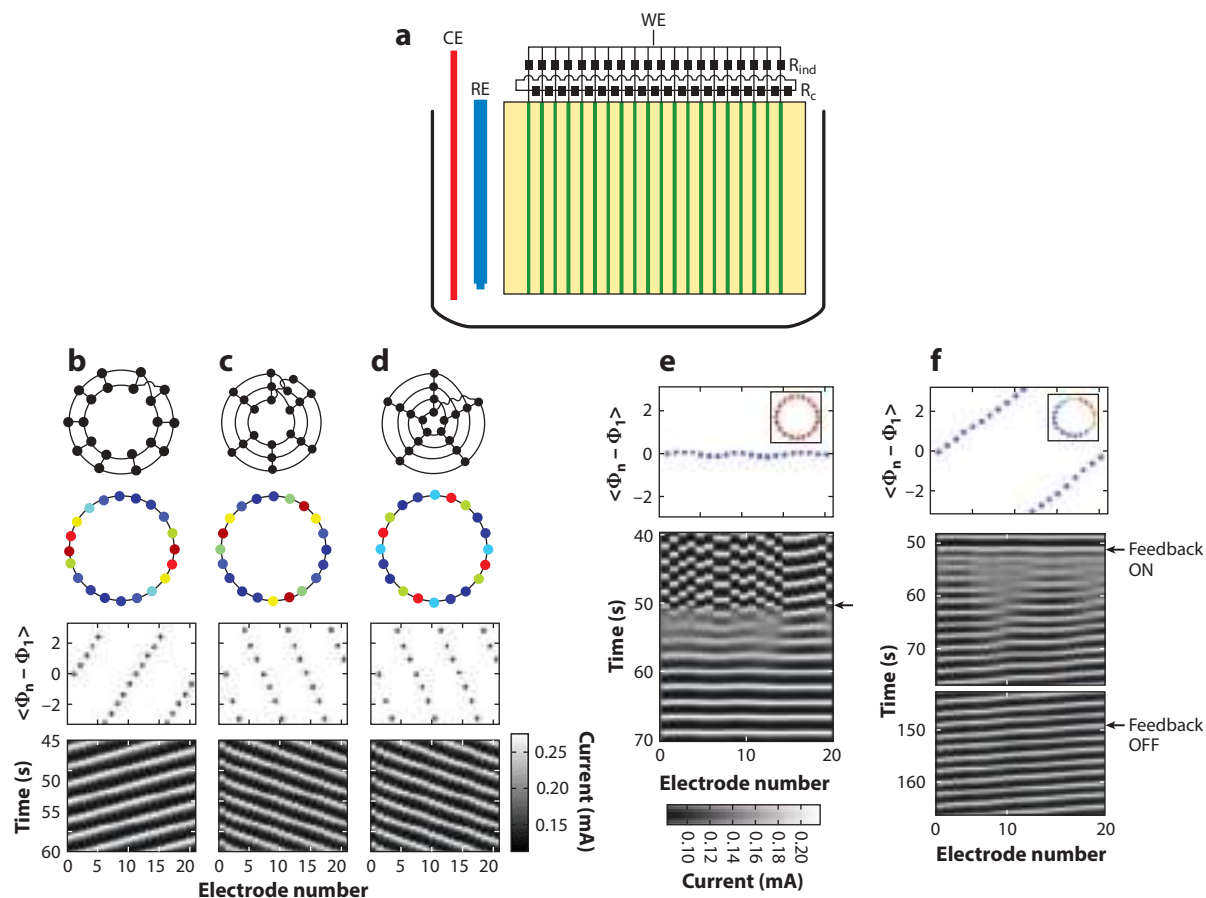
Figure 4

(*a*) An experimental setup with coupled working electrode arrays (WEs), the counterelectrode (CE), the reference electrode (RE), individual resistors attached to the electrodes (R_{ind}), and coupling resistances (R_c). (*b–d*) Rotating waves obtained with topologies and feedback: (*top to bottom*) different topologies, mean phase differences, and space/time plots for coupled oscillations in systems with different topologies. (*e*) An experiment started in the uncoupled state in which no synchronization was observed: (*top*) nearly zero phase difference after coupling and synchronization establishment and (*bottom*) space-time plot of the currents. The coupling was turned on at approximately $t = 50$ s; consequently, current oscillations synchronized quickly and remained stable. (*f*) Rotating wave with coupling: (*top*) phase difference and (*bottom*) space-time plot (adapted with permission from Reference 102).

synchronization states (**Figure 4b,c**). These results demonstrate the importance of biological network plasticity in obtaining a desired outcome at a certain moment. Ocampo-Espindola et al. (104) demonstrated the formation of chimera states (when coherent and incoherent dynamics coexist in a system) during nickel electrodissolution in sulphuric acid. This regime occurs when weak cross-coupling through collective resistance is present. These observations provide an understanding of mechanisms for the generation of chimeras in biological systems.

Oscillating chemical reactions [e.g., Belousov–Zhabotinsky (BZ) reaction] are another important model system for studying the synchronization of nonlinear oscillations. Basically, BZ reaction is the bromination of malonic acid by bromate in an acidic medium. This reaction does not proceed monotonically, and several mechanisms have been proposed to date (**Figure 5a**). This reaction may demonstrate several regimes, such as chaotic oscillation, chemical waves, and
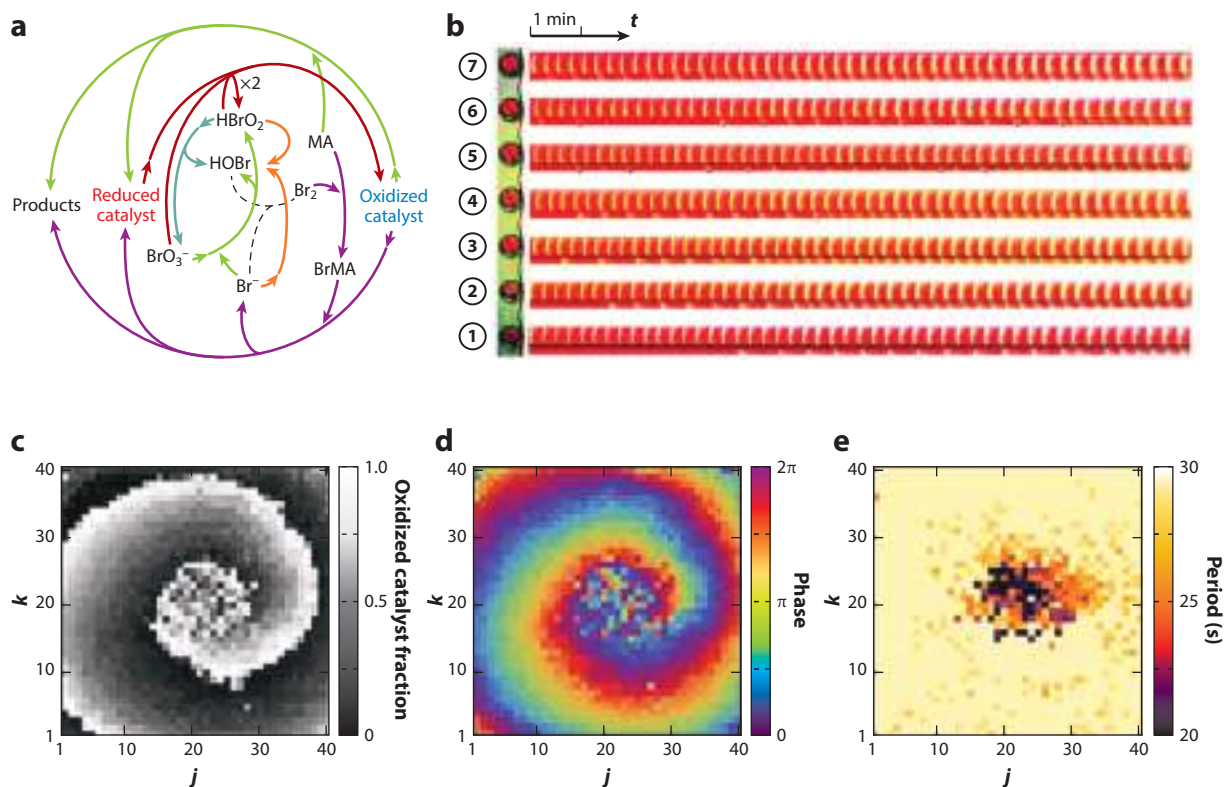
Figure 5

(*a*) A proposed scheme of BZ reaction processes: Solution color switching between red and blue occurs owing to changes in the concentration of either the reduced or the oxidized catalyst. (*b*) Synchronization patterns observed in a system of two droplets (large and small) in which BZ reaction proceeds; the oscillations in both coupled drops synchronize over time (adapted with permission from Reference 105; copyright 2016 Royal Society of Chemistry). (*c–e*) Spiral wave chimera in an array of coupled BZ oscillators and frequency-synchronized rotating spiral wave with aperiodic core oscillators: (*c*) spiral rotating around the incoherent core (700 s after initiation), (*d*) oscillator phases extracted from image *c*, and (*e*) period of the oscillators extracted from image *c* (adapted with permission from Reference 107). Abbreviations: BrMA, bromomalonic acid; BZ, Belousov–Zhabotinsky; MA, malonic acid.

spiral pattern formation. BZ reaction is characterized by complex temporal and spatiotemporal patterns. Depending on the reaction's geometry, phenomena that simulate signal processing with feedbacks, characteristic of biological systems, can be observed. BZ reaction ongoing inside contacting emulsion microdroplets arranged in a 1D array demonstrated synchronization owing to diffusion of components between the drops (105, 106) (**Figure 5b**). For instance, Totz et al. (107) studied a 2D 40 × 40 array of light-coupled BZ chemical oscillators, reporting erratic motion of the asynchronous spiral core, core growth and splitting, and transitions between chimera state and disordered oscillations. Each individual oscillator is represented here by an ion-exchange bead placed in BZ solution and loaded with a ruthenium photosensitive photocatalyst. Fluorescence intensity depends on the concentration of catalyst-reduced form, and thus corresponds to oscillation phase. By using catalyst-loaded particles distributed in BZ solution, chimeric and chimera-like states were also obtained (108) (**Figure 5c–e**). Despite the previous belief that chimeric states are possible only in systems with a large number of coupled oscillators, it was shown that two symmetrically diffusively coupled oscillators are sufficient to give rise to chimeric behavior (109). Chemical wave propagation in geometrically constrained media can be used for a variety of logic

operations (105, 110). Further, oscillating reactions' potential in terms of information storage capacity has been considered (111). To test this, an oscillating BZ reaction was carried out inside lipid droplets. Oscillations synchronized owing to activator diffusion through the lipid membrane and could be controlled by illumination owing to the photocatalyst present in the reaction mixture. Two stable rotational modes occur in this system (clockwise and anticlockwise) that allow reliable and light-controlled chemical memory units. Furthermore, a network of interacting but immiscible droplets in which BZ reaction takes place can be used as an information processing device (112). A chemical classifier made of droplets was designed in computer simulations using evolutionary algorithms and was used to distinguish between malignant and benign forms of cancer, demonstrating 97% accuracy.

Principles and patterns discovered in experiments with these systems open the way to creation of neuromorphic computers (113). Thus, our understanding of organism cognitive functions and development of novel computing devices mimicking these functions could benefit from study of synchronization patterns and chimera generations in artificial systems.

3. ION FLUXES AS INFORMATION CARRIERS

Impulse propagation in the nervous system occurs owing to electric signal transmission. The sodium–potassium molecular pump plays the main role in this process, removing sodium ions from the cell and introducing potassium ions into it, thus establishing the so-called action potential. Divalent magnesium and calcium ions also play important regulatory roles in cells. Inspired by this, the concept of iontronics uses the electronic properties of ionic motion and arrangement.

3.1. Ion Signaling in Living Cells

Inorganic ions play an important role in various biological functions. They participate in electron transfer, macromolecule complexation and functionalization, enzyme activation or inhibition, osmotic pressure regulation, and synthesis of biologically active molecules and energy carriers. In infochemistry, perhaps the most important function of ions in living cells is bioelectric, i.e., creation of a potential difference on the cell membrane that underlies the phenomenon of nerve impulse transmission in the body. In addition, ions have an important function in signaling, the mechanisms of which are an area of active study.

As demonstrated in experiments carried out in mouse cultured cells, Na^+ and Ca^{2+} induce neural cell myelination. It was revealed that increased sodium and potassium concentration correlates with myelin basic protein synthesis (114). Disorders of the myelin sheath in axons lead to sclerosis, autoimmune diseases, and impaired coordination and balance. Therefore, understanding the mechanism of ion signaling in the oligodendrocyte precursor cells where this process is located is of high importance.

Calcium signaling in articular cartilage has also been studied. In response to mechanical stimulation (load application), chondrocytes trigger intracellular calcium signals. Several signaling pathways have been considered (115). Calcium ions were demonstrated to be responsible for light adaptation in *Drosophila*. Changes in Ca^{2+} concentration upon illumination of photoreceptor cells have also been discussed (116). Inhibition of ion channels hinders tissue regeneration, evidencing the important role of cell signaling. For instance, blocking of calcium-activated chloride channels led to a reduction in cell proliferation, and blocking of potassium channels was associated with decreased phagocyte activity (117). Further, calcium ions also play an important role in gene expression.

The study of metal ions in the context of cell signaling has historically focused mainly (though not exclusively) on calcium ions. Chloride ions also have signal functions (118), and zinc ions have intracellular and extracellular regulatory functions in addition to their catalytic and structural functions in proteins (119). The effect of Zn^{2+} ions on human vascular cells has been studied to evaluate the processes occurring in the human body when Zn scaffolds are implanted (e.g., cardiovascular stent). Low Zn^{2+} concentrations have no impact on cell viability but promote cell adhesion, spreading, proliferation, and migration and enhance the expression of F-actin and vinculin. Cells treated with high concentrations of Zn^{2+} demonstrated the opposite behavior (120). Magnesium's and d-block metal's roles in signaling have been highlighted (121).

Recently, Liu et al. (122) demonstrated that neighboring biofilms can communicate and therefore coordinate growth using electrochemical signals, for instance, K^+ waves. This communication allows the two biofilms to share a limited nutrient by setting their growth phases accordingly.

It is therefore apparent that ions play a significant role in developmental signaling and in controlling various processes in living organisms. The efficiency and high selectivity of these processes are currently inspiring great interest in their application outside biological systems. In particular, ion signaling is slated for use in the next generation of electronics: iontronics. For this, ionic analogs of such electronic elements as a diode, memristor, and transistor are created.

3.2. Ionic Diodes

A diode is an electronic component that conducts current mainly in one direction—that is, it is characterized by asymmetric conductivity. Ion diodes are created based on substances that exhibit asymmetric ionic conductivity. Nanopores are often considered as candidates for design of ionic diodes. Asymmetric ion transport was observed through propylene carbonate conical pores filled with poly(methyl methacrylate) hydrogel doped with $LiClO_4$. This system, which has no liquid interfaces, demonstrates ionic current rectification and works as a solid-state ionic diode (123). However, because nanopore-based ionic diodes are inspired by ion channels of cells, such systems are studied mainly in aqueous solutions. Microhole supports asymmetrically covered by polymers with ionizable groups (ionomers) demonstrated diode behavior (124). Exhaustive research to determine electrolyte concentrations and the influence of diode geometry on functionality was performed employing a simulation model. Such a model is expected to allow prediction of better nanopore iontronic devices.

Aaronson et al. (125) presented a single-material ionic diode made of nonmodified reconstituted cellulose materials. Unfortunately, nanopores are disadvantaged by very high resistance, so that it is difficult to separate the signal from the background noise. Mesopores have been used as an alternative. Lin et al. (126) demonstrated anomalous ion transport through a conically shaped mesopore, the tip of which was filled with poly-L-lysine (PLL). The authors analyzed how charged polyelectrolytes can modulate ion transport at the nano- and mesoscale.

Diode behavior usually arises from the nanopore, asymmetry of which breaks symmetry of ion distribution in solution. Asymmetry is the basis of diode technology. For example, Zhao et al. (127) used asymmetric polyelectrolyte distribution to design an ionic diode, and Gao et al. (128) provided a platform for creating nanoscopic ionic channels from exfoliated 2D materials (e.g., graphene). Using this approach, they constructed Kirigami-nanofluidic diodes and circuits. Kirigami is a variation of origami that includes cutting rather than folding paper. Indeed, asymmetric edge lengths of exfoliated graphene sheets provided asymmetric interfacial resistances, resulting in ionic current rectification. Fine patterning was assumed to allow precise control of ion transport properties and construction of more sophisticated diode circuits able to realize information processing on a single 2D film. Synthetic alumina nanochannels with branched geometry

also exhibit diode behavior, owing to the fundamental asymmetry of the branched structure and surface charge distribution (129, 130) (**Figure 6**).

The creation of ionic analogs of p–n junctions offers another approach to constructing ionic diodes. An ionic diode made of nanocomposite electrodes demonstrated mechanical sensitivity and generated electrical output from mechanical stimuli. The nanocomposite electrodes were prepared by infiltrating ionic liquids into ionic polymeric matrices filled with multi-walled carbon nanotubes. The p-type side was prepared from Nafion membrane and n-type DF25 membrane. Mobile ions of ionic liquids can replace H^+ cations and Br^- anions in Nafion and DF25, respectively. A polycarbonate separator was also introduced to avoid shorting the circuit. The mechanical sensitivity of this device enables conversion of mechanical motions into electricity (131).

Stretchable ionic diodes made from polyelectrolyte hydrogels have been reported (132). As interest in soft and flexible devices increases, polymer iontronic alternatives to electronic components are a promising area of research. In addition to interest in flexible, wearable devices, the idea of integrating electronic devices into the human body is now attracting much attention. Since the information is transmitted by ion fluxes in the human body, and by electrons in the currently existing computing devices, it is important to perform the signal transfer in human–machine interfaces. In addition, because ion signals in organisms are rather weak, ways to enhance them must be developed. Recently, Lim et al. (133) presented a polyelectrolyte gel–based p–n ionic diode that can generate additional ionic current and thus amplify signal. Hydrogel ionic diodes demonstrate promise for use in flexible Zn-based batteries for wearable electronics (134) (**Figure 6e,f**).

An artificial nanofluidic diode that can perform simple logic calculations was designed from a system of two conical nanoporous polymer films. These nanoporous diodes mimic cell junction proteins and present possibilities for complex artificial information communication networks (135). Recently, Ali et al. (136) reported that a set of differently oriented single-pore membranes with different surface charges can operate like an arrangement of several ionic diodes connected in series or in parallel (**Figure 6a,b**). Thus, it is possible to implement circuits similar to those obtained in solid-state silicon electronics. Polyelectrolyte pore modification is a procedure by which one can adjust pore surface charge and design various ionic diode circuits.

Multiple stimuli-responsive diodes could perform various logic operations, and nanochannels with different functions could be combined in single nanofluidic diode chips for neuromorphic computers. An intellectual ionic diode was able to switch current direction, as demonstrated by Putra et al. (137). The diode was based on microporous cationic conductor Nafion interfaced at polyethylene-terephthalate and demonstrated potassium flux rectification. Precipitation of potassium ions in the form of perchlorate blocked ion flux and inverse diodes. Another mechanism of diode polarity change is based on ion mobility within the nanomembrane and the mechanical valve effect (138). Wang et al. (139) designed a light-responsive ionic rectifying 2D nanofluidic device based on spiropyran-modified layered graphene oxide membranes. Switching between low- and high-rectifying states can be performed rapidly via irradiation, thus enabling asymmetric ion transport. Xiao et al. (140) demonstrated light-triggered ion pumping through a carbon nitride nanotube membrane and against a concentration gradient.

A dual-responsive ionic diode has been designed using a track-etched polyethylene terephthalate nanopore surface coated with temperature- and pH-responsive PLL. PLL-coated channels are nonconductive at 70°C and pH 11.5 but can be switched to a conductive state by decreasing temperature or pH (141, 142). Zhang et al. (143) designed a light- and pH-sensitive artificial channel that closes in an acidic and dark environment and opens under illumination and in neutral pH. These nanofluidic diodes mimicking light-gated and pH-tunable ion channels play an important role in living cells. Further, PLL functionalization depth changes nanopore
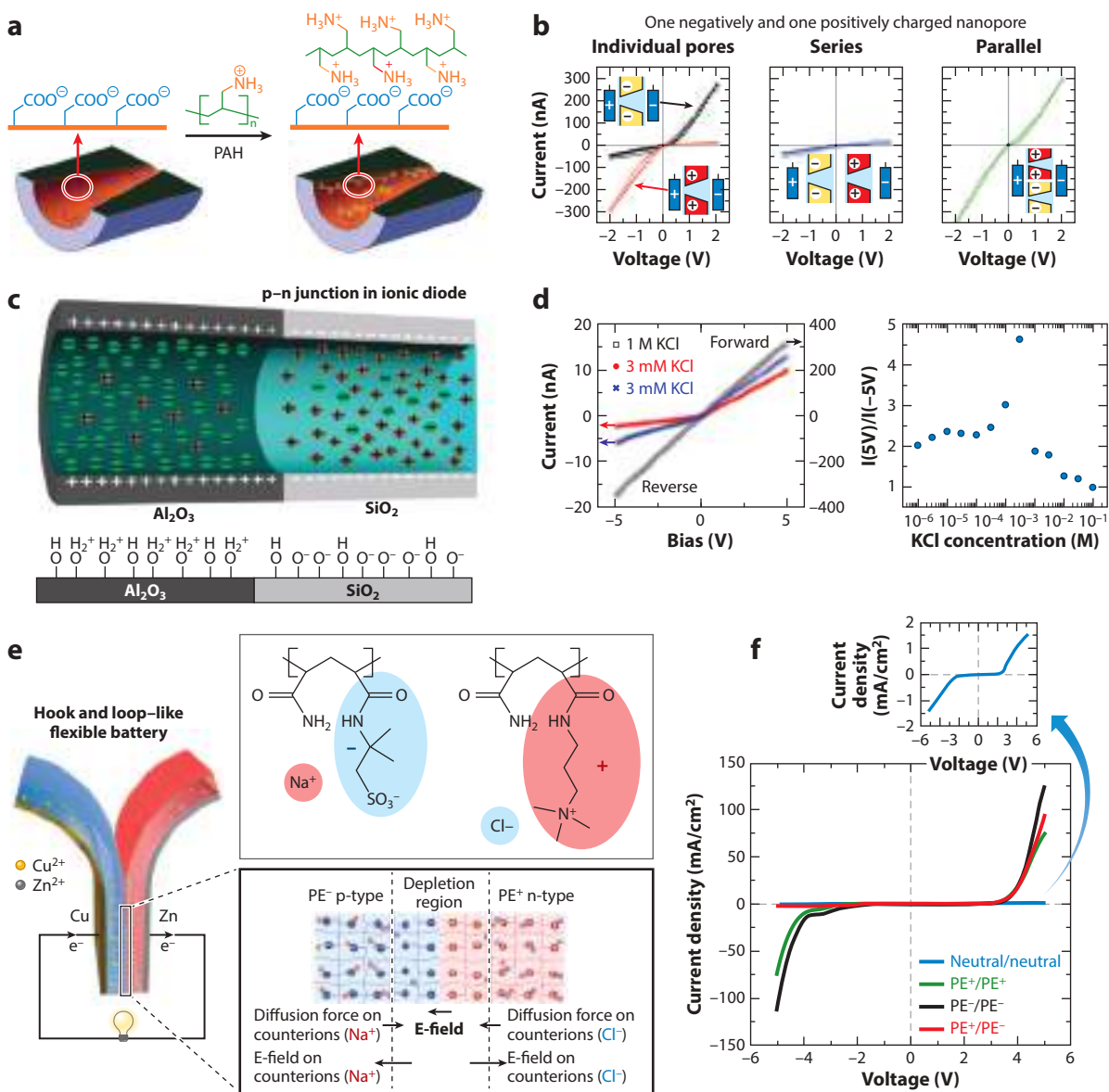
Figure 6

(*a*) A negatively charged polyanion (*left*) and positively charged polycation (*right*) coated pore surface of the conical nanofluidic diode. (*b*) The I–V curves for individual positive and negative pores separately, as well as their series and parallel connections (adapted with permission from Reference 136; copyright 2019 Royal Society of Chemistry). (*c*) An ionic diode made of heterostructured oxide nanotube heterojunction. (*d*) The current rectification of the nanotube diode in various solutions and current ratio of the forward and reverse direction at different KCl concentrations (adapted with permission from Reference 130; copyright 2009 American Chemical Society). (*e*) Schematic diagram of a flexible battery and chemical components of polyanion hydrogels and polycation hydrogels forming a hydrogel diode. (*f*) The current–voltage curves of diodes composed of two hydrogels with varying charges (adapted with permission from Reference 134).

conductivity, consequently enabling regulation of ion selectivity. As a result, cation or anion flux rectification can be performed, and switchable diodes can be obtained (144).

In the recent past, nanochannels were considered mainly for applications in energy conversion and water treatment (e.g., desalination), controlled mass release, and transport, but lately, attention has been shifting toward their use in various logic gate operations. As a result, ionic diodes hold promise for ion-based information-processing devices communicating with biological signals in physiological environments.

3.3. Ionic Memristors

Another electronic element, the development of an ionic analog of which is attracting a lot of attention, is the memristor. This element can change its resistance depending on the current flowing through it. Memristor behavior resembles the work of a biological synapse (145). Because when different signals pass, the memristor resistance changes in different ways, we can say that the signals have a certain weight. Thus, memristors can be considered as artificial synapses, and memristor-based artificial networks can be considered as neuroprocessors. Hewlett-Packard created the first memristor prototype in 2008, and even more than 10 years later, the technology is still in its infancy. The problem of reproducibility of resistance values from cycle to cycle still requires a solution. At the same time, new materials are considered from the point of view of the manifestation of memristive properties.

Oxygen-conducting oxides are generally considered as potential candidates for use in memristor devices. Amorphous oxides demonstrate higher oxygen conductivity compared with crystalline ones (146). A solid-state tantalum oxide memristic device was improved via addition of a porous ion-blocking graphene layer, which enhanced performance and allowed tuning of the resistive switching effect (147).

Memristor behavior has been observed in microtubules, protein intracellular structures that make up the cytoskeleton. Microtubules are hollow, polar cylinders 25 nm in diameter and a few micrometers in length. Microtubules were observed to work like biological memristors (148). It is assumed that these structures underlie the phenomenal memory of the amoeba, which does not have a nervous system as such. Microtubules also are considered to form bioelectric circuits to perform biologically inspired neuromorphic computing. Artificial nanochannel systems have been considered as well. A nanofluidic polydimethylsiloxane device demonstrated electrically controllable conductance and was considered an artificial synapse (149) (**Figure 7a**). To explore this, nanochannels were filled with a viscous ionic liquid and KCl water solution. Two immiscible liquids formed an interface inside the channel. Further, these interfaces were displaced by the external applied voltage. Thereby, a nanochannel-based memristor was realized (149, 150) (**Figure 7b,c**).

Artificial systems can simulate the behavior and functions of neurons and inspire neuromorphic computing. Owing to synaptic plasticity, it is possible to train living organisms, as well as to perform complex operations such as pattern recognition. Materials showing such properties can form the basis of neuromorphic or brain-inspired computing, where training and learning take place at the level of the material, not the program code.

4. INFOCHEMISTRY AND HEALTHCARE DIAGNOSTICS

The study of complex physicochemical processes requires reliable instruments with high statistical reliability. However, even with such instruments, the problem of obtaining a large amount of data remains. One of the reasons is the impossibility of fast delivery of the analyzed objects to the place of analysis. Another reason is the limited capabilities of instruments for streaming object analysis. That is why, in recent years, there has been an increasing return to portable chemical sensors as
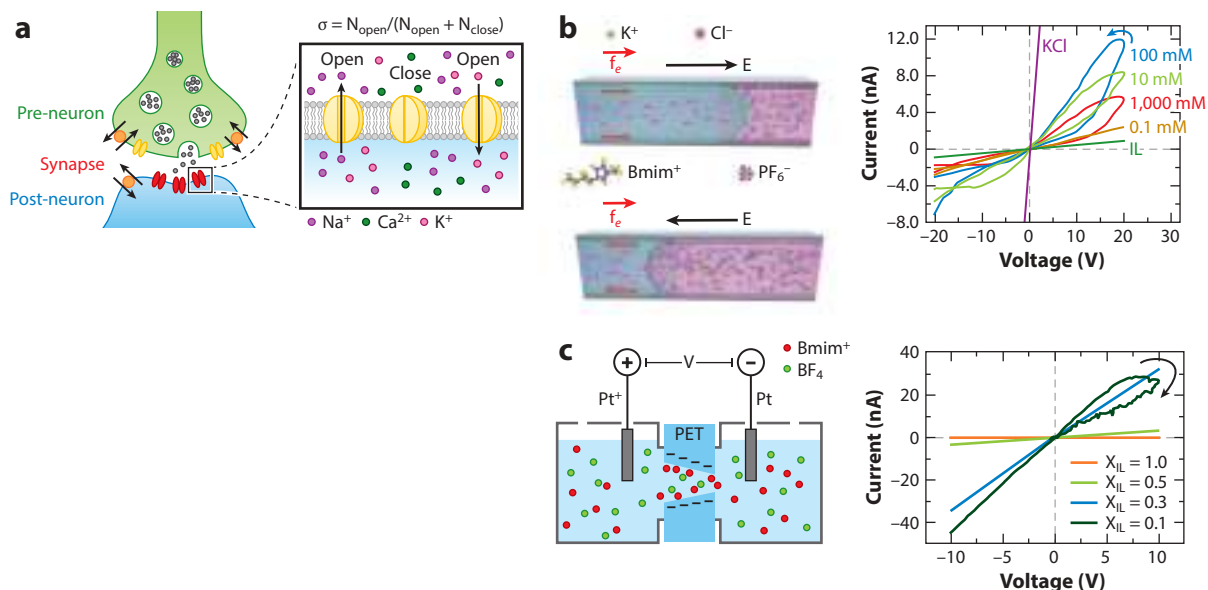
Figure 7

(*a*) Scheme of a biological synapse. (*b*) Scheme of ion and liquid transport in a nanochannel filled with KCl water solution and ionic liquid and I−V curves in solutions of KCl (adapted with permission from Reference 149; copyright 2019 American Chemical Society). (*c*) Ion transport through a single conical nanochannel and I–V curves for ion transport through a conical nanochannel with various molar fractions of ionic liquids in the electrolyte mixtures (adapted with permission from Reference 150; copyright 2017 Royal Society of Chemistry.

a data acquisition tool. Chemical sensors also meet the Internet of Things demand for collecting big data on complex systems.

Chemical sensors for collecting and analyzing information are used in industry, medical diagnostics, and ecology. In all these areas, sensors allow monitoring of the state of complex systems in dynamics. This achievement makes it possible to study a large number of processes that can occur simultaneously or sequentially. The information obtained on the concentration of products and reagents and the changing physical parameters of systems allows them to be studied at an entirely new level.

Chemical sensors that are used in an industry usually aid in study of artificially created complex systems. Medical diagnostics is of the greatest interest from the point of view of collecting information about complex biochemical processes. In studying biochemical processes and processes occurring in the body, it becomes possible to use the data obtained to create anthropomorphic systems and their programming. The principles and approaches of infochemistry make it possible to consider all the causes and correlations in the variable composition of biological fluids. The monitoring of a large number of parameters provides information about dynamic changes in the state of human health. Systematic analysis of big data enables creation of a healthcare fingerprint for timely diagnosis, therapy, and prevention of a wide range of diseases. An essential requirement for obtaining big data is the ability to continually monitor a large number of indicators.

4.1. Multisensor Electrochemical Platforms

Personalized diagnostics require rapid, quantitative, and informative analysis at the point of care. Sensor platforms meet this requirement and enable low-cost analysis. The sensor platform

Analyte	Recognition and transducing layer	Chemical-to-electrical signal transducer	Signal processing system
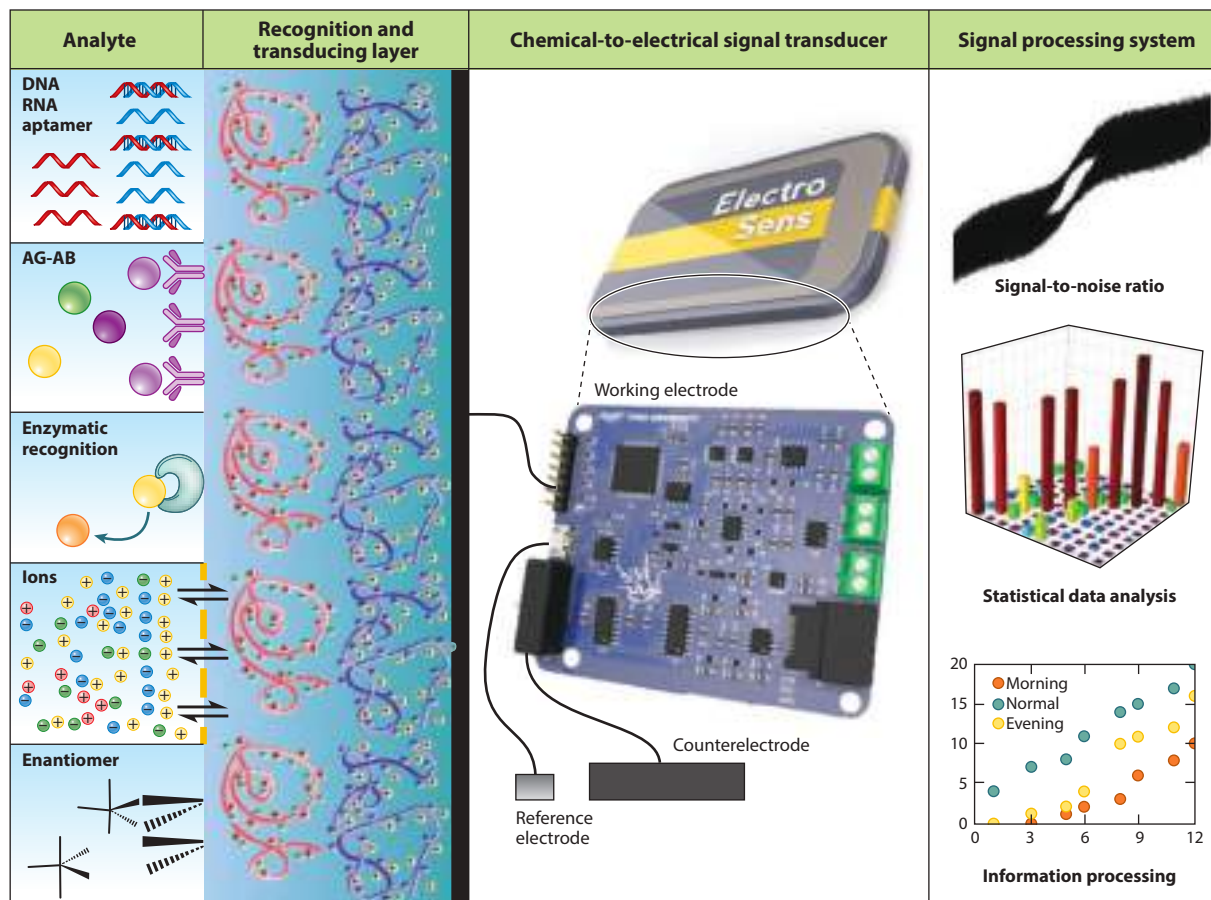
Figure 8

Principles of multisensor electrochemical platform construction.

consists of a sensitive layer, a transducer, and a data-recording and -processing system (**Figure 8**). Among the most common analytical methods in sensor platforms that used the selective interactions for response formation are Raman spectroscopy (151), UV-VIS spectroscopy (152, 153), and electrochemical methods of analysis [amperometry (154), cyclic voltammetry (155), potentiometry (156), and electrochemical impedance spectroscopy (157)]. Multielectrode electrochemical systems (158, 159) and multimodal sensing platforms (160, 161) allow control of many parameters (162, 163). Recognition-/sensitive-layer modification provides selectivity, signal stability, and the ability to integrate a sampling step directly into sensor design.

Multisensor electrochemical systems enable detection of heavy metals, such as zinc, in blood and urine samples, including at the sample-preparation stage (164) (**Figure 9a**). Another principal part of the electrochemical sensor platform is the electrochemical-to-electrical signal transducer potentiostat and its software. Potentiostats for portable sensor platforms require low-cost electronic components, the ability to transmit data over a distance, miniaturization, and the ability to integrate into everyday human life (165) (**Figure 9b**). Electrochemical multisensor systems allow analysis of sweat, blood, urine, saliva, and semen. Heavy metals, organic acids, and electrolyte and metabolite levels can be determined from blood and urine. Sweat is used to determine the level
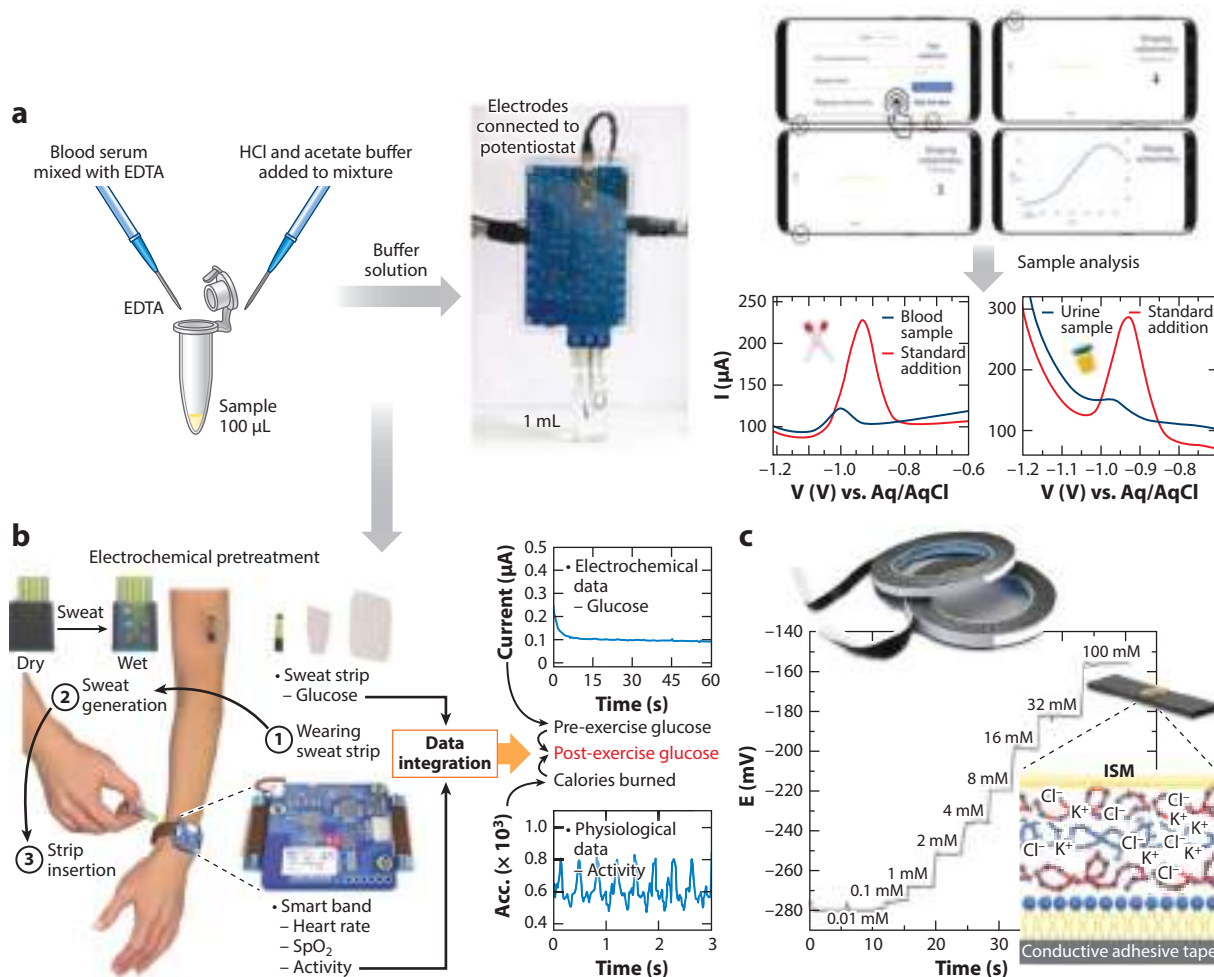
Figure 9

(*a*) Portative electrochemical sensing platform for Zn^{2+} detection by stripping voltammetry on the carbon fiber electrode (adapted from Reference 164; copyright 2020 American Chemical Society). (*b*) Electrochemical platform for glucose, heart rate, and activity control (adapted with permission from Reference 165). (*c*) Ionselective sensor for potassium and sodium detection by an integrated pseudo inner reference electrode (adapted from Reference 156; copyright 2019 American Chemical Society). Abbreviations: EDTA, ethylenediaminetetraacetic acid; ISM, ionselective membrane.

of lactate, potassium, sodium, and metabolites (166, 167). Saliva has a less representative composition, but it can indicate the state of the microflora (168) of the oral cavity and throat (169, 170), as well as the calcium content in the teeth (171). Miniaturized ion-selective electrodes based on cheap carbon electrode material and pseudo inner reference electrodes allow control of potassium and sodium levels in vivo (156) (**Figure 9c**).

Sperm is an essential reference for monitoring sexual activity and fertility (172). Fertility can be rapidly assessed indirectly via electrochemical detection of hydrogen peroxide to indicate oxidative stress, which, according to the World Health Organization, indirectly indicates male infertility (173). The stability of the signal measurement in the seminal fluid is provided by diamond nanoparticles (174).

These biological fluids are systems of complex and variable composition. In such systems, the influence of the matrix effect can be hard to determine. The engineering problem for express analysis of biological fluids lies in introducing additional, separate stages of sample preparation. Microtechniques can help solve this sample preparation problem. Membrane microfilters installed directly in front of the recognition layer allow the separation of blood plasma (175), which makes it possible to neutralize the influence of red blood cells. Microfluidic sample preparation constructs are used to separate low–molecular weight substances from protein structures or particles (176). Microfluidic separation is based on differentiated diffusion in laminar flow. Modified magnetic nanoparticles make it possible to concentrate the analyte on the electrode surface and neutralize the matrix effect (177).

Surface nanostructuring in the electrochemical sensor increases sensitivity and selectivity, improves other analytical characteristics, and allows sample preparation directly on the sensor's surface. Integration of miniaturization and sample preparation is an undoubted achievement for further developing engineering design of electrochemical multisensor platforms.

Despite all the advances listed here, sensor results do not have a systematic approach to assessing the information received. The reason for this lies in the complex interactions that are rather important for understanding fundamental chemical processes. In this case, the methods and approaches used in information technology to process big data can come to the rescue. These methods differ from the standard chemometric approach, which requires the analytical signal to be subjected to mandatory preliminary chemometric processing. The most pioneering chemometric approaches are the electronic tongue and electronic nose systems (178, 179). The most commonly used regression analysis allows discovery of similarities and building of predictive models based on them (180). And in the field of information technology, a fairly wide range of machine learning methods are used to build predictive models (181).

4.2. Machine Learning in Electrochemical Chemometrics

Machine learning techniques are crucial in modern information processing and predictions. These algorithms have found application in solving problems from various fields of chemistry. In theoretical chemistry, they can optimize quantum mechanical calculations and predict substance reactivity and catalytic ability. In organic and inorganic chemistry, they can find correlations between structure and spectra. Moreover, they are also used as decision-making algorithms in the chemical industry and as data analyzers in sensors. This variety of applications proves these algorithms' suitability for almost any field of chemistry.

However, the large number of algorithms, functions, and neural networks makes it challenging to choose the one needed to solve a specific problem. Both the essence of the solution and the type of data used must be considered. For this purpose, the type of training must be chosen—supervised, unsupervised, or reinforcement learning. There are methodologies to help choose the best machine learning method for a given model. Multilayer networks with a backpropagation algorithm are most suitable for solving complex chemical interactions because the main tasks are classification and modeling of physicochemical processes.

Machine learning serves as a classification method for characterizing the system via input parameters. However, the main roles of machine learning algorithms are parameter optimization and model correction. Such parameters can include almost any data, including voltammetric curves and infrared spectra. The relationship between the input data and the resulting response can be highly complex. Nevertheless, even in this case, neural networks can find the right solutions.

Control over the technological process is based on parameter analysis. Searching for correlation between parameters and product quality is a good task for machine learning algorithms. Various projects in biochemistry and pharmacology use neural networks. For example, models like SVM (support vector machine) can be used for chemical analysis of products to control industrial processes, saving labor time (182).

Spectroscopic methods, in particular mass and infrared spectroscopy, are actively used to identify the structures of various molecules. Spectra can be used to establish the structure of a substance. Reinforcement methods like ion mobility and liquid chromatography are also used to improve identification accuracy. However, machine learning can significantly simplify the identification of substances by spectroscopy and eliminate the need for additional methods. The relationship between spectra and structure is complicated, especially for new substances unavailable in databases. However, neural networks can detect these complex correlations and classify substances based on their spectra's analysis. In particular, several models can determine the taxonomy of molecules from their mass spectrum. In this case, it is possible to create a successful model for molecular classification (**Figure 10a**). Classification is provided from a large class of organic compounds to a subgroup—eicosanoids (183).

Machine learning is also gaining acceptance in the vast area of sensor design (184). It is incredibly widely used in electrochemical sensors because the sensors do not require large volumes of analytes and can detect low concentrations (185). Operation of such devices is based on obtaining voltammograms (186). The obtained voltammetric data provide a fingerprint of various molecules, because the redox peaks of substances on different electrodes will be resolved (187). Thus, they can be used to identify, e.g., various chemical toxins, heavy metals, and pesticides (188).

Machine learning algorithms can significantly simplify and speed up identification of various substances in liquids. Many uses for algorithms in the analysis and determination of these substances have been proposed. In particular, Dean et al. (187) proposed using models to assess the presence of explosives and heavy metals in water; the extensive databases of voltammograms for various metals and substances led to a high percentage of accuracy. Lu et al. (189) obtained similar data in studying heavy metals and pH, as well as the amount of suspended metal particles, in seawater, noting that large databases with high-quality data are necessary to achieve high accuracy. Large amounts of high-quality electrochemical data may also open the way to using deep learning networks to solve theoretical questions of electrochemistry (**Figure 10b**). In particular, Bond (190) proposed the use of machine learning techniques to predict the most appropriate kinetic modeling method. Bayesian methods allow appropriate Butler–Volmer or Marcus–Hush electrokinetic model parameters from voltammetric data (190).

Machine learning is increasingly being used to predict the catalytic activity of materials and to model catalytic processes (191). In particular, Chen et al. (192) proposed using a neural network to analyze density functional theory data on the catalytic reduction of CO_2 to CO. Such a method enables prediction of the adsorption processes on the surface of a catalyst made of gold nanoparticles, making it possible to estimate the entire surface (**Figure 10c**). Several other works posit the use of machine learning to develop improved technologies for catalyst production (e.g., 193).

Machine learning is also used for complex tasks, such as modeling protein interactions and establishing protein structure. Song et al. (194) analyzed several supervised learning models and assessed the contributions of different attributes to model training. Given the complexity of the model selection problem, the use of a single model does not give a good forecast; moreover, they found that predicting the path of interaction is much more complicated than assessing the final
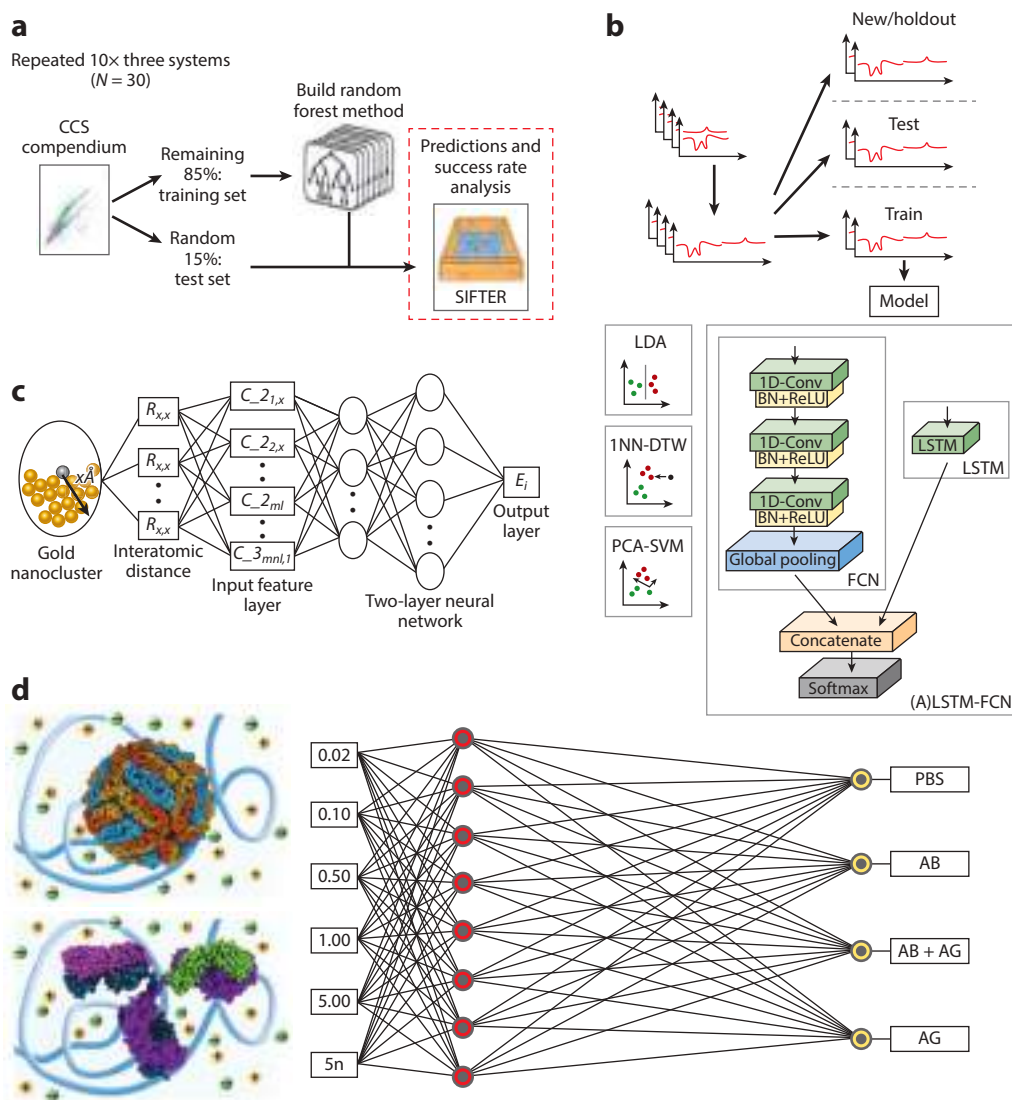
Figure 10

(*a*) Overall schematic of a SIFTER random forest machine learning workflow (adapted with permission from Reference 183; copyright 2020 American Chemical Society). (*b*) Schematic of data collection, preparation, and training. A schematic representation of each algorithm is shown (adapted with permission from Reference 187). (*c*) Overall structure of a neural network. A fully connected two-layer neural network with 30 nodes in the first layer and 50 nodes in the second layer fits the physical descriptor, with a total of 2,801 model parameters (153). (*d*) Multilayer perceptron model for a tick-borne antigen, antibody, and antigen–antibody complex (adapted with permission from Reference 196; copyright 2020 American Chemical Society). Abbreviation: 1NN-DTW, 1 nearest neighbor and dynamic time warping; AB, antibody; AG, antigen; CCS, collision cross section; FCN, fully convoluted networks; LDA, linear discriminant analysis; LSTM, long short-term memory; PBS, phosphate buffer solution; PCA-SVM, principal component analysis–support vector machine.

structure. Combining several models greatly increases the accuracy of structure estimation, but solving such complex problems requires the creation of databases with significantly diversified data (195).

In conclusion, machine learning can now help greatly in the development of various fields of chemistry. These methods are often used to analyze and interpret the data obtained to predict or estimate the amounts and structures of various chemicals. Machine learning for data prediction opens excellent opportunities for algorithmic production processes and a significant acceleration of data processing. One particularly important application could be sensor construction to detect various diseases by identifying antibodies and antigens (**Figure 10d**) in biological fluids (196). Machine learning could therefore provide significant advancements in chemistry and related disciplines.

4.3. Electrode Materials for Multielectrode Detection Systems

Another advantage of electrochemical and multimodal sensor platforms is the ability to create a large number of electrodes on one frame. The ease of multielectrode systems manufacturing allows adaptation of the electrode set for a specific range of analytes. Such versatility avoids the problem of comparing the results obtained on different setups.

Despite the rapid development of nanotechnology as a tool for creating multielectrode systems, there is promise in creating such a system from electrodes that will be cheap, easy to manufacture, and consistent with green chemistry principles. Simultaneously, advances have been made in lithographic methods for the manufacture of electrode arrays. Various methods have been proposed for the creation of miniature electrodes based on templates made via lithography. A developed electrode surface on a chip can be achieved via directed electrochemical growth (197). Applying high-frequency voltage triggers nucleation and directional growth of nanostructured dendrites between pairs of electrodes on a chip (**Figure 11a**).

It is also possible to create nanostructured electrodes based on lithographic templates via microchannel alignment (198). Microchannel alignment makes it possible to place precious metal (199) and semiconductor (200, 201) nanostructures on a microchip. Both of the above techniques enable creation of ensembles of electrodes of various morphologies and compositions on a chip. Use of such electrodes in vivo and in vitro requires electrode-inert biological fluids, high hydrogen overvoltage, biocompatibility, and long service life. Among biocompatible multielectrode systems made with low-cost materials, carbon fiber is outstanding in its properties (202). Such systems can include up to 64 individual carbon fiber electrodes (**Figure 11b**). The 64-channel multisensor system allows direct monitoring in a living organism (203). Electrodes based on conducting polymers are used to create such systems of various shapes and architectures (204). Nonconductive polymer fibers are coated with various conductive composites, allowing their use as multielectrode systems (205). Initially, multielectrode systems were developed for electroencephalographic and electrophysiological analysis. Such systems can be used in various multimodal sensor platforms because, with their help, it is possible to generate cascades of electrochemical processes that will affect the sensor response. In combination with machine learning methods, this will lead to increased selectivity and sensitivity of chemical sensors. Programming electrochemical reactions by varying the solution's composition and controlling the electrode surface state could make it possible to obtain characteristic photoelectrical responses (206) (**Figure 11c**). Multielectrode systems, consisting of electrodes modified with various sensitive layers, will determine a wide range of analytes in biological fluids. Multisensor electrochemical platforms based on such systems and machine learning algorithms for data processing will aid in health monitoring and preliminary medical diagnostics.
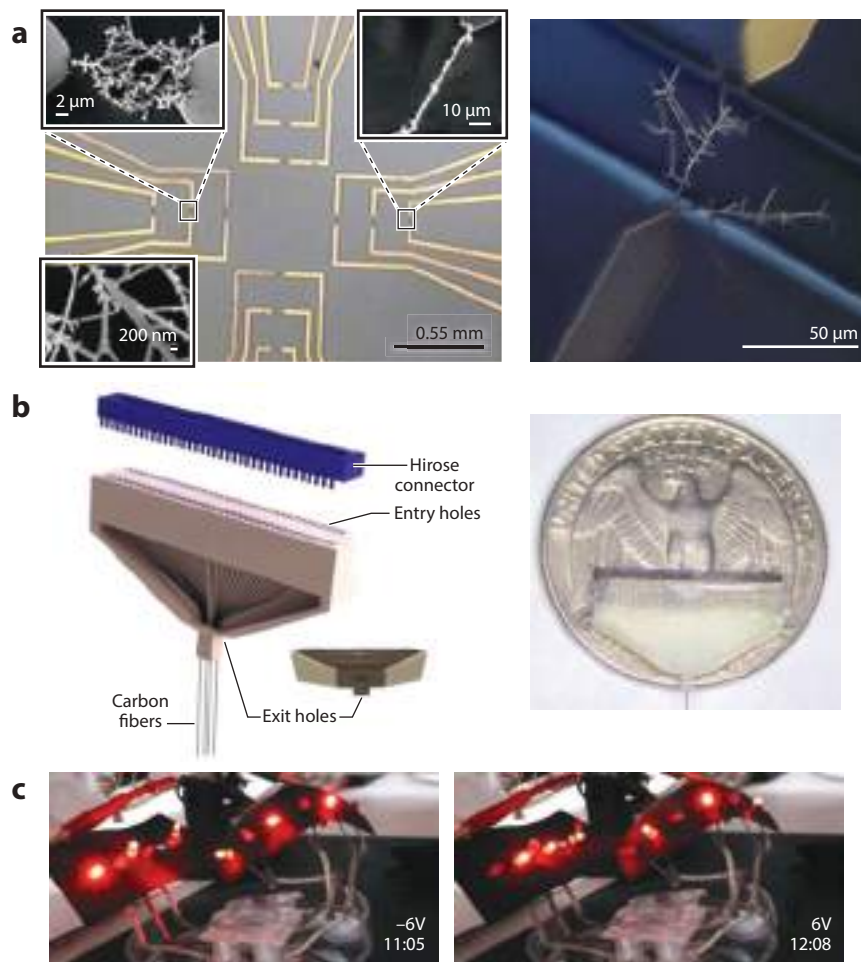
Figure 11

(*a*) A multisensor electrochemical system for the detection of glucose, hydrogen peroxide, and ethanol (adapted with permission from Reference 197). (*b*) A 64-carbon fiber electrode constructed for electrophysiological measurement (adapted with permission from Reference 203). (*c*) A multielectrode system for a chemically programmable signal with photodetection (206).

5. CONCLUSIONS

Elucidating the operating principles of chemical systems allows us to control the course of processes and predict possible results. Tools based on Boolean logic, mathematical statistics, and engineering describe the operation mechanisms of such systems. Also, we propose an approach in which the model systems are complex chemical systems. As a rule, nonlinear processes occur in such systems, the combination of which requires a detailed mathematical description. The use of a complex mathematical apparatus can lead to erroneous results and, subsequently, erroneous conclusions. Algebraic logic and modern methods of mathematical statistics are used to describe such systems in information technologies. Chemical descriptions based on simple logic gates and machine learning methods help explain the cascades of chemical systems and predict possible

resource paths. Such descriptions will find future application in the robotization of chemical bio-engineering.

We believe that a modern approach to the production of new knowledge should rely on inter-disciplinarity. Solving actual problems with the involvement of chemistry, physics, mathematics, and biology will be the main direction of science of the near future. From this point of view, info-chemistry, which unites fields of knowledge such as physics, chemistry, and biology, is undoubtedly at the forefront of scientific development. This developing field is faced with such urgent tasks as the design of synthetic cells and smart dynamic and self-regulated materials, development of devices for personal diagnostics, and nonlinear chemistry modeling.

DISCLOSURE STATEMENT

The authors are not aware of any affiliations, memberships, funding, or financial holdings that might be perceived as affecting the objectivity of this review.

ACKNOWLEDGMENT

LITERATURE CITED

1. Brinkman W, Haggan D, Troutman W. 1997. A history of the invention of the transistor and where it will lead us. *IEEE J. Solid-State Circ.* 32(12):1858–65

2. Jordan MI, Mitchell TM. 2015. Machine learning: trends, perspectives, and prospects. *Science* 349(6245):255–60

3. Li W, Lu W, Fuh J, Wong Y. 2005. Collaborative computer-aided design—research and development status. *Comput.-Aided Des.* 37(9):931–40

4. Venema L. 2011. Silicon electronics and beyond. *Nature* 479(7373):309

5. Keyes RW. 2005. Physical limits of silicon transistors and circuits. *Rep. Progress Phys.* 68(12):2701–46

6. Tkačik G, Bialek W. 2016. Information processing in living systems. *Annu. Rev. Condens. Matter Phys.* 7:89–117

7. Sweller J, Sweller S. 2006. Natural information processing systems. *Evol. Psychol.* 4(1). **https://doi.org/10.1177/147470490600400**

8. Panda D, Molla KA, Baig MJ, Swain A, Behera D, Dash M. 2018. DNA as a digital information storage device: Hope or hype? *3 Biotech* 8:239

9. Extance A. 2016. How DNA could store all the world's data. *Nature* 537(7618):22–24

10. Scholz A, Reid G, Vogel W, Bostock H. 1993. Ion channels in human axons. *J. Neurophysiol.* 70(3):1274–79

11. Nasrabadi NM. 2007. Pattern recognition and machine learning. *J. Electron. Imaging* 16(4):049901

12. Burstedde C, Klauck K, Schadschneider A, Zittartz J. 2001. Simulation of pedestrian dynamics using a two-dimensional cellular automaton. *Phys. A* 295(3–4):507–25

13. Abraham A, Das S, Roy S. 2008. Swarm intelligence algorithms for data clustering. *Soft Computing for Knowledge Discovery and Data Mining*, ed. O Maimon, L Rokach, pp. 279–313. New York: Springer Sci. Bus.

14. Gu J, Wang Z, Kuen J, Ma L, Shahroudy A, et al. 2018. Recent advances in convolutional neural networks. *Pattern Recognit.* 77:354–77

15. Handl J, Knowles J. 2007. An evolutionary approach to multiobjective clustering. *IEEE Trans. Evol. Comput.* 11(1):56–76

16. Ryzhkov NV, Andreeva DV, Skorb EV. 2019. Coupling pH-regulated multilayers with inorganic surfaces for bionic devices and infochemistry. *Langmuir* 35:8543–56

17. Szaciłowski K. 2012. *Infochemistry: Information Processing at the Nanoscale*. Chichester, UK: John Wiley & Sons

18. Thomas SW, Chiechi RC, LaFratta CN, Webb MR, Lee A, et al. 2009. Infochemistry and infofuses for the chemical storage and transmission of coded information. *PNAS* 106(23):9147–50

19. Kim C, Thomas SW, Whitesides GM. 2010. Long-duration transmission of information with infofuses. *Angew. Chem. Int. Ed.* 49(27):4571–75

20. Erbas-Cakmak S, Kolemen S, Sedgwick AC, Gunnlaugsson T, James TD, et al. 2018. Molecular logic gates: the past, present and future. *Chem. Soc. Rev.* 47(7):2228–48

21. Madhuprasad, Bhat MP, Jung H-Y, Losic D, Kurkuri MD. 2016. Anion sensors as logic gates: A close encounter? *Chemistry* 22(18):6148–78

22. Zaszczynska A, Sajkiewicz P, Gradys A. 2020. Piezoelectric scaffolds as smart materials for neural tissue engineering. *Polymers* 12(1):161

23. Li J-F, Liu W-S, Zhao L-D, Zhou M. 2010. High-performance nanostructured thermoelectric materials. *NPG Asia Mater.* 2(4):152–58

24. Polman A, Knight M, Garnett EC, Ehrler B, Sinke WC. 2016. Photovoltaic materials: present efficiencies and future challenges. *Science* 352(6283):aad4424

25. Shariat BS, Meng Q, Mahmud AS, Wu Z, Bakhtiari R, et al. 2017. Functionally graded shape memory alloys: design, fabrication and experimental evaluation. *Mater. Des.* 124:225–37

26. Li M-H, Keller P. 2009. Stimuli-responsive polymer vesicles. *Soft Matter* 5(5):927–37

27. Wu Y, Liu S, Tao Y, Ma C, Zhang Y, et al. 2014. New strategy for controlled release of drugs. Potential pinpoint targeting with multiresponsive tetraaniline diblock polymer vesicles: site-directed burst release with voltage. *ACS Appl. Mater. Interfaces* 6(3):1470–80

28. Chen T, Ferris R, Zhang J, Ducker R, Zauscher S. 2010. Stimulus-responsive polymer brushes on surfaces: transduction mechanisms and applications. *Prog. Polym. Sci.* 35(1–2):94–112

29. Peng S, Bhushan B. 2012. Smart polymer brushes and their emerging applications. *RSC Adv.* 2(23):8557–78

30. Ballauff M, Lu Y. 2007. "Smart" nanoparticles: preparation, characterization and applications. *Polymer* 48(7):1815–23

31. Moffitt MG. 2013. Self-assembly of polymer brush-functionalized inorganic nanoparticles: from hairy balls to smart molecular mimics. *J. Phys. Chem. Lett.* 4(21):3654–66

32. Xia L-W, Xie R, Ju X-J, Wang W, Chen Q, Chu L-Y. 2013. Nano-structured smart hydrogels with rapid response and high elasticity. *Nat. Commun.* 4:2226

33. Zhang F, Xiong L, Ai Y, Liang Z, Liang Q. 2018. Stretchable multiresponsive hydrogel with actuatable, shape memory, and self-healing properties. *Adv. Sci.* 5(8):1800450

34. Motornov M, Roiter Y, Tokarev I, Minko S. 2010. Stimuli-responsive nanoparticles, nanogels and capsules for integrated multifunctional intelligent systems. *Prog. Polym. Sci.* 35(1–2):174–211

35. Wohl BM, Engbersen JF. 2012. Responsive layer-by-layer materials for drug delivery. *J. Control. Release* 158(1):2–14

36. Silva APD, Mcclenaghan ND. 2004. Molecular-scale logic gates. *Chemistry* 10(3):574–86

37. Leung KC-F, Chak C-P, Lo C-M, Wong W-Y, Xuan S, Cheng CHK. 2009. Ph-controllable supramolecular systems. *Chemistry* 4(3):364–81

38. Zhang Q, Ko NR, Oh JK. 2012. Recent advances in stimuli-responsive degradable block copolymer micelles: synthesis and controlled drug delivery applications. *Chem. Commun.* 48(61):7542–52

39. Li Y, Rodrigues J, Tomás H. 2012. Injectable and biodegradable hydrogels: gelation, biodegradation and biomedical applications. *Chem. Soc. Rev.* 41(6):2193–221

40. Garnier T, Dochter A, Chau NTT, Schaaf P, Jierry L, Boulmedais F. 2015. Surface confined self-assembly of polyampholytes generated from charge-shifting polymers. *Chem. Commun.* 51(74):14092–95

41. Zhang Q, Weber C, Schubert US, Hoogenboom R. 2017. Thermoresponsive polymers with lower critical solution temperature: from fundamental aspects and measuring techniques to recommended turbidimetry conditions. *Mater. Horiz.* 4(2):109–16

42. Chhabra A, Kanapuram RR, Kim TJ, Geng J, Silva AKD, et al. 2013. Humidity effects on the wetting characteristics of poly(N-isopropylacrylamide) during a lower critical solution transition. *Langmuir* 29(25):8116–24

43. Collier TO, Anderson JM, Kikuchi A, Okano T. 2001. Adhesion behavior of monocytes, macrophages, and foreign body giant cells on poly (*N*-isopropylacrylamide) temperature-responsive surfaces. *J. Biomed. Mater. Res.* 59(1):136–43

44. Beharry AA, Woolley GA. 2011. Azobenzene photoswitches for biomolecules. *Chem. Soc. Rev.* 40(8):4422–37

45. Sadovski O, Beharry AA, Zhang F, Woolley GA. 2009. Spectral tuning of azobenzene photoswitches for biological applications. *Angew. Chem. Int. Ed.* 48(8):1484–86

46. Wang C, Hashimoto K, Tamate R, Kokubo H, Watanabe M. 2017. Controlled sol-gel transitions of a thermoresponsive polymer in a photoswitchable azobenzene ionic liquid as a molecular trigger. *Angew. Chem. Int. Ed.* 57(1):227–30

47. Chen M, Yao B, Kappl M, Liu S, Yuan J, et al. 2019. Entangled azobenzene-containing polymers with photoinduced reversible solid-to-liquid transitions for healable and reprocessable photoactuators. *Adv. Funct. Mater.* 30(4):1906752

48. Ryzhkov NV, Skorb EV. 2020. A platform for light-controlled formation of free-stranding lipid membranes. *J. R. Soc. Interface* 17:20190740

49. Maltanava HM, Poznyak SK, Andreeva DV, Quevedo MC, Bastos AC, et al. 2017. Light-induced proton pumping with a semiconductor: vision for photoproton lateral separation and robust manipulation. *ACS Appl. Mater. Interfaces* 9(28):24282–89

50. Poghossian A, Katz E, Schöning MJ. 2015. Enzyme logic AND-Reset and OR-Reset gates based on a field-effect electronic transducer modified with multi-enzyme membrane. *Chem. Commun.* 51(30):6564–67

51. Magri DC, Brown GJ, McClean GD, Prasanna De Silva A. 2006. Communicating chemical congregation: a molecular and logic gate with three chemical inputs as a "lab-on-a-molecule" prototype. *J. Am. Chem. Soc.* 128(15):4950–51

52. Uchiyama S, Kawai N, Silva APD, Iwai K. 2004. Fluorescent polymeric and logic gate with temperature and pH as inputs. *J. Am. Chem. Soc.* 126(10):3032–33

53. Radhakrishnan K, Tripathy J, Raichur AM. 2013. Dual enzyme responsive microcapsules simulating an "Or" logic gate for biologically triggered drug delivery applications. *Chem. Commun.* 49(47):5390–92

54. Szaciłowski K, Macyk W, Stochel G. 2006. Light-driven OR and XOR programmable chemical logic gates. *J. Am. Chem. Soc.* 128(14):4550–51

55. Chen L, Zeng X, Dandapat A, Chi Y, Kim D. 2015. Installing logic gates in permeability controllable polyelectrolyte-carbon nitride films for detecting proteases and nucleases. *Anal. Chem.* 87(17):8851–57

56. Deng H-H, Wang F-F, Liu Y-H, Peng H-P, Li K-L, et al. 2016. Label-free, resettable, and multi-readout logic gates based on chemically induced fluorescence switching of gold nanoclusters. *J. Mater. Chem. C* 4(29):7141–47

57. Saghatelian A, Völcker NH, Guckian KM, Lin VS-Y, Ghadiri MR. 2003. DNA-based photonic logic gates: AND, NAND, and INHIBIT. *J. Am. Chem. Soc.* 125(2):346–47

58. Ryzhkov NV, Nesterov P, Mamchik NA, Yurchenko SO, Skorb EV. 2019. Localization of ion concentration gradients for logic operation. *Front. Chem.* 7:419

59. Macyk W, Stochel G, Szaciłowski K. 2007. Photosensitization and the photocurrent switching effect in nanocrystalline titanium dioxide functionalized with iron(II) complexes: a comparative study. *Chemistry* 13(20):5676–87

60. Szaciłowski K, Macyk W, Hebda M, Stochel G. 2006. Redox-controlled photosensitization of nanocrystalline titanium dioxide. *Chem. Phys. Chem.* 7(11):2384–91

61. Furtado LFO, Alexiou ADP, Gonçalves L, Toma HE, Araki K. 2006. TiO$_2$-based light-driven XOR/INH logic gates. *Angew. Chem. Int. Ed.* 45(19):3143–46

62. Gawęda S, Stochel G, Szaciłowski K. 2008. Photosensitization and photocurrent switching in carminic acid/titanium dioxide hybrid material. *J. Phys. Chem. C* 112(48):19131–41

63. Pilarczyk K, Kwolek P, Podborska A, Gawęda S, Oszajca M, Szaciłowski K. 2016. Unconventional computing realized with hybrid materials exhibiting the photoelectrochemical photocurrent switching (PEPS) effect. In *Advances in Unconventional Computing*, Vol. 23. *Emergence, Complexity and Computation Advances in Unconventional Computing*, ed. A Adamatzky, pp. 429–67. Cham, Switz.: Springer

64. Ryzhkov NV, Yurova VY, Ulasevich SA, Skorb EV. 2020. Photoelectrochemical photocurrent switching effect on a pristine anodized Ti/TiO$_2$ system as a platform for chemical logic devices. *RSC Adv.* 10(21):12355–59

65. Li Z, Rosenbaum MA, Venkataraman A, Tam TK, Katz E, Angenent LT. 2011. Bacteria-based AND logic gate: a decision-making and self-powered biosensor. *Chem. Commun.* 47(11):3060–62

66. Guliyev R, Ozturk S, Kostereli Z, Akkaya EU. 2011. From virtual to physical: integration of chemical logic gates. *Angew. Chem. Int. Ed.* 50(42):9826–31

67. Braich RS. 2002. Solution of a 20-variable 3-SAT problem on a DNA computer. *Science* 296(5567):499–502

68. Smith LM, Corn RM, Condon AE, Lagally MG, Frutos AG, et al. 1998. A surface-based approach to DNA computation. *J. Comput. Biol.* 5(2):255–67

69. Lin S. 1965. Computer solutions of the traveling salesman problem. *Bell Syst. Tech. J.* 44(10):2245–69

70. Ouyang Q. 1997. DNA solution of the maximal clique problem. *Science* 278(5337):446–49

71. Faulhammer D, Cukras AR, Lipton RJ, Landweber LF. 2000. Molecular computation: RNA solutions to chess problems. *PNAS* 97(4):1385–89

72. Bonnet J, Yin P, Ortiz ME, Subsoontorn P, Endy D. 2013. Amplifying genetic logic gates. *Science* 340(6132):599–603

73. Siuti P, Yazbek J, Lu TK. 2013. Synthetic circuits integrating logic and memory in living cells. *Nat. Biotechnol.* 31(5):448–52

74. Pode Z, Peri-Naor R, Georgeson JM, Ilani T, Kiss V, et al. 2017. Protein recognition by a pattern-generating fluorescent molecular probe. *Nat. Nanotechnol.* 12(12):1161–68

75. Rout B, Milko P, Iron MA, Motiei L, Margulies D. 2013. Authorizing multiple chemical passwords by a combinatorial molecular keypad lock. *J. Am. Chem. Soc.* 135(41):15330–33

76. Kim K-W, Bocharova V, Halámek J, Oh M-K, Katz E. 2010. Steganography and encrypting based on immunochemical systems. *Biotechnol. Bioeng.* 108(5):1100–7

77. Ratner T, Reany O, Keinan E. 2009. Encoding and processing of alphanumeric information by chemical mixtures. *Chem. Phys. Chem.* 10(18):3303–9

78. Nenashkina A, Koltsov S, Zaytseva E, Brunova A, Pantiukhin I, Skorb EV. 2020. Storage of information using periodic precipitation. *ACS Omega* 5(14):7809–14

79. Rogers WB, Shih WM, Manoharan VN. 2016. Using DNA to program the self-assembly of colloidal nanoparticles and microparticles. *Nat. Rev. Mater.* 1:16008

80. Kanaras AG, Wang Z, Bates AD, Cosstick R, Brust M. 2003. Towards multistep nanostructure synthesis: programmed enzymatic self-assembly of DNA/gold systems. *Angew. Chem. Int. Ed.* 42(2):191–94

81. Chen G, Gibson KJ, Liu D, Rees HC, Lee J-H, et al. 2018. Regioselective surface encoding of nanoparticles for programmable self-assembly. *Nat. Mater.* 18(2):169–74

82. Loescher S, Walther A. 2020. Supracolloidal self-assembly of divalent Janus 3D DNA origami via programmable multivalent host/guest interactions. *Angew. Chem. Int. Ed.* 59(14):5515–20

83. Yin P, Choi HMT, Calvert CR, Pierce NA. 2008. Programming biomolecular self-assembly pathways. *Nature* 451(7176):318–22

84. Ong LL, Hanikel N, Yaghi OK, Grun C, Strauss MT, et al. 2017. Programmable self-assembly of three-dimensional nanostructures from 10,000 unique components. *Nature* 552(7683):72–77

85. Zhu H, Wang H, Shi B, Shangguan L, Tong W, et al. 2019. Supramolecular peptide constructed by molecular Lego allowing programmable self-assembly for photodynamic therapy. *Nat. Commun.* 10:2412

86. Xing P, Phua SZF, Wei X, Zhao Y. 2018. Programmable multicomponent self-assembly based on aromatic amino acids. *Adv. Mater.* 30(49):1805175

87. Mout R, Tonga GY, Wang L-S, Ray M, Roy T, Rotello VM. 2017. Programmed self-assembly of hierarchical nanostructures through protein-nanoparticle coengineering. *ACS Nano* 11(4):3456–62

88. Taniguchi Y, Sazali MAB, Kobayashi Y, Arai N, Kawai T, Nakashima T. 2017. Programmed self-assembly of branched nanocrystals with an amphiphilic surface pattern. *ACS Nano* 11(9):9312–20

89. Morphew D, Shaw J, Avins C, Chakrabarti D. 2018. Programming hierarchical self-assembly of patchy particles into colloidal crystals via colloidal molecules. *ACS Nano* 12(3):2355–64

90. Tóth-Szeles E, Horváth J, Holló G, Szűcs R, Nakanishi H, Lagzi I. 2017. Chemically coded time-programmed self-assembly. *Mol. Syst. Des. Eng.* 2(3):274–82

91. Zhang X, Zou J, Tamhane K, Kobzeff FF, Fang J. 2010. Self-assembly of pH-switchable spiral tubes: supramolecular chemical springs. *Small* 6(2):217–20

92. Liu H, Li C, Liu H, Liu S. 2009. pH-responsive supramolecular self-assembly of well-defined zwitterionic ABC miktoarm star terpolymers. *Langmuir* 25(8):4724–34

93. Ghosh A, Haverick M, Stump K, Yang X, Tweedle MF, Goldberger JE. 2012. Fine-tuning the pH trigger of self-assembly. *J. Am. Chem. Soc.* 134(8):3647–50

94. Fomina N, Johnson CA, Maruniak A, Bahrampour S, Lang C, et al. 2016. An electrochemical platform for localized pH control on demand. *Lab Chip* 16(12):2236–44

95. Ryzhkov NV, Mamchik NA, Skorb EV. 2019. Electrochemical triggering of lipid bilayer lift-off oscillation at the electrode interface. *J. R. Soc. Interface* 16(150):20180626

96. Rattay F. 1999. The basic mechanism for the electrical stimulation of the nervous system. *Neuroscience* 89(2):335–46

97. Kléber AG, Rudy Y. 2004. Basic mechanisms of cardiac impulse propagation and associated arrhythmias. *Physiol. Rev.* 84(2):431–88

98. Abrams DM, Strogatz SH. 2004. Chimera states for coupled oscillators. *Phys. Rev. Lett.* 93(17):174102

99. Hankins MJ, Gáspár V, Kiss IZ. 2019. Abrupt and gradual onset of synchronized oscillations due to dynamical quorum sensing in the single-cathode multi-anode nickel electrodissolution system. *Chaos* 29(3):033114

100. Sebek M, Kawamura Y, Nott AM, Kiss IZ. 2019. Anti-phase collective synchronization with intrinsic in-phase coupling of two groups of electrochemical oscillators. *Philos. Trans. R. Soc. A* 377(2160):20190095

101. dos Santos CGP, Machado EG, Kiss IZ, Nagao R. 2019. Investigation of the oscillatory electrodissolution of the nickel-iron alloy. *J. Phys. Chem. C* 123(39):24087–94

102. Sebek M, Kiss I. 2019. Plasticity facilitates pattern selection of networks of chemical oscillations. *Chaos* 29(9):083117

103. Sebek M, Kiss IZ. 2018. Spatiotemporal patterns on a ring network of oscillatory electrochemical reaction with negative global feedback. *Israel J. Chem.* 58(6–7):753–61

104. Ocampo-Espindola JL, Bick C, Kiss IZ. 2019. Weak chimeras in modular electrochemical oscillator networks. *Front. Appl. Math. Stat.* 5:36

105. Guzowski J, Gizynski K, Gorecki J, Garstecki P. 2016. Microfluidic platform for reproducible self-assembly of chemically communicating droplet networks with predesigned number and type of the communicating compartments. *Lab Chip* 16(4):764–72

106. Torbensen K, Ristori S, Rossi F, Abou-Hassan A. 2017. Tuning the chemical communication of oscillating microdroplets by means of membrane composition. *J. Phys. Chem. C* 121(24):13256–64

107. Totz JF, Rode J, Tinsley MR, Showalter K, Engel H. 2017. Spiral wave chimera states in large populations of coupled chemical oscillators. *Nat. Phys.* 14(3):282–85

108. Nkomo S, Tinsley MR, Showalter K. 2016. Chimera and chimera-like states in populations of nonlocally coupled homogeneous and heterogeneous chemical oscillators. *Chaos* 26(9):094826

109. Awal NM, Bullara D, Epstein IR. 2019. The smallest chimera: periodicity and chaos in a pair of coupled chemical oscillators. *Chaos* 29(1):013131

110. Steinbock O, Kettunen P, Showalter K. 1996. Chemical wave logic gates. *J. Phys. Chem.* 100(49):18970–75

111. Gizynski K, Gorecki J. 2017. Cancer classification with a network of chemical oscillators. *Phys. Chem. Chem. Phys.* 19(42):28808–19

112. Gizynski K, Gorecki J. 2017. Chemical memory with states coded in light controlled oscillations of interacting Belousov-Zhabotinsky droplets. *Phys. Chem. Chem. Phys.* 19(9):6519–31

113. Vanag VK. 2019. Hierarchical network of pulse coupled chemical oscillators with adaptive behavior: chemical neurocomputer. *Chaos* 29(8):083104

114. Friess M, Hammann J, Unichenko P, Luhmann HJ, White R, Kirischuk S. 2016. Intracellular ion signaling influences myelin basic protein synthesis in oligodendrocyte precursor cells. *Cell Calcium* 60(5):322–30

115. Lv M, Zhou Y, Chen X, Han L, Wang L, Lu XL. 2017. Calcium signaling of *in situ* chondrocytes in articular cartilage under compressive loading: roles of calcium sources and cell membrane ion channels. *J. Orthop. Res.* 36(2):730–38

116. Voolstra O, Huber A. 2019. Ca^{2+} signaling in *Drosophila* photoreceptor cells. In *Calcium Signaling*, ed. MS Islam, pp. 857–79. Adv. Exp. Med. Biol. Cham, Switz.: Springer Int.

117. Franklin BM, Voss SR, Osborn JL. 2017. Ion channel signaling influences cellular proliferation and phagocyte activity during axolotl tail regeneration. *Mech. Dev.* 146:42–54

118. Lüscher BP, Vachel L, Ohana E, Muallem S. 2020. Cl$^-$ as a bona fide signaling ion. *Am. J. Physiol. Cell Physiol.* 318(1):C125–36

119. Maret W. 2017. Zinc in cellular regulation: the nature and significance of "zinc signals." *Int. J. Mol. Sci.* 18(11):2285

120. Ma J, Zhao N, Zhu D. 2016. Bioabsorbable zinc ion induced biphasic cellular responses in vascular smooth muscle cells. *Sci. Rep.* 6:26661

121. Lazarou TS, Buccella D. 2020. Advances in imaging of understudied ions in signaling: a focus on magnesium. *Curr. Opin. Chem. Biol.* 57:27–33

122. Liu J, Prindle A, Humphries J, Gabalda-Sagarra M, Asally M, et al. 2015. Metabolic co-dependence gives rise to collective oscillations within biofilms. *Nature* 523(7562):550–54

123. Plett TS, Cai W, Thai ML, Vlassiouk IV, Penner RM, Siwy ZS. 2017. Solid-state ionic diodes demonstrated in conical nanopores. *J. Phys. Chem. C* 121(11):6170–76

124. Mathwig K, Aaronson BDB, Marken F. 2017. Ionic transport in microhole fluidic diodes based on asymmetric ionomer film deposits. *ChemElectroChem* 5(6):897–901

125. Aaronson BDB, He D, Madrid E, Johns MA, Scott JL, et al. 2017. Ionic diodes based on regenerated α-cellulose films deposited asymmetrically onto a microhole. *ChemistrySelect* 2(3):871–75

126. Lin C-Y, Combs C, Su Y-S, Yeh L-H, Siwy ZS. 2019. Rectification of concentration polarization in mesopores leads to high conductance ionic diodes and high performance osmotic power. *J. Am. Chem. Soc.* 141(8):3691–98

127. Zhao Y, Dai S, Chu Y, Wu X, Huang J. 2018. A flexible ionic synaptic device and diode-based aqueous ion sensor utilizing asymmetric polyelectrolyte distribution. *Chem. Commun.* 54(59):8186–89

128. Gao J, Koltonow AR, Raidongia K, Beckerman B, Boon N, et al. 2018. Kirigami nanofluidics. *Mater. Chem. Front.* 2(3):475–82

129. Kong Y, Fan X, Zhang M, Hou X, Liu Z, et al. 2013. Nanofluidic diode based on branched alumina nanochannels with tunable ionic rectification. *ACS Appl. Mater. Interfaces* 5(16):7931–36

130. Yan R, Liang W, Fan R, Yang P. 2009. Nanofluidic diodes based on nanotube heterojunctions. *Nano Lett.* 9(11):3820–25

131. Hou Y, Zhou Y, Yang L, Li Q, Zhang Y, et al. 2016. Flexible ionic diodes for low-frequency mechanical energy harvesting. *Adv. Energy Mater.* 7(5):1601983

132. Lee H-R, Woo J, Han SH, Lim S-M, Lim S, et al. 2018. A stretchable ionic diode from copolyelectrolyte hydrogels with methacrylated polysaccharides. *Adv. Funct. Mater.* 29(4):1806909

133. Lim S-M, Yoo H, Oh M-A, Han SH, Lee H-R, et al. 2019. Ion-to-ion amplification through an open-junction ionic diode. *PNAS* 116(28):13807–15

134. Duan J, Xie W, Yang P, Li J, Xue G, et al. 2018. Tough hydrogel diodes with tunable interfacial adhesion for safe and durable wearable batteries. *Nano Energy* 48:569–74

135. Wang Y, Zhai J. 2019. Cell junction proteins-mimetic artificial nanochannel system: basic logic gates implemented by nanofluidic diodes. *Langmuir* 35(8):3171–75

136. Ali M, Ramirez P, Nasir S, Cervera J, Mafe S, Ensinger W. 2019. Ionic circuitry with nanofluidic diodes. *Soft Matter* 15(47):9682–89

137. Putra BR, Carta M, Malpass-Evans R, McKeown NB, Marken F. 2017. Potassium cation induced ionic diode blocking for a polymer of intrinsic microporosity | nafion "heterojunction" on a microhole substrate. *Electrochim. Acta* 258:807–13

138. Rong Y, Song Q, Mathwig K, Madrid E, He D, et al. 2016. pH-induced reversal of ionic diode polarity in 300 nm thin membranes based on a polymer of intrinsic microporosity. *Electrochem. Commun.* 69:41–45

139. Wang L, Feng Y, Zhou Y, Jia M, Wang G, et al. 2017. Photo-switchable two-dimensional nanofluidic ionic diodes. *Chem. Sci.* 8(6):4381–86

140. Xiao K, Chen L, Chen R, Heil T, Lemus SDC, et al. 2019. Artificial light-driven ion pump for photoelectric energy conversion. *Nat. Commun.* 10:74

141. Li J, An P, Qin C, Sun C-L, Sun M, et al. 2020. Bioinspired dual-responsive nanofluidic diodes by poly-L-lysine modification. *ACS Omega*. 5(9):4501–6

142. Ali M, Ramirez P, Mafé S, Neumann R, Ensinger W. 2009. A pH-tunable nanofluidic diode with a broad range of rectifying properties. *ACS Nano* 3(3):603–8

143. Zhang Z, Wang L, Wang J, Jiang X, Li X, et al. 2012. Mesoporous silica-coated gold nanorods as a light-mediated multifunctional theranostic platform for cancer treatment. *Adv. Mater.* 24(11):1418–23

144. Lin C-Y, Ma T, Siwy ZS, Balme S, Hsu J-P. 2019. Tunable current rectification and selectivity demonstrated in nanofluidic diodes through kinetic functionalization. *J. Phys. Chem. Lett.* 11(1):60–66

145. Jo SH, Chang T, Ebong I, Bhadviya BB, Mazumder P, Lu W. 2010. Nanoscale memristor device as synapse in neuromorphic systems. *Nano Lett.* 10(4):1297–301

146. Schmitt R, Kubicek M, Sediva E, Trassin M, Weber MC, et al. 2018. Accelerated ionic motion in amorphous memristor oxides for nonvolatile memories and neuromorphic computing. *Adv. Funct. Mater.* 29(5):1804782

147. Lee J, Du C, Sun K, Kioupakis E, Lu WD. 2016. Tuning ionic transport in memristive devices by graphene with engineered nanopores. *ACS Nano* 10(3):3571–79

148. Tuszynski JA, Friesen D, Freedman H, Sbitnev VI, Kim H, et al. 2020. Microtubules as sub-cellular memristors. *Sci. Rep.* 10:2108

149. Zhang P, Xia M, Zhuge F, Zhou Y, Wang Z, et al. 2019. Nanochannel-based transport in an interfacial memristor can emulate the analog weight modulation of synapses. *Nano Lett.* 19(7):4279–86

150. Sheng Q, Xie Y, Li J, Wang X, Xue J. 2017. Transporting an ionic-liquid/water mixture in a conical nanochannel: a nanofluidic memristor. *Chem. Commun.* 53(45):6125–27

151. Kim N, Thomas MR, Bergholt MS, Pence IJ, Seong H, et al. 2020. Surface enhanced Raman scattering artificial nose for high dimensionality fingerprinting. *Nat. Commun.* 11:207

152. González-Morales D, Valencia A, Díaz-Nuñez A, Fuentes-Estrada M, López-Santos O, García-Beltrán O. 2020. Development of a low-cost Uv-Vis spectrophotometer and its application for the detection of mercuric ions assisted by chemosensors. *Sensors* 20(3):906

153. Wang X, Huang Z, Chen J, Luo Z, Xu Y, Duan Y. 2019. A colorimetric sensing platform based on site-specific endonuclease IV-aided signal amplification for the detection of DNA related to the human immunodeficiency virus. *Anal. Methods* 11(16):2190–96

154. Nikolaev KG, Ermakov SS, Offenhäusser A, Mourzina Y. 2017. Nonenzymatic determination of glucose on electrodes prepared by directed electrochemical nanowire assembly (DENA). *J. Anal. Chem.* 72(4):371–74

155. Nikolaev KG, Maybeck V, Neumann E, Ermakov SS, Ermolenko YE, et al. 2017. Bimetallic nanowire sensors for extracellular electrochemical hydrogen peroxide detection in HL-1 cell culture. *J. Solid State Electrochem.* 22(4):1023–35

156. Stekolshchikova AA, Radaev AV, Orlova OY, Nikolaev KG, Skorb EV. 2019. Thin and flexible ion sensors based on polyelectrolyte multilayers assembled onto the carbon adhesive tape. *ACS Omega* 4(13):15421–27

157. Zhang C, Su Y, Hu S, Jin K, Jie Y, et al. 2020. An impedance sensing platform for monitoring heterogeneous connectivity and diagnostics in lab-on-a-chip systems. *ACS Omega* 5(10):5098–104

158. Lee W, Someya T. 2019. Emerging trends in flexible active multielectrode arrays. *Chem. Mater.* 31(17):6347–58

159. Criscuolo F. 2020. *Wearable multi-electrode platform for ion sensing*. Thesis, Swiss Fed. Inst. Technol. Laussane, Laussane, Switz.

160. Stanley-Marbell P, Rinard M. 2020. Warp: a hardware platform for efficient multimodal sensing with adaptive approximation. *IEEE Micro*. 40:57–66

161. Al-Rawhani MA, Mitra S, Barrett MP, Cochran S, Cumming DRS, et al. 2020. Multimodal integrated sensor platform for rapid biomarker detection. *IEEE Trans. Biomed. Eng.* 67(2):614–23

162. Hanitra IN, Criscuolo F, Pankratova N, Carrara S, Micheli GD. 2020. Multichannel front-end for electrochemical sensing of metabolites, drugs, and electrolytes. *IEEE Sens. J.* 20(7):3636–45

163. Manickam P, Kanagavel V, Sonawane A, Thipperudraswamy SP, Bhansali S. 2019. Electrochemical systems for healthcare applications. In *Bioelectrochemical Interface Engineering*, ed. RN Krishnaraj, RK Sani, pp. 385–409. Hoboken, NJ: John Wiley & Sons

164. Nikolaev KG, Kalmykov EV, Shavronskaya DO, Nikitina AA, Stekolshchikova AA, et al. 2020. ElectroSens platform with a polyelectrolyte-based carbon fiber sensor for point-of-care analysis of Zn in blood and urine. *ACS Omega* 5(30):18987–94

165. Hong YJ, Lee H, Kim J, Lee M, Choi HJ, et al. 2018. Multifunctional wearable system that integrates sweat-based sensing and vital-sign monitoring to estimate pre-/post-exercise glucose levels. *Adv. Funct. Mater.* 28(47):1805754

166. Martín A, Kim J, Kurniawan JF, Sempionatto JR, Moreto JR, et al. 2017. Epidermal microfluidic electrochemical detection system: enhanced sweat sampling and metabolite detection. *ACS Sens.* 2(12):1860–68

167. Oh SY, Hong SY, Jeong YR, Yun J, Park H, et al. 2018. Skin-attachable, stretchable electrochemical sweat sensor for glucose and pH detection. *ACS Appl. Mater. Interfaces* 10(16):13729–40

168. Pasha SK, Kaushik A, Vasudev A, Snipes SA, Bhansali S. 2013. Electrochemical immunosensing of saliva cortisol. *J. Electrochem. Soc.* 161(2):B3077–82

169. Yin K, Pandian V, Kadimisetty K, Zhang X, Ruiz C, et al. 2020. Real-time colorimetric quantitative molecular detection of infectious diseases on smartphone-based diagnostic platform. *Sci. Rep.* 10:9009

170. Shi W, Li J, Wu J, Wei Q, Chen C, et al. 2020. An electrochemical biosensor based on multi-wall carbon nanotube-modified screen-printed electrode immobilized by uricase for the detection of salivary uric acid. *Anal. Bioanal. Chem.* 412(26):7275–83

171. Magar HS, Abbas MN, MB Ali, Ahmed MA. 2020. Picomolar-sensitive impedimetric sensor for salivary calcium analysis at POC based on Sam of Schiff base-modified gold electrode. *J. Solid State Electrochem.* 24(3):723–37

172. Tiegs AW, Scott RT. 2020. Evaluation of fertilization, usable blastocyst development and sustained implantation rates according to intracytoplasmic sperm injection operator experience. *Reprod. BioMed. Online* 41(1):19–27

173. Gosalvez J, Tvrda E, Agarwal A. 2017. Free radical and superoxide reactivity detection in semen quality assessment: past, present, and future. *J. Assist. Reprod. Genet.* 34(6):697–707

174. Blanco E, Vázquez L, del Pozo M, Roy R, Petit-Domínguez MD, et al. 2020. Evaluation of oxidative stress: nanoparticle-based electrochemical sensors for hydrogen peroxide determination in human semen samples. *Bioelectrochemistry* 135:107581

175. Yang X, Forouzan O, Brown TP, Shevkoplyas SS. 2012. Integrated separation of blood plasma from whole blood for microfluidic paper-based analytical devices. *Lab Chip* 12(2):274–80

176. Helton KL, Nelson KE, Fu E, Yager P. 2008. Conditioning saliva for use in a microfluidic biosensor. *Lab Chip* 8(11):1847–51

177. Castro-López V, Elizalde J, Pacek M, Hijona E, Bujanda L. 2014. A simple and portable device for the quantification of TNF-α in human plasma by means of on-chip magnetic bead-based proximity ligation assay. *Biosens. Bioelectron.* 54:499–505

178. Fei C, Ren C, Wang Y, Li W, Yin F, et al. 2021. Identification of the raw and processed *Crataegi* Fructus based on the electronic nose coupled with chemometric methods. *Sci. Rep.* 11:1849

179. Diouf A, Aghoutane Y, Burhan H, Sen F, Bouchikhi B, El Bari N. 2021. Tramadol sensing in non-invasive biological fluids using a voltammetric electronic tongue and an electrochemical sensor based on biomimetic recognition. *Int. J. Pharm.* 593:120114

180. Jiao T, Hassan MM, Zhu J, Ali S, Ahmad W, et al. 2021. Quantification of deltamethrin residues in wheat by Ag@ZnO NFs-based surface-enhanced Raman spectroscopy coupling chemometric models, *Food Chem.* 337:127652

181. Novati G, de Laroussilhe HL, Koumoutsakos P. 2021. Automating turbulence modelling by multi-agent reinforcement learning. *Nat. Mach. Intell.* 3:87–96

182. Nazarenko DV, Rodin IA, Shpigun OA. 2019. The use of machine learning in the analytical control of the preparations of medicinal plants. *Inorg. Mater.* 55(14):1428–38

183. Picache JA, May JC, McLean JA. 2020. Chemical class prediction of unknown biomolecules using ion mobility-mass spectrometry and machine learning: supervised inference of feature taxonomy from ensemble randomization. *Anal. Chem.* 92(15):10759–67

184. Shang C, Yang F, Huang D, Lyu W. 2014. Data-driven soft sensor development based on deep learning technique. *J. Process Control* 24(3):223–33

185. Kennedy GF, Zhang J, Bond AM. 2019. Automatically identifying electrode reaction mechanisms using deep neural networks. *Anal. Chem.* 91(19):12220–27

186. Peris-Díaz MD, Richtera L, Zitka O, Krężel A, Adam V. 2020. A chemometric-assisted voltammetric analysis of free and Zn(II)-loaded metallothionein-3 states. *Bioelectrochemistry* 134:107501

187. Dean SN, Shriver-Lake LC, Stenger DA, Erickson JS, Golden JP, Trammell SA. 2019. Machine learning techniques for chemical identification using cyclic square wave voltammetry. *Sensors* 19:2392

188. Aliramezani M, Norouzi A, Koch CR. 2020. A grey-box machine learning based model of an electrochemical gas sensor. *Sens. Actuators B* 321:128414

189. Lu H, Li H, Liu T, Fan Y, Yuan Y, et al. 2019. Simulating heavy metal concentrations in an aquatic environment using artificial intelligence models and physicochemical indexes. *Sci. Total Environ.* 694:133591

190. Bond AM. 2020. A perceived paucity of quantitative studies in the modern era of voltammetry: prospects for parameterisation of complex reactions in Bayesian and machine learning frameworks. *J. Solid State Electrochem.* 24(9):2041–50

191. Boucheikhchoukh A, Thibault J, Fauteux-Lefebvre C. 2020. Catalyst design using artificial intelligence: SO_2 to SO_3 case study. *Can. J. Chem. Eng.* 98(9):2016–31

192. Chen Y, Huang Y, Cheng T, Goddard WA. 2019. Identifying active sites for CO_2 reduction on dealloyed gold surfaces by combining machine learning with multiscale simulations. *J. Am. Chem. Soc.* 141(29):11651–57

193. Gu GH, Choi C, Lee Y, Situmorang AB, Noh J, et al. 2020. Progress in computational and machine-learning methods for heterogeneous small-molecule activation. *Adv. Mater.* 32(35):1907865

194. Song J, Zheng Y, Huang M, Wu L, Wang W, et al. 2019. A sequential multidimensional analysis algorithm for aptamer identification based on structure analysis and machine learning. *Anal. Chem.* 92(4):3307–14

195. Qi Y, Bar-Joseph Z, Klein-Seetharaman J. 2006. Evaluation of different biological data and computational classification methods for use in protein interaction prediction. *Proteins* 63(3):490–500

196. Ivanov AS, Nikolaev KG, Stekolshchikova AA, Tesfatsion WT, Yurchenko SO, et al. 2020. Tick-borne encephalitis electrochemical detection by multilayer perceptron on liquid metal interface. *ACS Appl. Bio Mater.* 3(11):7352–56

197. Nikolaev KG, Ermolenko YE, Offenhäusser A, Ermakov SS, Mourzina YG. 2018. Multisensor systems by electrochemical nanowire assembly for the analysis of aqueous solutions. *Front. Chem.* 6:256

198. Kisner A, Heggen M, Mayer D, Simon U, Offenhäusser A, Mourzina Y. 2014. Probing the effect of surface chemistry on the electrical properties of ultrathin gold nanowire sensors. *Nanoscale* 6(10):5146–55

199. Dan B, Wingfield TB, Evans JS, Mirri F, Pint CL, et al. 2011. Templating of self-alignment patterns of anisotropic gold nanoparticles on ordered SWNT macrostructures. *ACS Appl. Mater. Interfaces* 3(9):3718–24

200. Duan X, Niu C, Sahi V, Chen J, Parce JW, et al. 2003. High-performance thin-film transistors using semiconductor nanowires and nanoribbons. *Nature* 425(6955):274–78

201. Messer B, Song JH, Yang P. 2000. Microchannel networks for nanowire patterning. *J. Am. Chem. Soc.* 122(41):10232–33

202. Picollo F, Battiato A, Bernardi E, Plaitano M, Franchino C, et al. 2016. All-carbon multi-electrode array for real-time *in vitro* measurements of oxidizable neurotransmitters. *Sci. Rep.* 6:20682

203. Guitchounts G, Cox D. 2020. 64-Channel carbon fiber electrode arrays for chronic electrophysiology. *Sci. Rep.* 10:3830

204. Chen Y-H, Beeck MD, Vanderheyden L, Carrette E, Mihajlović V, et al. 2014. Soft, comfortable polymer dry electrodes for high quality ECG and EEG recording. *Sensors* 14(12):23758–80

205. Grozea C, Voinescu CD, Fazli S. 2011. Bristle-sensors—low-cost flexible passive dry EEG electrodes for neurofeedback and BCI applications. *J. Neural Eng.* 8(2):025008

206. Ivanov AS, Nikolaev KG, Novikov AS, Yurchenko SO, Novoselov KS, et al. 2021. Programmable soft-matter electronics. *J. Phys. Chem. Lett.* 12(7):2017–22

Review

Nanoparticles in Polyelectrolyte Multilayer Layer-by-Layer (LbL) Films and Capsules—Key Enabling Components of Hybrid Coatings

Ekaterina V. Lengert [1,2,*] , **Semyon I. Koltsov** [3] , **Jie Li** [1] , **Alexey V. Ermakov** [4] ,
Bogdan V. Parakhonskiy [1] , **Ekaterina V. Skorb** [3] **and Andre G. Skirtach** [1,*]

1 Department of Biotechnology, Ghent University, 9000 Ghent, Belgium; jiejieli.Li@UGent.be (J.L.);
   Bogdan.Parakhonskiy@UGent.be (B.V.P.)
2 Central Research Laboratory, Saratov State Medical University of V. I. Razumovsky,
   Ministry of Health of the Russian Federation, 410012 Saratov, Russia
3 IMTO (Information Technologies Mechanics and Optics), 191002 Sankt-Petersburg, Russia;
   koltsov@scamt-itmo.ru (S.I.K.); skorb@scamt-itmo.ru (E.V.S.)
4 Institute for Molecular Medicine, First Moscow State Medical University (Sechenov University),
   Moscow, 119992, Russia; ermakov_a_v_2@staff.sechenov.ru
* Correspondence: lengertkatrin@mail.ru (E.V.L.); Andre.Skirtach@UGent.be (A.G.S.)

Abstract: Originally regarded as auxiliary additives, nanoparticles have become important constituents of polyelectrolyte multilayers. They represent the key components to enhance mechanical properties, enable activation by laser light or ultrasound, construct anisotropic and multicompartment structures, and facilitate the development of novel sensors and movable particles. Here, we discuss an increasingly important role of inorganic nanoparticles in the layer-by-layer assembly—effectively leading to the construction of the so-called hybrid coatings. The principles of assembly are discussed together with the properties of nanoparticles and layer-by-layer polymeric assembly essential in building hybrid coatings. Applications and emerging trends in development of such novel materials are also identified.

---

1. Introduction

Versatile LbL (layer-by-layer) polyelectrolyte multilayer coatings have steadily drawn the increasing attention of researchers. This is driven by various factors including the versatility of the approach and an extensive range of applications, which is steadily continuing to increase. Originally, LbL was developed as planar layers [1]. In such an assembly [2], the structure of polyelectrolytes, the influence of water, pH, and salts on the LbL assembly have been investigated Various interactions and assembly methods [3,4] in the LbL assembly have been explored, including the electrostatic interaction, hydrogen bonding [5], while micrometre thick films have been also developed [6]. The extensive range of application of planar LbL coatings has included antifog [7] and ultraviolet (UV)-protective coatings [7], cell adhesion and tissue engineering [8]. A fundamental understanding of the interaction of polyelectrolytes has opened opportunities for versatile assembly of polymers incorporating diverse building blocks. Nanoparticles (NPs) have been explored as components of the LbL assembly in earlier publications [9–11] but their full potential has been recognised somewhat later, after enabling remote opening, increasing the efficiency of the effect of ultrasound on affecting the polyelectrolyte coatings, enhancing mechanical properties of capsules, extending the range of materials for sensors.

Originally developed for planar structures and substrates, the LbL approach has been transferred to spherical templates, which led to preparation of an LbL assembly freely suspended in water. This can be done by applying the LbL coatings onto colloidal particles, and subsequently dissolving the colloidal particle, which is also called a template for LbL assembly. The spherical shells, also called capsules, enable the polyelectrolytes to be freely suspended in an aqueous solution: the substrate holding the planar polyelectrolyte multilayers is thus not present. In this case, the zeta-potential of capsules can be easily measured, and polyelectrolytes are bound to each other directly, without a substrate. As a result, various stimuli can now be applied to control the LbL assembly [12], as it was shown, for example, studying the influence of pH and salt on the interaction of polyelectrolytes [13,14].

In this overview, we describe progress in the area of polyelectrolyte multilayer capsules and planar coatings with the emphasis on functionalization of LbL coatings with nanoparticles, which would constitute the so-called hybrid (organic coatings with incorporated inorganic components) [15–20]. We analyse the assembly of polyelectrolytes on both planar coatings and polyelectrolyte multilayer capsules. Furthermore, the assembly of nanoparticles is analysed, while the functionality of resultant structures is also described.

2. Functionalization of Polyelectrolyte Multilayers—Organic versus Inorganic Building Blocks

2.1. Incorporation of Dyes in Layer-by-Layer (LbL) Coatings—Bringing Multifunctionality through Organic Moieties

Various materials [21] can be incorporated into self-assembled LbL coatings. Although charged molecules have been traditionally employed in the LbL assembly, non-charged molecules or dyes can be ordered in LbL films by means of chemical bonding or by carriers. Pyrene molecules were shown to be incorporated in polyelectrolyte layers in a liposome-mediated process. In this regard, pyrene molecules were encapsulated into poly(acrylic acid)-stabilized cetyltrimethylammonium bromide micelles followed by LbL assembly of the micelles in a poly(diallyldimethylammonium chloride) (PDADMAC) framework [22], where optical signal is detected by detecting optical resonances of light propagating around a sphere, also referred to as whispery gallery modes. Moreover, the inclusion of dye into nanocomposite LbL-assembled film was found to be a simple method to provide spectroscopic analysis of stability (both structural and chemical) and adsorption properties of the film [23]. Additionally, fluorescent dyes bound to non-fluorescent particles via LbL films were shown to generate a strong whispering gallery modes signal for bioanalysis [24]. Incorporated in LbL layers electroactive dyes have also received substantial attention. It was shown that the way to incorporate electroactive anthraquinone dye to LbL films strongly influences its electrochemical properties and chemical properties [25]. Metachromic cationic dye methylene blue was investigated for organization in the LbL framework [26]. In addition, photocleavable chromophores [27], laser absorbing dye (IR-806) [28], bacteriorhodopsin [29], phthalocyanine [30], porphyrin [31,32], and naphthalocyanine [33] have been also incorporated in microcapsules for remote opening by laser light, but it was also noticed that inorganic nanoparticles appeared to be much more effective laser light absorbers

2.2. Incorporation of Nanoparticles in LbL Coatings—Hardness Enhancement and Additional Properties through Inorganic Building Blocks

Although nanoparticles have been perhaps most frequently used for LbL functionalization, various nanostructured building blocks, nanocomposite films with nanoparticles embedded in the layered structure have been shown to be a highly effective class of material to tune various properties (among which mechanical stiffness) with a high accuracy [34], Figure 1. Various methods have been used for LbL assembly with nanoparticles, where in addition to a dipping or incubation, spin-spray LbL assembly [35], spin-coating [36], spray assisted alignments [37], and cross-linking after infiltration [38] were used. Nanocomposite LbL films containing immobilized ZnO/SiO_2 nanoparticles were investigated to provide UV protection properties [39]. Alternating layers of cerium oxide nanoparticles (CONP)/alginate were fabricated on top of beta cells via LbL exhibiting robust antioxidant

activity and providing excellent protection to these cells upon exposure to 10^{-4} M of H_2O_2 without affecting the metabolism of the cells [40].
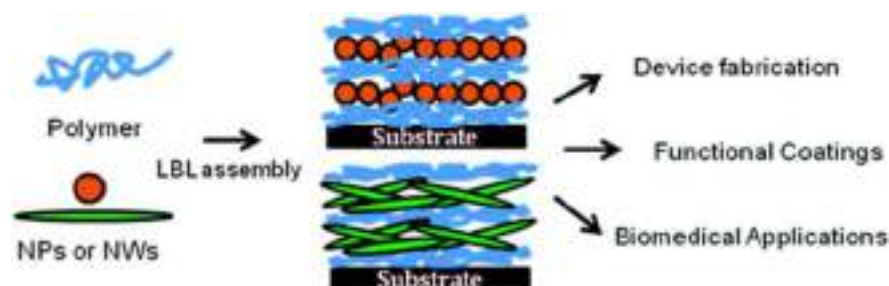

Figure 1. Schematics of incorporation of inorganic nanoparticles, nanowires and nanosheets in layer-by-layer (LbL) assembly. Reproduced with permission from [34]. Copyright 2008 American Chemical Society.

3. Planar LbL Coatings and Their Functionalization by Nanoparticles

Nanoparticles have been essential components of planar layers, where they were used for enhancement of mechanical properties, remote activation, controlling the stiffness of the coatings, for quantum dots incorporation and corrosion protection.

3.1. Enhancement of Mechanical Properties and Remote Acteivation of LbL Coatings

Mechanical stability of capsules and films plays an essential role in enabling practical applications. The addition of nanoparticles would thus increase the shell stiffness. It should be added that the same concept of strengthening mechanical properties of LbL by adding nanoparticles has been also shown for planar coatings. In regard with mechanical properties of planar coatings, mechanical properties of nanometre-thin [41] LbL films [42] (each LbL layer was reported to be 1–2 nm) resemble those of the substrate on which they are assembled (often glass, metal or plastic). But thicker LbL films [43], with a high molecular dynamic of polyelectrolytes [44], are rather soft, hindering cell growth in biomedical applications. One way to increase the stiffness of the coatings is to use chemical cross-linking [45,46]. Another possibility to improve the mechanical properties and enable the adherence of cells on the coatings is to functionalize the surface with metal nanoparticles [47]. Recently, particles and nanoparticles have been used to stimulate cell adhesion on the planar and soft hydrogel coatings relevant for osteoblasts and different types of cells [48].

3.2. Passive and Active Activation of LbL Coatings

Passively active coatings are those in which they or some of their components exhibit a certain functionality. For example, alternating layers of hyaluronic acid–dopamine conjugate with silver nanoparticles demonstrated a remarkable antibacterial [49,50] effect as well as improved adhesion, proliferation, and viability of cells to the surface, which promoted the formation of an apatite layer resembling bones [51]. In another example, incorporating of inorganic particles [52] into hybrid (organic-inorganic) coatings enabled effective cell growth, which is seen of a particular importance to various areas of tissue engineering [53].

An active functionality of nanoparticles was to functionalize the micrometre thick LbL coatings with nanoparticles and use them as active absorption centres for remote laser action. Nanoparticle functionalization of such a soft LbL coating is depicted in Figure 2 (left), where step-by-step assembly is presented for non-aggregated (red) and aggregated (blue) states of nanoparticles. Choosing proper aggregation state of nanoparticles and laser wavelength corresponding to the maximum absorption of NPs, one can locally cross-link the surface of films exposed to laser, Figure 2 (right). Even more drastic action of laser-nanoparticle interaction has been implemented in cell detachment [54], differentiation [55], and cell death induction [56].
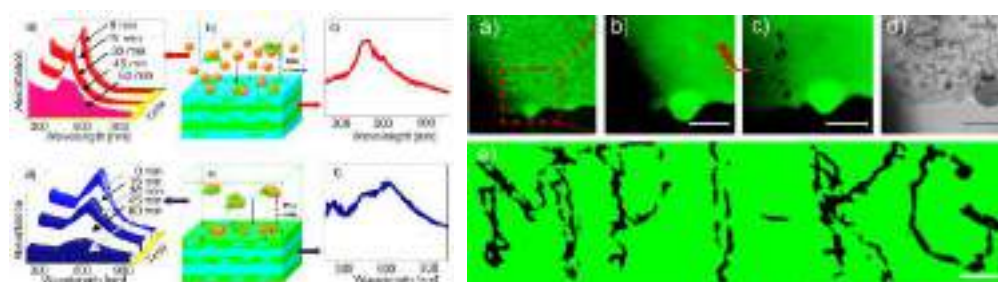
Figure 2. (**Left**) Kinetics of adsorption of non-aggregated (**a**–**c**) and aggregated (**d**–**f**) nanoparticles onto biocompatible poly-L-lysine (PLL)/hyaluronic acid (HA) films. (Adsorption on (PLL/HA)$_{24}$ films are shown in (**a**–**c**), while adsorption on (PLL/HA)$_{24}$PLL films is demonstrated in (**d**–**f**)). Ultraviolet–visible (UV/Vis) absorption spectra of the supernatant solution during adsorption in (**a**) and (**d**) were recorded at 15 min time intervals. Schematics of the interaction of nanoparticles and the films in non-aggregated and aggregated states are demonstrated in (**b**) and (**e**), and the corresponding UV/Vis absorption spectra of the films after nanoparticle adsorption are given in (**c**) and (**f**), respectively. (**Right**) Confocal laser scanning microscope images of a (PLL/HA)$_{24}$ film functionalized with aggregated gold nanoparticles (**a**). The zoomed-in area shown in (**b**) was exposed to a near-infrared (NIR) laser leaving characteristic dark spots, (**c**). The dark spots (**c**) affected by the near-IR laser can be also seen in the transmission image, (**d**). The scale bars in (**a**–**d**) correspond to 15 μm. The technique described in (**a**–**d**) is used to write MPI-KG (Max-Planck Institute of Colloids and Interfaces (German spelling)) (**e**), the scale bar here corresponds to 20 μm. Reproduced with permission from [57]. Copyright 2010 Wiley-VCH Verlag GmbH.

However, this is not the only functionality of the nanoparticles in the coatings—they can be also used to control the masking for fabricating Janus particles.

3.3. Assembling Janus Particles and Capsules Using LbL Coatings

Janus particles have at least two different surfaces referred to one structural unit [58]. Interest in Janus capsules is associated with a combination of delivery [12,59] for various therapies and self-propelled micro-/nanomotor approaches [60–62]. Applied to the encapsulation process, Janus particles combine different properties and provide a range of functions such as delivery, recognition, release of therapeutics, enzymatic activity, physical and chemical sensing [63,64]. In particular, drug delivery is focused on: (i) encapsulation of active chemicals [65], (ii) targeted delivery [66], and (iii) stimuli-responsive release [12]. Therefore, approaches for Janus structure creation aim for a high loading capacity [67] via hierarchical organization.

Methods for fabrication of the Janus particles can be grouped into three main approaches: direct synthesis, chemical modification of particles at biphasic interfaces, and topographically selective modification of particles [68–70]. Typically, the following methods are used for fabrication: sputtering [71], gel trapping [72], microcontact printing [73], and masking [74]. Another example of such an application is where nanoparticles were used to control the stiffness of the coatings, which, in turn, were used as a substrate-template for assembly of Janus particles and capsules [75]. The embedding has been regulated by the stiffness of the coatings, which is proportional to the concentration of nanoparticles incorporated into the surface of the coatings.

An interesting uncomplicated way of polyampholyte Janus-like particles formation was shown recently [76]. There, sites of molecules with opposite charge were pooled apart. The polyampholyte structure suggests that such Janus-like particles are dependent on both pH of the solution and its temperature. To create biocompatible Janus polyelectrolyte particles with a high monodispersity, the layer-by-layer technique was combined with multiphasic fabrication and patterned wettability [77]. Engineering self-propelled motors having a controllable speed can be of interest for many applications. For example, it was suggested to use bubble propulsion to move Janus polyelectrolyte particles [78]. Janus microcapsules were formed by grafting polyelectrolyte salt-responsive brushes onto preformed

(poly(styrene sulfonate) PSS/(polyallylamine hydrochloride) PAH)$_4$ microcapsule protected from one side. Depending on the presence of chlorate and polyphosphate anions brush modulation between hydrophobic and hydrophilic configurations was achieved. Upon gradually changed ion concentration, brushes could partially change their state, thereby adjusting the speed of the particle. In other words, it was possible to create particles with continuously propagating with adjustable speeds completely autonomously due to the surrounding chemical concentration gradients in the solution.

Recently, near-infrared (IR) irradiation was used to induce propulsion of Janus motors [79]. There, the particles constructed with erythrocyte membrane-cloak were used to ablate thrombus. Positively charged chitosan and negatively charged heparin were assembled using the LbL approach for building biocompatible and biodegradable capsules. The sensitivity to near infrared irradiation of capsules was achieved by using a sputtered gold layer on a part of the capsule. We note also that other polyelectrolyte systems modified with Au, e.g., hyaluronic acid (HA)/poly-L-lysine (PLL) (HA/PLL)$_{12}$ [75], became sensitive to near-infrared irradiation. Due to asymmetric coverage of particles with gold IR irradiation crates a local thermal gradient. That led to self-propulsion of the particles, based on thermophoresis effect. Consequently, the intensity of the irradiation directly influences the motile of the particles up to on-off switching behaviour. Besides Au, other nanoparticles, e.g., Pt, and enzymes, were assembled to self-propel capsules [80,81]. In addition, bending and rotational motions of micromotors were also implemented [82] in polymer tubes with poly(allylamine hydrochloride) as positively charged and poly(acrylic acid) as negatively charged polyelectrolytes. Alkaline treatment of one longitudinal side of the tube leads to asymmetry in action (swellability), thereby providing a bent motion. When placed in a fuel solution, such supramolecular structure demonstrates bending for soft connector tubes, and stable rotation for rigid angled ones. In addition, the connection angle determines the rotation velocity. It was noted that such structures could find their application in micro- and nano-machine engineering and biomedicine, such as microscale surgery and drug delivery.

Systematic description and comparison of the influence of grafting density onto interface properties [83] showed that swelling on planar and curved substrates upon changing of grafting density behave in different ways. In other applications, moving Janus capsules was suggested for separation of organics [84], where a reversible adsorption of organic dye by multilayered polyelectrolyte structure was shown. Thus, it is claimed to adsorb about 90% of dye species at pH higher than 9.0 and to release them back at the neutral pH value. The adsorption process is presumably ruled by electrostatic interaction of positive sites of polymer structure and the anionic form of dyes. Application of the above structures in water analysis has been proposed. Contrary to the approach used in classical drug delivery [85], a method of HeLa controlled transportation of cells was also presented. The system is based on relatively known and popular bubble-propelled particles, constructed of polyelectrolytes. It is reported that cells survive both the Janus particle attachment and subsequent movement in 5% H$_2$O$_2$ solution for over 20 min. A magnetic field is also claimed to be guideline technique by tuning the friction of moving object. Thereby, up to 90% of moderation could be achieved. Similarly, a high suitability of anisotropic shell for cell or cellular compartments has been also highlighted [86].

Janus capsules coated with leucocyte membranes were proposed as the possible treatment of some cancer cases [87]. The photothermal effect combined with a rapid water evaporation was used to deliver and attach capsules to the cancer cell wall and subsequently induce a damage to cells. Another publication [88] also highlights the possibility of coating Janus particles with leucocyte membrane to adhere to cancer cells. The second step of phagocytose is also observed for such cells labeled by Janus particles. Janus particles constructed to exhibit thermophoresis were applied for welding of mouse tissue via infrared laser heating [89] with the photothermal heating confined on single particles. Eventually, mechanical restoration of welded mouse tissue was proved with a set of mechanical characterization techniques.

Nanoparticle functionalization of planar LbL coatings has been shown to play an important role in controlling the patches of Janus particles and capsules, but nanoparticles have been also directly applied to release adsorbed materials on the surface coatings [90].

3.4. Corrosion Protection of the Coatings

Application of polyelectrolyte layer-by-layer deposition spurred interest in the field of corrosion protection as a possible way to replace toxic Cr(VI)-compounds [63]. One of the main advantages of polyelectrolyte structures is their light, pH, and humidity responsiveness, which would enable a self-healing process by changes of environment that existed at the beginning of the corrosion. Such a system seems to be useful both for steel alloys [91] and non-ferrous materials [63,64,92–94].

The protective layer can consist of pure polyelectrolytes [92] (optionally with corrosion protective additives) and could be multi-layered with sol-gel [64] and/or corrosion inhibitor coatings [91]. The more sophisticated way is based on creation micro- and nanocapsules with PE coatings. Capsules can be templated (the template is the dissolvable core) on SiO_2 particles [63,93,95], TiO_2 nanoparticles [95], nanotubes, and pure polyelectrolyte nanocapsules [96,97]. Different corrosive protection substances, such as benzotriazole [64,93–95] and its derivatives [97], and monomers for filling scratches for further induced polymerization, could be loaded inside these capsules. They are then incorporated in a more complex matrix such as sol-gel [93,95,98], epoxy [97] coatings, or polyelectrolyte multilayers [96]. Combined, these structures demonstrate mechanical strength, corrosion protection, and self-healing processes [99], triggered by initiation of corrosion or laser irradiation.

We highlight here the development of light-sensitive capsule-based active materials [95,100–102]. The principle of the approach is shown in Figure 3. Corrosion mitigating inhibitors encapsulated in the capsule with mesoporous core and light-controlled permeability of the shell have been used for developing coatings with self-healing functions, which are enabled by controllably releasing the inhibitor upon exposure to laser (infra-red) irradiation. Titania nanoparticles [100] can provide multilayers with photosensitivity. Thus, titania was used both as containers for loading benzotriazole (BTA) for corrosion inhibition and as photosensitive agents. Such capsules were then covered with polyelectrolytes, and they released inhibitor upon UV light irradiation.
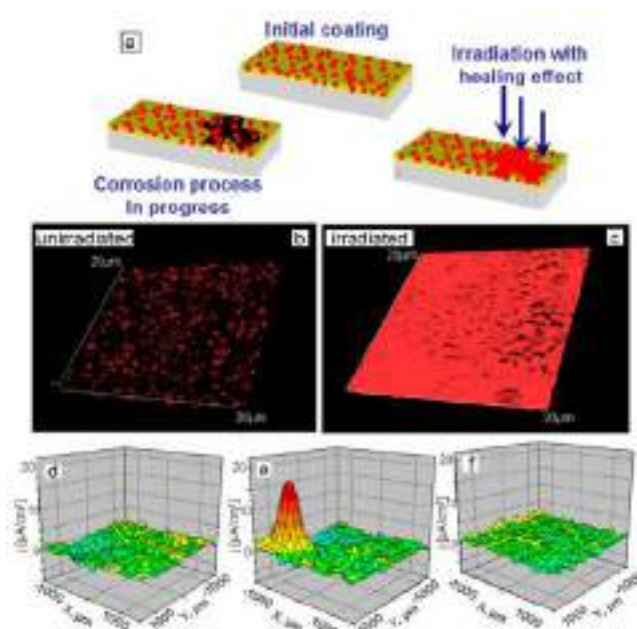
Figure 3. (**a**) Scheme of light-responsive protective coating. Luminescent confocal images of polyelectrolyte containers with titania cores incorporated into SiOx-ZrOx films. The images are obtained (**b**) before and (**c**) after UV irradiation. The particles in the figures correspond to aggregates of nanocontainers. Three-dimensional (3D) maps of the ionic currents above the surface area correspond to a mechanical defect in sol-gel coating loaded with TiO_2(benzotriazole)/(PEI/PSS)$_2$ containers: (**d**) at the beginning moment on the artificial defect; (**e**) after 64 h of corrosion; (**f**) is (**e**) after UV-irradiation and inhibitor release. Solution: 0.1 M NaCl. Reproduced with permission from [100]. Copyright 2009 The Royal Society of Chemistry.

The conformational structure of polyelectrolytes depends on the pH of the environment. Thus, change in pH for certain configurations will result in different permeability of the structure. Thereby, the system could demonstrate both self-healing and self-regulation behaviour when pH changes due to corrosion process starts self-healing process. The reversible changes of polyelectrolyte permeability could be explained by locally changed pH of the solution, as the consequence of photocatalytic degradation of water on the titania. The end of irradiation or corrosion cause thus system relaxation, and particle returns to their initial structure. Visualization of local pH gradient is possible by model physico-chemical properties—scanning ion-selective electrode technique (SIET) [103–105].

The inclusion of metal nanoparticles via LbL procedure enabled the synthesis of materials for unusual applications too. Electroactive (2 nm in diameter) polyelectrolyte-capped Pt nanoparticles assembled into LbL arrays have been used in catalytic production of H_2 [106]. Photocatalytic reduction [107] of noble metal particles on titania core [95] leads to dual-wavelength responsiveness: in the UV to near-IR regions of electromagnetic spectrum. It is possible to regulate photocatalytically (auto-catalytic) waves of enzymatic reactions [108], switch biofilm fluorescence [109], build a platform for a chemical logic device [110], and perform sustainable diagnostics [111–113]. The trend in the field of encapsulated systems is to combine different functions in one capsule matrix. One such functionality is to control the release of biocides together with corrosion inhibitors [114], while a prospective approach can lead to building self-regulating biocide systems [115].

3.5. Development of Sensors and Biosensors Based on Layer-by-Layer Assembled Coatings

Gold nanoparticles (AuNP) embedded into the polyelectrolyte matrices on the top of optical fibre exhibited a high accuracy pH sensing functionality based on the localized surface plasmon resonance (SPR) [116]. Measurement of pH shifts [117] was also implemented by incorporating gold nanorods, by detecting the surface plasmon shift of dispersed nanorods upon pH rise [118]. In another application, starch-stabilized silver nanoparticles in 3-n-propylpyridinium silsesquioxane chloride matrices were shown to function as SPR-based electrochemical sensors [119].

Hybrid materials assembled using carbon nanotubes and polyelectrolytes were shown to operate as effective membranes for the separation and rejection of ions [120]. Furthermore, the high electric conductivity of carbon nanotubes in a polymer framework allowed the development of multi-walled carbon nanotubes-based thin film electrodes transparent in the mid-IR (infrared) range [121].

It can be mentioned that sensory functions in planar coatings [122], Figure 4, represent a complementary area to those broadly implemented by polyelectrolyte multilayer capsules [123–125].

(a) (b)
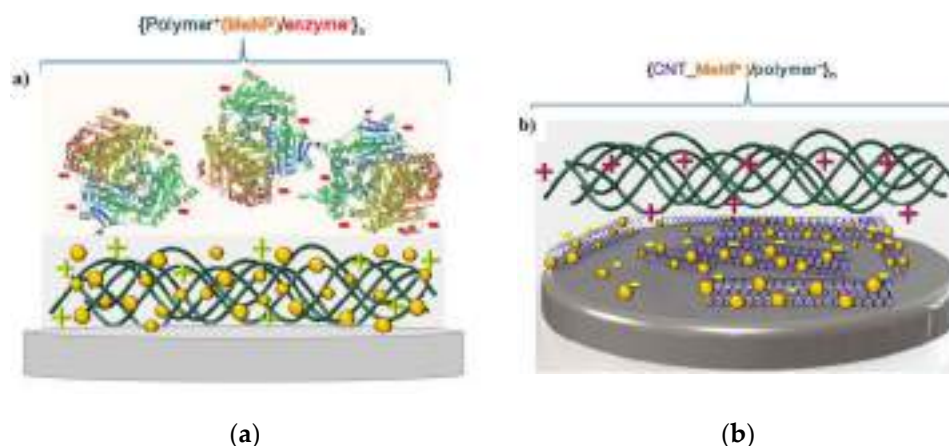
Figure 4. Schematics of LbL assemblies of: (**a**) polymer/nanoparticle (NP)/enzyme, and (**b**) carbon nanotube/NP/polymer sensors. Reproduced with permission from [122]. Copyright 2015 Elsevier.

3.6. Other Nanostructured Inorganic Building Blocks in LbL Planar Coatings

Recently, a variety of materials were applied to design advanced LbL coatings. Quercetin-loaded tripolyphosphate nanoparticles were ordered in a film (by an alternative with hyaluronic acid) resulting in a multilayer film capable to improve anticoagulation performance of surfaces [126]. Polysaccharides and nanogels were employed in polyelectrolyte multilayers proving that the presence of nanogel particles is beneficial for construction of a drug depot system [127]. Linear photochromic norbornene polymers assembled in LbL films exhibited a drastic decrease of the merocyanine band under a prolonged white light irradiation that potentially could be employed as photo-controlled drug depot system [128]. Bioactive thin films were prepared via encapsulation of biomacromolecules such as an enzyme (beta-lactamase, BlaP) into aluminosilicate halloysite nanotubes and their subsequent use for the fabrication of enzymatic coatings by LbL that potentially could act for effluent decontamination [129].

Application of quantum dots (QD) in capsules makes it possible to bring multifunctionality of encapsulation processes and sensor capabilities. Easily adjustable luminescence of QD has a high potential for applying QD-containing polyelectrolyte-based coatings and capsules for biological, particularly medical, and materials science as devices and theragnostic agents [130]. There are two trends in design of composite materials based on quantum dots and layer-by-layer technique. In the first approach, QD are incorporated into layer-by-layer films, Figure 5. For application of LbL technique, QDs are usually chemically modified with thioglycolic acid (TGA) [131], mercaptopropionic acid (MPA) [132], or mercaptoacetic acid (MAA) [133], and they have a negative zeta potential when cysteamine is applied [132].
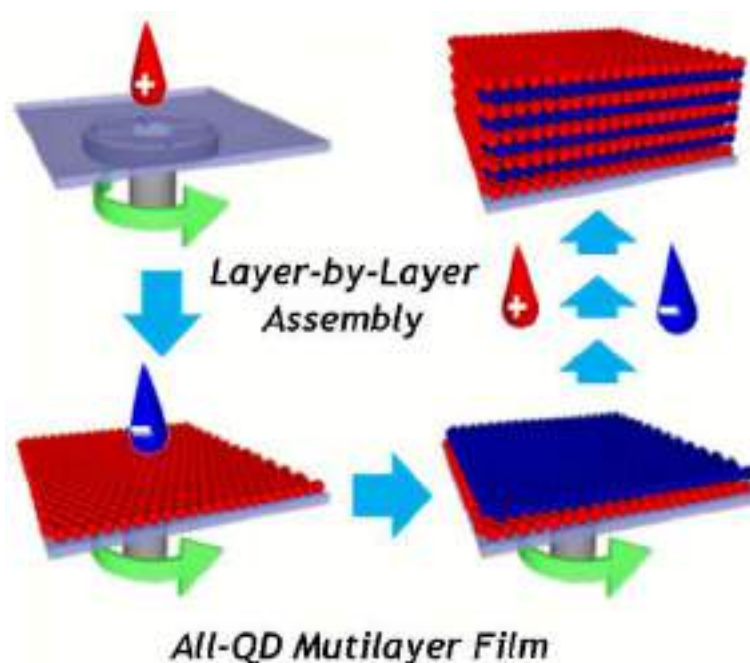
Figure 5. Schematic for the preparation of all-quantum dot (QD) multilayer films based on spin-assisted layer-by-layer assembly by sequentially depositing oppositely charged QDs (blue QDs and red QDs represent negatively charged QDs (QD-mercaptopropionic acid (MPA)) and positively charged QDs (QD-cysteamine (CAm)), respectively). Reproduced with permission from [132]. Copyright 2010 American Chemical Society.

The first approach has been conducted by reducing the toxicity of QDs, stabilization of dispersity, and optimization of distribution, while the QD optical properties were unaffected [134]. CdSe is the typical material for quantum dots, which are used for layer-by-layer coating functionalization. For example, MAA-treated QDs were coated by alternatively applying polyallylamine and polyvinyl sulfonic acid [133].

Materials prepared by the second approach find applications in designing flexible, organo-electronic devices [135]. Stabilization of QDs with polyelectrolytes provides the possibility of the energy transfer between bilayers of the charged polymers. The resulting film is reported to be sensitive for the detection of paraoxon [136] or deltamethrin. Incorporation of QD with graphene NPs in an alternative stacking manner in the PAH layers [137] leads to augmentation of the separation of charges and transport in GNs–CdS QDs composite film. A drawback of such methods is that CdSe nanoparticles undergo photooxidation in the polyelectrolyte matrix.

The LbL-assembled polyelectrolyte capsules can be functionalized with QD as biocompatible fluorescent agents for live-cell targeting [138–140]. In this case, polyelectrolyte film decreases the typical cytotoxic effect of the QD with the fluorescence properties remained. For example, compared to empty PLL/polyglutamic acid (PGA) capsules that do not influence the cell viability, CdTe- labelling of the same capsules displayed a higher cytotoxicity, but lower compared to pure CdTe QD [140]. A prospective field of engineering structures with semiconductor nanocrystals involves construction of complex ordered building blocks similar to those used in photonic crystals. Thus, demonstrated luminescence in both the IR and visible ranges from CdTe and HgTe [141] could be a starting point for development of sophisticated optoelectronics and optical telecommunications devices.

Biologically active QD-based hybrid nanocrystal/polyelectrolyte structures with an outer layer of anti-immunoglobulin G (anti-IgG) were shown to render some bio-specific properties to particles [142]. Considering the interesting info-chemistry [143,144], the optical coding and multiplexing can be achieved at different wavelengths and intensities by bringing in QDs in polyelectrolyte multilayers. To achieve that effect, it is possible to create bits of information by tuning the amount of red, green, and blue QD for achieving some characteristic colour ration. Combining these structures with some receptors makes it possible to identify various bio-processes [145], while gradient coatings [146] can stimulate combinatorial studies [99,147].

LbL were also functionalized by carbon-based fillers [148]. Polyelectrolyte-assisted layer-by-layer fabrication of carbon-containing coatings was proposed to order carbon fillers providing superior properties of the films. The unique combination of carbon materials properties together with versatility of the LbL assembly allows fabrication of multifunctional nanocomposite materials with improved mechanical, optical, thermal, electromagnetic, electrochemical properties [149]. The unique properties of graphene enabled high-performance capacitors and effective electromagnetic shielding [150]. A wide range of coatings functionalized by carbon fillers is aimed at the development of materials with a gas barrier function [151]. The change in permeability of microcapsules tuned by graphene oxide was also applied in drug delivery to reduce the permeability of low molecular substances [152]. Furthermore, coatings can be obtained on surfaces with complex shapes to provide additional functionality, for example, coatings containing arrays of closed cavities can be obtained (so-called microchambers) to store and release functional cargo in a controlled manner. Functionalisation of microchambers by graphene oxide enabled release on demand by near-infrared (NIR) laser in the "therapeutic window" [153], Figure 6. An unusual application of graphene oxide was shown by the binary hybrid-filled LbL coatings, composed of graphene oxide and β-FeOOH nanorods, which enabled the reduction of flammability of polyurethane foams [154]. AuNP assembled in unconventional LbL architectures enabled analysis of hybridization reactions with the ssDNA monitored via methylene blue as the electrochemical indicator. Such an architecture was used as DNA electrochemical biosensors [155] along with Pd nanoparticle-based RNA biosensor [156].
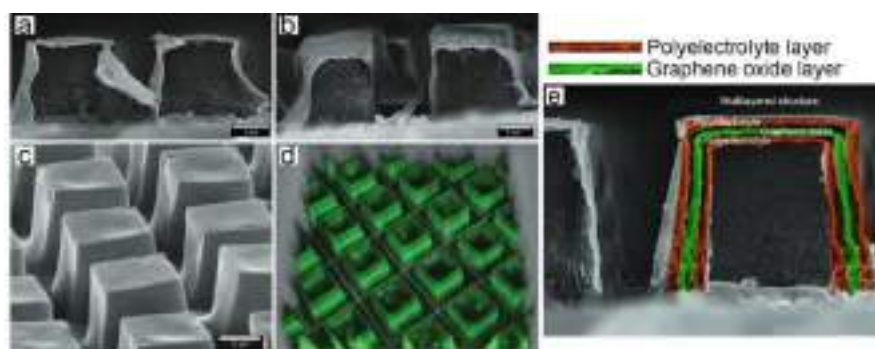
Figure 6. SEM (scanning electron microscopy) images of LbL-assembled microchambers constructed from a pure polyelectrolyte film (**a**) and functionalised by graphene oxide (**b**,**c**) and its corresponding confocal laser scanning microscopy (CLSM) image (**d**). Reproduced with permission from [153]. Copyright 2018 Wiley-VCH Verlag GmbH. (**e**) Schematics of the layered functionalization of microchambers by polyelectrolyte polymers and graphene.

In addition, carbon nanotubes and carbon-based fibres exhibit anisotropy upon ordering—a property useful in some applications, for example, in porous membranes [157]. It can be noted that many essential properties of LbL coatings, and particularly their permeability [158], depend on the concentration of polyelectrolytes, which was studied by the tangential streaming potential revealing that higher concentrations of polyelectrolytes are preferred for an effective adsorption [159]. In addition, some other nanostructured blocks, which extend functionalities of LbL coatings, include halloysites [160,161].

4. Spherical LbL Capsules and Their Functionalization by Nanoparticles

Nanoparticles have become an integral part of LbL assembly and have been also coated by LbL [162–164] and brushes [165] for producing nanocapsules, but frequently nanoparticles are incorporated into the shell of capsules and microcapsules. Many materials have been applied to functionalize multilayer capsules to control the surface properties of the shells; these include metal and magnetic NPs, carbon-based materials (graphene, nanotubes) click moieties, polymers as well as other biomolecules including proteins, peptides, nucleic acids, enzymes, etc.

4.1. Nanoparticle Incorporation into the Shell of LbL Capsules

Among various polymer-nanoparticle capsule systems, metal nanoparticles have been used most frequently [166,167]. AuNP were used as light-absorption centres of NIR light—the property used for release of encapsulated material from capsules. Alternative deposition of polymeric and AuNP layers in hybrid capsules, as shown in Figure 7 led to the possibility of an enhanced Raman microscopy-based detection [168]. The schematic of a capsule with alternatively deposited polymeric layers and nanoparticles is shown in Figure 7G. Another type of nanoparticle, $LaVO_4:Ln^{3+}$, has been used in polyethylene glycol (PEG)-functionalized or PEGylated polymer capsules fabricated using the LbL assembly for internalization by cells [169]. Dextran polymers with ferrocene or azobenzene groups were used for changing their electrical properties and conformational states reversibly with the aim to develop nano-capsules with on/off switching capabilities [170].
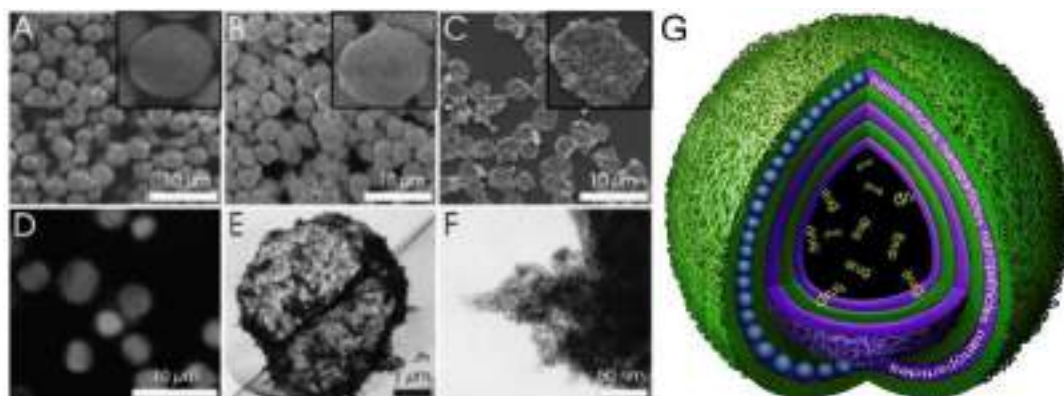
Figure 7. SEM images of (**A**) CaCO₃ microparticles containing fluorescein isothiocyanate (FITC)-dextran before LbL-coating and (**B**) after coating with four bilayers AuNP/PAH (polyallylamine hydrochloride). (**C**) SEM image of hollow (AuNP/PAH)₄ capsules obtained after the dissolution of the CaCO₃ core. (**D**) Confocal microscopy image of FITC-dextran filled (AuNP/PAH)₄ capsules. (**E**) TEM (transmission electron microscopy) images of a hollow (AuNP/PAH)₄ capsule and (**F**) the periphery of a hollow (AuNP/PAH)₄ capsule at a high magnification. Reproduced with permission from [168]. Copyright 2007 Wiley-VCH Verlag GmbH. (**G**) Schematic of a hybrid capsule with alternatively deposited polymeric layers (green) and nanoparticles (blue/pink) described in (**A**–**F**).

Besides metal nanoparticles, silica provides a physically robust, inert substrate with a strong resistance to damage when compared to bare polymer additives. The hybrid materials formed from hydrophilic polymers coated with thin silica layers are remarkably rigid and, at the same time, are capable of surface modification. Thus, straightforward and adoptable silane coupling reactions allow for functionalization of the surface while preserving the functionality of the core [171,172].

4.2. Supramolecular Functionalization and Click Chemistry

Supramolecular functionalization spurred development of the so-called "smart polymers" leading to new functionalities such as the reversibility of non-covalent interactions. Such functionality is expected to extend the range of stimuli for controlling the LbL assembled polymers [2]. Another enabling technology is click chemistry.

Click chemistry is the method of adding click-functionality to polymers with capability of forming covalent bonds within the polyelectrolyte multilayer films. This technique is applicable not only to polymers, biopolymers, proteins, but also to NPs. High stability and excellent physicochemical properties are some other advantages of LbL assembled using click chemistry. Polyelectrolyte multilayer films and capsules assembled using the 'click' chemistry have excellent biocompatibility which is particularly sought in drug delivery and tissue engineering [173]. An example of nanoparticle/polyelectrolyte multilayer assembly with click functionality is silver nanoparticle functionalized poly(N-isopropylacrylamide) (PNIPAM) nanocapsules, which were prepared combining the surface-initiated atom transfer radical polymerization (ATRP) and "click" chemistry approaches [174].

Fabrication of thin multilayer films was reported based on the 'click' chemistry approach possessing azide and alkyne modified poly(acrylic acid) [175]. Furthermore, biodegradable capsules were shown to be attractive candidates for biomedical applications [176]. Another example is poly(acrylic acid) (PAA) synthesized with alkyne (PAA-Alk) and azide (PAA-Az) moieties alternately deposited on silica particles and transformed into capsules by dissolving the silica template. Such capsules were shown to be pH-responsive confirmed by their reversible size changes upon cycling between basic and acidic solutions [177].

4.3. Release from Microcapsules by Laser Light, Magnetic Fields and Ultrasound

Laser light activation. Heat generation is at the core of the second law of thermodynamics and it drives various chemical reactions and processes. Applied to polyelectrolyte multilayer films and capsules, volume (global) heat is used to encapsulate molecules, but the local heating is used for the release from capsules [178]. Light-induced heat generation can be employed for opening of capsule shells and release of encapsulated molecules [28,179], which is particularly interesting for intracellular release, [180] multi-substance delivery [181] or endosomal escape [182]. This is because nanoparticles incorporated into the shells of capsules have been shown to control remotely by laser light [183] treatment of capsule shells modified by metal nanoparticles, heat is generated around NP causing a complete rupture or a permeability change of the capsule walls [184,185]. In this way, the remote release of tagged proteins from silver alginate microcapsules was demonstrated in vivo [186]. Silver-grafted poly-methacrylic acid, sodium salt (PMA) capsules loaded with an anticancer drug sorafenib tosylate (SFT) were used for controllable laser-induced release [187,188].

Various parameters (including the distribution of nanoparticles, which can be controlled by direct in-situ synthesis [189,190], their aggregation state, the power of illuminating laser) affect the responsiveness of the capsule to illuminating light. Aggregated NPs absorb more laser light, due to an increased absorption, generating more heat, thus lower laser powers are needed to achieve the release. At lower light intensity, the microcapsule shell is minimally affected upon the release of encapsulated cargo, and under some conditions (a low nanoparticle concentration on the polyelectrolyte multilayer shell and minimal laser intensity) the polymeric shell is not affected upon release. Various functionalities have been achieved upon releasing encapsulated drugs, including direction-specific release [191].

Graphene oxide functionalized microcapsules exhibited photothermal response and enhanced permeability of the shells by NIR laser treatment [192]. Polyelectrolyte microcapsules modified by photodynamic dye (zinc phthalocyanine) via thermal treatment were shown to provide selective therapy after internalization into cancer cells under treatment by NIR laser [193]. Also, microcapsules functionalized by single-wall carbon nanotubes were shown to release drugs in response to the NIR laser [194]. Emulsions have been also widely used for LbL coating [195]. Furthermore, microcapsules with a layer of AuNP fabricated by the oil-in-water Pickering emulsion method were proposed as biomedical theragnostic systems due to photothermal and sensor functionality [196].

Ultrasound effect. The use of ultra-sonication in medical applications has proved its effectiveness and opens a venue for the release of cargo without affecting healthy tissues, and that has been demonstrated both in vitro and in vivo. The disruption of the microcapsule shells occurs as a result of a cavitation in liquids under the action of ultrasound waves with a frequency of higher than 20 kHz. Ultrasound wave passing through a sound probe induces the formation of air micro-bubbles, which oscillate in the surrounding fluid and, finally, are destroyed, causing cavitation and the concentration of high energy in the fluid [12]. Applicability of ultrasound for nanoparticle-modified capsules opening has been widely investigated [197–199]. Recently, opening of metal NP-containing microcapsules was demonstrated by means of ultrasonication with parameters corresponding to those used in medical applications [200,201]. Ultrasound was also applied to release encapsulated materials from silver alginate hydrogel containers [202]. Polyelectrolyte microcapsules functionalized with magnetite and silica nanoparticles were shown to be raptured by high-intensity ultrasound and compared to each other enabling the conclusion that magnetite-based microcapsules are the most sensitive to sonication [203].

Furthermore, PAH/ PSS microcapsules containing nanoparticles in the shell were investigated in terms of sensitivity to ultrasonication in dependence on the location of magnetite within the shell. It was shown that capsules with iron oxide nanoparticles are readily ruptured [204]. Most ultrasonic approaches induce rapture of capsules via cavitation bubbles which means the unidirectional release of cargo. However, large capsules (above 300 μm) were shown to release cargo in a controllable and direction-specific manner by application of conventional ultrasound at frequencies between 1 and 4 MHz and intensity of a few W/cm^2 [205].

Hydrogel-based multilayer microcapsules composed of poly(methacrylic acid)/poly(N-vinylpyrrolidone) were shown to release cargo in response to ultrasonic treatment even without additional functionalization by nanoparticles enabling the release of 7 kDa G-quadruplex DNA [206], which was found to maintain their secondary structure. But addition of nanoparticles would further stimulate ultrasound based release, because they increase density in the walls. In addition, carbon dots synthesis within polyelectrolyte shell obtained via the hydrothermal method in the presence of the carbon-reach precursor was shown to stimulate ultrasound induced release [207].

Magnetic field-generated release. Biological tissues are transparent to magnetic fields which open a venue for designing targeted drug delivery systems based on microcapsules functionalized by magnetic nanoparticles facilitating the release of cargo in response to the magnetic field. For example, authors [208] observed rotation of (Co@Au) NPs coated by ferromagnetic gold imbedded into PAH/PSS shells under treatment by the magnetic field at 100–300 Hz. That accompanied by disruption of the shells and drastic increase in permeability of the capsules for model cargo fluorescein isothiocyanate (FITC)-labelled dextran.

Magnetic fields were shown not only to rapture magnetically responsive microcapsules, but also to enable delivery of microcapsules at a designated site or within a cell. Non-directional cell migration of phagocytosing cells was significantly inhibited when the cells were put in a magnetic field. Also, magnetic fields were used to retain magnetite containing microcapsules under flow conditions at the physiologic wall shear stress of 0.751 dyne cm^{-2}; under such conditions, release of drugs was achieved for more than 30 h [209]. Release of a model drug (doxycycline) was demonstrated by manipulating the permeability of microcapsules without causing a significant damage to the capsule shells. This was achieved as a result of a long-term treatment of the capsules by low frequency [181] alternating magnetic fields as a non-cytotoxic intracellular trigger [210].

Magnetic prednisolone microcapsules exhibiting the loading capacity of ~18% and encapsulation efficiency of up to 63% were successfully delivered to arthritic joints followed by prolonged drug release of 88.3% over 36 h [211]; 18 nm iron oxide cubes were embedded into the polyelectrolyte shell to exhibit photothermal effect followed by the release of the model drug in response to treatment by an alternating magnetic field [212]. Poly-L-lysine/poly glutamic acid nanocapsules functionalized by Fe_3O_4 nanoparticles were employed to mediate the hyperthermia effect from the radiofrequency magnetic field with maximum fields up to 0.025 T and frequencies up to 430 kHz, which led to increasing temperatures at the rate of 0.46 °C/min accompanied by disruption of capsule shells [213]. In addition, polyelectrolyte multilayer capsules functionalized with lipids were used for release upon application of a magnetic field [214].

Magnetic NPs have shown greater cytotoxicity in comparison to microcapsules containing an equivalent amount of magnetite [215]. Moreover, nanoparticles embedded into the shell lead to the remediation of organic compounds within the capsules [216].

4.4. Strengthening of Mechanical Properties of LbL Microcapsules by Nanoparticles

The mechanical stability of capsules [217] is one of the most important conditions for using them as delivery carriers. Various approaches have been used for mechanical characterization of capsules, including application of AFM (atomic force microscopy) for single-capsule measurement [218]. Polymeric microcapsules can be either strengthened by adding nanoparticles or, alternatively, another strategy can be considered where they would resemble red blood cells [219], because both carriers represent potent delivery systems [220]. It should be noted that particle elasticity and drug/intracellular delivery data point to a rather complex connection [221]. Additional studies of the elasticity of capsules involved atomic-force microscopy and Raman imaging confocal microscopy [222]. A method to handle agarose gel beads covered with assembled inwardly interweaved poly(allylamine) and poly(styrene sulfonate) was proposed [223], where an AFM colloidal probe technique was applied to measure elastic properties of capsules. To monitor the influence of the composition of mechanically deformed polyelectrolyte reflectometry techniques are useful. Thus, by analysing electron density and scattering

length density it is possible to find the thickness and density of the material. Overall and internal transformations are investigated via neutron and X-ray reflectometry, respectively [224]. Compared to classical measurements, which are dependent on the contact area, rheology investigation via pendant capsule elastometry has a number of advantages, since in this method there is no contact with capsules in situ, while surface tension provides information about viscoelastic properties of capsules [225]. A reference to software program written in C/C++ for analysis of pendant capsule elastometry data is also provided in [225].

There are several ways to overcome the challenge of capsule mechanical strength enhancement. Varying the number of polyelectrolyte layers, the molecular weight of polyelectrolytes, applying a thermal shrinking as well as nanoparticles incorporation were used for enhancing mechanical properties of polyelectrolyte shells. Increasing the number of polyelectrolyte layers is the simplest method to enhance mechanical stability [223,226], where the elastic modulus was reported to increase from to 10 to 190 kPa (and even higher) by creation of the corresponding shell structure of 10–24 μm or thicker. Polyelectrolyte molecular weight affects mechanical properties of capsules, and that was demonstrated for PDADMAC (molecular weight (MW) 13 kD) assembled with PSS (MW 70 kDa). The study is based on the axisymmetric shape analysis in the process of hydrostatic inflation with varying sodium chloride concentration in water [227] and demonstrates salo-plasticity. In other words, the higher the concentration of the salt, the higher the plasticization of assembled polymers. At certain point, type of response to deformation changes from elastic to plastic one. The complexation charge transfer from intrinsic to extrinsic lead to restoration of polymer mobility. That, in turn, results in a liquid-like interface, which is experimentally observed upon load. Another empirical fact is that the structure with a higher MW demands lower concentration of salt for plasticization. To rephrase it, a higher molecular weight leads to a lower melting point. That can be attributed to fewer electrostatic cross-linkages.

Crosslinking affects the mechanical properties of a capsule. For example, it was shown recently that synthesis of hollow polyelectrolyte capsules with ultraviolet-B-induced crosslinking was achieved by inclusion of thymine pendant groups in polyelectrolyte molecule [228]. One more recent example includes investigation of capsules crosslinked via amino/betaine dual-functional copolymers, also used for cell encapsulation [229]. Genipin-crosslinked capsules are significantly more stable as pipette aspiration tests showed. Thus, to simulate immune recognition a protein adhesion was carried out, where capsules were treated with FITC-labelled bovine serum albumin (BSA). The results show fine mechanical stability and very low binding of BSA to genipin-crosslinked capsules. Finally, sodium polyphosphate was used as a cross-linking agent for chitosan-modified cellulose capsules [230]. Hydrogen bonding affects the mechanical properties of capsules. For example, mechanically robust but soft spherical capsules based on a hydrogen-bonded (poly(N-vinylpyrrolidone) and (poly(methacrylic acid) were recently proposed [231]. The mechanical properties of capsules were evaluated via the method of osmotic pressure difference. The resulting elasticity lay in the range of Young's modulus that is common for elastomeric networks and was measured to be 97 ± 8 MPa. The deformation was induced by the osmotic pressure due to polystyrene sulfonate addition to the solution. Thus, hydrogen-bonded capsules showed recovery close to their initial shape within 12 h after the rinsing off the PSS. Investigation showed that capsules were capable of withstanding large deformations. This feature seems to be essential for the creation of adaptable delivery particles.

The approach of thermal shrinking of capsules [232] has been widely used for encapsulation of molecules and recently of enzymes [233], which found the optimal temperature for the encapsulation of enzymes. Temperature-dependence (in the range from 20 to 70 degrees °C) of mechanical properties of capsules (filled with air, oil, and water) was also studied by AFM [234]. Water significantly influences the thermal transition, e.g., as it was observed for PDADMAC/ PAA complexes [235], where the glass-transition temperature was investigated by differential scanning calorimetry. This thermal transition occurs at a lower temperature when hydration is increased and/or complexation pH is decreased. Nevertheless, for some systems the thermal transition appears to be only water dependent. Therefore, a hypothesis for the thermal transition (T-tr) was proposed involving are two steps of

hydrated capsule thermal transition. Both T-tr are due to restructuring of hydrogen bonds in the water-polyelectrolyte system and subsequent chain relaxation.

Although research on LbL planar coatings often preceded that on polyelectrolyte capsules, strengthening the capsule by nanoparticles was reported quite early. Indeed, strengthening of mechanical properties of capsules was performed by introduction of gold nanoparticles into the polymeric layers assigned to the introduction of an inorganic components and the formation of additional linkages of polymers [236]. Other examples of incorporation of nanoparticles include carbon nanotubes [237], graphene oxide [238], high stiffness cellulose nanofibrils [239], iron oxide nanoparticles [240], etc. It should be noted that the suspension of polyelectrolytes in polyelectrolyte multilayer capsules allows for a very sensitive assessment of polyelectrolyte multilayer properties [236].

4.5. Other Nanostructured Inorganic Building Blocks in LbL Microcapsules

Employment of carbon nanotubes as a filler in composite shells of polyelectrolyte microcapsules allowed reinforcement of their mechanical properties and tuning barrier properties together with the possibility of controlled opening by a NIR laser [237,241]. The conductivity of the polyelectrolyte films was also shown to be increased by carbon nanostructures (so-called carbon dots) via in situ "green" synthesis [242]. A similar procedure was applied to polyelectrolyte capsules in order to provide bright fluorescence induced by biocompatible carbon nanoparticles [207].

5. Conclusions and Perspectives

At the beginning of research on layer-by-layer assembly, nanoparticles carried rather auxiliary functions. In fact, they were simply other additives among available building blocks. This is evidenced by the first published results, where the focus lay on understanding the assembly and properties, and to a much lesser degree were applications investigated then. But during later research and development phases, nanoparticles emerged as key enabling components, which drove advances and pushed the development of many applications.

Nowadays, nanoparticles are broadly used in the LbL assembly, which serves as a matrix to order functional components in a predetermined manner with a high spatial resolution. This enables a variety of functionalities from smart coatings to drug-delivery systems. Introducing nanoparticles of a different nature into polyelectrolyte matrices is shown to produce alternative materials with superior properties for optical applications (light-emitting materials, light-harvesting materials), sensors, smart coatings including those with anti-corrosion function and improved mechanical properties or barrier function. These advances enabled the fabrication of multifunctional drug carriers with controllable and switchable parameters for advanced coatings in response to external stimuli. Several publications demonstrated possibilities of creating carriers for theranostics based on a combination of sensing properties with responsiveness towards external stimuli of different natures. For hybrid coatings containing nanoparticles, external stimuli have been also shown to control the surface cross-linking, its mechanical properties, corrosion functionality, etc.

Some disadvantages of adding nanoparticles are also identified. First, adding nanoparticles increases the costs and may prolong the time required for the LbL assembly. In addition, and specifically for biological applications, potential biocompatibility issues need to be addressed for some specific types of nanoparticle, for example for semiconductor quantum dots. But advantages of adding nanoparticles or nanocomponents are experienced particularly at a larger scope of applications. That is why the advantages of adding nanoparticles and nanocomponents completely outweigh these potential disadvantages.

Assessing future trends of research and development activities, one can say that nanoparticles have become indispensable components of the LbL assembly. Although some challenges remain for solving issues related to the circulation of drug carries within the body, targeting them to the site of interest, designing advanced coatings controllable by various stimuli, developing mechanisms for sensing physico-chemical parameters, and adjusting the influence of the system response to external

stimuli. Research work is underway to develop truly advanced coatings both on spherical and flat interfaces. In this regard, the LbL-assembly has proved to be a very versatile method assembly of coatings with an enormous potential for control of their properties and a rich mix of stimuli available for achieving that. Many scientific groups are working on this subject and many of those groups have had links and have been influenced by Helmuth Möhwald [243], whose dedication, profoundness, and accommodating way of thinking have encouraged many of his students, collaborators, followers, and researchers. His inspiration has influenced development in this area and will certainly do so in the future.

References

1. Decher, G. Fuzzy Nanoassemblies: Toward Layered Polymeric Multicomposites. *Science* **1997**, *277*, 1232–1237. [CrossRef]

2. Lvov, Y.; Decher, G.; Möhwald, H. Assembly, structural characterization, and thermal behavior of layer-by-layer deposited ultrathin films of poly(vinyl sulfate) and poly(allylamine). *Langmuir* **1993**, *9*, 481–486. [CrossRef]

3. Nuraje, N.; Asmatulu, R.; Cohen, R.E.; Rubner, M.F. Durable Antifog Films from Layer-by-Layer Molecularly Blended Hydrophilic Polysaccharides. *Langmuir* **2011**, *27*, 782–791. [CrossRef] [PubMed]

4. Richardson, J.J.; Bjornmalm, M.; Caruso, F. Technology-driven layer-by-layer assembly of nanofilms. *Science* **2015**, *348*, aaa2491. [CrossRef] [PubMed]

5. Kozlovskaya, V.; Shamaev, A.; Sukhishvili, S.A. Tuning swelling pH and permeability of hydrogel multilayer capsules. *Soft Matter* **2008**, *4*, 1499–1507. [CrossRef] [PubMed]

6. Zhang, J.; Senger, B.; Vautier, D.; Picart, C.; Schaaf, P.; Voegel, J.-C.; Lavalle, P. Natural polyelectrolyte films based on layer-by layer deposition of collagen and hyaluronic acid. *Biomaterials* **2005**, *26*, 3353–3361. [CrossRef]

7. Guin, T.; Cho, J.H.; Xiang, F.; Ellison, C.J.; Grunlan, J.C. Water-Based Melanin Multilayer Thin Films with Broadband UV Absorption. *ACS Macro Lett.* **2015**, *4*, 335–338. [CrossRef]

8. Gribova, V.; Auzely-Velty, R.; Picart, C. Polyelectrolyte Multilayer Assemblies on Materials Surfaces: From Cell Adhesion to Tissue Engineering. *Chem. Mater.* **2012**, *24*, 854–869. [CrossRef]

9. Kotov, N.A.; Dekany, I.; Fendler, J.H. Layer-by-Layer Self-Assembly of Polyelectrolyte-Semiconductor Nanoparticle Composite Films. *J. Phys. Chem.* **1995**, *99*, 13065–13069. [CrossRef]

10. Lee, D.; Rubner, M.F.; Cohen, R.E. All-Nanoparticle Thin-Film Coatings. *Nano Lett.* **2006**, *6*, 2305–2312. [CrossRef]

11. Lvov, Y.; Ariga, K.; Onda, M.; Ichinose, I.; Kunitake, T. Alternate Assembly of Ordered Multilayers of SiO_2 and Other Nanoparticles and Polyions. *Langmuir* **1997**, *13*, 6195–6203. [CrossRef]

12. Delcea, M.; Möhwald, H.; Skirtach, A.G. Stimuli-responsive LbL capsules and nanoshells for drug delivery. *Adv. Drug Deliv. Rev.* **2011**, *63*, 730–747. [CrossRef] [PubMed]

13. Déjugnat, C.; Haložan, D.; Sukhorukov, G.B. Defined Picogram Dose Inclusion and Release of Macromolecules using Polyelectrolyte Microcapsules. *Macromol. Rapid Commun.* **2005**, *26*, 961–967. [CrossRef]

14. Mauser, T.; Déjugnat, C.; Sukhorukov, G.B. Balance of Hydrophobic and Electrostatic Forces in the pH Response of Weak Polyelectrolyte Capsules. *J. Phys. Chem. B* **2006**, *110*, 20246–20253. [CrossRef]

15. Saveleva, M.S.; Eftekhari, K.; Abalymov, A.A.; Douglas, T.E.L.; Volodkin, D.V.; Parakhonskiy, B.V.; Skirtach, A.G. Hierarchy of Hybrid Materials—The Place of Inorganics-in-Organics in it, Their Composition and Applications. *Front. Chem.* **2019**, *7*, 179. [CrossRef]

16. Kaniewska, K.; Karbarz, M.; Katz, E. Nanocomposite hydrogel films and coatings—Features and applications. *Appl. Mater. Today* **2020**, *20*, 100776. [CrossRef]

17. Rial, R.; Liu, Z.; Ruso, J.M. Soft Actuated Hybrid Hydrogel with Bioinspired Complexity to Control Mechanical Flexure Behavior for Tissue Engineering. *Nanomaterials* **2020**, *10*, 1302. [CrossRef]

18. Park, M.-K.; Advincula, R.C. The Layer-by-Layer Assemblies of Polyelectrolytes and Nanomaterials as Films and Particle Coatings. In *Functional Polymer Films*; Wiley-VCH Verlag GmbH & Co. KGaA: Weinheim, Germany, 2011; pp. 73–112.

19. Ariga, K.; Hill, J.P.; Ji, Q. Organic-Inorganic Supramolecular Materials. In *Supramolecular Soft Matter*; John Wiley & Sons, Inc.: Hoboken, NJ, USA, 2011; pp. 43–55.

20. Katagiri, K. Organic-inorganic nanohybrid particles for biomedical applications. In *Bioceramics*; Elsevier: Amsterdam, The Netherlands, 2011; pp. 113–135.

21. Yan, X.; Zhu, P.; Li, J. Self-assembly and application of diphenylalanine-based nanostructures. *Chem. Soc. Rev.* **2010**, *39*, 1877–1890. [CrossRef]

22. Liu, X.; Zhou, L.; Geng, W.; Sun, J. Layer-by-Layer-Assembled Multilayer Films of Polyelectrolyte-Stabilized Surfactant Micelles for the Incorporation of Noncharged Organic Dyes. *Langmuir* **2008**, *24*, 12986–12989. [CrossRef]

23. Szabó, T.; Péter, Z.; Illés, E.; Janovák, L.; Talyzin, A. Stability and dye inclusion of graphene oxide/polyelectrolyte layer-by-layer self-assembled films in saline, acidic and basic aqueous solutions. *Carbon N. Y.* **2017**, *111*, 350–357. [CrossRef]

24. Olszyna, M.; Debrassi, A.; Üzüm, C.; Dähne, L. Label-Free Bioanalysis Based on Low-Q Whispering Gallery Modes: Rapid Preparation of Microsensors by Means of Layer-by-Layer Technology. *Adv. Funct. Mater.* **2019**, *29*, 1805998. [CrossRef]

25. Ma, W.; Zhang, Y.; Li, F.; Kou, D.; Lutkenhaus, J. Layer-by-Layer Assembly and Electrochemical Study of Alizarin Red S-Based Thin Films. *Polymers* **2019**, *11*, 165. [CrossRef] [PubMed]

26. Chakraborty, U.; Singha, T.; Chianelli, R.R.; Hansda, C.; Kumar Paul, P. Organic-inorganic hybrid layer-by-layer electrostatic self-assembled film of cationic dye Methylene Blue and a clay mineral: Spectroscopic and Atomic Force microscopic investigations. *J. Lumin.* **2017**, *187*, 322–332. [CrossRef]

27. Hu, X.; Qureishi, Z.; Thomas, S.W. Light-Controlled Selective Disruption, Multilevel Patterning, and Sequential Release with Polyelectrolyte Multilayer Films Incorporating Four Photocleavable Chromophores. *Chem. Mater.* **2017**, *29*, 2951–2960. [CrossRef]

28. Skirtach, A.G.A.G.; Antipov, A.A.; Shchukin, D.G.; Sukhorukov, G.B. Remote Activation of Capsules Containing Ag Nanoparticles and IR Dye by Laser Light. *Langmuir* **2004**, *20*, 6988–6992. [CrossRef]

29. Erokhina, S.; Benassi, L.; Bianchini, P.; Diaspro, A.; Erokhin, V.; Fontana, M.P. Light-Driven Release from Polymeric Microcapsules Functionalized with Bacteriorhodopsin. *J. Am. Chem. Soc.* **2009**, *131*, 9800–9804. [CrossRef]

30. Zeng, Y.; Wang, X.-L.; Yang, Y.-J.; Chen, J.-F.; Fu, J.; Tao, X. Assembling photosensitive capsules by phthalocyanines and polyelectrolytes for photodynamic therapy. *Polymer (Guildf)* **2011**, *52*, 1766–1771. [CrossRef]

31. Bédard, M.F.; Sadasivan, S.; Sukhorukov, G.B.; Skirtach, A. Assembling polyelectrolytes and porphyrins into hollow capsules with laser-responsive oxidative properties. *J. Mater. Chem.* **2009**, *19*, 2226–2233. [CrossRef]

32. Li, C.; Li, Z.-Y.; Zhang, J.; Wang, K.; Gong, Y.-H.; Luo, G.-F.; Zhuo, R.-X.; Zhang, X.-Z. Porphyrin containing light-responsive capsules for controlled drug release. *J. Mater. Chem.* **2012**, *22*, 4623–4626. [CrossRef]

33. Marchenko, I.V.; Borodina, T.N.; Trushina, D.B.; Nabatov, B.V.; Logachev, V.V.; Plotnikov, G.S.; Baranov, A.N.; Saletskii, A.M.; Ryabova, A.V.; Bukreeva, T.V. Incorporation of Naphthalocyanine into Shells of Polyelectrolyte Capsules and Their Disruption under Laser Radiation. *Colloid J.* **2018**, *80*, 399–406. [CrossRef]

34. Srivastava, S.; Kotov, N.A. Composite Layer-by-Layer (LBL) assembly with inorganic nanoparticles and nanowires. *Acc. Chem. Res.* **2008**, *41*, 1831–1841. [CrossRef] [PubMed]

35. Gittleson, F.S.; Hwang, D.; Ryu, W.-H.; Hashmi, S.M.; Hwang, J.; Goh, T.; Taylor, A.D. Ultrathin Nanotube/Nanowire Electrodes by Spin–Spray Layer-by-Layer Assembly: A Concept for Transparent Energy Storage. *ACS Nano* **2015**, *9*, 10005–10017. [CrossRef] [PubMed]

36. Danglad-Flores, J.; Eftekhari, K.; Skirtach, A.G.; Riegler, H. Controlled Deposition of Nanosize and Microsize Particles by Spin-Casting. *Langmuir* **2019**, *35*, 3404–3412. [CrossRef] [PubMed]

37. Hu, H.; Pauly, M.; Felix, O.; Decher, G. Spray-assisted alignment of Layer-by-Layer assembled silver nanowires: A general approach for the preparation of highly anisotropic nano-composite films. *Nanoscale* **2017**, *9*, 1307–1314. [CrossRef] [PubMed]

38. Zhou, Y.; Cheng, M.; Zhu, X.; Zhang, Y.; An, Q.; Shi, F. A facile method for the construction of stable polymer–inorganic nanoparticle composite multilayers. *J. Mater. Chem. A* **2013**, *1*, 11329–11334. [CrossRef]

39. Abd El-Hady, M.M.; Sharaf, S.; Farouk, A. Highly hydrophobic and UV protective properties of cotton fabric using layer by layer self-assembly technique. *Cellulose* **2020**, *27*, 1099–1110. [CrossRef]

40. Abuid, N.J.; Gattás-Asfura, K.M.; Schofield, E.A.; Stabler, C.L. Layer-by-Layer Cerium Oxide Nanoparticle Coating for Antioxidant Protection of Encapsulated Beta Cells. *Adv. Healthc. Mater.* **2019**, *8*, 1801493. [CrossRef]

41. Ghostine, R.A.; Jisr, R.M.; Lehaf, A.; Schlenoff, J.B. Roughness and Salt Annealing in a Polyelectrolyte Multilayer. *Langmuir* **2013**, *29*, 11742–11750. [CrossRef]

42. Buron, C.C.; Filiâtre, C.; Membrey, F.; Bainier, C.; Buisson, L.; Charraut, D.; Foissy, A. Surface morphology and thickness of a multilayer film composed of strong and weak polyelectrolytes: Effect of the number of adsorbed layers, concentration and type of salts. *Thin Solid Films* **2009**, *517*, 2611–2617. [CrossRef]

43. Lavalle, P.; Gergely, C.; Cuisinier, F.J.G.; Decher, G.; Schaaf, P.; Voegel, J.C.; Picart, C. Comparison of the Structure of Polyelectrolyte Multilayer Films Exhibiting a Linear and an Exponential Growth Regime: An in Situ Atomic Force Microscopy Study. *Macromolecules* **2002**, *35*, 4458–4465. [CrossRef]

44. Campbell, J.; Vikulina, A.S. Layer-By-Layer Assemblies of Biopolymers: Build-Up, Mechanical Stability and Molecular Dynamics. *Polymers* **2020**, *12*, 1949. [CrossRef] [PubMed]

45. Mzyk, A.; Lackner, J.M.; Wilczek, P.; Lipińska, L.; Niemiec-Cyganek, A.; Samotus, A.; Morenc, M. Polyelectrolyte multilayer film modification for chemo-mechano-regulation of endothelial cell response. *RSC Adv.* **2016**, *6*, 8811–8828. [CrossRef]

46. Schneider, A.; Francius, G.; Obeid, R.; Schwinté, P.; Hemmerlé, J.; Frisch, B.; Schaaf, P.; Voegel, J.-C.; Senger, B.; Picart, C. Polyelectrolyte Multilayers with a Tunable Young's Modulus: Influence of Film Stiffness on Cell Adhesion. *Langmuir* **2006**, *22*, 1193–1200. [CrossRef] [PubMed]

47. Schmidt, S.; Madaboosi, N.; Uhlig, K.; Köhler, D.; Skirtach, A.; Duschl, C.; Möhwald, H.; Volodkin, D.V. Control of cell adhesion by mechanical reinforcement of soft polyelectrolyte films with nanoparticles. *Langmuir* **2012**, *28*, 7249–7257. [CrossRef] [PubMed]

48. Abalymov, A.A.; Parakhonskiy, B.V.; Skirtach, A.G. Colloids-at-surfaces: Physicochemical approaches for facilitating cell adhesion on hybrid hydrogels. *Colloids Surf. A Physicochem. Eng. Asp.* **2020**, *603*, 125185. [CrossRef]

49. Kovačević, D.; Pratnekar, R.; Godič Torkar, K.; Salopek, J.; Dražić, G.; Abram, A.; Bohinc, K. Influence of Polyelectrolyte Multilayer Properties on Bacterial Adhesion Capacity. *Polymers* **2016**, *8*, 345.

50. Guo, S.; Kwek, M.Y.; Toh, Z.Q.; Pranantyo, D.; Kang, E.-T.; Loh, X.J.; Zhu, X.; Jańczewski, D.; Neoh, K.G. Tailoring Polyelectrolyte Architecture To Promote Cell Growth and Inhibit Bacterial Adhesion. *ACS Appl. Mater. Interfaces* **2018**, *10*, 7882–7891. [CrossRef]

51. Carvalho, A.L.; Vale, A.C.; Sousa, M.P.; Barbosa, A.M.; Torrado, E.; Mano, J.F.; Alves, N.M. Antibacterial bioadhesive layer-by-layer coatings for orthopedic applications. *J. Mater. Chem. B* **2016**, *4*, 5385–5393. [CrossRef]

52. Abalymov, A.A.; Van Der Meeren, L.; Saveleva, M.; Prikhozhdenko, E.; Dewettinck, K.; Parakhonskiy, B.; Skirtach, A.G. Cells-Grab-on Particles: A Novel Approach to Control Cell Focal Adhesion on Hybrid Thermally Annealed Hydrogels. *ACS Biomater. Sci. Eng.* **2020**, *6*, 3933–3944. [CrossRef]

53. Abalymov, A.A.; Parakhonskiy, B.; Skirtach, A.G. Polymer- and Hybrid-Based Biomaterials for Interstitial, Connective, Vascular, Nerve, Visceral and Musculoskeletal Tissue Engineering. *Polymers* **2020**, *12*, 620. [CrossRef]

54. Kolesnikova, T.A.; Kohler, D.; Skirtach, A.G.; Möhwald, H. Laser-Induced Cell Detachment, Patterning, and Regrowth on Gold Nanoparticle Functionalized Surfaces. *ACS Nano* **2012**, *6*, 9585–9595. [CrossRef] [PubMed]

55. Bai, J.; Zuo, X.; Feng, X.; Sun, Y.; Ge, Q.; Wang, X.; Gao, C. Dynamic Titania Nanotube Surface Achieves UV-Triggered Charge Reversal and Enhances Cell Differentiation. *ACS Appl. Mater. Interfaces* **2019**, *11*, 36939–36948. [CrossRef] [PubMed]

56. Xing, R.; Jiao, T.; Ma, K.; Ma, G.; Möhwald, H.; Yan, X. Regulating Cell Apoptosis on Layer-by-Layer Assembled Multilayers of Photosensitizer-Coupled Polypeptides and Gold Nanoparticles. *Sci. Rep.* **2016**, *6*, 26506. [CrossRef] [PubMed]

57. Skirtach, A.G.; Volodkin, D.V.; Möhwald, H. Bio-interfaces-Interaction of PLL/HA Thick Films with Nanoparticles and Microcapsules. *ChemPhysChem* **2010**, *11*, 822–829. [CrossRef]

58. De Gennes, P.-G. Soft Matter (Nobel Lecture). *Angew. Chem. Int. Ed. Engl.* **1992**, *31*, 842–845. [CrossRef]

59. Skorb, E.V.; Möhwald, H. 25th Anniversary Article: Dynamic Interfaces for Responsive Encapsulation Systems. *Adv. Mater.* **2013**, *25*, 5029–5043. [CrossRef]

60. Li, J.; Gao, W.; Dong, R.; Pei, A.; Sattayasamitsathit, S.; Wang, J. Nanomotor lithography. *Nat. Commun.* **2014**, *5*, 5026. [CrossRef]

61. Guix, M.; Meyer, A.K.; Koch, B.; Schmidt, O.G. Carbonate-based Janus micromotors moving in ultra-light acidic environment generated by HeLa cells in situ. *Sci. Rep.* **2016**, *6*, 21701. [CrossRef]

62. Dong, R.; Li, J.; Rozen, I.; Ezhilan, B.; Xu, T.; Christianson, C.; Gao, W.; Saintillan, D.; Ren, B.; Wang, J. Vapor-Driven Propulsion of Catalytic Micromotors. *Sci. Rep.* **2015**, *5*, 13226. [CrossRef]

63. Shchukin, D.G.D.G.; Zheludkevich, M.L.; Yasakau, K.a.; Lamaka, S.; Ferreira, M.G.S.M.G.S.; Möhwald, H. Layer-by-Layer Assembled Nanocontainers for Self-Healing Corrosion Protection. *Adv. Mater.* **2006**, *18*, 1672–1678. [CrossRef]

64. Andreeva, D.V.; Fix, D.; Möhwald, H.; Shchukin, D.G. Self-Healing Anticorrosion Coatings Based on pH-Sensitive Polyelectrolyte/Inhibitor Sandwichlike Nanostructures. *Adv. Mater.* **2008**, *20*, 2789–2794. [CrossRef] [PubMed]

65. Tong, W.; Song, X.; Gao, C. Layer-by-layer assembly of microcapsules and their biomedical applications. *Chem. Soc. Rev.* **2012**, *41*, 6103–6124. [CrossRef] [PubMed]

66. Vergaro, V.; Scarlino, F.; Bellomo, C.; Rinaldi, R.; Vergara, D.; Maffia, M.; Baldassarre, F.; Giannelli, G.; Zhang, X.; Lvov, Y.M.; et al. Drug-loaded polyelectrolyte microcapsules for sustained targeting of cancer cells. *Adv. Drug Deliv. Rev.* **2011**, *63*, 847–864. [CrossRef] [PubMed]

67. Zhao, T.; Chen, L.; Wang, P.; Li, B.; Lin, R.; Abdulkareem Al-Khalaf, A.; Hozzein, W.N.; Zhang, F.; Li, X.; Zhao, D. Surface-kinetics mediated mesoporous multipods for enhanced bacterial adhesion and inhibition. *Nat. Commun.* **2019**, *10*, 4387. [CrossRef] [PubMed]

68. Ling, X.Y.; Phang, I.Y.; Acikgoz, C.; Yilmaz, M.D.; Hempenius, M.A.; Vancso, G.J.; Huskens, J. Janus Particles with Controllable Patchiness and Their Chemical Functionalization and Supramolecular Assembly. *Angew. Chem. Int. Ed.* **2009**, *48*, 7677–7682. [CrossRef]

69. Pawar, A.B.; Kretzschmar, I. Fabrication, Assembly, and Application of Patchy Particles. *Macromol. Rapid Commun.* **2010**, *31*, 150–168. [CrossRef]

70. Yoshida, M.; Roh, K.-H.; Mandal, S.; Bhaskar, S.; Lim, D.; Nandivada, H.; Deng, X.; Lahann, J. Structurally Controlled Bio-hybrid Materials Based on Unidirectional Association of Anisotropic Microparticles with Human Endothelial Cells. *Adv. Mater.* **2009**, *21*, 4920–4925. [CrossRef]

71. Chen, R.T.; Muir, B.W.; Such, G.K.; Postma, A.; McLean, K.M.; Caruso, F. Fabrication of asymmetric "Janus" particles via plasma polymerization. *Chem. Commun.* **2010**, *46*, 5121–5123. [CrossRef]

72. Paunov, V.N.; Cayre, O.J. Supraparticles and "Janus" Particles Fabricated by Replication of Particle Monolayers at Liquid Surfaces Using a Gel Trapping Technique. *Adv. Mater.* **2004**, *16*, 788–791. [CrossRef]

73. Li, Z.; Lee, D.; Rubner, M.F.; Cohen, R.E. Layer-by-Layer Assembled Janus Microcapsules. *Macromolecules* **2005**, *38*, 7876–7879. [CrossRef]

74. Cui, J.-Q.; Kretzschmar, I. Surface-Anisotropic Polystyrene Spheres by Electroless Deposition. *Langmuir* **2006**, *22*, 8281–8284. [CrossRef] [PubMed]

75. Kohler, D.; Madaboosi, N.; Delcea, M.; Schmidt, S.; De Geest, B.G.; Volodkin, D.V.; Möhwald, H.; Skirtach, A.G. Patchiness of embedded particles and film stiffness control through concentration of gold nanoparticles. *Adv. Mater.* **2012**, *24*, 1095–1100. [CrossRef] [PubMed]

76. Xu, W.; Rudov, A.; Oppermann, A.; Wypysek, S.; Kather, M.; Schroeder, R.; Richtering, W.; Potemkin, I.I.; Wöll, D.; Pich, A. Synthesis of Polyampholyte Janus-like Microgels by Coacervation of Reactive Precursors in Precipitation Polymerization. *Angew. Chem. Int. Ed.* **2020**, *59*, 1248–1255. [CrossRef] [PubMed]

77. Kobaku, S.P.R.; Snyder, C.S.; Karunakaran, R.G.; Kwon, G.; Wong, P.; Tuteja, A.; Mehta, G. Wettability Engendered Templated Self-Assembly (WETS) for the Fabrication of Biocompatible, Polymer–Polyelectrolyte Janus Particles. *ACS Macro Lett.* **2019**, *8*, 1491–1497. [CrossRef]

78. Ji, Y.; Lin, X.; Wang, D.; Zhou, C.; Wu, Y.; He, Q. Continuously Variable Regulation of the Speed of Bubble-Propelled Janus Microcapsule Motors Based on Salt-Responsive Polyelectrolyte Brushes. *Chem. Asian J.* **2019**, *14*, 2450–2455. [CrossRef] [PubMed]

79. Shao, J.; Abdelghani, M.; Shen, G.; Cao, S.; Williams, D.S.; van Hest, J.C.M. Erythrocyte Membrane Modified Janus Polymeric Motors for Thrombus Therapy. *ACS Nano* **2018**, *12*, 4877–4885. [CrossRef] [PubMed]

80. Wu, Y.; Lin, X.; Wu, Z.; Möhwald, H.; He, Q. Self-Propelled Polymer Multilayer Janus Capsules for Effective Drug Delivery and Light-Triggered Release. *ACS Appl. Mater. Interfaces* **2014**, *6*, 10476–10481. [CrossRef]

81. Wu, Y.; Si, T.; Lin, X.; He, Q. Near infrared-modulated propulsion of catalytic Janus polymer multilayer capsule motors. *Chem. Commun.* **2015**, *51*, 511–514. [CrossRef]

82. Yoshizumi, Y.; Suzuki, H. Self-Propelled Metal–Polymer Hybrid Micromachines with Bending and Rotational Motions. *ACS Appl. Mater. Interfaces* **2017**, *9*, 21355–21361. [CrossRef]

83. Marschelke, C.; Raguzin, I.; Matura, A.; Fery, A.; Synytska, A. Controlled and tunable design of polymer interface for immobilization of enzymes: Does curvature matter? *Soft Matter* **2017**, *13*, 1074–1084. [CrossRef]

84. Lin, Z.; Wu, Z.; Lin, X.; He, Q. Catalytic Polymer Multilayer Shell Motors for Separation of Organics. *Chem. Eur. J.* **2016**, *22*, 1587–1591. [CrossRef] [PubMed]

85. Hu, N.; Zhang, B.; Gai, M.; Zheng, C.; Frueh, J.; He, Q. Forecastable and Guidable Bubble-Propelled Microplate Motors for Cell Transport. *Macromol. Rapid Commun.* **2017**, *38*, 1600795. [CrossRef] [PubMed]

86. Gilbert, J.B.; O'Brien, J.S.; Suresh, H.S.; Cohen, R.E.; Rubner, M.F. Orientation-Specific Attachment of Polymeric Microtubes on Cell Surfaces. *Adv. Mater.* **2013**, 5948–5952. [CrossRef] [PubMed]

87. He, W.; Frueh, J.; Wu, Z.; He, Q. Leucocyte Membrane-Coated Janus Microcapsules for Enhanced Photothermal Cancer Treatment. *Langmuir* **2016**, *32*, 3637–3644. [CrossRef] [PubMed]

88. He, W.; Frueh, J.; Wu, Z.; He, Q. How Leucocyte Cell Membrane Modified Janus Microcapsules are Phagocytosed by Cancer Cells. *ACS Appl. Mater. Interfaces* **2016**, *8*, 4407–4415. [CrossRef] [PubMed]

89. He, W.; Frueh, J.; Hu, N.; Liu, L.; Gai, M.; He, Q. Guidable Thermophoretic Janus Micromotors Containing Gold Nanocolorifiers for Infrared Laser Assisted Tissue Welding. *Adv. Sci.* **2016**, *3*, 1600206. [CrossRef]

90. Volodkin, D.; Skirtach, A.; Möhwald, H. Bioapplications of light-sensitive polymer films and capsules assembled using the layer-by-layer technique. *Polym. Int.* **2012**, *61*, 673–679. [CrossRef]

91. Andreeva, D.V.; Skorb, E.V.; Shchukin, D.G. Layer-by-Layer Polyelectrolyte/Inhibitor Nanostructures for Metal Corrosion Protection. *ACS Appl. Mater. Interfaces* **2010**, *2*, 1954–1962. [CrossRef]

92. Andreeva, D.V.; Fix, D.; Möhwald, H.; Shchukin, D.G. Buffering polyelectrolyte multilayers for active corrosion protection. *J. Mater. Chem.* **2008**, *18*, 1738–1740. [CrossRef]

93. Haneder, S.; Da Como, E.; Feldmann, J.; Lupton, J.M.; Lennartz, C.; Erk, P.; Fuchs, E.; Molt, O.; Münster, I.; Schildknecht, C.; et al. Controlling the Radiative Rate of Deep-Blue Electrophosphorescent Organometallic Complexes by Singlet-Triplet Gap Engineering. *Adv. Mater.* **2008**, *20*, 3325–3330. [CrossRef]

94. Grigoriev, D.O.; Köhler, K.; Skorb, E.; Shchukin, D.G.; Möhwald, H. Polyelectrolyte complexes as a "smart" depot for self-healing anticorrosion coatings. *Soft Matter* **2009**, *5*, 1426–1432. [CrossRef]

95. Skorb, E.V.; Skirtach, A.G.; Sviridov, D.V.; Shchukin, D.G.; Möhwald, H. Laser-Controllable Coatings for Corrosion Protection. *ACS Nano* **2009**, *3*, 1753–1760. [CrossRef] [PubMed]

96. Jafari, A.H.; Hosseini, S.M.A.; Jamalizadeh, E. Investigation of Smart Nanocapsules Containing Inhibitors for Corrosion Protection of Copper. *Electrochim. Acta* **2010**, *55*, 9004–9009. [CrossRef]

97. Kopeć, M.; Szczepanowicz, K.; Mordarski, G.; Podgórna, K.; Socha, R.P.; Nowak, P.; Warszyński, P.; Hack, T. Self-healing epoxy coatings loaded with inhibitor-containing polyelectrolyte nanocapsules. *Prog. Org. Coat.* **2015**, *84*, 97–106. [CrossRef]

98. Zhao, X.; Yuan, S.; Jin, Z.; Zhang, B.; Liu, N.; Chen, S.; Liu, S.; Sun, X.; Duan, J. Perfect Combination of LBL with Sol–Gel Film to Enhance the Anticorrosion Performance on Al Alloy under Simulated and Accelerated Corrosive Environment. *Materials* **2019**, *13*, 111. [CrossRef]

99. Fan, F.; Zhou, C.; Wang, X.; Szpunar, J. Layer-by-Layer Assembly of a Self-Healing Anticorrosion Coating on Magnesium Alloys. *ACS Appl. Mater. Interfaces* **2015**, *7*, 27271–27278. [CrossRef]

100. Skorb, E.V.; Sviridov, D.V.; Möhwald, H.; Shchukin, D.G. Light responsive protective coatings. *Chem. Commun.* **2009**, 6041–6043. [CrossRef]

101. Skorb, E.V.; Fix, D.; Andreeva, D.V.; Möhwald, H.; Shchukin, D.G. Surface-Modified Mesoporous SiO_2 Containers for Corrosion Protection. *Adv. Funct. Mater.* **2009**, *19*, 2373–2379. [CrossRef]

102. Skorb, E.V.; Shchukin, D.G.; Möhwald, H.; Sviridov, D.V. Photocatalytically-active and photocontrollable coatings based on titania-loaded hybrid sol–gel films. *J. Mater. Chem.* **2009**, *19*, 4931–4937. [CrossRef]

103. Ulasevich, S.A.; Brezesinski, G.; Möhwald, H.; Fratzl, P.; Schacher, F.H.; Poznyak, S.K.; Andreeva, D.V.; Skorb, E.V. Light-Induced Water Splitting Causes High-Amplitude Oscillation of pH-Sensitive Layer-by-Layer Assemblies on TiO_2. *Angew. Chem. Int. Ed.* **2016**, *55*, 13001–13004. [CrossRef]

104. Maltanava, H.M.; Poznyak, S.K.; Andreeva, D.V.; Quevedo, M.C.; Bastos, A.C.; Tedim, J.; Ferreira, M.G.S.; Skorb, E.V. Light-Induced Proton Pumping with a Semiconductor: Vision for Photoproton Lateral Separation and Robust Manipulation. *ACS Appl. Mater. Interfaces* **2017**, *9*, 24282–24289. [CrossRef] [PubMed]

105. Ryzhkov, N.V.; Skorb, E.V. A platform for light-controlled formation of free-stranding lipid membranes. *J. R. Soc. Interface* **2020**, *17*, 20190740. [CrossRef]

106. Fenoy, G.E.; Maza, E.; Zelaya, E.; Marmisollé, W.A.; Azzaroni, O. Layer-by-layer assemblies of highly connected polyelectrolyte capped-Pt nanoparticles for electrocatalysis of hydrogen evolution reaction. *Appl. Surf.·Sci.* **2017**, *416*, 24–32. [CrossRef]

107. Skorb, E.V.; Antonouskaya, L.I.; Belyasova, N.A.; Shchukin, D.G.; Möhwald, H.; Sviridov, D.V. Antibacterial activity of thin-film photocatalysts based on metal-modified TiO_2 and $TiO_2:In_2O_3$ nanocomposite. *Appl. Catal. B Environ.* **2008**, *84*, 94–99. [CrossRef]

108. Lanchuk, Y.; Nikitina, A.; Brezhneva, N.; Ulasevich, S.A.; Semenov, S.N.; Skorb, E.V. Photocatalytic Regulation of an Autocatalytic Wave of Spatially Propagating Enzymatic Reactions. *ChemCatChem* **2018**, *10*, 1798–1803. [CrossRef]

109. Nikitina, A.A.; Ulasevich, S.A.; Kassirov, I.S.; Bryushkova, E.A.; Koshel, E.I.; Skorb, E.V. Nanostructured Layer-by-Layer Polyelectrolyte Containers to Switch Biofilm Fluorescence. *Bioconjug. Chem.* **2018**, *29*, 3793–3799. [CrossRef]

110. Ryzhkov, N.V.; Yurova, V.Y.; Ulasevich, S.A.; Skorb, E.V. Photoelectrochemical photocurrent switching effect on a pristine anodized Ti/TiO_2 system as a platform for chemical logic devices. *RSC Adv.* **2020**, *10*, 12355–12359. [CrossRef]

111. Lanchuk, Y.V.; Ulasevich, S.A.; Fedotova, T.A.; Kolpashchikov, D.M.; Skorb, E.V. Towards sustainable diagnostics: Replacing unstable H_2O_2 by photoactive TiO_2 in testing systems for visible and tangible diagnostics for use by blind people. *RSC Adv.* **2018**, *8*, 37735–37739. [CrossRef]

112. Stekolshchikova, A.A.; Radaev, A.V.; Orlova, O.Y.; Nikolaev, K.G.; Skorb, E.V. Thin and Flexible Ion Sensors Based on Polyelectrolyte Multilayers Assembled onto the Carbon Adhesive Tape. *ACS Omega* **2019**, *4*, 15421–15427. [CrossRef]

113. Nikolaev, K.G.; Kalmykov, E.V.; Shavronskaya, D.O.; Nikitina, A.A.; Stekolshchikova, A.A.; Kosareva, E.A.; Zenkin, A.A.; Pantiukhin, I.S.; Orlova, O.Y.; Skalny, A.V.; et al. ElectroSens Platform with a Polyelectrolyte-Based Carbon Fiber Sensor for Point-of-Care Analysis of Zn in Blood and Urine. *ACS Omega* **2020**, *5*, 18987–18994. [CrossRef]

114. Andreeva, D.V.; Sviridov, D.V.; Masic, A.; Möhwald, H.; Skorb, E.V. Nanoengineered Metal Surface Capsules: Construction of a Metal-Protection System. *Small* **2012**, *8*, 820–825. [CrossRef] [PubMed]

115. Gensel, J.; Borke, T.; Pérez, N.P.; Fery, A.; Andreeva, D.V.; Betthausen, E.; Müller, A.H.E.; Möhwald, H.; Skorb, E.V. Cavitation Engineered 3D Sponge Networks and Their Application in Active Surface Construction. *Adv. Mater.* **2012**, *24*, 985–989. [CrossRef] [PubMed]

116. Rivero, P.J.; Goicoechea, J.; Hernaez, M.; Socorro, A.B.; Matias, I.R.; Arregui, F.J. Optical fiber resonance-based pH sensors using gold nanoparticles into polymeric layer-by-layer coatings. *Microsyst. Technol.* **2016**, *22*, 1821–1829. [CrossRef]

117. Tokarev, I.; Tokareva, I.; Minko, S. Optical Nanosensor Platform Operating in Near-Physiological pH Range via Polymer-Brush-Mediated Plasmon Coupling. *ACS Appl. Mater. Interfaces* **2011**, *3*, 143–146. [CrossRef]

118. Kozlovskaya, V.; Kharlampieva, E.; Khanal, B.P.; Manna, P.; Zubarev, E.R.; Tsukruk, V.V. Ultrathin Layer-by-Layer Hydrogels with Incorporated Gold Nanorods as pH-Sensitive Optical Materials. *Chem. Mater.* **2008**, *20*, 7474–7485. [CrossRef]

119. De Oliveira, R.D.; Calaça, G.N.; Santos, C.S.; Fujiwara, S.T.; Pessôa, C.A. Preparation, characterization and electrochemistry of Layer-by-Layer films of silver nanoparticles and silsesquioxane polymer. *Colloids Surf. A Physicochem. Eng. Asp.* **2016**, *509*, 638–647. [CrossRef]

120. Irigoyen, J.; Laakso, T.; Politakos, N.; Dahne, L.; Pihlajamäki, A.; Mänttäri, M.; Moya, S.E. Design and Performance Evaluation of Hybrid Nanofiltration Membranes Based on Multiwalled Carbon Nanotubes and Polyelectrolyte Multilayers for Larger Ion Rejection and Separation. *Macromol. Chem. Phys.* **2016**, *217*, 804–811. [CrossRef]

121. Stanojev, J.; Bajac, B.; Cvejic, Z.; Matovic, J.; Srdic, V.V. Development of MWCNT thin film electrode transparent in the mid-IR range. *Ceram. Int.* **2020**, *46*, 11340–11345. [CrossRef]

122. Barsan, M.M.; Brett, C.M.A. Recent advances in layer-by-layer strategies for biosensors incorporating metal nanoparticles. *TrAC Trends Anal. Chem.* **2016**, *79*, 286–296. [CrossRef]

123. McShane, M.; Ritter, D. Microcapsules as optical biosensors. *J. Mater. Chem.* **2010**, *20*, 8189–8193. [CrossRef]

124. Sukhorukov, G.B.; Rogach, A.L.; Garstka, M.; Springer, S.; Parak, W.J.; Muñoz-Javier, A.; Kreft, O.; Skirtach, A.G.; Susha, A.S.; Ramaye, Y.; et al. Multifunctionalized polymer microcapsules: Novel tools for biological and pharmacological applications. *Small* **2007**, *3*, 944–955. [CrossRef] [PubMed]

125. Van der Meeren, L.; Li, J.; Parakhonskiy, B.V.; Krysko, D.V.; Skirtach, A.G. Classification of analytics, sensorics, and bioanalytics with polyelectrolyte multilayer capsules. *Anal. Bioanal. Chem.* **2020**, *412*, 5015–5029. [CrossRef] [PubMed]

126. Wu, X.; Liu, C.; Chen, H.; Zhang, Y.; Li, L.; Tang, N. Layer-by-Layer Deposition of Hyaluronan and Quercetin-Loaded Chitosan Nanoparticles onto Titanium for Improving Blood Compatibility. *Coatings* **2020**, *10*, 256. [CrossRef]

127. Sydow, S.; de Cassan, D.; Hänsch, R.; Gengenbach, T.R.; Easton, C.D.; Thissen, H.; Menzel, H. Layer-by-layer deposition of chitosan nanoparticles as drug-release coatings for PCL nanofibers. *Biomater. Sci.* **2019**, *7*, 233–246. [CrossRef] [PubMed]

128. Campos, P.P.; Dunne, A.; Delaney, C.; Moloney, C.; Moulton, S.E.; Benito-Lopez, F.; Ferreira, M.; Diamond, D.; Florea, L. Photoswitchable Layer-by-Layer Coatings Based on Photochromic Polynorbornenes Bearing Spiropyran Side Groups. *Langmuir* **2018**, *34*, 4210–4216. [CrossRef] [PubMed]

129. Rouster, P.; Dondelinger, M.; Galleni, M.; Nysten, B.; Jonas, A.M.; Glinel, K. Layer-by-layer assembly of enzyme-loaded halloysite nanotubes for the fabrication of highly active coatings. *Colloids Surf. B Biointerfaces* **2019**, *178*, 508–514. [CrossRef]

130. Rogach, A.L. (Ed.) *Semiconductor Nanocrystal Quantum Dots*; Springer Vienna: Vienna, Austria, 2008; ISBN 978-3-211-75235-7.

131. Abd Rahman, S.; Ariffin, N.; Yusof, N.; Abdullah, J.; Mohammad, F.; Ahmad Zubir, Z.; Nik Abd Aziz, N. Thiolate-Capped CdSe/ZnS Core-Shell Quantum Dots for the Sensitive Detection of Glucose. *Sensors* **2017**, *17*, 1537. [CrossRef]

132. Bae, W.K.; Kwak, J.; Lim, J.; Lee, D.; Nam, M.K.; Char, K.; Lee, C.; Lee, S. Multicolored Light-Emitting Diodes Based on All-Quantum-Dot Multilayer Films Using Layer-by-Layer Assembly Method. *Nano Lett.* **2010**, *10*, 2368–2373. [CrossRef]

133. Jaffar, S.; Nam, K.T.; Khademhosseini, A.; Xing, J.; Langer, R.S.; Belcher, A.M. Layer-by-Layer Surface Modification and Patterned Electrostatic Deposition of Quantum Dots. *Nano Lett.* **2004**, *4*, 1421–1425. [CrossRef]

134. Nagaraja, A.T.; Sooresh, A.; Meissner, K.E.; McShane, M.J. Processing and Characterization of Stable, pH-Sensitive Layer-by-Layer Modified Colloidal Quantum Dots. *ACS Nano* **2013**, *7*, 6194–6202. [CrossRef]

135. Zimnitsky, D.; Jiang, C.; Xu, J.; Lin, Z.; Zhang, L.; Tsukruk, V.V. Photoluminescence of a Freely Suspended Monolayer of Quantum Dots Encapsulated into Layer-by-Layer Films. *Langmuir* **2007**, *23*, 10176–10183. [CrossRef] [PubMed]

136. Constantine, C.A.; Gattás-Asfura, K.M.; Mello, S.V.; Crespo, G.; Rastogi, V.; Cheng, T.-C.; DeFrank, J.J.; Leblanc, R.M. Layer-by-Layer Biosensor Assembly Incorporating Functionalized Quantum Dots. *Langmuir* **2003**, *19*, 9863–9867. [CrossRef]

137. Xiao, F.-X.; Miao, J.; Liu, B. Layer-by-Layer Self-Assembly of CdS Quantum Dots/Graphene Nanosheets Hybrid Films for Photoelectrochemical and Photocatalytic Applications. *J. Am. Chem. Soc.* **2014**, *136*, 1559–1569. [CrossRef] [PubMed]

138. Nifontova, G.; Ramos-Gomes, F.; Baryshnikova, M.; Alves, F.; Nabiev, I.; Sukhanova, A. Cancer Cell Targeting With Functionalized Quantum Dot-Encoded Polyelectrolyte Microcapsules. *Front. Chem.* **2019**, *7*, 34. [CrossRef] [PubMed]

139. Nifontova, G.; Efimov, A.; Agapova, O.; Agapov, I.; Nabiev, I.; Sukhanova, A. Bioimaging Tools Based on Polyelectrolyte Microcapsules Encoded with Fluorescent Semiconductor Nanoparticles: Design and Characterization of the Fluorescent Properties. *Nanoscale Res. Lett.* **2019**, *14*, 29. [CrossRef]

140. Adamczak, M.; Hoel, H.J.; Gaudernack, G.; Barbasz, J.; Szczepanowicz, K.; Warszyński, P. Polyelectrolyte multilayer capsules with quantum dots for biomedical applications. *Colloids Surf. B Biointerfaces* **2012**, *90*, 211–216. [CrossRef]

141. Rogach, A.L.; Kotov, N.A.; Koktysh, D.S.; Susha, A.S.; Caruso, F. II–VI semiconductor nanocrystals in thin films and colloidal crystals. *Colloids Surf. A Physicochem. Eng. Asp.* **2002**, *202*, 135–144. [CrossRef]

142. Wang, D.; Rogach, A.L.; Caruso, F. Semiconductor Quantum Dot-Labeled Microsphere Bioconjugates Prepared by Stepwise Self-Assembly. *Nano Lett.* **2002**, *2*, 857–861. [CrossRef]

143. Hashimoto, M.; Feng, J.; York, R.L.; Ellerbee, A.K.; Morrison, G.; Thomas III, S.W.; Mahadevan, L.; Whitesides, G.M. Infochemistry: Encoding Information as Optical Pulses Using Droplets in a Microfluidic Device. *J. Am. Chem. Soc.* **2009**, *131*, 12420–12429. [CrossRef]

144. Ryzhkov, N.V.; Andreeva, D.V.; Skorb, E.V. Coupling pH-Regulated Multilayers with Inorganic Surfaces for Bionic Devices and Infochemistry. *Langmuir* **2019**, *35*, 8543–8556. [CrossRef]

145. Han, M.; Gao, X.; Su, J.Z.; Nie, S. Quantum-dot-tagged microbeads for multiplexed optical coding of biomolecules. *Nat. Biotechnol.* **2001**, *19*, 631–635. [CrossRef] [PubMed]

146. Pinchasik, B.-E.; Tauer, K.; Möhwald, H.; Skirtach, A.G. Polymer Brush Gradients by Adjusting the Functional Density Through Temperature Gradient. *Adv. Mater. Interfaces* **2014**, *1*, 1300056. [CrossRef]

147. Sailer, M.; Barrett, C.J. Fabrication of Two-Dimensional Gradient Layer-by-Layer Films for Combinatorial Biosurface Studies. *Macromolecules* **2012**, *45*, 5704–5711. [CrossRef]

148. Ariga, K.; Ahn, E.; Park, M.; Kim, B. Layer-by-Layer Assembly: Recent Progress from Layered Assemblies to Layered Nanoarchitectonics. *Chem. Asian J.* **2019**, *14*, 2553–2566. [CrossRef] [PubMed]

149. Yu, A.; Zhang, X.; Zhang, H.; Han, D.; Knight, A.R. Preparation and electrochemical properties of gold nanoparticles containing carbon nanotubes-polyelectrolyte multilayer thin films. *Electrochim. Acta* **2011**, *56*, 9015–9019. [CrossRef]

150. Vallés, C.; Zhang, X.; Cao, J.; Lin, F.; Young, R.J.; Lombardo, A.; Ferrari, A.C.; Burk, L.; Mülhaupt, R.; Kinloch, I.A. Graphene/Polyelectrolyte Layer-by-Layer Coatings for Electromagnetic Interference Shielding. *ACS Appl. Nano Mater.* **2019**, *2*, 5272–5281. [CrossRef]

151. Liu, H.; Bandyopadhyay, P.; Kshetri, T.; Kim, N.H.; Ku, B.-C.; Moon, B.; Lee, J.H. Layer-by-layer assembled polyelectrolyte-decorated graphene multilayer film for hydrogen gas barrier application. *Compos. Part B Eng.* **2017**, *114*, 339–347. [CrossRef]

152. Kurapati, R.; Raichur, A.M. Graphene oxide based multilayer capsules with unique permeability properties: Facile encapsulation of multiple drugs. *Chem. Commun.* **2012**, *48*, 6013–6015. [CrossRef]

153. Ermakov, A.; Lim, S.H.; Gorelik, S.; Kauling, A.P.; de Oliveira, R.V.B.; Castro Neto, A.H.; Glukhovskoy, E.; Gorin, D.A.; Sukhorukov, G.B.; Kiryukhin, M.V. Polyelectrolyte-Graphene Oxide Multilayer Composites for Array of Microchambers which are Mechanically Robust and Responsive to NIR Light. *Macromol. Rapid Commun.* **2019**, *40*, 1700868. [CrossRef]

154. Pan, H.; Lu, Y.; Song, L.; Zhang, X.; Hu, Y. Construction of layer-by-layer coating based on graphene oxide/β-FeOOH nanorods and its synergistic effect on improving flame retardancy of flexible polyurethane foam. *Compos. Sci. Technol.* **2016**, *129*, 116–122. [CrossRef]

155. Gao, H.; Qi, X.; Chen, Y.; Sun, W. Electrochemical deoxyribonucleic acid biosensor based on the self-assembly film with nanogold decorated on ionic liquid modified carbon paste electrode. *Anal. Chim. Acta* **2011**, *704*, 133–138. [CrossRef] [PubMed]

156. Wu, X.; Chai, Y.; Yuan, R.; Su, H.; Han, J. A novel label-free electrochemical microRNA biosensor using Pd nanoparticles as enhancer and linker. *Analyst* **2013**, *138*, 1060–1066. [CrossRef] [PubMed]

157. Erokhina, S.; Ricci, V.; Iannotta, S.; Erokhin, V. Modification of the porous glass filter with LbL technique for variable filtration applications. *Colloids Surf. A Physicochem. Eng. Asp.* **2020**, *606*, 125459. [CrossRef]

158. Saveleva, M.S.; Lengert, E.V.; Gorin, D.A.; Parakhonskiy, B.V.; Skirtach, A.G. Polymeric and Lipid Membranes—From Spheres to Flat Membranes and vice versa. *Membranes* **2017**, *7*, 44. [CrossRef] [PubMed]

159. Egueh, A.-N.D.; Lakard, B.; Fievet, P.; Lakard, S.; Buron, C. Charge properties of membranes modified by multilayer polyelectrolyte adsorption. *J. Colloid Interface Sci.* **2010**, *344*, 221–227. [CrossRef] [PubMed]

160. Lvov, Y.; Wang, W.; Zhang, L.; Fakhrullin, R. Halloysite Clay Nanotubes for Loading and Sustained Release of Functional Compounds. *Adv. Mater.* **2016**, *28*, 1227–1250. [CrossRef] [PubMed]

161. Konnova, S.A.; Sharipova, I.R.; Demina, T.A.; Osin, Y.N.; Yarullina, D.R.; Ilinskaya, O.N.; Lvov, Y.M.; Fakhrullin, R.F. Biomimetic cell-mediated three-dimensional assembly of halloysite nanotubes. *Chem. Commun.* **2013**, *49*, 4208–4210. [CrossRef]

162. Dreaden, E.C.; Morton, S.W.; Shopsowitz, K.E.; Choi, J.-H.; Deng, Z.J.; Cho, N.-J.; Hammond, P.T. Bimodal Tumor-Targeting from Microenvironment Responsive Hyaluronan Layer-by-Layer (LbL) Nanoparticles. *ACS Nano* **2014**, *8*, 8374–8382. [CrossRef]

163. Häuser, M.; Langer, K.; Schönhoff, M. pH-Triggered release from surface-modified poly(lactic-co-glycolic acid) nanoparticles. *Beilstein J. Nanotechnol.* **2015**, *6*, 2504–2512. [CrossRef]

164. Schneider, G.; Decher, G. From Functional Core/Shell Nanoparticles Prepared via Layer-by-Layer Deposition to Empty Nanospheres. *Nano Lett.* **2004**, *4*, 1833–1839. [CrossRef]

165. Yang, Q.; Li, L.; Zhao, F.; Wang, Y.; Ye, Z.; Hua, C.; Liu, Z.; Bohinc, K.; Guo, X. Spherical Polyelectrolyte Brushes as Templates to Prepare Hollow Silica Spheres Encapsulating Metal Nanoparticles. *Nanomaterials* **2020**, *10*, 799. [CrossRef] [PubMed]

166. Yang, H.; Bradley, S.J.; Chan, A.; Waterhouse, G.I.N.; Nann, T.; Kruger, P.E.; Telfer, S.G. Catalytically Active Bimetallic Nanoparticles Supported on Porous Carbon Capsules Derived From Metal–Organic Framework Composites. *J. Am. Chem. Soc.* **2016**, *138*, 11872–11881. [CrossRef] [PubMed]

167. Zhao, W.; Wei, J.-S.; Zhang, P.; Chen, J.; Kong, J.-L.; Sun, L.-H.; Xiong, H.-M.; Möhwald, H. Self-Assembled ZnO Nanoparticle Capsules for Carrying and Delivering Isotretinoin to Cancer Cells. *ACS Appl. Mater. Interfaces* **2017**, *9*, 18474–18481. [CrossRef] [PubMed]

168. De Geest, B.G.; Skirtach, A.G.; De Beer, T.R.M.; Sukhorukov, G.B.; Bracke, L.; Baeyens, W.R.G.; Demeester, J.; De Smedt, S.C. Stimuli-Responsive Multilayered Hybrid Nanoparticle/Polyelectrolyte Capsules. *Macromol. Rapid Commun.* **2007**, *28*, 88–95. [CrossRef]

169. Jeyaraman, J.; Shukla, A.; Sivakumar, S. Targeted Stealth Polymer Capsules Encapsulating Ln^{3+}-Doped $LaVO_4$ Nanoparticles for Bioimaging Applications. *ACS Biomater. Sci. Eng.* **2016**, *2*, 1330–1340. [CrossRef]

170. Wajs, E.; Nielsen, T.T.; Larsen, K.L.; Fragoso, A. Preparation of stimuli-responsive nano-sized capsules based on cyclodextrin polymers with redox or light switching properties. *Nano Res.* **2016**, *9*, 2070–2078. [CrossRef]

171. Meaney, S.P.; Follink, B.; Tabor, R.F. Synthesis, Characterization, and Applications of Polymer–Silica Core–Shell Microparticle Capsules. *ACS Appl. Mater. Interfaces* **2018**, *10*, 43068–43079. [CrossRef]

172. Li, F.; Feng, Y.; Wang, Z.; Yang, L.; Zhuo, L.; Tang, B. Direct electrochemistry of horseradish peroxidase immobilized on the layered calcium carbonate–gold nanoparticles inorganic hybrid composite. *Biosens. Bioelectron.* **2010**, *25*, 2244–2248. [CrossRef]

173. De Geest, B.G.; Van Camp, W.; Du Prez, F.E.; De Smedt, S.C.; Demeester, J.; Hennink, W.E. Degradable multilayer films and hollow capsules via a "click" strategy. *Macromol. Rapid Commun.* **2008**, *29*, 1111–1118. [CrossRef]

174. Wu, T.; Ge, Z.; Liu, S. Fabrication of Thermoresponsive Cross-Linked Poly(N-isopropylacrylamide) Nanocapsules and Silver Nanoparticle-Embedded Hybrid Capsules with Controlled Shell Thickness. *Chem. Mater.* **2011**, *23*, 2370–2380. [CrossRef]

175. Such, G.K.; Quinn, J.F.; Quinn, A.; Tjipto, E.; Caruso, F. Assembly of ultrathin polymer multilayer films by click chemistry. *J. Am. Chem. Soc.* **2006**, *128*, 9318–9319. [CrossRef]

176. Ochs, C.J.; Such, G.K.; Yan, Y.; van Koeverden, M.P.; Caruso, F. Biodegradable Click Capsules with Engineered Drug-Loaded Multilayers. *ACS Nano* **2010**, *4*, 1653–1663. [CrossRef] [PubMed]

177. Such, G.K.; Tjipto, E.; Postma, A.; Johnston, A.P.R.; Caruso, F. Ultrathin, Responsive Polymer Click Capsules. *Nano Lett.* **2007**, *7*, 1706–1710. [CrossRef]

178. Parakhonskiy, B.V.; Parak, W.J.; Volodkin, D.V.; Skirtach, A.G. Hybrids of Polymeric Capsules, Lipids, and Nanoparticles: Thermodynamics and Temperature Rise at the Nanoscale and Emerging Applications. *Langmuir* **2019**, *35*, 8574–8583. [CrossRef] [PubMed]

179. Radt, B.; Smith, T.A.; Caruso, F. Optically Addressable Nanostructured Capsules. *Adv. Mater.* **2004**, *16*, 2184–2189. [CrossRef]

180. Skirtach, A.G.; Muñoz Javier, A.; Kreft, O.; Köhler, K.; Piera Alberola, A.; Möhwald, H.; Parak, W.J.; Sukhorukov, G.B. Laser-Induced Release of Encapsulated Materials inside Living Cells. *Angew. Chem. Int. Ed.* **2006**, *45*, 4612–4617. [CrossRef]

181. Brueckner, M.; Hollenbach-Latzko, S.; Reibetanz, U. Dual Transport of Active Substances with a Layer-by-Layer-Based Drug Delivery System to Terminate Inflammatory Processes. *Macromol. Biosci.* **2020**, *20*, 2000097. [CrossRef]

182. Brkovic, N.; Zhang, L.; Peters, J.N.; Kleine-Doepke, S.; Parak, W.J.; Zhu, D. Quantitative Assessment of Endosomal Escape of Various Endocytosed Polymer-Encapsulated Molecular Cargos upon Photothermal Heating. *Small* **2020**, *16*, 2003639. [CrossRef]

183. Borges, J.; Rodrigues, L.C.; Reis, R.L.; Mano, J.F. Layer-by-Layer Assembly of Light-Responsive Polymeric Multilayer Systems. *Adv. Funct. Mater.* **2014**, *24*, 5624–5648. [CrossRef]

184. Zograf, G.P.; Timin, A.S.; Muslimov, A.R.; Shishkin, I.I.; Nominé, A.; Ghanbaja, J.; Ghosh, P.; Li, Q.; Zyuzin, M.V.; Makarov, S.V. All-Optical Nanoscale Heating and Thermometry with Resonant Dielectric Nanoparticles for Controllable Drug Release in Living Cells. *Laser Photon. Rev.* **2020**, *14*, 1900082. [CrossRef]

185. Koryakina, I.; Kuznetsova, D.S.; Zuev, D.A.; Milichko, V.A.; Timin, A.S.; Zyuzin, M.V. Optically responsive delivery platforms: From the design considerations to biomedical applications. *Nanophotonics* **2020**, *9*, 39–74. [CrossRef]

186. Lengert, E.; Parakhonskiy, B.; Khalenkow, D.; Zečić, A.; Vangheel, M.; Monje Moreno, J.M.; Braeckman, B.P.; Skirtach, A.G. Laser-induced remote release in vivo in *C. elegans* from novel silver nanoparticles-alginate hydrogel shells. *Nanoscale* **2018**, *10*, 17249–17256. [CrossRef] [PubMed]

187. Neri, G.; Corsaro, C.; Fazio, E. Plasmon-Enhanced Controlled Drug Release from Ag-PMA Capsules. *Molecules* **2020**, *25*, 2267. [CrossRef] [PubMed]

188. Timin, A.S.; Gao, H.; Voronin, D.V.; Gorin, D.A.; Sukhorukov, G.B. Inorganic/Organic Multilayer Capsule Composition for Improved Functionality and External Triggering. *Adv. Mater. Interfaces* **2017**, *4*, 1600338. [CrossRef]

189. Parakhonskiy, B.V.; Bedard, M.F.; Bukreeva, T.V.; Sukhorukov, G.B.; Möhwald, H.; Skirtach, A.G. Nanoparticles on Polyelectrolytes at Low Concentration: Controlling Concentration and Size. *J. Phys. Chem. C* **2010**, *114*, 1996–2002. [CrossRef]

190. Anandhakumar, S.; Raichur, A.M. A facile route to synthesize silver nanoparticles in polyelectrolyte capsules. *Colloids Surf. B Biointerfaces* **2011**, *84*, 379–383. [CrossRef]

191. Bédard, M.F.; De Geest, B.G.; Möhwald, H.; Sukhorukov, G.B.; Skirtach, A.G. Direction specific release from giant microgel-templated polyelectrolyte microcontainers. *Soft Matter* **2009**, *5*, 3927–3931. [CrossRef]

192. Kaufman, G.; Montejo, K.A.; Michaut, A.; Majewski, P.W.; Osuji, C.O. Photoresponsive and Magnetoresponsive Graphene Oxide Microcapsules Fabricated by Droplet Microfluidics. *ACS Appl. Mater. Interfaces* **2017**, *9*, 44192–44198. [CrossRef]

193. Ermakov, A.V.; Verkhovskii, R.A.; Babushkina, I.V.; Trushina, D.B.; Inozemtseva, O.A.; Lukyanets, E.A.; Ulyanov, V.J.; Gorin, D.A.; Belyakov, S.; Antipina, M.N. In Vitro Bioeffects of Polyelectrolyte Multilayer Microcapsules Post-Loaded with Water-Soluble Cationic Photosensitizer. *Pharmaceutics* **2020**, *12*, 610. [CrossRef]

194. Saito, H.; Kato, N. Polyelectrolyte/carbon nanotube composite microcapsules and drug release triggered by laser irradiation. *Jpn. J. Appl. Phys.* **2016**, *55*, 03DF06. [CrossRef]

195. Szczęch, M.; Szczepanowicz, K. Polymeric Core-Shell Nanoparticles Prepared by Spontaneous Emulsification Solvent Evaporation and Functionalized by the Layer-by-Layer Method. *Nanomaterials* **2020**, *10*, 496. [CrossRef] [PubMed]

196. Hong, C.-S.; Park, J.H.; Lee, S.; Rhoo, K.Y.; Lee, J.T.; Paik, S.R. Fabrication of Protease-Sensitive and Light-Responsive Microcapsules Encompassed with Single Layer of Gold Nanoparticles by Using Self-Assembly Protein of α-Synuclein. *ACS Appl. Mater. Interfaces* **2018**, *10*, 26628–26640. [CrossRef] [PubMed]

197. Gao, H.; Wen, D.; Tarakina, N.V.; Liang, J.; Bushby, A.J.; Sukhorukov, G.B. Bifunctional ultraviolet/ultrasound responsive composite TiO$_2$/polyelectrolyte microcapsules. *Nanoscale* **2016**, *8*, 5170–5180. [CrossRef] [PubMed]

198. Novoselova, M.V.; Voronin, D.V.; Abakumova, T.O.; Demina, P.A.; Petrov, A.V.; Petrov, V.V.; Zatsepin, T.S.; Sukhorukov, G.B.; Gorin, D.A. Focused ultrasound-mediated fluorescence of composite microcapsules loaded with magnetite nanoparticles: In vitro and in vivo study. *Colloids Surf. B Biointerfaces* **2019**, *181*, 680–687. [CrossRef] [PubMed]

199. Hitchcock, J.; White, A.L.; Hondow, N.; Hughes, T.A.; Dupont, H.; Biggs, S.; Cayre, O.J. Metal-shell nanocapsules for the delivery of cancer drugs. *J. Colloid Interface Sci.* **2020**, *567*, 171–180. [CrossRef]

200. Stark, K.; Hitchcock, J.P.; Fiaz, A.; White, A.L.; Baxter, E.A.; Biggs, S.; McLaughlan, J.R.; Freear, S.; Cayre, O.J. Encapsulation of Emulsion Droplets with Metal Shells for Subsequent Remote, Triggered Release. *ACS Appl. Mater. Interfaces* **2019**, *11*, 12272–12282. [CrossRef]

201. White, A.L.; Langton, C.; Wille, M.-L.; Hitchcock, J.; Cayre, O.J.; Biggs, S.; Blakey, I.; Whittaker, A.K.; Rose, S.; Puttick, S. Ultrasound-triggered release from metal shell microcapsules. *J. Colloid Interface Sci.* **2019**, *554*, 444–452. [CrossRef]

202. Lengert, E.; Saveleva, M.; Abalymov, A.A.; Atkin, V.; Wuytens, P.C.; Kamyshinsky, R.; Vasiliev, A.L.; Gorin, D.A.; Sukhorukov, G.B.; Skirtach, A.G.; et al. Silver Alginate Hydrogel Micro- and Nanocontainers for Theranostics: Synthesis, Encapsulation, Remote Release, and Detection. *ACS Appl. Mater. Interfaces* **2017**, *9*, 21949–21958. [CrossRef]

203. Inozemtseva, O.A.; Voronin, D.V.; Petrov, A.V.; Petrov, V.V.; Lapin, S.A.; Kozlova, A.A.; Bratashov, D.N.; Zakharevich, A.M.; Gorin, D.A. Disruption of Polymer and Composite Microcapsule Shells under High-Intensity Focused Ultrasound. *Colloid J.* **2018**, *80*, 771–782. [CrossRef]

204. Stavarache, C.E.; Paniwnyk, L. Controlled rupture of magnetic LbL polyelectrolyte capsules and subsequent release of contents employing high intensity focused ultrasound. *J. Drug Deliv. Sci. Technol.* **2018**, *45*, 60–69. [CrossRef]

205. Kubiak, T.; Banaszak, J.; Józefczak, A.; Rozynek, Z. Direction-Specific Release from Capsules with Homogeneous or Janus Shells Using an Ultrasound Approach. *ACS Appl. Mater. Interfaces* **2020**, *12*, 15810–15822. [CrossRef] [PubMed]

206. Alford, A.; Tucker, B.; Kozlovskaya, V.; Chen, J.; Gupta, N.; Caviedes, R.; Gearhart, J.; Graves, D.; Kharlampieva, E. Encapsulation and Ultrasound-Triggered Release of G-Quadruplex DNA in Multilayer Hydrogel Microcapsules. *Polymers* **2018**, *10*, 1342. [CrossRef] [PubMed]

207. Gao, H.; Sapelkin, A.V.; Titirici, M.M.; Sukhorukov, G.B. In Situ Synthesis of Fluorescent Carbon Dots/Polyelectrolyte Nanocomposite Microcapsules with Reduced Permeability and Ultrasound Sensitivity. *ACS Nano* **2016**, *10*, 9608–9615. [CrossRef] [PubMed]

208. Lu, Z.; Prouty, M.D.; Guo, Z.; Golub, V.O.; Kumar, C.S.S.R.; Lvov, Y.M. Magnetic switch of permeability for polyelectrolyte microcapsules embedded with Co@Au nanoparticles. *Langmuir* **2005**, *21*, 2042–2050. [CrossRef]

209. Read, J.E.; Luo, D.; Chowdhury, T.T.; Flower, R.J.; Poston, R.N.; Sukhorukov, G.B.; Gould, D.J. Magnetically responsive layer-by-layer microcapsules can be retained in cells and under flow conditions to promote local drug release without triggering ROS production. *Nanoscale* **2020**, *12*, 7735–7748. [CrossRef]

210. Luo, D.; Poston, R.N.; Gould, D.J.; Sukhorukov, G.B. Magnetically targetable microcapsules display subtle changes in permeability and drug release in response to a biologically compatible low frequency alternating magnetic field. *Mater. Sci. Eng. C* **2019**, *94*, 647–655. [CrossRef]

211. Prabu, C.; Latha, S.; Selvamani, P.; Ahrentorp, F.; Johansson, C.; Takeda, R.; Takemura, Y.; Ota, S. Layer-by-layer assembled magnetic prednisolone microcapsules (MPC) for controlled and targeted drug release at rheumatoid arthritic joints. *J. Magn. Magn. Mater.* **2017**, *427*, 258–267. [CrossRef]

212. Carregal-Romero, S.; Guardia, P.; Yu, X.; Hartmann, R.; Pellegrino, T.; Parak, W.J. Magnetically triggered release of molecular cargo from iron oxide nanoparticle loaded microcapsules. *Nanoscale* **2015**, *7*, 570–576. [CrossRef]

213. Cristofolini, L.; Szczepanowicz, K.; Orsi, D.; Rimoldi, T.; Albertini, F.; Warszynski, P. Hybrid Polyelectrolyte/Fe$_3$O$_4$ Nanocapsules for Hyperthermia Applications. *ACS Appl. Mater. Interfaces* **2016**, *8*, 25043–25050. [CrossRef]

214. Katagiri, K.; Nakamura, M.; Koumoto, K. Magnetoresponsive Smart Capsules Formed with Polyelectrolytes, Lipid Bilayers and Magnetic Nanoparticles. *ACS Appl. Mater. Interfaces* **2010**, *2*, 768–773. [CrossRef]

215. Minaeva, O.V.; Brodovskaya, E.P.; Pyataev, M.A.; Gerasimov, M.V.; Zharkov, M.N.; Yurlov, I.A.; Kulikov, O.A.; Kotlyarov, A.A.; Balykova, L.A.; Kokorev, A.V.; et al. Comparative study of cytotoxicity of ferromagnetic nanoparticles and magnetitecontaining polyelectrolyte microcapsules. *J. Phys. Conf. Ser.* **2017**, *784*, 012038. [CrossRef]

216. Bezbaruah, A.N.; Shanbhogue, S.S.; Simsek, S.; Khan, E. Encapsulation of iron nanoparticles in alginate biopolymer for trichloroethylene remediation. *J. Nanopart. Res.* **2011**, *13*, 6673–6681. [CrossRef]

217. Gao, C.; Leporatti, S.; Moya, S.; Donath, E.; Möhwald, H. Stability and Mechanical Properties of Polyelectrolyte Capsules Obtained by Stepwise Assembly of Poly(styrenesulfonate sodium salt) and Poly(diallyldimethyl ammonium) Chloride onto Melamine Resin Particles. *Langmuir* **2001**, *17*, 3491–3495. [CrossRef]

218. Fery, A.; Weinkamer, R. Mechanical properties of micro- and nanocapsules: Single-capsule measurements. *Polymer (Guildf)* **2007**, *48*, 7221–7235. [CrossRef]

219. She, S.; Li, Q.; Shan, B.; Tong, W.; Gao, C. Fabrication of Red-Blood-Cell-Like Polyelectrolyte Microcapsules and Their Deformation and Recovery Behavior Through a Microcapillary. *Adv. Mater.* **2013**, *25*, 5814–5818. [CrossRef]

220. Kolesnikova, T.A.; Skirtach, A.G.; Möhwald, H. Red blood cells and polyelectrolyte multilayer capsules: Natural carriers versus polymer-based drug delivery vehicles. *Expert Opin. Drug Deliv.* **2013**, *10*, 47–58. [CrossRef]

221. Anselmo, A.C.; Mitragotri, S. Impact of particle elasticity on particle-based drug delivery systems. *Adv. Drug Deliv. Rev.* **2017**, *108*, 51–67. [CrossRef]

222. Dubreuil, F.; Elsner, N.; Fery, A. Elastic properties of polyelectrolyte capsules studied by atomic-force microscopy and RICM. *Eur. Phys. J. E Soft Matter* **2003**, *12*, 215–221. [CrossRef]

223. Pan, H.M.; Seuss, M.; Neubauer, M.P.; Trau, D.W.; Fery, A. Tuning the Mechanical Properties of Hydrogel Core–Shell Particles by Inwards Interweaving Self-Assembly. *ACS Appl. Mater. Interfaces* **2016**, *8*, 1493–1500. [CrossRef]

224. Frueh, J.; Rühm, A.; He, Q.; Möhwald, H.; Krastev, R.; Köhler, R. Elastic to Plastic Deformation in Uniaxially Stressed Polylelectrolyte Multilayer Films. *Langmuir* **2018**, *34*, 11933–11942. [CrossRef]

225. Hegemann, J.; Knoche, S.; Egger, S.; Kott, M.; Demand, S.; Unverfehrt, A.; Rehage, H.; Kierfeld, J. Pendant capsule elastometry. *J. Colloid Interface Sci.* **2018**, *513*, 549–565. [CrossRef] [PubMed]

226. Köhler, K.; Möhwald, H.; Sukhorukov, G.B. Thermal behavior of polyelectrolyte multilayer microcapsules: 2. Insight into molecular mechanisms for the PDADMAC/PSS system. *J. Phys. Chem. B* **2006**, *110*, 24002–24010. [CrossRef] [PubMed]

227. Cramer, A.D.; Dong, W.-F.; Benbow, N.L.; Webber, J.L.; Krasowska, M.; Beattie, D.A.; Ferri, J.K. The influence of polyanion molecular weight on polyelectrolyte multilayers at surfaces: Elasticity and susceptibility to saloplasticity of strongly dissociated synthetic polymers at fluid–fluid interfaces. *Phys. Chem. Chem. Phys.* **2017**, *19*, 23781–23789. [CrossRef] [PubMed]

228. Giménez, R.E.; Serrano, M.P.; Álvarez, R.M.S.; Martino, D.M.; Borsarelli, C.D. Fabrication and Characterization of Hollow Microcapsules from Polyelectrolytes Bearing Thymine Pendant Groups for Ultraviolet-B (UVB)-Induced Crosslinking. *ChemPlusChem* **2019**, *84*, 504–511. [CrossRef] [PubMed]

229. Hastings, D.E.; Stöver, H.D.H. Crosslinked Hydrogel Capsules for Cell Encapsulation Formed Using Amino/Betaine Dual-Functional Semibatch Copolymers. *ACS Appl. Polym. Mater.* **2019**, *1*, 2055–2067. [CrossRef]

230. Wu, Q.-X.; Xu, X.; Wang, Z.-L.; Yao, S.-J.; Tong, W.-Y.; Chen, Y. Effect of the cross-linking agent on performances of NaCS-CS/WSC microcapsules. *Colloids Surf. B Biointerfaces* **2016**, *147*, 416–421. [CrossRef]

231. Gupta, N.; Kozlovskaya, V.; Dolmat, M.; Kharlampieva, E. Shape Recovery of Spherical Hydrogen-Bonded Multilayer Capsules after Osmotically Induced Deformation. *Langmuir* **2019**, *35*, 10910–10919. [CrossRef]

232. Mueller, R.; Köhler, K.; Weinkamer, R.; Sukhorukov, G.B.; Fery, A. Melting of PDADMAC/PSS capsules investigated with AFM force spectroscopy. *Macromolecules* **2005**, *38*, 9766–9771. [CrossRef]

233. Van der Meeren, L.; Li, J.; Konrad, M.; Skirtach, A.G.; Volodkin, D.; Parakhonskiy, B.V. Temperature Window for Encapsulation of an Enzyme into Thermally Shrunk, $CaCO_3$ Templated Polyelectrolyte Multilayer Capsules. *Macromol. Biosci.* **2020**, *20*, 2000081. [CrossRef]

234. Mettu, S.; Zhou, M.; Tardy, B.L.; Ashokkumar, M.; Dagastine, R.R. Temperature dependent mechanical properties of air, oil and water filled microcapsules studied by atomic force microscopy. *Polymer (Guildf)* **2016**, *102*, 333–341. [CrossRef]

235. Zhang, Y.; Li, F.; Valenzuela, L.D.; Sammalkorpi, M.; Lutkenhaus, J.L. Effect of Water on the Thermal Transition Observed in Poly(allylamine hydrochloride)–Poly(acrylic acid) Complexes. *Macromolecules* **2016**, *49*, 7563–7570. [CrossRef]

236. Bédard, M.F.; Munoz-Javier, A.; Mueller, R.; del Pino, P.; Fery, A.; Parak, W.J.; Skirtach, A.G.; Sukhorukov, G.B. On the mechanical stability of polymeric microcontainers functionalized with nanoparticles. *Soft Matter* **2009**, *5*, 148–155. [CrossRef]

237. Yashchenok, A.M.; Bratashov, D.N.; Gorin, D.a.; Lomova, M.V.; Pavlov, A.M.; Sapelkin, A.V.; Shim, B.S.; Khomutov, G.B.; Kotov, N.A.; Sukhorukov, G.B.; et al. Carbon Nanotubes on Polymeric Microcapsules: Free-Standing Structures and Point-Wise Laser Openings. *Adv. Funct. Mater.* **2010**, *20*, 3136–3142. [CrossRef]

238. Del Mercato, L.L.; Guerra, F.; Lazzari, G.; Nobile, C.; Bucci, C.; Rinaldi, R. Biocompatible multilayer capsules engineered with a graphene oxide derivative: Synthesis, characterization and cellular uptake. *Nanoscale* **2016**, *8*, 7501–7512. [CrossRef] [PubMed]

239. Kaufman, G.; Mukhopadhyay, S.; Rokhlenko, Y.; Nejati, S.; Boltyanskiy, R.; Choo, Y.; Loewenberg, M.; Osuji, C.O. Highly stiff yet elastic microcapsules incorporating cellulose nanofibrils. *Soft Matter* **2017**, *13*, 2733–2737. [CrossRef] [PubMed]

240. Sciortino, F.; Thivolle, M.; Kahn, M.L.; Gaillard, C.; Chevance, S.; Gauffre, F. Structure and elasticity of composite nanoparticle/polymer nanoshells (hybridosomes). *Soft Matter* **2017**, *13*, 4393–4400. [CrossRef] [PubMed]

241. Chojnacka-Górka, K.; Rozpędzik, A.; Zapotoczny, S. Robust polyelectrolyte microcapsules reinforced with carbon nanotubes. *RSC Adv.* **2016**, *6*, 114639–114643. [CrossRef]

242. Ermakov, A.V.; Prikhozhdenko, E.S.; Demina, P.A.; Gorbachev, I.A.; Vostrikova, A.M.; Sapelkin, A.V.; Goryacheva, I.Y.; Sukhorukov, G.B. Composite multilayer films based on polyelectrolytes and in situ-formed carbon nanostructures with enhanced photoluminescence and conductivity properties. *J. Appl. Polym. Sci.* **2019**, *136*, 47718. [CrossRef]

243. Zhao, S.; Caruso, F.; Dähne, L.; Decher, G.; De Geest, B.G.; Fan, J.; Feliu, N.; Gogotsi, Y.; Hammond, P.T.; Hersam, M.C.; et al. The Future of Layer-by-Layer Assembly: A Tribute to ACS Nano Associate Editor Helmuth Möhwald. *ACS Nano* **2019**, *13*, 6151–6169. [CrossRef]

Coupling pH-Regulated Multilayers with Inorganic Surfaces for Bionic Devices and Infochemistry

Nikolay V. Ryzhkov,[†] Daria V. Andreeva,[‡] and Ekaterina V. Skorb*,[†]

[†]ITMO University, St. Petersburg 191002, Russian Federation

[‡]Centre for Advanced 2D Materials and Graphene Research Centre, National University of Singapore, 117546 Singapore

ABSTRACT: This article summarizes more than 10 years of cooperation with Prof. Helmuth Möhwald. Here we describe how the research moved from light-regulated feedback sustainable systems and control biodevices to the current focus on infochemistry in aqueous solution. An important advanced characteristic of such materials and devices is the pH concentration gradient in aqueous solution. A major part of the article focuses on the use of localized illumination for proton generation as a reliable, minimal-reagent-consuming, stable light-promoted proton pump. The in situ scanning vibration electrode technique (SVET) and scanning ion-selective electrode technique (SIET) are efficient for the spatiotemporal evolution of ions on the surface. pH-sensitive polyelectrolyte (PEs) multilayers with different PE architectures are composed with a feedback loop for bionic devices. We show here that pH-regulated PE multilayers can change their properties—film thickness and stiffness, permeability, hydrophilicity, and/or fluorescence—in response to light or electrochemical or biological processes instead of classical acid/base titration.
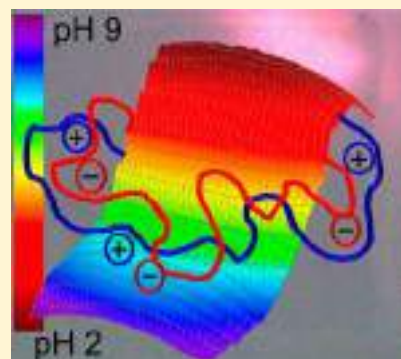
INTRODUCTION

For more than 10 years, the research was conducted with Prof. Helmuth Möhwald. In the beginning, functional materials for antibacterial coatings have been developed,[1−3] accompanied by corrosion protection[4−8] and then research focused on cell and tissue culturing,[9−15] keeping in mind the fundamental aspects of interfacial interactions for thin films.[16−20] Current interests include information processing with molecules in aqueous solution.[21] It is worth noting that the invention of the polyelectrolyte layer-by-layer (LbL) method was very important to surface science.[22−24]

Our work raised scientific questions related to the design and functions of the materials that, in many cases, were complex and included several aspects.[25] However, for fundamental understanding and modeling, the simpler the system, the better it was.[26] The focus of research was on developing new methods of making ensembles or approaches to mimicking biology. The range of problems includes the lack of understanding of reversible switching from one state to the other in the dynamic multilayers. "There is still an urgent need to understand the mechanisms for LbL assembly in multilayers", often noted Prof. Möhwald.

Processes at the interface of inorganic solids and polyelectrolytes (PEs) mimic a large variety of natural processes such as stimuli-responsive behavior,[27] self-healing,[28] actuation,[14] transport and delivery,[12] and pH buffering,[29] but predictive models beyond this are not well understood.[11−13] PEs multilayers are suitable for studying this, as they can be manipulated at will between glassy, rubbery hydrogels or organogels.[30] We investigate photocatalytically triggered local pH changes in titania/PEs LbL assembled interfaces mimicking natural processes in a novel design strategy for inorganic/polymer interfaces. We have shown recently that under the irradiation of TiO_2 a series of photocatalytic reactions lead to a local change in pH, which modulates the pH-sensitive LbL assembly. Prime questions are the following (i) How many photons are needed to locally change the pH on titania? (ii) What is the optimum LbL architecture for understanding proton trapping and storage and the pH gradient under local irradiation? (iii) How is reversible actuation of different assemblies for advanced applications achieved?

Here we address the feedback pH change on an inorganic surface (Figure 1): (i) the pH change due to the photocatalytic reaction of water splitting, (ii) the electrochemical process, (iii) the chemical or biochemical reaction network, and (iv) the biological process. Strong and weak PE assemblies, including charged biopolymers and hydrogels, can regulate the charge carrier generation[25] and the diffusion of ions at interfaces[31] and their lifetime and storage.[16] Fundamentally, a lot was known concerning dynamic changes in pH-regulated PEs when acid or base was added to a solution.[30] Developing various physico/chemical methods for monitoring ion diffusion in multilayers is important. The efficiency of the multilayers' response is investigated with atomic force microscopy, neutron reflectivity, in situ quartz crystal microbalance and ellipsometry, confocal laser scanning microscopy, and now, as
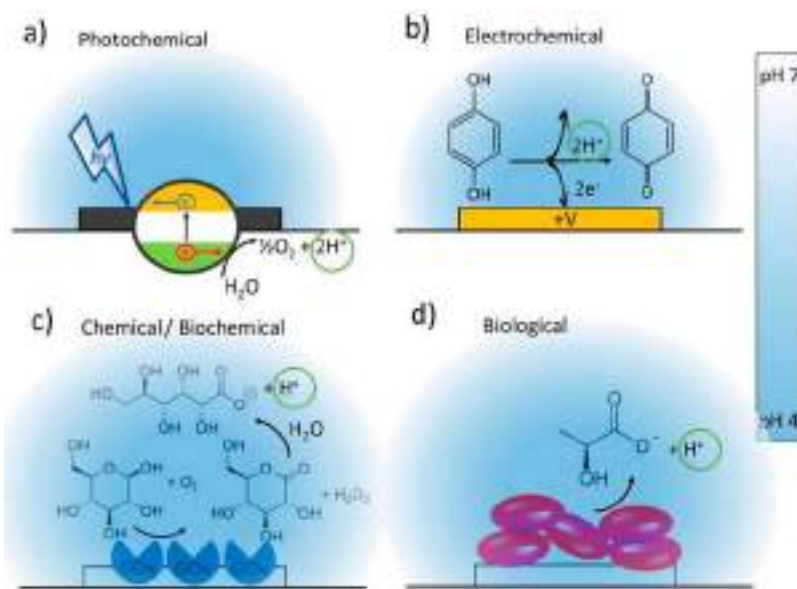
Figure 1. Approaches to the generation of a proton concentration gradient at an inorganic surface. (a) Photoelectrochemical water splitting on a semiconductor surface under supra band gap irradiation, (b) electrochemical oxidation of hydroquinone coupled with proton release, (c) catalytic oxidation of glucose by a substrate-immobilized enzyme (GOx) followed by local acidification, and (d) bacteria decreasing the pH of the surrounding media during the life cycle.

suggested by us, in situ scanning vibration electrode (SVET) and scanning ion-selective electrode techniques (SIET) for mapping the diffusion of ions over the surface. In particular, ion fluxes on the inorganic surface were investigated using SVET and SIET, which is a unique tool for the in situ characterization of local ionic currents above the surfaces.[32]

The use of light as an external stimulus to modulate the pH has great potential in the biosciences, medicine, and tissue engineering because of the possibility to irradiate micrometer-sized areas with fast on/off switching rates.[33] For local processes, one can further discuss ion propagation in horizontal and vertical directions depending on the nature of polymer and multilayer nanoarchitecture. The idea of the simultaneous irradiation of a system at various points moves us in the direction of a coupled network of nonlinear chemical reactions far from equilibrium.[34] However, the pH concentration gradient on the titania surface appears together with reactive oxygen species generation (ROS), which is still a challenge for modeling. Thus, we considered the idea of comparing knowledge for a photogenerated pH gradient and an electrochemical gradient.[35] A related question on the feasibility of the process is how many protons and photons or electrons are needed from the surface to locally change the pH from 7 to, for example, 4? The proton generation associated with water splitting or hydroquinone oxidation for the electrochemical process was studied using SVET/SIET.[35] The role of electrode modification by PEs for both photochemistry and electrochemistry is discussed. PEs drastically effect charge transfer on inorganic surfaces.

The instruments developed by us allow us to monitor information transfer in aqueous solution. We can use them to understand communication pathways in living matter when basic logic operations are suggested.[25] An important characteristic is the development of pH concentration gradients in solution. Here we present a strategy for both mentioned characteristics: (i) a controllable, sustainable pH concentration gradient in solution produced photochemically, electrochemi-

cally, or biochemically and controlled by multilayers as well as (ii) possible logic-operated materials. The synergy between components in such materials is important for the future green and sustainable way of controlling cells and tissue growth,[36] communication with bacterial colonies,[37] and the acceleration of autocatalytic processes[38] in solution and even developing a platform of transmembrane channels in bionic devices with a size-tuning bioinspired response.

We believe that it is now time to explain self-regulated feedback materials with appropriate general models and information exchange between programmable functional materials and bio-objects (e.g., tissue and biofilms) currently in focus in the "Infochemistry for self-organizing systems" group.[21] Interdisciplinary views on the problems from various sources—chemistry, physics, mathematics, and biology—help to solve complex issues and guides science development for the next generation. Infochemistry—entropy and information as well as storage and the possibly of storing information—is an experimental area of chemistry which deals with information storage[39−42] and processing[42−45] on a molecular level. In the group, we are working on different projects from the synthetic cell and biofilm programming to smart dynamic materials and materials for personal diagnostics, study, and modeling of nonlinear chemistry. The driving idea was that the LbL method of PE assembly, due to the simplicity of preparation, together with other functional inorganic components had a low barrier to entry synergy and could address both scientific and practical problems efficiently.

■ LIGHT−PH COUPLING ON TITANIA

Study of a Pristine Titania Surface. The titania nanotube layer is an efficient photocatalyst (the photocurrent and the open-circuit voltage are ca. 2 mA/cm^2)[32] due to an increased surface area and to the photoproduction of a high concentration of active species.[16,32] It is known that under supra band gap irradiation photoholes and photoelectrons are generated in a complex surface of nanotubes.[32] Consequently,

active species take part in a series of intensive photoreactions. H$^+$ and OH$^-$ are generated on different sites of a semi-conductor. During the irradiation of titania the local pH of media inside an irradiated spot can be shifted from neutral to acidic/basic and returned due to a fast recombination of species as seen in eqs 1 and 2.

$$TiO_2 + h\nu = e^-_{CB} + h^+_{VB} \tag{1}$$

$$h^+_{VB} + H_2O = OH^\bullet + H^+ \tag{2}$$
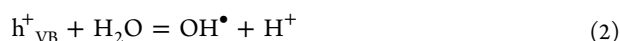
The photocurrent occurs because of the separation of photogenerated electron−hole pairs within the photoelectrode. Photoholes and photoelectrons are formed on the surface of titania. We proved experimentally that in our case[32] photo-holes inside an irradiated spot resulted in proton generation.

For pH-sensitive modulation with light, it is important to understand how photoinitiated processes on TiO$_2$ result in the conversion of light into ΔpH, including the localization of the effect. We suggest the application of the in situ SIET (Figure
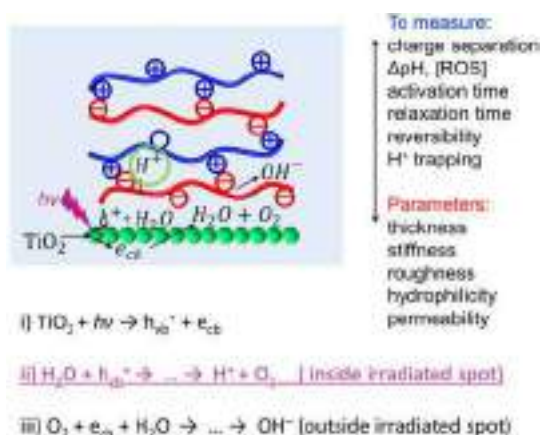
Figure 2. Surface decoration and photoinitiated light−pH coupled reactions. Primary and secondary photocatalytic reactions on TiO$_2$ resulting in a local change in pH (ΔpH). The reactions shown are (i) light-stimulated charge separation, (ii) a primary reaction with photoholes with the final production of protons and local surface acidification in the irradiated area, and (iii) the photoelectron reaction. ΔpH will affect the dynamic layers assembled on titania in terms of local changes in film thickness, stiffness, and permeability by regulating the time of dynamic layer activation, relaxation and reversibility. Reprinted from ref 16, Wiley.

3)[32] to map the migration of H$^+$ ions over TiO$_2$. SIET is a unique technique available for measuring in situ changes in ion concentrations locally in space and time. The main advantage of this unique method is that it allows measurements of local ΔpH near the surface without any pH-sensitive markers, which may potentially affect the photoreactions. Local pH means the activity of protons as measured by a SIET device[32] and can be associated with the dynamics of charged soft matter.

Maps of ΔpH were collected for pristine TiO$_2$ before illumination (Figure 3a), during illumination (Figure 3b), and 20 min after switching the illumination off (Figure 3c). The proton distribution maps show that protons were generated under irradiation. Thus, it is possible to couple light and pH, and we know how to visualize chemical processes in situ under local illumination. SIET allows measurement in a single point (Figure 3d) and scanning a line (Figure 3e), and together with X−Y maps, the Z map or line (Figure 3f) can be collected. It is

possible to change the position of an irradiated spot and its intensity (Figure 3g vs Figure 3h). We see that the pH concentration gradient map is changed (Figure 3i vs Figure 3b) during irradiation.

Light-Triggered Local pH Changes on Titania/PE Interfaces. LbL assembly can be an efficient structure for the fast trapping of photogenerated protons on TiO$_2$ (Figure 2).[16] The kinetics of the light−pH coupled actuation and modulation of LbL films and the study of the relaxation are important. We aim to answer the following key questions. (a) How can the photogeneration of charges in a solid be used to change the properties of soft matter? The photon absorption, carrier generation, chemical conversion to a pH−concentration gradient, lifetimes, and LbL stability should be elucidated. Subtopics are (b) the dependence on LbL architecture and (c) the nature of TiO$_2$ as a semiconductor, th eeffectiveness of doping, and the duration and intensity of irradiation.

The use of light-triggered local pH changes on titania/PE interfaces for the modulation of multilayers is illustrated in Figure 2. It is important to propose materials which can be sensitive to local changes in pH (ΔpH) and provide a high amplitude of response but do not undergo degradation in the presence of reactive oxygen species (ROS).

Of high priority are the following experiments: (i) the application of mathematical modeling of proton pumping by light on titania, (ii) the use of other semiconductors, (iii) multispot illumination and diffusion over the surface, and (iv) proton long-term trapping and release on demand by PE multilayers.

It is interesting to correlate the dynamic behavior of PEs with a proper model. Modeling for aqueous solutions is still a challenge. However, a novel model for the swelling of dry polyelectrolyte multilayers and water uptake from the air and its condensation in voids inside polyelectrolyte layers was proposed.[46,47] All-atom molecular dynamics simulations of salt diffusion in the polyelectrolyte assembly demonstrated the importance of water pockets in the structure of the multilayer.[48] Besides the ion hopping mode, the diffusing trajectories are found to present common features of a jump process, that is, subjection to PE relaxation and water pockets in the structure that open and close; thus, the ion can move from one pocket to another.[48]

The effect of the nonstoichiometry of PE multilayer ionic flux through the membrane was studied.[47] It was found that 1:1 stoichiometry of PEs in multilayers gives more predictable transport properties, whereas excess charges strongly affect the diffusion and permeability of ions through the multilayer. Ionic strength was shown to be an important parameter for determining the transport properties of multilayers.[47] At the same time, the overcompensation of charges in multilayers by small counterions may lead to the instability of the assembly.[48] It was also observed that pairs of weak PEs are more permeable to small molecules and ions, whereas multilayers assembled of strong PEs showed barrier properties.[49]

Models of diffusion and the prediction of the distribution of nanoparticles and ions inside polyelectrolyte layers were suggested.[50] Regulated transport properties of polyelectrolyte multilayers make them a powerful instrument for controlling the nucleation density, crystal orientation, and location of the growing crystals. The growing structures act as propagating fronts that leave in their wake a mineral film and eventually cover the whole surface.[51]
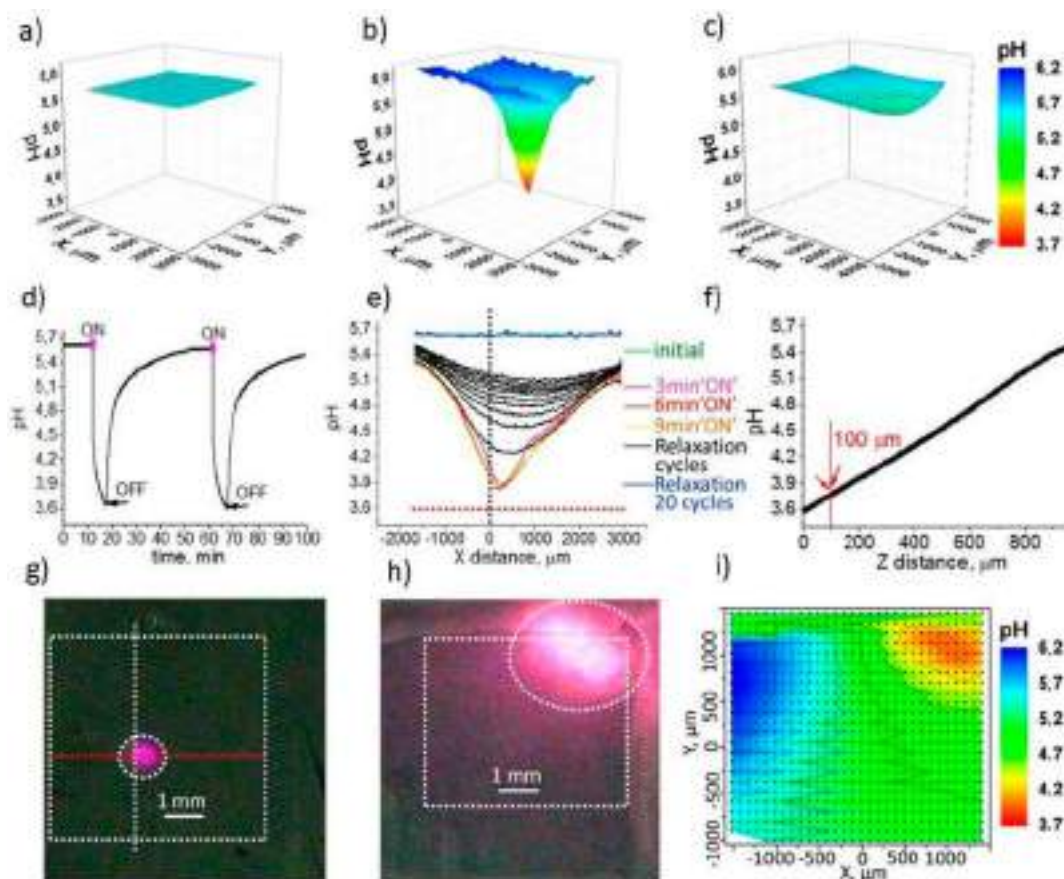
Figure 3. Light−pH coupling on the semiconductor surface. Maps obtained by in situ SIET to analyze local pH gradients generated on nanostructured TiO₂ (a) before irradiation, (b) during local irradiation, and (c) after irradiation (20 min of relaxation). (d) pH measurement inside an irradiation spot (shown in panel g) and single-spot time-evolution measurements on a titania layer after switching the light on and off. (e) Local pH measurements in a line (shown in panel g in red) before, during, and after irradiation (in which the maximum coincides with the position of the irradiation spot; the time of measurement of each line was 3 min). (f) pH in the Z direction during illumination inside the irradiated spot. (g) X−Y dashed lines shown in the optical image of the surface and the location of the focused irradiation spot on TiO₂ described above (panels a−e) mapped in panels a−c. (h) X−Y optical image with defocused light to show the flexibility of the method to change the intensity of illumination and its location and effect on the pH gradient of the surface with a corresponding (i) pH map with colored pH areas Reprinted from ref 32, Americal Chemical Society.

A kinetic study of polyelectrolyte molecules and counterion diffusion was preformed.[52] A better understanding of the influence of charged groups of polymers on the ionic conductivity was provided by the study of diffusion in polyelectrolyte hydrogels. It was indicated that zwitterionic PEs are more favorable to ion transportation.[53]

Regulated transport properties of polyelectrolyte assemblies allow us to design artificial ion channels gated by external stimuli. Biological channels were used to design stimuli-response artificial nanopores. An original approach to design a pH-gate nanopore based on LbL self-assembled PE multilayers was proposed.[54−59]

Gradient processes on the surface of the irradiated semiconductor/PEs have already played an important role in the regulation of cell behavior and the architecture of bionic devices. Recently, the preosteoblast cells' growth dynamics on the surface of mesoporous TiO₂ with the deposited layers of block copolymer micelles (BCM) and poly(acrylic acid) (PAA) has been investigated.[14] The consequence of the pH alteration after the irradiation of the material was the change in the polymer film stiffness—in the acidic media, the micelles swelled and drastically changed the thickness and Young's modulus of the polymer coating (Figure 4). We investigated the change in the BCM properties under the ΔpH generated by the vital bacteria.[16] To calculate the concentration of protons[16] needed for the activation of the layer of BCM, we assumed 1 cm² of TiO₂ to achieve pH 4 or $[H^+] = 10^{-4}$ M or 6×10^{19} L^{-1}, a coating with thickness of, for example, 150 nm in our case, that is, $V = 1.5 \times 10^{-8}$ L. The concentration of protons in the layers was then $[H^+] = 9 \times 10^{11}$ protons cm^{-2}, which is about 0.1% of the lattice sites of a typical solid (10^{15} lattice sites cm^{-2}). This means that only 0.1% of the surface atoms have to be charged to achieve pH 4 if no losses exist. Even at a low radiation intensity of 1 mW cm^{-2} = 10^{16} photons cm^{-2} s^{-1} for a quantum yield proton/photon conversion of 0.1%, the photons from 100 ms of irradiation can create enough protons on the TiO₂ surface to achieve LbL switching on the surface of TiO₂. This also means that fewer photoactive solids could create the same effect.

For the LbL assembly of the PEs without a TiO₂ coating, the change in stiffness under irradiation did not occur and the coating remained rigid. During 5 days of cultivation, the cells had a tendency to migrate from the "soft" part of the sample toward the "stiff" one (Figure 4). Thus, the manipulation of the mechanical modulus of the hybrid coatings can lead to the
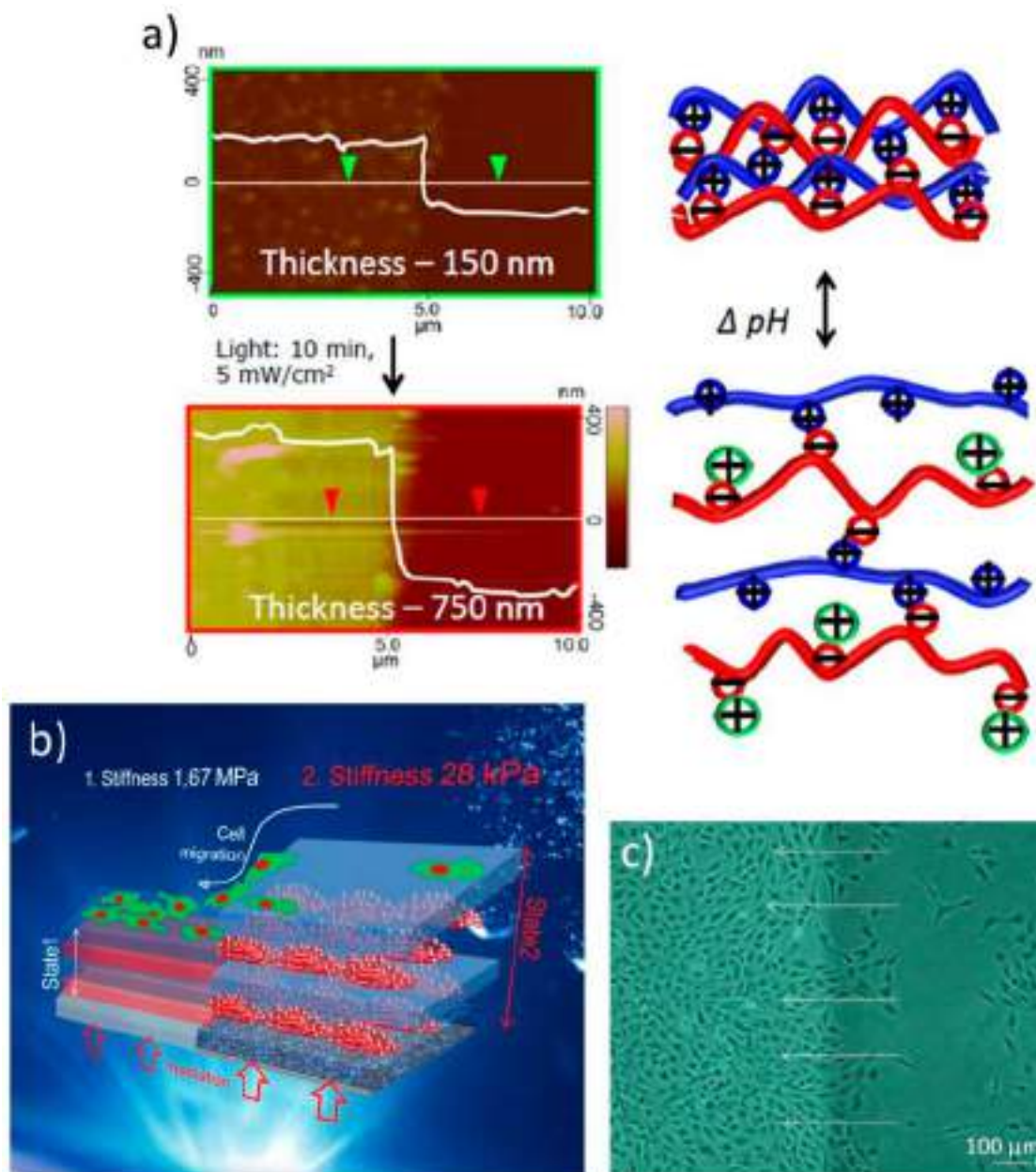
Figure 4. Example of photoswitchable LbL for bioapplication: (a) AFM images and schematic of change in the LbL thickness in response to irradiation (intensity of 5 mW/cm²) proving the changes in thickness from 150 to 750 nm and stiffness from 1.67 MPa to 28 kPa. Reprinted from ref 16, Wiley. (b) Suggestion for the use of such photoregulated lab-on-a-chip systems to guide cell migration and (c) the corresponding cell (osteoblast MC3T3-E1) migration experiment, with the number of the cells equal on both sides before irradiation. Adapted from ref 14, Wiley.

fabrication of stimuli-responsive materials for biological purposes.

The materials can be used for further applications. Several examples are shown in Figure 5. Delivery systems,[2] lab-on-a-chip systems,[60] light-healing materials,[20] and a buffering nanolayer[18] are proposed. All systems urgently need mathematical modeling; however, they have already demonstrated working sustainability and reliability for their suggested functions.

In Figure 5a, it is seen that titania based capsules can be opened locally, just on exposed areas.[2] The pH-sensitive complex adsorption/desorption process was shown on the example of protein tagged with histidine amino acid (poly-His-tag) with Ni-nitrilotriacetic acid (NTA) complex where the last

component was in the LbL assembly on the titanium-based chips covered with native titania[60] (Figure 5b). The interactions of the poly-His-tag protein with Ni-NTA are sensitive to pH. The short-term irradiation was used to switching the pH of the media. After turning the light on, the medium pH was 4. At such a pH value, the NTA-Ni²⁺/His-Tag dissociated and the protein desorbed from the surface. Turning the light off resulted in the reverse process—adsorption of the protein to the surface. The light regulation of the protein sorption can be used for biosensing and biomedical applications.

Recently Tsukruk et al.[61] suggested a nondestructive way to achieve the remote, reversible, light-controlled tunable permeability of an ultrathin PE assembly. PEs based on
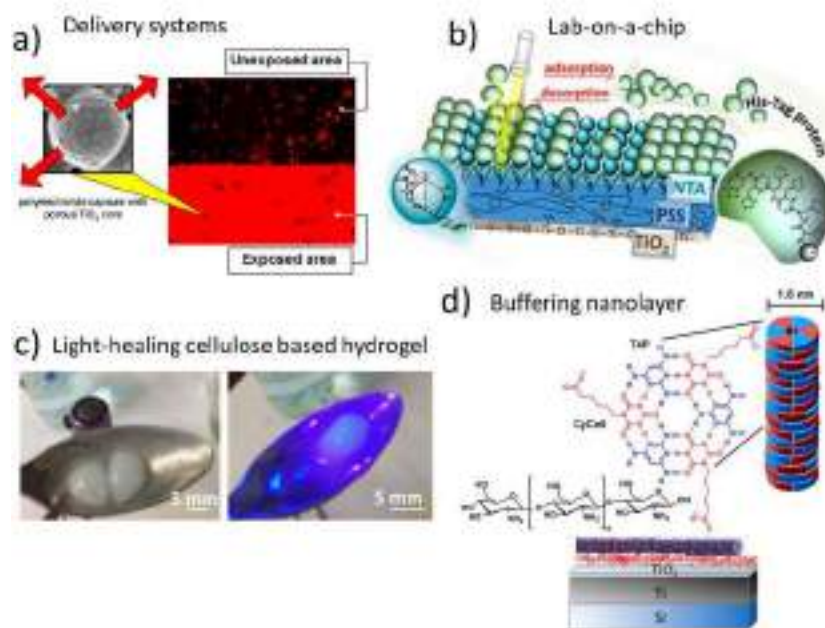
Figure 5. (a) Confocal kinetics study (fluorescence mode) of a release in the exposed area of chemical species from titania-based capsules. Reproduced from ref 2, Royal Chemical Society. (b) TiO_2 surface decorated with an LbL assembly of polystyrenesulfonate (PSS) and nickel−nitrilotriacetic acid (NTA) to bind (poly)histidine-tagged (His-Tag) proteins. Spatially resolved protein desorption is regulated by irradiation with light, causing a local pH shift that affects the pH-sensitive NTA/protein complex but not the PSS/NTA assembly. Adapted from ref 60, Wiley. (c) Light curing of a cellulose/titania-based hybrid (hydrogel). Optical images of a composite hydrogel cut (left) and light healing of the material after 15 min of irradiation (right). Adapted from ref 20. (d) Chitosan layer of 2 nm on the titania surface is efficient as a proton sponge and no disassembly of an unstable acidic medium CyCo6-TAP complex was observed due to a change in surface acidity. Adapted from ref 18, Royal Chemical Society.

Table 1

logic gate	gate	input	output	ref
OR	(PLL[a]/DNA)₇ multilayer	trypsin, deoxyribonuclease I	electrochemi-luminescense	78
	protamine/CS[b] capsules	trypsin hyaluronidase	drug release	77
	ITO/P4VP[c] film	Est[d], GOx[e]	electrode activity	50
	silica nanoparticles decorated with P2VP[f] shells	Est, GOx	size of particles/aggregates	79
	oil/water emulsion, stabilized by PS-b-P4VP-b-PEO[g] particles	Est, GOx	electrical conductivity of the emulsions obtained	84
	Est/GOx membrane	ethyl butyrate glucose	pH	47
AND	PLL/PAA[h]/PLL/DNA/PEI[i]/DNA/PLL/PAA/PLL/DNA multylayer	trypsin, deoxyribonuclease I	electrochemi-luminescense	78
	pDADMAC[j]/pAMPSA[k] diod	potential bias	fluorescence	76
	ITO/P4VP	Inv[l], GOx	electrode activity	83
	silica nanoparticles decorated with P2VP shells + sucrose and Ur[m]	Inv, GOx	size of particles/aggregates	79
	oil/water emulsion, stabilized by PS-b-P4VP-b-PEO particles	Inv, GOx	electrical conductivity of the emulsions obtained	84
	surface-immobilized HRP[n] and GOx	D- and L-N-acryloyl aspartic acid surface	catalytic activity	85
	multyenzimemembrane: Mut[o]/GOx/Inv/Ur	sucrose, O_2	pH	64
NAND	BSA[p]/MPA-AuNCs[q]	Fe^{2+}, H_2O_2	emission under UV	80
	5′-GCCAGAACCCAGTAGT-3′-fluorescein	5′-ACTACTGGGTTCTGGC-3′, ethidium bromide	fluorescence	81
NOR	BSA/MPA-AuNCs	Fe^{2+}, Fe^{3+}	emission under UV	80
INHIBIT	GO[r]/ABA[s]/TBA[t] complex	ATP[u], PDNA[v]/ trombine, PDNA	fluorescence	82
	5′-GCCAGAACCCAGTAGT-3′-fluorescein	5′-ACTACTGGGTTCTGGC-3′, Hoechst 33342, ethidium bromide	fluorescence	48

[a]PLL: poly-L-lysine. [b]CS: chondroitin sulfate. [c]P4VP: poly(4-vinylpyridine). [d]Est: esterase. [e]GOx: glucose oxidase. [f]P2VP: poly(2-vinylpyridine). [g]PS-b-P4VP-b-PEO: poly(styrene block 2 vinylpyridine block ethylene oxide) triblock copolymer. [h]PAA: poly(acrylic acid). [i]PEI: polyethylenimine. [j]pDADMAC: poly(diallyldimethylammonium chloride). [k]pAMPSA: poly(2-acrylamido-2-methyl-1-propanesulfonic acid). [l]Inv: invertase. [m]Ur: urease. [n]HRP: horseradish peroxidase, [o]Mut: methylmalonyl-CoA mutase. [p]BVA: bovine serum albumin. [q]MPA-AuNCs: mercaptopropionic acid−gold nanoclusters. [r]GO: graphene oxide. [s]ABA: 6-carboxy-fluorescein (FAM)-labeled adenosine triphosphate binding aptamer. [t]TBA: FAM-labeled thrombin binding aptamer. [u]ATP: adenosine triphosphate. [v]PDNA: FAM-free aptamer.
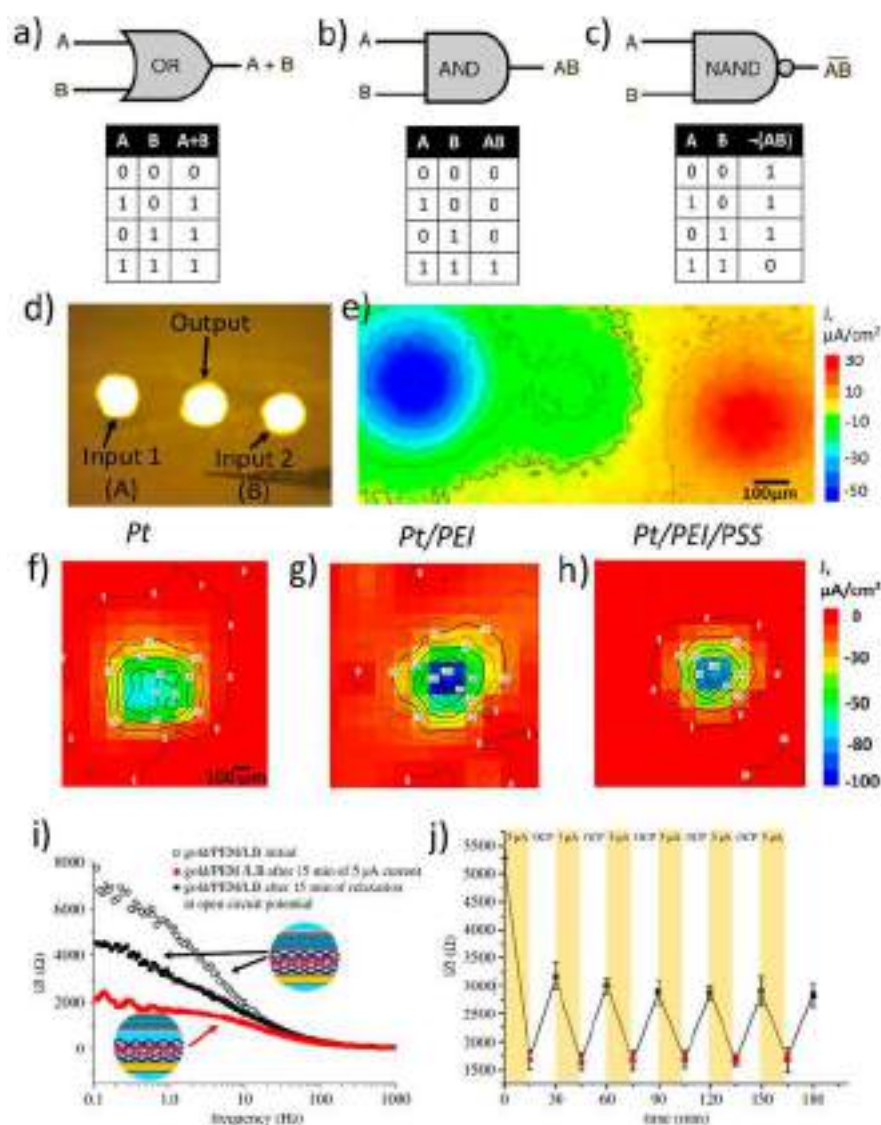
Figure 6. Basic logic gates and corresponding truth tables: (a) OR gate, (b) AND gate, (c) NAND gate, and (d) system of three gold electrodes embedded in an epoxy holder as a protopype of chemical computing iontronic device. Ion currents mapped by SVET in solution: (e) ion currents mapped by SVET in solution when positive and negative potentials are applied to input electrodes from panel d. Ion currents mapped by SVET in solution over an electrode under a negative potential bias: (f) bare Pt electrode, (g) Pt/PEI electrode, (h) Pt/PEI/PSS electrode, (i) impedance curves of both plots of impedance spectra for the gold/PEM/LB composite before passing 5 μA current, after 15 min of current passing, and after 15 min of relaxation, and (j) cycles of passing current and relaxation at open circuit potential associated with impedance oscillations at 1 Hz of the gold/PEM/LB composite due to lipid bilayer repulsion in acidified media via hydroquinone oxidation. Adapted from refs 62 and 35.

poly{[2-(methacryloyloxy)ethyl] trimethylammonium iodide} (PMETAI) star polyelectrolyte and poly(sodium 4-styrenesulfonate) (PSS) were prepared by an LbL technique.

Light-healing material (Figure 5c) is suggested by light−pH coupling.[20] The chitosan protection function against the supramolecular disassembly deposited on the surface of TiO₂ has been demonstrated[18] (Figure 5d). The combination of triaminopyrimidine (TAP) and cyanuric acid modified with a hexanoic acid side chain (CyCo6) is known to be reversely assembled−disassembled depending on pH. In our work, we showed that the assembly being deposited onto the TiO₂/chitosan surface after irradiation remained on the surface without destruction and disassembly. This confirms the hypothesis that the chitosan works as a buffering protective layer for trapping photogenerated H⁺.

LOGIC GATES

The proton generation via water splitting or hydroquinone oxidation for electrochemical process was studied using SVET/SIET.[35] The role of electrode modification by PEs for both photochemistry and electrochemistry was discussed.[62] PEs can regulate charge transfer on an inorganic surface. The rules of electrode coupling and inputs 1 and 2 vs output are planned for the photochemical process for logic operation. Notwithstanding, precise modeling is still a challenge, and several materials with electrochemical outputs were designed on the basis of polyelectrolyte LbL-assemblies and hydrogel films (Table 1). Thus, it is possible to regulate ion flux through polyelectrolyte membranes.

The generation of ion gradients on demand is an important task for electrochemistry. For example, proton fluxes may be

produced by electrochemical water splitting or hydroquinone oxidation.[63] The simplest example of information operating is switching functions according to Boolean logic using binary inputs and producing single binary output logic gates (Figure 6a−c). Various enzymatic logic gates yield an acidic medium as output. Shifting the medium back to neutral values enables one to reset the calculation results.[64−67] It also works in the reverse direction, using pH as input, with an electrochemical response that could be triggered according to Boolean logic. Several logic systems with electrochemical output were designed using polyelectrolyte LbL assemblies, hydrogel films, and grafted polymer brushes.[68−70] Microchip-based polyelectrolyte diodes poly(diallyldimethylammonium chloride)/poly(2-acrylamido-2-methyl-1-propanesulfonic acid) representing AND, OR, and NAND logic circuits were designed. Their functions are based on regulated ion transportation through the polyelectrolyte interface.[71]

Here we present (Figure 6d,e) materials that allow us to perform simple Boolean operations using ions as input or/and output signals.[70] Our model includes electrodes made of noble metals (Au or Pt) spatially organized in special way and immersed in an electrolyte solution where some electroactive probes may be introduced. By applying positive and negative potentials to electrodes, one is able to perform water splitting reactions or another pH-coupled redox processes. Herewith, oxidation and reduction processes may be spatially separated. As a result, the distribution of acidic and basic regions in solution that is close to the electrode surface may be realized in a special manner (Figure 6e). Furthermore, one of the electrodes may be assigned to the reading of electrochemical output. The electrochemical acidity change in the media may increase the activity of the "output electrode" toward the electrochemical probe if the electrode surface is modified by the pH-sensitive LbL assembly or polymer brush.

The current intensity of the oxidation or reduction of the electrochemical probe is registered as an output signal. In other words, in terms of logic gates input signals here are potential applied to a set of electrodes. Potential values higher than some cutoff are assigned as "1" input, and lower values are assigned as "0" input. Faradaic current registered at the output electrode above a certain threshold is assigned as "1", and lower values are assigned as "0". For example, poly(4-vinylpyridine) (P4VP) chains grafted to the electrode surface undergo a conformational change in the acidified surrounding medium. The permeability switches from the blocking regime to the previous regime, and an increase in output electrode activity is noticed.[72−74] A similar phenomenon was observed when the outermost layer of the polyelectrolyte assembly was presented by molecule turning from positive to negative at pH conditions changing from acidic to basic and vice versa.[74] Building blocks for such systems are not limited to pH-sensitive molecules. Structure changes may also be induced by complexation. Fortunately, LbL modification of the electrode surface provides an opportunity for the encapsulation of different chemicals and their release on demand. In summarizy, our future research direction will be focused on different geometries of input electrode arrays, varying applied potentials, and regimes of potential applications.

The surface of a noble metal electrode (Figure 6f−h) was subsequently modified by nanometer thin layers of polycation polyethylenimine (PEI) and polyanion poly(sodium 4-styrenesulfonate) (PSS). PEI is a proton sponge which stores electrochemically generated protons, whereas the PSS layer

serves as a cation exchange layer. The electrode was first covered by branched PEI to provide strong anchoring to the surface and to act as a positively charged terminating layer. The deposition of PSS was electrostatically driven by a underlying layer. Although the polymer multilayer assembly led to no change in redox processes at the electrode/electrolyte interface, both the anodic and cathodic activity of the Pt electrode measured by SVET[75] was higher for the polyelectrolyte-coated electrode than for a bare one. The gradient of released ions is characterized by a narrower spatial distribution, but if the polyelectrolyte membrane is relatively thick, then ion flux from the surface is suppressed.[35] There are various self-consistent theoretical descriptions of processes occurring in polyelectrolyte interfaces, but they are still not completely understood and there is still no general theory precisely predicting the effect of polyelectrolyte modification on electrode activity.

Until now, multicomponent coatings formed by multilayers of different polyelectrolyte compositions (strong−strong, strong−weak, weak−weak) had already been analyzed as nanolayers for corrosion protection. The mechanism of multilayer protective action is based on pH buffering polybase and polyacid complexes.[27,30] It was also demonstrated that polyelectrolyte layers can be used as an efficient pH-buffering protective layer for pH-sensitive soft materials.[76] By combining PEs of different molecular weights and strengths and containing different specific functional moieties, one can flexibly tune the spatial and temporal distribution of ionic fluxes through the membrane and perform independent handling by cations and anions. That fact opens prospects for developing futuristic biomimetic information processing using ions and molecules as signal carriers. A lot of effort has been made until now to develop alternative paths to information processing which are not based on solid-state electronics such as molecular logic gates[77] and DNA computing.[65]

Ryzhkov et al.[35] studied the proton generation on electrodes using in situ SVET, SIET, and electrochemical impedance spectroscopy (EIS) (Figure 6i). These methods are powerful instruments for the in situ observation of reversible processes in the multilayers (e.g., PEs and lipid bilayer/inorganic solid support interface (Figure 6i (insets)). EIS showed the reversible attachment/detachment of the lipid bilayer under acidic conditions as well as electrochemical proton release on the gold electrode due to hydroquinone oxidation (Figure 6j).

In situ studies of transmembrane channels often require a free-standing artificial analogue to biomembranes. Obtaining free-standing lipid membranes is still a challenge. In ref 35, the authors used an electrochemical approach for lipid bilayer detachment from a solid support via hydroquinone oxidation. LbL deposition of PEI and PSS on a gold electrode was performed to obtain a polymeric nanocushion of $[PEI/PSS]_3/$ PEI. The lipid bilayer was electrostatically deposited on the top of an underlaying polymer support from the dispersion of small unilamellar vesicles. Because lipid zwitterions demonstrate a pH-dependent surface charge density, the interactions between the polyelectrolyte support and the lipid bilayer can be regulated by pH. The recharging of lipid molecules can be also used for the design of materials with logic gates either individually or in the presence of enzyme.

Different enzymes are widely used as input signals in molecular logic gates. A logic network can be composed of three AND gates and an OR gate. Alcohol dehydrogenase,

glucose dehydrogenase, and glucose oxidase are three enzymes with gate functions. Nicotinamide adenine dinucleotide (NADH), acetaldehyde, glucose, and oxygen are four different inputs. The "successful" set of inputs, according to the logic scheme, yields an acidic medium and therefore increases the activity of the electrode modified by a pH-sensitive polymer brush and the current intensity of oxidation of the electrochemical probe.[67−70]

In ref 47, invertase and glucose oxidase or esterase and glucose oxidase were employed as inputs in AND and OR chemical computing networks, respectively. The logic gate here is the P4VP-modified ITO electrode. The positive output also gives a decrease in pH and a conformational change in the P4VP grafted to the electrode that leads to an increase in electrode activity. Urease enables one to reset the calculation results.[64,66]

Three input logic networks were designed using a poly(N,N-diethylacrylamide)-(poly(acrylic acid)-phenylboronic acid (PDEA-(PAA−PBA))-modified electrode with entrapped horseradish peroxidase (HRP). Inputs are pH, temperature, and fructose in solution. The pH sensitivity is attributed to the electrostatic interaction between the PAA and the electrochemical probe in solution at different pH values; the thermoresponsive behavior is attributed to a structural change in PDEA with temperature, and the fructose sensitivity is related to a structural change induced by the complexation between the PBA constituent and the sugar in solution. Thus, the electrochemical reduction of H_2O_2 catalyzed by HRP in the films and mediated by $K_3Fe(CN)_6$ in solution could be triggered according to Boolean logic of the presented scheme.[68]

The reduced graphene oxide/poly(N-isopropylacrylamide) (rGO/PNIPAA) composite electrode shows pH-, temperature-, and sulfate-sensitive behavior using ferrocene dicarboxylic acid ($Fc(COOH)_2$) oxidation. Responsive behavior for this system was mainly attributed to the transformation between rGO and GO in the films at different potentials. On the basis of this, a four-input-enabled OR (EnOR) logic gate network was established.[50] Analogous Boolean AND logic was realized using the (PAH/PAA)$_4$-(PDEA-HRP) multilayer.[69]

The biomimicking AND logic gate with a fluorescence response was designed. The simultaneous presence of both input signals ALT and AST runs the biocatalytic cascade with citrate as a final product. Citrate induces the dissolution of the alginate microspheres with loaded fluorescent dye.[77] Hence, smart drug delivery can be performed.

Smart release was also shown for species encapsulated in multilayers. OR and AND logic gates were designed. A PLL/DNA multilayer was employed as the OR logic gate for trypsin and Dnase I inputs. The introduction of PEI and PAA layers changes the type of gate to AND for the same inputs. Thus, Boolean logic gates capable of simultaneously sensing proteases and nucleases were suggested.[78]

Materials where the aggregation and dissociation of nanoparticles obey the Boolean logic of simple AND and OR gates were demonstrated.[79] Nanoparticles covered by poly(2-vinylpyridine) (P2VP) undergo protonation/deprotonation depending on the pH. The surface charge of the polymer shell changes from neutral to positive by the protonation and dissociation of particle aggregates. A pH change is produced here by the enzyme logic gate and happens in the presence of both glucose oxidase (GOx) and invertase in the case of the sucrose gate (AND logic) and in the presence

of GOx and esterase in the case of the ethyl-butirate-glucose gate (OR logic). The addition of urea gives the possibility to reset the system using urease.

Gold nanoclusters modified by bovine serum albumin/3-mercaptopropionic acid (BSA/MPA) were demonstrated to be a universal platform for creating Boolean gates with various types of logic. The same platform is able to demonstrate NAND, NOR, and IMPLICATION behavior depending on the input signals.[80]

Chemical computing based on performing simple logic operations provides a unique platform for detection systems. The AND−INH logic gate was suggested for trombine detection.[76] Much research is devoted to the design of DNA-based logic gates.[78,81,82]

Microchip-based polyelectrolyte diodes formed by poly(diallyldimethylammonium chloride)/poly(2-acrylamido-2-methyl-1-propanesulfonic acid) (pDADMAC/pAMPSA) showed AND, OR, and NAND logic circuits.[83]

The reversible inversion of emulsions was suggested to be an output signal of AND and OR enzymatic logic gates,[84] producing a pH shift in the water phase. The emulsion is stabilized by nanoparticles modified by a pH-sensitive polymer, and the water/oil emulsion is switched to oil/water as a positive response to the enzymatic gate. There are more examples in Table 1.

With respect to the perspectives of light-driven chemical information processing, the next step is the shifting focus from electrochemical inputs to incoming light signals. Light is considered to be the most efficient method of communication between chemical logic gates. One of the concepts combining iontronics technology and light-driven programmable logic gates is light−pH coupling. This phenomenon of the conversion of electromagnetic energy into an ion gradient may be realized on semiconductor surfaces as described above, and logic operation is not limited to electrochemical approaches but can be realized using light-regulated processes.

■ SELF-REGULATED SYSTEMS

Among the tendencies of smart material design, self-regulated materials and processes at interfaces play important roles in self-cleaning, self-healing, anticorrosion, autocatalysis, and antifouling. The following aspects should be addressed for the successful construction of materials with particular functionalities: (i) the choice of a material and its environment; (ii) the stability of the material under different environmental conditions; (iii) the mechanism of its degradation; (iv) strategies for the improvement of the material properties (e.g., stability); and (v) an attempt to make materials self-responsive. In this article, we discuss self-healing and self-cleaning materials and autocatalytic network design.

Self-healing materials can be attributed to the class of advanced materials due to the possibility to control feedback processes.[28] First, the nature of interfacial processes triggered by the local environment is important (e.g., a change in pH during the corrosion process).[11] Second, it is important to find proper PEs that could be useful for the stabilization ("healing") of the inorganic component damaged by the environment. Weak PEs are sensitive to pH changes and can selectively bind protons (e.g., chitosan and PEI).[18,86] The composition of the polymer multilayers is very important. For instance, the LbL approach can be used to optimize the architecture of the layers to provide both the effect of pH buffering and improved

material stability.[30] Self-healing has a broad spectrum of applications including corrosion protection,[86] elements of antifouling and antimicrobial coatings,[87] and bioinspired superhydrophobic interfaces.[88]

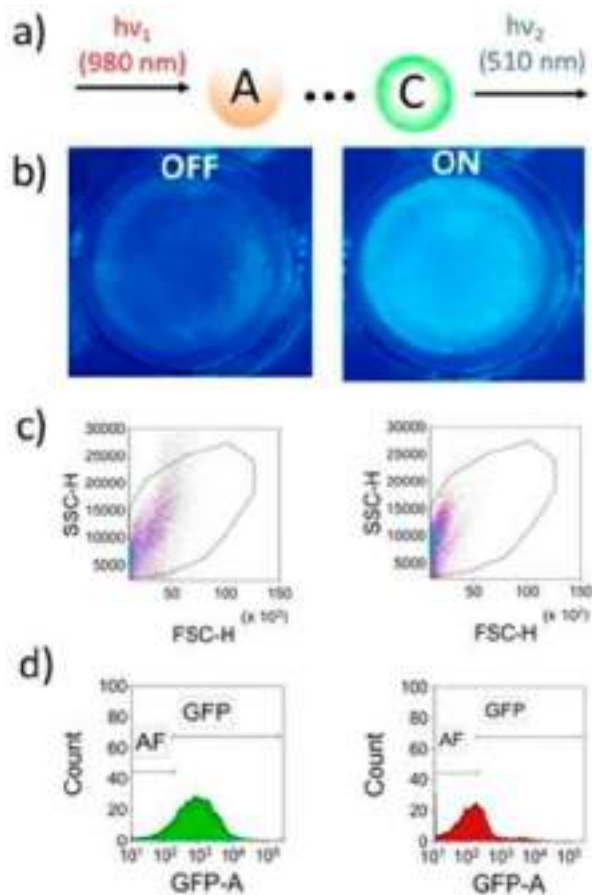Combined approaches have also been considered. In Figure 7, an example of a titania-based capsule (A) for the light-

Figure 7. (a) Scheme of *E. coli* XL-1 blue pBAD-GFPuv fluorescence activation by opened TiO$_2$/Ag/PE containers. (b) Inverse microscope image of *E. coli* XL-1 blue cultivated for 4 h on semiliquid agar with embedded TiO$_2$/Ag/PE containers before (left image) and after (right images) IR irradiation (wavelength, 980 nm; power, 2000 mV). (c, d) Cell fluorescence of GFP in a system with "closed" (left) and "open" (right) PE containers after incubating for 7 h. Adapted from ref 37, American Chemical Society.

stimulated (980 nm) delivery of chemical species is shown,[37] and bacterial metabolism (C) has feedback mechanisms which switch their fluorescence at 510 nm. In recent work by Nikitina et al.,[37] a new contribution to the design of PE capsules based on surface-modified mesoporous titania particles with deposited Ag nanoparticles to achieve chemical light up-conversion via biofilms is shown (Figure 7). The PE shell allows the slowing of the release kinetics of loaded L-arabinose and the switching of bacterial luminescence in a certain time. The hybrid TiO$_2$/Ag/PE capsule activated at 980 nm (IR) illumination demonstrated a 10 times faster release of L-arabinose as opposed to nonactivated containers. Fast IR-released L-arabinose switched the bacterial fluorescence which we monitored at 510 nm. The approach described herein can be used in many applications where targeted and delayed switching and light upconversion are required. Such complex

materials are very important for complex chemical network integration with biological networks such as enzymatic networks,[38] bacterial quorum sensing,[89] and synthetic biology,[90] suggesting them to be one working reaction network.

Enzymatic reactions can also be controlled using the light–pH coupling phenomenon. Surface modification by enzymes allows us to achieve affinity and improve the biological response of bioinert surfaces. The experiments with osteoblasts demonstrated that a titanium implant surface functionalized by a polyelectrolyte–enzyme interface had higher cell viability and triggered an osteogenic response.[91] Stimuli-responsive bio-interfaces open perspectives to smart materials for tissue engineering. Thus, the formation of trypsin from its precursor trypsinogen was chosen as an example of the pH-sensitive autocatalytic enzymatic reaction and was studied on the TiO$_2$/PSS/PEI hybrid and TiO$_2$ surface as a control[38] (Figure 8). The results indicated that the acidification of the media near pristine TiO$_2$ was the most possible explanation of trypsin suppressed formation in comparison to the hybrid system. In the latter case, the adsorption of trypsin was higher in comparison to that of pure TiO$_2$; however, it was less affected by the autocatalytic enzymatic reaction. Thus, varying the position of the polyelectrolyte layer in the LbL assembly can be served as an easy method of tuning the hybrid system's photoactivity.

Nowadays two important features, (i) bacterial metabolism regulation and stimulation and (ii) bacterial degradation due to a lethal concentration of reactive oxygen species (ROS), are being intensively discussed. It was shown[92] that because of the superoxide lifetime of ca. 20 min on the irradiated titania surface, the ROS is able to diffuse through the mesoporous film. The ROS photogenerated on titania could further penetrate the intracellular volume and alter the activity of the microorganisms. Both the photokilling of bacteria and profound changes in their metabolism can be attained depending on the exposures used. We are interested in changing the metabolism without bacterial deactivation. In our previous work it has been shown[92] that ROS produced on the titania surface effectively induces lytic cycles of lysogenic bacteria without killing them. To enhance the superoxide yield and bacterial adhesion, bimetallic Ag/Ni nanoparticles can be deposited in the pores of a titania film.[1] The main objective in this field of research is to develop programmable materials which interact with bacteria growing on the materials, posing the following questions: (i) What type of chemistry is suitable for communication with bacteria? (ii) How is two-sided communication designed (i.e., the processing of signals coming from both the bacterial signaling network and the synthetic chemical network)? (iii) How can synthetic chemistry influence and respond to bacterial activity?

Reversible oscillation of LbL films based on the high-amplitude actuation of BCM allows us to control cell behavior on the surface. Ulasevich et al. have successfully applied the switching of polyelectrolyte assembly by light[16] to control the behavior of supported cells.[14] In particular, the change in stiffness results in the migration of cells to a harder surface. A systematic study of the nanoscale surface design is needed to program significant bioresponses. BCM polyelectrolyte brushes adsorbed on the mesoporous surface demonstrated[93] an affective self-cleaning property of lactic bacteria. Lactic bacteria produced lactic acid and activated BCM: the polymer coating increased in its thickness and pushed the bacteria out of the
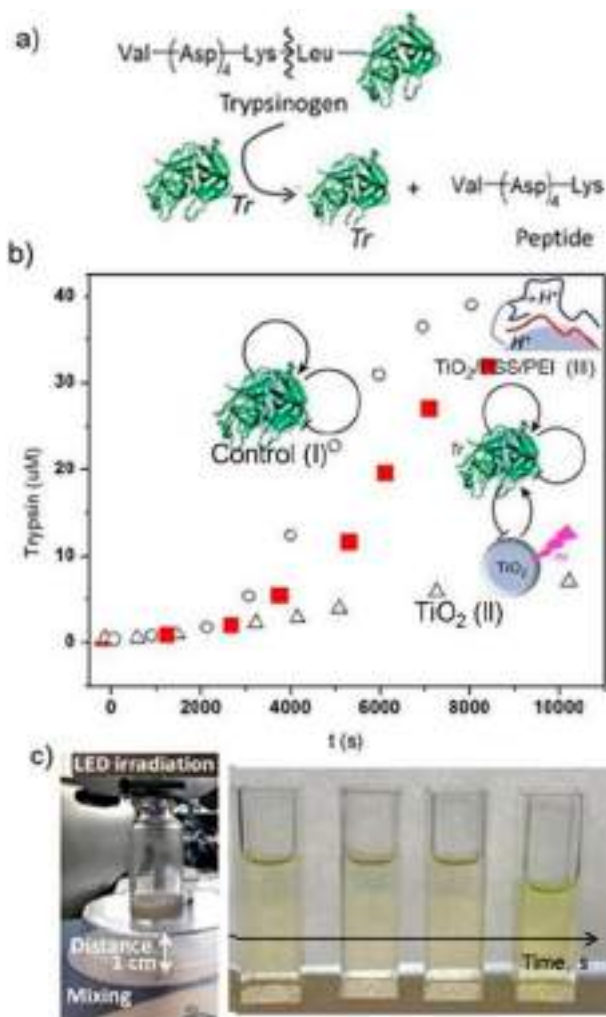
Figure 8. (a) Schematic of autocatalytic Tr-catalyzed Tg decomposition. (b) Conversion of the fluorogenic substrate monitored at λ_{ex} = 450 nm and λ_{em} = 520 nm. Each point is checked for 60 s with a time interval of 1 s, (I) for the Tr control reaction and reaction in the presence of (II) TiO$_2$ or (III) TiO$_2$/PSS/PEI under irradiation. (c) Photograph of (left) the reactor pointing to the glass flask spatially separated from the surface to decrease the effect of the temperature increase and (right) reaction monitoring over time, with the autocatalytic increase in fluorescence in test cuvettes. Adapted from ref 38, Wiley.

surface (Figure 9). In the discussed paper,[93] the authors focused on the synergy between feedback material and living bacteria that can be deactivated and more interestingly survive and interact with the feedback system in a predictive way. The lactic bacteria could reversibly be activated/deactivated on the surface as a result of the cyclic metabolic process in their life cycle.

CONCLUSIONS AND OUTLOOK

In the current article, only some examples of the types of materials and devices based on LbL assemblies are considered, which could be created within the research led by Prof. Möhwald. Prof. Möhwald said that the major motivation of the research was to understand internal interfaces in colloid systems and the elucidation of underlying mechanisms. Inspired by Prof. Möhwald, it is necessary to focus our efforts on the formal description of the materials, their combination,
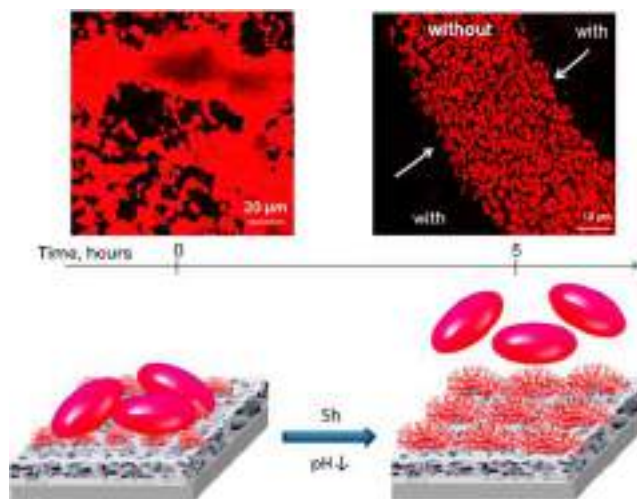
Figure 9. Confocal kinetic study (fluorescence mode) and schematic illustration of the pH-triggered self-cleaning behavior of the porous metal surface covered with pH-responsive micelles. As model cells, *Lactococcus lactis* 411 (*L. lactic*) bacteria (loaded with dye) were used. Bacteria decrease the pH, micelles respond to changes and increases in size, and bacteria detach from the surface, remaining just on surface without micelles. Adapted from ref 93, Wiley.

and their interaction with external stimuli and modeling. It is important to create a simple formalism which would allow the accessible transformation of the required logic and functions of the materials to the actual synthesis of the material (material genetics and logic). Novel artificial composites based on LbL assemblies that can mimic biofunctions, namely, stimuli-responsive behavior, are needed. Such composites should be composed of different classes of materials. Because of the unique architecture and synergy of the components, the possibility to achieve learning and self-adapting capabilities at the material level can be predicted. In such materials, even a small environmental perturbation might trigger pronounced structural and morphological changes. Layer-by-layer assemblies are built from hundreds of highly dynamic interfaces that might be extremely sensitive to environmental changes in the physiological range. At the macrolevel, the synergetic operation of all components allows the switch on/off functions on demand. Examples of the applications that can be targeted include, but are not limited to, self-healing, corrosion and photocorrosion protection, antifouling, antimicrobial coatings, stimuli-responsive membranes with logic gates, smart substrates for cell manipulation on demand and tissue nano-engineering, drug delivery, sensors, actuators and binders for implants, components of wearable electronics, and soft-power electronics.

AUTHOR INFORMATION

Corresponding Author
*E-mail: skorb@corp.ifmo.ru.
ORCID
Ekaterina V. Skorb: 0000-0003-0888-1693
Notes
The authors declare no competing financial interest.

ACKNOWLEDGMENTS

■ REFERENCES

(1) Skorb, E. V.; Antonouskaya, L. I.; Belyasova, N. A.; Shchukin, D. G.; Möhwald, H.; Sviridov, D. V. Antibacterial activity of thin-film photocatalysts based on metal-modified TiO_2 and TiO_2:In_2O_3 nanocomposite. *Appl. Catal., B* **2008**, *84*, 94−99.

(2) Skorb, E. V.; Shchukin, D. G.; Möhwald, H.; Sviridov, D. V. Photocatalytically-active and Photocontrollable Coatings Based on Titania-loaded Hybrid Sol-Gel Films. *J. Mater. Chem.* **2009**, *19*, 4931−4937.

(3) Skorb, E. V.; Antonouskaja, L. I.; Belyasova, N. A.; Sviridov, D. V. Photocatalysts for ecological disinfection based on titania modified by nanosilver particles. *Industry Catalysis* **2009**, *2*, 53−59.

(4) Skorb, E. V.; Skirtach, A.; Sviridov, D. V.; Shchukin, D. G.; Möhwald, H. Smart" Laser-Controllable Coatings for Corrosion Protection. *ACS Nano* **2009**, *3*, 1753−1760.

(5) Skorb, E. V.; Fix, D.; Andreeva, D. V.; Shchukin, D. G.; Möhwald, H. Surface Modified Mesoporous SiO_2 Containers for Corrosion Protection. *Adv. Funct. Mater.* **2009**, *19*, 2373−2379.

(6) Skorb, E. V.; Sviridov, D. V.; Möhwald, H.; Shchukin, D. G. Light-Controllable Nanocontainer-Coatings for Corrosion Healing. *Chem. Commun.* **2009**, 6041−6043.

(7) Grigoriev, D. O.; Köhler, K.; Skorb, E. V.; Shchukin, D. G.; Möhwald, H. Polyelectrolyte Complexes as "Smart" Depot for Self-Healing Anticorrosion Coatings. *Soft Matter* **2009**, *5*, 1426−1432.

(8) Skorb, E. V.; Shchukin, D. G.; Möhwald, H.; Andreeva, D. V. Ultrasound driven design of metal surfaces. *Nanoscale* **2010**, *2*, 722−727.

(9) Kopf, J.; Ulasevich, S. A.; Baidukova, O.; Zhukova, Y.; Dunlop, J. W. C.; Fratzl, P.; Rikeit, P.; Knaus, P.; Poznyak, S. K.; Andreeva, D. V.; Skorb, E. V. Ultrasonically produced porous sponge layer on titanium to guide cell behavior. *Adv. Eng. Mater.* **2016**, *18*, 476−483.

(10) Skorb, E. V.; Andreeva, D. V. Bio-inspired ultrasound assisted construction of synthetic sponges. *J. Mater. Chem. A* **2013**, *1*, 7547−7557.

(11) Skorb, E. V.; Andreeva, D. V. Surface nanoarchitecture for bio-applications: self-regulated intelligent surfaces. *Adv. Funct. Mater.* **2013**, *23*, 4483−4506.

(12) Skorb, E. V.; Möhwald, H. Dynamic Interfaces for Responsive Encapsulation Systems. *Adv. Mater.* **2013**, *25*, 5029−5043.

(13) Skorb, E. V.; Möhwald, H. Smart" surface capsules for delivery devices. *Adv. Mater. Interfaces* **2014**, *1*, 1400237.

(14) Ulasevich, S. A.; Brezhneva, N.; Zhukova, Y.; Möhwald, H.; Fratzl, P.; Schacher, F. H.; Sviridov, D. V.; Andreeva, D. V.; Skorb, E. V. Switching the Stiffness of Polyelectrolyte Assembly by Light to Control Behavior of Supported Cells. *Macromol. Biosci.* **2016**, *16*, 1422−1431.

(15) Zhukova, Z.; Ulasevich, S. A.; Dunlop, J.; Fratzl, P.; Möhwald, H.; Skorb, E. V. Ultrasound-driven titanium modification with formation of titania based nanofoam surfaces. *Ultrason. Sonochem.* **2017**, *36*, 146−154.

(16) Ulasevich, S. A.; Brezesinski, G.; Möhwald, H.; Fratzl, P.; Schacher, F. H.; Poznyak, S. K.; Andreeva, D. V.; Skorb, E. V. Light-Induced Water Splitting Causes High-Amplitude Oscillation of pH-Sensitive Layer-by-Layer Assemblies on TiO_2. *Angew. Chem., Int. Ed.* **2016**, *55*, 13001−13004.

(17) Skorb, E. V.; Möhwald, H. Ultrasonic approach for surface nanostructuring. *Ultrason. Sonochem.* **2016**, *29*, 589−603.

(18) Andreeva, D. V.; Kollath, A.; Brezhneva, N.; Sviridov, D. V.; Cafferty, B. J.; Möhwald, H.; Skorb, E. V. Using a chitosan nanolayer as an efficient pH buffer to protect pH-sensitive supramolecular assemblies. *Phys. Chem. Chem. Phys.* **2017**, *19*, 23843−23848.

(19) Brezhneva, N.; Nikitina, A.; Ryzhkov, N.; Klestova, A.; Vinogradov, A. V.; Skorb, E. V. Importance of buffering nanolayer

(20) Ulasevich, S. A.; Melnyk, I.; Andreeva, D. V.; Möhwald, H.; Skorb, E. V. Photomobility and photohealing of cellulose-based hybrids. *EPL.* **2017**, *119*, 38003.

(21) https://scamt.ifmo.ru/science/groups/infochemistry-of-self-organizing-systems/, accessed 03.03.2019.

(22) Decher, G. Fuzzy Nanoassemblies: Toward Layered Polymeric Multicomposites. *Science* **1997**, *277*, 1232−1237.

(23) Donath, E.; Sukhorukov, G. B.; Caruso, F.; Davis, S. A.; Möhwald, H. Novel hollow polymer shells by colloid-templated assembly of polyelectrolytes. *Angew. Chem., Int. Ed.* **1998**, *37*, 2201−2205.

(24) Lvov, Y.; Decher, G.; Möhwald, H. Assembly, structural characterization, and thermal behavior of layer-by-layer deposited ultrathin films of poly (vinyl sulfate) and poly (allylamine). *Langmuir* **1993**, *9*, 481−486.

(25) Ryzhkov, N. V.; Brezhneva, N.; Skorb, E. V. Feedback mechanisms at solid/polyelectrolyte interfaces for applied materials *Surf. Innovations* **2019**, *1*, .

(26) Whitesides, G. M. Toward a science of simplicity, *TED Talk* https://www.youtube.com/watch?v=GayY-mjZXrQ, dated 03.03.**2019**.

(27) Skorb, E. V.; Andreeva, D. V. Self-Healing Properties of Layer-by-Layer Assembled Multilayers. *Polym. Int.* **2015**, *64*, 713−723.

(28) Skorb, E. V.; Volkova, A.; Andreeva, D. V. Layer-by-layer assembled hybrid materials for sustainable applications. *Curr. Org. Chem.* **2014**, *18*, 2315−2333.

(29) Andreeva, D. V.; Fix, D.; Möhwald, H.; Shchukin, D. G. Self-healing anticorrosion coatings based on pH-sensitive polyelectrolyte/inhibitor sandwichlike nanostructures. *Adv. Mater.* **2008**, *20*, 2789−2794.

(30) Andreeva, D. V.; Skorb, E. V.; Shchukin, D. G. Layer-by-layer Polyelectrolyte/Inhibitor Nanostructures for Metal Corrosion Protection. *ACS Appl. Mater. Interfaces* **2010**, *2*, 1954−1962.

(31) Fares, H. M.; Schlenoff, J. B. Diffusion of Sites versus Polymers in Polyelectrolyte Complexes and Multilayers. *J. Am. Chem. Soc.* **2017**, *139*, 14656−14667.

(32) Maltanava, H.; Poznyak, S. K.; Andreeva, D. V.; Quevedo, M. C.; Bastos, A. C.; Tedim, J.; Ferreira, M. G. S.; Skorb, E. V. Light induced proton pumping with a semiconductor: vision for Photo-Proton lateral separation and robust manipulation. *ACS Appl. Mater. Interfaces* **2017**, *9*, 24282−24289.

(33) Shchukin, D. G.; Andreeva, D. V.; Skorb, E. V.; Möhwald, H. Emerging concepts in interfacial chemistry of hybrid materials. In *Supramolecular Chemistry of Hybrid Materials*; Rurack, K., Ed.; Wiley-VCH: Germany, 2010; pp 639−653.

(34) Grzybowski, B. A.; Huck, W. T. S. The nanotechnology of life-inspired systems. *Nat. Nanotechnol.* **2016**, *11*, 585−592.

(35) Ryzhkov, N. V.; Mamchik, N. A.; Skorb, E. V. Electrochemical triggering of lipid bilayer lift off oscillation at the electrode interface. *J. R. Soc., Interface* **2019**, *16*, 20180626.

(36) Zhukova, Y.; Skorb, E. V. Cell guidance on nanostructured metal based surfaces. *Adv. Healthcare Mater.* **2017**, *6*, 1600914.

(37) Nikitina, A. A.; Ulasevich, S. A.; Kassirov, I. S.; Bryushkova, E. A.; Koshel, E. I.; Skorb, E. V. Nanostructured Layer-by-Layer Polyelectrolyte Containers to Switch Biofilm Fluorescence. *Bioconjugate Chem.* **2018**, *29*, 3793−3799.

(38) Lanchuk, Y.; Nikitina, A.; Brezhneva, N.; Ulasevich, S. A.; Semenov, S. N.; Skorb, E. V. Photocatalytic Regulation of an Autocatalytic Wave of Spatially Propagating Enzymatic Reactions. *ChemCatChem* **2018**, *10*, 1798−1803.

(39) Thomas, S. W.; Chiechi, R. C.; LaFratta, C. N.; Webb, M. R.; Lee, A.; Wiley, B. J.; Zakin, M. R.; Walt, D. R.; Whitesides, G. M. W. Infochemistry and infofuses for the chemical storage and transmission of coded information. *Proc. Natl. Acad. Sci. U. S. A.* **2009**, *106*, 9147−9150.

(40) Kim, C.; Thomas, S. W.; Whitesides, G. M. Long-duration transmission of information with infofuses. *Angew. Chem., Int. Ed.* **2010**, *49*, 4571−4575.

(41) Palacios, M. A.; Benito-Peña, E.; Manesse, M.; Mazzeo, A. D.; LaFratta, C. N.; Whitesides, G. M.; Walt, D. R. InfoBiology by printed arrays of microorganism colonies for timed and on-demand release of messages. *Proc. Natl. Acad. Sci. U. S. A.* **2011**, *108*, 16510−16514.

(42) Fuerstman, M. J.; Garstecki, P.; Whitesides, G. M. Coding/decoding and reversibility of droplet trains in microfluidic networks. *Science* **2007**, *315*, 828.

(43) *Infochemistry: Information Processing at the Nanoscale*; Szaciłowski, K., Ed.; Wiley, 2012.

(44) Gizynski, K.; Gorecki, J. Chemical memory with states coded in light controlled oscillations of interacting Belousov−Zhabotinsky droplets. *Phys. Chem. Chem. Phys.* **2017**, *19*, 6519−6531.

(45) Smelov, P. S.; Vanag, V. K. A 'reader' unit of the chemical computer. *R. Soc. Open Sci.* **2018**, *5*, 171495.

(46) Löhmann, O.; Zerball, M.; von Klitzing, R. Water uptake of polyelectrolyte multilayers including water condensation in voids. *Langmuir* **2018**, *34*, 11518−11525.

(47) Zhang, R.; Duan, X.; Ding, M.; Shi, T. Molecular Dynamics Simulation of Salt Diffusion in Polyelectrolyte Assemblies. *J. Phys. Chem. B* **2018**, *122*, 6656−6665.

(48) Dautzenberg, H.; Jaeger, W.; Kötz, J.; Philipp, B.; Seidel, C. H.; Stscherbina, D. *Polyelectrolytes: Formation, Characterization and Applications.*; Hanser: Munich, 1994.

(49) Boroudjerdi, H.; Kim, Y. W.; Naji, A.; Netz, R. R.; Schlagberger, X.; Serr, A. *Phys. Rep.* **2005**, *416*, 129−199.

(50) Kelly, K. D.; Fares, H. M.; AbouShaheen, S.; Schlenoff, J. B. Intrinsic Properties of Polyelectrolyte Multilayer Membranes: Erasing the Memory of the Interface. *Langmuir* **2018**, *34*, 3874−3883.

(51) Nakouzi, E.; Fares, H. M.; Schlenoff, J. B.; Steinbock, O. Polyelectrolyte complex films influence the formation of polycrystalline micro-structures. *Soft Matter* **2018**, *14*, 3164−3170.

(52) Boyaciyan, D.; Braun, L.; Löhmann, O.; Silvi, L.; Schneck, E.; von Klitzing, R. Gold nanoparticle distribution in polyelectrolyte brushes loaded at different pH conditions. *J. Chem. Phys.* **2018**, *149*, 163322.

(53) Fu, J.; Fares, H. M.; Schlenoff, J. B. Ion-pairing strength in polyelectrolyte complexes. *Macromolecules* **2017**, *50*, 1066−1074.

(54) Ghoussoub, Y. E.; Zerball, M.; Fares, H. M.; Ankner, J. F.; von Klitzing, R.; Schlenoff, J. B. Ion distribution in dry polyelectrolyte multilayers: a neutron reflectometry study. *Soft Matter* **2018**, *14*, 1699−1708.

(55) Selin, V.; Ankner, J. F.; Sukhishvili, S. A. Diffusional response of layer-by-layer assembled polyelectrolyte chains to salt annealing. *Macromolecules* **2015**, *48*, 3983−3990.

(56) Fares, H. M.; Schlenoff, J. B. Equilibrium Overcompensation in Polyelectrolyte Complexes. *Macromolecules* **2017**, *50*, 3968−3978.

(57) Lee, C. J.; Wu, H.; Hu, Y.; Young, M.; Wang, H.; Lynch, D.; Xu, F.; Cong, H.; Cheng, G. Ionic Conductivity of Polyelectrolyte Hydrogels. *ACS Appl. Mater. Interfaces* **2018**, *10*, 5845−5852.

(58) Zhao, Y.; Janot, J. M.; Balanzat, E.; Balme, S. Mimicking pH-gated ionic channels by polyelectrolyte complex confinement inside a single nanopore. *Langmuir* **2017**, *33*, 3484−3490.

(59) Ma, T.; Gaigalas, P.; Lepoitevin, M.; Plikusiene, I.; Bechelany, M.; Janot, J. M.; Balanzat, E.; Balme, S. Impact of Polyelectrolyte Multilayers on the Ionic Current Rectification of Conical Nanopores. *Langmuir* **2018**, *34*, 3405−3412.

(60) Andreeva, D. V.; Melnyk, I.; Baidukova, O.; Skorb, E. V. Local pH Gradient Initiated with Light on TiO$_2$ for Light-Triggered Polyhistidine-Tagged Proteins Modulation. *ChemElectroChem* **2016**, *3*, 1306−1310.

(61) Xu, W.; Choi, I.; Plamper, F. A.; Synatschke, C. V.; Müller, A. H. E.; Tsukruk, V. V. Nondestructive Light-Initiated Tuning of Layer-by-Layer Microcapsule Permeability. *ACS Nano* **2013**, *7*, 598−613.

(62) Ryzhkov, N. V.; Mamchik, N. A.; Skorb, E. V. Interfaces in solution for ion gradient and logic operation. *Front. Chem.*, **2019**.

(63) Fomina, N.; Johnson, C. A.; Maruniak, A.; Bahrampour, S.; Lang, C.; Davis, R. W.; Kavusi, S.; Ahmad, H. An electrochemical platform for localized pH control on demand. *Lab Chip* **2016**, *16*, 2236−2244.

(64) Poghossian, A.; Katz, E.; Schöning, M. J. Enzyme logic AND-Reset and OR-Reset gates based on a field-effect electronic transducer modified with multi-enzyme membrane. *Chem. Commun.* **2015**, *51*, 6564−6567.

(65) Saghatelian, A.; Völcker, N. H.; Guckian, K. M.; Lin, V. S. Y.; Ghadiri, M. R. DNA-based photonic logic gates: AND, NAND, and INHIBIT. *J. Am. Chem. Soc.* **2003**, *125*, 346−347.

(66) Wang, X.; Zhou, J.; Tam, T. K.; Katz, E.; Pita, M. Switchable electrode controlled by Boolean logic gates using enzymes as input signals. *Bioelectrochemistry* **2009**, *77*, 69−73.

(67) Privman, M.; Tam, T. K.; Pita, M.; Katz, E. Switchable electrode controlled by enzyme logic network system: approaching physiologically regulated bioelectronics. *J. Am. Chem. Soc.* **2009**, *131*, 1314−1321.

(68) Liu, D.; Liu, H.; Hu, N. pH-, sugar-, and temperature-sensitive electrochemical switch amplified by enzymatic reaction and controlled by logic gates based on semi-interpenetrating polymer networks. *J. Phys. Chem. B* **2012**, *116*, 1700−1708.

(69) Wang, L.; Lian, W.; Yao, H.; Liu, H. Multiple-stimuli responsive bioelectrocatalysis based on reduced graphene oxide/poly (N-isopropylacrylamide) composite films and its application in the fabrication of logic gates. *ACS Appl. Mater. Interfaces* **2015**, *7*, 5168−5176.

(70) Yao, H.; Luo, X.; Yang, T.; Li, M.; Yang, B.; Lu, Y.; Liu, H. Triple-switchable biosensors and an AND logic gate based on binary assembly of weak polyelectrolyte multilayers and hydrogel films. *J. Electrochem. Soc.* **2016**, *163*, H1104−H1111.

(71) Han, J. H.; Kim, K. B.; Kim, H. C.; Chung, T. D. Ionic circuits based on polyelectrolyte diodes on a microchip. *Angew. Chem., Int. Ed.* **2009**, *48*, 3830−3833.

(72) Pennakalathil, J.; Kim, T. H.; Kim, K.; Woo, K.; Park, J. K.; Hong, J. D. Ion-permselective polyelectrolyte multilayer membrane installed with a pH-sensitive oxazine switch. *Langmuir* **2010**, *26*, 11349−11354.

(73) Ghostine, R. A.; Schlenoff, J. B. Ion diffusion coefficients through polyelectrolyte multilayers: temperature and charge dependence. *Langmuir* **2011**, *27*, 8241−8247.

(74) Rmaile, H. H.; Farhat, T. R.; Schlenoff, J. B. pH-Gated permeability of variably charged species through polyelectrolyte multilayer membranes. *J. Phys. Chem. B* **2003**, *107*, 14401−14406.

(75) Souto, R. M.; Lamaka, S. V.; González, S. Uses of scanning electrochemical microscopy in corrosion research. *Microscopy: Science, Technology, Applications and Education.* **2010**, *3*, 1769−1780.

(76) Skorb, E. V.; Andreeva, D. V. Layer-by-Layer approaches for formation of smart self-healing materials. *Polym. Chem.* **2013**, *4*, 4834−4845.

(77) Radhakrishnan, K.; Tripathy, J.; Raichur, A. M. Dual enzyme responsive microcapsules simulating an "OR" logic gate for biologically triggered drug delivery applications. *Chem. Commun.* **2013**, *49*, 5390−5392.

(78) Chen, L.; Zeng, X.; Dandapat, A.; Chi, Y.; Kim, D. Installing Logic Gates in Permeability Controllable Polyelectrolyte-Carbon Nitride Films for Detecting Proteases and Nucleases. *Anal. Chem.* **2015**, *87*, 8851−8857.

(79) Motornov, M.; Zhou, J.; Pita, M.; Gopishetty, V.; Tokarev, I.; Katz, E.; Minko, S. Chemical transformers" from nanoparticle ensembles operated with logic. *Nano Lett.* **2008**, *8*, 2993−2997.

(80) Deng, H. H.; Wang, F. F.; Liu, Y. H.; Peng, H. P.; Li, K. L.; Liu, A. L.; Xia, X.-H.; Chen, W. Label-free, resettable, and multi-readout logic gates based on chemically induced fluorescence switching of gold nanoclusters. *J. Mater. Chem. C* **2016**, *4*, 7141−7147.

(81) Saghatelian, A.; Völcker, N. H.; Guckian, K. M.; Lin, V. S. Y.; Ghadiri, M. R. DNA-based photonic logic gates: AND, NAND, and INHIBIT. *J. Am. Chem. Soc.* **2003**, *125*, 346−347.

(82) Wang, L.; Zhu, J.; Han, L.; Jin, L.; Zhu, C.; Wang, E.; Dong, S. Graphene-based aptamer logic gates and their application to multiplex detection. *ACS Nano* **2012**, *6*, 6659−6666.

(83) Han, J.-H.; Kim, K. B.; Kim, H. C.; Chung, T. D. Ionic Circuits Based on Polyelectrolyte Diodes on a Microchip. *Angew. Chem., Int. Ed.* **2009**, *48*, 3830−3833.

(84) Motornov, M.; Zhou, J.; Pita, M.; Tokarev, I.; Gopishetty, V.; Katz, E.; Minko, S. An integrated multifunctional nanosystem from command nanoparticles and enzymes. *Small* **2009**, *5*, 817−820.

(85) Ding, C.; Sun, H.; Ren, J.; Qu, X. Immobilization of enzyme on chiral polyelectrolyte surface. *Anal. Chim. Acta* **2017**, *952*, 88−95.

(86) Skorb, E. V.; Möhwald, H.; Andreeva, D. V. How can one controllably use of natural ΔpH in polyelectrolyte multilayers? *Adv. Mater. Interfaces* **2017**, *4*, 1600282.

(87) Andreeva, D. V.; Sviridov, D. V.; Masic, A.; Möhwald, H.; Skorb, E. V. Nanoengineered Metal Surface Capsules: Construction of a Metal-Protection System. *Small* **2012**, *8*, 820−825.

(88) Skorb, E. V.; Baidukova, O.; Andreeva, O. A.; Cherepanov, P. V.; Andreeva, D. V. Formation of polypyrrole/metal hybrid interfacial layer with self-regulation functions via ultrasonication. *Bioinspired, Biomimetic Nanobiomater.* **2013**, *2*, 123−129.

(89) Lentini, R.; Martín, N. Y.; Forlin, M.; Belmonte, L.; Fontana, J.; Cornella, M.; Martini, L.; Tamburini, S.; Bentley, W. E.; Jousson, O.; Mansy, S. S. Two-Way Chemical Communication between Artificial and Natural Cells. *ACS Cent. Sci.* **2017**, *3*, 117−123.

(90) Lanchuk, Y. V.; Ulasevich, S. A.; Fedotova, T. A.; Kolpashchikova, D. M.; Skorb, E. V. Towards sustainable diagnostics: replacing unstable H_2O_2 by photoactive TiO_2 in testing systems for visible and tangible diagnostics affordable by blind people. *RSC Adv.* **2018**, *8*, 37735−37739.

(91) Muderrisoglu, C.; Saveleva, M.; Abalymov, A.; Van der Meeren, L.; Ivanova, A.; Atkin, V.; Parakhonsky, B.; Skirtach, A. G. Nanostructured Biointerfaces Based on Bioceramic Calcium Carbonate/Hydrogel Coatings on Titanium with an Active Enzyme for Stimulating Osteoblasts Growth. *Adv. Mater. Interfaces* **2018**, *5*, 1800452.

(92) Skorb, E. V.; Andreeva, D. V.; Raiski, A. P.; Belyasova, N. A.; Möhwald, H.; Sviridov, D. V. Titanium Dioxide for Photocatalytic-assisted Prophage Induction to Lytic Cycle. *Photochem. Photobiol. Sci.* **2011**, *10*, 1974−1978.

(93) Gensel, J.; Borke, T.; Pazos-Perez, N.; Fery, A.; Andreeva, D. V.; Betthausen, E.; Müller, A. H. E.; Möhwald, H.; Skorb, E. V. Cavitation Engineered 3D Sponge Networks and Their Application in Active Surface Construction. *Adv. Mater.* **2012**, *24*, 985−989.

ice Publishing

Feedback mechanisms at inorganic–polyelectrolyte interfaces for applied materials

[1] **Nikolay V. Ryzhkov**
PhD student, ITMO University, St Petersburg, Russian Federation

[2] **Nadzeya Brezhneva**
PhD student, Chemistry Department, Belarusian State University, Belarus

[3] **Ekaterina V. Skorb**
Professor, ITMO University, St Petersburg, Russian Federation
(corresponding author: skorb@corp.ifmo.ru)
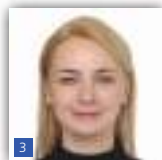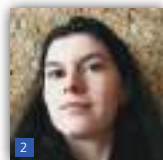
Non-linear processes at the interface between inorganic and polymeric species mimic a wide variety of natural processes such as stimulus-responsive behavior, self-healing, actuation, transport and delivery, and pH buffering. There are plenty of models describing phenomena at solid–polymer and polymer–liquid interfaces, but they do not provide complete understanding of the occurring processes. The authors analyze here recent progress in fundamental aspects of programmable materials based on polyelectrolyte feedback mechanisms on inorganic surfaces of applied materials in (*a*) photochemistry (focus on semiconductor–polyelectrolyte interfaces), (*b*) electrochemistry and (*c*) self-adaptive materials. The functionalization of the inorganic surface with polyelectrolyte layers provides an opportunity to construct novel hybrid materials with improved characteristics in comparison with pristine inorganic analogues. The importance of the transition from traditional to system thinking is highlighted, as well as the hierarchical scale of the time of polyelectrolyte responses due to complex overlapping between the processes of ion diffusion, chain site diffusion and self-diffusion.

1. Introduction

One of today's research interests focuses on the study of nature-mimicking interfaces of solid components and polymers (e.g. semiconductor–metal,[1] semiconductor–insulator,[2] semiconductor–polymer[3] and metal–polymer[4]). However, understanding the fundamental basis of the processes occurring on these interfaces is still a challenge, which substantially limits fabrication of novel high-performance devices and the improvement of already existing ones.[5] Such hybrid structures can be regarded as complex interfaces, and, under an external stimulus (e.g. electromagnetic irradiation and electric field) of an appropriate intensity, non-linear phenomena can take place in the system.[6,7] Particularly, ultraviolet (UV) or visible range irradiation can lead to the non-linear response of the semiconductor, leading to the appearance of the functions of intensity modulation,[8] harmonic generation,[9] spatial and temporal pulse shaping[10] and so on, providing opportunities for optical processing of information.[11] The non-linear phenomena at the semiconductor–polymer interface determine the non-linear optical properties of the hybrids[11] and the non-linear charge transfer at the inorganic–organic interface.[1,12] Also, an interesting stimulus-coupling phenomenon can take place on the semiconductor–soft matter interface.

Applying an external electromagnetic field can lead to the transformation of the initial energy of photons into a gradient of ions (particularly protons[13]), which can directly activate the pH-sensitive polymer component. Polyelectrolytes (particularly weak polyelectrolytes) are known to exhibit pH-tunable properties.[14] In fact, such hybrid systems exhibit several responses: (*a*) photocatalytic reactions on the irradiated semiconductor surface and the consequent acidification, (*b*) changes in the parameters of the polymeric pH-sensitive layer and (*c*) self-adaptive regulation (Figure 1).

In this paper, the authors focus on the analysis of stimulus-responsive solid–polyelectrolyte multilayer (PEM) interfaces with the further potential application of such structures in the design of smart materials. The photocatalytic activity of hybrids and the effect of the introduction of polyelectrolytes on the overall performance of the composite structure are discussed in Section 2.1. The electrochemical performance of multilayer-coated electrodes and their possible applications as well as the analysis of semiconductor–polyelectrolyte interfaces for photoelectrochemical applications are described in Section 2.2. Section 2.3 is devoted to the importance of self-adaptive systems.
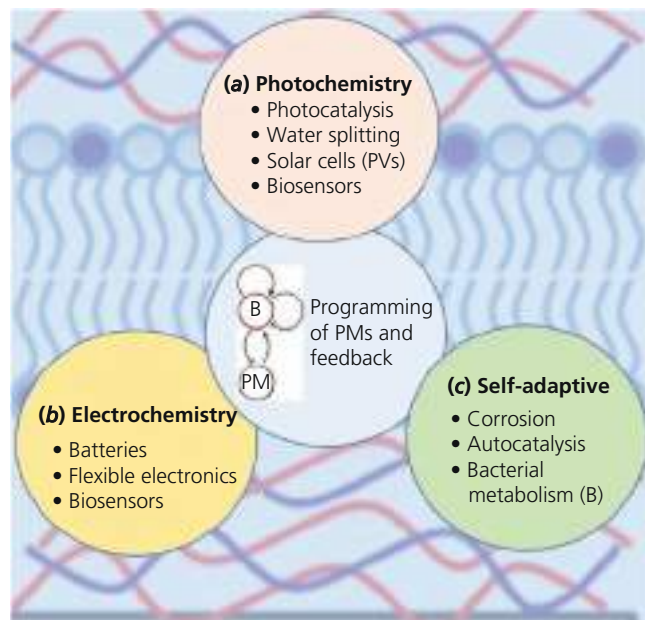
Surface Innovations

**Feedback mechanisms at
inorganic–polyelectrolyte interfaces for
applied materials**
Ryzhkov, Brezhneva and Skorb

Figure 1. Formation of a PM with feedback (so-called intelligent, smart or stimulus-responsive materials), highlighting external stimuli: (*a*) photoactivation, (*b*) electrochemical switching and (*c*) most advanced PMs designed as self-adaptive materials. The chosen applied areas for PMs are also highlighted. The inset in the center shows the possibility of using PMs for bacterial colonies' (B) activation or inhibition with simultaneous active change of PMs due to bacterial metabolism. The background highlights solid–polyelectrolyte interfaces and in some cases LB interfaces, which are important in the architecture of PMs with a submicron precision

2. Discussion

2.1 Basics of regulation of photocatalytic properties at interfaces

2.1.1 Photon-to-proton conversion at the semiconductor–polyelectrolyte interface

Hybrid systems based on semiconductors and polyelectrolytes could be divided into several categories (Table 1) – for example, hollow micro- and nano-objects (microcapsules,[17,18,20,24,26–28] nanofibers[16]), layer-by-layer (LbL) films,[19,21] self-assembled thin films,[22,23,30] surface-imprinted materials[31] or cross-linked composite materials.[25] Such systems are important for various applications (Figure 1) – for example, photocatalysis, water splitting, solar cells (photovoltaics (PVs)) and biosensors. Polyelectrolytes can be often exploited as a freestanding matrix for embedding semiconductor nanoparticles into their structure[25,28,29,32–34] or act as monolayers in LbL-assembled multilayers or self-assembled coatings along with semiconductor films.[16,19,21,35] Such hybrid systems possess, on the one hand, the properties of semiconductor materials – photocatalytic activity, chemical stability, absorbance in the UV range (for titanium dioxide (TiO_2) and zinc oxide (ZnO)) or visible range (cadmium sulfide (CdS) and cadmium selenide (CdSe)) and, on the other hand, the properties of the organic compartment – softness and flexibility.

Systems based on polyelectrolytes and semiconductors often exhibit synergistic effects – for example, enhancement of the semiconductor photocatalytic activity for environmental remediation applications (decomposition of dye or organic pollutants),[16–20,24,26–28] and increase in the biocidal activity of the hybrid antimicrobial materials.[21] Figure 2(a) demonstrates the materials under consideration and their feedback changes that determine a wide range of applications. The importance of the transition from traditional to system thinking ('dynamic thinking') (Figure 2(b)) is highlighted as well as the hierarchical scale of the time of polyelectrolyte responses due to complex overlapping between the processes of ion diffusion, chain site diffusion and self-diffusion. Introducing the term 'dynamic thinking' with regard to materials, the authors would like to emphasize the complexity of processes occurring in heterostructured solid–polyelectrolyte stimulus-responsive programmable materials (PMs) with synergetic effects of output and complex networks of feedback with non-linear time-dependent development.

Fares and Schlenoff,[36] Fares *et al.*,[37] Schlenoff[38] and Delgado and Schlenoff[39] in their studies discussed the diffusion processes in polyelectrolyte complexes and PEMs of certain architecture, taking into account small ion diffusion, site diffusion and polymer diffusion (Figure 2(c)). Both components – semiconductor and polyelectrolytes – affect each other. The topic under consideration includes the influence of photogenerated charges near the irradiated semiconductor surface on the properties of soft matter and the impact of soft matter on the photostimulated properties of the semiconductor. Photon absorption, generation of charge carriers under irradiation, chemical conversion into pH gradient, lifetimes and LbL stability are the general features considered in the characterization of semiconductor–polyelectrolyte systems. Titanium dioxide is not a specific semiconductor with the possibility of converting incident photons into a gradient of photogenerated species (particularly protons – light–pH coupling); however, this surface effect was studied in detail on titania.[19] Thus, titanium dioxide can be regarded as the first candidate for creating a predictive theory of light–pH coupling for advanced materials with a stimulus-responsive behavior. In the following, it will be possible to expand the discussion to other semiconductors – for example, silicon,[40] $A^{III}B^{V5}$ and even perovskites.[41]

Surface pH change was studied in situ with the scanning ion-selective electrode technique (SIET) (Figure 3).[42] For pH modulation with light, it is important to understand how photoinitiated processes on titanium dioxide result in the transformation of light into a pH change, including localization of the effect. SIET was applied to map the activity and migration of hydrogen (H^+) ions over the titanium dioxide surface. SIET is a unique technique available for measuring in situ changes in ion concentrations locally in space and time. The main advantage of this unique method is that it allows performing measurements of local pH changes near the surface without any pH-sensitive markers, which may potentially affect the photoreactions in the system. Maps of the pH were collected for pristine titanium dioxide before illumination (Figure 3(a)), during illumination

Table 1. Selected examples of semiconductor–polyelectrolyte applied systems

Semiconductor–polyelectrolyte hybrid system			Possible applications of the hybrid system	References
Semiconductor	Polyelectrolytes	Type of the system		
Titanium dioxide (TiO$_2$)	PAH, PSS	Hollow microcapsules – walls of PEMs with incorporated titania	Photocatalytic microreactors for microheterogeneous photoreduction of metal ions from aqueous solutions,[10,11,15] drug delivery systems, cosmetics and environmental engineering[14]	Walker et al.,[10] Ropp et al.,[11] Lonergan,[12] Skorb et al.,[13] Mamidala et al.[15]
Titanium dioxide	Chitosan	Surface-imprinted core–shell composite materials	Degradation of environmental organic pollutants	Pan et al.[16]
Titanium dioxide	PAH, PSS	Hybrid multilayered hollow nanofibers		Shchukin and Sviridov[17]
Titanium dioxide	PEI, PSS	Sprayed LbL assembly of titanium dioxide photocatalyst with polyelectrolytes for polyester textile functionalization	Antimicrobial textiles	Shchukin et al.[18]
Cadmium sulfide (CdS), titanium dioxide	Chitosan	Cross-linked composite films	Decolorization treatment of dye-containing effluents	Sun et al.[19]
Titanium dioxide	PAH, PSS	LbL-fabricated multilayer coating on wood surface	Multifunctional coatings for wood surface protection	Shchukin and Sukhorukov[20]
Titanium dioxide	Chitosan-grafted–poly(N-methylaniline)	Nanografted polymeric composites	Environmental remediation	Carre et al.[21]
Titanium dioxide	Chitosan	Sorbent beads	Wastewater treatment	Dal'Acqua et al.[22]
Cadmium sulfide	PDDA	Spherical nanosized particles	Photocatalytic removal of organic pollutants	Faria et al.[23]
Titanium dioxide	Poly(methacrylic acid–ethylene glycol dimethacrylate–3-(trimethoxysilyl) propylmethacrylate	Hollow composite microcapsules	Wastewater treatment	Shchukin et al.[24]
Titanium dioxide	PEI	Hybrid nanocomposites with multiwalled carbon nanotubes	Artificial photosynthetic systems	Zhu et al.[25]
Titanium dioxide, cadmium selenide (CdSe)	PAH, PAA, PEDOT:PSS	Self-assembled thin films	Hydrogen-producing devices	Timin et al.[26]
Titanium dioxide	PAH, PAA	Self-assembled thin films	Photocatalytic thin films	Gao et al.,[27] Bang et al.[28]
Titanium dioxide	PEI	Colloidal particles embedded in a polyethylene matrix		Essawy et al.[29]

(Figure 3(b)), 20 min after switching the illumination off and during 40 min of relaxation (Figure 3(c)). The proton distribution maps show that protons were generated under irradiation. Thus, it is possible to couple light and pH, and the authors know how to perform characterization of the system in situ and visualize chemical processes under local illumination.

2.1.2 Nanometer-thick polyelectrolyte layer regulates semiconductor functional properties

It is worth mentioning that LbL assembly allows the formation of an efficient structure for fast trapping of chemical species – for example, hydrogen ions (Table 1, Figure 4). The kinetics of light–pH-coupled actuation and modulation of LbL films and the study of the relaxation processes are in focus for the design of applied materials and PMs.

An increase in the photocatalytic activity in hybrid systems (e.g. poly (ethyleneimine) (PEI)-grafted multiwalled nanotubes in combination with titanium dioxide particles), particularly the enhancement of the titanium dioxide photoactivity in the UV range, can be explained by the auxochrome effect caused by the presence of –NH$_2$ groups in the polyelectrolyte.[48] The high self-decontaminating activity of PEI–titanium dioxide-based antimicrobial textiles was explained as due to the combination of the biocidal photocatalytic activity of titanium dioxide and biocidal activity of PEI.[21]

Vallejo-Montesinos et al.[49] reported a decrease in the photocatalytic activity of titanium dioxide–PEI particles embedded into a polyethylene matrix in comparison with that of a control sample containing pure titanium dioxide. The authors explain this passivation of photoactivity as due to the chemical affinity of the polyelectrolyte
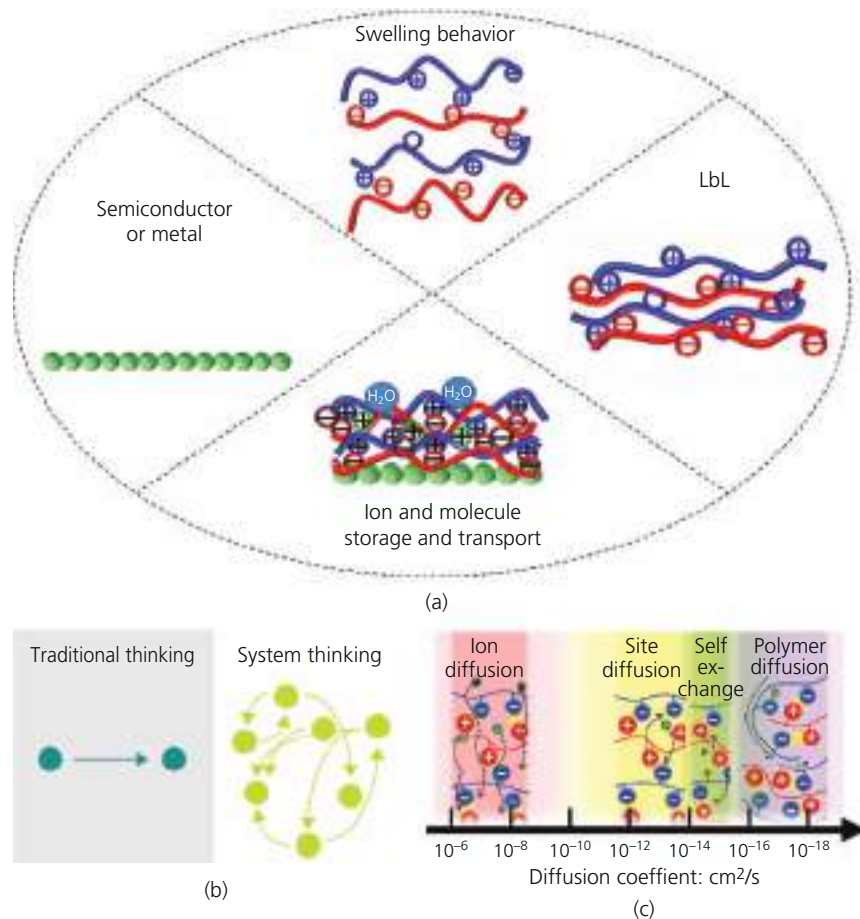
Figure 2. Schematic depiction of PM components and their dynamic thinking. (a) The solid (semiconductor or metal)–polyelectrolyte interface is in focus for its nanostructuring for a programmable swelling behavior, ion and molecule storage and transport against environmental changes and response to stimuli. (b) It is important in PM to transfer from traditional thinking to complex thinking. (c) Various time lines for diffusion coefficients in polyelectrolyte assembly that are important in predicting the PM response. Adapted from Fares and Schlenoff[36]

to the polymeric matrix and prevention of the floating of titanium dioxide particles to the surface of the composite during the preparation using an extrusion technique. The particles remained in the bulk of the composite due to the good integration of PEI-coated particles into the polymeric matrix, and these could not reach the surface so as to be irradiated and produce the photocatalytic activity.

Demonstrated recently in the authors' work[43,44] was the alteration in the titanium dioxide–polyelectrolyte hybrid photoactivity by variation of the chitosan or PEI buffer layer position in an LbL assembly. The combination of the external stimulus (in the authors' case, UV irradiation) and the consequent pH gradient formation near the irradiated surface of the semiconductor[42] can be regarded as stimulus-coupling activation of the semiconductor–polyelectrolyte hybrid system. Chitosan and PEI are known to exhibit 'proton sponge' properties by the trapping of hydrogen ions with NH_2 groups. Under UV irradiation of the hybrids, the 'photon-to-proton conversion' (i.e. the transformation of electromagnetic irradiation energy into proton flux on the irradiated surface of titanium dioxide

through a series of reduction/oxidation (red/ox) reactions with water) takes place. Recent work efficiently used the approach to control surface properties of titania.

Recently, the protection function against supramolecular disassembly of chitosan deposited on the surface of titanium dioxide has been demonstrated (Figures 4(a) and 4(b)).[43] The combination of triaminopyrimidine and cyanuric acid modified with a hexanoic acid side chain is known to be assembled–disassembled reversely with pH change in the surrounding media. In the authors' work, it was shown that the assembly deposited onto the titanium dioxide–chitosan surface after irradiation remained on the surface without being destroyed and disassembled. This led to the confirmation of the hypothesis exploiting chitosan as a buffering protective layer for trapping photogenerated hydrogen ions.

The generation of protons leads to a decrease in the subsurface pH value. Titanium dioxide is known to exhibit higher
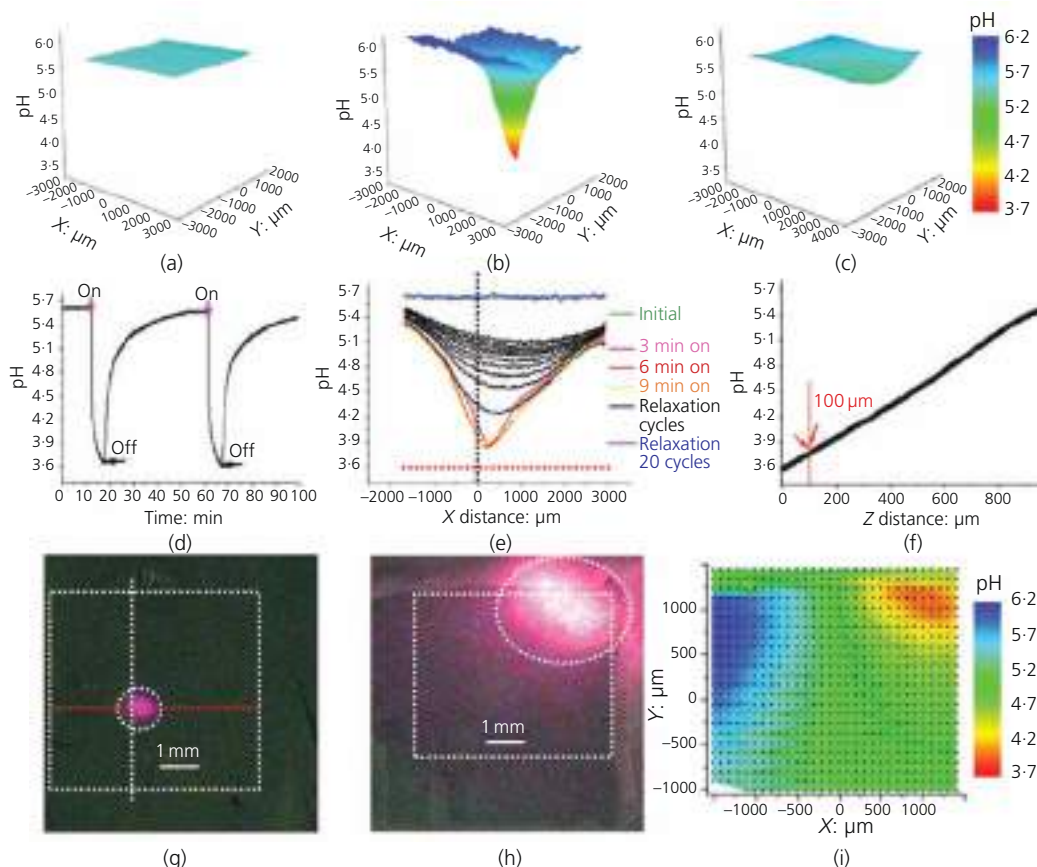
Figure 3. Light–pH coupling on a semiconductor surface. Maps obtained by the in situ SIET to analyze local pH gradients generated on nanostructured titanium dioxide: (a) before irradiation; (b) during local irradiation; (c) after irradiation (20 min of relaxation). (d) pH measurement inside an irradiation spot (shown in panel (g)) and single-spot time-evolution measurements on a titania layer after switching on and switching off the light. (e) Local pH measurements in a line (shown in panel (g) in (red)) before, during and after irradiation (the maximum coincides with the position of the irradiation spot; the time of measurement of each line was 3 min). (f) pH in the Z direction during illumination inside the irradiated spot. (g) X–Y dashed lines shown in the optical image of the surface and the location of the focused irradiation spot on titanium dioxide described earlier (panels (a)–(e)) and mapped in panels (a)–(c). (h) X–Y optical image with defocused light to show the flexibility of the method to change the intensity of illumination and its location and effect on the pH gradient of the surface with corresponding (i) pH map with color-pointed pH areas. Reprinted from Maltanava et al.[42]

photoactivity in the acidic medium, but, in the case of immediate binding of photogenerated protons by the PEI layer, the photoactivity can decrease. The authors showed that the titanium dioxide–poly(styrene sulfonate) (PSS)–PEI photocatalytic activity is around two times lower in comparison with that of titanium dioxide–PEI and around four times lower than in the case of pure titanium dioxide (Figures 4(c) and 4(d)). In the photoelectrochemical experiments, the authors also noticed a decrease in the photocurrent values. The authors assume that such decrease in the photoactivity can be related to the variation in buffering properties of PEI either deposited directly on the titanium dioxide surface or separated by a nanoscale-thick (~5 nm) PSS layer. Another demonstration of the mild photocatalytic activity of the titanium dioxide–PSS–PEI hybrid was described by Brezhneva et al.[44] Changes in the titania surface state can be efficiently controlled by impedance study (Figures 4(e) and 4(f)), resulting in either an increase or a decrease in photocatalytic properties. An important feature is detailed system modeling and prediction of applied characteristics against titanium dioxide–PSS–PEI hybrid and its architecture.

Titania is a good model semiconductor for studying the light–pH coupling effect due to its photocorrosion resistivity, stability and having one of the best-studied surface state chemistry in correlation with the surrounding medium. However, there are several other semiconductors (Table 1, Figures 4(g) and 4(h)). In Figures 4(g) and 4(h), it is highlighted that a PV element based on a zinc oxide/perovskite photoactive part in combination with PEI has $J_{sc} = 15 \cdot 6$ mA/cm^2.[45–47] Other polyelectrolytes were not tested, and even the role of PEI was not properly discussed for a predictive model. However, taking into account aforementioned facts, the probability of finding a proper nanoarchitecture for exploitation of perovskite and III–V semiconductor-based elements is high.

Surface Innovations

**Feedback mechanisms at
inorganic–polyelectrolyte interfaces for
applied materials**
Ryzhkov, Brezhneva and Skorb
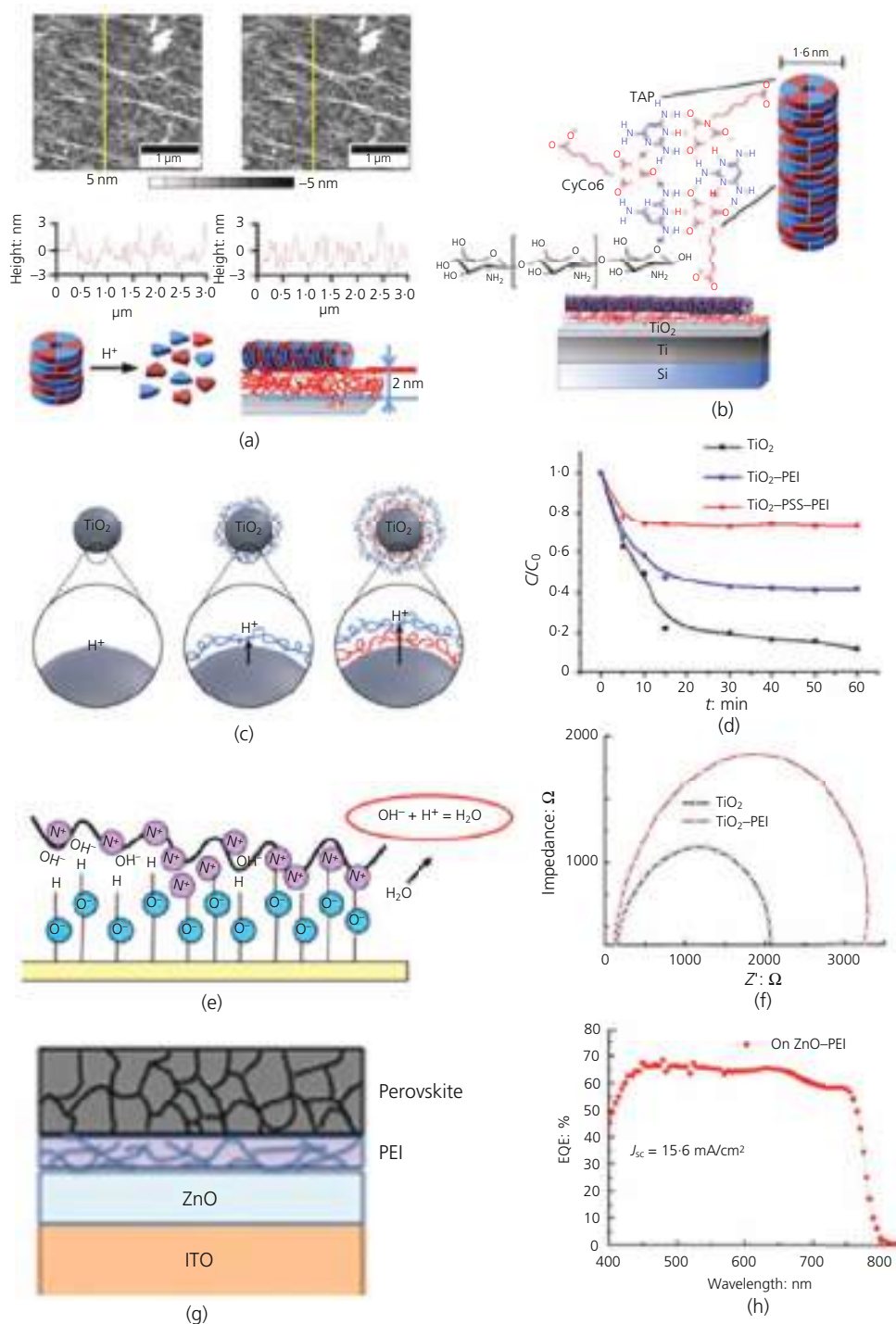
Figure 4. Effects of a nanometer-thick polyelectrolyte layer on semiconductor properties: (a, b) A 2 nm chitosan layer on the titania surface is efficient as a proton sponge, and no disassembly of the CyCo6–TAP complex was observed due to change of surface acidity (CyCo6, cyanuric acid modified with hexanoic acid side chain; TAP, triaminopyrimidine). Adapted from Andreeva et al.[43] (c, d) Highlight of the importance of the position of the polyelectrolyte proton sponge layer (here, PEI) in the interface of titania and LbL assembly of PEI and PSS, resulting in drastically different photoactivity. Adapted from Brezhneva et al.[44] (e, f) PEI also affects impedance and is used for modification of solar cells (adapted from Schouten et al.,[45] Muderrisoglu et al.[46] and Li et al.[47]), including (g, h) solar cells based on perovskites (adapted from Cheng et al.[41]). EQE, external quantum efficiency

The study of solar energy conversion and photoinduced bioactive sensors represents leading scientific fields, where interfaces play a decisive role for efficient applications. The key to tuning these interfaces specifically is a precise knowledge of interfacial structures and their formation on the microscopic, preferably atomic, scale. Supplie et al.[5] discussed how the area of III–V semiconductor development can be regarded within the frame of bioapplications and sensors. Supplie et al.[5] describe appropriate analysis techniques capable of monitoring critical physicochemical reactions in situ during non-vacuum preparation and photoactivity studies including well-defined inorganic epitaxial reference surfaces, buried interfaces and low-defect nucleation of disjunct epitaxial materials that were analyzed during preparation in a chemical vapor environment. In addition, the complex coupling of inorganic stable photoactive materials with responsive soft matter for bioactivity was also under consideration.

Enzymatic reactions can be also controlled using the light–pH coupling phenomenon. Surface modification by an enzyme allows achieving affinity and improving the biological response of bioinert surfaces. Experiments with osteoblasts demonstrated that the higher cell viability of a titanium implant surface functionalized by a polyelectrolyte–enzyme interface favors the osteogenic response.[45,46] Stimulus-responsive biointerfaces open perspectives to smart-material-based tissue engineering. Thus, the formation of trypsin from its precursor trypsinogen was chosen as an example of a pH-sensitive autocatalytic enzymatic reaction and was studied on a titanium dioxide–PSS–PEI hybrid and the titanium dioxide surface as a control.[50] The results indicated that the acidification of the surrounding media near the pristine titanium dioxide is the most possible explanation of the suppressed formation of trypsin in comparison with that in the hybrid system. In the latter case, the adsorption of trypsin was higher in comparison with that with pure titanium dioxide; however, polyelectrolyte layers deposition had less effect on the autocatalytic enzymatic reaction. Thus, varying the position of the polyelectrolyte layer in the LbL assembly can serve as an easy method of tuning the hybrid system photoactivity.

2.1.3 Complex thinking for switching biological response
The complex interactions of PMs with living objects, such as bacterial and yeast and human cells and tissues, are being discussed more and more. The proper design of drug delivery systems, as freestanding or surface capsules,[51–56] is a topic of high importance. The authors shall further focus on the following questions: (a) what a proper carrier is; (b) what type of chemistry is suitable for communication; (c) how to design two-sided communication – that is, processing of signals is performed by both the cell signaling network and synthetic chemical network; and (d) how to influence cells – for example, bacteria – with synthetic chemistry and how synthetic chemistry can response to bacteria.

In Figure 5(a), an example of a titania-based capsule for light-stimulated delivery of chemical species is shown,[57] and in Figure 5(b) it is pointed that bacterial metabolism has feedback mechanisms.[58] Nowadays there are many attempts to add chemical signals for biological signaling for various applications, from diagnosis and treatment of illnesses to modeling the understanding of complex system behaviors. In a recent work of Nikitina et al.,[59] a new contribution to the design of polyelectrolyte capsules based on surface-modified mesoporous titania particles with deposited silver (Ag) nanoparticles to achieve chemical light upconversion by way of biofilms was shown (Figures 5(c) and 5(d)). The polyelectrolyte shell allows slowing down the release kinetics of loaded L-arabinose and switching the bacterial luminescence in a certain time. The hybrid titanium dioxide–silver–polyelectrolyte capsule activated at 980 nm (infrared (IR)) illumination demonstrated ten times faster release of L-arabinose as opposed to non-activated containers. Fast IR release of L-arabinose switched bacterial fluorescence, which the authors monitored at 510 nm. The approach described herein can be used in many applications where delayed switching and light upconversion are required. Such complex thinking is very important for integration of complex chemical networks with biological networks – enzymatic networks,[50,60–63] bacterial quorum sensing[64–66] and synthetic biology[67–69] – suggesting them as one working reaction network.

Gradient processes on the surface of irradiated semiconductor–polyelectrolyte hybrids can also play an important role in the regulation of cell behavior. Recently, the dynamics of preosteoblast growth on the surface of mesoporous titanium dioxide with deposited layers of block-copolymer micelles (BCMs) and poly(acrylic acid) (PAA) has been investigated.[70] The consequence of pH alteration after irradiation of the system was a change in the polymer film stiffness – in the acidic media, the micelles swelled and drastically changed the thickness and the Young modulus of the polymer coating (Figure 6). Earlier, the change in BCM properties under ΔpH resulting from the bacterial vital activity was investigated.[71] For the LbL assembly of polyelectrolytes without titanium dioxide coating, a change in the stiffness under irradiation did not occur and the coating remained rigid. During 5 d of cultivation, the cells had a tendency to migrate from the 'soft' part of the sample toward the 'stiff' one (Figure 6). Thus, the manipulation of the mechanical modulus of the hybrid coatings can lead to the fabrication of stimulus-responsive materials for biological purposes.

Light is an attractive stimuli for the regulation of the gradient in time and space. It is easy to vary its intensity, duration and wavelength. However, in many cases, fundamental understanding of red/ox processes is needed. Studies of the electrochemical behavior of systems provide information about the quantity of the transferred electrons and processes at the electrodes.

2.2 Electrochemical studies of electrode–polyelectrolyte interfaces
2.2.1 Importance of multicycle behavior
Electrochemical cells usually consist of two electrodes immersed in a solution (liquid or solid) of electroactive species in
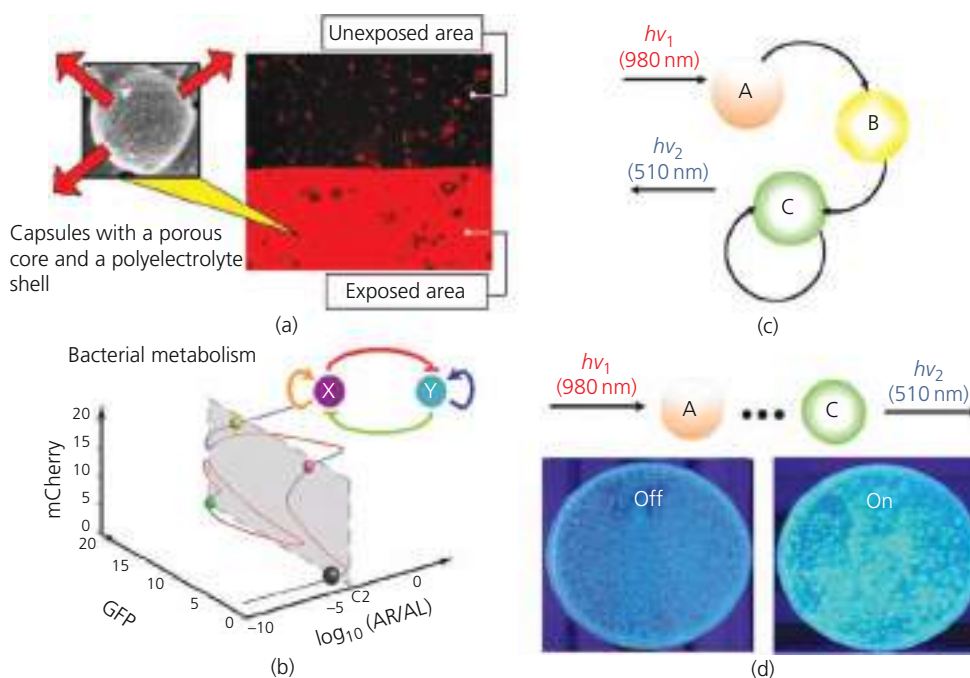
Figure 5. Complex thinking of polyelectrolyte capsules for switching biological response. (a) Titania capsules with a polyelectrolyte shell can be used for local light-stimulated delivery. The confocal image presents capsules loaded with rhodamine 6G and entrapped in a sol–gel matrix which releases the dye only in exposed areas. Adapted from Skorb et al.[57] (b) Bacterial metabolism is presented as having a non-linear start due to starting the fluorescence of green fluorescent protein (GFP) in response to L-arabinose activation. Adapted from Wu et al.[58] (c, d) A block schema of experiments where capsules (A) are nanostructured to release the needed concentration of L-arabinose (B) and switch bacteria metabolism (C), for use as a marker for switching of the fluorescence at 510 nm, which can be monitored by various methods. Shown here are photographs of petri dishes in off and on cycles. Adapted from Nikitina et al.[59] AR/AL, androgen receptor fluorescence

conductive media (electrolyte). The anode is where the oxidation reaction occurs, and the cathode is where the reduction reaction takes place. Since the fact that most electrochemical systems are heterogeneous, electrode reactions are related to electron transfer through the electrode–electrolyte interface. Thus, the characteristics of an electrode reaction are highly affected by the microstructure of the electrode surface, its cleanness, surface physics and chemistry. The non-faradaic impact of current flow is largely related to adsorption/desorption processes, solvent dipole reorientation and so on. Thereby, interfacial processes are of high importance in electrochemical systems.

LbL PEMs are traditional and ubiquitous components in designing interfaces with special properties. Recent progress in science provides understanding of fundamental principles of polyelectrolyte complexation and particle encapsulation due to electrostatic interactions.

As a result of the high ionization degree of polyelectrolytes, their deposition is a versatile and universal approach to creating the desired net charge on a surface. Concerning electrochemical applications, it is an attractive possibility to increase electrode selectivity and sensitivity as far as PEMs deposited on the top of the electrode surface form a strong electrostatic barrier to species of the same charge. Recently, it was demonstrated that the

permeability of polyelectrolyte films depends mostly on film composition rather than its thickness, and three different modes of interaction between PEMs on the top of electrodes and model electrochemical probes were observed – permeability, non-permeability and ion accumulation.[72]

For photochemical system, the light–pH coupling was discussed in detail earlier. For electrochemical systems, proton generation can be associated with hydroquinone oxidation (Figure 7(a)). Ryzhkov et al.[73] in their work studied proton generation on electrodes using the in situ scanning vibrating electrode technique (SVET) (Figures 7(b)–7(d), 7(k) and 7(m)), SIET (Figures 7(e), 7(f), 7(l) and 7(n)) and electrochemical impedance spectroscopy (EIS) (Figures 7(g) and 7(h)).

The methods are suggested to be powerful instruments for the in situ observation of reversible processes associated with the lipid bilayer (LB)–solid support interface (Figures 8(a)–8(c)). EIS highlighted the reversible disappearance of the LB's impact on impedance in acidic conditions set by dilute acid addition as well as by electrochemical proton release on the gold (Au) electrode due to hydroquinone oxidation. In situ studies of transmembrane channels often require a model bioinspired artificial LB decoupled from its underlying support. Obtaining freestanding lipid membranes is still a challenge. Ryzhkov et al.[73] suggested an
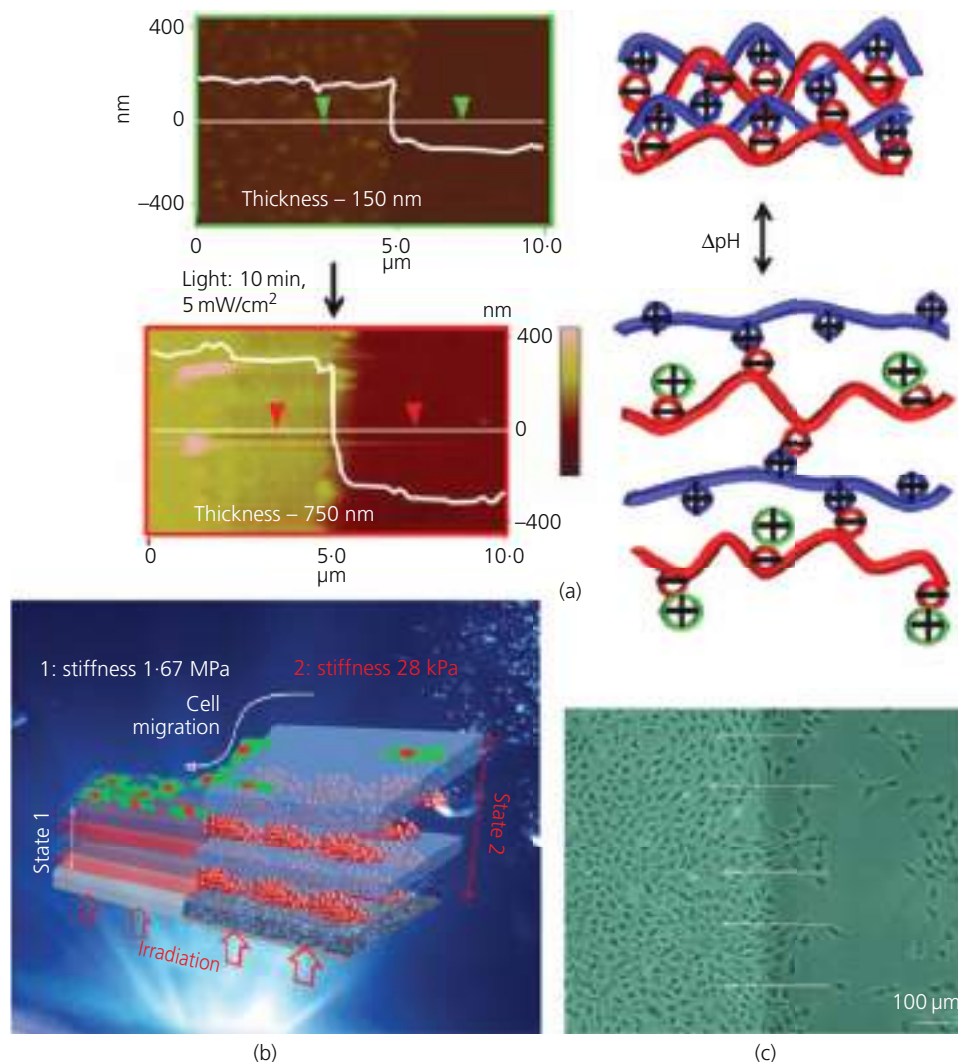
Figure 6. Example of photoswitchable LbL assembly for bioapplication. (a) Atomic force microscopy images and schematic illustration of change in LbL thickness in response to irradiation (intensity of 5 mW/cm^2) show a change in thickness from 150 to 750 nm as well as stiffness from 1·67 to 28 kPa. Adapted from Ulasevich et al.[71] (b) Suggestion of use of such photoregulated lab-on-a-chip in (a) to guide cell migration and (c) corresponding cell (osteoblast MC3T3-E1) migration experiment; note that, before irradiation, the numbers of cells were equal on both sides. Adapted from Ulasevich et al.[70]

electrochemical approach to LB separation from its solid support by way of hydroquinone oxidation. LbL deposition of PEI and PSS on a gold electrode was performed to obtain a polymeric nanocushion of [PEI–PSS]$_3$–PEI. The LB was deposited on the top of an underlying polymer support from the dispersion of small unilamellar vesicles due to their electrostatic attraction to the polymer support. Since lipid zwitterions demonstrate pH-dependent charge shifting, the separation distance between the polyelectrolyte support and LB can be adjusted by changing the environmental pH, leading to recharge of lipid molecules.

The outermost layer determining the net charge of the polyelectrolyte layer plays a crucial role in permeability properties of multilayered assembly completely blocking the diffusion of charged electroactive species. As it was demonstrated for pH-dependent charge-shifting electroactive species, permeability can be switched to non-permeability when the isoelectric point is crossed and the electroactive specimen involved in the electrode reaction becomes of the same charge as a terminating layer of the LbL assembly on the top of the electrode.[77] A similar behavior was observed when the outermost layer of a polyelectrolyte assembly was presented by molecule turning from being positively charged at pH 3 to negatively charged at pH 10 (Figures 8(d)–8(f)). Positive and negative electrochemical probes, $[Ru(NH_3)_6]^{3+}$ and $[Fe(CN)_6]^{3-}$, demonstrate a switch from the permeable regime to the non-permeable one and vice versa, respectively, shifting from basic to acidic condition.[78] PEMs of poly(diallyldimethylammonium chloride) (PDDA) and
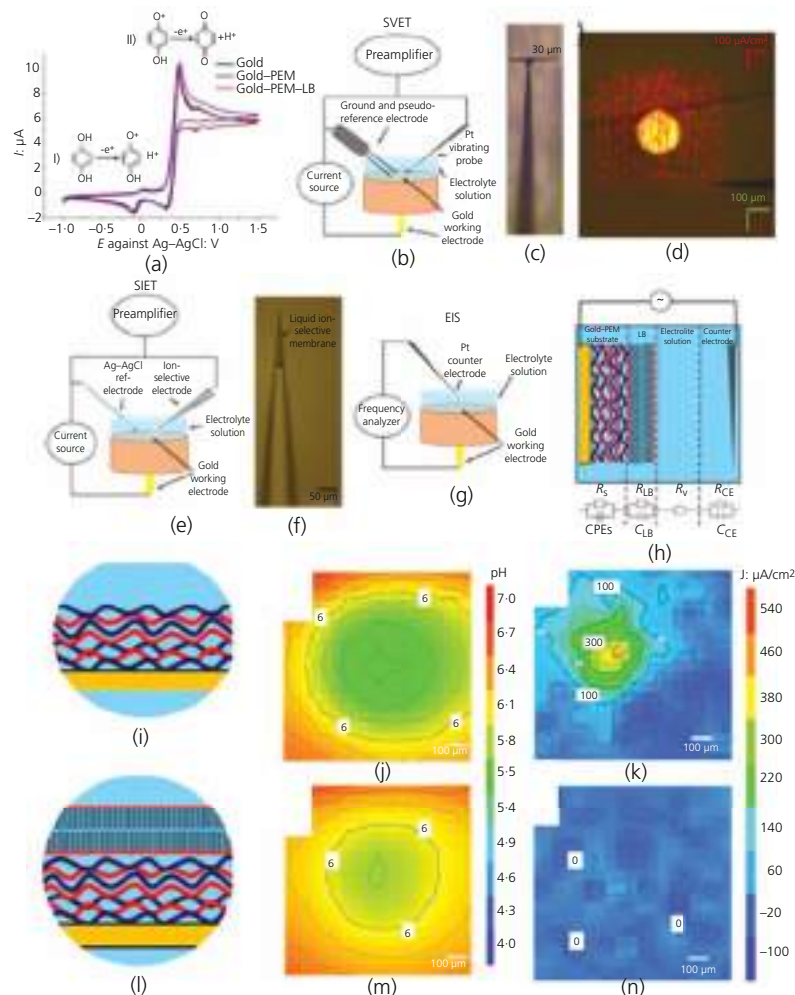
Figure 7. Possible methods and corresponding data for in situ spatiotemporal monitoring of feedback responses on a nanostructured surface. (a) Cyclic voltammetry curves of hydroquinone on a pure gold electrode and a gold electrode covered by a PEM and polymer-cushioned LB. (b) Scheme of SVET measurement. (c) Platinum (Pt)–iridium (Ir) vibrating probe. (d) Top view of the gold wire embedded in the epoxy holder. Red arrows represent ionic currents measured by SVET. The platinum vibrating electrode is seen at the right bottom of the image. (e) Schematic diagram of SIET measurement. (f) Glass capillary microelectrode with liquid ion-selective membrane. (g) Schematic diagram of EIS measurement. (h) Equivalent electrical scheme representing parts of the electrochemical system with the gold electrode covered by a PEM and a LB. (i–n) Schematic representation of the electrode structure; map of adjusted pH of electrode media after 5 μA current was passed through the electrode immersed in a 60 mM hydroquinone solution in 150 mM potassium nitrate (KNO$_3$), as measured by SIET; and anodic activity of the electrode immersed in a 60 mM hydroquinone solution in 150 mM potassium nitrate while 5 μA current was passed, as measured by SVET, for (i, j, k) gold–PEM and (l, m, n) gold–PEM–LB electrodes, respectively. Adapted from Ryzhkov et al.[73]

poly(4-styrenesulfonic acid-*co*-maleic acid) (PSS-MA) with strong and weak anionic groups become completely impermeable for both cationic and anionic probes at high pH and permeable for negative species in acidic conditions.[79]

Another regulation by light of the pH-sensitive complex adsorption/desorption process was shown in an example of protein tagged with the amino acid histidine amino acid (poly-His-tag) with a nickel (Ni)–nitrilotriacetic acid (NTA) complex where the last component was in the LbL assembly on the titanium-based chips covered with native titania[75] (Figures 8(g) and 8(h)). The interactions of the poly-His-tag protein with

nickel–NTA are pH sensitive. Short-term irradiation was used for switching the pH value of the subsurface surrounding media. After turning the light on, the pH value changed to 4 and the dissociation of NTA–Ni^{2+}/His-Tag occurred and the protein desorbed from the surface, which was confirmed by confocal laser fluorescence microscopy and quartz crystal microbalance analysis. Turning the light off resulted in the reverse process – adsorption of the protein to the surface. Thus, light regulation of protein sorption can have biosensing and biomedical applications.

The outermost polyelectrolyte layer of a multilayer determining its net charge plays a significant role in the interaction with

Surface Innovations

**Feedback mechanisms at
inorganic–polyelectrolyte interfaces for
applied materials**
Ryzhkov, Brezhneva and Skorb
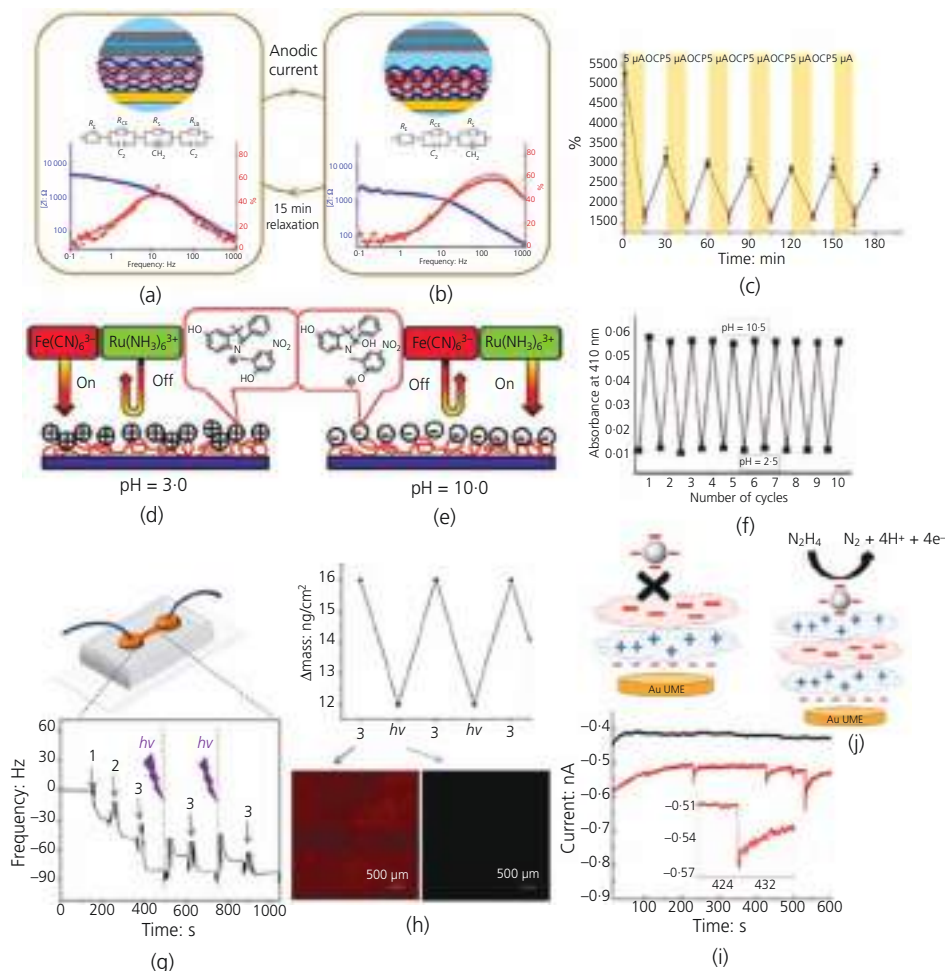
Figure 8. Examples chosen to highlight multicycle switching. (a, b) Impedance spectra of titanium dioxide–PEM–LB composites. The red curves are nine overlapping spectra registered in darkness immediately after 20 min of illumination; the blue curves are nine overlapping spectra registered after 20 min of relaxation in darkness. (c) Impedance oscillations during irradiation on–off cycles. Adapted from Ryzhkov et al.[73] (d–f) pH-dependent switching of electroactive LbL-based assembly. Adapted from Pennakalathil et al.[74] (g, h) Quartz crystal microbalance monitoring of adsorption and desorption on a chip of His-tag protein with corresponding confocal images of the surface with protein and without. Adapted from Andreeva et al.[75] Parts (i) and (j) highlight the possibility of having a reactive side against the activated state of PEM. Adapted from Castañeda et al.[76]

charged colloidal particles. If an experiment is performed in the solution of an electroactive specimen, every collision of a conductive particle with the PEM on the top of the electrode is followed by electron transfer. In the study of Pennakalathil et al.,[74] hydrazine oxidation was performed on poly-L-lysine (PLL)–poly-L-glutamic acid (PGA)-covered gold electrode in a dispersion of gold nanoparticles. Every collision of a nanoparticle with the PEM-covered electrode was followed by a current spike (Figures 8(i) and 8(j)).

Recent studies also aimed to reveal temperature and ionic strength effect on diffusion through PEMs.[80] The exact nature of ion transport through PEMs was discovered to be similar to the one through solid matter and coupled to the motion of the surrounding polyelectrolyte chains. Thus, this process is thermoactivated as it

was shown for PDDA–PSS multilayers.[80] Electrode modification by thermoresponsive polymer brushes that transform to a collapsed state during heating demonstrated simultaneous decrease in resistivity.[81] This approach can be used in the design of thermoresponsive switchable electrochemical sensors.

It was also shown that diffusion of the electroactive species to the electrode through polyelectrolyte layers can be significantly influenced by the nature of the supporting electrolyte.[82] EIS revealed that, for polyelectrolyte brushes grafted to the electrode surface, an increase in the salt concentration led to the collapsed state of the polymers, which blocked electron transport and decreased the conductivity of the composite. Nevertheless, swollen brushes allow good permeability of electroactive probes.[83]

Surface Innovations

**Feedback mechanisms at
inorganic–polyelectrolyte interfaces for
applied materials**
Ryzhkov, Brezhneva and Skorb

The aforementioned possibilities to change the permeability of the polymer layers on the top of the electrode surfaces open great perspectives on the design of electrochemical sensors with regulated selectivity, sensitivity and response time. This approach has been developed mainly in the design of amperometric biosensors. Due to the selective permeation of the target specimen through a PEM film of PAA/poly(vinyl sulphate) nanoarchitecture, the selectivity of the platinum (Pt) electrode to hydrogen peroxide (H_2O_2) in the presence of organic acids increased significantly.[84] Complete suppression of charged oxidizable compounds' permeability can be achieved by altering the number of the assembled layers. Modified electrodes semipermeably selective to hydrogen peroxide are suggested to be an attractive platform for glucose[85] and uric acid biosensors.[86]

It is now well recognized that nanoscale materials present significant enhancement in catalytic and sensing properties compared to bulk ones of the same composition. Thus, decoration of electrodes by metal nanoparticles draws much attention nowadays. LbL assembly, being a versatile and simple instrument of surface modification, is widely used for enhancing electrode efficiency due to nanostructuring.[87] Multilayered assemblies of PDDA and gold nanoparticles demonstrated a good response for arsenic (III) (As^{3+}) compounds, thus providing an opportunity for biosensor applications.[88] Recently, it has been reported that PEMs containing gold nanoparticles may exhibit stimulus-tunable electric conductivity. It was also demonstrated that the function of polyelectrolyte layers is not limited by particle immobilization. It was shown that humidity-responsive swelling of polyelectrolyte chains between encapsulated particles led to larger distances and lower electron tunneling probabilities.[89] It is important to note that conductivity may be both predetermined by deposition conditions and be changed while exploiting under external stimuli. The electrochemical response of multilayered assemblies of the charged polymer molecules and metal nanoparticles is significantly affected by the morphology of polymer layers. If multilayers of PSS–poly(allylamine)ferrocene (PA-FC) are organized in stratified layers, electron transport happens through the electron hopping from one metal particle to another separated by non-conductive polymer layers. In PGA–PA-FC multilayers, polyelectrolyte molecules are free to diffuse and their movement results in making metal impurities come in contact with each other and the electrode, enhancing electron transport and increasing the conductivity of the composite. In cross-linked PGA–PA-FC multilayers, the polyelectrolytes are no longer able to diffuse and electron transfer in these multilayers happens as in the case of PSS–PA-FC through electron hopping from one metal particle to another.[90] Thus, three different regimes of electron transfer can be observed from the electroactive specimen in solution to the electrode through the complex interfaces.

Another way to enhance electron transfer through polyelectrolyte layers is introducing specially modified polymers with electroactive moieties into the multilayered LbL assemblies. Poly(4-vinylpyridine) with a covalently attached osmium complex was suggested to be an electron transfer agent in a polyelectrolyte–lipid bioinspired composite.[91] Multilayers of PLL–PGA covering a gold electrode enhance electron transfer and induce increase in faradaic current without any introduction of the electroactive specimen into the multilayer structure.[76] Carbon nanotubes modified by PDDA layer demonstrated an increased catalytic performance to oxygen reduction similar to that of platinum catalysts. The main reason of such composite behavior was the strong electron-withdrawing ability of the polymer.[92]

In many cases, polyelectrolyte layers serve as a material that modulates the electrochemical response of the electrode. However, polyelectrolyte assemblies on the top of the electrode also serve as 'smart' dynamic materials responsive to electrochemical stimuli. Charged polymer molecules are highly sensitive to the surroundings. It is well known that they change conformation from linear to coiled during, for example, an increase in the ionic strength. Electrochemical control over the morphological transitions of polyelectrolytes is very attractive for guiding biological morphogenesis. A reversible thickness increase of about 5–10% may be reached through the penetration of chloride ions into the PEM resulting from $[Fe(CN)_6]^{4-}$ reduction and consequent appearance of non-compensated positive charges.[93] This phenomenon was used to demonstrate time-resolved control over the wettability of electrochemically addressable surface of polycationic poly(2-(methacryloyloxy) ethyltrimethylammonium chloride) (PMETAC) brushes with ferricyanide ions. Alternating application of negative and positive potentials induces reversible switches of PMETAC brushes between linear and coiled states simultaneously with the reduction and oxidation of $[Fe(CN)_6]^{3-}$ and $[Fe(CN)_6]^{4-}$. As a result, reversible changes in water contact angles may be observed.[94] It is well known that strong electric fields can promote dissociation of weak polyelectrolytes. Ionization of weak polyelectrolytes assembled on the top of the electrode surface under applied potential leads to enhanced intramolecular repulsion between the charged moieties of polymer molecules, which can promote conformational change. As a result, the switch from hydrophobic to hydrophilic state and vice versa can be performed. The swelling behavior of polystyrene-block-PAA under a negative bias led to an increase in the water contact angle.[95] Swelling and deswelling of polyelectrolyte layers under alternating applied potential can reversibly bend underlying supports due to conformational changes of polymers. A simple and versatile platform for electroactuation was demonstrated by employing a cantilever modified by PMETAC brushes,[96] Nanoactuation of PGA–poly(allylamine hydrochloride) (PAH) and carboxymethyl cellulose (CMC)–PDDA multilayers in similar conditions by potential application was also demonstrated.[97] It is interesting that ferrocyanide oxidation caused the swelling of PGA–PAH multilayers, whereas CMC–PDDA multilayers underwent contraction due to the presence of a positive and a negative Donnan potential, respectively. In the case of multilayers assembled from weak polyelectrolytes, morphological transitions

Surface Innovations

Feedback mechanisms at
inorganic–polyelectrolyte interfaces for
applied materials
Ryzhkov, Brezhneva and Skorb

may originate from pH change induced by water hydrolysis after potential application. Structural rearrangements of the weak polyelectrolyte molecules in an electrically induced pH gradient can lead to the creation of a porous structure.[98]

Although initially only artificial polyelectrolytes were suggested for LbL modification of electrodes, nowadays significant efforts are being made to expand this approach to biocompatible materials. Thin films of chitosan biopolymer susceptible to chemical modification by way of reactive functional groups were investigated due to several aspects. The first one is the switching net charge of the polymer film on the top of the electrode, and the second one is introduction of charge-based chemical recognition to amperometric sensors.[99] Modification of electrodes with biocompatible materials is a critical point for designing safe and reliable tissue–electrode interfaces of neuroprosthetic and cardiostimulating electrodes. Platinum electrodes modified by alternating layers of carbon nanotubes and poly(vinyl acetate) can serve as a new material for neural interfacing and significantly outperform materials available today in terms of electrochemical stability, low impedance and charge storage capacity.[100] Proteins and ferments assembled in multilayers on the top of electrodes have ushered a new era of electrochemical biosensors. Alternatively, immobilized poly(sodium 4-styrenesulfonate) and horseradish peroxidase (HRP) on zinc oxide nanorods exhibited a wide linear range and low detection limit of hydrogen peroxide without any electron transfer mediator.[101]

Another biocompatible hydrogen peroxide sensor based on HRP was assembled with a deoxyribonucleic acid (DNA) network. The last one greatly amplified the coverage of HRP molecules on the electrode surface and facilitated the charge carriers enhancing the electron transfer between HRP and the electrode. The biosensor showed fast response, high sensitivity, good reproducibility, long-term stability and an extremely low detection limit.[102] Direct electron transfer was observed for glucose oxidase immobilized on titanium dioxide. A glucose sensor with high sensitivity, low detection limit, good selectivity and long-term stability can be obtained without a mediator.[103] Experimental results showed that polyelectrolyte-stabilized colloidal gold can be used as a biocompatible matrix for enzyme immobilization.[104] It was demonstrated that chitosan-stabilized gold nanoparticles deposited on the top of a gold electrode enhanced the electron transfer ability. Protein molecules of myoglobin, hemoglobin and cytochrome c assembled on the top of these electrodes displayed an excellent electrocatalytic performance to the reduction of hydrogen peroxide and were stable as long-term sensors with reproducible measurements.[105] A densely packed gold nanoparticle platform combined with a multiple-enzyme-labeled detection antibody–magnetic bead bioconjugate was used as the basis for an ultrasensitive electrochemical immunosensor to detect cancer biomarkers in serum.[106]

Electrochemically triggered self-assembly of charge-shifting polyelectrolytes in nanoscale multilayers was demonstrated for many systems.[107] For example, an electrochemically generated pH gradient leads to the hydrolysis of anionic dimethylmaleic-modified PAH[108] or citraconic-modified PAH[109] to cationic PAH and its consequent assembly with anionic PSS.

Since polyelectrolyte assemblies are held together on the basis of electrostatic interaction, their stability is highly sensitive to influencing electrical fields. As reported by Zahn et al.,[110] release of DNA encapsulated in PEMs was triggered by the application of electrochemical potential. In the study of Si et al.,[111] calcein from vesicles embedded in polyelectrolyte layers was released and delivered to viable cells on the top of the assembly upon the application of an electrochemical stimulus.

A biocompatible method of selective detaching of three-dimensional cell-encapsulated hydrogel from a culture substrate was reported.[112,113] LbL assembly of PLL–hyaluronic acid with methacrylated chitosan on its top was deposited on an indium tin oxide (ITO) substrate. Heparin-based hydrogel fabricated on the top of the composite described earlier was detached by dissolution of the underlying PEM when applying an oxidative potential. The applied potential did not affect the viability or the function of the cells in the entire hydrogels.

To sum up, concerning the electrochemical aspects, LbL deposition of PEMs is a simple ways nanostructuring electrode surfaces. These complex structures can play an important role not only in tuning the structure of the electrodes on which surface they were deposited, but also in creating novel smart stimulus-responsive materials. External stimuli (electric field) to electrode–PEM hybrids can serve as a trigger for various processes – reversal switch of surface wettability, self-assembly of polyelectrolytes, release of the encapsulated substance and detachment of cell-encapsulated hydrogel. Thus, the diversity of the electric stimulus responses of such nanostructured hybrid material can find applications for biosensing, nanoactuation platforms and so on.

2.2.2 Photoelectrochemical applied devices

Taking into account the potential of polyelectrolyte layers for application in photoelectrochemical device fabrication, one should note that they can play an important role as templates for oxide semiconductor or metal film preparation.[114,115] Particularly, Lowman et al.[115] used LbL assembly of linear PEI and PAA as a framework for titanium dioxide porous layer preparation for the fabrication of dye-sensitized solar cells (DSSCs). The PEI layer can play an important role in the formation and growth of continuous, ultrasmooth and highly conductive silver coating for light-emitting diodes, photodetectors and optoelectronics.[116]

The combination of BCMs with PAA layers can be actuated by the pH gradient on the irradiated semiconductor surface described in the previous section. In the study of Lanchuk et al.,[117] the reaction of photoelectrochemical water splitting was used as the trigger for the actuation of deposited weak polyelectrolytes.

The illumination of the semiconductor with supraban energies causes the formation of photoelectrons and photoholes on the surface, followed by scavenging of oxygen molecules and surface hydroxyl groups, respectively. The photogenerated protons determine local acidification of the surface layer, which was confirmed by pH mapping by SIET.[42] The pH decrease leads to changes in the thickness and stiffness of the weak polyelectrolyte assembly; after fast switching, the system exhibited slow relaxation, which can potentially find applications in designing biomimicking materials.

A large number of papers are dedicated to the exploitation of semiconductor–polymer hybrid structures that can be used as an intermediate layer in organic or perovskite solar cells for their efficiency improvement.[118–123] One of the requirements for the efficient functioning of solar cells is the minimization of the barriers for charge transport across the active layer–electrode interface. Aliphatic polyelectrolytes containing amine groups (PEI and ethoxylated PEI (PEIE)) can be employed as an electron transport layer (ETL) to reduce the work function of the ITO and the interfacial energy barrier so as to facilitate the electron transfer between the active material and the electrode.

The deposition of PEI and PEIE resulted in the formation of a thin interfacial dipole between the active layer and the ETL. Also, composite materials based on semiconductor material (e.g. zinc oxide[118] and titanium dioxide[119]) with PEI or PEIE can act as the buffer cathode (i.e. ETL)[120,121] or as a protective layer in a hybrid organic–inorganic photocathode for hydrogen evolution operated in acidic conditions.[122]

Regarding the structure of inverted polymer solar cells, the interfacial layer is placed between the active layer material (e.g. fullerenes and conjugated polyelectrolytes (CPEs)) and the cathode (e.g. ITO). In the study of Jia et al.,[123] the ETL based on zinc oxide and PEI combined the advantages of both semiconductor and polymer components responsible for high charge carrier mobility and good film formation ability, respectively. The authors demonstrated that blending of PEI within the oxide film improved the surface roughness of the zinc oxide film, enhanced the structural order of zinc oxide in zinc oxide:PEI composite perpendicular to the surface of ITO the cathode and, consequently, significantly increased the mobility of electrons in the vertical direction with the content of PEI in the composite film up to 7 wt%. The use of zinc oxide–PEI composite in inverted solar and perovskite solar cells showed an improvement in power conversion efficiency (PCE) in comparison with the cases wherein only zinc oxide and PEI are used as cathode buffer layers.[123] In addition, the device stability (in comparison with the stability of the control device without the cathode buffer layer zinc oxide:PEI) also increased.

One of the ways to increase the PCE value is to employ multijunction solar cells instead of single-junction ones. However, the main obstacle for the arising applications of such devices is

interfacial losses between the hole-transporting layer (HTL) (e.g. poly(3,4-ethylenedioxythiophene) (PEDOT):PSS or molybdenum oxide nanoparticles) and the active polymer layers. Du et al.[124] showed that a multilayer consisting of HTL–zinc oxide–PEI possesses all the requirements needed for efficient intermediate layers in multijunction solar cells – high charge carrier recombination efficiency, high transparency and high physical robustness. In addition, tandem solar cells with this intermediate layer showed nearly no loss of V_{oc} and a function comparable to that of reference single-junction solar cells.

The deposition of PEI directly onto the surface of semiconductor films leads to the smoothening of the surface, decreasing the R_{ms} value. For the applications in solar cells, this fact can play an important role in the improvement of charge transfer. For example, the smooth interface morphology of a hybrid titanium dioxide–PEI film[91] can reduce interfacial defects of the semiconductor film followed by diminished light scattering and reflection. Additionally, a reduction in the recombination of charge carriers after polyelectrolyte deposition can also result from the smooth and featureless interface morphology. The magnification of the device short-circuit density J_{sc} is the consequence of titanium dioxide–PEI's positive effect on device performance in comparison with a pure titanium dioxide layer. Recombination dynamics and charge transport were measured using EIS (Figure 4(f)). The curve in the low-frequency region depends on the charge transport between the active layer and ITO electrode. Devices based on a PEI-modified titanium dioxide layer possess low charge transfer resistance in comparison with the pristine titanium dioxide-based device, demonstrating the probable facilitation of the electron transport from the ITO cathode to the active polymer-based layer and decreasing contact resistance.[125] The J–V measurements under dark conditions confirmed the suggestion of the electron transport enhancement in the case of titanium dioxide–PEI-modified solar cells.

Yan et al.[126] studied the effect of PEI layer deposition onto a titanium dioxide ETL on the device behavior. The authors altered the deposition of the polyelectrolyte on the top of the semiconductor coating, underneath it or in the bulk. It has been demonstrated that PEI deposition on the top of the titanium dioxide ETL facilitated the extraction of photogenerated electrons due to the formation of strong dipoles formed at the active layer–ETL interface, reduced energy barrier and, consequently, stabilized maximized efficiency. The maximum PCE value of the titanium dioxide–PEI-based device was c. 10%, whereas for pure titanium dioxide, the value was c. 9·5%. In another experiment, the authors blended titanium dioxide nanoparticles directly with PEI solution to obtain bulky functionalized titanium dioxide coating and estimated the impact on the performance of the solar cell. The optimal content of PEI turned out to be 10 wt%, which facilitated the dispersion and stabilization of titanium dioxide nanoparticles. With the use of lower or higher amounts of PEI, large aggregates of the semiconductor nanoparticles on the substrate were observed. Thus, the optimal concentration of PEI

Surface Innovations

Feedback mechanisms at
inorganic–polyelectrolyte interfaces for
applied materials
Ryzhkov, Brezhneva and Skorb

can lead to the formation to the cluster-free films, and, as a result, the highest PCE value is related to the optimal conditions of light absorption. The deposition of PEI underneath the titanium dioxide layer decreased the work function of the ITO (from 4·62 to 3·97 eV), facilitating charge extraction. Moreover, the softness of the polyelectrolyte in a viscous state permits penetration into the oxide layer, reducing its work function and reaching the highest efficiency. The preparation of the PEI–titanium dioxide–PEI triple layer where the polyelectrolyte was deposited both underneath and on the top of the titanium dioxide layer resulted in the reduction of J_{sc} and V_{oc} values – the authors suggest such reduction of the device parameters with the inhibiting nature of multiple PEI layers followed by hampering of electron transport.

Addition of a negatively charged polyelectrolyte – for example, PSS,[127] which supplies counter ions for positively charged PEI – and, consequently, the formation of an polyelectrolyte complex can lead to the tuning of the cathode work function, enhancement of the photocurrent and the device PCE value, resulting from the enhanced electron extraction at the PEI:PSS–active layer interface. The use of a titanium oxide (TiOx)–PEI:PSS bilayer system as an interfacial layer showed a decrease in series resistance, lowering the work function of the TiOx layer thus eliminating the energy barriers for electron transport and injection.

A special class of polyelectrolytes – CPEs – is interesting for solar cell applications as sensitizers due to their good absorption properties, adjustable bandgap and charge and exciton transport properties.[128,129] CPEs are π-conjugated polymers with ionic or ionizable groups on a π-conjugated backbone[130] and can be used as a light-harvesting material in DSSCs. Studies of CPE absorption onto the surface of semiconductor single crystals were performed in several works.[129–131] The nearly atomically flat surfaces of zinc oxide and titanium dioxide single crystals were used as model systems for the investigation of the CPE adsorption behavior. The proper choice of solvent, exposure time and concentration led to the necessary polymer chain length, surface coverage and thickness of the resulted film. The resulted polymer coating possesses the appropriate light absorption and electron injection properties for obtaining the incident photon-to-current and absorbed photon-to-current efficiency values adapted for further solar cell fabrication.[131] Zhu et al.[129] provided the conditions for avoiding aggregation of CPE molecules in the solution and after the adsorption on zinc oxide surface. The polyelectrolyte molecules were present as single unaggregated chains with a coiled conformation consisting of a helical structure, stabilized by π-interactions and hydrogen bonds between the carboxylic groups. This was confirmed by atomic force microscopy analysis. The unaggregated CPEs underwent efficient charge injection into the oxide semiconductor.

Fluorine-based CPEs as investigated by Pan et al.[130] produce interlayers with high transparency and smooth surface morphology with the decrease in the work function of a zinc oxide-coated ITO electrode. An ultrathin layer of CPE (~5 nm)

leads to the suppression of the charge carrier recombination and series resistance. The double interlayer zinc oxide–CPE structure allows preparation of high-performance organic PV devices.

In summary, the functionalization of the intermediate ETL of zinc oxide or titanium dioxide by polyelectrolyte layers can lead to the improvement in the performance of solar cell devices in comparison with non-modified zinc oxide and titanium dioxide analogs. Such hybrid structure can combine the advantages of both components – high electron affinity, transparency, air stability from one side and the ability of thin film formation from the other. The introduction of polyelectrolytes leads to the elimination of poor contacts on the ETL–active layer interfaces caused by the intrinsic surface defects of the inorganic semiconductor. Polyelectrolytes facilitate charge transport through the formation of dipole moments on the interface. Also, the degree of functional group ionization can lead to changes in charge carrier transport characteristics. Moreover, the important feature for the enhancement of the device performance is the formation of non-aggregated polyelectrolyte coating in order to obtain the maximum light absorbance and photoelectrochemical characteristics. That is why the precise control of film thickness and degree of polyelectrolyte aggregation is very important during the procedure of polyelectrolyte layer deposition or incorporation into the inorganic layer. The aforementioned factors open perspectives on the fabrication of high-performance solar cells or organic PVs based on the intermediate hybrid semiconductor–polyelectrolyte layer.

2.3 Self-regulated processes

Among trends in the design of smart materials, self-regulated materials and processes at interfaces play an important role, and the following aspects are under consideration: (a) the choice of the proper material and its environment; (b) stability of the material to the degradation under different environmental conditions; (c) mechanism of the degradation; (d) strategies for improvement of the material properties (e.g. stability); and (e) an attempt to make materials self-responsive during degradation. In this review, the authors discuss self-healing and self-cleaning materials and their autocatalytic network design.

Self-healing materials are a class of advanced materials that have the ability to control feedback processes, for example, at the solid–polyelectrolyte interface.[132] First, the nature of changes near the solid surface and in the local environment is important – for example, a change in pH during the corrosion process.[133] Second, it is important to find proper polyelectrolytes that could be responsible for stabilization ('healing') of the inorganic component damaged by the change in the surrounding medium. In this case, weak polyelectrolytes that are sensitive to pH alteration and can exhibit buffer properties (e.g. chitosan and PEI as representatives of the imine class) could be mentioned.[134] The composition of the PEMs should be also regarded. For instance, the LbL approach can be used for optimizing the architecture of the layers for providing both the

Surface Innovations

**Feedback mechanisms at
inorganic–polyelectrolyte interfaces for
applied materials**
Ryzhkov, Brezhneva and Skorb

effect of pH buffering and improved material stability.[135] Self-healing has a broad spectrum of applications, including corrosion protection,[132–137] elements of antifouling and antimicrobial coatings[138] and bioinspired superhydrophobic interfaces.[139]

The self-healing of metals by polyelectrolyte assemblies is associated with several factors[132–140] (Figure 9): (*a*) pH normalization through weak polyelectrolyte buffering; (*b*) the polyelectrolyte chain water-induced mobility; and (*c*) the possibility of release of organic molecules (healing agents). The versatile technology for the formation of self-regulated corrosion systems can be extended and optimized for novel trends and future needs.[132]

Today a particular research interest is paid to the area of systems that convert an input signal into a single output in a non-linear way.[141] From the chemical point of view, the oscillation reactions convert a steady supply of reactants into a periodic production of products. From the signal process point of view, one of the reactants is an input signal and one of the products is an output (Figure 10).[50,60–63] The oscillatory network first transits from steady output to oscillatory output and then back to a steady state. The presented oscillator in Figure 10 uses trypsinogen (zymogen of the proteolytic enzyme trypsin), a synthetic tripeptide

(a masked inhibitor for trypsin) and aminopeptidase (another proteolytic enzyme) as source materials. Oscillations result from the interaction between a positive feedback loop, which consists of an autocatalytic production of trypsin from trypsinogen, and a delayed negative feedback loop, which consists of trypsin inhibitor production. Interestingly, it was shown that titania–polyelectrolyte particles can drastically affect the network and propagation of the autocatalytic wave on the surface.[50] The challenges in this area include (*a*) predictive design of the interface chemical switches and oscillators and (*b*) computing cascades with bacterial signaling and metabolism.

In the field of model self-cleaning materials, antifouling coatings[139] and model microbiome systems[142,143] should be also mentioned. The effects of antibacterial evaluation suggest that the nanofunctionalized titanium dioxide coating possesses excellent antimicrobial activity.[142] An interdisciplinary approach includes the complementary experience in the development of PMs able to communicate with bacterial biofilms.

Can the behavior of bacterial communities (B) be manipulated by programming photoreactions on the surface of well-studied materials – for example, nanoengineered semiconductor composite
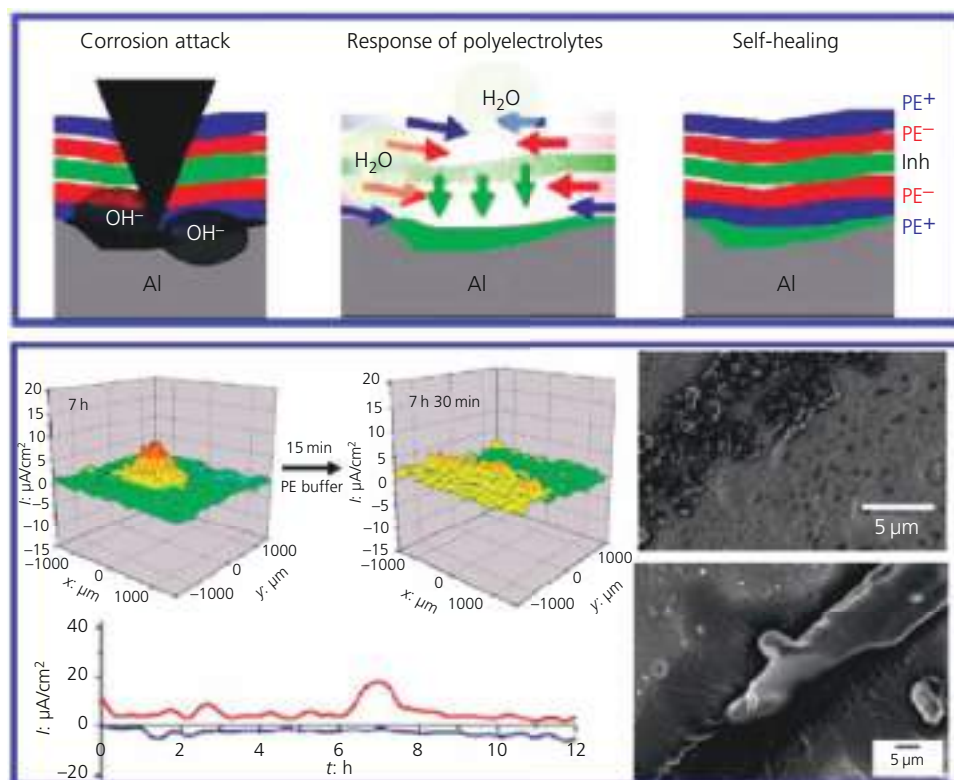
Figure 9. Corrosion zone self-healing mechanism based on LbL assembly of polyelectrolyte (PE): schematic diagram of corrosion attack with a change in pH and immediate response of polyelectrolytes with corrosion inhibitor in composition (Inh); corresponding SVET maps and graphs of minimum and maximum cathodic and anodic activities proving self-healing; scanning electron microscopy images of a corroded defect and progress of the healing of the defect with polyelectrolytes. Adapted from Andreeva *et al.*[135]

Surface Innovations

Feedback mechanisms at
inorganic–polyelectrolyte interfaces for
applied materials
Ryzhkov, Brezhneva and Skorb
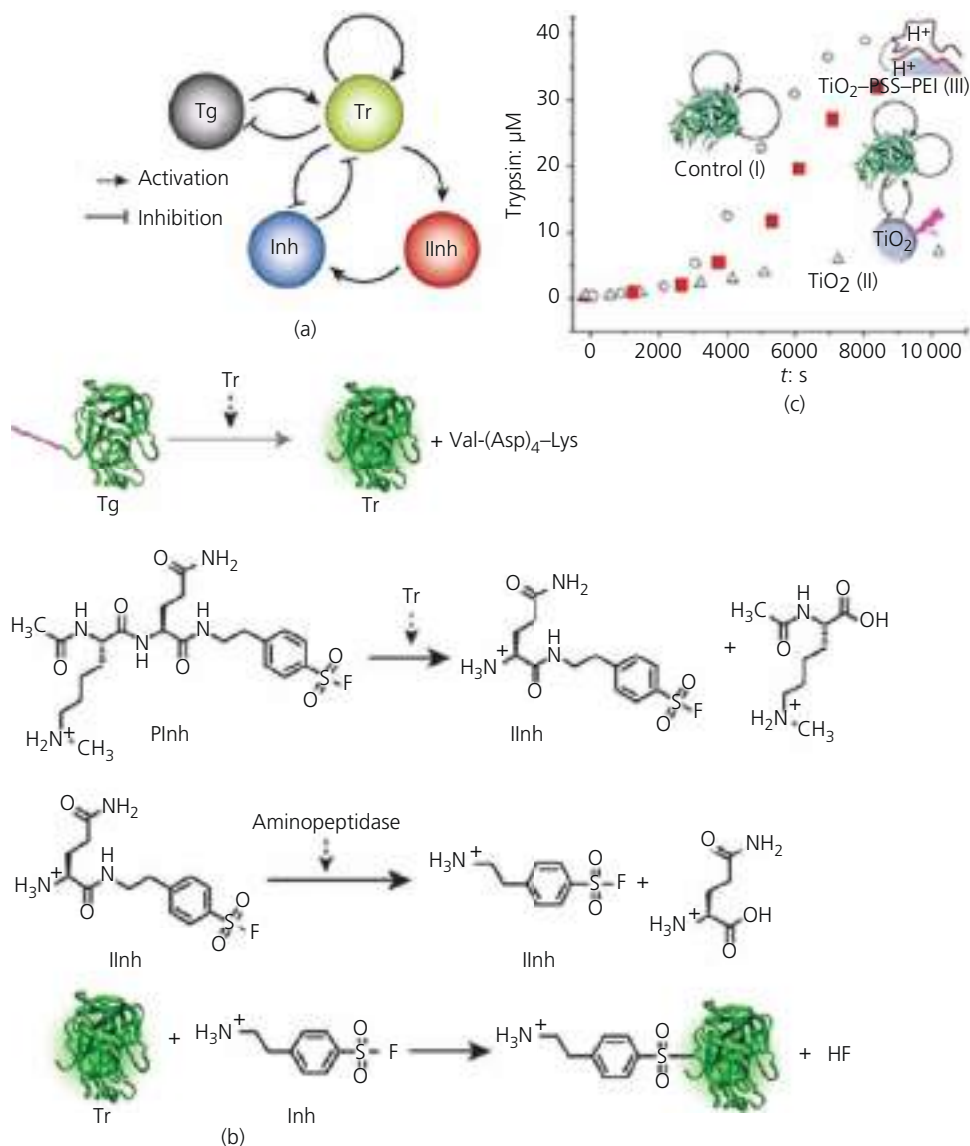
Figure 10. Autocatalytic trypsin (Tr) oscillator. (a) Depiction of the network of enzymatic reactions in the trypsin oscillator. (b) Specific reactions in the reaction network. Dashed arrows indicate catalysis. Reprinted with permission from Semenov et al.[61] (c) Inclusion of additional components into the trypsin oscillator drastically changes its kinetics: conversion of the fluorogenic substrate monitored at $\lambda_{ex} = 450$ nm and $\lambda_{em} = 520$ nm; each point is checked for 60 s with a time interval of 1 s. I, trypsin control reaction; II, III, reaction in the presence of titanium dioxide (II) or titanium dioxide–PSS–PEI (III) under irradiation. Reprinted with permission from Lanchuk et al.[50] IInh, intermediate inhibitor; Inh, inhibitor; PInh, proinhibitor; Tg, trypsinogen

surfaces (PM) (Figure 11(a))? If a bacteria/biofilm binary system can be regarded as a single unit (B), where bioreactions may activate or inhibit bacterial metabolism (Figure 11(b)), programming temporal reactions can be taken under consideration. Communication between bacteria of a given type by means of specific chemical species is becoming a rising topic of research,[144–151] Ion channels enable electrical communication within bacterial communities[144] (Figure 11(c)). Different types of bacteria communicate within biofilms[145] (Figure 11(d)). Thus, it should be possible to make them follow a given spatiotemporal program dictated by a photoresponsive material (Figure 11(e)).

Recently, Prindle et al.[144] have studied in detail the temporal synchronization and desynchronization of biofilm behavior (Figure 11(b)) in response to oscillations in potassium (K^+) ion concentration. However, there was not any study that could propose spatial localization of the programming signal in systems containing synthetic ionic channels. Ulasevich et al.[71] in their work aimed to fill this gap with photosensitive materials capable of locally controlled release of hydrogen and potassium ions with a further study of the resulting changes in biofilm growth and cell response.[70] Reversible oscillation of LbL films based on high-amplitude actuation of BCMs allows controlling the
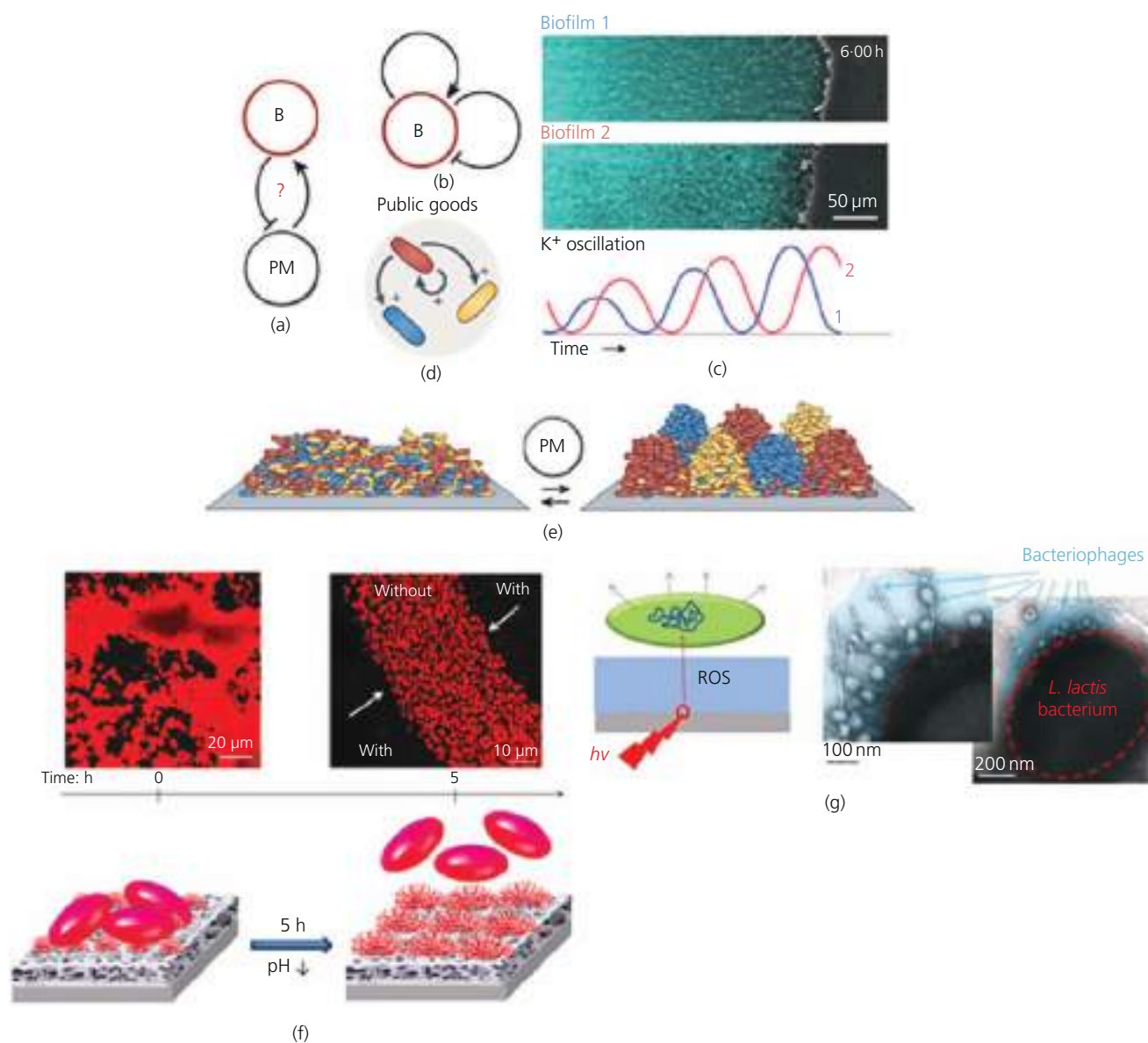
Figure 11. Taking microbial metabolism as part of a complex system for switching feedback stimuli between PMs and materials. (a) How to program bacterial communities is a key point in the authors' project. (b) A bacterial community has its own feedback mechanism – for example, (c) oscillation of potassium ions in time depending on chemical surroundings, (d) spatial structure, co-operation and competition in biofilms of different bacterial communities (shown in red, blue and yellow) to be programmed on the nanoengineered surface – for example, by photocontrolled local reactions. (c) is adapted from Prindle et al.,[144] and (d) and (e) are adapted from Rivera-Chavez and Bäumler.[145] (f) Self-controllable system. Confocal kinetic study (fluorescence mode) and schematic illustration of pH-triggered self-cleaning behavior of a porous metal surface covered with pH-responsive micelles. *Lactococcus lactis* 411 bacteria (loaded with dye) were used as model cells. Bacteria decrease the pH; micelles respond to the change and increase in size; and bacteria detach from the surface, remaining just on the surface without micelles. Adapted from Gensel et al.[146] (g) Schematic representations of a photoactuator employing photogeneration of ROS to alter cell metabolism (inducing apoptosis and proliferation or production of certain metabolites). Transmission electron microscopy image demonstrating the effect of ROS generated at titanium dioxide on the metabolism of lysogenic *L. lactis* bacteria (i.e. containing bacteriophage genes in their DNA). The opening of the cell envelope and the release of viruses is observed. Adapted from Skorb et al.[147]

cell behavior on the surface. Ulasevich et al.[71] have successfully applied switching of a polyelectrolyte assembly by light to control the behavior of supported cells.[70] In particular, the change in stiffness results in migration of cells to a harder surface.

A systematic study of nanoscale surface design is needed to program significant bioresponses. BCM polyelectrolyte brushes adsorbed on mesoporous surface demonstrated[146] an affective self-cleaning property of lactic bacteria. Lactic bacteria

Surface Innovations

**Feedback mechanisms at
inorganic–polyelectrolyte interfaces for
applied materials**
Ryzhkov, Brezhneva and Skorb

produced lactic acid and activated BCMs – the polymer coating increased in its thickness and pushed the bacteria out of the surface. Bassler's[148] paper focuses on the synergy between PMs and living bacteria that can be deactivated; however, more interestingly, bacteria survive and interact with PMs in a predictive way. Lactic bacteria could reversibly be activated/deactivated by PMs due to the cyclic metabolic process in their life cycle.

Nowadays two important features, (a) bacterial metabolism regulation and stimulation and (b) degradation of bacteria due to a lethal concentration of reactive oxygen species (ROS), are being intensively discussed. The ROS photogenerated on titania could further penetrate into the intracellular volume and alter the activity of the microorganisms. Both photokilling of bacteria and profound changes in their metabolism can be attained depending on the exposure used: the authors are interested in changing the metabolism without deactivation of bacteria. In the authors' previous work, it has been shown[147] (Figure 11(g)) that ROS produced on titania surface effectively induce lytic cycles of lysogenic bacteria without killing them. To enhance the superoxide yield and bacteria adhesion, bimetallic silver–nickel nanoparticles can be deposited in the pores of a titania film.[51] The main objective in this field of research is to develop PMs which interact with bacteria growing on the materials, opening the questions of (a) what type of chemistry is suitable for communication with bacteria; (b) how to design two-sided communication – that is, processing of signals coming from both the bacterial signaling network and synthetic chemical network; and (c) how can synthetic chemistry influences and responds to bacterial activity.

3. Conclusions

In this paper, several aspects of the inorganic (semiconductor or metal)–PEM interface usability are highlighted. Processes at interfaces are important for multiple-stimulus-responsive materials ('photon-to-proton conversion', where electromagnetic irradiation leads to the formation of photogenerated protons and thus a decrease in the pH value of the subsurface layer of the irradiated material). External stimuli can be regarded as triggers for the actuation of soft matter without its destruction. Polyelectrolyte deposition can impact differently on the photocatalytic activity of the hybrids – in some cases, polyelectrolytes and semiconductors can have a synergistic effect of photocatalytic activity enhancement, and, in the others, polymer coatings can suppress the photoactivity of the inorganic component. In general, the functionalization of the interfacial layers with polyelectrolytes in solar cells leads to the enhancement of the device performance due to the improved light absorption and enhanced electron transport from the active layer to the device. The aforementioned characteristics of the hybrids provide possibilities of their exploitation in various applications. Self-regulated systems are discussed together with the existing problems of interdisciplinary view to the problem of design of PMs 'living' together with biological networks.

REFERENCES

1. Xiang B, Li Y, Huy Pham C, Paesani F and Xiong W (2017) Ultrafast direct electron transfer at organic semiconductor and metal interfaces. *Science* **3(11)**: e1701508.
2. Zhang H, Guo X, Hui J *et al.* (2011) Interface engineering of semiconductor/dielectric heterojunctions toward functional organic thin-film transistors. *Nano Letters* **11(11)**: 4939–4946.
3. Bradley DDC (1991) Characterization of polymers for semiconductor applications. *Polymer International* **26(1)**: 3–16.
4. Skorb EV and Andreeva DV (2014) Layer-by-layer smart coatings for corrosion protection. In *Handbook of Smart Coatings for Corrosion Protection* (Hamdy AS (ed.)). Woodhead Publishing, Cambridge, UK, vol. 64, pp. 307–327.
5. Supplie O, May MM, Brückner S *et al.* (2017) In situ characterization of interfaces relevant for efficient photo-induced reactions. *Advanced Materials Interfaces* **4(21)**: 1601118.
6. Delcea M, Möhwald H and Skirtach AG (2011) Stimuli-responsive LbL capsules and nanoshells for drug delivery. *Advanced Drug Delivery Reviews* **63(9)**: 730–747.
7. Whitesides GM and Grzybowski B (2002) Self-assembly at all scales. *Science* **295(5564)**: 2418–2421.
8. Skorb EV, Skirtach A, Sviridov DV, Shchukin DG and Möhwald H (2009) 'Smart' laser-controllable coatings for corrosion protection. *ACS Nano* **3(7)**: 1753–1760.
9. Garmire E (1994) Nonlinear optics in semiconductors. *Physics Today*, May: pp. 42–48.
10. Walker BT, Flatten LC, Hesten HJ *et al.* (2018) Driven-dissipative non-equilibrium Bose–Einstein condensation of less than ten photons. *Nature Physics* **14**: 1173–1177.
11. Ropp C, Bachelard N, Barth D, Wang Y and Zhang X (2018) Dissipative self-organization in optical space. *Nature Photonics* **12(12)**: 739–743.
12. Lonergan MC (1997) A diode tunable based on an inorganic semiconductor/conjugated polymer interface. *Science* **278(5346)**: 2103–2106.
13. Skorb EV, Shchukin DG and Sviridov DV (2008) Hybrid silica–zirconia films loaded with titania nanoparticles and titania-based nanocontainers: novel materials for thin-film photocatalysts and photocontrollable coatings. In *Molecular and Nanoscale Systems for Energy Conversion* (Varfolomeev S (ed.)). Nova Science Publishers, New York, NY, USA, pp. 75–87.
14. Shchukin DG, Andreeva DV, Skorb EV and Möhwald H (2010) Emerging concepts in interfacial chemistry of hybrid materials. In *Supramolecular Chemistry of Hybrid Materials* (Rurack K (ed.)). Wiley-VCH, Weinheim, Germany, pp. 639–653.
15. Mamidala V, Nalla V, Maiti PS, Valiyaveettil and Ji W (2013) Charge transfer assisted nonlinear optical and photoconductive properties of CdS-AgInS$_2$ nanocrystals grown in semiconducting polymers. *Journal of Applied Physics* **113(12)**: 123107.
16. Pan C, Dong L, Ge L, Wang J and Gu Z (2009) Highly active TiO$_2$/polyelectrolytes hybrid multilayered hollow nanofibrous photocatalyst prepared from electrospun fibers using electrostatic layer-by-layer technique. *Journal of Macromolecular Science, Part B: Physics* **48(1)**: 92–105.
17. Shchukin DG and Sviridov DV (2006) Photocatalytic processes in spatially confined nanoreactors. *Journal of Photochemistry and Photobiology C: Photochemistry Reviews* **7(1)**: 23–29.
18. Shchukin DG, Ustinovich EA, Sukhorukov GB, Möhwald H and Sviridov DV (2005) Metallized polyelectrolyte microcapsules. *Advanced Materials* **17(4)**: 468–472.
19. Sun S, Deng T, Ding H, Chen Y and Chen W (2017) Preparation of nano-TiO$_2$-coated SiO$_2$ microsphere composite material

Surface Innovations

Feedback mechanisms at
inorganic–polyelectrolyte interfaces for
applied materials
Ryzhkov, Brezhneva and Skorb

and evaluation of its self-cleaning property. *Nanomaterials*
7(11): 367.
20. Shchukin DG and Sukhorukov GB (2004) Nanoparticle synthesis in
engineered organic nanoscale reactors. *Advanced Materials* **16(8)**:
671–682.
21. Carre G, Garnier L, Moeller-Sigert J *et al.* (2015) Antibacterial
textiles functionalized by layer-by-layer assembly of polyelectrolytes
and TiO₂ photocatalyst. *RSC Advances* **5(49)**: 38859–38867.
22. Dal'Acqua N, Scheffer FR, Boniatti R *et al.* (2013) Photocatalytic
nanostructured self-assembled poly(allylamine hydrochloride)/poly
(acrylic acid) polyelectrolyte films containing titanium dioxide-gold
nanoparticles for hydrogen generation. *Journal of Physical
Chemistry C* **117(44)**: 23235–23243.
23. Faria ACR, Vebber MC, Dal'Acqua N *et al.* (2017) Characterization
and application of self-assembled thin films of polyelectrolyte/TiO₂/
CdSe for hydrogen production. *International Journal of Hydrogen
Energy* **42(26)**: 16568–16578.
24. Shchukin DG, Ustinovich EA, Sviridov DV, Lvov YM and Sukhorukov GB
(2003) Photocatalytic microreactors based on TiO₂-modified
polyelectrolyte multilayer capsules. *Photochemical & Photobiological
Sciences* **2(10)**: 975–977.
25. Zhu H, Jiang R, Xiao L *et al.* (2013) CdS nanocrystals/TiO₂/
crosslinked chitosan composite: facile preparation, characterization
and adsorption–photocatalytic properties. *Applied Surface Science*
273: 661–669.
26. Timin AS, Muslimov AR, Lepik KV *et al.* (2016) Triple-responsive
inorganic–organic hybrid microcapsules as a biocompatible smart
platform for the delivery of small molecules. *Journal of Materials
Chemistry B* **4(45)**: 7270–7282.
27. Gao H, Wen D, Tarakina NV *et al.* (2016) Bifunctional ultraviolet/
ultrasound responsive composite TiO₂/polyelectrolyte microcapsules.
Nanoscale **8(9)**: 5170–5180.
28. Bang K, Lim H, Park S and Suh K (2015) A facile template-free
synthesis of pH-responsive polyelectrolyte/amorphous TiO₂
composite hollow microcapsules for photocatalysis. *RSC Advances*
5(73): 59257–59262.
29. Essawy AA, Sayyah SM and El-Nggar AM (2017) Wastewater
remediation by TiO₂-impregnated chitosan nano-grafts exhibited dual
functionality: high adsorptivity and solar-assisted self-cleaning. *Journal
of Photochemistry and Photobiology B: Biology* **173**: 170–180.
30. Vebber MC, Faria ACR, Dal'Acqua N *et al.* (2016) Hydrogen
production by photocatalytic water splitting using pol(allylamine
hydrochloride)/poly(acrylic acid)/TiO₂/copper chlorophyllin self-
assembled thin films. *International Journal of Hydrogen Energy*
41(40): 17995–18004.
31. Xiao G, Su H and Tan T (2015) Synthesis of core–shell bioaffinity
chitosan-TiO₂ composite and its environmental applications. *Journal
of Hazardous Materials* **283**: 888–896.
32. Renfigo-Herrera JA, Marin-Silva DA, Mendoza-Portillo E, Pinotti AN
and Pizzio (2018) Chitosan films containing TiO₂ nanoparticles
modified with tungstophosphoric acid for the photobleaching of
malachite green in solid–gas interfaces upon different wavelengths.
Molecular Catalysis **448**: 1–9.
33. Yang YH, Ren N, Zhang YH and Tang Y (2009) Nanosized cadmium
sulfide in polyelectrolyte protected mesoporous sphere: a stable and
regeneratable photocatalyst for visible-light-induced removal of
organic pollutants. *Journal of Photochemistry and Photobiology A:
Chemistry* **201(2–3)**: 111–120.
34. Pincus LN, Melnikov F, Yamani JS and Zimmerman JB (2018)
Multifunctional photoactive and selective adsorbent for arsenite and
arsenate: evaluation of nano titanium dioxide-enabled chitosan cross-
linked with copper. *Journal of Hazardous Materials* **358(15)**: 145–154.
35. Neela Priya D, Modak JM and Raichur AM (2009) LbL fabricated
poly(styrenesulfonate)/TiO₂ multilayer thin films for environmental
applications. *ACS Applied Materials & Interfaces* **1(11)**: 2684–2693.
36. Fares HM and Schlenoff JB (2017) Diffusion of sites versus
polymers in polyelectrolyte complexes and multilayers. *Journal of
the American Chemical Society* **139(41)**: 14656–14667.
37. Fares HM, Ghoussoub YE, Surmaitis RL and Schlenoff JB (2015)
Toward ion-free polyelectrolyte multilayers: cyclic salt annealing.
Langmuir **31(21)**: 5787–5795.
38. Schlenoff JB (2018) Site-specific perspective on interactions in
polyelectrolyte complexes: toward quantitative understanding.
Journal of Chemical Physics **149(16)**: 163314.
39. Delgado JD and Schlenoff JB (2017) Static and dynamic solution
behavior of a polyzwitterion using a Hofmeister salt series.
Macromolecules **50(11)**: 4454–4464.
40. Suzurikawa J, Nakao M, Kanzaki R and Takahashi H (2010)
Microscale pH gradient generation by electrolysis on a light-
addressable planar electrode. *Sensors and Actuators* **149(1)**: 205–211.
41. Cheng Y, Yang QD, Xiao J *et al.* (2015) Decomposition of
organometal halide perovskite films on zinc oxide nanoparticles.
ACS Applied Materials & Interfaces **7(36)**: 19986–19993.
42. Maltanava HM, Poznyak SK, Andreeva DV *et al.* (2017) Light-
induced proton pumping with a semiconductor: vision for
photoproton lateral separation and robust manipulation. *ACS Applied
Materials & Interfaces* **9(28)**: 24282–24289.
43. Andreeva DV, Kollath A, Brezhneva N *et al.* (2017) Using a chitosan
nanolayer as an efficient buffer to protect pH-sensitive
supramolecular assemblies. *Physical Chemistry Chemical Physics*
19(35): 23843–23848.
44. Brezhneva N, Nikitina A, Ryzhkov N *et al.* (2019) Importance of
buffering nanolayer position in layer-by-layer assembly on titania based
hybrid photoactivity. *Journal of Sol-Gel Science and Technology* **89(1)**:
92–100.
45. Schouten C, van den Beucken JJ, de Jonge LT *et al.* (2009) The
effect of alkaline phosphatase coated onto titanium alloys on bone
responses in rats. *Biomaterials* **30(32)**: 6407–6417.
46. Muderrisoglu C, Saveleva M, Abalymov A *et al.* (2018)
Nanostructured biointerfaces based on bioceramic calcium
carbonate/hydrogel coatings on titanium with an active enzyme
for stimulating osteoblasts growth. *Advanced Materials Interfaces*
5(19): 1800452.
47. Li Z, Zhang X, Liu C *et al.* (2016) Enhanced electron extraction
capability of polymer solar cells via employing electrostatically self-
assembled molecule on cathode interfacial. *ACS Applied Materials
& Interfaces* **8(12)**: 8224–8231.
48. Fusco C, Casiello M, Catucci L *et al.* (2018) TiO₂@PEI-grafted-
MWCNTs hybrids nanocomposites catalysts for CO₂
photoreduction. *Materials* **11(2)**: 307.
49. Vallejo-Montesinos J, Martinez JCL, Montejano-Carrizales JM
et al. (2017) Passivation of titanium oxide in polyethylene matrices
using polyelectrolytes as titanium dioxide surface coatings.
Mechanics, Materials Science & Engineering **8**: 38–50.
50. Lanchuk Y, Nikitina A, Brezhneva N *et al.* (2018) Photocatalytic
regulation of an autocatalytic wave of spatially propagating
enzymatic reactions. *ChemCatChem* **10(8)**: 1798–1803.
51. Skorb EV and Möhwald H (2013) Dynamic interfaces for responsive
encapsulation systems. *Advanced Materials* **25(36)**: 5029–5043.
52. Skorb EV and Möhwald H (2014) 'Smart' surface capsules for
delivery devices. *Advanced Materials Interfaces* **1(6)**: 1400237.
53. Skorb EV, Volkova A and Andreeva DV (2014) Layer-by-layer
assembled hybrid materials for sustainable applications. *Current
Organic Chemistry* **18(18)**: 2315–2333.
54. Skorb EV, Volkova A and Andreeva DV (2015) Layer-by-layer
approach for design of chemical sensors and biosensors. *Current
Organic Chemistry* **19(12)**: 1097–1116.
55. Skorb EV and Andreeva DV (2015) Self-healing properties of
layer-by-layer assembled multilayers. *Polymer International* **64(6)**:
713–723.

Surface Innovations

Feedback mechanisms at
inorganic–polyelectrolyte interfaces for
applied materials
Ryzhkov, Brezhneva and Skorb

56. Skorb EV and Andreeva DV (2013) Bio-inspired ultrasound assisted construction of synthetic sponges. *Journal of Materials Chemistry A* **1(26)**: 7547–7557.

57. Skorb EV, Shchukin DG, Möhwald H and Sviridov DV (2009) Photocatalytically-active and photocontrollable coatings based on titania-loaded hybrid sol–gel films. *Journal of Materials Chemistry* **19(28)**: 4931–4937.

58. Wu F, Su RQ, Lai YC and Wang X (2017) Engineering of a synthetic quadrastable gene network to approach Waddington landscape and cell fate determination. *eLife* **6**: e23702.

59. Nikitina AA, Ulasevich SA, Kassirov IS *et al.* (2018) Nanostructured layer-by-layer polyelectrolyte containers to switch biofilm fluorescence. *Bioconjugate Chemistry* **29(11)**: 3793–3799.

60. Semenov SN, Wong ASY, van der Made AM *et al.* (2015) Rational design of functional and tunable oscillating enzymatic networks. *Nature Chemistry* **7(2)**: 160–165.

61. Semenov SN, Ainla A, Skorb EV and Postma S (2018) Four-variable model of an enzymatic oscillator based on trypsin. *Israel Journal of Chemistry* **58(6–7)**: 781–786.

62. Pogodaev AA, Wong ASY and Huck WTS (2017) Photochemical control over oscillations in chemical reaction networks. *Journal of the American Chemical Society* **139(43)**: 15296–15299.

63. Wong ASY and Huck WTS (2017) Grip on complexity in chemical reaction networks. *Beilstein Journal of Organic Chemistry* **13(1)**: 1486–1497.

64. Sirasani G, Tong LC and Balskus EP (2014) A biocompatible alkene hydrogenation merges organic synthesis with microbial metabolism. *Angewandte Chemie International Edition* **53(30)**: 7785–7788.

65. Wallace S, Schultz EE and Balskus EP (2015) Using non-enzymatic chemistry to influence microbial metabolism. *Current Opinion in Chemical Biology* **25**: 71–79.

66. Lentini R, Martín NY, Forlin M *et al.* (2017) Two-way chemical communication between artificial and natural cells. *ACS Central Science* **3(2)**: 117–123.

67. Cornett EM, Campbell EA, Gulenay G *et al.* (2012) Molecular logic gates for DNA analysis: detection of rifampin resistance in *M. tuberculosis* DNA. *Angewandte Chemie International Edition* **51(36)**: 9075–9077.

68. Kim J and Winfree E (2011) Synthetic in vitro transcriptional oscillators. *Molecular Systems Biology* **7(465)**: 1–15.

69. Rondelez Y (2012) Competition for catalytic resources alters biological network dynamics. *Physical Review Letters* **108(1)**: 018102.

70. Ulasevich SA, Brezhneva N, Zhukova Y *et al.* (2016) Switching the stiffness of polyelectrolyte assembly by light to control behavior of supported cells. *Macromolecular Bioscience* **16(10)**: 1422–1431.

71. Ulasevich SA, Brezesinski G, Möhwald H *et al.* (2016) Light-induced water splitting causes high-amplitude oscillation of pH-sensitive layer-by-layer assemblies on TiO$_2$. *Angewandte Chemie International Edition* **55(42)**: 13001–13004.

72. Hoshi T, Saiki H and Anzai JI (2003) Amperometric uric acid sensors based on polyelectrolyte multilayer films. *Talanta* **61(3)**: 363–368.

73. Ryzhkov NV, Mamchik NA and Skorb EV (2019) Electrochemical triggering of lipid bilayer lift off oscillation at the electrode interface. *Journal of the Royal Society Interface* **16(150)**: 20180626.

74. Pennakalathil J, Kim TH, Kim K *et al.* (2010) Ion-permselective polyelectrolyte multilayer membrane in stalled with a pH-sensitive oxazine switch. *Langmuir* **26(13)**: 11349–11354.

75. Andreeva DV, Melnyk I, Baidukova O and Skorb EV (2016) Local pH gradient initiated by light on TiO$_2$ for light-triggered modulation of polyhistidine-tagged proteins. *ChemElectroChem* **3(9)**: 1306–1310.

76. Castañeda AD, Alligrant TM, Loussaert JA and Crooks RM (2015) Electrocatalytic amplification of nanoparticle collisions at electrodes modified with polyelectrolyte multilayer films. *Langmuir* **31(2)**: 876–885.

77. Zahn R, Vörös J and Zambelli T (2014) Tuning the electrochemical swelling of polyelectrolyte multilayers toward nanoactuation. *Langmuir* **30(40)**: 12057–12066.

78. Rmaile HH, Farhat TR and Schlenoff JB (2003) pH-gated permeability of variably charged species through polyelectrolyte multilayer membranes. *Journal of Physical Chemistry B* **107(51)**: 14401–14406.

79. Gu BX, Xu CX, Zhu GP *et al.* (2009) Layer-by-layer immobilized horseradish peroxidase on zinc oxide nanorods for biosensing. *Journal of Physical Chemistry B* **113(18)**: 6553–6557.

80. Spruijt E, Choi EY and Huck WT (2008) Reversible electrochemical switching of polyelectrolyte brush surface energy using electroactive counterions. *Langmuir* **24(19)**: 11253–11260.

81. Liu Y, Yin F, Long Y, Zhang Z and Yao S (2003) Study of the immobilization of alcohol dehydrogenase on Au-colloid modified gold electrode by piezoelectric quartz crystal sensor, cyclic voltammetry, and electrochemical impedance techniques. *Journal of Colloid and Interface Science* **258(1)**: 75–81.

82. Mani V, Chikkaveeraiah BV, Patel V, Gutkind JS and Rusling JF (2009) Ultra sensitive immunosensor for cancer biomarker proteins using gold nanoparticle film electrodes and multienzyme-particle amplification. *ACS Nano* **3(3)**: 585–594.

83. Zhao J, Bradbury CR and Fermín DJ (2008) Long-range electronic communication between metal nanoparticles and electrode surfaces separated by polyelectrolyte multilayer films. *Journal of Physical Chemistry C* **112(17)**: 6832–6841.

84. Cho C, Jeon JW, Lutkenhaus J and Zacharia NS (2013) Electric field induced morphological transitions in polyelectrolyte multilayers. *ACS Applied Materials & Interfaces* **5(11)**: 4930–4936.

85. Onda M, Lvov Y, Ariga K and Kunitake T (1996) Sequential actions of glucose oxidase and peroxidase in molecular films assembled by layer-by-layer alternate adsorption. *Biotechnology and Bioengineering* **51(2)**: 163–167.

86. Kelly KD, Fares HM, Shaheen SA and Schlenoff JB (2018) Intrinsic properties of polyelectrolyte multilayer membranes: erasing the memory of the interface. *Langmuir* **34(13)**: 3874–3883.

87. Maza E, Tuninetti JS, Politakos N *et al.* (2015) pH-responsive ion transport in polyelectrolyte multilayers of poly (diallyldimethylammonium chloride) (PDADMAC) and poly(4-styrenesulfonic acid-*co*-maleic acid) (PSS-MA) bearing strong-and weak anionic groups. *Physical Chemistry Chemical Physics* **17(44)**: 29935–29948.

88. Chirea M, García-Morales V, Manzanares JA *et al.* (2005) Electrochemical characterization of polyelectrolyte/gold nanoparticle multilayers self-assembled on gold electrodes. *Journal of Physical Chemistry B* **109(46)**: 21808–21817.

89. Lindholm-Sethson B, Gonzalez JC and Puu G (1998) Electron transfer to a gold electrode from cytochrome oxidase in a biomembrane via a polyelectrolyte film. *Langmuir* **14(23)**: 6705–6708.

90. Song Y, Wang L, Ren C, Zhu G and Li Z (2006) A novel hydrogen peroxide sensor based on horseradish peroxidase immobilized in DNA films on a gold electrode. *Sensors and Actuators B: Chemical* **114(2)**: 1001–1006.

91. Thotiyl MO, Basit H, Sánchez JA *et al.* (2012) Multi layer assemblies of polyelectrolyte–gold nanoparticles for the electrocatalytic oxidation and detection of arsenic (III). *Journal of Colloid and Interface Science* **383(1)**: 130–139.

92. Ghostine RA and Schlenoff JB (2011) Ion diffusion coefficients through polyelectrolyte multilayers: temperature and charge dependence. *Langmuir* **27(13)**: 8241–8247.

93. Hoshi T, Saiki H, Kuwazawa S *et al.* (2001) Selective permeation of hydrogen peroxide through polyelectrolyte multilayer films and its use for amperometric biosensors. *Analytical Chemistry* **73(21)**: 5310–5315.

Surface Innovations

Feedback mechanisms at
inorganic–polyelectrolyte interfaces for
applied materials
Ryzhkov, Brezhneva and Skorb

94. Ostendorf A, Cramer C, Decher G and Schönhoff M (2015) Humidity-tunable electronic conductivity of polyelectrolyte multilayers containing gold nanoparticles. *Journal of Physical Chemistry C* **119(17)**: 9543–9549.

95. Grieshaber D, Vörös J, Zambelli T *et al.* (2008) Swelling and contraction of ferrocyanide-containing polyelectrolyte multilayers upon application of an electric potential. *Langmuir* **24(23)**: 13668–13676.

96. Wang S, Yu D and Dai L (2011) Polyelectrolyte functionalized carbon nanotubes as efficient metal-free electrocatalysts for oxygen reduction. *Journal of the American Chemical Society* **133(14)**: 5182–5185.

97. Sénéchal V, Saadaoui H, Rodriguez-Hernandez J and Drummond C (2017) Electrowetting of weak polyelectrolyte-coated surfaces. *Langmuir* **33(20)**: 4996–5005.

98. Jan E, Hendricks JL, Husaini V *et al.* (2009) Layered carbon nanotube-polyelectrolyte electrodes outperform traditional neural interface materials. *Nano Letters* **9(12)**: 4012–4018.

99. Zhou F, Biesheuvel PM, Choi EY *et al.* (2008) Polyelectrolyte brush amplified electroactuation of microcantilevers. *Nano Letters* **8(2)**: 725–730.

100. Comminges C, Frasca S, Sütterlin M *et al.* (2014) Surface modification with thermoresponsive polymer brushes for a switchable electrochemical sensor. *RSC Advances* **4(81)**: 43092–43097.

101. Dochter A, Garnier T, Pardieu E *et al.* (2015) Film self-assembly of oppositely charged macromolecules triggered by electrochemistry through a morphogenic approach. *Langmuir* **31(37)**: 10208–10214.

102. Aytar BS, Prausnitz MR and Lynn DM (2012) Rapid release of plasmid DNA from surfaces coated with polyelectrolyte multilayers promoted by the application of electrochemical potentials. *ACS Applied Materials & Interfaces* **4(5)**: 2726–2734.

103. Graf N, Tanno A, Dochter A *et al.* (2012) Electrochemically driven delivery to cells from vesicles embedded in polyelectrolyte multilayers. *Soft Matter* **8(13)**: 3641–3648.

104. Chassepot A, Gao L, Nguyen I *et al.* (2012) Chemically detachable polyelectrolyte multilayer platform for cell sheet engineering. *Chemistry of Materials* **24(5)**: 930–937.

105. Gwon K, Kim M and Tae G (2014) A biocompatible method of controlled retrieval of cell-encapsulating microgels from a culture plate. *Integrative Biology* **6(6)**: 596–602.

106. Mani V, Chikkaveeraiah BV, Patel V, Gutkind JS and Rusling JF (2009) Ultrasensitive immunosensor for cancer biomarker proteins using gold nanoparticle film electrodes and multienzyme-particle amplification. *ACS Nano* **3(3)**: 585–594.

107. Zhu T, Sha Y, Yan J *et al.* (2018) Metallo-polyelectrolytes as a class of ionic macromolecules for functional materials. *Nature Communications* **9(1)**: 4329.

108. Schmidt DJ, Moskowitz JS and Hammond PT (2010) Electrically triggered release of a small molecule drug from a polyelectrolyte multilayer coating. *Chemistry of Materials* **22(23)**: 6416–6425.

109. Silva TR and Vieira IC (2016) A biosensor based on gold nanoparticles stabilized in poly(allylamine hydrochloride) and decorated with laccase for determination of dopamine. *Analyst* **141(1)**: 216–224.

110. Zahn R, Coullerez G, Vörös J and Zambelli T (2012) Effect of polyelectrolyte inter diffusion on electron transport in redox-active polyelectrolyte multilayers. *Journal of Materials Chemistry* **22(22)**: 11073–11078.

111. Si P, Ding S, Yuan J *et al.* (2011) Hierarchically structure one-dimensional TiO_2 for protein immobilization, direct electrochemistry, and mediator-free glucose sensing. *ACS Nano* **5(9)**: 7617–7626.

112. Feng JJ, Zhao G, Xu JJ and Chen HY (2005) Direct electrochemistry and electrocatalysis of heme proteins immobilized on gold nanoparticles stabilized by chitosan. *Analytical Biochemistry* **342(2)**: 280–286.

113. Sadman K, Wang Q, Chen SH, Delgado DE and Shull KR (2017) pH-controlled electrochemical deposition of polyelectrolyte complex films. *Langmuir* **33(8)**: 1834–1844.

114. Ghosh DS and Leo K (2017) Microcavity-enhanced semitransparent electrodes for oligothiophene small-molecule organic solar cells. *Advanced Electronic Materials* **3(5)**: 1600518.

115. Lowman GM, Tokuhisa H, Lutkenhaus JL and Hammond PT (2005) Dye sensitized solar cells incorporating polyelectrolyte multilayer composites. *Materials Research Society Symposium Proceedings* **836**: 1.5.1–1.5.6.

116. Skorb EV and Möhwald H (2016) Ultrasonic approach for surface nanostructuring. *Ultrasonics Sonochemistry* **29**: 589–603.

117. Lanchuk YV, Ulasevich SA, Fedotova TA, Kolpashchikov DM and Skorb EV (2018) Towards sustainable diagnostics: replacing unstable H_2O_2 by photoactive TiO_2 in testing systems for visible and tangible diagnostics affordable by blind people. *RCS Advances* **8(66)**: 37735–37739.

118. Chen HS, Lin SW, Jiang JM, Su YW and Wei KH (2015) Solution-processed zinc oxide/polyethyleneimine nanocomposites as tunable electron transport layers for highly efficient bulk heterojunction polymer solar cells. *ACS Applied Materials & Interfaces* **7(11)**: 6273–6281.

119. Yang D, Fu P, Zhang F *et al.* (2014) High efficiency inverted polymer solar cells with room-temperature titanium oxide/ polyethylenimine films as electron transport layers. *Journal of Materials Chemistry A* **2(41)**: 17281–17285.

120. Zhao XD, Li YQ, Xiang HY *et al.* (2017) Efficient color-stable inverted white organic light-emitting diodes with outcoupling-enhanced ZnO layer. *ACS Applied Materials & Interfaces* **9(3)**: 2767–2775.

121. Kim HH, Park S, Yi Y *et al.* (2015) Inverted quantum dot light emitting diodes using polyethylenimine ethoxylated modified ZnO. *Scientific Reports* **5**: 8698.

122. Rojas HC, Bellani S, Fumagalli F *et al.* (2016) Polymer-based photocathodes with a solution-processable cuprous iodide anode layer and a polyethyleneimine protective coating. *Energy and Environmental Science* **9(12)**: 3710–3723.

123. Jia X, Wu N, Wei J *et al.* (2016) A low-cost and low-temperature processable zinc oxide:polyethyleneimine (ZnO:PEI) nanocomposite as cathode buffer layer for organic and perovskite solar. *Organic Electronics* **38**: 150–157.

124. Du X, Lytken O, Killian MS *et al.* (2017) Overcoming interfacial losses in solution-processed organic multi-junction solar cells. *Advanced Energy Materials* **7(5)**: 1601959.

125. Li Z, Zhang X, Liu C *et al.* (2016) Enhanced electron extraction capability of polymer solar cells via employing electrostatically self-assembled molecule on cathode interfacial layer. *ACS Applied Materials & Interfaces* **8(12)**: 8224–8231.

126. Yan Y, Cai F, Yang L *et al.* (2017) Versatile device architectures for high performing light-soaking-free inverted polymer solar cells. *ACS Applied Materials & Interfaces* **9(38)**: 32678–32687.

127. Lin Z, Cang J, Zhang J *et al.* (2014) A work-function tunable polyelectrolyte complex (PEI:PSS) as a cathode interfacial layer for inverted organic solar cells. *Journal of Materials Chemistry A* **2(21)**: 7788–7794.

128. Subbiah J, Mitchell VD, Hui NKC, Jones DJ and Wong WWH (2017) A green route to conjugated polyelectrolyte interlayers for high-performance solar cells. *Angewandte Chemie International Edition* **56(29)**: 8431–8434.

129. Zhu X, Nepomnyashchii AB, Roitberg AE, Perkinson BA and Schanze KS (2013) Photosensitization of single-crystal ZnO by a conjugated polyelectrolyte designed to avoid aggregation. *Journal of Physical Chemistry Letters* **4(19)**: 3216–3220.

130. Pan Z, Leem G, Cekli S and Schanze KS (2015) Conjugated polyelectrolyte sensitized TiO_2 solar cells: chain-length and aggregation

effects on efficiency. *ACS Applied Materials & Interfaces* **7(30)**: 16601–16608.

131. Sambur JB, Averill CM, Bradley C *et al.* (2011) Interfacial morphology and photoelectrochemistry of conjugated polyelectrolytes adsorbed on single crystal TiO₂. *Langmuir* **1(27)**: 11906–11916.

132. Skorb EV and Andreeva DV (2015) Self-healing properties of layer-by-layer assembled multilayers. *Polymer International* **64(6)**: 713–723.

133. Skorb EV and Andreeva DV (2013) Surface nanoarchitecture for bio-applications: self-regulated intelligent surfaces. *Advanced Functional Materials* **23(36)**: 4483–4506.

134. Skorb EV, Möhwald H and Andreeva DV (2017) How can one controllably use of natural ΔpH in polyelectrolyte multilayers? *Advanced Materials Interfaces* **4(1)**: 1600282.

135. Andreeva DV, Skorb EV and Shchukin DG (2010) Layer-by-layer polyelectrolyte/inhibitor nanostructures for metal corrosion protection. *ACS Applied Materials & Interfaces* **2(7)**: 1954–1962.

136. Andreeva DV, Fix D, Moehwald H and Shchukin DG (2008) Self-healing anticorrosion coatings based on ph-sensitive polyelectrolyte/inhibitor sandwichlike nanostructures. *Advanced Materials* **20(14)**: 2789–2794.

137. Andreeva DV, Fix D, Moehwald H and Shchukin DG (2008) Buffering polyelectrolyte multilayers for active corrosion protection. *Journal of Materials Chemistry* **18(15)**: 1738–1740.

138. Lamaka SV, Shchukin DG, Andreeva DV *et al.* (2008) Sol–gel/polyelectrolyte active corrosion protection system. *Advanced Functional Materials* **18(20)**: 3137–3141.

139. Andreeva DV, Sviridov DV, Masic A, Möhwald H and Skorb EV (2012) Nanoengineered metal surface capsules: construction of a metal-protection system. *Small* **8(6)**: 820–825.

140. Skorb EV, Baidukova O, Andreeva OA, Cherepanov PV and Andreeva DV (2013) Formation of polypyrrole/metal hybrid interfacial layer with self-regulation functions via ultrasonication. *Bioinspired, Biomimetic and Nanobiomaterials* **2(3)**: 123–129.

141. SCAMT (Solution Chemistry of Advanced Materials and Technologies) (2019) https://scamt.ifmo.ru/science/groups/infochemistry-of-self-organizing-systems/ (accessed 05/03/2019).

142. Yu L, Li J, Wang D *et al.* (2015) Improved antimicrobial activity and bioactivity of porous CaP–TiO₂ coating through surface nanofunctionalisation. *Materials Technology* **30(6)**: B109–B114.

143. Lacasta AM, Cantalapiedra IR, Auguet CE, Penaranda A and Ramırez-Piscina L (1999) Modelling of spatio-temporal patterns in bacterial colonies. *Physical Review E: Statistical Physics, Plasmas, Fluids, and Related Interdisciplinary Topics* **59(6)**: 7036–7041.

144. Prindle A, Liu J, Asally M *et al.* (2015) Ion channels enable electrical communication in bacterial communities. *Nature* **527(7576)**: 59–63.

145. Rivera-Chavez F and Bäumler AJ (2015) The pyromaniac inside you: *Salmonella* metabolism in the host gut. *Annual Review of Microbiology* **69**: 31–48.

146. Gensel J, Borke T, Pazos-Perez N *et al.* (2012) Cavitation engineered 3D sponge networks and their application in active surface construction. *Advanced Materials* **24(7)**: 985–989.

147. Skorb EV, Andreeva DV, Raiski AP *et al.* (2011) Titanium dioxide for photocatalytic-assisted prophage induction to lytic cycle. *Photochemical & Photobiological Sciences* **10**: 1974–1978.

148. Bassler BL (1999) How bacteria talk to each other: regulation of gene expression by quorum sensing. *Current Opinion in Microbiology* **2(6)**: 582–587.

149. Miller MB and Bassler BL (2001) Quorum sensing in bacteria. *Annual Review of Microbiology* **55(1)**: 165–199.

150. Liu J, Prindle A, Humphries J *et al.* (2015) Metabolic co-dependence gives rise to collective oscillations within biofilms. *Nature* **523(7562)**: 550–554.

151. Skorb EV, Antonouskaya LI, Belyasova NA *et al.* (2008) Antibacterial activity of thin-film photocatalysts based on metal-modified TiO₂ and TiO₂:In₂O₃ nanocomposite. *Applied Catalysis B: Environmental* **84(1–2)**: 94–99.

How can you contribute?

To discuss this paper, please submit up to 500 words to the journal office at journals@ice.org.uk. Your contribution will be forwarded to the author(s) for a reply and, if considered appropriate by the editor-in-chief, it will be published as a discussion in a future issue of the journal.

ICE Science journals rely entirely on contributions from the field of materials science and engineering. Information about how to submit your paper online is available at www.icevirtuallibrary.com/page/authors, where you will also find detailed author guidelines.

ADVANCED
SCIENCE NEWS
www.advancedsciencenews.com

ADVANCED
HEALTHCARE
MATERIALS
www.advhealthmat.de

REVIEW

Cell Guidance on Nanostructured Metal Based Surfaces

Yulia Zhukova and Ekaterina V. Skorb*

Metal surface nanostructuring to guide cell behavior is an attractive strategy to improve parts of medical implants, lab-on-a-chip, soft robotics, self-assembled microdevices, and bionic devices. Here, we discus important parameters, relevant trends, and specific examples of metal surface nanostructuring to guide cell behavior on metal-based hybrid surfaces. Surface nanostructuring allows precise control of cell morphology, adhesion, internal organization, and function. Pre-organized metal nanostructuring and dynamic stimuli-responsive surfaces are used to study various cell behaviors. For cells dynamics control, the oscillating stimuli-responsive layer-by-layer (LbL) polyelectrolyte assemblies are discussed to control drug delivery, coating thickness, and stiffness. LbL films can be switched "on demand" to change their thickness, stiffness, and permeability in the dynamic real-time processes. Potential applications of metal-based hybrids in biotechnology and selected examples are discussed.

1. Introduction

From a materials point of view, metal-based surfaces can be initially designed to guide cell behavior "statically" or "dynamically" (**Figure 1**). Research on static systems typically fundamentally focusses on material properties that govern cell feedback and guide cell response by surface hydrophilicity, morphology, porosity, crystallinity, and chemical composition. To change just one material characteristic without changing others is challenging. For example, an increase of roughness is accompanied with a change of surface hydrophilicity. In our work, we discuss the possibility of cell behavior control by surface nanotopography on surfaces with the same chemical composition.

In addition to nanotopography, different chemical compositions of the surface may be also used to improve the material. Development of new biomaterials will come from an understanding of how differences in nanotopography and surface chemical composition change surface properties will aim the development of new biomaterials. One of the main challenges in the development of static materials is to have a synergy of factors determining a better material biocompatibility,

that in the case of medical implant nanostructuring outcome for a better patient recovery after implantation. We summarize some possible scenarios used nowadays in this review.

The methods used for surface nanostructuring are extremely important. The chosen method should provide optimization strategies, including non-equilibrium methods,[1] promising to control surface characteristics by duration and intensity of treatment and additives in solution, which may result in metal/polymer hybrids, or composite (titanium/hydroxyapatite (HA)).

Perhaps the most attractive strategy to guide cells is to use dynamic materials. All living systems are dynamic.[2] Dynamic processes found in life include the use of liquid flows,[3] concentration gradients,[4] molecular transport,[5] and environmental response.[6,7] We highlight examples of surface applications for guiding biomolecules in a continuous flow[7] and a controlled drug release,[8] as well as strategies to change surface stiffness and thickness.[9] Additional questions that will be examined are: How should nanostructuring of dynamic interfaces be planned? How can we achieve a controlled cell migration on the surface? How should we maintain chemical concentration gradients to direct drug delivery? In other words, the goal is to explain an interaction between dynamic nanostructured materials and cell behavior. In some examples, where non-biological systems are mentioned, the use of particles are used[10,11] to study collective migration.

While multiple dynamic systems are used to guide cell behavior, one very important challenge should also be mentioned. Toxicity level of the materials should be taken into account. Stimuli used to switch the materials to active states are limited. In this review, we discuss polyelectrolytes (PEs) Layer-by-Layer (LbL) assembly as a powerful example of dynamic coating and capsule shell for drug delivery capsules.[12–16] LbL systems are known as a straight-forward method to control the release of active species from "free" and "surface" capsules due to their stimuli-responsive ability.[16] LbL assembly has also been recently shown to be a promising candidate for the development of actuating coating, which can switch coating thickness and stiffness to guide cell migration on the surface.

2. Native Cell-Nanotopography Interactions

Recent advances in cell biology have resulted in an increased knowledge of the extracellular environment. Subendothelial extracellular matrix (ECM) is known to have a highly complex

Y. Zhukova, Prof. E. V. Skorb
Biomaterials Department
Max Planck Institute of Colloids and Interfaces
Am Mühlenberg 1, Potsdam 14424, Germany
E-mail: skorb@mpikg.mpg.de
Prof. E. V. Skorb
Laboratory of Solution Chemistry of Advanced Materials
and Technologies (SCAMT)
ITMO University
St. Petersburg 197101, Russian Federation

ADVANCED
HEALTHCARE
MATERIALS

www.advhealthmat.de

ADVANCED
SCIENCE NEWS

www.advancedsciencenews.com

REVIEW

surface geometry at the cellular and subcellular levels.[17] A hierarchical topography observed at the submicrometre level possesses many measurable features of the order of 100 nm.[18] For example, the basement membrane underlying the anterior corneal epithelium exhibits a complex topography rich of individual features, such as pores and fibers with dimensions ranging from 30 to 400 nm.[19] Moreover, the ECM molecules have nanodimensions. For example, collagen, the most abundant structural ECM protein, is approx. 300 nm long and 1.5 nm wide, and may assemble into fibrils with diameters between ca. 250–400 nm and several micrometers in length,[20] in vivo as well as in vitro.[21] Furthermore, focal adhesions have nanoscale structure and nanoscale connectivity to the cytoskeletal actin.[22] The adhesion of cells to nanotopographical surface involves nanoscale adhesion-localized structures, e.g. adhesion-related particles, which change in response to integrin clustering. Adhesion-related particles become aggregated when integrin clustering occurs, which in turn results in the formation of focal adhesions with an average integrin spacing of about 45 nm. Adhesion-related particles are linked to the actin cytoskeleton and, as a result, chemical inhibition of actin contraction causes a decrease in particle size, suggesting mechanosensitivity of the particles.[23,24] Thus, the interactions between biomaterials and host tissues are mainly controlled by the following nanoscale features: (1) cells grow on nanostructured extracellular matrices; (2) adsorbed proteins and their aggregates have nanodimensions; (3) biological events such as signaling and cell-substrate interactions occur at the nanometric level.

The nanotopographical cues present at the cellular level composing the extracellular environment, such as the size of ECM molecules and adsorbed proteins, peptide ligand spacing, have an impact on cell behavior. In recent studies multiple efforts have been made to improve and optimize titanium surface properties: (1) bioactivity (antibacterial capability) and biocompatibility (wettability, roughness, porosity, etc.); (2) osteogenic cell response and bone regeneration performance; (3) mechanical properties. To improve hydrophilicity, biological and antimicrobial properties, surface was additionally treated with ultraviolet irradiation,[25] coupled with calcium phosphates/hydroxyapatite,[26,27] enriched with silver-ions,[28] collagen-[29] and physical vapor deposition (PVD)-coated.[30] In vitro and in vivo studies with different cell cultures (human osteoblast-like MG63 cells,[31] MC3T3-E1,[32] human mesenchymal stem cells (hMSCs),[33] human periosteum-derived cells (hPDC),[34] immortalized mouse embryonic cells ME,[35] human gingival fibroblasts[30]) have indicated that addition of nanotopographical features enhance osteointegration and bioactivity of titanium surfaces. These efforts lead to the development of smart functional materials with modified nanotopography, aiming to improve the bioactive properties and to regulate cell performance on implant relevant surfaces for enhancement of healing and tissue regeneration.

Of special interest for this review are porous metal based surfaces, in particular titanium based one. We have recently started studying titanium surface from two perspectives. On the one hand, it is necessary to study titanium, its properties and ways to modify them, since it is one of the most important material used for implant production. On the other hand, due

Yulia Zhukova is currently a PhD candidate at the Max Planck Institute of Colloids and Interfaces in the Department of Biomaterials, and an associate member of Berlin-Brandenburg School for Regenerative Therapies (Germany). She received a Dipl. -Eng. in Biotechnology in 2010 from the Kaliningrad State Technical University (Russia) and a M.Sc. in Polymer Science in 2013 from Humboldt-Universität zu Berlin (Germany). Her current research focuses on advanced biomaterials and drug delivery systems for tissue engineering and regenerative medicine.

Ekaterina V. Skorb received her Ph.D in physical chemistry (2008) from Belarusian State University. Subsequently, she was postdoc and Alexander-von-Humboldt fellow at the Max Planck Institute of Colloids and Interfaces (MPIKG) with Prof. Helmuth Möhwald. From 2013 she has been working with Prof. Peter Fratzl (MPIKG) as an Independent Researcher. She was a Visiting Scholar in Harvard in Prof. George Whitesides group (2016-2017). From 2017 she is a professor at ITMO University leading a group of Infochemistry for Self-Adaptive Materials at SCAMT. Her current research interests are nonlinearity solids' engineering; spatiotemporal control of ion concentration gradients in dissipative systems for soft matter actuation and dynamic control of cell behavior.

to its photocatalytic activity nanostructured titanium dioxide is not a static substrate, and this dynamic property can be used for the development of smart biological systems.

3. Cell-Nanotopography Interactions on Metal Substrates

Various studies in surface structuring suggest that cells respond to nanotopography.[1,36–39] Park et al.[40] showed that behavior of MSCs seeded on TiO_2 nanotube layers is strongly dependent on the tube diameter, since both concentration and topography of cell adhesion sites are critical for integrin clustering. Whereas the tubes with the diameter of 15 nm present an optimum length scale for integrin clustering, 100 nm tubes prevent it and induce anoikis. Several studies[29–31] investigated nanostructure effect of the nanoporous alumina substrates on cell adhesion and growth behavior. Even though there were differences in cell types, epithelial cells preferred 30 nm sized alumina

ADVANCED
SCIENCE NEWS
www.advancedsciencenews.com

ADVANCED
HEALTHCARE
MATERIALS
www.advhealthmat.de

REVIEW
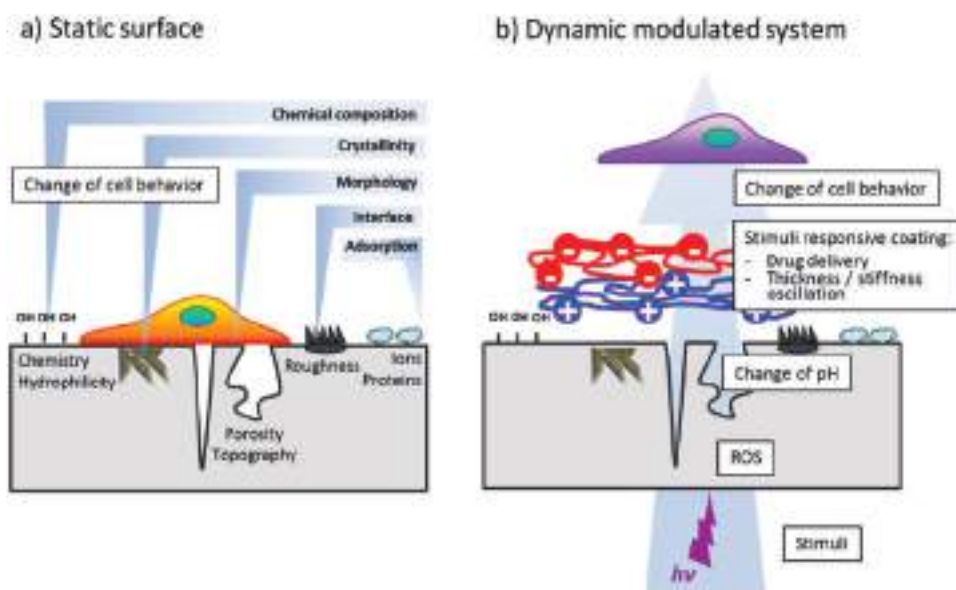
Figure 1. Nanostructured metal based surfaces, e.g. titanium-based, and polyelectrolyte multilayers for improvement of bioactive properties of lab-on-a-chip devices, implant relevant substrates: a) surface nanostructuring, "static" surface with specific surface chemistry, hydrophilicity, porosity, topography, roughness; b) formation of dynamic stimuli responsive systems, e.g. using Layer-by-Layer (LbL) assembly of oppositely charged polyelectrolytes (PEs), to spatiotemporally switch/activate surface during cells growth.

nanopores to the 40, 45, and 50 nm sized ones,[41] as well as the cell number of MG63 decreased gradually with the increase of pore size from 20 to 200 nm.[42] One plausible explanation could be that during the diffusion of ECM molecules into the nanoporous structures, the aggregates of ECM molecules were formed near the aperture region of the smaller nanopores. This hypothesis was confirmed by pre-soaking the surface with a collagen-containing culture medium that increased cell adhesion rates on the 30 nm sized nanoporous alumina compared to 40 and 45 nm sized one.[41] Thus, the adsorption of ECM molecules was influenced by the nanopore dimensions, where the optimal pore size varied for different cell types but its increase had similar negative effect on cell growth. Kant et al.[43] has shown how not only pore size, but also nanopore arrangement affects cell behavior. Porous anodic aluminum oxide (AAO) with nanopore gradient was produced with nonuniform anodization. Their study demonstrated that the pore organization had a direct influence on the orientation of neuronal cells, which is critical in nerve regeneration, where cell polarization is an important parameter in maintaining nerve function.

Dumas et al.[44] used a straight-forward femtosecond laser processing to produce hierarchical features consisted of controlled pattern of microgrooves and periodic oriented nanostructures. When the nanopore arrangement was orthogonal in relation to the microgrooves, a significant loss of cell alignment was observed, thereby indicating that MSCs were sensitive to the directional nanostructures in the microgrooves. Dalby et al.[45] used electron-beam lithography to demonstrate that neither order nor randomness successfully led to osteoinduction of MSCs. Their results demonstrated that highly ordered nanotopographies produce negligible cellular adhesion and osteoblastic differentiation. In contrast, controlled disorder produced spontaneous, abundant osteogenesis. These two studies stated that the use of disorder may be an effective strategy in promoting influence over at least MSCs for regenerative medicine and tissue engineering.

In this review, two nanotopographic geometries will be discussed more precisely together with fabrication methods relevant for further formation of composites and hybrids: sonochemically formed titania mesoporous surface layer (TMS) and titania nanotubular layer (TNT). Kopf et al.[46] reported the effect of these two nanotopographies on the behavior of C2C12 cells. **Figure 2** depicts that surface nanostructuring affects cell morphology: cells develop star-like morphology on TMS and spindle-like elongated morphology on TNT. Moreover, nanostructure influenced cell differentiation, indicating that nanotopography plays also an important role in cell differentiation of other cell types that should be considered in tissue engineering strategies. Thus, this study demonstrated the prospects of ultrasonically formed TMS to guide cell behavior in comparison to flat titania and TNT. The topographical parameters of the three compared substrates were: (1) surface roughness, which is similar for TNT and TMS and is higher than unmodified titania; (2) pore size; (3) regularity of the nanopore arrangement. To note, the open pore structures of TMS and TNT can be loaded with chemical moieties, allowing both topographically and chemically directed cell growth and migration.

Taken together, multiple studies reported that nanotopography, in particular, nanopore size, nanopore arrangement, and randomness, have an effect on cell behavior. At nanoscale, different cell types react specifically and in a differential manner to nanotopographical surface features. For example, whereas the mechanical stabilization through nanofeatures produced by surface topography could support stable adhesion and proliferation of osteoblastic cells, it could have lethal effect on neuronal cells.

ADVANCED
HEALTHCARE
MATERIALS
www.advhealthmat.de

ADVANCED
SCIENCE NEWS
www.advancedsciencenews.com

4. Metal Nanostructuring

Surface modifications have been developed to restructure the oxide layer formed on the bulk titanium surface using different oxidation treatments. In multiple studies titanium surface was modified by the combination of surface modification methods, e.g. combinations of mechanical and chemical methods (sand blasting and acid etching),[29] combination of two chemical methods (two step anodization method,[47] acid etching and subsequent controlled oxidation in hydrogen peroxide[48]), physicochemical methods (plasma electrolytic oxidation[49]). Using this approach, one can produce hierarchical micro-nano-porous or micro-nano-hybrid structures and multifunctional layers. In this review, we will provide chemical reactions and parameters specific for the electrochemical, sonochemical, and chemical etching of titanium.

4.1. Electrochemical Treatment

One of the promising and effective methods for modification of titanium-based orthopaedic implants is anodizing oxidation.[50] The mechanism of this method has been thoroughly studied (see reviews[51–53]). Anodization is based on different chemical reactions occurring at an electrode (an electron conductor) placed in an electrolyte (an ionic conductor):

at the interface between bulk Ti and Ti oxide:

$$Ti \leftrightarrow Ti^{2+} + 2e^- \tag{1}$$

at the interface between Ti oxide and electrolyte:

$$2H_2O \leftrightarrow 2O^{2-} + 4H^+ \tag{2}$$

$$2H_2O \leftrightarrow O_2 + 4H^+ + 4e^- \tag{3}$$

at both interfaces:

$$Ti^{2+} + 2O^{2-} \leftrightarrow TiO_2 + 2e^- \tag{4}$$

It is possible to control morphological parameters such as tube diameter, tube length, and tube separation by varying anodization parameters. The anodization parameters affecting the morphology of the resulting surface are: (1) anodization voltage is a key parameter controlling tube diameter; (2) electrolyte concentration equally affects pore diameter and length; (3) anodization time affects the surface features of nanotubes at the beginning of anodization; (4) inter-electrode spacing affects nanotube separation.

4.2. Sonochemical Surface Modification

We propose a perspective approach[54] to fabricate mesoporous metal surfaces (TMS) via treatment with high intensity ultrasound (HIUS) (**Figure 3**),[55] for example, for implant
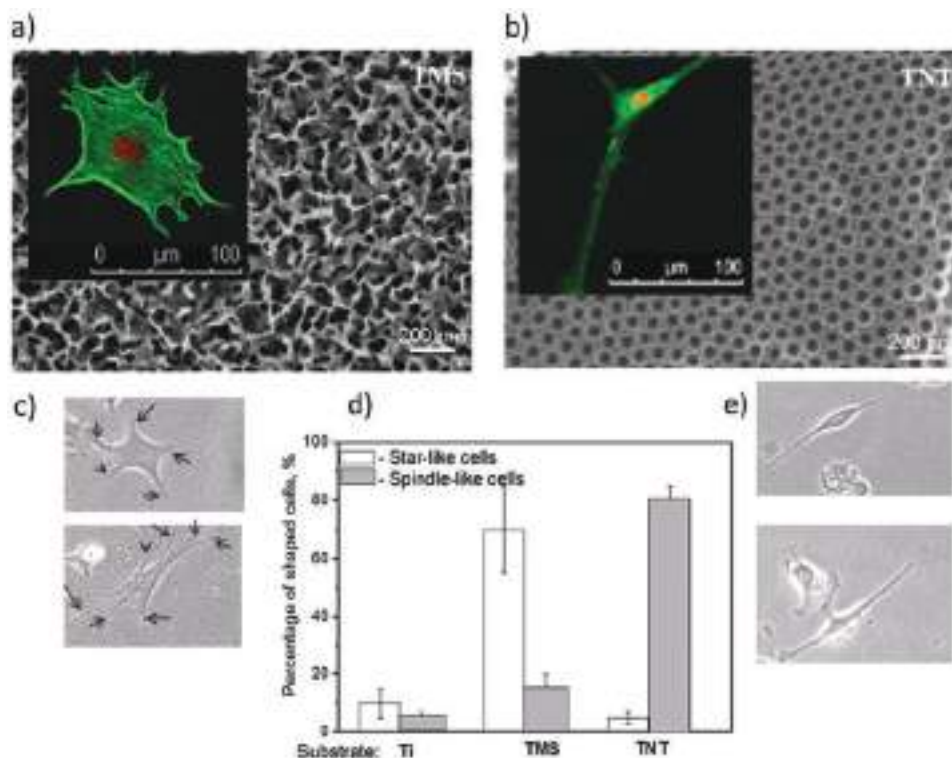
Figure 2. Scanning electron micrographs (SEM) showing mesoporous (TMS) (a) and nanotubular (TNT) (b) titania surfaces produced by sono-chemical and electrochemical treatments, respectively. Insets depict confocal microscopy images (green staining of actin cytoskeleton, red staining of cell nuclei) of cells developing specific morphologies on presented nanotopographies. C2C12 cells develop star-like (c) and spindle-like (e) shapes on TMS and TNT, respectively. Analysis of cell morphologies on these substrates indicates that unmodified Ti and TMS promote star-like shape of C2C12 (d). TNT promote elongated spindle-like morphology of C2C12 cells. Adapted with permission.[46]
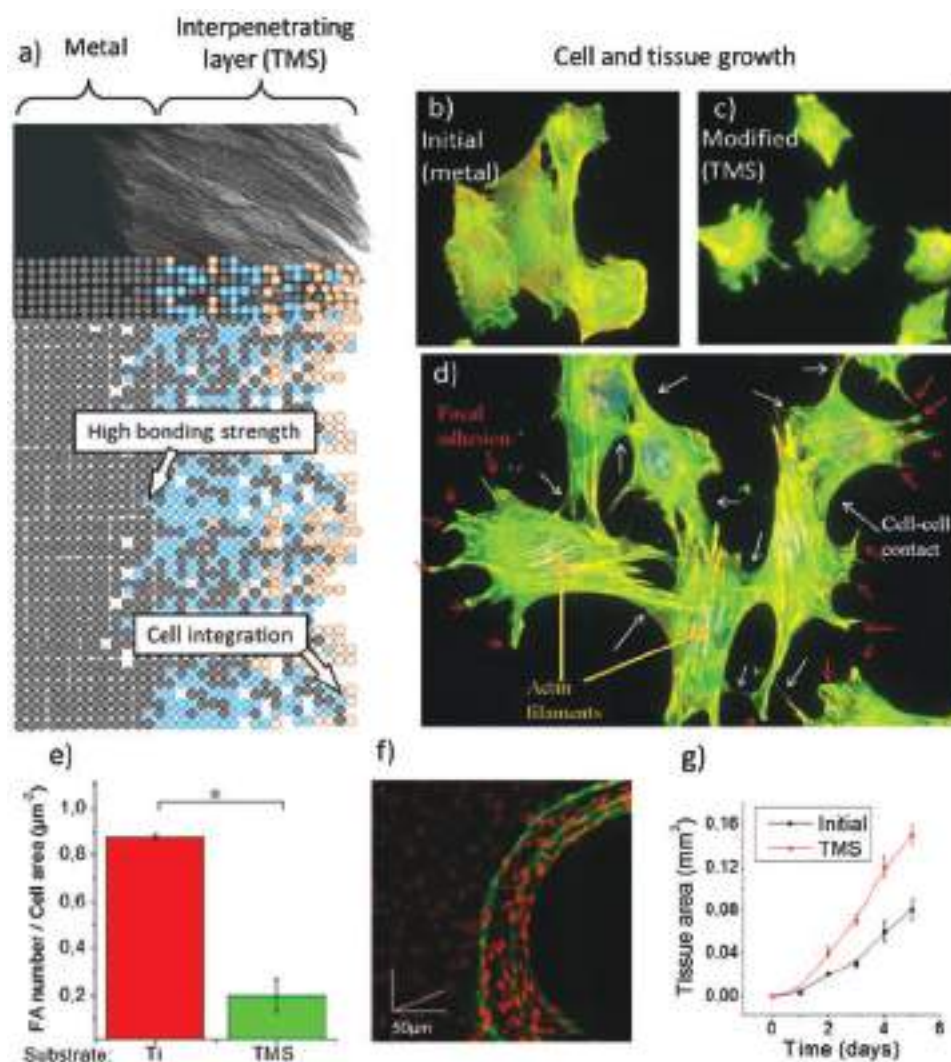
Figure 3. a) Nanostructured "static" layer has to perform well across two interfaces: between the bulk metal and interpenetrating layer and between the interpenetrating layer and the tissue. Produced with sonochemical treatment mesoporous titania surface (TMS) has high bonding strength to the bulk metal and can firmly integrate with cells at different stages of tissue formation. b–d) Confocal microscopy micrographs depicting individual cells grown on unmodified metal (b) and on TMS (c, d) shown at different stages of tissue growth. Single cells (c) have less focal contacts on TMS than on unmodified titanium (e). Effects of nanotopography on a single cell layer could also play a role in further tissue growth. Tissue formation in 3D cylindrical microchannels (f) was shown to be enhanced on TMS in comparison to unmodified titanium surface (g). Adapted with permission.[46]

improvement. As pointed in Figure 3a, during surface modification and formation of a nanostructured surface layer, the bonding strength with the metal implant matrix should be considered. Cells on nanostructured surface may have different communication (Figure 3b,c), cell-cell contact, and focal adhesion (FA) actin filament (Figure 3d). In Figure 3e, the FA number per cell area is significantly different on nanostructured surfaces, which may affect cell migration. Sonochemical treatment allows effective modification of 3D microdefects. In Figure 3f,g, the organization of MC3T3-E1 preosteoblasts tissue in 3D microdefects is shown, and tissue area formed on nanostructured surface is higher in comparison with unmodified surface.

Ultrasound is a unique energy source,[56] which provides energy localization with possible acoustic cavitation phenomena, i.e., the formation, growth, and implosive collapse of cavitation bubbles in a liquid. This collapse is able to produce intense local heating (hot spots with temperatures of roughly 5000 °C) and high pressures of about 500 atm.[56,57] At the liquid-solid interface, the collapse drives high-speed jets of liquid onto the surface, and the impact is sufficient to locally modify metals[58–60] and induces significant changes in surface morphology, composition, crystallinity and reactivity. HIUS has been used for the development of multifunctional nanomaterials such as bimetallic nanoparticles,[61–63] magnetic nanoparticles,[64] nanocomposites and hybrids,[65] mesoporous metal foams, and sponges.[66,67] HIUS offers a fast and versatile methodology for fabrication of nanostructured materials, both inorganic and organic,[68] that are often unavailable by conventional methods.[69]

HIUS induces a wide range of chemical and physical consequences. The chemical effects of ultrasound derive primarily

ADVANCED
HEALTHCARE
MATERIALS

www.advhealthmat.de

ADVANCED
SCIENCE NEWS

www.advancedsciencenews.com

REVIEW

from acoustic cavitation. The extreme temperatures and pressures induce sonolysis and generation of highly reactive radicals,[58–60] which chemically modifies the solid surface. Such extreme conditions induce acceleration of chemical reaction at the solid-liquid interface, increase of solids reactivity, thereby allowing to use less aggressive chemicals. The physical effects include: (1) improvement of mass transport from local turbulent flow and microstreaming; (2) generation of surface erosion and pitting at liquid-solid interfaces by shock waves and microjets; (3) generation of high-velocity interparticle collisions in liquid-solid slurries; (4) fragmentation of fragile solids to increase the surface area.[68]

The combination of physical and chemical effects allows a straight forward one-step modification of metal surfaces. The ultrasound-driven modification of metals in aqueous solutions results in the modification of outer surface properties such as roughness, surface area, and wettability,[66] and inner properties such as crystallinity,[70–72] amorphization, and phase structuring.[73,74]

Sonochemically modified metal based surfaces are highly hydrophilic[66] due to their high roughness and an active oxide layer on the metal surface. The surfaces are porous and attractive as surface encapsulation systems since no additional surface coating is required for encapsulation of bioactive molecules,[75–77] this will be discussed later. In experimental work, we use lab-scale substrates, however the method can be adapted for large-scale production.

4.3. Titanium Chemical Etching

Acid-etching is normally performed in acid mixtures such as H_2SO_4/H_2O_2,[78,79] oxalic acid/H_2O_2,[80] HF/HNO$_3$.[81] Chemical treatments such as acid etching and exposure to hydrogen peroxide and alkalis are known to produce textures on Ti surfaces. In most cases, however, these treatments result in topographic features on the micron scale. Yi et al.[78] show that chemical etching using H_2SO_4/H_2O_2 yields a nanotextured TiO$_2$ layer on Ti surface. The analysis of physicochemical values of treated surface such as roughness, oxide layer thickness, dimensions of nanopits, and Ti:O ratio indicates that the proposed method has shown high degree of reproducibility.[78] The mechanism by which mixtures of H_2SO_4/H_2O_2 create a nanotextured layer of TiO$_2$ is not completely understood. When Ti is exposed to H_2O_2, dissolution and oxidation of the metal occur. The H_2O_2/acid/Ti reaction leads to the formation of a porous TiO$_2$ layer. Variola et al.[79] has demonstrated that the properties of the nanotextured TiO$_2$ surfaces prepared by chemical oxidation in H_2SO_4/H_2O_2 mixture can be tailored by controlling the length of exposure to reactive mixture. Exposed surfaces of Ti are known to be spontaneously covered with a 3–6 nm layer of titanium oxide, mostly as TiO$_2$. According to a model for the oxide film proposed by McCafferty et al.[82] it is composed by three different layers: TiO (inner layer in contact with the metal), Ti$_2$O$_3$ (intermediate layer), and TiO$_2$ (outer layer). With increasing sputtering time, the etching solution reaches the suboxides TiO and Ti$_2$O$_3$, causing their transformation into TiO$_2$, and thereby increasing the thickness of the dioxide layer. When the underlying metal is exposed to the infiltrating solution, natural

passivation conditions are recreated, and initial native three-layered structure is reestablished. However, it is no longer in contact with the environment but rather with a nanoporous TiO$_2$ layer derived from suboxides transformation.

During the alkali treatment,[83] the surface-passive TiO$_2$ layer partially dissolves into alkaline solution due to the corrosive attack of hydroxyl groups:

$$TiO_2 + OH^- \rightarrow HTiO_3^- \tag{5}$$

This reaction proceeds simultaneously with the following hydration of Ti metal:

$$Ti + 3OH^- \rightarrow Ti(OH)_3^+ + 4e^- \tag{6}$$

$$Ti(OH)_3^+ + e^- \rightarrow TiO_2 \cdot H_2O + \cdot 0.5H_2 \uparrow \tag{7}$$

$$Ti(OH)_3^+ + OH^- \leftrightarrow Ti(OH)_4 \tag{8}$$
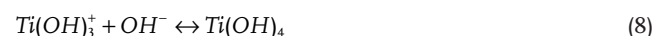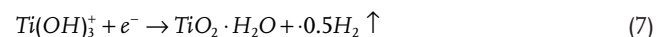
A further hydroxyl attack to hydrated TiO$_2$ produces negatively charged hydrates on the surfaces of the substrates as follows:

$$TiO_2 \cdot nH_2O + OH^- \leftrightarrow HTiO_3^- \cdot nH_2O \tag{9}$$
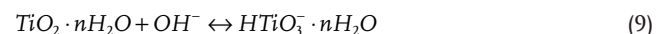
It is promising to use established composition for titanium etching in combination with non-equilibrium methods, e.g. HIUS treatment of Ti in NaOH.

4.4. Non-Equilibrium Methods for Advanced Composite Materials

The methods used for surface nanostructuring are extremely important. We highlight here a specific interest in nonlinearity solids' engineering and propose to exploit complex nonlinear dynamics to achieve superior technological functionalities, which may be difficult or even impossible to achieve with linear systems. The chosen method should provide the following optimization strategies with a promise to control surface characteristics by intensity and duration of treatment; additives in solution may result in metal/polymer hybrids or composite. The non-equilibrium methods could result in amorphous, metastable material structures that are possible to modify depending on various parameters. We will discuss some examples of non-equilibrium methods for surface modification. In particular, plasma deposition of hydroxyapatite (HA) coating on titanium,[26] photochemical local deposition of hydroxyapatite on titania,[27] and sonochemical method for the formation of different structures varying duration of ultrasonic irradiation[55] are discussed below.

HA can be used for the formation of bio-active coating with increased hydrophilicity. A porous HA-incorporated TiO$_2$ coating has been suggested by Ulasevich et al.[26] (**Figure 4**) to be formed using a plasma electrolytic oxidation coupled with electrophoretic deposition (PEO-EPD). Potassium titanium(IV) oxalate is decomposed by micro arcs generated on the anode producing TiO$_2$, while HA particles have been simultaneously
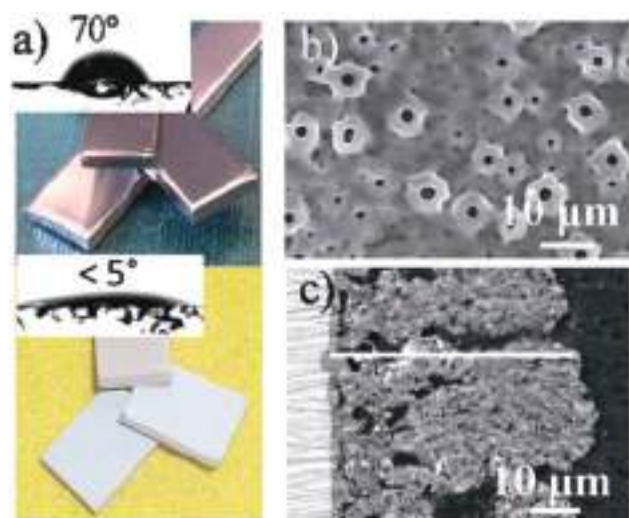
Figure 4. Importance of use methodologies which allow formation of composites or hybrids: a) images of the titanium samples before and after deposition of hydroxyapatite–incorporated TiO$_2$ coating on titanium using plasma electrolytic oxidation coupled with electrophoretic deposition treatment, inserts show contact angle values. b) SEM plan-view of the treated coating; c) SEM cross-sectional view of the sample. Adapted with permission.[26] Copyright 2016, Royal Society of Chemistry.

deposited on anode during EPD process. HA and TiO$_2$ particles have been coagulated into roundish conglomerates with the average diameter in a range of 200–600 nm and strong adhesion to the bulk material.

One more example of non-equilibrium method to deposit HA on TNT has been recently suggested by Ulasevich et al., a new method of photocatalytic deposition.[27] The method is based on a photo-triggered decomposition of the organophosphates such as triethylphosphate (TEP) on the TNT surface resulting in the formation of phosphate anions. HA is formed by the reaction of the phosphate anions and calcium cations presented in the solution, which is described by the following steps:

(1) TiO$_2$ photoactivation with the formation of photoholes (h^+_{vb}) and photoelectrons (e^-_{cb}),

$$TiO_2 + h\nu \rightarrow h^+_{vb} + e^-_{cb} \tag{10}$$

(2) radical (adsorbed 'ad') on surface on the TiO$_2$ surface and then released,

$$H_2O + h^+_w \rightarrow TiO_2 + OH^\bullet_{ad} + H^+ \tag{11}$$

(3) photodecomposition reactions,

$$TEP + OH^\bullet/h^+_{vb} \rightarrow PO_4^{3-} \tag{12}$$

(4) interaction of phosphate anions (product of TEP decomposition) with Ca^{2+} and OH$^-$ ions presented in the electrolyte with the formation of HA.

$$5Ca^{2+} + 3PO_4^{3-} + OH^- = Ca_5(PO_4)_3OH \tag{13}$$
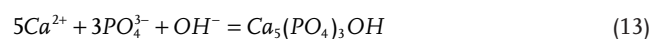
The initial nanotube diameter of ca. 60 nm was reported to decrease gradually during the photocatalytic deposition of HA and to depend on irradiation time.[27] The Glow Discharge Optical Emission Spectroscopy (GDOES) depth profile analysis revealed the uniform distribution of Ca and P elements within the TNT layer. Moreover, the photocatalytical deposition can be used for HA patterning of the surface using the local illumination. HA is formed on light-exposed area, while non-irradiated areas remain HA-free. Furthermore, the authors suggest the improvement of TNT biocompatibility with HA coating due to the following observations: (1) MC3T3-E1 cell density on HA-coated TNT was significantly higher than on uncoated TNT; (2) the adsorption of a protein mix, containing phosphorylase b, bovine serum albumin, ovalbumin, carbonic anhydrase II, soybean trypsin inhibitor A, and lysozyme, occurred faster on HA-rich regions than on an uncoated TNT. However, the enhancement of cell growth could be not only due to the HA bone-forming effect, but also due to the change of the pore size after the HA deposition. The proposed method of photocatalytic deposition of HA onto TNT favors one-step controlled deposition of HA only on irradiated areas.

Non-equilibrium methods for surface nanostructuring, e.g. HIUS treatment of Ti in NaOH, allow to make material with different composition for functionality, in comparison with Ti chemically etched in NaOH.[46] **Figure 5** shows that the HIUS treatment gives rise to several different morphological stages, starting with an untreated flat titanium (Figure 5a). Flat titanium is treated with HIUS in presence of an aqueous solution of NaOH. At the early stage of HIUS treatment in NaOH solution, a native titanium oxide layer is removed, mainly mechanically disrupted by HIUS, and a mesoporous titanium dioxide layer is formed on the exposed surface (Figure 5, stage I). The growth of titanate nanobelts perpendicularly from the titanium scaffold is displayed in Figure 5, Stage II, and finally, the formation of a complex hierarchical structure takes place (Figure 5, Stage III).

We have also shown that HIUS irradiation can be successfully applied as a "green chemistry" tool for the integration of ions, formation of composites into porous metal-based structure.[84] Formation of different cerium composites with aluminum by varying the sonication conditions is an example of a strategy for the formation of aluminum-cerium rich layer, where adhesion, anticorrosion properties, and composition are controlled just by duration and intensity of sonication.

5. Polyelectrolyte Layer-by-Layer (LbL) Assembly for Bio-Experiments

Deposition of alternating layers of oppositely charged polymers leads to the fabrication of layer-by-layer (LbL) thin films. In comparison to the Langmuir-Blodgett approach, self-assembled monolayers (SEMs), and soft lithography, the LbL approach is a versatile and straight-forward technique for the construction of well-defined multicomponent networks with nano- and meso-scale features. A great variety of compounds have been used for LbL deposition: polymers with charged groups, so-called, polyelectrolytes (PEs), block copolymers, hydrogels, etc.

ADVANCED
HEALTHCARE
MATERIALS
www.advhealthmat.de

ADVANCED
SCIENCE NEWS
www.advancedsciencenews.com

REVIEW
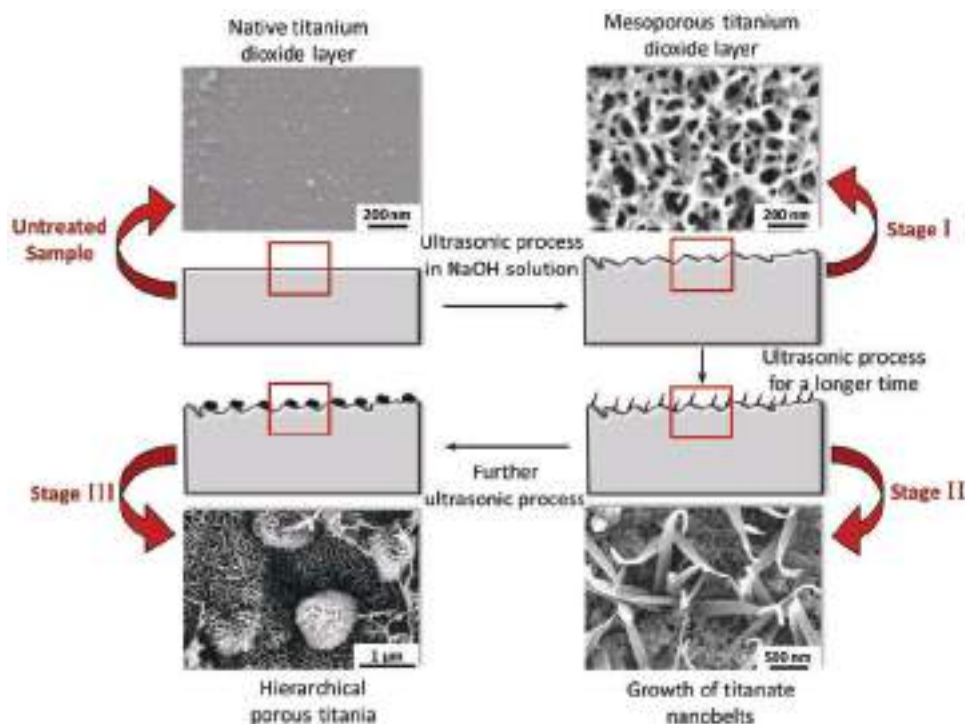
Figure 5. Schematic diagram of the morphological stages of the HIUS-alkali treated titanium surface: untreated flat titanium sample; mesoporous titanium dioxide layer (TMS) formed during the HIUS treatment in NaOH solution (Stage I); titanate nanobelts (Stage II) and hierarchical porous titania (Stage III) formed with further alkali treatment. Surface nanotopographies were observed by SEM. Adapted with permission.[55] Copyright 2016, Elsevier.

Various stimuli-responsive polyelectrolyte/polymer multilayer and related systems on the metal surface have been successfully used for the modulation of bacterial and cell behavior. Applications include: antibacterial coatings, drug and gene delivery, control of cell adhesion, cell sorting, production of the switchable cell culture substrates, etc. **Table 1** provides examples of compositions, stimuli-responsiveness, tested cell and bacteria types, and application areas of various chosen polyelectrolyte/polymer systems.

The bactericidal activity of the polyelectrolyte coating can be achieved in different ways: by incorporating an antibacterial component into the multilayer system,[85,86] or by the change of surface characteristics, e.g. hydrophilicity.[87] An antibacterial component can be incorporated into the polyelectrolyte system,[86] or can itself serve as one of the layer in LbL system.[85]

For instance, antibacterial coatings were constructed by direct assembly of tannic acid (TA) with one of the cationic antibiotics (tobramycin, gentamicin, or polymyxin B).[85] These films exhibit a controlled pH-triggered release upon acidification of the environment by pathogenic bacteria, such as *Staphylococcus epidermidis* (*S. epidermidis*) or *Escherichia coli* (*E. coli*). To elaborate biocidal activity of the thin film, a natural antibacterial peptide, gramicidin A, has been incorporated into polyelectrolyte assemblies, constructed from an anionic amphiphilic polysaccharide, hydrophobically modified carboxymethylpullulan (CMP-xC$_{10}$), and cationic poly(L-lysine) (PLL).[86] The use of the amphiphilic anionic derivative allows efficient solubilization of the peptide in aqueous solution without denaturation. Another approach exploits bacteria-responsive properties of the coating itself without involvement of potentially toxic cationic polymers or release of antimicrobial agents. Here, negatively charged LbL hydrogel films, consisting of chemically cross-linked poly(2-alkylacrylic acids) (PaAAs) with varying hydrophobicity, showed resistance to colonization by *Staphylococcus* epidermidis due to their hydrophobization in response to bacteria-induced acidification of the medium. Other examples of antibacterial polyelectrolyte systems are described in section 5.2.

Dextran-based LbL microcapsules has been used to deliver anti-inflammatory agents: alpha-2-macroglobulin (α2MG),[88] a protein with modulatory properties in inflammation, and C-type natriuretic peptide (CNP).[89] In both studies, the peptide could be stabilized through electrostatic interaction with the polyelectrolyte layers sufficient to allow diffusion of an active component in a manner responsive to the local environment. Protease-specific release of the model drugs has been shown from the protein/polyphenol based capsules, prepared by LbL assembly of bovine serum albumin (BSA) and tannic acid.[90] The susceptibility of the microcapsules to α-chymotrypsin resulted in release of an active component, while they clearly displayed resistance to trypsin due to inactivity of trypsin toward BSA. Moreover, a prominent example of LbL-assisted gene delivery has been demonstrated, where the surface of polished titanium disks was modified using the LBL technique with chitosan (CS), hyaluronic acid (HA), and cationic lipid-DNA (laminin γ2) complexes.[91] The gene coatings were successfully assembled on the titanium surface, and the final in vitro results demonstrated that this delivery system was able to control the release of plasmid DNA and to enhance cell adhesion. Furthermore, multilayer systems can be used to encapsulate cells and

ADVANCED
SCIENCE NEWS
www.advancedsciencenews.com

ADVANCED
HEALTHCARE
MATERIALS
www.advhealthmat.de

REVIEW

Table 1. Examples of polymer/polyelectrolyte multi-layered systems for the modulation of cell behavior.

System composition			Stimuli	Cell type/Bacteria	Ref.
Antibacterial coating					
TA	Cationic antibiotics (tobramycin, gentamicin, polymyxin B)	–	pH	S. epidermidis	[85]
				E. coli	
CMP-xC$_{10}$	PLL	Grami-cidin A	Biodegradation	E. faecalis	[86]
PaAAs	PMAA, PEAA, PPAA, PBAA	–	pH	S. epidermidis	[87]
PEI	PSS	TiO$_2$	Light	P. fluorescence (G(–))	[134]
				L. lactis (G(+))	
BCM	Ag	Al	Cell metabolism, pH	L. lactis	[28]
PSS	8HQ	Al	pH	E. Coli	[134]
Drug and gene delivery					
DS	PLA	α2MG	Biodegradation	Peripheral blood neutrophils and monocytes	[89]
DS	PLA	CNP	Biodegradation	Cartilage explants	[88]
TA	BSA	TRITC-BSA, THCP	Enzymatic degradation	Murine RAW264.7 macrophage cells	[90]
HA	CS	LDc	Biodegradation	HEK293, NH4	[91]
DOX		Al, TiO$_2$	pH, light, cell metabolism	MC3T3-E1 preosteoblast cell	[134,136]
DOX	PLL	TiO$_2$	Light	MC3T3-E1 preosteoblast cell	[136]
Control of cell adhesion, cell sorting					
HA	PLL	AuNPs	Mechanical reinforcement	L929 mouse fibroblasts	[93]
TPPAc-PLL	PEI	AuNPs	Laser irradiation	NIH3T3 fibroblasts	[94]
Poly(OEGMA-co-MEO$_2$MA)		–	Temperature	L929 mouse fibroblasts	[99,100]
PSS	PEDOT	PEDOT-S:H	Electric potential	Human primary keratinocytes and fibroblasts	[135]
BCM	PAA	TiO$_2$	Light	MC3T3-E1 preosteoblast cell	[9]
Cell/yeast encapsulation					
SF-PLL	SF-PGA	PEG	pH	Escherichia coli	[92]
				Bacillus subtilis	
PSS	PEI	SiO$_2^{SH}$		S. cerevisiae	[134]
Switchable cell culture substrates					
MZ140, MZ160		–	Temperature	L929 mouse fibroblasts	[95]
PNIPAM		–	Temperature	L929 mouse fibroblasts	[97]
Poly(MEO$_2$MA-co-OEGMA)		RGD	Temperature	L929 mouse fibroblasts	[98]
PNIPAAm-PEG(19%)-SH (P19)		Au	Temperature	L929 mouse fibroblasts, MG63 human osteosarcomas	[96]
BCM/PAA		TiO$_2$	Light	MC3T3-E1 preosteoblast cell	[9]

Abbreviations: α2MG, alpha-2-macroglobulin; AuNPs, gold nanoparticles. BCM, block copolymer micelles; BSA, bovine serum albumin. CMP-xC$_{10}$, carboxymethylpullulan derivatives; CNP, C-type natriuretic peptide; CS, chitosan. DS, dextran sulfate sodium salt. DOX, doxorubicin. E. coli, Escherichia coli; E. faecalis, Enterococcus faecalis. HA, hyaluronic acid; 8HQ, 8-hydroxyquinoline. LDc, liposome-DNA complexes. Poly(MEO$_2$MA-co-OEGMA) was synthesized using 2-(2-methoxyethoxy) ethyl methacrylate (MEO$_2$MA) and oligo(ethylene glycol) methacrylate, (OEGMA); MZ140, homopolymer microgel of NIPAM; MZ160, copolymer microgel of NIPAM and acrylic acid. Poly(OEGMA-co-MEO$_2$MA), random copolymers of 2-(2-methoxyethoxy)ethyl methacrylate (MEO$_2$MA) and oligo(ethylene glycol) methacrylate (OEGMA). PaAAs, poly(2-alkylacrylic acids); PBAA, poly(2-n-butylacrylic acid); PEAA, poly(2-ethylacrylic acid); PEDOT, poly-3,4-ethylendioxythiophen; PEDOT-S:H, poly(4-(2,3-dihydrothieno[3,4-b]-[1,4]-dioxin-2-yl-methoxy)-1-butanesulfonic acid; PEI, poly(ether imide); PLA, poly-L-arginine hydrochloride; PLL, poly-L-lysine; PMAA, polymethacrylic acid; PNIPAM, poly(N -isopropylacrylamide); PNIPAAm-PEG(19%)-SH (P19), poly(N-isopropylacrylamide)-poly(ethylene glycol)-thiol copolymer; PPAA, poly(2-n-propylacrylic acid); PSS, polystyrene sulfonate. RGD, arginine-glycine-aspartic acid. S. epidermidis, Staphylococcus epidermidis; SF-PGA, silk fibroin modified with with poly-L-glutamic acid; SF-PLL, silk fibroin (SF) modified with poly-L-lysine; SiO$_2^{SH}$, thiol-functionalized silica. TA, tannic acid; THCP, hydrophobic 3,4,9,10-tetra-(hectoxycarbonyl)-perylene; TRITC-BSA, hydrophilic-tetramethylrhodamine-isothiocyanatelabeled BSA; TPPAc-PLL, photosensitizer-coupled polypeptide (5-Mono(4-carboxyphenyl)-10, 15, 20-triphenyl porphine (TPPAc) -poly-L-lysine (PLL).

ADVANCED
HEALTHCARE
MATERIALS
www.advhealthmat.de

ADVANCED
SCIENCE NEWS
www.advancedsciencenews.com

REVIEW

yeasts. For example, the formation of robust and cytocompatible LbL shells has been shown on two types of bacterial cells (Gram-negative *E. coli* and Gram-positive *Bacillus subtilis*).[92]

A great variety of multilayer systems and triggers are used to control cell adhesion on the surface. Gold nanoparticles (AuNPs) are often used to achieve desired properties of the stimuli-responsive system. For example, negatively charged AuNPs have been used to mechanically reinforce the HA/PLL multilayers.[93] Due to the complexation of a large amount of oppositely charged AuNPs on the PLL film, the single deposition step lead to drastic changes of the film properties. In another prominent example, reactive oxygen species (ROS)-induced cell apoptosis is achieved on LbL assembled multilayers using photosensitizer-coupled polypeptides and AuNPs stabilized by type I collagen protein.[94] The photosensitive molecule is entrapped in the supporting film, which can be activated with laser illumination of a certain wavelength yielding ROS, responsible for triggering cell apoptosis. Therefore, cells located in the beam of the laser can provoke death, whereas other cells, in contact with the film but not illuminated by the laser, remain intact. Multiple studies demonstrated the fabrication of NIPAM-based thermoresponsive switchable cell culture substrates.[95–97] With a lower critical solution temperature (LCST) of 32 °C, PNIPAM is the currently most studied material for inducing surface changes between room and body temperature. Decreasing the temperature below the LCST of the polymer triggers the noninvasive detachment of cells from their cultivation substrate, thus, allowing control of adhesion of cells on synthetic substrates. However, PNIPAM is not a bio-inert polymer, which can interact with proteins. Therefore, a new class of thermoresponsive polymers with bio-repellent behavior constitute short oligo(ethylene glycol) methacrylates.[98–100] They exhibit thermoresponsive properties comparable to those of PNIPAM and the bio-repellent behavior due to hydrated PEG.

5.1. Modulation of Cell Behavior

Functional surface coatings made from triblock-terpolymer micelles demonstrate potential strategy for the development of stimuli-responsible LbL coatings. Triblock terpolymers consisting of a hydrophobic, a polyanionic, and a polycationic block are an interesting class of macromolecules due to their complex self-assembly in aqueous solution and their stimuli responsiveness.[101] Coatings are formed by dip-coating and the micellar form is retained upon adsorption. Whereas pH changes can trigger charge reversal for the quaternized polymer, micelles from the non-quaternized polymer are positively charged at all pHs, but can switch from crew-cut micelles to spherical polyelectrolyte brushes. In the first case, pH changes can trigger a novel morphological transition, the splitting into clusters of submicelles.[102] In the second case, no splitting occurs, but surface interactions are drastically altered. Thus, surfaces turn bacteria-repellent in acidic pH regime, which can be used as a self-regulated defense mechanism against fouling.[28] Moreover, these micelles can serve as building blocks for multilayers combining strong pH-sensitivity and full reversibility.[103]

We have recently shown the strategies to switch pH sensitive coating with light, based on the photocatalytic properties of TiO$_2$.[9,104,105] Firstly, it was important to understand how photoinitiated processes on TiO$_2$ result in local pH change on the surface. It is known that suprabandgap illumination of TiO$_2$ causes the generation of photoelectrons (e^-_{cb}) and photoholes (h^+_{vb}). The formed active species can then take part in a series of photocatalytic reactions:

$$TiO_2 + h\nu \rightarrow h^+_{vb} + e_{cb} \tag{14}$$

$$H_2O + h^+_{vb} \rightarrow \ldots \rightarrow H^+ + O_2 \tag{15}$$

$$O_2 + e_{cb} + H_2O \rightarrow \ldots \rightarrow OH^- \tag{16}$$

The photoholes convert the surface hydroxyl groups into protons, the electrons can be scavenged by any scavenging agent, in most cases by oxygen. During photocatalytic reactions both H$^+$ and OH$^-$ may be generated on different sites of titania. The in situ scanning ion selective electrode technique (SIET) allows mapping of the activity and migration of H$^+$ ions and provides the evidence that the acidification takes place at the irradiated spot and is reversible after switching off irradiation (**Figure 6**).[104]

Electromagnetic irradiation is a very attractive stimulus to actuate polymer systems due to its localization and remote control. However, only a limited number of stimuli-responsive polymers are able to undergo light-initiated transitions, their response is either rather weak or not reversible. In this context, "weak" PEs and hydrogels are very promising, since their morphology and polarity strongly depend on pH and they can be used for multilayer formation.[106–108]

When titania substrate is coated by a pH sensitive polymer, the photogenerated local pH modulates the properties of the polymer layer such as thickness, stiffness, permeability, etc.[9,104] The prominent example of the hybrid photosensitive system based on the mesoporous TiO$_2$ coated with a film assembled of polyelectrolyte layers and block copolymer micelles has been shown recently to affect the cell migration (**Figure 7**a,b).[9] High-amplitude switchable LbL multilayers are built from pH sensitive positively charged block copolymer micelles (BCM) and negatively charged poly(acrylic acid) (PAA) on TiO$_2$. In the biological experiment the multilayers were deposited on a transparent glass substrate half-covered with a photoactive TiO$_2$ layer. MC3T3-E1 preosteoblast cell line was cultivated on such substrate for 5 days, and on the 5th day the 'chip' was irradiated from the back side to eliminate the effect of UV on cells. Taken together, TiO$_2$ adsorbs light with production of photohole and photoelectron and the acidification of the titania surface happens. The generated protons are trapped by the BCM 'proton sponge', LbL is activated, and the change of its thickness and stiffness causes cell migration over the surface.

5.2. Antibacterial, Antifouling Properties

Various solutions have been recently proposed to improve antibacterial properties of titanium implants: embedment of Ag nanoparticles,[49] ion implantation of Ag,[48] Cu,[109] Zn[110] ions, silver doped hydroxyapatite coatings,[111] covalent coupling
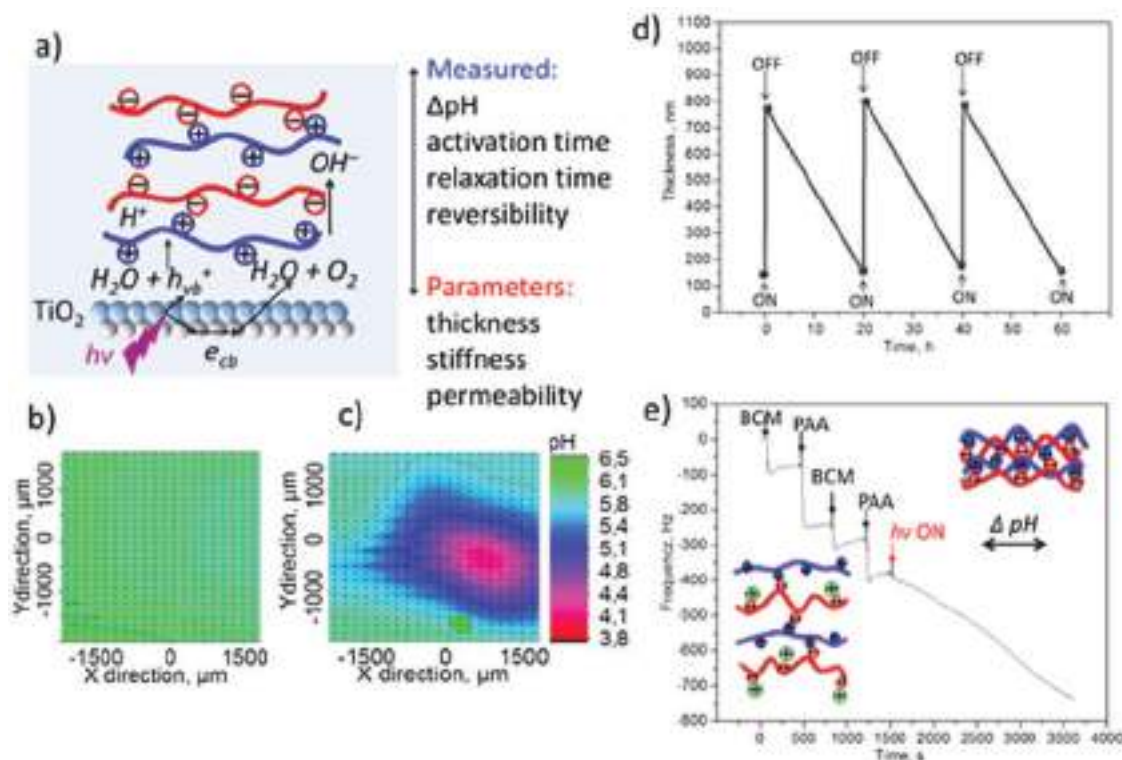
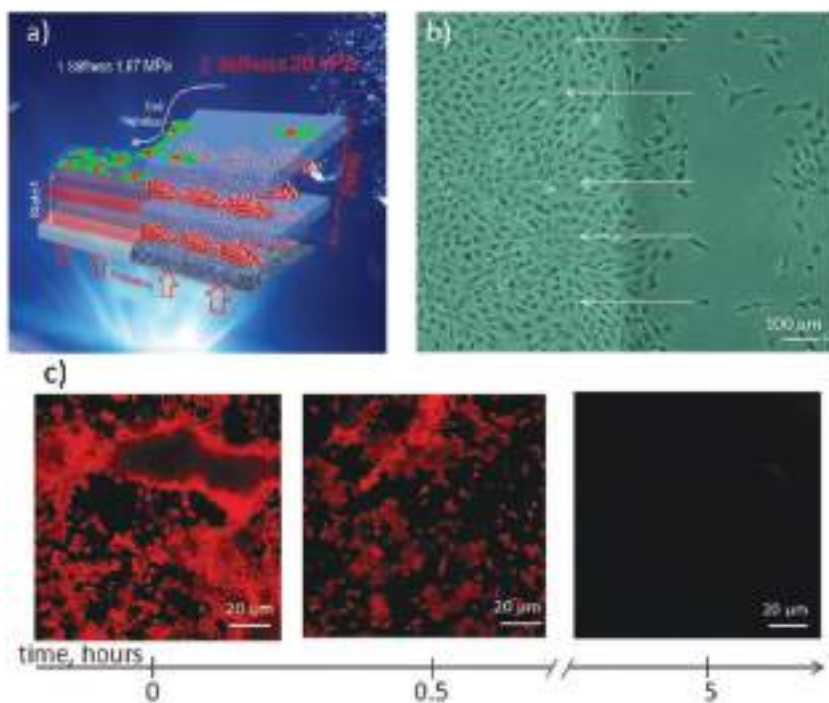**Figure 6.** a) Example of dynamic concept of modulation of multilayer coating on titania using light-pH coupled stimuli: TiO₂ is irradiated with light and ΔpH develops on its surface due to water splitting, assembled on top coating react to pH and changes its thickness, stiffness, permeability which can be used for drug delivery and reversibly actuating coatings. b, c) Maps of pH activity over the surface (b) before irradiation (no pH activity over the surface), (c) during irradiation (pronounce acidification in the center of irradiation spot which produces pH gradient over the surface). d) Special LbL architecture can result in formation of (d) reversible actuation in coating with increase its thickness under irradiation and then slow relaxation of coating when the light is switched off. e) Quartz crystal microbalance (QCM) measurements of LbL assembly and photoactivation by seconds-long pulse irradiation. Inset: schematic representation of the protonation of the LbL assembly of block copolymer micelles (BCM) and poly(acrylic acid) (PAA) increase of its thickness. When light is switched on (hν ON) the LbL start to uptake water changing its conformation with as suggested change in thickness, stiffness, and permeability. Localization of irradiation can result in gradient surface. Adapted with permission.[104]

of antibiotics such as tetracyclin[112] and vancomycin,[113] ZnO coatings,[114] immobilization of anhydride-functional silane,[115] chitosan/cefepime nanofiber coatings,[116] etc. Here we discuss two strategies: (1) release of biocide agent; (2) formation of stimuli responsive coating to "push" bacteria "off" the surface.

For example, the titania-assisted photocatalytic induction of bacteriophages to lytic cycle was reported to be an effective strategy.[117] Highly reactive radical species generated at TiO₂ surfaces under irradiation cause a release of phages from bacteria DNA. The straight-forward method allows the fast and effective method to module bacterial metabolisms without using complex polymer systems, but just due to the TiO₂ photo-catalytic properties.

One more approach is the formation of dynamically activated stimuli responsive coatings. Here we show an "intelligent" system, where the metabolic cycle of a *Lactic* bacteria switches coating to activated state (Figure 7c).[28] Coating is pH sensitive, *Lactic* bacteria produces lactic acid in their metabolic cycle, acid activates the coating, and bacteria are "pushed off" from the surface.

The two methods introduce different but very effective approaches to the development of metal-based dynamic systems with antimicrobial activity: delivery of active species and stimuli-responsive coating actuation.

5.3. Drug Delivery

To deliver active species such as growth factors, vitamins, enzymes or drugs, an "intelligent" encapsulation system based on metal surface are interesting. The encapsulation systems have been developed mainly in several directions – so-called, "free" capsules and capsules in coating immobilized on surfaces. For tissue engineering and implant applications systems formed on the surface via surface nanostructuring, so-called "surface" capsules, were suggested as favorable.[75–77] "Surface" capsules exhibit superior loading capacity, time-responsiveness, and extended release of encapsulated material. Many techniques were developed for modification of different surfaces to enable them to work as "surface" capsules.[118] To achieve controlled stimuli-responsive release of an active component, "surface" capsules may be covered with a protective PE layer. The PE complexes are universal encapsulation and carrier systems, which provide not only storage of the encapsulated material but also controlled release in response to external stimuli (pH,[119] ionic strength,[112] temperature,[113] light,[106–108] etc.).

A prominent example of the photocatalytically-active titania-based LbL coatings is shown in **Figure 8**.[106] The coatings were obtained by immobilization of loaded titania/PEs nanoparticles

ADVANCED
HEALTHCARE
MATERIALS
www.advhealthmat.de

ADVANCED
SCIENCE NEWS
www.advancedsciencenews.com

REVIEW

Figure 7. a, b) Examples of consequences of dynamic concept of modulation of multilayer coating on titania using light-pH coupled stimuli to regulate cells on the surface: during irradiation stiffness changes drastically and cells start to migrate through the surface. Adapted with permission from Ref. [9] c) Actuating coating can be used as antifouling one preventing bacteria growth on the surface, example of self-regulating system is presented, *Lactic* bacteria are grown on the surface and change pH, coating change its thickness fast and "push off" bacteria from the surface. Adapted with permission.[28]

into a sol-gel-derived matrix. By forming a PE shell on the mesoporous titania particles it is possible to fabricate nanoscale reservoirs, which can store relatively large organic molecules in their interior. The mesoporous titania particles were loaded with luminescent dye Rhodamine 6G before the deposition of the polyelectrolyte shell, and the light-driven release has been shown. Besides the drug delivery applications, the proposed hybrid coatings show high biocide and anti-corrosive
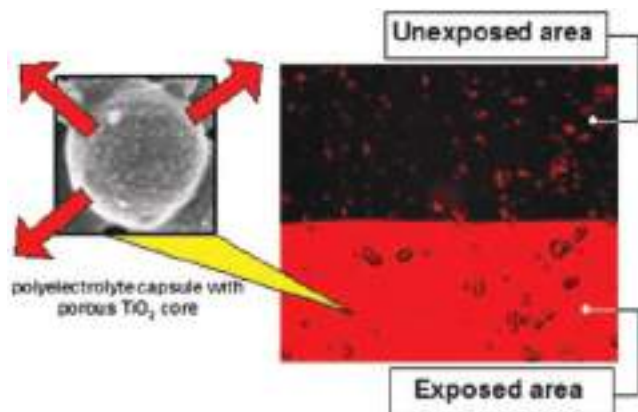
Figure 8. Titania-based capsules and LbL organized polyelectrolyte shell become permeable under irradiation and can locally release active species, which could regulate cell activity on the surface. Adapted with permission.[106] Copyright 2009, Royal Society of Chemistry.

properties.[106–108] A complementary technique was shown for AuNP-functionalized polymeric capsules on thick biocompatible hyaluronic acid (HA) and PLL films.[120,121] Film functionalization with AuNPs allows temperature control on the LbL coated supports, whereas integration of microcapsules in the film allows using the films as reservoirs with light-triggered release. Properties of a biomolecule-containing LbL films such as growth regime, thickness, loading capacity, and mobility of polymers within the film can be altered whether the synthetic or biopolymers constitute the PE film. For example, the thickness of linearly growing polystyrene sulfonate (PSS)/polyallylamine hydrochloride (PAH) increases a few nanometers per deposition step due to the strong polymer interaction and low mobility. In contrast, the thickness of the exponentially growing HA/PLL films is in the micrometer range due to the high mobility of polymers within the film. Similarly, low mobility of polymers within the PSS/PAH film leads to the adsorption of gold nanoparticles (AuNPs) or DNA molecules only on the terminating PAH layer. In contrast, high mobility of PLL in the HA/PLL film allows the AuNPs or DNA to adopt the thermodynamically most stable conformation, thereby inducing the film adsorption. Moreover, micrometer-sized objects, e.g. polyelectrolyte microcapsules, adsorb irreversibly on the HA/PLL film, whereas they can be easily removed from PSS/PAH by washing. Nano-sized AuNPs and DNA molecules form micrometer-sized aggregates on the HA/PLL film. The diffusion of AuNPs and DNA into the HA/PLL film is restricted at room temperature, but DNA diffusion is triggered by heating to 70 °C, leading to homogeneous filling of the film with DNA. Thus, these studies demonstrated the high loading capacity of HA/PLL film due to the enhanced PLL mobility and the "frozen in" structure of PSS/PAH, highlighting the fundamental difference between two systems.

Two types of pH-responsive encapsulation systems based on the surface metal sponges prepared by sonochemical treatment were proposed: a single-step system with a simultaneous activation and modification of the metal and active compound by HIUS, and a system where the metal sponge serves for the construction of PE surface capsules, allowing storage and release of the encapsulated substance (**Figure 9**).[75] In the first system the encapsulation is ensured via the chemisorption of the active compound and the surface –OH groups of the metal oxide layer. In contrast, in case of PE surface capsules there is no need in specific interactions between a metal and encapsulated compound, and therefore, it is a universal encapsulation and carrier system. Moreover, hybrid systems with polypyrrole are developed, allowing the efficient delivery and step-wise release of the low molecular weight active component.[65] pH-controlled release of the bone morphogenetic protein 2 (BMP-2) has been shown from the polyelectrolyte-modified porous titania surfaces

ADVANCED
SCIENCE NEWS
www.advancedsciencenews.com

ADVANCED
HEALTHCARE
MATERIALS
www.advhealthmat.de

REVIEW
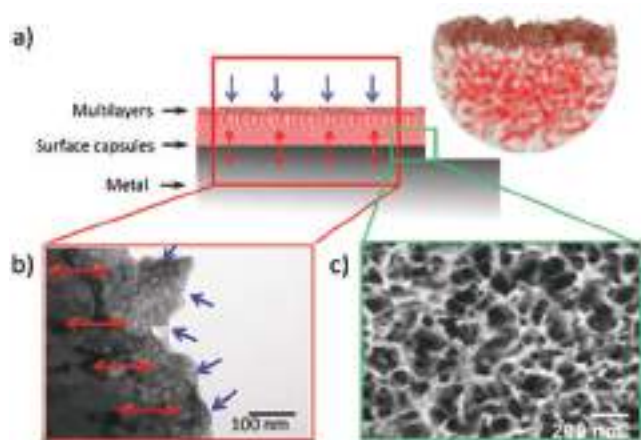
Figure 9. a) Schematic illustration of ultrasonically formed "surface capsules" loaded with an active agent and protected by a polyelectrolyte complex. b) Transmission electron microscopy (TEM) images of a surface capsule layer for chemical storage (blue arrows indicate the loading direction; red arrows indicate the interface between the bulk metal and capsules layer). c) SEM image of the sonochemically produced capsules layer (metal sponges) loaded with 8-hydroxyquinoline. Adapted with permission.[75]

formed via anodization.[122,123] Three different diffusion regimes could be determined from the BMP-2 release profiles from the PE multilayers: an initial burst release, a sustained release regime, and a depletion regime. After release from the

polyelectrolyte multilayer BMP-2 maintains its bioactivity, as determined by its ability to induce osteoblastic differentiation of myoblasts[123] and its effect on MC3T3-E1 preosteoblasts cell count and ALP activity.[124]

Dynamic protein delivery with possibility of its detection and reversible adsorption/desorption is shown in **Figure 10**.[82] Here a new principle of photo-assisted spatial desorption of (poly)histidine-tagged (His-Tag) proteins on a TiO_2 surface is suggested. Surface is decorated by LbL assembly of a strong polyelectrolyte PSS and nickel–nitrilotriacetic acid (NTA). The PSS/NTA multilayer architecture provides n-fold (n×NTA) binding efficiency for more precise protein recognition in comparison to existing molecular His-Tag protein recognition with one- and three-fold multiplication (1×NTA, 3×NTA). Spatially resolved desorption of proteins is regulated by non-photodestructive short-term low-intensity light irradiation. The local pH shift on irradiated TiO_2 selectively affects the pH-sensitive NTA/protein complex, but not the LbL assembly of PSS and NTA, which is stable in a broad pH range. The strategy opens prospects to proteins delivery as well as their detection, and purification. Importantly, preferable dynamic oscillation of coating properties is reversible.

5.4. Metal Nanoparticle-Laser Interactions for Cell Patterning and Detachment

The cell detachment from a culture substrate during cell harvesting still remains challenging. Different strategies available
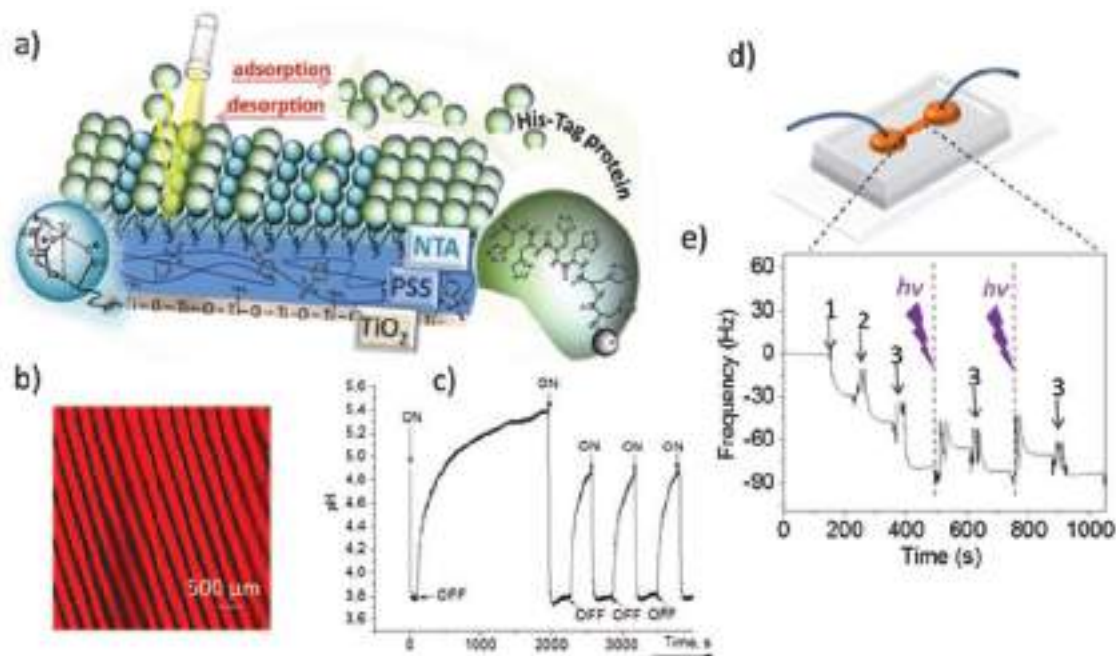
Figure 10. a) Schematic illustration of release of proteins from the surface using light-pH coupled stimuli on titania: LbL assembly of strong polyelectrolyte layers, polystyrene sulfonate (PSS), and pH-responsive and nickel-nitrilotriacetic acid (Ni^{2+}-NTA) layers for (poly)histidine-tagged (His-Tag) proteins recognition and manipulation. b) System TiO_2/(PSS/NTA/His-Tag)$_4$/PSS after irradiation through photomask allow local delivery/desorption of protein. c) Reversible and multicycle activity is pointed from real time evolution of the activity of H^+-ions over the TiO_2/PSS/NTA surface. "ON" is pointed time point of irradiation switched on and "OFF" – switched off. d) Microfluidic chamber to study His-Tag protein light induced modulation/desorption on TiO_2/LbL surface. e) QCM frequency change during the adsorption of (1) PSS, (2) NTA, (3) His-Tag protein; $h\nu$ corresponds to the moment of short term ((1)s) irradiation and results in protein desorption. Cycles of adsorption, light induced desorption are repeated several times. Adapted with permission.[105]

ADVANCED
HEALTHCARE
MATERIALS
www.advhealthmat.de

ADVANCED
SCIENCE NEWS
www.advancedsciencenews.com

REVIEW

for animal cell detachment are presented in the recent review (Simon, et al.).[125] Multiple factors should be considered when choosing cell-detachment method: (1) degree of cell adhesion characteristic to the tested cell line; (2) further application of detached cells; (3) process compatibility (physical or chemical); (4) process scale (5) reusability of the culture substrate, etc. To date, only a few alternative biomaterial platforms have been developed to improve the dynamic control over cell adhesion for tissue engineering and regenerative medicine.

In particular, the laser-triggered nanoengineered AuNP surfaces, also called plasmonic substrates, were used for targeted cell patterning. For example, Kolesnikova et al.[126] demonstrated a tunable nonthermal photochemical mechanism of NIH3T3 fibroblasts detachment and patterning on AuNP functionalized surfaces. ROS generated in a photocatalytic reaction could damage the cell membrane, thereby leading to cell detachment.

Recent elegant study introduced a new bottom-up approach to build plasmonic substrates for cell detachment and patterning using micellar block copolymer nanolithography (BCML).[127] In this study, inverse micelles of the block copolymer polystyrene-b-poly-2-vinylpyridine (PS-b-P2VP) containing Au. The substrates were used to grow murine and human cell types: tumoral (HeLa and A549) and non-tumoral (HUVEC) human cells; murine macrophage-like cell line (J774) and 3T3 fibroblasts. Irradiation with a 980 nm near infra-red (NIR) laser induced detachment of the tested cell types from nano-plasmonic substrates, with nearly complete viability of the detached cells. The photothermal effect was identified as the main cause of cell detachment. Taken together, the reported approach allows controlled and non-invasive cell patterning and detachment from light-responsive surfaces, suggesting its high relevance for biomedical research.

6. Prospects for Metal Based Hybrids

Recent developments in advanced metal modification techniques have enabled the fabrication of surface nanotopographies that encompass features and applications, highly important for implantology, regenerative therapies, and cell culture research. In brief, substrate engineering allows gaining basic knowledge on the effect of nanotopography on cell behavior; the technology can be applied for large-scale implant production and for the design of hybrid encapsulation systems; and such complex systems are dynamic and can be applied to guide cell behavior.

Firstly, cell-nanotopography interactions serve as a mechanism to precisely control cell functions. Cells respond to various physical and chemical cues of the adjacent substrate, which can be specifically designed to control particular cell response. Secondly, the straight-forward methods for metal, e.g. titanium, surface nanostructuring discussed in this minireview are fast, cheap and can be applied for large-scale manufacturing. They provide uniform access of the reactive substance to all surfaces, which could be applied for multifaceted devices with complex geometries such as dental screws and cardiovascular stents. For example, the self-organized nanotube arrays prepared by electrochemical anodization were grown in a radially outward direction on titanium mesh.[128] The nanotopographic cues produced

by these methods can be incorporated into relatively large geometrical areas making them attractive for commercial implant production. Moreover, titanium nanotopography can act synergistically with soluble factors to modulate the differentiation pathway. For instance we have recently reported the response of C2C12 cells on mesoporous titania and titania nanotubes, where the nanostructure of the material was observed to have an impact on the osteogenic differentiation, while it only moderately affects myogenic differentiation.[46] Furthermore, a metal matrix could be used for the construction of hybrid materials and surface encapsulation systems, described in detail elsewhere.[75–77] Hybrid materials (hybrids) are mainly composites consisting of organic molecules connected to a metal matrix. As a metal matrix serve such metal surfaces as Ti, steel and their alloys. In order to deliver active species such as growth factors, vitamins, enzymes or drugs, an "intelligent" encapsulation system based on metallic surface has to be designed. To avoid very fast release of bioactive molecules, surface capsules should be covered with a protective polymer film. For instance, an upload, storage, and controlled pH-triggered release of doxorubicin (anti-cancer drug) have been shown out of the sonochemically formed surface metal sponges.[75–77] By using the protective LbL assembled PEs, it was possible to achieve the controlled stimuli-responsive release of an active component.

The biocomposite materials can be used to enhance the efficiency of biomaterial for cell growth. Last but not least, patterning of the hybrid surface can be created in order to achieve the best environment for cell attachment, growth and differentiation. Both surface patterning and drug delivery systems will be able to provide spatial and temporal control over tissue growth. The main goal is to develop the conditions that best mimic the biological environment, provide support and control over tissue formation, which can be used for growth of cells of different types, co-cultures, and other complex systems.

In **Figure 11** we provide some examples of complex biomimetic systems. In the first example polymer-metal hybrid systems has been used to develop nature-inspired robotics (Figure 10a).[7] It was possible to create a biohybrid system that enabled an artificial ray to swim and phototactically follow a light cue. The muscoskeletal structure was reverse-engineered via a four-layered architecture: a three-dimensional elastomer [polydimethylsiloxane (PDMS)] body, cast via a titanium mold; a chemically neutral skeleton fabricated by means of thermal evaporation of gold through a custom designed shadow mask; a thin interstitial elastomer layer obtained by spin-coating; and last, a layer of aligned rat cardiomyocytes generated via microcontact printing of fibronectin. To reach reproducible and controlled locomotion, a layer of cardiomyocytes, which were engineered to respond to optical stimuli, was placed onto tissue. Thus, light-sensitive locomotion could be achieved without the need for neural coupling and coordination.

The next example of the application of hybrid polymer-metal system is the fabrication of the self-assembled muscle-MEMS (microelectromechanical) system.[129] The contractile myocytes were patterned on the Au/Cr/Si cantilevers with the help of thermally responsive PNIPAAm. The temperature response and myocyte growth inhibition of PNIPAAm made it possible to spatially pattern the myocytes. The removal of the PNIPAAm (dissolution in the medium) completely enables a release of the

**ADVANCED
SCIENCE NEWS**
www.advancedsciencenews.com

**ADVANCED
HEALTHCARE
MATERIALS**
www.advhealthmat.de

REVIEW
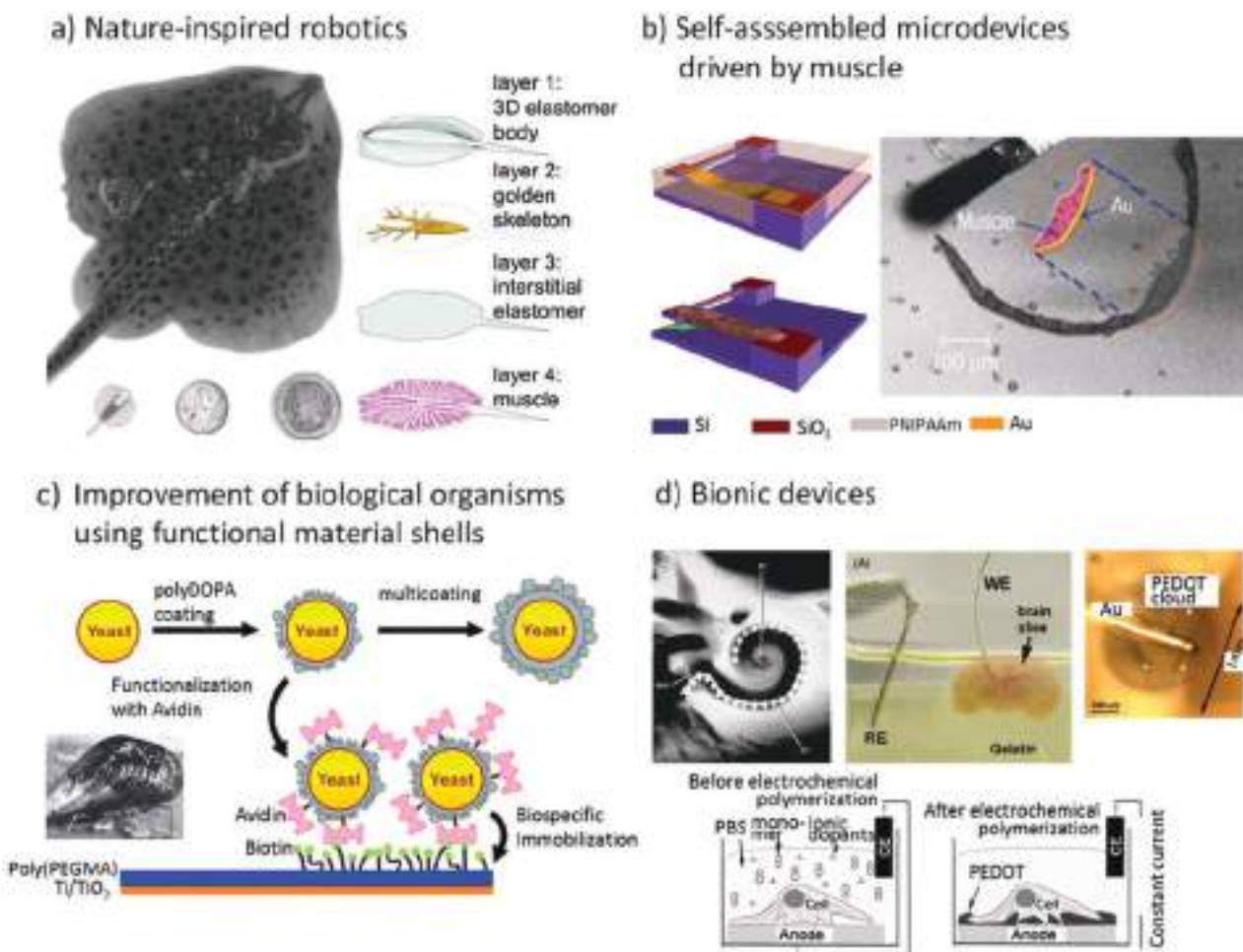
Figure 11. The prospects of using the metal-based polymer hybrid systems. a) Nature-inspired robotics. Tissue-engineered soft-robotic ray. Adapted with permission.[7] Copyright 2016, AAAS. b) Self-assembled microdevices, in particular, driven by muscle. Adapted with permission.[129] Copyright 2005, Nature Publishing Group. c) Improvement of biological organisms using functional material cells. Adapted with permission.[130] Copyright 2011, American Chemical Society. d) Fabrication of bionic devices for biomedical applications. Adapted with permission.[131] Copyright 2013, IOP. Abbreviations: DOPA, dihydroxyphenylalanine; PBS, phosphate-buffered saline; PEDOT, poly(3,4-ethylenedioxythiophene); Poly(PEGMA), poly(ethylene glycol) methacrylate.

self-assembled hybrid microdevice and its free movement. The nanometer-thin metal film played a crucial role in tailoring the shapes of muscle bundles and in bending movement of the mobile legs. The contraction of muscle bundles powered the motion of the device.

Moreover, inspired by biomineralization, an encapsulation approach of microorganisms has evolved from using inorganic materials in combination with polymer shell structures. For instance, mussel-inspired polydopamine (polyDOPA) shells were fabricated for the encapsulation of individual yeast cells.[130] By modifying the chemical reactivity of the polyDOPA shell towards amine and thiol functionalization, such as the functionalization with avidin, it was possible to achieve biospecific immobilization of yeasts on the biotin-functionalized substrate.

Hybrid devices, so-called "bionics", can be also discussed as an example.[103] It can serve as electrical conductors to transmit the charge into and out of biological systems. Inspired by a cochlear implant (bionic ear), a new paradigm for implantable electrodes based on conducting polymers was introduced, where a hybrod network was polymerized in situ throughout

living brain tissue.[131] The biological constituent of the composite was the living tissue. The hybrid network was produced by delivering the monomer solutions to electrode sites (Teflon-coated gold wire) implanted into the brain tissue. After polymerized, the polymer was formed on the electrode and grew out into the tissue.

In all there are two opinions among researchers worldwide concerning the approach to study such complex biological systems. The 1st approach suggests that the investigation should take into account only one factor/parameter affecting a particular chemical/biological event. Since biological systems are extremely complex and contain multiple parameters, which may have an influence on the process, one has to very precisely investigate the influence of each parameter separately. For instance, many models of physical systems implicitly account for multiple spatial scales by simplifying their boundary conditions into "black boxes" where assumptions about other spatial or temporal domains are summarized by governing equations.[132]

The 2nd approach suggests looking at the biological system explicitly accounting for more than one level of resolution

ADVANCED
HEALTHCARE
MATERIALS
www.advhealthmat.de

ADVANCED
SCIENCE NEWS
www.advancedsciencenews.com

REVIEW

across measurable domains of time, space, and/or function. There are several reasons for that. The general reason is that research nowadays is becoming more collaborative, multidisciplinary, involving multiple research groups and financial support worldwide, and allowing dealing with more complicated projects than earlier. Moreover, biological systems are inherently complex in nature and comprised of multiple functional dynamic networks to sustain an organism's normal development. It is often impossible to deduce the behavior and function of individual molecules, organisms, organs, etc. due to the non-linearity of pathways in biological networks. When designing new therapeutic products it is important to obtain a thorough understanding of the interaction between molecules and pathways.[133]

7. Conclusion

Native cell interactions are directly associated with the nano-topographical cues presented in the ECM. Similarly, the interactions between biomaterials and tissues are strongly controlled by the nanoscale features. Smart titanium-based materials with modified nanotopography and improved bioactive properties aim to regulate cell performance on implant relevant surfaces for enhancement of healing and tissue regeneration. In this review, we have discussed methods for titanium surface nanostructuring such as electrochemical treatment, sonochemical treatment, and chemical etching. These methods can be applied for large-scale manufacturing of complex implantable devices. In particular, we highlighted non-equilibrium sonochemical treatment as straight-forward method for the formation of hybrids and composite materials. Furthermore, we discussed the prospects of photoactive nanoporous titania surfaces for the development of smart titanium-polyelectrolyte assemblies.

LbL assembly is a versatile approach for the formation of dynamic, stimuli responsive systems for modulation of cells/biomolecules behavior on the surface, for antibacterial, antifouling, and drug delivery applications. Specific examples of metal based hybrid devices, i.e. "bionics", are discussed in the context of nature-inspired, biomimetic systems. Such devices should help researchers understand the general principles governing emergent properties and biological functions of complex systems. However, there is still no universal approach to study such complex systems: either by simplifying them to models or studying them as a complex network of multiple parameters. Nowadays both approaches have their place in the area.

[1] E. V. Skorb, D. V. Andreeva, *Adv. Funct. Mater.* **2013**, *23*, 4483.

[2] B. A. Grzybowski, W. T. S. Huck, *Nat. Nanotechnol.* **2016**, *11*, 585.

[3] J. W. Jeong, J. G. McCall, G. Shin, Y. Zhang, R. Al-Hasani, M. Kim, S. Li, J. Y. Sim, K. I. Jang, Y. Shi, D. Y. Hong, Y. Liu, G. P. Schmitz, L. Xia, Z. He, P. Gamble, W. Z. Ray, Y. Huang, M. R. Bruchas, J. A. Rogers, *Cell* **2015**, *162*, 662.

[4] M. Weitz, J. Kim, K. Kapsner, E. Winfree, E. Franco, F. C. Simmel, *Nat. Chem.* **2014**, *6*, 295.

[5] W. F. Paxton, S. Sundararajan, T. E. Mallouk, A. Sen, *Angew. Chem. Int. Ed.* **2006**, *45*, 5420.

[6] Y. Wei, S. Han, J. Kim, S. Soh, B. A. Grzybowski, *J. Am. Chem. Soc.* **2010**, *132*, 11018.

[7] S.-J. Park, M. Gazzola, K. S. Park, S. Park, V. Di Santo, E. L. Blevins, J. U. Lind, P. H. Campbell, S. Dauth, A. K. Capulli, F. S. Pasqualini, S. Ahn, A. Cho, H. Yuan, B. M. Maoz, R. Vijaykumar, J.-W. Choi, K. Deisseroth, G. V. Lauder, L. Mahadevan, K. K. Parker, *Science* **2016**, *353*, 158.

[8] T. Kumeria, H. Mon, M. S. Aw, K. Gulati, A. Santos, H. J. Griesser, D. Losic, *Colloids and Surfaces B: Biointerfaces* **2015**, *130*, 255.

[9] S. A. Ulasevich, N. Brezhneva, Y. Zhukova, H. Möhwald, P. Fratzl, F. H. Schacher, D. V. Sviridov, D. V. Andreeva, E. V. Skorb, *Macromol. Biosci.* **2016**, *16*, 1422.

[10] J. Yan, M. Han, J. Zhang, C. Xu, E. Luijten, S. Granick, *Nat. Mater.* **2016**, *15*, 1095.

[11] J. Zhang, S. Granick, *Faraday Discuss.* **2016**, *191*, 35.

[12] E. V. Skorb, D. V. Andreeva, *Polym. Chem.* **2013**, *4*, 4834.

[13] E. V. Skorb, D. V. Andreeva, *Polym. Int.* **2015**, *64*, 713.

[14] E. V. Skorb, A. V. Volkova, D. V. Andreeva, *Curr. Org. Chem.* **2015**, *19*, 1097.

[15] E. V. Skorb, A. V. Volkova, D. V. Andreeva, *Curr. Org. Chem.* **2014**, *18*, 2315.

[16] E. V. Skorb, H. Möhwald, D. V. Andreeva, *Adv. Mater. Intefaces* **2017**, *4*, 1600282.

[17] J. Engel, M. Chiquet, in *The Extracellular Matrix: an Overview*, Ed: P. R. Mecham, Springer, Berlin Heidelberg, **2011**.

[18] S. L. Goodman, P. A. Sims, R. M. Albrecht, *Biomaterials* **1996**, *17*, 2087.

[19] G. A. Abrams, S. L. Goodman, P. F. Nealey, M. Franco, C. J. Murphy, *Cell Tissue Res.* **2000**, *299*, 39.

[20] L. Bozec, G. van der Heijden, M. Horton, *Biophys. J.* **2007**, *92*, 70.

[21] K. Kadler, *Protein profile* **1995**, *2*, 491.

[22] M. J. Dalby, N. Gadegaard, R. O. C. Oreffo, *Nat. Mater.* **2014**, *13*, 558.

[23] P. Kanchanawong, G. Shtengel, A. M. Pasapera, E. B. Ramko, M. W. Davidson, H. F. Hess, C. M. Waterman, *Nature* **2010**, *468*, 580.

[24] I. Patla, T. Volberg, N. Elad, V. Hirschfeld-Warneken, C. Grashoff, R. Fassler, J. P. Spatz, B. Geiger, O. Medalia, *Nat. Cell Biol.* **2010**, *12*, 909.

[25] E. V. Skorb, L. I. Antonouskaya, N. A. Belyasova, D. G. Shchukin, H. Möhwald, D. V. Sviridov, *Appl. Catal. B* **2008**, *84*, 94.

[26] S. A. Ulasevich, A. I. Kulak, S. K. Poznyak, S. A. Karpushenkov, A. D. Lisenkov, E. V. Skorb, *RSC Advances* **2016**, *6*, 62540.

[27] S. A. Ulasevich, S. K. Poznyak, A. I. Kulak, A. D. Lisenkov, M. Starykevich, E. V. Skorb, *Langmuir* **2016**, *32*, 4016.

[28] J. Gensel, T. Borke, N. P. Pérez, A. Fery, D. V. Andreeva, E. Betthausen, A. H. E. Müller, H. Möhwald, E. V. Skorb, *Adv. Mater.* **2012**, *24*, 985.

[29] A. Diener, B. Nebe, F. Luthen, P. Becker, U. Beck, H. G. Neumann, J. Rychly, *Biomaterials* **2005**, *26*, 383.

[30] B. Grossner-Schreiber, M. Herzog, J. Hedderich, A. Duck, M. Hannig, M. Griepentrog, *Clin. Oral Impl. Res.* **2006**, *17*, 736.

[31] R. A. Gittens, R. Olivares-Navarrete, A. Cheng, D. M. Anderson, T. McLachlan, I. Stephan, J. Geis-Gerstorfer, K. H. Sandhage, A. G. Fedorov, F. Rupp, B. D. Boyan, R. Tannenbaum, Z. Schwartz, *Acta Biomater.* **2013**, *9*, 6268.

[32] S.-K. Moon, J.-S. Kwon, S.-H. Uhm, E.-J. Lee, H.-J. Gu, T.-G. Eom, K.-N. Kim, *Curr. Appl. Phys.* **2014**, *14*, S183.

[33] C.-M. Han, H.-E. Kim, Y.-H. Koh, *Surf. Coat. Technol.* **2014**, *251*, 226.

ADVANCED
SCIENCE NEWS

www.advancedsciencenews.com

ADVANCED
HEALTHCARE
MATERIALS

www.advhealthmat.de

REVIEW

[34] S. Amin Yavari, J. van der Stok, Y. C. Chai, R. Wauthle, Z. Tahmasebi Birgani, P. Habibovic, M. Mulier, J. Schrooten, H. Weinans, A. A. Zadpoor, *Biomaterials* **2014**, *35*, 6172.

[35] S.-E. Kim, S.-B. Lee, S.-W. Kwak, C.-K. Kim, K.-N. Kim, *Surf. Coat. Technol.* **2013**, *228*, S37.

[36] C. Selhuber-Unkel, T. Erdmann, M. López-García, H. Kessler, U. S. Schwarz, J. P. Spatz, *Biophys. J.* **2010**, *98*, 543.

[37] E. A. Cavalcanti-Adam, T. Volberg, A. Micoulet, H. Kessler, B. Geiger, J. P. Spatz, *Biophys. J.* **2007**, *92*, 2964.

[38] S. Oh, K. S. Brammer, Y. S. J. Li, D. Teng, A. J. Engler, S. Chien, S. Jin, *Proc. Natl. Acad. Sci. U. S. A.* **2009**, *106*, 2130.

[39] B. Trappmann, J. E. Gautrot, J. T. Connelly, D. G. T. Strange, Y. Li, M. L. Oyen, M. A. Cohen Stuart, H. Boehm, B. Li, V. Vogel, J. P. Spatz, F. M. Watt, W. T. S. Huck, *Nat. Mater.* **2012**, *11*, 642.

[40] J. Park, S. Bauer, K. von der Mark, P. Schmuki, *Nano Lett.* **2007**, *7*, 1686.

[41] S. H. Chung, S. J. Son, J. Min, *Nanotechnology* **2010**, *21*.

[42] Y. H. Song, Y. Ju, Y. Morita, G. B. Song, *J. Biosci. Bioeng.* **2013**, *116*, 509.

[43] K. Kant, S. P. Low, A. Marshal, J. G. Shapter, D. Losic, *ACS Appl. Mater. Interfaces* **2010**, *2*, 3447.

[44] V. Dumas, A. Rattner, L. Vico, E. Audouard, J. C. Dumas, P. Naisson, P. Bertrand, *J. Biomed. Mater. Res., Part A* **2012**, *100A*, 3108.

[45] M. J. Dalby, N. Gadegaard, R. Tare, A. Andar, M. O. Riehle, P. Herzyk, C. D. W. Wilkinson, R. O. C. Oreffo, *Nat. Mater.* **2007**, *6*, 997.

[46] J. Kopf, S. Ulasevich, O. Baidukova, Y. Zhukova, J. W. C. Dunlop, P. Fratzl, P. Rikeit, P. Knaus, S. K. Poznyak, D. V. Andreeva, E. V. Skorb, *Adv. Eng. Mater.* **2016**, *18*, 476.

[47] S. Grigorescu, V. Pruna, I. Titorencu, V. V. Jinga, A. Mazare, P. Schmuki, I. Demetrescu, *Bioelectrochemistry* **2014**, *98*, 39.

[48] S. Ferraris, A. Venturello, M. Miola, A. Cochis, L. Rimondini, S. Spriano, *Appl. Surf. Sci.* **2014**, *311*, 279.

[49] B. S. Necula, I. Apachitei, L. E. Fratila-Apachitei, E. J. van Langelaan, J. Duszczyk, *Appl. Surf. Sci.* **2013**, *273*, 310.

[50] C. Yao, T. J. Webster, *J. Nanosci. Nanotechnol.* **2006**, *6*, 2682.

[51] J. M. Macak, H. Tsuchiya, A. Ghicov, K. Yasuda, R. Hahn, S. Bauer, P. Schmuki, *Curr. Opin. Solid State Mater. Sci.* **2007**, *11*, 3.

[52] A. Ghicov, P. Schmuki, *Chem. Commun.* **2009**, 2791.

[53] R. K. Joshi, J. J. Schneider, *Chem. Soc. Rev.* **2012**, *41*, 5285.

[54] E. V. Skorb, D. V. Andreeva, *J. Mater. Chem. A* **2013**, *1*, 7547.

[55] Y. Zhukova, S. A. Ulasevich, J. W. C. Dunlop, P. Fratzl, H. Möhwald, E. V. Skorb, *Ultrason. Sonochem.* **2016**.

[56] K. S. Suslick, *Science* **1990**, *247*, 1439.

[57] S. Doktycz, K. Suslick, *Science* **1990**, *247*, 1067.

[58] E. V. Skorb, H. Möhwald, D. V. Andreeva, *Langmuir* **2016**, doi: 10.1021/acs.langmuir.6b02842.

[59] E. V. Skorb, H. Möhwald, *Ultrason. Sonochem.* **2016**, *29*, 589.

[60] D. G. Shchukin, E. Skorb, V. Belova, H. Möhwald, *Adv. Mater.* **2011**, *23*, 1922.

[61] E. V. Skorb, H. Möhwald, T. Irrgang, A. Fery, D. V. Andreeva, *Chem. Commun.* **2010**, *46*, 7897.

[62] J. Dulle, S. Nemeth, E. V. Skorb, T. Irrgang, J. Senker, R. Kempe, A. Fery, D. V. Andreeva, *Adv. Funct. Mater.* **2012**, *22*, 3128.

[63] P. V. Cherepanov, I. Melnyk, E. V. Skorb, P. Fratzl, E. Zolotoyabko, N. Dubrovinskaia, L. Dubrovinsky, Y. S. Avadhut, J. Senker, L. Leppert, S. Kummel, D. V. Andreeva, *Green Chem.* **2015**, *17*, 2745.

[64] O. Baidukova, H. Mohwald, A. S. Mazheika, D. V. Sviridov, T. Palamarciuc, B. Weber, P. V. Cherepanov, D. V. Andreeva, E. V. Skorb, *Chem. Commun.* **2015**, *51*, 7606.

[65] E. V. Skorb, O. Baidukova, A. Goyal, A. Brotchie, D. V. Andreeva, H. Möhwald, *J. Mater. Chem.* **2012**, *22*, 13841.

[66] E. V. Skorb, D. G. Shchukin, H. Möhwald, D. V. Andreeva, *Nanoscale* **2010**, *2*, 722.

[67] E. V. Skorb, D. Fix, D. G. Shchukin, H. Möhwald, D. V. Sviridov, R. Mousa, N. Wanderka, J. Schaferhans, N. Pazos-Perez, A. Fery, D. V. Andreeva, *Nanoscale* **2011**, *3*, 985.

[68] K. S. Suslick, G. J. Price, *Annu. Rev. Mater. Sci.* **1999**, *29*, 295.

[69] J. H. Bang, K. S. Suslick, *Adv. Mater.* **2010**, *22*, 1039.

[70] P. V. Cherepanov, I. Melnyk, D. V. Andreeva, *Ultrason. Sonochem.* **2015**, *23*, 26.

[71] P. V. Cherepanov, A. Kollath, D. V. Andreeva, *Ultrason. Sonochem.* **2015**, *26*, 9.

[72] P. V. Cherepanov, D. V. Andreeva, *Ultrason. Sonochem.* **2016**, doi: 10.1016/j.ultsonch.2016.05.006.

[73] E. V. Skorb, D. V. Andreeva, H. Möhwald, *Angew. Chem. Int. Ed.* **2012**, *51*, 5138.

[74] M. Virot, R. Pflieger, E. V. Skorb, J. Ravaux, T. Zemb, H. Möhwald, *J. Phys. Chem. C* **2012**, *116*, 15493.

[75] D. V. Andreeva, D. V. Sviridov, A. Masic, H. Möhwald, E. V. Skorb, *Small* **2012**, *8*, 820.

[76] E. V. Skorb, H. Möhwald, *Adv. Mater. Intefaces* **2014**, *1*, 1400237.

[77] E. V. Skorb, H. Möhwald, *Adv. Mater.* **2013**, *25*, 5029.

[78] J.-H. Yi, C. Bernard, F. Variola, S. F. Zalzal, J. D. Wuest, F. Rosei, A. Nanci, *Surf. Sci.* **2006**, *600*, 4613.

[79] F. Variola, J.-H. Yi, L. Richert, J. D. Wuest, F. Rosei, A. Nanci, *Bio-materials* **2008**, *29*, 1285.

[80] W. Zhang, Z. Li, Y. Liu, D. Ye, J. Li, L. Xu, B. Wei, X. Zhang, X. Liu, X. Jiang, *Int. J. Nanomed.* **2012**, *7*, 4459.

[81] F. He, F. Zhang, G. Yang, X. Wang, S. Zhao, *Oral Surg. Oral Med. Oral Pathol. Oral Radiol.* **2010**, *110*, e13.

[82] E. McCafferty, J. P. Wightman, *Appl. Surf. Sci.* **1999**, *143*, 92.

[83] H. M. Kim, F. Miyaji, T. Kokubo, T. Nakamura, *J. Biomed. Mater. Res.* **1996**, *32*, 409.

[84] E. Skorb, D. Shchukin, H. Möhwald, D. Andreeva, *Langmuir* **2010**, *26*, 16973.

[85] I. Zhuk, F. Jariwala, A. B. Attygalle, Y. Wu, M. R. Libera, S. A. Sukhishvili, *ACS Nano* **2014**, *8*, 7733.

[86] A. Guyomard, E. Dé, T. Jouenne, J.-J. Malandain, G. Muller, K. Glinel, *Adv. Funct. Mater.* **2008**, *18*, 758.

[87] Y. Lu, Y. Wu, J. Liang, M. R. Libera, S. A. Sukhishvili, *Biomaterials* **2015**, *45*, 64.

[88] N. J. Peake, A. M. Pavlov, A. D'Souza, B. Pingguan-Murphy, G. B. Sukhorukov, A. J. Hobbs, T. T. Chowdhury, *Biomacromolecules* **2015**, *16*, 524.

[89] D. F. Canova, A. M. Pavlov, L. V. Norling, T. Gobbetti, S. Brunelleschi, P. Le Fauder, N. Cenac, G. B. Sukhorukov, M. Perretti, *J. Controlled Release* **2015**, *217*, 284.

[90] M. V. Lomova, A. I. Brichkina, M. V. Kiryukhin, E. N. Vasina, A. M. Pavlov, D. A. Gorin, G. B. Sukhorukov, M. N. Antipina, *ACS Appl. Mater. Interfaces* **2015**, *7*, 11732.

[91] G. Yang, J. Zhang, W. Dong, L. Liu, J. Shi, H. Wang, *Sci. Rep.* **2016**, *6*, 23423.

[92] I. Drachuk, R. Calabrese, S. Harbaugh, N. Kelley-Loughnane, D. L. Kaplan, M. Stone, V. V. Tsukruk, *ACS Nano* **2015**, *9*, 1219.

[93] S. Schmidt, N. Madaboosi, K. Uhlig, D. Köhler, A. Skirtach, C. Duschl, H. Möhwald, D. V. Volodkin, *Langmuir* **2012**, *28*, 7249.

[94] R. Xing, T. Jiao, K. Ma, G. Ma, H. Möhwald, X. Yan, *Sci. Rep.* **2016**, *6*, 26506.

[95] K. Uhlig, T. Wegener, J. He, M. Zeiser, J. Bookhold, I. Dewald, N. Godino, M. Jaeger, T. Hellweg, A. Fery, C. Duschl, *Biomacromol.* **2016**, *17*, 1110.

[96] O. Ernst, A. Lieske, A. Holländer, A. Lankenau, C. Duschl, *Langmuir* **2008**, *24*, 10259.

[97] S. Schmidt, M. Zeiser, T. Hellweg, C. Duschl, A. Fery, H. Möhwald, *Adv. Funct. Mater.* **2010**, *20*, 3235.

ADVANCED
HEALTHCARE
MATERIALS

www.advhealthmat.de

ADVANCED
SCIENCE NEWS

www.advancedsciencenews.com

REVIEW

[98] K. Uhlig, H. Boerner, E. Wischerhoff, J.-F. Lutz, M. Jaeger, A. Laschewsky, C. Duschl, *Polymers* **2014**, *6*, 1164.

[99] E. Wischerhoff, K. Uhlig, A. Lankenau, H. G. Börner, A. Laschewsky, C. Duschl, J.-F. Lutz, *Angew. Chem. Int. Ed.* **2008**, *47*, 5666.

[100] K. Uhlig, B. Boysen, A. Lankenau, M. Jaeger, E. Wischerhoff, J.-F. Lutz, A. Laschewsky, C. Duschl, *Biomicrofluidics* **2012**, *6*, 024129.

[101] A. H. Groschel, A. Walther, T. I. Lobling, F. H. Schacher, H. Schmalz, A. H. E. Muller, *Nature* **2013**, *503*, 247.

[102] I. Dewald, J. Gensel, E. Betthausen, O. V. Borisov, A. H. E. Müller, F. H. Schacher, A. Fery, *ACS Nano* **2016**, *10*, 5180.

[103] J. Gensel, I. Dewald, J. Erath, E. Betthausen, A. H. E. Muller, A. Fery, *Chem. Sci.* **2013**, *4*, 325.

[104] S. A. Ulasevich, G. Brezesinski, H. Möhwald, P. Fratzl, F. H. Schacher, S. K. Poznyak, D. V. Andreeva, E. V. Skorb, *Angew. Chem. Int. Ed.* **2016**, *55*, 13001.

[105] D. V. Andreeva, I. Melnyk, O. Baidukova, E. V. Skorb, *ChemElectroChem* **2016**, *3*, 1306.

[106] E. V. Skorb, D. G. Shchukin, H. Möhwald, D. V. Sviridov, *J. Mater. Chem.* **2009**, *19*, 4931.

[107] E. V. Skorb, D. V. Sviridov, H. Möhwald, D. G. Shchukin, *Chem. Commun.* **2009**, 6041.

[108] E. V. Skorb, A. G. Skirtach, D. V. Sviridov, D. G. Shchukin, H. Möhwald, *ACS Nano* **2009**, *3*, 1753.

[109] M. Li, Z. Ma, Y. Zhu, H. Xia, M. Y. Yao, X. Chu, X. L. Wang, K. Yang, M. Y. Yang, Y. Zhang, C. B. Mao, *Adv. Healthcare Mater.* **2016**, *5*, 557.

[110] X. B. Zhao, J. S. Yang, J. You, *Bull. Mater. Sci.* **2016**, *39*, 285.

[111] S. Guimond-Lischer, Q. Ren, O. Braissant, P. Gruner, B. Wampfler, K. Maniura-Weber, *Biointerphases* **2016**, *11*, 011012.

[112] H. Davidson, M. Poon, R. Saunders, I. M. Shapiro, N. J. Hickok, C. S. Adams, *J. Biomed. Mater. Res., Part B* **2015**, *103*, 1381.

[113] V. Antoci Jr., C. S. Adams, J. Parvizi, H. M. Davidson, R. J. Composto, T. A. Freeman, E. Wickstrom, P. Ducheyne, D. Jungkind, I. M. Shapiro, N. J. Hickok, *Biomaterials* **2008**, *29*, 4684.

[114] G. Z. Li, Q. M. Zhao, H. L. Yang, Z. T. Liu, *Compos. Interfaces* **2016**, *23*, 125.

[115] M. Godoy-Gallardo, J. Guillem-Marti, P. Sevilla, J. M. Manero, F. J. Gil, D. Rodriguez, *Mater. Sci. Eng., C* **2016**, *59*, 524.

[116] A. B. Pebdeni, M. Sadri, S. B. Pebdeni, *RSC Advances* **2016**, *6*, 24418.

[117] E. V. Skorb, D. V. Andreeva, A. P. Raiski, N. A. Belyasova, H. Möhwald, D. V. Sviridov, *Photochem. Photobiol. Sci.* **2011**, *10*, 1974.

[118] A. M. Md Jani, D. Losic, N. H. Voelcker, *Prog. Mater Sci.* **2013**, *58*, 636.

[119] G. B. Sukhorukov, A. L. Rogach, B. Zebli, T. Liedl, A. G. Skirtach, K. Kohler, A. A. Antipov, N. Gaponik, A. S. Susha, M. Winterhalter, W. J. Parak, *Small* **2005**, *1*, 194.

[120] D. V. Volodkin, M. Delcea, H. Möhwald, A. G. Skirtach, *ACS Appl. Mater. Interfaces* **2009**, *1*, 1705.

[121] D. V. Volodkin, N. Madaboosi, J. Blacklock, A. G. Skirtach, H. Möhwald, *Langmuir* **2009**, *25*, 14037.

[122] A. M. Peterson, H. Möhwald, D. G. Shchukin, *Biomacromolecules* **2012**, *13*, 3120.

[123] C. Salvi, X. Lyu, A. M. Peterson, *Biomacromolecules* **2016**, *17*, 1949.

[124] A. M. Peterson, C. Pilz-Allen, T. Kolesnikova, H. Möhwald, D. Shchukin, *ACS Appl. Mater. Interfaces* **2014**, *6*, 1866.

[125] J. J. G.-C. M. Simon, *BioPharm International* **2016**, *29*, 26.

[126] T. A. Kolesnikova, D. Kohler, A. G. Skirtach, H. Möhwald, *ACS Nano* **2012**, *6*, 9585.

[127] J. J. Giner-Casares, M. Henriksen-Lacey, I. García, L. M. Liz-Marzán, *Angew. Chem. Int. Ed.* **2016**, *55*, 974.

[128] Q. Y. Zeng, M. Xi, W. Xu, X. J. Li, *Mater. Corros.* **2013**, *64*, 1001.

[129] J. Xi, J. J. Schmidt, C. D. Montemagno, *Nat. Mater.* **2005**, *4*, 180.

[130] S. H. Yang, S. M. Kang, K.-B. Lee, T. D. Chung, H. Lee, I. S. Choi, *J. Am. Chem. Soc.* **2011**, *133*, 2795.

[131] M. R.-B. Sarah, L. H. Jeffrey, C. M. David, *J. Neural Eng.* **2007**, *4*, L6.

[132] J. Walpole, J. A. Papin, S. M. Peirce, *Annu. Rev. Biomed. Eng.* **2013**, *15*, 137.

[133] H. P. Fischer, *Alcohol Research & Health* **2008**, *31*, 49.

[134] S. H. Yang, E. H. Ko, Y. H. Jung, I. S. Choi, *Angew. Chem. Int. Ed.* **2011**, *50*, 6115.

[135] K. M. Persson, S. Lönnqvist, K. Tybrandt, R. Gabrielsson, D. Nilsson, G. Kratz, M. Berggren, *Adv. Funct. Mater.* **2015**, *25*, 7056.

In Situ Characterization of Interfaces Relevant for Efficient Photoinduced Reactions

Oliver Supplie, Matthias M. May, Sebastian Brückner, Nadzeya Brezhneva, Thomas Hannappel,* and Ekaterina V. Skorb*

Solar energy conversion and photoinduced bioactive sensors are representing topical scientific fields, where interfaces play a decisive role for efficient applications. The key to specifically tune these interfaces is a precise knowledge of interfacial structures and their formation on the microscopic, preferably atomic scale. Gaining thorough insight into interfacial reactions, however, is particularly challenging in relevant complex chemical environment. This review introduces a spectrum of material systems with corresponding interfaces significant for efficient applications in energy conversion and sensor technologies. It highlights appropriate analysis techniques capable of monitoring critical physicochemical reactions in situ during non-vacuum preparation and photoactivity studies including well-defined inorganic epitaxial reference surfaces, buried interfaces, and low-defect nucleation of disjunct epitaxial materials that are analyzed during preparation in chemical vapor environment. Their surfaces are then modified and functionalized in gaseous and liquid environment. Finally, even more complex coupling of inorganic stable photoactive materials with responsive soft matter for bioactivity is reviewed. Interface formation, structure, and/or artificial photochemical interfacial reactions are scrutinized down to the atomic scale in real time, also accounting for equilibrium versus non-equilibrium, kinetically driven processes, in order to accelerate progresses in the realization of efficient energy materials and in the exploitation of photoinduced processes at interfaces.

1. Introduction

In his Nobel Lecture, Kroemer concisely coined the famous phrase "*Often it can be said, that the interface is the device.*"[1] This is particularly true for the semiconductor heterostructures

Dr. O. Supplie, Dr. S. Brückner, Prof. T. Hannappel
Institute for Physics
Technical University Ilmenau
98693 Ilmenau, Germany
E-mail: thomas.hannappel@tu-ilmenau.de
Dr. M. M. May
Department of Chemistry
University of Cambridge
Cambridge CB2 1EW, UK
N. Brezhneva, Prof. E. V. Skorb
Laboratory of Solution Chemistry of Advanced Materials
and Technologies (SCAMT)
ITMO University
197101 St. Petersburg, Russian Federation
E-mail: skorb@scamt.ru

which he pioneered and established. In general, interfaces do not only determine electronic properties of the final device; their atomic order also highly affects growth kinetics and defect formation. Moreover, the design of solid–liquid and hybrid interfaces determines their chemical reactivity and stability. In situ monitoring of interface preparation, formation, and interfacial reactions thus promises efficient process control. Paired with a detailed understanding of interface formation mechanisms, however, the true power of in situ control is to allow for specific modification and tuning of interface formation for the device of choice. There are several excellent reviews on in situ approaches covering wide ranges of materials from basic science to applications as well as varieties of preparation and analysis techniques.[2–11] As indicated in **Figure 1**, this review will be focused on in situ control over interfaces of materials that are relevant for photoinduced reactions in high-efficiency solar energy conversion and sensing applications with in situ control of semiconductor/polymer/biological interfaces. We will restrict the techniques to realistic and complex, non-ultrahigh-vacuum (UHV) ambient, where in situ control is most demanding—but also highly desired. The more complex the interfacial reactions are, the more important is the in situ characterization. Ex situ approaches can contribute to an indirect understanding of interface formation, but to understand and, finally, control the dynamic processes taking place, real-time measurements are appropriate. The challenge, we are facing, is twofold: On the one hand, increased interaction with the surrounding ambient causes higher complexity. Yet at the same time, it decreases the number of applicable techniques. On the other hand, those techniques are often elaborate and not necessarily easy to interpret. In a nutshell, we will discuss four main topics:

(i)   Surface preparation during growth of structures for high-efficiency solar energy conversion: World-record conversion efficiencies in both photovoltaics[12,13] and solar water splitting[14] are achieved with multijunction solar cells based on epitaxial III/V compound semiconductor structures. We will discuss in situ controlled preparation

**ADVANCED
SCIENCE NEWS**
www.advancedsciencenews.com

**ADVANCED
MATERIALS
INTERFACES**
www.advmatinterfaces.de

of relevant III/V and IV(100) surfaces in metalorganic vapor phase epitaxy (MOVPE).[15] MOVPE is the state-of-the-art industrially scalable technique for semiconductor epitaxy. Compared to vacuum-based techniques, MOVPE is demanding, given the involved complex physicochemical reactions and the presence of a carrier gas, which limits in situ methods mainly to optical approaches.

(ii) Preparation of buried interfaces during growth of structures for high-efficiency solar energy conversion: Based on the homoepitaxially prepared surfaces, we will discuss MOVPE in situ studies on multinary III/V compounds, their related buried heterointerfaces—such as tunnel junctions in multijunction solar cells—as well as III/V-on-IV heteroepitaxy.

(iii) Solid–liquid interfaces and electrochemical interface modification: The study of catalytic and electrochemical processes requires high spatial as well as temporal resolution. A great challenge for in situ techniques is the necessity to transport information through the liquid environment. Materials involved range from catalytically active metals, semiconductors, and photoelectrochemical applications to insulators used in surface passivation. Besides interfaces involving the III/V structures discussed above, some metallic and oxide-based materials and their interaction with gas phase and liquid water will be reviewed.

(iv) Semiconductor/polymer/biological interfaces for the development of spatiotemporal nanoscale machinery inspired by nature: Here, we review the coupling of inorganic stable photoactive materials with responsive soft matter for bioactivity. We discuss inspiration by nature as a general design concept for chemical networks—which consist of several inter-related single chemical reactions—for application in future "intelligent" systems. Lab-produced, artificial photochemical networks are discussed to provide reliable, inorganic semiconductors for new functions. Thus, we focus on a transformation of energy from electromagnetic irradiation into ion concentration gradients with in situ temporal control of the reaction network. Light is discussed here as an "on-demand" stimulation of the bioresponse, for which it is easy to control intensity, duration, and localization. Efficient actuation of pH-sensitive soft assemblies with light is shown as an example.

For the first part (Section 2), we will start from well-defined epitaxially prepared interfaces, such as InP(100) films and surfaces, which are relevant for high-efficiency solar energy conversion. The atomic order of these surfaces and their specific preparation in vacuum and MOVPE ambient have been studied and are now understood in great detail. They are perfectly suited to demonstrate the ideal interplay between in situ spectroscopy, density functional theory, and benchmarking to a broad range of surface science techniques. Based on their optical fingerprints, different atomically well-ordered surfaces can be specifically prepared. Following this approach, in situ control over surface preparation will be discussed for several important III/V compound semiconductor surfaces, such as GaAs and GaP, as well as for Ge and Si.

Building on these results, III/V materials will be combined to multinary compounds and III/V heterostructures, which are

Oliver Supplie studied physics at the Humboldt-Universität zu Berlin, Germany, and at the Uppsala Universitet, Sweden, as fellow of the Studienstiftung des deutschen Volkes. He received his PhD from the Humboldt-Universität for in situ studies on epitaxy and interface formation, which were performed at the Helmholtz-Zentrum Berlin and at the Ilmenau University of Technology, and which have been awarded by the European MRS and by the German Association of Crystal Growth DGKK. Funded by the German Research Foundation DFG, Oliver is currently postdoc in Ilmenau. Motivated by needs for advanced solar energy conversion and storage, his research interests include III/V-on-IV heteroepitaxy, surface science, and optics.

Thomas Hannappel is W3 full professor at the Institute of Physics, Ilmenau University of Technology. He was scientific director of the solar centre at the CIS Research Institute Erfurt, acting director of the Institute "Materials for photovoltaics" at the Helmholtz-Zentrum Berlin, acting department head at the Hahn-Meitner-Institute Berlin, and lecturer at the Free University Berlin; he started in situ studies on the Si/III–V interface at the NREL and received his PhD at the Berlin University of Technology with studies on photo-induced charge carrier dynamics performed at the Fritz-Haber-Institute of the Max-Planck-Society. Current research is focused on high-performance optoelectronic materials, crystal growth, critical interfaces, and solar energy conversion.

Ekaterina V. Skorb received her PhD in physical chemistry (2008). Subsequently, she was postdoc and AvH fellow at the Max Planck Institute of Colloids and Interfaces (MPIKG) with Prof. Helmuth Möhwald. From 2013, she has been working with Prof. Peter Fratzl (MPIKG) as a group leader. She was a Visiting Scholar in Harvard in Prof. George Whitesides group (2016–2017). From 2017 she is a professor at the ITMO University leading a group of Infochemistry for Self-Adaptive Materials at SCAMT. Her current research interests are spatiotemporal control of ion concentration gradients for soft matter actuation, biosensing, and dynamic control of cell behavior.

ADVANCED
SCIENCE NEWS

www.advancedsciencenews.com

ADVANCED
MATERIALS
INTERFACES

www.advmatinterfaces.de
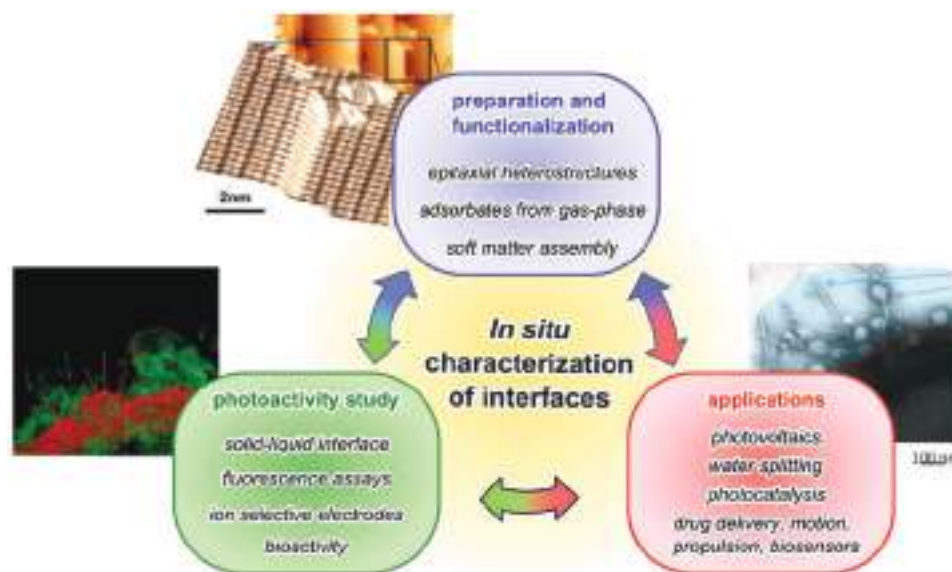
Figure 1. In this review, we focus on in situ studies on interfaces of materials, which are relevant for application in energy conversion and biosensing. We focus on in situ characterization during non-UHV preparation techniques and photoactivity aiming at control over interfacial reactions in real time. Inset images adapted with permission.[409,416]

studied with focus on their (buried) interfaces in the second part of this review (Section 3). This is of particular interest for semiconductor applications, where the sharpness of the heterointerface is of essential importance: Tunnel junctions will be addressed as well as heterointerfaces designed to suppress recombination of charge carriers. Appropriate interface preparation is also crucial for III/V heteroepitaxy on Si substrates, where crystal defects are easily introduced during III/V nucleation due to the different crystal structures involved. Here, we will demonstrate how in situ analysis enables detailed insights regarding the interface formation, which finally yields precise process control and fine interfacial tuning.

The structures discussed in Sections 2 and 3 are decisive for highly efficient solar energy conversion. Besides their applications in photovoltaic devices, they are promising ingredients for direct solar water splitting.[14,16–18] Corresponding modifications of their surfaces in liquid environments and by gases beyond MOVPE conditions will therefore be discussed in the third part of this review (Sections 4 and 5). The impact of these complex conditions on the surfaces is understood to a much lesser degree. Adsorption processes on well-defined surfaces, the focus of Section 4, try to bridge the gap between epitaxial surfaces in vacuum and in liquid ambient: While for the former, the application of various surface science techniques enabled an understanding on an atomistic level, this is much more challenging for the latter due to limited availability of applicable techniques. Here, we will first review studies on epitaxial reference surface discussed in part one, and second on noble metal surfaces. The next step directed toward applications for artificial photosynthesis in a water splitting device is to study the solid–liquid interface, which is the topic in Section 5. Emphasis will be put on how an electrochemical in situ modification enabled record solar-to-hydrogen efficiencies and how this approach may be transformed to other surfaces.

In the fourth part of this review (Sections 6–9), we will discuss nature inspired photochemical reactions beyond

applications of artificial photosynthesis: Photoinduced interfacial reactions also enable sensing applications focusing on modulation, detection, and deactivation of bacteria, pathogens, as well as biofilms and biomolecules. They also serve as platforms for systems for microfluidic biochips and autonomous soft robotics. Photochemical reactions to control hybrid interfaces will be detailed in Section 6. Different techniques for in situ detection of reactive oxygen species in TiO_2-based systems are discussed in Section 7. This is followed by studies on the photocatalytic degradation of organic species on TiO_2 in Section 8. Finally, Section 9 focuses on prospects for in situ modulation of soft matter and microorganisms without degradation.

2. Epitaxial Reference Surfaces

The attractiveness of the III/V semiconductor material class for a wide range of electro-optical applications is to a great extent owed to the possibility to smoothly tune their electronic structure via the composition of multinary compounds. **Figure 2** shows bandgaps and band offsets of the classical III/V semiconductors as a function of the lattice constant at room temperature and displays their approximated band alignment with respect to vacuum. The tunability of the bandgap allows absorption of a wide range of the solar spectrum. The combination of different materials enables high solar energy conversion efficiency: For a dual absorber structure, the limiting conversion efficiencies with dependence of the bandgaps of the subcells are plotted in **Figure 3**. The combination of III/V semiconductors with Si here promises efficiencies close to optimum, both for photovoltaic (PV) and water splitting application.[16,18–20] Such a tandem absorber device requires preparation of ideal structures in all involved interfaces, which are manifold as indicated in **Figure 4** for an InP-based solar cell optimized for the infrared.[21,22] It is therefore important to understand the surface formation step

Figure 2. a) Bandgaps of binary and ternary III/V compound semiconductors (line and symbol style indicate the nature of the bandgap), data from ref. [433]; b) Approximated conduction (turquois) and valence band (red) offsets (line and symbol style indicate the nature of the bandgap), data from refs. [20,433–436]; c) Solar spectrum AM1.5 ASTM-G-173-03. Data from ref. [437].

$$\frac{\Delta R}{R} \approx 2\mathrm{Re}\left(\frac{\Delta r}{r}\right). \tag{2}$$

For (100) faces of ideal cubic crystals, the bulk contribution is optically isotropic, which renders RAS an extremely interface and defect sensitive optical technique. Here, RAS is aligned such that $x = [0\bar{1}1]$ and $y = [011]$. To make RAS amplitudes intercomparable, they should be calibrated to a Si(110) reference.[23]

Contributions to RA spectra can be manifold, which renders RAS a versatile but also complicated analysis technique. Once the microscopic origin of the spectra is understood, they can act as qualitative and/or quantitative fingerprints for specific interfacial or defect-related properties. In order to understand the origin of the spectra, comparison to complementary surface science techniques ("benchmarking") is beneficial. Of course, such benchmarking should not affect the interface which is characterized, so—besides various other optical techniques applicable in MOVPE ambient—UHV based techniques are often applied. Most elegantly, samples are transferred contamination-free from MOVPE ambient to a mobile UHV shuttle,[24] which may in principle be attached to any UHV surface science chamber of interest, where the samples can be characterized in vacuo. Since RAS is also applicable in UHV, the state of the sample can be probed and verified after benchmarking as well.

2.1. InP(100)

InP has a long history as efficient photocathode in water splitting applications.[25,26] Recently, InP-based low bandgap tandem solar cells were suggested for multijunction solar cells (MJSCs) with more than three junctions[27–29] and applied in the current world record four-junction cell with conversion efficiencies exceeding 46%.[13,30,31] Here, InP(100) is of particular interest, since it may be considered as prototype surface regarding H-based MOVPE processing of phosphides, where hydrogen strongly affects the atomic surface structure compared to UHV preparation. InP(100) is also a valuable example for the fruitful combination of optical in situ spectroscopy, various complementary in system surface science techniques, and density functional theory (DFT) calculations, which lead to a very detailed understanding of the atomic and electronic surface structures. The atomic structure indeed has a significant impact on further surface functionalization, as will be discussed in Section 5.

2.1.1. Surface Reconstructions and Their Anisotropic Fingerprints

Depending on the P chemical potential (corresponding to In- vs P-rich conditions), two surface reconstructions typically occur

by step. We will thus first focus on surfaces of the important III/V semiconductors InP, GaP, and GaAs(100) as well as on the group IV substrates Si(100) and Ge(100). These are relevant for energy applications and are available as wafers, which facilitate the preparation of smooth and high-quality reference surfaces on homoepitaxially grown buffer layers.

MOVPE processing ambient hinders the application of electron-based techniques, so mostly optical techniques are applied in situ. In the following text, the linear optical technique reflection anisotropy spectroscopy[23] (RAS) will play an important role. RAS measures the difference in (complex) reflection along two mutually perpendicular crystal axes normalized to their mean reflection,

$$\mathbb{C} \ni \frac{\Delta r}{r} = \frac{r_x - r_y}{\frac{1}{2}(r_x + r_y)}. \tag{1}$$

Both real and imaginary parts can be measured, but mostly the real part (Re) is discussed here. In literature, reflectance, R, is discussed often instead of the complex Fresnel reflection amplitude coefficient, r. For $\Delta r \ll r$, the relation of RAS (complex number, r) and the corresponding reflectance anisotropy signal (real number, R) is[23]

**ADVANCED
SCIENCE NEWS**
www.advancedsciencenews.com

**ADVANCED
MATERIALS
INTERFACES**
www.advmatinterfaces.de

Figure 3. Theoretical efficiency limit for a two-junction absorber structure in the current-matched detailed balance limit operated as a,b) a photovoltaic cell (electric efficiency) and c) a water splitting device (solar-to-hydrogen efficiency) depending on the bandgap of the two subcells; calculated with YaSoFO[438]; In (a), the top absorber is assumed to be infinitely thick; In (b,c), the thickness of the top absorber is reduced to optimize current-matching with the bottom cell; The bandgap of Si is marked for the bottom cell and the inset on the right indicates the layer structures for a corresponding III/V-on-Si tandem cell with a GaP nucleation layer; for the water splitting device, a water layer of 1 mm thickness and an IrO$_2$ counter electrode with 1 Ω solution resistance were assumed.
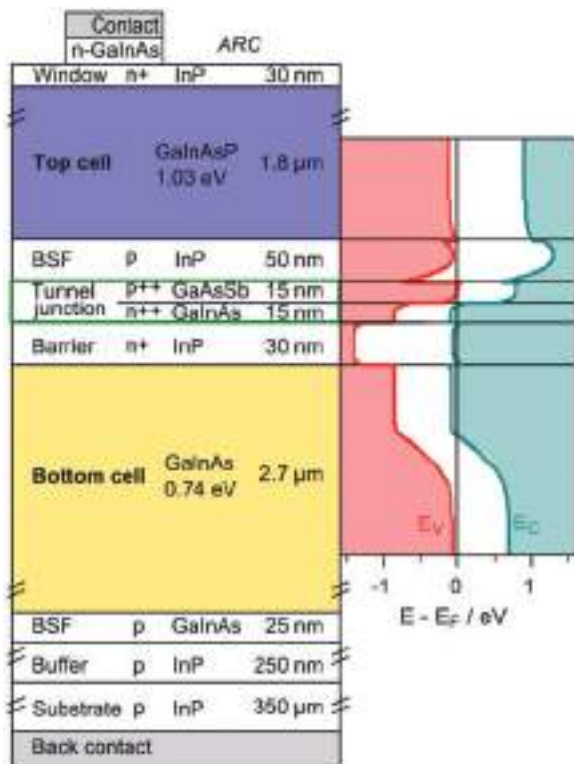
Figure 4. (left) Schematic of the stack and (right) approximated band diagram for an InP-based tandem solar cell optimized for absorption in the infrared as lower tandem in a four-junction solar cell (BSF = back surface field). Data from refs. [22,28].

in MOVPE ambient (cf. **Figure 5**) and they exhibit characteristically different RAS fingerprints (cf. **Figure 6**): (i) The P-rich (2 × 2)/c(2 × 4) surface consists of buckled P dimers stabilized by one H atom each,[32] while (ii) the In-rich (2 × 4) surface is terminated by a mixed dimer atop an In layer.[33] Figure 5 shows ball-and-stick models of these reconstructions and they are highlighted in the phase diagram in Figure 6b, which was obtained by DFT calculations.[32] Figure 6a displays the corresponding RA spectra obtained after homoepitaxial buffer growth and contamination-free transfer to UHV,[24] where they were measured at 20 K: The P-rich surface (violet) features a characteristic minimum P$_1$ at about 1.9 eV, an intense maximum P$_2$ at 3.2 eV slightly below the E$_1$ interband transition, a broad local maximum P$_3$ between 4.0 and 4.5 eV, as well as an additional peak at the E$_0'$ interband transition. The RA spectrum of the In-rich InP(100) surface (green) exhibits more features, the most prominent are two local minima around 2.0 eV (labeled In$_1$), a local maximum In$_2$ at about 2.4 eV, a local minimum In$_3$ close to the E$_1$ interband transition, a rather broad local maximum In$_4$ centered at about 3.7 eV, and another local maximum In$_4$ at the E$_0'$ interband transition. In particular, the spectral differences between P$_2$ and In$_2$/In$_3$ are suitable for in situ identification of the two surfaces. The dielectric function of InP[34] and its temperature dependence was measured in situ with ellipsometry,[35] which facilitates evaluation at real growth conditions.

Within the DFT–GW approximation (GWA), reasonable agreement of calculated and in situ RA spectra both for the In-rich[36,37] and the P-rich[32] InP(100) surface is achieved. The predicted spectral features help to clarify the microscopic origin of the RA spectra, which are best measured at low temperatures,[36,38,39] where peaks sharpen drastically.[35,40] However, so

ADVANCED
SCIENCE NEWS
www.advancedsciencenews.com

ADVANCED
MATERIALS
INTERFACES
www.advmatinterfaces.de
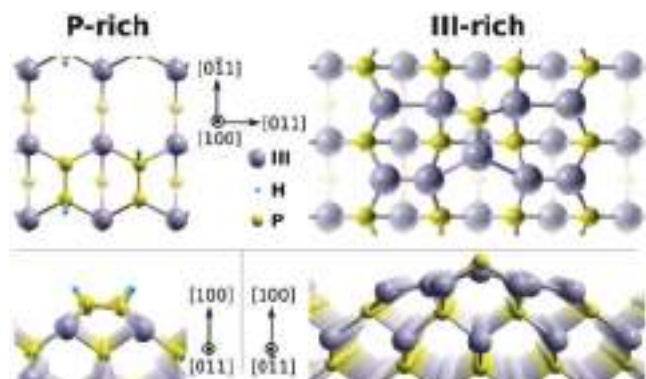
Figure 5. Surface reconstructions of (left) P-rich and (right) group-III-rich InP(100) resp. GaP(100) surfaces. The top row shows the top view and the bottom row side views in [0$\bar{1}$1] and [011] direction, respectively. Adapted from with permission.[50] Copyright 2014, ACS, reuse requests to be directed to the ACS.

far, the accuracy of DFT calculations is not sufficiently precise to predict RA spectra without any experimental feedback. Only in few specific cases, it is possible to deduce the given atomic surface structure from experimental in situ RA spectra by comparison to the theoretical ones.

2.1.2. The P-Rich InP(100) Surface

The P-rich InP(100) surface is an instructive example how the correlation of DFT and RAS enabled understanding the impact of the presence of H during MOVPE preparation: in situ RA spectra of both PH$_3$[35,41] and tertiarybutylphosphine (TBP)[42] prepared P-rich InP(100) surfaces show a characteristic line-shape that does not occur in H-free molecular beam epitaxy (MBE) ambient.[32,43] DFT calculations could relate the features P$_1$ and P$_2$ to optical transitions involving states induced by H termination of one H atom per P dimer.[32] The buckled P dimers of this "(2 × 1)-like" (2 × 2)-2D-2H reconstructed

surface[32] form zigzag lines and the buckling may flip causing a (2 × 2)/c(2 × 4) symmetry.[44,45] While dimer buckling may occur also on non H-terminated surfaces,[46] which would cause streaked (2 × 1)-like low energy electron diffraction (LEED) patterns just as for the H-terminated buckled P dimers, the existence of the P−H bonds was verified experimentally by in system Fourier transform infrared spectroscopy (FTIR) studies.[47] These studies also showed that RAS allows for in situ fine-tuning of the atomic order at the InP(100) surface:[47] The P-rich surface is commonly prepared by cooling under stabilization with the precursor TBP after homoepitaxial growth. When TBP supply is stopped at 300 °C, the surface is covered with excess P and precursor residuals.[48] Cycled heating to 360 °C (without precursor supply) and cooling to 300 °C (with precursor supply despite the very last cooling step) increases the atomic order at the surface,[47] which can be observed in situ by an increased intensity of P$_1$ along with a redshift of its energetic position.[42,48] In situ studies during InP:adsorbate interaction revealed that the H termination strongly increases the stability of the P-rich surface against O$_2$, yet not H$_2$O,[49,50] as will be discussed in more detail in Section 4.

2.1.3. The In-Rich InP(100) Surface

Given the different lineshapes of the anisotropic fingerprints of the two surface reconstructions, RAS enables to study the transformation from P-rich to In-rich surfaces in great detail:[48,51] Heating of the P-rich surface above 370 °C without P stabilization results in enhanced P desorption and P depletion of the surface.[48] RAS peaks originating from the occurrence of P dimers vanish and the lineshape changes toward that of the In-rich surface. **Figure 7** visualizes that the peaks at and below 2.5 eV of the RA spectrum of the In-rich surface can be attributed to transitions involving surface states related to the mixed dimer reconstruction.[36,37] The electronic orbitals for the corresponding surface states are shown in side view in Figure 7.
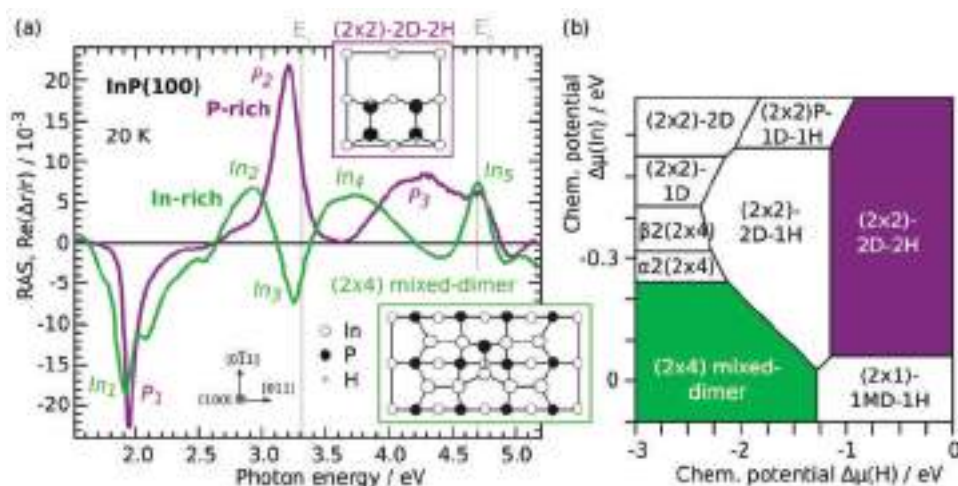
Figure 6. a) RAS of P-rich, (2 × 2)-reconstructed (violet) and In-rich, (2 × 4)-reconstructed (green) InP(100) surfaces, measured at 20 K, data from ref. [38]; the insets show ball-and-stick models of the corresponding surface reconstruction; gray vertical lines indicate the critical interband transitions of InP[439]; b) phase diagram depending on the In and H chemical potential, data from ref. [32].

ADVANCED
SCIENCE NEWS
www.advancedsciencenews.com

ADVANCED
MATERIALS
INTERFACES
www.advmatinterfaces.de
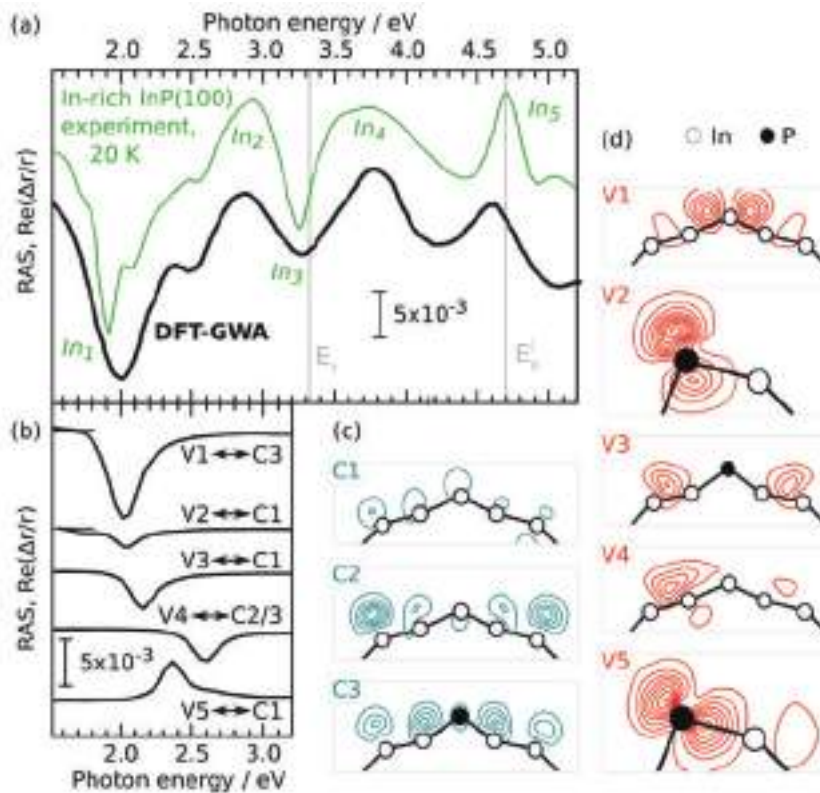
Figure 7. RAS of In-rich InP(100): a) comparison of experiment (green) and DFT–GWA calculation (black); b) contributions to the calculated RA spectrum from different transitions involving the surface states in the c) conduction and d) valence band; gray vertical lines indicate the critical interband transitions of InP.[439] Adapted with permission from.[36] (copyrighted by the American Physical Society). Data from refs. [36,38].

2.1.4. Experimental Verification of the Microscopic Origin of the Spectral Features

Further experimental indications for the origin of the contributions to the RA spectra of P-rich and In-rich InP(100) was obtained by analyzing their temperature-dependent phonon coupling:[40] Fitting this temperature dependence with an adequate model[52] yields the renormalization energy for each anisotropic contribution.[40] For the peaks P_1 and P_2 as well as In_3, the renormalization energy is similar to that of the InP bulk critical point energies, which implies an "intrinsic"[23] nature. Since the E_1 interband transition is close to P_2 and In_3, it was suggested that these anisotropies likely stem from surface modified bulk transitions.[40] P_1, in contrast, which is not in the vicinity of any critical interband transition, was attributed to a transition involving both bulk and surface states.[40] In_1 couples only weakly to phonons and was thus attributed to pure surface state transitions.[40]

The electronic structure of MOVPE-prepared InP(100) surfaces has been studied with in system ultraviolet photoelectron spectroscopy (UPS)[38] and with angular-resolved photoelectron spectroscopy after contamination-free transfer[24] to the BESSY-I synchrotron.[53] Occupied surface states with only little dispersion close to the valence band maximum (VBM) as well as occupied surface resonances were identified.[53] Performing

in system 2-photon photoemission (2PPE) studies on In-rich InP(100),[54] an occupied surface resonance was found about 0.2 eV below the VBM and two unoccupied dangling bond surface states were identified at 1.5 and 2.2 eV above the VBM near the Γ-point. The alignment of these states relative to the VBM agrees well with that of the surface states $V_{1,2}$, C_1, and C_2 predicted by DFT.[36] Electron dynamics of InP(100) and scattering from surface to bulk states were studied by applying pump-probe 2PPE at femtosecond timescale.[55–57]

As first observed for GaAs (see below), doping influences the RA spectrum of InP(100) via the linear electro-optic effect.[58]

2.2. GaP(100)

GaP is interesting for water splitting applications since its rather large bandgap of about 2.3 eV at room temperature might provide enough photovoltage.[59] However, due to this large bandgap and its indirect nature, thin GaP films are rather transparent and are thus not suitable as absorber layer for high efficiency solar energy conversion. However, GaP may be applied as window layer[60] in tandem configurations, as constituent of multinary compounds such as InGaP or GaAsP or when diluted with N and possibly As.[61] Moreover, GaP is almost lattice-matched to Si, which renders it an ideal candidate for pseudomorphic virtual III/V-on-Si substrates, as will be discussed in Section 3.

GaP(100) surfaces reconstruct analogously to the InP(100) surfaces discussed afore and also their optical in situ fingerprints are similar.[62] In H-based ambient, two surface reconstructions are typical: the P-rich surface (which occurs during growth and at rather low temperatures or when stabilized with TBP, respectively) and the Ga-rich surface (which forms when P desorbs preferentially at elevated temperatures). **Figure 8** compares the RA spectra of P-rich and Ga-rich GaP(100), which were prepared by MOVPE and measured in system at 20 K.[63] The spectrum of the P-rich surface (orange) exhibits a characteristic minimum P_1 at about 2.6 eV, an intense maximum P_2 at 3.7 eV slightly below the E_1 interband transition, a small local maximum P_3 at about 4.5 eV, as well as an local maximum P_4 at about 5eV. The RA spectrum of the Ga-rich GaP(100) surface (blue) exhibits a characteristic minimum Ga_1 slightly below 2.5 eV, a local maximum Ga_2 at about 3.2 eV, a local minimum Ga_3 close to the E_1 interband transition, a shoulder Ga_4 at about 4.2 eV, and a local maximum Ga_5 slightly above the E_0' interband transition. Compared to the RA spectra of the corresponding InP(100) surfaces,[38] those of GaP are shifted to higher energies. While the lineshape of the P-rich surfaces are very similar, Ga_1 is broader but exhibits less features than In_1.

ADVANCED
SCIENCE NEWS
www.advancedsciencenews.com

ADVANCED
MATERIALS
INTERFACES
www.advmatinterfaces.de
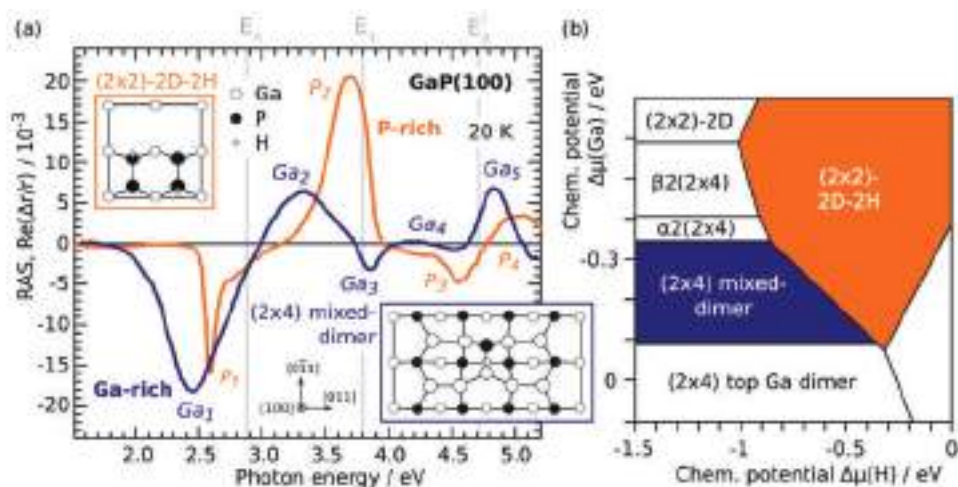
Figure 8. a) RAS of P-rich, (2 × 2)-reconstructed (orange) and Ga-rich, (2 × 4)-reconstructed (blue) GaP(100) surfaces, measured at 20 K, data from ref. [63]; the insets show ball-and-stick models of the corresponding surface reconstruction; gray vertical lines indicate the critical interband transitions of GaP[440]; b) Phase diagram depending on the Ga and H chemical potential, data from ref. [66].

In situ RA spectra of the Ga-rich GaP(100) surface were studied in combination with ab initio DFT calculations:[64] A mixed Ga–P dimer on top of a layer was suggested as ground state just as for In-rich InP(100). The surface reconstruction is (2 × 4) as confirmed by LEED on decapped[62] and contamination-free transferred[63] homoepitaxial surfaces. The corresponding surface state band structure exhibits several nonresonant surface states both in the valence and the conduction band.[37] Transitions involving these states cause the contributions to the RA spectrum below the E_1 interband transition: As predicted by DFT,[37] a series of occupied and unoccupied surface states was found was found experimentally applying in system 2PPE[65] and transitions involving them were assigned to Ga_1.[37,65] The presence of several anisotropic optical transitions can also explain the rather broad lineshape of Ga_1 compared to P_1. These spectral features vanish when the surface is exposed to oxygen and the surface states are quenched.[65] As we will see in Section 4, however, the surface states exhibit a much larger stability against oxidation by water. Peak Ga_2 stems from a surface modified bulk transition.[37]

For the P-rich GaP(100) surface, it was shown by ab initio DFT calculations,[66] that the lineshape of P_1 can be explained well by optical transitions involving surface states from the buckled, H-stabilized P dimer. These states and the corresponding RAS signals induced by optical transitions between occupied and nonoccupied surface states are shown in **Figure 9**. The presence of a surface state assigned to P_1 was also verified experimentally with in system 2PPE.[65] Just as for P-rich InP(100), the buckling of the dimer leads to a (2 × 2)/c(4 × 2) surface reconstruction (also referred to as (2 × 2)-2D-2H[66]), which causes streaks in the LEED patterns[63] and zigzag lines observed by scanning tunneling microscopy (STM).[45,63,66,67] At room temperature, the H atom is mobile and a flip-flop motion of the dimer can be detected by STM.[45]

Continuously measured RA spectra during annealing of the GaP(100) surface in H ambient showed that P starts desorbing preferentially at temperatures beyond about 490 °C and

that this causes a change from the P-rich to the Ga-rich surface reconstruction via an intermediate surface.[63,68] In contrast to InP(100), surface preparation in N_2-based ambient significantly impacts the surface formation.[51] Upon annealing in N_2, an additional intermediate surface phase occurs at temperatures above about 470 °C and below about 620 °C.[51]
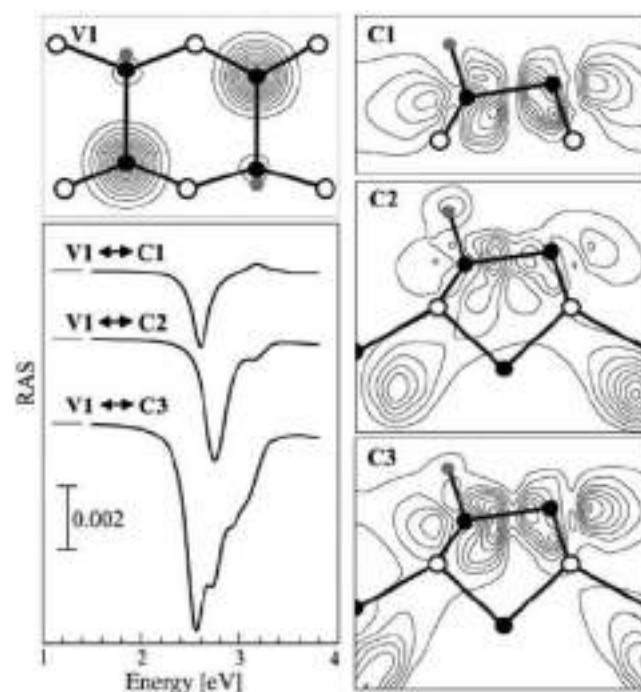
Figure 9. Orbital character of specific surface states of the P-rich, (2 × 2) reconstructed GaP(100) surface (at the k point of the Brillouin zone) and contributions of transitions between these states to peak P_1 in the RA spectrum of the P-rich, (2 × 2) reconstructed GaP(100) surface as calculated by DFT–GWA; Reproduced with permission.[66] Copyright 2003, The American Physical Society.

**ADVANCED
SCIENCE NEWS**
www.advancedsciencenews.com

**ADVANCED
MATERIALS
INTERFACES**
www.advmatinterfaces.de

2.3. GaAs(100)

GaAs is widely used in optoelectronics and it is the material of choice for record efficiency single-junction solar cells[12,69] as well as modules.[12,70] GaAs was used as active substrate in tandem absorber structures,[71,72] and due to the little lattice mismatch, growth of GaAs-based top absorber structures on Ge(100) is applied in the current industry standard InGaP/GaAs/Ge solar cells, achieving more than 40% conversion efficiency.[73–76] GaAs is also the first compound semiconductor that was grown epitaxially by MOVPE[15] and GaAs(100) surfaces were the first semiconductor surfaces studied in situ during MOVPE growth.[77] These first experiments studied growth kinetics and chemisorption with time resolved RAS.[77,78] RA spectra obtained in MOVPE ambient were often benchmarked to MBE-prepared GaAs(100) surfaces, where electron-based techniques are available.[78–80] Besides RAS, surface photoabsorption was applied in situ to compare the decomposition of the two typical precursors trimethylgallium and triethylgallium (TEGa).[81] Applying in situ RAS on GaAs(100), surface reconstructions of semiconductors were observed for the first time in atmospheric pressure demonstrating the potential of and the need for real-time growth monitoring due to complex surface structures and reactions.[82–84] Surface reconstructions similar to those known from UHV studies were found to occur also for MOVPE preparation in various process gases,[82] but, in general, surface reactions are more complex in MOVPE ambient.[85] In particular, surface reactions play a crucial role during initiation of GaAs homoepitaxy.[79,80,86,87]

Many different surface reconstructions were suggested for GaAs(100).[88–92] As for GaP(100) and InP(100) surfaces discussed above, spectral features of GaAs(100) surfaces were assigned to dimers on the surface[93,94] and the spectra vary strongly depending on the rate of As coverage on the surface.[95,96] Indeed, also calculations of the RAS lineshape for differently reconstructed GaAs(100) surfaces showed a strong dependence on the atomic structure of the surfaces.[97,98] However, the entire surface geometry needs to be taken into account to yield an adequate agreement with experimental data.[98] Excitonic effects were found negligible,[98] while surface strain can contribute to the RAS signal.[99,100] By comparison of RAS with DFT,[101] the As-rich surface was assigned to c(4 × 4) and (2 × 4) phases, while the Ga-rich surface reconstructs (4 × 2). Schmidt et al.[91] compared RA spectra obtained by DFT and in experiment, respectively. A mixed Ga–As dimer structure is energetically most favorable for "extreme" Ga-rich conditions,[91] and causes an RA spectrum similar to that experimentally observed for (n × 6) surface structures.[101] The (2 × 4) and c(4 × 4)

reconstructed GaAs(100) surface exhibits surface states, which contribute to the spectral RAS features below the E_1 bulk critical point.[80,101–103] The RA spectrum above E_1, in contrast, is assigned to surface modified bulk transitions.[102,104,105]

Figure 10 displays color-coded RA spectra during annealing in H_2 ambient. The development from the As-rich to the Ga-rich surface (via intermediate surface reconstructions) by desorption of As due to the increased temperature is clearly observable by the different RA spectra associated with the surface reconstructions. Here, the significant differences in the lineshapes enable to study the surface formation in situ with RA transients, which must be done with care in other cases since temperature induced spectral shifts occur as well.[40] Exploiting the in situ RA spectra of GaAs as a measure of crystal quality, process parameters could be tuned to increase the efficiency with regard to minimized material consumption[106] and precursor choice.[107]

Fermi-level pinning at the surface can be caused by impurity induced surface states and contributes to RAS via the linear electro-optic (LEO) effect.[108,109] Combined with precise knowledge about changes in the surface reconstruction on temperature and dopant adsorption, the LEO effect allows
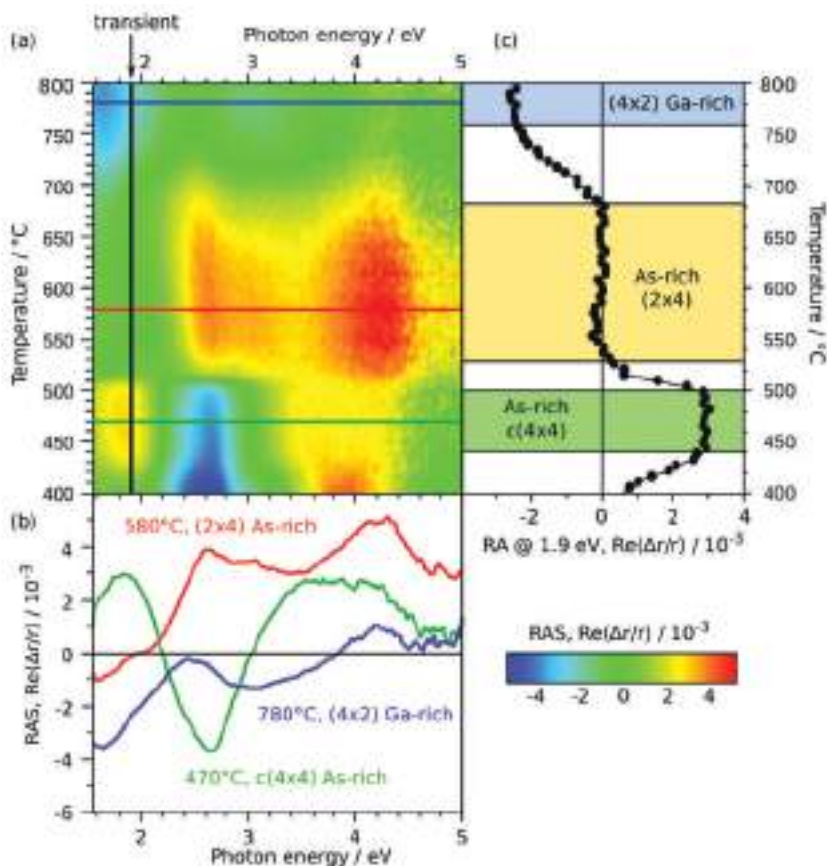
Figure 10. a) Color-coded RA spectra of GaAs(100) during annealing in H_2 ambient, where b) lines mark spectra extracted: With increasing temperature, the As-rich c(4 × 4) surface (green) transforms to the As-rich (2 × 4) surface (red) and finally to the Ga-rich (4 × 2) surface (blue). c) Despite the changing temperature (which causes shifts in the RAS signal), the surface formation can be followed in situ with a transient at 1.9 eV; data obtained by Dr. U. Seidel (formerly Hahn Meitner Institute, Berlin, Germany).

for in situ dopant quantification during MOVPE preparation.[101,110–112] Different regimes for C-doping were studied via their surface reconstructions.[113] Just as for InP and GaP, the temperature dependence of the dielectric function of GaAs[114] was measured by in situ ellipsometry in MOVPE ambient.[115]

A notable exception of the merely optical in situ approaches are the first MOVPE in situ STM images that were obtained at GaAs(100) surfaces at temperatures up to 650 °C and at atmospheric pressures.[116] Even though the limited resolution is a drawback compared to STM at ambient or cryogenic temperatures, the in situ STM approach was also used to study quantum dot formation.[117,118]

2.4. Multinary III/V Compounds

Ternary and quaternary III/V compound semiconductors are highly relevant in order to tune the bandgap, lattice constant, and optoelectronic properties as desired for the device of choice (cf. Figure 2). Multinary epilayers may be used as active parts of the device[119] (such as InGaAsP-based absorbers), as barrier layers to tune the band alignment, or simply as transition layers, for instance, to bridge lattice mismatch between two materials by graded buffers.[76,120] It is often useful to study constituents of multinary compounds individually.[121] For multinary compounds, optical real-time analysis can contribute to "control of thickness and stoichiometry during growth as well as monitoring the switching procedures during the growth of heterostructures."[122] For example, the MOVPE growth of entire laser and MJSC structures can be monitored in situ with RAS.[123,124] For multinary III/V compounds, the choice of a suitable growth regime is more important compared to the rather stable growth of binaries. Often, different growth conditions also relate to different surface structures, which can be observed with RAS. For InGaP, for example, bulk ordering was observed for P-rich growth conditions—which can be correlated with a characteristic RAS signal.[125,126]

A combined ex situ X-ray diffraction, ellipsometry, and in situ RAS study revealed that the In content in In$_x$Ga$_{1-x}$As can be obtained in situ since the composition of the uppermost layers affects the measured optical anisotropy:[127] As displayed in **Figure 11**, starting from a c(4 × 4) reconstructed GaAs(100) surface and its characteristic RA spectrum, the RAS lineshape changes toward that of (1 × 3) reconstructed InAs(100),[128] when the In content is increased.[127] In the same work, monolayer oscillations during InGaAs growth on GaAs(100) were observed.[127] Analysis of in situ RA spectra benefits from knowing the dielectric constants of the compound at growth temperature.[129] Similar to InGaAs, the stoichiometric dependence of the lineshape of the RAS signal enables evaluation of the As/P content of GaAsP(100) surfaces in situ, as indicated in **Figure 12**.[127,130]

The dependence of the RAS signal on the In and P content in InGaAs quantum wells (QWs) and strain compensating GaAsP layers was used also during MOVPE growth of laser diodes, and strain balancing was studied in situ via the RAS signal of GaAs.[131] For GaAsP QWs, the emission wavelength could be correlated to the amplitude of the RAS signal.[132] Similar to GaAs, the impact of doping on the RAS signal has been studied for multinary III/V compounds, such as InGaAs, AlGaAs, and
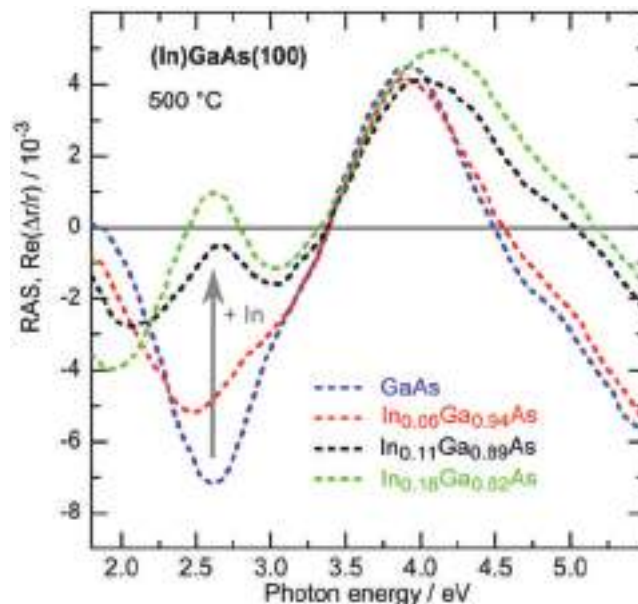
Figure 11. RA spectra of GaAs(100) and InGaAs(100) measured at 500 °C. The lineshape of the spectra depends on the stoichiometry; data from ref. [127].

AlGaInP.[58,132] Layer thickness, monolayer oscillations, and composition can be measured as well with in situ ellipsometry during MOVPE growth, as demonstrated, for instance, for InGaAs and AlGaAs.[133,134] AlGaAs was also studied with RAS in detail both in MOVPE[135] and in UHV.[136] With increasing complexity of quaternary compounds, composition and growth rate of InGaAsP and AlGaInP can be obtained combining in situ RAS and reflectance measurements during MOVPE growth.[137–140]

Broadening the range of compounds to dilute nitrides, it is worth to mention that the RAS signal of GaAsN also changes
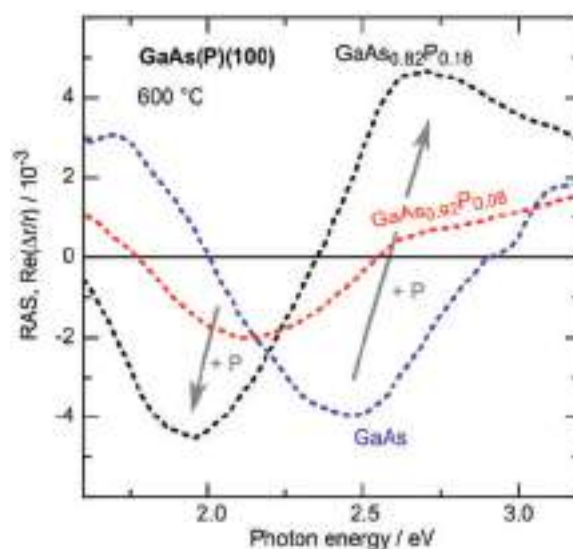
Figure 12. RA spectra of GaAs(100) and GaAsP(100) measured at 600 °C. The lineshape of the spectra depends on the stoichiometry; data from ref. [127].

**ADVANCED
SCIENCE NEWS**
www.advancedsciencenews.com

**ADVANCED
MATERIALS
INTERFACES**
www.advmatinterfaces.de

with the N content,[11,141] and reflectance measurements have been applied to yield the composition.[11,142] N incorporation into GaP at diluted concentration (grown heteroepitaxially on Si with about 2% N to yield lattice-matching at room temperature) was found to cause an additional contribution to the RAS signal at the E_1 interband transition of GaP, while the principal features of the surface reconstructions typical for GaP(100) could be preserved—if excess N at the surface was avoided.[20]

Besides the optical techniques commonly applied in situ during MOVPE preparation, in situ X-ray monitoring during InGaAs growth enabled determination of layer thickness and lattice mismatch as well as its temperature dependence.[143]

2.5. Nanostructures

A broad spectrum of microscopy techniques has also been applied for the in situ characterization of nanowires and nanostructures,[10] but mostly in vacuum environment. In practical MOVPE ambient, in situ reflectance during nanowire growth paired with optical modeling enables to determine the nanowire dimensions as well as their growth rate.[144] Interesting in situ approaches include in situ photoluminescence (PL), which was demonstrated to predict the emission wavelength of InGaN QW-based light emitting diodes (LEDs) already during growth.[145,146] Ostwald ripening of InAs quantum dots on GaAs(100) could be observed with in situ STM,[117] and a combined RAS/in situ STM study revealed the dependence of InGaAs quantum dot formation on different surface reconstructions.[118] InGaAs quantum dot formation and island nucleation were studied also by in situ ellipsometry.[147]

2.6. Si(100)

Regarding highly efficient tandem absorber structures for solar energy conversion, group IV substrates are often preferred over III/V substrates: Germanium, for example, is more suitable as substrate used in the industry, when manufacturing standard triple-junction solar cells, than GaAs, since the bandgap energy is lower and substrate costs are considerably cheaper. III/V-on-Si integration is considered to further reduce costs of solar cells,[61,148–152] to increase efficiency,[153] and is also desired for microelectronics.[154] In contrast to III/V crystal structures, both Si and Ge substrates do only have covalent bonds between two atoms of the identical kind and are thus nonpolar lattice structures. The step structure and atomic structure of Ge(100) and Si(100) surfaces therefore are highly important for subsequent low-defect heteroepitaxy of polar III/V semiconductors on nonpolar substrates: Steps of odd atomic height on the nonpolar substrate introduce antiphase disorder in subsequently grown, polar III/V epilayers.[155,156] Since both Si(100) and Ge(100) are dimerized under standard MOVPE preparation conditions, it is useful to express the step structure via the dimer orientation at the associated terraces. An established nomenclature[157] is that of A-type and B-type terraces (T_A and T_B) for (1×2) and (2×1) reconstructed surfaces, respectively, which is illustrated in **Figure 13**. Due to the tetrahedral coordination in the diamond lattice, the dimer orientation rotates by 90° on adjacent terraces separated by steps of mono- or odd-atomic height. Depending on the upper terrace, these are called S_A and S_B steps. Terraces separated by double-layer steps exhibit dimer rows in parallel to each other and are labeled D_A and D_B. In the following sections, we will discuss single-domain Si(100) and Ge(100) surface preparation, which enables III/V growth free of antiphase disorder.

2.6.1. Monohydride-Terminated Si(100) Surfaces

Surface Termination: Unreconstructed Si(100) surfaces exhibit two dangling bonds per Si atom because of the diamond crystal structure. To minimize the surface energy, buckled dimers form in UHV[158–160] and also the step structure at Si(100) misoriented toward [011] is governed by energetics: Biatomic B-type steps occur during annealing as predicted by theory,[157,161–164] while biatomic A-type steps are energetically less favorable than B-type steps as well as single atomic steps.[157] Their formation in UHV requires external forces.[165–168] Dependent on the temperature and H chemical potential (corresponding to H supply), Si(100) surfaces, which are exposed to atomic hydrogen in UHV, form differently H-passivated reconstructions.[162,169,170] Symmetric monohydride-terminated Si dimers with one H atom per Si atom form upon annealing in H_2 ambient.[171–174] H_2 process gas is also commonly used during MOVPE preparation. Indeed, attenuated total reflection (ATR)-FTIR measurements on MOVPE-prepared Si(100) surfaces have identified monohydride Si–H bonds at the surface[175,176] via measurement of their coupled stretch modes,[177,178] and tip-induced H desorption by STM has confirmed complete hydrogen coverage.[176] In situ RAS during cooling from 1000 °C in 950 mbar H_2 ambient verified that Si(100) is terminated by monohydrides at temperatures below 800 °C.[179] The dependence of the H coverage depends highly on MOVPE process temperature and reactor pressure.[179–181]

For such H-terminated Si(100) surfaces, energetics change drastically: Non-rebonded single-layer steps at monohydride-terminated Si(100) are energetically favorable,[182,183] as confirmed by STM studies in UHV in presence of atomic H.[184] In contrast, however, experiments show that S_A steps vanish in favor for biatomic steps during annealing in H_2 ambient.[185] Also, early H_2-based MOVPE experiments reported on antiphase domain (APD) free GaP growth on Si(100) with 2° misorientation,[186] which implies an unequal domain distribution at the Si surface. A prevailing majority domain with an unspecified type of step structure was also observed during MOVPE preparation of nominal Si(100) surfaces.[187] Quantitatively, FTIR studies surprisingly revealed a preference for the A-type domain after slow cooling in H_2,[175] which is considered the least favorable configuration in terms of energetics.

Surface Formation—Energetics versus Kinetics: The results discussed above imply a non-negligible impact of kinetic processes during MOVPE preparation of the Si(100) surfaces, which may counteract energetic considerations. Due to the strong anisotropy of the dimerized surface reconstruction, RAS is ideally suited to study Si(100) surface formation. While in principle also dimer induced strain[188] can contribute to RA spectra of Si(100),[189,190] the main bulk-like contribution is supposed to

ADVANCED
SCIENCE NEWS
www.advancedsciencenews.com

ADVANCED
MATERIALS
INTERFACES
www.advmatinterfaces.de
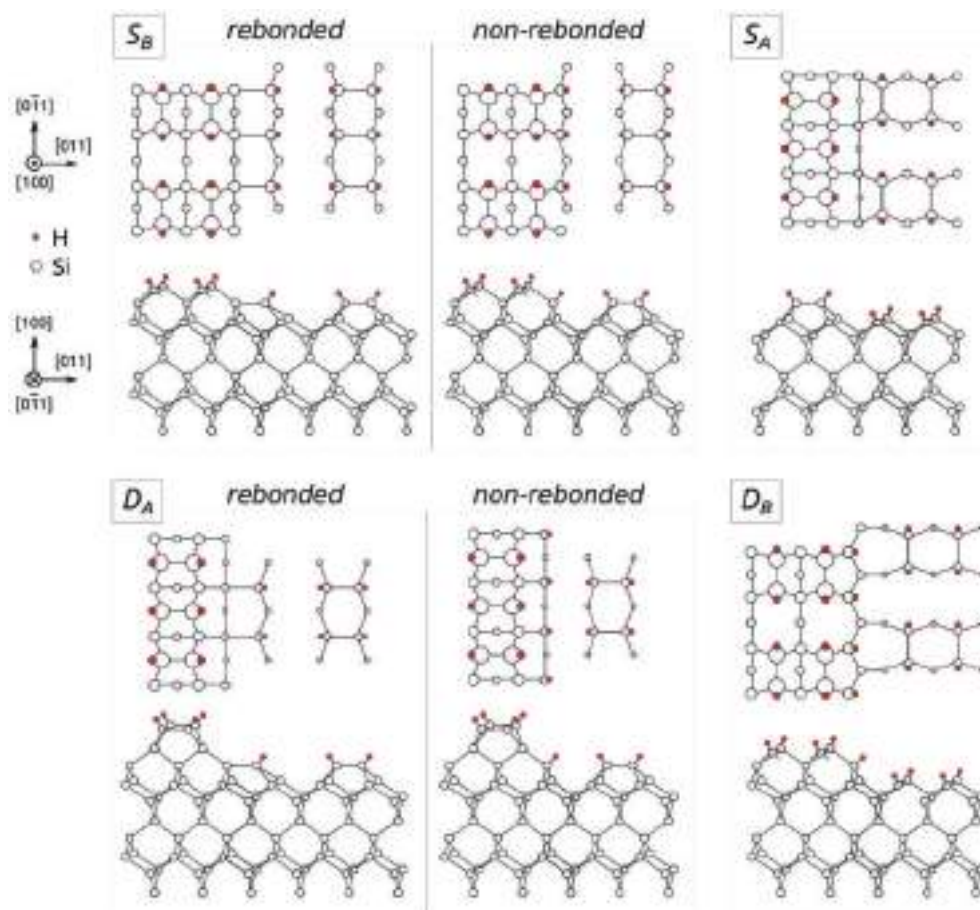
Figure 13. Single (top panel) and double-layer (bottom panel) step configuration at the monohydride-terminated Si(100) surface, shown in top view (first line in each panel) and side view (second line in each panel). At single-layer step edges S (or odd multiples), dimer rows on adjacent terraces are mutually perpendicular, while they are parallel across double-layer step edges D (or even multiples). The index A or B indicates whether the dimer rows on the upper terraces are aligned in parallel or perpendicular to the step edges, respectively. For S_B and D_A steps, also the rebonded configuration is shown; Data from ref. [157].

be induced by the anisotropic surface potential.[190,191] Differently H-terminated Si(100) surfaces exhibit RA spectra with different characteristic lineshapes.[191] They can thus be identified in situ. The fingerprint of the dimers at monohydride-terminated Si(100) surfaces (**Figure 14**a) consists of two peaks (at the E_1 and close to the E_2 interband transitions, respectively) and a shoulder in between.[191–193] This spectrum relates to the dimers at the terraces, which enables an in situ quantification of the domain ratio:[191,193] By definition of the RAS signal (Equation (1)), a 90° rotation of the dimer axis flips the sign of the spectrum. Contributions of domains consisting of dimers with mutually perpendicular dimer orientation thus cancel via inherent integration over the spot size. The measured sign of the signal then corresponds to the majority dimer orientation and its intensity yields the domain imbalance when scaled to a single-domain reference.[68,191,193]

In Figure 14a, the black RA spectrum corresponds to a monohydride-terminated Si(100) surface with a B-type majority domain and an A:B imbalance of about 40:60.[191] It was prepared in UHV with atomic H.[191] In strong contrast, in situ RAS reveals that the energetically less favored A-type terraces

form during annealing of Si(100) surfaces with 2° misorientation toward [011] in 950 mbar H_2 ambient (Figure 14, green line) under certain annealing conditions[193] after thermal deoxidation.[194] Despite sign and increased intensity (indicating a strong domain imbalance of A:B of about 0.85), the lineshapes of the RA signals of monohydride-terminated Si(100) are almost identical (Figure 14a), despite different magnitudes of misorientation. Step contributions to the signal[190] can thus be neglected here. Consequently, time-resolved RA measurements enable the observation of terrace formation in situ and demonstrate that thermal treatment with temperatures in the range of 730–750 °C is required for the development of such an A-type surface (Figure 14b).[193] The important point is, that this surface formation is dominated by kinetic processes rather than energetics. Strong interaction with the H_2 process gas[179] creates Si vacancies at the surface, which diffuse preferably along dimer rows on the anisotropic terraces.[195] If the terrace width is small compared to the vacancy diffusion length, T_B terraces retreat via vacancy annihilation at the end of the dimer rows,[165,168,195] as shown in Figure 14c. At larger terraces (lower offcut), single vacancies may coalesce to vacancy islands,[165,195]

**ADVANCED
SCIENCE NEWS**

www.advancedsciencenews.com

**ADVANCED
MATERIALS
INTERFACES**

www.advmatinterfaces.de
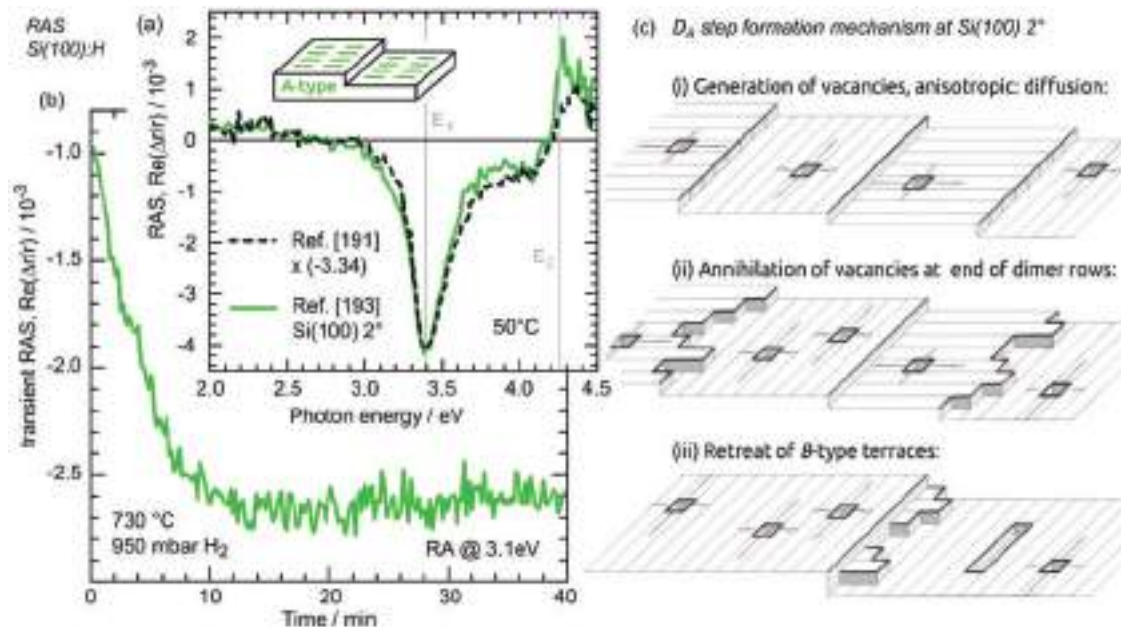
Figure 14. a) RA spectrum of a (1 × 2) reconstructed monohydride-terminated Si(100) surface with 2° misorientation toward [011] (about 85% A-type domains) from ref. [193] (green line, measured at 50 °C) compared to a flipped and scaled B-type surface from ref. [191]. (A:B = 40:60), b) time-resolved in situ RAS at the E_1 interband transition during annealing of Si(100) 2° → [011] in 950 mbar H_2 at 730 °C, c) schematic of the anomalous D_A step formation on Si(100) 2° → [011] surfaces Si vacancy generation and diffusion[193]; vertical gray lines indicate the interband transitions of Si.[441]

resulting in a Si layer-by-layer removal.[196] This can be observed in situ at Si(100) 0.1° as oscillations in transient RA measurements due to the dimer rotation at every subjacent terraces (**Figure 15**).[196] An activation energy of 2.8 ± 0.2 eV was derived via in situ RAS and attributed to SiH_x formation.[196,197] Since residuals at the step edges may remain, continued Si removal leads to roughened surfaces with frayed step edges.[196] In contrast to Si(100) 2°, annealing at about 730 °C in high H_2 pressure is not beneficial for almost nominal Si(100). The preparation route for Si(100) 2° is rather robust in a larger window of parameter variation and yields almost single-domain surfaces suitable for III/V nucleation.[198] It is important to realize that surface processes at Si(100) in hydrogen ambient also strongly depend on the misorientation: The formation of B-type Si surfaces is more likely on vicinal surfaces, where a step contribution can also occur in the RA spectra.[181]

2.6.2. Arsenic-Modified Si Surfaces

Despite the fact that arsenic (As) is present as residual in many application-relevant MOVPE reactors anyway, As-modification of Si(100) surfaces is of high interest for at least two reasons: (i) Compared to thermal deoxidation,[199] HF dipping plus processing in an As ambient can significantly reduce the thermal budget of the MOVPE Si process.[200,201] (ii) As in-diffusion into Si(100) is promising with regard to in situ preparation of Si p–n junctions,[202,203] while an As termination at the same time may prohibit Si in-diffusion into subsequently grown III/V epilayers.[204] Early UHV studies revealed that different process routes determine whether As either adsorbs additive on Si(100) (on top) or replaces Si atoms in the topmost layer(s), which

enabled the adjustment of the sublattice orientation of subsequently grown GaAs epilayers.[205] In situ RA spectra of these predominantly (1 × 2) and (2 × 1) reconstructed, As-modified Si(100) surfaces were assigned to optical transitions involving states induced by the As dimers.[206] This was questioned by MOVPE studies showing similar signals also on two-domain surfaces.[200,207] Recent results demonstrated MOVPE preparation of single-domain As-modified Si(100) surfaces[208,209] and suggest different microscopic origins for the two main anisotropic RAS contributions.[208]

X-ray photoelectron spectroscopy (XPS) results imply As intermixing in near-surface layers.[208] Similar to As-free systems, the RAS signal can be applied in situ to determine adequate temperature and As-pressure regimes for surface ordering, which is useful to avoid roughening or line defects that may occur.[200,208–210] For the MOVPE-prepared surface, it is still under debate, whether the surface is terminated by As or monohydride Si dimers on top of an As interlayer, a mix of both, or possibly Si—As heterodimers.[208] An increased intensity of the spectral contribution at the E_1 interband transition of Si in comparison to the UHV prepared surface, however, indicates that monohydride-termination dimers may in part be present. To resolve this question, in situ studies depending on the amount of As being offered in combination with FTIR are currently ongoing in our labs.

2.7. Ge(100)

Similar to Si(100), the influence of hydrogen was studied in situ during Ge(100) surface formation. In contrast to Si substrates in the complementary metal-oxide-semiconductor (CMOS)

ADVANCED
SCIENCE NEWS

www.advancedsciencenews.com

ADVANCED
MATERIALS
INTERFACES

www.advmatinterfaces.de
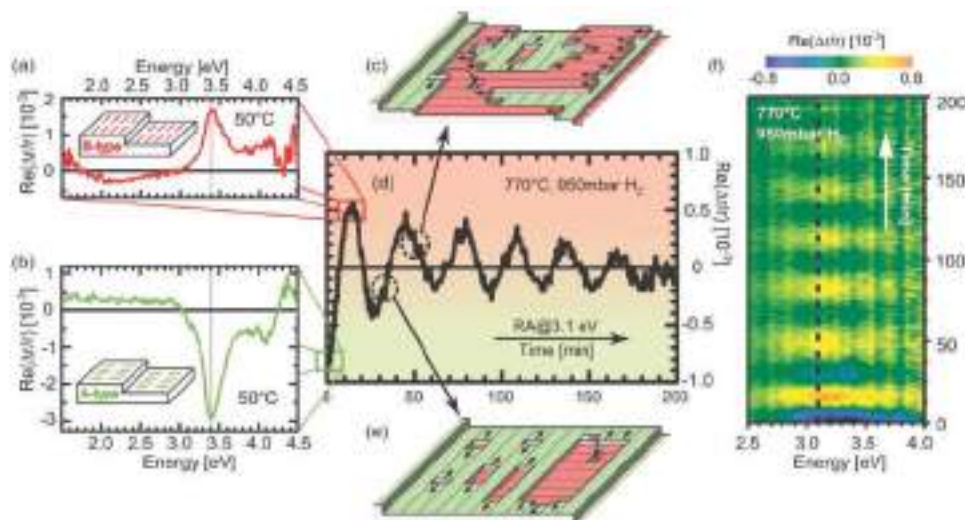
Figure 15. In situ RAS of almost exactly oriented Si(100) with 0.1° misorientation toward [011]: RA spectra of majority a) B-type and b) A-type domains after preparation in H_2 ambient (measured at 50 °C). d) RAS transient at the E1 interband transition extracted from f) continuously measured RAS during annealing at 770 °C in 950 mbar H_2 (41s per spectrum). c,e) The schematics indicate the vacancy formation causing the layer-by-layer removal process; Reproduced with permission.[196] Copyright the authors 2013, published under CC-BY 3.0 license.

technology, vicinal Ge surfaces are mostly applied in MJSC solar cell fabrication due to their tendency to form double-layer steps and due to the easier adjustment of appropriate doping concentrations. To reduce the surface energy, clean Ge surfaces reconstruct via the formation of dimers with (2×1), (2×2), or $c(4 \times 2)$ symmetry.[211] Monohydride termination along with a (2×1) reconstruction occurs during exposure to atomic H in UHV.[178] Assisted by benchmarking measurements to UHV-based surface science techniques, different RAS fingerprints were established for B-type monohydride-terminated and clean Ge(100) surfaces (cf. **Figure 16**).[212–214] This enabled in situ studies on the preparation of clean and monohydride terminated Ge(100) surfaces and the H desorption kinetics in MOVPE ambient, respectively.[215] From DFT calculations and comparison to experimental results,[216] however, the microscopic origin of the RA spectra could not yet be clarified due to lack of low temperature RAS data.

Thermal annealing in H_2 ambient enables complete removal of oxygen and other contaminations from oxidized "epiready" wafers.[214] Analogous to Si(100), Ge(100) surfaces are monohydride terminated after processing in H_2 ambient, as verified by FTIR measurements[214] (cf. **Figure 17**). The hydrogen coverage of the Ge surface during processing in H_2 ambient represents a dynamic balance of hydrogen adsorption and desorption events depending on the process parameters such as temperature and hydrogen pressure. Accordingly, Ge(100) is H-free in H_2 process gas ambient at a H_2 pressure of 100 mbar for temperatures above 370 °C, and thus corresponding process conditions are typically used for III/V nucleation (420–750 °C, 50–100 mbar H_2 pressure).[217–221] In contrast to Si(100), there is no indication for etching processes induced by the H_2 interaction. The vicinal Ge(100) substrates exhibited a clear (2×1)/B-type majority domain and mainly D_B double layer steps, respectively (see Figure 16). These findings serve as a reference point to study the influence of As and P on the surface structure of vicinal Ge(100) substrates.

With regard to III/V nucleation,[222–225] it is important to understand the impact of group V elements on the atomic order of the Ge(100) surface, since III/V-on-Si or III/V-on-Ge heteroepitaxy typically starts with exposure to group V precursors. Exposure of Ge(100) to As strongly affects the As dimer orientation, the height of steps, and the atomic configuration at the step edges,[226–228] which in turn affects the subsequent GaAs nucleation.[222–225] Process temperature, source, and partial pressure of arsenic are key parameters for the Ge(100):As surface preparation.[226,227] In particular, annealing in tertiarybutylarsine (TBAs) or AsH_3 at 650 °C resulted in a Ge(100):As surface with prevalence for As dimers oriented parallel to the step edges (Ge(100):As_B), while annealing at the same temperature in the presence of background As_4 from residual GaAs reactor coatings led to a surface with As dimers oriented perpendicular to the step edges (Ge(100):As_A). STM measurements (see Figure 16) revealed distinct differences in the step structure of Ge(100):As_B and Ge(100):As_A surfaces, in particular, formation of multiple layer steps due to step bunching after annealing in TBAs or AsH_3, which is known to etch the Ge(100) surface, and mainly quadruple-layer steps separating A-type terraces after annealing in background As_4, respectively.[226,229]

Characteristic RA spectra of vicinal Ge(100):As surfaces were established for MOVPE preparation applying TBAs and background As_4 as As sources (cf. Figure 16) and benchmarking to results from surface analysis by LEED, XPS, and STM.[229] The corresponding RA spectra contain contributions from both steps and terraces and enable in situ control over the domain formation.[229] While the rotation of the major As dimer orientation depending on the process conditions causes a flip of the characteristic features of the Ge(100):As RAS signal, additional differences in the RA spectra were assigned to the different step structures.[229] Temperatures in the range of 670 °C were found to be crucial for the formation of the surface structure.[229] Transient RAS measurements confirmed fast flipping of the

**ADVANCED
SCIENCE NEWS**
www.advancedsciencenews.com

**ADVANCED
MATERIALS
INTERFACES**
www.advmatinterfaces.de
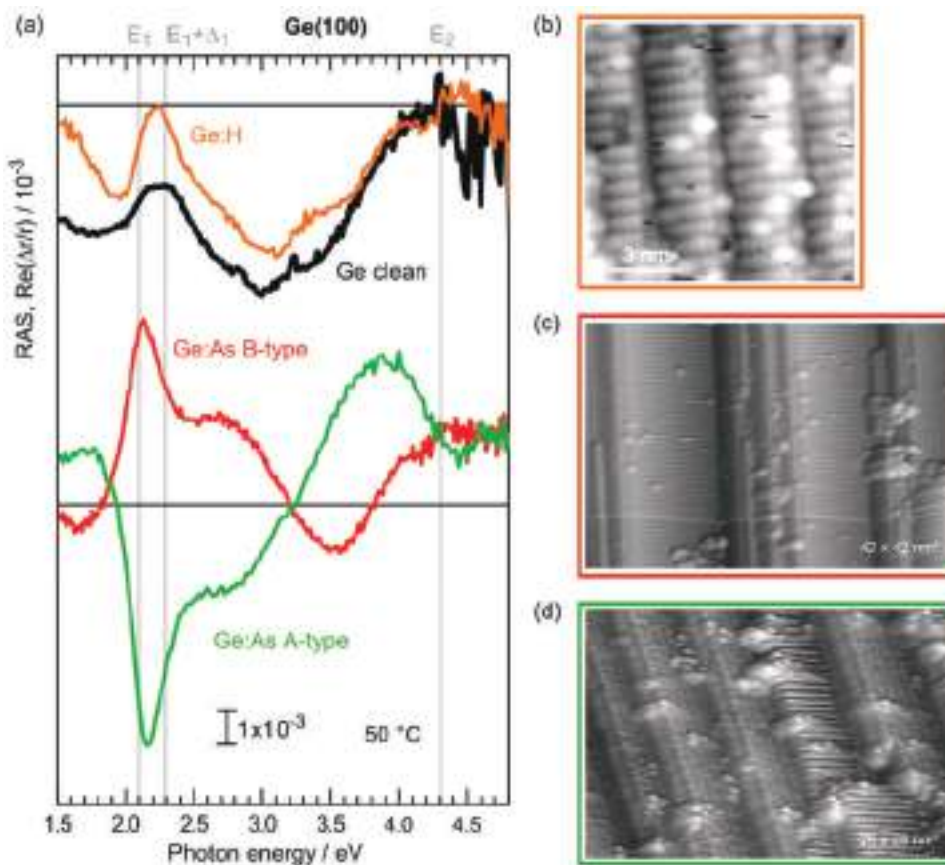
Figure 16. a) RA spectra of differently terminated vicinal Ge(100) surfaces: monohydride-terminated (orange), clean (black), A-type As-terminated (green) and B-type As-terminated; vertical lines indicate the interband transitions of Ge[52]; b–d) benchmarking of the monohydride, A-type As-terminated and B-type As-terminated surfaces, respectively, to STM; data from refs. [214,215,229].

major As dimer orientation on Ge(100) after changing the source of As (switching from As from precursor to background As_4). Similar to the observations on the Si(100) surface in H_2 ambient, surface energetics as well as kinetics compete during step and domain formation induced by thermal treatment and the interaction between the AsH_3 or As_4 and the Ge(100) surface. The in situ RAS measurements enable direct characteriza-

Figure 17. FTIR-ATR spectrum of the monohydride-terminated Ge(100) surface measured in vacuo after annealing in H_2 ambient; the absorption band can be assigned to Ge−H coupled stretch modes; data from ref. [214].

tion of the highly sensitive domain formation under different reactor conditions.

Nucleation of GaInP on Ge(100) in MOVPE environment is usually obtained by P termination of the Ge(100) surface prior to heteroepitaxy.[217,230,231] Phosphine (PH_3) and TBP are the two main P precursors used in MOVPE systems. Annealing under PH_3 at 300–450 °C in low pressure MOVPE systems leads to P termination of Ge(100) surfaces by one atomic layer.[232] LEED analysis of a P-terminated Ge(100) surface with 2° offcut prepared by PH_3 exposure in MOVPE ambient shows a (9×2) surface reconstruction.[231] In contrast to AsH_3, PH_3 does not etch the Ge surface.[233] TBP annealing results in a rather disordered P-terminated surface covered by about 1.5 monolayers (MLs) of P and carbon contamination.[230] The presence of carbon is attributed to byproducts of the TBP pyrolysis, since the Ge(100) surfaces are carbon free after H_2 annealing. The vicinal Ge(100) surface annealed in TBP exhibits a characteristic RA spectrum, which can be assigned to the P termination of the surface.[230] In situ RAS studies showed that the P termination is less stable during annealing in H_2 ambient than the As termination: P desorption takes place at temperatures around 430 °C as indicated by a transition from the RAS signal of the P terminated surface to the signal of the clean surface (see Figure 16).

Barrigon et al.[217] found that the morphology of InGaP nucleation layers on Ge correlates to a specific RAS feature,

**ADVANCED
SCIENCE NEWS**

www.advancedsciencenews.com

**ADVANCED
MATERIALS
INTERFACES**

www.advmatinterfaces.de

which enables optimization the InGaP nucleation route via transient in situ RA measurements.

3. Internal Interfaces of Epitaxial Heterostructures

The understanding of the atomic structure of the surfaces of III/V compounds is important particularly during switching processes and heterointerface formation.[58,130,234] There are different approaches to study the interface formation, of which we will choose three in the following text:

(i) One can focus on the atomic structure of the substrate layer prior to growth of the overlayer and analyze the impact on the properties of that layer. This will be exemplified for preparation of a tunnel junction in Section 4.1 and for III/V-on-Si heterointerfaces in Section 4.2.

(ii) If the top epilayers are sufficiently transparent, buried interfaces can be analyzed in situ with optical techniques.[235] Regarding RAS, a buried heterointerface may contribute in two ways:

(a) The interface itself may be optically anisotropic, for instance, due to strain, bonds along preferential directions, or bulk-termination effects similar to surfaces. Such interface anisotropies will be discussed for GaP/Si(100) in Section 4.2.3.

(b) The bare presence of the interface causes thickness-dependent Fabry–Pérot-like interference, which enters the RAS signal due to the normalization with the mean reflection. This can be exploited to obtain growth rates or dielectric constants, just as for reflectance measurements. If interference is considered adequately, antiphase disorder may be quantified from in situ RA spectra, as will be discussed in Section 4.2.4.

(iii) Spectra or transients can be measured continuously during nucleation and interface formation, respectively. Transient reflectance measurements, which are typically used to measure growth rates and surface roughness, can also be applied to determine the interfacial roughness.[235] Transient RAS measurements were applied to study GaP nucleation on Si,[236,237] and a recent example will be discussed in Section 4.2.3.

Due to the interference effects, care must be taken when analyzing RA spectra of heterostructures with regard to surface reconstructions. In simple heterostructures, interference can in principle be accounted for with an empirical approach:[68] If the reflectance signal of a reference surface of the overlayer material is available, one can calculate a so-called relative reflectance spectrum (reflectance of the heterostructure divided by that of the reference). Multiplication of the RAS signal with the relative reflectance signal corrects interference—under the assumption of isotropic interfaces (and identical apparatus function for the two reflectance measurements).[68]

Optical modeling, in contrast, enables the extraction of both the surface, interference, and "real" interface contributions from the RA spectra (cf. **Figure 18**). Assuming the anisotropies to be small, a Taylor expansion of the RAS signal yields an
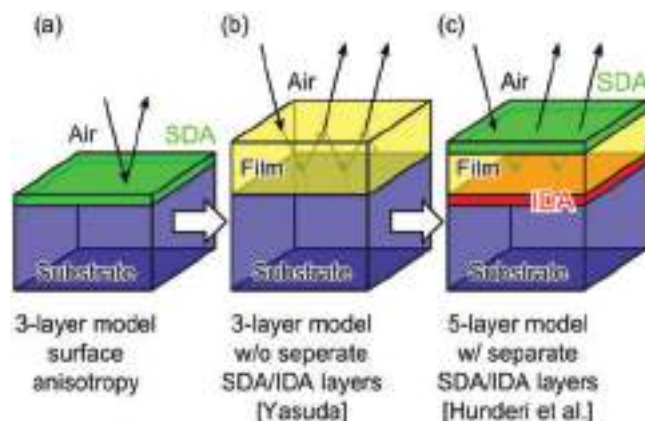
Figure 18. a) If the RAS signal stems from the surface of a sample, it may be expressed as surface dielectric anisotropy (SDA) assuming a thin optically anisotropic layer on an optically isotropic bulk[442]; b) In order to extract the SDA and the interface dielectric anisotropy (IDA) from RA spectra of heterostructures, Yasuda et al.[239] suggested a three-layer model to account for thickness dependent interference in the film; c) Hunderi et al.[242] extended this model to a five-layer model to account for the interference with additional layers for the SDA and IDA.

expression for the superposition of the surface, interface, and (overlayer) bulk anisotropies with prefactors that only depend on optical constants and the overlayer thickness.[238] Assuming that the actual anisotropies do not depend on the layer thickness, one yields a system of equation that can be solved for the anisotropic contributions. This three-layer approach was first demonstrated for ZnSe/GaAs(100)[239,240] and SiO₂/Si.[238,241] Surface and interface anisotropies have also been separated for AlAs/GaAs(100).[99] The three-layer model was extended to a five-layer model to study the interface between AlAs/GaAs(100),[242] and it was further modified to enable also fitting for the APD content of III/V-on-Si(100) heterostructures.[243]

3.1. III/V Heterostructures in Multijunction Cells

Strain and strain relaxation can be monitored in situ via the wafer curvature/bowing, which is particularly important for mismatched III/V heterostructures.[244,245] Interdiffusion can be studied with in situ ellipsometry to find optimized growth conditions for abrupt interfaces.[246] Interference-caused oscillations in RAS and reflectance measurements can be fitted to obtain the growth rate of the overlayers, and the intensity can be used to indicate the beginning of surface roughening.[247] Here, however, we will focus on in situ RAS studies related to the formation of heteroepitaxial junctions, which are applied in high-performance multijunction cells.

Inherent conversion losses in light absorbers originate from thermalization of electron–hole pairs generated by photons with energy larger than the bandgap and from radiation of photons with energy smaller than the bandgap of the semiconducting absorber material. These losses can be reduced, if multiple single-junction cells with different bandgaps are connected in series in monolithical stacks comprising a plurality of cells connected in series and deposited on substrates such as Si, Ge, GaAs, or InP. The cells are selected with appropriate bandgaps

**ADVANCED
SCIENCE NEWS**
www.advancedsciencenews.com

**ADVANCED
MATERIALS
INTERFACES**
www.advmatinterfaces.de

to efficiently generate photovoltage from a larger portion of the solar spectrum and to achieve current-matching in monolithic stacks. To facilitate photocurrent flow in a multijunction stack, tunnel junctions of low-resistivity materials are inserted between each adjacent semiconductor cell, and charge separating heterojunctions are introduced next to the contact layers to extract charge carrier selectively.[248] The theoretical upper limit of the conversion efficiency for a multiple solar cell configuration of infinitely many subcells with different bandgaps adds up to about 86%.[249] The formation of abrupt interfaces is of major importance at several positions in the layer structure of such multijunction solar cells. In particular, the performance of a tunnel junction critically depends on its spatial extension, i.e., the sharpness of its interfaces. Interfacial sharpness is also crucial for interfaces to charge separating contacts (so-called window and back surface field layers), which are directing the different charge carriers, electrons and holes, appropriately.

A low bandgap tandem (two-junction) solar cell was suggested almost a decade ago[27–29] as part of a four-junction solar cell: This two-junction tandem as lower part of the four-junction solar cell consists of an InGaAs bottom cell and InGaAsP top cell, both lattice-matched to InP, and can be optimized for absorption in the solar infrared spectrum underneath a well-established GaAs/InGaP top tandem. Such a low-bandgap tandem is part of the current record efficiency solar cell,[12,13,30,31] and its structure is shown schematically in Figure 4. The complete stack of the wafer-bonded InGaAs/InGaAsP//(In)GaAs/InGaP four-junction solar cell, comprises more than 20, partially delicate interfaces. Different leading groups in the high-performance photovoltaics field currently work on improving that type of multijunction solar cell for its development toward 50% conversion efficiencies.

The electronic structure across relevant interfaces in these cells highly depends on the atomic order and the sharpness of the heterointerface, which in turn requires an adequate preparation sequence. The interface formation does not only depend on the two materials to be combined but also on the sequence during growth. The transition from GaAs to InAs occurs quickly, for instance, while In segregation was suggested to extend the interface from InAs to GaAs over several monolayers.[120] When switching from As- to P-containing compositions, the carry-over of As into the subsequent P-containing layers is also well-known, such as for InGaAs/InGaP[250] or InGaAs/InP,[251–254] and is of particular interest for single interlayers of GaP in GaAs.[255] In the tandem structure optimized for the infrared (Figure 4), bandgaps of 1.03 eV (InGaAsP) and 0.73 eV (InGaAs) were utilized for the top and bottom subcell, respectively. It includes several critical interfaces (InP/InGaAs, InGaAs/InP, InGaAs/GaAsSb, GaAsSb/InP, InP/InGaAsP, GaAsP/InP) and, in particular, a specific interband tunnel junction including thin and highly doped layers of n-type InGaAs and p-type GaAsSb was used to connect the subcells.

The dependence of the RA spectrum on the InGaAs stoichiometry has been discussed above (Section 2.4). On the lattice constant of InP, however, the In content is significantly larger. **Figure 19** displays RA spectra of In$_{0.53}$Ga$_{0.47}$As grown on InP by MOVPE.[27] The lineshape was found to depend significantly upon annealing conditions, which can (similar to GaAs) be related to different surface reconstructions: By benchmarking to LEED, one As-rich (4 × 3) reconstructed surface, a group-III-rich (2 × 4) reconstructed surface and a group-III-rich (4 × 2) reconstructed surface was identified.[21] Transient RA measurements enabled identification of suitable process condition regimes for their preparation.[256] The transition from As-rich to group-III-rich surfaces, for instance, highly depends on the temperature at purging sequences.[256] For the (4 × 2)-reconstructed surface, surface states were also studied with energy-dependent UPS.[257]

The surface reconstruction of InGaAs(100) impacts the sharpness of the tunnel junction: Figure 19b shows the RA spectra of 2 nm thin GaAsSb layers grown on the three differently reconstructed InGaAs surfaces displayed in Figure 18a.[27] Their lineshape varies strongly depending on the InGaAs/InP template surface, even though all three GaAsSb(100) surfaces exhibit an As-rich c(4 × 4) surface reconstruction. XPS studies, however, revealed that the Sb content of the GaAsSb is too low when grown on As-rich, (4 × 3) reconstructed
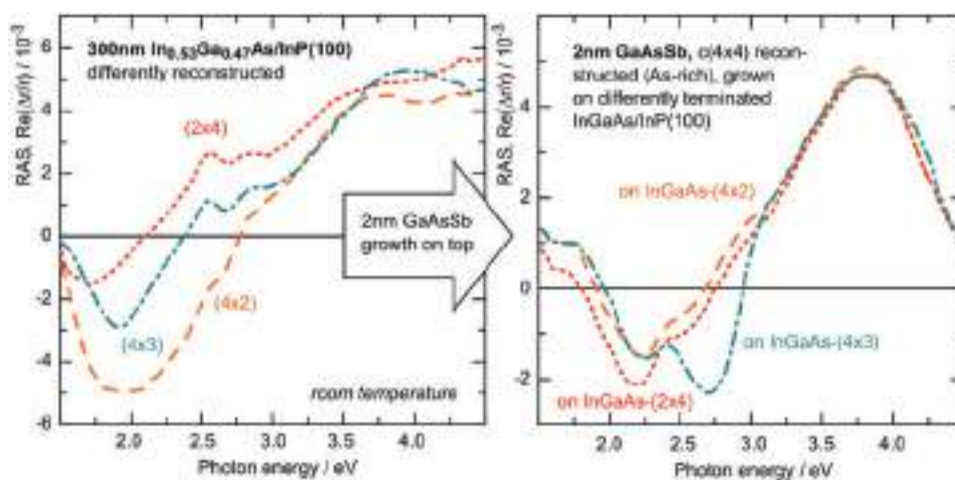
Figure 19. (left) RA spectra of differently reconstructed InGaAs surfaces (300 nm grown on InP(100)); (right) RA spectra of 2 nm GaAsSb grown on top of the differently reconstructed InGaAs/InP(100) samples. All GaAsSb surfaces reconstruct c(4 × 4) and are As-rich; data from ref. [27].

**ADVANCED
SCIENCE NEWS**
www.advancedsciencenews.com

**ADVANCED
MATERIALS
INTERFACES**
www.advmatinterfaces.de

InGaAs,[27] which may affect the RAS signal.[258,259] It was shown that sharper tunnel junctions can be prepared on the group-III-rich InGaAs(100) surface,[27] which increases the cell performance.[28]

For the same tandem structure, the impact of switching sequences on the interface recombination at the InGaAs/InP interface is crucial: The impact of different precursor switching sequences on the minority charge carrier lifetimes in the corresponding semiconducting layers has been correlated ex situ with time-resolved photoluminescence measurements of InP/InGaAs/InP double heterostructures.[29,254] For group-III-rich preparation, enhanced lateral homogeneity is achieved, which yields higher lifetimes compared to group-V-rich preparation.[254]

3.2. III/V/Si(100) Heterointerfaces

It is highly instructive to consider the formation of the III/V/Si(100) heterointerface as a three-step process, where each step has to be controlled precisely to yield well-ordered interface structures. First, the Si(100) surface has to be prepared such that it is mostly single-domain in order to avoid antiphase disorder already within the very first III/V epilayers (see Section 3). Second, during the actual nucleation phase, V-Si and/or III-Si bonds form within a nucleation layer of a thickness in the order of monolayers. In this step, it is not trivial to discriminate between the impact of precursor switching sequences and that of the residuals being present in practical growth ambient. Comparison of in situ signals obtained during and after Si surface preparation with clean reference signals therefore is highly valuable to determine when phase two actually begins.[260] Third, a "thicker" nucleation buffer is grown, which acts as virtual substrate layer for further integration of other III/V compounds, whose choice depends on the device of interest. Ideally, this buffer layer should exhibit defect densities as low as possible and a surface reconstruction suitable for subsequent epitaxy (see Section 2).

One of the most crucial challenges in III/V/Si(100) nucleation is rooted in the different crystal symmetries of Si (diamond) and III/V compounds (mostly zincblende), which is often referred to as "polar-on-nonpolar heteroepitaxy."[155] The choice of GaP as nucleating compound enables separation of the polarity issue from the other challenges, such as lattice-mismatch and diverging thermal expansion coefficients. GaP is an adequate candidate for the virtual substrate since it can be grown pseudomorphically up to several tens of nanometers. For optical applications, also the transparency of GaP compared to other III/V compounds can be advantageous.

3.2.1. The Significance of a Two-Temperature GaP-on-Si Nucleation Process

It is important to distinguish between the actual GaP nucleation phase (step two in the list above) and GaP buffer growth (step 3): Low-temperature migration enhanced epitaxy in MBE promotes 2D GaP nucleation on vicinal Si(100) substrates.[261,262] Also already in early MOVPE studies,[186] a two-step growth

process was found to suppress defects in the GaP layer.[186] Low temperature nucleation is beneficial to reduce interface roughening,[263–265] which was observed, e.g., by in situ ellipsometry[264] for nucleation at 600 °C. Detailed in situ studies—combining RAS, p-polarized reflectance spectroscopy, and laser light scattering during pulsed GaP nucleation by chemical beam epitaxy[237,266] as well as polarometry[267] in MOVPE—revealed that TBP reacts immediately upon adsorption on the growth surface,[237] and that the amount of Ga must be precisely balanced to minimize surface roughening, 3D nucleation, and Ga droplet formation.[237,266,267] 3D nucleation is also reduced when applying high V:III ratios.[268,269] More recently, GaP nucleation by MOVPE was studied in great detail ex situ with transmission electron microscopy (TEM): A pulsed nucleation sequence with alternating TBP and TEGa pulses at about 400 °C in combination with buffer layer growth above 570 °C was established.[220] As a result, virtual GaP/Si substrates free of islands, twin defects, and stacking faults can be achieved as long as Ga droplet formation can be avoided.[220,270]

3.2.2. Silicon Preparation in Presence of GaP Residuals

Specific preparation routes for single-domain Si(100) surfaces require balancing of energetic and kinetic driving forces which govern the step and terrace formation. In "clean" hydrogen ambient (free of III/V residuals, see Section 3), surface temperature and H_2 pressure have to be controlled precisely depending on the step density of the Si surface.[181] Outgassing of III/V residuals during Si surface preparation adds further complexity and in situ control becomes even more important. In situ mass spectrometry (MS) during annealing of the MOVPE reactor at 1000 °C/950 mbar H_2 after a standard GaP/Si process revealed that P- and Ga-related species can be detected even after 30 min.[260] How much this outgassing affects Si preparation also depends on the actual Si processing route: the desorption from reactor walls and from the susceptor is increased at higher temperatures. This is an issue particularly for the preparation route considered ideal for nominal Si(100) surfaces: A quick reduction of H_2 pressure at elevated temperatures is required to yield predominantly (1 × 2) reconstructed Si(100) surfaces, which increases the rate of desorbing species at a process stage where the H-stabilization is not yet stable.[179,196,260] The RA spectra of the Si surface still show the signature of the Si dimers at the Si E_1 interband transition and also modifications at lower and higher binding energies, which might be related to Ga species being adsorbed.[271] Regarding GaP growth on such "prenucleated" surfaces, antiphase disorder was increased which would be in line with both Si—P and Si—Ga bond domains being present at one terrace (see the next section).[260] If the amount of background GaP was further increased, no characteristic Si-related RAS signatures could be obtained anymore. Similarly, the (2 × 1) reconstruction of 2° misoriented Si(100) could only be observed in "clean" reactor ambient.[198] The preparation route for 2° misoriented Si(100)-(1 × 2), in contrast, bases on annealing at high H_2 pressure, which was found less critical and enabled more stable processing.[198,260] Based on this advanced Si surface preparation[193] and the low-temperature pulsed GaP nucleation,[220] in

**ADVANCED
SCIENCE NEWS**
www.advancedsciencenews.com

**ADVANCED
MATERIALS
INTERFACES**
www.advmatinterfaces.de

situ studies of single-domain GaP nucleation and the interface structure became feasible, as will be discussed in the following.

3.2.3. Single-Domain GaP Nucleation and Interface Structure

In situ RAS was applied in three different ways to study the GaP/Si interface: (i) RA spectra obtained directly prior to GaP nucleation and after GaP growth can be correlated[198] to indirectly conclude on the structure of the buried interface based on the assumption of an abrupt interface; (ii) surface and interface contributions to the final GaP/Si RA spectrum can be separated by optical modeling[243] in analogy to what was discussed for III/V heterostructures above; (iii) time-resolved RA yields real in situ information on the nucleation process.[272] While the optical modeling approach enables automated fitting for the APD content at the GaP/Si(100) surface,[243] the interpretation regarding the interfacial structures within all three approaches largely benefits from single-domain Si(100) substrates.

Approach (i) requires knowledge of the domain structure of the Si(100) surface prior to nucleation of the GaP sublattice as input. Assuming that the Si dimers break during nucleation, but that the Si atoms retain their lattice sites (i.e., an abrupt interface), one can conclude whether Si—P or Si—Ga bonds prevail at the interface. LEED patterns of a reference Si substrate and converged electron beam diffraction TEM of final GaP/Si structures were first used,[273] but both information can be obtained more directly with in situ RAS—which is particularly important for the correct description of the Si(100) surface.[198] RAS studies on Si(100) substrates with 2° misorientation toward [011]—whose preparation is less sensitive to residuals—revealed that the sublattice orientation of the GaP epilayer can be inverted by flipping the majority dimer orientation of the Si substrate from (1×2) to (2×1).[198] In both cases, this can be explained by Si—P bonds within the abrupt interface model.[198] Also ab initio DFT calculations predict that abrupt Si—P interfaces are energetically more favorable than abrupt Si—Ga interfaces over large ranges of chemical potential[198,274,275] and that TBP adsorption creates a "strong" Si—P bond.[276] Nevertheless, charge compensation at the buried interface requires interfacial intermixing due to the partial charges of Si—P and Si—Ga bonds, respectively.[277] Such compensated interfaces exhibit even lower formation energies than abrupt interfaces, independently on the chemical potential during nucleation.[198,275] Approach (i) cannot directly conclude on the atomic structure. Studies on almost exactly oriented Si(100), however, showed that it is possible to invert the GaP sublattice orientation also depending on the amount of Ga being available during nucleation.[198,260] Since RAS evidenced that the Si dimers prior to nucleation were aligned identically, this dependence on the chemical potential was interpreted as transition from Si—P to Si—Ga bonds depending on the chemical potential, which was predicted by DFT only for abrupt interfaces.

Approach (ii) revealed that the buried GaP/Si(100) heterointerface exhibits a characteristic optical anisotropy.[243,272] These findings also verify that the lineshape of the final GaP/Si(100) spectra is caused by internal reflection[68] and enable an advanced in situ quantification of antiphase disorder.[243] The presence of an interfacial anisotropy hints to a rather well-

ordered interface, but it cannot yet be concluded whether this is caused by interfacial bonds, which are aligned along one direction in projection on the (100) terrace plane,[242] or, for example, by strain in the surrounding Si or GaP matrix close to the interface[275,278,279] or by truncation of the bulk.[280,281]

Most recently, approach (iii) revealed that the GaP/Si(100) heterointerface forms already during the first (TBP, TEGa) pulse pairs at low temperature in rather P-rich conditions.[272] For the following discussion, see **Figure 20**. By measuring both transient RA during pulsed GaP nucleation and RA spectra after five and ten pulse pairs, respectively, it was shown that the Si-related RA signal vanishes with the first TBP pulse during GaP nucleation. A characteristic optical anisotropy evolves during further pulsed nucleation. This contribution to the RAS signal remains during further pulsing and annealing in TBP, when contributions associated to the GaP(100) surface start to superimpose. The lineshape of that nucleation-related signal exhibits significant similarity when compared to the interface-related anisotropy, which was deduced from thicker GaP/Si samples (cf. approach (ii)). This indicates that the interface which forms during pulsed nucleation does not significantly change upon further layer growth. In reference to earlier work,[236,237] pulse-related modulations in the RA transient during nucleation were assigned to a periodically consumed surface reaction layer. These findings are in line with XPS results, which imply that the interface forms within the first three pulse pairs and that every subsequent pulse pair adds a GaP bilayer.[272] The in situ RA spectra indicate that a GaP surface with the characteristic surface reconstruction related to buckled P dimers forms already after ten alternating (TBP,TEGa) pulses at low temperature and subsequent short annealing in TBP at 600 °C. Benchmarking to LEED revealed that these surfaces indeed exhibit the well-known $(2 \times 2)/c(4 \times 2)$ surface reconstruction—and that they are single-domain, which is highly relevant for their application as virtual substrates.[272] With regard to approach (i), the sublattice orientation of these thin single-domain layers implies Si—P bonds. This is confirmed by XPS: A second component in the Si and P photoemission lines can be ascribed to roughly 1 ML of Si—P bonds at the heterointerface.[272,275] Si—Ga bonds cannot entirely be excluded, but their contribution is only very weak, if any.[272,275]

Both Si and GaP surface preparation, as well as GaP nucleation can be controlled in situ with RAS. This seems to be of outmost importance to compare results obtained under different conditions in different reactors. Interface roughening was observed ex situ in recent work on GaP nucleation on almost nominal Si(100) and explained by a general faceting mechanism of the interface due to energetics.[282] This generalization and the performed DFT calculations, however, were questioned,[283] and the transfer from the used planar slabs[282] to real facets may not be trivial.

3.2.4. RAS of Virtual GaP/Si(100) Substrates and APD Quantification

Pseudomorphic GaP/Si(100) heterostructures exhibit RA spectra similar to GaP(100) since the main spectral features can be assigned to identical surface reconstructions,
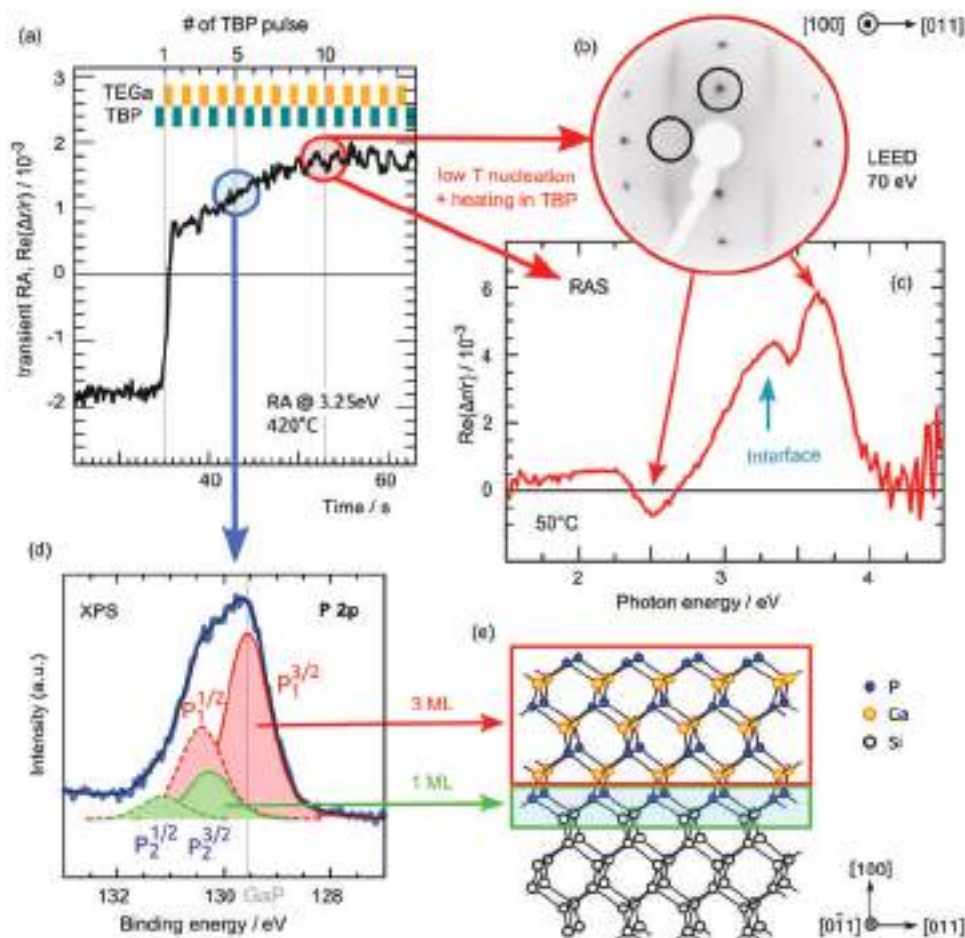
Figure 20. a) Time-resolved RA at 3.25 eV measured during pulsed GaP nucleation on majority A-type, monohydride-terminated Si(100) 2° at 420 °C. When stopped after ten pulse pairs and heated in TBP at 600 °C (where GaP growth would continue but was omitted here), a single-domain (2 × 1)-like LEED pattern with streaks along [0$\bar{1}$1] occurs, which is typical for the P-rich GaP(100) surface. c) The corresponding RA spectrum already shows the characteristic features of the P-rich GaP(100) surface and an additional contribution, which was assigned to the heterointerface[272]; d) XPS after five pulse pairs reveals a second component in the P 2p photoemission line, which can be attributed to Si—P bonds[272]; e) quantification of the XPS data yields about one monolayer (ML) of Si—P bonds and 3 ML GaP; data from ref. [272].

i.e., either P-rich (2 × 2)/c(4 × 2) or the Ga-rich (2 × 4).[68] By decomposing the spectral contributions, it was shown that the pure surface dielectric anisotropy of P-rich GaP/Si(100) indeed matches that of P-rich GaP(100).[243] Modifications of the lineshape due to interference and the anisotropy of the heterointerface (see above), however, are significant below the E_1 interband transition of GaP.[68,243] The intensity is additionally affected if antiphase disorder is present at the GaP/Si(100) surface: Antiphase disorder in the GaP epilayer implies surface domains of mutually perpendicular dimer domains.[218] Similar to the quantification of the domain content at Si(100) surfaces,[191,193] this causes a decreased intensity of the RAS signal.[218] Since GaP(100) exclusively shows bilayer steps, it can act as single-domain reference for scaling the spectra and thus the APD content can be obtained in situ. For correct scaling, however, interference due to internal reflection must be considered, which can be done either with an empirical approach[68] or by fitting.[243] Besides several ex situ approaches,[156,284–288] APDs have also been observed with in system low energy electron microscopy[289,290] and second harmonic generation.[291–293]

APDs at the buried interface also contribute to the interfacial electric fields.[294]

It is important to note that the APD content at the GaP/Si(100) surface is not necessarily identical to the domain imbalance at the Si(100) surface, since antiphase boundaries may annihilate during GaP growth by kinking.[262,295–297] The kinking depends on growth conditions,[296] and straight propagation is required to study the Si(100) surface indirectly.[298] For entirely APD-free GaP epilayers, single-domain Si(100) surfaces are required.[155] Single-domain RA spectra of GaP surfaces grown on preferentially A-type and B-type Si(100) surfaces, respectively, exhibit the opposite sign, which is caused by a sublattice inversion.[198]

Figure 21 juxtaposes RA spectra of differently terminated Si(100) surfaces directly prior to GaP nucleation and RA spectra of P-rich GaP/Si(100) obtained after GaP growth on the corresponding Si(100) surface. It can clearly be seen that the sublattice orientation of the majority domain in the GaP layer is determined by the prevalent dimer orientation on the Si(100) surface. The corresponding interface models are sketched in Figure 21 assuming abrupt interfaces.

**ADVANCED
SCIENCE NEWS**
www.advancedsciencenews.com

**ADVANCED
MATERIALS
INTERFACES**
www.advmatinterfaces.de
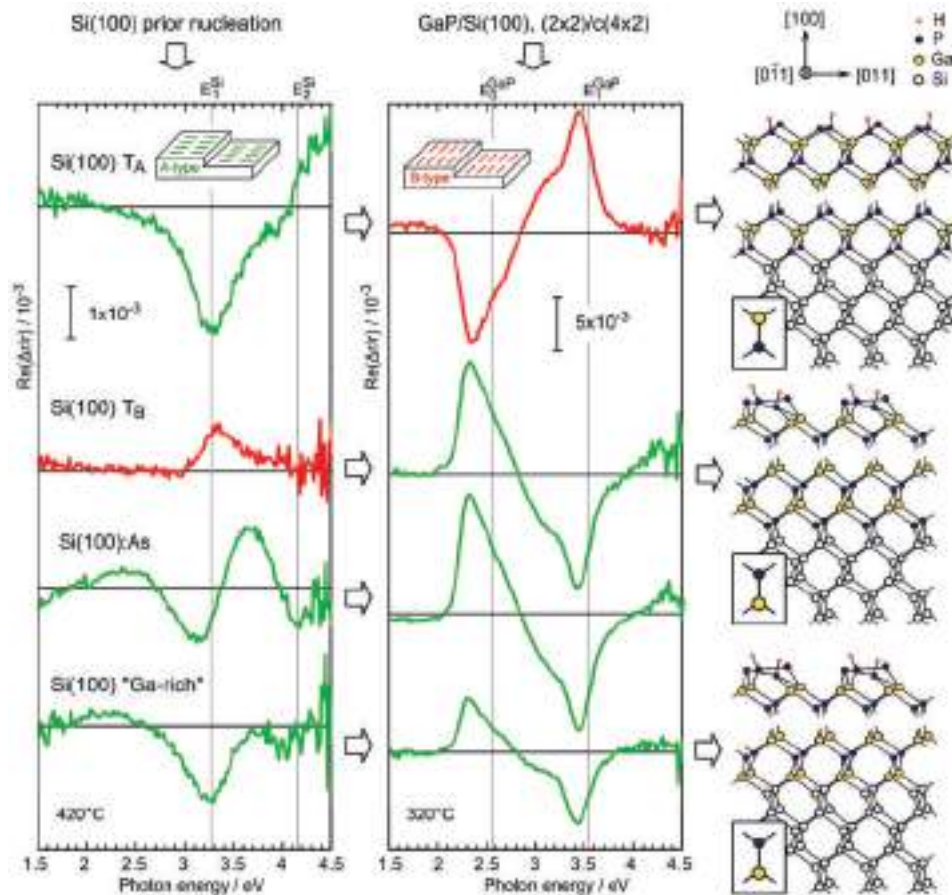
Figure 21. (left column) In situ RA spectra of differently terminated Si(100) surfaces obtained at 420 °C directly prior to pulsed GaP nucleation: (top) Si(100) 2° with majority A-type domains, (second line) Si(100) 2° with majority B-type domains, (third line) As-modified Si(100) 2° with majority A-type domains, and (bottom line) Si(100) 0.1° in a "Ga-rich" reactor[260] with A-type domains; (middle column) RA spectra of 35–40 nm GaP subsequently grown on the corresponding Si(100) surfaces; (right column) ball-and-stick models of the heterostructures assuming a simplified abrupt interface model. Adapted with permission.[301] Copyright 2016, Humboldt Universität zu Berlin. Data from refs. [193,198,208,260]; vertical lines indicate interband transitions for Si[441] and GaP.[440]

3.2.5. GaP Nucleation in Presence of As

GaP nucleation on As-modified Si(100) is studied less intense compared to monohydride-terminated Si(100). Recently, however, MOVPE growth of single-domain GaP epilayers on Si(100):As was reported.[208,209] Compared to GaP nucleation on monohydride-terminated Si(100), the GaP sublattice was inverted, as verified with LEED[209] and RAS.[208] Besides Si dimer orientation and (P,Ga) chemical potential during nucleation (see above), As modification thus is another possibility to choose the desired sublattice orientation. Moreover, due to the "prenucleation" of the Si surface with As, GaP nucleation on Si:As may not require a dedicated low-temperature nucleation step. At least this step was omitted in ref. [209] and recent TEM studies demonstrate that As-modification of the Si(100) surface prior to high temperature GaP nucleation reduces the defect density induced at the interface drastically.[299] When hydrofluoric acid (HF) dipping is applied rather than a sufficient thermal treatment to remove oxides from the surface,[199] annealing in As helps to reduce defects, which are assumed to originate from remaining contamination on the Si surface after

HF dipping.[201] Possibly, prior As-termination will also have an impact on the degradation of the bulk Si lifetime, which is often decreased in III/V MOVPE reactors.[300] XPS studies, however, imply increased intermixing,[208] so that the atomic structure of the GaP/Si:As interface may be more complex than in the Si−P case discussed above. Also, preliminary results on the GaP/Si(100):As interfacial dielectric anisotropy indicate an additional contribution.[301] Such less abrupt interfaces may enable the formation of an equal number of Si−As and Si−Ga, which would be beneficial with regard to interfacial charge compensation.[277]

4. Surfaces Modified by Adsorbates from Gas Phase

Postgrowth handling of devices and their application typically means that at least one surface is exposed to gases. While nitrogen in ambient air is generally acting as an inert gas, oxygen and water vapor can be considered the two most prominent reactive species that lead to the formation of new surface species. Ideally, these would passivate surface states acting as charge-carrier recombination states. But in reality, the modified

surface often develops new charge-carrier traps. Studies on adsorption and reaction mechanisms from the gas phase reveal the formation of these species and corrosion mechanisms as a function of well-controlled surface properties. As the in situ access to the semiconductor–liquid interface at sufficient surface sensitivity in an electrolyte is experimentally rather challenging, gas-phase adsorption experiments in UHV also constitute a possibility to bridge the gap between liquid environments and very well-defined surfaces in UHV. Depending on surface and adsorbate, they can reveal surface reactions that still persist at elevated pressures. Reliable analysis and reproducibility for these experiments greatly benefit if the starting point for adsorption experiments is a well-characterized surface such as described in Sections 2 and 3 above.

The same in situ techniques as mentioned in Section 2 can be employed here as well as vacuum-derived spectroscopy, such as near-ambient pressure XPS (NAP-XPS).[302] Time resolution combined with very high surface sensitivity is key to also allow for the analysis of reaction dynamics. In the following sections, we will review adsorption studies on some of the semiconductor surface systems treated above with a focus on water and oxygen exposure. We will see that reaction paths vary greatly with respect to the initial surface configuration and connect more traditional vacuum-based adsorption with recent trends in (near-)ambient pressure experiments.

4.1. General Aspects

When molecules adsorb on a solid surface from the gas phase, one can distinguish three different ways in which the molecules attach to the surface:

(a) In the case of physisorption, the molecules do not form a covalent or ionic bond with the surface, bonding is of van der Waals type such as in the case of water on $TiSe_2$.[303]

(b) Dissociative chemisorption denotes the case where the molecule breaks apart and at least one fragment forms a covalent bond with the surface, a prototype reaction is the oxidation of a surface from molecular oxygen.[304]

(c) During nondissociative chemisorption, a covalent bond is formed between adsorbate and surface, but the adsorbed molecule stays intact. An example here is water forming a covalent bond to a Si(100) surface by means of an oxygen lone pair.[305]

Coadsorption, where another species is adsorbed in a more or less rigid way, can greatly impact the effective surface interaction via blocking of sites or the promotion of dissociation,[306,307] which is the motive that clean and well-defined surfaces are of essential importance here. Two significant, inter-related quantities for the description of adsorption behavior are the sticking coefficient and the effective coverage in monolayers. The magnitude of the sticking coefficient gives the ratio between adsorbate molecules that stick on the surface to the impinging ones. The coefficient can be determined by the analysis of the saturation behavior of surface properties directly related to the adsorbate quantity of the surface as Langmuir isotherms or by molecular beam adsorption.[306,308,309] In the model of Langmuir adsorption, the surface

coverage increases monotonically with time, where the perfectly planar surface with a specific reactivity of each surface site reacts with the adsorbate under isothermal conditions.[306,308] Sticking coefficients cover several orders of magnitude, in the case of water from 10^{-4} for transition metal dichalcogenides to unity for Si(100)-(2 × 1).[305] Non-Langmuir behavior arises when the adsorbate on adjacent surface sites is interacting.[306]

The coverage q is typically defined in monolayers. The term ML can, however, be defined in various ways. From the perspective of the substrate, one ML is the occupation of every bulk basis site lying in the surface plane. In the case of cubic (100) surfaces discussed in Sections 2 and 3, the thickness of the ML is then a quarter of the lattice constant. From an adsorbate perspective, one can define one ML as a layer with the bulk density and thickness of one molecule. The quantity q can then be estimated by means of quantitative XPS,[50]

$$q = \frac{I}{e^{-d/(\lambda_0(E_o)\cos(\theta))} + I \cdot e^{-d/(\lambda_0(E_s)\cos(\theta))} - I - 1}. \tag{3}$$

Here, d is the overlayer thickness, λ_0 the electron attenuation length of the overlayer,[310] E_s, E_o the kinetic photoelectron energies of substrate and overlayer, and θ the angle against normal emission. The term $I = {I_{o,rel}}/{I_{s,rel}}$ is defined via the ratio $I_{o,s,rel} = {I_{o,s}}/{I_{o,s}^\infty}$ of measured intensity $I_{o,s}$ against the calculated intensity of an infinitely thick layer $I_{o,s}^\infty$.

Temperature is an important parameter in adsorption experiments. In the case of cleaved InP(110) surfaces, water adsorbs dissociatively at a temperature of 100 K with a near-unity sticking coefficient before at higher exposures an ice layer is observed.[311] Molecular water desorbs already at 150 K, and at room temperature "annealing," In oxide forms, with the oxygen substituting for the P. This demonstrates a wealth of temperature-dependent reactions of adsorbates with surfaces, but with the solid–liquid interface in mind, we will focus in the following text on room temperature processes.

4.2. Silicon Surfaces Exposed to Water, Oxygen, and Hydrogen

Silicon is probably the most intensively studied semiconductor surface regarding adsorption processes. This is partly owed to the fact that bulk crystals are readily available in the highest quality and well-defined surface terminations can be prepared by various methods, ranging from annealing in UHV to wet-chemical etching.[305,312] From an application point of view, the oxidation of Si is part of MOS technology and high-quality surface oxides benefit the device performance, moving critical interfaces to the interior of the device.[313–315]

Early experiments investigating water adsorption on Si relied on separate water adsorption followed by probing the modified surface with photoelectron spectroscopy. It was found that, for instance, the (2 × 1) reconstructed Si(100) surface features nondissociative chemisorption of H_2O with the oxygen oriented toward the surface at room temperature, but only in the case of well-ordered surfaces.[305] Less ordered surfaces show a dissociative chemisorption behavior forming OH bonds.[316] Unlike chemisorption of O_2, where the coverage is higher and the oxygen penetrates below the surface, the surface coverage

**ADVANCED
SCIENCE NEWS**

www.advancedsciencenews.com

**ADVANCED
MATERIALS
INTERFACES**

www.advmatinterfaces.de
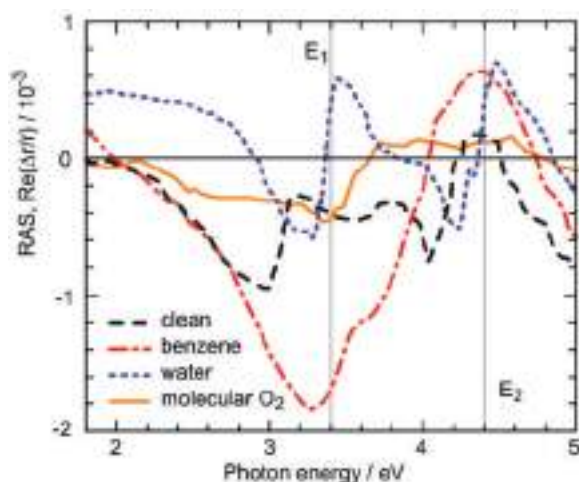
Figure 22. RAS for different adsorbates on the Si(100) surface. Data from ref. [318]. Vertical lines indicate the critical points of Si.[441]

is limited here to about half a monolayer.[305] Such a behavior cannot, however, be generalized to other Si surfaces as each one exhibits a distinct reaction kinetics and activity of surface sites,[317] emphasizing the requirement for well-ordered surfaces to study reaction mechanisms.

Reaction kinetics during adsorption can be revealed by means of time-resolved in situ spectroscopy, for instance, RAS, and also other optical and scanning probe techniques.[306] Due to the quantitative nature of RAS, the signal is directly proportional to the number of unaltered surface sites and one can derive the thermodynamics of Langmuir-like processes. As shown in **Figure 22**, the main spectral features of the clean (2 × 1) Si(100) surface are centered around the critical points of the Si band structure. With modifications by the adsorbate, signal shapes vary greatly for the different adsorbates such as molecular oxygen, benzene, or water for the Si(100) surface.[318] This shows that the optical signals are a convolution of optical anisotropy from the surface itself and the adsorbate molecule, which poses the challenge to distinguish and to identify the separate contributions from the experimental spectra. By means of in system STM, Witkowski et al.[318] found that water on nonhydrogenated (2 × 1) Si(100) adsorbs dissociatively, with OH attaching to one half of the dimer, and the remaining H on the other Si atom. This does to some extent contradict the findings of Schmeisser et al.,[305] where nondissociative adsorption was found. The reason for the discrepancy could be a) that the adsorption process itself by Schmeisser et al. was carried out at low temperature or b) a different step density (similar to Section 2.6.1), as Witkowski et al. used Si wafers with a higher miscut and, thus, increasing steps on the surface, while Schmeisser et al. did not report on this property of their samples.

The strength of bonding between surface and adsorbate can be evaluated by desorption experiments, either in the form of temperature-programed desorption or by using the energy of an intense (laser) light pulse to remove the surface species. In temperature-programed desorption experiments, the evaporated adsorbates or their fragments can be probed by in situ mass spectrometry, which allows for an identification of des-

orbed species, but does neither give spatial information nor direct information on the surface itself. In single-shot laser induced thermal desorption, on the other hand, the surface is analyzed by STM after desorption, which is feasible as the desorption process is frozen and the surface species not smeared out by diffusion, enabling high spatial resolution.[319,320]

4.3. InP Surfaces

InP has been used in solar water splitting applications for a long time, where its surface is inherently in close contact with water.[321] More recently, the (2 × 4) InP(100) surface (see Section 2.1) has been the starting point for a very efficient and stable photocathode.[16,322] The question arises whether the surface reconstruction of InP impacts the initial surface oxidation and if this is relevant for application of direct solar water splitting (solar-driven water photolysis).

For the oxidation of InP(100) surfaces by molecular oxygen, Chen et al. prepared the In-rich and the P-rich surface of InP(100), exposing them at different temperatures to oxygen pressures in the order of 10^{-5} mbar.[304] In situ RAS combined with in system photoelectron spectroscopy allowed them to correlate optical signatures to the oxygen uptake of the surface. They found that at room temperature, the P-rich surface exhibits a much slower oxygen uptake rate than the In-rich surface. After a dose of 10 kL, the oxygen coverage reached ≈1 ML for the In-rich surface, but only 0.1 ML for the P-rich surface. The oxygen uptake rate of P-rich InP(100) does, however, drastically increase for temperatures above 500 K. Even then, some optical anisotropy of the surface persists, which indicates that the surface does not completely lose its ordering. The In-rich surface, however, becomes almost completely optically isotropic already at 300 K. The results were interpreted as a dissociative chemisorption of O_2, inserting the oxygen in between both In–In and In–P bonds.[304]

To study the adsorption of water and to evaluate potential differences to oxygen, we prepared InP(100) surfaces as described in Section 2.1 and transferred them contamination-free to a UHV cluster equipped with XPS, LEED, and a separate adsorption chamber with an optical port for in situ RAS.[50] **Figure 23**a shows the resulting time-resolved spectrum for water exposure at room temperature. We see that, unlike for oxygen exposure (Figure 23b), the optical anisotropy of the surface is mostly conserved. The high-energetic feature I_5 related to a surface-modified bulk transition is even completely conserved, which shows that the water does not lead to subsurface oxidation, even after a water dose of 25 kL. Analysis of the resulting surfaces by XPS (**Figure 24**) shows that the predominant O 1s feature for H_2O exposure is an oxygen atom in between In and P (labeled O_I) with almost no In–O–In bonds, while for O_2 exposure, the In–O–In motive (labeled O_{II}) becomes much stronger. These assignments were corroborated by ultraviolet photoelectron spectroscopy of the P 3p and In 4d lines, where both adsorbates induced a modification of the P 3p line and the O2 exposure a relatively stronger oxide peak in the In 4d line.[50] No evidence for OH groups was found, so we assume a complete dissociation of the water. There is, however, a small signal at 527.8 eV binding energy, which might originate from oxygen bound to

**ADVANCED
SCIENCE NEWS**
www.advancedsciencenews.com

**ADVANCED
MATERIALS
INTERFACES**
www.advmatinterfaces.de
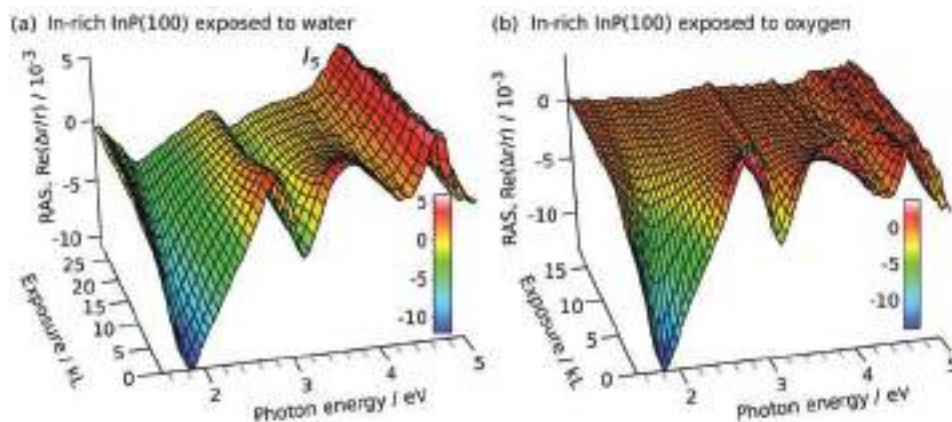
Figure 23. In situ RAS during the exposure of an In-rich surface to a) water and b) oxygen. Data from ref. [50]. I_5 denotes a feature related to a surface-modified bulk transition.

surface defects. Quantitative analysis after Equation (1) shows ≈0.25 ML oxygen after an H_2O dose of 25 kL, and ≈0.6 ML after 15 kL of O_2. The latter quantification is, however, subject to a relatively large error due to the subsurface diffusion of oxygen. The stability of the oxide was evaluated using temperature-programed desorption. A transfer of the samples back to the MOVPE reactor followed by annealing under RAS control showed that the In-rich surface modified by water could be completely restored by gently annealing to 570 K without the supply of precursors, while in the case of O_2 exposure, the initial optical anisotropy could not be recovered. These findings were also corroborated by UPS, where the valence band spectrum was also found to be completely recovered after annealing of the water-exposed surface. UPS also confirmed the evolution of a pronounced surface dipole for oxygen exposure (0.3 eV shift of the work function) and a weaker dipole for the water-modified surface (70 meV).[50] Features as the orientation of the water molecule on the surface can, depending on the system, also directly be derived from RAS if suitable calculations are available.[323]

A DFT study on water adsorbed to the In-rich surface by Wood et al.[324] showed that In–O–In bonds create in-gap states leading to surface charge carrier recombination, while In–O–P bonds avoid the trap state. Consequently, it appears that water

exposure electronically passivates the In-rich InP(100) surface, while oxygen exposure does not. The passivation is reversible, as the oxygen is only weakly bound to the surface, similar to "epi-ready" InP growth substrates. This finding explains the success of electrochemical in situ functionalization procedures for InP photocathodes,[16] where the surface is modified in an aqueous electrolyte and motivated the development of an electrochemical in situ surface modification routine for an AlInP surface of a photoelectrochemical tandem cell.[14] Later, an electronic surface passivation of In-based surfaces by water was also confirmed by in situ photoluminescence measurements on GaInP that enabled the observation of the electronic performance during water exposure.[325]

The P-rich InP(100) surface is, unlike for oxygen exposure,[304] surprisingly unstable upon water adsorption.[50] Thereby, the optical anisotropy of P-rich surfaces is irreversibly destroyed. Specific sites of the surface reconstruction being attacked by the polar water molecule could be the polar P–H bond or the lone pair of the P dimer. This again emphasizes that the initial surface reconstruction has a great impact on the initial interaction of InP(100) surfaces with adsorbates.

4.4. GaP Surfaces

GaP(100) surfaces are structurally and electronically closely related to InP(100) surfaces. Yet, their contact with water is not passivating the surface as in the case of InP, but leads to an unfavorable oxide, which hampers application in solar water splitting due to an unfavorable internal band offset between oxide and bulk.[59] Again, we prepared well-defined, Ga-rich, and P-rich GaP(100) surfaces to study their adsorption behavior with respect to water and oxygen. **Figure 25** juxtaposes in situ RAS of P-rich and Ga-rich GaP(100) during exposure to water.[326] We see that in both cases, some anisotropy is conserved and for the Ga-rich surface, the surface modified bulk transition as well, similar to the

Figure 24. X-ray photoelectron spectroscopy of the O 1s line after the exposure of the In-rich InP(100) surface to a) water and b) oxygen; data from ref. [50]. The inset in (a) shows the assignment of spectral features to oxygen binding sites.

**ADVANCED
SCIENCE NEWS**
www.advancedsciencenews.com

**ADVANCED
MATERIALS
INTERFACES**
www.advmatinterfaces.de
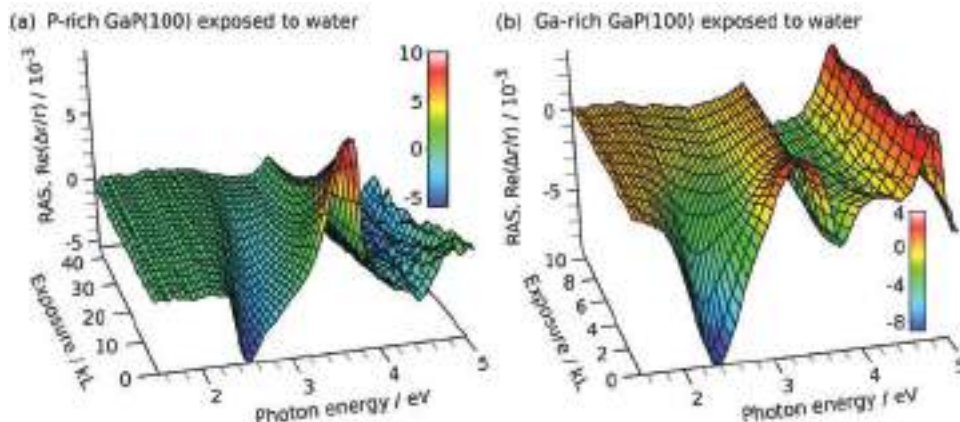
Figure 25. In situ RAS during the exposure of a) a P-rich and b) a Ga-rich GaP(100) surface to water. Data from ref. [326].

observations for In-rich InP(100). The Ga-rich surface is more reactive, as indicated by a more rapid reduction of the low-energy peak in the spectrum. A closer look on the RAS signal of the P-rich surface after exposure of water reveals the evolution of a new negative peak P_3 around 4.5 eV (**Figure 26**a). This peak is associated with a new c(2 × 2) surface reconstruction as revealed by LEED (blue-framed inset of Figure 26a).

Surprisingly, the new surface geometry does not involve any oxygen as it was evidenced by XPS (Figure 26b). Hence, water itself or the dissociated fragments oxygen or hydroxyl groups are not involved in the reordering of the surface. The lack of oxygen in the surface still holds true for the highest applied exposures of more than 100 kL and reveals an extraordinary inertness of the P-rich surface against oxidation by water, in stark contrast to the P-rich InP surface. The new superstructure could arise from a full dissociation of the water molecule, releasing oxygen and hydrogenating the surface, similar to what was found for hydrogen-exposed P-rich InP.[327] Further experimental and theoretical analysis is, however, required to understand this surface behavior and its spectral features.

The Ga-rich surface, on the other hand, features a mixture of dissociative chemisorption of water, forming hydroxyl groups, combined with the coadsorption of molecular water.[326] This

trend was confirmed by near-ambient pressure X-ray photoelectron spectroscopy of "sputter-annealed" GaP surfaces.[328,329] In NAP-XPS, a differentially pumped photoelectron spectrometer with a small aperture is brought very close to the sample surface, which allows exposing the sample to pressures in the order of 10 mbar during the measurement.[302] By these means, the chemical composition can be monitored in situ as a function of the pressure, further approaching ambient conditions at room temperature.

Kronawitter et al.[328] studied sputtered GaP(111) surfaces and found for pressures up to 10^{-4} mbar the same mixture of hydroxyl groups and coadsorbed molecular water as for the Ga-rich (100) surface,[326] which evidences some degree of similarity of the two surfaces with respect to water adsorption. Beyond 0.3 mbar, they find an additional photoelectron peak which they ascribe to interaction between OH and H_2O species. Zhang and Ptasinska investigated sputtered GaP(110) surfaces by NAP-XPS, also finding hydroxyl groups and molecular water, but, in addition, two more contributions, including Ga—O—Ga.[329] This could indicate that the Ga(111) surface is more prone to direct oxidation by water. Both studies do, unfortunately, lack in situ and also in system control of the surface after or rather during the sputtering procedure, e.g., by LEED,
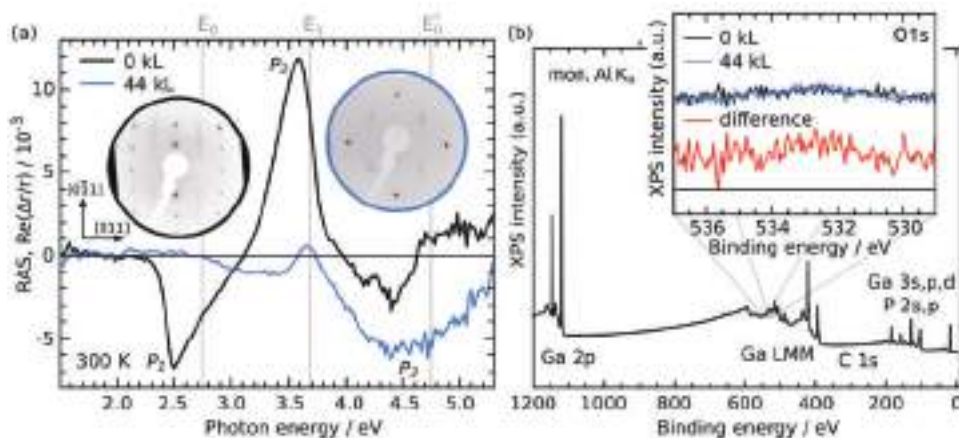
Figure 26. a) RAS and LEED of P-rich GaP(100) before and after water exposure. The critical point energies are labeled E_i, prominent features of the spectrum P_i. b) XPS of the P-rich surface after water exposure. Data from ref. [326].

**ADVANCED
SCIENCE NEWS**
www.advancedsciencenews.com

**ADVANCED
MATERIALS
INTERFACES**
www.advmatinterfaces.de

which can in principle lead to an overestimation of the reactivity of the surface due to defects[305] and contaminants such as carbon.

4.5. In Situ Studies on Noble Metal Surfaces

Noble metal surfaces are of interest for energy conversion applications, as they are very often used as (co-)catalysts in solar fuel production. A wealth of adsorption studies has been conducted regarding water, also organic compounds, probed in situ by methods such as X-ray absorption near edge structure, LEED, or surface enhanced Raman spectroscopy.[306,330–332] The information from these experiments provided crucial input for the development of theoretical methods to describe heterogeneous catalysis.[333] A famous example is the oscillatory process during carbon monoxide (CO) oxidation on Pt surfaces.[330] While it is beyond the scope of present review to cover the literature with respect to adsorption studies and we refer the reader to reviews in the literature,[306,334] we would like to highlight the extension of RAS in the form of reflection anisotropy microscopy as another example of in situ analysis to investigate CO oxidation on Pt(110).[335] Punckt et al. combined RAS with optical imaging, achieving spatial resolutions of better than 10 µm and a temporal resolution of 40 ms.[335] This setup revealed structural aspects of CO-poisoned islands of the Pt(110) surface and catalytic properties resolved in time and space. This technique is consequently also interesting for studies of catalytic properties at electrochemical interfaces.

5. The Solid–Liquid Interface

Further complexity in interface formation arises when liquids are introduced. The solid–liquid interface combines the world of the solid state with its crystal structure and extended Bloch states with the interfacial reactions and the dynamics of liquid environments and their redox levels. For heterogeneous catalysis, this interface is the key aspect.[333] The Helmholtz layer with its specifically adsorbed ions, the diffuse double layer, and the resulting potential drop in solid and electrolyte are closely connected to the surface properties of the solid.[336,337]

Corrosion sets in here and in catalysis or solar water splitting, charges have to be transferred over the solid–liquid interface.[338] Especially in the case of semiconductors, where additional properties such as space-charge layers and quasi-Fermi levels under illumination arise, the solid–liquid interface still holds many open questions. In the following text, we will briefly review some in situ spectroscopy methods with spatial resolution applied to semiconductor–electrolyte interfaces relevant for solar energy conversion and give an overview of recent methodological developments. Besides the epitaxial materials discussed in previous sections, metals are often applied as electrodes for water splitting and will partly be covered here as well.

The most common technique in electrochemistry is voltammetry, where the current passing through an electrode into the electrolyte is recorded as a function of the potential with respect to a reference such as a standard hydrogen electrode.[339] The technique is intrinsically in situ and provides feedback on energetics, kinetics, and in case of well-defined systems, submonolayer resolution for structurally induced features. A famous example is the surface reconstruction of Au single crystals, giving rise to specific signals.[340] To reveal charge-carrier dynamics in illuminated semiconductors, intensity modulated photocurrent spectroscopy can be employed. Here, the photocurrent of a semiconductor is treated as a time-dependent perturbation. A similar technique is (photo)electrochemical impedance spectroscopy, where the applied potential is perturbed under constant illumination.[341] These in situ techniques based on potential and current measurements do not directly provide spatial resolution or chemical information to analyze corrosion processes or bond formation in catalysis. So they have to be combined either with in system or ex situ analysis. An example of the latter one is shown in **Figure 27**, where illumination of the surface of an AlInP layer, which acts as window layer of a tandem absorber, initiated an oscillation of the open-circuit potential (OCP). Due to the lack of spatial resolution, the measured OCP is an average over the whole sample surface and from a well-defined oscillation, it follows that the whole surface is in the same state, which enables ex situ analysis. At the local extrema of the oscillation, the sample was brought to ex situ XPS to probe the state of the surface. Figure 27b shows that at the maximum of the oscillation, the oxide layer reaches
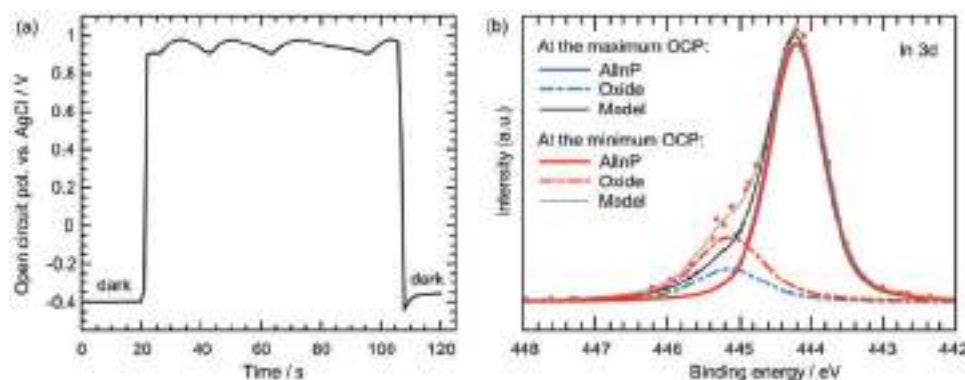
Figure 27. a) Open-circuit oscillations during functionalization of an AlInP surface for solar water splitting. b) XPS at different stages of the oscillation; data from ref. [14].

**ADVANCED
SCIENCE NEWS**
www.advancedsciencenews.com

**ADVANCED
MATERIALS
INTERFACES**
www.advmatinterfaces.de

a minimum, while at the minimum potential, the oxide layer is ≈0.4 nm thicker.[14] The oscillatory process is a photoelectrochemical layer-by-layer etching process, as the AlInP layer disappears after a number of oscillations, similar to the Si etching in MOVPE ambient described above (Figure 15). At the minimum surface oxide content, the process was aborted and directly followed by photoelectrochemical catalyst nanoparticle deposition, avoiding exposure to oxygen from ambient air, which would create charge-carrier recombination centers as discussed above. This step turned out to be crucial for the device performance, leading to an electronically and chemically passivated surface and thereby enabling efficient solar water splitting. It should be noted that such an oscillatory process, where the whole macroscopic, immersed surface is in the same microscopic phase, requires an atomically well-defined surface with a minimum of defects, for instance, epitaxial layers as described in Sections 2 and 3. An energy schematic for the resulting tandem device is presented in **Figure 28**, showing the band alignment of the heterostructure under illumination. Charges have to be transferred from the GaInP absorber of the top cell across the window layer to the phosphate layer and from there to the electrolyte supported by the catalyst. While the first buried interface between GaInP and AlInP is well-defined from growth,[342] the interface between highly n-doped GaInP and the PO_x species has to be adequately aligned to allow an efficient charge transfer. The energetic alignment between PO_x and the Rh nanoparticles is dominated by the n-type phosphate layer as long as the Rh nanoparticles are small and weakly interconnected.[14] This does, however, also require the PO_x compounds on the surface to be (electro)chemically stable, as the Rh nanoparticles cannot screen them completely from exposure to the electrolyte.

Oscillating electrochemical interfaces are, however, best studied by in situ methods to provide better temporal resolution and to ensure that the state of the surface is not perturbed by removal of the electrolyte during the transfer to subsequent analysis. Apart from the CO oscillations at Pt surfaces mentioned above,[330] which might be relevant for CO_2 reduction applications, the oxidation of Si in the electrolyte is also a prominent case of an oscillating electrochemical interface. Miethe and Krischer[343] studied the anodic oxidation of Si in a

fluoride-containing electrolyte by means of in situ ellipsometry. They find that the dissolution of p-type Si is spatially uniform, while n-type Si exhibits a patterned behavior.

Let us revisit the Au surface, which is a system well-suited for fundamental studies and method development, as it can be transferred to the electrolyte in a well-defined surface condition and is also stable in the liquid. Surface-enhanced infrared absorption spectroscopy employed by Ataka et al.[344] revealed the orientation of water molecules at the Au(111) surface as a function of the potential. From potentials below to above the potential of zero charge, water molecules reorient from the two hydrogen atoms close to the surface to hydrogen toward the solution, forming an ice-like structure with a following second layer of water.

Smith et al. studied the Au(110) surface by means of electrochemical RAS.[345,346] They identified signal shapes as a function of electrolyte and applied potential and found that the (1 × 3) Au(110) surface decays over time due to the accumulation of impurities at the interface (**Figure 29**). Time evolution of the optical anisotropy showed that the spectral features reveal a distinct decay behavior, related to the specific kinetics. They indicate that the impurities accumulating at the surface can be removed from the surface by a short positive potential pulse restoring the original spectrum. Their experiments demonstrate that RAS can also be a probe of surface species in the liquid electrolyte, and also show that the interpretation of spectra is very difficult, if there is no backing from theoretically derived spectroscopy.

Figure 28. Efficient unassisted water splitting: Energy schematic of the tandem layer structure under illumination yielding a solar-to-hydrogen efficiency of 14%. Solid black lines represent conduction and valence band edges, dashed black lines the Fermi level, and dashed blue (red) lines the quasi-Fermi levels of electrons (holes), and t_1, t_2 the tunnel junctions. Reproduced with permission.[14] Copyright 2015, the authors, published under CC-BY 4.0 license.

Figure 29. In situ RAS of the Au(110) surface. a) Spectra in H_2SO_4 directly after immersion and 24 h later. b) Time resolved transients at 2 and 2.6 eV; data from ref. [345].

**ADVANCED
SCIENCE NEWS**

www.advancedsciencenews.com

**ADVANCED
MATERIALS
INTERFACES**

www.advmatinterfaces.de

Spatial resolution—often at the cost of temporal resolution—can also be achieved by various scanning probe techniques such as scanning photocurrent microscopy or electrochemical scanning tunneling microscopy.[9] These techniques do, however, often have the disadvantage of a very limited temporal resolution, which impairs in situ control during surface processing.

The combination of intrinsic electrochemical methods with in situ spectroscopy at sufficiently high time, energy, and spatial resolution for process control can still be considered an evolving field. The future development of techniques and their adequate combination will help to further understand and precisely shape electrochemical interfaces.

6. Photochemical Reactions to Control Semiconductor/Polymer/Biological Interfaces

The solid–liquid interface was discussed above with a focus on its application in artificial photosynthesis. Inspiration by nature is not only useful for the conversion of sunlight into storable types of energy: Nature may act as a role model to construct even more complex, hybrid interfaces, where photoinduced interfacial reactions play an important role, a.o., in sensing applications. Novel strategies for intelligent materials and photoinduced interfacial reactions aim to build intelligent, i.e., bioactive, dynamic, nonequilibrium materials, acting as biosensors or chips varying their time characteristics: so-called life-inspired nanoscale machineries.[347–353] Strategies involve needs for effective energy conversion with the focus on oscillation reactions,[354] chemical networks,[355] autocatalytic[356] and autoamplification[357] reactions, which mimic living systems[358] using cell metabolic biomolecules[359] and ions, e.g., protons.[360] Biological systems solve such an energy management by developing unique sensory and adaptive capabilities,[361] transport mechanisms guided with ions,[362] proton gradients,[363] and chemical networks.[364] It is very attractive to utilize light for the modulation[351,352] of simple, reliable chemical reaction networks, because it is easy to control based on existing knowledge on reliable photosensitive material. The focus in this section is on well developed, reliable inorganic semiconductors and photoinduced surface reactions for new functions.

Intelligent interface architectures[365] provide new concepts of biocide materials, coatings, biosensors, and microfluidic chips. Our vision is to facilitate an in situ localization of gradients at certain sectors on a substrate to amplify or inhibit reactions and to control the polymer response for regulation of biomolecules, biofilms, and biosensing. In the following text, we focus on the possibility of efficient transformation of energy of electromagnetic irradiation into local ion gradients to actuate soft matter and biofilm formation. The strategy we suggest here is to combine in situ control of both the generation of ion concentration gradients on the semiconductor surface and of the film formation with time and spatial resolution (**Figure 30**) in order to achieve a network, which exhibits preferably several mechanisms for spatiotemporal switching,[366] amplification or inhibition,[356] activated depending on type and intensity of the external demand.[365,367]

Apart from photoinduced formation of ion gradients, we suggest an attractive strategy of amplification of concentrations of ions. One proton can, for example, provide several protons by autocatalysis. Control of ion and proton concentration gradients may be achieved by assembly of soft matter on the semiconductor surface, e.g., polyelectrolytes (PEs) by layer-by-layer (LbL) assembly. Prime issues are: (i) How many photons are needed to locally start the required chemical reaction on the surface? (ii) What is the optimum PEs LbL architecture to understand the basics of ion trapping and storage, the
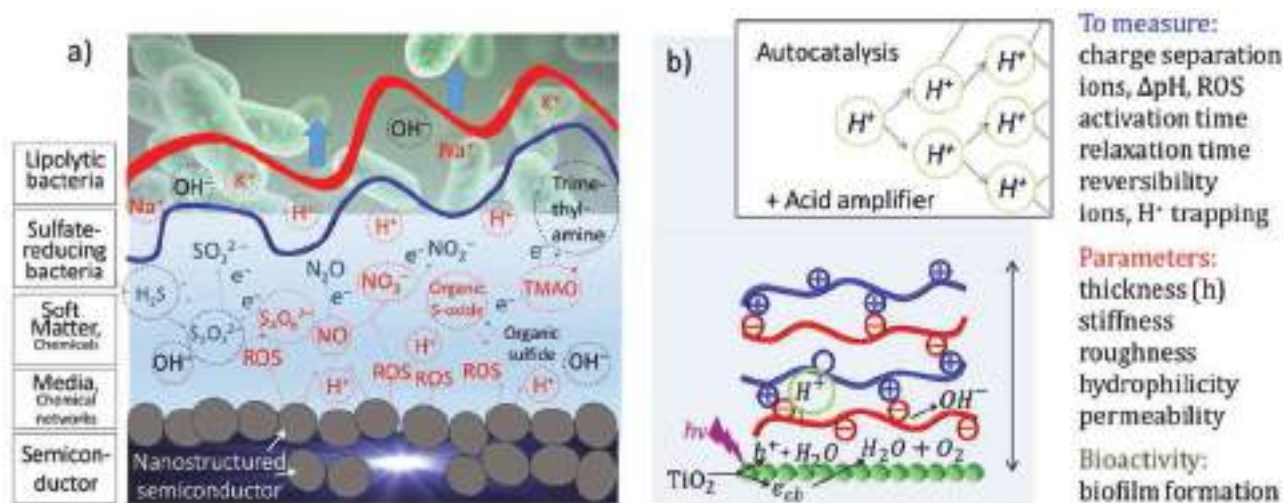
Figure 30. Possible photoreactions at semiconductor/polymer/biological interfaces straightforward for bioinspired nanoscale machinery. a) Schematic depiction of a photoresponsive system for a nanoscale machinery for biofilm regulation. It consists of semiconductor particles (grey), soft matter, and bacteria. Electromagnetic irradiation leads to the production of reactive oxygen species (ROS) and a local change of pH and other possible reactions depending on the initial composition of the solution and polymers used. The reactions affect the polymer film thickness, roughness, hydrophilicity, and local morphology. Possible gradients of species and film properties allow controlling biofilm formation. b) Surface decoration and photoinitiated light–pH coupled reactions: reactions on TiO_2 resulting in a local change of pH. Adapted with permission.[368] The inset shows that, besides the photogeneration of ions, such as protons, we are focusing on the possibility to amplify ion concentrations, e.g., by adding a chemical amplifier into the system. Abbreviation: TMAO, trimethylamine N-oxide.

gradients under local irradiation? (iii) How to achieve reversible actuation, faster or slower, of different LbL assemblies with controlled response times for bioapplications? To answer these questions, it is important to investigate both the change in the material and the system response in situ.

It is a challenging task to control spatiotemporal system gradients. Ulasevich et al.[368] proved that it is promising to use inorganic semiconductors to initiate a spatial-temporal gradient of pH on their surfaces.[368–370] An effective generation of proton gradients on TiO$_2$ surfaces under irradiation has been introduced[368–370] to control the bioactivity of the system for specific bioapplications of guiding cell migration on the surface[370] for coculturing biochips, and for protein recognition/modulation elements.[369]

For the specific examples and applications discussed here, the following key questions are important:

(a) How can the photogeneration of charges in a solid be used to initiate light-specific chemical reactions with time and space control? The question covers several topics, such as photon absorption,[371] carrier generation and mobility,[372] chemical conversion into reactive oxygen species (ROS),[373] ion gradients,[368] autocatalytic species to adjust amplification of ion gradients, such as a proton gradient,[374] as well as flexible positioning of the photoelectrode by the irradiation spot.[375]

(b) How do photogenerated ion gradients change the properties of the adjacent soft matter? The task is to "freeze" ion gradients locally,[376] to actuate soft matter,[368] to store ion carriers,[377] to release ions into the PEs LbL matrix,[369] and to control lifetimes, oscillations of mechanical properties, and LbL stability. Subquestions then concern (i) the dependence on PEs LbL architecture;[378–380] and (ii) the specificity for a semiconductor, effectiveness of doping, as well as duration and intensity of irradiation.[381]

(c) How does specific ion release at localized areas and change in morphology of the surface affect bacteria attraction and biofilm growth? The question concerns synergetic network regulation and spatiotemporal surface bioactivity to attract, deactivate, and affect their metabolism and desorb bacteria.[382] Subquestions are then related to (i) the mechanisms behind the effect of ROS on the bacteria;[383] (ii) the ion gradient to support growth of selective bacteria types located on certain areas;[384] and (iii) the effects of the surface-modified films as the photocontrollable bioactuators such as conformational transitions in the polymeric film.[369,370]

Concerning possible ion concentration gradients running in a network in parallel on semiconductor surfaces, we can ask if there is a universal strategy to predict possible ion concentration gradients and to suggest nanoscale machineries with chemical networks to control biofilms based on generation of ROS on well-known and controllable inorganic semiconductors. Here, life inspiration can be mentioned.[348,385] For example, it is known that, in order to trigger inflammation, the *Salmonella typhimurium* population[364] generates ROS with a subsequent production of electron (e⁻) acceptors. These electron acceptors enable *S. typhimurium* to use nutrients in the anaerobic environment. Some life-inspired transfer chain

reactions are mentioned in Figure 30a. It is interesting[364] that ROS generated by the inflammatory are known to exhibit "sulfur" pathways as they oxidize thiosulfate to $S_4O_6^{2-}$, providing a host-derived electron acceptor that supports growth of *S. typhimurium* by anaerobic respiration.[386] The reductase of *S. typhimurium* may reduce the tetrathionate ($S_4O_6^{2-}$) to thiosulfate($S_2O_3^{2-}$),[387] with further reduction to H$_2$S by sulfite reductase,[388] and thiosulfate reductase.[389]

"Sulfur" pathways in cells mentioned above are not the only inorganic exogenous electron acceptor pathways generated during inflammation.[364] Nitric oxide radical (NO) can react with superoxide ($O_2^- \cdot$), a ROS to form nitrate (NO_3^-) that boosts growth of *S. typhimurium* during gastroenteritis by nitrate respiration.[390] The pathogen uses energy taxis to migrate to spatial niches containing host-derived nitrate or tetrathionate.[391] How can we trace the pathogen on a semiconductor, e.g., TiO$_2$ surface? We suggest using photosystems to trace various inorganic "food" for pathogens (Figure 30a). We apply localized irradiation to trace their behavior or deactivate and detach them by localized ion concentration gradients, drug delivery, and time-controlled actuation of soft matter. Such nanoscale artificial machineries with parallel chemical reaction networks are on the frontiers of future technologies to trace spatiotemporal biomolecules, microorganisms, and cell pathways.

Today, a few parallel chemical reaction networks have already been designed for photoreactions on semiconductors. Further, we will give vivid examples of spatiotemporal light triggered gradients of protons on semiconductor surfaces.[368] Surprisingly, there are no data available to what extent the pH can be altered and how useful pH differences (ΔpH) can be before our recent study.[368] It has been shown that the pH can decrease from 7 to 4 very quickly and locally in the irradiated spot. It is thus a promising idea to use light–pH coupling for modulation of pH-sensitive organic molecules, and ΔpH to modulate pH-dependent soft matter with light on the surface of a semiconductor (Figure 30b).[368] pH-dependent polymers are a class of materials with tremendous structural variety.[392] One powerful example is "weak" PEs,[393] including biopolymers.[367] pH dependent polymers are also hydrogels,[394] which exhibit pronounced morphological changes in response to ΔpH and can also be used for multilayer formation.[395] It is the hot topic of recent works[368] to use LbL assemblies on photoactive TiO$_2$ surfaces, presented schematically in Figure 30b with the example of the successful modulation of LbL assembly thickness and with possible biomolecules,[369] biofilm detachment,[382] and cell migration[370] due to film actuation and pH sensitive bonds in LbL assemblies. In the first measurements, it was realized that the structural change induced by pH remains over hours after switching off the light and is advantageous for aims like cell growth and differentiation.[370]

One perspective is in situ modulation of photochemical processes on semiconductor surfaces. However, there are still a lot of challenges. Studies of the following issues are required to overcome existing scientific problems related to nanoscale electromagnetic energy transformation into ion concentration gradients: effects of nanoconfinement, chemical reaction networks in the system on formation of different ion gradients at localized areas under local irradiation of multipoints; energy exchange mechanisms in nanoscale energy storage and release

systems; formation of isolated conditions for ion gradients to avoid uncontrolled interaction with ambient environment; effective separation of photogenerated ions over the surface; diffusion length of the photoions in PE LbL multilayers in horizontal and vertical directions; and others.

The other promising idea is that ion and proton concentration gradients can be amplified drastically (Figure 30b, inset) due to nonlinear organic reactions to proliferate acidic molecules in soft matter.[374] We are sure, that this scientific field will grow further being unique to use reproducible light sensitive materials, e.g., inorganic semiconductors, for a new function of building blocks for nanoscale biomachineries[353] and biosensing.[369]

7. In Situ Techniques for the Detection of ROS and Ion Activity

In this review, we focus on in situ observation of interfacial chemical reactions on nanostructured semiconductor surfaces, such as TiO_2, involving ROS and ion generation, molecules generated in the system, such as hydroxyl radical, the singlet oxygen, "sulfur" pathways, polymer soft matter actuation, and bioresponse by fluorescence assays, scanning ion-selective electrode technique (SIET), μ-confocal photoluminescence (μ-CPL), and microorganism response. Advanced techniques are used to determine the spatiotemporal location of the photocatalytically active sites close to the surface. As an example, we summarize some examples of reactive compound detection in **Table 1**. It is interesting, that again life inspiration[364] can be used to find possible methods to detect ROS: ROS detection in a number of physiological[396–399] processes significantly improved due to paying high attention to microbiology.

7.1. Fluorescence Assays

In cell staining laser-induced fluorescence spectroscopy, fluorescent probes that correspond to exact processes are used.[400–402] The ROS effects occur through reactions with a large variety of cellular components including proteins, nicotinamide adenine dinucleotidephosphate, cysteine, tryptophan, glutathione, tyrosine, ascorbic acid, and nucleic acids, cholesterol, fatty acids, which cause membrane lipid peroxidation.[403] Nowadays, many species to guide biological pathways in situ are commercially available. For example, some probes are known to generate or detect various ROS, including singlet oxygen ($1O_2$), superoxide anion ($\cdot O_2^-$), hydroxyl radical (HO$\cdot$), various peroxides (ROOR') and hydroperoxides (ROOH), as well as NO.[404]

Several reviews discuss the chemistry of the different ROS and their fluorescence assays in photochemical processes.[404,405] We want to point out here, that in photochemistry, the future focus cannot only be on detection of photogenerated species and reaction pathways, but also on their localization within a certain surface area and on the time resolution of photochemical processes. In particular, in **Figure 31**, it is shown that it is very important to study localization of gradients on the surface, e.g., ion gradients.[406] A light-addressable photoelectrode suggested imaging with a fluorescence molecule and ion indicators.

Figure 31b describes an experimental setup for light-addressing imaging. pH imaging is possible with pH indicators, as shown in Figure 31c,d. In ref. [370], the fluorescent pH indicator 4,4′-(anthracene-9,10-diyldimethanediyl)dimorpholine, which exhibits $pK_a \approx 5.1$, was used. Other indicators are easy to adopt to study ions and molecules on inorganic semiconductor surfaces, but again the tendency of today is to rely on time and space resolution in order to enable studies of simultaneous reactions of different species, where each one affects the other. Taking into account the recent progress in experimental studies of cell and cell metabolism, it is clear that parallel networks are more than realistic to adopt the assays for photochemical reactions.

7.2. SIET

In situ SIET for mapping the photoactivity over the surface under local irradiation is new for the area[368–370] and its further development should be beneficial to the large scientific community working in this field. In particular, in refs. [368–370], the photogenerated proton activity over TiO_2 surface was monitored, as displayed in **Figure 32**. For the modulation of pH sensitive soft matter, biomolecules, and microorganisms with light, it is important to understand how photoinitiated processes on the semiconductor TiO_2 result in the transformation of light to an ion and in pH change, including localization of the effect. SIET is a very attractive technique with a sensitivity better than pH 0.2 units for mapping of the activity and migration of H^+ ions on a TiO_2 film in aqueous solution during local irradiation. SIET allows measurements of the concentration of specific ions (in particular in the mentioned case, H^+ ions) at a nearly constant microdistance over the surface.[407] In ref. [407], it is also mentioned that photoactivity is an important issue. Thus, to detect clear signals it is advantageous to a mesoporous TiO_2 layers with high photoactivity[368,408] compared to the lower photoactivities discussed in the following text for modulation of soft matter and biomolecules.[370]

SIET maps of a TiO_2 surface before and after irradiation are shown in Figure 32, confirming that it is possible for TiO_2 to release protons upon irradiation. Figure 32b displays how the pH in the center of the irradiated spot varies when switching on–off the local irradiation. The duration of irradiation correlates with the pH obtained: 5 s, 1 min, and 3 min of irradiation result in pH of 5.6, 4.5, and 4.0 peak values, respectively. The action of different photoelectrochemical reactions (Figure 30b) on the TiO_2 surface under illumination seems to be the only plausible explanation for the observed local acidification of the solution and confirms that TiO_2 is promising to demonstrate our concept to run reactions in parallel on a semiconductor to have ion and molecule gradients in time and space.

It is interesting to perform experiments with mobile flexible photoelectrode positions, where two or more semiconductor electrodes are placed in one Petri dish, and to shine the light on one of them or irradiate simultaneously several spots on the surface at different distances/locations, with different intensities and durations. The flexible spatial addressability, oscillations, and reversible changes are great advantages for nanoscale machineries. The next step may be the assembly of the actuating polymer soft matter on low-photoactive semiconductor surfaces by changing parameters in the system (Figure 30).

Table 1. Specific examples of detection of reactive species on semiconductors.

Analyzed material	Detected species	Methods for detection	Light source for sample irradiation	Reagents and additional features in methodology of photogenerated species detection	Reference
ZnO,[445,446] CeO_2,[446] Ag[447]	$OH^\bullet$, $O_2^{\bullet-}$, $^1O_2$	Colorimetric probe method (UV–vis[a] spectroscopy)	18 W black-light blue lamps[445]; 4 W compact UV lamp (365 nm)[446,447]	$=OH^\bullet$ indicator – p-nitrosodimethylaniline ($\lambda = 440$ nm),[445] p-chlorobenzoic acid[446,447]; $O_2^{\bullet-}$ indicator – 2,3-bis(2-methoxy-4-nitro-5-sulfophenyl)-2H-tetrazolium-5-carboxanilide ($\lambda = 470$ nm);[445][446,447] $^1O_2$ indicator – furfuryl alcohol[446,447]	[445–447]
TiO_2, ZnO	H_2O_2	Polarographic measurements; Fluorescence measurements; Iodide method	450 W Xe lamp	1) TiO_2 suspension (0.5 g L^{-1}) with $\lambda = 350$ nm and ZnO suspension (1×10^{-3} M; pH 7.7; O_2 bubbling) with $\lambda = 320$–330 nm 2) P-hydroxyphenylacetic acid, horseradish peroxidase and detection of dimerization of p-phenylacetic acid at $\lambda_{ex} = 315$ nm, $\lambda_{em} = 406$ nm 3) Iodide reagent (0.4 M KI, 0.06 M NaOH, $\approx 10^{-4}$ M $(NH_4)_2MoO_4$)	[448]
TiO_2,[449] TiO_2:Sm^{3+}[450]	OH	Fluorescence measurements	200 W high-pressure mercury lamp[449]; 160 W high-pressure mercury lamp[450]	Irradiation of TiO_2[449] or TiO_2:Sm^{3+} in terephthalic acid solution (5×10^{-4} M in 2×10^{-3} M NaOH solution) fluorescence emission ($\lambda_{ex} = 315$ nm) for 5 min[449] or 15 min.[450]	[449,450]
Cu_2O/SnO_2	H_2O_2	DPD[b] colorimetric method	300 W Xe lamp	N,N-diethyl-p-phenylenediamine, horseradish peroxidase:test solution phosphate buffer solution (0.5 M KH_2PO_4 and 0.5 M K_2HPO_4, pH of ≈ 6.0) with 0.01 g mL^{-1} DPD in 0.1 M H_2SO_4 solution and 1 mg mL^{-1} horseradish peroxidase; H_2O_2 quantification at $\lambda_{max} = 551$ nm.	[451]
$SrTiO_3$	$O_2^{\bullet-}$, $OH^\bullet$, $O^\bullet$	Nanoscale redox titration (SECM[c], SI-SECM[d])	300 W Xe lamp	$SrTiO_3$ illumination (in the 300–800 nm range) in 50×10^{-6} M $K_3[Fe(CN)_6]$, 100×10^{-3} M borate buffer solution, pH 9.3. SECM experiments – four-electrode configuration ($SrTiO_3$ (WE[e]), Ag/AgCl (3 M KCl) (RE[f]), 1mm Pt wire (CE[g]) with a 4 μm radius carbon fiber ultramicroelectrode or a 240 nm radius pyrolyzed carbon nanoelectrode.	[452,453]
W-$Mo/BiVO_4$	$OH^\bullet$	Nanoscale redox titration (SECM[c], SI-SECM[d])	300 W halogen bulb	Redox couple $IrCl_6^{2-/3-}$ as a titrant, Ag/AgCl (sat. KCl) (RE), 1 Pt wire (CE) using a 4 μm radius carbon fiber ultramicroelectrode positioned at 12 μm apart from the working electrode in 1×10^{-3} M K_2IrCl_6 and 0.1 M Na_2SO_4 pH 4.5.	[454]
TiO_2	H_2O_2	SECM	150 W Hg–Xe lamp	H_2O_2 microsensor – immobilizing horseradish peroxidase in an electron conducting hydrogel based on poly(4-vinylpyridine) with $[Os(bpy^h)_2Cl]^{3+/2+}$ redox centers on carbon fiber microelectrode. Independent monitoring of H_2O_2 formation on TiO_2 photoanode and indium tin oxide (ITO) cathode in phosphate-buffered saline (pH 7.4) using Pt wire (CE) and a saturated calomel electrode (RE) at 50 μm from the surface.	[455]
TiO_2	$O_2^{\bullet-}$	Method of chemiluminescent probe	150 W Xe arc lamp	TiO_2 suspension (4.3 mg mL^{-1} in 0.01 M NaOH, pH 11) with $\lambda_{exc} = 387$ or 360 nm, using different glass filters with intensities 40 and 3 mW cm^{-2}, respectively. Preaddition method – addition of 7×10^{-3} M luminol solution to TiO_2 suspension before the irradiation; postaddition method – immediately after irradiation.	[456]
TiO_2	$OH^\bullet$, $O_2^{\bullet-}$, H_2O_2	Continuous flow chemiluminescent analysis	500 W xenon light source	$O_2^{\bullet-}$ detection 0.1 mg mL^{-1} TiO_2 suspension, 1×10^{-6} M luminol. OH detection, addition of phthalhydrazide (1×10^{-6} M) into the photoreactor ($\bullet$OH capture), mixing with H_2O_2/$K_5Cu(HIO_6)_2$ (0.1×10^{-3} M) H_2O_2 detection, keeping TiO_2 suspension (0.01 mg mL^{-1}) in darkness for 30 min, and mixing with luminol (10×10^{-6} M)/$K_3Fe(CN)_6$ (0.01 M).	[457]

Table 1. Continued.

Analyzed material	Detected species	Methods for detection	Light source for sample irradiation	Reagents and additional features in methodology of photogenerated species detection	Reference
TiO₂,[458–460] ZnO,[458] SnO₂,[458] WO₃,[458] CdS,[458] ZnS,[458] BiVO4[458,460]	OH•	Photoluminescence,[458] fluorescence measurements[459]	350 W Xe arc lamp (365 nm),[458]	OH• detection under illumination with intensity about 5 mW cm⁻²[458] or in a range from 50 μW cm⁻² to 15 mW cm⁻²,[459] Photoluminescence of catalyst suspension[458] or TiO₂ film plate[459] in 10^{-3} M coumarin aqueous solution[458,459] or 5×10^{-4} M terephtalic acid in 2×10^{-3} M NaOH[458,459] at ambient temperature every 15 min,[458] 10 min, or 5 min[459] with $\lambda_{exc} = 332$ nm, $\lambda_{max} = 456$ nm (for coumarin) and $\lambda_{exc} = 315$ nm, $\lambda_{max} = 425$ nm (for terephtalic acid). O₂•⁻ detection[460] using 0.7×10^{-3} M luminol solution.	[458,460]
	O₂•⁻		200 W high-pressure mercury lamp[459]		
TiO₂/CdS	H₂S	Photoelectrochemical detection	500 W Xe lamp ($\lambda > 420$ nm)	Three-electrode system (TiO₂/CdS film (WE), Ag/AgCl (sat. KCl) (RE), Pt foil (CE)) in 0.5 M LiNO₃ solution containing 10×10^{-3} M Fe(CN)₆³⁻/⁴⁻ (pH = 6).	[461]
TiO₂	O₂	Photoelectrochemical detection, photoluminescence measurements	500 W high-pressure mercury lamp (365 nm)	Photocatalytic evolution of O₂ on TiO₂ rutile surfaces (WE) using in situ measurements of photocurrent, photoluminescence, and AFM using Pt plate (CE) and Ag/AgCl/KCl (RE) in 0.1 M HClO₄ solution.	[462]
TiO₂	•OH, ¹O₂	Single molecule fluorescent measurements	100 W Hg lamp (365 nm)	Detection of OH• diffused from the surface of pure TiO₂ to the PMMA[i] glass (intervening bandgap 12.5 μm) coated with 3-(p-hydroxyphenyl)-fluorescein and aminophenylfluorescein for OH• and terrilenediimide for ¹O₂ detection, respectively.	[463–466]
TiO₂/Ag, TiO₂/Ag/Ni	O₂•⁻	Photometric detection	125 W high-pressure mercury lamp	Deactivation of gram-positive and gram-negative bacteria. Illumination of samples under a thin layer of water with UV light for 10 min. Immediately after illumination, addition of the tetranitromethane aqueous solution in cuvette. Photometric detection of nitroform ($\lambda_{max} = 350$ nm).	[383]
TiO₂	H⁺	SIET[j]	UV LED[k] (365 nm)	Mapping of H⁺ activity over TiO₂ surface in solution under irradiation using pH microelectrode.	[368–370]
TiO₂,[467] TiO₂/Pd,[468] BiOI[469]	NO	Chemiluminescence NOₓ detection	500 W xenon arc mnnnnlamp[467] ; Solarsim 150,[468] LED lamp (448 nm)[469]	Irradiation of glass-fiber filters with TiO₂/Pd particles[468] or sample dish with TiO₂ suspension[467] or BiOI film on glass substrate[467] with solar light (420–700 nm) or visible light (448 nm),[469] with flowing air stream at a rate 3 L min⁻¹,[468] 1.2 L min⁻¹,[467] 1 L min⁻¹[469] containing 1 ppm,[468] 400 ppb,[467] 600 ppb[469] of NO.	[467–469]
WO₃/TiO₂	H₂S, SO₂	Pulsed flamed photometric detection	8 W blacklight tube (365 nm)	Irradiation of the reactor coated with TiO₂ aqueous suspension with flowing air stream (92 vol.% air, 15 ppm H₂S) with flow rate 200 or 500 mL min⁻¹	[470]
CdS	HS⁻, S₂O₃²⁻, SO₃²⁻	Spectrophotometric detection	1000 W mercury high-pressure lamp	HS⁻ detection: methylene blue ($\lambda_{max} = 670$ nm, $\varepsilon_{670} = 24\,600$ M⁻¹ cm⁻¹) a product of H₂S and N,N-dimethyl-n-phenylene-diamine interaction. SO₃²⁻ detection: formation of strongly colored compound ($\lambda_{max} = 590$ nm) in a reaction between SO₃²⁻ and fuchsine in the presence of formaldehyde in aqueous-alcoholic mixture S₂O₃²⁻ detection: reduction of I₃⁻ ($\lambda_{max} = 360$ nm, $\varepsilon_{360} = 24\,000$ M⁻¹ cm⁻¹) by sulfur(II–IV) compounds – products of CdS photocorrosion	[47]

a)UV–vis – ultraviolet-visible spectroscopy; b)DPD – N,N-diethyl-p-phenylenediamine; c)SECM – scanning electrochemical microscopy; d)SI-SECM – surface interrogation scanning electrochemical microscopy; e)WE – working electrode; f)RE – reference electrode; g)CE – counter electrode; h)bpy – 2,2'-bipyridine; i)PMMA – polymethylmethacrylate; j)SIET – scanning ion-selective microelectrode technique; k)LED – light emitting diode.
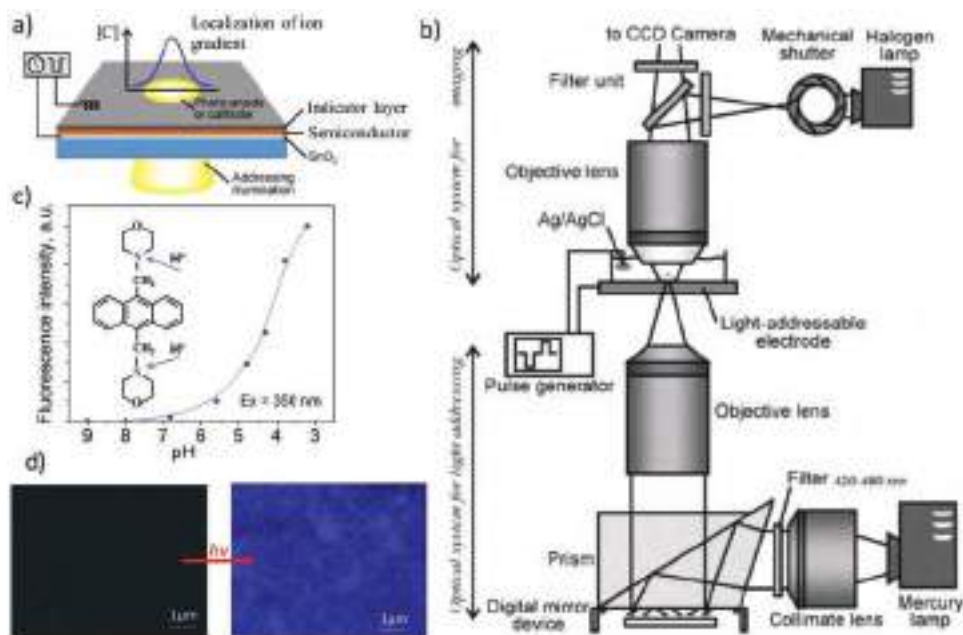
Figure 31. Possible system to detect in situ localized molecules or ion gradients under irradiation using fluorescent assays. a) Schematic diagram of ion gradient generation with a light-addressable photoelectrode. b) Experimental setup for in situ light addressing and ion imaging. Two separate optical systems can be used; a standard fluorescence upright microscope and a reduced projection exposure system equipped under the microscope stage. A patterned illumination reflected from a digital micromirror device may be projected onto the electrode substrate. Fluorescence emission of the ion, e.g., pH indicator, is monitored by a cooled charge-coupled device (CCD) camera attached to the microscope. The measured fluorescence intensities may be converted into ion concentration or pH changes using a calibration curve obtained in advance. Adapted with permission.[406] Copyright 2016, Elsevier. c) Calibration of the fluorescent pH indicator, and initial chemical formula to point to the protonation sites. d) Confocal fluorescence images of the surface of TiO_2, with the fluorescent pH dye (left) before and (right) after 10 s of irradiation.[370]
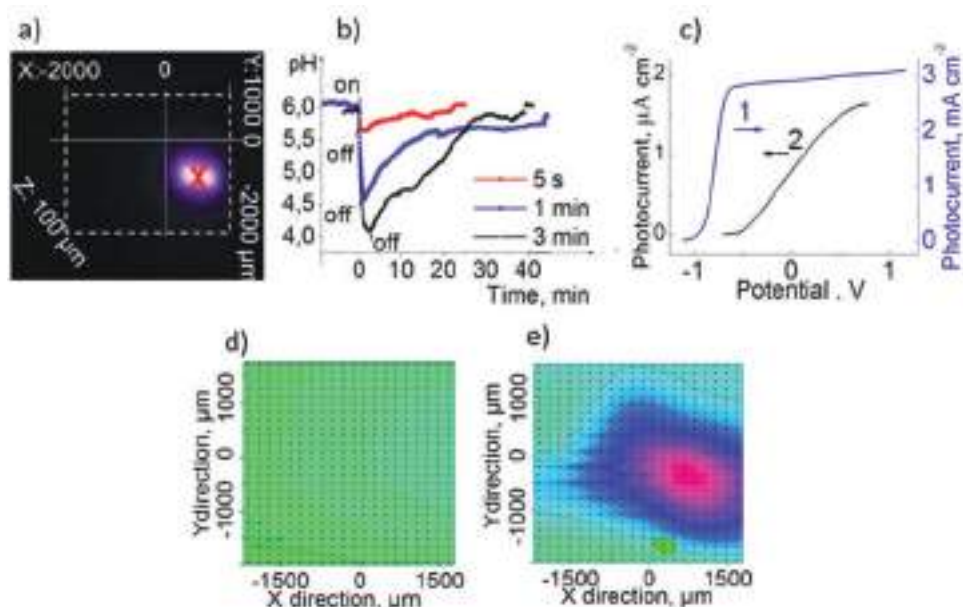
Figure 32. In situ local pH activity over a TiO_2 surface. a) Optical image of the surface during irradiation and measurements by the scanning ion selective electrode technique (SIET) for mapping of the activity of H^+ ions over the TiO_2 film under local irradiation. b) Temporal evolution of the pH over the mesoporous TiO_2 film in the center of the irradiation zone (X in (a); on—illumination is switched on, off—illumination is switched off). c) Photocurrent of low and high photoactivity TiO_2 indicating that for SIET study of the high photoactivity surface is more suited to detect the effect, but for soft matter actuation low photoactivity TiO_2 is preferable, not to degrade the polymer assembly. d,e) SIET maps of proton activity (d) before and (e) during the exposure of certain localized areas. Adapted with permission.[368]

ADVANCED
SCIENCE NEWS
www.advancedsciencenews.com

ADVANCED
MATERIALS
INTERFACES
www.advmatinterfaces.de

7.3. μ-CPL

One more technique that allows in situ monitoring of local changes is PL measurement with 3D micrometer resolution on nanostructured semiconductors: μ-CPL.[409] Again, its development should benefit the large scientific community working in this field. In particular, in ref. [409], the formation of mesoporous silicon by high intensity ultrasonic surface treatment was established (**Figure 33**) and displayed a strong PL activity. Numerous models[410–412] can be proposed to explain the PL of the modified silicon, including quantum confinement, surface states, defects in the oxide, and the formation of hydrogen-terminated bonds. It is important to study the nature of PL centers that can be changed in time, in situ.[409] One can monitor the PL signal in situ during aging of nanostructured silicon (Figure 33a,b), going from a nonoxidized structure to a partially oxidized one. Radiative recombination takes place within the surface amorphous layer (Figure 33c). Surface states localize electrons and holes, either separately or together with the formation of nanocrystalline Si in the porous matrix of SiO_x. One can change the character of the PL from green to red, for example, in samples exposed to water by aging and partially oxidizing the silicon, thus going through mostly hydrogen-terminated and/or nonterminated bonds to a partially oxidized Si structure.[409] The light emission by a single point on the silicon surface may be monitored by a 3D reconstruction of the porous μ-sized structure via μ-CPL. The dots, which are clearly visible in μ-CPL (Figure 33c), are probably formed due to the use of nonequilibrium high-intensity ultrasonic surface treatment[413] as a prospective method for surface modification. The positions of the dots are probably located on the spots where cavitation bubble collapse occurs along with a localization of a thermogradient on the surface[414] during surface modification due to high intensity ultrasonication.
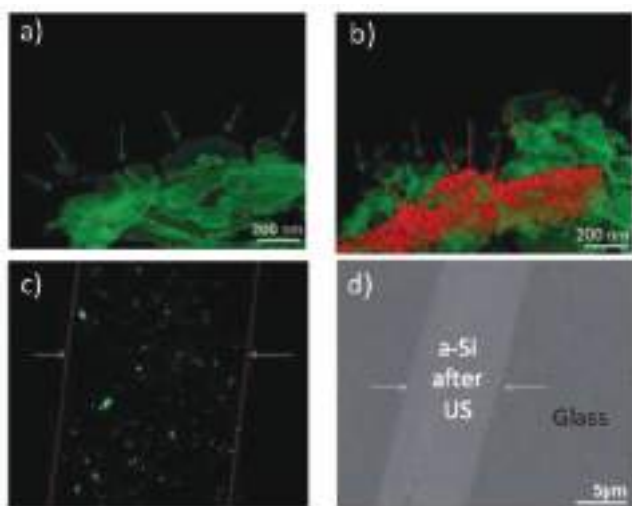
Figure 33. a–c) In situ μ-confocal photoluminescence (μ-CPL) spectra (fluorescence mode) of silicon after 30 min of sonochemical modification (20 kHz, 57 W cm⁻²) (a,b) of crystalline silicon wafer (a) immediately after modification, and (b) followed by aging; (c) amorphous silicon (a-Si) deposited on glass; d) corresponding scanning electron microscopy (SEM) picture; green and red arrows show side views of the PL spectra. Adapted with permission.[409]

It is promising to employ in situ methods in other areas and apply them to study of new aspects of the known photoreaction on semiconductor surface and in situ methods presented here are good examples.

7.4. Microorganism Response to Photogenerated Species

The photoproduced ROS could alter the activity of microorganisms penetrating into an intracellular volume, which is interesting for both photodestruction of bacteria[415] and nanoscale machineries discussed here (Figure 30a).

In particular, we address an example, where ROS photoproduced at TiO_2 under illumination effectively induces prophages in the lysogenic bacteria to the lytic cycle.[416] There was much discussion, how ROS affect microorganisms: whether they destroy the cell membrane or whether they affect nuclei of the cell or bacteria already before.[415] The mentioned experiment with lysogenic lactic bacteria[416] was planned in such a way not to deactivate or kill bacteria, but to use short term irradiation insufficient to kill bacteria to find out if ROS affect the deoxyribonucleic acid (DNA) of bacteria before their deactivation. In the case that ROS affect DNA stronger, they destroy the cell membrane via a prophage induction to the lytic cycle and cause release from the bacterium. From **Figure 34**, it is evident that photogenerated ROS are indeed released from a bacterium before it is deactivated, which means that DNA is affected faster than the cell membrane is destroyed.

It is also interesting to note that different microorganisms have different sensitivities to photogenerated species. At this point, an example can be drawn that Gram-positive (G(+)) bacteria are more sensitive to superoxide anions ($\cdot O_2^-$) in comparison with Gram-negative (G(−)) bacteria.[383] In particular, it was shown[383] that the yield of the superoxide could be enhanced by the bimetallic Ag/Ni nanoparticles deposited on TiO_2 and G(+) bacteria being in general more stable to ROS because of an additional lipid membrane, by contrast to G(−), that are more sensitive to ($\cdot O_2^-$).

We want to highlight here that microorganisms can also be used for in situ detection of the formation of photochemical reaction products, which immediately changes their behavior on the surface. The fact that microorganisms are very sensitive to photoinitiated processes makes the proposed concept (see Figure 30a) quite believable. This concept consists of guiding cell behavior on the surface. It would be extremely exciting if a spatiotemporal ion concentration gradient over the surface would guide cells locally promoting growth of one cell type (e.g., sulfur bacteria) and prevent the development of other cells to control biofilm formation and to detect selective biomolecules.

8. Photocatalytic Degradation of Organic Species on TiO_2

Recently, there has been a tendency among photocatalyst investigations concerning photodecomposition of chemical[373] and bacterial pollutants in an aqueous phase,[417] that are focused on photocatalytically active coatings[418] capable to remove adsorbed

**ADVANCED
SCIENCE NEWS**
www.advancedsciencenews.com

**ADVANCED
MATERIALS
INTERFACES**
www.advmatinterfaces.de
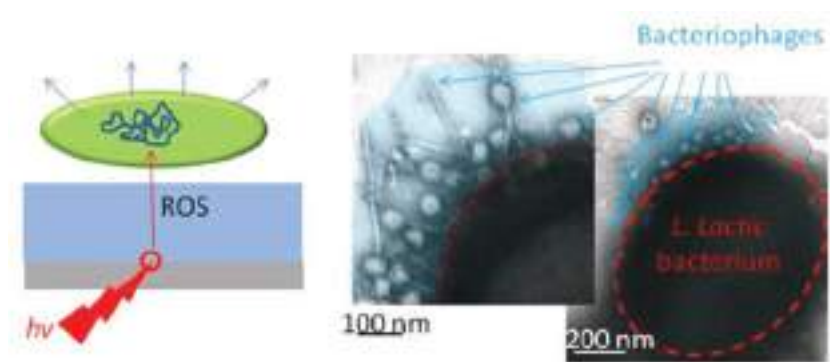
Figure 34. Schematic and transmission electron microscopy (TEM) image demonstrating the effect of ROS generated at a semiconductor on the metabolism of lysogenic lactic bacteria (i.e., containing a bacteriophage gene in their deoxyribonucleic acid (DNAs). The opening of the cell envelope and the release of viruses is observed. Adapted with permission.[416] Copyright 2011, Royal Society of Chemistry.

organic contaminants under solar or artificial illumination (so-called self-cleaning materials[418]).

The self-cleaning characteristics of semiconductors result not only from their strong oxidation power under irradiation, but also from the discovered phenomenon of the photoinduced superhydrophilicity inherent in the surface.[419] Thus, one may consider the contribution of a self-cleaning function combined with stability of the organized soft matter on a semiconductor for novel "intelligent" materials and nanoscale machineries.

When speaking about novel "intelligent" materials, the photocatalytic degradation of organic species can be mentioned as a negative process if one is interested in creating oscillating soft matter coatings[370] on the semiconductor surface without polymer degradation during irradiation. The potential degradation of the organic substances and polymer matrix triggered by ROS should always take into account photocatalytic systems.[420] The stability can be studied by means of a combination of spectroscopy with microscopy.[368] For example, FTIR[368,421] has proved to be an effective method for the investigation of the composition before and after irradiation.

In the following section, we will present examples using TiO$_2$ with a low photoactivity and a low-intensity as well as short-term irradiation that allows for in situ modulation[368] without degrading the polymer coating, in order to guide cell migration on the surface.[370] This point is a promising route to in situ control the biofilm on the surface[382] and to design new biosensors.[369]

9. Prospects for In Situ Modulation of Soft Matter and Microorganisms without Degradation

9.1. Reversible Oscillation of Soft Matter Properties: Thickness, Stiffness, Swelling

Here, we study the transformation of electromagnetic energy into spatiotemporal ion concentration gradients, where the inorganic semiconductor material is a light sensitive system, and PE LbL assembly. As a responsive element and with biofilm control, it is a prospective application for nanoscale machin-

eries and biosensing. It should be noted that we primarily aim here on the in situ characterization of changes in the material, formation of self-assembly, soft matter modulation, and light sensitive particle vortices.

In **Figure 35**, several methods are highlighted for in situ MS studies. Microchips covered with semiconductor and soft matter can be designed as microfluidic probe that allows real-time imaging of the electrode–liquid electrolyte interface (Figure 35a).[422] The same chips could be applied in an open cell for in situ quartz crystal microbalance (QCM) studies to follow both LbL assembly and photoactivation of the films (Figure 35c).[423] Photoactivation of the film can also be studied with the help of atomic force microscopy (AFM) (Figure 35d) with time resolution and localized at a certain area.

Recently, a specific LbL architecture for advanced bioapplications has been introduced: reversible oscillation of soft matter on semiconductor surface,[368] resulting in cell migration,[370] desorption from the surface,[382] and modulation of pH sensitive chemical bonds in LbL assemblies,[369] and drug chemical delivery.[420–424]

It is important to mention the high priority to monitor soft matter response on the surfaces (Figure 30) measuring charge separation, ion and ROS generation and localization, activation and relaxation time, process reversibility, as well as trapping of ions and molecules depending on various parameters, such as thickness, stiffness, roughness, hydrophilicity, and permeability. It is of high priority to obtain knowledge about the behavior of ion-enriched materials in nanoconfinement. Information about the stability of ion-enriched soft matter inside nanoconfined volumes and the interaction between different ion enriched reagents and ion migration will be obtained during further examinations. Knowledge of how to organize LbL assemblies with different ion contents, e.g., for different protonations, as well as of the assembly from different pH and ionic strength solutions for the formation of multifunctional gradient material with different affinities to store and exchange photogenerated ions is important. Systematic studies of the mechanism of film formation will be instructive in order to control biofilms on the surface.

9.2. Bioresponse due to Soft Matter Oscillation and Photoreactions

It has already been mentioned above and shown in **Figure 36** that some very specific "intelligent" systems were developed recently[370,382] to control system bioactivity, but unfortunately no general concept of biofilm regulation has been suggested yet. Reversible oscillation of LbL films based on high amplitude actuation of block copolymer micelles allows controlling cell behavior on a surface. In particular, change of stiffness results in migration of osteoblasts to a harder part of the surface (Figure 36a,b)[370,382] and in desorption of bacteria from the surface with time (Figure 36c).[382]

ADVANCED
SCIENCE NEWS
www.advancedsciencenews.com

ADVANCED
MATERIALS
INTERFACES
www.advmatinterfaces.de
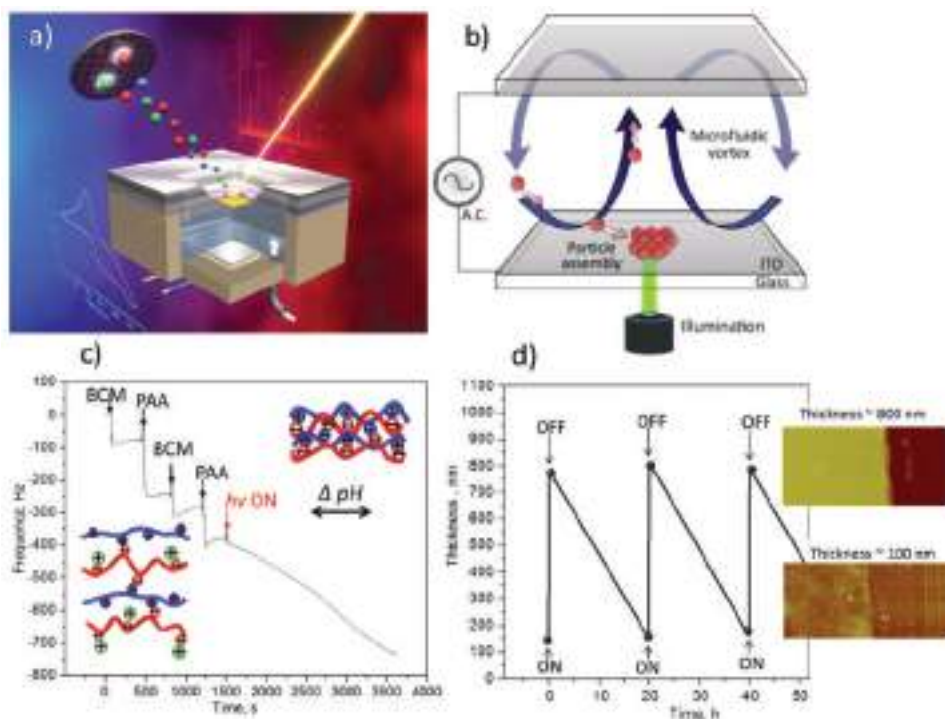
Figure 35. a) A microfluidic probe allows real-time imaging of the electrode–liquid electrolyte interface. Adapted with permission.[422] Copyright 2014, Royal Society of Chemistry. b) Prospective system to guide particle movement and real-time microfluidic vortex detection, i.e., by gas formation and effecting particle migration on a surface. Adapted with permission.[443] Copyright 2014, Elsevier. c) In situ quartz crystal microbalance (QCM) study of LbL PE assembly and its activation under irradiation resulting in water attraction into the LbL and d) LbL thickness change before and after irradiation. Abbreviation: BCM, block copolymer micelles; PAA, poly(acrylic acid) (PAA). Adapted with permission.[368,370]

Andreeva et al.[369] suggested a new principle of photoassisted spatial desorption of (poly)-histidine-tagged (His-Tag) proteins on a TiO$_2$ surface (**Figure 37**). Here, a semiconductor TiO$_2$ surface is decorated by an LbL assembly of a strong polyelectrolyte, namely, polystyrene sulfonate (PSS), and nickel–nitrilotriacetic acid (NTA). The PSS/NTA multilayer architecture provides n-fold ($n \times$ NTA) binding efficiency for more precise protein recognition in comparison to existing molecular His-Tag protein recognition with onefold and threefold multiplication. Spatially resolved desorption of proteins is regulated by non-photodestructive short-term low-intensity light irradiation. The local pH shift on irradiated TiO$_2$ selectively affects the pH-sensitive NTA/protein complex, but not the LbL assembly of PSS and NTA, which is stable in a broad pH range. It can be noted that in situ characterization of LbL organization and its following in situ modulation can be monitored by SIET, μ-CFM, and QCM (Figure 37).[369]

The examples discussed above clearly demonstrate that microorganisms are sensitive to both products of photoreactions, e.g., ROS, pH change in the system, and actuation of soft matter. This strongly supports our suggested concept to build a nanoscale machinery for controllable manipulation of microorganisms with biomolecules on a semiconductor surface. A systematic study of the design of such a nanoscale machinery is needed to modulate a pronounced bioresponse, to build a general concept, and to integrate the system into microfluidic chips or microbial biosensors. To have pronounced modulation of soft matter, different ion, e.g., proton, gradients need to be studied on surfaces in detailed manner.

One more important topic is the spatiotemporal delivery of ions for modern synthetic biology platforms (biofactories). The development of alternative, green transformation of electromagnetic energy into ion gradients and non-petrochemical feedstocks requires a new vision on industrial bioreactors, because more and more complex compounds (proteins, bacteria) are used in production now or will be used in the future. This calls for more precise control over the reactions occurring in bioreactors. Our systems for manipulation of biomolecules and bacteria provide controlled release of the necessary ions for bioobject activation exactly at the required bioreaction stage and place, which may cause a considerable biotechnology breakthrough in the future.

9.3. Chemical Delivery: Regulation of Soft Matter Permeability and Motion

An advantage of many microbial biosensors is that the immobilization of whole cells improves the stability of intracellular biorecognition elements, such as enzymes, because the enzyme is retained in the natural environment; moreover, the employment of genetically engineered microorganisms permits a drastic improvement of the sensitivity and selectivity of the resultant microbial biosensing devices. In order to integrate the microbial biorecognition elements into lab-on-chip devices, one needs to exert a remote control over adsorption and desorption of microbial cells as well as over their biochemistry, e.g., by delivering

**ADVANCED
SCIENCE NEWS**
www.advancedsciencenews.com

**ADVANCED
MATERIALS
INTERFACES**
www.advmatinterfaces.de
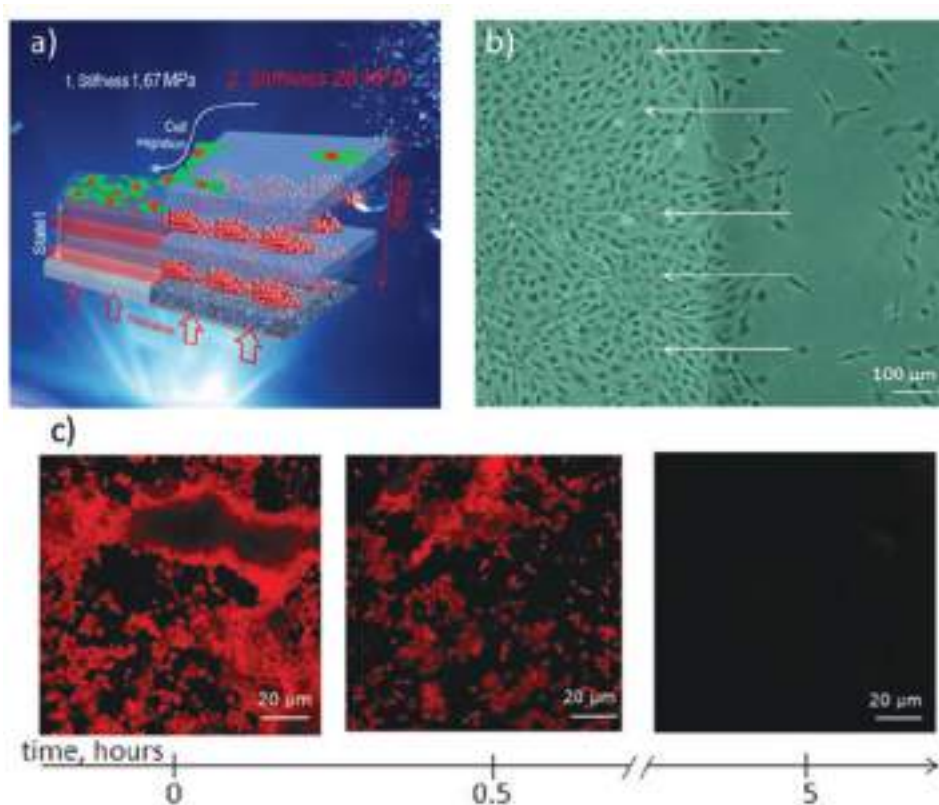
Figure 36. In situ bioresponse on soft matter actuation. a,b) Examples of consequences of a dynamic concept of modulation of a multilayer coating on titania using light–pH coupled stimuli to regulate cells on the surface: during irradiation the stiffness changes drastically and cells start to migrate across the surface. Adapted with permission.[370] Copyright. c) Actuating coating can be used as an antifouling approach preventing bacteria from growing on the surface. An example of a self-regulating system is presented: Lactic bacteria are grown on the surface and change the pH. The coating then changes its thickness fast and "pushes off" bacteria from the surface. Adapted with permission.[382]

different ions. To this end, the conformational transitions in the PE films induced by photocatalytic reactions occurring at the semiconductor surface in contact with the polyelectrolyte can be used. Thus, for example, in our previous works, we discussed the possibility of reversible photo-opening[425] of polyelectrolyte assemblies to affect the adsorbed microorganisms.[426] Indeed, self-oscillation of LbL films of different architectures provides a high gain for various bioapplications from protein and pathogenic cell recognition to cell detachment, migration, and construction of lab-on-chip elements. However, the development of a general concept for process regulation on "demand" is challenging—but possible and rewarding as well.

A prominent example of the photocatalytically active titania-based LbL coatings is shown in **Figure 38**a.[421] The coatings were obtained by the immobilization of loaded titania/PE nanoparticles into a sol–gel-derived matrix. By forming a PE shell on the mesoporous titania particles, it is possible to fabricate nanoscale reservoirs, which can store relatively large organic molecules in their interior. The mesoporous titania particles were loaded with the luminescent dye Rhodamine 6G before the deposition of the PE shell, and the light-driven release has been shown. Properties of biomolecule-containing LbL films, such as their growth regime, thickness, loading capacity, and mobility of polymers within the film, can be altered and synthetic polymers or biopolymers can constitute the PE film.

Two types of pH-responsive encapsulation systems based on surface metal sponges prepared by sonochemical treatment were proposed: (i) a single-step system with a simultaneous activation and modification of the metal and active compound by high-intensity ultrasound (HIUS), and (ii) a system where the metal sponge serves for the construction of PE surface capsules, allowing storage and release of an encapsulated substance.[426] In the first system, the encapsulation is ensured via the chemisorption of the active compound on the surface, i.e., −OH groups of the metal oxide layer. In contrast, in the case of PE surface capsules, there is no need of specific interactions between a metal and the encapsulated compound, and therefore, it is a universal encapsulation and carrier system. Moreover, hybrid systems with polypyrrole are developed, providing an efficient delivery and stepwise release of the low molecular weight active component.[425] Further examples have been analyzed in recent reviews,[366,367,380] proving that the strategy discussed is suitable to build probably even a light sensitive autonomous robot[427] for drug and cell delivery.

Photocatalytic reactions recently were used more and more for development of (nano)tools for autonomous and remotely guided catalytically self-propelled motion, as for example, shown in Figure 38b for InGaAs/GaAs/(Cr)Pt tubes.[428] The rolled-up tubes with diameters in the range of 280–600 nm move in hydrogen peroxide solutions with speeds as high

ADVANCED
SCIENCE NEWS
www.advancedsciencenews.com

ADVANCED
MATERIALS
INTERFACES
www.advmatinterfaces.de
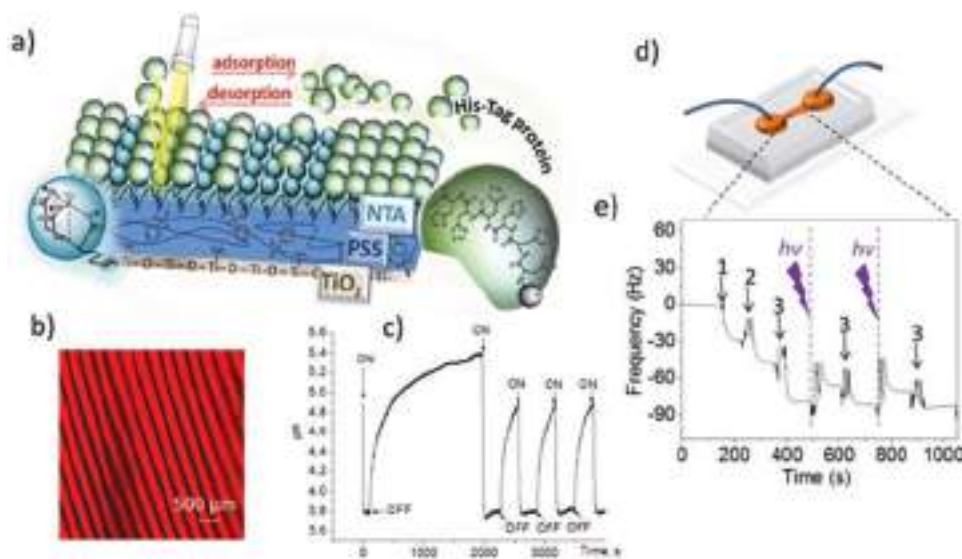
Figure 37. a) Schematic illustration of the release of proteins from the surface using light–pH coupled stimuli on titania: LbL assembly of strong polyelectrolyte layers, polystyrene sulfonate (PSS), and pH-responsive and nickel-nitrilotriacetic acid (Ni^{2+}-NTA) layers for (poly)histidine-tagged (His-Tag) protein recognition and manipulation. b) System TiO_2/(PSS/NTA/His-Tag)$_4$/PSS after irradiation through a photomask allows local delivery/desorption of proteins. c) Reversible and multicycle activity is detected from real-time evolution of the activity of H^+-ions over the TiO_2/PSS/NTA surface. "ON" is a time point of irradiation switched on and "OFF" – switched off. d) Microfluidic chamber to study His-Tag protein light induced modulation/desorption on the TiO_2/LbL surface. e) In situ QCM frequency change during the adsorption of (1) PSS, (2) NTA, (3) His-Tag protein; $h\nu$ corresponds to the moment of short term (1 s) irradiation and results in protein desorption. Cycles of adsorption, light induced desorption are repeated several times. Adapted with permission.[369]

as 180 µm s^{-1}. The effective transfer of chemical energy into translational motion has allowed these tubes to perform useful tasks such as transport of cargo.

Janus photocatalytic micromotors hold considerable promise for diverse practical applications. A highly efficient light-driven photocatalytic TiO_2–Au Janus micromotor with wireless steering and velocity control is shown in Figure 38c.[429] Unlike chemically propelled micromotors, which commonly require the addition of surfactants or toxic chemical fuels, the fuel-free Janus micromotor (diameter ≈1.0 µm) can be powered in pure water under an extremely low ultraviolet light intensity (2.5×10^{-3} W cm^{-2}), and with 40×10^{-3} W cm^{-2} they can reach a high speed of 25 body length s^{-1}, which is comparable to common Pt-based chemically induced self-electrophoretic Janus micromotors.

The concept of a surface combustion microengine is demonstrated on a microcantilever covered with a thin TiO_2 layer (Figure 38d,e).[428] Irradiation of this microengine produces controlled bending of the microcantilever as a result of differential stress produced by photocatalytic oxidation of organic molecules on the TiO_2 coating. Surface combustion based microengines would require less maintenance in minimally controlled field environment and could be potentially used in construction of miniature movable machines and conversion of solar energy to mechanical work, when extended to a large array of microcantilevers.

There is much attention nowadays to the development of light driven,[430] autonomous[431] soft robots (Figure 38f), and we suggest photocatalytic fuel production as an on-board fuel supply. Gas that may be generated from the fuel photodecomposition inflates fluidic networks downstream of the reaction sites, resulting in actuation.

10. Conclusion

After Kroemer's statement in his Nobel lecture in 2000,[1] today we can even more strongly note that the interface is still the device.[432] The increase in complexity is attended by the involvement of interfacial chemistry, different chemistry environments, liquids, and interfaces under operation in noninert ambient conditions. In this review, we have highlighted a variety of in situ spectroscopy routes to analyze the formation of surfaces and buried interfaces on the atomic scale in complex chemical surroundings during growth and preparation as well as during operation. On the example of several material systems such as III/V semiconductors, oxides, silicon, germanium, organic molecules, biomaterials, and hybrids of these materials as well as various examples of application with photoinduced reactions, we have shown that there are opportunities to scrutinize nucleation of materials, interface formation, growth, as well as more complex interfacial reactions.

Starting from clear and well-defined epitaxial interfaces in vapor phase ambient, such as InP(100) and GaP(100) surfaces, which are on the one hand highly relevant for record-breaking solar energy conversion and which on the other hand act as types of "drosophila" of atomic scale in situ control, we afterward illustrate their modification and chemical functionalization via different adsorbants, heterocontacts, and solid–liquid interfaces, involving industrially relevant and optoelectronic generic technology developments such as the growth of III/V compounds on silicon. These formation scenarios have been thoroughly studied by optical in situ spectroscopy (i.e., RAS) and benchmarked by a broad spectrum of relevance to the interfacial science. High-efficiency water splitting devices were

ADVANCED
SCIENCE NEWS
www.advancedsciencenews.com

ADVANCED
MATERIALS
INTERFACES
www.advmatinterfaces.de
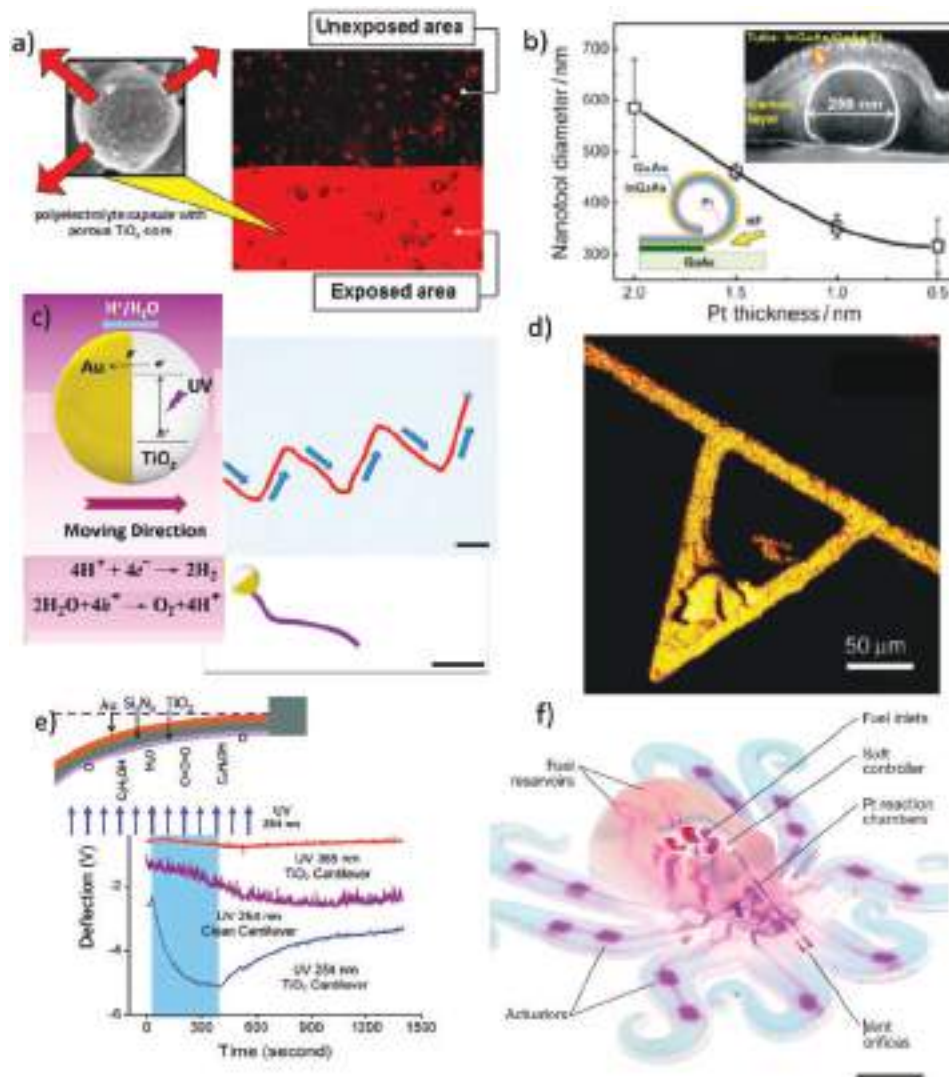
Figure 38. a) Titania-based capsules and LbL organized polyelectrolyte shell become permeable under irradiation and can locally release active components from the surface, which could regulate cell activity on the surface. Adapted with permission.[421] Copyright 2009, Royal Society of Chemistry. b) Scalability of the diameter of rolled-up nanotubes consisting of hybrid heteroepitaxial catalytic InGaAs (3 nm)/GaAs (3 nm)/Pt thin films. Bottom inset shows the rolled-up fabrication process by selective under-etching of the sacrificial AlAs (20 nm) layer. Top inset depicts a SEM image containing a focused ion beam cut of an individual tube composed of InGaAs/GaAs/Pt (0.5 nm). Adapted with permission.[444] Copyright 2012, American Chemical Society. c) Schematic of catalytic TiO_2–Au Janus micromotors powered by UV light in water and time-lapse images showing the stimuli guided propulsion of an Au–Ni–TiO_2 micromotor under 40×10^{-3} W cm^{-2} UV light. Scale bar, 10 µm. Adapted with permission.[429] Copyright 2016, American Chemical Society. d) The elemental distribution images of a TiO_2 modified microcantilever collected using secondary ion signals of Ti$^+$; and e) bending of a TiO_2 modified microcantilever exposed to UV radiations at 365 and 254 nm, and the bending of an unmodified microcantilever exposed to UV radiation at 254 nm (inset shows scheme for ethanol-fueled photocatalytic microengines based on TiO_2 modified AFM microcantilevers). Adapted with permission.[428] Copyright 2005, American Chemical Society. f) Fuel reaction is very prospective in semiconductor surface for fully soft, autonomous robot assembly, shown as example in image. Scale bar, 2 mm. Adapted with permission.[431] Copyright 2016, Nature Publishing Group.

achieved by an in situ controlled interface functionalization of well characterized surfaces of epitaxial semiconductor heterostructures. As a next step of surface functionalization, photochemical reactions at hybrid interfaces have been monitored in situ such as the detection of ROS, measured with specific ROS scavenging agents. Proton photogeneration has been studied with scanning probe in situ techniques such as scanning vibrating electrode technique, imaging mass spectrometry, and scanning ion-selective electrode.

However, there is still a huge challenge and a large and deep gap to be closed in the near and far future between the atomic scale understanding of model surfaces and interfaces, such as epitaxially prepared (100) surfaces, on the one hand and transient interfacial reactions under operation, such as in electrochemistry or ultrafast dynamics, on the other hand. There are many open tasks and questions that can be addressed by routes shown in this review. In photoelectrochemistry, solid–liquid interfaces are huge challenges with regard to efficient functionality,

stability/corrosion, and catalysis. In situ spectroscopy, such as near-ambient pressure photoelectron spectroscopies or RAS, will largely contribute to a microscopic understanding of the solid–liquid interface formation and functionalization. The key will be a detailed understanding of model systems and subsequent gradual lifting of the model character toward realistic application scenarios. In bioapplications, critical and conflicting requirements have to be addressed, such as having a sufficient defect concentration in the semiconductor to increase visible light absorption without limiting the carrier mobility too much via defect sites deep in the bandgap. For spatial separation of oxidation versus reduction, the carrier mobility should be very different for electrons and holes and on the organic side of biosensing, there is a competition between sensitivity, buffering, and stability. Also here, we believe that device design for such demanding applications strongly benefits from a detailed understanding of complex interfacial reactions, which in turn is best achieved by understanding the relevant processes starting from relatively easy model interfaces with increasing complexity of the final device structure. Thereby, the more complex the interface formation gets, the more important in situ characterization and in situ control over the involved processing steps become. Efforts for in situ characterization must be increased, in particular, combining spectroscopic and scanning probe techniques.

Conflict of Interest

The authors declare no conflict of interest.

[1] H. Kroemer, *Rev. Mod. Phys.* **2001**, *73*, 783.
[2] D. Aspnes, *Surf. Sci.* **1994**, *307*, 1017.
[3] J. F. McGilp, *Prog. Surf. Sci.* **1995**, *49*, 1.
[4] J.-T. Zettler, *Prog. Cryst. Growth Charact.* **1997**, *35*, 27.
[5] Z. Sobiesierski, D. I. Westwood, C. C. Matthai, *J. Phys.: Condens. Matter* **1998**, *10*, 1.
[6] W. Richter, *Appl. Phys. A: Mater. Sci. Process.* **2002**, *75*, 129.
[7] I. P. Herman, *Annu. Rev. Phys. Chem.* **2003**, *54*, 277.
[8] P. Weightman, D. S. Martin, R. J. Cole, T. Farrell, *Rep. Prog. Phys.* **2005**, *68*, 1251.
[9] D. V. Esposito, J. B. Baxter, J. John, N. S. Lewis, T. P. Moffat, T. Ogitsu, G. D. O'Neil, T. A. Pham, A. A. Talin, J. M. Velazquez, B. C. Wood, *Energy Environ. Sci.* **2015**, *8*, 2863.
[10] Q. Zhang, H. Li, L. Gan, Y. Ma, D. Golberg, T. Zhai, *Chem. Soc. Rev.* **2016**, *45*, 2694.
[11] M. Pristovsek, *Habilitation Thesis*, Technische Universität Berlin, Germany **2012**.
[12] M. A. Green, K. Emery, Y. Hishikawa, W. Warta, E. D. Dunlop, *Prog. Photovoltaics* **2016**, *24*, 905.
[13] T. Tibbits, P. Beutel, M. Grave, C. Karcher, E. Oliva, G. Siefer, A. Wekkeli, M. Schachtner, F. Dimroth, A. Bett, R. Krause, M. Piccin, N. Blanc, M. Muñoz-Rico, C. Arena, E. Guiot, C. Charles-Alfred, C. Drazek, F. Janin, L. Farrugia, B. Hoarau, J. Wasselin, A. Tauzin, T. Signamarcheix, T. Hannappel, K. Schwarzburg, A. Dobrich, in *Proceedings of the 29th European Photovoltaic Solar Energy Conference and Exhibition*, Amsterdam, The Netherlands **2014**, pp. 1975–1978.
[14] M. M. May, H.-J. Lewerenz, D. Lackner, F. Dimroth, T. Hannappel, *Nat. Commun.* **2015**, *6*, 8286.
[15] H. M. Manasevit, W. I. Simpson, *J. Electrochem. Soc.* **1969**, *116*, 1725.
[16] T. Hannappel, M. M. May, H.-J. Lewerenz, in *Photoelectrochemical Water Splitting, Materials, Processes and Architectures* (Eds: H.-J. Lewerenz, L. Peter), The Royal Society of Chemistry, Cambridge **2013**, pp. 223–265.
[17] O. Khaselev, J. A. Turner, *Science* **1998**, *280*, 425.
[18] S. Hu, C. Xiang, S. Haussener, A. D. Berger, N. S. Lewis, *Energy Environ. Sci.* **2013**, *6*, 2984.
[19] H. Döscher, O. Supplie, M. M. May, P. Sippel, C. Heine, A. G. Muñoz, R. Eichberger, H.-J. Lewerenz, T. Hannappel, *ChemPhysChem* **2012**, *13*, 2899.
[20] O. Supplie, M. M. May, H. Stange, C. Höhn, H.-J. Lewerenz, T. Hannappel, *J. Appl. Phys.* **2014**, *115*, 113509.
[21] U. Seidel, H.-J. Schimper, Z. Kollonitsch, K. Möller, K. Schwarzburg, T. Hannappel, *J. Cryst. Growth* **2007**, *298*, 777.
[22] A. Dobrich, *Dissertation thesis*, Freie Universität Berlin, Germany **2014**.
[23] D. E. Aspnes, A. A. Studna, *Phys. Rev. Lett.* **1985**, *54*, 1956.
[24] T. Hannappel, S. Visbeck, L. Töben, F. Willig, *Rev. Sci. Instrum.* **2004**, *75*, 1297.
[25] A. Heller, *Science* **1984**, *223*, 1141.
[26] A. G. Muñoz, C. Heine, M. Lublow, H. W. Klemm, N. Szabó, T. Hannappel, H.-J. Lewerenz, *ECS J. Solid State Sci. Technol.* **2013**, *2*, Q51.
[27] U. Seidel, B. Sagol, N. Szabó, K. Schwarzburg, T. Hannappel, *Thin Solid Films* **2008**, *516*, 6723.
[28] B. E. Sagol, U. Seidel, N. Szabó, K. Schwarzburg, T. Hannappel, *CHIMIA* **2007**, *61*, 775.
[29] N. Szabó, B. E. Sagol, U. Seidel, K. Schwarzburg, T. Hannappel, *Phys. Status Solidi RRL* **2008**, *2*, 254.
[30] F. Dimroth, M. Grave, P. Beutel, U. Fiedeler, C. Karcher, T. N. D. Tibbits, E. Oliva, G. Siefer, M. Schachtner, A. Wekkeli, A. W. Bett, R. Krause, M. Piccin, N. Blanc, C. Drazek, E. Guiot, B. Ghyselen, T. Salvetat, A. Tauzin, T. Signamarcheix, A. Dobrich, T. Hannappel, K. Schwarzburg, *Prog. Photovolt: Res. Appl.* **2014**, *22*, 277.
[31] F. Dimroth, T. N. D. Tibbits, M. Niemeyer, F. Predan, P. Beutel, C. Karcher, E. Oliva, G. Siefer, D. Lackner, P. Fuß-Kailuweit,

**ADVANCED
SCIENCE NEWS**

www.advancedsciencenews.com

**ADVANCED
MATERIALS
INTERFACES**

www.advmatinterfaces.de

A. W. Bett, R. Krause, C. Drazek, E. Guiot, J. Wasselin, A. Tauzin, T. Signamarcheix, *IEEE J. Photovoltaics* **2016**, *6*, 343.

[32] W. G. Schmidt, P. H. Hahn, F. Bechstedt, N. Esser, P. Vogt, A. Wange, W. Richter, *Phys. Rev. Lett.* **2003**, *90*, 126101.

[33] W. G. Schmidt, F. Bechstedt, N. Esser, M. Pristovsek, C. Schultz, W. Richter, *Phys. Rev. B* **1998**, *57*, 14596.

[34] D. E. Aspnes, A. A. Studna, *Phys. Rev. B* **1983**, *27*, 985.

[35] M. Zorn, T. Trepk, J.-T. Zettler, B. Junno, C. Meyne, K. Knorr, T. Wethkamp, M. Klein, M. Miller, W. Richter, L. Samuelson, *Appl. Phys. A: Mater. Sci. Process.* **1997**, *65*, 333.

[36] W. G. Schmidt, N. Esser, A. M. Frisch, P. Vogt, J. Bernholc, F. Bechstedt, M. Zorn, T. Hannappel, S. Visbeck, F. Willig, W. Richter, *Phys. Rev. B* **2000**, *61*, R16335.

[37] W. G. Schmidt, J. Bernholc, F. Bechstedt, *Appl. Surf. Sci.* **2000**, *166*, 179.

[38] T. Hannappel, L. Töben, S. Visbeck, H.-J. Crawack, C. Pettenkofer, F. Willig, *Surf. Sci.* **2000**, *470*, L1.

[39] N. Esser, W. G. Schmidt, C. Cobet, K. Fleischer, A. I. Shkrebtii, B. O. Fimland, W. Richter, *J. Vac. Sci. Technol., B: Microelectron. Nanometer Struct.–Process., Meas., Phenom.* **2001**, *19*, 1756.

[40] S. Visbeck, T. Hannappel, M. Zorn, J.-T. Zettler, F. Willig, *Phys. Rev. B* **2001**, *63*, 245303.

[41] J. Luo, J. Geisz, J. Olson, M.-C. Su, *J. Cryst. Growth* **1997**, *174*, 558.

[42] T. Hannappel, S. Visbeck, K. Knorr, J. Mahrt, M. Zorn, F. Willig, *Appl. Phys. A: Mater. Sci. Process.* **1999**, *69*, 427.

[43] K. B. Ozanyan, P. J. Parbrook, M. Hopkinson, C. R. Whitehouse, Z. Sobiesierski, D. I. Westwood, *J. Appl. Phys.* **1997**, *82*, 474.

[44] P. Vogt, T. Hannappel, S. Visbeck, K. Knorr, N. Esser, W. Richter, *Phys. Rev. B* **1999**, *60*, R5117.

[45] P. Kleinschmidt, H. Döscher, P. Vogt, T. Hannappel, *Phys. Rev. B* **2011**, *83*, 155316.

[46] L. Li, B.-K. Han, Q. Fu, R. F. Hicks, *Phys. Rev. Lett.* **1999**, *82*, 1879.

[47] T. Letzig, H.-J. Schimper, T. Hannappel, F. Willig, *Phys. Rev. B* **2005**, *71*, 033308.

[48] T. Hannappel, S. Visbeck, M. Zorn, J.-T. Zettler, F. Willig, *J. Cryst. Growth* **2000**, *221*, 124.

[49] M. M. May, O. Supplie, C. Höhn, W.-D. Zabka, H.-J. Lewerenz, R. van de Krol, T. Hannappel, *Proc. SPIE* **2013**, *8822*, 88220M.

[50] M. M. May, H.-J. Lewerenz, T. Hannappel, *J. Phys. Chem. C* **2014**, *118*, 19032 (https://doi.org/10.1021/jp502955m).

[51] H. Döscher, K. Möller, T. Hannappel, *J. Cryst. Growth* **2011**, *318*, 372.

[52] P. Lautenschlager, P. B. Allen, M. Cardona, *Phys. Rev. B* **1985**, *31*, 2163.

[53] A. Frisch, P. Vogt, S. Visbeck, T. Hannappel, F. Willig, W. Braun, W. Richter, J. Bernholc, W. Schmidt, N. Esser, *Appl. Surf. Sci.* **2000**, *166*, 224.

[54] L. Töben, T. Hannappel, R. Eichberger, K. Möller, L. Gundlach, R. Ernstorfer, F. Willig, *J. Cryst. Growth* **2003**, *248*, 206.

[55] L. Töben, L. Gundlach, R. Ernstorfer, R. Eichberger, T. Hannappel, F. Willig, A. Zeiser, J. Förstner, A. Knorr, P. H. Hahn, W. G. Schmidt, *Phys. Rev. Lett.* **2005**, *94*, 067601.

[56] L. Töben, L. Gundlach, T. Hannappel, R. Ernstorfer, R. Eichberger, F. Willig, *Appl. Phys. A: Mater. Sci. Process.* **2004**, *78*, 239.

[57] P. Sippel, J. M. Szarko, T. Hannappel, R. Eichberger, *Phys. Rev. B* **2015**, *91*, 115312.

[58] M. Arens, P. Kurpas, P. Ressel, M. Weyers, *Thin Solid Films* **1998**, *313–314*, 609.

[59] B. Kaiser, D. Fertig, J. Ziegler, J. Klett, S. Hoch, W. Jaegermann, *ChemPhysChem* **2012**, *13*, 3053.

[60] M. Feifel, T. Rachow, J. Benick, J. Ohlmann, S. Janz, M. Hermle, F. Dimroth, D. Lackner, *IEEE J. Photovoltaics* **2016**, *6*, 384.

[61] J. Geisz, J. Olson, D. Friedman, K. Jones, R. Reedy, M. Romero, *Proceedings of the 31st IEEE Photovoltaic Specialists Conference*, Lake Buena Vista, FL, USA **2005**, *61*, 695.

[62] N. Esser, W. Schmidt, J. Bernholc, A. Frisch, P. Vogt, M. Zorn, M. Pristovsek, W. Richter, F. Bechstedt, T. Hannappel, S. Visbeck, *J. Vac. Sci. Technol., B: Nanotechnol. Microelectron.: Mater., Process., Meas., Phenom.* **1999**, *17*, 1691.

[63] L. Töben, T. Hannappel, K. Möller, H. Crawack, C. Pettenkofer, F. Willig, *Surf. Sci.* **2001**, *494*, L755.

[64] A. M. Frisch, W. G. Schmidt, J. Bernholc, M. Pristovsek, N. Esser, W. Richter, *Phys. Rev. B* **1999**, *60*, 2488.

[65] P. Sippel, O. Supplie, M. M. May, R. Eichberger, T. Hannappel, *Phys. Rev. B* **2014**, *89*, 165312.

[66] P. H. Hahn, W. G. Schmidt, F. Bechstedt, O. Pulci, R. del Sole, *Phys. Rev. B* **2003**, *68*, 033311.

[67] N. Kadotani, M. Shimomura, Y. Fukuda, *Phys. Rev. B* **2004**, *70*, 165323.

[68] H. Döscher, T. Hannappel, *J. Appl. Phys.* **2010**, *107*, 123523.

[69] B. M. Kayes, H. Nie, R. Twist, S. G. Spruytte, F. Reinhardt, I. C. Kizilyalli, G. S. Higashi, *Proceedings of the 37th IEEE Photovoltaic Specialists Conference*, Seattle, WA, USA **2011**, *37*, 000004.

[70] L. S. Mattos, S. R. Scully, M. Syfu, E. Olson, L. Yang, C. Ling, B. M. Kayes, G. He, *Proceedings of the 38th IEEE Photovoltaic Specialists Conference,* Austin, TX, USA **2012**, *38*, 003187.

[71] T. Takamoto, M. Kaneiwa, M. Imaizumi, M. Yamaguchi, *Prog. Photovoltaics* **2005**, *13*, 495.

[72] J. M. Olson, S. R. Kurtz, A. E. Kibbler, P. Faine, *Appl. Phys. Lett.* **1990**, *56*, 623.

[73] A. Luque, *J. Appl. Phys.* **2011**, *110*, 031301.

[74] C. Fetzer, B. Jun, K. Edmondson, S. Khemthong, K. Rouhani, R. Cravens, R. Bardfield, M. Gillanders, *Proceedings of the 33rd IEEE Photovoltaic Specialists Conference*, San Diego, CA, USA **2008**, *33*, 1.

[75] W. Guter, J. Schöne, S. P. Philipps, M. Steiner, G. Siefer, A. Wekkeli, E. Welser, E. Oliva, A. W. Bett, F. Dimroth, *Appl. Phys. Lett.* **2009**, *94*, 223504.

[76] R. M. France, F. Dimroth, T. J. Grassman, R. R. King, *MRS Bull.* **2016**, *41*, 202.

[77] D. E. Aspnes, E. Colas, A. A. Studna, R. Bhat, M. A. Koza, V. G. Keramidas, *Phys. Rev. Lett.* **1988**, *61*, 2782.

[78] J. P. Harbison, D. E. Aspnes, A. A. Studna, L. T. Florez, M. K. Kelly, *Appl. Phys. Lett.* **1988**, *52*, 2046.

[79] D. Aspnes, *Mater. Sci. Eng., B* **1995**, *30*, 109.

[80] A. Balzarotti, M. Fanfoni, F. Patella, F. Arciprete, E. Placidi, G. Onida, R. D. Sole, *Surf. Sci. Lett.* **2003**, *524*, L71.

[81] T. Makimoto, Y. Yamauchi, N. Kobayashi, Y. Horikoshi, *Jpn. J. Appl. Phys.* **1990**, *29*, L645.

[82] I. Kamiya, D. E. Aspnes, H. Tanaka, L. T. Florez, J. P. Harbison, R. Bhat, *Phys. Rev. Lett.* **1992**, *68*, 627.

[83] D. E. Aspnes, I. Kamiya, H. Tanaka, R. Bhat, *J. Vac. Sci. Technol., B: Microelectron. Nanometer Struct.–Process., Meas., Phenom.* **1992**, *10*, 1725.

[84] I. Kamiya, H. Tanaka, D. E. Aspnes, M. Koza, R. Bhat, *Appl. Phys. Lett.* **1993**, *63*, 3206.

[85] K. Ploska, J.-T. Zettler, W. Richter, J. Jönsson, F. Reinhardt, J. Rumberg, M. Pristovsek, M. Zorn, D. Westwood, R. Williams, *J. Cryst. Growth* **1994**, *145*, 44.

[86] K. Deppert, J. Jönsson, L. Samuelson, *Thin Solid Films* **1993**, *224*, 133.

[87] M. Deura, M. Sugiyama, T. Nakano, Y. Nakano, Y. Shimogaki, *Jpn. J. Appl. Phys.* **2007**, *46*, 6519.

[88] J. Creighton, K. Baucom, *Surf. Sci.* **1998**, *409*, 372.

[89] S.-H. Lee, W. Moritz, M. Scheffler, *Phys. Rev. Lett.* **2000**, *85*, 3890.

[90] W. G. Schmidt, S. Mirbt, F. Bechstedt, *Phys. Rev. B* **2000**, *62*, 8087.

[91] W. Schmidt, F. Bechstedt, K. Fleischer, C. Cobet, N. Esser, W. Richter, J. Bernholc, G. Onida, *Phys. Status Solidi A* **2001**, *188*, 1401.

[92] I. Kamiya, D. E. Aspnes, L. T. Florez, J. P. Harbison, *Phys. Rev. B* **1992**, *46*, 15894.

[93] M. Wassermeier, I. Kamiya, D. E. Aspnes, L. T. Florez, J. P. Harbison, P. M. Petroff, *J. Vac. Sci. Technol., B: Microelectron. Nanometer Struct.–Process., Meas., Phenom.* **1991**, *9*, 2263.

[94] D. E. Aspnes, Y. C. Chang, A. A. Studna, L. T. Florez, H. H. Farrell, J. P. Harbison, *Phys. Rev. Lett.* **1990**, *64*, 192.

[95] U. Resch, S. Scholz, U. Rossow, A. Müller, W. Richter, A. Förster, *Appl. Surf. Sci.* **1993**, *63*, 106.

[96] M. J. Begarney, L. Li, C. H. Li, D. C. Law, Q. Fu, R. F. Hicks, *Phys. Rev. B* **2000**, *62*, 8092.

[97] S. J. Morris, J. M. Bass, C. C. Matthai, *Phys. Rev. B* **1995**, *52*, 16739.

[98] A. I. Shkrebtii, N. Esser, W. Richter, W. G. Schmidt, F. Bechstedt, B. O. Fimland, A. Kley, R. del Sole, *Phys. Rev. Lett.* **1998**, *81*, 721.

[99] L. F. Lastras-Martinez, D. Rönnow, P. V. Santos, M. Cardona, K. Eberl, *Phys. Rev. B* **2001**, *64*, 245303.

[100] L. F. Lastras-Martinez, J. M. Flores-Camacho, R. E. Balderas-Navarro, M. Chavira-Rodrguez, A. Lastras-Martinez, M. Cardona, *Phys. Rev. B* **2007**, *75*, 235315.

[101] W. G. Schmidt, F. Bechstedt, W. Lu, J. Bernholc, *Phys. Rev. B* **2002**, *66*, 085334.

[102] F. Arciprete, C. Goletti, E. Placidi, C. Hogan, P. Chiaradia, M. Fanfoni, F. Patella, A. Balzarotti, *Phys. Rev. B* **2004**, *69*, 081308.

[103] C. Goletti, V. Emiliani, S. Schintke, A. M. Frisch, N. Esser, B. O. Fimland, *Phys. Status Solidi B* **2005**, *242*, 2664.

[104] D. Paget, C. Hogan, V. L. Berkovits, O. E. Tereshchenko, *Phys. Rev. B* **2003**, *67*, 245313.

[105] F. Arciprete, C. Goletti, E. Placidi, P. Chiaradia, M. Fanfoni, F. Patella, C. Hogan, A. Balzarotti, *Phys. Rev. B* **2003**, *68*, 125328.

[106] R. Onitsuka, M. Sugiyama, Y. Nakano, *J. Cryst. Growth* **2010**, *312*, 1343.

[107] P. Kurpas, J. Jönsson, W. Richter, D. Gutsche, M. Pristovsek, M. Zorn, *J. Cryst. Growth* **1994**, *145*, 36.

[108] S. E. Acosta-Ortiz, A. Lastras-Martínez, *Phys. Rev. B* **1989**, *40*, 1426.

[109] Z. Sobiesierski, D. I. Westwood, M. Elliott, *Phys. Rev. B* **1997**, *56*, 15277.

[110] H. Tanaka, E. Colas, I. Kamiya, D. E. Aspnes, R. Bhat, *Appl. Phys. Lett.* **1991**, *59*, 3443.

[111] M. Pristovsek, S. Tsukamoto, N. Koguchi, B. Han, K. Haberland, J.-T. Zettler, W. Richter, M. Zorn, M. Weyers, *Phys. Status Solidi A* **2001**, *188*, 1423.

[112] M. Pristovsek, S. Tsukamoto, B. Han, J.-T. Zettler, W. Richter, *J. Cryst. Growth* **2003**, *248*, 254.

[113] M. Pristovsek, B. Han, J.-T. Zettler, W. Richter, *J. Cryst. Growth* **2000**, *221*, 149.

[114] M. Wassermeier, J. Behrend, J.-T. Zettler, K. Stahrenberg, K. Ploog, *Appl. Surf. Sci.* **1996**, *107*, 48.

[115] Z. A. Ibrahim, A. I. Shkrebtii, M. J. G. Lee, K. Vynck, T. Teatro, W. Richter, T. Trepk, T. Zettler, *Phys. Rev. B* **2008**, *77*, 125218.

[116] B. Rähmer, M. Pristovsek, M. Breusing, R. Kremzow, W. Richter, *Appl. Phys. Lett.* **2006**, *89*, 063108.

[117] R. Kremzow, M. Pristovsek, M. Kneissl, *J. Cryst. Growth* **2008**, *310*, 4751.

[118] M. Pristovsek, R. Kremzow, M. Kneissl, *Jpn. J. Appl. Phys.* **2013**, *52*, 041201.

[119] R. R. King, D. Bhusari, D. Larrabee, X.-Q. Liu, E. Rehder, K. Edmondson, H. Cotal, R. K. Jones, J. H. Ermer, C. M. Fetzer, D. C. Law, N. H. Karam, *Prog. Photovoltaics* **2012**, *20*, 801.

[120] J. Gupta, S. Watkins, R. Arés, G. Soerensen, *J. Cryst. Growth* **1998**, *195*, 205.

[121] M. Deura, Y. Shimogaki, Y. Nakano, M. Sugiyama, *J. Cryst. Growth* **2008**, *310*, 4736.

[122] W. Richter, J.-T. Zettler, *Appl. Surf. Sci.* **1996**, *100*, 465.

[123] P. Wolfram, E. Steimetz, W. Ebert, B. Henninger, J.-T. Zettler, *J. Cryst. Growth* **2003**, *248*, 240.

[124] N. A. Kalyuzhnyy, V. V. Evstropov, V. M. Lantratov, S. A. Mintairov, M. A. Mintairov, A. S. Gudovskikh, A. Luque, V. M. Andreev, *Int. J. Photoenergy* **2014**, *2014*, 836284.

[125] M. Zorn, P. Kurpas, A. I. Shkrebtii, B. Junno, A. Bhattacharya, K. Knorr, M. Weyers, L. Samuelson, J. T. Zettler, W. Richter, *Phys. Rev. B* **1999**, *60*, 8185.

[126] C. Krahmer, M. Philippens, M. Schubert, K. Streubel, *J. Cryst. Growth* **2007**, *298*, 18.

[127] M. Zorn, J. Jönsson, A. Krost, W. Richter, J.-T. Zettler, K. Ploska, F. Reinhardt, *J. Cryst. Growth* **1994**, *145*, 53.

[128] S. M. Scholz, A. B. Müller, W. Richter, D. R. T. Zahn, D. I. Westwood, D. A. Woolf, R. H. Williams, *J. Vac. Sci. Technol., B: Microelectron. Nanometer Struct.–Process., Meas., Phenom.* **1992**, *10*, 1710.

[129] A. Kussmaul, S. Vernon, P. C. Colter, R. Sudharsanan, A. Mastrovito, K. J. Linden, N. H. Karam, N. H. Karam, S. C. Warnick, M. A. Dahleh, *J. Electron. Mater.* **1997**, *26*, 1145.

[130] P. Kurpas, A. Oster, M. Weyers, A. Rumberg, K. Knorr, W. Richter, *J. Electron. Mater.* **1997**, *26*, 1159.

[131] F. Bugge, M. Zorn, U. Zeimer, A. Pietrzak, G. Erbert, M. Weyers, *J. Cryst. Growth* **2009**, *311*, 1065.

[132] M. Zorn, M. Weyers, *J. Cryst. Growth* **2005**, *276*, 29.

[133] T. Trepk, M. Zorn, J.-T. Zettler, M. Klein, W. Richter, *Thin Solid Films* **1998**, *313–314*, 496.

[134] J.-S. Lee, Y. Masumoto, *J. Cryst. Growth* **2000**, *221*, 111.

[135] K. Haberland, A. Kaluza, M. Zorn, M. Pristovsek, H. Hardtdegen, M. Weyers, J.-T. Zettler, W. Richter, *J. Cryst. Growth* **2002**, *240*, 87.

[136] S. J. Morris, J.-T. Zettler, K. C. Rose, D. I. Westwood, D. A. Woolf, R. H. Williams, W. Richter, *J. Appl. Phys.* **1995**, *77*, 3115.

[137] K. Haberland, A. Bhattacharya, M. Zorn, M. Weyers, J. T. Zettler, W. Richter, *J. Electron. Mater.* **2000**, *29*, 468.

[138] P. Wolfram, E. Steimetz, W. Ebert, N. Grote, J.-T. Zettler, *J. Cryst. Growth* **2004**, *272*, 118.

[139] M. Zorn, J.-T. Zettler, *Phys. Status Solidi B* **2005**, *242*, 2587.

[140] M. Zorn, J.-T. Zettler, A. Knauer, M. Weyers, *J. Cryst. Growth* **2006**, *287*, 637.

[141] R. Ehlert, F. Poser, N. Esser, P. Vogt, W. Richter, *Phys. Status Solidi B* **2005**, *242*, 2575.

[142] O. Reentilä, M. Mattila, M. Sopanen, H. Lipsanen, *J. Appl. Phys.* **2007**, *101*, 033533.

[143] T. Tsuchiya, T. Taniwatari, K. Uomi, T. Kawano, Y. Ono, *Jpn. J. Appl. Phys.* **1993**, *32*, 4652.

[144] M. Heurlin, N. Anttu, C. Camus, L. Samuelson, M. T. Borgström, *Nano Lett.* **2015**, *15*, 3597.

[145] C. Prall, C. Kaspari, F. Brunner, K. Haberland, M. Weyers, D. Rueter, *J. Cryst. Growth* **2015**, *415*, 1.

[146] C. Prall, M. Ruebesam, C. Weber, M. Reufer, D. Rueter, *J. Cryst. Growth* **2014**, *397*, 24.

[147] J.-S. Lee, S. Sugou, Y. Masumoto, *J. Appl. Phys.* **2000**, *88*, 196.

[148] F. Dimroth, T. Roesener, S. Essig, C. Weuffen, A. Wekkeli, E. Oliva, G. Siefer, K. Volz, T. Hannappel, D. Häussler, W. Jäger, A. W. Bett, *IEEE J. Photovoltaics* **2014**, *4*, 620.

[149] T. Roesener, H. Döscher, A. Beyer, S. Brückner, V. Klinger, A. Wekkeli, P. Kleinschmidt, C. Jurecka, J. Ohlmann, K. Volz, W. Stolz, T. Hannappel, A. W. Bett, F. Dimroth, *Proceedings of the 25th European Photovoltaic Solar Energy Conference and Exhibition*, Valencia, Spain 2010, pp. 964–968.

[150] T. J. Grassman, D. J. Chmielewski, S. D. Carnevale, J. A. Carlin, S. A. Ringel, *IEEE J. Photovoltaics* **2016**, *6*, 326.

[151] S. Almosni, C. Robert, T. Nguyen Thanh, C. Cornet, A. Létoublon, T. Quinci, C. Levallois, M. Perrin, J. Kuyyalil, L. Pedesseau, A. Balocchi, P. Barate, J. Even, J. M. Jancu, N. Bertru, X. Marie, O. Durand, A. Le Corre, *J. Appl. Phys.* **2013**, *113*, 123509.

[152] A. Rolland, L. Pedesseau, J. Even, S. Almosni, C. Robert, C. Cornet, J. M. Jancu, J. Benhlal, O. Durand, A. L. Corre, P. Rale, L. Lombez, J.-F. Guillemoles, E. Tea, S. Laribi, *Opt. Quantum Electron.* **2014**, *46*, 1397.

[153] S. R. Kurtz, P. Faine, J. M. Olson, *J. Appl. Phys.* **1990**, *68*, 1890.

[154] J. A. del Alamo, *Nature* **2011**, *479*, 317.

[155] H. Kroemer, *J. Cryst. Growth* **1987**, *81*, 193.

[156] S. F. Fang, K. Adomi, S. Iyer, H. Morkoc, H. Zabel, C. Choi, N. Otsuka, *J. Appl. Phys.* **1990**, *68*, R31.

[157] D. J. Chadi, *Phys. Rev. Lett.* **1987**, *59*, 1691.

[158] R. E. Schlier, H. E. Farnsworth, *J. Chem. Phys.* **1959**, *30*, 917.

[159] R. M. Tromp, R. J. Hamers, J. E. Demuth, *Phys. Rev. Lett.* **1985**, *55*, 1303.

[160] R. A. Wolkow, *Phys. Rev. Lett.* **1992**, *68*, 2636.

[161] D. E. Aspnes, J. Ihm, *Phys. Rev. Lett.* **1986**, *57*, 3054.

[162] Y. J. Chabal, K. Raghavachari, *Phys. Rev. Lett.* **1984**, *53*, 282.

[163] T. W. Poon, S. Yip, P. S. Ho, F. F. Abraham, *Phys. Rev. Lett.* **1990**, *65*, 2161.

[164] B. S. Swartzentruber, Y.-W. Mo, M. B. Webb, M. G. Lagally, *J. Vac. Sci. Technol., A* **1989**, *7*, 2901.

[165] P. Bedrossian, T. Klitsner, *Phys. Rev. Lett.* **1992**, *68*, 646.

[166] T. Doi, M. Ichikawa, S. Hosoki, K. Ninomiya, *Phys. Rev. B* **1996**, *53*, 16609.

[167] F. K. Men, W. E. Packard, M. B. Webb, *Phys. Rev. Lett.* **1988**, *61*, 2469.

[168] B. S. Swartzentruber, C. M. Matzke, D. L. Kendall, J. E. Houston, *Surf. Sci.* **1995**, *329*, 83.

[169] J. J. Boland, *Phys. Rev. Lett.* **1990**, *65*, 3325.

[170] J. E. Northrup, *Phys. Rev. B* **1991**, *44*, 1419.

[171] T. Aoyama, K.-I. Goto, T. Yamazaki, T. Ito, *J. Vac. Sci. Technol., A* **1996**, *14*, 2909.

[172] H. Bender, S. Verhaverbeke, M. Caymax, O. Vatel, M. M. Heyns, *J. Appl. Phys.* **1994**, *75*, 1207.

[173] K. W. Kolasinski, W. Nessler, A. de Meijere, E. Hasselbrink, *Phys. Rev. Lett.* **1994**, *72*, 1356.

[174] T. Komeda, Y. Kumagai, *Phys. Rev. B* **1998**, *58*, 1385.

[175] A. Dobrich, P. Kleinschmidt, H. Döscher, T. Hannappel, *J. Vac. Sci. Technol., B: Nanotechnol. Microelectron.: Mater., Process., Meas., Phenom.* **2011**, *29*, 04D114.

[176] H. Döscher, A. Dobrich, S. Brückner, P. Kleinschmidt, T. Hannappel, *Appl. Phys. Lett.* **2010**, *97*, 151905.

[177] Y. J. Chabal, A. L. Harris, K. Raghavachari, J. C. Tully, *Int. J. Mod. Phys. B* **1993**, *7*, 1031.

[178] Y. Chabal, *Surf. Sci.* **1986**, *168*, 594.

[179] S. Brückner, H. Döscher, P. Kleinschmidt, T. Hannappel, *Appl. Phys. Lett.* **2011**, *98*, 211909.

[180] P. Rosenow, R. Tonner, *J. Chem. Phys.* **2016**, *144*, 204706.

[181] S. Brückner, O. Supplie, A. Dobrich, A. Paszuk, P. Kleinschmidt, T. Hannappel, "Control over dimer orientations on vicinal Si(100) surfaces in hydrogen ambient: Kinetics vs. energetics", submitted to physica status solidi (b), **2017**.

[182] S. Jeong, A. Oshiyama, *Phys. Rev. Lett.* **1998**, *81*, 5366.

[183] F. A. Reboredo, S. B. Zhang, A. Zunger, *Phys. Rev. B* **2001**, *63*, 125316.

[184] A. R. Laracuente, L. J. Whitman, *Surf. Sci.* **2003**, *545*, 70.

[185] K. Kitahara, O. Ueda, *Jpn. J. Appl. Phys.* **1994**, *33*, L1571.

[186] J. M. Olson, M. M. Al-Jassim, A. Kibbler, K. M. Jones, *J. Cryst. Growth* **1986**, *77*, 515.

[187] B. Kunert, I. Németh, S. Reinhard, K. Volz, W. Stolz, *Thin Solid Films* **2008**, *517*, 140.

[188] J. A. Appelbaum, G. A. Baraff, D. R. Hamann, *Phys. Rev. B* **1976**, *14*, 588.

[189] K. Hingerl, R. E. Balderas-Navarro, A. Bonanni, P. Tichopadek, W. G. Schmidt, *Appl. Surf. Sci.* **2001**, *175–176*, 769.

[190] W. G. Schmidt, F. Bechstedt, J. Bernholc, *Phys. Rev. B* **2001**, *63*, 045322.

[191] M. Palummo, N. Witkowski, O. Pluchery, R. del Sole, Y. Borensztein, *Phys. Rev. B* **2009**, *79*, 035327.

[192] R. Shioda, J. van der Weide, *Appl. Surf. Sci.* **1998**, *130–132*, 266.

[193] S. Brückner, H. Döscher, P. Kleinschmidt, O. Supplie, A. Dobrich, T. Hannappel, *Phys. Rev. B* **2012**, *86*, 195310.

[194] H. Döscher, S. Brückner, A. Dobrich, C. Höhn, P. Kleinschmidt, T. Hannappel, *J. Cryst. Growth* **2011**, *315*, 10.

[195] Z. Zhang, H. Chen, B. C. Bolding, M. G. Lagally, *Phys. Rev. Lett.* **1993**, *71*, 3677.

[196] S. Brückner, P. Kleinschmidt, O. Supplie, H. Döscher, T. Hannappel, *New J. Phys.* **2013**, *15*, 113049.

[197] B. M. Gallois, T. M. Besmann, M. W. Stott, *J. Am. Ceram. Soc.* **1994**, *77*, 2949.

[198] O. Supplie, S. Brückner, O. Romanyuk, H. Döscher, C. Höhn, M. M. May, P. Kleinschmidt, F. Grosse, T. Hannappel, *Phys. Rev. B* **2014**, *90*, 235301.

[199] H. Döscher, S. Brückner, T. Hannappel, *J. Cryst. Growth* **2011**, *318*, 563.

[200] T. Hannappel, W. E. McMahon, J. M. Olson, *J. Cryst. Growth* **2004**, *272*, 24.

[201] W. E. McMahon, E. L. Warren, A. E. Kibbler, R. M. France, A. G. Norman, R. C. Reedy, J. M. Olson, A. C. Tamboli, P. Stradins, *J. Cryst. Growth* **2016**, *452*, 235.

[202] A. Paszuk, A. Dobrich, C. Koppka, S. Brückner, M. Duda, P. Kleinschmidt, O. Supplie, T. Hannappel, *J. Cryst. Growth* **2017**, *464*, 8.

[203] E. García-Tabarés, D. Martín, I. García, J. F. Leliévre, I. Rey-Stolle, *AIP Conf. Proc.* **2012**, *1477*, 5.

[204] Y. Kohama, K. Uchida, T. Soga, T. Jimbo, M. Umeno, *Appl. Phys. Lett.* **1988**, *53*, 862.

[205] R. D. Bringans, D. Biegelsen, L.-E. Swartz, *Phys. Rev. B* **1991**, *44*, 3054.

[206] L. Kipp, D. Biegelsen, J. Northrup, L.-E. Swartz, R. D. Bringans, *Phys. Rev. Lett.* **1996**, *76*, 2810.

[207] T. Bork, W. McMahon, J. Olson, T. Hannappel, *J. Cryst. Growth* **2007**, *298*, 54.

[208] O. Supplie, M. M. May, P. Kleinschmidt, A. Nägelein, A. Paszuk, S. Brückner, T. Hannappel, *APL Mater.* **2015**, *3*, 126110.

[209] E. L. Warren, A. E. Kibbler, R. M. France, A. G. Norman, P. Stradins, W. E. McMahon, *Appl. Phys. Lett.* **2015**, *107*, 082109.

[210] W. McMahon, I. Batyrev, T. Hannappel, J. Olson, S. Zhang, *Phys. Rev. B* **2006**, *74*, 033304.

[211] H. J. Zandvliet, *Phys. Rep.* **2003**, *388*, 1.

[212] T. Yasuda, L. Mantese, U. Rossow, D. E. Aspnes, *Phys. Rev. Lett.* **1995**, *74*, 3431.

[213] U. Rossow, L. Mantese, D. E. Aspnes, *J. Vac. Sci. Technol., B: Nanotechnol. Microelectron.: Mater., Process., Meas., Phenom.* **2000**, *18*, 2229.

[214] S. Brückel, E. Barrigón, O. Supplie, P. Kleinschmidt, A. Dobrich, C. Löbbel, I. Rey-Stolle, H. Döscher, T. Hannappel, *Phys. Status Solidi RRL* **2012**, *6*, 178.

[215] E. Barrigón, S. Brückner, O. Supplie, P. Kleinschmidt, I. Rey-Stolle, T. Hannappel, *Appl. Phys. Lett.* **2013**, *102*, 111608.

[216] S. Banerjee, J. F. McGilp, C. H. Patterson, *Phys. Status Solidi B* **2015**, *252*, 78.

[217] E. Barrigon, B. Galiana, I. Rey-Stolle, *J. Cryst. Growth* **2011**, *315*, 22.

[218] H. Döscher, T. Hannappel, B. Kunert, A. Beyer, K. Volz, W. Stolz, *Appl. Phys. Lett.* **2008**, *93*, 172110.

[219] W. He, S. L. Lu, J. R. Dong, Y. M. Zhao, X. Y. Ren, K. L. Xiong, B. Li, H. Yang, H. M. Zhu, X. Y. Chen, X. Kong, *Appl. Phys. Lett.* **2010**, *97*, 121909.

[220] K. Volz, A. Beyer, W. Witte, J. Ohlmann, I. Németh, B. Kunert, W. Stolz, *J. Cryst. Growth* **2011**, *315*, 37.

[221] B. Galiana, E. Barrigón, I. Rey-Stolle, V. Corregidor, P. Espinet, C. Algora, E. Alves, *Superlattices Microstruct.* **2009**, *45*, 277.

[222] Y. Li, L. Lazzarini, L. J. Giling, G. Salviati, *J. Appl. Phys.* **1994**, *76*, 57483.

[223] S. M. Ting, E. A. Fitzgerald, *J. Appl. Phys.* **2000**, *87*, 2618.

[224] H. W. Yu, E. Y. Chang, Y. Yamamoto, B. Tillack, W. C. Wang, C. I. Kuo, Y. Y. Wong, H. Q. Nguyen, *Appl. Phys. Lett.* **2011**, *99*, 171908.

[225] B. Galiana, I. Rey-Stolle, I. Beinik, C. Algora, C. Teichert, J. Molina-Aldareguia, P. Tejedor, *Sol. Energy Mater. Sol. Cells* **2011**, *95*, 1949.

[226] W. E. McMahon, J. M. Olson, *Phys. Rev. B* **1999**, *60*, 15999.

[227] W. E. McMahon, J. M. Olson, *Phys. Rev. B* **1999**, *60*, 2480.

[228] S. Gan, L. Li, M. J. Begarney, D. Law, B.-K. Han, R. F. Hicks, *J. Appl. Phys.* **1999**, *85*, 2004.

[229] S. Brückner, O. Supplie, E. Barrigón, J. Luczak, P. Kleinschmidt, I. Rey-Stolle, H. Döscher, T. Hannappel, *Appl. Phys. Lett.* **2012**, *101*, 121602.

[230] E. Barrigón, S. Brückner, O. Supplie, H. Döscher, I. Rey-Stolle, T. Hannappel, *J. Cryst. Growth* **2013**, *370*, 173.

[231] W. McMahon, A. Kibbler, J. Olson, *Surf. Sci.* **2004**, *571*, 146.

[232] Y. Shimamune, M. Sakuraba, T. Matsuura, J. Murota, *Appl. Surf. Sci.* **2000**, *162–163*, 390.

[233] W. McMahon, J. Olson, *J. Cryst. Growth* **2001**, *225*, 410.

[234] M. Zorn, J. Jönsson, W. Richter, J.-T. Zettler, K. Ploska, *Phys. Status Solidi A* **1995**, *152*, 23.

[235] K. Haberland, M. Zorn, A. Klein, A. Bhattacharya, M. Weyers, J.-T. Zettler, W. Richter, *J. Cryst. Growth* **2003**, *248*, 194.

[236] N. Dietz, U. Rossow, D. E. Aspnes, K. J. Bachmann, *J. Cryst. Growth* **1996**, *164*, 34.

[237] U. Rossow, N. Dietz, K. J. Bachmann, D. E. Aspnes, *J. Vac. Sci. Technol., B: Microelectron. Nanometer Struct.–Process., Meas., Phenom.* **1996**, *14*, 3040.

[238] T. Yasuda, *Thin Solid Films* **1998**, *313–314*, 544.

[239] T. Yasuda, K. Kimura, S. Miwa, L. H. Kuo, C. G. Jin, K. Tanaka, T. Yao, *Phys. Rev. Lett.* **1996**, *77*, 326.

[240] T. Yasuda, L. H. Kuo, K. Kimura, S. Miwa, C. G. Jin, K. Tanaka, T. Yao, *J. Vac. Sci. Technol., B: Nanotechnol. Microelectron.: Mater., Process., Meas., Phenom.* **1996**, *14*, 3052.

[241] T. Yasuda, D. E. Aspnes, D. R. Lee, C. H. Bjorkman, G. Lucovsky, *J. Vac. Sci. Technol., A* **1994**, *12*, 1152.

[242] O. Hunderi, J.-T. Zettler, K. Haberland, *Thin Solid Films* **2005**, *472*, 261.

[243] O. Supplie, T. Hannappel, M. Pristovsek, H. Döscher, *Phys. Rev. B* **2012**, *86*, 035308.

[244] M. Sugiyama, K. Sugita, Y. Wang, Y. Nakano, *J. Cryst. Growth* **2011**, *315*, 1.

[245] H. Sodabanlu, S. Ma, K. Watanabe, M. Sugiyama, Y. Nakano, *Appl. Phys. Express* **2012**, *5*, 062301.

[246] S. Sudo, Y. Nakano, M. Sugiyama, Y. Shimogaki, H. Komiyama, K. Tada, *Proceedings of the International Conference on Indium Phosphide and Related Materials*, Tsukuba, Japan **1998**, 485.

[247] Y. Wang, R. Onitsuka, M. Deura, W. Yu, M. Sugiyama, Y. Nakano, *J. Cryst. Growth* **2010**, *312*, 1364.

[248] P. Würfel, *Physics of Solar Cells*, Wiley-VCH, Weinheim **2009**.

[249] R. Brendel, J. H. Werner, H. J. Queisser, *Sol. Energy Mater. Sol. Cells* **1996**, *41*, 419.

[250] S. Ma, H. Sodabanlu, K. Watanabe, M. Sugiyama, Y. Nakano, *Jpn. J. Appl. Phys.* **2012**, *51*, 10ND09.

[251] J. Decobert, G. Patriarche, *J. Appl. Phys.* **2002**, *92*, 5749.

[252] N. L. Rowell, G. Yu, D. J. Lockwood, P. J. Poole, *J. Vac. Sci. Technol., A* **2004**, *22*, 897.

[253] J. Camassel, J. Laurenti, S. Juillaguet, F. Reinhardt, K. Wolter, H. Kurz, D. Grützmacher, *J. Cryst. Growth* **1991**, *107*, 543.

[254] A. Dobrich, K. Schwarzburg, T. Hannappel, *Sol. Energy Mater. Sol. Cells* **2016**, *148*, 25.

[255] H. Döscher, P. Hens, A. Beyer, L. Tapfer, K. Volz, W. Stolz, *J. Cryst. Growth* **2016**, *464*, 2.

[256] U. Seidel, T. Hannappel, *J. Cryst. Growth* **2008**, *310*, 2334.

[257] U. Seidel, E. Sagol, C. Pettenkofer, T. Hannappel, *Appl. Surf. Sci.* **2008**, *255*, 722.

[258] O. Pitts, S. Watkins, C. Wang, V. Fink, K. Kavanagh, *J. Cryst. Growth* **2003**, *254*, 28.

[259] O. Pitts, S. Watkins, C. Wang, *J. Cryst. Growth* **2003**, *248*, 249.

[260] O. Supplie, M. M. May, C. Höhn, H. Stange, A. Müller, P. Kleinschmidt, S. Brückner, T. Hannappel, *ACS Appl. Mater. Interfaces* **2015**, *7*, 9323.

[261] T. J. Grassman, M. R. Brenner, S. Rajagopalan, R. Unocic, R. Dehoff, M. Mills, H. Fraser, S. A. Ringel, *Appl. Phys. Lett.* **2009**, *94*, 232106.

[262] Y. Takagi, H. Yonezu, K. Samonji, T. Tsuji, N. Ohshima, *J. Cryst. Growth* **1998**, *187*, 42.

[263] V. K. Dixit, T. Ganguli, T. K. Sharma, S. D. Singh, R. Kumar, S. Porwal, P. Tiwari, A. Ingale, S. M. Oak, *J. Cryst. Growth* **2008**, *310*, 3428.

[264] K. A. Bell, M. Ebert, S. D. Yoo, K. Flock, D. E. Aspnes, *J. Vac. Sci. Technol., A* **2000**, *18*, 1184.

[265] T. Soga, T. Jimbo, M. Umeno, *J. Cryst. Growth* **1995**, *146*, 554.

[266] K. J. Bachmann, U. Rossow, N. Sukidi, H. Castleberry, N. Dietz, *J. Vac. Sci. Technol., B: Microelectron. Nanometer Struct.–Process., Meas., Phenom.* **1996**, *14*, 3019.

[267] X. Liu, I. K. Kim, D. E. Aspnes, *J. Vac. Sci. Technol., B: Microelectron. Nanometer Struct.–Process., Meas., Phenom.* **2007**, *25*, 1448.

[268] T. Soga, T. Suzuki, M. Mori, T. Jimbo, M. Umeno, *J. Cryst. Growth* **1993**, *132*, 134.

[269] T. Suzuki, T. Soga, T. Jimbo, M. Umeno, *J. Cryst. Growth* **1991**, *115*, 158.

[270] K. Werner, A. Beyer, J. Oelerich, S. Baranovskii, W. Stolz, K. Volz, *J. Cryst. Growth* **2014**, *405*, 102.

[271] S. Chandola, J. Power, T. Farrell, P. Weightman, J. McGilp, *Appl. Surf. Sci.* **1998**, *123–124*, 233.

[272] O. Supplie, M. M. May, G. Steinbach, O. Romanyuk, F. Grosse, A. Nägelein, P. Kleinschmidt, S. Brückner, T. Hannappel, *J. Phys. Chem. Lett.* **2015**, *6*, 464.

[273] A. Beyer, J. Ohlmann, S. Liebich, H. Heim, G. Witte, W. Stolz, K. Volz, *J. Appl. Phys.* **2012**, *111*, 083534.

[274] G. Steinbach, M. Schreiber, S. Gemming, *Nanosci. Nanotechnol. Lett.* **2013**, *5*, 73.

[275] O. Romanyuk, O. Supplie, T. Susi, M. M. May, T. Hannappel, *Phys. Rev. B* **2016**, *94*, 155309.

[276] A. Stegmüller, K. Werner, M. Reutzel, A. Beyer, P. Rosenow, U. Höfer, W. Stolz, K. Volz, M. Dürr, R. Tonner, *Chem. - Eur. J.* **2016**, *22*, 14920.

[277] W. A. Harrison, E. A. Kraut, J. R. Waldrop, R. W. Grant, *Phys. Rev. B* **1978**, *18*, 4402.

[278] T. Hanada, T. Yasuda, A. Ohtake, K. Hingerl, S. Miwa, K. Arai, T. Yao, *Phys. Rev. B* **1999**, *60*, 8909.

[279] E. Liarokapis, D. Papadimitriou, J. Rumberg, W. Richter, *Phys. Status Solidi B* **1999**, *211*, 309.

[280] R. del Sole, G. Onida, *Phys. Rev. B* **1999**, *60*, 5523.

[281] U. Rossow, L. Mantese, D. Aspnes, *Appl. Surf. Sci.* **1998**, *123*, 237.

[282] A. Beyer, A. Stegmüller, J. O. Oelerich, K. Jandieri, K. Werner, G. Mette, W. Stolz, S. D. Baranovskii, R. Tonner, K. Volz, *Chem. Mater.* **2016**, *28*, 3265.

[283] T. Hannappel, O. Supplie, M. M. May, P. Kleinschmidt, O. Romanyuk, *arXiv:1610.01758 [cond-mat.mtrl-sci]*, **2016**.

[284] R. Fischer, W. T. Masselink, J. Klem, T. Henderson, T. C. McGlinn, M. V. Klein, H. Morkoç, J. H. Mazur, J. Washburn, *J. Appl. Phys.* **1985**, *58*, 374.

[285] J. P. Gowers, *Appl. Phys. A: Mater. Sci. Process.* **1984**, *34*, 231.

**ADVANCED
SCIENCE NEWS**

www.advancedsciencenews.com

**ADVANCED
MATERIALS
INTERFACES**

www.advmatinterfaces.de

[286] T. N. Thanh, C. Robert, A. Létoublon, C. Cornet, T. Quinci, E. Giudicelli, S. Almosni, N. Boudet, A. Ponchet, J. Kuyyalil, M. Danila, O. Durand, N. Bertru, A. L. Corre, *Thin Solid Films* **2013**, *541*, 36.

[287] P. N. Uppal, H. Kroemer, *J. Appl. Phys.* **1985**, *58*, 2195.

[288] I. Németh, B. Kunert, W. Stolz, K. Volz, *J. Cryst. Growth* **2008**, *310*, 1595.

[289] H. Döscher, B. Borkenhagen, G. Lilienkamp, W. Daum, T. Hannappel, *Surf. Sci.* **2011**, *605*, L38.

[290] B. Borkenhagen, H. Döscher, T. Hannappel, G. Lilienkamp, W. Daum, *ECS Trans.* **2012**, *45*, 231.

[291] M. Lei, J. Price, W.-E. Wang, M. H. Wong, R. Droopad, P. Kirsch, G. Bersuker, M. C. Downer, *Appl. Phys. Lett.* **2013**, *102*, 152103.

[292] J. Amzallag, H. Benisty, S. Debrus, M. May, M. Eddrief, A. Bourdon, A. Chevy, N. Piccioli, *Appl. Phys. Lett.* **1995**, *66*, 982.

[293] K. Brixius, A. Beyer, J. Güdde, M. Dürr, W. Stolz, K. Volz, U. Höfer, *arXiv:1611.01307 [cond-mat.mes-hall]*, **2016**.

[294] K. Ishioka, K. Brixius, A. Beyer, A. Rustagi, C. J. Stanton, W. Stolz, K. Volz, U. Höfer, H. Petek, *Appl. Phys. Lett.* **2016**, *108*, 051607.

[295] M. Kawabe, T. Ueda, *Jpn. J. Appl. Phys.* **1987**, *26*, L944.

[296] I. Németh, B. Kunert, W. Stolz, K. Volz, *J. Cryst. Growth* **2008**, *310*, 4763.

[297] A. Beyer, B. Haas, K. I. Gries, K. Werner, M. Luysberg, W. Stolz, K. Volz, *Appl. Phys. Lett.* **2013**, *103*, 032107.

[298] H. Döscher, O. Supplie, S. Brückner, T. Hannappel, A. Beyer, J. Ohlmann, K. Volz, *J. Cryst. Growth* **2011**, *315*, 16.

[299] A. Navarro, P. C. E. García-Tabarés, B. Galiana, I. Rey-Stolle, C. Ballesteros, *J. Cryst. Growth* **2016**, *464*, 8.

[300] E. García-Tabarés, I. Rey-Stolle, *Sol. Energy Mater. Sol. Cells* **2014**, *124*, 17.

[301] O. Supplie, *Dissertation thesis*, Humboldt-Universität zu Berlin **2016**.

[302] U. Gelius, E. Basilier, S. Svensson, T. Bergmark, K. Siegbahn, *J. Electron Spectrosc. Relat. Phenom.* **1973**, *2*, 405.

[303] M. M. May, C. Brabetz, C. Janowitz, R. Manzke, *Phys. Rev. Lett.* **2011**, *107*, 176405.

[304] G. Chen, S. B. Visbeck, D. C. Law, R. F. Hicks, *J. Appl. Phys.* **2002**, *91*, 9362.

[305] D. Schmeisser, F. J. Himpsel, G. Hollinger, *Phys. Rev. B* **1983**, *27*, 7813.

[306] M. A. Henderson, *Surf. Sci. Rep.* **2002**, *46*, 1.

[307] J. M. White, S. Akhter, *Crit. Rev. Solid State Mater. Sci.* **1988**, *14*, 131.

[308] I. Langmuir, *J. Am. Chem. Soc.* **1918**, *40*, 1361.

[309] D. A. King, M. G. Wells, *Surf. Sci.* **1972**, *29*, 454.

[310] C. Powell, A. Jablonski, *J. Electron Spectrosc. Relat. Phenom.* **2010**, *178–179*, 331.

[311] O. Henrion, A. Klein, W. Jaegermann, *Surf. Sci.* **2000**, *457*, L337.

[312] T. Bitzer, H. Lewerenz, *Surf. Sci.* **1992**, *269–270*, 886.

[313] K. E. Bean, P. S. Gleim, *Proc. IEEE* **1969**, *57*, 1469.

[314] R. E. Blaha, W. R. Fahrner, *Phys. Status Solidi A* **1978**, *50*, 551.

[315] S. Katircioglu, *Surf. Sci.* **1987**, *187*, 569.

[316] K. Fujiwara, *Surf. Sci.* **1981**, *108*, 124.

[317] W. Ranke, Y. Xing, *Surf. Sci.* **1997**, *381*, 1.

[318] N. Witkowski, R. Coustel, O. Pluchery, Y. Borensztein, *Surf. Sci.* **2006**, *600*, 5142.

[319] M. Dürr, U. Höfer, *Surf. Sci. Rep.* **2006**, *61*, 465.

[320] N. Sano, T. Shibata, T. Kanki, T. Asano, *J. Chem. Eng. Jpn.* **2001**, *34*, 684.

[321] A. Heller, B. Miller, H. J. Lewerenz, K. J. Bachmann, *J. Am. Chem. Soc.* **1980**, *102*, 6555.

[322] H. J. Lewerenz, C. Heine, K. Skorupska, N. Szabó, T. Hannappel, T. Vo-Dinh, S. A. Campbell, H. W. Klemm, A. G. Muñoz, *Energy Environ. Sci.* **2010**, *3*, 748.

[323] A. Baghbanpourasl, W. G. Schmidt, M. Denk, C. Cobet, M. Hohage, P. Zeppenfeld, K. Hingerl, *Surf. Sci.* **2015**, *641*, 231.

[324] B. C. Wood, E. Schwegler, W. I. Choi, T. Ogitsu, *J. Phys. Chem. C* **2014**, *118*, 1062.

[325] J. L. Young, H. Döscher, J. A. Turner, T. G. Deutsch, *J. Phys. Chem. C* **2016**, *120*, 4418.

[326] M. M. May, O. Supplie, C. Höhn, R. van de Krol, H.-J. Lewerenz, T. Hannappel, *New J. Phys.* **2013**, *15*, 103003.

[327] T. Letzig, F. Willig, P. H. Hahn, W. G. Schmidt, *Phys. Rev. B* **2006**, *74*, 245307.

[328] C. X. Kronawitter, M. Lessio, P. Zhao, C. Riplinger, A. Boscoboinik, D. E. Starr, P. Sutter, E. A. Carter, B. E. Koel, *J. Phys. Chem. C* **2015**, *119*, 17762.

[329] X. Zhang, S. Ptasinska, *Phys. Chem. Chem. Phys.* **2015**, *17*, 3909.

[330] S. Ladas, R. Imbihl, G. Ertl, *Surf. Sci.* **1988**, *198*, 42.

[331] T. Bürgi, F. Atamny, A. Knop-Gericke, M. Hävecker, T. Schedel-Niedrig, R. Schlögl, A. Baiker, *Catal. Lett.* **2000**, *66*, 109.

[332] E. Savinova, D. Zemlyanov, B. Pettinger, A. Scheybal, R. Schlögl, K. Doblhofer, *Electrochim. Acta* **2000**, *46*, 175.

[333] J. K. Nørskov, *Top. Catal.* **1994**, *1*, 385.

[334] O. Björneholm, M. H. Hansen, A. Hodgson, L.-M. Liu, D. T. Limmer, A. Michaelides, P. Pedevilla, J. Rossmeisl, H. Shen, T. Gabriele, E. Tyrode, M.-M. Walz, J. Werner, H. Bluhm, *Chem. Rev.* **2016**, *116*, 7698.

[335] C. Punckt, F. S. Merkt, H. H. Rotermund, *New J. Phys.* **2007**, *9*, 213.

[336] R. Memming, G. Schwandt, *Angew. Chem., Int. Ed.* **1967**, *6*, 851.

[337] H. Gerischer, *Surf. Sci.* **1969**, *18*, 97.

[338] H. Gerischer, *J. Electroanal. Chem. Interfacial Electrochem.* **1983**, *150*, 553.

[339] A. J. Bard, L. R. Faulkner, *Electrochemical Methods: Fundamentals and Applications*, 2nd ed., Wiley, New York **2001**.

[340] D. Kolb, J. Schneider, *Electrochim. Acta* **1986**, *31*, 929.

[341] E. Ponomarev, L. Peter, *J. Electroanal. Chem.* **1995**, *397*, 45.

[342] F. Dimroth, R. Beckert, M. Meusel, U. Schubert, A. W. Bett, *Prog. Photovoltaics* **2001**, *9*, 165.

[343] I. Miethe, K. Krischer, *J. Electroanal. Chem.* **2012**, *666*, 1.

[344] K.-I. Ataka, T. Yotsuyanagi, M. Osawa, *J. Phys. Chem.* **1996**, *100*, 10664.

[345] C. I. Smith, P. Harrison, T. Farrell, P. Weightman, *J. Phys.: Condens. Matter* **2012**, *24*, 482002.

[346] C. I. Smith, P. Harrison, C. A. Lucas, Y. Grunder, S. D. Barrett, P. Weightman, *J. Phys.: Condens. Matter* **2016**, *28*, 015005.

[347] M. M. Lerch, M. J. Hansen, W. A. Velema, W. Szymanski, B. L. Feringa, *Nat. Commun.* **2016**, *7*, 12054.

[348] B. A. Grzybowski, W. T. S. Huck, *Nat. Nanotechnol.* **2016**, *11*, 584.

[349] H. Logtenberg, J. Areephong, J. Bauer, A. Meetsma, B. L. Feringa, W. R. Browne, *ChemPhysChem* **2016**, *17*, 1895.

[350] Y. Yan, S. C. Warren, P. Fuller, B. A. Grzybowski, *Nat. Nanotechnol.* **2016**, *11*, 603.

[351] N. Koumura, R. W. J. Zijlstra, R. A. van Delden, N. Harada, B. L. Feringa, *Nature* **1999**, *401*, 152.

[352] R. Eelkema, M. M. Pollard, J. Vicario, N. Katsonis, B. S. Ramon, C. W. M. Bastiaansen, D. J. Broer, B. L. Feringa, *Nature* **2006**, *440*, 163.

[353] T. Kudernac, N. Ruangsupapichat, M. Parschau, B. Macia, N. Katsonis, S. R. Harutyunyan, K. H. Ernst, B. L. Feringa, *Nature* **2011**, *479*, 208.

[354] R. Yoshida, T. Ueki, *NPG Asia Mater.* **2014**, *6*, e107.

[355] H. W. H. van Roekel, B. J. H. M. Rosier, L. H. H. Meijer, P. A. J. Hilbers, A. J. Markvoort, W. T. S. Huck, T. F. A. de Greef, *Chem. Soc. Rev.* **2015**, *44*, 7465.

[356] S. N. Semenov, L. J. Kraft, A. Ainla, M. Zhao, M. Baghbanzadeh, V. E. Campbell, K. Kang, J. M. Fox, G. M. Whitesides, *Nature* **2016**, *537*, 656.

**ADVANCED
SCIENCE NEWS**

www.advancedsciencenews.com

**ADVANCED
MATERIALS
INTERFACES**

www.advmatinterfaces.de

[357] S. N. Semenov, A. S. Y. Wong, R. M. van der Made, S. G. J. Postma, J. Groen, H. W. H. van Roekel, T. F. A. de Greef, W. T. S. Huck, *Nat. Chem.* **2015**, *7*, 160.

[358] X. M. He, M. Aizenberg, O. Kuksenok, L. D. Zarzar, A. Shastri, A. C. Balazs, J. Aizenberg, *Nature* **2012**, *487*, 21.

[359] M. Emond, T. L. Saux, J. F. Allemand, P. Pelupessy, R. Plasson, L. Jullien, *Chem. - Eur. J.* **2012**, *18*, 14375.

[360] M. Kato, J. Z. Zhang, N. Paul, E. Reisner, *Chem. Soc. Rev.* **2014**, *43*, 6485.

[361] F. Caschera, V. Noireaux, *Curr. Opin. Chem. Biol.* **2014**, *22*, 85.

[362] M. Forgac, *Nat. Rev. Mol. Cell Biol.* **2007**, *8*, 917.

[363] B. P. Pedersen, M. J. Buch-Pedersen, J. P. Morth, M. G. Palmgren, P. Nissen, *Nature* **2007**, *450*, 1111.

[364] F. Rivera-Chavez, A. J. Baumler, *Annu. Rev. Microbiol.* **2015**, *69*, 31.

[365] E. V. Skorb, A. V. Volkova, D. V. Andreeva, *Curr. Org. Chem.* **2015**, *19*, 1097.

[366] E. V. Skorb, D. V. Andreeva, *Adv. Funct. Mater.* **2013**, *23*, 4483.

[367] E. V. Skorb, H. Möhwald, *Adv. Mater.* **2013**, *25*, 5029.

[368] S. A. Ulasevich, G. Brezesinski, H. Möhwald, P. Fratzl, F. H. Schacher, S. K. Poznyak, D. V. Andreeva, E. V. Skorb, *Angew. Chem., Int. Ed.* **2016**, *55*, 13001.

[369] D. V. Andreeva, I. Melnyk, O. Baidukova, E. V. Skorb, *ChemElectroChem* **2016**, *3*, 1306.

[370] S. A. Ulasevich, N. Brezhneva, Y. Zhukova, H. Möhwald, P. Fratzl, F. H. Schacher, D. V. Sviridov, D. V. Andreeva, E. V. Skorb, *Macromol. Biosci.* **2016**, *16*, 1422.

[371] A. L. Linsebigler, G. Q. Lu, J. T. Yates, *Chem. Rev.* **1995**, *95*, 73.

[372] M. A. Henderson, I. Lyubinetsky, *Chem. Rev.* **2013**, *113*, 4428.

[373] E. V. Skorb, E. A. Ustinovich, A. I. Kulak, D. V. Sviridov, *J. Photochem. Photobiol., A* **2008**, *193*, 97.

[374] K. Ichimura, *Chem. Rec.* **2002**, *2*, 46.

[375] S. A. Ulasevich, S. K. Poznyak, A. I. Kulak, A. D. Lisenkov, M. Starykevich, E. V. Skorb, *Langmuir* **2016**, *32*, 4016.

[376] I. Richard, M. Thibault, G. D. Crescenzo, M. D. Buschmann, M. Lavertu, *Biomacromolecules* **2013**, *14*, 1732.

[377] R. V. Benjaminsen, M. A. Mattebjerg, J. R. Henriksen, S. M. Moghimi, T. L. Andresen, *Mol. Ther.* **2013**, *21*, 149.

[378] E. V. Skorb, D. V. Andreeva, *Polym. Int.* **2015**, *64*, 713.

[379] D. V. Andreeva, E. V. Skorb, D. G. Shchukin, *ACS Appl. Mater. Interfaces* **2010**, *2*, 1954.

[380] E. V. Skorb, H. Möhwald, *Adv. Mater. Interfaces* **2014**, *4*, 1600282.

[381] J. Schneider, M. Matsuoka, M. Takeuchi, J. L. Zhang, Y. Horiuchi, M. Anpo, D. W. Bahnemann, *Chem. Rev.* **2014**, *114*, 9919.

[382] J. Gensel, T. Borke, N. P. Perez, A. Fery, D. V. Andreeva, E. Betthausen, A. H. E. Muller, H. Möhwald, E. V. Skorb, *Adv. Mater.* **2012**, *24*, 985.

[383] E. V. Skorb, L. I. Antonouskaya, N. A. Belyasova, D. G. Shchukin, H. Möhwald, D. V. Sviridov, *Appl. Catal., B* **2008**, *84*, 94.

[384] C. D. Nadell, K. Drescher, K. R. Foste, *Nat. Rev. Microbiol.* **2016**, *14*, 589.

[385] G. M. Whitesides, *Interface Focus* **2015**, *5*, 20150031.

[386] S. E. Winter, P. Thiennimitr, M. G. Winter, B. P. Butler, D. L. Huseby, R. W. Crawford, J. M. Russell, C. L. Bevins, L. G. Adams, R. M. Tsolis, J. R. Roth, A. J. Baumler, *Nature* **2010**, *467*, 426.

[387] M. Hensel, A. P. Hinsley, T. Nikolaus, G. Sawers, B. C. Berks, *Mol. Microbiol.* **1999**, *32*, 275.

[388] C. J. Huang, E. L. Barrett, *J. Bacteriol.* **1991**, *173*, 1544.

[389] N. K. Heinzinger, S. Y. Fujimoto, M. A. Clark, M. S. Moreno, E. L. Barrett, *J. Bacteriol.* **1995**, *177*, 2813.

[390] C. A. Lopez, S. E. Winter, F. Rivera-Chavez, M. N. Xavier, V. Poon, S. P. Nuccio, R. M. Tsolis, A. J. Baumler, *mBio* **2012**, *3*, e00143.

[391] P. Louis, H. J. Flint, *FEMS Microbiol. Lett.* **2009**, *294*, 1.

[392] E. V. Skorb, H. Möhwald, D. V. Andreeva, *Adv. Mater. Interfaces* **2016**, *4*, 1600282.

[393] D. O. Grigoriev, K. Kohler, E. Skorb, D. G. Shchukin, H. Möhwald, *Soft Matter* **2009**, *5*, 1426.

[394] K. J. M. Bishop, C. J. Campbell, G. Mahmud, B. A. Grzybowski, *Stud. Multidiscip.* **2008**, *5*, 21.

[395] E. V. Skorb, A. V. Volkova, D. V. Andreeva, *Curr. Org. Chem.* **2014**, *18*, 2315.

[396] D. B. Zorov, C. R. Filburn, L. O. Klotz, J. L. Zweier, S. J. Sollott, *J. Exp. Med.* **2000**, *192*, 1001.

[397] D. B. Zorov, M. Juhaszova, K. W. Fishbein, S. J. Sollott, *Biophys. J.* **2001**, *80*, 500.

[398] D. B. Zorov, M. Juhaszova, S. J. Sollott, *Physiol. Rev.* **2014**, *94*, 909.

[399] Y. B. Liu, G. Fiskum, D. Schubert, *J. Neurochem.* **2002**, *80*, 780.

[400] L. A. Munishkina, A. L. Fink, *Biochim. Biophys. Acta, Biomembr.* **2007**, *1768*, 1862.

[401] W. E. Moerner, D. P. Fromm, *Rev. Sci. Instrum.* **2003**, *74*, 3597.

[402] P. Tinnefeld, M. Sauer, *Angew. Chem., Int. Ed.* **2005**, *44*, 2642.

[403] M. Hayyan, M. A. Hashim, I. M. AlNashef, *Chem. Rev.* **2016**, *116*, 3029.

[404] *The Molecular Probes Handbook—A Guide to Fluorescent Probes and Labeling Technologies* (Eds: I. Johnson, M. T. Z. Spence), 11th ed., Thermo Fisher Scientific, **2010**.

[405] A. Gomes, E. Fernandes, J. L. F. C. Lima, *J. Biochem. Biophys. Methods* **2005**, *65*, 45.

[406] J. Suzurikawa, M. Nakao, R. Kanzaki, H. Takahashi, *Sens. Actuators, B* **2010**, *149*, 205.

[407] D. Fix, E. V. Skorb, D. G. Shchukin, H. Möhwald, *Meas. Sci. Technol.* **2011**, *22*, 075704.

[408] J. Kopf, S. Ulasevich, O. Baidukova, Y. Zhukova, J. W. C. Dunlop, P. Fratzl, P. Rikeit, P. Knaus, S. K. Poznyak, D. V. Andreeva, E. V. Skorb, *Adv. Eng. Mater.* **2016**, *18*, 476.

[409] E. V. Skorb, D. V. Andreeva, H. Möhwald, *Angew. Chem., Int. Ed.* **2012**, *51*, 5138.

[410] F. Priolo, T. Gregorkiewicz, M. Galli, T. F. Krauss, *Nat. Nanotechnol.* **2014**, *9*, 19.

[411] J. D. Holmes, K. P. Johnston, R. C. Doty, B. A. Korgel, *Science* **2000**, *287*, 1471.

[412] L. T. Canham, *Nature* **2000**, *408*, 411.

[413] E. V. Skorb, H. Möhwald, *Ultrason. Sonochem.* **2016**, *29*, 589.

[414] E. V. Skorb, H. Möhwald, D. V. Andreeva, *Langmuir* **2016**, *32*, 11072.

[415] K. Sunada, T. Watanabe, K. Hashimoto, *J. Photochem. Photobiol., A* **2003**, *156*, 227.

[416] E. V. Skorb, D. V. Andreeva, A. P. Raiski, N. A. Belyasova, H. Möhwald, D. V. Sviridov, *Photochem. Photobiol. Sci.* **2011**, *10*, 1974.

[417] J. A. Byrne, P. S. M. Dunlop, J. W. J. Hamilton, P. Fernandez-Ibanez, I. Polo-Lopez, P. K. Sharma, A. S. M. Vennard, *Molecules* **2015**, *20*, 5574.

[418] Y. Paz, A. Heller, *J. Mater. Res.* **1997**, *12*, 2759.

[419] P. S. Foran, C. Boxall, K. R. Denison, *Langmuir* **2012**, *28*, 17647.

[420] E. V. Skorb, A. G. Skirtach, D. V. Sviridov, D. G. Shchukin, H. Möhwald, *ACS Nano* **2009**, *3*, 1753.

[421] E. V. Skorb, D. G. Shchukin, H. Möhwald, D. V. Sviridov, *J. Mater. Chem.* **2009**, *19*, 4931.

[422] B. W. Liu, X. Y. Yu, Z. H. Zhu, X. Hua, L. Yang, Z. Y. Wang, *Lab Chip* **2014**, *14*, 855.

[423] E. V. Skorb, D. V. Sviridov, H. Möhwald, D. G. Shchukin, *Chem. Commun.* **2000**, 6041.

[424] E. V. Skorb, D. Fix, D. V. Andreeva, H. Möhwald, D. G. Shchukin, *Adv. Funct. Mater.* **2009**, *19*, 2373.

[425] E. V. Skorb, O. Baidukova, A. Goyal, A. Brotchie, D. V. Andreeva, H. Möhwald, *J. Mater. Chem.* **2012**, *22*, 13841.

[426] D. V. Andreeva, D. V. Sviridov, A. Masic, H. Möhwald, E. V. Skorb, *Small* **2012**, *8*, 820.

**ADVANCED
SCIENCE NEWS**
www.advancedsciencenews.com

**ADVANCED
MATERIALS
INTERFACES**
www.advmatinterfaces.de

[427] M. Rogoz, H. Zeng, C. Xuan, D. S. Wiersma, P. Wasylczyk, *Adv. Opt. Mater.* **2016**, *4*, 1689.

[428] M. Su, V. P. Dravid, *Nano Lett.* **2005**, *5*, 2023.

[429] R. F. Dong, Q. L. Zhang, W. Gao, A. Pei, B. Y. Ren, *ACS Nano* **2016**, *10*, 839.

[430] S. J. Park, M. Gazzola, K. S. Park, S. Park, V. D. Santo, E. L. Blevins, J. U. Lind, P. H. Campbell, S. Dauth, A. K. Capulli, F. S. Pasqualini, S. Ahn, A. Cho, H. Y. Yuan, B. M. Maoz, R. Vijaykumar, J. W. Choi, K. Deisseroth, G. V. Lauder, L. Mahadevan, K. K. Parker, *Science* **2016**, *353*, 158.

[431] M. Wehner, R. L. Truby, D. J. Fitzgerald, B. Mosadegh, G. M. Whitesides, J. A. Lewis, R. J. Wood, *Nature* **2016**, *536*, 451.

[432] Editorial, *Nat. Mater.* **2012**, *11*, 91.

[433] I. Vurgaftman, J. R. Meyer, L. R. Ram-Mohan, *J. Appl. Phys.* **2001**, *89*, 5815.

[434] T. E. Fischer, *Phys. Rev.* **1966**, *142*, 519.

[435] W. N. Hansen, D. M. Kolb, *J. Electroanal. Chem. Interfacial Electrochem.* **1979**, *100*, 493.

[436] S. Tiwari, D. J. Frank, *Appl. Phys. Lett.* **1992**, *60*, 630.

[437] American Society for Testing and Materials (ASTM), Terrestrial reference spectra for photovoltaic performance evaluation. http://rredc.nrel.gov/solar/spectra/am1.5/

[438] M. M. May, D. Lackner, J. Ohlmann, F. Dimroth, R. van de Krol, T. Hannappel, K. Schwarzburg, *Sustainable Energy Fuels* **2017**, *1*, 492.

[439] P. Lautenschlager, M. Garriga, M. Cardona, *Phys. Rev. B* **1987**, *36*, 4813.

[440] S. Zollner, M. Garriga, J. Kircher, J. Humlicek, M. Cardona, G. Neuhold, *Phys. Rev. B* **1993**, *48*, 7915.

[441] P. Lautenschlager, M. Garriga, L. Vina, M. Cardona, *Phys. Rev. B* **1987**, *36*, 4821.

[442] J. D. E. McIntyre, D. E. Aspnes, *Surf. Sci.* **1971**, *24*, 417.

[443] A. Mishra, J. S. Kwon, R. Thakur, S. Wereley, *Trends Biotechnol.* **2014**, *32*, 415.

[444] A. A. Solovev, W. Xi, D. H. Gracias, S. M. Harazim, C. Deneke, S. Sanchez, O. G. Schmidt, *ACS Nano* **2012**, *6*, 1751.

[445] C. Kim, H. J. Park, S. Cha, J. Yoon, *Chemosphere* **2013**, *93*, 2011.

[446] Y. Li, W. Zhang, J. F. Niu, Y. S. Chen, *ACS Nano* **2012**, *6*, 5164.

[447] W. Zhang, Y. Li, J. F. Niu, Y. S. Chen, *Langmuir* **2013**, *29*, 4647.

[448] C. Kormann, D. W. Bahnemann, M. R. Hoffmann, *Environ. Sci. Technol.* **1988**, *22*, 798.

[449] K. Ishibashi, A. Fujishima, T. Watanabe, K. Hashimoto, *J. Photochem. Photobiol., A* **2000**, *134*, 139.

[450] Q. Xiao, Z. C. Si, J. Zhang, C. Xiao, X. K. Tan, *J. Hazard. Mater.* **2008**, *150*, 62.

[451] L. M. Liu, W. Z. Sun, W. Y. Yang, Q. Li, J. K. Shang, *Sci. Rep.* **2016**, *6*, 880.

[452] B. H. Simpson, J. Rodriguez-Lopez, *J. Am. Chem. Soc.* **2015**, *137*, 14865.

[453] B. H. Simpson, J. Rodriguez-Lopez, *Electrochim. Acta* **2015**, *179*, 74.

[454] H. S. Park, K. C. Leonard, A. J. Bard, *J. Phys. Chem. C* **2013**, *117*, 12093.

[455] H. Sakai, R. Baba, K. Hashimoto, A. Fujishima, A. Heller, *J. Phys. Chem.* **1995**, *99*, 11896.

[456] T. Hirakawa, H. Kominami, B. Ohtani, Y. Nosaka, *J. Phys. Chem. B* **2001**, *105*, 6993.

[457] D. B. Wang, L. X. Zhao, L. H. Guo, H. Zhang, *Anal. Chem.* **2014**, *86*, 10535.

[458] Q. J. Xiang, J. G. Yu, P. K. Wong, *J. Colloid Interface Sci.* **2011**, *357*, 163.

[459] K. Ishibashi, A. Fujishima, T. Watanabe, K. Hashimoto, *Electrochem. Commun.* **2000**, *2*, 207.

[460] S. Kohtani, K. Yoshida, T. Maekawa, A. Iwase, A. Kudo, H. Miyabe, R. Nakagaki, *Phys. Chem. Chem. Phys.* **2008**, *10*, 2986.

[461] H. Li, Y. Tian, Z. F. Deng, Y. Liang, *Analyst* **2012**, *137*, 4605.

[462] R. Nakamura, T. Okamura, N. Ohashi, A. Imanishi, Y. Nakato, *J. Am. Chem. Soc.* **2005**, *127*, 12975.

[463] T. Tachikawa, T. Majima, *Chem. Soc. Rev.* **2010**, *39*, 4802.

[464] K. Naito, T. Tachikawa, M. Fujitsuka, T. Majima, *J. Am. Chem. Soc.* **2009**, *131*, 934.

[465] T. Tachikawa, T. Majima, *J. Fluoresc.* **2007**, *17*, 727.

[466] K. Naito, T. Tachikawa, M. Fujitsuka, T. Majima, *J. Phys. Chem. C* **2008**, *112*, 1048.

[467] J. Z. Ma, H. M. Wu, Y. C. Liu, H. He, *J. Phys. Chem. C* **2014**, *118*, 7434.

[468] K. Fujiwara, U. Muller, S. E. Pratsinis, *ACS Catal.* **2016**, *6*, 1887.

[469] G. H. Dong, W. K. Ho, L. Z. Zhang, *Appl. Catal., B* **2015**, *168*, 490.

[470] A. Alonso-Tellez, D. Robert, V. Keller, N. Keller, *Environ. Sci. Pollut. Res.* **2014**, *21*, 3503.

[471] A. E. Raevskaya, A. L. Stroyuk, S. Y. Kuchmii, *J. Nanopart. Res.* **2004**, *6*, 149.

ADVANCED
SCIENCE NEWS
www.advancedsciencenews.com

ADVANCED
MATERIALS
INTERFACES
www.advmatinterfaces.de

PROGRESS REPORT

How Can One Controllably Use of Natural ΔpH in Polyelectrolyte Multilayers?

Ekaterina V. Skorb,* Helmuth Möhwald, and Daria V. Andreeva*

Most natural and synthetic polyelectrolytes (PEs) possess dissociable groups, and therefore the corresponding structures depend on pH. This enables manipulation of their properties, in special permeability, elasticity and swelling, and this can be made use of in many applications. The effect of individual polymer composition on the dissociation equilibrium is discussed. Different concentrations and pH values during the PE assembly affect concentration of charged groups per molecule on the dissociation equilibrium. Ionic strength also influences the protonation/deprotonation behavior of PE, that can be changed by adding different salt concentration but also varies with the concentration of charged groups in the polymer molecules. Electrostatic interactions of the polymer molecules strongly affect the dissociation equilibrium of weak PEs and, thus, layers architecture and properties that can be regulated by natural pH changes in such processes as self-healing, corrosion and antifouling, drug storage and delivery, etc.

1. Introduction

pH sensitive polyelectrolytes (PEs) multilayers with different PEs architecture are composed of at least one weak PE unit. The behavior of weak PE itself, and their assembly with either weak, or strong PEs are discussed.[1] Mostly discussed in the review are poly(ethyleneimine) (PEI), polyallylamine hydrochloride (PAH), and their bio-analog chitosan as polycations. Examples of negatively charged PEs are strong polystyrene sulfonate (PSS), and weak polyacrylic acid (PAA). Dissociation of weak PEs in aqueous medium is discussed for differently pH sensitive polymer assemblies. It is important that pH sensitive multilayers have weak PEs as one of the component, since the degree of their dissociation depends on the pH values and dissociation constant, pK_a for polyacids or pK_b for polybases.

The mechanism of proton migration within one PE layer or proton jumping between different layers is in focus. Potentiometric titration is presented as a method to reveal protonation steps. Proton trapping and release results in pH dependent swelling and morphological changes of the multilayers. pH dependent swelling of weak PEs is explained by the contribution of repulsive and attractive electrostatic interactions in the formation of collapsed and gel phases. The interplay between the pH buffering capacity, ion diffusion and proton migration over weak-weak PEs and strong-weak PEs assemlies is a question to focus. It is important to take into account the range of pH values, at which multilayers dissociate but maintain their integrity; as well as coupling of several stimuli for modulation of multilayers.[2]

The chosen applications are discussed based on the PEs pH sensitivity for very efficient non-viral gene transfer, anticorrosion coatings, drug delivery regulation and antimicrobial, antifouling coating development. The attractive idea of a pH gradient in PEs assemblies for both formation of bioactive materials and temporal switching of PE assemblies on a surface for regulation of biomolecules and cells is presented. Opportunities and challenges for further development toward an eventual goal to enable understanding, design and fabrication of ΔpH sensitive PEs assemblies, are essential for construction of dynamic interfaces and possible formation of self-regulation systems.

2. Materials for pH Sensitive Polyelectrolytes Multilayers

PEs are macromolecules that contain charged groups. Examples of positively charged PEs are PEI, quaternized poly(4-vinyl pyridine), poly(diallyldimethylammonium) chloride (PDADMAC), poly(4-vinylbenzyltrimethyl ammonium chloride), poly(L-lysine hydrochloride) (PLL), PAH, chitosan (CHI). Examples of negatively charged PEs are PSS, poly(methacrylic) acid (PMA), PAA, deoxyribonucleic acid (DNA), heparin (HEP), nafion, hyaluronic acid (HA), alginic acid (ALG), chondroitin sulfate (CSA), hyaluronan (HA) etc.

Oppositely charged PEs electrostatically interact in solution and release counter-ions. The driving force of these interactions is often a small negative enthalpy and an entropy gain due to the release of small mobile counter-ions.[1a,3] Additionally, pH sensitive hydrogen bonded systems are also known.[4]

In this review we use the term "polyelectrolytes" for all polymers that undergo chemical and/or physical association. Even

Dr. E. V. Skorb, Prof. H. Möhwald
Max Planck Institute of Colloids and Interfaces
Am Mühlenberg 1, 14424 Potsdam, Germany
E-mail: skorb@mpikg.mpg.de
Dr. D. V. Andreeva
Center for Soft and Living Matter
Institute of Basic Science
Ulsan Institute of Science and Technology
50 UNIST-gill, Uliju-gun, 44919 Ulsan, South Korea
E-mail: daria.baeumler@gmail.com

PROGRESS REPORT

neutral polymers can physically associate with small ions and became charged.[1a] One example is poly(ethylene glycol) that can gain charge in water by association of protons or small anions with its electronegative oxygens. Charged block-copolymers (BCPs)[5] have blocks with charged groups. Examples of charged BCPs are poly[(2-dimethylamino)ethylmethacrylate]-block-poly[di(ethylene-glycol) methylether methacrylate], (N,N-diethylacrylamide) -b-poly(N-isopropylacrylamide), poly(N-[3-(dimethylamino) propyl] acrylamide), etc. Polyampholytes[6] have both positive and negative charges in one molecule like poly(sodium 2-acrylamido-2-methyl-1-propanesulfonate-block-N-acryloyl-L-alanine) and some proteins. Zwitterionic polymers[7] contain functional groups pairing positive and negative charge, for example, carboxybetaine methacrylate and its derivatives.

Polymers with charged groups can be weak or strong.[1a] Strong PEs are dissociated in a broad pH range between 2 and 10. Thus, multilayers of strong PEs are not sensitive to pH changes in this range and can be decomposed at pH < 2 and pH > 10. In contrast, weak PEs can gradually dissociate depending on the pH values between 2 and 10. The degree of their dissociation depends on pH values and is quantified by a dissociation constant (pK_a for polyacids or pK_b for polybases). It is important that pH sensitive multilayers have weak PEs as one of the components of LbL assembly.[1a]

Figure 1 illustrates a pH dependent dissociation of the PE pairs of weak and strong PEs. We show here the simplest possible pH dependent association/dissociation of weak PEs. The pair formed by a weak positive PE and a strong negative PE is shown in Figure 1A. at a pH < pK_b of a weak polybase, both polymers are ionized and can electrostatically interact. The pair of a strong polybase and a weak polyacid (Figure 1B), is attracted at pH > pK_a, when the polyacid is ionized. The pair of two weak PEs (Figure 1C) can have two pH windows when the polymers are ionized and the pair is dissociated. At pK_a < pH the weak polybase is protonated; at pH > pK_b the weak polyacid is ionized. In the pH window pK_a > pH < pK_b, the weak PEs can associate.[1a]

3. Dissociation of Weak Polyelectrolytes in Aqueous Medium

Dissociation constants of PEs depend on a lot of parameters such as polymer architecture,[8] molecular weight,[9] charge density,[10] electrostatic repulsion between the charged groups,[10] hydrophobic interactions,[10] screening effect of salt.[11] Thus, in order to explain the complex behavior of the pK of PEs, an apparent dissociation constant is introduced. The apparent dissociation constant, pK_{app}, is used to explain the dissociation equilibrium in weak PEs. The Henderson-Hasselbalch equation is applied to discuss possible pH dependent shifts of pK_a or pK_b of weak PEs due to, for example, electrostatic interactions of the charged groups in branched or linear polymer chains or electrostatic screening, that can be caused by added salt molecules[11] or even by an increase in the concentration of dissolved polymer. Due to a complex pH dependent behavior of weak PEs we consider more closely the factors that can affect the dissociation equilibrium in weak PEs.[1a]

Ekaterina V. Skorb received her summa cum laude diploma in chemistry (2005) and PhD in physical chemistry (2008) from Belarusian State University (BSU). In 2010, she joined the Max Planck Institute of Colloids and Interfaces (MPIKG) as a Humboldt fellow. She is currently an independent researcher in the MPIKG and a privat docent at BSU. Her research interests include study of the processes in non-equilibrium/dynamic systems for stimuli-responsible materials, encapsulation, control of crystallization, nanomaterials, photochemistry and sonochemistry.

Helmuth Möhwald received his diploma in physics (1971) and his Ph.D (1974) from the University of Gottingen (Germany) for research in organic solids. After working as a postdoc at IBM, San Jose, an assistant professor at the University of Ulm, and a research scientist at Dornier Systems, he became an associate professor in biophysics at TU Munich (1981). From a chair in physical chemistry at the University of Mainz (1987), he became the founding director of the Max Planck Institute of Colloids and Interfaces in Potsdam (1993). His most recent honors are the Overbeek medal, the Gay-Lussac-Humboldt award (2007), an honorary doctorate from the University of Montpellier (2008), and the Wolfgang-Ostwald award (2009).

Daria Andreeva received her Ph.D (2002) from the Institute of Macromolecular Compounds Russian Academy of Science in chemistry and physics of polymers. After being an Alexander-von-Humboldt fellow at the Free University of Berlin, and working as a researcher in the Max Planck Institute of Colloids and Interfaces, she leaded a group in the University of Bayreuth (Germany). After finishing her habilitation in physical chemistry (2016), she joined the Center of Soft and Living Matter (South Korea). Her current interests are cavitation bubble-surface interactions, cavitation driven thermodynamically and kinetically restricted reactions and phase transformations in solids, processes in inorganic/polymer interfaces driven by local temperature, pressure and concentration gradients.
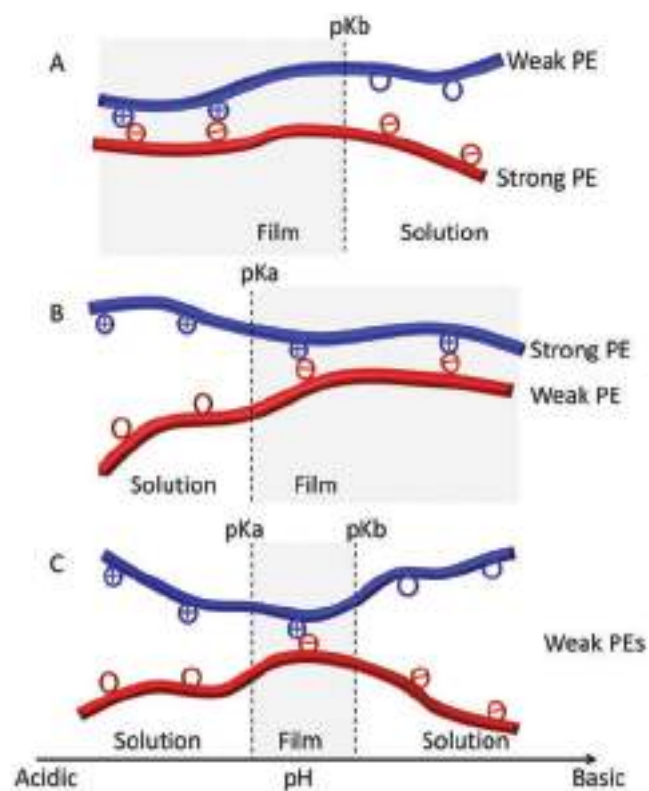
Figure 1. (A) pH dependent behavior of a weak polybase and a strong polyacid; (B) a strong polybase and a weak polyacid; (C) two weak PEs. In the simplest case, the association/dissociation process depends on pK values of weak PEs.[1a]

One of the factors that can affect the pK is the polymer architecture.[8] The protonation behavior of branched and linear polymer chains is different and can be explained by the presence of different charged groups in the linear and branched molecules using PEI. In the linear PEI chain primary amino groups are present. The branched PEI molecules have primary, secondary and tertiary amines and, additionally, can have different degree of branching. In general, the protonation/deprotonation behavior of weak PEs is a complex multi-step process, which has several dissociation equilibria. Thus, it is important to describe in details the protonation/deprotonation behavior of linear and branched molecules. Predictions of the protonation process of different polymer architectures are provided by Barkovec et al.[8] The predicted results are compared with the titration data.

Borkovec et al.[8] studied the effect of strong short-ranged electrostatic interactions between neighboring charged amino groups on the pK values of dendritic, comb-like and linear PEI. The authors used potentiometric titration to compare the predicted and experimental protonation/deprotonation behavior of comb-like PEI.

In order to explain a multi-step protonation of PEI Borkovec et al.[8] applied a model considering additionally to the pK a pair intersection interaction parameter or a free pair interaction energy, ε. The predicted titration curves were different for the branched and linear molecular architectures of PEI. At

high pH, for all polymer architectures the first protonation step occurred at pH ≈ pK = 10 due to independent binding of protons to the amino groups of PEI. For the linear PEI two protonation steps were calculated with a plateau when half charged groups in the polymer are protonated. For the comb-like PEI, Borkovec et al.[8] predicted three protonation steps with two plateaus. One plateau was characterized by half protonation of the polymer chains. The second one was predicted for the polymer with two-thirds protonated amines. The presence of a plateau was explained by the formation of an intermediate configuration of PEI, where every unprotonated moiety is in the vicinity of two protonated neighboring groups in the linear polymer and one protonated neighbor in the branched polymer. Thus, at pH ≈ pK – 2ε = 6 for the linear PEI, at pH ≈ pK – 3ε = 4 for dendrimers and at pH ≈ pK – ε = 8 for the comb-like PEI the pair interactions can be neglected and the protonation can continue. The second plateau in the comb-like molecules occurs when every unprotonated group is neighbored by three protonated groups at pH ≈ pK – 3ε = 4.[8]

Potentiometric titration of the comb-like molecules also revealed three protonation steps. First two steps occur pH 9.0–9.5 and pH 4.5–5.0. However, the protonation of the tertiary groups was not observed experimentally. It was proposed that this step might be in the very low pH range of –1.0 and +0.5. Nevertheless the experimental and predicted data have some discrepancy, it is clear that polymer architecture has a strong influence on the dissociation equilibrium of weak PEs and, thus, it is very important to consider the different pH-dependent behavior of polymer chains by construction of pH sensitive multilayers.[8]

The effect of polymer composition and also architecture on the dissociation equilibrium in polybases was studied by Suh et al.[10] It was shown, that modification of polyamines by hydrophobic lauryl groups led to the inhibition of the protonation of amino groups. Furthermore, the study of the protonation behavior of branched PEI and linear poly(allylamine) showed, that linear poly(allylamine) exhibited a low proton affinity in comparison to PEI. It was proposed that poly(allylamine) molecules had a cluster like micellar structure, in which hydrophilic and hydrophobic parts of the molecules were separated. Ammonium cations in the linear polymer were located at a relatively short distance to each other and are able to suppress deprotonation of one another.[10]

Suh et al.[10] also published interesting experimental data on a complex pH dependent behavior of different concentrations of polyamines. The authors studied the effect of different concentrations of dissolved polymer and also the effect of different concentration of charged groups per molecule on the dissociation equilibrium. This work elucidates the influence of ionic strength on the protonation/deprotonation behavior of polyamines, that can be changed by adding different salt concentration, but also is varied with the concentration of charged groups in the polymer molecules. Suh et al.[10] demonstrated that the pK_{app} of the polyamines decreased linearly as the pH was lowered. It was explained by an increased electrostatic suppression of the protonation process, when the concentration of positively charged groups in the polymer molecules was increased at lower pH values. Thus, the presence of protonated amino groups in a polymer electrostatically hinders the

subsequent protonation process. The authors propose that each amino group of the polymers can have a different pK value.

Thus Suh et al.[10] showed that the degree of protonation of PEI depended on the concentration of the polymer solution. The authors explained this phenomenon by the change in ionic strength that was observed in the deprotonated solutions of PEI. An increase in the concentration of the protonated amino groups led to an increase in the ionic strength of solution. The degree of protonation decreased with an increase in the concentration of dissolved polymer. This work clearly showed that the Debye length of dissolved weak PEs was strongly affected by concentration and nature of charged molecules in the solution. Screening of electrostatic interactions in polymer molecules strongly affected the dissociation equilibrium of weak PEs.[10]

Additionally, Burke and Barret[12] experimentally revealed a significant shift in the dissociation constants of multilayers of PAH and PAA in comparison to dilute solution values. It was found, that the number of layers, the pH of deposition solutions and ionic strength strongly affected pK_{app}. The pK_{app} of PAA and PAH increased with an increase in the pH of the assembly. However, for PAA the value of pK_{app} in the multilayers was much lower than in a dilute solution.

4. "Proton Sponge" Behavior of Polyamines

Recently, it was demonstrated, that polyamines exhibit an interesting proton binding property that is known in biology as "proton sponge" properties. First, this property was observed and described by research groups that worked on the development of biomimetic functional molecules for gene delivery.[13–16] However, till now "proton sponge" behavior is not well understood and is one of the questions that chemists seek to answer.[1a]

It was shown that polyamines and, especially, PEI were very efficient for non-viral gene transfer.[13–16] The gene transfer efficiency of PEI was attributed to its unique ability to overcome a specific barrier to gene transfer, lysosomal degradation. It was proposed that binding protons PEI molecules triggered the influx of chloride ions and, thus, increased the ionic strength inside the endosome. Due to a probable osmotic swelling the endosome underwent physical rupture.[14] In order to support this hypothesis, Akins et al.[13] compared the gene transfection efficiency of PEI and quaternized PEI. The authors proposed and experimentally proved that quaternized PEI exhibited lower effectivity.

During the last decade a lot of discussions have been evoked about the mechanism of PEI-assisted gene delivery.[16] The proton binding behavior of polyamines is not argued. However, Benjamensin et al.[16] proposed an alternative mechanism. The authors reported that the pH in lysosomes was not affected by the presence of PEI. The alternative mechanism is based on the pore formation in membranes due to an interaction between PEI and the membrane. Due to a "proton sponge" behavior of PEI the membrane tension can be increased. Thus, even if the mechanism of PEI-assisted gene delivery is an open question, it is clear, that polyamines possess a pronounced pH buffering capacity over almost the entire pH range that can be used for drug delivery and in anticancer therapy.[1a]

In order to avoid cytotoxic behavior of synthetic polyamines chitosan and its derivatives can be promising candidates.[1a] Richard et al.[17] indicated that chitosan had a similar capability to induce a "proton sponge" effect as PEI. The ionization behavior of chitosan and chitosan-DNA complexes is compared to that of PEI. Chitosan has even a higher buffering capacity than PEI in the lysosomal pH range, while the formation of chitosan-DNA complexes reduced the chitosan buffering capacity because of the negative electrostatic environment of nucleic acids that facilitates chitosan ionization.

Summarizing, "proton sponge" behavior of polyamines that is nothing else as buffering properties of weak PEs is a very interesting process that can be used for different bio applications. The proposed mechanism suggests that polycations can penetrate biological membranes and accumulate in lysosomes. Increase in the concentration of polyamines in lysosomes can definitely lead to an increase in osmotic pressure, swelling of lysosomes and their rapture. Thus, an interesting question, whether "proton sponge" properties of polyamines are important for gene delivery or weak polyamines just a useful carrier for DNA molecules that can bind, deliver and release genes on demand, is still open.[1a]

5. pH Dependent Swelling Behavior of Assembled Weak PEs

pH dependent swelling behavior of weak PEs was explained by the contribution of repulsive and attractive electrostatic interactions to the formation of collapsed and gel phases.[1a,18] Farhat et al.[19] analyzed the water content in the multilayers formed by a strong PSS and a weak PAH and found, that under ambient conditions the multilayer contained up to 10–20 wt.% of water.[19] Chi and Rubner[20] investigated the effects of charge density on swelling of weak positively charged PAH and negatively charged PAA. It was shown, that the multilayer thickness significantly increased, if the degree of ionization of the weak PE decreased below than 70–90% charged units.

A mechanism of the swelling/deswelling transitions of the pH dependent multilayers was proposed by Rubner et al.[21] It was shown, that the pH value, at which the multilayers were formed was important for the further swelling/deswelling behavior of the layers. Two different pH dependent swelling behaviors were observed. When the assembly is formed at $pH < pK_b$ and weak polybase is protonated, the film demonstrates a pH dependent swelling transition over the pH range of 2–10.5. When the layers are deposited at $pH > pK_b$, swelling/deswelling is determined by the elimination/reestablishment of hydrophobically associated PAH chain segments.

The experimental results of Rubner et al.[21] were supported by the predictions of Choudhury and Roy.[22] The study[22] revealed, that water can form hydrophilic and hydrophobic solvation shells in weak PEs. The hydrophilic solvation shell in PEI was calculated ≈0.35 nm. The hydrophobic solvation shell was ≈0.30 nm. It was shown that water molecules associated to polymer chains were ordered, and the ordering increased with the level of protonation. The unprotonated and protonated chains associate different number of water molecules. The

ADVANCED
SCIENCE NEWS
www.advancedsciencenews.com

ADVANCED
MATERIALS
INTERFACES
www.advmatinterfaces.de

PROGRESS REPORT

completely protonated molecules are hydrophilic and, thus, a thicker solvation shell can be expected.

Another interesting question is the mobility of associated water molecules in the multilayers.[1a] Schwartz and Schönhoff[23] analyzed ^{1}H spin relaxation by NMR for the investigation of the hydration of multilayers. The multilayers were formed by alternating adsorption of PSS and PAH. The experiments showed, that the adsorption of weak PAH layers led to an increase in ^{1}H spin relaxation rate, which can be an evidence of an increase in water mobility. On contrast, deposition of a strong PSS led to a decrease in ^{1}H spin relaxation rate and thus to a decrease in water mobility due to reduction in dynamic of bounded water molecules or to a decrease of the amount of water in the multilayers.[23]

Choudhury and Roy[22] calculated the relaxation time for the hydrogen bounded water molecules and water molecules, that were clustered due to hydrophobic interactions with polymer backbones. It was found, that for both water fractions the relaxation time of water molecules increased, when the polymer was protonated. These results were explained by the formation of a stronger hydrogen-bonding network in the charged system. However, if the second solvation shell was considered an increase in the relaxation time for the protonated chains was revealed. The authors proposed, that such interesting relaxation behavior of the associated water molecules can be explained by a tendency of water molecules to jump[1a] into a more favorable configuration closer to the hydrophilic centers of PEI.[22]

The self-diffusion coefficients were computed using the Einstein relationship. It was shown that the second solvation shell of the unprotonated chains has a self-diffusion coefficient $\approx 2.65 \times 10^{-5}$ cm^2 s^{-1} (at 300 K); for the first shell it is $\approx 1.16 \times 10^{-5}$ cm^2 s^{-1}. For the completely protonated system, the self-diffusion coefficients are $\approx 2.03 \times 10^{-5}$ cm^2 s^{-1}, $\approx 1.48 \times 10^{-5}$ cm^2 s^{-1}, respectively. These data prove the previously discussed tendency: electrostatic interaction in charged polymers triggers slower diffusion of water molecules, that are associated with charged groups and stimulates the diffusion of the second shell.[22]

In order to understand the relaxation properties of the multilayers it is important to understand whether the water molecules diffuse along the chain or jump to the solvation shell of another molecule.[1a] Choudhury and Roy[22] proposed that in the elongated protonated molecules the water molecules probably share their solvation shell with the nearest neighbors. In the unprotonated PEI coils the diffusion of water molecules can occur between different chains.

6. pH Dependent Morphological Changes of the Multilayers

In order to understand the order of magnitude of pH triggered conformational charges of PEs we would like to present studies of structural properties of weak PEs in protonated/deprotonated states. The different studies[22,24] showed that in unprotonated PEI chains the end-to-end distance was ≈ 2 nm and the radius of gyration (R_g) was ≈ 1 nm, which indicated the coiled form. For the elongated completely protonated system the end-to-end distance was ≈ 5.4 nm and R_g was ≈ 1.8 nm. These

parameters were calculated for 20-mer PEI. For 50-mer chains the end-to-end distance was ≈ 3.2 nm for unprotonated molecules and ≈ 8.5 nm for protonated molecules. R_g was ≈ 1.2 nm and ≈ 2.8 nm, correspondingly.[22]

In a number of studies amazing morphological changes with pH change were reported for multilayers formed by weak PEs.[1a] Rubner et al.[25] proposed a pH driven formation of microporous films of PAA and PAH. The mechanism is based on pH driven dissociation/association of polymer pairs. In result, the phase segregation and pore formation occur. The formation of pores was achieved by treatment of the PAA/PAH multilayers by acidic solution with pH = 2.4. The authors observed a significant increase in the thickness of the film. Then the relative density of the film was reduced.[25,26]

Dubas and Schlenoff[9] proposed a pH-assisted approach to the modulation of the morphology and properties of the PAA/PDADMAC pair. The films formed by low and high molecular weight PAA exhibited a pH dependent change of the thickness. The morphological changes were explained by pH dependent protonation/deprotonation behavior of a weak polyacid, PAA. The PAA molecules are more hydrophobic in the protonated state. It is interesting, that besides electrostatic interactions the PAA/PDADMAC pair can be associated via hydrogen bonding. Due to protonation of PAA the electrostatic interactions decrease, but the multilayers are stabilized by hydrogen bonds.

High-modulation morphological changes can be achieved by the deposition of charged block co-polymers on mesoporous metal surfaces.[1a,27,28] The mechanism of pH dependent high-amplitude changes of the LbL deposited block co-polymers and block co-polymer micelles is based on dissolution/collapse of the micellar core at different pH or pH dependent length and density of the micellar shell. Polymeric so-called nano-anemones were proposed by Webber et al.[29] These micelles contain poly(2-(dimethylamino) ethyl methacrylate)-block-poly(2-(diethylamino) ethyl methacrylate) (PDMA-b-PDEA). PDEA is molecularly dispersed at low pH and collapses at higher pH. Another interesting example of pH sensitive polymeric micelles are BMAADq core-shell-corona micelles.[30] The charge density of the MAA block and dissolution (at pH 4) or regeneration (at pH 7) of the shell can be adjusted by the pH of the solution. The mechanism of the reversible morphological change of these micelles is based on the electrostatic attraction/repulsion between protonated/deprotonated MAA and the positively charged quaternized poly(2-(dimethylamino) ethyl methacrylate) (Dq) blocks. The high-amplitude morphological changes of this system were used for the construction of antifouling coatings (**Figure 2**, and see also chapter 9).

7. pH Buffering Properties of PEs Assemblies and Suppression of Metal Corrosion

The unique pH dependent properties of the PE multilayers that are highlighted in the previous part are attractive for different applications. Corrosion protection is one of such application areas. Corrosion is a natural process of materials degradation or aging. The corroded surfaces loose their integrity and functions. PE multilayers are dynamic systems that can be used for
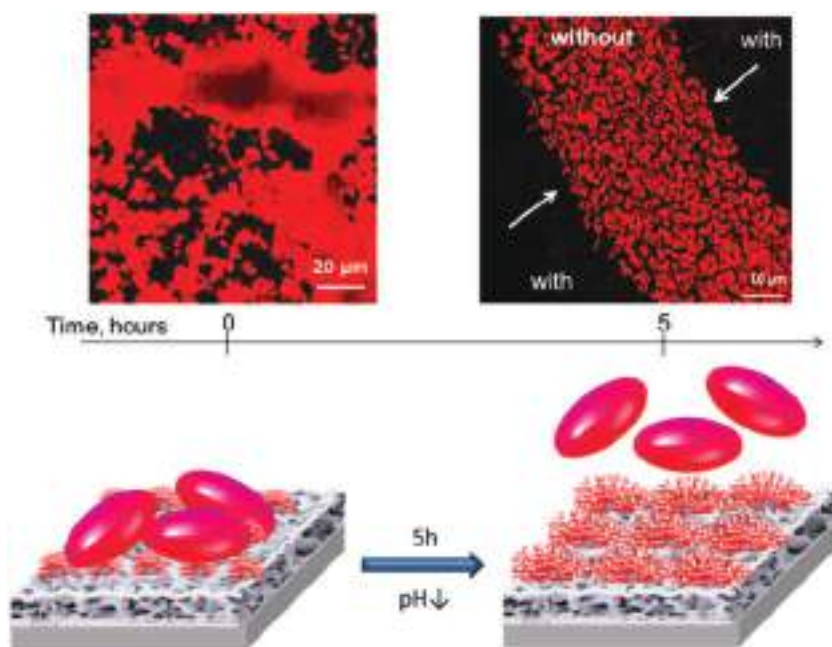
Figure 2. Confocal kinetic study (fluorescence mode) and schematic illustration of pH triggered self-cleaning behavior of the porous metal surface covered with pH responsive micelles. Labeled *Lactococcus Lactis 411* bacteria in their metabolic cycle decrease pH, micelles respond to change and increase in size, bacteria detach from the surface. Adopted with permission.[30]

the regulation of physicochemical processes on degraded surfaces. Swelling and high mobility of electrostatically bounded PE layers, pH buffering behavior of polyamines, high-amplitude morphological modulations are desirable features, that can be provided by PEs multilayers.[1a,31–36]

First, the unique pH buffering properties of polyamines can be used for the regulation of a corrosion degradation process. Metal corrosion begins, when the protection system on a surface is defected and cannot prevent a reaction of metal atoms with oxygen and humidity. It can happen due to mechanical scratch or impact of aggressive medium. Metal atoms are oxidized; this reaction is accompanied by release of H^+ on an anode. Thus, neutralization of corrosion induced local acidification can affect the kinetics of the degradation process. Such pH buffering activity of the PE multilayers can be realized by using the LbL deposited weak polyamines. As oppositely charged layers it is possible to use both strong negatively charged polymers and weak negatively charged PEs.[1a]

The layers of strong PEs are dense, probably less permeable in comparison with the film formed by weak PE. The multilayers could adhere to the surface, seal surface defects, and protect the surface from aggressive medium. Strong PEs can provide other mechanisms of anticorrosion protection.[37] For example, aluminium corrosion occurs when chlorides chemisorb onto the oxide surface and form soluble oxide-chloride complexes.[38] Thus, competitive adsorption of PEs can prevent the adsorption of aggressive anions by formation of a protective coating on the metal surface and can slow down the corrosion process.

Summarizing, strong and weak PEs can provide two mechanisms of corrosion protection of metals.[31–36] In order to reveal the contribution of these two mechanisms to the protection of

metals we compare the anticorrosion properties of three systems. LbL films of 10 bilayers of two strong PEs PSS and PDADMAC was used, two weak PEs PEI and PAA and a combination of the positively charged weak PEI and the negatively charged strong PSS.[1a,31–36] **Figure 3** shows maps of anodic and cathodic activity of the corroded metal surfaces. In situ visualization and time monitoring of corrosion degradation of metal surfaces protected by LbL films was performed using the scanning vibrating electrode technique (SVET, Applicable Electronics, USA; diameter of the Pt blackened electrode tip is 20 μm, the peak-to-peak amplitude is 60 μm, and the vibration frequency is 655 Hz). The SVET method allows monitoring local cathodic and anodic activity of the defects and in situ observation of healing behavior of the multilayers.[1a]

As seen in Figure 3 the multilayers formed by a pH buffer, PEI, and the relatively low permeable PSS demonstrate an excellent passivation of the corrosion process. The maps were recorded every 15 min, however no ionic flux can be detected. The experiments with the multilayers formed by two weak PEs, PEI and PAA, are very interesting, because it is possible to visualize pH buffering behavior of the weak PEs. The SVET images show that the multilayers can regulate the migration of ions up to 7 h, and then the ions are released into the media, which is detected by SVET in the medium. The next snapshot shows the passivation of the degradation process.[1a]

This experiment illustrates the dynamic behavior of the multilayers formed by weak PEs. Local environment can regulate the dynamics of structural relaxation in such systems. LbL assemblies of weak PEs regulate the diffusion of ions and simultaneously undergo pH triggered conformational changes of polymer chains and changes in the interchain distance. The relaxation process occurs by local pH neutralization and can be achieved by a pronounced pH buffering activity of pH sensitive materials. The water formed during neutralization leads to swelling of the polyelectrolyte multilayers and to enhancement of their mobility, resulting in faster diffusion of the polyelectrolyte chains and restructuring of the multilayers. This concept is confirmed by experiments with LbL assembled strong PEs. The multilayers of strong PEs are not efficient in corrosion protection of metal surfaces.[1a]

Additionally, as we already mentioned, PE multilayers are dynamic polymer systems due to electrostatic non-covalent interactions between oppositely charged polymers. Polymer segments are relatively mobile and restructuring of the LbL assemblies is possible in response to environmental change. pH changes following the corrosion process cause ionization of the functional groups of the PEs, which results in a lowered electrostatic interaction of the polymers as well as in an increased repulsion between uncompensated charges.[39,40] Ions can penetrate the layer structure to compensate the uncompensated charges.[41] The higher ionic concentration compared
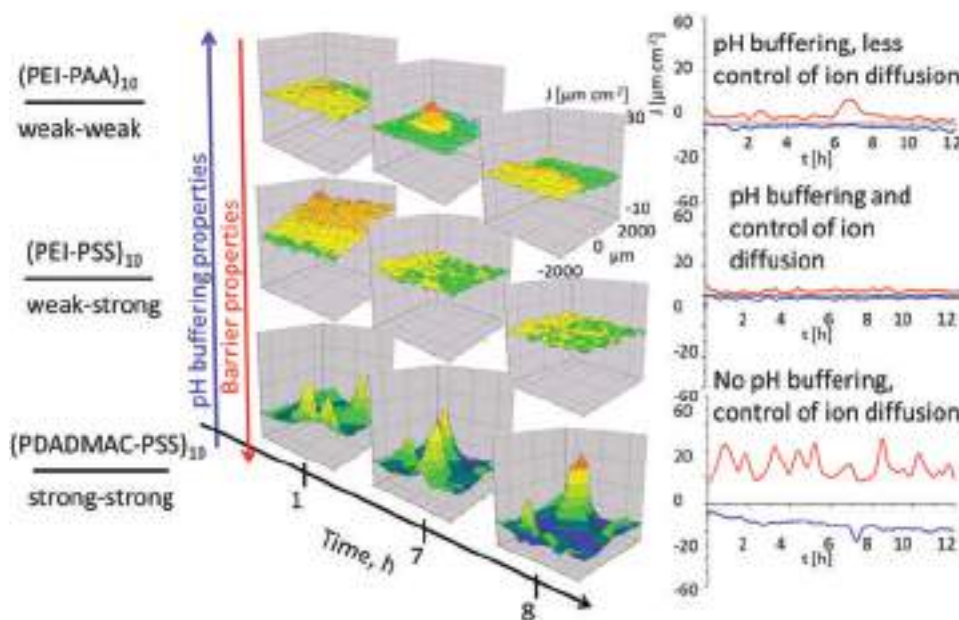
Figure 3. Illustration of the contribution of pH buffering and barrier properties of LbL assemblies. Three systems are compared: multilayers formed by 10 bilayers of two weak PEs, PEI and PAA; 10 bilayers of positively charged weak PEI and negatively charged strong PSS and; 10 bilayers of two strong PEs, PDADMAC and PSS. Time dependence of the current density changes of the damaged metal surfaces covered by PE multilayers obtained by using the scanning vibrating electrode technique (SVET): red curve – anodic current, blue curve – cathodic current (scale units: µA cm^{-2}, spatial resolution 150 µm, solution: 0.1 M NaCl). The snapshots are measured in 1, 7 and 8 h of the experiment time. Reproduced with permission.[1a] Adopted with permission.[36] Copyright 2010, American Chemical Society.

to the surrounding solution increases the osmotic pressure resulting in permeation of water into the polyelectrolyte multilayers. Thus, the PE multilayers start to swell, reorganize and heal surface defects that can appear during corrosion degradation.[1a]

8. Drug Delivery

Delivery systems based on pH responsive PE multilayers are developed to affect normal physiological process in the body (**Figure 4**) or to ensuring an optimum pH range according to
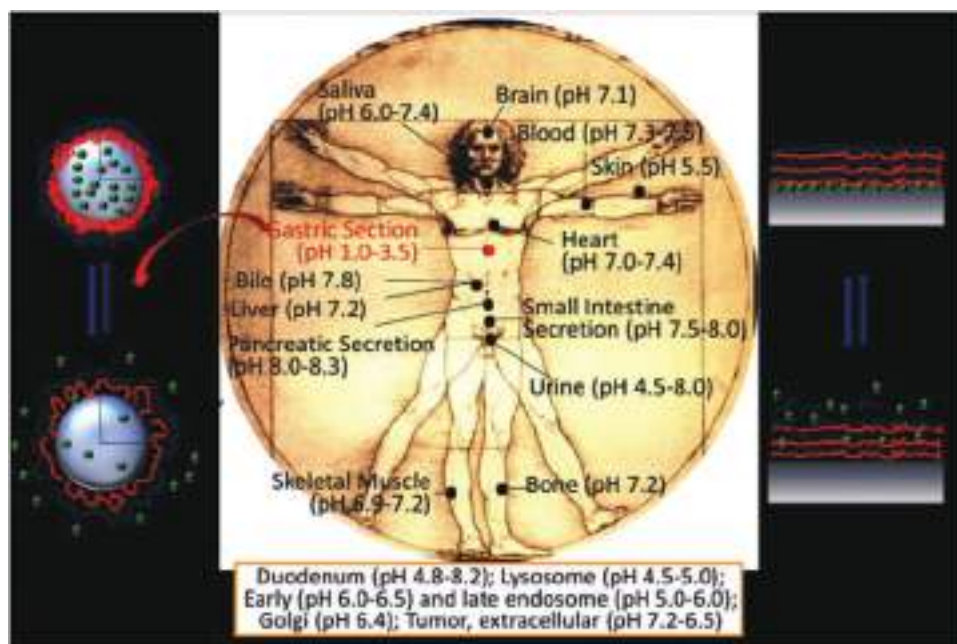
Figure 4. pH in body compartments together with pointed examples of "free" and "surface" capsules to be used to deliver drugs to the gastric section and implant development, correspondingly.

ADVANCED
MATERIALS
INTERFACES
www.advmatinterfaces.de

ADVANCED
SCIENCE NEWS
www.advancedsciencenews.com

the need. Here multidisciplinary knowledge is needed, an example being cancer tissue, which has been reported to be acidic extra-cellularly:[42] 1) to understand physiological environments; 2) suggest biocompatible multilayer design, where assembly increases the porosity, which is swelling under lower pH, but is stable in neutral one; 3) PE and delivered drug interaction, e.g. not to have later release of proteins or their denaturation; 4) experimental test loading/release behavior, stability, reversibility; 5) system fundamental understanding, modeling; 6) in vitro labora-tory tests with high significance; 7) in vivo tests. The cycle involves different scientific areas from fundamental computer models to chemistry, physics, biology and medi-cine state-of-art. Here our focus is on poly-electrolyte compositions, which change their properties under ΔpH: increase of porosity, swelling, water uptake, regulate ion migra-tion, hydrophilicity.

pH-dependent weak PEs are used for the release of chemicals from PE based capsules by changing their ionization (Figure 1), charge density resulting in the change of their microstructure – porosity, hydrophilicity, swelling behavior, water uptake, ion migration – triggered by natural pH-changes in the environment. Thus the permeability of cap-sules is tuned by a pH change. The changes in pH sensitive multilayers are preferably reversible returning the assembly to the initial state as soon as the pH is normalized.

It is especially important to take into account the change in pH in certain organs or diseased states to suggest optimal composition, physiological considerations. For example a pH change occurs along the gastrointestinal tract,[43] within the various body tissues (Figure 4). Drug encapsulation is devel-oping in two directions (Figure 4):[44] 1) "free" capsules with different sizes from micrometer to nanometer ranges; and 2) "surface" capsule formation for special surface nanoarchitec-ture connected with their applications. Both types of capsules are in focus to delivery application to guide chemicals with pH change.

It is of high priority (**Figure 5**) to control drug delivery (shown in red), having in mind the properties of PE, change in polymer mass (shown in green), mass of water (shown in blue), under different pH levels. As could be seen in Figure 5, from the graph, the amount of water absorbed by PEs can be well beyond the initial amount of polymer, even reaching ten times its value during the time interval shown. The water uptake depending on pH can be a key parameter to determine the swelling phenomenon and, as a consequence, the drug release from a matrix. A typical drug release profile via diffusion from PEs is shown in Figure 5, red circles on the right axis.[45] Release kinetics is faster at the beginning and tends to decrease with time, till all of the drug contained in the matrix reaches the dissolution medium. Release kinetics for pH sensitive sys-tems is strongly dependent from the pH: either capsule being in open or closed state. On the contrary, the mass of the drug still contained in the matrix is shown in Figure 5 as green stars,
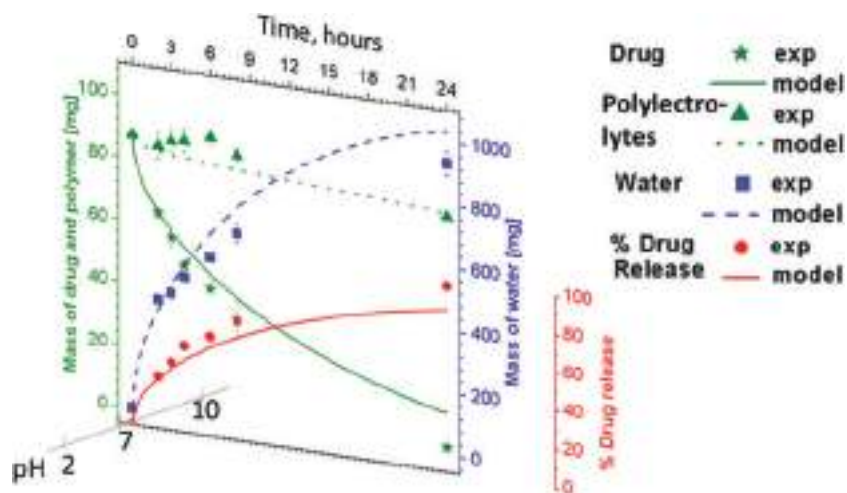
Figure 5. Example of important parameters for monitoring of polymer-based systems for drug delivery: drug and polymer mass evolutions (in green) and water mass evolution (in blue) together with the evolution of the percentage of drug released and suggestion to monitor the properties at various pH (in grey). Adopted with permission.[45] Published under CC-BY 3.0 licence 2016. Copyrighted by the authors.

on the left axis. It can be measured by the difference between the drug released and the initial amount of the drug.

Weak PEs multilayers were suggested by Sukhorukov et al.[46] for pH-controlled macromolecule delivery. Capsules were composed of 8 PSS (strong)/PAH (weak) layers. In such PEs assembly pH sensitivity can be first of all attributed to weak PE, PAH; and capsule stability to strong PE, PSS. Permeation and encapsulation of labeled-dextran macromolecules into PE capsules suggest, that capsules are more permeable ("open") at pH < 6.5 and less permeable ("closed") at pH > 7.5. The same capsules, (PSS/PAH)$_8$, were demonstrated[47] later to be open also at pH > 11. The mechanism of capsule opening is different in acidic and basic regions. Thus at pH > 11 it was shown that[47] PAH is less charged, and negative charges on PSS resulted in electrostatic repulsion, the capsule diameter increases, and in such a conformation the capsule is permeable.

It is an important issue to prepare capsules for different pH windows. Shutava et al.[48] suggested minimal permeability at pH 5.0–7.0 and maximal permeability at very high and very low pH capsules based on introducing tannic acid, a natural polyphenol, in PE assembly. Imoto et al.[49] reported acidic cap-sules composed of the weak and biodegradable polyelectrolytes chitosan and poly(G-glutamic acid) with fast release at acidic pH, and limited one at neutral and alkaline pH. Cuoma et al.[50] demonstrated the role of alginate or chitosan as the outer layer at liposome-templated PE capsules: chitosan as outer layer is stable only at acidic pH, alginate as outer layer remains stable at all the pH 4.6 to 8. The pH-optimum for the shrinking event was in the acidic range. Tong et al.[51] fabricated hollow bovine serum albumin capsules through a glutaraldehyde-mediated covalent LbL assembly method and subsequent core removal permeable for macromolecules at pH below 4.0 or above 10, while they remained impermeable in between.

Different pH during PE deposition is important to pro-vide certain capsule permeability and the capsule post-assem-bled film pH response. The PEs multilayers exhibit a history

ADVANCED
SCIENCE NEWS
www.advancedsciencenews.com

ADVANCED
MATERIALS
INTERFACES
www.advmatinterfaces.de

PROGRESS REPORT

dependent swelling behavior and molecular conformational memory[52] It was illustrated, that the same two PEs as PAH/PSS can be incorporated into a multilayer film with specifically designed molecular architectures (by virtue of assembly pH conditions), that enable them to be either virtually insensitive or highly responsive to small changes in post-assembly pH capable to deliver anionic dye molecules, e.g. rose bengal. Multilayer films assembled from PSS and PAH contained two design features: a weak PE with a pH-tunable charge density (PAH) and a strong PE with hydrophobic aromatic units (PSS). Multilayers fabricated at pH 9.5 were mostly pH sensitive; having initially relatively low degree of ionic cross-linking (see Figure 1), and a high extent of chain loops created sufficient "flexibility" for the system to access various conformational states. On contrary PAH/PSS assembled at 6.5/6.5 or 2.0/2.0 exhibits relatively pH-insensitive swelling behavior due to the relatively high degree of ionic cross-linking and interpenetration afforded by their molecular designs. Thus PAH/PSS multilayers formed at pH 9.5/9.5 are pH responsive and at, for example pH 6.5/6.5, are pH insensitive.

Delivering both macromolecules and low molecular weight species is an issue to solve. From the beginning in different groups the question was in focus. PE multilayers first were deposited onto colloids; a subsequent extraction of the colloidal template then yields hollow microcapsules.[53] The systems can be loaded with enzymes,[54] dyes[55] ions.[56] Simultaneously the core can remain and also be loaded with other chemicals. By Skorb et al.[57–59] various capsules with mesopours core and pH sensitive PE multilayered shell were suggested to be used for corrosion termination. It was discussed above that corrosion change pH of the surround medium which regulates release of active species from the capsules.

One more recent focus in the area of drug delivery is dual-, multi- loaded capsules: loading in one system several species. As an example, in the group of Tsukruk recently were reported[60] dual-loaded microcapsules based on assembly of star polymers. Sequential release of two types of molecules from the core (anionic FITC-dextran) and shell (cationic Rhodamine B molecule) of the microcapsules sequentially and independently is suggested due to different stimuli: pH decrease results in dextran release; increase in ionic strength to Rhodamine B release.

Examples for surface capsules can be implant materials. Nowadays implants preferably have biocide activity together with being in the body releasing active species, e.g. growth factors, to stimulate processes in cells.[61] To increase the loading capacity the surface is suggested to be structured to have porous surface layers. We recently compared two methods for metal surface structuring: ultrasonic surface treatment,[62–64] and anodization[65] to provide surface porous layer. It is also interesting in the area of surface capsules to have multi- responsive encapsulation systems. It was shown that effective use of this purpose magnesium based material which can provide multi-modal release.[66]

Taking together mentioned above notwithstanding there is state-of-art to have real system for delivery active species based on modulation of pH sensitive PE protonation, morphological changes, how specific interactions between different cations, e.g. H^+, Na^+, may influence deviations of ion concentrations, theory to solutions containing not only monovalent microions,

but multivalent ions Ca^{2+}, Mg^{2+}, Zn^{2+}, Fe^{3+}, interionic correlations, local pH deviation, e.g. induced by negatively charged microcapsules, etc. However even the behavior of the first suggested system (PAH/PSS)[46] is so variable and worth to discuss in regards of kinetic of proton migration, PE activation depending on PE multilayers architecture, initial parameters during assembly (pH, ionic strength, PE molecular weight, concentration, template core) together with other model systems to have further progress in this broad promising area.

9. Antimicrobial, Antifouling Coating

Architecture and stimuli-responsive behavior of pH responsive PE multilayers can reduce fouling in biomedical contexts. Fouling typically takes the form of biofilms,[67] whereas marine and industrial biofouling typically includes macrofouling[68] and inorganic fouling.[69] PE surfaces can be toxic for bacteria itself. It was shown,[70] that nanoparticles functionalized with cationic PAH, associated most significantly with bacterial surfaces and induced the greatest membrane damage and toxicity to bacteria. PEI also has a toxic effect for bacteria.[71] It was also proposed that the bactericidal effect results from the fact that hydrophobic polycationic chains were able to traverse and irreparably damage the bacterial cellular membrane, by interacting with and disrupting the negatively charged bacterial cell membrane followed by release of K^+ ions and other cytoplasmic constituents.[72] Here the importance of a thorough understanding of the specific molecular interactions between PE and cell is important and still under consideration. Thus already one top layer of PSS makes the system useful for cell growth, and allows the pH-controlled recovery of placenta-derived mesenchymal stem cell sheets.[73]

pH can be used for modulation of biocide activity of the surface, delivery and loading (**Figure 6**). Despite the PE multilayer research for biomolecule delivery, clinical translation has been limited and slow. Mechanisms of loading biomolecules and achieving controlled release through PEs are key issue not to have resulting toxicity of delivered biomolecules. E.g. delivered proteins can change their conformation being delivered, result in a negative effect. Here different types of biomolecules can be imagined like proteins, polypeptides, DNA, particles and viruses. The prospect of delivery of active species from surface capsules was already mentioned above. It was shown,[74] that effective encapsulation and release of biocide agent from surface capsules, is based on mesoporous metal sponges, to effect bacteria inactivation (**Figure 7**). Losic et al.[75] worked a lot with surface capsules to deliver several species with time-resolved release.

One more example (Figure 2) from our recent work[30] is an intelligent system, where it can be self-regulating from inorganic to organic architecture to have a pronounced effect on the cell metabolism with cell metabolism in turn affecting the PE assembly: use the cell metabolism as one of the external stimuli for self-cleaning. Ultrasonically formed silver/aluminum sponge-like surfaces as well as Ag free surfaces were used for a self-assembled immobilization of pH-responsive triblock terpolymer micelles. *Lactis* bacteria produce lactic acid in their life cycle and change the pH of the environment, PE micelles increase their corona size and push off the bacteria.
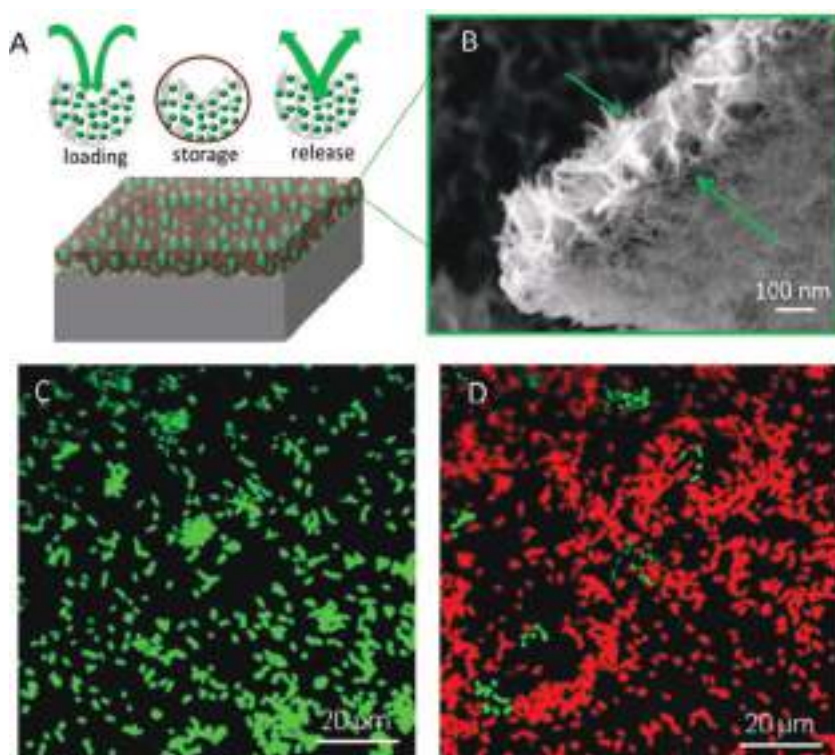
Figure 6. (A) Schematic illustration of upload, storage and release of active component and general view of capsules generated at the metal surface. (B) SEM image of the cross section of an aluminum sponge-like layer for loading with the biocide agent 8-hydroxyquinoline (8-HQ). (C, D) Confocal images show the inactivation of *E. coli* due to 8-HQ release from the surface capsule layer: (C) before release stimulation and (D) after release. Inactivated bacteria are red and live bacteria are green. Adopted with permission.[74]

much higher inactivation rate is attributed to gram-negative *P. fluorescens*. Gram-negative bacteria, like *P. fluorescens*, have a rather thin but highly resistant cell wall consisting of a single murein layer and a membrane made of lipopolysaccharides, phospholipids and proteins. This cell wall can be destroyed predominantly under attack of hydroxyl radicals, whereas superoxide ions only slightly contribute in this process.[77,79,80] By contrast, the cell envelope of *L. lactis* (gram-positive bacterium), which has a strong murein skeleton (more than 30 murein layers strengthened by inter-chain peptide bridges and molecules of teichoic acids) can be effectively destroyed not only by hydroxyl radicals but also by superoxide ions[77] These active oxygen species are long-lived ones[81] and capable to diffuse over the surface of the PE based coating; as result, not only cells contacting with titania particles but also those adhered at the titania-PE surface could exhibit deactivation under illumination. Moreover organisms, which are more sensitive to superoxide ions than OH, are affected with higher significance on TiO_2/PE than on TiO_2.

Antibacterial textiles functionalized by PE multilayers and TiO_2 photocatalyst was also suggested.[82] Looking precisely onto the results, it can be suggested, that indeed in top layer on TiO_2 is PEI, not PSS, which results in highest biocide activity of the textile. It is explained like PEI being polycationic agents induce the reorganization of the bilayer structure with the alignment of lipid head groups perpendicular to the bacterial membrane,[83] but can also confirmed our results[78] mentioned above, that PE under illumination generate ROS, that propagate due to trapping some of species in PE, but releasing lower time lived ones out. Moreover the effect is more significant under lower irradiation dose, since longer-term irradiation can result in PE photodecomposition. Highest biocide activity is easier to achieve on textile[82] covered with PEs/TiO_2, where titania is the last layer in the multilayer assembly (PEI/(PSS/TiO_2)$_n$). However the system of PEI as last layer seems to have a stronger influence on the propagation of the photogenerated species. This fact needs further investigation and discussion, since it is still expected in following the growth of use PEs multilayers propelled by the ease of film manufacture, low cost, mild assembly conditions, precise control of coating thickness, and versatility of coating materials to precise fundamental understanding and practical use for biomolecules, bacteria, cell detection and modulation in biosensing and antimicrobial surfaces.

The possibility to regulate cell adhesion was shown through patterned micelle adsorption. The antimicrobial activity clearly indicates antiseptic/disinfectant activity of the Ag/Al sponge surface. Moreover, it was show[76] that active species, e.g. release of reactive oxygen species (ROS), can result in detection of pathogenic *Lactis* bacteria releasing bacteriophages due to the effect of ROS the bacteria DNA. Different ROS has either stronger affect gram-positive bacteria than gram-negative: superoxide ions result in higher sensitivity of gram-negative bacteria.[77]

It was also shown, that PE assembly can affect ROS propagation from titania.[78] The antimicrobial properties against two different microorganisms: *P. fluorescens* (a fairly typical example of gram-negative bacterium) and *L. lactis* (a gram-positive bacterium). Light was used to generate ROS and following ΔpH on titania, but in this regime no inactivate microorganisms during the time scale of these disinfection experiments. Summarizing the results of the antimicrobial tests: the number of surviving bacteria exhibits a drastic decrease, when the cells are in contact with biocide films. The pronounced biocide activity of the coatings can be explained with generation of ROS and following ΔpH generation. Interestingly the release of superoxide-ions was higher and hydroxyl radicals were trapped in the matrix, which was confirmed by a much higher biocide activity against gram-positive *L. lactis* than against gram-negative *P. fluorescens*. By contrast, in contact with nanostructured individual sol TiO_2 film, with active release of hydroxyl redicals, a

10. pH Gradient in PEs Assemblies

Two main questions are relevant under this topic: (1) generation of pH gradients for biofabrication of membranes based on weak PEs; (2) change of pH with temporal and spatial control

ADVANCED
SCIENCE NEWS
www.advancedsciencenews.com

ADVANCED
MATERIALS
INTERFACES
www.advmatinterfaces.de
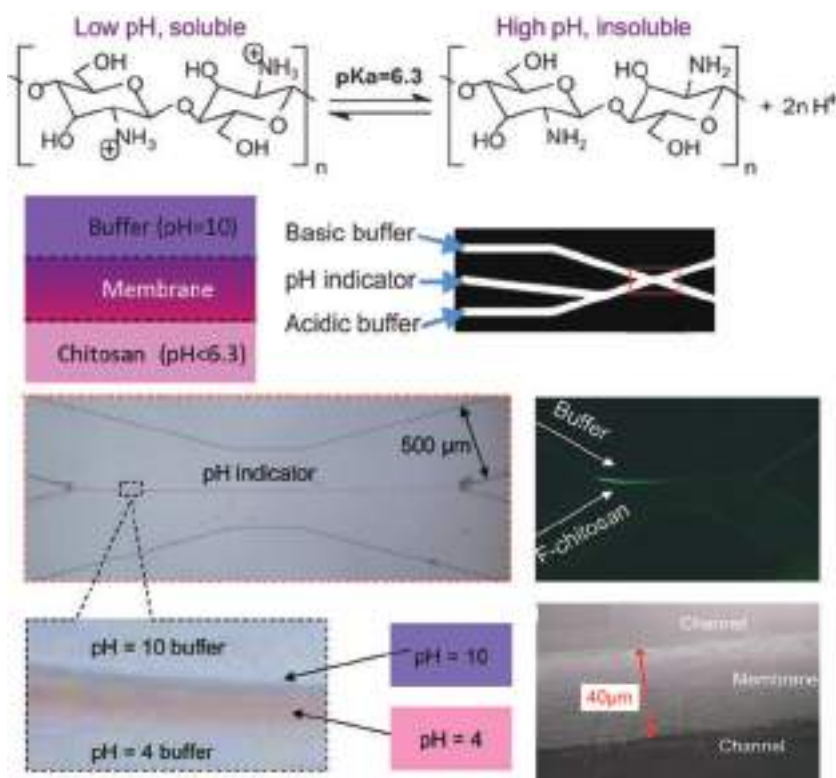
Figure 7. Generation of a pH gradient in microfluidics for in situ biofabrication of a straight chitosan membrane based on pH-responsive solubility of the polysaccharide chitosan. Adopted with permission.[85] Copyright 2011, Royal Society of Chemistry.

for manipulation with biomolecules and cells on the PEs surface.

Chitosan, a natural PE is an ideal example material, whose pH responsive properties make it uniquely valuable for biofabrication. Luo et al.[84] reported the in situ generation of pH gradients in microfluidic devices for biofabrication of chitosan membranes (Figure 7). The pH responsive polysaccharide chitosan was reported to form a freestanding hydrophilic membrane structure in microfluidic networks, where pH gradients were generated at the converging interface between an acidic chitosan solution and a basic buffer solution. As shown in Figure 7, chitosan at higher pH than the pKa of ≈6.3 become deprotonated, so that the polymer loses its charge and becomes insoluble. A simple and effective pumping strategy was devised to realize a stable flow interface, thereby generating a stable, well-controlled and localized pH gradient. Chitosan molecules were deprotonated at the flow interface, causing gelation and solidification of a freestanding chitosan membrane from a nucleation point at the junction of two converging flow streams to an anchoring point, where the two flow streams diverge to two output channels.

Chitosan was compared with PEI and heparin by Kirchhof et al.[85] Multilayers were prepared at three different pH values of 5, 7 and 9. The findings suggested that formation of PE gradients can be achieved by controlled variation of a simple parameter – the solution pH value. Water contact angle and quartz microbalance measurements show, that the resulting multilayers differ in terms of wetting behavior, layer mass and mechanical properties. The multilayer is then formed within a gradient generation microfluidic device. PEI or heparin solutions of pH 5 are introduced into one inlet, and the same solutions but at pH 9 into another inlet of the device. Behavior of the osteoblast cells on top of the multilayers proved the existence of a gradient in PEs density resulting in a cell gradient density promoting cell migration.

In the work[86] gradients of biochemical and physical cues were generated on PE films composed of hyaluronan (HA) and poly(L-lysine) (PLL) using a microfluidic device. Four different types of surface concentration gradients adsorbed onto the films were generated. These included surface concentration gradients of fluorescent PLL, fluorescent microbeads, a cross-linker, and one consisting of a polyelectrolyte grafted with a cell adhesive peptide. In all cases, reproducible centimeter-long linear gradients were obtained. Cell responses to the stiffness gradient and to the peptide gradient were studied: pre-osteoblastic cells were found to adhere and spread more along the stiffness gradient, which varied linearly from 200 kPa–600 kPa. Myoblast cell spreading also increased throughout the length of the increasing peptide gradient. This work demonstrates a method to modify PE films with concentration gradients of non-covalently bound biomolecules and with gradients in stiffness. The results highlight the potential of this technique to efficiently and quickly determine the optimal biochemical and mechanical cues necessary for specific cellular processes.

A gradient fabrication method for combinatorial surface studies that provides the equivalent of 5000 individual PEe multilayer film physicochemical conditions in a single 7 cm square film was suggested.[87] An automated layering instrument was built, which can generate a gradient of physical properties on a film in 1 dimension laterally by simultaneously changing both the location of PE adsorption and the layering conditions, such as pH or salt concentration of the PE dipping solutions. By rotating the substrate 90° after each deposition cycle, full 2-dimensional gradient combinatorial films were fabricated over many layers, spanning virtually all previous combinations of stable deposition pH and salt conditions for both PAH and PAA, a process which previously required more than 10 000 separate film samples. Surface spatial profiles of film thickness, surface energy (wettability), density (refractive index), and stiffness (modulus) were generated and correlated to assembly conditions. Optimal growth conditions were discovered not at the extremes of fabrication pH, but instead for PAH at a pH of 4–6 and for PAA at a pH around 4, demonstrating that these PE biosurfaces and this technique are suitable for optimizing high-throughput cellular growth.

Charge regulation in polyacid monolayers attached at one end to a planar surface was studied theoretically.[88] The polyacid layers were designed to mimic single-stranded DNA

ADVANCED
MATERIALS
INTERFACES
www.advmatinterfaces.de

ADVANCED
SCIENCE NEWS
www.advancedsciencenews.com

monolayers. The effects of the local pH and salt concentration on the protonation states of the polyacid layer are studied using a molecular mean-field theory that includes a microscopic description of the conformations of the polyacid molecule along with electrostatic interactions, acid base equilibrium, and excluded volume interactions. It was shown[88] that the degree of protonation can go all the way from 0% to 100%, when the bulk pH is kept fixed at 7 by changing the surface coverage of the polyacid and the bulk salt concentration. The effects of increasing protonation and the expulsion of the cations from the monolayer are reduced, when sodium ions are replaced by divalent magnesium ions. It was predicted that, in the case of a monovalent salt, NaCl, the amount of proton binding increases dramatically for high surface coverage of polyacid and low bulk salt concentration. When the polyelectrolyte is almost completely charge neutralized by bound protons, there is an expulsion of sodium from the layer.

Thin pH sensitive PAH/PAA PE film thickness gradients and spatial patterning via salt etching of multilayers was suggested by Rubner and Cohen et al.[89] The time- and concentration-dependent dissolution (etching) of PE multilayers immersed in NaCl solutions was observed. The PE film thickness decreased to a reproducible constant value, that depends upon the initial film thickness and the concentration of NaCl. As opposed to a "top-down" removal of PE chains from the film, the dissolution mechanism involved the diffusion and association of chains throughout the PEs, that leave the film in the form of PE complexes. Straightforward application of PE salt etching to pattern films, where the spatial position and amount of dissolved material are controlled, resulting in a multicolor reflector and a gradient-thickness film.

A promising topic are thin PE films, e.g. mixed PE brushes with a gradual change of the composition, ratio between two different oppositely charged surface-grafted weak PEs, across the sample.[90] The gradient of surface composition creates a gradient in surface charge density and, consequently, a gradient of the wetting behavior. The film was sensitive to pH and can be reversibly switched via pH change, consisting of poly(2-vinyl pyridine) (P2VP) and PAA.[91] This brush provided new possibilities to control surface properties upon a pH change. As compared to a neutral (nonelectrolyte) brush, electrostatic interactions may be explored as an additional parameter to regulate the response of a mixed brush. Theories predict that surface properties of a mixed PE brush are controlled by composition and charge ratio, degree of compensation of the total charge of the polymer. In the experiments previously reported[91] the mixed P2VPmix-PAA brush demonstrated switching behavior, where the top of the brush was occupied by negatively charged PAA at pH > 6.7 or positively charged P2VP chains at pH < 3.2. In conditions of electrical neutrality, both polymers formed a dense collapsed PE complex. The same composition gradient film was suggested by Ionov et al.[92]

In the works[93,94] both theory and experimental results of behavior of surface-anchored PAA brushes with gradient grafting density was studied. The theory[94] incorporated the acid-base equilibrium responsible for the charge regulation of the acrylic groups, as well as the conformations, size, shape, and charge distributions of all the molecular species. It was found, that the counterions adsorbed to the grafting

surface, overcompensating the charge of the polymer. The charge regulation within the polymer layer is determined by the interplay between the bulk pH, the ionic strength, and the density of polymer. The system tends to become uncharged with decreasing ionic strength of the solution and increasing polymer density. In all cases the charge regulation acts in order to minimize the electrostatic repulsions in the system. The local distribution of protons within the polymer layer is predicted to be very different from that of the bulk solution. The local pH within the polymer layer can be tuned by varying the solution ionic strength and the polymer surface coverage; the variation can be as large as two pH units, relative to the bulk pH.

Changing pH with spatial control remains difficult,[95] being possibly used in the design of biosensors, materials for lab-on-chip, organ-on-chip growth, etc., if the pH can be activated with other cell friendly external stimuli. A number of pH-responsive polymer films and hydrogels have been developed, biological systems typically do not tolerate substantial deviations in pH. Therefore, to apply such pH-responsive systems for biomedical or other sensitive applications, other stimuli, e.g. light, an electrochemical approach to alter local pH, while maintaining a constant, mild, bulk pH, can be effective.

Hammond et al.[96] suggested an elegant approach towards mechanomutable and reversibly swellable PE multilayer thin films controlled by electrochemically induced pH gradients. The polymer film comprised of PAH and PSS assembled at high pH (pH > 9.0), which is known to exhibit a large pH-induced swelling transition; however, relatively extreme bulk pH values (pH < 4 to swell, and pH > 10.5 to deswell) are required to manipulate the film. Negative electric potentials on gold electrodes coated with the PE film raised the local pH due to the potential induced reduction of dissolved oxygen and generation of hydroxide ions at the electrode surface. The in situ swelling state and mechanical properties of the film have been demonstrated to have 300% volume changes in the polymer thin films and had reversibly altered the mechanical properties over an order of magnitude (shear modulus between 1.9 MPa and 230 kPa, loss modulus between 620 kPa and 92 kPa, and effective indentation modulus between 19.2 MPa and 3.16 MPa).

It would be interesting to control the pH gradient via, for example, a local Red/Ox reaction of ions in the PEs assembly. Szleifer et al.[97] applied the theory to a single layer of pH sensitive PAH and the pH-independent osmium pyridine-bipyridine complex onto the Au surface modified by mercaptopropanesulfonate. The predictions from the molecular approach, validated by experimental studies, were the coupling between the protonation equilibrium of the amino groups in the polymer and sulfonate groups in the thiol and the redox equilibrium of the osmium redox sites. It was found,[97] that the variation of the film properties has a non-monotonic dependence on bulk pH and salt concentration. The film thickness shows a maximum with electrolyte ionic strength, whose origin is attributed to the balance between electrostatic amino-amino repulsions and amino-sulfonate attractions.

It would be attractive to use light to have a pH gradient, since light is a very convenient stimulus to control its localization, intensity and duration and, consequently, ratio of the generated pH gradient. By Ebara et al.[98] a photoinitiated proton releasing reaction of o-nitrobenzaldehyde (o-NBA) was suggested to have

ADVANCED
SCIENCE NEWS
www.advancedsciencenews.com

ADVANCED
MATERIALS
INTERFACES
www.advmatinterfaces.de

PROGRESS REPORT

pH responsive material separation. The surface trap and nanoparticles were both modified with the pH-responsive polymer poly(N-isorpopylacylamide-co-propylacrylic acid). The o-NBA-coated surface exhibited proton release upon light irradiation, allowing the buffered solution pH to decrease from 7.4 to 4.5 within 60 s. The low solution pH switched the polymer-modified surfaces to be more hydrophobic, which enabled the capture of the pH-sensitive polymer-coated nanoparticles onto the trap. When a photomask was utilized to limit the irradiation to a specific region, the polymer coated particle separation to only the exposed region. Via control of the irradiation, this technique enables not only prompt pH changes within the surface but also the capture of target molecules at specific channel locations. Reversibility and o-NBA stability were not discussed, although being important issues.

In our recent study[99] we suggested, that under irradiation of TiO$_2$ a series of photocatalytic reactions leads to a local change in pH, which modulates the pH sensitive PEs assembly. The efficiency of the multilayers' response was investigated with atomic force microscopy, in situ quartz crystal microbalance, confocal laser scanning microscopy and by in situ ion selective microelectrode technique for mapping the activity of protons over the surface under local irradiation. Strong and weak polyelectrolyte assemblies, including biopolymers, pH sensitive micelles were studied to regulate the diffusion of protons to have morphological changes in PEs assemblies. We have managed[100] to develop multilayers, which can be activated with light due to a pH change on the titania surface. The system is shown in **Figure 8**, irradiation in the experiment was done from back contact and adsorbed by a titania layer. In the scope of photocatalytic reactions on TiO$_2$ generation of protons was detected, which was trapped in PE assembly without proton release from the surface, but significant change in multilayer properties as thickness and stiffness. Initially the coating thickness is equal to 150 nm. Then the illumination is switched on and changes in thickness became 750 nm within 10 min of low intensity irradiation (5 mW cm^{-2}). The longer irradiation didn't result in further change of the film thickness. Colloidal probe atomic force microscopy measurements confirmed that the

LbL polymer assembly on the photoactive titania film became softer (ca. 28 kPa) during irradiation compared to the initial stiffness (ca. 1,67 MPa). In the bio-experiment cells (pre-osteoblast MC3T3) were cultivated on top of the surface. After 5 days the surface is irradiated from the bottom side. The part of the surface with titania layer activated PE assembly resulted in cell migration attributed to changes of the coating stiffness, which is known to be one of the critical parameters for the cells, and osteoblasts are known to prefer "harder" substrates. Here the following prospects for co-culturing on such a surface can be imagined: two cell lines with different preferences for substrate stiffness can be spatially separated over the surface being controlled in time.

11. Conclusions

ΔpH in polyelectrolyte multilayers results in a framework of interdependent phenomena. To find a predictive model for controllable use of a natural ΔpH to modulate surface properties for advanced applications, as anticorrosion, drug delivery, antifouling, and multifunction, it is important to focus first of all on single phenomenon. However the goal is a predictive model combining several experimental approaches with the succession of modeling approaches proposed to intelligent design of advanced systems.

The focus on ΔpH in polyelectrolyte multilayers can be suggested as the following. 1) Response of individual PEs to ΔpH, its protonation/deprotonation, is one important sub-question. 2) Multilayer architecture for basic systems, e.g. pH sensitive weak-weak, weak-strong assemblies, not pH sensitive strong-strong polyelectrolyte multilayers, and weak biopolymers, e.g. polysaccharides, polypeptides, proteins is an issue. 3) Many theoretical and experimental studies are oriented on spatially resolved diffusion of protons in multilayers in different directions. 4) How can the type of polyelectrolyte (strong – weak) affect pH buffering activity and barrier properties of films? 5) pH effect on polyelectrolyte chain mobility and conformation and, thus, on permeability, elasticity and swelling of
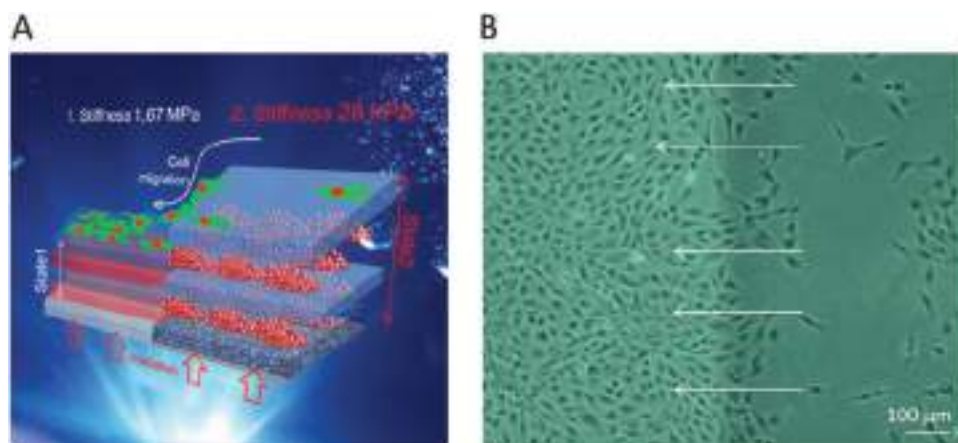
Figure 8. (A) Schematic of system for guided photocatalytic reactions on titania to produce a local pH gradient with fast trapping of formed protons and activation of pH sensitive modulation: change of stiffness from ≈2 MPa to ≈28 kPa and thickness from 150 nm to 750 nm results in cell migration over the surface. (B) Pre-osteoblast cells migrate towards the stiffer side of the substrates. Adopted with permission.[100]

films is important for design of new systems. 6) Intelligent systems can be designed for various advanced application. 7) Multi stimuli-responsive systems can be developed, for example, through the formation of hybrid pH sensitive colloid-polyelectrolyte assembly. In this review we highlight the questions to sketch the framework of multidisciplinary phenomena of the use of natural ΔpH in polyelectrolyte multilayers.

[1] a) D. V. Andreeva, *Habilitation Thesis*, Bayreuth **2016**; b) E. V. Skorb, D. V. Andreeva, *Polymer International*. **2015**, *64*, 713; c) E. V. Skorb, A. Volkova, D. V. Andreeva, *Current Organic Chem*. **2015**, *19*, 1097; d) E. V. Skorb, A. Volkova, D. V. Andreeva, *Current Organic Chem*. **2014**, *18*, 2315; e) E. V. Skorb, D. V. Andreeva, *Polymer Chemistry*. **2013**, *4*, 7547.

[2] a) T. Mauser, C. Déjugnat, G. B. Sukhorukov, *Macromol. Rapid Commun*. **2004**, *25*, 1781; b) M. Delcea, H. Möhwald, A. G. Skirtach, *Adv. Drug Delivery Rev*. **2011**, *63*, 730.

[3] a) G. Decher, J.-D. Hong, *Macromol. Symp*. **1991**, *46*, 321; b) G. Decher, J.-G. Hong, *BerBunsenges Phys. Chem*. **1991**, *95*, 1430.

[4] S. A. Sukhishvili, S. Granick, *JACS* **2000**, *122*, 9550.

[5] J.-F. Gohy, *Block copolymer micelles. In Block copolymers II*. V. Abetz, (Ed.). Springer **2005**.

[6] A. V. Dobrynin, R. H Colby, M. Rubinstein, *J. Pol. Sci. B: Pol. Phys*. **2004**, *42*, 3513.

[7] R. G. Ezell, A. B. Lowe, C. L. McCormick, Synthetic polyzwitterions: water-soluble copolymers and terpolymers. In *Polyelectrolytes and polyzwitterions: synthesis, properties, and application*. A. B. Lowe, C. L. MacCormick, (Eds.) ACS Symposium Series (Book 937), **2006**.

[8] G. J. M. Koper, R. C. van Duijvenbode, D. P. W. Stam, U. Steuerle, M. Borkovic, *Macromolecules* **2003**, *36*, 2500.

[9] S. T. Dubas, J. B. Schlenoff, *Macromolecules* **2001**, *34*, 3736.

[10] J. Suh, H.-J. Paik, B. K. Hwang, *Bioorg. Chem*. **1994**, *22*, 318.

[11] A. Katchalsky, P. Spitnik, *J. Polym. Sci*. **1947**, *2*, 432.

[12] S. E. Burke, C. J. Barrett, *Langmuir* **2003**, *19*, 3297.

[13] A. Akinc, M. Thomas, A. M. Klibanov, R. Lander, *J. Gene Med*. **2005**, *7*, 657.

[14] O. Boussif, F. Lezoualc'h, M. A. Zanta, M. D. Mergny, D. Scherman, B. Demeneix, J.-P. Behr, *Proc. Nat. Acad. Sci. USA* **1995**, *92*, 7297.

[15] A. Kichler, C. Leborgne, E. Coeytaux, O. Danos, *J. Gene Med*. **2001**, *3*, 135.

[16] R. V. Benjaminsen, M. A. Mattebjerg, J. R. Henriksen, S. M. Moghimi, T. L. Andresen, *Mol. Therapy* **2013**, *21*, 149.

[17] I. Richard, M. Thibault, G. De Crescenzo, M. D. Buschmann, M. Lavertu, *Biomacromolecules* **2013**, *14*, 1732.

[18] M. Annaka, T. Tanaka, *Nature* **1992**, *255*, 430.

[19] T. Farhat, G. Yassin, S. Dubas, S. Schlenoff, *Langmuir* **1999**, *15*, 6621.

[20] J. Choi, M. F. Rubner, *Macromolecules* **2005**, *38*, 116.

[21] K. Itano, J. Choi, M. F. Rubner, *Macromolecules* **2005**, *38*, 3450.

[22] C. K. Choudhury, S. Roy, *Soft Matt*. **2013**, *9*, 2269.

[23] B. Schwarz, M. Schönhoff, *Langmuir* **2002**, *18*, 2950.

[24] K. P. Sharma, C. K. Choudhury, S. Srivastava, H. Davis, P. R. Rajamohanan, S. Roy, G. Kumaraswamy, *J. Phys. Chem. B* **2011**, *115*, 9059.

[25] J. D. Mendelsohn, C. J. Barrett, V. V. Chan, A. J. Pal, A. M. Mayers, M. F. Rubner, *Langmuir* **2000**, *16*, 5017.

[26] J. Hiller, J. D. Mendelsohn, M. Rubner, *Nat. Mater*. **2002**, *1*, 59.

[27] A. Zhuk, R. Mirza, S. A. Sukhishvili, *ACS Nano* **2011**, *5*, 8790.

[28] I. Erel, Z. Zhu, A. Zhuk, S. A. Sukhishvili, *J. Colloid Interface Sci*. **2011**, *355*, 61.

[29] G. B. Webber, E. J. Wanless, S. P. Armes, Y. Tang, Y. Li, S. Biggs, *Adv. Mater*. **2004**, *16*, 1794.

[30] J. Gensel, T. Borke, N. Pazos-Pérez, A. Fery, A. V. Andreeva, E. Betthausen, A. Müller, H. Möhwald, E. V. Skorb, *Adv. Mater*. **2012**, *24*, 985.

[31] D. V. Andreeva, D. Fix, D. G. Shchukin, H. Möhwald, *Adv. Mater*. **2008**, *20*, 2789.

[32] D. V. Andreeva, D. Fix, H. Möhwald, D. G. Shchukin, *J. Mater. Chem*. **2008**, *18*, 1738.

[33] D. V. Andreeva, D. G. Shchukin, *Mater. Today* **2008**, *11*, 24.

[34] S. V. Lamaka, D. G. Shchukin, D. V. Andreeva, M. L. Zheludkevich, H. Möhwald, M. G. S. Ferreira, *Adv. Funct. Mater*. **2008**, *18*, 3137.

[35] D. Fix, D. V. Andreeva, Y. M. Lvov, D. G. Shchukin, H. Möhwald, *Adv. Funct. Mater*. **2009**, *19*, 1720.

[36] D. V. Andreeva, E. V. Skorb, D. G. Shchukin, *ACS Appl. Mater. Interf*. **2010**, *2*, 1954.

[37] T. R. Farhat, J. B. Schlenoff, *Electrochem. Solid State Lett*. **2002**, *5*, 13.

[38] L. Tomcsanyi, K. Varga, I. Bartik, G. Horanyi, E. Maleczki, *Electmchim. Acta* **1989**, *34*, 855.

[39] S. T. Dubas, J. B. Schlenoff, *Langmuir* **2001**, *17*, 7725.

[40] T. R. Farhat, J. B. Schlenoff, *Langmuir* **2001**, *17*, 1184.

[41] D. M. DeLongchamp, P. T. Hammond, *Chem. Mater*. **2003**, *15*, 1165.

[42] E. K. Rofstad, B. Mathiesen, K. Kindem, K. Galappathi, *Cancer Res*. **2006**, *66*, 6699.

[43] J. Fallingborg, *Dan. Med. Bull*. **1999**, *46*, 183.

[44] E. V. Skorb, H. Möhwald, *Adv. Mater*. **2013**, *25*, 5029.

[45] D. Caccavo, S. Cascone, G. Lamberti, A. A. Barba, A. Larsson, *Swellable Hydrogel-based Systems for Controlled Drug Delivery*, **2016**, http://dx.doi.org/10.5772/61792.

[46] G. B. Sukhorukov, A. A. Antipov, A. Voigt, E. Donath, H. Möhwald, *Macromol. Rapid Commun*. **2001**, *22*, 44.

[47] C. Dejugnat, G. B. Sukhorukov, *Langmuir* **2004**, *20*, 7265.

[48] T. Shutava, M. Prouty, D. Kommireddy, Y. Lvov, *Macromolecules* **2005**, *38*, 285068.

[49] T. Imoto, T. Kida, M. Matsusaki, M. Akashi, *Macromol. Biosci*. **2010**, *10*, 271.

[50] F. Cuomo, F. Lopez, A. Ceglie, L. Maiuro, M. G. Miguel, B. Lindman, *Soft Matter* **2012**, *8*, 4415.

[51] W. Tong, C. Gao, H. Möhwald, *Colloid. Polym. Sci*. **2008**, *286*, 1103.

[52] J. Hiller, M. F. Rubner, *Macromolecules* **2003**, *36*, 4078.

[53] F. Caruso, R. A. Caruso, H. Möhwald, *Science* **1998**, *282*, 1111.

[54] F. Caruso, D. Trau, H. Möhwald, R. Renneberg, *Langmuir* **2000**, *16*, 1485.

[55] X. Shi, F. Caruso, *Langmuir* **2001**, *17*, 2036.

[56] G. B. Sukhorukov, M. Brumen, E. Donath, H. Möhwald, *J. Phys. Chem. B* **1999**, *103*, 6434.

[57] E. V. Skorb, D. Fix, D. V. Andreeva, D. G. Shchukin, H. Möhwald, *Adv. Funct. Mater*. **2009**, *19*, 237.

[58] E. V. Skorb, A. Skirtach, D. V. Sviridov, D. G. Shchukin, H. Möhwald, *ACS Nano* **2009**, *3*, 1753.

[59] E. V. Skorb, D. V. Sviridov, H. Möhwald, D. G. Shchukin, *Chem. Comm*. **2009**, 6041.

[60] W. Xu, A. A. Steinschulte, F. A. Plamper, V. F. Korolovych, V. V. Tsukruk, *Chem. Mater*. **2016**, *28*, 975.

[61] E. V. Skorb, D. V. Andreeva, *Adv. Funct. Mater*. **2013**, *23*, 4483.

[62] E. V. Skorb, D. G. Shchukin, H. Möhwald, D. V. Andreeva, *Nanoscale* **2010**, *2*, 722.

[63] E. V. Skorb, D. Fix, D. G. Shchukin, H. Möhwald, D. V. Sviridov, R. Mousa, N. Wanderka, J. Schöferhans, N. Pazos-Perez, A. Fery, D. V. Andreeva, *Nanoscale* **2011**, *3*, 985.

[64] E. V. Skorb, H. Möhwald, T. Irrgang, A. Fery, D. V. Andreeva, *Chem. Comm*. **2010**, *46*, 7897.

ADVANCED
SCIENCE NEWS
www.advancedsciencenews.com

ADVANCED
MATERIALS
INTERFACES
www.advmatinterfaces.de

PROGRESS REPORT

[65] J. Kopf, S. A. Ulasevich, O. Baidukova, Y. Zhukova, J. W. C. Dunlop, P. Fratzl, P. Rikeit, P. Knaus, S. K. Poznyak, D. V. Andreeva, E. V. Skorb, *Adv. Eng. Mater.* **2016**, DOI: 10.1002/adem.201500456.

[66] E. V. Skorb, O. Baidukova, A. Brotchie, A. Goyal, D. V. Andreeva, H. Möhwald, *J. Mater. Chem.* **2012**, *22*, 13841.

[67] J. Chan, S. Wong (Eds.), *Biofouling Types, Impact and Anti-Fouling*, Nova Science Publishers, New York, USA, **2010**.

[68] M. Fingerman, R. Nagabhushanam, M. F. Thompson (Eds.), *Recent Advances in Marine Biotechnology*, Science Publishers Inc., Enfield, New Hampshire, **1999**.

[69] S. Shirazi, C.-J. Lin, D. Chen, *Desalination.* **2010**, *250*, 236.

[70] Z. V. Feng, I. L. Gunsolus, T. A. Qiu, K. R. Hurley, L. H. Nyberg, H. Frew, K. P. Johnson, A. M. Vartanian, L. M. Jacob, S. E. Lohse, M. D. Torelli, R. J. Hamers, C. J. Murphy, C. L. Haynes, *Chem. Sci.* **2015**, *6*, 5186.

[71] C. Wiegand, M. Bauer, U. C. Hipler, D. Fischer, *Int. J. Pharm.* **2013**, *456*, 165.

[72] N. Beyth, Y. Houri-Haddad, L. Baraness-Hadar, I. Yudovin-Farber, A. J. Domb, E. I. Weiss, *Biomaterials.* **2008**, *29*, 4157.

[73] O. Guillaume-Gentil, O. V. Semenov, A. H. Zisch, R. Zimmermann, J. Vörös, M. Ehrbar, *Biomaterials.* **2011**, *32*, 4376.

[74] D. V. Andreeva, D. V. Sviridov, A. Masic, H. Möhwald, E. V. Skorb, *Small.* **2012**, *8*, 820.

[75] M. S. Aw, J. Addai-Mensah, D. Losic, *J. Mater. Chem.* **2012**, *22*, 6561.

[76] E. V. Skorb, D. V. Andreeva, A. P. Raiski, N. A. Belyasova, H. Möhwald, D. V. Sviridov, *Photochem. Photobiol. Sci.* **2011**, *10*, 1974.

[77] E. V. Skorb, L. I. Antonouskaya, N. A. Belyasova, D. G. Shchukin, H. Möhwald, D. V. Sviridov, *Appl. Catal. B: Environmental.* **2008**, *84*, 94.

[78] E. V. Skorb, D. G. Shchukin, H. Möhwald, D. V. Sviridov, *J. Mater. Chem.* **2009**, *19*, 4931.

[79] M. Cho, H. Chung, W. Choi, J. Yoon, *Appl. Environ. Microbiol.* **2005**, *71*, 270.

[80] P.-C. Maness, S. Smolinski, D. M. Blake, Z. Huang, E. J. Wolfrum, W. A. Jakoby, *Appl. Environ. Microbiol.* **1999**, *65*, 4094.

[81] K. Ishibashi, A. Fujishima, T. Watanabe, K. Hashimoto, *J. Phys. Chem. B.* **2000**, *104*, 4934.

[82] G. Carre, L. Garnier, J. Moeller-Siegert, J.-P. Gies, V. Keller, P. Andre, N. Keller, *RSC Adv.* **2015**, *5*, 38859.

[83] A. M. Carmona-Ribeiro, L. D. de Melo Carrasco, *Int. J. Mol. Sci.* **2013**, *14*, 9906.

[84] X. Luo, D. L. Berlin, J. Betz, G. F. Payne, W. E. Bentley, G. W. Rubloff, *Lab Chip.* **2010**, *10*, 59.

[85] K. Kirchhof, A. Andar, H. B. Yin, N. Gadegaard, M. O. Riehle, T. Groth, *Lab Chip.* **2011**, *11*, 3326.

[86] J. Almodóvara, T. Crouzier, Š. Selimović, T. Boudou, A. Khademhosseini, C. Picart, *Lab Chip.* **2013**, *13*, 1562.

[87] M. Sailer, C. J. Barrett, *Macromolecules.* **2012**, *45*, 5704.

[88] M. J. Uline, Y. Rabin, I. Szleifer, *Langmuir.* **2011**, *27*, 4679.

[89] A. J. Nolte, N. Takane, E. Hindman, W. Gaynor, M. F. Rubner, R. E. Cohen, *Macromolecules.* **2007**, *40*, 5479.

[90] M. A. C. Stuart, W. T. S. Huck, J. Genzer, M. Müller, C. Ober, M. Stamm, G. B. Sukhorukov, I. Szleifer, V. V. Tsukruk, M. Urban, F. Winnik, S. Zauscher, I. Luzinov, S. Minko, *Nature Materials* **2010**, *9*, 101.

[91] N. Houbenov, S. Minko, M. Stamm, *Macromolecules.* **2003**, *36*, 5897.

[92] L. Ionov, N. Houbenov, A. Sidorenko, M. Stamm, I. Luzinov, S. Minko, *Langmuir* **2004**, *20*, 9916.

[93] T. Wu, P. Gong, I. Szleifer, P. Vl ek, V. Šubr, J. Genzer, *Macromolecules.* **2007**, *40*, 8756.

[94] P. Gong, T. Wu, J. Genzer, I. Szleifer, *Macromolecules.* **2007**, *40*, 8765.

[95] C. F. Lin, G. B. Lee, C. H. Wang, H. H. Lee, W. Y. Liao, T. C. Chou, *Biosens. Bioelectron.* **2006**, *21*, 1468.

[96] D. J. Schmidt, Y. Min, P. T. Hammond, *Soft Matter.* **2011**, *7*, 6637.

[97] M. Tagliazucchi, E. J. Calvo, I. Szleifer, *Langmuir.* **2008**, *24*, 2869.

[98] M. Ebara, J. M. Hoffman, A. S. Hoffman, P. S. Stayton, J. J. Lai, *Langmuir.* **2013**, *29*, 5388.

[99] S. A. Ulasevich, H. Möhwald, P. Fratzl, F. H. Schacher, F. H. Schacher, S. K. Poznyak, D. V. Andreeva, E. V. Skorb, *Angew. Chem., Int. Ed*, **2016**, DOI: 10.1002/anie.201603313.

[100] a) S. A. Ulasevich, N. Brezhneva, Y. Zhukova, H. Möhwald, P. Fratzl, F. H. Schacher, D. V. Sviridov, D. V. Andreeva, E. V. Skorb, *Macromol. Biosci.* **2016**, DOI: 10.1002/mabi.201600127; b) D. V. Andreeva, I. Melnyk, O. Baidukova, E. V. Skorb, *ChemElectroChem* **2016**, DOI: 10.1002/cels.201600268.

Effect of Cavitation Bubble Collapse on the Modification of Solids: Crystallization Aspects

Ekaterina V. Skorb,*,† Helmuth Möhwald,† and Daria V. Andreeva*,‡

†Max Planck Institute of Colloids and Interfaces, Am Mühlenberg 1, 14424 Potsdam, Germany

‡Center for Soft and Living Matter, Institute of Basic Science, Ulsan National Institute of Science and Technology, 50 UNIST-gill, Ulju-gun, 44919 Ulsan South Korea

ABSTRACT: This review examines the concepts how cavitation bubble collapse affects crystalline structure, the crystallization of newly formed structures, and recrystallization. Although this subject can be discussed in a broad sense across the area of metastable crystallization, our main focus is discussing specific examples of the inorganic solids: metal, intermetallics, metal oxides, and silicon. First, the temperature up to which ultrasound heats solids is discussed. Cavitation-induced changes in the crystal size of intermetallic phases in binary AlNi (50 wt % of Ni) alloys allow an estimation of local temperatures on surfaces and in bulk material. The interplay between atomic solid-state diffusion and recrystallization during bubble collapses in heterogeneous systems is revealed. Furthermore, cavitation triggered red/ox processes at solid/liquid interfaces and their influence on recrystallization are discussed for copper aluminum nanocomposites, zinc, titanium, magnesium-based materials, and silicon. Cavitation-driven highly nonequilibrium conditions can affect the thermodynamics and kinetics of mesoscopic phase formation in heterogeneous systems and in many cases boost the macroscopic performance of composite materials, notably in catalytic alloy and photocatalytic semiconductor oxide properties, corrosion resistance, nanostructured surface biocompatibility, and optical properties.
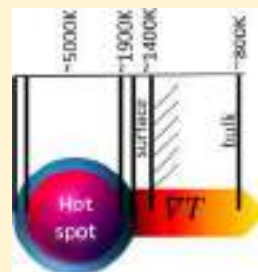
1. INTRODUCTION

A cavitation bubble collapse can modify solids by both recrystallization and interfacial solid-state reactions and phase transformations. Therefore, for a bottom-up modification of metals an important question is, up to which temperature can ultrasound heat a particle? Cavitation-induced temperature gradients are therefore the focus of this review because they provide unique conditions to trigger nonlinear processes in solids. The sonication medium is critical for both pathways of interfacial red/ox reactions and the generation and propagation of shock waves upon bubble collapse. A unique property of cavitation for materials science is that it might trigger kinetically and thermodynamically restricted processes in solids, for example, the formation of new phases in metal alloys that are not predicted by a phase diagram.

For advanced applications, reduction (hydrides) or oxidative (oxides) products are discussed. In this case, crystallization can follow the classical theory of nucleation with again some unique nature, e.g., ultrasound-induced changes of the metastability curve for bottom-up crystallization. Thus, sonochemically generated metal hydrides as prospects for hydrogen-storage materials are presented in one of the chapters.

Oxide phases in interpenetration metal foam layers for advanced catalytic and photocatalytic materials are discussed. Hybrids are pointed out as prospects to "seal against oxygen" the formed novel structures, especially if they are not stable in an oxygen atmosphere. In particular, single-step methodologies are proposed. The silicon modification is demonstrated from mechanoluminescence to amorphization, crystallization, and recrystallization. In conclusion, we summarize the advantage of novel materials synthesis and the unique nature of the ultrasonically assisted processes from the viewpoints of both top-down and bottom-up processes.

Sonochemical methodologies are presented as being time-relevant for the formation of various systems and for the control of their crystalline structures. Sonochemical methodologies have many advantages over conventional synthesis techniques because they are both environmentally friendly and cheap. Reactions that with other techniques would require the use of harsh reaction conditions (high temperature, high pressure, and organic solvents) can be carried out in aqueous systems under ambient conditions with ultrasound. Not only does this allow reactions to be carried out under milder conditions, but it also reduces the number of synthesis steps, permits the use of lower-purity chemicals, and gives higher yields. Ultrasound of high intensity can be used in a one-step formation of composite materials: interpenetrating metal—polymer hybrids, core—shell particles, two-layer composites, and multimetal composites.

There are great opportunities and challenges for further developments toward an eventual goal to enable an understanding of and the design and fabrication of encapsulation systems. We believe that this area will be explored further in the near future. The next step could be the formation of self-adaptive systems for needed applications with easy, low-cost, effective methodologies. Challenging but necessary is the

design of encapsulation systems for in vivo applications. The research concerns predominantly experiments among chemistry, physics, and in some cases biology.

2. UP TO WHICH TEMPERATURE CAN ULTRASOUND HEAT A PARTICLE?

The unique effect of cavitation on solids is based on the implosive collapse of nano- and microsized bubbles at solid and liquid interfaces.[1,2] Cavitation bubbles can be filled with plasma[3,4] and can be considered to be high-energy nano- and microreactors. Upon bubble collapse, energy is converted into mechanical (generation of microjets and shock waves), thermal (random movements of atoms, molecules, particles), and chemical energy (generation of free radicals and reactive oxygen species).[5]

The first important model of a collapsed bubble was proposed by Lord Rayleigh in 1917.[6] This model aimed to explain the cavitation damage in solids. On the basis of this model, an equation was proposed that allows a pressure and velocity prediction for collapsing vapor-filled cavities in a liquid under constant pressure. Thus, Rayleigh's work attempted to explain cavitation-driven erosion and thus the cavitation-driven processing of surfaces.

The first important question is, how high could the temperature be in collapsing bubbles? This point was addressed by Noltingk and Neppiras in 1950.[7,8] Noltingk and Neppiras proposed a thermal theory of bubble collapse. According to this so-called "hot spot" theory, extremely high temperatures can be created during bubble collapse at a high rate.

Ultrasonically triggered cavitation became a breakthrough technological approach to chemical synthesis in the early 1980s. According to Suslick,[9] "ultrasonic irradiation differs from traditional energy sources (such as heat, light, or ionizing radiation) in duration, pressure, and energy per molecule". A number of great works on the solid-state processing of solids and the sonochemical synthesis of matter have been published since that time. It is important to mention two publications of Suslick. Using different kinetics of synthesis of metal carbonyls, Suslick et al.[10] experimentally demonstrated the presence of several reaction zones in collapsing bubbles. The quenching of the hot spots in sonicated media that are macroscopically at ambient temperature and pressure is described by a thermal diffusion shell model yielding the development of a temperature gradient in a liquid.

Additionally, some other interesting physical effects of ultrasound in heterogeneous systems should be mentioned. First, Suslick and Doktycz[11] proposed that 10 μm metal particles collided in a sonicated liquid at roughly half the speed of sound. The temperature in the interfacial regions of the colliding particles reached ~3000 K. Surface melting was detected even in suspensions of molybdenum particles in an organic medium. Furthermore, near liquid–solid interfaces the asymmetric bubbles form high-speed jets of liquid.[12] High speed jets can proceed if the treated particles are larger than the size of cavitation bubbles.

Upon collapse, acoustic microbubbles form hot spots—regions with pressure of up to 500 atm, temperature of up to 5000 K, and a lifetime of a few nanoseconds.[13] A number of experimental data show that upon collapse of ultrasonically generated bubbles solid surfaces can be heated up to 2400 °C or higher, depending on the solvent.[14] This temperature is significantly higher than the bulk melting temperature of a wide variety of metals and even some metal oxides. However, fast

quenching from high temperatures exceeds rates of 10^{10} K/s. This might stimulate the development of a huge temperature gradient in the treated systems, and in the solid metal matrix fast quenching may lead to a significantly lower temperature of the metal core.

As mentioned before, the development of temperature gradients in a cavitating liquid was suggested by Suslick et al.[15] A thermal diffusion shell model describing the development of a temperature gradient in a liquid is schematically illustrated in Figure 1. Suslick et al.[15] found that in an ~200-nm-thick liquid shell around the hot spots the temperature decreased from ~5000 to ~1900 K.
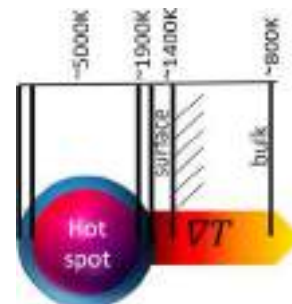
Figure 1. According to Suslick et al.,[15] in a ~200-nm-thick liquid shell around the hot spots the temperature decreased from ~5000 to ~1900 K. The temperature up to which surfaces and the bulk of the treated solids can be heated was estimated by Andreeva et al.[16] Reprinted from ref 1.

3. TEMPERATURE GRADIENT AND SOLID-STATE REACTIONS

It is obvious that the propagation of a huge temperature gradient is a unique means for the initiation of atomic diffusion and, therefore, solid-state reactions and phase-segregation processes. However, the main questions are the following: What is the temperature of surfaces and the bulk of ultrasonically treated particles? Can cavitation bubbles mesoscopically affect solids, and can cavitation-driven reactions be spatially resolved at the mesoscale? Additionally, it is interesting to determine up to which temperature the implosive collapse of clouds of cavitation bubbles can heat metal surfaces and metal bulk. Can the impact of cavitation on a metal surface trigger atomic diffusion and therefore affect the crystal size in metals or/and even trigger solid-state phase transformations in multiphase systems?[1]

To elucidate cavitation-driven diffusional processes in solid, multiphase metal-based heterogeneous materials, Andreeva et al.[16] used AlNi alloys as an interesting object with high potential in catalysis. AlNi alloys are mixtures of intermetallic compounds. Upon solidification from metal melts, the phases in such alloys nucleate and grow according to the phase diagrams. Depending on its composition, AlNi forms different mixtures of intermetallic compounds. In particular, upon cooling of an AlNi (50 wt % of Ni) melt, several phase transformations occur.[17] At 1133 °C, the AlNi phase completely transforms to the Al_3Ni_2 phase. Then, at 854 °C a slow transformation leads to the partial conversion of the Al_3Ni_2 phase to the Al_3Ni phase. This phase transformation proceeds relatively slowly, and complete transformation of the Al_3Ni_2 phase to Al_3Ni is kinetically restricted. Thus, the surface of conventionally prepared particles is covered with a phase that
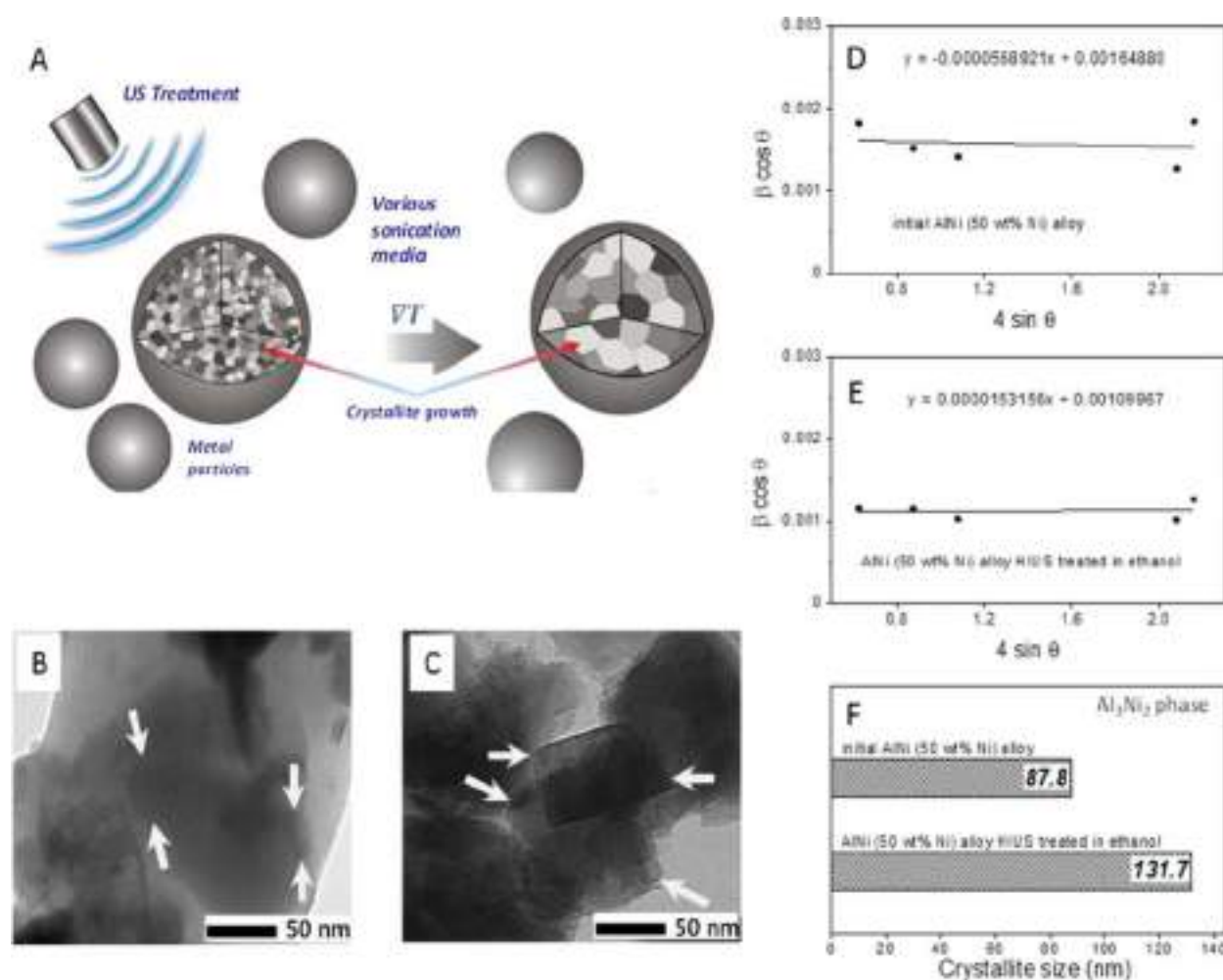
Figure 2. (A) Schematic illustration of crystal growth in cavitation at metal microparticles. TEM images of (B) initial and (C) HIUS-treated (in ethanol) AlNi (50 wt % Ni) alloys. The Williamson–Hall analysis of the Al_3Ni_2 intermetallic phase present in initial and HIUS-treated (in ethanol) AlNi (50 wt % Ni) alloys. (D, E) From the fit to the data, the strain (ε) is extracted from the slope and the crystallite size D is extracted from the y intercept of the fit. (F) Bar plot of Al_3Ni_2 intermetallic crystallite size. Adopted with permission from ref 20.

nucleates at lower temperature and has a lower surface tension.[18] However, the kinetically restricted transformations in AlNi alloys are thermodynamically favorable.[19] Thus, conventional approaches to the manipulation of composition and the microstructure of heterogeneous alloys, for example, aging, lead to the complete transformation of all phases into a thermodynamically favorable one. However, such materials lose their desirable hierarchical structure and heterogeneity.

An AlNi alloy with 50 wt % Ni solidified from a metal melt is covered with Al_3Ni and the Al phase. The Al_3Ni_2 phase is distributed in the matrix of the Al_3Ni phase. The composition-dependent surface properties of the ANi alloy including its efficiency in heterogeneous catalysis are passivated by Al and the Al_3Ni phase. Thus, the efficiency of the ultrasonically modified AlNi alloy in different catalytic processes can be established as a tool for monitoring the effects of ultrasound on the surface composition of solids. Along this line, Andreeva et al.[16,20–22] demonstrated that by using heterogeneous AlNi alloys it was possible to understand the mechanisms of ultrasound-assisted modification of solids.

One of the clearest evidences of the establishment of a temperature gradient in the particles is the growth of crystals as a consequence.[20] The crystal sizes were calculated before and after the cavitation treatment by the evaluation of powder X-ray diffraction (PXRD) patterns using the line shape analysis according to the Williamson-Hall (W–H) method (Figure 2). The size of crystals of the intermetallic phases in the treated alloy was nearly three and a half times as large (~320 nm for Al_3Ni_2), as compared to the size of the initial particles (~90 nm for Al_3Ni_2). Assuming diffusion-controlled crystal growth during the treatment period (1 h), we estimate the diffusion rate in AlNi (50 wt % of Ni) to be about ~10^{-18} m²/s. This value corresponds to self-diffusion in the metal matrix in the solid state. Thus, the evaluation of the kinetics of crystal growth showed that cavitation bubbles provide enough energy to the particles to trigger atomic diffusion in the metal matrix. However, the question arises as to whether the high-energy impact of cavitation bubbles on the metal surface is sufficient to modulate the composition of the AlNi alloy.

4. EFFECT OF SONICATION MEDIUM ON TEMPERATURE-DRIVEN CRYSTAL GROWTH

The kinetics of temperature-driven crystal growth depends on the sonication medium used.[1,16,21] It was revealed that during ultrasonic treatment the average minimum temperature, up to which ultrasound can heat the metal particles, increases in the order ethylene glycol < ethanol < decane (Figure 3A). On the basis of the obtained data, it was estimated that energy transfer
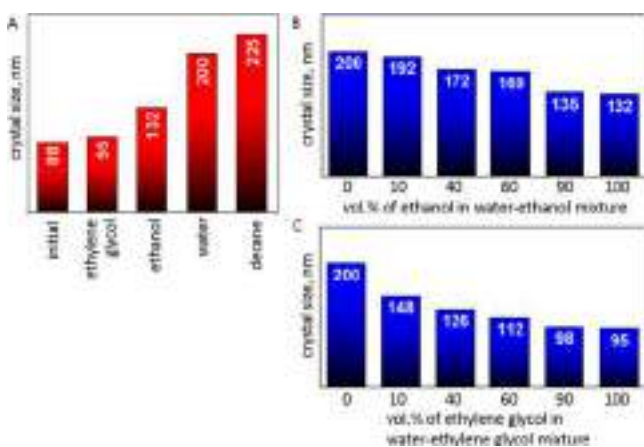
Figure 3. (A) Effect of sonication medium on the crystal size of the ultrasonically treated Al_3Ni_2 phase. The samples were sonicated for 60 min in ethylene glycol, ethanol, water, and decane. (B) Effect of vapor pressure of sonication media. The samples were treated in sonication media with variable volume fraction of ethanol in ethanol/water mixtures. (C) Effect of viscosity of sonication media. The samples were treated in ethylene glycol/water mixtures. Adopted with permission from ref 21.

from the collapsing cavitation bubble to the sonicated particle is ~17% more efficient in decane than in ethylene glycol. Thus, a relatively higher temperature on the metal surface in decane may be reached, which could trigger solid-state phase transformations—formation on the surface of the two thermodynamically favorable phases Al_3Ni_2 and AlNi.[1,16]

The temperature inside the cavitation bubble and the strength of its collapse depend on the physicochemical properties of the sonication medium.[1,24−27] A higher vapor pressure of the medium results in a lower temperature inside the cavitation bubble and weaker collapse. To investigate the effect of the vapor pressure of the medium on the kinetics of crystal growth, the metal particles were sonicated in media of various vapor pressures—water/ethanol mixtures. The calculated Al_3Ni_2 intermetallic crystallite size values vs sonication medium with different vapor pressures are shown in Figure 3B. Indeed, a gradual decrease in the crystal growth rate with a vapor pressure increase was observed.[21]

Another physical property that could influence the efficiency of energy transfer to sonicated matter and thus can affect the kinetics of crystal growth is viscosity.[24−27] A higher viscosity of the sonication medium might inhibit the energy propagation from a collapsing cavitation bubble. For this reason, the particles were treated with HIUS in media of various viscosities—water/ethylene glycol mixtures. As expected, upon monitoring the Al_3Ni_2 intermetallic crystal size (Figure 3C) it was observed (Figure 3B) that by increasing the viscosity of the sonication medium the efficiency of energy transfer to the sonication matter decreased, which led to slower kinetics of crystal growth.[21]

5. CAVITATION TRIGGERS KINETICALLY RESTRICTED TRANSFORMATIONS ON THE SURFACES OF HETEROGENEOUS SOLIDS

It is interesting that the thermal impact of ultrasound stimulates the pronounced compositional readjustment in alloys.[1,22] The phase transformations occur preferentially at solid−liquid interfaces and cannot be detected by a bulk PXRD but are clearly seen in the solid-state ^{27}Al nuclear magnetic resonance

(NMR) spectra. The skin effect, namely, the restricted ability of high-frequency electromagnetic fields to penetrate far into conducting as well as paramagnetic and ferromagnetic materials[28] such as aluminum, enhances the spectral intensity for intermetallic phases near surfaces, whereas that from the core of the particles is damped. In comparison with the results of the PXRD data, which are representative of the bulk or entire composition, the preferential segregation of intermetallic alloys near solid−liquid interfaces can be investigated. Thus, the interpretation of the spectral intensities yields the spatially resolved monitoring of ultrasonically induced phase transformations in the skin layer of AlNi alloys.[1] An analysis of the ^{27}Al NMR spectra revealed a decrease in the intensity of signals that are assigned to the Al_3Ni phase, an increase in the intensity of the Al_3Ni_2 signal, and the appearance of the signal assigned to the AlNi phase. Al_3Ni_2 forms from Al_3Ni at 854 °C, and AlNi forms from Al_3Ni_2 at 1133 °C. These changes are kinetically restricted but thermodynamically favorable. The enthalpies of formation of the intermetallic phases (ΔH(AlNi) $\approx$ −70 kJ/mol, ΔH (Al_3Ni_2) $\approx$ −65 kJ/mol, and ΔH (Al_3Ni) $\approx$ −45 kJ/mol)[29] confirm that the AlNi and Al_3Ni_2 phases are thermodynamically more stable than the Al_3Ni phase. Thus, we arrive at the picture in which the collapse of cavitation bubbles on/near metal surfaces triggers a local temperature increase up to 1133 °C, where the solid-state phase transformation proceeds. These phase transformations locally occur at the mesoscale. On the basis of the ^{27}Al NMR data, it was confirmed that the thermal impact of cavitation triggers kinetically restricted transformations on the surfaces of heterogeneous metal alloys.[1]

These results[1,22] showed that ultrasonic treatment leads to the formation of materials with a composition gradient. The composition of the surface of such materials is different from the composition of the core of the particles. This is one of the clear evidences of the propagation of a cavitation-driven huge temperature gradient. The solid-state transformations occurred on the surfaces of the particles, whereas in the particle core, crystal growth was observed.[1]

6. REDUCING VS OXIDIZING MEDIA: EFFECT OF CAVITATION ON THE FORMATION OF NEW CRYSTALLINE PHASES

Cavitation induces pressure changes; therefore, the oscillation of atoms leads to the cleavage of molecular bonds and the formation of free radicals and active species.[1,30] In aqueous media, the formation of both short-lived free radicals and reactive oxygen species with a longer lifetime occurs. Recently, it has been shown that even in aqueous media the cavitation-induced cleavage of water molecules produced both reductive and oxidative species (Figure 4). Thus, the pathways of sonochemical red/ox processes depend on the used systems.[31] This means that cavitation-induced interfacial red/ox reactions can yield the formation of new materials and/or phases.

Control of crystallinity can be achieved by exploiting different sonochemical modification pathways that occur in oxidizing and reducing media, namely, different interfacial red/ox reactions and surface etching by free radicals.[1,32,33] In water, the interfacial red/ox reactions might result in the continuous oxidation of the metal surface and the formation of new metal oxide phases. Water sonolysis yields the production of highly reactive species, including strong oxidants such as $^\bullet OH$, $^\bullet OOH$, and hydrogen peroxide.[34] These excited species chemically etch
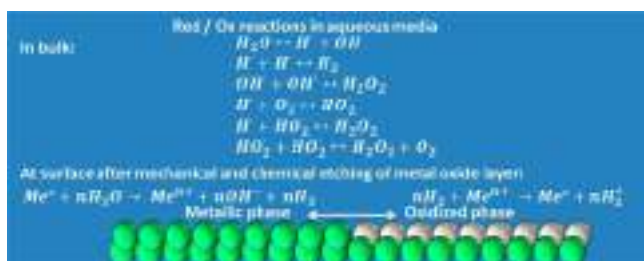
Figure 4. Sonochemical bulk reactions in aqueous media and possible interfacial red/ox reactions in ultrasonically treated metals. Reproduced from ref 1.

and oxidize metal surfaces. Thus, in an aqueous medium it might be possible to achieve the growth of new crystalline metal oxide phases.[1]

In a reducing medium (ethanol, ethylene glycol), the metal surface can be reduced by reducing agents that are generated by ultrasonically induced red/ox reactions.[1,35,36] The kinetics and mechanisms of ultrasonically triggered red/ox reactions depend on the reducing media. It is known that ethanol molecules can scavenge hydroxyl radicals and form the less active α-hydroxyethyl radical that prevents the metal surface from oxidizing.[1,37] In ethylene glycol, metal surfaces might be effectively reduced via the acoustically enhanced polyol mechanism. The even higher efficiency of ethylene glycol compared to that of ethanol in the ultrasound-assisted interfacial reduction might be explained by two possible reaction pathways.[1,23] First, we should consider the mechanism of reduction of metal surfaces by ultrasonically generated reducing agents. These agents, formed from ethylene glycol, are probably less mobile in the relatively viscous ethylene glycol, and thus recombination may not occur as fast. Thus, reduction in the more viscous medium of ethylene glycol might be more efficient as compared to that in less viscous ethanol. Second, ethylene glycol is a well-known strong reducing agent[1,38] and is

widely used for the reduction of noble metal compounds (known as the polyol process). It was shown that the polyol process is thermodynamically unfavorable and requires additional energy supplied to the system. In the presence of ethylene glycol, the reaction medium can be macroscopically heated to 60 °C.[1,39] This temperature is sufficient for lowering the oxidative potential of ethylene glycol, which promotes an easier reduction of metals.

Accordingly, the red/ox potential of media including an aqueous medium, ethanol, ethylene glycol, decane, and others is one of the factors responsible for the modulation of crystallinity, composition, and morphology of metal surfaces on demand. However, the role of the interfacial red/ox reactions in pathways of cavitation-driven modulation of the composition and morphology of metal surfaces is still an open question.[1]

Different crystal sizes observed for samples prepared in different sonication media are due to media-dependent kinetics of grain growth. The kinetics of atomic diffusion depends on the temperature gradient that develops in a metal matrix and is controlled by the sonication medium used. Slower crystal growth in ethylene glycol can serve as evidence of lower temperature of the metal matrix and thus a smaller impact of cavitation bubbles on the metal surface in a viscous sonication medium.[1,16,20−23] Additionally, it is also important to consider the effect of cavitation media on the formation of new crystalline phases via sonochemical interfacial red/ox reactions.

It was demonstrated that the impact of cavitation bubbles on metal surfaces can change the morphology and mechanical properties of metals. Light microscope (LM) images of the cross sections of the metal (here Al was used) layers treated for 1 min showed the presence of cracks in the Al layers[40] (Figure 5B2,3;D3). The formation of cracks in metal layers was explained by a decrease in the mechanical strength of the samples with larger crystals. The cross sections of the Al layers revealed the material segregation and destruction of layer integrity. The cross section of the Al layer treated for 10 min in
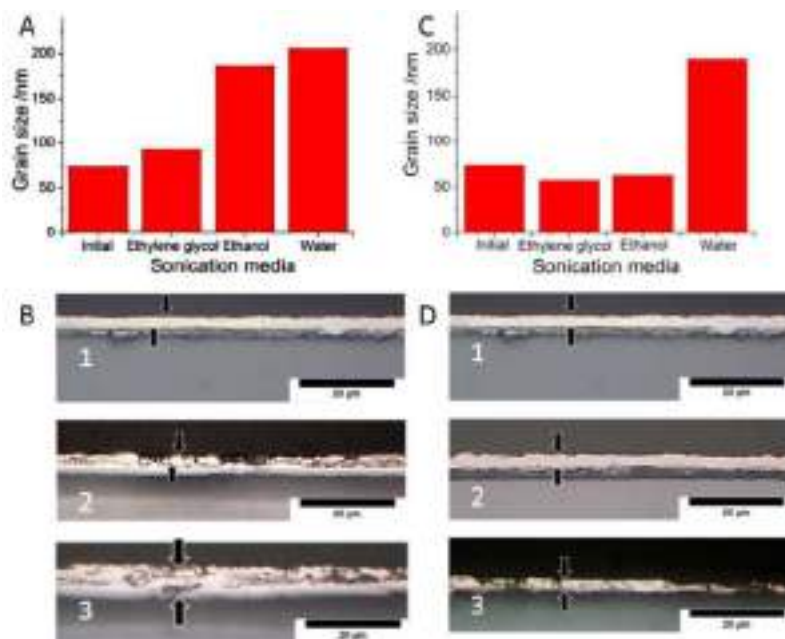
Figure 5. Grain size of initial Al and (A) 1 and (C) 10 min of ultrasonically treated Al in ethylene glycol, ethanol, and water and corresponding light microscope images of cross sections of the ultrasonically treated Al layers in (1) ethylene glycol, (2) ethanol, and (3) water for (B) 1 and 10 min (D) of sonication time. Reproduced from ref 1. Adopted with permission from ref 40.
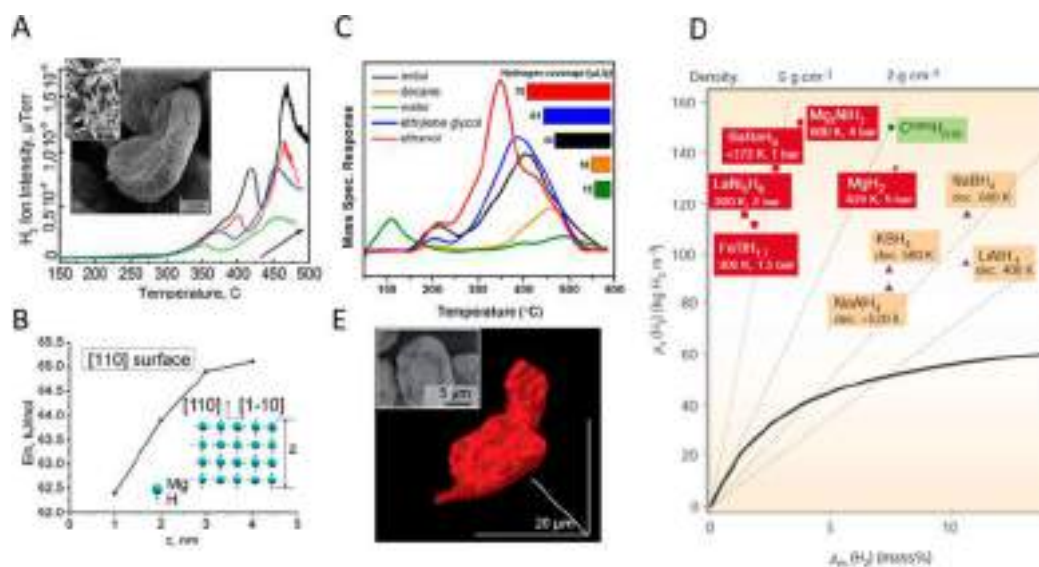
Figure 6. (A) Temperature-programmed desorption (TPD) of hydrogen from the sonogenerated magnesium−hydrogen nanostructure. Insets show electron microscopy (SEM) images of magnesium particles after sonication (scan rate 5 K/s). (B) Desorption energies of different slab thicknesses of hydrogen within the DFT level normalized per number of Mg atoms. Reproduced with permission from ref 45. (C) Effect on hydrogen TPD profiles for initial and HIUS-treated samples of AlNi (50 wt % Ni) particles in different sonication media. Reproduced with permission from ref 23. (D) Highlight of possible future structure likely to form sonochemically (in red) based on the graph of stored hydrogen per mass and per volume presented in ref 47: comparison of metal hydrides and some carbon nanotubes. Adopted from ref 46. (E) On the basis of ref 48, it can be expected that the sonochemically formed magnesium polypyrrole hybrid, shown in confocal (inset, SEM) images, has even more potential for hydrogen storage than those without polypyrrole. Reproduced with permission from ref 49.

reducing media (ethanol and ethylene glycol) has very smooth morphology (Figure 5D1,2). This correlates very well with the relatively small crystal size of these samples as estimated by XRD (Figure 5C) and ascribed to recrystallization and structure refinement.

The morphology of the cross sections of the samples sonicated in an oxidizing medium (water) reveals the formation of cracks and failures (Figure 5B3,D3) due to the formation of new phases. Therefore, the question arises as to whether it is possible to distinguish the contribution of chemical and physical effects on the modification process.[1]

Using X-ray photoelectron spectroscopy (XPS) surface analysis, the effects of reducing and oxidizing sonication media with different physicochemical properties on the surface composition of metal surfaces were compared.[21−23,41−43] As expected, the results indicated that the metallic/oxidized phase ratio increased for samples sonicated in reducing media.[21−23] In oxidizing media, the formation of metal oxide phases was established.[41−44]

Surprisingly, for AlNi (50 wt % of Ni) microparticles sonicated in an aqueous medium the presence of the Ni° peak was observed in the spectrum of the sample sonicated for 50 min and was not observed in the spectra of the samples sonicated for 40 and 60 min.[41] Such an interesting dependence of Ni° concentration on the surface vs sonication time was explained by a possible reduction process that occurred in the porous matrix even in the aqueous medium. The metallic phases are not only oxidized during ultrasonic treatment in water but also serve as effective donors of electrons and thus are responsible for producing H_2.[1]

7. SONOCHEMICALLY GENERATED METAL HYDRIDES AS PROSPECTS FOR HYDROGEN-STORAGE MATERIALS

The activation of metals by H_2 can be concomitantly triggered by the sonochemical process and is regulated by the medium or metal.[1] Reactive Al and Mg are not only oxidized during ultrasonic treatment in water but also serve as effective donors of electrons, resulting in H_2 production. Sonochemical modification of Al and Mg leads to the simultaneous formation of mesoporous metal frameworks and the generation of H_2 in the pores.[1] Magnesium as one of the most reactive metals can be discussed as a model.

The sonication of aqueous suspensions of Mg leads to the formation of highly active hydrogen containing magnesium of different compositions. Measurements of temperature-programmed desorption (TPD) of hydrogen (Figure 6A) reveal the presence of hydrogen in the sonicated Mg.[45] Moreover, several adsorbed hydrogen clusters can be suggested because there are at least two peaks visible in the spectrum. The calculated energy of hydrogen desorption is ca. 65.7 and 389.3 kJ. The concentration of the residual hydrogen in the sonicated and dried Mg powder was calculated to be ca. 1.13 mL mg^{-1}. Both Mg and MgH$_x$ clusters can be formed. Some of the possible geometries of MgH$_x$ were postulated recently by density functional theory (DFT) (B97) calculations.[45] Comparable to the system were hydrogen-enriched Mg$_{15}$H$_x$ clusters.

The extra hydrogen atoms are less strongly bound to the hydride structure and can therefore be released at lower temperatures. Mesoporous foam structures were formed with different nanosized units of MgH$_x$ slabs in the composition.[45] The energy of total hydrogen desorption from each slab within the hybrid PBE0 method was calculated by DFT for different thicknesses of MgH$_2$ crystal (100) slabs.[45] It was shown that complementary to our experimental data are slabs with a

thickness of between 2 and 3 nm. The entire dehydrogenation of MgH_2 slabs, the sum of desorption energies of all H layers, is about 65 kJ mol^{-1} for (110) with z = 3 nm (Figure 6B). This value is very close to the experimentally obtained value. The ΔH^o_{298} value of the entire dehydrogenation was calculated only for the 1 nm slab (110). It is 59.3 kJ mol^{-1}, whereas the electronic energy is 62.3 kJ mol^{-1}. The difference of 3 kJ mol^{-1} is vanishingly small, less than the error of application of different exchange correlation functionals. In such a way, the first peak of H_2 thermodesorption (65.7 kJ mol^{-1}) is most probably that of desorption of the whole hydrogen from MgH_2 nanoparticles of several nanometers in size. This is less than $\Delta H^o_{298}(MgH_2)$ = 76.46 kJ mol^{-1} as a result of the unique morphology of MgH_x produced sonochemically, and this is promising for solid hydrogen storage (Figure 6E).

For the AlNi (50 wt % of Ni) particles sonicated in water, a single low-temperature peak in the temperature-programmed desorption (TPD) profile might represent H_2 incorporated into the aluminum hydroxide matrix (Figure 6C).[1]

In contrast, it was shown that upon HIUS treatment of metal particles in reducing media the desorption maximum (peak 2) was shifted toward lower temperature. Thus, ultrasonic treatment led to the formation of hydrogen-containing phases with lower desorption energy values. The activation energy of hydrogen desorption was calculated to be 161 kJ for initial AlNi (50 wt % of Ni) particles and 92 kJ for those treated in ethanol. Additionally, the lower limit of H_2 volume present on the surface of the initial particles and the ultrasonically treated particles was estimated (Figure 6). The maximum hydrogen content was measured in the case of the sample treated in ethanol, whereas treatment in water led to a significant decrease in H_2 content. Thus, HIUS can be used for the tuning of metallic and oxidized phases in metal particles. It was shown[1,21−23] that the cavitation-driven modification of metal surfaces in ethanol significantly enhanced the electrochemical activity for hydrogen evolution reactions in comparison to that for initially inefficient metal surfaces. The cavitation-assisted enhancement of electrocatalytic properties of metal surfaces was explained by the formation of hydrogen-containing phases with relatively low hydrogen desorption activation energy.[1,44]

The pathways and kinetics of cavitation-driven sonochemical red/ox reactions depend on the media used. Choice of media is thus crucial for tuning the crystallinity, morphology, and composition of metal surfaces.[1] Although the use of water as a medium allows us to create an efficient hydrogenation catalyst,[41−43] switching to pure ethanol enables the activation of the same metal particles toward the electrocatalytic production of hydrogen.[21−23]

The following interplay for composite-metal-based hydrides can emerge if one follows the graph of storage of hydrogen per mass and per volume of different materials discussed in detail in ref 46. Sonochemical formation of nonequilibrium low-energy hydrides can be an attractive method that is economically and ecologically reasonable. Thus, following Figure 6E, one can consider studying composites of, for example, MgNi and FeTi after sonochemical treatment of the material.

Haas and Gedanken also highlighted[47] a combination of sonochemistry and electrochemistry, called sonoelectrochemistry, as a prospect for the formation of metallic (Mg) nanoparticles for hydrogen storage. Metallic magnesium particles (4 nm) were prepared by the sonoelectrochemical method. The precursors were the Grignard reagents, ethyl magnesium chloride, and butyl magnesium chloride, which were dissolved in THF or DBDG. In order to increase the ionic conductivity of the ether-based Grignard solutions, $AlCl_3$ was added to the solution. The $MgCl^+$ formed in this reaction was an electrochemically active species. The Mg deposition–dissolution is not a simple two-electron process of Mg ions but is in fact more complicated. The material deposited on the cathode was characterized as magnesium by XRD measurements. No active reducing agents are known to reduce a metal as active as Mg. The only way to chemically reduce Mg ions is to use another metal with a more negative reduction potential, such as Na or Li. It is therefore clear that only electrolytic methods could lead to the reduction of Mg ions. Sonoelectrochemistry is such a technique, which, in addition, produces the metal as a powder composed of nanoparticles. Moreover, the present method is considered to be a promising technique for the fabrication of a large number of nanometal particles. In the case of reactive metals, avoiding oxidation is a major task.

The sonochemical technique can help to obtain hydrides by "keeping out the oxygen", where the hydrides have a layer of polymer around them to prevent their oxidation under ambient conditions while enabling reversible hydrogen storage. Jeon et al.[48] demonstrated the presence of Mg in a gas-barrier polymer matrix. In this regard, attention also can be devoted to the direction of sononanoengineered magnesium–polypyrrole hybrids (Figure 6E).[49] The ultrasonically assisted preparation of metal–polypyrrole hybrids was suggested.[49,50] Hybrids were prepared through the sonication of metal and pyrrole without initiator or with the polymerization initiator in water and alcohol solutions. The properties of the obtained hybrids were found to depend on the ultrasonic conditions.

8. ULTRASOUND-INDUCED CHANGES IN THE METASTABILITY CURVE FOR BOTTOM-UP CRYSTALLIZATION

Sonochemistry is a unique tool for the synthesis of alloys, oxides, and intermetallics via high-temperature reduction. Because of a low-temperature solution chemistry synthesis route, a number of new metastable phases can be formed.[19−22] Sonochemical approaches facilitate the synthesis of nanoscale alloys and intermetallics. Colloidal metals, alloys, oxides, and intermetallic NPs synthesized through the bottom-up sonochemical approaches give rise to the smallest nanostructures owing to the accumulation of atoms and molecules via carefully controlled sonochemical reactions.[51]

In the bottom-up sonochemistry route, colloidal NPs are prepared from the reaction of molecular precursors, such as metal salts, metal–organic compounds, and metal–ligand complexes in a medium by chemical reduction of the corresponding metal salts with suitable reducing agents or by heating to an appropriate temperature in the presence of some stabilizing agents to regulate the growth of the NPs as well as induce a repulsive force opposed to the van der Waals forces, which in turn provides stable NPs in solution.[51] The commonly used stabilization procedure for NPs involves electrostatic, steric, and electrosteric stabilization using stabilizing agents such as ligands, surfactants, soft templates, and coordinating solvents.[52−54] As a consequence, NPs extracted from their growing reaction mixture are individually distinguishable and free-standing, having single or polycrystalline domains with the desired geometry and chemical composition, which generally reflects their characteristic properties. On the basis of the synthesis technique used to achieve NPs, they can also possess a monolayer of firmly surface-bound capping materials that

impart solubility in addition to stability to the particles and also regulate their interactions with the environment.[55]

The first stage of any crystallization process is nucleation, which is attributed to the appearance of a new phase, a nucleus in the metastable primary phase. The nucleus acts as a template for crystal growth.[55] Following classical nucleation theory,[56] a thermodynamic system tends to minimize its Gibbs free energy; in other words, it maximizes the entropy of the whole system. Sonochemistry is unique in one-pot high-temperature local chemistry and low-temperature solution chemistry with a number of new, possible metastable phases.[1]

Moreover, one can vary the initial composition of the sonication medium to induce the prospective formation of differently organized (Figure 7A) metal composites including
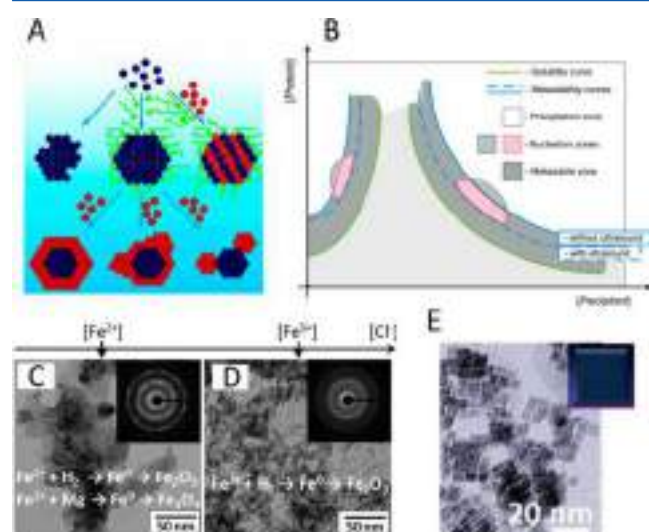
Figure 7. During the bottom-up approach for the formation of new crystalline structures, classical mechanisms (A) can interplay with sonochemical reactions and ultrasonic media. (A) Classical pathways for the synthesis of multimetallic core−shell or core−shell-like nanoparticles from metal precursors. Reproduced with permission from ref 59. (B) Influence of ultrasound on a protein crystallization phase diagram. Ultrasound changes the metastability curve, resulting in different crystal formation.[60] (C−E) Sonochemical synthesis from different precursors affects the formed structures. For example, we show TEM images of the (C) Fe_3O_4−Fe_2O_3 dendritic structure, and formation reactions with the two reducing agents, hydrogen and magnesium, are introduced as reducing agents with Fe^0 as the intermediate. (D) Fe_2O_3 magnetic rod-shaped nanoparticles and reaction-point hydrogen as the main reduction agent with Fe^0 as the intermediate. Insets show the electron diffraction of the samples. Reproduced with permission from ref 45. (E) The same reaction as in (D) in the presence of polymer can result in cubic Fe_2O_3 magnetic nanoparticles due to the process known from classical theory (A). Reproduced with permission from ref 61.

core−shell and intermetallic particles by varying the inorganic precursors and organic molecules in water-based or water-free media. Depending on the ultrasonic parameters,[57] one can expect different compositions of the formed material. In principle, the synthesis of multicomponent heterogeneous nanostructures, including dendrite, particle-on-particle, raspberry, and flower, is thermodynamically favored.[58] The synthesis is possible because the heterogeneous nucleation of a second component on the existing nanoparticle seed or core has a lower critical energy barrier; that is, the overall excess free energy is lower than for homogeneous nucleation. Depending

on the overall excess energy, which is largely related to the surface and interfacial energy terms, and the strain energy because of lattice mismatch at the interface, three different major types of nanostructures form, namely, layer-by-layer, island-on-wetting layer, and island growth modes (Figure 7A).[59] When the interfacial structures are not known or cannot be well-defined or the shape of the nanostructure is important, a generic description based on the morphology, such as raspberry, nanoflower, dendrite, particle-on-particle, and core−shell nanoparticles, is often used.

It is interesting that in a fact shown by Crespo et al.[60] ultrasound can be used as a nucleation promoter because it decreases the energy barrier for crystal formation (Figure 7B). Crystallization experiments were carried out with and without ultrasonic irradiation using commercial crystallization plates placed in temperature-controlled water baths. The nucleation-promoting effect introduced by ultrasound is reflected in the reduction of the metastable zone width, as measured by the isothermal microbatch technique. The same effect was confirmed by the increased number of conditions leading to the formation of crystals, when vapor diffusion techniques were carried out in the presence of ultrasound. By inducing faster nucleation, ultrasound leads to crystal growth at low super-saturation levels, which are known to yield better diffraction properties. In fact, XRD data sets show an improvement if ultrasound is used. Besides the immediate application of ultrasound in nucleation promotion, the diffraction results also suggest a promising application in crystal quality enhancement.

Besides the regulation of sonochemical parameters and the medium, template sonochemical synthesis to control bottom-up particle formation can be mentioned. In our group, we recently presented sonogenerated magnesium−hydrogen sponges (Sono-RHT) for effective reactive hard templating.[45] The formation of differently organized nanomaterials is possible by the variation of sonochemical parameters and solution composition: composite dendritic Fe_2O_3/Fe_3O_4 nanostructures (Figure 7C) starting with the Fe(II) precursor, Fe_2O_3 nanorods (Figure 7D) starting with the Fe(III) precursor, or iron-based nanocubes[61] (Figure 7E) starting with the Fe(III) precursor in the presence of pyrrole. As suggested for the reaction in all cases, Fe^{n+} + n electrons resulting in Fe(0) and then depending on the medium, Fe(0) can be oxidized because it is not stable under oxidative conditions. This may lead to metallic structure stabilization, e.g., by the formation of a metal/polypyrrole hybrid.[50]

Ultrasonic treatment suggests unique tools for the combination of top-down and bottom-up strategies. Thus, the sonochemical design of a cerium-rich anticorrosion nanonet-work on a metal surface was shown, when a metal surface was modified in the presence of cerium(III) aqueous solution.[62] An aluminum-based sponge layer was formed, where, depending on the ultrasonic intensity, either a cerium/aluminum nano-network with high adhesion to the metal and high corrosion resistance or a dense cerium oxide layer was obtained. In all, the question of forming novel oxide phases is very complex because it also works for top-down modification; however, the nucleation and oxide phase growth, also in a solid matrix, can be bottom-up.

9. OXIDE PHASE IN INTERPENETRATION METAL FOAM LAYER

Cavitation in aqueous media strongly affects the morphology and composition of particles and leads to the formation of new

crystalline phases that also exhibit excellent functional properties: catalytic and photocatalytic properties, corrosion resistance, optical properties, and biocompatibility of the nanostructured surface.

The general concept of ultrasound-driven modification of metals in water is as follows: the mechanism of modification of the metal structure under ultrasound irradiation is complex and involves a variety of aspects related to the thermal etching and oxidation of metal surfaces. Several groups of metals under different sonication conditions were investigated.[1,57,61]

Magnesium chosen here as the first example is ideal because it is liable to undergo oxidation and its melting point is within the range achievable by the ultrasonic processes (cavitation and interparticle collisions). The modification of magnesium proceeds through different stages, and at the end, we can achieve a total transformation of the metal to brucite.[63] It is a simple synthesis approach to the preparation of Mg(OH)$_2$ structures in water. Ultrasound irradiation constitutes a green and economical procedure for the synthesis of inorganic nanostructures without additional reagents and time-consuming chemistry. The formation of magnesium hydroxide is driven by the oxidation of the metal-caused byproducts of water sonolysis, i.e., free radicals. This process is accompanied by interparticle collisions and surface erosion. Magnesium hydroxide was obtained in deionized water via the ultrasound-assisted method, whereas the results of magnesium modification in ethanol showed no presence of magnesium hydroxide structures. A total conversion of magnesium to magnesium hydroxide was achieved at lower concentrations of magnesium in the solution. Platelets grew preferentially with an increasing magnesium concentration as well as in the presence of chloride ions.

One example of an active oxide material is titanium dioxide, formed by the oxidation of titanium. Titanium has been widely used as a biomaterial for various medical applications, and recently in our group we focused on the formation of metal-based foam layers with titanium dioxide in its composition for the treatment of implant surfaces or lab-on-a-chip devices.[64−67] In the study, we showed that a titania nanofoam on titanium can be formed under high intensity ultrasound (HIUS) treatment in alkaline solution. The physicochemical properties and morphology of the titania nanofoam are investigated in order to find optimal preparation conditions for producing surfaces with high wettability for cell culture studies and drug delivery applications. AFM and contact angle measurements reveal that the surface roughness and wettability of the surfaces depend nonmonotonously on the ultrasound intensity and duration of treatment, indicating a competition between HIUS-induced roughening and smoothening mechanisms. We finally demonstrate that superhydrophilic bio- and cytocompatible surfaces can be fabricated with short time ultrasonic treatment. The HRTEM shows the formation of TiO$_2$ nanocrystals in a porous matrix. A complex foam layer composition and titania structure with defects provide sensitivity of the formed titania to visible light: the photocurrent under visible light irradiation.[67]

One more example of a photoactive oxide structure formed under the HIUS treatment of metal is the treatment of zinc particles. During the treatment of Zn, a core−shell "hedgehog" consisting of a metallic zinc core covered by zinc oxide crystalline nanorods was shown.[68] The formation of an oxide layer can be controlled by the intensity and duration of sonication. Zinc oxide crystals (2 μm) formed by short-time

sonication exhibit tubular morphology. Probably because of their brittleness they are decomposed by further sonication. Long-term treatment (>30 min) stimulates the formation of stable oxide nanorods with length ~100 nm and diameter ~20 nm. The maximum surface area for Zn particles sonicated is 15 min are 22 m^2/g; samples sonicated for 30 and 90 min exhibit nonporous structure. Sonicated Zn particles might have a different structure because of the features of zinc oxide formed by sonication. The porosity of sonicated Zn is rapidly decreased with sonication time as a result of the transformation of tubular ZnO into ZnO nanorods. Some advanced photocatalytic nanostructured Zn[37], where ZnO nanorods are attached to the metallic Zn core, are presented below. Because of the hedgehog morphology, the novel zinc-based material exhibits increased surface area and high accessibility for substrate molecules and is a promising component of sensors, catalysts, active feedback coatings, and photovoltaic systems.

Shiju and Rothenberg et al.[42] showed that ultrasonically activated copper/aluminum CuAl alloys were excellent A^3 coupling catalysts. Additionally, partially oxidized porous CuAl composites can catalyze propane dehydrogenation at low temperatures.[43] The PXRD pattern of the initial alloy showed intense peaks for Al and CuAl$_2$. After sonication, the PXRD revealed the peaks corresponding to highly ordered Al(OH)$_3$ (bayerite) crystals and CuO, thus partial oxidation of the metallic phases. Surface analysis by XPS revealed the presence of mixed oxidation states for Cu on the catalyst surface. Seventy-two percent of the copper on the surface was oxidized to Cu$^+$, and the rest was oxidized to Cu^{2+}.

Material oxidation and simultaneous crystallization is an attractive area to study because ultrasonic treatment allows the formation of reactive oxygen species and their local delivery, providing the formation of porous structure. Moreover, high local temperature and pressure with a high heating/cooling rate are conditions for the crystallization of the oxide simultaneously with its formation without expensive postsynthesis structure annealing.

10. FROM MECHANOLUMINESCENCE TO AMORPHIZATION, CRYSTALLIZATION, AND RECRYSTALLIZATION

On the basis of the physicochemical behavior of crystalline or amorphous silicon under acoustic cavitation in water, one can follow the processes of amorphization, crystallizatio, and recrystallization vs parameters of ultrasonic treatment. These are the intensity and duration of the process[69] or media or the presence of a hydrogen donor to prevent oxidation and allow recrystallization in water for the case of silicon.[70]

In addition to local chemistry, the strain ultrasonically generated at the Si surface may modify the interatomic distances and lattice vibrational frequencies of the crystalline structure.[71] At atmospheric pressure, the untreated Si wafer exhibits a cubic diamond structure, and after sonication, Raman spectra[69] indicate the presence of polycrystalline Si (poly-Si).[72] Other sonicated areas were found to present a high-frequency Raman shift known to be influenced by the mechanical stress generated in the crystalline structure and reflecting a discrepancy in the distribution of the bond lengths of the sonicated Si.[71]

The amorphization of crystalline Si results from a structural destabilization of the Si structure and shows evidence of high atomic disorder at the surface of the sample.[71] TEM investigations confirmed the presence of a perfect diamond
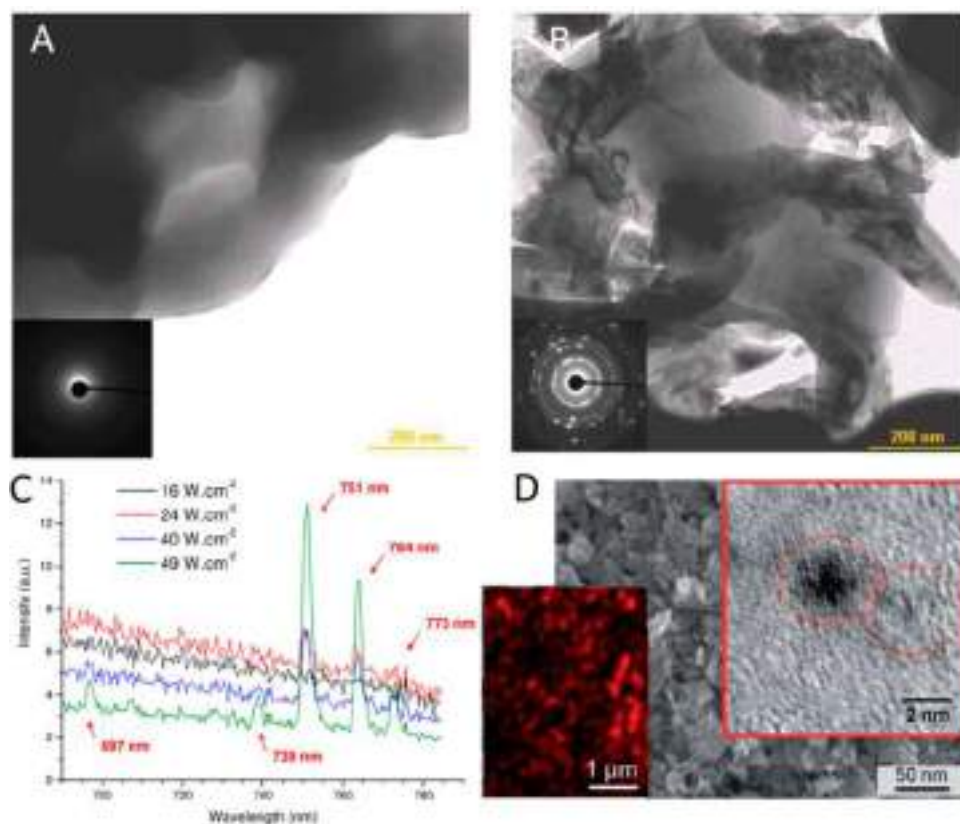
Figure 8. (A−C) Starting from crystalline silicon one obtains after 8 h of sonication (Ar, I_{ac} = 32 W cm^{-2}, 20 °C, H$_2$O, V = 250 mL) (A) an amorphous Si structure and (B) a polycrystalline Si structure, confirmed by bright-field TEM observation with ED. (C) Spectroscopic investigations reveal that argon (bubbling continuously through the liquid phase during experiments) can be ultrasonically excited via mechanoluminescence: normalized sonoluminescence spectra obtained during the sonication of a Si wafer in H$_2$O using different acoustic intensities (10 ± 1 °C, Ar, ~2 mm from the sonotrode, focusing near the surface), with magnification of the 690−790 nm region. Adopted and reproduced with permission from ref 69. (D) Sonication of amorphous silicon in water results in the formation of silicon quantum (HRTEM shown in right inset) dots in a matrix with optical activity (shown in left inset). Adopted and reproduced with permission from ref 70.

cubic single-crystalline structure for the untreated sample devoid of phase transformation. Measurements carried out on sonicated samples revealed the presence of a complex structure exhibiting complicated diffraction contrast because of the presence of a highly stressed and distorted structure (Figure 8A,B, electron diffraction patterns inserted for each image). The apparent porosity of the resulting sample is also increased. The corresponding electron diffractograms suggest the presence of several phases: (i) the initial crystalline structure, (ii) wide diffuse rings resulting from a randomized distribution of Si atoms within the investigated structures and corresponding to amorphous phase a-Si, and (iii) several concentric specklelike halo rings typical of poly-Si. TEM measurements were found[69] to be consistent with the μ-Raman investigations. Correlation of the various experimental results indicates the presence of mixed domains composed of crystalline, amorphous, and polycrystalline phases. The presence of a transition stage with several coexisting phases can be assumed. The presence of Si particles can result from the fragmentation of c-Si with ultrasound and their embedding in an amorphous phase (a-Si or a-SiOx) and from partial recrystallization, which may occur after amorphization and during sonication as a result of local sample heating and the generated solid friction during erosion. The different highlighted features show evidence of the complex stress state existing at the sonicated interface.

Spectroscopic investigations reveal that argon (bubbling continuously through the liquid phase during experiments) can be ultrasonically excited via mechanoluminescence, i.e., emission of light caused by mechanical action on a solid. This phenomenon was highlighted for the first time by Virot et al.[69] on an extended solid surface using these conditions and results from an interaction between the acoustically generated bubbles and the Si surface. According to the above observations, the mechanism of Ar excitation (Figure 8C) results from the strains generated at the Si surface and in its crystalline structure. Indeed, a Si phase transformation such as amorphization or metallization is known to accompany a drastic change in density, leading to volume expansion or contraction. Therefore, these local transformations are able to fracture, deform, and dislocate the Si (sub)surface. The generated strains and distortions affect the electron density of states (thus affecting the thermal and electrical properties of silicon), and Ar* emission probably goes with Si emission. The same mechanism may be involved when a-Si[70] under ultrasonic treatment is converted to optically active single nanocrystals c-Si (Figure 8D).

As the last example of phase transitions (crystalline−amorphous−crystalline) (Figure 9), an experiment on ~100 μm particles of silicon can be illustrated. Particles sonicated for 10 min exhibit a pronounced crystalline structure, and their size decreases to the submicrometer scale. The amorphization of
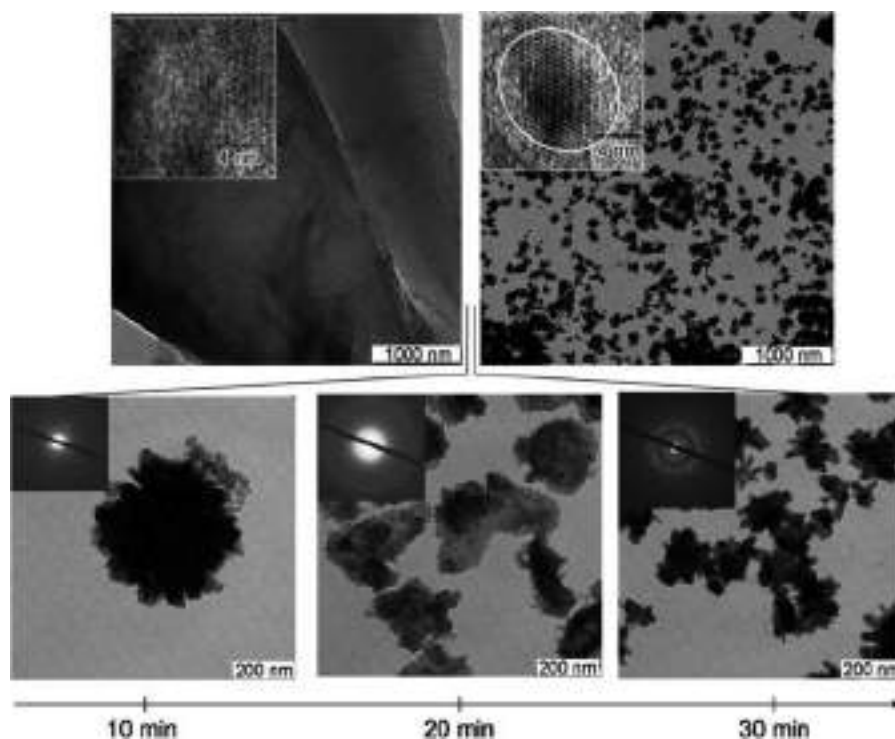
Figure 9. Starting from crystalline microparticles, one can follow different stages of silicon modification, crystalline ↔ amorphous ↔ crystalline with decreasing particle sizes to the nanometer scale. I_{ac} = 57 W cm^{-2}, 65 °C, H$_2$O with a hydrogen donor (Mg), and V = 250 mL.[70]

the particles is observed within 20 min of modification. Further exposure (>30 min) causes well-pronounced crystal growth from the amorphous phase in addition to a further size decrease. The observed phase transition (crystalline ↔ amorphous) is probably the main factor responsible for the ultrasound-assisted modification of silicon. Special conditions provided by high-intensity ultrasound could affect the melting and growth of the silicon crystals. The form of a solidified microstructure can be controlled by fast local heating and cooling cycles provided by cavitation. The crystal formation depends on the difference between the rates of attachment and detachment of atoms at the interface. The rate of attachment depends on the rate of diffusion in the liquid and is therefore affected by sonication.

11. OPEN ISSUES FOR FUTURE RESEARCH

Understanding the nature and conditions of nonlinear processes in open systems is important for the modulation of the microstructure of solids at a new level of complexity.[73] These nonlinear self-organization processes in solids promise new materials with applications among others in bio- and geosciences. One intriguing topic will be if cavitation generated by high-intensity ultrasound may trigger nonlinear processes in solids: a nonmonotonous dependence of the size of grains in the treated solids on sonication time and the oscillation of crystalline grain sizes vs time of ultrasonic treatment.[73] Control of solid surface heterogeneities for composite and hybrids due to processes in liquid during the sonication of surfaces is another issue.

Further study of hydrophilic/hydrophobic patterned surface modification following the work of Belova et al.[74−76] is interesting in controlling the crystallization of selected surface areas and localizing thermal effects on a sonicated surface. An enhanced lifetime by collective effects is achievable by

patterning if the density of surface nanobubbles or nano-droplets is larger or smaller on selective patterns and, correspondingly, their lifetime is longer or shorter. The correlation of surface nanodroplets as compared to surface nanobubbles in addition is attractive in controlling the liquid concentration in water and the gas concentration: liquid in liquid, gas in liquid, liquid/gas/liquid in liquid, and gas/liquid in liquid droplets and bubbles.

Nanobubbles as nuclei for cavitation bubbles and their organization on selected surface areas are an issue. Specific defects, such as pitting vs surface homogeneity, are expected to significantly reduce the lifetime of the surface bubbles and droplets.

It will be interesting to observe life cycles and diffusive dynamics of bubbles at different interfaces as well as see effects of bubble coalescence and splitting.

The influence of different forces and competing forces, e.g., cavitation-driven impact of shock heating and shear stress on surfaces, is the direction toward interplay crystallization. The capillary forces at the different phase contact lines deforming the interface are more and more in focus in the context of wetting the surface.

For model surfaces, as was mentioned in recent reviews of Lohse et al.,[77,78] efforts should be undertaken to control patterns and pits, preferably with a very high hydrophobicity of patterns to adsorb hydrophobic gas bubbles. Patterns and pit shapes, their lateral extension, and their spacing on the microscale and nanoscale offer weak spots on which the surface nanobubbles and nanodroplets will nucleate, similar to introducing controlled air-filled microcrevices and nanocrevices as weak spots in the study of cavitation bubbles.

The most tested systems for studies of the dynamics of bubbles at interfaces are model systems. However, advanced materials, e.g., those shown in our work on metal foams,[65]

sponges,[54,61] nanocomposites,[52,62] hybrids,[45,49,50] catalysts,[41–43,53] electrocatalysts,[21,22,44] photocatalysts,[68] and luminescent silicon,[70] are formed by simple sonication of particles or surfaces in liquid: fast, efficient, cheap, and robust methods with a focus on easy upscaling and a "green" medium. Thus, it is interesting to follow the dynamics of bubbles in real systems to correlate it to model systems with a dedicated theoretical explanation.

12. CONCLUSIONS

This review contributes to the understanding of the mechanisms involved during cavitation at the solid−liquid interface. High-power ultrasound was shown to induce interfacial changes in the physical, chemical, and structural properties of solids. The first important question of up to what temperature ultrasound can heat the particle must be answered to find what changes one can have in solid crystalline structures, involving either melting or solid-state diffusion. The influence of the solution on temperature-driven crystal growth is discussed. Cavitation can trigger kinetically restricted transformations on the surfaces of heterogeneous solids. Sonochemical reactions of oxidation and reduction can result in the formation of new phases that, as a result of locally extreme conditions, can occur in the crystalline phase. Thus, sonochemically generated metal hydrides are suggested as being future hydrogen-storage materials because of nonequilibrium low-temperature metal hydrides formed during sonication. Ultrasound can change the metastability for bottom-up crystallization, resulting in final crystalline structures different from thermodynamically driven ones. The gas discharge occurring at the solid−liquid interface revealed the stress and dramatic transformations created locally during sonication. These properties may provide an interesting route of investigations devoted to material functional properties vs crystallinity.

■ AUTHOR INFORMATION

Corresponding Authors
*E-mail: skorb@mpikg.mpg.de.
*E-mail: daria.baeumler@gmail.com.

Notes
The authors declare no competing financial interest.

■ REFERENCES

(1) The chapters 2−6 are parts of the habilitation thesis of Andreeva, D.V. Functional Polyelectrolyte Multilayers on Ultrasonically Modified Metal Surfaces. Bayreuth, 2016.

(2) Lorimer, J. P.; Mason, T. J. Sonochemistry Part 1 − The physical aspects. *Chem. Soc. Rev.* **1987**, *16*, 239−274.

(3) Nikitenko, S. I. Plasma Formation during Acoustic Cavitation: Toward a New Paradigm for Sonochemistry. *Adv. Phys. Chem.* **2014**, *2014*, 173878.

(4) Walton, A. J.; Reynolds, G. T. Sonoluminescence. *Adv. Phys.* **1984**, *33*, 595−660.

(5) Suslick, K. S.; Price, G. J. Applications of ultrasound to materials chemistry. *Annu. Rev. Mater. Sci.* **1999**, *29*, 295−326.

(6) Rayleigh, L. On the pressure developed in a liquid during the collapse of a spherical cavity. *Philosophical Magazine Series.* **1917**, *6*, 94−98.

(7) Noltingk, B. E.; Neppiras, E. A. Cavitation produced by ultrasonics. *Proc. Phys. Soc., London, Sect. B* **1950**, *63*, 674−685.

(8) Neppiras, E. A.; Noltingk, B. E. Cavitation produced by ultrasonics: Theoretical conditions for the onset of cavitation. *Proc. Phys. Soc., London, Sect. B* **1951**, *64*, 1032−1038.

(9) Suslick, K. S. Sonochemistry. *Science* **1990**, *247*, 1439−1445.

(10) Suslick, K. S.; Hammerton, D. A.; Cline, R. E. The sonochemical hot spot. *J. Am. Chem. Soc.* **1986**, *108*, 5641−5642.

(11) Doktycz, S. J.; Suslick, K. S. Interparticle collisions driven by ultrasound. *Science* **1990**, *247*, 1067−1069.

(12) Krefting, D.; Mettin, R.; Lauterborn, W. High-speed observation of acoustic cavitation erosion in multi-bubble systems. *Ultrason. Sonochem.* **2004**, *11*, 119−123.

(13) McNamara, W. B.; Didenko, Y. T.; Suslick, K. S. Sonoluminescence Temperatures During Multibubble Cavitation. *Nature* **1999**, *401*, 772−775.

(14) Ashokkumar, M.; Hall, R.; Mulvaney, P.; Grieser, F. Sonoluminescence from Aqueous Alcohol and Surfactant Solutions. *J. Phys. Chem. B* **1997**, *101*, 10845−10850.

(15) Didenko, Y. T.; McNamara, W. B.; Suslick, K. S. Hot Spot Conditions during Cavitation in Water. *J. Am. Chem. Soc.* **1999**, *121*, 5817−5818.

(16) Cherepanov, P. V.; Kollath, A.; Andreeva, D. V. Up to which temperature ultrasound can heat the particle? *Ultrason. Sonochem.* **2015**, *26*, 9−14.

(17) Batalu, D.; Cosmeliata, G.; Aloman, A. Critical Analysis of Al-Ni Phase Diagrams. *Metalurgia Inter.* **2006**, *11*, 36−45.

(18) Ilbagi, A.; Khatibi, P. D.; Henein, H.; Lengsdorf, R.; Herlach, D. M. Effect of cooling rate on solidification of Al-Ni alloys. *J. Physics: Conference Series* **2011**, *327*, 1−12.

(19) Shi, D. M.; Wen, B.; Melnik, R.; Yao, S.; Lia, T. J. First-principles studies of Al-Ni intermetallic compounds. *J. Solid State Chem.* **2009**, *182*, 2664−2669.

(20) Cherepanov, P. V.; Melnyk, I.; Andreeva, D. V. Effect of high intensity ultrasound on Al$_3$Ni$_2$, Al$_3$Ni crystallite size in binary AlNi (50 wt% of Ni) alloy. *Ultrason. Sonochem.* **2015**, *23*, 26−30.

(21) Cherepanov, P. V.; Ashokkumar, M.; Andreeva, D. V. Ultrasound assisted formation of Al-Ni electrocatalyst for hydrogen evolution. *Ultrason. Sonochem.* **2015**, *23*, 142−147.

(22) Cherepanov, P. V.; Melnyk, I.; Skorb, E. V.; Fratzl, P.; Zolotoyabko, E.; Dubrovinskaia, N.; Dubrovinsky, L.; Avadhut, Y. S.; Senker, J.; Leppert, L.; Kümmel, S.; Andreeva, D. V. The use of ultrasonic cavitation for near-surface structuring of robust and low-cost AlNi catalysts for hydrogen production. *Green Chem.* **2015**, *17*, 2745−2749.

(23) Cherepanov, P. V.; Andreeva, D. V. Phase structuring in metal alloys: Ultrasound-assisted top-down approach to engineering of nanostructured catalytic materials. *Ultrason. Sonochem.* **2016**, DOI: 10.1016/j.ultsonch.2016.05.006.

(24) Rae, J.; Ashokkumar, M.; Eulaerts, O.; von Sonntag, C.; Reisse, J.; Grieser, F. Estimation of ultrasound induced cavitation bubble temperatures in aqueous solutions. *Ultrason. Sonochem.* **2005**, *12*, 325−329.

(25) Ashokkumar, M. Sonochemical Synthesis of Inorganic Nanoparticles. In *Advanced Wet-Chemical Synthetic Approaches to Inorganic Nanostructures*; Cozzoli, P.D., Ed.;Transworld Research Network, 2008; pp 107−131.

(26) Ashokkumar, M.; Mason, T. Sonochemistry. *Kirk-Othmer Encylcopedia of Chemical Technology*; John Wiley & Sons, 2007.

(27) Tronson, R.; Ashokkumar, M.; Grieser, F. Comparison of the Effects of Water-Soluble Solutes on Multibubble Sonoluminescence Generated in Aqueous Solutions by 20- and 515-kHz Pulsed Ultrasound. *J. Phys. Chem. B* **2002**, *106*, 11064−11068.

(28) Blöchl, P. E. Projector augmented-wave method. *Phys. Rev. B: Condens. Matter Mater. Phys.* **1994**, *50*, 17953−17979.

(29) Nash, P.; Singleton, M. P.; Murray, J. L. *Phase Diagrams of Binary Nickel Alloys*; ASM International: Materials Park, OH, 1991; pp 3−11.

(30) Dharmarathne, L.; Ashokkumar, M.; Grieser, F. On the Generation of the Hydrated Electron during the Sonolysis of Aqueous Solutions. *J. Phys. Chem. A* **2013**, *117*, 2409−2414.

(31) Joseph, J. M.; et al. The sonochemical degradation of azobenzene and related azo dyes: rate enhancements via Fenton's reactions. *J. Phys. Chem. A* **2000**, *104*, 301−307.

(32) Ashokkumar, M.; Mulvaney, P.; Grieser, F. The Effect of pH on Multibubble Sonoluminescence from Aqueous Solutions Containing Simple Organic Weak Acids and Bases. *J. Am. Chem. Soc.* **1999**, *121*, 7355−7359.

(33) Cravotto, G.; Cintas, P. Harnessing mechanochemical effects with ultrasound-induced reactions. *Chem. Sci.* **2012**, *3*, 295−307.

(34) Petrier, C.; Lamy, M. F.; Francony, A.; Benahcene, A.; David, B. Sonochemical degradation of phenol in dilute aqueous solutions. *J. Phys. Chem.* **1994**, *98*, 10514−10520.

(35) Stricker, L.; Lohse, D. Radical production inside an acoustically driven microbubble. *Ultrason. Sonochem.* **2014**, *21*, 336−345.

(36) Misik, V.; Riesz, P. Probing the temperatures of cavitation regions. *Ultrason. Sonochem.* **1996**, *3*, 25−37.

(37) Phillis, J. W.; Estevez, A. Y.; O'Regan, M. H. Protective effects of the free radical scavengers, dimethyl sulfoxide and ethanol, in cerebral ischemia in gerbils. *Neurosci. Lett.* **1998**, *244*, 109−111.

(38) Bonet, F.; Guéry, C.; Guyomard, D.; Herrera Urbina, R.; Tekaia-Elhsissen, K.; Tarascon, J.-M. Electrochemical reduction of noble metallic compounds in ethylene glycol. *Int. J. Inorg. Mater.* **1999**, *1*, 47−51.

(39) Samiee, L.; Dehghani Mobarake, M.; Karami, R.; Ayazi, M. Developing of Ethylene Glycol as a New Reducing Agent for Preparation of Pd-Ag/PSS Composite Membrane for Hydrogen Separation. *J. Petroleum Sci. Technol.* **2012**, *2*, 25−32.

(40) Kollath, A.; Cherepanov, P. V.; Andreeva, D. V. Controllable manipulation of crystallinity and morphology of aluminium surface using high intensity ultrasound. *Applied Acoustics.* **2016**, *103*, 129−136.

(41) Dulle, J.; Nemeth, S.; Skorb, E. V.; Irrgang, T.; Senker, J.; Kempe, R.; Fery, A.; Andreeva, D. V. *Adv. Funct. Mater.* **2012**, *22*, 3128−3135.

(42) Dulle, J.; Thirunavukkarasu, K.; Mittelmeijer-Hazeleger, M. C.; Andreeva, D. V.; Shiju, N. R.; Rothenberg, G. Efficient three-component coupling catalysed by mesoporous copper-aluminum based nanocomposites. *Green Chem.* **2013**, *15*, 1238−1243.

(43) Schäferhans, J.; Gómez-Quero, S.; Andreeva, D. V.; Rothenberg, G. Efficient three-component coupling catalysed by mesoporous copper–aluminum based nanocomposites. *Chem. - Eur. J.* **2011**, *17*, 12254−12256.

(44) Cherepanov, P. V.; Andreeva, D. V. Ultrasound-Assisted Synthesis of Electrocatalysts for Hydrogen Production. In *Handbook of Ultrasonics and Sonochemistry*Ashokkumar, M., Ed.; Springer, 2016.

(45) Baidukova, O.; Möhwald, H.; Mazheika, A. S.; Sviridov, D. V.; Palamarciuc, T.; Weber, B.; Cherepanov, P. V.; Andreeva, D. V.; Skorb, E. V. Sonogenerated metal-hydrogen sponges for reactive hard templating. *Chem. Commun.* **2015**, *51*, 7606−7609.

(46) Schlapbach, L.; Züttel, A. Hydrogen-storage materials for mobile applications. *Nature* **2001**, *414*, 353−358.

(47) Haas, I.; Gedanken, A. Synthesis of metallic magnesium nanoparticles by sonoelectrochemistry. *Chem. Commun.* **2008**, 1795−1797.

(48) Jeon, K.-J.; Moon, H. R.; Ruminski, A. M.; Jiang, B.; Kisielowski, C.; Bardhan, R.; Urban, J. J. Air-stable magnesium nanocomposites provide rapid and high-capacity hydrogen storage without using heavy-metal catalysts. *Nat. Mater.* **2011**, *10*, 286−290.

(49) Skorb, E. V.; Baidukova, O.; Goyal, A.; Brotchie, A.; Andreeva, D. V.; Möhwald, H. Sononanoengineered magnesium−polypyrrole hybrid capsules with synergetic trigger release. *J. Mater. Chem.* **2012**, *22*, 13841−13848.

(50) Skorb, E. V.; Baidukova, O.; Andreeva, O. A.; Cherepanov, P. V.; Andreeva, D. V. Formation of polypyrrole/metal hybrid interfacial layer with self-regulation functions via ultrasonication. *Bioinspired, Biomimetic Nanobiomater.* **2013**, *2*, 123−129.

(51) Skorb, E. V.; Andreeva, D. V. Surface nanoarchitecture for bio-applications: self-regulated intelligent interfaces. *Adv. Funct. Mater.* **2013**, *23*, 4483−4506.

(52) Skorb, E. V.; Möhwald, H.; Irrgang, T.; Fery, A.; Andreeva, D. V. Ultrasound-Assisted Design of Metal Nanocomposites. *Chem. Commun.* **2010**, *46*, 7897−7899.

(53) Pazos- Perez, N.; Schäferhans, J.; Skorb, E. V.; Fery, A.; Andreeva, D. V. Ultrasound driven formation of metal-supported nanocatalysts. *Microporous Mesoporous Mater.* **2012**, *154*, 164−169.

(54) Skorb, E. V.; Fix, D.; Shchukin, D. G.; Möhwald, H.; Sviridov, D. V.; Mousa, R.; Wanderka, N.; Schöferhans, J.; Pazos- Perez, N.; Fery, A.; Andreeva, D. V. Sonochemical formation of metal sponges. *Nanoscale* **2011**, *3*, 985−993.

(55) Shchukin, D. G.; Skorb, E. V.; Belova, V.; Möhwald, H. Ultrasonic Cavitation at Solid Surfaces. *Adv. Mater.* **2011**, *23*, 1922−1934.

(56) *Nanochemistry: A Chemical Approach to Nanomaterials Front Cover: Edition 2*; Ozin, G. A., Arsenault, A. C., Cademartiri, L., Eds.; RSC Publ.: 2009; ISBN 978-1-84755-895-4.

(57) Skorb, E. V.; Möhwald, H. Ultrasonic approach for surface nanostructuring. *Ultrason. Sonochem.* **2016**, *29*, 589−560.

(58) Skorb, E. V.; Möhwald, H. "Smart" surface capsules for delivery devices. *Adv. Mater. Interfaces* **2014**, *1*, 201400237.

(59) Yang, H. Platinum-based electrocatalysts with core−shell nanostructures. *Angew. Chem., Int. Ed.* **2011**, *50*, 2674−2676.

(60) Crespo, R.; Martins, P. M.; Gales, L.; Rochac, F.; Damas, A. M. Potential use of ultrasound to promote protein crystallization. *J. Appl. Crystallogr.* **2010**, *43*, 1419−1425.

(61) Skorb, E. V.; Andreeva, D. V. Bio-inspired ultrasound assisted construction of synthetic sponges. *J. Mater. Chem. A* **2013**, *1*, 7547−7557.

(62) Skorb, E.; Shchukin, D.; Möhwald, H.; Andreeva, D. Ultrasound Driven Formation of Cerium-Rich Anticorrosion Nanonetwork on Aluminum Alloy Surface. *Langmuir* **2010**, *26*, 16973−16979.

(63) Baidukova, O.; Skorb, E. V. Ultrasound-assisted synthesis of magnesium hydroxide nanoparticles from magnesium. *Ultrason. Sonochem.* **2016**, *31*, 423−428.

(64) Ulasevich, S. A.; Poznyak, S.; Kulak, A. I.; Lisenkov, A.; Starykevich, M.; Skorb, E. V. Photocatalytic deposition of hydrox-yapatite onto titanium dioxide nanotubular layer with fine tuning of layer nanoarchitecture. *Langmuir* **2016**, *32*, 4016−4021.

(65) Zhukova, Y.; Ulasevich, S. A.; Dunlop, J. W. C.; Fratzl, P.; Möhwald, H.; Skorb, E. V. Ultrasound-driven titanium modification with formation of titania based nanofoam surfaces. *Ultrason. Sonochem.* **2016**, submitted for publication.

(66) Kopf, J.; Ulasevich, S. A.; Baidukova, O.; Zhukova, Y.; Dunlop, J. W. C.; Fratzl, P.; Rikeit, P.; Knaus, P.; Poznyak, S. K.; Andreeva, D. V.; Skorb, E. V. Ultrasonically produced porous sponge layer on titanium to guide cell behavior. *Adv. Eng. Mater.* **2016**, *18*, 476−483.

(67) Ulasevich, S. A.; Brezhneva, N.; Zhukova, Y.; Möhwald, H.; Fratzl, P.; Schacher, F. H.; Sviridov, D. V.; Andreeva, D. V.; Skorb, E. V. Ultrasound-driven titanium modification with formation of titania based nanofoam surfaces. *Macromol. Biosci.* **2016**, DOI: 10.1002/mabi.201600127.

(68) Dulle, J.; Nemeth, S.; Skorb, E. V.; Andreeva, D. V. Sononanostructuring of zinc based materials. *RSC Adv.* **2012**, *2*, 12460−12465.

(69) Virot, M.; Pflieger, R.; Skorb, E. V.; Ravaux, J.; Zemb, T.; Möhwald, H. Crystalline Silicon under Acoustic Cavitation: From Mechanoluminescence to Amorphization. *J. Phys. Chem. C* **2012**, *116*, 15493−15499.

(70) Skorb, E. V.; Andreeva, D. V.; Möhwald, H. Ultrasonically induced pathways of silicon modification towards a porous luminescent structure. *Angew. Chem., Int. Ed.* **2012**, *51*, 5138−5142.

(71) Unifantowicz, P.; Vaucher, S.; Lewandowska, M.; Kurzydłowski, K. J. Structural changes of silicon upon high-energy milling investigated by Raman spectroscopy. *J. Phys.: Condens. Matter* **2008**, *20*, 025205.

(72) Morris, M. A.; Morris, D. G. Ball- milling of elemental powders compound formation and or amorphization. *J. Mater. Sci.* **1991**, *26*, 4687−4696.

(73) Kollath, A.; Brezhneva, N.; Skorb, E. V.; Andreeva, D. V. Oscillations in solids driven by cavitation. *Phys. Chem. Chem. Phys.*, submitted for publication.

(74) Belova, V.; Gorin, D. A.; Shchukin, D. G.; Möhwald, H. Selective Ultrasonic Cavitation on Patterned Hydrophobic Surfaces. *Angew. Chem., Int. Ed.* **2010**, *49*, 7129−7133.

(75) Belova, V.; Shchukin, D. G.; Gorin, D. A.; Kopyshev, A.; Möhwald, H. A new approach to nucleation of cavitation bubbles at chemically modified surfaces. *Phys. Chem. Chem. Phys.* **2011**, *13*, 8015−8023.

(76) Belova, V.; Krasowska, M.; Wang, D.; Ralston, J.; Shchukin, D. G.; Möhwald, H. Influence of adsorbed gas at liquid/solid interfaces on heterogeneous cavitation. *Chem. Sci.* **2013**, *4*, 248−256.

(77) Lohse, D.; Zhang, X. Surface nanobubbles and nanodroplets. *Rev. Mod. Phys.* **2015**, *87*, 981−1035.

(78) Zhang, X.; Lohse, D. Perspectives on surface nanobubbles. *Biomicrofluidics* **2014**, *8*, 041301−041311.

CrossMark

Ultrasonic approach for surface nanostructuring

Ekaterina V. Skorb *, Helmuth Möhwald

Max Planck Institute of Colloids and Interfaces, Wissenschaftspark Golm, Am Mühlenberg 1, Golm 14424, Germany

A B S T R A C T

The review is about solid surface modifications by cavitation induced in strong ultrasonic fields. The topic is worth to be discussed in a special issue of surface cleaning by cavitation induced processes since it is important question if we always find surface cleaning when surface modifications occur, or vice versa. While these aspects are extremely interesting it is important for applications to follow possible pathways during ultrasonic treatment of the surface: (i) solely cleaning; (ii) cleaning with following surface nanostructuring; and (iii) topic of this particular review, surface modification with controllably changing its characteristics for advanced applications. It is important to know what can happen and which parameters should be taking into account in the case of surface modification when actually the aim is solely cleaning or aim is surface nanostructuring. Nanostructuring should be taking into account since is often accidentally applied in cleaning. Surface hydrophilicity, stability to Red/Ox reactions, adhesion of surface layers to substrate, stiffness and melting temperature are important to predict the ultrasonic influence on a surface and discussed from these points for various materials and intermetallics, silicon, hybrid materials. Important solid surface characteristics which determine resistivity and kinetics of surface response to ultrasonic treatment are discussed. It is also discussed treatment in different solvents and presents in solution of metal ions.

© 2015 Elsevier B.V. All rights reserved.

1. Introduction

The generation of bubbles by acoustic cavitation has been studied for many years [1–5] also because of great prospects of using "green" ultrasonic treatment for surface cleaning [6–8] and nanostructuring [9–15]. The mechanism of bubble formation (Table 1, inset) may be qualitatively understood as follows: in the zone of negative pressure of the sound wave small volumes of lower liquid density or gas clusters may expand to form bubble nuclei. These do not fully collapse during the high pressure phase and are further expanded in the next low pressure phases. This process continues until reaching a maximum critical diameter depending on ultrasound frequency and solvent [16]. These bubbles inside liquids upon collapse create transiently temperatures more than 5000 K, pressures higher than 1000 atm with cooling rates above 10^8 K/s. Hence there is the potential of performing high temperature and high pressure processes, but with a reactor near room temperature and ambient pressure. Much knowledge of a behavior of homogeneous bubble cavitation and collapse dependent on ultrasonic reactor parameters is obtained by studying single bubble systems [17–19]. Important ultrasonic reactor parameters are presented in Table 1: (i) frequency, intensity and duration of ultrasonic process; (ii) temperature, pressure and gas content; (iii) solution and chemical species which can be added to the solution.

For surface cleaning and nanostructuring the processes of homogeneous bubble oscillations and following collapse are studied in multi-bubble systems [20–22]. Shock waves created during bubble collapse create microscopic turbulences [23]. This phenomenon increases the transfer of mass across the solid surface, thus increasing the intrinsic mass-transfer coefficient, as well as possibly creating or modifying existing coatings, such as thick hybrid metal/polymer coatings [24]. Alternatively, this phenomenon may result in thinning/pitting of the film [25].

When the bubble collapse occurs near a solid surface that is several orders of magnitude more extended than the cavitation bubble [26], the collapse occurs asymmetrically [27] and bubble microjetting is formed perpendicular to the solid surface (Fig. 1). These microjets have an estimated speed of ca. several hundreds of m/s and lead to pitting and erosion of the surface [28].

Microscopic turbulences and jetting lead to an enhancement in heterogeneous reactions (secondary cavitation-assisted processes) with active species formed in the reactor. Thus, a part of the vaporized molecules from the surrounding medium can dissociate to form radical species, such as OH· and H·, for water sonolysis [29]. The radicals form by the hydrogen abstraction of RH additive

* Corresponding author.
  E-mail address: skorb@mpikg.mpg.de (E.V. Skorb).

Table 1
Important aspects for fundamental cavitation assisted modeling as reactor parameters and initial material. Inset shows the mechanism of the cycle of homogeneous generation of bubbles by acoustic cavitation, according to Ref. [16] approximate time of a cycle ca. 400 μs.

Fig. 1. (a) Schematic representation of the experimental ultrasonic device for controllable surface cleaning by cavitating bubbles. The gap between the glass slide and the silicon substrate $h = 100$ μm. The water column height is 5 mm. (b) A zoomed view of the same glass slide after exposure to cavitating bubbles from four pits in the cavitation cell described in this paper. The glass slide has sides of 10 mm. Reproduced with permission [6]. Copyright 2012, AIP Publishing.

molecules to form R· and/or by the pyrolysis of RH molecules during bubble collapse [30].

There are efforts directed to predict or model the consequences, cleaning or nanostructuring, of ultrasonic surface treatment. In the work of Rivas et al. [6] a special ultrasonic device with in situ processes control was studied with the ability to locally remove deposited layers from a glass slide in a controlled and rapid manner (Fig. 1). The cleaning takes place as the result of cavitating bubbles near the deposited layers and not due to acoustic streaming. The bubbles are ejected from air-filled cavities micromachined in a silicon surface, which, when vibrating ultrasonically, generate a stream of bubbles that travels to the layer deposited on an opposing glass slide. Depending on the pressure amplitude, the bubble clouds ejected from the micropits attain different shapes as a result of complex bubble interaction forces, leading to distinct shapes of the cleaned areas. Acoustic droplet vaporization uses ultrasound to induce a phase transition of liquid droplets that are near their boiling point thus plays important role for surface modifications espe-

cially in the cases of high-temperature vaporized droplets. Thus it is important to control the modification of the surfaces via the concentrations of additives in the system (monomer, polymer) and establish the role of initial cavitation in acoustic droplet vaporization in different solutions. It was shown that the cleaning rates for several inorganic and organic materials can be more efficient compared to conventional cleaning equipment.

The influence of dissolved gases, for example CO_2 [31], also can regulate cavitation intensity and consequently cleaning efficiency.

There is still not sufficient knowledge of view of (i) identified for both aspects of cleaning and nanostructuring separately mechanistic causes of cleaning and surface modifications (e.g. shock wave, jet, shear flow, local heating), (ii) one not always finds surface cleaning if one sees surface modification or vice versa, however aspects of cleaning and nanostructuring can be intimately connected.

In our studies and the review we have focused on studies of the consequences of processes that occur at the cavitation interface and solid surface. We focus on further prospects of selective
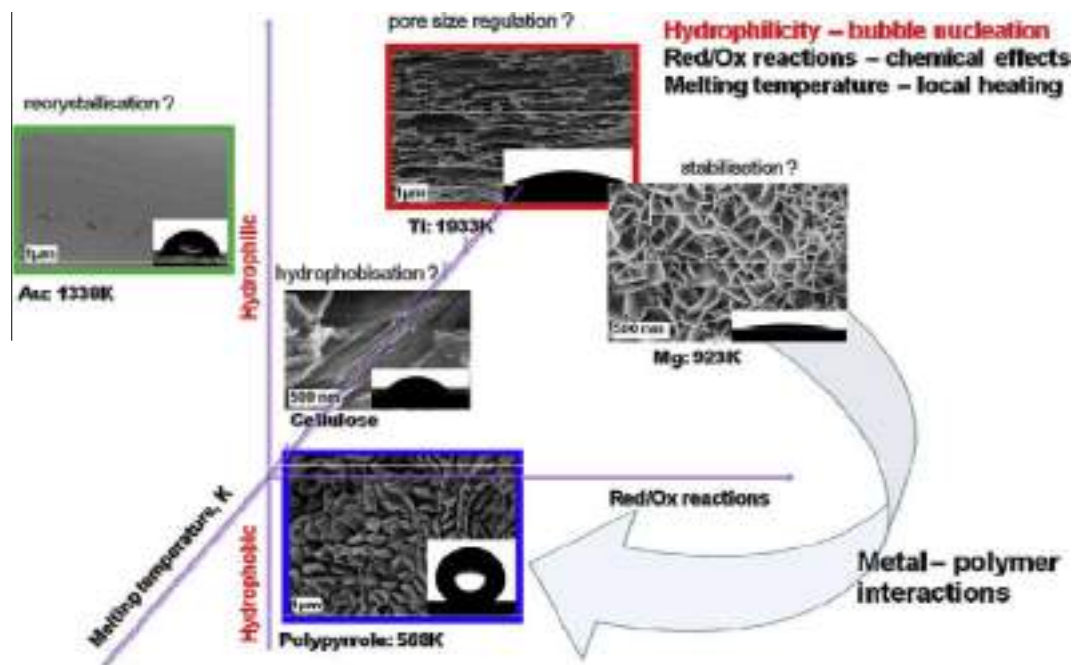
Fig. 2. SEM images of different materials after ultrasonic nanostructuring with points of correlation between surface properties and response of the surface to ultrasonic treatment. Surface hydrophilicity, stability to Red/Ox reactions, adhesion of surface layers to substrate, stiffness and melting temperature are important to predict ultrasonic effect on surfaces.

surface nanostructuring. Different types of surface (see following sections) were investigated metals and their alloys [9], polymers and hybrids [32], composites [13], glass [33] and silicon [12]. Thus, we have demonstrated the application of the cavitation-assisted approach for the development of novel advanced materials, with special emphasis on improving surface functionalities.

Many fundamental aspects of cavitation-assisted processes during surface modification are still unclear (see some questions in connection with reactor and surface parameters in Fig. 2), and in situ investigations (Fig. 3), together with a detailed study of each type of material and the prospects for their combinations, are necessary to elucidate the details of these reactions. The following central problems have been identified:

– To arrive at a mechanistic model of cavitation-assisted processes on solid surfaces. Physico-chemical properties at the surface are relevant for the surface response to ultrasound-assisted modification. Only a few authors have suggested models for a given type of material and its combination with other materials.
– To distinguish relationships between the primary and secondary effects of ultrasound, depending on the mechanical material properties and crystallinity. We therefore describe the progress in the area of soft and hard metal modification, because we expect (and some results have already shown this) that hard and soft metals exhibit different visible responses to ultrasonic exposure and could be building blocks for novel materials. Polymers are expected to exhibit a stronger response than hard materials such as Ti. For soft materials with low thermal conductivities local heating during ultrasonic processing may lead to a decrease or, oppositely, an increase in surface roughness because high local mobility may enable surface tension to flatten the surface. The bubble collapse causes hot spots, and the pressure pulses are also converted into heat; these effects may induce local melting. Thus, a crystalline surface may locally melt and become amorphous after cooling, as has been observed for biopolymers. Reactive species may be created in the solution and in the solid, which may cause a metal to

oxidize deeper inside the solid or a polymer to be destroyed or cross-linked. Concerning the influence of polymer surfaces, we have observed that ultrasonic treatment may render a surface hydrophobic/hydrophilic.
– To localize the effect of ultrasound. Thus, bubble nucleation may be controlled through patterning. A pressure pulse on a material may be focused on defects or grain boundaries. This fact necessitates the study of solids with a defined microstructure. Whether destruction proceeds along patterns, defects and grains is also relevant.
– To follow the kinetics of ultrasonic processes in complex multi-component systems. A solution to this issue is still unclear, but a solution is necessary because materials can be obtained with drastically varying hydrophilic/hydrophobic properties, roughness, porosity, crystallinity and, in the case of hybrids of metals and biopolymers, different nonlinear acoustic responses. The facts that the surface is made more hydrophobic or hydrophilic by ultrasound and that this further influences bubble nucleation may have interesting consequences for the time and space dependence of the treatment: the dose dependence becomes nonlinear and surface and gas specific and patterns can be reproduced with enhanced contrast to have, for example, defined protein/surface adhesion.
– To define intermediate steps of the process. If intermediate states of destruction can be produced, resembling, for example a porous solid, then new active surfaces may also be obtained.
– To provide scenarios of active surface construction based on pronounced responses of different materials, e.g. the metals and polymers, to ultrasound. These are required for implants connected to bone, metals (alloys of titanium and magnesium), and they therefore must be investigated to enable control of their structure and influence on the treatment (with or without additives in the system) of their surfaces. Protein and cell adhesion must also be investigated with respect to their dependence on the surface. Implants with the ability of sustained drug delivery due to the use of metals or hybrids with defined porosity for active chemical (such as drugs) storage and release by internal
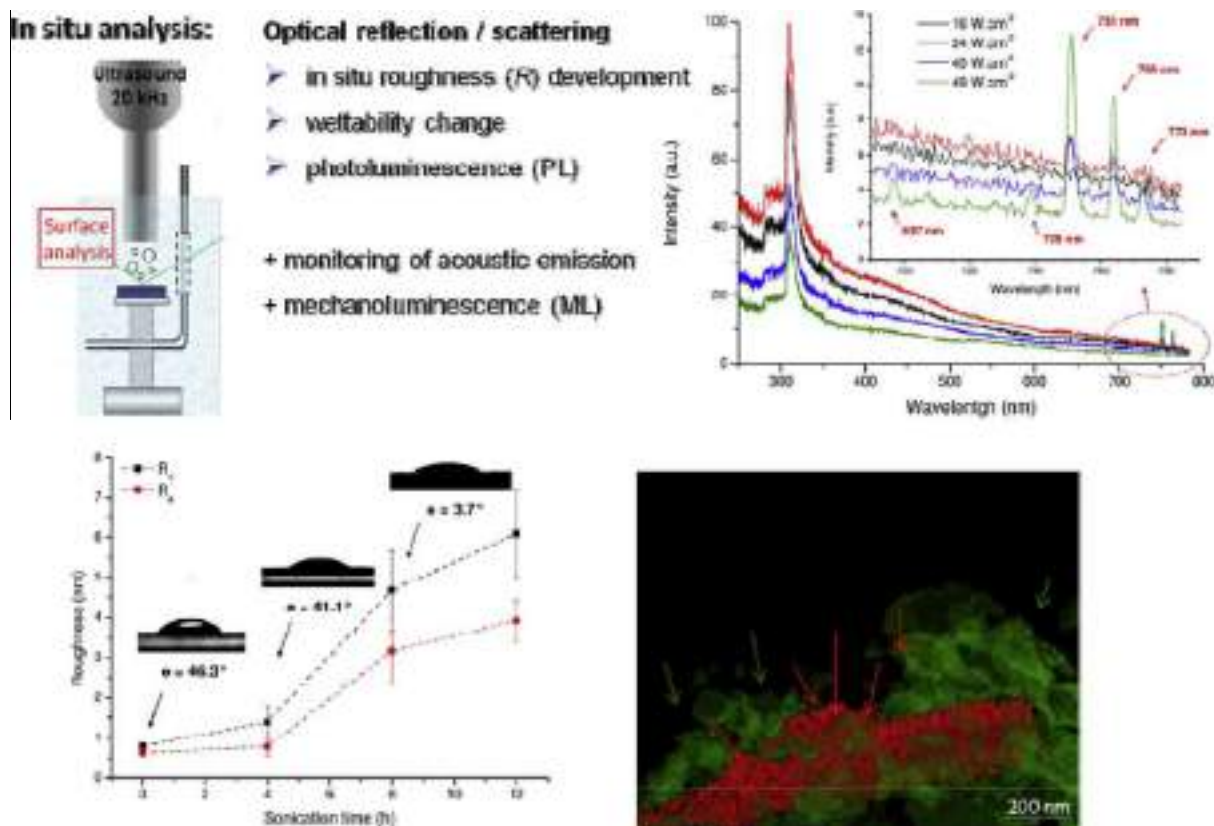
Fig. 3. In situ set up and obtained results for following theoretical calculations and predictions of consequences of ultrasonic surface treatment. Normalized sonoluminescence spectra obtained during sonication of a Si wafer in H_2O using different acoustic intensities. (Inset) Magnification of the 690–790 nm region. Measurements of the roughness and contact angle of the silicon wafer surface as a function of sonication time. Adapted with permission [50]. Copyright 2012, American Chemical Society. μ-Confocal photoluminescence spectra (fluorescent mode, side views) of silicon after ultrasonic modification and followed by ageing. Reproduced with permission [12]. Copyright 2012, Wiley.

(such as Mg dissolution) or external stimuli (pH, temperature, light) need further study. This research area is obviously very promising with respect to stem cell research.

In summary, ultrasonic chemistry carries many exciting prospects but is in its infancy with respect to our understanding and control of the process, which necessitates a multidisciplinary approach, which combines interface and colloid science, acoustics, inorganic, physical and polymer chemistry, and other disciplines for specific applications.

Sufficient experimental results, observations and experimental conclusions, will stimulate theoretical treatment and simulations. We find it important to highlight that processes on different hierarchical scale are taking part during surface modification and it is interesting to build up close cooperation between experiments and simulation of cavitation assisted processes. In Fig. 4 are presented some possible starting points for future simulations: hierarchical-multiscale examples of simulations of interaction between cavitation bubbles and surfaces by (i) electronic state; (ii) atomic scale; and (iii) pseudo-particles; (iv) continuum theory also can be applied to some processes (not shown in Fig. 4). Possible calculation methods are different for different hierarchy processes. Thus these are for (i) electronic state; kinetic Monte Carlo and molecular dynamic for (ii) atomic scale [34]; lattice Boltzmann method for (iii) pseudo-particles; and constitutive electric-plastic metal deformation, FEM [35], FFT [35] for continuum theory. Some important parameters to measure are reaction products, chemistry of cavitation-assisted processes for (i) electronic state; orientation of crystal, anisotropy, kinetics of defect nucleation, roughness, pore formation for (ii) atomic scale; penetration of liquid and gases

inside-outside the formed surface nanostructures, density and viscosity of liquid for (iii) pseudo-particles; and roughness, temperature, pressure, nature of solid surface (lattice parameters, phase diagram, nature of local bonds, elastic properties, patterns, defects) for (iv) continuum theory.

In the following chapters we will point mostly on our results of surface nanostructuring.

2. High intensity ultrasonic treatment of metal surfaces

We study the process of cavitation-assisted metal surface modification to suggest three sonochemical pathways: porous surfaces, surfaces with defined roughness and oxygen-free flat metal surfaces. Such surfaces are of importance for many sustainable applications from corrosion protection to biomaterials and lab-on-chip systems [36–38]. Initially, we use water as a solvent and vary the duration of the experiments at maximum intensity [9]. Solvents preventing oxidation [39,40] are also in focus (e.g., decane or IL or ionic liquid (IL)), which allow to understand, depending on the metal and the stage of modification, the intermediate metal surface states that are formed by the process.

The chosen metals, for example shown in Fig. 5, differ in their melting temperatures (see in Fig. 5) and crystal structures (not shown), e.g. hexagonal for Mg and Ti, and cubic for Au. These factors could influence the response of metals to physical cavitation-assisted effects, such as local melting and bond breakage. A cavitation-assisted chemical effect is also known, and our chosen metals thus exhibit different reactivity. In water solution, for
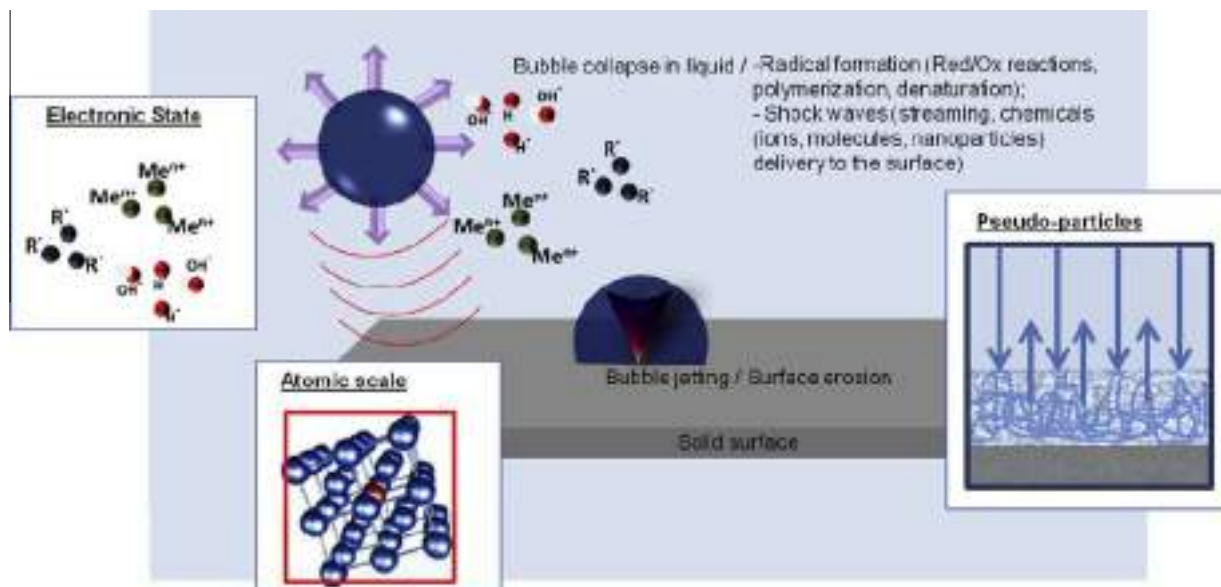
Fig. 4. Scheme of bubble collapse effects on the surface due to (i) symmetric collapse in liquid with formation of shock waves and liquid streaming; and (ii) asymmetric collapse with surface erosion. Insets show the complexity of the ultrasonic treatment of surfaces involving processes at different hierarchy scales: for theoretical calculations (i) electronic state; (ii) atomic scale; (iii) pseudo-particles.
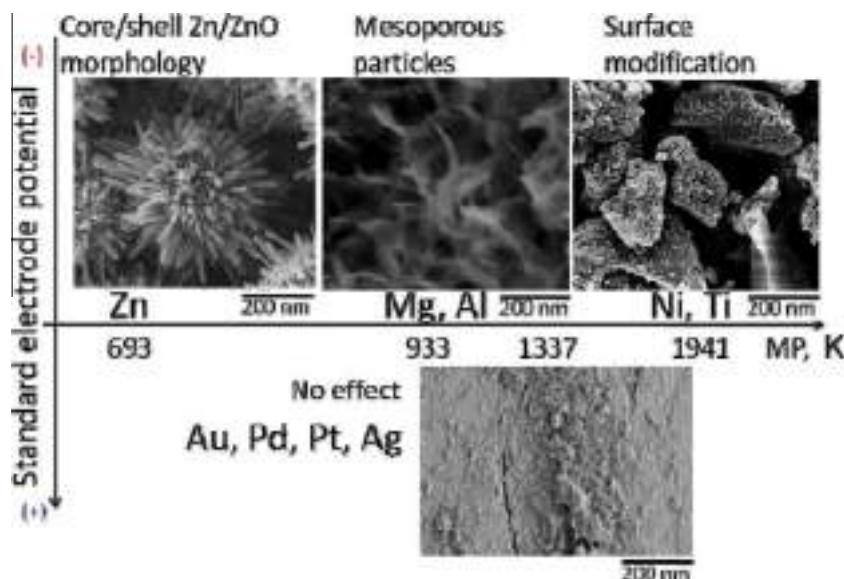
Fig. 5. Schematic presentation of the effect of acoustic cavitation on the modification of metal particles in water. Metals with low melting point (Zn) are completely converted into metal oxide. Al and Mg form mesoporous sponge-like structures. Metals with high melting points (Ni, Ti) exhibit surface modification under sonication. Nobel metals are resistant to ultrasound irradiation due to stability against oxidation. Y-axis represents the oxidation ability; X-axis – difference in melting point in Kelvin. SEM images correspond to 30 min of metal particles modification in pure water at 20 kHz, 57 W/cm^2. Adapted from Ref. [10,41,42] with permission from The Royal Society of Chemistry.

example, Zn, Mg, Al, Ni and Ti could be oxidized, and noble metals are stable against oxidation.

Smooth surfaces without oxide layers can be formed in the case of noble metal ultrasound exposure, even in water. Here, the physical response of noble metals could provide a means of cleaning and removing contaminants or of altering the local melting. Thus, the possibility of local recrystallization through high heating/cooling should be taken into account.

We are currently able to prepare metal sponges in water solution from active metals, Al and Mg, with thicknesses up to 500 nm and defined pore-size distributions [9–11]. The kinetics of the process is studied by controlling the surface roughness, hydrophilicity, component leaching, chemical composition and

crystallinity. At the beginning of the process, the control of cleaning and the following development of an outer layer with destruction of the initial oxide layer are in focus. One possible approach is to measure the zeta-potential indicating the surface charge. The inner structure can be further precisely controlled with possible stabilization of the formed mesoporous surface sponges through the formation of new oxide layers. The kinetics can be controlled by the total surface-sponge oxidation, which leads to the formation of metal surfaces with a thick mesoporous oxide layer [10]. The objective here is to stop the process of modification at a stage where the metal skeleton is stabilized by a thin oxide layer. Total conversion of the surface layer to oxide is possible. A good example is Zn modification [10,41,42] in water solution (Fig. 5). The control

over the surface characteristics is important [9,39], for example for control of morphology, porosity, oxidation, roughness and hydrophilicity depending on time of ultrasonic treatment (Fig. 6).

The experiments in solutions that lack oxidizing ability, such as IL or hydrocarbon liquids are a new focus (Fig. 7). The strategy can be as described for metal particles by the group of Suslick [39,40]. Metal plates can be irradiated in a hydrocarbon liquid (decane) and IL. The surfaces are initially highly crystalline; upon sonication, however, the surface could rapidly become amorphous.

Experiments with metal plates sonicated in hydrocarbon and IL in the presence of nano- or micro-metal particles can be performed. In this case, as was suggested in Ref. [43], one may expect particles collision and agglomeration to preferentially form metal surface sponges, as shown in Fig. 7. In comparison with the mesoporous-surface metal sponges prepared in water, the thick-

ness of the sponges in this case could be micro-sized deep. However such sponges are characterized by a wide-range of pore size distribution and much lower porosity in comparison to mesoporous oxide-stabilized sponges. Thus for aluminum oxide-stabilized sponges the porosity reached 80 m^2/g [44], and it was at the level ca. 1 m^2/g in the case of a sponge formed in IL [39]. However, in both cases it was shown that with time the porosity had a tendency to increase, reach a maximum and after that decrease.

The parameters as in Table 1 can be important for the following build of fundamental models. Their variation can provide experimental data for ultrasonic process modeling together with providing various nanostructured surfaces for sustainable applications.

The ultrasonic method for metal surface modification is really worth to investigate the scenario for surface cleaning and
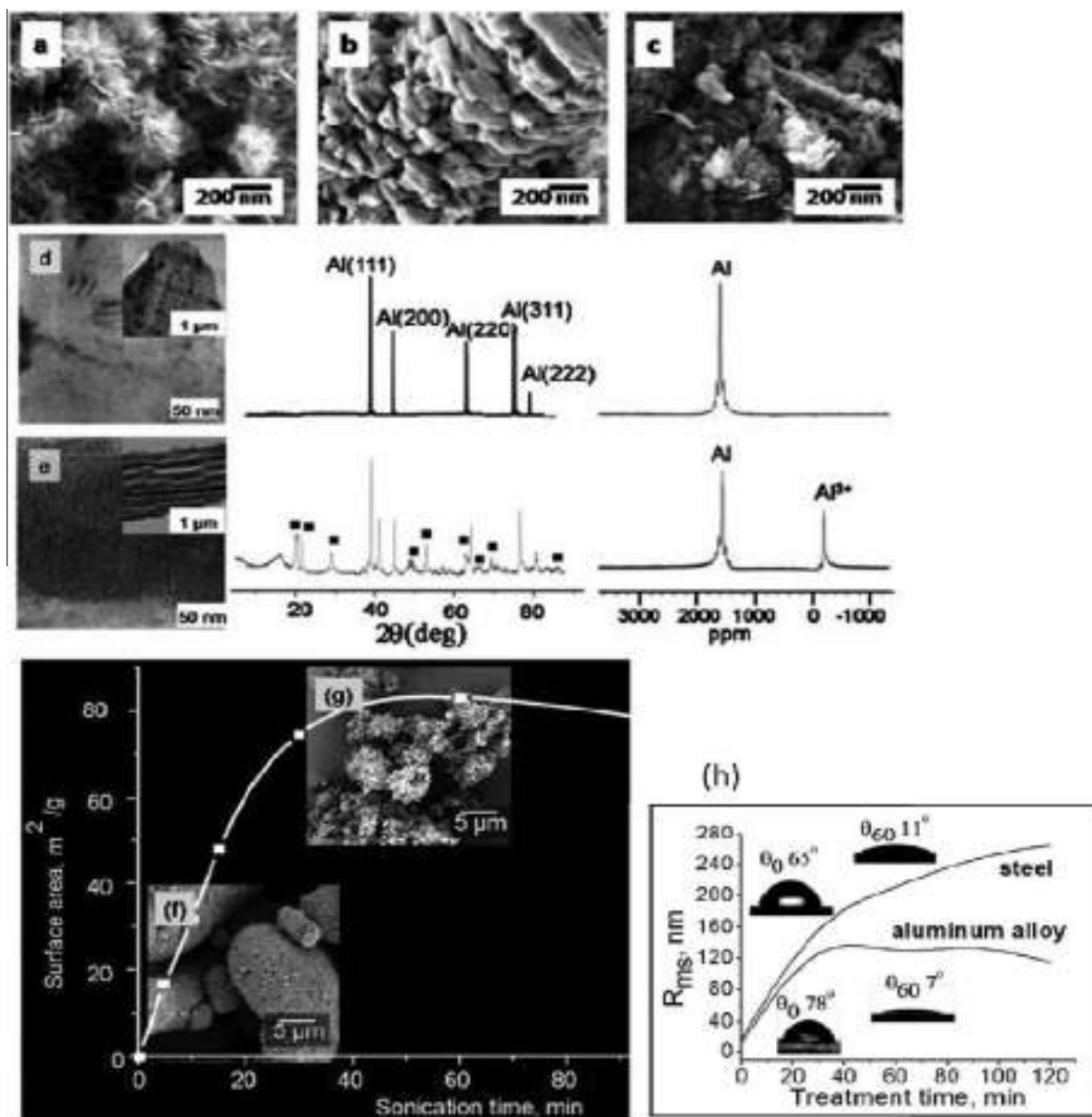
Fig. 6. SEM images of ultrasonically treated (20 kHz, 57 W/cm^2) aluminum particles for (a) 1 min, (b) 3 min, (c) 5 min. Influence of ultrasonication time on structural changes of the aluminum. TEM images, XRD (black squares show the peaks assigned to bayerite) and ^{27}Al MAS NMR spectra of (d) the initial aluminum and (e) after 60 min ultrasonic treatment. (f,g) Influence of the ultrasonication time on the specific surface area (BET analysis) and surface morphology of the Al (SEM images of particles treated for 5 min (f), 60 min (g)). Reproduced with permission [44] from The Royal Society of Chemistry. (h) Influence of ultrasonication time on plate roughness, insets show the water contact angles of the surface before and after ultrasonic treatment. Reproduced with permission [9] from The Royal Society of Chemistry.
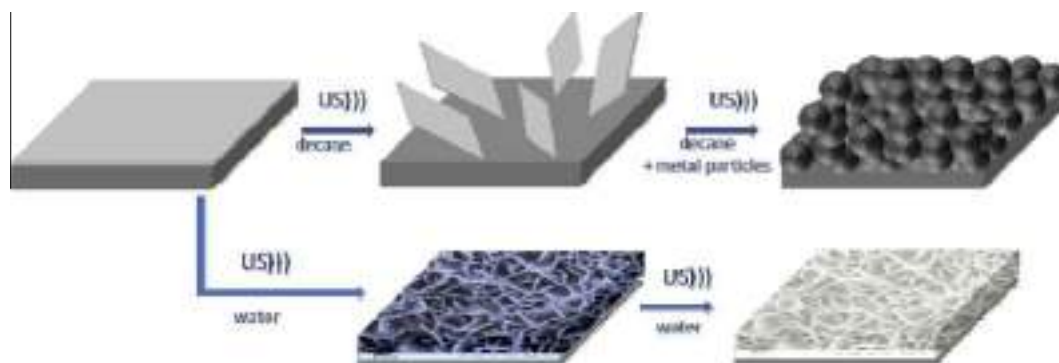
Fig. 7. Scheme of possible metal, for example magnesium, modification depending on the solution during the sonochemical process: UPPER – smooth oxide free metal surface (middle) design during the ultrasonic treatment (US) of a metal surface covered with a natural oxide layer (left) with the following surface sponge construction (right) in hydrocarbon liquid as a solution and presence of metal particle during the ultrasonic process; BELOW – surface metal sponge formation based on SEM and XRD study with intermediate structure of sponge with metal skeleton and in following the formation of oxide sponge on top of the metal plate.
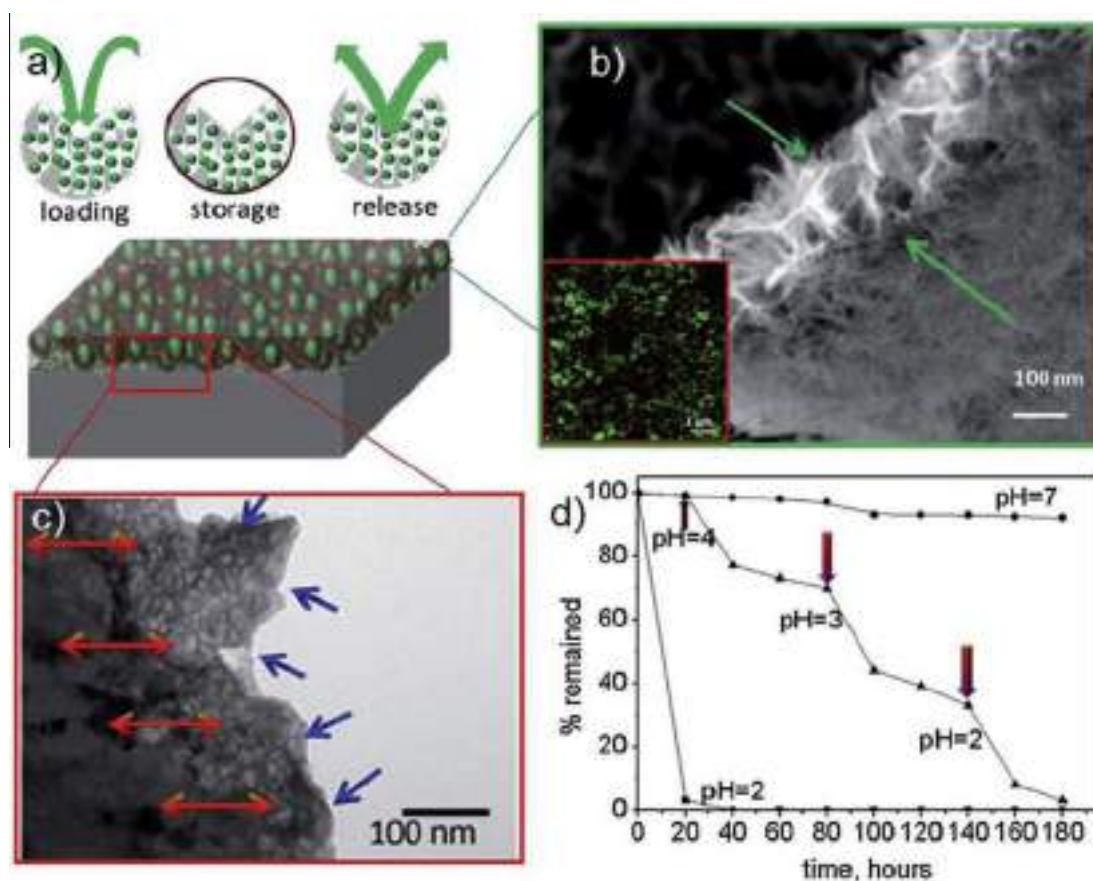
Fig. 8. (a) Schematic illustration of uploading, storage, and release of an active component (upper row) and general view of capsules generated at the metal surface (below). (b) SEM image of the cross-section of the aluminum sponge-like layer (indicated by arrows). Inset: luminescent confocal image (top view) of the surface capsules loaded with doxorubicin. (c) SEM image of the rough surface of the metal surface sponges. (d) Doxorubicin release under different pH (inset shows time-resolved release at acidic pH = 2). Reproduced with permission [45]. Copyright 2012, Wiley.

nanostructuring and regulating cavitation bubble dynamics and their interaction with surfaces, since the ultrasonic methodology is, indeed, unique [36], being highly economically and ecologically motivated in comparison with other known techniques. For example in Fig. 8 an ultrasonically generated metal sponge is used for effective surface capsule formation [37,38,45] to provide controllable, step-wise delivery of active chemicals (delivery of the antibiotic doxorubicin [45] is shown) or magnesium hydride for hydrogen storage and reactive hard templating [46].

Besides effective metal surface nanostructuring using physical and chemical effects of ultrasonic treatment, it is possible to design a device (Fig. 1) for cleaning [6] based on regulation of ultrasonically generated bubbles and their dynamics. The continuous and localized generation of acoustic cavitation bubbles can be accomplished by ultrasonically vibrating a silicon surface containing micropits [46]. When pouring liquid over the silicon substrate, individual gas bubbles can be entrapped in the pits; vibrating the surface ultrasonically resulted not only in acoustic streaming from
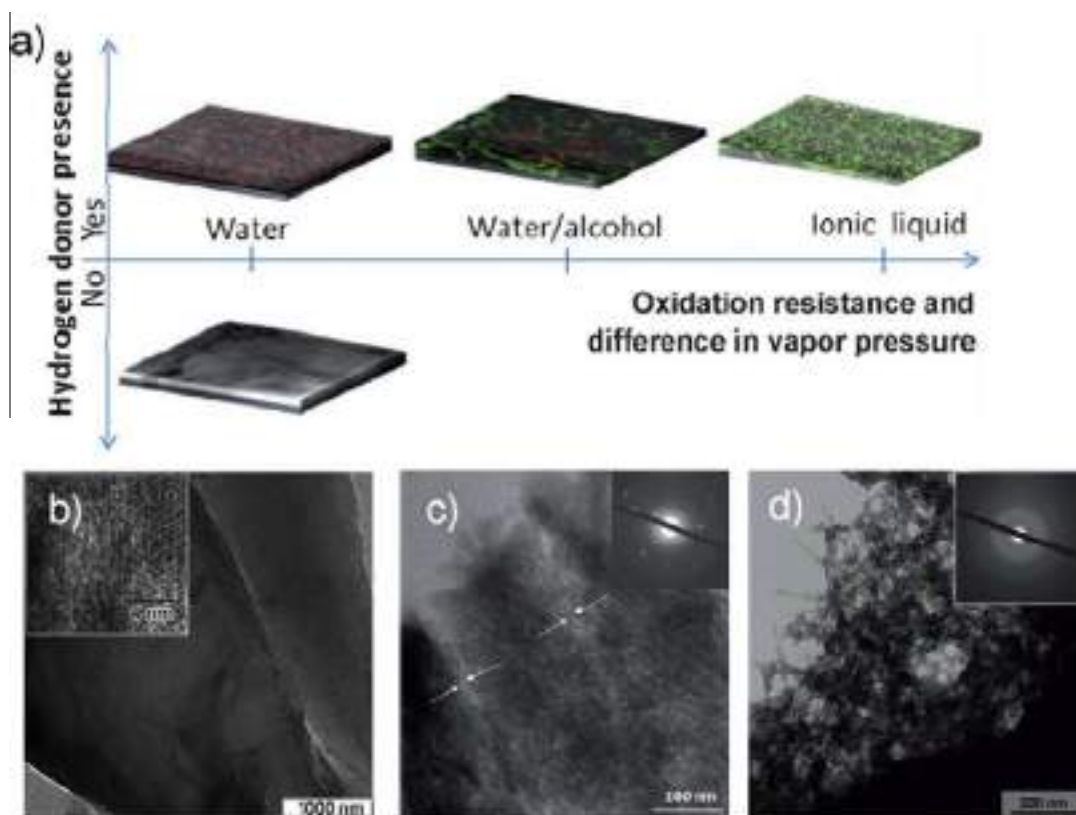
Fig. 9. (a) 3D schematic reconstruction, based on micro-confocal and TEM measurements of photoluminescence and porosity change, respectively, of Si after sonication in controlled solvent conditions. (b–d) TEM images of (b) initial crystalline silicon, (c) silicon after treatment in water, and (d) water/alcohol mixture. Insets presented evolution of (a) crystalline structure to (d) amorphous. Reproduced with permission [12]. Copyright 2012, Wiley.

the oscillating surface, but for large enough pressures also in pinch-off of gas bubbles from the micropits, as detailed elsewhere [47]. Water, ethanol, acetone were investigated [6] given their extensive use in general and ultrasonic cleaning applications of the cavitating bubbles for cleaning of the substrate opposite to silicon. It was shown that thin metal layers (Au shown in Fig. 8b) can be effectively removed in a certain local area, defined by the bubble cloud from the micropits.

To conclude this section, ultrasonic treatment is very prospective for both metal surface cleaning and nanostructuring and expected to be of increased interest for scientists from different fields from theory to application.

3. Silicon modification

We focus here on the ultrasound-assisted modification of silicon. For applications related to optics [48] or drug delivery [49], silicon suffers from an absence of intrinsic fluorescence and a lack of simple "green" modification techniques to render it suitable for such applications. In our study [12], we investigated the pronounced and controlled response of silicon surfaces to ultrasonic treatment, together with the formation of porous optically active silicon. The ultrasound-assisted method avoids the use of HF or similarly aggressive media, which are detrimental to the environment [48,49].

The ultrasound-assisted modification of silicon plates, in the form of both crystalline silicon wafers and amorphous silicon deposited onto glass, were studied [12]. In general, the interaction of cavitation bubbles with the silicon surface results in mechanical and chemical modification. As was already mentioned (see Table 1), the ultrasonic modification of solids is known to be controlled by

various sonication conditions, including the intensity and duration of sonication, the solvent, and the concentration and size of the sonicated species, oxidants, and reducing agents involved. The important innovation we introduce in our work [12] is the addition of hydrogen donors, such as in aqueous solutions magnesium particles or sodium borohydride, during ultrasonication, which has a dramatic influence on the process. The sonication of silicon species in water (Fig. 9), that does not contain a hydrogen donor, results in the formation of an oxidized surface caused by the oxidation of the silicon by-products of water sonolysis. The samples are characterized by a slight increase in their surface roughness and the absence of photoluminescence. The hydrogen donors slow down the surface oxidation processes, which are brought in by free radicals formed during water sonolysis, and stabilize the porous structure through the formation of silicon-terminated bonds. In this case, Si–H bonds could be formed as an alternative to, or together with, Si–O bonds. The illustration in Fig. 9a, based on a 3D reconstruction of TEM and μ-confocal measurements of the surface after high-intensity ultrasonic exposure, shows our general concept of a single-step "green" method for the construction of surfaces with different porosities. Without a reducing agent present during modification in water, neither porous nor luminescent structures were observed. However, in the presence of a reducing agent, luminescent structures with a range of porosities (25–40% in water, 60–70% in water/alcohol mixtures, and 40–50% in an ionic liquid) were detected. Furthermore, the differences in porosities correlate with differences in photoluminescence (green or red).

Moreover it was shown [12,50] that ultrasonic treatment (20 kHz, 57 W/cm^2) affects the surface crystal structure (Fig. 9b–d, insets): (i) provides amorphization of crystalline structures; and (ii) alternatively possibility to crystalline the amorphous.
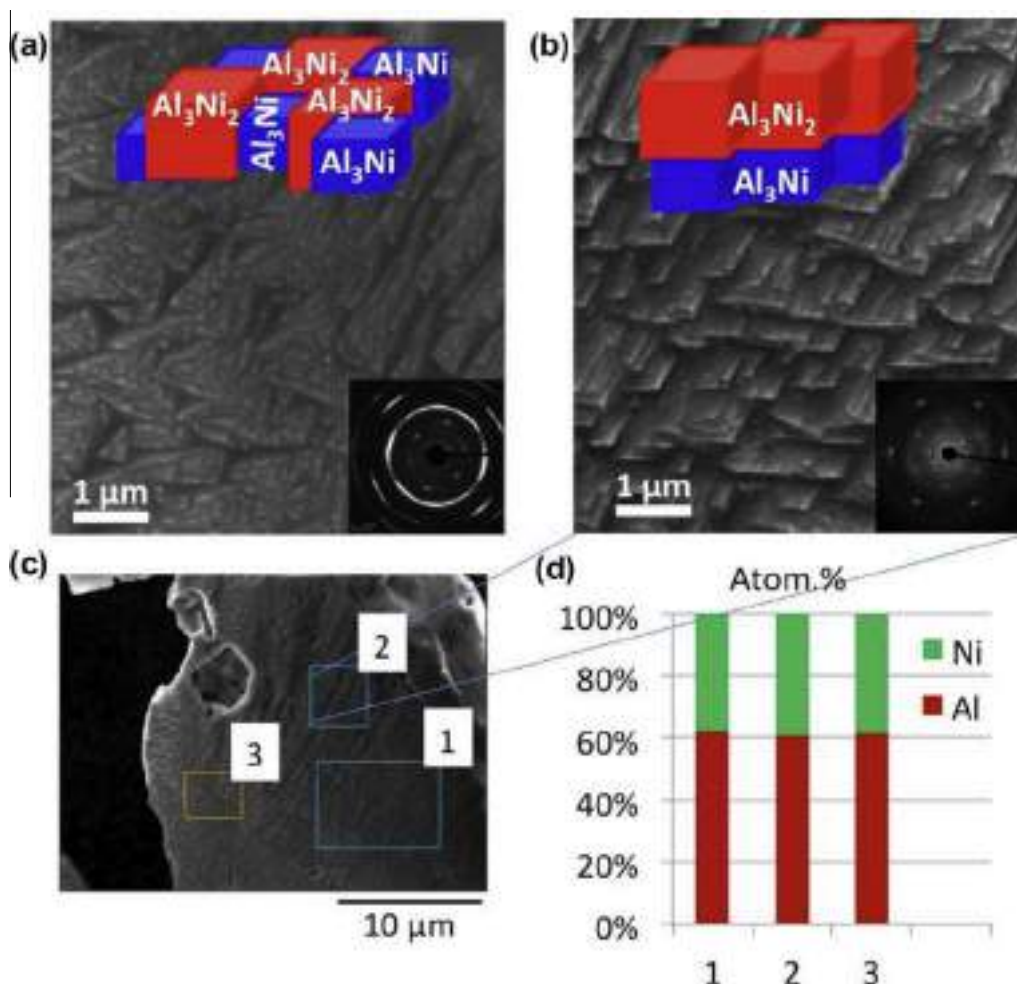
Fig. 10. Scanning electron microscopy images taken from the surface of AlNi (50 wt.% Ni) before (a) and after (b) ultrasonication. The inserts show selected area electron diffractions, which demonstrates the tendency to form larger intermetallic crystals after the ultrasonic treatment. The sketches illustrate the random phase distribution in the initial AlNi particles and the preferential clustering of the Al_3Ni_2 phase upon treatment. Energy dispersive X-ray analysis of the metal surface after ultrasonication proves the formation of Al_3Ni_2 at the surface, where aluminum to nickel is 3:2. Reproduced with permission [55]. Copyright 2015, from The Royal Society of Chemistry.

Crystalline samples modified for 20 min reveal partial surface amorphization (Fig. 9b–d), which later converts into a completely amorphous microporous silicon structure.

A detailed study of Rivas et al. [51] correlates Si erosion to its crystalline structure in an ultrasonic device employing micropits [52]. Together with controlling the ultrasonic reactor parameters (Table 1), an ultrasound device enables the control of the location and amount of cavitation bubbles and the surface modification effects on a millimeter scale [6,51,52]. It was observed [51] that the concerted effect of various sources of damage formation such as jetting, shock waves, direct bubble impact, and surface stress corrosion can all cause the damage observed for the three crystallographic silicon surfaces studied, although each of the three surfaces has a different resistance to erosion. For (1 0 0) silicon, and under the current working conditions, the incubation time was of the order of 50 min, whereas for (1 1 0) and (1 1 1) apparently the incubation period is larger than the total 180 min sonication.

Spectroscopic investigations reveal [50] (Fig. 3) that argon (bubbling continuously through the liquid phase during experiments) can be ultrasonically excited via mechanoluminescence, i.e., emission of light caused by mechanical action on a solid. This phenomenon is highlighted being important and showing that material from the solid surface can affect the bubbles.

Here it is worth to discuss the advantage of in-situ analysis to monitor ultrasonic treatment. A simple possible set up for in situ monitoring is presented in Figs. 1 and 3. The in situ control allows to follow the kinetics, which, in most cases, is nonlinear. It enables to directly measure the formed surface structure and its development with time.

4. Ultrasonic assisted formation of composite materials

4.1. Metal alloy treatment

Ultrasonic treatment of metal alloys with components of different sensitivity to ultrasound results in formation of multi-metal nanocomposites after ultrasonic nanostructuring [10,44,53–57]. The ultrasonic nanostructuring of metal alloys is based on microphase separation in an alloy due to different phase response to ultrasound. Thus, if alloy particles consisting of an ultrasound-resistant compound and a sensitive one are treated, one would expect that novel nanocomposite structures are developed. We tested Al/Ni, Al/Pd, Al/Fe and Al/Pd/Cu systems [10,44,53]. Indeed, the treatment of the aqueous alloy with highly-intense ultrasound leads not only to the formation of porous structure from more active metal aluminum but also results in phase segregation, yielding ultrasound-resistant nickel, palladium and copper nanoparticles homogeneously distributed in the porous matrix.

Simultaneously BET analysis even reveals a more porous structure formation in the case of nanocomposites compared to
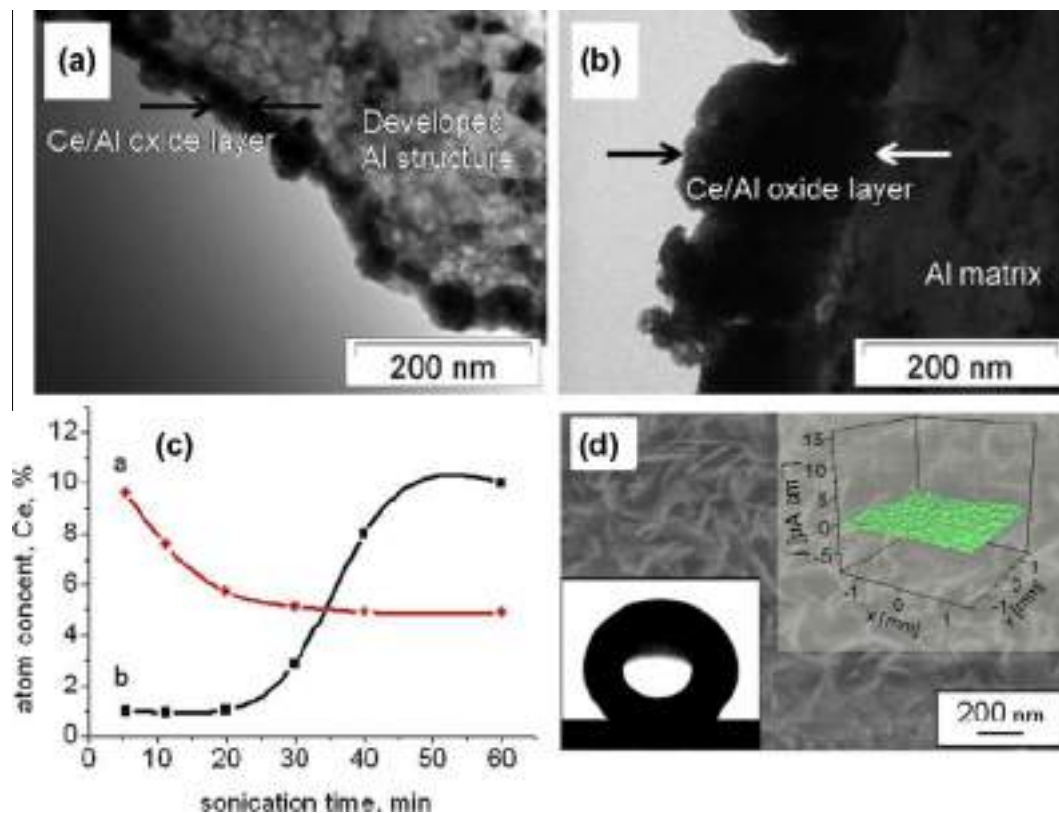
Fig. 11. Transmission electron microscopy (TEM) image of the cross section of aluminum covered by (a) a cerium/aluminum nanonetwork and (b) a dense cerium oxide layer. (c) Dependence of the atomic concentrations of cerium on ultrasonic treatment time (measured by energy dispersive X-ray spectrometry). The samples were sonicated at 57 W/cm^2 in 0.5 M cerium (III) nitrate solution (a) and at 30 W/cm2 in 0.5 M cerium (III) nitrate solution (b).The dense cerium oxide layer is shown by the arrows. Reproduced with permission [50]. Copyright 2012, American Chemical Society. (d) SEM image of an aluminum plate covered by layered double hydroxide laurate, inset shows the water contact angle on this surface and 3D current density maps of the surface after 12 h immersion in 0.1 M NaCl. Reproduced from Ref. [9] with permission from The Royal Society of Chemistry.

individual active metals: the surface area in this case amounted to 125 m^2/g for the AlNi, 280 m^2/g for the Al/Pd, 210 m^2/g for those of Al/Pd/Cu after 60 min of modification and ca. 80 m^2/g in the case of aluminum.

The formed nanostructures are highly prospective for various fields of catalysis, electrocatalysis, hydrogen storage materials, etc. The group of Andreeva focuses on developing such nanostructures to be effective in these areas [53–57]. Recently, it has been argued that structuring of near-surface regions in metal alloys is of great importance for achieving enhanced catalytic activities of intermetallic compounds [54,55]. Upon controlled ultrasonic nanostructuring of intermetallic phases in AlNi alloys [55], the preferential orientation of Al$_3$Ni$_2$ (100) hexagonal crystal planes at the surface was achieved (Fig. 10) in ethanol solution. AlNi powder (4 g) was dispersed in 40 mL ethanol and sonicated for 60 min operated at 20 kHz with a maximum output power of 1000 W. The maximum intensity was calculated to be 140 W cm^{-2} at mechanical amplitude of 140 μm. To avoid overheating during sonication the experiment was carried out in a homemade thermostatic cell connected to a thermostat. The temperature was monitored during the treatment and kept at 298 K. The ultrasonic treatment of AlNi particles causes a remarkable modification of morphology and surface composition in the AlNi alloys. The compositional and morphological changes are clearly visible in Fig. 10. The ultrasonically induced clustering of intermetallic phases in the modified AlNi particles is also schematically illustrated in Fig. 10. It is of high importance that the development of an ultrasonically induced temperature gradient within the surface of an alloy can stimulate additional crystal growth [54,55]. The Al$_3$Ni$_2$ and Al$_3$Ni crystallites in ultrasonically treated AlNi are nearly twice as large (131 nm for Al$_3$Ni$_2$; 113 nm for Al$_3$Ni), as compared to pristine particles (87 nm for Al$_3$Ni$_2$; 56 nm for Al$_3$Ni). Assuming diffusion-controlled crystal growth during the treatment period (1 h), the diffusion rate in the AlNi (50 wt.% of Ni) was estimated to be about 2×10^{-18} m^2/s. The reference experiments (heating the particles in an oven for 1 h at different temperatures showed that the observed atomic diffusion proceeds at an average temperature in the particle interior that is equal to about $T \approx 823$ K [55].

In summary alloy treatment could provide selective intermetallic phase separation and growth. For example the formation of the Al$_3$Ni$_2$ phase on the surface of AlNi alloys is kinetically restricted [58], but the thermal shock processing of the metal surface by ultrasonically generated cavitation bubbles creates large local temperature gradients in the AlNi particles to overcome kinetic barriers. Moreover estimation of local surface treatment could be done by following the eutectics reaction of intermetallic alloys. Collapsing cavitation bubbles may heat the surface above 1000 K, thus, triggering the near-surface transformation of the catalytically inactive Al$_3$Ni phase into beneficial Al$_3$Ni$_2$ [55]. In the particle interior, the estimated mean temperature reaches ca. 800 K, which is well below the phase transition temperature, but still enough for substantial solid-state diffusion and crystal growth.

4.2. Treatment in solutions containing metal ions, nanoparticles

During ultrasonic treatment to clean or modify the surface one should take into account that if any additives are presented in the solution they could be involved as in the bubble dynamics [16], as in formed surface structures [10,13,14]. There are pros and cons in that.
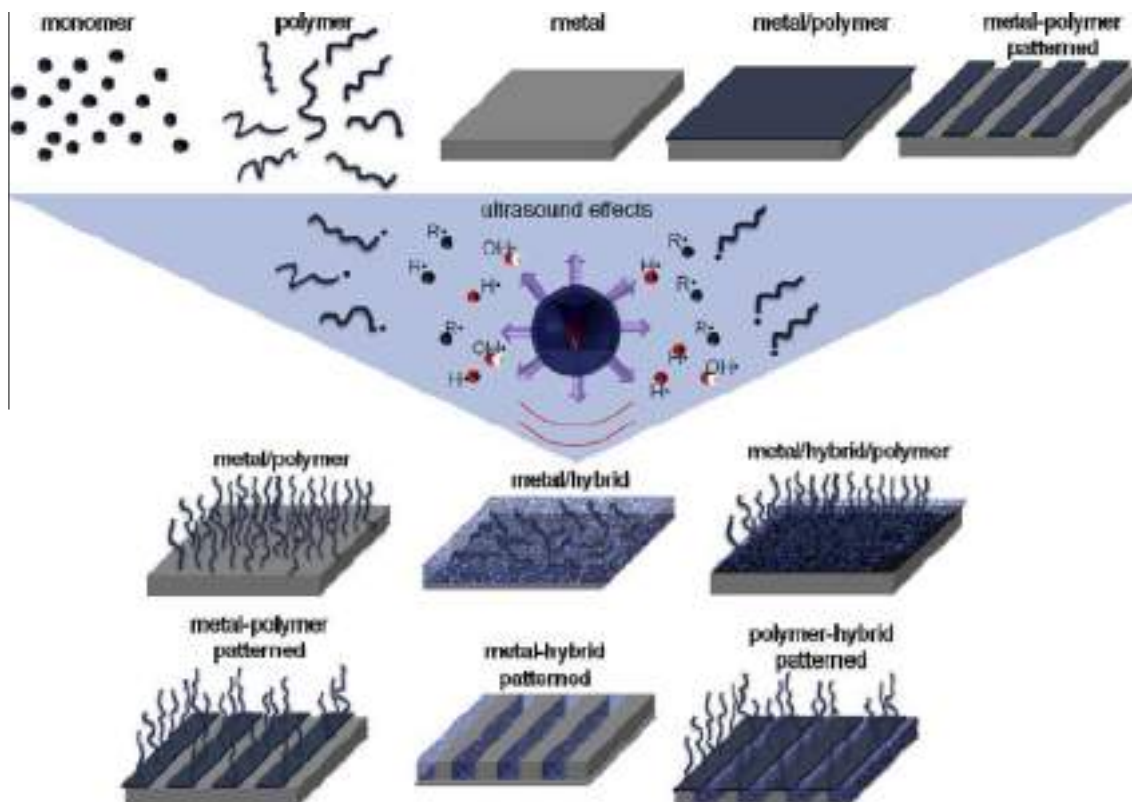
Fig. 12. Schematic presentation of possible research objects containing the material combination (individual not shown): initial materials – monomer, polymer, metal, metal/polymer, and metal-polymer-patterned surface – UPPER part; possible ultrasonic effects in the reactor – physical (shock waves and liquid jets) and chemical (formation of radicals from monomer and polymer and sonolysis of the liquid (here, water shown)) – MIDDLE part; some examples of systems which could be expected after applying ultrasonic exposure: polymers could be attached to the metal (here shown as a brush formation on the surface); the metal and polymer could form a porous hybrid system; on the surface of a metal, a thin hybrid (metal/polymer) layer could be formed with subsequent polymer attachment to the hybrid (here, brush formation is shown); and in the case of an initial patterned surface, the combination of approaches is possible – LOWER part of the scheme. Reproduced with permission [38] Copyright 2014, Wiley.

The advantages can be clearly seen, when ultrasonic treatment of aluminum surfaces was performed in cerium (III) aqueous solution under different intensities of treatment [13]. Salts of transition and rare-earth metals (Ce, Co, Mo) have been proposed as alternatives to carcinogenic chromate inhibitors [59] due to their low toxicity, economic efficiency, and sufficient cathodic inhibition of metal corrosion [60]. The ultrasonic treatment results in two types of cerium-enriched surface nanostructures (Fig. 11) which correlate with two tested ultrasonic intensities: (i) cerium/aluminum oxide nanonetwork, where cerium oxide is formed at lower intensity of ultrasonic treatment; and (ii) aluminum oxide interlaced in a mixed layer strongly connected to the metal surface. A combination of microscopic and spectroscopic methods was applied to study structure and morphology of the coatings as well as to optimize the ultrasound-assisted preparation method. The anticorrosion activity of the novel cerium/aluminum oxide system is more pronounced for the samples prepared at higher intensity (57 W/cm^2 in comparison to 30 W/cm^2) of ultrasound and characterized by formation of a Al/Ce nanonetwork interfacial layer (Fig. 11a), well adhering to the matrix. At lower intensity of sonication surface oxidation is dominating and the novel layer has poor adhesion to the matrix (Fig. 11b), which results in low anticorrosion properties.

The other example presented in Fig. 11d is the treatment of aluminum in laurate solution [9]. It was already mentioned above (Fig. 6h) that aluminum is characterized by increased hydrophilicity of the surface after ultrasonic treatment. It should be also noted that superhydrophilicity can help in formation of superhydrophobic surfaces involving surface modification of our developed struc-

ture [61], for example by sodium laurate [62]. In principle a porous layer on aluminum could be considered as layered material such as anionic clay e.g. layered double hydroxide. This layered double hydroxide in our case plays the role of an inorganic host, which can be modified to reach surface superhydrophobicity due to formation complex structure by attachment of laurate under low intensity sonication to the porous surface and formation of layered double hydroxide laurate. The formed structure is shown in Fig. 11d. Treatment in sodium laurate results in a surface bonded laurate film showing induced superhydrophobicity with water contact angle 163° (Fig 11d, inset). It the case of unmodified aluminum the layered double hydroxide layer exhibits very poor adhesion, contrarily in the case of high intensity designed aluminum the layer adhesion was very high even after 1 month of corrosion test. Measurements (Fig. 11d inset) by the scanning vibrating electrode technique [63] revealed a very high corrosion resistance with simultaneous self-healing ability [9].

The other attractive approach is intercalation of active centers into the porous matrix, e.g. noble metals. Examples can be also based on metal sponge formation with noble particles in their structures [14,64,65]. The pre-sonicated metal sponge (Al) was mixed with a noble metal nanoparticle dispersion. The mixture was sonicated with high intensity ultrasound. The resulting materials find applications in effective catalysis [14], SERS [64], and biocide surfaces [65].

To conclude, the ultrasonic treatment of multicomponent structures, e.g. metal alloys, or in solutions with additives, e.g. metal ions salts or nanoparticles, involves many ultrasonically initiated primary and secondary processes and reactions. To model and
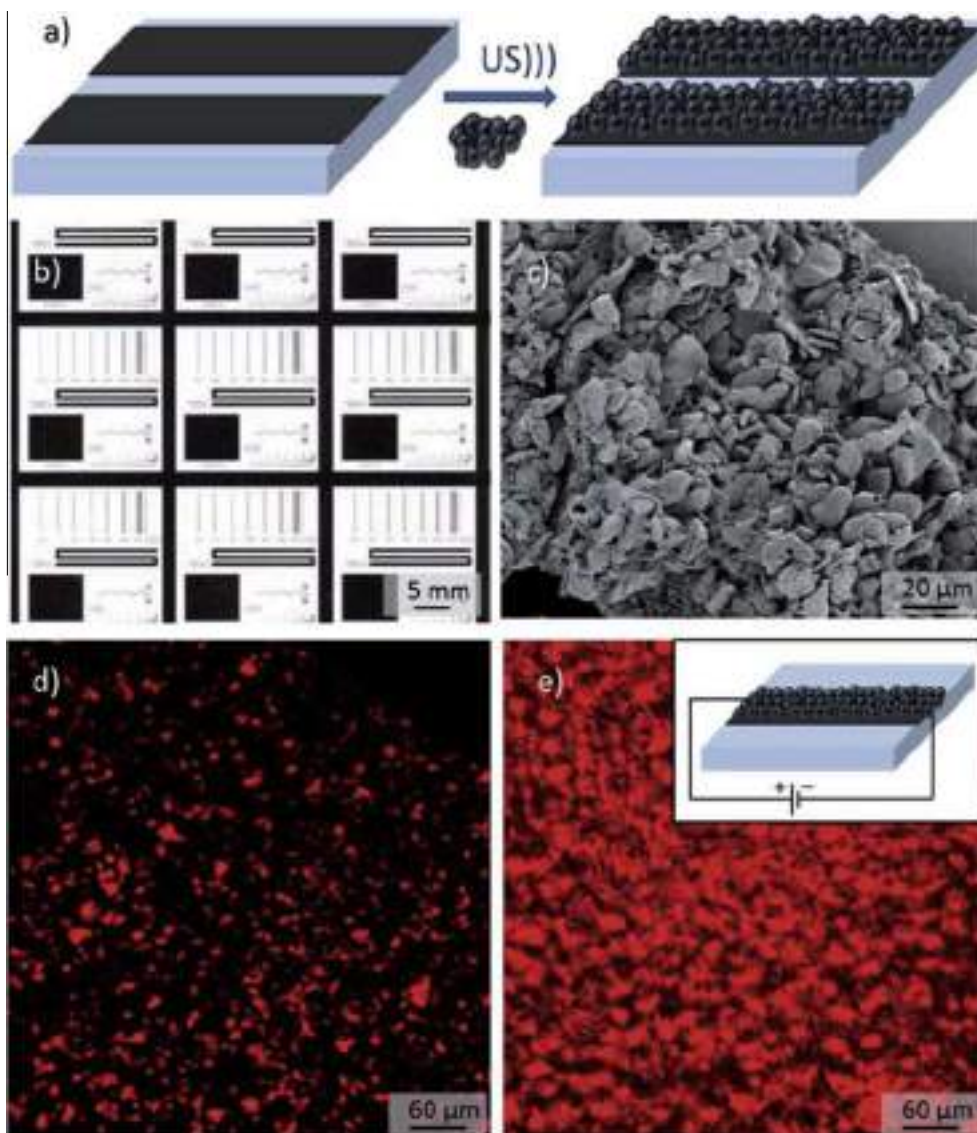
Fig. 13. (a) Schematic representation of the process of sonoimpregnation (5 min) of hybrid particles on a patterned surface. (b) Optical image of the initial nickel patterned ITO glass electrode. (c) SEM image of a patterned sonoimpregnated surface of a Rh6G-loaded hybrid. (d) Confocal microscopy image (fluorescent mode) of (c). (e) Is (d) after electric current flow (shown schematically in the inset). Reproduced from Ref. [32] with permission from The Royal Society of Chemistry.

understand all processes is still a challenge and in-situ investigation, mentioned in the previous part, are of high priority concerning complex structures and solutions with additives.

5. Formation of metal hybrids with polymers

Advanced approaches for structure engineering of interfaces/surfaces to generate new properties and applications are of high priority. The surface modifications and functionalization can be expanded to the construction of hybrid material.

The advantage of ultrasonic treatment is the possibility to form hybrids together with surface cleaning and following nanostructuring, e.g. metals with polymer hybrids performing ultrasonic treatment in solution containing monomers, polymers (Table 1). The presence of monomer or polymer molecules in the sonochemical reactor can influence the cavitation process [16]. Organic molecules are able to accumulate at the gas/liquid interface of cavitation microbubbles. The center of the bubble exhibits high temperatures and pressures, whereas the bulk liquid remains under

normal conditions. A transition zone also exists between these two states. Molecules are present in both the transition zone and the outer liquid phase. The time required for the orientation of long-chain molecules in the gas/liquid interface is longer than that required for short-chain molecules and longer than the bubble lifetime.

However, organic molecules near the bubble interface influence the cavitation process, which increases surface pressure, decreases the lifetime of the cavitation bubble, and leaves the molecule in the correct orientation and chemical state for transport and attachment to the surface [66]. Five main effects of cavitation are known for monomers and polymers: the formation of free radicals during the cavitation process, polymerization, chain reorientation, polymer decomposition and the involvement of organics in chemical processes, such as oxidation and bond breakage [67,68].

Despite the great interest [69] in the prospective field of metal–polymer interactions by high-intensity ultrasound through cavitation-assisted processes, a general lack of knowledge persists about such processes. Fig. 12 shows a schematic representation of
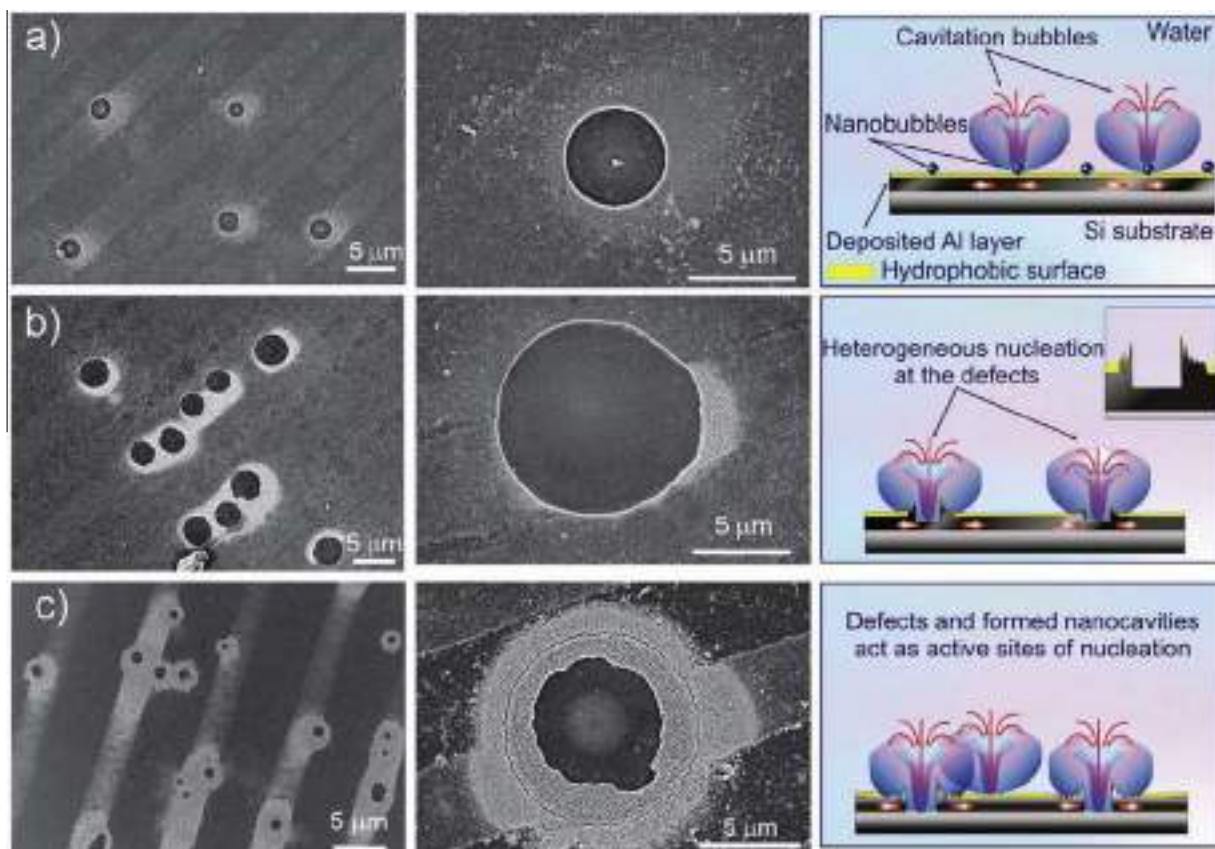
Fig. 14. SEM images of patterned Si with 100 nm of sputtered Al layer after ultrasonic treatment: (a) at 10 min of sonication, (b) at 20 min of sonication, (c) at 40 min of sonication. First column: overview images of the sonicated surfaces (thickness of the hydrophobic stripes is about 8 μm; hydrophilic stripes, 20 μm). Second column: high magnification images (3000×) of the formed defects on hydrophobic surfaces. Third column: sketch of the cavitation process on the hydrophobic surface. Reproduced with permission [70]. Copyright 2011, The Royal Society of Chemistry.

the main initial surfaces and some hypothesized consequences of sonochemical surface modification. Three main possible methods of metal-polymer interaction have been postulated: (1) the attachment of polymer molecules to a metal surfaces or a thin metal-oxide layer on the metal; (2) the formation of a hybrid, which simultaneously interacts with and modifies the metal, and polymer or monomer attachment with subsequent polymerization, or monomer polymerization and subsequent polymer attachment; (3) the formation of a thin hybrid layer on the metal surface and the subsequent attachment of the polymer (either initially present or formed from the monomer during the process of sonication).

In our group we developed active metal, e.g. Mg or Al, polypyrrole hybrids [32,69]. We proposed a novel method [32,69] of formation of a polymer/metal hybrid interfacial layer with switchable properties by using ultrasonication. Intense ultrasonication leads to formation of a rough metal interface and triggers free radical polymerization of monomers in the interfacial region of the metal surface. Thus, the polymer layer exhibits excellent adhesion to the bulk metal. The novel concept was demonstrated for a model polypyrrole/aluminum system [32]. Hydrophilic/hydrophobic properties and corrosion resistance, also due to doping/dedoping of polypyrrole of the interfacial layers, can be adjusted for a particular application. The proposed method can serve as a platform for formation of interfaces with self-regulating properties: self-healing, switchable hydrophilicity.

Magnesium–polypyrrole hybrid capsules loaded with the organic fluorophore rhodamine 6G (Rh6G) were developed [32]. The hybrids were prepared through sonication of magnesium and pyrrole without initiator or with Fe(III) as the polymerization initiator in water and alcohol solutions. The properties of the obtained hybrids, as well as the dye-loading efficiency, were found to depend on the ultrasonic conditions. The fluorophore release from the free or surface sonoimmobilised capsules in aqueous solutions of different pH values and under electric current was studied. Effective pH-responsive release, including step-wise release, was confirmed for the hybrid system. The electric current was also shown to trigger the release of hybrid capsules sonoimmobilised onto a Ni patterned ITO surface (Fig. 13).

It is interesting that together with synthesis, removal/cleaning of the surface from biofilms and polymers (hydrogels) are simultaneously possible, for example, using the ultrasonic device shown in Fig. 8 [6]. Biofilms are known to be able to adhere strongly to a substrate. Many of the MCF-7 cells of biofilm grown on a glass slide had been detached due to the induced cavitation cloud. However, optical visualization does not give any information on the cells around the area that was cleaned. Those cells might have been lysed through sonoporation. The method of dead-live staining could provide information on the viability of the remaining cells.

Control of cavitation is also suggested by means of hybrid patterned surfaces [15,70,71]. Thus cavitation at the solid surface normally begins with nucleation, in which defects or assembled molecules located at a liquid–solid interface act as nucleation centers and are actively involved in the evolution of cavitation bubbles. A simple approach to evaluate the behavior of cavitation bubbles based on sonication of patterned substrates with a small roughness (less than 3 nm) and controllable surface energy was proposed. A mixture of octadecylphosphonic acid (ODTA) and octadecanethiol (ODT) was stamped on the Si wafer coated with

different thicknesses of an aluminum layer (20–500 nm). The growth mechanism of cavitation bubble nuclei and the evolution of individual pits (defects) formed under sonication on the modified surface were investigated (Fig. 14). An activation behavior as a function of Al thickness, sonication time, ultrasonic power and temperature was reported. In the process cooperativity was introduced, as initially formed pits further reduce the energy to form bubbles. Furthermore, cavitation on the patterns is a controllable process, where up to 40–50 min of sonication time only the hydrophobic areas are active nucleation sites. The study provides a convincing proof of a theoretical approach on nucleation.

Organic–inorganic hybrid nanocompounds or porous metal organic frameworks have been investigated and shown be possible to be synthesized in cavitation assisted reactions [72].

In summary, ultrasonic chemistry carries many exciting prospects but is in its infancy with respect to our understanding and control of the process, which necessitates a multidisciplinary approach for specific applications. Concerning the latter, the focus for hybrids is bubble nucleation through hybrid patterned surfaces [15], biomaterials and biomimetic [42].

6. Conclusions

There have been many developments in recent years in application of ultrasonic cleaning/treatment of different solid surfaces. Ultrasonic nanostructuring results in new types of advanced materials. Using high intensity ultrasound is ecologically friendly and allows one to achieve high temperature and high pressure nonequilibrium conditions locally on a microlevel with a bulk reactor near room temperature. Important solid surface characteristics which determine solid surface resistivity and kinetics of surface response to ultrasonic cleaning/treatment are discussed. The current achievements of the application of ultrasonic approach for the modification of solid-state materials can be summarized according to the following main directions:

(1) There are two main concepts explaining the interaction of the cavitation bubble with solid surface: collapse of the single cavitation bubble at solid surface resulting in the bubble jetting and concerted collapse of bubble clusters.
(2) Surface hydrophilicity, stability to Red/Ox reactions, adhesion of surface layers to the substrate, melting temperature are important to predict the influence of ultrasound on the surface.
(3) Ultrasonic treatment of metals, silicon can be used for the development of active chemically-stabilized surface sponge-like structures, recrystallization of the surfaces, formation of metal nanoalloys.
(4) The collapsing cavitation bubbles may heat the surface above 1000 K and trigger the near-surface transformation of solids and intermetallics (analyzed based on modification of AlNi alloy particles). In the particle interior, the estimated mean temperature can then be ca. 800 K, which is below the phase transition temperature, but still high enough for substantial solid-state diffusion and crystal growth.
(5) The ultrasonic treatment in solution with additives, besides possible phase transformation of bulk materials, results in incorporation of metal ions/nanoparticles into the bulk structure and formation of functional layers.
(6) The main focus of the ultrasonic treatment of hybrids may be devoted to stimulated reorganization of polymers, partial oxidation, cross-linking, crystallinity, changes of the outer polymer layers and hybrid development. Interesting prospects of selective nanostructuring can thus be derived.

References

[1] M. Ashokkumar, T.J. Mason, Sonochemistry, in: Kirk-Othmer Encyclopedia of Chemical Technology, Wiley, 2000.
[2] J.H. Bang, K.S. Suslick, Applications of ultrasound to the synthesis of nanostructured materials, Adv. Mater. 22 (2010) 1039–1059.
[3] C.E. Brennen, in: Cavitation and Bubble Dynamics, Oxford University Press, 1995.
[4] L.H. Thompson, L.K. Doraiswamy, Sonochemistry: science and engineering, Ind. Eng. Chem. Res. 38 (1999) 1215–1249.
[5] M.A. Margulis, in: Sonochemistry Basis, High School, Moscow, 1984.
[6] D.F. Rivas, B. Verhaagen, J.R.T. Seddon, A.G. Zijlstra, L.-M. Jiang, L.W.M. Sluis, M. Versluis, D. Lohse, H.J.G.E. Gardeniers, Localized removal of layers of metal, polymer, or biomaterial by ultrasound cavitation bubbles, Biomicrofluidics 6 (2012) 034114–034120.
[7] M. Hauptmann, H. Struyf, S. De Gendt, C. Glorieux, S. Brems, Importance of bubble size control in ultrasonic surface cleaning by pulsed high-frequency sound fields, ECS J. Solid State Sci. Technol. 3 (2014) N3032–N3040.
[8] N. Bremond, M. Arora, C.D. Ohl, D. Lohse, Cavitation on surfaces, J. Phys. Condens. Matter. 49 (2005) S3603–S3608.
[9] E.V. Skorb, D.G. Shchukin, H. Möhwald, D.V. Andreeva, Ultrasound driven design of metal surfaces, Nanoscale 2 (2010) 722–727.
[10] E.V. Skorb, D. Fix, D.G. Shchukin, H. Möhwald, D.V. Sviridov, R. Mousa, N. Wanderka, J. Schöferhans, N. Pazos-Perez, A. Fery, D.V. Andreeva, Formation of oxide-stabilized mesoporous metal sponges by ultrasound, Nanoscale 3 (2011) 985–993.
[11] D.G. Shchukin, E.V. Skorb, V. Belova, H. Möhwald, Ultrasonic cavitation at solid surfaces, Adv. Mater. 23 (2011) 1922–1934.
[12] E.V. Skorb, D.V. Andreeva, H. Möhwald, Ultrasonically induced pathways of silicon modification towards a porous luminescent structure, Angew. Chem. Int. Ed. 51 (2012) 5138–5142.
[13] E.V. Skorb, D.G. Shchukin, D.V. Andreeva, Ultrasound driven formation of cerium-rich anticorrosion nanonetwork on aluminum alloy surface, Langmuir 26 (2010) 16973–16979.
[14] N. Pazos-Perez, J. Schäferhans, E.V. Skorb, A. Fery, D.V. Andreeva, Ultrasound driven formation of metal-supported nanocatalysts, Micropor. Mesopor. Mater. 154 (2012) 164–169.
[15] V. Belova, D.A. Gorin, D.G. Shchukin, H. Möhwald, Selective ultrasonic cavitation on patterned hydrophobic surfaces, Angew. Chem. Int. Ed. 49 (2010) 7129–7133.
[16] G.J. Price, Current Tends in Sonochemistry, Royal Society of Chemistry, Cambridge, U.K., 1992.
[17] Y. Didenko, K.S. Suslick, The energy efficiency of formation of photons, radicals, and ions during single bubble cavitation, Nature 418 (2002) 394–397.
[18] D.J. Flannigan, K.S. Suslick, Plasma formation and temperature measurement during single-bubble cavitation, Nature 434 (2005) 52–55.
[19] D. Radziuk, H. Möhwald, K.S. Suslick, Single bubble perturbation in cavitation proximity of solid glass: hot spot versus distance, Phys. Chem. Chem. Phys. 16 (2014) 3534–3541.
[20] W.B. McNamara, Y.T. Didenko, K.S. Suslick, Sonoluminescence temperatures during multi-bubble cavitation, Nature 401 (1999) 772–775.
[21] N. Bremond, M. Arora, C.D. Ohl, D. Lohse, Controlled multi-bubble surface cavitation, Phys. Rev. Lett. 96 (2006) 224501.
[22] J. Rooze, E.V. Rebrov, J.C. Schouten, J.T.F. Keurentjes, Dissolved gas and ultrasonic cavitation – a review, Ultrason. Sonochem. 20 (2013) 1–11.
[23] H. Xu, B.W. Zeiger, K.S. Suslick, Sonochemical synthesis of nanomaterials, Chem. Soc. Rev. 42 (2013) 2555–2567.
[24] E.V. Skorb, H. Möhwald, in: S. Manickam, M. Ashokkumar (Eds.), Cavitation: A Novel Energy Efficient Technique for the Generation of Nanomaterials, Pan Stanford Publishing, Singapore, 2011.
[25] V. Belova, D.A. Gorin, D.G. Shchukin, H. Möhwald, Controlled effect of ultrasonic cavitation on hydrophobic/hydrophilic surfaces, ACS Appl. Mater. Interfaces 3 (2011) 417–425.
[26] J.L. Luche, A few questions on the sonochemistry of solutions, Ultrason. Sonochem. 4 (1997) 211–215.
[27] A.A. Ndiaye, R. Pflieger, B. Siboulet, J. Molina, J.F. Dufreche, S.I. Nikitenko, Nonequilibrium vibrational excitation of OH radicals generated during multibubble cavitation in water, J. Phys. Chem. A. 116 (2012) 4860–4867.
[28] F.R. Young, in: Cavitation, Imperial College Press, 1999.
[29] A.V. Volkova, S. Nemeth, E.V. Skorb, D.V. Andreeva, Highly efficient photodegradation of organic pollutants assisted by sonoluminescence, Photochem. Photobiol. (2014). PHP-2014-08-RA-0199.

[30] I. Masselin, X. Chasseray, L. Durand-Bourlier, J.-M. Lainé, P.-Y. Syzaret, D. Lemordant, Effect of sonication on polymeric membranes, J. Membr. Sci. 181 (2001) 213–220.

[31] S. Brems, M. Hauptmann, E. Camerotto, A. Pacco, H. Struyf, P. Mertens, C. Gottschalk, S. De Gendt, The influence of dissolved carbon dioxide on cavitation intensity in ultrasound cleaning systems, Jpn. J. Appl. Phys. 52 (2013) 066602–66607.

[32] E.V. Skorb, O. Baidukova, A. Brotchie, A. Goyal, D.V. Andreeva, H. Möhwald, Sononanoengineered magnesium – polypyrrole hybrid capsules with synergetic trigger release, J. Mater. Chem. 22 (2012) 13841–13848.

[33] M. Virot, T. Chave, S.I. Nikitenko, D.G. Shchukin, T. Zemb, H. Möhwald, Acoustic cavitation at the water-glass interface, J. Phys. Chem. C 114 (2010) 13083–13091.

[34] N. Zaafarani, D. Raabe, R.N. Singh, F. Roters, S. Zaefferer, Three-dimensional investigation of the texture and microstructure below a nanoindent in a Cu single crystal using 3D EBSD and crystal plasticity finite element simulations, Acta Mater. 54 (2006) 1863–1876.

[35] N. Zaafarani, D. Raabe, F. Roters, S. Zaefferer, On the origin of deformation-induced rotation patterns below nanoindents, Acta Mater. 56 (2008) 31–42.

[36] E.V. Skorb, D.V. Andreeva, Surface nanoarchitecture for bio-applications: self-regulated intelligent surfaces, Adv. Funct. Mater. 23 (2013) 4483–4506.

[37] E.V. Skorb, H. Möhwald, Dynamic interfaces for responsive encapsulation systems, Adv. Mater. 36 (2013) 5029–5043.

[38] E.V. Skorb, H. Möhwald, "Smart" surface capsules for delivery devices, Adv. Mater. Interface 1 (2014) 1400237, http://dx.doi.org/10.1002/admi.201400237R1.

[39] S.J. Doktycz, K.S. Suslick, Interparticle collisions driven by ultrasound, Science 247 (1990) 1067–1069.

[40] K.S. Suslick, S.B. Choe, A.A. Cichowlas, M.W. Grinstaff, Sonochemical synthesis of amorphous iron, Nature 353 (1991) 414–416.

[41] J. Dulle, S. Nemeth, E.V. Skorb, D.V. Andreeva, Sononanostructuring of zinc-based materials, RCS Adv. 2 (2012) 12460–12465.

[42] E.V. Skorb, D.V. Andreeva, Bio-inspired ultrasound assisted construction of synthetic sponges, J. Mater. Chem. A 1 (2013) 7547–7557.

[43] K.S. Suslick, J.J. Gawienowski, P.F. Schubert, H.H. Wang, Sonochemistry in non-aqueous liquids, Ultrasonics 22 (1994) 33–36.

[44] E.V. Skorb, H. Möhwald, T. Irrgang, A. Fery, D.V. Andreeva, Ultrasound-assisted design of metal nanocomposites, Chem. Commun. 46 (2010) 7897–7899.

[45] D.V. Andreeva, D.V. Sviridov, A. Masic, H. Möhwald, E.V. Skorb, Nanoengineered metal surface capsules: construction of a metal–protection system, Small 8 (2012) 820–825.

[46] O. Baidukova, H. Möhwald, A.S. Mazheika, D.V. Sviridov, T. Palamarciuc, B. Weber, P.V. Cherepanov, D.V. Andreeva, E.V. Skorb, Sonogenerated metal-hydrogen sponges for reactive hard templating, Chem. Commun. 51 (2015) 7606–7609.

[47] N. Bremond, M. Arora, C.D. Ohl, D. Lohse, Cavitation on patterned surfaces, Phys. Fluids 17 (2005) 091111.

[48] L.T. Canham, Gaining light from silicon, Nature 408 (2000) 411–412.

[49] Y.Y. Li, F. Cunin, J.R. Link, T. Gao, R.E. Betts, S.H. Reiver, V. Chin, S.N. Bhatia, M.J. Sailor, Polymer replicas of photonic porous silicon for sensing and drug delivery applications, Science 299 (2003) 2045–2047.

[50] M. Virot, R. Pflieger, E.V. Skorb, J. Ravaux, T. Zemb, H. Möhwald, Crystalline silicon under acoustic cavitation: from mechanoluminescence to amorphization, J. Phys. Chem. C 116 (2012) 15493–15499.

[51] D.F. Rivas, J. Betjes, B. Verhaagen, W. Bouwhuis, T.C. Bor, D. Lohse, H.J.G.E. Gardeniers, Erosion evolution in mono-crystalline silicon surfaces caused by acoustic cavitation bubbles, J. Appl. Phys. 113 (2013) 064902–64913.

[52] D.F. Rivas, B. Verhaagen, J.R.T. Seddon, A.G. Zijlstra, L.-M. Jiang, L.W.M. Sluis, M. Versluis, D. Lohse, H.J.G.E. Gardeniers, Biomicrofluidics 6 (2012) 034114.

[53] J. Dulle, S. Nemeth, E.V. Skorb, T. Irrgang, J. Senker, R. Kempe, A. Fery, D.V. Andreeva, Sonochemical activation of Al/Ni hydrogenation catalyst, Adv. Funct. Mater. 22 (2012) 3128–3135.

[54] P.V. Cherepanov, I. Melnyk, D.V. Andreeva, Effect of high intensity ultrasound on Al_3Ni_2, Al_3Ni crystallite size in binary AlNi (50 wt% of Ni) alloy, Ultrason. Sonochem. 23 (2015) 26–30, http://dx.doi.org/10.1016/j.ultsonch.2014.07.022.

[55] P.V. Cherepanov, I. Melnyk, E.V. Skorb, P. Fratzl, E. Zolotoyabko, N. Dubrovinskaia, L. Dubrovinsky, Y. Avadhut, J. Senker, L. Leppert, S. Kümmel, D.V. Andreeva, The use of ultrasound for near-surface structuring of robust and low-cost AlNi catalysts for hydrogen production, Green Chem. 17 (2015) 2745–2749.

[56] J. Schäferhans, S. Gomez-Quero, D.V. Andreeva, G. Rothenberg, Novel and effective copper–aluminum propane dehydrogenation catalysts, Chem. Eur. J. 17 (2011) 12254–12256.

[57] J. Dulle, K. Thirunavukkarasu, C. Marjo, M.C. Mittelmeijer-Hazeleger, D.V. Andreeva, N. Raveendran Shiju, G. Rothenberg, Efficient three-component coupling catalysed by mesoporous copper–aluminum based nanocomposites, Green Chem. 15 (2013) 1238–1243.

[58] D. Batalu, G. Cosmeliata, A. Aloman, Critical analysis of AlNi phase diagrams, Metall. Inter. 11 (2006) 36–45.

[59] P. Patnaik, Handbook of Inorganic Chemical Compounds, McGraw-Hill, New York, 2003.

[60] S.V. Oleinik, Y.I. Kuznetsov, Corrosion inhibitors in conversion coatings, Prot. Met. 43 (2007) 391–397.

[61] E.V. Skorb, L.I. Antonouskaya, N.A. Belyasova, D.G. Shchukin, H. Möhwald, D.V. Sviridov, Antibacterial activity of thin-film photocatalysts based on metal-modified TiO_2 and $TiO_2:In_2O_3$ nanocomposite, Appl. Catal. B: Environ. 84 (2008) 94–99.

[62] F. Zhang, L. Zhao, H. Chen, S. Xu, D.G. Evans, X. Duan, Superhydrophobic layered double hydroxide films on aluminum, Angew. Chem. 120 (2008) 2500–2503.

[63] D. Fix, E.V. Skorb, D.G. Shchukin, H. Möhwald, Quantitative analysis of scanning electric current density and pH-value observations in corrosion studies, Meas. Sci. Technol. 22 (2011) 075704–075710.

[64] N. Pazos-Perez, T. Borke, D.V. Andreeva, R.A. Alvarez-Puebla, Silver coated aluminium microrods as highly colloidal stable SERS platforms, Nanoscale 3 (2011) 3265–3268.

[65] J. Gensel, T. Borke, N. Pazos-Perez, A. Fery, D.V. Andreeva, E. Betthausen, A.H.E. Müller, H. Möhwald, E.V. Skorb, Cavitation engineered 3D sponge networks and their application in active surface construction, Adv. Mater. 24 (2012) 985–989.

[66] H. Destaillats, T.W. Alderson, M.R. Hoffmann, Applications of ultrasound in NAPL remediation, Environ. Sci. Technol. 35 (2001) 3019–3024.

[67] P. Riesz, D. Berdahl, C.L. Christman, Free radical generation by ultrasound in aqueous and nonaqueous solutions, Environ. Health Perspectives 64 (1985) 233–252.

[68] M. Zeng, H.N. Gao, Z.Q. Wu, L.R. Fan, T.H. Zheng, D.F. Zhou, J. Macromol. Sci. A Pure Appl. Chem. 47 (2010) 1042.

[69] E.V. Skorb, O. Baidukova, O.A. Andreeva, P.V. Cherepanov, D.V. Andreeva, Formation of polypyrrole/metal hybrid interfacial layer with self-regulation functions via ultrasonication, Bioinspired Biomimetic Nanobiomater. 2 (2013) 123–129.

[70] V. Belova, D.G. Shchukin, D.A. Gorin, A. Kopyshevc, H. Möhwald, A new approach to nucleation of cavitation bubbles at chemically modified surfaces, Phys. Chem. Chem. Phys. 13 (2011) 8015–8023.

[71] V. Belova-Magri, A. Brotchie, C. Cairós, R. Mettin, H. Möhwald, Micropatterning for the control of surface cavitation: visualization through high-speed imaging, ACS Appl. Mater. Interfaces 7 (2015) 4100–4108.

[72] M.Y. Masoomi, A. Morsali, Morphological study and potential applications of nanometal–organic coordination polymers, RCS Adv. 3 (2013) 19191–19218.

Self-healing properties of layer-by-layer assembled multilayers

Ekaterina V Skorb[a] and Daria V Andreeva[b*]

Abstract

The review is focused on the formation and the self-healing properties of polymer and hybrid multilayers formed via the layer-by-layer approach. In the first part of the review the recent developments in the construction of polymer multilayers are highlighted. In the second part the design and the self-healing properties of inorganic − polymer hybrid multilayers are described. It is shown that self-healing multilayers have a broad spectrum of applications including corrosion protection, as elements of antifouling and antimicrobial coatings and bio-inspired superhydrophobic interfaces. It is demonstrated that dynamic functional interfaces have a complex hierarchical organization of non-covalently bonded polymers and colloidal particles. Mechanisms of self-healing behavior of the multilayers and the role of water and external stimuli (pH, ionic strength and temperature, light) in swelling of multilayers and rearrangement of polymer segments are discussed. Future trends, perspectives and research strategies for the design of 'smart' self-assemblies with self-healing properties are proposed.
© 2015 Society of Chemical Industry

Keywords: multilayers; layer-by-layer; self-healing; stimuli responsive material; hybrid

INTRODUCTION

Stimuli responsive multilayers are self-assemblies of polyelectrolytes[1,2] and/or block copolymers,[3,4] hydrogels,[5,6] colloidal particles,[7,8] nanotubes,[9,10] clays,[11,12] low molecular weight active compounds[13,14] etc. The multilayers are dynamic nanonetworks with stimuli responsive properties.[15,16] Reversible stimuli responsive behavior of the multilayers is possible due to non-covalent (electrostatic,[17,18] hydrogen bonding,[19,20] hydrophobic interactions[21] etc.) intermolecular and intramolecular bonding in the layers.

Reversible stimuli responsive properties of the self-assembled multilayers are a key factor for the broad application area of these materials. The multilayers are used for the formation of active layers in corrosion protection systems[22−28] and antifouling,[29] antimicrobial and antifungal[30−32] coatings. The self-assembled nanonetworks are effective components for the construction of selective, highly sensitive and multifunctional sensors and biosensors.[33−35] Pharmaceutical and biomedical applications of hybrid multilayers include the design of 'smart' drug delivery systems[36−40] and the functionalizing and protection of implants' surfaces.[41] Stimuli responsive multilayered systems can be applied as important elements of regenerative medicine.[39,40] Furthermore, such systems can provide a suitable extracellular microenvironment for cell growth and tissue engineering.[39,40]

The dynamic nature of hybrid multilayers is used in a broad spectrum of applications and is the basis of many research strategies. Deposition of multilayers on surfaces provides solids with biofunctions and biocompatibility.[41] One of the important properties of nature is its ability to self-heal or self-repair, i.e. the regeneration/restoration of damaged integrity and functions of a system.[42−45] The multilayer assembly as a dynamic polymer system is able to heal/restore defects due to the mobility of non-covalent bonded layers.[15] Mobility as well as permeability

and elasticity of the multilayers are affected by the number of unbound mobile chains in the multilayers.[46,47] External stimuli (pH, ionic strength, humidity, light and temperature) determine the presence of associated/dissociated functional groups in polymer chains, the degree of swelling of polymer networks[48−50] and thus the mobility of multilayers and their ability to heal damaged areas.

The initial concept of self-healing properties of multilayers was suggested by Sackmann et al.[51] The concept is based on the investigation of the properties of substrate-supported lipid bilayers by Tamm and McConnell.[52] In a series of works Stackmann et al.[51,53,54] demonstrated that soft hydrated hydrophilic biopolymers served as effective lubricating layers for the formation of defect-free lipid − protein bilayers.[51] The bilayers could move over these supporting layers and thus heal possible defects in their structure.[53,54] The multilayers in these works were formed via the Langmuir − Blodgett approach.

Later Legras et al.[55] pointed out in a review that among other self-assembly methods (Langmuir − Blodgett approach,[56] self-assembly monolayers,[57] formation of hyper-branched polymer films,[58] polymer grafting[59] etc.) the tendency for self-healing was unique for the layer-by-layer (LbL) approach. It was shown that stepwise alternating deposition of oppositely charged species, the so-called LbL process, was a unique self-assembly approach to the formation of multilayers that were able to heal surface defects.[55]

---

* Correspondence to: Daria V Andreeva, Physical Chemistry II, University of Bayreuth, DE-95440 Bayreuth, Germany.
  E-mail: daria.andreeva@uni-bayreuth.de

a Max Planck Institute of Colloids and Interfaces, DE-14424 Potsdam, Germany

b Physical Chemistry II, University of Bayreuth, DE-95440 Bayreuth, Germany

Dr Ekaterina V. Skorb is an Associate Professor at the Belarusian State University and Independent Researcher at the Max Planck Institute of Colloids and Interfaces in Potsdam. The focus of work in her laboratory is surface nanostructuring and the development of advanced stimuli responsive composites for tissue engineering, drug delivery and 'lab-on-chip' systems.

Dr Daria V. Andreeva is a docent at the Department of Physical Chemistry II, University of Bayreuth. In 1999 she was a UNESCO fellow, in 2003 an Alexander-von-Humboldt fellow. Since 2009 she has been an assistant within the Elite Study Program Macromolecular Science (Elite Network Bavaria). Her research is focused on sonochemical and self-assembly approaches to the formation of metal and metal/polymer composites.

The unusual tendency of LbL self-assemblies to self-healing of surface defects and inhomogeneity was attributed to the surface coverage by layers of charged macromolecules.

In the last decade, stimuli responsive LbL assembled multilayers were found to be useful for the design of functional coatings with self-healing ability. The LbL approach is a versatile and easy technique that is adjustable to different substrates and to different classes of low and high molecular weight compounds. Thus, it is a suitable approach to the design of hybrid materials that mimic nature.

In this review we focus on the formation and self-healing properties of hybrid multilayers formed using the LbL technique. The review has two parts, schematically illustrated in Fig. 1. The first part highlights the formation of polymer interfaces with self-healing properties (Fig. 1(a)). The multilayers are applied for the decoration of surfaces and for supplying surfaces with self-healing properties. Technologically this is important for the formation of an active protective coating, e.g. for corrosion protection of metals. Such coatings are a good alternative to passive barrier coatings that lose their properties after chemical or mechanical damage. The second part (Fig. 1(b)) is focused on the formation and self-healing properties of hybrid multilayers formed by the LbL assembly of polymers and colloidal particles. Such multilayers are designed for modification of different substrates including wood, polymers, ceramics etc. and can also be used as free-standing films.

SELF-HEALING THIN FILMS: MULTILAYERS ON SURFACES

Polymer multilayers deposited on a surface have been successfully used for the design of active protective coatings with self-repairing or self-healing properties. In this case, LbL modified surfaces are active components of corrosion protective systems, antifouling, antimicrobial, antifungal coatings, systems with tuned hydrophobicity etc. In Table 1 we summarize the data on compositions and application areas of polymer-based multilayers with self-healing properties.
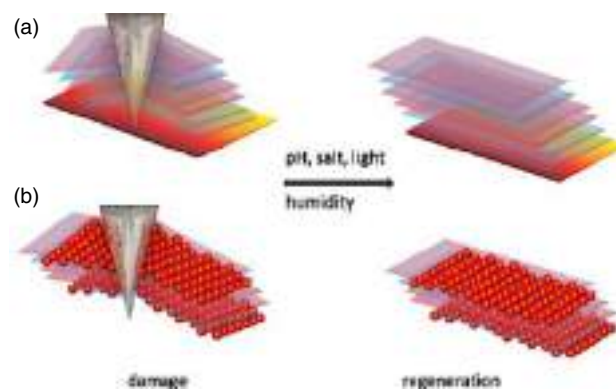
Figure 1. Schematic illustration of hybrid multilayers with self-healing properties: (a) surface decorated by multilayers; (b) polymer/colloidal particle assemblies with self-healing properties.

Self-healing mechanisms of LbL assembled multilayers

The self-healing behavior of the multilayers is based on water-induced mobility of polymer chains.[46,47] In aqueous media or a humid atmosphere the multilayers adsorb water.[48−50] In the swollen state surface defects can be eliminated by rearrangement of polymer chains, and the integrity and functions of damaged multilayers are restored. As we see in Table 1 the existing self-healing systems mostly consist of 'weak' polyelectrolytes or at least one polyelectrolyte in the system is 'weak'. The pronounced water-induced self-healing process is observed for 'weak – strong' and 'weak – weak' polyelectrolyte pairs, hydrogels and block copolymers (BCPs).

A hydrogel is a hydrophilic polymer network.[69−71] It was proposed by South and Lyon[72] that mechanically damaged hydrogel films are characterized by a heterogeneous distribution of charges. Water-induced mobility of polymer segments leads to rearrangement of polymer chains and the restoration of destroyed interactions. As alternatives to hydrogels, hydrogen bonded multilayers of poly(vinyl pyrrolidone) (PVPON) and poly(acrylic acid) (PAA) were proposed.[67] It was shown[67] that the hydrogen bonded multilayers exhibit swelling-induced mechanical instability similar to hydrogels. In contrast to covalently crosslinked hydrogels the layers are bonded by reversible hydrogen bonding. Due to the reversible character of bonding hydrogen bonded multilayers are suitable components for self-healing coatings.

The self-healing activity of the multilayers can be triggered or accelerated by external stimuli (pH, ionic strength, light, temperature).[48−50] pH is one of the external stimuli for reversible swelling/deswelling of layers of 'weak' polyelectrolytes,[24−27] BCPs,[18,19,46,48] pH sensitive hydrogels[65,66] and polymer brushes.[50] Highly sensitive pH dependent multilayers were prepared using 'weak' polyelectrolytes, e.g. poly(allylamine hydrochloride) (PAH) or poly(ethyleneimine) (PEI) and PAA. PAH/PAA multilayers demonstrate a transition from a highly crosslinked, ion-paired network at pH 5.5 to a swollen, highly hydrated network with fixed positive charges at pH 2.0 (Fig. 2(a)).[74]

For BCPs and BCP micelles (BCMs) pH change triggers reversible dissolution/collapse of micellar core or tune length and the density of the micellar shell. For example, Webber et al.[73,75] demonstrated a 'nano-anemone' effect of poly(2-(dimethylamino) ethyl methacrylate)-block-poly(2-(diethylamino)ethyl methacrylate) (PDMA-b-PDEA). PDEA is molecularly dispersed at low pH and collapsed at higher pH (Fig. 2(b)). pH sensitive triblock terpolymercore-shell-corona micelles (BMAADq) consist of

Table 1. Composition and application area of self-healing polymer-based multilayers

Composition of multilayers		Additional component	Stimuli	Application area	Ref.
PAH-SPEEK	PAA	POTS	Humidity	Super hydrophobic surfaces	[60]
PAH-SPEEK	PAA	POTS, PFOS	Humidity		[61]
bPEI	PAA	Triclosan	Water	Antibacterial coating	[62]
bPEI	PAA	–	Water	–	[63]
PEI	PSS	8-Hydroxyquinoline	pH, ionic strength	Corrosion protection	[24,26,27]
PEI	PSS	–	pH, ionic strength	Corrosion protection	[25,64]
PEI, PDADMAC	PSS, PAA	8-Hydroxyquinoline	pH, ionic strength	Corrosion protection	[64]
–	PSS	8-Hydroxy-quinoline, benzotriazole	pH, ionic strengh	Corrosion protection; antibacterial coating	[32]
PDADMAC	p-NIPAm-AAc		Water	Antifouling biocoating	[65,66]
BMAADq micelles	–	–	pH	Antibacterial, self-recovery, self-cleaning	[29]
PVPON	PAA	–	Water/ethanol	–	[67]
PEI	PVDMA	n-decylamine	pH	superhydrophobic surfaces	[68]

PAH-SPEEK, complexes of poly(allylamine hydrochloride) and sulfonated poly(ether ether ketone); POTS, 1H,1H,2H,2H-perfluorooctyltriethoxysilane; PFOS, perfluorooctanesulfonic acid lithium salt; PAA, poly(acrylic acid); bPEI, branched poly(ethyleneimine); PEI, poly(ethyleneimine); PSS, poly(styrene sulfonate); PDADMAC, poly(diallyldimethylammonium chloride); p-NIPAm-AAc, poly(N-isopropylacrylamide)-co-acrylic acid; BMAADq, triblock terpolymer micelles consisting of polybutadiene (B), poly(methacrylic acid) (MAA) and quaternized poly(2-(dimethylamino)ethyl methacrylate) (Dq), $B_{800}MAA_{200}Dq_{285}$ (subscripts denoting the degrees of polymerization of the corresponding blocks); PVPON, poly(vinyl pyrrolidone); PVDMA, poly(vinyl-4,4-dimethylazlactone).
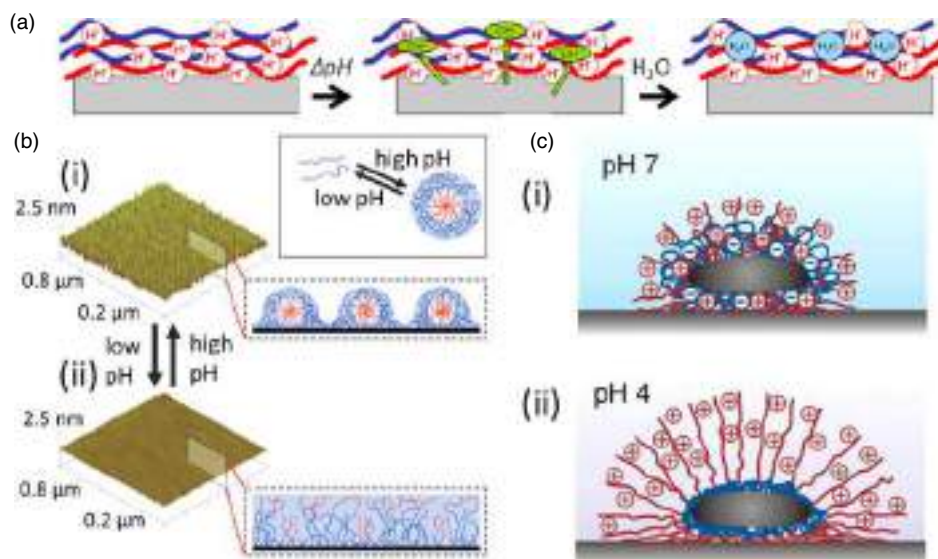
Figure 2. Schematic illustration of mechanisms of pH dependent self-healing behavior. (a) Polyelectrolyte multilayers. (b) Core/shell BCMs at pH > 7 (i) and pH < 7 (ii); represented with permission from [73]. (c) Core/shell/corona micelles at pH 7 (i) and pH 4 (ii); reproduced with permission from [29]. Copyright 2004, 2012, Wiley.

polybutadiene (B), poly(methacrylic acid) (MAA) and quaternized poly(2-(dimethylamino)ethyl methacrylate) (Dq).[76] Accordingly, the charge density of the MAA block and dissolution (at pH 4) or regeneration (at pH 7) of the shell can be adjusted by the pH of the solution. The mechanism of the reversible morphological changes of the BMAADq micelles is based on the attraction/repulsion between pH dependent charged/uncharged MAA and the positively charged Dq blocks (Fig. 2(c)).

Hydrogels can exhibit pH and temperature dependent phase transitions. Response to pH is induced in a hydrogel by the formation of copolymers with PAA, e.g. poly(N-isopropylacrylamide)-co-acrylic acid (p-NIPAm-AAc).[65,66,71] At pH < 4.5 the AAc groups are protonated, and at pH > 4.5 the AAc groups are deprotonated. For both pH- and temperature-triggered morphological changes of hydrogels hydration is a major factor

that controls reversible coulombic interactions in polymer networks and thus their self-healing behavior.[65–67,71,73] Poor mechanical properties of hydrogels restrict their use in the formation of multilayers. A number of technological solutions, namely crosslinking of layers[69] and LbL deposition of colloidal particles together with hydrogels,[66] have been proposed in order to enhance the mechanical properties of hydrogel-containing multilayers.

Temperature change stimulates pronounced morphological changes of hydrogels, BCPs and BCMs. In BCPs and PCMs p-NIPAm is responsible for sensitivity of the multilayers to temperature change. p-NIPAm chains are molecularly dispersed at temperatures below 32 °C (lower critical solution temperature) and collapsed in aqueous solution at temperatures above 32 °C. The temperature dependent volume phase transitions of micellar
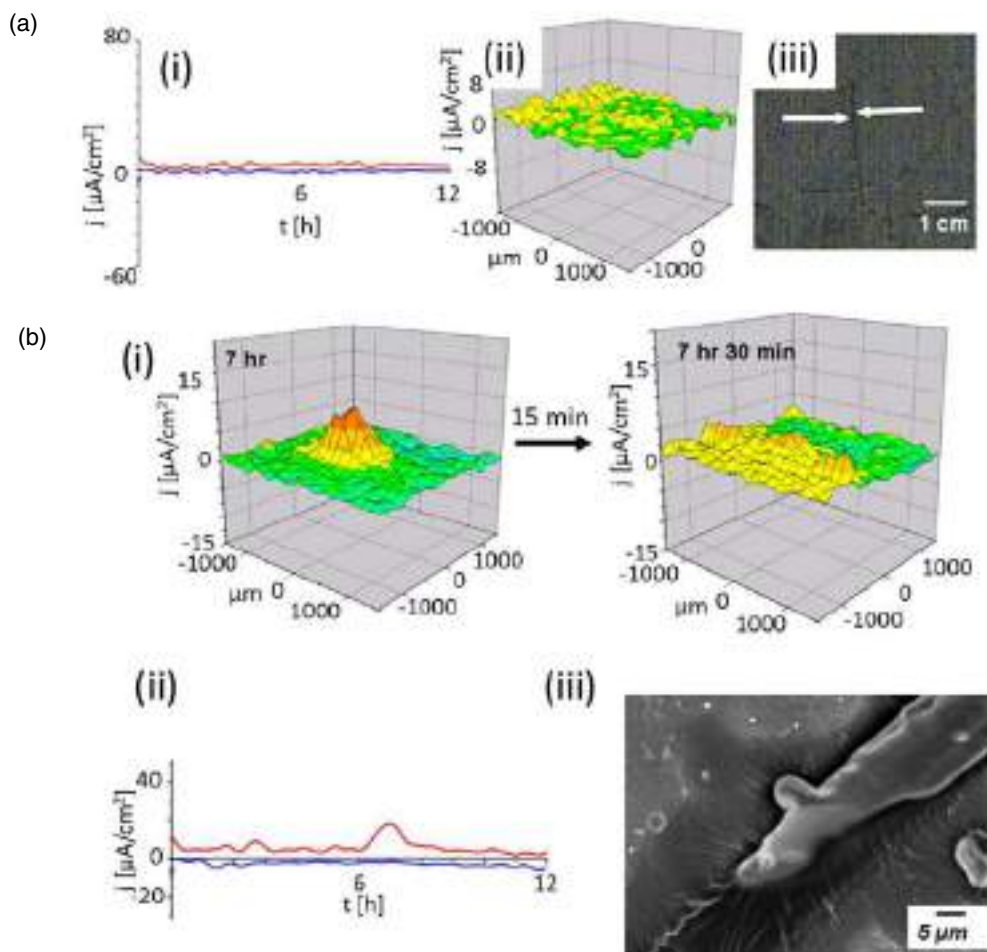
Figure 3. (a) Time dependence of the current density changes of a damaged aluminium alloy covered by a PEI–PSS 10-bilayer coating obtained by using the SVET: red curve, anodic current; blue curve, cathodic current (scale units µA cm^{-2}, spatial resolution 150 µm, solution 0.1 mol L^{-1} NaCl) (i). Snapshot measured after 3 h of the experiment time (ii). Photograph of the behavior of the damaged surface during the SVET experiments. The scratch is highlighted by arrows (iii). (b) SVET measurements of the ionic currents above the surface of the damaged aluminium alloy covered by the PEI–PAA 10-bilayer coating (scale units µA cm^{-2}, spatial resolution 150 µm, solution 0.1 mol L^{-1} NaCl). Experiment time 7 h (left); experiment time 7 h 30 min (right) (i). Time dependence of the current density changes of the scratched aluminium alloy covered by the PEI–PAA 10-bilayer coating: red curve, anodic current; blue curve, cathodic current (ii). SEM image of the surface of the PEI–PAA coating after 12 h immersion in 0.1 mol L^{-1} NaCl. Reproduced with permission from [64]. Copyright 2010, American Chemical Society.

cores of BCMs and crosslinked hydrogels result in reversible swelling/deswelling of the layers.[48,77,78]

The presence of salt in the medium leads to charge screening effects: it degreases repulsion forces between the charges and stimulates coil conformation of the chains.[77−79] Higher salt concentration (up to 1 mol L^{-1} NaCl) leads to increased water content in the multilayers.[80] Small counterions can penetrate the layers and compensate charges.[81] The higher ionic concentration compared to the surrounding solution increases the osmotic pressure and results in permeation of water into the multilayers. Thus, the polyelectrolyte multilayers start to swell and increase their mobility.[82−84]

Self-healing multilayers and their application
Anticorrosion coatings
The pH dependent self-healing activity of LbL deposited multilayers of 'weak' and 'strong' polyelectrolytes were studied on a polyelectrolyte based anticorrosion protection system.[24−27,64] The self-healing efficiency of LbL multilayers of polyelectrolytes on commercial aluminium alloys, magnesium alloys and stainless

steel was monitored by the scanning vibrating electrode technique (SVET). The SVET mapping of local cathodic and anodic activity of the damaged area proved the healing activity of the multilayers. As seen in Fig. 3(a) the multilayers formed by 'weak'–'strong' polyelectrolytes of PEI and poly(styrene sulfonate) (PSS) demonstrate a very fast self-healing response. The multilayers formed by two 'weak' polyelectrolytes (PEI/PAA) demonstrate a slower response. The degradation/healing cycles can be detected by SVET (Fig. 3(b)).[64] In addition to the self-healing mechanisms that are described in the above section, the unique pH buffering activity of the 'weak' − 'strong' and 'weak' − 'weak' polyelectrolyte multilayer system is important for suppression of corrosion propagation in metals.[24−27]

Assembled in multilayers polyelectrolytes have a relatively large number of functional groups and can reversibly entrap low molecular weight compounds.[24,64] Healing agents (corrosion inhibitors) deposited as components of the multilayers can be released on demand. External stimuli, pH, temperature, light etc., as well as chemical reactions following the corrosion degradation, change the degree of dissociation of the polyelectrolytes and therefore

control the concentration of bonded and unbonded healing agents in the multilayers. Thus, healing agents could be encapsulated into the multilayers and locally released at a particular time.

Superhydrophobic surfaces with self-healing activity

Superhydrophobic multilayers with self-healing properties were developed by Sun et al.[60,61] The nanoscaled hierarchical structured surface was prepared by LbL deposition of complexes of PAH and sulfonated poly(ether ether ketone) (SPEEK) with PAA. 1H,1H,2H,2H-perfluorooctyltriethoxysilane (POTS) was deposited via chemical vapor deposition and used as a hydrophobic layer and a healing agent.[60] Damage of the hydrophobic POTS layer triggered swelling of the multilayers and rearrangement of the polyelectrolyte chains. Thus, POTS molecules migrated to the surface and healed defects. It was mentioned that the proposed bio-inspired self-healing process mimics wax production by plants. The self-healing multilayers with enhanced properties were designed by LbL spraying of PAH-SPEEK and PAA with two healing agents: POTS and perfluorooctanesulfonic acid lithium salt (PFOS).[61] Use of spraying technology for deposition of the layers significantly simplifies the deposition process. Spraying can also help to re-encapsulate the self-healing agent.

Superhydrophobic surfaces with self-healing properties were also produced by LbL assembled covalently crosslinked branched PEI (bPEI) and the amine-reactive polymer poly(vinyl-4,4-dimethylazlactone) (PVDMA).[68] Reaction of the multilayers with n-decylamine leads to superhydrophobicity of the surface. The enhanced healing process was detected at lower pH and proved the importance of PEI protonation for the healing properties of the multilayers.

Antimicrobial, antifouling coating with self-healing properties

Several strategies for the construction of antimicrobial coatings with self-healing properties have been proposed. First, antimicrobial agents can be encapsulated into the stimuli responsive multilayers.[62] For example, triclosan (5-chloro-2-(2,4-dichlorophenoxy)-phenol) solubilized in cetyltrimethylammonium bromide (CTAB) micelles was entrapped into bPEI/PAA multilayers. It was shown that triclosan in CTAB micelles does not affect the water-induced interdiffusion of polyelectrolytes and the films demonstrated healing and antimicrobial properties.[62]

However, antimicrobial agents could affect the homogeneity and stability of the self-healing multilayers. A novel approach for the encapsulation of active agents was developed using sonochemical activation of metal surfaces.[32] Ultrasonically treated porous metal surface 'surface capsules' can be loaded with antimicrobial agents and then sealed by LbL assembled multilayers (Fig. 4(a)). The metal/polymer hybrid surfaces were produced by encapsulation of antiseptic agent and corrosion inhibitor, 8-hydroxyquinoline, and corrosion inhibitor, benzotriazole.[32]

An innovative self-cleaning antifouling coating was designed by the deposition of BCMs on ultrasonically activated surfaces.[29] The self-healing activity of the hybrid BMAADq/metal surface was triggered by living products of bacteria (Fig. 4(b)). This spectacular cell-cleaning surface effect is based on a pH-triggered desorption of the bacteria due to changes in morphology of the charged quaternized poly(2-(dimethylamino)ethyl methacrylate) (Dq) corona of the micelles. The lactic acid produced by Lactococcus lactis decreases the local pH of the metal/micelle/bacteria interface. At pH 4 the length of the charged corona increases[76]
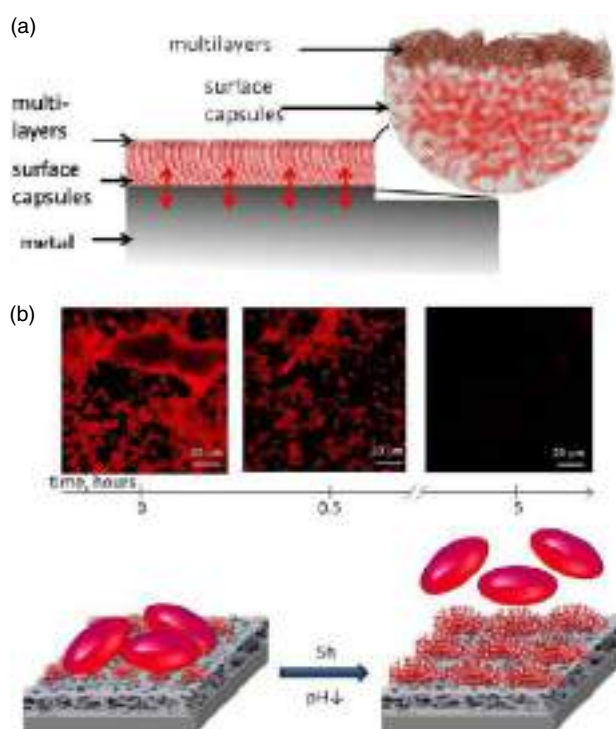
Figure 4. (a) Schematic illustration of ultrasonically formed 'surface capsules' loaded with healing agent and sealed by polyelectrolyte multilayers. Adopted with permission from [32]. (b) Confocal kinetic study (fluorescence mode) and schematic illustration of pH-triggered self-cleaning behavior with micelles on a covered porous Al surface. As model cells *Lactococcus Lactis 411* bacteria (loaded with dye) were used. Reproduced with permission from [29]. Copyright 2012, Wiley.

and the adsorbed bacteria are detached from the surface. Thus, pH-regulated self-cleaning of the metal/micelle network was achieved.

Summarizing, recent studies have demonstrated that LbL assembled multilayers are very promising self-healing elements of functional coatings including anticorrosion systems, superhydrophobic surfaces, and antimicrobial and antifouling protection systems. The use of the multilayers for the design of 'smart' devices and active surfaces can enhance their durability and exploitation time. A number of studies showed that polyelectrolytes, hydrogels, BCPs and BCMs can be used for the formation of self-healing multilayers. However, additional investigation should elucidate mechanisms of self-healing and quantify the response of multilayers.

SELF-HEALING HYBRID COLLOID — POLYMER ASSEMBLIES

In this section we describe two strategies of hybrid colloid–polymer assemblies for self-healing applications with some recent specific examples of the developed systems. The first strategy is incorporation of colloidal particles into multilayers (Fig. 1(b)). The second strategy is the possibility of LbL assembly on colloidal particles for development of capsules for self-healing application. Colloidal particles can affect the most important structural functions of a system such as stiffness, strength, fracture toughness, ductility, fatigue strength, energy absorption, damping, thermal stability, as well as self-healing ability and sensitivity to different stimuli. The chosen hybrid colloid–polymer assemblies for self-healing are summarized in Table 2.

Table 2. Hybrid colloid–polymer assemblies for self-healing

Composition of polymers					
Polymer 1	Polymer 2	Colloidal particles	Stimuli	Application area	Ref.
bPEI	PAA	AgNPs	Humidity	Electrically conductive coatings	[85,86]
PAH	PSS	AuNPs	Humidity	Polymeric membrane	[87]
PMMA	PLA	$TiCl_4$ (TiO_2) Al_2O_3	Atmospheric moisture	Electronic devices	[88]
lipid 1	lipid 2	Janus nanoparticles	Humidity, pH, temperature	Biomembrane	[89]
PVA	PSS	LDH	Water	Oxygen barrier film	[90]
PDADMAC	–			Fugitive network scaffold	[91]
PAM	PAA	Graphene	Temperature	Shape memory systems	[92]
PVDF-HFP	FAS	SiO_2	Water	Superamphiphobic fabric	[93]
PEI	PSS	TiO_2	pH, ionic strength, light	Corrosion protection	[30,94]
PEI	PSS	TiO_2 AgNPs	pH, ionic strength, light	Corrosion protection	[94,95]
PEI	PSS	SiO_2	pH, ionic strength	Corrosion protection	[31]

NPs, nanoparticles; PMMA, poly(methyl methacrylate); PLA, poly(lactic acid); LDH, layered double hydroxide; PVA, poly(vinylalcohol); PVDF-HFP, poly(vinylidene fluoride hexafluoropropylene; FAS, fluoroalkyl silane.

Incorporation of colloidal particles into multilayers

To provide systems with advanced functionality or stimuli sensitivity the LbL assembled multilayers often combine polymeric materials with inorganic nanoparticles. Nanoparticles are a mobile component that can autonomously migrate[96] to the damaged area after a fracture occurs. The driving force for particle expulsion from the polymeric matrix is the gain in conformational entropy of the polymer chains. Important parameters for the process are particle nature, size, surface functionalization and concentration in the LbL composite. Spontaneous percolation of nanoparticles during a fracture can be used for the recovery of functional properties such as mechanical performance or electrical conductivity, as well as light emission.[97] Nanoparticles can also affect the swelling/deswelling and mobility of the polyelectrolyte or provide the LbL composite with multi-stimuli sensitivity: together with pH sensitivity the system can sense other stimuli, such as light, electromagnetic field, ultrasound etc.

The self-healing behavior of polyelectrolyte multilayers has been discussed in the first part of this review. Metal nanoparticles as well as metal ions can affect the interdiffusion of polyelectrolyte chains – the mobility of the polyelectrolyte chains within the assembly for lateral diffusion to heal scratches. Silver nanoparticles aided the self-healing of bPEI and PAA polyelectrolyte multilayers[85] (Fig. 5(a)) and speeded the ability of the multilayer assembly to heal defects. This enhancement of property does not seem to be due to changes in mechanical properties but rather to enhanced affinity to water and plasticization that enables the film to swell better.

The propagation of cracks in electrically conductive materials leads to unexpected breakdown of functions of the surface. A facile way of fabricating healable LbL composite electrically conductive film was demonstrated recently[86] for a system of silver nanowires (AgNWs) in multilayers of bPEI and PAA–hyaluronic acid (PAA–HA) blend (AgNWs/(bPEI/PAA–HA) (Fig. 5(b)).

Unlike the rough bPEI/PAA films[98] the introduction of highly water-absorbing HA makes the bPEI/PAA–HA films flat, transparent and highly flexible with conveniently achieved healability by depositing AgNWs on top of the films. The water-enabled healability of the underlying LbL assembly is successfully imparted to conductive films of AgNWs, which can achieve convenient
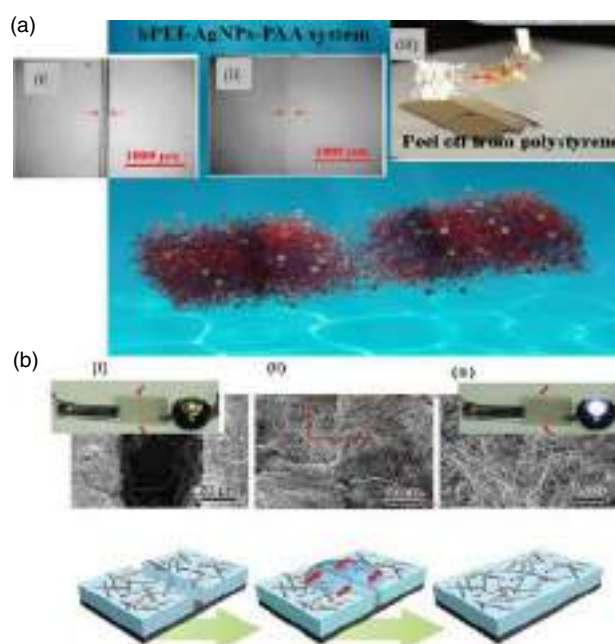
Figure 5. Different shaped silver nanoparticles (AgNPs) for self-healing systems. (a) Schematic illustration and study of the increase of self-healing of bPEI-PAA polyelectrolyte multilayers with spherical AgNPs: scratch before (i) and after (ii) healing for the coating bPEI-AgNPs-PAA. The 'healed' film contains segments of bPEI-PAA, bPEI-Ag$^+$-PAA and bPEI-AgNPs-PAA (from left to right) and can be peeled off from the polystyrene substrate (iii). Reproduced with permission from [85]. Copyright 2014, Royal Chemical Society. (b) Water-enabled healing of electrical conductivity of Ag nanowires, (NWs)/(bPEI/PAA–HA)*50 system: schematic and film with a cut before (i) and after (ii, iii) being healed. Insets present film healing and recovery of electrical conductivity: no light from damaged film (i), and light from the LED bulb comes on after healing (ii). Reproduced with permission from [86]. Copyright 2012, Wiley.

multiple healing of cuts in conductive films. The healable conductive films have high conductivities as a result of the use of AgNWs. Transparent healable conductive films, which have conductivities much higher than those of the usually used indium tin oxide (ITO) on glass, are also fabricated by the same method.

It should be mentioned that gold nanoparticles (AgNPs) can provide coatings with biocide activity[29] which can be used as discussed above for the development of antifouling, antibacterial coatings. Moreover noble nanoparticles make it possible to switch/activate polyelectrolyte LbL composites with light.[8]

AuNPs are also used to affect the self-healing properties of LbL assemblies. Nanocomposite membranes prepared by LbL assembly of polymeric materials with AuNP intralayers[87] have been reported. The membranes were composed of a central layer sandwiched between nine bilayers of two alternating polyelectrolytes: PAH and PSS. After plastic deformation, the membranes showed complete and autonomous recovery of their properties on a time scale of hours, which was possible by means of a reversible polymer – nanoparticle self-organization process.

Multilayer composites that utilize polymeric and brittle inorganic films are essential components for extending the lifetimes and exploiting the flexibility of many electronic devices. However, crack formation within the brittle inorganic layers as well as the flexing of these multilayer composite materials allows the influx of atmospheric water, a major source of device degradation. In the study by Jiang *et al.*[88] the reactive metal oxide precursor $TiCl_4$ is encapsulated within the pores of a degradable polymer, poly(lactic acid) (PLA). Electrospun PLA fibers are found to be reactive to atmospheric water leading to hydrolysis of the degradable polymer shell and subsequent release of the reactive metal oxide precursor. Release of the reactive $TiCl_4$ from the pores results in hydrolysis of the metal oxide precursor, forming solid titanium oxides at the surface of the fibers. The efficacy of this self-healing delivery system is also demonstrated by the integration of these reactive fibers in the polymer planarization layer, poly(methyl methacrylate) (PMMA), of a multilayer film, upon which an alumina barrier layer is deposited.[88] The introduction of nanocracks in the alumina barrier layer leads to the release of the metal oxide precursor from the pores of the fibers and the formation of titanium dioxide nanoparticles within the crack and upon the thin film surface. In this study the first delivery system that may find utility for the self-healing of multilayer barrier films through the site-specific delivery of metal oxide nanoparticles through smart reactive composite fibers was established.

Janus nanoparticles, composed of hydrophobic and hydrophilic portions, have been studied as active components for a lipid bilayered membrane with self-healing properties.[89] During external compressive stress on the membrane surface in an aqueous environment, Janus nanoparticles can self-assemble on the edge of a pore, with hydrophilic ends facing the inside of the pore. This assembly lasts for a long time and allows further repeatable pore opening and closing with lower stress intensity than for the first cycle. This happens without affecting membrane integrity and represents a sensible enhancement of the healing ability with respect to a bare lipid bilayered membrane. Pore opening can also be triggered by other parameters such as pH or temperature.

Ceramic and oxide particles in an LbL assembly can affect the self-healing functionality. Thus hybrid films were fabricated via LbL assembly of layered double hydroxide (LDH) nanoplatelets and PSS followed by subsequent permeation of poly(vinylalcohol) (PVA) providing excellent oxygen barrier performance with humidity-triggered self-healing capability[90] (Fig. 6(a)).

A method for tailoring local mechanical properties near channel surfaces of vascular structural polymers for high structural performance in microvascular systems was suggested recently by White's group[91] (Fig. 6(b)), while synthetic vascularized materials were composed of the LbL assembly of PDADMAC/halloysite
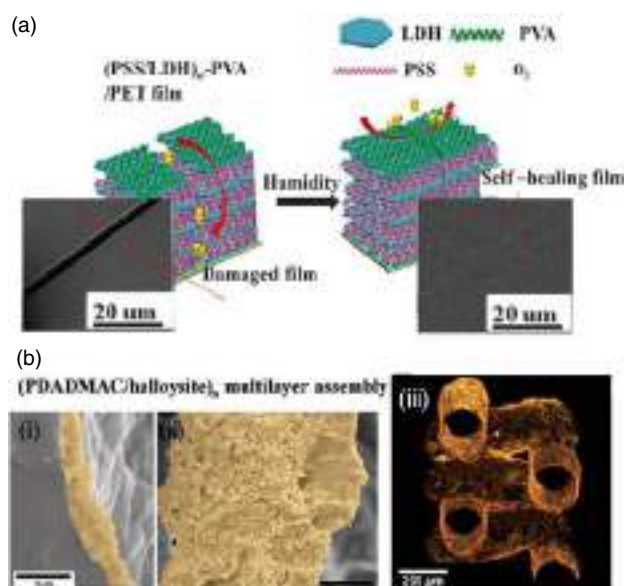
Figure 6. (a) Schematic illustration of the fabrication of layered double hydroxide (LDH) nanoplatelets and PSS followed by subsequent permeation of poly(vinylalcohol) (PVA) ((LDH – PSS)$_n$ – PVA) film on a polyester substrate serving as an oxygen barrier film with self-healing ability together with the corresponding SEM images of a damaged (LDH – PSS)$_{20}$ – PVA film and a self-healing one after 75 h. Reproduced with permission from [89]. Copyright 2014, Royal Chemical Society. (b) Microvascular networks using LbL assembly of PDADMAC with halloysite nanotubes. SEM images (i, ii) of cross-sections showing the matrix-embedded PDADMAC/halloysite reinforcement at 10 bilayers (i) and 80 bilayers (ii). Micro-computed tomography reconstruction of (PDADMAC/halloysite)$_{80}$ multilayer deposited onto a fugitive network scaffold. Reproduced with permission from [90]. Copyright 2014, Royal Chemical Society.

multilayers. Taking inspiration from biological tissues such as dentin and bone, the mechanical deficiencies can be mitigated by complex hierarchical structural features near to channel surfaces. By employing electrostatic LbL assembly to deposit films containing halloysite nanotubes onto scaffold surfaces followed by matrix infiltration and scaffold removal, it was possible to controllably deposit nanoscale reinforcement onto 200 μm diameter channel surface interiors in microvascular networks. High resolution strain measurements on reinforced networks under load verify that the halloysite reduces strain concentrations and improves mechanical performance.

Shape memory systems are another important area of self-healing composites.[100,101] Modeling of shape memory polymer response and shape recovery loss was recently published.[102 – 104] A variety of composite polymer materials with shape memory effect were designed in Mather's group.[105 – 107] Polymer composites were prepared using polymerization-induced phase separation[105] and were used for the construction of shape memory polymeric webs via electrospinning[106] and even for the construction of shape memory polymeric foams.[107] For the formation of shape memory self-healing nanoscale materials the LbL approach might be a novel technological approach.

Multilayered materials with shape memory effect and self-healing ability based on graphene and a copolymer of poly(acrylamide-*co*-acrylic acid) (PAM-PAA) have been demonstrated (Fig. 7(a)).[92] It is known that PAM forms intermolecular hydrogen bonds with PAA only at low temperature, while it dissociates at a certain temperature, the so-called 'zipper effect'.[108] Therefore, PAM-PAA is suitable as the soft phase in a hard – soft

719
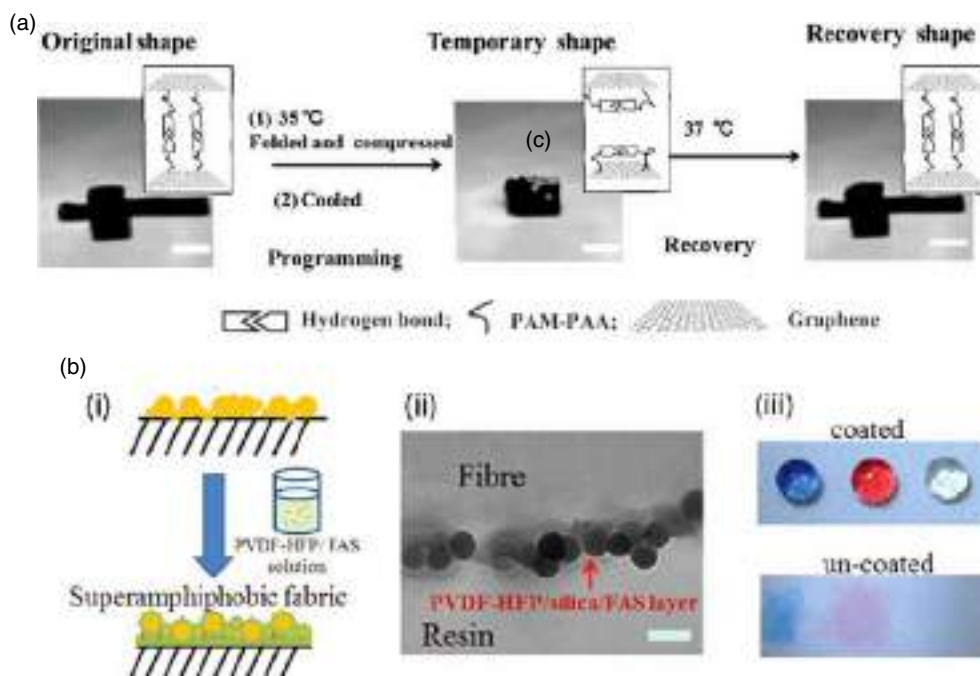
Figure 7. Self-healing hybrid LbL shape memory systems (a) and superhydrophobic material (b). (a) Graphene enhances the shape memory of the PAM-PAA system. Photographs of the shape memory behavior of an unfolded cube box. Scale 10 mm. Insets show the scheme of shape memory G-PAM-PAA involving the transformation of intermolecular and intramolecular hydrogen bonding in the hard – soft two-phase system. Reproduced with permission from [91]. Copyright 2013, Wiley. (b) Self-healing superamphiphobic fabrics of hybrid LbL coating on fabric based on SiO$_2$ and fluoro-containing polymer (poly(vinylidene fluoride hexafluoropropylene) (PVDF-HFP)) and fluoroalkyl silane (FAS). Scheme of dip-coating of fabric/SiO$_2$ for the formation of superhydrophobic coating (i). Cross-sectional TEM images of PVDF-HPF/FAS/silica nanoparticle coated polyester fiber (scale bar 200 nm) (ii). Photograph of blue-colored water, red-colored hexadecane and clear soybean oil on the coated and uncoated polyester fabrics (iii).

two-phase system. However, PAM-PAA itself has poor shape memory ability due to low mechanical strength.

Graphene, a one-atom-thick layer of carbon, has attracted considerable attention in recent years owing to its remarkable structure and properties, such as high mechanical stiffness and electrical and thermal conductivity.[109,110] The unique two-dimensional plate-like structure of graphene makes it very suitable for self-healing composite systems[111] as the hard phase in the hard – soft two-phase system. The shape memory effect of the composites can be tuned by the content of graphene sheets. The composite design combines reversible and nonreversible crosslinking in a shape memory system. The hydrogen bond network serves as reversible crosslinking in the soft phase of the hard – soft two-phase system. The soft polymer chains are immobilized on a hard sheet (stiffness and toughness) as nonreversible crosslinking.

The hard sheet can not only immobilize polymer chains to ensure the stable shape but also contribute to the high modulus and stiffness of materials. The intermolecular hydrogen bonding network of the soft segments between the hard sheets was formed in permanent shape and dissociated in a temporary shape. Then, the polymer chains were aggregated and the new intramolecular hydrogen bonding was formed by the soft segments in the hard sheet to stabilize the temporary shape. When the temperature increased, the intramolecular hydrogen bonding of the soft segments in the hard sheet was dissociated, and the intermolecular hydrogen bonding network of the soft segments between the hard sheets was formed again to recover the permanent shape[92] (Fig. 7(a)).

A robust, superamphiphobic fabric with a novel self-healing ability to auto-repair from chemical damage was suggested by

Zhou et al.[93] The hybrids of poly(vinylidene fluoride hexafluoropropylene (PVDF-HFP), fluoroalkyl silane (FAS) and modified silica nanoparticles were prepared by a two-step LbL technique (Fig. 7(b)). The coated fabrics can withstand at least 600 cycles of standard laundry and 8000 cycles of abrasion without apparently changing the superamphiphobicity. The coating is also very stable to strong acid/base, ozone and boiling treatments. After being chemically damaged, the coating can restore its super liquid-repellent properties by a short-time heating treatment or room temperature ageing.

Summarizing, the synergetic functionality of inorganic – organic components of LbL assembly opens a broad avenue for the design of multifunctional, sensitive to multi-stimuli systems, suggesting broad self-healing prospects and the use of materials in various fields: electronic, sensing and (bio-)sensing, corrosion and (bio-)corrosion protection, smart textile design and, shape memory materials etc.

LbL composite capsules for self-healing

'Active' self-healing coating means that the coating is designed to react/be sensitive to various internal or external stimuli (Fig. 8).[112,113] It was suggested that incorporation of LbL composite capsules[30,31,114] in a protection coating could be an effective strategy in the construction of active protection systems with self-healing properties.

Classical capsules consist of an inorganic core and polyelectrolyte shell. The polyelectrolyte shell has the following functions: (i) the shell provides long-term storage of an encapsulated healing agent; (ii) it supplies the system with stimuli responsive properties and (iii) additional functions, e.g. pH buffering effect etc.
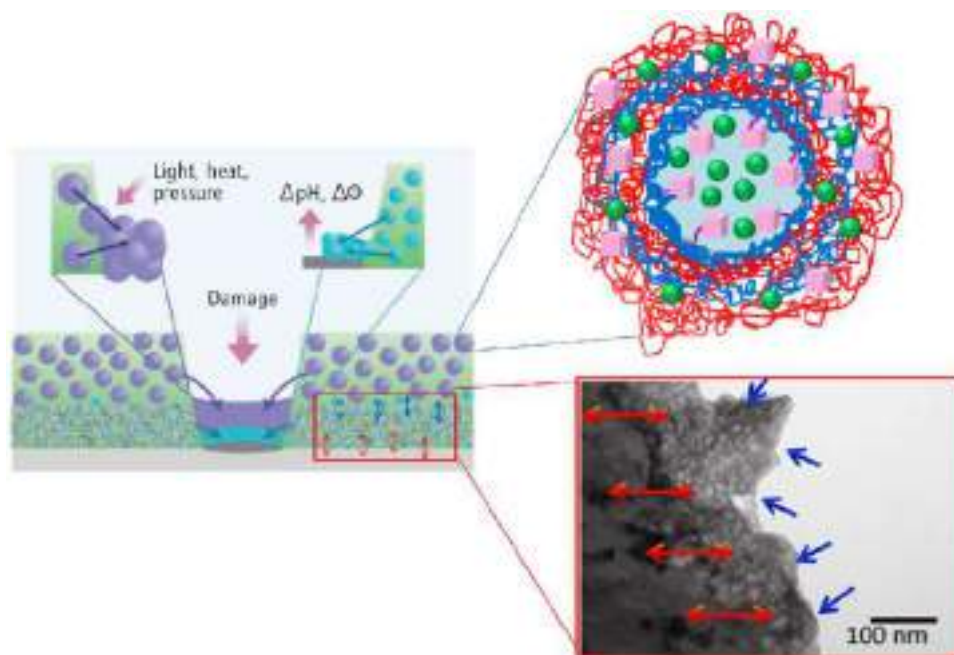
Figure 8. Schematic of active smart self-healing coating. LbL capsules with inorganic core are suggested to be effective integrated into a micron-sized coating; surface capsules built on, for example, a surface sponge layer (shown in cross-section TEM image, red arrows indicate good sponge layer adhesion to bulk metal, here aluminium) are effective to be built up on metal. Active species or sensing chemicals, nanoparticles, depending on the functionalities required can be encapsulated into the capsule core or be integrated into the polyelectrolyte shell. The sensitivity of the capsule shell can be adjusted to different stimuli (e.g. pH changes or changes in the electrochemical potential, φ) for opening and release of the encapsulated active material by nanoengineering of the LbL shell components and structure. Reproduced with permission from [105], Copyright 2013, Science Publishing Group; [32], Copyright 2012, Wiley.

Active species or sensing chemicals, nanoparticles, can be encapsulated into the capsule core or integrated into the polyelectrolyte shell (Fig. 8).[94,95,115,116] The triggering mechanism of active species release is local changes of the pH value caused, for example, by corrosion process.

Mesoporous nanoparticles such as oxides and ceramics, e.g. SiO_2,[31] TiO_2,[95] ZnO,[117] $CaCO_3$,[118] were used for delivery of healing agents to damage area. In the groups of Lvov[119−122] and Shchukin[28] the LbL shell was optimized to natural halloysite nanotubes for the formation of self-healing systems.

Composite self-healing materials were prepared using a combination of loading with self-healing agent capsules and shape memory alloy wires.[123] It was shown that exploring several mechanisms of crack repair significantly improves the ability of materials to self-recovery. The formation of multifunctional materials can be achieved using the LbL approach. Multilayers and LbL capsules can be constructed using different building blocks. Thus, the proposal by White et al.[123] of the concept of a combination of several components with different mechanisms of self-healing is very interesting for LbL technology.

As an alternative to 'free' capsules 'surface' capsules were proposed. This interesting encapsulation system has already been discussed in the first part of this review and is illustrated in Figs 4 and 8. In brief, the ultrasonically formed 'surface' capsules[32] are able to solve the problem of homogeneous distribution of healing and adhesion of surface capsule to bulk material. Moreover the surface capsules can be modified in complex composite nanostructures. It was shown[124] effective formation of Ce-Al nanocomposite, loading of porous metal surface with AgNPs.[29]

The sensitivity of LbL shells is adjustable to several stimuli. For example, TiO_2/$(PEI/PSS)_2$ capsules are sensitive to pH and light.[30,94]
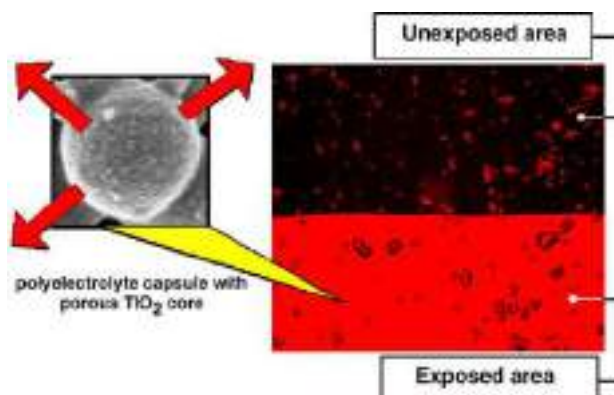
Figure 9. SEM image of TiO_2/$(PEI/PSS)_2$ multi-stimuli (pH and UV irradiation) responsive capsule. Confocal study of the possibility of local release of active chemicals from TiO_2/$(PEI/PSS)_2$ capsules into sol–gel anticorrosion coating: the UV laser trace confirms that localization of release is possible. Reproduced with permission from [30]. Copyright 2009, Royal Chemical Society.

The polyelectrolyte shell itself is sensitive to pH changes. However, the pH initiated release of encapsulated species is relatively slow in comparison to light (UV) stimulated release which is faster and is possible due to UV light absorption of the titania core. Light is interesting as a stimulus since it is very easy to control spatially and energetically. Figure 9 shows release of dye from such capsules upon UV irradiation of the modified surfaces.

LbL capsules are very interesting objects to develop complex systems with self-healing properties. Capsules can be used as elements for multifunctional systems. Different types of capsules with different healing agents can be incorporated in one coating.

721

The chemical nature of the shell provides the system with multi-sensitivity to different stimuli.

OUTLOOK AND PERSPECTIVES

Strategies for future development of self-healing multilayers involve fundamental and practical aspects. Regarding the fundamental aspects, the mechanism of self-healing in multilayers has still open questions that can be addressed in future studies. The importance of the partial disintegration of multilayers in aqueous media and desorption/reabsorption mechanism for the self-healing process is not elucidated very well. Other important questions are sensitivity of the polymer layers to internal stimuli, amplitude of their response and reusability. Nevertheless, stimuli responsive polymers are responsive to external stimuli (light, pH, ionic strength, humidity etc.). The amplitude of their response (change in thickness and morphology) could be insufficient for practical use. Thus, understanding of time and space dependent propagation of stimuli in multilayers is necessary for the focused design of self-healing materials. We should not forget that exposure of multilayers to external stimuli can often cause degradation of the polymers and restrict their application. In particular, electromagnetic irradiation can cause the *in situ* formation of reactive oxygen species and free radicals that trigger polymer degradation. Physical and chemicals processes that external stimuli trigger in multilayers should be addressed in future.

Considering the use of 'new' materials, biocompatible BCPs, hydrogels and colloidal particles are prospective building blocks for the construction of self-healing multilayers. These materials should exhibit self-healing properties at physiological conditions. Protocols for the LbL deposition of non-toxic biocompatible polymers and colloids should be developed.

Improved properties can be achieved by a combination of building blocks that provide different self-healing mechanisms in one system. From this point of view, organic–inorganic hybrid multilayers and capsules are very promising for the tuning of stimuli responsive properties of LbL assemblies for particular applications. Future developments will be based on multicomponent hierarchically organized interfaces that combine properties of functional materials and devices together with the multi-trigger stimuli response of the system. Multifunctionality can be achieved by tailoring composition, structure, physicochemical and mechanical properties at the nanometer scale. Combination of stimuli responsive building blocks provides advances for system intelligence and multifunctionalization.

In future, the application area of self-healing multilayers might be significantly extended. Development of sensors, biosensors, catalysts, membranes, implants etc. with self-healing properties and optimization of the already-existing self-healing anticorrosion, antifouling, antimicrobial and superhydrophobic coatings will enhance durability and prolong exploitation of different devices are aims of future studies.

CONCLUSIONS

In this review we have highlighted the self-healing properties of stimuli responsive multilayers. We demonstrated that interfaces adapted to self-regeneration and self-regulation require a complex hierarchical organization of dynamic non-covalently bonded polymers and colloidal particles. LbL technology for the construction of self-healing interfaces is an extremely exciting approach. Via LbL assembly a variety of hybrid multilayers can be designed and prepared. Up to now self-healing multilayers have been proposed for anticorrosion systems, antifouling and antimicrobial coatings, and superhydrophobic surfaces. However, versatile LbL technology for the formation of hybrid dynamic multilayers can be extended and optimized for novel trends and future needs.

REFERENCES

1 Decher G and Hong J-D, *Macromol Symp* **46**:321 (1991).
2 Decher G and Hong J-G, *BerBunsenges Phys Chem* **95**:1430 (1991).
3 Zhu Z and Sukhishvili SA, *J Mater Chem* **22**:7667 (2012).
4 Xu L, Zhu Z and Sukhishvili SA, *Langmuir* **27**:409 (2011).
5 Schmidt S, Hellweg T and Klitzing Rv, *Langmuir* **24**:12595 (2008).
6 Jones CD and Lyon LA, *Macromolecules* **33**:8301 (2000).
7 Pajor-Swierzy A, Kolasonska-Sojka M and Warszynski P, *Colloid Polym Sci* **292**:455 (2014).
8 Skirtach AG, Dejungnat C, Braun D, Susha AS, Rogach AL, Parak WJ et al., *Nano Lett* **5**:1371 (2005).
9 Loh KJ, Kim J, Lynch JP, Kam NWS and Kotov NA, *Smart Mater Struct* **16**:429 (2007).
10 Frueh J, Nakashima N, He Q and Möhwald H, *J Phys Chem B* **116**:12257 (2012).
11 Zhuk A, Mirza R and Sukhishvili SA, *ACS Nano* **5**:8790 (2011).
12 Veerabadran NG, Mongayt D, Torchilin V, Price RR and Lvov YM, *Macromol Rapid Commun* **30**:99 (2009).
13 Yoo D, Lee J-K and Rubmer MF, *Res Soc Symp Proc* **413**:395 (1996).
14 Tadeschi C, Caruso F, Möhwald H and Kirstein S, *J Am Chem Soc* **122**:5841 (2000).
15 Skorb EV and Andreeva DV, *Polym Chem* **4**:4834 (2013).
16 Skorb EV, Volkova AV and Andreeva DV, *Curr Org Chem* **18**:2315 (2014).
17 Schlenoff JB, Ly H and Li M, *J Am Chem Soc* **120**:7626 (1998).
18 Sukhishvili SA, *Curr Opin Colloid Interface Sci* **10**:37 (2005).
19 Erel I, Zhu Z, Zhuk A and Sukhishvili SA, *J Colloid Interface Sci* **355**:61 (2011).
20 Yang SY and Rubner MF, *J Am Chem Soc* **124**:2100 (2002).
21 Kotov NA, *Nanostruct Mater* **12**:789 (1999).
22 Loh KJ, Kim J, Lynch JP, Kam NWS and Kotov NA, *Smart Mater Struct* **16**:429 (2007).
23 Westcott SL, Kotov NA, Ostrander JW, Mamedov AA, Reust DK and Roark JP, *NSTI-Nanotech* **3**:288 (2004).
24 Andreeva DV, Fix D, Shchukin DG and Möhwald H, *Adv Mater* **20**:2789 (2008).
25 Andreeva DV, Fix D, Möhwald H and Shchukin DG, *J Mater Chem* **18**:1738 (2008).
26 Andreeva DV and Shchukin DG, *Mater Today* **11**:24 (2008).
27 Lamaka SV, Shchukin DG, Andreeva DV, Zheludkevich ML, Möhwald H and Ferreira MGS, *Adv Funct Mater* **18**:3137 (2008).
28 Fix D, Andreeva DV, Lvov YM, Shchukin DG and Möhwald H, *Adv Funct Mater* **19**:1720 (2009).
29 Gensel J, Borke T, Pazos-Pérez N, Fery A, Andreeva AV, Betthausen E et al., *Adv Mater* **24**:985 (2012).
30 Skorb EV, Shchukin DG, Möhwald H and Sviridov DV, *J Mater Chem* **19**:4931 (2009).
31 Skorb EV, Fix D, Andreeva DV, Shchukin DG and Möhwald H, *Adv Funct Mater* **19**:2373 (2009).
32 Andreeva DV, Sviridov DV, Masic A, Möhwald H and Skorb EV, *Small* **8**:823 (2012).
33 Saetia K, Schnorr JM, Mannarino M, Kim SY, Rutledge GC, Swager TM et al., *Adv Funct Mater* **24**:492 (2014).
34 Lee SW, Kim BS, Chen S, Shao-Horn Y and Hammond P, *J Am Chem Soc* **131**:671 (2009).
35 Lee M, Zine N, Baraket A, Zabala M, Campabadal F, Caruso R et al., *Sens Actuators B* **175**:201 (2012).
36 Skorb EV, Baidukova O, Goyal A, Brotchie A, Andreeva DV and Möhwald H, *J Mater Chem* **22**:13841 (2012).
37 Yan Y, Such G, Johnston APR, Lomas H and Caruso F, *ACS Nano* **5**:4252 (2011).
38 Andreeva DV, Gorin DA, Shchukin DG and Sukhorukov GB, *Macromol Rapid Commun* **27**:931 (2006).
39 Chong S-F, Sexton A, De Rose R, Kent SJ, Zelikin AN and Caruso F, *Biomaterials* **30**:5178 (2009).
40 De Geest BG, Willart MA, Hammad H, Lambrecht BN, Pollard C and Bogaert P, *ACS Nano* **6**:2136 (2012).
41 Skorb EV and Andreeva DV, *Adv Funct Mater* **23**:4483 (2013).

42 Hager MD, Greil P, Leyens C, Van der Zwaag S and Schubert US, *Adv Mater* **22**:5424 (2010).

43 White SR, Sottos NR, Geubelle PH, Moore JS, Kessler MR, Sriram SR *et al.*, *Nature* **409**:794 (2001).

44 Burattini S, Greenland BW, Chappell D, Colquhoun HM and Hayes W, *Chem Soc Rev* **39**:1973 (2010).

45 Zhu M, Rong MZ and Zhang MQ, *Polym Int* **63**:1741 (2014).

46 Lu Y, Sarshar MA, Du K, Chou T, Choi C-H and Sukhishvili SA, *ACS Appl Mater Interfaces* **5**:12617 (2013).

47 Vogt C, Ball V, Mutterer J, Schaaf P, Voegel J-C, Senger B *et al.*, *J Phys Chem B* **116**:5269 (2012).

48 Tan WS, Cohen RE, Rubner MF and Sukhishvili SA, *Macromolecules* **43**:1950 (2010).

49 Minko S, Muller M, Motornov M, Nitschke N, Grundke K and Stamm M, *J Am Chem Soc* **125**:3896 (2003).

50 Costa RR, Custodio A, Arias FJ, Rodriguez-Cabello JC and Mano JF, *Small* **7**:2640 (2011).

51 Elender G, Kfihner M and Sackmann E, *Biosens Bioelectron* **11**:565 (1966).

52 Tamm LK and McConnell HM, *Biophys J* **47**:105 (1985).

53 Merkel R, Sackmann E and Evans E, *J Phys France* **50**:1535 (1989).

54 Sigl H, Brink G, Seufert M, Schulz M, Wegner G and Sackmann E, *Eur Biophys J* **25**:249 (1997).

55 Bertrand P, Jonas A, Laschewsky A and Legras R, *Macromol Rapid Commun* **21**:319 (2000).

56 Morizumi T, *Thin Solid Films* **1–2**:413 (1998).

57 Tsukruk V and Rebeker DH, *Polymer* **36**:1791 (1995).

58 Liu Y, Xu P, Zuo Z, Cheng Z, Lee D-W and Li X, *J Mater Chem* **22**:18004 (2012).

59 Senaratne W, Andruzzi L and Ober CK, *Biomacromol* **6**:2427 (2005).

60 Li Y, Li L and Sun J, *Angew Chem Int Ed* **49**:6129 (2010).

61 Li Y, Chen S, Wu M and Sun J, *Adv Mater* **26**:3344 (2014).

62 Wang X, Wang Y, Bi S, Wang Y, Chen X, Qiu L *et al.*, *Adv Funct Mater* **24**:403 (2014).

63 Wang X, Liu F, Zheng X and Sun J, *Angew Chem Int Ed* **50**:11378 (2011).

64 Andreeva DV, Skorb EV and Shchukin DG, *ACS Appl Mater Interfaces* **2**:1954 (2010).

65 Jones CD and Lyon LA, *Macromolecules* **33**:8301 (2000).

66 Park CW, South AB, Hu X, Verdes C, Kim J-D and Lyon LA, *Colloid Polym Sci* **289**:583 (2011).

67 Han Q, Li C, Guan Y, Zhu XX and Zhang Y, *Polymer* **55**:2197 (2014).

68 Manna U and Lynn DM, *Adv Mater* **25**:5104 (2013).

69 Liang X, Kozlovskaya V, Chen Y, Zavgorodnya O and Kharlampieva E, *Chem Mater* **24**:3707 (2012).

70 Quinn JF and Caruso F, *Langmuir* **20**:20 (2004).

71 Serpe MJ, Jones CD and Lyon LA, *Langmuir* **19**:8759 (2003).

72 South AB and Lyon LA, *Angew Chem Int Ed* **49**:767 (2010).

73 Webber GB, Wanless EJ, Armes SP, Tang Y, Li Y and Biggs S, *Adv Mater* **16**:1794 (2004).

74 Han L, Yin J, Wang L, Chia K-K, Cohen R, Rubner MF *et al.*, *Soft Matter* **8**:8642 (2012).

75 Webber GB, Wanless EF, Armes SP, Tang Y, Li Y and Biggs S, *Adv Mater* **16**:1794 (2004).

76 Betthausen E, Drechsler M, Förtsch M, Schacher FH and Müller AHE, *Soft Matter* **7**:8880 (2011).

77 Tan WS, Zhu Z, Sukhishvili SA, Rubner MF and Cohen RE, *Macromolecules* **44**:7767 (2011).

78 Lundin M, Solaqa F, Thormann E, Macakova L and Blomberg E, *Langmuir* **27**:7537 (2011).

79 Schoeler B, Kumaraswamy G and Caruso F, *Macromolecules* **35**:889 (2002).

80 Carriere D, Krastev R and Schönhoff M, *Langmuir* **20**:11465 (2004).

81 DeLongchamp DM and Hammond PT, *Chem Mater* **15**:1165 (2003).

82 Dubas ST and Schlenoff JB, *Langmuir* **17**:7725 (2001).

83 Farhat TR and Schlenoff JB, *Langmuir* **17**:1184 (2001).

84 Farhat TR and Schlenoff JB, *Solid State Lett* **5**:13 (2002).

85 Huang X, Bolen MJ and Zacharia NS, *Phys Chem Chem Phys* **16**:10267 (2014).

86 Li Y, Chen S, Wu M and Sun J, *Adv Mater* **24**:4578 (2012).

87 Jiang C, Markutsya S, Pikus Y and Tsukruk VV, *Nat Mater* **3**:721 (2004).

88 Liu HA, Gnade BE and Balkus KJ, *Adv Funct Mater* **18**:3620 (2008).

89 Alexeev A, Uspal WE and Balazs AC, *ACS Nano* **2**:1117 (2008).

90 Dou Y, Zhou A, Pan T, Han J, Wei M, Evans DG *et al.*, *Chem Commun* **50**:7136 (2014).

91 Olugebefola SC, Hamilton AR, Fairfield DJ, Sottos NR and White SR, *Soft Matter* **10**:544 (2014).

92 Dong J, Ding J, Weng J and Dai L, *Macromol Rapid Commun* **34**:659 (2013).

93 Zhou H, Wang H, Niu H, Gestos A and Lin T, *Adv Funct Mater* **23**:1664 (2013).

94 Skorb EV, Sviridov DV, Möhwald H and Shchukin DG, *Chem Commun* **40**:6041 (2009).

95 Skorb EV, Skirtach A, Sviridov DV, Shchukin DG and Möhwald H, *ACS Nano* **3**:1753 (2009).

96 Gupta S, Zhang Q, Emrick T, Balazs AC and Russell TP, *Nat Mater* **5**:229 (2006).

97 Amendola V and Meneghetti M, *Nanoscale* **1**:74 (2009).

98 Wang X, Liu F, Zheng X and Sun J, *Angew Chem Int Ed* **50**:11378 (2011).

99 Pazos-Pérez N, Borke T, Andreeva DV and Alvarez-Puebla A, *Nanoscale* **3**:3265 (2011).

100 Hu J, Zhu Y, Huang H and Lu J, *Prog Polym Sci* **37**:1720 (2012).

101 Meng H and Li G, *Polymer* **54**:2199 (2013).

102 Shojaei A and Li GQ, *Proc R Soc Lond A Math Phys Eng Sci* **470**:20140199 (2014).

103 Yang Q and Li G, *J Polym Sci B Polym Phys* **52**:1429 (2014).

104 Yang QX and Li GQ, *Smart Mater Struct* **23**:105032 (2014).

105 Torbati AH, Nejad HB, Ponce M, Sutton JP and Mather PT, *Soft Matter* **10**:3112 (2014).

106 Torbati AH, Mather RT, Reeder JE and Mather PT, *J Biomed Mater Res B* **102B**:1236 (2014).

107 Nejad HB, Baker RM and Mather PT, *Soft Matter* **10**:8066 (2014).

108 Katano H, Maruyama A, Sanui K, Ogata N, Okano T and Sakurai Y, *J Control Release* **16**:215 (1991).

109 Lee C, Wei X, Kysar JW and Hone J, *Science* **321**:385 (2008).

110 Allen MJ, Tung VC and Kaner RB, *Chem Rev* **110**:132 (2010).

111 Kan L, Xu Z and Gao C, *Macromolecules* **44**:444 (2011).

112 Shchukin D and Möhwald H, *Science* **341**:1458 (2013).

113 Yang Y and Urban MW, *Chem Soc Rev* **42**:7446 (2013).

114 Samadzadeh M, Boura SH, Peikan M, Kasiriha SM and Ashrafi A, *Prog Org Coat* **68**:159 (2010).

115 Skorb EV and Möhwald H, *Adv Mater Interfaces* DOI: 10.1002/admi.201400237R1 (2014).

116 Skorb EV and Möhwald H, *Adv Mater* **36**:5029 (2013).

117 Kolesnikova TA, Gorin DA, Fernandes P, Kessel S, Khomutov GB, Fery A *et al.*, *Adv Funct Mater* **20**:1189 (2010).

118 Yashchenok AM, Delcea M, Videnova K, Jares-Erijman EA, Jovin TM, Konrad M *et al.*, *Angew Chem Int Ed* **49**:8116 (2010).

119 Abdullayev E and Lvov Y, *J Mater Chem* **20**:6681 (2010).

120 Abdullayev E and Lvov Y, *J Nanosci Nanotechnol* **11**:10007 (2011).

121 Abdullayev E, Joshi A, Wei W, Zhao Z and Lvov Y, *ACS Nano* **6**:7216 (2012).

122 Abdullayev E, Abbasov V, Tursunbayeva A, Portnov V, Ibrahimov H, Mukhtarova G *et al.*, *ACS Appl Mater Interfaces* **5**:4464 (2013).

123 Neuser S, Michaud V and White SR, *Polymer* **53**:370 (2012).

124 Skorb EV, Shchukin DG and Andreeva DV, *Langmuir* **26**:16973 (2010).

www.MaterialsViews.com

ADVANCED
MATERIALS
INTERFACES

www.advmatinterfaces.de

REVIEW

"Smart" Surface Capsules for Delivery Devices

Ekaterina V. Skorb* and Helmuth Möhwald

This review describes emerging trends, basic principles, applications, and future challenges for designing next generation responsive "smart" surface capsules. Advances and importance of "surface" capsules which are not deposited onto the surface but are built into the surface are highlighted for selective applications with specific examples of surface sponge structures formed by high intensity ultrasonic surface treatment (HIUS). Surface capsules can be adapted for biomedical applications, membrane materials, lab-on-chip, organ-on-chip, and for template synthesis. They provide attractive self-healing anticorrosion and antifouling prospects. Nowadays delivery systems are built from inorganic, organic, hybrid, biological materials to deliver various drugs from low molecular weight substances to large protein molecules and even live cells. It is important that capsules are designed to have time prolonged release features. Available stimuli to control capsule opening are physical, chemical and biological ones. Understanding the underlying mechanisms of capsule opening by different stimuli is essential for developing new methods of encapsulation, release, and targeting. Development of "smart" surface capsules is preferable to respond to multiple stimuli. More and more often a new generation of "smart" capsules is designed by a bio-inspired approach.

1. Introduction

Encapsulation systems nowadays find a great number of advanced applications. Capsules can be adapted for biomedical applications: drug delivery, tissue engineering, cell encapsulation, theranostics. They are used for sensing, membrane materials, for template synthesis and provide attractive self-healing anticorrosion and antifouling prospects. Active chemicals, cells, biomolecules are encapsulated to prevent their interaction with an aggressive environment or to regulate their activity. They can be regulated by internal or external stimuli. Time prolongated activity is possible for "smart" capsules to achieve needed advanced functionalities. Material types used for capsule formation are all available species from synthetic systems to natural or bio-mimetic species, live cells. There are also a

great number of methodologies for capsule design available for the time being in synthetic chemistry.

The capsules can be used as "free" suspended particles or being integrated/developed into the surface ("surface" capsules) (**Figure 1**). This paper reviews the state of the art of surface capsules with advanced functionalities produced using new strategies, including HIUT. Before focusing on surface capsules, brief summary on classic "free" capsules provided. The past decade, a variety of capsules have been designed and produced through creative combinations of emerging technologies, soft matter physics, and chemistry. These new approaches have provided tremendous control over the size, shape, structure, and materials.[1]

"Free" capsules can be composed of differently formed empty core and shell membranes and permit the encapsulation of freely suspended materials in the interior of an enclosed membrane (Figure 1a). The inner compartment of a capsule can be used to encapsulate active species that are then release upon the breakup of the shell membrane, e.g., because of chemical, physical or biological stimuli. Membrane engineering through optimization of the composition and structure can be used to design impermeable shell membranes, or selectively permeable shell membranes that permit the passage of molecules smaller than a critical size. Hollow capsules, e.g., polymer capsule, can be fabricated be self-assembly, layer-by-layer assembly, single-step polymer adsorption, bio-inspired assembly, surface polymerization, and ultrasound assembly. These techniques can be applied to prepare polymer capsules with diverse functionality and physicochemical properties, which may fulfill specific requirements in various areas.[2]

Porous particles comprise a single body of materials without distinct layers and they enable active species to be directly embedded in the body. There are in Figure 1b, left shown two examples of formation of "free" encapsulation systems based on porous particles. The mesoporous silica (MCM 41) is shown in left image (Figure 1b, left) as effective carrier for encapsulation of active species, e.g., corrosion inhibitor.[3] Such carriers as $CaCO_3$ nanosheets and layered nanostructures (e.g., layered double hydroxide (LDH)), one-dimensional nanostructures, nanotubes such as carbon nanotubes, tubule aluminosilicates (halloysites) can be mentioned.[4] Important the particle used as a body for encapsulate active chemical possesses a huge surface

Dr. E. V. Skorb, Prof. H. Möhwald
Max Planck Institute of Colloids and Interfaces
Wissenschaftspark Golm
Am Mühlenberg 1, Golm 14424, Germany
E-mail: skorb@mpikg.mpg.de

REVIEW
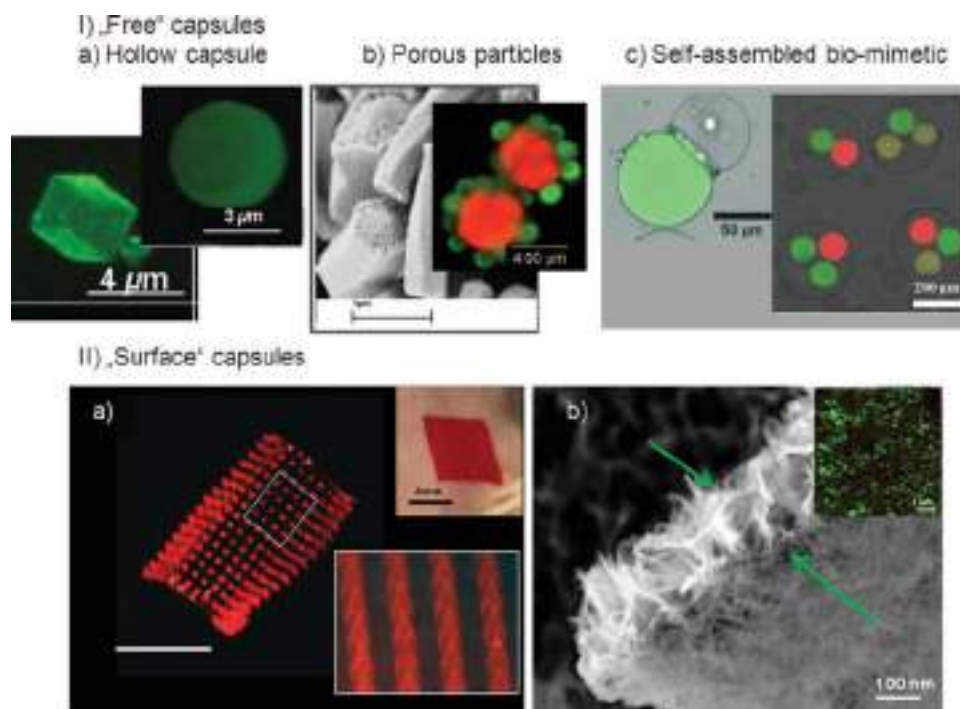
Figure 1. I) "Free" capsule systems. a) Confocal images of three dimensional (3D) reconstructed cubic (CdCO$_3$ cores) and spherical (SiO$_2$ cores) microcapsules. Reproduced with permission.[3a] Copyright 2011, American Chemical Society. b) SEM image of mesoporous silica used for active chemicals delivery (left) and fluorescent confocal image of multicompartment capsules based on porous CaCO$_3$ particle (red labeled) with SiO$_2$ (green labeled). Reproduced with permission.[3b,5a] Copyright 2009 and 2010, Wiley c) Vesicles templated by double-emulsion drops: confocal microscopy image of the dumbbell-shaped polymersomes containing two distinct materials in separate lumens (left); multiple vesicles-in-vesicle structures (right). Reproduced with permission.[6] Copyright 2011, American Chemical Society. II) "Surface" capsule systems. a) A curled microneedle array, showing the flexibility of the array. Scale bar is 1 cm. Inset below shows higher resolution brightfield macroscopic images of a microneedle patch. Reproduced with permission.[17] Copyright 2013, Wiley. Above inset show injection of microneedle array into skin. Reproduced with permission.[17] Copyright 2012, Wiley. b) Sonochemical metal surface nanostructuring for the formation of "surface" metal sponge for encapsulation of active chemicals (inset show confocal fluorescent microscopy of doxorubicin loaded surface (top-view)). Reproduced with permission.[3] Copyright 2012, Wiley.

area, large pore volume, and cage-type porous structure, leading to efficient materials sequestration from solution.

The second example is shown the promise of multicomponent systems for drug delivery based on CaCO$_3$ particle (Figure 1b, right).[5] Subcompartmentalization was achieved by decorating a larger subcontainer with smaller subcompartments (liposomes). It was found that porosity, ionic strength, and particle concentration are critical factors controlling the adsorption of nanoparticles (NPs) and liposomes onto the larger inner core of capsules. The simultaneous incorporation of small and large molecules, for example, an enzyme and its substrate, in the same particle or capsule so as to induce a specific biochemical reaction in a well-defined three-dimensional architecture was possible. Enhanced mechanical stability of the particles in comparison with hollow capsules is a characteristic feature of this system. Furthermore, it was shown that an enzyme-substrate reaction can occur in the same porous CaCO$_3$ particle upon disruption of the outer subcompartments; thus the substrate is released while the enzyme is maintained in the confined and protected volumes of the capsules.

Important issues need to be addressed in the fields of soft matter and biomedical science. Biological systems are very complex, and no panacea microcarrier is available that is useful for all purposes with optimal performances. Each application is associated with specific optimal conditions under which a

capsule application should function, such as the release profiles of one or multiple drugs, or biological specification. Last years it becomes increasanly important the application of bio-mimetic concept for the understanding and design of novel applicable bio-materials (Figure 1, Ic). In Figure 1 it is presented vesicles templated dumbbell-shaped polymersomes containing two distinct materials in separate lumens (left) and multiple vesicles-in-vesicle structures (right).[6] Formation of such self-organized bio-compatible systems is increased area of scientific interest.

We can't touch all available materials used for capsule development, methodologies and application in our review. However, we can guide to some specific examples which illustrate modern trends. In particular as a guideline we choose the sonochemical approach to show how one methodology can be used to design various materials (**Figure 2**): oxides, metals, silicon, polymers, hybrids, etc.[7] We highlight the importance of cooperation between synthetic chemistry with theoretical modeling to design process the regulation and effective use of a powerful methodology for design of various types of effective encapsulation systems.

Capsules can be engineered in one step or, as in most cases, nanostructured in several steps. We discuss the most effective universal methodologies which are used for multi-step capsule adaptation to a needed application. Thus self-assembled monolayers (SAM)[8] are effective for nanostructuring of a

www.MaterialsViews.com

ADVANCED
MATERIALS
INTERFACES
www.advmatinterfaces.de

REVIEW
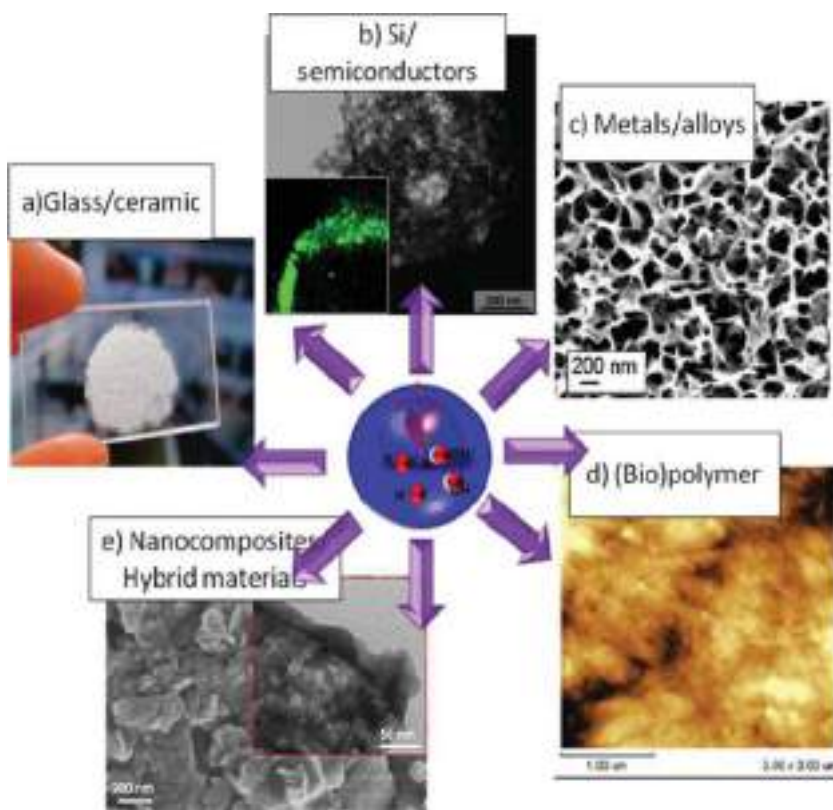
Figure 2. Example how one methodology, sonochemical material treatment, can provide effective modification of various materials which in following can be effectively adapted for a design of "smart" capsules. Materials with different properties after sonochemical treatment: a) optic image of silica glass (Reproduced with permission.[143b] Copyright 2012, Americal Chemical Society); b) TEM image of porous silicon formed in water-alcohol solution. The inset shows its micro-confocal photoluminescence (Reproduced with permission.[143a] Copyright 2012, Wiley); c) SEM image of sonochemically formed aluminium surface sponge (Reproduced with permission.[14a] Copyright 2010, Royal Society of Chemistry); d) AFM tapping-mode image in air of bacterial cellulose thin film; e) SEM and TEM images of formed hybrid magnesium/polypyrrole implant structure in ethanol + pyrrole solution. Frequency of 20 kHz; I_{ac} = 40–60 W cm^{-2}, except for the case of biopolymers (d) where I_{ac} was less than 20 W cm^{-2}.

surface (termination of corrosion, cell metabolism regulation, drug delivery, antifouling, etc.). There are examples which point to the importance of changes in interfacial properties or of release of biocide to regulate the cell behavior on the surface: 1) cell detachment from the surface after a change of interfacial properties via a stimuli-responsive change in polymer surface conformation; and 2) stimuli-responsive release of biocide from "surface" capsules for antifouling surface activity.

The construction and optimisation of systems with synergetic properties are now of high actuality. Sonochemical, cavitation-assisted, processes for active "surface" encapsulation system construction are at the frontier of different fields of science, such as nanometre-scale engineering and biotechnology (implants, antifungal and antibacterial systems) and therefore are presented here as example. In Figure 3, the patterning of surfaces with simultaneous formation in selected patterned "surface" capsules is presented as prospective and interesting for the formation of neighbouring regions with different adsorption abilities with respect to biological objects. Surface micro-patterning techniques, can be used for controlling cell adhesion and cell-microenvironment interactions, such as homotypic and heterotypic cell–cell interactions.[11] Formation of encapsulation regions in a patterned way is preferable. To regulate adhesion, sonochemically modified patterned surfaces, as shown in Figure 3 can be used. The patterned array system can be fabricated by a photolithography technique.[12] A change in interfacial properties, e.g., wettability and functional terminal groups regulate cell adhesion and protein adsorption. To demonstrate the hypothesis, patterned arrays with additional functional terminal groups, such as an amine (NH$_2$) group (3-aminopropyltriethoxysilane), a methyl (CH$_3$) group (trichlorovinylsilane), and a fluorocarbon (CF$_3$) group (trichloro(perfluorooctyl)silane), can be used. The contact angle can be measured to determine the hydrophilic and hydrophobic properties. Bacteria adhesion and feedback properties of patterned surfaces in the following can be regulated as described, for example, in Figure 3, Example 1.

Unlike traditional patterning methods, the presented systems contain feedback properties through the design of loaded capsule patterns (Figure 3, example 2). Mesoporous metal sponges are effective bases for the construction of surface-attached capsules for the storage of active components and their stimuli controlled release.[13,14] Sonochemically formed metal-polyelectrolyte capsules loaded with active chemicals introduce the possibility of providing metal surfaces with important properties, including high biocide activity, anti-friction properties, and the ability to release active components to stimulate activities of attached cells, such as in stem-cell research. Different

surface of synthesized inorganic materials, e.g., oxides, silicon, metals, to follow the regulation of physico-chemical capsule properties, for example hydrophilicity. Layer-by-Layer (LbL) organization[9,10] of oppositely charged polyelectrolytes is discussed as very effective universal methodology for the formation of a capsule shell for both "free" and "surface" capsules. We discuss in this review the pore architecture, e.g., regular oriented 1D-nanotubes or 3D- mesoporous organization. The importance to have pronounced release kinetics for "smart" surface capsules is highlighted. Some other possibilities for effective design are mentioned, e.g., sol-gel methodology and plasma polymer deposition, thermal coatings, to achieve a needed functionality. Thus the techniques are suggested as promising to provide an effective variation of the interfacial properties.

For the time being there are two types of responsive surface encapsulation systems (**Figure 3**): 1) capsules should have such functionalization, for example by SAM, to have stimuli-changeable interfacial properties (hydrophilic/hydrophobic or surface layer thickness, functional groups); 2) capsules should be able to release encapsulated material to activate processes on the

Figure 3. Example 1. Formation of a patterned surface with defined ability to adsorb biological objects: scheme of patterned surface (right part) and confocal microscopy study of adsorption to the surfaces with suppressed (left) and high bacteria (*E. Coli*) adhesion ability (right). Example 2. Scheme based on AFM images of polished aluminium (a) before modification; (b) sonochemically modified aluminium; (c) aluminium with incorporated surface metal/polymer capsule loaded by active chemicals (AC); complexation between AC and the polyelectrolyte (PE) prevent the release of the chemicals in the pore; (d) aluminium protected on the top by polymer or sol-gel film; (e) SEM top view of sonochemically formed surface metal-based core for subsequent surface capsule construction; (f) optical observation of complex AC (biocide)/PE(PSS) stability at different pH levels: left is at pH = 7 (turbid) and right is at pH = 10 (clear); (g) TEM image of aluminium with surface-formed capsules for AC storage. The right inset shows biocide activity of the surface with capsules loaded with a biocide agent before and after its release. *E. Coli* was visualised with LIVE/DEAD *BacLight*, which allows inactivated (red) and living (green) bacteria to be distinguished. Reproduced with permission.[13] Copyright 2012, Wiley.

ultrasonic intensities result in the formation of structures with different features that determine their subsequent use for active surface construction. At a lower sonication intensity (30 W/cm^2), just an increase in the surface roughness was observed, without the formation of a base for subsequent capsule construction. However, as shown in Figure 3 (Example 2), high-intensity sonication (57 W/cm^2) of metal surfaces results in the formation of highly porous surfaces. The thickness of the modified mesoporous layer, as estimated by TEM analysis of the ultramicrotomed plates, is about 200 nm with a pore size of approximately 7 nm. This layer exhibits strong adhesion to the surface and is continuous; it is therefore a promising surface capsule support. The pores of the sonochemically formed metal (here, aluminium) surface are loaded with biocide,[13] and the pores are then closed using a complexation reaction between the active incorporated agent and the polyelectrolyte.[15] Thus, the constructed smart surface capsules formed by the walls of the metal pores and polyelectrolytes are effective for the prolonged storage of the active component. The metal walls

provide the high stability and adhesion of the capsules to the metal plate; the polyelectrolytes are responsible for the loading and release of the active species (here, biocide) on demand. The smartness and possibility to trigger biocide release from the system by adjusting the pH level is evident in Figure 3f (left image, neutral pH, turbid due to complexation). The ability to destroy the complex and to release biocides when necessary is a high priority. In the described case, the pH change could be an effective trigger for the destruction of the complex. In Figure 3f (right image, alkaline pH, clear), the destruction of the complex is evident. In the right insets of Figure 3, the surface before and after the biocide release and its effective influence on *E. Coli* bacteria is shown.[13] In this case a high biocide activity of the surface is evident.

Means to control capsule opening are physical (temperature, laser light, electric and magnetic field, ultrasound, and mechanical action), chemical (ionic strength, pH, electrochemical and solvent) and biological stimuli (enzymes and receptors).[5b] For the time being the attention of scientists

focuses on the direction of designing of encapsulation systems which are sensitive to more than one stimulus. The capsule sensitivity to external/internal stimuli is based on the sensitivity of its building block. Most common stimuli are acting on the soft organic part of the system. Stimuli responsive macromolecules are capable of conformational and chemical changes on receiving a stimulus (T, pH, ionic strength, electromagnetic irradiation or magnetic field, electric potential, chemical composition or applied mechanical force). The discussed systems are planar films, coatings and non-planar capsules, micelles, as well as combinations of two non-planar in planar systems (surface capsules + coating). Different architectures and fundamental approaches in the area provide specific advanced applications which are also highlighted in the review. Different architecture provides control of dynamics (system response) and amplitude of changes of the interfacial properties, reversibility of the changes and the intensity of the external signal that could trigger the changes. The inorganic part of the encapsulation system, for example mesoporous particles themselves or being a core of polyelectrolyte 3D capsule, could be bonded with an encapsulated chemical with relatively mobile bonds (chemisorbed). The release from such systems is responsive to external or internal stimuli. This review discusses trends and challenges in designing next generation carriers. There is high attention for bio-mimicking both encapsulation material and release processes. There are some background ideas presented in the review.

This review provides an overview of the various encapsulation materials and techniques that have been proposed to control the release of (bio-)active molecules of interest in biomedicine and drug delivery, optical materials, bio-sensors and biomembranes, template for synthesis, surface coatings, sensing, self-healing and antifouling surfaces. Some specific examples of advanced applications are presented in the review. Finally, an outlook on future directions and a glimpse into the current developments are provided.

2. Basic Properties of "smart" Surface Capsules

Significant recent application driven progress has been made with regards to the main properties of "smart" surface capsules. In particular, for advanced applications multifunctional capsules are in focus with the possibility of multi-component delivery and multi trigger stimuli response of the capsule system.[16] The main properties of capsules are their interaction with active components to deliver: 1) loading, 2) storage and 3) release (**Figure 4**).

Active components can i) be material of the capsule (see following section), ii) be composite or hybrid capsule which can provide several materials to deliver, iii) be loaded into capsules, or iii) active materials to deliver can be capsule building blocks and loaded materials (**Figure 5**).

Loading of capsules with active material can be performed through a manifold of mechanisms and strategies. They can be physically entrapped (Figure 5a) in capsules[3] or adsorbed to the capsule material by specific interactions, non-covalent or covalent binding via degradable linkers[13] and subsequently released via diffusion, swelling, erosion, degradation or a
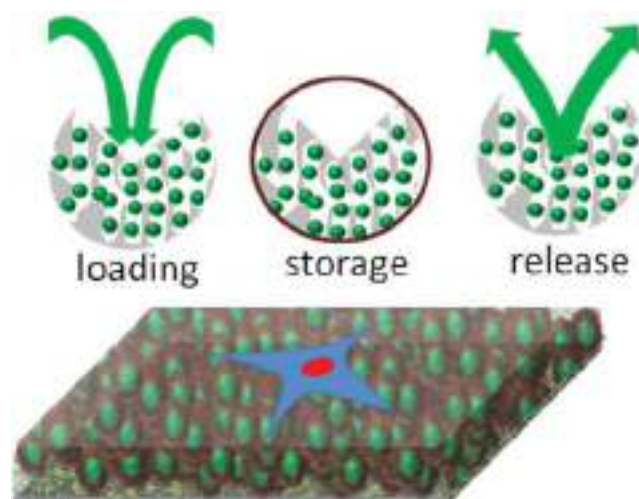
Figure 4. Scheme of the processes of loading, storage and release of active components, shown for a single capsule (upper row); active feedback surface design, which will influence surface adhering biological objects, e.g., cells and bacteria (below). Reproduced with permission.[13] Copyright 2012, Wiley.

specific trigger such as pH, temperature, etc. Also, a combination of multiple delivery systems can be used to achieve multimodular release of multiply active substances.[16] Depending on the loading/release mechanism, different release profiles can be obtained.

Physical entrapment of active species in a capsule is a frequently applied technique for local delivery.[3] Its relative simplicity represents a clear advantage over more sophisticated encapsulation/release methods and the majority of encapsulation systems rely on this loading process. Loading is done by incubation of the preformed capsule with the species of interest or by adding the species to the capsule forming premateral, e.g., for polymer capsules monomers/prepolymers.

The release mechanism in the case of physically entrapped species depends on both the characteristics of the capsule material and the active substance. If there are pores and they are bigger than the dynamic radius of the loaded molecules, diffusion is the driving force for release, with a diffusion rate depending on the loaded molecule size and the 'free-volume' in the capsule.[18] For most cases relatively slow release due to diffusion is of interest to retain a high quantity of loaded materials after capsule formation. However, the active species, e.g., protein, should be released in sufficiently high concentration
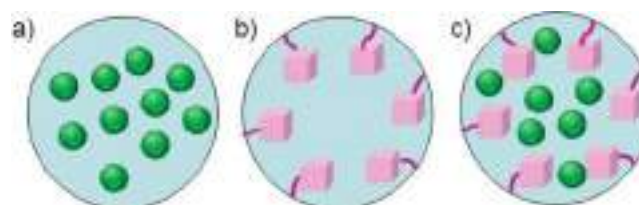
Figure 5. Examples of possible loading mechanism: a) physical entrapment of encapsulated materials into capsule; b) chemical bonding of material to capsule; c) multi-modal loading: one of component is physically entrapped into capsule and one is chemically bonded. Moreover active components can be material of capsule.

REVIEW

to initiate the necessary function/response of cells. Simultaneously the concentration of released species should not be higher than the toxic limit. Thus the majority of the gel based encapsulation systems[18] reported to date exhibit diffusion controlled release, following Higuchi's kinetics, implying that the release is proportional to the square root of time. This release profile was shown to be particularly beneficial for the delivery of several growth factors for tissue engineering applications.

On the other hand, when the pores are smaller than the loaded molecule diameter, degradation of capsule material (free or surface) is needed for release. For example, hydrogel encapsulation systems can be swelling-controlled depending on water uptake and changes in drug diffusivity within the matrix. Swelling increases polymer flexibility and makes pores bigger, resulting in higher mobility of active molecules. As a consequence, release depends on Fickian diffusion, polymer disentanglement and dissolution in water.[19] The other example can be erosion-controlled systems, e.g., biodegradable magnesium implants[20] or of biodegradable polymers.[21] In these systems, the mobility of active molecules in the homogeneous nondegraded matrix is limited and release is then governed by the degradation rate of the capsule material and porosity increase.

Covalent binding is another loading mechanism (Figure 5b).[13] Let's take as example proteins as active encapsulated chemicals. Mostly exploiting their reactive amine and thiol groups, they can be covalently bound to polymer matrices via functional groups like hydroxy, amine, carboxyl groups that, if not naturally present in the structure of the polymer, have to be introduced by functionalization reactions, blending or co-polymerization. The release of the protein can be provided either via hydrolysis, reduction reactions or (cell-mediated) enzymatic cleavage. This type of mechanism leads to on-demand release of loaded proteins, mimicking the enzymatic activity naturally occurring in the 'healthy' extracellular matrix (ECM).[18] However, stability and maintenance of biological activity of the protein may be an issue. It is important to remain an active species in active conformation, e.g., one should be careful that after release protein escapes denaturation and inactivation. The release mechanism from capsules can be adjusted by diffusion, swelling, erosion, internal or external stimuli or combinations thereof.

The design of "smart" capsules may offer the possibility to deliver multiple species with independent release rates and loading (Figure 5c).[16] It is still a challenge to develop capsules with multiple species delivery. An appropriate control over temporal and spatial release is of high priority for such systems. Encapsulating various compounds with different physiochemical properties and achieving their synchronized and sustained release seem too hard to realize.

However, currently technologies are available that have a proven potential of modulation of release profiles according to the specific application needs. These include traditional diffusion/swelling/degradation mediated release on-demand, affinity, covalent binding based delivery and special surface nanostructuring. Some specific examples are presented later.

A sustained multi-delivery system for herbal medicines was suggested recently.[22] An injectable nanoparticulate system based on poly(ethylene glycol)-poly(lactic-co-glycolide) (PEG–PLGA) platforms was prepared for co-encapsulation and sustained release of four active components (ginkgolides A, B, C and bilobalide) in Ginkgo biloba extract. Carriers were screened by a macrophage uptake experiment for their ability of long-circulation. Sustained and synchronized release of four components from an encapsulation system was observed both in vitro and in vivo. The half-life times of four terpenoid compounds were also significantly improved by incorporation into carriers. The results indicated that despite the physiochemical properties of the compounds themselves, the release of ginkgo terpenes depends mainly on the degradation of PEG–PLGA based platforms. The reported system might be a potent drug carrier for injectable delivery of multiple drug components, especially those found in herbal medicines.

It was shown[23] that structural swelling of bicontinuous cubic lipid/water phases is essential for overcoming the nanoscale constraints for encapsulation of large therapeutic molecules in network-type lipid carriers. SAXS scans permitted monitoring of tuning of the diameters of the aqueous nanochannel compartments in cubosome structures by external stimuli and membrane curvature modulating agents. They revealed that coexisting nanochannel structures and intermediate states can be typical for multicomponent amphiphilic mixtures subjected to thermal treatment. The encapsulation of small proteins occurs without perturbation of the cubosome structure. The entrapment of proteins with sizes bigger than the water channel diameters occurs via a "nanopocket defects" mechanism and spontaneous nanocubosome generation in the interior of the cubic lipid/protein assembly. Further questions that require investigations should consider the role of the structural asymmetry of the double diamond-type nanochannel network for protein loading and release, the conformation of the entrapped proteins, the mechanism of fragmentation and steric stabilization of the cubosomes by biocompatible polymers, their functionalization for targeted delivery of therapeutic proteins, and the interaction with the cellular environment.

Multifunctional capsules are also achievable by making capsules sensitive to different stimuli. Thus one capsule can be sensitive to more than one stimulus. For example the formed magnesium-polypyrrole capsules are sensitive simultaneously to pH (due to Mg) and electric current flow (due to the conductivity of polypyrrole).[24]

It is also clear that for different applications capsules made from different materials are needed. Metals have to be protected from corrosion. Polymers are used for single component capsules or as one of the capsule components. Silica, especially, mesoporous silica, such as MCM-41, is often suggested to deliver active substances due to the unique nature of mesoporous systems. Mesoporous luminescent Si is used when capsules need to be visualized, for example to follow their track in the body. Light carbon structures, carbon nanotubes, are used as capsule material. Calcium carbonate and other ceramics can be effective to deliver different substances.

Specific applications are required for integration of capsules on surfaces. Examples of such applications are corrosion protection, implants and antifouling surfaces, sensors and membranes, lab-on-chip and organ-on-chip systems. Recently it was suggested that for such applications it is of high priority to incorporate capsules into surfaces: "surface capsules".[13,25] The following advanced features can be mentioned for "surface"

capsules in comparison with "free capsules" which are used to be integrated in coatings: 1) regular "surface" capsule distribution throughout the surface; 2) possibility of multicomponent loading; 3) spatially resolved encapsulation. Examples of such surface capsules layers for metal surfaces are: 1) anodized oxide layers on metal surfaces, e.g., on aluminum, anodic aluminum oxide (AAO), or on titanium, titanium dioxide nanotube (TNT), with the formation of a porous layer with oriented nanotubes (Me-1D);[26] 2) metal surface mesoporous sponge layers (Me-meso).[13] Both Me-1D and Me-meso have their advantages. Thus Me-1D can be very precise for control of release kinetics, time-resolved release of multi-components which are loaded into Me-1D. Me-meso due to the complex mesoporous nature of the sponge layer provides all advantages for mesoporous silica or titania: high free volume, time prolonged storage of even physically entrapped species.

3. "Free" and "Surface" Capsules

Mostly when one mentions capsules for delivery devices, one means "free", "classical" capsules which are used being either in the suspension or integrated into a coating. There are numbers of papers, including some competent reviews,[27] which present "free" encapsulation systems for delivery devices in their variation: different size, shape, texture, compartments, etc. In the presented review we point on "surface" encapsulation systems. There are some tendencies of "free" capsules which can be used to design also "surface" encapsulation systems. Some ideas and background are presented below.

In background of polymer "free" capsules there are two main approaches to produce polymer capsules; template-free and template-assisted techniques.[2] It is now feasible to prepare polymer capsules of diverse size, composition, morphology, and properties. Recent trend in the organization of encapsulation system is self-assembled biomimetic (Figure 1, Ic). An attractive option for the design of delivery systems is to mimic structures already present in vivo. Thus, a great deal of research has focused on the design of liposome-based systems.[28] The structure of a liposome consists of a vesicle assembled from a lipid bilayer, with an aqueous interior and a hydrophobic membrane. Lipids are readily degradable in vivo, allowing the components of the delivery system to be removed easily from the body. Vesicles templated by double-emulsion drops: confocal microscopy image of the dumbbell-shaped polymersomes containing two distinct materials in separate lumens (left); multiple vesicles-in-vesicle structures (right) are presented as the example for such systems highliting also possibility of multi-component delivery by this systems. Self-assembling during the formation of advanced systems relies on either the spontaneous ordering of molecules into engineered structures (polymer complexes, liposomes, micelles, and polymersomes) or the templated-assembly, e.g., of LbL.[2] Biological mimics, such as virus-like particles,[29] have also found application.

Various nanotechnological nanocarrier systems for cancer therapy are focusing on recent development in polyelectrolyte capsules for targeted delivery of antineoplastic drugs against cancer cells.[30] Biodegradable polyelectrolyte microcapsules (PMCs) are supramolecular assemblies of particular interest

for therapeutic purposes, as they can be enzymatically degraded into viable cells, under physiological conditions. Incorporation of small bioactive molecules into nano-to-microscale delivery systems may increase drug's bioavailability and therapeutic efficacy at single cell level giving desirable targeted therapy. LbL self-assembled PMCs are efficient microcarriers that maximize drug's exposure enhancing antitumor activity of neoplastic drug in cancer cells. They can be envisaged as novel multifunctional carriers.

Due to its versatility and ease of use the layer-by-layer (LbL) assembly technique has been under intensive investigation for delivery applications.[31] Especially the development of responsive LbL materials has advanced significantly in recent years. Responsiveness plays an important role in many delivery applications, either for loading of therapeutics or controlled and triggered release.

Nanoengineered multifunctional capsules with tailored structures and properties are of particular interest due to their multifunctions and potential applications in diverse fields.[16] The past decade has witnessed a rapid increase of research concerning the new fabrication strategies, functionalization and applications of multifunctional capsules. The advances in assembly of capsules by the LbL technique can be introduced with focus on tailoring the properties of hydrogen-bonded multilayer capsules by cross-linking, and fabrication of capsules based on covalent bonding and bio-specific interactions. The multi-compartmental capsules can transform providing advanced applications, e.g., drug carriers, biosensors and bioreactors.

Embedding of nanoparticles into "free" capsules opens up the opportunities to navigate the capsules with magnetic field and in-situ trigger the release of encapsulated material in response to the physical stimuli, such as light and ultrasound.[32]

Self-healing property is in focus. Thus capsules is obtained by adding healing agents to the material to be repaired, and intrinsic materials, where self-healing is achieved by the material itself through its chemical nature. The crosslinking chemistries used in self-healing materials is in focus.[33]

Some specific features of specifically bonded capsules can be potentially interesting for their application. For example, capsules assembled through the use of neutral or polar hydrogen bonding interactions have the ability to orient and control the position of the encapsulated guest molecules represents their stand-out feature.[34]

The field of metallosupramolecular self-assembly has emerged as a promising research area for the development of intricate, three-dimensional structures of increasing complexity and functionality.[35] The advent of this area of research has strongly benefited from design principles that considered the ligand geometry and metal coordination geometry, thus opening up routes towards rationally designed architectures. Three classes of metallosupramolecular assemblies can be mentioned: architectures formed through the combination of a single ligand and metal, heteroleptic structures and heterometallic structures.

Often a surface layer is degradable and itself can be an active layer to provide release of material or being the released material, e.g., "surface" capsules-microneedles (Figure 1, IIa). "Surface" capsules, as was mentioned above, can be formed by

surface nanostructuring and encapsulation of active species into a surface (Figure 1, IIb).

Large biomolecules, such as peptides, proteins, antibodies, and nucleic acids can be too large, fragile, or insoluble for delivery by traditional "free" capsule routes.[36] In this case the delivery into the body is desired not by oral delivery, but by hypodermic injection. A novel and mild technique for the production of microneedles for the delivery was suggested (Figure 1, IIa).[37] The "surface" needles are made of biodegradable and water-soluble polymers with the drug encapsulated in the polymer needle matrix. After application, the needle patch remains in the skin for a short time period that allows the polymer to dissolve while it releases the drug. This simple approach enables an inexpensive and fast fabrication process. Large, fragile biomacromolecules could be incorporated into microneedle matrices for successful delivery through the skin. The group of Prausnitz[38] has demonstrated the efficacy of microneedle vaccines in vivo; they showed for a mouse that a single dose of influenza vaccine with microneedles exhibited immune response superior to the same dose administered intramuscularly. Microneedles have been applied for administration of a human growth hormone.[39] It is important to achieve really access to controllable release with high efficacy profiles of drug as well as to control of the behavior of the devices under storage at various conditions to assess their robustness over time. Microneedles as "surface" capsules may be expanded to treat many disease models that are currently unexplored, including skin and breast cancers. A novel transdermal-based approach of "surface" capsule microneedles could serve as an avenue for a local and possibly systemic, yet minimally invasive, therapy.

Degradable hydrogels are another possibility for "surface" delivery. Hydrogels can be coated on the surface and be carriers for active species. Moreover available patterning techniques have been used to adjust the surface area and consequently modulate the release profiles of the biomolecules from hydrogels in a spatially resolved manner.[40] Deviation from the expected release behavior is observed when a specific stimulus – typically temperature, pH, presence of certain molecules – leads to a physical or chemical change in the network structure, for instance, hydrogels swell or shrink in response to a certain trigger thereby modulating the release of encapsulated drugs/ proteins. The techniques are effectively used for advanced applications, e.g., tissue engineering.

The other possibility in developing of "surface" capsule arrays is surface nanostructuring with the formation of a porous surface with the free volume to be loaded with active chemicals. Thus pore formation during high intensity ultrasonic surface treatment was shown for various metals.[13,14] Moreover the effective variation of the pore structure is possible through variation of parameters of sonication. Great advantage of the synthetic methodology is a large number of synthetic parameters which can be optimized to tune surface nanostructuring in a controllable manner. Our study has shown that high power ultrasonic surface treatment results from the interplay of conceptually different mechanisms. 1 – There is physical impact due to a pressure wave and a jet impinging on the surface and deep into it, while 2 – extreme temperatures and pressures create highly reactive radicals derived from the solution, dissolved gas or additive. The ultrasound-driven modification of metals in water-based solutions leads to the development of an outer surface and, following the modification of the inner structure of the metals, an increase in the specific surface area. Metal surfaces are simultaneously oxidised, and the pore structure is stabilised. We have demonstrated the potential of formation of surface metal sponges together with defined roughness variation (**Figure 6**). It is worth to note here, that the effect of erosion of the metals has long been regarded a possible damage mechanism due to high pressure, casting of metals during the ultrasonic process. Melt impingement and erosion have also been proposed to be an important step leading to soldering. The present analysis, based on existing erosion theories, has shown that the use of cavitation assisted processes for pronounced formation of mesoporous structures or any
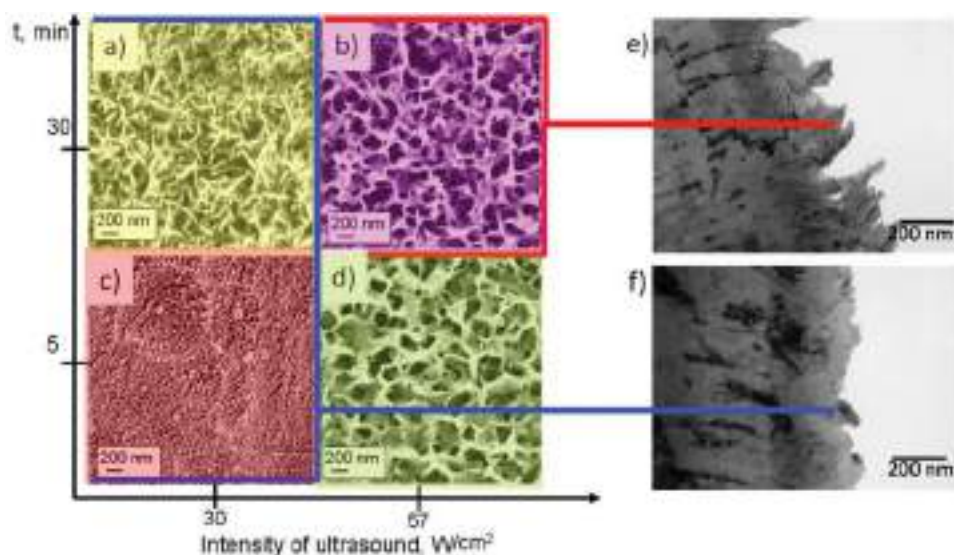
Figure 6. High intensity ultrasound for metal surface nanostructuring. Electron microscopy images of aluminium after sonochemical modification at different intensities and duration. Reproduced with permission.[14] Copyrights 2009, Royal Society of Chemistry.

www.MaterialsViews.com

ADVANCED
MATERIALS
INTERFACES
www.advmatinterfaces.de

REVIEW

pronounced metal structures, has not been shown before our recent studies. Moreover the methodology might be very interesting (see below) to provide single-step hybrids and effective loading of porous structures with active chemicals.

Another possibility is to use surface oriented nanotube arrays for delivery of active chemicals, e.g., formed by anodization. Pore formation during anodization is reported for selected metals including Al, Ti Ta, Hf, W, Zr, Nb (frequently called valve metals) and their alloys, under appropriate experimental conditions. The process is influenced by the type of electrolyte, the electrolyte concentration, pH, temperature, applied voltage and current, as well as the surface pre-texturing. Tuning the pore to nanotube morphology is possible by changing the anodization parameters.

Nanotube "surface" carriers were selected for drug delivery due to their unique features, such as low fabrication cost, controllable pore/nanotube structure, tailored surface chemistry and high surface area. Mechanical stability, chemical inertness, biocompatibility, controllable pore size and pore volumes, along with tunable surface chemistry have made nanotubes of Si, AAO and TNT an excellent platform for loading a large amount of drugs and facilitating their controlled release. Elegant work was presented by the Losic group[41] where an anodized nanotube layer is used as "surface" capsule layer. Thus insoluble drugs can be encapsulated into micelles and then micelles are encapsulated into AAO for therapeutic implants.[41a] The release kinetics from the suggested encapsulation system was especially useful in bone implant therapies that require a large initial dose followed by a prolonged dose over a few weeks. Additionally, by applying a plasma polymer film on the top of AAO, the release could be extended considerably, the burst release almost suppressed and zero order drug release kinetics over a period of more than 4 weeks was achieved.

It is very exiting that two types of micelles with different hydrophilicity can be effectively loaded into nanotubes by layer post functionalization with spatially resolved matter (**Figure 7**). Thus after growing of the first nanotube layer and its modification to make the surface hydrophobic, e.g., by silanization, the formation of an encapsulation layer for hydrophobic micelles is provided. The following further growth of the nanotube layer then provides a hydrophilic surface which can be loaded by hydrophilic micelles. The micelles can be released in a time-controllable manner. In all "surface" drug delivery is interesting because of the stimuli-responsiveness.
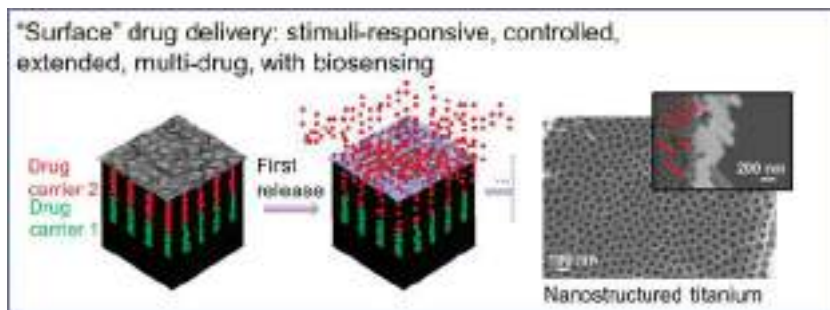
Figure 7. Example of formation of "smart" surface encapsulation system based on grown of TNT on titanium by its anodization. It is pointed the advanced features highly preferable and possible for "surface" drug delivery.

4. Engineering of Encapsulation Systems

Advanced approaches for structure engineering of interfaces/surfaces to generate new properties and applications are of high priority. The surface modifications and functionalization expanded significantly the number of applications of already developed encapsulation systems both as "free" and "surface" capsules. Thus for example some surface is chemical instable, e.g., some inorganic oxides, in acidic environment which is a disadvantage for some applications. This limitation can be overcome by changing the surface properties and by adding new surface functionalities. Emerging techniques for the fabrication and nanostructuring of capsules: self-assembly, layer-by-layer assembly, single-step polymer adsorption, bio-inspired assembly, surface polymerization, and anodisation, ultrasound assembly or structuring.

There is the strategy of the design of surface dynamic encapsulation system presented in **Figure 8**. It is suggested that the porous surface layer, e.g., meso-Me or AAO, TNT, can be encapsulation layer to deliver active chemical. Release of active chemical is prevented by LbL hybrids coating. LbL may response to different stimuli. The physical changes of the multilayers are possible. The thickness and roughness of the multilayers can be changed The mobility of the polyelectrolytes within the multilayers can be expected. Besides physical changes, chemical changes in multilayers are possible, e.g., change of pH and ion fluxes from the surface. The stimuli are preferable to varies simultaneously (i) response of dynamic layer and (ii) release of active species which provide, for example, of bio-response of adsorbed on surface microorganisms (cells, tissue, bacteria and viruses).

Surface chemistry plays a key role in targeted delivery. One of the major breakthroughs in this area was the finding of a way of surface nanostructuring for capsules for a chosen application. For example, hydrophobic capsules coated with hydrophilic polymer molecules, such as polyethylene glycol (PEG) can resist serum protein adsorption and prolong the particle's systemic circulation.[42] For the formation of delivery devices the surfaces of encapsulation systems can be nanostructured by different methods: electrochemical anodization, sonochemical methodologies, laser irradiation, etc.[18] Moreover targeted delivery is achieved by surface functionalization of capsule material with polyelectrolytes;[43] polymers to achieve mechanostereochemical[44] pore closure or coating prevented any molecule diffusion; biocompatible substances such as hydroxyapatite;[45] biomolecules,[46] such as peptides and antibodies. Thus surfaces can be modified via modification with organic molecules with the desired functionality. The surface modification techniques that have been explored to improve the surface properties and to add new functionality can be divided into two groups: wet chemical synthesis and gas-phase techniques. Examples of wet chemical approaches are self-assembly processes (silanes, organic acids), layer-by-layer deposition, sol-gel processing, polymer grafting. Gas-phase surface modification techniques used for surface
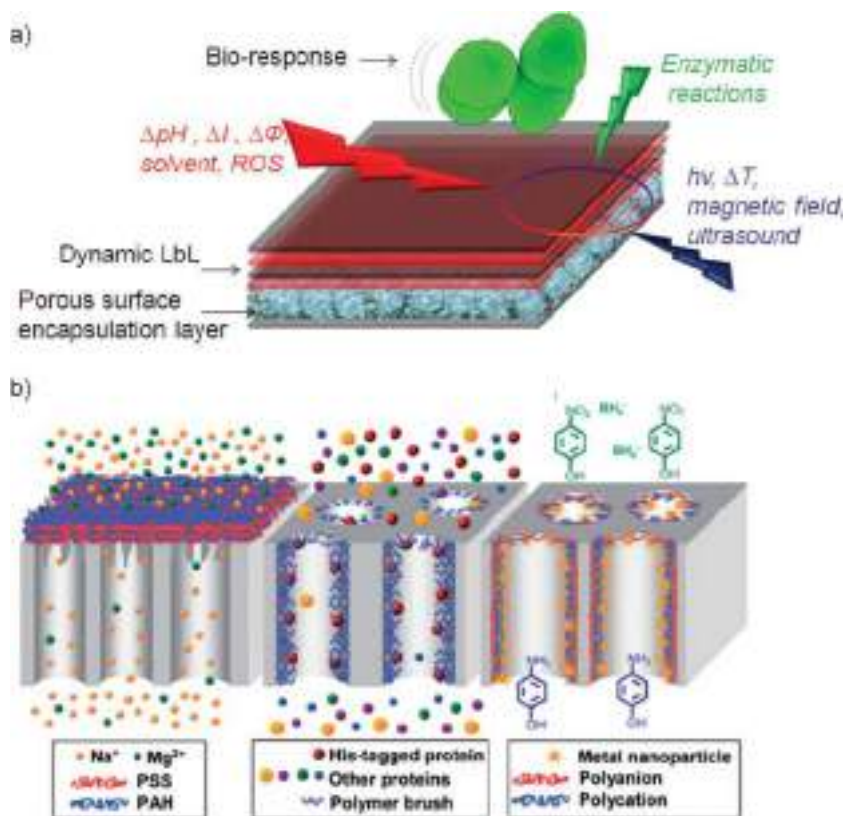
Figure 8. "Surface" capsule systems. a) Schematic of design of encapsulation system based on porous surface layer, e.g., surface metal sponge, with encapsulation into it active molecules and control the release of active molecules with dynamic layers, e.g., polyelectrolytes LbL hybrids sensitive to different stimuli, e.g., physical, chemical and biological, to provide response of cells on top of such surface. b) Nanostructuring of surface encapsulation system to regulate release behavior or sensing properties. Reproduced with permission.[9] Copyrights 2012, Royal Society of Chemistry.

modifications include thermal chemical vapor deposition, vapor metal deposition, plasma processing and polymerization.

Interfacial interactions of encapsulation systems are often manipulated with self-assembled monolayers (SAMs). There are passive and active SAMs known. Passive SAMs change surface chemistry; however does not response to any stimuli. Active SAMs are sensitive to various stimuli: physical, chemical and biological.

The first monolayer of SAMs were prepared with alkyl siloxanes,[47] and soon the coupling with thiol groups became very popular. These are able to form strong and specific noncovalent coordination bonds with gold, which result in the formation of a monolayer of thiolate molecules on a gold-coated substrate.[48] Especially alkanethiols with long, saturated, unbranched alkyl chains are known to self-assemble into well-defined monolayers on gold through both sulfur-gold coordination bonds and van der Waals interactions between alkyl chains.[49] An advantage for formation of complex multifunctional encapsulation systems is the synthetic flexibility of alkanethiols for providing various terminal groups enables presentation of a variety of ligands on a surface for tailoring surface properties.[50] Moreover the substances attached to the capsule by thiol groups can be released on demand. Release of alkanethiolates is known

to be possible by electrical potentials, both reductively and oxidatively (**Figure 9**).[51]

Alkylsilanes on inorganic surfaces are presenting hydroxyl groups. Silane derivatives with functional head groups and hydrolysable silane head groups are used for the modification of inorganic substrates bearing hydroxyl groups, including silicon oxide, quartz, glass, and oxides of various metals such as Al, Cu, Sn, Ti, Fe, Zn. The reactive functional head groups allow introduction of other compounds to the capsule surface to afford another class of widely used substrates with tunable surface properties, like SAMs of alkanethiolates on gold.[52] Silane-based modification of surfaces requires a more elaborate treatment than alkanethiolate SAMs on gold. However, alkylsilane on SiO_2 is more chemically and thermally stable than thiolates on gold surfaces due to the strong covalent linkage between hydroxyl groups on the surface and the silane head groups.

Examples of passive SAMs are PEG and poly(ethylene oxide) polyethelenoxide (PEO) systems. The SAMS are used to provide possible encapsulation systems with antifouling properties.[53] A monolayer of oligo(ethylene glycol) groups ensures that the surfaces are inert to nonspecific protein adsorption.[54] The inertness of the surface is an essential factor for biological applications using cells and biomolecules such as proteins, which tend to bind nonspecifically to any artificial surface. Passive SAMs are widely used in microfluidics, but it is becoming clear[55] that greater functionality can be provided in more sophisticated systems with the use of active SAMs that can change their surface chemistry in response to stimuli such as pH, heat, light, applied voltages, etc.
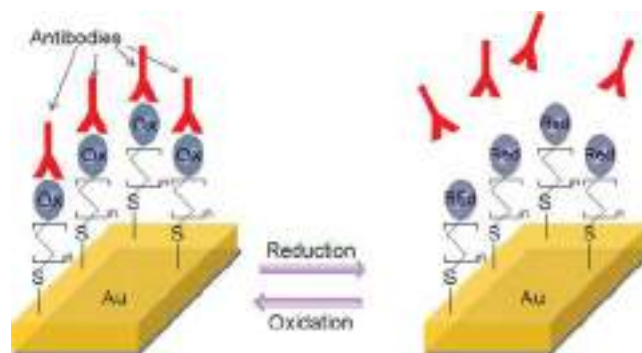
Figure 9. Stimuli for regulation of drug delivery. Electrochemical: antibodies have a high affinity for benzoquinone but not for its reduced form, hydroquinone. They can thus be reversibly attached to an electrode and released in solution through the oxidation and reduction, respectively, of the quinone moiety. Adopted from.[51] Copyright the Nature Publishing Group.

www.MaterialsViews.com

ADVANCED
MATERIALS
INTERFACES

www.advmatinterfaces.de

REVIEW

An example of a thermo sensitive active material with this switchable SAMs is an end-tethered monolayer of poly(Nisopropylacrylamide) (PNIPAM). This polymer exhibits a lower critical solution temperature (LCST), a temperature above which the polymer becomes insoluble, in water at about 35 °C.[56] At room temperature, the polymer swells in water to create a relatively hydrophilic surface with a water contact angle that can be as low as 30°. Above the LCST, the water is expelled, the polymer collapses, and the surface becomes hydrophobic in air.[57] Such systems can be effective used for delivery of proteins whose adsorption to SAMs depends on temperature. At room temperature, the adsorption of large globular proteins such as human serum albumin (HSA) is negligible on a tethered PNIPAM and is comparable to that on PEO SAMs. Above the LCST, HSA adsorption is extensive. Complete protein monolayers form at rates comparable to those seen on hydrocarbon-terminated octadecyltrichlorosilane surfaces. For large globular proteins such as HSA, complete desorption is normally observed on cooling the PNIPAM films to room temperature.

SAMs with specifically designed electroactive groups have been successfully employed to control functionalities in response to an applied potential. Especially electroactive functionalized surfaces based on the hydroquinone (HQ)/benzoquinone (BQ) redox couple have provided real-time control over molecular-level interactions between surfaces and cells or biomolecules such as peptides, carbohydrates, DNA, and proteins.[58,59] The group of Mrksich[59] reported various dynamic substrates that can electrochemically regulate interfacial interactions with proteins and cells. First, they demonstrated electrochemical release of immobilized ligands from the surface. Quinone ester groups tethered to ligands such as biotin and RGD (Arg-Gly-Asp) peptide were presented on SAMs on gold. On reduction to the corresponding HQ by an electrical potential, an intramolecular cyclization reaction ensued to give a lactone with release of the ligands. This allowed electrochemical control of specific binding of streptavidin to the monolayer and selective release of cells from the substrate on demand.[60] Mrksich et al. also introduced HQ-presenting monolayers, on which electrochemical oxidation provided BQ that acted as a molecular handle for immobilizing diene-modified molecules through Diels–Alder cycloaddition.[61] Next, they expanded their strategy to the construction of a dynamic substrate with two dynamic properties: release of one ligand followed by immobilization of another.

Azobenzene chemistry provides active dynamic modulation of surface characteristics by photoswitching by means of reversible trans-cis isomerization.[62] For example chymotrypsin delivery is possible by such a system.[63] Photochemical exposure with UV (or visible) light reversibly controls the geometry of the trans-form of azobenzene, which shows a low affinity towards chymotrypsin, or cis-form azobenzene, which strongly binds to chymotrypsin, leading to photochemical dynamic modulation of the protease binding to the surface.

o-Nitrobenzyl groups have been widely used for construction of phototriggering substrates that reveal various functional groups such as free amine and carboxylic acid.[64] Light irradiation induces cleavage of the bond at the benzylic position with the release of a caging molecule. Thus for example, Maeda and co-workers introduced a method for photoactivation of selective regions of a substrate for cell adhesion using photocleavable 2-nitrobenzyl-presenting substrate and bovine serum albumin (BSA).[65]

Benzophenone chemistry also provides photosensitive active SAMs. Under the illumination at 330–365 nm wavelength light, the photoactivation takes place repeatedly without loss of activity of benzophenone, which is chemically and photochemically robust enough to be handled in ambient light and under biological conditions. For example, benzophenone was used for photoactivated immobilization of biomolecules onto the inner wall of a capillary (internal diameter of 100 mm).[66] In the presence of biomolecules, an inner capillary surface with benzophenone that is irradiated to immobilize biomolecules can be used as a capillary bioassay system, with applications that include DNA hybridization and immunoassays. Bailey et al. introduced an approach to generate multicomponent immobilized biomolecular patterns and gradients on surfaces by sequential exposures of benzophenone -presenting substrates.[67]

Enzyme-triggered activation of surfaces is an attractive research theme in the area of dynamic substrate construction, because enzymes in living systems dictate cellular behavior and precisely control many functions of systems by performing biochemical conversions. Cutinase, a serine esterase, is one example. It can change a surface property from being redox-inactive to redox-active. SAMs of 4-hydroxyphenyl valerate-terminated alkanethiolate were treated with cutinase, and the acyl group was removed from the surface by cutinase to give HQ. The redox activity of the resulting HQ was then monitored to quantify the enzyme activity.[68] Control over surface properties has also been reported for proteolytic enzymes such as protease K, matrix metalloproteinase, trypsin, chymotrypsin, a-thrombin, and elastase.[69] Todd et al.[70] designed an enzyme-responsive surface that presented a Fmoc-protected RGD peptide precursor (Fmoc-AARGD), which prevented adhesion of cells due to poor accessibility of the RGD sequence to the integrin receptor caused by a bulky Fmoc group. Treatment with elastase broke the peptide bond between the two alanine residues, which revealed ARGD and thus activated the surface to a cell-adhesive state. Electrochemical monitoring of thrombin and trypsin activity was demonstrated by using a monolayer grafted with ferrocene-labeled enzyme substrate peptides.[71] In the presence of proteases, the electroactive reporter ferrocene was cleaved and diffused away from the surface. Analysis of the electric current signal then enables quantification of ferrocene-labeled peptides on the surface, and thus proteolytic enzyme activity can be assayed.

SAM layers can be the effective first layer for synthesis of longer functional chains to achieve a needed functionality, including multi-functionality, which was widely developed in the group of Minko.[72] Thus hybrid brushes composed of two liquid polymers, poly(dimethylsiloxane) (PDMS) and a highly branched ethoxylated polyethylenimine (EPEI), were synthesized on Si wafers by the "grafting to" method and by applying a combinatorial approach (fabrication of gradient brushes).[73] The combinatorial approach revealed a strong effect of "layer assisted tethering", which allowed us to synthesize hybrid brushes twice as thick as the reference homopolymer brushes. The hybrid brushes are stable thin films that can rapidly and

ADVANCED
MATERIALS
INTERFACES
www.advmatinterfaces.de

Materials
Views
www.MaterialsViews.com

reversibly switch between hydrophilic and hydrophobic states in water and air, respectively. The switching in water affects a rapid release of amino functional groups which can be used to regulate adhesion and reactivity of the material. The switching in air rapidly returns the brush to a hydrophobic state. The hybrid brush is hydrophilic because of two mechanisms: (1) exposure of EPEI chains to the brush-water interface under water, and (2) retention of some fraction of water via swollen EPEI chains (the EPEI chains swell by 2–3 times), which are conserved by a PDMS cap in air. The hybrid brush is wettable under water, and at the same time, the brush is nonwettable in air, because water droplets are trapped in a metastable state when the water contact angle is above 90°.

In some cases passive layers can be active due to their release from the substrate. Jiang et al.[74] prepared patterned monolayers with 1-octadecanethiols amongst oligo(ethylene glycol)-terminated alkanethiols which were inert to nonspecific adsorption of proteins and cell adhesion. Cells were allowed to selectively attach to the patterned region where extracellular matrix (ECM) proteins were coated. On electrochemical treatment of the monolayer the oligo(ethylene glycol)-terminated alkanethiolates were released and the inertness of the monolayer was compromised. ECM proteins, either in the culture medium or secreted by cells, were then adsorbed onto the surface, and cell migration took place across the entire surface.

In order for an encapsulation systems to be usable in a reversible protein trap, at least three requirements must be met: (i) the polymer used form an encapsulation system needs to be in a configuration that supports the stimuli, e.g., desired thermal, activated phase transition, (ii) the layer must be robust and strongly attached to the surface, and (iii) protein adsorption must be reversible and rapid.

Many elegant studies have been performed using the Layer-by-layer (LbL) technique.[9,10,75] The LbL deposition procedure involves the step-wise electrostatic assembly of oppositely charged species (e.g., polyelectrolytes and inhibitors or others: proteins, nanoparticles) on the substrate surface with nanometer scale precision and allows the formation of a coating with multiple functionality. The coating properties can be controlled by the number of deposition cycles and the types of polyelectrolytes used. Polyelectrolytes are macromolecules carrying a relatively large number of functional groups that are charged or could become charged under certain circumstances. The macromolecules may be polycations and/or polyanions depending on the charged groups. Depending on the degree of dissociation the polyelectrolytes can be "weak" or "strong". The LbL layers could also be hydrogen-bonded, for example poly(methacrylic acid) and poly-(vinylpyrrolidone) can be self-assembled and form multilayers due to formation of intermolecular hydrogen bonds. The response of the hydrogen bonded systems to external stimuli is due to the introduced electrostatic charges into ionisable groups within the layers.

Polyelectrolytes exhibit very good adhesion to the substrate surface. The conformation of polyelectrolytes is mostly dependent on their nature and adsorption conditions and much less dependent on the substrate and charge density of the substrate surface. Polyelectrolyte coatings are expected to cover many kinds of surfaces including non-ionic and apolar substrates.

One should have in mind that the charge of encapsulation systems, which is essential for the systems LbL modified by charged polyelectrolytes affects the functions. Thus positively charged particles have been shown to exhibit higher internalization by macrophages and dendritic cells compared to neutral or negatively charged particles.[76]

Sol-gel chemistry is known for encapsulation system nanostructuring. Thus "surface" encapsulation systems can be formed by the sol-gel assembly process. The process involves the hydrolysis of precursor solutions. The precursor solution and the surfactant play significant roles in the self-assembly process of sol-gel structures forming. The profit of using the sol-gel technique is (1) high purity materials are synthesized at relatively low temperature, (2) homogenous and multi-component structure are obtained by mixing precursor solutions and (3) processing parameters can be controlled allowing the synthesis of materials with different properties such as structure, thermal stability and surface reactivity (using precursors with additional functional groups).[77] An example can be the work of Yamaguchi et al.[78] They employed a rather simple fabrication procedure of spotting precursor solutions containing cationic cetyltrimethylammonium bromide as structure directing agent and tetraethoxysilane as the silica source onto the anodized aluminum surface, and obtained aligned and columnar ordered silica nanochannels.

To provide sustained release of poorly soluble drugs from implants, extended drug release based on applying a thin plasma polymer film on the top of nanotubes arrays after drug loading.[79] A plasma polymer layer with different thickness deposited on nanotube arrays allows control over pore diameter and hence rate of drug release. It was possible to achieve favorable zero order release kinetics from AAO implants by controlling the deposition of a plasma polymer layer.

Self-ordering and biomimetics are of high relevance for synthetic chemistry, including in the development of encapsulation systems. The most significant feature of nature-designed structures is their multifunctionality and creation through unique genetically guided self-ordering, -organization, -assembly processes. The spontaneous organization of small individual subunits into larger scale ordered and stable structures, is ubiquitous in nature.[80] Self-assembly and self-organized (or self-ordered) fabrication processes are recognized as cost effective, and the most elegant route in nanotechnology leads to the generation of complex and functional nanostructured materials.[81] Several synthetic approaches based on chemical, electrochemical, sol–gel and hydrothermal methods involving self-organization have been explored for their synthesis using both top-down and bottom-up approaches.[82]

Using one inspirational system one can come up with a set of new approaches to the synthesis of materials at the hierachical scale. Thus echinoderms, provide new approaches to the synthesis of ordered, oriented crystalline materials at the nanoscale. The same organism also inspires the design of tunable nano- and microlens structures. The novel, hybrid hydrogel-actuated nanospines and nano traps act similar to echinoderm skin. One can also consider how to generate unusual chirality on the assembly.[83] These bioinspired structures have the potential for use in a variety of fields, including actuators for controlled release, self-healing artificial muscles.

Obviously, echinoderms provide new, bioinspired concepts in materials chemistry, nanotechnology, and engineering.

Diatom structures, e.g., silica based structures as well as titania, are important for development of capsules for delivery devices. For the time being diatoms have enormous ecological importance on this planet and display a diversity of patterns and structures at the nano- to millimetre scale. Diatoms are unicellular, eukaryotic, photosynthetic algae that are found in aquatic environments. Diatom nanotechnology for capsules emphasizes recent advances in diatom biomineralization, biophotonics, photoluminescence, microfluidics, compustat domestication, multiscale porosity, silica sequestering of proteins, detection of trace gases, controlled drug delivery and computer design.[84] More sophisticated drug-delivery systems, such as self-propelled swimming microrobots, could also benefit from the unique properties of diatom frustule structures.[85] Designing of microdevices that can travel inside the human body and carry out a range of complex medical procedures, such as monitoring, drug delivery and cell repair[86] is discussed. Recent developments in micro- and nanoscale engineering have led to the realization of various miniature mobile robots, but one can have an intriguing opportunity to integrate whole biological organisms or their parts.[87]

Porous structures from the molecular to the macro-level are widely used in nature.[88] These pore structures with their elegant and intricate designs have played pivotal roles in many biological processes. These processes include transport of nutrients through the cell wall, selective transport of small or specific molecules or solutes, energy or charge transport, gas adsorption, ion exchange, signalling, and many other activities. It is therefore not surprising that the concept of mimicking porous, complex structures has attracted a considerable amount of attention in materials science. Important are the control of the free volume and shape arrangements.

Shape of capsules and parts for delivery device have come into focus next. First capsules of interest were mostly spherical in shape. However, the biological world is mostly non-spherical in shape. The peculiar shape of the different biological entities plays an important role for their function.[89] Bacteria and viruses exhibit a variety of peculiar shapes. For example, rod-shaped *Escherichia coli* and *Tobacco mosaic* virus and *Bacillus anthraci*, spiral-shaped *Campylobacter jejuni*, and bullet-shaped *Rabies* virus.[90] This initiates also studies of capsules which are not spherical in shape or with complex pore organization. The major problem in performing experiments with particles of different shapes was the difficulty in their fabrication. However, with recent advances in materials science and technology, this limitation is being addressed. Some of the methods for fabrication of anisotropic shapes include self-assembly,[91] lithography,[92] nonwetting template molding,[93] microfluidics,[94] and sonochemical synthesis.[14,95]

Some examples of anisotropic particles that have been already fabricated include PEG-based trapezoids, bars, cubes, cones, discs, cylinders, and many other shapes fabricated by the top-down particle replication in nonwetting template technology.[96] Dendukuri et al. have developed a high through put continuous-flow lithographic technique that combines the advantages of microscope projection lithography and microfluidics to form morphologically complex polymeric particles

suitable for encapsulation systems of a variety of different shapes. Some of the shapes generated by this technique include rings, triangles, cylinders, cuboids, polygonal structures, and curved particles.[97] Various shaped particles bearing segregated hydrophilic and hydrophobic sections have also been synthesized using the same technique.

Here again we can show that the sonochemical nanostructuring (sononanostructuring) is very prospective, as it enables modification of many different materials (Figure 2). But also the shape and texture of the resulting material can be manipulated,which in the following will be shown to be very prospective for encapsulation systems for "free" and "surface" capsules. Thus zinc particles, could be used to form a core@shell "hedgehog" zinc-based material by a "green" ultrasound method.[95] The core@shell "hedgehogs" consist of a metallic zinc core covered by zinc oxide nanorods. Due to the "hedgehog" morphology, the novel zinc-based material exhibited increased surface area, high accessibility for substrate molecules and could be a promising component of sensors, catalysts, active feedback coatings, and photovoltaic systems.

A direct replica method enabled to synthesize an array of plastic micro-objects of different shapes, such as cones, bicones, hollow cylinders, rings, test tubes, clubs, and vases. Dimethyl formamide-based colloidal nanoparticles with tunable size and shape have been fabricated by wet chemical methods.[98]

Such complex shaped capsules with diverse physical features will open up new avenues in engineering carriers for drug delivery and imaging. They can also be used as models to study the importance of shape in biological functions of organisms, such as bacteria and viruses, since the film stretching method can efficiently mimic many peculiar shapes exhibited by biological entities.

To go back to our strategy to use high intensity ultrasound as prospective for the formation of "surface" encapsulation systems, not just for the modification of individual materials (Figure 2), but simultaneous formation of advanced hybrid systems on example of formation special metal-polymer interaction by sonochemical intelligent nanoengineering.

Since the early work of Lord Rayleigh it is known that ultrasound may form cavitation bubbles inside liquids. Upon bubble collapse transiently temperatures more than 5000 K, pressures higher than 1000 atm with cooling rates above 10^8 K/sec are created.[99–101] Hence there is the potential of performing high temperature and high pressure chemistry, but with a reactor near room temperature and ambient pressure. Structures may also be formed and quenched far from equilibrium. The most pronounced effects of ultrasound on liquid–solid systems are mechanical and chemical, and these effects are attributed to symmetric and asymmetric cavitation collapses. Recent modelling has confirmed that symmetric bubble collapse in a liquid medium causes shock waves with high pressures in addition to high gas temperatures in the collapsed cavities. These high-pressure, high-temperature conditions exist for short time, however being enough for active surface modification. Such extreme conditions can be effectively used for active surface construction.[13,14,100]

Shock waves also potentially create microscopic turbulences.[101] This phenomenon increases the transfer of mass across the solid, thus increasing the intrinsic mass-transfer

ADVANCED
MATERIALS
INTERFACES
www.advmatinterfaces.de

Materials
Views
www.MaterialsViews.com

REVIEW

coefficient, as well as possibly creating or modifying existing coatings, such as thick hybrid metal/polymer coatings.[102] Alternatively, this phenomenon may result in thinning/pitting of the film.[103] When the bubble collapses occur near a solid surface that is several orders of magnitude more extended than the cavitation bubbles,[104] the collapses occur asymmetrically[105] and solvent microjets are formed perpendicular to the solid surface. These microjets have an estimated speed of ca. several hundreds of m/s and lead to pitting and erosion of the surface.[106] Moreover, this behaviour leads to an enhancement in heterogeneous reactions (secondary cavitation-assisted processes) with active species formed in the reactor. Thus, a part of the vaporised molecules from the surrounding medium can be dissociated to form radical species, such as OH• and H•, for water sonolysis.[107] The radicals form by the hydrogen abstraction of RH additive molecules to form R• and/or by the pyrolysis of RH molecules during bubble collapse.[108] Recent studies[109] have suggested scenarios and provided prospective defined cavitation pathways for surface modifications based on their responses to ultrasound. Different responses result from differences in the surfaces' hydrophilic/hydrophobic properties or chemical reactivity. Thus, comparison of bubble formation on hydrophobic and hydrophilic surfaces with those formed in the bulk reveals a stronger response on the hydrophobic part of a patterned surface than on the hydrophilic part. If a surface changes its hydrophilicity/hydrophobicity during a sonochemical process, it is clear that the surface response to ultrasound becomes nonlinear.

The presence of monomer or polymer molecules in the sonochemical reactor can influence the cavitation process. Organic molecules are able to accumulate at the gas/liquid interface of cavitation microbubbles. The centre of the bubble exhibits high temperatures and pressures, whereas the bulk liquid remains under normal conditions. A transition zone also exists between these two states.[102]

Molecules are present in both the transition zone and the outer liquid phase. The time required for the orientation of long-chain molecules in the gas/liquid interface is longer than that required for short-chain molecules and longer than the bubble lifetime.[110] However, organic molecules near the bubble interface influence the cavitation process, which increases surface pressure, decreases the lifetime of the cavitation bubble, and leaves the molecule in the correct orientation and chemical state for transport and attachment to the surface.[111] Five main effects of cavitation are known for monomers and polymers: the formation of free radicals during the cavitation process,[112] possible polymerisation,[113] possible chain reorientation,[114] polymer decomposition[115] and the possible involvement of organics in chemical processes, such as oxidation and bond breakage.[24]

Despite the great interest in the prospective field of controlling the metal–polymer interactions by high-intensity ultrasound through cavitation-assisted processes, a general lack of knowledge persists about such processes. A few reports have concentrated on the characterisation of the chemical interactions between metals and untreated polymer surfaces, and a few others have concentrated on plasma-treated polymer surfaces. From the studies on untreated polymer surfaces, several general observations can be made. Typically, for polymers that do not contain carbon–oxygen or carbon–nitrogen functionalities, little to no chemical interaction is observed, irrespective of the reactivity with metal.[116] For reactive metals, such as Al, Mg, Cr, and Ni, extensive chemical interactions can occur, typically with oxygen atoms in oxygen-containing polymers.[117] For metals with moderate chemical reactivity, such as Cu, Ti and Ag, chemical interactions were found to be polymer dependent.[118] Thus, for example, titanium is interesting to study because its moderate chemical reactivity allows discrimination between weakly and strongly interacting nucleation sites on the polymer surface.

Figure 10 shows a schematic representation of the main initial surfaces and some hypothesised consequences of sonochemical surface modification. Three main possible methods of metal-polymer interaction have been postulated: 1) the attachment of polymer molecules to metal surfaces or thin metal-oxide layers on the metal; 2) the formation of a hybrid, which simultaneously interacts with and modifies the metal, and polymer or monomer attachment with subsequent polymerisation, or monomer polymerisation and subsequent polymer attachment; 3) the formation of a thin hybrid layer on the metal surface and the subsequent attachment of the polymer (either initially present or formed from the monomer during the process of sonication).

Many fundamental aspects of cavitation-assisted processes during surface modification are still unclear, and in situ investigations, together with a detailed study of each type of material and the prospects for their combinations, are necessary to elucidate the details of these reactions. The following central problems have been identified:

– To arrive at a mechanistic model of cavitation-assisted processes on solid surfaces. Physico-chemical properties of the surface are relevant for the surface's response to ultrasound-assisted modification. Only a few authors have suggested models for a given type of material and its combination with other materials.

– To distinguish relationships between the primary and secondary effects of ultrasound, depending on the mechanical material properties and crystallinity. One might expect (and some results have already shown) that hard and soft metals exhibit different visible responses to ultrasonic exposure and can be building blocks for novel materials. Polymers are expected to exhibit a stronger response than hard materials such as Ti. For soft materials with low thermal conductivities, local heating during ultrasonic processing may lead to a decrease or, oppositely, an increase in surface roughness because high local mobility may enable surface tension to flatten the surface. The bubble collapse causes hot spots, and the pressure pulses are also converted into heat; these effects may induce local melting. Thus, a crystalline surface may locally melt and become amorphous after cooling, as has been observed for biopolymers. Reactive species may be created in the solution and in the solid, which may cause a metal to oxidise deeper inside the solid or a polymer to be destroyed or cross-linked. Concerning the influence of polymer surfaces, we have observed that ultrasonic treatment may render a surface hydrophobic/hydrophilic.

– To localize the effect of ultrasound. Thus, bubble nucleation may be controlled through patterning. A pressure pulse on
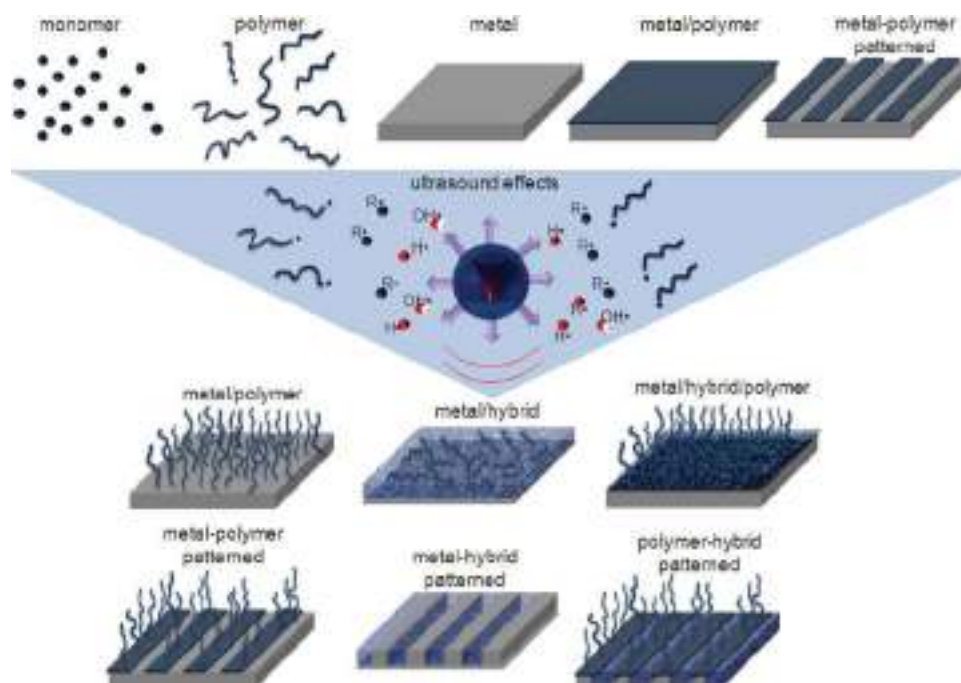
Figure 10. Schematic presentation of the research objects containing the material combination (individual not shown): initial materials – monomer, polymer, metal, metal/polymer, and metal-polymer-patterned surface – UPPER part; possible ultrasonic effects in the reactor – physical (shock waves and liquid jets) and chemical (formation of radicals from monomer and polymer and sonolysis of the liquid (here, water shown)) – MIDDLE part; and some examples of systems which could be expected after applying ultrasonic exposure: polymers could be attached to the metal (here shown as a brush formation on the surface); the metal and polymer could form a porous hybrid system; on the surface of a metal, a thin hybrid (metal/polymer) layer could be formed with subsequent polymer attachment to the hybrid (here, brush formation is shown); and in the case of an initial patterned surface, the combination of approaches is possible – LOWER part of the scheme.

a material may be focused on defects or grain boundaries. This fact necessitates the study of solids with a defined microstructure. Whether destruction proceeds along patterns, defects and grains is also relevant.

– To follow the kinetics of sonochemistry in complex multicomponent systems. A solution to this issue is still unclear, but a solution is necessary because materials can be obtained with drastically varying hydrophilic/hydrophobic properties, roughness, porosity, crystallinity and, in the case of hybrids of metals and biopolymers, different nonlinear acoustic responses. The facts that the surface is made more hydrophobic or hydrophilic by ultrasound and that this further influences bubble nucleation may have interesting consequences for the time and space dependence of the treatment: the dose dependence becomes nonlinear and surface and gas specific and patterns can be reproduced with enhanced contrast to have, for example, defined protein/surface adhesion.

– To control the modification of the surfaces via the concentrations of additives in the system (monomer, polymer) and to establish the role of initial cavitation in acoustic droplet vaporisation in different solutions.

– To define intermediate steps of the process. If intermediate states of destruction resembling a porous solid can be produced, then new active surfaces may also be produced.

– To provide scenarios of active surface construction based on pronounced responses of the metals and polymers to ultrasound. These are required for implants connected to

bone, metals (alloys of titanium and magnesium), and they therefore must be investigated for the possibility of controlling their structure and influencing the treatment (with or without additives in the system) of their surfaces. Protein and cell adhesion must also be investigated with respect to their interactions with a surface. Implants with the possible ability of sustained drug delivery due to the use of metals or hybrids with defined porosity for active chemical (such as drugs) storage and release by an internal (such as Mg dissolution) or external stimuli (pH, temperature, light) need further study. This research area is obviously very promising with respect to stem cell research.

In summary, ultrasonic chemistry carries many exciting prospects but is in its infancy with respect to our understanding and control of the process, which necessitates a multidisciplinary approach that combines interface and colloid science, acoustics, inorganic, physical and polymer chemistry, and other disciplines for specific applications. Concerning the latter, the focus in the following is laid on biomaterials and construction of hybrid materials. Moreover, to have real progress in fabricating intelligent materials, e.g., capsules, design by certain methodology (high intensity ultrasonic one), it is of high priority to have strong collaboration between different scientific fields. Thus after enough data concerning the effect different materials is collected, this might stimulate theoretical treatment and simulations. In **Table 1** are presented some possible starting points[119] for future simulations of high intensity

Table 1. Hierarchical-multiscale: examples of simulations of interaction between cavitation bubble and metal / metal-polymer / polymer / hybrid surface.

Hierarchical-multiscale	Electronic state	Atomic scale	Pseudo-particles	Continuum theory
Possible calculation methods	– quantum mechanics chemical reactions thermodynamic properties	– kinetic Monte Carlo molecular dynamic	– lattice Boltzmann method	– constitutive electric-plastic metal deformation –FEM –FFT
Some important parameters	Reaction products, chemistry of cavitation-assisted processes	Orientation of crystal, anisotropy, kinetics of defect, nucleation, roughness, porous formation	Penetration of liquid and gases inside-outside the formed porous structures, density and viscosity of liquid	Roughness (R), temperature, pressure, nature of metal / metal-polymer/polymer/hybrid (lattice parameters, phase diagram, nature of local bonds, elastic properties, patterns, defects)

ultrasonic treatment for metal surface modification needed to design hybrid materials by different pathways, such as presented in **Figure 11**. In particular hierarchical-multiscale examples are presented of simulations of interaction between cavitation bubbles and metal/metal-polymer/polymer/hybrid surfaces. Thus for each hierarchy level different theories can be applied: electronic state; atomic scale; pseudo-particles and continuum theory. Possible calculation methods are shown as well as some important process parameters are pointed out. One could imagine the very high level of cooperation which is needed between different groups to establish real progress in intelligent materials design with deep understanding of the process of construction of intelligent materials.

5. Materials for Capsules

Nowadays a wide variety of available materials are suitable for use as delivery devices. One must take into account the needed application to select one of the systems for encapsulation. In some cases polymer capsules are needed: synthetic or natural polymers for encapsulation systems. However in other cases, e.g., "free" capsules to be introduced into anticorrosion coatings, long term mechanical stability of capsules is needed and either mesoporous inorganic materials are used as main component to deliver active chemicals or hybrids of inorganic/polymeric materials are used for capsule construction. Oxides, calcium carbonate and other ceramics are known to be used as capsule cores to store in their porous interior active chemicals and deliver active chemicals to a desired area. Silicon formation and modification for encapsulation systems are known especially for systems where advanced properties of luminescent silicon are needed. Carbon based structures are used as mechanically stable light weight material. Metal based structures are developed for delivery devices. More often, as was already mentioned above, to have intellectual encapsulation systems post functionalization of individual materials is needed, for example to provide pore closure. After modification the final capsules in most cases consist of a hybrid mixture of components used for capsule formation. A separate topic for cell related application is cell encapsulation or bio-production of capsules by cells. In the following chapter we will mention some specific examples of different systems.

5.1. Polymer Capsules

Polymers as materials for the formation of "free" hollow polymer capsules are the most established class of materials.The variation of known and available systems is amazing: at least one paper was published every day during last year with mentioning the keyword "polymer capsule". This is because different applications, e.g., different drugs delivery, sensors, reactors, templates, catalysts, are besides need in require variations of size, composition, morphology and, specific polymers. The use of synthetic polymers offers the opportunity to fine tune their chemical structure to achieve a modular release, which is an advantage for the intelligent encapsulation systems. Natural polymer networks can be also tailored, but just to some extent by changing polymer concentration and crosslink density. Development of hybrid networks in which natural polymers are synthetically modified or combined with synthetic polymers, has been proposed to combine beneficial properties of both kinds of polymers with respect to mechanical properties, tailorability in terms of biodegradability as well as biocompatibility and cytocompatibility.

Very powerful and an increased area of scientific interest, for example for "surface" capsules, are hydrogels to be used for encapsulation systems. The possibility to tailor the release kinetics of proteins from hydrogels can be achieved through the use of excipients or by changing the crosslinking density of the polymer network. The geometry of the hydrogel-based depot also affects the release rate and the duration. Generally, the bigger the device, the longer the diffusion distances and the longer the release consequently lasts.

5.1.1. Synthetic Polymers Systems

Interesting as capsule materials are advanced nanoengineered polymers which can provide capsules with advanced additional functionality via their structuring and functional characteristics. Examples are in the area of conductive polymers, such as e.g., polypyrrole, polyaniline. Electrically conducting polymers have been the subject of continuous research and development due to their potential applications in many technological areas such as rechargeable batteries, sensors, electromagnetic interference shielding, electrochromic display devices, smart windows, molecular devices, energy storage systems, membrane gas separation, and so on.[120]
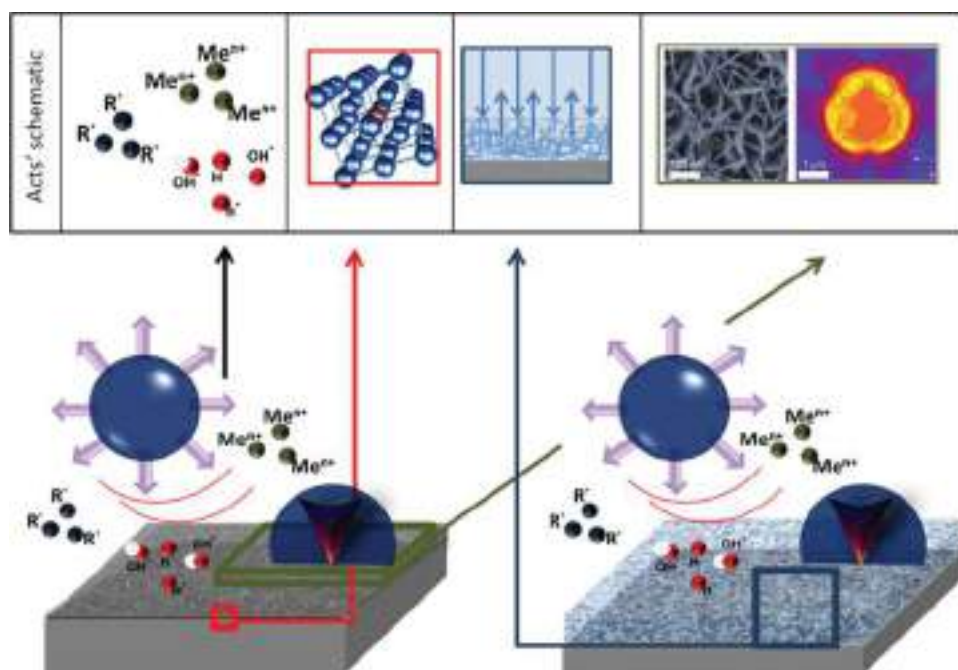
Figure 11. Schematic presentation of the possible objects for simulation. The ultrasound affects the initial and modified materials differently, i.e., non-linear response to cavitation assisted processes is observed. Upper part shows examples of possible to simulations systems in hierarchical-multiscale. Start point (upper row, right images) can be continuum theory as comparison of R experimental (obtained with in situ setup) with R simulated; and on the origin of deformation-induced rotation patterns below cavitation jets as indents.

Polypyrrole microcapsules were successfully prepared by electrochemical polymerization of pyrrole on the surface of stainless steel electrodes.[121] The size of the capsules and the thickness of the polypyrrole shell (up to complete filling of the capsule with grown polypyrrole) can be varied by changing both the scan speed of the electrode potential and potential range. The polypyrrole shell of the microcapsule exhibits very strong barrier properties in acidic media at 2 < pH < 7 and a high permeability at pH > 7, providing effective encapsulation of low molecular weight species at low pH values. The capsules can be used on the surface of "steel" providing a "surface" encapsulation system or being detached from the steel as "free" capsules.

Intensive works with some other polymers are known due to their unique properties providing in the following capsule functionality and stimuli response. Poly(N-isopropylacrylamide) (PNIPAM)[122] is known to open capsules in response to several stimuli: pH, T. Among the various synthetic polymers studied for the delivery of growth factors in tissue repair, PEG-based networks play a prominent role.[123] Mostly studied for LbL systems are such synthetic polymers as poly(styrene sulfonate) sodium salt (PSS), poly(ethyleneimine) (PEI), poly(allylamine) (PAH), poly(diallyldimethylammonium) chloride (PDADMAC), poly(meth)acrylic acid (PMA/PAA). The synthetic polymers are used in their different combination to achieve the needed functionality. Here the detailed work on the combination of "week-week", "week-strong", "strong-strong" polyelectrolytes for self-healing LbL can be mentioned.[124]

Microgels/nanogels possess high water content, biocompatibility, and desirable mechanical properties.[125] They are crosslinked polymeric particles, which can be considered as hydrogels if they are composed of water soluble/swellable polymer chains. They offer unique advantages for polymer-based drug delivery systems: a tunable size from nanometers to micrometers, a large surface area for multivalent bioconjugation, and an interior network for the incorporation of biomolecules. Present and future microgel applications require a high degree of control over properties. They include stability for prolonged circulation in the blood stream, novel functionality for further bioconjugation, controlled particle size with uniform diameter, and biodegradability for sustained release of drugs for a desired period of time and facile removal of empty devices. Nowadays various synthetic strategies for the preparation of microgels/nanogels are known, including photolithographic and micromolding methods, continuous microfluidics, modification of biopolymers, and heterogeneous free radical and controlled/living radical polymerizations.

In all it is important to know that for a particular application a particular system should be chosen and adapted, for example allowing to go from in vitro to in vivo study.

5.1.2. Natural Polymers for Encapsulation Systems

Natural polymers offer a degree of functionality not available for many synthetic polymers, such as tailorability in terms of biodegradability as well as biocompatibility and cytocompatibility. There is a large number of systems based on natural polymers available today. Some examples are presented below. The main classes of natural polymers studied formulations are polysaccharides, proteins/polypeptides, DNA, liposomes.[126] Examples of polysaccharides used for capsule formation are chitosan,[127] dextran,[128] alginate,[129] hyaluronic acid.[130]

Chemistry offers tools to modulate the structure of natural polymers without a negative effect on their advanced properties. Thus even after extraction and some modification one can use, e.g., silk protein, for advanced encapsulation systems with bio-fuctionality.[131]

Natural polymers are especially prospective for tissue engineering and other bio-applications, e.g., for the physical encapsulation of growth factors. Taking hydrogels as example, hydrogels designed with natural polymers as building blocks display multiple advantages over synthetic polymer networks with respect to their biocompatibility, biodegradability and good cell adhesion properties. Therefore, extensive work is available on biopolymer-based hydrogels for cell and growth factor encapsulation in regenerative medicine.[132]

Lipids and lipopolymers self-assembled into biocompatible nano- and mesostructured functional capsules offer many potential applications in medicine and diagnostics.[133]

5.2. Inorganic Materials

Inorganic materials are extensively used to provide encapsulation systems: from hollow particles to, which is mostly the case, porous substances to encapsulate and store active chemicals. Here again functionality of the inorganic material and its following nanostructuring, e.g., SAM or LbL, provide space for capsule optimization taking into account needed properties and functionalities. Thus capsules can be controlled in vivo, which is very important for material circulation in the body, by loading of mesoporous luminescent Si with the drug.[134] Capsules can be dissolved without negative effect to the body: $CaCO_3$ for delivery of insulin,[135] magnesium[24] biodegradable implants.

5.2.1. Oxides, Calcium Carbonate and Other Ceramics

Oxides are extensively used for formation of delivery devices. Thus mesoporous silica provides an excellent matrix for guest molecules, due to several attractive features among their textural and chemical properties, which play an important role in the loading and release of molecules, i.e., they govern the host-guest interactions between the bio-ceramic matrix and organic guest.[44] The SiO_2 for capsules provides a combination of structural, mechanical, chemical and optical features that might both overcome challenges associated with conventional delivery of therapeutic agents and have advantages over existing delivery systems. Among the important characteristics, these materials present high surface area (ca. 1000 m^2g^{-1}), large pore volume (ca. 1 cm^3g^{-1}), regular and tunable mesopore diameter (2–50 nm) and pore channel systems homogeneously organized in 2D and 3D mesostructures,[136] biocompatibility and biodegradability of silica based capsules make them a promising biomaterial for drug-delivery applications. They can be easily functionalized, protected and designed for controlled drug release through nanosized pores or by embedment in the silica.[137] The preparation of ultra-high-purity and fraction-free silica capsules from raw material is possible using simple separation procedures. These microcapsules are proposed as excellent natural porous materials for delivery applications.

Magnetic particles such as iron oxide nanoparticles find many applications as contrast agents, in magnetic cell sorting, and immunoassays in pathology laboratories.[138] For example recently it was shown to use polymer-shelled magnetic microbubbles on the interplay of shell structure with low- and high-frequency mechanics of multifunctional magnetic microbubbles.[139] Efforts are underway to develop magnetic particles for controlled and directed transport of therapeutics as well as hyperthermia treatment for cancerous tumors.[140]

5.2.2. Silicon Formation and Modification for Encapsulation Systems

Porous Si exhibits a number of properties that make it an attractive material for controlled drug delivery applications. Subsequently, porous Si or porous SiO_2 (prepared from porous Si by oxidation) host matrices have been employed to demonstrate in vitro release of the steroid dexamethasone, ibuprofen, cis-platin, doxorubicin, and many other drugs.[141] With a free volume that can be in excess of 80%, porous Si can carry cargo such as proteins, enzymes, drugs or genes. It can also carry nanoparticles, which can be equipped with additional homing devices, sensors, or cargoes. The tailored pore sizes and volumes that are controllable from the scale of microns to nanometers; a number of convenient chemistries exist for the modification of porous Si surfaces that can be used to control the amount, identity, and in vivo release rate of drug payloads and the resorption rate of the porous host matrix; the material can be used as a template for organic and biopolymers, to prepare composites with a designed nanostructure; and finally, the optical properties of photonic structures prepared from this material provide a self-reporting feature that can be monitored in vivo.

Usually porous Si is prepared by electrochemical etching. Thus porous Si is a product of an electrochemical anodization of single crystalline Si wafers in an aggressive hydrofluoric acid electrolyte solution. Pore morphology and pore size can be varied by controlling the current density, the type and concentration of dopant, the crystalline orientation of the wafer, and the electrolyte concentration in order to form macro-, meso-, and micropores. Pore sizes ranging from 1 nm to a few microns can be prepared.

The group of Sailor with co-workers[142] showed the prospects of post-anodization ultrasonic treatment of silicon to provide detachment of mesoporous luminescent layers/microparticles with their following use for drug delivery. A procedure for generating colloidal suspensions of Si that exhibit luminescence, attributed to quantum confinement effects, was described. Samples of n- or p-type Si that have been electrochemically etched to form porous Si can be ultrasonically dispersed into methylene chloride, acetonitrile, methanol, toluene, or water solvents, forming a suspension of fine Si particles that luminesce. Transmission electron microscopy analyses show that the Si particles have irregular shapes, with diameters ranging from many micrometers to nanometers. Luminescent, composite polystyrene/Si films can be made by the addition of polystyrene to a toluene suspension of the Si nanoparticles and casting of the resulting solution onto a glass

slide. Simultaneously the prospects of sonochemical treatment of luminescent microparticles in different solvents to change their luminescent nature were shown.

Recently a concept of sonochemically regulated construction of submicron and micron porous silicon with unique mechanical, optical and drug delivery properties as initial material micron-Si particles, crystalline, or amorphous, p- or n- type, were suggested.[143] An experiment on ~100 μm particles of silicon proved the formation of nanocrystalline Si and its subsequent phase transitions (crystalline–amorphous–crystalline) without oxidation in water solution in the presence of hydrogen donor material. Thus the 10-min-sonicated particles exhibit a pronounced crystalline structure, and their size decreases to the submicron scale. The amorphisation of the particles is observed within 20 min of modification. Further exposure (>30 min) causes well-pronounced crystal growth from the amorphous phase in addition to a further size decrease. The observed phase transition (crystalline ↔ amorphous) is probably the main factor responsible for ultrasound-assisted modification of silicon. Special conditions provided by high-intensity ultrasound could affect the melting and growth of the silicon crystals. The form of a solidified microstructure can be controlled by fast local heating and cooling cycles provided by cavitation. The crystal formation depends upon the difference between the rates of attachment and detachment of atoms at the interface. The rate of attachment depends on the rate of diffusion in the liquid and is, therefore, affected by sonication.

5.2.3. Carbon Based Structures

Carbon-based encapsulation systems attract particular interest, since they are chemically inert, but can be surface-functionalized for the grafting of active chemicals: nucleic acids, peptides, and proteins. Moreover such systems can be loaded with other active chemical, providing multi-loading capacity. Thus, carbon nanotubes,[144] fullerenes,[145] graphene[146] and nanodiamonds[147] have been studied for drug delivery.

The size, geometry, and surface characteristics of single-wall nanotubes (SWNTs), multiwall nanotubes (MWNTs), and C_{60} fullerenes makes them appealing for drug carrier usage. SWNTs and C_{60} fullerenes have diameters on the order of 1 nm, about half the diameter of the average DNA helix. MWNTs have diameters ranging from several nanometers to tens of nanometers depending on the number of walls in the structure. Fullerenes and carbon nanotubes are typically fabricated using electric arc discharge, laser ablation, chemical vapor deposition, or combustion processes. The application of these nanomaterials in the fields of vaccine delivery, gene delivery, small molecule transporters, and targeted delivery is being explored.

5.2.4. Metal Based Structures

"Surface" encapsulation systems, mentioned above, are built on the surface of mesoporous sonochemically treated metals[13,14] or anodized structures[41] and are prospective for such applications as implants, lab-on-chip and organ-on-chip growth, formation of anticorrosion and antifouling surfaces.

Moreover when linked to or embedded within polymeric drug carriers, metal nanoparticles can be used as thermal release triggers when irradiated with infrared light or excited by an alternating magnetic field.[148] Biomolecular conjugation methods of metals include bifunctional linkages, lipophilic interaction, silanization, electrostatic attraction, and nanobead interactions.[108]

Gold nanoparticles have received great attention in the synthesis of multifunctional drug delivery carriers due to the unique capability of attachment of thiol-derivatized molecules.[48] Not only can gold nanoparticles be decorated with a targeting ligand, hydrophilic polymers such as PEG for imparting stealth properties and therapeutics (drug or nucleic acids), but they can also be imaged using contrast imaging techniques. Moreover, once the gold nanoparticles are targeted to the diseased site, such as tumor, hyperthermia treatment can be used for tumor destruction.

5.3. Composites and Hybrids

It is clear that a variety of particle platforms have been developed for a wide spectrum of applications, and they have unique advantages and limitations. Combinations of materials have also been developed to benefit from the advantages of various materials while addressing the limitations of these materials. For example, inorganic nanoparticles possess unique optical and magnetic properties, but lack favorable bulk mechanical properties and surface processing characteristics. In contrast, polymeric particles offer flexibility with respect to manipulation of surface chemistry, bulk mechanical properties, and particle geometry.

Core@shell particles with an inorganic core (quantum dots, iron oxide nanoparticles) and polymeric shell have been developed, which can be used for therapeutic delivery and imaging.[149] Additional functionalities, such as luminescence of the core, can be easily introduced. Similarly, $CaCO_3$-polystyrene composites have been developed where $CaCO_3$ provides required strength and polystyrene provides compatibility.

Liposomes and polymeric nanoparticles are the two most widely researched drug delivery platforms. Attempts have been made to combine the advantages of both systems. For example, polymeric nanoparticles have been encapsulated within fusogenic liposomes to regulate the intracellular pharmacokinetics of gene-based drugs by protecting them from enzymatic and hydrolytic degradation.[150]

The group of Zhitomirsky[151] has made progress in constructing effective chitosan composite encapsulation systems. They use electrophoretic deposition for the fabrication of chitosan-carbon nanotube-hydroxyapatite and hydroxyapatite-$CaSiO_3$-chitosan composite encapsulation systems. The use of chitosan enabled the co-deposition of hydroxyapatite and carbon nanotubes or $CaSiO_3$ particles and offered the advantage of room temperature processing of composite materials. The thickness of the individual layers was varied in the range of 0.1–20 μm. A layered composite chitosan – multiwalled carbon nanotube surface encapsulation system was in the range of 0.5–10 μm which could be manipulated by variation of the deposition voltage and deposition time.

ADVANCED
MATERIALS
INTERFACES

www.advmatinterfaces.de

Materials Views

www.MaterialsViews.com

REVIEW

Intelligent design of "smart" encapsulation systems based on inorganic materials is required nowadays following functionalization. Thus silica based capsules provide flexibility for the design of complex drug-delivery vehicles through functionalization with sensing biomolecules or immunotargeting bioreceptors, optically active dyes (for imaging) and/or magnetic nanoparticles (for controlled movement to target diseased tissue or cancer cells).[84] There is interest in nanorobotic delivery systems. In regards to their physical and structural properties, porous silica capsules are ideal microscale bodies for designing these future robotic devices for delivery, e.g., biomedical applications. However, the self-propelled function is missing here, and to introduce mobility, one could attach bacteria to the diatom in addition to, or instead of, the gliding motility of diatoms themselves. Many bacteria propel themselves along in a fluid by rotating their corkscrew-like tails, called flagella, at relatively high speeds, and as robust machines. These flagellae can easily be integrated with other microscopic components and do not need to be purified or reconstituted. The bacteria motors work using a simple chemical energy source (glucose) and are naturally sensitive to the environment (e.g., metal ions, ethylene diamine tetraacetic acid [EDTA]), which means that nanobot movement can be controlled. Of course, in the dark parts of our bodies, we might want to use motile apochlorotic diatoms.

5.4. Biological Objects: Cell Encapsulation and Capsule Formation by Cells

Live cell encapsulation technologies are in trend. Several major important features for cell encapsulation can be mentioned: complete encapsulation, mechanical stability, selective permeability, e.g., for immune isolation, suitable extracellular microenvironment for optimal cellular functions. One should be aware that enhancement of one advantage does not decrease the other function. For example, a thick membrane with good immune isolation and mechanical stability often leads to poor nutrient/oxygen supply for cellular functions.

There are numbers of techniques for cell encapsulation: ionic gelation, complex coacervation, interfacial precipitation. Methods have been developed to encapsulate various primary cells or cell lines for different tissue engineering or therapeutic applications.

The materials used for cell encapsulation have to be biocompatible. Cross-linked chitosan, collagen, agarose microspheres, ceramic-based materials and their combination with polymers, e.g., polyethylenimine, poly-acrylic acid, different compositions of methacrylates, polylysin, sodium alginate, hydrogels and polyelectrolytes.

Preferably material for cell encapsulation should be not only biocompatible but also biodegradable. For example biodegradable self-reporting nanocomposite films of poly(lactic acid) nanoparticles engineered by layer-by-layer assembly were suggested.[152] In particular, multilayer assemblies of biodegradable poly(lactic acid) (PLA) nanoparticles based on hydrogen-bonding or electrostatic interactions were designed and fabricated. Moreover, gold nanoparticles can be effectivly grown within the PLA nanoparticle assemblies either through

UV-irradiation or under mild reducing conditions to create biodegradable nanocomposites with distinct optical response, which allows monitoring biodegradation of the films. The nanocomposite coatings of PLA nanoparticles were enzymatically degraded by a-chymotrypsin. The biodegradation process can be colorimetrically monitored with UV-vis spectroscopy thus opening the way for facile and real-time monitoring useful for biotechnology applications.

The material used for cell encapsulation is selected according to the following application for a specific cell line and can have advanced functionality, e.g., be stimuli responsive. Thus encapsulation of liver microsomes into a thermosensitive hydrogel for characterization of drug metabolism and toxicity was demonstrated.[153] The thermosensitivity of the hydrogel (Pluronic F127-acrylamide-bisacrylamide hydrogel) was studied using a swelling ratio and protein release assay to verify its ability to encapsulate microsomes. The metabolic activity of microsomes encapsulated in gels was investigated by detecting the metabolites of hydrogel-compatible substrates, including dextromethorphan, chloroxazone and testosterone. The classical anticancer prodrug cyclophosphamide was chosen as a model drug for the study of drug metabolism and the prediction of drug effects. When the microsomes encapsulated in the hydrogel were used in the cell culture system, the drug induced a higher level of apoptosis in MCF-7 cells compared with traditional microsomes.

Hydrogel functionalization and its variety provides space for optimization of the material used for cell encapsulation. There are studies how synthetic materials affect a natural cell and its metabolism. An example of such a research can be the analysis of the influence of encapsulation of cardiac stem cells (CSCs) within matrix enriched hydrogel capsules on cell survival, post-ischemic cell retention and cardiac function.[154] Transplantation of ex vivo proliferated CSCs is an emerging therapy for ischemic cardiomyopathy but outcomes are limited by modest engraftment and poor long-term survival. The effect of single cell microencapsulation to increase CSC engraftment and survival after myocardial injection was explored. Transcript and protein profiling of human atrial appendage sourced CSCs revealed strong expression the pro-survival integrin dimers – thus rationalizing the integration of fibronectin and fibrinogen into a supportive intra-capsular matrix. Encapsulation maintained CSC viability under hypoxic stress conditions and, when compared to standard suspended CSC, media conditioned by encapsulated CSCs demonstrated superior production of pro-angiogenic/cardioprotective cytokines, angiogenesis and recruitment of circulating angiogenic cells. Intra-myocardial injection of encapsulated CSCs after experimental myocardial infarction favorably affected long-term retention of CSCs, cardiac structure and function. Single cell encapsulation prevents detachment induced cell death while boosting the mechanical retention of CSCs to enhance repair of damaged myocardium.

There are numbers of studies to induce regeneration of organs by cell injection. However mostly cells are difficult to inject without their damage. Thus cells are encapsulated before being injected. For example, injectable calcium phosphate–alginate–chitosan microencapsulated MC3T3-E1 cell paste for bone tissue engineering in vivo was suggested.[155] The study aimed to develop alginate–chitosan microencapsulated mouse

osteoblast MC3T3-E1 cells to evaluate the osteogenic potential of a calcium phosphate cement complex with these cells, and trace the implanted MC3T3-E1 cells in vivo. MC3T3-E1 cells were embedded in alginate microcapsules, cultured in osteogenic medium for some days, and then covered with chitosan before mixing with a paste of calcium phosphate cement. The construct was injected into the dorsal subcutaneous area of nude mice. Lamellar-bone-like mineralization, newly formed collagen and angiogenesis were observed after 4 weeks. After 8 weeks, areas of newly formed collagen expanded with further absorption of osteoid-like structures. Cell tracing in vivo showed that implanted MC3T3-E1 cells were clearly visible after 2 weeks. The in vivo results indicate that the injectable encapsulated cells are promising for bone tissue engineering applications.

R. Grass' group in Zurich suggested an effective method of reversible DNA encapsulation in silica to produce radical oxygen species (ROS)-resistant and heat-resistant synthetic DNA 'fossils'.[156] In particular, the protocol describes a method for encapsulating DNA into amorphous silica (glass) spheres, mimicking the protection of nucleic acids within ancient fossils. In the approach, DNA encapsulation is achieved after the ammonium functionalization of silica nanoparticles. Within the glass spheres, the nucleic acid molecules are hermetically sealed and protected from chemical attack, thereby withstanding high temperatures and aggressive ROS. The encapsulates can be used as inert taggants to trace chemical and biological entities. The protocol is applicable to short double-stranded and single-stranded DNA fragments, genomic DNA and plasmids. The nucleic acids can be recovered from the glass spheres without harm by using fluoride-containing buffered oxide etch solutions. Special emphasis is placed on a protocol of the safe handling of the buffered hydrogen fluoride solutions. After dissolution of the spheres and subsequent purification, the nucleic acids can be analyzed by standard techniques (gel electrophoresis, quantitative PCR and sequencing).

An important issue is the development of encapsulation devices as an effective platform for implantation of genetically engineered cells in allogeneic conditions, which could be adapted to the chronic administration of recombinant proteins. An example of a successful device is a high-capacity cell encapsulation system suggested for the implantation of allogeneic myoblasts, which survive at high density for at least one year.[157] The system is developed as flat sheet device. It is based on permeable polypropylene membranes sealed to a mechanically resistant frame which confines cells seeded in a tailored biomimetic hydrogel matrix. In order to quantify the number of cells surviving in the device and optimize initial conditions leading to high-density survival, devices containing C2C12 mouse myoblasts expressing a luciferase reporter in the mouse subcutaneous tissue were implanted. It was shown that the initial cell load, hydrogel stiffness and permeable membrane porosity are critical parameters to achieve long-term implant survival and efficacy. Optimization of these parameters leads to the survival of encapsulated myogenic cells at high density for several months, with minimal inflammatory response and dense neovascularization in the adjacent host tissue.

One cell can be a capsule for the other one. Thus bacteria are effective capsules for bacteriophages. When a stimulus is applied the bacteriophage can be released from the bacteria. It was shown for example that titania and ROS generated on it under actinic irradiation provide release of bacteriophages from *Lactic* bacteria.[158]

Capsules can be formed by cells. Vesicles released by eukaryotic cells act as capsule used by cells to exchange biomolecules as transmembrane receptors and genetic information.[159]

Cell-derived vesicles as a bio-platform for the encapsulation of theranostic nanomaterials.[160] Endothelial cells were loaded with different types of nanoparticles solely or in combination. The cells were then incubated to form in the cell vesicles around the nanoparticles. Then the release of biogenic vesicles loaded with nanoparticles was triggered. Functional nanoparticles were encapsulated in a cell-camouflaged nanoplatform. A cell-camouflaged nanoplatform enclosing such nanoparticles represents the concept of cell-released vesicles as a universal nanoencapsulation platform.

6. Stimuli Response of Capsules

Materials science and chemical biology provide a variety of choices for stimuli triggered capsule behavior. Materials with "dynamicity" whereby surface properties can be modulated by an internal and external stimulus on user demand have been actively exploited for the past decade. These switchable materials with dynamic properties are widely used for a number of applications such as micro/nanoarrays, biomolecule immobilization, basic cell studies, and tissue engineering on a variety of materials. Stimuli to control capsule opening are physical (temperature, laser light, electric and magnetic field, ultrasound, and mechanical action), chemical (ionic strength, pH, electrochemical and solvent) and biological ones (enzymes and receptors).

In the past years, design of novel bio-responsive capsules that release drugs in response to an intracellular signal, in particular acidic pH and redox potential due to enzymatic reactions, has received great interest.[161] pH controls the linear charge density of an adsorbing polymer as well as the charge density of the previously adsorbed polymer layer. Bio-capsules which are pH sensitive, are usually designed to destabilize vehicles and to release drugs in endosomal and/or lysosomal compartments, which have pH values typically as low as 5.5 and 4.5, respectively. In comparison, redox-responsive capsules are mostly intended to disassemble and release drugs in the cytosol which contains 2 to 3 orders higher levels of glutathione (GSH) tripeptide (approximately 2–10 mM) than the extracellular fluids (approximately 2–20 μM).[162] Glutathione (GSH)-responsive systems were suggested as effective nano-vehicles for targeted intracellular drug and gene delivery.[163] GSH/glutathione disulfide (GSSG) is the major redox couple in animal cells that determines the anti-oxidative capacity of cells.[164] GSH/GSSG is kept reduced by nicotinamide adenine dinucleotide phosphate (NADPH) and glutathione reductase. The intracellular level of GSH is also dependent on other redox couples such as NADH/NAD+, NADPH/NADP+ and thioredoxin$_{red}$/thioredoxin$_{ox}$. This significant difference in GSH level has rendered GSH-responsive submicron capsules most appealing for targeted intracellular drug delivery. It should further be noted that

ADVANCED
MATERIALS
INTERFACES

www.advmatinterfaces.de

Materials
Views

www.MaterialsViews.com

REVIEW

the endosomal compartment is also redox-active, and the redox potential is modulated by a specific reducing enzyme gam-mainterferon-inducible lysosomal thiol reductase in the copresence of a reducing agent such as cysteine (but not GSH).[165]

Moreover, the redox-active lysosome contains also low-mass iron that is kept in a reduced state (Fe^{2+}) by the acidic interior and high concentrations of thiols such as cysteine within lysosome.[166] GSH-responsive encapsulation systems such as micelles, nanoparticles, polymersomes, nanogels, dendrimers, and nano-sized nucleic acid complexes for controlled delivery of anti-cancer drugs (e.g., doxorubicin and paclitaxel), photosensitizers, anti-oxidants, peptide and protein drugs, or nucleic acids (e.g., DNA, siRNA, and antisense oligodeoxynucleotide) were suggested. The unique disulfide chemistry has enabled novel and versatile design of multifunctional delivery systems to overcome both extracellular and intracellular barriers. It is anticipated that GSH-responsive nano-vehicles have enormous potential in targeted cancer therapy.

The encapsulation systems based on reduction-sensitive polymers have attracted a lot of attention for diverse biomedical applications including controlled drug delivery, gene delivery and diagnostic imaging.[167] It has to be noted, however, that only in the last couple of years exploding progress has been made in the capsule design for triggered intracellular drug release It should further be noted that many of the reported systems are not based on biodegradable and/or biocompatible materials, which are nevertheless the first requirement for most

biomedical applications. In the future, more efforts should be directed to development of novel cell-sensitive degradable polymers and copolymers including polyesters, polycarbonates, polypeptides, poly(ester amide)s and poly(ester urethane)s. Notably, recently there have appeared interesting reports on the synthesis of reduction-sensitive stepwise cleavable star polymers,[168] biodegradable polyurethanes derived from L-arabinitol,[169] and cascade degradable linear polymers.[170]

Lipids and lipopolymers self-assembled into biocompatible nano- and mesostructured functional capsules offer many potential applications in medicine and diagnostics due to their stimuli response. Thus recently it was demonstrated[171] how high-resolution structural investigations of bicontinuous cubic templates made from lyotropic thermosensitive liquid-crystalline materials have initiated the development of innovative lipidopolymeric self-assembled nanocarriers. Such structures have tunable nanochannel sizes, morphologies, and hierarchical inner organizations and provide capsules for the predictable loading and release of therapeutic proteins, peptides, or nucleic acids. It was shown that structural studies of swelling of bicontinuous cubic lipid/water phases are essential for overcoming the nanoscale constraints for encapsulation of large therapeutic molecules in multicompartment lipid carriers. The findings were generalized to control the stability and the hydration of the water nanochannels in liquid crystalline lipid capsules to confine therapeutic biomolecules within these structures. It was done by analyzing the influence of amphiphilic and soluble
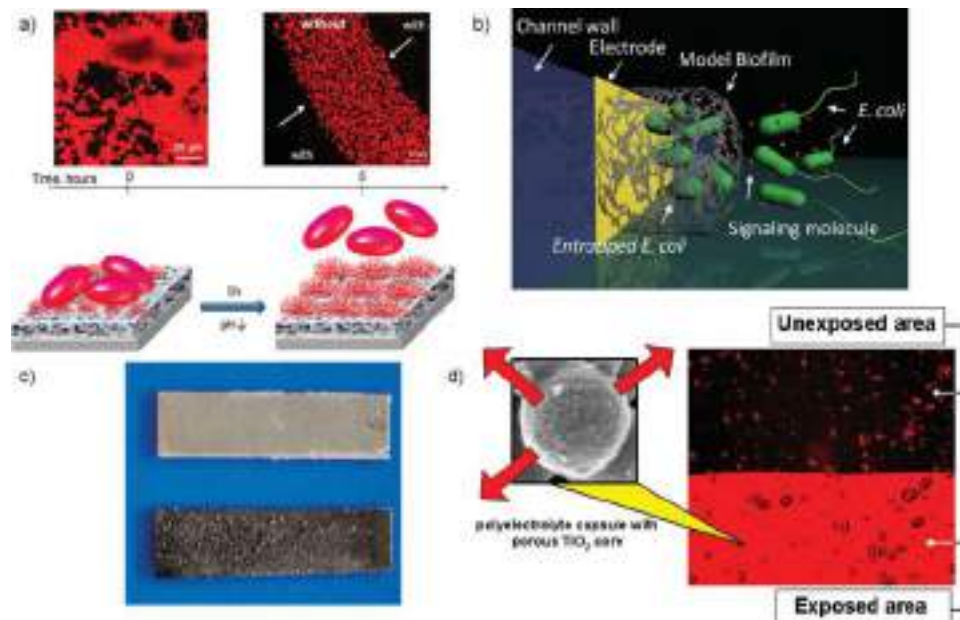
Figure 12. Examples of application of surface encapsulation systems. a) Self-controllable system of biocide coating: confocal kinetic study (fluorescence mode) and schematic illustration of pH triggered self-cleaning behavior of the porous metal surface covered with pH responsive micelles. As model cells *Lactococcus Lactis 411* bacteria (loaded with Rh6G) were used. Bacteria decrease pH, micelles respond to change and increase in size, bacteria detach from the surface. Reproduced with permission.[14d] Copyright 2012, Wiley. b) The functionality of stimuli-responsive polysaccharide alginate is demonstrated by biofabricating 3D cell-gel biocomposites: mimicking the formation of biofilms, for interrogating phenotypes of *E. coli* bacterial populations. Reproduced with permission.[172] Copyright 2012, Wiley. c) Long-term corrosion test: aluminum alloy covered by the LbL hybrid of PE/inhibitor coating (above) and unmodified aluminum plate (below). Reproduced with permission.[124a] Copyrights 2009, Wiley. d) Micrograph of the edge of the laser beam trace at the surface of LbL surface hybrid system which is polyelectrolyte capsules containing titania in silica-zirconia film. The red area corresponds to the release of the Rhodamine 6G from the capsules. Reproduced with permission.[43c] Copyrights 2009, Royal Chemical Society.

www.MaterialsViews.com

ADVANCED
MATERIALS
INTERFACES

www.advmatinterfaces.de

REVIEW

additives (e.g., poly(ethylene glycol)monooleate, octyl gluco-side, proteins) on the nanochannels' size in a diamond (D)-type bicontinuous cubic phase of the lipid glycerol monooleate. At body temperature, the long-living stability of swollen states, corresponding to a diamond cubic phase with large water channels was shown. With the application of a thermal stimulus, the system becomes progressively more ordered into a double-diamond cubic lattice formed by a bicontinuous lipid membrane. High-resolution freeze-fracture electron microscopy indicates that nanodomains are induced by the inclusion of proteins into nanopockets of the supramolecular cubosomic assemblies. These results contribute to the understanding of the structure and dynamics of functionalized self-assembled lipid nanosystems during stimuli-triggered liquid crystal based capsule phase transformations.

Enzymes, as an external stimulus for inducing capsule switching, can offer unprecedented opportunities for applications including tissue engineering, drug delivery, and biosensors.

7. Conclusion

Over the past several years, significant progress has been made with regards to structural engineering of capsules. Much of this progress has been application driven. Examples of some advanced applications are presented in **Figure 12**. In this review, we have pointed out some important aspects for "smart" surface capsule design of different materials with attention to capsules with various stimuli sensitivities, multifunctionality and -loading capacity. Fabrication of complex encapsulation systems in surface nanostructures combined with control over surface functionality is expected to lead to unique nanostructures and nanodevices with unprecedented functional properties for the next generation devices including the exploration of their application with a focus on the different research area ranging from medicine to material science and electronics. Access to complex structures is achieved by available advanced modern methodologies of synthesis of capsule cores or the following capsule modification with, e.g., polymer grafting, SAM, LbL, sol-gel methodology. Examples of innovative surface modification approaches and their impact on properties of the resulting materials as well as applications enabled by these surface modifications have been highlighted. As one powerful and prospective methodology for both formation of encapsulation systems and the following nanostructuring, the sonochemical approach is highlighted throughout the review. This approach can be effective for the design of various materials: oxides, metals, silicon, polymers, hybrids, etc. It is an instructive example to highlight the importance of cooperation between synthetic chemistry with theoretic modeling to design process regulation and effective use of a powerful methodology for design of various types of effective encapsulation systems.

Acknowledgements

of interaction between cavitation bubble and metal/metal-polymer/polymer/hybrid surface.

[1] a) T. S. Shim, S.-H. Kim, S.-M. Yang, *Part. Part. Syst. Charact.* **2013**, *30*, 9.

[2] a) J. Cui, M. P. van Koeverden, M. Müllner, K. Kempe, F. Caruso, *Adv. Col. Interface Sci.* **2013**, DOI: 10.1016/j.cis.2013.10.012; b) Y. Yan, M. Björnmalm, F. Caruso, *Chem. Mater.* **2014**, *26*, 452; c) G. K. Such, A. P. R. Johnston, F. Caruso, *Chem. Soc. Rev.* **2011**, *40*, 19.

[3] a) E. V. Skorb, D. Fix, D. V. Andreeva, D. G. Shchukin, H. Möhwald, *Adv. Funct. Mater.* **2009**, *19*, 2373; b) O. Shchepelina, M. O. Lisunova, I. Drachuk, V. V. Tsukruk, *Chem. Mater.* **2012**, *24*, 1245.

[4] a) K. Ariga, J. Qingmin, J. M. McShane, Y. M. Lvov, A. Vinu, P. Jonathan, J. P. Hill, *Chem. Mater.* **2012**, *24*, 728; b) V. Vergaro, F. Scarlino, C. Bellomo, R. Rinaldi, D. Vergara, M. Maffia, F. Baldassarre, G. Giannelli, X. C. Zhang, Y. M. Lvov, et al. *Adv. Drug Del. Rev.* **2011**, *63*, 847.

[5] a) D. Volodkin, A. Skirtachb, H. Möhwald, *Polym. Int.* **2012**, *61*: 673; b) A. P. R. Johnston, G. K. Such, F. Caruso, *Angew. Chem. Int. Ed.* **2010**, *49*, 2664.

[6] a) A. Perro, C. Nicolet, J. Angy, S. Lecommandoux, J. F. Le Meins, A. Colin, *Langmuir* **2011**, *27*, 9034; b) S. H. Kim, H. C. Shum, J. W. Kim, J. C. Cho, D. A. Weitz, *J. Am. Chem. Soc.* **2011**, *133*, 15165.

[7] L. Richert, P. Lavalle, E. Payan, X. Z. Shu, G. D. Prestwich, J.-F. Stoltz, P. Schaaf, J. C. Voegel, C. Picart, *Langmuir* **2004**, *20*, 448.

[8] A. Bunge, M. Fischlechner, M. Loew, A. Arbuzova, A. Herrmann, D. Huster, *Soft Matter* **2009**, *5*, 3331.

[9] a) I. Drachuk, O. Shchepelina, M. Lisunova, S. Harbaugh, N. Kelley-Loughnane, M. Stone, V. V. Tsukruk, *ACS Nano* **2012**, *6*, 4266; b) A. V. Dobrynin, M. Rubinstein, *Prog. Polym. Sci.* **2005**, *30*, 1049; c) G. Such, A. P. R. Johnston, F. Caruso, *Chem.. Soc. Rev.* **2011**, *40*, 19.

[10] a) C. Holmes, J. Daoud, P. O. Bagnaninchi, M. Tabrizian, *Adv. Health. Mater.* **2014**, *3*, 572; b) S. De Koker, R. Hoogenboom, B. G. De Geest, *Chem. Soc. Rev.* **2012**, *41*, 2867; c) B. M. Wohl, L. F. J. Engbersen, *J. Control. Rel.* **2012**, *158*, 2; d) W. J. Tong, X. X. Song, C. Y. Gao, *Chem Soc. Rev.* **2012**, *41*, 6103.

[11] a) M. Dubey, K. Emoto, H. Takahashi, D. G. Castner, D. W. Grainger, *Adv. Funct. Mater.* **2009**, *19*, 3046; b) D. Liu, C. A. C. Abdullah, R. P. Sear, J. L. Keddie, *Soft Matter* **2010**, *6*, 5408; c) D. I. Rozkiewicz, Y. Kraan, M. W. T. Werten, F. A. Wolf, V. Subramaniam, B. J. Ravoo, D. N. Reinhoudt, *Chem. Eur. J.* **2006**, *12*, 6290.

[12] a) K. Suzuki, B. W. Smith, *Microlithography: Science and Technology, Second Edition (Optical Science and Engineering)*, CRC Press, N. Y., USA **2007**; b) E. V. Skorb, T. V. Byk, V. G. Sokolov, T. V. Gaevskaya, D. V. Sviridov, C.-H. Noh, *Chemistry of High Energy* **2008**, *42*, 127; c) E. V. Skorb, D. Grützmacher, C. Dais, V. Guzenko, V. G. Sokolov, T. V. Gaevskaya, D. V. Sviridov, *Nanotechnology* **2010**, *21*, 315301; d) E. V. Skorb, T. V. Byk, V. G. Sokolov, T. V. Gaevskaya, D. V. Sviridov, C.-H. Noh, K. Y. Song, Y. N. Kwon, S. H. Cho, *J. Photochem. Photobiol. A: Chem.* **2008**, *193*, 56.

[13] D. V. Andreeva, D. V. Sviridov, A. Masic, H. Möhwald, E. V. Skorb, *Small* **2012**, *8*, 820.

[14] a) E. V. Skorb, D. G. Shchukin, H. Möhwald, D. V. Andreeva, *Nanoscale* **2010**, *2*, 722; b) E. V. Skorb, D. G. Shchukin,

REVIEW

H. Möhwald, D. V Andreeva, *Langmuir* **2010**, *26*, 16973; c) E. V. Skorb, D. Fix, D. G. Shchukin, H. Möhwald, D. V. Sviridov, R. Mousa, N. Wanderka, J. Schäferhans, N. Pazos-Pérez, A. Fery, D. V. Andreeva, *Nanoscale* **2011**, *3*, 985; d) J. Gensel, T. Borke, N. Pazos-Pérez, A Fery, D. V. Andreeva, E. Betthausen, A. Müller, H. Möhwald, E. V. Skorb, *Adv. Mater.* **2012**, *24*, 985; e) E. V. Skorb, D. V. Andreeva, *J. Mater. Chem. A* **2013**, *1*, 7547.

[15] D. O. Grigoriev, K. Köhler, E. V. Skorb, D. G. Shchukin, H. Möhwald, *Soft Matter.* **2009**, *5*, 1426.

[16] a) Y. F. Poon, Y. Cao, Y. Liu, V. Chan, M. B. Chan-Park, *ACS Appl Mater Interfaces.* **2010**, *2*, 2012; b) Z. Zhao, L. Yin, G. Yuan, L. Wang, *Langmuir* **2012**, *28*, 2704; c) Z. Zhu, S. A. Sukhishvili, *J. Mater. Chem.* **2012**, *22*, 7667.

[17] J. Li, L. He, J. Wang, Z. T. Zhang, J. Shi, X. Z. Zhang, Y. P. Cao, Y. Chen, *Express Polym. Lett.* **2014**, *8*, 143.

[18] R. Censi, P. Martino, T. Vermonden, W. E. Hennink, *J. Control. Release* **2012**, *161*, 680.

[19] B. A. Miller-Chou, J. L. Koenig, *Prog. Polym. Sci.* **2003**, *28*, 1223.

[20] E. V. Skorb, D. V. Andreeva, *Adv. Funct. Mater.* **2013**, *23*, 4483.

[21] E. V. Skorb, D. V. Andreeva, *Polymer Chemistry* **2013**, *4*, 7547.

[22] L. Han, Y. Fu, A. J. Cole, J. Liu, J. Wang, *Fitoterapia* **2012**, *83*, 721.

[23] A. Angelova, B. Angelov, R. Mutafchieva, S. Lesieur, P. Couvreur, *Accounts Chem. Res.* **2011**, *44*, 147.

[24] E. V. Skorb, O. Baidukova, A. Goyal, A. Brotchie, D. V. Andreeva, H. Möhwald, *J. Mater. Chem.* **2012**, *22*, 13841.

[25] E. V. Skorb, H. Möhwald, *Adv. Mater.* **2013**, *36*, 5029.

[26] a) A. Santos, T. Kumeria, D. Losic, *Trend. Anal. Chem.* **2013**, *44*, 25; b) A. M. M. Jani, D. Losic, N. H. Voelcker, *Prog. Mat. Sci.* **2013**, *58*, 636; c) K. Gulati, M. S. Aw, D. Findlay, D. Losic, *Therap. Deliv.* **2012**, *3*, 857; d) G. Jeon, S. Y. Yang, J. K. Kim, *Mater. Chem.* **2012**, *22*, 14814; e) R. K. Joshi, J. J. Schneider, *Chem. Soc. Rev.* **2012**, *41*, 5285.

[27] a) M. Delcea, H. Möhwald, A. G. Skirtach, *Adv. Drug Deliv. Rev.* **2011**, *63*, 730; b) J. Cui, M. P. Koeverden, M. Müllner, K. Kempe, F. Caruso, *Adv. Col. Inter. Sci.* DOI: 10.1016/j.cis.2013.10.012; c) T. S. Shim, S.-H. Kim, S.-M. Yang, *Part. Part. Syst. Charact.* **2013**, *30*, 9.

[28] H. Lee, S. M. Dellatore, W. M. Miller, P. B. Messersmith, *Science* **2007**, *318*, 426. 9.

[29] A. Postma, Y. Yan, Y. Wang, A. N. Zelikin, E. Tjipto, F. Caruso, *Chem. Mater.* **2009**, *21*, 3042.

[30] Y. Lvov, K. Ariga, I. Ichinose, T. Kunitake, *J. Am. Chem. Soc.* **1995**, *117*, 6117.

[31] a) S. A. Sukhishvili, *Current opinion Coll. Interfaces Sci.* **2005**, *10*, 37–44; b) J. Hiller, J. D. Mendelsohn, M. F. Rubner, *Nature Mater.* **2001**, *1*, 59.

[32] Z. Estephan, Z. Quin, D. Lee, J. Crocker, S.-J. Park, *NanoLetters* **2013**, *13*, 4449.

[33] a) M. D. Hager, P. Greil, C. Leyens, S. Van der Zwaag, U. S. Schubert, *Adv. Mater.* **2010**, *22*, 5424; b) S. Burattini, B. W. Greenland, D. Chappell, H. M. Colquhoun, W. Hayes, *Chem. Soc. Rev.* **2010**, *39*, 1973; c) E. V. Skorb, A. Volkova, D. V. Andreeva, **2014**; d) J. A. Syrett, C. R. Becer, D. M. Haddleton, *Polym. Chem.* **2010**, *1*, 978.

[34] L. Adriaenssens, P. Ballester, *Chem Soc. Rev.* **2013**, *42*, 3261.

[35] M. M. J. Smulders, I. A. Riddell, C. Browne, J. R. Nitschke, *Chem Soc. Rev.* **2013**, *42*, 1728.

[36] a) E. M. Enlow, C. Luft, M. E. Napier, J. M. DeSimone, *Nano. Lett.* **2011**, *11*, 808; b) S. P. Sullivan, N. Murthy, M. R. Prausnitz, *Adv. Mater.* **2008**, *20*, 933.

[37] a) K. A. Moga, L. R. Bickford, R. D. Geil, S. S. Dunn, A. Pandya, Y. Wang, J. H. Fain, C. F. Archuleta, A. T. O'Neill, J. M. De Simone, *Adv. Mater.* **2013**, *25*, 5060; b) K. Tsioris, W. K. Raja, E. M. Pritchard, B. Panilaitis, D. L. Kaplan, F. G. Omenetto, *Adv. Funct. Mater.* **2012**, *22*, 330.

[38] S. P. Sullivan, D. G. Koutsonanos, M. del Pilar Martin, J. W. Lee, V. Zarnitsyn, S. O. Choi, N. Murthy, R. W. Compans, I. Skountzou, M. R. Prausnitz, *Nat. Med.* **2010**, *16*, 915.

[39] J. W. Lee, S. O. Choi, E. I. Felner, M. R. Prausnitz, *Small* **2011**, *7*, 531.

[40] a) L. Pescosolido, W. Schuurman, J. Malda, P. Matricardi, F. Alhaique, T. Coviello, P. R. Van Weeren, W. J. A. Dhert, W. E. Hennink, T. Vermonden, *Biomacromol.* **2011**, *12*, 1831; b) W. S. R. Censi, J. Malda, G. di Dato, P. E. Burgisser, W. J. A. Dhert, C. F. van Nostrum, P. di Martino, T. Vermonden, W. E. Hennink, *Adv. Funct. Mater.* **2011**, *21*, 1833; c) T. M. Seck, F. P. W. Melchels, J. Feijen, D. W. Grijpma, *J. Control. Release* **2010**, *148*, 34.

[41] a) M. S. Aw, S. Simovic, J. Addai-Mensaha, D. Losic, *J. Mater. Chem.* **2011**, *21*, 7082; b) M. S. Aw, M. Kurian, D. Losic, *Chem. A. Europ.* **2013**, *19*, 12586.

[42] K. D. Sattler, *Handbook of Nanophysics: Nanomedicine and Nanorobotics*, CRC Press, Taylor & Francis Group, USA **2011**.

[43] a) E. V. Skorb, D. Fix, H. Möhwald, D. G. Shchukin, *Adv. Funct. Mater.* **2009**, *19*, 2373; b) E. V. Skorb, D. Sviridov, H. Möhwald, D. G. Shchukin, *Chem. Comm.* **2009**, *40*, 6041; c) E. V. Skorb, D. G. Shchukin, H Möhwald, D. V. Sviridov, *J. Mater. Chem.* **2009**, *19*, 4931.

[44] K. K. Coti, M. E. Belowich, M. Liong, M. W. Ambrogio, Y. A. Lau, H. A. Khatib, J. I. Zink, N. M. Khashab, J. F. Stoddart, *Nanoscale* **2009**, *1*, 16.

[45] H.-W. Kim, J. C. Knowles, H.-E. Kim, *Wiley InterScience* **2004**, 240.

[46] L. Chen, C. Y. Tang, D. Z. Chen, C. T. Wong, C. P. Tsui, *Compos. Sci. Technol.* **2011**, *71*, 1842.

[47] J. Sagiv, *J. Am. Chem. Soc.* **1980**, *102*, 92.

[48] A. Ulman, *Chem. Rev.* **1996**, *96*, 1533.

[49] C. D. Bain, E. B. Troughton, Y. T. Tao, J. Evall, G. M. Whitesides, R. G. Nuzzo, *J. Am. Chem. Soc.* **1989**, *111*, 321.

[50] J. C. Love, L. A. Estroff, J. K. Kriebel, R. G. Nuzzo, G. M. Whitesides, *Chem. Rev.* **2005**, *105*, 1103.

[51] a) R. M. Penner, *Nat. Chem.* **2010**, *2*, 251; b) I. Choi, Y.-K. Kim, D.-H. Min, S. Lee, W.-S. Yeo, *J. Am. Chem. Soc.* **2011**, *133*, 16718.

[52] S. Onclin, B. J. Ravoo, D. N. Reinhoudt, *Angew. Chem.* **2005**, *117*, 6438.

[53] I. Choi, W.-S. Yeo, *ChemPhysChem* **2013**, *14*, 55.

[54] M. Mrksich, G. M. Whitesides, *ACS Symp. Ser.* **1997**, *680*, 361.

[55] a) G. V. Kaigala, R. D. Lovchik, E. Delamarche, *Angew. Chem. Int. Ed.* **2012**, *51*, 11224; b) R. Pelton, *J. Col. Interface Sci.* **2010**, *348*, 673.

[56] S. Schmidt, M. Zeiser, T. Hellweg, C. Duschl, A. Fery, H. Möhwald, *Adv. Funct. Mater.* **2010**, *20*, 3235.

[57] H. M. Zareie, C. Boyer, V. Bulmus, E. Nateghi, T. P. Davis, *ACS Nano* **2008**, *2*, 757.

[58] M. Mrksich, G. M. Whitesides, *Annu. Rev. Biophys. Biomol. Struct.* **1996**, *25*, 55.

[59] a) D. H. Min, M. Mrksich, *Curr. Opin. Chem. Biol.* **2004**, *8*, 554; b) C. D. Hodneland, Y. S. Lee, D. H. Min, M. Mrksich, *Proc. Natl. Acad. Sci. USA* **2002**, *99*, 5048; c) M. N. Yousaf, B. T. Houseman, M. Mrksich, *Angew. Chem. Int. Ed.* **2001**, *40*, 1093.

[60] a) W. S. Yeo, M. N. Yousaf, M. Mrksich, *J. Am. Chem. Soc.* **2003**, *125*, 14994; b) W. S. Yeo, M. Mrksich, *Adv. Mater.* **2004**, *16*, 1352.

[61] M. N. Yousaf, M. Mrksich, *J. Am. Chem. Soc.* **1999**, *121*, 4286.

[62] a) D. Liu, Y. Xie, H. Shao, X. Jiang, *Angew. Chem. Int. Ed.* **2009**, *48*, 4406; b) G. B. Demirel, N. Dilsiz, M. A. Ergun, M. Cakmak, T. Caykara, *J. Mater. Chem.* **2011**, *21*, 10415; c) P. Wan, P. Xing, Y. Chen, L. Chi, X. Zhang, *Chem. Commun.* **2011**, *47*, 5994; d) Y.-H. Gong, C. Li, J. Yang, H.-Y. Wang, R.-X. Zhuo, X.-Z. Zhang, *Macromolecules* **2011**, *44*, 7499.

[63] D. Pearson, A. J. Downard, A. Muscroft-Taylor, A. D. Abell, *J. Am. Chem. Soc.* **2007**, *129*, 14862.

www.MaterialsViews.com

ADVANCED
MATERIALS
INTERFACES
www.advmatinterfaces.de

REVIEW

[64] a) J. Nakanishi, Y. Kikuchi, S. Inoue, K. Yamaguchi, T. Takarada, M. Maeda, *J. Am. Chem. Soc.* **2007**, *129*, 6694; b) S. Petersen, J. M. Alonso, A. Specht, P. Duodu, M. Goeldner, A. del Campo, *Angew. Chem. Int. Ed.* **2008**, *47*, 3192; c) S. Kaneko, H. Nakayama, Y. Yoshino, D. Fushimi, K. Yamaguchi, Y. Horiike, J. Nakanishi, *Phys. Chem. Chem. Phys.* **2011**, *13*, 4051.

[65] J. Nakanishi, Y. Kikuchi, T. Takarada, H. Nakayama, K. Yamaguchi, M. Maeda, *J. Am. Chem. Soc.* **2004**, *126*, 16314.

[66] M. Y. Balakirev, S. Porte, M. Vernaz-Gris, M. Berger, J. P. Arie, B. Fouque, F. Chatelain, *Anal. Chem.* **2005**, *77*, 5474.

[67] C. R. Toh, T. A. Fraterman, D. A. Walker, R. C. Bailey, *Langmuir* **2009**, *25*, 8894.

[68] W. S. Yeo, M. Mrksich, *Angew. Chem. Int. Ed.* **2003**, *42*, 3121.

[69] S. J. Todd, D. Farrar, J. E. Gough, R. V. Ulijn, *Soft Matter* **2007**, *3*, 547.

[70] S. J. Todd, D. J. Scurr, J. E. Gough, M. R. Alexander, R. V. Ulijn, *Langmuir* **2009**, *25*, 7533.

[71] J. Adjmian, A. Anne, G. Cauet, C. Demaille, *Langmuir* **2010**, *26*, 10347.

[72] a) H. Kuroki, I. Tokarev, S. Minko, *Ann. Rev. Mater. Res.* **2012**, *48*, 343; b) J. Genzer, *Soft Matter Gradient Surfaces*, Wiley-VCH, **2012**; c) A. Grigoryev, Y. Roiter, I. Tokarev, I. Luzinov, S. Minko, *Adv. Funct. Mater.* **2013**, *23*, 870.

[73] M. Motornov, R. Sheparovych, I. Tokarev, Y. Roiter, S. Minko, *Langmuir* **2007**, *23*, 13.

[74] X. Y. Jiang, R. Ferrigno, M. Mrksich, G. M. Whitesides, *J. Am. Chem. Soc.* **2003**, *125*, 2366.

[75] E. V. Skorb, D. V. Andreeva, *Polymer Chem.* **2013**, *4*, 7547.

[76] A. Verma, F. Stellacci, *Small* **2010**, *6*, 12.

[77] Z. X. Li, J. C. Barnes, A. Bosoy, J. F. Stoddart, J. I. Zink, *Chem. Soc. Rev.* **2012**, *41*, 2590.

[78] A. Yamaguchi, F. Uejo, T. Yoda, T. Uchida, Y. Tanamura, T. Yamashita, N. Teramae, *Nat. Mater.* **2004**, *3*, 337.

[79] S. Simovic, D. Losic, K. Vasilev, *Chem. Commun.* **2010**, *46*, 1317.

[80] G. Whitesides, J. Mathias, C. Seto, *Science* **1991**, *254*, 1312.

[81] E. Gomar-Nadal, J. Puigmarti-Luis, D. B. Amabilino, *Chem. Soc. Rev.* **2008**, *37*, 490.

[82] K. Lee, W. Wagermaier, A. Masic, K. P. Kommareddy, M. Bennet, I. Manjubala, S.-W. Lee, S. B. Park, H. Cölfen, P. Fratzl, *Nat. Comm.* **2012**, *3*, 725.

[83] a) A. Sidorenko, T. Krupenkin, A. Taylor, P. Fratzl, J. Aizenberg, *Science* **2007**, *315*, 487; b) B. Pokroy, A. K. Epstein, M. C. M. Gulda Persson, J. Aizenberg, *Adv. Mater.* **2009**, *21*, 463; c) B. Pokroy, S. H. Kang, L. Mahadevan, J. Aizenberg, *Science* **2009**, *323*, 237.

[84] R. Gordon, D. Losic, M. A. Tiffany, S. S. Nagy, F. A.S. Sterrenburg, *Trends in Biotechnol.* **2005**, *27*, 117.

[85] M. Sitti, *Nature* **2009**, *458*, 1121.

[86] J. Xi, J. J. Schmidt, C. D. Montemagno, *Nature Mater.* **2005**, *4*, 180.

[87] a) V. Arabagi, B. Behkam, E. Cheung, M. Sitti, *J. Appl. Phys.* **2011**, *109*, 114702; b) B. Behkam, M. Sitti, *Appl. Phys. Lett.* **2008**, *93*, 223901; c) S. A. Amin, D. H. Green, D. Al Waheeb, A. Gärdes, C. J. Carrano, *Biomater.* **2012**, *25*, 135.

[88] P. Fratzl, J. W. C. Dunlop, R. Weinkamer, *Materials Design Inspired by Nature*, RSC Publishing, **2013**.

[89] M. Delcea, N. Sternberg, A. M. Yashchenok, R. Georgieva, H. Bäumler, H. Möhwald, A. G. Skirtach, *ACS Nano* **2012**, *6*, 4169.

[90] K. D. Young, *Microbiol. Molec. Biol. Rev.* **2006**, *70*, 660.

[91] a) J. F. Galisteo-López, M. Ibisate, R. Sapienza, L. S. Froufe-Pérez, Á. Blanco, C. López, *Adv. Mater.* **2011**, *23*, 30; b) S. N. Fejer, D. Chakrabarti, D. J. Wales, *Soft Matter* **2011**, *7*, 3553.

[92] D. Dendukuri, D. C. Pregibon, J. Collins, T. A. Hatton, P. S. Doyle, *Nat. Mater.* **2006**, *5*, 365.

[93] J. P. Rolland, B. W. Maynor, L. E. Euliss, A. E. Exner, G. M. Denison, J. M. DeSimone, *J. Am. Chem. Soc.* **2005**, *127*, 10096.

[94] S. Q. Xu, Z. H. Nie, M. Seo, P. Lewis, E. Kumacheva, H. A. Stone, P. Garstecki, D. B. Weibel, I. Gitlin, G. M. Whitesides, *Angew. Chem. Int. Ed.* **2005**, *44*, 724.

[95] J. Dulle, S. Nemeth, E. V. Skorb, D. V. Andreeva, *RCS Advances* **2012**, *2*, 12460.

[96] a) J.-W. Kim, R. J. Larsen, D. A. Weitz, *J. Am. Chem. Soc.* **2006**, *128*, 14374; b) J.-W. Kim, R. J. Larsen, D. A. Weitz, *Adv. Mater.* **2007**, *19*, 2005.

[97] D. Dendukuri, D. C. Pregibon, J. Collins, T. A. Hatton, P. S. Doyle, *Nat. Mater.* **2006**, *5*, 365.

[98] K. Nogi, M. Hosokawa, M. Naito, T. Yokoyama, *Nanoparticle Technology Handbook*, Elsevier, Oxford, GB, **2012**.

[99] a) K. S. Suslick, L. A. Crum, *Encyclopedia of Acoustics*, Ed: M. J. Crocker, Wiley & Sons. Inc., N. Y., **1995**; b) M. A. Margulis, In: *Sonochemistry basis*, High School, Moscow, **1984**; c) L. H. Thompson, L. K. Doraiswamy, *Ind. Eng. Chem. Res.* **1999**, *38*, 1215.

[100] D. G. Shchukin, E. V. Skorb, V. Belova, H. Möhwald, *Adv. Mater.* **2011**, *23*, 1922.

[101] F. G. Hammitt, *Cavitation and multiphase flow phenomena*, McGraw-Hill Book Co., N.Y., **1980**.

[102] D. G. Shchukin, H. Möhwald, *Phys. Chem. Chem. Phys.* **2006**, *8*, 3496.

[103] V. Belova, D. G. Shchukin, D. A. Gorin, A. Kopyshev, H. Möhwald, *Phys. Chem. Chem. Phys.* **2011**, *13*, 8015.

[104] J. L. Luche, *Ultrason. Sonochem.* **1997**, *4*, 211.

[105] T. J. Mason, *Chem. Soc. Rev.* **1997**, *26*, 443.

[106] a) F. R. Young, *Cavitation*, Imperial College Press, **1999**; b) H. Soyamaa, M. Futakawa, *Tribol. Lett.* **2004**, *17*, 27; c) H. Suzuki, M. Futakawa, T. Shobu, T. Wakui, T. Naoe, *J. Nucl. Sci. Technol.* **2010**, *47*, 136.

[107] J. G. Adewuyi, *Environ. Sci. Technol.* **2005**, *39*, 8557.

[108] M. M. Caruso, D. A. Davis, Q. Shen, S. A. Odom, N. R. Sottos, S. R. White, J. S. Moore; *Moore, Chem. Rev.* **2009**, *109*, 5755.

[109] V. Belova, D. A. Gorin, D. G. Shchukin, H. Möhwald, *Angew. Chem. Int. Ed.* **2010**, *49*, 7129.

[110] J. Z. Sostaric, P. Riesz, *J. Am. Chem. Soc.* **2001**, *123*, 11010.

[111] H. Destaillats, T. W. Alderson, M. R. Hoffmann, *Environ. Sci. Technol.* **2001**, *35*, 3019.

[112] H. Endo, *J. Acoust. Soc. Am.* **1994**, *95*, 2409.

[113] M. Zeng, H. N. Gao, Z. Q. Wu, L. R. Fan, T. H. Zheng, D. F. Zhou, *J. Macromol. Sci. A Pure Appl. Chem.* **2010**, *47*, 1042.

[114] A. V. Mohod, P. R. Gogate, *Ultrasonic Sonochem.* **2011**, *18*, 727.

[115] K. Zhang, B.-J. Park, F.-F. Fang, H. J. Choi, *Molecules* **2009**, *14*, 2095.

[116] a) L. J. Gerenser, K. E. Goppert-Berarducci, *Metallized Plastics, Fundamental and Applied Aspects*, Ed.: K. L. Mittal, Plenum Press, N. Y., **1992**; b) H. V. Boenig, *Plasma Science and Technology*, Cornell Press, Ithaca, **1982**; c) J. M. Burkstrand, *Phys. Rev.* **1979**, *B20*, 4853.

[117] a) J. L. Jordan, C. A. Kovac, J. F. Morar, R. A. Pollak, *Phys. Rev.* **1987**, *B36*, 1369; b) S. C. Freilich, F. S. Ohuchi, *Polymer* **1987**, *28*, 1908; c) A. J. Pertsin, Y. M. Pashunin, *Appl. Surf. Sci.* **1991**, *47*, 115; d) H. M. Meyer, S. G. Anderson, L. Atanasoska, J. H. Weaver, *Vac. Sci. Technol.* **1988**, *A6*, 30.

[118] a) L. J. Gerenser, *J. Adhesion Sci. Technol.* **1993**, *7*, 1019; b) J. M. Burkstrand, *J. Appl. Phys.* **1981**, *52*, 4795.

[119] a) N. Zaafarani, D. Raabe, F. Roters, S. Zaefferer, *Acta Mater.* **2008**, *56*, 31; b) N. Zaafarani, D. Raabe, R. N. Singh, F. Roters, S. Zaefferer, *Acta Mater.* **2006**, *54*, 1863; c) C. Zambaldi, D. Raabe, *Acta Mater.* **2010**, *58*, 3516; d) E. Demir, D. Raabe, N. Zaafarani, S. Zaefferer, *Acta Mater.* **2009**, *57*, 559; e) F. Varnik, D. Raabe, *Modelling Simul. Mater. Sci. Eng.* **2006**, *14*, 857; f) D. Raabe, *Modelling Simul. Mater. Sci. Eng.* **2004**, *12*, R13; g) M. Gross, F. Varnik, D. Raabe, *EPL* **2009**, *88*, 26002; h) M. Gross, F. Varnik, D. Raabe, I. Steinbach, *Phys. Rev. E* **2010**, *81*, 051606.

[120] a) G. P. Wang, L. Zhang, J. J. Zhang, *Chem. Soc. Rev.* **2012**, *41*, 797; b) D. V. Andreeva, Z. Pientka, L. Brozova, M. Bleha, G. A. Polotskaya, G. K. Elyashevich, *Thing Solid Films* 2002, 406, 54.

[121] B. Parakhonskiy, D. Andreeva, H. Möhwald, D. G. Shchukin, *Langmuir* **2009**, *25*, 4780.

[122] J. F. Wang, L. Lin, Q. F. Cheng, L. Jiang, *Angew. Chem. Int. Ed.* **2012**, *51*, 4676.

[123] K. Knop, R. Hoogenboom, D. Fischer, U. S. Schubert, *Angew. Chem. Int. Ed.* **2010**, *49*, 6288.

[124] a) D. V. Andreeva, D. Fix, D. G. Shchukin, H. Möhwald, *Adv. Mater.* **2008**, *20*, 2789; b) E. V. Skorb, D. G. Shchukin, H. Möhwald, D. V. Andreeva, *Langmuir* **2010**, *26*, 16973.

[125] J. K. Oh, R. Drumright, D. J. Siegwart, K. Matyjaszewski, *Prog. Polym. Sci.* **2008**, *33*, 448.

[126] a) C. G. Palivan, O. Fischer-Onaca, M. Delcea, F. Itel, W. Meier, *Chem. Soc. Rev.* **2012**, *41*, 2800; b) T. A. Kolesnikova, A. G. Skirtach, H. Mohwald, *Exp. Op. Drug Deliv.* **2013**, *10*, 47.

[127] S. F. Yan, S. Q. Rao, J. Zhu, Z. C. Wang, Y. Zhang, Y. R. Duan, X. S. Chen, J. B. Yin, *Inter. J. Pharmac.* **2012**, *427*, 443.

[128] G. F. Luo, X. D. Xu, J. Zhang, J. Yang, Y. H. Gong, Q. Lei, H. Z. Jia, C. Li, R. X. Zhuo, X. Z. Zhang, *ACS Appl. Matre. Inter.* **2012**, *4*, 5317.

[129] L. Gao, J. B. Fei, J. Zhao, W. Cui, Y. Cui, J. B. Li, *Chem.-A Europ. J.* **2012**, *18*, 3185.

[130] H. Y. Yoon, H. Koo, K. Y. Choi, S. J. Lee, K. Kim, I. C. Kwon, J. F. Leary, K. Park, S. H. Yuk, J. H. Park, K. Choi, *Biomaterials* **2012**, *33*, 3980.

[131] M. P. Neubauer, C. Blüm, E. Agostini, J. Engert, T. Scheibel, A. Fery, *Biomater. Sci.* **2013**, *1*, 1160.

[132] a) Y. F. Wen, J. K. Oh, *RCS Advances* **2014**, *4*, 229; b) A. T. Neffe, C. Wischke, M. Racheva, A. Lendlein, *Exp. Rev. Med. Dev.* **2013**, *10*, 813; c) R. Agarwal, V. Singh, P. Jurney, L. Shi, S. V. Sreenivasan, K. Roy, *ACS Nano* **2012**, *6*, 2524.

[133] A. Schroeder, D. A. Heller, M. M. Winslow, J. E. Dahlman, E. James, G. W. Pratt, R. Langer, T. Jacks, D. G. Anderson, *Nat. Rev. Cancer* **2012**, *12*, 39.

[134] E. J. Anglin, L. Cheng, W. R. Freeman, M. J. Sailor, *Adv. Drug Delivery Rev.* **2008**, *60*, 1266.

[135] D. V. Volodkin, R. von Klitzing, H. Möhwald, *Angew. Chem. Int. Ed.*. **2010**, *49*, 9258.

[136] a) J. M. Rosenholm, C. Sahlgren, M. Linden, *Nanoscale* **2010**, *2*, 1870; b) M.-H. Kim, H.-K. Na, Y.-K. Kim, S.-R. Ryoo, H. S. Cho, K. E. Lee, H. Jeon, R. Ryoo, D.-H. Min, *ACS Nano* **2011**, *5*, 3568; c) I. I. Slowing, B. G. Trewyn, S. Giri, V. S. Y. Lin, *Adv. Funct. Mater.* **2007**, *17*, 1225; d) A. Popat, S. B. Hartono, F. Stahr, J. Liu, S. Z. Qiao, G. Q. Lu , *Nanoscale* **2011**, *3*, 2801; e) Q. He, J. Shi, *J. Mater. Chem.* **2011**, *21*, 5845.

[137] R. Guillet-Nicolas, A. Popat, J.-L. Bridot, G. Monteith, S. Z. Qiao, F. Kleitz, *Angew. Chem. Int. Ed.* **2013**, *52*, 2318.

[138] a) L. H. Reddy, J. L. Arias, J. Nicolas, P. Couvreur, *Chem. Rev.* **2012**, *112*, 5818; b) S. Parveen, R. Misra, S. K. Sahoo, *Nanomed.-Nanotechnol. Biol. Med.* **2012**, *8*, 147.

[139] M. Poehlmann, D. Grishenkov, S. V. V. N. Kothapalli, J. Harmark, H. Hebert, A. Philipp, R. Hoeller, M. Seuss, C. Kuttner, S. Margheritelli, G. Paradossi, A. Fery, *Soft Matter.* **2014**, *10*, 214.

[140] Z. L. Cheng, A. Al Zaki, J. Z. Hui, V. R. Muzykantov, A. Tsourkas, *Science* **2012**, *338*, 903.

[141] E. J. Anglin, L. Cheng, W. R. Freeman, M. J. Sailor, *Adv. Drug Deliv. Rev.* **2008**, *60*, 1266–1277.

[142] J. L. Heinrich, C. L. Curtis, G. M. Credo, K. L. Kavanagh, M. J. Sailor, *Science* 1992, *25*, 66.

[143] a) E. V. Skorb, D. V. Andreeva, H. Möhwald, *Angew. Chem. Int. Ed.* **2012**, *51*, 5138; b) M. Virot, R. Pflieger, E. V. Skorb, J. Ravaux, T. Zemb, H. Möhwald, *J. Phys. Chem. C.* **2012**, *116*, 15493.

[144] M. P. Monopoli, C. Aberg, A. Salvati, K. A. Dawson, *Nature Nanotechnol.* **2012**, *7*, 779.

[145] R. G. Mendes, A. Bachmatiuk, B. Buchner, G. Cuniberti, M. H. Rummeli, *J. Mater. Chem. B.* **2013**, *1*, 401.

[146] a) T. Kuila, S. Bose, A. K. Mishra, P. Khanra, N. H. Kim, J. H. Lee, *Progr. Mater. Sci.* **2012**, *57*, 1061; b) K. Yang, L. Z. Feng, X. Z. Shi, Z. Liu, *Chem. Soc. Rev.* **2013**, *42*, 530.

[147] V. N. Mochalin, O. Shenderova, D. Ho, Y. Gogotsi, *Nature Nanotechnol.* **2012**, *7*, 11.

[148] E. V. Skorb, A. Skirtach, D. V. Sviridov, D. G. Shchukin, H Möhwald, *ACS Nano* **2009**, *3*, 1753.

[149] M. F. Shao, F. Y. Ning, J. W. Zhao, M. Wei, D. G. Evans, X. Duan, *J. Am. Chem. Soc.* **2012**, *134*, 1071.

[150] N. Kamaly, Z. Y. Xiao, P. M. Valencia, A. F. Radovic-Moreno, O. C. Farokhzad, *Chem. Soc. Rev.* **2012**, *41*, 2971.

[151] a) K. Grandfield, F. Sun, M. FitzPatrick, M. Cheong, I. Zhitomirsky, *Surf. Coat. Technol.* **2009**, *203*, 1481; b) X. Pang, T. Casagrande, I. Zhitomirsky, *J. Coll. Interf. Sci.* **2009**, *330*, 323.

[152] V. H. Orozco, V. Kozlovskaya, E. Kharlampieva, B. L. López, V. V. Tsukruk, *Polymer* **2010**, *51*, 4127.

[153] H. Yang, Y. Zheng, B. Zhao, T. Shao, Q. Shi, N. Zhou, W. Cai, *Biomaterials* **2013**, *34*, 9770.

[154] A. E. Mayfield, E. L. Tilokee, N. Latham, B. McNeill, B.-K. Lam, M. Ruel, E. J. Suuronen, D. W. Courtman, D. J. Stewart, D. R. Davis, *Biomaterials* **2014**, *35*, 133.

[155] P. Qiao, J. Wang, Q. Xie, F. Li, L. Dong, T. Xu, *Mater. Sci. Engineer. C* **2013**, *33*, 4633.

[156] D. Paunescu, M. Puddu, J. O. B. Soellner, P. R. Stoessel, R. N. Grass, *Nature Prot.* **2013**, *8*, 2440.

[157] A. Lathuilière, S. Cosson, M. P. Lutolf, B. L. Schneider, P. Aebischer, *Biomaterials* **2014**, *35*, 779.

[158] E. V. Skorb, D. V. Andreeva, A. P. Raiski, N. A. Belyasova, H. Möhwald, D. V. Sviridov, *Photochem. Photobiol. Sci.* **2011**, *10*, 1974.

[159] E. van der Pol, A. N. Böning, P. Harrison, A. Sturk, R. Nieuwland, *Pharmacol. Rev.* **2012**, *64*, 676.

[160] A. K. A. Silva, R. Corato, T. Pellegrino, S. Chat, G. Pugliese, N. Luciani, F. Gazeaua, C. Wilhelm, *Nanoscale* **2013**, *5*, 11374.

[161] a) C. J. F. Rijcken, O. Soga, W. E. Hennink, C. F. van Nostrum, *J. Control. Release* **2007**, *120*, 131; b) F. H. Meng, Z. Y. Zhong, J. Feijen, *Biomacromol.* **2009**, *10*, 197; c) V. Torchilin, *Eur. J. Pharm. Biopharm.* **2009**, *71*, 431.

[162] F. Q. Schafer, G. R. Buettner, *Free Radic. Biol. Med.* **2001**, *30*, 1191.

[163] R. Cheng, F. Feng, F. Meng, C. Deng, J. Feijen, Z. Zhong, *J. Control. Release* **2011**, *152*, 2.

[164] G. Wu, Y.-Z. Fang, S. Yang, J. R. Lupton, N. D. Turner, *J. Nutr.* **2004**, *134*, 489.

[165] B. Arunachalam, U. T. Phan, H. J. Geuze, P. Cresswell, *Proc. Natl Acad. Sci. USA* **2000**, *97*, 745.

[166] T. Kurz, J. W. Eaton, U. T. Brunk, *Antioxid. Redox. Signal.* **2010**, *13*, 511.

[167] a) F. H. Meng, W. E. Hennink, Z. Y. Zhong, *Biomaterials* **2009**, *30*, 2180; b) G. Saito, J. A. Swanson, K. D. Lee, *Adv. Drug Deliv. Rev.* **2003**, *55*, 199.

[168] a) X. B. Jiang, Y. M. Chen, F. Xi, *Macromolecules* **2010**, *43*, 7056; b) J. Q. Liu, H. Y. Liu, Z. F. Jia, V. Bulmus, T. P. Davis, *Chem. Commun.* **2008**, 6582.

[169] M. V. de Paz, F. Zamora, B. Begines, C. Ferris, J. A. Galbis, *Biomacromol.* **2010**, *11*, 269.

[170] M. A. Dewit, A. Beaton, E. R. Gillies, *J. Polym. Sci. Polym. Chem.* **2010**, *48*, 3977.

[171] A. Angelova, B. Angelov, R. Mutafchieva, S. Lesieur, P. Couvreur, *Accounts Chem. Res.* **2011**, *44*, 147.

[172] Y. Cheng, C.-Y. Tsao, H.-C. Wu, X. Luo, J. L. Terrell, J. Betz, G. F. Payne, W. E. Bentley, G. W. Rubloff, *Adv. Funct. Mater.* **2012**, *22*, 519.

25th Anniversary Article: Dynamic Interfaces for Responsive Encapsulation Systems

Ekaterina V. Skorb* and Helmuth Möhwald

Encapsulation systems are urgently needed both as micrometer and sub-micrometer capsules for active chemicals' delivery, to encapsulate biological objects and capsules immobilized on surfaces for a wide variety of advanced applications. Methods for encapsulation, prolonged storage and controllable release are discussed in this review. Formation of stimuli responsive systems via layer-by-layer (LbL) assembly, as well as via mobile chemical bonding (hydrogen bonds, chemisorptions) and formation of special dynamic stoppers are presented. The most essential advances of the systems presented are multifunctionality and responsiveness to a multitude of stimuli – the possibility of formation of multi-modal systems. Specific examples of advanced applications – drug delivery, diagnostics, tissue engineering, lab-on-chip and organ-on-chip, bio-sensors, membranes, templates for synthesis, optical systems, and antifouling, self-healing materials and coatings – are provided. Finally, we try to outline emerging developments.

1. Introduction

Interfaces are most important on one hand to understand and control colloidal systems with their large fraction of specific surface, on the other hand most processes start at an interface, and therefore they determine many physical and chemical properties. From a basic science point of view they exhibit peculiarities as low-dimensional systems and are anisotropic systems where molecules can be oriented. Macromolecules like proteins and peptides may change their secondary and tertiary structure and thus their function at interfaces. Within the strategy of building and understanding hierarchical structures they are positioned at the lowest length scale which one may also consider the base. Accordingly the main aim is to understand and to control molecular interfaces as regards structure, dynamics and properties. As an offspring of this the knowledge could be used to prepare complex films, coated colloids and capsules.

As a general trend in interface research an increase in complexity for advanced functional systems develops. Planar and non-planar interfaces mostly contain several substances of

proteins, polypeptides or nanoparticles, polyelectrolytes that are responsive to external stimuli or convert internal chemical and biochemical signals into optical, electrical, thermal and mechanical signals. Small molecules at the interface with their dynamics are relevant for drug delivery systems, self-healing materials, coating, tissue engineering, etc. This concerns reorganization of molecules, their diffusion as well as collective motion like flow under a surface pressure gradient.

Encapsulation of responsive active species is developing in two directions (Section 3): 1) capsules with different sizes from micrometer to nanometer ranges or encapsulation of biological objects; and 2) surface capsule formation for special surface nanoarchitecture connected with their applications. The complex encapsulation system could contain inorganic (silica or titania, Si, carbon or titanium nanotubes, halloysites, $CaCO_3$, etc.) and organic parts (low molecular weight species, natural (protein, peptides) or synthetic (polyelectrolytes, micelles) polymer substances together with some life objects (neurons cells, stem cells, yeasts, spores, bacteria, etc.)) (Section 4).

Stimuli responsive systems are based on the sensitivity of their building blocks (Section 5). Most common stimuli are determined by the soft organic part of the system. Stimuli responsive macromolecules are capable of conformational and chemical changes on receiving an external signal (T, pH, ionic strength, electromagnetic irradiation or magnetic field, electric potential, chemical composition or applied mechanical force). The discussed systems are planar films, coatings, non-planar capsules and micelles; as well as combinations of two non-planar in planar systems (surface capsules + coating) (**Figure 1**). Different architectures and fundamental approaches in the area provide specific advanced applications which are also highlighted in this review. Responsive planar polymer surfaces can be grafted polymer thin films or self-organized monolayers, thin films of polymer networks and self-assembled multilayered thin films. Different architecture provides control of dynamics (system response) and amplitude of changes of the interfacial properties, reversibility of the changes and the intensity of the external signal that could trigger the changes. The inorganic part of encapsulation systems, for example mesoporous particles themselves or being a core of polyelectrolyte 3D capsules, could be bonded with an encapsulated chemical with relatively weak bonds or chemisorbed. The release from such systems is responsive to external or internal stimuli.[1] This review discusses trends and challenges in designing next generation

Dr. E. V. Skorb, Prof. H. Möhwald
Max Planck Institute of Colloids and Interfaces
Wissenschaftspark Golm, Am Mühlenberg 1
Golm, 14424, Germany
E-mail: skorb@mpikg.mpg.de
Dr. E. V. Skorb
Chemistry Department
Belarusian State University
Leningradskaya str. 14, Minsk, 220030, Belarus
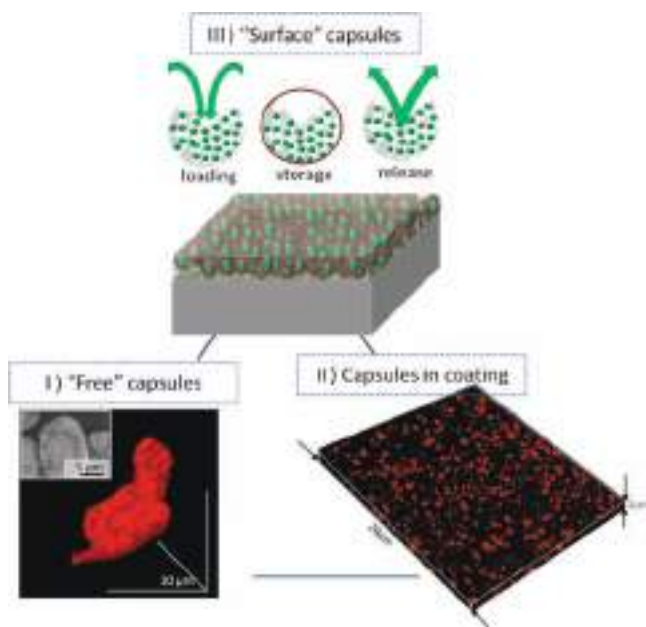
Figure 1. Three types of encapsulation systems. (I) "Free" capsules of different sizes from submicron to micron scale can be based on mesoporous carriers (e.g., SiO_2, TiO_2, Si) or 1D tubular structures (e.g., halloysites, carbon nanotubes), polymer or hybrid material. A magnesium/polypyrrole capsule is presented as an example. Reproduced with permission.[2e] Copyright 2012, Royal Society of Chemistry. (II) Capsules can be introduced into a coating (e.g., sol-gel, polymer, between polyelectrolytes layers) after their synthesis. Confocal fluorescent 3D image of titania based capsules in sol-gel SiO_x-ZrO_x coating. (III) "Surface " capsules are formed in a surface via its nanostructuring (e.g., formation of mesoporous surface sponges well adhering to the bulk material, anodization process with formation of 1D oriented nanotubes). Reproduced with permission.[2a] Copyright 2012, Wiley.

Ekaterina V. Skorb received her diploma degree in chemistry at Belarusian State University in 2005. She got her PhD from the same university in physical chemistry in the area of photochemistry in 2008. She came to the Max Planck Institute of Colloids and Interfaces as a Humboldt fellow in 2010. She is currently a senior lecturer at Belarusian State University and an independent researcher in the Max Planck Institute of Colloids and Interfaces. Her research interests include study of the processes on dynamic interfaces, fabrication and characterization of stimuli-responsive encapsulation systems, nanomaterials, drug delivery systems for "smart intelligent" nanoarchitecture.

Helmuth Möhwald received his diploma in physics (1971) and PhD (1974) from the University of Gottingen (Germany) for research in organic solids. In 1981 he became associate professor in biophysics at TU Munich and in1987 a chair in physical chemistry at the University of Mainz. He became founding director of the Max Planck Institute of Colloids and Interfaces in Potsdam in 1993. His main research interests include chemistry and physics in confined spaces, dynamics at interfaces, and supramolecular interactions.

carriers for a broad range of applications both in vivo and in vitro.

One specific task in designing intelligent systems is to provide systems with multi trigger stimuli response – multi-modal systems – to mimic of natural systems. A multi-responsive system can be achieved (i) with combining in one system the sub-organization of blocks responsive to different stimuli; (ii) with spatially and temporally resolved release from multi-chemical delivery systems. Moreover mimicking both encapsulation and release processes would be of high priority. There are some background ideas presented in Section 6.

Responsive encapsulation systems are finding an increasingly large number of applications in biomedicine and drug delivery, optical materials, bio-sensors and bio-membranes, templates for synthesis, surface coatings, photonics, self-healing and antifouling surfaces. Some specific examples of advanced applications are presented in Section 7, which focuses on recent developments including highlights in use of multi-modal systems for specific applications.

2. Principles of Encapsulation Systems

Use of encapsulation systems has been started before people did understand the principle of their intelligent design and nano-organization. Thus dairies on use of perfumes which smell differently during a day, drug pills with prolonged action, go back to many centuries. Nowadays encapsulation is an imperative technology in pharmacy, food industry and medicine. Recent progress in science provides understanding of design principles and fundamental scientific background of encapsulation systems for wider areas of advanced applications including further progress in drug delivery, diagnostics, tissue engineering, lab-on-chip and organ-on-chip, membranes, templates for synthesis, optical systems, bio-sensors, antifouling, self-healing materials and coatings. The encapsulation systems have been developed mainly in two directions to be used as "free" systems (Figure 1I) or being immobilized on surfaces (Figure 1II). Most recently[2] it was suggested that if specific applications are connected with use of planar surfaces – self-healing, antifouling surfaces, material for tissue engineering, implants – it would be more reasonable to provide systems where surface capsules are not immobilized,
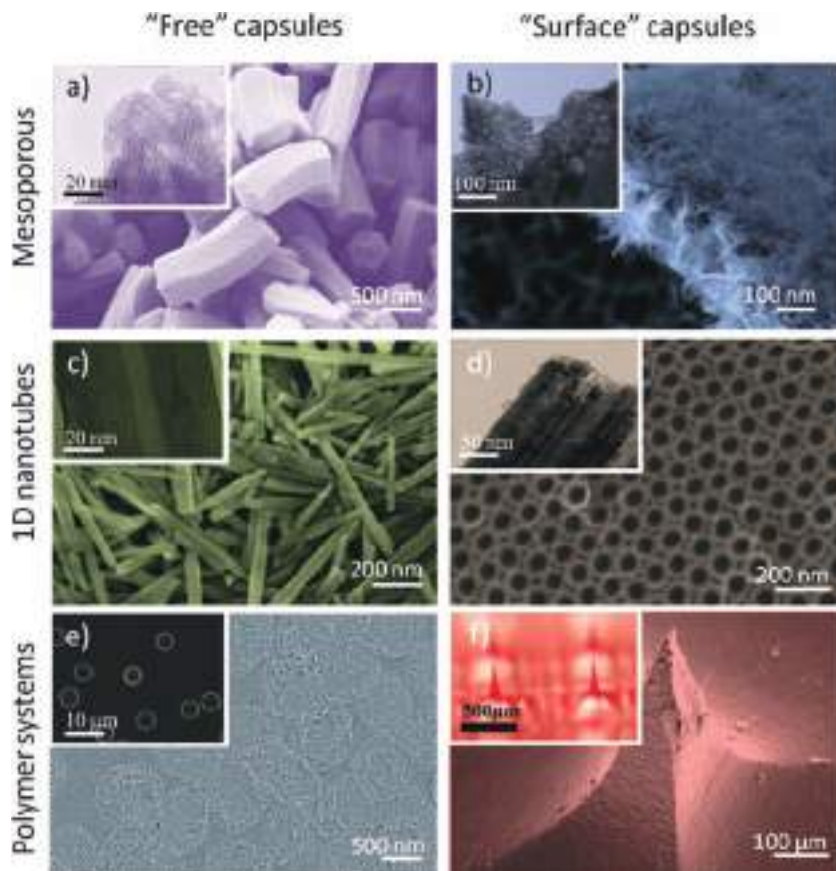
Figure 2. Example of materials for "free" and "surface" capsules. a) SEM and TEM (inset) of mesoporous silica. Reproduced with permission.[32] Copyright 2009,Wiley. b) SEM and TEM (inset) of surface metal sponges. Reproduced with permission.[2a] Copyright 2012,Wiley. c) SEM and TEM (inset) of halloysites. Reproduced with permission.[11a] Copyright 2012, Wiley. d) SEM and TEM (inset) of surface titanium nanotubes. e) SEM and scanning confocal fluorescence microscopy image (inset) of fluorescently labeled domain-like capsules of polydiallyldimethyl ammoniumchlorid/molybdate.[36] Copyright 2009, Royal Society of Chemistry. f) SEM and optical image (inset) of drug-loaded silk microneedles.[13] Copyright 2012, Wiley.

Mesoporous carriers are often used as core of encapsulation systems (**Figure 2**a,b).[5] The core material is variable and depends on the desired potential application. It could be, for example, highly luminescent biocompatible silicon,[6] highly porous silica particles (MCM-41, MCM-48, etc.)[7] or photosensitive mesoporous titania,[8] biocompatible and biodegradable calcium carbonate,[9] metal sponges for anticorrosion, antifouling, lab-on-chip and tissue engineering materials,[2] $CdCO_3$ and $MnCO_3$,[10] etc. 1D nanotubes (Figure 2c,d) with defined kinetics of diffusion from oriented channels and being excellent templates for synthesis are also very prospective to be the core of encapsulation systems: natural tubule halloysites,[11] surface anodized aluminum or titanium layers,[12] carbon nanotubes.[13] Some specific features of inorganic carriers can be mentioned. i) In some cases stabilization of "free" inorganic carriers (Figure 1I) is needed to avoid aggregation, and ii) during immobilization of them in coating (Figure 1II) they can have low compatibility with organic coating and decrease coating adhesion and long term stability. Simultaneously they can be effectively used in sol-gel coatings.[11] Inorganic carriers are shape constant and thermostable at high temperatures, in comparison with most polymer systems.

Polymers are traditional and ubiquitous components in designing drug delivery carriers (Figure 2e,f).[14] The main properties of polymers depend on such parameters as their molecular weight, the persistence length and grafting ratio/charge density of functional groups.[15] These parameters determine the melting temperature of polymers, their thermal properties, hydrodynamic radius, and configuration. Complexation of polymers due to opposite charges is used in assembling polyelectrolyte multilayers, while their alternative deposition leads to layer-by-layer (LbL) films which can be constructed either on planar substrates[16] or on nonplanar (spherical,[9,17] cubes,[10] etc.) templates. Assembling LbL layers on non-planar templates followed by dissolution of the templates resulted in the production of 3D polymer capsules with semipermeability. The capsule permeability depends on nature of polymers used for LbL and number of layers. Combination of inorganic carriers and organic LbL for formation of capsules allow to decrease number of LbL without negative effect to diffusion from such capsules.[8] Moreover an advantage of an inorganic carrier, e.g., constant shape, is achievable for the hybrid system, in comparison with pure polymer capsules which can deform dramatically during their immobilization inside coating.

Polymer capsules with strong barrier properties in acidic media could be prepared by conductive polymers through their chemical or electrochemical synthesis, e.g., polypyrrole capsules

but formed in surface vis-à-vis surface nanostructuring with existing methodology (Figure 1III). Examples of possible methods for surface nanostructuring are highlighted in a recent review:[1a] electrochemical surface modification, plasma etching technologies, laser induced surface modification, chemical etching, sol-gel route and bio-inspired ultrasound assisted methodology. Direct formation of encapsulation systems in a surface provides an effective manner for submicron delivery vehicles for prolonged release of easily diffusing low molecular weight substances: corrosion inhibitors, biocide agents.[2a]

Typically encapsulation systems are from submicron to micrometer ranges. The size range is particularly important for in vivo applications because only nanometer-sized delivery vehicles can be used for circulation.[3] Micrometer sized capsules are still very attractive objects because of the simplicity, of superior loading capacity, and large surface area for modification. In addition capsules of several hundred of micrometers may provide the development of the manner of release and reveal the feasibility of direction-specific release.[4]

were successfully prepared on stainless steel electrodes,[18a] by in situ polymerization of pyrrole in polymer matrix[18b] or by LbL deposition of polyelectrolytes and polypyrrole.[18c] The size of the capsule and the thickness of the polypyrrole shell (up to their complete filling with grown polypyrrole) can be varied by changing both the scan speed of the electrode potential and potential range.

Capsules made of cross-linked polymers and liquid core are also attracting great attention.[19] Thus three types of polymers with high cross-link density – polyurethane, polyurea, and polyamide – can be examples of systems enabling storage of low molecular weight substances. The structure of the resulting capsules depends on the type of polymer. Polyurethane and polyurea formed "compact" microcapsules, while in the case of polyamide nanoscale core@shell structures were formed. "Compact" morphologies form due to the high affinity of the liquid capsule component to the polymer; core@shell morphology is formed when the affinity is low. Application of the Hansen solubility parameters approach allows prediction and control of the morphology of capsules made of cross-linked polymers.

Thermal conversion in polymers, e.g., conversion of the polyamide layers into polyimide coatings, provides an effective manner for encapsulation.[20] The thickness of the polyamide/polyimide shells can be size variable.

Emulsion carriers can be used as core of encapsulation systems.[21] Various shells around emulsion droplets can be mentioned: polyelectrolytes,[22] nanoparticles,[23] proteins,[24] enzymes,[25] etc. The layer growth is governed by their electrostatic, hydrogen bonding, hydrophobic, etc. forces and allows the formation of nanostructured shells.

The combination of two acoustic phenomena (emulsification and cavitation) provides versatile ultrasonic assisted ways for microcapsule formation.[26] The yield of microspheres strongly depends on the temperature/time profile of the solution during irradiation. In the preparation of protein microspheres by ultrasound, the sizes of microspheres are affected by the sonication variables, such as energy input and sonication time.[27] It was found that the mean sizes of the ultrasonically prepared emulsions decrease with the increase of sonication time and sonication amplitude.[28] The dispersion of emulsion size during ultrasonic fabrication is caused by the uneven distribution of acoustic energy in the ultrasonic vessel and the region with intensive energy is restricted to areas close to the sound emitting surface of the ultrasonic probe producing the emulsion particles with the minimal size. Far from this area the acoustic energy decreases sharply, which results in the formation of big microspheres.

Nowadays one can choose the right encapsulation system: i) for specific application, e.g., "free" capsule or planar system, capsule sizes; ii) taking into account conditions which will be applied to form final system, e.g., high temperature, bent fracture during formation of anticorrosion coatings; (iii) biocompatibility and kinetics of (bio)degradation; (iv) achieved encapsulation efficiency, e.g., high free volume, pore sizes; (v) with low cost and (vi) high stability.

3. Encapsulation and Release

There are several possibilities for encapsulation of needed material. The chosen method for encapsulation depends on 1) nature of species to encapsulate, e.g., low molecular weight substance[7,8] or macromolecule,[29] biological object,[30] hydrophilic/hydrophobic agent; [31] 2) capsule material, e.g., possibility of hydrogen or chemical bonding,[2a] electrostatic interaction;[16,17] 3) limitation of capsule sizes, e.g., in some cases nanocarriers can be toxic or, on contrary, needed for circulation;[4] 4) time-dependent release, e.g., either just prolonged release is needed with slow release or stimuli responsive release;[1] 5) spatially dependent release, e.g., localization of release profile,[8] etc. Moreover encapsulation could happen i) after capsules are already formed (for example, mesoporous systems,[32] trapping in LbL capsules using physico-chemical stimuli which influence the interaction of polymers and, correspondingly, the permeability of capsules;[33] ii) together with capsules' formation (adsorption in porous $CaCO_3$ core followed by LbL polyelectrolyte deposition and core dissolution,[33] emulsions;[22] iii) capsule shell or core could be an active material (molybdate based capsules for corrosion protection;[34] and iv) combined approach (combination of mentioned i-iii, or several encapsulation systems in one, e.g., multicompartmental and anisotropic micro- and nanocapsules.[35]

In the case of mesoporous carriers if they are placed to the solution containing active agent the pores suitable in size for encapsulation of dissolved agent are loaded with it due to a concentration gradient (**Figure 3**).[31] Surface phenomena and surface tension determine the process.[36] The exact nature of the bonding depends on the species involved, but the adsorption process is generally classified as physisorption[37] (e.g., weak van der Waals forces) or chemisorption[2a] (characteristic of covalent bonding), it may also occur due to electrostatic attraction.[17] Oxygen-containing compounds (Si, silica and titania, metal sponges, etc.) are typically hydrophilic and polar. Carbon-based compounds are typically hydrophobic and non-polar, including materials such as activated carbon and graphite. Polymer-based compounds are polar or non-polar functional groups in a polymer matrix. Mesoporous carriers could be in the form of 3D capsules[5] or surface immobilized.[7] Due to complex pore shape the prolonged release is possible even without formation of any protective shell. There is an attractive possibility to prevent release by relatively dynamic chemical bonding between mesoporous carrier and encapsulated agent without any other shell.[2a]

Thus silicon, metal sponges, SiO_2 and TiO_2 mesoporous carriers could chemisorb species through oxygen bridges.[2a,5,6] Moreover there is an attractive possibility to chemically graft organic species by direct oxygen free surface-carbon bonding, for example Si–C bonding[38] by thermal hydrosilylation. The process is the "alkanethiols on gold" analogue reaction of the silicon system, allowing the chemist to place a wide variety of organic functional groups on a silicon or porous silicon surface.[39] The main requirement of the reaction is that the surface provides hydrogen bonding, e.g., in the case of mesoporous silicon[40] or metal sponges.[2]

For 1D carriers, e.g., halloysites,[11] carbon nanotubes[13] or surface titanium nanotubes,[12] in the case of unprotected systems there is a limitation of the proposed delivery systems. In particular the quantity of chemisorbed material is too low compared to the mesoporous systems. A direct diffusion of physically encapsulated molecules is relatively fast. The release
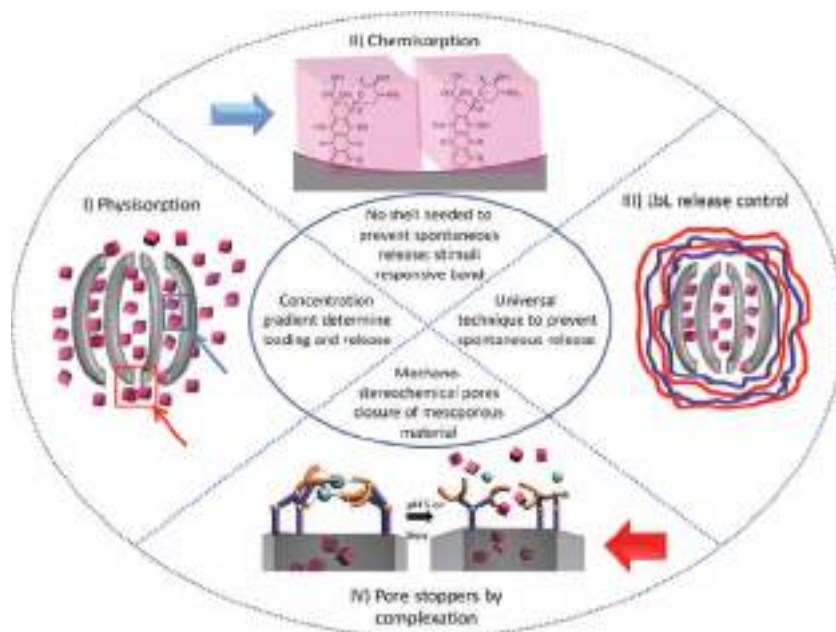
Figure 3. Encapsulation and release methodology. Scaffold for encapsulation is shown in grey. Encapsulated active species are shown as pink cubes. (I) Physisorption is widely used for material encapsulation into all types of encapsulation systems. (II) Chemisorption, example of doxorubicin molecule shown, as a prospective strategy for encapsulation systems. (III) Poly-electrolytes layer-by-layer (LbL) assembly is a universal technique to prevent release from all types of encapsulation systems. LbL provides ease, reversible, stimuli responsive loading and release prospects. (IV) Illustration of stopper design: a nanogate composed of two iminodi-acetic acid molecules and a metal ion (blue spheres) on mesoporous silica nanoparticles. Reproduced with permission.[68] Copyright 2013, American Chemical Society. The blue arrow in (I) highlights increased in (II) channel for chemisorption of molecules. The red arrow in (I) presents possible place for (IV) stoppers.

kinetics depends on the structure dimensions and geometry. There are suggestions that at a size scale of 100 nm and larger, diffusion of drug molecules is largely insensitive to tube diameter and the total drug release is dependent only on the tube length.[41] Nevertheless this high burst release can be beneficial for some applications (e.g., preventing bone infection in the cases of implant with drug loaded titanium nanotubes) in the case if it does not exceed optimal therapeutic dosage.

A versatile universal approach to prevent physisorbed encapsulation agent diffusion from the mentioned mesoporous carriers and 1D tubular structures is formation of a protective LbL assembly shell (Figure 3III).[8] 3D polyelectrolyte capsules were initially suggested to be prepared by LbL adsorption of oppositely charges polyelectrolyte molecules around micron or submicron inorganic template cores with following core dissolution.[16] Although LbL coating of uncharged colloids was reported,[42] the charge still remains one of the main prerequisites in assembling polyelectrolyte multilayers.[43] Later on it was suggested that the core could be left and be advanced for certain applications: self-healing,[1,44] multi-component loading and time resolved drug delivery,[45] antifouling and anticorrosion surfaces,[1,2,46] etc. Moreover the number of layers which was enough to protect release of the encapsulated material could be decreased: two bilaers were enough to prevent release from mesoporous silica and titania capsules.[10] Although for LbL assembly and shell components synthetic polyelectrolytes,[19]

were initially suggested, nowadays the approach is expanded to biocompatible poly-ions,[47] proteins,[48] deoxyribonucleic acid,[49] lipids,[50] multivalent ions,[51] small dye molecules,[52] charged nanoparticles,[53] dendrimers,[54] micelles.[55] The diversity of possible building-blocks is most promising for functionalization. Recently by Zhang et al.[56] it was shown interesting approach to use LbL assembly of azulene-based supra-amphiphiles for reversible encapsulation of organic molecules in water by charge-transfer inter-action: the loading capacity can be regulated by change of the layer pairs, selective pyrene uptake is capable by recognizing the hydrophobic template molecule in water, the reloading process increases with increasing of temperature.

An example of such functionalization development is a new class of polyelectrolytes with modular biological functionality and tunable physicochemical properties which have been engineered to abrogate cytotoxicity. Highly permeable, hydrogen-bonded multilayers allowing gentle cell encapsulation using non-toxic, non-ionic and biocompatible components such as poly(N-vinylpyrrolidone) and tannic acid which were earlier exploited on abiotic surfaces but never assembled on cell surfaces were also presented recently.[30b] Encapsulation of *Saccharomyces cerevisiae* yeast cells with lightly cross-linked polymethacrylic acid was suggested.[30a] Neuron cellular uptake of biodegradable and synthetic polymeric microcapsules was demonstrated in situ.[30d] With the examples it is seen that nowadays encapsulation is not limited just for active molecules, but also expanded to biological objects with prospects of mimicking natural processes.

Porous thin layers of hydrogel films exhibit stimuli-dependent, e.g., pH-dependent, porosity and can be used as LbL for pore closure of encapsulation systems.[57] Thus, increase of pH and subsequent swelling of porous gel films causes the growth of a pore size, and at decreased pH the polymers demonstrate the opposite behavior. More and more attention is directed to hydrogels based on natural polymers.[58] Thus hydrogels designed with natural polymers as building blocks display multiple advantages over synthetic polymer networks with respect to their biocompatibility, biodegradability and good cell adhesion properties. The main classes of natural polymers studied in hydrogel formulations are polysaccharides (e.g., alginate,[59] dextran,[60] hyaluronan,[61] chitosan[62]), proteins/polypeptides[63] (e.g., collagen,[64] fibrin[65] and gelatin.[66]

Release control is also achievable with complex stoppers (Figure 3IV). Thus controllable release of benzotriazole from halloysite nanotubes could be achieved by the formation of metal-benzotriazole complex caps (stopper) at halloysite tube endings by the interaction of leaking benzotriazole and metal ions from the bulk solution.[67a,b] The suggested method requires only a short rinsing of benzotriazole-loaded halloysite

nanotubes with an aqueous solution containing metal ions. Formation of stoppers at halloysite tubes is suggested through using Cu(II) ions. The release rate depends on a number of parameters, such as the chemistry and morphology of halloysite samples, the concentration and type of metal ion, and the concentration of benzotriazole available.

There are impressive developments in the area of supramolecular chemistry, i.e., host–guest complexes,[67c] and mechanostereochemical phenomena (e.g., cucurbits[67d–f] and bistable rotaxanes) to use them for pore closure of mesoporous materials (Figure 3IV),[68] e.g., MCM-41, etc. The feature in focus is stimuli response of the host-guest complexes, stimulated by changes in pH, light and redox potentials, magnetic field, in addition to enzymatic catalysis. Complexes of low molecular weight substances with polyelectrolytes can be also used for pore closure of a mesoporous system, e.g., benzotriazole or 8-hydrohyquinoline with sodium polystyrene sulfonate.[2a,34]

Additional functionalization in some cases needs double-, multi- encapsulation systems. Thus, for example, it was suggested to use micellar drug carriers to encapsulate hydrophobic drugs into titanium nanotubes.[12] An electrostatically mediated liposome-fused mesoporous system was suggested.[69] The negatively charged drugs are absorbed into the pores of silica. To increase cargo retention, the positively charged silica

is fused with an anionic liposome, 1,2-dioleoyl-sn-glycero-3[phospho-L-serine], followed by further lipid exchange with a cationic liposome, 1,2-dioleoyl-3-trimethylammoniumpropane.

4. Prospects of Stimuli Response

To gain fundamental knowledge on "smart" stimuli responsive systems with regulated release and/or interface behavior, e.g., cell/surface interaction, prompt feedback effects are important aims. In particular, specific applications, e.g., interaction with life systems need dedicated adaptive stimuli of nanoengineered systems.

System design is such a way to provide regulated release materials following a change in stimuli (**Figure 4**) (pH, temperature, ionic strength and solvent, electromagnetic and magnetic field, ultrasound, mechanical action, biological species, e.g., enzymes and cell receptors, etc). Stimuli to choose depend on system applications. Moreover multi-trigger systems are of high priority. Simultaneously one should avoid systems are too complicated to understand fundamental aspects of their stimuli response. Since parts of the system would affect at each other.

Chemically encapsulated species can be detached through chemical stimuli, pH, ionic strength, solvent; or biological stimuli, enzymes, cell receptors.[1] Physical stimuli, e.g., electromagnetic irradiation could be also applied resulting in following chemical changes. Under electromagnetic irradiation with suitable wavelength on titania (Figure 4b)[8,70] or on Au nanoparticles[71] production of reactive oxygen species takes place which could influence the stability of chemisorbed bonds and encapsulated species can be released on demand by irradiation. Moreover production of reactive species affects the system responsive behavior. It is known that self-healing ability of the titania surface could be optimized through immobilization of noble nanoparticles.[72] In particular, the nanostructured photocatalysts TiO_2, $TiO_2:In_2O_3$, TiO_2/Ag, and $TiO_2/Ag/Ni$ prepared as thin film on ceramic substrates by spraying oxide sols with subsequent silver photodeposition and electroless nickel deposition were screened for their antibacterial efficiency against *P. fluorescens* and *L. lactis*. The photocatalysts show higher activity against *L. lactis* than *P. fluorescens* that can be explained in terms of different morphologies of gram positive and gram negative cell envelopes. Gram positive bacteria were more sensitive to $O_2\bullet^-$. Probably, active species initiate different deactivation mechanisms of OH• due to cell wall degradation/mineralisation, and $O_2\bullet^-$ affects the cell nucleus. In some cases over exposure can be a problem and provide system degradation. When TiO_2 is used as capsule carrier in introduced in anti-corrosion coating during over irradiation the
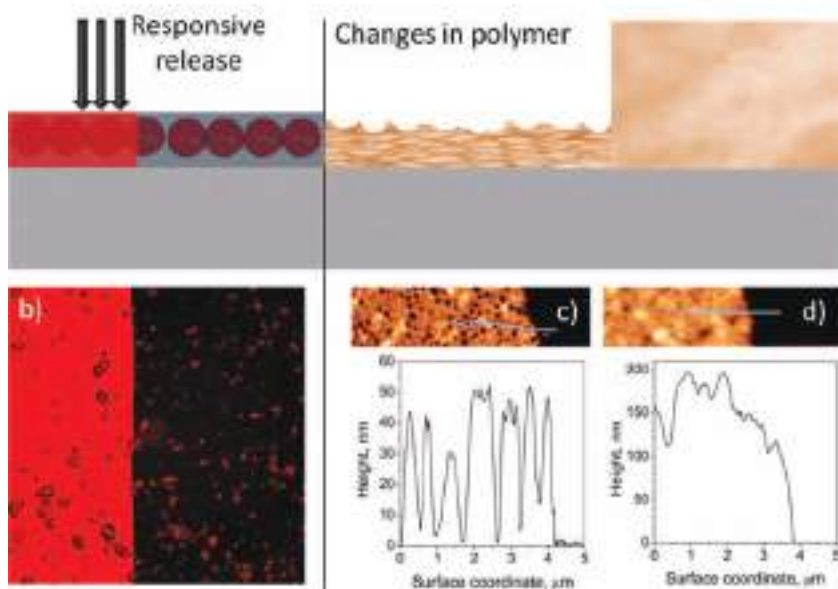
Figure 4. Stimuli responsive systems. a) Different stimuli (physical, chemical or biological) could provide system activation as shown in left release from encapsulation system or shown in right provide changes in responsive polymer part. b) Scanning confocal fluorescence microscopy image of coating immobilized titania-polyelectrolyte capsules after laser irradiation. There is release on irradiated part (left) and capsules are stable in nonirradiated surface (right). Reproduced with permission.[8a] Copyright 2009, Royal Society of Chemistry. c, d) SPM topography images and cross-section profiles of a porous gel membrane (c) at pH 2 – open pores, the thickness of the swollen film is 1.2 times the thickness of the dry film and (d) at pH 5.5 – closed pores, the thickness of the swollen film is 5 times the thickness of the dry film. Reproduced with permission.[83] Copyright 2012, Royal Society of Chemistry.

anticorrosion coating can be slowly degraded due to photocatalytic activity of titania.

One more attractive possibility of laser-induced cell detachment on gold nanoparticle functionalized surfaces was demonstrated recently.[71] It is interesting that the selective cell detachment from nanoengineered gold nanoparticle surfaces, triggered by laser irradiation, occurs in a nonthermal manner. It was shown that detachment is attributed to a photochemical mechanism due to production of reactive oxygen species under illumination of gold nanoparticles by green laser light. It was also demonstrated that cells migrate from unirradiated areas leading to their reattachment and surface recovery which is important for controlled spatial organization of cells in wound healing and tissue engineering.

Stimuli responsive release systems based on LbL encapsulation were developed extensively in recent decades and highlighted several times in competent reviews.[1,2,4a,14,15,21,73] Uncontrollable release can be regulated with all types of stimuli – chemical, biological, and physical – by proper LbL design. Thus centers of adsorption of electromagnetic irradiation centers between LbL, e.g., Au nanoparticles,[74] or titania,[8] provide LbL sensitivity to electromagnetic irradiation. It is very important that LbL system can resealed after stimuli stop which allows step-wise release for LbL based capsules.[75] The material response to external stimuli is reversible and several transitions forwards and backwards are possible. Polyelectrolytes are a class of polymers which carry charged functional groups; these groups avail a variety of control of physical–chemical properties as biodegradability, pKa or the glass transition temperature of the polymer complex. Thus LbL themselves can be sensitive to pH.[32] LbL films prepared from the aqueous polyelectrolyte solutions can increase their thickness by adding salt to these solutions.[76] The reason for such changes in thickness of the film is a different conformation of the polyelectrolyte chains. They are flat and parallel to the substrate without salt, meanwhile in the solutions with higher salt concentration the chains form loops and then are adsorbed at the interface.[77] Therefore, the polyelectrolyte density of the films prepared from solutions without salt is considered to be lower than the polyelectrolyte density of films made with a salt additive.[78]

Polymer protection prepared from polypyrrole shells of the microcontainers exhibits very strong barrier properties in acidic media at 2<pH<7 and a high permeability at pH>7, providing effective encapsulation of low molecular weight species at low pH values.[18]

As advanced surface encapsulation systems which are capsules formed in surfaces metal sponges are suggested (Figure 2b). The encapsulation possibilities inside the surface carrier were already mentioned together with regulation of release properties, especially from surface capsules, e.g., mesoporous metal sponges.[2] Real-time control and reversibility of biomolecule/surface interactions at interfaces are an increasingly important goal for a range of scientific fields and applications. A further step in advanced intelligent systems is surface functionalization with various nonspecific or specific functional groups for engineering surface response. In general, hydrophilic surfaces that are nonreactive to proteins or cells are alternated by adding functional molecules that can undergo conformational changes or phase transitions in such a way that they expose demanded molecular fragments or even phases at the interface upon external signal.[79] In many cases, hydrophobic fragments,[80] electrically charged groups,[81] polypeptide chains,[82] micelles[2d] or hydrogels[83] were used for the stimuli-triggered exposure at interfaces. In this way, nonspecific hydrophobic and electrostatic interactions or specific antibody-antigen interactions were switched on to bind proteins and cells by external signals.[84] This interaction could be irreversible or reversible, if a proper balance between attractive interactions and steric repulsion was achieved in the latter case. By using new design techniques, response times from surfaces can now be tuned smoothly from seconds to hours.

A specific example of stimuli-responsive thin films protective for surface drug carriers involves macromolecules that are grafted chemically to a surface at sufficiently high grafting densities, so that the polymer chains experience excluded volume repulsions and adopt a stretched conformation. There is a disadvantage of the grafting of stimuli responsive polymers to the surface: limitation of the surface material. Use of special building blocks, e.g., stimuli responsive micelles,[2d] adsorbed at different surfaces together with LbL methodology provide universal control and help solving the problem.

The field of stimuli-responsive, smart or switchable systems has generated much research interest due to its potential to attain unprecedented levels of control over bioobjects (biomolecules, bacteria, cells) adsorption processes and interactions at engineered interfaces, including the control over reversibility of adsorption. Advances in this field are particularly relevant to applications in the areas of biosensing, chromatography, drug delivery, lab-on-chip, organ-on-chip, regenerative medicine. The control over bioadsorption and desorption processes at interfaces is often used to control subsequent events such as cell–surface interactions.[32] Considerable research interest has been directed at systems that can be reversibly switched between interacting and non-interacting states and used thus for switching, on and off, bio-interfacial interactions such as protein adsorption. Such switchable coatings often incorporate features such as temporal resolution, spatial resolution and reversibility. Switchable interfaces employ stimuli such as light, temperature, electric potential, pH and ionic strength to control protein adsorption/desorption and cell attachment/detachment.

Thermal variations of the material environment have been used to induce the reconstruction of the polymer brushes and their properties. For example, poly(N-isopropylacrylamide) (PNIPAM) brushes possess a lower critical solution temperature (LCST), above which the material is insoluble, at about 35 °C in water.[85] The polymer expands in water at room temperature and its surface becomes hydrophilic.[86] Above the LCST, the polymer collapses and its surface gets less hydrophilic. This responsive characteristic can be used in the regulation of protein adsorption at the substrate surface. Thus, at room temperature protein adsorption on the PNIPAM film is negligible, while above the LCST the film surface becomes more hydrophobic and interacts more strongly with the proteins.[87] Some zwitterionic polymer brushes possessing an upper critical solution temperature (UCST), above which the polymer is miscible, tend to change their wetting characteristics oppositely with temperature.[88]

Polymer nanoparticles which have a network structure and therefore possess properties of hydrogels are called nanogels.[89] They also demonstrate heat responsive behavior.[90] The PNIPAM–polysaccharide (grafted) copolymer nanogel dissolves in cold water and congregates into nanogels because of collapse of the PNIPAM chains at high temperature.

Thin hydrogel films (Figure 4c-d)[91] together with the above LbL polyelectrolyte multilayer nanonetwork[46c] are examples of systems which exhibit sensitivity to pH changes. The rise of pH leads to ionization of the weakly acid segments of hydrogels as in polyelectrolytes the functional groups of the weak polymers.[92] It causes the repulsion between uncompensated charges and in order to balance these charges the concentration of the counter ions inside the system increases. As a result, the osmotic pressure grows, causing water infiltration and swelling and therefore increasing their mobility. The decrease of pH leads to protonation, reduction of osmotic pressure, expulsion of water and shrinking of the polymer structures.

The change in electric potential across polyelectrolyte gels induces changes in their conformation.[93] This property of polyelectrolyte gels was demonstrated on a polyacrylamide gel, across which an electrical field was applied. With an application of the electric field a force was produced on H^+ as well as on the negatively charged acrylic acid groups, which caused the shift of the gel towards the positive electrode. This shift created a stress along the gel axis with its minimum at the negative electrode and the maximum at the positive one and, as a result, the gel was deformed. With the increase of the voltage above 2,15 V the gel completely collapsed, and one could obtain the original form when the electric field was removed.

Novel biocompatible hybrid-materials composed of iron-ion-cross-linked alginate with embedded protein molecules have been designed for signal-triggered drug release.[94] Electrochemically controlled oxidation of Fe^{2+} ions in the presence of soluble natural alginate polymer and drug mimicking protein (bovine serum albumin) results in the formation of an alginate-based thin-film cross-linked by Fe^{3+} ions at the electrode interface with the entrapped protein.

Altering of surface composition and physical properties of the material can be achieved through the change of a surrounding medium. For example, mixed polymer brushes made of polystyrene and poly(2-vinylpyridine) macromolecules were found to alter the surface composition and wettability after changing the solvents.[78] Further, mixed brushes prepared from polystyrene and poly(methylmethacrylate) change their surface topography in different solutions, and it stimulates the local motion of different objects adsorbed on the surface.[95] Also, poly(ethyleneimine)–poly(dimethylsiloxane) mixed brushes, hydrophilic in water switch to hydrophobic state in air.[96]

Ultrasound has the potential for control of the permeability of encapsulation systems.[97] Polyelectrolyte microcapsules with zinc oxide nanoparticles in their shell proved to have potential as drug-delivery systems with the possibility of opening under the action of ultrasound. Moreover a way to localize capsules with magnetic particles under the ultrasonic horn and their stimuli opening were demonstrated.

Targeting by a magnetic field is one of the main functions of magnetic nanoparticles incorporated into capsules. Furthermore, the therapeutic performance of capsules can be enhanced if magnetic field triggered release is achieved.[98]

It was mentioned above that laser can be stimuli to provide catalytic activity of gold to provide formation of reactive oxygen species.[71] Simultaneously laser-induced remote release can be based on localized heating of the polymeric component in hybrids in the vicinity of metal nanoparticles absorbing laser light.[74] Thus, the polyelectrolyte multilayer becomes mobile above the glass temperature of the polyelectrolyte complex. It should be noted that excessive heating is undesirable for living cells, but it is desirable for cancer treatment. Besides noble nanoparticles, to make surface light switchable special molecules can be suggested. For example, azobenzene molecules, which undergo transitions from cis- to trans-configuration upon exposure to light close the pores in a cooperative way thus entrapping molecules inside, e.g., a porous surface.

Recent studies[1] also aimed to use processes in functional systems to provide stimuli release in a certain time period (**Figure 5**). Thus the possibility to use the cell metabolism to initiate stimuli response is extremely interesting as an example of self-responsive system.[2d] *Lactic* bacteria in their life cycle produce lactic acid and decrease the pH without using external stimuli. If a special stimulus sensitive system is included in the design of the surface where bacteria are grown, bacteria affect the material resulting in system response. pH responsive
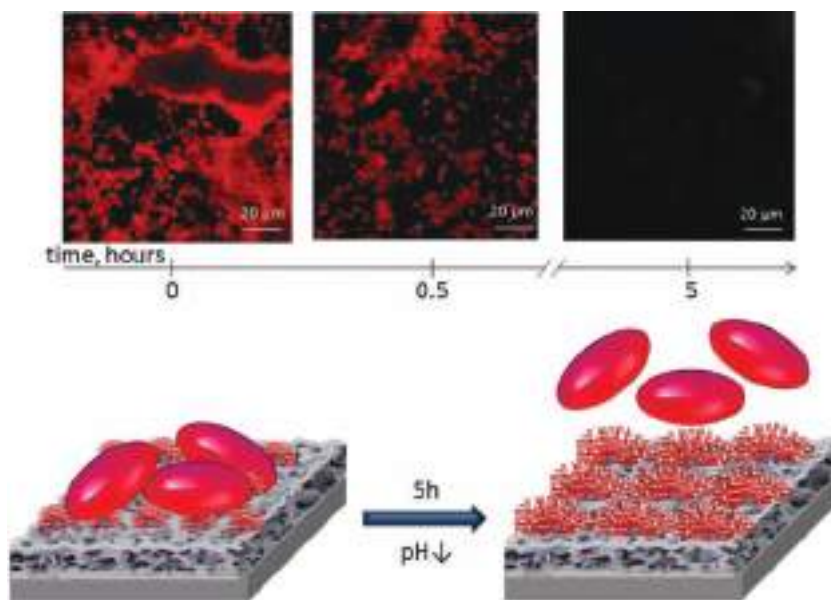
Figure 5. Self-controllable system. Confocal kinetic study (fluorescence mode) and schematic illustration of pH triggered self-cleaning behavior of the porous metal surface covered with pH responsive micelles. As model cells *Lactococcus Lactis 411* bacteria (loaded with Rh6G) were used. Bacteria decrease pH, micelles respond to change and increase in size, bacteria detach from the surface. Reproduced with permission.[2d] Copyright 2012, Wiley.
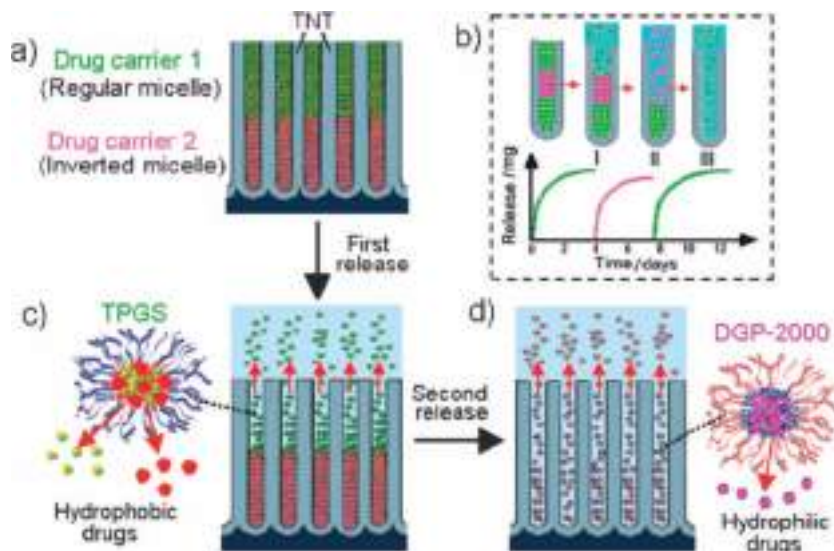
Figure 6. Multi-drug delivery. Scheme of multi-drug release using titania nanotube arrays (TNT) and polymer micelles as drug carriers. (a) TNT loaded with two types of polymer micelles, a regular micelle (TPGS) encapsulated with hydrophobic and inverted micelle (DGP 2000) encapsulated with hydrophilic drug; (b) scheme of sequential drug release with layered drug carriers with details of two step drug release in (c) and (d). Reproduced with permission.[45] Copyright 2012, Royal Society of Chemistry.

micelles which could increase their corona size depending on pH, being part of a responsive system could "push off" the bacteria from the surface.

5. Multi-Modal Systems

It is likely that future developments will be based on multicomponent and multifunctional, hierarchically organized interfaces that combine properties of functional materials and devices together with multi trigger stimuli response of the system. Multifunctionality achieved by tailoring the composition, structural, physico-chemical and mechanical properties at the nanometer scale and combination of stimuli responsive building blocks provides advances for system intelligence and multifuctionalization. However the effect of system blocks to each other should be clear. One should avoid unpredictable complexity. Thus nature uses very complex systems where each blocks improve each other. The multi-modal system needs to be totally understood from fundamental point of view to be used in real functional systems.

Multi-modal systems which are available consist of building blocks sensitive to different stimuli or one block sensitive to several stimuli (**Figure 6**). Thus a multi-modal system can be achieved: (i) with material responsive to several stimuli; (ii) with a hybrid system whose components are sensitive to different stimuli, or (iii) with special nano-organized assembly into encapsulation systems, e.g., micelles, nanotubes.

In the case of polyelectrolyte multilayer films, pH sensitivity of the material can be combined with response to altering ionic strength in order to trigger conformational transitions. The earlier mentioned PNIPAM brushes alter their shape in response to changes in pH, temperature and ionic strength.[85b] One more

example of a multi-trigger responsive layer is a redox-polymer-modified electrode. It was found that the variations of the layer properties are dependent on pH, solution ionic strength and applied electrode potential.[99] Some nanogels can also reversibly respond to different triggers, for instance, temperature- and redox-sensitive nanoparticles.[100]

One of the background ideas is to combine in one system the nanoblocks responsive to different stimuli. An example of a hybrid system can be surface organized magnesium-polypyrrole hybrids.[2e] An active chemical release of such a hybrid is achievable by pH-change or an electric field. Functionalization by magnetic and metal nanoparticles produces capsules which respond to multiple stimuli.

Double- or multi-responsive systems can be based just on the polymer architecture. Random copolymers are used to tailor the transition point depending on two independent parameters, for example, pH and temperature. In contrast block copolymers tend to self-assemble reversibly and form micelles depending on the environmental conditions. The micelles are then either stabilized through strong non-covalent interaction (e.g., ionic) or fixed through subsequent crosslinking. In both cases, one obtains a nano-object, which can be utilized as a micellar responsive drug delivery system, but it can also mimic biological entities like vesicles.[101]

Moreover multifuctionality can be attributed to multicomponent system loading with different species and their time resolved release. Thus polymer micelles as drug carriers encapsulated with drugs were loaded at the bottom of titanium nanotube array structures, and their delayed release was obtained by loading blank micelles (without drug) on the top (Figure 6).[45] Delayed and time-controlled drug release was successfully achieved by controlling the ratio of blank and drug-loaded micelles. The concept was demonstrated using four different polymer micelles (regular and inverted) loaded with water-insoluble (indomethacin) and water-soluble drugs (gentamicin).

An elegant approach on the multimodal release of different proteins from the same hydrogel was reported.[102] An injectable PEGylated fibrin gel designed for the release of platelet-derived growth factor BB (PDGF-BB) and TGF-β1 gene with distinct kinetics. Growth factors were loaded into PEGylated fibrin gels via 3 mechanisms: entrapment, conjugation through a homobifunctional amine reactive PEG linker, and physical adsorption on the fibrin matrix. PDGF-BB was entrapped during thrombin-mediated crosslinking leading to its diffusion-controlled release over 2 days. TGF-β1 was both conjugated through the PEG linker and bound to the matrix via physical adsorption, increasing the release time of TGF-β1 up to 10 days. Further, the release rate was highly correlated to gel degradation rate, indicating that TGF-β1 release was degradation-controlled.

A new system with nanogate supported on silica[103] is capable of simultaneously delivering both large and small
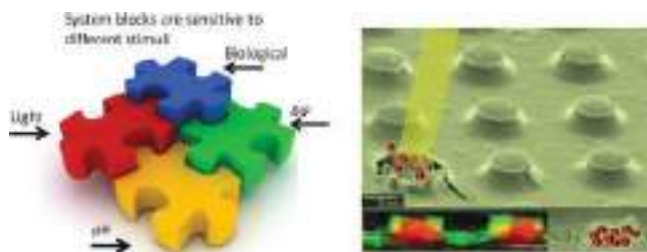
Figure 7. Multi-responsive system. (Left) Hierarchical organization of stimuli responsive system is presented as puzzle where each block is responsive to certain stimuli. (Right) SEM and Raman (inset below) images of an example of multi-modal system: a composite polyelectrolyte film made of poly(allylammonium)-poly(styrene sulfonate) multilayers and gold nanoparticles incorporated between subsequent stacks of polyelectrolytes. The film shaped as microchambers is loaded with colloid particles or oil-soluble molecules. A focused laser beam (shown in yellow) is used for remotely addressing the individual microchambers and site-specific release of the loaded cargo (shown in red). Reproduced with permission.[104] Copyrights 2013, Wiley.

molecules. The system can be expanded as a delivery system for a broad combination of cargo molecules and metal ions for biological application. In neutral conditions, the nanogate remains closed and cargo is stored, but the addition of acid opens the nanogate, releasing both metal ions and large cargo molecules. Controlled cargo release was also demonstrated by activation through competitive binding. By changing both the metal ion and/or the choice of nanogate, the pH responsiveness can be tuned to allow for biological pH activation.

Individually addressable patterned multilayer microchambers for site-specific release-on-demand was demonstrated.[104] Patterned arrays of light-responsive microchambers were suggested as candidates for specific demand of chemicals. A composite film was made of poly(allylammonium)-poly(styrene sulfonate) multilayers and gold nanoparticles incorporated between subsequent stacks of polyelectrolytes. The film shaped as microchambers was loaded with colloid particles or oil-soluble molecules and chemical release with electromagnetic irradiation was demonstrated (**Figure 7**).

6. Specific Examples of Advanced Applications

The mission of modern science is to concentrate on basic science with transfer technology and knowledge towards applications. Responsive systems can be introduced into many products at a relatively low cost. New design strategies for responsive materials establish an enabling technology for drug delivery,[96] diagnostics,[105] stem cell stimulation,[106] lab-on-chip and organ-on-chip,[107] bio-membranes and bio-sensors,[108] template for synthesis,[109] optical systems,[74,110] antifouling,[2a] self-healing materials and coatings.[8,32,46,111]

Providing added functionality can enhance the value of a product significantly – for example, materials that are capable of repairing themselves in less than an hour can be used in many coatings applications ranging from decoration, anticorrosion protection to biomedical industries. High-value materials in, for example, the automotive and aerospace industries require increasingly sophisticated eco-friendly coatings
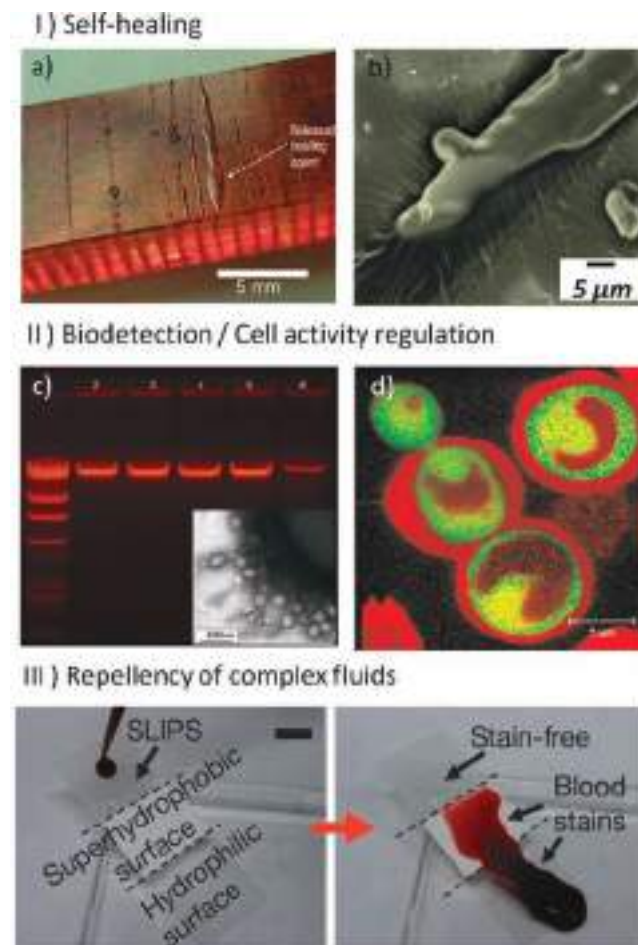
Figure 8. Few examples of advanced applications. (I) Self-healing surfaces: a) composite structure after cracks in the coating, (b) SEM image of polyelectrolyte multilayer healing ability. Reproduced with permission.[111,46c] Copyrights 2007, Nature Publishing Group; 2010, American Chemical Society. (II) Bioregulation: a) bacteriophage detection, b) pH-responsive LbL nanoshells for direct regulation of (yeast) cell activity.[105,30a] Copyrights 2011, Royal Society of Chemistry; 2012, American Chemical Society. (III) Bioinspired self-repairing slippery surfaces with pressure-stable omniphobicity for repellency of blood.[31] Copyrights 2011, Nature Publishing Group.

for improved performance, self-healing, and durability, and in this respect recent developments in stimuli responsive systems are most promising, making the coating "active" on macro and microlevels (**Figure 8**I). Standard anticorrosion coatings developed so far passively prevent the interaction of corrosive species with the metal which require thicker coatings and does not solve the "cut-edge" problem. The next generation of stimuli responsive protective coatings should be much thinner and possess self-healing or self-curing effects in the scratched (damaged) areas. This requires development of components of the coatings reacting to external or internal impact (pH, humidity changes, or distortion of the coating integrity, etc.) and, if possible, able to combine the self-healing property with other functionality (e.g., detection, controlled reflection, self-cleaning).[8,32,46]

Antibiotic-releasing silk biomaterials for infection prevention and treatment was demonstrated recently.[112] The release of penicillin and ampicillin from loaded silk films, silk microspheres suspended in silk hydrogels and bulk-loaded silk hydrogels was investigated and the in vivo efficacy was demonstrated in a murine infected-wound model. Special design of surface silk microneedles which contain an active chemical was also successfully used for controlled-release drug delivery (Figure 2f).[113] The degradation rate of silk fibroin and the diffusion rate of the entrained molecules can be controlled simply by adjusting post-processing conditions. It was shown that room temperature and aqueous-based micromolding allows for the bulk loading of these microneedles with labile drugs. The drug release rate is decreased 5.6-fold by adjusting the post-processing conditions of the microneedles, mainly by controlling the silk protein secondary structure. Antibiotic loaded silk microneedles were manufactured and used to demonstrate a 10-fold reduction of bacterial density after their application.

Tuning and switching adhesion between stimuli-responsive materials, proteins and cells has been explored for the control of cell and protein adhesion,[114] and used for tissue engineering and bioseparation. Thus muscle tissues in heart and skeletal muscle require orientational structures for expressing their functions effectively in vivo.[115] Thermoresponsive polymer surfaces[116] provide normal human dermal fibroblasts aligning on the physicochemically patterned surfaces simply by one-pot cell seeding. Furthermore, the aligned cells were harvested as a tissue-like cellular monolayer, called "cell sheet" only by reducing temperature. The cell sheet harvested from the micropatterned surface possessed a different shrinking rate between vertical and parallel sides of the cell alignment, maintaining the alignment of cells and related ECM proteins, promising to show the mechanical and biological aspects of cell sheets harvested from the functionalized thermoresponsive surfaces.

Different sensitivity of different microorganisms, e.g., bacteria and bacteriophages,[106] provide effective instrumentation to manipulate their live cycles. In particular it was shown that the kinetic activity of the deactivation of bacteriophages dramatically exceeds that of bacterial deactivation. This allows to suggest a procedure of photocatalytic lysogenic bacteria detection (Figure 8IId).

Encapsulation of lubricant into porous surfaces[31] was demonstrated yielding a robust synthetic surface that repels various liquids: self-repairing slippery surfaces with pressure-stable omniphobicity. The slippery surfaces are useful in fluid handling and transportation, optical sensing, medicine, and as self-cleaning and antifouling materials operating in extreme environments (Figure 8III).

Biocompatible stimuli-responsive hydrogel porous membranes via phase separation of a polyvinyl alcohol and Na-alginate intermolecular complex was demonstrated.[83] Ion cross-linked porous alginate thin films were fabricated from mixtures of sodium alginate and polyvinyl alcohol in an aqueous solution. The porous membranes are a pH-sensitive material whose pore diameter can be tuned by changes in pH. The membranes are mechanically robust and can be transferred onto the surface of porous substrates.

Reversible swelling-shrinking transitions in polyelectrolyte brushes and hydrogel thin film plasmonic biosensors for monitor pH changes,[117] the concentration of cholesterol,[118] and the concentration of glucose using the enzymatic reaction of glucose oxidase[82] were also demonstrated. In all extensive work is available on biopolymer-based hydrogels for cell and growth factor encapsulation in regenerative medicine.[119]

Biomedical systems that can deliver multiple growth factors in a multimodal mode and provide desirable pore structure and porosity to potentially encapsulate cells, have considerable potential as future therapeutic tools in tissue engineering.[1a]

There are just few examples presented, however it goes without saying that the concepts presented in this review will be beneficial for many new applications in the future because they will allow for the introduction of new aspects and possibilities in the field of conventional materials. Many important applications may be developed on the basis of implementation of biomimetic concepts into responsive surfaces in the near future. We foresee development of smart surfaces that can, for example, recognize specific biological signals, selectively separate biological molecules, release functional groups or proteins, and change mechanical properties.

7. Conclusions

In this review we highlighted the roles of dynamic interfaces for responsive encapsulation systems. Interfaces adapted to self-control and self-regulation requires a complex hierarchical organization of stimuli responsive nanoorganized blocks. However to have background knowledge from a basic science point of view lower detentions or building blocks for "intelligent" systems deserve scientific attention. Thus prospective materials for encapsulation with suggestions concerning loading and release strategies to provide systems for advanced applications. In living systems nature broadly exploits the principles of hierarchical organization for self-control and stimuli responsive switching and self-regulation. However, synthetic intelligence is still a challenge. Even more challenging is in vivo design. The research concerns predominantly experiments between chemistry, physics and in some cases biology.

Switchable interfaces have been demonstrated for a variety of applications. Some examples are presented in the review. Advantages that are expected from such switchable interfaces include speed, ease, reversibility, temporal and spatial control over interfacial interactions and events. Whilst there has been much excitement generated in this area, in many cases the understanding of the underlying mechanisms is still limited and needs to be extended.

There are great opportunities and challenges for further developments, toward an eventual goal to enable understanding, design and fabrication of encapsulation systems. We believe that the area will be explored further in nearest future. A next step in dynamic interface construction can be self-adaptive systems for needed applications.

[1] a) E. V. Skorb, D. V. Andreeva, *Adv. Funct. Mater.* **2013**, DOI: 10.1002/adfm.201203884; b) E. V. Skorb, D. V. Andreeva, *Polym. Chem.* **2013**, DOI: 10.1039/c3py00088e.

[2] a) D. V. Andreeva, D. V. Sviridov, A. Masic, H. Möhwald, E. V. Skorb, *SMALL* **2012**, *8*, 820; b) E. V. Skorb, D. Fix, D. G. Shchukin, H. Möhwald, D. V. Sviridov, R. Mousa, N. Wanderka, J. Schöferhans, N. Pazos- Perez, A. Fery, D. V. Andreeva, *Nanoscale* **2011**, *3*, 985; c) E. V. Skorb, D. G. Shchukin, D. V. Andreeva, *Langmuir* **2010**, *26*, 16973; d) J. Gensel, T. Borke, N. Pazos- Perez, A. Fery, D. V. Andreeva, E. Betthausen, A. H. E. Müller, H. Möhwald, E. V. Skorb, *Adv. Mater.* **2012**, *24*, 985; e) E. V. Skorb, O. Baidukova, A. Goyal, A. Brotchie, D. V. Andreeva, H. Möhwald, *J. Mater. Chem.* **2012**, *22*, 13841.

[3] a) R. Cheng, F. Feng, F. Meng, C. Deng, J. Feijen, Z. Zhong, *J. Control. Release* **2011**, *152*, 2; b) L. Han, Y. Fu, A. J. Cole, J. Liu, J. Wan, *Fitoterapia* **2012**, *83*, 721; c) R. P. Brinkhuis, F. P. J. T. Rutjes, J. C. M. Hest, *Polym. Chem.* **2011**, *2*, 1449; d) H.-N. Nguyen, S.-P. Wey, J.-H. Juang, K. Sonaje, Y.-C. Ho, E.-Y. Chuang, C.-W. Hsu, T.-C. Yen, K.-J. Lin, H.-W. Sung, *Biomaterials* **2011**, *32*, 2673.

[4] a) M. Delcea, H. Möhwald, A. G. Skirtach, *Adv. Drug Delivery Rev.* **2011**, *63*, 73; b) T. A. Kolesnikova, A. G. Skirtach, H. Möhwald, *Expert Opin. Drug Delivery* **2013**, *10*, 47; c) L. J. Cock, S. Koker, B. G. Geest, J. Grooten, C. Vervaet, J. P. Remon, G. B. Sukhorukov, M. N. Antipina, *Angew. Chem. Int. Ed.* **2010**, *49*, 6954; d) B. G. De Geest, G. B. Sukhorukov, H. Möhwald, *Expert Opin. Drug Deliv.* **2009**, *6*, 613.

[5] a) D. G. Shchukin, D. V. Andreeva, E. V. Skorb, H. Möhwald, In: *Supramolecular Chemistry of Hybrid Materials*, Ed. K. Rurack, Wiley-VCH, Germany, **2010**, 639–653; b) E. V. Skorb, D. G. Shchukin, D. V. Sviridov, In: *Molecular and Nanoscale Systems for Energy Conversion*, Ed. V. Varfolomeev, Nova Science Publishers, N.Y., **2008**, 75–87; c) D. Borisova, H. Möhwald, D. G. Shchukin, *ACS Nano* **2011**, *5*, 1939.

[6] E. J. Anglin, L. Cheng, W. R. Freeman, M. J. Sailor, *Adv. Drug Delivery Rev.* **2008**, *60*, 1266.

[7] K. K. Coti, M. E. Belowich, M. Liong, M. W. Ambrogio, Y. A. Lau, H. A. Khatib, J. I. Zink, N. M. Khashab, J. F. Stoddart, *Nanoscale* **2009**, *1*, 16.

[8] a) E. V. Skorb, D. G. Shchukin, H. Möhwald, D. V. Sviridov, *J. Mater. Chem.* **2009**, *19*, 4931; b) E. V. Skorb, A. Skirtach, D. V. Sviridov, D. G. Shchukin, H. Möhwald, *ACS Nano* **2009**, *3*, 1753; c) E. V. Skorb, D. V. Sviridov, H. Möhwald, D. G. Shchukin, *Chem. Comm.* **2009**, *1*, 6041.

[9] a) D. Volodkin, A. Skirtach, H. Möhwald, *Polym. Int.* **2012**, *61*, 673; b) D. V. Volodkin, A. I. Petrov, M. Prevot, G. B. Sukhorukov, *Langmuir* **2004**, *20*, 3398.

[10] O. Shchepelina, M. O. Lisunova, I. Drachuk, V. V. Tsukruk, *Chem. Mater.* **2012**, *24*, 1245.

[11] a) W. Wei, E. Abdullayev, A. Hollister, D. Mills, Y. M. Lvov, *Macromol. Mater. Eng.* **2012**, *297*, 645; b) D. Fix, D. V. Andreeva, Y. M. Lvov, D. G. Shchukin, H. Möhwald, *Adv. Funct. Mater.* **2009**, *19*, 1720.

[12] K. Gulati, M. S. Aw, D. Findlay, D. Losic, *Therapeutic Delivery* **2012**, *3*, 857.

[13] a) R. Singh, H. S. Nalwa, *J. Biomed. Nanotechnol.* **2011**, *7*, 489; b) E. Heister, V. Neves, C. Lamprecht, S. R. P. Silva, H. M. Coley, J. McFadden, *Carbon* **2012**, *50*, 622.

[14] S. Koker, R. Hoogenboom, B. G. De Geest, *Chem. Soc. Rev.* **2012**, *41*, 2867.

[15] M. A. C. Stuart, W. T. S. Huck, J. Genzer, M. Müller, C. Ober, M. Stamm, G. B. Sukhorukov, I. Szleifer, V. V. Tsukruk, M. Urban, F. Winnik, S. Zauscher, I. Luzinov, S. Minko, *Nat. Mater.* **2010**, *9*, 101.

[16] G. Decher, *Science* **1997**, *277*, 1232.

[17] a) F. Caruso, R. A. Caruso, H. Möhwald, *Science* **1998**, *282*, 1111; b) E. Donath, G. B. Sukhorukov, F. Caruso, S. A. Davis, H. Möhwald, *Angew. Chem. Int. Ed.* **1998**, *37*, 2202; c) G. B. Sukhorukov, E. Donath, S. Davis, H. Lichtenfeld, F. Caruso, V. I. Popov, H. Möhwald, *Polym. Adv. Technol.* **1998**, *9*, 759; d) G. B. Sukhorukov, M. Brumen, E. Donath, H. Möhwald, *J. Phys. Chem. B* **1999**, 6434.

[18] a) B. Parakhonskiy, D. Andreeva, H. Möhwald, D. Shchukin, *Langmuir* **2009**, *25*, 4780; b) D. V. Andreeva, Z. Pientka, L. Brozová, M. Bleha, G. A. Polotskaya, G. K. Elyashevich, *Thin Solid Films* **2002**, *406*, 54; c) D. V. Andreeva, D. A. Gorin, D. G. Shchukin, G. B. Sukhorukov, *Macromol. Rap. Comm.* **2006**, *27*, 931.

[19] A. Latnikova, D. O. Grigoriev, H. Möhwald, D. G. Shchukin, *J. Phys. Chem. C* **2012**, *116*, 8181.

[20] D. V. Andreeva, D. G. Gorin, H. Möhwald, G. B. Sukhorukov, *Langmuir* **2007**, *23*, 9031.

[21] E. M. Shchukina, D. G. Shchukin, *Cur. Opinion Colloid Interface Sci.* **2012**, *17*, 281.

[22] D. O. Grigoriev, T. Bukreeva, H. Möhwald, D. G. Shchukin, *Langmuir* **2008**, *24*, 999.

[23] M. F. Haase, D. O. Grigoriev, H. Möhwald, D. G. Shchukin, *Adv. Mater.* **2012**, *24*, 2429.

[24] L. M. C. Sagis, R. Ruiter, F. J. Rossier, M. J. Ruiter, K. Schroen, A. C. Aelst, H. Kieft, R. Boom, E. Linden, *Langmuir* **2008**, *24*, 1608.

[25] K. Ariga, Q. Ji, J. P. Hill, *Adv. Polym. Sci.* **2010**, *229*, 51.

[26] K. Landfester, J. Eisenblätter, R. Rothe, *JCT Res.* **2004**, *1*, 65.

[27] Y. Han, D. Radziuk, D. G. Shchukin, H. Möhwald, *J. Mater. Chem.* **2008**, *18*, 5162.

[28] Y. Han, D. Radziuk, D. G. Shchukin, H. Möhwald, *Macromol. Rapid Commun.* **2008**, *29*, 1203.

[29] a) Z. She, M. N. Antipina, J. Li, G. B. Sukhorukov, *Biomacromolecules* **2010**, *11*, 1241; b) Z. She, C. Wang, J. Li, G. B. Sukhorukov, M. N. Antipina, *Biomacromolecules* **2012**, *13*, 2174; c) A. Angelova, B. Angelov, R. Mutafchieva, S. Lesieur, P. Couvreur, *Acc. Chem. Res.* **2011**, *44*, 147; d) R. Palankar, A. G. Skirtach, O. Kreft, M. Bedard, M. Garstka, K. Gould, H. Möhwald, G. B. Sukhorukov, M. Winterhalter, S. Springer, *Small* **2009**, *5*, 2168.

[30] a) I. Drachuk, O. Shchepelina, M. Lisunova, S. Harbaugh, N. Kelley-Loughnane, M. Stone, V. V. Tsukruk, *ACS Nano* **2012**, *6*, 4266; b) V. Kozlovskaya, S. Harbaugh, I. Drachuk, O. Shchepelina, N. Kelley-Loughnane, M. Stoneb, V. V. Tsukruk, *Soft Matter.* **2011**, *7*, 2364; c) J. T. Wilson, W. Cui, V. Kozlovskaya, E. Kharlampieva, D. Pan, Z. Qu, V. R. Krishnamurthy, J. Mets, V. Kumar, J. Wen, Y. Song, V. V. Tsukruk, E. L. Chaikof, *J. Am. Chem. Soc.* **2011**, *133*, 7054; d) A. M. Pavlov, A. V. Sapelkin, X. Huang, K. M. Y. P'ng, A. J. Bushby, G. B. Sukhorukov, A. G. Skirtach, *Macromol. Biosci.* **2011**, *11*, 848; e) B. Franz, S. S. Balkundi, C. Dahl, Y. M. Lvov, A. Prange, *Macromol. Biosci.* **2010**, *10*, 164; f) S. S. Balkundi, N. G. Veerabadran, D. M. Eby, G. R. Johnson, Y. M. Lvov, *Langmuir* **2009**, *25*, 14011.

[31] T.-S. Wong, S. H. Kang, S. K. Y. Tang, E. J. Smythe, B. D. Hatton, A. Grinthal, J. Aizenberg, *Nature* **2011**, *477*, 443.

[32] E. V. Skorb, D. Fix, D. V. Andreeva, D. G. Shchukin, H. Möhwald, *Adv. Funct. Mater.* **2009**, *19*, 2373.

[33] K. Ariga, Y. M. Lvov, K. Kawakami, Q. Ji, J. P. Hill, *Adv. Drug Del. Rev.* **2011**, *63*, 762.

[34] D. O. Grigoriev, K. Köhler, E. V. Skorb, D. G. Shchukin, H. Möhwald, *Soft Matter.* **2009**, *5*, 1426.

[35] M. Delcea, A. Yashchenok, K. Videnova, O. Kreft, H. Möhwald, A. G. Skirtach, *Macromol. Biosci.* **2010**, *10*, 465.

[36] B. Bhushan, Y. C. Jung, *Progress Mater. Sci.* **2011**, *56*, 1.

[37] M.-C. Desjonqueres, D. Spanjaard, *Concepts in Surface Physics*, Springer, **2002**.

[38] K. A. Kilian, T. Bocking, K. Gaus, M. Gal, J. J. Gooding, *Biomaterials* **2007**, *28*, 3055.

[39] J. M. Buriak, *Chem. Rev.* **2002**, *102*, 1272.

REVIEW

[40] E. V. Skorb, D. V. Andreeva, H. Möhwald, *Angew. Chem. Int. Ed.* **2012**, *51*, 5138.

[41] L. Peng, A. D. Mendelsohn, T. J. Latempa, S. Yoriya, C. A. Grimes, T. A. Desai, *Nano Lett.* **2009**, *9*, 1932.

[42] K. Ariga, J. P. Hill, Q. Ji, *Phys. Chem. Chem. Phys.* **2007**, *9*, 2319.

[43] F. Caruso, G. B. Sukhorukov, *Multilayer Thin Films*, Wiley-VCH Verlag, Weinheim, **2003**.

[44] E. V. Skorb, D. G. Shchukin, *New Corrosion Protection Concepts.* In: European Coatings Tech Files, Ed. G. Gehrenkemper, Vincentz Network GmbH & Co, Germany, **2010**.

[45] M. S. Aw, J. Addai-Mensaha, D. Losic, *Chem. Commun.* **2012**, *48*, 3348.

[46] a) D. V. Andreeva, D. Fix, D. G. Shchukin, H. Möhwald, *Adv. Mater.* **2008**, *20*, 2789; b) D. V. Andreeva, D. Fix, H. Möhwald, D. G. Shchukin, *J. Mater. Chem.* **2008**, *18*, 1738; c) D. V. Andreeva, E. V. Skorb, D. G. Shchukin, *ACS Appl. Mater. Interfaces* **2010**, *2*, 1954.

[47] D. B. Shenoy, A. A. Antipov, G. B. Sukhorukov, H. Möhwald, *Biomacromolecules* **2003**, *4*, 265.

[48] F. Caruso, H. Möhwald, *J. Am. Chem. Soc.* **1999**, *121*, 6039.

[49] O. I. Vinogradova, O. V. Lebedeva, K. Vasilev, H. F. Gong, J. Garcia-Turiel, B. S. Kim, *Biomacromolecules* **2005**, *6*, 1495.

[50] Z. H. An, C. Tao, G. Lu, H. Möhwald, S. Zheng, Y. Cui, J. B. Li, *Chem. Mater.* **2005**, *17*, 2514.

[51] I. L. Radtchenko, G. B. Sukhorukov, S. Leporatti, G. B. Khomutov, E. Donath, H. Möhwald, *J. Colloid Interface Sci.* **2000**, *230*, 272.

[52] Z. F. Dai, A. Voigt, S. Leporatti, E. Donath, L. Dähne, H. Möhwald, *Adv. Mater.* **2001**, *13*, 1339.

[53] a) F. Caruso, H. Lichtenfeld, M. Giersig, H. Möhwald, *J. Am. Chem. Soc.* **1998**, *120*, 8523; b) N. A. Kotov, I. Dekany, J. H. Fendler, *J. Phys. Chem.* **1995**, *99*, 13065; c) C. Jiang, H. Ko, V. V. Tsukruk, *Adv. Mater.* **2005**, *17*, 2127.

[54] A. J. Khopade, F. Caruso, *Biomacromolecules* **2002**, *3*, 1154.

[55] a) L. Xu, Z. Zhu, S. A. Sukhishvili, *Langmuir* **2011**, *27*, 409; b) Z. Zhu, S. A. Sukhishvili, *ACS Nano* **2009**, *3*, 3595; c) J. Gensel, I. Dewald, J. Erath, E. Betthausen, A. H. E. Müller, A. Fery, *Chem. Sci.* **2013**, *4*, 32.

[56] J. Zhang, F. Li, B. Yuan, Q. Song, Z. Wang, X. Zhang, *Langmuir* **2013**, *29*, 6348.

[57] I. Tokarev, M. Orlov, S. Minko, *Adv. Mater.* **2006**, *18*, 2458.

[58] a) M. Rinaudo, *Polym. Int.* **2008**, *57*, 397; b) T. Coviello, P. Matricardi, C. Marianecci, F. Alhaique, *J. Control. Release* **2007**, *119*, 5; c) R. Censi, P. Martino, T. Vermonden, W. E. Hennink, *J. Control. Release* **2012**, *161*, 680.

[59] a) E. A. Silva, D. J. Mooney, *Biomaterials* **2010**, *31*, 1235; b) L. Pescosolido, T. Piro, T. Vermonden, T. Coviello, F. Alhaique, W. E. Hennink, P. Matricardi, *Carbohydr. Polym.* **2011**, *86*, 208.

[60] a) S. R. Van Tomme, W. E. Hennink, *Expert Rev. Med. Devices* **2007**, *4*, 147; b) S. G. Lévesque, M. S. Shoichet, *Bioconjug. Chem.* **2007**, *18*, 874.

[61] G. Kogan, L. Šoltés, R. Stern, P. Gemeiner, *Biotechnol. Lett.* **2007**, *29*, 17.

[62] a) N. Bhattarai, J. Gunn, M. Q. Zhang, *Adv. Drug Deliv. Rev.* **2010**, *62*, 83; b) M. Ishihara, K. Obara, S. Nakamura, M. Fujita, K. Masuoka, Y. Kanatani, B. Takase, H. Hattori, Y. Morimoto, M. Ishihara, T. Maehara, M. Kikuchi, *J. Artif. Organs* **2006**, *9*, 8; c) M. Amidi, E. Mastrobattista, W. Jiskoot, W. E. Hennink, *Adv. Drug Deliv. Rev.* **2010**, *62*, 59; d) R. Zhang, W. Li, H. Möhwald, W. Sui, Z. Wang, C. Gao, *J. Colloids Interfaces Sci.* **2012**, *372*, 40.

[63] a) Y. Tabata, A. Nagano, Y. Ikada, *Tissue Eng.* **1999**, *5*, 127; b) H. Teles, T. Vermonden, G. Eggink, W. E. Hennink, F. A. de Wolf, *J. Control. Release* **2010**, *147*, 298.

[64] P. Y. Lee, Z. Li, L. Huang, *Pharm. Res.* **2003**, *20*, 1995.

[65] S. E. Sakiyama-Elbert, J. A. Hubbell, *J. Control. Release* **2000**, *69*, 149.

[66] a) S. Young, M. Wong, Y. Tabata, A. G. Mikos, *J. Control. Release* **2005**, *109*, 256; b) Z. Patel, H. Ueda, M. Yamamoto, Y. Tabata, A. Mikos, *Pharm. Res.* **2008**, *25*, 2370.

[67] a) E. Abdullayev, Y. Lvov, *J. Mater. Chem.* **2010**, *20*, 6681; b) E. Abdullayev, R. Price, D. Shchukin, Y. Lvov, *Appl. Mater. Interfaces* **2009**, *7*, 1437; c) J. Zhang, Y. Liu, B. Yuan, Z. Wang, M. Schçnhoff, X. Zhang, *Chem. Eur. J.* **2012**, *18*, 14968; d) Y.-L. Sun, B.-J. Yang, S. X.-A. Zhang, Y.-W. Yang, *Chem. Eur. J.* **2012**, *18*, 9212; e) C. R. Thomas, D. P. Ferris, J.-H. Lee, E. Choi, M. H. Cho, E. S. Kim, J. F. Stoddart, J.-S. Shin, J. Cheon, J. I. Zink, *J. Am. Chem. Soc.* **2010**, *132*, 10623.

[68] D. Tarn, M. Xue, J. I. Zink, *Inorg. Chem.* **2013**, *52*, 2044.

[69] J. Liu, X. Jiang, C. Ashley, C. J. Brinker, *J. Am. Chem. Soc.* **2009**, *131*, 7567.

[70] a) K. Katagiri, K. Koumoto, S. Iseya, M. Sakai, A. Matsuda, F. Caruso, *Chem. Mater.* **2009**, *21*, 195; b) E. V. Skorb, E. A. Ustinovich, A. I. Kulak, D. V. Sviridov, *J. Photochem. Photobiol. A: Chem.* **2008**, *193*, 97.

[71] T. A. Kolesnikova, D. Kohler, A. G. Skirtach, H. Möhwald, *ACS Nano* **2012**, *6*, 9585.

[72] E. V. Skorb, L. I. Antonouskaya, N. A. Belyasova, D. G. Shchukin, H. Möhwald, D. V. Sviridov, *Appl. Catal. B: Environmental.* **2008**, *84*, 94.

[73] a) K. Ariga, Q. Ji, M. J. McShane, Y. M. Lvov, A. Vinu, J. P. Hill, *Chem. Mater.* **2012**, *24*, 728; b) M. M. de Villiers, D. P. Otto, S. J. Strydom, Y. M. Lvov, *Adv. Drug Del. Rev.* **2011**, *63*, 701.

[74] a) A. G. Skirtach, D. V. Volodkin, H. Möhwald, *ChemPhysChem* **2010**, *4*, 822; b) M. F. Bedard, B. G. De Geest, A. G. Skirtach, H. Möhwald, G. B. Sukhorukov, *Adv. Col. & Int. Sci.* **2010**, *158*, 2; c) B. V. Parakhonsky, M. Bedard, T. V. Bukreeva, G. B. Sukhorukov, H. Möhwald, A. G. Skirtach, *J. Phys. Chem. C* **2010**, *114*, 1996.

[75] a) M. F. Bedard, D. Braun, G. B. Sukhorukov, A. G. Skirtach, *ACS Nano* **2008**, *2*, 1807; b) A. G. Skirtach, M. F. Bedard, P. Karageorgiev, G. B. Sukhorukov, H. Möhwald, *J. Am. Chem. Soc.* **2008**, *130*, 11572.

[76] R. Steitz, V. Leiner, R. Siebrecht, R. v. Klitzing, *Colloid Surf. A* **2000**, *163*, 63.

[77] R. Klitzing, H. Möhwald, *Macromolecules* **1996**, *29*, 6901.

[78] J. Draper, I. Luzinov, S. Minko, I. Tokarev, M. Stamm, *Langmuir* **2004**, *20*, 4064.

[79] H. Kuroki, I. Tokarev, S. Minko, *Annu. Rev. Mater. Res.* **2012**, *42*, 343.

[80] a) K. Kikuchi, K. Sumaru, J. Edahiro, Y. Ooshima, S. Sugiura, T. Takagi, T. Kanamori, *Biotechnol. Bioeng.* **2009**, *103*, 552; b) O. Hoy, B. Zdyrko, R. Lupitskyy, R. Sheparovych, D. Aulich, J. Wang, E. Bittrich, K.-J. Eichhorn, P. Uhlmann, K. Hinrichs, M. Müller, M. Stamm, S. Minko, I. Luzinov, *Adv. Funct. Mater.* **2010**, *20*, 2240.

[81] C. L. Yeung, P. Iqbal, M. Allan, M. Lashkor, J. A. Preece, P. M. Mendes, *Adv. Funct. Mater.* **2010**, *20*, 2657.

[82] I. Tokarev, I. Tokareva, V. Gopishetty, E. Katz, S. Minko, *Adv. Mater.* **2010**, *22*, 1412.

[83] V. Gopishetty, I. Tokarev, S. Minko, *J. Mater. Chem.* **2012**, *22*, 19482.

[84] J. Lahann, S. Mitragotri, T. N. Tran, H. Kaido, J. Sundaram, I. S. Choi, H. Saskia, G. A. Somorjai, R. Langer, *Science* **2003**, *299*, 371.

[85] a) R. Pelton, *Adv. Colloid Interface Sci.* **2000**, *1*, 85; b) E. Wischerhoff, K. Uhlig, A. Lankenau, H. G. Borner, A. Laschewsky, C. Duschl, J.-F. Lutz, *Angew. Chem. Int. Ed.* **2008**, *47*, 5666.

[86] D. L. Huber, R. P. Manginell, M. A. Samara, B.-I. Kim, B. C. Bunker, *Science* **2003**, *301*, 352.

[87] H. Lakhiari, T. Okano, N. Nurdin, C. Luthi, P. Descouts, D. Muller, J. Jozefonvicz, *Biochim. Biophys. Acta* **1998**, *1379*, 303.

[88] O. Azzaroni, A. Brown, W. Huck, *Angew. Chem. Int. Ed.* **2006**, *45*, 1770.

[89] J. K. Oh, R. Drumright, D. J. Siegwart, K. Matyjaszewski, *Prog. Polym. Sci.* **2008**, *33*, 448.

[90] N. Morimoto, X.-P. Qiu, F. M. Winnik, K. Akiyoshi, *Macromolecules* **2008**, *41*, 5985.

[91] L. Zarzar, P. Kim, J. Aizenberg, *Adv. Mater.* **2011**, *23*, 1442.

[92] K. Itano, J. Choi, M. Rubner, *Macromolecules* **2005**, *38*, 3450.

[93] F. Zhou, P. M. Biesheuvel, E.-Y. Choi, W. Shu, R. Poetes, U. Steiner, W. T. S. Huck, *Nano Lett.* **2008**, *8*, 725.

[94] Z. Jin, G. Güven, V. Bocharova, J. Halámek, I. Tokarev, S. Minko, A. Melman, D. Mandler, E. Katz, *ACS Appl. Mater. Interfaces* **2012**, *4*, 466.

[95] S. Santer, A. Kopyshev, J. Donges, H.-K. Yang, J. Rühe, *Adv. Mater.* **2006**, *18*, 2359. 92.

[96] a) M. Motornov, R. Sheparovych, I. Tokarev, Y. Roiter, S. Minko, *Langmuir* **2007**, *23*, 13; b) T. K. Tam, M. Ornatska, M. Pita, S. Minko, E. Katz, *J. Phys. Chem. C* **2008**, *112*, 8438.

[97] a) A. A. Antipov, G. B. Sukhorukov, S. Leporatti, I. L. Radtchenko, E. Donath, H. Möhwald, *Colloid Surf. Physicochem. Eng. Asp.* **2002**, *198*, 535; b) T. A. Kolesnikova, D. A. Gorin, P. Fernandes, S. Kessel, G. B. Khomutov, A. Fery, D. C. Shchukin, H. Möhwald, *Adv. Funct. Mater.* **2010**, *20*, 1189.

[98] W. Wang, L. Liu, X. J. Ju, D. Zerrouki, R. Xie, L. H. Yang, L. Y. Chu, *ChemPhysChem*, **2009**, *10*, 2405.

[99] M. Tagliazucchi, E. Calvo, I. Szleifer, *Langmuir* **2008**, *24*, 2869.

[100] N. Morimoto, F. Winnik, K. Akiyoshi, *Langmuir* **2007**, *23*, 217.

[101] Z. Zhu, S. A. Sukhishvili, *J. Mater. Chem.* **2012**, *22*, 7667.

[102] C. T. Drinnan, G. Zhang, M. A. Alexander, A. S. Pulido, L. J. Suggs, *J. Control. Release* **2010**, *147*, 180.

[103] D. Tarn, M. Xue, J. I. Zink, *Inorg. Chem.* **2013**, *52*, 2044.

[104] M. V. Kiryukhin, S. R. Gorelik, S. M. Man, G. S. Subramanian, M. N. Antipina, H. Y. Low, G. B. Sukhorukov, *Macromol. Rapid Commun.* **2013**, *34*, 87.

[105] E. V. Skorb, D. V. Andreeva, A. P. Raiski, N. A. Belyasova, H. Möhwald, D. V. Sviridov, *Photochem. Photobiol. Sci.* **2011**, *10*, 1974.

[106] a) I. Choi, W.-S. Yeo, *ChemPhysChem* **2013**, *14*, 55; b) S. F. M. v. Dongen, P. Maiuri, E. Marie, C. Tribet, M. Piel, *Adv. Mater.* **2013**, *25*, 1687.

[107] a) A. Sidorenko, T. Krupenkin, A. Taylor, P. Fratzl, J. Aizenberg, *Science* **2007**, *315*, 487; b) O. Kuksenok, V. V. Yashin, A. C. Balazs, *Soft Matter* **2007**, *3*, 1138.

[108] a) S. J. Lue, J. J. Hsu, T. C. Wei, *J. Membrane Sci.* **2008**, *321*, 146; b) C. Y. Jiang, S. Markutsya, Y. Pikus, V. V. Tsukruk, *Nature Mater.* **2004**, *3*, 721; c) H. C. Chiu, Y. W. Lin, Y. F. Huang, C. K. Chuang, C. S. Chern, *Angew. Chem. Int. Ed.* **2008**, *47*, 1875; d) K. Ch. Daoulas, M. Müller, *Adv. Polym. Sci.* **2009**, *224*, 197.

[109] a) E. Abdullayev, K. Sakakibara, K. Okamoto, W. Wei, K. Ariga, Y. Lvov, *ACS Appl. Mater. Interfaces* **2011**, *3*, 4040; b) E. V. Skorb, D. V. Andreeva, *J. Mater. Chem. A* DOI:10.1039/C3TA01695G.

[110] a) I. B. Burgess, L. Mishchenko, B. D. Hatton, M. Kolle, M. Loncar, J. Aizenberg, *J. Am. Chem. Soc.* **2011**, *133*, 12430; b) J. Aizenberg, *MRS Bulletin*, **2010**, *35*, 323.

[111] K. S. Toohey, N. R. Sottos, J. A. Lewis, J. S. Moore, R. S. White, *Nat. Mater.* **2007**, *6*, 581.

[112] E. M. Pritchard, T. Valentin, B. Panilaitis, F. Omenetto, D. L. Kaplan, *Adv. Funct. Mater.* **2012**, *23*, 854.

[113] K. Tsioris, W. K. Raja, E. M. Pritchard, B. Panilaitis, D. L. Kaplan, F. G. Omenetto, *Adv. Funct. Mater.* **2012**, *22*, 330.

[114] a) M. P. Lutolf, J. L. Lauer-Fields, H. G. Schmoekel, A. T. Metters, F. E. Weber, G. B. Fields, J. A. Hubbell, *Proc. Natl Acad. Sci. USA* **2003**, *100*, 5413; b) C. D. H. Alarcon, T. Farhan, V. L. Osborne, W. T. S. Huck, C. Alexander, *J. Mater. Chem.* **2005**, *15*, 2089.

[115] M. H. Ross, G. I. Kaye, W. Pawlina, *Histology: a Text and Atlas: With Cell and Molecular Biology*, 4th ed.; Lippincott Williams & Wilkins: Baltimore, MD, **2003**.

[116] H. Takahashi, M. Nakayama, K. Itoga, M. Yamato, T. Okano, *Biomacromolecules* **2011**, *12*, 1414.

[117] I. Tokareva, S. Minko, J. H. Fendler, E. Hutter, *J. Am. Chem. Soc.* **2004**, *126*, 15950.

[118] I. Tokareva, I. Tokarev, S. Minko, E. Hutter, J. H. Fendler, *Chem. Commun.* **2006**, *1*, 3343.

[119] R. Censi, P. Martinoa, T. Vermonden, W. E. Hennink, *J. Control. Release* **2012**, *161*, 680.

Bio-inspired ultrasound assisted construction of synthetic sponges

Ekaterina V. Skorb[*ab] and Daria V. Andreeva[c]

A porous material with a system of cavities can be considered as a sponge. The amazing mechanical, optical, electrical and sorption properties of sponge-like silicon-, carbon- and metal-based materials arose interest in novel synthetic pathways of formation of the sponges which in addition gained value in many energy and climate related issues. Here, we present a prospective bio-inspired approach to fabricate synthetic sponges *via* intensive ultrasonication. Ultrasound of high intensity triggers formation of cavitation bubbles in liquid in a controlled way. Cavitation happens when a rapid change in pressure occurs. Cavitation in nature occurs in fast streams, produced by some shrimps, and in the xylem of plants. Ultrasonically induced cavitation bubbles can be considered as chemical microreactors providing high temperature and pressure at the microscopic scale and trigger formation of active species (including free radicals) from dissolved molecules. In the context of chemistry, cavitation has the unique potential of locally catalyzing high-temperature (up to 5000 K) and high-pressure (several hundreds of bars) reactions, while the system remains macroscopically near room temperature and ambient pressure. Ultrasound of high intensity has already been applied for the synthesis of structured organic and inorganic materials and composites. In this review we summarize the latest achievements in the application of ultrasonication for the formation of hierarchically ordered 3-D networks (sponges). The prospects of applications of sonochemically formed composites in catalysis, optics, hydrogen storage and corrosion protection are highlighted.

Introduction

Hierarchically ordered 3-D networks (sponges) have great potential for biomedical, optical and catalytic applications as sensors and energy storage materials.[1–5] The characteristic features of synthetic sponges, namely electrical/thermal conductivity (metal sponges), mechanical and thermal stability (inorganic sponges), and relatively low density compared to bulk materials have led to a wide range of applications in photovoltaics, fuel cells, sensing, separation and biotechnology.[1–13] Porous materials can be formed by using a template or by a template-free method. For example, porous metals with large pores (200 μm to 2 mm) can be produced through a process of casting, powder metallurgy, and sputter deposition.[6] Approaches to fabricate microporous sponges with controlled porosity are based on electroplating into self-assembled liquid crystal surfactants,[7] colloidal crystals,[8] and porous block copolymers.[9] Mesoporous sponges have been synthesized by

chemical reduction,[10] plasma spraying[11] and electrodeposition[12] followed by template decomposition, *etc.*[9] The methods are usually multistage and involve a sacrificial second phase, which increases production costs because of the formation of the template and its subsequent removal, combined with waste generation, especially when up-scaling the procedure. Thus, environmentally friendly and inexpensive methods of production of sponges are still required.

The interest in ultrasound and cavitation effects dates back to over more than 100 years. The first report of cavitation concerned the notice that the propeller of a submarine was pitted and eroded.[14] Since the early work of Lord Rayleigh it is known that ultrasound may form cavitation bubbles in liquid which upon collapse create transiently temperatures around 5000 K, pressures around 1000 atm with cooling rates above 10^8 K s^{-1}.[15] One of the most basic concepts of sonochemistry is that free radicals are formed as a result of the cavitation and microbubble collapse which are created during the rarefaction (or negative pressure) period of sound waves. There is also the concept of rectified diffusion (the growth of microbubbles due to unequal transfer of mass across the interface during bubble oscillation).[16] It was also shown that bubble-induced microstreaming is one of the factors that leads to the well-known ultrasonic cleaning effects in heterogeneous systems.[17,18] Later on the understanding of the physical effects of ultrasound in

a Max Planck Institute of Colloids and Interfaces, Wissenschaftspark Golm, Am Mühlenberg 1, 14476 Golm, Germany. E-mail: skorb@mpikg.mpg.de; Fax: +49 331567 9202; Tel: +49 331567 9233

b Chemistry Department, Belarusian State University, Leningradskaya str. 14, Minsk, 220030, Belarus

c Physical Chemistry II, University of Bayreuth Universitatstr, 30, Bayreuth, 95440, Germany

This journal is © The Royal Society of Chemistry 2013

J. Mater. Chem. A, 2013, **1**, 7547–7557 | **7547**

liquid systems was also increasing. It was hypothesized that microjets formed during asymmetric cavitation.[19] Moreover the sonolysis of water was found to give rise to sonochemistry.[20]

Ultrasonic frequencies range from 20 kHz to 1 GHz. It is known that the threshold for cavitation increases with frequency. Thus the higher frequencies are typically used for ultrasonic diagnostics, the lower ones in chemistry. They encompass wavelengths between 10 cm and 1 μm and hence do not directly interact at the molecular level. The mechanism of bubble formation may be qualitatively understood as follows: in the zone of negative pressure of the sound wave small volumes of lower liquid density or containing gas clusters may expand to form certain bubble nuclei. These do not fully collapse during the high pressure phase and are further expanded in the next low pressure phases. This process continues until reaching a maximum critical diameter depending on the ultrasound frequency and solvent. In the following upon a very quick adiabatic cavitation collapse the mechanical ultrasonic energy is converted into mechanical energy of matter, chemical energy, heat and, under certain conditions, light. The mechanical ultrasonic energy can be scattered, adsorbed and reflected by the interfaces, particles and matter. Thus, chemical and physical transformations of matter can be triggered. Solvents, additives (free radical scavengers, surfactants, reduction agents, oxidants), nanoparticles or ions significantly influence the physical and chemical processes in the sonicated media. Organic molecules, nanoparticles and ions near the bubble interface influence the cavitation process by increasing the surface pressure, decreasing the lifetime of the cavitation bubble.[21] For surfactants, monomers and polymers the following key aspects should be considered: the formation of free radicals during the cavitation process,[22] polymerization of monomers triggered by sonogenerated free radicals,[23] chain reorientation,[24] polymer decomposition,[25] oxidation and bond breakage.[26] Thus, ultrasonically assisted modification of solids in the presence of organic and inorganic compounds could lead to formation of composites.[27]

Recent studies have suggested scenarios of sonochemical modification of solids.[28–34] The great advantage of the sonochemical approach is that the morphology, composition and functionality of particles modified by using ultrasound can be controlled by the process conditions (reaction media, duration and intensity of sonication). The mechanism of ultrasound-assisted modification of solids is based on sonochemical effects (interfacial red/ox reactions triggered by sonogenerated free radicals) and sonomechanical effects (mechanical impact on the material via interparticle collisions and collisions with cavitation bubbles) of ultrasound. Both aspects still need to be systematically investigated with respect to their relevance for a particular functionality.

The following key aspects of formation of sponge-like materials via ultrasonication should be considered before starting the synthetic procedure.

(1) First of all interfacial red/ox reactions in the presence of different solvents with different properties (viscosity, density, surface tension, vapor pressure) and in the presence of additives, gases, free radical scavengers, and hydrogen donors. The

temperature inside the cavitation bubble, type and concentration of free radicals depend on the used reaction media.

(2) The pore formation in solids treated by ultrasound could rely on the interplay of sonochemical and sonomechanical factors: the generation of H_2 inside pores and defects, chemical etching of a metal surface by free radicals and sonomechanical structuring of the metal surface due to interparticle collisions in ultrasonic fields should be considered. The contribution of the sonochemical and sonomechanical effects to pore formation can be tuned by sonication of particles in the presence of different solvents and additives.

(3) Phase segregation in multi-component systems can be observed. For example, in the ultrasonic field some intermetallic phases in metal alloys undergo a complex impact of sonogenerated free radicals, high temperatures and pressures, mechanical stress due to interparticle collisions and formation of microjets. Thus, the ultrasound treatment of solids could lead to formation of new phases (via oxidation metal oxides, carbides etc.) and/or in situ reduction (metallic particles).

Furthermore, ultrasound of high intensity can be used in a one step formation of composite materials: interpenetrating metal–polymer hybrids, core–shell particles, two-layered composites, multi-metal composites, etc. Composite materials can be formed by (i) ultrasound-assisted incorporation of materials in pre-formed sponges, (ii) ultrasound-assisted in situ synthesis of materials in pre-formed sponges, and (iii) one step method of formation of composites from multi-component systems.
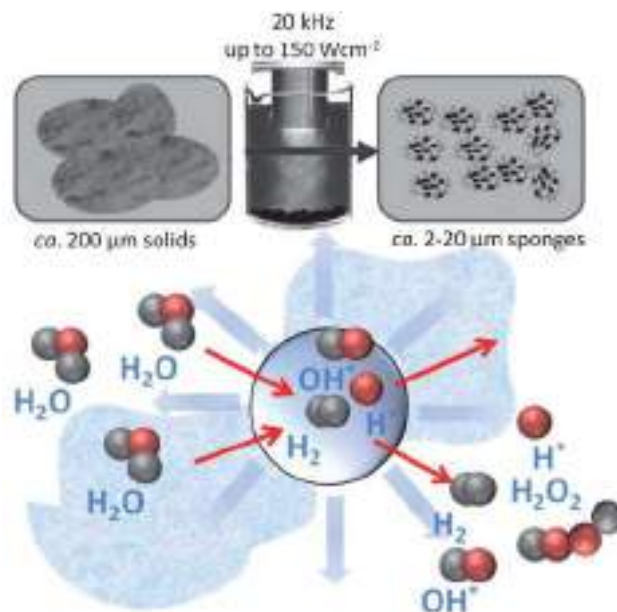
Fig. 1 Schematic illustration of the synthesis of sponge like materials triggered by ultrasound (above) and the formation of active species by water sonolysis during cavitation bubble collapse (bottom). During aluminum modification the physical effect relies on mechanical effects of cavitation bubbles on Al particles e.g. erosion, fragmentation and destruction of the native oxide layer due to shock waves generated by cavitation bubble collapse; particle collision and breakage due to the intensive turbulent liquid flow caused by bubble collapse; melting and recrystallisation. In water possible reactions for Al is oxidation and formation of a novel thin smooth oxide layer protected metal skeleton of sponge; reduction processes are also possible due to formation of hydrogen species.

In this review we highlight generic principles of relevance for the different aspects of ultrasonication for constructing hierarchically ordered 3-D networks and elucidate design strategies for controlling morphology and properties of synthetic sponges (Fig. 1).

Sonochemical formation of metal sponges

The mechanism of modification of a metal structure under ultrasound irradiation is complex and involves a variety of aspects related to melting, solidification of metals, selective etching and oxidation of the metal surface. It is known that transformation of liquid into solid involves the creation of curved solid–liquid interfaces (leading to capillarity effects) and the microscopic flow of heat.[28–41] The shape of a solidified microstructure depends on the cooling conditions. Special conditions provided by ultrasound of high intensity affect the crystallization process in metal particles and, therefore, influence the metal structure. Surface oxidation during ultrasound irradiation is another important aspect in the formation of pores, having a crucial role in the stabilization of the metal structure cast under ultrasound irradiation.

Ultrasound modification of Zn, Al and Mg particles (Fig. 2) starts with oxidation of the metal surface and formation of a rough metal oxide (hydroxide) layer with the formation of pits followed by development of an inner structure. The XRD patterns evidence that bayerite $Al(OH)_3$ with an admixture of boehmite $AlO(OH)$ are formed during sonication of aluminum. The ^{27}Al MAS NMR spectra of the samples treated by ultrasound exhibit two signals that can be assigned to Al and Al^{3+}, respectively.[35] It is important to note that during ultrasound irradiation formation of a porous metallic structure covered by a thin oxide layer takes place which is proved by the presence of the

peaks assigned to Al^0 in XRD patterns and NMR spectra even after long term ultrasound treatment. The latest results of 3 Dimensional Field Ion Microscopy also confirm the metallic structure covered with an oxide (hydroxide) layer.[35]

Monitoring of the effects of ultrasound on solids can be demonstrated by using >100 μm aluminum particles. Aluminum has a relatively low melting point (933 K) and could undergo plastic deformations in response to ultrasonic stress. Furthermore, the aluminum surface is oxidized under ambient conditions. The >100 μm aluminum particles can be considered as surfaces for 5 μm cavilation bubbles formed at 20 kHz. We observed the following dynamics of the particle modification. The surface of the aluminum particles after 1 min of sonication has a cell-like morphology of aluminum oxide. After 3 min of sonication decomposition of particles and formation of a lamellar morphology takes place. The initial 100 μm Al particles change into 200 nm thick lamellae in 60 minutes. The TEM image also demonstrates the formation of 50–100 nm channels between lamellae. It is interesting to note that the metal oxide layer formed within the first minute of sonication is removed by longer (>1 min) treatment. The surface of porous aluminium lamellae is covered by a smooth thin aluminum oxide. Probably this morphology of aluminum oxide is more stable and can resist the impact of ultrasonic cavitation. Within 5 min of sonication formation of a porous inner structure became noticeable. The roughness of the surfaces of the aluminum particles increased. The BET isotherms showed that in the first 5 min the formation of mesopores is stimulated. After 10 min of ultrasound treatment we observe both micropores and mesopores. The average pore diameter estimated by BET is about 4 nm for the 60 min treated aluminum particles. Further increase of irradiation time leads to regression of structure development. SEM images and BET analysis demonstrate a
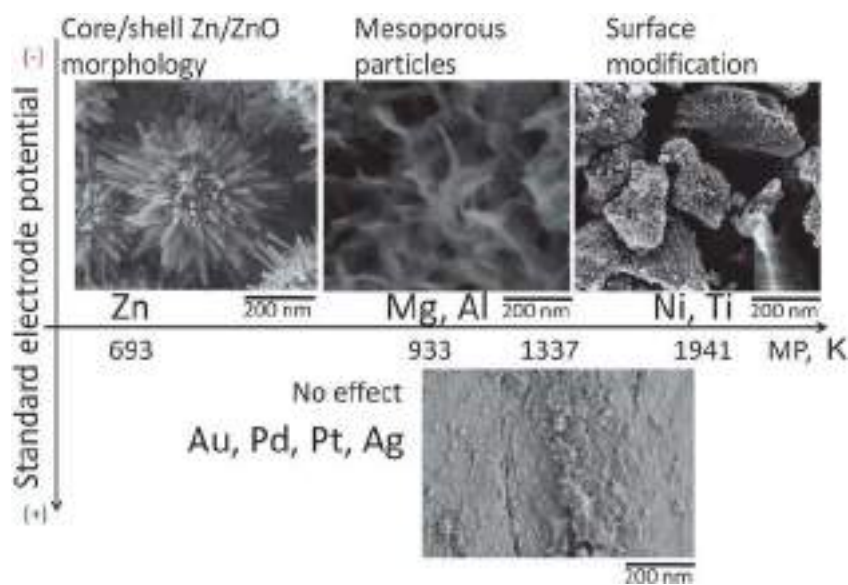
Fig. 2 Schematic presentation of the effect of acoustic cavitation on the modification of metal particles in water. Metals with low melting point (Zn) are completely converted into metal oxide. Al and Mg form mesoporous sponge-like structures. Metals with high melting points (Ni, Ti) exhibit surface modification under sonication. Nobel metals are resistant to ultrasound irradiation due to stability against oxidation. Y-axis represents the oxidation ability; X-axis – difference in melting point in Kelvin. Frequency of 20 kHz; $I_{ac} = 57$ W cm^{-2}. Adapted from ref. 35 and 37 with permission from The Royal Society of Chemistry.

decrease of porosity, surface smoothing and fusion of the particles after 2 h sonication due to total Al oxidation.

The modification pathways of solids as well as their morphology after ultrasonic treatment are different for each material. The XRD patterns and BET analysis of Mg after ultrasonic treatment prove the formation of the sponge-like morphology and development of a hydroxide phase on the metal surface. Sonication of magnesium leads to formation of a more porous structure with higher surface area in comparison with Al. The surface areas for 30 min sonicated Mg and Al are 69 m^2 g^{-1} and 54 m^2 g^{-1}, respectively. Furthermore, Mg sponges are characterized by larger pores than Al sponges: the average pore diameter is ~14 nm in the case of magnesium and ~4 nm in the case of aluminum.

Zinc based particles exhibit a completely different morphology after sonochemical treatment. It is shown in ref. 35 the ultrasound stimulated formation of zinc oxide on the surface of zinc particles. The formation of the oxide layer can be controlled by the intensity and duration of sonication. Thus zinc oxide crystals may exhibit tubular morphology. Probably due to their brittleness they can be decomposed by further sonication. In the case of initial Zn particles with size ca. 50 μm long-term treatment (>30 min) provided total metal oxidation with the formation of stable oxide nanorods with length ≈100 nm and diameter of approximately 20 nm.[35] The maximum surface area for 15 min sonicated Zn particles was 22 m^2 g^{-1}, 30 and 90 min sonicated samples exhibit an unporous structure. Sonicated Zn particles might have a different structure due to features of zinc oxide formed by sonication. The porosity of the sonicated Zn is rapidly decreased with sonication time due to transformation of tubular ZnO into ZnO nanorods. Some advanced photocatalytic nanostructured Zn,[37] where ZnO nanorods are attached to the metallic Zn core, were also formed, see the example in Fig. 2.

The metals with higher (compared to Mg and Al) melting points (Ni, 1723 K and Ti, 1941 K) exhibit changes in the interfacial layer during longer time of ultrasonic exposure. If the time of treatment is chosen as an optimal one for the formation of an aluminum sponge the surface structure development is observed in the case of Ni and Ti particles. The BET and TEM data show no evidence of formation and development of an inner structure.

The noble metals (Au, Pd, Ag, Pt) that have a special place due to their low tendency to oxidation exhibit the highest resistance to ultrasound irradiation (among the mentioned metals) and form neither a porous structure nor a developed surface after sonication, even in cases where their melting points are actually lower than the those of metals that can be modified slightly (like Ni or Ti). Therefore, surface oxidation plays a crucial role in the stabilization of the metal structure developed under ultrasound irradiation.

The formation of sponges from 'hard' (Ni, Ti) and noble metals could be done through particle collision and following agglomeration through the methodology presented by Suslick's group.[38–40] The idea was tested for transition metals. In particular, a series of transition metal powders were used to probe the maximum temperatures and speeds reached during such interparticle collisions. Metal particles that were irradiated in

hydrocarbon liquids with ultrasound underwent collisions at roughly half the speed of sound and generated local effective temperatures between 2600 °C and 3400 °C at the point of impact for particles with an average diameter of ~10 μm. As the malleable particles are irradiated, profound changes in particle aggregation and morphology are observed. Upon sonication the particle surface is smoothed quite rapidly. At the same time, the extent of aggregation increases dramatically. The authors attribute both effects to interparticle collisions driven by the turbulent flow created by the ultrasonic field. The increased aggregation accounts for the eventual decrease in the observed surface area and probably also causes the small diminution in activity observed after lengthy sonication. Moreover these changes in surface morphology are associated with a dramatic change in surface composition. Auger electron spectra depth profiles obtained on Ni samples before and after sonication show that in the case of sonication of such metals in hydrocarbon liquids a thick oxide coat is found to exist before the ultrasonic irradiation, and after 1 h of ultrasonic irradiation in octane the oxide layer becomes thinner. The total surface areas differ dramatically for the sponges formed as shown in ref. 35 and 41 and as lately discussed by K. S. Suslick et al.[38–40] Thus for aluminum sponges the maximum porosity reached 80 m^2 g^{-1}, and it was at the level ca. 1.00 m^2 g^{-1} in the case of a nickel sponge. However, in both cases it was shown that with time the porosity had a tendency to increase, reach a maximum and then decrease.

It should be also noted that if organic solutions are used the metals which formed sponges in aqueous solution (Al, Mg) or have tendency to total oxidation (Zn) obey the same rules as 'hard' metals. Thus it was shown for Zn powder with an average diameter of 5 μm that after 30 min ultrasonic exposure at 15 °C in freshly distilled decane (17 ml, 20% by weight) under Ar at 20 kHz and 50 W cm^{-2} small particles connect to one another with great force, producing interparticle melting (sintering). It was suggested that the effect originates from the rapid cooling of the effectively molten collision zone as the colliding particles rebound immediately after the impact.

Combining sonochemical and reactive hard template approaches

Synthesis of nanostructured materials by using a "reactive hard template" (RHT) approach was first introduced in 2007 by A. Thomas et al.[42] with great advantage of omitting high temperatures or harsh reagents for the removal of template. According to this method the reaction-confining matrix could be simultaneously a reagent in the synthesis of the nanostructures. The RHT concept, which combines the advantages of hard templating[43,44] with an in situ decomposition, i.e., removal of the template[42,44,45] is an advanced area of materials science and synthetic chemistry due to its high economic efficiency. Herein we combine both RHT and sonochemical approaches to synthesise hierarchically structured materials and propose a novel method of template-assisted synthesis of nanostructures by using sonochemistry (sono-RHT, Fig. 3).
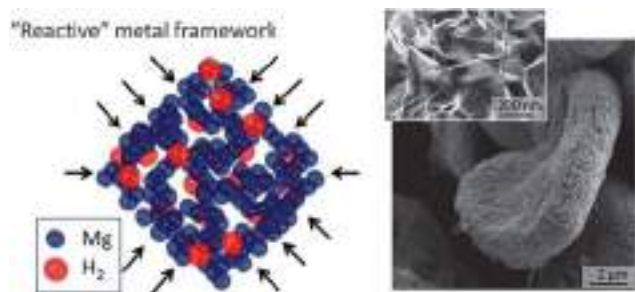
Fig. 3 Reactive hard template (RHT) nature: the left image shows the scheme of a porous magnesium framework which contains hydrogen molecules – "reactive" metal framework, arrows in the scheme point to the possibility to introduce different chemical precursors into the RHT. Right images are SEM images of a Mg particle after sonochemical modification. Adapted from ref. 27 with permission from The Royal Society of Chemistry.

The sonochemical oxidation in water of "reactive" metals (Al, Mg) is followed by the production of a highly concentrated reducing agent, e.g. hydrogen, on the metal surface. The "reactive" Al and Mg are not only oxidized during ultrasonic treatment in water, but also serve as effective donors of electrons and, thus, are responsible for H_2 production. Thus sonochemical modification of Al and Mg leads to simultaneous formation of mesoporous metal frameworks and generation of H_2 in the pores. Both Mg and MgH_x clusters can be formed. The sonochemically formed mesoporous framework of "reactive" metals combines functionality of a template material and a reagent. The use of the "reactive" metal frameworks as the RHT for the synthesis of nanostructures is schematically illustrated in Fig. 3.

A general sono-RHT synthetic procedure of nanostructures includes the following steps: (i) sonochemical formation of the mesoporous metal RHT; (ii) ultrasound assisted loading of the RHT with chemical precursors for nanoparticle synthesis; (iii) reduction of precursors catalyzed by the sonoactivated metal surface; (iv) RHT decomposition due to the electrochemical processes stimulated by ultrasound. Herein, we demonstrate the sono-RHT for the synthesis of hierarchically structured materials.

Magnesium as one of the most reactive metals was used as a model "reactive" metal for the proof of the principles of sono-RHT. Sonication of aqueous suspensions of Mg leads to formation of highly active magnesium hydrates of different composition. The magnesium hydrides are rapidly decomposed under extreme conditions during sonication in water with production of H_2, thus, magnesium is a promising material that can be used for the sono-RHT synthesis.

The combination of the sonochemical approach and the RHT concept leads to the formation of a variety of nanomaterials in aqueous solutions. The structures that can be obtained are affected by the preparation conditions. The acoustic cavitation in water and the shape-defining effect of the "reactive" template material provide the special thermodynamic and kinetic conditions for synthesis of nanostructures of particular morphology. We demonstrated the formation of magnetic nanorods, dendritic and spherical magnetic iron based particles. Due to the presence of Fe^0 the system can be

used to catalyze the synthesis of carbon nanomaterials. As one of the prospects of the method we would like to highlight the formation of biocompatible hybrid nanostructures, for example the hybrid with polypyrrole.

Silicon sponge design and organization

In a concept of sonoregulated construction of submicron and micron silicon sponges (Fig. 4) with unique mechanical, optical and drug delivery properties as initial material micron-Si particles, crystalline, or amorphous, p- or n-type, were suggested.[46] The system had three components: initial Si micron sized particles, a solvent and a hydrogen donor (Mg or Al, as described above).

It should be mentioned here that the work is in strong connection with sono-RHT (see above). Thus magnesium is a highly reactive metal in water solution:

$$Mg + 2H_2O \rightarrow Mg(OH)_2 + H_2\uparrow$$
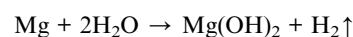
Then hydrogen can be involved in the ultrasonic process and form additional hydrogen radicals, for example through the reaction with hydroxyl radicals formed in the sonochemical reactor due to water sonolysis:[47]

$$H_2\uparrow + OH^. \rightarrow H_2O + H^.$$
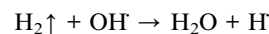
An experiment on ~100 μm particles of silicon proved[46] the formation of nanocrystalline Si and its subsequent phase transitions (crystalline–amorphous–crystalline) without
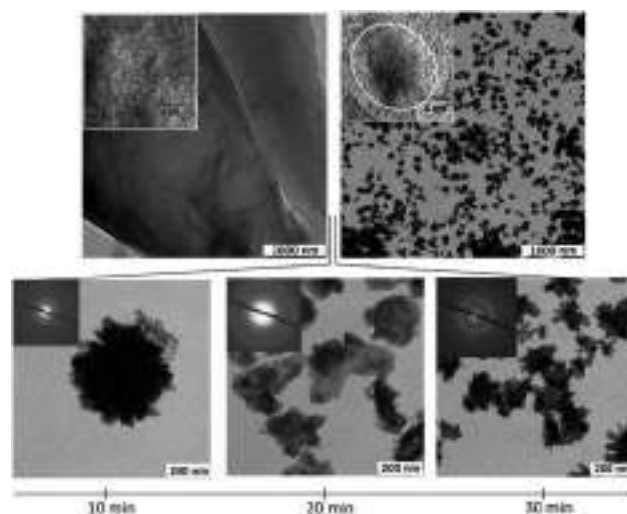
Fig. 4 TEM images of μ-sized silicon particles modified via ultrasonication (20 kHz, 57 W cm^{-2}) in aqueous solution in the presence of a hydrogen-donor material (here, magnesium) before and after a 35 min modification (upper left and right image, respectively). The HRTEM images (upper insets) show the crystalline structure. The bottom images are the TEM/ED images vs. modification time (10 min (left), 20 min (middle) and 30 min (right)). The observed modification kinetic is faster than those observed with plates. Reprinted from ref. 46 with permission. Copyright @ 2012 WILEY-VCH Verlag GmbH & Co. KGaA, Weinheim.

oxidation in water solution in the presence of a hydrogen donor material (Mg) (Fig. 4). Thus the 10 min sonicated particles exhibit a pronounced crystalline structure, and their size decreases to the submicron scale. The amorphisation of the particles is observed within 20 min of modification. Further exposure (>30 min) causes well-pronounced crystal growth from the amorphous phase in addition to a further size decrease. The observed phase transition (crystalline ↔ amorphous) is probably the main factor responsible for ultrasound-assisted modification of silicon. Special conditions provided by high-intensity ultrasound could affect the melting and growth of the silicon crystals. The form of a solidified microstructure can be controlled by fast local heating and cooling cycles provided by cavitation. The crystal formation depends upon the difference between the rates of attachment and detachment of atoms at the interface. The rate of attachment depends on the rate of diffusion in the liquid and is, therefore, affected by sonication.

Moreover the work[46] demonstrated the formation of porous silicon with unique optical properties by a "green" method of ultrasonication including: (i) the one-step formation of silicon with a purposefully variable porous structure, (ii) the formation of photoluminescent centres and defect states that could be centres for charge separation, and (iii) the possibility of patterned surface-selective modification. The ultrasonic modification of solids is known to be controlled by various sonication conditions, including the intensity and duration of sonication, the solvent, and the concentration and size of the sonicated species, oxidants and reducing agents.

Mesoporous metal nanocomposites

The following two ultrasound assisted strategies can be distinguished: (i) a one-step method was developed to produce metal nanocomposites from metal alloys under ultrasound irradiation; (ii) catalytic metal nanoparticles are incorporated and homogeneously distributed inside the porous matrix maintaining their initial morphology, structure and properties.

The sonochemical nanostructuring of metal alloys[41,48] is based on microphase separation in an alloy due to different phase response to ultrasonic effects. Thus, if alloy particles consisting of an ultrasound-resistant compound and a sensitive one are treated, one would consequently expect that novel nanocomposite structures are developed. We tested Al/Ni, Al/Pd, Al/Fe, Al/Cu and Al/Pd/Cu systems. Indeed, the treatment of the aqueous alloy dispersions with highly intense ultrasound leads not only to the formation of porous structure but also results in phase segregation yielding ultrasound-resistant nickel, palladium and copper oxide nanoparticles homogeneously distributed in the porous matrix.

Simultaneously BET analysis even reveals the more porous structure formation in the case of nanocomposites: the surface area in this case amounted to 280 m^2 g^{-1} for the Al/Pd particles and 210 m^2 g^{-1} for those of Al/Pd/Cu after 60 min of modification. Thus, the phase segregation process in multi-metal

systems stimulates the formation of mesoporous structures by sonication. Such nanocomposites could be used as catalysts.

The sonochemical activation of Al/Ni and Al/Cu alloys and formation of Al/Ni based hydrogenation catalyst[48] and Al/Cu oxide dehydrogenation catalyst[49] were studied in detail (Fig. 5).

It was shown that sonochemical treatment of Al/Cu alloys with the content of Cu up to 25 wt% leads to the formation of catalytically active and stable metal oxide phase. The Al/Cu oxide catalyst was very efficient in propane dehydrogenation reaction.[49]

The initial 1 : 1 Al/Ni alloy consists of Al$_3$Ni$_2$ and Al$_3$Ni intermetallides. Collapse of cavitation bubbles generated by ultrasound is followed by high local (μm^2 area) temperature (up to 5000 K) and high rate of heating/cooling processes – special cooling conditions for metals could affect the microstructure of an alloy. Moreover, it was discussed above that active metals, here aluminum, could be not just oxidized itself during ultrasonic treatment in water solution, but also could serve as an effective donor of the reducing agent (H$_2$).[48] The finding is extremely important for Al/Ni catalysts activated *in situ* during preparation. As a result catalyst activation in H$_2$ could be expected during catalyst formation without the total transformation of metallic nickel to oxide or even during the reduction process, also in the matrix pores. The components in XPS at 852.3 and 854.0 are associated with metallic Ni and NiO.[50] The peak positions are indicative of partial reduction of Ni in the process. 5 min after sonication the
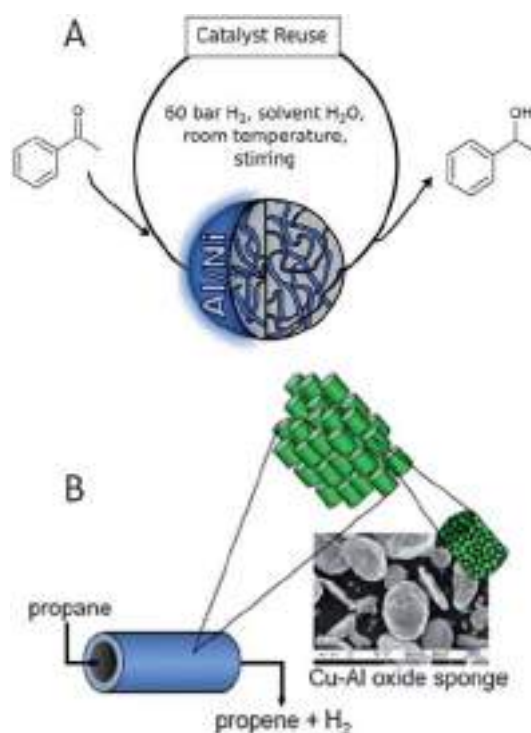
Fig. 5 Application of the sonochemically activated (A) Al/Ni and (B) Al/Cu particles in hydrogenation and dehydrogenation reactions. Adapted from ref. 48 and 49 with permission. Copyright @ 2011 and 2012 WILEY-VCH Verlag GmbH & Co. KGaA, Weinheim.

same oxide is seen as before oxidation, however within 50 min nickel is in the metallic state. The formation of metallic nickel could be explained due to catalyst centers' (Ni) *in situ* activation in H_2 which is formed in the process of partial matrix (aluminum) oxidation. A conceptual novelty of the proposed ultrasound assisted Al/Ni catalyst preparation is self-control of red/ox reactions during modification with structure optimization for maximum catalytic efficiency. The oxide peak positions indicate surface oxide reoxidation and transformation of the initial oxide to bayerite structure. The aluminum peak position/transformation is attributed to both phases: metallic aluminum as well as the novel reoxidized aluminum layer.

Summarizing the results: at the initial stages of sonication of the alloy particles the increase of oxide phase could be attributed to oxidation of metals and the formation of porous structure. In the final product metallic Ni was detected by XPS. We propose that hydrogen generated during oxidation of aluminum could reduce nickel. Thus, it can be concluded that the sonochemically activated Al/Ni catalyst is composed of an unmodified Al/Ni skeleton with surface modified aluminum (oxidized) and catalytic active nickel centers (reduced) regularly distributed in this matrix. The formation of a several nm thick metal oxide layer plays an important role in the structure stabilization without any negative effect on its future catalytic activity. Furthermore, the sonogenerated oxide layer provides excellent stability to the catalyst during its exploitation. The sonicated Al/Ni can be stored and used under ambient

conditions in comparison to RANEY® nickel that is pyrophoric and requires special storage conditions.[51,52]

The unique morphology of the sonoactivated Al/Ni system (presence of metallic Ni and sonogenerated metal oxides) provides easy and efficient catalytic performance of the material. First of all the catalyst does not require pre-activation before use. If the catalyst is pre-activated for 24 h in a hydrogen atmosphere (solid catalyst material) no increase in the catalytic activity is observed. Then, the sonoactivated Al/Ni can be a good alternative to the commercial RANEY® nickel. Thus Al/Ni has high conversion ability of acetophenone to 1-phenylethanol (70 bar H_2 pressure) at room temperature.

Ultrasound can be used for incorporation of active particles into a porous support. The method suggests a multi-step single pot methodology (Fig. 6).[53] According to this method the pre-sonicated and dried metal sponge (Al) particles were mixed with pre-synthesised noble metal nanoparticle dispersion. The mixture was sonicated with high intensity ultrasound for different time intervals. After that the solution, comprising mesoporous Al particles (Fig. 6A and B) filled with small noble metal nanoparticles, was centrifuged, the supernatant discarded and dried in an oven at 85 °C for 24 h. The final structure can be seen in the TEM image (Fig. 6C).

Zinc-based materials: sono-nanoarchitecture

We proposed an easy ultrasound-driven method for modification of zinc particles, so-called top-down "sononanostructuring" (see also below). In particular here, attention should be paid to core–shell "hedgehog" zinc-based materials. The general concept of ultrasound-driven modification of zinc particles is shown in Fig. 7.[37]

During the treatment of zinc particles the following phenomena could be observed (Fig. 7A): (I) formation of cavitation bubbles in the aqueous suspension of zinc particles; (IIa) red/ox reactions at the interfacial regions; (IIb) interparticle collisions; (III) generation of the core–shell "hedgehog" zinc. Moreover (IV) total oxidation with total conversion to the oxide structure is possible (not shown in the sketch).

Zn particles of the size *ca.* 4 μm and *ca.* 50 μm were used for the study. The sonicated Zn particles consist of the metallic Zn core covered by ZnO nanorods. The core–shell morphology can be clearly seen in the TEM image of the cross-section of the modified Zn particle (Fig. 7B). The nanorods are attached perpendicularly to the Zn core. The SEM image (Fig. 7C) shows that the nm long rods homogeneously cover the metal surface, forming so-called "hedgehogs" from Zn particles.

The nanostructured semiconductor zinc-based material demonstrated here could be a promising component in the construction of a whole range of composite systems for photocatalysis, gas sensing, photovoltaic, *etc.* The metallic nature of the Zn core could be applied to the formation of corrosion protection systems.
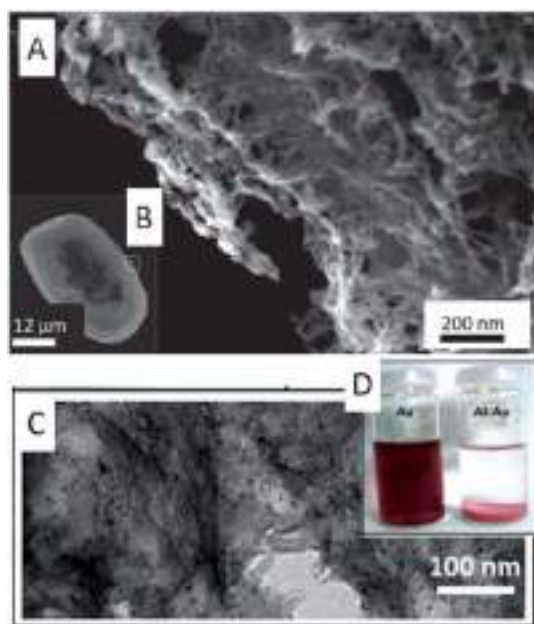
Fig. 6 (A) Scanning electron microscopy (SEM) image of mesoporous aluminum particles after sonication. (B) Low magnification SEM image of (A). (C) TEM image of a microtomed mesoporous bimetallic (Al–Au) particle. (D) The linear digital photographs of Au nanoparticle suspensions before (left) and after (right) the ultrasound-assisted loading into Al nanostructures. The particles sediment due to their incorporation into the Al sponge particles. Adapted from ref. 53 with permission. Copyright @ 2012 Elsevier.
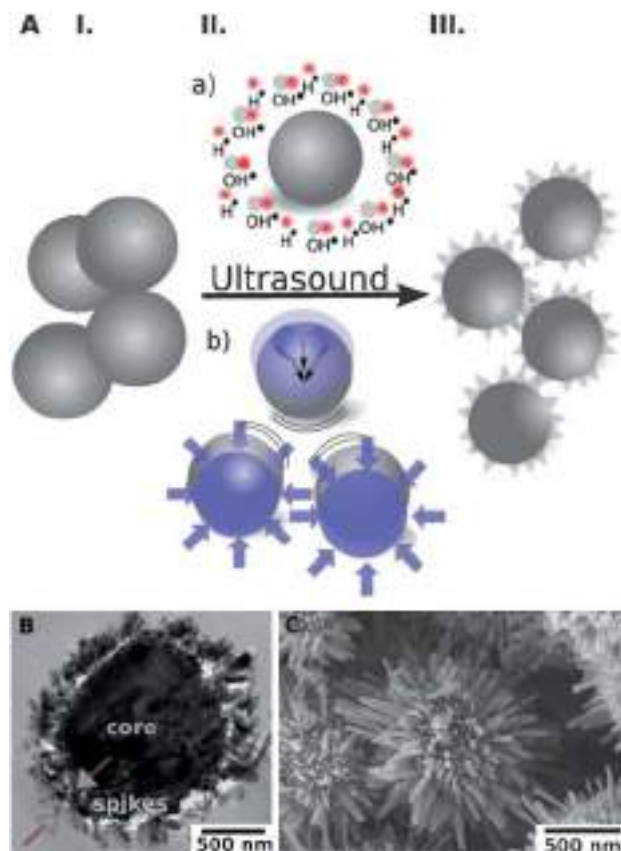
Fig. 7 (A) Sonochemical modification of zinc particles: (I) initial particles; (II) (a) chemical aspects due to surface oxidation; (b) physical aspects are caused by interparticle collisions and surface impinging by high velocity microjets providing preferable directions of etching; (III) formation of "hedgehog" zinc particles. (B and C) TEM (B, 10 min US) and SEM (C, 15 min US) images of the core–shell "hedgehog" structure: the metal core and the oxide nanorods attached to the core after treatment. Reprinted from ref. 37 with permission from The Royal Society of Chemistry.

Fig. 8 (a) 3D confocal microscopy reconstruction of the sononanoengineered magnesium–polypyrrole hybrid loaded with the fluorophore Rhodamine 6G (Rh6G) (fluorescence mode); the inset shows the SEM of the hybrid. (b) Time-resolved release of Rh6G from porous magnesium (Mg–Rh6G) and hybrid capsules (Mg–Rh6G–Ppy) in aqueous solution at neutral pH. (c) Rh6G release after 60 minutes in aqueous solution at different acidic pH values. (d) Time resolved release under initial pH = 4 and two step-wise pH changes: pH change 1 to pH = 3, pH change 2 to pH = 1. (e) Confocal microscopy images (fluorescence mode) of sonoimpregnated onto Ni pattern Mg–Rh6G–Ppy capsules into a Ni pattern. (f) is (e) after an electric current flow as in the inset scheme. Adapted from ref. 27 with permission from The Royal Society of Chemistry.

Hybrid material formation: capsules with synergetic trigger release

The ultrasonic assisted preparation and characterisation of magnesium–polypyrrole (Mg–Ppy) hybrid capsules are presented in Fig. 8.[27]

Hybrids were prepared through sonication of magnesium and pyrrole without or with a polymerisation initiator in water and alcohol solutions. The hybrids' morphology, potential, chemical composition, sonoinduced phase transformation and fluorescence properties were studied. The properties of the obtained hybrids, as well as the capsule loading efficiency, were found to depend on ultrasonic conditions.

The hybrid capsules with synergetic trigger release are expected to be of great interest for the next decade, since time and space resolved release of active chemicals (labeling fluorescent dyes, drugs, vitamins, antibodies, *etc.*) could provide further successful use of encapsulation systems in the construction of medical devices, corrosion termination and as surfaces for stem cell research. The suggested[27] hybrid systems, the components of which are sensitive to different factors (such

as Mg to pH change, and polypyrrole to change in the electrical potential) represent ideal candidates in the design of such capsules. We have presented a sonochemical approach for the formation of such hybrids, which has great potential due to its ecologically friendly nature and low amount of process steps, additives and reagents.

The fluorophore release from the free or surface sonoimmobilised capsules in aqueous solution of different pH values and under electrical current flow was also studied. An effective pH responsive release, including step-wise release, was confirmed for the hybrid system. An electrical current flow was also shown to trigger the release of hybrid capsules sonoimmobilised onto the Ni patterned ITO surface.

Surface capsules: bio-active surfaces

We report a novel encapsulation system (Fig. 9) based on a sonochemically formed sponge-like layer that could solve crucial problems of surface engineering and surface protection: adhesion of a protective system to the surface and release of an active compound on demand. The novel concept opens
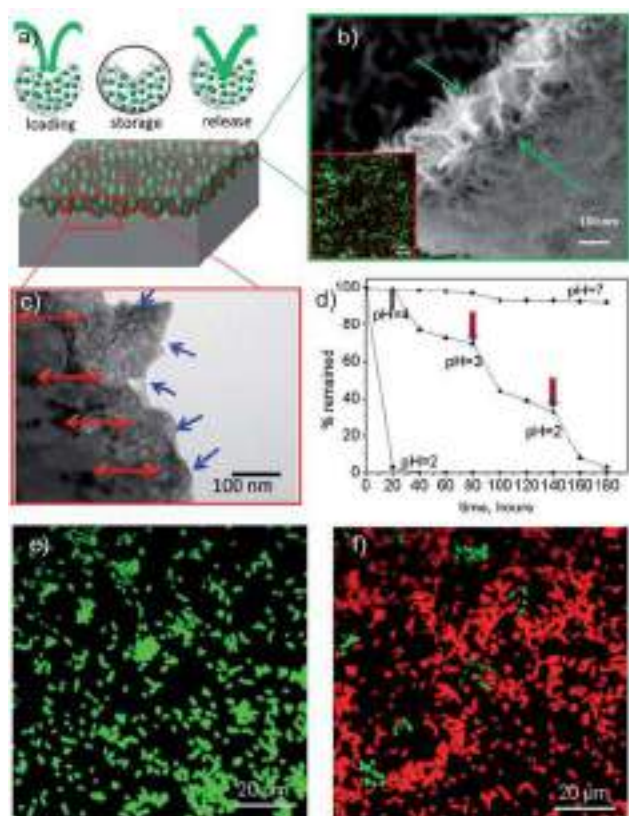
Fig. 9 (a) Schematic illustration of upload, storage and release of an active component and general view of capsules generated at the metal surface. (b) SEM image of the cross-section of an aluminum sponge-like layer and a luminescence confocal image of the surface capsules loaded with doxorubicin. (c) TEM image of aluminum with a surface capsule layer for chemical storage (blue arrows show the loading direction, red arrows show the interface between bulk metal and capsules' layer). (d) Doxorubicin release at different pH. (e and f) Confocal images show the inactivation of *E. coli* due to 8-hydroxyquinoline release from the surface capsule layer: (e) before release stimulation and (f) after release. Inactivated bacteria are red and alive bacteria are green. Adapted from ref. 56 with permission. Copyright @ 2012 WILEY-VCH Verlag GmbH & Co. KGaA, Weinheim.

capsules can be formed and loaded by ultrasound treatment of the metal surface in the presence of an active component. As a model (Fig. 9) encapsulation of a fluorescent antibiotic (doxorubicin) is presented. To achieve successful formation of surface capsules loaded with doxorubicin, the aluminum surface was sonicated in aqueous solution of doxorubicin in a thermostatted flow cell at 20 kHz and an intensity of 57 W cm^{-2}. The pH dependent release from such capsules is shown in Fig. 9d. At pH = 7 the encapsulation system is very stable and a negligible release from the capsules can be detected. At pH 4–2 we monitored the step-wise release of chemisorbed doxorubicin. Thus, the generation of a pH responsive encapsulation system on a metal surface can be performed in a single-step mode.

According to the Type II capsules the surface sponges can be used for construction of metal–polyelectrolyte capsules for storage of active chemicals and their release on demand. The pores of metal sponges can be simply sealed by polyelectrolyte complexes.[57] The polyelectrolyte complexes are a universal encapsulation/carrier system and provide safe storage of active chemicals and their release in response to external stimuli (pH,[58] ionic strength,[59] temperature,[60] light[61]). In this case, we do not need a specific interaction (chemisorption) between the metal surface and the active chemical. The upload/release of the active chemical in Type II capsules can be controlled by the formation of a complex between chemical and polyelectrolyte.[54] The complex has one or two pH windows (pH regions of complex instability) and provides an easy way to upload/release manipulation. The surface capsules loaded with 8-hydroxyquinoline (8-HQ) provide long-term antiseptic activity to the metal surface (Fig. 9e and f).

Nanoarchitectures in 3-D top-down and bottom-up organisation

A top-down and a bottom-up concept of synthesis of a hierarchically ordered 3-D network can be realized by using ultrasonication. The ultrasound based approach allows synthesis of functional sponges for the construction of complex submicron and micron 3-D networks (Fig. 10).

The questions are if we can achieve submicron (Fig. 10, I) and micron (Fig. 10, III) scale hierarchically ordered 3-D networks. Results shown in Fig. 10, III prove that our idea is more than realistic. The submicron organization is possible. Nanoparticles are building blocks in the case of submicron sponges. There is now in focus the possibility to regulate the nanoparticle morphology during the sonochemical process.

Submicron sponges can be considered as building blocks of mesotechnology. The micron scale organization of sonochemically formed aluminium submicron sponges in the presence of a surfactant with stepwise decrease of intensity during the ultrasonication leads to construction of parallel sheets (Fig. 10, IIIa). If the intensity remains constant we can organize aluminium particles in mesoscopic ellipsoids under the same conditions (Fig. 10, IIIb).

prospects in metal nanoengineering and surface protection as well as in encapsulation and polyelectrolyte applications.

In general, the suggested encapsulation system[54,55] consists of the following components: the sonochemically formed surface metal sponges adhering to the bulk metal (Fig. 9) which can be loaded with a variety of agents (corrosion inhibitors, biocides, enzymes, DNA fragments, antibodies) and a protective coating. Thus, the loaded metal sponges have the functionality of porous capsules. Compared to existing encapsulation systems[56] the surface capsules are a continuation of the bulk metal, modified metal layer used for encapsulation is strongly adhered to the unmodified metal part (Fig. 9c, shown with red arrows), and do not need to be immobilized on the surface or incorporated into a protective coating. Furthermore, the rough surface of the metal capsules provides excellent adhesion to the protective coating.

In particular in ref. 54 two types of encapsulation systems based on the surface metal sponges are suggested. The simultaneous activation/modification of the metal surface and active chemical by ultrasound is suggested in Type I. The metal

Fig. 10 (I) Schematic presentation of ultrasonic effects (ultrasonic bubble collapse (blue bubble in I) as liquid jets on a surface and as shock waves in solution, generation of free radicals (red small bubbles in I) in time) on μ-sized initial particles (shown in grey) and questions concerning the possibility to have 3-D organized submicron sponges due to surface imprinting, breakage, interparticle collisions and chemical surface modification by free radicals with different reactor parameters. It was shown by us that the units (can be called "spicules" as in a biosponge) for submicron sponge organization can have different shape, as in (II) TEM images, depending on parameters in the sonochemical reactor during their synthesis: (I and IIa) star-like for the special case of Si modification in the presence of a hydrogen donor in water solution. (IIb) Spherical: simple or complex as was shown for carbon during graphite Mg-template assisted modification in water solution; (IIc) cubic monodispersed for metal nanoparticles in water solution during sonication when at a certain step of modification we introduce pyrrole to the solution and decrease the power. (III) Possibility to organize 3-D micron sponges as shown in the scheme and SEM images for Al modification in the presence of surfactant (IIIa) parallel layers; (IIIb) ellipsoid hollow structure. Frequency of 20 kHz; I_{ac} = 20–60 W cm^{-2}.

Conclusions

A major challenge in the fabrication of micron and submicron organized sponges is the achievement of their advanced properties and defined structure. Our strategy is based on biological concepts of sponge organization and its improved mechanics with a high variety of ultrasonic energy pathways for building sponge units from metals, silicon, composites and hybrids. The advantages of the presented methodologies: (i) use of simple precursors such as micron sized particles; (ii) easy handling compared with traditional methods; (iii) facile and fast synthesis; (iv) controlled growth of active materials by increased or limited pore spaces; (v) excellent performance.

The following main issues are under discussion.

To understand energetic aspects of ultrasonic processes in the presence of solids.

The presence of solid surfaces itself affects the acoustic field and cavitation bubble stability.

Cavitation assisted processes of sponge formation and organization have non-linear character which should be taken into account.

Due to extreme conditions such as high local pressure, high temperature and high heating/cooling rate some not

thermodynamically, but kinetically stable structures (nanoparticles, submicron and micron sponges) could be expected.

The possibility to achieve advanced properties (like those of sea sponges) as improved mechanics are in focus for the sonogenerated sponges through their organization in the presence of additives such as polymers with different chain lengths.

Special liquid streaming is caused by ultrasound which influence sponge organization the same way as sea sponges adapt their shape for optimal water flow.

Acknowledgements

Notes and references

1 *Emerging technologies and techniques in porous media*, ed. D. B. Ingham, Springer, 2004, p. 507.
2 *Porous Media: Applications in Biological Systems and Biotechnology*, ed. K. Vafai, CRC Press, 2010, p. 599.

7556 | *J. Mater. Chem. A*, 2013, **1**, 7547–7557

This journal is © The Royal Society of Chemistry 2013

3 J.-R. Li, R. J. Kuppler and H.-C. Zhou, *Chem. Soc. Rev.*, 2009, **38**, 1477.

4 J. Lee, J. Kim and T. Hyeon, *Adv. Mater.*, 2006, **18**, 2073.

5 W. Tianchi, X. Dangsheng and Z. Tianle, *Carbon*, 2010, **48**, 2435.

6 National Science Foundation, (28 December 2007), Retrieved 22 January 2009, http://www.sciencedaily.com/releases/2007/12/071220111513.htm.

7 G. S. Attard, P. N. Bartlett, N. R. B. Coleman, J. M. Elliott, J. R. Owen and J. H. Wang, *Science*, 1997, **278**, 838.

8 O. D. Velev, P. M. Tessier, A. M. Lenhoff and E. W. Kaler, *Nature*, 1999, **401**, 548.

9 H. Maeda, Y. Kusunose, M. Terasaki, Y. Ito, C. Fujimoto, R. Fujii and T. Nakanishi, *Chem.–Asian J.*, 2007, **2**, 350.

10 H. Masuda and K. Fukuda, *Science*, 1998, **268**, 1466.

11 Y. Yusuke, M. Toshiyuki, Y. Tokihiko, K. Kazuyuki and O. Tetsuya, *J. Mater. Chem.*, 2005, **15**, 1987.

12 A. Devasenapathi, H. Ng, C. M. S. Yu and S. W. Lim, *J. Mater. Sci.*, 2005, **40**, 5463.

13 J. Erlebacher, M. J. Aziz, A. Karma, N. Dimitrov and K. Sieradzki, *Nature*, 2001, **410**, 450.

14 J. I. Thornycroft and S. W. Barnaby, *Min. Proc. Inst. Chem. Eng.*, 1895, **122**, 51.

15 L. Rayleigh, *Philos. Mag.*, 1917, **34**, 94.

16 E. N. Harvey, D. K. Barnes, W. D. McElroy, A. H. Whitely, D. C. Pease and K. W. J. Cooper, *J. Cell. Comp. Physiol.*, 1994, **24**, 1.

17 S. A. Elder, *J. Acoust. Soc. Am.*, 1959, **31**, 54.

18 S. A. Elder, J. Kolb and W. L. Nyborg, *J. Acoust. Soc. Am.*, 1954, **26**, 933.

19 C. F. Naude and A. T. Ellis, *J. Basic Eng.*, 1961, **83**, 648.

20 K. Makino, M. M. Mossoba and P. Riesz, *J. Phys. Chem.*, 1983, **87**, 1369.

21 D. G. Shchukin and H. Möhwald, *Phys. Chem. Chem. Phys.*, 2006, **8**, 3496.

22 H. Endo, *J. Acoust. Soc. Am.*, 1994, **95**, 2409.

23 M. Zeng, H. N. Gao, Z. Q. Wu, L. R. Fan, T. H. Zheng and D. F. Zhou, *J. Macromol. Sci., Part A: Pure Appl.Chem.*, 2010, **47**, 1042.

24 A. V. Mohod and P. R. Gogate, *Ultrason. Sonochem.*, 2011, **18**, 727.

25 K. Zhang, B.-J. Park, F.-F. Fang and H. J. Choi, *Molecules*, 2009, **14**, 2095.

26 M. A. Margulis, *Sonochemistry basis*, High School, Moscow, 1984.

27 E. V. Skorb, O. Baidukova, A. Goyal, A. Brotchie, D. V. Andreeva and H. Möhwald, *J. Mater. Chem.*, 2012, **22**, 13841.

28 L. H. Thompson and L. K. Doraiswamy, *Ind. Eng. Chem. Res.*, 1999, **38**, 1215.

29 K. S. Suslick and L. A. Crum, *Encyclopedia of Acoustics*, ed. M. J. Crocker, Wiley & Sons. Inc., N. Y., 1995.

30 D. V. Andreeva, E. V. Skorb and D. G. Shchukin, *ACS Appl. Mater. Interfaces*, 2010, **2**, 1954.

31 E. V. Skorb, D. G. Shchukin, H. Möhwald and D. V. Andreeva, *Nanoscale*, 2010, **2**, 722.

32 E. V. Skorb, D. G. Shchukin, H. Möhwald and D. V. Andreeva, *Langmuir*, 2010, **26**, 16973.

33 D. G. Shchukin, E. V. Skorb, V. Belova and H. Möhwald, *Adv. Mater.*, 2011, **23**, 1922.

34 E. V. Skorb and D. G. Shchukin, in *European Coatings Tech Files*, ed. G. Gehrenkemper, Vincentz Network GmbH & Co, Germany, 2010.

35 E. V. Skorb, D. Fix, D. G. Shchukin, H. Möhwald, D. V. Sviridov, R. Mousa, N. Wanderka, J. Schäferhans, N. Pazos-Pérez, A. Fery and D. V. Andreeva, *Nanoscale*, 2011, **3**, 985.

36 A. Weissler, *J. Am. Chem. Soc.*, 1959, **81**, 1077.

37 J. Dulle, S. Nemeth, E. V. Skorb and D. V. Andreeva, *RSC Adv.*, 2012, **2**, 12460.

38 K. S. Suslick and D. J. Casadonte, *J. Am. Chem. Soc.*, 1987, **109**, 3459.

39 K. S. Suslick, D. J. Casadonte and S. J. Doktycz, *Solid State Ionics*, 1989, **32/33**, 444.

40 K. S. Suslick and G. J. Price, *Annu. Rev. Mater. Sci.*, 1999, **29**, 295.

41 E. V. Skorb, H. Möhwald, T. Irrgang, A. Fery and D. V. Andreeva, *Chem. Commun.*, 2010, **46**, 7897.

42 A. Fischer, M. Antonietti and A. Thomas, *Adv. Mater.*, 2007, **19**, 264.

43 A. H. Lu and F. Schuth, *Adv. Mater.*, 2006, **18**, 1793.

44 A. Thomas, F. Goettmann and M. Antonietti, *Chem. Mater.*, 2008, **20**, 738.

45 A. Fischer, Y.-S. Jun, A. Thomas and M. Antonietti, *Chem. Mater.*, 2008, **20**, 7383–7389.

46 E. V. Skorb, D. V. Andreeva and H. Möhwald, *Angew. Chem., Int. Ed.*, 2012, **51**, 5138.

47 J. G. Adewuyi, *Environ. Sci. Technol.*, 2005, **39**, 8557.

48 J. Dulle, S. Nemeth, E. V. Skorb, T. Irrgang, J. Senker, R. Kempe, A. Fery and D. V. Andreeva, *Adv. Funct. Mater.*, 2012, **22**, 3128.

49 J. Schäferhans, J. Gomez-Quero, D. V. Andreeva and G. Rothenberg, *Chem.–Eur. J.*, 2011, **17**, 12254.

50 S. R. Kirumakki, B. G. Shpeizer, G. V. Sagar, K. V. R. Chary and A. Clearfield, *J. Catal.*, 2006, **242**, 319.

51 J. Masson, P. Cividino and J. Court, *Appl. Catal., A*, 1997, **161**, 191.

52 P. Mars, T. V. D. Mond and J. J. Scholten, *Ind. Eng. Chem. Prod. Res. Dev.*, 1962, **1**, 161.

53 N. Pazos-Pérez, J. Schäferhans, E. V. Skorb, A. Fery and D. V. Andreeva, *Microporous Mesoporous Mater.*, 2012, **154**, 164.

54 D. V. Andreeva, D. V. Sviridov, A. Masic, H. Möhwald and E. V. Skorb, *Small*, 2012, **8**, 820.

55 J. Gensel, T. Borke, N. Pazos-Pérez, A. Fery, D. V. Andreeva, E. Betthausen, A. Müller, H. Möhwald and E. V. Skorb, *Adv. Mater.*, 2012, **24**, 985.

56 E. V. Skorb, D. Fix, D. V. Andreeva, D. G. Shchukin and H. Möhwald, *Adv. Funct. Mater.*, 2009, **19**, 2373.

57 D. V. Andreeva, E. V. Skorb and D. G. Shchukin, *ACS Appl. Mater. Interfaces*, 2010, **2**, 1954.

58 T. Shutava, M. Prouty, D. Kommireddy and Y. Lvov, *Macromolecules*, 2005, **38**, 2850.

59 D. Schmaljohann, *Adv. Drug Delivery Rev.*, 2006, **58**, 1655.

60 M. A. C. Stuart, W. T. S. Huck, J. Genzer, M. Müller, C. Ober, M. Stamm, G. B. Sukhorukov, I. Szleifer, V. V. Tsukruk, M. Urban, F. Winnik, S. Zauscher, I. Luzinov and S. Minko, *Nat. Mater.*, 2010, **9**, 101.

61 E. V. Skorb, A. Skirtach, D. V. Sviridov, D. G. Shchukin and H. Möhwald, *ACS Nano*, 2009, **3**, 1753.

This journal is © The Royal Society of Chemistry 2013

J. Mater. Chem. A, 2013, **1**, 7547–7557 | **7557**

Polymer Chemistry
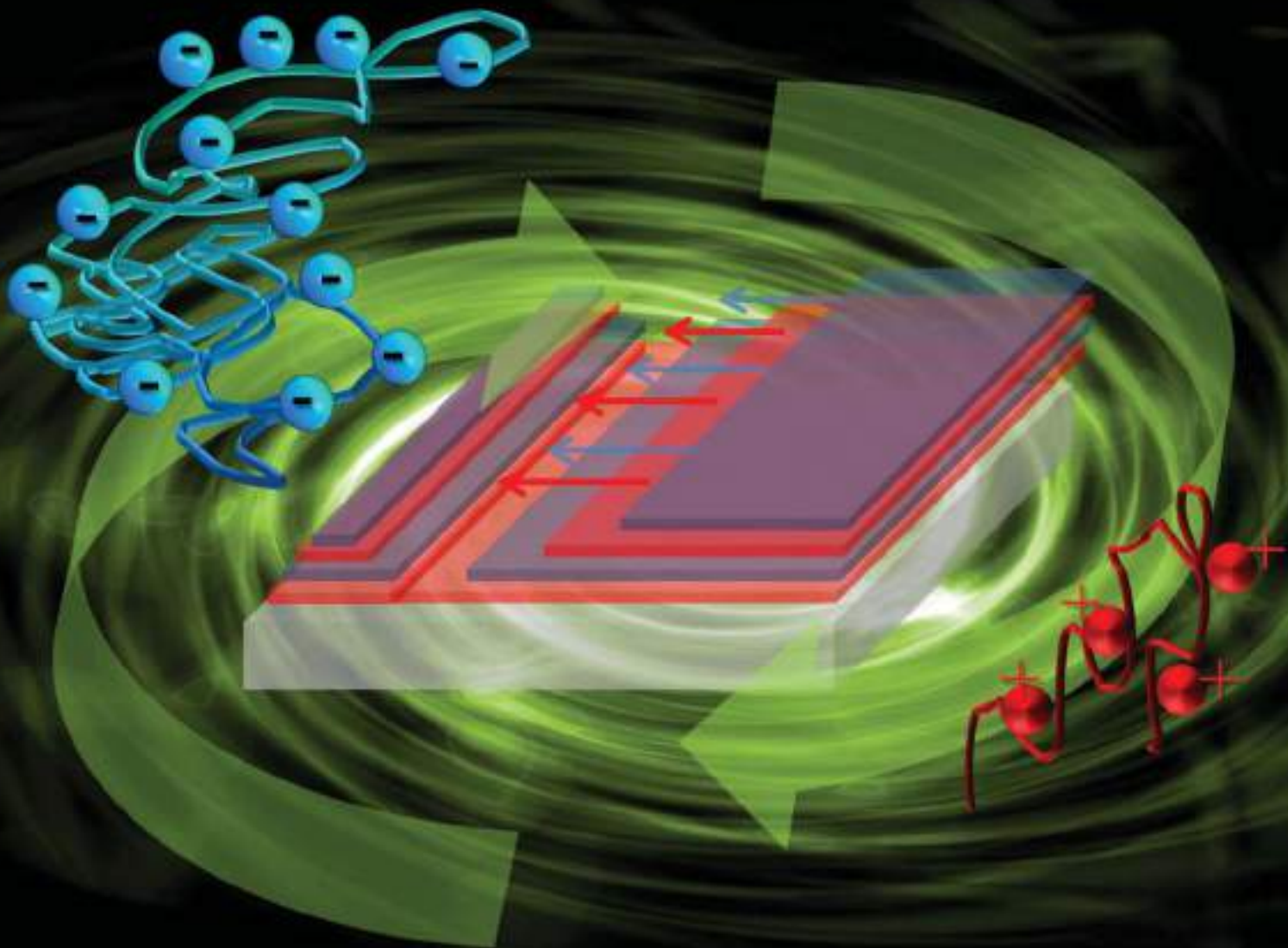
Themed issue: Self-healing polymers

RSC Publishing

REVIEW ARTICLE
Ekaterina V. Skorb and Daria V. Andreeva
Layer-by-Layer approaches for formation of smart self-healing materials

Polymer Chemistry

RSCPublishing

REVIEW

Layer-by-Layer approaches for formation of smart self-healing materials

Ekaterina V. Skorb[ab] and Daria V. Andreeva[*c]

This review is focused on the current achievements in application of Layer-by-Layer techniques for formation of materials with self-healing properties. We addressed the questions related to choice of materials for the Layer-by-Layer deposition, general aspects of multilayer formation, deposition techniques, and the mechanisms of self-healing of the multilayers. Layer-by-Layer deposited polyelectrolytes, hydrogels, conducting polymers, inorganic particles, hybrid organic–inorganic particles, and healing agents show great potential in formation of self-healing materials. In general, a non-covalently bonded Layer-by-Layer system exhibits high mobility of its components in response to external stimuli (humidity, T, pH, ionic strength, light, *etc.*) and, thus, can restore its integrity and heal defects. The review highlights the recent examples of Layer-by-Layer based design of self-healing materials for corrosion protection and biomedical application.

aChemistry Department, Belarusian State University, Leningradskaya str. 14, Minsk, 220030, Belarus

bMax Planck Institute of Colloids and Interfaces, Wissenschaftspark Golm, Am Mühlenberg 1, 14424 Golm, Germany

cPhysical Chemistry II, University of Bayreuth, Universitatstr., 30, Bayreuth, 95440, Germany. E-mail: daria.andreeva@uni-bayreuth.de; Fax: +49 921552731; Tel: +49 921552750

Introduction

Stimuli responsive materials are known as "smart" materials or the materials with self-healing or self-repairing ability.[1–4] A great variety of charged and non-charged compounds including polyelectrolytes,[4–7] clays,[8] nanoparticles,[9] nanotubes,[10] micelles,[11] bio molecules,[12] low molecular weight self-healing agents,[13] *etc.* could be used for contraction of functional multilayers. The Layer-by-Layer (LbL) deposition of organic and inorganic compounds on a surface leads to modification of its interfacial region and alteration of its properties. The surface charges morphology, hydrophobicity, wetting, adhesion, biocompatibility[14–16] as well as loading capacity of the interfacial layer can be altered by deposition of the multilayers.[17] Added to this is the easy formation of a nanostructure with multi-functionality by the LbL technique. Due to simple and uniform LbL deposition of a variety of components the LbL approaches for formation of materials

Ekaterina V. Skorb received her Diploma degree in Chemistry from Belarusian State University (Belarus), where she also did her PhD in Photochemistry. She came to the Max Planck Institute of Colloids and Interfaces as a Humboldt fellow in 2010. She is currently a Senior Lecturer at Belarusian State University (Belarus) and an Independent Researcher in the Max Planck Institute of Colloids and Interfaces (Germany). Her research interests include fabrication and characterization of functional hybrid materials, nanomaterials, stimuli-responsive interfaces, drug delivery systems for "smart intelligent" nanoarchitecture.

Daria V. Andreeva is an Academic Assistant at the Department of Physical Chemistry II of the University of Bayreuth. She got her PhD in the Institute of Macromolecular Compounds Russian Academy of Science in 2002. The PhD thesis concerned the formation of gas separation polymer membranes. In 2004–2005, she was an Alexander-von-Humboldt fellow in Free University of Berlin. In 2005–2009, she worked in the Max Planck Institute of Colloids and Interfaces on the development of Layer-by-Layer approaches for encapsulation and corrosion protection of metal surfaces. Her research interests are in the field of organic–inorganic composites, stimuli responsive interfaces, and surface nanostructuring.
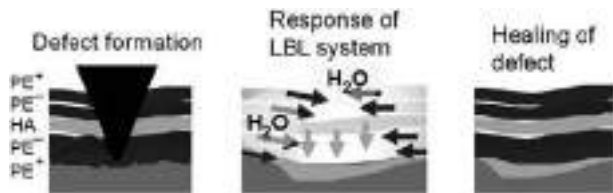
Fig. 1 Schematic illustration of the self-healing behaviour of LbL films (positively charged polyelectrolytes, PE⁺, negatively charged polyelectrolytes, PE⁻ and healing agent, HA) stimulated by water penetration into the multilayers. The healing agent released from the multilayers and healed surface defects. Finally, the multilayers restore film integrity. Adapted with permission from ref. 68. Copyright © 2010, American Chemical Society.

have a broad range of applications in the fields of sensing,[18] electroluminescence,[19] biosensing,[20,21] separation,[14,22] catalysis,[23] drug delivery,[24] interfacial nanoengineering,[25] etc.

The initial interest in the LbL technique arose from the electrostatic LbL assembly proposed by Iler in 1966.[26] In 1997 *Science* published a famous article "Fuzzy nanoassemblies toward layer polymer multicomposites".[4] Since that time the LbL concept has attracted the attention of many scientific groups all over the world. The LbL approach for deposition of various compounds serves as a platform for focused design of materials with particular architecture, properties and functions. One of these functions could be the self-healing ability. In this review we focus on the application of the LbL technique as one of the methods of construction of "smart" materials with self-healing functions.

LbL approaches for construction of an artificial self-healing material is an emerging field of materials science, biomimetic chemistry and supramolecular chemistry. The self-healing behaviour of LbL formed materials can be understood by using a dynamic polymer system concept.[27–30] In general, polymers have great potential in self-healing due to high mobility of the polymer chains under physiological conditions.[1] Dynamic polymer materials exhibit reversible properties due to the presence of reversible covalent bonds (thermodynamically driven bond breaking and reformation) and non-covalent (hydrogen bonding, electrostatic interactions, etc.) intermolecular interactions.[29,30] The self-healing potential of the LbL deposited multilayers is based on the mobility of the components of the multilayers which is sensitive to external stimuli. Self-healing of LbL films is schematically illustrated in Fig. 1. The mobility as well as permeability and elasticity of the multilayers are determined by the nature of the multilayers and external conditions (pH, ionic strength, T, light, etc.). In this review we summarize the recent achievements in development, formation and application of "smart" self-healing materials prepared via LbL techniques. The main aspects of mechanisms of self-healing of LbL films are addressed.

A general LbL concept

Materials overview

Despite a great variety of compounds that are used or potentially could be used for LbL deposition, polyelectrolytes are

considered as key components of the LbL systems. Indeed, the self-healing activity of LbL films to a great extent relies on properties of the polyelectrolytes involved in the LbL film formation.

Polyelectrolytes are macromolecules carrying a relatively large number of functional groups that are charged or could become charged under certain circumstances. The properties of these polymers in solutions and on charged surfaces were thoroughly addressed.[31] In brief, the morphology and properties of the LbL deposited polyelectrolyte layers depend on the solvent, solution dielectric constant, salt concentration, pH and interactions of the polymer with the substrate.[32–34]

The ionomers may be polycations and/or polyanions depending on the charged groups. Depending on the degree of dissociation the polyelectrolytes can be "weak" or "strong". The most extensively studied "weak" polyelectrolytes are polyethylene imine (PEI), poly(acrylic acid) (PAA), and polyallylamine hydrochloride (PAH). Among "strong" polyelectrolytes polystyrene sulfonate (PSS) and poly(diallyldimethylammonium) chloride (PDADMAC) are model polymers used for the investigation of multilayers formation and functions. These polymer pairs form multilayers due to electrostatic interactions.[35–37] They often are used as model systems for the investigation of behaviour, properties and nanoarchitecture of the LbL films in response to pH and ionic strength. Besides the multilayers formed by electrostatic interactions, LbL layers could also be hydrogen-bonded.[38,39] Poly(methacrylic acid) and poly(vinylpyrrolidone) can be self-assembled and form multilayers due to formation of intermolecular hydrogen bonds.[38] The PAA and polyacrylamide (PAAm) pair was stabilized by imidization in order to form stable stimuli responsive hydrogen bonded multilayers.[39] The response of the hydrogen bonded systems to external stimuli is due to the introduced electrostatic charges into ionisable elements within the layers.

Besides pH and ionic strength it was shown that temperature change and light can be used for triggering the healing activity of a material.[40,41] In general, the LbL films are kinetically stabilized during their preparation.[41] A temperature increase can provide enough energy to overcome the kinetic barriers and to stimulate the rearrangements of the multilayers. Sukhorukov et al.[41] demonstrated that the films consisting of PDADMAC and PSS can change their thickness and permeability between 30 and 50 °C. In order to provide the multilayers with light sensitivity[42–47] azobenzene derivatives can be LbL assembled. One of the examples is the poly(1-(4-(3-carboxy-4-hydroxy phenylazo) benzene-sulfonamido)-1,2-ethanediyl) sodium salt which has photosensitive groups in the side chains.[43,44] Such photosensitive polyelectrolytes could be used for construction of multilayers responsive to light as an external stimulus. Another approach for formation of light sensitive multilayers is loading particles sensitive to light[45] into the multilayers.

Polyelectrolytes are usually a basic component of the LbL formed multilayers. Other polymers (conducting polymers, hydrogels, photosensitive and biocompatible polymers), nanoparticles, nanotubes, clays, healing agents, etc. can be LbL deposited together with polyelectrolytes and, thus, supply the LbL materials with desirable functions. Temperature-responsive

nanolayers can be formed by LbL deposition of hydrogels poly(*N*-isopropylacrylamide) (PNIPAM),[48–51] poly(*N*-vinylcaprolactam) (PVCL)[52–54] and their copolymers. Hydrogels exhibit pronounced temperature response in a very narrow temperature range.[55] PNIPAM is soluble in water below 32 °C and precipitates at higher temperatures. The temperature responsive multilayers are formed by LbL deposition of PNIPAM or PVCL and their copolymers together with various polyelectrolytes. The multilayers can be prepared *via* formation of intermolecular covalent bonds,[56] electrostatic interactions[51] or hydrogen bonds.[56] The self-assemblies of PNIPAM and PAA,[56] PVCL and poly(vinyl methyl ether) were formed *via* hydrogen bonding.[55] The covalently bonded systems exhibit a high stability compared to electrostatically bonded multilayers. In general, hydrogels are extremely promising components for the LbL construction of self-healing materials. Non-covalently bonded hydrogels use secondary interactions such as hydrogen bonding, ionic and hydrophobic association for healing of damaged areas. In cross-linked hydrogels the main healing factor is the presence of water in the system.

Conducting polymers (polyaniline, polypyrrole, *etc.*) demonstrated self-healing behaviour based on several mechanisms.[57] Due to their conductive and oxidative properties conducting polymers can directly passivate degradation of metal surfaces. Additionally, these polymers are stimuli responsive materials that are suitable for LbL deposition.[58–63] Nanoarchitecture of the layers formed by conducting polymers can be changed in response to external stimuli. The conducting polymers can incorporate and release healing agents *via* a doping/dedoping process.

LbL deposition of low molecular weight compounds, nanoparticles, nanotubes, clays, DNA, *etc.* can provide multilayers with additional functions. For example, metal nanoparticles incorporated into an LbL film provide the multilayers with light responsive properties.[64,65] Carbon nanotube/polyelectrolyte multilayers exhibit sensing activity and can be used for sensing of corrosion damage.[10] The inorganic clays were successfully incorporated into an anticorrosion multilayer coating mostly for improvement of mechanical properties of the coatings.[8] LbL deposited TiO_2 (ref. 66) yields to formation of photosensitive materials. Nanoparticles added to the polymers can migrate to damaged areas and heal nanocracks. The healing agents (for example, corrosion inhibitors) can be also used as a component of LbL systems.[67,68] The multilayer systems formed by different combinations of "weak" and "strong" polyelectrolytes sensitive to different stimuli could be used for entrapment of low molecular weight compounds. Polyelectrolytes assembled in multilayers have a relatively large number of functional groups and can reversibly entrap healing agents. External stimuli, such as pH, temperature, light, *etc.*, change the degree of dissociation of polyelectrolytes, control the concentration of bonded and un-bonded species in the multilayers and, therefore, trigger the release of healing agents on demand.

Construction of self-healing materials by using the LbL technique

The unique blend of features that are relevant to surface nanoengineering aligns the LbL technique with soft-

lithography,[69] the Langmuir–Blodgett technique,[70] self-assembled monolayers,[71] *etc.* Compared to other methods the LbL technique does not require sophisticated equipment for the formation of the multilayers. The deposition procedure is relatively fast and versatile, could be adjusted to a substrate with different charge, texture and morphology.[25,35–37,72]

The layer formation process is entropically driven by the release of counterions.[35] The growth of multilayers is a result of electrostatic attraction and repulsion between charged chains. The growth of multilayers under different conditions can be studied *in situ* by using the quartz crystal microbalance with dissipation monitoring, and *ex situ* using X-ray reflectivity, zeta potential measurements, microscopic and spectroscopic methods.

There are two key factors – pH and ionic strength – to control the LbL growth of the multilayers. These factors affect the conformation of the deposited polyelectrolytes and, thus, the thickness of the multilayers.[73–93] The sketch in Fig. 2 is a schematic illustration of the LbL deposition of oppositely charged polyelectrolytes. The sketch shows the deposition of relatively linear polymer molecules and formation of well-defined polymer nanolayers. In reality, polyelectrolyte chains penetrate into each other. Depending on pH and ionic strength differently coiled polyelectrolyte chains can be deposited. Thus, the thickness of the multilayers consisting of the same polymers but prepared at different pH and ionic strength can vary from tens to hundreds of nanometers. The deposition parameters should be experimentally found for each particular system.

Presence of salts in the deposition solution leads to charge screening effects, degreases repulsion forces between the charges and stimulates coil conformation of the chains.[86,87] Higher salt concentration (up to 1 M NaCl) leads to increased water content in the multilayers.[88] Deposition of weak polyelectrolytes is strongly affected by the pH of the polymer solution. pH influences the dissociation of weak polyelectrolytes and, thus, the charge density of the polyelectrolytes can be controlled by pH values. A higher amount of the deposited chitosan was observed at pH 4. These films exhibited higher hydrophobicity and more pronounced antibacterial properties in comparison to the chitosan/heparin films prepared at pH 6.[91]

It was shown[89] that the thickness and morphology of the films can be changed by post-treatment under different conditions. The post-treatment of the layers by solutions with high
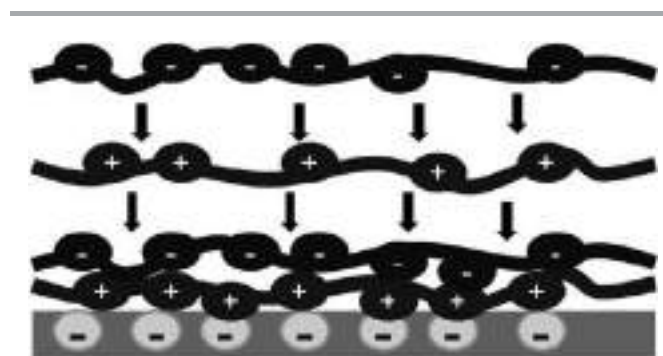
Fig. 2 Sketch of multilayer growth on a negatively charged surface.

salt concentrations has an annealing effect and results in smoothing of the interfacial layer. It was shown that depending on pH different amounts of the polymer can be deposited.[90] The multilayers of PSS/PAH exposed to low pH were thicker and more permeable compared to the as-prepared film.[74,92] The mechanism of annealing was explained by rearrangement of polymer segments, by salt ions and formation of new polymer–polymer interactions resulting in a new film morphology.[93]

Layer deposition generally starts with immersion of a substrate in an aqueous solution of a charged polyelectrolyte.[37] The LbL technique allows homogeneous film formation on different surfaces including non-ionic and non-polar substrates.[73–75] Deposition of multilayers and their properties do not depend on the substrate morphology, thus, many substrates from planar surfaces to particles and tubes can be covered by multilayers.[76–79] The first deposited layer is called the "anchoring" layer.[81] The anchoring layer should exhibit very good adhesion to the substrate surface and be able to seal surface defects. During the next adsorption step the polyelectrolyte molecules adsorb to the oppositely charged surface.

Technologically, the LbL technique is the step-wise assembly of oppositely charged species on a substrate.[82,83] In general, the sequential immersion of a substrate in solutions of the LbL components (polymers, nanoparticles, *etc.*) leads to formation of LbL assemblies. Each deposition cycle is followed by surface rising with a solvent in order to remove the unbound compounds. The deposition cycles are repeated in order to deposit a particular number of layers.

Three convenient techniques can be used for the LbL deposition: spraying, spin coating and dip coating. The comparison of these three methods was profoundly studied and carefully addressed in the literature.[94–101]

The dip coating technique includes the following steps: (1) immersion of substrates in the dipping solutions; (2) equilibrium time 10–20 min, and (3) rinsing of the substrate with a solvent. It is a well-established procedure of LbL film formation.[94] At the same time it is a time-consuming process that requires building up of robotic lines.[94] Additionally, this method needs a relatively large quantity of the material for each deposition step. At the same time, dip coating is the only method that could be used for formation of polyelectrolyte capsules and deposition of LbL films on spheres, particle, tubes, *etc.*

Spraying is an alternative method of formation of LbL films on planar substrates. This method was described in detail and compared to the dip coating method in ref. 94. Development of spraying for LbL deposition is an important step in application of LbL techniques. In this case, the working and rinsing solutions are supplied by spraying. The procedure includes (1) two spraying sequences per single layer; (2) waiting time to remove the solution excess; (3) spraying with rinsing solution; (4) waiting time again. The main advantage of spraying is the significant reduction of time needed for multilayer formation. Kolasinska *et al.*[94] demonstrated that the time needed for preparation using spraying can be reduced by a factor of 60 compared to dipping.

Spin coating[95,96] is a relatively new deposition procedure for the multilayer formation. Spin coater requires excess polymer solution to be applied to a substrate before spinning.[95] Then the solvent is rapidly expelled from the surface and the dissolved component forms a layer. The time and rate of spinning should be adjusted for a particular system.[96] The procedure is very fast. Uniform films can be prepared within a few hours. Saving of time for equilibrium achieving (tens of minutes for dip coating in comparison to a couple of seconds for spin coating deposition) was explained by convection and hydrodynamic stress provided by fast spinning.[95] The main disadvantage of this method is its restriction to planar surfaces. It cannot be used for different shapes of substrates, for example, for LbL modification of spheres, particles, bubbles.

In summary, all methods (spraying, spinning and dip coating) can be adjusted to a particular substrate. The morphology and functionality of the LbL films depend on the preparation method. The films formed by spraying, spin coating and dip coating demonstrated significantly different thickness and roughness. It has been found that spraying and dip coating lead to formation of relatively thick and rough films. The spin coating method of layer deposition leads to formation of thinner multilayers due to the shear forces applied during sample spinning.[99] Therefore, all preparation methods result in successful modification of the surface by the polyelectrolytes. All deposition methods are easy to implement and can be up-scaled. Compared to other methods dip coating is time consuming since each adsorption and rinsing step usually takes several minutes. In order to accelerate and automate the LbL deposition process, spray deposition[100,101] and spin coating[99] have been found as good alternatives for shortening the deposition time and are suitable for up-scaling.

The mechanism of self-healing in LbL deposited multilayers

The mechanism of self-healing of LbL deposited multilayers is based on the mobility of the components of the multilayers which are sensitive to external stimuli. The number of unbound mobile chains in the multilayers is a key factor in the degree of mobility of the polyelectrolyte multilayers. pH and ionic strength are two factors that are essential for the swelling behaviour of the multilayers.[102,103] pH and ionic strength are two external stimuli that can affect the water content in the multilayers and, thus, mobility of the polyelectrolyte chains.[104]

A number of investigations have provided important knowledge on the mobility of multilayers and factors influencing it. Hammond *et al.*[105] deposited viruses as probes on an LbL film in order to visualize the mobility of the layers under different conditions. It was shown that pH is one of the external stimuli that could control the mobility of the "weak" polyelectrolytes in the multilayers. Thus, dissociation of "weak" polyions in response to pH change can be proposed as an important aspect of self-healing application of the multilayers. The charge density of "strong" polyelectrolytes is constant over a broad pH range.[35–39]

Experiments (different scattering techniques, microscopy and spectroscopy studies, *etc.*) demonstrate that water in the multilayers influences molecular interactions in the layers and, thus, mobility of the layers. It was experimentally shown that the water

fraction in the multilayers can be controlled by ionic strength,[89] pH[106–108] and the type of the adsorbed polyelectrolytes.[103] The water fraction was higher in the PSS layers compared to PAH layers.[106] Furthermore, if the outermost layer of the film is PSS it swells more than the film with PAH on the top.[106] Different water content in the components of the multilayers was studied by neutron reflectometry.[109] A photobleaching method was used to study the influence of water on the mobility of polyelectrolyte–lipid multilayers. A diffusion coefficient of the order of 10^{-10} cm^2 s^{-1} was measured in swollen lipid layers. The screening of the interaction of lipid and polyelectrolyte was found as an important factor influencing the mobility of the multilayers.[110]

Several studies have investigated the diffusion of charged and uncharged molecules in multilayers. In poly(L-lysine) and hyaluronic acid multilayers diffusion of biomolecules with different hydrodynamic radii and charge was studied.[111] Diffusion of the molecules in the multilayers occurred due to electrostatic interactions between the molecules and the polymer matrix. The uncharged molecules exhibited size-independent exclusion. Lavalle et al.[102] studied the mobility of a fluorescein labelled protein in the multilayers by fluorescence recovery after photobleaching and demonstrated that the mobility of the protein within the film depends on its concentration. Thus, proteins in the multilayers diffuse from the high-concentration region to the low-concentration regions. The same dynamics could be expected for other compounds (self-healing agents) deposited in multilayers. In this case, damage of the multilayer integrity can trigger diffusion of healing agents and LbL deposited nanoparticles to the defected area and healing of defects at the nanoscale level.

Another mechanism of self-healing provided by LbL materials is based on the ability of the multilayers to load/release healing agents on demand. Various techniques for loading and release of active compounds by using LbL materials were proposed for biomedical and industrial applications.[112,113] It was shown that DNA can be released from the LbL films under physiological conditions.[114] Low molecular weight healing agents including ions can be incorporated into a multilayer system.[8,67,68] In this case, the LbL film is able to regulate loading and release of these compounds. The multilayer systems formed by "weak" and "strong" polyelectrolytes sensitive to different stimuli could be used for entrapment of low molecular weight healing agents. Polyelectrolytes assembled in multilayers have a relatively large number of functional groups and can reversibly non-covalently bind low molecular weight compounds. Healing agents deposited as a component of the polyelectrolyte film can be released on demand. External stimuli (pH, ionic strength, light, T, etc.) can trigger their release and delivery to a defected area. Moreover external stimuli change the degree of dissociation of polyelectrolytes and, therefore, affect the concentration of bonded and un-bonded species in the multilayers.

Self-healing materials formed by using LbL approaches

Polyelectrolytes as key self-healing materials

Polyelectrolyte multilayers have a pronounced self-healing effect due to their mobility in response to environmental change. External stimuli such as pH, ionic strength, temperature, light, etc. affect ionization of the functional groups of the polyelectrolytes which results in a lowered electrostatic interaction of the polymers as well as in an increased repulsion between uncompensated charges.[75,115] Water and counter ions can penetrate the layer structure to compensate the charges.[116] The higher ionic concentration compared to the surrounding solution increases the osmotic pressure resulting in penetration of water into the polyelectrolyte multilayers. Thus, the polyelectrolyte multilayers start to swell and, therefore, increase their mobility.

Recently a novel corrosion protection system consisting of "weak" and "strong" polyelectrolytes was proposed.[117–119] This system demonstrated pH dependent self-healing activity. It is interesting that "weak"–"weak", "weak"–"strong" and "strong"–"strong" polyelectrolytes showed different healing properties.[117–119]

The scanning vibrating electrode technique[120] (SVET from Applicable Electronics, USA; diameter of the Pt blackened electrode tip is 20 μm, the peak-to-peak amplitude is 60 μm, and the vibration frequency is 655 Hz) was applied for in situ monitoring of the healing behaviour of the multilayers. The SVET allows monitoring local cathodic and anodic activity of the defects and in situ observation of degradation or healing processes. At the beginning of the SVET experiments the samples were scratched and immersed into aggressive media.

The system of two "weak" polyelectrolytes PEI and PAA demonstrated a pronounced self-healing ability (Fig. 3A and B). The scratched metal plates covered by PEI/PAA were immersed into 0.1 M NaCl solution for 12 h. During this time the beginning of degradation processes of the metal surface (the peaks on the curves and on the map of the ion current monitoring) was detected by SVET. However, the PEI/PAA system suppresses
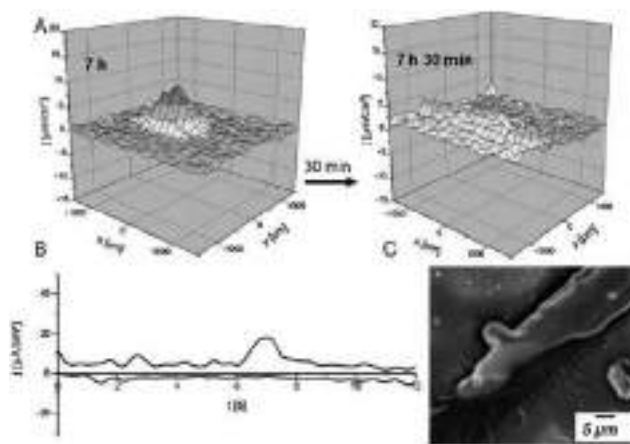
Fig. 3 (A) Scanning vibrating electrode measurements of the ionic currents above the surface of the scratched aluminum alloy covered by the PEI/PAA-ten-bilayer-coating (scale units: μA cm^{-2}, spatial resolution 150 μm, solution: 0.1 M NaCl). Experiment time is 7 h (left); experiment time is 7 h 30 min (right); (B) time dependence of the current density changes of the scratched aluminum alloy covered by the PEI/PAA-ten-bilayer-coating: upper curve – anodic current, lower curve – cathodic current; and (C) scanning electron microscopy image of the surface of the PEI/PAA coating after 12 h of immersion in 0.1 M NaCl. Adapted with permission from ref. 68. Copyright © 2010, American Chemical Society.

propagation of degradation. The intensive degradation process detected at 6 h of the experiment was completely suppressed at 8 h of the experiment that can be seen in the current density maps (Fig. 3A). The mechanism of self-healing of polyelectrolyte multilayers was explained by high mobility of the nanolayers triggered by water penetration into the multilayers. The SEM image of the defected area that partly recovered after immersion in 0.1 M NaCl solution can be seen in Fig. 3C. It was shown[121] that immersion of the protected substrates in water or even spraying water on the substrate leads to the pronounced healing effect. The authors[121] proposed that water could be an easier external stimulus triggered healing process in the multilayers in comparison to light irradiation or thermal treatment. These results prove the self-healing behaviour of the polyelectrolyte multilayers in aggressive media. In contrast to the system formed with the "weak" polyelectrolytes the "strong–strong" polyelectrolyte multilayers formed by PDADMAC and PSS did not exhibit healing properties.[68] Fig. 4B demonstrates the defect propagation on the aluminum surface covered by PDADMAC/PSS. To provoke degradation of the surface the polyelectrolyte coating was scratched before immersion. Both anodic (peak) and catholic peaks (gaps) (Fig. 4A) appear with experiment time resulting in defect propagation throughout the whole surface of the sample. Both strong polyelectrolytes carry high charge densities over a broad pH range. Therefore, interaction between them is too strong to be altered by pH change.

Recently,[122] the LbL concept was applied for formation of superhydrophobic surfaces with self-healing ability. In this case, an elegant solution was proposed for overcoming defect formation in superhydrophobic coatings. The rough surface formed by PAH, sulfonated poly(ether ether ketone) (SPEEK) and PAA multilayers was covalently bonded to hydrophobic 1H,1H,2H,2H-perfluorooctyl triethoxysilane (POTS). After damage of the hydrophobic layer, the hydrophilic PAH–SPEEK/PAA multilayers could swell in a humid environment that leads to increased chain mobility. The covalently attached hydrophobic POTS molecules could diffuse in the swollen polymer matrix to the surface due to rearrangement of polyelectrolyte chains. The diffused fluoroalkyl chains heal the defects in the hydrophobic outermost layer of the PAH–SPEEK/PAA multilayers. Thus, the authors[122] could successfully combine the superhydrophobic and self-healing properties by using LbL deposited polyelectrolyte multilayers.

The LbL multilayers of biopolymers can promote the healing ability of bio substrates (implants, stents).[46,47] The LbL deposited chitosan/heparin multilayers on stents lead to formation of the biocompatible surfaces that could accelerate the healing process after implantation. The multilayers of biocompatible chitosan and heparin could promote re-endothelialization and fast healing process after stent implantation.[47]

Beside pH and ionic strength, temperature and light can be external stimuli triggering the self-healing activity of multilayers. A special example is application of ethylene-co-methacrylic acid (EMAA) for formation of self-healing materials.[123]

The optical photographs of the LbL formed temperature responsive multilayers consisting of EMAA and PEI can be seen in Fig. 5. Zacharia and Huang[123] showed that the multilayers undergo temperature dependent reversible bonding. The collaborative work of the groups of Tsukruk and Müller[124] resulted in a non-destructive light responsive LbL system consisting of poly{[2-(methacryloyloxy)ethyl]trimethyl ammonium iodide} (PMETAI) star-like polymer and PSS with incorporated

Fig. 4 (A) Time dependence of the corrosion propagation of the scratched aluminum alloy covered by the PDADMAC/PSS-ten-bilayer-coating obtained by using the scanning vibrating electrode technique: upper curve – anodic current, lower curve – cathodic current (scale units: µA cm^{-2}, spatial resolution 150 µm, solution: 0.1 M NaCl); and (B) scanning electron microscopy image of the scratch covered by corrosion products. Adapted with permission from ref. 68. Copyright © 2010, American Chemical Society.

Fig. 5 The PEI/EMAA multilayer being pulled off the substrate. Reprinted with permission from ref. 123. Copyright © 2012, American Chemical Society.

hexacyanocobaltate ions. Changes in nanoarchitecture of the multilayers were observed due to the effect of the light-induced ionic state of cobalt on the morphology of ion-selective PMETAI. The expansion/shrinkage behaviour of the LbL films was controlled by ratio multivalent vs. monovalent ion concentration. Thus, this light dependent mobility of the chains can be potentially used for formation of self-healing materials.

Hydrogels in LbL formed self-healing materials

Application of hydrogels as a component of the LbL films for formation of self-healing materials is a very perspective approach in surface nanoengineering. Hydrogels exhibit pronounced morphological changes in response to external stimuli (temperature and humidity).[55] Stimuli responsive properties of PNIPAM and its co-polymers with poly(acrylic acid) and poly(vinylamine) have been widely addressed during the last few decades.[42,49–51] Other examples of hydrogels are less toxic and biocompatible PVCL[53] and its co-polymers. The mechanism of self-healing of hydrogels is based on morphological changes of the hydrogel containing layers in response to external stimuli.[125] At temperatures below 32 °C PNIPAM absorbs water and swells. At temperatures above 32 °C PNIPAM desorbs water and transforms to a hydrophobic state.[54]

Recently, South and Lyon[125] proposed that hydration can be a major factor that stimulates reversible Coulombic interactions in hydrogels and, thus, their self-healing behaviour. Healing processes are stimulated by hydration of the polymer.

A disadvantage of self-healing and other applications of hydrogels is the poor mechanical properties of the films formed by the hydrogel. The uncontrollable rearrangements or even dissolution of hydrogels upon usage significantly restrict their application as self-healing materials.[126] The LbL approach of formation of "smart" films containing hydrogels is a promising technological solution. It was demonstrated that the intermolecular interaction in PVCL and poly(2-hydroxypropylacrylate) layers was stronger than intramolecular interactions.[126] Strong intermolecular interaction is one of the key factors for formation of a stable LbL assembly.

Stability and "smart" properties of self-assembled PNIPAM, its co-polymers and polyelectrolytes were thoroughly investigated. Temperature dependent changes in the nanoarchitecture of the hydrogel containing LbL assemblies were reported by Sukhishvili and Zhu,[49] Schlenoff and Jaber,[51] Caruso and Quinn[42] and Lyon et al.[50] Below we will highlight some recent examples of application of LbL deposited hydrogels as self-healing materials.

The self-assembly of PDADMAC, gold nanoparticles (Au NPs) and poly(N-isopropylacrylamide-co-acrylic acid) hydrogel particles was proposed by Lyon et al.[127] The authors demonstrated reversible self-healing ability and improved mechanical properties. Au NPs provided additional reinforcement to the multilayers. At the same time, the NPs did not hinder the mobility of the polymer layers. Thermoresponsive multilayers of cross-linked PVCL were proposed by Kharlampieva et al.[53] This very interesting approach is based on LbL deposition of PVCL/poly-(methacrylic acid) (PMAA). After cross-linking of PVCL layers

PMAA was removed. Finally, highly reversible thermoresponsive behaviour was observed for the single component cross-linked PVCL multilayers. Formation of pH responsible multilayers containing PMAA copolymers was demonstrated by the groups of Vladimir Tsukruk.[128] This research reported very sophisticated experiments on pH stimulated manipulation of hydrogel-containing multilayers. The LbL hydrogel multilayers demonstrated very promising results in pH controlled cell growth and functions. Thus, it was shown to have a great advantage in application of LbL assembled hydrogels in biomedical application, tissue engineering and biomimetic approaches.

Conducting polymers as components of self-healing multilayers

Conducting polymers could be LbL deposited together with polyelectrolytes via a reversible doping/dedoping process. The self-healing behaviour of conducting polymers was suggested by Wessling.[57] Conducting polymers in the self-healing multilayers can have several functions. First of all conducting polymers are able to heal the defects and works like a healing agent.[63]

Conducting polymers (polypyrrole, polyaniline) could passivate the metal substrates and, thus, prevent their degradation in aggressive media. Kowalski, Ohtsuka and Ueda[63] studied the self-healing ability of polypyrrole on steel surface. Conducting polymers can load and release healing agents via a doping/dedoping process.[60,62] It was also shown that model dyes[58] and healing agents,[63] for example, phosphomolybdate ions could release from the systems containing polypyrrole in damage zones and heal defects. Fig. 6 illustrates the release of a model dye rhodamine 6G (Rh6G) from polypyrrole layers. The curves prove the pH dependent release of the dye. The conducting polymers transfer from a compact (neutral) state to a gel (oxidized) state due to swelling of the polymer matrix during oxidation.[60] Furthermore, hydrophilic properties and, thus, swelling and loading capacity of conducting polymers can be controlled by doping/dedoping reactions. The permeability of LbL films containing polypyrrole can be tuned by pH. Polypyrrole layers exhibit very strong barrier properties in acidic media at $2 < pH < 7$ and a high permeability at $pH > 7$.[60] Thus, polypyrrole layers can be used for non-specific immobilization of healing agents due to barrier properties of the polypyrrole
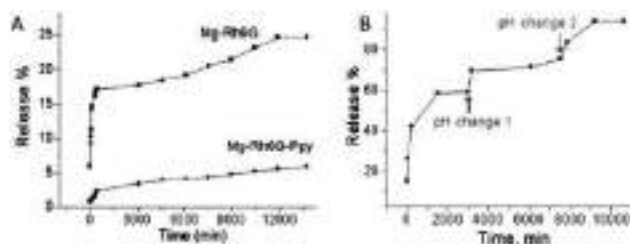
Fig. 6 (A) Time-resolved release of Rh6G from porous magnesium (Mg–Rh6G) without polypyrrole and the hybrid layer (Mg–Rh6G–Ppy) in aqueous solution at neutral pH. (B) Time resolved release under initial pH = 4 and two step-wise pH changes: pH change 1: to pH = 3, pH change 2: to pH = 1. Adapted from ref. 58 with permission from The Royal Society of Chemistry.

layers. Additionally conducting polymers can be used as a sensor that could register mechanical damage.[129]

LbL deposition of healing agents as a component of multilayers

LbL deposited multilayers can be considered as a carrier for low molecular weight compounds.[130] The sensitivity of the polyelectrolyte film to a variety of physical, chemical and mechanical impacts (like pH-shift or mechanical defects) is responsible for the regulated release of healing agents entrapped in multilayers. External stimuli (pH, temperature, light, *etc.*) change the degree of dissociation of polyelectrolytes and, therefore, control the concentration of bonded and un-bonded species in the film.

Active species deposited as a component of the polyelectrolyte nanonetwork can be released on demand. Furthermore the loading and release properties of "weak" polyelectrolyte multilayers could be considered as a function of pH. This tendency of polyelectrolyte multilayers was studied by using a model system consisting of PAH/PAA films loaded with methylene blue dye.[74] At acidic pH the dye can diffuse into PAH/PAA multilayers. The amount of the loaded dye increased linearly with increasing film thickness. Release studies demonstrated a pH-sensitive release mechanism.

In self-healing systems instead of dyes healing agents can be trapped in polyelectrolyte multilayers.[131–133] For example, 8-hydroxyquinoline (8HQ) was deposited as a positively charged component of PEI/PSS multilayers on the aluminium alloy surface.[17] The sketch of the polyelectrolyte multilayers with the deposited inhibitor is illustrated in Fig. 7A. Fig. 7B and C demonstrate a high level of passivation of surface degradation

in aggressive media. No evidence of the degradation process was registered visually and by using SVET. The samples with LbL polymer/inhibitor protection exhibit excellent resistance to degradation. No products of degradation can be seen in the substrates protected by the inhibitor–polymer multilayer in long term tests.

A very interesting and novel approach is the application of the LbL coating for protection and functionalizing of ultrasonically activated metal surfaces.[131–136] Such surfaces, so-called "surface sponges",[135,136] exhibit a mesoporous structure, high roughness and surface area. The surface sponges can be loaded with corrosion inhibitors and covered by polyelectrolyte multilayers. The local changes in pH accompanying the corrosion process leads to the disintegration of the healing agent and polyelectrolyte nanolayers. The inhibitor can release from the multilayers and heal the degradation pits. When the pH returns to the initial value, the nanolayers are assembled again due to recovery of multilayers.

The biodegradable multilayers were proposed as a carrier for antibiotics at the implant–tissue interface. Cefazolin was loaded in poly(L-lysine)/poly(L-glutamic acid) (PLL/PLGA) nanofilms on stainless steel disks.[57] PLL/PLGA multilayers were loaded with cefazolin by immersing them in a cefazolin solution (pH 7) for 20 min. Antibacterial activity against *S. aureus* and surface adhesion properties to bacteria and osteoblasts were studied. The pronounced inhibiting growth of bacteria in presence of cefazolin and biocompatibility of the surface to osteoblasts were achieved due to the LbL films. Thus, the cefazolin loaded multilayers could provide healing ability due to antibacterial properties and biocompatibility.

The LbL approach in formation of hybrid self-healing materials

Hybrid materials formed by LbL consist of inorganic particles and polyelectrolyte multilayers. Incorporation of particles into multilayers leads to enhanced mechanical properties of the multilayers[8,127] and provides the systems with additional stimuli responsive properties[9,17,65,137] (light, ultrasound, magnetic and electric field). Incorporation of porous particles results in high loading capacity of the self-healing system. In particular, LbL deposition of inorganic particles and polyelectrolytes could significantly expand the range of stimuli that could affect film nanoarchitecture. LbL deposition of metal NPs results in sensitivity of the multilayers in the UV light to near-IR region and to ultrasound waves. Incorporation of inorganic components into multilayers enhances mechanical properties of the multilayers.

Recently, Shchukin[138–146] and co-workers proposed a novel LbL approach for formation of hybrid self-healing materials. Inorganic porous particles are used as carriers for low molecular weight active agents (healing compounds, corrosion inhibitors, antibiotics, *etc.*). In order to provide the carriers with stimuli responsive properties they are covered by LbL films. These self-healing systems can be added to all types of coating. The hybrid system incorporated into a coating is schematically illustrated in Fig. 8A. Compatibility of the hybrid particles with
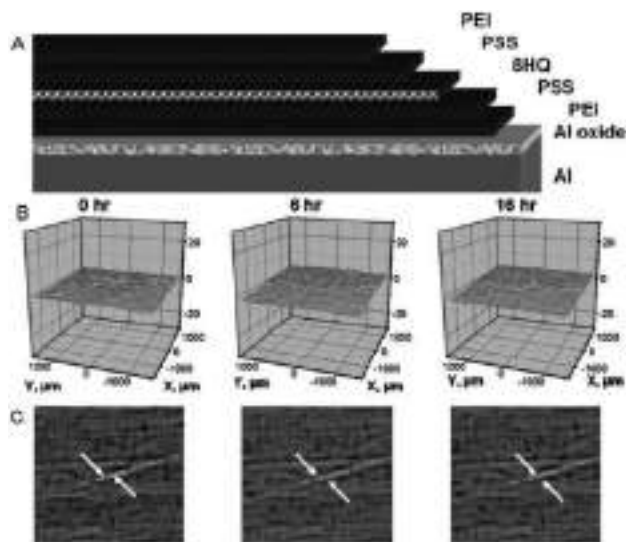
Fig. 7 (A) Schematic illustration of the PEI/PSS/8HQ self-healing system on aluminium surface; (B) scanning vibrating electrode technique (SVET) measurements of the ionic currents above the surface of the scratched aluminum alloy covered by the polyelectrolyte/inhibitor coating (scale units: μA cm⁻², spatial resolution 150 μm, solution: 0.1 M NaCl); (C) optical photographs of the behaviour of the scratched surface during the SVET experiments (the scratch is shown by the arrows). Adapted with permission from ref. 13. Copyright © 2008 WILEY-VCH Verlag GmbH & Co. KGaA, Weinheim.
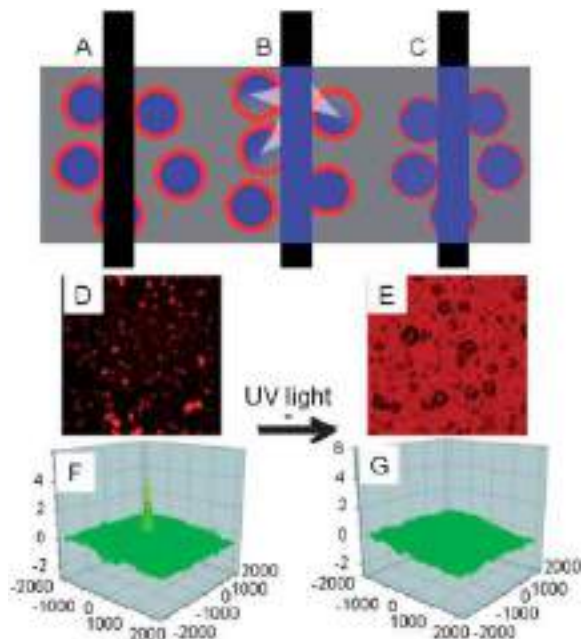
Fig. 8 Schematic illustration of the release of healing agents from the hybrid LbL systems: (A) inorganic carriers loaded with healing agent (blue) and covered by polyelectrolyte multilayers (red) (the black bar indicates hypothetic damage); (B) release of the healing agent in response to mechanical rapture (black bar); (C) release of the healing agent in response to chemical trigger (black bar) (pH, light, T). (D and E) Confocal images of polyelectrolyte–titania hybrids (in luminescent mode). The images are obtained (D) before and (E) after UV illumination. The particles in the figures correspond to the aggregates. Scanning vibrating electrode measurements of the ionic currents above the surface of polyelectrolyte–titania hybrids incorporated into an $SiO_x:ZrO_x$ hybrid film (aluminium alloy is a substrate) (F) after 12 hours of degradation; (G) after UV-irradiation and release of healing agent. Scale units: $\mu A\ cm^{-2}$, spatial resolution 150 μm. Solution: 0.1 M NaCl. The figures D–G are reproduced from ref. 146 with permission from The Royal Society of Chemistry.

commercial coatings can be achieved by adjustment of the surface chemistry of the multilayers.

The advantages of this approach are clear from technological and economical points of view: easy formation and storage, high loading capacity for healing agents, homogeneous distribution in the coating matrix. Titania, silica particles, clays were proposed as carriers for healing agents.

Incorporation of titania[146] provides multilayers with photosensitivity. The multilayers assembled by PEI/PSS were used as "smart" multilayers for protection of porous titania loaded with a healing agent (benzotriazole (BTA)) or model dye (rhodamine 6G) (Fig. 8D–G). A very interesting and perspective UV light-driven release of the encapsulated chemicals was successfully demonstrated. The reversible release can be attributed to local changes in pH due to photocatalytic processes occurring in the titania. pH changes triggered by photocatalysis lead to conformational transitions in the polyelectrolyte multilayers. Thus, the system is characterized by both self-healing and self-regulation properties. Loading of healing agents in porous inorganic particles can dramatically increase the concentration of healing agents in the multilayers and provide homogeneous distribution of healing agents in self-healing materials.

An example of formation of "smart" multilayers with high loading capacity is LbL deposition of hollow nanotubes. Natural nanotubes, halloysites, aluminosilicate clay could be loaded with healing agents.[147] The halloysite nanotubes, loaded with BTA was modified by PAH/PSS multilayers. The release of the entrapped inhibitor from PAH/PSS/halloysite/BTA was controlled by a pH dependent permeability of the polyelectrolyte multilayers. A similarly high level of damage protection was observed for the polyelectrolyte multilayer/silica NP/BTA.[148] The BTA content in the resulting SiO_2-based system was up to 95 mg g^{-1} of SiO_2 NPs. Biocompatible hybrid self-healing materials can be formed by using porous calcium carbonate particles and LbL films of biopolymers.[149] Porous calcium carbonate microparticles can be loaded with healing agents, LbL covered by biopolymers and used in bionanoengineering of biomaterials with self-healing properties.

Conclusions

The LbL approaches for formation of "smart" self-healing materials with stimuli-responsive properties are in focus in the review. Stimuli responsive behaviour, which is intrinsic to natural systems, is becoming a key requirement for advanced artificial materials and devices, presenting a substantial scientific and engineering challenge. Synthetic materials capable of responding to external or internal stimuli represent one of the most exciting and emerging areas of fundamental scientific interest. External or internal stimuli (pH, T, ionic strength, humidity, electric or magnetic potential, etc.) alter surface properties, in particular, the surfaces suggested to be formed by LbL deposition of: (i) polyelectrolytes; (ii) hydrogels; (iii) conducting polymers; and (iv) healing agents. A special case is the formation of (iv) hybrid materials with self-healing ability via LbL approach.

The "smart" polyelectrolyte multilayers offer a broad range of applications in the fields of nonlinear optics, light emission, sensing, separation, bioadhesion, biocatalytic activity, drug delivery and can be used in mimetic chemistry.

In summary, we believe that the area will be developed drastically in the nearest future. Thus, for example, next step is the use of LbL self-healing materials as building blocks for nanoarchitecture of "intelligent" surfaces.[136,137]

Notes and references

1 (a) M. D. Hager, P. Greil, C. Leyens, S. Van der Zwaag and U. S. Schubert, *Adv. Mater.*, 2010, **22**, 5424; (b) S. Burattini, B. W. Greenland, D. Chappell, H. M. Colquhoun and W. Hayes, *Chem. Soc. Rev.*, 2010, **39**, 1973; (c) B. C.-K. Tee, C. Wang, R. Allen and Z. Bao, *Nat. Nanotechnol.*, 2012, **7**, 825.

2 S. R. White, N. R. Sottos, P. H. Geubelle, J. S. Moore, M. R. Kessler, S. R. Sriram, E. N. Brown and S. Viswanathan, *Nature*, 2001, **409**, 794.

3 Y. Zhao, J. Fickert, K. Landfester and D. Crespy, *Small*, 2012, **8**, 2954.

4 G. Decher, *Science*, 1997, **277**, 1232.

5 Y. Lvov, K. Ariga, I. Ichinose and T. Kunitake, *J. Am. Chem. Soc.*, 1995, **117**, 6117.

6 G. Decher, B. Lehr, K. Lowack, Y. Lvov and J. Schmitt, *Biosens. Bioelectron.*, 1994, **9**, 677.

7 G. B. Sukhorukov, J. Schmitt and G. Decher, *Ber. Bunsen-Ges.*, 1996, **100**, 948.

8 S. L. Westcott, N. A. Kotov, J. W. Ostrander, A. A. Mamedov, D. K. Reust and J. P. Roark, *NSTI Nanotech 2004, NSTI Nanotechnol. Conf. Trade Show*, 2004, **3**, 288.

9 A. G. Skirtach, A. A. Antipov, D. G. Shchukin and G. B. Sukhorukov, *Langmuir*, 2004, **20**, 6988.

10 K. J. Loh, J. Kim, J. P. Lynch, N. W. S. Kam and N. A. Kotov, *Smart Mater. Struct.*, 2007, **16**, 429.

11 Z. Zhu and S. Sukhishvili, *J. Mater. Chem.*, 2012, **22**, 7667.

12 J. Blacklock, A. Vetter, A. Lankenau, D. Oupicky and H. Möhwald, *Biomaterials*, 2010, **31**, 7167.

13 D. V. Andreeva, D. Fix, D. G. Shchukin and H. Möhwald, *Adv. Mater.*, 2008, **20**, 2789.

14 J. Hiller, J. D. Mendelsohn and M. F. Rubner, *Nat. Mater.*, 2001, **1**, 59.

15 E. Kharlampieva, V. Kozlovskaya and S. A. Sukhishvili, *Adv. Mater.*, 2009, **21**, 3053.

16 N. Kotov, I. Dékány and J. H. Fendler, *J. Phys. Chem.*, 1995, **99**, 13065.

17 M. Krasowska, M. Kolasinska, P. Warszyński and K. Małysa, *J. Phys. Chem. C*, 2007, **111**, 5743.

18 C. Y. Jiang, S. Markutsya and V. V. Tsukruk, *Langmuir*, 2004, **20**, 882.

19 M. Gao, C. Lesser, S. Kirstein, H. Mohwald, A. L. Rogach and H. Weller, *J. Appl. Phys.*, 2000, **87**, 2297.

20 O. Mermut and C. J. Barrett, *Analyst*, 2001, **126**, 1861.

21 G. B. Suchorukov, A. L. Rogach, B. Zenli, T. Liedl, A. G. Skirtach, K. Köhler, A. A. Antipov, N. Gaponik, A. S. Suscha, M. Winterhalter and W. J. Parak, *Small*, 2005, **1**, 194.

22 K. C. Krogman, J. L. Lowery, N. S. Zacharia, G. C. Rutledge and P. T. Hammond, *Nat. Mater.*, 2009, **8**, 512.

23 L. Ouyanga, D. M. Dotzauera, S. R. Hogga, J. Macanásb, J. F. Lahitteb and M. L. Bruening, *Catal. Today*, 2010, **156**, 100.

24 D. V. Andreeva, D. G. Gorin, H. Möhwald and G. B. Sukhorukov, *Langmuir*, 2007, **23**, 9031.

25 M. A. C. Stuart, W. T. S. Huck, J. Genzer, M. Muller, C. Ober, M. Stamm, G. B. Sukhorukov, I. Szleifer, V. V. Tsukruk, M. Urban, F. Winnik, S. Zauscher, I. Luzinov and S. Minko, *Nat. Mater.*, 2009, **9**, 101.

26 R. K. Iler, *J. Colloid Interface Sci.*, 1966, **21**, 569.

27 J. A. Syrett, C. R. Becer and D. M. Haddleton, *Polym. Chem.*, 2010, **1**, 978.

28 T. Ono, S. Fujii, T. Nobori and J.-M. Lehn, *Chem. Commun.*, 2007, 46.

29 M. W. Urban, *Nat. Chem.*, 2012, **4**, 80.

30 K. Imato, M. Nishihara, T. Kanehara, Y. Amamoto, A. Takahara and H. Otsuka, *Angew. Chem., Int. Ed.*, 2012, **51**, 1138.

31 A. V. Dobrynin and M. Rubinstein, *Prog. Polym. Sci.*, 2005, **30**, 1049.

32 P. Ott, J. Gensel, S. Roesler, K. Trenkenschuh, D. V. Andreeva, A. Laschewsky and A. Fery, *Chem. Mater.*, 2010, **22**, 3323.

33 A. A. Antipov and G. B. Sukhorukov, *Adv. Colloid Interface Sci.*, 2004, **111**, 49.

34 W. B. Stockton and M. F. Rubner, *Macromolecules*, 1997, **30**, 2717.

35 G. Decher and J. D. Hong, *Macromol. Symp.*, 1991, **46**, 321.

36 G. Decher and J. D. Hong, *Ber. Bunsen-Ges. Phys. Chem.*, 1991, **95**, 1430.

37 G. Decher, J. D. Hong and J. Schmitt, *Thin Solid Films*, 1992, **210–211**, 831.

38 S. A. Sukhishvili and S. Granick, *J. Am. Chem. Soc.*, 2000, **122**, 9550.

39 S. Y. Yang and M. F. Rubner, *J. Am. Chem. Soc.*, 2002, **124**, 2100.

40 Z. Zhao, L. Yin, G. Yuan and L. Wang, *Langmuir*, 2012, **28**, 2704.

41 K. Köhler, D. G. Shchukin, H. Möhwald and G. B. Sukhorukov, *J. Phys. Chem. B*, 2005, **109**, 18250.

42 J. F. Quinn and F. Caruso, *Langmuir*, 2004, **20**, 20.

43 P. Fischer, A. Laschewsky, E. Wischehoff, X. Arys, A. Jonas and R. Legras, *Macromol. Symp.*, 1999, **137**, 1.

44 K. G. Yager and C. J. Barrett, *Curr. Opin. Solid State Mater. Sci.*, 2001, **5**, 487.

45 I. Alessandri, M. Ferroni and L. E. Depero, *ChemPhysChem*, 2009, **10**, 1017.

46 B. Thierry, F. M. Winnik, Y. Merhi, J. Silver and M. Tabrizian, *Biomacromolecules*, 2003, **4**, 1564.

47 S. Meng, Z. Liu, L. Shen, Z. Guo, L. L. Chou, W. Zhong, Q. Du and J. Ge, *Biomaterials*, 2009, **30**, 2276.

48 K. Glinel, G. B. Sukhorukov, H. Möhwald, V. Khrenov and K. Tauer, *Macromol. Chem. Phys.*, 2003, **204**, 1784.

49 Z. Zhu and S. A. Sukhishvili, *ACS Nano*, 2009, **3**, 3595.

50 M. J. Serpe, C. D. Jones and L. A. Lyon, *Langmuir*, 2003, **19**, 8759.

51 J. A. Jaber and J. B. Schlenoff, *Macromolecules*, 2005, **38**, 1300.

52 I. Erel-Unal and S. A. Sukhishvili, *Macromolecules*, 2008, **41**, 8737.

53 V. Kozlovskaya, J. Baggett, B. Godin, X. Liu and E. Kharlampieva, *ACS Macro Lett.*, 2012, **1**, 384.

54 X. Liang, V. Kozlovskaya, Y. Chen, O. Zavgorodnya and E. Kharlampieva, *Chem. Mater.*, 2012, **24**, 3707.

55 A. Phadkea, C. Zhanga, B. Armanb, C.-C. Hsuc, R. A. Mashelkard, A. K. Leled, M. J. Tauberc, G. Aryab and S. Varghesea, *Proc. Natl. Acad. Sci. U. S. A.*, 2012, **109**, 4383.

56 S. Y. Yang, D. Lee, R. E. Cohen and M. F. Rubner, *Langmuir*, 2004, **20**, 5978.

57 B. Wessling, *Adv. Mater.*, 1994, **6**, 226.

58 E. V. Skorb, O. Baidukova, A. Goyal, A. Brotchie, D. V. Andreeva and H. Möhwald, *J. Mater. Chem.*, 2012, **22**, 13841.

59 D. V. Andreeva, Z. Pientka, L. Brozová, M. Bleha, G. A. Polotskaya and G. K. Elyashevich, *Thin Solid Films*, 2002, **406**, 54.

60 B. Parakhonskiy, D. Andreeva, H. Möhwald and D. Shchukin, *Langmuir*, 2009, **25**, 4780.

61 G. K. Elyashevich, E. Y. Rosova, D. V. Andreeva, G. A. Polotskaya, M. Trchová and Z. Pientka, *J. Appl. Polym. Sci.*, 2005, **97**, 1410.

62 D. V. Andreeva, D. A. Gorin, D. G. Shchukin and G. B. Sukhorukov, *Macromol. Rapid Commun.*, 2006, **27**, 931.

63 D. Kowalski, M. Ueda and T. Ohtsuka, *J. Mater. Chem.*, 2010, **20**, 7630.

64 B. Radt, T. A. Smith and F. Caruso, *Adv. Mater.*, 2004, **16**, 2184.

65 M. F. Bedard, B. G. De Geest, A. G. Skirtach, H. Mohwald and G. B. Sukhorukov, *Adv. Colloid Interface Sci.*, 2010, **158**, 2.

66 K. Katagiri, K. Koumoto, S. Iseya, M. Sakai, A. Matsuda and F. Caruso, *Chem. Mater.*, 2009, **21**, 195.

67 D. V. Andreeva, D. Fix, H. Möhwald and D. G. Shchukin, *J. Mater. Chem.*, 2008, **18**, 1738.

68 D. V. Andreeva, E. V. Skorb and D. G. Shchukin, *ACS Appl. Mater. Interfaces*, 2010, **2**, 1954.

69 Y. Xia, J. A. Rogers, K. E. Paul and G. M. Whitesides, *Chem. Rev.*, 1999, **99**, 1823.

70 F. M. Vinnik, *Polymer*, 1990, **31**, 2125.

71 S. M. Barlow and R. Raval, *Surf. Sci. Rep.*, 2003, **50**, 201.

72 P. Bertrand, A. Jonas, A. Laschewsky and R. Legras, *Macromol. Rapid Commun.*, 2000, **21**, 319.

73 T. G. Vargo, J. M. Calvert, K. J. Wynne, J. K. Avlyanov, A. G. MacDiarmid and M. F. Rubner, *Supramol. Sci.*, 1995, **2**, 169.

74 J. D. Mendelsohn, C. J. Barrett, V. V. Chan, A. J. Pal, A. M. Mayes and M. F. Rubner, *Langmuir*, 2000, **16**, 5017.

75 S. T. Dubas and J. B. Schlenoff, *Macromolecules*, 1999, **32**, 8153.

76 D. Yoo, S. S. Shiratori and M. F. Rubner, *Macromolecules*, 1998, **31**, 4309.

77 M. Ferreira and M. F. Rubner, *Macromolecules*, 1995, **28**, 7107.

78 Y. Lvov, K. Ariga, I. Ichinose and T. Kunitake, *J. Chem. Soc., Chem. Commun.*, 1995, 2313.

79 J. Ramsden, Y. M. Lvov and G. Decher, *Thin Solid Films*, 1995, **261**, 343.

80 M. Toda, A. N. Itakura, S. Igarashi, K. Büscher, J. S. Gutmann, K. Graf and R. Berger, *Langmuir*, 2008, **24**, 3191.

81 M. Kolosinska, R. Krastew and P. Warsynski, *J. Colloid Interface Sci.*, 2007, **305**, 45.

82 M. Lösche, J. Schmitt, G. Decher, W. C. Bouwmann and K. Kjaer, *Macromolecules*, 1998, **31**, 8893.

83 J. Schmitt, T. Grunewald, G. Decher, P. S. Pershan, K. Kjaer and M. Lösche, *Macromolecules*, 1993, **26**, 7058.

84 J. H. Fendler, *Chem. Mater.*, 1996, **8**, 16161624.

85 X. Arys, A. M. Jonas, B. Laguitton, A. Laschewsky, R. Legras and E. Wischerhoff, *Thin Solid Films*, 1998, **329**, 734.

86 M. Lundin, F. Solaqa, E. Thormann, L. Macakova and E. Blomberg, *Langmuir*, 2011, **27**, 7537.

87 B. Schoeler, G. Kumaraswamy and F. Caruso, *Macromolecules*, 2002, **35**, 889.

88 D. Carriere, R. Krastev and M. Schönhoff, *Langmuir*, 2004, **20**, 11465.

89 S. T. Dubas and J. B. Schlenoff, *Langmuir*, 2001, **17**, 7725.

90 S. S. Shiratori and M. F. Rubner, *Macromolecules*, 2000, **33**, 4213.

91 J. H. Fu, J. Ji, W. Y. Yuan and J. C. Shen, *Biomaterials*, 2005, **26**, 6684.

92 A. Fery, B. Scholer, T. Cassagneau and F. Caruso, *Langmuir*, 2001, **17**, 3779.

93 R. A. McAloney, V. Dudnik and M. C. Goh, *Langmuir*, 2003, **19**, 3947.

94 M. Kolasinska, R. Krastev, T. Gutberlet and P. Warszynski, *Langmuir*, 2009, **25**, 1224.

95 C. J. Lefaux, J. A. Zimberlin, A. V. Dobrynin and P. T. Mather, *J. Polym. Sci., Part B: Polym. Phys.*, 2004, **42**, 3654.

96 M. Kiel, S. Mitzscherling, W. Leitenberger, S. Santer, B. Tiersch, T. K. Sievers, H. Möhwald and M. Bargheer, *Langmuir*, 2010, **26**, 18499.

97 J. B. Schlenoff, S. T. Dubas and T. Farhat, *Langmuir*, 2000, **16**, 9968.

98 A. Izquierdo, S. S. Ono, J.-C. Voegel, P. Schaaf and G. Decher, *Langmuir*, 2005, **21**, 7558.

99 P. A. Chiarelli, M. S. Johal, D. J. Holmes, J. L. Casson, J. M. Robinson and H. L. Wang, *Langmuir*, 2002, **18**, 168.

100 C. H. Porcel, A. Izquierdo, V. Ball, G. Decher, J.-C. Voegel and P. Schaaf, *Langmuir*, 2005, **21**, 800.

101 J. Seo, J. L. Lutkenhaus, J. Kim, P. T. Hammond and K. Char, *Langmuir*, 2008, **24**, 7995.

102 C. Vogt, V. Ball, J. Mutterer, P. Schaaf, J.-C. Voegel, B. Senger and P. Lavalle, *J. Phys. Chem. B*, 2012, **116**, 5269.

103 G. Ladam, P. Schaad, J. C. Voegel, P. Schaaf, G. Decher and F. Cuisinier, *Langmuir*, 2000, **16**, 1249.

104 S. T. Dubas and J. B. Schlenoff, *Langmuir*, 2001, **17**, 7725.

105 P. J. Yoo, N. S. Zacharia, J. Doh, K. T. Nam, A. M. Belcher and P. T. Hammond, *ACS Nano*, 2008, **2**, 561.

106 M. Schönhoff, V. Ball, A. R. Bausch, C. Dejugnat, N. Delorme, K. Glinel, R. v. Klitzing and R. Steitz, *Colloids Surf., A*, 2007, **303**, 14.

107 J. J. Harris and M. L. Bruening, *Langmuir*, 2000, **16**, 2006.

108 J. A. Hiller and M. F. Rubner, *Macromolecules*, 2003, **36**, 4078.

109 A. Zhuk, J. F. Ankler and S. A. Sukhishvili, *Soft Matter*, 2013, **9**, 410.

110 J. E. Wong, F. Rehfeldt, P. Haenni, M. Tanaka and R. V. Klitzig, *Macromolecules*, 2004, **37**, 7285.

111 K. Uhlig, N. Madaboosi, S. Schmidt, M. S. Jäger, J. Rose, C. Duschl and D. V. Volodkin, *Soft Matter*, 2012, **8**, 11786.

112 A. G. Skirtach, A. M. Yashchenok and H. Moehwald, *Chem. Commun.*, 2011, **47**, 12736.

113 J. Zhang, L. S. Chua and D. M. Lynn, *Langmuir*, 2004, **20**, 8015.

114 D. V. Volodkin, N. Madaboosi, J. Blacklock, A. G. Skirtach and H. Möhwald, *Langmuir*, 2009, **25**, 14037.

115 T. R. Farhat and J. B. Schlenoff, *Langmuir*, 2001, **17**, 1184.

116 D. M. DeLongchamp and P. T. Hammond, *Chem. Mater.*, 2003, **15**, 1165.

117 J. Lackmann, T. Niendorf, M. Maxisch, R. Regenspurger, G. Grundmeier and H. J. Maier, *J. Mater. Sci.*, 2012, **47**, 151.

118 R. Farhat and J. B. Schlenoff, *Electrochem. Solid-State Lett.*, 2002, **5**, 13–15.

119 S. V. Lamaka, D. G. Shchukin, D. V. Andreeva, M. L. Zheludkevich, H. Möhwald and M. G. S. Ferreira, *Adv. Funct. Mater.*, 2008, **18**, 3137.

120 R. Oltra, V. Maurice, R. Akid and P. Marcus, *Local Probe Techniques for Corrosion Research*, ISBN: 1420054058, 2007, p. 182.

121 X. Wang, F. Liu, X. Zheng and J. Sun, *Angew. Chem., Int. Ed.*, 2011, **50**, 11378.

122 Y. Li, L. Li and J. Sun, *Angew. Chem., Int. Ed.*, 2010, **49**, 6129.

123 H.-C. Huang and N. S. Zacharia, *ACS Macro Lett.*, 2012, **1**, 209.

124 W. Xu, I. Choi, F. A. Plamper, C. V. Synatschke, A. H. E. Müller and V. V. Tsukruk, *ACS Nano*, 2013, **7**, 598.

125 A. B. South and L. A. Lyon, *Angew. Chem., Int. Ed.*, 2010, **49**, 767.

126 Z. Zhao, L. Yin, G. Yuan and L. Wang, *Langmuir*, 2012, **28**, 2704.

127 C. W. Park, A. B. South, X. Hu, C. Verdes, J.-D. Kim and L. A. Lyon, *Colloid Polym. Sci.*, 2011, **289**, 583.

128 I. Drachuk, O. Shchepelina, M. Lisunova, S. Harbaugh, N. Kelley-Loughnane, M. Stone and V. V. Tsukruk, *ACS Nano*, 2012, **6**, 4266.

129 K. A. Williams, A. J. Boydston and C. W. Bielawski, *J. R. Soc., Interface*, 2007, **4**, 359.

130 A. J. Chung and M. F. Rubner, *Langmuir*, 2002, **18**, 1176.

131 A. P. Esser-Kahn, S. A. Odom, N. R. Sottos, S. R. White and J. S. Moore, *Macromolecules*, 2011, **44**, 5539.

132 E. V. Skorb, D. G. Shchukin, H. Möhwald and D. V. Andreeva, *Langmuir*, 2010, **26**, 16973.

133 E. V. Skorb, D. G. Shchukin, H. Möhwald and D. V. Andreeva, *Nanoscale*, 2010, **2**, 722.

134 D. V. Andreeva, *Int. J. Mater. Res.*, 2011, **102**, 597.

135 E. V. Skorb, D. Fix, D. G. Shchukin, H. Möhwald, D. V. Sviridov, R. Mousa, N. Wanderka, J. Schäferhans, N. Pazos-Pérez, A. Fery and D. V. Andreeva, *Nanoscale*, 2011, **3**, 985.

136 J. Gensel, T. Borke, N. Pazos-Pérez, A. Fery, D. V. Andreeva, E. Betthausen, A. Müller, H. Möhwald and E. V. Skorb, *Adv. Mater.*, 2012, **24**, 985.

137 D. V. Andreeva, D. V. Sviridov, A. Masic, H. Möhwald and E. V. Skorb, *Small*, 2012, **8**, 820.

138 D. G. Shchukin, D. A. Gorin and H. Möhwald, *Langmuir*, 2006, **22**, 7400.

139 D. Fix, D. V. Andreeva, Y. M. Lvov, D. G. Shchukin and H. Moehwald, *Adv. Funct. Mater.*, 2009, **19**, 1720.

140 E. V. Skorb, D. Fix, D. V. Andreeva, H. Möhwald and D. G. Shchukin, *Adv. Funct. Mater.*, 2009, **19**, 2373.

141 D. V. Andreeva and D. G. Shchukin, *Mater. Today*, 2008, **11**, 24.

142 M. J. Hollamby, D. Fix, I. Dönch, D. Borisova, H. Möhwald and D. G. Shchukin, *Adv. Mater.*, 2011, **23**, 1361.

143 Y. S. Han, D. Shchukin, P. Fernandes, R. C. Mutihac and H. Möhwald, *Soft Matter*, 2010, **6**, 4942.

144 E. V. Skorb, D. Sviridov, H. Möhwald and D. G. Shchukin, *Chem. Commun.*, 2009, **40**, 6041.

145 E. V. Skorb, A. Skirtach, D. V. Sviridov, D. G. Shchukin and H. Möhwald, *ACS Nano*, 2009, **3**, 1753.

146 E. V. Skorb, D. G. Shchukin, H. Möhwald and D. V. Sviridov, *J. Mater. Chem.*, 2009, **19**, 4931.

147 E. Abdullayev, R. Price, D. G. Shchukin and Y. Lvov, *ACS Appl. Mater. Interfaces*, 2009, **1**, 1437.

148 E. V. Skorb, D. Fix, H. Möhwald and D. G. Shchukin, *Adv. Funct. Mater.*, 2009, **19**, 2373.

149 G. B. Sukhorukov, D. V. Volodkin, A. M. Günther, A. I. Petrov, D. B. Shenoy and H. Möhwald, *J. Mater. Chem.*, 2004, **14**, 2073.

www.MaterialsViews.com

ADVANCED
FUNCTIONAL
MATERIALS
www.afm-journal.de

FEATURE ARTICLE

Surface Nanoarchitecture for Bio-Applications: Self-Regulating Intelligent Interfaces

Ekaterina V. Skorb* and Daria V. Andreeva

The surface nanoarchitecture provides spatially and temporally resolved stimuli response of the material, and offers defined control over the behavior of biomolecules and cells at the solid-liquid interface. Here, the focus is on metal-based systems that are interesting for biomedical applications. Intelligence of the surface is suggested to be achieved through its nanostructuring for stimuli responsive properties. Spatial and temporal cell performance at the surface, provided by the surface nanoarchitecture, offers advanced bio-applications of metal-based materials, such as implantation, lab-on-chip and organ-on-chip, biosensors, smart biomaterials and drug delivery systems. Spatial control is achieved by surface patterning. Temporal control is accessed through the application of stimuli responsive switchable surface chemistry, sensitive to external parameters: temperature, pH, light, electric and magnetic field, ionic strength, surrounding medium (hydrogels in water), multi-trigger response, and response to products of the cell metabolism. The key issue is the prospect in the formation of self-regulating "intelligent" surface cell interactions: biomimetic of natural systems.

1. Introduction

Nanostructured surfaces that provide effective control over biomolecules/cell/tissue deposition, growth and release can be considered as self-regulated "intelligent" surfaces (**Figure 1**). Recently, significant efforts and challenges have been directed to produce active surfaces with pronounced stimuli sensitive and feedback properties to achieve self-regulation.[1] One of the successful examples are antifouling and self-healing coatings.[1] To achieve self-regulation of inorganic surfaces one needs to endow them active agents that are released on demand. An efficient, versatile and simple way towards formation of self-regulated surfaces is the formation of porous interfaces. The porous interfacial layer is a surface encapsulation system with stimuli responsive loading

and release.[1,2] The approach of application of the porous interface for construction of self-regulated surfaces is schematically illustrated in Figure 1. In addition, such kind of the surfaces can provide control of biomolecules/microorganism/cell positioning, adhesion, spreading, growth and migration on surfaces which may have highest relevance in areas like implantation, lab-on-chip and organ-on-chip, biosensors, stem cell research.

Here we focus on titanium, magnesium, steel and their alloys as important metals for bioengineering, human implants. Implantable metal based devices such as orthopedic implants,[3a] vascular stents,[3b] and dental implants are widely used in medicine.[3c] Additionally, the porous metal interface can serve as a drug-delivery platform and stimuli responsive material (Figure 1). Noble metals being deposited on indium tin oxide (ITO) glass or silicon are discussed in the context of biosensors or lab-on-chip technology. Formation of metal based composites and hybrids provide complex morphology, regulated porosity, wettability and adhesion of self-regulated surfaces. Thus, fine tuning of elasticity, hydrophilic/hydrophobic properties, sorption capacity can be achieved. Moreover biocompatibility of metal based materials can be increased through, for example, formation of metal-hydroxyapatite composites or more complex composite metal (hydroxyapatite-carbon nanotubes).

Various design strategies have been suggested to direct the adhesion of cells to selected areas of a substrate.[4] One particularly versatile approach to control cell attachment and patterning is the physical or chemical adsorption of functional molecules such as extracellular matrix proteins and pH-, temperature-, electrically sensitive polymers to selected areas of a substrate. The development of patterning techniques coupled with functional surface chemistry has enabled the formation of surfaces with stringent control over the adsorption of biomolecules and cells in space. Furthermore, the development of switchable surfaces that are responsive to a particular signal and that switch between disparate properties, such as hydrophobic/hydrophilic, positive/negative charge or even swollen/condensed layers, has added a new dimension to biomolecule manipulation. Besides switchable hybrids examples can be found in "smart" chemical (drug, vitamin, growth factors, biomolecules) delivery (Figure 1, bottom).

Elasticity, morphology, porosity, wettability of the components of the hybrid systems has to be considered in order to

Dr. E. V. Skorb
Max Planck Institute of Colloids and Interfaces
Wissenschaftspark Golm
Am Mühlenberg 1, Golm 14424, Germany
E-mail: skorb@mpikg.mpg.de
Dr. E. V. Skorb
Chemistry Department
Belarusian State University
Leningradskaya str. 14, Minsk, 220030, Belarus
Dr. D. V. Andreeva
Chair of Physical Chemistry II
University of Bayreuth
Universitätsstr. 30, Bayreuth 95440, Germany

design bio-active surfaces.[5] By formation of hybrid systems initial "hard" metals can be changed to a soft elastic surface (Figure 1, right) by physical or chemical adsorption of organic polymer molecules/biomolecules. The inorganic-organic hybrid materials formed by using metal surfaces modified by polymers can adapt to the environment, change wettability and adhesion to the surface depending on the external conditions. Furthermore, the polymers deposited on a metal surface can convert chemical and biochemical signals into optical, electrical, thermal and mechanical signals, and so forth. A broad spectrum of available natural and synthetic polymers is available for formation of hybrid systems. These hybrid systems are perspective for construction of mimetic bio-interfaces, controlled drug-delivery and release systems, and stimuli responsive coatings.[1,2] Proteins and peptide chains, DNA, RNA, oligonucleotides, lipids and polysaccharides, as well as larger assemblies of these biomolecules, in particular living cells, can be used as building blocks for formation of the hybrids. The synthetic stimuli-responsive macromolecules are capable of conformational and chemical changes on receiving an external (T, pH, light, electric and magnetic field, ionic strength, surrounding medium (hydrogels in water) and multi-trigger response) or internal (cell metabolism) signals.[6]

2. Selected Materials

The bio-functional metal surfaces (**Figure 2**) for implantation are mostly composed of Ti, Mg, steel and their alloys. Metals should be biocompatible (Ti and its alloy) and preferably also biodegradable (Mg, Fe, Zn and Mo alloys).[7] For bio-electronic devices conductivity (noble metals) could be also a key factor. A porous metal matrix could be formed by surface anodization (Figure 2a), plasma or laser treatment (Figure 2b), chemical etching (Figure 2d), sol-gel route (Figure 2e,f), ultrasonic technique (**Figure 3**).

Biomimetic composite and hybrid materials are widely used in nature to sustain life and maintain biological function providing a specific morphology and functionality.[8] The issue of the composite is another effect to provide stimuli response of the surface. Hydroxyapatite-metal composites are an example of such materials. Hydroxyapatite is the major mineral phase in bone. Synthetic analogies can provide better integration of metallic surfaces with bone after implantation.[9] Thus, the stabilized composite of metal and apatite may improve biocompatibility and promote osteointegration. Moreover, there is a tendency to use carbon materials (carbon nanotubes, graphene layer) to further improve tensile strength, fracture toughness and mechanical properties of the surface.[10] For example, carbon nanotubes have excellent mechanical properties to strengthen and toughen hydroxyapatite. Studies of bioactive mineral–carbon composites show an expansion of potential applications to fields ranging from interdisciplinary science to practical engineering such as the fabrication of reinforced bone-implantable materials. The photocatalytically active mixed oxide composite systems can be formed by using, for example, $TiO_2:In_2O_3$.[11] Additional to the photocatalytically active composites with biocide activity are antifouling corrosion stable hydrophobic layered double hydroxides on metal surfaces (Figure 3e).[12]

Ekaterina V. Skorb received her Diploma degree in Chemistry at Belarusian State University (Belarus) in 2005. She obtained her PhD from the same university in Physical Chemistry in the area of Photochemistry in 2008. She came to the Max Planck Institute of Colloids and Interfaces (Germany) as a Humboldt fellow in 2010. She is currently a Senior Lecturer at Belarusian State University and an Independent Researcher in the Max Planck Institute of Colloids and Interfaces. Her research interests include study of the processes on non-equilibrium interfaces, fabrication and characterization of functional stimuli-responsive hybrid materials, nanomaterials, drug delivery systems for "smart intelligent" nanoarchitecture.

Daria V. Andreeva is an Academic Assistant at the Department of Physical Chemistry II of the University of Bayreuth. She obtained her PhD in the Institute of Macromolecular Compounds Russian Academy of Science in 2002. The PhD thesis concerned the formation of gas separation polymer membranes. In 2004–2005, she was an Alexander-von-Humboldt fellow in Free University of Berlin. In 2005–2009, she worked in the Max Planck Institute of Colloids and Interfaces on the development of layer-by-layer approaches for encapsulation and corrosion protection of metal surfaces. Her research interests are in the field of organic–inorganic composites, stimuli responsive interfaces, and surface nanostructuring.

Hybrid materials (hybrids) are composites consisting of a combination of several compounds at the nanometer or molecular level. Commonly one of these compounds is inorganic and the other one–organic. Such submicron scale materials organization/combination can result in characteristics in between the original phases or even new properties. Here, described hybrids are composed of organic molecules connected to a metal matrix by:[13] (1) physical adsorption (via van der Waals or electrostatic interactions) (Figure 2h); (2) physical entrapment (loading of material inside pores of metal matrix) (Figure 1, below); and (3) covalent attachment (Figure 2g). The organics could be (i) biomolecules,[14a] for example, proteins and peptide chains, DNA, RNA, oligonucleotides, lipids and polysaccharides, cells, and drugs;[14b] (ii) stimuli responsive synthetic systems, for example, polyethylene glycol/oxide (PEG/PEO), polysiloxanes,[14c] poly(N-isopropylacrylamide)

![Materials Views logo]
www.MaterialsViews.com

ADVANCED
FUNCTIONAL
MATERIALS
www.afm-journal.de
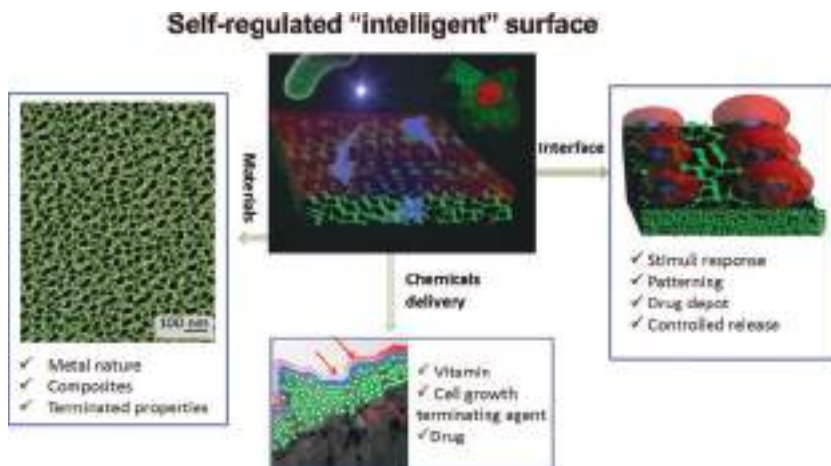
Figure 1. Design strategy for intelligent surfaces. Left: nanostructured metal surface (scanning electron microscope (SEM) image of a modified metal surface of potential implants), platform for optimization/modification of metal surfaces by formation of organic/inorganic composites. Right: formation of feedback coatings. Soft matter (micelles, hydrogels, polymer films) sensitive to external stimuli, for example, T, pH, light, electrical, magnetic field, grafted/adsorbed on the porous metal matrix. Bottom: generated porous nanonetwork well adhering to bulk metal as a universal encapsulation system suitable for multicomponent loading and time-resolved release. The metal surface capsules can be loaded with active agents, such as corrosion inhibitors, vitamins and drugs, enzymes, DNA fragments, or antibodies.

(PNIPAAM),[14d] copolymer systems,[14e] mixed polymers,[14f] micelles,[6] stimuli-responsive nanogels,[14g] and so forth.

2.1. Metals for Implant Biosurfaces and Fundamental Studies

At present, a wide range of materials are used in medical applications, including metals, ceramics, and polymers.[15] All bio-inspired materials for implants must fulfill the required specifications of biocompatibility, biofunctionality, biodurability and biosafety in short, medium and long term.[16]

The earliest records of the use of metallic implants in surgery go back to the 16th century.[17] Through the end of the 19th century, however, the attempts to introduce metal pieces into a human body were largely unsuccessfull focusing more on surgery-related infection.[18] Metal implants started to be widely developed after Lister's introduction of antiseptic surgical techniques in the 1880s,[19] sharply reducing the incidence of infection and making it possible to distinguish the tissue reaction to an implant from inflammation attributable to infection.

Titanium and its alloys, such as the dental alloy Ti-6Al-4V and others (e.g., Ti-5Al-2.5Fe, Ti-6Al-7Nb) are well known for implants because of their superior mechanical properties, hardness, corrosion resistance and biocompatibility.[20] After long term use, the alloys could release toxic components even from a corrosion resistant material.[21] The titanium alloys do not corrode in the body due to their passivation by a thin surface layer of metal oxide. However, metal ions could slowly diffuse through the oxide layer and accumulate in the tissue. For Ti-6Al-4V alloy, the ion release kinetics, as well as the presence of vanadium ions, may play a major role in influencing the osteoblast behavior. Co-Cr alloys are often used for stents.[22] For such alloys the chromium oxide layer, Cr_2O_3, provides good

corrosion protection and the possibility of self-healing.[23] However, the problem related to toxicity of chromium ions is severe.

Nanostructuring of the implant surface can provide a change of the metal ion release profile. Metal ion release studies and surface analyses were performed by C. H. Ku et al.[24] on untreated and triton treated titanium alloys. In vitro experiments (from 72 h up to 4 weeks) show an accelerated peak of alkaline phosphatase activity on the control sample which to some extent can be evidence of Al ion release from the alloy. Osteonectin, osteopontin, and osteocalcin gene expression (at week 1) as well as total protein amount (until week 4) were not affected by the surface treatments.

An oxide layer on the surfaces of the implants is one of the main factors that are responsible for the biocompatibility of implants and the protection of their surface. After metal implantation the tissue is in contact with the native oxide layer and not with the metal or metal alloys themselves.[25] The metal oxide layer has a self-healing activity and can be recovered after its chemical or mechanical damage. In oxidizing media as in the human body fluid the metal oxide layer can rebuild in milliseconds after damaging. Moreover oxide surfaces have an important role in the formation of hybrids. The metal oxide surfaces can be used as apatite inducer providing apatite nucleation.[26] Porous metal oxide layers are commonly formed on the surfaces of alloy implants, passivating and fixing the implants to bone via bony ingrowths into the porous structure, promoting osseo/osetointegration.[27] A freshly formed oxide layer could provide chemical attachment of active chemicals through, for example, oxygen[28] bridges (Figure 2g): formation of hybrids and drug delivery systems.

Titanium implants with defined size and geometry of 3D micropores used in model experiments provide special terminated properties and chemistry.[29]

One of the key aspects in the mimic of the "intelligent" surfaces is the switchable stimuli response of the blocks used for the surface nanoarchitecture.[30] A representative example of metals with stimuli responsive properties is a shape memory alloy, nitinol. Nitinol is the equiatomic intermetallic compound Ni-Ti, containing to 60 wt.% of Ni and the rest Ti with less than 1 wt.% inclusions, for example, Co, Cr, Mn, Fe. Nitinol exhibits good biocompatibility and corrosion resistance in vivo. It belongs to a very special group of shape memory alloys: materials that can return to their original shape after having been plastically deformed.[31] The shape memory effect in nitinol is related to the nanocrystallographically reversible structural change: martensitic transformation. The martensitic transformation is induced by temperature changes. The transformation temperature[32] strongly depends on the alloy composition: an increase in Ni content above the stoichiometric composition results in a decrease in the transition temperature. The same effect can be achieved by adding cobalt as a substitute

FEATURE ARTICLE
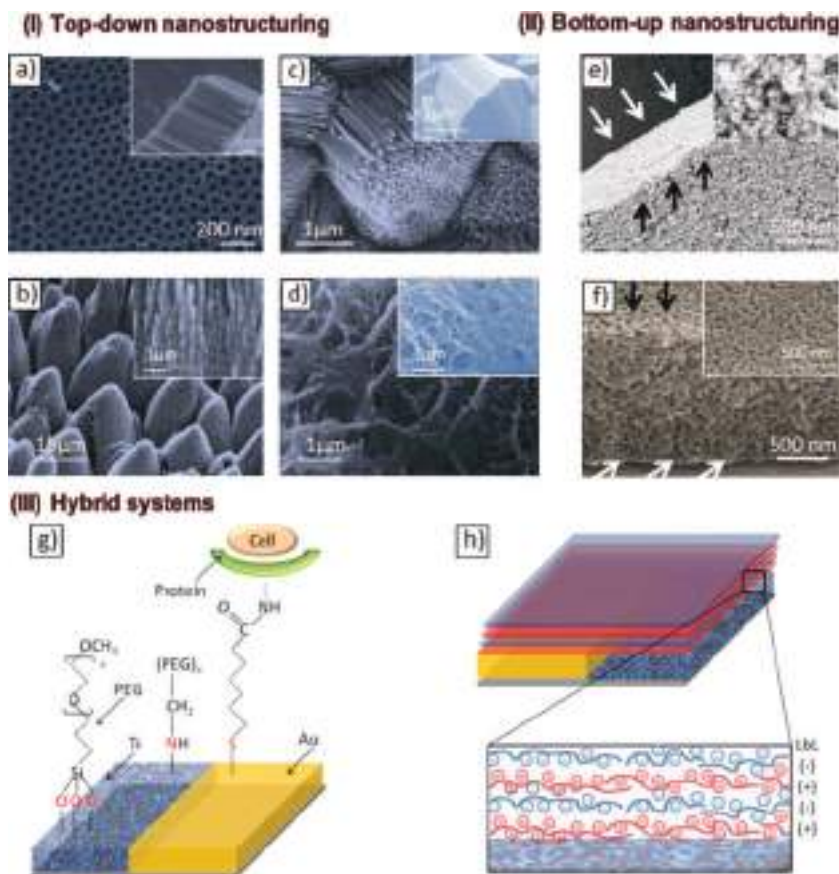
Figure 2. Materials for intelligent surfaces: nanostructured metal based surfaces formed by I) top-down and II) bottom-up nanostructuring. In particular, a) SEM images of titanium nanotube arrays formed by anodization. b) Titanium surface textured with femtosecond laser pulses. Reproduced with permission.[69] Copyright 2011, Wiley Periodicals, Inc. c) Titanium disk surfaces after plasma treatment. Reproduced with permission.[78] Copyright 2006, Materials Research Society. d) Surface characteristics of the inner pores of chemically etched titanium. e) Sol-gel titania film. f) Cross-section of gold-titania particle layer prepared by a sol-gel template route. Reproduced with permission.[84] Copyright 2009, American Chemical Society. (III) Examples of hybrid systems. A schematic representation of patterned (Ti/Au) surface modification with g) self-assembled monolayer through sulfur bridges on Au, and oxygen- amide- linking on Ti, and h) layer-by-layer (LbL). The possibility to guide cell adhesion is highlighted.

to have effective clinical implantation, and (ii) pathway of the products of corrosion, for example, metal ions, nanoparticles, gas bubbles are travelling in the body. Nearly all patients benefited from the treatment with magnesium implants.[33] Although some patients experienced subcutaneous gas cavities caused by rapid implant corrosion, some patients had no pain, and almost no infections were observed during the postoperative follow up. Researchers and clinicians should be warned from all the historical reports that Mg is a special lightweight metal that needs specific knowledge, careful professional handling and experience-based design for its successful bio application. A recent patent claimed a stent with a base body consisting of a core of a biocorrosive alloy selected from the group composed of Mg, Fe, Zn and Mo, with a diffusion layer containing Mn and Se covering the core. Thus, several Mg alloys have been investigated, including the ones containing minor quantity (up to 10 wt.%) of other metals in composition,[36] for example, Al, Mn, Y, Zn, or more significant quantity of another metal, for example, Mg-Li (60:40) alloys. Pure Fe,[37a] and its alloy with Mn[37b] were also investigated as biodegradable ones. The potential can be expanded by the development of well based science behind the technology, since before taking the materials into applications, the understanding of the degradation mechanisms in vitro and in vivo must be fully developed. Thus, one of the issues regarding human health is the release of metal ions, nanoparticles from an alloy due to degradation of implanted materials through oxidation and/or hydrolysis or corrosion, which accelerates exposure of materials. The question of the safety of biodegradable metals placed in the body also requires specific attention. However, at the moment, the list of potential medical applications for biodegradable metals seems limited, but their potential is obvious.

for Ni. The martensite transformation in nitinol brings about an abrupt change in Young's modulus and yield stress. This provides the rare ability to tailor the properties of nitinol to a specific application by slightly changing the alloy composition. One could image great prospects of such alloys for constructing the switchable stimuli responsive material and self-healing materials.

There are two classes of materials that have been proposed for biodegradable stents:[33,34a] (i) polymers from the lactic acid, glycolic and caprolactone families[34b,c] and (ii) metals, either Mg-based[34d,e] or Fe-based alloys.[35] In this article the focus is on metal based materials which have superior mechanical properties. The development of biodegradable metal implants is breaking the paradigm in which metallic biomaterials must be corrosion-resistant. It is a challenging topic to fundamentally understand the behavior of the implants since two main issues need to be understood: (i) corrosion kinetics

There are investigations[38] which elucidate the biocompatibility and microstructure variation of steel alloys with Al and Mn, etc. in composition and favourable mechanical characteristics. A recast layer can be formed on the alloy surface, following electro-discharge machining. Nanocarbide was introduced on the recast layer following electro-discharging. The nanocarbide phase is important and has significant roles in forming a nanostructured oxide layer which further increases the alloy biocompatibility.

To provide models for confining proteins and cells, tissue behavior on surfaces, some well defined nanoarchitectured surfaces are needed. Metal deposited layers on glass or ITO conductive glass are in focus. Such layered systems are very convenient to manipulate with well defined variation of one parameter such as defined surface morphology, patterning,

Materials Views
www.MaterialsViews.com

ADVANCED
FUNCTIONAL
MATERIALS
www.afm-journal.de

FEATURE ARTICLE
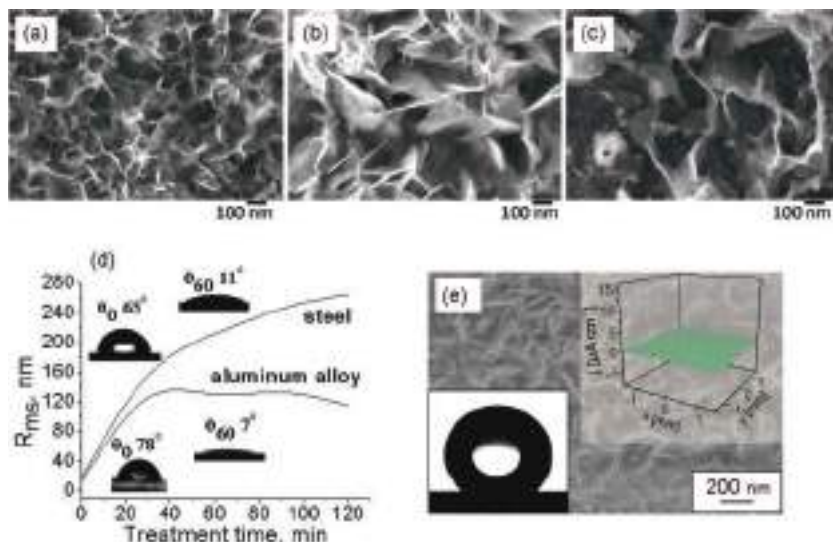
Figure 3. SEM images of a) aluminium, b) magnesium alloys and c) stainless steel after 40 min of sonochemical modification. d) Influence of sonication time on plate roughness, insets show the water contact angles of the surface before and after sonication. e) SEM image of a metal composite plate covered by layered double hydroxide laurate, insets show water contact angles onto this surface, and scanning vibrating electrode measurement of 3D current density map confirms the induced corrosion stability of the composite. Reproduced with permission.[12] Copyright 2010, Royal Society of Chemistry.

porosity, pore size and distance between them, surface conductivity, and so forth. They provide excellent models to follow and stimulate an attachment especially due to chemical bonding (on gold through sulphur bridges, on titanium, Al, Mg through oxygen bridges, amide linking, etc. (Figure 2g)). Well defined layered systems are very prospective for fundamental studies of biological objects, design of lab-on-chip and organ-on-chip, biosensors.

2.2. Methodology Used for Metal Surface Nanostructuring

In recent years, various processing routes have been developed for the synthesis of nanostructured metal-based systems such as anodization,[39a] plasma etching,[39b] sol-gel route,[39c] chemical reactions in liquid and gas,[39d] ultrasonic irradiation.[39e] All mentioned methods besides the sol-gel route are top-down (Figure 2a–d,3) methodologies of nanostructuring;[40] thus, an initially microscopic surface texture is modified to submicron architecture. The sol-gel approach (Figure 2e,f)[40] provides a microscopic system by sub-system organisation (using nanoblocks). Some examples of nanostructures include nanotubes, nanorods, nanowires, nanofibers, nanobelts, nanoribbons, nanowhiskers, nanoneedles, lamellar and hierarchical dendrites, and so forth.[41] Notwithstanding existing available techniques for metal surface nanostructuring, just a few were tested and totally understood for their effect on cell behavior.

2.2.1. Electrochemical Surface Modification

Electrochemical modification of metals is one of the well known methods of metal nanostructuring. There are several competing possibilities to modify morphology and porosity of metal surfaces in electric fields. One can distinguish: (i) electropolishing pretreatment with formation of a surface with different roughness; and (ii) anodization aiming at formation of a porous interfacial layer.

Electrochemical modification of aluminum and titanium is the most popular example of the electrochemical nanofabrication approach. Other transition metals, also potentially interesting for implantation (e.g., Ta, Nb, Hf, Zr, W) can be effectively nanostructured by the electrochemical method. It is well known that during the anodization of a metal, there are two processes: field-enhanced oxidation of metal and field-enhanced oxide dissolution.[42] There ate two interfaces: solution/oxide and oxide/metal. Oxidation occurs at the metal/oxide interface when the oxygen containing ions (O^{2-}/OH^-) are transported from the solution to the oxide layer. At the same time, metal ions (e.g., Al^{3+}) migrate from the metal to the solution/oxide interface and dissolve into the solution. Since the electric field can enhance the migration of the metal ion, the latter process is called field-enhanced dissolution.

The metal oxide interfacial layer is responsible for bioapplication and cell integration with a metal. The anodic oxide interface involves generally an amorphous or a crystalline metal oxide layer.[43] During the Ti electrochemical modification formation of anatase and rutile was observed.[44] Anatase and rutile are able to induce various apatite structures in vitro. The type of electrolyte solution during oxidation[45] can affect metal nanostructuring and, thus, cell–material interactions. A commercially pure titanium substrate was nanostructured by an anodization process using different electrolyte solutions, for example, HF, H_3PO_4 and H_2SO_4.[45] Bioactive bulk TiO_2 films were produced in presence of different electrolytes. Rough surface morphology, high surface energy, thicker oxide layer and low values of contact angles were important factors for optimal cell/material interaction. It was shown that each of the surfaces prepared at different conditions exhibits different cell–material interactions. Colonization of the cells was shown with a distinctive cell-to-cell attachment in the HF anodized surface. Good cellular adherence with the extracellular matrix extensions in between the cells was observed for samples anodized in H_3PO_4 electrolyte. The TiO_2 layer grown in H_2SO_4 electrolyte did not show significant cell growth on the surface, and some cell death was also observed. Cell adhesion and differentiation, living cell density and proliferation were more pronounced on anodized surfaces in comparison with the initial ones. Similar to cell–material interaction, variations in mineral deposition behavior were also demonstrated for films grown in different electrolytes. Moreover, ions introduced in the interfacial layer during electrochemical modification in presence of different electrolytes,[46] have a significant impact on the functionality of the material. For example, nitrogen and carbon doping of

TiO_2 can shift titania absorption into the visible light spectrum, providing change of surface stimuli to electromagnetic irradiation.[47]

Since nanotube materials have been introduced by Zwilling et al.[48] they have attracted great attention also for bio-applications. Electrochemical surface modification is one of the most promising top-down synthetic approaches for fabrication of highly ordered one dimensional (1D) nanotube materials. The properties of nanotube modified surfaces depend on the diameters of the nanotubes, their length and wall thickness. Electrochemical growth of a nanotube on a metal surface is a relatively simple, low cost method of production of highly organized and uniform nanostructures with controllable dimensions and unique properties. Furthermore, interest in nanotubular titanium dioxide was significantly increased due to unique photocatalytic properties of the material. The photocatalytic materials exhibit antibacterial self-cleaning activity of the surfaces[49] or UV response of the interfacial layer for implantable drug delivery, stem cell-differentiation, and anti-cancer treatment. Additional to photocatalytic properties, charge transfer, molecular transport and loading capacity of nanotubes are important for bio-application. The tube formation is also an electrolyte sensitive process. The length of the nanotubes can be controlled by varying the anodization time. The diameter of the tubes is adjusted by changing the applied anodization voltage. The growth rate of the nanotubes is variable, for example, by ultrasonic excitation in the electrochemical bath.[50] The electrical field intensity at the pore bottom is much higher than that at the wall, and metals, for example, aluminum, can be consumed at a high rate near the bottom of the pore, allowing continuous growth of the pore depth. In contrast, for anodized titanium the final thickness of the porous oxide film does not increase with the anodizing time.[48] Titanium oxide can be etched at a high rate in HF solution even in the absence of an anodizing voltage. If the etching rate of the oxide in solution is comparable with that of the field-enhanced dissolution, the titanium oxide either in the wall or at the pore bottom can dissolve at a balanced rate resulting in a constant pore depth. Uniform long titania nanotube arrays of various pore sizes (ca. 20–100 nm), lengths, outer diameters (90–220 nm), and wall thicknesses (7–34 nm) have been reported[51] by tailoring electrochemical anodization conditions.[52] Moreover, dependent upon the titanium alloy used, metal composites can be readily introduced. It was mentioned above that in HF formation of a nonporous surface is possible, however HF can be suitable also for formation of nanotubes et al.[48] The nanotubular titania structuring can be achieved by using a mixture of H_3PO_4 and HF solutions with ultrasonic excitation.[53] Recently, Losic and co-workers[54] published a method of self-ordering electrochemical synthesis of titanium nanotubes with defined pore size and depth of the anodization (determine length of nanotubes). In particular, it was shown that nanotubes with desired nanotube diameters (70–180 nm) and length (5–200 μm) can be fabricated using anodization in NH_4F/ethyleneglycol electrolyte by controlling the anodization voltage and time (Figure 2a).

By using electrochemical treatment of nitiol,[55] the problem of uncontrollable release of Ni can be solved. Electropolishing pretreatment and photoelectrocatalytic Fenton's oxidation of nitiol in presence Fe^{2+}/H_2O_2 has been studied. By using this method, a titania layer with a Ni-free zone near the surface and a graded interfacial structure between the titania layer and the NiTi substrate can be formed. These layers successfully suppress Ni ion release from the alloy, although this film has a porous structure on the nanometer scale.

Thus, electrochemical modification of metal surfaces can help to avoid introduction and release of toxic compounds from the implant surface and to improve biocompatibility of the metal by controllable formation of an oxide layer. The chemically active oxide layer can be a source of oxygen bridges, amide-linkage for formation of stable hybrids. The porous network of the metal oxide layer can be used as a drug depot for controlled local drug delivery and release on demand.

2.2.2. Plasma Etch Technologies

The plasma etching is widely used for continuous cleaning of surfaces by physical and/or chemical processes.[56] (i) Dry plasma etching-substrates are immersed in a reactive gas (plasma). The layer to be etched is removed by chemical reactions and/or physical means (ion bombardment). (ii) Wet plasma etching-substrates are immersed in a reactive solution. One of the advantages of plasma etching is that nanostructuring with small extension of the surfaces can be achieved. High energy provides both thermodynamically and kinetically stable surfaces.

In all, etching in a discharge environment is achieved by providing active species, which react with the substrate forming volatile compounds. In plasma etching, the reactive species are ions and activated neutrals, created in an electrical discharge. The process usually takes place inside a reactor under well controlled environmental parameters like, for example, pressure, temperature and feed gas flow. The following processes are observed: chemical etching, ion enhanced etching, physical etching, trenching, sidewall passivation and mask erosion. It is still a challenge to describe in detail a rather complex system as plasma etching.[57]

Examples of chemical reactions, which are relevant for plasma etching with the reaction of etch agent with the surface,[58] are CF_4, BCl_3, HCl, Cl_2 for Al; CF_4, Cl_2 for Ti and its alloys; SF_6, CF_4, NF_3, Cl_2, O_2 for W and O_2, SO_2, CF_4 for polymers. Thus the proper etching gas composition is important. For example, aluminum is not etched by fluorine, because AlF_3 is not volatile, chlorine is used. $AlCl_3$, the etch product, is highly corrosive to the remaining aluminum film, and must be removed quickly after plasma etching. Native aluminum oxide is an etch resistant barrier, which is removed by H_2 plasma reduction and/or by sputtering by bombardment with Ar at high energies. A bombardment mixture which includes the additional components Ar, O_2 usually enhances the etch rate of the surface[59] and can provide the following increase of possible nanostructures. This was the proof for the concept of ion enhanced chemical etching,[58–60] which is the foundation of plasma etching. It is extremely interesting that by using plasma etching it is possible to introduce some elements at the atomic level on the metal surface.

Wet etching has several important methodological advantages: simple equipment, high throughput (batch process), high selectivity.[61] For uncoated metals, a high-voltage (>1000 V)

www.MaterialsViews.com

ADVANCED
FUNCTIONAL
MATERIALS
www.afm-journal.de

FEATURE ARTICLE

pulsed discharge method of preparation of thin anodic films on valve metals under conditions of extremely high rates of the film growth was also studied, for example, for titanium[62a,b] and for aluminium[62c] The peculiarities of this method have been demonstrated with the anodic oxidation of titanium in sulfuric acid solutions, H_3PO_4. Ammonium pentaborate aqueous solution was used as the electrolyte for aluminium hot pulsed discharge modification, since alumina films prepared by the conventional anodization methods in that electrolyte are well-studied. Thus, the previously discussed electrolytes usually suitable for anodization can be also used for electric discharges. A light flash at the electrode was generated upon pulsed anodization of metals. The emission spectra consist of narrow lines assigned to electronically excited O, H and metal atoms, indicating that hot plasma is created at the electrode surface.

The plasma technique is also widely used for the deposition of nanocomposite coatings and hybrid formation.[63] Moreover, plasma treatment was effectively used for further regulation of pore diameters after anodization to slow down release of encapsulated materials.[64]

2.2.3. Laser-Induced Surface Modification

The development of laser-induced modification[65] of metal surfaces leads to formation of micrometer, sub-micrometer, and nano-scale surface textures. The laser technique can be used for removal of organic molecules from the surface.[66]

A porous metal interface can be formed by laser-induced melting or sintering of metal particles on the metal surfaces.[67] By using a laser, porous layers can be formed on metallic constructions of different shape. The laser technologies have been used to first pattern grooves and ridges onto silicon and titanium.[68] A single-step ultrafast-laser texturing process has been developed. The surface structured by using this method is illustrated in (Figure 2b).[69] The textured titanium samples remained completely hydrophilic with no measurable contact angle even after several weeks in normal atmosphere. An increase in mesenchymal stem cell number was observed on laser-modified surfaces in comparison with an untreated control titanium surface. Extensive formation of cellular bridges by stromal cells between pillars shows the favorable response of differentiated cells to the surface and the promotion of their attachment.

Biocompatibility of the micropatterned NiTi surface produced by femtosecond laser was studied.[70] It was shown that grooves and ripples covered by nanoparticles were formed on the sample surfaces. The crystal structure was not changed by laser treatment. However, the cell culture test proved that the micro-patterns were beneficial to improve the biocompatibility of NiTi alloys: the growth of osteoblasts oriented along the grooves, a large amount of synapses and filopodia were formed due to ripples, holes and nanoparticles on the alloy surface, and the proliferation rate and alkaline phosphatase content of cells were increased after laser treatment.[70]

Besides formation of nanostructured porous surfaces, effective polishing can be achieved by, for example, excimer laser titanium surface treatment.[66]

After the irradiation of a material by short laser pulses of frequencies close to the ablation threshold, periodic structures frequently appear in the form called laser-induced periodic surface structures.[71–73]

2.2.4. Chemical Etching

The mechanism of chemical etching consists of three elementary steps: (i) adsorption of reactive species on the surface; (ii) etch product formation (chemical reaction); (iii) etch product desorption. In general, just simple thermodynamic calculation and comparison of red/ox potentials suggest suitable reagents for chemical etching.[74] Most etching chemical agents (oxidation agent) for particular metal are well known.[74] However, it is still a challenge to predict the surface morphology and chemistry after chemical etching.[75a] It is even more difficult to optimize parameters during modification, for example, concentration, duration of modification, activation steps. Thus, there is still a great area of material science and engineering with hope to have unique functional surfaces.

The alkali-treated titanium[75b] without heat treatment leads to formation of an unstable reactive surface layer capable of bone-bonding. In Takemoto et al.,[76] treatment of titanium in a dilute hydrochloric acid (HCl) leads to the formation of a porous layer known as titanate gel layer.[77] Comparison between three types[78] of surface treatment was demonstrated: (a) alkali and heat treatment (Figure 2d, inset); (b) alkali, hot water, and heat treatment; and (c) alkali, dilute HCl, hot water, and heat treatment (Figure 2d). The porous bioactive titanium implant prepared by treatment had the highest osteoinductivity, with induction of a large amount of bone formation within 3 months.

Chemical treatment of titanium with a mixture of H_2SO_4/H_2O_2 can uniquely generate sponge-like networks of nanopits within the surface layer of titanium-based metals.[79] The mixture of H_2SO_4/H_2O_2 firstly triggers the surface etching and its oxidation in a controlled manner.

It has been reported[80] that the titanate gel layer can also be produced using H_2O_2 treatment on the surface of pure titanium. It was shown that the surface of Ti–6Al–4V alloy was modified using various concentrations of H_2O_2 and subsequently heat treated. A porous anatase titania layer was formed on the surface of Ti–6Al–4V alloy upon treatment with 15 wt% and 25 wt% of H_2O_2. In vitro characterization revealed that the treatment of Ti–6Al–4V alloy significantly improved the bioactivity of the material.[81]

2.2.5. Sol-Gel Route

The sol-gel method is one of the suitable ways of preparing films of metal oxides or crystalline materials.[40] For preparing crystalline materials, this method includes crystallization and/or transformation processes. The precursors generally consist of fine particles which are amorphous or crude crystallites. Precursors with various microstructures can be prepared by the hydrolysis and sol-gel conditions, yielding various degrees of crystallization and transformation. The various microstructures enable to control the transition behavior of precursors and produce a desirable structure. The addition of seeds to precursors or using double alkoxides as raw material are ways of controlling the microstructure of precursors, so as to obtain ceramics

FEATURE ARTICLE

with desirable properties by the sol-gel method.[82] The titania layer can be also formed by the sol-gel route (Figure 2e).

The sol-gel route (often combined with templating self-organized supramolecular assemblies of small molecules, surfactants, and block copolymers) is used for synthesis of porous materials of various sizes, morphology and highly ordered 3D porous structures.[83] A 3D template composed of self assembled amphiphilic diblock copolymer nanoparticles with diameter below 100 nm provides well ordered film formation (Figure 2f).[84] For example, Janus and core/shell nanoparticles could be self-assembled and well-ordered on the substrate using a vertical immersion method.

The future studies could be directed towards the formation of special structures specifically designed for enhancing sensing properties such as vertically aligned, flower-like, and hierarchical dendrites with the loading of nanoparticles, biocides, drugs, and so forth. Special attention should be paid to the operating temperature for a given metal-oxide and surface configuration, such that the balance between biocompatibility, stimuli response and power consumption can be optimized.

2.2.6. Bio-Inspired Ultrasound Assisted Methodology

There is a perspective bio-inspired approach to fabricate synthetic porous materials via intensive ultrasonication.[85] Ultrasound of high intensity triggers the formation of cavitation bubbles in liquid in a controlled way. Cavitation happens when a rapid change in pressure occurs. In nature, cavitation occurs in fast streams, produced in some shrimps and in the xylem of plants. The cavitation erosion of metal surfaces is known for a long time causing erosion of ocean propellers. Simultaneously, it is also known that surfaces and particles are often exposed to ultrasound in an ultrasonic bath for cleaning. Effects of ultrasound on the surface depend on its intensity, duration of the process, conditions of the sonoreactor (solvent, additives, sonotrode position, etc.)

The most pronounced effects of ultrasound on liquid–solid systems are mechanical and chemical, and these effects are attributed to symmetric and asymmetric cavitation bubble collapses.[86] The symmetric bubble collapse in a liquid medium causes shock waves with high pressures in addition to "hot spots" (high local temperatures in the range of thousands atm and K). The pressure on a material may be focused on defects or grain boundaries. Thus, solid metals with a defined microstructure can provide defined nanostructuring. Moreover, the bubble collapse causes a hot spot, the pressure pulse is also converted into heat, and this may cause local melting. A crystalline surface may locally melt and become amorphous after cooling. Shock waves also potentially create microscopic turbulences.[87] This phenomenon increases the transfer of mass across the solid, therefore, increasing the intrinsic mass-transfer coefficient. Ultrasonically generated active species, for example, radical species such as OH· and H·, for water sonolysis,[88] provide effective surface etching, possibly creating a nanostructured surface, such as metal based surface sponges well adhering to the bulk metal.[2a,5e] By asymmetric bubble collapse close to the surface, solvent microjets are formed perpendicular to the solid surface.[89] These microjets have an estimated speed of 100 m s^{-1} and lead to pitting and erosion of the surface. Moreover, the impact of microjets in the metal surface leads to an enhancement in free radical-assisted heterogeneous red/ox reactions (secondary cavity-assisted processes).

The ultrasound-driven modification of metals in aqueous solutions results in the modification of an outer surface (roughness, surface area, surface chemistry) the inner structure of the metals (crystallinity, amorphization, phase separation) (Figure 3).[12,90] The modification of metals by ultrasound depends on the nature of the metal. We have shown that metals with relatively high reactivities (Zn, Al, Mg) could be oxidized during the sonochemical process. The control of the oxidation process allows the formation of mesoporous metals that consist of a metal skeleton stabilised with an oxide layer.[90b] Phase segregation via ultrasonication was also observed in alloys.[90c,d] Beside formation of metal oxide phase, the ratio of the intermetallic phases in the Al/Ni, Al/Fe can be ultrasonically changed. It was shown that the ultrasound-induced red/ox reactions in metal alloys can be applied for design of effective and stable catalysts.[90c,d] Selective oxidation of one component of the alloy (Al) is followed by hydrogen release and reduction of the second component (Ni).[90c]

The ultrasonically formed surface with defined mesoporous metal sponges[2a,5e,90e] can serve as a platform for the construction of surface-attached capsules for the storage of active components and their stimuli controlled release. Even more prospective is the possibility of sonochemical formation of hybrid structures with regulated releases of encapsulated agent.

2.3. Composite and Hybrid Materials

It was already mentioned above that together with individual metals their alloys are used for implant formation (Section 2.1). The alloys, in comparison with the individual metals, have better mechanical and biodegradation properties. To achieve other advanced functionalities, biomimetic composite and hybrid materials are suggested as very prospective materials. In focus for bio-application are (i) natural, and (ii) engineered composite materials (composites) which are made from two or more constituent materials with significantly different physical or chemical properties. Natural and engineered materials can be combined to form co-composites. Hybrid materials are composites consisting of several compounds at the nanometer or molecular level. Commonly, one of these compounds is inorganic and the other one organic. Such sub-micrometer scale materials organization/combination can result in characteristics in between the original phases or even new properties. Here we focus on hydroxyapatite (HA), carbon based materials, and metal/polymer hybrids.

2.3.1. Biomimetic Composites with Hydroxyapatite

High priority nanocomposites for bio-application are bio-active calcium phosphate materials, for example, brushite, hydroxyapatite, fluoridated hydroxyapatite, and so forth. The hydroxyapatites have received considerable attention as materials for implants and bone augmentation procedures, since they chemically bond directly to bones[91] and in the formation of a strong bone implant interface. Nanostructured bio-metals

can provide better integration with synthetic and natural hydroxyapatite. Moreover, the combination of the high mechanical strength of metals with the osteoconductive properties of calcium phosphates make hydroxyapatite coatings on titanium implants widely used in orthopedic surgery.

The cellular responses depend upon the physical and chemical characteristics of the surface and upon its chemical composition, crystallinity and particle size.[92] The effect of hydroxyapatite surface roughness and generally surface texture on cellular response is a developed area from a practical and fundamental point of view. The oxide layer on a metal is important to provide different nanocomposites. A chemical treatment of the titanium surface would inhibit the negative effect of titanium processing on amorphous layer formation and subsequently hydroxyapatite precipitation. The plasma-spray process, electrophoretic deposition, sputter deposition, and sol–gel methods were used for forming titanium-hydroxyapatite (HA) composites.[93] Additionally, the biomimetic approach was used. It has four main advantages:[94] (i) it is a low-temperature process applicable to any heat-sensitive substrate, including polymers; (ii) it forms bone-like apatite crystals having high bioactivity and good resorption characteristics; (iii) it is evenly deposited on, or even into, porous or complex implant geometries; and (iv) it can incorporate bone growth-stimulating factors.

Hydroxyapatite being deposited on metal surface can be a protective layer which regulats the kinetics of biodegradation of metals. Thus the hydroxyapatite layer can slow down degradation of magnesium-based implants.[95] The method for formation of a dense, strong, and thick calcium-phosphate coating on titanium and porous tantalum implants using a two-step biomimetic procedure was elaborated.

Apatite deposition on surfaces of titanium specimens is a general phenomenon related to surface contact. Some chemical species[96] were released from the titanium surfaces, and, as a result, the properties of the simulated body fluid between the two contact surfaces and/or the properties of the contact surfaces themselves were altered during soaking so as to favour apatite deposition. Oxide-covered titanium is simple in terms of composition. The species that may be released are H^+ or OH^- ions and the ions related to titanium.[97] Obviously, the accumulation of OH^- ions on the surface would lead to a more negatively charged surface that is believed necessary for apatite nucleation.[98] The release of titanium hydroxide and OH^- ions from the titanium surfaces and their accumulation inside the confined space between the two contact surfaces were suggested to be responsible for the apatite deposition.

The titanium treated in NaOH can form hydroxycarbonated apatite after exposition to simulated body fluid.[99] The hydroxycarbonated apatite layer, however, was inhomogeneous and non-uniform even after 20 days in a synthetic body fluid (SBF). Acid etching of titanium in HCl under inert atmosphere leads to the formation of a uniform micro-roughened surface that provides improved conditions for in situ hydroxycarbonated apatite formation. After alkali treatment in NaOH the apatite nucleation was homogeneous and the thickness of the precipitated hydroxycarbonated apatite layer increased continuously with time. The treatment of titanium by a two step HCl and NaOH treatment is a suitable method provided the titanium surface with bone-bonding ability. The process of apatite formation on chemically treated titanium is supposed to be similar to that on bioactive glasses.

Composite with hydroxyapatite can provide geometric control of loading and release of material from the surface. For example, the metal based porous layer can be loaded with an active agent and then hydroxyapatite can provide either control of release or be loaded with other agents.

2.3.2. Composites with Carbon-Based Materials: Carbon Nanotubes, Graphene-Based Materials

The carbon-based materials have a great potential for bio-applications: formation of implant materials (improved mechanics), and biosensors (fast electron transfer kinetics).

Carbon nanotubes are attractive materials in materials science and engineering due to their advantageous mechanical properties including high tensile strength, high resilience, flexibility and other unique structural, electrical and physicochemical properties.[100] Currently, carbon nanotubes are used in several biomedical applications including cancer therapy, treatment of the central nervous system, and tissue engineering applications including bone tissue engineering, sensing cellular behavior, augmenting cellular behavior, cell tracking, and labeling.[101] Furthermore, the composite with carbon nanotubes acts as an excellent reinforcement material with enhanced strength, toughness and flexural strength for major load bearing applications. Moreover, the bioactivity of hydroxyapatite is not affected by the incorporation of carbon nanotubes.[102]

2.3.3. Hybrid Systems

There are two types of interactions between metals and organic molecules in hybrids: (i) chemical bonding, for example, self-assembled monolayers (SAMs); and (ii) physical interaction, for example, electrostatic layer-by-layer (LbL). In an intelligent system, the hybrids could regulate: (i) the surface-cell interface, (ii) the terminating properties (elasticity, hydrophilicity); (iii) drug loading and release; and (iv) stimuli response.

The 1980s showed an explosion of interest in SAMs-densely packed, oriented monolayer films of long-chain surfactants that spontaneously chemisorb from solution onto solid surfaces.[103] SAMs are ideal models for the study of fundamental processes at organic surfaces, such as wetting, adsorption, adhesion, chemical reactivity and, as result, surface bio-applications.[104] They also can be considered as models for explanation of physical principles that govern the assembly of other supramolecular structures, such as membranes and micelles. Potential applications of SAMs are in the traditional areas of surface chemistry-adhesion, wetting, corrosion and lubrication. The SAMs, often made from amphiphilic hydrocarbon molecules, are expected to function as a barrier to prevent the uncontrollable leaching of drugs from the metal substrate.[105] Three categories of molecules are mostly used for this purpose: fatty acids with carboxylic end groups that form electrostatic interactions with metal substrates, alkylthiols that are used for gold, copper or steel substrate by metal-sulfur bonding, alkyl phosphonates and alkylsilanes that react with the metal oxide from the metal, and metal alloy substrates.

The multicomponent nanonetwork formed by polyelectrolyte multilayers using the LbL technique could offer new opportunities for formation of stimuli response interfaces with self-regulation and self-healing properties.[106] The LbL deposition procedure involves the step-wise electrostatic assembly of oppositely charged species (e.g., polyelectrolytes and inhibitors or others: proteins, nanoparticles) on the substrate surface with nanometer scale precision, and allows the formation of a coating with multiple functionality. The coating properties can be controlled by the number of deposition cycles and the types of polyelectrolytes used. Polyelectrolytes exhibit very good adhesion to the substrate surface and are able to seal surface defects, be sensitive to external stimuli[107] (pH, T, ionic strength) and show self-healing properties. The conformation of polyelectrolytes is mostly dependent on their nature and adsorption conditions and much less dependent on the substrate and charge density of the substrate surface. Polyelectrolyte coatings are expected to cover many kinds of surfaces including non-ionic and a polar substrates. Polyelectrolyte multilayers offer a broad range of applications in the fields of nonlinear optics, light emission, sensing, separation, bioadhesion, biocatalytic activity, corrosion protection, drug delivery, and specific bio-applications based on surface modifications.

Metal hybrids with conducting polymers could be also used for formation of self-healing surfaces sensitive to electric fields. Electrically conducting polymers, for example, biocompatible polypyrrole, have been the subject of continuous research and development due to their potential applications in many technological areas including bio-applications.[108]

Comparing different nanoarchitectures one should consider the dynamics of stimuli response and the amplitude of changes of the materials' properties, reversibility of the changes, and the intensity of the external signal that could trigger the changes. Reconstructable surfaces fall into several categories: (i) grafted polymer thin films (here referred to as polymer brushes); (ii) thin films of polymer networks; (iii) self-assembled multilayered thin films, and (iv) block-copolymer self-organisation on different surfaces depending on their physico-chemical characteristics.

Some of the methods described above have great advantage because of the possibility of single step formation of composites and hybrids. For example, the formation of a metal/polymer interpenetrating hybrid nanocomposite was demonstrated for aluminium with ultrasonic high intensity treatment.[109] An initial sonochemically induced increase in the hydrophilicity can aid in the formation superhydrophobic surfaces by chemical modification of the ultrasonically formed structure. As an example, sodium laurate[110] was attached to the surface with ultrasonic assistance forming a layered double-hydroxide laurate with a water contact angle of 163°, Figure 3e. In the case of unmodified aluminium, the double-hydroxide layer exhibits very poor adhesion properties. In contrast, adhesion of the double-hydroxide layer on a sonicated surface is very strong.

Effective magnesium/polypyrrole hybrid systems were formed by the sonochemical methodology to provide an example of multi-stimuli-responsive systems: (i) sensitive to pH due to magnesium biocorrosion, and (ii) electric fields due to the conductive nature of polypyrrole.

3. Active Cell-Surface Interfaces

The cell adhesion, proliferation, differentiation or apoptosis on a solid surface, including metal implants, mainly depends on its surface physico-chemical properties including elasticity, morphology and roughness, texture, porosity, and wettability.[111] After implantation the implant surface is in contact with body fluids and interacts with a number of proteins and different cell types.[112] In addition, implant surface-specific cellular responses are the result of a complex biological system that includes protein adsorption, receptor-ligand binding, and signal transduction.[113] The implant should present a surface that will induce osseointegration. The methodology to control surface-cell interactions is based on physicochemical, morphological and biochemical approaches.[114] According to the physicochemical approach, surface energy, surface charge, and surface composition were altered in order to improve the bone-implant interface. Glow discharge was used to increase the surface free energy in order to increase tissue adhesion.[115] However, increased surface energy does not lead to selectively increased adhesion of particular cells and tissues and bone-implant interfacial strength.[116] Also, both positively and negatively charged surfaces were observed to promote bone formation.[117] Alterations in surface morphology and roughness were used to regulate cell and tissue response of implants. The mechanical interlocking surfaces with grooves and pits can induce "contact guidance", whereby the direction of the cell movement is affected by the morphology of the substrate.[118]

The aim of biochemical surface modification is to immobilize proteins, enzymes or peptides on biomaterials for the purpose of inducing specific cell and tissue responses or to control the tissue-implant interface with molecules delivered directly to the interface. One approach to biochemical surface modification applies cell adhesion molecules.[119] In accordance with a second approach to control cell-biomaterial interactions, one uses biomolecules having demonstrated osteotropic effects.[120]

For biomolecules delivery to the tissue-implant interface, it is essential that local cell populations interact with the biomolecules in order to initiate cellular events, and that concentrations of biomolecules are greater than threshold levels for cellular activity.[121]

To control exposure and concentration, retention and/or release of biomolecules from implants, the surfaces can be altered using different methods, including adsorption and covalent immobilization.[122]

3.1. Terminated Properties

In the past few years, interest in regulating bioactivity has shifted to exploration of nanostructured biomaterials.[123] Several reports showed that nanometer-scale surface features can influence cellular attachment, differentiation, and alignment.[124] A simple surface treatment can generate multifunctional nanostructured interfacial layer that could selectively control cell growth. Ideally the surfaces promote the growth of certain cells and inhibit the undesirable growth of other cells without the addition of any exogenous biological or pharmacological agents.

www.MaterialsViews.com

ADVANCED
FUNCTIONAL
MATERIALS
www.afm-journal.de

FEATURE ARTICLE
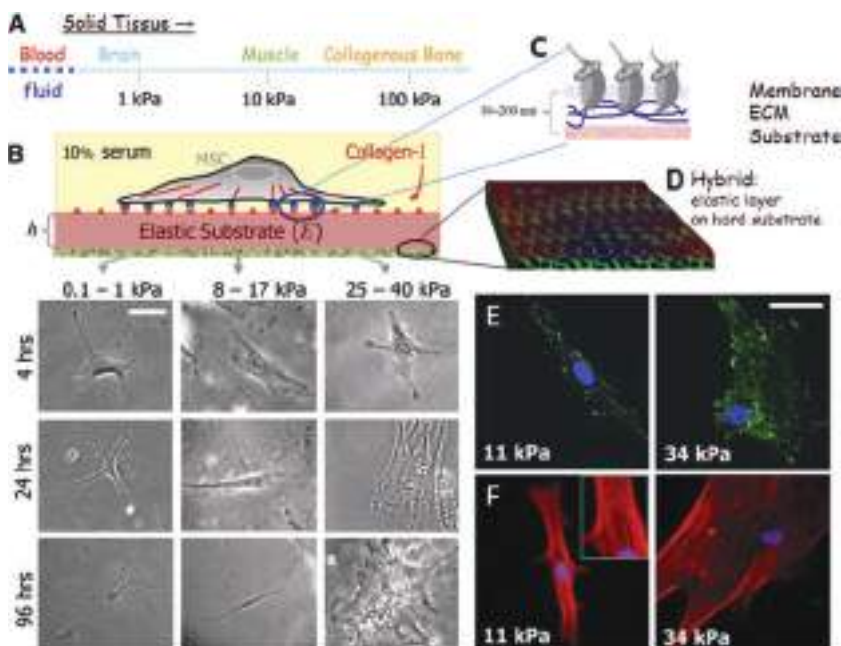
Figure 4. Tissue elasticity and differentiation of naive mesenchymal stem cells (MSCs). A) Solid tissues exhibit a range of stiffness, as quantified by the elastic modulus, (*E*–elasticity of micro-environment). B) In vitro gel system allows for control of *E* through crosslinking, control of cell adhesion by covalent attachment of collagen-I, and control of thickness. MSCs of a standard expression phenotype are initially small and round but develop increasingly branched, spindle, or polygonal shapes when grown on matrices, respectively, in the range typical of Ebrain (0.1–1 kPa), Emuscle (8–17 kPa), or stiff crosslinked-collagen matrices (25–40 kPa). Adhesions grow and cytoskeletal organization increases with substrate stiffness. C) Extra cellular matrix (ECM); D) Hybrids for elasticity regulation. E) Paxillin-labeled adhesions grow from undetectable diffuse ''contacts'' on myogenic gels (11 kPa). On the stiffest, osteogenic gels (34 kPa), the adhesions are long and thin and slightly more peripheral than they appear on glass. (F) F-actin organization shows a similar trend, from diffused on soft gels to progressively organized on stiffer substrates (as stress fibers). Scale bar is 20 μm. Reproduced with permission.[127] Copyright 2006, Elsevier.

The mechanism of the selective cell growth is based on surface structuring regulating the terminated properties or their active chemical local controllable delivery without negative effect on the surrounding environment.

A significant challenge in implantology is the design of biomaterials[125] that actively promote functional regeneration of the host tissue, and avoiding undesirable tissue responses. This requires selective control of interactions at the tissue/implant interface, a series of complex events that depend on synergistic parameters[126] including surface chemistry, elasticity, topography (morphology and porosity), and energy. To date, efforts have focused on defining how microtexture influences the molecular and cellular events of tissue repair.

3.1.1. Elasticity

In specific examples, it is highlighted that microenvironments appear as very important factors in stem cell lineage specification. The stem cell specification is difficult to adequately characterize or to control with soft tissues. Naive mesenchymal stem cells (MSCs) were shown to specify the lineage and commit to phenotypes with extreme sensitivity to tissue level elasticity (**Figure 4**).[127] Soft matrices that mimic brain are neurogenic. Stiffer matrices that mimic muscle are myogenic. Comparatively, rigid matrices that mimic collagenous bone are osteogenic. During an initial week in culture, reprogramming of these lineages is possible with addition of soluble induction factors. After several weeks in culture, the cells commit to the lineage specified by matrix elasticity, consistent with the elasticity-insensitive commitment of differentiated cell types. Inhibition of nonmuscle myosin II blocks all elasticity directed lineage specifications–without strongly perturbing many other aspects of cell functions. The results have significant implications for understanding physical effects of the in vivo microenvironment and also for therapeutic uses of stem cells.

3.1.2. Morphology

The major role of surface roughness of Ti and its alloys in cell response is elucidated in the literature.[128] Osteoblast-like cells attach more readily to a rough Ti surface. Synthesis of extracellular matrix and subsequent mineralization were found to be enhanced on rough or porous Ti.[129]

Surface nanostructuring could be used for regulation of osteoblast response and bone growth.[130] The ability to control the lateral spacing of these structures is important.[131] Micrometer scale features and optimized lateral spacing enhance cell attachment, spreading, and differentiation by providing higher surface energy and improved hydrophilicity of smooth titanium surfaces. The superimposed sub-micrometer scale features appear to enhance production of local factors that modulate differentiation and other cellular responses.[132] Certain patterns of the surfaces have also been able to control cell growth, being more preferable to adhesion of osteoblasts than to that of other cell types.[133]

In addition, the importance of nanometer scale roughness on bone cell function has been shown by creating ceramic substrates of the same crystallinity, crystal phase, and chemistry, altering only in degree of nanometer surface features.[134] Nanoscale roughness on these nanophase ceramics improved both osteoblastic and osteoclastic responses, whilst simultaneously inhibiting fibroblast function.

A key tenet of bone tissue engineering is the development of scaffold materials that can stimulate stem cell differentiation in the absence of chemical treatment.[135] Nanoscale disorder to stimulate human mesenchymal stem cells leads to formation of bone mineral in vitro in the absence of osteogenic supplements. This approach has similar efficiency to that of cells cultured with osteogenic media. In addition, the current studies show that topographically treated mesenchymal stem
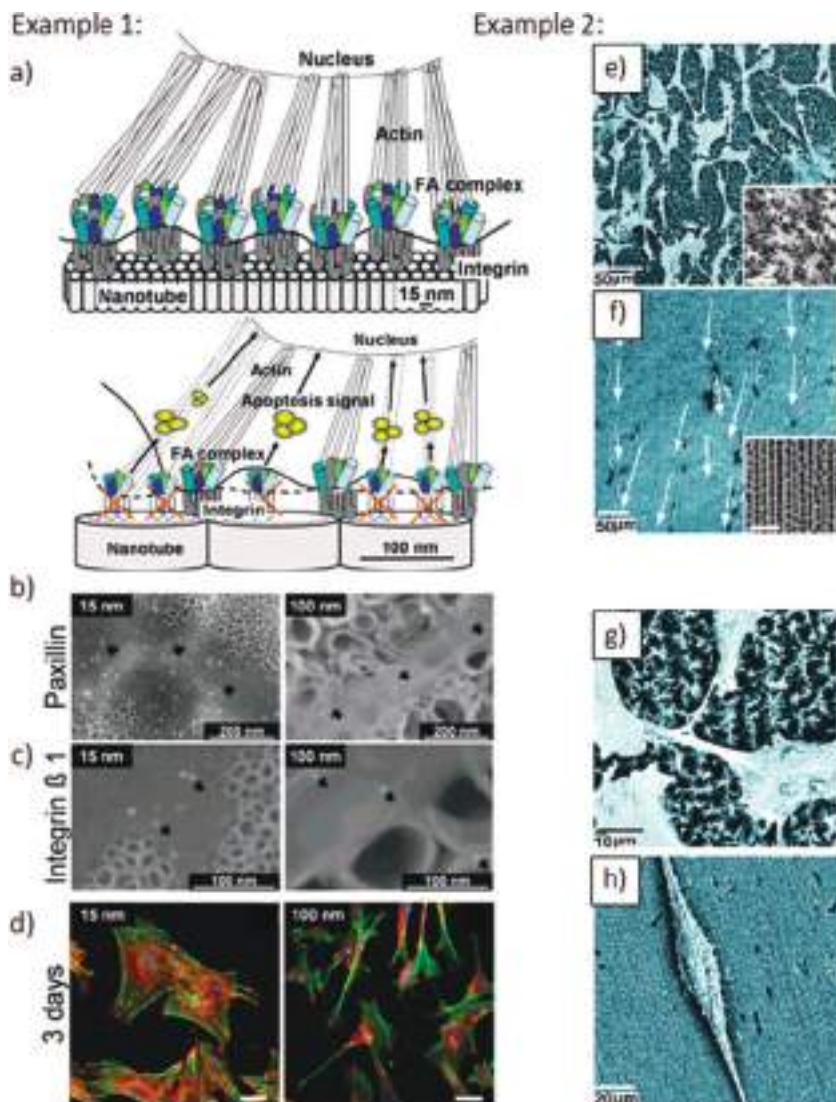
Figure 5. Example 1: focal contact formation, differentiation, and apoptosis of mesenchymal stem cells on 15 and 100 nm nanotubes. a) Nanoscale spacing directs cell fate: hypothetical model showing the lateral spacing of focal contacts on nanotubes of different diameters. A spacing of 15 nm seems optimal for integrin assembly into focal contacts, thus inducing assembly of actin filaments and signaling to the nucleus. Nanotubes larger than 70 nm diameter do not support focal contact formation and cell signaling, thus leading to apoptosis (anoikis). b) Analysis of focal contacts by SEM using immunogold staining with paxillin, and c) β1-integrin antibodies reveal dense packing of paxillin in focal contacts on 15 nm tubes, while labeling was sparse on 100 nm tubes. d) At 3 days, cells are well spread on 15 nm tubes (d, right), but develop a migratory morphology on 100 nm tubes with few focal contacts and stress fibers (d, left). Reproduced with permission.[138] Copyright 2007, American Chemical Society. Example 2: morphological changes of neuroblastoma cells grown on anodized aluminum (AAO). e) Polygonal morphology of cells on pores with nanobrushes showing randomly oriented cells with extensive cell to cell interconnection. Inset shows underlying surface with partially collapsed brushes. f) Elevated linear morphology of cells with orientation on which follows orientation of pores (lines). Inset shows underlying surface with aligned pores. SEM images of single neuroblastoma cells grown on different pore morphologies of AAO: g) pores with nanobrushes show an extensive branching and interconnection of cells; h) aligned pores show a linear morphology of neuroblastoma cells directed by aligned pores. Reproduced with permission.[140] Copyright 2010, American Chemical Society.

cells have a distinct differentiation profile compared with those treated with osteogenic media, which has implications for cell therapies.

3.1.3. Porosity

The mesoporous surfaces promote[136] both early and longer-term osteogenic events in cell cultures and, therefore, imparting bioactive properties to the materials. It is possible (1) to modulate the formation of nanopores in a titanium alloy (Ti6Al4V), and (2) to control the growth of common cell types on the implant metal. Osteogenic cells were evaluated because they are critical for the successful integration of implants in bone. Fibroblastic cell can form a fibrous capsule, weaken the bone/implant interface, and represent a major complication for permanent implants, ultimately requiring their replacement. Smooth muscle cells were investigated because their hypertrophy and proliferation are widely known to contribute to the restenosis of blood vessels after corrective surgery.[137] In all cases, culture intervals corresponding to initial stages of cell colonization were examined, as these are critical for biomaterial integration at any site of implantation.

TiO_2 nanotubes with different diameter were studied to direct cell vitality (**Figure 5**).[138] Self-assembled layers of vertically oriented TiO_2 nanotubes with defined diameters between 15 and 100 nm can regulate adhesion, spreading, growth, and differentiation of mesenchymal stem cells. The nanotubes with a spacing <30 nm and a diameter ≈15 nm provided an effective length scale for accelerated integrin clustering/focal contact formation and strongly enhanced cellular activities compared to smooth TiO_2 surfaces. Cell adhesion and spreading were severely impaired on nanotube layers with a tube diameter > 50 nm, resulting in dramatically reduced cellular activity and a high extent of programmed cell death. Thus, on a TiO_2 nanotube surface, a lateral spacing geometry with openings of 30–50 nm represents a critical borderline for cell fate.

In current trends of diagnostics with microchip biosensors prospects of porous material, nanoporous material, for example, anodized aluminium oxides and ultrasonically modified metal were demonstrated.[139a] In the work of the Losic group,[139b] a microchip biosensor based on nanoporous alumina coated with gold was suggested for detection of circulating tumour cells. Moreover, porous anodic aluminum oxide with mesoporous gradients consisting of a spatial distribution of pore diameters was fabricated using a nonuniform anodization process to design a surface with multifunctional gradients (structural, optical, wetting). This is important for application in microfluidics, diagnostics, drug delivery,

Materials
Views
www.MaterialsViews.com

ADVANCED
FUNCTIONAL
MATERIALS
www.afm-journal.de

and cell manipulation.[140] The pore gradient surface and neuro-blastoma cell exhibit potential for pore topography directed cell growth and hence possess biological relevance (Figure 5e,f). Pore gradients fabricated by this method open opportunities to design cell culture platforms with desired structural, chemical, and growth factor controlled cell growth and differentiation.

3.1.4. Hydrophilic/Hydrophobic Properties

A number of studies provide the evidence that enhancing the hydrophilic properties of the surface enhances cell spreading and cell adhesion. On the other hand, some authors reported that cells have greater adhesion and proliferation on hydro-phobic surfaces or on surfaces with intermediate contact angles. Materials able to integrate with bone, for example, titanium and hydroxyapatite, are hydrophilic.[141,142] On the other hand, many polymers used for tissue engineering are hydrophobic in their native state, and require surface modification or wetting proce-dures before cell seeding.

For instance, Webster and colleagues demonstrated that aqueous contact angles were three times smaller (i.e., more wettable) when the alumina grain size was decreased from 167 to 24 nm.[143] They also reported that the adsorption of vit-ronectin, which stimulates osteoblast adhesion, increased on nanophase ceramics with greater wettability. Moreover, when vitronectin adsorbed on nanophase ceramics, it was unfolded to a larger extent that on conventional ceramics, which exposed larger numbers of osteoblast adhesive epitopes to the absorbed proteins.

Increased wettability of hybrids has been achieved through the use of nanophase ceramics in order to increase bone cell function. Specifically, Kay and colleagues demonstrated that nanosized titania particles embedded in poly(lactic-co-glycolic acid) promoted osteoblast adhesion compared with convention-ally sized titania (100 nm) in poly(lactic-co-glycolic acid).[144]

In a recent study, Cai et al.[145] investigated the influence of titanium films with micro- and nanoscale topography (by varying the deposition rate and the film thickness) on protein adsorption and cell growth. They studied their chemical com-position, surface topography and wettability and found that the films shared the same surface chemistry but exhibited very dif-ferent topographies. Interestingly, they found no statistically significant differences in protein adsorption, however, albumin and fibrinogen adsorption only were measured. Also, no statis-tically significant influences of surface roughness on osteoblast proliferation and cell viability were detected in their study.

"Hot" specific examples here are bio-inspired self-repairing slippery surfaces with pressure-stable omniphobicity (SLIPS)[146] for, e.g., antifluidic drag, antibiofouling. Thus, most state-of-the-art liquid repellent surfaces are modeled after lotus leaves, which, due to their rough, waxy surface and con-tact angle characteristics, are known to exhibit superhydropho-bicity and self-cleaning, as water droplets remove contaminants from their surfaces when they roll-off. The SLIPS technology, inspired by the Nepenthes pitcher plant, provides unique capa-bilities that are unmatched by any other liquid-repellent surface technologies. SLIPS can be optimized for extreme tempera-ture and pressure conditions, rapid self-healing, biocompat-ibility, and chemical inertness, and so forth. In particular, the

biocompatibility of SLIPS and its ability to repel biological fluids allow its application in antifouling coatings for medical devices and instruments, and even for marine vessels. Its pressure resistance is well-suited for deep-sea exploration. It is anticipated that SLIPS can serve as omniphobic materials capable of meeting emerging needs in biomedical fluid han-dling, fuel transport, anti-fouling, anti-icing, self-cleaning win-dows and many more areas that are beyond the reach of current technologies.

3.2. Surface Drug Depot

The nanostructured surfaces can be used for regulated drug delivery. There are four main strategies to design a surface drug depot: (i) the porous metal interface can accumulate pharmaceutical compounds,[5e,139] (ii) immobilization drugs in a porous scaffold[109,147] (iii) an organic component, for example, micelles, of a metal-organic hybrid can immobilize drugs,[139] and (iv) combine the above strategies to provide multicomponent drug delivery systems sensitive to different stimuli.

In the group of D. Losic[148,54] nanotube arrays (on plates, wires) are suggested as a drug career. Several advanced strat-egies are suggested for drug loading: (i) chemical bonding of active substances to the wall of titanium nanotubes; (ii) loading of tubes with micelles which contain hydrophobic drugs; (iii) step-wise loading with a certain amount of drug in well ordered 1D nanotube arrays; and (iv) multicomponent loading in ano-dized metal. Besides release control through pore size regula-tion, or temporally resolved release due to spatially resolved loading in 1D tubes magnetic fields suggested to control release can be highlighted for the application of intelligent surfaces. Thus magnetic field responsive drug delivery systems using titania nanotube arrays loaded with polymer micelles can serve as drug-carriers due to the special inner tube nanoarchitecture with magnetic nanoparticles loaded at the bottom of the nano-tubes **Figure 6**.

Mesoporous metal sponges are effective bases for the con-struction of surface-attached capsules for the storage of active components and their stimuli controlled release.[139] Sono-chemically formed metal-polyelectrolyte capsules **Figure 7**[5e] loaded with active chemicals introduce the possibility of pro-viding metal surfaces with important properties, including high biocide activity, anti-friction properties, and the ability to release active components to stimulate activities of attached cells, such as in stem-cell research. Different ultrasonic intensities result in the formation of structures with different features that deter-mine their subsequent use for active surface construction. The pores of the sonochemically formed metal surface are loaded with biocide and then closed using a complexation reaction between the active incorporated agent and the polyelectro-lyte.[149] Thus, smart surface capsules formed by the walls of the metal pores and polyelectrolytes for the prolonged storage of the active component were constructed. The metal walls provide the high stability and adhesion of the capsules to the metal plate; the polyelectrolytes are responsible for the loading and release of the active species on demand. Our system offers an elegant approach to trigger biocide release by adjusting the

**ADVANCED
FUNCTIONAL
MATERIALS**
www.afm-journal.de

*Materials
Views*
www.MaterialsViews.com

FEATURE ARTICLE
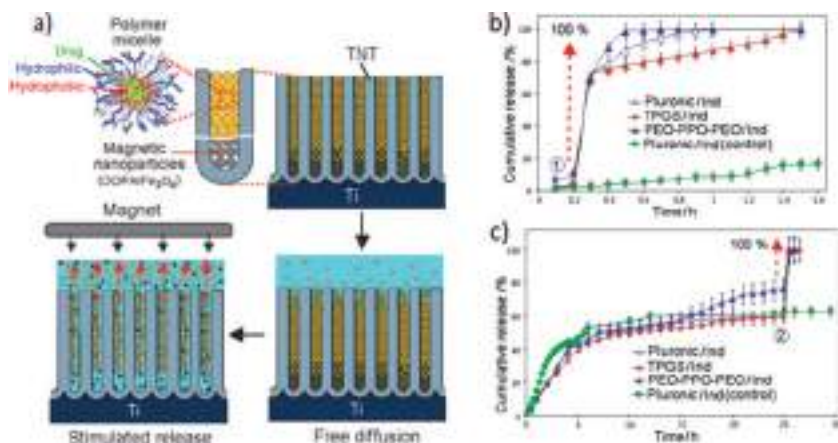
Figure 6. a) Scheme of the magnetic stimuli-responsive drug release from titanium nanotubes which integrate polymer micelles as drug carriers loaded with poorly soluble drugs and magnetic nanoparticles. The release is achieved by applying an external magnetic field. b,c) Release profiles of magnetic field triggered release of drug (indomethacin (Ind)) encapsulated in polymer micelles (TPGS, Pluronic and PEO-PPO-PEO). Non-triggered release with Pluronic-Ind was used as a control. Reproduced with permission.[54] Copyright 2012, Royal Society of Chemistry.

mobility of the pH sensitive complex. Moreover, it allows the release of the biocide in a controlled way, which is of high priority (regulated local release). . The possibility of bacteria deactivation due to silver release from sonochemically formed surface capsules was also shown.[2a]

Ultrasonic assisted surface immobilization of magnesium/polypyrrole capsules allows formation of stimuli response systems for release of active chemicals.[109] The hybrid materials can respond to several stimuli. Due to magnesium, the hybrid is sensitive to pH change. Polypyrrole is sensitive to electric field. In this case, no external coating is needed, since ultrasonic induced particle collisions allow melting of metal based capsules in the metal substrate, in particular, Ni patterns on ITO.

Mesoporous silica, titania or $CaCO_3$ based capsules can be homogeneously distributed on the surface by using the sol-gel approach or through formation of polymer hybrid coatings.[147] Micrometer-sized polyelectrolyte capsules made with the LbL technique are not suitable for deposition in sol-gel coating due to their instability in the coating. However nanosized polymer micelles are also promising candidates.

3.3. Patterning

The development of a number of high-resolution patterning techniques coupled with functional surface chemistry has enabled the formation of surfaces that offer stringent control over the adsorption of biomolecules and cells in space.[150] Specific strategies for the surface patterning of biomolecules include photolithography, laser ablation, robotic spotting, electron beam lithography, microcontact printing, templating, imprint lithography, soft-lithography, microfluidics, microelectronics, magnetic forces, and so forth.[151] Each of the techniques has its inherent advantages and limitations, for example, electron beam lithography enables high-resolution periodic patterns but is time-consuming.[152]

Patterned surfaces that contain (i) a well-defined surface geometry/topology, can be obtained with additional (ii) localized chemical functionalities being useful in a large field of applications,[153] for example, tissue engineering, cell behavior investigations, co-cultivating of different cells types, artificial growth of neuron networks, and so on. Such surface is urgent for a fundamental understanding between surface cell interactions with precise variation of selected trigger parameters.

A specific example of an attempt to control human mesenchymal cell differentiation using nanoscale symmetry and disorder is the work of M. J. Dalby and co-workers.[154] The nanotopographies had well defined holes and periodic distances between them. In particular, five different patterns were used, all with either absolute or average center-center spacing of 300 nm: (1) square array; (2) hexagonal array; (3) disordered square array with dots displaced randomly by up to 50 nm on both axes from their position in a true square; (4) disordered square array with dots displaced randomly by up to 20 nm on both axes from their position in a true square; (5) pits placed randomly over a 150 μm by 150 μm field, repeated to fill a 1 cm^2 area. It would seem likely that one of the initial events in substrate induced stem cell differentiation is the ability of the cells to form mature febrile-like adhesions. The nanotopographies modulated the ability of the osteoprogenitor cells to form very long (>8 μm) fibrillar-like adhesions, with square arrays and hexagonal arrays resulting in shorter adhesions and disordered square arrays with dots displaced randomly by up to 50 nm resulting in longer adhesion. It was also shown that the type of patterning is important for the initial stages of the tissue growth; however after formation of a dense layer of tissue on the substrate the cell growth follows the classical type.

The principle of chemical surface special functionalization for bio-applications can be demonstrated by using polyethylene glycol (PEG) (Figure 2g), polyethylene oxide (PEO), and so on, and selective surface grafting for, e.g., antifouling applications.[155] Cell manipulation on a surface can be achieved through proteins. Synthetic polymers can be combined with protein, for example, photolithographic techniques were used to create PEG hydrogel scaffolds which can be modified with various biomolecules such as peptides, growth factors, and other signaling molecules;[156] this system can be applied in basic science to investigate various aspects of cell locomotion to advance our knowledge in wound healing, inflammation, embryogenesis, and tumor cell metastasis.

Surface manipulation using biomolecules currently permits spatial control over the biomolecule position via patterned surface (i) chemistry or (ii) topography. It is expected that for self-regulated intelligent systems deposition of biomolecules is a strong instrument of nanoarchitecture control for stimuli responsive surfaces.

www.MaterialsViews.com

ADVANCED
FUNCTIONAL
MATERIALS
www.afm-journal.de

FEATURE ARTICLE
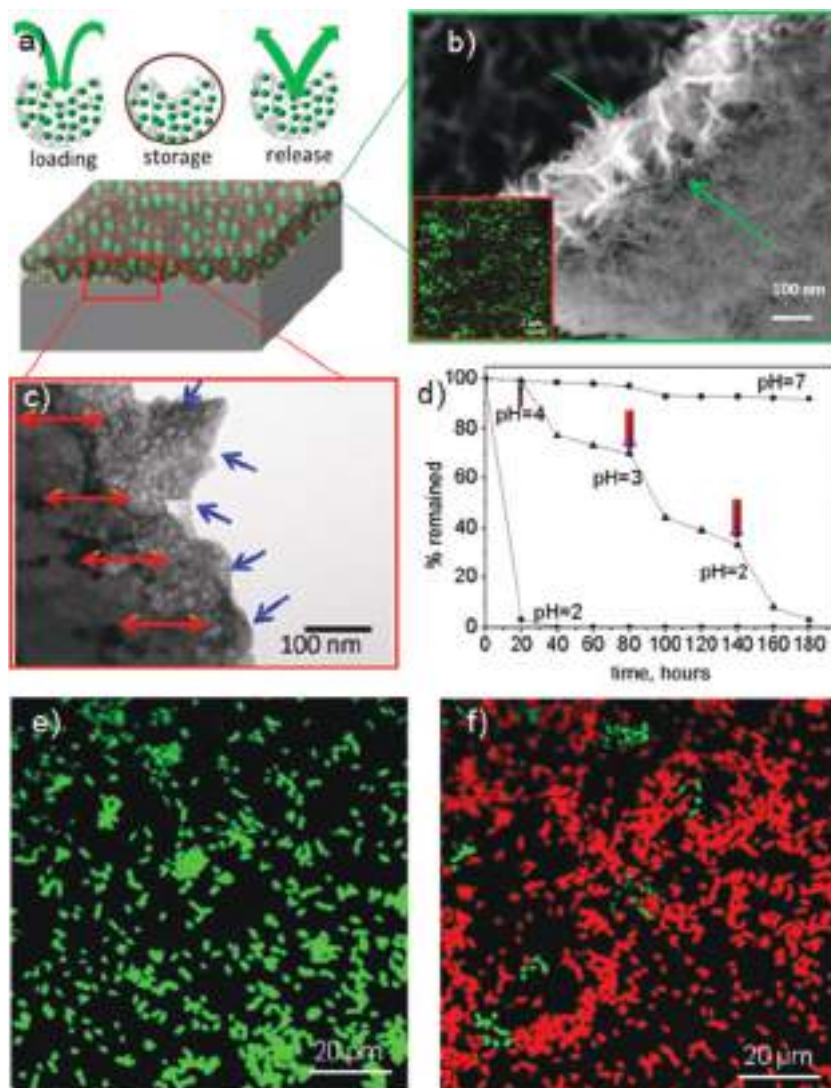
Figure 7. a) Schematic illustration of upload, storage and release of active component and general view of capsules generated at the metal surface. b) SEM image of the cross section of an aluminum sponge-like layer and luminescence confocal image of the surface capsules loaded with doxorubicin. c) Transmission electron microscopy image of aluminum with surface capsule layer for chemical storage (blue arrows show the loading direction, red arrows show the interface between bulk metal and capsules' layer). d) Doxorubicin release under different pH. e,f) Confocal images show the inactivation of *E. coli* due to 8-hydroxyquinoline release from the surface capsule layer: e) before release stimulation and f) after release. Inactivated bacteria are red and alive bacteria are green. Reproduced with permission.[5e] Copyright 2012, Wiley-VCH.

3.4. Stimuli Sensitive Response

Stimuli responsive behavior, which is intrinsic to natural systems, is becoming a key requirement for advanced artificial materials and devices, presenting a substantial scientific and engineering challenge (Figure 6–10). Intelligent surfaces are able to control the behavior of biomolecules (proteins, peptides, lipids, polysaccharides, cells, etc.) in both space and time. External stimuli (pH, T, ionic strength, humidity, electric or magnetic potential) alter surface properties. In particular, surfaces in response to external stimuli can exhibit (i) changes in adhesion, growth and desorption of cells, (ii) adhesion, mobility and desorption of biomolecules (iii) loading/release of active chemicals (drugs, antifouling and anticorrosion agents). Moreover, the adsorption/desorption/morphology of biomolecules (DNA, proteins, etc.) and cells (bacteria, fibroblast and osteoblast, etc.) onto the surface may be self-regulated by their metabolism (biomimetic of natural system). The possible environmental conditions for this purpose are limited due to the biomedical setting of drug delivery as application. Synthetic materials capable of responses to external or internal stimuli represent most exciting and emerging areas of fundamental scientific interest. In most trends, stimuli responsive changes of a system are inherent to an organic component of a hybrid. However, biodegradation of metal components of a hybrid can also provide release of an active chemical.

3.4.1. Thermo-Response

Temperature-responsive polymers and hydrogels can be utilized for the preparation of so-called (i) cell adhesion switchable surface, and (ii) "smart" drug delivery systems (**Figure 8,9**a).[155,157] Temperature-responsive systems exhibit a volume phase transition at a certain temperature, which causes a sudden change in solvation. Polymers, which become insoluble upon heating, have a so-called lower critical solution temperature (LCST). Systems, which become soluble upon heating, may have an upper critical solution temperature (UCST). There are also systems, which exhibit both LCST and UCST behavior, but that is usually not occurring within the setting of the intended biomedical applications. Most applications use the change from, for example, room temperature to body temperature in order to induce a change in the physical properties for gelation, especially in topical applications and in injectable biodegradable scaffolds. In vitro applications in cell culture are also using the stimulated swelling and collapsing of hydrogels with their change in surface properties.

Typical LCST polymers are based on *N*-isopropylacrylamide (NIPAM),[158] *N,N*-diethylacrylamide,[159] methylvinylether,[160] and *N*-vinylcaprolactam[161] as monomers. A typical UCST system is based on a combination of acrylamide and acrylic acid,[162] PEO-*b*-poly(propylene oxide) block copolymers (PEO-*b*-PPO), PEO-*b*-PPO-b-PEO and PEG-*b*- poly lactic-*co*-glycolic acid-b-PEG.[163]

Thermoresponsive poly(*N*-isopropylacrylamide) (PNIPAM) microgel films[164] allow controlled detachment of adsorbed cells at a temperature change. Cell response occurs on the time scale of several minutes, is reversible, and allows harvesting of cells in a mild fashion.

FEATURE ARTICLE

(I) Regulation of biomolecules adhesion
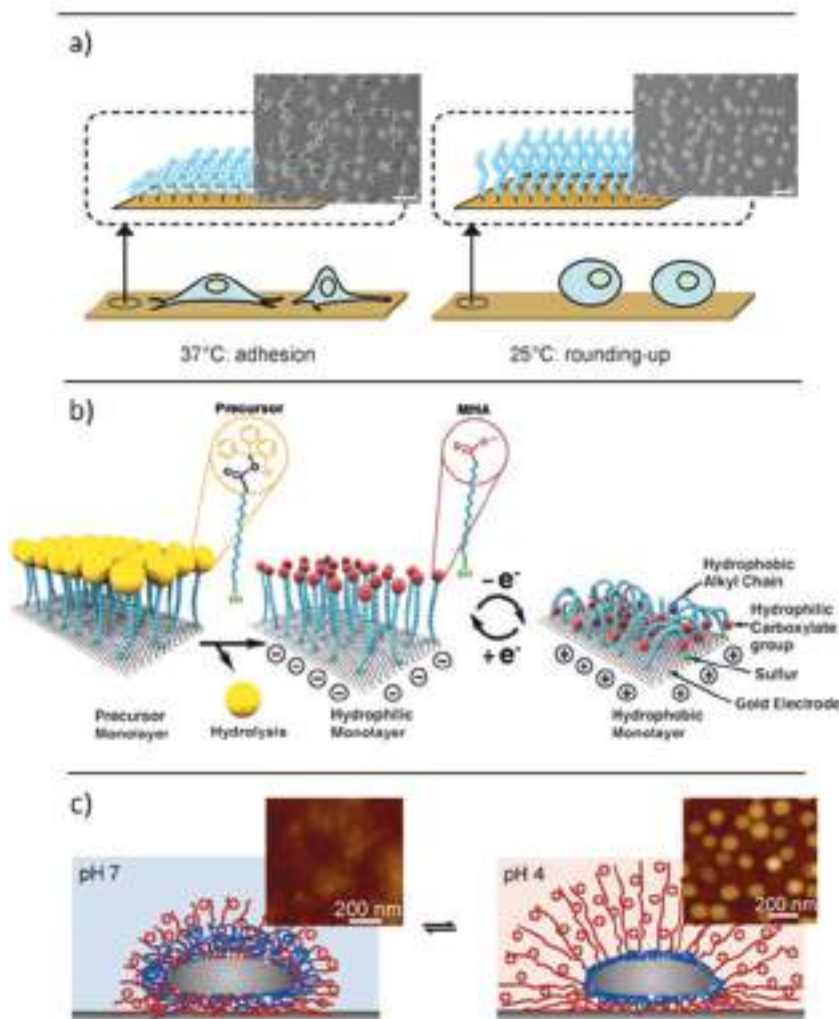
Figure 8. Part I: Stimuli for regulation of biomolecule adhesion. a) Thermo-response and phase-contrast microscopy images of L929 mouse fibroblasts behavior of polymer grafted gold substrates coatings at different temperatures. Reproduced with permission.[155] Copyright 2008, Wiley-VCH. b) Electrochemical transition between straight (hydrophilic) and bent (hydrophobic) molecular conformations. Reproduced with permission.[176] Copyright 2003, American Association for the Advancement of Science. c) Surface immobilization of pH-responsive triblock terpolymer micelles on a porous aluminum surface formed by ultrasonication: schematic representation of adsorbed micelles on the porous surface depicting their pH-dependent morphology. Insets show atomic force microscopy images of a sponge-like metal surface before and after adsorption of micelles. Reproduced with permission.[2a] Copyright 2012, Wiley-VCH.

The fact that microgels are attached non-covalently allows using them on a broad variety of (charged) surfaces and is a major advantage as compared to approaches relying on covalent attachment of active films. PNIPAM derivatives undergo a sharp coil to globule transition in water at 32 °C, changing from a hydrophilic state below this temperature to a hydrophobic state. Cell cultures, which prefer more hydrophobic surfaces, on such responsive PNIPAM surfaces can be directly associated with hydrophilic and hydrophobic surface properties. Cells are able to attach to PNIPAM at physiological conditions because of hydrophobicity of PNIPAM modified surface. The cells can

be detached due to increased hydrophilicity at low temperature.

Novel smart substrates advantageously combine some features of PNIPAM surfaces (i.e., stimuli response) and PEG surfaces (i.e., bio-repellence at room temperature). Zareie et al.[165] reported on a temperature-responsive SAM based on the synthesis of an oligo(ethylene glycol) (OEG) molecule modified with a phenyl-methyl-trithiocarbonyl-propionic acid 2-dithiopyridyl-ethyl ester that exhibited a LCST of 37 °C. The widespread, successful application of OEG molecules for formation of low-fouling layers makes this molecule an attractive starting point for generating surfaces with switchable low-fouling properties (Figure 8a).[155] Thermoresponsive OEG–Au surfaces allow efficient control over cell-adhesion within a convenient and easily achievable temperature range (25–37 °C).

Thermo responsive LBL films can provide an effective base for formation of hybrid systems for drug delivery. Temperature treatment turns out to be a unique tool to precisely tune the permeability of polyelectrolyte multilayers or also complex micelles containing LbL.[157]

Nanoparticles incorporated in LBL films can absorb electromagnetic irradiation and, thus, provide drug delivery systems with thermo responsive properties.[166]

3.4.2. pH-Response

pH variation is well known and a fundamentally investigated stimulus to switch either (i) cell adhesion[2a] or (ii) sorption capacity of delivery systems[167] (Figure 8,9c). In the extracellular tissue tumour tissue has extracellularly a pH of 6.5–7.2, thus slightly lower than the physiological pH of 7.4.[168] After cellular uptake of the drug, release can be achieved in the lysosomes at pH of 4.5–5.0. Hydrolytic enzymes, such as cathepsin B, are also frequently utilized for drug release. The nanometer size of the drug conjugates or micellar structures allow passive targeting of the pharmaceutical compounds.[169] An ideal "intelligent" surface has internal regulation adapted to a particular application.

pH responsive compounds have ionizable functional groups capable of donating or accepting protons upon pH changes. Electrostatic repulsion between generated charges causes alterations of the hydrophobic volume along a polymer chain. The following mechanisms of response of polyelectrolyte multilayers (Figure 2h, 8c) to external stimuli as pH change can be proposed: (i) the polyelectrolytes have pH-buffering activity and can stabilize the pH in the metal surface; (ii) the active chemical can be released pH dependently from the

www.MaterialsViews.com

ADVANCED
FUNCTIONAL
MATERIALS
www.afm-journal.de

FEATURE ARTICLE

(II) Regulation of drug delivery
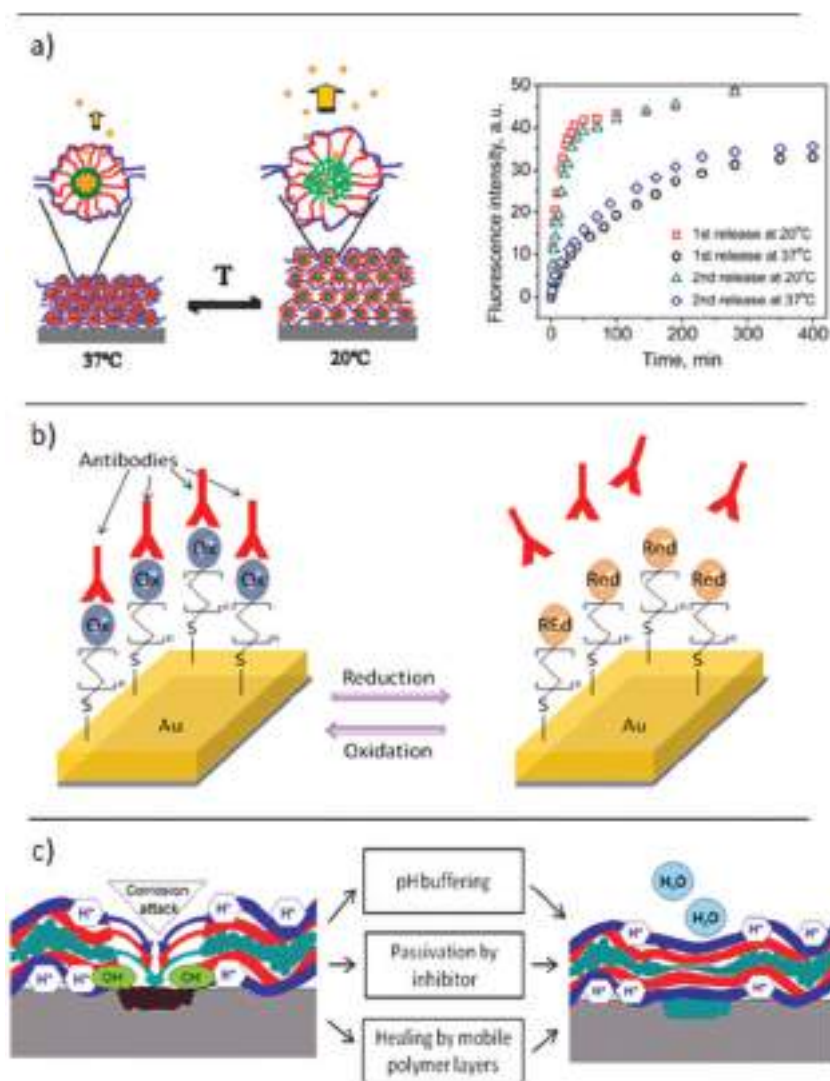
Figure 9. Part II: Stimuli for regulation of drug delivery. a) Reversible temperature-triggered swelling of stimuli-responsive block copolymer micelle layers. Release kinetics of pyrene from micelle layers of pH 5.0 buffer solution at 20 °C and 37 °C. Reproduced with permission.[157] Copyright 2009, American Chemical Society. b) Antibodies have a high affinity for benzoquinone but not for its reduced form, hydroquinone. They can thus be reversibly attached to an electrode and released in solution through the oxidation and reduction. Adapted with permission.[177b] Copyright 2010, Nature Publishing Group. c) Schematic mechanism of self-healing effect based on LbL hybrid. Reproduced with permission.[167a] Copyright 2008, Wiley-VCH.

polyelectrolyte multilayers; (iii) polyelectrolytes forming the coating are relatively mobile and have the tendency to seal the mechanical cracks of the coating.[167]

Recently, Peterson et al.[170] demonstrated pH-controlled release of proteins from polyelectrolyte-modified anodized titanium surfaces for implant applications. A polyelectrolyte coating of poly-L-histidine and poly(methacrylic acid) was used for sustained release of negatively charged species (morphogenetic proteins such as BMP-2) under physiological conditions. This complex demonstrated pH-dependent release, with maximum release at pH 5–6, but low levels of sustained release

at pH 7–8. Smaller initial burst release and higher amounts of sustained release were observed when lower molecular weight poly(methacrylic acid) was used.

For certain designs of cell surface interactions, it is preferable to have surface contact with developed morphology metal based surfaces, not with polymer layers, or a stable matrix is required. In particular, two types of encapsulation systems based on surface metal sponges have been suggested.[5e] The simultaneous activation/modification of the metal surface and incorporation of active chemicals by ultrasound are suggested in Type I. The metal capsules can be formed and loaded by ultrasound treatment of the metal surface in presence of an active component. As a model (Figure 7) encapsulation of a fluorescent antibiotic (doxorubicin) was presented. The pH dependent release from such capsules is shown in **Figure 10**d. At pH = 7 the encapsulation system is very stable and release from the capsules is negligible. At pH 4-2 we monitored a step-wise release of chemisorbed doxorubicin. At pH lower than 2 the release continues due to degradation of the metal oxide and dissolution of aluminum. Thus, the generation of a pH responsive encapsulation system on a metal surface can be performed in a single-step mode.

According to the Type II capsules, the surface sponges can be used for construction of metal-polyelectrolyte capsules for storage of active chemicals and their release on demand. The pores of metal sponges can be simply sealed by polyelectrolyte complexes.[149] The polyelectrolyte complexes are a universal encapsulation/carrier system and provide safe storage of active chemicals and their release in response to external stimuli, here pH. In this case, one does not need a specific interaction (chemisorption) between metal surface and active chemical. The upload/release of the active chemical in Type II capsules can be controlled by the formation of a complex between chemical and polyelectrolyte. The complex has one or two pH

windows (pH regions of complex instability) and provides an easy way of upload/release manipulation. The surface capsules loaded with 8-hydroxyquinoline (8-HQ) provide long-term antiseptic activity of the metal surface (Figure 7d,e). The metal surface contaminated by *E. Coli* bacteria before and after biocide release is shown in Figure 7e,f, correspondingly. Live and dead bacteria visualization proofs high biocide activity of the metal surface with 8-HQ-loaded capsules.

Recently, bacterial detachment from the surface initiated regulated by bacteria themselves was shown.[2a] Thus, on a metal surface a special type of pH responsive micelles[6b,c] was

**ADVANCED
FUNCTIONAL
MATERIALS**

www.afm-journal.de

*Materials
Views*

www.MaterialsViews.com
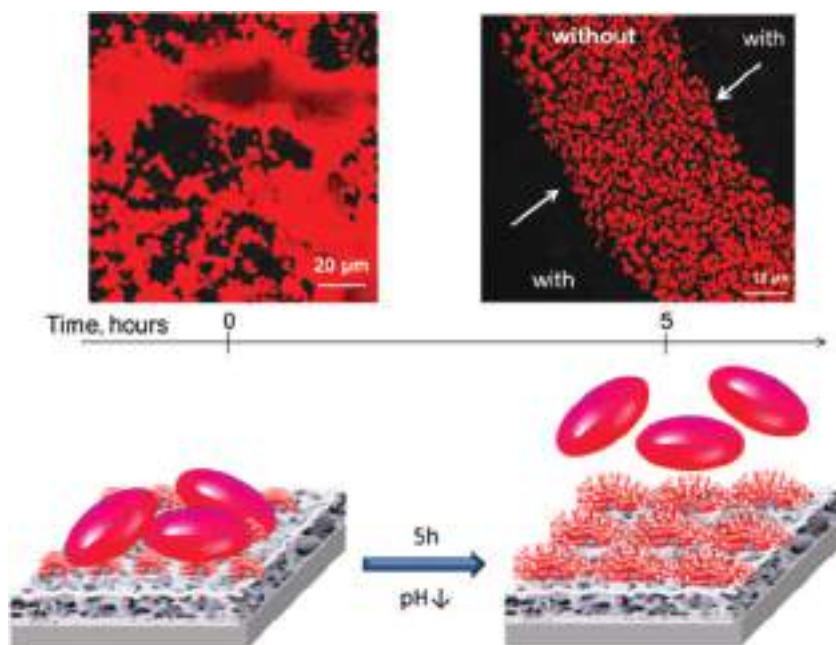
Figure 10. Synergetic surface activity: variation of cell adhesion through patterning with pH-responsive triblock terpolymer micelles and self-cleaning by antiseptic/disinfectant properties of porous Ag/Al surface. As model cells, *L. lactis 411* bacteria were used to present the idea of self-controllable intelligent surfaces. Reproduced with permission.[2a] Copyright 2012, Wiley-VCH.

immobilised. The micelles change their corona sizes depending on pH. Increase of micelle's corona size results in effective bacteria detachment from the surface at low pH.

Hydrogels change the orientation depending on pH, which is a significant prospective for both (i) control of biomolecules' surface behavior, and (ii) drug delivery targeting. A novel chemo-mechanical hybrid actuation system that enables pH-responsive reversible motion of microstructures in liquid has been demonstrated recently.[171] Inspired by biological actuators, the system is a composite of passive structural skeletal elements, put in motion by a poly(acrylic acid-*co*-acrylamide) hydrogel muscle that swells and contracts in response to chemical signals. The dynamics and mechanism of actuation were studied using electrochemically generated pH gradients that allow visualization of the hydrogel volume-phase transition and translation into movements of the microstructures.

3.4.3. Electro-Magnetic Irradiation

An electromagnetic field initiated by light could be an effective stimulus for (i) biomolecule detachment as well as (ii) drug delivery. The mechanism of surface sensitivity to light is based on light adsorption around adsorbed centers; for example, semiconductors such as TiO_2 absorbed effectively UV light, doped TiO_2 or its composites can be adapted also to the visible region, noble metal nanoparticles absorb IR light.[172]

Titanium covered with a native oxide layer has been selected to focus on intelligent metal surfaces. Moreover, it was mentioned that the layer can be modified to have different crystallinity, morphology, porosity, and so on, which can have a critical role also for the photocatalytic activity inherent to TiO_2. The

latter can be used to impart antiviral, antibacterial, and fungicidal properties, and effectively inhibit biofilm formation on the surface of TiO_2 implants. Titanium dioxide is known to be activated upon exposure to ultraviolet light, where irradiation of the surface promotes electrons from the valence band to the conduction band leaving a positively charged hole. As electrons and holes migrate, potent oxidative species, such as OH· and $O_2\cdot^-$, are produced.[173] The quantity of each species can be regulated by, for example, modification of the surface with metallic, bimetallic particles or formation of mixed oxide composites which can have a significant role to increase antibacterial activity selectively either to gram negative bacteria or gram positive ones.[173b] In particular, the nanostructured photocatalysts TiO_2, TiO_2:In_2O_3, TiO_2/Ag, and TiO_2/Ag/Ni prepared as thin film on ceramic substrates by spaying oxide sols with subsequent silver photodeposition and electroless nickel deposition were screened for their antibacterial efficiency against *P. fluorescens* and *L. lactis*.[173b] The photocatalysts show higher activity against *P. fluorescens* than *L. lactis* that can be explained in terms of different morphologies of gram positive and gram negative cell envelopes. Gram positive bacteria were more sensitive to $O_2\cdot^-$. Probably, active species initiate different deactivation mechanisms of OH· due to cell wall degradation/mineralisation, and $O_2\cdot^-$ affects the cell nucleus.

For the preparation of hybrid systems sensitive to UV-light mesoporous TiO_2 can be added to, for example, an LbL surface layer. The LbL method in this system can locally enable switching to open/close state by UV-irradiation. It was shown that short-term mild irradiation results in reversible permeability changes due to local variations in pH due to photocatalytic processes occurring at the titania surface.[147c,d] The irreversible decomposition of the LbL film is also possible after long term strong UV irradiation due to photodecomposition of polyelectrolytes.

Different sensitivity of different microorganisms, for example, bacteria and bacteriophages,[173c] provide effective instrumentation to manipulate their live cycles. In particular it was shown that the kinetic activity of the deactivation of bacteriophages dramatically exceeds that of bacterial deactivation. This allows to suggest a procedure of photocatalytic lysogenic bacteria detection including the following steps: (a) daily obtaining lysogenic bacteria cultures by standard methods; (b) cultivation of lysogenic bacteria in a sterile physiological solution and addition of the nanodispersed titania photocatalyst to the resultant suspension; (c) UV-irradiation of the mixed suspension; (d) seeding of the irradiated culture by a standard two-layer method with the subsequent crops incubated for some days; (e) calculation of the number of negative colonies and concentration of phages (plaque forming unit per mL). This is a strong example of providing the stimuli to affect the metabolism of microorganisms, which is of high priority for intelligent surface design and biomimetic of natural systems.

www.MaterialsViews.com

ADVANCED
FUNCTIONAL
MATERIALS
www.afm-journal.de

FEATURE ARTICLE

Laser-induced remote release is based on localized heating of the polymeric component in hybrids in the vicinity of metal nanoparticles absorbing laser light.[147b,d,174] Thus, the polyelectrolyte multilayer becomes mobile above the glass temperature T_g of the polyelectrolyte complex. It should be noted that excessive heating is undesirable for living cells, but it is desirable for cancer treatment. Besides noble nanoparticles, to make surface light switchable special molecules can be suggested. For example, azobenzene molecules, which undergo transitions from cis- to trans-configuration upon exposure to light close the pores in a cooperative way thus entrapping molecules inside, e.g., a porous surface.

One more attractive possibility of laser-induced cell detachment on gold nanoparticle functionalized surfaces was demonstrated recently.[175] It is interesting that the selective cell detachment from nanoengineered gold nanoparticle surfaces, triggered by laser irradiation, occurs in a nonthermal manner. It was shown that detachment is attributed to a photochemical mechanism due to production of reactive oxygen species under illumination of gold nanoparticles by green laser light. It was also demonstrated that cells migrate from unirradiated areas leading to their reattachment and surface recovery which is important for controlled spatial organization of cells in self-healing and tissue engineering.

3.4.4. Electric or Magnetic Field, Electrochemical Activation

Electric fields can be also used to protonate/deporotonate SAM of acid-terminated thiols. Lahann et al.[176] developed a surface coating on Au that transduced conformational changes in a low-density SAM, initiated by a voltage bias into wettability changes (Figure 8b). The self-assembled surfaces offer exciting opportunities when applied to the manipulation of biomolecules.

The uptake and release of antibodies from modified electrodes (Figure 9b) were described by Sivan and co-workers.[177] In these experiments, antibodies were selected such that they recognize and bind strongly to n-decanethiolbenzoquinones, but have a lower affinity for their reduced form (hydroquinones). This enabled the electrochemical control of their release: antibodies were attached to a benzoquinone monolayer self-assembled on a gold electrode, and subsequently released and re-attached on successive electrochemical reduction and oxidation.

Polypyrrole finds vast applications in biosensors, controlled drug delivery, gas sensors, artificial muscles, and so on.[178] For biological applications, polypyrrole has advantages as it is biocompatible, stable and conductive.[179] Thus, besides using metals to provide sensitivity to electrical potential, biocompatible polypyrrole can be used for the same purpose. Its conductive nature allows an applied current to be switched on and off reversibly, to facilitate the controlled delivery of drugs or the release of other chemicals. In addition, due to its stability, it can protect the capsules used in controlled release systems from degradation before reaching the target site. These properties of polypyrrole help to overcome the present problem of achieving efficient low molecular weight active component delivery. Thus, it was shown that hybrid Mg-polypyrrole composites immobilized onto ITO provide release of encapsulated active agent under electric currents.[109]

Magnetic field effects are very similar to the effects of lasers since both represent various components of electromagnetic fields. In the case of magnetic fields, magnetic nanoparticles serve as absorbing centers producing localized heating centers and inducing release. Recently, the group of Losic[54] demonstrated a very prospective way of magnetic-responsive delivery of drug-carriers using titania nanotube arrays (Figure 6). It was shown that a rapid (1–1.5 h) triggered release of drug encapsulated polymer micelles as drug-carriers with 100% release can be achieved at desirable times of the drug release process. The release of polymer micelles from titania nanotubes is proven to be generic by exploring three types of amphiphilic micelles, and indomethacin, a hydrophobic drug entrapped inside the lipophilic core of micelles. This strategy is particularly valuable for drug-releasing implants in orthopaedics and bone surgery, where on-demand release is needed under conditions (infections) where no time delay can be afforded for drugs to be administered by conventional therapy.

3.4.5. Solvent and Ionic Strength

The permeability of polyelectrolyte complexes or micelles on surfaces can also be changed by adding an organic solvent or salt to the aqueous suspension.[180] The decrease in the dielectric constant of the medium increases the strength of the electrostatic interactions between the polyion chains and, thus, leads to a collapse of the polymers. As a result, the LbL are much more permeable than the initial films. It can be noted that solvent used during film manufacture also plays an important role.[181] However, contrary opinions exist about the reversibility of the solvent treatment. For the influence of salt on the properties of polyelectrolyte complexes two concentration ranges have to be distinguished. At very low ionic strength, the complex does not change, but its permeability increases due to a partial breakage of ionic bonds. At higher salt concentrations, the electrostatic interactions between the oppositely charged polyions are sufficiently weakened to enable their rearrangements. Although addition of salt increases the permeability of the polyelectrolyte layer, an opposite effect can be achieved if one polymer in the pair possesses hydrophobic groups, for example poly(styrenesulfonate sodium salt) (PSS). Upon increase of ionic strength, the electrostatic interaction between the charged groups decreases.[182] Moreover, low salt concentrations can even inhibit fusion of layers upon heating.

Altogether a change of ionic strength can be a suitable stimulus due to the difference in ionic strength at environmental conditions and, for instance, in the human body. Thus, for example, the system can be designed in a way to have release of drug after material implanting into the body.

3.4.6. Multi-Trigger Response

One advanced trend for stimuli responsive surfaces is the development of a system that can respond to several external and/or internal stimuli in an intelligent way and mimic natural systems. A double-responsive system can be achieved (i) with a hybrid system whose components are sensitive to different stimuli, or (ii) with special nano-organized assembly into micelles, hydrogel. A background idea is to combine in

ADVANCED
FUNCTIONAL
MATERIALS
www.afm-journal.de

Materials
Views
www.MaterialsViews.com

FEATURE ARTICLE

one system the nanoblocks responsive to different stimuli. An example of a hybrid system can be surface organized magnesium-polypyrrole hybrids.[109] An active chemical release from such a hybrid is achievable by pH-change (due to magnesium biodegradation) or an electric field (due to the conductivity of polypyrrole). It can be noted that functionalization by magnetic and metal nanoparticles produces capsules which response to multiple stimuli. Double- or multi-responsive systems can be based just on the polymer architecture. Random copolymers are used to tailor the transition point depending on two independent parameters, for example, pH and temperature. In contrast block copolymers tend to self-assemble reversibly and form micelles depending on the environmental conditions. The micelles are then either stabilised through strong non-covalent interaction (e.g., ionic) or fixed through subsequent crosslinking. In both cases, one obtains a nano-object, which can be utilized as a micellar responsive drug delivery system, but it can also mimic biological entities like vesicles.[183]

Summarizing: (i) noble metal nanoparticles and nanorods can provide surface plasmon resonance in the visible region of the electromagnetic spectrum; (ii) magnetic nanoparticles can guide a system, (iii) semiconductor particles, (iv) quantum dots, (v) carbon nanostructures, (vi) biomolecules, antibodies and targeting molecules, (vii) stimuli micelles, etc., and their combination can provide intelligent systems with multi-trigger response.

3.4.7. Self-Regulated Processes: Biomimetic of Natural Systems

The last example (Figure 10) from our recent work[2a] provides nice support of the presented idea: use the cell metabolism as one of the stimuli. In particular, the novelty of this work is the design of the 3D designed surfaces with both space- and time-dependent functionality. The different surface functionality and reactivity can be controlled by surface patterning and formation of a sponge with active component in its composition. Ultrasonically formed silver/aluminum sponge-like surfaces as well as Ag-free surfaces were used for a self-assembled immobilization of pH-responsive triblock terpolymer micelles. The self-induced regulation which can be assumed as successful step in mimicking natural systems and antibacterial properties were tested by using *L. lactis 411* bacteria as a model system. These types of bacteria produce lactic acid in their life cycle and change the pH of the environment. The micelles change their conformation and bacteria are "pushed off" from the surface. The possibility to regulate cell adhesion was shown through patterned micelle adsorption. The antimicrobial activity clearly indicates antiseptic/disinfectant activity of the Ag/Al sponge surface.

4. Conclusions

In this article, the latest achievements in construction of "intelligent" systems that could mimic biofunctions are highlighted. Interfaces adapted to self-control and self-regulation require a complex hierarchical organization of stimuli responsive nano-organized blocks. In living systems, nature broadly exploits the principles of hierarchical organization for self-control and

stimuli responsive switching and self-regulation. However, synthetic intelligence is still a challenge. Even more challenging is in vivo design.

We demonstrated how the blocks can be nanostructured and combined to provide system response to environmental changes, stimuli switchability. We focused on metal surfaces, that usually passive surface widely used for implantation. However, as shown in the here, nanostructuring of metal interfacial layer can provide novel characteristics that are attractive for intelligent surfaces. The potential of hybrids and composites for formation of active interfaces is also demonstrated. Polymer systems are suggested as nanoblocks for hierarchical organization in combination with metals.

The design of the 3D architecture surfaces with both space- and time-dependent functionality (cell attraction, pH- trigged self-cleaning, antiseptic/disinfection) is a modern issue in bio-nanoingineering and materials science. Spatial and temporal biomolecule performance at the surface provided by the surface nanoarchitecture offers advanced bio-applications of metal based materials, such as implantation, organ-on chip and lab-on-chip, biosensors, smart biomaterials, drug delivery systems.

We believe that the area will be explored further in nearest future. A next step in active surface construction can be the surfaces that are applicable for a generation of entire organs due to spatially and temporally resolved co-culture growth regulated by morphology and functions of the interfacial layer.

[1] a) M. J. Harrington, A. Masic, N. Holten-Andersen, J. H. Waite, P. Fratzl, *Science* **2010**, *328*, 216; b) S. R. White, N. R. Sottos, P. H. Geubelle, J. S. Moore, M. R. Kessler, S. R. Sriram, E. N. Brown, S. Viswanathan, *Nature* **2001**, *409*, 794; c) D. V. Andreeva, D. Fix, H. Möhwald, D. G. Shchukin, *Adv. Mater.* **2008**, *20*, 2789; d) E. V. Skorb, D. G. Shchukin, in *European Coatings Tech Files*, (Ed: G. Gehrenkemper), Vincentz Network GmbH & Co, Germany **2010**.

[2] a) J. Gensel, T. Borke, N. Pazos Pérez, A. Fery, D. V. Andreeva, E. Betthausen, A. H. E. Müller, H. Möhwald, E. V. Skorb, *Adv. Mater.* **2012**, *24*, 985; b) D. L. Huber, R. P. Manginell, M. A. Samara, B. I. Kim, B. C. Bunker, D. L. Huber, R. P. Manginell, M. A. Samara, B. I. Kim, B. C. Bunker, *Science* **2003**, *301*, 352; c) F. Caruso, R. A. Caruso, H. Möhwald, *Science* **1998**, *282*, 1111; d) M. A. C. Stuart, W. T. S. Huck, J. Genzer, M. Müller, C. Ober, M. Stamm, G. B. Sukhorukov, I. Szleifer, V. V. Tsukruk, M. Urban, F. Winnik, S. Zauscher, I. Luzinov, S. Minko, *Nat. Mater.* **2010**, *9*, 101; e) D. E. Discher, A. Eisenberg, *Science* **2002**, *297*, 967; f) T. M. Allen, P. R. Cullis, *Science* **2004**, *43*, 1818.

[3] a) M. Long, H. J. Rack, *Biomaterials* **1998**, *19*, 1621; b) E. C. Keeley, J. A. Boura, C. L. Grines, *Lancet* **2003**, *361*, 13; c) L. Guehennec, A. Soueidan, P. Layrolle, Y. Amouriq, *Dent. Mater.* **2007**, *23*, 844.

[4] a) P. Kollmannsberger, C. M. Bidan, J. W. C. Dunlop, P. Fratzl, *Soft Matter* **2011**, *7*, 9549; b) W. Tan, T. A. Desai, Biomed. *Microdevices* **2003**, *5*, 235; c) H. Kaji, K. Tsukidate, T. Matsue, M. Nishizawa, *J. Am. Chem. Soc.* **2004**, *126*, 15026; d) E. Kharlampieva, V. Kozlovskaya, S. A. Sukhishvili, *Adv. Mater.* **2009**, *21*, 3053.

[5] a) R. Singhvi, A. Kumar, G. P. Lopez, G. N. Stephanopoulos, D. I. C. Wang, G. M. Whitesides, D. E. Ingber, *Science* **1994**, *264*, 696; b) U. Hersel, C. Dahmen, H. Kessler, *Biomaterials* **2003**, *24*, 4385; c) S.-H. Lee, J. J. Moon, J. L. West, *Biomaterials* **2008**, *29*, 2962; d) P. Roach, D. Farrar, C. C. Perry, *J. Am. Chem. Soc.* **2006**, *128*, 3939; e) D. V. Andreeva, D. V. Sviridov, A. Masic, H. Möhwald, E. V. Skorb, *Small* **2012**, *8*, 820.

[6] a) C. M. Schilli, M. F. Zhang, E. Rizzardo, S. H. Thang, Y. K. Chong, K. Edwards, G. Karlsson, A. H. E. Muller, *Macromolecules* **2004**, *37*, 7861; b) E. Betthausen, M. Drechsler, M. Förtsch, F. H. Schacher, A. H. E. Müller, *Soft Matter* **2011**, *7*, 8880; c) J. Gensel, E. Betthausen, C. Hasenöhrl, K. Trenkenschuh, M. Hund, F. Boulmedais, P. Schaaf, A. H. E. Müller, A. Fery, *Soft Matter* **2011**, *23*, 11144.

[7] R. P. McLaughlin, J. C. Bennett, H. Trevisi, *Systemized Orthodontic Treatment Mechanics*, Mosby, Edinburgh **2001**.

[8] a) B. M. Novak, *Adv. Mater.* **1993**, *5*, 422; b) C. Sanchez, G. J. D. A. Soler-Illia, F. Ribot, T. Lalot, C. R. Mayer, V. Cabuil, *Chem. Mater.* **2003**, *13*, 3061; c) P. Judeinstein, C. Sanchez, *J. Mater. Chem.* **1996**, *6*, 511; d) N. Tran, T. J. Webster, *WIREs Nanomed. Nanobiotechnol.* **2009**, *1*, 336.

[9] Y. Z. Yang, K. H. Kim, J. L. Ong, *Biomaterials* **2005**, *26*, 327.

[10] a) E. W. Keefer, B. R. Botterman, M. I. Romero, A. F. Rossi, G. W. Gross, *Nat. Nanotechnol.* **2008**, *3*, 434; b) K. L. Elias, R. L. Price, T. J. Webster, *Biomaterials* **2002**, *23*, 3279; c) S. Kim, C. B. Park, *Adv. Funct. Mater.* **2012**, DOI: 10.1002/adfm.201201994; d) L. Zhang, T. J. Webster, *Nano Today* **2009**, *4*, 66.

[11] a) E. V. Skorb, T. V. Byk, V. G. Sokolov, T. V., Gaevskaya, D. V. Sviridov, C.-H. Noh, *Chem. High Energy* **2008**, *42*, 127; b) E. V. Skorb, V. G. Sokolov, T. V. Gaevskaya, D. V. Sviridov, *Theor. Exper. Chem.* **2009**, *45*, 40; c) S. A. Zhdanok, S. V. Gorbatov, A. A. Mikhailov, F. V. Plevako, K. F. Plevako, S. V. Shushkov, E. V. Skorb, V. G. Sokolov, T. V. Gaevskaya, D. V. Sviridov, *J. Engineer. Phys. Thermophys.* **2009**, *81*, 213; d) T. V. Byk, V. G. Sokolov, T. V. Gaevskaya, E. V. Skorb, D. V. Sviridov, C.-H. Noh, K. Y. Song, Y. N. Kwon, S. H. Cho, *J. Photochem. Photobiol. A: Chem.* **2008**, *193*, 56.

[12] E. V. Skorb, D. G. Shchukin, H. Möhwald, D. V. Andreeva, *Nanoscale* **2010**, *2*, 722.

[13] L. T. Jonge, S. C. G. Leeuwenburgh, J. G. C. Wolke, J. A. Jansen, *Pharmacol. Res*, **2008**, *25*, 2357.

[14] a) T. Okano, N. Yamada, M. Okuhara, H. Sakai, Y. Sakurai, *Biomaterials* **1995**, *16*, 297; b) E. Wischerhoff, T. Zacher, A. Laschewsky, E. D. Rekak, *Angew. Chem. In. Ed.* **2000**, *112*, 4771; c) K. L. Prime, G. M. Whitesides, *J. Am. Chem. Soc.* **1993**, *115*, 10714; d) A. M. Jonas, K. Glinel, R. Oren, B. Nysten, W. T. S. Huck, *Macromolecules* **2007**, *40*, 4403; e) J.-F. Lutz, P. Akdemir, A. Hoth, *J. Am. Chem. Soc.* **2006**, *128*, 13046.

[15] T. G. Kim, H. Shin, D. W. Lim *Adv. Funct. Mater.* **2012**, *22*, 2446.

[16] H. Hermawan, D. Dubé, D. Mantovani, *Acta Biomater.* **2010**, *6*, 1693.

[17] A. Mirskii, *Surgery from past to present. History remarks*, Science, Moscow, **2000**.

[18] N. N. Znamenskii, Dental implantation, 4th Pirogov's forum, 1891.

[19] U. W. Herr, *J. Urol.* **2007**, *177*, 457.

[20] R. M. Pilliar, *Biomaterials* **1991**, *12*, 95.

[21] a) N. C. Blumenthal, V. Cosma., *Biomed. Mater. Res.* **1989**, *23*, 13; b) I. Gorman, *J. Endourol.* **1997**, *11*, 383.

[22] R. V. Marrey, R. Burgermeister, R. B. Grishaber, R. O. Ritchie, *Biomaterials* **2006**, *27*, 1988.

[23] Y. Okazaki, E. Gotoh, *Biomaterials* **2005**, *26*, 11.

[24] C. H. Ku, D. P. Pioletti, M. Browne, P. J. Gregson, *Biomaterials* **2002**, *23*, 1447.

[25] Y. T. Sul, C. B. Johansson, S. Petronis, A. Krozer, Y. Jeong, A. Wennerberg, T. Albrektsson, *Biomaterials* **2002**, *23*, 491.

[26] F. Lindberg, J. Heinrichs, F. Ericson, P. Thomsen, H. Engqvist, *Biomaterials* **2008**, *29*, 3317.

[27] S. D. Cook, N. Thongpreda, R. C. Anderson, R. J. Haddad, *J. Biomed. Mater. Res.* **1988**, *22*, 287.

[28] *Polymer grafting and crosslinking*, (Eds: A. Bhattacharya, J. W. Rawling, R. Paramita), Wiley & Sons, Inc., Hoboken, New Jersey, **2009**.

[29] K.-H. Frosch, F. Barvencik, C. H. Lohmann, V. Viereck, H. Siggelkow, J. Breme, K. Dresing, K. M. Stürmer, *Cells Tissues Organs* **2002**, *170*, 214.

[30] J. B. Park, in *The Biomedical Engineering Handbook*, (Ed: J. B. Bronzino), CRC Press, Boca Raton, FL **1995**.

[31] M. Schillinger, S. Sabeti, C. Loewe, P. Dick, J. Amighi, W. Mlekusch, O. Schlager, M. Cejna, J. Lammer, E. Minar, *New Eng. J. Medicine* **2006**, *354*, 1879.

[32] D. A. Porter, K. E. Easterling, *Phase Transformations in Metals and Alloys*, Chapman and Hall, London **1992**.

[33] F. Witte, *Acta Biomater.* **2010**, *6*, 1680.

[34] a) B. Heublein, G. Hausdorf, *EPO, EP1270023*, **2002**; b) H. Tamai, K. Igaki, E. Kyo, K. Kosuga, A. Kawashima, S. Matsui, H. Tamai, T. Tsuji, S. Motohara, H. Uehata, *Circulation* **2000**, *102*, 399; c) T. Tsuji, H. Tamai, K. Igaki, E. Kyo, K. Kosuga, T. Hata, M. Okada, T. Nakamura, H. Komori, S. Motohara, H. U°ehata, *Curr. Interv. Cardiol. Rep.* **2001**, *3*, 10; d) P. Peeters, M. Bosiers, J. Verbist, K. Deloose, B. Heublein, *J. Endovasc. Ther.* **2005**, *12*, 1; e) J. Levesque, H. Hermawan, D. Dube, D. Mantovani, *Acta Biomater.* **2008**, *4*, 284.

[35] a) M. Peuster, P. Wohlsein, M. Brugmann, M. Ehlerding, K. Seidler, C. Fink, H. Brauer, A. Fischer, G. Hausdorf, *Heart* **2001**, *86*, 563; b) R. Waksman, R. Pakala, R. Baffour, R. Seabron, D. Hellinga, F. O. Tio, *J. Interv. Cardiol.* **2008**, *21*, 15; c) H. Hermawan, D. Dubé, D. Mantovani, *Acta Biomater.* **2010**, *6*, 1693.

[36] a) J. Levesque, D. Dube, M. Fiset, D. Mantovani, *Mater. Sci. Forum.* **2003**, *426*, 521; b) A. Bolz, T. Popp, *USPTO, US20016287332*, **2001**.

[37] a) M. Peuster, C. Hesse, T. Schloo, C. Fink, P. Beerbaum, C. Schnakenburg, *Biomaterials* **2006**, *27*, 4955; b) H. Hermawan, H. Alamdari, D. Mantovani, D. Dubé, *Powder Metall.* **2008**, *51*, 38.

[38] S. Picard, J. B. Memet, R. Sabot, J. L. Grosseau-Poussard, J. P. Riviere, R. Meilland, *Mater. Sci. Eng. A* **2001**, *303*, 163.

[39] H. M. Kim, F. Miyaji, T. Kokubo, T. Nakamura, *J. Biomed. Mater. Res.* **1996**, *32*, 409.

[40] L. Zhang, T. Webster, *Nano Today* **2009**, *4*, 66.

[41] M. M. Arafat, B. Dinan, S. A. Akbar, A. S. M. A. Hasseb, *Sensors* **2012**, *12*, 7207.

[42] Alfa Aesar website: http://www.alfa.com, (accessed April 2013).

[43] J.-Y. Aralom, T. P. Hoar, *Electrochim. Acta* **1970**, *15*, 877.

[44] B. Yang, M. Uchida, H.-M. Kim, X. Zhang, T. Kokubo, *Biomaterials* **2004**, *25*, 1003.

[45] K. Das, S. Bose, A. Bandyopadhyay, *Acta Biomater.* **2007**, *3*, 573.

[46] C. Richter, L. Menon, *Energy Environ. Sci.* **2010**, *3*, 427.

[47] A. Fujishima, X. T. Zhang, D. A. Tryk, *Surface Sci. Rep.* **2008**, *63*, 515.

[48] V. Zwilling, E. Darque-ceretti, A. Boutry-Forveille, D. David, M. Y. Perrin, M. Aucouturier, *Interface Annu.* **1999**, *27*, 629.

[49] K. Sunada, Y. Kikuchi, K. Hashimoto, A. Fujishima, *Env. Sci. Technol.* **1998**, *32*, 726.

ADVANCED
FUNCTIONAL
MATERIALS
www.afm-journal.de

www.MaterialsViews.com

FEATURE ARTICLE

[50] M. Mahmood, Z. Li, D. Casciano, M. V. Khodakovskaya, T. Chen, A. Karmakar, E. Dervishi, Y. Xu, T. Mustafa, F. Watanabe, A. Fejleh, M. Whitlow, M. Al-Adami, A. Ghosh, A. S. Biris, *J. Cellular Molec. Medic.* **2011**, *15*, 2297.

[51] J. C. Yu, J. Lin, D. Lo, S. K. Lam, *Langmuir* **2000**, *16*, 7304.

[52] a) R. Sharma, P. P. Das, M. Misra, V. Mahajan, J. P. Bock, *Nanotechnology* **2009**, *20*, 075704; b) M. Kitano, K. Funatsu, M. Anpo, *J. Phys. Chem. B* **2006**, *110*, 25266.

[53] K. S. Raja, M. Misra, K. Paramguru, *Electrochim. Acta* **2005**, *51*, 154.

[54] M. S. Aw, J. Addai-Mensah, D. Losic, *J. Mater. Chem.* **2012**, *22*, 6561.

[55] P. K. Chu, J. Y. Chen, L. P. Wang, N. Huang, *Mater. Sci. Engineer.* **2002**, *36*, 143.

[56] K. Subramani, D. Wismeijer, *In. J. Oral Max. Impl.* **2012**, *27*, 1043.

[57] T. Witvrouwen, S. Paulussen, B. Sels, *Plasma Proc.* **2012**, *9*, 750.

[58] J. Kuppers, *Surf. Sci. Rep.* **1995**, *22*, 249.

[59] C. C. Hsu, M. A. Nierode, J. W. Coburn, D. B. Graves, *J. Phys. D Appl. Phys.* **2006**, *39*, 3272.

[60] M. R. Gonçalves, T. Makaryan, F. Enderle, S. Wiedemann, A. Plettl, O. Marti, P. Ziemann, *Beilstein J. Nanotechnol.* **2011**, *2*, 448.

[61] *Principles of Plasma Discharges and Materials Processing*, (Eds: M. A. Lieberman, A. J. Lichtenberg), John Wiley & Sons Inc., New York **1994**.

[62] a) S. K. Poznyak, D. V. Talapin, A. I. Kulak, *J. Electroanal. Chem.* **2005**, *579*, 299; b) A. D. Lisenkov, A. N. Salak, S. K. Poznyak, M. L. Zheludkevich, M. G. S. Ferreira, *J. Phys. Chem. C* **2011**, *115*, 18634.

[63] P. Kingshott, H. Thissen, H. J. Griesser, *Biomaterials* **2002**, *23*, 2043.

[64] K. Vasilev, Z. Poh, K. Kant, J. Chan, A. Michelmore, D. Losic, *Biomaterials* **2010**, *31*, 532.

[65] a) B. Nayak, M. Gupta, K. Kolasinski, *App. Phys. A Mater.* **2008**, *90*, 399; b) B. Nayak, M. Gupta, K. Kolasinski, *Nanotechnology* **2007**, *18*, 195302.

[66] M. Bereznai, I. Pelsoczi, Z. Toth, K. Turzo, M. Radnai, Z. Bor, A. Fazekas, *Biomaterials* **2003**, *24*, 4197.

[67] a) R. Stamp, P. Fox, W. O'Neill, E. Jones, C. Sutcliffe, *J. Mater. Sci. Mater. Med.* **2009**, *20*, 1839; b) I. Shishkovsky, *Appl. Surf. Sci.* **2009**, *255*, 9902; c) J. V. Rau, A. Generosi, S. Laureti, V. S. Komlev, D. Ferro, S. N. Cesaro, B. Paci, V. R. Albertini, E. Agnostinelli, S. M. Barinov, *ACS Appl. Mater. Interfaces* **2009**, *1*, 1813.

[68] a) S. Mwenifumbo, M. Li, J. Chen, A. Beye, W. Soboyejo, *J. Mater. Sci. Mater. Med.* **2007**, *18*, 9; b) M. Hirao, K. Sugamoto, N. Tamai, K. Oka, H. Yoshikawa, Y. Mori, T. J. Saski, *J. Biomed. Mater. Res. A* **2005**, *73*, 213.

[69] J. R. Bush, B. K. Nayak, L. S. Nair, M. C. Gupta, C. T. Laurencin, *J. Biomed. Mater. Res. B* **2011**, *97B*, 299.

[70] M. Djouder, T. E. Itina, D. Deghiche, O. Lamrous, *Appl. Surf. Sci.* **2012**, *261*, 337.

[71] a) V. I. Emel'yanov, V. I. Konov, V. N. Tokarev, V. N. Seminogov, *J. Opt. Soc. Am. B* **1989**, *6*, 104; b) F. Keilmann, Y. H. Bai, *Appl. Phys. A* **1982**, *29*, 9; c) A. M. Ozkan, A. P. Malshe, T. A. Railkar, W. D. Brown, M. D. Shirk, P. A. Molian, *Appl. Phys. Lett.* **1999**, *75*, 3716; d) A. Y. Vorobyev, V. S. Makin, C. Guo, *J. Appl. Phys.* **2007**, *101*, 034903.

[72] X. J. Wu, T. Q. Jia, F. L. Zhao, M. Huang, N. S. Xu, H. Kuroda, Z. Z. Xu, *Appl. Phys. A* **2007**, *86*, 491.

[73] M. Djouder, T. E. Itina, D. Deghiche, O. Lamrous, *Appl. Surf. Sci.* **2012**, *258*, 2580.

[74] *Inorganic Chemistry*, (Ed: Y. D. Tretjakov) Akademiya, Moscow **2004**.

[75] S. Nishiguchi, T. Nakamura, M. Kobayashi, H.-M. Kim, F. Miyaji, T. Kokubo, *Biomaterials* **1999**, *20*, 491.

[76] M. Takemoto, S. Fujibayashi, M. Neo, J. Suzuki, T. Matsushita, T. Kokubo, T. Nakamura, *Biomaterials* **2006**, *27*, 2682

[77] a) H. M. Kim, F. Miyaji, T. Kokubo, S. Nishiguchi, T. Nakamura, *J. Biomed. Mater. Res.* **1999**, *45*, 100; b) T. Kokubo, F. Miyaji, H. M. Kim, T. Nakamura, *J. Am. Ceram. Soc.* **1996**, *79*, 1127; c) A. K. Shukla, R. Balasubramaniam, *Corros. Sci.* **2006**, *48*, 1696.

[78] K. H. Sandhage, S. A. Dregia, S. A. Akbar, *J. Mater. Res.* **2006**, *21*, 1822

[79] A. Nanci, J. D. Wuest, L. Peru, P. Brunet, V. Sharma, S. Zalzal, M. D. McKee, *J. Biomed. Mater. Res.* **1998**, *40*, 324.

[80] M. Karthega, N. Rajendran, *Appl. Surf. Sci.* **2010**, *256*, 2176.

[81] J. M. Wu, H. Satoshi, K. Tsuru, A. Osaka, *Scr. Mater.* **2002**, *46*, 101.

[82] a) H. Dislich, *Angew. Chem. Int. Ed.* **1971**, *10*, 363; b) R. Roy, *Science* **1987**, *238*, 1664.

[83] a) Y. Xia, B. Gates, Y. Yin, Y. Lu, *Adv. Mater.* **2000**, *12*, 693; b) B. Gates, Y. Yin, Y. Xia, *Chem. Mater.* **1999**, *11*, 2827.

[84] W.-J. Shin, F. Basarir, T.-H. Yoon, J.-S. Lee, *Langmuir* **2009**, *25*, 3344.

[85] E. V. Skorb, D. V. Andreeva, *J. Mater. Chem. A* **2013**;

[86] a) D. G. Shchukin, E. V. Skorb, V. Belova, H. Möhwald, *Adv. Mater.* **2011**, *23*, 1922; b) E. V. Skorb, D. V. Andreeva, H. Möhwald, *Angew. Chem. Int. Ed.* **2012**, *51*, 5138.

[87] K. S. Suslick, L. A. Crum, in *Encyclopedia of Acoustics*, (Ed.: M. J. Crocker), Wiley & Sons. Inc., New York **1995**.

[88] J. G. Adewuyi, *Environ. Sci. Technol.* **2005**, *39*, 8557.

[89] L. H. Thompson, L. K. Doraiswamy, *Ind. Eng. Chem. Res.* **1999**, *38*, 1215.

[90] a) E. V. Skorb, D. G. Shchukin, D. V. Andreeva, *Langmuir* **2010**, *26*, 16973; b) E. V. Skorb, H. Möhwald, T. Irrgang, A. Fery, D. V. Andreeva, *Chem. Commun.* **2010**, *46*, 7897; c) J. Dulle, S. Nemeth, E. V. Skorb, T. Irrgang, J. Senker, R. Kempe, A. Fery, D. V. Andreeva, *Adv. Funct. Mater.* **2012**, *22*, 3128; d) J. Schäferhans, S. Gomez-Quero, D. V. Andreeva, G. Rothenberg, *Chem. Eur. J.* **2011**, *17*, 12254; e) D. V. Andreeva, *Inter. J. Mater. Res.* **2011**, *102*, 597; f) M. Virot, R. Pflieger, E. V. Skorb, J. Ravaux, T. Zemb, H. Möhwald, *J. Phys. Chem. C* **2012**, *116*, 15493.

[91] P. Fratzl, *Science* **2012**, *335*, 177.

[92] D. D. Deligianni, N. D. Katsala, P. G. Koutsoukos, Y. F. Missirlis, *Biomaterials* **2001**, *22*, 87.

[93] a) P. Ducheyne, W. Raemdonck, J. C. Heughebaert, M. Heughebaert, *Biomaterials* **1986**, *7*, 97; b) J. L. Ong, L. C. Lucas, W. R. Lacefield, E. D. Rigney, *Biomaterials* **1992**, *13*, 249; c) B. Ben-Nissan, C. S. Chai, K. A. Gross, *Bioceramics* **1997**, *10*, 175.

[94] a) C. Du, P. Klasens, R. E. Haan, J. Bezemer, F. Z. Cui, K. Groot, P. Layrolle, *J. Biomed. Mater. Res.* **2002**, *59*, 535; b) S. Leeuwenburgh, P. Layrolle, F. Barrere, J. Schoonman, C. A. Blitterswijk, K. Groot, *J. Biomed. Mater. Res.* **2001**, *56*, 208; c) P. Layrolle, C. Valk, R. Dalmeijer, C. A. Blitterswijk, K. Groot, *Bioceramics* **2001**, *13*, 391.

[95] S. Yang, Z. Shaoxiang, L. Jianan, Z. Changli, Z. Xiaonong, *Acta Biomater.* **2010**, *6*, 1736.

[96] S. B. Cho, F. Miyaji, T. Kokubo, K. Nakanishi, N. Soga, T. Nakamura, *J. Biomed. Mater. Res.* **1996**, *32*, 375.

[97] K. E. Healy, P. Ducheyne, *J. Biomed. Mater. Res.* **1992**, *26*, 319.

[98] P. Li, C. Ohtsuki, T. Kokubo, K. Nakanishi, N. Soga, K. Groot, *J. Biomed. Mater. Res.* **1994**, *28*, 7.

[99] L. Jonasova, F. A. Muller, A. Helebrant, J. Strnad, P. Greil, *Biomaterials* **2004**, *25* 1187.

[100] S. Iijima, *Nature* **1991**, *354*, 56.

[101] Y. Zhang, Y. Bai, B. Yan, *Drug Discovery Today* **2010**, *15*, 428.

[102] R. Rajesh, N. Senthilkumar, A. Harihasubramanian, Y. D. Ravichandran, *Int. J. Pharm. Pharm. Sci.* **2012**, *4*, 23.

www.MaterialsViews.com

ADVANCED
FUNCTIONAL
MATERIALS
www.afm-journal.de

FEATURE ARTICLE

[103] A. Ulman, *Introduction to Ultrathin Organic Films*, Academic Press, Boston **1991**.

[104] a) C. Redon, F. Brochard-Wyatt, E Rondelez, *Phys. Rev. Lett.* **1991**, *66*, 715; b) K. L. Prime, G. M. Whitesides, *Science* **1991**, *252*, 1164; c) M. K. Chdudhury, G. M. Whitesides, *Science* **1992**, *225*, 1230.

[105] R. M. Penner, *Nature* **2010**, *2*, 251.

[106] a) M. A. C. Stuart, W. T. S. Huck, J. Genzer, M. Müller, C. Ober, M. Stamm, G. B. Sukhorukov, I. Szleifer, V. V. Tsukruk, M. Urban, F. Winnik, S. Zauscher, I. Luzinov, S. Minko, *Nat. Mater.* **2010**, *9*, 101; b) E. V. Skorb, D. V. Andreeva, *Polym. Chem.* **2013**, DOI: 10.1039/C3PY00088E.

[107] a) G. Decher, *Science* **1997**, *277*, 1232; b) Y. Lvov, F. Caruso, *Anal. Chem.* **2001**, *73*, 4212; c) J. Hiller, J. D. Mendelsohn, M. F. Rubner, *Nat. Mater.* **2001**, *1*, 59; d) S. Srivastava, N. Kotov, *Acc. Chem. Res.* **2008**, *41*, 1831; e) E. Kharlampieva, V. Kozlovskaya, S. A. Sukhishvili, *Adv. Mater.* **2009**, *21*, 1.

[108] a) R. A. Green, N. H. Lovell, L. A. Poole-Warren, *Biomaterials* **2009**, *30*, 3637; b) D. V. Andreeva, D. A. Gorin, D. G. Shchukin, G. B. Sukhorukov, *Macromol. Rapid Commun.* **2006**, *27*, 931; c) D. V. Andreeva, Z. Pientka, L. Brozová, M. Bleha, G. A. Polotskaya, G. K. Elyashevich, *Thin Solid Films* **2002**, *406*, 54.

[109] E. V. Skorb, O. Baidukova, A. Goyal, A. Brotchie, D. V. Andreeva, H. Möhwald, *J. Mater. Chem.* **2012**, *22*, 13841.

[110] a) E. V. Skorb, D. Fix, D. G. Shchukin, H. Möhwald, D. V. Sviridov, R. Mousa, N. Wanderka, J. Schäferhans, N. Pazos-Pérez, A. Fery, D. V. Andreeva, *Nanoscale* **2011**, *3*, 985; b) J. Dulle, S. Nemeth, E. V. Skorb, T. Irrgang, J. Senker, R. Kempe, A. Fery, D. V. Andreeva, *Adv. Funct. Mater.* **2012**, *22*, 3128; c) N. Pazos-Perez, J. Schäferhans, E. V. Skorb, A. Fery, D. V. Andreeva, *Microporous Mesoporouw Mater.* **2012**, *154*, 164.

[111] a) M. M. Stevens, J. H. George, *Science* **2005**, *310*, 1135; b) V. Karageorgiou, D. Kaplan, *Biomaterials* **2005**, *26*, 5474.

[112] A. Ianuzzi, S. M. Kurtz, W. Kane, P. Shah, R. Siskey, A. Ooij, R. Bindal, R. Ross, T. Lanman, K. Buttner-Janz, J. Isaza, *Spine* **2010**, *35*, E1310.

[113] Y. Kawazoe, H. Shimogawa, A. Sato, M. Uesugi, *Angew. Chem. Int. Ed.* **2011**, *50*, 5478.

[114] K. Nagase, J. Kobayashi, T. Okano, *J. Royal Soc. Interface* **2009**, *6*, S293.

[115] H. Chen, Y. X. Zhang, D. Li, X. Y. Hu, L. Wang, W. G. McClung, J. L. Brash, *J. Biomed. Mater. Res. A.* **2009**, *90A*, 940.

[116] L. J. Zhang, T. J. Webster, *Nano Today* **2009**, *4*, 66.

[117] K. M. Hennessy, B. E. Pollot, W. C. Clem, M. C. Phipps, A. A. Sawyer, B. K. Culpepper, S. L. Bellis, *Biomaterials* **2009**, *30*, 1898.

[118] B. D Boyan, C. H. Lohmann, D. D. Dean, V. L. Sylvia, D. L. Cochran, Z. Schwartz, *Annu. Rev. Mater. Res.* **2001**, *31*, 357.

[119] D. M. D. Ehrenfest, P. G. Coelho, B.-S. Kang, Y.-T. Sul, T. Albrektsson, Tomas, *Trends Biotechnol.* **2010**, *28*, 198.

[120] J. T. Buijs, G. Pluijm, *Cancer Lett.* **2009**, *273*, 177.

[121] K. Kashiwagi, T. Tsuji, K. Shiba, *Biomaterials* **2009**, *30*, 1166.

[122] I. Banerjee, R. C. Pangule, R. C. Kane, *Adv. Mater.* **2011**, *23*, 690.

[123] M. M. Stevens, J. H. George, *Science* **2005**, *310*, 1135.

[124] a) M. S. Lord, C. Modin, M. Foss, M. Duch, A. Simmons, F. S. Pedersen, B. K. Milthorpe, F. Besenbacher, *Biomaterials* **2006**, *27*, 4529; b) A. S. G. Curtis, N. Gadegaard, M. J. Dalby, M. O. Riehle, C. D. W. Wilkinson, G. Aitchison, *IEEE Trans. Nano-Biosci.* **2004**, *3*, 61; c) W.-J. Li, R. Tuli, X. Huang, P. Laquerriere, R. S. Tuan, *Biomaterials* **2005**, *26*, 5158; d) R. Kriparamanan, P. Aswath, A. Zhou, L. Tang, K. T. Nguyen, *J. Nanosci. Nanotechnol.* **2006**, *6*, 1905.

[125] N. D. Spencer, M. Textor, in *Materials in Medicine*, (Eds: M. O. Speidel, P. Uggowitzer), ETH, Zurich, Switzerland **1997**.

[126] a) S. Margel, E. A. Vogler, L. Firment, T. Watt, S. Haynie, D. Y. Sogah, *J. Biomed. Mater. Res.* **1993**, *27*, 1463; b) A. J. Engler, L. Richert, J. Y. Wong, C. Picart, D. E. Discher, *Surf. Sci.* **2004**, *570*, 142; c) K. Anselme, M. Bigerelle, B. Noel, E. Dufresne, D. Judas, A. Iost, P. Hardouin, J. Biomed. *Mater. Res.* **2000**, *49*, 155; d) E. A. Vogler, *J. Biomater. Sci. Polym. Ed.* **1999**, *10*, 1015.

[127] A. Engler, S. Sen, H. L. Sweeney, D. E. Discher, *Cell* **2006**, *126*, 677.

[128] K. T. Bowers, J. C. Keller, B. A. Randolph, D. G. Wick, C. M. Michaels. *Int. J. Oral. Maxillofac. Implants* **1992**, *7*, 302.

[129] B. D. Boyan, T. W. Hummert, D. D. Dean, Z. Schwartz, *Biomaterials* **1996**, *17*, 137.

[130] a) D. Perrin, S. Szmukler-Moncler, C. Echikou, P. Pointaire, J. Bernard, *J. Clin. Oral. Implants Res.* **2002**, *13*, 465; b) G. Zhao, A. Raines, M. Wieland, Z. Schwartz, B. Boyan, *Biomaterials* **2007**, *28*, 2821.

[131] D. Khang, J. Lu, C. Yao, K. Haberstroh, T. Webster, *Biomaterials* **2008**, *29*, 970.

[132] O. Zinger, G. Zhao, Z. Schwartz, J. Simpson, M. Wieland, D. Landolt, B. Boyan, *Biomaterials* **2005**, *26*, 1837.

[133] L. Richert, F. Vetrone, J. H. Yi, S. F. Zalzal, J. D. Wuest, F. Rosei, A. Nanci, *Adv. Mater.* **2008**, 1488.

[134] E. Batur, E. Taylor, E. Alpaslan, T. J. Webster, *Nanotechnology* **2011**, *22*, 295102.

[135] M. J. Dalby, N. Gadegaard, R. Tare, A. Andar, M. O. Riehle, P. Herzyk, C. D. W. Wilkinson, R. O. C. Oreffo, *Nat. Mater.* **2007**, *6*, 997.

[136] L. Richert, F. Vetrone, J.-H. Yi, J. D. Wuest, F. Rosei, A. Nanci, *Adv. Mater.* **2008**, *20*, 1488.

[137] P. M. Vanhoutte, H. Shimokawa, E. H. C. Tang, M. Feletou, *Acta Physiol.* **2009**, *196*, 193.

[138] J. Park, S. Bauer, K. Mark, P. Schmuki, *Nano Lett.* **2007**, *7*, 1686.

[139] a) N. Pazos Perez, T. Borke, D. V. Andreeva, R. Alvarez Pueblo, *Nanoscale* **2011**, *3*, 3265; b) K. Tushar, M. D. Kurkuri, K. R. Diener, L. Parkinson, D. Losic, *Biosens. Bioelectron.* **2012**, *35*, 167.

[140] K. Kant, S. P. Low, A. Marshal, J. G. Shapter, D. Losic, *Appl. Mater. Interfaces* **2010**, *2*, 3447.

[141] F. Rupp, L. Scheideler, D. Rehbein, D. Axmann, J. Gels-Gerstorfer, *Biomaterials* **2004**, *25*, 1429.

[142] R. Löbbicke, M. Chanana, H. Schlaad, C. Pilz-Allen, C. Gunter, H. Möhwald, A. Taubert, *Biomacromolecules* **2011**, *12*, 3753

[143] T. J. Webster, C. Ergun, R. H. Doremus, R. W. Siegel, R. Bizios, *J. Biomed. Mater. Res.* **2009**, *51*, 475.

[144] S. Kay, A. Thapa, K. M. Haberstroh, T. J. Webster, *Tissue Eng.* **2002**, *8*, 753.

[145] K. Y. Cai, M. Muller, J. Bossert, A. Rechtenbach, K. D. Jandt, *Appl. Surf. Sci.* **2005**, *250*, 252.

[146] T.-S. Wong, S. H. Kang, S. K. Y. Tang, E. J. Smythe, B. D. Hatton, A. Grinthal, J. Aizenberg, *Nature* **2011**, *477*, 443.

[147] a) E. V. Skorb, D. Fix, D. V. Andreeva, D. G. Shchukin, H. Möhwald, *Adv. Funct. Mater.* **2009**, *19*, 2373; b) E. V. Skorb, A. Skirtach, D. V. Sviridov, D. G. Shchukin, H. Möhwald, *ACS Nano* **2009**, *3*, 1753; c) E. V. Skorb, D. G. Shchukin, H. Möhwald, D. V. Sviridov, *J. Mater. Chem.* **2009**, *19*, 4931; d) D. Fix, E. V. Skorb, D. G. Shchukin, H. Möhwald, *Meas. Sci. Technol.* **2011**, *22*, 075704; e) E. V. Skorb, D. V. Sviridov, H. Möhwald, D. G. Shchukin, *Chem. Commun.* **2009**, *40*, 6041.

[148] a) A. M. MdJani, I. M. Kempson, D. Losic, N. H. Voelcker, *Angew. Chem. Int. Ed.* **2010**, *49*, 7933; b) K. Vasilev, Z. Poh, K. Kan, J. Chan, A. Michelmore, D. Losic, *Biomaterials* **2010**, *31*, 532.

[149] D. O. Grigoriev, K. Köhler, E. V. Skorb, D. G. Shchukin, H. Möhwald, *Soft Matter* **2009**, *5*, 1426.

[150] A. S. Blawas, W. M. Reichert, *Biomaterials* **1998**, *19*, 595.

[151] A. L. Hook, N. H. Voelcker, H. Thissen, *Acta Biomater.* **2009**, *5*, 2350.

[152] E. V. Skorb, D. Grützmacher, C. Dais, V. Guzenko, V. G. Sokolov, T. V. Gaevskaya, D. V. Sviridov, *Nanotechnology* **2010**, *21*, 315301.

[153] a) L. A. Kerrigan, J. T. Kadonaga, *Current Protocols in Molecular Biology*, John Wiley & Sons, New York **2001**; b) M. Motherway, K. F. Tipton, A. D. McCarthy, I. Couee, J. Irwin, *Current Protocols in Protein Science*, John Wiley & Sons, New York **2002**.

[154] R. J. McMurray, N. Gadegaard, P. M. Tsimbouri, K. V. Burgess, L. E. McNamara, R. Tare, K. Murawski, E. Kingham, R. O. C. Oreffo, M. J. Dalby, *Nat. Mater.* **2011**, *10*, 637.

[155] E. Wischerhoff, K. Uhlig, A. Lankenau, H. G. Borner, A. Laschewsky, C. Duschl, J.-F. Lutz, *Angew. Chem. Int. Ed.* **2008**, *47*, 5666.

[156] W. Wu, J. Shen, P. Banerjee, S. Zhou, *Adv. Funct. Mater.* **2011**, *21*, 2830.

[157] Z. Zhu, S. A. Sukhishvili, *ACS Nano* **2009**, *3*, 3595.

[158] M. Shibayama, T. Norisuye, S. Nomura, *Macromolecules* **1996**, *29*, 8746.

[159] I. Idziak, D. Avoce, D. Lessard, D. Gravel, X. X. Zhu, *Macromolecules* **1999**, *32*, 1260.

[160] L. M. Mikheeva, N. V. Grinberg, A. Y. Mashkevich, V. Y. Grinberg, L. T. M. Thanh, E. E. Makhaeva, A. R. Khokhlov, *Macromolecules* **1997**, *30*, 2693.

[161] K. Van Durme, S. Verbrugghe, F. E. Du Prez, B. Van Mele, *Macromolecules* **2004**, *37*, 1054.

[162] T. Aoki, M. Kawashima, H. Katono, K. Sanui, N. Ogata, T. Okano, Y. Sakurai, *Macromolecules* **1994**, *27*, 947.

[163] D. Schmaljohann, *Adv. Drug Delivery Rev.* **2006**, *58*, 1655.

[164] S. Schmidt, M. Zeiser, T. Hellweg, C. Duschl, A. Fery, H. Möhwald, *Adv. Funct. Mater.* **2010**, *20*, 3235.

[165] H. M. Zareie, C. Boyer, V. Bulmus, E. Nateghi, T. P. Davis, *ACS Nano* **2008**, *2*, 757.

[166] D. Volodkin, A. Skirtach, H. Möhwald, *Polym. Int.* **2012**, *61*, 673.

[167] a) D. V. Andreeva, D. Fix, D. G. Shchukin, H. Möhwald, *Adv. Mater.* **2008**, *20*, 2789; b) D. V. Andreeva, E. V. Skorb, D. G. Shchukin, *Appl. Mater. Interfaces* **2010**, *2*, 1954; c) D. G. Shchukin, D. V. Andreeva, E. V. Skorb, H. Möhwald, in *Supramolecular Chemistry of Hybrid Materials*, (Ed: K. Rurack), Wiley-VCH, Weinheim, Germany **2010**.

[168] K. Na, Y. H. Bae, in: *Polymeric Drug Delivery Systems*, (Ed: G. S. Kwon), Taylor & Francis, Boca Raton, FL **2005**.

[169] A. G. Skirtach, A. M. Yashchenok, H. Möhwald, *Chem. Commun.* **2011**, *47*, 12736.

[170] A. Peterson, D. Shchukin, H. Möhwald, *Biomacromolecules* **2012**, *13*, 3120.

[171] L. D. Zarzar, P. Kim, J. Aizenberg, *Adv. Mater.* **2011**, *23*, 1442.

[172] A. Fujishima, X. Zhang, *Chimie* **2006**, *9*, 750.

[173] a) E. V. Skorb, E. A. Ustinovich, A. I. Kulak, D. V. Sviridov, *J. Photochem. Photobiol. A: Chem.* **2008**, *193*, 97; b) E. V. Skorb, L. I. Antonouskaya, N. A. Belyasova, D. G. Shchukin, H. Möhwald, D. V. Sviridov, *Appl. Catal. B* **2008**, *84*, 94; c) E. V. Skorb, D. V. Andreeva, A. P. Raiski, N. A. Belyasova, H. Möhwald, D. V. Sviridov, *Photochem. Photobiol. Sci.* **2011**, *10*, 1974.

[174] a) A. G. Skirtach, A. A. Antipov, D. G. Shchukin, G. B. Sukhorukov, *Langmuir* **2004**, *20*, 6988; b) B. Radt, T. A. Smith, F. Caruso, *Adv. Mater.* **2004**, *16*, 2184; c) E. V. Skorb, D. G. Shchukin, D. V. Sviridov, in *Molecular and Nanoscale Systems for Energy Conversion*, (Eds: S. Varfolomeev, L. Krylova, C. E. Zaikov), Nova Science Publishers, New York **2008**.

[175] T. A. Kolesnikova, D. Kohler, A. G. Skirtach, H. Möhwald, *ACS Nano* **2012**, *6*, 9585.

[176] J. Lahann, S. Mitragotri, T. N. Tran, H. Kaido, J. Sundaram, I. S. Choi, H. Saskia, G. A. Somorjai, R. Langer, *Science* **2003**, *299*, 371.

[177] a) A. Artzy Schnirman, E. Zahavi, H. Yeger, R. Rosenfeld, I. Benhar, Reiter, *Nano Lett.* **2008**, *8*, 3398; b) R. M. Penner, *Nat. Chem.* **2010**, *2*, 251.

[178] M. Gerard, A. Chaubey, B. D. Malhotra, *Biosens. Bioelectron.* **2002**, *17*, 345; J. Janata, M. Josowicza, *Nat. Mater.* **2003**, *2*, 19; T. Mirfakhrai1, J. D. W. Madden, R. H. Baughman, *Mater. Today* **2007**, *10*, 30.

[179] R. A. Green, N. H. Lovell, L. A. Poole-Warren, *Biomaterials* **2009**, *30*, 3637.

[180] a) C. Gao, H. Möhwald, J. Shen, *ChemPhysChem* **2004**, *5*, 116; b) A. Fery, B. Scholer, T. Cassagneau, F. Caruso, *Langmuir* **2001**, *17*, 3779; c) H. Y. Zhang, Z. Q. Wang, Y. Q. Zhang, X. Zhang, *Langmuir* **2004**, *20*, 9366.

[181] H. Y. Zhang, Z. Q. Wang, Y. Q. Zhang, X. Zhang, *Langmuir* **2004**, *20*, 9366.

[182] M. Delcea, H. Möhwald, A. G. Skirtach, *Adv. Drug Delivery Rev.* **2011**, *63*, 730.

[183] S. Keller, I. Sauer, H. Strauss, K. Gast, M. Dathe, M. Bienert, *Angew. Chem. Int. Ed.* **2005**, *44*, 5252.

к научному докладу на соискание ученой степени

доктора химических наук

СКОРБ ЕКАТЕРИНА ВЛАДИМИРОВНА

По теме:

РЕАКЦИОННО-ДИФФУЗИОННЫЕ ХИМИЧЕСКИЕ ПРОЦЕССЫ НА ГРАНИЦЕ МЕТАЛЛОВ ИЛИ ПОЛУПРОВОДНИКОВ С ПОЛИМЕРНЫМИ НАНОСЛОЯМИ

Специальность 1.4.4 - физическая химия

Санкт-Петербург – 2022

Soft Hydrogel Actuator for Fast Machine-Learning-Assisted Bacteria Detection

Filipp V. Lavrentev, Igor S. Rumyantsev, Artemii S. Ivanov, Vladimir V. Shilovskikh, Olga Yu. Orlova, Konstantin G. Nikolaev, Daria V. Andreeva, and Ekaterina V. Skorb*

Cite This: https://doi.org/10.1021/acsami.1c22470

Read Online

ACCESS | Metrics & More | Article Recommendations | Supporting Information

ABSTRACT: We demonstrate that our bio-electrochemical platform facilitates the reduction of detection time from the 3-day period of the existing tests to 15 min. Machine learning and robotized bioanalytical platforms require the principles such as hydrogel-based actuators for fast and easy analysis of bioactive analytes. Bacteria are fragile and environmentally sensitive microorganisms that require a special environment to support their lifecycles during analytical tests. Here, we develop a bio-electrochemical platform based on the soft hydrogel/ eutectic gallium—indium alloy interface for the detection of *Streptococcus thermophilus* and *Bacillus coagulans* bacteria in various mediums. The soft hydrogel-based device is capable to support bacteria' viability during detection time. Current—voltage data are used for multilayer perceptron algorithm training. The multilayer perceptron model is capable of detecting bacterial concentrations in the 10^4 to 10^8 cfu/mL range of the culture medium or in the dairy products with high accuracy (94%). Such a fast and easy biodetection is extremely important for food and agriculture industries and biomedical and environmental science.

KEYWORDS: *hydrogel, interface, lactic acid bacteria, eGaIn, multilayer perceptron*
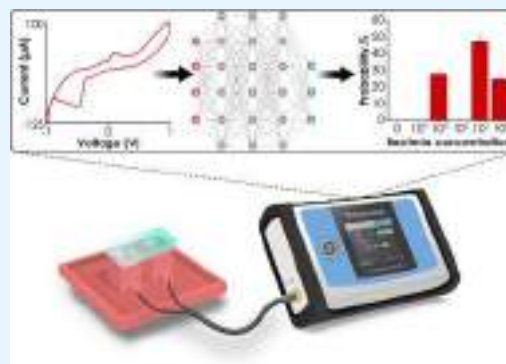
INTRODUCTION

Currently, machine learning approaches, and in particular deep learning, are very popular when processing and analyzing large amounts of data.[1] Deep networks are flexible function approximators that, with enough training data, can be trained to recognize patterns in data.[2] This approach is increasingly used to analyze a large number of biological images[3–5] and has found its application to simulate molecular mechanisms[6] and automatic annotation of animal behavior.[1,7] However, our approach is to use deep learning to analyze the current—voltage characteristic data.

Hydrogels are increasingly used in various fields: flexible electronics,[8,9] sensing,[10–12] wound dressing,[13,14] and energy saving.[15,16] Soft biomimetic interfaces involving hydrogels and liquid metals and alloys play an important role in gaining more and more information about various complex biosystems. Among all complex biosystems, the potential of the "good" microbiome is of greatest interest.[17] Certain lactic acid bacteria have beneficial effects on human health, cure gastrointestinal disorders, and strengthen the host's immune system.[18,19] Bacterial viability is generally considered an essential metric for optimal probiotic functionality.[20] It is believed that they must enter the gastrointestinal tract alive and in sufficient quantities [10^7–10^8 colony-forming units (cfu)/mL] for their benefits to be evaluated.[21,22] Earlier, we developed a fermented milk product with the spore-forming probiotic *Bacillus coagulans*

and auxiliary culture *Streptococcus thermophilus* in its composition.[23]

During development, it was crucial to control the number of viable bacteria during storage. Various methods, which have certain disadvantages, are used to count the number of viable bacteria. For all these methods, bacteria must be grown selectively in a cultural medium. This medium must contain certain substances and have a specific pH and a suitable oxygen level (or lack of oxygen for anaerobic bacteria).[24,25] However, these methods do not take into account the possibility of transition to a viable but uncultivated state in which bacteria do not multiply but are metabolically active.[26,27] Selective staining with membrane-permeable fluorescent dyes to identify live and dead bacteria require manual counting.[28,29] Application of deep learning methods for bacteria image processing allows a great gain in data analysis and may be implemented for very sensitive methods, such as holographic microscopy; however, it still requires training with selective staining and specific microscopy setup.[30] The real-time

polymerase chain reaction method is complicated and does not allow distinguishing the DNA of living cells from dead ones.[31] Some other approaches were tried, such as counting bacteria on a microfluidic chip by implementation of differential resistive pulse sensing (RPS).[32] However, this method has disadvantages in recognizing solutions with a high and low concentration of bacteria. Also, the possibility of separating live and dead bacteria by the RPS method has not been proven.

Currently, electrochemical methods are widely applied for numerous analytical tasks in colloid science and analysis of small biological objects. A cyclic electrochemical method combined with artificial neural network analysis allows us to estimate thin-layer parameters with the focus on a number of small point defects and their development.[33] The electrochemical impedance spectroscopy (EIS) method applied to a biopolymer-coated substrate also shows a high sensitivity for hole-like defects and the corrosion caused by biofilm inhomogeneity.[34] Considering the bacteria behavior resembling an inhomogeneous biofilm, it can be a great achievement to apply cyclic voltammetry for the detection and enumeration of bacteria attracting considerable attention for their intrinsic advantages, including fast response, simple equipment, and high specificity.[35−37] State-of-the-art research suggests that electrochemical sensors will inevitably become a viable alternative to conventional methods in the near future. EIS is a method for studying conductive materials and phase boundaries.[38] This method applies a low amplitude, variable frequency cyclic function to the transducer and uses the resulting current to calculate the impedance.[38] Initially, the EIS method was used to quantify the total biomass in samples;[39] later, its application to electrodes modified with DNA probes or antibodies was a breakthrough in the selectivity of the method.[40] The conductometric method, such as EIS, does not need labels as a means of rapid detection of bacteria, which simplifies sensor preparation.[41] However, its detection rates are still low compared to traditional methods.[43] There are hydrogel-based systems that are used to detect various biological molecules.[8] This technique has already proven itself well as a selective analysis for the tick-borne encephalitis virus.[10] We propose a soft flexible hydrogel/liquid metal actuator for bacteria monitoring in different mediums and products. Such a device provides faster and cheaper bacteria quantitative analysis in comparison with the existing techniques.

■ EXPERIMENTAL SECTION

Materials. Agar (powder) was purchased from Sigma-Aldrich. MRS broth (de Man, Rogosa, Sharpe) (powder) was purchased from HiMedia, India. Commercial probiotic preparation LactoSpore as a source of the spores of *B. coagulans* MTCC 5856 was used. The authenticity of the strain of *B. coagulans* in LactoSpore has been established through genotyping and phenotypic characterization. LactoSpore contains a mixture of ellipsoidal terminal spores and vegetative cells. During cultivation in MRS broth nutrient medium, all spores germinated into vegetative cells. The starter culture of *S. thermophilus* TA 40 (TA 40 LYO 50 DCU) is purchased from Danisco, France. Phosphate-buffered saline (PBS) tablets were purchased from Rosmedbio. A eutectic alloy of gallium−indium was purchased from Megaclassic Company.

Methods. *Preparation of the Hydrogel.* To prepare the gel, 0.1 g of agar was added to 9 mL of PBS, and then, this solution was stirred and sterilized at 121 °C. To prevent the death of bacteria, the solution was cooled down to 45−50 °C and poured into a Petri dish to 1 mL of bacteria suspension (inoculant). The inoculant was prepared in advance by separating the overnight cultivation of *S. thermophilus* and

B. coagulans bacteria in a nutrient medium MRS with the addition of lactose (5 g/L). Then, the inoculants with two bacteria were mixed 1:1. To obtain various concentrations of bacteria, 1 mL of inoculant was serially diluted in 9 mL of 0.01 M PBS. 1 mL of fermented milk product was dispersed and mixed with 9 mL of agar solution with PBS to prepare gel samples with yogurt. Counting the number of viable bacteria in the inoculum and dilutions was performed by counting the cfu on the plates.

Scanning Electron Microscopy Images of Mixed Gallium Oxide and Lactate Insoluble Film. Scanning electron microscopy (SEM) studies were performed with a Hitachi S-3400N scanning electron microscope. Images were acquired for an insoluble film formed on the eGaIn electrode surface at an operating voltage of 5 kV. A mixed gallium oxide−lactate film was prepared by the placing of the hydrogel with bacteria on the liquid metal electrode. Under the applied voltage, gallium is oxidizing and lactic acid produced by bacteria interacts with gallium cations. The formed film is transferred on a silicon wafer with a layer of excess gallium−indium alloy which was used as a background. Elemental compositions of acquired films were estimated by means of energy-dispersive X-ray (EDX) spectroscopy. The spectra acquisition conditions were as follows: 5 kV accelerating voltage, 0.2 nA beam current, and 120 s dwell time per spectrum. In order to avoid film degradation, spectra were acquired from an area of 15 μm^2.

Density Functional Theory Calculation. The quantum chemical calculations and full geometry optimization of all model structures were carried out using the ORCA 4.2.1 program package.[42] Convergence tolerances for geometry optimization procedure: energy change = 5.0000×10^{-6} Eh, maximal gradient = 3.0000×10^{-4} Eh/bohr, RMS gradient = 1.0000×10^{-4} Eh/bohr, maximal displacement = 4.0000×10^{-3} bohr, and rms displacement = 2.0000×10^{-3} bohr. Grid4 and FinalGrid5 specifications were used in all cases. Symmetry operations have not been applied during the geometry optimization procedure for all model structures. The Hessian matrices were calculated for all optimized model structures in order to prove the location of correct minima on the potential energy surfaces (no imaginary frequencies in all cases) and to estimate the thermodynamic parameters, the latter being calculated at 298.15 K and 1.00 atm (Table S1).

Training Set Construction. Current−voltage ($I-V$) characteristic curves were measured using Keithley 6430. For the database, the $I-V$ curves were measured three times at 400 points per cycle for three independent samples per concentration range in the voltage sweep mode in the following potential values: −0.02 to 0.02 V, −0.1 to 0.1, −0.5 to 0.5, −1 to 1, and −5 to 5 V. The $I-V$ characteristics for all samples with different concentrations of bacteria are shown in Figure S2. The database for the concentration of bacteria is compiled on the basis of the parameters of electrochemical processes—voltage and current. Voltage ranges were chosen as descriptors. The data themselves represent the values of the currents obtained from the entire cyclic volt−ampere curve. Since it was required to obtain the same amount of data from each sample, the speed was different in each voltage range. For voltage ranges of 0.02, 0.1, 0.5, 1.0, and 5.0 V, it was, respectively, 1, 5.2, 27, 57.1, and 285.7 mV/s. Thus, each sample in the database is represented by five descriptors with 2400 points in each of them; whole database consists of 72 000 experimental points.

Then, the database underwent a binary normalization process, as a result of which all current values took values from 0 to 1. This training method was used to train the multilayer perceptron model.

Machine Learning Model. For machine learning calculations, Weka v3.8.4 (Waikato Environment for Knowledge Analysis) is used. Dividing the data into a training set (90%) and a test set (10%) allows the accuracy of the model to be checked. The predictive model is trained on the database. Such a data set consists of columns filled with attributes that determine the answers.[44] Since the peaks of the redox potential are individual for hydrogel compositions, currents are attributes and bacteria concentrations are classes. Machine learning models use attributes and find statistical weights for them to predict classes. The multilayer perceptron model was chosen due to its relatively low complexity and low-cost performance. For data
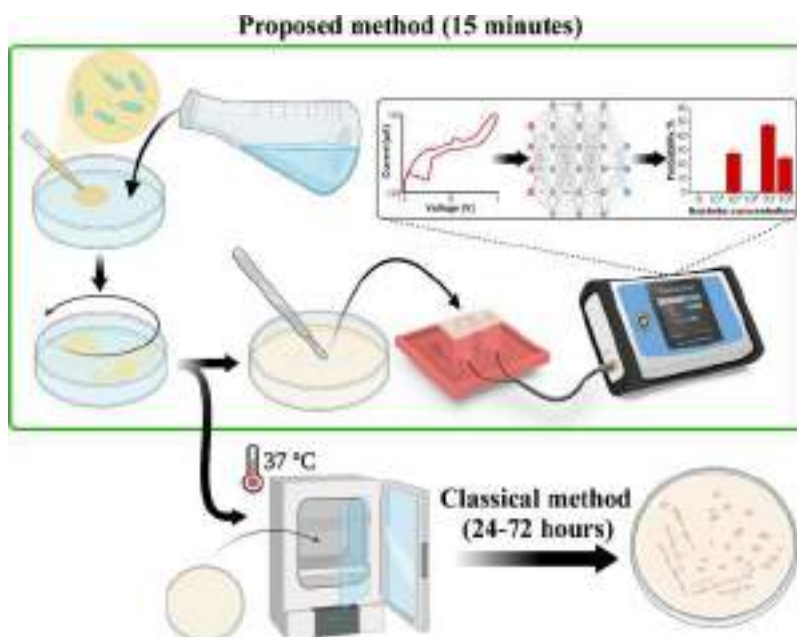
Figure 1. Brief scheme of the machine-learning-assisted electrochemical platform for determining the concentration of bacteria in comparison with the classical method.
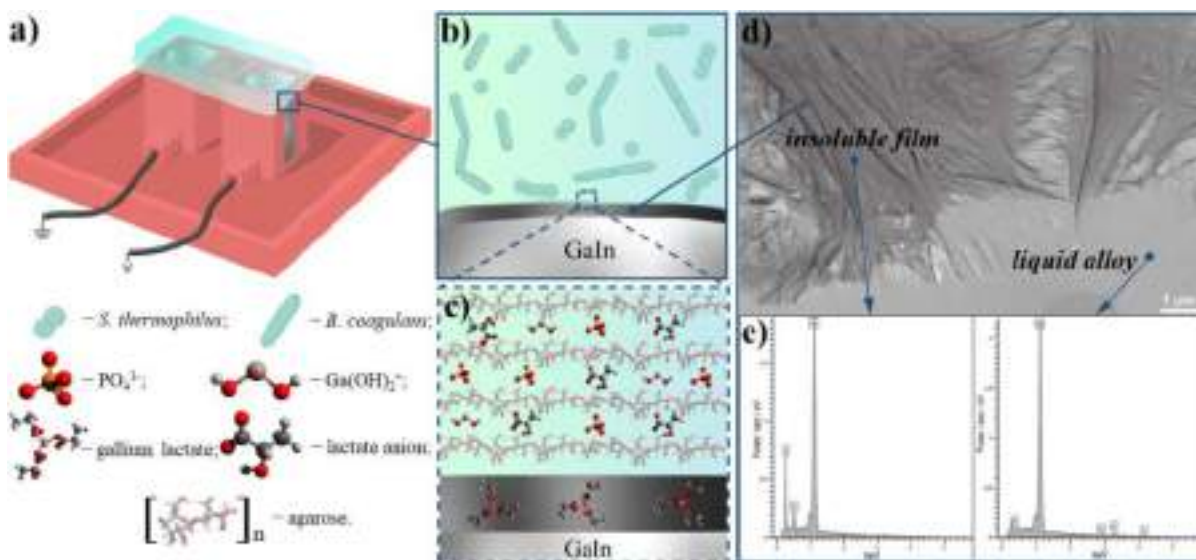
Figure 2. (a) Scheme of the electrochemical system. (b) Formation of the primary metabolite of lactic acid by bacteria *S. thermophilus* and *B. coagulans* in the gel structure. (c) Interaction of lactate anions with eGaIn with the formation of insoluble reaction products on the electrode surface. (d) SEM image of an insoluble film formed on the eGaIn electrode surface (view from top). (e) EDX spectra of alloy and film surfaces.

processing by a supervised learning method, a multilayer perceptron model with the following parameters was used: learning rate—0.1, momentum—0.1, random seed—0, the number of hidden layers—3, and the number of nodes in the hidden layer—12, each of which is a weighting factor. The nodes alternately generate an activation potential

$$z = \sum_{i=1}^{N} x_i w_i + b$$

where z is the activation potential, x is the descriptor value, w is the weighting factor of the node, and b is the bias.

The values of the activation function are assessed using the activation function, which is sigmoid. Through this process, objects are classified. The weights (w_i) during the training of the model are fitted using the backpropagation method. In the course of its operation, the model uses the input data, corresponds to the result, and compares it with the original answers, after which the weights are adjusted taking into account the error gradient (E)

$$\Delta w_{i,j} = \eta \frac{\partial E}{\partial w_{i,j}} + \gamma \Delta w_{i,j}^{t-1}$$

where η—training time and γ—momentum.

■ RESULTS AND DISCUSSION

We propose using of the $I-V$ characteristics at the interface between the eutectic gallium–indium alloy (eGaIn) electrode and the hydrogel (Figure 1) to detect *S. thermophilus* and *B. coagulans* bacterial concentrations in the range from 10^4 to 10^8 cfu/mL.

C
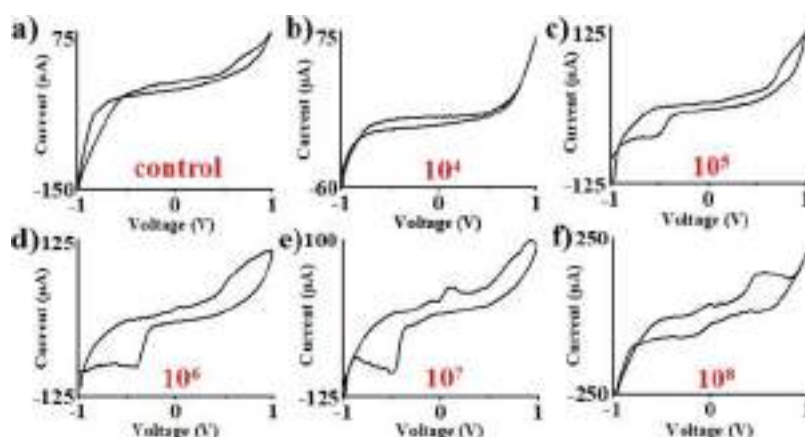
Figure 3. Characteristic curves of $I-V$ characteristics with 400 points per cycle for gels with different concentrations of *S. thermophilus* and *B. coagulans* bacteria (0.01 M PBS pH 7.4) in a voltage range of −1 to 1 V. (a) $I-V$ curve for a gel without bacteria. (b) $I-V$ curve for a gel with 10^4 bacteria per milliliter. (c) $I-V$ curve for a gel with 10^5 bacteria per milliliter. (d) $I-V$ curve for a gel with 10^6 bacteria per milliliter. (e) $I-V$ curve for a gel with 10^7 bacteria per milliliter. (f) $I-V$ curve for a gel with 10^8 bacteria per milliliter.

Considering that water (or other liquid) accounts for 12% of the structure of a bacterium, its population increase will affect the electrical conductivity and dielectric constant of a suspension. Accordingly, any suspension with bacteria can be analyzed by statistically measuring its electrochemical behavior using the cyclic voltammetry method. Due to the formation of various redox states on the electrode−electrolyte interface, different signals will occur on the $I-V$ curves. Analysis of the data obtained may indirectly indicate the presence of a certain number of bacteria. For the full spectrum of generation of redox states, it is necessary to use an electrode material capable of electric current-induced polymorphic transition in a given voltage range. One such material is eGaIn alloy, which consists of 75 wt % Ga and 25 wt % In.[45] This alloy has been successfully used to create flexible electronics due to its low melting point, high electrical conductivity, nontoxicity, and low saturated vapor pressure. Gallium is quickly passivated in air, forming a thin oxide film on its surface, which has a higher resistivity than the pure metal. This electrochemical approach has a clear advantage over the plate counting because it is easier and faster and can reduce human error.

The electrochemical system presented in Figure 2a consists of hydrogels and two eGaIn electrodes. The hydrogel is based on 0.01 M PBS. Since the measurement is performed in a hydrogel, the composition of the gel includes the bacteria *S. thermophilus* and *B. coagulans* MTCC 5856 at various concentrations. Before being added to the hydrogel, the bacteria were cultured in MRS liquid nutrient medium to maintain viability. Homofermentative lactic acid bacteria carry out the microbiological synthesis of lactic acid during fermentation (Figure 2b). The bacteria used in this study contain only L-lactate dehydrogenase and therefore form the L-isomer of lactic acid. When a potential difference is applied, gallium is oxidized and its $Ga(OH)^{2+}$ cations begin to diffuse into the hydrogel. Indium cations do not exist in such a system because of their reduction by gallium. The formal oxidation potential of gallium is −0.529 V, however, in aqueous media, the formal oxidation potential of gallium shifts to 0.319 V.[8] In the hydrogel, gallium cations interact with bacteria, their metabolites, and cultural medium anions (Figure 2c).

Most of the gallium complexes and compounds formed in the system are soluble. However, gallium oxide, lactate, and phosphate are insoluble. As a result, a film of $Ga(CH_3CH-$ $(OH)COO)_3$ and Ga_2O_3 is formed on the electrode surface. In the presence of a small amount of lactic acid, gallium lactate crystallizes in the form of thin plates.[46] Due to the fact that the reaction in the electrochemical cell proceeds very quickly, the formation of gallium lactate crystals of a distinguishable size does not occur in the system. The formation of an insoluble oxide lactate layer is proved by the SEM images (Figure 2d). The images clearly show the contrast between the solid film of gallium compounds and the liquid alloy in the fissure, formed during sample deposition on a wafer. EDX spectra of alloy and film surfaces show a significant excess of the carbon and oxygen amounts in the film (Figures 2e and S1). Presumably, it verifies the presence of the oxide and lactate, which constituted the insoluble layer. Moreover, the corrugated surface indicates that the surface layer is solid, and the surface tension is unable to restore the smooth surface with a minimal amount of energy. However, the transparency of a layer at higher accelerating voltages limits the thickness by no more than tens of nanometers.

Due to the absence of gallium phosphate, we provide some quantum chemical computations to evaluate the thermodynamic favorability of binding between gallium cations and lactate and dihydrophosphate anions. The level of theory for calculations is B3LYP/def2-TZVPP. For theoretical studies of reactions, the dihydrophosphate anion $(H_2PO_4^-)$ was considered as a model particle due to the order of phosphoric acid dissociation constants $K_{a1} = 7.5 \times 10^{-3}$, $K_{a2} = 6.2 \times 10^{-8}$, and $K_{a3} = 4.8 \times 10^{-13}$. Results of DFT calculations are presented in Tables S1 and S2 and reveal that the formation of gallium lactate is much more thermodynamically favorable than the formation of gallium dihydrophosphate. The difference of reactions' ΔG is about 39 kJ/mol. That is the reason for the absence of phosphorus in the EDX spectra of the insoluble film.

Resistance of the gallium lactate layer determines the $I-V$ curve of the sample since this insoluble layer has the higher resistance in system. The dissolution potential of gallium oxide and gallium lactate increases with the increase in film resistance. The presence of various concentrations of bacteria in the hydrogel also changes the $I-V$ curve. The interaction of gallium cations with various concentrations of bacteria leads to the formation of lactate and phosphate films in different ratios. Redox processes of the formation and decomposition of the

D
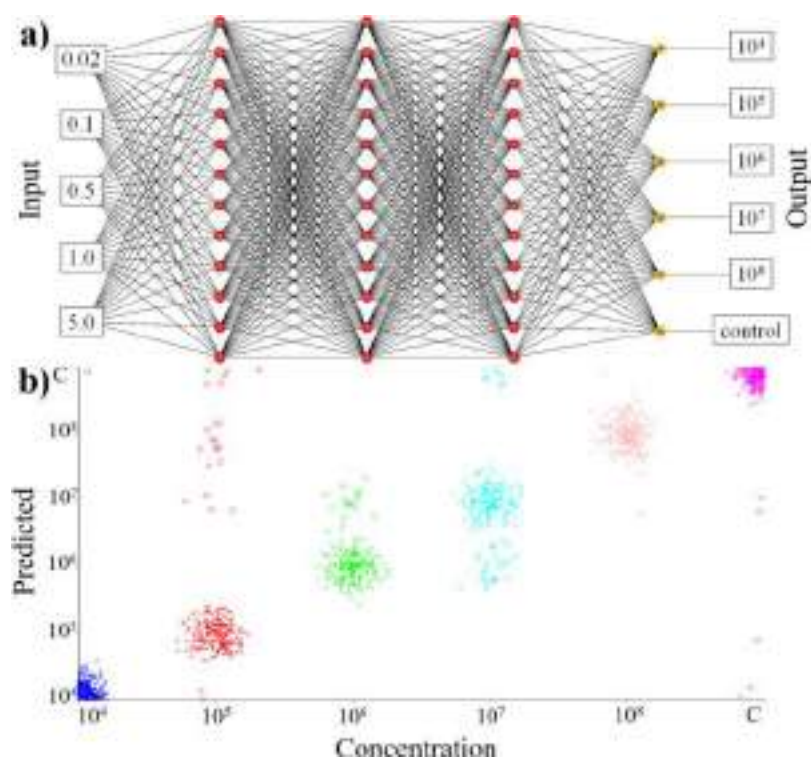
Figure 4. (a) Scheme of multilayer perceptron with three hidden layers. Three hidden layers with 12 nodes are used to describe the relationship of current−voltage data from the input layer and sample compound data from the output layer. (b) Prediction error graph—the axes show the actual and predicted values, and the correct values are indicated by crosses (C—control).
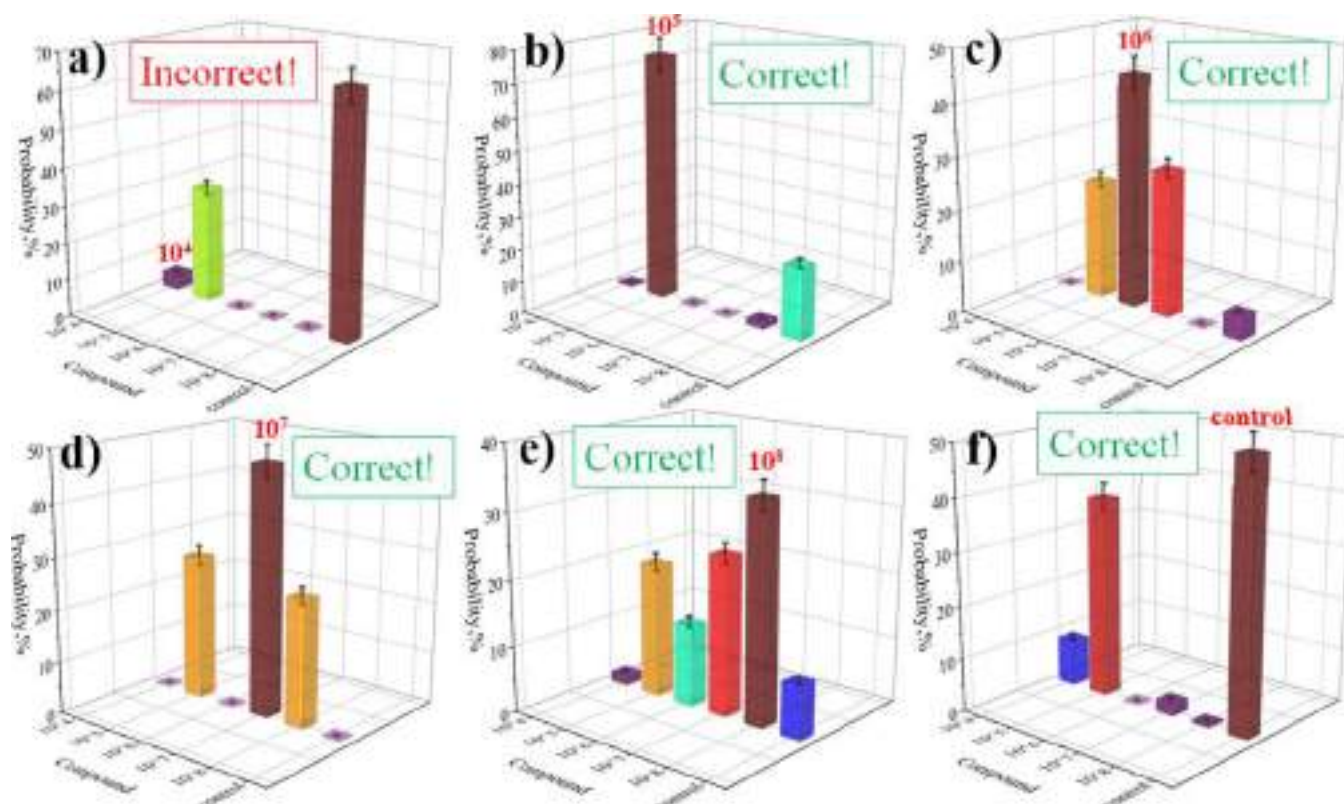
Figure 5. Results of the prediction of samples with different concentrations of *S. thermophilus* and *B. coagulans* bacteria, obtained on the model of a multilayer perceptron. (a) Graph for the sample with bacteria concentration 10^4 cfu/mL. (b) Graph for the sample with bacteria concentration 10^5 cfu/mL. (c) Graph for the sample with bacteria concentration 10^6 cfu/mL. (d) Graph for the sample with bacteria concentration 10^7 cfu/mL. (e) Graph for the sample with bacteria concentration 10^8 cfu/mL. (f) Graph for the sample without bacteria.

E

film with different constituents determine the shape of the $I-V$ characteristic peaks, which differ in the potential range of 0.02–5 V.

Various machine learning methods can solve many biological and chemical issues, in particular, for optimizing metabolic network models and their analysis, as well as predicting complications of diabetes.[47,48] We apply the feed-forward deep neural network model (multilayer perceptron) for logical data analysis.[49] Also, training of the machine learning model is performed using an error backpropagation algorithm.[50] Multilayer perceptron allows the detection of individual states at the eGaIn/hydrogel interface that depend on the hydrogel composition.

The applied voltage ranges for the database are −0.02 to 0.02, −0.1 to 0.1, −0.5 to 0.5, −1 to 1, and −5 to 5 V. Collected $I-V$ characteristics (Figure 3) correspond for a two-electrode system/hydrogel interface. Final database consists of six data points—PBS control and five concentration ranges (10^4 to 10^8 cfu/mL). Each data point includes 12 000 experimental points which are evenly distributed in five descriptors by voltage ranges. New experimental points from independent experiments are sequentially added to the database until the samples are successfully classified. The collected data were split into a training data set (90%) and a test data set (10%) to test the accuracy of the model.

This proportion is optimal from the point of view of preserving large amounts of data and does not require a significant reduction in the test set. The multilayer perceptron model is trained with the following parameters: learning rate—0.1, momentum—0.1, the number of hidden layers—3, and the number of nodes in the hidden layer—12 (Figure 4a). Classification errors (Figure 4b) also indicate a high accuracy in determining the composition of hydrogels. An excellent determination accuracy of 94% is achieved.

In five out of six cases, the trained multilayer perceptron model obtained correct results with the highest probabilities (Figure 5). Certain difficulties arose with the determination of the concentration of bacteria 10^4 (Figure 5a). From $I-V$ curves, it is visible that the concentration of 10^4 has a similar appearance to the control sample without bacteria (Figure S2). This uncertainty arises from the multiple responses to phosphate anions, lactate, and other compounds at low concentrations. This is accompanied by the presence of a weak useful signal. This disadvantage can be compensated by the expansion of the database. Further addition of statistically significant values to the database will lead to a decrease in the statistical error.

The collected database was used to determine the concentration of *S. thermophilus* and *B. coagulans* bacteria in a yogurt sample as an analyte to assess the potential for applying the proposed approach to dairy products. The multilayer perceptron model trained on the collected database gives the correct result with the highest probability (Figure 6).

CONCLUSIONS

We have proposed a soft biomimetic monitoring device that can detect bacteria of various concentrations with 15 min time versus a traditional period of 3 days. The device can be used to determine the concentration of a wide range of bacteria. In its essence, our approach is essential for microbiological analysis at various levels. The main advantage is to use a one-time collected database and machine learning algorithm that avoids calibration every time. The multilayer perceptron algorithm

Figure 6. Graph with the result of the yogurt sample compound prediction.

shortens the bacteria detection time and has the highest percentage of accuracy, which increases the statistical reliability of predictions. The proposed reliable method can be used to solve a wide range of complex biological problems. The presented experimental concept can be further applied to miniaturized monitoring systems.

ASSOCIATED CONTENT

⬛ Supporting Information

The Supporting Information is available free of charge at https://pubs.acs.org/doi/10.1021/acsami.1c22470.

> SEM image of an insoluble film formed on the eGaIn electrode surface with EDX analysis showing a distribution map of Ga, C, and O; example of $I-V$ curves of different modes and gel with various concentrations used for a database; calculated Gibbs free energy change for reactions proceeding in a hydrogel; and Cartesian atomic coordinates for all optimized model structures (PDF)

> Data set used for the machine learning approach is provided (XLSX)

AUTHOR INFORMATION

Corresponding Author

Ekaterina V. Skorb − *Infochemistry Scientific Center of ITMO University, St. Petersburg 191002, Russia;* ⊙ orcid.org/0000-0003-0888-1693; Email: skorb@itmo.ru

Authors

Filipp V. Lavrentev − *Infochemistry Scientific Center of ITMO University, St. Petersburg 191002, Russia*

Igor S. Rumyantsev − *Infochemistry Scientific Center of ITMO University, St. Petersburg 191002, Russia*

Artemii S. Ivanov − *Institute for Functional Intelligent Materials, National University of Singapore, Singapore 117544, Singapore; Department of Materials Science and Engineering, National University of Singapore, Singapore 117575, Singapore*

Vladimir V. Shilovskikh − *Infochemistry Scientific Center of ITMO University, St. Petersburg 191002, Russia*

Olga Yu. Orlova − *Infochemistry Scientific Center of ITMO University, St. Petersburg 191002, Russia*

Konstantin G. Nikolaev − *Infochemistry Scientific Center of ITMO University, St. Petersburg 191002, Russia*

Daria V. Andreeva − *Institute for Functional Intelligent Materials, National University of Singapore, Singapore 117544, Singapore; Department of Materials Science and Engineering, National University of Singapore, Singapore 117575, Singapore*

Complete contact information is available at:
https://pubs.acs.org/10.1021/acsami.1c22470

Notes
The authors declare no competing financial interest.

◼ ACKNOWLEDGMENTS

◼ REFERENCES

(1) Vogt, N. Machine Learning in Neuroscience. *Nat. Methods* **2018**, *15*, 33.

(2) Speiser, A.; Müller, L.-R.; Hoess, P.; Matti, U.; Obara, C. J.; Legant, W. R.; Kreshuk, A.; Macke, J. H.; Ries, J.; Turaga, S. C. Deep Learning Enables Fast and Dense Single-Molecule Localization with High Accuracy. *Nat. Methods* **2021**, *18*, 1082−1090.

(3) Belthangady, C.; Royer, L. A. Applications, Promises, and Pitfalls of Deep Learning for Fluorescence Image Reconstruction. *Nat. Methods* **2019**, *16*, 1215−1225.

(4) Weigert, M.; Schmidt, U.; Boothe, T.; Müller, A.; Dibrov, A.; Jain, A.; Wilhelm, B.; Schmidt, D.; Broaddus, C.; Culley, S.; Rocha-Martins, M.; Segovia-Miranda, F.; Norden, C.; Henriques, R.; Zerial, M.; Solimena, M.; Rink, J.; Tomancak, P.; Royer, L.; Jug, F.; Myers, E. W. Content-Aware Image Restoration: Pushing the Limits of Fluorescence Microscopy. *Nat. Methods* **2018**, *15*, 1090−1097.

(5) Gómez-de-Mariscal, E.; García-López-de-Haro, C.; Ouyang, W.; Donati, L.; Lundberg, E.; Unser, M.; Muñoz-Barrutia, A.; Sage, D. DeepImageJ: A User-Friendly Environment to Run Deep Learning Models in ImageJ. *Nat. Methods* **2021**, *18*, 1192−1195.

(6) AlQuraishi, M.; Sorger, P. K. Differentiable Biology: Using Deep Learning for Biophysics-Based and Data-Driven Modeling of Molecular Mechanisms. *Nat. Methods* **2021**, *18*, 1169−1180.

(7) Kabra, M.; Robie, A. A.; Rivera-Alba, M.; Branson, S.; Branson, K. JAABA: Interactive Machine Learning for Automatic Annotation of Animal Behavior. *Nat. Methods* **2013**, *10*, 64−67.

(8) Ivanov, A. S.; Nikolaev, K. G.; Novikov, A. S.; Yurchenko, S. O.; Novoselov, K. S.; Andreeva, D. V.; Skorb, E. V. Programmable Soft-Matter Electronics. *J. Phys. Chem. Lett.* **2021**, *12*, 2017−2022.

(9) Ding, Y.; Tang, H.; Zhang, C.; Li, W.; Li, G.; Zhang, Y.; Xu, C.; Zhao, F.; Guo, Q.; Guo, C. F.; Xiang, X. D. High-Throughput Screening of Self-Healable Polysulfobetaine Hydrogels and their Applications in Flexible Electronics. *Adv. Funct. Mater.* **2021**, *31*, 2100489.

(10) Ivanov, A. S.; Nikolaev, K. G.; Stekolshchikova, A. A.; Tesfatsion, W. T.; Yurchenko, S. O.; Novoselov, K. S.; Andreeva, D. V.; Rubtsova, M. Y.; Vorovitch, M. F.; Ishmukhametov, A. A.; Egorov, A. M.; Skorb, E. V. Tick-Borne Encephalitis Electrochemical Detection by Multilayer Perceptron on Liquid-Metal Interface. *ACS Appl. Bio Mater.* **2020**, *3*, 7352−7356.

(11) Jia, Z.; Müller, M.; Schönherr, H. Towards Multiplexed Bacteria Detection by Enzyme Responsive Hydrogels. *Macromol. Symp.* **2018**, *379*, 1600178.

(12) Gevorkian, A.; Morozova, S. M.; Kheiri, S.; Khuu, N.; Chen, H.; Young, E.; Yan, N.; Kumacheva, E. Actuation of Three-Dimensional-Printed Nanocolloidal Hydrogel with Structural Anisotropy. *Adv. Funct. Mater.* **2021**, *31*, 2010743.

(13) Zhang, H.; Sun, X.; Wang, J.; Zhang, Y.; Dong, M.; Bu, T.; Li, L.; Liu, Y.; Wang, L. Multifunctional Injectable Hydrogel Dressings for Effectively Accelerating Wound Healing: Enhancing Biomineralization Strategy. *Adv. Funct. Mater.* **2021**, *31*, 2100093.

(14) Zhu, T.; Jiang, C.; Wang, M.; Zhu, C.; Zhao, N.; Xu, J. Skin-Inspired Double-Hydrophobic-Coating Encapsulated Hydrogels with Enhanced Water Retention Capacity. *Adv. Funct. Mater.* **2021**, *31*, 2102433.

(15) Cheng, T.; Zhang, Y. Z.; Wang, S.; Chen, Y. L.; Gao, S. Y.; Wang, F.; Lai, W. Y.; Huang, W. Conductive Hydrogel-Based Electrodes and Electrolytes for Stretchable and Self-Healable Supercapacitors. *Adv. Funct. Mater.* **2021**, *31*, 2101303.

(16) Mandal, S.; Kumari, S.; Kumar, M.; Ojha, U. Supplementary Networking of Interpenetrating Polymer System (SNIPSy) Strategy to Develop Strong & High Water Content Ionic Hydrogels for Solid Electrolyte Applications. *Adv. Funct. Mater.* **2021**, *31*, 2100251.

(17) Lufton, M.; Bustan, O.; Eylon, B.-h.; Shtifman-Segal, E.; Croitoru-Sadger, T.; Shagan, A.; Shabtay-Orbach, A.; Corem-Salkmon, E.; Berman, J.; Nyska, A.; Mizrahi, B. Living Bacteria in Thermoresponsive Gel for Treating Fungal Infections. *Adv. Funct. Mater.* **2018**, *28*, 1801581.

(18) Nagpal, R.; Kumar, A.; Kumar, M.; Behare, P. V.; Jain, S.; Yadav, H. Probiotics, Their Health Benefits and Applications for Developing Healthier Foods: A Review. *FEMS Microbiol. Lett.* **2012**, *334*, 1−15.

(19) Parvez, S.; Malik, K. A.; Ah Kang, S.; Kim, H.-Y. Probiotics and Their Fermented Food Products Are Beneficial for Health. *J. Appl. Microbiol.* **2006**, *100*, 1171−1185.

(20) Maukonen, J.; Alakomi, H.-L.; Nohynek, L.; Hallamaa, K.; Leppämäki, S.; Mättö, J.; Saarela, M. Suitability of the Fluorescent Techniques for the Enumeration of Probiotic Bacteria in Commercial Non-Dairy Drinks and in Pharmaceutical Products. *Food Res. Int.* **2006**, *39*, 22−32.

(21) Kurmann, J. A.; Rasic, J. L. *The Health Potential of Products Containing Bifidobacteria*; Robinson, R. K., Ed.; Elsevier Applied Sciences: London, 1991.

(22) Bouhnik, Y. Survie et effets chez l'homme des bactéries ingérées dans les laits fermentés. *Lait* **1993**, *73*, 241−247.

(23) Lavrentev, F. V.; Ashikhmina, M. S.; Ulasevich, S. A.; Morozova, O. V.; Orlova, O. Y.; Skorb, E. V.; Iakovchenko, N. V. Perspectives Of Bacillus Coagulans Mtcc 5856 In The Production Of Fermented Dairy Products. *LWT* **2021**, *148*, 111623.

(24) Tortora, G.; Funke, B.; Case, C. *Microbiology: An Introduction*; Pearson: London, 2016; Vol. 12.

(25) Corry, J.; Curtis, G.; Baird, R. *Handbook of Culture Media for Food Microbiology*; Elsevier Science.: Amsterdam, 2003; Vol. 2.

(26) Xu, H.-S.; Roberts, N.; Singleton, F. L.; Attwell, R. W.; Grimes, D. J.; Colwell, R. R. Survival and Viability of NonculturableEscherichia Coli AndVibrio Cholerae in the Estuarine and Marine Environment. *Microb. Ecol.* **1982**, *8*, 313−323.

(27) Lahtinen, S. J.; Ahokoski, H.; Reinikainen, J. P.; Gueimonde, M.; Nurmi, J.; Ouwehand, A. C.; Salminen, S. J. Degradation of 16S RRNA and Attributes of Viability of Viable but Nonculturable Probiotic Bacteria. *Lett. Appl. Microbiol.* **2008**, *46*, 693−698.

(28) Johnson, M. B.; Criss, A. K. Fluorescence Microscopy Methods for Determining the Viability of Bacteria in Association with Mammalian Cells. *J. Visualized Exp.* **2013**, *79*, 50729.

(29) Boulos, L.; Prévost, M.; Barbeau, B.; Coallier, J.; Desjardins, R. LIVE/DEAD BacLight: application of a new rapid staining method for direct enumeration of viable and total bacteria in drinking water. *J. Microbiol. Methods* **1999**, *37*, 77−86.

(30) Verduijn, J.; van der Meeren, L.; Krysko, D. v.; Skirtach, A. G. Deep Learning with Digital Holographic Microscopy Discriminates Apoptosis and Necroptosis. *Cell Death Discovery* **2021**, *7*, 229.

(31) Kramer, M.; Obermajer, N.; Bogovič Matijašić, B.; Rogelj, I.; Kmetec, V. Quantification of Live and Dead Probiotic Bacteria in Lyophilised Product by Real-Time PCR and by Flow Cytometry. *Appl. Microbiol. Biotechnol.* **2009**, *84*, 1137−1147.

(32) Song, Y.; Zhang, H.; Chon, C. H.; Chen, S.; Pan, X.; Li, D. Counting Bacteria on a Microfluidic Chip. *Anal. Chim. Acta* **2010**, *681*, 82−86.

(33) Finke, A.; Escobar, J.; Munoz, J.; Petit, M. Prediction of Salt Spray Test Results of Micro Arc Oxidation Coatings on AA2024

Alloys by Combination of Accelerated Electrochemical Test and Artificial Neural Network. *Surf. Coat. Technol.* **2021**, *421*, 127370.

(34) Kumari, S.; Tiyyagura, H. R.; Douglas, T. E. L.; Mohammed, E. A. A.; Adriaens, A.; Fuchs-Godec, R.; Mohan, M. K.; Skirtach, A. G. ANN Prediction of Corrosion Behaviour of Uncoated and Biopolymers Coated Cp-Titanium Substrates. *Mater. Des.* **2018**, *157*, 35−51.

(35) Lazcka, O.; Campo, F. J. D.; Muñoz, F. X. Pathogen Detection: A Perspective of Traditional Methods and Biosensors. *Biosens. Bioelectron.* **2007**, *22*, 1205−1217.

(36) Huang, Y.-M.; Hsu, H.-Y.; Hsu, C.-L. Development of Electrochemical Method to Detect Bacterial Count, Listeria Monocytogenes, and Somatic Cell Count in Raw Milk. *J. Taiwan Inst. Chem. Eng.* **2016**, *62*, 39−44.

(37) Zhang, X.; Jiang, Y.; Huang, C.; Shen, J.; Dong, X.; Chen, G.; Zhang, W. Functionalized Nanocomposites with the Optimal Graphene Oxide/Au Ratio for Amplified Immunoassay of E. Coli to Estimate Quality Deterioration in Dairy Product. *Biosens. Bioelectron.* **2017**, *89*, 913−918.

(38) Barsoukov, E.; Macdonald, J. R. *Impedance Spectroscopy: Theory, Experiment, and Applications*; John Wiley & Sons: New Jersey, 2018; Vol. *560*.

(39) Grimnes, S.; Martinsen, Ø. G. *Bioimpedance and Bioelectricity Basics*, 2nd ed.; Academic Press: Oxford, 2008; Vol. *435*.

(40) Mirsky, V. M.; Riepl, M.; Wolfbeis, O. S. Capacitive monitoring of protein immobilization and antigen-antibody reactions on monomolecular alkylthiol films on gold electrodes. *Biosens. Bioelectron.* **1997**, *12*, 977−89.

(41) Enami, M.; Amin, M.; Shabani, P.; Gashtil, M. R. Design and Fabrication of a Conductometry System for Fast Detection of Pathogenic Bacteria in Human Urine. *Int. J. Enteric. Pathog.* **2020**, *8*, 32−36.

(42) Neese, F. The ORCA Program System. *Wiley Interdiscip. Rev.: Comput. Mol. Sci.* **2012**, *2*, 73−78.

(43) Radke, S. M.; Alocilja, E. C. A High Density Microelectrode Array Biosensor for Detection of E. Coli O157:H7. *Biosens. Bioelectron.* **2005**, *20*, 1662−1667.

(44) Gasteiger, J.; Zupan, J. Neural Networks in Chemistry. *Angew. Chem., Int. Ed. Engl.* **1993**, *32*, 503−527.

(45) Wang, C.; Wang, C.; Huang, Z.; Xu, S. Materials and Structures toward Soft Electronics. *Adv. Mater.* **2018**, *30*, 1801368.

(46) Dudley, H. C.; Garzoli, R. F. Preparation and Properties of Gallium Lactate. *J. Am. Chem. Soc.* **1948**, *70*, 3942−3943.

(47) Cuperlovic-Culf, M. Machine Learning Methods for Analysis of Metabolic Data and Metabolic Pathway Modeling. *Metabolites* **2018**, *8*, 4.

(48) Dagliati, A.; Marini, S.; Sacchi, L.; Cogni, G.; Teliti, M.; Tibollo, V.; De Cata, P.; Chiovato, L.; Bellazzi, R. Machine Learning Methods to Predict Diabetes Complications. *J. Diabetes Sci. Technol.* **2018**, *12*, 295−302.

(49) Behler, J. First Principles Neural Network Potentials for Reactive Simulations of Large Molecular and Condensed Systems. *Angew. Chem., Int. Ed.* **2017**, *56*, 12828−12840.

(50) Schneider, G.; Wrede, P. Prediction of the Secondary Structure of Proteins from the Amino Acid Sequence with Artificial Neural Networks. *Angew. Chem., Int. Ed. Engl.* **1993**, *32*, 1141−1143.

Spatiotemporal Regulation of Hydrogel Actuators by Autocatalytic Reaction Networks

Arpita Paikar, Alexander I. Novichkov, Anton I. Hanopolskyi, Viktoryia A. Smaliak, Xiaomeng Sui, Nir Kampf, Ekaterina V. Skorb, and Sergey N. Semenov*

Regulating hydrogel actuators with chemical reaction networks is instrumental for constructing life-inspired smart materials. Herein, hydrogel actuators are engineered that are regulated by the autocatalytic front of thiols. The actuators consist of two layers. The first layer, which is regular polyacrylamide hydrogel, is in a strained conformation. The second layer, which is polyacrylamide hydrogel with disulfide crosslinks, maintains strain in the first layer. When thiols released by the autocatalytic front reduce disulfide crosslinks, the hydrogel actuates by releasing the mechanical strain in the first layer. The autocatalytic front is sustained by the reaction network, which uses thiouronium salts, disulfides of β-aminothiols, and maleimide as starting components. The gradual actuation by the autocatalytic front enables movements such as gradual unrolling, screwing, and sequential closing of "fingers." This actuation also allows the transmission of chemical signals in a relay fashion and the conversion of a chemical signal to an electrical signal. Locations and times of spontaneous initiation of autocatalytic fronts can be preprogrammed in the spatial distribution of the reactants in the hydrogel. To approach the functionality of living matter, the actuators triggered by an autocatalytic front can be integrated into smart materials regulated by chemical circuits.

1. Introduction

Hydrogel actuators have attracted much interest in the materials research community because of their potential applications in soft robotics,[1] drug delivery systems,[2] microvalves,[3] and sensors.[4] Actuation is typically driven by a mechanical response (e.g., swelling/shrinking) of a hydrogel material to external non-specific

stimuli such as temperature,[5] pH,[6] metal ions,[7] or ion strain.[8] Nevertheless, the complexity of motion executed by these actuators is limited by two factors: i) the whole volume of the material responses simultaneously to the stimuli; ii) the response lacks temporal regulation (that is, the response coincides with the stimulus, when the stimulus is ON, the response is ON, and no delays, periodicities, or other complex temporal patterns take place). To overcome these limitations, actuation should be spatially and temporarily regulated.

Inspired by biological organisms where responses are controlled by biochemical signaling networks,[9] researchers have been developing hydrogel materials and actuators that are autonomously regulated by synthetic chemical reaction networks.[10] Initially, the research focused on using the Belousov–Zhabotinsky (BZ) reaction—the best-known chemical oscillator—or its close analogs to create periodical swelling/shrinking hydrogels.[11] Lately, however, the focus has moved towards using de novo enzymatic,[12] DNA,[13] and organic[14] reaction networks to regulate hydrogel materials. These reaction networks provide control over individual interactions between the system's components and therefore, they are more desirable than the BZ reaction from a design standpoint. Schulman, Gracias, and co-workers demonstrated the selective actuation of various parts of the hydrogel by specific DNA strands.[13b] Walther and co-workers[14a–c,15] and Huck and co-workers[12a] pioneered temporal control of sol–gel transitions by organic or enzymatic reaction networks. Pojman, Taylor, and co-workers demonstrated spatiotemporal regulation of gelation by an autocatalytic front.[12b,16] Nevertheless, autonomous spatiotemporal regulation of hydrogel actuators by de novo reaction networks remains elusive.

In this work, we regulated the actuation of disulfide-containing hydrogel materials by autocatalytic fronts that release thiols. These actuators can perform complex motions (that is, gradual unrolling, wave movement, or sequential actuation) otherwise inaccessible to hydrogel actuators without an external control.

2. Results and Discussion

Designing hydrogel actuators that can be regulated by the autocatalytic front requires developing two compatible

A. Paikar, A. I. Novichkov, A. I. Hanopolskyi, V. A. Smaliak, X. Sui,
N. Kampf, S. N. Semenov
Department of Molecular Chemistry and Materials Science
Weizmann Institute of Science
Rehovot 7610001, Israel
E-mail: sergey.semenov@weizmann.ac.il
X. Sui
Department of Chemical Research Support
Weizmann Institute of Science
Rehovot 7610001, Israel
E. V. Skorb
Infochemistry Scientific Center
ITMO University
Saint Petersburg 191002, Russia

**ADVANCED
SCIENCE NEWS**
www.advancedsciencenews.com

**ADVANCED
MATERIALS**
www.advmat.de

components: i) a hydrogel with a mechanical response to a chemical stimulus and ii) a chemical reaction network that releases this chemical stimulus in the autocatalytic front. Thiol-based chemistry is clean, predictable, and it is actively used for designing reaction networks.[17] Therefore, we decided to develop hydrogels with mechanical response to thiols, which were previously unknown, to the best of our knowledge.

Making two-layer hydrogels is a common strategy to introduce mechano-responsive properties into hydrogel materials.[4c] Typically, one layer is irresponsive to stimuli (e.g., temperature, pH), whereas another layer swells or shrinks in response to the stimuli. Swelling/shrinking requires the hydrogel to exchange water freely with the environment; therefore, it has to be submerged in aqueous media. However, this approach is inapplicable for spatially resolved regulation of hydrogels by chemical reaction networks because the reactants leak into the surrounding solution. Therefore, we integrated a mechano-responsive system into hydrogel by first accumulating a mechanical strain into the material and then releasing it in response to stimuli (**Figure 1**).[5b] To accumulate strain, we first bend an irresponsive hydrogel layer (polyacrylamide crosslinked by N,N'-methylenebisacrylamide (BAM)) and then fabricate the thiol-responsive layer (polyacrylamide crosslinked by N,N'-bis(acryloyl)cystamine (BAC)). The deformation of the first layer creates the strain, whereas the second layer maintains it. When hydrogel comes into contact with thiols, the disulfide crosslinks break, the second layer softens,[18] and the first layer returns to its original shape, releasing the mechanical strain. If thiols are released by an autocatalytic front, the disulfide crosslinks will be gradually reduced, and the mechanical actuation will follow the autocatalytic front (Figure 1a).

To generate controllable autocatalytic fronts, the chemistry must satisfy at least two criteria: (i) It should be autocatalytic and (ii) it should not be prone to spontaneous activation (beginning autocatalytic growth without the deliberate addition of autocatalysis). The majority of the known thiol-based autocatalytic systems have rates of spontaneous activation that are too high for application in the proposed system.[17c] Nevertheless, the system recently published by us has appropriate qualities.[17d] It consists of thiouronim salt **1** derived from thiocholine, N,N'-bis(2-cyanoethyl)cystamine (**3a**), and maleimide (**Figure 2**). Although we originally synthesized **3a** to enable a cascade cyclization with the formation of pyrimidine derivatives, the mixture of this compound with **1** exhibited unexpectedly high (several times higher than for regular cystamine) stability against spontaneous activation. As a result, the mixture of **1**, **3a**, and maleimide can resist spontaneous activation for more than 7 h.

Figure 2 summarizes the chemistry of this reaction network. The spontaneous activation is caused by the release of thiocholine (**2**) in two processes: i) hydrolysis of **1** and ii) direct aminolysis of **1** by the amine groups in **3a**. To prevent spontaneous activation, we added sub-stoichiometric amounts of maleimide, which reacts almost instantly with thiols. Together, the release of thiols by hydrolysis and aminolysis and their consumption by maleimide form a "trigger." This trigger initiates autocatalysis as soon as all maleimide is consumed. By controlling the amount of maleimide, we can regulate the timing of autocatalysis. We hypothesized that having secondary amine in **3a** instead of the
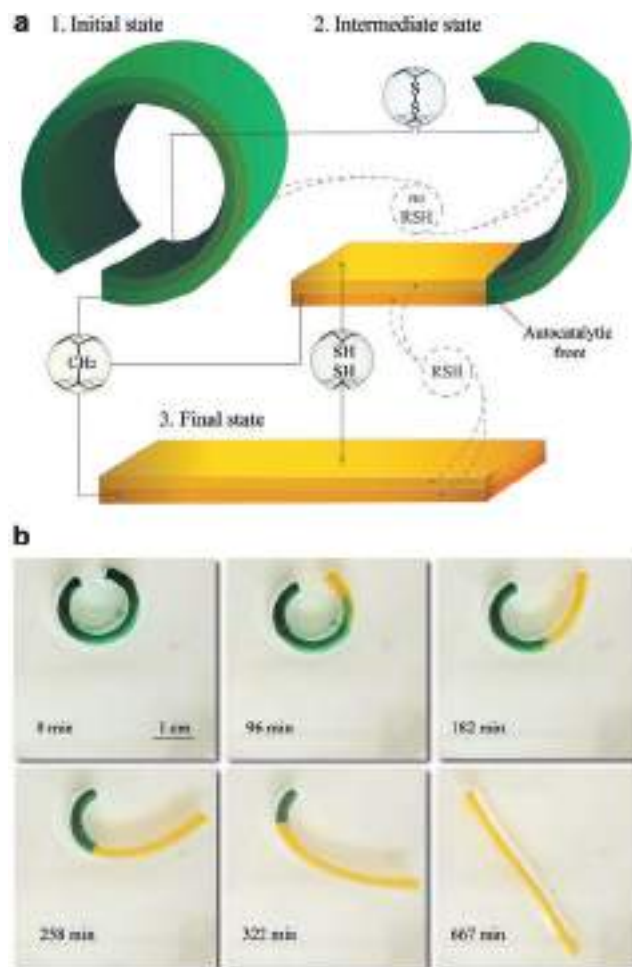
Figure 1. Actuation driven by an autocatalytic front. a) A schematic diagram showing the shape change that follows the reduction of the disulfide crosslinks in the autocatalytic front. b) An experiment that represents changes shown in the diagram (see also Video S1, Supporting Information). For details about the autocatalytic chemistry and the experimental set-up, see Figure 2 and Figure 3. Briefly, the double-layer hydrogel was immersed in a cyclohexane/tetrachloroethylene mixture to achieve near-zero buoyancy, and autocatalysis was initiated from one side of the hydrogel.

primary amine in cystamine strongly reduces the aminolysis rate; the hydrolysis rate is already slow for **1**. Therefore, we can achieve long delay times (7–10 h) using small (20% of the **1**) quantities of maleimide. To test this hypothesis, we compared the delay time—an interval from the time that the reagent was mixed until the autocatalytic release of thiols—for three mixtures containing **1** (0.1 M), maleimide (0.02 M), and 0.1 M of cystamine, of **3a**, or of N,N'-dimethylcystamine (**3b**) in 0.5 M phosphate buffer (PB) pH 7.5. The solution with cystamine, a primary amine, produced thiols within 4 h, whereas solutions with **3a** and **3b** lasted for 8 and 9 h, respectively, before releasing thiols. Thus, disulfides of β-aminothiols with secondary amines must be used for experiments requiring long delay times.

Details about the mechanism underlying the autocatalytic formation of guanidines can be found in our previous report.[17d] Briefly, the direct attack of **3a** or **3b** on **1** is very slow,

**ADVANCED
SCIENCE NEWS**

www.advancedsciencenews.com

**ADVANCED
MATERIALS**

www.advmat.de
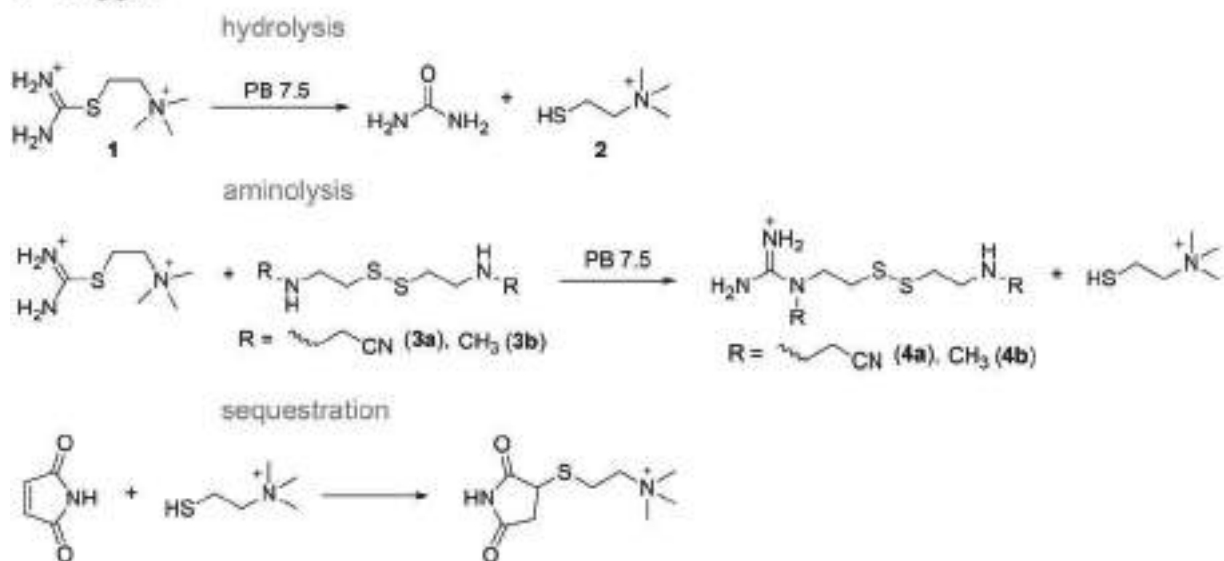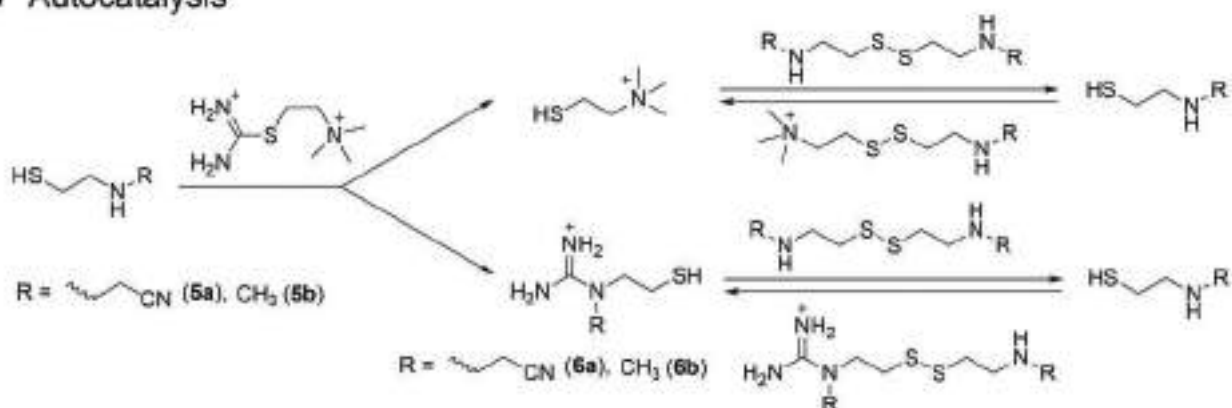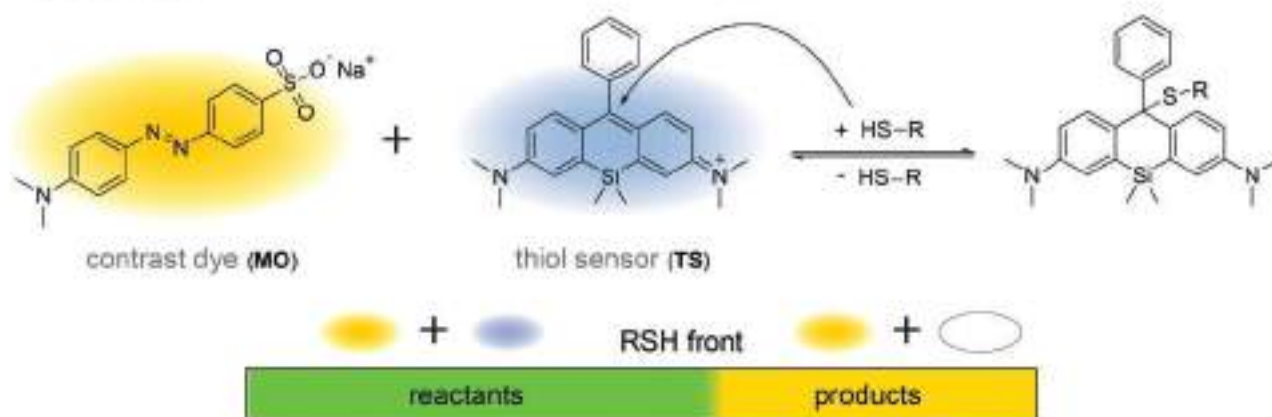
Figure 2. Chemistry of the reaction network. a) A series of reactions responsible for the delay time between mixing reagents and the beginning of the autocatalysis. b) The mechanism underlying the autocatalytic production of thiols. c) The system of dyes that we used to visualize the autocatalytic front.

whereas the thiol-assisted formation of guanidine from *N*-(2-cyanoethyl)cysteamine (**5a**) or *N*-methylcysteamine (**5b**) is a rapid process that releases thiocholine and 1-(2-cyanoethyl)-1-(2-mercaptoethyl)guanidine (**6a**) or 1-(2-mercaptoethyl)-1-methylguanidine (**6b**), all of which bear thiol groups. These thiols can exchange with **3a** or **3b**, producing two molecules of **5a** or

5b, thus, causing exponential growth of the concentration of all thiols in the solution.

To detect the propagation of the autocatalytic wave concomitantly with recording the movements of the hydrogel, we used a system of dyes consisting of methyl orange (**MO**) (0.8×10^{-3} M) and thiol sensor (**TS**) (0.3×10^{-3} M). A thiol sensor is a triarylmethane-based dye that reversibly reacts with thiols.[19] In its unreacted form, the sensor is a fully conjugated molecule with a bright blue color. Reaction with thiols breaks conjugation and decolorizes the molecule. Methyl orange keeps hydrogels visible in videos even when **TS** is decolorized. Mixing the yellow-orange color of **MO** and the blue color of **TS** yields a green color; thus, the propagation of the autocatalytic front results in the transition from green (**TS** + **MO**) to yellow-orange (**MO**).

Bilayer hydrogels were prepared by the sequential casting of a layer of acrylamide hydrogel with *N,N*′-methylenebisacrylamide (BAM) crosslinks and a layer of acrylamide hydrogel with disulfide-containing *N,N*′-bis(acryloyl)cystamine (BAC) crosslinks. Two molds for hydrogels were made: one for the first single layer and one for the bilayer. The first mold provides the shape that the gel has to adopt after the reduction of disulfides. The second mold provides the starting shape of the bilayer hydrogel. Therefore, the first layer of acrylamide hydrogel must be deformed before being put into the mold for a bilayer hydrogel. The mechanical strain that accumulates because of this deformation is released during the reduction of disulfides. For the majority of shapes used in this work, the strain is of flexural type, but in the helical shape, because of the combination of bending and twisting, the strain is of mixed nature. The most general way of preparing these molds is by casting polydimethylsiloxane (PDMS) into 3D printed molds (Figure S1, Supporting Information); PDMS is a perfect material for the molds because its transparency enables photoinitiation of the polymerization of acrylamide, and its flexibility aids in removing hydrogels. Typically, we prepare the regular acrylamide hydrogel for the first layer by photopolymerization (LED 360 nm) of a water solution containing 9.7% of acrylamide (AAm), 0.4% of BAM, and 0.2% of 2,2-azobis(2-methylpropionamidine)dihydrochloride (AAPH) as the initiator. The second layer was prepared analogously, by using 1.2% of BAC instead of BAM. For some shapes, 3D printing was unnecessary, and we used metal and glass masters and molds (see the Supporting Information) to prepare these bilayer hydrogels.

We loaded hydrogels with the autocatalytic mixture by soaking it in the PB (0.5 M, pH 7.5) containing **1** (0.11 M), **3a**, or **3b** (0.11 M), and maleimide (0.033 M) for 2 h (**Figure 3**a). All concentrations were calculated by considering the volume of hydrogels. Next, for most experiments, we placed hydrogels in a mixture of cyclohexane and tetrachloroethylene (≈2:1), ensuring that the density matched the density of the hydrogel to minimize the effect of gravity on the movement of hydrogels. We initiated autocatalysis from one edge of the hydrogels by adding small crystals of cysteamine hydrochloride and recorded videos of their movement using a USB camera (Figure 3a).

We designed several shapes that highlight the gradual actuation of the hydrogels by an autocatalytic front. The basic shape is a ring. Two transformations are possible using a ring shape: i) from ring to flat (unrolling) and ii) from flat to ring (rolling). Figure 1b and Video S1, Supporting Information show

the unrolling of the 5 cm piece of the hydrogel consisting of a 1 mm layer of regular polyacrylamide hydrogel (the outer part of the ring) and a 1.7 mm layer of the disulfide crosslinked hydrogel (the inner part of the ring). As expected from the design, the unrolling was gradual, with movement following the autocatalytic front. The use of **3b** instead of **3a** in the autocatalytic mixture did not change the behavior of this actuator (Video S2, Supporting Information); therefore, we used **3a** in most of the remaining experiments.

Next, we demonstrated how an autocatalytic front could govern the sequential activation of actuators (Figure 3b-top, Video S3, Supporting Information). To this end, we designed a "hand" hydrogel device with four "fingers." Each finger consists of an actuator that is transformed from a flat to a curved shape. When four of these fingers were attached to a joint base and autocatalysis was initiated from one side of the base, the fingers banded sequentially following the front.

Next, we designed two "complex" shapes: spiral and wave (Figure 3b-middle and Figure 3b-bottom; Videos S4 and S5, Supporting Information). Both of these shapes generate complex movement—gradual screwing or periodic actuation in different directions—when regulated by an autocatalytic front.

We created a "spiral" shape by first casting a polyacrylamide gel (1.55 mm thick) in a spiral mold, then flattering it in a straight, 2.8 mm-thick mold and casting disulfide hydrogel on top of it. Thus, in its initial state, the gel is only partially bended; however, it gradually screws into the spiral as the autocatalytic front propagates.

We created a "wave" shape by placing a 1.25 mm-thick wave-shaped layer of polyacrylamide into a 2.5 mm-thick wave-shaped mold in antiphase to the original mold; then, we filled the voids with a solution of acrylamide and BAC and finally, we polymerized the mixture. Thus, when an autocatalytic wave propagates, the gel periodically moves in opposite directions.

A quantitative analysis of the videos reveals that the autocatalytic front propagates at a rate of 6–7 mm h^{-1}. Previous studies showed that thiol autocatalysis can be satisfactorily described by second-order autocatalysis by combining the concentrations of all thiols (**2**, **5a** or **5b**, **6a** or **6b**) into one variable *SH*, and by considering **1** as the limiting substrate.[17d] The one-dimensional reaction-diffusion equation will take the form

$$\frac{\partial[SH]}{\partial t} = D\frac{\partial^2[SH]}{\partial x^2} + k[SH]([1]_0 - [SH]) \tag{1}$$

where *D* is a representative diffusion coefficient of thiols, *k* is the autocatalytic rate constant, and $[1]_0$ is the initial concentration of **1**.

This equation belongs to the Fisher–Kolmogorov–Petrovsky–Piskunov class of equations,[20] which have a solution in the form of a travelling wave. The rate of propagation (*v*) of this wave is given by

$$v = 2\sqrt{Dk[1]_0} \tag{2}$$

Here $k = 0.21$ s^{-1} M^{-1} is obtained by conducting the kinetics experiment (see in Figure S10, Supporting Information). $D = 5.10^{-10}$ m^2 s^{-1} is obtained by conducting the DOSY experiments for cystamine (see Figure S11, Supporting Information), which
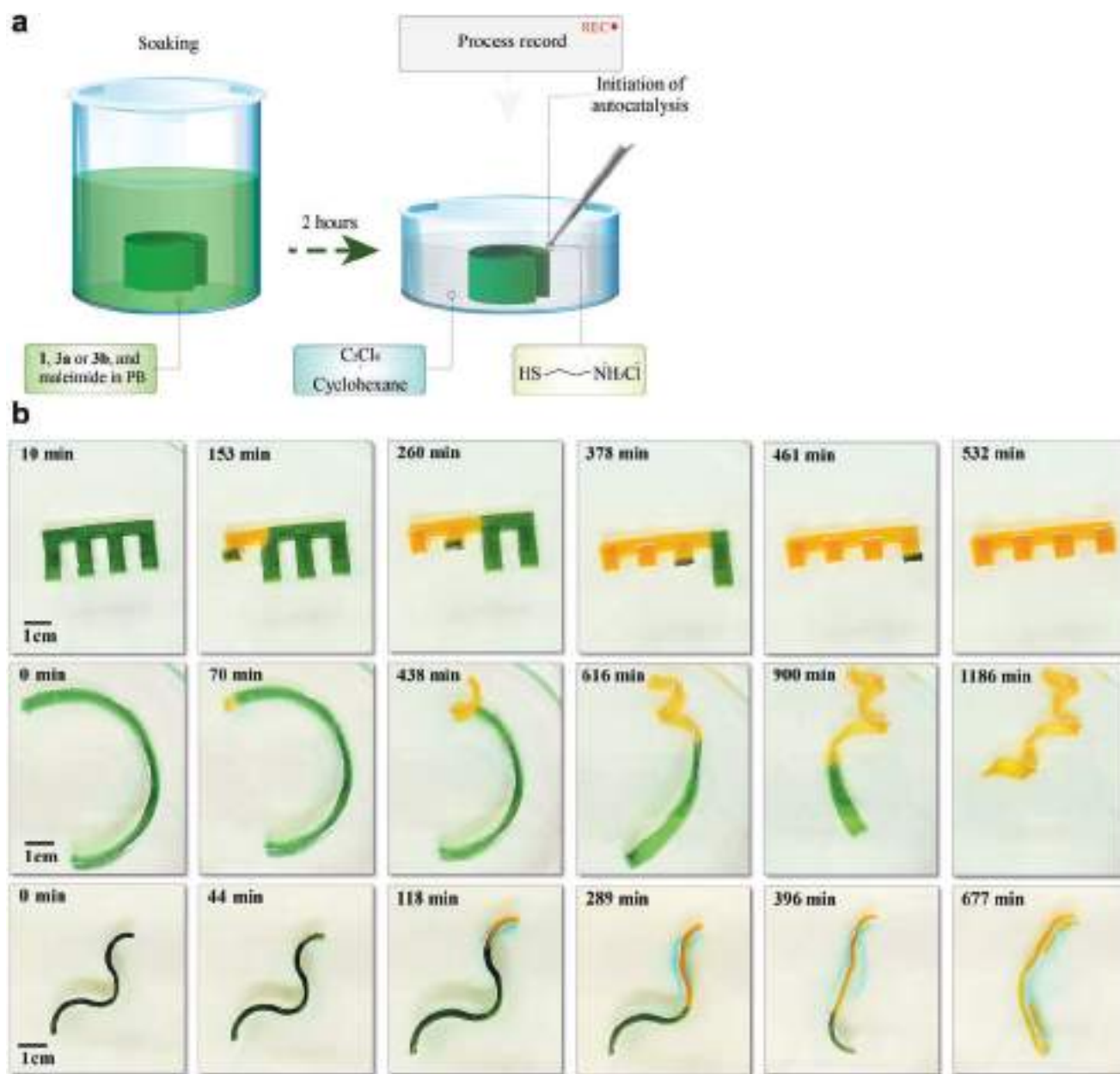
Figure 3. Experiments demonstrating complex motion enabled by an autocatalytic front. a) Schematics that show the procedures that preceded the recording in the actuation experiments: soaking the hydrogel in the autocatalytic mixture (typically: **1** 0.11 M, **3a** 0.11 M, maleimide 0.033 M, in 0.5 M PB pH 7.5); initiation of the autocatalysis. b) From top to bottom: sequential actuation of "fingers" (see also Video S3, Supporting Information); gradual screwing of the spiral (see also Video S4, Supporting Information); periodic movement in the "wave" (see also Video S5, Supporting Information).

because of its molecular weight and composition represents well the thiol-bearing molecules from this study. $[1]_0 = 0.077$ M is obtained by subtracting the maleimide concentration (0.033 M) from the initial concentration of **1** (0.11 M). Using these numbers results in a rate of 10 mm h^{-1}. This rate is in reasonable agreement with the experimental value of 6–7 mm h^{-1}. Somewhat slower than predicted propagation of the autocatalysis can be explained by the effect of maleimide, which is neglected in the model and whose diffusion counteracts the propagation of the front. The rates observed in our experiments are significantly lower than in BZ-based systems, where the wave velocity

reaches 360 mm h^{-1} at room temperature.[21] Nevertheless, these rates are similar to those found in copper-catalyzed azide–alkyne click autocatalysis (3.9 mm h^{-1}),[22] urea–urease autocatalysis (5–6 mm h^{-1}),[16] or predator–prey DNA-based reaction networks (5–20 mm h^{-1}).[23] This trend reflects the much faster rates for inorganic redox reactions than for biochemical and organic reactions.

Next, we probed some additional functionality of autocatalysis-driven hydrogel actuators. First, we tested whether actuators can function in air. To this end, we suspended the ring actuator on the spatula placed across the beaker (**Figure 4**

Figure 4. Experiments demonstrating the special features of hydrogels actuated by the autocatalytic front. From top to bottom: actuation in the air (100% humidity) of the hydrogel piece suspended on a spatula (autocatalysis was initiated from two sides of the hydrogel piece) (see also Video S6, Supporting Information); a relay system where actuation of one piece of hydrogel initiates the actuation of another (see also Video S7, Supporting Information); a delayed electrical switch created by actuating hydrogel (see also Video S8, Supporting Information). A thin copper wire was inserted into the hydrogel and contacted a brass plate when the hydrogel was actuated.

top; Video S6, Supporting Information). Activation of the autocatalytic front from two sides of the hydrogel resulted in an unclamping motion. In addition to functionality in air, this experiment also demonstrated how motion can be controlled by choosing multiple activation points for autocatalysis. This flexibility in choosing activation points expands the range of the possible types of motions for autocatalysis-driven hydrogels. The experiment in Figure 4 was conducted in an artificially humidified atmosphere. The experiments in open air or artificially dry environments (Videos S9 and S10, Supporting Information) show that drying influences but does not qualitatively change the behavior of this actuator in air.

The propagation of the autocatalytic front can be viewed as the propagation of a chemical signal. Thus, we decided to demonstrate a "relay" effect where one hydrogel actuator activates the actuation of another actuator. To this end, we fabricated three small (9.5 mm external diameter) ring actuators from a 0.7 mm layer of regular polyacrylamide and a 1.2 mm layer of the disulfide-crosslinked polyacrylamide hydrogel. Then, we placed three actuators in a series such that the first actuator uses the brass ring as a support to push the second actuator, which will push the third actuator (Figure 4 middle; Video S7, Supporting Information). As the video demonstrates, the autocatalysis and actuation in the second actuator started only after the first actuator touched it and the autocatalytic front reached the contact point. The same transmission occurred between the second and the third actuators.

Also, we showed how actuation can transform a chemical signal into an electrical signal (Figure 4 bottom; Video S8, Supporting Information). Briefly, we inserted a copper wire into the ring actuator, connected this wire to one of the battery contacts, connected a lamp to the battery and a brass block, and placed the ring actuator in such a way that the copper wire does not touch the brass block, but it will touch it when the hydrogel actuates. The system performed as expected. The autocatalytic front, initiated from one side of the hydrogel, induced actuation that put the wire into contact with the brass block and switched the lamp on about 4 h after the experiment began.

Finally, we demonstrated how to preprogram points of the activation and its timing by chemical reaction networks (**Figure 5**; Video S11, Supporting Information). It has been demonstrated with various chemistries that the first-order release of a signaling molecule combined with its fast sequestration (molecular titration) form a "trigger" circuit,[14a–c, 24] which controls the timing of the release of the signaling molecule. In the case of the thiol chemistry from this work, the first-order reaction that releases signaling molecules is mainly the hydrolysis of the thiouronium salt (**1**), while the sequestration is the reaction of thiocholine (**2**) with maleimide (Figure 2a). To preprogram points and timing of activation, we introduced acetylthiocholine—a molecule that hydrolyses with the release of thiocholine faster than the thiouronium salt—at the desired points by applying agarose stamps containing acetylthiocholine (0.8 M) to the bilayer acrylamide hydrogel. We used the ring actuator and applied agarose stamps at three points: sides and the

**ADVANCED
SCIENCE NEWS**

www.advancedsciencenews.com

**ADVANCED
MATERIALS**

www.advmat.de
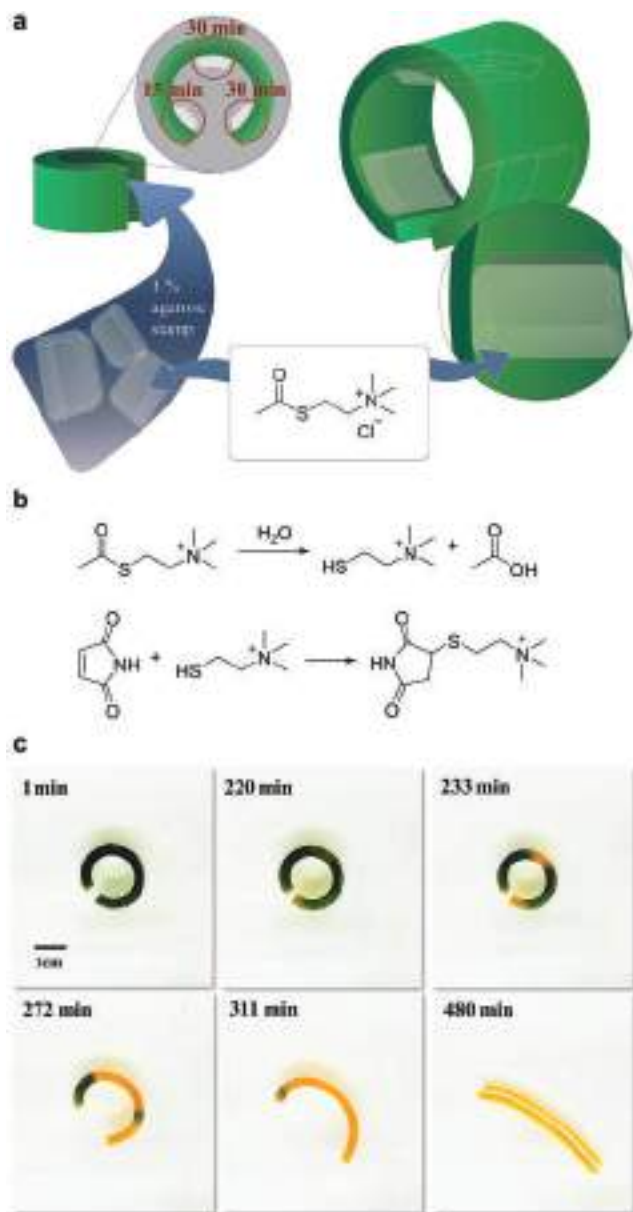
Figure 5. Preprogramming of the timing and location of the initiation of the autocatalytic front. a) A schematic diagram showing the injection of acetylthiocholine by diffusion from agarose stamps containing 0.8 M solution of acetylthiocholine. Time labels indicate for how long stamps were in contact with the hydrogel ring. b) A set of reactions constituting the "trigger" chemical circuit based on the acetylthiocholine. c) An experiment that shows delayed spontaneous initiation of the autocatalysis at predefined locations (see also Video S11, Supporting Information).

middle. On the right side and in the middle, the stamps were applied for 30 min while on the left side for 15 min (Figure 5a). The fast hydrolyzing acetylthiocholine (Figure 5b) at high concentration shortened triggering time from 10 to 3 h 20 min at the right side and in the middle (Figure 5c). The autocatalysis started spontaneously at these places and then propagated in all directions by the autocatalytic wave. The left side showed signs of activation only at the end of the process. Therefore, in this design, we can control (i) points of activation by choosing

points where the stamp is applied; (ii) timing of activation by choosing for how long we apply the stamps or concentration of acetythiocholine in the stamps. This experiment makes a simple demonstration of how actuation regulated by an autocatalytic front is coupled to chemical circuits.

To better understand the behaviors of the hydrogel actuators, we characterized regular polyacrylamide hydrogels, disulfide-crosslinked polyacrylamide hydrogels, and reduced disulfide-crosslinked polyacrylamide hydrogels by scanning electron microscopy (SEM), tensile stress measurements, and rheological measurements. To avoid the presence of the salt of buffer and nonvolatile thiols, we used ammonia and ethanethiol to prepare reduced hydrogel for the SEM experiments. We prepared four types of samples for SEM by lyophilization: all three hydrogels individually and the bilayer structure with one layer that reduced the disulfide crosslinked gel (1 mm of each layer). SEM images showed porous structures for both regular and disulfide-crosslinked hydrogels (**Figure 6**a,b). Although these two types of hydrogel have a distinctive appearance, they have similar porosity. Since the reduction of disulfide crosslinks caused the collapse of the porous structure during lyophilization, leaving only large ($\approx$100 µm) voids (Figure S7, Supporting Information), we performed SEM of a bilayer stack with reduced disulfides (Figure 6c) while using a lesser amount of ethanethiol. The images show the expansion of pores, which is an expected consequence of reducing the disulfide crosslinks.

Tensile stress and rheological measurement provide direct information on how the thiols released by the autocatalytic front affect the mechanical properties of the disulfide-crosslinked hydrogel. Analysis of tensile stress measurements for the regular and the disulfide-crosslinked hydrogels (Figure 6d; Figure S8, Supporting Information), up to 20% elongation, which is the region most relevant for small elongations experienced by hydrogels during bending, resulted in a Young's modulus of 15 ± 2 kPa and 16 ± 1 kPa (errors reflect 95% confidence intervals), respectively. To reveal the effect of thiols under conditions maximally close to the actuation experiments, we soaked disulfide crosslinked hydrogel in 0.5 M PB containing **1** (0.1 M), **3a** (0.1 M), and maleimide (3×10^{-3} M) and let autocatalysis (activated at multiple points) consume the whole piece of the hydrogel. At this point, we started measuring the tensile stress for this sample. The Young's modulus for this sample gradually dropped from 9 to 1.4 kPa during the first half-hour because of the reduced disulfides. In the context of the actuation of bilayer hydrogels, the drop in Young's modulus means that the reduced disulfide layer does not maintain deformation in the regular polyacrylamide layer.

The influence of thiols goes beyond the partial reduction of disulfide crosslinks. It makes the remaining disulfide bonds dynamic. Hydrogels with dynamic crosslinks adopt their shape after deformation.[25] We tested this adaptation in the reduced hydrogel sample by elongating it by 50%, keeping it at this elongation for 30 min, and then releasing it. The hydrogel returned to 132% of its original length; 65% of the deformation was irreversible. In addition to the drop in Young's modulus, this adaptation to the enforced shape might play a role in the actuation.

The rheological measurements determined the frequency dependence of the elastic (G') and viscous (G'') moduli, measuring

**ADVANCED
SCIENCE NEWS**

www.advancedsciencenews.com

**ADVANCED
MATERIALS**

www.advmat.de
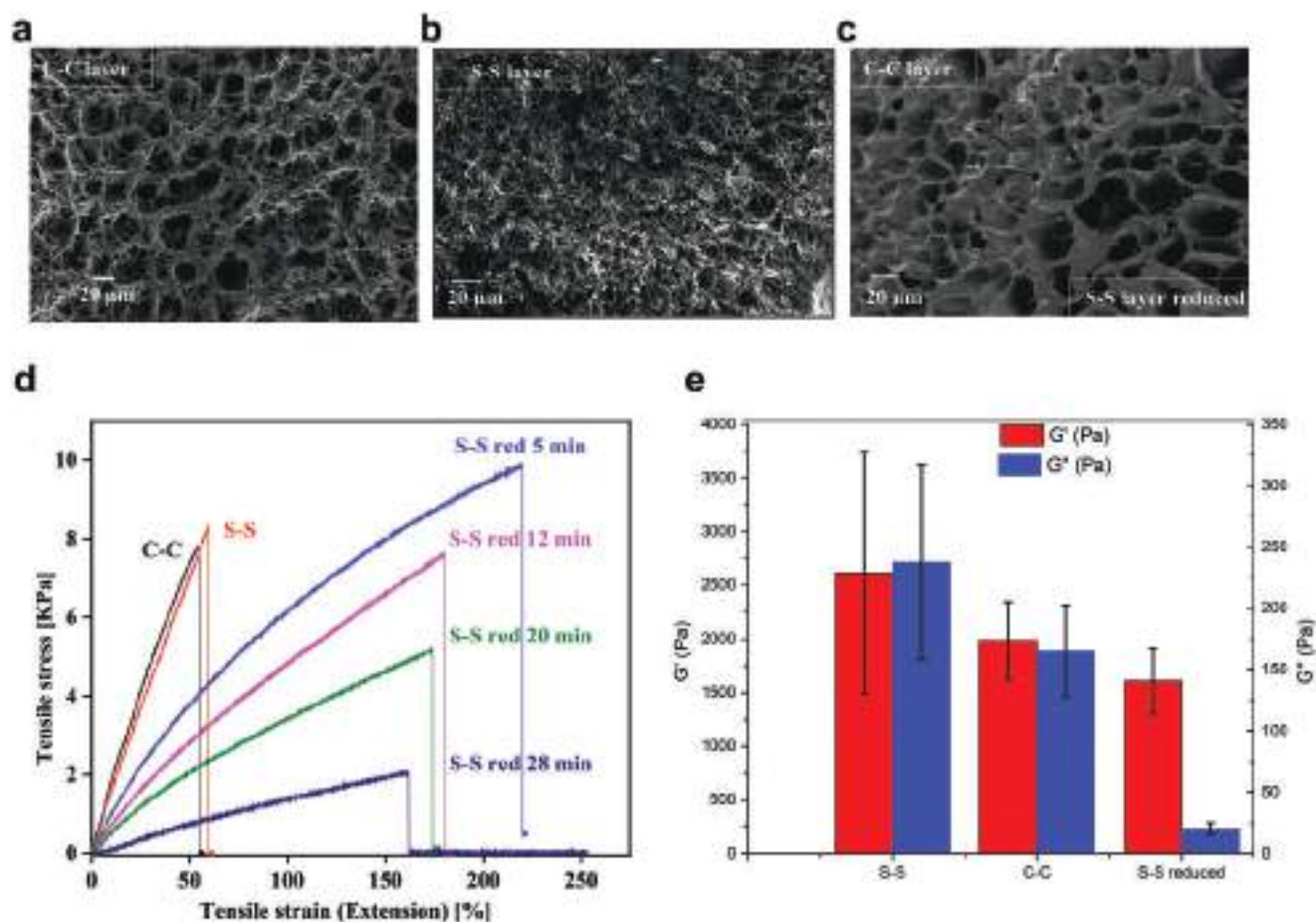
Figure 6. Physical characterization of hydrogels. a–c) Scanning electron microscopy (SEM) images of BAM-crosslinked (denoted as C–C), disulfide-crosslinked (denoted as S–S), and reduced bilayer polyacrylamide hydrogels correspondingly. d) Representative curves from tensile stress measurements. See the Supporting Information for the complete data set. e) Summary of the elastic (storage, in red) G' and viscous (loss, in blue) G'' moduli taken at 1 Hz of the S–S, C–C, and the partially reduced S–S polyacrylamide hydrogels (measurements were made in triplicate, the error bars represent standard deviations).

the stress response of the gels with frequencies varying from 1 to 30 Hz (Figure S9, Supporting Information). All samples exhibited gel-like behavior where G' is higher than G'' (Figure 6e). A comparative analysis of G' revealed that both the disulfide-crosslinked and regular polyacrylamide hydrogels were stiffer (2615 ± 1129 Pa and 1982 ± 361 Pa, respectively) than the reduced hydrogel (G' of 1604 ± 302 Pa). In addition, the G'' values revealed that the viscous part of the fully crosslinked gels is significantly higher than after the crosslinking reduction. This change is due to the larger pores formed after the disulfide bond reduction (in line with the SEM image in Figure 6c) leading to the low drag of the matrix on the solvent fluid. The rheological data confirm that the reduction of disulfide crosslinks changes the hydrogel's microscale structure and its viscoelastic properties. These changes are the underlying reason behind the actuation.

3. Conclusions

This work demonstrated autonomous spatiotemporal regulation of hydrogel actuators by a rationally engineered thiol-based

chemical reaction network that sustains autocatalytic fronts. In contrast to actuation regulated by light, which also provides spatiotemporal resolution,[26] the chemical regulation does not require external control. This mode of regulation of actuation provides three main advantages: i) it enables gradual motions that are inaccessible for actuators in which the whole hydrogel actuates simultaneously, ii) it enables the transfer of chemical signals or the transformation of chemicals to other types (e.g., electrical) of signals, and iii) it opens up the possibility to integrate these actuators into large devices regulated by chemical circuits. In this work, we have already shown how a simple "trigger" circuit regulates the timing of spontaneous initiation of the autocatalysis at specific points.

To the best of our knowledge, this work is the only example of autonomous regulation of actuation with nonlinear chemistry other than BZ reaction.[11] Although still less rich than BZ reaction in terms of dynamics behaviors,[27] the thiols chemistry happens at much milder conditions and is more modular. BZ chemistry happens in 1 M sulfuric acid and involves a strong oxidant, potassium bromate, while thiol chemistry works at neutral pH and mild redox environments. BZ reaction has a very complex mechanism with more than

**ADVANCED
SCIENCE NEWS**

www.advancedsciencenews.com

**ADVANCED
MATERIALS**

www.advmat.de

50 reactions involved.[28] In contrast, we designed thiol-based reaction networks from the individual reactions; thus, it is possible to adjust some fragments of a chemical network to reach desirable performance as was demonstrated here with modification of the "trigger" part of the chemical network.

In the current form, this system also has some disadvantages: (i) actuation is slow, (ii) the forces are small, and (iii) actuation is irreversible. However, we think that these challenges can be overcome by future developments in the actuator's design as well as the chemistry that governs them.

This system can be developed in several directions. The first direction is making actuation reversible by eliminating the need for accumulated strain in the hydrogel. This goal would require designing the chemistry of two layers so that their swelling changes significantly in response to the release of thiols or other products of the autocatalytic reaction. The second direction is miniaturization. Decreasing the dimensions of hydrogels will increase the force they can generate per unit of weight as well as increase actuation speed because the velocity of autocatalytic fronts is independent of the hydrogel size. The third direction is to use non-uniformly distributed reagents, which has been illustrated here by injecting acetythiocholine at specific point on the hydrogel in order to regulate initiation of the autocatalysis. The fourth change, which is more radical than the previous three, is to make the system open by introducing a fluidic feeding system. The feeding system can refill the reagents and enable further rounds of autocatalysis, whereas re-oxidation can restore disulfide crosslinks.

Based on this system, we can formulate a general approach for developing hydrogel actuators regulateded by an autocatalytic front. First, autocatalytic chemistry must be optimized. The rate of spontaneous activation has to be slow enough to provide a delay of autocatalysis that is sufficient (hours in our experiments) for an autocatalytic front to travel a required distance (centimeters in our experiments). Sequestering molecules such as maleimide provide some control over the delay of autocatalysis; however, their amount is limited by the concentration of substrates, and slow background reactions are necessary for long traveling distances of autocatalytic fronts. Second, strained bilayer hydrogels with crosslinks breakable by desired chemistry have to be designed. Using the outlined strategy, it should be possible to design hydrogel actuators based on acid,[17a,29] base,[30] or enzymatic autocatalysis.[31]

In a broader context of designing stimuli-responsive materials, the hydrogel actuators regulated by autocatalytic fronts can serve as building blocks integrated into large systems that involve many types of stimuli, responses, and chemical signaling channels. These systems will bring synthetic soft materials regulated by reaction networks closer in functionality to living matter.

4. Experimental Section

Synthesis: 1)   We synthesized thiouronim salt (**1**),[17d] *N*,*N*′-bis(2-cyanoethyl)cystamine (**3a**),[17d] and thiol sensor (**TS**)[19] following the published protocols.

2)   *N*,*N*′-dimethylcystamine (**3b**): (i) *N*-methylaminoethanol (5 g, 67 mmol) was dissolved in 50 mL of chloroform and SOCl$_2$ (10 mL) was added by portions on ice. The mixture was stirred for 6 h at room temperature, concentrated, and quenched with ethanol (100 mL) and then concentrated again. The residue was recrystallized from ethanol to form pure *N*-(2-chloroethyl)-methylamine hydrochloride. Yield: 4.7 g (36 mmol, 54%). ^{1}H NMR (400 MHz, D$_2$O, δ): 3.83 (t, 2H, *J* = 5.7 Hz), 3.39 (t, 2H), 2.72 (s, 3H). (Caution! In basic conditions, this compound can alkylate itself with the formation of nitrogen mustards, which are blistering agents.)

(ii) The product of the previous reaction (4.7 g, 36 mmol) was dissolved in 50 mL of H$_2$O and 50 mL of MeOH. Anhydrous Na$_2$S$_2$O$_3$ (5.6 g, 36 mmole) was added to the reaction and the mixture was refluxed for 48 h. HCl (10N, 20 mL) was then added and the mixture was stirred for 2 h. After the solvent evaporated, the product was extracted with methanol. I$_2$ solution in methanol was added dropwise until the persistent brown color appeared. After methanol evaporated, the product was recrystallized from ethanol/water. Yield: 4 g (3.7 g, 81%). ^{1}H NMR (300 MHz, D$_2$O, δ): 3.36 (t, 2H, *J* = 6.7 Hz), 2.96 (t, 2H, *J* = 6.7 Hz), 2.68 (s, 3H). ^{13}C NMR (300 MHz, D$_2$O, δ): 47.03, 32.86, 31.90. HRMS (ESI) *m*/*z*: [M+H]$^+$ calcd. for C$_6$H$_{16}$N$_2$S$_2$: 181.0755; found 181.0842.

Fabrication of the Ring Actuator: First, we prepared the regular acrylamide hydrogel with 1 mm thickness for the first layer by photopolymerization (λ = 360 nm) of a water solution containing 9.7% of acrylamide (AAm), 0.4% of *N*,*N*′-methylenebisacrylamide (BAM), and 0.2% of 2,2-azobis(2-methylpropionamidine)dihydrochloride (AAPH) as an initiator. Then, the gel was cut into pieces with a dimension of $50 \times 9 \times 1$ mm and carefully placed inside the ring-shaped PDMS mold (20 mm outer diameter, 2.7 mm thickness) to the outer wall. Next, the mold void was filled with a water solution of acrylamide (9.7%), *N*,*N*′-bis(acryloyl) cystamine (BAC) (1.2%), and 2,2-azobis(2-methylpropionamidine) dihydrochloride (AAPH) (0.2%) and photopolymerized using UV light (λ = 360 nm) for 30 sec. Finally, we removed the bilayer ring of the gel with a thickness of 2.7 mm from the mold; the outer side was made with BAM crosslinks and the inner side was made with disulfide crosslinks. The details of the fabrication of this bilayer hydrogel can be found in Video S12, Supporting Information. Next, we soaked the gel in the autocatalytic solution (containing 0.11 M of thiouronim salt **1**, 0.11 M of either *N*,*N*′-bis(2-cyanoethyl)cystamine (**3a**), or *N*,*N*′-dimethylcystamine (**3b**), 0.033 M of maleimide, 0.3×10^{-3} M of thiol sensor, and 0.8×10^{-3} M of methyl orange in a 0.5 M PB solution of pH 7.5) for 2 h. Then, we immersed the gel in a crystallizing dish containing cyclohexane and tetrachloroethane ($\approx$2:1 ratio). We initiated autocatalysis on one edge of the ring with a small crystal of cysteamine and covered the dish with a glass plate. Finally, the whole process was monitored under camera and the video was recorded for a few hours.

Fabrication of Other Actuators: In all cases, first, the BAM crosslinked gel was prepared with a specific thickness. Then, it was placed inside the PDMS mold and the mold gap was filled with the solution for disulfide crosslinked hydrogel, and the solution was irradiated with UV for 30 s for photopolymerization. Then, the desired structure was obtained and the same procedure was followed as in the ring structure. (For detailed description of the fabrication of each actuator, see Supporting Information).

Tensile Test: We prepared samples of BAM crosslinked and disulfide crosslinked hydrogels by photopolymerization of 1 mm-thick layers of solutions of acrylamide (9.7%), AAPH (0.2%), and BAM (0.4%) or BAC (1.2%) correspondingly. To prepare samples of hydrogels with partially reduced disulfide crosslinks, we reduced disulfide crosslinked samples using the same autocatalytic solution as we used in actuation experiments just before the measurements. Tensile tests were performed on a universal testing system (Instron 5965), equipped with a 10 N load cell. The hydrogel samples were cut into $1 \times 1 \times 30$ mm^3 strips, and the gauge length was 10 mm. The speed of the crosshead was 5 mm min^{-1}. For statistical reasons, about 10 specimens were tested for each type of sample.

Scanning Eectron Microscopy: 1 mm-thick layers of both BAM and disulfide crosslinked hydrogels, which were prepared as described for tensile measurements, were cut into square pieces and frozen using liquid nitrogen and then subjected to lyophilization overnight. A few pieces of disulfide gel were immersed in the alkaline solution (using NH$_3$) of ethanethiol (0.2 M)

**ADVANCED
SCIENCE NEWS**

www.advancedsciencenews.com

**ADVANCED
MATERIALS**

www.advmat.de

for 2–3 min and then freeze dried in a lyophilizer. For the bilayer reduced gel, we first prepared one bilayer gel as described for the ring actuator, then cut it into square pieces and reduced disulfides using alkaline ethanethiol solution (this time less amount (0.1 m) taken) as described previously. Then, we freeze dried it and observed it under a scanning electron microscope. The topology of the lyophilized samples was analyzed under a high-resolution scanning electron microscope (Gemini 500, Zeiss), using an Everhart-Thornley detector. Samples were introduced to the SEM chamber without any sputtering. The images were taken at 1 kV acceleration voltage, with a 3–4 mm working distance.

Rheological Measurements: Three types of gels (i.e., BAM crosslinked, disulfide crosslinked, and reduced disulfide crosslinked) were prepared as described for tensile measurements. A sample (2 cm in diameter and 1 mm thickness) was placed on the lower serrated plate of the rheometer, ensuring that it covered the entire surface with no air bubbles present. Storage (G') and loss (G'') moduli were measured using a Thermo Scientific rheometer in a plate–plate (P20 Ti S L) configuration using the HAAKE MARS III system at 25 ± 0.1 °C (with a constant working load of 0.4 N). Dynamic frequency sweep analysis was conducted to measure the frequency-dependent G' and G'' moduli of various gels in the range of 0.1–30 Hz and an amplitude of 1 Pa. The data are presented as the average (±STDEV) taken @1 Hz (a linear regime of the frequency sweep trace) from at least three samples from two different preparations.

Conflict of Interest

The authors declare no conflict of interest.

Data Availability Statement

The data that support the findings of this study are available from the corresponding author upon reasonable request.

[1] a) G. H. Kwon, J. Y. Park, J. Y. Kim, M. L. Frisk, D. J. Beebe, S. H. Lee, *Small* **2008**, *4*, 2148; b) G. M. Whitesides, *Angew. Chem., Int. Ed.* **2018**, *57*, 4258; c) F. Ilievski, A. D. Mazzeo, R. F. Shepherd, X. Chen, G. M. Whitesides, *Angew. Chem., Int. Ed.* **2011**, *50*, 1890.

[2] T. S. Shim, S. H. Kim, C. J. Heo, H. C. Jeon, S. M. Yang, *Angew. Chem., Int. Ed.* **2012**, *51*, 1420.

[3] D. J. Beebe, J. S. Moore, J. M. Bauer, Q. Yu, R. H. Liu, C. Devadoss, B. H. Jo, *Nature* **2000**, *404*, 588.

[4] a) Z. Hu, X. Zhang, Y. Li, *Science* **1995**, *269*, 525; b) X. Le, W. Lu, J. Zhang, T. Chen, *Adv. Sci.* **2019**, *6*, 1801584; c) J. Shang, X. Le, J. Zhang, T. Chen, P. Theato, *Polym. Chem.* **2019**, *10*, 1036; d) L. Ionov, *Mater. Today* **2014**, *17*, 494.

[5] a) Y. Tan, D. Wang, H. Xu, Y. Yang, X. L. Wang, F. Tian, P. Xu, W. An, X. Zhao, S. Xu, *ACS Appl. Mater. Interfaces* **2018**, *10*, 40125; b) Y. Osada, A. Matsuda, *Nature* **1995**, *376*, 219.

[6] a) L. Zhao, J. Huang, Y. Zhang, T. Wang, W. Sun, Z. Tong, *ACS Appl. Mater. Interfaces* **2017**, *9*, 11866; b) O. Erol, A. Pantula, W. Liu, D. H. Gracias, *Adv. Mater. Technol.* **2019**, *4*, 1900043.

[7] E. Palleau, D. Morales, M. D. Dickey, O. D. Velev, *Nat. Commun.* **2013**, *4*, 2257.

[8] N. Bassik, B. T. Abebe, K. E. Laflin, D. H. Gracias, *Polymer* **2010**, *51*, 6093.

[9] B. N. Kholodenko, *Nat. Rev. Mol. Cell Biol.* **2006**, *7*, 165.

[10] a) H. W. van Roekel, B. J. Rosier, L. H. Meijer, P. A. Hilbers, A. J. Markvoort, W. T. Huck, T. F. de Greef, *Chem. Soc. Rev.* **2015**, *44*, 7465; b) A. Walther, *Adv. Mater.* **2020**, *32*, 1905111; c) R. Merindol, A. Walther, *Chem. Soc. Rev.* **2017**, *46*, 5588.

[11] a) R. Yoshida, *Adv. Mater.* **2010**, *22*, 3463; b) S. Maeda, Y. Hara, R. Yoshida, S. Hashimoto, *Angew. Chem., Int. Ed.* **2008**, *47*, 6690; c) S. Maeda, Y. Hara, T. Sakai, R. Yoshida, S. Hashimoto, *Adv. Mater.* **2007**, *19*, 3480; d) R. Yoshida, T. Takahashi, T. Yamaguchi, H. Ichijo, *J. Am. Chem. Soc.* **1996**, *118*, 5134; e) T. Mikanohara, S. Maeda, Y. Hara, S. Hashimoto, *Adv. Rob.* **2014**, *28*, 457.

[12] a) S. G. J. Postma, I. N. Vialshin, C. Y. Gerritsen, M. Bao, W. T. S. Huck, *Angew. Chem., Int. Ed.* **2017**, *56*, 1794; b) E. Jee, T. Bansagi Jr, A. F. Taylor, J. A. Pojman, *Angew. Chem., Int. Ed.* **2016**, *55*, 2127.

[13] a) J. Fern, R. Schulman, *Nat. Commun.* **2018**, *9*, 3766; b) A. Cangialosi, C. Yoon, J. Liu, Q. Huang, J. Guo, T. D. Nguyen, D. H. Gracias, R. Schulman, *Science* **2017**, *357*, 1126.

[14] a) T. Heuser, E. Weyandt, A. Walther, *Angew. Chem., Int. Ed.* **2015**, *54*, 13258; b) L. Heinen, A. Walther, *Soft Matter* **2015**, *11*, 7857; c) T. Heuser, A. K. Steppert, C. M. Lopez, B. Zhu, A. Walther, *Nano Lett.* **2015**, *15*, 2213; d) J. P. Wojciechowski, A. D. Martin, P. Thordarson, *J. Am. Chem. Soc.* **2018**, *140*, 2869.

[15] a) X. Fan, A. Walther, *Angew. Chem., Int. Ed.* **2021**, *60*, 11398; b) X. Fan, A. Walther, *Angew. Chem., Int. Ed.* **2021**, *60*, 3619.

[16] M. M. Wrobel, T. Bansagi, S. K. Scott, A. F. Taylor, C. O. Bounds, A. Carranzo, J. A. Pojman, *Biophys. J.* **2012**, *103*, 610.

[17] a) A. I. Hanopolskyi, V. A. Smaliak, A. I. Novichkov, S. N. Semenov, *ChemSystemsChem* **2020**, *3*, 2000026; b) B. J. Cafferty, A. S. Y. Wong, S. N. Semenov, L. Belding, S. Gmur, W. T. S. Huck, G. M. Whitesides, *J. Am. Chem. Soc.* **2019**, *141*, 8289; c) S. N. Semenov, L. J. Kraft, A. Ainla, M. Zhao, M. Baghbanzadeh, C. E. Campbell, K. Kang, J. M. Fox, G. M. Whitesides, *Nature* **2016**, *537*, 656; d) A. I. Novichkov, A. I. Hanopolskyi, X. Miao, L. J. W. Shimon, Y. Diskin-Posner, S. N. Semenov, *Nat. Commun.* **2021**, *12*, 2994; e) X. Miao, A. Paikar, B. Lerner, Y. Diskin-Posner, G. Shmul, S. N. Semenov, *Angew. Chem. Int. Ed.* **2021**, *60*, 20366; f) X. Sun, E. V. Anslyn, *Angew. Chem., Int. Ed.* **2017**, *56*, 9522.

[18] H. A. Aliyar, P. D. Hamilton, N. Ravi, *Biomacromolecules* **2005**, *6*, 204.

[19] K. Umezawa, M. Yoshida, M. Kamiya, T. Yamasoba, Y. Urano, *Nat. Chem.* **2017**, *9*, 279.

[20] M. El-Hachem, S. W. McCue, W. Jin, Y. Du, M. J. Simpson, *Proc.: Math., Phys. Eng. Sci.* **2019**, *475*, 20190378.

[21] L. Howell, E. Osborne, A. Franklin, E. Hebrard, *J. Phys. Chem. B* **2021**, *125*, 1667.

[22] S. N. Semenov, L. Belding, B. J. Cafferty, M. P. S. Mousavi, A. M. Finogenova, R. S. Cruz, E. V. Skorb, G. M. Whitesides, *J. Am. Chem. Soc.* **2018**, *140*, 10221.

[23] A. Padirac, T. Fujii, A. Estevez-Torres, Y. Rondelez, *J. Am. Chem. Soc.* **2013**, *135*, 14586.

[24] a) J. Fern, D. Scalise, A. Cangialosi, D. Howie, L. Potters, R. Schulman, *ACS Synth. Biol.* **2017**, *6*, 190; b) S. N. Semenov, A. J. Markvoort, W. B. L. Gevers, A. Piruska, T. F. A. de Greef, W. T. S. Huck, *Biophys. J.* **2013**, *105*, 1057.

[25] B. Fan, K. Zhang, Q. Liu, R. Eelkema, *ACS Macro Lett.* **2020**, *9*, 776.

[26] a) Y. Chen, C. Chen, H. U. Rehman, X. Zheng, H. Li, H. Liu, M. S. Hedenqvist, *Molecules* **2020**, *25*, 4246; b) X. Qian, Y. Zhao, Y. Alsaid, X. Wang, M. Hua, T. Galy, H. Gopalakrishna, Y. Yang, J. Cui, N. Liu, M. Marszewski, L. Pilon, H. Jiang, X. He, *Nat. Nanotechnol.* **2019**, *14*, 1048; c) C. Li, A. Iscen, H. Sai, K. Sato, N. A. Sather, S. M. Chin, Z. Alvarez, L. C. Palmer, G. C. Schatz, S. I. Stupp, *Nat. Mater.* **2020**, *19*, 900; d) X. Lu, S. Guo, X. Tong, H. Xia, Y. Zhao, *Adv. Mater.* **2017**, *29*, 1606467.

[27] I. R. Epstein, B. Xu, *Nat. Nanotechnol.* **2016**, *11*, 312.

[28] L. Gyorgyi, T. Turanyi, R. J. Field, *J. Phys. Chem.* **1990**, *94*, 7162.

[29] K. Ichimura, *Chem. Rec.* **2002**, *2*, 46.

[30] K. Arimitsu, K. Ichimura, *J. Mater. Chem.* **2004**, *14*, 336.

[31] a) J. F. Pechere, H. Neurath, *J. Biol. Chem.* **1957**, *229*, 389; b) S. N. Semenov, A. J. Markvoort, T. F. A. de Greef, W. T. S. Huck, *Angew. Chem., Int. Ed.* **2014**, *53*, 8066.

Nanoparticles

All-Dielectric Nanostructures with a Thermoresponsible Dynamic Polymer Shell

Anna A. Nikitina[+], Valentin A. Milichko[+], Alexander S. Novikov, Artem O. Larin, Proloy Nandi, Utkur Mirsaidov, Daria V. Andreeva, Mikhail V. Rybin, Yuri S. Kivshar, and Ekaterina V. Skorb*

Abstract: We suggest a new strategy for creating stimuli-responsive bio-integrated optical nanostructures based on Mie-resonant silicon nanoparticles covered by an ensemble of similarity negatively charged polyelectrolytes (heparin and sodium polystyrene sulfonate). The dynamic tuning of the nanostructures' optical response is due to light-induced heating of the nanoparticles and swelling of the polyelectrolyte shell. The resulting hydrophilic/hydrophobic transitions significantly change the shell thickness and reversible shift of the scattering spectra for individual nanoparticles up to 60 nm. Our findings bring novel opportunities for the application of smart nano-materials in nanomedicine and bio-integrated nanophotonics.

All-dielectric nanophotonics[1–3] have recently emerged as a new paradigm in optics with the multitude of Mie-type resonances governing various linear and nonlinear optical properties of non-plasmonic (silicon, germanium, gallium arsenide, etc.) nanoparticles (NPs), nanostructures, and metasurfaces. These structures are highlighted by high refractive index, low optical losses within the visible and infrared ranges, as well as compatibility to the complementary metal-oxide-semiconductors (CMOS) technology.[4] Tuning all-dielectric nanostructures' electronic and optical properties provides a powerful platform for highly-efficient nanophotonic devices such as optical switches and smart sensors.[5–8] Great prospects for the all-dielectric nanostructures for real-life applications[9] are the stimuli-responsive optical nano-materials in nanomedicine[10] and bio-integrated nanophotonics.[5,7,8,11–15]

Based on previous experimental results, to achieve optical properties tuning of different all-dielectric nanostructures the mechanical stretching,[16–19] thermo-optical effect,[20,21] liquid crystals coating,[22–24] phase transition[25] and ultrafast light pumping[26,27] are used. However, the mentioned approaches have disadvantages, as they need strong external stimuli, for example, illumination by intense pulsed irradiation, which leads to a significant physical alteration of organic surroundings.[28]

To perform bio integration of the NPs, different strategies as functionalization or decoration by polyelectrolytes (PE) can be realized. Generally, the structural rearrangement mechanism in PE is rather uniform and is known in polymer physics as the coil-globule transition, defined as the reversible transition of macromolecules from an expanded coil state through an ideal coil state to a collapsed globule state.[29–31] Triggers of such transitions in polymers can be restricted to chemical (pH,[23] ionic strength,[32] solvent[33]), physical (temperature[34,35]) stimuli, and a mechanical impact.[36] The present research focuses on swelling of the PE shell.

High-modulation morphological swelling can be achieved by the deposition of pH-sensitive charged block copolymers, block-copolymer micelles, and the formation of PE brushes.[37] The mechanism of high-amplitude changes of the PE shell is based on the expansion/collapse of macromolecules, thus regulating the whole shell's length and density.[29,36]

In a well-known thermo-responsible system based on Au NP and poly-(N-isopropyl acrylamide) (PNIPAM) the shell usually collapses due to temperature. Köhler et al.[38,39] described the similar shrink for poly-(diallyldimethylammonium chloride) (PDADMAC) and poly-(sodium 4-styrenesulfonate) (PSS) assembly. Simultaneously, recently the PNIPAM swelling was also achieved.[40]

In this work, we present a new concept of assembly of similarly charged PE[41,42] on the surface of optically resonant silicon NPs, allowing the dynamic and reversible swelling of this polymer shell due to light-induced heating of the NPs.[43] At the same time, the contribution of hydrophilic repulsive and hydrophobic attractive forces of negatively charged heparin (Hep) and PSS[44] for reversible swelling is discussed.

We used a mixture of negatively charged Hep and PSS for decoration of positively charged crystalline Si NPs (Support-

---

[*] A. A. Nikitina,[+] Dr. V. A. Milichko,[+] A. O. Larin, Dr. M. V. Rybin,
Prof. Y. S. Kivshar, Prof. E. V. Skorb
ITMO University
9 Lomonosova street, 191002 St. Petersburg (Russia)
E-mail: skorb@itmo.ru

Dr. V. A. Milichko[+]
Université de Lorraine, Institut Jean Lamour, UMR CNRS 7198
54011 Nancy (France)

Dr. A. S. Novikov
Institute of Chemistry, Saint Petersburg State University
Universitetskaya Nab., 7/9, 199034 St. Petersburg (Russia)

P. Nandi, Prof. U. Mirsaidov
Centre for BioImaging Sciences, Department of Biological Sciences,
National University of Singapore (Singapore)

Prof. U. Mirsaidov, Prof. D. V. Andreeva
Department of Materials Science and Engineering, National University of Singapore (Singapore)

Dr. M. V. Rybin
Ioffe Institute
194021 St Petersburg (Russia)

Prof. Y. S. Kivshar
Research School of Physics, Australian National University, Canberra
ACT 2601, (Australia)

[+] These authors contributed equally to this work.

Supporting information and the ORCID identification number(s) for the author(s) of this article can be found under:
https://doi.org/10.1002/anie.202101188.

ing Information, Figure S1) dispersed in water. Hep is a polysaccharide widely used for drug delivery, regenerative medicine, and sensing due to its biocompatibility. The strategy proposed for the exploitation of polysaccharides suggests their incorporation in multilayers. Such multilayered materials provide target surfaces with desirable adhesion properties to biomolecules and cells and can be used to uptake, deliver, and release biomolecules on demand.[45–48] However, the potential of heparin for the formation of temperature-sensitive interfaces has not been previously explored. We have conducted many tests and experimentally found the best optimal thermo-responsible system of swelling behavior to combine both negatively charged PSS and Hep. The PE shell is usually formed by oppositely charged PE.[41] However, we have experimentally developed the PE shell system on Si NP, allowing us to achieve reversible swelling of the PE shell.

In Figure 1 a, the process of the PE shell of Hep and PSS reversible thermo-guided swelling upon irradiation by visible

light is schematically illustrated. Surprisingly, such an assembly started swelling during the temperature increase compared with the similar system of oppositely charged PE.[38,39] The swelling was also confirmed by the optical (Figure 1 b) and transmission electron microscopy (TEM) (Figure 1 c,d). Among many particles (Figure 1 e), the single one was chosen and analyzed individually.

To evaluate the thermodynamic favorability for the hydrophobic/hydrophilic interaction of the PE shell, we performed quantum chemical calculations using density functional theory (DFT) (M06-2X/6-31G* level of theory; for details, see the Supporting Information, Computational section and Tables S1 and S2). The results of calculations revealed that self-assembly of a functional monomeric unit of associate Hep/PSS via hydrogen bonding N−H···O, O−H···O, C−H···O, and O−H···Ph is thermodynamically favorable (by 7.9 kcal mol^{-1} in terms of Gibbs free energies, Figure 2 c). This fact proves the relevance of the favorable association between the same charged species (Figure 2 a–c), guided by hydrophobic effects on substrate specificity.

We then investigated the tuning of the optical response of single NPs placed on silica substrate in an air atmosphere. Figure 3 demonstrates experimental results of measuring the scattering light in the dark field geometry from single NPs covered by PDADMAC/Hep/PSS before, during, and after light-induced heating. The laser source (Supercontinuum Fianium SC400-6 with a tunable wavelength of 400–850 nm, 60 MHz repetition rate, a pulse duration of 6 ps, and an FWHM of 10 nm) was utilized to heat each NP. Depending on the NP diameter,[8,49] the pumping wavelength was tuned with an intensity of 1 to 5 mW cm^{-2}.[50] In our case, the mechanism of light-induced heating is based on the concept of conversion

Figure 1. a)–d) Representation of the application of thermo-responsive Si NP/Hep/PSS (a), optical (b) and bright-field TEM images of a hybrid system before (c) and after (d) irradiation. Hydrophilic parts of molecules are shown in red, and hydrophobic blocks are presented in green. e) Optical image of various particles. Note that for the scattering spectra the response of single particle is used and analyzed.

Transformation	ΔE	ΔH	ΔG
Hep + PSS → Hep/PSS	-25.0	-24.0	-7.9

Figure 2. Representation of optimized geometries for functional units of polymers proving the favorable assembly of same charged Hep and PSS: Hep (a), and monomer of PSS (b) and their association (Hep/PSS) with calculated values of ΔE, ΔH, and ΔG (in kcal mol^{-1}) (c).

12738 www.angewandte.org

© 2021 Wiley-VCH GmbH

Angew. Chem. Int. Ed. **2021**, *60*, 12737 –12741
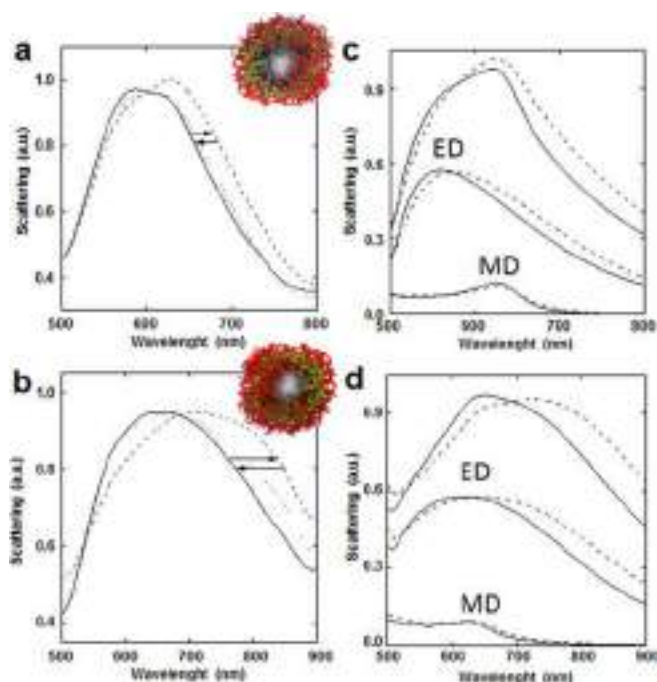
Figure 3. Scattering spectra for the single silicon NPs with thermo-responsive polymers shell in dark field geometry: a) Si NP/PDADMAC/Hep/PSS, b) Si NP/Hep/PSS. Red arrows demonstrate the spectrum shift due to the light-induced heating by visible light (550 nm) with the intensity of 3 mWcm^{-2}, while the blue ones demonstrate the reversible process. c),d) Approximation of the scattering spectra before (black curves) and during (dash curves) light-induced heating using Mie theory for (c) Si NP/PDADMAC/Hep/PSS and (d) Si NP/Hep/PSS. The multipolar expansion demonstrates the electric and magnetic dipole (ED and MD) contributions to the entire spectra.

of light energy to heat through resonant interaction with silicon NP having multiple Mie resonances.[51] The NPs nonzero absorption coefficient within the visible range and its high refractive index provide irradiated NPs heating up to 1000 K[7] This energy then transfers to the surroundings of the NPs,[4] i.e., the polymer shell.

Based on the experiment results, a significant red shift of the spectra can be observed. The driving force for the shrinkage is the decrease in the water/PE interface. Here, light-induced heating reduced the interaction between PDADMAC and PSS, causing the spectrum's observed shift. Simultaneously, Hep and PSS deposited as a mixture for the negatively charged layer show surprisingly high stability with swelling during temperature increase.

To describe the observed behavior of the single NP (Figures 3 a, b), we approximated the experimental scattering spectra to simulated curves evaluated using Mie theory for the case of core–shell NPs. For each NP, the silicon core diameter was set to 190 nm according to TEM measurements. Data for the refractive index of crystalline silicon were used according to the literature,[52] and the real part of the polymer shell refractive index was assumed to be $n = 1.5$. Our fitting procedure yielded the shell absorption index (i.e., the imaginary part of the refractive index) and the outer radius of the NPs. The obtained parameters are listed in the Supporting Information, Table S3. The simulated curves

shown in Figure 3 c,d are in reliable agreement with the experimental data. Besides the scattering intensity, we also display the electric and magnetic dipole (ED and MD) contributions to the entire spectra. The magnetic resonance variation related to the shell modification is negligible since the electric field is localized predominantly within the silicon core volume.

The multipolar expansion demonstrates that the broadband electric dipole resonance causes a significant contribution to the scattering spectra shift. Unlike its magnetic counterpart, the electric dipole's electric field penetrates the polyelectrolyte shell layer, which is tuned practically under laser illumination. It should be noted that the thermally responsive polymer shell was previously used to adjust the plasmon resonance.[37–39] This effect enables all-dielectric NPs to tune electric and magnetic resonances with different efficiency, allowing the intriguing effect of resonance overlapping and scattering spectrum reshaping.[11]

The maximal shift of Mie-type resonance, 60 nm, is achieved for the Si NP/Hep/PSS without PDADMAC, where we accelerate the hydrophobic effect and charge repulsion. Figure 4a shows that for the NPs without PDADMAC, the polymer shell relaxes to the original thickness faster than the ones with PDADMAC. The system's relaxation closer to the initial states takes several tens of minutes, while the complete relaxation should be achieved for hours (Figure 4b). The effect of the shift of optical resonances for Si NP/Hep/PSS can be explained by considering hydrophobic-hydrophilic interactions. At the initial stage, hydrophilic groups (sulfo- and hydroxyl groups) are adsorbed onto
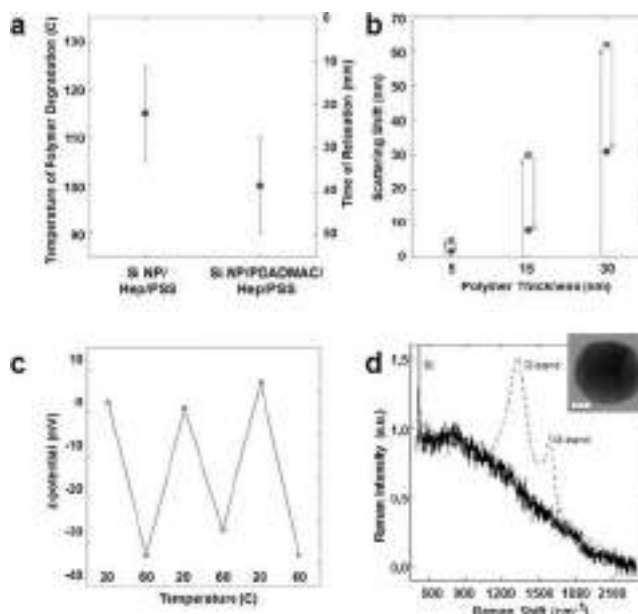
Figure 4. a) Thermal stability and relaxation time of samples Si NP/Hep/PSS and Si NP/PDADMAC/Hep/PSS. b) Dependence of the maximal spectral shift for system on shell thickness under the heating up to 90°C by light. c) Z-potential changes over successive cycles of heating and cooling. d) The Raman spectrum of the silicon NPs with thermally responsive polymers shell before (black curve) and after (dash curve) extreme heating up to 130°C. Inset shows the TEM of silicon NPs after overheating. The scale bar corresponds to 100 nm.

a silicon surface, and hydrophobic groups are outside pointing towards the solution. In solution, both forms of Hep exist in a dynamic equilibrium.[53] When the temperature increases, the equilibrium shifts favoring Hep/PSS conformation change, forcing hydrophobic and hydrophilic groups to swap the place.[31]

To confirm the hypothesis mentioned above, we performed zeta-potential measurements (Figure 4c). When the solution was heated in situ from 20°C to 60°C, we observed the PE shell's relaxation several times, proving the reversibility of the response. During the heating, zeta-potential also decreased from −5 to −60 mV. The increase of the thickness from 5 nm to 30 nm yields an increase in resonance tuning efficiency from 5 to 60 nm under the heating (Figure 4b). Therefore, we analyzed the maximum temperature (up to 90°C) to achieve perfect tuning while preserving the polymers' initial structure and composition. However, increasing the temperature to achieve the maximal tuning can lead to polymer carbonization, as seen by pronounced D and G-bands of carbon in Figure 4d. Our observation shows the possibility to control Mie resonance by the PE shell engineering and demonstrates that these hybrid systems can have a compassionate optical response which is easily manipulated through temperature. This polyelectrolyte assembly design is fundamental for applying the system with a high-density shell and paves the way for next generation nanophotonic systems.

In summary, we report on the design and realization of stimuli-responsive bio-integrated nanostructures based on optically resonant silicon NPs covered by an ensemble of similarly charged polyelectrolytes such as heparin and sodium polystyrene sulfonate. The nanostructures' dynamic tuning optical scattering spectra by light is due to light-induced heating of the NPs and concomitant swelling of the polyelectrolyte shell. Herein, the maximal shift (60 nm), higher thermal stability (up to 120 C), and faster relaxation rate (20 min) are observed for Si NP/Hep/PSS structure. We have also revealed that the hydrophilic/hydrophobic transitions lead to a significant change in the shell thickness and reversible shift of scattering spectra at mild conditions. Our findings have both fundamental importance and potential for in vivo application as smart nanomaterials in nanomedicine and bio-integrated nanophotonics.

Conflict of interest

The authors declare no conflict of interest.

[1] D. W. Lee, B. R. Yoo, *J. Ind. Eng. Chem.* **2016**, *38*, 1–12.
[2] H. C. Y. Yu, A. Argyros, G. Barton, M. A. van Eijkelenborg, C. Barbe, K. Finnie, L. Kong, F. Ladouceur, S. McNiven, *Opt. Express* **2007**, *15*, 9989.
[3] A. I. Kuznetsov, A. E. Miroshnichenko, M. L. Brongersma, Y. S. Kivshar, B. Luk'yanchuk, *Science* **2016**, *354*, 846.
[4] J. H. Bahng, S. Jahani, D. G. Montjoy, T. Yao, N. Kotov, A. Marandi, *ACS Nano* **2020**, *14*, 17203–17212.
[5] A. A. Krasilin, K. Volodina, A. A. Sukhova, M. I. Petrov, D. A. Zuev, V. A. Dyachuk, V. A. Milichko, *J. Biophotonics* **2018**, *11*, 1–6.
[6] N. Bontempi, K. E. Chong, H. W. Orton, I. Staude, D. Y. Choi, I. Alessandri, Y. S. Kivshar, D. N. Neshev, *Nanoscale* **2017**, *9*, 4972–4980.
[7] O. Yavas, M. Svedendahl, P. Dobosz, V. Sanz, R. Quidant, *Nano Lett.* **2017**, *17*, 4421–4426.
[8] V. A. Milichko, D. A. Zuev, D. G. Baranov, G. P. Zograf, K. Volodina, A. A. Krasilin, I. S. Mukhin, P. A. Dmitriev, V. V. Vinogradov, S. V. Makarov, P. A. Belov, *Laser Photonics Rev.* **2018**, *12*, 1700227.
[9] N. I. Zheludev, Y. S. Kivshar, *Nat. Mater.* **2012**, *11*, 917–924.
[10] Z. Li, Y. Yin, *Adv. Mater.* **2019**, *31*, 1807061.
[11] J. L. Liu, T. Liu, J. Pan, S. Liu, G. Q. M. Lu, *Annu. Rev. Chem. Biomol. Eng.* **2018**, *9*, 389–411.
[12] X. Liu, F. Zhang, X. Jing, M. Pan, P. Liu, W. Li, B. Zhu, J. Li, H. Chen, L. Wang, J. Lin, Y. Liu, D. Zhao, H. Yan, C. Fan, *Nature* **2018**, *559*, 593–598.
[13] J. F. Li, Y. J. Zhang, S. Y. Ding, R. Panneerselvam, Z. Q. Tian, *Chem. Rev.* **2017**, *117*, 5002–5069.
[14] M. Ha, J. H. Kim, M. You, Q. Li, C. Fan, J. M. Nam, *Chem. Rev.* **2019**, *119*, 12208–12278.
[15] C. Kinnear, T. L. Moore, L. Rodriguez-Lorenzo, B. Rothen-Rutishauser, A. Petri-Fink, *Chem. Rev.* **2017**, *117*, 11476–11521.
[16] P. Gutruf, C. Zou, W. Withayachumnankul, M. Bhaskaran, S. Sriram, C. Fumeaux, *ACS Nano* **2016**, *10*, 133–141.
[17] S. M. Kamali, E. Arbabi, A. Arbabi, Y. Horie, A. Faraon, *Laser Photonics Rev.* **2016**, *10*, 1002–1008.
[18] S. M. Kamali, A. Arbabi, E. Arbabi, Y. Horie, A. Faraon, *Nat. Commun.* **2016**, *7*, 11618.
[19] W. Park, J. B. Lee, *Appl. Phys. Lett.* **2004**, *85*, 4845–4847.
[20] M. Rahmani, L. Xu, A. E. Miroshnichenko, A. Komar, R. Camacho-Morales, H. Chen, Y. Zárate, S. Kruk, G. Zhang, D. N. Neshev, Y. S. Kivshar, *Adv. Funct. Mater.* **2017**, *27*, 1700580.
[21] T. Lewi, H. A. Evans, N. A. Butakov, J. A. Schuller, *Nano Lett.* **2017**, *17*, 3940–3945.
[22] J. Sautter, I. Staude, M. Decker, E. Rusak, D. N. Neshev, I. Brener, Y. S. Kivshar, *ACS Nano* **2015**, *9*, 4308–4315.
[23] J. Bohn, T. Bucher, K. E. Chong, A. Komar, D. Y. Choi, D. N. Neshev, Y. S. Kivshar, T. Pertsch, I. Staude, *Nano Lett.* **2018**, *18*, 3461–3465.
[24] A. Komar, Z. Fang, J. Bohn, J. Sautter, M. Decker, A. Miroshnichenko, T. Pertsch, I. Brener, Y. S. Kivshar, I. Staude, D. N. Neshev, *Appl. Phys. Lett.* **2017**, *110*, 071109.
[25] C. H. Chu, M. L. Tseng, J. Chen, P. C. Wu, Y. H. Chen, H. C. Wang, T. Y. Chen, W. T. Hsieh, H. J. Wu, G. Sun, D. P. Tsai, *Laser Photonics Rev.* **2016**, *10*, 986–994.
[26] S. Makarov, S. Kudryashov, I. Mukhin, A. Mozharov, V. Milichko, A. Krasnok, P. Belov, *Nano Lett.* **2015**, *15*, 6187–6192.
[27] M. R. Shcherbakov, S. Liu, V. V. Zubyuk, A. Vaskin, P. P. Vabishchevich, G. Keeler, T. Pertsch, T. V. Dolgova, I. Staude, I. Brener, A. A. Fedyanin, *Nat. Commun.* **2017**, *8*, 17.

[28] M. A. C. Stuart, W. T. S. Huck, J. Genzer, M. Müller, C. Ober, M. Stamm, G. B. Sukhorukov, I. Szleifer, V. V. Tsukruk, M. Urban, F. Winnik, S. Zauscher, I. Luzinov, S. Minko, *Nat. Mater.* **2010**, *9*, 101–113.

[29] M. O. Gallyamov, I. S. Chaschin, A. I. Gamzazade, A. R. Khokhlov, *Macromol. Chem. Phys.* **2008**, *209*, 2204–2212.

[30] O. E. Philippova, E. V. Volkov, N. L. Sitnikova, A. R. Khokhlov, J. Desbrieres, M. Rinaudo, *Biomacromolecules* **2001**, *2*, 483–490.

[31] A. R. Khokhlov, P. G. Khalatur, *Curr. Opin. Colloid Interface Sci.* **2005**, *10*, 22–29.

[32] N. V. Ryzhkov, N. A. Mamchik, E. V. Skorb, *J. R. Soc. Interface* **2019**, *16*, 20180626.

[33] D. O. Grigoriev, K. Karen, E. Skorb, D. G. Shchukin, M. Helmuth, *Soft Matter* **2009**, *5*, 1426–1432.

[34] E. V. Skorb, A. G. Skirtach, D. V. Sviridov, D. G. Shchukin, H. Möhwald, *ACS Nano* **2009**, *3*, 1753–1760.

[35] B. V. Parakhonskiy, W. J. Parak, D. Volodkin, A. G. Skirtach, *Langmuir* **2019**, *35*, 8574–8583.

[36] M. Delcea, H. Möhwald, A. G. Skirtach, *Adv. Drug Delivery Rev.* **2011**, *63*, 730–747.

[37] S. A. Ulasevich, G. Brezesinski, H. Möhwald, P. Fratzl, F. H. Schacher, S. K. Poznyak, D. V. Andreeva, E. V. Skorb, *Angew. Chem. Int. Ed.* **2016**, *55*, 13001–13004; *Angew. Chem.* **2016**, *128*, 13195–13198.

[38] K. Köhler, D. G. Shchukin, H. Möhwald, G. B. Sukhorukov, *J. Phys. Chem. B* **2005**, *109*, 18250–18259.

[39] R. Mueller, K. Köhler, R. Weinkamer, G. Sukhorukov, A. Fery, *Macromolecules* **2005**, *38*, 9766–9771.

[40] S. T. Jones, Z. Walsh-Korb, S. J. Barrow, S. L. Henderson, J. Del Barrio, O. A. Scherman, *ACS Nano* **2016**, *10*, 3158–3165.

[41] E. V. Skorb, H. Möhwald, D. V. Andreeva, *Adv. Mater. Interfaces* **2017**, *4*, 1600282.

[42] A. A. Nikitina, S. A. Ulasevich, I. S. Kassirov, E. A. Bryushkova, E. I. Koshel, E. V. Skorb, *Bioconjugate Chem.* **2018**, *29*, 3793–3799.

[43] P. A. Dmitriev, S. V. Makarov, V. A. Milichko, I. S. Mukhin, A. S. Gudovskikh, A. A. Sitnikova, A. K. Samusev, A. E. Krasnok, P. A. Belov, *Nanoscale* **2016**, *8*, 5043–5048.

[44] J. J. Richardson, B. L. Tardy, H. Ejima, J. Guo, J. Cui, K. Liang, G. H. Choi, P. J. Yoo, B. G. De Geest, F. Caruso, *ACS Appl. Mater. Interfaces* **2016**, *8*, 7449–7455.

[45] E. V. Skorb, H. Möhwald, *Adv. Mater.* **2013**, *25*, 5029–5043.

[46] S. Backert, M. Neddermann, G. Maubach, M. Naumann, *Helicobacter* **2016**, *21*, 19–25.

[47] S. Boddohi, C. E. Killingsworth, M. J. Kipper, *Biomacromolecules* **2008**, *9*, 2021–2028.

[48] L. Sun, X. Xiong, Q. Zou, P. Ouyang, R. Krastev, *J. Appl. Polym. Sci.* **2017**, *134*, 1–10.

[49] G. P. Zograf, M. I. Petrov, D. A. Zuev, P. A. Dmitriev, V. A. Milichko, S. V. Makarov, P. A. Belov, *Nano Lett.* **2017**, *17*, 2945–2952.

[50] I. S. Altman, D. Lee, J. D. Chung, J. Song, M. Choi, *Phys. Rev. B Condens. Matter Mater. Phys.* **2001**, *63*, 161402.

[51] C. Zhang, Y. Xu, J. Liu, J. Li, J. Xiang, H. Li, J. Li, Q. Dai, S. Lan, A. E. Miroshnichenko, *Nat. Commun.* **2018**, *9*, 2964.

[52] M. A. Green, M. J. Keevers, *Prog. Anesth. Mech. Prog. Photovolt. Res. Appl.* **1995**, *3*, 189–192.

[53] B. Mulloy, M. J. Forster, *Glycobiology* **2000**, *10*, 1147–1156.

Layer-By-Layer Polyelectrolyte Assembly for the Protection of GaP Surfaces from Photocorrosion

Nikolay V. Ryzhkov, Olesya Ledovich, Lara Eggert, Andreas Bund, Agnieszka Paszuk, Thomas Hannappel, Konstantin Klyukin, Vitaly Alexandrov, and Ekaterina V. Skorb*

ACCESS		Metrics & More		Article Recommendations

ABSTRACT: Polyelectrolyte layer-by-layer assemblies are known as protective coatings for corrosion inhibition. Here, we demonstrate that polyelectrolyte multilayers of poly-(ethyleneimine) (PEI) and poly(styrene sulfonate) (PSS)—(PEI/PSS)$_x$—adsorbed at the GaP(100) photocathode surface remarkably mitigate the photocorrosion of GaP without decreasing its photoconversion efficiency. The activity of the polybase−polyacid complex is based on buffering pH changes at the solid−liquid interface. We carried out ab initio molecular dynamics-based simulations of the GaP(100) surface in contact with liquid water and demonstrated that an increase in the proton concentration enhances GaP dissolution. We used the scanning vibrating electrode technique (SVET) to characterize the distribution of photocorrosion activity areas over bare and polyelectrolyte-coated GaP surfaces and we showed that a polyelectrolyte coating impedes the dissolution kinetics. Data obtained using the SVET were compared to photoetched pores on the semiconductor surface. Voltammetric and chronoamperometric measurements were also performed to evaluate photoconversion efficiencies before and after the application of the protective coatings.

KEYWORDS: polyelectrolytes, layer-by-layer assembly, proton sponge, III−V semiconductors, photocorrosion
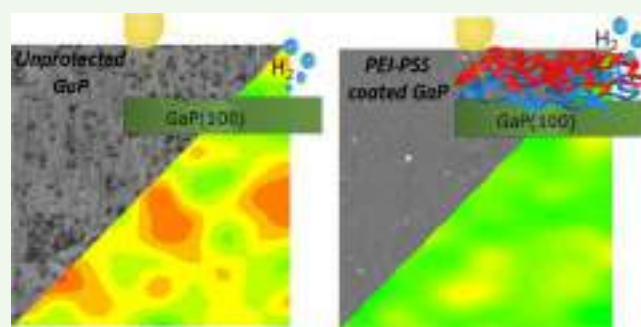
■ INTRODUCTION

Energy conversion using solar irradiation is a perspective and sustainable way to obtain clean and renewable fuels.[1] World-record conversion efficiencies in both photovoltaics[2] and solar water splitting[3] are achieved with multijunction solar cells based on III-V compound semiconductor structures. Despite the outstanding efficiency of hydrogen production under solar light irradiation,[4] the widespread use of these materials is limited by their oxidative corrosion.[5,6]

A promising photocathode for solar-to-hydrogen conversion is GaP, as its band gap is well-aligned to the water reduction accompanied by hydrogen production.[7] However, emerging holes can trigger the anodic dissolution of the material (Figure 1a) according to eq 1 in acidic solutions[8]

$$GaP + 3H_2O + 6h^+ = Ga^{3+} + 3H^+ + H_3PO_3 \qquad (1)$$
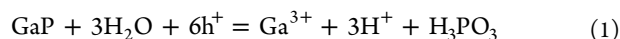
and according to eq 2 in alkali ones[8]

$$GaP + 4OH^- + 3h^+ = GaO_2^- + P + 2H_2O \qquad (2)$$
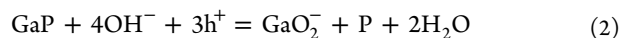
Indeed, photocathodes made of GaP are reported to be unstable and the rate of photodegradation depends significantly on the electrolyte's nature.[6] Previous observations indicated that GaP is quite unstable under both acidic and basic conditions, whereas GaP photocorrosion is significantly

suppressed at neutral pH.[9] It is obvious that the photo-electrochemical decomposition of water on the photoelectrode leads to pH changes at the interface. Thus, high-value III−V semiconductor materials require pH buffering at the semi-conductor/solution interface for improved performance and durability.

Based on this, a very effective solution for the deposition of protective coatings is the layer-by-layer (LbL) procedure, which involves the stepwise electrostatic assembly of oppositely charged polymer molecules and allows the formation of coatings with multiple functionalities.[10,11] LbL-assembled polyelectrolyte coatings have been proven to efficiently protect metals from corrosion.[12,13] The phenomen-on of their anticorrosion performance can be explained by three mechanisms: (i) weak polyelectrolytes exhibit a pH-buffering activity and can stabilize the pH level;[14,15] (ii) protons occurring at the solid−liquid interface and assisting
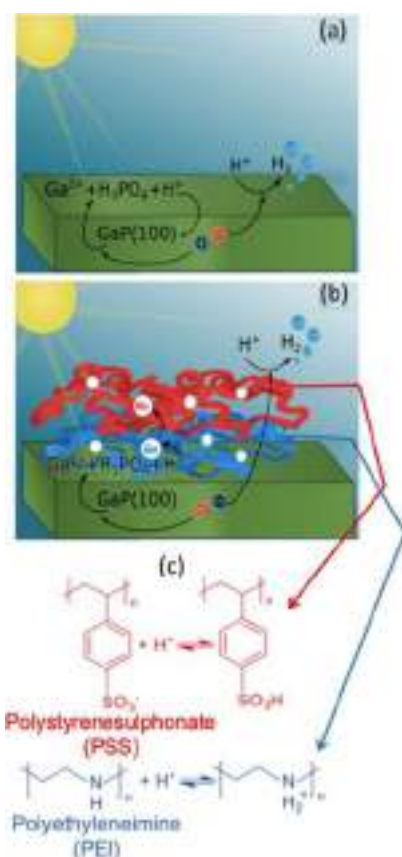
Figure 1. Schematic representation of photoinitiated processes at the (a) GaP−water solution interface: light-induced charge separation occurs in GaP; the electrons captured by protons in the water solution lead to hydrogen evolution and holes lead to anodic dissolution of GaP and local acidification of corrosive area, promoting further corrosion. As a result, under illumination, the photoelectrode surface is etched and the photocurrent and the photoconversion efficiency decrease; (b) PEI/PSS-protected GaP(100) surface: protons produced during GaP anodic dissolution are captured by PEI, proton "sponge" weak polyelectrolyte, and then PSS, strong polyelectrolyte; as a result, pH-buffering at the GaP/water solution interface inhibits semiconductor anodic dissolution, surface etching occurs to a lesser extent, and the photocurrent is stabilized.

corrosion can be captured by polyelectrolyte molecules,[16] and (iii) the polyelectrolytes that form the coating are relatively mobile[17] and have the tendency to seal and eliminate mechanical cracks of the coating, performing self-healing. All the mechanisms mentioned above could also be useful for III−V semiconductor photocorrosion protection. Furthermore, nanometer-thick polyelectrolyte multilayers are optically transparent[18] and permeable for water and smaller ions,[19] which is important in solar water-splitting applications. Recent studies also showed that polyelectrolyte layer formation on top of photoelectrodes of various natures does not lead to impedance growth.[20,21] In this paper, we studied the stability of bare and polyelectrolyte-coated p-type GaP(100) during operation under solar light. Hereby, in this paper, we focus on the control of the photochemical response of the hybrid system based on GaP, which can significantly change its long-term performance in the aqueous solution.

A smart multilayered system consisting of a strong−weak polyelectrolyte assembly deposited on GaP(100) substrates providing pH buffering at the semiconductor−solution interface is observed to prevent photocorrosion of the photoelectrode material. We also present the calculations that justify our strategy for protecting the material against corrosion by its interface pH-buffering. Anodic dissolution of GaP under illumination in solution is characterized in situ. Also, the effects of photocorrosion on material morphology and performance are shown.

RESULTS AND DISCUSSION

GaP Dissolution Mechanism and pH-Buffering Strategy to Inhibit GaP Photocorrosion. When cathodic hydrogen production and the anodic process described in (1) occur simultaneously, they can be combined to obtain the overall scheme of the corrosion process at the GaP−water solution interface when this is irradiated

$$GaP + 3H_2O + 3H^+ = Ga^{3+} + H_3PO_3 + 3H_2 \qquad (3)$$
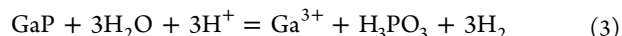
Equation 3 shows that protons are converted to hydrogen and drive the process of photoelectrode dissolution.

To demonstrate the critical role that an acidic environment may play in facilitating the dissolution of GaP, we have also
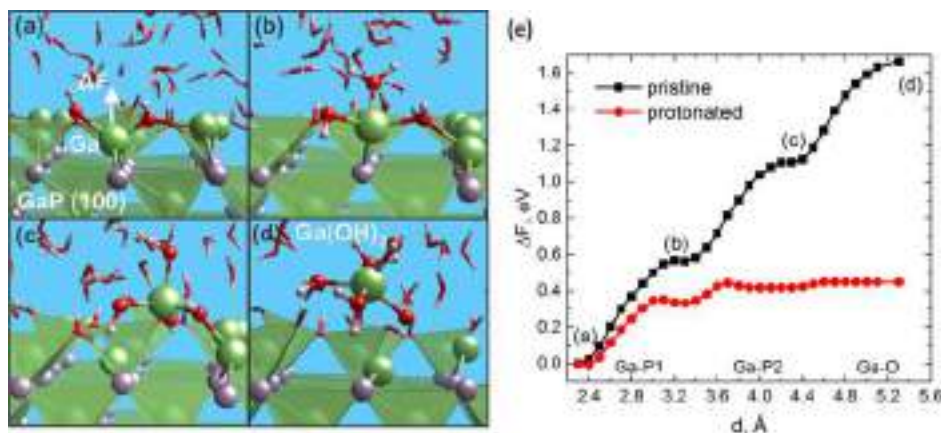
Figure 2. (a−d) Scheme showing the identified mechanism of Ga dissolution from the GaP (100) surface in an aqueous solution (color scheme: Ga—green, P—gray, O—red, and H—white): (a) Ga−P bond breaking, (b) Ga−H₂O bond formation, (c) second Ga−P bond breaking and Ga release to the surface, (d) Ga−O bond breaking and desorption of a Ga(OH)₃ complex; (e) corresponding free-energy profiles for the pristine and protonated GaP (100) surfaces in contact with water. The graph is composed of three parts corresponding to breaking the two Ga−P and single Ga−O bonds chosen as collective variables in each interval.
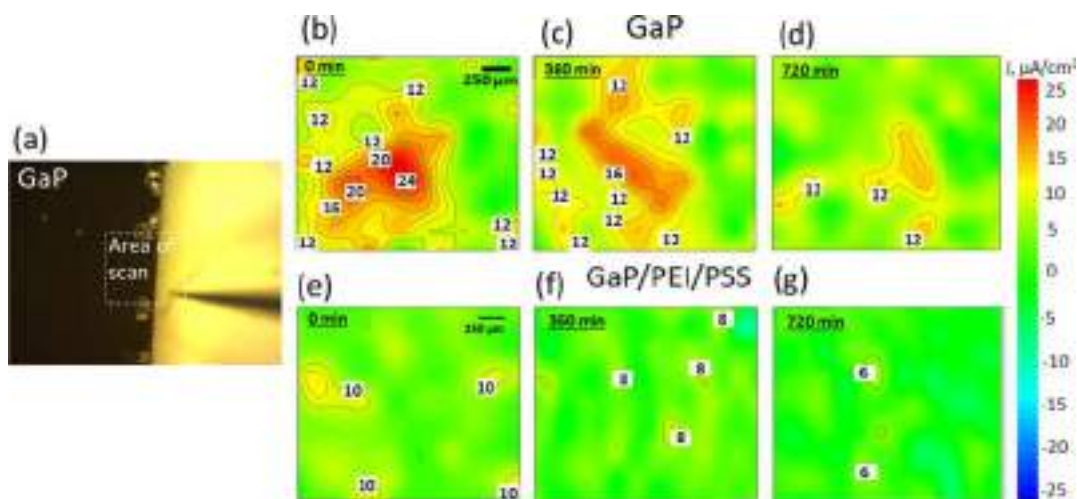
Figure 3. (a) Optical image of the GaP photoelectrode scanned using an SVET probe. The scanned area at the edge of the GaP specimen is shown by the white dotted frame, (b−d) series of long-term SVET scans over the pristine GaP surface at an open circuit obtained after (b) 1−15 min of illumination, (c) 360−375 min of illumination, and (d) 705−720 min of illumination, (e−g) series of long-term SVET scans over the GaP/PEI/PSS surface at an open circuit obtained after (e) 1−15 min of illumination, (f) 360−375 min of illumination, and (g) 705−720 min of illumination, SVET scans were registered in 0.05 M NaCl solution.

undertaken ab initio molecular dynamics (AIMD)-based simulations of the GaP (100) surface in contact with liquid water. Previous AIMD calculations of the pristine GaP and InP (100) surfaces[23,24] exposed to water have identified surface hydroxylation motifs and revealed distinct hydrogen-bond strength and proton-transfer dynamics at the two semiconductor/water interfaces. Our AIMD simulations started with a fully equilibrated Ga-rich GaP (100)/water interface where we observed a combination of free and bridging chemisorbed hydroxyl groups and molecular water. These surface groups are found to be in dynamic equilibrium because of the facile local proton transfer, in full agreement with prior AIMD simulations.[23,24] To demonstrate an effect of surface protonation on GaP dissolution kinetics, we examined the dissolution of Ga from a representative interfacial configuration, as shown in Figure 2. Here, Ga is coordinated by one bridging OH, one free OH, and two subsurface P atoms. To estimate activation barriers of Ga dissolution, we applied a slow-growth approach in combination with the thermodynamic integration technique as implemented in VASP (see the Computational Methodology section).

We first modeled Ga dissolution under pH-neutral conditions and found that Ga dissolution starts with the subsequent breaking of the two Ga−P bonds. After the first bond is broken (Figure 2a), Ga forms a new bond with the nearest H_2O molecule resulting in a metastable state (Figure 2b) with a very flat minimum characterized by an activation barrier of 0.61 eV. Then, the system overcomes a barrier of 0.51 eV, which involves the breaking of the second Ga−P bond, dissociation of H_2O, and release of Ga to the surface (Figure 2c). The last dissolution step is the desorption of $Ga(OH)_3$ from the surface into solution by breaking the remaining Ga−O bond. This step takes about 0.56 eV to break a single Ga−O bond (Figure 2c,d). Figure 2e (black line) shows a free energy profile for the pristine GaP (100) surface in contact with water.

To evaluate the impact of local pH changes on Ga dissolution rates, we then introduced additional protons to the system. These protons can diffuse into the semiconductor interior and protonate subsurface P atoms adjacent to the

dissolving Ga atoms disrupting the Ga−P bond topology. Herein, we did not examine the mechanism and kinetics of proton diffusion through the surface; however, this process was demonstrated for other semiconductor materials.[25] Moreover, proton transfer into the subsurface will be facilitated after the dissolution process has started and in the presence of surface irregularities. As seen in Figure 2e (red line), protonation of P atoms weakens the structural Ga−P bonds leading to more stable intermediate states and considerably lower activation barriers. It is found that after a subsequent protonation of adjacent P atoms, the cumulative dissolution barrier drops down to 0.48 eV, which should result in dissolution kinetics that are several orders of magnitude enhanced relative to pH-neutral conditions.

The magnitude of the effect at medium pH values is seen from our AIMD-based simulations of dissolution barriers discussed above. The predicted difference in interfacial behavior may be achieved by the pH-buffering performance of polyelectrolyte layers on the semiconductor surface.

We thus conclude that the strategy to prevent GaP photocorrosion is pH stabilization at the semiconductor−liquid interface. This could be achieved by the formation of a coating with a pronounced pH-buffering activity on the semiconductor surface. Nanometer-thick[26] LbL-assembled coatings are good candidates.[15] They do not prevent charge transfer at the solid−liquid interface maintaining photoconversion efficiency[20,21] but inhibit direct interaction of GaP with protons in solution, impeding corrosion. Branched cationic polyethyleneimine (PEI) was used as a first layer. This polymer is a weak polybase exhibiting buffering properties because the closely spaced amino groups are able to take up H^+ ions from the solution.[27] Because PEI has a limited buffer capacity, its single layer on the GaP photoelectrode surface will not give the desired long-term effect. Therefore, poly(sodium-4-stereenesulphonate) (PSS) was deposited on top of the GaP/PEI. PSS is a strong polyanion and cation-exchange polymer which, in combination with PEI, allows better pH-buffering the semiconductor/solution interface. Our strategy to prevent GaP photocorrosion by depositing buffering multilayers combining

proton "sponge" and proton conductive layers is demonstrated in Figure 1b.

GaP Photocathode Corrosion Inhibition. With proton consumption from solution and their conversion to H_2, pH of the near-electrode region is expected to shift to basic values.[22] Because acidic electrolytes (e.g., 1 M H_2SO_4) are usually utilized to produce hydrogen, it is unlikely that a strongly alkaline medium is formed at the interface. Therefore, further we focused on corrosion processes in acidic electrolytes. In this case, protons in solution can serve not only as acceptors of photoelectrons but also interact with the material of the photoelectrode, contributing to its photocorrosion.

Furthermore, according to eq 1, gallium phosphide photo-anodic dissolution is accompanied by acidification at the photoelectrode–solution interface in areas where corrosion process is localized. As will be shown later (Figures 3 and 4),
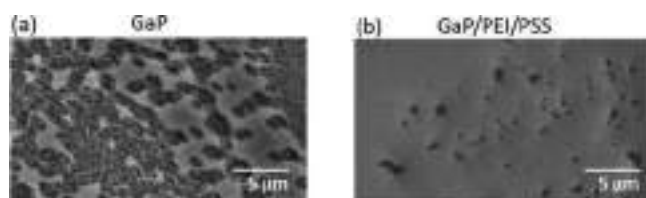
Figure 4. SEM images of the photoelectrode surface for (a) pristine GaP after 12 h of illumination in 1 M KCl, (b) GaP/PEI/PSS after illumination under mild conditions of 1 M KCl.

corrosion does not occur on the entire surface of the illuminated photoelectrode but only in some regions (e.g., where crystal defects are localized). Therefore, even in neutral electrolytes, a local shift of pH toward lower values can occur in places where corrosion processes are localized. These locally formed protons can influence corrosion processes before being converted to hydrogen.

To demonstrate the validity of the model considered in the previous chapter and the protective performance of the proposed polyelectrolyte coating of $(PEI/PSS)_x$ architecture, we performed an SVET analysis of pristine- and polyelec-trolyte-protected photoelectrode surfaces under illumination in the electrolyte solution. This technique allows us to visualize the distribution of anodic and cathodic activity regions by measuring the electric field in a solution near the sample surface. The measurements by SVET were carried out under open-circuit conditions. The reason is an external electric field arising in the solution upon polarization of the photoelectrode.

It might be so high that the electric fields arising during corrosion could not be recorded using an SVET device.

The uniformly illuminated (visible irradiation, 11,000 lumen) area at the edge of the planar GaP specimen was studied by SVET in 0.05 M NaCl solution at pH ~7. The scanned area included both the space above the photoactive sample and the spaces above the region without the sample; thus, the test and control samples were studied simultaneously under the same conditions during a single experiment (Figure 3a).

Over a pristine GaP sample, anodic activity spots were observed. The interfacial reactions occurring at open-circuit potential can be attributed to the anodic dissolution of the photoelectrode material coupled with photocathodic proton reduction according to the scheme from Figure 1a. It is worth noting that despite the uniform illumination, the areas of anode activity are localized only in some parts of the sample (Figure 3b). This supports the assumption that the observed anode activity is related to the dissolution of the photo-electrode because of its photocorrosion. Lattice defects introduce energy states within the valence band which are more likely to be populated with the photoexcited holes. Therefore, photocorrosion initially starts and evolves at lattice defects. This determines the pattern of the anodic activity observed on the SVET scan. The sample was scanned continuously for 12 h, allowing us to observe the evolution of the GaP photoanodic dissolution (Figure 3b–d).

Photocorrosion is observed during the early times of illumination. We suppose that it occurs under open-circuit conditions because there is no way of holes outflow but photoelectrode material self-oxidation. Also, we can conclude that anodic dissolution fades over time possibly because of the surface passivation, accompanying the photocorrosion of the GaP under neutral-pH conditions.[9]

When the GaP photoelectrode surface is coated by a polyelectrolyte multilayer of PEI/PSS, anodic dissolution is suppressed according to SVET scanning. Absolute values of the anodic activity in terms of ionic current are 2.5 times lower and the anodic activity localization area is more than 10 times smaller (Figure 3e–g). Photocorrosion processes usually develop fast after disruption of the surface atomic order. However, polyelectrolyte coatings being adaptive and dynamic materials respond to local changes in pH and ionic strength by polymer network reorganization.[28] Apparently, coating self-healing occurs[29] and stable low anodic activity is observed over polyelectrolyte-coated GaP.
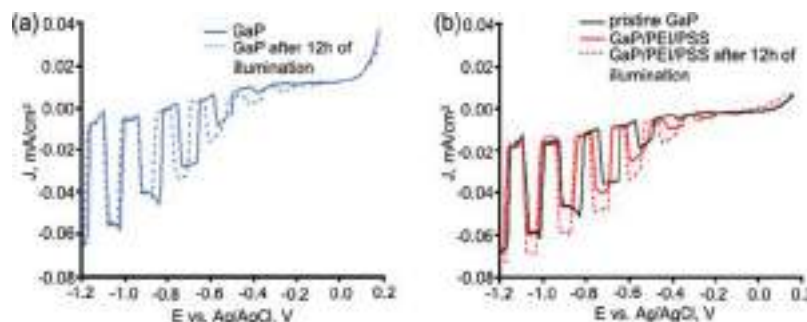
Figure 5. (a) Current–potential curves under chopped illumination of pristine GaP(100), black line—previously unused GaP specimen and black dotted line—the same specimen after 12 h of operation under illumination (11,000 lumen) in 1 M KCl solution; (b) current–potential curves under chopped illumination of: black line—previously unused pristine GaP, red line—the same specimen of GaP after PEI/PSS deposition, and red dotted line—GaP/PEI/PSS after 12 h of operation under illumination (11,000 lumen) in 1 M KCl solution.
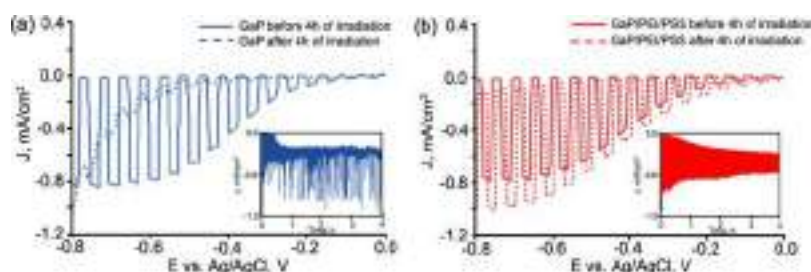
Figure 6. Current−potential curves registered in 1 M H$_2$SO$_4$ solution under chopped illumination (11,000 lumen) of (a) pristine GaP, black line—before irradiation and black dotted line—the same specimen after 4 h illumination at −0.6 V vs Ag/AgCl; (b) GaP/PEI/PSS red line—before irradiation and red dotted line—the same specimen after 4 h illumination at −0.6 V vs Ag/AgCl; insets are chronopotentiometry curves during 4 h under chopped illumination at −0.6 V vs Ag/AgCl.

The effects of photocorrosion on the morphology of the photoelectrode at the microscopic level were studied by SEM. Figure 4a demonstrates the surface of the GaP photoelectrode after 12 h of illumination under neutral conditions. Although the initial GaP surface was smooth and relatively featureless, the formation of pores was observed after operation under illumination in agreement with maps of photoanodic activity registered using the SVET (Figure 3b−d). Despite the passivation of the surface over time, significant surface defects are formed. After depositing a protective layer, anodic dissolution is suppressed according to SVET data (Figure 3e−g) and the photoelectrode surface is etched in a lower degree (Figure 4b).

Thus, the deposition of a buffering polyelectrolyte multilayer allows us to suppress the anodic dissolution of GaP, and nanometer-thick polyelectrolyte PEI/PSS coating provides effective photocorrosion inhibition.

Photocurrent Degradation Prevention. The effect of polyelectrolyte layers on the photoactivity of GaP photocathodes was studied under chopped visible irradiation (11,000 lumen) in a three-electrode cell in 1 M KCl. Figure 5 demonstrates typical I−V plots. Cathodic photocurrent steadily increases with the potential becoming more negative whether polyelectrolytes are deposited on top of the surface or not. Polyelectrolyte layers neither affect the absorption of light by a semiconductor nor have a significant photosensitizing effect and almost the same profile of voltammetry curves was observed for bare (Figure 5a) and polyelectrolyte-coated GaP (Figure 5b). Furthermore, we observed that for the polyelectrolyte-coated GaP photoelectrode, a slight increase in the photocurrent values was observed. We suppose that it is due to surface area increase after rough polyelectrolyte coating formation.[21] For both bare and PEI/PSS-coated photoelectrodes, no photocurrent degradation during long-term operation under constant illumination (11,000 lumen) and −0.6 V versus Ag/AgCl polarization was observed. Thus, in the photo-electrochemical cell, in the mild ambience photocathode surface, etching does not lead to a decrease in the photoconversion efficiency and photocurrent degradation.

However, at neutral pH, photocurrent density values are rather small compared to recent reports for acidic solutions where proton conversion is the most effective.[4] Furthermore, we studied the ability of buffering polyelectrolyte layers to protect GaP from photocorrosion under acidic conditions (1 M H$_2$SO$_4$). Here, photocurrents increased by an order of magnitude because of the higher efficiency of proton-to-hydrogen conversion and a lower nonradiative recombination rate of photoexcited charge carriers. Nonetheless, under such conditions, the anodic dissolution of the photocathode leads rather quickly to photocurrent degradation. Figure 6a demonstrates the photocurrent decrease after photoelectrode operation at −0.6 V versus Ag/AgCl under illumination by visible light with 11,000 lumen intensity for 4 h, evidencing its significant photodegradation and the decrease in photo-conversion efficiency in comparison with neutral conditions (Figure 5a). The photocurrent density is lower for pristine GaP photoelectrodes after long-time irradiation (Figure 6a), whereas for PEI/PSS-protected photocathodes, the effect of photocurrent decrease after operation under illumination is not so pronounced (Figure 6b).

Such a difference in the behavior of the photoelectrode in different electrolytes is in agreement with previously proposed mechanisms of GaP photocorrosion.[30] It was previously reported that during GaP anodic dissolution, Ga is going into solution in the form of hydroxide.[6] Meanwhile, this compound is not soluble in solutions of medium pH.[9,30] Thus, anodic oxidation of GaP under neutral conditions leads to the formation of a Ga(OH)$_3$ passivating layer, preventing further dissolution.[8] We suppose that it is a reason why we observed photoanodic activity decay on SVET scans (Figure 3b−d) and no significant photocurrent degradation in KCl solution of neutral pH for the bare GaP sample (Figure 5a). However, the passivation layer can be dissolved by acids and fresh electrode surface proceeds to corrode under illumination resulting in significant photocurrent degradation (Figure 6a).

With the time of irradiation for both samples (coated and uncoated with polyelectrolytes), an increase in the dark cathodic current was observed (Figure 6 a,b insets). For bare GaP, the growth of the dark current is observed mainly during the first hour, while for the sample coated with polyelectrolytes, this process is more extended in time and an increase in the dark current is observed for 1.5−2 h before stabilization. It should be noted that this is not a unique process; such changes have previously been shown in photoelectrodes based on Cr$_2$O$_3$,[31] for example. We suppose that this phenomenon could be explained by electrons leaking to defect and surface states emerging during photocorrosion of GaP.

Thereby, buffering with polyelectrolyte layers does not only prevent GaP dissolution in neutral media under illumination but also preclude its photodegradation and photoconversion efficiency decrease in strongly acidic media.

■ CONCLUSIONS

We have demonstrated an efficient strategy of soft matter assemblies for photocorrosion protection, particularly addressing III−V semiconductor systems. The smart coating

assembled from weak proton "sponge" polycation PEI and strong polyanionic cationite PSS prevents anodic etching of p-type Zn-doped GaP photocathodes and enables its prolonged photoactivity. The mechanism of polyelectrolyte multilayer protective action is based on the pH-buffering capacity of a polyelectrolyte multilayer. The effect has been demonstrated on a surface relevant for water splitting devices, but it is expected to be applicable to many types of interfacial processes where pH-buffering is important.

■ MATERIALS AND METHODS

Chemicals and Materials. Poly(ethyleneimine) (PEI, $M_w \sim 70$ kDa) and poly(styrene sulfonate) (PSS, $M_w \sim 500$ kDa) were obtained from Sigma-Aldrich. Reagent-grade NaCl (99.5%) was obtained from Merck. All chemicals were used without further purification. p-type GaP (100) wafers with ±0.5° offcut Zn-doped to 1.8 to 2.3 × 10^{18} cm^{-3} were obtained from the Institute of Electronic Materials Technology (Warsaw, Poland).

Computational Methodology. Simulations were performed employing a $10.90 \times 10.90 \times 21.35$ Å^3 box comprising the GaP slab and a vacuum gap of ~10 Å. The surface was hydroxylated in accordance with previous studies[23,24] and the vacuum gap was filled with 34 H_2O to obtain a water density of ~1 g/cm^3. To evaluate dissolution barriers, we applied Born-Oppenheimer molecular dynamics (BOMD) simulations in combination with slow-growth and Blue Moon ensemble techniques[32] within the plane-wave density-functional-theory formalism as implemented in the VASP code.[33] All simulations were performed employing the Perdew–Burke–Ernzer-hof (PBE)[34] functional along with the projector-augmented wave (PAW) formalism and DFT-D3 van der Waals correction.[35] A 1.0 fs time step in the BOMD simulations and the hydrogen mass of 3 a.m.u. were used. To keep the charge neutrality of the simulation cell with additional protons into aqueous solution, we removed one/two protons from the absorbed water on the opposite side of the GaP slab. The Nose–Hoover thermostat was used to keep the simulation temperature around 300 K.[36] The trajectories obtained using the slow-growth approach as the energetically favorable reaction pathways were used for subsequent Blue Moon ensemble-based thermodynamic integrations to estimate activation barriers. A set of windows along each reaction pathway was chosen with a step of 0.1 Å between adjacent windows. Configurations in each window were additionally equilibrated during 2 ps, while the next 2 ps were used to collect and average the energy gradients along the reaction direction. A similar computational scheme was employed in a series of recent studies.[37−39]

Polyelectrolyte Multilayer Assembly. A single p-GaP (100) wafer was cut into several parts. Polyelectrolyte layers were deposited on top of GaP using the classical LbL technique. The procedure of multilayer assembly consists of depositing alternating layers of oppositely charged materials with wash steps in between. In our case, it was accomplished by alternating immersion of the GaP specimen in a polyelectrolyte (PEI and PSS) in ambient light. Semiconductor plates were immersed in 2 mg/mL polyelectrolyte solution in 0.5 M NaCl for 15 min in ambient light. After the deposition of each layer, the specimen was rinsed with water and dried in air steam. To obtain more dense PEI coverage, the GaP plate was twice immersed in PEI solution before PSS deposition. Eventually, PEI/PSS coating was obtained on top of the GaP substrate.

Local Photo-electrochemical Study. Photoactivity of pristine- and polyelectrolyte-covered, p-type, Zn-doped GaP(100) was studied under irradiation using the SVET. This method allows the observation of the material's electrochemical activity with micrometer spatial resolution and outstanding sensitivity. The potential, ΔV, between two points at a distance Δr from each other was measured for these purposes. It is realized using a vibrating (with amplitude Δr) probe scanning the surface of the irradiated specimen. To perform the SVET study, a system from Applicable Electronics (USA) under control of

ASET program (Scienceware, USA) was used. Pristine- or polyelectrolyte-covered GaP(100) samples under investigation were attached to an epoxy holder using adhesive tape. The surface of the photoelectrode was uniformly illuminated by visible light (luminous power 11,000 lumen) and scanned using the vibrating probe. The scanning area was selected on the edge of the specimen. As a vibrating probe for the SVET experiments, insulated Pt−Ir microprobes (Microprobe Inc., USA) with a platinum black spherical tip of 30 μm diameter were applied. The probe was vibrating in two directions parallel and perpendicular to the specimen surface 150 μm above it. The amplitude of vibration was 30 μm, and vibration frequencies of the probe were 136 Hz (perpendicular to the surface) and 222 Hz (parallel to the surface). Data were presented in terms of ionic currents. The ionic current density was mapped on a 40 × 40 grid in a 0.05 M NaCl solution. The time of acquisition for each SVET data point was 0.6 s.

Photocurrent Measurements. Photo-electrochemical measurements were performed in a handmade 3D-printed cell with the PalmSens4 potentiostat (Netherlands) in a three-electrode cell with pristine- or polyelectrolyte-modified GaP(100) as working electrodes, an Ag/AgCl (KCl sat.) reference electrode, and a Pt wire as a counter electrode. Specimen of GaP was made in contact with the copper plate from the back unpolished side, pressed against it, and fixed to obtain stable ohmic contact. Photocurrent measurements were performed in 1 M KCl or 1 M H_2SO_4 solution under chopped illumination by visible light. Measurements were carried out in two regimes: potential scan from 0.2 to −1.2 V versus Ag/AgCl and chronoamperometry at −0.6 V versus Ag/AgCl. Prior measurement, each specimen was equilibrated in solution at OCP for 5−10 min in the dark.

■ AUTHOR INFORMATION

Corresponding Author

Ekaterina V. Skorb − *ITMO University, St. Petersburg 191002, Russian Federation;* ⊙ orcid.org/0000-0003-0888-1693; Email: skorb@itmo.ru

Authors

Nikolay V. Ryzhkov − *ITMO University, St. Petersburg 191002, Russian Federation*

Olesya Ledovich − *ITMO University, St. Petersburg 191002, Russian Federation*

Lara Eggert − *Technical University Ilmenau, Ilmenau 98693, Germany*

Andreas Bund − *Technical University Ilmenau, Ilmenau 98693, Germany;* ⊙ orcid.org/0000-0001-9837-2408

Agnieszka Paszuk − *Technical University Ilmenau, Ilmenau 98693, Germany*

Thomas Hannappel − *Technical University Ilmenau, Ilmenau 98693, Germany*

Konstantin Klyukin − *Department of Chemical and Biomolecular Engineering, University of Nebraska-Lincoln, Lincoln, Nebraska 68588, United States;* ⊙ orcid.org/0000-0001-8325-8725

Vitaly Alexandrov − *Department of Chemical and Biomolecular Engineering, University of Nebraska-Lincoln, Lincoln, Nebraska 68588, United States;* ⊙ orcid.org/0000-0003-2063-6914

Complete contact information is available at:
https://pubs.acs.org/10.1021/acsanm.0c02768

Notes

The authors declare no competing financial interest.

REFERENCES

(1) Hisatomi, T.; Kubota, J.; Domen, K. Recent Advances in Semiconductors for Photocatalytic and Photoelectrochemical Water Splitting. *Chem. Soc. Rev.* **2014**, *43*, 7520−7535.

(2) Dimroth, F.; Grave, M.; Beutel, P.; Fiedeler, U.; Karcher, C.; Tibbits, T. N. D.; Oliva, E.; Siefer, G.; Schachtner, M.; Wekkeli, A.; Bett, A. W.; Krause, R.; Piccin, M.; Blanc, N.; Drazek, C.; Guiot, E.; Ghyselen, B.; Salvetat, T.; Tauzin, A.; Signamarcheix, T.; Dobrich, A.; Hannappel, T.; Schwarzburg, K. Wafer Bonded Four-Junction GaInP/ GaAs//GaInAsP/GaInAs Concentrator Solar Cells with 44.7% Efficiency. *Prog. Photovoltaics Res. Appl.* **2014**, *22*, 277−282.

(3) Cheng, W.-H.; Richter, M. H.; May, M. M.; Ohlmann, J.; Lackner, D.; Dimroth, F.; Hannappel, T.; Atwater, H. A.; Lewerenz, H.-J. Monolithic Photoelectrochemical Device for Direct Water Splitting with 19% Efficiency. *ACS Energy Lett.* **2018**, *3*, 1795−1800.

(4) Standing, A.; Assali, S.; Gao, L.; Verheijen, M. A.; Dam, D. V.; Cui, Y.; Notten, P. H. L.; Haverkort, J. E. M.; Bakkers, E. P. A. M. Efficient Water Reduction with Gallium Phosphide Nanowires. *Nat. Commun.* **2015**, *6*, 7824.

(5) Pishgar, S.; Strain, J. M.; Gulati, S.; Sumanasekera, G.; Gupta, G.; Spurgeon, J. M. Investigation of the Photocorrosion of n-GaP Photoanodes in Acid with in situ UV-Vis Spectroscopy. *J. Mater. Chem. A* **2019**, *7*, 25377−25388.

(6) Butler, M. A.; Ginley, D. S. P-Type GaP as a Semiconducting Photoelectrode. *J. Electrochem. Soc.* **1980**, *127*, 1273.

(7) Tee, S. Y.; Win, K. Y.; Teo, W. S.; Koh, L.-D.; Liu, S.; Teng, C. P.; Han, M.-Y. Recent Progress in Energy-Driven Water Splitting. *Adv. Sci.* **2017**, *4*, 1600337.

(8) Meek, R. L.; Schumaker, N. E. Anodic Dissolution and Selective Etching of Gallium Phosphide. *J. Electrochem. Soc.* **1972**, *119*, 1148.

(9) Madou, M. J.; Cardon, F.; Gomes, W. P. Anodic Processes at the n- and p-Type GaP Electrodes. *Berichte der Bunsengesellschaft für physikalische Chemie* **1977**, *81*, 1186−1190.

(10) Ryzhkov, N. V.; Andreeva, D. V.; Skorb, E. V. Coupling PH-Regulated Multilayers with Inorganic Surfaces for Bionic Devices and Infochemistry. *Langmuir* **2019**, *35*, 8543−8556.

(11) Ryzhkov, N. V.; Brezhneva, N.; Skorb, E. V. Feedback mechanisms at inorganic-polyelectrolyte interfaces for applied materials. *Surf. Innovations* **2019**, *7*, 145−167.

(12) Andreeva, D. V.; Skorb, E. V.; Shchukin, D. G. Layer-by-Layer Polyelectrolyte/Inhibitor Nanostructures for Metal Corrosion Protection. *Appl. Mater. Interfaces* **2010**, *2*, 1954−1962.

(13) Skorb, E. V.; Skirtach, A. G.; Sviridov, D. V.; Shchukin, D. G.; Möhwald, H. Laser-Controllable Coatings for Corrosion Protection. *ACS Nano* **2009**, *3*, 1753−1760.

(14) Andreeva, D. V.; Fix, D.; Möhwald, H.; Shchukin, D. G. Buffering Polyelectrolyte Multilayers for Active Corrosion Protection. *J. Mater. Chem.* **2008**, *18*, 1738.

(15) Brezhneva, N.; Nikitina, A.; Ryzhkov, N.; Klestova, A.; Vinogradov, A. V.; Skorb, E. V. Importance of Buffering Nanolayer Position in Layer-by-Layer Assembly on Titania Based Hybrid Photoactivity. *J. Sol. Gel Sci. Technol.* **2018**, *89*, 92−100.

(16) Tago, T.; Shibata, H.; Nishide, H. Proton Conductivity in the Dry Membrane of Poly(Sulfonic Acid) and Polyamine Layer-by-Layer Complex. *Chem. Commun.* **2007**, 2989.

(17) Fares, H. M.; Schlenoff, J. B. Diffusion of Sites versus Polymers in Polyelectrolyte Complexes and Multilayers. *J. Am. Chem. Soc.* **2017**, *139*, 14656−14667.

(18) Hiller, J. A.; Mendelsohn, J. D.; Rubner, M. F. Reversibly Erasable Nanoporous Anti-Reflection Coatings from Polyelectrolyte Multilayers. *Nat. Mater.* **2002**, *1*, 59−63.

(19) Antipov, A. A.; Sukhorukov, G. B.; Möhwald, H. Influence of the Ionic Strength on the Polyelectrolyte Multilayers' Permeability. *Langmuir* **2003**, *19*, 2444−2448.

(20) Ryzhkov, N. V.; Skorb, E. V. A Platform for Light-Controlled Formation of Free-Stranding Lipid Membranes. *J. R. Soc. Interface* **2020**, *17*, 20190740.

(21) Ulasevich, S.; Ryzhkov, N. V.; Andreeva, D. V.; Özden, D. S.; Piskin, E.; Skorb, E. V. Light-to-Heat Photothermal Dynamic Properties of Polypyrrole-Based Coating for Regenerative Therapy and Lab-on-a-Chip Applications. *Adv. Mater. Interfaces* **2020**, *7*, 2000980.

(22) Jin, J.; Walczak, K.; Singh, M. R.; Karp, C.; Lewis, N. S.; Xiang, C. An Experimental and Modeling/Simulation-Based Evaluation of the Efficiency and Operational Performance Characteristics of an Integrated, Membrane-Free, Neutral PH Solar-Driven Water-Splitting System. *Energy Environ. Sci.* **2014**, *7*, 3371−3380.

(23) Wood, B. C.; Schwegler, E.; Choi, W. I.; Ogitsu, T. Hydrogen-Bond Dynamics of Water at the Interface with InP/GaP(001) and the Implications for Photoelectrochemistry. *J. Am. Chem. Soc.* **2013**, *135*, 15774−15783.

(24) Wood, B. C.; Schwegler, E.; Choi, W. I.; Ogitsu, T. Surface Chemistry of GaP(001) and InP(001) in Contact with Water. *J. Phys. Chem. C* **2014**, *118*, 1062−1070.

(25) Ghosh, S.; Soudackov, A. V.; Hammes-Schiffer, S. Role of Proton Diffusion in the Nonexponential Kinetics of Proton-Coupled Electron Transfer from Photoreduced ZnO Nanocrystals. *ACS Nano* **2017**, *11*, 10295−10302.

(26) Shiratori, S. S.; Rubner, M. F. pH-Dependent Thickness Behavior of Sequentially Adsorbed Layers of Weak Polyelectrolytes. *Macromolecules* **2000**, *33*, 4213−4219.

(27) Curtis, K. A.; Miller, D.; Millard, P.; Basu, S.; Horkay, F.; Chandran, P. L. Unusual Salt and PH Induced Changes in Polyethylenimine Solutions. *PLoS One* **2016**, *11*, No. e0158147.

(28) Ryzhkov, N. V.; Brezhneva, N.; Skorb, E. V. Feedback mechanisms at inorganic-polyelectrolyte interfaces for applied materials. *Surf. Innovations* **2019**, *7*, 145−167.

(29) Skorb, E. V.; Andreeva, D. V. Self-Healing Properties of Layer-by-Layer Assembled Multilayers. *Polym. Int.* **2015**, *64*, 713−723.

(30) Memming, R.; Schwandt, G. Electrochemical Properties of Gallium Phosphide in Aqueous Solutions. *Electrochim. Acta* **1968**, *13*, 1299−1310.

(31) Sekizawa, K.; Oh-Ishi, K.; Morikawa, T. Photoelectrochemical Water-Splitting over a Surface Modified p-Type Cr2O3 Photocathode. *Dalton Trans.* **2020**, *49*, 659−666.

(32) Sprik, M.; Ciccotti, G. Free Energy from Constrained Molecular Dynamics. *J. Chem. Phys.* **1998**, *109*, 7737−7744.

(33) Shi-Gang, S.; Yan, L.; Nan-Hai, L.; Ji-Qian, M. Kinetics of Dissociative Adsorption of Formic-Acid on Pt(100), Pt(610), Pt(210) and Pt(110) Single-Crystal Electrodes in Perchloric-Acid Solutions. *J. Electroanal. Chem.* **1994**, *370*, 273−280.

(34) Perdew, J. P.; Burke, K.; Ernzerhof, M. Generalized Gradient Approximation Made Simple. *Phys. Rev. Lett.* **1996**, *77*, 3865−3868.

(35) Ehrlich, S.; Moellmann, J.; Reckien, W.; Bredow, T.; Grimme, S. System-Dependent Dispersion Coefficients for the DFT-D3 Treatment of Adsorption Processes on Ionic Surfaces. *ChemPhysChem* **2011**, *12*, 3414−3420.

(36) Martyna, G. J.; Klein, M. L.; Tuckerman, M. Nosé-Hoover chains: The canonical ensemble via continuous dynamics. *J. Chem. Phys.* **1992**, *97*, 2635−2643.

(37) Klyukin, K.; Rosso, K. M.; Alexandrov, V. Iron Dissolution from Goethite (α-FeOOH) Surfaces in Water by Ab Initio Enhanced Free-Energy Simulations. *J. Phys. Chem. C* **2018**, *122*, 16086−16091.

(38) Leung, K. First-Principles Modeling of Mn(II) Migration above and Dissolution from LixMn2O4 (001) Surfaces. *Chem. Mater.* **2016**, *29*, 2550−2562.

(39) Xiao, H.; Goddard, W. A.; Cheng, T.; Liu, Y. Cu metal embedded in oxidized matrix catalyst to promote CO_2 activation and CO dimerization for electrochemical reduction of CO_2. *PNAS* **2017**, *114*, 6685.

Polyelectrolyte Substrate Coating for Controlling Biofilm Growth at Solid–Air Interface

Nikolay V. Ryzhkov, Anna A. Nikitina, Peter Fratzl, Cécile M. Bidan,* and Ekaterina V. Skorb*

Because bacteria–surface interactions play a decisive role in bacteria adhesion and biofilm spreading, it is essential to understand how biofilms respond to surface properties to develop effective strategies to combat them. Polyelectrolyte coating is a simple and efficient way of controlling surface charge and energy. Using polyelectrolytes of various types, with different molecular weights and polyelectrolyte solutions of various pH provides a unique approach to investigate the interactions between biofilms and their substrate. Here, the formation of *Escherichia coli* biofilms at a solid–air interface is explored, whereby charge and interfacial energy are tuned using polyelectrolyte coatings on the surface. Cationic coatings are observed to limit biofilm spreading, which remain more confined when using high molecular weight polycations. Interestingly, biofilm surface densities are higher on polycationic surfaces despite their well-studied bactericidal properties. Furthermore, the degree of polyelectrolyte protonation also appears to have an influence on biofilm spreading on polycation-coated substrates. Finally, altering the interplay between biomass production and surface forces with polyelectrolyte coatings is shown to affect biofilm 3D architecture. Thereby, it is demonstrated that biofilm growth and spreading on a hydrogel substrate can be tuned from confined to expanded, simply by coating the surface using available polyelectrolytes.

1. Introduction

Biofilms are surface-attached complex 3D structures of bacterial cells embedded in a self-produced fibrous biopolymer matrix. These adhesive living systems are known for their

N. V. Ryzhkov, A. A. Nikitina, Prof. E. V. Skorb
Infochemistry Scientific Center of ITMO University
ITMO University
Lomonosova str. 9, St. Petersburg 191002, Russia
E-mail: skorb@itmo.ru

Prof. P. Fratzl, Dr. C. M. Bidan
Biomaterials Department
Max Planck Institute of Colloids and Interfaces
Am Mühlenberg 1, 14424 Potsdam, Germany
E-mail: cecile.bidan@mpikg.mpg.de

The ORCID identification number(s) for the author(s) of this article can be found under https://doi.org/10.1002/admi.202001807.

consequences on human health[1,2] and industrial processes[3,4] as well as antibiotics resistance.[5] Various approaches to inhibition of biofilm formation and their eradication were developed.[6] Biofilm formation at an interface is determined by several phenomena, e.g., the initial adhesion of single bacteria to the surface and the further biofilm growth and spreading due to cell proliferation and biopolymer production.[7] Therefore, surface energy and electrostatic interactions with the substrate are two key determinants of biofilm formation. On this basis, a common strategy to fight bacterial colonization is the functionalization of surfaces that are prone to biofilm fouling.[6,8] For instance, surface hydrophilization[9] and low surface energy strategies[10] were considered. Surface topology was also modified to influence bacterial colonization, as recently reviewed in detail.[11]

Polyelectrolyte coatings allow changing the surface energy, charge, and mechanical characteristics of various substrates easily.[12,13] Therefore, polyelectrolyte assemblies are often considered for possible application as antibacterial coatings. However, understanding the fundamental principles of bacteria–surface interactions remains of high importance.[14–16] Due to the negative charges found on their external membrane, bacteria tend to tightly attach to positively charged surfaces.[17] It was demonstrated that biofilm spreading rate was decreasing with increasing strength of adhesion.[17] One possible explanation is that bacteria elongation preceding cell division is obstructed by strong electrostatic binding to the surface.[18] Besides this, it is also known that positively charged molecules (and polycations to a greater extent) exhibit antibacterial properties due to their ability to disrupt membranes of bacterial cells.[19] In contrast, negatively charged surfaces provide less stable bacterial cell contact with the surface,[18] so that the initial adhesion step is difficult but further biofilm spreading meets less obstacle.

In addition to help preventing healthcare and industry-related issues, investigating biofilm formation is beneficial to understand the development of biological tissues,[20] cell adaptability,[21] and communication[22] since some morphogenesis principles are common with higher organisms' tissues. Furthermore, colonies and biofilms of non-pathogenic microorganisms are considered to be promising to design hybrid living materials[23–27] challenging to get synthetically. Revealing

**ADVANCED
SCIENCE NEWS**
www.advancedsciencenews.com

**ADVANCED
MATERIALS
INTERFACES**
www.advmatinterfaces.de

the nature of bacteria–surface interactions and identifying the principles of biofilm adaptation to surface conditions are also essential to support further progresses in such contexts.

Polyelectrolytes are charged polymers that are able to change their characteristics in response to external stimuli such as temperature,[28] light,[29] ionic strength,[30] and pH.[31,32] It was recently demonstrated that reversible oscillation of polyelectrolyte layer-by-layer assemblies based on high amplitude actuation of block copolymer micelles allows controlling cell behavior on a surface. Their pH responsiveness was also used via light–pH coupling[33] to control the behavior of mammalian cells.[34,35]

Here, we chose an *Escherichia coli* strain (*E. coli* AR3110)[36] to study biofilm formation on polyelectrolyte-modified agar gels. *E. coli* AR3110 bacteria were shown to produce and assemble an extracellular matrix mainly composed of phosphoethanolamine cellulose and amyloid fibers.[36,37] We found that the patterns of ridges and wrinkles emerging during biofilm growth on solid depend on the nature of the polyelectrolyte used, its molecular weight, and the pH of the solution in which it was prepared. Macroscopic spatiotemporal characterizations of the biofilms were performed to assess the influence of the physicochemical properties of the substrates on biofilms morphology. We believe that the phenomena discovered in our study can make a significant contribution to understanding the adaptability of biological tissues and be used in the development of approaches to the directed biosynthesis of functional materials. In addition, the data shown will help to develop more effective ways to prevent biofilm growth in both medical and industrial contexts.

2. Results and Discussion

We used various polyelectrolytes to modify the surface properties of the nutritive substrate in order to control *E. coli* AR3110 biofilm growth. Therefore, we chose several polyelectrolytes,

namely polyethyleneimine (PEI; weak polycation), poly(sodium 4-styrenesulphonate) (PSS; strong polyanion), poly(allylamine hydrochloride) (PAH; weak polycation), and poly(acrylic acid) (PAA; weak polyanion) (Figure S1, Supporting Information). We varied the conditions of polyelectrolyte deposition by using different molecular weights of the polycations. The molecular weight allows affecting the transformation from glassy and rubbery states of the polyelectrolyte.[38] Various pH in the polyelectrolyte solutions were used for their deposition.

2.1. Polycationic Surfaces Impair Biofilm Spreading and Limit Their Growth

Polyelectrolyte solutions used for coating deposition were adjusted to pH 7. Detailed insight of biofilm morphogenesis on the various polyelectrolyte coatings were obtained by capturing images every 30 min and gathering them in time-lapse videos (see Videos, Supporting Information). **Figure 1**a demonstrates the appearance of biofilms growing on bare and polyelectrolyte coated agar substrates at various time points. Differences in the speed of biofilm spreading and, in their phenotype, depending on the polyelectrolyte used could be observed. Daily measurements of projected biofilm area were plotted as a function of time (Figure 1b).

Figure 1a,b shows that biofilm growth kinetics was similar on a bare Luria-Bertani (LB) agar and on PSS- or PAA-coated LB agar throughout the entire observation time. They demonstrate synchronous growth and the same projected area throughout the observation period as well as the same final mass after 4 days of growth. In contrast, cationic polymers were observed to significantly reduce biofilm spreading over the substrate. In particular, *E. coli* biofilms grown on PEI ($M_w = 25\,000$) or PAH ($M_w = 17\,000$) covered agar substrate after 4 days of incubation had on average a diameter ≈2.5 times smaller than control biofilms grown on bare agar substrates.
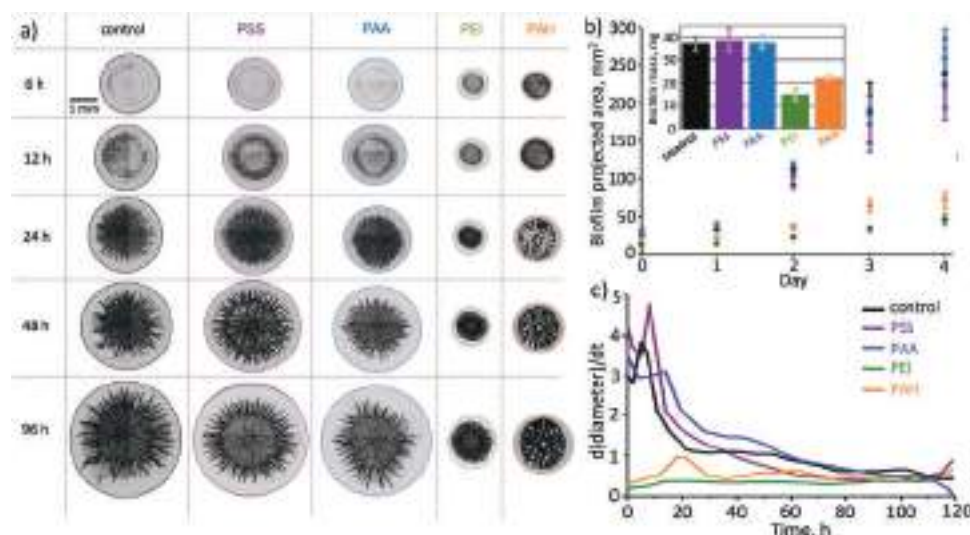
Figure 1. a) Bright-field snapshots of biofilms growing on bare control and polyelectrolyte-covered (PSS, PAA, PEI (M_w 25 000), PAH (M_w 17 000)) agar substrates at designated times. b) Biofilm projected area plotted versus incubation time and biofilm mass data (inset): biofilms grown on PAA, PSS coatings, and control surface demonstrate the same values of the projected area ($p > 0.1$) and mass ($p = 0.8$), whereas PEI and PAH coatings promote smaller biofilm area ($p < 0.002$) throughout the observation period and final mass ($p < 2 \times 10^{-5}$), herewith PEI reduces biofilm spreading more than PAH ($p < 0.003$ for area and $p = 8 \times 10^{-4}$ for mass). c) Derivative plot of biofilm versus time of growth.

After inoculation, biofilm growth rate on the control as well as on polyanion-coated surfaces (PAA and PSS) were higher than on polycation-coated surfaces (PEI and PAH). The biofilm projected area of biofilm growing on a pristine agar surface (as well as on PSS and PAA coated) increase by about 30% on the first day, and 300% on the second day with a subsequent slowdown (Figure 1b). But for biofilms growing on PEI- and PAH-coated agar, significantly slower growth rate was observed. On the first day, biofilms grew by only 8% and 12%, respectively, whereas on the second day by 57% (PEI) and 70% (PAH) (Figure 1b). After 4 days of culture, biofilms grown on polycationic surfaces occupied less than 20% of control biofilm area (Figure 1b inset). Kymograph-like space–time plots showing changes of biofilm diameter as a function of time were extracted from time-lapse videos (Figure S2a, Supporting Information). The temporal evolution of biofilm diameter was additionally plotted for each type of polyelectrolyte coating (Figure S2b, Supporting Information).

Derivative plots were also obtained to better visualize and quantify the growth rate (Figure 1c). Biofilms growing on positively charged surfaces (PEI- and PAH-coated agar) were characterized by a slow growth at an almost constant rate (with a small maximum for PEI). Biofilms growing on negatively charged surfaces first grow faster reaching a maximum growth rate between 5 and 7 h after inoculation, and subsequently slowed down to reach similar growth rates as those observed on positively charged surfaces (less pronounced for PAA in this experiment) (Figure 1c).

After 4 days of growth, biofilms were removed from the nutritive substrates and weighted. The average mass of biofilms grown on surfaces covered by various polyelectrolytes is displayed in the insert in Figure 1b. The biofilms grown on PEI and PAH were 2 to 2.5 times lighter than the ones grown on the control surfaces, although their area was more than five times lower (Figure 1b). In other words, biofilm growing on polycation-coated substrates was two times denser than biofilm growing on bare control or PSS- and PAA-covered surfaces ($32-33$ vs $14-19$ mg cm^{-2}) (Figure S3a, Supporting Information). Interestingly, PEI and PAH constrained biofilm spatial expansion but did not impair biomass production to the same degree.

It has been reported that polycations exhibit antibacterial properties, i.e., interact with and disrupt bacterial cell membranes.[39,40] But PEI and PAH coatings were reported to exhibit weak bactericidal activity since they do not contain the quaternary amino groups most toxic to bacteria.[14,41] Indeed, biofilms inoculated from bacterial suspension in nutritive media mixed with polycation solution revealed no bactericide effect of polycation. It was evidenced by the fact that biofilms grew equally regardless of the nature of the polyelectrolyte when a bare agar plate was inoculated with bacterial suspension mixed with these polyelectrolyte solutions (Figure S4, Supporting Information). Hence, the reason for limited biofilm spreading on polycationic surfaces rather lies in interfacial effects than in polyelectrolyte toxicity. We assume that biofilm spreading is impaired by strong electrostatic attachments, which prevent elongation and division of the bacteria along the plane of the solid-air interface.[17,42] A so-called "arrested growth"[43] behavior was consistently observed for biofilms forming on PEI- and PAH-coated substrates. Concerning surface energy, it was reported that surface charging usually improves wetting

properties[44] without clear correlation between the sign of charge and wettability.[12] However, some studies report that polyelectrolyte multilayers with terminating polycations tend to be more hydrophobic,[45] which also may have an impact in our case. Our observations are expected to hold for both negatively charged gram-positive and gram-negative bacteria, which were shown to both adhere faster on positively charged surfaces compared to negatively charged ones. However, the effects may be slightly altered in gram-positive bacteria, which were shown to better grow on positive surfaces compared to gram-negative bacteria in dynamic conditions.[18] However, it should be noted that the shape of the bacterial cell may also play a role in the process under investigation, so it is difficult to make unambiguous assumption about how polyelectrolyte coatings affect the growth of biofilms of bacteria with different cell membrane structures without taking into account many other factors. Therefore, in this study, we focused on studying the effects on a single bacteria type: *E. coli* AR 3110.

2.2. High-Molecular-Weight Coatings Suppress Biofilm Spreading

Since polyanionic coatings did not significantly affect biofilm morphogenesis, we further focused on polycations. PEI of several molar weights was used to coat the surface of the nutritive LB agar biofilm substrates. Biofilm images were acquired daily during the culture period and the projected biofilm area was measured and plotted against time (**Figure 2**). The increase of molar weight of the polycations resulted in a decreasing speed of biofilm spreading.

In comparison to bare substrates (control), biofilms reached 50–60% of the control projected area when grown on low molecular weight ($M_w = 1300$) PEI-coated substrates, 20–30% on medium molecular weight ($M_w = 25\,000$) PEI-coated substrates, and only ≈10% on high molecular weight ($M_w = 750\,000$) PEI-coated substrates (Figure 2a).

The ratio of the mass of biofilms grown on PEI coated substrate to the control conditions was 0.7, 0.4, and 0.25 for low, medium, and high molecular weight PEI, respectively, (Figure 2a inset). Area density, in contrast, increased from 23 to 35 mg cm^{-2} upon transition from the surface modified by low weight PEI to high weight PEI (Figure S3b, Supporting Information).

Similar to PEI, increasing PAH molecular weight in PAH-coated LB agar substrates from 17 000 to 65 000 led to a decrease of the projected area and the mass of the biofilms grown on their surface (Figure 2b and inset) and an increase of the area density (30 mg cm^{-2} for low molecular weight vs 40 mg cm^{-2} for high molecular weight polymer) (Figure S3c, Supporting Information).

This is consistent with the data on the dependence of the hydrophobicity of polyelectrolyte coatings on their molecular weight. For alkylated PEI derivatives antibacterial activity was revealed to depend on the molecular weight of the polymer.[14] Low molecular weight polymers were reported to have negligible, if any, antibacterial activity.[14] Indeed, for PEI and PAH, each repeat unit of both polycations carries two hydrophobic CH groups together with protonatable and potentially hydrophilic NH groups. Hence, polymer molecular weight increase promotes worse wettability.

**ADVANCED
SCIENCE NEWS**
www.advancedsciencenews.com

**ADVANCED
MATERIALS
INTERFACES**
www.advmatinterfaces.de
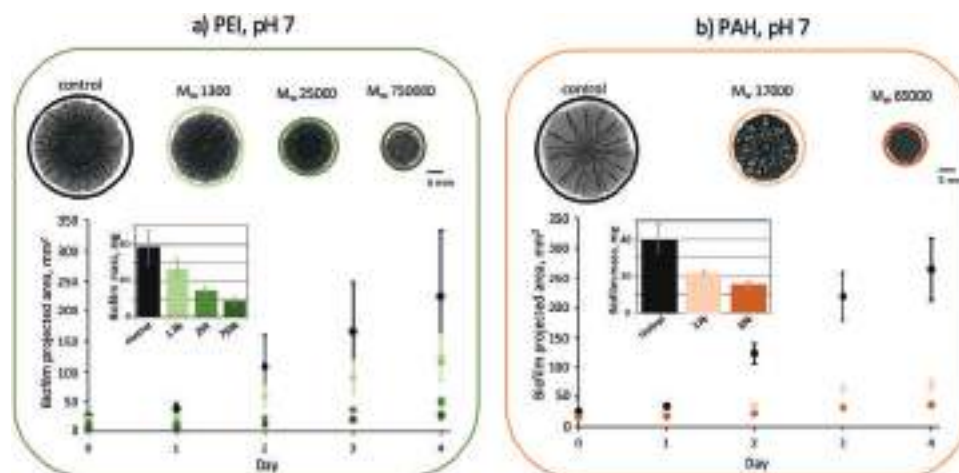
Figure 2. Effect of polyelectrolyte molecular weight: a) bright-field images (top) of biofilms grown for 4 days on bare nutritive agar substrate and substrate covered by PEI with average $M_w = 1300$, average $M_w = 25\,000$, and average $M_w = 750\,000$; biofilm projected area versus incubation time (bottom), inset demonstrates biofilm mass data after 4 days of growth; the area and mass of a biofilm grown on PEI coating with medium molecular weight is less than on low molecular weight ($p < 3 \times 10^{-4}$ and $p < 2 \times 10^{-5}$, respectively) and more than on high molecular weight coating ($p < 7 \times 10^{-7}$ and $p < 5 \times 10^{-5}$, respectively). b) Bright-field images (top) of biofilms grown for 4 days on bare nutritious agar substrate and substrate covered by PAH with average $M_w = 17\,000$, average $M_w = 65\,000$; biofilm projected area versus incubation time (bottom), inset demonstrates biofilm mass data after 4 days of growth; the area and mass of a biofilm grown on high molecular weight PAH coating is less than on low molecular weight coating ($p < 2 \times 10^{-7}$ and $p < 0.002$, respectively).

2.3. The pH of the Polyelectrolyte Solutions Used to Coat the Agar Has a Conditional and Limited Effect on Biofilm Spreading

Branched PEI is known for its buffering capacity. It is a weak polycation highly sensitive to pH of surrounding media and responding to it by charge and conformational alterations.[46,47] We deposited PEI ($M_w = 25\,000$) from solutions of various pH (**Figure 3**a). This molecular weight was chosen for giving

a clear effect on biofilm morphology, while leaving the possibility to observe further limitation of biofilm spreading. Indeed, with the more effective $M_w = 750\,000$, further biofilm growth limitation induced by pH changes would be difficult to quantify due to their size similar to the initial drop of bacteria suspension. At all studied pH (3, 5, 7, and 9), biofilm growth was much reduced compared with the control experiment on bare agar substrate, for which the pH of the aqueous phase in
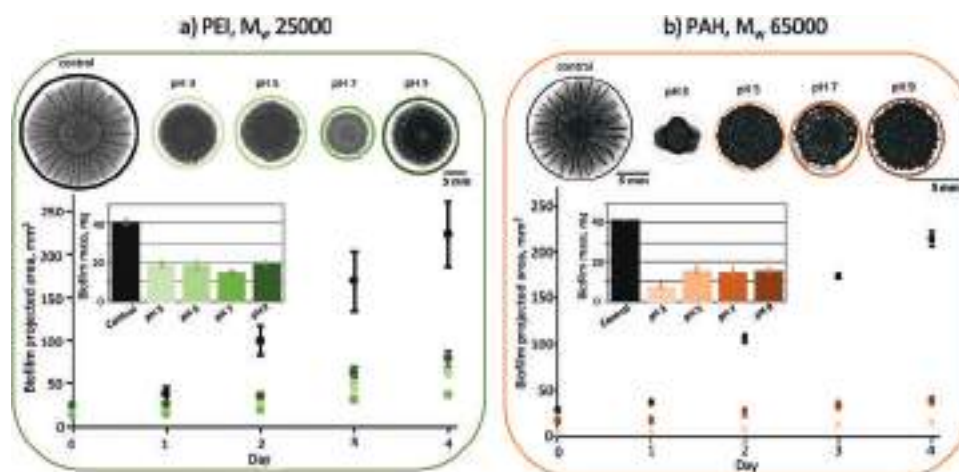
Figure 3. Effect of the pH of the polyelectrolyte solutions: a) bright-field images (top) of biofilms grown for 4 days on bare nutritive agar substrate and substrate covered by PEI with average $M_w = 25\,000$ and pH 3, 5, 7, and 9; biofilm area versus incubation time (bottom); and biofilm mass data after 4 days of incubation (inset); PEI coating applied from solution with pH 7 limits biofilm spreading as well as mass production to the greatest degree ($p < 6 \times 10^{-4}$ and $p = 1 \times 10^{-5}$, respectively), whereas areas and masses of biofilms grown at PEI coating applied from solutions with pH 3, 5, and 9 are equal ($p > 0.01$ and $p > 0.06$, respectively). b) Bright-field images (top) of biofilms grown for 4 days on bare nutritious agar substrate and substrate covered by PAH with average $M_w = 65\,000$ and pH 3, 5, 7, and 9; biofilm area versus incubation time (bottom); and biofilm mass data after 4 days of incubation (inset); PAH coating applied from solution with pH 3 limits biofilm spreading as well as mass production to the greatest degree ($p < 3 \times 10^{-6}$ and $p = 0.001$, respectively), whereas areas and masses of biofilms grown at PAH coatings applied from solutions with pH 5, 7, and 9 are equal ($p > 0.06$ and $p > 0.8$, respectively).

**ADVANCED
SCIENCE NEWS**

www.advancedsciencenews.com

**ADVANCED
MATERIALS
INTERFACES**

www.advmatinterfaces.de

the hydrogel was estimated between 7 and 8 using pH paper. Surprisingly, the effect was particularly pronounced on the substrate coated with a neutral PEI solution of pH 7. In this case, the projected area of the biofilms on the fourth day was 2 to 2.5 times smaller and their mass was ≈20% lower compared to the biofilms obtained with all the other tested pH. Moreover, the area density of biofilms grown on PEI coatings was maximum at pH 7 (34 vs 25–30 mg cm^{-2} for other studied pH) (Figure S3d, Supporting Information). Here, we can also note that depositing a drop of basic or acidic solution (without polyelectrolyte) on the agar surface prior to inoculation did not affect further biofilm growth and spreading (Figure S5, Supporting Information).

We believe that the observed phenomenon can be explained by the non-monotonicity of changes in the properties of PEI as a function of pH. A freshly prepared solution of PEI in 0.5 M NaCl has a pH 9. The polymer charge increases with decreasing pH. Due to PEI protonation, the surface coated at pH 7 carries a more positive net charge in comparison to the surface coated at pH 9, and thus is more favorable to the adhesion of negatively charged bacteria. As a result, biofilm spreading on the surface coated at pH 7 is limited to a greater extent. With further protonation, the protonability of amine groups decreases due to electrostatic repulsion of protons from already protonated amine groups.[48] As a result, more protons and chloride ions are found in solution as HCl is added to reach lower pH values. Eventually, chloride ions screen the positive charges of protonated amines, which leads to a decrease of the positive net charge. Therefore, agar substrates coated with PEI at pH 3 and 5 are expected to present lower positive net charges compared to pH 7 and thereby weaker electrostatic interactions with bacteria. Consistently, a better spreading of biofilm over these surfaces coated at pH 3 and 5 was observed in comparison to pH 7.

PAH is another weak polyelectrolyte with a pKa from 8.5 to 9 and has buffering capacity.[49,50] Low molecular weight PAH (M_w = 17 000) demonstrated ambiguous data on pH-dependence (Figure S6, Supporting Information). However, for high molecular weight PAH (M_w = 65 000), biofilm spreading was impaired to the greatest degree on a surface coated with a PAH solution of pH 3. On such an acidic surface, the biofilm spread over approximately one-third of the projected area and weighted approximately half of the mass compared to biofilms growing on surfaces modified with PAH from solutions with less acidic pH (from 5 to 9) (Figure 3b). On PAH coatings, the largest value of biofilm area density was obtained at pH 3 (54 mg cm^2 vs 40 for pH 5–9) (Figure S3e, Supporting Information). Thus, we found that the polycations that inhibit the spreading of biofilms also presented a pH-dependent effect on biofilm growth.

Decreasing the pH of PAH solution gradually increases the degree of PAH molecule protonation. Unlike branched PEI, protonated amino groups of the PAH are not located in the backbone and are thus more accessible to protonation. Therefore, protonation is accompanied by a monotonous increase of polymer molecule positive charge and gradual conformational transition from coiled to extended. As a result, the hydrophobicity and the charge of surfaces coated by PAH increase as the pH decreases.

Polyanions did not exhibit such an effect and biofilms grown on surfaces modified with PAA and PSS were similar to control samples. To reveal pH dependence of polyanion coatings, solutions of weak polyanion–polyacrylic acid (PAA, pKa = 4.5–6.5[51,52]) with various pH were prepared and used to coat agar substrates where biofilms were grown. When the carboxyl groups are protonated, the polymer is overall hydrophobic. On the other hand, when deprotonated, the surface is expected to be less hydrophobic. Hence, PAA-coated agar is expected to be more hydrophobic in comparison with a less protonated and more negatively charged PAA surface at higher pH. In contrast to this assumption, we did not observe any influence of PAA coating pH on biofilm spreading (Figure S7, Supporting Information). Apparently, the charge effect prevails over the wettability of the surface on which the biofilm grows. As long as the surface charge remains negative, the biofilm hydrophobicity does not constitute a major obstacle to biofilm growth.

2.4. Polyelectrolyte Coating Affects Biofilm Wrinkling Patterns

Mechanical and adhesive properties of the biofilms were shown to determine their morphology.[53] The different biofilm sizes and shapes obtained on the different types of polyelectrolyte coatings may thus provide insights into the biofilm properties involved in the effects observed and thereby provide new hints on how to control them. After inoculation of bare agar substrates, *E. coli* AR3110 expanded and formed circular biofilms with disordered wrinkling patterns in the center and radial folds on the outside. Biofilms grown on PSS or PAA coated substrates were also characterized by more disorganized patterns in the core and radial wrinkles emerging at the periphery (**Figure 4**a,b). In contrast, biofilms grown on PEI- and PAH-coated substrates developed a more compact morphology characterized by very dense networks of poorly organized wrinkles (Figure 4a,c). It was reported that periodical radial wrinkles developing in biofilms originate from tangential compressive stresses that accumulate during growth and cannot be released otherwise, while radial stresses are released by biofilm expansion.[53] These conclusions are in line with our observation that the wrinkling patterns obtained on various surfaces vary from periodic radial folds with low density (on bare substrates, PSS and PAA) to very dense and disordered folding patterns (on PEI and PAH). This qualitative observation is supported by the calculation of the biofilm area density (biofilm mass/biofilm projected area), which appears to vary accordingly from ≈20 mg cm^{-2} in control conditions or on polyanionic surfaces to values greater than 40 mg cm^{-2} on polycationic surfaces (Figure S8, Supporting Information, inset). It highlights that despite a lower mass, biofilms subjected to constrained spreading on polycationic coatings have a higher area density compared to control surfaces and polyanionic coatings. This observation indicates that the interfacial interactions with the substrate affect the biofilm lateral spreading in a greater extent than biomass production. The mechanism of radial stress relaxation through biofilm expansion along the surface[53] is thus less effective in cases of confined spreading like on polycationic surfaces, so that compressive stresses are expected to build up in both radial and circumferential directions and lead to the observed disordered and dense wrinkling pattern (Figure 4a,c).
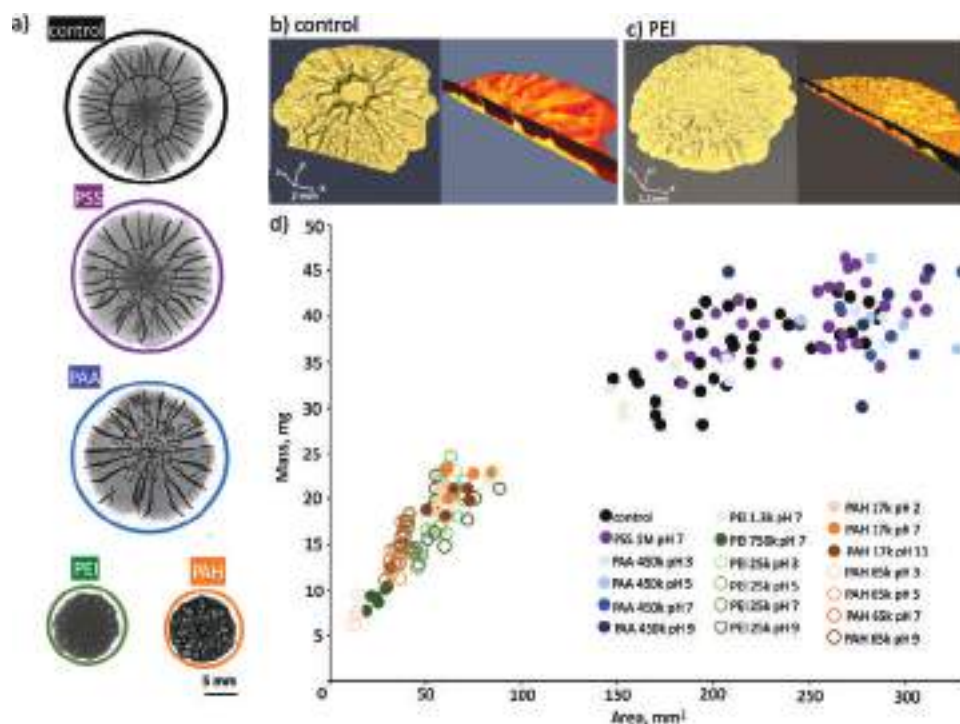
Figure 4. a) Bright-field images of biofilms grown for 4 days on a bare nutritive agar substrate PSS-, PAA-, PEI-, and PAH-coated substrates; b,c) X-ray microtomographies of biofilms grown on b) a bare agar substrate and c) a PEI-coated agar substrate; d) scatter diagram of mass and area for biofilms growing on substrates coated by various polyelectrolytes of different molecular weight and pH.

To better understand the link between biofilm morphology and the properties of the underlying surface, we plotted each biofilm mass as a function of their projected area for all the conditions tested (Figure 4d). Two data clusters are clearly separated by a gap at areas between 100 and 150 mm^2: one corresponds to biofilm confined spreading on polycationic coatings and the other corresponds to biofilm expanded spreading on bare agar substrates or polyanionic coatings. Biofilms grown on PEI coatings with M_w 25 000 and pH 3, 5, and 9 were found to have no statistically significant differences in area and mass ($p > 0.01$) and, therefore, were combined into one group. Similarly, we combined the data for biofilms grown on PAH coatings with M_w 17 000 and separately for biofilms grown on PAH with M_w 65 000 and pH 5, 7, and 9. Data for PSS, PAA, and control were also combined following the same criterion. In Figure S8 (Supporting Information) one can see that the data are divided into a larger number of clusters with varying degrees of positive correlation within each of them. Figure S8 (Supporting Information) shows that the clusters corresponding to biofilms grown on PAH M_w 65 000 (pH 5, 7, and 9) and PEI M_w 25 000 (pH 7) overlap significantly and have similar values of density but different phenotypes: disordered wrinkled cores and radial wrinkled shells on PEI and completely disordered wrinkling on PAH (Figure 3). Similarly, clusters formed by biofilms of different phenotypes grown on PAH M_w 17 000 and PEI M_w 25 000 (pH 3, 5, and 9) also intersect. Thus, the effect of polyelectrolyte coatings on biofilm 3D architecture is not limited to creating obstacles to lateral spreading on the surfaces but has a more complex nature, which is still unclear. In that context, it will be worthwhile to explore further how the polyelectrolyte coating affect biofilm composition and if polyelectrolytes from the coating interact with biofilm matrix components. The simple experimental protocol for systematic studies of the effect of polyelectrolyte coatings on biofilm growth established in this work will be the ideal tool to address this new question with various bacteria types, shapes, and matrices, in a near future.

3. Conclusion

E. coli AR3110 biofilms were grown on polyelectrolyte-coated agar substrates. Polyelectrolyte coating is a convenient approach to modify surface charge and energy to influence biofilm formation at solid–air interfaces in static conditions. It was demonstrated that polycationic surfaces impair biofilm spreading on their substrate. It was also surprisingly observed that polycation coatings, which are considered to be antibacterial, lead to the formation of denser biofilms. Increasing the molecular weight of the polycations used to coat the substrate impairs biofilm spreading even more. For weak polyelectrolyte coatings, pH dependence of biofilm spreading over such coatings revealed that more protonated surfaces prevent biofilm spreading to larger extent thus confirming the role of charges. In addition, it was shown that polyelectrolyte coating influences both the area of spreading and (to a smaller extent) the amount of produced biomass, thereby influencing the 3D architecture of biofilm growing on a particular substrate. We, thus, demonstrated that biofilm spreading can be confined or extended by modifying the substrate with common polyelectrolytes.

**ADVANCED
SCIENCE NEWS**

www.advancedsciencenews.com

**ADVANCED
MATERIALS
INTERFACES**

www.advmatinterfaces.de

4. Experimental Section

Chemicals: Branched PEI (M_w = 1300, M_w = 25 000, and M_w = 750 000), PAH (M_w = 17 000, M_w = 65 000), PSS (M_w = 1 000 000), and PAA (M_v = 450 000) were purchased from Sigma-Aldrich. LB (Luria/Miller) nutrient media from Roth was used to obtain a bacterial suspension. Microcolonies were grown on LB agar (Luria/Miller) from Roth. The biofilms were grown on 15 cm diameter plates of NaCl-free LB agar containing 10 g L^{-1} tryptone from casein, 1.25 g L^{-1} yeast extract, and 18 g L^{-1} bacteriologic agar (all from Roth).

Substrate Preparation: NaCl-free LB agar solutions were prepared from the ingredients listed above and autoclaved. The solutions were then kept warm in a water bath at 55 °C for 1 h before pouring 100 mL per 15 cm petri dish. After solidification of the agar, the plates were sealed with parafilm and kept upside down for 2 days at room temperature. Several 2 mg mL^{-1} solutions of polyelectrolytes were prepared in 0.5 M NaCl. The pH of each solution was adjusted to the desired values by dropping NaOH and HCl. Further, polyelectrolyte solutions with adjusted pH were sterilized using filtration and UV irradiation. The surface of each large NaCl-free LB agar plate was virtually divided into nine sections. One of the sections was not coated with polyelectrolytes. Having such a control in each plate enables to account for the interplate variability of biofilm phenotypes caused by parameters not considered in the experiment (e.g., humidity in the laboratory). On each of the eight remaining sections, 50 µL of the corresponding polyelectrolyte solution was deposited with a pipette and allowed to spontaneously spread over the surface. The polyelectrolyte films obtained on the agar surface were finally left to dry for 30–40 min without the lid of the plate.

Biofilm Culture: *E. coli* AR3110 bacteria (kindly provided by the Microbiology Lab of the Humboldt University, Berlin, Germany) were used. Bacterial suspension was routinely obtained by growing single microcolonies overnight in liquid LB medium. Each section of the polyelectrolyte coated NaCl-free LB agar plates (including control) were inoculated with 5 µL of bacterial suspension as a single round drop (without bubbles). After the inoculation drop had dried on the surface of the agar, the plates were closed, sealed with parafilm, turned upside down, and incubated at 28 °C for up to 4 days. All these steps were performed under a sterile laminar flow.

Biofilm Characterization: Once a day, each inoculated plate was imaged with a regular scanner. The biofilm images were analyzed using ImageJ[54] to quantify biofilm growth by measuring the projected biofilm area as a function of culture time. For detailed macroscopic spatiotemporal characterizations of biofilm geometry, a separate series of growth experiments was carried out in a specially designed transparent incubator installed on the stage of a stereomicroscope (Zeiss AxioZoom.V16). Each of the nine biofilms growing on the same plate was imaged separately every 30 min for 4 days. The images of each biofilm were then combined to produce time-lapse videos. Part of the biofilms was scanned with an X-ray microtomography scanner (EasyTom, RX Solutions), provided with a micro-focus tube (XRay150, RX-Solutions). Image stacks were reconstructed in the X-ACT software (RX-Solutions). For visualization, slice conjunction and 3D rendering were performed in Amira (Version 6.5, FEI). After 4 days of growth, each biofilm was removed from the nutritive substrate, placed in a separate tube, and weighted. The obtained mass values were averaged and presented with their standard deviation.

Statistics: Between 10 and 15 experiments were carried out in each of the conditions studied. The data are presented as mean values with standard deviations. The null hypothesis regarding the equivalence of data obtained under different experimental conditions was tested using one-way analysis of variance. Differences in experimental data with $p < 0.01$ were considered to be statistically significant.

Supporting Information

Supporting Information is available from the Wiley Online Library or from the author.

Conflict of Interest

The authors declare no conflict of interest.

Data Availability Statement

The data that support the findings of this study are available from the corresponding author upon reasonable request.

[1] K.-Y. Ha, Y.-G. Chung, S.-J. Ryoo, *Spine* **2005**, *30*, 38.
[2] D. Pavithra, M. Doble, *Biomed. Mater.* **2008**, *3*, 034003.
[3] J. J. Kelly, N. Minalt, A. Culotti, M. Pryor, A. Packman, *PLoS One* **2014**, *9*, e98542.
[4] D. Kregiel, *Food Control* **2014**, *40*, 32.
[5] P. S. Stewart, J. W. Costerton, *Lancet* **2001**, *358*, 135.
[6] D. Huang, J. Wang, K. Ren, J. Ji, *Biomater. Sci.* **2020**, *8*, 4052.
[7] G. O'toole, H. B. Kaplan, R. Kolter, *Annu. Rev. Microbiol.* **2000**, *54*, 49.
[8] L. Liu, H. Shi, H. Yu, S. Yan, S. Luan, *Biomater. Sci.* **2020**, *8*, 4095.
[9] Y. F. Yang, L. S. Wan, Z. K. Xu, *Water Sci. Technol.* **2010**, *61*, 2052.
[10] J. Lee, J. Yoo, J. Kim, Y. Jang, K. Shin, E. Ha, S. Ryu, B. G. Kim, S. Wooh, K. Char, *ACS Appl. Mater. Interfaces* **2019**, *11*, 6550.
[11] S. Guo, M. Y. Kwek, Z. Q. Toh, D. Pranantyo, E. T. Kang, X. J. Loh, X. Zhu, D. Jańczewski, K. G. Neoh, *ACS Appl. Mater. Interfaces* **2018**, *10*, 7882.
[12] K. Hänni-Ciunel, G. H. Findenegg, R. V. Klitzing, *Soft Mater.* **2007**, *5*, 61.
[13] N. V. Ryzhkov, D. V. Andreeva, E. V. Skorb, *Langmuir* **2019**, *35*, 8543.
[14] K. Lewis, A. M. Klibanov, *Trends Biotechnol.* **2005**, *23*, 343.
[15] X. Zhu, X. J. Loh, *Biomater. Sci.* **2015**, *3*, 1505.
[16] N. V. Ryzhkov, N. Brezhneva, E. V. Skorb, *Surf. Innovations* **2019**, *7*, 145.
[17] B. Gottenbos, H. C. V. D. Mei, H. J. Busscher, *J. Biomed. Mater. Res.* **2000**, *50*, 208.
[18] B. Gottenbos, *J. Antimicrob. Chemother.* **2001**, *48*, 7.
[19] N. Kawabata, M. Nishiguchi, *Appl. Environ. Microbiol.* **1988**, *54*, 2532.
[20] B. D. Wood, M. Quintard, S. Whitaker, *Biotechnol. Bioeng.* **2002**, *77*, 495.
[21] C. D. L. Fuente-Núñez, F. Reffuveille, L. Fernández, R. E. Hancock, *Curr. Opin. Microbiol.* **2013**, *16*, 580.
[22] H. Gu, S. Hou, C. Yongyat, S. D. Tore, D. Ren, *Langmuir* **2013**, *29*, 11145.
[23] V. E. Johansen, L. Catón, R. Hamidjaja, E. Oosterink, B. D. Wilts, T. S. Rasmussen, M. M. Sherlock, C. J. Ingham, S. Vignolini, *Proc. Natl. Acad. Sci. USA* **2018**, *115*, 2652.
[24] X. Jin, I. H. Riedel-Kruse, *Proc. Natl. Acad. Sci. USA* **2018**, *115*, 3698.

**ADVANCED
SCIENCE NEWS**

www.advancedsciencenews.com

**ADVANCED
MATERIALS
INTERFACES**

www.advmatinterfaces.de

[25] P. Q. Nguyen, Z. Botyanszki, P. K. R. Tay, N. S. Joshi, *Nat. Commun.* **2014**, *5*, 4945.

[26] M. Florea, H. Hagemann, G. Santosa, J. Abbott, C. N. Micklem, X. Spencer-Milnes, L. D. A. Garcia, D. Paschou, C. Lazenbatt, D. Kong, H. Chughtai, K. Jensen, P. S. Freemont, R. Kitney, B. Reeve, T. Ellis, *Proc. Natl. Acad. Sci. USA* **2016**, *113*, E3431.

[27] J. Huang, S. Liu, C. Zhang, X. Wang, J. Pu, F. Ba, S. Xue, H. Ye, T. Zhao, K. Li, Y. Wang, J. Zhang, L. Wang, C. Fan, T. K. Lu, C. Zhong, *Nat. Chem. Biol.* **2018**, *15*, 34.

[28] L. Xu, Z. Zhu, S. A. Sukhishvili, *Langmuir* **2011**, *27*, 409.

[29] Q. Yi, G. B. Sukhorukov, *Adv. Colloid Interface Sci.* **2014**, *207*, 280.

[30] A. A. Antipov, G. B. Sukhorukov, H. Möhwald, *Langmuir* **2003**, *19*, 2444.

[31] C. Déjugnat, G. B. Sukhorukov, *Langmuir* **2004**, *20*, 7265.

[32] W. Tong, C. Gao, H. Möhwald, *Macromolecules* **2006**, *39*, 335.

[33] S. A. Ulasevich, G. Brezesinski, H. Möhwald, P. Fratzl, F. H. Schacher, S. K. Poznyak, D. V. Andreeva, E. V. Skorb, *Angew. Chem., Int. Ed.* **2016**, *55*, 13001.

[34] S. A. Ulasevich, N. Brezhneva, Y. Zhukova, H. Möhwald, P. Fratzl, F. H. Schacher, D. V. Sviridov, D. V. Andreeva, E. V. Skorb, *Macromol. Biosci.* **2016**, *16*, 1422.

[35] J. Gensel, T. Borke, N. P. Pérez, A. Fery, D. V. Andreeva, E. Betthausen, A. H. E. Müller, H. Möhwald, E. V. Skorb, *Adv. Mater.* **2012**, *24*, 985.

[36] D. O. Serra, A. M. Richter, R. Hengge, *J. Bacteriol.* **2013**, *195*, 5540.

[37] W. Thongsomboon, D. O. Serra, A. Possling, C. Hadjineophytou, R. Hengge, L. Cegelski, *Science* **2018**, *359*, 334.

[38] Y. Zhang, P. Batys, J. T. O'Neal, F. Li, M. Sammalkorpi, J. L. Lutkenhaus, *ACS Cent. Sci.* **2018**, *4*, 638.

[39] T. Ikeda, H. Hirayama, H. Yamaguchi, S. Tazuke, M. Watanabe, *Antimicrob. Agents Chemother.* **1986**, *30*, 132.

[40] D. J. Phillips, J. Harrison, S.-J. Richards, D. E. Mitchel, E. Tichauer, A. T. Hubbard, C. Guy, I. Hands-Portman, E. Fullam, M. I. Gibson, *Biomacromolecules* **2017**, *18*, 1592.

[41] M. Wyrtwal, P. Koczurkiewicz, K. Wójcik, M. Michalik, B. Kozik, M. Żylewski, M. Nowakowska, M. Kepczynski, *J. Biomed. Mater. Res., Part A* **2013**, *102*, 721.

[42] G. Harkes, J. Dankert, J. Feijen, *J. Biomater. Sci., Polym. Ed.* **1992**, *3*, 403.

[43] S. Trinschek, K. John, S. Lecuyer, U. Thiele, *Phys. Rev. Lett.* **2017**, *119*, 078003.

[44] L. K. Koopal, *Adv. Colloid Interface Sci.* **2012**, *179*, 29.

[45] M. Elzbieciak, M. Kolasinska, P. Warszynski, *Colloids Surf., A* **2008**, *321*, 258.

[46] A. V. Harpe, H. Petersen, Y. Li, T. Kissel, *J. Controlled Release* **2000**, *69*, 309.

[47] K. A. Curtis, D. Miller, P. Millard, S. Basu, F. Horkay, P. L. Chandran, *PLoS One* **2016**, *11*, e0158147.

[48] J. Suh, H. J. Paik, B. K. Hwang, *Bioorg. Chem.* **1994**, *22*, 318.

[49] J. Goicoechea, F. J. Arregui, J. M. Corres, I. R. Matias, *J. Sens.* **2008**, *2008*, 142854.

[50] S. W. Cranford, C. Ortiz, M. J. Buehler, *Soft Matter* **2010**, *6*, 4175.

[51] A. S. Michaels, O. Morelos, *Ind. Eng. Chem.* **1955**, *47*, 1801.

[52] J. Choi, M. F. Rubner, *Macromolecules* **2005**, *38*, 116.

[53] J. Yan, C. Fei, S. Mao, A. Moreau, N. S. Wingreen, A. Košmrlj, H. A. Stone, B. L. Bassler, *eLife* **2019**, *8*, e43920.

[54] J. Schindelin, I. Arganda-Carreras, E. Frise, V. Kaynig, M. Longair, T. Pietzsch, S. Preibisch, C. Rueden, S. Saalfeld, B. Schmid, J.-Y. Tinevez, D. J. White, V. Hartenstein, K. Eliceiri, P. Tomancak, A. Cardona, *Nat. Methods* **2012**, *9*, 676.

2001807 (8 of 8)

Nanoscale

Silver melamine thin film as a flexible platform for SERS analysis†

Anastasia Nenashkina,[a] Semyon Koltsov,[a] Olga Yu. Orlova,[a] Anna A. Nikitina,[a] Demid A. Kirilenko,[a,b] Daria V. Andreeva,[c] Maria Blanco-Formoso,[d] Nicolas Pazos-Perez, [iD][d] Ramon Alvarez-Puebla [iD][d,e] and Ekaterina V. Skorb [iD]*[a]

New SERS detection platforms are required for the quick and easy preparation of sensing devices for food, agriculture, and environmental science. For quantitative sensing, it is important that a sensing material, in addition to efficient sensing, provides extraction and concentration of the target molecules such as toxic pesticides or healthy vitamins. We design such films adopting the Liesegang rings formation process that includes the reaction–diffusion of silver nitrate and melamine followed by the precipitation of different intermediates and their reduction by light in a pectin medium. Surprisingly, we find that the presence of melamine provides an excellent substrate for the extraction of pollutants at the solid-liquid interface giving rise to a powerful but easy and fast method for the quantification of fruits' quality. The complex silver and melamine containing films show high sensitivity even at relatively low silver concentrations.

Introduction

Nanostructured silver is one of the most efficient materials for surface enhanced Raman scattering (SERS).[1–3] Silver nanoparticles have been fabricated by different methods. Colloidal synthesis, for example, allows the formation of nanoparticles (NPs) with a defined size and shape.[4–7] These particles can be employed directly in solution for the acquisition of average SERS or used for the fabrication of optically active thin films, where the particles interact to form electromagnetic hot spots (hot spot SERS).[8–10] Also, optically active platforms can be obtained by using physical methods such as chemical vapor deposition[11] or sputtering.[12] All these methods, however, require appropriate analytes with a high affinity for the silver surfaces to yield strong signals. Thus, several alternatives have been developed to increase the retention of molecules onto the plasmonic substrates, the most popular being the combination of metallic nanoparticles with different polymers.[13] Also, new waveguide-based SERS platforms, made of gold, have been reported.[14] Such technology is outstanding with relatively low

SERS backgrounds, achieving high signal-to-background ratios. Further work suggests also the decreasing of laser-induced photon background of waveguide media.[15]

Recently, we[16] demonstrated the use of reaction–diffusion systems for the formation of programmable transparent flexible thin films with silver patterns. The thicker part of the ring in the films could be compared with well-known selective gold etching techniques,[17] but reaction–diffusion appears to be easier and cheaper. Here we take advantage of reaction–diffusion to prepare heavily loaded thin films of melamine and silver. These films are flexible, resistant and can be prepared without significant effort on large surfaces. The presented structure has several layers and these are distributed radially, which should allow the optimal thickness to be determined with one sample, therefore it is probably more advantageous than self-assembly.[18] Surprisingly, the presence of melamine provides an excellent substrate for the extraction of pollutants at the solid-liquid interface giving rise to a powerful but easy and fast method for the quantification of, for example, pollutants in fruits. Moreover, melamine allows the silver concentration to be minimized for the formation of thin film as a flexible platform for SERS analysis.

[a]ITMO University, Lomonosova str. 9, 191002 Saint Petersburg, Russian Federation. E-mail: skorb@itmo.ru
[b]Ioffe Institute, Politekhnicheskaya str. 26, 194021 St-Petersburg, Russian Federation
[c]Department of Materials Science and Engineering, National University of Singapore, 117575 Singapore
[d]Department of Physical Chemistry, Universitat Rovira i Virgili, 43007 Tarragona, Spain
[e]ICREA, Passeig Lluis Companys 23, 08010 Barcelona, Spain
†Electronic supplementary information (ESI) available. See DOI: 10.1039/d0nr08543j

Results and discussion

Silver particles (AgNPs) are formed in the reaction–diffusion system primarily due to the reaction of silver nitrate and melamine or pectin, particularly its galacturonic acid monomer (Fig. 1A and B).

Pectin is a part of agar water gel, which is the medium of the reaction. The initially white precipitation is then decomposed by light, forming particles of different sizes.

From a certain point, separated bands of precipitation could be seen. This is a phenomenon known as Liesegang rings or bands.[19–21] Basically, they are formed due to the supersaturation process and limited delivery of reactants to the reaction center because of diffusion limitations.[22] Liesegang rings formed with silver nitrate are relatively common and described in the literature.[16,23,24] It would be interesting to find a practical application of the formed material, and, here, we suggest how to use thin flexible films for SERS. Moreover, the films were additionally optimized for higher SERS signals by adding melamine. The process of gradient structure formation is demonstrated in time-series photos and kymograms (Fig. 2).

The kymograms (Fig. 2B and D) are the representation of the same crossline of growing rings/zones as a function of time.
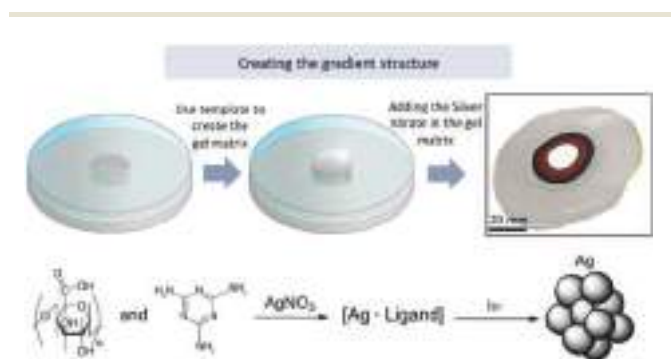
Fig. 1 Formation of silver-based films with gradient structure. In a Petri dish patterned with a hollow cylinder agar gel is filled with silver nitrate and a schematic of the process. After air drying a thin, flexible, free standing film is formed and shown in the right upper corner.

From the kymograms it is clear that the formed rings are stable and have a constant location over time. The gradient structure starts with the zone of NPs. They do not agglomerate due to time stability. The zones have white–yellow–red–brown–black color gradient corresponding to the formed silver-based structure. The color becoming reddish represents the increase of the concentration and size of nanoparticles. Then black bands are formed. The farther the zone is from the center, the wider it is. The occurrence of zones depends on time as follows: $x = f(\sqrt{t})$. This behavior is common for classical non-linear periodic precipitate structures.[21–23] As shown in Fig. 2B and D, the size of pattern propagation and the simulation results are in very good agreement. The size of the formed AgNPs depends on the initial local concentration of silver nitrate. The summary of the reaction is as follows: upon diffusion of the silver salt, Ag^+ ions react with pectin and melamine to form a white precipitation.[24,25] Then it decomposes due to light irradiation, forming AgNPs followed by their aggregation.

Reaction–diffusion takes time. For a Petri dish with a diameter of 9 cm, it could take more than 24 h to occur in the whole volume. Notably, half of the reaction is over in less than 8 h (see the ESI video†). This behavior is due to the square root dependence of the location on time for the diffusive reagents.

In the model, we summarize the possible reactions of silver to average the binding of the silver with the ligand. To model the precipitation, we used the classical nucleation and growth model.[25,26] [L] stands for the galacturonic acid monomer or melamine, $n \gg m$:

Formation of the intermediate:

$$Ag^+ + [L] \rightarrow [AgL]_{(solvated)} \tag{1}$$

Nucleation process:

$$m[AgL] \rightarrow [AgL]_{m \ (nuclear)} \tag{2}$$
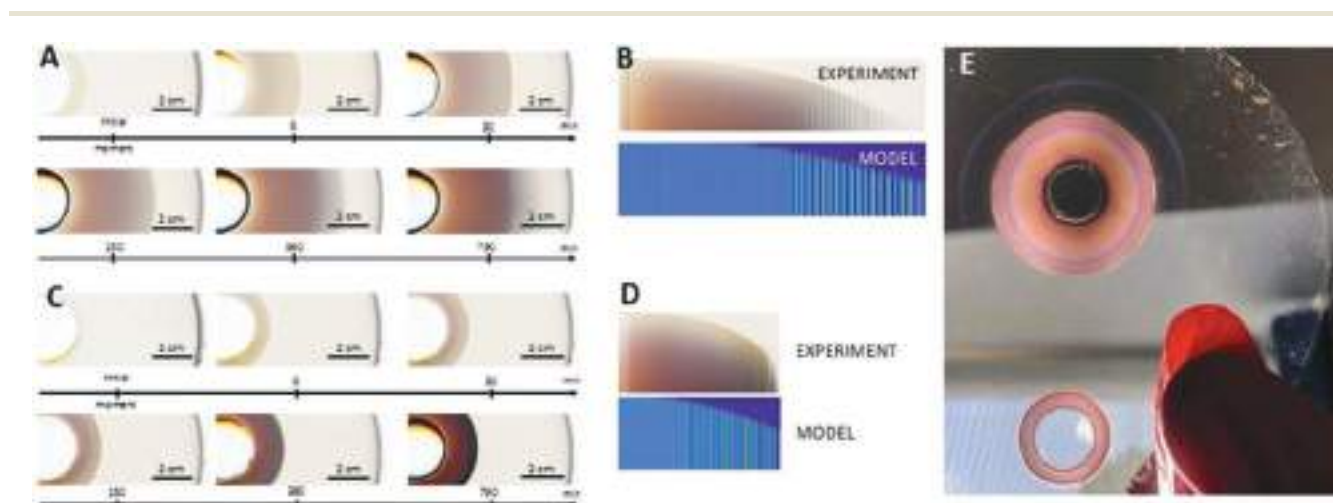
Fig. 2 (A–D) Spatiotemporal assembly of gradient silver based structures, and time series photos of gradient structure formation for the system with 2 wt% (A and B) and 0.2 wt% (C and D) of silver nitrite, respectively. (B and D) Photos based kymogram (upper brown pattern) and Matlab modelled behaviour (below blue pattern) for 2 wt% and 0.2 wt%, respectively. (E) Photo of silver melamine thin film as a flexible platform for 2 wt% (top pattern) and 0.2 wt% (bottom pattern), respectively.

Precipitate growth:

$$[AgL]_{m \ (nuclear)} + n[AgL] \rightarrow [AgL]_{n \ (solid)} \qquad (3)$$
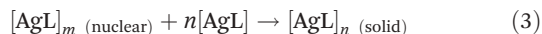
The following set of differential equations describes the reaction–diffusion:

$$\frac{\partial c_{in}}{\partial t} = D_{in} \frac{\partial^2 c_{in}}{\partial x^2} - k_1 c_{in} c_{out}$$

$$\frac{\partial c_{out}}{\partial t} = D_{out} \frac{\partial^2 c_{out}}{\partial x^2} - k_1 c_{in} c_{out}$$

$$\frac{\partial c}{\partial t} = D_{int} \frac{\partial^2 c}{\partial x^2} + k_1 c_{in} c_{out} - k_2 \theta(c - c^\star)c - k_3 cp$$

$$\frac{\partial p}{\partial t} = k_2 \theta(c - c^\star) + k_3 cp$$

where c_{in} is the concentration of ligands, c_{out} is the concentration of silver nitrate, and p is the concentration of the solid salt. D_{in}, D_{out}, D_{int} are diffusion coefficients for the average ligand, silver ions, and their salt respectively; k_1, k_2, k_3 are kinetic coefficients for the formation of intermediate particles (reaction (1)), the formation of nucleation centers (reaction (2)), and formation of Liesegang rings (LRs) due to precipitation growth (reaction (3)); c^* is a threshold concentration of salt precipitation. We used the following values to simulate the formation of these periodic assemblies: L = 10 a.u. (length of the test tube used), τ = 0.001 a.u. (time step), D_{in} = 1 a.u., D_{out} = 1 a.u., D_{int} = 0.1 a.u., k_1 = 1000 a.u., k_2 = 1 a.u., k_3 = 10 000 a.u., c^* = 0.01 a.u., c_{in} = 0.5 a.u., c_{out} = 5 a.u. Numerical simulations based on these equations were performed and are shown in Fig. 2B and D (lower blue patterns).

Interestingly, precipitation inside the film seems to have no effect at the surface of the resulting thin film (Fig. 3). The height mode of atomic force microscopy (AFM) showed that no difference between a band and pure dry gel is observed. This fact implies that silver nanoparticles tend to grow inside the gel rather than on its surface. Thus, the average roughness of the samples lies in the range of 2–10 nm.

Transmission electron microscopy (TEM) (Fig. 4) was employed to characterize the dispersion and morphology of the AgNPs that are grown in 1 mM melamine solution. Thus, we observe silver nanoparticles with an average size of about 50 nm of relatively small dispersion. This type of particle is formed as an entire seed with clear grains (Fig. 4 below). The dark band zone consists of silver nanoparticle agglomerates and individual particles up to 150 nm in diameter (Fig. 4 right upper corner).

Thus, the self-organized structure provides us with a variety of particle sizes. At the zone closest to the centre, silver nanoparticles tend to be stable. The farther the zone of particle formation, the bigger the particles that tend to dominate. This behaviour could be explained by an excess of silver ions at an area that is close to the centre. That excess results in a strong electrical double layer (EDL) that is formed on the surface of silver particles due to the absorbance of silver ions.[27,28] The EDL prevents agglomeration of the particles. At the same time, particles far from the centre are surrounded by a lower concentration of silver ions due to their dilution and run-off in the reaction. The EDL, therefore, is smaller and is not enough to prevent agglomeration.[27,28]
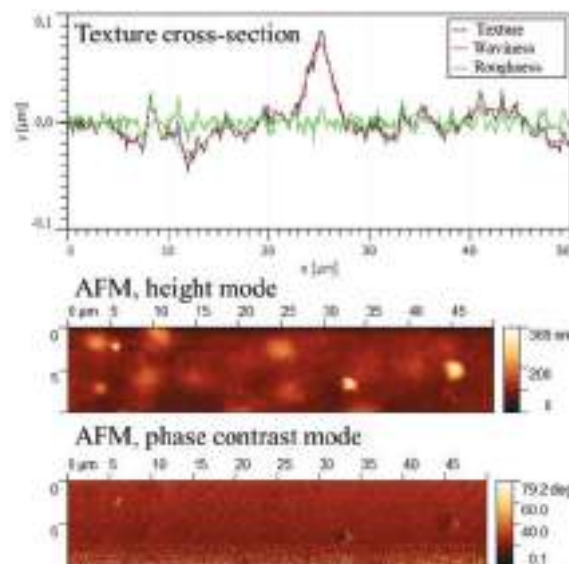
Fig. 3 The AFM texture of the surface and the phase-contrast of the gradient structure. The roughness is ~5.5 nm, and phase contrast shows no drastic differences in the substances with and without reaction–diffusion systems.
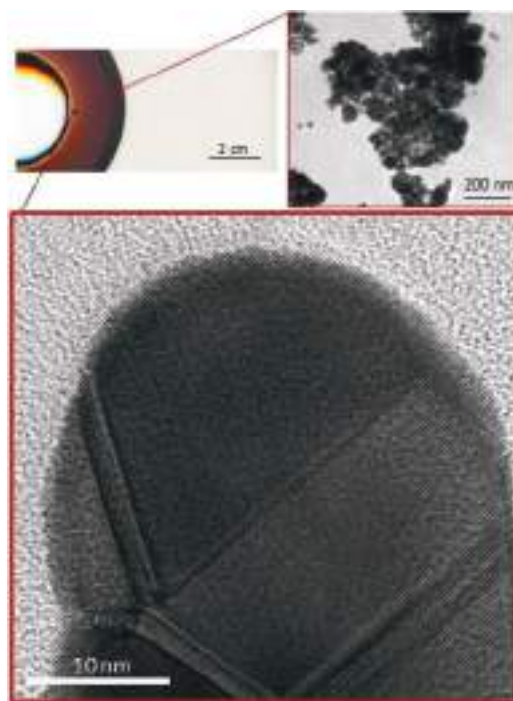
Fig. 4 Silver nanoparticle composition of the gradient structure, synthesized in the presence of 1 mM melamine. Pale yellow zone corresponds for rare nanoparticles of ~50 nm in diameter with clear grains; dark-reddish zone states for agglomerates of silver particles up to 150 nm in diameter.

Fig. 5 (A) SERS spectrum of benzenethiol absorbed by silver particles on the film acquired with a NIR laser (785 nm) and SERS mapping of a large area of the film and the intensity of the 1072 cm^{-1} (in plane CH deformation). (B) SERS spectra of thiram at different concentrations after transfer of the pesticide from the apple surface to the film by spraying ethanol. Correlation of the peak area of the CS stretching with the thiram concentration.

Elemental composition analysis by EDX presented the strongest signal from the silver (Ag) region and weaker signals from C, O atoms from the organic matrix (see the ESI Fig. 2† for detailed information). The optical properties of the structured films were investigated by Raman spectroscopy using benzenethiol (BT) in the gas phase as reported (Fig. 5A). All the samples exhibit the characteristic fingerprint of BT,[29] however, the addition of melamine during the silver growth process results in an increased enhancement factor of over 20-fold. This fact indicates, first, that melamine interacts with the nanoparticle surfaces giving rise to a more efficient packing of nanoparticles and, thus, improved hot spots. Secondly, the melamine coating improves the molecular trapping of the analyte facilitating its capture. For more detailed data, please see the ESI, Fig. S1.†

To check the signal intensity homogeneity through the radial cross-section of the sample, a large mapping was carried out on the film. Fig. 5A shows the evolution of the intensity of the 1072 cm^{-1} (in plane CH deformation) band of BT. Notably, from the center to the outer limits, the signal rapidly increased, reaching a stable maximum in the darker areas for several centimeters and decreasing again in the outer limits. This can be correlated with the concentration and the agglomeration of the colloid nanoparticles. Thus, as the nanoparticles interact as the aggregate to produce efficient hot spots, subsequently, the signal increases.

With these properties in mind, we designed an experiment to fully exploit these silver films as reactive strips for fast pollutant/pesticide detection in food (Fig. 5B).

First, we contaminated the surface of an apple with thiram, a known fungicide and ectoparasiticide extensively used to prevent fungal diseases in seed, crops and fruits. After air

drying, we placed a piece of the film on the apple and sprayed ethanol (into the uncovered side) to transfer the thiram from the apple surface to the film.

Then, to ensure reproducibility,[30,31] three different films for each concentration were studied by SERS. The vibrational spectra of thiram show the dominant vibrational modes are SS and CS stretching modes (555 and 1369 cm^{-1}, respectfully) with minor contributions of the CNC scissoring (441 cm^{-1}), CS asymmetric stretching (930 cm^{-1}), and CN stretching (1138 cm^{-1}).[32] The vibrational pattern is clearly recognized for concentrations as low as the nM regime; and, by correlating the peak area of the CS stretching mode (1369 cm^{-1}) with concentration, a linear relation can be established from 10^{-5} to 10^{-6} M. Note that the similar intensity provided by the samples with concentrations 10^{-4} and 10^{-5} M indicate the saturation of the silver surfaces. These detection limits are competitive with those provided by classical techniques (chromatography, polarography, voltamperometry or luminescence),[33] but with the advantages of speed, cost and the possibility of sample acquisition in the field with no or very little preparation.

Conclusions

We developed multifunctional flexible silver films that allow the extraction and concentration of target substances and minimizing the concentration of silver for efficient SERS sensing and biodetection. We adopted the Liesegang rings formation process for the formation of multifunctional complex films, and the preparation conditions were additionally optimized for higher SERS signal. We applied the model to

propose a possible reaction of silver and to the average bonding of the silver with the ligand. In short, the adopted Liesegang process is based on the reaction–diffusion of silver nitrate and melamine, the precipitation of different intermediates and the reduction of intermediates by light in a pectin medium. Our results show that melamine provides an excellent substrate for the extraction of pollutants at the solid–liquid interface. Furthermore, the SERS pattern is clearly recognized for concentrations as low as the nM regime and the detection limit is similar to those that can be obtained from time consuming and costly chromatography, polarography, voltamperometry or luminescence. Additionally, our technique is even applicable in the field with no or very little preparation. Thus, the new SERS detection platform can be integrated into different devices for food-related applications, agricultural needs, and environmental control.

Experimental

Materials

In the experiment the following reagents were used. Silver nitrate, 99%, agar (A1296), benzene thiol, and melamine were purchased from Sigma Aldrich. The type of agar is crucial for reproducibility. All aqueous solutions were prepared by using highly pure water from Millipore Elix (18 MΩ cm^2 cm^{-1}).

Methods

Films of standard comparison (Fig. 1A). First, a hollow tube of 1.5 cm in diameter is placed in the centre of a Petri dish. Then 20 ml of 1% agar is poured in the Petri dish, d = 90 mm. In the case of melamine-containing sample preparation 1 mM solution of melamine instead of pure water should be used. Once the hot solution has gelled, the tube is removed and the resulting hole is filled with $AgNO_3$ solution (0.2–2 wt%). Having closed the dish to prevent evaporation, it is left for 24 h under constant "daylight" irradiation. The last step is to leave the dry agar in a ventilated oven at 38 °C.

Characterization of the prepared silver based structure. To measure the particles and their composition we used SEM, EDX and TEM. Squares of the structured agar film of about 5 × 5 mm were cut and then placed on a silicon wafer watered with isopropyl alcohol. After complete evaporation of the alcohol, measurements were made.

To investigate the particles *via* TEM a non-dried structure was taken and dissolved in hot brine. The resulting solution was centrifuged, then the precipitate was washed with water. The process was repeated three times. The resulting precipitate was sent for TEM investigation.

A target-oriented approach was utilized for the optimization of the analytical measurements. Before measurements the samples were mounted on a 4 mm copper grid with a carbon film and fixed in a grid holder. The sample morphology was studied using a transmission electron microscope. Images were acquired in a Jeol JEM-2100F (accelerating voltage 200 kV, point-to-point resolution 0.19 nm).

SERS measurements: SERS was collected with a Renishaw Invia system with a 785 nm laser and a high-resolution grating of 1200 g cm^{-1}. The laser beam was focused at the Au film through a 50× objective, providing a sample area of 1 μm^2, with power at the sample of 3 mW and acquisition time of 1 s. Maps were acquired using a 10× objective with the Renishaw StreaLine accessory with power at the sample of 300 mW. For BT, the analyte was retained in the gas phase by depositing the film in a closed Petri dish with 100 μL of ethanolic solution of BT (10^{-4} M) placed close to but separately from the film for 30 min. In the case of thiram, ethanolic solutions from 10^{-4} to 10^{-10} M were prepared and sprayed on different apples. After air-drying, a piece of film was placed on each apple's surface and sprayed with ethanol to transfer the pesticide.

Kymogram of the prepared silver based structures. A kymogram is a type of graphical representation of data when one of the axes of the picture is for the *x*-coordinate, and the second axis is for time. In other words, a kymogram is a number of the same one-pixel lines of the same photo exposure in different time points, with lines located under each other. To create it we first made 400 images of the gel with the reaction occurring with two-minute steps by using a high-definition transmission scanner for films. Then, by means of the ImageJ package software, we created a stack of images and sliced them into a kymogram.

Modelling of the prepared silver based structures. We did a 1D kymogram-like mathematical description in the MatLab package software. The MatLab code is enclosed in the ESI.†

Conflicts of interest

There are no conflicts to declare.

Acknowledgements

References

1 J. Zhao, A. O. Pinchuk, J. M. McMahon, S. Li, L. K. Ausman, A. L. Atkinson and G. C. Schatz, *Acc. Chem. Res.*, 2008, **41**, 1710–1720.
2 J. Langer, *et al.*, *ACS Nano*, 2020, **14**, 28–117.

3   N. Pazos-Perez, T. Borke, D. V. Andreeva and R. A. Alvarez-Puebla, *Nanoscale*, 2011, **3**, 3265–3268.

4   J. Reguera, J. Langer, D. J. de Aberasturi and L. M. Liz-Marzán, *Chem. Soc. Rev.*, 2017, **46**, 3866–3885.

5   F. C. Meldrum, N. A. Kotov and J. H. Fendler, *Langmuir*, 1994, **10**, 2035–2040.

6   D. Radziuk, D. G. Shchukin, A. Skirtach, H. Möhwald and G. Sukhorukov, *Langmuir*, 2007, **23**, 4612–4617.

7   E. V. Skorb, D. V. Sviridov, H. Möhwald and D. G. Shchukin, *Chem. Commun.*, 2009, 6041–6043.

8   N. P. W. Pieczonka and R. F. Aroca, *Chem. Soc. Rev.*, 2008, **37**, 946–954.

9   M. Tebbe, P. Cherepanov, E. V. Skorb, S. K. Poznyak, J. G. de Abajo, A. Fery, D. V. Andreeva, R. A. Alvarez Puebla and N. Pazos-Perez, *Part. Part. Syst. Charact.*, 2014, **31**, 1134–1140.

10 M. Mueller, M. Tebbe, D. V. Andreeva, M. Karg, R. A. Alvarez Puebla, N. Pazos Perez and A. Fery, *Langmuir*, 2012, **28**, 9168–9173.

11 E. V. Skorb, V. G. Sokolov, T. V. Gaevskaya and D. V. Sviridov, *Theor. Exp. Chem.*, 2009, **45**, 40–43.

12 T. R. Jensen, M. D. Malinsky, C. L. Haynes and R. P. Van Duyne, *J. Phys. Chem. B*, 2000, **104**, 10549–10556.

13 R. A. Alvarez-Puebla and L. M. Liz-Marzán, *Chem. Soc. Rev.*, 2012, **41**, 43–51.

14 N. Turk, A. Raza, P. Wuytens, H. Demol, M. Van Daele, C. Detavernier, A. Skirtach, K. Gevaert and R. Baets, *Nanomaterials*, 2019, **9**, 1–14.

15 K. Reynkens, S. Clemmen, A. Raza, H. Zhao, J. S.-D. Peñaranda, C. Detavernier and R. Baets, *Opt. Express*, 2020, **28**, 33564.

16 A. Nenashkina, S. Koltsov, E. Zaytseva, A. Brunova, I. Pantiukhin and E. V. Skorb, *ACS Omega*, 2020, **5**, 7809–7814.

17 L. Zhang, C. Guan, Y. Wang and J. Liao, *Nanoscale*, 2016, **8**, 5928–5937.

18 Y. Wu, W. Yu, B. Yang and P. Li, *Analyst*, 2018, **143**, 2363–2368.

19 S. Prager, *J. Chem. Phys.*, 1956, **25**, 279–283.

20 J. B. Keller and S. I. Rubinow, *J. Chem. Phys.*, 1981, **74**, 5000–5007.

21 D. Walgraef, *Spatio-Temporal Pattern Formation*, Springer, 1996.

22 R. A. Schibeci and C. Carlsen, *J. Chem. Educ.*, 2009, **65**, 365.

23 B. A. Grzybowski, *Chemistry in Motion. Reaction–Diffusion Systems for Micro- and Nanotechnology*, John Wiley & Sons Ltd. Registered, Evanston, 1st edn, 2009.

24 E. Nakouzi and O. Steinbock, *Sci. Adv.*, 2016, **2**, e1601144.

25 I. Lagzi, B. Kowalczyk and B. A. Grzybowski, *J. Am. Chem. Soc.*, 2010, **3113**, 1–6.

26 B. Chopard, P. Luthi and M. Droz, *Phys. Rev. Lett.*, 1994, **72**, 1384–1387.

27 S. S. Zumdahl, *Chemical Principles*, Heath, Lexington, 1995.

28 P. W. Atkins and J. De Paula, *Physical chemistry*, Oxford, 2002.

29 R. Holze, *Phys. Chem. Chem. Phys.*, 2015, **17**, 21364–21372.

30 J. Xu, S. Shang and S. Jiang, *Composites, Part B*, 2019, **177**, 107376.

31 J. Xu, X. Li, Y. Wang, T. Hua, R. Guo, D. Miao and S. Jiang, *Cellulose*, 2020, **27**, 941–954.

32 A. Mariño-López, M. Blanco-Formoso, L. N. Furini, A. Sousa-Castillo, E. Tiryaki, M. Pérez-Lorenzo, M. Testa-Anta, V. Salgueiriño, N. A. Kotov, R. A. Alvarez-Puebla and M. A. Correa-Duarte, *Langmuir*, 2019, **35**, 4110–4116.

33 V. K. Sharma, J. S. Aulakh and A. K. Malik, *J. Environ. Monit.*, 2003, **5**, 717–723.
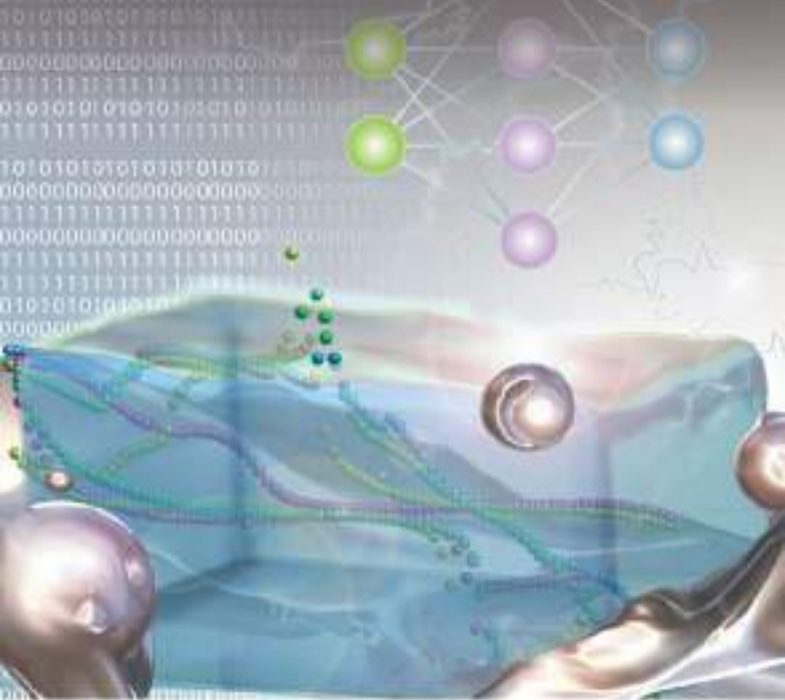
Programmable Soft-Matter Electronics

Artemii S. Ivanov, Konstantin G. Nikolaev, Alexander S. Novikov, Stanislav O. Yurchenko, Kostya S. Novoselov, Daria V. Andreeva, and Ekaterina V. Skorb*

Read Online

ACCESS | Metrics & More | Article Recommendations | SI Supporting Information

ABSTRACT: The hydrogels of the polyelectrolytes polyethylenimine and poly(acrylic acid) are used to form a thin-layer interface on the gallium−indium eutectic alloy's surface. The proposed method of gradually increasing the applied voltage reveals the possibility of formation of electronic components: diode, capacitor, resistor, and memristor. The components can be changed to each other many times. A multilayer perceptron model with one hidden layer and 12 nodes allows identifying hydrogels' composition and automatically setting the desired architecture of electronic components. The design of electronic components makes it possible to easy-to-produce new electronic parts and programmable soft-matter electronics.
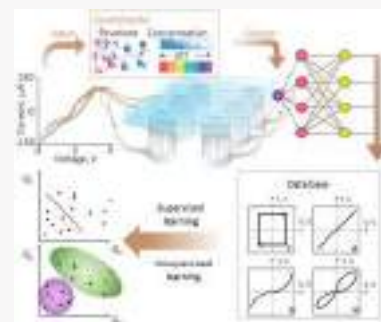
These days the importance of soft-matter-based electronics rapidly increases.[1−3] Because of its outstanding properties (like flexibility[4] and stretchability[5]), this type of electrical component can find potential applications for constructing portable[6] and wearable electronics[7] and biocompatible devices.[8] However, it is a complicated issue to find materials with available electric and mechanical properties. There are three types of such materials: conductive polymers,[9] liquid metals,[8] and hydrogels.[10,11]

Today, the most common liquid metals are eutectic gallium−indium alloys (eGaIn of 75 wt % Ga and 25 wt % In) and galinstan (68.5 wt % Ga, 21.5 wt % In, and 10.0 wt % Sn).[12] Both have high conductivity and a melting point less than 20 °C (for eGaIn it is 16 °C).[8] On the air, gallium is passivated by a thin oxide layer with a higher resistivity than the pure metal.[13,14] Film thickness is the critical factor in controlling current−voltage (I−V) characteristics of the electrical components based on these alloys.[15−17] For this purpose, hydrogels doped with different chemical compounds are used.[18]

The polyelectrolyte-based hydrogels[19] activate the rectification currents for the diode interface.[20] In previous studies, the addition of polyelectrolytes to hydrogels was considered only to form asymmetric I−V behavior.[21−23] We consider the addition of polyelectrolytes in the hydrogel to regulate pH and thus activate gallium oxidation processes. As the concentration of gallium ions increases, the insoluble film grows faster under an applied voltage. A different thickness of this film in different voltage ranges determines different electrical behaviors in one chemical system.[24,25]

In the present work, the one hydrogel interface provides four components at once—a capacitor, a resistor, a diode, and a memristor—with the ability to switch between them. We describe the electrochemistry of these switching processes and suggest a model in which it is possible to convert electrical behaviors by varying the voltage. Machine learning methods can design complex architectures by using a combination of electronic components. A system based on eGaIn and polyelectrolyte hydrogels will change the architecture directly on the board. Here, we propose a new system trained by a multilayer perceptron model based on liquid metals and hydrogels.

We propose a prototype of a chemical perceptron (Figure 1). A perceptron model is one of the simplest algorithms in machine learning and refers to the supervised and unsupervised learning and binary classification. Such a device can be used to analyze the composition of the gels from the obtained I−V curves and is also able to predict electrical behavior from the composition of the used gels.[26,27] The perceptron consists of input, output, and hidden layers between which the signal is redistributed (Figure 1a).

The electrochemical system consists of six electrodes of eGaIn interconnected by hydrogels (Figure 1b). When current flows through hydrogels, it is redistributed between them, and the values of these currents are the weight characteristics of the signals, the total value of which is estimated. This total signal is processed by using the multilayer perceptron model created using the database (Figure 1b). As a result, it is possible to obtain a reliable answer about the composition of the used
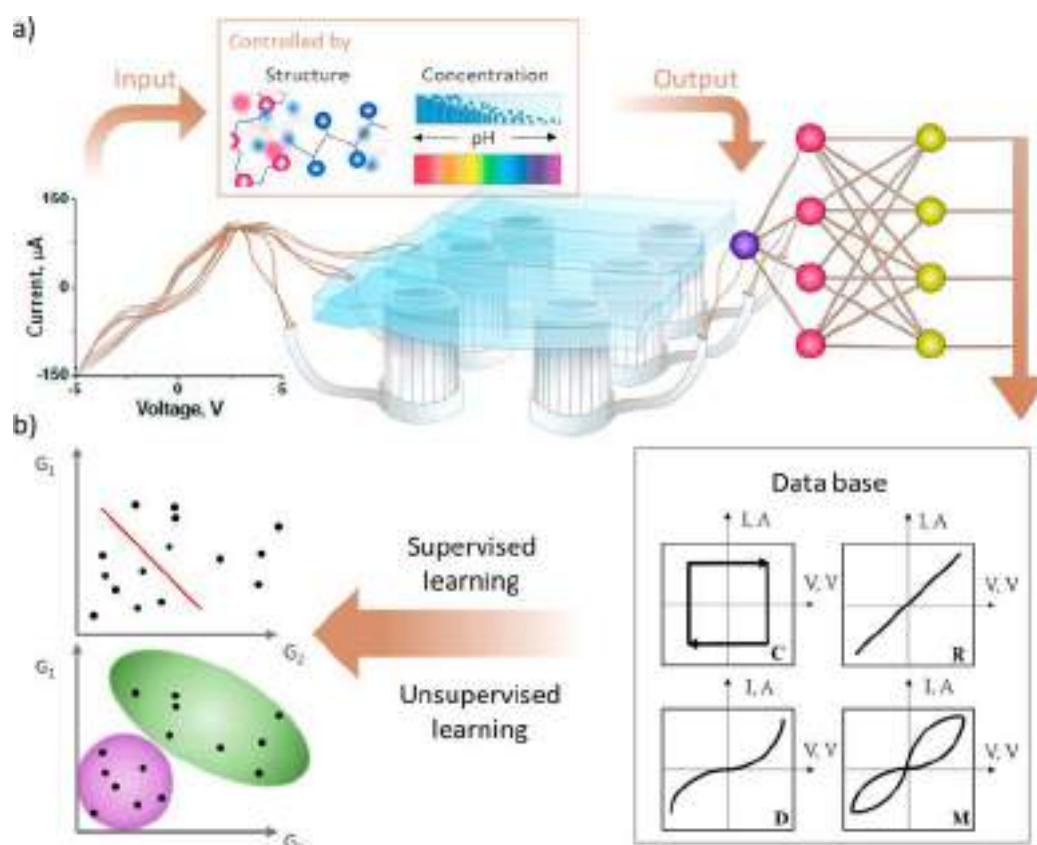
Figure 1. (a) An input signal in the form of an electric current passes through two hidden layers and converts into an output signal. The hidden layers are eGaIn electrodes connected by hydrogels of various compositions. (b) Machine-learning-based composition analysis scheme. The output signal is processed by using classification and clustering models; as a result, the composition of the used hydrogels is predicted with high accuracy.

hydrogels: the presence or absence of a buffer, the value of pH, and the used polyelectrolyte—poly(acrylic acid) (PAA) or polyethylenimine (PEI).

In the described soft-matter-based chemical perceptron, the classification is performed in terms of $I-V$ characteristic curves determined with the properties of constitutes. Therefore, one can formulate the direct and inverse problems to solve which chemical perceptron is suitable. The direct problem is related to the proper choice of the experiment's gel set and conditions providing a given response in the system, e.g., a particular form of $I-V$. The background for the immediate problem is that the gels' electrochemical parameters and interfaces directly affect the currents' features under the externally applied voltage. On the contrary, the inverse problem deals with a known response of a particular component's system and unknown properties. In our case, this is a chemical composition of an unknown gel.

In this case, the system's response is compared to the $I-V$'s obtained during supervised learning (the measurements with known gels), thus providing the classification of the points (properties) in the generalized space of parameters.

Several databases for the model training are composed. All of them are compiled according to the $I-V$ characteristics obtained from a two-electrode system on which hydrogels of individual compositions were tested. The design of the electrochemical cell is shown in detail in Figure 2a,b.

The electrochemical system is constructed of two eGaIn electrodes, which contacted with an electric circuit. The source meter unit Keithley 6430 is a voltage source in the circuit and simultaneously a measurement instrument. A circuit is created by the hydrogel, which lay on two electrodes. Gel fully covers
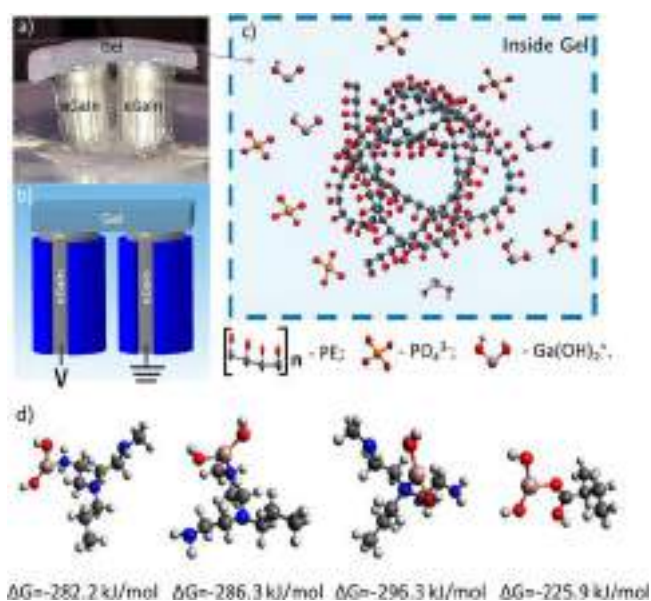
Figure 2. (a) Photograph of chemical system, where hydrogel is a conductor between two eGaIn electrodes. (b) Schematic model of chemical system. (c) Diffusion of ions and polyelectrolytes inside the gel. (d) Binding energies and geometries of the dihydroxygallium(III) species interactions with polyelectrolytes (ωB97X-D3/6-311++G** level of theory).

the surface of eGaIn electrodes. The hydrogel is a 1 wt % agar solution doped with polyelectrolytes and phosphate saline
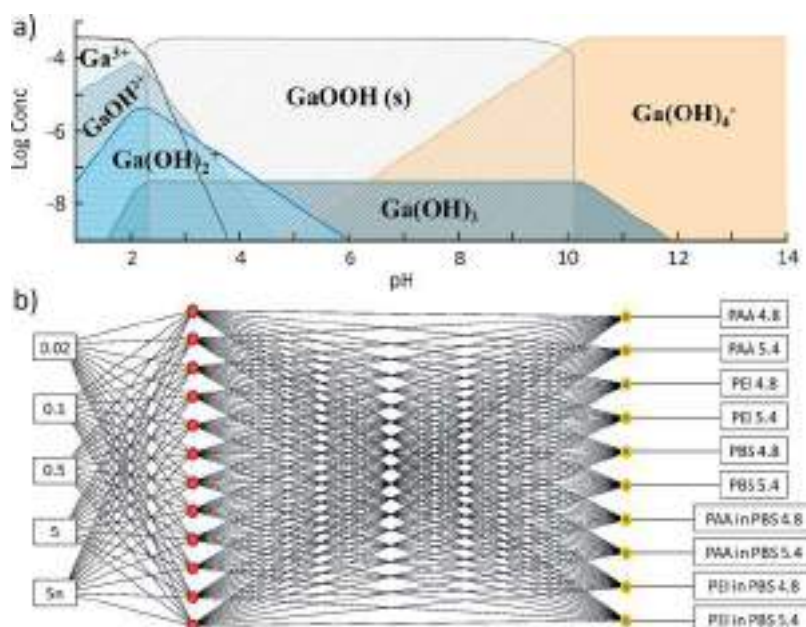
Figure 3. (a) Relative gallium fraction concentrations depend on total gallium amount (0.38 mM) generated on electrode at 5 V. (b) Scheme of a multilayer perceptron using current values to determine gel compositions.

buffer. 0.1 g of agar and 10 μL of 1 wt % polyelectrolyte solution were added into 10 mL of water. In the case of PEI 1 M HCl is added for pH adjustment. Then the mixture is stirred and heated. The heated mixture is poured in the Petri dish and cooled to form a gel. The composition of the gel is shown in Figure 2c.

When current flows through the electrodes, gallium is oxidized and turns into Ga^{3+}. Indium in the alloy is always reduced by the gallium and does not participate in chemical reactions. In this case, gallium is characterized by forming an oxide film on the surface upon contact with an aqueous solution. This reaction is thermodynamically favorable (about -949 kJ/mol) and proceeds upon direct contact of the eGaIn alloy with the hydrogel to form α-Ga_2O_3 (hydrated form) (Figure S1). The formal oxidation potential of gallium is -0.529 V. The two-electrode system (Figure 2a) assumes the occurrence of opposite reactions on the eGaIn electrodes. In aqueous media, the formal oxidation potential of gallium shifts to the anodic region and becomes equal to 0.319 V. This potential of redox process value strongly depends on pH and concentration of soluble gallium forms ($E_o = 0.319 - 0.1182$pH $+ 0.0197 \log(C$ (gallium dissolved species))). Following this and the diagram of the ratio of the fractions of gallium forms, the pH values 4.8 and 5.4 were chosen at which the generation of the dissolved form of gallium, gallyl ion ($Ga(OH)_2^+$), will occur (Figure 3 and Figure S2). The generation of soluble forms of gallium provides a complexation reaction with polyelectrolyte macromolecules, which prevents an uneven oxide film on the electrode surface. The 0.07 M phosphate buffer enhances the formation of an insoluble layer of gallium compounds. In the presence of PO_4^{3-} anions, gallium phosphate competitively forms, as a result of which, when the potential is applied, the mixed oxide–phosphate layer forms faster than the oxide layer. The thickness of the mixed oxide–phosphate layer drops with an increase in voltage. Also, since the gels are in direct contact with each other, the interaction between them occurs with the interfacial formation of a polyelectrolyte associate, which prevents PAA

and PEI diffusion. Local gallium ions release from polyelectrolytes use to prevent bacterial growth.[28,29] The inclusion of gallium ions in the layers of polyelectrolytes is performed to prevent gallium oxide formation. This achievement became possible because polyelectrolytes can form complexes and ion pairs with multivalent metals.[30,31]

To evaluate the thermodynamic favorability for the association of PAA and PEI with gallium cations, quantum chemical calculations at the ωB97X-D3/6-311++G** and B3LYP/aug-cc-pVDZ levels of theory are performed. For theoretical studies of gallium reactions, the dihydroxy gallium-(III) species are considered as model systems since according to the Pourbaix diagram it is the most stable cation in the pH range from 4.8 to 6.[32] Results of DFT calculations are presented in Table S1 and S2 and reveal that coordination of PAA and PEI to $Ga(OH)_2^+$ is highly thermodynamically favorable (Figure 2d). The presence and interaction between the discussed species affect I–V's.

I–V's are obtained in different voltage ranges (Figure S3) and used for the database (Supporting Information). When measurements are in the -0.02 to 0.02 V and -0.1 to 0.1 V ranges, curves characteristic of the capacitor are obtained. When recording curves in the range up to 0.5 V, no electrochemical reactions occur on the electrode surface. The obtained characteristic corresponds to the thickness of the chemically formed oxide film. With increasing voltage to the ranges -0.5 to 0.5 V and -1 to 1 V, we obtain curves characteristic of a resistor with nonlinear resistance. Applying a voltage above 0.5 V leads to an increase in the concentration of the soluble form of $Ga(OH)_2^+$ and a proportional increase in the GaOOH oxide film's thickness, which transforms into Ga_2O_3. With a further increase in voltage to -5 to 5 V and repeating cycles, diode behavior is observed. This change is because, at low currents, gallium ionization is weakly expressed, and oxide film does not grow. With a further increase in the applied potential, gallium oxidation accelerates, and the film thickness increases rapidly, which contributes to an increase in the layer resistance (Figure S1). A single application of the
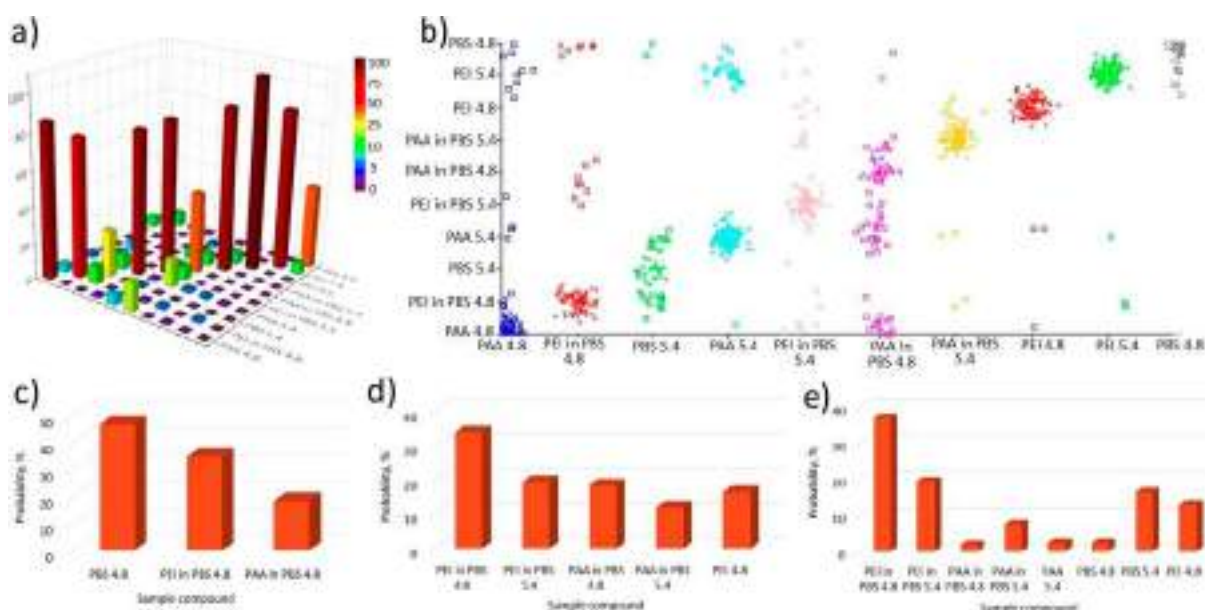
Figure 4. (a) Confusion histogram for multilayer perceptron classification. (b) Prediction error graph. The axes show the actual and predicted values; the correct values are indicated by crosses and the errors by squares. (c−e) Result of the three gels (shown in Figure 1b) composition analysis (c) by the range of −0.02 to 0.02 V; (d) by the ranges of −0.02 to 0.02 V, −0.1 to 0.1 V, and −0.5 to 0.5 V; and (e) by analysis of all data set −0.02 to 0.02 V, −0.1 to 0.1 V, −0.5 to 0.5 V, −5 to 5 V, and (−5 to 5 V)n.

reduction potential of −7 to 7 V can partially dissolve the oxide layer that elicits the diode−resistor transition. However, since it is impossible to dissolve the film completely, the manifestation of capacitor properties is no longer possible. When a voltage higher than 1 V is applied, electrochemical decomposition of water does not occur since an oxide film's growth increases the resistance in the circuit and decreases the actual value of the applied voltage. The diagram shown in Figure 3a displays the content of the fractions of the forms of gallium compounds during the electric generation of 0.38 mM of the total gallium content in the hydrogel. The gallium content is calculated from the peak area at a 5 V sweep. This sweep achieves the limiting diffusion current in the system and maximum of total dissolved gallium concentration. According to the equation

$$C(Ga_{total\ dissloved}) = \frac{S_{anodic\ peak}}{FzvV}$$

where $S_{anodic\ peak}$ is the anodic peak area, V the volume of the hydrogel, F Faraday's constant, z the charge value, and v the voltage sweep rate. In addition, at −0.5 to 0.5 V and −1 to 1 V and a single −5 to 5 V, the system is characterized by diode behavior. Finally, with multiple voltage sweeps in the range (−5 to 5 V)n, a large film thickness leads to the appearance of memristor behavior. The dissolution of the oxide−phosphate film by a single application of the reduction potential triggers the system's diode-like behavior. All current−voltage collected data were put in the system training.

The artificial neural network in chemistry can solve a wide range of tasks such as pattern recognition and classification, approximation, prediction, and others.[33] The multilayer perceptron models are the most widely used neural networks that consist of one input layer, one output layer, and one or more hidden layers.[34−36] The Weka 8.3.4 program, a multilayer perceptron model, was applied for the analysis (Figure 3b). For the raw database, all points of the $I-V$ curve are taken. One layer and 12 multilayer perceptron model classes are used to

describe the relationship between input and output data. The data of measured current at different voltage sweep serve as input data. The hydrogel compositions are the output parameters. The confusion matrix (Figure 4a) depicts correspondence between predicted and real hydrogel composition for the trained model. The diagonal matrix values are superior to all others, which indicates the correct operation of the trained model. Classification errors (Figure 4b) also indicate a high accuracy in determining the composition of hydrogels. We also compared different classifiers and clustering models, among which the multilayer perceptron showed the highest accuracy, 82% (Table S3). Low clustering accuracy is presumably associated with poor data differentiability. Clustering accuracy for the expectation-maximization (EM) method is improved by integrating data and obtaining areas between the curves (Figure S2).

An ensemble of three electrodes and three gels of various compositions is used to verify the proposed model's operation. Surprisingly, the composition of the hydrogels is accurately detected with reduced input data. The low voltage sweep −0.02 to 0.02 V allows uncovering the composition of hydrogels (Figure 4c). Characteristic low voltage sweep indicates chemical composition. Such achievement is due to the specific interaction of polyelectrolytes in hydrogels and the eGaIn alloy. As a result of this specific interaction, either the formation of a thick oxide film or the oxide film dissolution and the formation of complex compounds on the alloy surface occur.

$I-V$ sweep data as an input for the ranges of −0.02 to 0.02 V, −0.1 to 0.1 V, and −0.5 to 0.5 V allow only two out of three compositions to be determined (Figure 4d,e). The range of $I-V$ scans corresponding to the range used for training the system allows us to determine the statistical weights corresponding to the magnitude of the current flow in the system. Visualization of the flow of electric current through hydrogels of various compositions using photodiodes confirms the analysis of $I-V$ characteristics (Figure 5a). With increasing
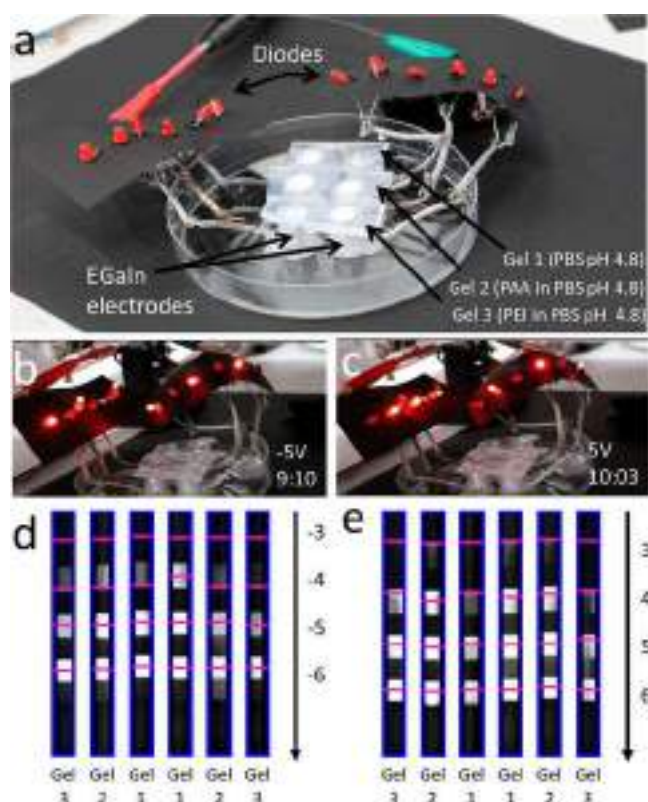
Figure 5. (a) Photograph of electrochemical multielectronic component system. (b) Set of experiments with different values of applied voltage −5 V forward current direction and (c) 5 V reverse current direction. (d) Kymograms for the each of six hydrogel outputs at cathodic voltage switching. (e) Kymograms for the each of six hydrogel outputs at anodic voltage switching.

voltage, an increase in the glow intensity of the diodes is observed. However, as the oxide film grows, the glow intensity decreases (Figure 5b,c). Because of the different compositions of hydrogels, the decrease in intensity is uneven. Also, there is a redistribution of the current in the circuit. Therefore, even with the same voltage, the intensity changes. Video S1 demonstrates the uneven distribution of the signal between gels of various compositions. The electrochemical system with diodes is designed to visualize the effect of changes in various parameters. A quantitative assessment of the intensity of the diodes' glow using kymograms proves the asymmetric current flow (Figure 5d,e). The data in Table S4 confirm the current flow's irregularity at six points, three of which are "input" and three are "output".

In conclusion, we have proposed a chemical self-switchable electronic system capable of operating as a capacitor, resistor, diode, and memristor. The self-switchable interface is achieved by controlling the formation of an insoluble film of gallium oxide or salt. Based on this interface, a chemical hydrogel perceptron is created. It is possible to predict the electrical response by using input in the form of a hydrogel composition and determine the composition by the electrical response.

Our results deliver a groundbreaking approach to engineering soft-matter-based elements for information treatment since the perceptron model is among the simplest but crucial ones for this purpose. This approach paves the way for future experiments and theoretical studies: from experiments with complex geometries and types of gels to theoretical analysis of

which kind of problems can be in principle formulated and solved with the soft-matter-based logical devices.

■ ASSOCIATED CONTENT

Ⓢ Supporting Information

The Supporting Information is available free of charge at https://pubs.acs.org/doi/10.1021/acs.jpclett.1c00007.

> DFT calculations data; comparison of the different classification models (PDF)
>
> Video S1 (MP4)
>
> Training and education data set for the machine learning (XLSX)

■ AUTHOR INFORMATION

Corresponding Author

Ekaterina V. Skorb − *Infochemistry Scientific Center, ITMO University, Saint Petersburg 191002, Russia;* ⊙ orcid.org/0000-0003-0888-1693; Email: skorb@itmo.ru

Authors

Artemii S. Ivanov − *Infochemistry Scientific Center, ITMO University, Saint Petersburg 191002, Russia*

Konstantin G. Nikolaev − *Infochemistry Scientific Center, ITMO University, Saint Petersburg 191002, Russia*

Alexander S. Novikov − *Infochemistry Scientific Center, ITMO University, Saint Petersburg 191002, Russia;* ⊙ orcid.org/0000-0001-9913-5324

Stanislav O. Yurchenko − *Bauman Moscow State Technical University, Moscow 105005, Russia;* ⊙ orcid.org/0000-0001-6821-904X

Kostya S. Novoselov − *Department of Materials Science and Engineering, National University of Singapore, Singapore 117575, Singapore*

Daria V. Andreeva − *Department of Materials Science and Engineering, National University of Singapore, Singapore 117575, Singapore*

Complete contact information is available at:
https://pubs.acs.org/10.1021/acs.jpclett.1c00007

Notes

The authors declare no competing financial interest.

■ REFERENCES

(1) Rich, S. I.; Wood, R. J.; Majidi, C. Untethered soft robotics. *Nat. Electron* **2018**, *1* (2), 102−112.

(2) Bartlett, M. D.; Dickey, M. D.; Majidi, C. Self-healing materials for soft-matter machines and electronics. *NPG Asia Mater.* **2019**, *11* (1), 21.

(3) Kazem, N.; Hellebrekers, T.; Majidi, C. Soft multifunctional composites and emulsions with liquid metals. *Adv. Mater.* **2017**, *29* (27), 1605985.

(4) Gong, S.; Yap, L. W.; Zhu, B.; Cheng, W. Multiscale soft-hard interface design for flexible hybrid electronics. *Adv. Mater.* **2020**, *32* (15), No. e1902278.

(5) Stoyanov, H.; Kollosche, M.; Risse, S.; Wache, R.; Kofod, G. Soft conductive elastomer materials for stretchable electronics and voltage controlled artificial muscles. *Adv. Mater.* **2013**, *25* (4), 578−583.

(6) Majidi, C. Soft-matter engineering for soft robotics. *Adv. Mater. Technol.* **2018**, *4* (2), 1800477.

(7) Shi, Y. L.; Wang, C. J.; Yin, Y. F.; Li, Y. H.; Xing, Y. F.; Song, J. Z. Functional soft composites as thermal protecting substrates for wearable electronics. *Adv. Funct. Mater.* **2019**, *29* (45), 1905470.

(8) Wang, C.; Wang, C.; Huang, Z.; Xu, S. Materials and structures toward soft electronics. *Adv. Mater.* **2018**, *30* (50), No. e1801368.

(9) Rong, Q.; Lei, W.; Liu, M. Conductive hydrogels as smart materials for flexible electronic devices. *Chem. - Eur. J.* **2018**, *24* (64), 16930−16943.

(10) Chiechi, R. C.; Weiss, E. A.; Dickey, M. D.; Whitesides, G. M. Eutectic gallium-indium (EGaIn): a moldable liquid metal for electrical characterization of self-assembled monolayers. *Angew. Chem., Int. Ed.* **2008**, *47* (1), 142−144.

(11) Shay, T.; Velev, O. D.; Dickey, M. D. Soft electrodes combining hydrogel and liquid metal. *Soft Matter* **2018**, *14* (17), 3296−3303.

(12) Bowers, C. M.; Liao, K.-C.; Yoon, H. J.; Rappoport, D.; Baghbanzadeh, M.; Simeone, F. C.; Whitesides, G. M. Introducing ionic and/or hydrogen bonds into the SAM//Ga_2O_3 top-interface of $AgTS/S(CH_2)_nT//Ga_2O_3/EGaIn$ junctions. *Nano Lett.* **2014**, *14* (6), 3521−3526.

(13) Koo, H. J.; So, J. H.; Dickey, M. D.; Velev, O. D. Towards all-soft matter circuits: prototypes of quasi-liquid devices with memristor characteristics. *Adv. Mater.* **2011**, *23* (31), 3559−64.

(14) Daeneke, T.; Khoshmanesh, K.; Mahmood, N.; de Castro, I. A.; Esrafilzadeh, D.; Barrow, S. J.; Dickey, M. D.; Kalantar-Zadeh, K. Liquid metals: fundamentals and applications in chemistry. *Chem. Soc. Rev.* **2018**, *47* (11), 4073−4111.

(15) Baghbanzadeh, M.; Pieters, P. F.; Yuan, L.; Collison, D.; Whitesides, G. M. The rate of charge tunneling in EGaIn junctions is not sensitive to halogen substituents at the self-assembled monolayer//Ga_2O_3 interface. *ACS Nano* **2018**, *12* (10), 10221−10230.

(16) Ai, Y.; Kovalchuk, A.; Qiu, X.; Zhang, Y.; Kumar, S.; Wang, X.; Kühnel, M.; Nørgaard, K.; Chiechi, R. C. In-place modulation of rectification in tunneling junctions comprising self-assembled monolayers. *Nano Lett.* **2018**, *18* (12), 7552−7559.

(17) Park, S.; Yoon, H. J. New Approach for large-area thermo-electric junctions with a liquid eutectic gallium−indium electrode. *Nano Lett.* **2018**, *18* (12), 7715−7718.

(18) Cayre, O. J.; Chang, S. T.; Velev, O. D. Polyelectrolyte diode: nonlinear current response of a junction between aqueous ionic gels. *J. Am. Chem. Soc.* **2007**, *129* (35), 10801−10806.

(19) Lu, C.; Chen, X. All-temperature flexible supercapacitors enabled by antifreezing and thermally stable hydrogel electrolyte. *Nano Lett.* **2020**, *20* (3), 1907−1914.

(20) Gao, D.; Lee, P. S. Rectifying ionic current with ionoelastomers. *Science* **2020**, *367* (6479), 735−736.

(21) So, J. H.; Koo, H. J.; Dickey, M. D.; Velev, O. D. Ionic current rectification in soft-matter diodes with liquid-metal electrodes. *Adv. Funct. Mater.* **2012**, *22* (3), 625−631.

(22) Kim, B. J.; Um, S. H.; Song, W. C.; Kim, Y. H.; Kang, M. S.; Cho, J. H. Water-gel for gating graphene transistors. *Nano Lett.* **2014**, *14* (5), 2610−2616.

(23) Kim, K. K.; Hong, S.; Cho, H. M.; Lee, J.; Suh, Y. D.; Ham, J.; Ko, S. H. Highly sensitive and stretchable multidimensional strain sensor with prestrained anisotropic metal nanowire percolation networks. *Nano Lett.* **2015**, *15* (8), 5240−5247.

(24) Koo, H. J.; Velev, O. D. Ionic current devices-recent progress in the merging of electronic, microfluidic, and biomimetic structures. *Biomicrofluidics* **2013**, *7* (3), 031501.

(25) Dickey, M. D. Stretchable and soft electronics using liquid metals. *Adv. Mater.* **2017**, *29* (27), 1606425.

(26) Brown, K. A.; Brittman, S.; Maccaferri, N.; Jariwala, D.; Celano, U. Machine learning in nanoscience: big data at small scales. *Nano Lett.* **2020**, *20* (1), 2−10.

(27) Wang, P.; Nasir, M. E.; Krasavin, A. V.; Dickson, W.; Zayats, A. V. Optoelectronic synapses based on hot-electron-induced chemical processes. *Nano Lett.* **2020**, *20* (3), 1536−1541.

(28) Herron, M.; Schurr, M. J.; Murphy, C. J.; McAnulty, J. F.; Czuprynski, C. J.; Abbott, N. L. Gallium-loaded dissolvable microfilm constructs that provide sustained release of Ga^{3+} for management of biofilms. *Adv. Healthcare Mater.* **2015**, *4* (18), 2849−2859.

(29) Bonifacio, M. A.; Cometa, S.; Dicarlo, M.; Baruzzi, F.; de Candia, S.; Gloria, A.; Giangregorio, M. M.; Mattioli-Belmonte, M.; De Giglio, E. Gallium-modified chitosan/poly(acrylic acid) bilayer coatings for improved titanium implant performances. *Carbohydr. Polym.* **2017**, *166*, 348−357.

(30) Staňo, R.; Nová, L.; Uhlík, F.; Košovan, P. Multivalent counterions accumulate in star-like polyelectrolytes and collapse the polymer in spite of increasing its ionization. *Soft Matter* **2020**, *16* (4), 1047−1055.

(31) Ermoshkin, A. V.; Olvera de la Cruz, M. Polyelectrolytes in the presence of multivalent ions: gelation versus segregation. *Phys. Rev. Lett.* **2003**, *90* (12), 125504.

(32) Pourbaix, M. Atlas of electrochemical equilibria in aqueous solution. *NACE* **1974**, *307*.

(33) Gasteiger, J.; Zupan, J. Neural networks in chemistry. *Angew. Chem., Int. Ed. Engl.* **1993**, *32* (4), 503−527.

(34) Akter, T.; Desai, S. Developing a predictive model for nanoimprint lithography using artificial neural networks. *Mater. Des.* **2018**, *160*, 836−848.

(35) Martinez-Blanco, M. D.; Ornelas-Vargas, G.; Solis-Sanchez, L. O.; Castaneda-Miranada, R.; Vega-Carrillo, H. R.; Celaya-Padilla, J. M.; Garza-Veloz, I.; Martinez-Fierro, M.; Ortiz-Rodriguez, J. M. A comparison of back propagation and generalized regression neural networks performance in neutron spectrometry. *Appl. Radiat. Isot.* **2016**, *117*, 20−26.

(36) Patel, J.; Choi, S. K. Classification approach for reliability-based topology optimization using probabilistic neural networks. *Struct. Multidiscip O* **2012**, *45* (4), 529−543.

ADVANCED MATERIALS INTERFACES
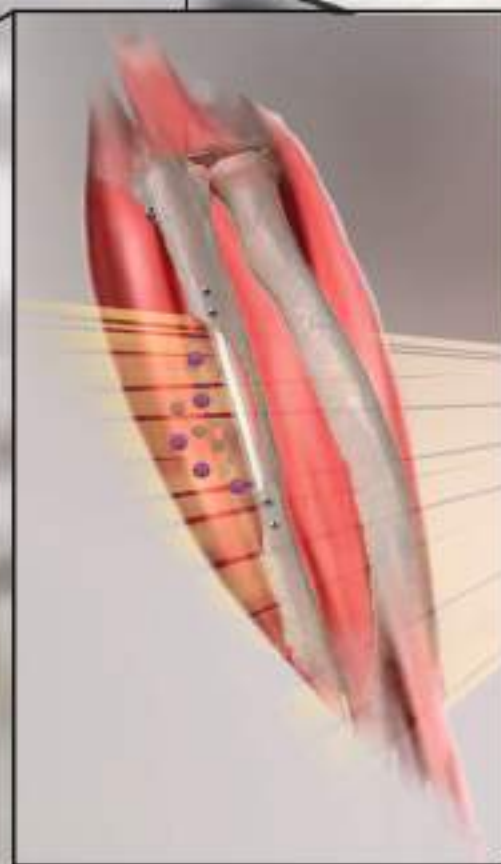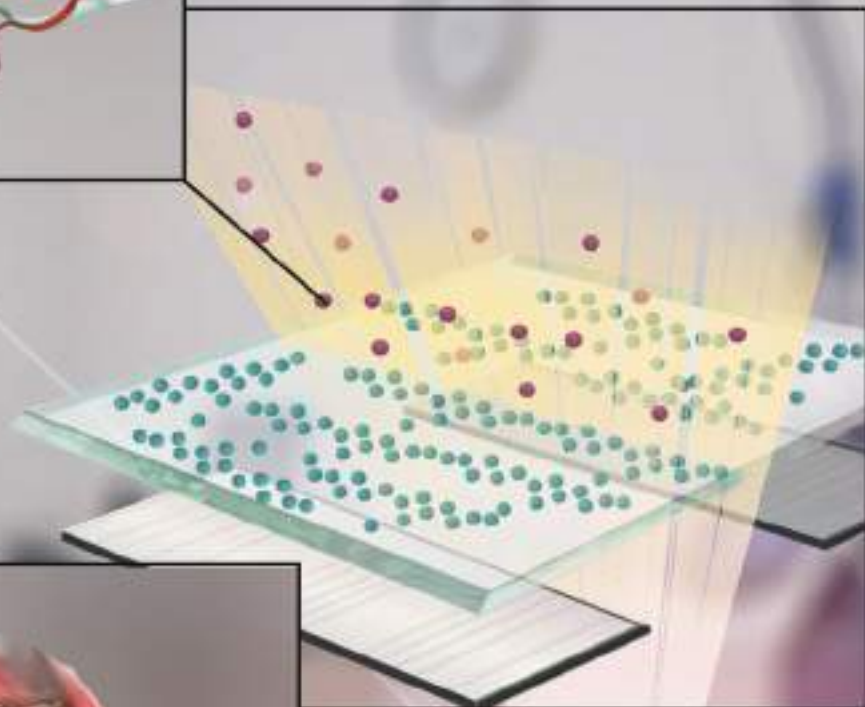
Light-to-Heat Photothermal Dynamic Properties of Polypyrrole-Based Coating for Regenerative Therapy and Lab-on-a-Chip Applications

Sviatlana Ulasevich,* Nikolay V. Ryzhkov, Daria V. Andreeva, Dilek Sura Özden, Erhan Piskin, and Ekaterina V. Skorb*

Targeted delivery and release of biomolecules, e.g., bone morphogenetic protein (BMP-2), are gaining high interest due to the application for tissue engineering, diagnostics, surface-enhanced therapy and lab-on-a-chip. Here, a new hybrid temperature-responsive system consisting of polypyrrole (PPy) layer, mesoporous titania surface (TMS), and BMP-2 is proposed. The PPy layer has the light-to-heat photothermal property. Dynamic behavior of the PPy layer in response to light can regulate release of BMP-2. The PPy-based coatings on TMS have shown to be efficient for storage of BMP-2 and can be tuned to release BMP-2 under irradiation. Moreover, the possibility of local delivery and generation of a gradual release of BMP-2 for regulated cell growth is shown. Furthermore, the fabricated surfaces possess excellent biocompatibility and low cytotoxicity for MC3T3-E1 cells. It is shown that the released BMP-2 can effectively promote osteogenic differentiation of MC3T3-E1 cells. Thus, the TMS/PPy–BMP-2 is suggested to prolong targeted release of the BMP-2 for more than 25 days which stimulates osteoblasts' proliferation. The new stimuli-responsive hybrid system is promising for targeted, localized, sustained drug release and application in bone tissue engineering.

1. Introduction

Developing tissue engineering technologies relies on biomaterials that physically support tissue growth and stimulate specific cell functions. Among these biomaterials, polymer-based materials are universal in every aspect of life and used for a wide variety of biomedical applications.[1,2] Especially, hybrid materials based on metal surfaces and stimuli-responsive polymers are interesting for the formation of multifunctional surfaces on commercially available implants and lab-on-a-chip devices.

The deposition of stimuli-responsive hybrids on titanium's surface can significantly increase the performance and lifetime of titanium implants. Since polymer-coated titanium surfaces function as a semipermeable membrane which protects the incorporated therapeutics, at certain conditions, therapeutics can be loaded into the metal surface and released in response to the biological environment, for example, at particular pH or upon light or/and heat treatment.

Uptake/release of therapeutics on demand can be achieved by the deposition of stimuli-responsive polymeric coatings.[3,4] Light is an efficient noninvasive stimulus which can initiate phase transitions in stimuli-responsive biomaterials.[5] Here, we use polypyrrole (PPy) which is known to have light-to-heat photothermal dynamic properties.[6–9] For the first time, we show that a mild light-to-heat conversion properties of PPy can be used for the delivery of therapeutics to cells and for the enhancement of cells' proliferation. Furthermore, PPy is a material of choice for biomedical applications because it exhibits in vitro and in vivo compatibility.[10] So being biocompatible and electrically conductive, PPy surfaces can modulate cellular activities, including cell adhesion, migration, DNA synthesis, and protein secretion.[8–12] Therefore, among other conductive polymers, PPy is known to be applied in medicine.[16,17] The conductivity of the PPy and its ability to absorb near-infrared radiation make it interesting for the construction of biosensors. In particular, it was shown that PPy is compatible with many biological sensing molecules such as enzymes, antibodies.[13]

Dr. S. A. Ulasevich, N. V. Ryzhkov, Prof. E. V. Skorb
Infochemistry Scientific Center of ITMO University
ITMO University
Lomonosova str. 9, St. Petersburg 191002, Russia
E-mail: saulasevich@itmo.ru; skorb@itmo.ru
Prof. D. V. Andreeva
Department of Materials Science and Engineering
National University of Singapore
Singapore 117575, Singapore
Dr. D. S. Özden
Chemical Engineering Department and Bioengineering Division
Center for Bioengineering and Biyomedtek/Nanobiyomedtek
Hacettepe University
Beytepe, Ankara 06800, Turkey
Prof. E. Piskin
NanoBMT
Nanobiyomedtek Biyomedikal and Biyoteknoloji San.Tic., Ltd.Sti.
Bilkent University
56 Cyberpark, Bilkent, Ankara 06800, Turkey

ADVANCED
SCIENCE NEWS
www.advancedsciencenews.com

ADVANCED
MATERIALS
INTERFACES
www.advmatinterfaces.de

Recently, research groups have already used PPy to enhance mechanical properties and biocompatibility of implants.[14–16] So being biocompatible and electrically conductive, PPy films were applied in experiments with muscle, bone, cardiac, and nerve cells because of their perfect mechanical match between PPy molecules and tissues. For in vivo studies, implanted PPy triggers minimal tissue inflammation.[14] Furthermore, it was shown that PPy can even increase the growth of regenerating axons.[15,16] Additionally, rigid PPy molecules can be doped with biocompatible synthetic and natural polymers to improve films' processability. Kai et al. constructed a polypyrrole/poly(caprolactone)/gelatin electrospun conductive nanofibrous membrane as a scaffold for reconstruction of damaged myocardium and cardiac tissues. Addition of lower-melting temperature and glass-transition polymer, polycaprolactone, into PPy networks enhances elastic properties of PPy.[17] Furthermore, Wang and co-workers showed that polypyrrole/poly(D,L-lactide) composite tissue scaffolds implanted subcutaneously or intramuscularly in rats provide immune cell infiltration compared to FDA-approved poly(lactic acid-co-glycolic acid) material.[18] Sajesh et al. constructed PPy–alginate blend with chitosan scaffold and assessed the scaffold for cell viability, cytocompatibility, and mineralization with MG-63 cells.[19,20]

Besides the applications for tissue scaffolds engineering,[17–21] tests in simulated body fluid solution have shown that PPy enhances also the anticorrosion resistance of implants.[22–24] The conductivity of PPy and its sensitivity to near-infrared light as well as its ability to respond upon receiving a specific electronic signal, can be used for actuators[25,26] and targeted delivery.[5,22–28] Recently, a lot of interesting works were published on electrically controlled release of bioactive molecules from PPy-based materials.[11,27–33] Electrochemical synthesis of PPy, which is generally performed by application of constant current (galvanostatic), constant potential (potentiostatic), or potential scanning or sweeping methods, allows simultaneous encapsulation of bioactive molecules via doping process.[14] The PPy-based nanocontainers, nanocarriers, or capsules can be used for encapsulation of antibiotics, enzymes, and proteins.[27–33] Furthermore, PPy is prospective for engineering biocompatible barrier "skin" shell for the encapsulation of water soluble and low molecular weight therapeutics.[4]

PPy carriers have attracted much interest as carriers for electrochemical immobilization of therapeutics.[11,33] In particular, Sirivisoot et al. demonstrated the release of dexamethasone sodium phosphate and penicillin/streptomycin from nanostructured PPy film polymerized on multi-walled (MW) carbon nanotubes (NT) were grown out of anodized nanotubular Ti (MWNT–Ti).[34] Similarly, they used nanostructured PPy for the incorporation of Dex and penicillin/streptomycin coating on commercially pure titanium via electrochemical deposition. They showed that titanium/PPy surfaces with encapsulated penicillin and dexamethasone provide necessary adhesion of osteoblast and fibroblast by applying voltage.[32–34] Wang et al.[35] have shown that hollow PPy nanocapsules loaded with antitumor agent doxorubicin are pH-sensitive, and release more than half of the encapsulated drug within 15 h at a pH of 4.5. It is also shown that the release can be further regulated by applying near-infrared light. Park et al.[36] have studied PPy nanoparticles (NPs) doped with hyaluronic acid for preferential release of doxorubicin at lysosomal pH < 5.[37,38]

Despite many articles about PPy-based biocompatible materials and biomedical devices, the photothermal behavior of PPy has not been explored. It was proposed[6] that the broadband light absorption of the PPy shell enables efficient light-to-heat conversion upon irradiation, allowing the dynamic motion of colloids via light-irradiation-induced Marangoni flow. It was shown that the light-triggered water evaporation rate was higher for the PPy-coated surfaces. Furthermore, Winnik and co-workers[7] designed the composites containing PPy for the adsorption of near-infrared (NIR) radiation and the conversion of the energy of the radiation into heat. They applied PPy composites to localize heating for hot-melt adhesives. Phase transition was shown for the PPy-modified NPs.[7] Liu and co-workers[8] proposed to use PPy for the design of PPy-based biocompatible photothermal light-to-heat transducer. Photothermal therapy used PPy as a photothermal agent with a strong adsorption in NIR light.[36] Liu and co-workers[36] mentioned that "optical absorbing agents "cook" cancer under light." Our aim is to propose a mild nondistractive approach to in vivo manipulate osteoblasts on the surface of titanium implants. Thus, here, we used the ability of PPy to respond to near-infrared light and convert it into a slight temperature increase.[6–9] We applied this effect to trigger the release of therapeutics on demand but not harmful for living cells.

In our study, we have developed a hybrid stimuli-responsive layer based on PPy and mesoporous titania surface (TMS) obtained by sonochemical treatment of titanium. Sonochemical nanostructuring of titanium surface was used to obtain the rough surface with structure providing better adhesion and osseointegration.[37–49] Comparing with other methods, sonochemical surface modification can be applied as a time and energy saving approach to the fabrication of functional nanostructured surfaces.[42–45]

Sonochemical surface treatment bases on the collapse of cavitation bubbles near solid/liquid interfaces. Cavitation leads to generation and propagation of shock waves and high-pressure- and temperature-induced decomposition of sonication medium. In water, cavitation causes water sonolysis. The products of water decomposition are responsible for interfacial red/ox reactions. The redox reactions lead to the formation of titania layer during the treatment.[40–47] Since cavitational reactions are quenched extremely fast, the dissolution and oxidation of titanium proceed at highly nonequilibrium conditions. As a result, disordered porous structure is formed. In our study, a novel method based on sonochemical surface treatment of titanium was developed.

Sonochemically formed TMS layer was fabricated using high-intensity ultrasound treatment together within alkali 5 M NaOH. This technique provides the generation and spread of cavitation along the surface of the metal and creates large heat gradients in metals. Thus, the materials with compositional gradients and porous morphology and nonequilibrium nanostructures are formed at macroscopically environmental conditions. The use of ultrasonic cavitation is for near-surface structuring of robust and low-cost AlNi catalysts for hydrogen production.[48] The formation of TMS can be explained by the special kinetics of sonochemical reactions triggered by shock waves due to ultrasound-induced cavitation bubble collapse.[50–53]

Such mesoporous titania layer formed on bulk titanium due to ultrasound-induced cavitation is suitable to attach

biomolecules into nanostructured surfaces such as growth factors, tissue specific proteins, drug molecules, nanoparticles, nanoemulsions which can be applied to enhance cellular activity and bone combination.[4,42,49–57] The sonochemical nanostructuring is an important step to achieve the better adhesion of the stimuli-responsive polymer to the substrate, whereas the wettability of the surface plays an important role for biological systems in terms of adsorption of proteins, cell adhesion, and cell movements.[40–44]

The porous structure of the titanium scaffold can provide satisfactory microenvironments for cell migration, proliferation, differentiation, angiogenesis, and vascularization for the bone regeneration process. It is known[58] that surface topography substantially affects the macroscopic behavior of a material. At the cellular level, biological responses, such as the orientation and migration of cells and the cellular production of organized cytoskeletal arrangements, are directly affected by the surface topography.

Here, we propose a new approach for the modification of the surfaces of titanium/titanium alloy implants. The modified titanium surface can act both as a carrier for therapeutics and as a support for the deposition of stimuli-responsive coatings. Stimuli-responsive coating can change their permeability on demand and regulate release of therapeutics in response to environment.[2]

In this research, TMS helps to solve crucial PPy-based coating drawback of breakdown of hybrid material properties due to rigidity and fragility of PPy. As a result, cell culture on TMS/(PPy–polystyrene sulfonate (PSS)) can be effective than Glass/PPy. The viabilities of MC3T3-E1 cells are incubated on the different substrates. Bone morphogenic protein (BMP-2) was encapsulated directly in TMS matrix. Owing to the low cytotoxicity, high specific surface area, and high absorption characteristics of TMS, BMP-2 can efficiently load and protect. The idea of our approach is to trigger the protein release by irradiation. Therefore, we apply light-to-heat photothermal dynamic properties[6–9] of polypyrrole-based coating to regulate encapsulation and release of the protein on demand for regenerative therapy and lab-on-a-chip applications. The light-to-heat conversion can stimulate the release of BMP-2 from the pores of TiO_2. The advantage of our approach is noncontact switching of our system whereas for electrically controlled release, we need to make a contact with electrode or power supply.

2. Results and Discussion

2.1. Preparation of TMS Surface

TMS was formed by cavitation-assisted dissolution and oxidation of titanium surface in alkaline solution. Clouds of cavitation bubbles were produced by using a high-intensity ($\approx$200 W cm^{-2})-focused ultrasound operated at 20 kHz. The chemical effect of sonication could be explained by reactive oxygen species (ROS) generation due to bubbles' collapse in a liquid. These ROS species can be further involved in secondary reactions oxidizing the titanium. Taking into account exceedingly high temperatures ($\approx$5100 K), pressures ($\approx$20 MPa) created

during the acoustic cavitation,[11,48–51,59] we can assume that oxidizing of titanium undergoes according to Equations (1)–(8)

$$Ti^0 + OH^- + 5H_2O \rightarrow \left[Ti(H_2O)_5\, OH^- \right]^{3+} + 4e^- \tag{1}$$

$$2[Ti(H_2O)_5\, OH]^{3+} \rightarrow [Ti_2(H_2O)_8(OH_2)^{6+} + 2H_2O] \tag{2}$$

$$\alpha - TiO_2 \cdot 2H_2O \rightarrow \beta - TiO_2 \cdot H_2O + H_2O \tag{3}$$

$$\beta - TiO_2 \cdot H_2O \rightarrow TiO_2 + H_2O \tag{4}$$

$$2Ti^0 + 6H_3O^+ + 6H_2O \rightarrow 2\left[Ti(H_2O)_6 \right]^{3+} + 3H_2 \tag{5}$$

$$\left[Ti(H_2O)_6 \right]^{3+} + 3OH^- = Ti(OH)_3 + 6H_2O \tag{6}$$

$$4Ti(OH)_3 + O_2 + (x-6)H_2O = 4TiO_2 \cdot xH_2O \tag{7}$$

$$Ti^0 + 2NaOH + H_2O \rightarrow Na_2TiO_3 + 2H_2 \tag{8}$$
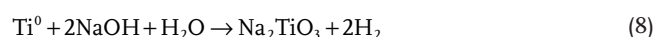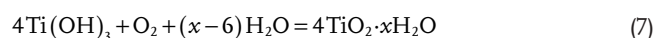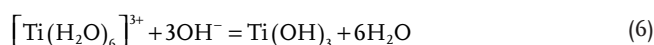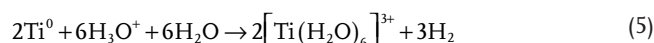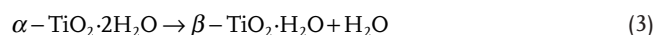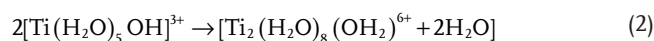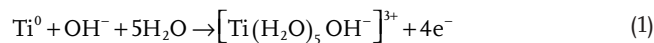
At the next stage, the polycondensation of $[Ti(H_2O)_5OH^-]^{3+}$ ions occurs with the formation of oligomeric hydroxo- and oxoderivatives. The as-precipitated α-titanic acid contains a significant amount of bridging OH— groups. Its formula unit is α-$TiO_2 \cdot 2H_2O$. On the aging of the titanic acid (Equation (3)), the hydroxyl bridges convert into O— bridges. The β-titanic acid (β-$TiO_2 \cdot xH_2O$, $x = 1$) contains a smaller number of OH— groups and water molecules due to additional Ti—O—Ti bonds. Heating of β-titanic acid leads to its complete dehydration and all OH— bridges turn to O— bridges (Equation (4)).

In addition, adverse reactions can occur (Equations (5)–(8)). During the sonochemical treatment, the electrolyte acquires a slight violet color, which may be due to the formation of $[Ti(H_2O)_6]^{3+}$ ions. The color of the aqua complexes is associated with the transition of the electron from t_{2g} to the e_g orbital with the absorption of energy corresponding to the splitting energy $\Delta_0 = 20\,300$ cm^{-1}, i.e., yellow-green part of the visible spectrum.

These ions react with hydroxyl ions to form a dark violet precipitate of $Ti(OH)_3$ (Equation (6)). In the presence of oxygen, it is further oxidized according to Equation (7), followed by polycondensation. Furthermore, since there is a local temperature and pressure increase, the reaction (8) can take place.

Figure 1 shows the steps of stimuli-responsive coatings fabrication. The titania substrate was obtained using the sonochemical treatment. Then, samples were annealed at 450 °C to remove any organic contaminants and provide crystallization of titania layer.

The BMP-2 was loaded into the mesoporous titania matrix (Figure 1b). To control the release of the protein and its biological activity, the PPy-based coating was deposited. The PPy layer is modified with PSS to form a layer-by-layer assembly shown in Figure 1h. Since PPy has a high surface energy, its molecules can be attached to surfaces. The PSS was deposited by layer-by-layer assembly technique through electrostatic interaction between positively charged PPy and negatively charged PSS. However, there is also a possibility of the formation of hydrogen bonds between hydrogen atom at nitrogen in the PPy structure and the oxygen atom in —SO$_3$H group.[60–63] Developing our system, we choose the PSS due to its ability to act

**ADVANCED
SCIENCE NEWS**
www.advancedsciencenews.com

**ADVANCED
MATERIALS
INTERFACES**
www.advmatinterfaces.de
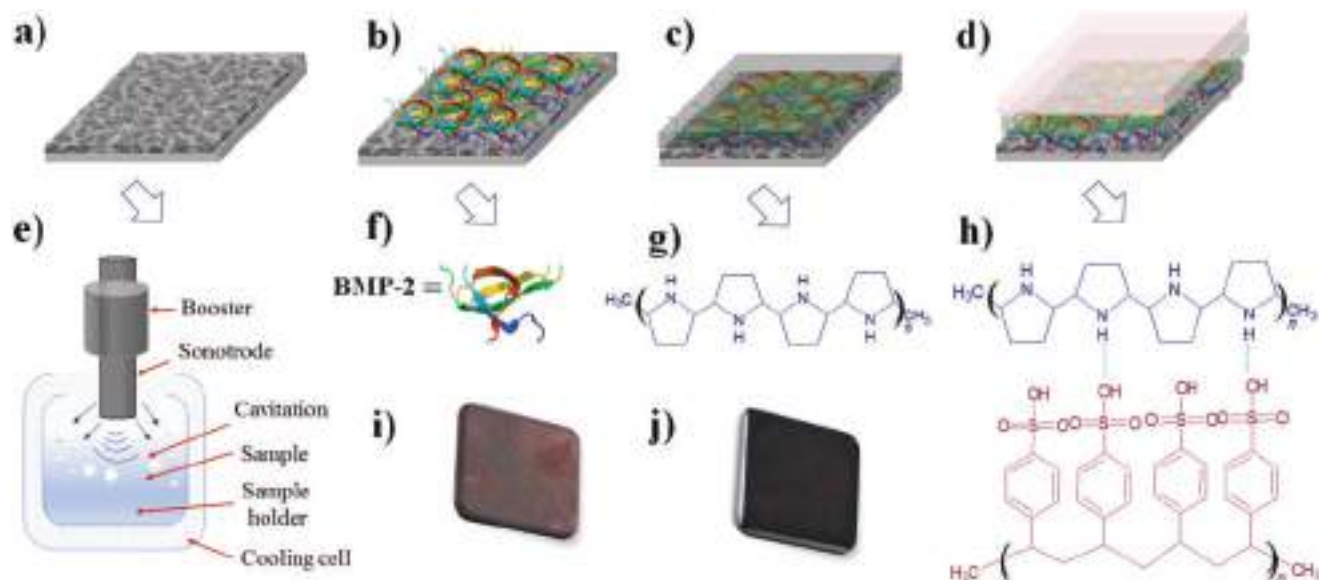
Figure 1. The scheme of the process steps of stimuli-responsive coatings fabrication: a) the schematic image of TMS; b) the schematic image of BMP-2 protein loaded in TMS; c) the schematic image of PPy layer deposited on TMS; d) the schematic image of PSS layer deposited on TMS/PPy; e) the scheme of the sonication cell; f) molecular structure of BMP-2 protein; g) molecular structure of PPy; h) the scheme of the interaction between PPy and PSS molecules; i) the photo of TMS; j) the photo of TMS/(PPy–PSS) sample.

as a dopant and ensure enhanced processability of rigid PPy.[53] The PSS is found to be biocompatible upon implantation.[63,64] Besides, we want to create a cheap reproducible system, and PSS is one of the cheapest reagents compared to, for example, poly(caprolactone) or poly(D,L-lactide). The sonochemical nano-structuring is an important step to achieve the better adhesion of the stimuli-responsive polymer to the substrate, whereas the wettability of the surface plays an important role for biological systems in terms of adsorption of proteins, cell adhesion, and cell movements.[53,54]

Figure 2 shows the initial smooth titanium surface. To compare the surface morphology, we decided to measure the mean roughness (Ra) that is the arithmetic average of the absolute values of the roughness profile ordinates. This parameter gives a good general description of the height variations in the surface. For example, the roughness of initial titanium is $\approx 8 \pm 2$ nm. While the sonochemical treatment leads to the formation of a rough titania layer of sponge-like structure (Figure 2b–f). The Ra parameter of TMS surface is $\approx 11 \pm 2$ nm. Thus, the roughness of TMS is 1.4 times higher compared to the initial
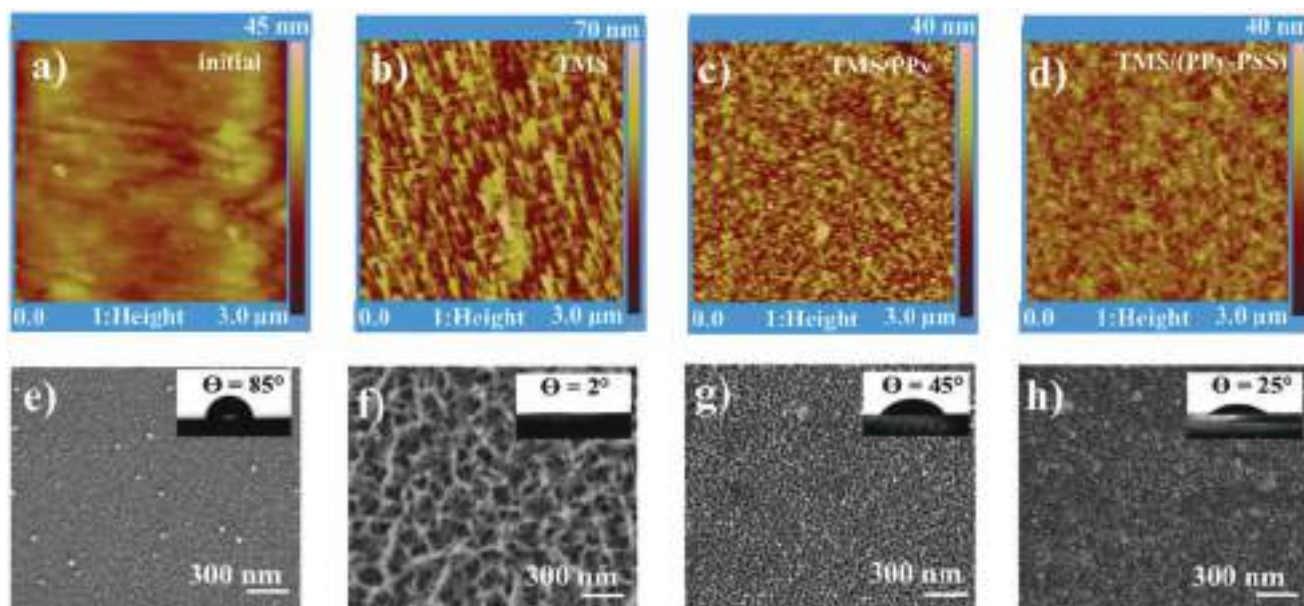
Figure 2. a–d) AFM and e–h) SEM images of initial titanium surface (a,e); TMS surface (b,f); TMS modified by PPy layer (c,g); TMS/(PPy–PSS) sample (d,h). The insets show the water contact angle values.

**ADVANCED
SCIENCE NEWS**

www.advancedsciencenews.com

**ADVANCED
MATERIALS
INTERFACES**

www.advmatinterfaces.de

titanium surface. And, we can conclude that sonication leads to mechanical etching of titanium surface which causes the formation of a mesoporous structure on titanium.

To evaluate the hydrophobic/hydrophilic properties of the surface, we measured the contact angle value. The initial surface of polished titanium has a contact angle value of 85° ± 5°. As shown in Figure 2, the wettability changes according to the surface treatment, and the contact angle value of TMS is ≈2° ± 2°. The increase of the hydrophilic properties of TMS could be explained by the formation of a rough hydrophilic surface of the titanium oxide.

The PPy was deposited as a thin layer polymer onto the TMS and did not significantly change the morphology of TMS. The contact angle value increases to 45° ± 5° but the surface is still hydrophilic. Interestingly, the deposition of PSS layer on TMS/PPy has decreased the contact angle value up to 25° ± 5°. It could be concerned with the redistribution of hydrophilic–hydrophobic sections of the polymer chains due to the intermolecular and intramolecular interaction between PPy and PSS.

Before loading BMP-2 into the pores, we check the stability and anticorrosion resistance of the fabricated coating. Electrochemical impedance spectroscopy revealed corrosion resistance of both samples bare TMS and TMS/(PPy–PSS) with both demonstrating impedance at high frequencies and capacitive behavior at low frequencies. Both the surfaces demonstrate impedance behavior at high frequencies and capacitive behavior at low frequencies. **Figure 3** shows impedance curve of Bode plots for bare TMS and TMS/(PPy–PSS). In terms of the Bode plots, TMS/(PPy–PSS) shows the highest impedance value (0.01 Hz, Figure 3a) and the largest frequency width of the maximum phase angle (85°, Figure 3), while TMS demonstrates the lowest impedance value (0.01 Hz, Figure 3) and the smaller frequency width of the maximum phase angle (70°, Figure 3). Impedance decrease was observed for the polymer covered TMS in comparison with the bare one at low frequencies which are in range of biosignal frequency.[57,58] Apparently, this indicates a greater roughness of the surface coated with a conductive polymer, which makes the area of the conductive surface more accessible to the electrolyte. An increase in roughness is also visible in the atomic force microscopy (AFM) images (Figure 2a,b,e).
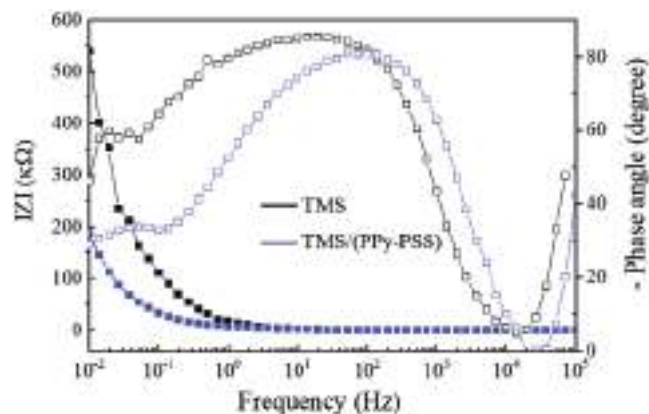
Figure 3. Bode plots of electrochemical impedance spectroscopy (EIS) plots of TMS and TMS/(PPy–PSS). Black curves correspond to TMS sample, gray curves correspond to TMS/(PPy–PSS) sample.

It should be noted that cell adhesion is a very important issue for the developing biomaterials.[65–69] The influence of the local properties, such as the local hardness and stability on the interaction with cells, has not been yet fully understood and exploited. This is particularly relevant for hydrogels, very promising materials with, unfortunately, in many cases, poor cell adhesion properties, attributed mostly to their softness. There are several approaches to increase the adhesion of the material: i) by functionalizing them with particles and performing a thermal treatment,[65,66] and ii) by nanostructuring the initial surface morphology.[65–69] Here, we use sonochemical treatment for nanostructuring the support of our hybrid material. To examine cell adhesion on the fabricated surfaces, we compare the cell viability on flat and rough coatings. It should be mentioned that PPy layer was not attached on the smooth glass surface. Here, TMS helps to solve crucial PPy-based coating drawback of breakdown of hybrid material properties due to rigidity and fragility of PPy. As a result, cell culture on TMS/(PPy–PSS) is more effective than Glass/PPy. The viabilities of MC3T3-E1 cells are incubated on the different substrates. In **Figure 4**a, the surfaces displayed low cytotoxicity. Confocal images show that the cells cultured on TMS and TMS/(PPy–PSS) spread better and extended more filopodia compared to cells on the flat glass surface (Figure 4b–d). Here, TMS revealed not only larger surface areas but also higher surface roughness that provides better adhesion of PPy-based coating to the surface mostly due to physical interlocking. The deposition of PPy does not change the surface morphology drastically. As a result, cell culture on TMS/PPy is more effective than flat surface/PPy for preosteoblast's adhesion. On day 8, cells were stained and imaged for each surface condition. Results for preosteoblasts are shown in Figure 4. In all cases, cells were alive and formed a thick cell layer after 8 days.

As shown in **Figure 5**, external signals mediating fundamental cellular functions are communicated by distinct classes of membrane-bound proteins. Moreover, plasma membrane acts as a platform for accepting extracellular signals (chemical, electrical, or mechanical), and bringing the signals internally by activating the membrane-associated proteins as well as intracellular secondary messengers. For example, in response to external signals that activate cell movement, membrane receptors and membrane bound guanine nucleotide exchange factors induce some enzymes that moderate signaling pathways forcing to activation of motility machinery, especially, the actin polymerization machinery.[69–73] One class of membrane proteins known as cell adhesion molecules play an essential role in linking the cell to its extracellular environment, which combines neighboring cells as well as the extracellular matrix. Two most-studied cell adhesion molecules include the integrin and cadherin family of proteins; while integrins center to the leading edge of motile cells and moderate adhesions between the cellular cytoskeleton and extracellular matrix that creates traction forces for cell motility, cadherins ease cellular organization into tissues by collaborating with cadherin family proteins on neighboring cell membranes and mechanically pairing the cytoskeletal structures of cells forming the tissue.[60]

AFM has been used to compare the relative thickness of BMP-2 adsorbed onto TMS/(PPy–PSS). As shown in **Figure 6**a, a greater thickness of BMP-2 is evident on PPy–PSS layer in
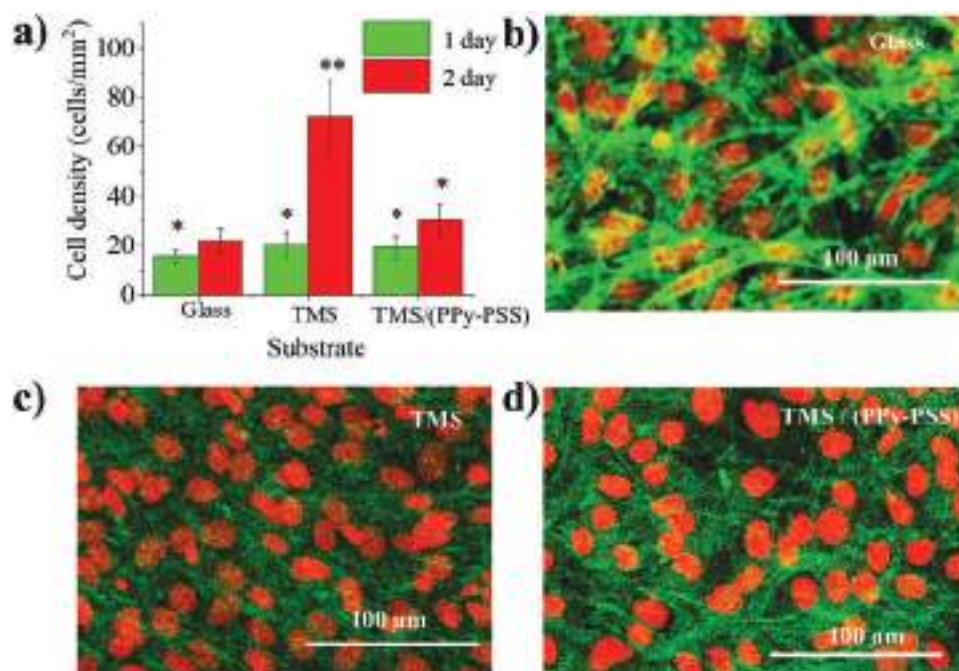
Figure 4. a) Cell viabilities of MC3T3-E1 cells seeded on different substrates for 1 and 2 days. Initial cell seeding of 6×10^3 cells cm^{-2}. All the results were repeated 4 times and presented as mean ± SD. * indicates $p < 0.05$, ** indicates $p < 0.10$. b–d) Fluorescent confocal laser scanning microscopy of stained MC3T3-E1 after 8 days on flat surface of glass (b), rough TMS (c), and TMS/(PPy–PSS) sample (d). Scale bar is 100 µm.

comparison to the rough TMS surface with an initial roughness is altered from ≈11 ± 2 to ≈14 ± 2 nm. AFM line scans across the protein adsorbed pattern (not shown here) indicate the difference in thickness to be from ≈23 ± 2 to 26 ± 2 nm. BMP-2 release results are given in Figure 6b,c. The cumulative release profiles are almost identical for TMS and TMS/(poly-ʟ-histidine (PL)–poly(methacrylic acid) (PMMA))₅. The PL–PMMA coating was used as a control because this type of polyelectrolyte assembly has demonstrated excellent results in the research.[72]

Figure 7b shows the percentage of total bone morphogenetic protein 2 released at each time point. Here, more than 40% of BMP-2 release occurs in the first day from the TMS and TMS/(PL–PMMA)₅. While, TMS/(PPy–PSS) sample inhibits the release and the amount of the released BMP-2 is ≈10%. Thus, 60% of BMP-2 release from TMS and TMS/(PL–PMMA)₅ is achieved after 5 days (Figure 6b,c). After 25 days, more than 80% of BMP-2 is released from TMS and TMS/(PL–PMMA)₅ as compared to 40% from the TMS/(PPy–PSS).

Thus, TMS/(PPy–PSS) is shown to be both more efficient to prevent BMP-2 release in comparison with previously suggested[70] for prolonged BMP-2 release (PL/PMMA)₅. Since PPy has a low permeability,[71–74] it can be said that PPy-based coating with PSS as an supporting polymer gives a dense composite structure for layer by layer composition. This composite structure provides capsule formation for entrapping low molecular weight and/or water-soluble compounds so that delivery can be controlled.[54–59,70–73]

Figure 6d shows that the cell proliferation rate increased in the case of TMS with loaded BMP-2 compared to TMS without BMP-2. At the same time, cell proliferation is significantly lower for TMS/(PPy–PSS) with loaded BMP-2 that corresponds to previously obtained BMP-2 release data. To evaluate if BMP-2 could stimulate the osteogenesis in vitro, we use alizarin red staining to identify the mineralization (not shown here). All samples have had positive red color, indicating the calcium deposition. The TMS–BMP-2 sample has had the highest positive result for red calcium deposition. These coatings should result in improved osseointegration of an implanted titanium device.

The local release from TMS/(PPy–PSS) sample was examined by confocal microscope. The study of local release was carried out in two ways. In the first method (Figure 7a), we used a magnesium tape of $12 \times 2 \times 0.3$ mm as a stencil. A photomask was placed on the surface of the sample and irradiated using an IR flashlight (850 nm, 40 mW cm^{-2}) for 10 min. The distance between the sample surface and the light source was 1 cm. The thickness of the polymer coating through which the light passed was about 400 nm. Then, we examined the release of Rhodamine-labeled BMP-2 by a confocal microscope.

Figure 7 shows a dark strip, the thickness of which is comparable to the thickness of the stencil (2 mm). At the same time, a glow of Rhodamine B is observed on the surface. Gradually, the edges of the strip are eroded, which may be due to the diffusion of BMP-2 into the PSS layer. After carrying out this experiment, we decided to conduct the experiment with cell cultures. As previously shown, the PPy–PSS layer inhibits the release of BMP-2. We suggested that irradiation will lead to a local change of the pH on the surface of titanium dioxide that will change the conformation of the PPy. The loaded BMP-2 will release into the PSS layer and then BMP-2 will diffuse into the environment. In this regard, the autoclaved sample was irradiated through a stencil for 10 min and then cells were seeded on the sample. In 5 days, we can see more cells on the irradiated side of the sample compared to the nonirradiated side (Figure 7d,e).
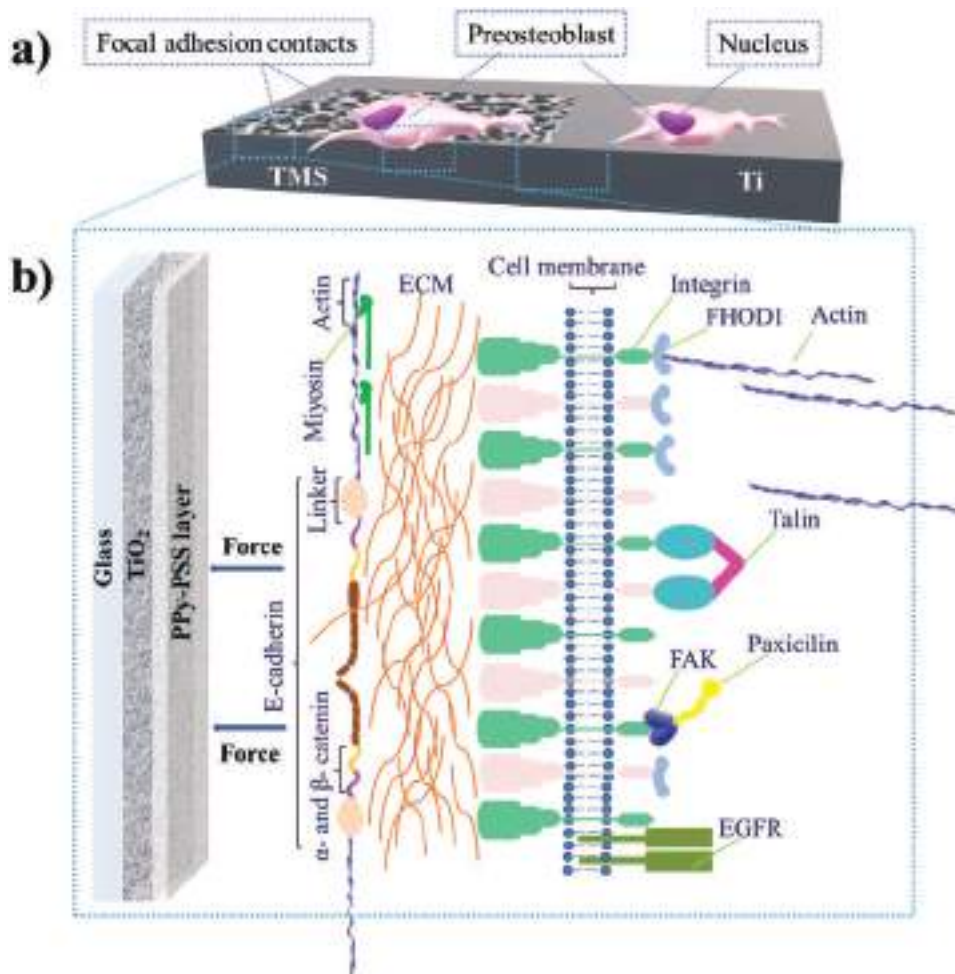
Figure 5. a) The schematic illustration of MC3T3-E1 behavior during their formation of focal adhesion contacts on different topography of mesoporous and smooth titanium surface. b) The model of direct mechanotransduction identifying the direct link between an extracellular matrix (ECM) and cell membrane. Membranes serve as an interface between the cell and its environment. Cell adhesion molecules embedded in the membrane, such as integrin or E-cadherin, allow interactions with the ECM and neighboring cells, respectively. Abbreviations: TiO_2 – ultrasonically generated titanium dioxide mesoporous surface, PPy – polypyrrole, PSS – polysodiumstyrenesulfonate, FHOD1 – FH1/FH2 domain-containing protein 1, FAK – focal adhesion kinase, EGFR – epidermal growth factor receptor.

In the second way, we tried to release the BMP-2 using a focused IR beam (850 nm, 200 mW cm^{-2}) to create a 3D gradient of BMP-2 concentrations. For these purposes, we took a titanium plate with defects cut out in it in the form of a triangle. The sample was modified sonochemically. Since the electrolyte is concentrated, the porous coating is uniformly formed both on the surface and in the bulk of the defects. Then, BMP-2 was loaded into the pores of the sample and modified with polymer layers. Before seeding the cells, the beam was focused on the corner of the triangle and irradiated for 10 min (Figure 7b). Then, cells were seeded, as in the previous case. Figure 7f shows the higher proliferation rate and the defect overgrowth thickness is about 100 µm in the irradiated corner, while the defect overgrowth thickness in the control and in nonirradiated corners is approximately the same and equal to 80 µm. Thus, it is shown that the coatings obtained are promising for the development of local and delayed delivery of active agents.

3. Conclusion

In summary, we demonstrated a hybrid TMS/(PPy–PSS) system for slow targeted release of bone morphogenic protein. Ultrasound-assisted method has been applied to form the mesoporous titania surface that was used to attach the stimuli-responsive polymer coating. The TMS/(PPy–PSS) coatings have demonstrated the ability for sustained release of BMP-2. Cells cultured on BMP-2-eluting samples have demonstrated the higher proliferation rate corresponding to BMP-2 release rate. The pH-sensitivity of PPy has been demonstrated on the example of local BMP-2 release triggered by photoactive TMS film. The PPy–PSS coating on TMS is effective to control preosteoblast cell growth. This hybrid of TMS/(PPy–PSS) system can be used in the biomedical area and it could be prospective for lab-on-a-chip applications, fundamental study of the effects of surface encapsulation to guide cell migration.

ADVANCED
SCIENCE NEWS
www.advancedsciencenews.com

ADVANCED
MATERIALS
INTERFACES
www.advmatinterfaces.de
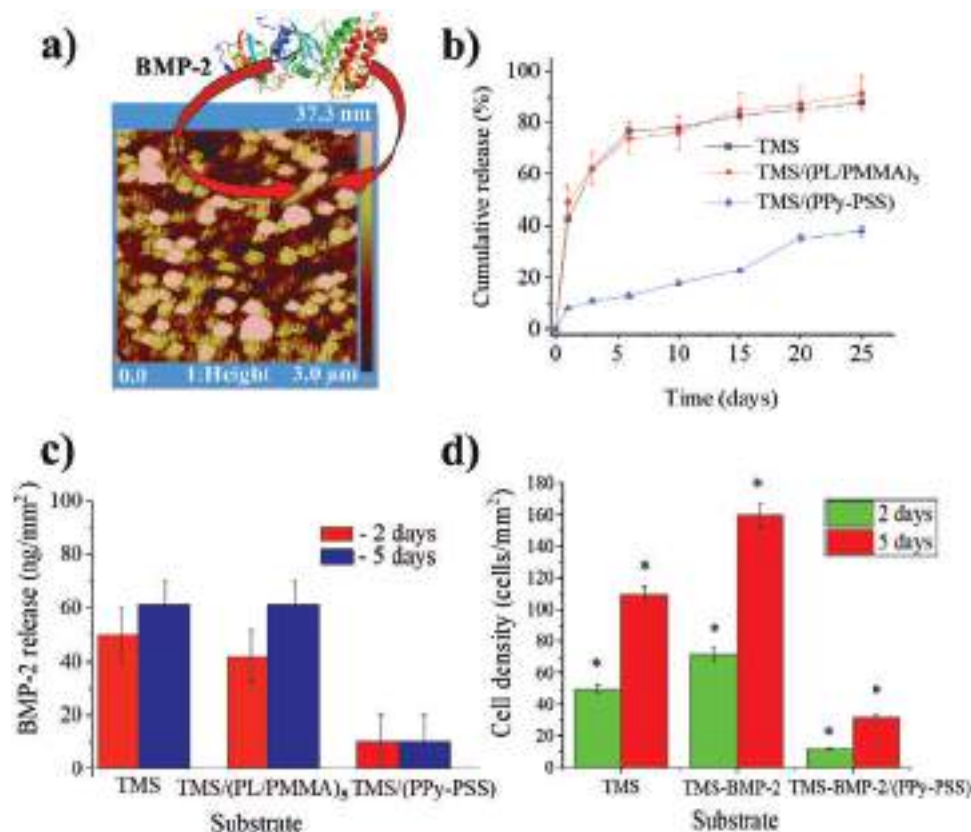
Figure 6. a) AFM image of TMS/(PPy–PSS) sample with loaded BMP-2. b) In vitro release profiles of BMP-2 protein from TMS, TMS/(PL–PMMA)$_5$, TMS/(PPy–PSS). c) Release of BMP-2 from TMS, TMS/(PL–PMMA)$_5$, and TMS/(PPy–PSS) samples for 2 and 5 days. d) Cell density of MC3T3-E1 cells seeded on different substrates for 2 and 5 days. Initial cell seeding of 6×10^3 cells cm^{-2}. All the results were repeated 4 times and presented as mean $\pm$ SD. Measurements were carried out in triplicates (* indicates $p < 0.05$).

4. Experimental Section

Preparation of TMS Surface: Structuring of titanium surface was made using sonochemical treatment. The titanium samples of $20 \times 20 \times 0.5$ mm were previously polished and washed with deionized water, acetone, and ethanol consecutively to eliminate any contaminants. Afterward, titanium samples were ultrasonically treated in 5 м NaOH solution using the ultrasonic processor UIP1000hd (Hielscher Ultrasonics, Germany) operated at 20 kHz. The apparatus was equipped with the sonotrode BS2d22 (head area 3.8 cm^2) and the booster B4-1.4, magnifying the working amplitude 1.42 times. The mechanical amplitude was ≈81 µm. The generated intensity was of 200 W cm^{-2}. The maximum power input was 760 W resulting from the multiplication of the intensity with the frontal area (with 3.8 cm^2) of the used sonotrode. Titanium samples were fixed in a homemade Teflon holder and treated for 5 min.

For cell experiments, transparent samples were used. Titanium was deposited onto a pretreated glass surface using vacuum spraying. Then, titanium was nanostructured sonochemically as described above. After titanium nanostructuring, all samples were heated at 450 °C for 3 h to enhance the crystallinity and conductivity of the titania layer.

BMP-2 Loading into TMS Surfaces: The fabricated TMS samples were immersed in BMP-2 solution (1 µg mL^{-1}) at vigorous shaking at room temperature for 48 h. After the final loading, the resulting surfaces were washed thoroughly with water to avoid the BMP-2 adsorption outside the pores and finally dried under vacuum. To evaluate the BMP-2 loading capacity, BMP-2-loaded samples were immersed in 6 mL phosphate buffered saline (PBS) (pH 4.5). The release amount of BMP-2 was evaluated with enzyme-linked immunosorbent assay (ELISA). The BMP-2 amount loaded in the pores of TMS matrix was 100 ng mm^{-2}.

Polymer/Polyelectrolyte Coating: After loading the BMP-2 into the TMS pores, the PPy polymer was intended to be deposited onto the TMS surface to achieve stimulated release. For this reason, PPy and polysodiumstyrenesulfonate polymers were chosen to provide the desired release. The BMP-2-loaded TMS samples were immersed in 10 wt% PPy milli-Q water solution for 15 min to deposit the first layer. Then, samples were taken out, washed with milli-Q water to remove uncoated PPy, and dried in a N$_2$ beam. The second layer was deposited from PSS solution (2 mg mL^{-1} in 0.5 м NaCl, PSS: 70 000 MW) during 15 min. After each deposition, the samples were washed in milli-Q water and dried. The samples were covered from 1 up to 3 bilayers (PPy–PSS)$_3$.

BMP-2 Release Study: The BMP-2-loaded TMS samples were immersed in 3 mL of the simulation media (0.9 wt% NaCl solution) at a constant temperature (37 °C). Then, 300 µL of aliquots were taken at fixed time intervals from the water under the sample. The released concentration of BMP-2 was estimated using ELISA method. The stimuli-controlled release was performed using IR-flashlight (850 nm, 40 mW cm^{-2}) during 10 min. To study the local release, the sample was illuminated through a stencil-plate. For visualization of the release, Rhodamine B-labeled BMP-2 was used. The Rhodamine-labeled BMP-2 was obtained via the reaction of BMP-2 with the dye at a ratio of 1 mol of BMP-2 to 20 mol of Rhodamine. The reaction was conducted in a sodium bicarbonate buffer (50×10^{-3} м) at pH 7 for 2 h. The result product was purified using a Sephadex G25 column (Sigma-Aldrich). The degree of labeling was estimated using Agilent Cary 50 spectrophotometer (Agilent, USA) at a wavelength of 550 nm. The visualization of release was done using Leica TCS SP confocal laser scanning microscope (Leica, Germany).

Surface Characterization: Field-emission scanning electron microscope (SEM) Zeiss Leo 1550 Gemini (Zeiss, Germany) at the operating voltage of 3 kV was used for structural and morphological characterization of
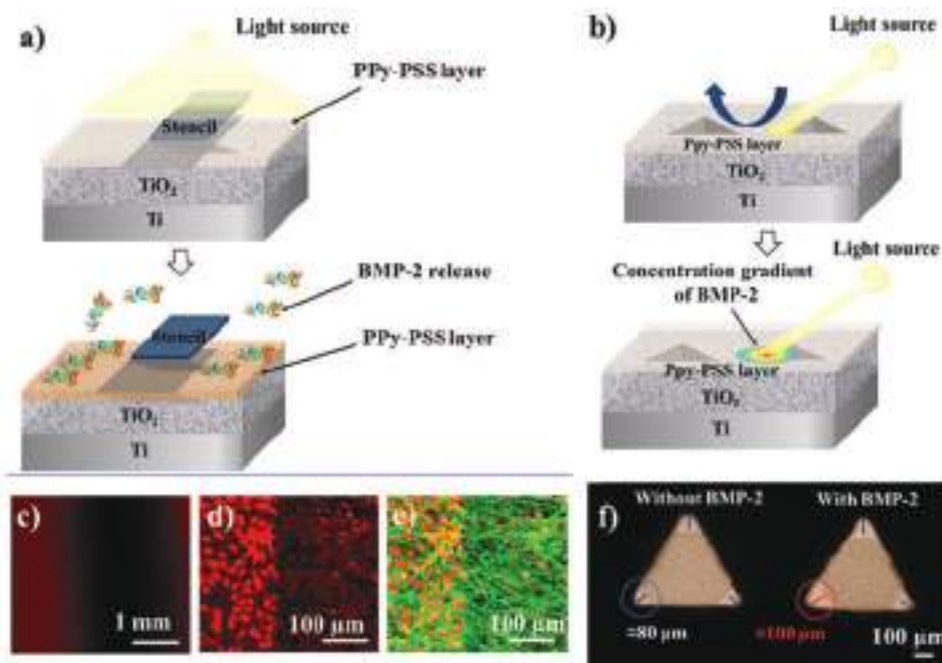
Figure 7. a) Scheme of sample irradiation for local BMP-2 release using a stencil and an irradiation. b) The scheme of spot irradiation of the sample for local delivery of BMP-2 using a focused beam. c) Confocal image of TMS/(PPy–PSS) sample containing Rhodamine-labeled BMP-2 after irradiation of the sample through a stencil for 10 min. d) Confocal image of cell nuclei seeded on the TMS/(PPy–PSS) after 5 days of cultivation. e) Confocal images of MC3T3-E1 cells seeded on the TMS/(PPy–PSS) after 5 days of cultivation. The sample was previously irradiated through a stencil. f) Images of an optical inverse microscope of MC3T3-E1 cells grown in a defect after the local release of BMP-2. Scale 100 μm. Measurements were carried out in triplicates (* indicates $p < 0.05$).

prepared TMS samples. The TMS samples were mounted onto the holder with a double-sided conductive tape and coated with carbon layer of 3 nm thick using a vacuum evaporator. High-resolution transmission electron microscopy (HRTEM) was performed by Philips CM30 TEM microscope operated at 300 kV.

AFM measurements were performed in air at room temperature in tapping mode with microcantilevers OMCL-AC160TS-W (Olympus, Japan). Resonance frequency was 247 kHz; spring constant was 42 N m^{-1}. Atomic force microscopy images of a scan size 3×3 μm^2 were done on three different places on the sample. Image analysis was carried out with the software Nanoscope V614r1. The surface roughness was calculated by the software as an arithmetic average of the absolute values of the surface height deviations measured from the mean plane.

Surface wettability analysis was performed using optical tensiometer G23 M (Krüss, Germany) equipped with a digital camera and image analysis software which analyzed the static contact angles after the application of a drop of 5 μL distilled water on the TMS samples to determine their hydrophilic/hydrophobic property.

In Vitro Cytocompatibility Study: Murine preosteoblastic cells MC3T3-E1 (provided by the Ludwig Boltzmann Institute of Osteology, Vienna, Austria) were seeded with the density of 6×10^3 cells cm^{-2} on the surface of the TMS/(PPy–PSS) samples and cultured for 8 days in an Alpha-MEM (Sigma-Aldrich, St. Louis, MO) supplemented with 10% fetal calf serum (PAA laboratories, Linz, Austria), 0.1% ascorbic acid (Sigma-Aldrich, St. Louis, MO), and 0.1% gentamicin (Sigma-Aldrich, Steinheim, Germany) according to protocol described in ref. [35]. Cells were incubated at 37 °C in humidified 5% CO$_2$, and the medium was changed every 2–3 days.

Cell Staining: The TMS samples with PPy–PSS coating were washed with PBS, afterward fixed with 4 wt% paraformaldehyde and permeabilized with 0.1% Triton X100 (Sigma-Aldrich, Steinheim, Germany) for 15 min. Then, samples were incubated for 1 h in a 1:20 solution of Alexa flour 488 phalloidin (Invitrogen, Eugene, OR, USA) in a dark hood at 4 °C. Then, the samples were washed in PBS and stained for nuclei with 1:300 solution of TO-PRO-3 iodide (Invitrogen, OR, USA) for 5 min according the protocol described in ref. [40]. Alizarin red staining was used to evaluate the mineralization ability of BMP-2. The MC3T3-E1 cells on TMS, TMS–BMP-2, and TMS/(PPy–PSS) with BMP-2 were stained and analyzed at 8 days after BMP-2 release according to protocol described in paper.[46] The quantitative alizarin red staining was estimated by spectrophotometry at 562 nm.

Confocal Laser Scanning Microscopy: Images of cell nuclei and actin cytoskeleton cells were obtained using Leica TCS SP confocal laser scanning microscope (Leica, Germany) with a 100× oil immersion objective and numerical aperture 1.4 to acquire confocal scanning fluorescence microscopy images. Ar-ion (488, 514 nm) and a He–Ne laser (543 nm) were used as an excitation source.

Impedance Spectroscopy: Electrochemical studies of uncoated and polymer–polyelectrolyte-coated TMS samples were performed with an IVIUM potentiostat in a three-electrode arrangement with a Pt counter electrode and saturated silver chloride as reference electrode and samples as working electrodes. Each sample was fixed with conductive glue from the corners of sample to be attached with a small cylindrical glass bottle (10 mL volume). The testing solution was PBS at room temperature. The amplitude was 10 mV versus open-circuit potential and range of frequencies from 100 kHz to 0.01 Hz were adjusted.

Statistics: Cell culture experiments were reproduced at least 3 times using three samples of each group. All obtained values were presented as mean ± standard deviation (SD). Statistical analysis was performed using ANOVA (* $p < 0.05$).

Conflict of Interest

The authors declare no conflict of interest.

Keywords

mesoporous titania, polyelectrolytes, polymer coating, polypyrrole, ultrasonic treatment

[1] J. H. Collier, J. P. Camp, T. W. Hudson, C. E. Schmidt, *J. Biomed. Mater. Res.* **2000**, *50*, 574.

[2] A. Lendlein, A. R. Langer, *Science* **2002**, *296*, 1673.

[3] G. D. Venkatasubbu, S. Ramasamy, V. Ramakrishnan, J. Kumar, *Adv. Powder Technol.* **2013**, *24*, 947.

[4] D. V. Andreeva, D. A. Gorin, D. G. Shchukin, G. B. Sukhorukov, *Macromol. Rapid Commun.* **2006**, *27*, 931.

[5] S. A. Ulasevich, N. Brezhneva, Y. Zhukova, H. Möhwald, P. Fratzl, F. H. Schacher, E. V. Skorb, *Macromol. Biosci.* **2016**, *16*, 1422.

[6] Y. Asaumi, M. Rey, N. Vogel, Y. Nakamura, S. Fujii, *Langmuir* **2020**, *36*, 2695.

[7] F. Li, M. A. Winnik, A. Matvienko, A. Mandelis, *J. Mater. Chem.* **2007**, *17*, 4309.

[8] K. Yang, H. Xu, L. Cheng, C. Sun, J. Wang, Z. Liu, *Adv. Mater.* **2012**, *24*, 5586.

[9] K. M. Au, M. Chen, S. P. Armes, N. Zheng, *Chem. Commun.* **2013**, *49*, 10525.

[10] G. Shi, Z. Zhang, M. Rouabhia, *Biomaterials* **2008**, *29*, 3792.

[11] E. V. Skorb, O. Baidukova, A. Goyal, A. Brotchie, D. V. Andreeva, H. Möhwald, *J. Mater. Chem.* **2012**, *22*, 13841.

[12] D. V. Andreeva, Z. Pientka, L. Brozová, M. Bleha, G. A. Polotskaya, G. K. Elyashevich, *Thin Solid Films* **2002**, *406*, 54.

[13] J.-C. E. Vidal, E. Garcia-Ruiz, J.-R. J. M. A. Castillo, *Microchim. Acta* **2003**, *143*, 93.

[14] S. Kim, L. K. Jang, M. Jang, S. Lee, J. G. Hardy, J. Y. Lee, *ACS Appl. Mater. Interfaces* **2018**, *10*, 33032.

[15] S. J. Chen, D. Y. Wang, C. W. Yuan, X. D. Wang, P. Y. Zhang, X. S. Gu, *J. Mater. Sci.* **2000**, *19*, 2157.

[16] P. M. George, A. W. Lyckman, D. A. LaVan, A. Hegde, Y. Leung, R. Avasare, C. Testa, P. M. Alexander, R. Langer, M. Sur, *Biomaterials* **2005**, *26*, 3511.

[17] D. Kai, M. P. Prabhakaran, G. Jin, S. Ramakrishna, *J. Biomed. Mater. Res., Part A* **2011**, *99A*, 376.

[18] G. Shi, M. Rouabhia, Z. Wang, L. H. Z. Dao, *Biomaterials* **2004**, *25*, 2477.

[19] K. M. Sajesh, R. Jayakumar, R. S. V. Nair, K. P. Chennazhi, *Int. J. Biol. Macromol.* **2013**, *62*, 465.

[20] F. Song, W. Jie, T. Zhang, W. Li, Y. Jiang, L. Wan, B. Liu, *RSC Adv.* **2016**, *6*, 92804.

[21] B. Rikhari, S. P. Mani, N. Rajendran, *Carbohydr. Polym.* **2018**, *189*, 126.

[22] J. Liao, Y. Zhang, G. Tan, G. C. Ning, *Surf. Coat. Technol.* **2013**, *228*, S41.

[23] M. Mîndroiu, C. Ungureanu, R. Ion, R. V. Pîrvu, *Appl. Surf. Sci.* **2013**, *276*, 401.

[24] A. M. Kumar, N. Rajendran, *Ceram. Int.* **2013**, *39*, 5639.

[25] D. Samanta, N. Hosseini-Nassab, R. N. Zare, *Nanoscale* **2016**, *8*, 9310.

[26] D. H. S. M. Richardson-Burns, J. L. Hendricks, C. Sequera, D. C. Martin, *Adv. Funct. Mater.* **2007**, *17*, 79.

[27] N. Hosseini-Nassab, D. Samanta, Y. Abdolazimi, J. P. Annes, R. N. Zare, *Nanoscale* **2017**, *9*, 143.

[28] J. Chen, X. Li, J. Li, L. Huang, T. Ren, S. Zhong, *Mater. Sci. Eng. C* **2018**, *89*, 316.

[29] M. Liu, N. Xu, W. Liu, *RCS Adv.* **2016**, *6*, 84269.

[30] A. Anderson, J. Davis, *Electroanalysis* **2015**, *27*, 872.

[31] A. Moquin, R. Hanna, T. Liang, H. Erguven, E. R. Arndtsen, A. Kakkar, *Chem. Commun.* **2019**, *55*, 9829.

[32] B. Parakhonskiy, D. Andreeva, H. Möhwald, D. G. Shchukin, *Langmuir* **2009**, *25*, 4780.

[33] W. R. Stauffer, X. T. Cui, *Biomaterials* **2006**, *27*, 2405.

[34] S. Sirivisoot, R. Pareta, T. J. Webster, *Nanotechnology* **2011**, *22*, 085101.

[35] Y. Wang, Y. Xiao, R. Tang, *Chem. - Eur. J.* **2014**, *20*, 11826.

[36] D. Park, Y. Cho, S. H. Goh, Y. Choi, *Chem. Commun.* **2014**, *50*, 15014.

[37] D. Samanta, J. L. Meiser, R. N. Zare, *Nanoscale* **2015**, *7*, 9497.

[38] G. K. Elyashevich, E. Y. Rosova, D. V. Andreeva, G. A. Polotskaya, M. Trchová, Z. Pientka, *J. Appl. Polym. Sci.* **2005**, *97*, 1410.

[39] D. O. Dinc, M. Yilmaz, S. Cetin, M. Turk, E. Piskin, *Surf. Innovations* **2019**, *7*, 249.

[40] A. Wennerberg, T. Albrektsson, *Clin. Oral Implants Res.* **2009**, *20*, 172.

[41] M. Vallet-Regí, *Chem. - Eur. J.* **2006**, *12*, 5934.

[42] J. Kopf, S. Ulasevich, O. Baidukova, Y. Zhukova, J. W. Dunlop, P. Frazl, *Adv. Eng. Mater.* **2016**, *18*, 476.

[43] Y. Zhukova, S. A. Ulasevich, J. W. Dunlop, P. Fratzl, H. Möhwald, E. V. Skorb, *Ultrason. Sonochem.* **2017**, *36*, 146.

[44] E. Kuvyrkov, N. Brezhneva, S. A. Ulasevich, E. V. Skorb, *Ultrason. Sonochem.* **2019**, *52*, 437.

[45] V. Belova, D. A. Gorin, D. G. Shchukin, H. Möhwald, *Angew. Chem., Int. Ed.* **2010**, *49*, 7129.

[46] R. J. Chung, K. L. Ou, W. K. Tseng, H. L. Liu, *Surf. Coat. Technol.* **2016**, *303*, 283.

[47] X. Xu, M. Sun, D. Wang, W. Bu, Z. Wang, Y. Shen, H. Sun, *Nanoscale* **2019**, *11*, 21953.

[48] P. V. Cherepanov, I. Melnyk, E. V. Skorb, P. Fratzl, E. Zolotoyabko, N. Dubrovinskaia, L. Dubrovinsky, Y. S. Avadhut, J. Senker, L. Leppert, S. Kümmel, D. V. Andreeva, *Green Chem.* **2015**, *17*, 2745.

[49] C. Yu, C. Y. Jimmy, M. Chan, *J. Solid State Chem.* **2009**, *182*, 1061.

[50] K. Okitsu, Y. Mizukoshi, H. Bandow, Y. Maeda, T. Yamamoto, Y. Nagata, *Ultrason. Sonochem.* **1996**, *3*, S249.

[51] M. M. Mdleleni, T. Hyeon, K. S. Suslick, *J. Am. Chem. Soc.* **1998**, *120*, 6189.

[52] A. M. Peterson, H. Möhwald, D. G. Shchukin, *Biomacromolecules* **2012**, *13*, 3120.

[53] E. V. Skorb, D. G. Shchukin, H. Möhwald, D. V. Andreeva, *Nanoscale* **2010**, *2*, 722.

[54] J. Aizenberg, J. C. Weaver, M. S. Thanawala, V. C. Sundar, D. E. Morse, P. Fratzl, *Science* **2005**, *309*, 275.

[55] G. B. Street, S. E. Lindsey, A. I. Nazzal, K. J. Wynne, *Mol. Cryst. Liq. Cryst.* **1985**, *118*, 137.

[56] J. Gensel, T. Borke, N. P. Pérez, A. Fery, D. V. Andreeva, E. Betthausen, E. V. Skorb, *Adv. Mater.* **2012**, *24*, 985.

[57] D. V. Andreeva, D. V. Sviridov, A. Masic, H. Möhwald, E. V. Skorb, *Small* **2012**, *8*, 820.

[58] R. Sameni, G. D. Clifford, *Open Pacing, Electrophysiol. Ther. J.* **2010**, *3*, 4.

[59] *Inorganic Chemistry* (Eds: Y. D. Tretyakov, A. A. Drozdov, V. P. Zlomanov, G. N. Mazo, F. M. Spiridonov), Vol. *3*, Publishing Center "Academy,", Moscow, Russia **2007**, p. 352.

[60] W. Qi, L. Duan, K. W. Wang, X. H. Yan, Y. Cui, Q. He, J. Li, *Adv. Mater.* **2008**, *20*, 601.

[61] W. Qi, X. Yan, L. Duan, Y. Cui, Y. Yang, J. Li, *Biomacromolecules* **2009**, *10*, 1212.

[62] J. N. Cha, H. Birkedal, L. E. Euliss, M. H. Bartl, M. S. Wong, T. J. Deming, G. D. Stucky, *J. Am. Chem. Soc.* **2003**, *125*, 8285.

[63] D. H. Kim, S. M. Richardson-Burns, J. L. Hendricks, D. C. Sequera, D. C. Martin, *Adv. Funct. Mater.* **2007**, *17*, 79.

[64] M. Tomczykowa, M. E. Plonska-Brzezinska, *Polymers* **2019**, *11*, 350.

[65] C. Zhong, J. Feng, X. Lin, Q. Bao, *Int. J. Nanomed.* **2017**, *12*, 1215.

[66] A. Abalymov, L. V. der Meeren, M. Saveleva, E. Prikhozhdenko, K. Dewettinck, B. Parakhonskiy, A. G. Skirtach, *ACS Biomater. Sci. Eng.* **2020**, *6*, 3933.

[67] B. Guadarrama, D. Bello, A. Fouillen, A. Badia, A. Nanci, *ACS Appl. Mater. Interfaces* **2020**, *12*, 14924.

[68] C. Muderrisoglu, M. Saveleva, A. Abalymov, L. V. der Meeren, A. Ivanova, V. Atkin, B. Parakhonskiy, A. G. Skirtach, *Adv. Mater. Interfaces* **2018**, *5*, 1800452.

[69] G. Fang, K. Huang, J. Niu, T. Kuang, Y. Zheng, Z. Gu, J. Zou, *Int. J. Biol. Macromol.* **2020**, *151*, 1126.

[70] J. I. Rosales-Leal, M. A. Rodríguez-Valverde, G. Mazzaglia, P. J. Ramón-Torregrosa, L. Díaz-Rodríguez, O. García-Martínez, M. A. Cabrerizo-Vílchez, *Colloids Surf., A* **2010**, *365*, 222.

[71] A. Hall, *Science* **1998**, *279*, 509.

[72] P. S. Murray, R. Zaidel-Bar, *Biol. Open* **2014**, *3*, 1183.

[73] A. M. Peterson, C. Pilz-Allen, T. Kolesnikova, H. Möhwald, D. Shchukin, *ACS Appl. Mater. Interfaces* **2014**, *6*, 1866.

[74] R. V. Parthasarathy, V. P. Menon, C. R. Martin, *Chem. Mater.* **1997**, *9*, 560.

Oscillating of physicochemical and biological properties of metal particles on their sonochemical treatment

Sviatlana A. Ulasevich[b], Elena I. Koshel[b], Ilya S. Kassirov[a], Nadzeya Brezhneva[b], Liubov Shkodenko[b], Ekaterina V. Skorb[b,*]

[a] *Saint-Petersburg Pasteur Institute, Mira st.14, St. Petersburg, 197101, Russia*
[b] *ITMO University, Lomonosova st. 9, St. Petersburg 191002, Russia*

ABSTRACT

Different metal particles are increasingly used to target bacteria as an alternative to antibiotics. Despite numerous data about treating bacterial infections, the utilization of metal particles in antibacterial coatings for implantable devices and medicinal materials promoting wound healing. The antibacterial mechanisms of nanoscale and microscale particles are poorly understood, but the currently accepted mechanisms include oxidative stress induction, metal ion release, and non-oxidative mechanisms. Thus, investigation of the antibacterial mechanisms of nanostructured metal particles is very important for the development of more effective antimicrobial materials. However, it is very difficult to develop a proper model for revealing the antibacterial mechanisms due to difficulty to choose a method that allows obtaining materials of various properties under approximately the same conditions. In this paper, we propose a green and feasible technique to create critical conditions for modification of zinc particles at highly non-equilibrium states. We demonstrate that the sonication process can be useful for fabrication the materials with oscillating physical, chemical and antibacterial properties. We believe this method besides medical applications can be also used in natural science basic research as an experimental tool for modelling the physical and chemical processes. After the sonication, the zinc particles exhibit a different surface morphology and amount of leached Zn^{2+} ions compared to initial ones. It has been revealed that oscillations of the Zn^{2+} ions concentration lead to oscillation the antibacterial properties. Thus, the properties of the materials can be easily altered by adjusting the ultrasound energy dissipated via varying the sonication.

1. Introduction

The investigation of the antibacterial mechanisms of nanoscale and microscale particles is very important for the development of more effective antimicrobial materials [1]. Despite the abundance of literature on antimicrobial effects [2–5], the antibacterial mechanisms are still poorly understood. However, evaluating novel antibacterial mechanisms of action can be difficult and is uncommon in assessments of nanoscale and microscale metal particles due to the diversity of chemical approaches for fabrication of these particles [5–7]. It is very difficult to obtain the chemical compounds of various properties under approximately the same conditions. It causes another difficult task to develop a proper model for revealing the antibacterial mechanisms.

In this paper, we propose a green and feasible technique to create critical conditions for modification of metal particles at highly non-equilibrium states. We demonstrate that the sonication process can be

useful for fabrication the materials with oscillating physical, chemical and antibacterial properties. We believe this method besides medical applications can be also used in natural science basic research as an experimental tool for modelling the physical and chemical processes.

The interest in application of ultrasonic cavitation for cleaning and surface treatment processes has increased greatly in the last decades [8]. There are many papers about cavitation phenomena and studying the details of the mechanism of cavitation bubble formation, oscillating growth, and consequent collapse [9–11]. Great numbers of research works have been dedicated to investigation of cavitation bubble physical properties such as internal temperature and pressure [12–14]. Ultrasonic treatment can be effectively used for the preparation of stable suspensions of reagents as well as at intermediate stages of the synthesis of complex nanocomposites in liquid and viscous solutions [15–20]. It was previously shown [21–23] that high intensity ultrasound could be also used for the fabrication of microstructure in metal

---
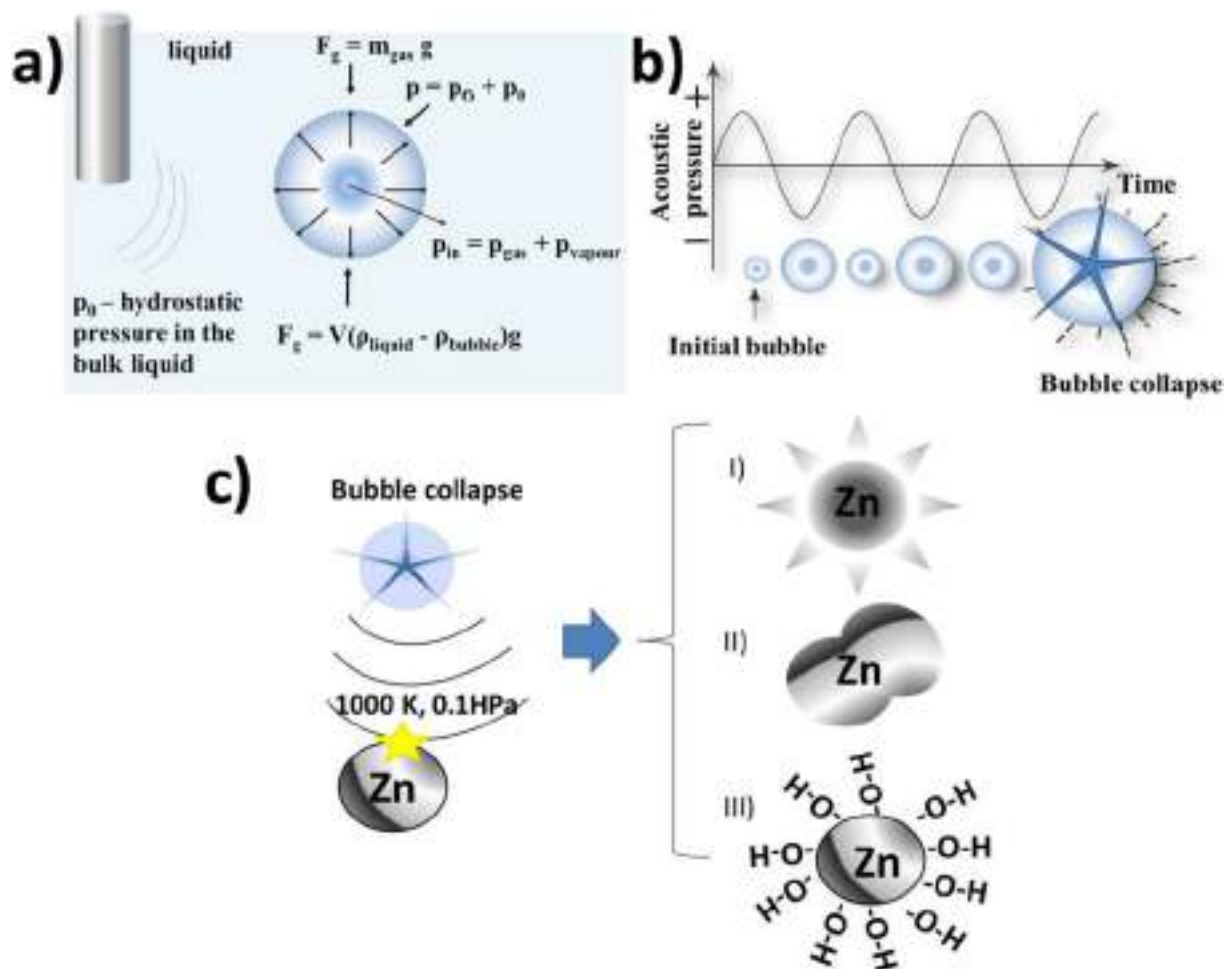
Fig. 1. The schematic illustrations of: a) cavitation bubble formation during sonication process and forces applied to it; b) acoustic cavitation oscillating process; c) sonochemical modification of zinc particles: (I) formation of "hedgehog" zinc particles; (II) physical modifications caused by bubble collapse and shock waves action leading to melting and recrystallization; (III) chemical aspects due to surface oxidation by active species formed by water sonolysis during cavitation bubble collapse. In water possible reactions for zinc oxidation and formation of a novel thin smooth oxide layer protected metal skeleton of sponge; reduction processes are also possible due to formation of hydrogen species.

alloys at a nanometer scale as well as for a new simple route of synthesizing Nd_2O_3 nanostructures [24] or Nd_2O_3-SiO_2 nanocomposites [25] from its inorganic precursors. The acoustic cavitation can be a great alternative to existing complex methods of synthesis of these oxides. Chemical reactions may be driven with the created hot spots appeared after the collapse of bubbles with very short lifetimes. Authors [25] produced the Nd_2O_3-SiO_2 nanocomposites with enhanced photocatalytic activity through simple and rapid sonochemical route in the presence of putrescine as a new basic agent, for the first time. It was demonstrated that shape, size and photocatalytic activity of the sonochemically fabricated neodymium oxide were under the influence of the type of capping agent. Thus, ultrasonic treatment can be used as a striking tool to produce materials with controlled shape and grain size. Besides, the ultrasonic treatment allowed to vary and optimize the mole ratio of Si: Nd to obtain the best Nd_2O_3-SiO_2 nanocomposites on the shape, size and photocatalytic activity [24–26].

Since properties of materials are under the influence of shape and grain size, the fabrication of materials with controlled shape and grain size has become an especially substantial research field. We think the use of high-intensity ultrasonic technique for metal nanostructuring is very perspective. Great advantage of our methodology is a large number of synthetic parameters which can be optimized to tune the surface morphology in a controllable manner.

Ultrasound-assisted structuring of the phase in metal alloys relies on several mechanisms including interfacial red/ox reactions, mechanical impact and temperature driven solid state phase transformations which affect surface composition and morphology of metals [21]. Ultrasonically induced temperature gradient occurs due to bubble collapse. This bubble's explosion leads to the 3D-formation of chaotically ordered nanoscale structures that look like sponges or foams [27]. Physical and chemical properties of sonication medium strongly effect on the structuring pathways as well as morphology and composition of catalysts [21,22]. It was previously shown that ultrasonic treatment of metal particles can affect its microstructure, morphology as well as composition [9,28–30]. However, the mechanisms of ultrasonically produced modification of solid heterogeneous systems are still under the question. Moreover, an interesting point is unique properties of modified materials.

In this paper, we demonstrated non-linear behavior of physicochemical and bactericidal properties of ultrasonic modified zinc particles. The aim of the research is to study the influence of sonication parameters on physicochemical and antimicrobial properties of fabricated particles and reveal the mechanism of such phenomena.

Zinc particles are chosen as a model of studying the oscillating nature of physicochemical properties because its potential bio-applications due to its physiochemical properties, biocompatibility and biosafety approach [31–35]. There are various mechanisms for the antimicrobial activity of zinc nanoparticles. T. Gordon et al. [36]
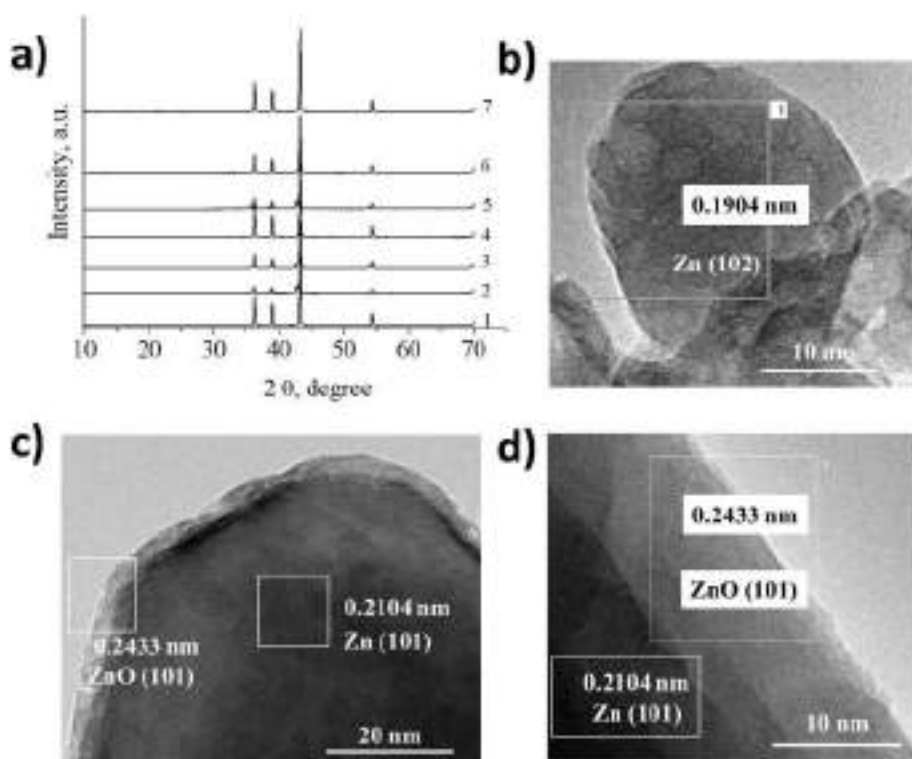
Fig. 2. a) XRD patterns of non-treated (1) and sonochemically treated zinc particles during 3 min (2), 5 min (3), 10 min (4), 15 min (5), 30 min (6) and 90 min (7). All peaks are indexed with the zinc phase where the bars correspond to the diffraction peaks according to the JCPDS card number: for Wüstite 00-006-0615 [55]; b–d) TEM images of the sonochemically treated zinc particles obtained at a power of 143 W (b) and 625 W (c, d).
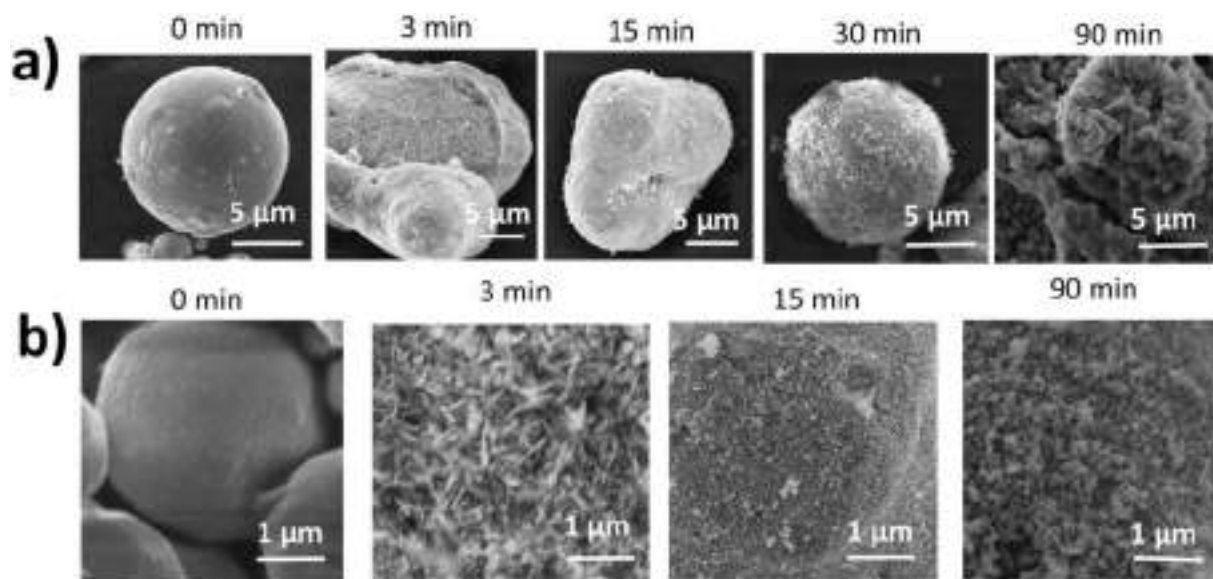
Fig. 3. a) SEM images of the sonochemically treated zinc particles obtained during different sonication time; b) SEM images of zinc particles' surface after sonochemical treatment.

assumed that the antibacterial activity of the zinc particles could be mediated by the ZnO phase formed on the surface of the particle. The antibacterial activity of the zinc oxide nanostructures was found to be dependent on nanoparticle size and surface defects which in turn are shape-dependent. The major reason for this biocidal activity has been proposed to arise from the release of reactive oxygen species (ROS) from the surface of ZnO when in solution. Generated ROS and hydrogen peroxide molecules on ZnO particles penetrate the cell membrane and kill the bacteria [37–39]. Besides, the antibacterial activity of zinc particles could be explained by mechanical damage, cellular internalization and release of Zn^{2+} ions. Zinc ions could inhibit multiple activities of bacteria, such as transmembrane proton translocation, glycolysis and acid tolerance [37,39,40]. Thus, further conclusive studies are needed to determine the exact antibacterial mechanism of zinc particles.

To clarify the mechanism of zinc antibacterial activity we use ultrasound treatment. We assume that ultrasound-assisted structuring of zinc particles relies on several mechanisms including mechanical modification, interfacial red/ox reactions and temperature driven solid-state phase transformations that affect surface composition and morphology of metals. High-speed liquids jets and shockwaves generated as a result of cavitation bubbles collapse via sonication can activate the redox reactions, interparticle collisions, melting and recrystallization resulting to zinc oxide layer formation and the core-shell "hedgehog" structure [31] fabrication.

Fig. 4. The scheme of the reactions: a) between Zn^{2+} and eriochrome black T in water solution (pH = 10); b–c) between $ZnIn^-$ and Ethylenediaminetetraacetic acid (EDTA) in water solution (pH = 10); d) schematic illustration of release experiment; e) the time dependence of concentration of Zn^{2+} ions leached from zinc particles treated sonochemically during different sonication time.

2. Experimental section

2.1. Preparation of zinc particles

Five grams of the zinc powder (zinc powder, purity, ≥99%, Sigma Aldrich) were dispersed in ultrapure water (50 mL) and sonicated using the ultrasonic processor UIP1000hd (Hielscher Ultrasonics, Germany) operated at 20 kHz. The maximum intensity (at 20% of amplitude) was calculated to be 57 W/cm² at the mechanical amplitude of 81 μm (at 100%). The apparatus was equipped with the sonotrode BS2d18 with a head area of 2.5 cm². The booster B2-2.2 magnifies the working amplitude in 2.2 times. Sonication was performed in the sonication cell at constant cooling and the temperature was in a range of 273–313 K monitored by the temperature sensor inserted in the electrolyte. The sonication time was 3 min, 10 min, 15 min, 30 min, 60 min and 90 min to study the efficiency of ultrasonic waves' action on zinc particles. After the treatment, the zinc particles were washed up with distilled water and dried at 120 °C for 24 h.

2.2. Sample characterization

The structural and morphological characterization of prepared zinc samples was performed using the field-emission scanning electron microscope Tescan Vega3 (TESCAN ORSAY HOLDING, Czech Republic) at the operating voltage of 5 kV. The zinc particles were fixed onto the holder with a double-sided conductive tape. TEM images were obtained on a JEOL JEM-2010 Fx high resolution transmission electron microscope (HRTEM, 200 kV).

X-ray diffraction (XRD) measurements were carried out with an Advanced D8 Bruker diffractometer (Bruker, Germany), using a focused and monochromatized CuKα1 source radiation (λ = 1.5406 Å).

The BET adsorption/desorption isotherm was determined by nitrogen sorption at 77 K using a Surface area and pore size analyzer Quantachrome NOVA 1200 e Micromeritics (Quantachrome
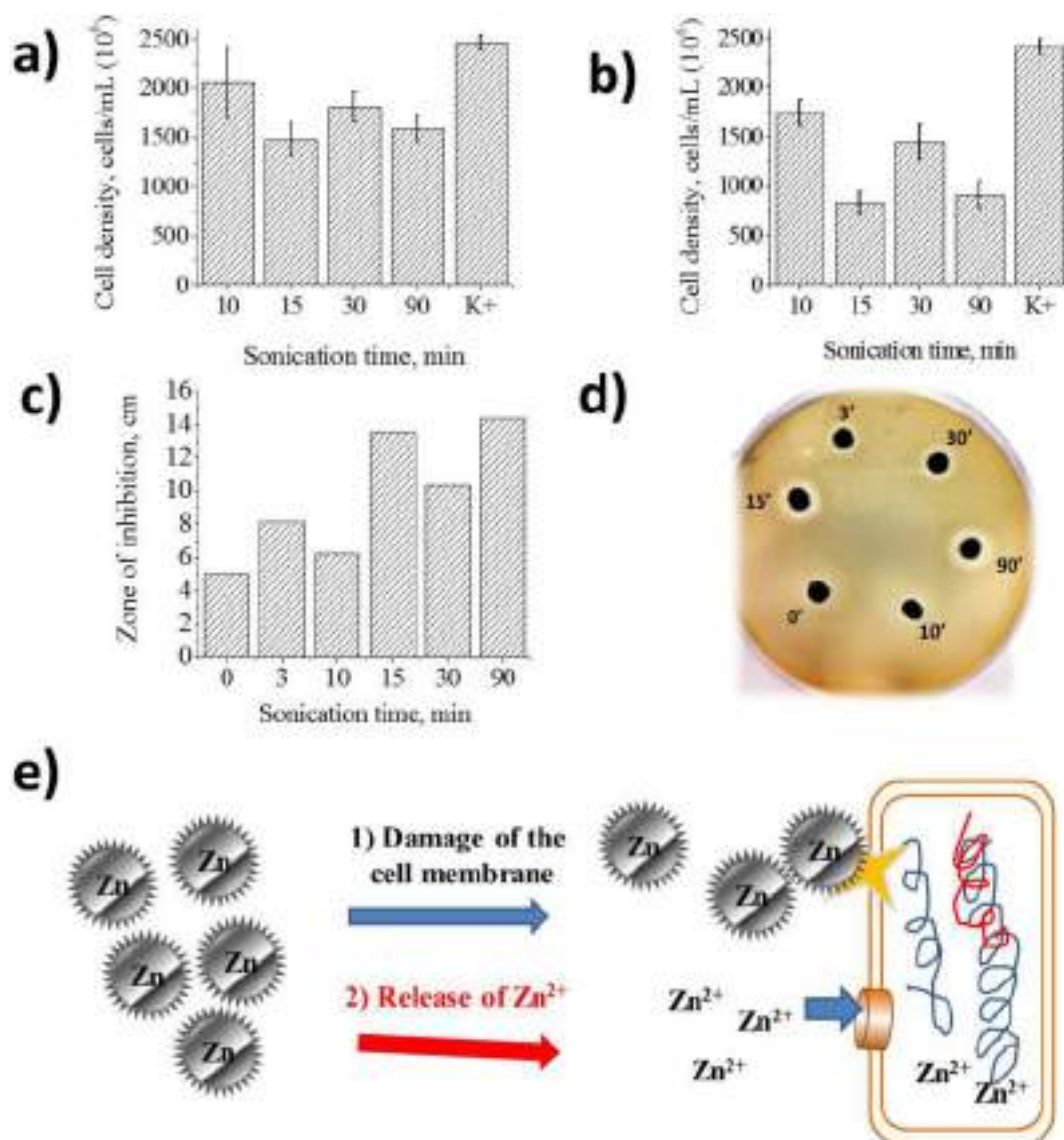
Fig. 5. a–b) Oscillation of antibacterial activity of zinc nanoparticles sonochemically treated at different time: 10 min, 15 min, 30 min and 90 min (K$^+$ – control probe) against *E. coli* after incubation with zinc nanoparticles at concentration of 0.001 g/mL (a) and 0.01 g/mL (b). The mean ± standard deviation is indicated; Data represent mean value ± confidence interval of 3 independent experiments, p < 0.05; c) the dependence of inhibition zone diameter on sonication time of treatment zinc nanoparticles at the concertation of 1 g/mL via well diffusion test; d) the photo of inhibition zone diameter of zinc particles treated sonochemically in water solution at the concertation of 1 g/mL during different sonication time: 0 min, 3 min, 10 min; 15 min; 30 min and 90 min; e) scheme of the possible antibacterial mechanisms of sonochemically treated zinc particles. Clear correlation of maximum Zn^{2+} ions release and related biocide activity is proved for 15 min and 90 min treated samples.

Instrument, USA). The weight of freeze–dried samples was around 0.36 g. All samples were degassed under vacuum at 180 °C for 4 h before N$_2$ adsorption.

In the leaching process, 50 mg of sonicated zinc powder was added to 25 g of distilled water for 24 h in 250 mL conical flask. One milliliter solution sample was taken using a syringe filter of 1 mm pore size. The amount of Zn^{2+} ions was determined by titration with EDTA solution in the presence of the indicator Eriochrome Black T.

2.3. Bacterial strains

The biological studies were conducted on resistant strain of *E. coli* Nova Blue Tc^R.

2.4. An analysis of the antimicrobial activity of particles

To determine the ability of zinc particles to suppress the growth of microorganisms, the agar/disk diffusion test was used and the minimum inhibitory concentration of particles (MIC) was determined. For agar diffusion test 5 μL of particles at concentrations of 1.0 g/mL was added to the grown lawn and incubated for 24 h at 37 °C. At the end of the incubation, the inhibition zone of bacterial growth was fixed. The experiments were carried out in triplicate.

To determine the minimum inhibitory concentration (MIC), use the standard dilution method. For this, the particles were added to bacterial cell suspensions of density 10^6 cells/mL to final particle concentrations of 0.001, 0.01, 0.1 g/mL. After 24 h of incubation at 37 °C, the cell density in the suspensions was analyzed using a spectrophotometer at a wavelength of 550 nm and recalculate in CFU/ml (PromEcoLab, Russia).

2.5. Statistics

Bacteria culture experiments were reproduced at least three times

using three samples of each group. Obtained data were averaged with the standard error of the mean. Statistical analysis was performed using ANOVA (*p < 0.05).

3. Results and discussion

In this paper, we use a sonochemical nanostructuring of zinc particles followed by studying its physical and chemical properties. Besides, ultrasound-driven technique was used to clarify the mechanism of zinc antibacterial activity. The advantage of this method is a possibility to vary the topography, chemical composition, ξ-potential, surface area of the nanostructured particles easily by changing the parameters of sonication such as intensity of ultrasound, frequency, duration of treatment and electrolyte (solvent, additives) used for treatment [41–43].

An ultrasound provides energy localization with possible acoustic cavitation phenomena, such as the formation, the growth, and the implosive collapse of cavitation bubbles in a liquid [44–47]. When ultrasound passes through the liquid medium, an acoustic bubble is forming (Fig. 1). The pressure caused by the surface tension force and the hydrostatic pressure in the bulk liquid outside affect the bubble. The inner pressure of the bubble is composed of liquid's vapor pressure and pressure of gasses dissolved in a liquid. It is assumed that pressure and temperature inside the bubble are always uniform, and therefore is time-dependent. The bubble has a spherical shape preserved during all the process, with radius oscillating through time under ultrasound (Fig. 1b). Passing through a liquid medium ultrasound waves induce molecular motion through a series of compression and rarefaction cycles [48,49]. Preexisting micro-bubbles of gas dissolved into the liquid medium grow in size due to rectified diffusion with each succeeding expansion and rare faction half-cycle until they become unstable and violently collapse (Fig. 1b). Rectified diffusion is phenomena of bubble growth under the influence of increased gas exchange area and larger inward flux during expansion [11–13].

There are three mechanisms of metal phase structuring during ultrasound-assisted treatment (Fig. 1c). The mechanical one is structuring of the surface morphology by acting of shock waves, micro-jets, turbulence and shear forces. The physical effect produced by bubble collapse leads to intense local heating, hot spots with temperatures of roughly 5000 K and high pressures of about 0.1 HPa [44,45,49]. It can cause local melting of the metal particles. The chemical one includes interfacial red/ox reactions initiated by water sonolysis (Fig. 1c). The water sonolysis occurs via ultrasonic cavitation. The bubble collapse acts as a localized "hot spot" with singular conditions of high temperature and pressure followed by short-life. The molecules of water and gases are broken (sonochemistry) and chemical processes such as bond cleavage occur. Water is decomposed into a hydrogen atom and hydroxyl radical according Eq. (1). This process is described in many papers [50,51]. The presence of radicals is proved by a-(4-pyridyl-1-oxide)-N-tert-butylnitrone and 5,5-dimethyl-1-pyrroline N-oxide (DMPO) trap OH· radicals. Besides, generated ROS can oxidize the etching zinc surface [46,47]. We assume the process under go via next oxidation-reduction reactions:

$$H_2O \xrightarrow{ultrasonication} H^{\cdot} + OH^{\cdot} \tag{1}$$

$$Zn^0 + 4 OH^- - 2 e^- \rightarrow [Zn(OH)_4]^{2-} \tag{2}$$

$$[Zn(OH)_4]^{2-} \rightarrow Zn(OH)_2 + 2OH^- \tag{3}$$

$$[Zn(OH)_4]^{2-} \xrightarrow{condensation} ZnO_2 \times H_2O + 2OH^- \tag{4}$$
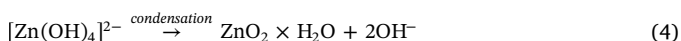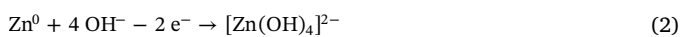
During sonication bubble collapse may cause water sonolysis (Eq. (1)) resulting OH· and H· formation. Active radicals react with Zn producing $[Zn(OH)_4]^{2-}$ (Eqs. (2)–(3)) and during the time this system condense as zinc oxide (Eq. (4)).

The XRD patterns (Fig. 2a) of the nanostructured zinc particles

prepared at different sonication times of 3, 10, 15, 30, 60 and 90 min indicate high crystallinity. The peaks at 2θ = 36.32°, 39.03°, 43.26° and 54.33° are assigned to (002), (100), (101), and (102), indicating that the samples are composed of zinc with hexagonal closest packed structure [52–54]. No other characteristic peaks of any impurities have been detected. To study nanoscale zinc particles' structure formed during sonochemical treatment a high-resolution transmission electron microscopy was used. Fig. 2b shows a homogenous structure consisted of zinc (102) crystallites. TEM images (Fig. 2c, d) clearly show core-shell morphology for the zinc particles obtained after sonochemical treatment at a higher power of 625 W. The core is composed by zinc (102) or zinc (101) phases, whereas the shell is composed by a ZnO (101) phases. We assume this structure could be explained by chemical reactions between zinc surface and ROS formed as a result of water sonolysis take place followed by zinc hydroxide complex formation. Rapid warming of sample leads to its partial phase transformation into ZnO (101) [55–57]. Since in our paper, we have studied the mechanism of the antibacterial activity of zinc particles, it was necessary to exclude the effect of oxide. For these purposes, all zinc particles are obtained at a total power less or equal than 143 W.

In our research, Zn particles of size ca. 5 μm and ca. 25 μm are used. It should be mentioned the influence of particles' size can be rather significant. The smaller particles' size the bigger surface area we have. The big surface area leads to an increase in the released cations. However, we herein are interested in studying of the microscale particles' properties to reveal the mechanism of zinc antibacterial activity and exclude the influence of nanoscale size. The initial Zn particles are round and smooth (Fig. 3a). During the sonication process the morphology of zinc particles changes starting rough and porous (Fig. 3b). There are some nanoneedles appeared on the surface of particles. As shown in Fig. 2 after 90 min of sonication zinc particles look as "hedgehogs". The surface morphology changes drastically. The BET surface area of sonochemically treated zinc particles increases in 8 times compared to BET surface value of non-treated particles (not shown here). There are some oscillations of the surface morphology (Fig. 3b). As shown, the sonication of zinc particles for 3 min causes the formation of little needles on it. Further sonication destroys the obtained structure by shock waves and high-speed jets and the surface becomes smooth again. Then, after "smoothing" the zinc surface is structured again via the sonication process. It is interesting that the oscillation of the physicochemical properties of zinc particles occurs during sonochemical treatment at different powers. In our experiments, the total power output of an ultrasonic unit depends on the sonotrode frontal area S and ultrasonic intensity. We have varied the intensity of the ultrasound altering the total output power in a range of 143–625 W. Oscillations of the physicochemical properties of ultrasonically modified zinc particles remain on increasing the total output power. However, the frequency of properties' oscillations decreases on increasing of ultrasonic intensity. Besides, a phase of zinc oxide appears after the ultrasonic treatment of zinc particles at the power higher than 143 W.

As sonochemical treatment of metals could make it possible to enhance the ability of metals to release ions in a bacteria medium we have measured the amount of released Zn^{2+} ions. The amount of leached Zn^{2+} ions was checked by complexation titration using eriochrome black T as an indicator and ethylenediaminetetraacetic acid (EDTA) as a reagent. This method is mainly based on substances that change color when creating complexes with determined metals (Fig. 4a). For example, eriochrome black T is blue when free in a solution with pH of 7–11. The solution is pink when eriochrome black T forms a complex with zinc (pH = 10). It is important that formation constant for these complexes is low enough, so that titrant reacts with complexed ions first. Thus, when EDTA is added in a solution the ZnY^{2-} complex is formed and eriochrome black T is released (Fig. 4c). The ZnY^{2-} complex is colorless, while eriochrome black T is blue. The presence of unreacted blue eriochrome black T, colorless ZnY^{2-} complex and pink $ZnIn^-$ complex gives violet color, when whole amount of Zn^{2+} ions

reacts with EDTA, the solution becomes blue. Immersion of sonochemically treated zinc particles in a medium solution reveals nonlinear dependence of Zn^{2+} concentration on sonication time (Fig. 4e).

Fig. 5a shows that the dependence of antibacterial properties on sonication time has nonlinear character, but generally the antibacterial efficiency of zinc nanostructured particles is higher. The most significant antimicrobial effect is evident for samples obtained at 15 min and 90 min of sonication that correlates with the results of diffusion analysis in agar (Fig. 5a, c). There is no significant difference in antibacterial activity between zinc particles fabricated after 15 min and particles fabricated after 90 min as well as highest zinc ion release quantity. Antimicrobial activity of zinc particles taken at higher concentration demonstrates the same tendency (Fig. 5b). During first 15 min of sonication the antibacterial activity increases and after 15 min of sonication it decreases slightly, then, after 30 min of sonication, it increases again. A bactericidal effect of an antimicrobial agent could be caused by damage of cell membrane, resulting outflow of protoplasmic inclusions [58].

What are the antibacterial mechanisms of acting of sonochemically treated zinc particles? As mentioned above, there are various mechanisms for the antimicrobial activity of zinc particles reported in the literature [36–40,59,60]. The zinc surface could be oxidized to zinc oxide during sonochemical process. First mechanism of antimicrobial activity of sonicated zinc nanoparticles is based on generation of ROS on the ZnO surface. These ROS cause fatal damage of DNA, cell membranes and cellular proteins leading to bacteria inactivation [59]. However, X-ray spectra have shown the absence of ZnO phase, so this mechanism is not likely in this paper. In addition, all experiments were carried out without UV-illumination during experiment. Thus, there are two possible antibacterial mechanisms based on properties of zinc surface and Zn^{2+} ions release (Fig. 5e).

The second mechanism deals with direct interaction of zinc particle and cell membrane (Fig. 5e). We propose that cavitation driven gradients create critical conditions for modification of zinc particles at highly non-equilibrium conditions. The followed relaxation of the system can amplify to the development of spontaneous heterogeneities in systems [9,27,45]. Thus, we can conclude that surface morphology of the zinc particles could also strongly affect on the antibacterial properties and modulation of morphological structure in heterogeneous systems can be achieved. Oscillating of the antibacterial activity could be concerned with changing of the surface morphology and as a result BET surface area. The highest BET surface area we have the highest amount of leached Zn^{2+} ions are present in a solution.

If we compare SEM images of zinc particles sonicated at 15 min and 90 min, we can see completely different morphology while antibacterial activity of samples is approximately the same. At the same time, the histogram of leached Zn^{2+} ions corresponds completely to antibacterial activity and inhibition zone diameter. Thus, we can conclude that release of Zn^{2+} ions plays an important part in bactericidal mechanism.

The antibacterial activity exhibited by zinc particles could be also explained by leaching of soluble Zn^{2+} ions when Zn particles are immersed in water or solution with bacteria due to pH changes as a result of antibacterial activity (Fig. 4e, Fig. 5e). The latter, in turn, exert a destructive effect on the bacterial cell wall, linking to the active groups that make up its composition [59]. It should be mentioned that amount of released Zn^{2+} ions corresponds with oscillations of antibacterial activity. Thus, the antibacterial properties of sonochemically fabricated zinc particles are based on the leaching of Zn^{2+} ions.

4. Conclusions

We propose that cavitation driven gradients create critical conditions for modification of zinc particles at highly non-equilibrium states. After the sonication, the zinc particles exhibit a different surface morphology and microstructure comparing to initial ones. The unique cavitation driven approach leads to the oscillation of surface morphology

and concentration of leached Zn^{2+} ions as well as antibacterial properties. The question of correlation of functional properties and both 1) Zn based particles morphology and 2) zinc ions release. Here, it is proven that highest biocide activity is for 15 min and 90 min treated zinc particles that correlated very nicely with zinc ion release. Simultaneously morphology of 15 min and 90 min treated zinc particles are different: smooth and rough correspondingly. Thus, one can conclude that most effect of zinc based particles biocide activity is due to zinc ion release and the ultrasonic treatment is a perspective method for a fabrication of the gradients of physical and chemical properties in different materials. It can be used for the hierarchical organization in metal particles and the construction of functional interfaces on demand. This method can be used for modulation and amplification of the generation of spontaneous heterogeneities in systems.

Declaration of competing interest

We wish to confirm that there are no known conflicts of interest associated with this publication and there has been no significant financial support for this work that could have influenced its outcome.

Acknowledgements

References

[1] C.S. Rempe, K.P. Burris, S.C. Lenaghan, C.N. Stewart, The potential of systems biology to discover antibacterial mechanisms of plant phenolics, Front. Microbiol. 8 (2017) 422.

[2] A.J. Huh, J.Y. Kwon, "Nanoantibiotics": a new paradigm for treating infectious diseases using nanomaterials in the antibiotics resistant era, J. Control. Release 156 (2011) 128–145.

[3] A.V. Crua, D. Medina, B. Zhang, M.U. González, Y. Huttel, J.M. García-Martín, T.J. Webster, Comparison of cytocompatibility and anticancer properties of traditional and green chemistry-synthesized tellurium nanowires, Int. J. Nanomedicine 14 (2019) 3155.

[4] J.M. Silvan, I. Zorraquin-Peña, D. Gonzalez de Llano, M. Moreno-Arribas, A.J. Martinez-Rodriguez, Antibacterial activity of glutathione-stabilized silver nanoparticles against Campylobacter multidrug-resistant strains, Front. Microbiol. 9 (2018) 458.

[5] M. Goudarzi, N. Mir, M. Mousavi-Kamazani, S. Bagheri, M. Salavati-Niasari, Biosynthesis and characterization of silver nanoparticles prepared from two novel natural precursors by facile thermal decomposition methods, Sci. Rep. 6 (2016) 32539.

[6] S. Mortazavi-Derazkola, S. Zinatloo-Ajabshir, M. Salavati-Niasari, Novel simple solvent-less preparation, characterization and degradation of the cationic dye over holmium oxide ceramic nanostructures, Ceram. Int. 41 (8) (2015) 9593–9601.

[7] M. Amiri, M. Salavati-Niasari, A. Akbari, T. Gholami, Removal of malachite green (a toxic dye) from water by cobalt ferrite silica magnetic nanocomposite: herbal and green sol-gel autocombustion synthesis, Int. J. Hydrog. Energy 42 (2017) 24846–24860.

[8] E.V. Skorb, H. Möhwald, Ultrasonic approach for surface nanostructuring, Ultrason. Sonochem. 29 (2016) 589–603.

[9] P.V. Cherepanov, A. Kollath, D.V. Andreeva, Up to which temperature ultrasound can heat the particle? Ultrason. Sonochem. 26 (2015) 9–14.

[10] D.V. Andreeva, P.V. Cherepanov, Y.S. Avadhut, J. Senker, Rapidly oscillating microbubbles force development of micro-and mesoporous interfaces and composition gradients in solids, Ultrason. Sonochem. 51 (2019) 439–443.

[11] M.A. Margulis, M. Arkad'evich, Sonochemistry and Cavitation, Gordon and Breach Publishers, 1995.

[12] J.P. Lorimer, T.J. Mason, Sonochemistry. Part 1 – the physical aspects, Chem. Soc. Rev. 16 (1987) 239–274.

[13] J. Rae, M. Ashokkumar, O. Eulaerts, C. von Sonntag, J. Reisse, F. Grieser, Estimation of ultrasound induced cavitation bubble temperatures in aqueous solutions, Ultrason. Sonochem. 12 (2005) 325–329.

[14] V. Misik, N. Miyoshi, P. Riesz, EPR spin-trapping study of the sonolysis of H_2O/D_2O mixtures: probing the temperatures of cavitation regions, J. Phys. Chem. 99 (1995) 3605–3611.

[15] M. Fatemeh, M. Salavati-Niasari, In vitro comparative study of pure hydroxyapatite nanorods and novel polyethylene glycol/graphene oxide/hydroxyapatite nanocomposite, J. Nanopart. Res. 16 (9) (2014) 2604.

[16] M. Amiri, A. Akbari, M. Ahmadi, A. Pardakhti, M. Salavati-Niasari, Synthesis and in vitro evaluation of a novel magnetic drug delivery system; proecological method for the preparation of $CoFe_2O_4$ nanostructures, J. Mol. Liq. 249 (2018) 1151–1160.

[17] M. Amiri, A. Pardakhti, M. Ahmadi-Zeidabadi, A. Akbari, M. Salavati-Niasari, Magnetic nickel ferrite nanoparticles: green synthesis by Urtica and therapeutic effect of frequency magnetic field on creating cytotoxic response in neural cell lines, Colloids Surf. B: Biointerfaces 172 (2018) 244–253.

[18] F. Mohandes, M. Salavati-Niasari, Freeze-drying synthesis, characterization and in vitro bioactivity of chitosan/graphene oxide/hydroxyapatite nanocomposite, RSC Adv. 4 (49) (2014) 25993–26001.

[19] M. Amiri, M. Salavati-Niasari, A. Akbari, A magnetic CoFe$_2$O$_4$/SiO$_2$ nanocomposite fabricated by the sol-gel method for electrocatalytic oxidation and determination of L-cysteine, Microchim. Acta 184 (3) (2017) 825–833.

[20] M. Amiri, M. Salavati-Niasari, A. Pardakhty, M. Ahmadi, A. Akbari, Caffeine: a novel green precursor for synthesis of magnetic CoFe$_2$O$_4$ nanoparticles and pH-sensitive magnetic alginate beads for drug delivery, Mater. Sci. Eng. C 76 (2017) 1085–1093.

[21] P.V. Cherepanov, D.V. Andreeva, Phase structuring in metal alloys: ultrasound-assisted top-down approach to engineering of nanostructured catalytic materials, Ultrason. Sonochem. 35 (2017) 556–562.

[22] J. Dulle, S. Nemeth, E.V. Skorb, T. Irrgang, J. Senker, R. Kempe, A. Fery, D.V. Andreeva, Sonochemical activation of Al/Ni hydrogenation catalyst, Adv. Funct. Mater. 22 (2012) 3128–3135.

[23] P.V. Cherepanov, I. Melnyk, D.V. Andreeva, Effect of high intensity ultrasound on Al$_3$Ni$_2$, Al$_3$Ni crystallite size in binary AlNi (50 wt% of Ni) alloy, Ultrason. Sonochem. 23 (2015) 26–30.

[24] S. Zinatloo-Ajabshir, S. Mortazavi-Derazkola, M. Salavati-Niasari, Sonochemical synthesis, characterization and photodegradation of organic pollutant over Nd$_2$O$_3$ nanostructures prepared via a new simple route, Sep. Purif. Technol. 178 (2017) 138–146.

[25] S. Zinatloo-Ajabshir, S. Mortazavi-Derazkola, M. Salavati-Niasari, Nd$_2$O$_3$-SiO$_2$ nanocomposites: a simple sonochemical preparation, characterization and photocatalytic activity, Ultrason. Sonochem. 42 (2018) 171–182.

[26] S. Zinatloo-Ajabshir, M. Salavati-Niasari, Sonochemical-assisted synthesis of pure nanocrystalline tetragonal zirconium dioxide using tetramethylethylenediamine, Int. J. Appl. Ceram. Technol. 11 (4) (2014) 654–662.

[27] P.V. Cherepanov, I. Melnyk, E.V. Skorb, P. Fratzl, E. Zolotoyabko, N. Dubrovinskaia, L. Dubrovinsky, Y.S. Avadhut, J. Senker, L. Leppert, S. Kuemmel, D.V. Andreeva, The use of ultrasonic cavitation for near-surface structuring of robust and low-cost AlNi catalysts for hydrogen production, Green Chem. 17 (2015) 2745–2749.

[28] E.V. Skorb, H. Möhwald, D.V. Andreeva, Effect of cavitation bubble collapse on the modification of solids: crystallization aspects, Langmuir 32 (2016) 11072–11085.

[29] P.V. Cherepanov, M. Ashokkumar, D.V. Andreeva, Ultrasound assisted formation of Al-Ni electrocatalyst for hydrogen evolution, Ultrason. Sonochem. 23 (2015) 142–147.

[30] S.J. Doktycz, K.S. Suslick, Interparticle collisions driven by ultrasound, Science 247 (1990) 1067–1069.

[31] J. Dulle, S. Nemeth, E.V. Skorb, D.V. Andreeva, Sononanostructuring of zinc based materials, RCS Adv. 2 (2012) 12460–12465.

[32] H. Mirzaei, M. Darroudi, Zinc oxide nanoparticles: biological synthesis and biomedical applications, Ceram. Int. 43 (2017) 907–914.

[33] N. Padmavathy, R. Vijayaraghavan, Enhanced bioactivity of ZnO nanoparticles—an antimicrobial study, Sci. Technol. Adv. Mater. 9 (2008) 035004.

[34] E. Malka, I. Perelshtein, A. Lipovsky, Y. Shalom, L. Naparstek, N. Perkas, A. Gedanken, Eradication of multi-drug resistant bacteria by a novel Zn-doped CuO nanocomposite, Small 9 (2013) 4069–4076.

[35] A.M. Allahverdiyev, E.S. Abamor, M. Bagirova, M. Rafailovich, Antimicrobial effects of TiO$_2$ and Ag$_2$O nanoparticles against drug-resistant bacteria and leishmania parasites, Future Microbiol. 6 (2011) 933–940.

[36] T. Gordon, B. Perlstein, O. Houbara, I. Felner, E. Banin, S.T. Margel, Synthesis and characterization of zinc/iron oxide composite nanoparticles and their antibacterial properties, Colloids Surf. A Physicochem. Eng. Asp. 374 (2011) 1–8.

[37] M. Ramani, S. Ponnusamy, C. Muthamizhchelvan, From zinc oxide nanoparticles to microflowers: a study of growth kinetics and biocidal activity, Mater. Sci. Eng. C 32 (2012) 2381–2389.

[38] R. Yuvakkumar, J. Suresh, A.J. Nathanael, M. Sundrarajan, S.I. Honga, Novel green synthetic strategy to prepare ZnO nanocrystals using rambutan (Nephelium lappaceum L.) peel extract and its antibacterial applications, Mater. Sci. Eng. C 41 (2014) 17–27.

[39] A.A. Alswat, M.B. Ahmad, T.A. Saleh, M.Z.B. Hussein, N.A. Ibrahim, Effect of zinc oxide amounts on the properties and antibacterial activities of zeolite/zinc oxide nanocomposite, Mater. Sci. Eng. C 68 (2016) 505–511.

[40] J. Niu, Z. Tang, H. Huang, J. Pei, H. Zhang, G. Yuan, W. Ding, Research on a Zn-Cu alloy as a biodegradable material for potential vascular stents application, Mater. Sci. Eng. C 69 (2016) 407–413.

[41] E.V. Skorb, D.V. Andreeva, Surface nanoarchitecture for bio-application self-regulation intelligent interfaces, Adv. Funct. Mater. 23 (2013) 4483–4506.

[42] E.V. Skorb, O. Baidukova, A. Brotchie, A. Goyal, D.V. Andreeva, H. Möhwald, Sononanoengineered magnesium–polypyrrole hybrid capsules with synergetic trigger release, J. Mater. Chem. 22 (2012) 13841–13848.

[43] Y. Zhukova, S.A. Ulasevich, J.W.C. Dunlop, P. Fratzl, H. Möhwald, E.V. Skorb, Ultrasound-driven titanium modification with formation of titania based nanofoam surfaces, Ultrason. Sonochem. 36 (2017) 146–154.

[44] E.V. Skorb, D.G. Shchukin, H. Möhwald, D.V. Andreeva, Ultrasound-driven design of metal surface nanofoams, Nanoscale 2 (2010) 722–727.

[45] J. Kopf, S.A. Ulasevich, O. Baidukova, Y. Zhukova, J.W.C. Dunlop, P. Fratzl, Ultrasonically produced porous sponge layer on titanium to guide cell behavior, Adv. Eng. Mater. 18 (2016) 476–483.

[46] E.V. Skorb, H. Möhwald, "Smart" surface capsules for delivery devices, Adv. Mater. Interfaces 1 (2014) 1400237.

[47] D.V. Andreeva, D.V. Sviridov, A. Masic, H. Möhwald, E.V. Skorb, Nanoengineered metal surface capsules: construction of a metal-protection system, Small 8 (2012) 820–825.

[48] J.J. Royer, N. Monnin, N. Pailot-Bonnetat, L.O. Filippov, I.V. Filippova, T. Lyubimova, Thermodynamics of ultra-sonic cavitation bubbles in flotation ore processes, J. Phys. Conf. Ser. 879 (2017) 012024.

[49] M. Ashokkumar, T.J. Mason, Sonochemistry, Kirk-Othmer Encyclopedia of Chemical Technology, 2000.

[50] T.-P.A. Ricardo, E.A. Serna-Galvis, Sonolysis, Advanced Oxidation Processes for Waste Water Treatment, Academic Press, 2018, pp. 177–213.

[51] H. Yanagida, Y. Masubuchi, K. Minagawa, T. Ogata, J.I. Takimoto, K. Koyama, A reaction kinetics model of water sonolysis in the presence of a spin-trap, Ultrason. Sonochem. 5 (4) (1999) 133–139.

[52] R.W.G. Wyckoff, New York rocksalt structure, Crystal Structures 1, Interscience Publishers, New York, 1963, pp. 85–237.

[53] A.W. Hull, W.P. Davey, Graphical determination of hexagonal and tetragonal crystal structures from x-ray data, Phys. Rev. 17 (1921) 549.

[54] M.J. Akhtar, M. Ahamed, S. Kumar, M.M. Khan, J. Ahmad, S.A. Alrokayan, Zinc oxide nanoparticles selectively induce apoptosis in human cancer cells through reactive oxygen species, Int. J. Nanomedicine 7 (2012) 845.

[55] J. Lohr, A.A. De Almeida, M.S. Moreno, H. Troiani, G.F. Goya, T.E. Torres Molina, L.C. Nagamine, Effects of Zn substitution in the magnetic and morphological properties of Fe-oxide-based core–shell nanoparticles produced in a single chemical synthesis, J. Phys. Chem. 123 (2) (2018) 1444–1453.

[56] P.M. Perillo, M.N. Atia, D.F. Rodríguez, Studies on the growth control of ZnO nanostructures synthesized by the chemical method, Matéria (Rio de Janeiro) 23 (2) (2018).

[57] P. Bindu, T. Sabu, Estimation of lattice strain in ZnO nanoparticles: X-ray peak profile analysis, J. Theor. Appl. Phys. 8 (4) (2014) 123–134.

[58] K. Steffya, G. Shanthi, A.S. Maroky, S. Selvakumar, Enhanced antibacterial effects of green synthesized ZnO NPs using Aristolochia indica against Multi-drug resistant bacterial pathogens from Diabetic Foot Ulcer, J. Infect. Public Health 11 (2018) 463–471.

[59] K.R. Raghupathi, R.T. Koodali, A.C. Manna, Size-dependent bacterial growth inhibition and mechanism of antibacterial activity of zinc oxide nanoparticles, Langmuir 27 (2011) 4020–4028.

[60] E.A.S. Dimapilisa, C.-S. Hsu, R.M.O. Mendoza, L. Ming-Chun, Zinc oxide nanoparticles for water disinfection, Sustain. Environ. Res. 28 (2018) 47–56.

Check for updates

Photoelectrochemical photocurrent switching effect on a pristine anodized Ti/TiO₂ system as a platform for chemical logic devices†

Nikolay V. Ryzhkov, Veronika Yu. Yurova, Sviatlana A. Ulasevich and Ekaterina V. Skorb *

We report here the effect of the photoelectrochemical photocurrent switching (PEPS) observed on highly-ordered pristine anodized Ti/TiO₂ for the first time. At negative potential bias, blue irradiation gives cathodic photocurrent, whereas anodic photocurrent was observed for ultraviolet irradiation. We believe this phenomenon is due to the electron pathway provided by Ti^{3+} defect states.

Titanium dioxide, being one of the most studied materials, still draws much attention from researchers.[1,2] It is considered to be a very promising material due to its high chemical stability, nontoxicity, and its unique properties. Due to stable and robust photoactivity, titania is widely used in the design of solar cells[3] and photocatalytic applications.[4] In addition to the fact that titanium dioxide occurs in several crystalline modifications, it can also be obtained in various forms, such as, for example, nanotubes,[5] nanofibers,[6] and nanosheets.[7] The photocatalytic performance of TiO_2 is highly dependent on crystallinity,[8] phase content, form, and preparation method.[9] It was reported that highly ordered arrays of TiO_2 nanotubes are characterized by short charge transport distance and little carrier transport loss.[5] Therefore, electrochemically fabricated TiO_2 nanotube arrays are preferable compared to random non-oriented titania.[10] Great varieties of photoelectrochemical behaviour can be achieved by doping[11] and surface modification.[12,13]

An interesting feature has recently been demonstrated for highly ordered arrays of TiO_2 nanotubes obtained by double stepwise electrochemical anodization of a titanium foil (Ti/TiO_2). Together with our colleagues observed that localized illumination of Ti/TiO_2 surface in water solution triggers proton flux from irradiated area.[14] The photocatalytic activity of TiO_2 is based on photogenerated electron–hole pairs. Under the electric field of Ti/TiO_2 Schottky junction and due to upward surface band bending, efficient spatial charge separation occurs, and photoexcited holes (h^+) reach TiO_2 – solution interface. The h^+, which is a strong oxidizing agent, can react with water, and a pronounced pH gradient arises due to water photolysis. Thus, titanium dioxide can be used to trigger local ion fluxes, and proton release is associated with anodic photocurrent. The use of the light-pH coupling effect

to control pH-sensitive soft matter was previously demonstrated.[15,16] Complementary species, H^+ and OH^-, annihilating when occurring simultaneously, extend chemical arithmetic with subtraction operation opening way to pure chemical calculations.[17] Ion fluxes consideration as information transducers in solution were proposed[18] and performing simple logic operations was demonstrated.[19] This phenomenon opens perspectives to biomimetic information processing and developing effective human–machine interfaces.[20]

Photoelectrodes using light and potential as inputs and yielding photocurrents are being considered as the basis for logic devices. In this way, optical computing compatible with existing silicon-based devices may be performed.

Logic operations are described by Boolean algebra operating with truth values denoted 0 (false) and 1 (true). Elementary logical operations are modelled by logic gates producing single binary output from multiple binary inputs and physically implemented by some switch. As for photoelectrode based information processing, the photoelectrochemical photocurrent switching (PEPS) effect is utilized. This effect is that under appropriate external polarization or/and illumination by light with appropriate photon energy, switching between anodic and cathodic photocurrent may be observed for n-type semiconductors and the opposite for p-type.[21,22]

Without further modification, this effect was observed for a very limited number of materials, such as bismuth orthovanadate, lead molybdate, V–VI–VII semiconductors, and some others. To show this effect, the majority of semiconductors require electronic structure perturbation creating new electron pathways. A convenient solution is specific modifier adsorption onto the semiconductors' surface, providing a sufficient level of electronic coupling. Photoelectrodes made of nanocrystalline TiO_2 modified by cyanoferrate,[13,23] and ruthenium[24] complexes, thiamine, folic acid,[25] and carminic acid[26] demonstrated PEPS behavior.

ITMO University, 9, Lomonosova street, Saint Petersburg, 191002, Russia. E-mail: skorb@itmo.ru

† Electronic supplementary information (ESI) available: Additional details concerning experimental conditions. See DOI: 10.1039/d0ra00205d

RSC Advances

Surprisingly, we observed the PEPS effect on non-modified Ti/TiO$_2$ obtained by anodation of Ti plates.

Highly ordered arrays of anatase Ti/TiO$_2$ were obtained. Crystallinity was proved by XRD (Fig. S1a†). Fig. 1a shows a SEM image of TiO$_2$ nanotube arrays obtained as described above. According to SEM image, an average pore diameter is *ca.* 60 nm. As reported, highly ordered TiO$_2$ nanotubes possess a short charge transport distance and little carrier transport loss. Therefore, highly ordered TiO$_2$ nanotube arrays fabricated by electrochemical anodization of titanium may exhibit some enhanced capacity of electron transfer than non-oriented ones of random mixture.[10]

According to Mott–Schottky analysis, at potential bias more positive than −0,697 V *vs.* Ag/AgCl reference electrode upwards band bending occurs (Fig. S2†). Heat treatment in a nonoxidizing atmosphere leads to Ti^{3+} formation. Appearance of Ti^{3+} self-doping was proved by EDX analysis (Fig. S1b†). It was previously reported that Ti^{3+} introduces gap states which act as recombination centers and pathways for electron transfer.[27–29] Ti^{3+} species in reduced TiO$_2$ introduce a gap state between valence and conduction bands.[27,28]

We studied dependence of photocurrent on applied potential. Ultraviolet irradiation (365 nm) gave positive photocurrent for all potentials studied in range from −0.6 V to 0.6 V *vs.* Ag/AgCl reference electrode (Fig. S3†). The photocurrent increases as the potential becomes more positive, but eventually saturates. The dependence of the current on the potential under blue irradiation (405 nm) had a different character. Sigmoid function with inflection point at 0–0.2 V was observed for blue light.

It should be noticed that photocurrent plotted against time on Fig. 2–4 as well as against potential on Fig. S3† is $\Delta I = I_{\text{under illumination}} - I_{\text{in darkness}}$. Steady state current values were used for calculations.

At +300 mV *vs.* Ag/AgCl irradiation by both blue and ultraviolet light give anodic photocurrent (Fig. 2a and c). The UV-irradiation ($\lambda = 365$ nm, 5 mW cm^{-2}) excites electron directly to the conduction band (CB) of TiO$_2$, which is further transferred to conducting titanium support (Fig. 2b). When Ti/TiO$_2$ electrode in thermodynamic equilibrium with electrolyte, an upward surface band bending occurs at the semiconductor–liquid junction. This phenomenon obstructs electron injection

Fig. 2 Photocurrent curves under chopped irradiation by (a) 365 nm UV LED, (c) 405 nm blue LED at applied potential bias +300 mV *vs.* Ag/AgCl, and corresponding scheme of electron pathway at +300 mV polarization under irradiation by (b) 365 nm UV LED and (d) 405 nm blue LED.

from the conduction band into the electrolyte and forces electron drift to conducting substrate. The fast and steady photocurrent production/extinction upon light on/off indicates efficient charge separation and low recombination.
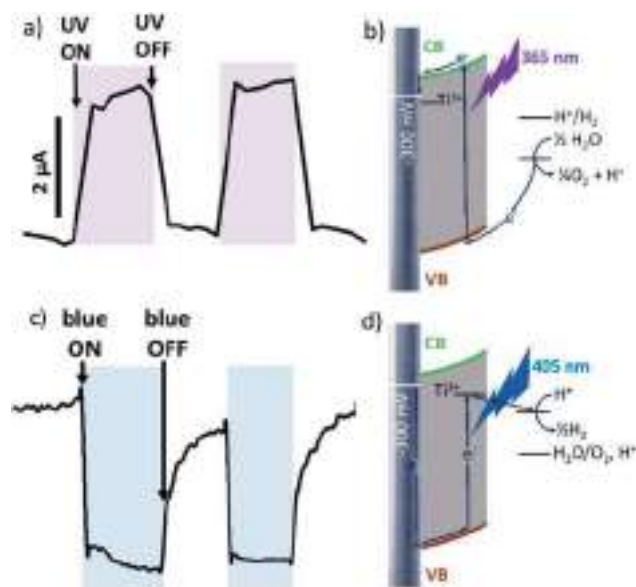
Fig. 3 Photocurrent curves under chopped irradiation by (a) 365 nm UV LED, (c) 405 nm blue LED at applied potential bias −300 mV *vs.* Ag/AgCl, and corresponding scheme of electron pathway at −300 mV polarization under irradiation by (b) 365 nm UV LED and (d) 405 nm blue LED.

Fig. 1 (a) SEM image of the TiO$_2$ nanotubes array. The inset shows cross-section view. (b) Scheme of a cell for photocurrent measurements experiment, CE – counter electrode, RE – reference electrode, WE – working electrode.
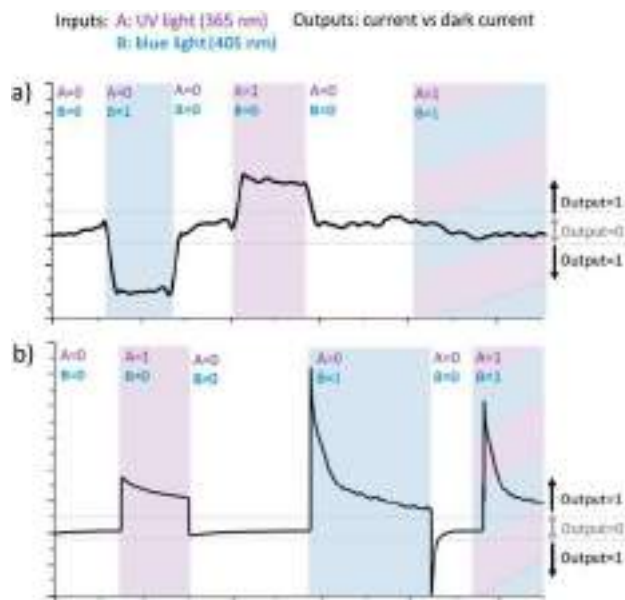
Fig. 4 (a) XOR logic realized on negatively polarized (−0.3 V) pristine Ti/TiO$_2$ by two source irradiation, input A – UV light (365 nm), input B – blue light (405 nm); blue light gives anodic photocurrent, UV – cathodic photocurrent. The current, significantly different from the dark one, is taken as output 1, otherwise − 0. When irradiated by blue and UV light simultaneously, anodic and cathodic current compensate each other, and no total photocurrent observed. Thus output 0, when both inputs are 1 (b) OR logic realized on positively polarized (+0.3 V) non-modified Ti/TiO$_2$ by two sources of irradiation. Irradiation by any of them, blue or UV, gives anodic photocurrent.

Blue light ($\lambda = 405$ nm, 70 mW cm^{-2}) is characterized by lower energy than UV-irradiation, which is not sufficient to excite the electron to CB. But electron excited by blue light can be trapped by Ti^{3+} located close to the conduction band and transferred to conduction support from these levels (Fig. 2c). An initial current spike following by an exponential decrease suggesting a fast recombination process. It should be also noticed than when irradiation is switched off photocurrent 'overshoots' as the remaining surface holes continue to recombine with electrons.

At more negative potential (−300 mV vs. Ag/AgCl, for example) applied to non-modified anodized Ti/TiO$_2$ photoelectrode, we observed anodic photocurrent during irradiation by UV light (Fig. 3a) whereas blue irradiation gave anodic photocurrent (Fig. 3c). Excitation within bandgap by UV-irradiation leads to cathodic photocurrent (Fig. 3b). In the case of irradiation by blue light, electron trapping by Ti^{3+} occurs in the same manner as at +300 mV polarization. But at negative polarization, the energy landscape is such that electron transport to electron donor in solution is preferable (Fig. 3d). As a result, cathodic current occurs.

Thereby, photoelectrode activity of non-modified anodized Ti/TiO$_2$ can be switched from anodic to cathodic and vice versa by applying various potentials and various photon energies. This is the effect of photoelectrochemical photocurrent switching.

Thereby, when Ti/TiO$_2$ is irradiated simultaneously by blue and UV light being negatively polarized, competition between cathodic and anodic photocurrents occurs. Returning to Boolean logic, the PEPS effect allows us to perform annihilation of two input signals and implement optoelectronic XOR logic gate. XOR logic operation outputs true (1) only when input values are different and yield zero otherwise.

It is necessary to assign logic values to input and output signals to analyse the system based on Ti/TiO$_2$ PEPS effect in terms of Boolean logic. Logical 0 and 1 are assigned to off and on states of the LEDs, respectively. Different wavelengths (365 and 405 nm) correspond to two different inputs of the logic gate. In the same way, we can assign logic 0 to the state when photocurrent is not generated and logic 1 to any nonzero photocurrent intensity irrespectively on its polarization (cathodic or anodic).

Fig. 4 demonstrates how different types of Boolean logic are realized by irradiation of Ti/TiO$_2$. Light sources are denoted here as inputs, UV light – A and blue light – B. If the corresponding light source is switched ON and illuminates photoelectrode Ti/TiO$_2$, this input is '1', otherwise, it's '0'. The photocurrent is read as output. It's considered to be '1' if significantly differs from dark value and '0' otherwise.

At −300 mV vs. Ag/AgCl, pulsed irradiation with UV diode (365 nm, 5 mW cm^{-2}) results in anodic photocurrent, which is consistent with electron excitation to CB and transfer to conducting support. Irradiation with blue LED (405 nm) gives cathodic photocurrent due to electron capture by Ti^{3+} states following by transferring to electron acceptor in solution. Simultaneous irradiation with two LEDs with adjusted intensity yields zero net current as anodic and cathodic photocurrents compensate effectively (Fig. 4a).

At positive potentials, pulsed irradiation with UV diode gives anodic photocurrent pulses, as well as the blue one. It is interesting to note that when two sources of light are simultaneously irradiated, the photocurrents created by each of them individually do not summarize. At +300 mV, photocurrent output under the influence of two light inputs (365 nm and 405 nm) follows OR logic giving positive output if at least one of inputs is positive (Fig. 4b).

Fig. 5 demonstrates the reconfigurable logic system which characteristics can be changed via an appropriate polarization of the photoelectrode regarded as programming input. Two irradiation sources are considered as inputs. OR/XOR logic is realized depending on programming input.

In summary, PEPS effect on modified nanocrystalline TiO$_2$ was previously discussed a lot.[13,23–26] In this work we report the same phenomenon for pristine anodized Ti/TiO$_2$ system. Due to substructure of Ti/TiO$_2$ system, it shows characteristic response to various range of illumination, including visible range and polarization. The Ti/TiO$_2$ system is a simple and robust model of chemical logic gates. Suggested mimicking of logic functions in aqueous solutions allows further integration of element into communication with living objects[16] vs. intrinsically associated photooxidation and degradation, but rather activation for needed function.[30]

Fig. 5 A reconfigurable logic system based on non-modified Ti/TiO₂. Light sources are inputs. The choice between XOR and OR function is determined by programming input of potential bias. At +300 mV OR logic is realized, at −300 − XOR logic. Corresponding truth table is presented.

Experiment

Highly ordered arrays of photoactive crystalline TiO₂ nanotubes can be obtained by double two-stage anodization of titanium substrates in ethylene glycol electrolyte containing fluoride ions. Double anodization involves forming a first anodization layer and an adjacent second anodization layer on an angled surface, the interface between the two anodization layers being regular and uniform. Anodization was performed via two stages where at the first stage the anode was linearly polarized from 0 to 40 V, and then at the second stage, the electrode was polarized at a constant voltage of 40 V. The as prepared Ti/TiO₂ were treated ultrasonically in ethanol for 0.5–1 min to remove the debris and annealed at 450 °C for 3 hours.

For Mott–Schottky analysis potential was scanned from −1.0 to +0.4 with increment 0.04 V and 3 minutes delay for equilibration of each potential. Potential were oscillating with amplitude 0.005 V and frequency 1000 Hz.

Photocurrent measurements were performed in 3-electrode cell with Ti/TiO₂ nanotubes plate as working electrode, Pt counter electrode and Ag/AgCl reference electrode. During each measurement desired potential bias was applied and after establishing a constant stable dark current working electrode was illuminated by UV LED (365 nm) or blue LED (405 nm) or both light sources simultaneously.

For Boolean logic implementation light intensity was adjusted the light intensity was adjusted in such a way that under −0.3 V polarization photoresponses on UV and blue light annihilate.

Conflicts of interest

There are no conflicts to declare.

Acknowledgements

Notes and references

1 E. Zghab, M. Hamandi, F. Dappozze, H. Kochkar, M. S. Zina, C. Guillard and G. Berhault, *Mater. Sci. Semicond. Process.*, 2020, **107**, 104847.
2 R. Nebel, K. M. Macounová, H. Tarábková, L. Kavan and P. Krtil, *J. Phys. Chem. C*, 2019, **123**, 10857.
3 J. R. Jennings, A. Ghicov, L. M. Peter, P. Schmuki and A. B. Walker, *J. Am. Chem. Soc.*, 2008, **130**, 13364.
4 S. P. Albu, A. Ghicov, J. M. Macak, R. Hahn and P. Schmuki, *Nano Lett.*, 2007, **7**, 1286.
5 K. Lee, A. Mazare and P. Schmuki, *Chem. Rev.*, 2014, **114**, 9385.
6 A. Kumar, R. Jose, K. Fujihara, J. Wang and S. Ramakrishna, *Chem. Mater.*, 2007, **19**, 6536.
7 W. Q. Fang, J. Z. Zhou, J. Liu, Z. G. Chen, C. Yang, C. H. Sun, G. R. Qian, J. Zou, S. Z. Qiao and H. G. Yang, *Chem.–Eur. J.*, 2011, **17**, 1423.
8 J. Zhang, P. Zhou, J. Liu and J. Yu, *Phys. Chem. Chem. Phys.*, 2014, **16**, 20382.
9 S. K. Choi, S. Kim, S. K. Lim and H. Park, *J. Phys. Chem. C*, 2010, **114**, 16475.
10 P. Roy, S. Berger and P. Schmuki, *Angew. Chem., Int. Ed.*, 2011, **50**, 2904.
11 A. Ghicov, J. M. Macak, H. Tsuchiya, J. Kunze, V. Haeublein, L. Frey and P. Schmuki, *Nano Lett.*, 2006, **6**, 1080.
12 N. Brezhneva, A. Nikitina, N. Ryzhkov, A. Klestova, A. V. Vinogradov and E. V. Skorb, *J. Sol-Gel Sci. Technol.*, 2019, **89**, 92.
13 W. Macyk, G. Stochel and K. Szaciłowski, *Chem.–Eur. J.*, 2007, **13**, 5676.
14 H. M. Maltanava, S. K. Poznyak, D. V. Andreeva, M. C. Quevedo, A. C. Bastos, J. Tedim, M. G. S. Ferreira and E. V. Skorb, *ACS Appl. Mater. Interfaces*, 2017, **9**, 4282.
15 S. A. Ulasevich, G. Brezesinski, H. Möhwald, P. Fratzl, F. H. Schacher, S. K. Poznyak, D. V. Andreeva and E. V. Skorb, *Angew. Chem., Int. Ed.*, 2016, **55**, 13001.
16 S. A. Ulasevich, N. Brezhneva, Y. Zhukova, H. Möhwald, P. Fratzl, F. H. Schacher, D. V. Sviridov, D. V. Andreeva and E. V. Skorb, *Macromol. Biosci.*, 2016, **16**, 1422.

17 P. Banda, C. Teuscher and D. Stefanovic, *J. R. Soc., Interface*, 2014, **11**, 20131100.

18 N. V. Ryzhkov, N. A. Mamchik and E. V. Skorb, *J. R. Soc., Interface*, 2019, **16**, 20180626.

19 N. V. Ryzhkov, P. Nesterov, N. A. Mamchik, S. O. Yurchenko and E. V. Skorb, *Front. Chem.*, 2019, **7**, 419.

20 N. V. Ryzhkov, D. V. Andreeva and E. V. Skorb, *Langmuir*, 2019, **35**, 8543.

21 K. Pilarczyk, P. Kwolek, A. Podborska, S. Gawęda, M. Oszajca and K. Szaciłowski in *Advances in Unconventional Computing*, ed. A. Adamatzky, Springer, Cham, 2017, pp.429–467.

22 M. ce Long, R. Beranek, W. min Cai and H. Kisch, *Electrochim. Acta*, 2008, **53**, 4621.

23 K. Szaciłowski, W. Macyk, M. Hebda and G. Stochel, *ChemPhysChem*, 2006, **7**, 2384.

24 L. F. O. Furtado, A. D. P. Alexiou, L. Gonçalves, H. E. Toma and K. Araki, *Angew. Chem., Int. Ed.*, 2006, **45**, 3143.

25 S. Gawęda, G. Stochel and K. Szaciłowski, *Chem.–Asian J.*, 2007, **2**, 580.

26 S. Gawęda, G. Stochel and K. Szaciłowski, *J. Phys. Chem. C*, 2008, **112**, 19131.

27 M. Nolan, S. D. Elliott, J. S. Mulley, R. A. Bennett, M. Basham and P. Mulheran, *Phys. Rev. B: Condens. Matter Mater. Phys.*, 2006, **77**, 235424.

28 C. Di Valentin, G. Pacchioni and A. Selloni, *J. Phys. Chem. C*, 2009, **113**, 20543.

29 J. Weidmann, T. Dittrich, E. Konstantinova, I. Lauermann, I. Uhlendorf and F. Koch, *Sol. Energy Mater. Sol. Cells*, 1999, **56**, 153.

30 E. V. Skorb, D. V. Andreeva, A. P. Raiski, N. A. Belyasova, H. Möhwald and D. V. Sviridov, *Photochem. Photobiol. Sci.*, 2011, **10**, 1974.

Author for correspondence:
Ekaterina V. Skorb
e-mail: skorb@itmo.ru

THE ROYAL SOCIETY
PUBLISHING

A platform for light-controlled formation of free-stranding lipid membranes

Nikolay V. Ryzhkov and Ekaterina V. Skorb

ITMO University, Lomonosova str. 9, 191002 Saint Petersburg, Russia

NVR, 0000-0002-6557-0018; EVS, 0000-0003-0888-1693

The engineering of artificial cells is one of the most significant scientific challenges. Thus, controlled fabrication and *in situ* monitoring of biomimetic nanoscale objects are among the central issues in current science and technology. Studies of transmembrane channels and cell mechanics often require the formation of lipid bilayers (LBs), their modification and their transfer to a particular place. We present here a novel approach for remotely controlled manipulation of LBs. Layer-by-layer deposition of polyethyleneimine and poly(sodium 4-styrenesulfonate) on a nanostructured TiO_2 photoanode was performed to obtain a surface with the desired net charge and to enhance photocatalytic performance. The LB was deposited on top of a multi-layer positive polymer cushion by the dispersion of negative vesicles. The separation distance between the electrostatically linked polyelectrolyte cushion and the LB can be adjusted by changing the environmental pH, as zwitterionic lipid molecules undergo pH-triggered charge-shifting. Protons were generated remotely by photoanodic water decomposition on the TiO_2 surface under 365 nm illumination. The resulting pH gradient was characterized by scanning vibrating electrode and scanning ion-selective electrode techniques. The light-induced reversible detachment of the LB from the polymer-cushioned photoactive substrate was found to correlate with suggested impedance models.

1. Introduction

One of the central issues of modern science and technology is to mimic the structure and, hence, properties of living systems by non-living matter [1–3]. Since compartmentalization is considered to be a critical step in the origin of life, obtaining and manipulating artificial lipid membranes draws much attention [4,5]. In general, there are three model systems for studying cellular membranes [6,7]: supported lipid bilayers (SLBs), giant unilamellar vesicles (GUVs) and black lipid membranes (BLMs). The presence of SLBs is the major drawback of supported membranes. It is unclear how support affects the structure, function and incorporation of membrane proteins. Using polymer-cushioned membranes partially reduces coupling with the support. The volatile nature of GUVs complicates their usage, while the spherical surface is also a disadvantage for some analytical techniques. Disadvantages of BLMs are that they have insufficient long-term stability and that residual organic solvents such as hexane are present in the membranes.

The approach of local release of free-standing bilayers proposed here may be employed for studying the properties of cellular membranes, for functional studies of membrane proteins such as ion channels, pumps and transporters and also for cell mechanics investigations. In the case of SLBs, the LB and support are held together by electrostatic interactions [8]. Since phospholipids are known to demonstrate pH-dependent charge-shifting behaviour [9], biomimetic lipid–polyelectrolyte composites are strongly affected by the pH of the surrounding medium [10]. Based on neutron reflectivity data [11–13], the lipid bilayer (LB) is firmly attached to the oppositely charged underlying support, which is made up of strong polyelectrolytes. At the isoelectric point, the components are repelled, and the interaction switches from attraction to repulsion. With a pH lower than the lipid molecule's isoelectric point, the separation distance
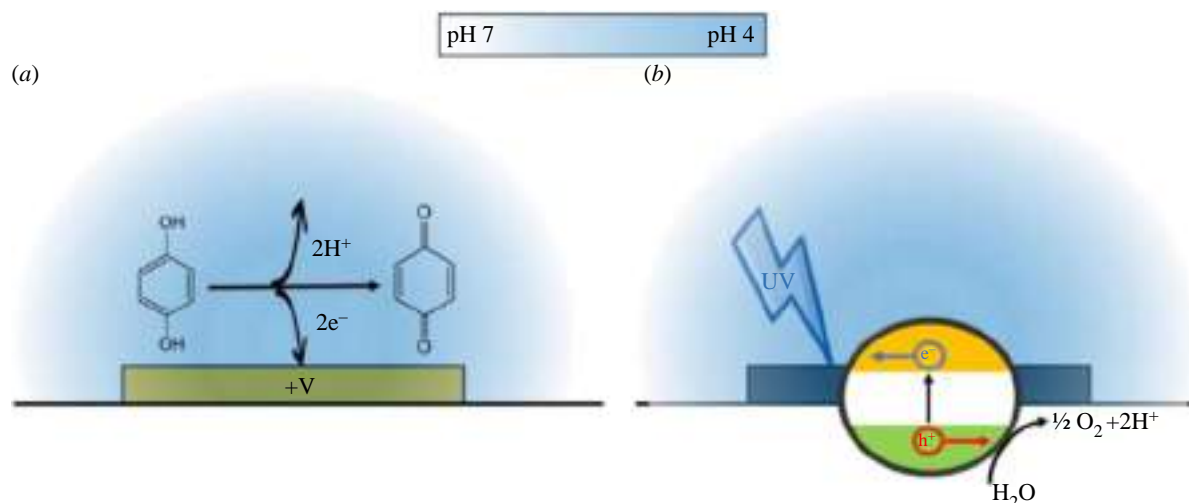
Figure 1. (a) Electrochemical generation of proton flux from the electrode–solution interface via a hydroquinone oxidation reaction, which is coupled with proton release. (b) Photoelectrochemical decomposition of water on the surface of photoexcited TiO_2, due to the *n*-type conductivity of nanostructured Ti/TiO_2 photoexcited holes, is captured by surface states. Water splitting with proton release occurs at the TiO_2–solution interface inside the irradiated spot, whereas electrons—being major charge carriers—are transferred to bulk titanium. (Online version in colour.)

between the lipid membrane and the polymer cushion increases [11]. Manipulating the interaction strength may also be useful for developing nanoactuators.

There are numerous strategies for modifying the pH of a solution [14–16]. A photochemical one is considered to be extremely promising because it allows pH changes to be performed remotely without chemical contamination. By irradiating the surface of semiconductors, acidity can be changed remotely and locally with high resolution [17]. Nanostructured titania (TiO_2) was demonstrated to be an extremely efficient photocatalyst [18]. It provides an effective and controllable way to transform electromagnetic energy into local pH change [17]. Effectively manipulating pH-sensitive soft matter deposited on TiO_2 was performed by 365 nm irradiation [19–21].

In this article, we develop ideas that we have previously proposed [10] and introduce a novel approach to designing photostimulated adaptive biointerfaces. We have already demonstrated electrochemically triggered reversible LB lift-off from the underlying conducting substrates covered by polyelectrolytes via hydroquinone oxidation coupled with proton release (figure 1a). Here, we present light-triggered reversible LB lift-off from the underlying polymer-cushioned [22] photoactive anodized TiO_2 substrate, in which 365 nm light of $5\,mW\,cm^{-2}$ intensity promotes the separation of electrons and holes. Under the field of the Schottky junction with the environment, holes reach the semiconductor–environment interface and react with surrounding water media to form proton flux (figure 1b).

Phosphatidylcholine bilayers (LB) supported by a polyelectrolyte multi-layer (PEM) of polyethyleneimine (PEI) and poly(sodium 4-styrenesulfonate) (PSS) were obtained by the vesicle rupture [23–25] and layer-by-layer (LbL) technique [26] on top of TiO_2. The light-induced activity and resulting proton concentration close to the surface under localized 5 mm irradiation were studied using a scanning vibrating electrode technique (SVET) and a scanning ion-selective electrode technique (SIET). We report here increasing the light-to-ΔpH conversion efficiency of a TiO_2/PEM photoelectrode in comparison with bare TiO_2. Electrochemical spectroscopy also revealed that, in the acidic conditions generated by photoelectrochemical water

splitting, the LB impact impedance [27–29] of the TiO_2/PEM/LB composite disappears. Owing to proton diffusion, the local pH returns to an initial bulk value when irradiation is switched off. As a result, the LB attaches back to the PSS/PEI cushion, and we observed impedance growth.

Semiconductor surfaces covered by PEMs and LBs provide a unique platform for light-triggered remote manipulation of LBs. This approach seems to be promising for bilayer array patterning [8,30]. Free-standing lipid membranes can be obtained for studying transmembrane proteins [31,32], modelling cell mechanics [33,34] and studying flexoelectricity phenomena [35]. Creating free-standing lipid membranes would also be advantageous for cell culturing and tissue engineering [36,37].

2. Results and discussion

2.1. pH effects on lipid molecules

Depending on the intended application, the properties of vesicles may be optimized. Electrostatic interactions are key for vesicles' attraction to the underlying support, and, because of the short radius of curvature, small vesicles tend to rupture [23]. Thus, small charged vesicles are perfect for bilayer formation from vesicle dispersion. When prepared, lipid vesicles had a bimodal size distribution representing small unilamellar vesicles (100 nm in diameter) and large aggregates of vesicles (5 μm). Liposomes of the order of 10–100 nm in size are well suited for the deposition of lipid layers [38]. Usually, an extrusion procedure is used to obtain liposomes of the desired size [39]. Alternatively, centrifugation may be employed to obtain homogeneously sized, single-lamellar phospholipid vesicles [40]. Centrifugation was used to separate the large fraction of the lipid vesicles (figure 2a inset).

The small lipid unilamellar vesicle dispersion thus obtained in water (pH 7) was strongly negative (ζ-potential approx. −35 mV) (figure 2a) and stable for weeks at 4°C [41].

Taking the lipid charge into account, we covered the TiO_2 surface with PEM of (PSS/PEI)$_3$ architecture, with the outer PEI layer giving a net positive charge.

The lipid–polyelectrolyte assembly is held together by electrostatic forces. Changing the charge of the species, one
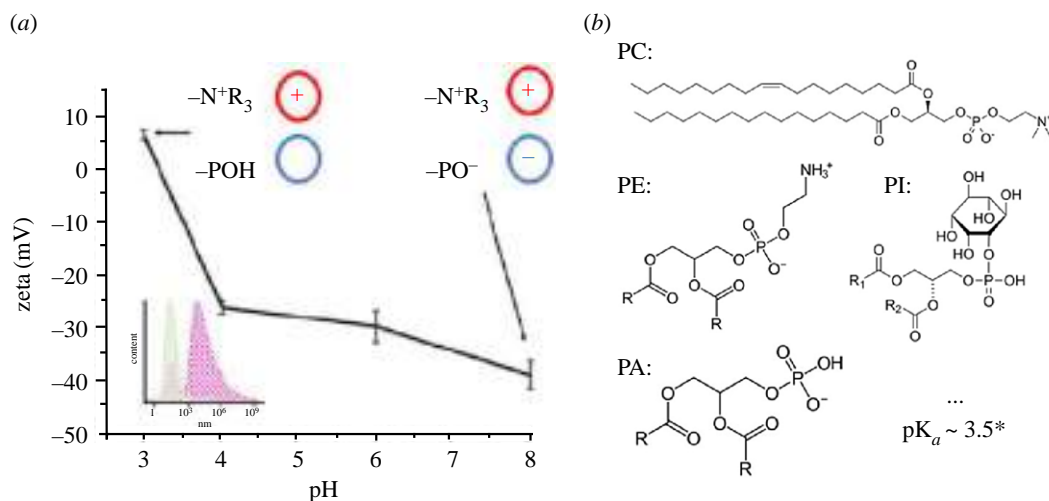
Figure 2. (a) ζ-potential of lipid vesicles obtained from soy lecithin at different pH values adjusted by diluted HCl and NaOH solutions; at pH 3 vesicles are positive. Inset—size distribution of lipid vesicles: pink, before centrifugation; green, after centrifugation. Content value normalized to content of the predominant component. (b) Main components of soy lecithin: PC, phosphatidylcholine; PE, phosphatidylethanolamine; PI, phosphatidylinositol; and PA, phosphatidic acid. The charged moieties are positive N^+R_3 and/or negative PO^- when the dissociated pK_a of the dissociating phosphate group is reported to be less than or equal to 3.5. (Online version in colour.)

can vary the strength of electrostatic interaction. Phospholipid molecules forming soy lecithin contain positively and negatively charged moieties, $-PO^-$ and N^+R_3, which can take part in equilibrium processes with H^+ and OH^- (figure 2b),

$$- PO^- + H^+ = -POH$$
$$N^+R_3 + OH^- = NR_3OH.$$
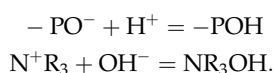
Thus, the $-PO^-$, $-POH$, N^+R_3 and NR_3OH groups are in equilibrium, and the pH and acid–base constants determine their concentration,

$$K_a = \frac{a_H + a_{PO^-}}{a_{POH}} \quad \text{and} \quad K_b \frac{a_N +_{R_3} a_{OH^-}}{a_{NR_3OH}}. \quad (2.1)$$

The pK_a of the phosphate group on phosphatidylcholine was reported to be approximately 3.5 [42,43]. Therefore, under neutral conditions, phosphate groups are deprotonated. The amine group of the phospholipids always remains in a positively charged state. In this case, some components of soy lecithin carry only a negative charge, which is not compensated by a positive amine group (e.g. phosphatidylinositol and phosphatidic acid). As a result, lipid structures are negative in neutral media. Under acidic conditions, a positive net charge of lipid vesicles is due to protonated phosphate groups (figure 2a). Consequently, the interaction mode between lipid assembly and underlying strong polyelectrolyte support (always positive) switches from attraction to repulsion, which varies the pH of the surrounding medium.

2.2. Multi-layer formation

When obtained, nanostructured TiO_2 has a tubular nanostructure (figure 3a). After PEM assembly composed of polycationic PEI and polyanionic PSS (figure 3b), superhydrophilic titania nanotubes with a water contact angle of 11°–12° (figure 3d) become less hydrophilic, with a contact angle of 35° (figure 3e). LB deposition yields better wettability with the TiO_2/PEM/LB composite than with the TiO_2/PEM architecture. During LB self-assembly, the hydrophobic hydrocarbon tails are inside the bilayer and the hydrophilic charged groups are outside (figure 3c), which determines more hydrophilic properties of

lipid-covered substrates (figure 3f). Surface roughness is a fundamental parameter, so the surface topography of the multi-layered structures under investigation was evaluated (figure 3g–i).

Atomic force microscopy (AFM) images were taken after each step of assembly to study the changes in morphology upon adsorption of polyelectrolytes and lipids on the surface of the titania nanotubes. In figure 3g, the formation of nanostructured dots is observed, which correlates with the nanotubular morphology of anodized TiO_2 found by scanning electron microscope (SEM) analysis (figure 3a). By contrast, the surface topography of the polyelectrolyte-covered specimen is flatter and smoother (figure 3h). Figure 3i shows a topographic image of the TiO_2/PEM substrate after lipid vesicle adsorption. Figure 3i demonstrates surface features of larger diameter and with higher roughness than in figure 3h. The most likely explanation for the very large surface features in figure 3i is that these are lipid agglomerations on the surface of the PEM. At the same time, figure 3i also demonstrates a flat domain formation. This fact, together with the quartz crystal microbalance (QCM) data (figure 3c) demonstrating vesicle adsorption, rupture and fusion, proves the formation of LBs on selected areas of polyelectrolyte-cushioned nanostructured TiO_2.

2.3. Electrochemical impedance spectroscopy

Electrochemical impedance spectroscopy can serve as an accessible approach to evaluate the process where lipid membranes are involved, as continuous LBs possess high impedance [28,29,42]. Under an open-circuit potential, no Faradaic processes occur, so elements of Ohmic resistance and capacitance are sufficient to describe the impedance of the electrochemical system. Electronic supplementary material, figure S1a demonstrates an equivalent electrical circuit describing the TiO_2/PEM/LB composition. R_E corresponds here to the Ohmic resistance of the electrolyte solution, R_S, for the Ohmic resistance of the TiO_2/PEM solid support, CPE_S ($CPE_S = 1/4 \exp(\alpha j\pi/2)/Q\omega N$, where j is the imaginary unit number, ω is frequency, and Q and N are independent frequency parameters). R_{LB} and C_{LB} are related to the Ohmic resistance and capacitance of LB, respectively. The contribution of the counter-electrode is also considered (R_{CE} and
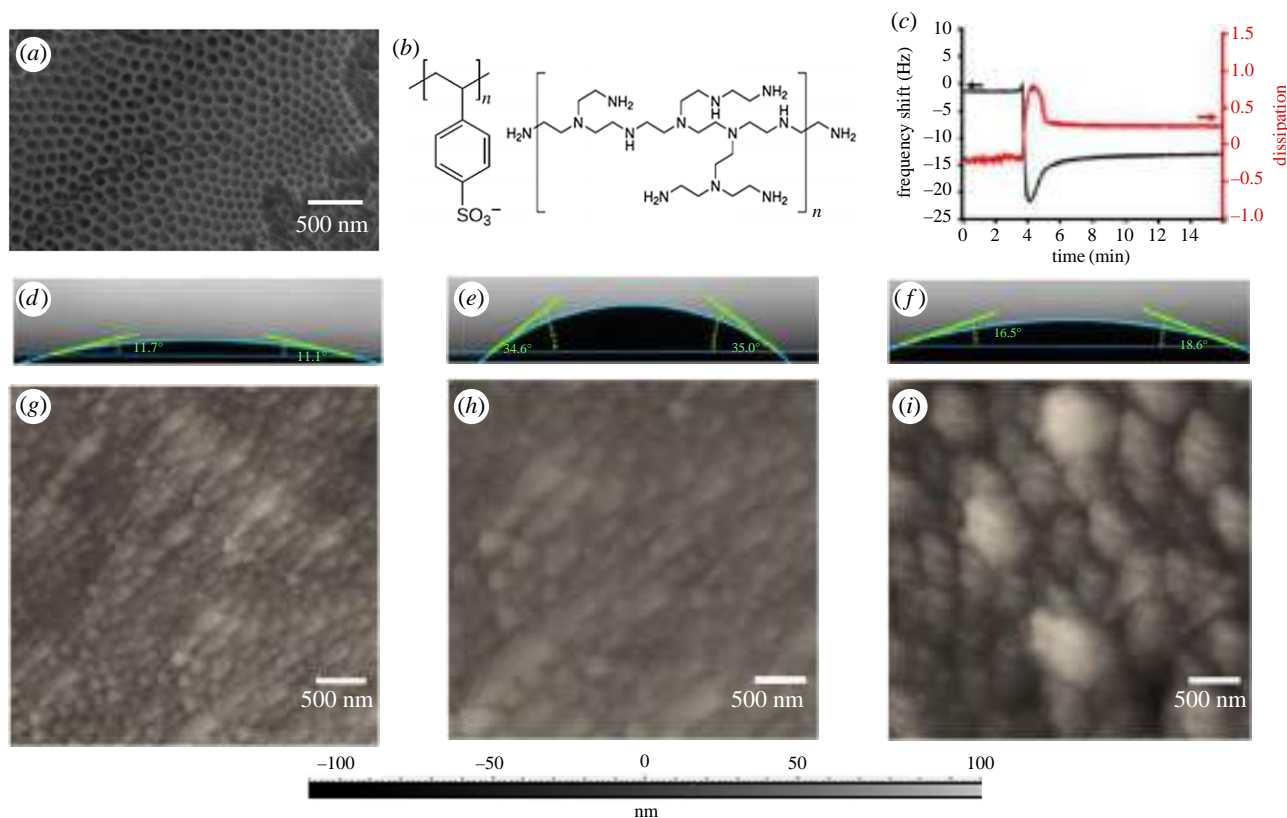
Figure 3. Polyelectrolyte–lipid multi-layer formation on top of the nanostructured TiO_2 surface. (a) SEM image of anodized TiO_2. (b) Structural formulae of the polyelectrolytes used for the formation of the polyelectrolyte cushion; left, poly(styrenesulphonate), PSS; right, branched poly(etheleneimine), PEI. (c) QCM analysis of LB formation on top of the PEM cushion. Injection of the lipid vesicle suspension leads to a frequency shift of −30 Hz, followed by an increase of 10 Hz almost without delay. This behaviour corresponds to vesicle adsorption followed by their rupture and release of the water contained inside. Simultaneously there is a sharp increase in the dissipation factor followed by its decrease, which corresponds to a highly rough surface due to vesicle adsorption followed by formation of a continuous bilayer after vesicle rupture, fusion and reorganization. (d–f) Water contact angle measurements of (d) bare TiO_2, (e) TiO_2/PEM, (f) TiO_2/PEM/LB. (g,h) AFM scans of the surface of (g) bare TiO_2, (h) TiO_2/PEM, (i) TiO_2/PEM/LB. (Online version in colour.)

C_{CE}). In the case of TiO_2/PEM, the LB impact is excluded (electronic supplementary material, figure S1b). This model, which is based on an approximation of the distinct interfaces and the layered structure of the composite, allows us to describe processes at the PEM-LB interface with appropriate accuracy. Low resistances and the very large capacitances reported for the lipid layer of the composite multi-layer support the above interpretation of the AFM results (figure 3g–i) and demonstrate lipid aggregate deposition and partial bilayer formation on the rough surface of the polymer-cushioned TiO_2.

2.4. pH-responsive lipid bilayer

Electronic supplementary material, figure S2a demonstrates the impedance characterization of TiO_2/PEM/LB under neutral conditions. The impedance characteristics of the TiO_2/PEM/LB composite changed dramatically when the surrounding medium reached pH 3 as a result of dilute HCl being added dropwise (electronic supplementary material, figure S2b). The equivalent circuit, without taking the lipid impact into account (electronic supplementary material, figure S1b), fits an experimental spectrum of TiO_2/PEM/LB at pH 3 (electronic supplementary material, figure S2b). Under neutral conditions, the LB has a significant impact on total impedance, represented by resistivity R_{LB} and capacity C_{LB} in parallel, and the equivalent circuit from electronic supplementary material, figure S1a should be employed to fit the experimental data. Relatively low resistance seems to be consistent with there not being perfect surface coverage. The fitting parameters are summarized in

electronic supplementary material, table S1. These results demonstrate that the impact of the LB on the impedance of TiO_2/PEM/LB disappears under acidic conditions. This means that the LB leaves the region of the TiO_2/PEM diffuse double-layer electric field propagation. Protonation of lipid phosphate groups leads to charge-shifting from negative to positive. As a result, positive lipid membranes drift away from the TiO_2/(PSS/PEI)$_3$ support, which has a positive PEI outer layer. Most likely, the protonated lipid layer, which is not very firmly attached to the positive underlying support, was swept away by fluid flow during solution exchange; this is why the disappearance of the lipid impact under acidic conditions was irreversible when the acidity of the surrounding medium was adjusted back to neutral pH by adding diluted NaOH solution.

Impedance measurements for the TiO_2/PEM composite were also taken to demonstrate the stability of the PEM (electronic supplementary material, figure S2c,d). Neither the impedance spectrum nor the equivalent circuit and best-fitting parameters undergo any significant changes when the environmental acidity changes from pH 7 to pH 3. A combination of R_E, R_S and CPE_S may describe the TiO_2/PEM impedance (electronic supplementary material, figure S1b), and the corresponding numerical values summarized in electronic supplementary material, table S1 do not vary significantly. Any minor differences in impedance between neutral and acidic conditions are due to a decrease in the Ohmic resistance of the solution as a result of the increase in concentration of the conducting protons.
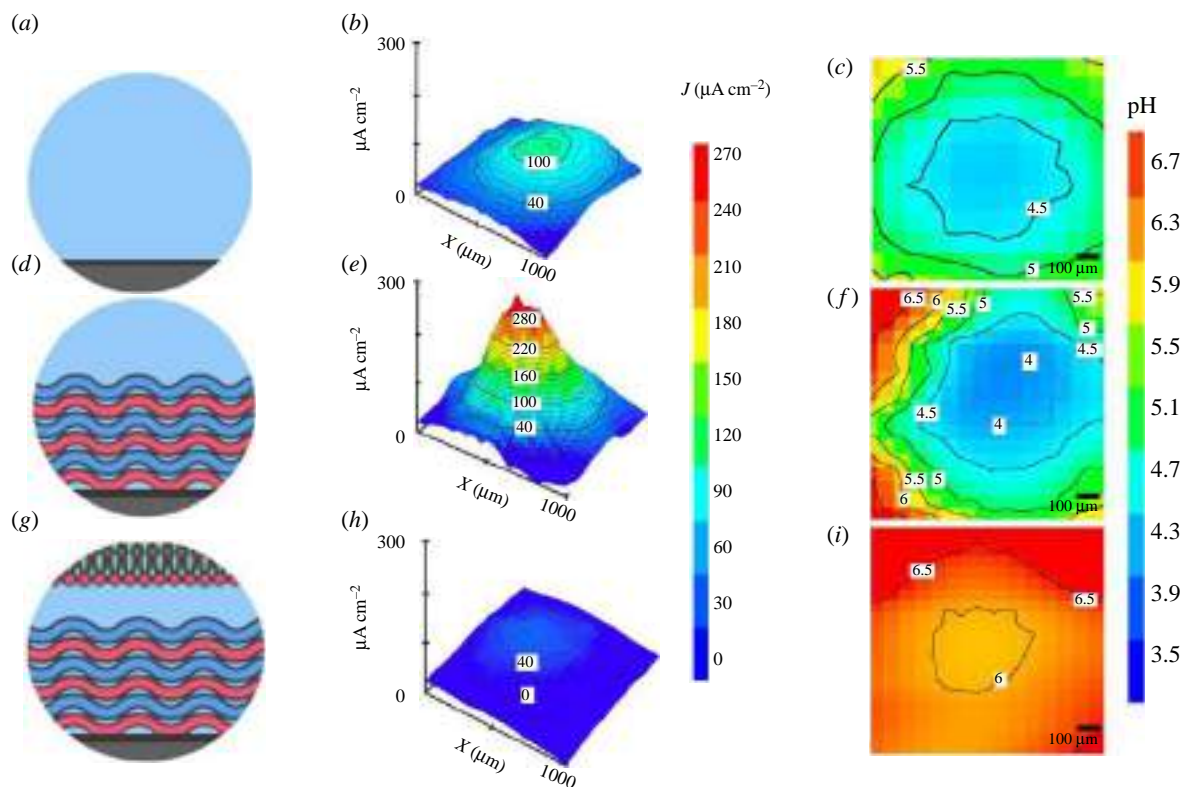
Figure 4. Schematic of the photoelectrode–solution interface, anodic activity (current density map) and a pH map of the water solution close to the photoelectrode surface for (a–c) TiO₂, (d–f) TiO₂/PEM and (g–i) TiO₂/PEM/LB measured by (b,e,h) SVET and (c,f,i) SIET in 50 mM NaCl under 365 nm 5 mW cm⁻² irradiation. (Online version in colour.)

2.5. The enhanced photocatalytic performance of TiO₂/(PSS/PEI)₃

A significant proton concentration can be obtained by light-induced water splitting on a locally irradiated TiO₂ surface. The map of photoanodic activity and the resulting pH gradient inside and around the irradiated spot on the TiO₂ surface (figure 4a) were visualized by SVET and SIET (figure 4b,c, respectively). Light-initiated water splitting on a nanostructured titania photoanode enabled us to shift pH from the initial 6.5–7 to 4.5 (figure 4c). It was previously reported that PEI works like a proton sponge and leads to a more pronounced pH gradient on the surface of the illuminated TiO₂ [44]. SVET and SIET gave insight on the effects of a (PSS/PEI)₃ multilayer on the photocatalytic performance of the underlying TiO₂. We revealed that the PEM of (PSS/PEI)₃ on top of a TiO₂ photoanode (figure 4d) significantly increases its photocatalytic activity (figure 4e) from 120 to 320 μA cm⁻². The map of pH is in agreement with ionic current data. The local pH inside the irradiated area of TiO₂/(PSS/PEI)₃ drops from approximately 7 to less than 4 (figure 4f). Narrow localization of the acidification phenomenon should also be noted for TiO₂/(PSS/PEI)₃ under 365 nm 5 mW cm⁻² illumination. Thus, one can remotely change the local pH from neutral to acidic with high spatial resolution by irradiating the photoactive surface of TiO₂ modified by a PEM of special nanoarchitecture [45].

2.6. Light-triggered lipid bilayer lift-off

As discussed above, irradiation of TiO₂/PEM gives an acidic pH inside the irradiated spots close to the surface. A LB adsorbed on top of the TiO₂/PEM composite (figure 4g) almost completely suppresses the ionic current from the surface of the photocatalyst (figure 4h). Thus, lipid phosphate groups adsorb most of the photoelectrochemically generated protons and recharge.

Following this assumption, the pH map obtained by SIET revealed no significant pH shift over irradiated TiO₂/PEM/LB (figure 4i).

Photocurrent and pH measurements were performed versus time at one point inside the irradiated spot (figure 5a) to investigate the dynamic behaviour of TiO₂/PEM/LB and TiO₂/PEM under illumination and the stability of the polymer assembly and LB to photodegradation. Figure 5b demonstrates a rapid photocurrent response at the very moment that irradiation occurs, and current density returned to dark values immediately after turning off the irradiation.

In accordance with the current density maps, the steady-state current density value for TiO₂/(PSS/PEI)₃ is twice as high as that for the bare photoactive substrate, and for TiO₂/(PSS/PEI)₃/LB it is twice as low. As one may see for TiO₂/(PSS/PEI)₃ and TiO₂/(PSS/PEI)₃/LB, the photocurrent is stable with time. Thus, the PEM and LB are not degraded by irradiation at least during 20 min of irradiation.

Figure 5c demonstrates the pH evolution with time of irradiation. For TiO₂ as well as for TiO₂/(PSS/PEI)₃, the pH drops rapidly the moment illumination is turned on and gradually decreases within the next 10 min; it then stabilizes at approximately 4.5 and 3.5–4, respectively. After 20 min in 'darkness', the local proton concentration close to the irradiated area decreases. Thus TiO₂/(PSS/PEI)₃ provides a platform for reversible manipulation of the pH-sensitive matter assembled on top of it.

Experimental impedance spectra of TiO₂ substrates coated with a (PSS/PEI)₃ polymer cushion before and immediately after irradiation under open circuit conditions are almost identical (figure 6a,b). Electronic supplementary material, table S2 summarizes the fitting parameters used to describe experimental data from figure 6.

Thus, irradiation of TiO₂/PEM does not trigger any changes in the PEM, whereas the pH-sensitive LB is significantly affected
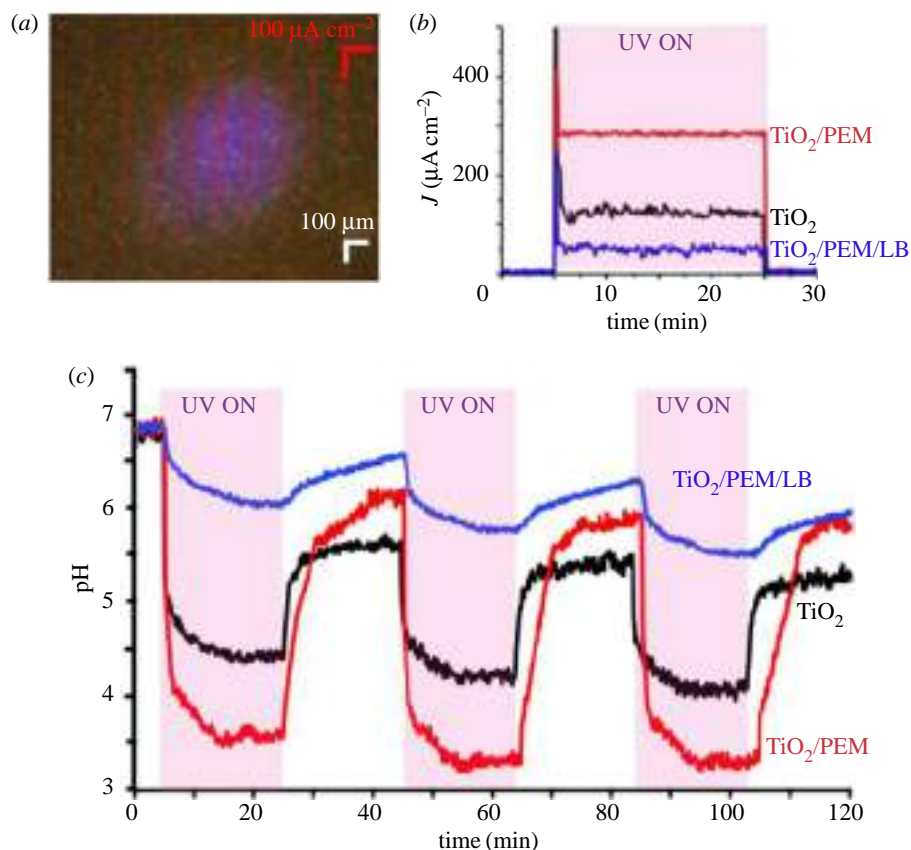
Figure 5. (a) View of the irradiated spot on the surface of specimen; red arrows indicate the direction and magnitude of the ionic current measured at each point. (b) Time evolution of the pH in the centre of the irradiated spot on the surface of the TiO₂, TiO₂/PEM and TiO₂/PEM/LB composites. (c) Time evolution of the ionic current normal to the surface of the TiO₂, TiO₂/PEM and TiO₂/PEM/LB composites. (Online version in colour.)

by the light-induced pH gradient. Local acidification by light-induced water splitting (figure 7) has the same effect on pH-sensitive species as the acidification of the bulk solution (electronic supplementary material, figure S2a,b). As can be seen from the presented spectra (figure 7a,b), after irradiation of TiO₂/(PSS/PEI)₃/LB the parabolic phase curve (figure 7a) of the Bode plots transforms to an S-shaped curve (figure 7b) and the |Z| curve shifts to lower values. The equivalent circuit without LB impact should be employed to successfully fit experimental data of TiO₂/(PSS/PEI)₃/LB after irradiation with ultraviolet (UV) light. The acidification of the bulk solution by diluted HCl triggers the same behaviour in the lipid layer (electronic supplementary material, figure S2a,b). At the same time, it should be noted that the S-shaped phase curve is typical for TiO₂/(PSS/PEI)₃ regardless of irradiation and the bulk pH (electronic supplementary material, figure S2b,c; figure 6a,b). Thus, when the lipid layer is on top of the TiO₂/PEM, the resulting composite demonstrates a much more resistive behaviour. The LB impact on impedance disappears after a short time of irradiation, whereas the PEM of PSS/PEI is not significantly affected by a light-induced pH decrease.

There is a redistribution of excess protons throughout the solution after the light is turned off (figure 5c). Lipid molecules at pH close to neutral return to the initial negative non-protonated state, and the LB is attracted back to the oppositely charged underlying support (figure 7a). The best-fitting parameters are presented in electronic supplementary material, table S3.

Thus, reversible lift-off of the lipid membrane from the underlying support can be performed by alternating periods of irradiation and relaxation in 'darkness'. Apart from the

solution exchange method of pH adjustment, the photoelectrochemical one is not associated with any significant fluxes that are able to remove protonated lipid molecules that are loosely bonded to a positive polymer cushion.

The LB on top of the TiO₂/PEM substrate shows resistive behaviour (approx. 120 ohm). Immediately after 20 min of UV irradiation, the impedance was observed to be two times lower under the same conditions. After 20 min of relaxation, the impedance increased to 100–110 ohm (figure 8a). During further cycles of irradiation and relaxation in 'darkness', the oscillating behaviour of impedance was observed. Figure 8b demonstrates the oscillatory behaviour of impedance during light on–off cycles. pH oscillations take place as a result of local proton release and their diffusion during irradiation and relaxation in darkness, respectively. As a result, oscillations of the lipid molecule's charge and the strength of the electrostatic forces between the LB and its underlying support occur. Sustainability of the LB and reversibility of the process were demonstrated for at least 10 cycles.

2.7. A platform for encapsulation

Light-controlled manipulation by the LB described above provides an instrument to capture species from solution and 'encapsulate' them under a LB. To prove this concept, we performed encapsulation of a model electroactive probe under a LB and tested the efficiency of encapsulation by electrochemical methods. A TiO₂/PEM/LB composite photoelectrode was immersed in a solution of $[Ru(NH_3)_6]^{3+}$, being a model electrochemical probe [46,47], and a cyclic redox process was carried out. Owing to incomplete coating with the LB, the TiO₂
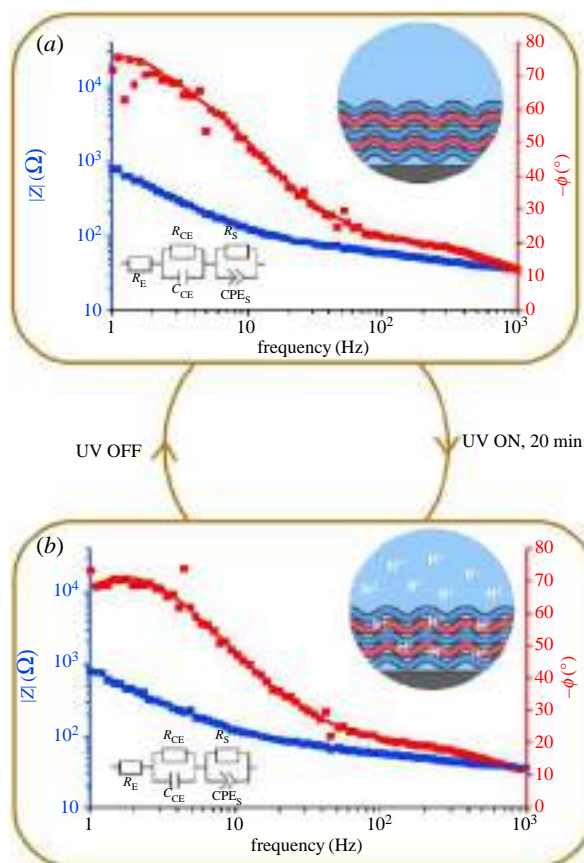
Figure 6. Scheme of TiO₂/PEM composite behaviour during irradiation on–off cycles. Bode plots of impedance spectra, schematic of the object under investigation (top inset) and the equivalent electrical circuit used for fitting experimental data (bottom inset) of (*a*) a relaxed TiO₂/PEM composite before irradiation as well as after 20 min of relaxation after irradiation is switched off and (*b*) immediately after irradiation is switched off. (Online version in colour.)

Figure 7. Scheme of the cyclic process of reversible LB detachment from polymer-cushioned titania associated with lipid recharge due to their protonation as a result of TiO₂ photocatalytic activity. Bode plots of impedance spectra, schematic of the object under investigation (top inset) and the equivalent electrical circuit used for fitting experimental data of (*a*) a relaxed TiO₂/PEM/LB composite before irradiation as well as after 20 min of relaxation after irradiation is switched off and (*b*) TiO₂/PEM/LB after 20 min of illumination. Experimental data are indicated by dots; fitted data are solid lines. (Online version in colour.)

electrode surface was still available for electron transfer with the dissolved electrochemical probe. The cyclic redox process revealed the inequality of the anodic and cathodic current absolute values, evidencing the irreversibility of the redox process with $[Ru(NH_3)_6]^{3+} = [Ru(NH_3)_6]^{2+}$ on the TiO₂/PEM/LB electrode. The reason for this is the inequality of the diffusion of the differently charged cations to the electrode surface, carrying a net negative charge under neutral conditions. In accordance with the results stated above, the oxidized form of the cation tends to be closer to the electrode surface. As a result, the cathodic current is more pronounced in the cycling process.

Under irradiation, proton generation at the TiO₂–solution interface occurs. Lipid molecules capture photogenerated protons. Consequently, the lipid layer recharges and detaches from the supporting polyelectrolyte layers. As a result, electroactive cations are pushed away from the electrode surface following electron transfer suppression. Cathodic current decays much more quickly than an anodic one. The $[Ru(NH_3)_6]^{3+}$ cation carrying more positive charge is involved in the reduction process, whereas less positive $[Ru(NH_3)_6]^{2+}$ oxidizes. Thus, the oxidized state of the electrochemical probe is more sensitive to lipid recharge from negative to positive. A total of 20 consecutive cycles of the $[Ru(NH_3)_6]^{3+} = [Ru(NH_3)_6]^{2+}$ redox process at the TiO₂/PEM/LB electrode during irradiation revealed gradual current decay (figure 9*a*). Complete suppression of electron transfer between the electrode and the soluble species happens after a further 20 minutes of irradiation. During relaxation in

darkness, the evolution of $[Ru(NH_3)_6]^{3+} = [Ru(NH_3)_6]^{2+}$ cyclic voltammograms on the TiO₂/PEM/LB electrode occurs in the opposite direction, returning to the initial state. Strong polyelectrolytes do not undergo protonation in acidic pH adjusted by water photolysis. Thus, the TiO₂/PEM photoelectrode with no lipid on top demonstrates stable values of anodic as well as cathodic current during irradiation (electronic supplementary material, figure S3a). When the lipid layer attaches back to the polyelectrolyte support, it captures electroactive ions from the solution and holds them underneath on the surface of the PEM-cushioned TiO₂. After a procedure including irradiation and relaxation in the $[Ru(NH_3)_6]^{3+}$ solution, the TiO₂/PEM/LB specimen was removed from the electroactive cation solution and rinsed with water five times. Furthermore, a cyclic voltammogram (CV) was obtained in a pure NaCl solution. Nevertheless, peaks of $[Ru(NH_3)_6]^{3+} = [Ru(NH_3)_6]^{2+}$ redox process were observed (figure 9*b*). CVs, in this case, were similar to those obtained for TiO₂/PEM/LB where $[Ru(NH_3)_6]^{3+}$ was embedded in PEM during the deposition stage (electronic supplementary material, figure S3b).

A kinetic study of the $[Ru(NH_3)_6]^{3+} = [Ru(NH_3)_6]^{2+}$ cyclic redox process at TiO₂/PEM/LB before and after irradiation was performed. The redox process on TiO₂/PEM/LB without irradiation corresponds to the criteria for a
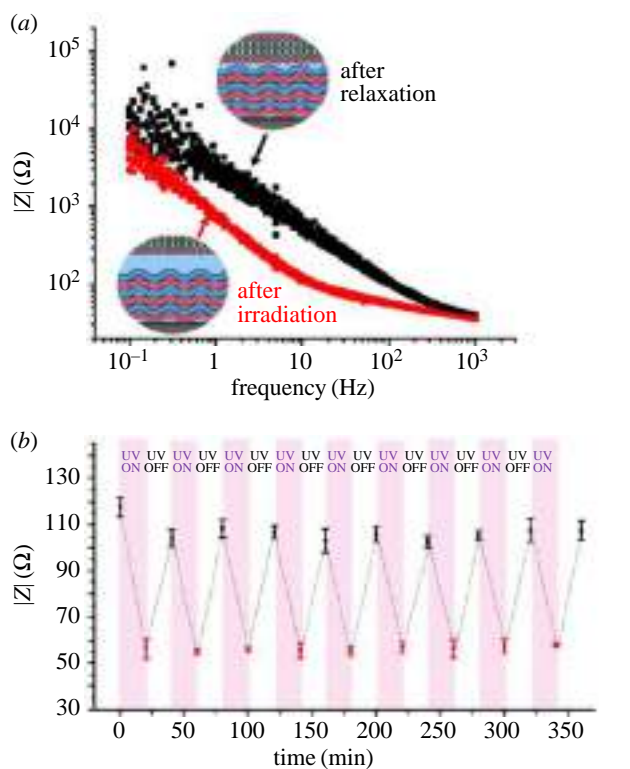
Figure 8. (a) Impedance spectra of TiO$_2$/PEM/LB composites. Red, nine overlapping spectra registered in darkness immediately after 20 min of illumination; black, nine overlapping spectra registered after 20 min relaxation in darkness. (b) Impedance oscillations during irradiation on–off cycles. (Online version in colour.)

diffusion-controlled process which follows the linear dependence of peak current on $v^{1/2}$ (v-scan rate, demonstrated only for anodic current because for cathodic determination of the baseline is difficult because of the preceding peak) (electronic supplementary material, figure S3c,e). After irradiation of the TiO$_2$/PEM/LB photoanode, a slight increase in the peak amplitude was observed, and linear dependence of the peak current on v relates to the adsorption kinetics (electronic supplementary material, figure S3d,e). A set of control experiments was performed (electronic supplementary material, figure S4). Thus, capturing and encapsulation of soluble species can be achieved by irradiation of TiO$_2$/PEM/LB composites in solutions.

3. Conclusion

Phospholipids are known to be charge-shifting molecules sensitive to pH. Thus, it is possible to affect the coulombic forces determining the interaction of lipids with a charged underlying support. As it is negative in neutral media, a phosphatidylcholine bilayer was deposited on a positive PEI capping layer of a polyelectrolyte cushion on nanostructured TiO$_2$. Owing to protonation of the phosphate group, lipids become less negatively charged, and the strength of the electrostatic attraction weakens. Consequently, the separation distance between the LB and its underlying support increases. Impedance spectroscopy measurements were employed to demonstrate this effect. It was demonstrated that the LB impact on the impedance of a TiO$_2$/PEM/LB composite disappears with an increase in proton concentration, evidencing lipid layer lift-off from support. A new
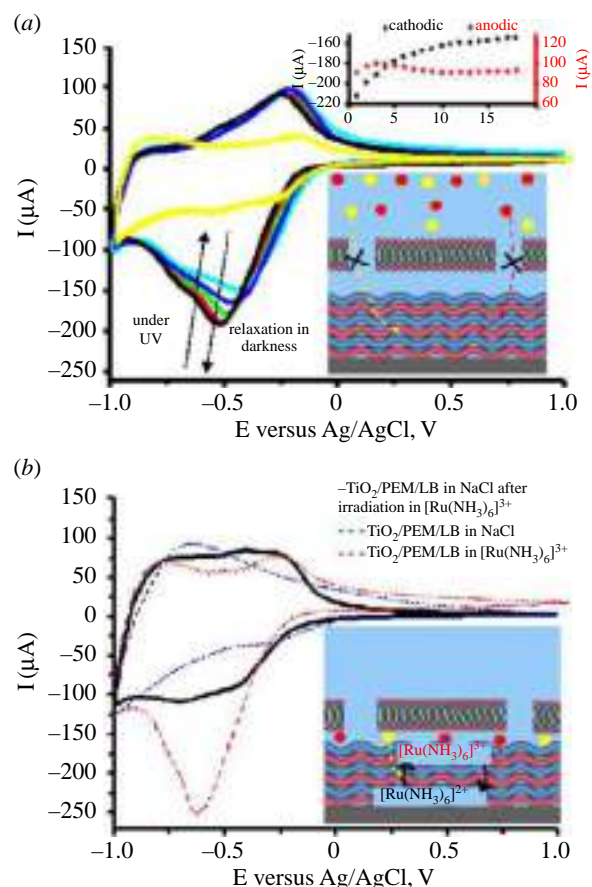
Figure 9. (a) Cyclic voltammograms (CVs) of the $[Ru(NH_3)_6]^{3+} = [Ru(NH_3)_6]^{2+}$ redox process on a TiO$_2$/PEM/LB electrode; 20 consecutive cycles with a 70 mV s^{-1} scan rate; each fifth is present. Current decrease, from black to cyan during irradiation; current increase, from cyan to black during relaxation in darkness. The yellow graph is after 20 min of irradiation, and electron transfer is almost completely suppressed. Top inset is evolution of anodic and cathodic currents extracted from 20 consecutive cycles. (b) 70 mV s^{-1} cycling of $[Ru(NH_3)_6]^{3+} = [Ru(NH_3)_6]^{2+}$ encapsulated underneath a lipid bilayer (black graph) on a TiO$_2$/PEM/LB electrode and comparison with the CV of $[Ru(NH_3)_6]^{3+} = [Ru(NH_3)_6]^{2+}$ bulk solution in 0.5 M NaCl (red doted line) and pure 0.5 NaCl (blue dotted line) at the TiO2/PEM/LB electrode. (Online version in colour.)

approach for a light-controlled free-standing lipid membrane fabrication is presented here. Because of anodic water photolysis on the surface of the TiO$_2$/PEM, the pH of the surrounding medium adjusted to the irradiated spot decreased to approximately 3.5–4 from an initial 7 and reversible LB lift-off from the irradiated TiO$_2$/PEM composite was observed.

4. Experimental section

4.1. Chemicals and materials

Branched PEI (M$_w$ 70 kDa) 30% water solution was purchased from Alfa Aesar, PSS (M$_w$ 500 kDa) was purchased from Polysciences Inc. Liquid soy lecithin (Lecisoy 400) was obtained from Cargill, USA. Reagent grade NaCl (99.5%) was obtained from Merck and hexane from Ekos-1, Russia. All chemicals were used as received without any purification. Titanium plates (99.6% purity) with a thickness of 1 mm were used. $[Ru(NH_3)_6]Cl_3$ from Sigma Aldrich was used as an electrochemically active probe.

Titania nanotubes were obtained by anodization of Ti plates etched in HF:HNO₃ 1 : 2 solution. Ti plate was used as an anode and Pt plate of the same area as a cathode. Electrolyte solution contained 0.75 wt% of NH₄F and 2 wt% of distilled water in ethylene glycol. Anodization was carried out at a constant voltage of 40 V for 1 h, followed by 10 min ultrasonication in 1M HCl. After the second anodation in the same conditions, substrates were kept under ethanol overnight and annealed at 450°C for 3 h.

4.2. Nanoarchitecting of TiO₂/PEM and TiO₂/PEM/LB multi-layered films

For the preparation of the small lipid unilamellar vesicle dispersion, the following procedure was performed. Soy lecithin solution in hexane (10 mg ml⁻¹) was kept under vacuum for solvent evaporation for at least 3 h. After removing any hexane traces, a thin lipid film was obtained on the vessel bottom. This film was rehydrated with distilled water to a final 10 mg ml⁻¹ concentration with simultaneous sonication in an ultrasonic bath for 15 min. To determine the size and the charge of the prepared vesicles, dynamic light scattering and ζ-potential measurements were conducted on a Photocor Compact-ζ analyser. Separation of different sized fractions of lipid vesicles was performed by centrifugation at 14 000 r.p.m. for 20 min.

The polyelectrolyte cushion was deposited using the classical LbL technique. PEI as a polycation solution and PSS as a polyanion solution were prepared by dissolving 2 mg ml⁻¹ in a 0.5 M solution of NaCl in deionized water. Six layers were deposited on titania nanotubes under a vacuum, resulting in the PEM architecture (PSS/PEI)₃. Each deposition was followed by rinsing with water.

To obtain TiO₂/PEM/LB with an embedded electroactive [Ru(NH₃)₆]³⁺probe, after each layer of PSS the specimen was immersed in 0.5 mM [Ru(NH₃)₆]Cl₃ solution in 0.5 M NaCl for 20 min under a vacuum.

Polymer-modified substrates were immersed in a 10 mg ml⁻¹ dispersion of small lipid unilamellar vesicles for 1 h to obtain a LB on top of the polyelectrolyte cushion. Vesicles attached to the oppositely charged surface of the PEM then ruptured, fused, and spread on the surface, forming a continuous bilayer. The procedure described was followed by rinsing with ionized water. As prepared, TiO₂/(PSS/PEI)₃ and TiO₂/(PSS/PEI)₃/LB were kept under water before further measurements. Each stage of multi-layer deposition was followed by QCM measurement using a Q-Sense AB (Sweden), AFM studies were carried out with a Solver Next microscope (Russia), and water contact angles were measured using drop shape analyser (Kruss DSA25, Germany).

4.3. Local photoelectrochemical study

Photocatalytic activity of nanostructured titania and acidity changes inside the irradiated spot close to the TiO₂ surface were studied by SVET and SIET.

SVET here is a unique tool to characterize the photoanodic activity and local ionic currents in solution. SIET measures gradients of ion concentrations. High precision and spatial resolution may be achieved for both methods.

The system from Applicable Electronics (USA) under control of the ASET program (Sciencewares, USA) was used to perform SVET and SIET measurements. SVET and SIET measurements were performed on samples glued to an epoxy support.

Adhesive tape was used to insulate each sample, leaving a 0.25 cm² window exposed to the electrolyte solution.

As a vibrating probe for SVET experiments, insulated Pt-Ir microprobes (Microprobe Inc., USA) with a platinum black spherical tip of 30 μm in diameter were applied. The probe vibrated in two directions parallel and perpendicular to the specimen surface and 150 μm above it. The amplitude of vibration was 30 μm; vibration frequencies of the probe were 136 Hz (perpendicular to the surface) and 222 Hz (parallel to the surface). The only perpendicular component was used for treating and presentation of data.

The local pH measurements were carried out using glass capillary microelectrodes with an apex tip diameter of 2 μm that were prepared from borosilicate glass capillaries with an outer diameter of 1.5 mm. Capillaries were silanized by injecting 200 μl of N,N-dimethyltrimethylsililamine in the glass preparation chamber at 200°C before filling. Silanized capillaries were filled with Hydrogen Ionophore I Cocktail B (Sigma), which served as a proton-selective membrane, and 0.1 M KCl + 0.01 M KH₂PO₄ internal solution. Ag/AgCl/KCl (sat) was used as an external reference electrode. The pH-selective microelectrodes were calibrated using commercially available pH buffers and demonstrated a linear Nernstian response −53 to −55 mV pH⁻¹ in a pH range from 4 to 8. The local activity of H⁺ was detected 25 μm above the surface.

A low-intensity (5 mW cm⁻²) light-emitting diode (365 nm, ThorLabs) focused in a spot (approx. 0.5 mm²) was used to trigger photo-induced processes.

The local pH and ionic current density were mapped on a 15 × 15 grid in a 0.05 M NaCl solution under open-circuit potential conditions. The time evolution of the photocatalytic processes was measured at one point in the centre of the irradiated spot. The time of acquisition for each SVET and SIET data point was 0.6 and 2.5 s, respectively.

4.4. Electrochemical impedance spectroscopy measurements

Electrochemical measurements were performed using a Compactstat instrument (Ivium, Netherlands) in a quartz three-electrode electrochemical cell with a volume of approximately 50 ml filled by 0.05 M NaCl. TiO₂ substrates covered by a LB and/or PEM were used as working electrodes, Pt wire served as a counter-electrode, and Ag/AgCl/3M KCl served as the reference electrode. Impedance spectra for frequencies between 1 Hz and 1 kHz with an AC modulation amplitude of 5 mV were recorded at a bias potential set equal to the open-circuit potential of the working electrode. The surface of the samples exposed to electrolyte was also 0.25 cm². Experiments were performed in 0.05 M NaCl on TiO₂/PEM and TiO₂/PEM/LB at pH 7 and pH 3, adjusted by dilute HCl, and later at bulk pH 7 before and after UV irradiation. Impedance data were treated as Bode plots, and fitting procedures were performed by equivalent circuit analysis mode of the standard Ivium software.

4.5. Cyclic voltammetry

CV experiments were performed using a PalmSence4 potentiostat. TiO₂ substrates covered by a LB and/or PEM were used as working electrodes, Pt wire was used as a counter-electrode, and Ag/AgCl/3M KCl served as the reference electrode. Potential cycling from −1 to 1 V was performed with a scan rate of 70 mV s⁻¹ in 0.5 M NaCl and also in the presence of

0.5 mM [Ru(NH$_3$)$_6$]Cl$_3$ as the electroactive probe. Measurements were carried out before irradiation and after irradiation by 365 nm LED for 20 min, and after 20 min of relaxation in darkness. For each condition, four consecutive scans were obtained; the fourth was used to represent the data. To follow the time evolution of the current during irradiation and relaxation 20 consecutive cycles were obtained, and the peak current changes were tracked. For the kinetic study, the scan rate was varied from 5 to 150 mV s^{-1}, and the peak current was plotted against the scan rate.

4.6. Statistical analysis

Acidity data were recalculated from the measured electrochemical potentials in accordance with calibration. All other data are presented as obtained. For microelectrode mapping, each experiment was reproduced three times; one of the typical maps is given. One of five characteristic impedance spectra is also provided for each studied system. Numerical values extracted from impedance fitting are expressed as mean ± s.e.m., $n = 5$.

References

1. Blain JC, Szostak JW. 2014 Progress toward synthetic cells. Annu. Rev. Biochem. 83, 615–640. (doi:10.1146/annurev-biochem-080411-124036)

2. Dzieciol AJ, Mann S. 2012 Designs for life: protocell models in the laboratory. Chem. Soc. Rev. 41, 79–85. (doi:10.1039/C1CS15211D)

3. Ryzhkov N, Andreeva DV, Skorb EV. 2019 Coupling pH-regulated multilayers with inorganic surfaces for bionic devices and infochemistry. Langmuir 35, 8543–8556. (doi:10.1021/acs.langmuir.9b00633)

4. Han X, Studer A, Sehr H, Geissbühler I, Di Berardino M, Winkler FK, Tiefenauer LX. 2007 Nanopore arrays for stable and functional free-standing lipid bilayers. Adv. Mater. 19, 4466–4470. (doi:10.1002/adma.200700468)

5. Tanaka M, Sackmann E. 2005 Polymer-supported membranes as models of the cell surface. Nature 437, 656–663. (doi:10.1038/nature04164)

6. Kiessling V, Domanska MK, Murray D, Wan C, Tamm LK. 2008 Supported lipid bilayers: development and applications in chemical biology. In Wiley encyclopedia of chemical biology (ed. TP Begley), pp. 1–12. Hoboken, NJ: John Wiley & Sons.

7. Goldup A, Ohki S, Danielli JF. 1970 Black lipid films. In Recent progress in surface science, vol. 3 (eds JF Danielli, AC Riddiford, MD Rosenberg), pp. 193–260. New York, NY: Academic Press.

8. Castellana ET, Cremer PS. 2006 Solid supported lipid bilayers: from biophysical studies to sensor design. Surf. Sci. Rep. 61, 429–444. (doi:10.1016/j.surfrep.2006.06.001)

9. Hafez IM, Ansell S, Cullis PR. 2000 Tunable pH-sensitive liposomes composed of mixtures of cationic and anionic lipids. Biophys. J. 79, 1438–1446. (doi:10.1016/S0006-3495(00)76395-8)

10. Ryzhkov NV, Mamchik NA, Skorb EV. 2019 Electrochemical triggering of lipid bilayer lift-off oscillation at the electrode interface. J. R. Soc. Interface 16, 20180626. (doi:10.1098/rsif.2018.0626)

11. Singh S, Junghans A, Tian J, Dubey M, Gnanakaran S, Chlistunoff J, Majewski J. 2013 Polyelectrolyte multilayers as a platform for pH-responsive lipid bilayers. Soft Matter 9, 8938–8948. (doi:10.1039/c3sm51651b)

12. Majewski J, Wong JY, Park CK, Seitz M, Israelachvili JN, Smith GS. 1998 Structural studies of polymer-cushioned lipid bilayers. Biophys. J. 75, 2363–2367. (doi:10.1016/S0006-3495(98)77680-5)

13. Wong JY, Majewski J, Seitz M, Park CK, Israelachvili JN, Smith GS. 1999 Polymer-cushioned bilayers. I. A structural study of various preparation methods using neutron reflectometry. Biophys. J. 77, 1445–1457. (doi:10.1016/S0006-3495(99)76992-4)

14. Dochter A, Garnier T, Pardieu E, Chau NTT, Maerten C, Senger B, Schaaf P, Jierry L, Boulmedais F. 2015 Film self-assembly of oppositely charged macromolecules triggered by electrochemistry through a morphogenic approach. Langmuir 31, 10 208–10 214. (doi:10.1021/acs.langmuir.5b02749)

15. Garnier T, Dochter A, Chau NTT, Schaaf P, Jierry L, Boulmedais F. 2015 Surface confined self-assembly of polyampholytes generated from charge-shifting polymers. Chem. Commun. 51, 14 092–14 095. (doi:10.1039/C5CC04477D)

16. Rodon Fores J et al. 2017 Localized supramolecular peptide self-assembly directed by enzyme-induced proton gradients. Angew. Chem. Int. Ed. 56, 15 984–15 988. (doi:10.1002/anie.201709029)

17. Maltanava HM, Poznyak SK, Andreeva DV, Quevedo MC, Bastos AC, Tedim J, Ferreira MGS, Skorb EV. 2017 Light-induced proton pumping with a semiconductor: vision for photoproton lateral separation and robust manipulation. ACS Appl. Mater. Interfaces 9, 24 282–24 289. (doi:10.1021/acsami.7b05209)

18. Macak JM, Zlamal M, Krysa J, Schmuki P. 2007 Self-organized TiO2 nanotube layers as highly efficient photocatalysts. Small 3, 300–304. (doi:10.1002/smll.200600426)

19. Andreeva DV, Melnyk I, Baidukova O, Skorb EV. 2016 Local pH gradient initiated by light on TiO$_2$ for light-triggered modulation of polyhistidine-tagged proteins. ChemElectroChem. 3, 1306–1310. (doi:10.1002/celc.201600268)

20. Ulasevich SA, Brezhneva N, Zhukova Y, Möhwald H, Fratzl P, Schacher FH, Sviridov DV, Andreeva DV, Skorb EV. 2016 Switching the stiffness of polyelectrolyte assembly by light to control behavior of supported cells. Macromol. Biosci. 16, 1422–1431. (doi:10.1002/mabi.201600127)

21. Ulasevich SA, Brezesinski G, Möhwald H, Fratzl P, Schacher FH, Poznyak SK, Andreeva DV, Skorb EV. 2016 Light-induced water splitting causes high-amplitude oscillation of pH-sensitive layer-by-layer assemblies on TiO$_2$. Angew. Chem. Int. Ed. 55, 13 001–13 004. (doi:10.1002/anie.201604359)

22. Ryzhkov NV, Brezhneva N, Skorb EV. 2019 Feedback mechanisms at inorganic–polyelectrolyte interfaces for applied materials. Surf. Innov. 7, 145–167. (doi:10.1680/jsuin.19.00006)

23. Wen C, Wan M, Li X, He Q, Gaoand L, Fang W. 2017 Formation mechanism and properties of polyelectrolyte multilayer-supported lipid bilayers: a coarse-grained molecular dynamics study. ACS Omega 2, 910–917. (doi:10.1021/acsomega.7b00198)

24. Shao J, Wen C, Xuan M, Zhang H, Frueh J, Wan M, Gao L, He Q. 2017 Polyelectrolyte multilayer-cushioned fluid lipid bilayers: a parachute model. Phys. Chem. Chem. Phys. 19, 2008–2016. (doi:10.1039/C6CP06787E)

25. Diamanti E, Gregurec D, Romero G, Cuellar JL, Donath E, Moya SE. 2016 Lipid layers on polyelectrolyte multilayers: understanding lipid–polyelectrolyte interactions and applications on the surface engineering of nanomaterials. J. Nanosci. Nanotechnol. 16, 5696–5700. (doi:10.1166/jnn.2016.11752)

26. Richardson JJ, Björnmalm M, Caruso F. 2015 Technology-driven layer-by-layer assembly of nanofilms. Science 348, aaa2491. (doi:10.1126/science.aaa2491)

27. Diamanti E, Gregurec D, Rodríguez-Presa MJ, Gervasi CA, Azzaroni O, Moya SE. 2016 High resistivity lipid bilayers assembled on polyelectrolyte multilayer cushions: an impedance study. Langmuir 32, 6263–6271. (doi:10.1021/acs.langmuir.6b01191)

28. Steinem C, Janshoff A, Ulrich WP, Sieberand M, Galla HJ. 1996 Impedance analysis of supported lipid bilayer membranes: a scrutiny of different preparation techniques. *Biochim. Biophys. Acta.* **1279**, 169–180. (doi:10.1016/0005-2736(95)00274-X)

29. Wiegand G, Arribas-Layton N, Hillebrandt H, Sackmann E, Wagner P. 2002 Electrical properties of supported lipid bilayer membranes. *J. Phys. Chem. B* **106**, 4245–4254. (doi:10.1021/jp014337e)

30. Orth RN, Kameoka J, Zipfel WR, Ilic B, Webb WW, Clark TG, Craighead HG. 2003 Creating biological membranes on the micron scale: forming patterned lipid bilayers using a polymer lift-off technique. *Biophys. J.* **85**, 3066–3073. (doi:10.1016/S0006-3495(03)74725-0)

31. Purrucker O, Hillebrandt H, Adlkofer K, Tanaka M. 2001 Deposition of highly resistive lipid bilayer on silicon–silicon dioxide electrode and incorporation of gramicidin studied by AC impedance spectroscopy. *Electrochim. Acta* **47**, 791–798. (doi:10.1016/S0013-4686(01)00759-9)

32. Yang TH, Yee CK, Amweg ML, Singh S, Kendall EL, Dattelbaum AM, Shreve AP, Brinker CJ, Parikh AN. 2007 Optical detection of ion-channel-induced proton transport in supported phospholipid bilayers. *Nano Lett.* **7**, 2446–2451. (doi:10.1021/nl071184j)

33. Ding Y, Wang J, Xu GK, Wang GF. 2018 Are elastic moduli of biological cells depth dependent or not? Another explanation using a contact mechanics model with surface tension. *Soft Matter* **14**, 7534–7541. (doi:10.1039/C8SM01216D)

34. Ding Y, Xu GK, Wang GF. 2017 On the determination of elastic moduli of cells by AFM based indentation. *Sci. Rep.* **7**, 45575. (doi:10.1038/srep45575)

35. Bruhn DS, Lomholtand MA, Khandelia H. 2016 Quantifying the relationship between curvature and electric potential in lipid bilayers. *J. Phys. Chem. B* **120**, 4812–4817. (doi:10.1021/acs.jpcb.6b03439)

36. Gwon K, Kim M, Tae G. 2014 A biocompatible method of controlled retrieval of cell-encapsulating microgels from a culture plate. *Integr. Biol.* **6**, 596–602. (doi:10.1039/c4ib00006d)

37. Chassepot A *et al.* 2012 Chemically detachable polyelectrolyte multilayer platform for cell sheet engineering. *Chem. Mater.* **24**, 930–937. (doi:10.1021/cm2024982)

38. Schönherr H, Johnson JM, Lenz P, Frank CW, Boxer SG. 2004 Vesicle adsorption and lipid bilayer formation on glass studied by atomic force microscopy. *Langmuir* **20**, 11 600–11 606. (doi:10.1021/la049302v)

39. Mayer LD, Hope MJ, Cullis PR. 1986 Vesicles of variable sizes produced by a rapid extrusion procedure. *Biochim. Biophys. Acta Biomembr.* **858**, 161–168. (doi:10.1016/0005-2736(86)90302-0)

40. Barenholz Y, Gibbes D, Litman BJ, Goil J, Thompson TE, Carlson FD. 1977 A simple method for the preparation of homogeneous phospholipid vesicles. *Biochemistry* **16**, 2806–2810. (doi:10.1021/bi00631a035)

41. Choo N-J, Hwang LY, Solandt JJR, Frank CW. 2013 Comparison of extruded and sonicated vesicles for planar bilayer self-assembly. *Materials* **6**, 3294–3308. (doi:10.3390/ma6083294)

42. Scholfield CR. 1981 Composition of soybean lecithin. *J. Am. Oil. Chem. Soc.* **58**, 889–892. (doi:10.1007/BF02659652)

43. Dijkstra AJ, Segers JC. 2007 Production and refining of oils and fats. In *The lipid handbook* (eds FD Gunstone, JL Harwood, AJ Dijkstra), pp. 178–180, 3rd edn, ch. 3. Boca Raton, FL: CRC Press.

44. Skorb EV, Moehwald H, Andreeva DV. 2017 How can one controllably use of natural δph in polyelectrolyte multilayers?. *Adv. Mater. Interfaces* **4**, 1600282; 1–15. (doi:10.1002/admi.201600282)

45. Brezhneva N, Nikitina A, Ryzhkov N, Klestova A, Vinogradov AV, Skorb EV. 2019 Importance of buffering nanolayer position in layer-by-layer assembly on titania based hybrid photoactivity. *J. Sol-gel Sci. Technol.* **89**, 92–100. (doi:10.1007/s10971-018-4728-5)

46. Ghita M, Arrigan DWM. 2004 Electrochemical overoxidation of polyindole and its cation-permselective behavior. *Electroanalysis* **16**, 979–987. (doi:10.1002/elan.200302938)

47. Moriss CA, Chen C-C, Baker LA. 2012 Transport of redox probes through single pores measured by scanning electrochemical-scanning ion conductance microscopy (SECM-SICM). *Analyst* **137**, 2933–2938. (doi:10.1039/c2an16178h)

Humidity-Driven Transparent Holographic Free-Standing Polyelectrolyte Films

Konstantin G. Nikolaev, Sviatlana A. Ulasevich, Olga Luneva, Olga Yu. Orlova, Daria Vasileva, Semen Vasilev, Alexander S. Novikov, and Ekaterina V. Skorb*

Cite This: *ACS Appl. Polym. Mater.* 2020, 2, 105−112

Read Online

ACCESS | Metrics & More | Article Recommendations | Supporting Information

ABSTRACT: In the present work, transparent holographic poly(diallyldimethylammonium chloride) (PDADMAC)/heparin and PDADMAC/poly(styrenesulfonate) (PSS) films were synthesized via polyelectrolyte coacervates. PDADMAC/heparin films were obtained without temperature treatment. Thin holographic free-standing films with a 1 μm grating period and uniform surface of a polyelectrolyte complex were readily and quickly made by pressing polyelectrolyte coacervate, the hydrated viscoelastic fluid-like form of polyelectrolyte complex precursor, between a flat surface and holographic mask. Heparin replaces PSS in film composition to prepare the sheer film. Thus, the PDADMAC/heparin holographic film demonstrates transparency and reversible response for humidity under diffraction detection. In addition to diffraction humidity signal measurements, the cobalt(II) chloride was impregnated in polyelectrolyte coacervate to make an additional colorimetric signal response. In this case, the free-standing film serves both as the substrate for the hygroscopic salt and as a diffraction humidity sensor. The PDADMAC/heparin/Co(II) chloride film demonstrates a linear humidity range from 50 to 90%. Additionally, due to hydrated inorganic salt ion size, cobalt chloride prevents film porosity, which initiates under film swelling. Based on the results and calculations obtained, the study proposes the mechanism of water incorporation, including the reptation model and polyelectrolyte complex behavior. Results of density functional theory calculations prove that binding of cobalt aqua complexes $[Co(H_2O)_6]^{2+}$ with the dimeric associates heparin/PDADMAC via noncovalent interactions (hydrogen bonds) additionally is much more energetically favorable compared with the alternative association of heparin/PDADMAC with water molecules.

KEYWORDS: polyelectrolytes, swelling, hygroscope, holographic film, humidity sensor

INTRODUCTION

Polyelectrolyte complexation and coacervation products have been paid much attention in the last few decades[1−3] due to their properties as they are readily produced, environmentally friendly, and their synthesis corresponds to several principles of "green chemistry" (i.e., they do not require organic solvents).[4−9] These complexes can serve as a drug delivery system for enzymes and DNA because such molecules can readily be incorporated into polyelectrolyte (PE) complexes.[10] These PE complexes can be also applied for membrane production,[11] biosensor construction,[6,12] enzyme immobilization, and microcapsules preparation.[13−15] There are three classes of materials: coacervates, soluble complexes, and nonequilibrium complexes.[16] Oppositely charged polyelectrolytes in aqueous solutions could form a liquid polymer phase, which is frequently named the complex coacervate, and a polymer-poor state.[17−19] Such complexes can form free-standing films.[20] Currently, there is a growing practical interest in free-standing polyelectrolyte films because of their ubiquitousness in terms of properties and application. Mixing of neutral polymers is controlled with proper forces between them and by their entropy of blending. The entropy value,

more sluggish for polymers than for small molecules, is unlikely to be overcome even with a predilection for polymers to associate with themselves. However, when aqueous solutions of polyelectrolytes with repeatable charged units are blended, the significant amount of entropy decrease of the counterion (and water) leads to polyelectrolyte complexation with molecular-level blending, which is constant and expected for a wide range of polyelectrolytes.[21] Such a process is time, temperature, and salt concentration dependent.[22−24] In addition to the experimental results, here we made thermodynamic calculations for the hydration processes and presence of cobalt complex in free-standing film.

The mildness of these complexes grows with increasing salt concentration and temperature. These advantages allow the complexation process to occur at room temperature. Most of the synthetic PEs demonstrate stoichiometric complexation.

There are many proposed mechanisms of complexation based on the characteristics of the ion groups, molecular weights, and external conditions of the reaction.[18,24−29] The complexation process is characterized with the clearest dependence on the molecular weight and dissociation force. At this stage, polyelectrolytes are poorly coupled and well-hydrated and demonstrate fluid-like behavior. Therefore, PE coacervate freely make PE complexes. The poly(diallyldimethyl-ammonium chloride) (PDADMAC)/poly(styrenesulfonate) (PSS) polyelectrolyte couple demonstrates PE coacervate behavior.

Nevertheless, such a polyelectrolyte couple has a limitation due to the reduction of the ionic cross-linking between chains in adjacent layers associated with the transition between intrinsic to extrinsic compensation to the interaction polyelectrolyte.[30] We propose replacement of one of them for the weak polyelectrolyte to avoid rigidity. Additionally, the application of polymer free-standing film demands the incorporation of metal complexes and structures.[6,31−37]

In the present work, we suggest forming PDADMAC/PSS, PDADMAC/heparin, and PDADMAC/heparin/CoCl$_2$ PE free-standing films to demonstrate properties of PE coacervates for the formation a unique holographic architecture based on thermodynamic calculations.

■ RESULTS AND DISCUSSION

The method of polyelectrolyte complex via PE coacervate formation is appropriate for fast free-standing film preparation. Holographic free-standing polyelectrolyte films were produced from a mix of oppositely charged PE solutions, as described by Kelly et al.[17] for the PDADMAC/PSS free-standing film. These PEs can form coacervate complexes with one or more oppositely charged ions, forming PE complexes as a consequence of strong electrostatic (Coulomb's) interactions and hydrogen bonding. Thus, after mixture of PDADMAC and PSS solutions, which are oppositely charged, secondary binding forces such as Coulomb interactions occur immediately. This is the first step of PE complex mechanism formation. This stage of the reaction is very rapid. The second step involves the formation of hydrogen bonds and the correction of the distortions of the polymer chains to define new conformation of the polymer chains. The third step includes the aggregation of secondary complexes, mainly through hydrophobic interactions and PE coacervate formation. The properties of PE complexes obtained depend on numerous factors, in particular ionic strength and stoichiometry. PE complexes form together with ion-pairing interactions, Pol$^+$Pol$^-$, between oppositely charged units on macromolecules. The ionic strength of the polyelectrolytes has a significant impact on the final size of the PE complexes. The removal of complexed ion pairs causes the critical salt concentration for coacervation. An increase in ionic strength induces a decrease in the average diameter of the blobs, which could be related to the increase in chain flexibility. The following equation applies: Pol$^+$Cl$^-$·xH$_2$O + Pol$^-$Na$^+$·yH$_2$O → Pol Pol·iH$_2$O + Na$^+$ + Cl$^-$ + zH$_2$O.

The as-prepared white precipitate of PDADMAC/PSS was washed with water. Then, the PE complex PDADMAC/PSS needed to dissolve in water and dry at 50 °C in the oven (Figure S1). Then, the PDADMAC/PSS complex was dissolved in KBr to form a gel.[38] The interaction in solutions between electrostatically complementary polyelectrolytes with high charge density on the circuits leads to the formation of PE

complexes capable of a 1:1 ratio of oppositely charged groups being released from the solution in the form of relatively little solvated precipitates, called stoichiometric PE complexes. They are insoluble in any of the known solvents and capable of swelling to a limited extent in water.[29] After coacervation, the system was divided into two liquid phases, one of which was enriched with macromolecular components and called coacervate. The second phase was an almost pure dispersion medium, called an equilibrium fluid. A coacervate, along with an equilibrium liquid, is called a coacervate system. Coacervate complexes are very sensitive to the presence of extraneous electrolytes. The ability of low molecular weight salts to destroy coacervate complexes is due to the shielding effect of small ions, and the electrolyte efficiency is more due to the charge of the cation or anion. The precipitate was added in the potassium bromide solution to dissolve it and form a coacervate. The coacervate gel was placed between two glass slides and dried in this position overnight at ambient temperature. One of the glass slides was covered by the holographic template to form a holographic pattern. The holographic film prepared (Figure S2) had low transparency because of melted polyelectrolyte complex with high hydrophobicity. Such an effect is aligned with PSS molecular structure. Under charge compensation inside strong PEs, the PE complexes, and the aromatic part of PSS, there is high hydrophobicity, and therefore, PE complexes swelled and formed an opaque film. Such an effect prevents applying the PE complexes as free-standing "green" holographic films and in other optical devices.[35,39]

Heparin is a strong polyelectrolyte and has the same sulfonic group as PSS. Heparin was used instead of PSS to form PE complexes in an equimolar ratio. The relation charge density to the molecular weight for heparin is smaller than that for PSS, and it could influence the coacervation process.[40] Therefore, we set the equimolar ratio. The PDADMAC/heparin film required modification of the original methodology because the heating limitation is over 40 °C. The white precipitate formed after mixing PDADMAC and heparin was decanted and washed with deionized water. Then, the PDADMAC/heparin precipitate was dissolved in deionized water. A holographic template was placed on the bottom of the Petri dish, into which coacervate was poured. This system was dried under vacuum overnight at ambient temperature (Figure 1). As a result, the transparent holographic film was prepared (Figure
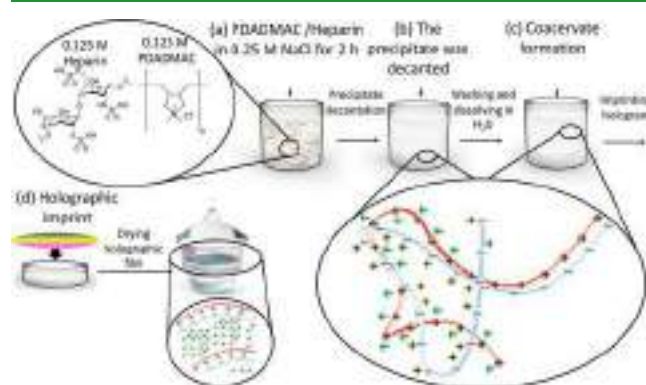
Figure 1. Scheme of PDADMAC/heparin free-standing holographic film synthesis through the precipitate formation stage (a), decantation process (b), coacervate formation (c), and holographic imprint technique (d).
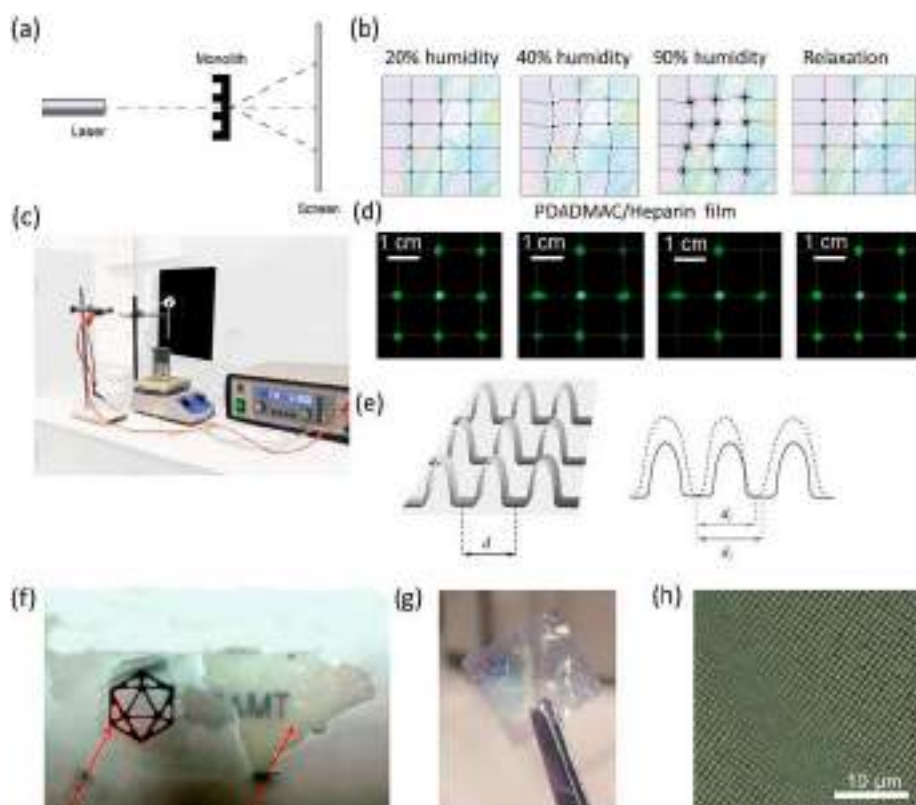
Figure 2. Diffraction humidity test measurement setup (a–e): common scheme of holographic film geometric parameter measurement (a, c), proposed changes in grating period (b, e), and spot size changes during humidity measurements from 20 to 90% and after relaxation (d). PDADMAC/heparin (left) and PDADMAC/PSS (right) synthesized films (f). PDADMAC/heparin free-standing holographic film photo (g) and optical microscope image (h).

2). Atomic force microscopy (AFM) and scanning electron microscopy (SEM) images showed that the structured film has a high reproducibility of a grating period (Figure 3). For the
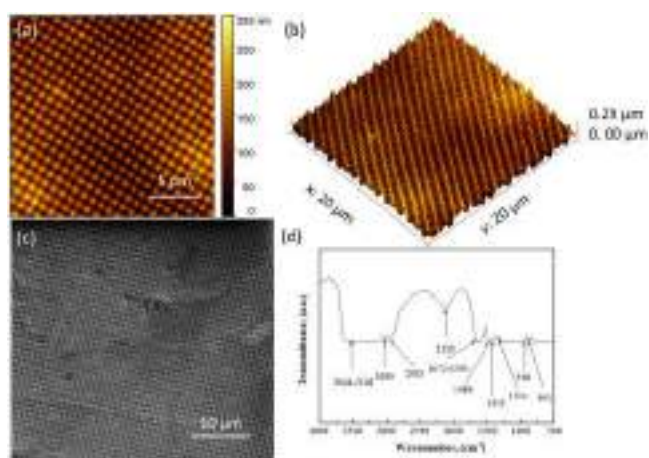
Figure 3. PDADMAC/heparin holographic film AFM images (a, b), SEM image (c), and FTIR spectrum (d).

proof of PE complex formation, the Fourier transform infrared (FTIR) spectra are shown in Figure 3. The molecular structure of the PDADMAC/heparin complex has characteristic peaks of $-OH$ at 3648–3102 and 3030 cm^{-1}. The asymmetric stretching peak at 2929 cm^{-1}, $-CH_n-$, and symmetrical C–H bending vibration at 1480 cm^{-1} correspond to the characteristic bands of PDADMAC. The characteristic peaks

at 1654–1594 cm^{-1} are related to the stretching vibration of NR_4 and $C(CH_3)_2^+$ of PDADMAC. The peaks at 1413 and 1334 cm^{-1} indicate the carboxylate groups of heparin. The presence of these radicals, asymmetric stretching peak at $-CH_n-$, symmetrical bending vibration at C–H, the stretching vibration of NR_4 and $C(CH_3)_2^+$ of PDADMAC, and the carboxylate group peaks of heparin confirm the composition of the PDADMAC/heparin complex. The FTIR spectrum, which is shown in Figure S3, corresponds to the PDADMAC/PSS complex. The characteristic peaks of $-OH$ are 3543–3273 and 3031 cm^{-1}. The characteristic peak at 1641 cm^{-1} is related to the stretching vibration of $-NR_4$ and $-C(CH_3)$ of PDADMAC. Appearing at asymmetric vibrations at 1198 cm^{-1} and symmetric vibrations at 1021 cm^{-1}, the characteristic PSS peaks confirm the sulfonic group.. Out-of-plane deformation vibration of $=C-H$ has signals at 836, 686, and 621 cm^{-1}. The characteristic PDADMAC peaks are symmetrical $-CH_n-$ (2927 cm^{-1}) and symmetrical C–H bending vibration (1467 cm^{-1}). The stretching vibration of NR_4 and $C(CH_3)$ of PDADMAC are also seen. The characteristic peaks of the sulfonic group, out-of-plane deformation vibration of $=C-H$ of PSS, symmetrical peaks of $-CH_n-$ (2927 cm^{-1}), and the symmetrical C–H bending vibration (1467 cm^{-1}) of PDADMAC confirm that the polyelectrolyte complex consists of bonded PDADMAC and PSS.

The ordered structure depending on humidity and the degree of exposure can change its conformation. The film structure changes as soon as the humidity value changes. A blur of the holographic pattern can be used as a sensor of

humidity (Figure 2a and Figure 2c). It is possible to use a blur of the holographic pattern as the sensor of humidity. The test with laser beam diffraction was conducted. The results from pictures of the screen are represented in Figure 2. As the holographic polyelectrolyte films were placed in conditions of changing humidity, they absorbed water molecules, which caused the geometry change of diffraction grating. Before humidity influence on the sample, the diffraction pattern shows a uniform deviation of the laser points from the direction of the main beam. The diffraction pattern of the PDADMAC/heparin holographic film shows eight points. The homogeneity of the holographic pattern and the absence of defects confirm that under laser diffraction the deviation of points occur in the same direction. Figure 2d shows the state of the diffraction pattern of exposure to 20% moisture. After exposure to 40% humidity, four points became less bright, and four points blurred (Figure 2d). Because the polyelectrolyte film was shrinking due to changes in humidity, points at horizontal and vertical directions became partially blurred and deviated (Figure 2b). Figure 2d also demonstrates the picture of diffraction after 90% humidity treatment. It is seen that dots of horizontal and vertical deviations became blurred spots. In the absence of moisture, the film takes its original form, and the diffraction pattern is similar to the diffraction pattern of the first type before exposure to moisture. The diffraction pattern (Figure 2d) confirms the reversibility of the system. According to the data presented, we can conclude that the PDADMAC/heparin holographic film is more stable than the PDADMAC/PSS holographic film (Figure S3). The change in the diffraction pattern of the film of the first type is slower than that of the film of the second type.

We measured the grating period from the AFM image for PDADMAC/PSS holographic film and SEM image for PDADMAC/heparin holographic film (Table 1). Based on

Table 1. Theoretical Calculation of Spot Size for PDADMAC/PSS Holographic Film and PDADMAC/Heparin Holographic Film Based on the Grating Period

type of film	grating period (d, μm)	spot size (y, cm)
PDADMAC/PSS	1.33 ± 0.04	0.204 ± 0.005
PDADMAC/heparin	1.01 ± 0.02	0.260 ± 0.005

small-angle approximation using eq 1, the spot sizes (Table 1) were calculated.

$$y \approx \frac{m\lambda D}{d} \qquad (1)$$

where y is the spot size, λ is the laser wavelength, m is the order, D is the distance to screen, and d is the grating period. We measured the spot size for each state of the polyelectrolyte structure with a change in humidity with using the program for PDADMAC/PSS holographic film and PDADMAC/heparin holographic film. From eq 1, the grating period was calculated according to the spot size changing (Tables 2 and 3). From Tables 1 and 2, it can be seen that the grating period before exposure to humidity and the grating period during relaxation at ambient temperature have the same value, which undermines the system's reversibility. These data confirm that our system is reversible and suitable for holographic film application.

The CoCl$_2$ aquacomplex was added to the PE complex structure to demonstrate compatibility with holographic film

Table 2. Grating Period Changes at Varying Humidity Level for PDADMAC/PSS Holographic Film

humidity (%)	spot size (y, cm)	grating period (d, μm)
20	0.204 ± 0.004	1.30 ± 0.02
40	0.224 ± 0.002	1.18 ± 0.01
90	0.264 ± 0.002	1.00 ± 0.01
relaxation (20)	0.204 ± 0.005	1.30 ± 0.03

Table 3. Grating Period Changes at Varying Humidity Level for PDADMAC/Heparin Holographic Film

humidity (%)	spot size (y, cm)	grating period (d, μm)
20	0.226 ± 0.003	1.18 ± 0.02
40	0.326 ± 0.003	0.82 ± 0.01
90	0.399 ± 0.002	0.670 ± 0.003
relaxation (20)	0.226 ± 0.004	1.18 ± 0.02

admixtures and enhance humidity response. The transition metal complex salts are widely used in polymer films due to their optical activity. The concentration of chloride ions from cobalt salt is taken into account to save the ionic strength during the PE complex formation. The cobalt ion has no effect on the coacervation process due to aquacomplex Co(H$_2$O)$_6$$^{2+}$ formation, which prevents interaction of the cobalt ion with polyelectrolyte following the Hofmeister range.[41] The PDADMAC/heparin/CoCl$_2$ film also demonstrates transparency because the complex salt has no dissociation in the PE complex. The PDADMAC/heparin/CoCl$_2$ film demonstrates an additional optical humidity response. The advantage of such a modification is prevention of porosity film formation. This effect can be explained by the hygroscopic property of cobalt chloride salt. In contrast with free-standing polyelectrolyte films with sodium chloride and other alkali metals,[31] where under film swelling porosity arises, the film with cobalt chloride is not porous, as under film swelling water is mainly incorporated in a metal complex. The water bonded with the metal complex has an ionic radius higher than that of alkali metal ions, which prevents porosity (Figure S4). To evaluate the thermodynamic favorability for the formation of various supramolecular associates in the chemical systems under study, we performed quantum chemical calculations using density functional theory (DFT) (for details, see the Computational Details section and Supporting Information, Tables S4 and S5). The results of our quantum chemical calculations reveal that (i) self-assembly of PDADMAC and heparin to dimeric associates heparin/PDADMAC is thermodynamically profitable (by 43.7 kcal/mol in terms of Gibbs free energies); (ii) binding of cobalt aquacomplexes [Co(H$_2$O)$_6$]$^{2+}$ with these dimeric associates heparin/PDADMAC via noncovalent interactions (hydrogen bonds) is much more energetically favorable compared with alternative association of heparin/PDADMAC with water molecules (as in the case of heparin/PDADMAC/[Co(H$_2$O)$_6$]$^{2+}$. We located the structure with two imaginary frequencies; from Table 4, it is obvious that the difference in ΔE, ΔH, and ΔG values in the cases of hypothetical transformations H$_2$O + heparin/PDADMAC→ heparin/PDADMAC···H$_2$O and [Co(H$_2$O)$_6$]$^{2+}$ + heparin/PDADMAC→ heparin/PDADMAC···[Co(H$_2$O)$_6$]$^{2+}$ is dramatic, and removal of small imaginary frequencies does not change the thermodynamics estimation qualitatively.

As humidity increases, cobalt chloride changes the color from blue to purple to pink.[42] Such striking changes in color

Table 4. Calculated Values of ΔE, ΔH, and ΔG (in kcal/mol)

transformation	ΔE	ΔH	ΔG
PDADMAC + heparin → heparin ···PDADMAC	−59.3	−57.9	−43.7
H_2O + heparin···PDADMAC → heparin ···PDADMAC···H_2O	−42.6	−41.2	−28.0
$[Co(H_2O)_6]^{2+}$ + heparin···PDADMAC→ heparin···PDADMAC···$[Co(H_2O)_6]^{2+}$	−120.8	−120.4	−103.4

make cobalt chloride useful as a humidity indicator in weather instruments.[43] Moreover, the mechanism of swelling for the transition metal complex salt with PE complexes is shown in Figures 4a−d. The metal complex allows the formation of
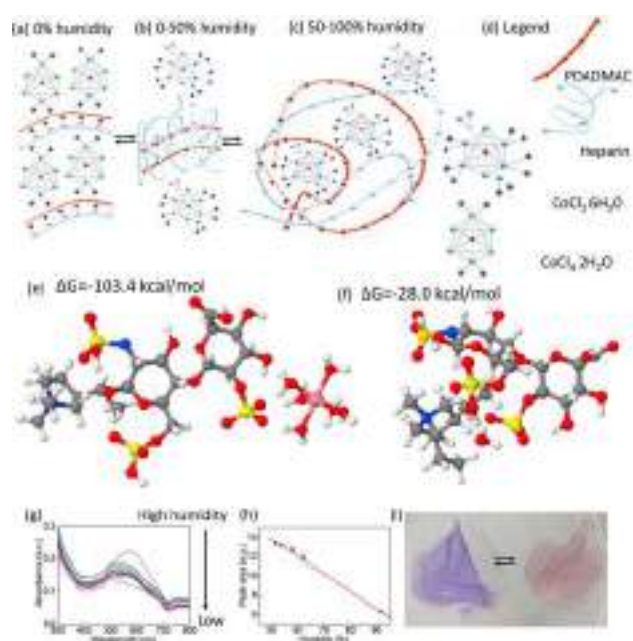
Figure 4. Proposed mechanism of PDADMAC/heparin/CoCl$_2$ film swelling during humidity measurements: from the dried film with salt crystals (a) to reptation model for the PE complex melt (b), blob formation at high humidity (c), and legend for schematics (d). Representation of optimized geometries for model structures formed of PDADMAC/heparin/Co(H$_2$O)$_6^{2+}$ (e) and PDADMAC/heparin with a water molecule (f). UV−vis spectra for the PDADMAC/heparin/CoCl$_2$ film at several humidity levels (g) and calibration curve for the peak area dependence on humidity (h). The optical image of PDADMAC/heparin/CoCl$_2$ film color transition depends on humidity (i).

polyelectrolyte melt at a dried state (Figure 4a) at a 20% room humidity level. This film corresponds to the polymer reptation model (Figure 4b), and with humidity increasing, the PDADMAC/heparin/CoCl$_2$ forms the blobs (Figure 4c). Such an advantage provides evidence for the reversibility of the free-standing holographic film proposed. Cobalt is a transition metal that is capable of forming a wide range of stable, colored metal complexes, most of them with an octahedral crystalline structure. The anhydrous, blue-colored cobalt(II) chloride changes the color in response to humidity, thus forming the hydrated, pink-colored hexaaquocobalt(II) ion. The reverse process can be obtained by dehydration in the oven. These phenomena can be explained by the d−d orbital electron transition of cobalt(II) and have been detected

through UV−vis absorption spectroscopy. The results make it evident that the anhydrous, blue-colored cobalt(II) complex shows three absorption bands in the visible spectral region of 500−700 nm. The hydration of the cobalt(II) compound is accompanied by a decrease of the absorption peaks, which can be observed at 660 nm. In the present study, this decrease was measured as a function of humidity (Figures 4e−g). Free-standing PDADMAC/heparin/CoCl$_2$ film data absorbance spectra were evaluated. The linear humidity dependence on the absorption peak area was demonstrated from 50 to 90%. Such a film can be reversibly dried and used multiple times for humidity measurements.

■ CONCLUSION

The research proposes the method for PDADMAC/heparin and PDADMAC/heparin/CoCl$_2$ holographic film with the reproducible grating period. Such an approach allows ready and quick preparation of a free-standing film via coacervation without temperature treatment. The method proposed can be used for the free-standing film preparation with specific geometry. Hydration processes were observed experimentally and simultaneously calculated with the DFT model. The results obtained prove the preliminary cobalt aquacomplex formation and its interaction with the polyelectrolyte complex. PDADMAC/heparin film demonstrates a humidity response sensing with relaxation. Cobalt(II) chloride as a dopant in polyelectrolyte coacervate adds the additional parameter for quantitative humidity sensing. Such a sensor allows measurement of humidity levels from 50 to 90%. The mechanism of PE complex swelling, including the reptation model and polyelectrolyte melt behavior, is proposed.

■ METHODS

Chemicals. Poly(diallyldimethylammonium chloride) (PDAD-MAC; molar mass 200 000−350 000 g mol^{-1}) and poly(4-styrenesulfonic acid, sodium salt) (PSS; molar mass 70 000 g mol^{-1}) were purchased from Sigma-Aldrich. Heparin (pharmacy, 5000 medical units) was bought from the pharmacy and was preliminarily concentrated. Sodium chloride (NaCl; purity ≥99.99%) and potassium bromide (KBr) were purchased from Merck. Cobalt(II) chloride (CoCl$_2$) was from LenReactiv. All salt solutions were prepared using Milli-Q (18.2 MΩ·cm). Holographic film (1000 grooves/mm) was from Edmund Optics.

Instruments. *Infrared Spectroscopy (IR).* IR spectra were performed using an FTIR spectrometer (FSM 1201, Infraspek, Russia). Spectra were recorded in a range of 500−4000 cm^{-1} at a scan rate of 50 cm^{-1}/min. A Memmert UF30 Plus oven was used.

UV−Vis Spectrophotometry. UV−vis spectrophotometry was used to characterize the optical properties of the PE films. Measurements were carried out using a two-beam scanning spectrophotometer with high-resolution (Spectrophotometer UV-1800, Shimadzu, Japan). UV−vis spectra were recorded in the range of 200−800 cm^{-1} at an average scan rate.

Atomic Force Microscopy (AFM). The surface topology of holographic PE films was measured using an atomic force microscope (Ntegra Prima, NT-MDT, Russia). A 20 × 20 μm, 10 × 10 μm, and 5 × 5 μm area was scanned to obtain sufficient patterns for reliable statistics. The measurements were conducted at room temperature (298 K) with a Ti/Pt coated tip.

Scanning Electron Microscopy (SEM). A Tescan Vega 3 scanning electron microscope with a classical tungsten thermocathode and XM object chamber (sample height of 145 mm and at 3−5 kV) was used to image the surface of PE complex films.

Green Laser. A 50 mW green laser pointer with a 532 nm wavelength was used to perform the laser diffraction test. The test was done in a dark room to better visualize the laser beam diffraction by

the holographic film. For this purpose, a holographic film with a thickness of 0.5 mm was produced. Both the green laser and holographic films were fixed at the same level, and the holographic plane of the material was situated perpendicularly to the direction of the laser beam. The rays outgoing from the film were depicted in the black sector, and the distance between the film and the picture was 5 cm. To observe hygroscopic properties of the holographic monolith, it was placed in a medium with several humidities, and photographs of the screen were taken at 10 s of treatment. Finally, the holographic film was dried in an oven and put in the installation again.

Free-Standing Film Holographic Architecture Fabrication. Polyelectrolyte free-standing films were prepared via PE complex formation by the simultaneous mixing of aqueous solutions of polycation and polyanion. The gel was placed between two glass slides and dried in this position overnight at ambient temperature. One of two glass slides was covered by the holographic template to form a holographic pattern.

Humidity Measurements. The laser diffraction test was performed in a dark room to ensure maximum visibility of the diffraction of the laser beam by a holographic monolith. The green laser was fixed at the same level as the holographic sample that was located perpendicular to the direction of laser radiation. The diffracted rays emanating from the monolith fell on a black screen. The distance between the sample and the screen was 5 cm. The holographic film was placed in an environment with 90% humidity to consider the hygroscopic properties of the monolith. Finally, the humidity was changed to the initial level, and the relaxation strain of the sample was observed. UV−vis humidity was measured by calculating the dependence of peak area and color from film susceptibility to moisture. The film was kept at an equal distance above heated water for 10, 30, and 60 s from 30 to 60°. After that, UV−vis spectra were obtained, and peak areas were calculated.

Computational Details. The full geometry optimization of all model structures was carried out at the DFT level of theory using the M06-2X functional (54% of Hartree−Fock exchange, recommended for the study of main group thermochemistry)[44] with the help of the Gaussian 09 program package.[45] Calculations were performed using the fully relativistic energy-consistent Stuttgart/Cologne pseudopotentials MDF10 that described ten core electrons and the appropriate contracted basis sets for the cobalt atoms[46] and the standard 6-31G* basis sets for all other atoms. No symmetry restrictions were applied during the geometry optimization procedure. The Hessian matrices were calculated analytically for all optimized model structures to prove the location of correct minima on the potential energy surface (no imaginary frequencies in all cases, except heparin/PDADMAC··· $[Co(H_2O)_6]^{2+}$) and to estimate the thermodynamic parameters, the latter being calculated at 25 °C. The Cartesian atomic coordinates for all optimized equilibrium model structures are presented in the Supporting Information, Table S6.

ASSOCIATED CONTENT

Ⓢ Supporting Information

The Supporting Information is available free of charge at https://pubs.acs.org/doi/10.1021/acsapm.9b01151.

Scheme of the preparation process, additional SEM and AFM images, thermodynamic calculation results, and XYZ coordinate molecule data (PDF)

Special Issue Paper

This paper is an additional article for *ACS Appl. Polym. Mater.* **2020**, *2*, issue 1, "Young Investigators Forum".

AUTHOR INFORMATION

Corresponding Author

Ekaterina V. Skorb − *ITMO University, St. Petersburg, Russian Federation;* ⓘ orcid.org/0000-0003-0888-1693; Email: skorb@itmo.ru

Other Authors

Konstantin G. Nikolaev − *ITMO University, St. Petersburg, Russian Federation*

Sviatlana A. Ulasevich − *ITMO University, St. Petersburg, Russian Federation*

Olga Luneva − *ITMO University, St. Petersburg, Russian Federation*

Olga Yu. Orlova − *ITMO University, St. Petersburg, Russian Federation*

Daria Vasileva − *Ural Federal University, Ekaterinburg, Russian Federation*

Semen Vasilev − *Ural Federal University, Ekaterinburg, Russian Federation, and University of Limerick, Limerick, Ireland;* ⓘ orcid.org/0000-0002-3103-1438

Alexander S. Novikov − *Saint Petersburg State University, Saint Petersburg, Russian Federation;* ⓘ orcid.org/0000-0001-9913-5324

Complete contact information is available at:
https://pubs.acs.org/10.1021/acsapm.9b01151

Notes

The authors declare no competing financial interest.

REFERENCES

(1) Guzmán, E.; Ruano, M.; Ortega, F.; Rubio, R. G. Stratified Interpolyelectrolyte Complexes: Fabrication, Structure and Properties. In *Polyelectrolytes: Thermodynamics and Rheology*; Visakh, P. M., Bayraktar, O., Picó, G. A., Eds.; Springer International Publishing: Cham, 2014; pp 299−347.

(2) Frueh, J.; Gai, M.; Halstead, S.; He, Q. Structure and Thermodynamics of Polyelectrolyte Complexes. In *Polyelectrolytes: Thermodynamics and Rheology*; Visakh, P. M., Bayraktar, O., Picó, G. A., Eds.; Springer International Publishing: Cham, 2014; pp 19−86.

(3) Dias, R. S.; Stokke, B. T. Polyelectrolyte Complexes. In *Polyelectrolytes: Thermodynamics and Rheology*; Visakh, P. M., Bayraktar, O., Picó, G. A., Eds.; Springer International Publishing: Cham, 2014; pp 275−298.

(4) Gucht, J. v. d.; Spruijt, E.; Lemmers, M.; Cohen Stuart, M. A. Polyelectrolyte complexes: Bulk phases and colloidal systems. *J. Colloid Interface Sci.* **2011**, *361* (2), 407−422.

(5) Tchoe, Y.; Chung, K.; Lee, K.; Jo, J.; Chung, K.; Hyun, J. K.; Kim, M.; Yi, G.-C. Free-standing and ultrathin inorganic light-emitting diode array. *NPG Asia Mater.* **2019**, *11* (1), 37.

(6) Xue, Q.; Wang, Q.; Han, Z.; Tang, N.; Zhou, C.; Pan, W.; Wang, Y.; Duan, X. Printed Highly Ordered Conductive Polymer Nanowires Doped with Biotinylated Polyelectrolytes for Biosensing Applications. *Adv. Mater. Interfaces* **2019**, *6* (18), 1900671.

(7) Gai, M.; Frueh, J.; Kudryavtseva, V. L.; Mao, R.; Kiryukhin, M. V.; Sukhorukov, G. B. Patterned Microstructure Fabrication: Polyelectrolyte Complexes vs Polyelectrolyte Multilayers. *Sci. Rep.* **2016**, *6*, 37000.

(8) Skorb, E. V.; Möhwald, H.; Andreeva, D. V. How Can One Controllably Use of Natural ΔpH in Polyelectrolyte Multilayers? *Adv. Mater. Interfaces* **2017**, *4* (1), 1600282.

(9) Fernández-Peña, L.; Guzmán, E.; Leonforte, F.; Serrano-Pueyo, A.; Regulski, K.; Tournier-Couturier, L.; Ortega, F.; Rubio, R. G.; Luengo, G. S. Effect of molecular structure of eco-friendly glycolipid biosurfactants on the adsorption of hair-care conditioning polymers. *Colloids Surf., B* **2020**, *185*, 110578.

(10) Meka, V. S.; Sing, M. K. G.; Pichika, M. R.; Nali, S. R.; Kolapalli, V. R. M.; Kesharwani, P. A comprehensive review on polyelectrolyte complexes. *Drug Discovery Today* **2017**, *22* (11), 1697−1706.

(11) Abdu, S.; Sricharoen, K.; Wong, J. E.; Muljadi, E. S.; Melin, T.; Wessling, M. Catalytic Polyelectrolyte Multilayers at the Bipolar Membrane Interface. *ACS Appl. Mater. Interfaces* **2013**, *5* (21), 10445−10455.

(12) Ermakov, S. S.; Nikolaev, K. G.; Tolstoy, V. P. Novel electrochemical sensors with electrodes based on multilayers fabricated by layer-by-layer synthesis and their analytical potential. *Russ. Chem. Rev.* **2016**, *85* (8), 880−900.

(13) Bourganis, V.; Karamanidou, T.; Kammona, O.; Kiparissides, C. Polyelectrolyte complexes as prospective carriers for the oral delivery of protein therapeutics. *Eur. J. Pharm. Biopharm.* **2017**, *111*, 44−60.

(14) Petrova, A. V.; Chernyakov, D. D.; Poshina, N. D.; Gofman, V. I.; Romanov, P. D.; Mishanin, I. A.; Golovkin, S. A.; Skorik, A. Y. Electrospun Bilayer Chitosan/Hyaluronan Material and Its Compatibility with Mesenchymal Stem Cells. *Materials* **2019**, *12* (12), 1−17.

(15) Argudo, P. G.; Guzman, E.; Lucia, A.; Rubio, R. G.; Ortega, F. Preparation and Application in Drug Storage and Delivery of Agarose Nanoparticles. *Int. J. Polym. Sci.* **2018**, *2018*, 1−9.

(16) Sing, C. E. Development of the modern theory of polymeric complex coacervation. *Adv. Colloid Interface Sci.* **2017**, *239*, 2−16.

(17) Kelly, K. D.; Schlenoff, J. B. Spin-Coated Polyelectrolyte Coacervate Films. *ACS Appl. Mater. Interfaces* **2015**, *7* (25), 13980−13986.

(18) Fares, H. M.; Schlenoff, J. B. Equilibrium Overcompensation in Polyelectrolyte Complexes. *Macromolecules* **2017**, *50* (10), 3968−3978.

(19) Kim, S.; Huang, J.; Lee, Y.; Dutta, S.; Yoo, H. Y.; Jung, Y. M.; Jho, Y.; Zeng, H.; Hwang, D. S. Complexation and coacervation of like-charged polyelectrolytes inspired by mussels. *Proc. Natl. Acad. Sci. U. S. A.* **2016**, *113* (7), E847.

(20) Delaney, K. T.; Fredrickson, G. H. Theory of polyelectrolyte complexation—Complex coacervates are self-coacervates. *J. Chem. Phys.* **2017**, *146* (22), 224902.

(21) Tirrell, M. Polyelectrolyte Complexes: Fluid or Solid? *ACS Cent. Sci.* **2018**, *4* (5), 532−533.

(22) Sing, C. E.; Zwanikken, J. W.; Olvera de la Cruz, M. Effect of Ion-Ion Correlations on Polyelectrolyte Gel Collapse and Reentrant Swelling. *Macromolecules* **2013**, *46* (12), 5053−5065.

(23) Fu, J.; Fares, H. M.; Schlenoff, J. B. Ion-Pairing Strength in Polyelectrolyte Complexes. *Macromolecules* **2017**, *50* (3), 1066−1074.

(24) Chremos, A.; Douglas, F. J. The Influence of Polymer and Ion Solvation on the Conformational Properties of Flexible Polyelectrolytes. *Gels* **2018**, *4* (1), 1−16.

(25) Fares, H. M.; Schlenoff, J. B. Diffusion of Sites versus Polymers in Polyelectrolyte Complexes and Multilayers. *J. Am. Chem. Soc.* **2017**, *139* (41), 14656−14667.

(26) Liu, Y.; Momani, B.; Winter, H. H.; Perry, S. L. Rheological characterization of liquid-to-solid transitions in bulk polyelectrolyte complexes. *Soft Matter* **2017**, *13* (40), 7332−7340.

(27) Ghoussoub, Y. E.; Zerball, M.; Fares, H. M.; Ankner, J. F.; von Klitzing, R.; Schlenoff, J. B. Ion distribution in dry polyelectrolyte multilayers: a neutron reflectometry study. *Soft Matter* **2018**, *14* (9), 1699−1708.

(28) Reurink, D. M.; Haven, J. P.; Achterhuis, I.; Lindhoud, S.; Roesink, H. D. W.; de Vos, W. M. Annealing of Polyelectrolyte Multilayers for Control over Ion Permeation. *Adv. Mater. Interfaces* **2018**, *5* (20), 1800651.

(29) Fares, H. M.; Wang, Q.; Yang, M.; Schlenoff, J. B. Swelling and Inflation in Polyelectrolyte Complexes. *Macromolecules* **2019**, *52* (2), 610−619.

(30) Guzmán, E.; Maestro, A.; Llamas, S.; Álvarez-Rodríguez, J.; Ortega, F.; Maroto-Valiente, A.; Rubio, R. G. 3D solid supported inter-polyelectrolyte complexes obtained by the alternate deposition of poly(diallyldimethylammonium chloride) and poly(sodium 4-styrenesulfonate). *Beilstein J. Nanotechnol.* **2016**, *7* (1), 197−208.

(31) Ghostine, R. A.; Shamoun, R. F.; Schlenoff, J. B. Doping and Diffusion in an Extruded Saloplastic Polyelectrolyte Complex. *Macromolecules* **2013**, *46* (10), 4089−4094.

(32) Yetisen, A. K.; Naydenova, I.; da Cruz Vasconcellos, F.; Blyth, J.; Lowe, C. R. Holographic Sensors: Three-Dimensional Analyte-Sensitive Nanostructures and Their Applications. *Chem. Rev.* **2014**, *114* (20), 10654−10696.

(33) Abhyankar, N.; Ghoussoub, Y. E.; Wang, Q.; Dalal, N. S.; Schlenoff, J. B. Ion Environments in Mn2+-Doped Polyelectrolyte Complexes: Dilute Magnetic Saloplastics. *J. Phys. Chem. B* **2016**, *120* (27), 6771−6777.

(34) Ryabchun, A.; Lancia, F.; Nguindjel, A.-D.; Katsonis, N. Humidity-responsive actuators from integrating liquid crystal networks in an orienting scaffold. *Soft Matter* **2017**, *13* (44), 8070−8075.

(35) Bang, K.; Jang, C.; Lee, B. Curved holographic optical elements and applications for curved see-through displays. *J. Inf. Disp.* **2019**, *20* (1), 9−23.

(36) Qin, S.; Xiang, S.; Eberle, B.; Xie, K.; Grunlan, J. C. High Moisture Barrier with Synergistic Combination of SiOx and Polyelectrolyte Nanolayers. *Adv. Mater. Interfaces* **2019**, *0* (0), 1900740.

(37) Yildirim, E.; Zhang, Y.; Lutkenhaus, J. L.; Sammalkorpi, M. Thermal Transitions in Polyelectrolyte Assemblies Occur via a Dehydration Mechanism. *ACS Macro Lett.* **2015**, *4* (9), 1017−1021.

(38) O'Neal, J. T.; Wilcox, K. G.; Zhang, Y.; George, I. M.; Lutkenhaus, J. L. Comparison of KBr and NaCl effects on the glass transition temperature of hydrated layer-by-layer assemblies. *J. Chem. Phys.* **2018**, *149* (16), 163317.

(39) Ahmed, R.; Butt, H. Diffractive Surface Patterns through Single-Shot Nanosecond-Pulsed Laser Ablation. *ACS Photonics* **2019**, *6* (7), 1572−1580.

(40) Noda, I.; Takahashi, Y. Viscoelastic properties of polyelectrolyte solutions. *Berichte der Bunsengesellschaft für physikalische Chemie* **1996**, *100* (6), 696−702.

(41) Salomäki, M.; Tervasmäki, P.; Areva, S.; Kankare, J. The Hofmeister Anion Effect and the Growth of Polyelectrolyte Multilayers. *Langmuir* **2004**, *20* (9), 3679−3683.

(42) Russell, A. P.; Fletcher, K. S. Optical sensor for the determination of moisture. *Anal. Chim. Acta* **1985**, *170*, 209−216.

(43) Otsuki, S.; Adachi, K. Humidity dependence of visible absorption spectrum of gelatin films containing cobalt chloride. *J. Appl. Polym. Sci.* **1993**, *48* (9), 1557−1564.

(44) Zhao, Y.; Truhlar, D. G. The M06 suite of density functionals for main group thermochemistry, thermochemical kinetics, non-covalent interactions, excited states, and transition elements: two new functionals and systematic testing of four M06-class functionals and 12 other functionals. *Theor. Chem. Acc.* **2008**, *120* (1), 215−241.

(45) Frisch, M. J.; Trucks, G. W.; Schlegel, H. B.; Scuseria, G. E.; Robb, M. A.; Cheeseman, J. R.; Scalmani, G.; Barone, V.; Mennucci, B.; Petersson, G. A.; Nakatsuji, H.; Caricato, M.; Li, X.; Hratchian, H. P.; Izmaylov, A. F.; Bloino, J.; Zheng, G.; Sonnenberg, J. L.; Hada, M.; Ehara, M.; Toyota, K.; Fukuda, R.; Hasegawa, J.; Ishida, M.; Nakajima, T.; Honda, Y.; Kitao, O.; Nakai, H.; Vreven, T.; Montgomery, Jr., J. A.; Peralta, J. E.; Ogliaro, F.; Bearpark, M.; Heyd, J. J.; Brothers, E.; Kudin, K. N.; Staroverov, V. N.; Keith, T.; Kobayashi, R.; Normand, J.; Raghavachari, K.; Rendell, A.; Burant, J. C.; Iyengar, S. S.; Tomasi, J.; Cossi, M.; Rega, N.; Millam, J. M.; Klene, M.; Knox, J. E.; Cross, J. B.; Bakken, V.; Adamo, C.; Jaramillo, J.; Gomperts, R.; Stratmann, R. E.; Yazyev, O.; Austin, A. J.; Cammi, R.; Pomelli, C.; Ochterski, J. W.; Martin, R. L.; Morokuma, K.; Zakrzewski, V. G.; Voth, G. A.; Salvador, P.; Dannenberg, J. J.; Dapprich, S.; Daniels, A. D.; Farkas, O.; Foresman, J. B.; Ortiz, J. V.; Cioslowski, J.; Fox, D. J. *Gaussian 09*, Revision C.01; Gaussian, Inc.: Wallingford, CT, 2010.

(46) Dolg, M.; Wedig, U.; Stoll, H.; Preuss, H. Energy-adjusted ab initio pseudopotentials for the first row transition elements. *J. Chem. Phys.* **1987**, *86* (2), 866−872.

ACS OMEGA

Article

ElectroSens Platform with a Polyelectrolyte-Based Carbon Fiber Sensor for Point-of-Care Analysis of Zn in Blood and Urine

Konstantin G. Nikolaev, Evgeniy V. Kalmykov, Daria O. Shavronskaya, Anna A. Nikitina, Anna A. Stekolshchikova, Ekaterina A. Kosareva, Artemiy A. Zenkin, Igor S. Pantiukhin, Olga Yu. Orlova, Anatoly V. Skalny, and Ekaterina V. Skorb*

Cite This: *ACS Omega* 2020, 5, 18987−18994

Read Online

| ACCESS | | 📊 Metrics & More | | 📰 Article Recommendations | | 🅢 Supporting Information |

ABSTRACT: In this paper, we describe an electrochemical sensing platform—ElectroSens—for the detection of Zn based on self-assembled polyelectrolyte multilayers on the carbon fiber (CF) electrode surface. The CF-extended surface facilitates the usage of a small volume electrochemical cell (1 mL) without stirring. This approach allows making a low-cost three-electrode platform. Working electrode modification with layer-by-layer assembly of polyethyleneimine (PEI), poly(sodium 4-styrenesulfonate) (PSS), and mercury nitrate layers eliminates solution toxicity and provides stable stripping voltammetry measurements. The stable, robust, sustainable, and even reusable Ag/AgCl reference electrode consists of adsorbed 32 PEI-KCl/PSS-KCl bilayers on the CF/silver paste separated from the outer solution by a polyvinyl chloride membrane. The polyelectrolyte-based sensor interface prevents adsorption of protein molecules from biological liquids on the CF surface that leads to a sensitivity increase of up to 2.2 μA/M for Zn^{2+} detection and provides a low limit of detection of 4.6×10^{-8} M. The linear range for Zn detection is 1×10^{-7} to 1×10^{-5} M. A portable potentiostat connected via wireless to a smartphone with an android-based software is also provided. The ElectroSens demonstrates reproducibility and repeatability of data for the detection of Zn in blood and urine without the digestion step.

INTRODUCTION

Deficiency of vitamins and minerals (trace elements) is a severe global health problem, partly because of logistical difficulties in assessing the state of trace elements in a population.[1] Zinc is an essential trace element (micronutrient) which plays an essential role in human physiology. Inorganic cofactors in biological systems, more precisely Zn(II) metal ions, are the most widespread in mechanisms of diverse functions of proteins and their complexes.[2] The pathological effects of zinc deficiency include the occurrence of skin lesions, growth retardation, impaired immune function, and impaired healing. In epidemiological situations, a quick assessment of the state of the human immune system is required. Determining the zinc content is more easy to carry out than an immune analysis because the cost of such a rapid test is lower. Such a rapid test will allow an assessment of the immune status in those cases when it is impossible to provide the population with the necessary test systems, for example, as in the case of COVID-19.[3]

Stripping voltammetry (SV) analysis is a powerful and straightforward tool for continuous monitoring of trace target metal species.[4−6] The determination of zinc in biological samples is usually carried out by the method of anodic SV (ASV). As working electrodes (WEs), carbon,[7] copper,[8,9] bismuth,[10] and glassy carbon modified with mercury salts are used. Despite the advantages of precipitating heavy metals in the

mercury amalgam, this method is rarely used because of the toxicity of mercury.[11] Electrodes are modified with mercury salts using polyelectrolytes (PEs) soluble in organic solvents, which not only lead to the high saturation of PEs with mercury ions but also lead to toxic waste, which does not comply with the principles of "green chemistry" and does not allow scaling such processes. Water-soluble PE assemblies[12−14] also have the ability to be saturated with oppositely charged ions[15] and are also able to hold them despite thermodynamic equilibrium. The use of water-soluble PEs as a method for immobilizing mercury salts on the surface of a WE will allow scaling the process of electrode modification.[16] Pulsed electroanalytical methods, such as differential-pulse ASV[11] and square-wave ASV (SWASV),[5,17] are used for reducing the noise-to-signal ratio and increasing the resolution of the anodic peaks.

For zinc detection by the method of ASV in biological fluids, various methods of sample preparation and signal acquisition are used. Deproteinization of samples by sodium ethylenediamine-

tetraacetate (EDTA) was proposed by Zakharchuk et al.[18] Such a method has the advantage of eliminating the matrix effect of biological molecules and breaking up zinc from complexes. The Metexchange solution (ESA Inc.), which is a mixture made up of chromium chloride (1.07 wt %), calcium acetate (1.43 wt %), and mercuric ions, was used for Zn detection by stripping it on the Bi electrode.[19] Screen-printed modified electrodes without sample preparation for the Zn SV detection in sweat[20] are demonstrated.

Carbon fiber (CF)[21,22] is an outstanding class of carbon materials, with carbon atoms bonded together into crystals that are aligned parallel to the long axis of the fiber. Aligning the crystals gives the fiber a high strength to volume ratio. Fibrous materials are widely used in the field of electrochemistry and composite materials because of their carrier mobility, electrical conductivity, environmental stability, excellent mechanical properties, low weight, and high-temperature resistance, as well as the possibility of production at low cost. Conductive fiber fabrics provide an excellent class of substrates for the development of wearable sensors,[23,24] as they will be in constant contact with the skin.[25,26]

We propose an electroanalytical platform—ElectroSens (Figure 1)—for zinc detection based on a CF electrode modified with water-soluble PEs [polyethyleneimine (PEI) and poly(sodium 4-styrenesulfonate) (PSS)] and mercury nitrate, as well as a cheap and stable Ag/AgCl reference electrode (RE) based on the CF and the adsorbed layers of PEs. Such a platform is prospective for a wide range of analyses (Figure S1); however, the biggest issues are robustness and sustainability as well as assay cost. Here, we solve all the issues.

■ RESULTS AND DISCUSSION

The electroanalytical system for SWASV Zn detection comprises a three CF electrode-based system, sample pretreatment kit, a potentiostat (Figure 1a), software for the smartphone (Figure 1b), and a cloud database (Figure 1c). The potentiostat sends the data to the smartphone by Bluetooth for data processing, and then data are collected in the MongoDB cloud database.

The electrochemical sensing platform is a three-electrode system connected to a minipotentiostat (Figure 2a,b) and a kit

Figure 1. Electrochemical platform for the Zn detection in blood and urine consists of an electrochemical sensing platform (a three CF electrode-based system, sample pretreatment kit, and a potentiostat) (a), software for the smartphone (b), and data storage cloud system (c) (see also Supporting Information for self-written software and video example of its application during analysis).

Figure 2. Electrochemical platform setup: an insulated CF WE, an RE, and a CE (a), connected to the minipotentiostat (b). Scheme of the WE (c) and RE (d) modification using LbL assembly of PEs.

for pretreatment. For the steady heavy metal deposition on the WE, mercury salts were used for the electrode modification.[27] At the deposition stage, mercury ions reduce to the metallic mercury and other heavy metal deposits form a solution in the amalgam. Because of the toxicity of mercury, the bismuth and copper WEs are used in modern sensors for heavy metal detection. Nevertheless, mercury-modified electrodes have advantages over these two metals. For example, copper and bismuth have a smaller working voltage window than mercury. Electroconductive polymers were used for electrode modification by mercury salts. A disadvantage of such a method is using organic solvents for the modifier preparation. We propose to use the water-soluble PEs for the electrode modification with mercury salts.[28] Modification with PE multilayers (Figure 2e)

for the mercury immobilization (Figure 2c) is applied for the WE. The CF surface has the ability to adsorb PEI and PSS because of the specific chemical or Van der Waals interactions.[29]

Mercury is able to form amino complexes with organic molecules. PEI was used as a complexing agent. PEI exhibits a high degree of surface affinity. As a counterion, a strong PSS PE was used. This allows the formation of a well-studied PEI/PSS complex.[30] The PEI/PSS complex facilitates the diffusion of heavy metal ions but at the same time prevents the protein surface from blocking the electrode surface, which causes the damping of the analytical signal.[31,32] The layer-by-layer (LbL) assembly method for the deposition of PEs is widely used in the fabrication of biosensors because of its ability to selectively hold and pass various ions through multilayers.[33] PE multilayers also have the potential to be used for the stable RE construction (Figure 2d). For reference electrode construction, PEI/PSS multilayers were placed between the CF/Ag paste/AgCl interface and the PVC membrane (Figure 2d). Potassium chloride addition into the PE layers leads to a pseudointernal solution.[16] PEI,[34] as a positively charged PE, prevents diffusion of potassium ions from the inner solution to outer media. This pseudointernal electrode solution coupled with the CF/Ag paste/AgCl interface forms an ion-to-electron transfer system. This approach enables us to produce a low-cost miniaturized RE.

For the simulation of 3 M KCl internal solution in the RE, we vary the concentrations of KCl in the PE containing deposition solutions (Figure 3a) and a number of (PEI/PSS) bilayers (Figure 3b). The number of PEI/PSS bilayers varies from 4 to 32. The concentration of KCl in the PE deposition solutions varies from 0.1 to 1 M (Figure 3a). The electrode modified with eight bilayers of PEI/PSS in 1 M KCl solution demonstrates stable electrode potential values. We use this RE modification: CF/Ag paste/AgCl/(PEI/PSS)$_8$, 1 M KCl, for the electroanalytical measurements. Stability measurements during storage require 7 days of conditioning time and demonstrate stable electrode potential values (vs the commercial Ag/AgCl RE) for the proposed miniaturized RE. A 3 M KCl solution was used for storage and conditioning of the RE.

Modification of the working CF electrode by PEs and mercury salt provides a thin layer of amalgam. Water-soluble PEs, which are used for the electrode modification, have the ability to form a complex with mercury ions. PEI was used for removing mercury from wastewaters by mercury(II) complexation with PEI amino groups.[35] Interaction of PSS with Hg^{2+} is caused by a strong polyanion−cation complexation.[36] We consider two options for LBL deposition of PEs with mercury salt. The first case is the mutual deposition of PEs and mercury nitrate: (PEI(Hg-$(NO_3)_2$)/PSS(Hg$(NO_3)_2$))$_n$. The second option is the separate deposition of each layer: (PEI/Hg^{2+}/PSS/Hg^{2+})$_n$.

We evaluate both of these cases by scanning electron microscopy (SEM) (Figure 4) and quartz-crystal microbalance (QCM) methods (Figure 5). Figure 4a,b shows the SEM images of the bare CF surface. A commercially produced CF has an average diameter of CF equal to 5 μm. We can observe the changes at the modified CF surface that are formed by LBL deposition with one PEI/PSS bilayer (Figure 4c,d). The CF surface after LBL deposition is fully covered by PEs. The SWASV Zn detection has no influence on the CF-modified surface (Figure 4e,f).

This was confirmed using the mapped energy-dispersive X-ray (EDX) elemental spectra (Figure 4g,k). The presence of nitrogen before measurements (Figure 4h) demonstrates the
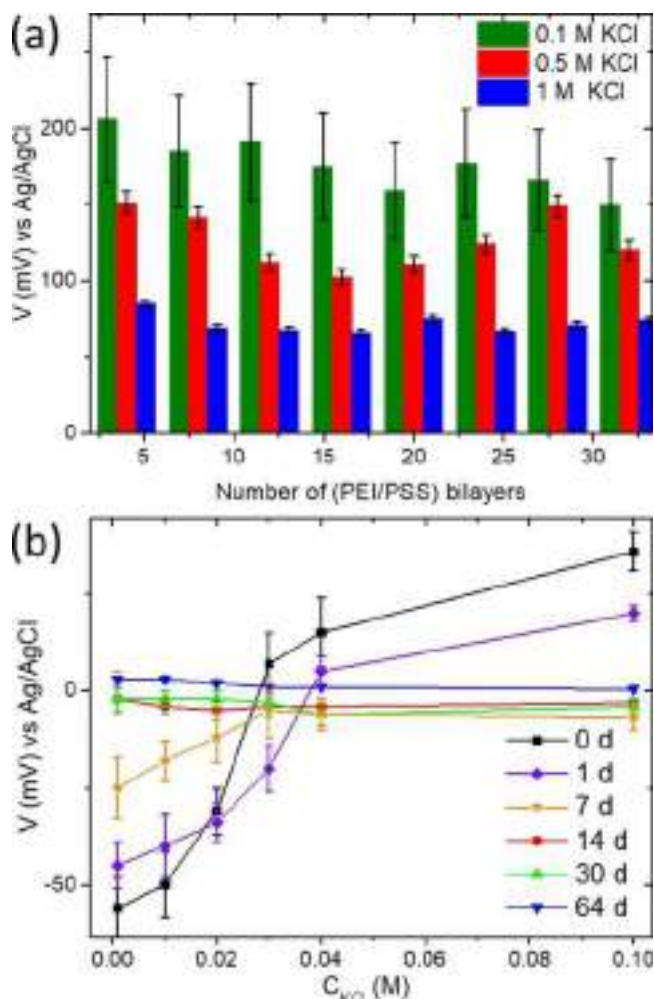
Figure 3. RE signal vs the commercial Ag/AgCl RE for the different PE layers deposited in 0.1, 0.5, and 1 M KCl (a). RE signal recorded vs the commercial Ag/AgCl electrode during storage in 3 M KCl (b).

adsorption of PEI on the CF surface as well as the presence of sulfur proves strong adsorption of PSS (Figure 4i). The mapped EDX spectrum of mercury shows uniform codeposition of the mercury nitrate together with PEs (Figure 4j).

The CF surface after LBL deposition is fully covered by PEs, which was confirmed using the mapped EDX elemental spectra (Figure 4g,k). The presence of nitrogen before measurements (Figure 4h) demonstrates the adsorption of PEI on the CF surface as well as the presence of sulfur proves strong adsorption of PSS (Figure 4i).

The mapped EDX spectrum of mercury shows uniform codeposition of mercury nitrate together with PEs (Figure 4j). Post-SWASV Zn detection using the mapped EDX spectrum demonstrates that signals from sulfur (Figure 4m) and mercury (Figure 4n) remain the same. In Figure 4l, we can observe a decrease in the nitrogen signal caused by its complexation with metallic mercury. Full coverage of the CF by PEs and the uniform mercury distribution prove the formation of a thick film on the CF surface. Such a modification facilitates the surface deposition for heavy metal SWASV determination. PE adsorption, together with mercury salt, was proved by QCM measurements. Except for the first and third harmonics, which had high noise levels, the higher harmonics overlapping with each other involve normalized changes in the frequency for the
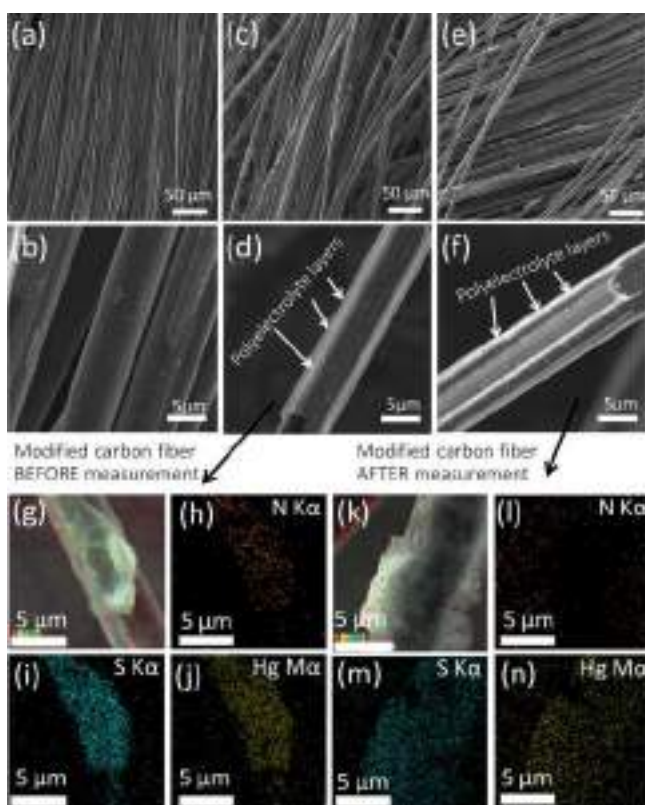
Figure 4. SEM images of the CF electrode (a,b), PEs−Hg^{2+}-modified CF electrode (c,d), and modified CF after electrochemical measurements (e,f). Mapped EDX spectra of the PEs−Hg^{2+}-modified CF electrode after modification (g) and separate mapped EDX spectra of nitrogen (h), sulfur (i), and mercury (j). EDX spectra obtained after electrochemical measurements of the modified CF electrode (k) and mixed EDX spectra of nitrogen (l), sulfur (m), and mercury (n).

fifth harmonic versus time. The normalization was obtained by dividing the change in frequency by its harmonic number. Figure 5a shows the deposition of PEI and PSS, together with mercury nitrate. Serial deposition of PEs with different mercury nitrate concentrations is shown in Figure 5a.

The deposition of the two bilayers of PEs with 1.6 mg/mL of mercury(II) (Figure 5a) leads to a shift of about 200 MHz. Lower frequency changes are observed for the deposition of two bilayers with 6 to 12 mg/mL mercury(II) solution (Figure 5a). An unstable behavior of the adsorbed layers with 1.6 to 12 mg/mL Hg^{2+} explains PE complexation with others and breaks away from the surface. This PE complexation depends on the salt concentration in the adsorbed PE layers.[37,38]

In spite of a lower frequency shift (about 100 MHz), PE layer adsorption with 6 mg/mL Hg^{2+} exhibits a stable frequency signal and a plateau after second bilayer deposition, which is evidence of full surface coverage. The scheme of separate PE layers and mercury deposition controlled by QCM is shown in Figure 5b. Separate deposition leads to the frequency signal stabilization caused by the absence of interaction of mercury ions with PEs in the solution before deposition. Two bilayers (($PEI/Hg^{2+}/PSS/Hg^{2+})_2$) reach the same frequency value as for the PE layers deposited together with mercury salt. We observe no significant changes in the scheme of deposition, excluding unnecessary additional LBL steps. Strong PE complexation with mercury is proved and shown in Figure 5c,d. For this purpose, we wash the twotypes of adsorbed layers subsequently with zinc nitrate and

deionized (DI) water. The layers deposited with 1.6 to 12 mg/mL demonstrate an unstable behavior and the removal of the adsorbed layers caused a change in the total ionic strength of the adsorbed PE layers.[38,39] The stable behavior of the PE layers deposited with 6 mg/mL Hg^{2+} explains the charge compensation between the surface, PEs, and mercury(II).[40] For the SWASV Zn detection, deposition of the two PE bilayer with 6 mg/mL Hg^{2+} is appropriate.

Electrochemical behavior of different deposited PEs−Hg^{2+} bilayers on the GF electrode investigated by SWASV in the acetate buffer solution (pH 3.6) is shown in Figure S3. Conditions for SWASV pretreatment are 60 s of cleaning at −1.4 V and 60 s of deposition at −1.5 V. Anodic square-wave sweep is from −1.5 to 0.6 V with a 50 mV amplitude and a 50 Hz frequency. The frequency value and amplitude correspond to those reported in previous works.[10,17] A reduction in capacitive currents caused by the oxidation of impurities in real blood and urine samples was observed under the proposed square-wave sweep conditions. We observe the mercury anodic dissolution peak at about 0.4 V for both types of PEs−Hg^{2+} bilayers. The Hg^{2+} peak current value for the CF/($PEI/Hg^{2+}/PSS/Hg^{2+})_2$ is equal to 257 μA. For the CF/($PEI(Hg^{2+})/PSS(Hg^{2+}))_2$, this peak magnitude is equal to 453 μA. Zn addition to the background solution till 1×10^{-5} M concentration leads to the appearance of a Zn anodic peak at −1.0 V. We observe slightly decreasing mercury peak current at 0.4 V in the case of CF/($PEI/Hg^{2+}/PSS/Hg^{2+})_2$ deposition after Zn addition. Greater peak current of mercury for the CF/($PEI(Hg^{2+})/PSS(Hg^{2+}))_2$ modification than for CF/($PEI(Hg^{2+})/PSS(Hg^{2+}))_2$ LBL adsorption indicates the amount of immobilized mercury in the PE layers. For the SWASV Zn detection, the CF/($PEI(Hg^{2+})/PSS(Hg^{2+}))_2$ is a convenient method because of the high amount of immobilized mercury and absence of mercury removal from the PE layers. The CF is a micrometer-sized electrode, and therefore, the semispherical diffusion mechanism is realized in the electrochemical cell. Because of this fact, we realize the electroanalysis of Zn without stirring.

The primary parameter for SWASV Zn analysis is the deposition time for the electrochemical pretreatment. We set all SWASV parameters described above, excluding potential sweep. Potential sweep is from −1.5 to 0.0 V for the regular mercury film surface on the CF electrode. Deposition time varies from 30 to 300 s (Figure 6a). The Zn concentration in the electrochemical cell is 1×10^{-5} M. The plateau of the Zn peak area (inset Figure 6a) appears at 240 s.

Nevertheless, we observe the plateau at 60 s (inset Figure 6a). For obtaining the calibration curve, we set the deposition time to be 60 s. In Figure 6b, SWAS voltammograms for the Zn concentration range from 1×10^{-7} to 5×10^{-4} M are presented. The calibration curve is shown in the inset of Figure 6b.

The linear range for the proposed sensor is equal to 1×10^{-7} to 1×10^{-5} M ($R^2 = 0.9986$). Sensitivity is found to be 2.2 ± 0.3 μA/M. The limit of detection is 4.6×10^{-8} M. The detection limit is estimated by adding three times the standard deviation of the blank signal to its mean value. The concentration of zinc in the blood and urine samples depends on a large number of parameters: age, gender, diet, health status, and so forth. The zinc content in the urine sample can reach 10 μM[41] and in the blood sample 1 μM.[42] We used the modified pretreatment technique reported by Zakharchuk et al.[18] for blood and urine samples. This method does not include sample digestion. Zn^{2+} extraction is achieved by the addition of 40 μL of 0.1 M EDTA to 100 μL of blood or urine and mixing for 1 h at room temperature
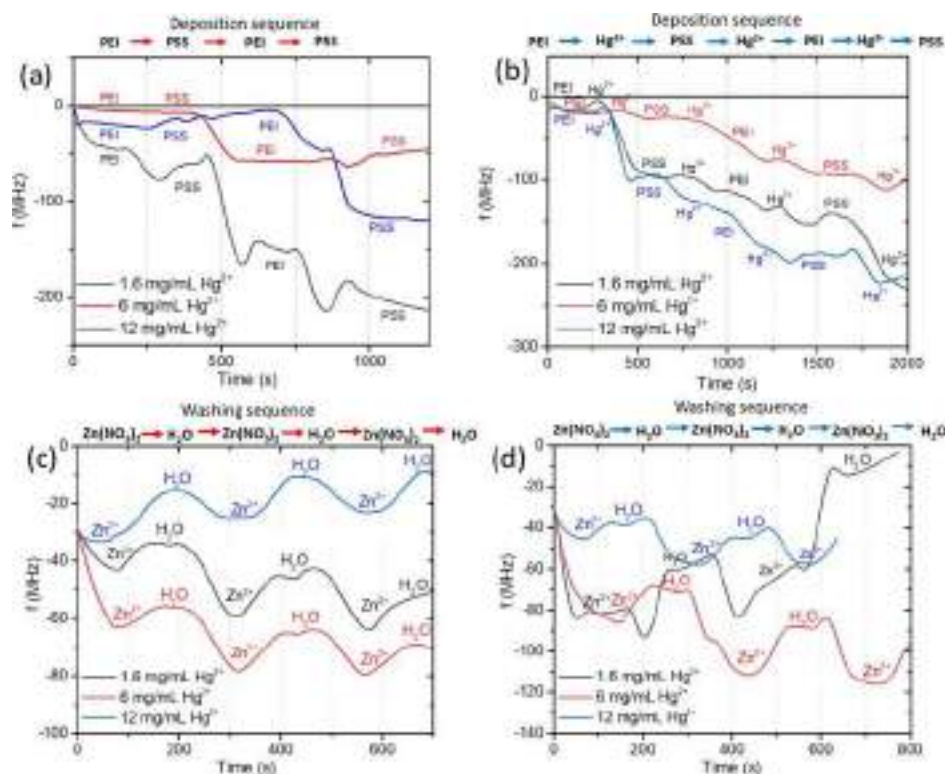
Figure 5. Results of QCM measurements for the adsorbed PE layers by two schemes: $(PEI(Hg(NO_3)_2)/PSS(Hg(NO_3)_2))_2$ (a) and $(PEI/Hg^{2+}/PSS/Hg^{2+})_2$ (b). Mercury erosion from PE layers carried out using zinc nitrate and DI water for the $(PEI(Hg(NO_3)_2)/PSS(Hg(NO_3)_2))_2$ (c) and $(PEI/Hg^{2+}/PSS/Hg^{2+})_2$ (d) layers.

(Figure 7). Then, 40 μL of 1 M NaCl and 20 μL 1 M HCl are added to the mixture. The obtained mixture is left for 30 min at room temperature. For the SWASV measurements, 800 μL of acetate buffer solution is added. The deposition time for the samples of blood and urine is increased up to 90 s. Figure 7 depicts the pretreatment process and SWAS voltammograms for the detection of Zn^{2+} in blood and urine samples. The standard addition of Zn^{2+} realizes the Zn^{2+} evaluation in blood and urine. The reference Zn assay in blood and urine is carried out by inductively coupled plasma−mass spectrometry (ICP MS) heavy metal analysis. Each sample was measured three times. Based on the data obtained, the standard deviation was estimated. The comparison results are shown in Table 1.

The standard deviations of the results obtained by the proposed method are in good agreement with the standard deviations of the results obtained by the ICP MS method. The estimated results presented in Table 1 demonstrate the possibility of accurate detection of Zn^{2+} in blood and urine without the digestion step. This together with the proposed minipotentiostat and software is advantageous for the point-of-care analysis.

CONCLUSIONS

To summarize, the goal of this study was to describe an easy-to-produce electrochemical platform that can be integrated into the point-of-care analysis. The three-electrode cell consisting of a modified WE with $(PEI(Hg^{2+})/PSS(Hg^{2+}))_2$ layers and a reference CF/Ag paste/AgCl/$(PEI(KCl)/PSS(KCl))_8$ electrode allows to determine the zinc(II) concentration in blood and urine samples. We propose together with a minipotentiostat and a software program an electroanalytical system for continuous monitoring of a wide range of analytes. LbL

assembly was efficiently used for the application. Finally, the bioassay could becarried out using undiluted human blood and urine with no digestion or a long-time pretreatment process.

EXPERIMENTAL SECTION

Chemicals and Materials. CFs with 450 g/m^2 of area density were produced by M-Carbo (Minsk, Belarus). PEI (M_W ~ 750 000, 50% (w/v) solution), poly(sodium 4-styrenesulfonate) (PSS, M_W ~ 1 000 000), sodium chloride, and zinc nitrate hexahydrate were purchased from Sigma-Aldrich (USA). 2-Nitrophnyl octyl ether (o-NPOE) and high-molecular-weight poly(vinyl chloride) (PVC) were purchased from Sigma-Aldrich. Hydrochloric acid (HCl) and potassium chloride (KCl) were obtained from Fluka. Tetrahydrofuran solution (THF, 45% in H$_2$O) was provided by Sigma-Aldrich. Silver conductive glue (Kontakt, Keller) and nail polish were purchased from local stores. HCl and KCl solutions were prepared using DI water. Acetic acid, hydrochloric acid, and sodium acetate were acquired from LenReactiv (Russia). Mercury nitrate monohydrate was purchased from Kubancvet-met (Russia). Sodium ethylenediaminetetraacetate (EDTA) was purchased from Helicon (Russia). All solutions were prepared using DI water (>18.0 MΩ cm, Milli-Q gradient system, Millipore, Burlington, MA).

Scanning Electron Microscopy. The morphology of the CF electrodes was studied using a scanning electron microscope (Tescan Vega-3, Czech Republic).

QCM Measurements. Gold sensors (5 MHz, Au-coated) were purchased from Shenzhen RenLux Crystal Co., Ltd. (China). Sensors were cleaned with Piranha solution before each measurement. QCM measurements were carried out on a Gamry Potentiostat (Gamry Instruments, USA) using flow
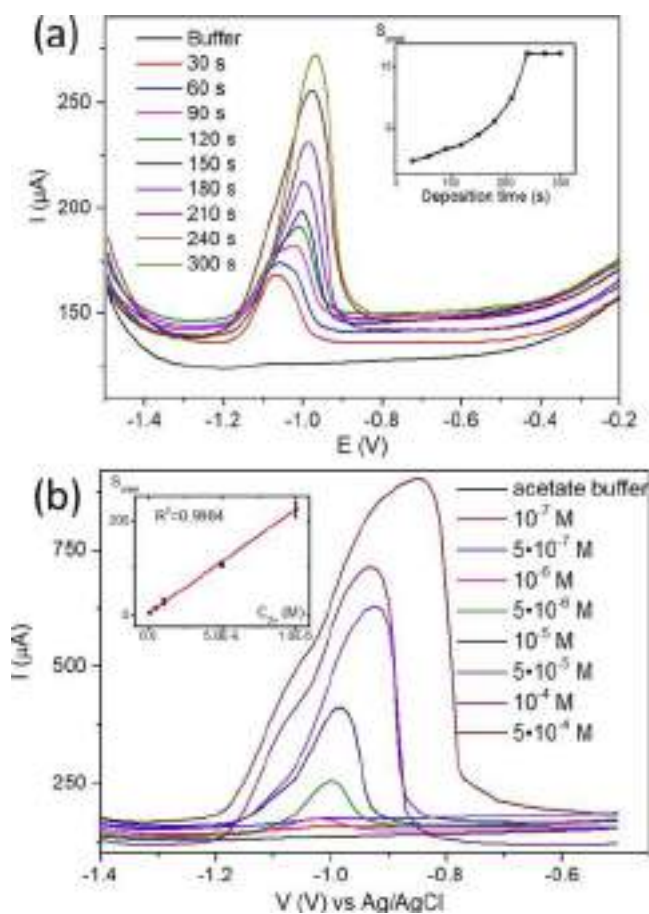
Figure 6. SWASV Zn deposition time dependence for the CF/$(PEI(Hg^{2+})/PSS(Hg^{2+}))_2$ electrode (a) and SWAS voltammograms (b) and calibration curve (inset b).

Figure 7. Scheme of electroanalysis of Zn^{2+} in blood and urine with the proposed sensing platform.

Table 1. Calculation Results for the Zn^{2+} Detection in the Real Samples

sample	ICP−MS (ppm) ($n = 3$, $p = 0.95$)	SWASV (ppm) ($n = 3$, $p = 0.95$)
urine	0.6 ± 0.1	0.5 ± 0.2
blood	6.4 ± 2.1	5.9 ± 2.9

modules. PE solutions were flowed into the modules at 10 rpm using a Heildolph 5101 peristaltic pump. For QCM experiments, PE solutions were prepared at a concentration of 2 mg/mL. LbL assembly was tracked for three different $Hg(NO_3)_2$ concentrations: 1.6, 6, and 12 mg/mL. PEs were alternately deposited on the gold sensor. Between the adsorption steps (5 min), the sensor was rinsed with deionized water (2 min). In other experiments, PEs were deposited with aqueous solutions (2 mg/mL). Between the adsorption steps, the sensor was rinsed with $Hg(NO_3)_2$ (2 min). Swelling experiments on $Zn(NO_3)_2$ were carried out using the following procedure: salt solution (0.1 M in H_2O/acetate buffer 90:10) was flown for 1 min through the modules, after rinsing with deionized water.

Overall Potentiostat Scheme. The overall system was based on the ARM Cortex-M4 74 MHz CPU microcontroller with an analog part, which includes an ultralow bias current DiFET operational amplifier, a gain selectable amplifier, an analog switch, a precision operational amplifier, a programmable gain instrumentation amplifier, and an ultralow offset voltage operational amplifier (Figure S2). The sensor data are processed byusing the chip built into the potentiostat circuit, Bluetooth was chosen for wireless communication of the sensor with the user's smartphone because bluetooth low energy (BLE) has low power consumption and is implemented in all modern devices as a standard communication mode. In this way, our device is compatible with all smartphones without any specialized hardware.

Potentiostat Software Design. The application (https://drive.google.com/file/d/1_zEojyo0MhxXjmrLe_ofLQTb9uyC60Py/view) is written in Java for Android mobile OS. Standard libraries—Bluetooth and BluetoothSocket for working with BLE—were used in development. Third-party libraries: Retrofit—for client−server interaction and Gson were used for data conversion. The SQLite database is used to store the test results on the device. Details are provided in Supporting Information.

CF-based electrode preparation, composition, and connection are highlighted in Figure 2.

Ag/AgCl RE Construction. CF was cut into 80 mm length pieces, which were covered with nail polish, leaving 15 mm uncovered at both ends. Then, the applied coat of nail polish was dried according to the instruction. Following this step, one of the ends was coated with silver conductive glue and left to dry in air for 30 min.

After that, the end, coated with silver, was immersed into 1 M HCl and rinsed with deionized water. Thus, AgCl-coated CF was obtained. The working area of the electrode in the following

was modified using the LbL assembly. It was plunged sequentially for 30 s into the PEI solution at first and then into the PSS solution. The tight end was rinsed between dips with deionized water. Finally, 64 layers (32 layers of PEI and 32 layers of PSS) were assembled. The free end of the CF was attached to a paper clip. The precursor of the membrane was prepared by dissolving 0.5 g of the membrane components (335 mg of o-NPOE and 165 mg of PVC) in 1 mL of THF. The mixture was stirred for 20 min before using it. The prepared mixture can be stored at 4 ± 2 °C. The part of the fiber, coated with polymers, was dipped into the membrane mixture four times with 2 min breaks for drying. Then, the electrode was hung vertically for membrane setting for 40−90 min at room temperature.

WE Modification. CF was partially insulated with nail polish. One of the uninsulated parts was covered with PE-assembled multilayers and mercury salt. The LbL technique was used for the CF electrode modification. The LbL assembly of PEI and PSS layers was carried out using the aqueous solutions with a concentration of 2 mg/mL. Each PE was deposited for 5 min, and then the CF electrode was washed for 1 min with DI water. Concentration of the Hg^{2+} deposition solution was varied from 1.6 to 12 mg/mL. Between each layer deposition, the electrode was rinsed with DI water (Figure S3).

Electrochemical Assay. The SWASV technique was used for zinc detection. For this purpose, the three-electrode system consisting of a working CF-modified electrode, a reference CF-based Ag/AgCl electrode, and a CF counter electrode (CE) was used. An electrochemical cell volume of 1 mL was used. The acetate buffer (pH 3.6) was set as the background solution. All electroanalytical measurements were repeated at least three times for the statistical evaluation of the results.

ASSOCIATED CONTENT

Supporting Information

The Supporting Information is available free of charge at https://pubs.acs.org/doi/10.1021/acsomega.0c02279.

Common scheme of the ElectroSens approach, potentiostat circuit board, and CF-modified electrode electrochemical measurement results (PDF)

Example of application of self-written software during analysis (MP4)

AUTHOR INFORMATION

Corresponding Author

Ekaterina V. Skorb − Infochemistry Scientific Center of ITMO University, St. Petersburg 191002, Russian Federation; orcid.org/0000-0003-0888-1693; Email: skorb@itmo.ru

Authors

Konstantin G. Nikolaev − Infochemistry Scientific Center of ITMO University, St. Petersburg 191002, Russian Federation

Evgeniy V. Kalmykov − Infochemistry Scientific Center of ITMO University, St. Petersburg 191002, Russian Federation

Daria O. Shavronskaya − Infochemistry Scientific Center of ITMO University, St. Petersburg 191002, Russian Federation

Anna A. Nikitina − Infochemistry Scientific Center of ITMO University, St. Petersburg 191002, Russian Federation

Anna A. Stekolshchikova − Infochemistry Scientific Center of ITMO University, St. Petersburg 191002, Russian Federation

Ekaterina A. Kosareva − Infochemistry Scientific Center of ITMO University, St. Petersburg 191002, Russian Federation

Artemiy A. Zenkin − Infochemistry Scientific Center of ITMO University, St. Petersburg 191002, Russian Federation

Igor S. Pantiukhin − Infochemistry Scientific Center of ITMO University, St. Petersburg 191002, Russian Federation

Olga Yu. Orlova − Infochemistry Scientific Center of ITMO University, St. Petersburg 191002, Russian Federation

Anatoly V. Skalny − Infochemistry Scientific Center of ITMO University, St. Petersburg 191002, Russian Federation

Complete contact information is available at:
https://pubs.acs.org/10.1021/acsomega.0c02279

Author Contributions

The manuscript was written through contributions of all authors. All authors have given approval to the final version of the manuscript.

Notes

The authors declare no competing financial interest.

ACKNOWLEDGMENTS

REFERENCES

(1) Gernand, A. D.; Schulze, K. J.; Stewart, C. P.; West, K. P.; Christian, P. Micronutrient deficiencies in pregnancy worldwide: health effects and prevention. *Nat. Rev. Endocrinol.* **2016**, *12*, 274−289.

(2) Gombart, A. F.; Pierre, A.; Maggini, S. A review of micronutrients and the immune system—working in harmony to reduce the risk of infection. *Nutrients* **2020**, *12*, 236.

(3) Skalny, A.; Rink, L.; Ajsuvakova, O. P.; Aschner, M.; Gritsenko, V. A.; Alekseenko, S.; Svistunov, A. A.; Petrakis, D.; Spandidos, D. A.; Aaseth, J.; Tsatsakis, A. Zinc and respiratory tract infections: Perspectives for COVID-19 (Review). *Int. J. Mol. Med.* **2020**, *46*, 17−26.

(4) Ward Jones, S. E.; Chevallier, F. G.; Paddon, C. A.; Compton, R. G. General Theory of Cathodic and Anodic Stripping Voltammetry at Solid Electrodes: Mathematical Modeling and Numerical Simulations. *Anal. Chem.* **2007**, *79*, 4110−4119.

(5) da Silva, S. M.; Squissato, A. L.; Rocha, D. P.; Vasconcellos, M. L. S.; de, Q.; Ferreira, R.; Richter, E. M.; Munoz, R. A. A. Improved anodic stripping voltammetric detection of zinc on a disposable screen-printed gold electrode. *Ionics* **2020**, *26*, 2611.

(6) Ermakov, S. S.; Sheremet, A. A.; Moskvin, L. N. Determination of zinc in aqueous solutions by a combined no-standard electrochemical method with preliminary electrolytic separation of copper. *Russ. J. Appl. Chem.* **2008**, *81*, 420−422.

(7) Wang, J.; Lu, J.; Hocevar, S. B.; Farias, P. A. M.; Ogorevc, B. Bismuth-Coated Carbon Electrodes for Anodic Stripping Voltammetry. *Anal. Chem.* **2000**, *72*, 3218−3222.

(8) Pei, X.; Kang, W.; Yue, W.; Bange, A.; Heineman, W. R.; Papautsky, I. Disposable Copper-Based Electrochemical Sensor for Anodic Stripping Voltammetry. *Anal. Chem.* **2014**, *86*, 4893−4900.

(9) Kang, W.; Pei, X.; Rusinek, C. A.; Bange, A.; Haynes, E. N.; Heineman, W. R.; Papautsky, I. Determination of Lead with a Copper-Based Electrochemical Sensor. *Anal. Chem.* **2017**, *89*, 3345−3352.

(10) Gao, W.; Nyein, H. Y. Y.; Shahpar, Z.; Fahad, H. M.; Chen, K.; Emaminejad, S.; Gao, Y.; Tai, L.-C.; Ota, H.; Wu, E.; Bullock, J.; Zeng, Y.; Lien, D.-H.; Javey, A. Wearable Microsensor Array for Multiplexed Heavy Metal Monitoring of Body Fluids. *ACS Sens.* **2016**, *1*, 866−874.

(11) Opoka, W.; Jakubowska, M.; Baś, B.; Sowa-Kućma, M. Development and Validation of an Anodic Stripping Voltammetric Method for Determination of Zn2+ Ions in Brain Microdialysate Samples. *Biol. Trace Elem. Res.* **2011**, *142*, 671−682.

(12) Skorb, E. V.; Anna, V. V.; Daria, V. A. Layer-by-Layer Approach for Design of Chemical Sensors and Biosensors. *Curr. Org. Chem.* **2015**, *19*, 1097−1116.

(13) Ryzhkov, N. V.; Mamchik, N. A.; Skorb, E. V. Electrochemical triggering of lipid bilayer lift-off oscillation at the electrode interface. *J. R. Soc., Interface* **2019**, *16*, 20180626.

(14) Andreeva, D. V.; Kollath, A.; Brezhneva, N.; Sviridov, D. V.; Cafferty, B. J.; Möhwald, H.; Skorb, E. V. Using a chitosan nanolayer as an efficient pH buffer to protect pH-sensitive supramolecular assemblies. *Phys. Chem. Chem. Phys.* **2017**, *19*, 23843−23848.

(15) Brezhneva, N.; Nikitina, A.; Ryzhkov, N.; Klestova, A.; Vinogradov, A. V.; Skorb, E. V. Importance of buffering nanolayer position in Layer-by-Layer assembly on titania based hybrid photo-activity. *J. Sol-Gel Sci. Technol.* **2019**, *89*, 92−100.

(16) Stekolshchikova, A. A.; Radaev, A. V.; Orlova, O. Y.; Nikolaev, K. G.; Skorb, E. V. Thin and Flexible Ion Sensors Based on Polyelectrolyte Multilayers Assembled onto the Carbon Adhesive Tape. *ACS Omega* **2019**, *4*, 15421−15427.

(17) Anastasiadou, Z.; Panagiotis, J.; Stella, G. Square wave anodic stripping voltammetry determination of eco-toxic metals in samples of biological and environmental importance. *Open Chem.* **2010**, *8*, 999−1008.

(18) Zakharchuk, N. F.; Saraeva, S. Y.; Kolyadina, L. I.; Sudaeva, O. I.; Brainina, K. Z. Direct Measurements of Cadmium, Lead and Copper in Whole Blood Using the Stripping Voltammetric Method with Modified Thick-Film Graphite Electrodes. *Chem. Sustainable Dev.* **2003**, *11*, 775−786.

(19) Jothimuthu, P.; Wilson, R. A.; Sukavasi, S.; Herren, J.; Wong, H.; Beyette, F. R.; Heineman, W. R.; Papautsky, I. In Lab-on-a-chip sensor for measuring zinc in blood serum. *SENSORS, 2010 IEEE*, Nov 1−4, 2010; IEEE, 2010; pp 1222−1225.

(20) Crew, A.; Cowell, D.; Hart, J. Development of an anodic stripping voltammetric assay, using a disposable mercury-free screen-printed carbon electrode, for the determination of zinc in human sweat. *Talanta* **2008**, *75*, 1221−1226.

(21) Lim, G. N.; Ross, A. E. Purine Functional Group Type and Placement Modulate the Interaction with Carbon-Fiber Micro-electrodes. *ACS Sens.* **2019**, *4*, 479−487.

(22) Farajikhah, S.; Innis, P. C.; Paull, B.; Wallace, G. G.; Harris, A. R. Facile Development of a Fiber-Based Electrode for Highly Selective and Sensitive Detection of Dopamine. *ACS Sens.* **2019**, *4*, 2599−2604.

(23) Sweilam, M. N.; Varcoe, J. R.; Crean, C. Fabrication and Optimization of Fiber-Based Lithium Sensor: A Step toward Wearable Sensors for Lithium Drug Monitoring in Interstitial Fluid. *ACS Sens.* **2018**, *3*, 1802−1810.

(24) Li, W.; Chen, R.; Qi, W.; Cai, L.; Sun, Y.; Sun, M.; Li, C.; Yang, X.; Xiang, L.; Xie, D.; Ren, T. Reduced Graphene Oxide/Mesoporous ZnO NSs Hybrid Fibers for Flexible, Stretchable, Twisted, and Wearable NO$_2$ E-Textile Gas Sensor. *ACS Sens.* **2019**, *4*, 2809−2818.

(25) Yang, C.; Trikantzopoulos, E.; Nguyen, M. D.; Jacobs, C. B.; Wang, Y.; Mahjouri-Samani, M.; Ivanov, I. N.; Venton, B. J. Laser Treated Carbon Nanotube Yarn Microelectrodes for Rapid and Sensitive Detection of Dopamine in Vivo. *ACS Sens.* **2016**, *1*, 508−515.

(26) Zhu, W.; Zhang, Y.; Gong, J.; Ma, Y.; Sun, J.; Li, T.; Wang, J. Surface Engineering of Carbon Fiber Paper toward Exceptionally High-Performance and Stable Electrochemical Nitrite Sensing. *ACS Sens.* **2019**, *4*, 2980−2987.

(27) Brainina, K.; Henze, G.; Stojko, N.; Malakhova, N.; Faller, C. Thick-film graphite electrodes in stripping voltammetry. *Fresenius. J. Anal. Chem.* **1999**, *364*, 285−295.

(28) Roeser, J.; Heinrich, B.; Bourgogne, C.; Rawiso, M.; Michel, S.; Hubscher-Bruder, V.; Arnaud-Neu, F.; Méry, S. Dendronized Polymers with Silver and Mercury Cations Recognition: Complexation Studies and Polyelectrolyte Behavior. *Macromolecules* **2013**, *46*, 7075−7085.

(29) Lee, A. A.; Kostinski, S. V.; Brenner, M. P. Controlling Polyelectrolyte Adsorption onto Carbon Nanotubes by Tuning Ion-Image Interactions. *J. Phys. Chem. B* **2018**, *122*, 1545−1550.

(30) Sharma, V.; Sundaramurthy, A. Multilayer capsules made of weak polyelectrolytes: a review on the preparation, functionalization and

applications in drug delivery. *Beilstein J. Nanotechnol.* **2020**, *11*, 508−532.

(31) Mauser, T.; Déjugnat, C.; Möhwald, H.; Sukhorukov, G. B. Microcapsules Made of Weak Polyelectrolytes: Templating and Stimuli-Responsive Properties. *Langmuir* **2006**, *22*, 5888−5893.

(32) Delcea, M.; Möhwald, H.; Skirtach, A. G. Stimuli-responsive LbL capsules and nanoshells for drug delivery. *Adv. Drug Delivery Rev.* **2011**, *63*, 730−747.

(33) Van der Meeren, L.; Li, J.; Parakhonskiy, B. V.; Krysko, D. V.; Skirtach, A. G. Classification of analytics, sensorics, and bioanalytics with polyelectrolyte multilayer capsules. *Anal. Bioanal. Chem.* **2020**, *412*, 5015.

(34) Nestler, P.; Paßvogel, M.; Ahrens, H.; Soltwedel, O.; Köhler, R.; Helm, C. A. Branched Poly(ethylenimine) as Barrier Layer for Polyelectrolyte Diffusion in Multilayer Films. *Macromol* **2015**, *48*, 8546−8556.

(35) Uludag, Y.; Özbelge, H. Ö.; Yilmaz, L. Removal of mercury from aqueous solutions via polymer-enhanced ultrafiltration. *J. Membr. Sci.* **1997**, *129*, 93−99.

(36) Yasri, N. G.; Sundramoorthy, A. K.; Chang, W.-J.; Gunasekaran, S. Highly Selective Mercury Detection at Partially Oxidized Graphene/Poly(3,4-Ethylenedioxythiophene): Poly(Styrene-sulfonate) Nano-composite Film-Modified Electrode. *Front. Mater.* **2014**, *1*, 33.

(37) Bago Rodriguez, A. M.; Binks, B. P.; Sekine, T. Emulsions Stabilized with Polyelectrolyte Complexes Prepared from a Mixture of a Weak and a Strong Polyelectrolyte. *Langmuir* **2019**, *35*, 6693−6707.

(38) Nikolaev, K. G.; Ulasevich, S. A.; Luneva, O.; Orlova, O. Y.; Vasileva, D.; Vasilev, S.; Novikov, A. S.; Skorb, E. V. Humidity-Driven Transparent Holographic Free-Standing Polyelectrolyte Films. *ACS Appl. Polym. Mater.* **2020**, *2*, 105−112.

(39) Yang, M.; Shi, J.; Schlenoff, J. B. Control of Dynamics in Polyelectrolyte Complexes by Temperature and Salt. *Macromolecules* **2019**, *52*, 1930−1941.

(40) Wang, Q.; Schlenoff, J. B. The Polyelectrolyte Complex/Coacervate Continuum. *Macromol* **2014**, *47*, 3108−3116.

(41) Tinkov, A. A.; Skalnaya, M. G.; Ajsuvakova, O. P.; Serebryansky, E. P.; Chao, J. C. J.; Aschner, M.; Skalny, A. V. Selenium, Zinc, Chromium, and Vanadium Levels in Serum, Hair, and Urine Samples of Obese Adults Assessed by Inductively Coupled Plasma Mass Spectrometry. *Biol. Trace Elem. Res.* **2020**, DOI: 10.1007/s12011-020-02177-w.

(42) Crăciun, E. C.; Bjørklund, G.; Tinkov, A. A.; Urbina, M. A.; Skalny, A. V.; Rad, F.; Dronca, E. Evaluation of whole blood zinc and copper levels in children with autism spectrum disorder. *Metab. Brain Dis.* **2016**, *31*, 887−890.

Article

Storage of Information Using Periodic Precipitation

Anastasia Nenashkina, Semyon Koltsov, Ekaterina Zaytseva, Anastasia Brunova, Igor Pantiukhin, and Ekaterina V. Skorb*

Cite This: *ACS Omega* 2020, 5, 7809−7814

Read Online

ACCESS | Metrics & More | Article Recommendations | SI Supporting Information

ABSTRACT: In the present work, transparent flexible thin polymer films with silver patterns have been created. The resulting structures made by the printing method represent a new alternative approach for recording, protecting, and transmitting information as well as for nonlinear gradient material formation. An alphabet for process automatization was created, and an automated system for recording and reading information was developed. To protect the information, we suggest the usage of a classic XOR function: the idea of scrambling is to demonstrate the simple and clear example of coding the ITMO University logo, and the code is provided. Additionally, the resulting samples are functional gradient materials with peaks of surface plasmon resonance. In the following, automated peak decoding by UV−vis spectroscopy allows an additional physicochemical method for structure decoding.
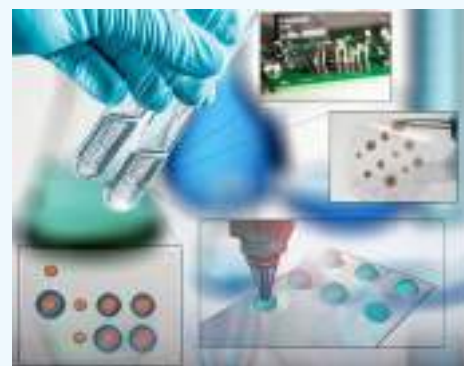
INTRODUCTION

In recent times, because of the constant increase in speed and the amount of produced information in our planet increases the interest in developing alternative information storage technologies.[1] Technologies from electronic,[2] optical,[3] and magnetic methods,[4] to low molecular weight molecules,[5] high molecular weight molecules,[6] and biologically derived systems[7] are used to store information.

One of the most popular and used methods of chemical information storing is DNA encoding.[8] The coding technique of DNA-based storage and the one in modern computers differ in their alphabets. Thus, there are bases A, C, T, and G in DNA instead of "1" and "0" in a computer. Four different signals of DNA bases results in a large number of chemical information encoding ways.

Storing information in DNA has some advantages, such as huge data storage density, the stability of the carrier (at low temperatures), the ability to create an error correction mechanism, and the ability to solve some computational problems much faster than on a modern binary computer.[9] However, it does not have the capability to rewrite information, and further clear development is needed. Nowadays, all attempts of experimental chemical information storage and processing are growing areas of infochemistry.[10−12]

Another way of information coding is encoding the m-SMS molecule, which includes three fluorescent groups (fluorescein, sulforhodamine B, and Nile blue).[5] The main idea is to convert the text to numbers using a public alphanumeric code to obtain a numeric sequence. Moreover, such a method can be considered for further development of chemical computing. These systems are capable of writing any messages by

sequentially adding chemical inputs. Reading is accomplished using a hand-held spectrometer.

In the group of Whitesides,[13] the way of chemical encoding based on matching a single pulse of light with an alphanumeric symbol was suggested.

The ignited metals emit light at different wavelengths.[14,15] It makes possible to discern which metal was burned and to encode the message.

Important is that, notwithstanding very low resolution, the proof of concept of alternative ways is shown. Here, we also focus on proof of concept for our system, and simultaneously, we show a prospective way of UV−vis spectroscopy for decoding the information. The advantages of stimuli-responsive materials are also mentioned.

Rules of coding and decoding are clearly presented. The main disadvantage of such a system is that peaks corresponded to some metals can overlap, so one needs to avoid some sequences. Another procedure is based on a common, small set of molecules (for instance, 32 oligopeptides) to write binary information.[6] It minimizes the time and difficulty of the synthesis of new molecules. This way consists of writing messages in an eight-bit American Standard Code for Information Interchange (ASCII), converting them to an equivalent molecular code and store them in an array plate

(four bytes per spot). "Writing" is performed by first translating information into binary. Binary information is converted to oligopeptides immobilized on a self-assembled monolayer, for storage. A MALDI-TOF mass spectrometer analyzes ("reads") these plates. A program decodes the information in the spectra and generates a bit string that is used to regenerate the original text.

Mankind is confidently moving toward the creation of nanocomputers for various applications: from sensors that can control our metabolism to the creation of powerful fit-hand quantum computers. Minimization is especially important for information technologies. It is demanded to create materials that combine a minimum volume in space and a high recording density. Notwithstanding that the high recording density is needed, the proof of concept in majority cases is done for model systems. Here, we focus on the system where, in the long run, the high recording density is possible and show proof of concept and procedure from automated coding, create the program, and suggest prospects for material science with automatization of formation, writing, and reading. We suggest using functional gradient materials[16−19] as a new storage medium that in the following can be stimuli-responsive media.

Functional gradient materials are composite or single-phase materials, which change their functional properties uniformly or stepwise in at least one dimension of a particle, film, or bulk sample. The functional gradient materials have found applications in various scientific fields such as the aerospace plane,[20] ceramic engines,[21] optics,[22] nuclear fusion,[23] and medicine.[24] The incredible potential of printing inspires us to engender a new information media based on functional gradient materials.

Here, we present a novel approach with rules of coding and decoding, encrypting the data as well as a prospective way for functional nonlinear materials. Thus, a potential printing way for the flexible film with silver patterns is described. Both coding and a way to provide information security is highlighted together with material science prospects. Future prospects are suggested.

■ RESULTS AND DISCUSSION

The material made of agar and silver from silver nitrate was used for the investigation (Figure 1). The gradient structure is formed because of the diffusion of silver nitrate (active substance) into 1 wt % agar gel.[25,26] During the diffusion of silver ions through agar, Liesegang rings (LRs) are formed. LR formation is a phenomenon of space-separated precipitation; when due to a combination of supersaturation, nucleation, and diffusion limitation separate bands, rings of precipitation are formed.[27] The resolution during wet-stamping can be increased drastically.[28] Here, we focus on the main principle of the reaction.

For the experiment, 1 wt % agar solution was used as the carrier matrix. In a Petri dish with a diameter of 90 mm, 4 mL of hot agar solution was added and uniformly distributed over the surface. The matrix was completely gelled and ready to use within 1−3 min. After that, silver solutions at various concentrations were applied dropwise to the surface: 0, 0.2, 0.5, 1 and 2 wt %. The drop volume was 3.36 μL.

As the silver nitrate passes through the gel, it reacts with the galacturonic acid monomers contained in the pectin of the agar.[25] The resulting white salt decomposes under light irradiation with the formation of silver nanoparticles and dark silver particles. The diffusion reaction proceeds from 1 to
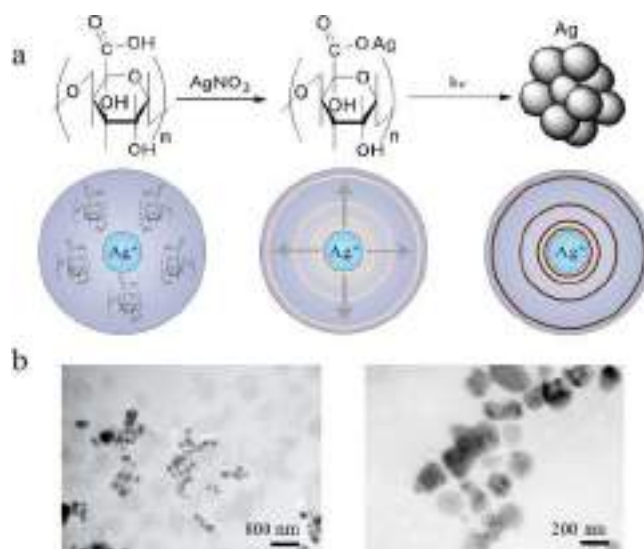
Figure 1. Diffusion reaction of the Ag$^+$ ions occurs in the agar gel with formation of the silver-based NPs (a). TEM images of the silver-based NPs (b).

2 h under the irradiation of the visible spectrum, and further light does not affect the structure. Transmission electron microscopy (TEM) (Figure 1b) images were captured for the confirmation of the particle size. When concentration rises, the dispersion of the particle size is increased.[26]

Alphabets for the transliteration for the writing process is presented in the table in Figure 2a. The alphabets are based on LR phenomena that allow creating a distinguishable pattern. Different positions of silver particles zones and their total amount in the formed pattern make it possible to recognize several different signals. Positioning is controlled by varying the concentration of silver nitrate. This behavior of changing band position with the changing electrolyte concentration is known as Matalon−Packter[29] low. Using this fundamental diffusion regularities is a new way to store and transmit information.

The alphabet was created (Figure 2a−c). Each letter corresponds to a combination of three digits from the set 0, 1, 2, 3, and 4 (Figure 2a). Each digit corresponds to a certain concentration; 0 states for zero concentration (Figure 2b). The choice of the number of symbol coding digits and five different signals let us code $5^3 = 125$ different symbols. This amount is enough to encode 105 basic symbols of the English text. To enlarge the symbol capacity, we need just to add one more concentration that will lead to $6^3 = 216$ different symbols or to use four digits to code, so we get $5^4 = 625$ symbols.

To protect the information, we suggest using a classic XOR function as a special way to coded messages to prevent information leak. Thus, a cipher will be transmitted rather than a message, and only those who have the key will be able to solve it.

The XOR function is a digital logic gate (yes or no type) that gives a true (1 in our case) output when the number of true inputs is odd. Particularly, it gives 0 when two variables are equal and 1 when they differ. For binary notation, if the input is 1, 1 or 0, 0, we get 0, and for 0, 1 or 1, 0, we get 1. It is both an associative and a commutative operation, which means that neither the order nor the grouping of operands affects the results.[30] Thus, applying the formula $B_i = A_i \oplus B_{i-n} \oplus B_{i-m}$ to the original message, it can always be restored using the

Figure 2. Alphabet encoded table (a). Inorganic LRs with concentrations corresponding to numbers from 1 to 4 in the program code (concentration of the active substance $AgNO_3$ from top to bottom: 0.2, 0.5, 1, and 2%) (b). Corresponding numbers in the program code (0 is not shown and corresponds to 0% of the active substance, i.e. empty space) (c).

formula $A_i = B_i \oplus B_{i-n} \oplus B_{i-m}$. The whole process is called scrambling (Figure 3a−f). Parameters m and n can be changed to generate different keys.
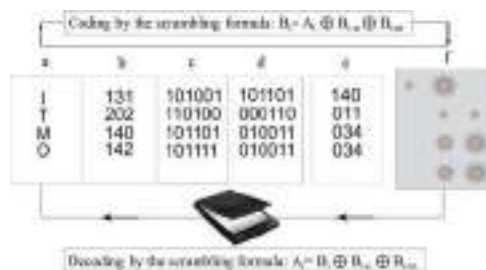
Figure 3. Three-stage coding system (a−f). Coding word (a). According to the table of correspondences (Figure 2a) of combinations of different concentrations to symbols, the initially coded word is obtaining (b).Received message is transferring to the binary number system (c). Scrambling, getting a new sequence (d).Sequence is translating back to the fifth number system (e). Result of experiments obtained by the inkjet printing (f). Received pattern is recognized by the printer as the initial word.

To encode the word "ITMO", we used the following algorithm: (1) according to the table of combinations of different concentrations to symbols: "ITMO" = 131 202 140 142 (Figure 3b); (2) the received message was translated in binary notation, letter by letter, padding it with zeros to seven characters, if necessary: "ITMO" = 0101001 0110100 0101101 0101111 (Figure 3c); (3) the message was scrambled with the given keys (in our case 3 and 5), getting a new sequence 0101101 1011001 1010001 1110110 (Figure 3d); and (4) this sequence was transferred back to the fifth number system, as a result of which we get 140 324 311 433 (Figure 3e). The message is recorded directly into the Petri dish or by robotic printing (Figure 3f). To decode the encoded message, the inverse algorithm is used (Figure 3f−a).

To automate the process of the message reading and decryption, a program was written. This program allows using a scanner as a reading equipment (Figure 4). Thus, reading

Figure 4. Process of creating thin-film information media (a,b). Jet printing, (a) 1—replaceable cartridges with various concentrations of active substance ($AgNO_3$), 2—droplet application process, and 3—robotic printer. Machine reading process (b), 1—scanner, 2—sheet with coded information (each drop has its own digit in the code), and 3—photos of the resulting drops (concentration of the active substance from top to bottom: 0.2, 0.5, 1, and 2% of the $AgNO_3$). Scale by 1 mm.

occurs quickly, and human decoding errors are prevented. Also, the modern scanners because of its high resolution are supposed to be able to read nanoscale (~500 nm and more) features of the films. To eliminate the human factor, to completely automate the process, and to enlarge signal capacity, a robotic printing method is proposed here (Figure 4a). For creating messages using the printing method, replaceable cartridges with silver nitrate solutions of various concentrations are proposed. The cartridges are made of tinted glass or a completely opaque material so that the silver nitrate salt does not decompose. A thin, transparent agar layer is charged to the printer as a substrate. LRs are formed after

droplets were applied to the surface. Silver nanoparticles (NPs) are formed under irradiation.[31] The dried film is read by a scanner, which decodes it into a finished message using a scrambling formula (Figure 4b).

The formed silver NPs exhibit a phenomenon known as surface plasmon resonance (SPR). The SPR is an optical property that takes place when light interacts with conductive nanoparticles that are smaller than the incident wavelength. This behavior is explained to be the interaction of the silver nanoparticle surface electron cloud with a certain value wavelength light corresponding to the resonance frequency. Silver NPs are especially efficient at absorbing and scattering light. The SPR peak wavelength of such NPs can be tuned from 400 (violet light) to 530 nm (green light) by changing the particle size. UV−vis spectra can be used to increase the resolution for the suggested method, allowing the decoding of the formed structure.

Further development will lead to the formation of diffraction patterns upon light transmission. Using controlled patterning by means of Liesegang phenomena, we possibly will manage to create a diffraction grid. Thus, we will be able (i) to read both intensity and the position of light and (ii) to use lasers to read less than 300 nm size features, and therefore, the storage density will increase.

One could think of more insights into programming by controlling the concentration of silver nanoparticles or by, for example, direct synthesis or precipitation of existing ones. Some additional material can be compared with the polymer with silver NPs: NP redistribution controlling into polyelectrolyte multilayers by temperature,[32] AgNPs in situ formation on the elliptical vaterite beads and its potential effect on surface-enhanced Raman scattering.[33]

Moreover, it is possible to use gradient polymeric coatings[34] or tunable wettability[35] to help in controlling the deposition of gradients and further increase the resolution for information coding.

With a change in the concentration of the active substance, the characteristic peak of SPR also changes. Various shapes provide us with different SPR plots, as shown in Figure 5a.

Dried films were easily removed from the Petri dish. Such material distinguished for its flexibility, lightness and with the silver NPs contained in it, has a high optical density (Figure 5b). As stated above, with a change in the concentration of the active substance, the characteristic peak of SPR also changes. Therefore, a new alternative method of encoding and protecting information is proposed (Figure 5a). Plots with SPR peaks were obtained for describing the system (Figure 5a).[36] As can be seen, the peaks correspond to the wavelengths from 445 to 519 nm, which is common for silver nanoparticles. Depending on the conditions of the reaction, the sizes of nanoparticles can vary and can aggregate in different ways; because of this, the characteristic wavelength and peak width also shift. Therefore, a method for encoding and decrypting a message by creating characteristic peaks is also provided. In this case, the Agilent Cary 60 UV−vis spectrophotometer becomes the reader. For such a method, we are supposed to create special nozzles for the spectrophotometer, with the help of which it becomes possible to read messages of very small sizes and without mistakes.

The film with nanoparticles can be stable upon most presumable environmental conditions, including stability up to 250 °C.[37] We have heated our samples up to 200 °C and maintain and did not observe visible changes neither in agar
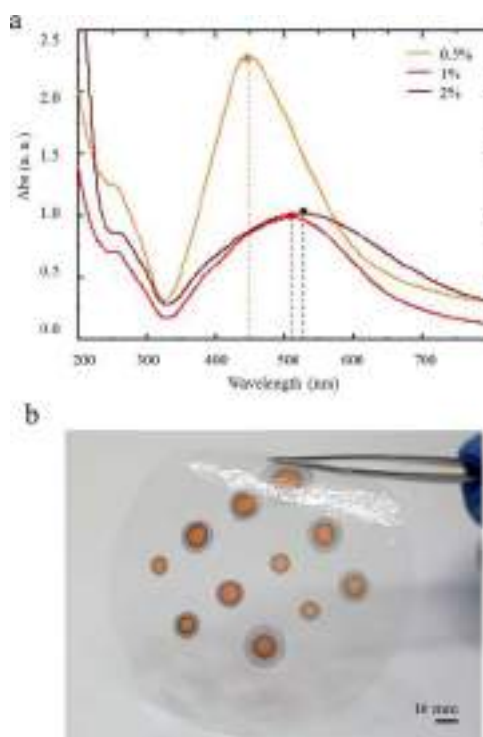
Figure 5. Alternative coding method (a,b). Plots correlated with the SPR response, which differ within various concentrations of the active substance ($AgNO_3$) at the plot (a). Lowest concentration (here is 0.5%) corresponds to a wavelength of 445 nm and peaks of the 1 and 2% active substance run through the 505 and 519 nm, respectively. The SPR peak width indicates particle uniformity. The resulting film is thin and flexible (b). These samples were used for obtaining plasmon resonance peaks (plot on the left).

degradation nor in silver particle positions. The film can be bent many times. The films are highly flexible and robust. The formed structure is also stable under irradiation (405 nm, 5 mW/cm^2 for 24 h). The material is stable under wet conditions, and after soaking in water, it retains the pattern.

■ CONCLUSIONS

In conclusion, we developed a printed, flexible film with silver patterns: the functional gradient materials. We created a new alphabet for coding information in the structure of the film. Each silver pattern contains silver NPs that exhibit the phenomenon of SPR. The program for automated information coding and scrambling is presented. The simple structure imaging can be used for decoding patterns using the scanner as the reading equipment. In addition, by decoding the patterned structure, the SPR peak wavelength of the formed silver nanoparticles—which can be tuned from 400 nm (violet light) to 530 nm (green light) by changing the particle size—can be decoded by UV−vis spectrophotometry. Because of the possibility of creating nanostructures based on the obtained gradient material, microsensor sources of information transfer can be developed in the future.

■ METHODS

Chemicals. Agar (A1296, powder, CAS number: 9002-18-0) and silver nitrate (Nnitric acid silver(I) salt, molecular weight: 169.87, CAS number: 7761-88-8) were purchased from Sigma-Aldrich. Pure water from Millipore Elix (18 MΩ·

cm^2/cm) was used to prepare the necessary solutions for the experiment.

Instruments. *UV−VIS Spectrophotometry.* UV−vis spectrophotometry was used to characterize the optical properties of the thin films. Measurements were carried out using a two-beam scanning spectrophotometer with a high resolution spectrophotometer UV-1800 (Schimadzu, Japan). Spectra were recorded in a range of 200−800 cm^{-1} at a medium scan rate.

Transmission Electron Microscopy. Before measurements, the samples were mounted on a 3 mm copper grid with a carbon film and fixed in a grid holder. The morphology of the samples was studied using the Hitachi transmission electron microscope. Images were acquired in the bright-field TEM mode at 100 kV accelerating voltage.[38]

Other Equipment. The scanner Canon CanoScan 9000F Mark II is used as the reading medium.

Experimental Thin-Film Fabrication. For creating an experimental model, 1% Agar A1296 solution was used as the carrier matrix. In a Petri dish with a diameter of 90 mm, 4 mL of hot agar solution was added and uniformly distributed over the surface. The matrix was completely gelled and ready for use within 1−3 min. After that, silver solutions with various concentrations were applied dropwise with a drop volume of 3.36 μL to the surface. The diffusion reaction proceeds from 2 to 5 h under irradiation of the visible spectrum.

ASSOCIATED CONTENT

SI Supporting Information

The Supporting Information is available free of charge at https://pubs.acs.org/doi/10.1021/acsomega.9b03954.

> Scanning electron microscopy images for Ag NPs in the agar matrix and program code written in C-sharp for reading received structures by scanner (PDF)

AUTHOR INFORMATION

Corresponding Author

Ekaterina V. Skorb − ITMO University, St. Petersburg 191002, Russian Federation; ⬤ orcid.org/0000-0003-0888-1693; Email: skorb@itmo.ru

Authors

Anastasia Nenashkina − ITMO University, St. Petersburg 191002, Russian Federation

Semyon Koltsov − ITMO University, St. Petersburg 191002, Russian Federation

Ekaterina Zaytseva − ITMO University, St. Petersburg 191002, Russian Federation

Anastasia Brunova − ITMO University, St. Petersburg 191002, Russian Federation

Igor Pantiukhin − ITMO University, St. Petersburg 191002, Russian Federation

Complete contact information is available at:
https://pubs.acs.org/10.1021/acsomega.9b03954

Notes

The authors declare no competing financial interest.

ACKNOWLEDGMENTS

REFERENCES

(1) *Digital Memory Studies: Media Pasts in Transition*, 1st ed.; Hoskins, A., Ed.; Tailor and Francis: New York, 2018; pp 326.

(2) Iraci, J. The Soaking Resistance of Electronic Storage Media. *Restaurator* 2017, 38, 33−75.

(3) Gu, M.; Li, X.; Cao, Y. Optical Storage Arrays: A Perspective for Future Big Data Storage. *Light: Sci. Appl.* 2014, 3, No. e177.

(4) Stein, I. Analysis of Noise from Magnetic Storage Media. *J. Appl. Phys.* 1963, 34, 1976−1990.

(5) Sarkar, T.; Selvakumar, K.; Motiei, L.; Margulies, D. Message in a Molecule. *Nat. Commun.* 2016, 7, 11374.

(6) Cafferty, B. J.; Ten, A. S.; Fink, M. J.; Morey, S.; Preston, D. J.; Mrksich, M.; Whitesides, G. M. Storage of Information Using Small Organic Molecules. *ACS Cent. Sci.* 2019, 5, 911−916.

(7) Adamatskiy, A. Identification of probabilistic cellular automata. *Sov. J. Comput. Syst. Sci.* 1992, 30, 118−123.

(8) Song, T.; Eshra, A.; Shah, S.; Bui, H.; Fu, D.; Yang, M.; Mokhtar, R.; Reif, J. Fast and Compact DNA Logic Circuits Based on Single-Stranded Gates Using Strand-Displacing Polymerase. *Nat. Nanotechnol.* 2019, 14, 1075−1081.

(9) Bornholt, J.; Lopez, R.; Carmean, D.; Ceze, L.; Seelig, G.; Strauss, K. A DNA-Based Archival Storage System. *IEEE Micro* 2017, 37, 637−649.

(10) *Information Theory and the Central Limit Theorem*, 1st ed.; Johnson, O., Ed.; Imperial College Press: London, 2004, pp 208.

(11) Ryzhkov, N. V.; Andreeva, D. V.; Skorb, E. V. Coupling pH-Regulated Multilayers with Inorganic Surfaces for Bionic Devices and Infochemistry. *Langmuir* 2019, 35, 8543−8556.

(12) Ryzhkov, N. V.; Nesterov, P.; Mamchik, N. A.; Yurchenko, S. O.; Skorb, E. V. Localization of ion concentration gradients for logic operation. *Front. Chem.* 2019, 7, 419.

(13) Hashimoto, M.; Feng, J.; York, R. L.; Ellerbee, A. K.; Morrison, G.; Thomas III, S. W.; Mahadevan, L.; Whitesides, G. M. Infochemistry: Encoding Information as Optical Pulses Using Droplets in a Microfluidic Device. *J. Am. Chem. Soc.* 2009, 131, 12420−12429.

(14) Kim, C.; Thomas, S. W.; Whitesides, G. M. Long-Duration Transmission of Information with Infofuses. *Angew. Chem., Int. Ed.* 2010, 49, 4675−4679.

(15) Park, K. M.; Kim, C.; Thomas, S. W., III; Yoon, H. J.; Morrison, G.; Mahadevan, L.; Whitesides, G. M. New encoding schemes with infofuses. *Adv. Mater.* 2011, 23, 4851−4856.

(16) Bhavar, V.; Singh, R.; Kattire, P.; Thakare, S.; Patil, S.; Singh, R. K. P. A Review on Functionally Gradient Materials (FGMs) and Their Applications. *IOP Conf. Ser.: Mater. Sci. Eng.* 2017, 229, 012021.

(17) Skorb, E. V.; Andreeva, D. V. Surface Nanoarchitecture for Bio-Applications: Self-Regulating Intelligent Interfaces. *Adv. Funct. Mater.* 2013, 23, 4483−4506.

(18) Skorb, E. V.; Möhwald, H.; Andreeva, D. V. How Can One Controllably Use of Natural ΔpH in Polyelectrolyte Multilayers? *Adv. Mater. Interfaces* 2017, 4, 1600282.

(19) Lanchuk, Y.; Nikitina, A.; Brezhneva, N.; Ulasevich, S. A.; Semenov, S. N.; Skorb, E. V. Photocatalytic Regulation of an Autocatalytic Wave of Spatially Propagating Enzymatic Reactions. *ChemCatChem* 2018, 10, 1798−1803.

(20) Wang, H.; Chen, M.-L.; Zhu, M.; Wang, Y.; Dong, B.; Sun, X.; Zhang, X.; Cao, S.; Li, X.; Huang, J.; Zhang, L.; Liu, W.; Sun, D.; Ye, Y.; Song, K.; Wang, J.; Han, Y.; Yang, T.; Guo, H.; Qin, C.; Xiao, L.; Zhang, J.; Chen, J.; Han, Z.; Zhang, Z. Gate tunable giant anisotropic resistance in ultra-thin GaTe. *Nat. Commun.* 2019, 10, 2302.

(21) Caccia, M.; Tabandeh-Khorshid, M.; Itskos, G.; Strayer, A. R.; Caldwell, A. S.; Pidaparti, S.; Singnisai, S.; Rohskopf, A. D.; Schroeder, A. M.; Jarrahbashi, D.; Kang, T.; Sahoo, S.; Kadasala, N. R.; Marquez-Rossy, A.; Anderson, M. H.; Lara-Curzio, E.; Ranjan, D.;

Henry, A.; Sandhage, K. H. Ceramic-metal composites for heat exchangers in concentrated solar power plants. *Nature* **2018**, *562*, 406−409.

(22) Drescher, L.; Kornilov, O.; Witting, T.; Reitsma, G.; Monserud, N.; Rouzée, A.; Mikosch, J.; Vrakking, M. J. J.; Schütte, B. Extreme-Ultraviolet Refractive Optics. *Nature* **2018**, *564*, 91−94.

(23) Pease, R. S. Controlled Nuclear Fusion Reactions. *Nature* **1958**, *182*, 1051−1053.

(24) Skorb, E. V.; Andreeva, D. V. Layer-by-Layer Approaches for Formation of Smart Self-Healing Materials. *Polym. Chem.* **2013**, *4*, 4834−4845.

(25) Shankar, S.; Tanomrod, N.; Rawdkuen, S.; Rhim, J.-W. Preparation of Pectin/Silver Nanoparticles Composite Films with UV-Light Barrier and Properties. *Int. J. Biol. Macromol.* **2016**, *92*, 842−849.

(26) Ivanova, N. V.; Trofimova, N. N.; Es'kova, L. A.; Babkin, V. A. The Study of the Reaction of Pectin-Ag(0) Nanocomposites Formation. *Int. J. Carbohydr. Chem.* **2012**, *2012*, 1−9.

(27) Prager, S. Periodic Precipitation. *J. Chem. Phys.* **1956**, *25*, 279−283.

(28) Bensemann, I. T.; Fialkowski, M.; Grzybowski, B. A. Wet Stamping of Microscale Periodic Precipitation Patterns. *J. Phys. Chem. B* **2005**, *109*, 2774−2778.

(29) Schibeci, R. A.; Carlsen, C. An Interesting Student Chemistry Project: Investigating Liesegang Rings. *J. Chem. Educ.* **1988**, *65*, 365−366.

(30) *Hardware Protection through Obfuscation*, 1st ed.; Tehranipoor, M. M.; Bhunia, S.; Forte, D., Eds.; Springer Publishing Company: e-book, 2017; pp 352.

(31) Alsawafta, M.; Wahbeh, M.; Truong, V.-V. Plasmonic Modes and Optical Properties of Gold and Silver Ellipsoidal Nanoparticles by the Discrete Dipole Approximation. *J. Nanomater.* **2012**, *2012*, 457968.

(32) Parakhonskiy, B. V.; Bedard, M. F.; Bukreeva, T. V.; Sukhorukov, G. B.; Möhwald, H.; Skirtach, A. G. Nanoparticles on Polyelectrolytes at Low Concentration: Controlling Concentration and Size. *J. Phys. Chem. C* **2010**, *114*, 1996−2002.

(33) Kamyshinsky, R.; Marchenko, I.; Parakhonskiy, B.; Yashchenok, A.; Chesnokov, Y.; Mikhutkin, A.; Gorin, D.; Vasiliev, A.; Bukreeva, T. Composite Materials Based on Ag Nanoparticles in Situ Synthesized on the Vaterite Porous Matrices. *Nanotechnology* **2019**, *30*, 035603.

(34) Pinchasik, B.-E.; Tauer, K.; Möhwald, H.; Skirtach, A. G. Polymer Brush Gradients by Adjusting the Functional Density Through Temperature Gradient. *Adv. Mater. Interfaces* **2014**, *1*, 1300056.

(35) Muzammil, I.; Li, Y.; Lei, M. Tunable Wettability and PH-Responsiveness of Plasma Copolymers of Acrylic Acid and Octafluorocyclobutane. *Plasma Processes Polym.* **2017**, *14*, 1700053.

(36) Van Lierop, D.; Krpetić, Ž.; Guerrini, L.; Larmour, I. A.; Dougan, J. A.; Faulds, K.; Graham, D. Positively Charged Silver Nanoparticles and Their Effect on Surface-Enhanced Raman Scattering of Dye-Labelled Oligonucleotides. *Chem. Commun.* **2012**, *48*, 8192−8194.

(37) Ouyang, Q.-Q.; Hu, Z.; Li, S.-D.; Quan, W.-Y.; Wen, L.-L.; Yang, Z.-M.; Li, P.-W. Thermal Degradation of Agar: Mechanism and Toxicity of Products. *Food Chem.* **2018**, *264*, 277−283.

(38) Kachala, V. V.; Khemchyan, L. L.; Kashin, A. S.; Orlov, N. V.; Grachev, A. A.; Zalesskiy, S. S.; Ananikov, V. P. Target-Oriented Analysis of Gaseous, Liquid and Solid Chemical Systems by Mass Spectrometry, Nuclear Magnetic Resonance Spectroscopy and Electron Microscopy. *Russ. Chem. Rev.* **2013**, *82*, 648−685.

Letter

Tick-Borne Encephalitis Electrochemical Detection by Multilayer Perceptron on Liquid−Metal Interface

Artemii S. Ivanov, Konstantin G. Nikolaev, Anna A. Stekolshchikova, Weini T. Tesfatsion, Stanislav O. Yurchenko, Kostya S. Novoselov, Daria V. Andreeva, Maya Yu. Rubtsova, Mikhail F. Vorovitch, Aydar A. Ishmukhametov, Alex M. Egorov, and Ekaterina V. Skorb*

Cite This: *ACS Appl. Bio Mater.* 2020, 3, 7352−7356

Read Online

ACCESS | Metrics & More | Article Recommendations | SI Supporting Information

ABSTRACT: This work depicts an electrochemical hydrogel−eutectic gallium indium alloy interface for the detection of tick-borne encephalitis (TBE) virus. This interface allows recording of nonlinear current−voltage responses, depending on the composition of the hydrogel. The current−voltage data for the machine learning model are trained by a multilayer perceptron. This model accurately recognizes the TBE antibody, antigen, and an antibody−antigen complex in mixture with interfering bovine serum albumin with 93% accuracy. Thus, this interface can be used as a convenient method for expressed viruses and pathogens detection.
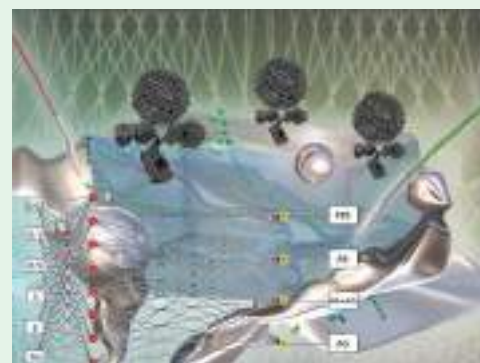
KEYWORDS: *tick-borne encephalitis, eGaIn, multilayer perceptron, biomolecules, viruses detection*

Rapid and sensitive detection of viral infections associated with human diseases is of great importance in a variety of applications, such as biomedical investigations,[1] pathogen identification,[2] and early clinical diagnosis.[3−5] There are viruses such as influenza viruses, human immunodeficiency virus (HIV), severe acute respiratory syndrome coronavirus (SARS-CoV19), and different flaviviruses, having the potential to cause global problems, including pandemic.[6,7]

TTick-borne encephalitis (TBE) virus is a member of the flavivirus genus and one of the critically important human pathogens.[8,9] Up to 10,000 cases of TBE disease are registered in Europe and Asia annually.[10] Virus carriers can be not only ticks but also animals. In this regard, the development of rapid, cheap, and straightforward methods for detecting TBE virus is relevant. Selective determination of viruses in biological fluids is one of the problems of using methods for rapid analysis. The polymerase chain reaction assay method was previously proposed for the determination of TBE RNA.[11] Enzyme-linked immunosorbent assay with electrochemical detection allows determination of TBE antibodies using indirect stripping voltammetric analysis.[12] Simultaneously, the assay needs calibration each time, which is time-consuming.[13] The idea here is a method with machine learning instead of calibration each time.

In laboratory analysis, gel permeation chromatography is used for these purposes. This method allows the effective separation of macromolecules in biological fluids by size.[14] Gel permeation chromatography has a unique separation mecha-nism based on differences in the molecular size of the sample components.[15,16] Microscale systems for purification and separation of biological fluids are microfluidic systems based on liquid chromatography methods.[17] For the precision manufacture of microfluidic devices, as well as devices for their operation, high costs are required, which increases the cost of analysis. For on-site analysis, the use of simple devices that do not require complex manipulations is required and suggested here by us.

We propose using the current−voltage (*I*−*V*) characteristics of the eutectic gallium indium alloy (eGaIn)/hydrogel interface (Figure 1) for the selective assay of TBE antibody (AB), antigen (AG), and an antibody−antigen (AB−AG) complex in the presence of an interfering agent.

The electrochemical analysis, namely, voltammetry, allows the formation of various redox states at the electrode−electrolyte interface.[18] A logical analysis of the obtained data may indirectly indicate the presence of a particular virus, antibodies, or their associated form. For the full spectrum of redox state generation, it is required to use an electrode
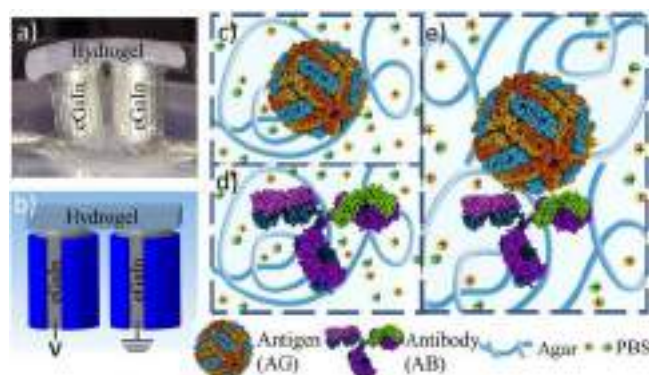
Figure 1. (a) Photograph of the electrochemical system. (b) Scheme of the electrochemical system. (c) AG in the media of agar and PBS. (d) AB in the media of agar and PBS. (e) AB−AG interaction in media of agar and PBS.

material that is capable of forming polymorphic states. One such material is eGaIn alloy.[19] eGaIn alloy consists of 75 wt % Ga and 25 wt % In. This alloy is successfully used to create flexible electrical components due to its high electrical conductivity, nontoxicity, low saturated vapor pressure, and low melting point. On the air, gallium is passivated by a thin oxide layer that has a higher resistivity than the pure metal.[20,21] A soft-matter electric system consisting of hydrogels and two eGaIn electrodes is presented in Figure 1. Hydrogel doped with PBS and AB, AG, or complex AG−AB lays on top of the electrodes and connects them. When current flows through the eGaIn alloy and hydrogel, gallium is oxidated and $Ga(OH)^{2+}$ cations diffuse into the gel. Indium cations do not exist in such a system due to their reduction by gallium. Then insoluble layer of $GaPO_4$ appears on the boundary between alloy and hydrogel after interaction with PO^{4-} anions. Resistance of gallium phosphate layer determines the $I-V$ curve of the sample. However, the presence of AB, AG, or AB−AG changes the $I-V$ curve. Interactions of gallium cations with these substances lead to the formation of complex compounds $AB\cdots Ga(OH)^{2+}$, $AG\cdots Ga(OH)^{2+}$, $AB-AG\cdots Ga(OH)^{2+}$. Such complexes exist due to the amine and thiol groups in AB and AG molecules. Redox processes of formation and decay of such substances determine peaks formed in $I-V$ curves, which are different in the potential range 0.02−5 V. Different forms of hysteresis loops, which are individual for each compound, are used for composition identification.

For logical analysis,[22] we propose use of a feedforward deep neural network model (multilayer perceptron).[23,24] The backpropagation algorithm does the training of such a machine learning model.[25] Different computer and machine learning methods are able to solve a lot of biological and chemical problems, in particular, establishing the structure of proteins and their interactions, as well as predicting the effect of mutations on their assembly.[26,27]

Multilayer perceptron supervised learning allows the detection of individual states on an eGaIn/hydrogel interface that depends on hydrogel composition. A database is necessary for model training.[28] In the database columns consist of attributes by which responses are determined. Since the redox peaks are individual for hydrogel compositions, currents are attributes and compositions are responses. This approach can be used to detect diseases and their stages using $I-V$ curves as a fingerprint for identifying AB, AG, and AB−AG complexes.

For gel preparation, 0.05 g of agar is added into 5 mL of phosphate-buffered saline, and then this solution is stirred and heated. The solution is poured into a Petri dish and cooled to 45 °C. Then 2×10^3 particles/mL AG buffered gel is prepared. In the case of AB, we prepare a 1:3000 solution by adding 1.67 μL of antibody solution into 5 mL of buffered gel (0.01 M phosphate buffer with pH 7.4). Also, for an AB−AG solution, both substances are added simultaneously. Collected $I-V$ characteristics (Figure 2) correspond for the two-electrode system/hydrogel interface.
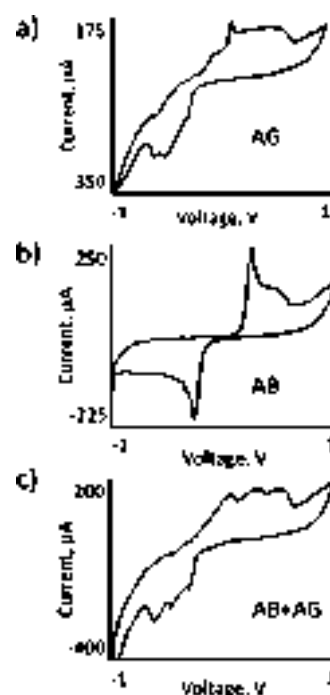
Figure 2. Characteristic $I-V$ curves with 200 points per cycle for different gels in a voltage range of −1 to 1 V. (a) $I-V$ curve for a gel with AG 2×10^3 (0.01 M PBS, pH 7.4) particles/mL. (b) $I-V$ curve for a gel with AB diluted 1:3000 (0.01 M PBS, pH 7.4). (c) $I-V$ curve for a gel with AB + AG (0.01 M PBS, pH 7.4).

The used ranges for database are −0.02 to 0.02 V, −0.1 to 0.1 V, −0.5 to 0.5 V, −1 to 1 V, and −5 to 5 V, and $(-5 \text{ to } 5 \text{ V})_n$. The full database for the machine learning experiment is provided in the Supporting Information (SI) as well as plotted $I-V$s shown in Figure S1. The division of data on the training set (90%) and test set (10%) allows one to verify the accuracy of the model. This separation allows one to save a sufficiently large number of values for training the model and does not overly reduce the test set. The multilayer perceptron model is trained with the following parameters: learning rate, −0.1; momentum, −0.8; the number of nodes in the hidden layer, −8 (Figure 3). The determination accuracy of 93% is achieved!

The system trained on pure samples is tested to determine AG and AB in samples with an interfering agent. The interfering agent—bovine serum albumin (BSA) with concentration range from 0.05 to 1 wt %—serves as a blocking agent to prevent nonspecific interactions between analytes, substrates, and electrode surfaces.[29] The concentration of BSA in test samples was 0.07 wt %. The multilayer perceptron trained model demonstrates the ability to recognize the hydrogel system, consisting of AG, AB, their complex, and BSA (Figure 4).
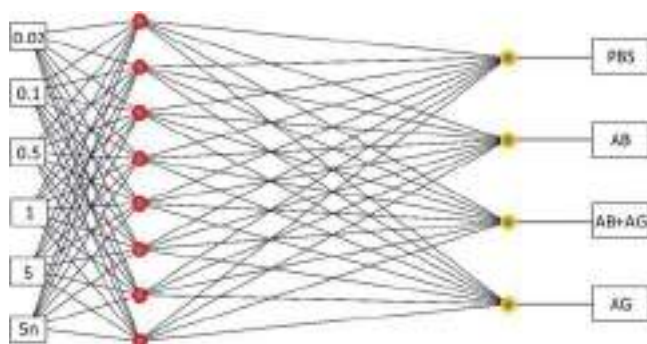
Figure 3. Scheme of multilayer perceptron with one hidden layer. One hidden layer with eight nodes is used to describe the relationship of current−voltage data from the input layer and sample compound data from the output layer.

In all cases (Figure 4), the perceptron model obtained the correct results with the highest probabilities. Some uncertainty appeared with the identification of AG and AG−AB complex due to the presence of AG in both samples. From $I-V$ curves it is visible that AG and AG−AB have similar oxidation−reduction peaks (Figure 2). However, these peaks and current values are different enough for identification of sample compounds by machine learning methods. Also, further addition of statistically significant values to the database will lead to a decrease of the statistical error.

In conclusion, we suggested a system that can detect AB, AG, and AB−AG complex in the presence of the interfering agent. This is of high importance for the approach of complex fluids analysis. The method uses a one-time collected database and machine learning algorithm that allows avoiding calibration each time. A multilayer perceptron algorithm reduces the analyte detection time and improves the statistical reliability of predictions. The proposed reliable method could be used for the resolution of the wide range of complex biological systems. We show the proof-of-concept, which in the following can be applied for miniaturized test systems with a portative potentiostat. Such an electrochemical system demonstrates a new approach to the detection of virus diseases and pathogens.

■ ASSOCIATED CONTENT

Ⓢ Supporting Information

The Supporting Information is available free of charge at https://pubs.acs.org/doi/10.1021/acsabm.0c00954.

All data sets used for the system training (PDF)

Dataset used for the machine learning approach (XLSX)

■ AUTHOR INFORMATION

Corresponding Author

Ekaterina V. Skorb − *Infochemistry Scientific Center, ITMO University, Saint Petersburg 191002, Russian Federation;* ⓞ orcid.org/0000-0003-0888-1693; Email: skorb@itmo.ru
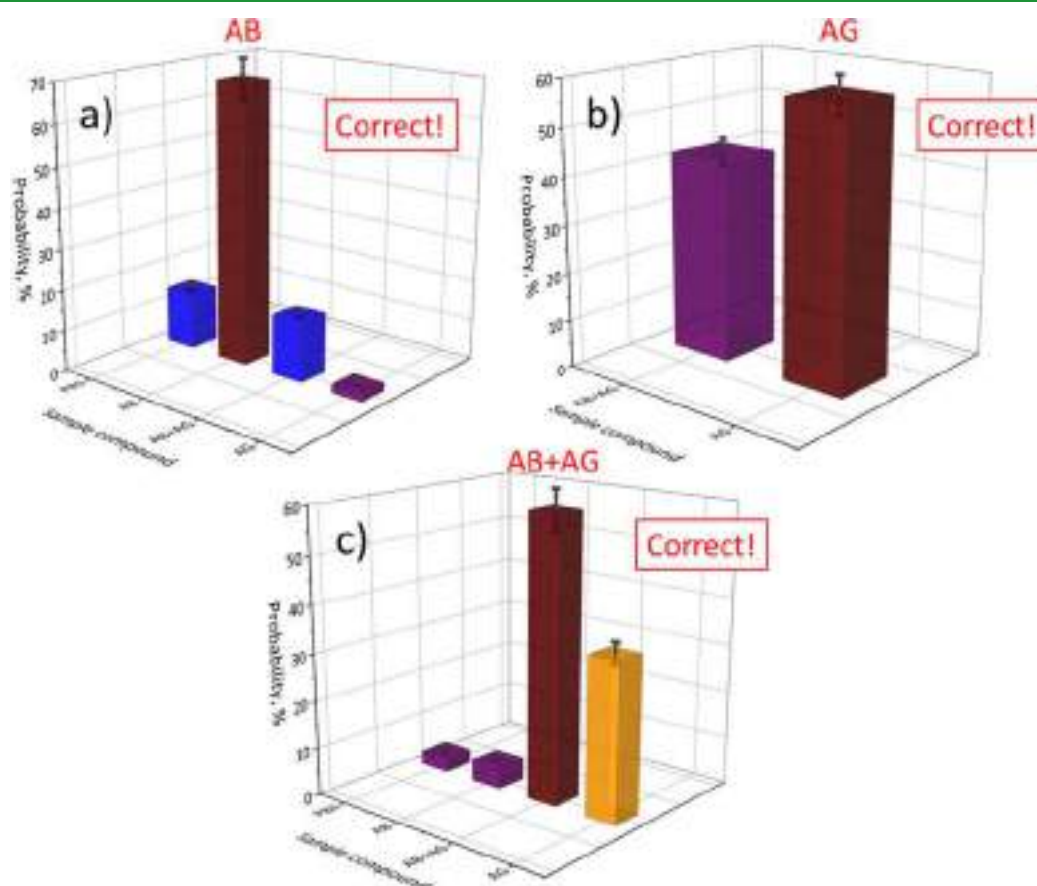
Figure 4. Prediction results for sample compounds in the presence of BSA obtained by multilayer perceptron model. (a) Graph for the sample with AG. (b) Graph for the sample with AB. (c) Graph for the sample with AB−AG complex.

Authors

Artemii S. Ivanov − *Infochemistry Scientific Center, ITMO University, Saint Petersburg 191002, Russian Federation*

Konstantin G. Nikolaev − *Infochemistry Scientific Center, ITMO University, Saint Petersburg 191002, Russian Federation*

Anna A. Stekolshchikova − *Infochemistry Scientific Center, ITMO University, Saint Petersburg 191002, Russian Federation*

Weini T. Tesfatsion − *Infochemistry Scientific Center, ITMO University, Saint Petersburg 191002, Russian Federation*

Stanislav O. Yurchenko − *Bauman Moscow State Technical University, Moscow 105005, Russian Federation;* ⊚ orcid.org/0000-0001-6821-904X

Kostya S. Novoselov − *Department of Materials Science and Engineering, National University of Singapore, Singapore 117575 Singapore*

Daria V. Andreeva − *Department of Materials Science and Engineering, National University of Singapore, Singapore 117575 Singapore*

Maya Yu. Rubtsova − *Faculty of Chemistry, M. V. Lomonosov Moscow State University, Moscow 119991, Russian Federation*

Mikhail F. Vorovitch − *Federal State Budgetary Scientific Institution "Chumakov Federal Scientific Center for Research and Development of Immune-and-Biological Products of Russian Academy of Sciences" (FSBSI "Chumakov FSC R&D IBP RAS"), Moscow 108819, Russian Federation; Sechenov First Moscow State Medical University, 119991 Moscow, Russian Federation*

Aydar A. Ishmukhametov − *Federal State Budgetary Scientific Institution "Chumakov Federal Scientific Center for Research and Development of Immune-and-Biological Products of Russian Academy of Sciences" (FSBSI "Chumakov FSC R&D IBP RAS"), Moscow 108819, Russian Federation; Sechenov First Moscow State Medical University, 119991 Moscow, Russian Federation*

Alex M. Egorov − *Faculty of Chemistry, M. V. Lomonosov Moscow State University, Moscow 119991, Russian Federation; Federal State Budgetary Scientific Institution "Chumakov Federal Scientific Center for Research and Development of Immune-and-Biological Products of Russian Academy of Sciences" (FSBSI "Chumakov FSC R&D IBP RAS"), Moscow 108819, Russian Federation*

Complete contact information is available at:
https://pubs.acs.org/10.1021/acsabm.0c00954

Notes

The authors declare no competing financial interest.

■ REFERENCES

(1) Park, J.-K.; Xiao, Y.; Ramuta, M. D.; Rosas, L. A.; Fong, S.; Matthews, A. M.; Freeman, A. D.; Gouzoulis, M. A.; Batchenkova, N. A.; Yang, X.; Scherler, K.; Qi, L.; Reed, S.; Athota, R.; Czajkowski, L.; Han, A.; Morens, D. M.; Walters, K.-A.; Memoli, M. J.; Kash, J. C.; Taubenberger, J. K. Pre-existing immunity to influenza virus hemagglutinin stalk might drive selection for antibody-escape mutant viruses in a human challenge model. *Nat. Med.* **2020**, *26*, 1240−1246.

(2) Gao, Z.; Ovchinnikova, O. G.; Huang, B.-S.; Liu, F.; Williams, D. E.; Andersen, R. J.; Lowary, T. L.; Whitfield, C.; Withers, S. G. High-Throughput "FP-Tag" Assay for the Identification of Glycosyltransferase Inhibitors. *J. Am. Chem. Soc.* **2019**, *141* (6), 2201−2204.

(3) Smith, S. J.; Nemr, C. R.; Kelley, S. O. Chemistry-Driven Approaches for Ultrasensitive Nucleic Acid Detection. *J. Am. Chem. Soc.* **2017**, *139* (3), 1020−1028.

(4) Jiang, X.; Loeb, J. C.; Manzanas, C.; Lednicky, J. A.; Fan, Z. H. Valve-Enabled Sample Preparation and RNA Amplification in a Coffee Mug for Zika Virus Detection. *Angew. Chem., Int. Ed.* **2018**, *57* (52), 17211−17214.

(5) Gao, X.; Li, S.; Ding, F.; Fan, H.; Shi, L.; Zhu, L.; Li, J.; Feng, J.; Zhu, X.; Zhang, C. Rapid Detection of Exosomal MicroRNAs Using Virus-Mimicking Fusogenic Vesicles. *Angew. Chem., Int. Ed.* **2019**, *58* (26), 8719−8723.

(6) Lavizzari, A.; Klingenberg, C.; Profit, J.; Zupancic, J. A. F.; Davis, A. S.; Mosca, F.; Molloy, E. J.; Roehr, C. C.; The International Neonatal COVID-19 Consortium. International comparison of guidelines for managing neonates at the early phase of the SARS-CoV-2 pandemic. *Pediatr. Res.* **2020**, DOI: 10.1038/s41390-020-0976-5.

(7) Zhang, X.; Dhawane, A. N.; Sweeney, J.; He, Y.; Vasireddi, M.; Iyer, S. S. Electrochemical Assay to Detect Influenza Viruses and Measure Drug Susceptibility. *Angew. Chem., Int. Ed.* **2015**, *54* (20), 5929−5932.

(8) Makenov, M.; Karan, L.; Shashina, N.; Akhmetshina, M.; Zhurenkova, O.; Kholodilov, I.; Karganova, G.; Smirnova, N.; Grigoreva, Y.; Yankovskaya, Y.; Fyodorova, M. First detection of tick-borne encephalitis virus in Ixodes ricinus ticks and their rodent hosts in Moscow, Russia. *Ticks Tick Borne Dis* **2019**, *10* (6), 101265.

(9) Holding, M.; Dowall, S. D.; Medlock, J. M.; Carter, D. P.; McGinley, L.; Curran-French, M.; Pullan, S. T.; Chamberlain, J.; Hansford, K. M.; Baylis, M.; Vipond, R.; Hewson, R. Detection of new endemic focus of tick-borne encephalitis virus (TBEV), Hampshire/Dorset border, England, September 2019. *Eurosurveillance* **2019**, *24* (47), 1900658.

(10) Strokach, A.; Corbi-Verge, C.; Teyra, J.; Kim, P. M. Predicting the Effect of Mutations on Protein Folding and Protein-Protein Interactions. *Methods Mol. Biol.* **2019**, *1851*, 1−17.

(11) Veje, M.; Studahl, M.; Norberg, P.; Roth, A.; Möbius, U.; Brink, M.; Bergström, T. Detection of Tick-Borne Encephalitis Virus RNA in Urine. *J. Clin. Microbiol.* **2014**, *52* (11), 4111.

(12) Khristunova, E.; Barek, J.; Kratochvil, B.; Korotkova, E.; Dorozhko, E.; Vyskocil, V. Electrochemical immunoassay for the detection of antibodies to tick-borne encephalitis virus by using various types of bioconjugates based on silver nanoparticles. *Bioelectrochemistry* **2020**, *135*, 107576.

(13) Wu, Y.; Tilley, R. D.; Gooding, J. J. Challenges and Solutions in Developing Ultrasensitive Biosensors. *J. Am. Chem. Soc.* **2019**, *141* (3), 1162−1170.

(14) Mena, J. A.; Ramírez, O. T.; Palomares, L. A. Quantification of rotavirus-like particles by gel permeation chromatography. *J. Chromatogr. B: Anal. Technol. Biomed. Life Sci.* **2005**, *824* (1), 267−276.

(15) Moscato, B. M.; Zhu, B.; Landis, C. R. GPC and ESI-MS Analysis of Labeled Poly(1-Hexene): Rapid Determination of Initiated Site Counts during Catalytic Alkene Polymerization Reactions. *J. Am. Chem. Soc.* **2010**, *132* (41), 14352−14354.

(16) Mason, A. F.; Coates, G. W. Gel Permeation Chromatography as a Combinatorial Screening Method: Identification of Highly Active Heteroligated Phenoxyimine Polymerization Catalysts. *J. Am. Chem. Soc.* **2004**, *126* (35), 10798−10799.

(17) Grinias, J. P.; Kennedy, R. T. Advances in and prospects of microchip liquid chromatography. *TrAC, Trends Anal. Chem.* **2016**, *81*, 110−117.

(18) Deng, X.; Galli, F.; Koper, M. T. M. In Situ Electrochemical AFM Imaging of a Pt Electrode in Sulfuric Acid under Potential Cycling Conditions. *J. Am. Chem. Soc.* **2018**, *140* (41), 13285−13291.

(19) Wang, C.; Wang, C.; Huang, Z.; Xu, S. Materials and Structures toward Soft Electronics. *Adv. Mater.* **2018**, *30* (50), 1801368.

(20) Koo, H.-J.; So, J.-H.; Dickey, M. D.; Velev, O. D. Towards All-Soft Matter Circuits: Prototypes of Quasi-Liquid Devices with Memristor Characteristics. *Adv. Mater.* **2011**, *23* (31), 3559−3564.

(21) Daeneke, T.; Khoshmanesh, K.; Mahmood, N.; de Castro, I. A.; Esrafilzadeh, D.; Barrow, S. J.; Dickey, M. D.; Kalantar-zadeh, K. Liquid metals: fundamentals and applications in chemistry. *Chem. Soc. Rev.* **2018**, *47* (11), 4073−4111.

(22) Behler, J. First Principles Neural Network Potentials for Reactive Simulations of Large Molecular and Condensed Systems. *Angew. Chem., Int. Ed.* **2017**, *56* (42), 12828−12840.

(23) Akter, T.; Desai, S. Developing a predictive model for nanoimprint lithography using artificial neural networks. *Mater. Des.* **2018**, *160*, 836−848.

(24) Patel, J.; Choi, S.-K. Classification approach for reliability-based topology optimization using probabilistic neural networks. *Struct. Multidiscip. Optim.* **2012**, *45* (4), 529−543.

(25) Schneider, G.; Wrede, P. Prediction of the Secondary Structure of Proteins from the Amino Acid Sequence with Artificial Neural Networks. *Angew. Chem., Int. Ed. Engl.* **1993**, *32* (8), 1141−1143.

(26) Abalymov, A.; Van der Meeren, L.; Skirtach, A. G.; Parakhonskiy, B. V. Identification and Analysis of Key Parameters for the Ossification on Particle Functionalized Composites Hydrogel Materials. *ACS Appl. Mater. Interfaces* **2020**, *12* (35), 38862−38872.

(27) Rinderspacher, B. C.; Elward, J. M. Enriched optimization of molecular properties under constraints: an electrochromic example. *Mol. Syst. Des. Eng.* **2018**, *3* (3), 485−495.

(28) Gasteiger, J.; Zupan, J. Neural Networks in Chemistry. *Angew. Chem., Int. Ed. Engl.* **1993**, *32* (4), 503−527.

(29) Sun, Y.-S.; Zhu, X. Characterization of Bovine Serum Albumin Blocking Efficiency on Epoxy-Functionalized Substrates for Micro-array Applications. *J. Lab. Autom.* **2016**, *21* (5), 625−631.

Macromolecular
Materials
and Engineering
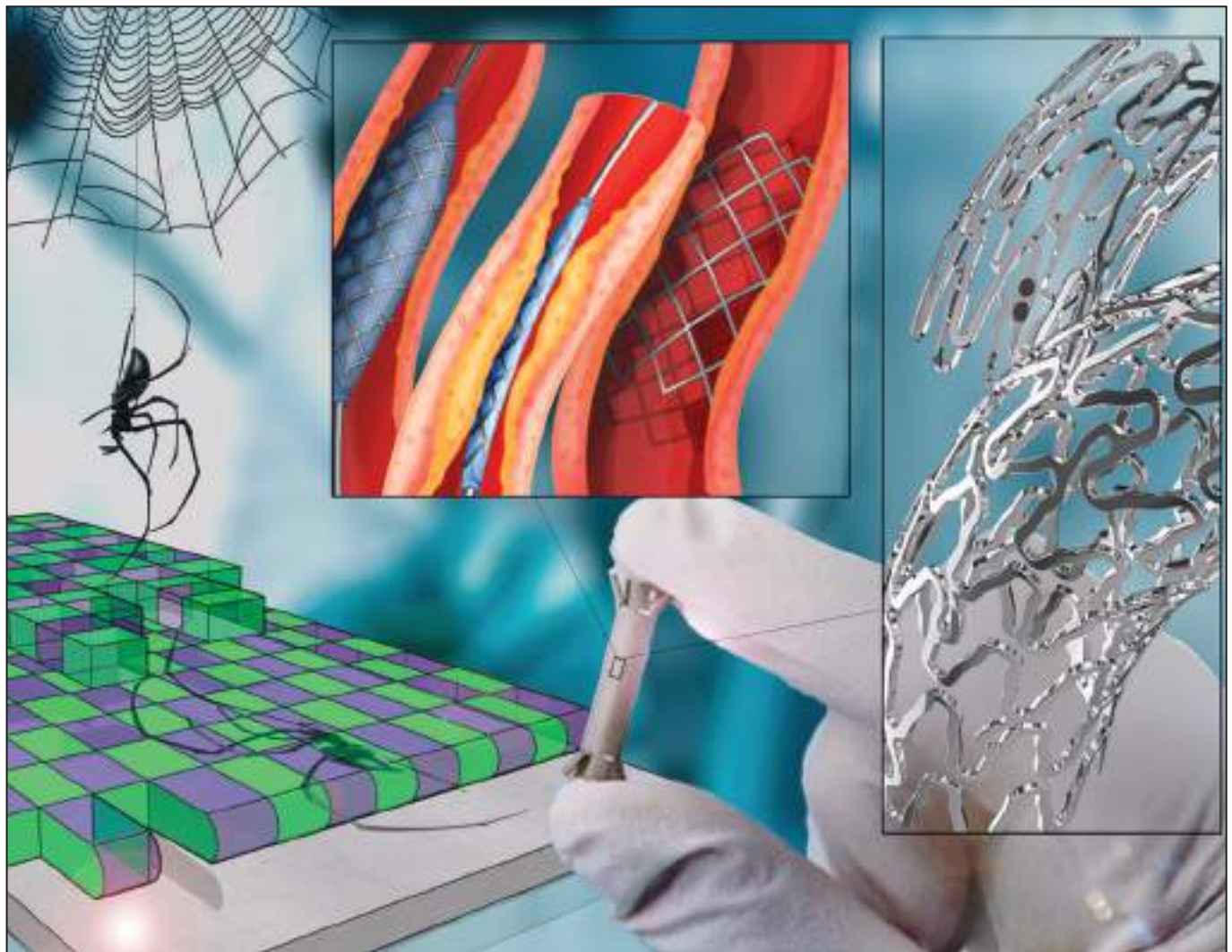
Natural Silk Film for Magnesium Protection: Hydrophobic/Hydrophilic Interaction and Self-Healing Effect

Sviatlana A. Ulasevich, Anastasia V. Nenashkina, Nikolai V. Ryzhkov, Grigorii Kiselev, Valeria Nikolaeva, Aleksandra Kiseleva, Kseniia Mosina, Ekaterina V. Skorb,* and Elena F. Krivoshapkina*

Biodegradable implants are required in order to provide successful treatment of injuries. Temporary magnesium-based implants with particular properties are needed in cases when it is desirable not only to maintain vital activity, but also to initiate the self-healing process of damaged bones or tissues as well. Unfortunately, the use of magnesium alloys is limited due to the fast biodegradability of the applied material. The aim of this research is to improve the corrosion resistance of magnesium alloys by sonochemical treatment in silk solution followed by additional layer-by-layer deposition of natural silk on the magnesium surface. The sonication process is carried out at a frequency of 20 kHz during 5–10 min, while the duration of the silk layer deposition is 15 min. The corrosion behavior of magnesium substrates modified by natural silk layer-by-layer assembly is studied. Magnesium substrates sonochemically treated in silk solution demonstrate three times better corrosion resistance compared to control samples sonochemically treated in water. Additional deposition of a silk layer enhances obtained corrosion resistance by 18 times, resulting in a 54-fold increase overall.

1. Introduction

Over the last few years, magnesium alloys have gained some attention due to their potential applications as biodegradable implants in the biomedical field, specifically in orthopedics.[1–3] To appreciate the prospects of magnesium alloys in such applications, understanding of the physiological roles of magnesium in the human body is essential.[2] It is well known that magnesium ions are the fourth most abundant cations in mammals after sodium, potassium, and calcium. Also, magnesium is the second most prevalent intracellular cation.[4,5] Inside mammalian cells, magnesium plays essential roles including the following ones: regulating calcium and sodium ion channels, stabilizing deoxyribonucleic acid, being a cofactor and catalyst for many enzymes, and stimulating cell growth and proliferation.[4,6]

Magnesium alloys are composed of lightweight metals that possess mechanical properties close to natural bones. They also reduce stress-shielding effects due to appropriate elastic modulus of the current implant.[7] The degradation rate of magnesium-based implants is adapted to the bone healing process. Furthermore, degradation products of magnesium alloys are nontoxic to the human body as opposed to the majority of metallic biomaterials. Moreover, Mg^{2+} ions are components of bone tissues, being the fourth most frequent ion in the human body and vital to metabolism.[8] Additionally, magnesium alloys may sustain the integrity under physiological pressure for 12 to 18 weeks, enhancing bone tissue recovery.[9]

The unfortunate inconvenience of magnesium implant application is that pure magnesium undergoes corrosion under effect of environmental pH (7.4–7.6) quite fast,[10] according to the following anodic (Equation (1)) and cathodic (Equation (2)) reactions. In addition, the reaction described by Equation (3) can occur near the cathode surface.[11]

$$Mg - 2e^- \rightarrow Mg^{2+} \tag{1}$$

$$2H_2O + 2e^- \rightarrow H_2 + 2OH^- \tag{2}$$

$$Mg^{2+} + 2OH^- \rightarrow Mg(OH)_{2(s)} \tag{3}$$
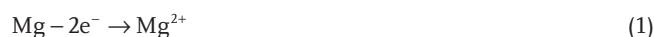
The hydrogen gas, being released in large amounts during a short period, is one of the main issues for clinical demands. It is known that hydrogen gas development is the reason for substantial gas bubbles appearance around implant surfaces, causing separation of tissue layers.[10,13]

Additionally, magnesium hydroxide is unstable in the presence of chloride ions, components of human blood. In the presence of chloride ions, magnesium hydroxide undergoes a conversion into magnesium chloride, which dissolves in aqueous solutions.[12]

The result of the abovementioned negative factors is a so-called biodegradation of the material, when implant quickly dissolves under physiological pH before the body tissue is regenerated. One of the methods to control the biodegradation

Dr. S. A. Ulasevich, A. V. Nenashkina, N. V. Ryzhkov, G. Kiselev, V. Nikolaeva, A. Kiseleva, K. Mosina, Prof. E. V. Skorb, Prof. E. F. Krivoshapkina
ITMO University
9, Lomonosova Street, Saint Petersburg 191002, Russian Federation
E-mail: skorb@itmo.ru; kef@scamt-itmo.ru

**ADVANCED
SCIENCE NEWS**
www.advancedsciencenews.com

**Macromolecular
Materials and Engineering**
www.mme-journal.de

process is deposition of polyelectrolyte coatings on the metal surface.[13–23] Polyelectrolyte assembly prevents the interaction of corrosive species with the metal surface[13–15] and possesses pH-buffering activity to provide a possibility of stabilizing pH on the metal surface in the corrosion area.[16–18]

In this article, we establish a novel, smart, multilayer anticorrosion system that consists of a pH-sensitive natural polymer silk film deposited on magnesium alloy surfaces pretreated by sonication. The novelty of the method lies in sonochemical treatment of magnesium alloy in spider silk solution. We suggest there are several processes during this treatment. First, the structuring of the magnesium surface and pore formation occur. Then, fragments of spider silk molecules incorporate simultaneously into pores and structure of the magnesium surface. For better corrosion resistance we also use additional layer-by-layer assembly of spider silk layers. This coating is suggested to improve corrosion resistance of magnesium-based alloys.

In several reports, silkworm silk has been already successfully applied as a natural polymer-based source for coating of metallic implants.[24,25] Although silkworms are domesticated[26] and their silk has been used in industry for over thousands of years in order to develop textiles,[27] spider silk constitutes equally crucial material to investigate.[28] Silkworms and spiders produce various types of silks, each type represented different values of tensile strength and elasticity.[29] Therefore, for two types of insects, protein structure and fibers architecture may differ, which inflects modifications in silk properties.[30] Mechanical strength of spider silk accordingly seems to sufficiently surpass that of silkworms, making it a favorable material to produce sustainable bio-implants for human body.[31]

Spider silk is a natural biopolymer consisting of numerous spider silk proteins named spidroins. Effective formation of these composites is implemented in glands, where distinctive cells generate liquid silk proteins in the lumen of the body.[32] After being secreted in the narrow duct, aqueous solution undergoes transformation to solid state under changes in temperature, pressure, and pH.[28,32] Hierarchical structure of spidroins is represented by repetitive sequences composed of 150–500 amino acids[33] and edged by non-repetitive N- and C-terminal regions.[34,35] Those repetitive blocks, which are rich in alanine, are packed in a certain way to form extra stable crystalline secondary structures named β-sheets.[36] Crystallites are distributed in the amorphous regions that are formed of glycine enriched secondary structures: random coil conformations, α-helices, and β-turns.[37] Namely, β-sheets are responsible for the great toughness of silk, while random coil conformations and α-helices make fibers elastic.[38] Biocompatibility and biodegradability should be mentioned as well; spider silk is known to be applied in various biomedical fields from tissue engineering to cancer therapy.[38,39]

In addition to enhanced mechanical properties and biocompatibility, a tough yet flexible silk coating may prevent quick Mg^{2+} release into the human body, prolonging the period of implant service. Furthermore, the presence of biocompatible nanocomposite may accelerate bone or tissue healing processes and reduce the immune response as well. Therefore, the properties of silk make it a suitable candidate for implant modification, providing a strong and flexible "shield" between the body and magnesium-based material.

2. Results and Discussion

2.1. Corrosion Study of Magnesium Based Implants Modified by Natural Spider Silk

The design of a novel anticorrosion system is schematically shown in **Figure 1**. A thin natural oxide film that is not sufficient to protect the magnesium against corrosion usually covers the magnesium surface. Therefore, we decided to form a thick protective oxide layer using ultrasonic treatment in distilled water (control sample) at a frequency of 20 kHz during 10 min. It is generally expected that the surface pretreatment produces a porous oxide layer on the metal surface with the roughness sufficient for mechanical interlocking. Sonication provides an opportunity to incorporate different ions and even molecules. For these purposes, we decided to treat magnesium alloy in a silk solution (Figure 1b, picture (1)). After sonochemical modification, the sample should be rinsed in water and dried (Figure 1b, picture (2)). Studies of various sonication durations (from 1 to 30 min) revealed that 10 min is optimal for obtaining the best corrosion resistance. Sonication time less than 10 min does not show proper corrosion resistance while the longer duration of sonication demonstrates quite the same values of corrosion resistance. Moreover, since silk solution has pH of 4.0, long sonication leads to dissolving the magnesium implant. Therefore, there is no need to use sonication longer than 10 min. To enhance the corrosion resistance, an additional layer of silk is deposited by dipping the sample in the silk solution for 15 min (Figure 1b, picture (3)).

Natural spider silk was obtained from *Linothele fallax*. Scanning electron microscopy (SEM) image (**Figure 2**a) shows long fibers of natural silk of different diameters. Natural spider silk fibers have smooth surfaces with noticeable furrows aligned across the fiber axis. The Fourier transform infrared spectroscopy (FTIR) spectrum of the natural spider silk fibers (Figure 2b) reveals characteristic bands of polypeptide absorbance: amide I (1650 cm^{-1}) and amide II (1540 cm^{-1}) are two main absorption bands, which are observed due to stretching of $C = O$ bonds (amide I) and planar deformation vibrations of the $N–H$ bond (amide II). A clear band at 1230 cm^{-1} is detected because of mixed $C–N$ stretching and $N–H$ bending vibrations of amino acids of the spidroins. A clear band is also observed at about 3300 cm^{-1} due to stretching vibrations of the $N–H$ bond. Prior to the implant modification, the bioactivity of spider silk was also studied. Figure 2c shows that natural spider silk does not seem to possess any biological activity, making web from *Linothele fallax* a sufficient biocompatible material for broad biomedical applications. Figure 2d shows the analysis of the secondary structure of the proteins in the silk according to a method described by Madurga et al.[40] The contribution of secondary structures is obtained from the mathematical processing of the amide I band. In this type of web, there is a relatively large number of β-structures, which play an important role in the strength characteristics of the web.

It should be mentioned that natural spider silk does not dissolve easily due to its very complicated polymer structure containing different sets of proteins. The solution of spider silk is characterized by dynamic light scattering (DLS) analysis (Figure 2e). Large aggregates were removed by centrifuging at
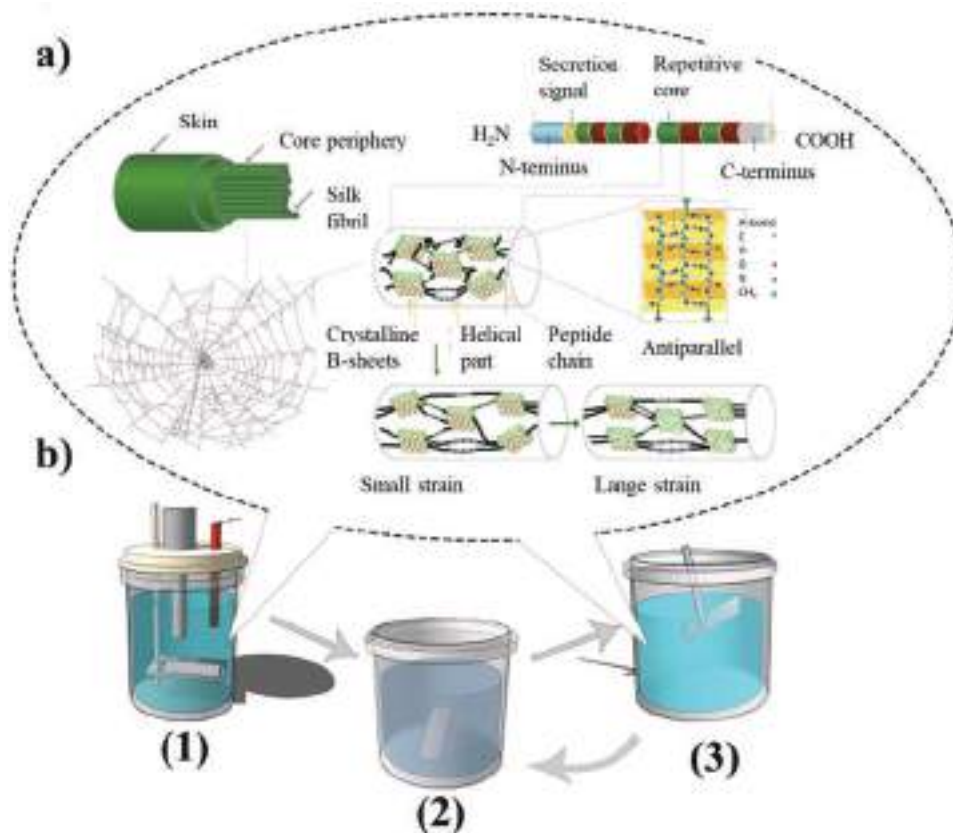
Figure 1. a) Schematic structure of spider silk; b) Schematic representation of magnesium ultrasonic treatment in the silk solution at 20 kHz for 10 min (1) followed by rinsing in distilled water (2) and layer-by-layer silk deposition by dipping into the silk solution at a pH = 4.0 (3).

6000 rpm for 6 min. The major protein particles have a mean hydrodynamic diameter of 147.0 ± 2.2 nm. The extent protein globules that are also present in the silk solution at 25 °C have the smallest mean hydrodynamic diameter of 1.5 ± 0.2 nm.

2.2. Corrosion Study of Magnesium Based Implants Modified by Natural Spider Silk

The SEM images (**Figure 3**) of the modified samples fabricated by sonication of the magnesium surface in water show rough porous structures. The surface obtained by sonochemical treatment in the silk solution looks similar (Figure 3b), while sonochemical treatment followed by layer-by-layer silk deposition leads to uniform deposition of silk on the substrate surface. Magnification shows the fragments of spider silk on the magnesium surface (Figure 3c). In the case of sonochemical treatment in the silk solution, silk molecules do not form a continuous coating but rather are randomly bunched on the surface. Figure 3d–f show the micro-morphologies of the surfaces of the modified samples after the corrosion test in 3.5 wt% NaCl solution.

Figure 3d,e show that the morphology of the initial sample surface exhibits a porous structure, which is composed of tiny erect laminas. The morphology of the samples sonochemically treated in water and in the silk solution changes drasti-

cally (Figure 3d,e), while morphology of the sample additionally covered by a silk layer changes a little. In Figure 3f, we can see the fragments of the initial structure.

Moreover, for the initial sample, damage is found on most of the surface, and pitting corrosion initially takes place at the edges of the sample. However, for the silk covered sample, no obvious corrosion damage is observed during first 2 min compared to the samples without a silk layer. This demonstrates that after ultrasonic modification in the silk solution and additional deposition of the silk layer, the corrosion resistance of magnesium samples can be greatly improved as advised by the further potentiodynamic polarization tests.

The potentiodynamic polarization curves of the initial and modified samples are shown in **Figure 4**a. Figure 4 presents the logarithm of the passive current density (logI) as a function of the applied voltage (values are summarized in **Table 1**). The corrosion potential (E_{corr}) is the potential at which the anodic and cathodic reaction rates are equal. The measurement current approaches zero at the corrosion potential because all electrons released by dissolving the metal are consumed by reduction reactions. The Tafel slopes method is used to measure the corrosion potential. As shown in Table 1 and Figure 4a (curve 1), the E_{corr} of magnesium sonochemically treated in water is −1.385 V, and the calculated corrosion rate equals 10.74 mm/year. The corrosion potential values of magnesium alloy correspond to the literature data and lie in a range from
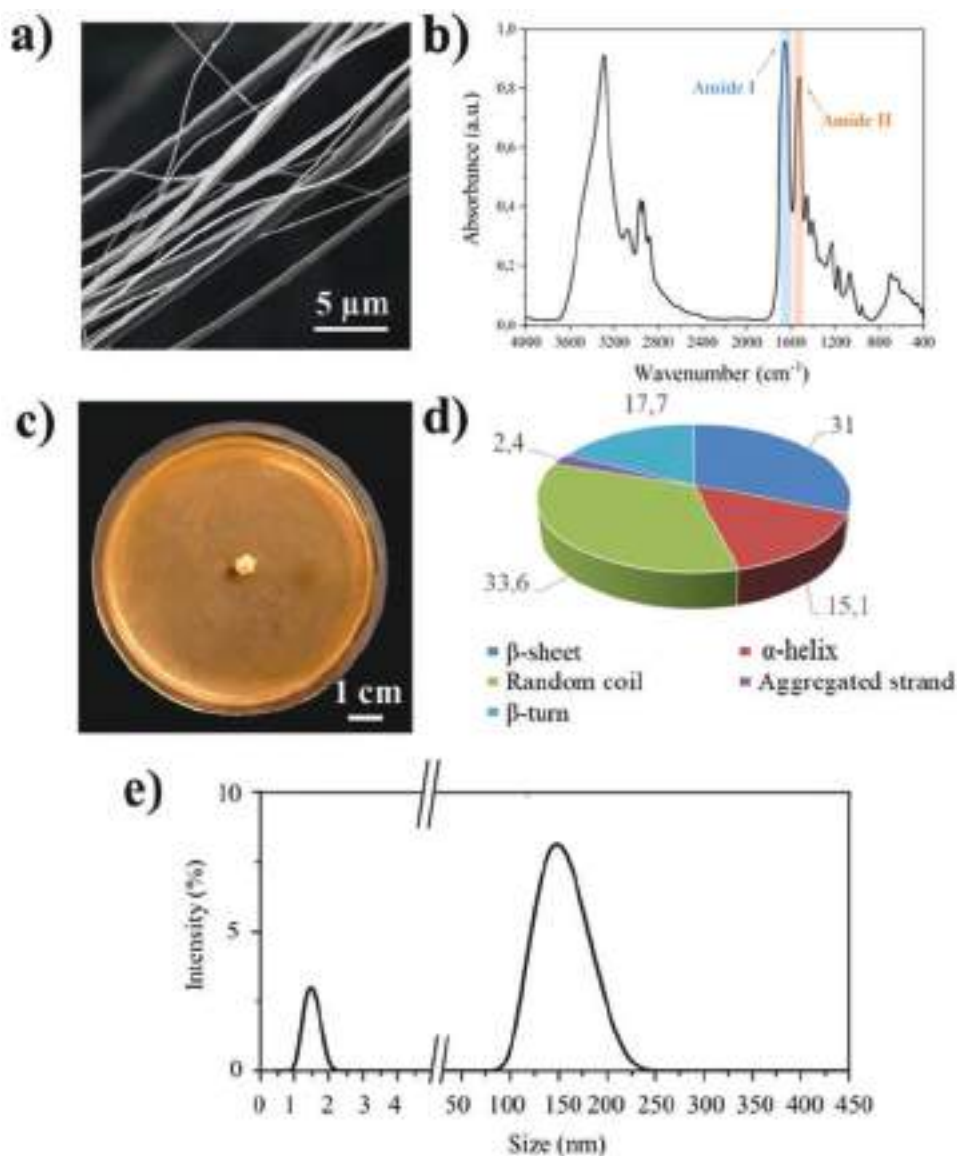
Figure 2. a) SEM image of natural spider silk fibers; b) FTIR spectrum of natural spider silk fibers; c) Bioactivity test of natural spider silk sample; scale bar is 1 cm; d) Percentage of secondary structures in spider silk proteins; e) DLS-analysis of prepared silk solution.

−1.3 to −1.52 V due to different content of the magnesium alloy.[24,25,41–43] Sonochemical treatment in the silk solution changes E_{corr} to −1.518 V, while the corrosion rate decreases to 3.27 mm/year. Thus, sonochemical treatment in the silk solution leads to a threefold increase in corrosion resistance. Additional modification of the sample ultrasonically treated in the silk solution changes the E_{corr} to −1.594 V, and the corrosion rate decreases to 0.20 mm/year. An additional deposition of a silk layer on the sample sonochemically-modified in the silk solution increases corrosion resistance of magnesium alloys by 54 times compared to the control sample that was ultrasonically treated in distilled water. Deposition of more than one additional silk layer on magnesium surface does not affect the corrosion resistance values of the magnesium implant. According to the results in Figure 4a, the sample modified by silk possesses the noblest corrosion potential. These findings

demonstrate that one additional silk layer provides the best corrosion resistance of magnesium alloys and optimal surface protection (Table 1). Better corrosion resistance of magnesium alloy modified by spider silk corresponds well to the literature data.[24] Although reports suggest that the values of corrosion current density vary, there is, however, a general trend of their declining by two orders of magnitude. A similar phenomenon has been described in the papers.[24,25,41]

Figure 4b shows photos of the samples ultrasonically treated in the silk solution without coating (right) and coated by the silk layer (left). Corrosion defects can be observed after 1 h of immersion in 3.5 wt% NaCl on the unmodified magnesium surface, whereas the sample with the silk film does not exhibit any visible signs of corrosion attack.

The schematic representation of the mechanism of corrosion protection of silk-modified magnesium alloys is shown in
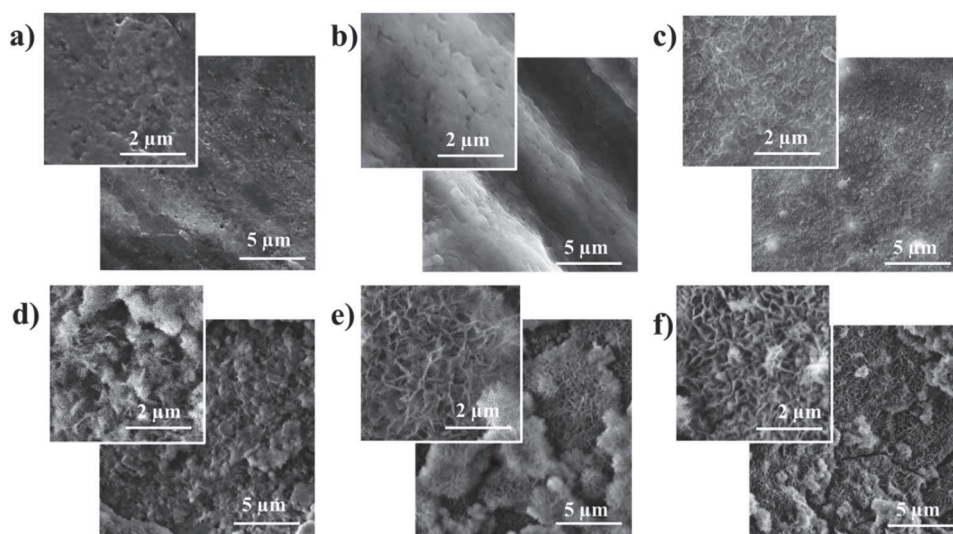
Figure 3. SEM images of magnesium surface a–c) before and d–f) after the corrosion test in 3.5 wt% NaCl; a,d) Control magnesium sample sonochemically treated in distilled water; b,e) Magnesium sample sonochemically treated in the silk solution; c,f) Magnesium sample sonochemically treated in the silk solution and additionally modified by a silk layer. Sonication process is carried out at a frequency of 20 kHz for 10 min. The additional silk layer is deposited by dipping the sample in the silk solution for 15 min.

Figure 4c. We assume that the effect of corrosion resistance can be based on three possible mechanisms.

The first mechanism may be due to the presence of –NH and –NH$_2$ groups in the silk molecule structure. Additionally, the silk layer can possess pH-buffering activity and can stabilize the pH between values of 5 and 7.5 on the metal surface in corrosive media. The second mechanism may be related to hydrophilic/hydrophobic interactions within the silk structure as the corrosion processes are followed by changes of the pH value in the corrosive area and metal degradation.[44] Spider silk molecules have both hydrophobic and hydrophilic parts. The squares indicate the various sections of spider silk (shown in Figure 4). The crystalline regions are hydrophobic which aids the loss of water during solidification of spider silk.[45] The squares indicate the hydrophilic parts of spider silk that mainly are due to hydroxyl and amino groups. However, these segments are intermixed with one another within spider silk so that it is difficult to disentangle them into some separate fragments. In this regard, in Figure 4 they are displayed as squares. In addition, under the influence of external factors the polymer silk chains can bend in any direction. This, combined with the fact that the abovementioned sections also constantly reassemble, prevents the corrosion. Depending on the external condition, silk molecules can organize themselves reversibly, preventing corrosion. The third mechanism is based on the fact that silk forms relatively mobile structures. These structures have the tendency to seal and eliminate the mechanical cracks of the coating. Self-healing or self-curing of the corrosion-damaged areas can be performed by three mechanisms: pH neutralization, passivation of the damaged metal surface by inhibitors entrapped between silk layers, and reparation of the coating.

In conclusion, we developed a novel method of anticorrosion protection, including the surface ultrasonic treatment and deposition of the silk layer.

3. Conclusion

Surface analyses were carried out on the silk coating deposited on sonochemically treated magnesium surface. The SEM data indicated that silk deposits on the magnesium surface and forms uniform layer. Moreover, silk deposition promotes the oxidization of the magnesium surface, and the longer the sonication time is, the thicker the oxide layer. After silk modification, the corrosion resistance of magnesium alloys is improved after modification of their surface with silk. Hybrid effects of sonochemical oxidative protection combined with silk layer-by-layer assembly possess the best corrosion resistance. Magnesium substrates sonochemically treated in silk solution demonstrate three times better corrosion resistance compared to control samples sonochemically treated in water. Ultrasonic treatment followed by the additional deposition of silk layer-by-layer assembly enhances the corrosion resistance by 54 times compared to the control samples.

4. Experimental Section

Materials: In order to have a constant access to biomaterial the research group developed an insectarium on the base of laboratory. There are 50 species of *Linothele fallax*, a Bolivian curtain-web spider with enlarged abdomen, which takes half of the spider body. Thus, the amount of silk produced is substantially bigger in comparison with typical orb-web spiders, making *Linothele fallax* a suitable candidate as a web supplier for numerous experiments. Magnesium (≥99.5% Mg basis), sodium chloride (purity ≥99.5%), trifluoroacetic acid (TFA, purum. ≥99%, purified by redistillation, for protein sequencing) were patched from Sigma-Aldrich. Prior to experiment magnesium plates were polished to delete the oxide layer and degreased in acetone followed by drying at 90 °C.

Silk Solution Preparation: Before film preparation, the 30 mg of natural spider silk was washed twice with ethanol and isopropanol to get rid of mechanical impurities in the spider silk. Washed spider silk material

ADVANCED
SCIENCE NEWS
www.advancedsciencenews.com

Macromolecular
Materials and Engineering
www.mme-journal.de
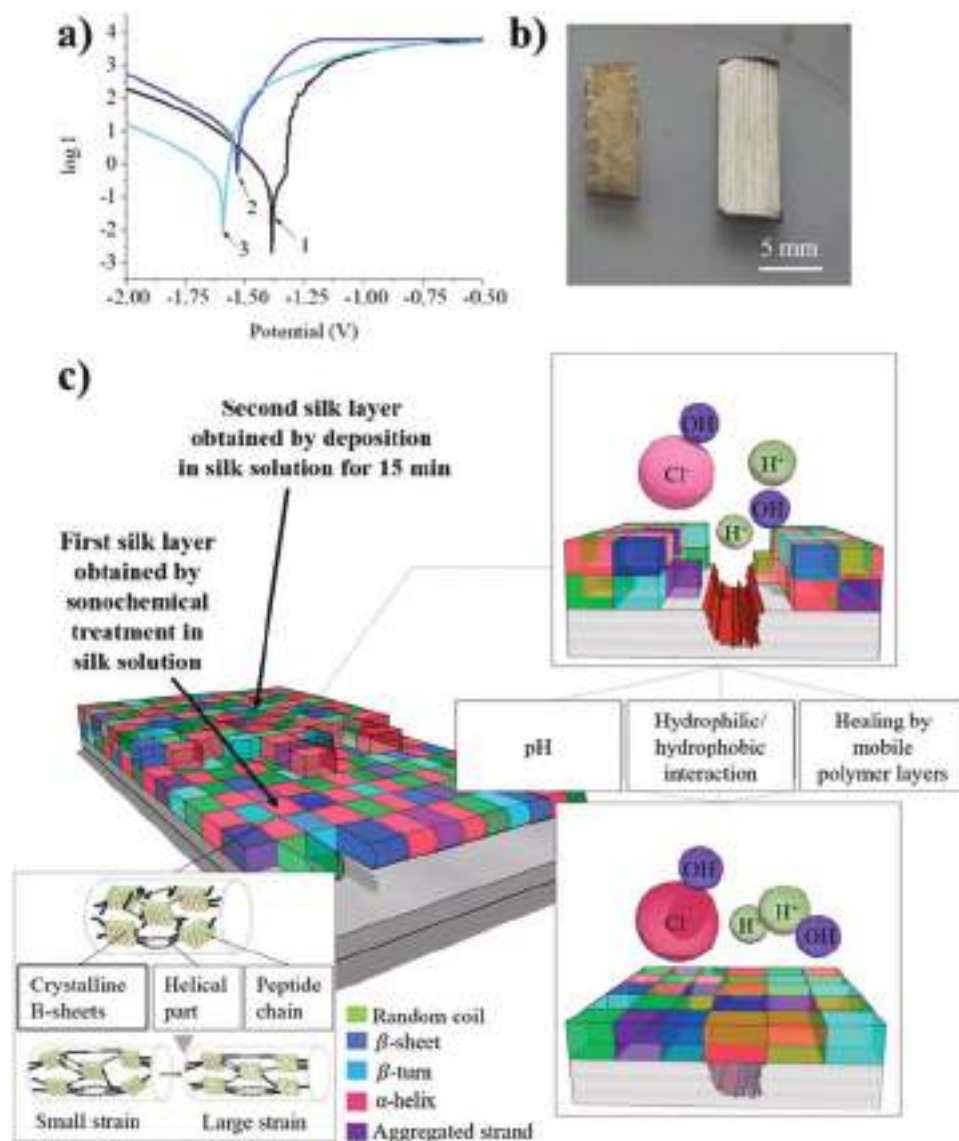
Figure 4. a) Potentiodynamic polarization curves of control magnesium sample sonochemically treated in distilled water (1) magnesium sample sonochemically treated in a silk solution (2) magnesium sample sonochemically treated in the silk solution and additionally modified by a silk layer (3) in 3.5 wt% NaCl solution saturated with Mg^{2+}; b) Photos of unmodified magnesium plate (left) and magnesium plate ultrasonically modified and covered by the silk coating (right) after corrosion test; c) Scheme of the silk polymer coating on the ultrasonically modified magnesium surface and schematic mechanisms of corrosion protection provided by the silk layers.

was dried under vacuum for 12 h. Then, 25 mg of resulted dried sample was dispersed in 500 µL of concentrated trifluoroacetic acid (TFA)[46] by constant mixing at 500 rpm at 25 °C. A curtain-type of spider web possess enhanced structural stability in comparison with silk fibers from the *Bombyx mori* silkworm. It is, therefore, difficult to treat spider silk with solvents such as formic acid[47] or chaotropic salts,[48] which are normally used for silkworm silk dissolution. In contrast, TFA appears to effectively break the polymer structure of spider silk. Additionally, TFA dissolves silk instantaneously, reducing the duration of the experiment. Complete dissolution of spider silk occurs in 3 h. The pH value of as-prepared silk solution is 1.0. To increase the pH value until 4.0, the silk solution was dialyzed for 24 h.

Fourier Transform Infrared Spectroscopy: FTIR analysis was used to investigate silk secondary structure. Spectra were acquired with a Shimadzu IRPrestige-21 FTIR spectrometer (Shimadzu, Japan) equipped with a DLaTGS detector. The spectra were measured in the range from 4000–400 cm^{-1} in transmission mode. Dry samples (105 °C, 2 h) were treated with crystalline KBr (2 mg of sample:700 mg of KBr) and then pressed into a disk. The data were obtained at a resolution of 0.5 cm^{-1} with 20 cumulated scans and a signal-to-noise ratio of 40 000:1. The data were processed using software provided by the manufacturer (Shimadzu).

Morphology of Silk Fibers and Modified Magnesium Alloys: Scanning electron microscopy (SEM) was used to study the morphology of fibers and modified magnesium surface. The SEM micrographs of the samples were obtained using Vega Tescan 3 at an operating voltage of 5 keV. Samples were fixed on a carbon tape.

Dynamic Light Scattering Analysis: The dynamic light scattering (DLS) method was applied to determine the size distribution of peptide nanoparticles in a prepared solution. The DLS measurements were carried out using a Mavern Zetasizer.

Table 1. The relationship between the corrosion current density, corrosion potential, polarization resistance, and corrosion rate of the modified magnesium samples.

Parameters	Sample 1 (Control)	Sample 2	Sample 3
Electrolyte content	Distilled water (pH = 6.0)	Silk solution (pH = 4)	Silk solution (pH = 4)
Sonication time [min]	10	10	10
Sonication frequency [kHz]	20	20	20
Additional silk layer	no	no	yes
E_{corr} [V]	−1.385	−1.518	−1.594
I_{corr} [µA]	82.20	12.86	1.08
I_{corr} per surface area [A cm^{-2}]	2.35×10^{-4}	7.14×10^{-5}	4.32×10^{-6}
Polarization resistance	1657	2355	24 500
Anodic β Tafel constant	0.392	0.091	0.074
Cathodic β Tafel constant	1.58	0.30	0.34
Corrosion rate [mm/year]	10.74	3.27	0.20
Relation of the corrosion rate (sample)/ corrosion rate (control)	1	3.3	54.2

Modification of Magnesium Alloys: Preliminary degreased magnesium plates were ultrasonically treated at a frequency of 20 kHz during 5–10 min in a solution of spider silk (Table 1). The sonication was carried out using a sonicator USG-5522 (BSUIR, Belarus) in the initial and dialyzed silk solutions at pH of 1.0 and 4.0, respectively. The maximum output power of 100 W, the maximum ultrasound intensity was calculated to be 20 W cm^{-2} at the mechanical amplitude of 25 µm (at 100%). The sonotrode was made of stainless steel (head area 4.52 cm^2). Sonication was performed in the sonication cell at constant temperature of around 313.15 K monitored by the temperature sensor inserted in the electrolyte. The sonication parameters are chosen according to the preliminary results that suggest the best performance in modification of magnesium alloy. After sonication, the samples were rinsed three times in water and dried at 20 °C. The additional silk layer on the surface of ultrasonically modified sample was deposited by dipping into the dialyzed silk solution for 15 min.

Corrosion Behavior Study: To evaluate the corrosion behavior of magnesium-based silk modified implants, potentiodynamic polarization tests were performed using a PalmSens4 potentiostat system (PalmSens BV, The Netherlands). The tests were carried out in a 3.5 wt% NaCl solution saturated with Mg(OH)$_2$, and the scan rate was 1 mV s^{-1}. The result analyses were calculated using Program software PSTrace 5 (PalmSens Compact Electrochemical Interfaces, The Netherlands) in application of corrosion mode. The corrosion potential was calculated using Tafel slope method where the anodic and cathodic Tafel slopes intersect. The corrosion rate in mm/year was calculated according to the standart practice described in the ASTM Standart G 102. In addition, the morphology of the samples after corrosion test was observed using SEM.

Biological Activity: Biological activity tests were performed in a petri dish using agar diffusion method. Bacteria culture *Staphylococcus aureus* (209 P strain) was incubated in pre-prepared LB nutrient medium (Lennox) for 24 h at 37 °C in a shaker-incubator. Then 150 µL of *Staphylococcus aureus* bacterial suspension was incubated into agar plate. Samples of natural spider silk were placed in the middle of the inoculated plate followed by further incubation at 37 °C for 18 h. After that, the inhibition zone of bacterial growth was measured.

Conflict of Interest

The authors declare no conflict of interest.

[1] F. Witte, *Acta Biomater.* **2015**, *23*, S28.
[2] P. C. Banerjee, S. Al-Saadi, L. Choudhary, S. E. Harandi, R. Singh, *Materials* **2019**, *12*, 136.
[3] M. Niinomi, *Metall. Mater. Trans.* **2002**, *3*, 33.
[4] G. Radenković, D. Petković, *Biomater. Clin. Pract. Adv. Clin. Res. Med. Devices* **2003**, *1*, 49.
[5] H. Waizy, J. M. Seitz, J. Reifenrath, A. Weizbauer, F. W. Bach, A. Meyer-Lindenberg, B. Denkena, H. Windhagen, *J. Mater. Sci.* **2013**, *48*, 39.
[6] J. Vormann, *Mol. Aspects Med.* **2003**, *24*, 27.
[7] F. Witte, V. Kaese, H. Haferkamp, E. Switzer, A. Meyer-Lindenberg, *Biomaterials.* **2005**, *26*, 17.
[8] M. Pogorielov, E. Husak, A. Solodivnik, S. Zhdanov, *Interv. Med. Appl. Sci.* **2017**, *9*, 1.
[9] Z. G. Huan, M. A. Leeflang, J. Zhou, L. E. Fratila-Apachitei, J. Duszczyk, *J. Mater. Sci. Mater. Med.* **2009**, *21*, 9.
[10] G. Song, *Corros. Sci.* **2007**, *49*, 4.
[11] D. V. Andreeva, E. V. Skorb, D. G. Shchukin, *ACS Appl. Mater. Interfaces* **2010**, *2*, 1954.
[12] G. Song, D. S. T. John, J. Nairn, *Corros. Sci.* **2004**, *39*, 1983.
[13] D. V. Andreeva, D. Fix, H. Möhwald, D. G. Shchukin, *Adv. Mater.* **2008**, *20*, 2789.
[14] D. Fix, D. V. Andreeva, Y. M. Lvov, D. G. Shchukin, H. Möhwald, *Adv. Funct. Mater.* **2009**, *19*, 1720.

**ADVANCED
SCIENCE NEWS**

www.advancedsciencenews.com

**Macromolecular
Materials and Engineering**

www.mme-journal.de

[15] E. V. Skorb, D. Fix, D. V. Andreeva, H. Möhwald, D. G. Shchukin, *Adv. Funct. Mater.* **2009**, *19*, 2373.

[16] D. V. Andreeva, E. V. Skorb, D. G. Shchukin, *ACS Appl. Mater. Interfaces* **2010**, *2*, 7.

[17] S. V. Lamaka, D. G. Shchukin, D. V. Andreeva, M. L. Zheludkevich, H. Möhwald, M.G.S. Ferreira, *Adv. Funct. Mater.* **2008**, *18*, 3137.

[18] E. V. Skorb, D. V. Andreeva, *Polym. Chem.* **2013**, *4*, 4834.

[19] E. V Skorb, D. Fix, D. G. Shchukin, H. Möhwald, D. V. Sviridov, R. Mousa, N. Wanderka, J. Schäferhans, N. Pazos-Pérez, A. Fery, D. V. Andreeva, *Nanoscale* **2011**, *3*, 985.

[20] E. V. Skorb, A. G. Skirtach, D. V. Sviridov, D. G. Shchukin, H. Möhwald, *ACS Nano* **2009**, *3*, 1753.

[21] D. O. Grigoriev, K. Köhler, E. Skorb, D. G. Shchukin, H. Möhwald, *Soft Matter* **2009**, *5*, 1426.

[22] D. V. Andreeva, D. V. Sviridov, A. Masic, H. Möhwald, E. V. Skorb, *Small* **2012**, *8*, 6.

[23] E. V. Skorb, D. V. Andreeva, *Polym. Int.* **2015**, *64*, 713.

[24] P. Wang, P. Xiong, J. Liu, S. Gao, T. Xi, Y. Cheng, *J. Mater. Chem. B* **2018**, *6*, 967.

[25] P. Xiong, Z. Jia, M. Li, W. Zhou, J. Yan, Y. Wu, Y. Cheng, Y. Zheng, *ACS Biomater. Sci. Eng.* **2018**, *4*, 3163.

[26] M. Farokhi, F. Mottaghitalab, Y. Fatahi, A. Khademhosseini, David L. Kaplan, *Trends Biotechnol.* **2018**, *36*, 907.

[27] W. Huang, S. Ling, C. Li, F. G. Omenetto, D. L. Kaplan, *Chem. Soc. Rev.* **2018**, *47*, 6491.

[28] R. V. Lewis, *Chem. Rev.* **2006**, *106*, 3762.

[29] M. Heim, D. Keerl, T. Scheibel, *Angew. Chem., Int. Ed.* **2009**, *48*, 3584.

[30] F. Vollrath, D. Porter, *Polymer* **2009**, *50*, 5623.

[31] M. Andersson, J. Johansson, A. Rising, *Int. J. Mol. Sci.* **2016**, *17*, 1290.

[32] A. Rising, G. Hjalm, W. Engstrom, J. Johansson, *Biomacromolecules* **2006**, *7*, 3120.

[33] M. Humenik, T. Scheibel, A. Smith, *Prog. Mol. Biol. Transl. Sci.* **2011**, *103*, 135.

[34] F. Vollrath, *Curr. Biol.* **2006**, *16*, R925.

[35] J. Gosline, P. Guerette, C. Ortlepp, K. Savage, *J. Exp. Biol.* **1999**, *202*, 3295.

[36] M. Zhang, Y. Zhang, W. Wu, A. Zhang, Z. Pan, *Adv. Mater. Res.* **2011**, *175-176*, 127.

[37] D. Saravanan, *Artic. Des. Sch.* **2006**, *5*, 1.

[38] O. Tokareva, M. Jacobsen, M. Buehler, J. Wong, D. L. Kaplan, *Acta Biomater.* **2014**, *10*, 1612.

[39] K. Jastrzebska, K. Kucharczyk, A. Florczak, E. Dondajewska, A. Mackiewicz, H. Dams-Kozlowska, *Reports Pract. Oncol. Radiother.* **2015**, *20*, 2.

[40] R. Madurga, A. M. Gañán-Calvo, G. R. Plaza, G. V. Guinea, M. Elices, J. Pérez-Rigueiro, *Green Chem.* **2017**, *19*, 3380.

[41] P. Xiong, Z. Jia, W. Zhou, J. Yan, P. Wang, W. Yuan, Y. Li, Y. Cheng, Z. Guan, Y. Zhengl, *Acta Biomater.* **2019**, *92*, 336.

[42] Z. Wang, W. Zhao, C. Qin, Y. Cui, *Mater. Res.* **2012**, *15*, 51.

[43] C.-J. Pan, L.-Q. Pang, Y. Hou, Y.-B. Lin, T. Gong, T. Liu, W. Ye, H.-Y. Ding, *Appl. Sci.* **2016**, *7*, 33.

[44] M. L. Zheludkevich, D. G. Shchukin, K. A. Yasakau, H. Mohwald, M. G. S. Ferreira, *Chem. Mater.* **2007**, *19*, 402.

[45] O. S. Rabotyagova, P. Cebe, D. L. Kaplan, *Biomacromolecules* **2009**, *10*, 229.

[46] T. Asakura, H. Matsuda, N. Kataoka, A. Imai, *Biomacromolecules* **2017**, *18*, 1965.

[47] J. W. Seo, H. Kim, K. H. Kim, S, Q. Choi , H. J. Lee, *Adv. Funct. Mater.* **2018**, *28*, 1870250.

[48] D. N. Rockwood, R. C. Preda, T. Yücel, X. Wang, M. L. Lovett, D. L. Kaplan, *Nat. Protoc.* **2011**, *6*, 1612.

Thin and Flexible Ion Sensors Based on Polyelectrolyte Multilayers Assembled onto the Carbon Adhesive Tape

Anna A. Stekolshchikova,[†] Anton V. Radaev,[‡] Olga Yu. Orlova,[†] Konstantin G. Nikolaev,[†] and Ekaterina V. Skorb*,[†] [ID]

[†]ITMO University, Lomonosova str. 9, St. Petersburg 191002, Russian Federation
[‡]Chromas Core Facility, St. Petersburg University, Research Park 2/5, Oranienbaum Highway, St. Petersburg 198504, Russian Federation

ABSTRACT: A novel flexible ion-selective sensor for potassium and sodium detection was proposed. Flexible ion-selective electrodes with pseudo-liquid internal solution on contrary to the system with a solid contact provided a more stable analytical signal. Such advantages were achieved because of polyelectrolyte (PEI/PSS) layers adsorption on the conduct substrate with a layer-by-layer technique. Such an approach demonstrated that ion-selective electrodes save sensitivity with Nernstian dependence: 56.2 ± 1.4 mV/dec a_{Na^+} and 56.3 ± 1.9 mV/dec a_{K^+}, as well as a fast time of response for potassium (5 s) and sodium (8 s) was shown. The sensing platform proposed demonstrates a better time of response and is close to the Nernstian value of sensitivity with a sensor low cost. The results proposed confirm a pseudo-liquid junction for the ion-selective electrode. Biocompatibility of an ion-selective sensing platform was demonstrated at potassium potentiometric measurements in *Escherichia coli* biofilms. Potassium levels in a biofilm were measured with potentiometry and showed agreement with the previous results.
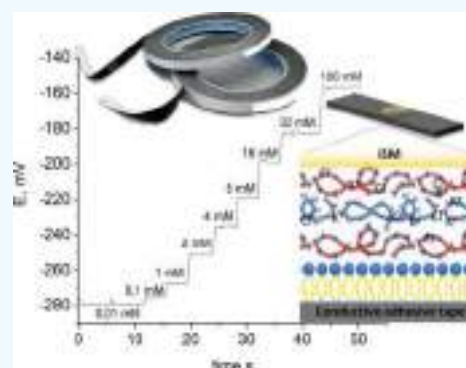
INTRODUCTION

Real-time, wearable, minimally invasive monitoring is used in medical diagnosis and professional sport.[1−5] The application on sensors becomes hard because of dilution of the biomarkers of interest, as well as variability in salinity, pH, and other physicochemical variables which directly impact the readout of real-time biosensors.[6−13] Such parameters as sodium (Na^+),[14] potassium (K^+),[15] calcium (Ca^{2+}), and others[16−18] are analyzed in professional sports. Electrolyte ions in aqueous solutions are usually measured using a potentiometric method with ion-sensitive membranes.[18] Potentiometric ion-selective electrodes (ISEs) have already been in use for half-a-century, mainly in physiological studies.[19] Typical ISEs are liquid contact electrodes. Until recently, ISE devices were non-compatible with the principles of miniaturization and portability. Both the internal solution and the internal electrode are strived to be eliminated to be replaced by the solid contact.[20,21] However, elimination of the internal reference system and its replacement with the solid contact resulted in insufficient long-term stability of ISE potentials and in poor piece-to-piece reproducibility.[19,22] We suppose that polyelectrolyte multilayers formed by layer-by-layer assembly[23,24] have hydration activity[25−28] and can serve as the inner electrode solution in potentiometric sensors.[29−31] This paper describes the design and fabrication of a flexible ion-sensing electrochemical adhesive tape (AT)-based analytical device for potentiometric measurements of potassium and sodium ions. This sensing platform has a carbon AT that contains ISEs with conventional ion-selective membranes (ISMs) immobilized within a polyelectrolyte multilayer as the pseudo-inner solution and ion-to-electron transducer. Within the polyelectrolyte layers, potassium chloride is used as an ion source. Carbon ATs are cheap flexible electronic conductors. The required selectivity for the target analyte is achieved by using a suitable ionophore.

Because of unique properties such as light weight, low cost, high flexibility, excellent elasticity, and figure moulding, the flexible carbon conductive AT could serve as an ideal platform for personalized wearable devices.

RESULTS AND DISCUSSION

Flexible ISEs consisted of ISMs and ATs modified through lipid and polyelectrolyte layers (Figure 1a−e). The adhesive carbon tape was used as a substrate because of its mechanical reliability, adhesive effect, and conductivity. Carbon conductivity allows this material to be used as an inner electrode.[32] The scheme of the ion-selective AT used as a flexible conducting platform (0.8 × 3.5 cm) is presented in Figure 1d.

Deposition of the polyelectrolyte layers was carried out by a layer-by-layer method,[26,33] which is more preferable for polyelectrolyte adsorption, as it does not require specific expensive equipment[31] and is more accessible. This method
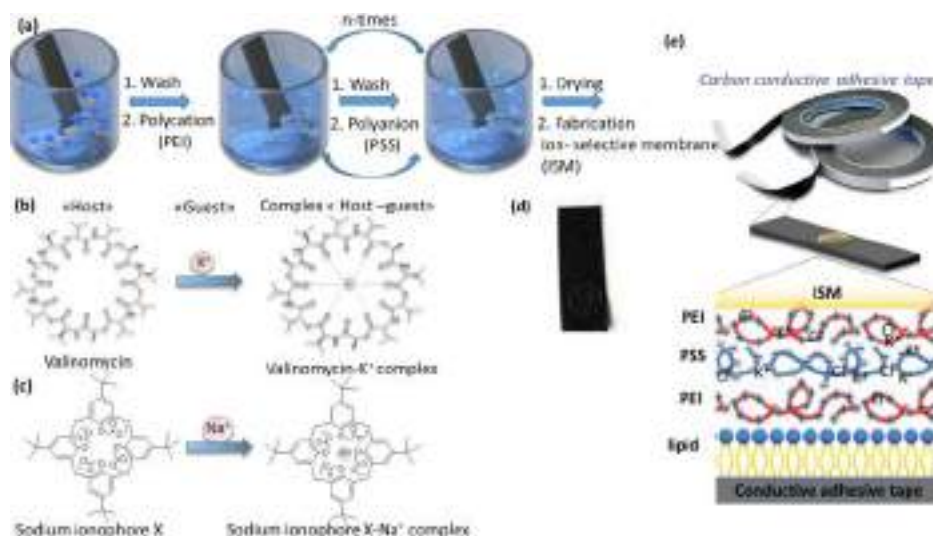
Figure 1. Experimental design, device architecture, and fabrication procedure of the self-powered wearable noninvasive sensor. (a) The polyelectrolyte LBL assembly on the adhesive type. (b) Structure of the antibiotic valinomycin, which was used as the ionophore for the potassium ISM with a complex "host−guest". (c) Sodium ionophore X and its complexation with the sodium ion. (d) Carbon conductive AT as the initial substrate. (e) Common scheme of the ISM, composition with polyelectrolytes multilayers, lipid layer, carbon conductive AT.
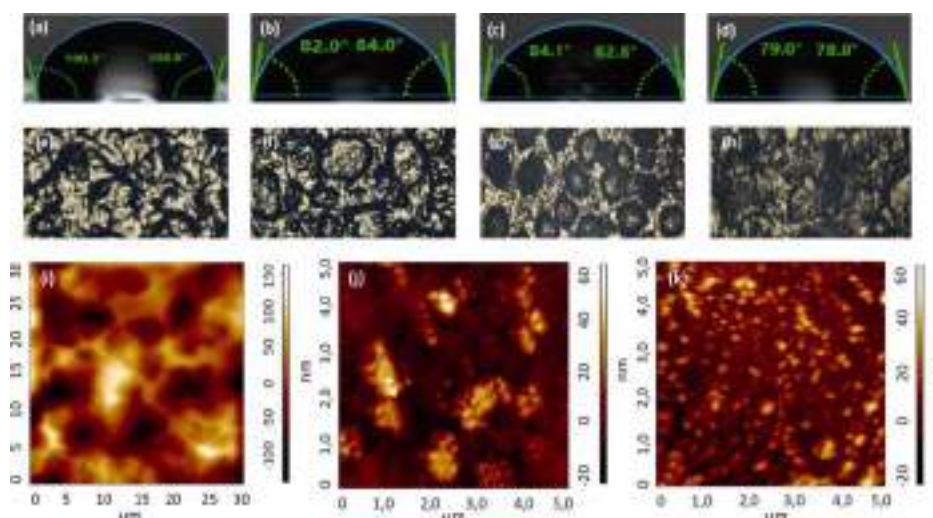
Figure 2. Characterization of morphology surface of electrodes. Water contact angles of wetting for (a) bare adhesive tape (AT), (b) lipid bilayer deposited on top of AT (AT/lip), (c) composite with polyelectrolyte layer of PEI, deposited on top of lipid layer (AT/lip/PEI) (d) composite with polyelectrolyte layer of PSS, deposited on top of PEI layer; optic images of (e) AT, (f) AT/lip, (g) AT/lip/PEI (h) AT/lip/PEI/PSS/PEI; AFM images of (i) AT/lip/PEI, (j) ITO/lip/PEI, (k) ITO/lip/PEI/PSS.

allows to create fairly uniform and thin films on the surface of the substrate. The number of layers was taken from the literature data.

The polyelectrolyte layers were deposited on the substrates with a partially negative or positive charge.[34] The surface of the AT did not have a partial charge; therefore, to obtain polyelectrolyte composites, lipid vesicles were deposited as the first modifying layer.[35] The stage of the lipid layer setting was monitored by measuring the water contact angle. As seen from Figure 2, a hydrophobic substrate with a water contact angle of 100−110° (Figure 2a) became more hydrophilic with a contact angle of 82−84° after the assembly of the lipid layer (Figure 2b). Overlaying the lipid layer gave better wettability of the AT. Hydrophobic hydrocarbon tails were attached to the surface of the AT, and hydrophilic negatively charged heads were faced outside and interacted with the positively charged polyelectrolytes. When the positively charged (PEI)

polyelectrolytes assembled on the lipid layer, the contact angle slightly increased (Figure 2c), but after adsorption of the PSS (negatively charged polyelectrolyte), the contact angle decreased to 79−78° (Figure 2d).

Each step of the multilayer architecture assembly was controlled by morphology by atomic force microscopy (AFM).[36] This method allows the control of surface parameters such as roughness and smoothness. These characteristics influence further stages of surface modification. For the ISM immobilization need not only be wetted surface but uniform. According to the AFM data on the surface of the AT, it is not always possible to create a sufficiently even layer of polyelectrolytes. This could be explained by the original structure of the AT surface. As can be seen from Figure 2e, a layer of glue on the surface of the substrate applied to the carbon tape rather unevenly. The thickness of the adhesive in some places of the AT sometimes exceeds the thickness of the
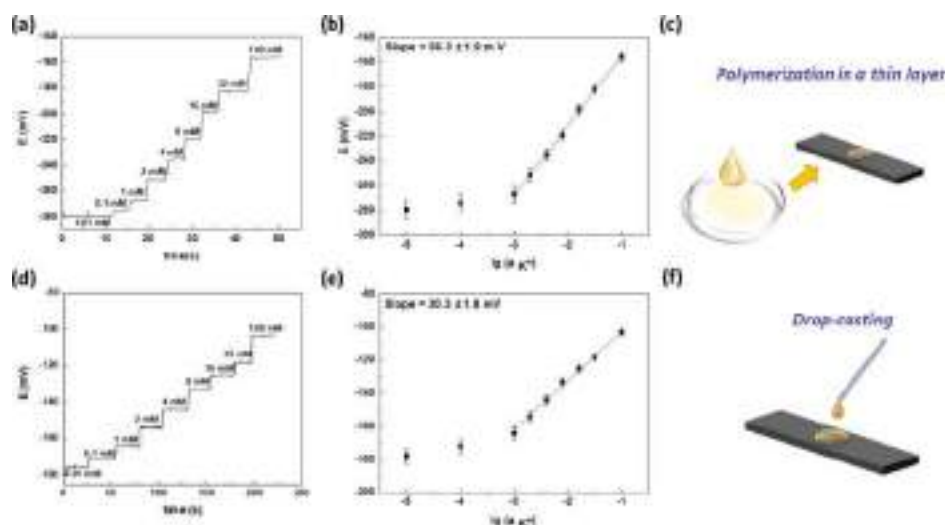
Figure 3. Analytical measurements of ISEs: (a) potentiometric response ISEs with ISMs which are prepared by polymerization a thin layer method, (b) calibration plot for the potassium ISE with an ISM which is prepared by polymerization in the thin layer method ($y = 56.3x - 98.9$, $n = 3$ $P = 0.95$), (c) representation of the preparation of the ISM by polymerisation in a thin film layer with a Petri dish, (d) potentiometric response ISE with an ISM which is prepared by a drop casting method (e) calibration plot for the potassium ISE with an ISM which is prepared by a drop casting method ($y = 30.3x - 71.7$, $n = 3$ $P = 0.95$), (f) representation of the drop casting method on the adhesive type.
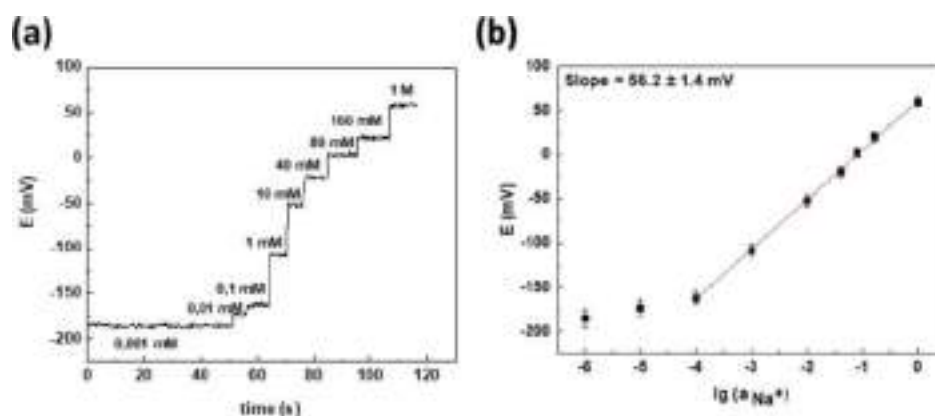
Figure 4. (a) Potentiometric response for sodium ISE and (b) corresponding calibration plot after addition of the standard sodium chloride solution ($y = 56.2x + 61.8$).

polyelectrolyte layer, therefore, it is not possible to see the real structure of the substrate surface with polyelectrolytes deposited. In order to compare the AFM images obtained for the AT, AFM photographs with polyelectrolyte layers, deposited on the indium tin oxide (ITO) flexible substrate, were removed. As seen from Figure 2i−k, the structure of the deposited polyelectrolytes on the AT and on the substrate is quite similar. Thus, according to the AFM data obtained for the two different substrates with the same quantity of polyelectrolytes, the PEI layer is deposited on the substrate by small conglomerates, and the PSS layer precipitates fairly evenly. Deposition of polyelectrolyte layers on top of the AT/lipid layer composite leads to an increase of roughness.

The adsorbed polyelectrolyte layers are hydrated[25,37] and can be used as a liquid internal reference system. For this purpose, we provide polyelectrolyte layer adsorption from the potassium chloride decimolar solution. This technique allows adding more water in a layer as polyelectrolytes swell[38] in saline solution. The number of layers was set to form a charge barrier between the inner solution and membrane.[39] PEI,[39] as the positively charged polyelectrolyte, prevents diffusion of

potassium ions from the inner solution to outer media. This approach allows stable pseudo-inner electrode potential. Thus, we used consistent PEI/PSS/PEI layers. To avoid capacitor-like behavior, we did not prepare more layers. By adding potassium chloride into the polyelectrolyte layer, we achieved the pseudo-internal solution as a part of ISEs. This pseudo-internal electrode solution coupled with a carbon paste on the AT forms an ion-to-electron transfer system. This approach enables the production of low cost ISEs with high potential stability and signal reproducibility.

The potentiometric measurements of electrolytes such as K^+ and Na^+ require the addition of an ISM which is generally a plasticized polymer doped with an ionophore. It is a compound that can selectively bind to the ions of interest via coordinate bonds. In our investigation, an ISM was prepared by mixing a polymeric phase (PVC) with a plasticizer (o-NPOE). To make this material sensitive to Na^+ and K^+ ions, it was doped with a highly hydrophobic ionic site (KTpClPB), sodium ionophore X, and potassium ionophore I, respectively. AT-based ISEs for two target analytes, namely, K^+ and Na^+, were prepared and tested individually.

Table 1. Analytical Characteristics of the Wearable ISEs for Potassium and Sodium Detection[a]

substrate material	type of transducing	sensitivity, mV/dec a_{Na^+}	linear range, M	limit of detection	response time, s	reference
		Sodium				
adhesive carbon tape	inner solution	56.2 ± 1.4	10^{-4} to 10^{0}	4.0×10^{-4}	8	present work
textile/polyurethane/CNTs	solid contact	59.4	10^{-4} to 10^{-1}	$10^{-4.9}$		43
carbon tattoo	solid contact	63.7	10^{-4} to 10^{-1}		10	41
carbon/PEDOT/PET	solid contact	54.8	10^{-4} to 10^{-1}			42
		Potassium				
adhesive carbon tape	inner solution	56.3 ± 1.9	10^{-3} to 10^{-1}	3.9×10^{-5}	5	present work
textile/polyurethane/CNTs	solid contact	56.5	10^{-4} to 10^{-1}	$10^{-4.9}$		43
carbon/PEDOT/PET	solid contact	53.9	10^{-4} to 10^{-1}			42
CNTs/cotton	solid contact	54.9	10^{-4} to 10^{-1}	10^{-5}	60	44

[a]CNTs—carbon nanotubes, PEDOT—poly(3,4-ethylenedioxythiophene); PET—polyethylene terephthalate.
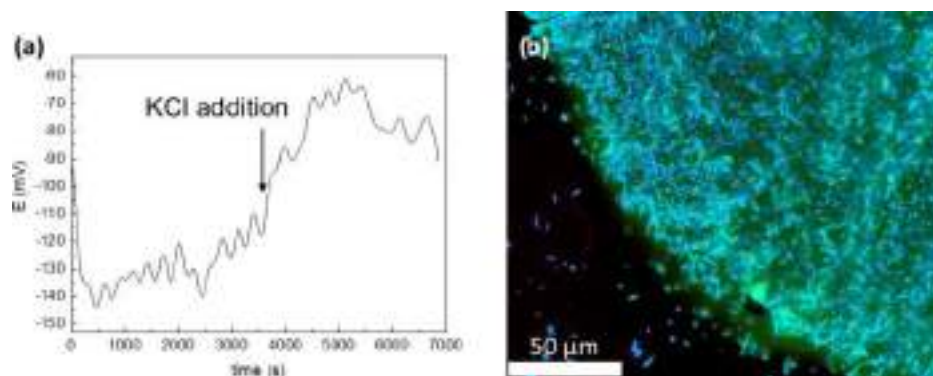
Figure 5. (a) Potentiometric potassium chloride disruption response for *the E. coli* colony on the conductive sensor and (b) bacteria imaging with biomarkers thioflavin S and propidium.

In each experiment, potassium and sodium ISEs were dipped into standard solutions of salt (NaCl and KCl respectively), while the concentration of the solution was changed in steps and the open-circuit potentials were monitored continuously using a potentiostat. Electromotive force (EMF) was measured between the ISE and a commercial Ag/AgCl reference electrode. Both Figures 3a and 4a show the time trace of potentiometric response for the prepared AT-based electrodes of K^+ and Na^+ ions, when the activity of the primary analyte increased. K^+ ion concentration in human sweat lies in the range of 1 to 16 mM. The calibration plots for potassium ions (Figure 3b) show a Nernstian response between 10^{-3} and 10^{-1} M indicating that the membrane is working as expected.

The method of preparation and deposition of the ISM on AT/Lip/Poly was found to have an effect on sensor performance. The best sensitivity (56.3 ± 1.9 mV/decade) and stability of potential were obtained using a polymerization method in a thin film (Figure 3a−c). From the above, it was concluded that it is better to make a membrane in a Petri dish (Figure 3d−f).

Na^+ ion concentration in human sweat is in the range of 10 to 160 mM (Figure 4b). Average sensitivity of ISEs in this range (10^{-4} to 1 M) was found to be 56.2 ± 1.4 mV/decade, which was close to the value expected for the detection of monovalent ions using ideal ISMs (59.2 mV/decade) (Figure 4b). Analytical characteristics of ISEs are shown in Table 1. The results obtained showed good agreement with the literature.[20,40] The proposed sensing platform demonstrated a better time of response and was close to the Nernstian value of sensitivity with a low sensor cost. The results confirm the proposed pseudo-liquid junction for the ISE. The sodium ISE demonstrates lower response time in comparison with the carbon tattoo sensor of the solid contact type.[41] Sensitivity of the proposed sodium sensor is close to other sensors based on the same carbon material[17,41,42] and flexible textile.[43] Linear range for sodium potentiometric sensor was higher, because was constructed pseudo-inner solution, which provide stable work of sensor. This pseudo-inner solution potassium ISE showed a much lower response time (5 s) in contrast with the carbon textile-based ion-selective sensor (60 s).[44] Sensitivity, limit of detection, and linear range of the potassium-selective electrode with pseudo-inner solution were compared with ion-selective solid contact sensors based on carbon[42−44] and flexible substrates such as textile[43] and cotton.[44]

To demonstrate sensor application for monitoring in real samples, oscillations[45] in the bacteria biofilm under expansion were observed.[46] Such oscillations are usually observed by using a Nernstian fluorescent dye.[47] Bacteria have many ion channels, such as sodium, chloride, calcium-gated, and potassium ones and ionotropic glutamate receptors, similar to those found in neurons. *Escherichia coli* was used to control potassium ions under biofilm living. For this purpose, the biofilm was directly grown on the ISE surface. EMF was refined because of resistance increase before measurements and after biofilm growth. Then, potentiometric measurements of such systems were provided (Figure 5). Standard potassium chloride (0.1 M, 100 μL) addition to bacteria was performed to create disturbance. According to the potassium ISE calibration curve, potassium concentration in the biofilm was calculated and established as 190 mM. This value corresponds with the potassium level in the biofilm, varying from 200 to 400 mM,[48] found in the literature. After standard potassium addition, its concentration increased dramatically to 1.3 M. Such essential and disproportional potassium levels could be

explained with potassium pumping by the biofilm from the solution to the gap between the ISE and biofilm. Nevertheless, the proposed sensor demonstrated good stability and biocompatibility during measurements, as the *E. coli* biofilm showed life-sustaining activity after potentiometric measurements (Figure 5b).

CONCLUSIONS

We offer a wearable sensor by using PEI/PSS multilayers as inner ISE solution together with a low-cost adhesive carbon tape as a sensitive transducer. Its high sensitivity and durability are obtained using a novel approach to the preparation of polyelectrolyte multilayers as a unique platform for sensing application. The sodium and potassium ion-selective sensor shows combined superiority of high sensitivity, fast response, and high durability. In addition, the low-cost strain sensor based on the adhesive carbon tape shows sensitive response to bacteria potassium oscillations. This wearable sensing platform can monitor various human health indicators, including electrolytes. The sensitivity and suitability for making potentiometric sensors of the demonstrated sensing platform may enable a wide range of applications in intelligent devices.

METHODS

Chemicals. Valinomycin (potassium ionophore I), 4-*tert*-butylcalix[4]arene-tetraacetic acid tetraethyl ester (sodium ionophore X), potassium tetrakis(4-chlorophenyl)borate (KTpClPB), 2-nitrophenyl octyl ether (o-NPOE), and poly-(vinyl chloride) high molecular weight (PVC) were all purchased from Sigma-Aldrich. Tetrahydrofuran (THF) and hexane were purchased from Ekos-1, Russia. Potassium chloride (KCl), sodium chloride (NaCl), and phosphate-buffered saline were from Merk. Liquid soya lecithin Lecisoy 400 was purchased from Cargill, USA. Branched polyethyle-neimine (PEI, M_w 70 kDa) 30% water solution was purchased from Alfa Aesar, and polysterenesulfonate (PSS, M_w 500 kDa)—from Polysciences, Inc.

Fabrication of the AT-Based Platform (ATP). A conventional conductive double-sided carbon tape (8 mm width, 3.5 cm height, 150 μm thickness) purchased from Tescan (Czech Republic) was used as the initial substrate. To increase the hydrophilicity the AT was immersed in a dispersion of lipid vesicles.

To prepare small unilamellar vesicle (SUV) solution, the following procedure was performed: soy lecithin solution in hexane (10 mg mL^{-1}) was kept under vacuum for solvent evaporation at least for 3 h. After removing any hexane traces, a thin lipid film on the bottom of the vessel was obtained. The resulting lipid film was rehydrated by using distilled water for final 10 mg/mL concentration with simultaneous sonication in an ultrasonic bath for 15 min.

To obtain the results, the lipid bilayer on top of the conductive double-sided adhesive carbon tape was immersed in a 10 mg/mL dispersion of SUV for 1 h. Vesicles attached to the oppositely charged surface of the AT then ruptured, fused, and spread on the surface forming a continuous bilayer. The procedure described was followed by rinsing with large quantity of distilled water and drying under an air steam.

The polyelectrolyte multilayer film was deposited on top of the lipid bilayer. Polyelectrolytes films were assembled using a layer-by-layer technique. Three layers of positively charged PEI and negatively charged PSS were assembled from solutions with a polyelectrolyte concentration of 2 mg mL^{-1} in 0.1 M KCl. A concentration of 2 mg/mL of polyelectrolytes was used, as it gives optimum thickness films. For each layer deposition, surfaces were incubated during 15 min at room temperature in the polyelectrolyte solution. Each step of polyelectrolyte deposition was followed by a washing step with distilled water.

Fabrication of the ISM. The potassium ISM contained 1.4 wt % of valinomycin, 0.3 wt % of KTpClPB, 32.8 wt % of PVC, and 65.5 wt % NPOE. The sodium ISM contained 0.99 wt % of sodium ionophore X, 0.25 wt % of KTpClPB, 32.92 wt % of PVC, and 65.84 wt % of o-NPOE. The membranes were prepared by dissolving the mixture into 1.5−4 mL of THF. ISM coatings on the ATP were prepared by two different methods: drop casting and thin film polymerization. For thin film polymerization, we poured the THF solution into a Petri dish and allowed the THF to evaporate over 24 h. We then cut the membrane into small circular pieces (3 mm in diameter) and conditioned them by soaking overnight in chloride solutions of the corresponding ions (10^{-3} M K$^+$, 10^{-1} M Na$^+$). A volume of 40 μL of the membrane cocktail was applied at once by drop casting onto the electrode (into the orifice left by the plastic mask). The membrane was dried for 24 h. The volume of the membrane cocktail applied was optimized for the fabrication of a membrane approximately 3 mm in diameter. The electrodes were conditioned in proper saline solution: 0.001 M KCl or 0.1 NaCl prior to and between measurements, which were performed at room temperature.

***E. coli* ATCC Growing on the Potassium ISE.** *E. coli* ATCC night culture was used for biofilm preparation. The biofilm was grown on the potassium ISE for 24 h at 38 °C in an LB broth (LENNOX). Prior to potentiometric measurements, the ISE with the biofilm was rinsed with deionized water.

Characterization of the AT-Based ISE. Characterization of the electrode surface morphology was observed by using an atomic force microscope Solver Next (NT-MDT, Russia) in semi-contact mode. Wettability of the obtained composites was characterized by contact angle measurements using a drop shape analyzer Kruss DSA25 (Germany).

Electrochemical measurements were performed using a CompactStat instrument (Ivium, Netherlands) in a standard two-electrode cell at room temperature (22 °C). The AT-based electrode was used as the working electrode and a 3 M Ag/AgCl/KCl (type 6.0733.100, Metrohm AG) as the reference electrode. The membrane was fully covered by the solution, but there was no direct contact between the exposed carbon adhesive-tape and the solution. The activity coefficients were calculated by the Debye−Hückel approximation. After the measurements, the electrodes were air-dried and stored with using storage corresponding salt solution. Several calibration curves with the primary analyte in highly concentrated background standard solutions (1−16 mM for potassium ions, 20−160 mM for sodium ions) were prepared. Knowing the concentration of the standard solutions and the limit of detection, the selectivity coefficient was obtained. The electrochemical cell volume was 20 mL. The background solution for bacteria measurements was phosphate-buffered solution (pH 7.2).

AUTHOR INFORMATION

Corresponding Author

*E-mail: skorb@itmo.ru.

ORCID

Ekaterina V. Skorb: 0000-0003-0888-1693

Notes

The authors declare no competing financial interest.
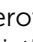
■ REFERENCES

(1) Gao, W.; Ota, H.; Kiriya, D.; Takei, K.; Javey, A. Flexible Electronics toward Wearable Sensing. *Acc. Chem. Res.* **2019**, *52*, 523−533.

(2) Jeong, Y. R.; Lee, G.; Park, H.; Ha, J. S. Stretchable, Skin-Attachable Electronics with Integrated Energy Storage Devices for Biosignal Monitoring. *Acc. Chem. Res.* **2019**, *52*, 91−99.

(3) Yang, Y.; Gao, W. Wearable and flexible electronics for continuous molecular monitoring. *Chem. Soc. Rev.* **2019**, *48*, 1465−1491.

(4) Koga, H.; Nagashima, K.; Huang, Y.; Zhang, G.; Wang, C.; Takahashi, T.; Inoue, A.; Yang, H.; Kanai, M.; He, Y.; Uetani, K.; Nogi, M.; Yanagida, T. Paper-based disposable molecular sensor constructed from oxide nanowires, cellulose nanofibers, and pencil-drawn electrodes. *ACS Appl. Mater. Interfaces* **2019**, *11*, 15044.

(5) Hamedi, M. M.; Ainla, A.; Güder, F.; Christodouleas, D. C.; Fernández-Abedul, M. T.; Whitesides, G. M. Integrating Electronics and Microfluidics on Paper. *Adv. Mater.* **2016**, *28*, 5054−5063.

(6) Shiwaku, R.; Matsui, H.; Nagamine, K.; Uematsu, M.; Mano, T.; Maruyama, Y.; Nomura, A.; Tsuchiya, K.; Hayasaka, K.; Takeda, Y.; Fukuda, T.; Kumaki, D.; Tokito, S. A Printed Organic Amplification System for Wearable Potentiometric Electrochemical Sensors. *Sci. Rep.* **2018**, *8*, 3922.

(7) Brothers, M. C.; DeBrosse, M.; Grigsby, C. C.; Naik, R. R.; Hussain, S. M.; Heikenfeld, J.; Kim, S. S. Achievements and Challenges for Real-Time Sensing of Analytes in Sweat within Wearable Platforms. *Acc. Chem. Res.* **2019**, *52*, 297−306.

(8) Sekar, M.; Pandiaraj, M.; Bhansali, S.; Ponpandian, N.; Viswanathan, C. Carbon fiber based electrochemical sensor for sweat cortisol measurement. *Sci. Rep.* **2019**, *9*, 403.

(9) Wang, Y.; Wang, X.; Lu, W.; Yuan, Q.; Zheng, Y.; Yao, B. A thin film polyethylene terephthalate (PET) electrochemical sensor for detection of glucose in sweat. *Talanta* **2019**, *198*, 86−92.

(10) Smith, R. E.; Totti, S.; Velliou, E.; Campagnolo, P.; Hingley-Wilson, S. M.; Ward, N. I.; Varcoe, J. R.; Crean, C. Development of a novel highly conductive and flexible cotton yarn for wearable pH sensor technology. *Sens. Actuators, B* **2019**, *287*, 338−345.

(11) Li, P.; Zhang, D.; Wu, Z. Flexible MoS2 sensor arrays for high performance label-free ion sensing. *Sens. Actuators, A* **2019**, *286*, 51−58.

(12) Oh, S. Y.; Hong, S. Y.; Jeong, Y. R.; Yun, J.; Park, H.; Jin, S. W.; Lee, G.; Oh, J. H.; Lee, H.; Lee, S.-S.; Ha, J. S. Skin-Attachable, Stretchable Electrochemical Sweat Sensor for Glucose and pH Detection. *ACS Appl. Mater. Interfaces* **2018**, *10*, 13729−13740.

(13) Bae, C. W.; Toi, P. T.; Kim, B.-Y.; Lee, W. I.; Lee, H. B.; Hanif, A.; Lee, E. H.; Lee, N.-E. Fully Stretchable Capillary Microfluidics-integrated Nanoporous Gold Electrochemical Sensor for Wearable Continuous Glucose Monitoring. *ACS Appl. Mater. Interfaces* **2019**, *11*, 14567.

(14) Buono, M. J.; Ball, K. D.; Kolkhorst, F. W. Sodium ion concentration vs. sweat rate relationship in humans. *J. Appl. Physiol.* **2007**, *103*, 990−994.

(15) Kassal, P.; Sigurnjak, M.; Steinberg, I. M. Paper-based ion-selective optodes for continuous sensing: Reversible potassium ion monitoring. *Talanta* **2019**, *193*, 51−55.

(16) Promphet, N.; Rattanawaleedirojn, P.; Siralertmukul, K.; Soatthiyanon, N.; Potiyaraj, P.; Thanawattano, C.; Hinestroza, J. P.; Rodthongkum, N. Non-invasive textile based colorimetric sensor for the simultaneous detection of sweat pH and lactate. *Talanta* **2019**, *192*, 424−430.

(17) Parrilla, M.; Cuartero, M.; Crespo, G. A. Wearable potentiometric ion sensors. *TrAC, Trends Anal. Chem.* **2019**, *110*, 303−320.

(18) Cuartero, M.; Parrilla, M.; Crespo, G. A. Wearable potentiometric sensors for medical applications. *Sensors* **2019**, *19*, 363.

(19) Bakker, E.; Pretsch, E. Nanoscale potentiometry. *TrAC, Trends Anal. Chem.* **2008**, *27*, 612−618.

(20) Lan, W.-J.; Zou, X. U.; Hamedi, M. M.; Hu, J.; Parolo, C.; Maxwell, E. J.; Bühlmann, P.; Whitesides, G. M. Paper-Based Potentiometric Ion Sensing. *Anal. Chem.* **2014**, *86*, 9548−9553.

(21) Sempionatto, J. R.; Martin, A.; García-Carmona, L.; Barfidokht, A.; Kurniawan, J. F.; Moreto, J. R.; Tang, G.; Shin, A.; Liu, X.; Escarpa, A.; Wang, J. Skin-worn Soft Microfluidic Potentiometric Detection System. *Electroanalysis* **2019**, *31*, 239−245.

(22) Jaworska, E.; Lewandowski, W.; Mieczkowski, J.; Maksymiuk, K.; Michalska, A. Critical assessment of graphene as ion-to-electron transducer for all-solid-state potentiometric sensors. *Talanta* **2012**, *97*, 414−419.

(23) Tan, Y.; Yildiz, U. H.; Wei, W.; Waite, J. H.; Miserez, A. Layer-by-Layer Polyelectrolyte Deposition: A Mechanism for Forming Biocomposite Materials. *Biomacromolecules* **2013**, *14*, 1715−1726.

(24) Suran, S.; Balasubramanian, K.; Raghavan, S.; Varma, M. M. Spatially resolved observation of water transport across nano-membranes using bright-field nanoscopy. *Appl. Phys. Lett.* **2018**, *113*, 043701.

(25) Schönhoff, M.; Ball, V.; Bausch, A. R.; Dejugnat, C.; Delorme, N.; Glinel, K.; Klitzing, R. v.; Steitz, R. Hydration and internal properties of polyelectrolyte multilayers. *Colloids Surf., A* **2007**, *303*, 14−29.

(26) Skorb, E. V.; Volkova, A. V.; Andreeva, D. V. Layer-by-Layer Approach for Design of Chemical Sensors and Biosensors. *Curr. Org. Chem.* **2015**, *19*, 1097−1116.

(27) Farhat, T.; Yassin, G.; Dubas, S. T.; Schlenoff, J. B. Water and Ion Pairing in Polyelectrolyte Multilayers. *Langmuir* **1999**, *15*, 6621−6623.

(28) Ryzhkov, N. V.; Mamchik, N. A.; Skorb, E. V. Electrochemical triggering of lipid bilayer lift-off oscillation at the electrode interface. *J. R. Soc., Interface* **2019**, *16*, 20180626.

(29) Andreeva, D. V.; Kollath, A.; Brezhneva, N.; Sviridov, D. V.; Cafferty, B. J.; Möhwald, H.; Skorb, E. V. Using a chitosan nanolayer as an efficient pH buffer to protect pH-sensitive supramolecular assemblies. *PCCP* **2017**, *19*, 23843−23848.

(30) Prudnikova, K.; Utz, M. Polyelectrolyte hydrogels as electro-mechanical transducers. In *Frontiers in Sensing: From Biology to Engineering*; Barth, F. G., Humphrey, J. A. C., Srinivasan, M. V., Eds.; Springer Vienna: Vienna, 2012; pp 351−361.

(31) Rivero, P. J.; Goicoechea, J.; Arregui, F. J. Layer-by-layer nano-assembly: A powerful tool for optical fiber sensing applications. *Sensors* **2019**, *19*, 683.

(32) Mikhelson, K. N. Modern Trends in the ISEs Theory and Applications. In *Ion-Selective Electrodes*; Mikhelson, K. N., Ed.; Springer Berlin Heidelberg: Berlin, Heidelberg, 2013; pp 125−134.

(33) Ermakov, S. S.; Nikolaev, K. G.; Tolstoy, V. P. Novel electrochemical sensors with electrodes based on multilayers fabricated by layer-by-layer synthesis and their analytical potential. *Russ. Chem. Rev.* **2016**, *85*, 880−900.

(34) Lu, W.; Luo, Y.; Chang, G.; Liao, F.; Sun, X. Layer-by-layer self-assembly of multilayer films of polyelectrolyte/Ag nanoparticles for enzymeless hydrogen peroxide detection. *Thin Solid Films* **2011**, *520*, 554−557.

(35) Elizarova, I. S.; Luckham, P. F. Layer-by-layer adsorption: Factors affecting the choice of substrates and polymers. *Adv. Colloid Interface Sci.* **2018**, *262*, 1−20.

(36) Kozhuharov, S.; Maroni, P.; Borkovec, M. In situ Imaging of Single Polyelectrolyte Chains with the Atomic Force Microscope. *Chimia* **2019**, *73*, 17−20.

(37) Andreeva, D. V.; Skorb, E. V.; Shchukin, D. G. Layer-by-Layer Polyelectrolyte/Inhibitor Nanostructures for Metal Corrosion Protection. *ACS Appl. Mater. Interfaces* **2010**, *2*, 1954−1962.

(38) Brezhneva, N.; Nikitina, A.; Ryzhkov, N.; Klestova, A.; Vinogradov, A. V.; Skorb, E. V. Importance of buffering nanolayer position in Layer-by-Layer assembly on titania based hybrid photoactivity. *J. Sol-Gel Sci. Technol.* **2019**, *89*, 92−100.

(39) Nestler, P.; Paßvogel, M.; Ahrens, H.; Soltwedel, O.; Köhler, R.; Helm, C. A. Branched Poly(ethylenimine) as Barrier Layer for Polyelectrolyte Diffusion in Multilayer Films. *Macromolecules* **2015**, *48*, 8546−8556.

(40) Novell, M.; Parrilla, M.; Crespo, G. A.; Rius, F. X.; Andrade, F. J. Paper-Based Ion-Selective Potentiometric Sensors. *Anal. Chem.* **2012**, *84*, 4695−4702.

(41) Bandodkar, A. J.; Molinnus, D.; Mirza, O.; Guinovart, T.; Windmiller, J. R.; Valdés-Ramírez, G.; Andrade, F. J.; Schöning, M. J.; Wang, J. Epidermal tattoo potentiometric sodium sensors with wireless signal transduction for continuous non-invasive sweat monitoring. *Biosens. Bioelectron.* **2014**, *54*, 603−609.

(42) Alizadeh, A.; Burns, A.; Lenigk, R.; Gettings, R.; Ashe, J.; Porter, A.; McCaul, M.; Barrett, R.; Diamond, D.; White, P.; Skeath, P.; Tomczak, M. A wearable patch for continuous monitoring of sweat electrolytes during exertion. *Lab Chip* **2018**, *18*, 2632−2641.

(43) Parrilla, M.; Cánovas, R.; Jeerapan, I.; Andrade, F. J.; Wang, J. A Textile-Based Stretchable Multi-Ion Potentiometric Sensor. *Adv. Healthcare Mater.* **2016**, *5*, 996−1001.

(44) Guinovart, T.; Parrilla, M.; Crespo, G. A.; Rius, F. X.; Andrade, F. J. Potentiometric sensors using cotton yarns, carbon nanotubes and polymeric membranes. *Analyst* **2013**, *138*, 5208−5215.

(45) Liu, J.; Prindle, A.; Humphries, J.; Gabalda-Sagarra, M.; Asally, M.; Lee, D.-y. D.; Ly, S.; Garcia-Ojalvo, J.; Süel, G. M. Metabolic co-dependence gives rise to collective oscillations within biofilms. *Nature* **2015**, *523*, 550.

(46) Prindle, A.; Liu, J.; Asally, M.; Ly, S.; Garcia-Ojalvo, J.; Süel, G. M. Ion channels enable electrical communication in bacterial communities. *Nature* **2015**, *527*, 59.

(47) Kralj, J. M.; Hochbaum, D. R.; Douglass, A. D.; Cohen, A. E. Electrical Spiking in Escherichia coli Probed with a Fluorescent Voltage-Indicating Protein. *Science* **2011**, *333*, 345.

(48) Sharma, R.; Shimada, T.; Mishra, V. K.; Upreti, S.; Sardesai, A. A. Growth Inhibition by External Potassium of Escherichia coli Lacking PtsN (EIIANtr) Is Caused by Potassium Limitation Mediated by YcgO. *J. Bacteriol.* **2016**, *198*, 1868.

PAPER

Check for updates

Light-controllable systems based on TiO$_2$-ZIF-8 composites for targeted drug release: communicating with tumour cells†

Aziza Sharsheeva, [ID] [a] Vadim A. Iglin, [ID] [a] Pavel V. Nesterov, [ID] [a] Oleg A. Kuchur, [ID] [a] Elizaveta Garifullina, [ID] [a] Evamarie Hey-Hawkins, [ID] [b] Sviatlana A. Ulasevich, [ID] [a] Ekaterina V. Skorb, [ID] [a] Alexandr V. Vinogradov [ID] [a] and Maxim I. Morozov [ID] ⋆[a]

Drug delivery systems based on the zeolitic imidazolate framework ZIF-8 have recently attracted viable research interest owing to their capability of decomposing in acidic media and thus performing targeted drug delivery. *In vivo* realization of this mechanism faces a challenge of relatively slow decomposition rates, even at elevated acidic conditions that are barely achievable in diseased tissues. In this study we propose to combine drug delivery nanocomposites with a semiconductor photocatalytic agent that would be capable of inducing a local pH gradient in response to external electromagnetic radiation. In order to test this principle, a model drug-releasing nanocomposite comprising photocatalytic titania nanotubes, ZIF-8, and the antitumor drug doxorubicin has been investigated. This system was demonstrated to release the drug in a quantity sufficient for effectively suppressing IMR-32 neuroblastoma cells that were used as a model diseased tissue. With locally applied UV irradiation, this result was achieved within 40 minutes, which is a relatively short time compared to the release duration in systems without photocatalyst, typically taking from several hours to several days.

Introduction

Neuroblastoma (IMR-32) is a neuroendocrine tumour that occurs in the sympathetic nervous system, which leads to tumours in the adrenal glands and/or in the sympathetic trunk and affects mainly young children. Tumours are known to grow and form metastases, disrupting the work of bone marrow, the liver, lymph nodes, *etc.*[1] When the disease is detected at the early stages (I–IV), chemotherapy or surgery is prescribed. However they do not always lead to recovery. Besides, the main problem of chemotherapy is its destructive effect on the patient's body, leading to short-term survival.[2] The side effects of such therapy can be effectively minimized in a system of targeted drug delivery to the tumour tissue and/or metastases, while not affecting the healthy cells.

Nanomaterials with effective drug encapsulation, controllable self-assembly and biocompatibility are considered to be promising for antitumor therapy.[3] Their unique nanoscale size

and distinctive bioeffects may help to solve the current chemotherapeutic barriers in cancer treatment. Metal–organic frameworks (MOFs) are crystalline solids assembled by the connection of metal ions or clusters through organic linkers whose structures are held together by strong metal–ligand bonding or by weaker bonding forces.[4] They naturally have flexible structures that in combination with the many different types of bridging ligands allow designing a large diversity of functional frameworks with various architectures and properties. The versatility of MOFs has led to their broad application in gas separation and/or storage,[5] sensors,[6] nonlinear optics[7] and catalysis.[4] Furthermore, extraordinarily high surface area, tunable pore size, and intrinsic biodegradability make them attractive for targeted drug delivery.[8–11]

Zeolitic imidazolate frameworks (ZIFs) represent a new and special class of MOFs comprising imidazolate linkers and metal ions with structures similar to conventional aluminosilicate zeolites.[12–15] Among this class, ZIF-8 (Zn(mim)$_2$, mim = 2-methyl-imidazolate) possesses a large pore cavity (11.6 Å)[16] and highly developed surface area (*ca.* 1630 m^2 g^{-1}).[13,14] In addition, ZIF-8 is capable of decomposing in acidic media.[12] These properties make this framework attractive for drug encapsulation, transportation, and selective pH-mediated release.[16–20] The pH-mediated release is an essential feature of antitumor drug carriers, as tumour extracellular substance is known to be relatively more acidic

^{a} Laboratory of Solution Chemistry of Advanced Materials and Technologies, ITMO University, Lomonosova str. 9, St.Petersburg, 191002, Russian Federation. E-mail: morozov@scamt-itmo.ru

^{b} Faculty of Chemistry and Mineralogy, Institute of Inorganic Chemistry, Leipzig University, D-04103 Leipzig, Germany

† Electronic supplementary information (ESI) available. See DOI: 10.1039/c9tb01377f

compared to normal tissues.[21,22] Antitumoral agents such as doxorubicin (DOXO) can be structurally incorporated by binding to the surface of ZIF-8 and released upon increasing the acidity of the surrounding medium.[17,18] Importantly, the resultant nanocomposite DOXO-ZIF-8 demonstrates lower cytotoxicity compared to pure doxorubicin,[17] which is one of the key aspects of improving the drug's therapeutic profile by the means of engineered nanocarriers.[23] Further improvements in engineered DOXO-ZIF-8 nanocomposites concern various functional additives and modifiers such as polyacrylic acid, Au nanoclusters, and magnetic Fe_3O_4 nanoparticles. They enhance the pH sensitivity and can be used for various cancer imaging techniques, such as magnetic resonance, X-ray computer tomography, and fluorescence.[24] Despite many advantages, the rate of drug release by such nanocomposites is relatively slow, typically requiring several hours to several days for releasing reasonable amounts of doxorubicin at pH varying between 5.0 and 7.4.[16,17,24–26]

In this regard we address here a possibility of enhancing the release efficiency of anticancer drug nanocomposites by combining them with a photocatalytic agent enabling additional control of the drug release kinetics by external UV illumination. As a prototype model, we propose depositing the DOXO-ZIF-8 nanocomposite particles onto highly-ordered titanium dioxide nanotubes (TNTs) that are known for both excellent biocompatibility[27] and photocatalytic activity.[28,29] In particular, TNTs were shown to convert the external electromagnetic energy into a local pH gradient at their surface.[30–33] Thus, implementation of the photosensible TNTs in antitumor drug delivery systems should enable an additional control of the pH-mediated drug release by using UV light for acceleration. Here, we address the preparation of DOXO-ZIF-8-TNT nanocomposite, and investigation of its structural and chemical integrity, as well as functionality. Functional kinetics of the controllable drug release and the resultant cytotoxic effect on IMR-32 cells are thus of primary interest.

Materials and methods

Formation of TiO_2 nanotubes

Titanium plates (99.99% trace metals basis) with a thickness of 1.5 mm and an area of 4 cm^2 were preliminarily polished in a mixture of hydrofluoric and nitric acids taken in a volume ratio of 1:2. Prior to anodizing, the non-active surface of the electrode was protected with a chemically resistant mask. The electrolyte was prepared on the basis of ethylene glycol with addition of 2 vol% of distilled water and 0.75 wt% of ammonium fluoride. Anodization was carried out at a constant voltage of 40 V for 1 h using an AC–DC power supply PS8160-04DT (EA Elektro-Automatik, Germany) and Winkler platinum electrode.

After the first anodization, the prepared titania layer was removed using an ultrasonic bath Grad 40-35 with distilled water. The second anodization was processed in order to obtain a highly regular structure of TNTs. The as-prepared coating was rinsed in ethanol and dried. In order to develop higher crystallinity, the samples were finally annealed in air at 450 °C for 3 h.

Synthesis of ZIF-8 crystals and ZIF-8-TNT nanocomposites

To obtain ZIF-8-TNT nanocomposites, the TNTs samples were immersed in a solution of 293 mg of $Zn(OAc)_2 \cdot 2H_2O$ and 1.08 g of Hmim in 30 mL of deionized water for 48 h, without stirring, thus adopting the method by Jian et al.[34] The process was performed at room temperature (ca. 25 °C). The molar ratio of $Zn/Hmim/H_2O$ was adjusted towards optimal morphology of the resulting ZIF-8 product, though two different topologies (sod, dia) were obtained within the final coating layer (Fig. S1, ESI†). After washing for 4 h in phosphate buffer (pH = 7.4), the obtained TNT-ZIF-8 plates were dried at 50 °C for 24 h. Similarly, the control batches of ZIF-8 particles were synthesized by the same procedure and collected as a precipitate.

Incorporation of doxorubicin onto ZIF-8 and ZIF-8-TNT plates

In order to incorporate doxorubicin onto the ZIF-8-TNT samples, a solution of 3 mg of doxorubicin hydrochloride in 3 mL of DI water was prepared, and then the ZIF-8-TNT plates were immersed in the solution for 24 hours, without stirring. The process was performed at room temperature, as suggested in a previous study.[17] The obtained DOXO-ZIF-8-TNT samples were washed in phosphate buffer (pH = 7.4) for 1 h. The amount of doxorubicin adsorbed onto ZIF-8 was estimated by UV-vis spectroscopy. The control batches of DOXO-ZIF-8 nanocomposites were prepared in the same way.

The whole processing chain is schematically illustrated in Fig. 1.

Material characterization and analysis

The microstructure of the obtained materials was analyzed using a TESCAN MAIA 3 scanning electron microscope.

Energy dispersive X-Rays Spectrometry (EDX) was carried out using an Inca X-ACT Spectrometer (Oxford Instruments).

X-ray diffraction (XRD) analysis was performed using a Rigaku SmartLab 3 diffractometer, with CuKα radiation (λ = 1.5418 Å).

Fourier-transform infrared (FTIR) spectra were obtained using a Thermo Scientific Nicolet 5700 FTIR-spectrometer, in ATR mode.

SVET/SIET instrumentation and measurements

Scanning Vibrating and Ion-selective Electrode Techniques (SVET-SIET instrumentation, Applicable Electronics, LLC) were employed for measuring the ionic current density and mapping the pH distribution near the surface–solution interface.[35]
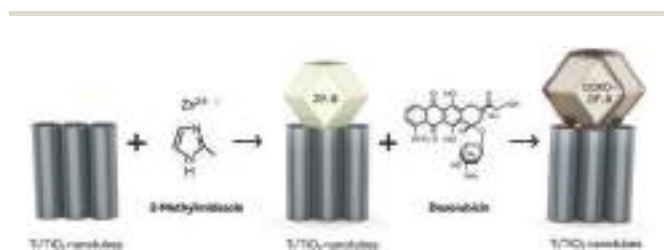
Fig. 1 Schematic of TNT–ZIF-8–DOXO assembly.

The electrochemical cell used by SVET is schematically shown in Fig. 2a. The electric signal is collected by a system of three electrodes (working, reference, and grounding). The working microelectrode is made of a platinum–iridium alloy with an insulating sheath along its entire length except for the platinum tip with a diameter of approximately 10 μm. The platinum tip vibrates with an amplitude of 10 μm at a distance of 150 μm from the sample surface. While vibrating at each area of interest, the working tip probes the electric field near the surface by measuring the potential difference ΔV between two points distanced by Δd. The measured voltage fluctuation between the working and reference electrodes is then amplified and converted into the current density using Ohm's law and the conductivity of the solution as the conversion factor. The vibration also serves for mixing the solution near the probe and thus preventing any stationary redox process at the tip.[36] Preliminary calibration is a routine, in which several measurements are performed at various fixed positions of the working electrode in the stationary (non-vibrating) regime.

Samples of TNT, ZIF-8-TNT, and DOXO-ZIF-8-TNT were fixed on an epoxy resin and placed into an aqueous solution of 0.05 M NaCl. Measurements of the current density were carried out iteratively at a fixed area of the sample. This area was subjected to external UV light irradiation applied as a step function and the resulting response of ionic current excitation and relaxation was characterized.

Generation of H$^+$ ions was characterized using a Scanning Ion-selective Electrode Technique (SIET). This method realizes the concept of local potentiometry, based on the relationship between the measured potential difference and the activity of a hydrogen ion.[35] The measurements were performed with two microelectrodes: reference and H$^+$-selective. The H$^+$-selective microelectrode (Fig. 2b) was prepared using single-barrel glass capillaries filled with injected N,N-dimethyltrimethyl-silamine. The membrane of the microelectrode (ion-selective cocktail) consists of 0.5 wt% polyvinyl chloride, 9.9 wt% tridodecyl-amine, 88.9 wt% benzyl-2-nitrophenyl ether and 0.7 wt% potassium tetrakis-(4-chlorophenyl)borate. The reference electrode was prepared using a silver wire coated by silver chloride.

The experimental SIET setup is schematically shown in Fig. 2c. The ion-selective electrode was attached to a microelectro-mechanical system controlling the tip position near the sample surface, thus allowing for scanning regime. The local activity of the H$^+$ cations was measured at a height of 50 μm from the sample surface within an area of ca. 2.25 mm^2.

In vitro study of the drug loading and release profile

The system DOXO-ZIF-8-TNT is relatively stable in water. Evaluation of drug adsorption by ZIF-8-TNT was performed using UV-vis spectroscopy (single-beam spectrometer Cary 8454 UV-vis). The quantity of the adsorbed doxorubicin was determined using the calibration curve of doxorubicin in water. In order to evaluate the amount of doxorubicin in DOXO-ZIF-8-TNT, the samples were placed in cuvettes with water (2 mL) and subjected to UV irradiation until full release (ca. 150 min, 37 ± 0.5 °C). Thus the loading or release efficiency under other conditions was evaluated correspondingly, as percentage of the fully released amount.

MTT-assay for interaction of IMR-32 neuroblastoma cells with nanocomposites under UV-irradiation

Interaction of neuroblastoma cells with TNTs, ZIF-8-TNT and DOXO-ZIF-8-TNT nanocomposites under UV-irradiation was investigated using a reduction assay of 3-(4,5-dimethyl-2-thiazolyl)-2,5-diphenyl-2H-tetrazolium bromide (MTT). To perform this test, the samples with nanocomposite coatings were placed in 12-well plates along with the IMR-32 neuroblastoma cells (10^5 cells mL^{-1} for adherent cells) and incubated at 37 °C for 72 h. For the control experiment, a certain amount of the IRM-32 cells was incubated solely to serve as a reference. After the first 24 h of incubation, all the samples with cells were irradiated using a UV source (365 nm) placed at a distance of 10 cm. The light exposition time varied within 5–40 min for the purpose of the experiments. The LED element of a DLR-6 lamp (25 W, 13 000 lm) was used as a source of UV light. Upon irradiation, the samples were returned to incubation. The incubated product was tested by adding 0.2 mL of MTT (5 mg mL^{-1}) for 2 hours, and then the MTT-formazan product was dissolved in 10 mL of DMSO and the absorbance was measured at 570 nm using a plate reader Infinite F50 (Tecan). To improve cell visibility, trypan blue solution (0.4 wt%) was added as cell stain.

Results and discussion

SEM and XRD characterization

Scanning electron microscopy (SEM) images of the titania nanotubes and the composite TNT-ZIF-8 assemblies are shown in Fig. 3. The images demonstrate the vertical arrangement of titania nanotubes (Fig. 3a and b), with a coating thickness of ca. 5 μm (inset in Fig. 3a) and an average pore diameter of ca. 70 nm (Fig. 3b). The calculated geometric surface of TNTs has been estimated as 529 cm^2. The TNT-ZIF-8 nanocomposite is a uniform coating of ZIF-8 with two different topologies on TNTs (Fig. 3c). The major volume fraction of a ZIF-8 layer is

Fig. 2 Scheme of the (a) SVET cell, (b) ion-selective electrode, and (c) SIET cell.
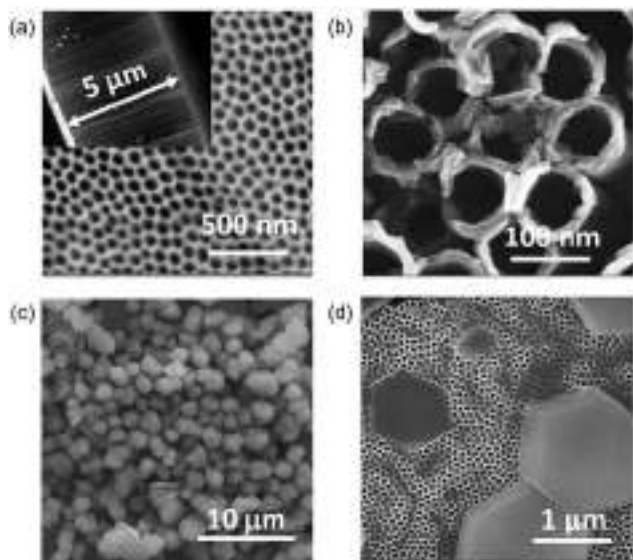
Fig. 3 SEM images of TNTs (top-view) (a and b) and TNTs with deposited ZIF-8 (c and d); the inset in (a) shows the cross-section view of the TNT layer.

crystals with a characteristic shape of rhombic dodecahedron (Fig. 3d). The minor volume fracture that is also visible in Fig. 3c has a flake-like morphology. The final identification of the ZIF-8 topologies has been performed using X-ray diffraction analysis.

X-ray diffraction (XRD) patterns have been obtained for all the prepared materials. The XRD spectrum of ZIF-8 is shown in Fig. 4a. Two ZIF-8 polymorphs with sodalite (sod, CCDC code: VELVOY)[12,37] and diamondoid (dia, CCDC code: OFERUN10)[14,38] topologies have been identified. In contrast to the SEM image (Fig. 3c), the manifestation of the dia-ZIF-8 topology is stronger on the XRD pattern, likely due to much higher density of dia-ZIF-8 compared to sod-ZIF-8 (calculated values 1.58 g cm^{-3} vs. 0.95 g cm^{-3}, correspondingly).[14] The observed variety of topologies in the obtained material has no substantial effect on the functionality of ZIF-8 as a drug carrier. The topologically different polymorphs have identical local structure[39] and therefore similar intrinsic reactivity of the tetrahedral Zn nodes. This has recently been demonstrated by in-depth DFT analysis of the reactivity among different ZIF-8 polymorphs.[39] In particular, the difference in the reaction energies for the formation of a linker vacancy in sod-ZIF-8 and dia-ZIF-8 has been evaluated below 1 kcal mol^{-1},[40] which is well beyond the accuracy limits of standard DFT approaches.[41] Furthermore, DFT calculations point to a substantial reactivity enhancement of the under-coordinated Zn sites on the external surface compared to those within the bulk ZIF-8,[40,42] thus allowing for a more efficient coordination of doxorubicin at the surface of the ZIF-8 carrier.[17]

Fig. 4b illustrates the XRD patterns of DOXO, ZIF-8-DOXO, TNT, TNT-ZIF-8, and TNT-ZIF-8-DOXO. Pure doxorubicin was an amorphous powder and showed no apparent XRD reflections. The XRD patterns of pure ZIF-8 and DOXO-ZIF-8 are nearly identical, thus confirming no effect on the structural integrity of the host ZIF-8 upon adsorption of doxorubicin.[17]
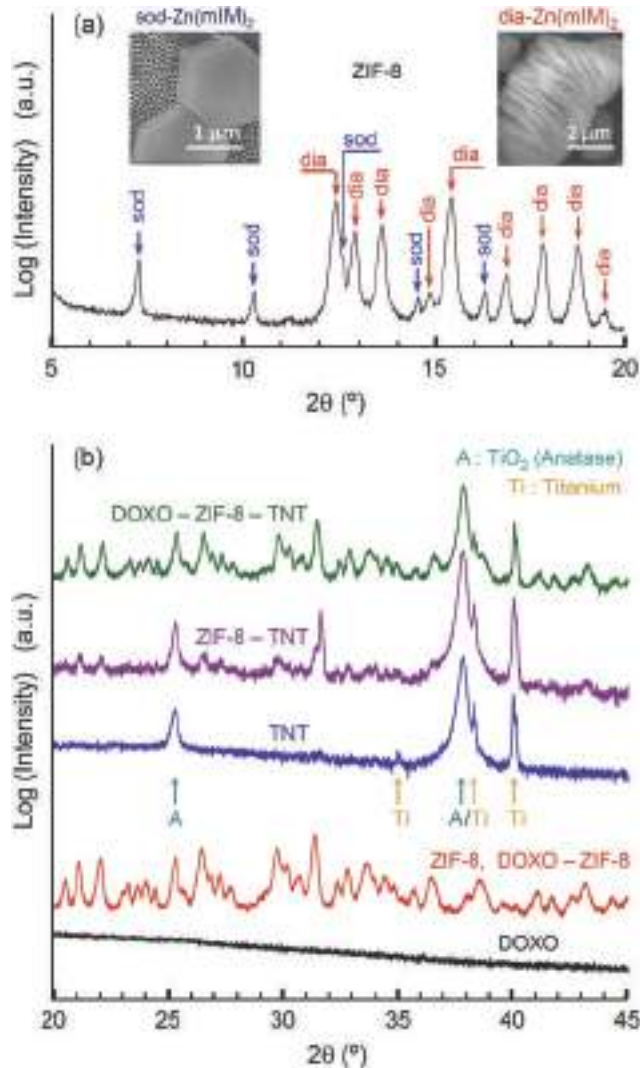
Fig. 4 XRD patterns of experimentally obtained materials: (a) ZIF-8 (insets illustrate the topologies of identified polymorphs); (b) DOXO, DOXO-ZIF-8, TNT, TNT-DOXO-ZIF-8, and DOXO-ZIF-8-TNT.

The patterns of all the multilayer assemblies include traces of the bottom titanium substrate, then the layers of TiO$_2$ (anatase) nanotubes, ZIF-8, and ZIF-8-DOXO, as shown in Fig. 4b. The peaks of titanium (Ti) and anatase-TiO$_2$ (A) phases are indexed according to JCPDS cards #5-682 and #21-1272, correspondingly. Thus, each layer of the nanocomposite manifests itself on the XRD pattern by the series of individual reflections, slightly shadowing the peak intensities resulting from the layers underneath. Hence, the structural integrity of all the layers is shown to remain unaltered at all the processing stages.

FTIR analysis

Fourier-transform infrared spectroscopy (FTIR) has been used as complementary analysis providing deeper insight into the chemical arrangement of elements in the obtained materials. The FTIR spectra obtained for TNT, ZIF-8, ZIF-8-TNT, DOXO, and DOXO-ZIF-8-TNT are shown in Fig. 5a. The TNT pattern includes the distinctive peak at 663 cm^{-1}, associated with the
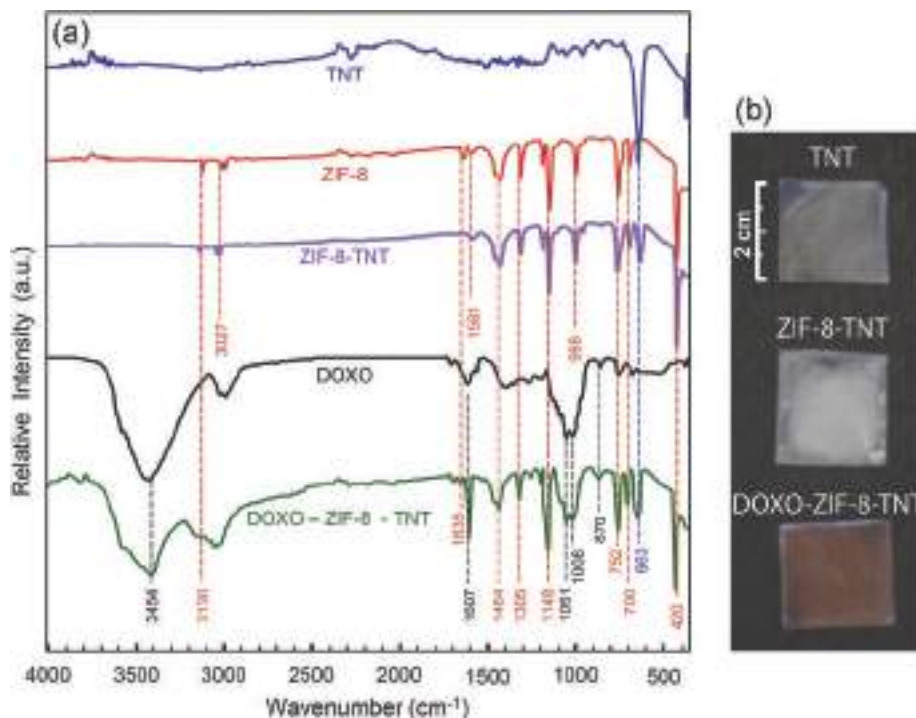
Fig. 5 (a) Infrared spectra for TNT, ZIF-8, DOXO, and DOXO-ZIF-8-TNT; (b) images of TNT, ZIF-8-TNT and DOXO-ZIF-8-TNT.

Ti–O–Ti stretch.[43,44] ZIF-8 yields a series of bands interpreted[17,45] as aromatic and aliphatic C–H asymmetric stretching vibrations (3130 and 3027 cm^{-1}), C=C (Imidazole ring) stretch mode (1635 cm^{-1}), and C=N stretch vibration (1581 cm^{-1}). The signals at 1305–1464 cm^{-1} correspond to the entire ring stretching, while the band at 1148 cm^{-1} is associated with an aromatic C–N stretching mode. The absorption band at 420 cm^{-1} is associated with the Zn–N stretching mode. The observed spectrum is thus consistent with the previous FTIR analysis.[45] The FTIR spectrum of ZIF-8-TNT includes all the characteristic bands observed in ZIF-8 and TNT, thus confirming the structural integrity of the composite. FTIR data for pure doxorubicin have also been reported previously;[17,46] they are consistent with the data obtained in this study. The following band assignment has been suggested:[17,46] the characteristic stretching vibration of the O–H and N–H bonds (3454 cm^{-1}), the axial deformation of C–H (3027 cm^{-1}) and C–O (1607 cm^{-1}) bonds, and stretching of the alcohol group (1008–1200 cm^{-1}). Finally, the FTIR pattern of DOXO-ZIF-8-TNT confirms the chemical integrity of the constituting components, as all their characteristic bands persist in the spectrum of the nanocomposite (TNT: Ti–O–Ti (663 cm^{-1})); ZIF-8: C–H (3000–3200 cm^{-1}), C=C ((imidazole ring) (1635 cm^{-1}), C–N (1148 cm^{-1}), Zn–N (420 cm^{-1}); DOXO: O–H and N–H bonds (3454 cm^{-1}), C–H (3000–3200 cm^{-1}), C=C (aryl) (1607 cm^{-1}), C–O–C (1008–1200 cm^{-1})). Despite this, encapsulation of doxorubicin by TNT-ZIF-8 was evidenced by the contrast change of colour: the crystals of doxorubicin were pale orange in the solution, while ZIF-8 crystals on the TNT substrate were white. Upon adsorption, the surface of a DOXO-ZIF-8-TNT nanocomposite became reddish-brown (mahogany), see Fig. 5b. This supports the mechanism of ZIF-8-TNT formation by adhesion of the hydrophobic ZIF-8 crystals[47] on the amphiphilic TNT surface.[48] The crystals of ZIF-8 were not leached when the ZIF-8-TNT composite was immersed in water. Doxorubicin is a relatively large molecule to be encapsulated in the pores of ZIF-8. As suggested by Vasconcelos et al.,[17] the adsorption scenario is based on interaction of doxorubicin with the Zn^{2+} cations at the surface of ZIF-8. Seemingly, at the surface of ZIF-8, two imidazolate ligands are replaced by water molecules that are, in turn, the most likely candidates to be replaced by doxorubicin. The tetrahedral coordination geometry of the cation is thus maintained throughout these transformations. As discussed previously, this scenario is in line with DFT analyses of the undercoordinated Zn node reactivity on the external surface and within the bulk of ZIF-8.[40,42]

SVET/SIET

The Scanning Vibrating Electrode Technique (SVET) measures the current density in the vicinity of the interface between solid and liquid phases. Fig. 6a illustrates the behaviour of current density measured at the surface of TNTs, ZIF-8-TNT, and DOXO-ZIF-8-TNT in response to excitation by external UV irradiation. In all the cases, application of the UV light pulse ignited an intensive redistribution of electric charges with an immediate increase of the current density, followed by a slow relaxation process until a new equilibrium is established with steady current. The decaying period lasted for 5–15 min depending on the material. As shown in Fig. 6b for the case of DOXO-ZIF-8-TNT, this relaxation can be described in terms of the second-order rate equation. To get more insight into the mechanism of the current formation, an experiment with scanning H$^+$ ion-selective potentiometry was carried out.
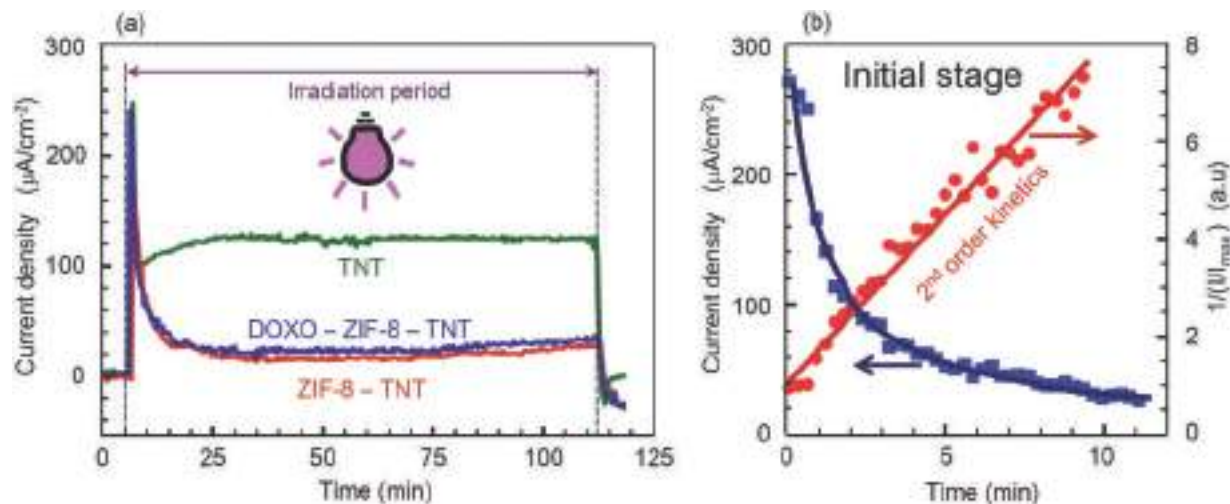
Fig. 6 (a) Excitation and relaxation of electric current at the surface of TNT, ZIF-8-TNT, and DOXO-ZIF-8-TNT in response to UV irradiation; (b) Relaxation of electric current in DOXO-ZIF-8-TNT and its interpolation with the 2nd order rate equation.

The results are shown in Fig. 7. In this experiment, samples of TNTs, ZIF-8-TNT, and DOXO-ZIF-8-TNT were subjected to UV irradiation covering some local area at the surface of the samples (Fig. 7a). The activity of H^+ ions within the selected area has been measured by SIET and the resultant maps of pH distribution are shown for TNT (Fig. 7b), ZIF-8-TNT (Fig. 7c), and DOXO-ZIF-8-TNT (Fig. 7d).

Comparison of the SVET (Fig. 6a) and SIET (Fig. 7b–d) experiments indicates relatively high ionic current and narrow distribution of the hydrogen ions around the irradiated epicentre on TNTs (Fig. 7b). In contrast, in the cases of ZIF-8-TNT and DOXO-ZIF-8-TNT the ionic current is weaker (Fig. 6a), while the distribution of hydrogen ions is broader (Fig. 7c and d). This suggests that some of the hydrogen ions are absorbed into the upper layers. This is plausible, since the structure of ZIF-8 is porous and includes basic amino groups that may attract protons.

The origin of photoinduced protons and ionic current in the aqueous medium at the interface with titania has been a subject of several research studies[30–33,49,50] addressing the photocatalytic dissociation of water. In particular, the following processes have been figured out. Irradiation of titania with energy exceeding the band gap results in generation of electron–hole couples (e^-, h^+).
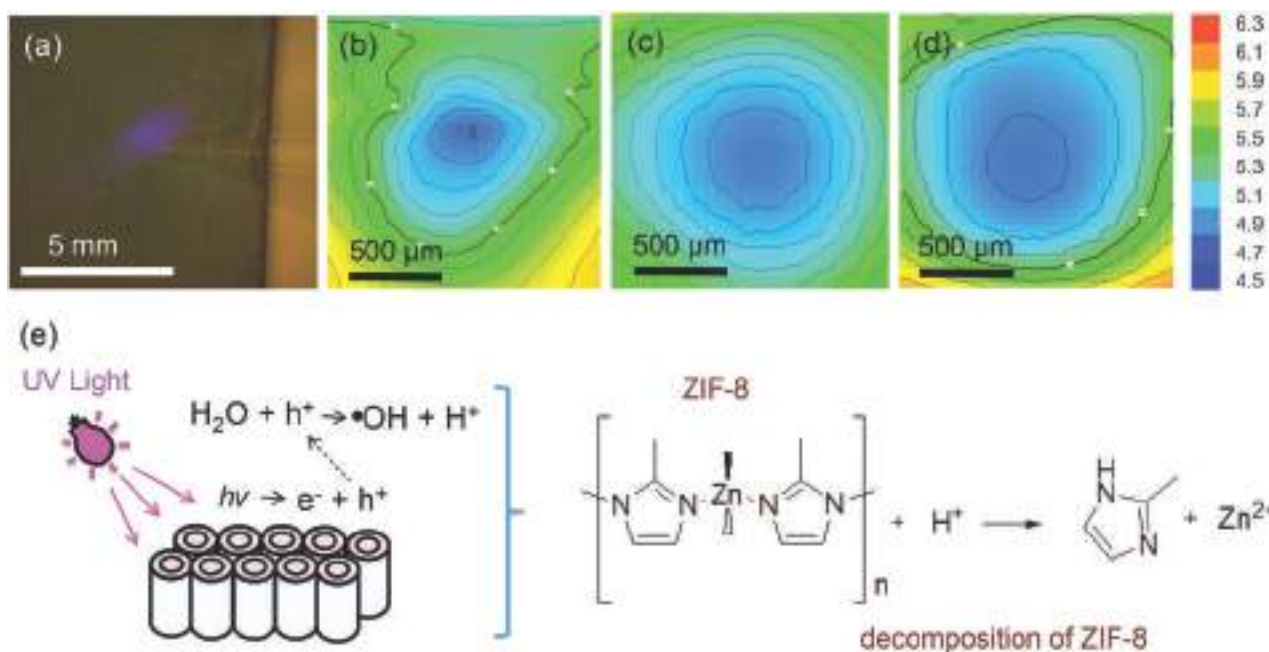
Fig. 7 SIET study of proton activity at the surface of TNTs and TNT-ZIF-8-DOXO: (a) surface of a sample with UV-irradiated area; (b–d) SIET maps for pH distribution within the irradiated area for (b) TNTs, (c) TNT-ZIF-8, and (d) TNT-ZIF-8-DOXO samples; (e) mechanism of photocatalytic decomposition of ZIF-8 at the irradiated surface of TNTs.

The transfer of holes from bulk to surface is faster by one or two orders of magnitude than that of electrons,[50,51] hence the photoinduced holes likely first reach and interact with water molecules. Thus, the initial stage of the photocatalytic process is suggested to be:[49]

$$H_2O + h^+ \rightarrow \,^\bullet OH + H^+$$

The hydroxyl radical is a reactive oxygen species that may undergo further photoinduced reactions[50] producing various species, including H^+ and OH^-. However, an important feature is the possibility to control their localization by focusing the light. Formation of a local pH gradient with the minimum at the epicentre of the irradiated interface has been demonstrated in a series of publications by the means of SIET.[31–33]

In this study, SIET mapping of the H^+ localization within the irradiated area on TNT (Fig. 7b) and DOXO-ZIF-8-TNT (Fig. 7c) samples suggests that the presence of a ZIF-8 intermediate layer leads to a larger number of protons distributed along the irradiated surface. The lower SVET current in ZIF-8-TNT and DOXO-ZIF-8-TNT compared to TNT (Fig. 6) indicates that ZIF-8 reduces the photoinduced pH gradient and the associated ionic current along the normal to the irradiated surface. These observations suggest penetration of the photoinduced protons into the structure of ZIF-8. In turn, the protonation of ZIF-8 leads to it decomposition. The protons mainly interact with the mim ligands, the terminal group in the ZIF-8 structure, while the resulting change in acidity is accompanied by a simultaneous change in the concentration of Zn^{2+}.[52] The whole process chain is schematically shown in Fig. 7d.

Release kinetics of doxorubicin

Since the photocatalytic activity of titania agents affects decomposition of ZIF-8 via the surrounding aqueous medium, it allows for controllable release of doxorubicin from the DOXO-ZIF-8-TNT nanocomposite. The time dependence of the process

Fig. 8 Kinetics of the doxorubicin release efficiency in DOXO-ZIF-8-TNT with and without UV irradiation (365 nm) at 25 °C and 37 °C. The inset shows the initial stage of the process.

in a PBS buffer solution with pH = 7.4 is shown in Fig. 8 for the cases with and without UV irradiation, as well as for two different temperatures, 25 °C (ambient temperature) and 37 °C (human body temperature). Within the chosen time scale, no notable drug release was observed in the absence of UV light. In contrast, irradiation is shown to accelerate the drug release process, so the full release was achieved within 120 min at 25 °C and 90 min at 37 °C, correspondingly. The photoinduced release demonstrated two distinct stages with the different rate regimes. The initial stage (Fig. 8, inset) lasted for several minutes and likely corresponded to the period of ionic current relaxation registered by an SVET experiment (Fig. 6b). Thus the main stage of the photoinduced drug release corresponds to the regime of steady ionic current generation (Fig. 6a and 8).

In the absence of UV irradiation, the full release of the drug from DOXO-ZIF-8-TNT in a buffer solution with pH = 7.4 took 41 and 29 days at temperatures 25 °C and 37 °C, correspondingly. This indicates rather strong chemical bonding between DOXO and ZIF-8 in the nanocomposite. In particular, it demonstrates a superior stability under ambient conditions compared to DOXO-MIL-100, a composite based on a non-toxic iron(III) carboxylate MOF, in which the drug release completes within 14 days under similar conditions.[8]

To elucidate better the role of ZIF-8 in drug loading and release by DOXO-ZIF-8-TNT, a control MOF-free experiment on DOXO loading and release on pure TNTs has been fulfilled. In this case, TNTs demonstrated a smaller loading capacity: ca. 0.25 mg cm^{-2} vs. ca. 0.71 mg cm^{-2} in the case of ZIF-8-TNT. In addition, the DOXO-TNT nanocomposite demonstrated a relatively poorer stability in buffer solution (pH 7.4, 37 °C) compared to DOXO-ZIF-8-TNT: the complete drug release occurred within 5 hours (Fig. S2a, ESI†) vs. 29 days (Fig. S2b, ESI†). Furthermore, the observed stability of DOXO-TNT is apparently weaker compared to various nanocomposites based on TiO$_2$ nanoparticles, which were reported[53–55] to release well below 20% of the drug under similar experimental conditions.

Kinetics of all the processes addressed in this study are summarized in Fig. 9 with appropriate axis scales related to the most applicable rate order. For the processes occurring under UV irradiation, two regimes can be distinguished kinetically: (1) the initial stage, in which the first portion of transient photoinduced charge undergoes relaxation (Fig. 6b and 9a, b) and (2) the main stage, in which the local current caused by the photoinduced charge is steady (Fig. 6a and 9c, d). The kinetics of the current density relaxation measured by SVET at the initial stage appeared to be of the second-order rate (Fig. 9a). The fact that it is different from the physical model of electrostatic charge decay rather indicates the chemical origin of the process. Indeed, the physical model of charge relaxation would presume the first-order rate, an exponential decay with the time constant $\tau = RC$, where R and C are the effective resistance and capacitance of the aqueous solution within the area of characterization. The corresponding initial period of the drug release is characterized by the pseudo first-order rate (Fig. 9b). This is rather typical for reactions occurring in systems with a TiO$_2$ catalyst.[56–58] Nonetheless, the main stage of the drug release from DOXO-ZIF-8-TNT
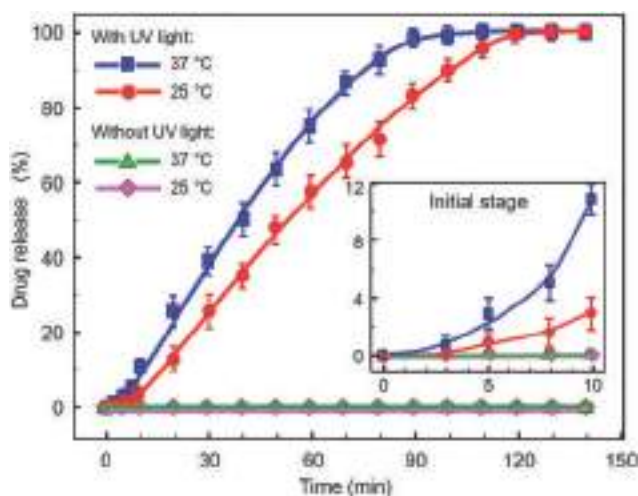
6816 | J. Mater. Chem. B, 2019, 7, 6810–6821

This journal is © The Royal Society of Chemistry 2019
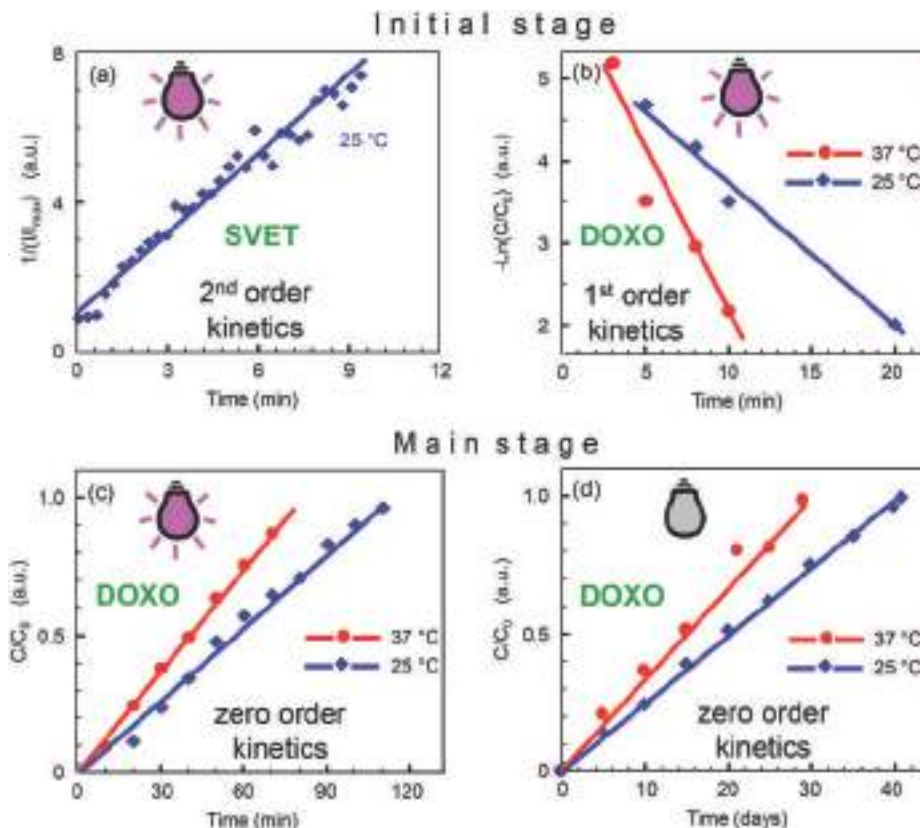
Fig. 9 Kinetics of various processes involved in drug release from DOXO-ZIF-8-TNT: (a) SVET current, (b) initial stage of photoinduced drug release; (c and d) main stage of drug release with (c) and without (d) UV irradiation.

appears to be rate-independent, irrespective of the irradiation on/off regime (Fig. 9c and d). This indicates a diffusion-limited heterogeneous reaction, likely controlled by the rate of proton penetration into the metal–organic framework. It is, however, difficult to elucidate the particular limiting factors for both stages, as the whole process of doxorubicin release involves a multiple chain of physical and chemical interactions. The key stages are shown in Fig. 7e, while intermediate processes may limit the rate. In particular, these can be the proton transport into ZIF-8, proton interaction with imidazolate linkers or destruction and decomposition of the framework, whose products may begin competing with TNTs for photon absorption, etc.

In this study, we do not address kinetics of the earlier processes occurring in TiO$_2$-related systems within the sub-millisecond period, such as photogeneration of electrons and holes, their transfer and interaction with water, etc. They have been investigated and reported elsewhere.[50,51]

The UV light induced decomposition of ZIF-8 on a TNT plate was investigated by SEM/EDX analysis. The result is shown in Fig. S3 (ESI†). Prior to irradiation, the shape of an arbitrarily chosen sod-ZIF-8 crystal along with the distribution of Zn and Ti elements was characterized (Fig. S3a, ESI†). The next characterization was carried out after 90 min of exposure to UV-irradiation at 37 °C in a PBS buffer solution with pH = 7.4, in order to examine the decomposition ZIF-8-TNT under the conditions sufficient for full release of doxorubicin by the DOXO-ZIF-8-TNT system (Fig. 8).

This treatment resulted in partial degradation of ZIF-8 crystals on TNT. As shown in Fig. S3b (ESI†), they lost their sharpness, while the distribution of Zn atoms became broader, partially leaving the crystal boundaries and encompassing the surrounding area; no apparent changes was observed for Ti distribution.

In order to get more insight into the decomposition process, an FTIR analysis was performed with the UV irradiated sample of ZIF-8-TNT. Prior to the analysis, the sample was dried for 4 hours at 60 °C and then stored in a vacuum drier (ca. 0.1 atm) for another 4 hours. The FTIR analysis confirmed the partial decomposition of ZIF-8 on TNT induced by UV irradiation, as demonstrated in Fig. S4 (ESI†). The relative intensity of the absorption band associated with the Zn–N stretching mode (420 cm^{-1}) decreased, though it did not disappear entirely. In addition, a new broad band (2700–3400 cm^{-1}) appeared in the spectrum, likely pointing to the presence of O–H and/or N–H stretch modes. Supposedly, the N–H bond may result from interaction between protons and mim ligands, while the hydroxyl group may be bonded to zinc (Fig. 7e).

These results are consistent with the previous studies[52,59,60] addressing in-depth analyses of ZIF-8 decomposition in various media.

Interaction of IMR-32 neuroblastoma cells with ZIF-8-TNT and DOXO-ZIF-8-TNT under UV irradiation

In this section we address the effect of photoinduced release of doxorubicin on the IMR-32 neuroblastoma cell line cultivated

This journal is © The Royal Society of Chemistry 2019

J. Mater. Chem. B, 2019, 7, 6810–6821 | 6817
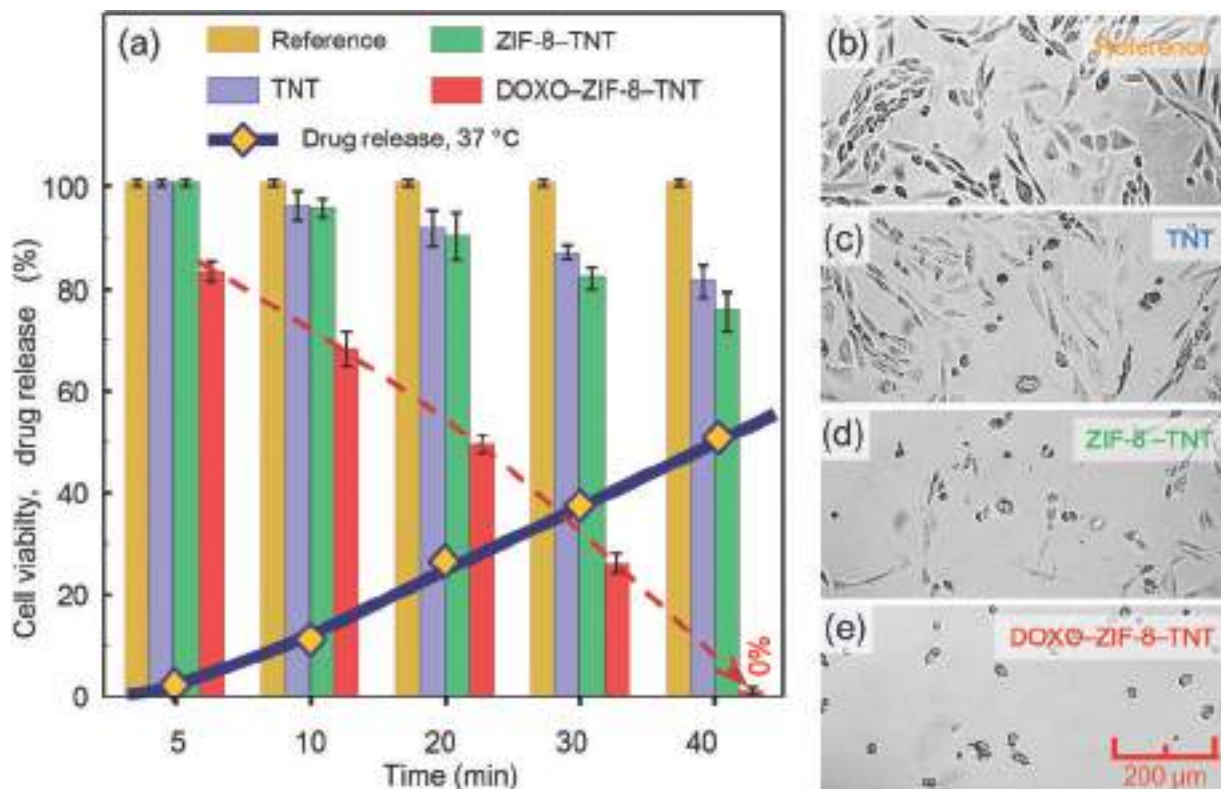
Fig. 10 Viability of IMR-32 neuroblastoma cells incubated on TNTs, ZIF-8-TNT, DOXO-ZIF-8-TNT, and solely (reference) under UV irradiation: (a) chart for percentage of viable cells and doxorubicin release measured at various time periods; and (b–e) optical microscope images of cells incubated solely (b), and on TNTs (c), ZIF-8-TNT (d), and DOXO-ZIF-8-TNT (e) after 40 min exposure to UV light.

on the developed DOXO-ZIF-8-TNT composite materials and compare it with the cytotoxicity of other materials and conditions used in this study. The results of the corresponding MTT assays are presented in Fig. 10. The bar chart of cell viability (Fig. 10a) shows that 40 min exposure to UV irradiation alone is not toxic for the cells, as the reference batch demonstrated nearly 100% viability. In combination with TNTs, the UV light affected the local acidity, which was not well tolerated by the cells. In particular, only 81% and 75% of cells survived on TNT and ZIF-8-TNT surfaces during the same period of light exposure. Finally, the introduction of doxorubicin into the system reduced the cell viability to zero: no apparently viable cells were observed after irradiating on DOXO-ZIF-8-TNT. This result was achieved within 40 min, with *ca.* 50% (0.35 mg) of doxorubicin released. Photos (with 100× magnification) of the cells exposed to 40 min UV irradiation solely, as well of the cells on TNT, ZIF-8-TNT and DOXO-ZIF-8-TNT plates are shown in Fig. 10b–e, correspondingly.

Conclusions

In this study we have investigated the possibility to enhance the control of pH-mediated release of a drug in a class of promising drug delivery systems based on ZIF-8. This class has numerous advantages in encapsulation, transportation and selective

targeted release of various drugs, which have recently attracted tangible research interest. Although several actionable engineering solutions have advanced the functional efficacy of the system, one of the key advantages, namely the selective targeted release, still remains challenging. The problems in question are: (1) the relatively slow rate of drug release, ranging from several hours to several days depending on the pH level, ranging from 5.0 to 7.4 in most of the *in vitro* assays; and (2) the relevancy of such assays, since the extracellular pH of most known tumours barely achieves this range. Using a model system of DOXO-ZIF-8-TNT, we demonstrated that the effective drug release sufficient for effectively suppressing the viability of tumour cells can be achieved in just under an hour. For this purpose, we introduced a photocatalytic semiconductor, TNTs, into a nanocomposite and demonstrated the possibility to enhance the pH gradient in the targeted zone by illumination with photon energy exceeding the band gap. In the examined model system, we used the nanocomposite material prepared on titanium plates and UV light irradiation. These features are obviously not suitable for immediate practical implementation, while we believe the proposed concept is prospective for further design of drug delivery systems based on ZIF-8. Thus, engineering a system in which a semiconductor photocatalytic agent would be implemented in the form of nanoparticles and respond to the electromagnetic energy with an effective penetration depth shall be addressed in further research.

Conflicts of interest

There are no conflicts to declare.

Acknowledgements

References

1 G. M. Brodeur, Neuroblastoma: Biological Insights into a Clinical Enigma, *Nat. Rev. Cancer*, 2003, **3**(3), 203–216, DOI: 10.1038/nrc1014.

2 D. Neill, D. Hughes, J. A. Edwardson, B. K. Rima and D. Allsop, Human IMR-32 Neuroblastoma Cells as a Model Cell Line in Alzheimer's Disease Research, *J. Neurosci. Res.*, 1994, **39**(4), 482–493, DOI: 10.1002/jnr.490390415.

3 M. Ferrari, Cancer Nanotechnology: Opportunities and Challenges, *Nat. Rev. Cancer*, 2005, **5**(3), 161–171, DOI: 10.1038/nrc1566.

4 A. Corma, H. García and F. X. Llabrés i Xamena, Engineering Metal Organic Frameworks for Heterogeneous Catalysis, *Chem. Rev.*, 2010, **110**(8), 4606–4655, DOI: 10.1021/cr9003924.

5 S. Ma and H.-C. Zhou, Gas Storage in Porous Metal–Organic Frameworks for Clean Energy Applications, *Chem. Commun.*, 2010, **46**(1), 44–53, DOI: 10.1039/B916295J.

6 L. E. Kreno, K. Leong, O. K. Farha, M. Allendorf, R. P. Van Duyne and J. T. Hupp, Metal–Organic Framework Materials as Chemical Sensors, *Chem. Rev.*, 2012, **112**(2), 1105–1125, DOI: 10.1021/cr200324t.

7 L. R. Mingabudinova, V. V. Vinogradov, V. A. Milichko, E. Hey-Hawkins and A. V. Vinogradov, Metal–Organic Frameworks as Competitive Materials for Non-Linear Optics, *Chem. Soc. Rev.*, 2016, **45**(19), 5408–5431, DOI: 10.1039/C6CS00395H.

8 P. Horcajada, T. Chalati, C. Serre, B. Gillet, C. Sebrie, T. Baati, J. F. Eubank, D. Heurtaux, P. Clayette and C. Kreuz, *et al.*, Porous Metal-Organic-Framework Nanoscale Carriers as a Potential Platform for Drug Delivery and Imaging, *Nat. Mater.*, 2010, **9**(2), 172–178, DOI: 10.1038/nmat2608.

9 L. Wang, M. Zheng and Z. Xie, Nanoscale Metal–Organic Frameworks for Drug Delivery: A Conventional Platform with New Promise, *J. Mater. Chem. B*, 2018, **6**(5), 707–717, DOI: 10.1039/C7TB02970E.

10 M.-X. Wu and Y.-W. Yang, Metal–Organic Framework (MOF)-Based Drug/Cargo Delivery and Cancer Therapy, *Adv. Mater.*, 2017, **29**(23), 1606134, DOI: 10.1002/adma.201606134.

11 X. Gao, X. Hai, H. Baigude, W. Guan and Z. Liu, Fabrication of Functional Hollow Microspheres Constructed from MOF Shells: Promising Drug Delivery Systems with High Loading Capacity and Targeted Transport, *Sci. Rep.*, 2016, **6**, 37705, DOI: 10.1038/srep37705.

12 K. S. Park, Z. Ni, A. P. Côté, J. Y. Choi, R. Huang, F. J. Uribe-Romo, H. K. Chae, M. O'Keeffe and O. M. Yaghi, Exceptional Chemical and Thermal Stability of Zeolitic Imidazolate Frameworks, *Proc. Natl. Acad. Sci. U. S. A.*, 2006, **103**(27), 10186–10191, DOI: 10.1073/pnas.0602439103.

13 R. Banerjee, A. Phan, B. Wang, C. Knobler, H. Furukawa, M. O'Keeffe and O. M. Yaghi, High-Throughput Synthesis of Zeolitic Imidazolate Frameworks and Application to CO_2 Capture, *Science*, 2008, **319**(5865), 939–943, DOI: 10.1126/science.1152516.

14 Q. Shi, Z. Chen, Z. Song, J. Li and J. Dong, Synthesis of ZIF-8 and ZIF-67 by Steam-Assisted Conversion and an Investigation of Their Tribological Behaviors, *Angew. Chem., Int. Ed.*, 2011, **50**(3), 672–675, DOI: 10.1002/anie.201004937.

15 B. Chen, Z. Yang, Y. Zhu and Y. Xia, Zeolitic Imidazolate Framework Materials: Recent Progress in Synthesis and Applications, *J. Mater. Chem. A*, 2014, **2**(40), 16811–16831, DOI: 10.1039/C4TA02984D.

16 C.-Y. Sun, C. Qin, X.-L. Wang, G.-S. Yang, K.-Z. Shao, Y.-Q. Lan, Z.-M. Su, P. Huang, C.-G. Wang and E.-B. Wang, Zeolitic Imidazolate Framework-8 as Efficient pH-Sensitive Drug Delivery Vehicle, *Dalton Trans.*, 2012, **41**(23), 6906–6909, DOI: 10.1039/C2DT30357D.

17 I. B. Vasconcelos, T. G. da Silva, G. C. Gare Militão, T. A. Soares, N. M. Rodrigues, M. O. Rodrigues, N. B. da Costa, R. O. Freire and A. S. Junior, Cytotoxicity and Slow Release of the Anti-Cancer Drug Doxorubicin from ZIF-8, *RSC Adv.*, 2012, **2**(25), 9437–9442, DOI: 10.1039/C2RA21087H.

18 C. Adhikari, A. Das and A. Chakraborty, Zeolitic Imidazole Framework (ZIF) Nanospheres for Easy Encapsulation and Controlled Release of an Anticancer Drug Doxorubicin under Different External Stimuli: A Way toward Smart Drug Delivery System, *Mol. Pharm.*, 2015, **12**(9), 3158–3166, DOI: 10.1021/acs.molpharmaceut.5b00043.

19 K. Liang, R. Ricco, C. M. Doherty, M. J. Styles, S. Bell, N. Kirby, S. Mudie, D. Haylock, A. J. Hill, C. J. Doonan and P. Falcaro, Biomimetic mineralization of metal-organic frameworks as protective coatings for bio macromolecules, *Nat. Commun.*, 2015, **6**, 7240, DOI: 10.1038/ncomms8240.

20 W. Liang, R. Ricco, N. K. Maddigan, R. P. Dickinson, H. Xu, Q. Li, C. J. Sumby, S. G. Bell, P. Falcaro and C. J. Doonan, Control of Structure Topology and Spatial Distribution of Biomacro-molecules in Protein@ZIF-8 Biocomposites, *Chem. Mater.*, 2018, **30**(3), 1069–1077, DOI: 10.1021/acs.chemmater.7b04977.

21 K. Engin, D. B. Leeper, J. R. Cater, A. J. Thistlethwaite, L. Tupchong and J. D. McFarlane, Extracellular pH Distribution in Human Tumours, *Int. J. Hyperthermia*, 1995, **11**(2), 211–216, DOI: 10.3109/02656739509022457.

This journal is © The Royal Society of Chemistry 2019

J. Mater. Chem. B, 2019, **7**, 6810–6821 | **6819**

22 M. Stubbs, P. M. J. McSheehy, J. R. Griffiths and C. L. Bashford, Causes and Consequences of Tumour Acidity and Implications for Treatment, *Mol. Med. Today*, 2000, **6**(1), 15–19, DOI: 10.1016/S1357-4310(99)01615-9.

23 R. R. Patil, S. A. Guhagarkar and P. V. Devarajan, Engineered Nanocarriers of Doxorubicin: A Current Update, *Crit. Rev. Ther. Drug Carr. Syst.*, 2008, **25**(1), 1–61.

24 R. Bian, T. Wang, L. Zhang, L. Li and C. Wang, A Combination of Tri-Modal Cancer Imaging and in Vivo Drug Delivery by Metal–Organic Framework Based Composite Nanoparticles, *Biomater. Sci.*, 2015, **3**(9), 1270–1278, DOI: 10.1039/C5BM00186B.

25 H. Zheng, Y. Zhang, L. Liu, W. Wan, P. Guo, A. M. Nyström and X. Zou, One-Pot Synthesis of Metal–Organic Frameworks with Encapsulated Target Molecules and Their Applications for Controlled Drug Delivery, *J. Am. Chem. Soc.*, 2016, **138**(3), 962–968, DOI: 10.1021/jacs.5b11720.

26 C. Cheng, C. Li, X. Zhu, W. Han, J. Li and Y. Lv, Doxorubicin-Loaded Fe_3O_4-ZIF-8 Nano-Composites for Hepatocellular Carcinoma Therapy, *J. Biomater. Appl.*, 2019, **33**(10), 1373–1381, DOI: 10.1177/0885328219836540.

27 Y. Wang, C. Wen, P. Hodgson and Y. Li, Biocompatibility of TiO_2 Nanotubes with Different Topographies, *J. Biomed. Mater. Res., Part A*, 2014, **102**(3), 743–751, DOI: 10.1002/jbm.a.34738.

28 J. M. Macak, M. Zlamal, J. Krysa and P. Schmuki, Self-Organized TiO_2 Nanotube Layers as Highly Efficient Photocatalysts, *Small*, 2007, **3**(2), 300–304, DOI: 10.1002/smll.200600426.

29 S. P. Albu, A. Ghicov, J. M. Macak, R. Hahn and P. Schmuki, Self-Organized, Free-Standing TiO_2 Nanotube Membrane for Flow-through Photocatalytic Applications, *Nano Lett.*, 2007, **7**(5), 1286–1289, DOI: 10.1021/nl070264k.

30 M. Domaschke, X. Zhou, L. Wergen, S. Romeis, M. E. Miehlich, K. Meyer, W. Peukert and P. Schmuki, Magnéli-Phases in Anatase Strongly Promote Cocatalyst-Free Photocatalytic Hydrogen Evolution, *ACS Catal.*, 2019, **9**(4), 3627–3632, DOI: 10.1021/acscatal.9b00578.

31 S. A. Ulasevich, G. Brezesinski, H. Möhwald, P. Fratzl, F. H. Schacher, S. K. Poznyak, D. V. Andreeva and E. V. Skorb, Light-Induced Water Splitting Causes High-Amplitude Oscillation of PH-Sensitive Layer-by-Layer Assemblies on TiO_2, *Angew. Chem., Int. Ed.*, 2016, **55**(42), 13001–13004, DOI: 10.1002/anie.201604359.

32 H. M. Maltanava, S. K. Poznyak, D. V. Andreeva, M. C. Quevedo, A. C. Bastos, J. Tedim, M. G. S. Ferreira and E. V. Skorb, Light-Induced Proton Pumping with a Semiconductor: Vision for Photoproton Lateral Separation and Robust Manipulation, *ACS Appl. Mater. Interfaces*, 2017, **9**(28), 24282–24289, DOI: 10.1021/acsami.7b05209.

33 N. V. Ryzhkov, P. Nesterov, N. A. Mamchik, S. O. Yurchenko and E. V. Skorb, Localization of Ion Concentration Gradients for Logic Operation, *Front. Chem.*, 2019, **7**, DOI: 10.3389/fchem.2019.00419.

34 M. Jian, B. Liu, R. Liu, J. Qu, H. Wang and X. Zhang, Water-Based Synthesis of Zeolitic Imidazolate Framework-8 with High Morphology Level at Room Temperature, *RSC Adv.*, 2015, **5**(60), 48433–48441, DOI: 10.1039/C5RA04033G.

35 A. Bastos, Application of SVET/SIET Techniques to Study Healing Processes in Coated Metal Substrates, in *Handbook of Sol-Gel Science and Technology*, ed. L. Klein, M. Aparicio and A. Jitianu, Springer International Publishing, Cham, 2017, pp. 1–57, DOI: 10.1007/978-3-319-19454-7_138-2.

36 O. Dolgikh, A. Demeter, S. V. Lamaka, M. Taryba, A. C. Bastos, M. C. Quevedo and J. Deconinck, Simulation of the Role of Vibration on Scanning Vibrating Electrode Technique Measurements Close to a Disc in Plane, *Electrochim. Acta*, 2016, **203**, 379–387, DOI: 10.1016/j.electacta.2016.01.188.

37 A. Phan, C. J. Doonan, F.-J. Uribe-Romo, C. B. Knobler, M. O'Keeffe and O. M. Yaghi, Synthesis, Structure, and Carbon Dioxide Capture Properties of Zeolitic Imidazolate Frameworks, *Acc. Chem. Res.*, 2010, **43**(1), 58–67, DOI: 10.1021/ar900116g.

38 C. Mottillo, Y. Lu, N.-H. Pham, M. J. Cliffe, T.-O. Do and T. Friščić, Mineral neogenesis as an inspiration for mild, solvent-free synthesis of bulk microporous metal–organic frameworks from metal (Zn, Co) oxides, *Green Chem.*, 2013, **15**, 2121–2131, DOI: 10.1039/C3GC40520F.

39 M. Eddaoudi, D. F. Sava, J. F. Eubank, K. Adila and V. Guillerm, Zeolite-like metal-organic frameworks (ZMOFs): design, synthesis, and properties, *Chem. Soc. Rev.*, 2015, **44**, 228–249, DOI: 10.1039/c4cs00230j.

40 C. Han, C. Zhang, N. Tymińska, J. R. Schmidt and D. S. Sholl, Insights into the Stability of Zeolitic Imidazolate Frameworks in Humid Acidic Environments from First-Principles Calculations, *J. Phys. Chem. C*, 2018, **122**(8), 4339–4348, DOI: 10.1021/acs.jpcc.7b12058.

41 K. D. Vogiatzis, M. V. Polynski, L. K. Kirkland, J. Townsend, A. Hashemi, C. Liu and E. A. Pidko, Computational Approach to Molecular Catalysis by 3d Transition Metals: Challenges and Opportunities, *Chem. Rev.*, 2019, **119**(4), 2453–2523, DOI: 10.1021/acs.chemrev.8b00361.

42 C. Chizallet and N. Bats, External Surface of Zeolite Imidazolate Frameworks Viewed Ab Initio: Multifunctionality at the Organic−Inorganic Interface, *J. Phys. Chem. Lett.*, 2010, **1**(1), 349–353, DOI: 10.1021/jz900192x.

43 M. Ocaña, V. Fornés, J. V. G. Ramos and C. J. Serna, Factors Affecting the Infrared and Raman Spectra of Rutile Powders, *J. Solid State Chem.*, 1988, **75**(2), 364–372, DOI: 10.1016/0022-4596(88)90176-4.

44 A. M. Peiró, J. Peral, C. Domingo, X. Domènech and J. A. Ayllón, Low-Temperature Deposition of TiO_2 Thin Films with Photocatalytic Activity from Colloidal Anatase Aqueous Solutions, *Chem. Mater.*, 2001, **13**(8), 2567–2573, DOI: 10.1021/cm0012419.

45 Y. Zhang, Y. Jia, M. Li and L. Hou, Influence of the 2-Methylimidazole/Zinc Nitrate Hexahydrate Molar Ratio on the Synthesis of Zeolitic Imidazolate Framework-8 Crystals at Room Temperature, *Sci. Rep.*, 2018, **8**(1), 9597, DOI: 10.1038/s41598-018-28015-7.

46 A. Rudra, R. M. Deepa, M. K. Ghosh, S. Ghosh and B. Mukherjee, Doxorubicin-Loaded Phosphatidylethanolamine-Conjugated Nanoliposomes: In Vitro Characterization and Their Accumulation in Liver, Kidneys, and Lungs in Rats, *Int. J. Nanomed.*, 2010, **5**, 811–823, DOI: 10.2147/IJN.S13031.

47 K. Zhang, R. P. Lively, C. Zhang, R. R. Chance, W. J. Koros, D. S. Sholl and S. Nair, Exploring the Framework Hydrophobicity and Flexibility of ZIF-8: From Biofuel Recovery to Hydrocarbon Separations, *J. Phys. Chem. Lett.*, 2013, **4**(21), 3618–3622, DOI: 10.1021/jz402019d.

48 Y.-Y. Song, F. Schmidt-Stein, S. Bauer and P. Schmuki, Amphiphilic TiO_2 Nanotube Arrays: An Actively Controllable Drug Delivery System, *J. Am. Chem. Soc.*, 2009, **131**(12), 4230–4232, DOI: 10.1021/ja810130h.

49 S. Tan, H. Feng, Y. Ji, Y. Wang, J. Zhao, A. Zhao, B. Wang, Y. Luo, J. Yang and J. G. Hou, Observation of Photocatalytic Dissociation of Water on Terminal Ti Sites of $TiO_2(110)$-1 × 1 Surface, *J. Am. Chem. Soc.*, 2012, **134**(24), 9978–9985, DOI: 10.1021/ja211919k.

50 M. A. Henderson, A Surface Science Perspective on TiO_2 Photocatalysis, *Surf. Sci. Rep.*, 2011, **66**(6), 185–297, DOI: 10.1016/j.surfrep.2011.01.001.

51 A. Yamakata, T. Ishibashi and H. Onishi, Water- and Oxygen-Induced Decay Kinetics of Photogenerated Electrons in TiO_2 and Pt/TiO_2: A Time-Resolved Infrared Absorption Study, *J. Phys. Chem. B*, 2001, **105**(30), 7258–7262, DOI: 10.1021/jp010802w.

52 H. Zhang, D. Liu, Y. Yao, B. Zhang and J. Lin, Stability of ZIF-8 Membranes and Crystalline Powders in Water at Room Temperature, *J. Membr. Sci.*, 2015, **485**, 103–111, DOI: 10.1016/j.memsci.2015.03.023.

53 M. Yin, E. Ju, Z. Chen, Z. Li, J. Ren and X. Qu, Upconverting Nanoparticles with a Mesoporous TiO_2 Shell for Near-Infrared-Triggered Drug Delivery and Synergistic Targeted Cancer Therapy, *Chem. – Eur. J.*, 2014, **20**, 14012–14017, DOI: 10.1002/chem.201403733.

54 S. Shen, L. Wu, J. Liu, M. Xie, H. Shen, X. Qi, Y. Yan, Y. Ge and Y. Jin, Core–shell structured $Fe_3O_4@TiO_2$-doxorubicin nanoparticles for targeted chemo-sonodynamic therapy of cancer, *Int. J. Pharmaceut.*, 2015, **486**, 380–388, DOI: 10.1016/j.ijpharm.2015.03.070.

55 L. Zeng, Y. Pan, Y. Tian, X. Wang, W. Ren, S. Wang, G. Lu and A. Wu, Doxorubicin-loaded $NaYF_4$:Yb/Tm–TiO_2 inorganic photosensitizers for NIR-triggered photodynamic therapy and enhanced chemotherapy in drug-resistant breast cancers, *Biomaterials*, 2015, **57**, 93–106, DOI: 10.1016/j.biomaterials.2015.04.006.

56 C.-R. Lee, H.-S. Kim, I.-H. Jang, J.-H. Im and N.-G. Park, Pseudo First-Order Adsorption Kinetics of N719 Dye on TiO_2 Surface, *ACS Appl. Mater. Interfaces*, 2011, **3**(6), 1953–1957, DOI: 10.1021/am2001696.

57 V. R. Djokić, J. Vujović, A. D. Marinković, P. Rada, D. O. E. Janaćković, A. E. Onjia and D. Ž. Mijin, A Study of the Photocatalytic Degradation of the Textile Dye CI Basic Yellow 28 in Water Using a P 160 TiO_2-Based Catalyst, *J. Serb. Chem. Soc.*, 2012, **77**(12), 1747–1757, DOI: 10.2298/JSC121015130D.

58 Y. Ye, Y. Feng, H. Bruning, D. Yntema and H. H. M. Rijnaarts, Photocatalytic Degradation of Metoprolol by TiO_2 Nanotube Arrays and UV-LED: Effects of Catalyst Properties, Operational Parameters, Commonly Present Water Constituents, and Photo-Induced Reactive Species, *Appl. Catal., B*, 2018, **220**, 171–181, DOI: 10.1016/j.apcatb.2017.08.040.

59 M. A. Luzuriaga, C. E. Benjamin, M. W. Gaertner, H. Lee, F. C. Herbert, S. Mallick and J. J. Gassensmith, ZIF-8 degrades in cell media, serum, and some – but not all – common laboratory buffers, *Supramol. Chem.*, 2019, **31**(8), 485–490.

60 M. J. Velásquez-Hernández, R. Ricco, F. Carraro, F. T. Limpoco, M. Linares-Moreau, E. Leitner, H. Wiltsche, J. Rattenberger, H. Schröttner, P. Frühwirt, E. M. Stadler, G. Gescheidt, H. Amenitsch, C. J. Doonan and P. Falcaro, Degradation of ZIF-8 in phosphate buffered saline media, *CrystEngComm*, 2019, **21**, 4538–4544, DOI: 10.1039/C9CE00757A.

Localization of Ion Concentration Gradients for Logic Operation

Nikolay V. Ryzhkov[1], Pavel Nesterov[1], Natalia A. Mamchik[1], Stanislav O. Yurchenko[2] and Ekaterina V. Skorb[1]*

[1] Laboratory of Solution Chemistry of Advanced Materials and Technologies, ITMO University, Saint Petersburg, Russia,
[2] Terahertz Technology Lab, Bauman Moscow State Technical University, Moscow, Russia

Adjustment of the environmental acidity is a powerful method for fine-tuning the outcome of many chemical processes. Numerous strategies have been developed for the modification of pH in bulk as well as locally. Electrochemical and photochemical processes provide a powerful approach for on-demand generation of ion concentration gradients locally at solid-liquid interfaces. Spatially organized in individual way electrodes provide a particular pattern of proton distribution in solution. It opens perspectives to iontronics which is a bioinspired approach to signaling, information processing, and storing by spatial and temporal distribution of ions. We prove here that soft layers allow to control of ion mobility over the surface as well as processes of self-organization are closely related to change in entropy. In this work, we summarize the achievements and discuss perspectives of ion gradients in solution for information processing.

Keywords: interface, polyelectrolyte multilayers, pH-gradient, logic gates, iontronics

INTRODUCTION

Nobel laureate Herbert Kroemer stated that "the interface is the device" in reference to heterogeneous semiconductor structures. But this idea also inspired the development of interfacial science beyond the physics of heterostructures. Interfaces play a significant role in many physical and chemical processes. There is a wide variety of procedures for surface treatment and the modification of functional interfaces. Decher et al. (1992) described alternately exposing of charged substrates to positively and negatively charged macromolecules in order to obtain functional multilayered coatings. Layer-by-layer (LbL) assembled coatings and capsules have found various applications due to the versatility of multilayer formation technique and a variety of charged compounds which may be incorporated into it (Decher et al., 1998; Ryzhkov et al., 2019a). Polyelectrolyte multilayers are traditional components of biomaterial surface coatings (Zhukova et al., 2017), membranes for separation (Rmaile et al., 2003), as well as cargoes for drug encapsulation and delivery (Nikitina et al., 2018).

Polyelectrolyte multilayers are also considered to be an appropriate model mimicking the structure and properties of biological membranes (Zhu and Szostak, 2009). A lipid bilayer supported by a polyelectrolyte cushion provides a platform for modeling and investigating many cellular processes. Nowadays, transport processes in polyelectrolyte layers has garnered much attention. Due to their selective ionic permeability (Tanaka and Sackmann, 2005), one may perform dynamic polarization across the membrane. This process simulates neuron polarization during nerve conduction, thereby modeling information processing in living systems.

Development of a reliable model infallibly mimicking biological way of information processing is still a challenge. A lot of efforts are put to mimic biological way of computation by artificial

matter. The simplest example of information operations is switching functions following Boolean logic—logic gates. Logic gates use binary inputs and produce a single binary output. By now, several systems based on polyelectrolytes that perform information processing according to Boolean logic and using ionic signals (particularly protons) have been developed. Motornov et al. (2008) designed an enzyme-based hybrid system of pH-responsive nanoparticles assembling and disassembling following AND/OR Boolean logic. Motornov et al. (2009) also developed a pH-responsive Pickering emulsion coupled with specific enzymatic reactions performing AND and OR logic. Han et al. (2009) developed microchip polyelectrolyte diodes representing AND, OR, and NAND logic based on ion transportation through the polyelectrolyte interface. Thus, applicability of iontronic devices were demonstrated.

Reversible conformational changes of polymer brushes atop an electrode modulated by pH and influencing charge transport behavior are wifely exploited for designing biomimetic iontronic calculating devices. A more detailed mechanism is described as follows. For example, sucrose in the presence of both invertase (Input A) and glucose oxidase (Input B) results in a decrease in pH, transforming into gluconic acid (AB). The described system performs AND Boolean logic. OR logic can be designed using an ethyl butyrate-glucose mixture. Acidification of the medium (A+B) in this case can be achieved either by the oxidation of ethyl butyrate to butyric acid by esterase (Input A) or by the oxidation of glucose to gluconic acid by glucose oxidase (Input B). In brief, enzymatic inputs run a cascade of reactions leading to a pH shift to acidic values. The electrode surface with grafted shrunk poly-4-vinyl pyrrolidone (P4VP) at neutral pH is not electrochemically active because of the blocking effect of the polymer film. Output "1" of the logic operations yielded a pH drop to acidic conditions, resulting in the protonation and swelling of the P4VP polymer allowing penetration of a soluble redox probe to the conducting support. Thus, one may perform amperometry or impedance spectroscopy study for output detection. Wang et al. (2009) designed the system described above. Different groups employed a large variety of enzymes and electrode coatings for realizing a similar approach to designing biochemical logic gates. Privman et al. (2008), Katz and Minko (2015), and Poghossian et al. (2015) developed enzyme-based biocomputing systems coupled with pH-responsive membranes and electrodes. As a result, they obtained bioelectronic devices switchable by logically processed biomolecular signals. Reversible pH-responsive on-off behavior performing Boolean logic was suggested for designing novel multi switchable electrochemical biosensors based on electrodes covered by polymer network (Liu et al., 2012) or polymer brushes (Li et al., 2014) and electrodes made of inorganic-polymer composites (Wang et al., 2015).

Significant progress in DNA and molecular logic operations was made in recent years. However, various issues remain unresolved. For example, information transfer through live-machine interfaces: living matter conducts electricity mostly using ions, while machines conduct electricity mostly using electrons (Yang and Suo, 2018). It's of high importance nowadays because technologies at the interface between natural and artificial plays a central role in science. We suggest here a

strategy for performing iontronic logic operations at interfaces in solutions and present it's modeling by the electrochemical and photochemical system and how they can be related to Shannon's entropy. Having an array of electrodes and applying potential bias according to some program, one may realize the spatial distribution of acidic and basic areas in water solutions close to an electrode in a unique pattern with micrometer resolution. It's key to iontronic information processing. Designating current density higher than some value as logic input "1" and pH lower than some cut-off as logic output "1," we may design different logic gates varying the geometry of input electrodes, the position of response point and cut-off values. We present here the simplest AND logic gate performed by a couple of microelectrodes and discuss assembling of individual logic gates in concatenated logic cascades and complex branching networks by multielectrode arrays.

Having an array of electrodes and applying potential, oxidation, and reduction processes may be localized at particular electrodes and hence spatially separated. Protons propagating from parental electrode serve as information transmitters. Moreover, we have demonstrated that polyelectrolyte modification of electrode surface may lead to amplification and better localization of ion fluxes and hence signal amplification and can be related to self-organization *vs.* Shannon's entropy. All this discussion is also extrapolated to polyelectrolyte modified photoelectrodes under irradiation.

ENHANCING ELECTROCHEMICALLY PRODUCED IONIC SIGNALS BY POLYELECTROLYTE ASSEMBLIES

Electrochemistry provides one with a powerful approach for the on-demand local generation of ionic signals. For example, proton fluxes may be produced by electrochemical hydroquinone oxidation (Fomina et al., 2016). Due to their proton-coupled electron transfer, low redox potential, and relative chemical stability, quinones are widely used as the electroactive species for the controlled generation/consumption of protons (Dochter et al., 2015; Garnier et al., 2015). Naturally occurring hydroquinone compounds play a significant role in electron/proton transfer of many biological processes (Jeyanthi et al., 2016). Thus, the quinone/hydroquinone transition serves as an essential electrochemical model for the development of biomimetic systems. Its changing molecular structure allows for its electrochemical properties to be tuned (Peduto et al., 2017). But characteristics of an electrode reaction are highly affected by the microstructure of the electrode surface, since the fact that electrochemical systems under investigation are heterogeneous and electrode reaction is related to electron transfer through the electrode-electrolyte interface.

Electrode surface influences diffusion of electrochemical reactants and products as well as Faradaic process. In case of hydroquinone oxidation, horizontal and vertical proton propagation is supposed to be a three-dimensional pH wave. It originates from the ion source and weakens as it moves

away. Fick's laws describe diffusion and postulate that ionic flux goes from regions of higher concentration to areas with a lower one. Furthermore, the magnitude of the driving force determining ion movement is proportional to the concentration gradient. Ion fluxes and the concentration of a particular ion close to the surface of the electrodes were investigated using Scanning Vibrating Electrode Technique (SVET) and Scanning Ion-Selective Electrode Technique (SIET), unique tools for the characterization of local ionic currents in solution and ion concentration gradient measurement, respectively (Souto et al., 2010). SVET allows the electric field in a solution to be measured for the visualization of anodic and cathodic areas on surfaces with nA precision and μm spatial resolution (**Figure 1a**). During SVET-analysis, a vibrating Pt-probe (**Figure 1b**) scans the surface, estimating its electrical potential in amplitude points of its vibration and then recalculates it in ionic currents. SIET is based on potentiometric principles. A glass capillary microelectrode with the ion-selective membrane in the tip scans the surface, measuring the concentration of a particular ion.

We have studied the effect of polyelectrolyte assembly on top of an electrode on the propagation of electrochemically generated protons. The system under investigation is a working electrode (WE) gold or platinum wire embedded in an epoxy resin so that its round section was brought into contact with a solution (**Figure 1c**). System may be also extended to several electrodes (**Figures 1d,e**). Electrochemical reaction is coupled with proton release. The pH-wave propagation is driven by a concentration gradient. Further, the surface of the noble metal electrode (WE) was subsequently modified with nanometer-thin layers of the polycation polyethyleneimine (PEI) and the polyanion poly(sodium 4-styrenesulfonate) (PSS). PEI is considered to be a proton sponge that stores electrochemically generated protons while the PSS layer serves as a cation exchange layer. The electrode was first covered by branched PEI to provide secure anchoring to the surface and to act as a positively charged terminating layer. Deposition of PSS was then carried out via electrostatic interaction with the underlying layer. Although polymer multilayer assembly leads to no change in redox processes at electrode/electrolyte interface, both the anodic and cathodic activity of the Pt electrode measured by SVET is higher for one that is polyelectrolyte coated than for a bare one (**Figures 1f,g**). It is worth noting that a terminating PEI layer resulted in more pronounced anodic/cathodic activity. However, if this polyelectrolyte membrane is thick enough, ion flux from the surface is suppressed (Ryzhkov et al., 2019b).

Since LbL polyelectrolyte assemblies contain many uncompensated charges, ions cannot freely pass through the membrane. Although it is still passive transport down their concentration gradient, ion movement pathways are more complex and cannot be explained by simple diffusion. We consider polyelectrolyte LbL assemblies as a convenient tool for controlling the transmission of the ion signal. Strong and weak polyelectrolyte assemblies, including charged biopolymers and hydrogels, can regulate charge carrier generation, the diffusion of ions at interfaces, lifetime and storage (Ryzhkov et al., 2019a). There is still no general theory precisely predicting electrode response to polyelectrolyte modification. Until now,

multicomponent coatings formed by multilayers of different polyelectrolyte compositions (strong–strong, strong–weak, weak–weak) have been analyzed as nanolayers for corrosion protection. The mechanism of multilayer protective action is based on pH buffering polybasic and polyacid complexes (Andreeva et al., 2010; Skorb and Andreeva, 2015). It has also been demonstrated that polyelectrolyte layers can be used as an efficient pH-buffering protective layer for pH-sensitive soft materials (Skorb and Andreeva, 2013). It is expected that by combining polyelectrolytes of different molecular weights, strengths, and with different specific functional moieties, one can flexibly tune spatial and temporal distribution of ionic fluxes through the membrane and perform independent handling by cations and anions. That fact opens up prospects for developing futuristic biomimetic information processing using ions as signal carriers.

DISCUSSION OF SOFT MATTER ASSEMBLIES FOR CONTROLLING ION FLUXES

LbL deposition of polyelectrolyte multilayers is a universal approach to designing interfaces with unique properties. Its impact is not limited by enhancement of ion fluxes described above. Different effects may be achieved by polyelectrolytes of different nature. Recent progress in science provides an understanding of polyelectrolyte complexation principles. Despite the apparent simplicity of the assembly procedure, the processes occurring in the multilayers are incredibly complex. Polyelectrolyte layers in multilayered structures are not perfectly stratified, and polymer chains of polycations and polyanions are significantly interpenetrated (Schönhoff, 2003). Much attention is drawn to the dynamics and internal structure of polyelectrolyte multilayers and studying of internal diffusion (Fares and Schlenoff, 2017; Selin et al., 2017). Various parameters such as ionic strength (Steitz et al., 2000), charge density (Steitz et al., 2001), pH, and temperature (Karg et al., 2008) influence the internal structure of polyelectrolyte film. Several models of diffusion in ultrathin polyelectrolyte films were suggested (Klitzing and Möhwald, 1996; Farhat and Schlenoff, 2001). Three different modes of interaction of polyelectrolyte multilayers and small ionic species were observed—permeability, non-permeability, and ions accumulation. It was also found that the permeability of polyelectrolyte membranes depends mostly on film composition rather than its thickness (Hoshi et al., 2003). The outermost layer of polyelectrolyte LbL assembly carry out excess non-compensated charge and plays a crucial role in permeability properties blocking penetration of similarly charged small species (Rmaile et al., 2003). Fu et al. (2017) demonstrated that pairs of weak polyelectrolytes tend to transport small molecules or ions more, whereas multilayers assembled from strong polyelectrolytes are less permeable. Kelly et al. (2018) demonstrated that ion flux through the membrane is significantly affected by the stoichiometry of the polyelectrolyte multilayer. An excess of some component, polycation, or polyanion, changes diffusion
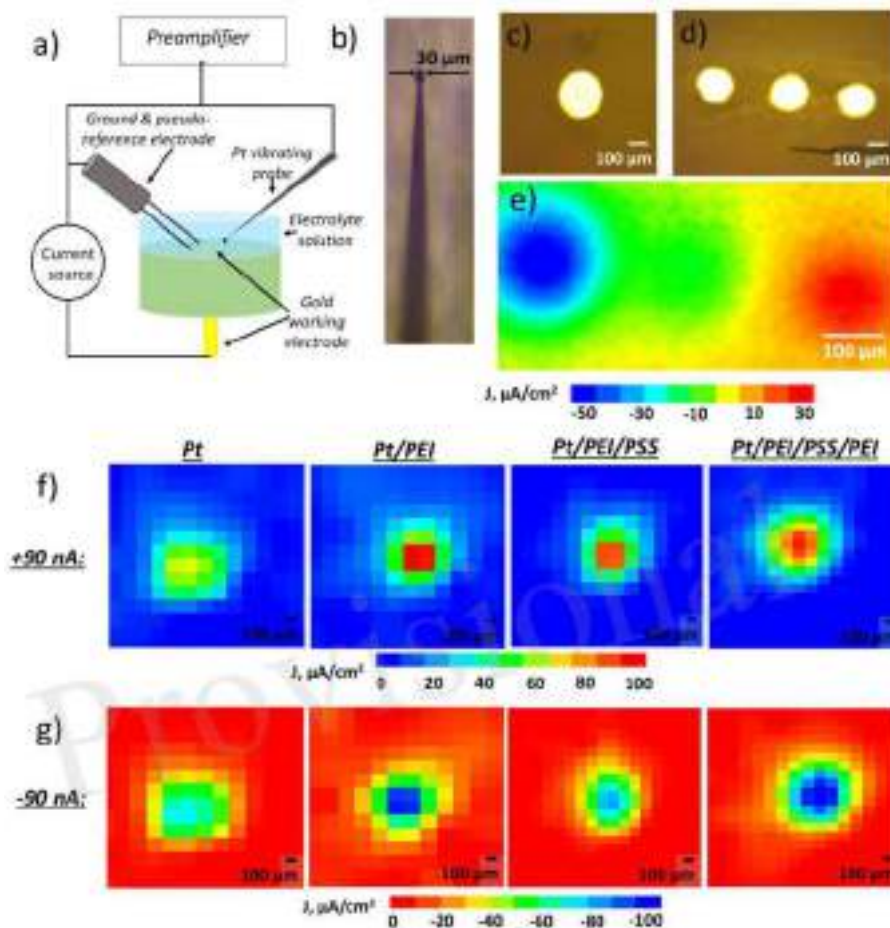
FIGURE 1 | (a) Schematic of scanning vibrating electrode technique (SVET) for determining an ionic current that can be used together with scanning ion selective electrode (SIET). (b) Pt-Ir vibrating probe for SVET, (c) top view of gold electrode embedded in epoxy resin, (d) top view of working electrodes (WE) embedded in epoxy resin (e) ion currents mapped by SVET in solution over three WEs, left electrode is negatively polarized (−90 nA), right one—positively (+90 nA), red demonstrates areas of positive ionic current in solution related to anodic activity and blue—areas of negative ionic current in solution and cathodic activity on the surface, (f,g) ionic current over one WE under either positively [in (f)] or negatively [in (g)] on pristine Pt or Pt covered with different polyelectrolyte multilayers—Pt/ polyethylenimine (Pt/PEI), Pt/PEI/ poly(sodium 4-styrenesulfonate) (Pt/PEI/PSS), and Pt/PEI/PSS/PEI—number of layers affects drastically on the ionic current.

and permeability of ions through the polyelectrolyte multilayer. Ion transportation through polyelectrolyte multilayers can be described similarly to solid matter permeability. Thus, the action of surrounding polyelectrolyte chains affects diffusion through polyelectrolyte assemblies significantly and diffusion is thermoactivated (Spruijt et al., 2008). Internal interfaces predetermine the properties of polyelectrolyte multilayers, and one should therefore keep in mind the composition and structure of the multilayer, the internal layer chemistry, and interactions between components when designing functional polyelectrolyte multilayers (Brezhneva et al., 2019). The means of changing the permeability of polymer layers mentioned above have already found extensive use in the development of semipermeable separating membranes and electrochemical sensors with improved selectivity, sensitivity, and response time.

Thus, polyelectrolyte multilayers are a powerful instrument for the regulation of ion-fluxes. By varying membrane composition, enhanced ion transport, accumulation, and delayed release can be realized.

PH-WAVE PROPAGATION AS A BASIS FOR IONTRONICS

Precise control over electrochemically generated ion fluxes open perspectives for flexible and reliable approach for transition from machine way of information processing (via electrons) to biological one (via ions) and developing technologies at the interface between natural and artificial (wearable and implantable devices, for example).

Our interest is focused on information transfer in aqueous solutions and the prospective for communication with living matter. Here, we demonstrate a proof of concept of basic logic operations that use ions as input and/or output signals which allows unequivocal output reading. The system under

investigation is presented by an array of gold or platinum electrodes particularly embedded in an epoxy resin and immersed in the electrolyte solution. The simplest model systems containing two electrodes are shown in **Figure 2**.

By applying positive and negative potentials to the electrodes one is able to carry out a pH coupled redox process (e.g., hydroquinone oxidation). Herewith, oxidation and reduction processes may be spatially separated. As a result, the distribution of acidic and basic areas in a solution adjusted to an electrode surface may be realized particularly. Anodic and cathodic activity are localized directly at the electrodes while the resulting pH gradient is more spatially blurred. The desired localization of the proton wave may be achieved via electrode functionalization by polymer assembly. The electrodes may be designated as inputs and the acidity of the space between the electrodes as output in terms of logic gates. Simple AND logic operations (**Figure 2a**) may be performed. The main processor of any computing device is basically a bunch of interconnected logic gates, thus performing these simple logic operations is an important step toward biomimetic iontronic calculations. The open-circuit potential applied to the input electrode (**Figure 2b**) is designated as input "0" and hydroquinone oxidation potential (0.70 vs. SHE) as input "1." The acidity of the solution between the electrodes is read as an output signal. A pH lower than some threshold, for example, 5.0, is designated as output "1" with anything lower being "0." Two "0" inputs provide "0" output (**Figure 2c**). If only one of the electrodes is polarized, the resulting pH wave does not reach the output area, and pH > 5.0. Therefore, the output signal is "0" (**Figure 2d**). Otherwise, if both input electrodes are polarized, generated protons propagate to the output area, making the pH there significantly acidic, <5.0, giving signal "1" in output area (**Figure 2e**).

In general, the model system described above may be extended to several dozen electrodes. As such, some electrodes may be assigned as inputs while others are for the reading of the electrochemical output. We started with three microelectrodes (**Figure 1d**) and, by SVET, demonstrated that the independent polarization of electrodes might be performed, while no effect of the bipolar electrode was observed in the studied potential window (**Figure 1e**).

What we plan to do next is to cover the output electrode with pH sensitive film, grafted P4VP or P2VP brushes for example (Pennakalathil et al., 2010; Ghostine and Schlenoff, 2011). This thin polymer layer in its non-protonated state is collapsed and acts as an insulator, inhibiting direct electron transfer from the electrode to the electrochemically active specimen in solution and vice versa. If only one input electrode is active, the resulting proton wave does not reach the output electrode. The polymer layer still blocks the electrode surface and no current is observed during polarization. When both inputs are "1" (applied potential of hydroquinone oxidation), then the resulting proton wave reaches the output electrode, making the surrounding media acidic enough to protonate the blocking polymer layer atop the output electrode. As a result, polymer conformation changes from collapsed to swelled, allowing penetration of hydroquinone to the electrode. Thus,

an anodic current of hydroquinone oxidation may be registered at the output electrode. A Faradaic current registered at the output electrode above a certain threshold is assigned as "1" and lower as "0." Thus, switching of output electrode activity may be performed according to Boolean logic. It is worth noting that in this case some autocatalysis may be shown, and the acidification of the area close to the output electrode leads to electrochemical generation of more protons. Thus, signal amplification and signal transmission from one location to another realizing specific pathways through the electrode network may be performed.

Our future research direction will be focused on different geometries of input electrode array, varying applied potentials and passed currents, and regimes of application (constant current, pulses, etc.). Another direction is the development of novel approaches for output electrode modification for ensuring disambiguation of output response reading.

SELF-ORGANIZATION VS. SHANNON'S ENTROPY

Fundamental concept of information theory is Shannon's entropy. Entropy in this case is a measure of unpredictability of the state, or equivalently, of its average information content. We suggest here description of described above approach to designing of iontronic devices in terms of Shannon's entropy.

Idea here is a correlation of soft matter components (polyelectrolytes and lipid layers) of living cell and our biomimetic model (**Figures 3A,B**). We took photochemical system (**Figure 3C**) (Maltanava et al., 2017) shown previously as the analogy to electrochemically induced proton gradients in aqueous electrolytes and collect SIET pH maps for pristine working electrode (WE) (System I), WE covered with polyelectrolyte multilayers (System II) and WE covered with polyelectrolyte multilayers and lipid layer on top (System III).

Processes of self-organization are known to be closely related to change in entropy of the system (Haken, 2006). Typically, this occurs with spatial change in thermodynamic (as temperature, density, and pressure) as well as chemical parameters and, in particular, ion composition of the system. In our case, the changes of temperature, density, and pressure are negligible, while the local electrochemical influence affects directly the ion-distribution in the solution. Note that the spatial pH-redistribution occurs self-consistently, being accompanied by local electric potential redistribution during the free-energy minimization of the system. In result, the self-organization and the redistribution of pH-fields are directly associated with each other and, thus, the change of entropy can be illustrated using the fields of pH.

According to its definition, the Shannon's entropy is (Haken, 2006).

$$S = -\sum_i p_i \log_2 p_i \qquad (1)$$
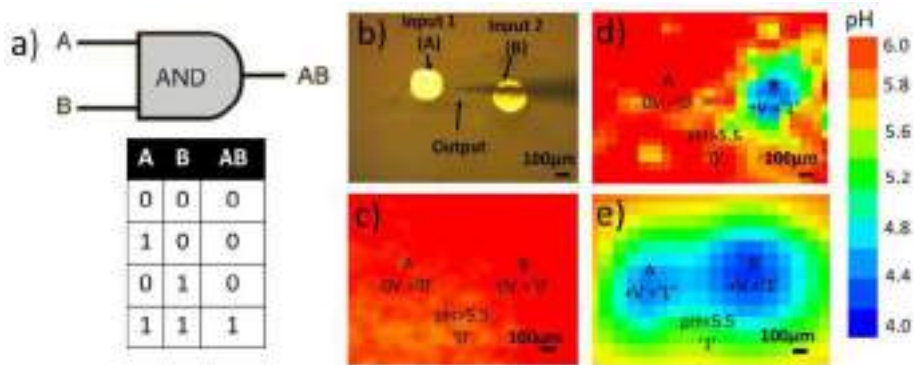
FIGURE 2 | (a) Basic AND logic gate and corresponding truth table, **(b)** system of two WEs embedded in epoxy holder, **(c–e)** 2D pH-maps via SIET of two input electrodes in hydroquinone solution during polarization of electrodes in different regimes and interpretation in terms of logic gates, positive polarization +V is determined as input "1," no polarization 0V as input "0," pH >5.0 is determined as output "0" and pH<5.0 as output "1," **(c)** no potential applied, both inputs are "0," as a result, no pH drop – output "0," **(d)** positive potential is applied to the right electrode "1," left one is not polarized "0," resulting pH drop localized on right electrode and doesn't propagate to output area "0" **(e)** positive potential applied to both electrodes "1," resulting proton wave reaches output area giving output "1".
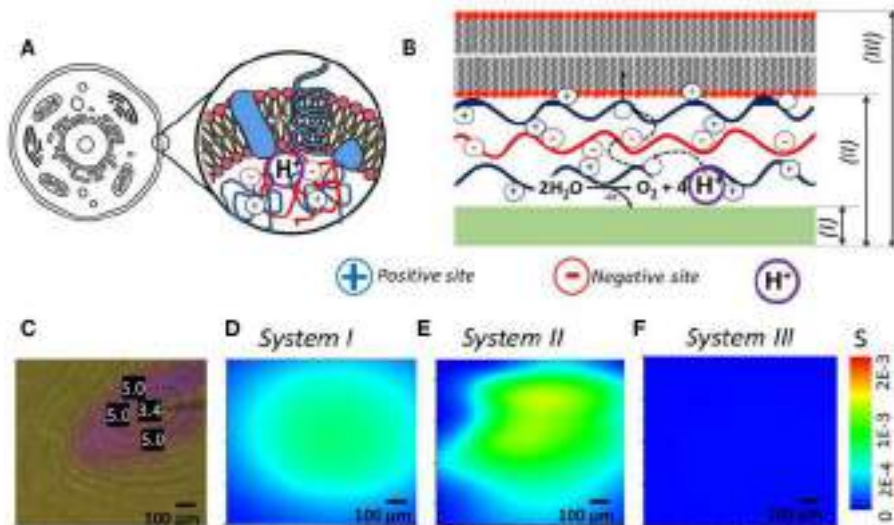
FIGURE 3 | (A,B) Idea of cell prototype system that consists of polyelectrolyte assembly or coacervates, reactions inside that are protected from environment by lipid bilayers. **(C)** System with local gradient of pH initiated by light (measured pH values are shown in units in photo). **(D–F)** Recalculated into Shannon's entropy SIET pH maps of—**(D)** pristine WE, **(E)** WE covered with polyelectrolytes, and **(F)** WE covered with polyelectrolytes and lipid bilayer—processes of self-organization are closely related to change in entropy of the system.

where $0 < p_i < 1$ is the probability to measure some observable value i. In a case of a lot of observable independent values (e.g., set of p-values at different spatial points), corresponding summation over them should be performed in the right hand side of Equation (1).

The particular physical sense of the probability p depends on the system's nature and plays an important role for interpretation of the results. For instance, p can be related to the probability of some molecular dipole orientation or electric charge in case of electric systems, an electron spin orientation or magnetic polarization in magnetic systems, a particular state of photons in optical systems, or concentration of chemicals in reacting systems (Haken, 2006). In the same manner, this approach could be naturally expanded to solutions, to consider p in sense of probability that an observed ion in the solution is an H^+ or OH^- ion (whose concentrations are related with each other). In other words, we may use the parts of H^+ and OH^- ions as the probabilities p_H and p_{OH}, to calculate corresponding contribution to the Shannon's entropy associated with the pH in a given spatial area of measurement. One should note that, generally speaking, the pH distribution provides the same information as the field of electric potential, since they are consistently related with each other in the solution.

The probability to observe H^+ cations in a solution during a measurement is simply related to the cation concentration in the system and pH of the solution as $p_H = C_H/C_0 = 10^{-pH}$, where $C_0 = 1M$ is a normalizing concentration. For OH^- anions, we have $p_{OH} = C_{OH}/C_O = 10^{pH-14}$, since $p_H \, p_{OH} = 10^{-14}$. From here, by substitution of this expression for p into Equation (1), we readily obtain the pH-related part of the Shannon's entropy as

$$S = \log_2 10 \, (pH \, 10^{-pH} + pOH \, 10^{-pOH})$$
$$= \log_2 10 \, (pH \, 10^{-pH} + (14 - pH) \, 10^{\,pH-14}) \qquad (2)$$

Equation (2) determines the contribution to Sannon's entropy, associated with pH measured in a small volume (which we consider as a subsystem of a large system herein the pH-measurement is performed). At pH = 7, Equation (2) exhibits a local minimum. Note that Equation (2) is symmetric relatively pH = 7 and, at pH < 6.8 (pH > 7.2), the first (second) term in the parenthesizes becomes negligible.

The total entropy for given discrete spatial distribution of pH (distribution of the system states) can be calculated with summation over the S-values in all spatial points of the system. This situation with discrete distribution of pH field is typical for experiments we performed, since the size of a "cell" (small open volume of the solution) wherein pH is measured is determined by the electrode size.

The approach based on Equation (2) is convenient for analysis of self-organization phenomena (related to change in pH-distributions) and their interpretation in terms of entropy fields. This can be illustrated using results of our measurements of pH fields in different systems. For instance, taking spatial distribution of cations determined experimentally in cases of bare electrode, as well as for electrode covered by polyelectrolyte multilayer (PEI/PSS)₃ and lipid bilayer, we obtained the spatial distributions of entropy $S(x, y)$ represented in **Figures 3D–F**. Interestingly, huge difference is observed for obtained the spatial distributions of entropy that can be associated with various soft matter components for controlling ion fluxes.

CONCLUDING REMARKS AND OUTLOOK

In this perspective, we highlight information processing and signaling by spatial and temporal distribution of ions. A model electrochemical and photochemical system creating local ion-fluxes were demonstrated.

Electrodes spatially organized in a particular manner allows propagation of pH waves to be triggered and spatial distribution of H^+ according to a particular pattern to be realized. Proton diffusion from two sources is reported to model the AND logic gate. We are currently studying how the system geometry influences the pattern of proton concentration and developing a simulation that predicts pH pattern depending on the working electrode geometry and vice versa, namely suggesting electrode geometry depending on desired pH pattern.

The LbL assembly of polyelectrolyte multilayers is suggested as an instrument to control horizontal and vertical ion propagation with ability to correlate it with the spatial distributions of entropy. The experiments we have described are only a small sample of the full range of polyelectrolyte materials that can be assembled on top of electrodes and tested for ion conduction ability.

EXPERIMENTAL SECTION

Three-electrode electrochemical cells (working electrode, Pt counter electrode and Ag/AgCl reference electrode) were utilized as model electrochemical and photoelectrochemical systems. Working electrode was presented by gold or platinum wire (0.2 mm in diameter, 2–3 cm length) embedded in epoxy resin so that circular cross-section of wire exposed to outside media on flat surface of obtained holder. Anodized TiO_2 (1.5 cm²) under low intensity light-emitted diode (365 nm) irradiation focused in spot (~0.25 cm²) was utilized as working photoelectrode. The anodic and cathodic activity of electrode under polarization in water solution as well as photoactivity of illuminated TiO_2 was studied by SVET and generated pH gradients by SIET. To perform the SVET and SIET measurements, a system from Applicable Electronics (USA) modulated by an ASET program (Sciencewares, USA) was used. As a vibrating probe for SVET experiments, an insulated Pt-Ir microprobe (Microprobe Inc., USA) with a platinum black spherical tip 30 μm in diameter was used. The probe was made to vibrate both parallel and perpendicular to the specimen surface at a height of 150 μm. The amplitude of vibration was 30 μm, while the probe vibrated at frequencies of 136 Hz (perpendicular to surface) and 225 Hz (parallel to surface). Only the perpendicular component was used in the treatment and presentation of the data. The environmental pH measurements by SIET were carried out using glass-capillary microelectrodes filled with Hydrogen Ionophore Cocktail I (Sigma) based liquid pH-selective membrane and $KCl + KH_2PO_4$ internal solution. Ag/AgCl/KCl (sat) was used as the external reference electrode. The pH-selective microelectrodes were calibrated using commercially available pH buffers and demonstrated a linear Nernstian response—55 to−58 mV/pH—in a pH range from 3 to 8. The local activity of H^+ was detected 25 μm above the surface. Instrumentation allows to measure voltage with nV precision level, and measure extremely low ion concentration gradients. Step motors allow to study electrochemical activity of material with micrometer spatial resolution and high-resolution maps were obtained. Electrochemical systems were studied in 60 mM hydroquinone solution in 150 mM KNO_3, photoelectrochemical one without addition of hydroquinone.

The deposition of the polyelectrolyte multylayers onto the surface of working electrode was performed using the classical Layer-by-Layer technique. Two mg/ml each branched polyethylenimine (PEI, Mw 70 kDa, 30% water solution purchased from Alfa Aesar) and polystyrene sulfonate (PSS, Mw 500 kDa purchased from Polysciences Inc.,) were dissolved in 0.5 M aqueous NaCl to make polycation and polyanion solutions respectively. Each layer took 20 min to be deposited after which it was rinsed with excess distilled water and then steam-dried. On top of polyelectrolyte modified TiO_2 lipid bilayer was also deposited from 10 mg/ml dispersion of Lecisoy 400 vesicles for 1 h. Further electrochemical characterization

of modified electrodes and photoelectrodes were performed as described above.

SVET data presented as obtained, SIET data recalculated according to previous calibration. Mapping for each experimental condition were reproduced at least three times, one of typical maps is presented.

AUTHOR CONTRIBUTIONS

NR and ES contributed conception and design of the study. SY contributes discussion and writing of Shannon's entropy vs. H^+ concentration gradient part. NR, NM, and PN performed experimental work and treatment of the data. NR wrote the first draft of the manuscript. ES coordinated the study and helped draft the manuscript.

FUNDING

REFERENCES

Andreeva, D. V., Skorb, E. V., and Shchukin, D. G. (2010). Layer-by-layer polyelectrolyte/inhibitor nanostructures for metal corrosion protection. *ACS Appl. Mater. Interfaces* 2, 1954–1962. doi: 10.1021/am1002712

Brezhneva, N., Nikitina, A., Ryzhkov, N., Klestova, A., Vinogradov, A. V., and Skorb, E. V. (2019). Importance of buffering nanolayer position in Layer-by-Layer assembly on titania based hybrid photoactivity. *J. Sol-Gel Sci. Technol.* 89:92. doi: 10.1007/s10971-018-4728-5

Decher, G., Eckle, M., Schmitt, J., and Struth, B. (1998). Layer-by-layer assembled multicomposite films. *Curr. Opin. Colloid Interface* 3, 32–39. doi: 10.1016/S1359-0294(98)80039-3

Decher, G. H. J. D., Hong, J. D., and Schmitt, J. (1992). Buildup of ultrathin multilayer films by a self-assembly process: III. Consecutively alternating adsorption of anionic and cationic polyelectrolytes on charged surfaces. *Thin Solid Films* 210, 831–835. doi: 10.1016/0040-6090(92)90417-A

Dochter, A., Garnier, T., Pardieu, E., Chau, N. T. T., Maerten, C., Senger, B., et al. (2015). Film self-assembly of oppositely charged macromolecules triggered by electrochemistry through a morphogenic approach. *Langmuir* 31, 10208–10214. doi: 10.1021/acs.langmuir.5b02749

Fares, H. M., and Schlenoff, J. B. (2017). Diffusion of sites versus polymers in polyelectrolyte complexes and multilayers. *J. Am. Chem. Soc.* 139, 14656–14667. doi: 10.1021/jacs.7b07905

Farhat, T. R., and Schlenoff, J. B. (2001). Ion transport and equilibria in polyelectrolyte multilayers. *Langmuir* 17, 1184–1192. doi: 10.1021/la001298+

Fomina, N., Johnson, C. A., Maruniak, A., Bahrampour, S., Lang, C., Davis, R. W., et al. (2016). An electrochemical platform for localized pH control on demand. *Lab Chip* 16, 2236–2244. doi: 10.1039/C6LC00421K

Fu, J., Fares, H. M., and Schlenoff, J. B. (2017). Ion-pairing strength in polyelectrolyte complexes. *Macromolecules* 50, 1066–1074. doi: 10.1021/acs.macromol.6b02445

Garnier, T., Dochter, A., Chau, N. T. T., Schaaf, P., Jierry, L., and Boulmedais, F. (2015). Surface-confined self-assembly of polyampholytes generated from charge-shifting polymers. *Chem. Commun.* 51, 14092–14095. doi: 10.1039/C5CC04477D

Ghostine, R. A., and Schlenoff, J. B. (2011). Ion diffusion coefficients through polyelectrolyte multilayers: temperature and charge dependence. *Langmuir* 27, 8241–8247. doi: 10.1021/la2015258

Haken, H. (ed.). (2006). *Information and Self-Organization. A Macroscopic Approach to Complex Systems*. Berlin: Springer.

Han, J. H., Kim, K. B., Kim, H. C., and Chung, T. D. (2009). Ionic circuits based on polyelectrolyte diodes on a microchip. *Angew. Chem.* 121, 3888–3891. doi: 10.1002/ange.200900045

Hoshi, T., Saiki, H., and Anzai, J. I. (2003). Amperometric uric acid sensors based on polyelectrolyte multilayer films. *Talanta* 61, 363–368. doi: 10.1016/S0039-9140(03)00303-5

Jeyanthi, V., Anbu, P., Vairamani, M., and Velusamy, P. (2016). Isolation of hydroquinone (benzene-1, 4-diol) metabolite from halotolerant Bacillus methylotrophicus MHC10 and its inhibitory activity towards bacterial pathogens. *Bioprocess. Biosyst. Eng.* 39, 429–439. doi: 10.1007/s00449-015-1526-0

Karg, M., Pastoriza-Santos, I., Rodriguez-Gonzalez, B., Klitzing, R., Wellert, S., and Hellweg, T. (2008). Temperature, pH, and ionic strength induced changes of the swelling behavior of PNIPAM– poly (allylacetic acid) copolymer microgels. *Langmuir* 24, 6300–6306. doi: 10.1021/la702996p

Katz, E., and Minko, S. (2015). Enzyme-based logic systems interfaced with signal-responsive materials and electrodes. *Chem. Commun.* 51, 3493–3500. doi: 10.1039/C4CC09851J

Kelly, K. D., Fares, H. M., Abou Shaheen, S., and Schlenoff, J. B. (2018). Intrinsic properties of polyelectrolyte multilayer membranes: erasing the memory of the interface. *Langmuir* 34, 3874–3883. doi: 10.1021/acs.langmuir.8b00336

Klitzing, R. V., and Möhwald, H. (1996). A realistic diffusion model for ultrathin polyelectrolyte films. *Macromolecules* 29, 6901–6906. doi: 10.1021/ma960240s

Li, Z., Wang, H., Song, X., Yan, J., Hu, H., and Yu, B. (2014). Dual-responsive polymer brushes as an electrochemical logic gate. *J Electroanal Chem.* 719, 7–13. doi: 10.1016/j.jelechem.2014.01.030

Liu, D., Liu, H., and Hu, N. (2012). pH-, sugar-, and temperature-sensitive electrochemical switch amplified by enzymatic reaction and controlled by logic gates based on semi-interpenetrating polymer networks. *J. Phys. Chem. B* 116, 1700–1708. doi: 10.1021/jp209788g

Maltanava, H. M., Poznyak, S. K., Andreeva, D. V., Quevedo, M. C., Bastos, A. C., Tedim, J., et al. (2017). Light-induced proton pumping with a semiconductor: vision for photoproton lateral separation and robust manipulation. *ACS Appl. Mater. Interfaces* 9, 24282–24289. doi: 10.1021/acsami.7b05209

Motornov, M., Zhou, J., Pita, M., Gopishetty, V., Tokarev, I., Katz, E., et al. (2008). "Chemical transformers" from nanoparticle ensembles operated with logic. *Nano Lett.* 8, 2993–2997. doi: 10.1021/nl802059m

Motornov, M., Zhou, J., Pita, M., Tokarev, I., Gopishetty, V., Katz, E., et al. (2009). An integrated multifunctional nanosystem from command nanoparticles and enzymes. *Small* 5, 817–820. doi: 10.1002/smll.200801550

Nikitina, A. A., Ulasevich, S. A., Kassirov, I. S., Bryushkova, E. A., Koshel, E. I., and Skorb, E. V. (2018). Nanostructured layer-by-layer polyelectrolyte containers to switch biofilm fluorescence. *Bioconjug. Chem.* 29, 3793–3799. doi: 10.1021/acs.bioconjchem.8b00648

Peduto, A., Scuotto, M., Krauth, V., Roviezzo, F., Rossi, A., Temml, V., et al. (2017). Optimization of benzoquinone and hydroquinone derivatives as potent inhibitors of human 5-lipoxygenase. *Eur. J. Med. Chem.* 127, 715–726. doi: 10.1016/j.ejmech.2016.10.046

Pennakalathil, J., Kim, T. H., Kim, K., Woo, K., Park, J. K., and Hong, J. D. (2010). Ion-permselective polyelectrolyte multilayer membrane installed with a pH-sensitive oxazine switch. *Langmuir* 26, 11349–11354. doi: 10.1021/la1007044

Poghossian, A., Katz, E., and Schöning, M. J. (2015). Enzyme logic AND-Re set and OR-Reset gates based on a field-effect electronic transducer modified with multi-enzyme membrane. *Chem. Commun.* 51, 6564–6567. doi: 10.1039/C5CC01362C

Privman, M., Tam, T. K., Pita, M., and Katz, E. (2008). Switchable electrode controlled by enzyme logic network system: approaching physiologically regulated bioelectronics. *J. Am. Chem. Soc.* 131, 1314–1321. doi: 10.1021/ja8088108

Rmaile, H. H., Farhat, T. R., and Schlenoff, J. B. (2003). pH-Gated permeability of variably charged species through polyelectrolyte multilayer membranes. *J. Phys. Chem.* 107, 14401–14406. doi: 10.1021/jp035921l

Ryzhkov, N. V., Brezhneva, N., and Skorb, E. V. (2019a). Feedback mechanisms at solid/polyelectrolyte interfaces for applied materials. *Surface Innovat.* 7, 145–167. doi: 10.1680/jsuin.19.00006

Ryzhkov, N. V., Mamchik, N. A., and Skorb, E. V. (2019b). Electrochemical triggering of lipid bilayer lift-off oscillation at the electrode interface. *J. R. Soc. Interface* 16:20180626. doi: 10.1098/rsif.2018.0626

Schönhoff, M. (2003). Self-assembled polyelectrolyte multilayers. *Curr. Opin. Colloid Interface* 8, 86–95. doi: 10.1016/S1359-0294(03)00003-7

Selin, V., Ankner, J. F., and Sukhishvili, S. A. (2017). Nonlinear layer-by-layer films: effects of chain diffusivity on film structure and swelling. *Macromolecules* 50, 6192–6201. doi: 10.1021/acs.macromol.7b01218

Skorb, E. V., and Andreeva, D. V. (2013). Layer-by-Layer approaches for formation of smart self-healing materials. *Polym. Chem.* 4, 4834–4845. doi: 10.1039/c3py00088e

Skorb, E. V., and Andreeva, D. V. (2015). Self-healing properties of layer-by-layer assembled multilayers. *Polymer Int.* 64, 713–723. doi: 10.1002/pi.4899

Souto, R. M., Lamaka, S. V., and González, S. (2010). "Uses of scanning electrochemical microscopy in corrosion research," in *Microscopy: Science, Technology, Application and Education*, eds A. Mendez-Vilas and J. Diaz (Badajos: Formatex Research Center), 1769–1780.

Spruijt, E., Choi, E. Y., and Huck, W. T. (2008). Reversible electrochemical switching of polyelectrolyte brush surface energy using electroactive counterions. *Langmuir* 24, 11253–11260. doi: 10.1021/la801994b

Steitz, R., Jaeger, W., and Klitzing, R. V. (2001). Influence of charge density and ionic strength on the multilayer formation of strong polyelectrolytes. *Langmuir* 17, 4471–4474. doi: 10.1021/la010168d

Steitz, R., Leiner, V., Siebrecht, R., and Klitzing, R. V. (2000). Influence of the ionic strength on the structure of polyelectrolyte films at the solid/liquid interface. *Colloids Surf. A* 163, 63–70. doi: 10.1016/S0927-7757(99)00431-8

Tanaka, M., and Sackmann, E. (2005). Polymer-supported membranes as models of the cell surface. *Nature* 437, 656–663. doi: 10.1038/nature04164

Wang, L., Lian, W., Yao, H., and Liu, H. (2015). Multiple-stimuli responsive bioelectrocatalysis based on reduced graphene oxide/poly (N-isopropylacrylamide) composite films and its application in the fabrication of logic gates. *ACS Appl. Mater. Interfaces* 7, 5168–5176. doi: 10.1021/am5075002

Wang, X., Zhou, J., Tam, T. K., Katz, E., and Pita, M. (2009). Switchable electrode controlled by Boolean logic gates using enzymes as input signals. *Bioelectrochemistry* 77, 69–73. doi: 10.1016/j.bioelechem.2009.06.012

Yang, C., and Suo, Z. (2018). Hydrogel ionotronics. *Nat. Rev. Mater.* 3, 125–142. doi: 10.1038/s41578-018-0018-7

Zhu, T. F., and Szostak, J. W. (2009). Coupled growth and division of model protocell membranes. *J. Am. Chem. Soc.* 131, 5705–5713. doi: 10.1021/ja900919c

Zhukova, Y., Hiepen, C., Knaus, P., Osterland, M., Prohaska, S., Dunlop, J. W. C., et al. (2017). The role of titanium surface nanostructuring on preosteoblast morphology, adhesion and migration. *Adv. Health Mater.* 6:1601244. doi: 10.1002/adhm.201601244

Mathematical Analysis of a Prototypical Autocatalytic Reaction Network

Ekaterina V. Skorb [1] and Sergey N. Semenov [2],*

[1]   ChemBio Cluster, ITMO University, Lomonosova St. 9, Saint Petersburg 191002, Russia; skorb@corp.ifmo.ru
[2]   Department of Organic Chemistry, Weizmann Institute of Science, Rehovot 76100, Israel
*   Correspondence: sergey.semenov@weizmann.ac.il

Abstract: Network autocatalysis, which is autocatalysis whereby a catalyst is not directly produced in a catalytic cycle, is likely to be more common in chemistry than direct autocatalysis is. Nevertheless, the kinetics of autocatalytic networks often does not exactly follow simple quadratic or cubic rate laws and largely depends on the structure of the network. In this article, we analyzed one of the simplest and most chemically plausible autocatalytic networks where a catalytic cycle is coupled to an ancillary reaction that produces the catalyst. We analytically analyzed deviations in the kinetics of this network from its exponential growth and numerically studied the competition between two networks for common substrates. Our results showed that when quasi-steady-state approximation is applicable for at least one of the components, the deviation from the exponential growth is small. Numerical simulations showed that competition between networks results in the mutual exclusion of autocatalysts; however, the presence of a substantial noncatalytic conversion of substrates will create broad regions where autocatalysts can coexist. Thus, we should avoid the accumulation of intermediates and the noncatalytic conversion of the substrate when designing experimental systems that need autocatalysis as a source of positive feedback or as a source of evolutionary pressure.

Keywords: Autocatalysis; reaction networks; origin of life; Michaelis-Menten kinetics; numerical simulations; self-replication

1. Introduction

Autocatalytic reactions are of profound importance for at least three problems in the chemical sciences: (i) chemical evolution and the origin of life, [1–6] (ii) dissipative chemical systems [7–9], and (iii) chemical signaling and information processing systems [10]. Autocatalytic self-replication is an element needed for Darwinian selection. Biological evolution is driven by cellular division and life most likely originates from prebiotic reactions that involve some form of self-replication and autocatalysis [1,11–14]. Dissipative systems, such as chemical and biological oscillators and Turing structures [15–18], often require autocatalytic reactions as a source of positive feedback. Finally, biochemical signaling systems need autocatalysis for signal amplification [10].

The importance of autocatalysis for determining the origin of life is twofold [19]. At the initial stages of prebiotic evolution, where organic building blocks accumulated, autocatalysis is a possible solution for the "mixtures" problem [20–22], which involves a low abundance of any particular reaction product from diverse starting materials because of the statistical distribution of the reaction products. Autocatalysis would accelerate the formation of a limited set of products and consume starting materials for forming these products, thus avoiding the formation of the complex mixture. At later stages of prebiotic evolution, autocatalysis serves as a driving force for the natural selection of information carriers [2,12,14,23]. It amplifies the fittest carriers against others. Many variations of information carriers have been proposed such as rybozimes [24], autocatalytic sets of polypeptides [1,2,12,14,22],

or vesicles carrying compositional information [23], but autocatalysis is always a driving force behind the evolution of these species.

Direct autocatalysis, which is a process whereby a product directly catalyzes its own production through formation of only short-living intermediates, is often differentiated from network autocatalysis, where multiple stable products cooperatively accelerate their own production [25–29]. Because of its high mechanistic versatility compared with direct autocatalysis, network autocatalysis has become a basis for a variety of models for determining the origin of life [1,2,11,12,14,23,30]. Nevertheless, the functional properties (e.g., the ability to evolve) of a particular network depend on their kinetic behavior which [31,32], consequently, depend on the structure of the network [33]. Therefore, it is important to analyze the kinetics of specific and chemically plausible autocatalytic reaction networks [34–36].

Semenov, Whitesides, and coworkers have recently published two autocatalytic reactions that can be reduced to a catalytic cycle, followed by the noncatalytic conversion of one product of this catalytic cycle to the catalyst itself (Figure 1) [37,38].
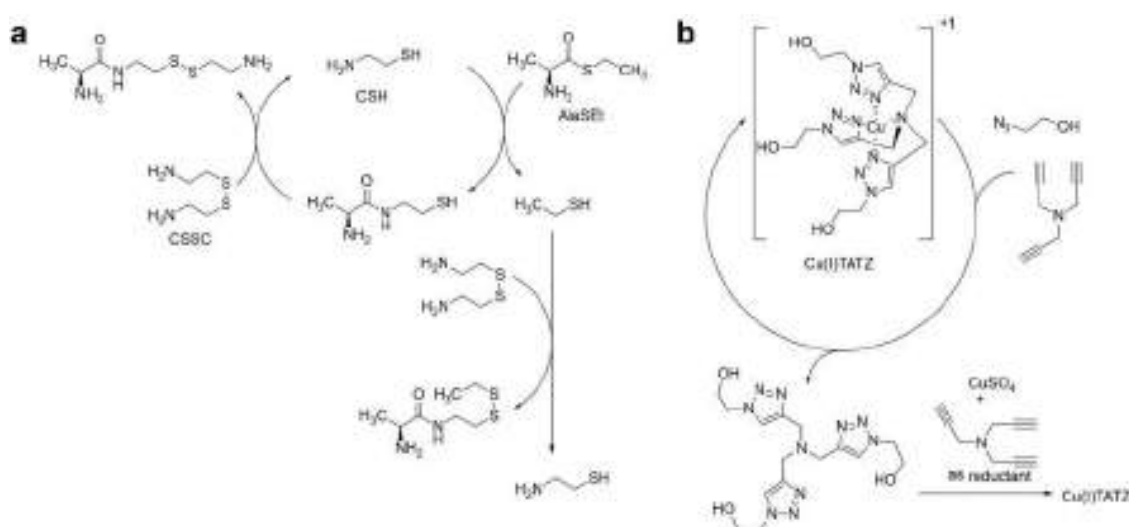
Figure 1. Schemes that represent (**a**) the thiol-based autocatalytic reaction and (**b**) the copper-catalyzed azide-alkine cycloaddition-based autocatalytic reaction as a catalytic cycle coupled to a non-catalytic reaction that converts one of the products of catalytic transformation into the catalyst itself. Examples of autocatalysts are cysteamine (CSH) and a copper complex (Cu(I)TATZ).

In the first example, we can separate a catalytic cycle of cysteamine (CSH), which catalyzed the acylation of cystamine (CSSC) by a thioester; this is followed by converting one of its byproducts, ethanethiol, into CSH (Figure 1a) [37]. In the second example, the catalytic cycle of the copper-catalyzed azide-alkyne cycloaddition reactions is followed by the formation of a catalytically active complex from triazole derivatives (Figure 1b) [38]. Because of the abundance of catalytic reactions in nature, we speculate that these motifs might be among the most common autocatalytic motifs in simple (i.e., non-biological) reaction networks.

Here, we would like to analyze the kinetic behavior of one type of these motifs where the Michaelis-Menten-type catalysis is coupled to one additional irreversible reaction (Figure 2).

We decided to analyze this particular motif because the Michaelis-Menten scheme can be applied to many catalytic reactions and possibility to reduce extended motifs to this motif by considering only rate-limiting steps. We would like to determine under which conditions this reaction network can be used in place of quadratic autocatalysis in experiments investigating chemical evolution and chemical systems with nonlinear kinetics and whether the kinetics of this network will always cause mutual exclusion of competing replicators.
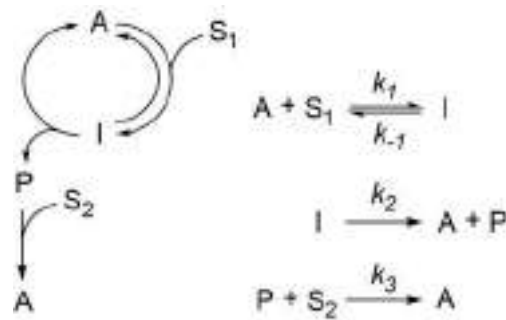
Figure 2. The autocatalytic reaction network analyzed here.

2. Results and Discussion

2.1. Analysis of Kinetics for a Network with an Infinite Supply of Substrates

Equations (1)–(3) with constant S_1 and S_2 describe the network in this approximation:

$$\frac{dA}{dt} = -k_1 S_1 A + (k_2 + k_{-1})I + k_3 S_2 P \tag{1}$$

$$\frac{dI}{dt} = k_1 S_1 A - (k_2 + k_{-1})I \tag{2}$$

$$\frac{dP}{dt} = k_2 I - k_3 S_2 P \tag{3}$$

Let us first consider two of the simplest cases: (i) when quasi-steady-state approximation (QSSA) can be applied to I ($\frac{dI}{dt} = 0$) and P ($\frac{dP}{dt} = 0$) and (ii) when QSSA can be applied to A ($\frac{dA}{dt} = 0$) and P ($\frac{dP}{dt} = 0$). Simple calculations (see the Appendix A) show that in the first case the reaction is perfectly autocatalytic with the effective rate constant $k_e = k_1 S_1 k_2 / (k_2 + k_{-1})$:

$$\frac{dA}{dt} = \frac{k_1 S_1 k_2}{(k_2 + k_{-1})} A \tag{4}$$

Obviously, in a situation with a limited amount of S_1, the reaction will behave as quadratic autocatalysis with rate constant k_e.

In the second case, the reaction is entirely autocatalytic for I with k_2 as the autocatalytic constant (see the Appendix A):

$$\frac{dI}{dt} = k_2 I \tag{5}$$

Let us next look at a situation where we apply QSSA only to I. This situation is important for experimental systems because it has been shown that many catalytic reactions follow Michaelis–Menten kinetics, which implies QSSA for I. The equations (1)–(3) can be reduced to the second order Equation (6) on P:

$$\frac{d^2P}{dt^2} + k_3 S_2 \frac{dP}{dt} - \frac{k_3 S_2 k_1 S_1 k_2}{(k_2 + k_{-1})} P = 0 \tag{6}$$

From 6, with initial conditions $P(0) = 0$ and $A(0) = A_0$, we can derive an expression for A (see the Appendix A for details).

$$A(t) = \frac{A_0}{\sqrt{k_3 S_2 (k_3 S_2 + 4k_1 S_1 k_2 / (k_2 + k_{-1}))}} \left((k_3 S_2 + \lambda_1)e^{\lambda_1 t} - (k_3 S_2 + \lambda_2)e^{\lambda_2 t} \right)$$
$$\lambda_{1/2} = \frac{-k_3 S_2 \pm \sqrt{k_3 S_2 (k_3 S_2 + 4k_1 S_1 k_2 / (k_2 + k_{-1}))}}{2} \tag{7}$$

Note that for physical (positive) rate constants and concentrations, λ_1 is always positive and λ_2 is always negative. The first term in Equation (7) has a positive exponent (λ_1) and has the higher coefficient in front of the exponent other than the second term, and therefore, it will dominate from the beginning. Chemically, this equation means that if intermediates of the catalytic cycle do not accumulate in significant amounts, the reaction will behave as exponential autocatalysis from the beginning of the experiment and any deviations from exponential growth will decay over time.

Next, we will examine a situation where we do not have an accumulated product of the catalytic cycle because of the substantially high rate of its conversion to the autocatalyst. This situation is described by QSSA with $\frac{dP}{dt} = 0$ and cannot be reduced to the second order differential equation; instead, we need to solve a system involving two equations:

$$\frac{dA}{dt} = -k_1 S_1 A + (2k_2 + k_{-1})I \tag{8}$$

$$\frac{dI}{dt} = k_1 S_1 A - (k_2 + k_{-1})I \tag{9}$$

For the initial conditions, A(0) = A_0 and I(0) = 0; this system has a solution:

$$A(t) = A_0(C_1 e^{\lambda_1 t} + C_2 e^{\lambda_2 t})$$
$$\lambda_{1/2} = \frac{-k_1 S_1 - k_2 - k_{-1} \pm \sqrt{(k_1 S_1 + k_2 + k_{-1})^2 + 4k_1 S k_2}}{2} \tag{10}$$

Both the C_1 and C_2 coefficients are positive and $C_1 + C_2 = 1$ (for an exact expression of C_1 and C_2, see the Appendix A). The value λ_1 is always positive and λ_2 is always negative for any positive rate constants. Therefore, the value of the decaying term, $A_0 C_2 e^{\lambda_2 t}$, will not exceed that of A_0. These calculations indicate that if in an experimental system the product P does not accumulate and A_0 is much smaller than the concentration of the substrate, S_1, this system will behave as an almost perfect quadratic autocatalysis.

Finally, we will briefly examine a situation where we do not apply any QSSA. For an autocatalyst A, the solution has a general form:

$$A(t) = C_1 e^{\lambda_1 t} + C_2 e^{\lambda_2 t} + C_3 e^{\lambda_3 t} \tag{11}$$

If any part of λ_{1-3} is positive, then A will grow exponentially after an initial lag period (the term with a positive exponent will dominate in Equation (11)). As we show in the Appendix A, because rate constants are positive, one of the λ_{1-3} values must be positive. Thus, independently of rate constants and after some lag period, this reaction network will produce exponential growth. Experimental systems are limited by the amounts of the substrates S_1 and S_2 and might not have time to reach an exponential phase, especially with a high initial concentration of A.

2.2. Competition of the Autocatalysts of Two Different Autocatalytic Networks for Common Substrates

To describe a practically interesting situation, we analyzed the competition between two autocatalytic networks in a continuously stirred tank reactor (CSTR). Network 1 consists of A_1, I_1, and P_1 and network 2 consists of A_2, I_2, and P_2; they compete for common substrates S_1 and S_2. Here, the system is defined by:

$$\frac{dA_1}{dt} = -k_1 S_1 A_1 + (k_2 + k_{-1})I_1 + k_3 S_2 P_1 - k_0 A_1 \tag{12}$$

$$\frac{dI_1}{dt} = k_1 S_1 A_1 - (k_2 + k_{-1} + k_0)I_1 \tag{13}$$

$$\frac{dP_1}{dt} = k_2 I_1 - (k_3 S_2 + k_0)P_1 \tag{14}$$

$$\frac{dA_2}{dt} = -k_1' S_1 A_2 + (k_2' + k_{-1}') I_2 + k_3' S_2 P_2 - k_0 A_2 \tag{15}$$

$$\frac{dI_2}{dt} = k_1' S_1 A_2 - (k_2' + k_{-1}' + k_0) I_2 \tag{16}$$

$$\frac{dP_2}{dt} = k_2' I_1 - (k_3' S_2 + k_0) P_2 \tag{17}$$

$$\frac{dS_1}{dt} = -(k_1 A_1 + k_1' A_2 + k_0) S_1 + k_{-1} I_1 + k_{-1}' I_2 + k_0 S_{10} \tag{18}$$

$$\frac{dS_2}{dt} = -(k_3 P_1 + k_3' P_2 + k_0) S_2 + k_0 S_{20}, \tag{19}$$

where S_{10} and S_{20} are the concentrations at which S_1 and S_2 are supplied to the reactor.

We should mention at this point that if networks compete only for substrate S_1 and S_2 is considered to be in an unlimited supply (i.e., we consider Equations (12)–(18) with S_2 being constant), autocatalysts A_1 and A_2 cannot coexist at a steady state if any difference between the rate constants of the reactions of the networks exists (see the Appendix A). The model with constant S_2 describes experimental systems where S_2 is in a big excess in relation to S_1 or where conversion of P to A is a monomolecular reaction.

If S_2 is variable, we cannot draw a simple conclusion about coexistence and need to use numerical analysis. We analyzed 12–19 using Mathematica script (see the Appendix A). Figure 3a shows concentrations of A_1 and A_2 at t = 2000 where, in most cases, the system reaches a steady state. We set all constants to unity, the initial concentrations of A_1 and A_2 to 0.001, k_0 to 0.1, and varied k_1 and k_3, which characterize reactions with substrates. The graph has two characteristic futures: (i) autocatalysts A_1 and A_2 do not coexist, if one has a nonzero concentration and another falls to zero; (ii) competition is not sensitive to k_3 as soon as k_3 is sufficiently high. These features mean that these networks can undergo Darwinian evolution and that this evolution will be more sensitive to improvements in k_1 than in k_3.

An important difference between model 12–19 and plausible chemical systems is the presence of the noncatalytic conversion of substrates to autocatalysts in many experimental systems. To consider these reactions, we have to add $k_4 S_1$ and $k_4' S_1$ to Equations (12) and (13) correspondingly, and subtract both these terms from Equation (18). We performed a numerical analysis of the modified equations with the same parameters as in Figure 3a and with k_4 and k_4' set to 0.01 (Figure 3b). The graph shows that autocatalysts can coexist and the region of coexistence is higher for low k_3 values. Thus, we should avoid accumulating P in experimental systems with noncatalytic background reactions. We also explored how k_2 and k_{-1} influence the competition between two replicators (Figure 3c,d). The plots demonstrate that k_2, which represents k_{cat} in a classical Michaelis-Menten scheme, has a stronger influence on the competition than k_3 does, but it is less important than k_1. Interestingly, simultaneously varying k_2 and k_{-1} produces almost a symmetrical plot, which indicates their equal contribution to the competition between replicators (Figure 3d). Overall, the data indicate that k_1, which is responsible for initiating the catalytic cycle, has the greatest effect on the competition, whereas k_3, which is responsible for an axillary reaction that produces an extra molecule in the catalyst, has a minimum effect.
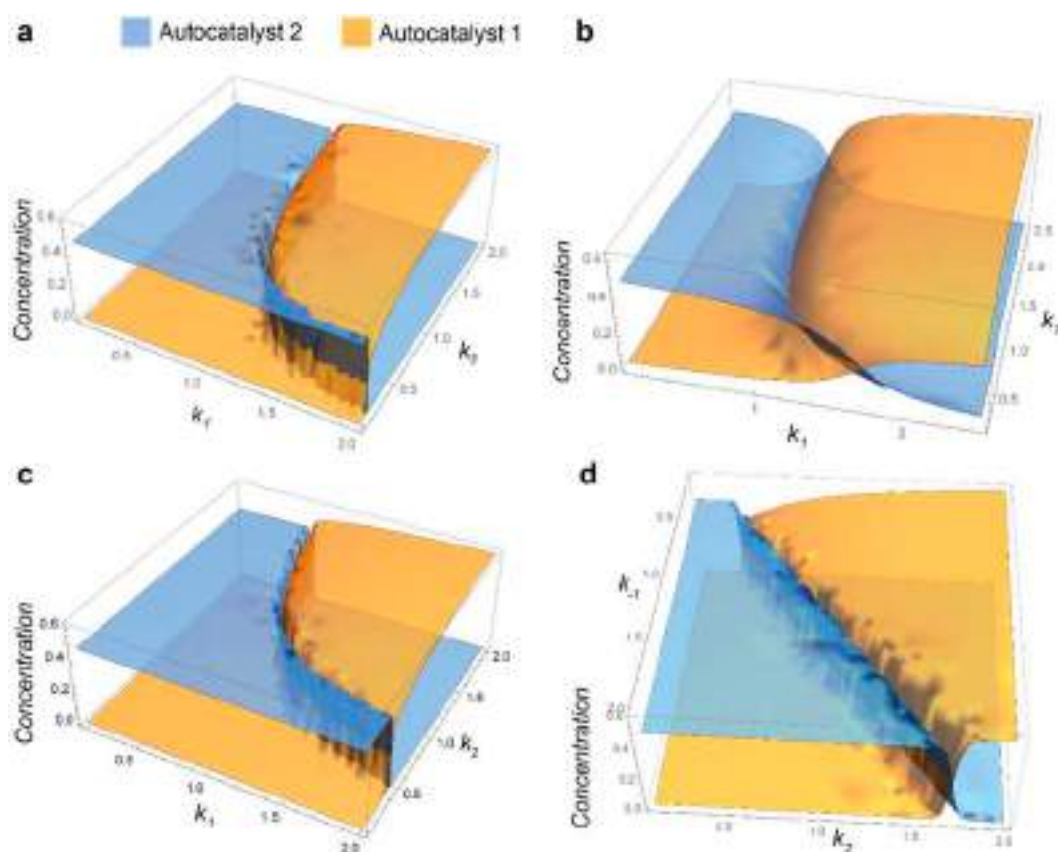
Figure 3. Competition between replicators A_1 and A_2 in continuously stirred tank reactor (CSTR). (**a**) The system is based on Equations (12)–(19). All reaction rate constants except k_1 and k_3 are set to 1; k_0 is set to 0.1, S_{10} and S_{20} are set to 1, and k_1 and k_3 are varied from 0.1 to 2. (**b**) When considering the noncatalytic formation of A_1 and A_2 with $k_4 = k_4' = 0.01$, other parameters are identical to *a*. (**c**) The system is based on Equations (12)–(19). All reaction rate constants except k_1 and k_2 are set to 1; k_0 is set to 0.1, S_{10} and S_{20} are set to 1, and k_1 and k_2 are varied from 0.1 to 2. (**d**) The system is based on Equations (12)–(19). All reaction rate constants except k_{-1} and k_2 are set to 1; k_0 is set to 0.1, S_{10} and S_{20} are set to 1, and k_{-1} and k_2 are varied from 0.1 to 2. In all plots, the concentrations of replicators A_1 and A_2 are plotted at t = 2000, $A_1(0) = 0.001$, $A_2(0) = 0.001$.

3. Conclusions

In this work, we determined, as precisely as possible, where and how to use reactions in experimental systems, which are based on the scheme shown in Figure 2. The results provide two main conclusions: (i) As soon as an intermediate of catalytic I or an intermediate product P does not accumulate in the reaction (at least one of them can be described by QSSA), the reaction kinetics does not deviate from exponential autocatalysis after a short lag period. (ii) The competition between these networks results in the mutual exclusion of autocatalysts if the noncatalytic formation of autocatalysts is negligible. Therefore, although these networks are not direct autocatalysts from a mechanistic perspective, they will behave as simple quadratic autocatalysts in most experimental systems.

Finally, if some variable information in autocatalyst A is transferred to product P and then retained during conversion of P to A, the network fulfills the conditions for Darwinian evolution. Interestingly, an experimental system from Otto's group is [39,40], in a way, already following this mechanism. The growth of the supramolecular stacks, which is catalyzed by the terminus of the stack, is the catalytic step with information transfer; breaking the stack, which generates an extra terminus, is a P to A step that retains the information.

Appendix A

I. Equations (2)–(3) at $\frac{dI}{dt} = 0$ and $\frac{dP}{dt} = 0$ give:

$$k_1 S_1 A - (k_2 + k_{-1})I = 0 \tag{A1}$$

$$k_2 I - k_3 S_2 P = 0 \tag{A2}$$

$$I = \frac{k_1 S_1 A}{k_2 + k_{-1}} \tag{A3}$$

$$P = \frac{k_2 k_1 S_1 A}{k_3 S_2 (k_2 + k_{-1})} \tag{A4}$$

Substitution of (A3) and (A4) into (1) gives Equation (4)

Equations (1) and (3) at $\frac{dA}{dt} = 0$ and $\frac{dP}{dt} = 0$) give:

$$- k_1 S_1 A + (k_2 + k_{-1})I + k_3 S_2 P = 0 \tag{A5}$$

$$P = \frac{k_2 I}{k_3 S_2} \tag{A6}$$

$$A = -\frac{(2k_2 + k_{-1})I}{k_1 S_1} \tag{A7}$$

Substitution of (A7) into (2) gives Equation (5)

II. Equation (6) at $P(0) = 0$ and $A(0) = A_0$ => $\frac{dP}{dt}(0) = \frac{k_1 S_1 k_2}{(k_2 + k_{-1})} A_0$ has a solution:

$$P(t) = \frac{A_0 k_1 S_1 k_2}{(k_2 + k_{-1}) \sqrt{k_3 S_2 (k_3 S_2 + 4k_1 S_1 k_2 / (k_2 + k_{-1}))}} (e^{\lambda_1 t} - e^{\lambda_2 t});$$
$$\lambda_{1/2} = \frac{-k_3 S_2 \pm \sqrt{k_3 S_2 (k_3 S_2 + 4k_1 S_1 k_2 / (k_2 + k_{-1}))}}{2} \tag{A8}$$

Considering that:

$$A(t) = \frac{(k_2 + k_{-1})}{k_1 S_1 k_2} \left(k_3 S_2 P + \frac{dP}{dt} \right) \tag{A9}$$

A(t) is described by Equation (7).

III. In Equation (10) coefficients C_1 and C_2 are expressed by:

$$C_1 = \frac{k_1 S_1 - k_2 - k_{-1} + \sqrt{(k_1 S_1 + k_2 + k_{-1})^2 + 4k_1 S_1 k_2}}{2\sqrt{(k_1 S_1 + k_2 + k_{-1})^2 + 4k_1 S_1 k_2}}$$
$$C_2 = \frac{k_2 + k_{-1} - k_1 S_1 + \sqrt{(k_1 S_1 + k_2 + k_{-1})^2 + 4k_1 S_1 k_2}}{2\sqrt{(k_1 S_1 + k_2 + k_{-1})^2 + 4k_1 S_1 k_2}} \tag{A10}$$

IV.   Equations (1)–(3) are linear and a solution for this linear system of ODE has the following form:

$$\begin{pmatrix} A \\ I \\ P \end{pmatrix} = C_1 e^{\lambda_1 t}\widetilde{\nu}_1 + C_2 e^{\lambda_2 t}\widetilde{\nu}_2 + C_3 e^{\lambda_3 t}\widetilde{\nu}_3 \tag{A11}$$

where λ_1, λ_2, and λ_3 are eigenvalues, and $\nu_{1\text{-}3}$ are the corresponding eigenvectors of the matrix:

$$\begin{pmatrix} -k_1 S_1 & k_2 + k_{-1} & k_3 S_2 \\ k_1 S_1 & -k_2 - k_{-1} & 0 \\ 0 & k_2 & -k_3 S_2 \end{pmatrix} \tag{A12}$$

λ_1, λ_2, and λ_3 are roots of the equation:

$$\lambda^3 + (k_1 S_1 + k_2 + k_{-1} + k_3 S_2)\lambda^2 + k_3 S_2 (k_1 S_1 + k_2 + k_{-1})\lambda - k_1 S_1 k_3 S_2 k_2 = 0 \tag{A13}$$

From Vieta's formula:

$$\lambda_1 \lambda_2 \lambda_3 = k_1 S_1 k_3 S_2 k_2 \tag{A14}$$

Because k_1, k_2, k_3, S_1, S_2 are positive, one of the $\lambda_{1\text{-}3}$ values must be positive.

V.   Steady-state conditions for 12-19 are as follows:

$$A_1\left(-k_1 S_1 + \frac{(k_2 + k_{-1})k_1 S_1}{k_2 + k_{-1} + k_0} + \frac{k_2 k_1 S_1 k_3 S_2}{(k_3 S_2 + k_0)(k_2 + k_{-1} + k_0)} - k_0\right) = 0 \tag{A15}$$

$$A_2\left(-k'_1 S_1 + \frac{(k'_2 + k'_{-1})k'_1 S_1}{k'_2 + k'_{-1} + k_0} + \frac{k'_2 k'_1 S_1 k'_3 S_2}{(k'_3 S_2 + k_0)(k'_2 + k'_{-1} + k_0)} - k_0\right) = 0 \tag{A16}$$

If we consider S_2 to be constant and the reaction rates are different for two networks, this system of equations does not have solutions where both A_1 and A_2 are nonzero.

VI.   Mathematic script that generates the plot 3A. Plots 3B-C were generated by modifying this script.

```
k0 = 0.1; k1 = 1; k1r = 1; k2 = 1; k3 = 1; k1z = 1; k1rz = 1; k2z = 1; k3z = 1; S01 = 1; S02
= 1; s = ParametricNDSolve[{a'[t] == -a[t]*(i*k1*s1[t] + k0) + b[t]*(k2 + k1r) + h*k3*s2[t]*p[t],
b'[t] == i*k1*a[t]*s1[t] - b[t]*(k2 + k1r + k0), p'[t] == k2*b[t] - (h*k3*s2[t] + k0)*p[t], a1'[t] ==
-a1[t]*(k1z*s1[t] + k0) + b1[t]*(k2z + k1rz) + k3z*s2[t]*p1[t], b1'[t] == k1z*a1[t]*s1[t] - b1[t]*(k2z
+ k1rz + k0), p1'[t] == k2z*b1[t] - (k3z*s2[t] + k0)*p1[t], s1'[t] == -i*k1*a[t]*s1[t] - k1z*a1[t]*s1[t]
+ k1r*b[t] + k1rz*b1[t] - k0*s1[t] + k0*S01, s2'[t] == -h*k3*p[t]*s2[t] - k3z*p1[t]*s2[t] - k0*s2[t] +
k0*S02, a[0] == 0.001, a1[0] == 0.001, b[0] == p[0] == b1[0] == p1[0] == 0, s1[0] == s2[0] == 1 },
{a, b, p, a1, b1, p1, s1, s2}, {t, 0, 2000}, {i, h}]; Plot3D[{a[i, h][2000] /. s, a1[i, h][2000] /. s}, {i, 0.1,
2}, {h, 0.1, 2}, PlotStyle -> Opacity[0.7], Mesh -> None, AxesStyle -> 16]
```

References

1.   Eigen, M. Selforganization of matter and the evolution of biological macromolecules. *Naturwissenschaften* **1971**, *58*, 465–523. [CrossRef]

2.   Eigen, M.; Schuster, P. Hypercycle—Principle of Natural Self-Organization. B. Abstract Hypercycle. *Naturwissenschaften* **1978**, *65*, 7–41. [CrossRef]

3.   Sievers, D.; Von Kiedrowski, G. Self Replication of Complementary Nucleotide-Based Oligomers. *Nature* **1994**, *369*, 221–224. [CrossRef] [PubMed]

4.   Li, T.; Nicolaou, K.C. Chemical self-replication of palindromic duplex DNA. *Nature* **1994**, *369*, 218–221. [CrossRef]

5.   Lee, D.H.; Granja, J.R.; Martinez, J.A.; Severin, K.; Ghadiri, M.R. A self-replicating peptide. *Nature* **1996**, *382*, 525–528. [CrossRef]

6. Ashkenasy, G.; Jagasia, R.; Yadav, M.; Ghadiri, M.R. Design of a directed molecular network. *Proc. Natl. Acad. Sci. USA* **2004**, *101*, 10872–10877. [CrossRef]

7. Whitesides, G.M.; Grzybowski, B. Self-assembly at all scales. *Science* **2002**, *295*, 2418–2421. [CrossRef] [PubMed]

8. Nicolis, G.; Prigogine, I. *Self-Organization in Nonequilibrium Systems: From Dissipative Structures to Order Through Fluctuations*; Wiley: New York, NY, USA, 1977; pp. 40–233.

9. Field, R.J.; Noyes, R.M. Oscillations in chemical systems. IV. Limit cycle behavior in a model of a real chemical reaction. *J. Chem. Phys.* **1974**, *60*, 1877–1884. [CrossRef]

10. Kholodenko, B.N. Cell-signalling dynamics in time and space. *Nat. Rev. Mol. Cell Bio.* **2006**, *7*, 165–176. [CrossRef]

11. Dyson, F.J. A Model for the Origin of Life. *J. Mol. Evol.* **1982**, *18*, 344–350. [CrossRef]

12. Vasas, V.; Fernando, C.; Santos, M.; Kauffman, S.; Szathmary, E. Evolution before genes. *Biol. Direct* **2012**, *7*. [CrossRef]

13. Nghe, P.; Hordijk, W.; Kauffman, S.A.; Walker, S.I.; Schmidt, F.J.; Kemble, H.; Yeates, J.A.M.; Lehman, N. Prebiotic network evolution: Six key parameters. *Mol. Biosyst.* **2015**, *11*, 3206–3217. [CrossRef]

14. Kauffman, S.A. Autocatalytic sets of proteins. *J. Theor. Biol.* **1986**, *119*, 1–24. [CrossRef]

15. Epstein, I.R.; Pojman, J.A. *An Introduction to Nonlinear Chemical Dynamics: Oscillations, Waves, Patterns, and Chaos*; Oxford University Press: New York, NY, USA, 1998; pp. 17–324.

16. Dekepper, P.; Epstein, I.R.; Kustin, K. A Systematically Designed Homogeneous Oscillating Reaction - the Arsenite-Iodate-Chlorite System. *J. Am. Chem. Soc.* **1981**, *103*, 2133–2134. [CrossRef]

17. Lengyel, I.; Epstein, I.R. Modeling of Turing Structures in the Chlorite Iodide Malonic-Acid Starch Reaction System. *Science* **1991**, *251*, 650–652. [CrossRef] [PubMed]

18. Turing, A.M. The Chemical Basis of Morphogenesis. *Philos. T. Roy. Soc. B* **1952**, *237*, 37–72.

19. Lifson, S. On the crucial stages in the origin of animate matter. *J. Mol. Evol.* **1997**, *44*, 1–8. [CrossRef]

20. Hordijk, W.; Hein, J.; Steel, M. Autocatalytic Sets and the Origin of Life. *Entropy* **2010**, *12*, 1733–1742. [CrossRef]

21. Eschenmoser, A. Etiology of potentially primordial biomolecular structures: From vitamin B12 to the nucleic acids and an inquiry into the chemistry of life's origin: A retrospective. *Angew. Chem. Int. Ed. Engl.* **2011**, *50*, 12412–12472. [CrossRef]

22. Hordijk, W.; Steel, M. Chasing the tail: The emergence of autocatalytic networks. *Biosystems* **2017**, *152*, 1–10. [CrossRef]

23. Markovitch, O.; Lancet, D. Excess Mutual Catalysis Is Required for Effective Evolvability. *Artif. Life* **2012**, *18*, 243–266. [CrossRef] [PubMed]

24. Lincoln, T.A.; Joyce, G.F. Self-Sustained Replication of an RNA Enzyme. *Science* **2009**, *323*, 1229–1232. [CrossRef] [PubMed]

25. Plasson, R.; Brandenburg, A.; Jullien, L.; Bersini, H. Autocatalyses. *J. Phys. Chem. A* **2011**, *115*, 8073–8085. [CrossRef]

26. Hinshelwood, C.N. On the Chemical Kinetics of Autosynthetic Systems. *J. Chem. Soc.* **1952**, 745–755. [CrossRef]

27. Blackmond, D.G. An examination of the role of autocatalytic cycles in the chemistry of proposed primordial reactions. *Angew. Chem. Int. Ed. Engl.* **2009**, *48*, 386–390. [CrossRef]

28. Bissette, A.J.; Fletcher, S.P. Mechanisms of Autocatalysis. *Angew. Chem. Int. Ed.* **2013**, *52*, 12800–12826. [CrossRef]

29. Hordijk, W.; Steel, M.; Dittrich, P. Autocatalytic sets and chemical organizations: Modeling self-sustaining reaction networks at the origin of life. *New J. Phys.* **2018**, *20*, 015011. [CrossRef]

30. Hordijk, W.; Steel, M.; Kauffman, S. The structure of autocatalytic sets: Evolvability, enablement, and emergence. *Acta Biotheor.* **2012**, *60*, 379–392. [CrossRef]

31. Szathmary, E. The origin of replicators and reproducers. *Philos. Trans. R. Soc. Lond B Biol. Sci.* **2006**, *361*, 1761–1776. [CrossRef]

32. Szathmáry, E. Simple growth laws and selection consequences. *Trends in Ecology & Evolution* **1991**, *6*, 366–370.

33. Wagner, N.; Ashkenasy, G. How Catalytic Order Drives the Complexification of Molecular Replication Networks. *Isr. J. Chem.* **2015**, *55*, 880–890. [CrossRef]

34. Ashkenasy, G.; Hermans, T.M.; Otto, S.; Taylor, A.F. Systems chemistry. *Chem. Soc. Rev.* **2017**, *46*, 2543–2554. [CrossRef] [PubMed]

35. Ludlow, R.F.; Otto, S. Systems chemistry. *Chem. Soc. Rev.* **2008**, *37*, 101–108. [CrossRef]

36. Dadon, Z.; Wagner, N.; Alasibi, S.; Samiappan, M.; Mukherjee, R.; Ashkenasy, G. Competition and cooperation in dynamic replication networks. *Chemistry* **2015**, *21*, 648–654. [CrossRef]

37. Semenov, S.N.; Kraft, L.J.; Ainla, A.; Zhao, M.; Baghbanzadeh, M.; Campbell, C.E.; Kang, K.; Fox, J.M.; Whitesides, G.M. Autocatalytic, bistable, oscillatory networks of biologically relevant organic reactions. *Nature* **2016**, *537*, 656–660. [CrossRef] [PubMed]

38. Semenov, S.N.; Belding, L.; Cafferty, B.J.; Mousavi, M.P.S.; Finogenova, A.M.; Cruz, R.S.; Skorb, E.V.; Whitesides, G.M. Autocatalytic Cycles in a Copper-Catalyzed Azide-Alkyne Cycloaddition Reaction. *J. Am. Chem. Soc.* **2018**, *140*, 10221–10232. [CrossRef]

39. Carnall, J.M.A.; Waudby, C.A.; Belenguer, A.M.; Stuart, M.C.A.; Peyralans, J.J.P.; Otto, S. Mechanosensitive Self-Replication Driven by Self-Organization. *Science* **2010**, *327*, 1502–1506. [CrossRef]

40. Sadownik, J.W.; Mattia, E.; Nowak, P.; Otto, S. Diversification of self-replicating molecules. *Nat. Chem.* **2016**, *8*, 264–269. [CrossRef]

THE ROYAL SOCIETY
PUBLISHING

Electrochemical triggering of lipid bilayer lift-off oscillation at the electrode interface

Nikolay V. Ryzhkov, Natalya A. Mamchik and Ekaterina V. Skorb

ITMO University, 9 Lomonosova Street, St Petersburg 191002, Russian Federation

NVR, 0000-0002-6557-0018

In situ studies of transmembrane channels often require a model bioinspired artificial lipid bilayer (LB) decoupled from its underlaying support. Obtaining free-standing lipid membranes is still a challenge. In this study, we suggest an electrochemical approach for LB separation from its solid support via hydroquinone oxidation. Layer-by-layer deposition of polyethylenimine (PEI) and polystyrene sulfonate (PSS) on the gold electrode was performed to obtain a polymeric nanocushion of $[PEI/PSS]_3/PEI$. The LB was deposited on top of an underlaying polymer support from the dispersion of small unilamellar vesicles due to their electrostatic attraction to the polymer support. Since lipid zwitterions demonstrate pH-dependent charge shifting, the separation distance between the polyelectrolyte support and LB can be adjusted by changing the environmental pH, leading to lipid molecules recharge. The proton generation associated with hydroquinone oxidation was studied using scanning vibrating electrode and scanning ion-selective electrode techniques. Electrochemical impedance spectroscopy is suggested to be a powerful instrument for the *in situ* observation of processes associated with the LB–solid support interface. Electrochemical spectroscopy highlighted the reversible disappearance of the LB impact on impedance in acidic conditions set by dilute acid addition as well as by electrochemical proton release on the gold electrode due to hydroquinone oxidation.

1. Introduction

A vital parameter necessary for the completion of various chemical processes in solution chemistry [1,2] and biochemistry [3] is the acidity at which the reactions take place. Fine-tuning the environmental acidity serves as a powerful regulatory method, influencing the outcome of these processes [4,5] and allowing for the desired effects to be achieved. pH-sensitive systems play a significant role in the design of those smart materials that respond to external stimuli [6] such as soft robots [7], self-organizing structures [8,9] and nanocapsules [10,11]. The acidity of the environment greatly affects those systems held together by electrostatic interactions [12].

Numerous strategies have been developed for modifying the pH of a solution on both large and small scales. Recent reports have included photochemical [13], enzymatic [14] and electrochemical [8,9] approaches to pH adjustment. Faraday's laws of electrolysis show that electrochemically adjusting the pH of a system enables quantitative control over the generation of pH-determining ions. Precise spatiotemporal control can be performed due to the high localization of reactions on the electrode surface.

Owing to their proton-coupled electron transfer [15], low redox potential and relative chemical stability quinones are widely used as the electroactive species for the controlled generation/consumption of protons [8,9]. Naturally occurring hydroquinone compounds play a major role in electron/proton transfer of many biological processes [16,17]. Thus, the quinone/hydroquinone transition serves as an important electrochemical model for the development

of biomimetic systems. Its changing molecular structure allows for its electrochemical properties to be tuned [18].

Designing artificial composites that mimic living matter is of utmost importance to modern science. Many attempts have been made to imitate the structure and properties of biological membranes by use of artificial polyelectrolyte–lipid composites [19,20]. A lipid bilayer (LB) supported by a polyelectrolyte cushion provides a platform for the investigation of many cellular processes [21,22].

Typically, polyelectrolyte multilayers (PEM) are assembled by various adaptations of the classical layer-by-layer (LbL) technique. The basis of the LbL technique is the cyclical alternating deposition of oppositely charged components. Many variations of this method exist [23]. Two of the most developed techniques for LB formation are the Langmuir–Blodgett/Langmuir–Schaefer method [24] and deposition from the dispersion of vesicles in water [25,26]. The latter, technically simple and versatile, involves the adsorption of the dispersed vesicles to an oppositely charged surface, rupture of said vesicles and spreading to form a continuous bilayer [27,28].

It is well known that the phospholipid membrane is attached to the underlaying polyelectrolyte cushion by a combination of electrostatic forces and hydrophobic interactions [24]. Polyelectrolyte multilayer assemblies are held together by electrostatic forces as well [29]. Therefore, biomimetic lipid–polyelectrolyte composites are strongly affected by the pH of the surrounding medium. Repelling of the components can be achieved when the isoelectric point of some component is reached and the interaction switches from attraction to repulsion. It has been shown that by making the environmental pH acidic, the distance between the LB and the underlaying support can be varied [30]. Structural characterization by neutron reflectometry revealed that, due to the pH-sensitivity of lipids, the distance between the polymeric cushion and the LB can be reversibly adjusted by as much as 300 nm [31] by simply varying the pH of aqueous environment. Molecular dynamic simulations later confirmed this. Such manipulation of the intermolecular interactions between the lipid membrane and its underlaying support and the subsequent distance between them may be useful in obtaining free-standing lipid membranes for the study of transmembrane proteins. This allows for the denaturation of these proteins to be avoided while simultaneously affording the use of specific analytical techniques not available for black lipid membranes [32]. Since mechanic properties of lipid membrane are highly dependent on fabrication approach, free-standing lipid membranes detached from underlaying polymer support could be useful model for the understanding of cell mechanics [33,34]. Electrotriggered lipid lift-off may also be considered as an alternative to phospholipid bilayer arrays patterning [24] and study of the lipid membrane's flexoelectricity [35].

Here we report the electrochemically triggered reversible LB lift-off from the underlying conducting substrates covered by polyelectrolytes via hydroquinone oxidation coupled with proton release (figure 1). We have conducted electrochemical studies on a phosphatidylcholine bilayer supported by a polyelectrolyte multilayer of polyethylenimine (PEI) and poly(sodium 4- styrenesulfonate) (PSS) on top of gold, obtained by the vesicle rupture and LbL techniques respectively. The anodic activity and proton concentration in close proximity to the gold electrode during the oxidation of hydroquinone to quinone was studied by use of the scanning vibrating electrode technique (SVET) and scanning ion-selective electrode technique (SIET). It has been demonstrated that the polyelectrolyte layers show a decrease in conductivity after LB assembly [36]. Electrochemical impedance spectroscopy (EIS) has become a widely used technique in the study of lipid layer formation and characterization [37]. Electrochemical spectra have revealed that a dense LB atop a polyelectrolyte multilayer can attain extremely high resistance and capacitance values [38].

Here we suggest EIS to be a powerful instrument for the routine analysis of the LB. It serves as a viable alternative to neutron reflectivity—a technique that is not always readily available and limited to flat, smooth specimens. Electrochemical spectroscopy revealed that in the acidic conditions generated by the quinone/hydroquinone redox reaction, the LB impact in impedance of gold/PEM/LB composites disappears. Its lift-off can be attributed to its electrostatic repulsion from its underlaying support [31]. The process described above is observed to be reversible. After a short relaxation time, the proton concentration decreases, returning to near the starting concentration due to diffusion, causing the LB to go back, followed by impedance growth.

2. Experiment

2.1. Chemicals
Branched PEI (Mw 70 kDa) 30% water solution purchased from Alfa Aesar; poly(sodium 4-styrenesulfonate) (PSS, Mw 500 kDa) purchased from Polysciences Inc.; liquid soya lecithin Lecisoy 400 containing mostly phosphatidylcholines obtained from Cargill, USA; reagent grade NaCl (99.5%) obtained from Merck and hexane from Ekos-1, Russia. All chemicals were used as received without any purification. Gold wire, 0.2 mm in diameter, was purchased from Agar (UK). Pieces of gold wire of 2–3 cm length were embedded in epoxy resin so that circular cross-section of gold wire exposed to outside media on the flat surface of the obtained holder. Prior to the assembly process, the gold substrates were rinsed with acetone then ethanol and, subsequently, in an excess of distilled water.

2.2. Polyelectrolyte multilayered film formation
The deposition of the polyelectrolyte cushion onto the gold embedded in the epoxy resin was performed using the classical LbL technique 2 mg ml^{-1} each PEI and PSS were dissolved in 0.5 M aqueous NaCl to make polycation and polyanion solutions, respectively. Each layer took 20 min to be deposited after which it was rinsed with excess distilled water and then steam-dried. A total of seven layers were deposited, resulting in a [PEI/PSS]$_3$/PEI polyelectrolyte multilayer.

2.3. Lipid vesicles preparation and characterization
For the preparation of the lipid small unilamellar vesicles (SUV) solution following procedure was performed. A soy lecithin solution in hexane (10 mg ml^{-1}) was kept under vacuum for solvent evaporation for at least 3 h. After removing any hexane traces, a thin lipid film on the bottom of the vessel was obtained. The resulting lipid film was rehydrated using distilled water for a final 10 mg ml^{-1} concentration
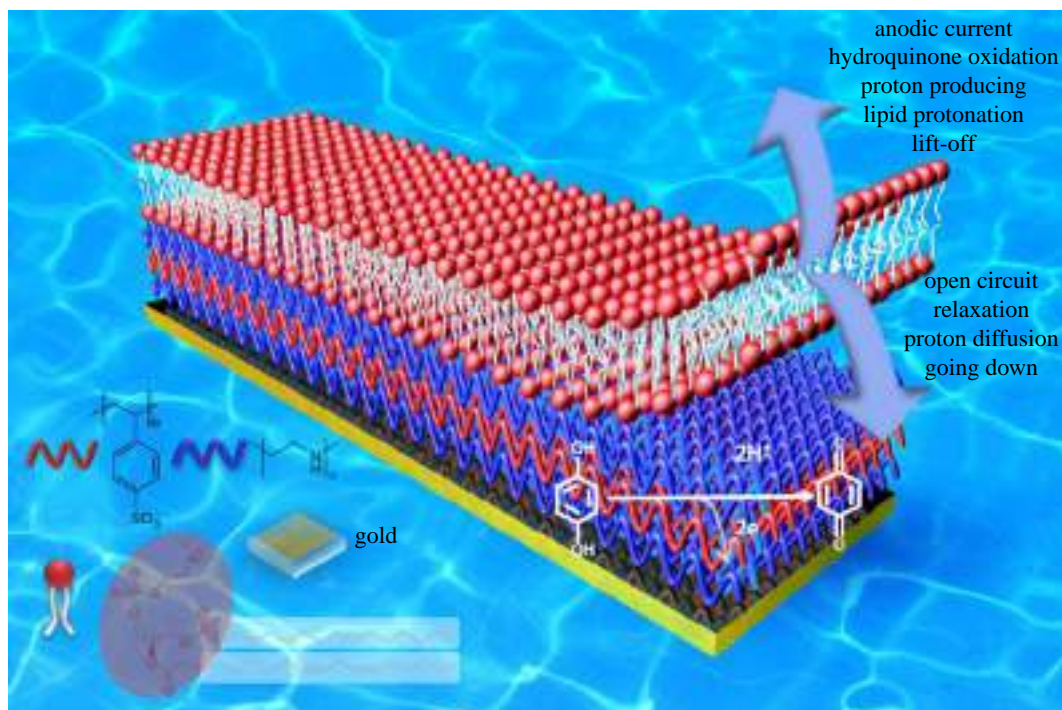
Figure 1. Local acidification of medium in close proximity to the electrode surface during the electrochemical oxidation of hydroquinone to quinone and the resulting lift-off of the LB from its underlying support due to electrostatic repulsion after lipid recharge due to protonation. (Online version in colour.)

with simultaneous sonication in an ultrasonic bath for 15 min. In order to determine the size and charge of the prepared vesicles, dynamic light scattering (DLS) and ζ-potential measurements were conducted with a Photocor Compact-Z analyser. Centrifugation at 14 000 r.p.m. for 20 min was performed to separate the different sized fractions in lipid vesicles suspension.

2.4. Lipid bilayer deposition

To obtain the model LB atop a polyelectrolyte cushion, modified substrates were immersed in 10 mg ml^{-1} dispersion of SUV for 1 h. Vesicles attached themselves to the oppositely charged PEM surface then ruptured, fused and spread on the surface, forming a continuous bilayer. The resulting structure was then rinsed with a large quantity of distilled water. LB formation as well as PEI/PSS multilayer formation were followed by QCM-D monitoring (Q-Sense AB).

2.5. Acidity adjusting

Two approaches to adjusting the pH were tested. By adding dilute solutions of NaOH and HCl, pH 3 and 7 were gained. The alternative method was the electrogeneration of protons via the oxidation of 60 mM hydroquinone solutions in 150 mM KNO$_3$ at a constant electric current of 5 μA. Owing to the proton-coupled electron transfer of the quinone/ hydroquinone redox system, pH gradient occurs in close proximity to the electrodes during oxidation and reduction processes (figure 2a).

2.6. SVET-SIET measurements

The anodic activity of gold immersed in a hydroquinone solution under an applied positive potential was studied by SVET and generated pH gradients by SIET which enables voltage measurement with nV precision level, electrochemical activity of material to be studied with micrometre spatial resolution and the measurement of extremely low ion concentration gradients [39]. To perform the SVET and SIET measurements, a system from Applicable Electronics (USA) modulated by an ASET program (Sciencewares, USA) was used. As a vibrating probe for SVET (figure 2b) experiments, an insulated Pt-Ir microprobe (Microprobe Inc., USA) with a platinum black spherical tip 30 μm in diameter was used (figure 2c). The probe was made to vibrate both parallel and perpendicular to the specimen surface at a height of 150 μm. The amplitude of vibration was 30 μm, while the probe vibrated at frequencies of 136 Hz (perpendicular to surface) and 225 Hz (parallel to surface). Only the perpendicular component was used in the treatment and presentation of the data (figure 2d). The environmental pH measurements by SIET (figure 2e) were carried out using glass capillary microelectrodes filled with Hydrogen Ionophore Cocktail I (Sigma) based liquid pH-selective membrane and KCl + KH$_2$PO$_4$ internal solution (figure 2f). Ag/AgCl/KCl (sat) was used as the external reference electrode. The pH-selective microelectrodes were calibrated using commercially available pH buffers and demonstrated a linear Nernstian response −55 to −58 mV pH^{-1}—in a pH range from 3 to 8. The local activity of H$^+$ was detected 25 μm above the surface. The local pH and ionic current density were mapped on a 11 × 11 grid in a 150 mM KNO$_3$ solution containing 60 mM hydroquinone.

2.7. Electrochemical impedance spectroscopy

Electrochemical measurements were performed using potentiostat Compactstat.e (Ivium, Netherlands). The polyelectrolyte multilayer and LB covered gold substrates were used as working electrodes, Pt wire as a counter electrode and an Ag/AgCl/ 3 M KCl reference electrode in a quartz electrochemical cell with a volume of approximately 50 ml filled by 150 mM KNO$_3$ containing 60 mM hydroquinone (figure 2g). The distance between the working and counter electrode was approximately 15 mm. Deposition of the PEM and lipid were
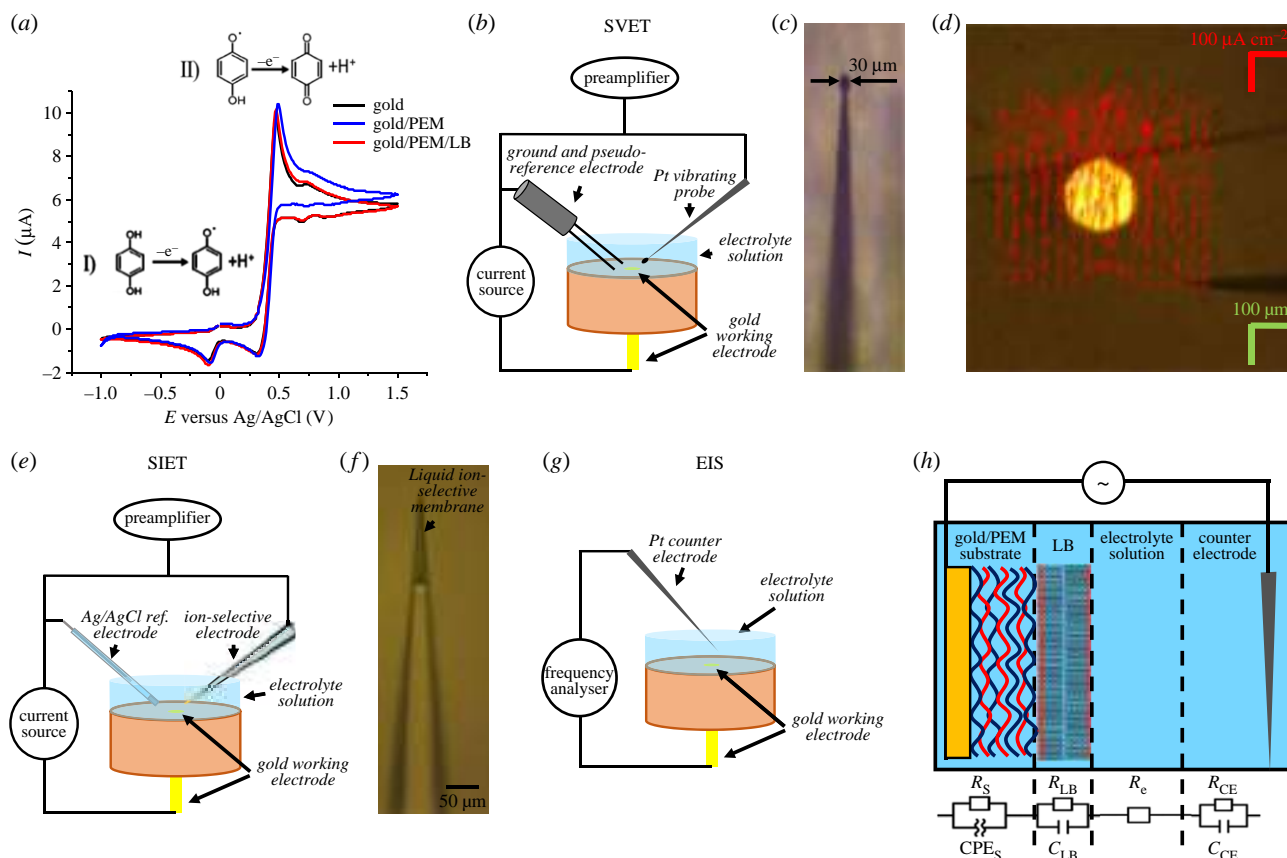
Figure 2. (*a*) Cyclic voltammetry curves of hydroquinone on a pure gold electrode and a gold electrode covered by a polyelectrolyte multilayer and polymer cushioned LB, (*b*) scheme of SVET measurement, (*c*) Pt-Ir vibrating probe, (*d*) top view of gold wire embedded in epoxy holder, red arrows are representative of ionic currents measured by SVET, the platinum vibrating electrode is seen at the right bottom of the image, (*e*) schematic of SIET measurement, (*f*) glass capillary microelectrode with liquid ion-selective membrane, (*g*) schematic of EIS measurement, (*h*) equivalent electrical scheme representing parts of electrochemical system with gold electrode covered by a polyelectrolyte multilayer and LB. (Online version in colour.)

performed as described above. Impedance spectra for frequencies between 0.1 and 1000 Hz with an AC modulation amplitude of 5 mV were recorded at a bias potential set equal to the open circuit potential of the working electrode. Data analysis was performed using standard Ivium software (figure 2*h*).

3. Results and discussion

Owing to the proton-coupled electron transfer of the quinone/hydroquinone redox system, a pH gradient occurs in close proximity to the electrodes during oxidation and reduction processes. A two-step hydroquinone oxidation takes place (figure 2*a*) where each step and each peak on cyclic voltammetry corresponds to one electronic process— the release of one proton. The oxidation of hydroquinone happens at an oxidative potential of about 0.5–0.6 V while the electrolysis of water requires a minimum of 1.5 V. According to the rules of stoichiometry, the same acidification can be achieved via both methods: water electrolysis and the oxidation of hydroquinone to 1,4-benzoquinone. The latter is preferable because of its lower oxidative potential. It was calculated that hydroquinone oxidation leads to a pH of 3.6 at the surface of electrode and gradually increases to neutral (pH ∼ 7) away from it [40]. It is important that CVA curves are not affected by further deposition of polyelectrolyte layers and LB formation (figure 2*a*). Since molecules of hydroquinone and quinone are rather small and uncharged

they are able to pass freely through the LB and polyelectrolytes, a feat impossible for large molecules and ions.

The anodic activity of the gold electrode and the pH gradients were visualized using scanning microelectrode techniques SVET and SIET (figure 3). The microelectrode measurements demonstrated that the oxidation of quinone to hydroquinone on a bare gold electrode (figure 3*a*) leads to the local acidification, pH decrease to approximately 4 from initial 7 (figure 3*b*) in accordance with theoretical modelling [41]. An ionic current of more than $500 \, \mu A \, cm^{-2}$ was observed over the surface of the electrode (figure 3*c*).

Further assembly of a biomimetic nanocomposite simulating a living cell membrane was done using the LbL technique (electronic supplementary material, figure S1). The electrode was first covered by branched PEI to provide strong anchoring to the surface and to act as a positively charged terminating layer. Deposition of PSS was then carried out, making a surface negative. Eventually, a gold/(PEI/PSS)₃PEI multilayered composition was obtained (figure 3*d*). The choice of terminating layer (positive PEI) is predetermined by the necessity of further LB formation from lipid vesicles suspension. It is of utmost importance that the lipid be oppositely charged to the capping layer of the polymer cushion for strong attachment of lipid vesicles, their rupture and complete coverage of the surface when forming a defect-free self-organized LB on top of polymer support. Lipid vesicles obtained from soy lecithin consisting mostly of phosphatidylcholine were observed to be negative (ζ-potential approx. −35 mV) at neutral pH.
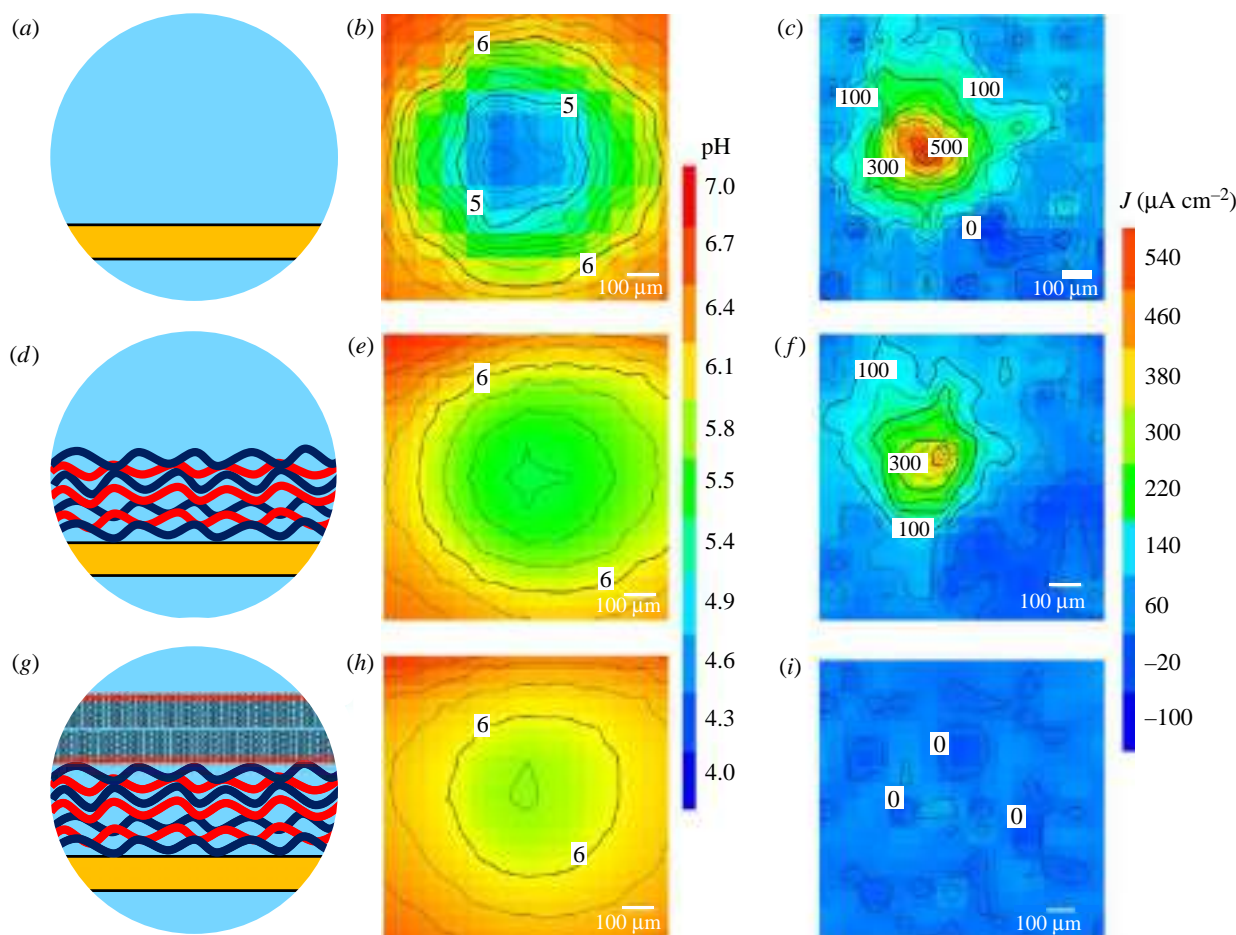
Figure 3. Schematic of electrode structure, pH map of adjusted to electrode media after passing 5 μA current through electrode immersed in a 60 mM hydroquinone solution in 150 mM KNO$_3$ measured by SIET, anodic activity of electrode immersed in a 60 mM hydroquinone solution in 150 mM KNO$_3$ during 5 μA current passing measured by SVET, respectively, for bare gold (a–c), gold/PEM (d–f), gold/PEM/LB (g–i). (Online version in colour.)

Owing to their short radius of curvature, small vesicles are more likely to rupture. Thus size distribution of lipid vesicles significantly affects their stability. As prepared vesicles have bimodal size distribution representing small unilamellar vesicles (SUV) with 100 ± 11 nm and large aggregates of vesicles 5.0 ± 0.5 μm and large fractions can be separated by centrifugation. Negative small vesicles are stable for weeks when stored at 4°C in a fridge.

Although polymer multilayer assembly leads to no change in redox processes at the electrode/hydroquinone solution interface, anodic activity measured by SVET is significantly lower for polyelectrolyte coated gold than for a bare one (figure 3f). During the oxidation of hydroquinone to 1,4-benzoquinone two electrons are transferred to the electrode and release of two protons occurs. Positive protons are repelled by and attracted to the uncompensated positive and negative charges of PEI and PSS, respectively. Since the polyelectrolyte multilayer consists of alternating PEI and PSS layers, the diffusion of charged ions is difficult. The ionic current 250 μm above the surface where it was measured is therefore lower than for a bare gold electrode. The polyethylenimine layer serving as a proton sponge [42] is responsible for the higher pH during hydroquinone oxidation on the gold/PEM electrode in comparison to pure gold (figure 3e).

To obtain polyelectrolyte/lipid composites, lipid vesicles which are negative in neutral media were deposited at pH

7 on the positive PEI capping layer of the polymer cushion obtained by LbL deposition on gold (figure 3g). The LB, which is impermeable to charged species, blocks the ion current from the gold surface (figure 3i), causing all protons released during hydroquinone oxidation to be concentrated beneath the LB and proton concentration above it to be rather low (figure 3h). Whereas strong polyelectrolyte molecules are not pH-sensitive, PSS is one which dissociates in an extremely wide pH range. With its isoelectric point being much lower than that of the lipid [43], PEI is always protonated in aqueous solution [42]. Zwitterionic lipid molecules are able to adsorb protons. Phospholipid molecules forming soy lecithin contain positively and negatively charged moieties, –PO$^-$ and N$^+$R$_3$, which can take part in equilibrium processes H$^+$ and OH$^-$.

$$- \text{PO}^- + \text{H}^+ = -\text{POH}$$

$$\text{N}^+\text{R}_3 + \text{OH}^- = \text{NR}_3\text{OH}.$$

Thus -PO$^-$, -POH, N$^+$R$_3$ and NR$_3$OH groups are in equilibrium and the concentration of each is determined by pH and acid–base constants:

$$K_a = \frac{a_{\text{H}} + a_{\text{PO}^-}}{a_{\text{POH}}} \quad \text{and} \quad K_b = \frac{a_{\text{N}^+\text{R}_3} a_{\text{OH}^-}}{a_{\text{NR}_3\text{OH}}}.$$

Because of the constant value, the amine group of phospholipids always remains in a positively charged state. The
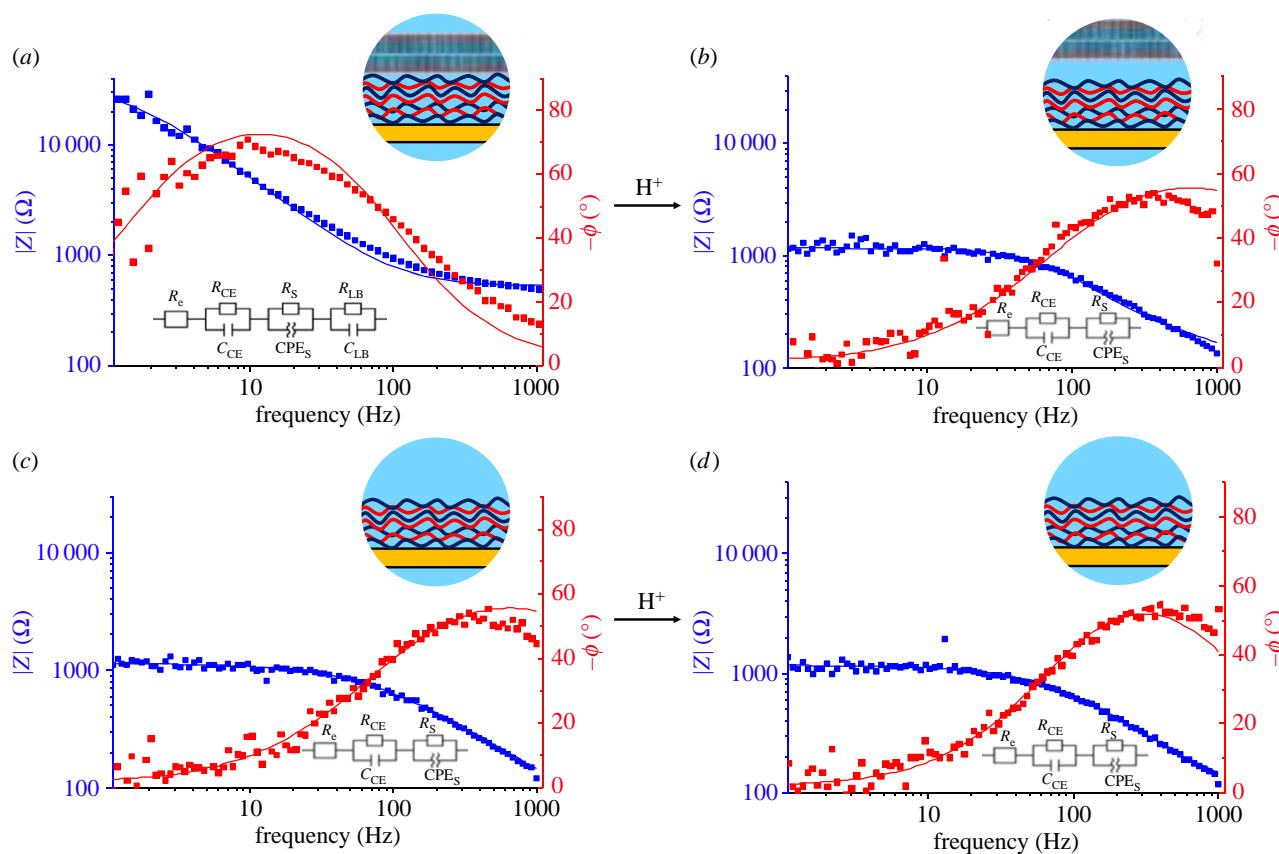
Figure 4. Bode plots for impedance spectra of (a) gold/[PEI/PSS]$_3$/LB in neutral conditions, (b) gold/[PEI/PSS]$_3$/LB in acidic conditions set by dilute HCl addition to solution, (c) gold/[PEI/PSS]$_3$ in neutral conditions, (d) gold/[PEI/PSS]$_3$ in acidic conditions set by addition of dilute HCl to the solution, top insets are schematics of processes occurring on the electrode, bottom insets are equivalent electrical schematics used to fit experimental data. (Online version in colour.)
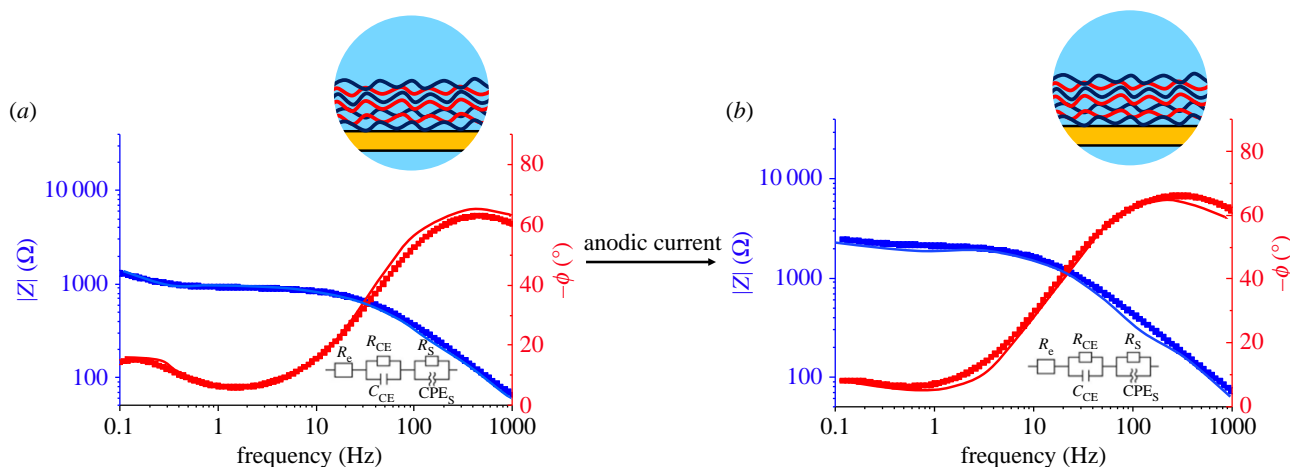
Figure 5. Bode plots for impedance spectra of gold/PEM in 60 mM hydroquinone solution (a) in neutral conditions before passing electrical current and (b) after 15 min of passing galvanostatic current of 5 µA followed by local acidification due to hydroquinone oxidation coupled with protons release. (Online version in colour.)

pKa of the phosphate group for phosphatidylcholine was reported to be approximately 3.5 [44]. Therefore, at pH 7 a_{PO^-} in 10^3–10^4 higher than a_{POH}, and at pH 3 the protonated state starts to prevail. Thus, at neutral conditions phosphate groups exist in the deprotonated state. As some components of soy lecityhin in this case carry only negative charge, which is not compensated by the positive amine group (e.g. phosphatidylinositol and phosphatidic acid) [45], there is negative net charge of lipid structures. In acidic media, due to protonated phosphate groups, positive net charge occurs.

The pH-dependence of lipid vesicles was demonstrated by ζ-potential measurements (electronic supplementary material, figure S2). Phospholipid vesicles adjusted by diluted HCl to pH 5, 3 and 2 demonstrate exponential growth of charge, becoming positive in pH lower than 4 and keeping constant size distribution. Thus, the protonation of lipids followed by their recharge from initially being strongly negative to only slightly negative and even positive at low pH occurs, whereas PSS is still negative and PEI, which is on top of the polymer cushion, is still positive. Such charge-shifting behaviour
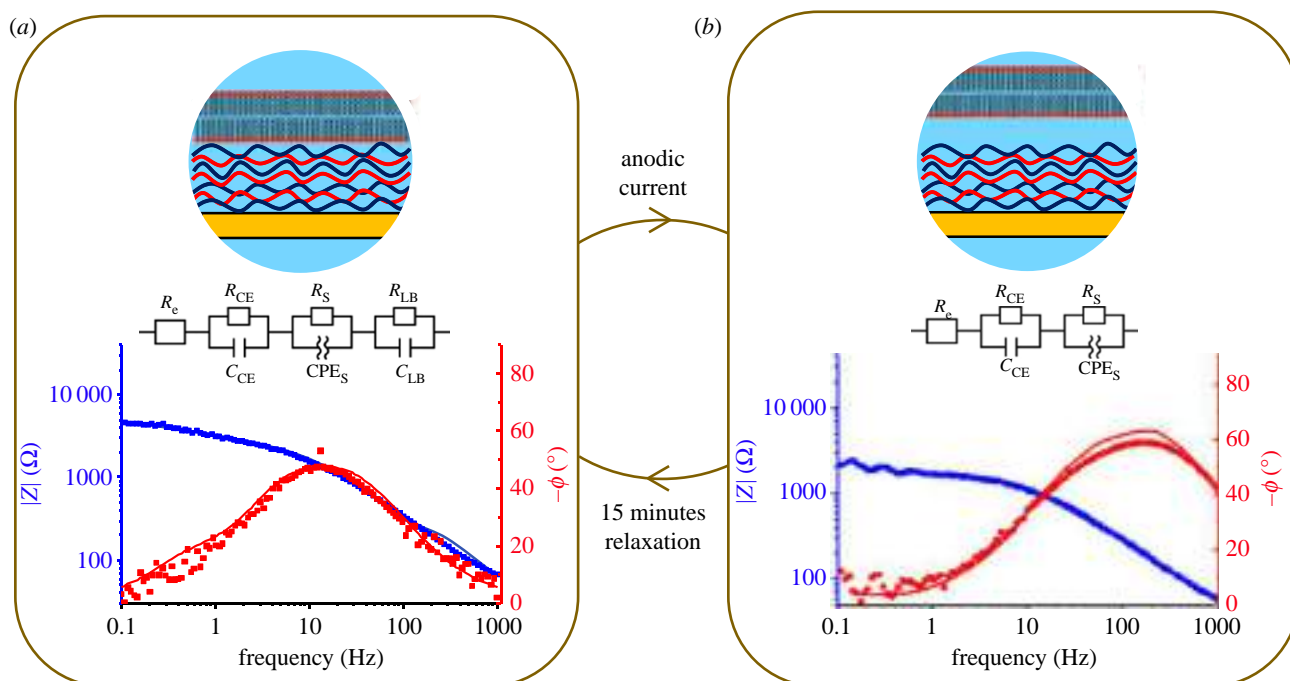
Figure 6. Plots of impedance spectra of gold/PEM in 60 mM hydroquinone solution (a) before passing electrical current, (b) after 15 min of passing galvanostatic current of 5 μA followed by local acidification due to hydroquinone oxidation coupled with protons release and relaxation to the initial state (a) after 15 min at open circuit potential. (Online version in colour.)

Table 1. Best-fitted parameters of impedance data of gold/PEM composite before and after passing 5 μA current.

	before	after
R_S (Ω)	15 ± 6	80 ± 17
R_{CE} (Ω)	640 ± 20	640 ± 45
C_{CE} (F)	$2.3 \pm 0.1 \times 10^{-3}$	$2.3 \pm 0.1 \times 10^{-3}$
R_{WE} (Ω)	910 ± 10	2200 ± 70
Q_{WE} (Siemens × second)	$9.8 \pm 0.5 \times 10^{-6}$	$9.7 \pm 0.5 \times 10^{-6}$
N	0.85	0.84

leads to differing strengths of electrostatic interactions between the LB and its underlaying support, causing LB lift-off from the polymeric cushion due to Coulombic repulsion in strong acidic pH [31]. Neutron reflectometry is suggested to be a powerful instrument in the investigation of the dynamic behaviour of polymer–lipid composites and the separation distance can be determined within nanometre precision [31]—but only for extremely flat and smooth species. EIS can serve as a more accessible and less expensive alternative for the qualitative evaluation of the process because continuous LBs are characterized by high resistivity. Experiments were performed on the gold/PEM and gold/PEM/LB working electrodes at pH 7 and pH 3, adjusted by dilute HCl (figure 4) and later at pH 7 before and after running a galvanostatic 5 μA current (figures 5 and 6).

Under an open circuit potential, no Faradaic processes are involved and the impedance of the electrochemical system may be described in terms of Ohmic resistance and capacitance. An equivalent electrical circuit describing gold/PEM/LB composition is given in figure 4a (bottom inset). R_E corresponds here to the Ohmic resistance of the electrolyte solution, R_S for the Ohmic resistance of the gold/PEM solid

support, CPE$_S$ (CPE$_S$ = 1/4 exp($\alpha j\pi/2$)/$Q\omega N$, where j is the unit imaginary number, ω is frequency, while Q and N are frequency independent parameters) is for the gold/PEM imperfect capacitance representing its significantly rough surface, R_{LB} and C_{LB} are related to the Ohmic resistance and capacitance LB, respectively. The contribution of the counter electrode is also considered (R_{CE} and C$_{CE}$) [36]. When the pH of the surrounding medium was adjusted to 3 by adding dilute HCl dropwise, the impedance characteristics of the gold/PEM/lipid composite change dramatically. The equivalent electrical circuit described above does not suitably describe the impedance of the system under these new conditions and changes that have occurred cannot be attributed to R_S. Another equivalent electrical circuit that does not take into account the contributions of the LB (R_{LB} and C_{LB}) was therefore employed. The plots of the impedance spectra of gold/PEM/LB composite in neutral and acidic conditions are both shown in figure 4a,b. These results demonstrate that in acidic conditions the LB drifts away from the gold/PEM support due to lipid protonation and recharge from negative to positive, resulting in the repulsion of the positive protonated LB from the positive underlaying PEI. To demonstrate the stability of the polyelectrolyte multilayer, impedance measurements for the gold/PEM composite were also taken. It was observed that neither the impedance spectrum nor equivalent cirquit and best-fitting parameters undergo any changes when the environmental acidity changes from pH 7 to pH 3. Gold/PEM impedance may be described by a combination of R_E, R_S and CPE$_S$ (figure 4c,d, bottom insets). Any minor differences in impedance between neutral and acidic conditions can be related to a decrease in the Ohmic resistance of the solution due to an increase in the concentration of the conducting protons. It is important to emphasize that the S-shaped phase curve and parabolic impedance curves for gold/PEM electrodes are similar to those obtained for gold/PEM/lipid electrodes in acidic conditions.
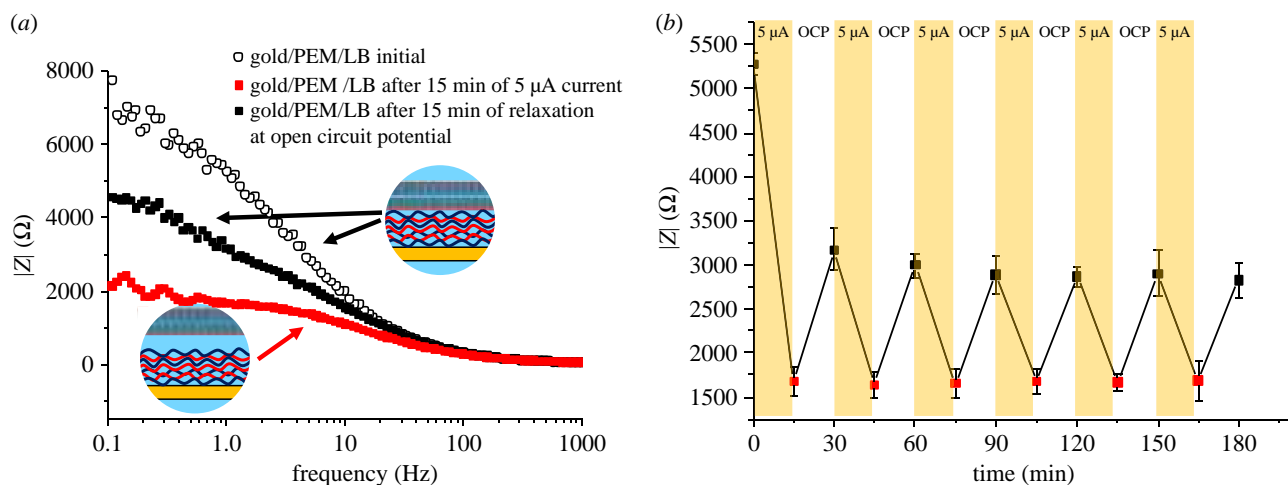
Figure 7. (a) Impedance curves of Bode plots of impedance spectra of gold/PEM/LB composite before passing 5 μA current, after 15 min of current passing and after 15 min of relaxation, (b) cycles of passing current and relaxation at open circuit potential associated with impedance oscillations at 1 Hz of gold/PEM/LB composite due to LB repulsion in acidified media via hydroquinone oxidation. (Online version in colour.)

Table 2. Best-fitted parameters of impedance data of gold/PEM/LB composite before and after passing 5 μA current.

	before current	after current	after relaxation
R_S (Ω)	50 ± 10	60 ± 30	38 ± 9
R_{CE} (Ω)	70 ± 30	60 ± 10	110 ± 50
C_{CE} (F)	$9 \pm 3 \times 10^{-5}$	$7 \pm 2 \times 10^{-4}$	$3.7 \pm 1 \times 10^{-3}$
R_{WE} (Ω)	260 ± 60	700 ± 120	1000 ± 100
Q_{WE} (Siemens × second)	$1.5 \pm 0.4 \times 10^{-3}$	$4 \pm 2 \times 10^{-5}$	$9 \pm 1 \times 10^{-5}$
N	0.90	0.74	0.87
R_{LB} (Ω)	470 ± 40		160 ± 20
C_{LB} (F)	$1.1 \pm 0.1 \times 10^{-4}$		1.56×10^{-1}

Passing a 5 μA electrical current through the solution and the resulting acidification of the surrounding medium does not influence the impedance characteristics of the gold/PEM electrode much (figure 5). Experimental impedance of gold substrates coated by the PEI/PSS polymer cushion before passing the current (figure 5a) and immediately after in open circuit conditions (figure 5b) are almost identical as well as fitting parameters according to equivalent circuit described above for gold/PEM composite (figure 5a,b, bottom insets, table 1). As for hydroquinone oxidation and release of protons, measuring the impedance of the gold/PEM/LB before and after passing an electrical current show significant differences (figure 6a,b). Local acidification using electrochemical proton-coupled electron transfer have the same effect on pH-sensitive species as the acidification of bulk solution (figure 4a,b). Local acidification leads to the 'disappearance' of the contribution of the LB on the total impedance, presented by R_{LB} and C_{LB} elements of the equivalent cirquit (figure 6a). After current passing and 15 min relaxation followed by the diffusion of excess protons from adjoined to electrode media and pH retrieval to bulk value lipid molecules come back to the initial not protonated state and are attracted back to the oppositely charged underlying support (figure 6a). The best-fitting parameters are presented in table 2. Reversibility is a distinguishing feature of LB lift-off triggered by electrochemical protonation. Apart from the solution exchange method of pH adjustment, hydroquinone

oxidation is not associated with any significant fluxes able to remove protonated lipid molecules loosely bonded to a positive polymer cushion. Figure 7 demonstrates the oscillatory behaviour of impedance during direct current on–off cycles. As is evident, the LB on the top of the gold/PEM substrate demonstrates resistive behaviour (greater than 5000 Ω at 1 Hz oscillation of open circuit potential with amplitude of 5 mV). Immediately after 15 min of passing current, the impedance was observed to be approximately 2000 Ω under open circuit potential with the same conditions. After 15 min of relaxation, the impedance increases to 3000–3500 Ω but never returns to its starting value (figure 7a). During further cycles of passing current and relaxation, the oscillating behaviour of impedance was observed. Owing to proton release from hydroquinone oxidation during passing current followed by reversible lipid protonation and its recharge, oscillation of electrostatic forces between the LB and its underlaying support occurs. Sustainability of the LB and reversibility of the process was demonstrated for at least six cycles during a period of 3 h (figure 7b).

4. Conclusion

Phospholipids are known to be charge-shifting molecules highly sensitive to pH. Thus, it is possible to control the electrostatic interaction of lipids with a charged underlaying

support. A phosphatidylcholine bilayer, which is negative in neutral media, was deposited on a positive PEI capping layer of a polyelectrolyte cushion on a gold electrode. Lipids, which themselves are negatively charged in neutral media, strongly attached to underlaying support, become positive due to protonation of the phosphate group compensating the negative charge of the zwitterion, lowering electrostatic attraction. As a result, the separation distance between the LB and its underlaying support increases. Impedance spectroscopy measurements have demonstrated their effectiveness for supported LB characterization. When the lipid layer is deposited on a thin polymer cushion, the resulting composite demonstrates much more resistive behaviour. It was shown that the LB impact in impedance disappears with an increase in proton concentration.

Presented here is a new electrochemical approach for a free-standing lipid membrane fabrication. Owing to the proton-coupled oxidation of hydroquinone, the pH of the surrounding medium decreased to 3–4 from an initial 7. Reversible LB lift-off was observed during electrotriggered acidification of the surrounding medium and relaxation

cycles whereas the polymer cushion was proven not to undergo any changes during hydroquinone oxidation and local acidification.

References

1. Sukhishvili SA. 2005 Responsive polymer films and capsules via layer-by-layer assembly. *Curr. Opin. Colloid Interface Sci.* **10**, 37–44. (doi:10.1016/j.cocis.2005.05.001)

2. Blackburn OA, Tropiano M, Natrajan LS, Kenwright AM, Faulkner S. 2016 Luminescence of a binuclear europium complex bearing a 4-nitrophenolate chromophore: a different way of seeing pH dependence. *Chem. Commun.* **52**, 6111–6114. (doi:10.1039/C6CC02078J)

3. Idili A, Vallée-Bélisle A, Ricci F. 2014 Programmable pH-triggered DNA nanoswitches. *J. Am. Chem. Soc.* **136**, 5836–5839. (doi:10.1021/ja500619w)

4. Ulasevich SA, Brezesinski G, Möhwald H, Fratzl P, Schacher FH, Poznyak SK, Andreeva DV, Skorb EV. 2016 Light-induced water splitting causes high-amplitude oscillation of pH-sensitive layer-by-layer assemblies on TiO$_2$. *Angew. Chem. Int. Ed.* **55**, 13 001–13 004. (doi:10.1002/anie.201604359)

5. Andreeva DV, Melnyk I, Baidukova O, Skorb EV. 2016 Local pH gradient initiated with light on TiO$_2$ for light-triggered polyhistidine-tagged proteins modulation. *ChemElectroChem.* **3**, 1306–1310. (doi:10.1002/celc.201600268)

6. Lu Y, Wu Y, Liang J, Libera MR, Sukhishvili SA. 2015 Self-defensive antibacterial layer-by-layer hydrogel coatings with pH-triggered hydrophobicity. *Biomaterials* **45**, 64–71. (doi:10.1016/j.biomaterials.2014.12.048)

7. Li X, Cai X, Gao Y, Serpe MJ. 2017 Reversible bidirectional bending of hydrogel-based bilayer actuators. *J. Mater. Chem. B.* **5**, 2804–2812. (doi:10.1039/C7TB00426E)

8. Dochter A, Garnier T, Pardieu E, Chau NTT, Maerten C, Senger B, Schaaf P, Jierry L, Boulmedais F. 2015 Film self-assembly of oppositely charged macromolecules triggered by electrochemistry

through a morphogenic approach. *Langmuir* **31**, 10 208–10 214. (doi:10.1021/acs.langmuir.5b02749)

9. Garnier T, Dochter A, Chau NTT, Schaaf P, Jierry L, Boulmedais F. 2015 Surface confined self-assembly of polyampholytes generated from charge-shifting polymers. *Chem. Commun.* **51**, 14 092–14 095. (doi:10.1039/C5CC04477D)

10. Bae Y, Fukushima S, Harada A, Kataoka K. 2003 Design of environment-sensitive supramolecular assemblies for intracellular drug delivery: polymeric micelles that are responsive to intracellular pH change. *Angew. Chem. Int. Edit.* **115**, 4788–4791. (doi:10.1002/ange.200250653)

11. Shchukin DG, Shchukina E. 2014 Capsules with external navigation and triggered release. *Curr. Opin. Pharm.* **18**, 42–46. (doi:10.1016/j.coph.2014.09.002)

12. Sukhorukov GB, Antipov AA, Voigt A, Donath E, Möhwald H. 2001 pH-controlled macromolecule encapsulation in and release from polyelectrolyte multilayer nanocapsules. *Macromol. Rapid Commun.* **22**, 44–46. (doi:10.1002/1521-3927(20010101)22:1<44::AID-MARC44>3.0.CO;2-U)

13. Maltanava HM, Poznyak SK, Andreeva DV, Quevedo MC, Bastos AC, Tedim J, Ferreira MGS, Skorb EV. 2017 Light-induced proton pumping with a semiconductor: vision for photoproton lateral separation and robust manipulation. *ACS Appl. Mater. Interfaces* **9**, 24 282–24 289. (doi:10.1021/acsami.7b05209)

14. Rodon FJ et al. 2017 Localized supramolecular peptide self-assembly directed by enzyme-induced proton gradients. *Angew. Chem. Int. Edit.* **56**, 15 984–15 988. (doi:10.1002/anie.201709029)

15. Laviron E. 1984 Electrochemical reactions with protonations at equilibrium: part X. The kinetics of

the p-benzoquinone/hydroquinone couple on a platinum electrode. *J. Electroanal. Chem. Interfacial Electrochem.* **164**, 213–227. (doi:10.1016/S0022-0728(84)80207-7)

16. Peduto A et al. 2017 Optimization of benzoquinone and hydroquinone derivatives as potent inhibitors of human 5-lipoxygenase. *Eur. J. Med. Chem.* **127**, 715–726. (doi:10.1016/j.ejmech.2016.10.046)

17. Jeyanthi V, Anbu P, Vairamani M, Velusamy P. 2016 Isolation of hydroquinone (benzene-1, 4-diol) metabolite from halotolerant *Bacillus methylotrophicus* MHC10 and its inhibitory activity towards bacterial pathogens. *Bioprocess. Biosyst. Eng.* **39**, 429–439. (doi:10.1007/s00449-015-1526-0)

18. Nagaraja C, Venkatesha TV. 2018 The influence of electron donating tendency on electrochemical oxidative behavior of hydroquinone: experimental and theoretical investigations. *Electrochem. Acta* **260**, 221–234. (doi:10.1016/j.electacta.2017.12.035)

19. Buddingh BC, van Hest JC. 2017 Artificial cells: synthetic compartments with life-like functionality and adaptivity. *Acc. Chem. Res.* **50**, 769–777. (doi:10.1021/acs.accounts.6b00512)

20. Zhu TF, Szostak JW. 2009 Coupled growth and division of model protocell membranes. *J. Am. Chem. Soc.* **131**, 5705–5713. (doi:10.1021/ja900919c)

21. Dzieciol AJ, Mann S. 2012 Designs for life: protocell models in the laboratory. *Chem. Soc. Rev.* **41**, 79–85. (doi:10.1039/C1CS15211D)

22. Tanaka M, Sackmann E. 2005 Polymer-supported membranes as models of the cell surface. *Nature* **437**, 656–663. (doi:10.1038/nature04164)

23. Richardson JJ, Björnmalm M, Caruso F. 2015 Technology-driven layer-by-layer assembly of nanofilms. *Science* **348**, aaa2491. (doi:10.1126/science.aaa2491)

24. Castellana ET, Cremer PS. 2006 Solid supported lipid bilayers: from biophysical studies to sensor design. *Surf. Sci. Rep.* **61**, 429–444. (doi:10.1016/j.surfrep.2006.06.001)

25. Richter RP, Bérat R, Brisson AR. 2006 Formation of solid-supported lipid bilayers: an integrated view. *Langmuir* **22**, 3497–3505. (doi:10.1021/la052687c)

26. Shao J, Wen C, Xuan M, Zhang H, Frueh J, Wan M, Gao L, He Q. 2017 Polyelectrolyte multilayer-cushioned fluid lipid bilayers: a parachute model. *Phys. Chem. Chem. Phys.* **19**, 2008–2016. (doi:10.1039/C6CP06787E)

27. Diamanti E, Gregurec D, Romero G, Cuellar JL, Donath E, Moya SE. 2016 Lipid layers on polyelectrolyte multilayers: understanding lipid–polyelectrolyte interactions and applications on the surface engineering of nanomaterials. *J. Nanosci. Nanotechnol.* **16**, 5696–5700. (doi:10.1166/jnn.2016.11752)

28. Moya S, Donath E, Sukhorukov GB, Auch M, Bäumler H, Lichtenfeld H, Möhwald, H. 2000 Lipid coating on polyelectrolyte surface modified colloidal particles and polyelectrolyte capsules. *Macromolecules* **33**, 4538–4544. (doi:10.1021/ma9914974)

29. Andreeva DV, Kollath A, Brezhneva N, Sviridov DV, Cafferty BJ, Möhwald H, Skorb EV. 2017 Using a chitosan nanolayer as an efficient pH buffer to protect pH-sensitive supramolecular assemblies. *Phys. Chem. Chem. Phys.* **19**, 23 843–23 848. (doi:10.1039/C7CP02618H)

30. Hafez IM, Ansell S, Cullis PR. 2000 Tunable pH-sensitive liposomes composed of mixtures of cationic and anionic lipids. *Biophys. J.* **79**, 1438–1446. (doi:10.1016/S0006-3495(00)76395-8)

31. Singh S, Junghans A, Tian J, Dubey M, Gnanakaran S, Chlistunoff J, Majewski J. 2013 Polyelectrolyte multilayers as a platform for pH-responsive lipid bilayers. *Soft Matter.* **9**, 8938–8948. (doi:10.1039/c3sm51651b)

32. Orth RN, Kameoka J, Zipfel WR, Ilic B, Webb WW, Clark TG, Craighead HG. 2003 Creating biological membranes on the micron scale: forming patterned lipid bilayers using a polymer lift-off technique. *Biophys. J.* **85**, 3066–3073. (doi:10.1016/S0006-3495(03)74725-0)

33. Ding Y, Wang J, Xu GK, Wang GF. 2018 Are elastic moduli of biological cells depth dependent or not? Another explanation using a contact mechanics model with surface tension. *Soft Matter* **14**, 7534–7541. (doi:10.1039/C8SM01216D)

34. Ding Y, Xu GK, Wang GF. 2017 On the determination of elastic moduli of cells by AFM based indentation. *Sci. Rep.* **7**, 45575. (doi:10.1038/srep45575)

35. Bruhn DS, Lomholt MA, Khandelia H. 2016 Quantifying the relationship between curvature and electric potential in lipid bilayers. *J. Phys. Chem. B.* **120**, 4812–4817. (doi:10.1021/acs.jpcb.6b03439)

36. Diamanti E, Gregurec D, Rodríguez-Presa MJ, Gervasi CA, Azzaroni O, Moya SE. 2016 High resistivity lipid bilayers assembled on polyelectrolyte multilayer cushions: an impedance study. *Langmuir* **32**, 6263–6271. (doi:10.1021/acs.langmuir.6b01191)

37. Steinem C, Janshoff A, Ulrich WP, Sieber M, Galla HJ. 1996 Impedance analysis of supported lipid bilayer membranes: a scrutiny of different preparation techniques. *Biochim. Biophys. Acta.* **1279**, 169–180. (doi:10.1016/0005-2736(95)00274-X)

38. Purrucker O, Hillebrandt H, Adlkofer K, Tanaka M. 2001 Deposition of highly resistive lipid bilayer on silicon–silicon dioxide electrode and incorporation of gramicidin studied by AC impedance spectroscopy. *Electrochim. Acta* **47**, 791–798. (doi:10.1016/S0013-4686(01)00759-9)

39. Bastos A. 2017 Application of SVET/SIET techniques to study healing processes in coated metal substrates. In (eds L Klein, M Aparicio, A Jitianu) *Handbook of sol-gel science and technology*. Cham, Switzerland: Springer.

40. Johnson EK, Adams DJ, Cameron PJ. 2010 Directed self-assembly of dipeptides to form ultrathin hydrogel membranes. *J. Am. Chem. Soc.* **132**, 5130–5136. (doi:10.1021/ja909579p)

41. Fomina N, Johnson CA, Maruniak A, Bahrampour S, Lang C, Davis RW, Kavusi S, Ahmad H. 2016 An electrochemical platform for localized pH control on demand. *Lab. Chip.* **16**, 2236–2244. (doi:10.1039/C6LC00421K)

42. Richard I, Thibault M, De Crescenzo G, Buschmann MD, Lavertu M. 2013 Ionization behavior of chitosan and chitosan–DNA polyplexes indicate that chitosan has a similar capability to induce a proton-sponge effect as PEI. *Biomacromol.* **14**, 1732–1740. (doi:10.1021/bm4000713)

43. Schulze A, Maitz MF, Zimmermann R, Marquardt B, Fischer M, Werner C, Went M, Thomas I. 2013 Permanent surface modification by electron-beam-induced grafting of hydrophilic polymers to PVDF membranes. *RSC Adv.* **3**, 22 518–22 526 (doi:10.1039/c3ra43659d)

44. Gunstone FD, Harwood JL, Dijkstra AJ. 2007 *The lipid handbook with CD-ROM*, pp. 179–180. Boca Raton, FL: CRC press.

45. Scholfield CR. 1981 Composition of soybean lecithin. *J. Am. Oil. Chem. Soc.* **58**, 889–892. (doi:10.1007/BF02659652)

Sonochemical nanostructuring of titanium for regulation of human mesenchymal stem cells behavior for implant development

Evgeny Kuvyrkov[a], Nadzeya Brezhneva[b], Sviatlana A. Ulasevich[b], Ekaterina V. Skorb[b,*]

[a] Republican Scientific and Practical Center of Transfusiology and Medical Biotechnologies, Minsk 220053, Belarus
[b] ITMO University, St. Petersburg 192001, Russia

ABSTRACT

The influence of surface nanotopography of sonochemically generated mesoporous titania coatings (TMS) on the adhesion, proliferation, and osteogenic differentiation of human mesenchymal stem cells (hMSCs) have been investigated *in vitro* for the first time. It has been revealed that adhesion and proliferation of hMSCs is higher on disordered TMS surfaces compared to smooth polished titania surface after five days of incubation. Surprisingly, the sonochemically generated disordered nanotopography induces the differentiation of hMSCs into osteogenic direction in the absence of osteogenic medium in 14 days of incubation. Thus sonochemical nanostructuring of titanium based implants stimulates the regenerative process of bone tissue.

1. Introduction

Clinical investigations are conducted to prove the regenerative capacity of human mesenchymal stem cells (hMSCs) [1]. However, it is already obvious that the transplantation of adult stem cells cannot repair all damages of tissues and organs without supporting implants. The surface of these implants mimics the biological state of tissue in human body. The injection of cells in the injury place is not efficient as it does not provide the long presence of cells in the defect area and consequently the stimulating impact on the tissue regeneration [2,3]. Because of that implants with inserted cells need to be transplanted. Independently of the therapeutic way, the necessary condition for bone regeneration is the carrier having an adhesive surface and triggering the osteogenic signaling. Attached stem cells response with the differentiation into osteoblasts.

Nanoengineering of titanium implant surface is perspective to develop an artificial tissue niche. Titanium is a preferable material because of the most suitable biocompatibility for human tissues, as well as strength, and corrosive resistance in physiological environment compared to others [3]. It is necessary that implants surface has a good adhesion and triggers the osteogenic differentiation of attached cells into osteoblasts. It has been shown that biological response of cells depends on the unique features of surface, such as a topography, chemical composition, surface energy and charge, mimic the extracellular matrix of nature tissue [4]. Modern nanostructured coatings are foam which mimics nature tissues. This specie weakens a weight on nature

tissue thereby decreasing the risk of thrombosis and inflammatory reactions. It also minimizes the risk of implant destruction in the place where a bone and an implant are jointed extending the time of implant using. Moreover, it increases the speed of osteosynthesis and the quality of its integration with the tissues of recipient, as well as minimized the risk of rejection after implantation due to the better functional activity of hMSCs on these coatings.

Besides, the biologically active substances can be inserted in the pores of nanostructured coatings with the possibility of multi-component loading and the controlled release of content [5]. As shown these coatings provide the local controlled prolonged release of antibiotics and chemotherapeutic drugs in sufficiently high concentrations preventing the expanse of infectious and oncological diseases without general intoxication of organism [6,7]. These systems are able to reduce the duration of patient rehabilitation and to minimize postoperative complications in patients thereby providing the improvement of their health and increase in the efficiency of current treatment methods for the defects of bones.

In this paper we use sonochemistry for titanium surface nanostructuring. There is a lot of applications of ultrasound, for example, for oil recovery [8,9] and oil–water de-emulsification [10]. The system for oil recovery is consisted of several injection wells surrounding a production well and all processes take part in oil. Ultrasonic generator and transducer have been used operating at 20 kHz and 350 W of output power.

In our paper the ultrasonication generates high-speed liquid jets and

shockwaves formed on the collapse of cavitation bubbles near a surface. In these conditions the redox reactions take place leading to titania layer formation. Simultaneously, titanium dioxide dissolves partially in alkaline solution generating the pores distributed disorderly. The method offers a fast and versatile tool for the fabrication of nanostructured materials, both inorganic and organic [11], that are often unavailable by conventional methods [12]. The major advantage of this technique is that the propagation of cavitation generates large local temperature gradients in solids, resulting in materials with a porous layer and disordered nanostructures at room conditions. Moreover, an external ultrasound irradiation can be used to trigger the release of encapsulated biomolecules through pores in nanostructured coating [13].

We focus on the implant coating which can stimulate the differentiation of hMSCs into osteogenic direction without chemical inductors. These coatings will be able to accelerate an osteosynthesis on a metal surface. Stimulating the osteogenic differentiation of stem cells by these osteoinductive materials can be the alternative method of regenerative process induction of bone tissue. It was described medical materials in the literature [14,15], but there is no data about implants that possess the bone substitution or stimulate the osteogenic differentiation of stem cells in the absence of osteogenic inductors. In addition, the sonochemically generated mesoporous coatings on the basis of titanium dioxide can provide an ingrowth of bone-tissue extracellular matrix into a metal surface to improve an osteointegration between a bone and a metal. Also, the ultrasonically generated TMS are attractive for the surface delivery of biomolecules to maintain cellular function and viability.

Here, for the first time, we discuss the influence of sonochemically generated mesoporous coatings on the basis of titanium dioxide on the adhesion, proliferation, and osteogenic potential of hMSCs.

2. Experimental section

2.1. Preparation of TMS surface

Titanium samples were ultrasonically treated in 100 mL of 5 M NaOH (Sigma-Aldrich) solution using the ultrasonic processor UIP1000hd (Hielscher Ultrasonics, Germany) operated at 20 kHz with the maximum output power of 1000 W. The apparatus was equipped with the sonotrode BS2d18 (head area 2.5 cm^2) and the booster B2-2.2, magnifying the working amplitude 2.2 times.

Titanium samples of 1×1 cm^2 size were fixed into homemade Teflon holder and were treated at 60%-intensity for 15 min. The distance between the sonotrode and treated sample was 1.5 cm. The maximum intensity was calculated to be 250 W/cm^2 at the mechanical amplitude of 187 µm (at 100%). Sonication was performed in the sonication cell at constant temperature of around 333 K monitored by the temperature sensor inserted in the electrolyte. The sonication parameters were chosen according to preliminary results shown best modification of titania surface and described in our previous research [16,17]. Sonication was performed at 333 K to increase the effectiveness of sonication. The intensity per surface area of sonotrode of ultrasound unit depends on temperature.

Prior to sonication, the titanium samples were chemically polished in a mixture of concentrated HF (50 wt%) and HNO$_3$ (65 wt%) taken at a volume ratio of 2:1 for 3–5 s and rinsed with deionized water Milli-Q water (18 MΩ·cm) was used for preparing all aqueous solutions. As-prepared samples were annealed at 450 °C for 3 h. Prior to cellular experiments all samples were washed 3 times for 15 min in 75% ethanol and Milli-Q water and dried, then they were sterilized by heat at 170–180 °C for 2 h.

2.2. Surface characterization

The structural and morphological characterization of prepared TMS

samples was performed using the field-emission scanning electron microscope Zeiss Leo 1550 Gemini (Zeiss, Germany) at the operating voltage of 3 kV. The TMS plates were mounted onto the holder with a double-sided conductive tape and coated with carbon layer of 3 nm thick using a vacuum evaporator. High-resolution transmission electron microscopy (HRTEM) was performed by TEM in a Philips CM30 operated at 300 kV.

Atomic force microscopy measurements were carried out in air at room temperature in tapping mode with micro cantilevers OMCL-AC160TS-W (Olympus, Japan). Resonance frequency was 247 kHz; spring constant was 42 N/m. Atomic force micrographs of a scan size 5×5 µm^2 were made on three different places on the sample. Image analysis was carried out with the software Nanoscope V614r1. The surface roughness was quantified by the software as an arithmetic average ofthe absolute values of the surface height deviations measured from the mean plane.

X-ray diffraction (XRD) measurements were carried out with an Advanced D8 Bruker diffractometer (Bruker, Germany), using a focused and monochromatized CuKα source.

2.3. Contact angle measurements

The hydrophilicity/hydrophobicity of obtained samples was determined by the contact angle of wettability on an air–water-substrate interface using the optical tensiometer G23 M (Krüss, Germany) equipped with a digital camera and image analysis software. The measurements were performed using 1 µL of Milli-Q water droplet placed on the sample surface from the syringe at room temperature. The procedure was repeated three times on at least three samples of each surface type and average contact angle value was calculated.

2.4. MTT-test

MTT is a tetrazolium dye (3-(4,5-dimethylthiazol-2-yl)-2,5-diphenyltetrazolium bromide) used in a colorimetric assay for the detection of cell viability. Pre-warmed Dulbecco's modified essential medium without phenol red (Sigma, USA) was brought to hMSCs attached to TMS surfaces. Human fat tissue-derived MSCs are provided by Stem Cells Bank in the Republican Scientific and Practical Center of Transfusiology and Medical Biotechnologies (Minsk, Republic of Belarus). The human fat tissue-derived MSCs from 1 hematologic healthy donor were explored. This cellular line was expanded up to passage 3–4. The aqueous solution of MTT (Sigma Aldrich) with 5 mg/mL concentration was added at a volume ratio of 1:10. HMSCs were incubated in a carbon dioxide incubator NU-4850 Autoflow Ir Water-Jacketed CO$_2$ Incubator (Nuaire, UAS) with 5% carbon dioxide and 95% relative air humidity at 37 °C for 3 h. Dimethylsulfoxide (Sigma, USA) was added after removing the liquid. Blue formazan crystals formed by cell mitochondrial dehydrogenase that reduced MTT were extracted for 20 min at 37 °C in dark. The dimethylsulfoxide solution of formazan was thoroughly pipetted, then it was transferred in tube. After pipetting the aliquots of the solution were brought in 96-well plate (Sarstedt, Germany). Dimethylsulfoxide solution was used as a control. The extinction of extracted formazan was defined by the optical method at λ = 570 nm using the absorption light detection reader ELX800 (Biotek Instruments, USA) with the software GEN 5 V.1.10. The extinction of formazan E_{570} was calculated as a difference between the extinction of formazan dissolved in dimethylsulfoxide and the extinction of dimethylsulfoxide. Measurements were performed in duplicate for 4 independent repeats.

2.5. Living fluorescence staining of cells and confocal laser scanning microscopy

After removal of the complete growth media the cells were rinsed twice with pre-warmed Dulbecco's phosphate buffered saline (Sigma,

USA) for 1 min. The solution of fluorescence vital dye for the membranes of cells CellTracker Green (Thermofisher Scientific, USA) diluted with the pre-warmed Dulbecco's modified essential medium without phenol red (Sigma, USA) at a volume ratio of 1:1000 was brought. The cells were incubated in a carbon dioxide incubator NU-4850 Autoflow Ir Water-Jacketed CO_2 Incubator (Nuaire, USA) with 5% carbon dioxide and 95% relative air humidity at 37 °C for 30 min in dark. Then the cells were rinsed tree times with pre-warmed Dulbecco's phosphate buffered saline (Sigma, USA) for 10 min. The exciting-emission light detection microscope LEICA TCS SPE (Leica, Germany) with the image software LAS AF was used to perform confocal laser scanning microscopy.

2.6. Culturing of hMSCs

The hMSCs were seeded on the TMS surfaces at a specific cellular density of 12000 cells/cm². The samples were located in a 24-well plate under pre-warmed complete growth medium consisting of 10% human AB group serum (Republican Scientific and Practical Center of Transfusiology and Medical Biotechnologies, Republic of Belarus), 0.1% gentamicin (Sigma, USA) and alpha-modified essential medium with 2 mM L-glutamine and nucleosides (Sigma, USA). The hMSCs were incubated in a carbon dioxide incubator NU-4850 Autoflow Ir Water-Jacketed CO_2 Incubator (Nuaire, USA) with 5% carbon dioxide and 95% relative air humidity at 37 °C for 24 h.

For proliferation, after the attachment of hMSCs to the TMS surfaces in 24 h the culture medium had been removed as described above. The hMSCs were rinsed twice with pre-warmed Dulbecco's phosphate buffered saline (Sigma, USA) for 1 min. The pre-warmed complete growth medium consisting of 10% human AB group serum (Republican Scientific and Practical Center of Transfusiology and Medical Biotechnologies, Republic of Belarus), 0.1% gentamicin (Sigma, USA) and alpha-modified essential medium with 2 mM L-glutamine and nucleosides (Sigma, USA) was brought and the hMSCs were incubated for 5 days.

For osteogenic differentiation, the hMSCs were seeded on the TMS surfaces at a cell density of 10,000 cells/cm². The materials were located in 24-well plate under the culture medium in absence of osteogenic inductors. The culture medium was Dulbecco's modified essential medium consisting of 4.5 g/L of glucose, 2 mM L-glutamine (Sigma, USA) with 2% human AB group serum (Republican Scientific and Practical Center of Transfusiology and Medical Biotechnologies, Republic of Belarus) and 0.1% gentamicin (Sigma, USA). The incubation time for osteogenic differentiation of hMSCs was 14 days. The culture medium was replaced in 2–3 days after 2 times rinsing the hMSCs with pre-warmed Dulbecco's phosphate buffered saline (Sigma, USA) for 1 min.

2.7. Quantitative real-time polymerase chain reaction

Total RNA was isolated by the use of TRI-reagent extraction with the following DNase treatment according to the manufacturer's instructions of Sigma Corporation, USA. cDNA was synthesized using Revertaid Reverse Transcriptase (Thermofisher Scientific, USA) by thermocycler Applied Biosystems Gene Amp Pcr Systems 2700 (Applied Biosystems, USA) in compliance with the program: 25 °C for 10 min, 50 °C for 30 min, 85 °C for 5 min. Quantitative reverse transcriptase polymerase chain reaction was carried out by the means of the thermocycler Cfx96 Touch™ Real-Time PCR Detection System (BIO-RAD, USA) in accordance with the program: 50 °C for 2 min, 95 °C for 10 min, 40 cycles consisting of 95 °C for 15 s, 60 °C for 30 s, 75 °C for 10 s. The alkaline phosphatase (ALP) and osteocalcin (OSC) transcript expression were normalized versus glyceraldehyde-3-phosphate dehydrogenase (GAPDH). The expression level of tissue-specific genes was calculated with the $2^{-\Delta\Delta CT}$-method [16]. The gene-specific primers information was following: ALP forward primer sequence 5′-ACAACTACCAGGCGC AGTCT-3′, ALP reverse primer sequence 5′-CAGAACAGGACGCTC

AGG-3′, amplicon size 260 bp; OSC forward primer sequence 5′-GCCC TCACACTCCTCGCC-3′, OSC reverse primer sequence 5′-CTACCTCGCT GCCCTCCTG-3′, amplicon size 130 bp; GAPDH forward primer sequence 5′-TCAAGGCTGAGAACGGGAA-3′, GAPDH reverse primer sequence 5′-TGGGTGGCAGTGATGGCA-3′, amplicon size 376 bp.

2.8. Statistics

Cell culture experiments were reproduced at least three times using three samples of each group. Obtained data were averaged with the standard error of the mean. Statistical analysis was performed using ANOVA (*p < 0.05).

3. Results and discussion

We have developed a novel method of sonochemical surface nanostructuring to treat the implant surface and improve its characteristics. The advantage of this method is a possibility to vary the topography, chemical composition, hydrophilicity, roughness of the nanostructured surfaces easily by changing the sonochemical treatment parameters related to a high intensity ultrasound and electrolyte (solvent, additives) used for treatment. The high intensity ultrasound treatment processing is characterized by various ultrasound parameters (amplitude, intensity, frequency), and the duration of treatment [17]. An ultrasound provides energy localization with possible acoustic cavitation phenomena, i.e., the formation, the growth, and the implosive collapse of cavitation bubbles in a liquid (Fig. 1). This collapse is able to produce intense local heating, hot spots with temperatures of roughly 5000 K and high pressures of about 0.1 HPa [18,19]. Besides generating the reactive oxygen species (ROS) that oxidized the titanium surface, ultrasonically generated oxidation–reduction reactions provide effective surface etching that result in obtaining the titanium dioxide layer of 1 μm thick according to Eqs. (1)–(5) [20,21].

$$Ti^0 + OH^- - 4e^- \rightarrow Ti(OH)^{3+} \tag{1}$$

$$2Ti(OH)^{3+} + 6H_2O + 6e^- \rightarrow 2TiO_2 \cdot 2H_2O + 3H_2 \tag{2}$$

$$Ti(OH)^{3+} + 2H_2O + OH^- + 2e^- \leftrightarrow TiO_2 \cdot 2H_2O + H_2 \tag{3}$$

$$Ti(OH)^{3+} + 3OH^- \leftrightarrow Ti(OH)_4 \tag{4}$$

$$Ti(OH)_4 \xrightarrow{condensation} TiO_2 \cdot xH_2O + (2-x)H_2O \tag{5}$$
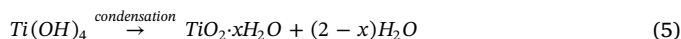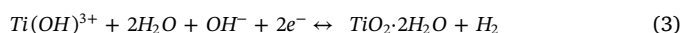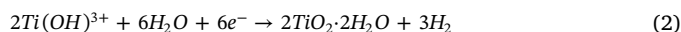
By bubble collapse close to the surface, solvent microwaves are formed perpendicular to the solid surface. These microwaves collide against the solid surface with the estimated speed of 100 m/s and lead to its nanostructuring (Fig. 1b).

The porous TiO_2 layer formed on bulk titanium has an excellent double-side adhesion [17]. The porous nanostructure of TMS surface can provide the incorporation of bio-macromolecules into surface [21,22], such as tissue-specific proteins, growth factors, polymeric micelles, etc, while still allowing for cellular survival and bone integration [23–25]. The important technological step in the preparation of samples is heating after sonochemical treatment to remove any organic contamination and to crystallize a surface of titanium dioxide layer. Titanium polished and annealed at 450 °C was used as a reference sample. Fig. 2a shows the XRD pattern of polished TiO_2 before and after thermal treatment up to 450 °C. All peaks at 2θ values of 35.1°, 38.5°, 40.3°, and 53.13° are associated with titanium support [26]. Energy-dispersive analysis reveals the presence of oxygen in the resulting film and atomic ratio between Ti and O ratio is 1:1. Higher intensity of peak at 2Θ: 38.5° compared to the peak at 2Θ of 40.3° can be attitude to a phase transition of titanium to high-temperature β-phase [26]. The XRD pattern of TMS reveals one intense peak corresponding to deposited titanium phase and a wide peak in the range of 2θ values from 20° to 30° (Fig. 2b). This broadened peak may be explained by several factors: (i) indicate small size of TiO_2 crystallites, (ii) amorphousness of titania
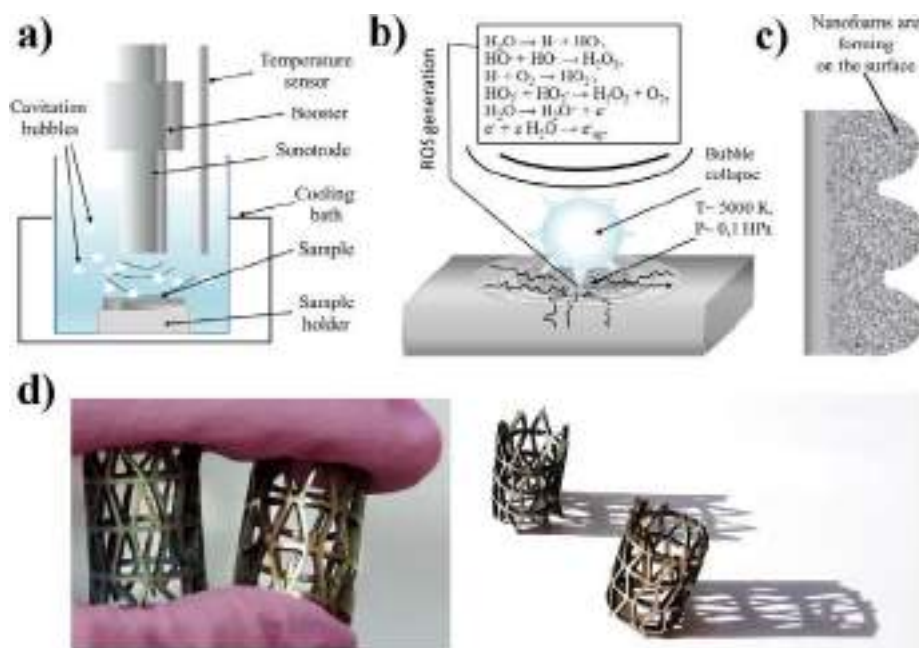
Fig. 1. The schematic illustration of the sonication cell (a), Schematic illustration of the surface structuring process taking place during the ultrasonic treatment of a titanium surface in aqueous alkaline solution (b) and formed surface (c), photo of titanium implants (d): the greenish one (the left sample in the hand) is implant after ultrasonic treatment, the yellowish one (the sample is situated on right) is non-modified implant.

layer, (iii) atomic structure disorder of titania layers, as well as the presence of various phase structures of TiO_2 [21]. This suggestion is also confirmed by EDX analysis. The atomic ratio of Ti/O in TMS coating is of 1:1.4. Besides, a selected-area electron diffraction pattern from TMS shows diffraction ring that have a d-spacing of 2.38 Å, which can be identified to be the (0 0 4) reflection of anatase phase (not shown). In Fig. 2c we can see the smooth surface of titanium dioxide layer. The boundaries of titanium crystallites are visible. Rounded craters with average diameter of 1 μm can be formed during the chemical polishing of titanium in places of surface defects. The TMS surface has a sponge-like structure (Fig. 2d).

The water contact angle measurements (Fig. 3a) indicate that surface of thermally treated titanium has a contact angle value of ca. 70° ($p < 0.05$) similar to contact angle of initial polished titanium surface (ca. 80°). The contact angle value of TMS surface is ca. 15° (Fig. 3b).

The surface wettability (hydrophilicity/hydrophobicity) is crucial in determining the biological response to the implanted materials. It affects the protein adsorption, platelet adhesion or activation and cellular adhesion [24,25]. The TMS surface wettability is therefore assessed by measuring the water contact angle. High contact angle values ($> 90°$), are associated with hydrophobic surfaces with low surface energy and decreased water-material interaction. While an increased surface energy and water-material interaction with low water contact angles correlates to hydrophilic surface. Georgi et al. [27] has demonstrated increased cell proliferation with increasing material surface wettability (water sessile drop method). Webb et al. [28] has shown that cell attachment and spreading are significantly greater on hydrophilic surfaces than on hydrophobic surfaces, and that moderately hydrophilic
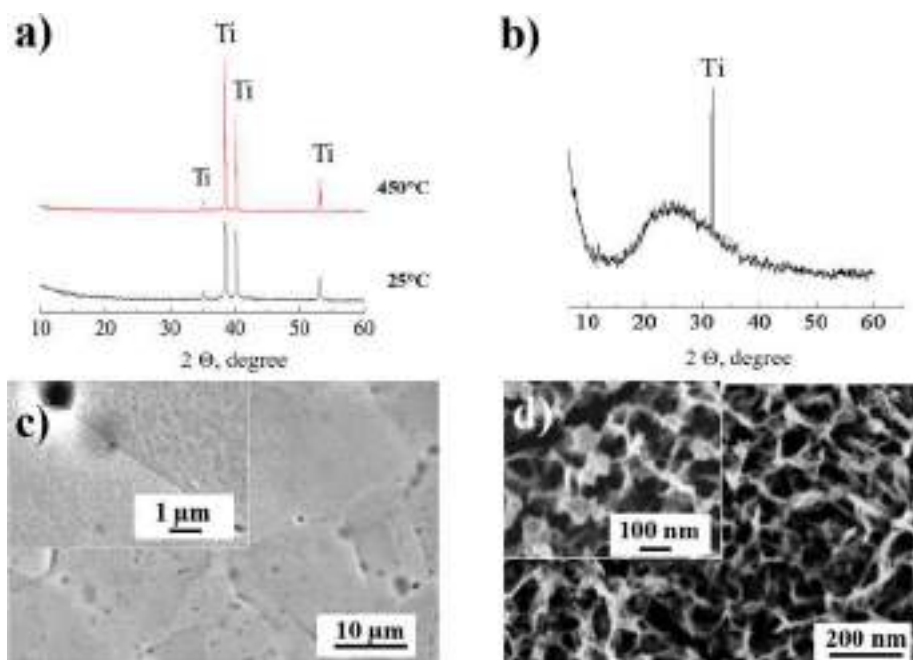
Fig. 2. The XRD patterns of titania coating fabricated by thermal treatment of polished titanium (a) and sonochemical treatment of polished titanium (b); SEM images of polished titanium surface (c) and sonochemically generated mesoporous titanium dioxide surface (d).
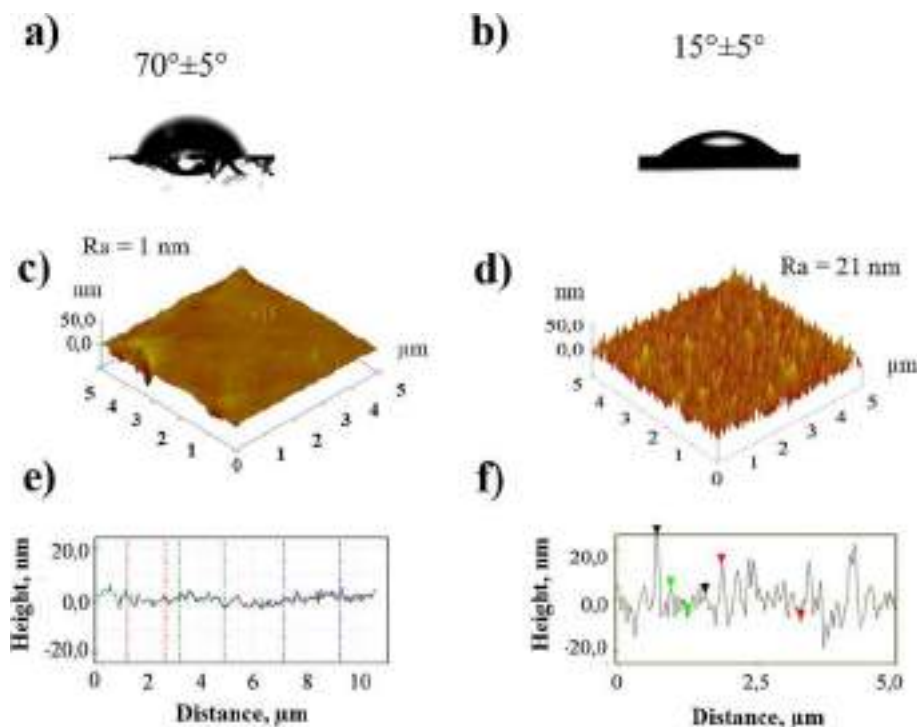
Fig. 3. The contact angle value of polished titanium (a) and sonochemically generated mesoporous titanium dioxide surface (b); AFM pictures of the polished titanium surface (c) and TMS surface (d). The scan size area was fixed to $50 \times 50\ \mu m^2$; AFM profiles of polished titanium (e) and TMS (f) surface.

surfaces promoted the highest level of cell attachment. Thus the implant wettability is a considerable factor for its success and tissue integration. Fig. 3 shows that sonochemical treatment allows to increase the surface hydrophilicity drastically. The superhydrophilic TMS has shown a stronger influence on the behavior of hMSCs compared with polished titanium surface.

Another important factor affecting the adhesion and proliferation of cells is the roughness of the surface. As mentioned above the surface of polished titanium is very smooth that corresponds to AFM data (Fig. 3c–f). The Ra parameter of polished titanium surface is 1 nm, while the Ra parameter of TMS surface is approximately 20 nm. It is worth to mention that surface roughness in the range from 10 nm to 10 μm may influence the interface biology, since it is of the same order in size as cells and large biomolecules [29]. Thus TMS coating is expected to be promising for cell proliferation and differentiation.

To investigate the adhesion and proliferation of hMSCs, MTT-test with the following colorimetry is carried out. The mitochondrial dehydrogenase of vital cells reduces water-soluble MTT of yellow color into the water-insoluble blue crystals of formazan. Meanwhile coenzyme of nicotinamide adenine dinucleotide (phosphate) (NAD(P)H, i.e., NADH and NADPH) oxidizes during donating of hydride ion H^- ($H^- \rightleftarrows H^+ + 2e^-$). This biochemical oxidation–reduction reaction occurring in living cells is described in Fig. 4. The adhesion and proliferation of hMSCs on TMS are evaluated in the extinction of formazan. The blue crystals of formazan are extracted with dimethylsulfoxide and the extinction is measured colorimetrically at 570 nm opposite dimethylsulfoxide. The dependence between the extinction of formazan and the concentration of cells reduced MTT has a linear relation. The smooth surface of polished titanium is used as a control. The values of extinction for formazan reduce by the hMSCs in 24 h and 5 days of culturing on the material surface are shown in Fig. 5. The extinction of formazan formed by hMSCs in 24 h of culturing on chemical polished titania and TMS surfaces does not differ (Fig. 5a). In 5 days, the extinction of formazan is higher on TMS surface than on the smooth surface of polished titanium. Consequently, the proliferation of hMSCs is faster on the TMS compared with the polished titanium. The same value of formazan

extinction in 24 h of hMSCs culturing confirms the equal number of these type cells attached to each surface of material (Fig. 5). The ability of cells to attach to solid surfaces depends on the hydrophilic-hydrophobic properties of the surface, a surface tension and charge, as well as its structure in an incipient stage. The adsorption of serum proteins to the surface of material provides the more robust adhesion of cells [30,31]. The formazan extinction is higher on TMS than on the smooth surface of polished titanium in 5 days. Consequently, the proliferation of hMSCs is faster on the TMS compared with the smooth surface of polished titanium. The extinction of formazan in 5 days of cellular culturing exceed it in 24 h as evidence that hMSCs culture grew on each TMS surface.

The method of confocal laser scanning microscopy has been used after living fluorescence staining of cells to visualize the hMSCs on the TMS surface (Fig. 6). Fig. 6 shows the cells of roundish and spindle-like shape after 24 h of cultivating. The cells form the monolayer of adhesive cells on the polished titanium and TMS surfaces on the 5-th day and isolated colonies are indistinguishable as it is noted in crop of high density. The seen phenotypic characteristics of cells prove the presence of hMSCs on all interest surfaces of materials. Also, we can state visually that the number of cells increased in 5 days after adhesion indicating the growth of cellular culture on all interest surfaces of materials.

To evaluate the osteogenic potential of hMSCs on the TMS, the genes of osteogenic proteins that are unique or prevail components into extracellular matrix of bone tissue, in particular, osteocalcin and alkaline phosphatase, have been chosen as markers. Osteocalcin is a non-collagen protein found in dentin and bones. This protein is excreted by only osteoblasts and is used as the marker of bone formation [32]. Alkaline phosphatase is hydrolytic enzyme that accepts phosphate groups from nature biopolymers. There is many amount of this enzyme into bones. Alkaline phosphatase provides the mineralization exchange into bone tissue [33]. The hMSCs are incubated on TMS surfaces in the medium without osteogenic inductors to research the surface nanotopography influence of TMS on the osteogenic potential of this cellular line. The negative control is titanium in the medium without osteogenic inductors. The positive control is titanium in the osteogenic medium.
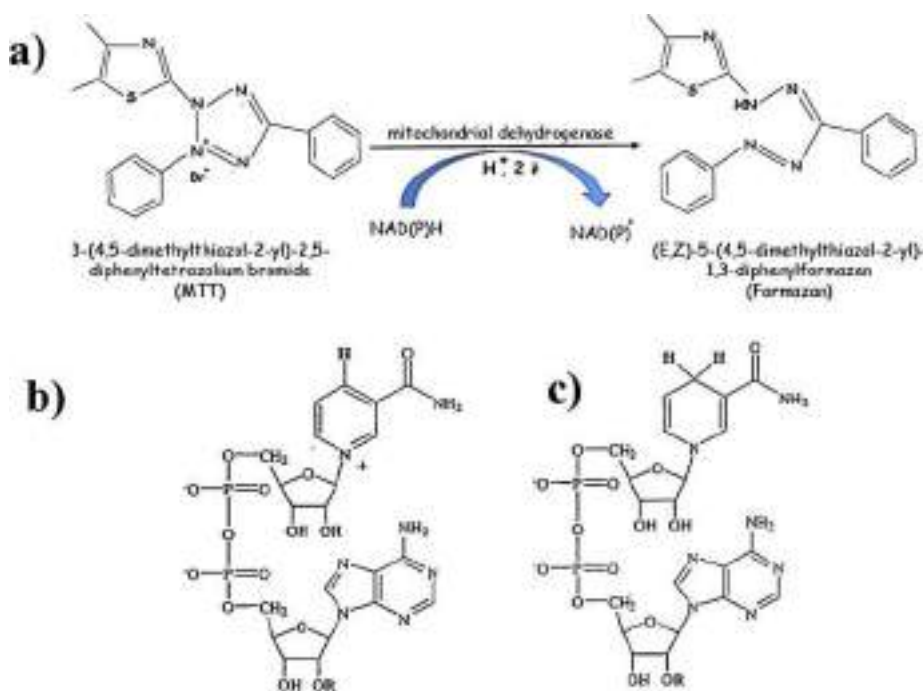
Fig. 4. Reduction of MTT by mitochondrial dehydrogenase in living cells (a); NAD^+: R = H. $NADP^+$: R = PO_3^{2-} (b); NADH: R = H. NADPH+: R = PO_3^{2-} (c). Abbreviations: NAD(P)H (i.e., NADH and NADPH) – reduced form of nicotinamide adenine dinucleotide (phosphate), NAD(P)$^+$ (i.e., NAD^+ and $NADP^+$) – oxidized form of nicotinamide adenine dinucleotide (phosphate).

To analyze the osteogenic differentiation of hMSCs, the expression level of tissue-specific genes, such as osteocalcin and alkaline phosphatase, was measured by the use of quantitative reverse transcription polymerase chain reaction as described in Methods. The expression of alkaline phosphatase and osteocalcin gene into hMSCs under the different conditions of culturing in 14 days is represented in Fig. 7. We have found that hMSCs cultured on the TMS have statistically higher genetic expression of alkaline phosphatase and osteocalcin compared to expression observed at 14 days in hMSCs on the smooth surface of polished titanium without osteogenic inductors. But the expression level of these important genes is lower than from the positive control (smooth surface of polished titanium with osteogenic inductors). Besides, the TMS stimulate the differentiation of hMSCs into osteoblasts. Thus, the coating having disorder nanotopography is preferable for the osteogenic differentiation of hMSCs. Fig. 7 proves that TMS surfaces stimulate the differentiation of hMSCs into osteoblasts. However, it is still not clear if the change of the surface is promoted by sonication itself or by the action of alkaline solution used or the combination of both. In order to show clearly the effect of sonication we have prepared the surfaces of polished titanium and treated in 5 M NaOH for 3 h (ATT), blasted titanium after immersion in water for 3 h (MST) and surface of blasted titanium after immersion in 5 M NaOH for 3 h (MSAT). All these samples were studied to check the osteogenic potential of hMSCs cultured in Dulbecco's modified essential medium with 2% human AB group serum in absence of osteofactors (Fig. 7c,d). According to analysis after 14 days, there is no critical osteoblast genes

expression on all these surfaces (see the picture in paper manuscript). Detail quantification of critical osteogenic markers by qRT-PCR has not been statistically significant difference in genetic expression on MSATT compared with ATT and MST.

It can be explained that revealed regularities in the proliferation and osteogenic potential of hMSCs are related to the focal adhesion contacts of spindle-like cells to the nanostructured surfaces of materials [33]. As known, nanotopography plays the key role in the regulation of focal adhesion, the sites of cellular attachment to a substrate [34]. Nanotopography modulates the ability of hMSCs to form very long, more 8 µm, fibrillary-like adhesions, with order surface resulting in shorter adhesions and disorder surface resulting in longer adhesions [35,36]. These dynamic adhesions are subject to the complex regulation involving integrin binding to extracellular matrix compounds, and the reinforcement of the adhesion plaque by the recruitment of additional proteins. Such alters impact on cytoskeletal tension through the reorganization of cytoskeletal components changing the shape of nucleus, chromosomal arrangement, and gene transcription, and ultimately the growth and differentiation of cells [37,38]. This mechanism of direct transduction is schematically shown in Fig. 8. As we can see a local force applied to integrin through the extracellular matrix (ECM) is concentrated at focal adhesions and channeled to filamentous (F)-actin. It is bundled by α-actinin and made tense by myosin II, which generates prestress. F-actins are connected to microtubules (MTs) through actin-crosslinking factor 7 (AcF7), and to intermediate filaments (IFs) through Plectin 1. MTs is connected with IFs and IFs with nesprin 3 on
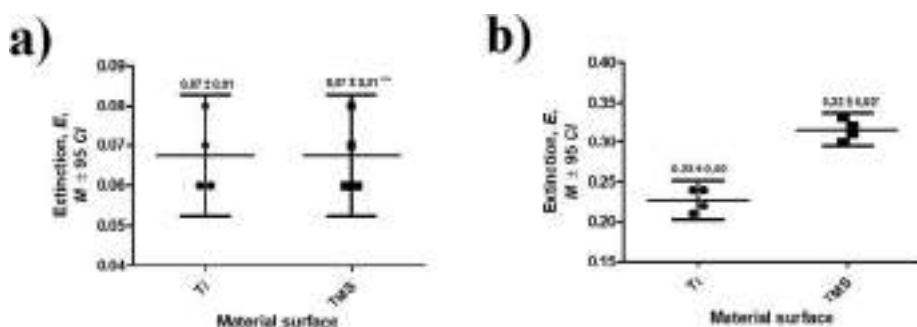
Fig. 5. The extinction of formazan formed by hMSCs in 24 h (a) and 5 days (b) culturing on the chemically polished and TMS surface. Data represent mean value ± confidence interval of 4 independent experiments. Symbol 'ns' indicates that confidence intervals are blocked for $p < 0.05$. Symbol '*' indicates that confidence intervals are not blocked for $p < 0.05$. Abbreviations: Ti – smooth surface of polished titanium, TMS – sonochemically generated titania mesoporous surface.
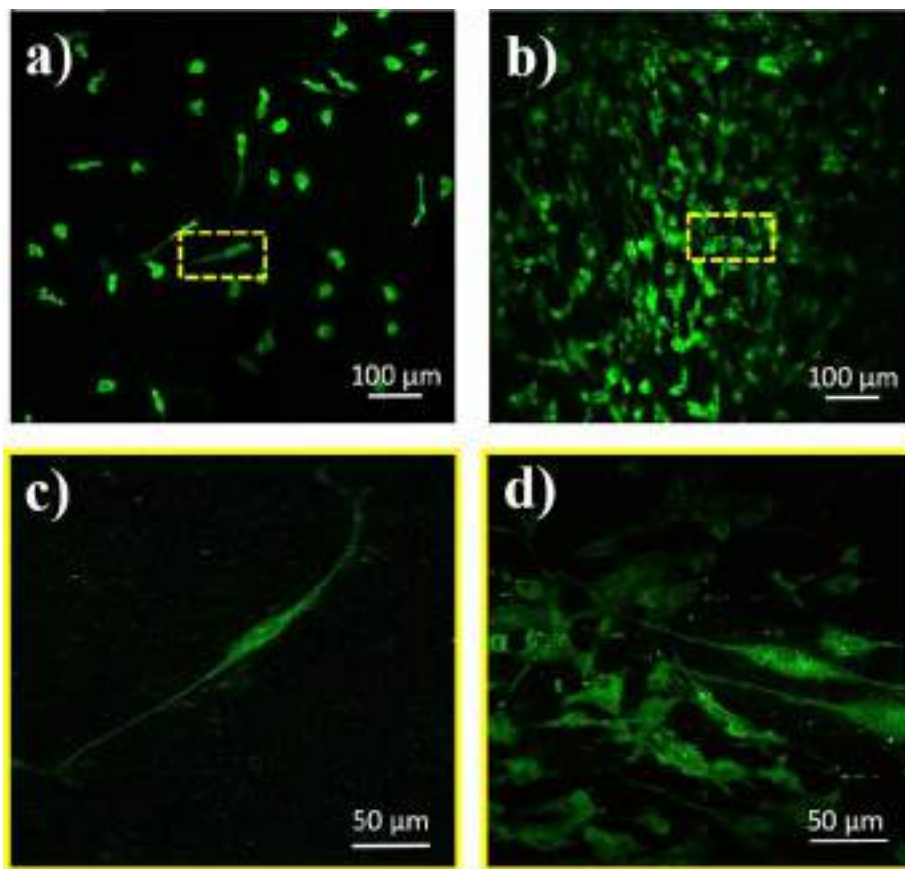
Fig. 6. Confocal microscopy images of hMSCs on the chemically polished titanium (a, c) and TMS surface (b, d) during their culturing: a – 24 h, b – 5 days, c – 24 h; d – 5 days.
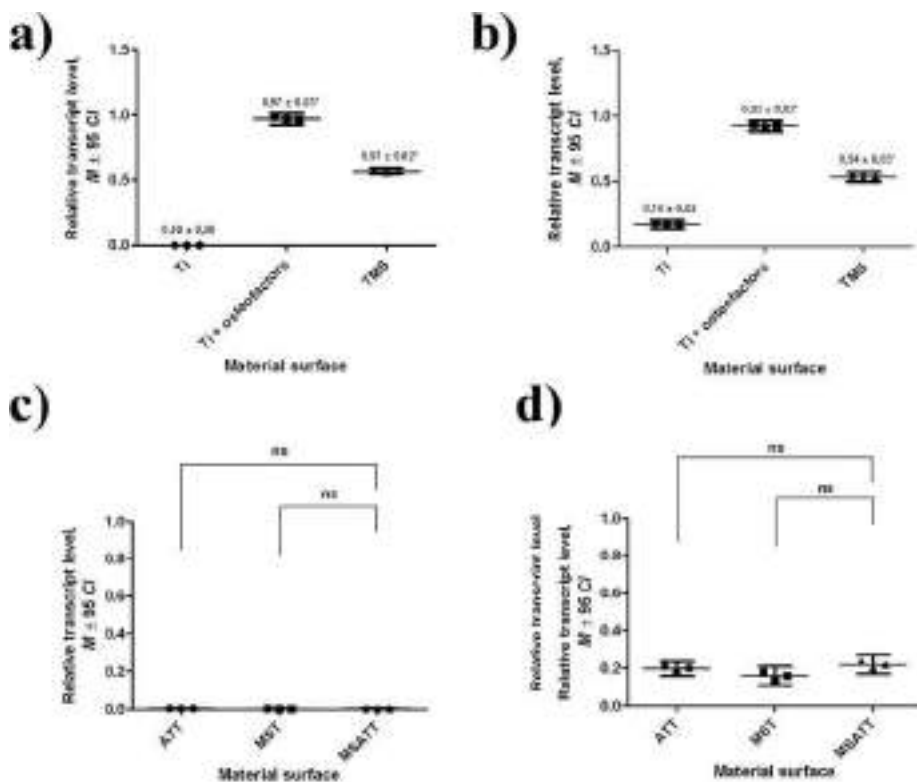
Fig. 7. The expression of osteoblast markers by human mesenchymal stem cells cultured osteocalcin (a, c) and alkaline phosphatase gene (b, d) after 14 days of incubation. Data represent mean value (M) ± confidence interval (CI) of 3 independent experiments. Symbol * indicates that confidence intervals are not blocked for $p < 0.05$. Symbol "ns" indicates that confidence intervals are blocked. Abbreviations: Ti – smooth chemically polished titania surface in medium without osteogenic factors, Ti + osteofactors – smooth chemically polished titania surface in osteogenic medium, TMS – ultrasonically obtained titania surface in medium without osteogenic factors, ATT – polished titanium treated in 5 M NaOH for 3 h, MST – blasted titanium after immersion in water for 3 h, MSATT – blasted titanium after immersion in 5 M NaOH for 3 h.
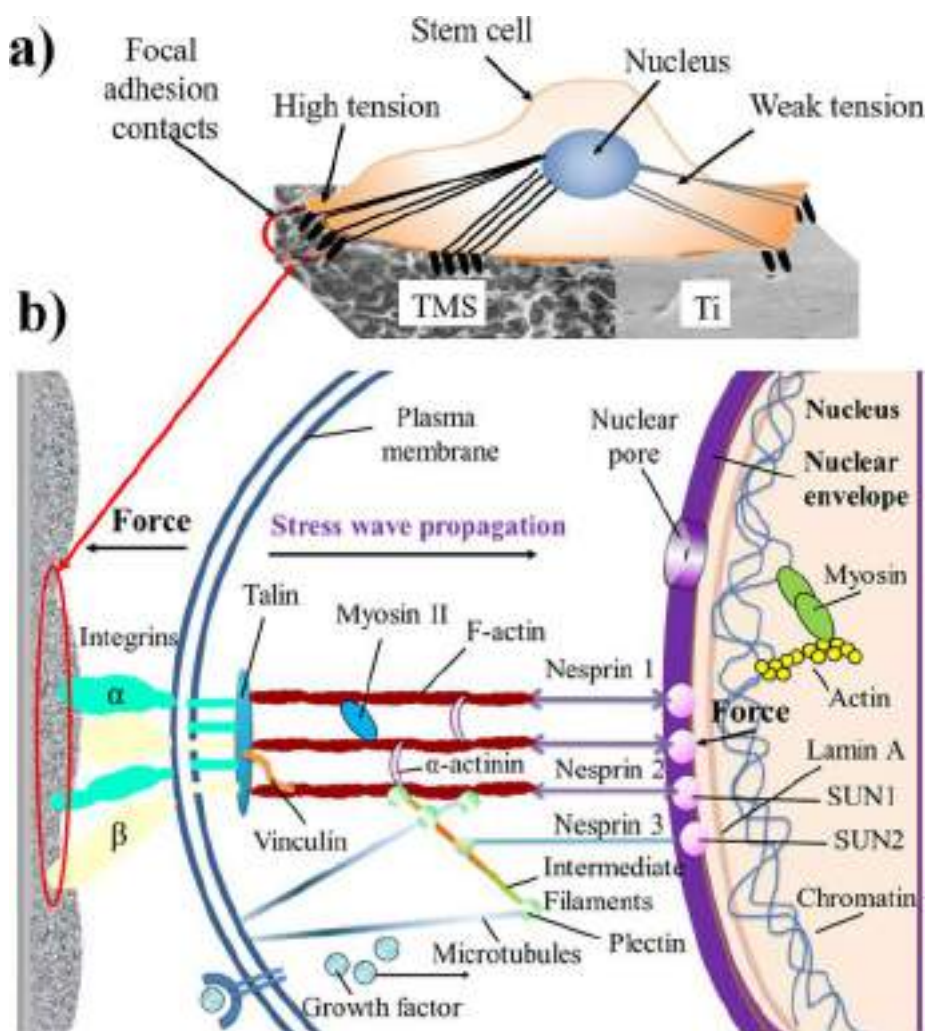
Fig. 8. The schematic illustration of hMSCs behavior during their formation of focal adhesion contacts on different nanotopography of sponge-like and smooth surface (a); The model of direct mechanotransduction identifying the direct link between an extracellular matrix (ECM) and the nucleus of cell. A force applied to integrins via the ECM can be channeled to the nucleus through focal adhesion interaction with the cytoskeletal proteins microfilaments, intermediate filaments and microtubules. Cytoskeletal interactions with the nucleus can lead to changes in gene expression via chromatin remodeling. (b). Abbreviations: Ti – smooth chemically polished titania; TMS – ultrasonically generated titanium dioxide mesoporous surface.

the outer nuclear membrane by Plectin 1. F-actin is connected to the inner nuclear membrane protein SUN1 by Nesprin 1 and nesprin 2; nesprin 3 connects Plectin 1 to SUN1 (also known as UNC84A)) and SUN2 (known as UNC84B). Nuclear actin and myosin (and nuclear titin) might help to form the nuclear scaffold, control gene positioning and regulate nuclear prestress. The force channeled into the nuclear scaffold might directly affect gene activation within milliseconds of surface deformation. By contrast, it takes seconds for growth factors to alter nuclear functions by eliciting chemical cascades of signaling, which are mediated by motor-based translocation or chemical diffusion. Thus, the changes in focal adhesion contacts and integrin binding alter indirectly the cellular signaling cascades that mediate the regulation of genetic expression [39–41].

We think that long focal adhesions and higher intracellular tension of hMSCs cultured on the TMS surface induce the moderate levels of extracellular signal-regulated kinase (ERK) signaling, which are enough to promote cell differentiation with a cell cycle arrest [39,42]. In contrast, small adhesions and the intracellular tension of weak level associated with smooth titanium exert the affect only cell proliferation [40,42]. Extracellular signal–regulated kinase signaling, that is critical for cell cycle progression and differentiation, induces different cellular responses as the result of the duration and magnitude of signaling [42,43]. It has been reported the surface of polymethylmethacrylate with the nanoscale disorder pores with average pore diameter of 50 nm formed by electronic laser lithography induces the differentiation of hMSCs into osteogenic direction [35]. Besides, we have showed recently that mouse myoblasts C2C12 cultured on the TMS turn the

fibroblast-like shape of their cytoskeleton into star-like inherent to osteoblasts [19].

4. Conclusions

In this study, the influence of surface nanotopography of sonochemically generated mesoporous titania coatings (TMS) on the adhesion, proliferation, and osteogenic differentiation of hMSCs has been investigated. We have found that disordered TMS surface obtained by sonochemical treatment provides good hMSCs adhesion, maintain their proliferation, and induce the osteoblast differentiation of this cellular line in the absence of osteogenic factors. The TMS surfaces demonstrate ca. 1.4 times higher the extinction of formazan formed by hMSCs after 5 days of cultivation and ca. 3 times better osteogenic differentiation of hMSCs compared to chemically polished titanium. The disorder TMS are expected to be applied in 3D implants to stimulate the growth of bone tissue. Thus, the method is a prospective for development of implants.

Acknowledgements

This work was financially supported by the Ministry of Health of the Republic of Belarus funding via the research program "Fundamental and Applied Sciences – Medicine" (state registration № 20170224), Republic of Belarusian Republican Fundamental Research (grant № X17PM-004) and RSF grant № 17-79-20186 (part of sonochemical surface nanostructuring). ITMO Fellowship and Professorship Program

References

[1] H.K. Salem, C. Thiemermann, Mesenchymal stromal cells: current understanding and clinical, Stem Cells 28 (2010) 585–596.

[2] R.V. Deev, A.Y. Drobyshev, I.Y. Bozo, A.A. Isaev, Ordinary and activated bone grafts: applied classification and the main features, BioMed Res. Int. 2015 (2015) 1–19.

[3] E.V. Skorb, D.V. Andreeva, Surface nanoarchitecture for bio-application self-regulation intelligent interfaces, Adv. Funct. Mater. 23 (2013) 4483–4506.

[4] H.N. Kim, A. Jiao, N.S. Hwang, M.S. Kim, D.H. Kang, Nanotopography-guided tissue engineering and regenerative medicine, Adv. Drug. Deliv. Rev. 65 (2013) 536–558.

[5] E.V. Skorb, H. Möhwald, Dynamic interfaces for responsive encapsulation systems, Adv. Mater. 36 (2013) 5029–5043.

[6] M. Ma, M. Kazemzadeh-Narbat, Y. Hui, S. Lu, C. Ding, D.D. Chen, Local delivery of antimicrobial peptides using self-organized TiO_2 nanotube arrays for peri-implant infections, J. Biomed. Mater. Res. 100A (2012) 278–285.

[7] K. Gulati, M.S. Aw, D. Losic, Nanoengineered drug-releasing Ti wires as an alternative for local delivery of chemotherapeutics in the brain, Int. J. Nanomedicine 7 (2012) 2069–2076.

[8] M. Mohsin, M. Meribout, An extended model for ultrasonic-based enhanced oil recovery with experimental validation, Ultrason. Sonochem. 23 (2014) 413–423.

[9] M. Mohsin, M. Meribout, Oil–water de-emulsification using ultrasonic technology, Ultrason. Sonochem. 22 (2015) 573–579.

[10] M. Mohsin, M. Meribout, Antenna array design for enhanced oil recovery under oil reservoir constraints with experimental validation, Energy 66 (2014) 868–880.

[11] E.V. Skorb, H. Möhwald, D.V. Andreeva, How can one controllably use of natural ΔpH in polyelectrolyte multilayers? Adv. Mater. Interfaces 4 (2017) 1600282 1–15.

[12] Y. Zhukova, E.V. Skorb, Cell guidance on nanostructured metal based surfaces, Adv. Healthcare Mater. 6 (2017) 1600914.

[13] E.V. Skorb, O. Baidukova, A. Brotchie, A. Goyal, D.V. Andreeva, H. Möhwald, Sononanoengineered magnesium – polypyrrole hybrid capsules with synergetic trigger release, J. Mater. Chem. 22 (2012) 13841–13848.

[14] A. Wilkinson, R.N. Hewitt, L.E. McNamara, D. McCloy, R.M. Dominic Meek, M.J. Dalby, Biomimetic microtopography to enhance osteogenesis in vitro, Acta Biomater. 7 (2011) 2919–2925.

[15] H. Seeherman, J. Wozney, R. Lee, Bone morphogenetic protein delivery systems, Spine 27 (2002) 16–23.

[16] T.D. Schmittgen, K.J. Livak, Analyzing real-time PCR by the comparative CT method, Nat. Protoc. 3 (2008) 1101–1108.

[17] Y. Zhukova, S.A. Ulasevich, J.W.C. Dunlop, P. Fratzl, H. Möhwald, E.V. Skorb, Ultrasound-driven titanium modification with formation of titania based nanofoam surfaces, Ultrason. Sonochem. 36 (2017) 146–154.

[18] E.V. Skorb, D.G. Shchukin, H. Möhwald, D.V. Andreeva, Ultrasound-driven design of metal surface nanofoams, Nanoscale 2 (2010) 722–727.

[19] J. Kopf, S.A. Ulasevich, O. Baidukova, Y. Zhukova, J.W.C. Dunlop, P. Fratzl, Ultrasonically produced porous sponge layer on titanium to guide cell behavior, Adv. Eng. Mater. 18 (2016) 476–483.

[20] S.G. Kumar, K.S.R. Koteswara Rao, Polymorphic phase transition among the titaniacrystal structures using a solution-based approach: from precursor chemistry to nucleation process, Nanoscale 6 (2014) 11574–11632.

[21] E.V. Skorb, H. Möhwald, "Smart" surface capsules for delivery devices, Adv. Mater. Interfaces 1 (2014) 1400237.

[22] D.V. Andreeva, D.V. Sviridov, A. Masic, H. Möhwald, E.V. Skorb, Nanoengineered metal surface capsules: construction of a metal-protection system, Small 8 (2012) 820–825.

[23] J. Park, S. Bauer, K. Mark, P. Schmuki, Nanosize and vitality: TiO_2 nanotube diameter directs cell fate, Nano Lett. 7 (2007) 1686–1691.

[24] J. Macak, H. Tsuchiya, A. Ghicov, K. Yasuda, R. Hahn, S. Bauer, TiO_2 nanotubes: self-organized electrochemical formation, properties and applications, Curr. Opin. Solid State Mater. 11 (2007) 3–18.

[25] M.J. Dalby, N. Gadegaard, R.O.C. Oreffo, Harnessing nanotopography and integrin–matrix interactions to influence stem cell fate, Nat. Mater. 13 (2014) 558–569.

[26] ICPDS – International Centre for Diffraction Data, 1999, [44-1288].

[27] F. Georgi, T.G. Grinnel, Studies on the biocompatibility of materials: fibroblast reorganisation of substratum-bound fibronectin on surfaces varying in wettability, J. Biomed. Mater. Res. 30 (1996) 385–391.

[28] K. Webb, V. Hlady, P.A. Tresco, Relative importance of surface wettability and charged functional groups on NIH 3T3 fibroblasts attachment, spreading, and cytosqueletal organization, J. Biomed. Mater. Res. 241 (1998) 422–430.

[29] J.I. Rosales-Leal, M.A. Rodríguez-Valverde, G. Mazzaglia, P.J. Ramón-Torregrosa, L. Diaz-Rodriguez, O. Garcia-Martinez, M.A. Cabrerizo-Vílchez, Effect of roughness, wettability and morphology of engineered titanium surfaces on osteoblast-like cell adhesion, Colloids Surf. A Physicochem. Eng. Asp. 365 (2010) 222–229.

[30] O. Mashinchian, L.A. Turner, M.J. Dalby, S. Laurent, M.A. Shokrgozar, S. Bonakdar, Regulation of stem cell fate by nanomaterial substrates, Nanomedicine 10 (2015) 829–847.

[31] N.K. Lee, Endocrine regulation of energy metabolism by the skeleton, Cell 3 (2007) 456–459.

[32] H.M. Khandwala, S. Mumm, M.P. Whyte, Low serum alkaline phosphatase activity and pathologic fracture: case report and brief review of hypophosphatasia diagnosed in adulthood, Endocr. Pract. 12 (2007) 676–681.

[33] M.J. Dalby, N. Gadegaard, R. Tare, A. Andar, M.O. Riehle, P. Herzyk, The control of human mesenchymal cell differentiation using nanoscale symmetry and disorder, Nat. Mater. 6 (2007) 997–1003.

[34] J. Yang, L.E. McNamara, N. Gadegaard, E.V. Alakpa, K.V. Burgess, R.M.D. Meek, Nanotopographical induction of osteogenesis through adhesion, bone morphogenic protein cosignaling, and regulation of microRNAs, ACS Nano 8 (2014) 9941–9953.

[35] J. Lee, F. Hong, S. Kwon, S.S. Kim, D.O. Kim, H.S. Kang, Activation of p38 MAPK induces cell cycle arrest via inhibition of Raf/ERK pathway during muscle differentiation, Biochem. Biophys. Res. Commun. 298 (2002) 765–771.

[36] B. Wang, T. Du, Y. Wang, C. Yang, S. Zhang, X. Cao, Focal adhesion kinase signaling pathway is involved in mechanotransduction in MG-63 Cells, Biochem. Biophys. Res. Commun. 410 (2011) 671–676.

[37] N. Wang, J.D. Tytell, D.E. Ingber, Mechanotransduction at a distance: mechanically coupling the extracellular matrix with the nucleus, Nat. Rev. Mol. Cell. Biol. 10 (2009) 75–82.

[38] S.Y. Hong, Y.M. Jeon, H.J. Lee, J.G. Kim, J.A. Baek, J.C. Lee, Activation of RhoA and FAK induces ERK-mediated osteopontin expression in mechanical force-subjected periodontal ligament fibroblasts, Mol. Cell. Biochem. 335 (2010) 263–272.

[39] B. Wang, Y. Gao, Z. Xiao, B. Chen, J. Han, J. Zhang, Erk1/2 promotes proliferation and inhibits neuronal differentiation of neural stem cells, Neurosci. Lett. 461 (2009) 252–257.

[40] J. Li, G. Wang, C. Wang, Y. Zhao, H. Zhang, Z. Tan, MEK/ERK signaling contributes to the maintenance of human embryonic stem cell self-renewal, Differentiation 75 (2007) 299–307.

[41] S. Meloche, J. Pouyssegur, The ERK1/2 mitogen-activated protein kinase pathway as a master regulator of the G1- to S-phase transition, Oncogene 26 (2007) 3227–3239.

[42] H.A. Coller, What's taking so long? S-phase entry from quiescence versus proliferation, Nat. Rev. Mol. Cell. Biol. 8 (2007) 667–670.

[43] M. Ebisuya, K. Kondoh, E. Nishida, The duration, magnitude and compartmentalization of ERK MAP kinase activity: mechanisms for providing signaling specificity, J. Cell. Sci. 118 (2005) 2997–3002.

CrossMark

Importance of buffering nanolayer position in Layer-by-Layer assembly on titania based hybrid photoactivity

Nadzeya Brezhneva[1] · Anna Nikitina[1] · Nikolay Ryzhkov[1] · Anastasiya Klestova[1] · Alexandr V. Vinogradov[1] · Ekaterina V. Skorb[1]

Abstract

Nanoarchitecture of layer-by-layer (LbL) films is a convenient and simple way to control the photoelectrochemical properties of the semiconductor films. Hereby, we used the combination of polystyrenesulfonate (PSS) and polyethyleneimine (PEI) deposited on the TiO_2 film for controlling the photochemical response of the hybrid system. Photogenerated protons on the TiO_2 surface are responsible for the acidity change near the irradiated surface. We investigated that the photogenerated protons being absorbed by PEI spatially separated from the TiO_2 surface with the nanoscale-thick PSS layer (with thickness ca. 5 nm) lead to the sufficient decrease in photoactivity of the hybrid system TiO_2/PSS/PEI ca. 4 times in comparison with pristine TiO_2. PEI nanolayer being deposited directly on the TiO_2 surface can decrease the photoactivity of the system ca. 2–2.5 times.

Graphical Abstract

We show that the photoactivity of the sol–gel titania can be regulated by self-assembly of polyelectrolyte nanolayersand nanoarchitecture of these layers. The work highlights the importance of well-defined colloidal units for inkjet printing of gradient surface.
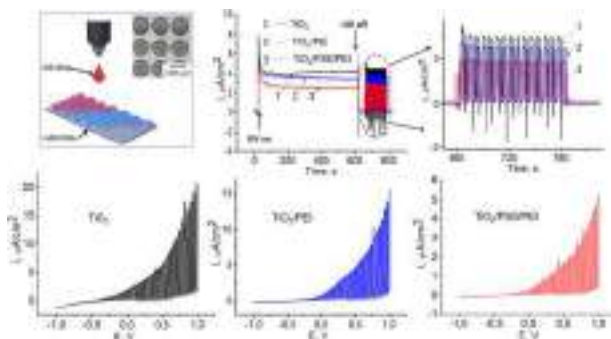
These authors contributed equally: Nadzeya Brezhneva and Anna Nikitina

✉ Anna Nikitina
nikitina@scamt-itmo.ru

1 Laboratory of Solution Chemistry of Advanced Materials and Technologies (SCAMT), ITMO University, Lomonosova str. 9, St. Petersburg 197101, Russian Federation

Highlights

- Deposition of TiO$_2$ photoactive layer by inkjet printing.
- Investigation of photoactivity of the hybrid system based on titanium dioxide and polyelectrolyte layers (polystyrenesulfonate PSS, polyethyleneimine PEI).
- Variation in "proton sponge" activity of PEI depending on the distance from TiO$_2$ surface.
- PEI nanolayer being deposited directly on the TiO$_2$ surface can decrease the photoactivity of the system ca. 2–2.5 times, nanoarchitecture PSS/PEI – 4–4.5 times in comparison with pristine TiO$_2$.

Keywords TiO$_2$ · Layer-by-layer assembly · Photoactivity · Sol–gel · Polyelectrolytes

1 Introduction

Polyelectrolyte multilayers present an interesting type of coatings for the surface modification of materials to obtain functional interfaces [1, 2] and find the applications in the field of anticorrosion coatings [3], membranes [4], drug delivery systems [5], antimicrobial coatings [6], and microfluidics [7, 8]. The layer-by-layer (LbL) technique is a very attractive tool for a control over the nanoscale thickness, composition, and properties of the formed films and nowadays is widely used due to the simplicity of the deposition procedure and cost-effectiveness of the method used [9]. It has been shown [10] that it is possible to create the multilayer films with a desired set of properties by using the appropriate assembly technology. The great advantages of the LbL assembly are the possibilities to deposit polymer films on substrates of different shapes and sizes, tune the properties of the films by regulating the number of layers and consequence of deposited layers.

The preparation of novel hybrid materials based on organic and inorganic constituents is explained by the new trends of materials science and engineering. Titanium dioxide appears to be a widely studied semiconductor often used as a photocatalyst in different processes including water or air purification due to its low cost, non-toxicity, chemical stability. One of the modern methods for the nanostructured TiO$_2$ thin films preparation includes inkjet printing as one of the techniques to prepare thin films from liquids. It proves to be a modern and clean method of liquid deposition and preparing the patterns on the surface of the substrate [11].

The inkjet printing serves as a convenient tool for functional materials and devices preparation [12]. In general, the use of nanocrystalline colloids containing the minimum of amorphous phase can be suitable for different objects fabrication, including electronic devices [13], light-emitting diodes [14], and sensors [15]. The sol–gel technique provides an opportunity of preparing crystalline materials under ambient pressure and temperature [16]. Recently, it has been demonstrated that the inkjet printing can be applied to the production of photocatalytic coatings based on TiO$_2$ on polymer films [17].

During irradiation of TiO$_2$ surface with the supra-band gap energy light ($E > 3.2$ eV in the case of anatase modification) leads to the generation of photoelectrons (e$^-$) and photoholes (h$^+$). The photoholes are involved in the process of H$_2$O molecules oxidation, finally leading to the formation of oxygen and protons according to Eqs. (1)–(3). The photoelectrons are involved in the reduction reaction of oxygen molecules where in the presence of water molecules they can be transformed into OH$^-$.

$$TiO_2 \rightarrow h^+ + e^-, \tag{1}$$

$$H_2O + h^+ \rightarrow \ldots \rightarrow O_2 + H^+, \tag{2}$$

$$O_2 + e^- + H_2O \rightarrow \ldots \rightarrow OH^-. \tag{3}$$
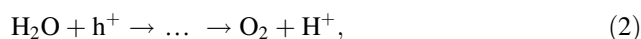
The generation of H$^+$ species leads to the decrease in the subsurface pH value. Recently, the possibility to create local pH change caused by the irradiation of TiO$_2$ surface has been demonstrated [18]. By using scanning ion-selective electrode technique the authors demonstrated the localization of the light energy conversion into the acidification of the subsurface semiconductor layer. Analysis of the pH maps which image the pH value distribution along the semiconductor surface has showed that he pH value above the non-irradiated surface of the TiO$_2$ comprise ca. 6.5 and in the region of the focused light beam spot during irradiation ca. 4.

The possibility of photon-to-proton conversion (i.e., the transformation of the electromagnetic irradiation energy into the proton flux on the irradiated surface of TiO$_2$ through the number of photocatalytic reactions with water) provides the efficient nondestructive soft matter actuation when the latter was deposited on the TiO$_2$ surface using the LbL technique. Weak polyelectrolytes are known to exhibit drastic response to pH consisted in their morphology and polarity change [19]. Ulasevich et al. [20] have recently demonstrated that pH sensitive weak polymers layers deposited on the TiO$_2$ surface demonstrated the changes in the properties of the deposited polymer coating without its destruction under photocatalytic reactions on the semiconductor surface. The thickness of the coating increased as a result of changes in polymer properties—under pH

changes these polyelectrolytes alter their conformation, swell and change the stiffness of the coating. According to the colloidal probe atomic force microscopy the coating with LbL assembly of weak polyelectrolytes becomes softer —from 1.67 MPa of the initial coating to 28 kPa after irradiation. In fact, the possibility of switching the pH-sensitive polymers (actuation) by light was demonstrated.

Nanoarchitecture of the surface provides the possible use of such systems as "intelligent" surfaces: they were used for the regulation of cell migration [20], adsorption/desorption of proteins [21]. Also, an interesting buffering effect of chitosan has been investigated [22]. The chitosan nanolayer is served as a protector of the supramolecular assembly deposited on the TiO$_2$ surface preventing its destruction. The deposited nanolayer served as a proton sponge that efficiently absorbs protons from the irradiated surface of the semiconductor preventing pH-dependent disorder of supramolecular assembly. Another interesting example of proton sponges among polyelectrolytes is polyethyleneimine (PEI) which is known to be used for non-viral gene delivery and due to the extraordinary cationic charge and buffering capacity for complexation with nucleic acids and lysosomal/endosomal release [23]. Such polyelectrolyte has been used in the artificial photosynthetic system with high stability in the wide pH range and improved H$_2$ generation from neutral aqueous solutions with the use of enzyme hydrogenase as a catalyst under visible-light irradiation [24]. The PEI can also play an important role in the durability of electrochemical catalyst. It has been investigated that the electrochemical active surface area of the carbon black electrode modified with Pt nanoparticles after 1200 cycle operation decreased more significantly in comparison with that modified with PEI [25]. Nevertheless, despite the mentioning of buffering layer and the effect of "proton sponge" it is unclear how the position of PEI nanolayer can affect the photochemical properties of TiO$_2$ and TiO$_2$-based hybrid materials. It does not seem clear, how can the nanoarchitecture of the deposited polyelectrolytes containing buffering nanolayer of PEI. In this paper, we investigate the importance of buffering nanolayer (PEI) position in LbL assembly on the photocurrent value and further photoactivity of the TiO$_2$/polyelectrolyte system. Photoactive layer of TiO$_2$ for the further LbL deposition has been obtained by the inkjet printing that serves as a convenient tool for functional materials and devices preparation.

2 Experimental section

2.1 Materials

In the experiment the following reagents were used. Titanium (IV) isopropoxide (TTIP, 97%), 2-propanol (IPA,

99.5%), nitric acid (HNO$_3$, 65%), sodium chloride (NaCl, > 99%), polystyrenesulfonate (PSS, M_w = 1,000,000, powder), polyethyleneimine (PEI, M_w = 750,000, 50%wt/v solution) and Rhodamine 6 G (Rh6G, 95%) were purchased from Sigma Aldrich. All aqueous solutions were prepared by using highly pure water from Millipore Elix (18 MΩ·cm²/cm). Ninety six percent ethanol was purchased from ChimMed, Russia. Ninety eight percent ethylene glycol was purchased from LenReactiv, Russia. n-Si wafers were used as substrates (d = 150 mm).

2.2 Preparation of aTiO$_2$sol

The TiO$_2$ sol was prepared as it was described before [16]. TTIP mixed with 2-propanol 4:3 (v/v) was added drop by drop into the HNO$_3$ solution (0.8 ml of 65% acid was mixed with 100 ml of deionized water) and kept under constant stirring at 80 °C for 1 h followed by cooling down and stirring at room temperature for the next 3 days.

2.3 Preparation of TiO$_2$ solution

The obtained TiO$_2$ sol was evaporated in a rotary evaporator under reduced pressure at 50 °C. Then the particles were dried in the desiccator and TiO$_2$ xerogel powder was obtained. A water-based solution for titania layer deposition contained 20 wt% of TiO$_2$powder and was prepared by dissolving the appropriate amount of titania particles in the mixture of deionized water or water: ethylene glycol 1:3 (v/v) mixture.

For printing TiO$_2$ inks, before loading into a printer, TiO$_2$ ink was degassed and passed through the 0.2 μm syringe filter to remove any large aggregates or particles. The ink was printed using FUJIFILM Dimatix Materials Printer DMP-2850 on n-silicon wafer treated beforehand by plasma cleaner. To obtain the optimum coverage thickness the inkjet depositions were performed on a silicon wafer heated to 40 °C with an inter-droplet distance of 40 μm. Two layers of 25 × 25 mm^2 square patterns were printed with 90 s delay between layers.

2.4 Characterization of the prepared TiO$_2$particles

The obtained TiO$_2$ particles were tested by dynamic light scattering technique using Photocor Compact analyzer (Russia). The morphology of TiO$_2$particleswas obtained by scanning electron microscope (SEM) Tescan Vega-3(Czech Republic). The samples for high resolution transmission electron microscopy (HRTEM) were prepared by dispersing small amounts of samples in ethanol to form a homogeneous suspension. A drop of the suspension was deposited on a carbon-coated copper grid for HRTEM observations (FEI TECNAI G2 F20 operating at 200 kV).

The X-ray diffraction pattern of the sample was obtained using Bruker D8 Advance equipment with Cu Kα ($\lambda = 1.5418$ Å).

2.5 Deposition of polyelectrolyte multilayers onto the TiO₂

PSS and PEI were dissolved in 1 M NaCl solution to the concentration 2 mg/ml. The pH of the polyelectrolyte solution was adjusted by 1 M HCl or 1 M NaOH solution. In the case of TiO₂ particles the 50 mg of the powder was mixed with 1 ml of polyelectrolyte solution and then stirred in shaker for 5 min followed by the centrifugation at the rotor speed 10,000 min^{-1} for 10 min. The excess of the polyelectrolyte was removed by washing the samples with distilled water and then repeatedly centrifuged. The deposition of polyelectrolytes onto the n-Si/TiO₂ substrates was performed by the dip-coating technique. The samples were immersed into the solution of polyelectrolyte for 15 min followed by washing of the sample with distilled water.

2.6 Photocatalytic activity study of TiO₂ particles

The photocatalytic study was performed using UV hand lamp (365 nm, 8 W, Herolab, Germany). The as-prepared solutions of 5×10^{-6} M Rhodamine 6G (Rh6G) and 2×10^{-5} M Methylene blue (MB) were used for the photocatalytic experiments. The appropriate amount of TiO₂ particles was mixed with the solution of the dye. The mixture was stirred in the quartz beaker during 1 h in the dark place so as to reach the equilibrium of the dye sorption/desorption process. After that the mixture was irradiated during 1 h with sampling at certain time intervals. The TiO₂ particles were separated from the dye solution by centrifugation. The concentration of dyes after irradiation was estimated using spectrophotometer Varian Cary (USA). The calibration curve for each dye was constructed by measuring the absorbance of the dye at different concentrations.

Detection of the photogenerated reactive oxygen species (ROS) was carried out using chemiluminescent analysis with luminol solution. Pristine TiO₂ particles and TiO₂-particles covered with polyelectrolytes were irradiated in distilled water by the UV lamp (365 nm, 8 W, Herolab, Germany) during 60 min. The aliquot of 20 µl was taken every 10 min and added to the quartz cuvette with luminol solution. Luminol solution was prepared by dissolving 100 mg of luminol in 50 ml of 0.25 M NaOH solution. The chemiluminescence intensity was measured by a Cary Eclipse 5301 (Agilent Technologies, USA) fluorescence spectrophotometer. The excitation of the luminescence was carried out at 310 nm and emission spectra were measured at 380 nm.

2.7 Photoelectrochemical measurements

The photoelectrochemical measurements were performed with the Autolab potentiostat PGStat302N (Netherlands) in the three-electrode cell with n-Si/TiO₂ with or without deposited polyelectrolyte layers as a working electrode, Ag/AgCl(KCl sat.) as a reference electrode and Pt wire as a counter electrode. A 365 nm UV LED was used as the light source, for light beam focusing the focusing lens at a distance 2 cm from the electrochemical cell were used. The solution of 0.05 M Na₂SO₄ was used as a working electrolyte.

3 Results and discussions

The ink for inkjet printer was made from TiO₂ xerogel. According to SEM (Fig. 1a), the obtained xerogel is shapeless and is presented by aggregates with the average size ca. 0.1–0.4 µm. As shown in the HRTEM image (Fig. 1b), the interplanar distance presented in TiO₂ is 0.35 nm that corresponds to the biggest peak 101 according to the literature data [25, 26]. The XRD pattern shows the presence of anatase phase with small amount of brookite phase (Fig. 1c). The obtained TiO₂ particles are characterized by the isoelectric point (IEP) value of 6.7 (Fig. 1d). As it is known, the IEP is the value of pH at which the negative and positive charges compensate each other. In the acidic region of pH the particles are positively charged and in the alkaline region with pH values greater than the value of IEP—negatively charged. In our experiment varying the pH differently charged polyelectrolytes were deposited on the particles surface. At the pH = 2 the particles are positively charged, that is why PSS was selected as the first layer for deposition (Fig. 2a). At the pH = 9 the particles are negatively charged and PEI was deposited directly on the TiO₂ surface (Fig. 2b).

An important feature of adsorption in solutions of electrolytes is its electrostatic nature [26]. According to Helmholtz model, the spatial separation of charges near the surface can be regarded as a double electric layer consisting of potential-determining ions directly bound to the surface, counter ions in adjusted medium and co-ions displaced in volume. The surface plane that divides solid from liquid with charge density σ_0 is characterized by potential φ_0. Centers of counter ions associated with surface charges density, σ_β, are assumed to be exposed to potential φ_β. The distribution of ions in the diffuse layer governed only by electrostatic forces and thermal motion is affected by the

Fig. 1 a SEM image, **b** HRTEM image, **c** XRD, and **d** the electrokinetic study of the TiO$_2$ particles
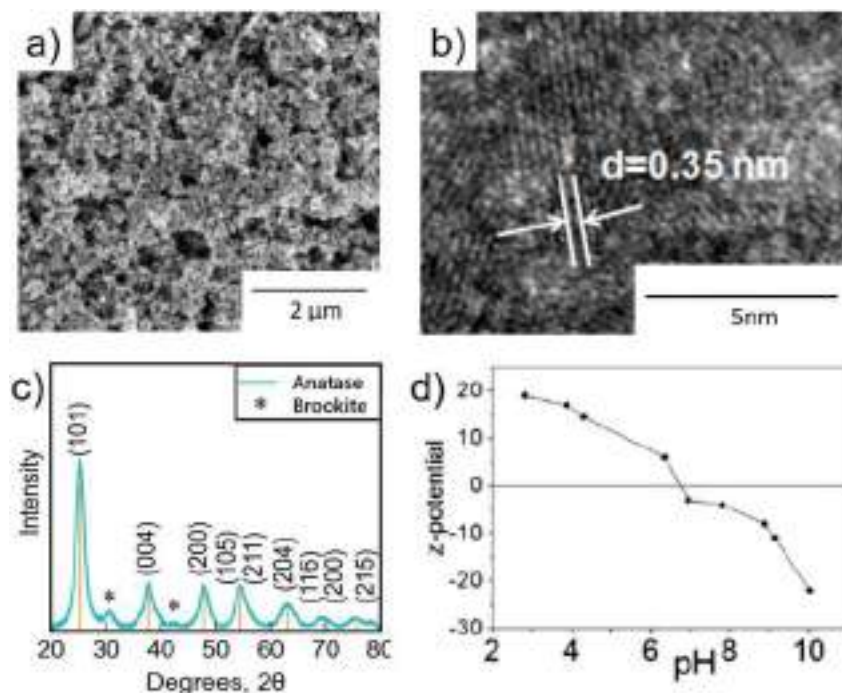
electrostatic potential φ$_d$, diffuse layer charge density is denoted as σ$_d$.

From electroneutrality requirement, it follows that

$$\sigma_0 + \sigma_\beta + \sigma_d = 0. \tag{4}$$

According to the Gouy–Chapman theory, in the case of (1:1) symmetrical electrolytes the relationship between the surface charge density and the electrostatic potential of the diffuse layer φ$_d$ is given by

$$\rho_\delta = -\sqrt{8\varepsilon\varepsilon_0 kTn_0}\sinh\left(\frac{ze\varphi_d}{2kT}\right) \tag{5}$$

or

$$\varphi(x) \approx \frac{4kT}{ze}\tanh\left(\frac{ze\varphi_d}{4kT}\right)e^{-x}, \tag{6}$$

where ϰ is Debye–Hückel parameter given by

$$\frac{1}{-} = \sqrt{\frac{\varepsilon\varepsilon_0 kT}{2z^2 e^2 n_0}}, \tag{7}$$

where ze is the charge of ion, ε_0 is the dielectric constant, ε is the permeability, k is the Boltzmann constant, T is the absolute temperature, and n_0 is the ion concentration.

This theory makes it possible to describe the phenomenon of charge change of a surface, during LbL assembly of polyelectrolytes. Amount of adsorbed PSS macromolecules on pristine TiO$_2$ surface positive at pH=2 is limited by the electrostatic repulsion which suppresses further adsorption. Consequent deposition of PEI can be considered in the terms described above with starting charge parameter φ$_0$—

equal to negative φ$_d$ for TiO$_2$/PSS composition. When deposition is carried out at pH=9 TiO$_2$ surface is negatively charged, thus adsorption of PEI is available and occurs till amount of PEI is not enough for its electrostatic repulsion from TiO$_2$/PEI surface and PEI excess is in diffusion layer.

It is known that TiO$_2$ has higher photoactivity under lower pH [27]. Recently, it has been shown that local irradiation of the TiO$_2$ surface leads to the local acidification followed by the pH change [28]. Thus if we regulate acidic media near TiO$_2$ surface we increase its photoactivity, but if all generated protons will be immediately trapped by proton sponge layer that is spatially separated from titania, the photoactivity should be decreased. This schematically is illustrated in Fig. 2. We tested photoactivity for our systems. We observed a significant decrease in the photoactivity of TiO$_2$/PSS/PEI in comparison with pure TiO$_2$ during the photocatalytic degradation of Rh6G and MB dyes. During the irradiation of the TiO2 surface the photoelectrons move toward the surface and are scavenged by the oxygen molecules forming O$_2$- superoxide-anion radicals. The photoholes generated in the valence band react with the surface hydroxyl groups OH$^-$ and form hydroxyl (OH·) and hydroperoxyl radicals (HO$_2$·). These reactive oxygen species (ROS) take part in the degradation of the dyes into the simpler molecules. As shown in Fig. 3a, b, the deposited layer of PEI decreases the photoactivity of the system ca 2-2.5 times, whereas the layers of PSS and PEI decrease the dye degradation ca. 4–4.5 times in comparison with pristine TiO$_2$. The quantity of ROS amount generated during the irradiation of pristine TiO$_2$ particles and hybrid

Fig. 2 The change of TiO$_2$ particles zeta-potential after the deposition of PEI **a**, PSS/PEI **b**, and **c** schematic of importance of PEI position to control acidification of titania surface
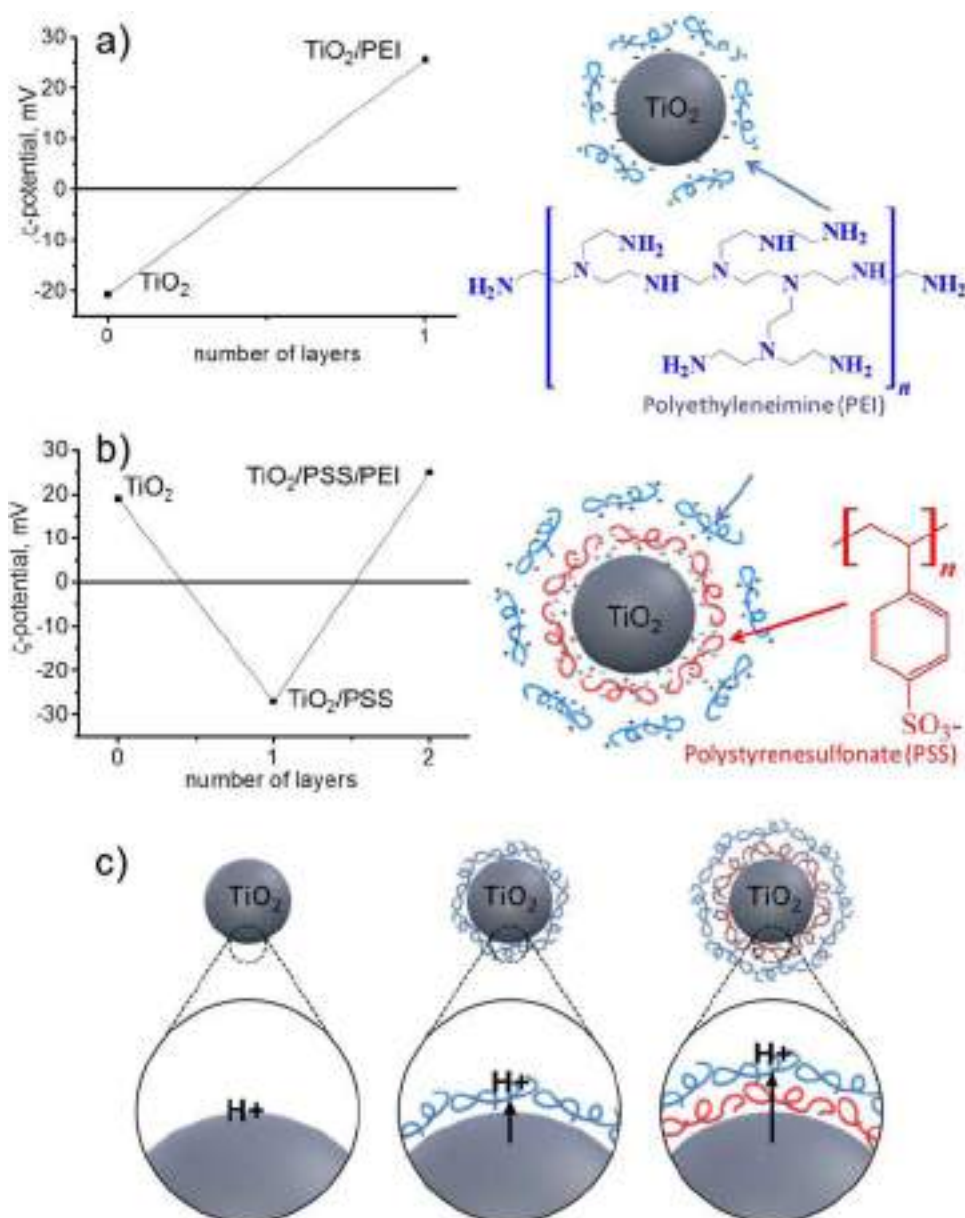
particles with polyelectrolyte coatings was estimated using chemiluminescence spectra with luminol solution. For pure TiO2 particles after 20 min of irradiation the ROS amount comprised 0.04 mol/l, for TiO$_2$/PEI – 4.4×10^{-3} mol/l, TiO$_2$/PSS/PEI – 1.33×10^{-4} mol/l.

The stability of the PEI and PSS/PEI layers on TiO$_2$ surface under UV irradiation were detected using IR spectroscopy (Fig. 3c). As it shown there are no evident changes in IR spectra before and after UV-irradiation.

In following we analyze the question—how can the deposited buffer PEI nanolayer and its position in the LbL assembly can affect the photocatalytic activity of the system? For this we suggest as model TiO$_2$ based film or inkjet printer system [29] on the n-Si substrate can be also suitable for LbL assembly deposition with their further activation by

light. PEI proton sponge layer is suggested to be placed either on TiO$_2$ or separated from TiO$_2$ with PSS layer. In Fig. 4a it is schematically highlighted potentially promising approach of inkjet printing the surface with different photoactivity. Figure 4c shows typical photocurrent–potential plots measured under chopped illumination of the TiO$_2$ electrodes in 0.05 M Na$_2$SO$_4$ solution with pH 6. The photocurrent for pure TiO$_2$ increased steadily with the increasing potential of the working electrode, and a photocurrent density of 20 μA/cm^2 (1.0 V vs. Ag/AgCl) was obtained. Compared to that of pure TiO$_2$, the deposited PEI nanolayer leads to the decrease in photocurrent, ca. 15 μA/cm^2 (1.0 V vs. Ag/AgCl). The deposition of PSS layer onto TiO$_2$ prior to the deposition of PEI leads to more significant deterioration of the photocurrent by approximately 75 %

Fig. 3 Photocatalytic degradation of Rhodamine 6G **a** and Methylene Blue **b** on the TiO₂, TiO₂/PEI and TiO₂/PSS/ PEI particles; IR-FT spectra of TiO₂/PSS/PEI layers before and after UV irradiation **c**
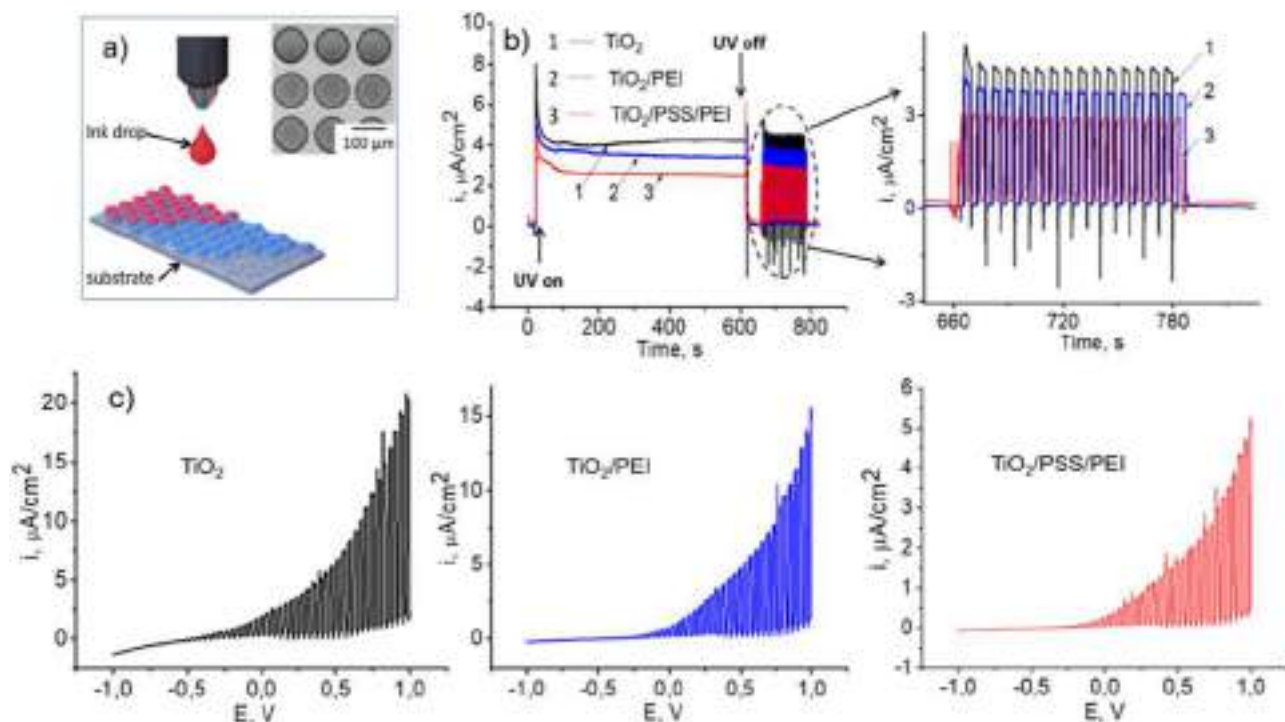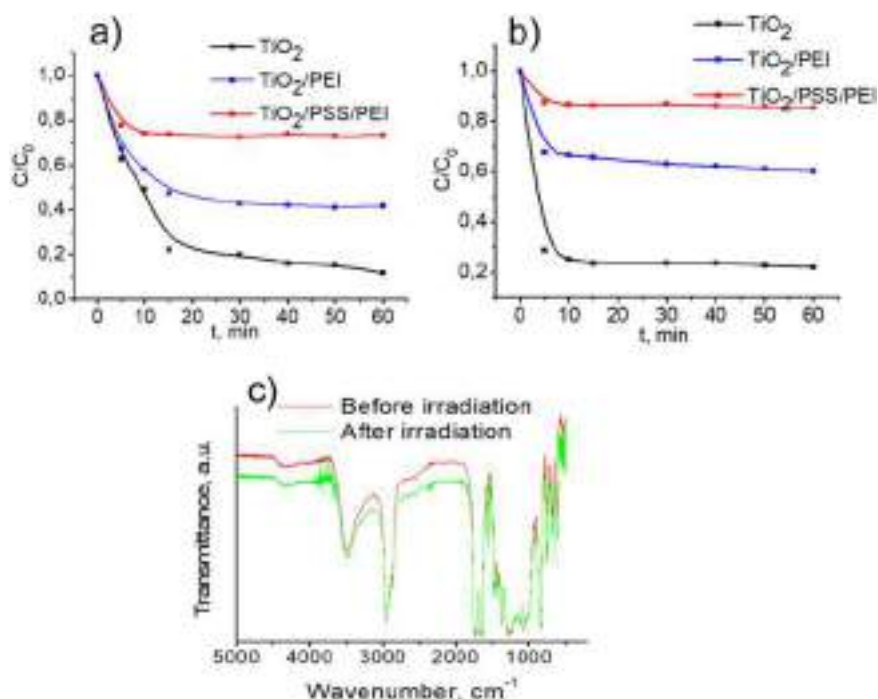
Fig. 4 a The schematic illustration of TiO₂ film preparation by inkjet printing. Inset—SEM image of the obtained print, **b** chronoampero-metric measurements of the samples at +0.25 V in 0.05 M Na₂SO₄, **c** i–V curves under chopped illumination on TiO₂ film and coated with polyelectrolytes

(ca. 4.5 µA/cm² at 1.0 V vs. Ag/AgCl) in comparison with pure TiO₂.

The chronoamperometric curves were measured at the potential +0.25 V (Fig. 4b). As it can be observed from Fig. 4b in the moment of light switching the great excitement of the photocurrent value takes place demonstrating the rapid initial generation of electron–hole pairs. The photocurrent decrease over the first minutes of the irradiation is observed and it can be related to the charge recombination within the film as the photoholes migrate toward the surface to

combine with Red/Ox species in the solution, the photo-electrons move to the opposite direction. Then the photo-current reaches the steady-state value when the photocharge generation and recombination reach equilibrium. As it can be observed from Fig. 4b, the photocurrent reaches its steady-state value at different time of irradiation in the case of pristine TiO_2 and after the deposition of polyelectrolyte layers. After the deposition of PEI layer, the equilibrium between the rates of charge generation and its recombina-tion reach equilibrium faster than in the case of pristine TiO_2. The deposited PEI slightly affects the photocurrent steady-state value but when it is separated from the TiO_2 film with the nanometer thick layer of PSS (which thickness comprises ca. 5 nm) the photocurrent decreases drastically. This may be related to different buffer activities of the PEI layer [30]. When it is deposited directly on the TiO_2 surface it may absorb the photogenerated protons less effectively in the case of that deposited onto the PSS layer. In the moment of the switching the light off the photocurrent reaches the cathodic values which can be attributed to the discharging of the double layer on the Si substrate. The obtained inkjet prints with different chemistries can potentially find appli-cation as planar batteries that can produce gradient currents and can easily charge/discharge.

4 Conclusions

In this paper, the possibility of TiO_2-based photoactive layers preparation has been demonstrated for pristine TiO_2 or TiO_2 modified by polyelectrolytes. By varying the nanoarchitecture of the deposited polyelectrolyte layers it has been shown that the photoactivity of the titanium dioxide film can be changed drastically. The influence of the composition and the consequence of the PEI buffering layer deposition on the photocatalytic and photoelec-trochemical properties of titanium dioxide have been investigated. The PEI nanolayer can decrease the photo-activity of the system up to 2–2.5 times, the nanoarchi-tecture of the deposited polyelectrolyte PSS/PEI decreases photocatalytic activity of TiO_2/PSS/PEI in comparison with pure TiO_2 ca. 4–4.5 time. This can be related to the different "proton-sponge" activity that exhibit PEI nanolayer either being deposited directly onto the TiO_2 surface or being separated from it with the nanolayer of PSS.

Compliance with ethical standards

Conflict of interest The authors declare that they have no conflict of interest.

References

1. Decher G, Schlenoff JB (2006) Multilayer thin films: sequential assembly of nanocomposite materials. Wiley-VCH, Weinheim
2. Mauser T, Dejugnat C, Sukhorukov G (2004) Reversible pH-dependent properties of multilayer microcapsules made of weak polyelectrolytes. Macromol Rap Commun 25:1781–1785
3. Andreeva DV, Sviridov DV, Masik A, Möhwald H, Skorb EV (2012) Nanoengineered metal surface capsules: construction of a metal-protection system. Small 8:820–825
4. Ilyas S, de Grooth J, Nijmeijer K, de Vos WM (2014) Multi-functional polyelectrolyte multilayers as nanofiltration membranes and as sacrificial layers for easy membrane cleaning. J Colloid Interface Sci 446:386–393
5. Jiang B, Barnett JB, Li B, (2009) Advances in polyelectrolyte multilayer nanofilms as tunable drug delivery systems Nano-technol Sci Appl 2:21–27
6. Séon L, Lavalle P, Schaaf P, Boulmedais F (2015) Polyelectrolyte multilayers: a versatile tool for preparing antimicrobial coatings. Langmuir 31(47):12856–12872
7. Minnikanti S, Gangopadhyay, Reyes DR (2014) Polyelectrolyte multilayers in microfluidic systems for biological applications. Polymers 6(8):2100–2115
8. Berwald S & Meier-Haack J (2002). In: Tripathy SK, Kumar J, Nalwa HS (eds) Applications of polyelectrolytes and theoretical models. American Scientific Publication, Stevenson Ranch, CA
9. Decher G (1997) Fuzzy nanoassemblies: toward layered poly-meric multicomponents. Science 277(5330):1232–1237
10. Richardson JJ, Bjornmalm M, Caruso F (2014) Technology-driven layer-by-layer assembly of nanofilms. Science 348:aaa2491
11. Grubb PM, Subbaraman H, Park S, Akinwande D, Chen RT (2017) Inkjet printing of high performance transistors with micron order chemically set gaps. Sci Rep 1202. https://doi.org/10.1038/s41598-017-01391-2
12. Alamán J, Alicante R, Peña JI, Sánchez-Somolinos C (2016) Inkjet printing of functional materials for optical and photonic applications. Materials (Basel) 9(11):910
13. Gao M, Li L, Song Y (2017) Inkjet printing wearable electronic devices. J Mater Chem C 5:2971–2993
14. Mehta S, Murugeson S, Prakash BD (2016) Microbes based printing for fabrication of microlenses for organic light emitting diodes. Org Electron 35:199–207
15. Safaryan SM, Yakovlev AV, Vinogradov AV, Vinogradov VV (2017) Inkjet printing of the chromogen free oxidase based optical biosensors. Sens Actuators B: Chem 251:746–752
16. Yakovlev AV, Milichko AV, Vinogradov VV, Vinogradov AV (2016) Inkjet color printing by interference nanostructures. ACS Nano 10:3078–3086
17. Langlet M, Kim A, Audier M, Herrmann J (2002) Sol–gel pre-paration of photocatalytic TiO_2 films on polymer substrates. J Sol–Gel Sci Technol 25:223–234
18. Maltanava HM, Poznyak SK, Andreeva DV, Quevedo MC, Bastos AC, Tedim J, Ferreira MGS, Skorb EV (2017) Light-induced proton pumping with a semiconductor: vision for pho-toproton lateral separation and robust manipulation. ACS Appl Mater Interf 9(28):24282–24289
19. Gensel J, Borke T, Pazos-Perez N, Fery A, Andreeva DV, Bet-thausen E, Müller AHE, Möhwald H, Skorb EV (2012) Cavitation engineered 3D sponge networks and their application in active surface construction. Adv Mater 24:985
20. Ulasevich SA, Brezhneva N, Zhukova Y, Möhwald H, Fratzl P, Schacher FH, Sviridov DV, Andreeva DV, Skorb EV (2016) Switching the stiffness of polyelectrolyte assembly by light to control behavior of supported cells. Macromol Biosci 16:1422–1431

21. Andreeva DV, Melnyk I, Baidukova O, Skorb EV (2016) Local pH gradient initiated by light on TiO$_2$ for light-triggered modulation of polyhistidine-tagged proteins. ChemElectroChem 3:1306–1310

22. Andreeva DV, Kollath A, Brezhneva N, Sviridov DV, Cafferty BJ, Möhwald H, Skorb EV (2017) Using a chitosan nanolayer as an efficient pH buffer to protect pH-sensitive supramolecular-assemblies. PhysChemChemPhys 19:23843–23848

23. Moffatt S, Wiehle S, CristianoR J (2016) A multifunctional PEI-based cationic polyplex for enhanced systemic p53-mediated gene therapy. Gene Ther 13:1512–1523

24. Liang W-J, Wang F, Wen M, Jian J-X, Wang X-Z, Chen B, Tung C-H, Wu L-Z, (2015) Branched polyethylenimine improves hydrogen photoproduction from a CdSe quantum dot/[FeFe]-hydrogenase mimic system in neutral aqueous solutions. Chem - A Eur J 21(8):3187–3192

25. Park SH, Yang HN, Lee DC, Park KW, Kim WJ (2014) Electrochemical properties of polyethyleneimine-functionalized Pt-PEI/carbon black as a catalyst for polymer electrolyte membrane fuel cell. ElectrochimActa 125:141–148

26. Nakamura M, Sato N, Hoshi N, Sakata O (2011) Outer Helmholtz plane of the electrical double layer formed at the solid electrode-liquid interface ChemPhysChem 12:1430–1434

27. Skorb EV, Ustinovich EA, Kulak AI, Sviridov DV (2008) Photocatalytic activity of TiO$_2$:In$_2$O$_3$nanocomposite films towards the degradation of arylmethane and azo dyes. JPhotochemPhotobiol A: Chem 193:97–102

28. Maltanava H, Poznyak SK, Andreeva DV, Quevedo MC, Bastos AC, Tedim J, Ferreira MGS, Skorb EV (2017) Light induced proton pumping with a semiconductor: vision for PhotoProton lateral separation and robust manipulation. ACS Appl Mater Interfaces 9:24282–24289

29. Yakovlev AV, Milichko VA, Vinogradov VV, Vinogradov AV (2016) Inkjet color printing by interference nanostructures. ACS Nano 10(3):3078–3086

30. Skorb EV, Möhwald H, Andreeva DV (2017) How can one controllably use of natural ΔpH in polyelectrolyte multilayers? Adv Mater Interfaces 4(1):1600282. 1-15

Nanostructured Layer-by-Layer Polyelectrolyte Containers to Switch Biofilm Fluorescence

Anna A. Nikitina, Sviatlana A. Ulasevich, Ilia S. Kassirov, Ekaterina A. Bryushkova, Elena I. Koshel, and Ekaterina V. Skorb*

ITMO University, St. Petersburg 191002, Russian Federation

ABSTRACT: The development of stimuli-responsive nanocontainers is an issue of utmost importance for many applications such as targeted drug delivery, regulation of the cell and tissue behavior, making bacteria have useful functions and here converting light. The present work shows a new contribution to the design of polyelectrolyte (PE) containers based on surface modified mesoporous titania particles with deposited Ag nanoparticles to achieve chemical light upconversion via biofilms. The PE shell allows slowing down the kinetics of a release of loaded L-arabinose and switching the bacteria luminescence in a certain time. The hybrid $TiO_2/Ag/PE$ containers activated at 980 nm (IR) illumination demonstrate 10 times faster release of L-arabinose as opposed to non-activated containers. Fast IR-released L-arabinose switch bacteria fluorescence which we monitor at 510 nm. The approach described herein can be used in many applications where the target and delayed switching and light upconversion are required.
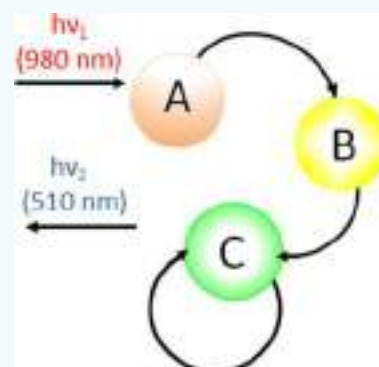
INTRODUCTION

During the last few decades, there has been increasing interest in the development of stimuli responsive materials for effective drug, peptide, protein, and DNA delivery.[1] These materials can amplify, suppress, modulate, or combine signals that they receive from the environment by incorporating in physico-chemical positive and negative feedback and delay mechanisms. The fabrication of functional hybrid materials comprised of nanoscale building blocks represents one way in which nanotechnology can contribute to biology and medicine ranging from drug delivery systems and targeted gene therapy to biosensors. Active chemicals, cells, and biomolecules are encapsulated to delay their activity, preventing interaction with aggressive environments.[2] A system based on stimuli responsive materials could even be used to regulate the microorganisms[3] quorum sense[4] and networking.[5] In our previous work, we were able to successfully design containers sensitive to ultraviolet (UV),[6] visible (vis),[7] and infrared (IR)[2] light, as well as couple light and temperature,[6] irradiation, and pH[8] to regulate cellular metabolisms of free and surface encapsulation systems.[9] Here we aim to make cells become fluorescent, opening novel direction for chemical light upconversion by biofilms triggered by nanoarchitectured smart containers.

Nowadays, the application of bacteria is of great interest. For example, purple nonsulfur bacteria can be used for hydrogen production during photoheterotrophic growth on a variety of organic substrates.[10] Photosynthetic bacteria are widely distributed around the world and can be used for wastewater treatment as they convert the organic carbon in wastewater to valuable biomass and pigments. There are some bioelectrochemical systems that exploit the ability of exoelectrogenic microbes to respire through transfer of electrons outside the cell.[11] Exoelectrogenic bacteria transfer electrons to the anode either through direct contact (via highly conductive nanowires or membrane-associated proteins)[12] or by using soluble electron shuttles.[13] Recently, several attempts have been made in the field of biological upconversion to use lanthanide-doped upconversion nanocrystals (UCNs) on the cell surface through copper-free click cyclization.[14] IR-light-sensitive UCNs doped with neodymium ions that can be activated by IR-laser excitation were attached to the tag through a modified dibenzyl cyclooctyne moiety. Upon 808 nm light illumination, the upconverted emission at 480 nm from UCNs could activate the light-gated channel rhodopsin-2 proteins (ChR2)[15] and therefore manipulate cation influx (e.g., Ca^{2+}) across the cell membrane to remotely regulate physiological processes under living conditions.

RESULTS AND DISCUSSION

Herein, we present a simple approach to the chemicobiological switching of bacteria fluorescence with IR light using nanoarchitectured container initiators and a metabolic bacteria pathway. It is based on feedback IR activation of the container (Scheme 1) with a substance that can effect bacteria metabolism to switch its bioluminescence. Containers (Scheme 1A) are nanoarchitectured for response to IR, and have controllable porosity for active molecule load and the ability to regulate the porosity and slow down intrinsic release by a polyelectrolyte (PE) shell. After irradiation of the containers at 980 nm, active molecules are released (Scheme 1B, L-arabinose). Active molecules switch the bacterial

Scheme 1. Signal Processing in a Biocompatible System That Communicates with Bacteria through Small Organic Molecules and Possesses Delayed Switching of Bioluminescence[a]
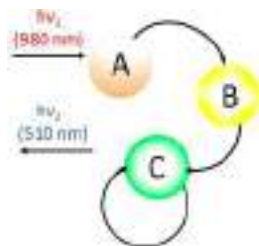
[a]The system is activated by IR-irradiation. (A) $TiO_2/Ag/PE$ container initiator loaded with L-arabinose; (B) L-arabinose releases from the container and switches bacterial (C) illumination through interfering with the bacterial metabolic network; (C) *Escherichia coli* XL-1 Blue pBAD-GFPuv (*E. coli*).

metabolism in the needed direction; here switching the fluorescent gene, we can detect light at 510 nm (Scheme 1C).

We use a known bacteria metabolic pathway to prove our idea. We study our system on the bacteria strain *Escherichia coli* (*E. coli*) XL-1 Blue with pBAD-GFPuv plasmid, which contains a gene for the synthesis of a green fluorescent protein (GFP) that is under the control of an arabinose promoter P_{BAD}. When L-arabinose is added to the nutrient medium, GFP synthesis is activated and the cells begin to fluoresce in the green spectrum (507 nm).[16−18] The excitation of fluorochrome in the protein has two peaks: 395 and 478 nm. The optimal concentration of arabinose in a medium for the induction of fluorescence is

0.1%. This highly fluorescent protein shows an emission peak at 510 nm with a quantum efficiency of 0.85, which is comparable to that of fluorescein.[17] The fluorescence of GFP is attributed to the chromophore that is formed as a result of a post-translational cyclization reaction and the subsequent oxidation of three amino acids, Ser65-Tyr66-Gly67, present in the protein.

Thus, we can switch chemicobiological upconversion even in complex biological models. These systems could find its applications in medicine, lab-on-chip technology, and when studying the specific regulation membrane-associated activities *in vivo*.[18]

The fluorescence induction by released from containers L-arabinose was studied in detail and carefully calibrated using a cytofluorimeter and cell culturing (Figure 1). The number of fluorescent cells and their fluorescence level, depending on the concentration of L-arabinose, were analyzed in a liquid medium and on Petri dishes in dense agar medium (Figure 1b−e). Under optimized conditions, the fluorescence emitted by GFP can be related to the concentration of L-arabinose present in the medium. Figure 1e−g shows significant GFP fluorescence at L-arabinose concentration of 0.01 wt % and after 7 h of incubation. The curve has a plateau after the concentration of 0.1 wt %.

Based on calibration we developed PE containers (Figure 2) able to release more than 0.01 wt % of L-arabinose at 980 nm. For this purpose, we optimize containers previously suggested by us[2,6] for loading and IR-release of L-arabinose. It should be mentioned that L-arabinose is a low-weight molecule and its size is much smaller than polyelectrolytes' size. In this regard, L-arabinose might penetrate through the PE shell. However, we
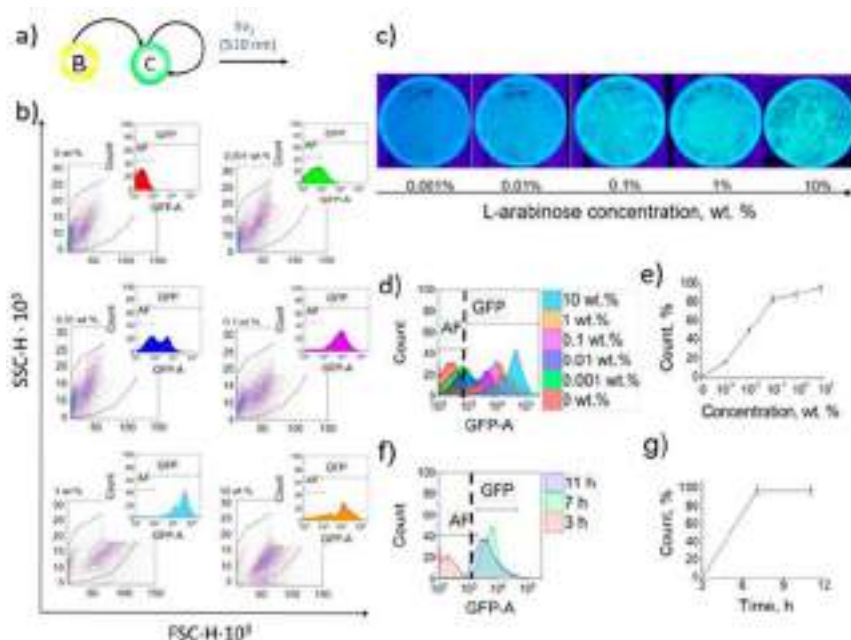
Figure 1. Calibration of *E. coli* XL-1 Blue pBAD-GFPuv response to L-arabinose. (a) Scheme of the bacteria switching by L-arabinose. (b) Calibration of the bacteria fluorescence in the presence of L-arabinose using flow cytometry. The colors in DotPlot mean that there is a large amount of events in points X and Y (green color means maximal number of events, blue−medium, violet−minimum numbers of events). Forward-scattered light (FSC) is proportional to cell-surface area or size. Side-scattered light (SSC) is proportional to cell granularity or internal complexity. Data were analyzed using Kaluza-analyzer 2.0 program. Inset shows the GFP fluorescence (higher than a control) in a cell system with L-arabinose. (c) Photos of Petri dishes (*d* = 90 mm) with separate bacterial colonies grown with an addition of L-arabinose at a concentration of 0.001, 0.01, 0.1, 1.0, and 10.0 wt %. (d,e) Overlay (d) and dependence (e) of the number of fluorescent cells on the L-arabinose concentration obtained from cytoflow data. (f,g) Dependence of GFP fluorescence on time after addition of 0.01 wt % of L-arabinose.
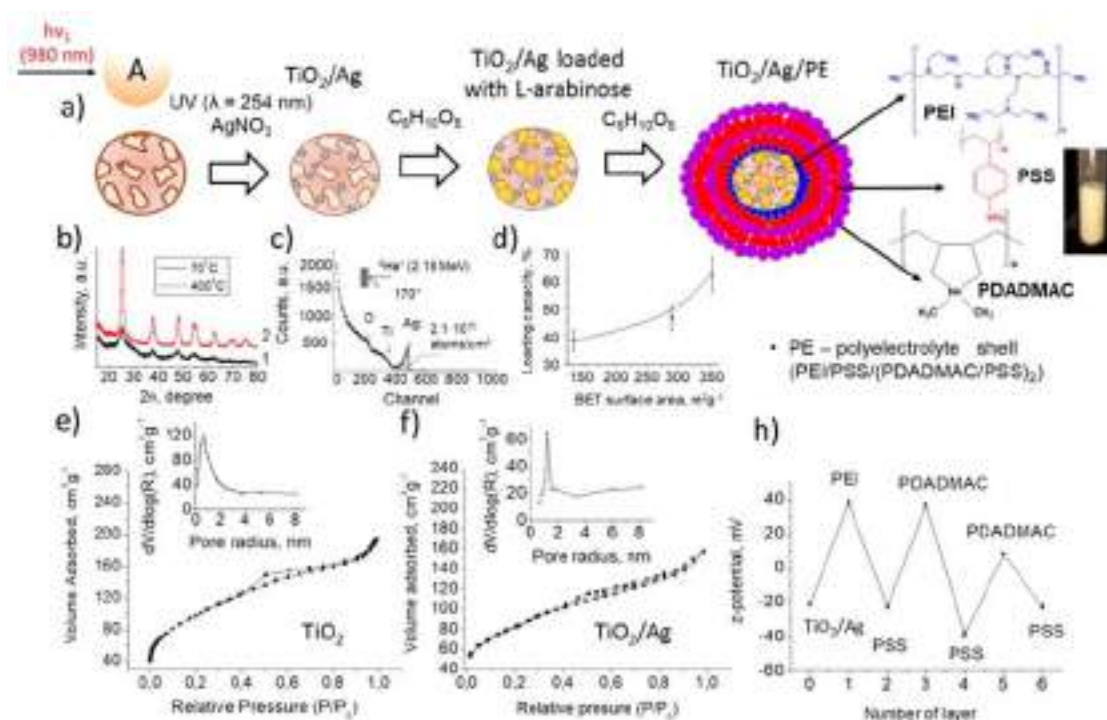
Figure 2. (a) Scheme of TiO$_2$/Ag/PE containers loaded with L-arabinose synthesis; inset shows the photo of TiO$_2$/Ag/PE containers. (b) XRD patterns of pristine TiO$_2$ powders dried at 70 °C (1) and 400 °C (2). (c) RBS data of the TiO$_2$/Ag powder. (d) Dependence of L-arabinose loading capacity value on BET surface area of pristine TiO$_2$ powder. (e) Nitrogen adsorption−desorption isotherms for TiO$_2$ powder obtained by oxidative destruction of TiC with nitric acid. Inset shows an average pore radius distribution in TiO$_2$. (f) Nitrogen absorption−desorption isotherms and corresponding pore size distributions (inset) of TiO$_2$/Ag powder. (h) zeta (ζ)-potential of particles during TiO$_2$/Ag/PE container nanoengineering.

have calibrated the system, as shown in Figure 1, to determine the optimal number of PE layers. As a result, we have selected the system with TiO$_2$/Ag/PEI/PSS/PDADMAC/PSS/PDAD-MAC/PSS structure. Three PE bilayers without IR-irradiation drastically slow down the release of L-arabinose at a concentration sufficient to activate the fluorescence of bacteria, but under IR-irradiation the PE shell opens and the concentration of released L-arabinose becomes enough to activate the fluorescence of bacteria. Using the system with less than three PE bilayers is not enough to suppress the penetration of L-arabinose in high concentrations. At the same time, increasing the number of PE layers reduces the colloid system stability and leads to a nonuniform distribution of the nanocontainers in the bacterial medium.

Titania, due to its unique photocatalytic properties coupled with a large surface area and high porosity, is a prospective material for the container core.[8,9] The synthesis of a mesoporous TiO$_2$ core has been carried out using a template-free method of a mild one-step oxidation reaction between nitric acid and titanium carbide, as a Ti-containing precursor, at 70 °C. The oxidation of black TiC powder by concentrated nitric acid gives a yellowish finely dispersed powder (Figure 2a, inset). The X-ray patterns of the synthesized nanoparticles dried at 70 °C and annealed at 400 °C are shown in Figure 2b. The strongest peak was observed for the (1 0 1) reflection at 2θ: 25.2°. Prominent peaks were also observed at 2θ: 37.9°, 48.0°, 54.7° that corresponds to (0 0 4), (2 0 0), and (2 1 1) reflections. All characteristic peaks are attributed to the anatase phase (JCPDS#21−1272). No peaks of rutile or brookite phases have not been detected. The mean crystallite size of TiO$_2$ is

calculated by the width of the (101) peak using Debye−Scherrer equation.[19] The mean crystallite size of TiO$_2$ increases from about 4 nm to about 7.4 nm on increasing the treatment temperature from 70 °C up to 400 °C.

To make the container sensitive to IR, silver nanoparticles were photocatalytically deposited onto TiO$_2$ using the method previously suggested by us.[20,21] The Rutherford backscattering spectrometry (RBS) spectrum of TiO$_2$/Ag show the width of Ti, O, and Ag concentration peaks (Figure 2c). The average amount of deposited Ag atoms is ca. 2×10^{15} atoms per cm^2.

Figure 2d shows the dependence of the value of the L-arabinose loading capacity inside the pore of particles on the surface area value. As we can see, the maximal loading capacity (more than 60%) corresponds to 350 m$^2 \cdot$g^{-1}. For design of the containers, we have decided to use TiO$_2$ powders with maximal surface area. How does the deposition of silver affect the surface area?

The mesoporous structure of TiO$_2$ and TiO$_2$/Ag powders has been investigated using N$_2$ adsorption−desorption isotherm measurements (Figure 2e,f). This kind of isotherm belongs to IV type with lag loop in the characteristics of the mesoporous solid which, in addition to the pore condensation step, shows an increase in adsorption at a high relative pressure due to textural porosity indicating the existence of very small particles.[6,20] BET surface area and total pore volume of initial TiO$_2$ powder reaches the values of 350 m^2 g^{-1} and 0.300 cm^3 g^{-1}, respectively. The pore size is distributed in a narrow range between 0.2 and 8.0 nm with an average pore size of about 1.0−2.0 nm. Silver deposition leads to a decrease in the surface area and pore volume to 287 m$^2 \cdot$g^{-1} and 0.129 cm^3 g^{-1}, respectively (Figure 2e,f insets), that indicates

clogging the pores with deposited silver particles. The pore size distribution remains the same, but the average pore size range is about 1.7−1.8 nm. Thus, TiO$_2$/Ag is suitable for L-arabinose loading.

The fabrication of a polyelectrolyte shell around the TiO$_2$/Ag core by the layer-by-layer (LbL) assembly (Figure 2a) of oppositely charged PE allows one to prevent the spontaneous release of loaded L-arabinose. The PE shell lends controlled release properties to the prepared containers. The opening of the shell can only be induced by changing the surrounding temperature value to the hot region (which happens when the containers are irradiated with an IR Laser at a wavelength of 980 nm), while at room temperature the PE shell remains intact preventing undesired leakage of the entrapped L-arabinose. When the containers are irradiated, the Ag nanoparticles serve as absorbing centers in the shells of the containers and heat up.[2,6,15,21] Being in contact with thermosensitive PE silver nanoparticles activates the PE shell followed by L-arabinose release.

The release kinetics of the entrapped L-arabinose into water at neutral pH is represented in Figure 3. As seen from Figure 3a, there is no absorbance peak of L-arabinose before IR-irradiation, but it appears after IR-irradiation during 2 min indicating the release of the L-arabinose from the prepared containers. Figure 3b shows the release profile of L-arabinose from initial TiO$_2$ (plot 1) and TiO$_2$/Ag/PE containers before

Figure 3. (a) Scheme of TiO$_2$/Ag/PE container activation by 980 nm laser. (b) UV−vis spectra of release solution before (1) and after (2) IR-irradiation (wavelength: 980 nm, power: 2000 mV) of TiO$_2$/Ag/PE capsules with L-arabinose. (c) L-Arabinose release (%) from initial TiO$_2$ particles (1) and TiO$_2$/Ag/PE capsules before (2) and after (3) IR-irradiation. (d) Percent ratio of L-arabinose release during 30 min from initial TiO$_2$ particles (1) and TiO$_2$/Ag/PE capsules before (2) and after (3) IR-irradiation. Abbreviations: PE − polyelectrolytes shell (PEI/PSS/(PDADMAC/PSS)$_2$); IR − IR-irradiation with a wavelength of 980 nm for 2 min.

(plot 2) and after (plot 3) IR-irradiation. Looking at the results reported in Figure 3 it is possible to conclude that the encapsulation efficiency (defined as effective loading/theoretical loading ratio) is always high (>90%). It is obvious that initial TiO$_2$ particles being immersed in water release the L-arabinose immediately. About 20% of the loaded L-arabinose is released during the first 30 min while TiO$_2$/Ag/PE containers release less than 10% (Figure 3c). It proves that the PE shell prevents the spontaneous release of L-arabinose. Approximately 90% of L-arabinose releases in water after 300 min of immersing TiO$_2$ containers in water while TiO$_2$/Ag/PE containers release about 70%. It should be mentioned that the activation of PE containers by IR light leads to fast release of L-arabinose.

Approximately 90% of L-arabinose is present in water 30 min after opening the containers. It could be modified by changing the PE conformation of the shell as well as altering the binding affinity between the polymer and the L-arabinose molecule.

The induction of cells' fluorescence by containers was studied under the conditions previously selected during the calibration using the flow cytometer. Preliminary analysis of a dense agar medium demonstrated the effectiveness of containers for delivery and control of L-arabinose release (not shown here). Using this method, it is possible to perform a visual assessment of the operation of the system. The fluorescence of experimental samples with opened containers visually corresponds to that of the control samples, where arabinose is added at a concentration of 0.1 wt %. More relevant results are obtained using the PE containers in a semiliquid agar, rather than in a dense one. This may be due to the mechanical action of the agar medium on the PE shell preventing the opening of the containers. It could also be explained by bad diffusion of L-arabinose through the dense agar layer. According to the scheme (Figure 4a), near-IR illumination at a wavelength of 980 nm will penetrate the bacteria and semiliquid agar activated by PE containers.

The opened PE containers release the L-arabinose that activates the synthesis of GFP leading to fluorescence with an emission at 510 nm. As shown in Figure 4b, there is no fluorescence of *E. coli* cultivated in semiliquid agar embedded with "closed" PE containers. In contrast, activation by IR-illumination leads to highly visible fluorescence after 7 h of activation. Based on the results of this experiment, it can be concluded that when using the developed system of active compounds release from containers, a controlled change in metabolic processes within the biofilm is possible. In this case, the bacterial biofilm is a macrocolony formed on an agar medium.

The optimum concentration of L-arabinose in the medium is found to be 0.1 wt % and can be achieved using designed PE containers. DotPlot data did not show a critical displacement of the cell population, which indicates that there is no significant effect of the containers on the viability of the cells. Thus, these PE capsules could also provide the delayed bioluminescence and act as personalized nanomedicines for various pathological disorders in the future.

We believe that our system can find its application in photodynamic therapy, which is a noninvasive method of care for the face and body. We think photodynamic therapy is very promising, as it uses narrow-band nonthermal light energy to activate the processes of natural cellular renewal and skin regeneration.

Figure 4. (a) Scheme of *E. coli* XL-1 Blue pBAD-GFPuv fluorescence activation by opened TiO$_2$/Ag/PE containers. (b) Negative microscope image of *E. coli* XL-1 Blue cultivated for 4 h on semiliquid agar with embedded TiO$_2$/Ag/PE containers before (left image) and after (right images) IR-irradiation (wavelength: 980 nm, power: 2000 mV). (c,d) Cell fluorescence of GFP in a system with "closed" (left) and "opened" (right) PE containers after incubating for 7 h.

CONCLUSION

In summary, we introduced a novel and simple strategy based on feedback between nanoarchitectured PE containers and bacteria to achieve nonphotonic chemicobiological upconversion: upon 980 nm light irradiation, a blue light (at 510 nm) from *E. coli* XL-1 could be emitted. There are several key points: (1) the system of controlled release of biomolecules from the containers works successfully in a biological system; (2) the containers themselves do not have a significant effect on bacterial cells, as can be seen from flow cytometry data; (3) the developed materials can induce metabolic processes in both plankton cells and in biofilms (in the macrocolony model); (4) the developed methods can be used to test similar systems in biological objects. The present strategy provides a site-specific and effective approach of using the living bacteria.

METHODS

Materials. Titanium carbide (TiC, 99.5% (metals basis)) was purchased from Alfa-Aesar. Polyethylenimine (PEI, $M_W \sim$ 750 000, 50% (w/v) solution), poly(sodium 4-styrenesulfonate) (PSS, $M_W \sim$ 1 000 000), Poly(diallyldimethylammonium chloride, (PDADMAC, $M_w \sim$ 200 000−350 000, 20% (w/v) solution in H$_2$O), L-arabinose (≥98%), sodium chloride, absolute ethanol, and HNO$_3$ were purchased from Sigma−Aldrich and used without further purification. The water was purified before use in a three stage Millipore Milli-Q Plus 185

purification system and had a resistivity higher than 18.2 MΩ cm^{-1}.

Synthesis of Surface-Modified Mesoporous TiO$_2$ Containers Loaded with L-Arabinose. Surface-modified mesoporous TiO$_2$ containers consist of a TiO$_2$/Ag core and a polyelectrolyte (PE) shell. A yellowish powder of TiO$_2$ was obtained by oxidizing 1.5 g of TiC (in black powder form) with concentrated nitric acid. The 4 M HNO$_3$ was added dropwise into a three-neck round-bottom flask with TiC at a rate of 2 drops per second. The synthesis was carried out in a water bath at 70 °C for 1 h. Then the yellowish precipitate was separated by filtration and washed 3 times with ethanol. As-prepared TiO$_2$ was dried at 70 °C in air and annealed at 200 °C (the heating rate was 10 °C·min^{-1}). Silver nanoparticles were deposited onto the photocatalytic TiO$_2$ surface during UV illumination (wavelength of 254 nm, power 5 W cm^{-2}) for 30−90 s in 10 μM AgNO$_3$ aqueous solution (Figure 1 a, the second stage).

L-Arabinose was loaded in the pores of TiO$_2$/Ag nanoparticles from 10 wt % solution of L-arabinose under vacuum for 1 h. The TiO$_2$/Ag particles were separated by centrifugation and then dried. The loading process was repeated two times (Figure 1a, the third stage). The PE shell was formed using Layer-by-Layer (LbL) deposition. Polyelectrolytes were dissolved in 1 M NaCl at a concentration of 2 mg·mL^{-1}. A positive PEI layer was deposited at the first stage mixing of the negatively charged TiO$_2$/Ag (0.5 wt %) solution with 2 mL of 2 mg mL^{-1} PEI solution for 15 min. Then, the TiO$_2$/Ag/PEI sample was washed three times by centrifugation at 5000 rpm for 5 min in 1 wt % L-arabinose solution to prevent the release of the loaded L-arabinose. This washing procedure was performed after each stage of PE deposition. The second PE layer was formed from a negatively charged PSS. The third layer was made from 2 mg mL^{-1} PDADMAC solution. The fourth layer was carried out from 2 mg mL^{-1} PSS solution. The procedure was repeated twice. The formation of the oppositely charged PE layers was determined by ζ-potential measurements (Figure 1f) using Photocor Compact-Z analyzer (Photocor, Russian Federation). The resulting PE shell consisted of PEI/PSS/PDADMAC/PSS/PDADMAC/PSS and as-prepared containers have a TiO$_2$/Ag/PEI/PSS/PDADMAC/PSS/PDADMAC/PSS structure (Figure 2a, the fourth stage).

L-Arabinose Release Studies. L-Arabinose release studies were performed on both "closed" and "opened" containers. L-Arabinose-loaded "closed" containers of 10 mg were placed in a quartz cuvette with 3 mL of Milli-Q water. At predetermined time intervals, 3 mL aliquots of aqueous suspension were centrifuged at 5000 rpm for 1 min and 2.8 mL of transparent solution separated from precipitate was subjected to the UV−vis analysis described above. The amount of released L-arabinose was calculated using an appropriate calibration curve. L-Arabinose release studies from "opened" containers were carried out using the same protocol, only on the containers previously activated by IR-irradiation for 2 min. ASP-SL IR Laser with a wavelength of 980 nm and output power of 1−2000 mW was used as an IR-irradiation source.

Nanoparticle Yield, Drug Loading, and Encapsulation Efficiency. The loading capacity of TiO$_2$/Ag/PE containers was calculated using the following equation:

$$\%LC = (\text{Weight of entrapped substance}$$
$$/\text{weight of nanoparticles}) \times 100\% \qquad (1)$$

The quantitative analysis of L-arabinose release was carried out with a Spectrophotometer UV-1800 (Schimadzu, Japan). Concentration determination was performed using UV detection at 278 nm, and was based on a previously created calibration curve. Encapsulation efficiency was expressed as a percentage of substance in the fabricated nanoparticles with respect to the initial amount of substance used for the preparation of nanoparticles:

$$\%EE = (\text{weight of substance in nanoparticles}$$
$$/\text{weight of substance fed initially}) \times 100\% \qquad (2)$$

Characterization Methods. The TiO_2 crystal structure was examined by X-ray diffraction on a PANalytical X'Pert PRO MRD (Multi-Purpose Research Diffractometer, Holland) with modular construction using Cu Kα-radiation. The recording speed was $0.4°$ min^{-1}. The qualitative and quantitative presence of Ag atoms in TiO_2/Ag powder were studied by the Rutherford backscattering spectrometry (RBS) technique using 2.18 MeV $^4He^+$ ions; the detector was placed at an angle of $170°$ with respect to incident beam direction. The BET adsorption/desorption isotherm was determined by nitrogen sorption at 77 K using a Surface area and pore size analyzer Quantachrome NOVA 1200 e Micromeritics (Quantachrome Instrument, USA). The weight of the freeze–dried samples was around 0.36 g. All samples were degassed under vacuum at 180 °C for 4 h before N_2 adsorption. Particle size and ζ-potential were measured using particle size and zeta potential analyzer Photocor Compact-Z (Photocor, Russian Federation). *Escherichia coli* XL-1 Blue with pBAD-GFPuv plasmid were used in this study. The strain used contains a gene for the synthesis of a green fluorescent protein (GFP) that is under the control of an arabinose promoter PBAD. When L-arabinose is added to the nutrient medium, GFP synthesis is activated and the cells begin to fluoresce in the green spectrum (510 nm).

Bacterial Test on Agar Medium and Quantitative Analysis on a Flow Cytometer. *Escherichia coli* XL-1 Blue with pBAD-GFPuv plasmid were used in this study. The strain used contains a gene for the synthesis of a green fluorescent protein (GFP) that is under the control of an arabinose promoter PBAD. When L-arabinose is added to the nutrient medium, GFP synthesis is activated and the cells begin to fluoresce in the green spectrum (507 nm). The excitation of fluorochrome in the protein has two peaks: 395 and 478 nm.

At the first stage, the system was tested visually by culturing bacteria on a dense and semidense LB agar medium. When calibrating the fluorescence dependence on the arabinose concentration, the latter was added directly to the medium at concentrations of 0.001, 0.01, 0.1, 1.0, and 10.0%. To analyze the fluorescence induction by arabinose from capsules, the latter were applied from above to the agar medium. The capsules were treated with an IR Laser at a wavelength of 980 nm for 2 min. Night cultures of *E. coli* with cell density 10^3 and 10^6 were inoculated on dense and semidense agar media in order to obtain isolated colonies and biofilms (macrocolonies), respectively. The dishes were incubated for 24 h at 37 °C. The results were analyzed visually using a UV-transilluminator.

For a more detailed quantitative analysis, bacterial cells were examined using flow cytometry. When calibrating the fluorescence dependence on the L-arabinose concentration, the latter was added directly to the medium at concentrations of 0.001, 0.01, 0.1, 1.0, and 10.0%. To analyze the fluorescence induction by L-arabinose from capsules, the latter were previously opened by IR Laser treatment for 2 min at a wavelength of 980 nm. After laser treatment, the capsule suspension was added to the medium at a concentration such that the concentration of released L-arabinose reached a value of 0.1%, the optimum concentration according to literature and our calibration. For preparation of control samples, the capsules were not previously opened and added to the culture medium unopened. After this, night cultures of *E. coli* with cell density 10^6 were inoculated in immunology plates. The samples were incubated at 37 °C for 24 h. After incubation, the samples were analyzed using a flow cytometer NovoCyte (ACEA Biosciences, USA) with parameters for FITC (excitation-488 nm, emission-525 nm). Each experiment was repeated three times. Fluorescence-based methods can also be used to enumerate bacteria. In the food and biotechnology industries, for instance, the automated counting of pure cultures by flow cytometry is well established.[22,23]

■ **AUTHOR INFORMATION**

Corresponding Author
*E-mail: skorb@corp.ifmo.ru.
ORCID ⊙
Ekaterina V. Skorb: 0000-0003-0888-1693

Notes
The authors declare no competing financial interest.

■ **REFERENCES**

(1) De Geest, B. G., De Koker, S., Sukhorukov, G. B., Kreft, O., Parak, W. J., Skirtach, A. G., Demeester, J., De Smedt, S. C., and Hennink, W. E. (2009) *Soft Matter 5*, 282−291.
(2) (a) Skorb, E. V., and Andreeva, D. V. (2015) *Polym. Int. 64*, 713−723. (b) Skorb, E. V., and Möhwald, H. (2013) *Adv. Mater. 25*, 5029−5043. (c) Zhang, X. H., Zhang, X. D., Lou, S. T., Zhang, Z. X., Sun, J. L., and Hu, J. (2004) *Langmuir 20*, 3813−3815.
(3) Bukreeva, T. V., Parakhonsky, B. V., Skirtach, A. G., Susha, A. S., and Sukhorukov, G. B. (2006) *Crystallogr. Rep. 51*, 863−869.
(4) Khalil, A. S., and Collins, J. J. (2010) *Nat. Rev. Genet. 11* (5), 367.
(5) (a) Lanchuk, Y., Nikitina, A., Brezhneva, N., Ulasevich, S. A., Semenov, S. N., and Skorb, E. V. (2018) *ChemCatChem 10* (8), 1798−1803. (b) Semenov, S. N., Ainla, A., Skorb, E. V., and Postma, S. (2018) *Isr. J. Chem. 58*, 781.
(6) (a) Skorb, E. V., Skirtach, A., Sviridov, D. V., Shchukin, D. G., and Möhwald, H. (2009) *ACS Nano 3*, 1753−1760. (b) Radziuk, D., Shchukin, D. G., Skirtach, A., Möhwald, H., and Sukhorukov, G. (2007) *Langmuir 23*, 4612−4617.
(7) Maltanava, H., Poznyak, S. K., Andreeva, D. V., Quevedo, M. C., Bastos, A. C., Tedim, J., Ferreira, M. G. S., and Skorb, E. V. (2017) *ACS Appl. Mater. Interfaces 9*, 24282−24289.
(8) (a) Ulasevich, S. A., Brezhneva, N., Zhukova, Y., Möhwald, H., Fratzl, P., Schacher, F. H., Andreeva, D. V., and Skorb, E. V. (2016) *Macromol. Biosci. 16*, 1422−1431. (b) Ulasevich, S. A., Brezesinski, G., Möhwald, H., Fratzl, P., Schacher, F. H., Poznyak, S. K., Andreeva, D.

V., and Skorb, E. V. (2016) *Angew. Chem., Int. Ed.* 55, 1−5. (c) Andreeva, D. V., Melnyk, I., Baidukova, O., and Skorb, E. V. (2016) *ChemElectroChem* 3, 1306−1310.

(9) Skorb, E. V., and Möhwald, H. (2014) *Adv. Mater. Interfaces 1*, 1400237.

(10) Golomysova, A., Gomelsky, M., and Ivanov, P. S. (2010) *Int. J. Hydrogen Energy* 35, 12751−12760.

(11) Ahn, Y., and Logan, B. E. (2010) *Bioresour. Technol.* 101, 469−475.

(12) Lovley, D. R. (2008) *Curr. Opin. Biotechnol.* 19, 564−571.

(13) Logan, B. E. (2009) *Nat. Rev. Microbiol.* 7, 375.

(14) Ai, X., Lyu, L., Zhang, Y., Tang, Y., Mu, J., Liu, F., Zhou, Y., Zuo, Zh., Liu, G., and Xing, B. (2017) *Angew. Chem., Int. Ed.* 56, 3031−3035.

(15) Nagel, G., Szellas, T., Huhn, W., Kateriya, S., Adeishvili, N., Berthold, P., Ollig, D., Hegemann, P., and Bamberg, E. (2003) *Proc. Natl. Acad. Sci. U. S. A.* 100, 13940−13945.

(16) Santala, V., Karp, M., and Santala, S. (2016) *FEMS Microbiol. Lett.* 363, 125.

(17) Hoffman, R. M. (2005) *Nat. Rev. Cancer* 5, 796.

(18) Shetty, R. S., Ramanathan, S., Badr, I. H. A., Wolford, J. L., and Daunert, S. (1999) *Anal. Chem.* 71 (4), 763−768.

(19) Campardelli, R., Della Porta, G., Gomez, V., Irusta, S., Reverchon, E., and Santamaria, J. (2013) *J. Nanopart. Res.* 15, 1987.

(20) Skorb, E. V., Antonouskaya, L. I., Belyasova, N. A., Shchukin, D. G., Möhwald, H., and Sviridov, D. V. (2008) *Appl. Catal., B* 84, 94−99.

(21) Skorb, E. V., Fix, D., Andreeva, D. V., Möhwald, H., and Shchukin, D. G. (2009) *Adv. Funct. Mater.* 19, 2373−2379.

(22) Papadimitriou, S., and Bikiaris, D. (2009) *J. Controlled Release* 138, 177−184.

(23) Gunasekera, T. S., Attfield, P., and Veal, D. A. (2000) *Appl. Environ. Microbiol.* 66, 1228−1232.

Eu modified Cu₂O thin films: Significant enhancement in efficiency of photoelectrochemical processes through suppression of charge carrier recombination

Sanjib Shyamal[a], Paramita Hajra[a], Harahari Mandal[a], Aparajita Bera[a], Debasis Sariket[a], Ashis Kumar Satpati[b], Mikalai V. Malashchonak[c], Alexander V. Mazanik[c], Olga V. Korolik[c], Anatoly I. Kulak[d], Ekaterina V. Skorb[e,f], Arjun Maity[g,h], Eugene A. Streltsov[c], Chinmoy Bhattacharya[a,*]

[a] Indian Institute of Engineering Science & Technology, Shibpur, Howrah 711103 West Bengal, India
[b] Analytical Chemistry Division, Bhabha Atomic Research Centre, Trombay, Mumbai 400085, India
[c] Belarusian State University, Nezavisimosti Av. 4, 220030 Minsk, Belarus
[d] Institute of General and Inorganic Chemistry, National Academy of Sciences of Belarus, Surganov St. 9/1, 220072 Minsk, Belarus
[e] Harvard University, Department of Chemistry & Chemical Biology, Oxford Street, Cambridge 02138, MA, United States
[f] ITMO University, St. Petersburg 197101, Russian Federation
[g] DST/CSIR Innovation Centre, National Centre for Nanostructured Materials, Pretoria 0001, South Africa
[h] University of Johannesburg, Department of Applied Chemistry, South Africa

GRAPHICAL ABSTRACT
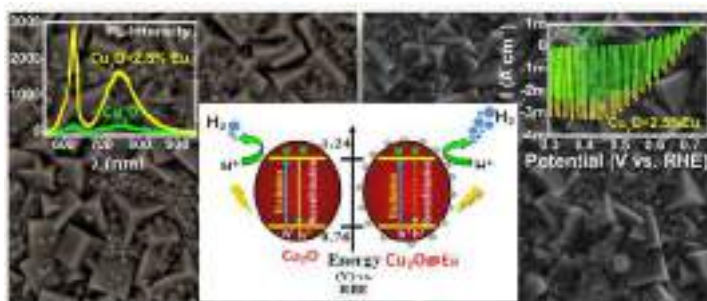
ARTICLE INFO

ABSTRACT

We propose a simple way to increase incident photon-to-current conversion efficiency (IPCE, Y) for electrodeposited p-type Cu₂O films through addition of Eu(III) to the electrodeposition bath. This is the first reported enhancement of photocurrent for Cu₂O modified with a rare-earth element. Our study is based on hypothesis that a large ionic radius of Eu(III) promotes its precipitation in form of inclusions of another phase, which act as getter centers leading to purification of host material from detrimental impurities and, correspondingly, to increase in lifetime of non-equilibrium charge carriers. SEM, EDX and XRD analyses indicate that addition of Eu (III) results in some increase of Cu₂O crystallite size and growth of a secondary Eu containing phase without changing the Cu₂O lattice parameters. Electrochemical impedance spectroscopy indicates invariance of acceptor concentration and flat band potential for Eu modified films. Remarkable increase of charge carriers' lifetime,

which manifests in the growth of Cu_2O exciton photoluminescence (PL) intensity and PL decay constant, leads to increased IPCE for the Eu modified films. Optimization of Eu(III) concentration in the electrodeposition bath allows attaining the cathodic photocurrent as high as $3.2\,mA\,cm^{-2}$ ($35\,mW\,cm^{-2}$ Xe lamp illumination), which is as $\approx 40\%$ greater than that for the pure Cu_2O film and corresponds to $Y \approx 100\%$ at wavelength $\lambda < 450\,nm$.

1. Introduction

Hydrogen evolution from renewable sources such as sunlight and water will be extremely important when the fossil-fuel supplies become depleted or when the environmental consequences of their burning are no longer acceptable. Nowadays, cuprous oxide (Cu_2O) is considered as an attractive material for the photoelectrochemical hydrogen production [1]. With a direct band gap of $\approx 2\,eV$, Cu_2O absorbs a significant part of the solar spectrum (maximal theoretical photocurrent density equals to $14.7\,mA\,cm^{-2}$ under AM1.5 illumination). Availability, low toxicity, as well as favorable energy band positions for solar water splitting are obvious advantages of this semiconductor.

Since Cu_2O usually possesses *p*-type conductivity, it is of interest for solar energy primarily as a photocathode for water photoelectrolysis (hydrogen production), photoreduction of carbon dioxide (hydrocarbonate anions) [2,3], or in solid-state hetorojunction solar cells with ZnO [4] or TiO_2 [5,6]. Currently, the electrochemical deposition of Cu_2O films [1,4–41] dominates among other known chemical and physical methods (thermal and radical oxidation of copper, sputtering, SILAR, CVD, $Cu(OH)_2$ reduction, spray pyrolysis). Electrodeposition is a simple, technological, non-wasteful and inexpensive way to form thin Cu_2O films on different large-area conducting substrates (including those with a complex geometric configuration).

The most common approach to electrosynthesis of Cu_2O is based on use of aqueous solutions containing copper salt (e.g., $CuSO_4$), ligand (most often, lactate anion) and alkali (NaOH) as main components. The copper is stabilized by complexing with lactate ion, and the pH can be raised to alkaline values. Formation of Cu_2O at a cathode occurs as a result of consecutive electrochemical and chemical processes [39]. Faradaic reduction of Cu(II) complexes gives rise to formation of Cu(I) in a cathodic space. Since Cu(I) does not form stable chelate complexes with bidentate ligands, lactate complex is destroyed in an alkaline medium with formation of a Cu_2O deposit.

It was demonstrated that cuprous oxides deposited at solution pH below 7.5 are *n*-type semiconductors, while cuprous oxides deposited at a solution pH above 9.0 possess *p*-type conductivity [31]. Use of solutions without lactate anions enables one to form *n*-Cu_2O in a slightly acidic medium (pH from 5.2 to 6.4) containing acetate buffer [32]. Variation of electrodeposition conditions (solution pH, deposition potential and temperature, concentration of dopants) allows in turn formation of *p*-Cu_2O/*n*-Cu_2O homojunction solar cells [32–34].

Polycrystalline deposits with a random orientation of grains are formed on most conductive substrates. Cu_2O crystallites have a characteristic cubic shape and a typical size of several micrometers. However, Cu_2O epitaxial structures can be grown on single crystalline substrates, in particular, Au [14], InP [15,16], Si [17]. Moreover, along with electrosynthesis of polycrystalline and epitaxial films, the methods for formation of Cu_2O nanowires, nanotubes and nanorods [18–21], as well as structures with a complex morphology [22–27] are developed.

Unfortunately, practical use of the Cu_2O photoelectrodes is limited by two essential drawbacks. The first one is photocorrosion instability in aqueous solutions (Cu_2O is thermodynamically unstable both to oxidation and reduction processes [1,38]). One of the promising ways to enhance photocorrosion hardness of the Cu_2O photocathodes in hydrogen evolution processes is protection of surface by thin ZnO and TiO_2 films formed by the atomic layer deposition [1,20,29]. Additionally, electrocatalytic properties of the surface can be improved by deposition of Pt [1,29] or RuO_x [20].

The second problem related to solar energy applications of

electrodeposited Cu_2O films is a rather small diffusion length of minority charge carriers (typically, a few tens of nanometers for electrons), which is much less than the depth of light penetration. As a consequence, the reported values of quantum efficiency for the photocathodes based on the electrodeposited Cu_2O films are usually significantly less than 100% ($\approx 1\%$ [24], $\approx 26\%$ [28], $\approx 70\%$ [20]) making relevant a looking for methods of charge recombination suppression. Our previous studies have demonstrated that properties of the electrodeposited Cu_2O films can be improved by variation of electrolyte composition [35,36]. Nevertheless, origins of these effects are not completely understood and require further research.

The goal of this study is to increase IPCE for electrodeposited Cu_2O films, whereas questions related to corrosion stability are outside of the scope of this work. We propose to improve the quantum efficiency by addition of europium (III) nitrate into electrodeposition solution containing copper (II) sulfate and lactic acid. Choice of Eu as a modifying additive is determined by the following reasons. Firstly, Eu^{3+} has the largest ionic radius among all lanthanides (0.109 nm), which exceeds significantly radius of Cu^+ (0.077 nm). This enables one to suppose that europium will not incorporate into the Cu_2O crystal lattice forming getter centers in the electrodeposited films and, hence, suppressing charge recombination in them. Similar approaches are applied often to improve parameters of different semiconductor materials and devices. For example, creation of internal getters in silicon wafers is widely used to increase lifetime and diffusion length of charge carriers due to bulk purification from detrimental impurities, which act as recombination centers [42,43]. Secondly, sufficiently negative standard electrode potential ($E^0_{Eu^{3+}/Eu^0} = -1.99\,V$) excludes the formation of metallic europium under cathodic electrode polarization.

There are some works devoted to the effects of Eu modifications for different semiconductors (Tables S1 and S2, Supplementary material). It has been noticed that addition of Eu improves the emission spectra of the host semiconductors, like TiO_2 [SR1-SR7], ZnO [SR8-SR11], ZnS [SR12-SR14], CdS [SR14, SR15], SiO_2 [SR16], $BaNb_2V_2O_{11}$ [SR17] etc. Among these, only some of them have reported change in photocatalytic activity of the semiconductors measured in terms of removal of pollutants [SR3], degradation of phenol [SR4, SR6], chloroform [SR7] and decoloration of dyes [SR17] and not describing the water splitting behavior. There are a rather limited number of publications dedicated to influence of rare-earths on the Cu_2O film morphology, and to the best of our knowledge, the idea to improve photoelectrochemical properties of Cu_2O films by creation of getter centers using rare-earth elements has not been suggested before.

It will be demonstrated below that an optimization of Eu(III) concentration in the electrodeposition bath enables to reach IPCE values close to 100% for the Cu_2O photocathodes.

2. Experimental section

2.1. Film preparation

2.1.1. Materials

Europium nitrate $Eu(NO_3)_3 \cdot 5H_2O$ (99.9%) was purchased from Sigma-Aldrich. Copper sulfate $CuSO_4 \cdot 5H_2O$, dipotassium hydrogen phosphate K_2HPO_4, lactic acid $CH_3CHOHCOOH$, potassium hydroxide KOH, Triton X-100 surfactant TX-100, sodium sulfate Na_2SO_4, sodium acetate CH_3COONa, acetic acid CH_3COOH were purchased from Merck (AR grade). The FTO-coated conducting glass substrates (20 Ω/sq, Kintech Technologies, Shanghai) were cleaned by subsequent

sonication in the soap solution, ethanol and deionized water.

2.1.2. Fabrication of photoelectrodes

Cu$_2$O thin films were electrodeposited from the mixture of copper sulfate and europium nitrate in a basic solution. Concentration of Cu^{2+} ions in the solution was equal to 0.2 M. Europium nitrate (0, 0.5, 1.25, 2.5, 5, or 10% with respect to the Cu^{2+} concentration) was dissolved in water with the subsequent addition of dipotassium hydrogen phosphate followed by copper sulfate, lactic acid, potassium hydroxide and TX-100 surfactant. The films were deposited at a constant current density of -0.1 mA cm^{-2} using a DC constant current source meter (Metravi, India) in a two-electrode configuration (a Pt foil served as the counter electrode) at 30 °C for 180 min.

2.2. Film characterization

The thickness of the Cu$_2$O films prepared with different concentrations of Eu(III) in electrolyte was determined gravimetrically to remain within 0.5 ± 0.02 µm; the density of Cu$_2$O was taken in calculations equal to 6.0 g/cc [44].

The surface morphology and elemental composition of the Cu$_2$O films were studied through scanning electron microscopy (SEM) and energy dispersive X-ray (EDX) analysis using a LEO 1455 VP Scanning Electron Microscope. Transmission spectra of the prepared thin films were measured using a MC122 spectrophotometer (Proscan Special Instruments, Belarus). The phase composition was identified by the X-ray diffraction (XRD) analysis at a scan rate of 0.5° min^{-1} using a Rigaku ULTIMA IV diffractometer (Bragg–Brentano geometry, Cu Kα emission). X-ray photoelectron spectra were obtained using a Thermo Scientific K-alpha spectrometer (Al K$_\alpha$ monochromatic X-ray source, Ar

gun for surface etching).

Photoluminescence (PL) and Raman spectra were recorded at room temperature using a Nanofinder HE (LOTIS TII, Belarus – Japan) confocal spectrometer. DPSS CW laser (473 nm) was used as an excitation source. Optical power was attenuated down to 10 µW to minimize the thermal impact on the samples. Incident beam was focused on the sample surface with a 100X Olympus lens (NA = 0.95). Backscattered light was dispersed on a 600 lines mm^{-1} diffraction grating with a spectral resolution better than 3 cm^{-1} (0.1 nm in the wavelength scale) and detected using a thermostated CCD matrix with a signal acquisition time typically equal to 60 s. Calibration was performed by means of a built-in gas-discharge lamp to an accuracy better than 3 cm^{-1} (0.1 nm). Lifetime of the photogenerated charge carriers was determined from PL decay kinetics at an excitation wavelength of 505 nm (Horiba, Deltadiode) with 625 emission wavelength and the spectral FWHM in continuous mode < 2 nm with the help of multifunctional time correlated single-photon counting (TCSPC) spectrophotometer (Model 1057, Fluorolog, Horiba Scientific Tech. USA).

2.3. Electrochemical impedance measurements

The electrochemical impedance measurements were carried out in pH 4.9 acetate buffer solution with 0.1 M Na$_2$SO$_4$ as supporting electrolyte with the help of Autolab-302, PG-Stat FRA-II (Metrohm, Netherlands) using the similar cell setup as detailed below. Variation of capacitance at the semiconductor-electrolyte interface (the Mott-Schottky analysis) was determined in the potential range from 0.78 to 0.28 V vs. RHE at a frequency of 1000 Hz and ac RMS amplitude of 10 mV.
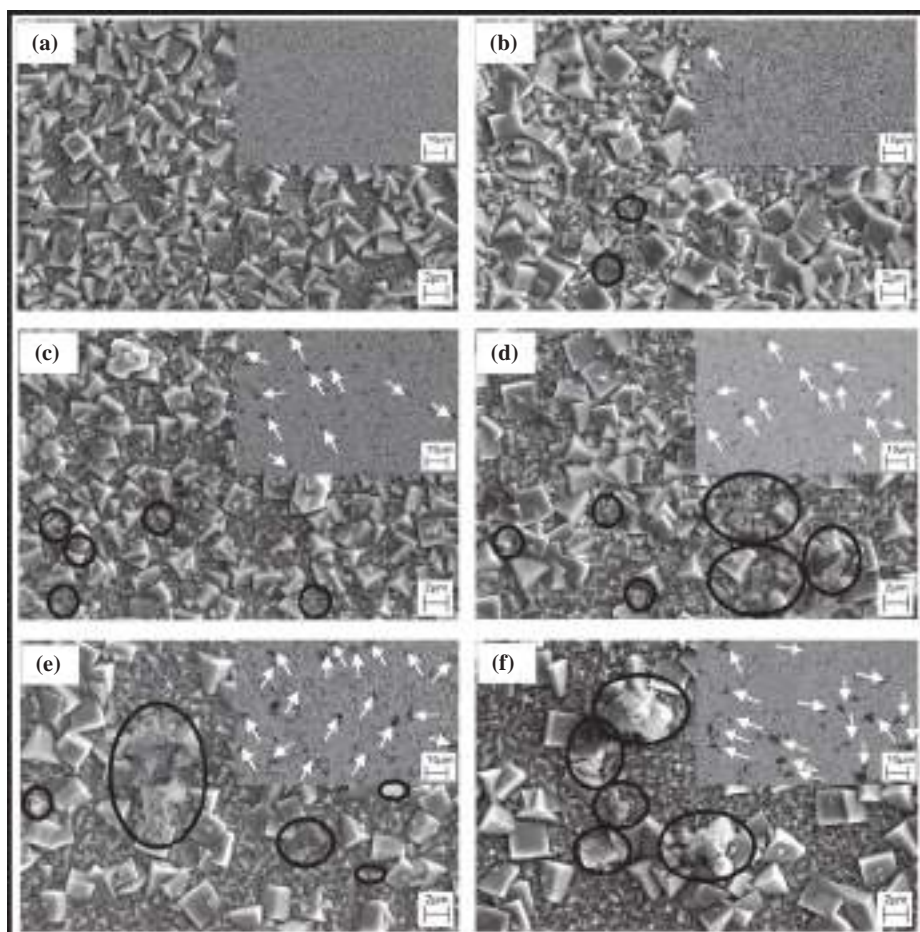
Fig. 1. SEM images of the Cu$_2$O films showing some precipitates (marked with black circles) along with cubic Cu$_2$O crystals. Images in the backscattering mode are given in insets indicating the presence of another phase (arrows). Eu(III) concentration in the electrolyte is 0% (a), 0.5% (b), 1.25% (c), 2.5% (d), 5% (e), and 10% (f).

2.4. Photoelectrochemical measurements

The photoelectrochemical properties of the prepared Cu_2O films were studied in a borosilicate glass cell with a three-electrode configuration containing a Pt rod counter and a saturated Ag/AgCl as the reference electrode. The potentials hereafter reported have been converted to the reversible hydrogen electrode (RHE). The Cu_2O working electrodes were exposed through an O-ring with a surface area of $0.27\ cm^2$. Linear sweep voltammetry (LSV) was carried out using a CHI-650E potentiostat within the potential range of 0.78–0.28 V vs. RHE with a scan rate of $10\ mV\ s^{-1}$. The photoresponse was measured under periodically chopped irradiation from Xe-arc lamp (Hammaan, India) as a white-light source with an incident beam intensity of $35\ mW\ cm^{-2}$, through an electrolyte containing $0.1\ M\ Na_2SO_4$ in $0.2\ M$ sodium acetate buffer (pH 4.9). Photocurrents were also measured under illumination of $100\ mW\ cm^{-2}$ using similar experimental setup to verify the effect of incident power on the PEC process.

Stability of the semiconductors undergoing photoelectrochemical H_2 evolution reaction was determined through chronoamperometry at a fixed applied potential of 0.4 V vs. RHE under constant illumination of $35\ mW\ cm^{-2}$, using similar cell configuration. The results were further verified through repeated LSV scan under periodic chopped illumination with calculation of relative deterioration of photocurrent.

PEC action spectra were measured with a high-intensity grating monochromator (spectral resolution 1 nm), a 250 W halogen lamp and a light chopper. The spectral dependences of IPCE were determined from the photocurrent and optical power of the incident monochromatic beam. The films were illuminated from the electrolyte side.

3. Results and discussion

3.1. SEM, EDX, XRD, XPS and optical characterization of Cu_2O films

SEM images demonstrate that the films are formed by cubic grains of different dimensions (Fig. 1), similar to earlier observations for the electrodeposited Cu_2O films reported by many authors. The size of the cubic grains increases to some extent with a gradual addition of Eu(III) to the electrolyte. The films deposited in presence of Eu(III) indicate some precipitates (marked with black circles) along with the main phase. These precipitates are formed possibly due to the growth of hydrated europium oxide or europium hydroxide [45] in the alkaline electrodeposition bath (pH 12–13). The SEM images obtained in the backscattering mode (insets in Fig. 1) indicate intense black spots (marked with arrows) arising from the different chemical phases as compared to the Cu_2O matrix. The pure Cu_2O films do not show such black spots, and their amount increases with a gradual rise of Eu(III) concentration in the electrodeposition bath.

EDX spectra taken under electron beam excitation of different spots on the film surface show that the "cubic" shaped particles contain primarily Cu and O without Eu (Fig. 2a) for all the films under investigation. However, for the films deposited in presence of Eu(III), EDX spectra show a definite amount of Eu (along with Cu, O from the underlaying Cu_2O grains and Sn from the FTO substrate), when secondary phase inclusions of irregular shape (marked as red circles in Fig. 1) are excited by the electron beam.

XRD patterns demonstrate peaks corresponding to the cubic Cu_2O structure (standard JCPDS file No. 05-0667) without noticeable change in their positions (Fig. 3). The absence of any peaks corresponding to Eu containing phases and retaining of "pure" Cu_2O crystallinity indicate that Eu is present in the films in amorphous forms and not being incorporated into the Cu_2O lattice. Additionally, a few peaks also appeared from the FTO substrate (standard JCPDS file No. 46-1088). The diffraction patterns demonstrate the strongest peak at $2\theta = 36.39°$ corresponding to the (*hkl*) value of (1 1 1) along with the others, (1 1 0), (2 0 0), (2 2 0), (3 1 1), and (2 2 2) for all the samples. The gradual increase of Eu(III) concentration in the electrodeposition bath leads to a

slight decrease in full width at half maxima (FWHM) for all peaks indicating the rise in grain size, particularly, for initial addition of Eu(III), as presented in Table 1. There is no significant modification of the film texture due to Eu(III) addition to the electrodeposition bath. One can suppose that the observed increase of grain size is related to decrease in number of electrocrystallization centers due to aggregation of defects by the europium containing inclusions.

In the Raman spectra, one can see the peaks at ≈ 216, ≈ 236, ≈ 300, ≈ 412, ≈ 498, ≈ 650, and $\approx 796\ cm^{-1}$ (Fig. 4). The two most intense peaks at ≈ 216 and $\approx 650\ cm^{-1}$ correspond to the two-phonon and one-phonon scattering processes in Cu_2O, respectively [46]. The latter band can be deconvoluted into two peaks at $632\ cm^{-1}$ and $650\ cm^{-1}$, which is a consequence of TO–LO splitting for polar oscillations.

Peak fitting by Lorentz lines has demonstrated that a gradual rise of Eu(III) concentration in the bath does not affect their position and width, which is consistent with the XRD analysis and points to conservation of Cu_2O intra-grain properties. At the same time, there is a clear increasing trend in the intensity of the two-phonon band at $\approx 216\ cm^{-1}$ relative to that for the one-phonon band at $\approx 650\ cm^{-1}$. Such effect, as well as an overall increase of Raman signal intensity, could be correlated to the strengthening of electron-phonon interaction in the films electrodeposited from Eu(III) containing solutions pointing to crystal quality improvement and being in a qualitative agreement with XRD and PL results (as discussed in the subsequent sections).

Raman peaks at ≈ 236, ≈ 412, ≈ 498, and $\approx 796\ cm^{-1}$ do not correspond to symmetry-allowed one-phonon scattering processes in Cu_2O, CuO or $Eu(OH)_3$ phases [46–48]. The position of the peak at $\approx 300\ cm^{-1}$ allows interpreting it as arising from one-phonon scattering in CuO [47], however, the absence of peak at $\approx 344\ cm^{-1}$ inherent to CuO in the measured spectra testifies in favor of its other nature. Tentatively, all these peaks could be explained by the presence
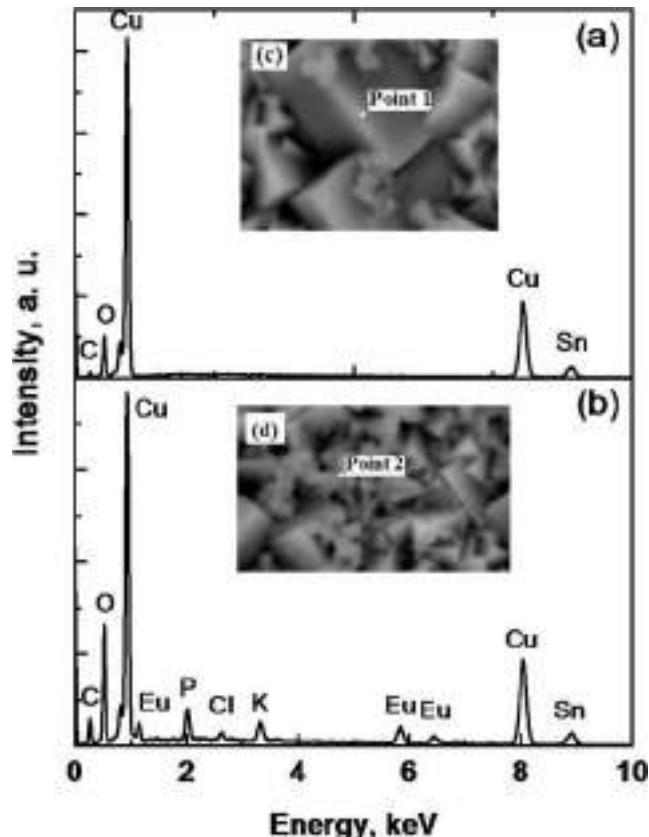
Fig. 2. EDX spectra from (a) cubic grain and (b) inclusion of irregular type for the Cu_2O film (Eu(III) concentration in the electrolyte of 2.5%). SEM images of corresponding surface regions are given in (c) and (d).
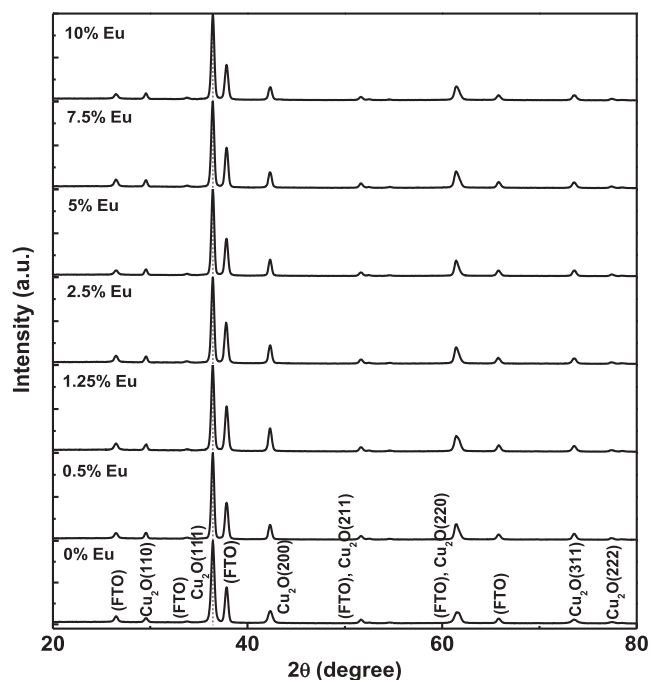
Fig. 3. XRD patterns of Cu$_2$O films deposited from electrolytes with different Eu(III) concentrations.

Fig. 4. Raman spectra of Cu$_2$O films deposited from electrolytes with different Eu(III) concentrations.

of some amorphous inclusions on the surface of the films. Meanwhile, they were observed by some researchers for Cu$_2$O films prepared using different techniques [49–51]. All these peaks are symmetry-forbidden in Cu$_2$O, and their observation points to relaxation of the symmetry-based selection rules. The most probable origin of symmetry breaking is presence of point defects (copper split vacancies) in the lattice [51]. The intensity of symmetry forbidden peaks (I_{SF}) relative to intensity of symmetry-allowed peaks (I_{SA}) inherent to Cu$_2$O changes from point to point for each sample, and no correlation between Eu(III) concentration in the electrodeposition bath and I_{SF}/I_{SA} ratio has been established.

XPS data show that addition of Eu(III) gives rise to increased intensity of the peaks corresponding to Cu(II) (Fig. 5a-c) [52]. Growth of Cu(II) content in the films could be explained by the known effect of coprecipitation of different hydroxides (Eu and Cu, in our case). However, in our experiments Cu(II) does not participate in photoelectrochemical processes because we used pH4.9 acetate buffer (acetic acid – sodium acetate) solutions, where Cu(II) is known to be selectively leached out [13]. As is seen from Fig. 5d, even after photoelectrochemical measurements, europium demonstrates peaks at ≈1135 and 1164 eV, which correspond to 3d$_{5/2}$ and 3d$_{3/2}$ electrons, respectively, and point to +3 oxidation stage [53]. This means that photocurrent increase for the Eu modified films (see below) is not related to reduction of Eu^{3+} cations.

The photoluminescence spectra of the films demonstrate two distinct bands (Fig. 6a). The high-energy band (≈625 nm) has a

complicated structure and corresponds to phonon-assisted exciton recombination, whereas low-energy one (≈750 nm) is known to be related to the oxygen vacancies [54]. The fundamental possibility to observe the exciton PL at room temperature is related to extremely high exciton Rydberg energy in Cu$_2$O (about 0.1 eV) [55]. However, it should be noted that no exciton PL was registered in number of works devoted to Cu$_2$O indicating a high crystalline perfectness of our films. Fitting of exciton band with three Gauss lines shows only slight (within 2.5 nm) change of its position with Eu(III) concentration in the electrodeposition bath, which correlates with invariance of band gap energy obtained from the Tauc analysis (see below). Fig. 6b demonstrates that the introduction of Eu(III) into the electrolytic bath leads to significant increase in intrinsic PL intensity for the Cu$_2$O films by approximately one order of magnitude, which means suppression of nonradiative recombination processes in the matrix. TCSPC measurements (Fig. S1, Supporting material) reveal that the lifetime of the charge carriers for pure Cu$_2$O appears as 91 ps and increases more than two fold (up to 206 ps) for the material deposited in presence of an optimized amount (2.5%) of Eu(III) in the electrodeposition bath. The observed increase in lifetime correlates qualitatively with the grain size enlargement, as discussed in SEM analysis and is further confirmed through variation of peak width in XRD patterns (Fig. 6b). At the same time, the relative change of the grain size in the films is rather slight, whereas the PL intensity increases dramatically, suggesting the contribution of additional mechanisms to explain this effect. As it was mentioned in Introduction, a large ionic radius of Eu^{3+} reduces its

Table 1
Results of XRD analysis for Cu$_2$O films: FWHM of (1 1 1) peak, calculated lattice parameter and grain size values, as well as intensity ratios for different peaks with respect to that of the strongest (1 1 1) peak depending on Eu(III) concentration in electrolyte.

Eu(III) concentration in electrolyte, %	(1 1 1) peak FWHM in 2θ scale, deg	Lattice parameter, nm	Grain size, nm	$I_{(200)}/I_{(111)}$ (theor = 0.37) JCPDS file No. 05-0667	$I_{(220)}/I_{(111)}$ (theor = 0.27) JCPDS file No. 050667
0	0.353	0.4268	39	0.186	0.238
0.5	0.300		50	0.181	0.283
1.25	0.315		46	0.284	0.315
2.5	0.308		48	0.227	0.295
5	0.299		50	0.192	0.259
10	0.311		47	0.165	0.268
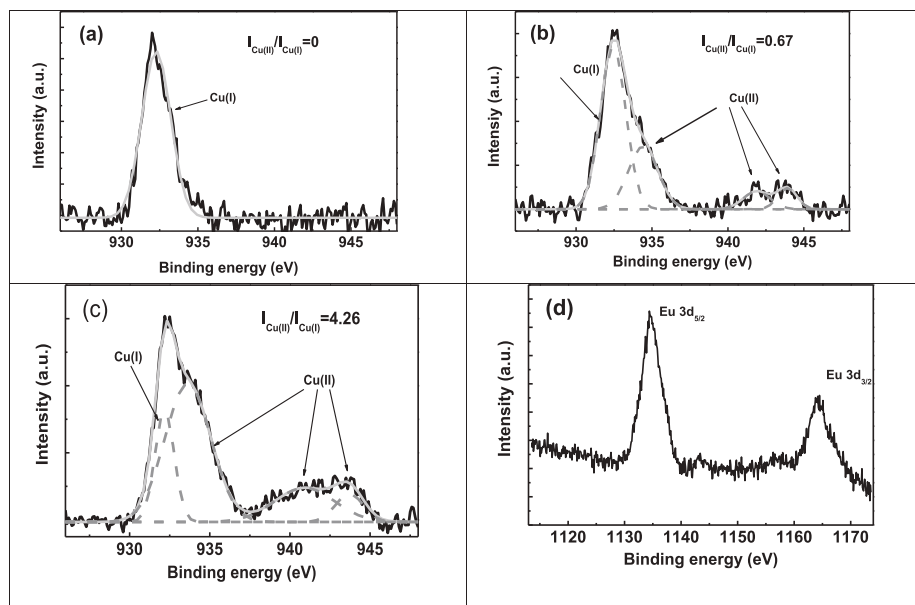
Fig. 5. XPS Cu 2p$_{3/2}$ high resolution spectra for the as-grown Cu$_2$O films deposited from electrolytes with Eu(III) concentrationsof 0% (a), 2.5% (b), and 10% (c); Eu 3d high resolution spectrum for the Cu$_2$O film(Eu(III) concentration in the electrolyte of 2.5%) after photoelectrochemical measurements.

solubility in the host lattice (Cu$_2$O) promoting precipitation in the form of separate phase inclusions. These precipitates can act as gettering centers for detrimental impurities giving rise to purification of Cu$_2$O grains. Subsequently, this leads to a prominent suppression of charge carrier recombination in the Cu$_2$O films and thereby PL enhancement, similar to our earlier observations for chalcogenide semiconductors [56]. Formation of precipitates is well known to be favorable at grain boundaries; therefore, their passivation can be tentatively considered as an additional possible mechanism of recombination suppression.

3.2. Impedance analysis

Variation of space-charge capacitance with applied potential (Mott-Schottky plot)at a typical frequency of 1000 Hz is presented in Fig. 7. Negative slopes demonstrate *p*-type conductivity of all Cu$_2$O films. The acceptor concentration (N_A) and the flat-band potential (E_{fb}) were estimated from the slope and intercept at potential axis, respectively, using the Mott-Schottky equation [57] with the relative dielectric permittivity of Cu$_2$O taken as 7.5 [58]. From the figure it is evident that the bulk properties, i.e. the acceptor concentration ($N_A = 8.6 \times 10^{16}$ cm^{-3}), as well as the flat band potential ($E_{fb} = 0.62$ V
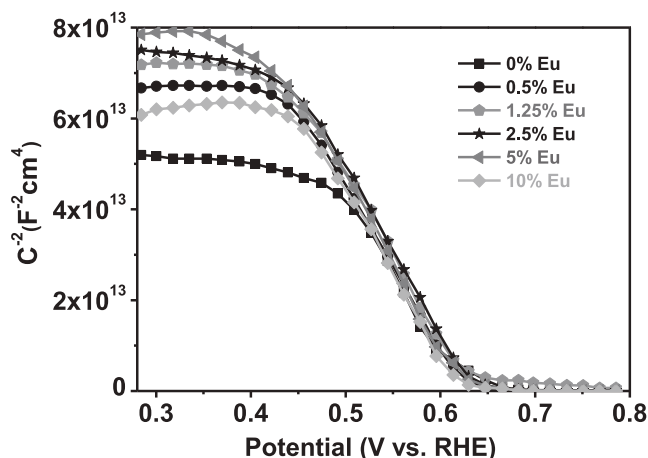
Fig. 7. Mott–Schottky plot at a typical ac frequency of 1000 Hz for Cu$_2$O films deposited from electrolytes with different Eu(III) concentrations.
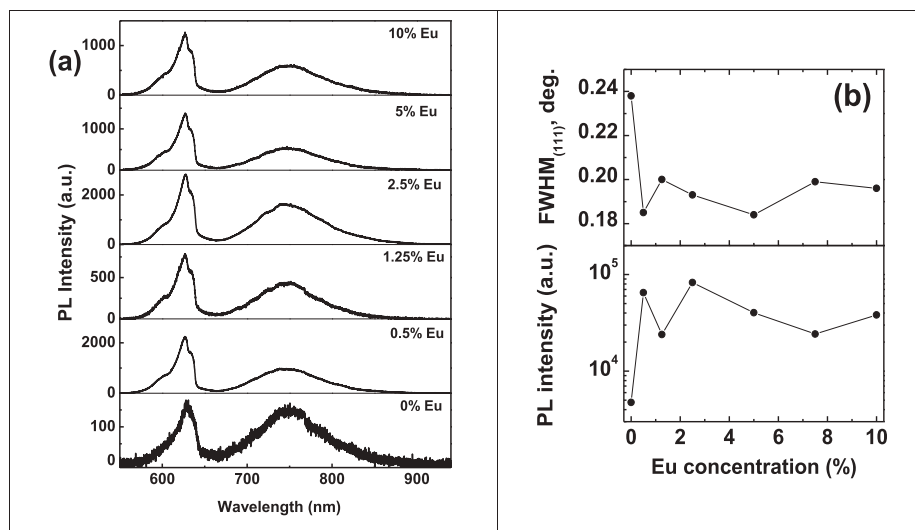
Fig. 6. (a) PL spectra of Cu$_2$O films deposited from electrolytes with different Eu(III) concentrations; (b) FWHM of Cu$_2$O (1 1 1) reflex and wavelength integrated intensity of Cu$_2$O exciton PL band vs. Eu(III) concentration in electrolyte.

vs. RHE) remain almost constant for all the films in depending of Eu(III) concentrations in the electrodeposition bath. Constancy of N_A points to absence of europium induced ion doping effect. The position of the conduction band (–1.74 V vs. RHE) as estimated from the experimental N_A, E_{fb} data and E_g value for direct allowed optical transitions (see below) is at more cathodic potential side compared to that required for reduction of H_2O indicating applicability of the present semiconductor for cathodic hydrogen evolution. Note that the calculated N_A value is overestimated to some extent because the geometrical surface area used in the Mott-Schottky equation is smaller as compared to the real surface area of the "Cu_2O-electrolyte" interface (Fig. 1).

3.3. Photoelectrochemical properties of Cu_2O films

The performances of the Cu_2O films were measured in terms of photocurrent through linear sweep voltammograms (Fig. 8) in 0.1 M Na_2SO_4–0.2 M acetate buffer solution (pH 4.9) under illumination with intensity of 35 mWcm^{-2}. The maximal output photocurrents for each of the electrodes, as measured from the respective LSV plots, are presented in Fig. 8 inset. It is evident that the photocurrent increases with a gradual addition of Eu(III) to the electrodeposition bath and reaches a maximum of 3.2 mA cm^{-2} at 2.5% Eu(III) concentration, beyond which it decreases again. The highest photocurrent observed for the Cu_2O film deposited from a solution containing 2.5% Eu(III) exceeds by 35–40% the photocurrent for the film obtained without Eu(III). Electrochemical behavior of the bare Eu-containing phases (i.e. film deposited from the said electrochemical bath in absence of Cu^{2+}) was evaluated through LSV under periodic illumination. Insignificant variation of current throughout the working potential range (as demonstrated by a nearly straight line plot in Fig. 8) indicates that the material reveals no PEC activity. The enhancement of photocurrent due to Eu(III) addition is observed also at higher intensity of incident light (100 mW cm^{-2} illumination, Fig. S2), although the photocurrent increases sublinearly with the light intensity.

Since we have not taken any measure to improve stability of the Eu modified Cu_2O films under illumination, the photocurrent demonstrated rather rapid decay (Fig. S3), which correlates with earlier experiments reported by other authors [59]. Stability of the

semiconductor was tested through periodic voltammetry under chopped illumination (Fig. S3, inset), and it was found with the increase in the number of LSV pattern that the rate of photocurrent decrease is reduced after 2nd successive scans. Time instability of the photocurrent is contributed by the reduction of Cu_2O to metallic Cu, which was even visually observed through formation of black spots over the surface when the electrode was immersed in electrolytic media under illumination. SEM analysis of the sample prepared with optimized Eu(III) concentration after polarization studies indicates some specific changes of the surface morphology, as presented in Fig. S4a. The XRD pattern (Fig. S4b) shows reflexes at 43.7, 50.2 and 74.3° corresponding to elemental Cu, which also supports the above observations. Similar results were also reported in literature [13].

Fig. 9 presents the variation of IPCE for the Cu_2O films in 0.1 M Na_2SO_4 solution (pH 4.9 acetate buffer solution) when a fixed potential of 0.4 V vs. RHE was held. The maximal IPCE value of ~100% was recorded for the Cu_2O film deposited from electrolyte with 2.5% Eu(III) concentration, which can be considered as optimal, whereas the "pure" Cu_2O exhibits only 40% IPCE.

Since the Cu_2O films reveal a pronounced light scattering effect (Fig. S5a), we used IPCE instead transmittance spectra for determination of band gap energy E_g taking into account that IPCE is proportional to the absorption coefficient near the absorption edge. Another advance of using IPCE spectra is determined by minimization of impact of absorption mechanisms unrelated to PEC reactions [60,61]. As is seen from Fig. S5b, where the Tauc plots are given for direct allowed optical transitions, the variation of Eu(III) concentration in the electrodeposition bath has only slight impact on E_g indicating that the increase of photocurrent in the Eu-modified films is not related to E_g decrease, and suppression of charge carriers recombination is the most plausible reason of the observed effect.

One can see from Fig. 9 that the maximal enhancement of IPCE is attained for long wavelength light, when majority of electron-hole pairs are generated outside of the space charge region (SCR) and high lifetime values are required for participation of carriers in PEC reactions. However, the similar enhancement of IPCE due to Eu(III) addition to the electrodeposition bath is observed also for a short wavelength light, which is absorbed mainly in the thin near-surface part of film. Fig. 10
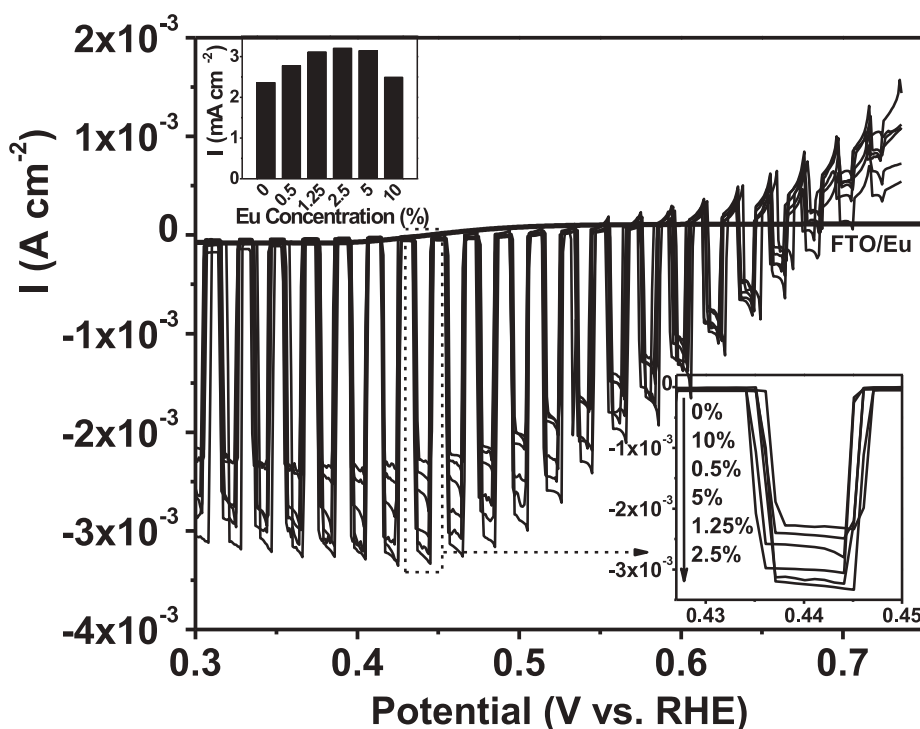
Fig. 8. LSV plots measured in pH 4.9 acetate buffer solution under UV–visible illumination (Xe: 35 mW cm^{-2}) for Cu_2O films deposited from electrolytes with different Eu (III) concentrations; inset: variation of the maximal photocurrent with Eu(III) concentration in deposition electrolyte.
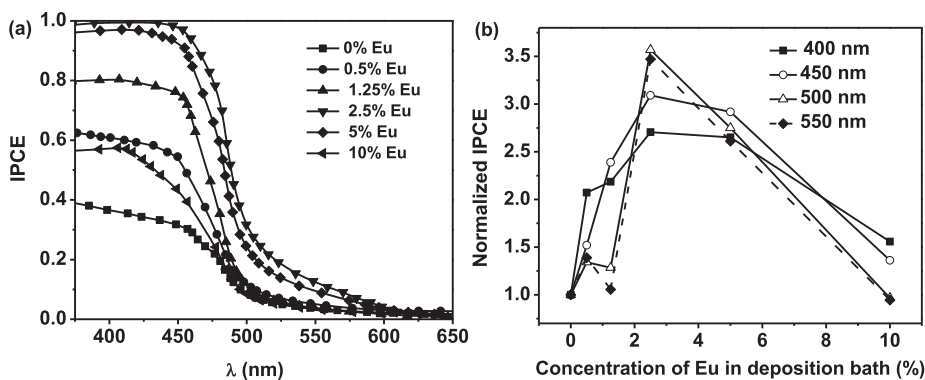
Fig. 9. (a) IPCE spectra for cathodic photocurrent for Cu$_2$O films deposited from electrolytes with different Eu(III) concentrations; (b) IPCE values derived from spectra presented in (a) and normalized to the corresponding values for the films grown without Eu(III) *vs* Eu(III) concentration in electrodeposition bath.
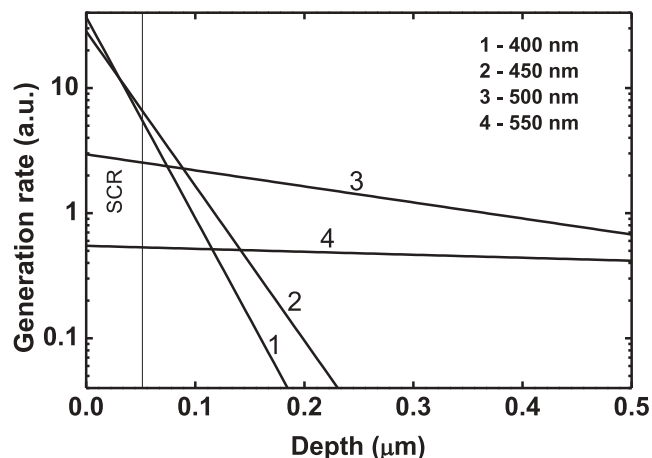
Fig. 10. Generation rate of electron-hole pairs depending on the depth for different wavelengths.

demonstrates in-depth profiles for generation rate of electron-hole pairs calculated using absorption coefficient values taken from [62]. The SCR width at potential of 0.4 V vs. RHE was estimated as $W_{scr} \approx 50$ nm from the Mott-Schottky plot (Fig. 7). In particular, for $\lambda = 400$ nm, 85% quanta are absorbed within the SCR. From this point of view, it seems strange that increase in lifetime of charge carriers influences remarkably on IPCE at this wavelength. To explain the afore-said contradiction, one should take into account that a conventional assumption about absence of recombination loss for the charge carriers generated within SCR is valid only if the following condition is true:

$$L_{dr} = \mu\tau E >> W_{scr}. \tag{1}$$

Here L_{dr} is the drift length of carriers, and μ and τ are their mobility and lifetime, respectively. According to the Poisson equation, the average electric field strength in SCR is

$$E = \frac{eN_A}{\varepsilon_0\varepsilon}\frac{W_{SCR}}{2} \approx 2.7\cdot10^6 \text{ Vm}^{-1}. \tag{2}$$

Taking from [24] $\mu \approx 5$ cm^{2}V^{-1}s^{-1} and $\tau \approx 90$ ps from our TCSPC experiments, we obtain $L_{dr} \approx 120$ nm, which is comparable with W_{SCR} and points to possibility of recombination of charge carriers generated within SCR.

Thus, the improved PEC performance of the Eu modified Cu$_2$O films over the pure material can be explained in the following way: (i) increase in size of the Cu$_2$O crystallites to some extent with a gradual addition of Eu(III) to the electrolytic bath leading to better coverage of the surface area and lowering of grain-boundary recombination; (ii) formation of a distinct Eu-containing precipitates which can act as gettering centers for detrimental impurities giving rise to purification of Cu$_2$O grains; (iii) this process in turn suppresses charge carrier recombination in the semiconductor matrix with increasing lifetime of

the carriers; (iv) the photogenerated electrons in the conduction band therefore have more opportunity to participate in photoelectrochemical reduction of H$_2$O to generate H$_2$.

4. Conclusions

We have reported for the first time the electrodeposition of rare earth (Eu) modified *p*-type Cu$_2$O thin films. Presence of an optimized Eu(III) concentration in the electrodeposition bath (2.5% in respect to Cu(II) concentration) provides the highest photocurrent of 3.2 mA cm^{-2} (~100% quantum efficiency at $\lambda < 450$ nm) compared to 2.3 mA cm^{-2} for pure Cu$_2$O, measured at 0.4 V vs. RHE under 35 mW cm^{-2} illumination in the aqueous electrolyte (pH 4.9 buffer). XRD studies indicate single-phase composition of the films, whereas SEM-EDX analysis demonstrates the inclusions of Eu containing secondary phase on their surface. Electrochemical impedance Mott-Schottky analysis also indicates no change in bulk properties of all the Eu modified films, as their acceptor concentration and flat band potential remain invariant. The presence of Eu(III) in the bath influences the material in different ways such as an increased grain size with passivation of non-radiative recombination centers, which significantly enhance the photoluminescence emissions (by order of magnitude) through suppression of non-radiative recombination of the photogenerated charge carriers. Increase of carrier lifetime in the Eu modified films provides their improved photoelectrochemical properties compared to the pure Cu$_2$O.

Appendix A. Supplementary data

Supplementary data associated with this article can be found, in the online version, at http://dx.doi.org/10.1016/j.cej.2017.11.004.

References

[1] A. Paracchino, V. Laporte, K. Sivula, M. Grätzel, E. Thimsen, Nat. Mater. 10 (2011) 456–461.
[2] X. An, K. Li, J. Tang, ChemSusChem 7 (2014) 1086–1093.
[3] A.D. Handoko, J. Tang, Int. J. Hydrogen Energy 38 (2013) 13017–13022.
[4] S.S. Jeong, A. Mittiga, E. Salza, A. Masci, S. Passerini, Electrochim. Acta 53 (2008) 2226–2231.
[5] P.E. de Jongh, D. Vanmaekelbergh, J.J. Kelly, Chem. Mater. 11 (1999) 3512–3517.
[6] K. Kardarian, D. Nunes, P.M. Sberna, A. Ginsburg, D.A. Keller, J.V. Pinto, J. Deuermeier, A.Y. Anderson, A. Zaban, R. Martins, E. Fortunato, Sol. Energy Mater. Sol. Cells 147 (2016) 27–36.
[7] A.E. Rakhshani, A.A. Al-Jassar, J. Varghese, Thin Solid Films 148 (1987) 191–201.
[8] A.E. Rakhshani, J. Varghese, Sol. Energy Mater. 15 (1987) 237–248.
[9] T.D. Golden, M.G. Shumsky, Y. Zhou, R.A. VanderWerf, R.A. Van Leeuwen, J.A. Switzer, Chem. Mater. 8 (1996) 2499–2504.
[10] P.E. de Jongh, D. Vanmaekelbergh, J.J. Kelly, J. Electrochem. Soc. 147 (2000) 486–489.
[11] T. Mahalingam, J.S.P. Chitra, S. Rajendran, M. Jayachandran, M.J. Chockalingam, J. Cryst. Growth 216 (2000) 304–310.
[12] W. Zhao, W. Fu, H. Yang, C. Tian, M. Li, Y. Li, L. Zhang, Y. Sui, X. Zhou, H. Chen, G. Zou, CrystEngComm 13 (2011) 2871–2877.
[13] A. Paracchino, J.C. Brauer, J.-E. Moser, E. Thimsen, M. Grätzel, J. Phys. Chem. C 116 (2012) 7341–7350.
[14] E.W. Bohannan, M.G. Shumsky, J.A. Switzer, Chem. Mater. 11 (1999) 2289–2291.
[15] R. Liu, E.W. Bohannan, J.A. Switzer, F. Oba, F. Ernst, Appl. Phys. Lett. 83 (2003) 1944–1946.
[16] R. Liu, F. Oba, E.W. Bohannan, F. Ernst, J.A. Switzer, Chem. Mater. 15 (2003) 4882–4885.
[17] J.A. Switzer, R. Liu, E.W. Bohannan, F. Ernst, J. Phys. Chem. B 106 (2002) 12369–12372.
[18] X. Liu, Y. Zhou, Appl. Phys. A 81 (2005) 685–689.
[19] J.-H. Zhong, G.-R. Li, Z.-L. Wang, Y.-N. Ou, Y.-X. Tong, Inorg. Chem. 50 (2011) 757–763.
[20] J. Luo, L. Steier, M.-K. Son, M. Schreier, M.T. Mayer, M. Grätzel, Nano Lett. 16 (2016) 1848–1857.
[21] Y.H. Lee, I.C. Leu, C.L. Liao, S.T. Chang, M.T. Wu, J.H. Yen, K.Z. Fung, Electrochem. Solid State Lett. 9 (2006) A207–A210.
[22] M.J. Siegfried, K.-S. Choi, Angew. Chem. 117 (2005) 3282–3287.
[23] C.J. Engel, T.A. Polson, J.R. Spado, J.M. Bell, A. Fillinger, J. Electrochem. Soc. 155 (2008) F37–F42.
[24] C.M. McShane, K.-S. Choi, J. Am. Chem. Soc. 131 (2009) 2561–2569.
[25] S. Bijani, M. Gabás, L. Martínez, J.R. Ramos-Barrado, J. Morales, Thin Solid Films 515 (2007) 5505–5511.
[26] M.J. Siegfried, K.-S. Choi, Angew. Chem. Int. Ed. 47 (2008) 368–372.
[27] L. Ma, Y. Lin, Y. Wang, J. Li, E. Wang, M. Qiu, Y. Yu, J. Phys. Chem. C 112 (2008) 18916–18922.
[28] J.N. Nian, C.C. Hu, H. Teng, Int. J. Hydrogen Energy 33 (2008) 2897–2903.
[29] A. Paracchino, N. Mathews, T. Hisatomi, M. Stefik, S. Tilley, M. Grätzel, Energy Environ. Sci. 5 (2012) 8673–8681.
[30] L.C. Wang, N.R. de Tacconi, C.R. Chenthamarakshan, K. Rajeshwar, M. Tao, Thin Solid Films 515 (2007) 3090–3095.
[31] L. Wang, M. Tao, Electrochem. Solid-State Lett. 10 (2007) H248–H250.
[32] K. Han, M. Tao, Sol. Energy Mater. Sol. Cells 93 (2009) 153–157.
[33] C. Zhu, M.J. Panzer, A.C.S. Appl, Mater. Interfaces 7 (2015) 5624–5628.
[34] C.M. McShane, W.P. Siripala, K.-S. Choi, J. Phys. Chem. Lett. 1 (2010) 2666–2670.
[35] S. Shyamal, P. Hajra, H. Mandal, J.K. Singh, A.K. Satpati, S. Pande, C. Bhattacharya, A.C.S. Appl, Mater. Interfaces 7 (2015) 18344–18352.
[36] S. Shyamal, P. Hajra, H. Mandal, A. Bera, D. Sariket, A.K. Satpati, S. Kundu, C. Bhattacharya, J. Mater. Chem. A 4 (2016) 9244–9252.
[37] K. Mizuno, M. Izaki, K. Murase, T. Shinagawa, M. Chigane, M. Inaba, A. Tasaka, Y. Awakura, J. Electrochem. Soc. 152 (2005) C179–C182.
[38] L. Wu, L.-k Tsui, N. Swami, G. Zangari, J. Phys. Chem. C 114 (2010) 11551–11556.
[39] M. Pourbaix Atlas of Electrochemical Equilibria in Aqueous Solutions, 2nd English ed. 1974 Houston National Association of Corrosion Engineers 384.
[40] Z. Zang, A. Nakamura, J. Temmyo, Optics Express 21 (2013) 11448–11454.
[41] Z. Zang, A. Nakamura, J. Temmyo, Mater. Lett. 92 (2013) 188–191.
[42] D. Gilles, E.R. Weber, S.K. Hahn, Phys. Rev. Lett. 64 (1990) 196–199.
[43] A.Y. Liu, C. Sun, V.P. Markevich, A.R. Peaker, J.D. Murphy, D. Macdonald, J. Appl. Phys. 120 (2016) 193103–193110.
[44] W.M. Haynes (Ed.). CRC Handbook of Chemistry and Physics, 96th ed., Boca Raton, 2015-16.
[45] Atlas of E-pH diagrams, Geological Survey of Japan Open File Report No.419, Naoto TAKENO, May 2005.
[46] P.F. Williams, S.P.S. Porto, Phys. Rev. B 8 (1973) 1782–1785.
[47] H. Hagemann, H. Bill, W. Sadowski, E.M. Walker, Solid State Commun. 73 (1990) 447–451.
[48] J.-G. Kang, Y. Jung, B.-K. Min, Y. Sohn, Appl. Surf. Sci. 314 (2014) 158–165.
[49] J.C. Hamilton, J.C. Farmer, R.J. Anderson, J. Electrochem. Soc. 133 (1986) 739–745.
[50] K. Reimann, K. Syassen, Phys. Rev. B 39 (1989) 11113.
[51] T. Sander, C.T. Reindl, M. Giar, B. Eifert, M. Heinemann, C. Heiliger, P.J. Klar, Phys. Rev. B 90 (2014) 045203.
[52] M.C. Biesinger, L.W.M. Lau, A.R. Gerson, R. St, C. Smart, Appl. Surf. Sci. 257 (2010) 887–898.
[53] D. Li, X. Zhang, L. Jin, D. Yang, Opt. Express 18 (2010) 27191–27196.
[54] Y. Wang, S. Li, H. Shi, K. Yu, Nanoscale 4 (2012) 7817–7824.
[55] E.F. Gross, N.A. Karryjew, Dokl. Akad. Nauk SSSR 84 (1952) 471–474.
[56] V. Grivickas, K. Gulbinas, V. Gavryushin, V. Bikbajevas, O.V. Korolik, A.V. Mazanik, A.K. Fedotov, Phys. Status Solidi RRL 8 (2014) 639–642.
[57] A.J. Bard, L.R. Faulkner, Electrochemical Methods Fundamentals and Application, second ed., John Wiley & Sons, New York, 2001.
[58] F. Pei, S. Wu, G. Wang, M. Xu, Y.S. Wang, L. Chen, J. Korean Phys. Soc. 55 (2009) 1243–1249.
[59] C. Li, Y. Li, J.J. Delaunay, A.C.S. Appl, Mater. Interfaces 6 (2014) 480–486.
[60] E.A. Bondarenko, E.A. Streltsov, M.V. Malashchonak, A.V. Mazanik, A.I. Kulak, E.V. Skorb, Adv. Mater. (2017), http://dx.doi.org/10.1002/adma.201702387.
[61] M.V. Malashchonak, E.A. Streltsov, D.A. Kuliomin, A.I. Kulak, A.V. Mazanik, Mater. Chem. Phys. 201 (2017) 189–193.
[62] C. Malerba, F. Biccari, C.L.A. Ricardo, M. D'Incau, P. Scardi, A. Mittiga, Sol. Energy Mater. Sol. Cells 95 (2011) 2848–2854.

Autocatalytic Cycles in a Copper-Catalyzed Azide−Alkyne Cycloaddition Reaction

Sergey N. Semenov,[†,⊥] Lee Belding,[†] Brian J. Cafferty,[†] Maral P.S. Mousavi,[†] Anastasiia M. Finogenova,[†] Ricardo S. Cruz,[†] Ekaterina V. Skorb,[†,∥] and George M. Whitesides*,[†,‡,§]

[†]Department of Chemistry and Chemical Biology, Harvard University, 12 Oxford Street, Cambridge, Massachusetts 02138, United States

[‡]Kavli Institute for Bionano Inspired Science and Technology, School of Engineering and Applied Sciences, Harvard University, 29 Oxford Street, Cambridge, Massachusetts 02138, United States

[§]Wyss Institute for Biologically Inspired Engineering, Harvard University, 60 Oxford Street, Cambridge, Massachusetts 02138, United States

S *Supporting Information*

ABSTRACT: This work describes the autocatalytic copper-catalyzed azide−alkyne cycloaddition (CuAAC) reaction between tripropargylamine and 2-azidoethanol in the presence of Cu(II) salts. The product of this reaction, *tris*-(hydroxyethyltriazolylmethyl)amine $(N(C_3N_3)_3)$, accelerates the cycloaddition reaction (and thus its own production) by two mechanisms: (i) by coordinating Cu(II) and promoting its reduction to Cu(I) and (ii) by enhancing the catalytic reactivity of Cu(I) in the cycloaddition step. Because of the cooperation of these two processes, a rate enhancement of >400× is observed over the course of the reaction. The kinetic profile of the autocatalysis can be controlled by using different azides and alkynes or ligands (e.g., ammonia) for Cu(II). When carried out in a layer of 1% agarose gel, and initiated by ascorbic acid, this autocatalytic reaction generates an autocatalytic front. This system is prototypical of autocatalytic reactions where the formation of a product, which acts as a ligand for a catalytic metal ion, enhances the production and activity of the catalyst.
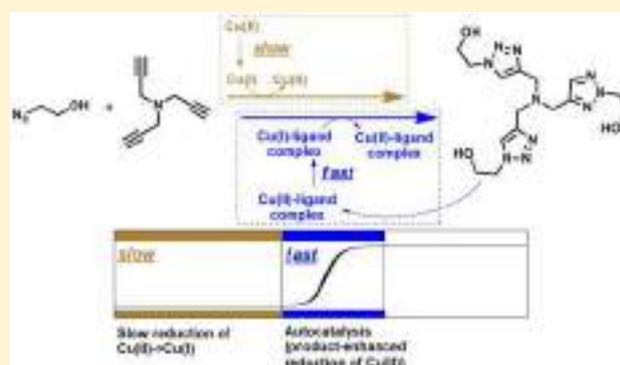
INTRODUCTION

Autoamplification and autocatalysis are important, although surprisingly uncommon, types of processes in chemistry.[1] Biological cellular division is, in a sense, a type of autoamplification. Flames and explosions are autocatalytic, as is the formose reaction,[2,3] silver-halide photography,[4] photolithography using chemically amplified photoresists,[5−7] crystallization, electroless deposition of metals,[8] the Soai reaction,[9−12] the formaldehyde−sulfite reaction,[13,14] and the removal of the 9-fluorenylmethoxycarbonyl (Fmoc) protecting group.[15] The Belousov−Zhabotinsky (BZ) reaction (the best known oscillating chemical reaction) has autocatalysis as a core element,[13,16,17] as does a reaction based on the Kent ligation, a reaction that we have designed to oscillate.[18]

This work describes an autocatalytic, copper-catalyzed, azide−alkyne cycloaddition (CuAAC) reaction that uses the designed reduction of Cu(II) to Cu(I) to generate autocatalysis. We can view the reaction as an autocatalytic cycle driven by the formation of a ligand that promotes the reduction of Cu(II) to Cu(I), where Cu(I) is the catalytic metal ion. This autocatalytic organic reaction has the potential to be applied to a broad range of substrates and represents a potentially general mechanism to use in the design of autocatalytic cycles.

Autoamplification and autocatalysis have been suggested as processes that contribute to the solution of two core problems in consideration of the origin of life, that is, "dilution" and "mixtures".[19,20] Although Eschenmoser, Sutherland, De Duve, Breslow, Wächtershäuser, Morowitz, and many others have famously demonstrated how simple, plausible prebiotic molecules (e.g., cyanide, formaldehyde, formamide, sulfur dioxide, hydrogen sulfide, carbon dioxide, others) can convert, usually, under *carefully* controlled laboratory conditions, into the more complex molecules that make up metabolism (or fragments of them),[2,21−28] it remains unclear how, or if, dilute solutions containing complex mixtures of these, and other, compounds would do so. One possible solution to these problems is for reactions to occur in enclosed or dimensionally constrained spaces (including, but not restricted to, liposomes or vesicles, water droplets in oil, cracks in rocks, evaporating ponds, freezing water) or adsorbed on surfaces.[29−32] A second

Scheme 1. Simplified Scheme Describing the Reactions That Are Involved in the Autocatalytic Formation of *tris*-(Hydroxyethyltrizolylmethyl)amine ($N(C_3N_3)_3$), *bis*-(Hydroxyethyltrizolylmethyl)propargylamine ($N(C_3)(N_3C_3)_2$), and (Hydroxyethyltrizolylmethyl)dipropargylamine ($N(C_3)(N_3C_3)_2$) from Tripropargylamine (1) and 2-Azidoethanol (2) in the Presence of CuSO_4[a]
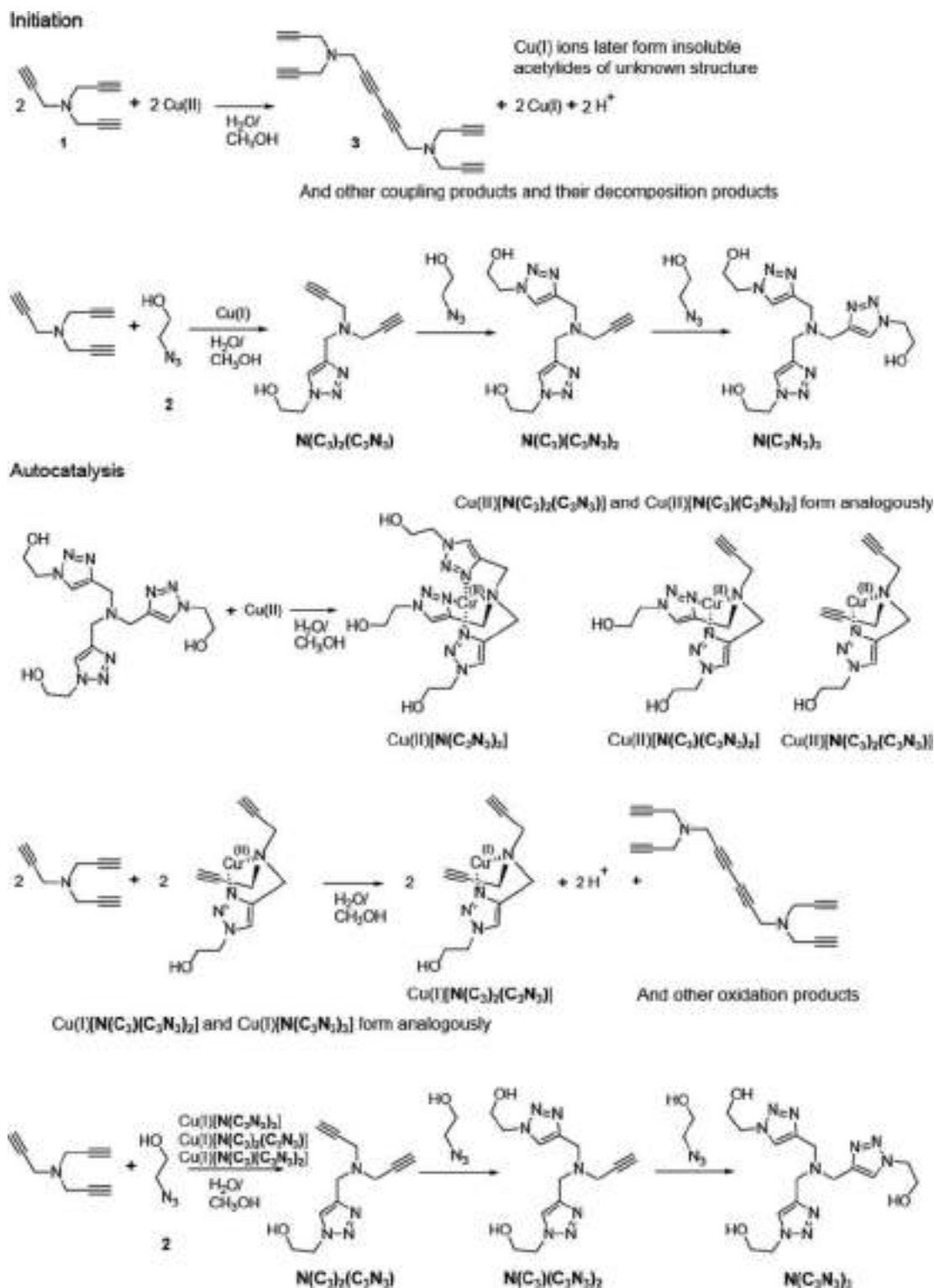
[a]The scheme uses the conversion of **1** to **3** to illustrate one plausible route for the initial reduction of Cu(II) to Cu(I) and does not consider alternative products from the oxidative coupling of **1** or the nature of the Cu(I) species in the initiation step. The abbreviations we use for the compounds (e.g., $N(C_3N_3)_3$) are indicated in bold-face text on the figure.

solution to the problem of dilution/mixtures is autocatalysis and autoamplification. Autoamplifying reactions, by providing very efficient conversion of specific reactants to specific products, might provide one mechanism for generating high local
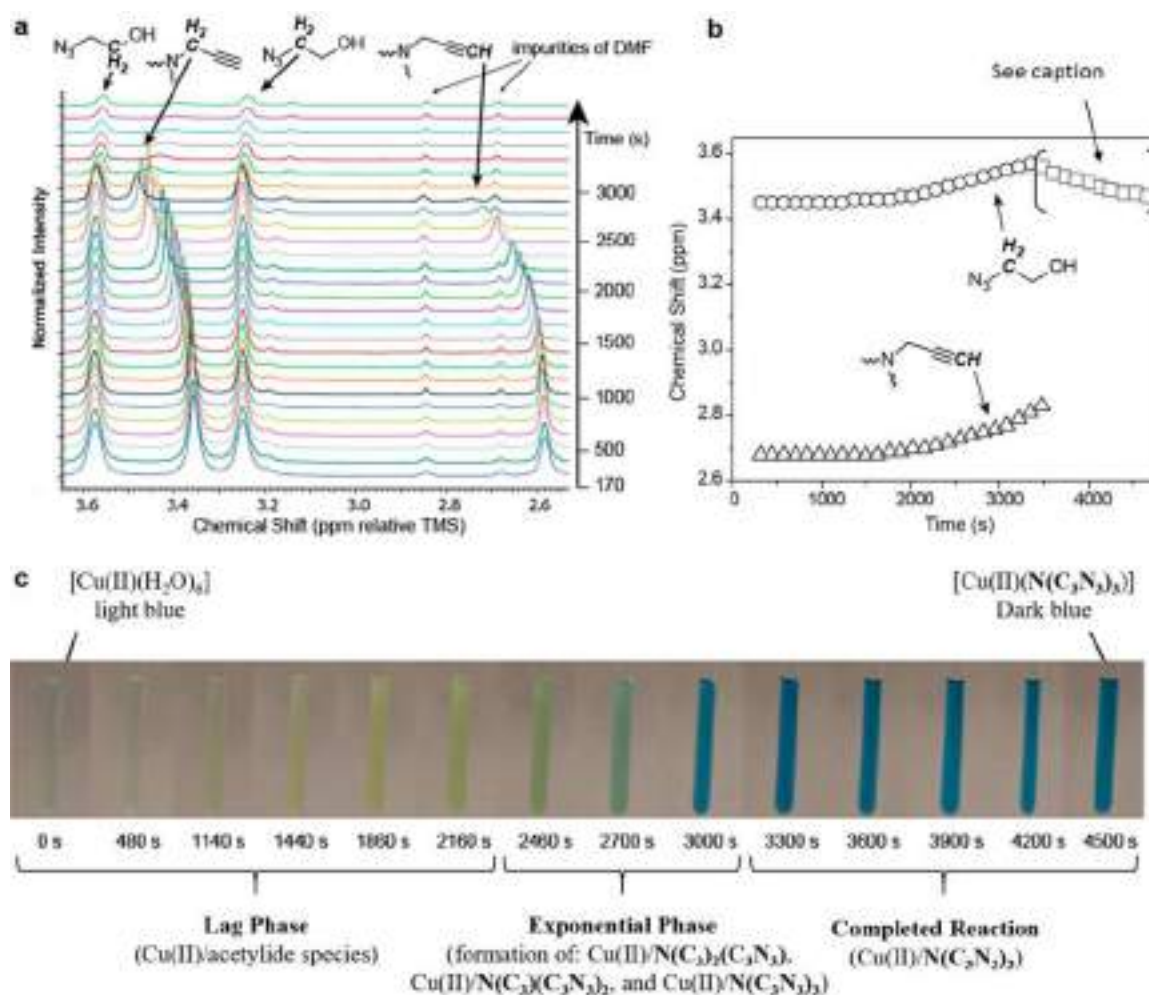
Figure 1. Time course of the reaction between tripropargylamine (**1**), 2-azidoethanol (**2**), and CuSO$_4$. Concentrations were estimated by integrating the alkyne proton against a *tert*-butanol internal standard. (a) ^{1}H NMR spectra showing the disappearance of the proton signals of **1** and **2** over time. (b) Plot of the chemical shifts of **1** during the first 3300 s of the reaction. After 3300 s, the alkyne protons (~2.6 ppm) disappear, and the propargylic protons (~ 3.4 ppm) change (bracketed region); this change indicates the formation of a small amount of a new species (□, whose structure we have not defined). (c) Images of an NMR tube containing the reaction mixture at different times. Standard reaction conditions were **1** (109 mM), **2** (309 mM), and CuSO$_4$ (43 mM) in a mixture of D$_2$O/CD$_3$OD (9:4, v:v) at 25 °C.

concentrations of these products. Autocatalysis thus might provide a route to increase the availability of particular molecules (or sets of molecules) important for the emergence of life.[1,33−37]

Multireaction systems that make up metabolism[38] do not ordinarily use direct autocatalysis, that is, processes in which a catalytic entity catalyzes its own production. Instead, complex autocatalytic cycles usually require multiple reactions to support autoamplification.[1,2,18,39,40] Acid-catalyzed hydrolysis of esters,[41] formation of trypsin from trypsinogen,[42] autophosphorylation of protein kinase CK2,[43] and oxidation of oxalic acid by permanganate are examples of direct autocatalysis.[44] The reverse Krebs cycle,[40,45] blood coagulation cascade,[46] thiol autocatalytic reaction,[18] and the formose reaction are examples of autocatalytic cycles.[2]

Although the subject of autoamplification/catalysis has been a subject of core interest in chemistry, it has proven very difficult to design new autocatalytic cycles from organic reactions. Despite the extraordinary versatility of organic chemistry, autocatalytic reactions are surprisingly rare, and almost all have been discovered by accident.[2,3,9,47] The literature on autocatalytic reactions directly relevant to the one we have

developed here is large but not predictive (at least so far) of new reactions.[1] Template-directed reactions, which were pioneered by von Kiedrowski and Rebek,[48−51] are an exception. These reactions are designed largely based on the rules of molecular recognition. They suffer, however, from product inhibition and small (usually less than an order of magnitude) difference in rates of templated and random reaction pathways and from structural complexity of the starting material.[52] Zubarev et al., in search of prebiotic precursors to the citric acid cycle, used computational approaches to propose plausible autocatalytic cycles in the chemistry of carboxylic acids.[40,53] Our group recently designed a simple autocatalytic cycle based on chemistry of organic thiols,[18] and Otto and co-workers developed, after initial incidental discovery, mechanochemical autocatalysis in assemblies of cyclic disulfides.[54]

Early work by Finn,[55] Fokin,[56] and Binder[57] suggested that the cycloaddition step of Cu(I)-catalyzed click reactions can be autocatalytic. Finn[55] and Fokin[56] noticed that *tris*-(triazolylmethyl)amines form Cu(I) complexes that are more reactive catalysts for cycloaddition and, therefore, suggested that the formation of *tris*-(triazolylmethyl)amines from *tris*-(alkynylmethyl)amines proceeds autocatalytically. Although

the kinetics of this autocatalysis has not been characterized, Binder reported a CuAAC-based polymerization that might also have proceeded autocatalytically, and Devaraj demonstrated that a CuAAC reaction can promote the autocatalytic formation of vesicles and nanoparticles.[58,59] These examples, which begin from catalytically active Cu(I) compounds, however, describe only modest rate enhancements (less than an order of magnitude) over the course of the reactions.

Our motivation for examining an autocatalytic copper-catalyzed click reaction, based on the reduction of an inactive Cu(II) starting material to a catalytically active Cu(I) species, was as follows: (i) Fokin[56] noted that tris-(triazolylmethyl)-amine ligands appeared to stabilize Cu(I) from disproportionation and increased the redox potential of Cu(I)/Cu(II) by nearly 300 mV. (ii) Zhu[60] observed that the CuAAC reaction proceeds with $Cu(OAc)_2$ in the absence of any added reducing agent and that the addition of 2 mol % of tris-(triazolylmethyl)-amine ligands increased the rate of the reaction. He suggested that "tris(triazolylmethyl)amine ligands may increase the thermodynamic driving force for the reduction of Cu(II) during the induction period to rapidly produce a highly catalytic Cu(I) species for the AAC reactions."[60]

The focus of this manuscript is on the participation of multiple reactions (reaction networks) to generate a strong autocatalytic rate enhancement, which is an important kinetic parameter for generating dynamic behaviors, such as oscillations and multistability, and for creating conditions for chemical evolution.

■ RESULTS AND DISCUSSION

We hypothesized that we could design an autocatalytic reaction with an initial reaction rate that is negligible, thereby creating a larger difference between the initial and final rates of the reaction by using, as a starting material, a water-soluble and catalytically inactive Cu(II) salt ($CuSO_4$). For increasing the concentration of the catalytic species, the triazole formed in this reaction must be a ligand that promotes the reduction of Cu(II) to Cu(I), where Cu(I) is required to form the active catalyst, which is likely a dynamic ensemble of multinuclear Cu(I) species. Scheme 1 outlines the major features of the system of reactions we have examined.

Kinetic Studies of the Reaction of Tripropargylamine with 2-Azidoethanol in the Presence of CuSO₄. We tested our hypothesis by allowing tripropargylamine (**1**) to react with 2-azidoethanol (**2**) and $CuSO_4$, in a water:methanol mixture (9:4; v:v) and monitored the reaction by ^{1}H NMR spectroscopy. We performed this reaction by adding a solution of **1** (109 mM) in CD_3OD to a solution of **2** (309 mM) and $CuSO_4$ (43 mM) in D_2O at room temperature (Figure 1a). The low concentrations of reactants, compared to previous studies,[55,56] allowed us to overcome issues with product inhibition[61,62] and to characterize the kinetics of the reaction in detail. Simple visual observation of the reaction showed an initially pale blue, almost clear, solution containing hydrated Cu(II) ions, which remained unchanged for ~20 min, before the solution became more opaque and, after ~50 min, changed to a dark blue color, a color typical of Cu(II) triazole complexes (Figure 1c). This apparent incubation period, followed by a relatively sudden change of color (associated with the formation of Cu(II) triazole complexes), suggested that the reaction among **1**, **2**, and $CuSO_4$ has an autocatalytic character.

Monitoring a reaction by NMR is often impractical in the presence of paramagnetic Cu(II) ions. Fortunately, however, the NMR signals of **1** and **2**, though slightly broad, were sufficiently sharp for quantitative spectroscopy and could be accurately integrated against an internal standard of tert-butanol. The reaction products, mono-, bis-, and tris-(triazolylmethyl)amines, however, were not visible in the NMR spectrum when Cu(II) ions were present.

To examine the kinetics of the reaction, we followed the disappearance of the alkyne proton of **1** at 2.6 ppm (Figure 1a). We used this proton to monitor the progress of the reaction because it appears in a clear region of the NMR spectrum and H-D exchange was negligible during an hour at pH 4.7 (which corresponds to the pH of the initial reaction mixture, see Supporting Information for details). The kinetic profile of the reaction resembled that of a typical autocatalytic reaction with a lag phase, exponential phase, and saturation phase (Figure 2a). The exponential phase was accompanied by a shift (of only partly identified origin) in the resonance frequency of the protons of **1** (Figure 1b), which correlated with the change in color of the solution to dark blue. We determined the final composition of the reaction mixture by reducing all remaining Cu(II) to $[Cu(I)(CN)_x]^{(x-1)-}$ with an excess of potassium cyanide[63,64] and analyzing the mixture by ^{1}H NMR spectroscopy. The final product of the reaction was the tripodal ligand tris-(2-hydroxyethyltriazolylmethyl)amine (which we abbreviate as $\mathbf{N(C_3N_3)_3}$), which formed in 85% yield (as determined by ^{1}H NMR); the methylene signal adjacent to the amine was integrated relative to an internal tert-butanol standard.

If a reaction is autocatalytic, then addition of the autocatalyst to the reaction will shorten its lag phase. We performed an NMR kinetics experiment, identical in form to the one described above, but with the addition of $\mathbf{N(C_3N_3)_3}$ (1 mol % relative to **1**) and observed a decrease in the duration of the lag phase by a factor of 3 (Figure 2a).

We also tested the reaction in a $H_2O:CH_3OH$ (9:4, v:v) mixture by monitoring the change in absorption at 650 nm (Figure 2b) because Cu(II)-triazolylmethylamine complexes absorb light more strongly at this wavelength than unbound Cu(II) (i.e., the aqua complex) (Figure S2). Unexpectedly, in the reaction without any added autocatalyst, there was no detectable reaction within the first 6000 s, and autocatalysis began only after 7000 s (~2 h) (Figure 2c; details of this difference in rate are discussed in a following section). The addition of 1 mol % (relative to **1**) of the autocatalyst—the mixture of complexes of mono-, bis-, and tris-(triazolylmethyl)-amines with copper from the previously complete reaction—shortened the lag phase to 1800 s, and the addition of 5 or 10 mol % of the autocatalyst completely eliminated the lag phase (Figure 2c).

During the reaction of **1** (109 mM), **2** (309 mM), and $CuSO_4$ (43 mM) in a $H_2O:CH_3OH$ (9:4, v:v) mixture, the pH of the solution increased from 4.7 to 6.2. To test whether this increase of 1.5 pH units contributed to autocatalysis, we ran the reaction in acetate buffer (340 mM) but under otherwise identical reaction conditions. The buffered reaction gave similar kinetics to that of the unbuffered reaction, suggesting that the change in pH does not contribute strongly to autocatalysis (Figure S3).

Propagation of an Autocatalytic Reaction Front. Autocatalytic reactions form autocatalytic fronts when they take place without mixing.[65] The observation of an autocatalytic front provides additional support for autocatalysis, as opposed to other mechanisms for delayed activation. For instance, simple CuAAC reactions accelerated by tris-triazolyl ligands can have observable lag phases.[66] Because the catalytic species in CuAAC reactions are multinuclear, and under most circumstances only a
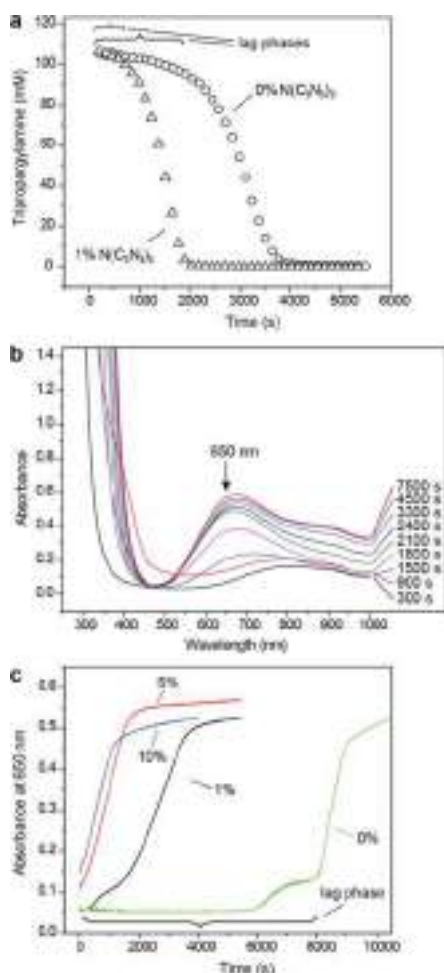
Figure 2. Experiments showing elimination of the lag period with the addition of an autocatalyst in the reaction among **1** (109 mM), **2** (309 mM), and CuSO$_4$ (43 mM). (a) Plot showing the disappearance of the alkyne proton of **1** (at 2.6 ppm) over time, as determined by ^{1}H NMR. The numbers above the traces show the mol % of *tris*-(2-hydroxyethyltriazolylmethyl)-amine (**N(C$_3$N$_3$)$_3$**) added relative to **1**. All reactions were performed in a mixture of D$_2$O/CD$_3$OD (9:4, v:v) at 25 °C in an NMR tube, and the concentration of tripropargylamine was calculated by integrating the alkyne proton against a *tert*-butanol internal standard. (b) UV−vis absorption spectra at various time points during the reaction with 1 mol % of autocatalyst (the mixture of complexes of *mono*-, *bis*-, and *tris*-(triazolylmethyl)amines with copper) added relative to **1** in a H$_2$O/CH$_3$OH (9:4, v:v) mixture at 25 °C. Copper complexes of triazolylmethylamines absorb at 650 nm. (c) UV−vis analysis of the reaction using the same conditions as in (b) performed by measuring the absorption at 650 nm. The numbers above the traces show the approximate mol % of the autocatalyst (the mixture of complexes of *mono*-, *bis*-, and *tris*-(triazolylmethyl)amines with copper from a reaction that had previously reached completion) relative to **1**.

fraction of the total copper present is a part of the operational catalyst, the required evolution of catalyst speciation may result in an observable lag phase. We demonstrated that the autocatalytic CuAAC reaction formed an autocatalytic reaction front by performing the reaction in a layer of 1% agarose gel (1 mm thick) in H$_2$O:CH$_3$OH (9:4, v:v) loaded with **1** (125 mM), **2** (309 mM), and CuSO$_4$ (84 mM). We initiated autocatalysis by adding a small (∼0.1 mm) crystal of ascorbic acid (which rapidly reduces Cu(II) to Cu(I)) (Figure 3a and Supplementary Video). Initially, the agarose gel appeared clear with weak blue
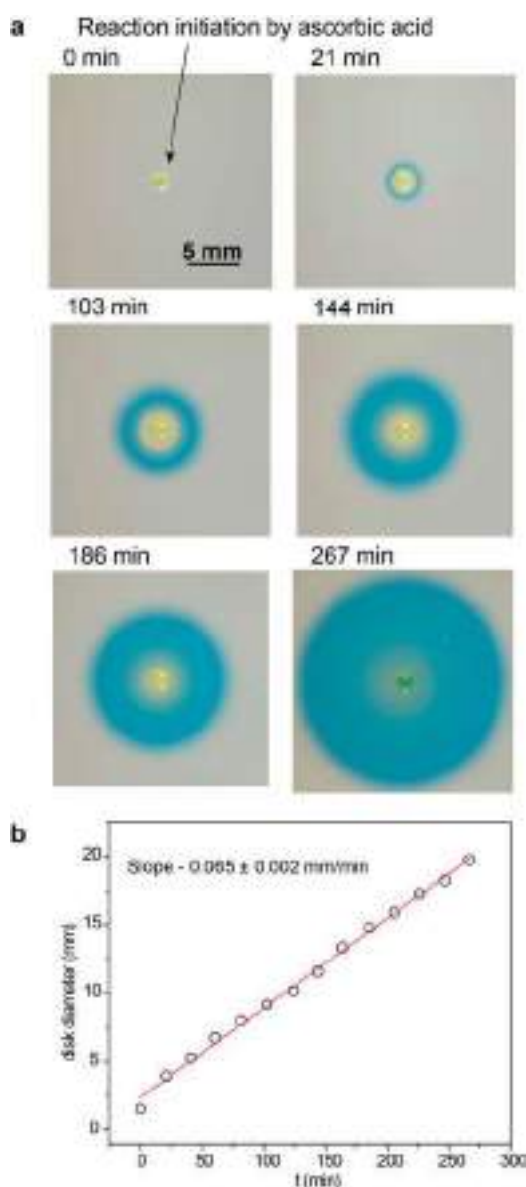
Figure 3. Reaction front driven by the autocatalytic copper catalyzed azide−alkyne cycloaddition. (a) Photographs of the reaction propagating in 1 mm thick agarose gel loaded with **1** (125 mM), azidoethanol (320 mM), and CuSO$_4$ (84 mM). We initiated the reaction at the central point in the gel using a crystal of ascorbic acid. The yellow color comes from the reduced Cu(I) species; the blue color comes from the Cu(II) complex with **N(C$_3$N$_3$)$_3$** (Cu(II) **N(C$_3$N$_3$)$_3$**) and indicates progress of the reaction. (b) Graph showing that the reaction front propagates with constant velocity.

coloring. When the ascorbic acid was added, the area in contact with the crystal turned yellow because Cu(II) was reduced to Cu(I) (which, in the presence of alkynes, forms polynuclear Cu(I) acetylide complexes that are yellow). The area in contact with Cu(I) subsequently underwent the CuAAC reaction, and as triazolyl ligands were produced, the gel turned to a dark blue color associated with Cu(II)/triazolyl complexes. The area closest to the ascorbic acid crystal used to initiate the reaction remained yellow because Cu(II) was being continuously reduced to Cu(I). The autocatalytic front propagated radially with constant velocity (as illustrated by the time/space plot, Figure 3b) at a rate of 0.0325 ± 0.0010 mm/min. Propagation of the reaction front continued for 4 h with a final radius of 10 mm.
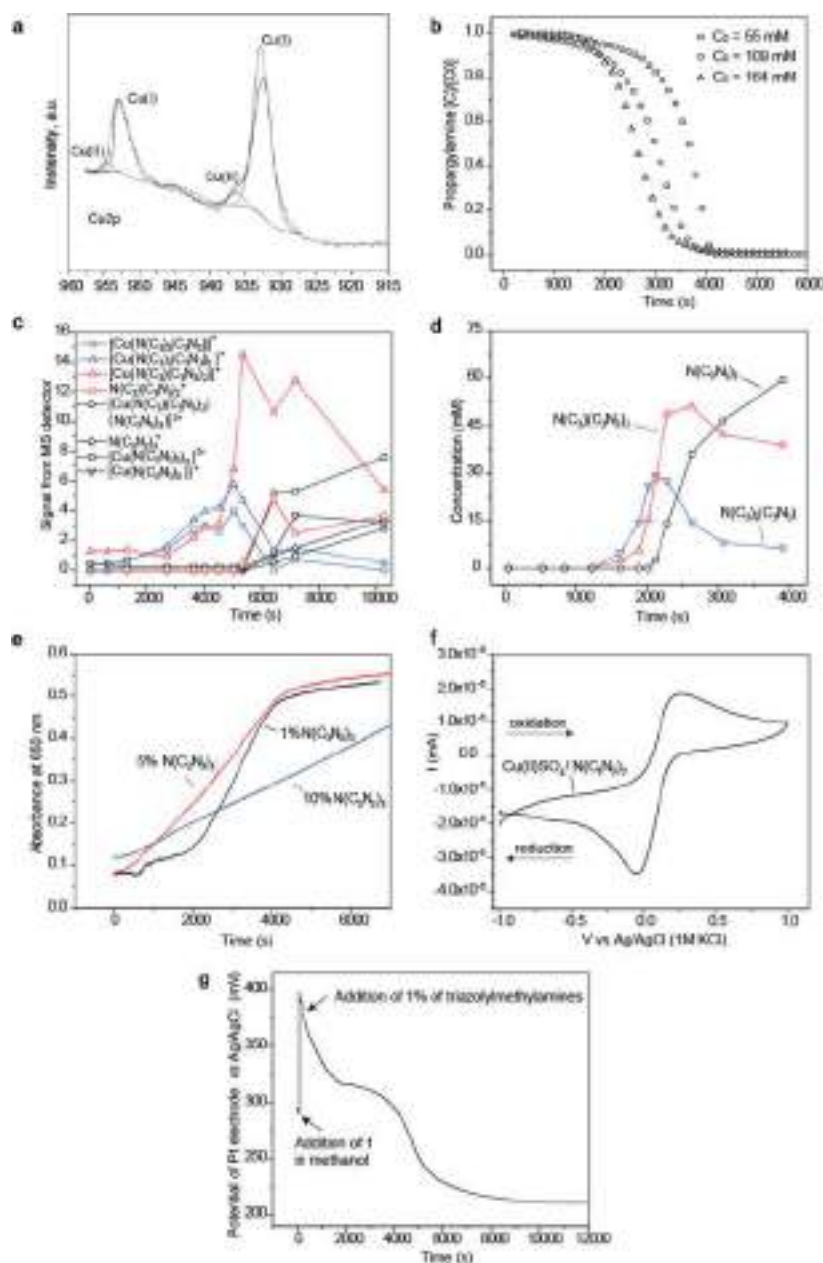
Figure 4. Mechanistic studies of the reaction among **1**, **2**, and CuSO$_4$. (a) XPS data showing the presence of Cu(I) in the precipitate formed in the reaction of **1** (109 mM) and CuSO$_4$ (43 mM) in a D$_2$O/CD$_3$OD (9:4, v:v) mixture. (b) ^{1}H NMR kinetic experiments for the reaction among **1**, **2** (309 mM), and CuSO$_4$ (43 mM) in a D$_2$O/CD$_3$OD (9:4 v:v) mixture at 25 °C starting from different amounts of **1**. The concentration of tripropargylamine was calculated by integrating the alkyne proton against a *tert*-butanol internal standard. (c) Changes in intensity of ESI-MS signals of some triazole species during the autocatalytic CuAAC reaction. The reaction was carried out under the same conditions as the experiment shown in panel (d). (d) Change in concentrations of N(C$_3$)$_2$(C$_3$N$_3$), N(C$_3$)(C$_3$N$_3$)$_2$, and N(C$_3$N$_3$) in the reaction of **1** (109 mM), **2** (309 mM), and CuSO$_4$ (43 mM) determined by NMR measurements. Samples were removed from the reaction and quenched by addition to 2 wt % aqueous solutions of KCN. (e) UV−vis analysis of reactions with different starting concentrations of N(C$_3$N$_3$)$_3$. The reaction contained **1** (109 mM), **2** (309 mM), and CuSO$_4$ (43 mM) in H$_2$O/CH$_3$OH (9:4 v:v) mixture at 25 °C. (f) Cyclic voltammogram (scan rate, 100 mV/s) of CuSO$_4$ (5 mM), Na$_2$SO$_4$ (50 mM), and N(C$_3$N$_3$)$_3$ (10 mM) in H$_2$O/CH$_3$OH (9:4 v:v). (g) Change in potential of a Pt wire electrode vs a Ag|AgCl reference electrode (1.0 M KCl as reference solution) during the reaction of **1** (109 mM), **2** (309 mM), and CuSO$_4$ (43 mM) in a H$_2$O/CH$_3$OH (9:4 v:v) mixture at 25 °C. The reaction was initiated by 1 mol % of triazolylmethylamines.

Two characteristics of the autocatalytic CuAAC reaction described here make it suitable for the study of dynamic phenomena in reaction-diffusion systems: (i) a low rate of spontaneous activation and (ii) an easy detection by color change. We note that organic autocatalytic reactions (i.e., autocatalytic reaction of thiols and template-directed reactions)[18,51] usually have rates of spontaneous activation that prevent prolonged observation of an autocatalytic front. For example, an autocatalytic reaction front driven by the template-directed cycloaddition of a nitrone to an alkene propagated only for ~20 min before the reaction spontaneously activated in bulk.[52] By contrast, for the system described in this paper, spontaneous activation beyond the propagating front was only observed after 300 min.

Mechanism of the Reaction of Tripropargylamine with 2-Azidoethanol in the Presence of CuSO$_4$. *Initiation of the Reaction.* Our initial hypothesis was that autocatalysis would require the addition of a reducing reagent to convert Cu(II) to Cu(I). In fact, this reduction proceeded in the presence of only **1** and **2**: no additional reducing agent was required. Because the reduction of Cu(II) to Cu(I) by alkynes is a well-known reaction and is the basis for the Eglinton coupling,[67] we propose that **1** (either as an alkyne or a tertiary amine) acts as a reducing agent in the reaction. To test this hypothesis, we mixed **1** (109 mM) and CuSO$_4$ (43 mM) in D$_2$O:CD$_3$OD in the absence of azide **2**. The yellow precipitate expected for a Cu(I) acetylide formed within an hour. X-ray photoelectron spectroscopic (XPS) data confirmed the presence of Cu(I), carbon, and nitrogen in this precipitate (Figure 4a and Figure S4).

To determine which functional group of **1** (the alkyne or amine) acts as the reducing agent, we examined two model reactions: (i) We allowed propargyl alcohol (500 mM) to react with CuSO$_4$ (43 mM) in acetate buffer (200 mM, pH 4.7) at 60 °C for 2 min, and (ii) we allowed triethylamine (110 mM) to react with CuSO$_4$ (43 mM) in acetate buffer (200 mM, pH 4.7) at 60 °C for 2 min. The reaction with propargyl alcohol resulted in the reduction of Cu(II) to Cu(I) and formation of a yellow precipitate of Cu(I) acetylide, whereas no reaction was observed with triethylamine. ESI-MS data from the reaction of **1**, **2**, and CuSO$_4$ in H$_2$O:CH$_3$OH showed the presence of butadiyne **3** in the reaction mixture (M + Na$^+$, 283.1). We therefore infer that the reduction of Cu(II) to Cu(I) by the alkyne functionality of **1** is likely the initiation step for the cycloaddition between the azide and alkyne. To support this proposal, we demonstrated that increasing the starting concentration of **1** decreased the duration of the lag phase (Figure 4b). We note, however, that the reduction in the lag phase may be partially influenced by the increased concentration of the tertiary amine, which could be functioning to depolymerize unreactive and highly aggregated Cu(I) acetylides.[62]

Catalytic Properties of Cu(I) Complexes with tris-Triazolylmethylamines. To investigate the contribution of *tris*-triazolylmethylamine ligands on the acceleration of the Cu(I)-catalyzed cycloaddition reaction, we performed a control experiment in which Cu(I) was added at the start of the reaction and was maintained in the reduced state by the presence of 2× excess (relative to the concentration of CuSO$_4$) of ascorbic acid (Figure S5). Reactions initiated with Cu(I) at 43 mM proceeded at rates that were too large to be monitored by NMR. To decrease the rate of the reaction to a rate that is compatible with NMR analysis, and especially to monitor the initial stages of the reaction, we decreased the concentration of copper to 2 mM. Because Cu(I) was present at the beginning of the reaction, we saw no lag phase. We did, however, observe a slight (~2×) increase in rate during the initial stages of the reaction; the observation is compatible with autocatalysis. Because the initial concentration of Cu(I) was lower, the speciation of Cu(I) (which may have a significant impact on the rate of the cycloaddition[68]) will have been different, and thus, the rate (and change in rate over time) is not necessarily directly comparable with our other experiments. Nevertheless, this increase in rate, although small compared to our systems that use Cu(II) as a precursor, is probably analogous to the rate enhancement reported by Fokin[56,62] and is comparable to that reported by Binder.[57]

Role of Intermediate Cycloaddition Products. The simplified sequence of reactions summarized in Scheme 1 proposes the sequential formation of *mono-*, *bis-*, and *tris*-(2-hydroxyethyltriazolylmethyl)amines. We investigated the roles of these species in autocatalysis. First, we used ESI-MS to monitor the reaction (see Experimental Section for details) and observed that (2-hydroxyethyltriazolylmethyl)-dipropargylamine (N(C$_3$)$_2$(C$_3$N$_3$)) and *bis*-(2-hydroxyethyltriazolylmethyl)propargylamine (N(C$_3$)(C$_3$N$_3$)$_2$) were the major species formed during the initial stages of the reaction (i.e., during the lag phase); N(C$_3$)(C$_3$N$_3$)$_2$ was the major species formed during the exponential phase, and *tris*-(2-hydroxyethyltriazolylmethyl)amine (N(C$_3$N$_3$)$_3$) was formed in significant quantities only near the end of the reaction (once almost all of the tripropargylamine had been consumed; Figure 4c). Second, we measured the kinetics of the reaction by NMR spectroscopy by collecting 100 μL samples, quenching them in KCN solution (2 wt % in D$_2$O:CD$_3$OD) and measuring their NMR spectra (Figure S6). KCN quenches the reaction by converting all Cu(II) to [Cu(I)(CN)$_x$]$^{(x-1)-}$, which is not an active catalyst for cycloaddition. This system also permits recording of ^{1}H NMR spectra, where N(C$_3$)$_2$(C$_3$N$_3$), N(C$_3$)-(C$_3$N$_3$)$_2$, and N(C$_3$N$_3$)$_3$ are visible and resolvable. The results show that no triazole compounds are formed (above the detection limit of NMR spectroscopy: ~1 mM) until 800 s (rate < 1.25 × 10^{-3} mM/s), and that the maximum rate of formation of triazoles, at ~2000 s, is ~0.5 mM/s (Figure 4d, Figure S9). Thus, we observed a rate enhancement of more than 400×, which explains the prolonged propagation of the autocatalytic front without spontaneous reaction outside of the reaction front. Consistent with the MS data, N(C$_3$)(C$_3$N$_3$)$_2$ was the major species formed during the exponential phase (Figure 4d). This result might be, at least partially, a consequence of product inhibition by bidentate chelation of two N(C$_3$)(C$_3$N$_3$)$_2$ ligands to Cu(I),[62] effectively trapping the active Cu(I) catalyst in a stable, inactive form and briefly isolating N(C$_3$)(C$_3$N$_3$)$_2$ from further reaction.

Both the MS and NMR experiments suggest that the formation of N(C$_3$N$_3$)$_3$ from N(C$_3$)(C$_3$N$_3$)$_2$ is not cooperative because N(C$_3$N$_3$)$_3$ is not formed in the earlier stages of the reaction. The NMR data, however, suggested that the formation of N(C$_3$)(C$_3$N$_3$)$_2$ from N(C$_3$)$_2$(C$_3$N$_3$) is, to some extent, cooperative because N(C$_3$)$_2$(C$_3$N$_3$) did not accumulate in the mixture and was quickly converted to N(C$_3$)(C$_3$N$_3$)$_2$.

To understand the roles of the N(C$_3$)$_2$(C$_3$N$_3$), N(C$_3$)-(C$_3$N$_3$)$_2$, and N(C$_3$N$_3$)$_3$ in the autocatalytic process, we studied the effect of adding them to the initial reaction mixture on the kinetics of this reaction (Figure 4e and Figure S7). Adding a small amount of N(C$_3$N$_3$)$_3$ (1 mol % relative to **1**) resulted in a kinetic curve that is effectively indistinguishable from that obtained by adding 1 mol % (relative to **1**) of the mixture from the completed reaction (i.e., a mixture of N(C$_3$)$_2$(C$_3$N$_3$), N(C$_3$)(C$_3$N$_3$)$_2$, and N(C$_3$N$_3$)$_3$ and their copper complexes). Adding either 5 or 10 mol % of N(C$_3$N$_3$)$_3$ eliminated the lag phase but also decreased the maximum slope of the kinetic curve. When 10 mol % of N(C$_3$)$_2$(C$_3$N$_3$) or N(C$_3$)(C$_3$N$_3$)$_2$ was added to the reaction, the lag phase (which included the interval from 0−4000 s for N(C$_3$)$_2$(C$_3$N$_3$) and from 0−1000 s for N(C$_3$)(C$_3$N$_3$)$_2$; Figure S7) was not completely eliminated, although the slopes of the kinetic curves were higher than in the experiment with 1 mol % of N(C$_3$N$_3$)$_3$. This observation suggested that N(C$_3$N$_3$)$_3$ is the most active of these three species in accelerating the reduction of Cu(II) to Cu(I), although

$N(C_3)(C_3N_3)_2$ might play a more important role in catalyzing the CuAAC reaction. We note here, however, that the exact mechanism for the reduction of Cu(II) to Cu(I), and the nature of the species involved, are not known.

Electrochemical Studies. We hypothesized that triazolylmethylamines stabilize Cu(I) against disproportionation in water/methanol mixtures. Cu(I) ions disproportionate in water, or water/methanol mixtures, to Cu(II) and Cu(0).[69] As a consequence of the tendency for Cu(I) to disproportionate, the cyclic voltammogram (CV) obtained from $CuSO_4$ (5 mM) in a mixture of $H_2O:CH_3OH$ (9:4, v:v) gave two oxidation and reduction peaks (Figure S8). The CV of $CuSO_4$ (5 mM) and $N(C_3N_3)_3$ (10 mM) in a mixture of $H_2O:CH_3OH$ (9:4, v:v), however, gave only one peak (Figure 4f) corresponding to the reduction of Cu(II) to Cu(I). The ligand $N(C_3N_3)_3$ pushes the redox potential of the reduction of Cu(I)/Cu(0) to negative values to the extent that we do not observe this peak within the 2 V potential window. This shift in the $E°_{Cu(I)/Cu(0)}$ makes the disproportionation of Cu(I) unfavorable ($E_{disproportionation} = E_{Cu(I)/Cu(0)} - E_{Cu(II)/Cu(I)}$) and stabilizes Cu(I) in the complex with $N(C_3N_3)_3$. This stabilization of the catalytically active Cu(I) ions in solution facilitates the cycloaddition reaction.

To monitor the redox reactions taking place during the autocatalytic reaction, we recorded the open-circuit potential of the solution. We monitored the potential of a Pt wire (relative to a Ag/AgCl reference electrode) during the reaction among **1** (109 mM), **2** (309 mM), and $CuSO_4$ (43 mM) in a $H_2O:CH_3OH$ mixture. Figure 4g shows the resulting potential curve, which has four characteristic features: (i) an initial spike in potential, immediately after the addition of **1**, (ii) an 80 mV drop in potential after the addition of 1% triazolylmethylamines (500−2000 s), (iii) a period of approximately constant potential (2000−4000 s), and (iv) a 100 mV drop in potential starting at 4000 s. The potential drop at 4000 s correlated with a color change from pale to dark blue. Although unambiguous interpretation of open circuit potential measurements is difficult, the second drop in potential (4500 s) might plausibly originate from an increase in the concentration of Cu(I) caused by the chemical reduction of Cu(II) during the autocatalytic process.

Inverse Solvent Kinetic Isotope Effect. We observed (based on the duration of the lag phase) an apparent inverse solvent kinetic isotope effect (KIE) in the reaction among **1**, **2**, and $CuSO_4$ (that is, the lag phase ended earlier in $D_2O:MeOD$ (9:4, v:v) than in $H_2O:MeOH$ (9:4, v:v)). The lag phase ends at ~1500 s (~25 min) in $D_2O/MeOD$ (Figure 2b) and after 7000 s (~116 min) in $H_2O/MeOH$ under otherwise identical reaction conditions (Figure 2b). Because we believe that the lag phase is a consequence of the slow reduction of Cu(II) to Cu(I), the observed solvent kinetic isotope effect likely involves the alkyne-mediated reduction of Cu(II) to Cu(I). The details of the mechanism and intermediate species of the reduction of Cu(II) to Cu(I) by terminal alkynes are complex and are still under considerable debate[70] (as are the details of the mechanism and intermediate species of the CuAAC reaction[71]). The processes that are believed to be involved (hybridization changes, reductive elimination, and/or transition metal C−H activation), however, are chemical processes often associated with KIEs.[72]

We hypothesized that, in deuterated solvent and in the presence of copper, the alkyne protons of **1** may exchange with deuterium from D_2O and/or MeOD and that the deuterated product **1**-d$_3$ (i.e., tripropargylamine with its three alkyne protons replaced with deuterium) may be the origin of the observed inverse KIE. We thus ran the reaction among **1**-d$_3$, **2**,

and $CuSO_4$ in a mixture of $H_2O:MeOH$ (9:4, v:v) and monitored the reaction by UV/vis spectroscopy at 650 nm (Figure 5). As a control, we also ran the reaction among **1**-d$_3$, **2**, and $CuSO_4$ in a mixture of $D_2O:MeOD$ (9:4, v:v).
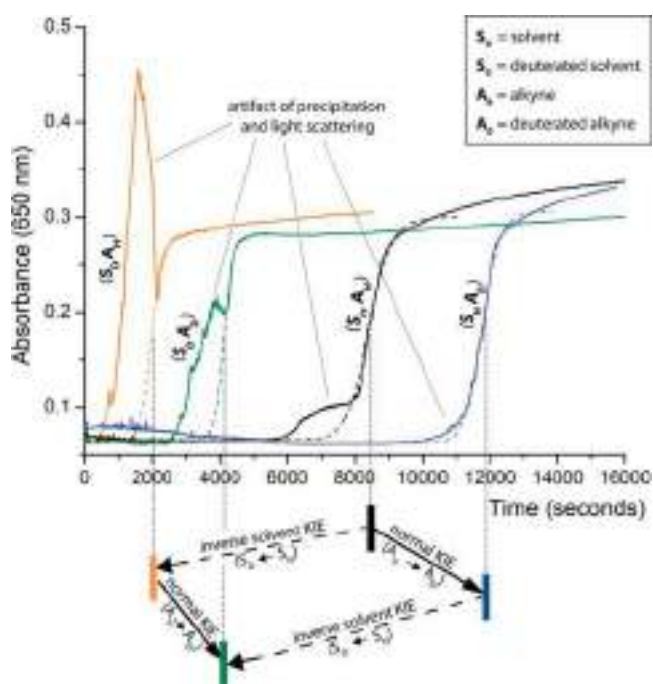
Figure 5. (top) Reaction progress monitored by UV/vis spectroscopy at 650 nm of four different reactions. In all forms, the starting concentrations were **1** or **1**-d$_3$ (109 mM), **2** (309 mM), and $CuSO_4$ (43 mM) in a mixture of $H_2O:MeOH$ or D_2O and MeOD (9:4, v:v). The dashed lines are sigmoidal fits to the data omitting the region containing the artifact of precipitation and light scattering. (bottom) Representation of how the two kinetic isotope effects (KIEs) plausibly and approximately independently influence the lag phase of these four reactions. The position of the colored bars corresponds to the approximate duration of the lag phase on the x-axis.

Figure 5 shows the reaction progress of four different reactions run under the same reaction conditions: (1) **1**-d$_3$, **2**, and $CuSO_4$ in a mixture of $H_2O:MeOH$ (9:4, v:v), (2) **1**-d$_3$, **2**, and $CuSO_4$ in a mixture of $D_2O:MeOD$ (9:4, v:v), (3) **1**, **2**, and $CuSO_4$ in a mixture of $H_2O:MeOH$ (9:4, v:v), and (4) **1**, **2**, and $CuSO_4$ in a mixture of $D_2O:MeOD$ (9:4, v:v).

If **1**-d$_3$ were causing the observed inverse KIE, the duration of the lag phase of the reaction involving **1**-d$_3$ and $H_2O/MeOH$ would resemble that observed in the reaction of **1** and $D_2O/MeOD$. Figure 5, however, shows that the lag phase for the reaction with **1**-d$_3$ in $H_2O/MeOH$ was even longer than that using **1** in $H_2O/MeOH$, ending after ~11000s (183 min). This observed normal KIE supports the involvement of the alkyne proton in the lag phase (reduction of Cu(II) to Cu(I)) but also indicates that it is not the origin of the observed inverse KIE. Furthermore, the control reaction among **1**-d$_3$, **2**, and $CuSO_4$ in a mixture of $D_2O:MeOD$ (9:4, v:v) had a longer lag phase than that of **1** in $D_2O/MeOD$. Thus, although the alkyne displays a normal KIE and is involved in the lag phase, the observed inverse solvent KIE is not affected by the alkyne proton. The idea that these two KIEs act independently is supported by the effect of isotopic substitution of the alkyne (**1**-d$_3$) on the duration of the lag phase, which was roughly the same for both solvent systems.

Figure 5 indicates that these reactions show a spike in absorbance as the lag phase ends. This absorbance peak corresponds to the formation of precipitates, which we expect are insoluble Cu(I) intermediates. The intensity of this absorbance peak (and thus the degree of precipitation) also correlates with the duration of the lag phase (reactions with shorter lag phases have larger absorbance peaks). We attribute this observation to the fact that shorter lag phases have more rapid formation of Cu(I) intermediates, which thus accumulate in larger concentrations (and thus precipitate to larger extents).

Given that the inverse solvent KIE is not affected by the alkyne proton but is still involved in the reduction of Cu(II), we suspected that D_2O and/or MeOD may influence the reduction potential of the $Cu(II)/N(C_3N_3)_3$ complex. We did not, however, see a change in the cyclic voltammogram (scan rate, 100 mV/s) of $CuSO_4$ (5 mM), Na_2SO_4 (50 mM), and $N(C_3N_3)_3$ (10 mM) in D_2O/CH_3OD (9:4; v:v) as compared to that in H_2O/CH_3OH (9:4; v:v) (Figure 4f). We can thus only speculate that these deuterated solvents influence the rate of reduction of Cu(II) to Cu(I) through an isotope-dependent solvation effect that reduces the activation free energy of electron transfer.[73] We have thus not identified the origin of the negative KIE at this time. Because this mechanistic feature, although interesting, is secondary to the focus of the work, we leave it unresolved.

Summary of the Mechanism. We summarize our current inferences concerning the mechanism of the autocatalytic CuAAC reaction as follows: The reaction starts with an initial, slow, reduction of hydrated Cu(II) to Cu(I), where an alkyne serves as the reducing agent. The reduction of Cu(II) to Cu(I) by the acetylenic group of $N(CH_2C{\equiv}CH)_3$ (1) leads to the initial Cu(I) complexes that are catalytically active in the cycloaddition. The products of the initial and subsequent cycloadditions—$N(C_3)_2(C_3N_3)$, $N(C_3)(C_3N_3)_2$, and $N\text{-}(C_3N_3)_3$ (Scheme 1)—form coordination complexes with Cu(I) and Cu(II). Uncoordinated Cu(I) is unstable in water/methanol solutions and disproportionates. Here, the triazolyl amine ligands form stable and soluble complexes with Cu(I), which maintain copper in its catalytically active oxidation state, Cu(I), in solution. The formation of $N(C_3)_2(C_3N_3)$, $N(C_3)\text{-}(C_3N_3)_2$, and $N(C_3N_3)_3$ also accelerate the reduction of Cu(II) to Cu(I), although the exact reasons for this acceleration are unclear and might involve intermediates in the CuAAC reaction.

Thus, formation of the Cu(I) species, the catalytically active species in the click (cycloaddition) reaction, is promoted by the formation of ligands that are the product of that reaction. The reaction cycle is autocatalytic because the production, and stability in solution, of Cu(I) is promoted by the aminotriazolyl ligands, and production of the aminotriazolyl ligands is accelerated by Cu(I) (Scheme 2). The Cu(I) species that are formed in the reduction process might, however, be initially catalytically inactive and require extra steps to rearrange into catalytically active complexes. An additional contribution to autocatalysis, although probably a less important one, comes from the increased activity of Cu(I) in the CuAAC reaction when it is complexed with an aminotriazolyl ligand. As the CuAAC reaction (catalyzed by Cu(I)) progresses, more aminotriazolyl ligands are produced. The aminotriazolyl ligands coordinate Cu(I) (in addition to Cu(II)) to form a more reactive Cu(I) catalyst, which in turn accelerates the rate of formation of the aminotriazolyl ligands.

On the basis of this reaction profile, we have developed a numerical model involving six simplified reactions to describe

Scheme 2. Proposed Important Steps in the Autocatalytic Reaction between Propargylamines and Azides in Water or Water/Methanol in the Presence of Cu(II) Salts
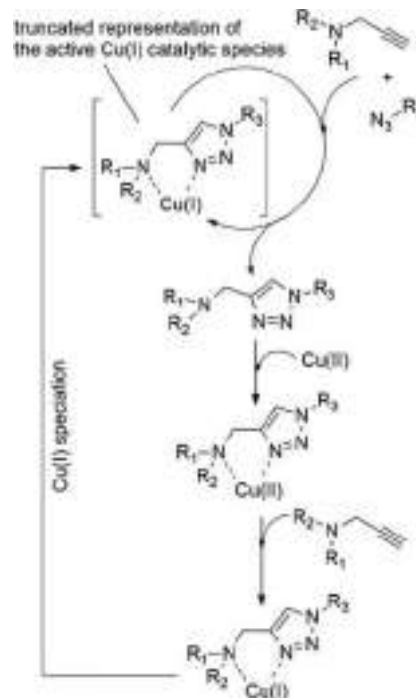
the proposed mechanism (see Supporting Information for details). The numerical solution of these equations shows kinetics that resemble the experimental data (Figure S9). This type of modeling shows that a plausible kinetic scheme (with adjustable rate constants) can model the observed data adequately. As with all similar weakly constrained models, "compatibility" is not "proof", but the goodness of fit of the simulated data, using physically plausible values of rate constants, provides further support for the general scheme proposed.

Substrate Scope. The reaction mechanism outlined in Scheme 2 suggests that autocatalysis is not dependent on the structure of the azide. To test the dependence of the structure of the substrate on autocatalysis, we ran the reaction with two additional azides: tetraethylene glycol diazide (4) and benzyl azide (5). In the first experiment, we allowed 1 (309 mM), 4 (150 mM), and $Cu(SO_4)$ (43 mM) to react in a mixture of D_2O/CD_3OD (9:4, v:v). The concentration of 4 was reduced (relative to the reactions with 2) to maintain the same relative concentration of azide. In the second experiment, we allowed 1 (309 mM), 5 (309 mM), and $Cu(NO_3)_2 \cdot 3H_2O$ (43 mM) to react in pure CD_3OD. We used a different solvent in this experiment because benzyl azide is insoluble in the water/methanol (9:4, v:v) mixture, and we used a different source of Cu(II) to increase its solubility in CD_3OD. Both the reaction with azide 4 and that with azide 5 gave sigmoidal kinetics with lag phases and exponential growth phases that were similar to those observed with 2 (Figure 6a). We therefore conclude that the structures of the azide component have only a weak influence on the kinetics of the reaction and that the reaction can tolerate a variety of substituted azides.

We also tested the reaction of 2 (327 mM) with propargylamine (309 mM) and $CuSO_4$ (43 mM) in a water/methanol (9:4, v:v) mixture. The reaction displays sigmoidal kinetics, but
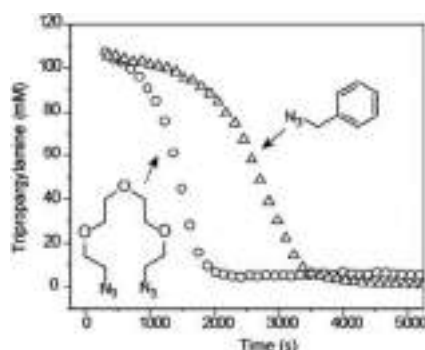
Figure 6. Scope of the autocatalytic CuAAC reaction. ^{1}H NMR kinetics experiments for the reaction between **1** (109 mM), CuSO$_4$ (43 mM), and tetraethylene glycol diazide (**4**, 150 mM) or benzylazide (**5**, 260 mM). The experiment with **4** was conducted in a D$_2$O/CD$_3$OD (9:4, v:v) mixture at 25 °C. The experiment with **5** was conducted in pure CD$_3$OD. The concentration of alkyne was calculated by integrating the alkyne proton against a *tert*-butanol internal standard.

the formation of precipitates and the combination of copper speciation, disproportionation of Cu(I) complexes, and depolymerization of insoluble Cu poly acetylides make an unambiguous interpretation of this sigmoidal kinetic curve challenging (Figure S10 and Supplementary Discussion).

Displacing Ammonia from Cu(II) Ions. A possible extension of the autocatalytic cycle (Scheme 2) is the displacement of a ligand that binds to Cu(II) (such as ammonia) by the triazolylmethylamines formed in the reaction (Scheme 3). The release of a free ligand opens a new path to couple autocatalysis to independent chemical reactions.

We ran the reaction of **1**, **2**, and CuSO$_4$ in the presence of ammonia (240 mM) and ammonium chloride (430 mM) and monitored the reaction by ^{1}H NMR. The disappearance of **1** followed an approximately sigmoidal curve characteristic of an autocatalytic reaction (Figure 7). The formation of precipitates during intermediate stages of the reaction may be the cause of the deviation of the course of the reaction from the expected sigmoid. When the reaction was complete, the solution was pale yellow, which is in contrast to the bright blue color of reactions without ammonia. The most plausible explanation for this difference in color is a faster reduction of Cu(II) aminotriazolyl complexes in the presence of ammonia, perhaps as a result of the increased pH of the solution. Reduction of Cu(II) thus happens faster than cycloaddition, and all copper is reduced to yellow Cu(I) complexes. When exposed to air, the color of the complete reaction mixture changes back to blue. This experiment demonstrated that we can extend the scope of the autocatalytic CuAAC reaction to reactions that involve complexes of Cu(II). This experiment also provided further evidence that autocatalysis is not a consequence of an increase in pH during the reaction because the reaction remains
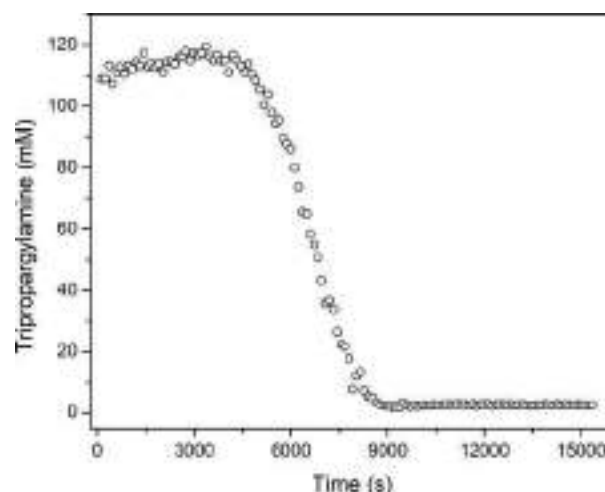
Figure 7. ^{1}H NMR kinetic experiments for the reaction among propargylamine (109 mM), azidoethanol (309 mM), CuSO$_4$ (43 mM), NH$_3$ (240 mM), and NH$_4$Cl (430 mM). Experiments were conducted in a D$_2$O/CD$_3$OD (9:4 v:v) mixture at 25 °C. The concentration of tripropargylamine was calculated by integrating the alkyne proton against a *tert*-butanol internal standard.

autocatalytic when performed in an ammonia/ammonium chloride buffer.

■ CONCLUSIONS

This work describes an autocatalytic system where coupling the CuAAC reaction and the reduction of Cu(II) to Cu(I) affords a large rate enhancement over the course of the reaction. We consider this system of reactions as prototypical of autocatalytic cycles. In this example, a classical catalytic cycle (the CuAAC reaction) is coupled to a process (the reduction of Cu(II) to Cu(I)) that generates an extra molecule of the catalyst, a process that "amplifies" the number of molecules of catalyst (in principle, exponentially) and that underlies the mechanism of all autocatalytic reactions. This system is driven by the catalytic formation of a product that, by acting as a ligand, enhances the production and activity of the catalyst. This characteristic of the product(s) is achieved by (i) the formation of a nucleophilic triazole ring from a non-nucleophilic azido group and (ii) the formation of a chelate ligand from a monodentate ligand. Specifically, the organic azide group from azidoethanol (which does not bind strongly to copper ions) converts to a triazole (which does coordinate strongly to copper ions) and a monodentate tripropargylamine converts to a tetradentate triazolylmethylamine (which bind tightly to Cu(I) and Cu(II) ions).

The autocatalytic CuAAC reaction is compatible with a range of substrates and can, in principle, generate polymeric/oligomeric products. We illustrated two subtypes of the

Scheme 3. Substitution of Ammonia from Cu(II) Ammonia Complex by N(C$_3$N$_3$)$_3$ Ligand
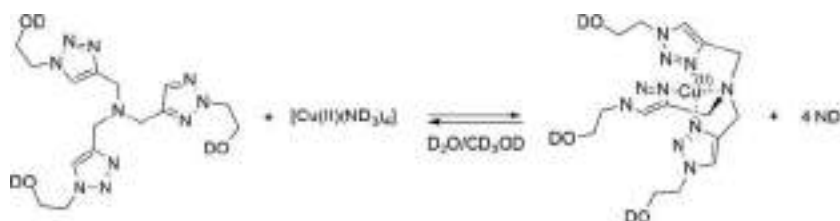
autocatalytic cycle (see Scheme S1): (i) the product ligand forms the active catalyst from a solvated metal ion, and (ii) the product ligand forms a complex from a metal ion containing an ancillary ligand that is released upon complexation.

This reaction will aid in the development and understanding of chemical reaction networks. This and other work examining mechanisms of autocatalysis may also help to form a better picture of the processes that led to the emergence of life on earth because similar processes (kinetically, although certainly in this case not in molecular detail) might generate autocatalysis in mixtures of molecules (for example, alkynes and nitriles, or metal ions bound to peptides) that may have been important for the origin of life.[74−76]

■ ASSOCIATED CONTENT

Ⓢ Supporting Information

The Supporting Information is available free of charge on the ACS Publications Web site. The Supporting Information is available free of charge on the ACS Publications website at DOI: 10.1021/jacs.8b05048.

> Experimental details of syntheses and kinetics experiments and details of the kinetic model describing autocatalysis (PDF)
>
> Supplementary video of the propagating autocatalytic front (MPG)

■ AUTHOR INFORMATION

Corresponding Author

*gwhitesides@gmwgroup.harvard.edu

ORCID Ⓞ

Sergey N. Semenov: 0000-0002-5829-2283
George M. Whitesides: 0000-0001-9451-2442

Present Addresses

[⊥]S.N.S.: Department of Organic Chemistry, Weizmann Institute of Science, Rehovot 76100, Israel
[∥]E.V.S.: SCAMT Laboratory, ITMO University, St. Petersburg 197101, Russian Federation.

Notes

The authors declare no competing financial interest.

■ ACKNOWLEDGMENTS

■ REFERENCES

(1) Bissette, A. J.; Fletcher, S. P. *Angew. Chem., Int. Ed.* **2013**, *52*, 12800−12826.
(2) Breslow, R. *Tetrahedron Lett.* **1959**, *1*, 22−26.
(3) Boutlerow, A. M. *Comptes Rendus Chimie* **1869**, *53*, 145−147.
(4) James, T. H.; Mees, C. E. K. *The theory of the photographic process*, 4th ed.; Macmillan: New York, 1977; xvii, p 714.
(5) Ichimura, K. *Chem. Rec.* **2002**, *2*, 46−55.
(6) Kruger, S.; Revuru, S.; Higgins, C.; Gibbons, S.; Freedman, D. A.; Yueh, W.; Younkin, T. R.; Brainard, R. L. *J. Am. Chem. Soc.* **2009**, *131*, 9862.
(7) Kruger, S. A.; Higgins, C.; Cardineau, B.; Younkin, T. R.; Brainard, R. L. *Chem. Mater.* **2010**, *22*, 5609−5616.
(8) Mallory, G. O.; Hajdu, J. B. American Electroplaters and Surface Finishers Society. *Electroless plating: fundamentals and applications*; The Society: Orlando, FL, 1990; viii, p 539.
(9) Soai, K.; Shibata, T.; Morioka, H.; Choji, K. *Nature* **1995**, *378*, 767−768.
(10) Soai, K.; Kawasaki, T. *Top. Curr. Chem.* **2007**, *284*, 1−33.
(11) Soai, K.; Kawasaki, T. *Chirality* **2006**, *18*, 469−478.
(12) Blackmond, D. G. *Proc. Natl. Acad. Sci. U. S. A.* **2004**, *101*, 5732.
(13) Kovacs, K.; McIlwaine, R. E.; Scott, S. K.; Taylor, A. F. *J. Phys. Chem. A* **2007**, *111*, 549−551.
(14) Kovacs, K.; McIlwaine, R. E.; Scott, S. K.; Taylor, A. F. *Phys. Chem. Chem. Phys.* **2007**, *9*, 3711−3716.
(15) Arimitsu, K.; Ichimura, K. *J. Mater. Chem.* **2004**, *14*, 336−343.
(16) Belousov, B. P. *Sbornik Referatov po Radiatsionni Meditsine* **1958**; Vol. *145*, p 1
(17) Gyorgyi, L.; Turanyi, T.; Field, R. J. *J. Phys. Chem.* **1990**, *94*, 7162−7170.
(18) Semenov, S. N.; Kraft, L. J.; Ainla, A.; Zhao, M.; Baghbanzadeh, M.; Campbell, C. E.; Kang, K.; Fox, J. M.; Whitesides, G. M. *Nature* **2016**, *537*, 656−660.
(19) Hordijk, W.; Hein, J.; Steel, M. *Entropy* **2010**, *12*, 1733−1742.
(20) Eigen, M.; Schuster, P. *Naturwissenschaften* **1978**, *65*, 7−41.
(21) Patel, B. H.; Percivalle, C.; Ritson, D. J.; Duffy, C. D.; Sutherland, J. D. *Nat. Chem.* **2015**, *7*, 301−307.
(22) Eschenmoser, A. *Tetrahedron* **2007**, *63*, 12821−12844.
(23) De Duve, C. *Singularities: Landmarks on the Pathways of Life*; Cambridge University Press: Cambridge, UK, 2005.
(24) Ricardo, A.; Carrigan, M. A.; Olcott, A. N.; Benner, S. A. *Science* **2004**, *303*, 196.
(25) Smith, E.; Morowitz, H. J. *Proc. Natl. Acad. Sci. U. S. A.* **2004**, *101*, 13168−13173.
(26) Huber, C.; Wächtershäuser, G. *Science* **1997**, *276*, 245−247.
(27) Cody, G. D.; Boctor, N. Z.; Filley, T. R.; Hazen, R. M.; Scott, J. H.; Sharma, A.; Yoder, H. S. *Science* **2000**, *289*, 1337−1340.
(28) Butch, C.; Cope, E. D.; Pollet, P.; Gelbaum, L.; Krishnamurthy, R.; Liotta, C. L. *J. Am. Chem. Soc.* **2013**, *135*, 13440−13445.
(29) Morowitz, H. J.; Heinz, B.; Deamer, D. W. *Origins Life Evol. Biospheres* **1988**, *18*, 281−287.
(30) Monnard, P.-A.; Kanavarioti, A.; Deamer, D. W. *J. Am. Chem. Soc.* **2003**, *125*, 13734−13740.
(31) Burcar, B.; Pasek, M.; Gull, M.; Cafferty, B. J.; Velasco, F.; Hud, N. V.; Menor-Salván, C. *Angew. Chem., Int. Ed.* **2016**, *55*, 13249−13253.
(32) Hazen, R. M.; Sverjensky, D. A. *Cold Spring Harbor Perspect. Biol.* **2010**, *2*, a002162.
(33) Pross, A. *Origins Life Evol. Biospheres* **2005**, *35*, 151−166.
(34) Kauffman, S. A. *At Home in the Universe: The Search for Laws of Self-organization and Complexity*; Oxford University Press, 1995.
(35) Eigen, M.; Schuster, P. *The Hypercycle: A Principle of Natural Self-Organization*; Springer: Berlin, Heidelberg, 1979.
(36) Eschenmoser, A. *Angew. Chem., Int. Ed.* **2011**, *50*, 12412−12472.
(37) Hordijk, W.; Steel, M. *BioSystems* **2017**, *152*, 1−10.
(38) Barenholz, U.; Davidi, D.; Reznik, E.; Bar-On, Y.; Antonovsky, N.; Noor, E.; Milo, R. *eLife* **2017**, *6*, 1.
(39) Lincoln, T. A.; Joyce, G. F. *Science* **2009**, *323*, 1229−1232.
(40) Zubarev, D. Y.; Rappoport, D.; Aspuru-Guzik, A. *Sci. Rep.* **2015**, *5*, 1.
(41) Xu, Y.; Chen, Q.; Zhao, Y. J.; Lv, J.; Li, Z. H.; Ma, X. B. *Ind. Eng. Chem. Res.* **2014**, *53*, 4207−4214.
(42) Neurath, H.; Dreyer, W. J. *Discuss. Faraday Soc.* **1955**, *20*, 32−43.
(43) Donella-Deana, A.; Cesaro, L.; Sarno, S.; Brunati, A. M.; Ruzzene, M.; Pinna, L. A. *Biochem. J.* **2001**, *357*, 563−567.
(44) Launer, H. F. *J. Am. Chem. Soc.* **1932**, *54*, 2597−2610.
(45) Morowitz, H. J.; Kostelnik, J. D.; Yang, J.; Cody, G. D. *Proc. Natl. Acad. Sci. U. S. A.* **2000**, *97*, 7704−7708.
(46) Davie, E. W.; Fujikawa, K.; Kisiel, W. *Biochemistry* **1991**, *30*, 10363−10370.
(47) Flegeau, E. F.; Bruneau, C.; Dixneuf, P. H.; Jutand, A. *J. Am. Chem. Soc.* **2011**, *133*, 10161−10170.
(48) von Kiedrowski, G. *Angew. Chem., Int. Ed. Engl.* **1986**, *25*, 932−935.
(49) Sievers, D.; von Kiedrowski, G. *Nature* **1994**, *369*, 221−224.

(50) Tjivikua, T.; Ballester, P.; Rebek, J. *J. Am. Chem. Soc.* **1990**, *199*, 46.

(51) Wintner, E. A.; Conn, M. M.; Rebek, J. *J. Am. Chem. Soc.* **1994**, *116*, 8877−8884.

(52) Bottero, I.; Huck, J.; Kosikova, T.; Philp, D. *J. Am. Chem. Soc.* **2016**, *138*, 6723−6726.

(53) Rappoport, D.; Galvin, C. J.; Zubarev, D. Y.; Aspuru-Guzik, A. *J. Chem. Theory Comput.* **2014**, *10*, 897−907.

(54) Carnall, J. M. A.; Waudby, C. A.; Belenguer, A. M.; Stuart, M. C. A.; Peyralans, J. J. P.; Otto, S. *Science* **2010**, *327*, 1502−1506.

(55) Chan, T. R.; Hilgraf, R.; Sharpless, K. B.; Fokin, V. V. *Org. Lett.* **2004**, *6*, 2853−2855.

(56) Dohler, D.; Michael, P.; Binder, W. H. *Macromolecules* **2012**, *45*, 3335−3345.

(57) Flory, P. J. *Principles of Polymer Chemistry*; Cornell University Press, 1953.

(58) Hardy, M. D.; Yang, J.; Selimkhanov, J.; Cole, C. M.; Tsimring, L. S.; Devaraj, N. K. *Proc. Natl. Acad. Sci. U. S. A.* **2015**, *112*, 8187−8192.

(59) Brea, R. J.; Devaraj, N. K. *Nat. Commun.* **2017**, *8*, 730.

(60) Kuang, G.-C.; Michaels, H. A.; Simmons, J. T.; Clark, R. J.; Zhu, L. *J. Org. Chem.* **2010**, *75*, 6540−6548.

(61) Rostovtsev, V. V.; Green, L. G.; Fokin, V. V.; Sharpless, K. B. *Angew. Chem., Int. Ed.* **2002**, *41*, 2596.

(62) Rodionov, V. O.; Presolski, S. I.; Diaz Diaz, D.; Fokin, V. V.; Finn, M. G. *J. Am. Chem. Soc.* **2007**, *129*, 12705−12712.

(63) Parkash, R.; Zýka, J. *Microchem. J.* **1972**, *17*, 309−317.

(64) Roof, R. B., Jnr; Larson, A. C.; Cromer, D. T. *Acta Crystallogr., Sect. B: Struct. Crystallogr. Cryst. Chem.* **1968**, *24*, 269−273.

(65) Epstein, I. R.; Pojman, J. A. *An introduction to nonlinear chemical dynamics: oscillations, waves, patterns, and chaos*; Oxford University Press: New York, 1998; xiv, p 392.

(66) Rodionov, V. O.; Presolski, S. I.; Gardinier, S.; Lim, Y.-H.; Finn, M. G. *J. Am. Chem. Soc.* **2007**, *129*, 12696−12704.

(67) Eglinton, G.; Galbraith, A. R. *J. Chem. Soc.* **1959**, 889.

(68) Rodionov, V. O.; Fokin, V. V.; Finn, M. G. *Angew. Chem., Int. Ed.* **2005**, *44*, 2210−2215.

(69) Rorabacher, D. B.; Schroeder, R. R., Electrochemistry of Copper. In *Encyclopedia of Electrochemistry*; John Wiley and Sons, Inc., 2007; pp 992−1046.

(70) Zhang, G.; Yi, H.; Zhang, G.; Deng, Y.; Bai, R.; Zhang, H.; Miller, J. T.; Kropf, A. J.; Bunel, E. E.; Lei, A. *J. Am. Chem. Soc.* **2014**, *136*, 924−926.

(71) Jin, L.; Tolentino, D. R.; Melaimi, M.; Bertrand, G. *Sci. Adv.* **2015**, *1*, e1500304.

(72) Gómez-Gallego, M.; Sierra, M. A. *Chem. Rev.* **2011**, *111*, 4857−4963.

(73) Farver, O.; Zhang, J.; Chi, Q.; Pecht, I.; Ulstrup, J. *Proc. Natl. Acad. Sci. U. S. A.* **2001**, *98*, 4426.

(74) Wachtershauser, G. *Proc. Natl. Acad. Sci. U. S. A.* **1990**, *87*, 200−204.

(75) Scintilla, S.; Bonfio, C.; Belmonte, L.; Forlin, M.; Rossetto, D.; Li, J. W.; Cowan, J. A.; Galliani, A.; Arnesano, F.; Assfalg, M.; Mansy, S. S. *Chem. Commun.* **2016**, *52*, 13456−13459.

(76) Beinert, H. *JBIC, J. Biol. Inorg. Chem.* **2000**, *5*, 2−15.

Full Paper

Four-Variable Model of an Enzymatic Oscillator Based on Trypsin

Sergey N. Semenov,*[a, b, c] Alar Ainla,[d] Ekaterina V. Skorb,[e] and Sjoerd G. J. Postma[b]

Abstract: This paper describes a four-variable model for an enzymatic oscillator based on trypsin. Variables in this model are concentrations of the essential proteins (trypsin and trypsinogen) and small molecules (masked and active inhibitors of trypsin) within the network. Importantly, to simplify the model, non-essential side reactions are neglected and essential reactions are assumed to follow first or second order kinetics. Numerical solutions of this reduced model semi-quantitatively reproduce experimentally determined periods, amplitudes, and phase shifts of oscillations in the concentrations of several species in the network. Moreover, linear stability analysis shows that oscillations in the trypsin oscillator emerge and disappear through Hopf bifurcation. The model will be helpful in situations where simplicity is necessary such as detailed analysis of dynamics and modeling of reaction-diffusion systems.

Keywords: Chemical Oscillator · Trypsin · Reaction Networks · Linear Stability Analysis

1. Introduction

Biochemical oscillators are fundamentally important for all forms of life. Bacterial cells multiply in periodic, oscillatory cycles of cell division.[1] Many organisms, from cyanobacteria to vertebrates, follow day-night cycles using circadian clocks.[2] Oscillations of calcium concentration in the cytoplasm are part of cellular signaling and glycolytic oscillations are part of the regulation of metabolism.[2b,3] Moreover, heartbeats and periodic contractions of intestines are controlled by oscillations in muscle cells.[2b]

Despite the abundance of oscillations in biology,[4] a design of a *de-novo* enzymatic oscillator was not accomplished up until recently. Huck and coworkers published the first bottom-up engineered enzymatic oscillator in 2015.[5] The oscillator is built around the proteolytic enzyme trypsin, which is formed autocatalytically from its inactive precursor trypsinogen.[6] The autocatalytic production of trypsin is coupled to its self-induced delayed destruction in a delayed negative feedback loop. Crucially, the negative feedback loop contains small molecules that are amenable by organic synthesis. Importantly, by changing the molecular structure of these small molecules, it was shown that the oscillator can become more robust, resilient,[7] or light-controlled.[8]

The model of this oscillator considers all known reactions in the system, including undesired side reactions, uses the Michaelis-Menten equation to model rates of enzymatic reactions with small molecular substrates, and considers the trypsin-trypsinogen complex as an independent variable.[5] This level of detail is necessary to reach the closest fit of the numerical simulations to experimental data. Nevertheless, the complexity of a detailed model has a number of drawbacks: (i) it hinders qualitative understanding of the nature of oscillations, (ii) it makes analytical linear stability analysis impractical, (iii) it is too complicated for the implementation into

reaction-diffusion models which are necessary to model the formation of chemical patterns and other phenomena involving diffusion.[9]

In this work, we present a four-variable model for the trypsin oscillator, perform its linear stability analysis, and discuss its abilities and limitations to explain existing experimental data.

2. Results and Discussion

Chemical description of the oscillator. As mentioned above, the enzyme trypsin is at the core of the oscillator (Figure 1a). Trypsin (**Tr**) catalyzes its own production by cleaving a hexapeptide fragment from trypsinogen (**Tg**, the catalytically inactive precursor of trypsin).[6,10] Trypsin also triggers the negative feedback. The source of this negative feedback is a

[a] S. N. Semenov
Department of Chemistry and Chemical Biology, Harvard University, 12 Oxford Street, MA 02138, USA
E-mail: semenovmsu@gmail.com
[b] S. N. Semenov, S. G. J. Postma
Institute for Molecules and Materials, Radboud University Nijmegen, Heyendaalseweg 135, 6525 AJ Nijmegen, The Netherlands
[c] S. N. Semenov
Department of Organic Chemistry, Weizmann Institute of Science, Rehovot 76100, Israel
[d] A. Ainla
INL – International Iberian Nanotechnology Laboratory, Avenida Mestre José Veiga s/n, 4715-330 Braga, Portugal
[e] E. V. Skorb
SCAMT Laboratory, ITMO University, St. Petersburg 197101, Russian Federation

⌨ Supporting information for this article is available on the WWW under https://doi.org/10.1002/ijch.201700146

Full Paper
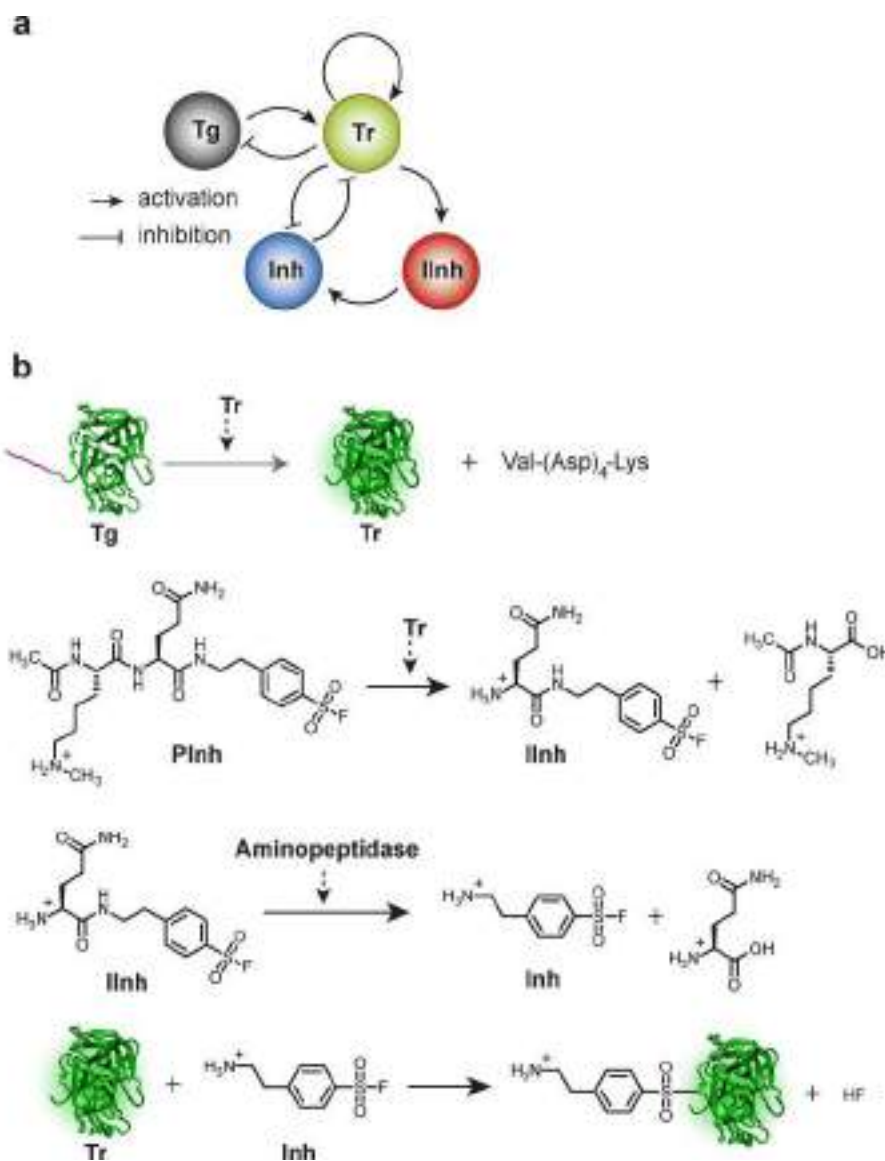
Figure 1. Trypsin oscillator **a**. Depiction of the network of enzymatic reactions in the trypsin oscillator. **b**. Specific reactions in the reaction network. Dashed arrows indicate catalysis.

specially designed tripeptide proinhibitor (**PInh**) which contains three parts: (i) 4-(2-aminoethyl)benzensulfonyl fluoride (AEBSF), a trypsin inhibitor; (ii) glutamine; (iii) Nε-methyl-Nα-acetyl-L-lysine (Figure 1b).[5,7] Cleavage of acetyl-methyl-lysine from the proinhibitor, which is catalyzed by trypsin, initiates the loop. Cleavage of glutamine from the intermediate inhibitor (**IInh**), which is catalyzed by aminopeptidase, releases AEBSF (**Inh**), an irreversible trypsin inhibitor.[11] This step ensures a controllable delay between the formation of trypsin and its inhibition. AEBSF reacts stoichiometrically and irreversibly with trypsin through nucleophilic substitution of fluorine on the sulfonylfluoride group by nucleophilic serine in the active site of trypsin. Formation of the catalytically inactive conjugate of AEBSF with trypsin closes the negative

feedback loop. Importantly, all reactions happen in a continuously stirred tank reactor (CSTR). Trypsinogen, small amounts of trypsin, proinhibitor, and aminopeptidase are continuously supplied to the reactor at fixed rates and concentrations. Moreover, all content of the CSTR is continuously washed away through an outlet.

Four-variable model of the trypsin oscillator. Figure 1b shows four core chemical reactions of the oscillator: (i) autocatalytic formation of trypsin; (ii) initiation of the negative feedback loop; (iii) delay; (iv) inhibition of trypsin. We aimed to construct a minimal model that will capture these basic features of the oscillator. Therefore, we made three assumptions about these core reactions. First, the autocatalytic formation of trypsin can be described as a second-order

reaction with rate constant K_{Tg}. This assumption implies that the Michaelis-Menten expression $k_{cat}/(K_m + [Tg])$ does not change significantly during the oscillatory reaction. Second, the concentration of proinhibitor does not change significantly during the reaction and, thus, the rate of formation of the intermediate inhibitor can be described by a first-order reaction from the concentration of trypsin with a rate constant K_{PInh}. This assumption implies that $k_{cat}[PInh]/(K_m + [PInh])$ does not change significantly during the oscillatory reaction. Third, formation of the inhibitor is a first-order reaction from the intermediate inhibitor with the rate constant K_{IInh}. This assumption implies that $k_{cat}[Aminopeptidase]/(K_m + [IInh])$ is constant throughout the oscillations. The experimentally determined K_M for the aminopeptidase reaction is 3 mM and $[IInh]$ does not exceed 0.2 mM during the sustained phase of the oscillations.[5] For that reason, we can approximate the inhibitor formation by a first-order reaction. Finally, we also neglected all end products and added washout of all compounds with constant k_0 (flow rate/reactor volume), supply of trypsinogen with constant flux $k_0[Tg_0]$, where $[Tg_0]$ is the concentration of trypsinogen in the incoming flow, and supply of trypsin with constant flux $k_0[Tr_0]$, where $[Tr_0]$ is the concentration of trypsin in the incoming flow. The reaction of trypsin with the inhibitor is a second-order reaction with the rate constant K_I (Figure 2).

With all these assumptions, the model has four variables: trypsin, intermediate inhibitor, inhibitor, and trypsinogen. The system of four differential equations (1a–d, *vide infra*) fully describes the evolution of these variables in time.

To estimate the rate constants in these equations we used rate constants from the detailed model and computed simplified rate constants using the Michaelis-Menten equation.[5] The calculations gave the following values: $K_{Tg} =$

50 mM^{-1}h^{-1}, $K_{PInh} = 46.2$ h^{-1} (estimated for $[PInh] = 1.54$ mM), $K_{IInh} = 1.98$ h^{-1} (estimated for aminopeptidase activity 0.33 U mL^{-1}), $K_I = 43$ mM^{-1}h^{-1}. Using these parameters with $[Tg_0] = 0.168$ mM, $[Tr_0] = 0.0002$ mM, and $k_0 = 0.22$ h^{-1} our model demonstrates sustained oscillations in trypsin concentration with a period of 6.5 h and a peak-to-peak amplitude of 0.006 mM (Figure 3a). This period and

Figure 3. Simulations based on the four-variable model. **a**. Comparison of experimental data and numerical modeling. Modeling parameters: $K_{Tg} = 50$ mM^{-1}h^{-1}, $K_{PInh} = 46.2$ h^{-1}, $K_{IInh} = 1.98$ h^{-1}, $K_I = 43$ mM^{-1}h^{-1}, $[Tg_0] = 0.168$ mM, $[Tr_0] = 0.0002$ mM, and $k_0 = 0.22$ h^{-1}. Experimental data were taken from ref [5], conditions: $[Tg_0] = 0.168$ mM, $[Tr_0] = 0.0002$ mM, $[PInh_0] = 1.54$ mM, $Amp_0 = 0.33$ U mL^{-1}. Positions of the first peaks were aligned for clarity of the presentation. **b**. The evolution of the concentrations of key compounds (Tr, green; Intermediate Inhibitor, red; Inhibitor, blue) during oscillations. Modeling parameters are identical to a. Control-theoretic diagram (top) shows the relation between phases of oscillations.

Figure 2. Full reaction set, including supply and removal by flow, that represents the four-variable model. The variables are indicated in red.

Full Paper

amplitude are similar to the ones which we observed in the experiment with the same concentrations of incoming reagents and the same flow rate.[5]

$$d[Tr]/dt = K_{Tg}[Tg][Tr] + k_0[Tr_0] - k_0[Tr] - K_I[Tr][Inh]$$
(1a)

$$d[IInh]/dt = K_{PInh}[Tr] - k_0[IInh] - K_{IInh}[IInh]$$
(1b)

$$d[Inh]/dt = K_{IInh}[IInh] - K_I[Tr][Inh] - k_0[Inh]$$
(1c)

$$d[Tg]/dt = -K_{Tg}[Tg][Tr] + k_0[Tg_0] - k_0[Tg]$$
(1d)

The amplitudes of oscillations of intermediate inhibitor and inhibitor and shifts of their peaks relative to each other and to trypsin also qualitatively resemble experimental data. Therefore, we can use the model to describe oscillations in terms of three key variables: trypsin; intermediate inhibitor, and inhibitor (Figure 3b). The oscillatory cycle starts from the autocatalytic production of trypsin accompanied by the production of intermediate inhibitor in the reaction catalyzed by trypsin. In the next phase, intermediate inhibitor is converted into inhibitor which reacts with trypsin. Finally, flow washes out inhibitor and the cycle repeats. This view of oscillations as a sequence of stages where one stage triggers another is similar to the control-theoretical diagrams used to describe an oscillator based on thiols.[12] Although this approach is simplified, it already demonstrates the difference in structures of these two oscillators, which is mainly the presence of a delay step in the trypsin oscillator. In contrast, autoamplification and inhibition happen within one phase of oscillations in the thiol system, but are decoupled into two separate phases in the trypsin network.

Next, we performed a linear stability analysis of the reduced model to describe the dynamic behavior predicted by the model, and to compare this behavior with the experimentally observed trends.

Linear stability analysis. We performed linear stability analysis using a standard procedure.[13] We calculated steady states of trypsin [Tr], intermediate inhibitor [IInh], inhibitor [Inh], and trypsinogen [Tg] concentrations from the kinetic equations (1a–d) (see supporting information). To analyze the stability of these steady states we used the Jacobian matrix (J), and determined the eigenvalues (λ) such that $|J{-}I\lambda| = 0$:

$$(J - I\lambda) = \begin{pmatrix} K_{Tg}[Tg]-k_0-K_I[Inh]-\lambda & 0 & -K_I[Tr] & K_{Tg}[Tg] \\ K_{PInh} & -K_{IInh}-k_0-\lambda & 0 & 0 \\ -K_I[Inh] & K_{IInh} & -K_I[Tr]-k_0-\lambda & 0 \\ -K_{Tg}[Tg] & 0 & 0 & -K_{Tg}[Tr]-k_0-\lambda \end{pmatrix}$$
(2)

We found only one physically meaningful, positive, steady state for all tested parameters. We, however, do not exclude that, within seven-parameters space, regions with multiple positive steady states exist. Figure 4a shows the stability of this steady state as a function of k_0, which reflects flow in a reactor. Increasing k_0 from 0 to high values causes a transition from a stable state to an unstable state, at $k_0 = 0.0118$ h^{-1}, and another transition from the unstable state to a new stable state
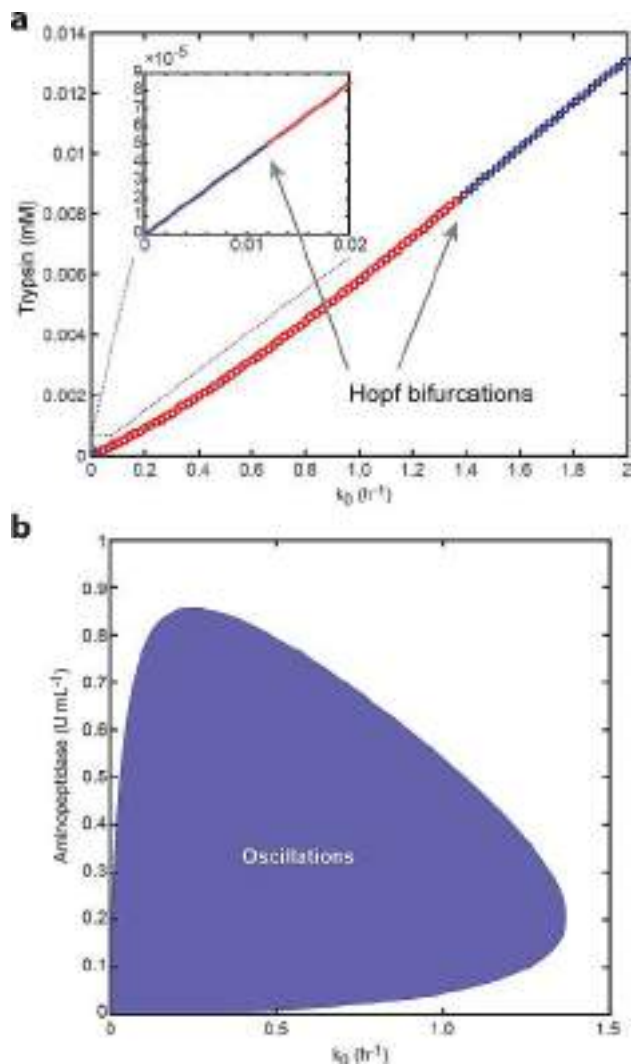
Figure 4. Results of the linear stability analysis of the four-variable model. **a**. Stability of steady states as function of k_0. The graph shows steady states, which were calculated from the model ($K_{Tg} = 50$ mM^{-1}h^{-1}, $K_{PInh} = 46.2$ h^{-1}, $K_{IInh} = 1.98$ h^{-1}, $K_I = 43$ mM^{-1}h^{-1}, $[Tg_0] = 0.168$ mM, $[Tr_0] = 0.0002$ mM), and their stability (blue crosses indicate stable states, red circles indicate unstable states). **b**, A phase plot computed from the four-component model. Aminopeptidase activity is calculated as $K_{IInh}/6$.

at $k_0 = 1.36$ h^{-1}. Real parts of the eigenvalues go through zero at both transitions. Thus, they happen *via* an Andronov–Hopf bifurcation.[14] Steady states on both sides of the oscillatory region are stable focuses (the system, when perturbed, returns to the stable state by orbiting around it) which cause damped oscillations as confirmed by experiments. Figure 4b shows the analysis of the k_0 / [Aminopeptidase] phase plane, where aminopeptidase activity is calculated as $K_{IInh}/6$, where 6 comes from an estimation of the k_{cat}/K_m for the aminopeptidase-catalyzed reaction. We defined an oscillatory region as a region with an unstable steady state and confirmed the presence of a stable orbit by numerical simulations at various

points within the parameter space. The oscillatory region forms an island that qualitatively resembles simulations with the detailed model, but predicts preservation of sustained oscillations at two times higher flow rates and aminopeptidase activities than the detailed model and experiments. Perhaps, side reactions and Michaelis-Menten kinetics of enzymatic reactions destabilize the oscillator at high flow rates and aminopeptidase activities in experiments. Apparent sustained oscillations at $k_0 = 0$ and aminopeptidase activity $= 0$ are the result of limited resolution of the plot.

This analysis shows that the trypsin oscillator behaves in a qualitatively different way as compared to the thiol oscillator and a pH-based organic oscillator where oscillations emerge through a Hopf bifurcation and end through a saddle-node bifurcation.[12,15] We did not find any phase plane where the state diagram (one is shown in Figure 4b) will have a cross-shape with a bistability region that is characteristic for many oscillatory systems.[16]

Wong *et al.* experimentally demonstrated that the oscillatory region grows by increasing K_{PInh} and K_I by changing the lysine and sulfonylfluoride fragments of the proinhibitor.[7b] We tested the influence of K_{PInh} and K_I on the region of stable oscillations in the simple model (Figure 5) and observed that higher values of K_{PInh} and K_I indeed move the borders of the region of sustained oscillations to higher flow rates.

3. Conclusions

In summary, we reduced a numerical model of the enzymatic oscillator based on trypsin to four variables. This simplified model qualitatively captures the oscillatory dynamics of three key species in the oscillator: trypsin, intermediate inhibitor, and active inhibitor. The model correctly predicts directions of changes in the region of stable oscillations with changes in individual rate constants. Overall, however, it overestimates the stability of the oscillator to changes in flow rates, especially to high flow rates, in comparison to experiments and the detailed model. Neither the incorporation of side reactions or full Michaelis-Menten kinetics of enzymatic reactions were essential for oscillations to emerge in a model of the trypsin system.

The simplified model helps to identify how oscillations of trypsin form and disappear through Hopf bifurcation and will be helpful in situations where numerical simulations are difficult such as in the presence of mass transfer by diffusion or convection.

The trypsin, thiols, and organic pH oscillators have different reaction network topologies. The thiol oscillator has two negative feedback loops, based on a weak and a strong inhibitor, while the trypsin network has one delayed negative feedback loop. These topologies do not exclude each other and can be combined in one system that has two negative feedback loops, one of which is delayed. For example, we can add an additional strong feedback loop to the herein described trypsin oscillator using soybean trypsin inhibitor. Potentially, this hybrid system will be more robust to changes in external and internal parameters than individual systems. It provides an interesting target for experimental studies, which can first be probed with the computational models at hand.

4. Computational Detail

Numerical integration of kinetic equations was performed with COPASI program.[17] Linear stability analysis was performed with MATLAB scripts, which are supplied with the manuscript.

Figure 5. Overlay of phase plots at different K_{PInh}, and K_I. Modeling parameters: $K_{Tg} = 50$ mM^{-1}h^{-1}, $K_{IInh} = 1.98$ h^{-1}, $[Tg_0] = 0.168$ mM, $[Tr_0] = 0.0002$ mM.

References

[1] a) J. J. Tyson, *P. Natl. Acad. Sci. USA* **1991**, *88*, 7328–7332; b) J. E. Ferrell, T. Y. C. Tsai, Q. O. Yang, *Cell* **2011**, *144*, 874–885.
[2] a) M. Nakajima, K. Imai, H. Ito, T. Nishiwaki, Y. Murayama, H. Iwasaki, T. Oyarna, T. Kondo, *Science* **2005**, *308*, 414–415; b) P. E. Rapp, *J. Exp. Biol.* **1979**, *81*, 281–306; c) S. Panda, M. P. Antoch, B. H. Miller, A. I. Su, A. B. Schook, M. Straume, P. G. Schultz, S. A. Kay, J. S. Takahashi, J. B. Hogenesch, *Cell* **2002**, *109*, 307–320.

Full Paper

[3] a) E. E. Selkov, *Eur. J. Biochem.* **1968**, *4*, 79–86; b) A. Boiteux, A. Goldbeter, B. Hess, *P. Natl. Acad. Sci. USA* **1975**, *72*, 3829–3833.

[4] J. J. Tyson, K. C. Chen, B. Novak, *Curr. Opin. Cell Biol.* **2003**, *15*, 221–231.

[5] S. N. Semenov, A. S. Y. Wong, R. M. van der Made, S. G. J. Postma, J. Groen, H. W. H. van Roekel, T. F. A. de Greef, W. T. S. Huck, *Nat. Chem.* **2015**, *7*, 160–165.

[6] H. Neurath, W. J. Dreyer, *Discuss. Faraday Soc.* **1955**, 32–43.

[7] a) A. S. Y. Wong, S. G. J. Postma, I. N. Vialshin, S. N. Semenov, W. T. S. Huck, *J. Am. Chem. Soc.* **2015**, *137*, 12415–12420; b) A. S. Y. Wong, A. A. Pogodaev, I. N. Vialshin, B. Helwig, W. T. S. Huck, *J. Am. Chem. Soc.* **2017**, *139*, 8146–8151.

[8] A. A. Pogodaev, A. S. Y. Wong, W. T. S. Huck, *J. Am. Chem. Soc.* **2017**, *139*, 15296–15299.

[9] a) A. M. Turing, *Philos. Trans. R. Soc. London Ser. B* **1952**, *237*, 37–72; b) V. Castets, E. Dulos, J. Boissonade, P. Dekepper, *Phys. Rev. Lett.* **1990**, *64*, 2953–2956; c) S. Soh, M. Byrska, K. Kandere-Grzybowska, B. A. Grzybowski, *Angew. Chem. Int. Ed.* **2010**, *49*, 4170–4198; d) I. R. Epstein, T. Bansagi, V. K. Vanag, *Science* **2011**, *331*, 1309–1312; e) S. G. J. Postma, I. N. Vialshin, C. Y. Gerritsen, M. Bao, W. T. S. Huck, *Angew. Chem. Int. Ed.* **2017**, *56*, 1794–1798; f) S. N. Semenov, S. G. J. Postma, I. N. Vialshin, W. T. S. Huck, *Chem. Commun.* **2014**, *50*, 3089–3092.

[10] J. P. Abita, M. Delaage, Lazdunsk. M, *Eur. J. Biochem.* **1969**, *8*, 314-&.

[11] S. G. J. Postma, D. te Brinke, I. N. Vialshin, A. S. Y. Wong, W. T. S. Huck, *Tetrahedron* **2017**, *73*, 4896–4900.

[12] S. N. Semenov, L. J. Kraft, A. Ainla, M. Zhao, M. Baghbanza-deh, C. E. Campbell, K. Kang, J. M. Fox, G. M. Whitesides, *Nature* **2016**, *537*, 656–660.

[13] I. R. Epstein, J. A. Pojman, *An introduction to nonlinear chemical dynamics: oscillations, waves, patterns, and chaos*, Oxford University Press, New York, **1998**.

[14] a) Yu. A. Kuznetsov, *Elements of applied bifurcation theory*, 3rd ed., Springer, New York, **2004**; b) S. H. Strogatz, *Nonlinear dynamics and chaos : with applications to physics, biology, chemistry, and engineering, Second edition. ed.*, Westview Press, a member of the Perseus Books Group, Boulder, CO, **2015**.

[15] K. Kovacs, R. E. McIlwaine, S. K. Scott, A. F. Taylor, *J. Phys. Chem. A* **2007**, *111*, 549–551.

[16] a) J. Boissonade, P. Dekepper, *J. Phys. Chem.* **1980**, *84*, 501–506; b) M. Orban, P. Dekepper, I. R. Epstein, K. Kustin, *Nature* **1981**, *292*, 816–818.

[17] S. Hoops, S. Sahle, R. Gauges, C. Lee, J. Pahle, N. Simus, M. Singhal, L. Xu, P. Mendes, U. Kummer, *Bioinformatics* **2006**, *22*, 3067–3074.

PAPER

Towards sustainable diagnostics: replacing unstable H_2O_2 by photoactive TiO_2 in testing systems for visible and tangible diagnostics for use by blind people

Yulia V. Lanchuk, [a] Sviatlana A. Ulasevich, [a] Tatiana A. Fedotova, [b] Dmitry M. Kolpashchikov [ab] and Ekaterina V. Skorb *[a]

Blind and color blind people cannot use colorimetric diagnostics; the problem is especially severe in rural areas where high temperatures and the absence of electricity challenge modern diagnostics. Here we propose to replace the unstable component of a diagnostic test, H_2O_2, with stable TiO_2. Under UV irradiation, TiO_2 forms reactive oxygen species that initiate polymerization of acrylamide causing liquid-to-gel transition in an analyte-dependent manner. We demonstrate that specific DNA sequences can be detected using this approach. This development may enable the detection of biological molecules by users with limited resources, for example in developing countries or for travelers in remote areas.

An ideal diagnosis, including diagnosis for infectious diseases, should meet the ASSURED criteria: (i) affordable by those at risk of infection; (ii) sensitive; (iii) specific; (iv) user-friendly; (v) rapid, and robust, for example not requiring refrigerated storage; (vi) equipment-free; (vii) delivered to those who need it.[1]

Analytic methods with visually detectable outputs (*e.g.* color change) satisfy criteria (iv) and (vi), and are therefore among the most common. Indeed, pregnancy tests, test strips for measuring acetone and glucose in urine for diabetic people, and pH strips are known to be the best to make the analysis easiest in data output. However, such methods cannot be used by the visually impaired.

Recently, we described an alternative output signal that cannot only be detected by sight, but also by touch and applied it in the detection of adenosine triphosphate (ATP) and deoxyribonucleic acid (DNA).[2] The method is based on the analyte-dependent radical polymerization of acrylamide into polyacrylamide in the presence of hydrogen peroxide (H_2O_2). H_2O_2 serves as a source of radicals. The test uses affordable reagents and does not require any instrumentation for signal readout. Such test systems can be adopted for detection of a wide variety of biological analytes. Unfortunately, H_2O_2 is subject to light decomposition and should be refrigerated for long term storage; it is also prone to exploding at high concentrations. Therefore, substituting H_2O_2 with a more stable ingredient would increase the shelf life of the test system and make it

usable in those environments with limited access to refrigeration. This work is devoted to addressing the ASSURED criterion (v): we substituted perishable H_2O_2 with stable titania (TiO_2) as an alternative source of initiators of radical polymerization.

Recently we demonstrated the possibility of converting electromagnetic energy into pH gradients[3] or generating reactive oxygen species (ROS) using TiO_2,[3,4] which makes this approach attractive for controlling interactions between chemical networks. Moreover, combining several functional chemical networks can result in a network with new functions. We have also shown that the pH gradient on titania can be used for regulating enzymatic reaction networks.[5] In this work, we were interested in using photogenerated ROS (such as superoxide anion $O_2^{\bullet -}$, hydroxyl radical $^{\bullet}OH$, and hydrogen peroxide H_2O_2) (Fig. 1) to initiate radical polymerization with the aim of making a visual and tactile portable sensor for the detection of biologically important molecules (DNA, RNA, ATP). Under ultraviolet (UV) irradiation, TiO_2 splits water, which results in the generation of a high concentration of ROS and free radicals.[6]

The sensing system is based on deoxyribozyme sensor that produces ROS in the presence of a specific analyte, thereby triggering the radical polymerization of acrylamide into polyacrylamide. The buffer contained acetylacetone, H_2O_2, 40% acrylamide/bisacrylamide, hemin and a split deoxyribozyme sensor with peroxidase-like activity (PxR).[2] In the presence of the specific analyte sequence (A1 in this study), the sensor hybridized with the analyte and formed PxR, which bound hemin and decomposed H_2O_2 to ROS. The latter oxidized acetylacetone to the acetylacetone radical, which initiated the polymerization of acrylamide, resulting in liquid-to-gel conversion. Here, the aim of the research is to increase the system sustainability by

[a] *ITMO University, Lomonosova St. 9, 191002, St. Petersburg, Russian Federation. E-mail: skorb@corp.ifmo.ru*

[b] *Chemistry Department University of Central Florida, Orlando, FL, USA*
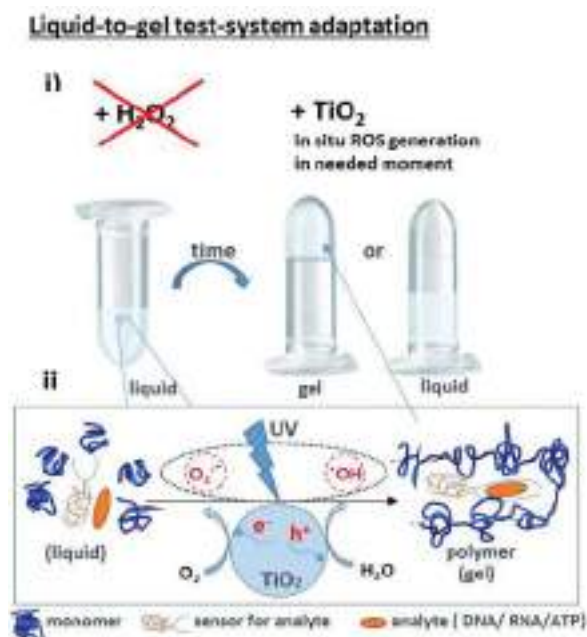
Fig. 1 (i) A portable sensor based on a light-induced liquid-to-gel transition for polymer by radical polymerization on TiO_2 particles. The details of the sensor design are shown in Fig. 5; (ii) ROS formation on titania *via* reactions with photogenerated photohole (h^+) and photoelectron (e^-).

changing H_2O_2 to TiO_2 particles. Noteworthy is that the system is externally controlled by UV light, since TiO_2 produces ROS only upon irradiation.

Firstly, we quantified the TiO_2-derived ROS with the aim of finding the optimal conditions for the generation of the minimum amount of ROS needed for the polymerization. We used luminol chemiluminescence (CL) calibrated with hydrogen peroxide. Luminol (5-amino-2,3-dihydro-1,4-phthalazinedione) is a widely used CL reagent and has CL emission at different wavelengths depending on the conditions.[6] Traditionally, luminol CL is observed in the presence of H_2O_2 in alkaline solutions (Fig. 2), which is catalyzed by metal ions, metal complexes or vitamins.[7–10]

The luminol CL signaling is conveniently used for the detection of ROS (particularly superoxide anion, hydrogen peroxide, hydroxyl radical) in biological systems.[11–16]

Irradiation of TiO_2 suspensions of different concentrations (0.03 M and 0.06 M) at two wavelengths (365 nm and 254 nm) revealed more ROS being formed upon irradiation at 254 nm – as was expected (Fig. 3).

According to the data obtained, the minimum concentration of TiO_2 needed to trigger polymerization after 5 min of irradiation at 365 nm was 1.25 mM (Fig. 4). We therefore used these conditions in the following experiments, since short irradiation time and longer wavelength of UV-A irradiation are less damaging to the DNA-based biosensor component than UV-C light with wavelength of 254 nm. It should be noted that control experiments were made without TiO_2 particles and polymerization did not occur. Next, we optimized the conditions for the analyte-dependent activation of PxR resulting in
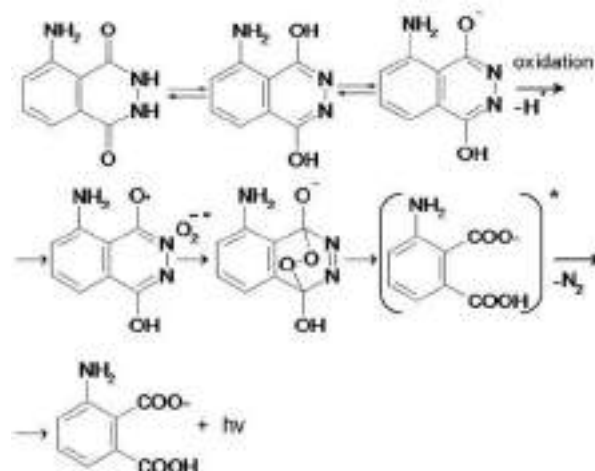
Fig. 2 Mechanism of chemiluminescence of luminol and $O_2^{-\cdot}$.

acrylamide polymerization. If polymerization occurs, the gel will stick to the bottom of the inverted tubes (Fig. 5).[2] To demonstrate the general applicability of the approach, we designed a sensor for an analyte of biomedical significance, nucleic acids, as an example. A sequence of 16S rRNA, which
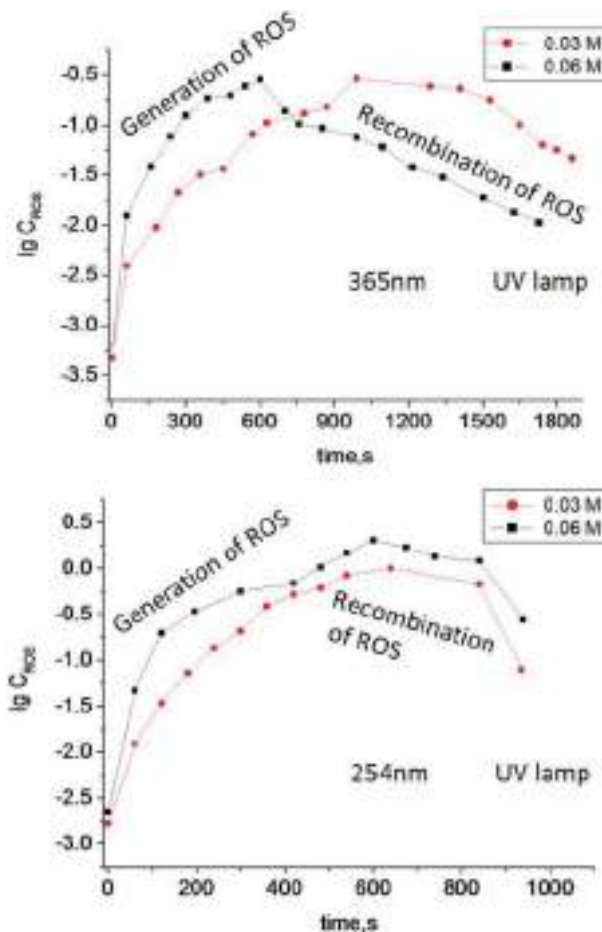
Fig. 3 Log concentration of ROS generated in TiO_2 suspensions of different concentration (0.03 M and 0.06 M) under irradiation by UV light with different wavelengths *vs.* irradiation time.
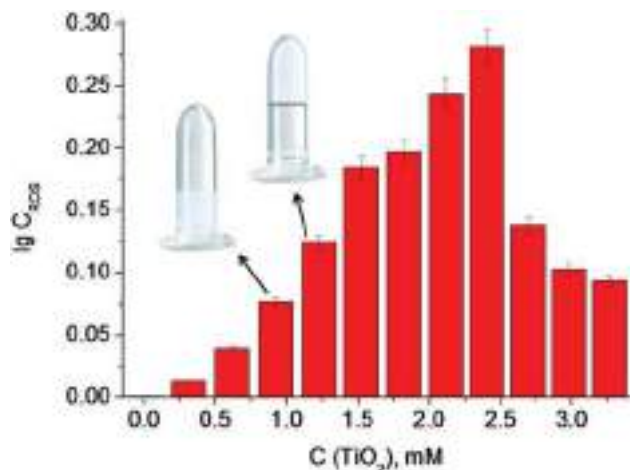
Fig. 4 The dependence of the log concentration of ROS generated on TiO$_2$ particles on TiO$_2$ suspension concentration. Inserts show the minimum concentration of TiO$_2$ particles in a suspension (therefore minimum concentration of ROS generated on TiO$_2$ particles), needed for the gel formation.

was represented in this study by synthetic A1 sequence (5′-CAT TAC TCA CCC GTC CGC CAC TCG TCA GCG AAG CAG CAA GCT GCT TCC TGT TAC CGT TCG), of pathogenic *E. coli* O157:H7 was chosen as the target analyte,. The binding of A1 to PxR1 and PxR2 stabilized the G-quadruplex structure, which then binds to hemin and catalyzes the polymerization (Fig. 5A).

Firstly, we tested the influence of hemin concentration on polymer formation. Gel fragments were observed in the presence of hemin at the concentration higher than 5×10^{-8} M (Table 1). No gel fragments were observed in the absence of TiO$_2$ or hemin (two control experiments). Gel formation was

Table 1 Influence of hemin concentration on polymer formation

No.	1	2	3	4	5	6
C, M	10^{-9}	2.5×10^{-8}	5×10^{-8}	7.5×10^{-8}	10^{-7}	2.5×10^{-7}
Gel	−	−	−	+	+	+

observed in the system with the buffer components, hemin and TiO$_2$.

Sample 1 (negative control) with a hemin concentration of 5×10^{-8} M shows no gel formation (Fig. 5c), sample 2 (positive control) contained already formed G-quadruplex which triggered the polymerization reaction. Sample 3 contained separated RNA fragments of PxR1 and PxR2 without A1 analyte: no gel formation was observed. The presence of A1 analyte in sample 4 resulted in polymerization. Therefore, we achieved analyte-dependent polymer formation without using H$_2$O$_2$. This development is pivotal for the future development of H$_2$O$_2$-free tests systems for nucleic acid analysis employable by blind and color blind people.

Reactions on the surface are very attractive when considering the development of a robust sensor. The surface layer of anodized titania nanotubes (TNT) is suitable for surface ROS generation.[17] To understand how much ROS were generated on TNT surfaces, experiments with luminol CL were conducted (Fig. 6). A benefit of using light is the ability to control reaction networks with an external stimulus. To check our hypothesis of using TNT as a good alternative source of ROS and understand how much photogenerated ROS are needed for radical polymerization, we experimented with the buffer solution (Fig. 6B) (neither analyte nor sensor for the analyte were present). Polymerization was completed after 15 min of UV irradiation (365

Fig. 5 Polymerization-based visual and tactile detection of A1 analyte. (A) Sensor design: RNA strands PxR1 and PxR2 bind A1 sequence and form a G-quadruplex structure, which then binds to hemin (green oval) and catalyzes the radical polymerization of the acrylamide solution. The dotted lines represent triethylene glycol linkers. (B and C) Inverted test-tubes with radical polymerization of acrylamide initiated by reactive oxygen species generated on TiO$_2$ particles under UV light 365 nm. (B) Systems with different concentrations of hemin (Table 1). (C) All samples contained hemin of 5×10^{-8} M (1); (2) with G-quadruplex; (3) with RNA strands PxR1 (1 μM) and PxR2 (1 μM); (4) with PxR1 and PxR2 and RNA (1 μM).

Fig. 6 (A) Log concentration of ROS generated on TiO$_2$ nanotubes (TNT) under UV irradiation at different wavelengths *vs.* time. (B) Radical polymerization of acrylamide initiated by ROS generated on TNT under UV irradiation at 365 nm.

nm), which proves the use of TNT as an alternative robust surface for ROS generation. This polymerized gel can also find its application as protective coating against unfavorable environment.

In order to demonstrate this hypothesis, a photolithography displaying the name of our laboratory was made (Fig. 7).

Nowadays, methods for the detection of biological analytes are under continuous development.[18,19] Sensors usually display their readings on a screen or by some visual means. This interface is not user-friendly for the visually impaired. Here, we report improvement on an alternative method that can be used for the tactile detection of biological analytes and, therefore, is more user-friendly for blind people. Using this method, we can detect nucleic acids as well as analytes that are used in the diagnosis of infectious diseases. The use of PxR-based (or PxD, *etc.*) sensors are widely spread in the detection of a wide variety of analytes, including small molecules, metal ions and proteins.[20]

It should be noted that all the analytes can be detected with high specificity, even at room temperature, which is important in practice. The main disadvantage of this assay is its sensitivity to atmospheric oxygen, which inhibits polymerization[16] and makes the analysis difficult. We hope that future progress in creating special equipment for carrying out such experiments in an oxygen-free environment may help to solve this problem.

The toxicity of liquid acrylamide can be easily circumvented by wearing gloves. We also consider that the reported assay in this article is very promising beyond tactile-like sensors. For example, the liquid-to-gel transition can be used with light in the regulation of liquid flow in the channels of (micro)fluidic devices.

In conclusion, point-of-care diagnostic systems should be cost efficient, easy to transport, robust and sustainable among other characteristics. To improve these qualities, we replaced unstable hydrogen peroxide component with stable and robust titania in the liquid-to-gel testing system. The ability to trigger the system by light irradiation is an attractive alternative to traditional tests in which the reaction is triggered by the addition of analytes. We hope that the method developed in this study will make home test-systems available to blind and color blind persons.

Experimental section

Materials

Hombikat UV100 (>99% anatase, 5 nm particle size, supplied by Sachtleben Chemie); luminol, hemin, DMSO (99.9%, anhydrous (max. 0.005% H_2O)) and sodium hydroxide (NaOH) were acquired from Sigma Aldrich. Millipore water (Milli-Q Plus 185) was used for preparation of aqueous solutions and sample washing. RNAse-free water was purchased from Fisher Scientific, Inc. (Pittsburgh, PA) and used for all buffers and for the stock solutions of oligonucleotides. The oligonucleotides were obtained from Integrated DNA Technologies, Inc. (Coralville, IA). The oligonucleotides were dissolved in water and stored at −20 °C until needed. Stock concentrations of oligonucleotides were calculated by measuring the absorption of the solutions at 260 nm by using a Perkin-Elmer Lambda 35 UV/Vis spectrometer (San Jose, CA). Extinction coefficients of oligonucleotides were calculated by using OligoAnalyzer 3.1 software (Integrated DNA Technologies, Inc.). All experiments were carried out in the buffer, containing 50 mM HEPES pH 6.6., 50 mM $MgCl_2$, 20 mM K^+, 120 mM NaCl, 1% DMSO v/v, 0.03% w/v Triton X 100, 38% w/v acrylamide, 2% w/v bisacrylamide, 127 mM acetylacetone.

Chemiluminescence measurements

3 mL of TiO_2 suspension (0.03 M and) or a drop of pure water (100 μL) on TNT was irradiated with the UV lamp (with different wavelength 365 nm and 254 nm) and every minute a 10 μL aliquot of the irradiated solution was taken and added to a cuvette with 2 mL of 0.2% luminol in 1% NaOH solution for CL measurements. The fluorescence spectra were measured from 380 to 550 nm at the excitation wavelength of 310 nm. The widths of emission and excitation slits were set at 10.0 and 10.0. The fluorescence spectra were measured by a Cary Eclipse fluorescence spectrophotometer equipped with a 1.0 cm quartz cell.

Polymerization in tubes

1 mL liquid in a tube contained 50 mM HEPES pH 6.6, 50 mM $MgCl_2$, 20 mM K^+, 120 mM NaCl, 1% DMSO v/v, 0.03% w/v Triton X 100, 38% w/v acrylamide, 2% w/v bisacrylamide, 127 mM acetylacetone and 5×10^{-8} M hemin. 3 mL of TiO_2 suspension was irradiated under UV light at 365 nm during 15 min and then added to the tube with all the components. The final concentration of TiO_2 in tube was 1.25 mM. Tactile readout is possible if the samples are placed on a piece of filter paper. The experiment was carried out in box with argon due to the fact that oxygen inhibits the polymerization reaction.[16]
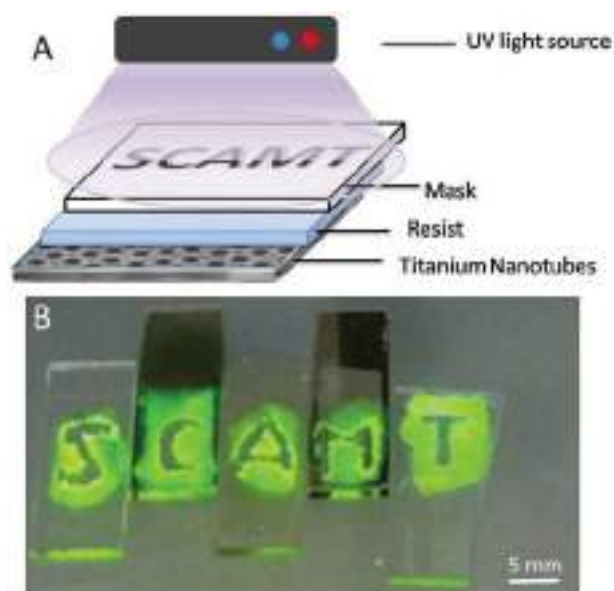
Fig. 7 (A) Scheme of photolithography process (negative resist) by radical polymerization of acrylamide initiated by ROS generated on TiO_2 anodized surface (TNT) under UV light 365 nm; (B) experiment of polymerization of test-sample on TNT allows further test improvement.

Polymerization on the surface

The drop on the TNT contained reaction buffer: 50 mM HEPES pH 6.6, 50 mM MgCl$_2$, 20 mM K$^+$, 120 mM NaCl, 1% DMSO v/v, 0.03% w/v Triton X 100, 38% w/v acrylamide, 2% w/v bisacrylamide, 127 mM acetylacetone, 5×10^{-8} M hemin. Experiment was carried out in box with argon due to the fact that oxygen inhibits the polymerization reaction. Radical polymerization of acrylamide was initiated by ROS generated on TNT under UV irradiation at 365 nm during 15 min. Photolithography was made the same way with photomasks.

Conflicts of interest

There are no conflicts to declare.

Acknowledgements

References

1 P. K. Drain, E. P. Hyle, F. Noubary, K. A. Freedberg, D. Wilson, W. Bishai, W. Rodriguez and I. V. Bassett, *Lancet Infect. Dis.*, 2014, **14**, 239–249.

2 T. A. Fedotova and D. M. Kolpashchikov, *Chem. Commun.*, 2017, **53**, 12622–12625.

3 (*a*) S. A. Ulasevich, G. Brezesinski, H. Möhwald, P. Fratzl, F. Schacher, S. K. Poznyak, D. V. Andreeva and E. V. Skorb, *Angew. Chem., Int. Ed.*, 2016, **55**, 13001–13004; (*b*) H. Maltanava, S. K. Poznyak, D. V. Andreeva, M. C. Quevedo, A. C. Bastos, J. Tedim, M. G. S. Ferreira and E. V. Skorb, *ACS Appl. Mater. Interfaces*, 2017, **9**, 24282–24289; (*c*) E. V. Skorb and H. Möhwald, *Adv. Mater.*, 2013, **36**, 5029–5043; (*d*) D. V. Andreeva, I. Melnyk, O. Baidukova and E. V. Skorb, *ChemElectroChem*, 2016, **3**, 1306–1310.

4 Y. V. Lanchuk, A. A. Nikitina, N. Y. Brezhneva, S. A. Ulasevich, S. N. Semenov and E. V. Skorb, *ChemCatChem*, 2018, **10**, 1798–1803.

5 E. V. Skorb, L. I. Antonouskaya, N. A. Belyasova, D. G. Shchukin, H. Möhwald and D. V. Sviridov, *Appl. Catal., B*, 2008, **84**, 94–99.

6 K.-D. Gundermann and F. McCapra, *React. Struct.: Concepts Org. Chem.*, 1987, **23**, 84–87.

7 J. Guo, H. Cui, W. Zhou and W. Wang, *J. Photochem. Photobiol., A*, 2008, **193**, 89–96.

8 W. Chen, L. Hong, A.-L. Liu, J.-Q. Liu, X.-H. Lin and X.-H. Xia, *Talanta*, 2012, **99**, 643–648.

9 N. Yang, H. Song, X. Wan, X. Fan, Y. Su and Y. Lv, *Analyst*, 2015, **140**, 2656–2663.

10 J. Du, Y. Li and J. Lu, *Talanta*, 2002, **57**, 661–665.

11 M. Nakano, *Methods Enzymol.*, 1990, **186**, 585–591.

12 R. P. Brandes and M. Janiszewski, *Kidney Int.*, 2005, **67**, 1662–1664.

13 A. Gomes, E. Fernandes and J. L. F. C. Lima, *J. Biochem. Biophys. Methods*, 2005, **65**, 45–80.

14 K. Faulkner and I. Fridovich, *Free Radical Biol. Med.*, 1993, **15**, 447–451.

15 C. Lu, G. Song and J.-M. Lin, *Trends Anal. Chem.*, 2006, **25**, 10.

16 O. Emery, T. Lalot, M. Brigodiot and E. Marechal, *J. Polym. Sci., Part A: Polym. Chem.*, 1997, **35**, 3331–3333.

17 (*a*) Y. Zhukova and E. V. Skorb, *Adv. Healthcare Mater.*, 2017, **6**, 1600914; (*b*) Y. Zhukova, C. Hiepen, P. Knaus, M. Osterland, S. Prohaska, J. W. C. Dunlop, P. Fratzl and E. V. Skorb, *Adv. Healthcare Mater.*, 2017, **6**, 1601244; (*c*) S. A. Ulasevich, S. Poznyak, A. I. Kulak, A. Lisenkov, M. Starykevich and E. V. Skorb, *Langmuir*, 2016, **32**, 4016–4021.

18 A. J. Gormley, R. Chapman and M. M. Stevens, *Nano Lett.*, 2014, **14**, 6368–6373.

19 M. Ikeda, T. Tanida, T. Yoshii, K. Kurotani, S. Onogi, K. Urayama and I. Hamachi, *Nat. Chem.*, 2014, **6**, 508–518.

20 (*a*) X. Yang, T. Li, B. Li and E. Wang, *Analyst*, 2010, **135**, 71–75; (*b*) J. J. Kosman and B. Juskowiak, *Anal. Chim. Acta*, 2011, **707**, 7–17; (*c*) L. Neo, K. Kamaladasan and M. Uttamchandani, *Curr. Pharm. Des.*, 2012, **18**, 2048–2057; (*d*) B. T. Roembke, S. Nakayama and H. O. Sintim, *Methods*, 2013, **64**, 185–198; (*e*) D. Chang, S. Zakaria, M. Deng, N. Allen, K. Tram and Y. Li, *Sensors*, 2016, **16**, E2061; (*f*) D. L. Ma, C. Wu, Z. Z. Dong, W. S. Tam, S. W. Wong, C. Yang, G. D. Li and C. H. Leung, *ChemPlusChem*, 2017, **82**, 8–17; (*g*) K. Shahsavar, M. Hosseini, E. Shokri, M. R. Ganjali and H. Ju, *Anal. Methods*, 2017, **9**, 4726–4731.

Photocatalytic Regulation of an Autocatalytic Wave of Spatially Propagating Enzymatic Reactions

Yulia Lanchuk,[a] Anna Nikitina,[a] Nadzeya Brezhneva,[a] Sviatlana A. Ulasevich,[a] Sergey N. Semenov,[b] and Ekaterina V. Skorb*[a]

Bioinspiration is an attractive way to develop new robust chemistry. In biological cell, chemical reactions form complex networks (e.g. signaling and metabolic) that communicate with each other and control cell division, growth, and interaction with environment. Thus, combining multiple chemical subsystems into a single network is an attractive way to design a chemical system with new functions. In this paper, we combined two chemical networks: i) a photocatalytic oxidation/ reduction on TiO_2 particles, and ii) an autocatalytic formation of enzyme trypsin (Tr) from its precursor trypsinogen (Tg). Moreover, we put the combined network in hydrogel media, where all reactions are coupled to diffusion, to achieve a photocatalytic regulation of an autocatalytic wave. We showed that TiO_2 particles affected the fluorescence quenching of Tr, but, without irradiation, had no effect on the autocatalytic formation of Tr. With irradiation, however, a cascade of photocatalytic reactions causes media acidification that suppress the autocatalytic formation of Tr and propagation of the autocatalytic wave.

Nature uses pH gradients to regulate chemical networks.[1] Buffering capacity is a well-known function of biomolecules.[2] In our recent work, we studied, in detail, the process of local pH changes by irradiation of a TiO_2 surface, suggesting titania as a robust surface for light controlled proton pumping.[3] We used the phenomena of light-pH coupling on titania for a non-destructive modulation of pH-sensitive layers,[4] adsorption/ desorption of proteins,[5] control of preosteoblast migration,[6] bacteria assembly,[7] self-healing of hydrogel,[8] and even a regulation of a "prebiotic nucleotides" assembly.[9] In this context, we got interested in using pH gradients on titania for regulating biomolecular reaction networks. The coupling of pH oscillators to pH-dependent complexation equilibria proposes an especially attractive way to construct new oscillatory reactions.[10]

[a] Y. Lanchuk, A. Nikitina, N. Brezhneva, Dr. S. A. Ulasevich, Prof. E. V. Skorb
Infochemistry for Self-Adaptive Materials
SCAMT Laboratory, ITMO University
St. Petersburg 197101 (Russian Federation)
E-mail: skorb@corp.ifmo.ru

[b] Dr. S. N. Semenov
Chemistry and Chemical Biology
Harvard University
02138 Cambridge, MA (USA)

The ORCID identification number(s) for the author(s) of this article can be found under https://doi.org/10.1002/cctc.201702005.

This manuscript is part of a Special Issue on "Supported Molecular Catalysts".

In this paper, we studied coupling of the photocatalytic titania based system with pH dependent enzymatic network (Figure 1). The enzymatic system was previously studied in detail in the group of Huck.[11] The network is built around autocatalytic formation of trypsin (Tr) from trypsinogen (Tg).
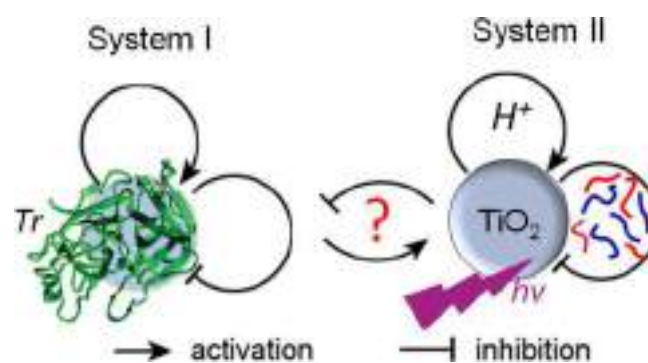
Figure 1. Schematic of a combination of two network of chemical reactions: (System I) Enzymatic autocatalytic Tr-system, and (System II) Photocatalytic reactions on titania regulated by change of particle photoactivity via polyelectrolytes' buffering. The question is how the one network changes behavior of the other one.

Here, it is important to note that the Tr network is sensitive to pH, and, thus, our photocatalytic system and the Tr network might interact through pH. Tr has highest proteolytic activity at pH 8 and loss its activity under acidification. Therefore, activity of Tr should respond to pH changes which are caused by photocatalytic reactions on titania. The main issue to take into account is that besides a local change in pH, there are reactive oxygen species (ROS) generated on titania that might deactivate biomolecules.[4] Importantly, assembly of polyelectrolytes (e.g. polyethylenimine) on titania particles might control photoactivity of titania particles and buffer changes in pH by locally absorbing of protons.

First, we studied how TiO_2 particles affect fluorescence quenching of Tr, and the mechanism of interaction between TiO_2 and Tr. The interaction was analyzed by fluorescence[12] quenching under different concentrations of titania particles and temperatures between 298 and 308 K. The fluorescence emission spectra were collected in the range of 290–400 nm, upon excitation at 278 nm. Tr has a strong fluorescence with an emission peak at 336 nm, owing to its tryptophan residue. The effect of different concentrations of titania on Tr fluorescence intensities is shown in Figure 2. The fluorescence intensity was decreasing with increasing concentration of titania,
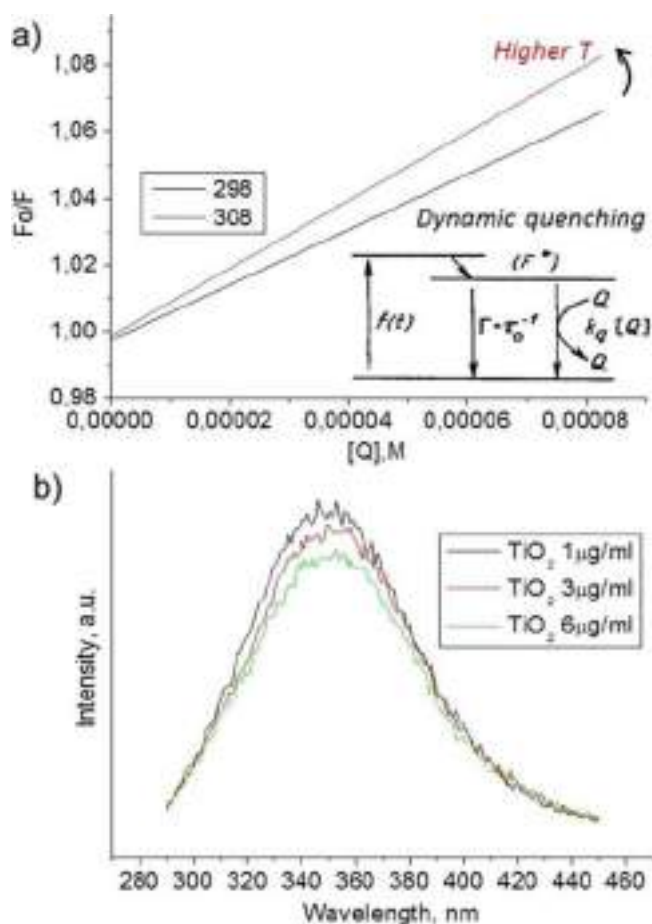
Figure 2. Study of fluorescence quenching of Tr, $\lambda_{ex} = 278$ nm and $\lambda_{em} = 290–400$ nm in the presence of TiO$_2$ particles at different a) temperatures of 298 K and 308 K. Inset shows schematic mechanism of dynamic quenching. b) Example of spectra for different particles concentration at 298 K.

which means effective fluorescence quenching of the intrinsic fluorescence of the protein. The fluorescence quenching data could be analyzed according to the Stern–Volmer Equation (1).

$$F_0/F = 1 + K_q\tau_0[Q] = 1 + K_{sv}[Q] \qquad (1)$$

For which F_0 and F mean the fluorescence intensities before and after the addition of particles. K_q, τ_0, $[Q]$, and K_{sv} are the constant of molecular quenching, the average lifetime of Tr without quencher, the concentration of quencher, and the Stern–Volmer quenching constant, respectively. Data are presented as F_0/F dependence from $[Q]$ (Figure 2a). It is seen the F_0/F linearly depends on the concentration of titania, that indicates the existence in solution of one type of fluorophore equally available for the quencher. Fluorescence quenching processes are generally described by two main mechanisms: 1) static quenching and 2) dynamic fluorescence quenching.[13] Static quenching involves a long-lasting formation of a complex between the fluorophore and quencher, which is sometimes referred to a dark complex. Dynamic quenching involves collisions between the two molecules with the fluorophore losing kinetic energy. Dynamic quenching is dependent on

diffusion. Since the increase of temperature results in an increase of diffusion coefficients, the linear dependence of the quenching efficiency from the quencher concentration for a higher temperature should be above that for a lower temperature (Figure 2). Contrarily, in the case of the static quenching, the stability of the complex decreases when temperature increases and the dependence of the quenching efficiency from the quencher concentration for higher temperature is below that for lower temperature. In our case, we see dynamic quenching, however, further study is needed to analyze lifetime changes. Previous studies have determined the lifetime is 10 ns at $\lambda_{ex} = 278$ nm.[14]

Concerning thermodynamic parameters for binding, there are four types of non-covalent interactions that play a major role in the binding: hydrogen bonding, ionic interactions, van der Waals forces, and hydrophobic interactions.[15] Some thermodynamic parameters, such as the standard enthalpy change (ΔH°), standard entropy change (ΔS°), and Gibbs free energy change (ΔG°), are functions of the binding constant (K) [Eqs. (2) and (3)].

$$\Delta G^\circ = -RT \ln K \qquad (2)$$

$$\Delta S^\circ = \frac{\Delta H^\circ - \Delta G^\circ}{T} \qquad (3)$$

For our cases, ΔG° had a negative value, indicating that the binding of Tr to particles was spontaneous ΔS° was positive, and ΔH° was negative, indicating that binding was exothermic. Recently, Momeni et al.[12] have discussed the temperature dependence of Tr interaction with TiO$_2$ nanoparticles. Ross et al.[16] have found that negative ΔH° and ΔS° are associated with van der Waals and hydrogen bonding, while the positive ΔH° and ΔS° values are evidence for hydrophobic interaction. When ΔH° and ΔS° are very low negative or positive values it is discussed as electrostatic interaction.[16] Our study of the Tr binding with TiO$_2$ based particles clearly proved that Tr absorbs on the surface of the titania particles.

Further, we studied a photocatalytic effect of a TiO$_2$ network on a Tr network. During autocatalytic formation of Tr from Tg, Tr cleaves the peptide bond between lysine and leucine in the termini of the polypeptide chain of trypsinogen (Tg).[11] This cleavage generates a molecule of catalytically active Tr and releases a hexapeptide fragment, which blocks the active side of the trypsinogen molecule. Here, we tested the influence of the TiO$_2$ based system on the autocatalytic formation of Tr from Tg (Figure 3a).

In a control experiment, we dissolved Tg (1 mg mL^{-1}, corresponding to 42 μM) in Tris buffer (100 mM, pH 8) containing CaCl$_2$ (20 mM) and initiated the autocatalytic reaction with an aliquot of Tr (2.15 μM in final mixture) (Figure 3b(I)). The reaction proceeded with continuous stirring at 298 K. We took aliquots of the solution at different time points and determined trypsin concentrations with a fluorogenic assay using bis-(Cbz-L-Arg)-Rhodamine as a substrate. To measure Tr activity, disposable cuvettes (path length 2.00 cm) were filled with 3 mL of the fluorogenic substrate bis-(Cbz-L-Arg)-Rhodamine (5.1 μM in 50 mM Tris buffer, pH 8). To this solution, 10 μL of the reaction
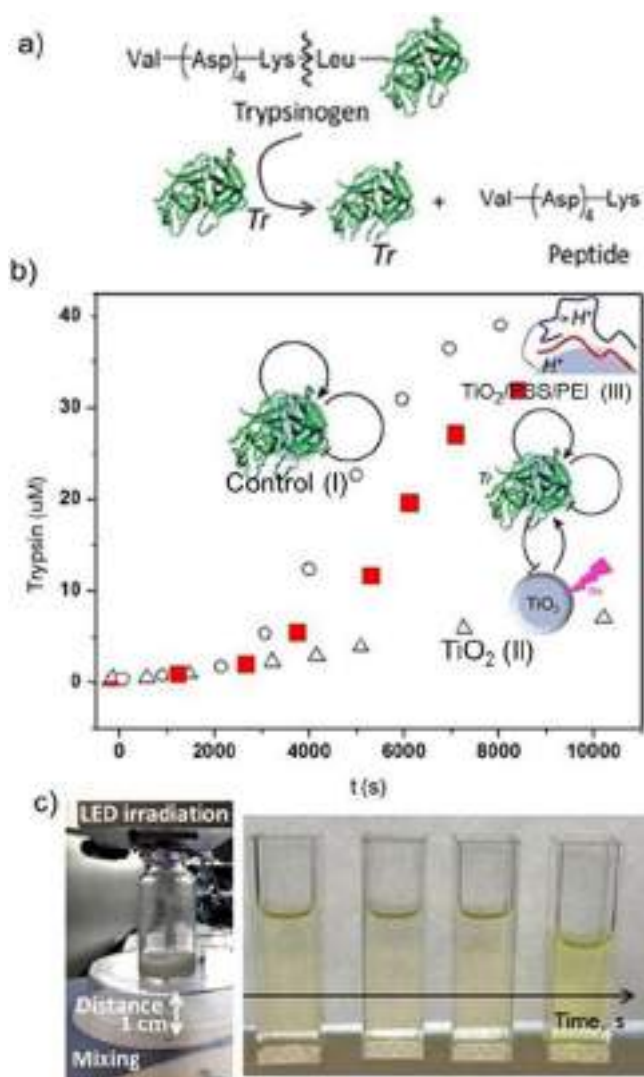
Figure 3. a) Schematic of autocatalytic *Tr*-catalyzed *Tg* decomposition. b) Conversion of the fluorogenic substrate monitored at $\lambda_{ex}=450$ nm and $\lambda_{em}=520$ nm, each point is checked for 60 seconds with a time interval of 1 second, (I) for *Tr* control reaction, (II, III) reaction in the presence of (I) TiO$_2$ or (III) TiO$_2$/PSS/PEI under irradiation. c) Photo of (left) the reactor pointed that the glass flask spatially separated from the surface to decrease effect of temperature increase, and (right) reaction monitoring over time, autocatalytic increase of fluorescence in test cuvettes.

mixture was added. Conversion of the fluorogenic substrate was monitored and the rate of the *Tr* formation was similar to previously reported data.[11]

In the next experiment, we added a TiO$_2$ suspension (3 μg mL^{-1}) to the reaction mixture that contained the same concentrations of *Tg* and *Tr* in the same buffer as in the control experiment described above (Figure 3 b(II)). We irradiated the mixture during the reaction with UV light (365 nm from LED source) and monitored the concentration of trypsin with the fluorogenic assay. We observed substantial suppression of the formation of *Tr* with its rate being slower than in the absence of TiO$_2$ and irradiation. For individual TiO$_2$ particles, a slower rate of reaction may be attributed to a significant pH change: we determined, by indicator paper, that the pH of the reacting

solution after 3 hours of irradiation was around 5. This acidification of the reacting solution by photochemical reactions on TiO$_2$ is the most probable cause for the suppressed formation of *Tr* from *Tg*. Interestingly, notwithstanding that adsorption of *Tr* is higher on hybrid TiO$_2$ particles in comparison to pristine TiO$_2$, it affected autocatalytic reaction milder than pristine TiO$_2$.

Protons that are generated on TiO$_2$ can be buffered by layer-by-layer (LbL) assembly of the polyelectrolytes—polystyrene sulfonate (PSS)/ polyethylenimine (PEI)—around TiO$_2$.[17] Details of buffering properties polyelectrolyte shell around nanoparticle we described earlier work.[18] Here we formed TiO$_2$/PSS/PEI particles and added them at concentration of 3 μg mL^{-1} to the reaction mixture (Figure 3 b(III)). The observed suppression of the formation of *Tr* with its rate being slower than that in the absence of hybrid particles of TiO$_2$, however higher than in the presence of pristine TiO$_2$. Our hypothesis is that we changed the photoactivity of titania by its modification with polyelectrolytes. For regulation of organic reactions, we are interested in pH gradients rather than high photoactivity. In other words, we want to use titania photochemistry not for photodegradation and photodestruction, but for photoactivation and programing of other systems. Thus, regulation of photoactivity of titania by LbL assembly is a powerful tool for programming titania based systems.

We highlight in Figure 4 possible approaches (to measure and parameters) suggested by us in our previous work[4] and modified for the present study. Here, for TiO$_2$ we focus mostly on photoactivity and photogenerated[3] H$^+$ accumulation either near TiO$_2$ surface or trapping by PEI layer that is LbL
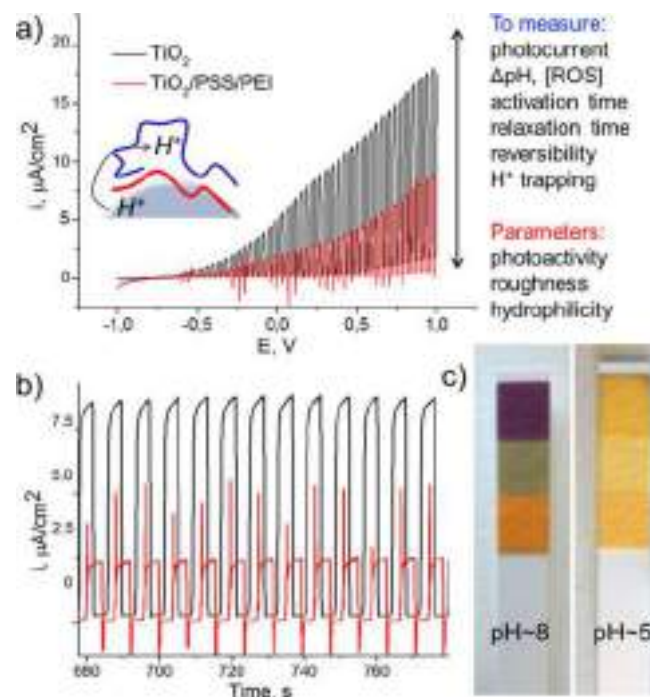
Figure 4. a,b) Photocurrent at a TiO$_2$ photoelectrode measured under irradiation (LED 365 nm, I = 5 mW cm^{-2}) at 0.25 V vs. Ag/AgCl before and after LbL deposition of PSS/PEI on n-Si support. Electrolyte was 0.1 M KOH with 0.2 M glycine. c) Paper pH indicator reaction for the Tris buffer before and after 3 hours irradiation in the presence of TiO$_2$ (3 μg mL^{-1}) particles.

spatially separated from titania by PSS. It is known that TiO$_2$ has higher photoactivity under lower pH.[19] Thus if we regulate acidic media near TiO$_2$ surface we increase its photoactivity, but if all generated protons will be immediately trapped by proton sponge layer that is spatially separated from titania, the photoactivity should be decreased. This schematically is illustrated as a positive feedback on photoactivity of protons and a negative feedback of polyelectrolytes (Figure 1).

Transient photocurrent response curves of TiO$_2$ film and TiO$_2$/PSS/PEI film were exanimated by photoelectrochemical test device under irradiation ($\lambda_{LED} = 365$ nm) using n-Si or ITO as a support (Figure 4a,b). As shown in Figure 4a, the photocurrent value increases rapidly at a maximum value when the light turned on due to the separation of electron-hole pairs at the heterostructure-electrolyte interface. The current value drops when the light turned off, which is attributed to the recombination of electron-hole pairs. Notably, the TiO$_2$/PSS/PEI film shows much lower photocurrent than TiO$_2$ one. We propose that the surface states responsible for photoactivation might be the surface states associated with the acidification at the titania surface.[3] It is known that PEI has proton sponge ability.[18] Hence, under irradiation, an association of protons either on TiO$_2$ are possible, or PEI. The proposed mechanism is supported by photocurrent measurements showing a weaker photocurrent on TiO$_2$/PSS/PEI vs. a pristine TiO$_2$ (Figure 4a,b).

Interestingly, for the hybrid system of TiO$_2$/PSS/PEI a pronounced spike-like shape of the transient can be in this case attributed to surface recombination processes.[19] The shape of the transient states for hybrid TiO$_2$/PSS/PEI indicates upon switching-on the light a sharp "overshoot" appears due to the very fast photoresponse of a hybrid. However, the relatively slower photocurrent response of pristine titania sets immediately on and dominates the photocurrent under steady state illumination for hybrid lower than for TiO$_2$. Similarly, when the light is interrupted, the rapid photoresponse of the hybrid vanishes again immediately "overshoot".

The mild photoactivity of TiO$_2$/PSS/PEI might be an advantage for the regulation of enzymatic reactions without decomposition of reaction components. For example, the Tr-system works in a Tris buffer (pH 8, Figure 4c (left)), TiO$_2$ being a strong photocatalyst might decompose components of a buffer, that we observed as a decrease of pH (Figure 4c (right)) after 3 hours of irradiation of 10 mL pf TRIS buffer with 3 µg mL^{-1} TiO$_2$ particles at LED irradiation 365 nm (5 mW cm^{-2}). On the contrary, having the same photoactivity center (TiO$_2$), it doesn't happen for the system of TiO$_2$/PSS/PEI. It should also be noted that the presence of a proton on TiO$_2$ was shown by us before[3] as well as efficient pH-buffering of 2 nm chitosan layer.[9]

Finally, we characterized enzymatic reaction-diffusion network coupled to the TiO$_2$ based system in a hydrogel[20] media (Figure 5). Autocatalytic formation of Tr from Tg can sustain autocatalytic reaction front.[21] We hypothesized that photochemical reactions on TiO$_2$ can suppress this autocatalytic front (Figure 5). To test this hypothesis, we casted a layer of agarose hydrogel (1 mm thick, 1 wt% agarose) which contained suspension of TiO$_2$ (3 µg mL^{-1}) and soaked this gel in the Tris
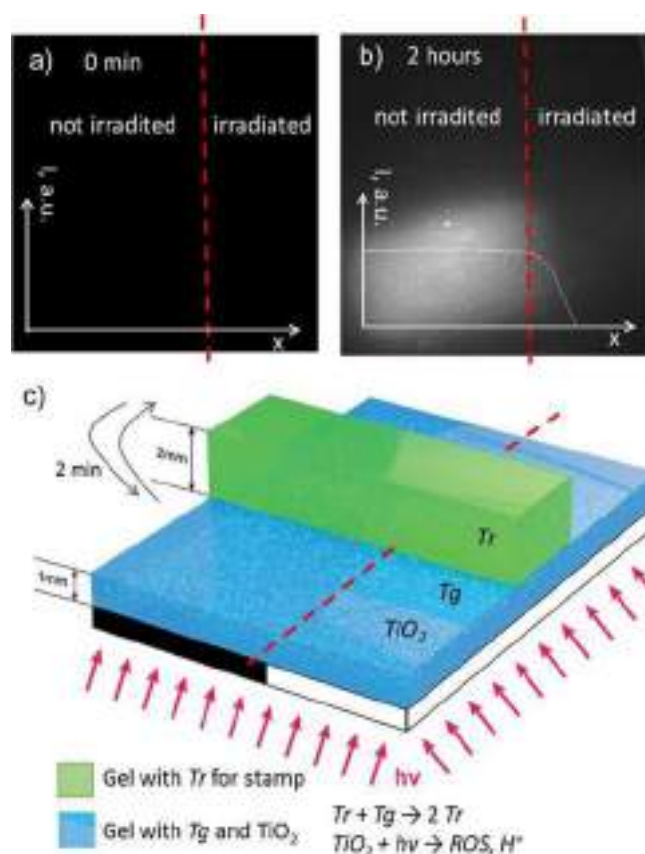
Figure 5. Spatial propagation of enzymatic activity: a,b) processing of experimental fluorescent microscopy data at a) initial moment after 2 min activation of Tg by Tr and after 2 hours of reaction progress; c) schematic description of wet stamping experiment. Red dash line corresponds to border of irradiation through the photomask and clear indicates that propagation front of enzymatic reaction is drastically different for photoactivated systems and area without photoactivation.

buffer (20 mM, pH 8) containing Tg (2 mg mL^{-1}, 83 µM), CaCl$_2$ (20 mM), soybean Tr inhibitor (STI, 2 µM), and bis-(Cbz-L-Arg)-Rhodamine (5.1 µM).

We cut approximately 1 cm by 2 cm piece of this hydrogel, irradiated half of this piece for 20 minutes with UV light, and placed it under the fluorescence microscope equipped with yellow fluorescent protein (YFP) filter cube. To initiate autocatalytic reaction front we placed a 6 mm by 2 mm by 1 mm piece of agarose hydrogel (3 wt%) that contained Tr (43 µM) on the hydrogel that contained Tr for 2 minutes. We positioned the Tr containing hydrogel in a way that Tr diffused in both irradiated and not irradiated areas of the bottom hydrogel. Fluorescence imaging showed that trypsin activity developed and autocatalytic front propagated only on the not-irradiated areas.

To summarize, it is an attractive idea to combine different functional chemical networks in one network for achieving new functions. Combining individual steps does not necessarily have a synergetic effect.

A hybrid TiO$_2$ system has mild photocatalytic characteristics and lower photocurrent in comparison to pristine TiO$_2$. In the long run, the system of pristine TiO$_2$ may be too aggressive to

control biochemical reactions without oxidizing chemicals in the reaction media, and the hybrid systems, which control reactions by local change of pH without photodegradation, will be an optimum solution for interface with biochemistry. Coupled systems that are similar to the *Tr/* TiO$_2$ system presented here are interesting for studying effects of reactions on surfaces of semiconductor nanoparticles on enzymatic activity, for providing measures of the toxic effects of nanoparticles on the target organism, for studying molecular mechanisms that underlie toxicity, and as model networks for studying synergy between photocatalytic and autocatalytic reactions.

Experimental Section

Materials. Silicon (n-type Si) wafers (100) were from CrysTech Kristralltechnologie. Titanium (IV) isopropoxide (purity of 97%), polystyrenesulfonate (PSS, $M_w = 1000000$, powder) and polyethyleneimine (PEI, Mw = 750000, 50% wt/v solution), bovine pancreas trypsin (purity of 99%) were from Sigma Aldrich. Absolute ethanol and isopropanol AnalR NORMAPUR from VWR Chemicals was used as received. Nitric acids was purchased from EMD. Hydrochloric acid (1 M, HCl) and sodium hydroxide (1 M, NaOH) were acquired from Grüssing. Millipore water (Milli-Q Plus 185) was used for preparation of aqueous solutions and sample washing.

Preparation of a TiO$_2$ sol. The TiO$_2$ sol was prepared as it was described before in Ref. [22]. 16 mL of titanium (IV) isopropoxide mixed with 12 mL of isopropanol was added drop by drop into the HNO$_3$ solution (0,8 mL of 65% acid was mixed with 100 mL of deionized water) and kept under constant stirring at 80 °C for 1 hour followed by cooling down and stirring at room temperature for the next 3 days.

Deposition of polyelectrolyte multilayers onto the TiO$_2$. PSS, and PEI were dissolved in 1 M NaCl solution to the concentration 2 mg mL^{-1}. The pH of the polyelectrolyte solution was adjusted by 1 M HCl or 1 M NaOH solution. In the case of TiO$_2$ particles the 50 mg of the powder was mixed with 1 mL of polyelectrolyte solution and then stirred in shaker for 5 min followed by the centrifugation at the rotor speed 10000 min^{-1} for 10 min. The excess of the polyelectrolyte was removed by washing the samples with distilled water and then repeatedly centrifuged. The deposition of polyelectrolytes onto the Si (ITO)/TiO$_2$ substrates was performed by dip-coating technique. The samples were immersed into the solution of polyelectrolyte for 15 min followed by the washing of the sample with distilled water.

Photoelectrochemical measurements. The photoelectrochemical measurements were performed with the Autolab potentiostat PGStat302N (Netherlands) in the three-electrode cell with n-Si/TiO$_2$ with or without deposited polyelectrolyte layers as a working electrode, Ag/AgCl (KCl sat.) as a reference electrode and Pt wire as a counter electrode. A 365 nm UV LED was used as the light source, for light beam focusing the focusing lens at a distance 2 cm from the electrochemical cell was used. 0.1 M KOH with 0.2 M glycine solution was used as a working electrolyte.

Fluorescence measurements. For fluorescence quenching experiments, the intrinsic fluorescence of tryptophan residues in trypsin was carried in the presence TiO$_2$ particles at different concentrations and temperatures. The fluorescence spectra were measured from 290 to 400 nm with the excitation wavelength at 278 nm.

The widths of emission and excitation slits were set at 5.0 and 3.0, respectively. The fluorescence spectra were measured by a Shimadzu RF-5301 fluorescence spectrophotometer equipped with a temperature controller and a 2.0-mm quartz cell. Bovine pancreas trypsin was dissolved in a Tris-HCl buffer (50 mM and pH 8.0) to become 0.1 mg mL^{-1} in concentration. Solution was equilibrated for 2 min at 298 K or 308 K. To obtain the binding parameters, data were analyzed by the modified Stern–Volmer equation. Particles were suspended in deionized water.

Autocatalytic enzymatic network. In control experiment, we dissolved *Tg* (1 mg mL^{-1}, corresponding to 42 μM) in Tris buffer (100 mM, pH 8) containing CaCl$_2$ (20 mM) and initiated the autocatalytic reaction with an aliquot of *Tr* (2.15 μM in final mixture). The reaction proceeded with continuous stirring at 298 K. We took aliquots of the solution at different time points and determined trypsin concentrations with a fluorogenic assay using bis-(Cbz-L-Arg)-Rhodamine as a substrate. To measure *Tr* activity, disposable cuvettes (path length 2.00 cm) were filled with 3 mL of the fluorogenic substrate bis-(Cbz-L-Arg)-Rhodamine (5.1 μM in 50 mM Tris buffer, pH 8). To this solution, 10 μL of the reaction mixture was added. Conversion of the fluorogenic substrate was monitored and the rate of the *Tr* formation was similar to previously reported data.[11]

Reaction—diffusion in gel: control of autocatalytic wave. To test this hypothesis, we casted a layer of agarose hydrogel (1 mm thick, 1 wt% agarose) which a contained suspension of TiO$_2$ (3 μg mL^{-1}) and soaked this gel in the Tris buffer (20 mM, pH 8) containing *Tg* (2 mg mL^{-1}, 83 μM), CaCl$_2$ (20 mM), soybean *Tr* inhibitor (STI, 2 μM), and bis-(Cbz-L-Arg)-Rhodamine (5.1 μM). We cut approximately 1 cm by 2 cm piece of this hydrogel, irradiated half of this piece for 20 minutes, and placed it under the fluorescence microscope equipped with yellow fluorescent protein (YFP) filter cube. To initiate autocatalytic reaction front we placed a 6 mm by 2 mm by 1 mm piece of agarose hydrogel (3 wt%) that contained Tr (43 μM) on the hydrogel that contained Tr for 2 minutes. We positioned the Tr containing hydrogel in a way that Tr diffused in both irradiated and not irradiated areas of the bottom hydrogel.

Conflict of interest

The authors declare no conflict of interest.

[1] E. V. Skorb, D. V. Andreeva, *Adv. Funct. Mater.* **2013**, *23*, 4483–4506.
[2] a) E. V. Skorb, H. Möhwald, D. V. Andreeva, *Adv. Mater. Interfaces* **2017**, *4*, 1600282; b) O. Supplie, M. M. May, S. Brückner, N. Brezhneva, T. Hannappel, E. V. Skorb, *Adv. Mater. Interfaces* **2017**, *4*, 1601118.
[3] H. Maltanava, S. K. Poznyak, D. V. Andreeva, M. C. Quevedo, A. C. Bastos, J. Tedim, M. G. S. Ferreira, E. V. Skorb, *ACS Appl. Mater. Interfaces* **2017**, *9*, 24282–24289.

[4] S. A. Ulasevich, G. Brezesinski, H. Möhwald, P. Fratzl, F. Schacher, S. K. Poznyak, D. V. Andreeva, E. V. Skorb, *Angew. Chem. Int. Ed.* **2016**, *55*, 13001 – 13004; *Angew. Chem.* **2016**, *128*, 13195 – 13198.

[5] D. V. Andreeva, I. Melnyk, O. Baidukova, E. V. Skorb, *ChemElectroChem* **2016**, *3*, 1306 – 1310.

[6] S. A. Ulasevich, N. Brezhneva, Y. Zhukova, H. Möhwald, P. Fratzl, F. H. Schacher, D. V. Sviridov, D. V. Andreeva, E. V. Skorb, *Macromol. Biosci.* **2016**, *16*, 1422 – 1431.

[7] J. Gensel, T. Borke, N. Pazos-Perez, A. Fery, D. V. Andreeva, E. Betthausen, A. H. E. Müller, H. Möhwald, E. V. Skorb, *Adv. Mater.* **2012**, *24*, 985 – 989.

[8] S. A. Ulasevich, I. Melnyk, D. V. Andreeva, H. Möhwald, E. V. Skorb, *EPL* **2017**, *119*, 38003.

[9] D. V. Andreeva, A. Kollath, N. Brezhneva, D. V. Sviridov, B. J. Cafferty, H. Möhwald, E. V. Skorb, *Phys. Chem. Chem. Phys.* **2017**, *19*, 23843 – 23848.

[10] K. Kurin-Csörgei, I. R. Epstein, M. Orbán, *Nature* **2005**, *433*, 139 – 142.

[11] S. N. Semenov, A. S. Y. Wong, R. M. Made, S. G. J. Postma, J. Groen, H. W. H. Roekel, T. F. A. de Greef, W. T. S. Huck, *Nat. Chem.* **2015**, *7*, 160 – 165.

[12] L. Momeni, B. Shareghi, A. A. Saboury, M. Evini, *Monatsh. Chem.* **2017**, *148*, 199 – 207.

[13] *Principles of Fluorescence Spectroscopy* (Ed.: J. R. Lakowicz), Springer, **2007**.

[14] a) J. R. Lakowicz, G. Weber, *Biochemistry* **1973**, *12*, 4161 – 4170; b) W. R. Ware, *J. Phys. Chem.* **1962**, *66*, 455 – 458.

[15] W.-R. Wang, R.-R. Zhu, R. Xiao, H. Liu, S.-L. Wang, *Biol. Trace Elem. Res.* **2011**, *142*, 435.

[16] P. D. Ross, S. Subramanian, *Biochemistry* **1981**, *20*, 3096.

[17] a) E. V. Skorb, D. G. Shchukin, H. Möhwald, D. V. Sviridov, *J. Mater. Chem.* **2009**, *19*, 4931 – 4937; b) E. V. Skorb, D. Fix, D. V. Andreeva, D. G. Shchukin, H. Möhwald, *Adv. Funct. Mater.* **2009**, *19*, 2373 – 2379; c) E. V. Skorb, A. Skirtach, D. V. Sviridov, D. G. Shchukin, H. Möhwald, *ACS Nano* **2009**, *3*, 1753 – 1760; d) E. V. Skorb, D. V. Sviridov, H. Möhwald, D. G. Shchukin, *Chem. Commun.* **2009**, 6041 – 6043.

[18] Y. Zhukova, E. V. Skorb, *Adv. Health. Mater.* **2017**, *6*, 1600914.

[19] R. Beranek, *Adv. Phys. Chem.* **2011**, 786759.

[20] a) S. N. Semenov, S. G. J. Postma, I. N. Vialshin, W. T. S. Huck, *Chem. Commun.* **2014**, *50*, 3089 – 3092; b) S. N. Semenov, A. J. Markvoort, W. B. L. Gevers, A. Piruska, T. F. A. de Greef, W. T. S. Huck, *Biophys. J.* **2013**, *105*, 1057 – 1066.

[21] S. N. Semenov, A. J. Markvoort, T. F. A. de Greef, W. T. S. Huck, *Angew. Chem. Int. Ed.* **2014**, *53*, 8066 – 8069; *Angew. Chem.* **2014**, *126*, 8204 – 8207.

[22] A. V. Yakovlev, A. V. Milichko, V. V. Vinogradov, A. V. Vinogradov, *ACS Nano* **2016**, *10*, 3078 – 3086.

PCCP

Physical Chemistry Chemical Physics

rsc.li/pccp

ROYAL SOCIETY
OF **CHEMISTRY**

PCCP

Check for updates

Bismuth oxysulfide film electrodes with giant incident photon-to-current conversion efficiency: the dynamics of properties with deposition time

Evgeny A. Bondarenko,[a] Eugene A. Streltsov, [iD] *[a] Alexander V. Mazanik, [iD] [a] Anatoly I. Kulak, [iD] [b] Vytautas Grivickas,[c] Patrik Ščajev[c] and Ekaterina V. Skorb [iD] *[d]

It was demonstrated in our previous work that the photoelectrochemical (PEC) reduction processes occur with a giant incident photon-to-current conversion efficiency (IPCE $\gg$ 100%) at bismuth oxysulfide (BOS) semiconductor films in aqueous solutions containing acceptors of photoelectrons ($[Fe(CN)_6]^{3-}$). The anomalously high IPCE was related to the photoconductivity of the semiconductor. In this work, we analyze the dynamics of the chemical and phase composition of BOS films with variation of their deposition time, as well as the dependence of photocurrent on the film thickness and wavelength of the incident light. We demonstrate that in the case of illumination with a short-wavelength light (λ = 465 nm), the photocurrent is reduced down to a complete disappearance with an increase in the film thickness in the range of 0.3–1.3 μm, and for a fixed thickness of the bismuth oxysulfide film, the photocurrent decreases with the reduction of the wavelength indicating that photogeneration of the charge carriers over the entire thickness of the film is necessary for the giant IPCE effect. Using the light induced transient grating (LITG) method, the lifetime of the charge carriers (τ) was determined in the range of 25–80 ps depending on the film thickness, whereas the diffusion coefficient (D) does not exceed 1 cm^2 s^{-1} meaning that the charge transport across the films is determined only by drift.

Introduction

Bismuth oxysulfides (BOSs) represent a new promising class of layered materials with a pronounced anisotropy of properties. $Bi_4O_4S_3$ is of interest as a superconductor,[1–3] whereas Bi_2O_2S, $Bi_9O_{7.5}S_6$ and Bi_2OS_2 exhibit attractive photoelectrical properties.[4–8] Recently, we prepared a new type of BOS films, which possess a layered structure. They are formed by several tens of nanometers thick platelet-like crystals with a lateral size of a few micrometers. It was demonstrated that bismuth and sulfur atoms in this material have +3 and −2 oxidation states, respectively. According to the chemical analysis, for 0.67 μm films, the Bi/S molar ratio equals 1.11, indicating the simplest chemical formula as $Bi_{10}O_6S_9$.[9]

The prepared BOS films revealed the effect of giant incident photon-to-current conversion efficiency (IPCE) under visible light illumination.[9] The discovered effect consists of a significant acceleration of the photoelectrochemical (PEC) cathodic process, for which the IPCE reaches up to 2500%. The effect is observed in aqueous solutions containing an acceptor of photoelectrons, *e.g.*, $[Fe(CN)_6]^{3-}$, starting from its certain minimal concentration ($c > 10^{-3}$ M).[9] A remarkable influence of the photoconductivity on the efficiency of the cathodic faradaic process is a distinctive feature of the prepared BOS photoelectrodes. In other words, the giant IPCE is determined by the reduction of the BOS film resistivity under illumination, which provides the charge carriers from an external circuit the possibility to take part in the photoreduction process.[9]

The unique photoelectrochemical properties of the BOS films suggest a relevance of further research devoted to unraveling the mechanisms responsible for the giant IPCE effect. As any PEC process taking place on the semiconductor electrode, the aforementioned giant IPCE is related to the charge transfer in a semiconductor, discharge of electroactive particles, mass transfer in solution, *etc.* Obviously, revealing the limiting stages of the process including ones for the solid state will make it possible to control the PEC behavior of the

[a] *Belarusian State University, Nezalezhnastsi Av. 4, Minsk 220030, Belarus.*
  E-mail: StreltEA@bsu.by

[b] *Institute of General and Inorganic Chemistry, National Academy of Sciences of Belarus, Minsk 220072, Belarus*

[c] *Institute of Photonics and Nanotechnology, Vilnius University, Sauletekio ave. 3, LT-10257 Vilnius, Lithuania*

[d] *Infochemisry Group; SCAMT Laboratory, ITMO University, St. Petersburg 197101, Russian Federation. E-mail: skorb@corp.ifmo.ru*

system, which is necessary for the development of materials with desired functional properties.

This work is aimed at unraveling the influence of the film thickness and light wavelength on the giant IPCE effect. By varying the wavelength of the incident light at a fixed film thickness, one can obtain uniform photogeneration of charge carriers over the entire semiconductor or only in a subsurface layer. A similar result can be achieved using a monochromatic light and varying the film thickness. As it will be demonstrated below, the generation of photocharges over the entire film is necessary for the realization of the giant IPCE effect.

Experimental

Preparation of bismuth oxysulfide films

The BOS films were grown on FTO substrates using the chemical bath deposition (CBD) technique developed by us earlier.[9] Briefly, the deposition was done at 100 °C using an aqueous solution containing 0.021 M $Bi(NO_3)_3$, 0.731 M triethanolamine, 0.207 M thiourea and 0.162 M NH_3. The deposition time (t_{dep}) was varied in the range from 20 to 200 min. The detailed physical–chemical characterization of the films was presented in our previous research.[9]

Measurement conditions and equipment

X-ray diffraction (XRD) studies were carried out using an Empyrean diffractometer (PANalytical, Netherlands; Cu Kα source with a Ni-filter, 0.01 degree step). The scanning electron microscopy (SEM) study was performed using a Zeiss Leo 1550 (Germany) field emission microscope. The thickness of the films was determined from the cross-sectional SEM images. The elemental composition of the BOS films was established from the energy-dispersive X-ray spectra (EDX) recorded using a Zeiss Leo 1455 microscope (Germany) with an Aztec Energy Advanced X-Max 80 X-ray analyzer (Oxford instruments, United Kingdom). Transmission spectra were recorded using a MC122 spectrometer (Proscan Special Instruments, Belarus).

Photoelectrochemical measurements were performed using a P-8 potentiostat (Elins, Russia) in a three-electrode cell with a platinum counter electrode and a saturated silver chloride reference electrode (+0.201 V *vs.* SHE). Polarization curves were obtained at a potential scan rate of 20 mV s^{-1}. The samples were illuminated from the substrate side to minimize the light absorption in the electrolyte.

As a light source, a 250 W halogen lamp was employed. The light with a required wavelength was selected using a MDR-2 monochromator (Russia). The intensity of the monochromatic light was determined using a calibrated OPT101 photodiode.

For the determination of the charge carriers' lifetime and ambipolar diffusion coefficient, the light induced transient grating (LITG) method was used.[10,11] LITG investigations were conducted by the scheme described in detail elsewhere.[12] Briefly, excitation was accomplished by an Ekspla Nd:YLF laser

with 10 ps pulse duration and 0.527 µm wavelength (the second harmonic). The laser was operating with a 10 Hz repetition rate and the energy was attenuated by a half-wave plate and a Glan prism. A holographic beam splitter and two focal lenses were employed to adjust a 100% contrast of the interference grid-pattern at the spatial period Λ (varied in the 1–5 µm range). The excitation spot diameter was 320 µm. As a probe, the 1.053 µm wavelength of the first harmonic pulse was delayed by 30 cm optical delay line with a quadruple beam pass. The probe beam was projected into the centrum of the excited spot and the transmitted I_T and the diffracted I_D parts were detected by 16 bit CAN detectors. The compression of noise fluctuation was achieved using the normalization of the diffracted beam to the transmitted one by 10 pulse averaging under the 5% tolerance interval for the excitation pulse energy.

Results and discussion

Characterization of bismuth oxysulfide films

Fig. 1a shows the dependence of the BOS film thickness (d) on the deposition time. The fastest growth of the thickness is observed during the first 60 min of deposition, whereas the subsequent deposition during 2 hours is characterized by a significantly lower rate of the thickness increase. When the film thickness reaches 0.8 µm, the growth practically finishes due to depletion of the bismuth precursor in the CBD solution. Therefore, the films with $d > 0.8$ µm were deposited in two stages by subsequent soaking of the substrates in two identical solutions.

The dependence of the optical absorption on the deposition time (Fig. 1b) qualitatively correlates with a kinetic curve. It is clearly seen that the most significant growth of the light absorption is inherent to the first 60 min of film deposition, whereas the subsequent growth leads only to a slight increase of the absorption coefficient. In spite of wavelength-dependent scattering, which hinders a correct determination of the absorption edge, there is its gradual red shift with the deposition time. As is seen from the inset of Fig. 1a, this fact correlates with the change of film colour, indicating the reduction of the band gap energy (E_g). As the band gap energy of Bi_2O_3 (2.6–2.8 eV[13–15]) is known to be significantly higher than the E_g of Bi_2S_3 (1.2–1.3 eV[16–18]), the increase in the sulfur content during the film growth could be the reason for the observed red shift of the absorption edge. To confirm this hypothesis, we performed an EDX analysis of the films deposited during different time periods. As shown in Fig. 1c, the increase of the deposition time results in the increase of the sulfur to bismuth ratio in the films.

The observed variation of the chemical composition of the BOS films with deposition time could be explained with the chemical reactions occurring during the synthesis. At the initial stage, the dissolution of the bismuth salt in triethanolamine leads to the formation of a bismuth chelate complex with a 1:1 metal-to-ligand ratio:[19]

$$Bi^{3+} + 4N(C_2H_4OH)_3 \rightarrow Bi(N(C_2H_4O)_3) + 3[NH(C_2H_4OH)_3]^+$$

(1)

This journal is © the Owner Societies 2018

Phys. Chem. Chem. Phys., 2018, **20**, 20340–20346 | **20341**
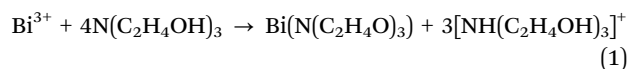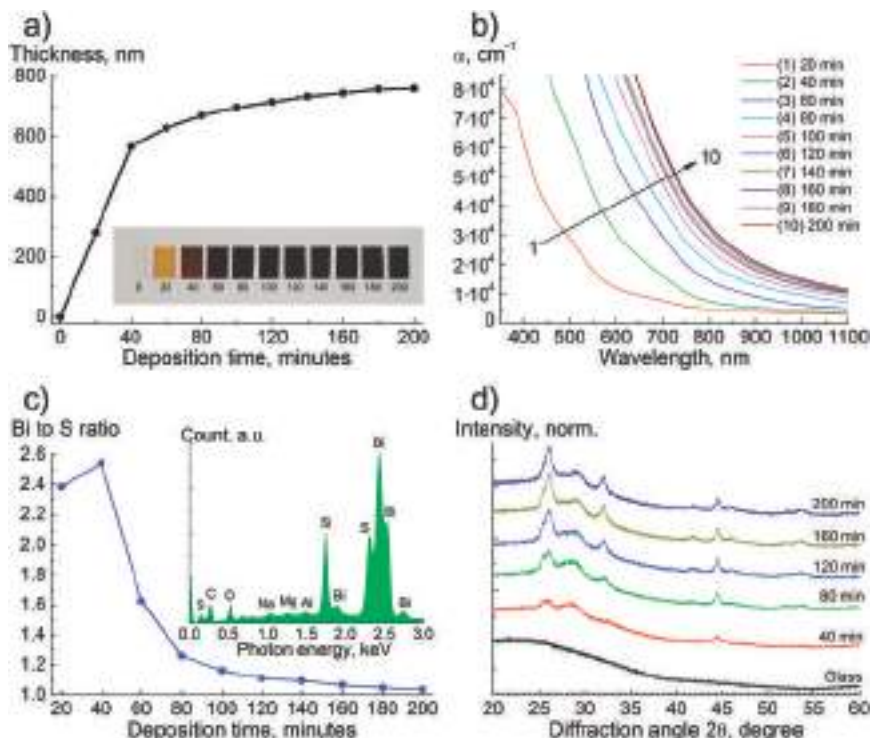
Fig. 1   (a) Thickness of the BOS films vs. deposition time (inset: photographs of the films); (b) absorption spectra; (c) Bi/S atomic ratio derived from EDX vs. deposition time (inset: EDX spectrum of the BOS film on glass, t_{dep} = 180 min); (d) XRD patterns.

Then, two competing processes could take place under heating. On the one hand, in basic aqueous solution (pH ∼ 9.2), the bismuth complex is subjected to hydrolysis with the formation of hydrated oxide:[20]

$$2Bi(N(C_2H_4O)_3) + 3nH_2O \rightarrow Bi_2O_3 \cdot nH_2O + 2N(C_2H_4OH)_3 \tag{2}$$
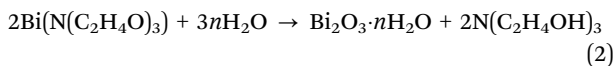
On the other hand, thiourea also hydrolyses under these conditions, and the products of its decomposition react with the bismuth complex resulting in the precipitation of Bi_2S_3:[21]

$$2Bi(N(C_2H_4O)_3) + 3SC(NH_2)_2 + 6OH^- + 3H_2O$$
$$\rightarrow Bi_2S_3 + 2N(C_2H_4OH)_3 + 6NH_3 + 3CO_3^{2-} \tag{3}$$
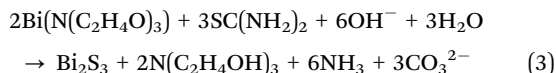
Both these above-mentioned reactions give rise to the formation of bismuth oxysulfide. As hydrolysis of the chelate complex dominates at the initial deposition stages, the content of sulfur in the films increases with the deposition time.

The XRD patterns of the BOS film and glass are given in Fig. 1d. As we pointed out earlier,[9] a large width of the lines may originate from a high defect density in the films. Moreover, the broadening of the reflexes can be caused by the low thickness of the plate-like crystals and tensile/compressive strains due to their curvature. Note that the intensity of the lines practically does not alter with t_{dep}. Thereby, the crystalline phase does not undergo any significant changes during the CBD process. The enrichment of the film by oxygen on the initial deposition stage could be related

to the formation of the amorphous phase being "sulfidized" by further film formation. Moreover, this phase could be subjected to partial crystallization. This process influences the total concentration of intrinsic defects in the films and, correspondingly, the recombination of the photocharges (see below).

In spite of the variation of the chemical composition of the BOS films with the deposition time, their surface microstructures do not show any remarkable changes (Fig. 2).

The films are formed by platelet-needle-like aggregates, which are randomly oriented relative to each other.
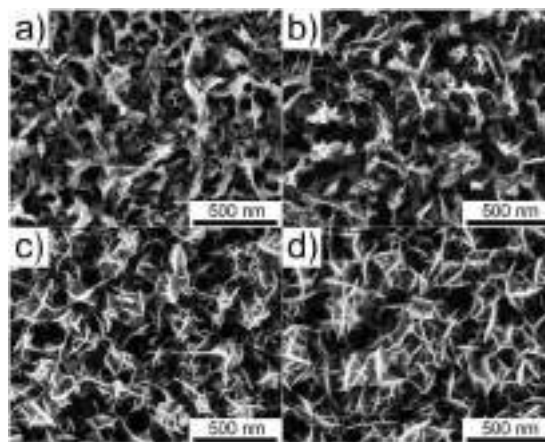
Fig. 2   SEM images of the BOS films deposited for 40 (a), 60 (b), 80 (c) and 100 min (d).

20342 | Phys. Chem. Chem. Phys., 2018, 20, 20340–20346

This journal is © the Owner Societies 2018
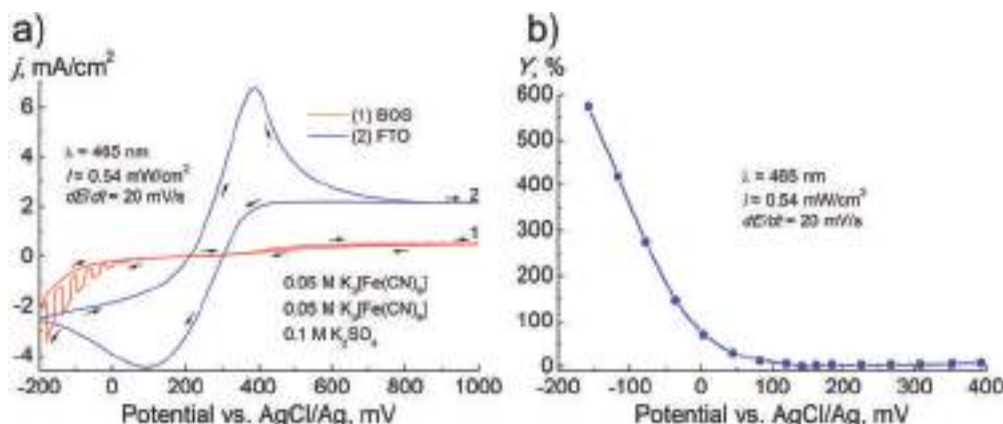
Fig. 3 CV curves of the BOS film (t_{dep} = 80 min) and the FTO electrode as a reference (a); IPCE vs. electrode potential of the same BOS film (b).

Photoelectrochemical investigations

The cyclic voltammograms (CVs) of the BOS films in $[Fe(CN)_6]^{3-}/[Fe(CN)_6]^{4-}$ containing solution exhibit the giant IPCE effect towards negative electrode potentials (Fig. 3). An abnormally high PEC activity was observed in the cathodic reduction of $[Fe(CN)_6]^{3-}$. For comparison, the CV curve of the reference FTO electrode is given.

The cathodic current (both in the dark and under illumination) is related to the reduction of complex anions:

$$[Fe(CN)_6]^{3-} + e = [Fe(CN)_6]^{4-} \qquad (4)$$
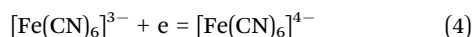
It is clearly seen that the FTO electrode is characterized by high electrocatalytic activity in the processes of $[Fe(CN)_6]^{4-}$ anodic oxidation and $[Fe(CN)_6]^{3-}$ cathodic reduction. A "classical" shape of the CV curve of the FTO electrode points to the transition of the electrochemical process from the kinetic to the diffusion regime, when the electrode potential is shifted away from the equilibrium value.[22] After deposition of the BOS film on the surface of the FTO substrate, the aforementioned dark anodic process is blocked. This fact enables one to conclude that the BOS films are rather dense and contain no crossing macropores and macrovoids, avoiding an immediate contact of the solution with the FTO substrate.

Fig. 4 shows dependences of the cathodic photocurrent and the dark current on the film thickness. As is seen, for a relatively low thicknesses of the BOS films ($d < 0.4$ μm), the dark current is dominating. The maximal photocurrent is at $d = 0.7$–0.8 μm, and just in the same thickness range, a sharp decrease of the dark current was observed.

Any electrochemical process is known to be multistage and includes the process of charge transfer in the semiconductor for the subsequent discharge of electroactive particles at the interface between the electrode and the electrolyte. As we pointed out earlier,[9] the BOS films illumination leads to a sharp increase in their conductivity. Since the aqueous solutions containing the $[Fe(CN)_6]^{3-}/[Fe(CN)_6]^{4-}$ redox-system strongly absorb visible light, the photoelectrodes were illuminated from the FTO-substrate side.

In this case, the generation rate is maximal near the FTO/BOS interface and decays with motion into the depth of the film. As is known, the depth of light penetration into a material is about α^{-1}, where α is the absorption coefficient. The d to α^{-1} ratio can be changed not only by varying the film thickness under a constant wavelength λ, but also by changing λ at a constant thickness of the BOS film. For the films with $d = 1.3$ μm, the photocurrent is absent in the case of a blue light illumination,
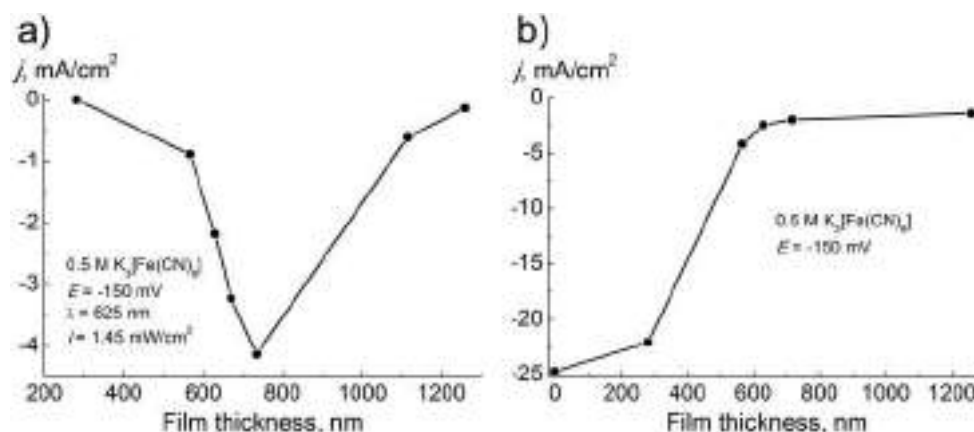
Fig. 4 Cathodic photocurrent (a) and dark current (b) vs. BOS film thickness.
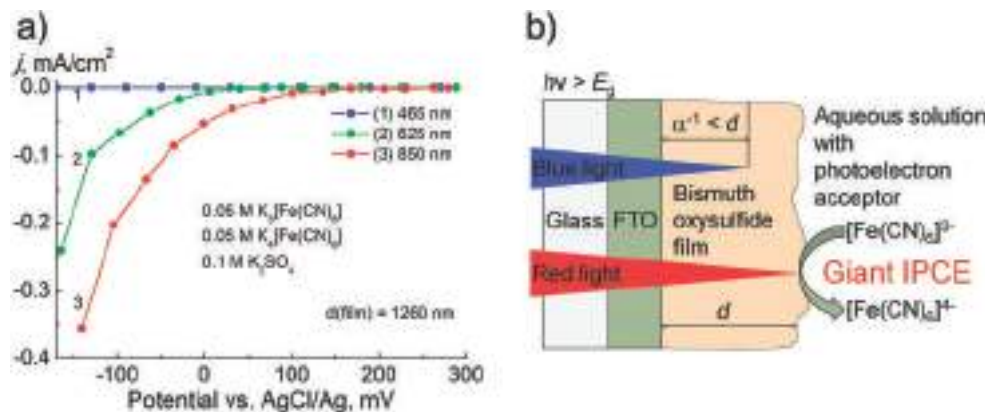
Fig. 5 Photopolarization curves of the BOS film (t_{dep} = 180 + 80 min) under monochromatic illumination at different wavelengths (a); scheme illustrating the difference between short- and long-wavelength illuminations (b).

whereas a red light generates photocurrent, the value of which increases with increasing wavelength (Fig. 5a).

It can be concluded that for the observation of the giant IPCE, the film thickness has to be smaller as compared to the depth of photocharges generation. This fact can be easily explained from the following simple consideration. One can demonstrate that the ratio of film resistances for the cases of a short ($\alpha^{-1} \ll d$) and a long-wavelength ($\alpha^{-1} \approx d$) illumination can be estimated as follows:

$$\frac{R_{SW}}{R_{LW}} = \frac{\Delta N}{\beta N_0} \gg 1 \qquad (5)$$

where ΔN and N_0 are the concentrations of the photogenerated and equilibrium charge carriers, respectively (we assume a high excitation level, *i.e.* $\Delta N \gg N_0$), and $\beta > 1$ is the ratio between the depths of photocharges generation in the cases of a long-wavelength and a short-wavelength illumination.

The influence of the wavelength on the photocurrent value is illustrated in Fig. 5b. As it was indicated above, the films are rather dense, and the 1D description is appropriate. For a short-wavelength illumination, the $\alpha^{-1} < d$ relation is true, and the photocharges are generated in a rather thin layer near the FTO substrate. There is a "dark" film layer with a thickness of about $d - \alpha^{-1}$, which possesses a high resistivity. In contrast, in the case of a long-wavelength light, the photocharges are generated over all the film volume, and there is no "dark" layer with high resistivity.

Light induced transient grating measurements

Note that passing of current through the BOS films is determined by the drift of charge carriers, whereas their diffusion can be neglected. This follows from the results of the LITG studies presented below. In LITG measurements, the concentration of the photogenerated charge carriers induced by the interference grid-pattern can be expressed as $\Delta N_{(t=0)}(1 + \cos(2\pi x/\Lambda)) \times \exp(-\alpha z)$, where $\Delta N_{(t=0)}$ is the maximal carrier concentration at the zero time for overlapping pump/probe pulse, α is the absorption coefficient, Λ is the grating period, and the coordinates x and z refer to the in-plane and out-of-plane directions, respectively.[23]

$\Delta N_{(t=0)}$ is proportional to the incoming pump intensity I_{inc}: $\Delta N_{(t=0)} \sim \alpha I_{inc}(1 - R)/h\nu$, where R is the optical reflection coefficient, and $h\nu$ = 2.36 eV is the photon energy. The absorption coefficient at 527 nm wavelength is determined from Fig. 1b to be about $\alpha = 2$–5×10^4 cm^{-1}. The latter value allows to estimate the excited carrier concentration to be $\Delta N_{(t=0)} = 5 \times 10^{18}$–$10^{20}$ cm^{-3} for I_{inc} in the 0.1–1 mJ cm^{-2} fluence range. The excited carriers induce a change in the complex refractive index of the material, which can be described by the classical Drude–Lorentz model. Customarily, the diffraction occurs by a change in the real part of the refractive index Δn_{FC}, which is proportional to ΔN with a coefficient n_{eh} counted for a single e–h pair.[24] In most semiconductors, n_{eh} is of the order of 10^{-22} cm^3.[23] The LITG erasure is monitored by measuring the time-dependence of the diffraction efficiency: $DE(t) = I_D(t)/I_T(t)$. Assuming an exponential decay, $DE(t)$ can be expressed as:[12]

$$DE(t) = \left(\frac{\pi n_{eh}\Delta N_{(t=0)}}{\alpha\lambda}\right)^2 \exp\left(\frac{2t}{\tau_G}\right) \qquad (6)$$

$$\frac{1}{\tau_G} = \frac{1}{\tau} + \frac{4\pi^2 D}{\Lambda^2} \qquad (7)$$

where τ_G is the grating erasure time. The first and second terms in (7) are determined by the charge carriers' recombination and diffusion between fringes in the layer plane direction, respectively. As is seen from (7), the recombination lifetime τ and the diffusion coefficient D can be determined from transients recorded at different Λ values. For a high excitation level, when the concentrations of electrons and holes are equal, the ambipolar diffusion coefficient can be expressed as $D = 2D_e D_h/(D_e + D_h)$, where D_e and D_h are the diffusivities of the electrons and of holes, respectively.

As is seen in Fig. 6, the lifetime of the charge carriers does not exceed 80 ps. The absence of any visible changes in the grating erasure time τ_G for different grating periods Λ enables one to estimate the upper limit of the ambipolar diffusion coefficient detection substantially below 1 cm^2 s^{-1}. This allows to evaluate the diffusion length of $(D\tau)^{1/2} < 90$ nm being substantially smaller than the sample thickness. This means
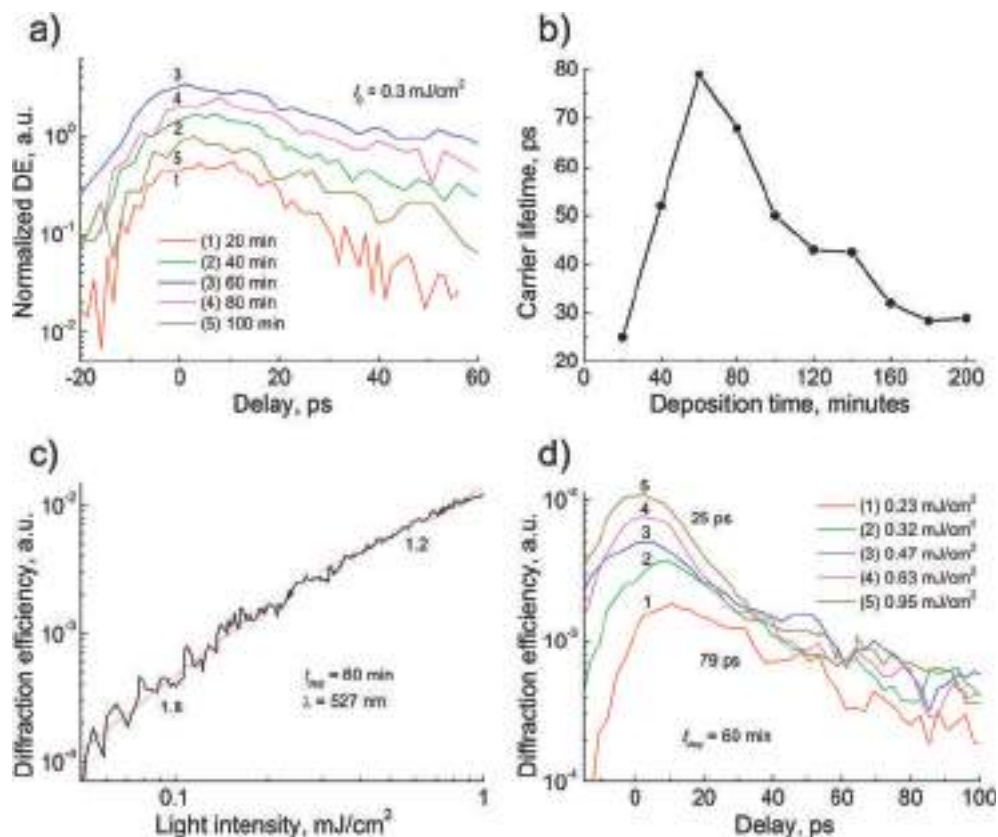
Fig. 6 LITG decay transients at a fluency of 0.3 mJ cm^{-2} for the BOS films prepared with different deposition times (a); carrier lifetime at 0.3 mJ cm^{-2} vs. deposition time (b); diffraction efficiency vs. fluency for a film with t_{dep} = 60 min (c); LITG decay transients for the same BOS film at different light fluence (d).

that the charge transport at the medium excitation across the films is determined only by drift. The LITG slope at low carrier concentrations is close to 2, which indicates the linear generation of free carriers (eqn (6)). The slope reduction at high excitations is plausibly related to the carrier lifetime reduction, see Fig. 6d, down to the probe duration of 10 ps due to the enhanced non-radiative Auger recombination ($1/\tau = C\Delta N^2$) with Auger coefficient $C \sim 5 \times 10^{-30}$ cm^6 s^{-1}. A C value of $\sim 10^{-30}$ cm^6 s^{-1} is typical for semiconductors with a direct bandgap of ~ 1.5 eV.[25]

The decrease of lifetime with increasing excitation level is in agreement with our previous results, which indicated a gradual reduction of the IPCE with an increase in the incident light intensity.[9] The observed decrease in the medium injection life-time with the deposition time ($t_{dep} > 60$ min, when the phase composition is stabilized, see Fig. 1c) could be explained by the change in the S to Bi atom ratio, which seems to be responsible for the increase in concentration of the intrinsic defects in the films. Another alternative explanation is that the fine-grained modification of their microstructures (Fig. 2c and d) can enhance the carrier recombination at the grain boundaries.

Conclusions

The dynamics of the properties of CBD grown bismuth oxysulfide films with their deposition time has been investigated. In particular,

a red shift of the absorption edge with the deposition time (film thickness) has been revealed, which is related to the enrichment of the films by sulfur established by the EDX analysis. The modification of the chemical composition of the BOS films during their deposition is determined by different rates of simultaneously occurring reactions of the hydrolysis of the bismuth triethanolamine complex and thiourea in aqueous solution.

In the case of illumination of the BOS electrode with a short-wavelength light (λ = 465 nm), the photocurrent is reduced down to a complete disappearance with an increase of the films thickness in the range of 0.3–1.3 μm, while for a fixed thickness of the semiconductor film, the photocurrent decreases with decreasing wavelength. This means that photo-generation of the charge carriers over the entire thickness of the film is necessary for the registration of the giant IPCE effect. The photocharges generated over the entire depth of the BOS film enhance its conductivity providing the electron transport from an external circuit to the interface between the electrode and the electrolyte, where the photoelectrochemical reaction takes place.

Using the light-induced transient grating method, the life-time of the charge carriers was determined to be 25–80 ps depending on the film thickness, whereas the diffusion coefficient does not exceed 1 cm^2 s^{-1}, which corresponds to the upper limit of the diffusion length of approximately 90 nm. Such small values

of the diffusion length mean that the charge transport across the films is determined only by drift.

Conflicts of interest

There are no conflicts to declare.

Acknowledgements

References

1 Y. Mizuguchi, H. Fujihisa, Y. Gotoh, K. Suzuki, H. Usui, K. Kuroki, S. Demura, Y. Takano, H. Izawa and O. Miura, *Phys. Rev. B: Condens. Matter Mater. Phys.*, 2012, **86**, 220510(R).

2 W. A. Phelan, D. C. Wallace, K. E. Arpino, J. R. Neilson, K. J. Livi, C. R. Seabourne, A. J. Scott and T. M. McQueen, *J. Am. Chem. Soc.*, 2013, **135**, 5372.

3 G. Liu, D. Li, S. Li, J. Wang, W. Liu and Z. Zhang, *Phys. C*, 2015, **510**, 27.

4 A. L. Pacquette, H. Hagiwara, T. Ishihara and A. A. Gewirth, *J. Photochem. Photobiol., A*, 2014, **277**, 27.

5 X. Zhang, Y. Liu, G. Zhang, Y. Wang, H. Zhang and F. Huang, *ACS Appl. Mater. Interfaces*, 2015, **7**, 4442.

6 S. Meng, X. Zhang, G. Zhang, Y. Wang, H. Zhang and F. Huang, *Inorg. Chem.*, 2015, **54**, 5768.

7 A. Miura, Y. Mizuguchi, T. Takei, N. Kumada, E. Magome, C. Moriyoshi, Y. Kuroiwa and K. Tadanaga, *Solid State Commun.*, 2016, **227**, 19.

8 E. Koyama, I. Nakai and K. Nagashima, *Acta Crystallogr., Sect. B: Struct. Sci.*, 1984, **40**, 105.

9 E. A. Bondarenko, E. A. Streltsov, M. V. Malashchonak, A. V. Mazanik, A. I. Kulak and E. V. Skorb, *Adv. Mater.*, 2017, **29**, 1702387.

10 P. Baronas, P. Ščajev, V. Čerkasovas, G. Kreiza, P. Adomėnas, O. Adomėnienė, K. Kazlauskas, C. Adachi and S. Juršėnas, *Appl. Phys. Lett.*, 2018, **112**, 033302.

11 P. Ščajev, S. Miasojedovas, A. Mekys, D. Kuciauskas, K. G. Lynn, S. K. Swain and K. Jarašiūnas, *J. Appl. Phys.*, 2018, **123**, 025704.

12 P. Ščajev, R. Aleksiejunas, S. Miasojedovas, S. Nargelas, M. Inoue, C. Qin, T. Matsushima, C. Adachi and S. Juršėnas, *J. Phys. Chem. C*, 2017, **121**(39), 21600.

13 L. Leontie, M. Caraman, M. Delibaş and G. I. Rusu, *Mater. Res. Bull.*, 2001, **36**, 1629.

14 Y. Yan, Z. Zhou, Y. Cheng, L. Qiu, C. Gao and J. Zhou, *J. Alloys Compd.*, 2014, **605**, 102.

15 Z. Bian, J. Zhu, S. Wang, Y. Cao, X. Qian and H. Li, *J. Phys. Chem. C*, 2008, **112**, 6258.

16 L. M. Peter, *J. Electroanal. Chem. Interfacial Electrochem.*, 1979, **98**, 49.

17 J. Grigas, E. Talik and V. Lazauskas, *Phys. Status Solidi B*, 2002, **232**, 220.

18 J. Lukose and B. Pradeep, *Solid State Commun.*, 1991, **78**, 535.

19 W. T. Miller, *J. Am. Chem. Soc.*, 1940, **62**, 2707.

20 T. P. Gujar, V. R. Shinde, C. D. Lokhande, R. S. Mane and S. H. Han, *Appl. Surf. Sci.*, 2005, **250**, 161.

21 G. Hodes, *Chemical Solution Deposition of Semiconductor Films*, Marcel Dekker, New York, 2003.

22 R. G. Compton and C. E. Banks, *Understanding Voltammetry*, Imperial College Press, London, 2011.

23 H. J. Eichler, P. Gunter and D. W. Pohl, *Laser-Induced Dynamic Grattings*, Springer-Verlag, New York, 1986.

24 B. R. Bennett, R. A. Soref and J. A. D. Alamo, *IEEE J. Quantum Electron.*, 1990, **26**, 113.

25 K. A. Bulashevich and S. Y. Karpov, *Phys. Status Solidi C*, 2008, **5**, 2066.

Ultrasound-driven titanium modification with formation of titania based nanofoam surfaces

CrossMark

Yulia Zhukova *, Sviatlana A. Ulasevich, John W.C. Dunlop, Peter Fratzl, Helmuth Möhwald, Ekaterina V. Skorb

Max Planck Institute of Colloids and Interfaces, Am Mühlenberg 1, 14476 Potsdam, Germany

ABSTRACT

Titanium has been widely used as biomaterial for various medical applications because of its mechanical strength and inertness. This on the other hand makes it difficult to structure it. Nanostructuring can improve its performance for advanced applications such as implantation and lab-on-chip systems. In this study we show that a titania nanofoam on titanium can be formed under high intensity ultrasound (HIUS) treatment in alkaline solution. The physicochemical properties and morphology of the titania nanofoam are investigated in order to find optimal preparation conditions for producing surfaces with high wettability for cell culture studies and drug delivery applications. AFM and contact angle measurements reveal, that surface roughness and wettability of the surfaces depend nonmonotonously on ultrasound intensity and duration of treatment, indicating a competition between HIUS induced roughening and smoothening mechanisms. We finally demonstrate that superhydrophilic bio-and cytocompatible surfaces can be fabricated with short time ultrasonic treatment.

© 2016 Elsevier B.V. All rights reserved.

1. Introduction

Artificial heart valves and joint components, dental implants, orthopedic screws, pacemaker cases, vascular stents are commonly used biomedical applications of titanium-based implants [1]. Titanium is a bioinert metal, it induces a tolerable reaction in the host tissue, shows an adequate resistance to the corrosive *in-vivo* environment, and has the necessary strength, ductility and endurance limit to withstand loading experienced in everyday life [2]. Intense research is still being pursued in the development of new titanium alloys with enhanced biocompatibility and lower elastic modulus closer to bone [3]. Due to its outstanding properties, Ti and its alloys up to nowadays represent the standard in orthopedic surgery and implantology, in particular, of permanent load-bearing implants [4]. Modifications of the surface at the nanoscale have an effect on the chemical reactivity of a biomedical material affecting biomolecular, ionic and other interactions of the surface with the tissue [6]. Such changes in surface properties, altered by ultrasonic modification, may change wetting properties, leading to different protein adsorption, or influence bone mineralization [5]. Recent advances in regenerative therapies and surface science suggest, that cell adhesion to the implant surface can be regulated by various features of the underlying adhesive substrate, such as its chemical composition, physical properties, and topography (for more information about surface modification strategies and cellular recognition of these surfaces see these review papers [5,6]). Recent studies in surface nanostructuring suggest that cells respond to nanotopography [7].

The high mechanical strength and inertness of titanium is also the main issue when trying to nanostructure it. Straight-forward known surface treatments of Ti and its alloys (Ti6Al4V) can be divided into three main groups: mechanical, chemical and physical methods [4]. Polishing, machining, blasting belong to the mechanical methods. Chemical manufacturing methods for surface modification are acid- and alkali-treatments, anodic oxidation. Physical methods can be represented by plasma spray treatment [8], ion implantation [9] and laser treatments [10]. These methods can be used either individually or in combination with other treatments, and cause the formation of different nanotopographies with inhomogeneous features. However, the majority of methods for surface nanostructuring are expensive, time consuming, or difficult to apply for large scale implant production [11]. Parameters, which are required for large-scale manufacturing, are the following: 1) ability to simultaneously reach all surfaces in devices with complex geometries (e.g. femoral stems, dental screws and cardiovas-

* Corresponding author.
  E-mail address: yulia.zhukova@mpikg.mpg.de (Y. Zhukova).

cular stents); 2) possibility to modify at the nanoscale commercially available biocompatible metals and implants; 3) simple integration into industrial process lines [4]. According to the above mentioned features, chemical treatments seem to be attractive for large-scale manufacturing, because they provide uniform access of the reactive substance to all surfaces, but this leaves often unwanted residuals. In addition chemical treatment needs further processing in the case of annealing of crystalline materials at high temperatures. Thus, it is important to find an alternative technology with minimum chemicals addition for nanoscale modification of titanium, which could be applied for multifaceted devices with complex geometries such as dental screws and cardiovascular stents of potentially partially crystalline materials.

Ultrasound is used in different areas, from surface modification to capsules' opening and diagnostics. High intensity ultrasound (HIUS) is a promising method for the production of nanostructured materials. Ultrasound is a unique energy source [12] which provides energy localization with possible acoustic cavitation phenomena, i.e., the formation, growth, and implosive collapse of cavitation bubbles in a liquid. This collapse is able to produce intense local heating (hot spots with temperatures of roughly 5000 °C) and high pressures of about 500 atm [12]. At the liquid-solid interface, the collapse drives high-speed jets of liquid into the surface, whose impact is sufficient to locally melt most metals [12,13] and induces significant changes in surface morphology, composition, and reactivity. On contrary to the ultrasound power used for disruption of carriers [14,15], the ultrasound power used in our study for surface modification is at least 3 times higher.

The strategy we demonstrate here combines the extreme conditions provided for short times by HIUS with a dedicated short term chemical treatment, in special we combine HIUS with an alkali surface treatment. The alkali surface treatment [16] showed an effect analogous to heat treatment on the bone-bonding ability of alkali-treated titanium. Additional treatment with ultrasound [17] can be an attractive method for the production of a partially crystalline titania nanofoam layer strongly adhering to the substrate. It has been used for the development of multifunctional nanomaterials such as bimetallic nanoparticles [18,19], magnetic nanoparticles [20], nanocomposites [21], mesoporous metal surfaces and sponges [22]. The effect of ultrasound irradiation on the surface morphology and physicochemical properties has been demonstrated in various studies [23,24]. Metal based surfaces irradiated by HIUS are highly hydrophilic [25] due to their high roughness, and an active oxide layer is formed on the metal surface. The surfaces are porous and attractive as surface encapsulation systems, since no additional surface coating is required for encapsulation of bioactive molecules [26]. High intensity ultrasound (HIUS) offers a fast and versatile methodology for fabrication of nanostructured materials, both inorganic and organic [27], that are often unavailable by conventional methods [28].

This paper contributes to the understanding of the mechanisms involved in titanium surface modification in alkali solution during HIUS. The morphology and chemical properties of the nanostructured surfaces produced by the sonochemical method extensively depend on the various treatment parameters related to HIUS and alkali treatment. HIUS processing is characterized by various ultrasound parameters (amplitude, intensity, frequency), and duration of treatment, which can be summarized as the energy input into the system. Alkali treatment is characterized by the nature and concentration of the electrolyte solution. In this study, we test the effect of HIUS energy input and alkali treatment on morphology and physicochemical properties of the titanium surface. Furthermore, we investigate the cytocompatibility of the nanostructured titanium surfaces to show prospects of nanostructured materials for bio-application.

2. Experimental section

2.1. Materials

A titanium layer (99.9%) of thickness 400 nm was deposited on glass or silicon substrates by means of Electron Beam Physical Vapor Deposition (EB-PVD). The size of the substrates was (*approx.*) 1×1 cm^2 to fit the homemade Teflon sample holder used for HIUS. Prior to sonication, the metal plates were degreased with isopropanol and rinsed with Milli-Q water (18 MΩ·cm).

Bulk titanium or its alloys, although being very tough, can be used for modification. In our experiments with cell studies it is advantageous to use a nanoscale-thick Ti layer on a glass substrate rather than bulk titanium, since the optical observation of the cell growth requires transparent samples. The formed titania nanofoam layer on glass is transparent enough to observe cell adhesion and growth on the surface. Closest to bulk titanium are thicker layers, 400–150 nm. Thus, as model we use a 400 nm deposited layer on glass or on silicon for atomic force microscopy study.

2.2. Fabrication of nanostructured surfaces

Samples were ultrasonically treated in presence of sodium hydroxide using the ultrasonic processor UIP1000hd (Hielscher Ultrasonics GmbH, Germany) with a maximum output power of 1000 W. The apparatus was equipped with a sonotrode BS2d18 (head area 2.5 cm^2) and a booster B2-2.2, magnifying the working amplitude 2.2 times. Sonication parameters are controlled and presented in Fig. 1. Sonication was performed at *ca.* 20 kHz and constant temperature of around 333 K monitored by the thermo sensor inserted into the working solution. In order to investigate the effect of preparation conditions on the morphology of nanostructured titanium surfaces, samples were treated with ultrasound of different amplitude (60, 70, 80%) for different time periods (3, 5, 7, 10, and 15 min). The maximum intensity was calculated to be 250 W cm^{-2} at mechanical amplitude of 187 μm (at 100%). After treatment the samples were additionally rinsed with isopropanol and water.

The calculation of the energy corresponding to each ultrasonic intensity and duration of treatment is given below. Firstly, according to operating instructions for UIP1000hdT, the maximal mechanical amplitude at 100% for the sonotrode BS2d18 without booster is 85 μm. With an enhancing booster B2-2.2, the maximal
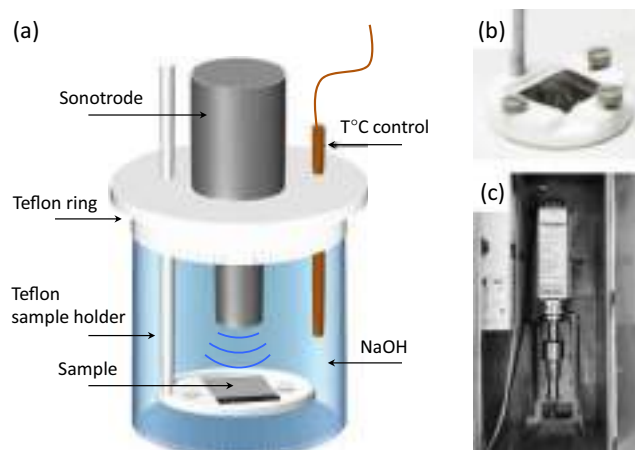
Fig. 1. (a) Experimental setup; (b) Homemade Teflon sample holder; (c) Ultrasonic processor UIP1000hd (Hielscher Ultrasonics GmbH, Germany) equipped with a sonotrode BS2d18 and booster B2-2.2. Sonotrode BS2d18: diameter 18 mm, approx. length 125 mm; booster B2-2.2: booster B2-2.2: diameter 70 mm, approx. length 115 mm.

mechanical amplitude was increased by a factor of 2.2 and A_{100} = 187 µm, which correspond to the maximal ultrasonic intensity I_{100} = 250 W cm^{-2}. The equipment was operated at three amplitudes 80, 70 and 60%, which correspond to ultrasonic intensities I_1 = 200, I_2 = 175 and I_3 = 150 W cm^{-2}. The total power output of an ultrasonic unit is the product of the sonotrode frontal area S and ultrasonic intensity (Eq. (1)).

$$P[\text{W}] = I[\text{W cm}^{-2}] \times S[\text{cm}^2] \tag{1}$$

The energy E is the product of the corresponding power output P and the time of exposure t:

$$E[\text{W s}] = P[\text{W}] \times t[\text{s}] \tag{2}$$

After rearranging, Eq. (2) becomes:

$$E[\text{W s}] = I[\text{W cm}^{-2}] \times S[\text{cm}^2] \times t[\text{s}] \tag{3}$$

The values of energy corresponding to ultrasonic intensities and durations of treatment are given in Table 1.

2.3. Atomic force microscopy (AFM)

AFM measurements were carried out in air at room temperature in tapping mode with micro cantilevers OMCL-AC160TS-W (Olympus, Japan). Typical cantilever values: resonance frequency 300 kHz; spring constant 42 N/m. Atomic force micrographs of a scan size 3×3 µm^2 were made on three different places on the sample. Image analysis was carried out with the software Nanoscope V614r1. Quantitative data about the surface roughness, height profile, and three-dimensional projections of the micrographs were obtained using this software. The surface roughness was quantified by the software as an arithmetic average of the absolute values of the surface height deviations measured from the mean plane:

$$R_a = \frac{1}{N}\sum_{j=1}^{N}|Z_j| \tag{4}$$

2.4. Water contact angle measurements

The contact angle was measured using the homemade system described in Ref. [29]. Measurements were performed with a 1 µl water droplet deposited onto the titanium substrates with a syringe from the top. During the process, the contact angles, from the left θ_L and from the right θ_R, are continuously monitored. After that, the average contact angles $\overline{\theta_L}$ and $\overline{\theta_R}$, $\Delta\theta$ and an average contact angle $\overline{\theta}$ were calculated as follows:

$$\left|\overline{\theta_R} - \overline{\theta_L}\right| = \Delta\theta \tag{5}$$

$$\frac{\overline{\theta_R}}{2} + \frac{\overline{\theta_L}}{2} = \overline{\theta} \tag{6}$$

Untreated titanium substrates were used as a control.

Table 1
Energy of sonication used at different amplitudes and exposure times.

Energy, [W s]			
Exposure time, [min]	Ultrasonic intensity, [W cm^{-2}]		
	150 (at 60%)	175 (at 70%)	200 (at 80%)
3	27,000	31,500	36,000
5	45,000	52,500	60,000
7	63,000	73,500	84,000
10	90,000	105,000	120,000
15	135,000	157,500	180,000

2.5. Scanning electron microscopy (SEM)

Prior to microscopy the samples were sputtered with gold. SEM was conducted with a Gemini Leo 1550 instrument (Leo Elektronenmikroskopie GmbH, Germany) at an operating voltage of 3 keV.

2.6. Transmission electron (high-resolution) microscopy (TEM, HRTEM)

Transmission electron microscopy (TEM) measurements were performed on a Zeiss EM 912 Omega (Carl Zeiss AG, Germany) transmission electron microscope operated at 300 kV and equipped with an electron-diffraction (ED) unit. High-resolution transmission electron microscopy (HRTEM) was performed by TEM in a Philips CM30 operated at 300 kV. The samples were ultramicrotomed (Leica EM FC6) and placed onto carbon-coated copper grids.

2.7. Cell culture studies

A mouse calvarial preosteoblast cell line MC3T3-E1 was obtained from the Ludwig Boltzmann Institute, Vienna, Austria. Preosteoblasts were cultured in α-MEM supplemented with 10% (by volume) fetal calf serum (FCS), 4500 mg glucose, 0.1% (by volume) gentamycin, 0.1% (by volume) ascorbic acid, and maintained at 37 °C with 5% CO$_2$ in humidified atmosphere. Cells were passaged in total three times every 24 h by a dilution factor of 1/6. After reaching confluence, cells were removed from the culture vessels by incubating with pronase for 3–5 min and seeded onto glass and TMS surfaces at 6000 cells/cm^2. Three samples were tested per substrate type, three independent experiments were conducted. All surfaces and scaffolds were autoclaved before cell culture experiments. After 3 h of growth optical images were obtained with a phase contrast microscope.

2.8. Actin cytoskeleton staining

The surfaces were washed with phosphate buffer saline (PBS), fixed with 4% paraformaldehyde in PBS, and permeabilized with buffered Triton-X100 (Sigma-Aldrich, Steinheim, Germany) for 10 min at room temperature. The scaffolds were then thoroughly washed with PBS and stained for 60–90 min with phalloidin Alexa488 (Invitrogen, Oregon, USA) (1:20) in dark at 4 °C. After that scaffolds were thoroughly washed with PBS again, and stained for nuclei with TO-PRO3 iodide (Invitrogen, Oregon, USA) (1:300) for 5 min at room temperature. The scaffolds were washed with PBS, mounted with Fluoro-Mount in inverted position on the glass slides, and examined via confocal microscopy (Leica Microsystems, Mannheim, Germany).

3. Results and discussion

In this study, we test first the effect of processing parameters, such as HIUS energy input and alkali treatment, on morphology and physicochemical properties of the titanium surface, then the cytocompatibility of the nanostructured surfaces. The focus is on formation of a nanofoam layer. In water Ti exhibits minor nanofoam layer formation after 60 min of sonication [30]. Ti has a high melting point, and the physical effect of melting is prevalent over other effects of ultrasonic irradiation, therefore one can observe a slight increase in surface roughness. However, by additional treatment in NaOH one can enhance the chemical effects of ultrasonic treatment.

The HIUS treatment gives rise to four different morphological stages (Fig. 2), starting with an untreated flat titanium (Fig. 2,
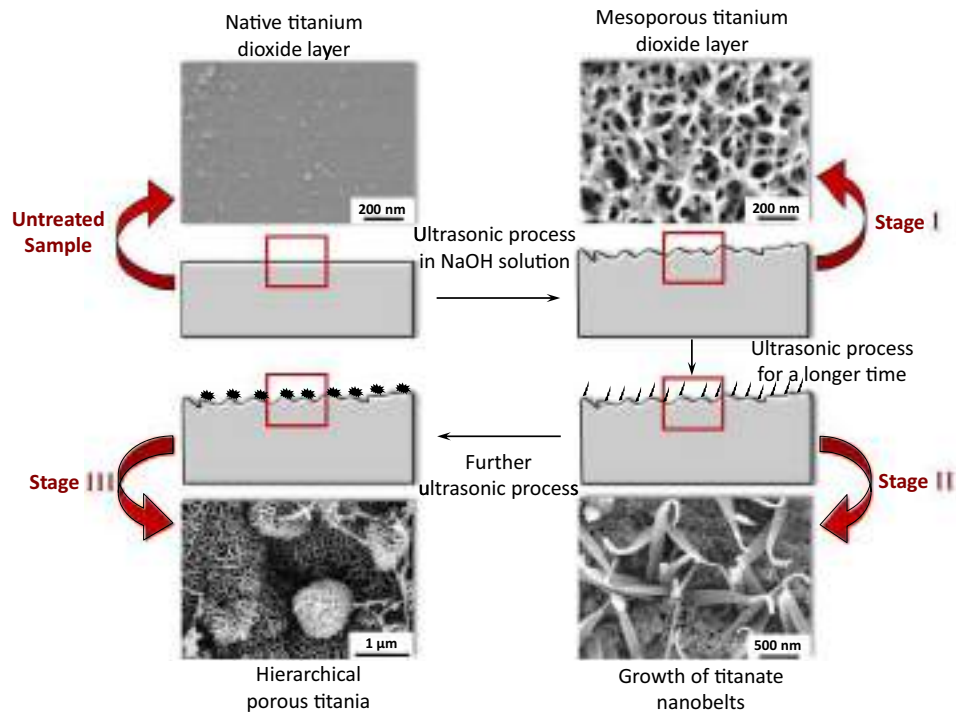
Fig. 2. Schematic diagram of the morphological stages of the HIUS-alkali treated titanium surface: untreated flat titanium (Untreated Sample); mesoporous titanium dioxide layer formed during the HIUS treatment in NaOH solution (Stage I); titanate nanobelts (Stage II) and hierarchical porous titania (Stage III) formed with further alkali treatment. Surface nanotopographies were observed by SEM.

untreated sample). It has a native oxide layer mainly composed of the stable oxide TiO_2 and is typically 3–7 nm thick [31]. Flat titanium is treated with HIUS in presence of an aqueous solution of NaOH. In the early stage of HIUS treatment in NaOH solution, a native titanium oxide layer is removed, mainly mechanically disrupted by HIUS and a mesoporous titanium dioxide layer is being formed on the exposed surface (Fig. 2, stage I). With further alkali treatment more hydroxyls attack hydrated TiO_2, leading to negatively charged hydrates on the metal surface:
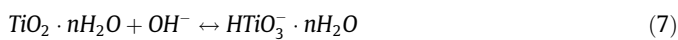
$$TiO_2 \cdot nH_2O + OH^- \leftrightarrow HTiO_3^- \cdot nH_2O \qquad (7)$$

The growth of titanate nanobelts perpendicularly from the titanium scaffold is displayed in Fig. 2, Stage II, and finally, the formation of a complex hierarchical structure takes place (Fig. 2, Stage III). For biological applications mesoporous titanium with the pronounced nanofoam layers was used. In previous work on aluminium alloys [32], the strongest adhesion was observed before the layer formed at Stage I. Moreover, together with the strongest adhesion, the layer formed after Stage I covered the surface uniformly. This will be discussed further being the most promising as novel strategy for titanium implant treatment.
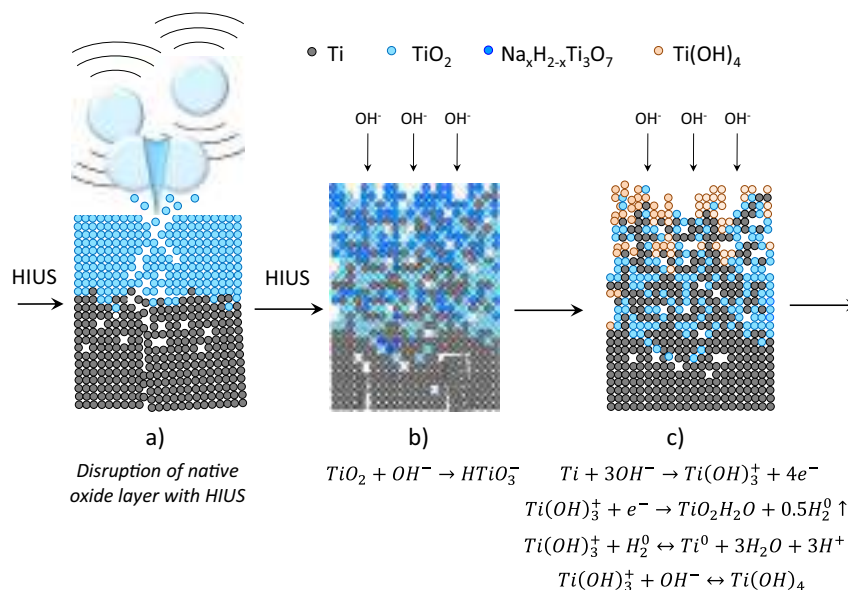
Fig. 3. Schematic illustration of the structuring process taking place during the HIUS treatment of a titanium surface in aqueous solution of NaOH.
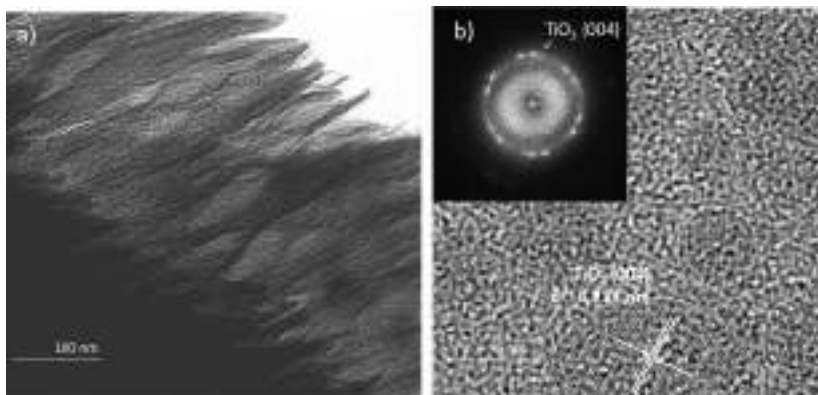
Fig. 4. (a) TEM images of areas of an interpenetration layer of amorphous titania well adhering to titanium with inclusions of (b) shown in HRTEM and electron diffraction (ED) crystalline TiO_2.

What are the effects of high intensity ultrasonic treatment one can use to overcome a TiO_2 layer? The titanium covered with a native layer (Ti/TiO_2) is shown in Fig. 3a. Due to physical impact, bubble collapse with high energy jets, the oxide layer is expected to break [12]. The sonochemical etching during treatment in alkali medium is obvious. The early study of Ziemniak et al. [33] showed the solubility behavior of TiO_2 in alkali media, e.g. in aqueous sodium hydroxide. The main oxidation state is Ti^{4+}, although due to sonochemical non-equilibrium conditions one can expect also the states Ti^{3+} and Ti^{2+}, that are less stable, as intermediate resulting in an advanced nanostructured surface with an interesting morphology for cell growth studies. In basic solution the negative charge on the titanium surface increases with increasing pH [31]. It was shown [27,28], that during the hydrothermal alkali treatment the passive protective TiO_2 layer partially dissolves into alkaline solution because of the impact of the hydroxyl groups:

$$TiO_2 + OH^- \rightarrow HTiO_3^- \qquad (8)$$

In our study, the native oxide layer breaks up due to the physical effect of HIUS and, contrary to the hydrothermal treatment, results in interplay between reactions with TiO_2 and Ti with formation of an interpenetrating "domain-like" layer of complex structure (Fig. 3b). The reaction proceeds simultaneously with the hydration of TiO_2 (Eq. (8)) and Ti:

$$Ti + 3OH^- \rightarrow Ti(OH)_3^+ + 4e^- \qquad (9)$$

$$Ti(OH)_3^+ + e^- \rightarrow TiO_2 \cdot H_2O + 0.5H_2 \uparrow \qquad (10)$$

$$Ti(OH)_3^+ + 3H_2 \rightarrow Ti^0 + 3H_2O + 3H^+ \qquad (11)$$

$$Ti(OH)_3^+ + OH^- \leftrightarrow Ti(OH)_4 \qquad (12)$$
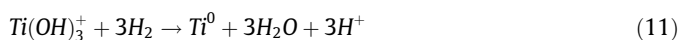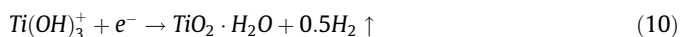
High-intensity ultrasound induces a wide range of chemical and physical consequences. The chemical effects of ultrasound derive primarily from acoustic cavitation. The extreme temperatures and pressures induce sonolysis and generation of highly reactive radicals [12], which chemically transforms the solid surface. This allows acceleration of a chemical reaction at the solid-liquid interface, reactivity enhancement of the solids, and permits use of less aggressive chemicals. The physical effects include (1) improvement of mass transport from local turbulent flow and microstreaming, (2) generation of surface erosion and pitting at liquid-solid interfaces by shock waves and microjets, (3) generation of high-velocity interparticle collisions in liquid-solid slurries, and (4) fragmentation of fragile solids to increase the surface area [27]. The combination of physical and chemical effects allows a one-step straight forward modification of metal surfaces.

Thus, the final structure, shown in Fig. 3c, should be hydrophilic due to surface –OH groups. In contrast to surfaces experiencing hydrothermal treatments, the layer of formed oxidized structure can be partially crystalline due to the high energy of the HIUS applied to the system and extreme heating/cooling rates known for the process. The low magnification TEM image of the cross section of the film-substrate interface points to adhesion of the formed interpenetration layer to titanium (Fig. 4a). The HRTEM and ED micrographs detected the TiO_2 (004) peak which correspond to anatase (Fig. 4b). This experimental observation correlates to the hydration of Ti in alkali solution (Eq. (10)).

The intensity and duration of ultrasound treatment significantly affect the formation of a mesoporous titania surface. At ultrasound intensities $150–200\ W\ cm^{-2}$ formation of a "domain-like" structure starts to form due to the development of the TiO_2 layer. Maturation mainly develops with the increase of duration and intensity of ultrasonication (Fig. 5). Surface roughness R_a and contact angle of three points on the surface are plotted vs. time (Fig. 5a, c) and vs. energy (Fig. 5b, d) for different ultrasound
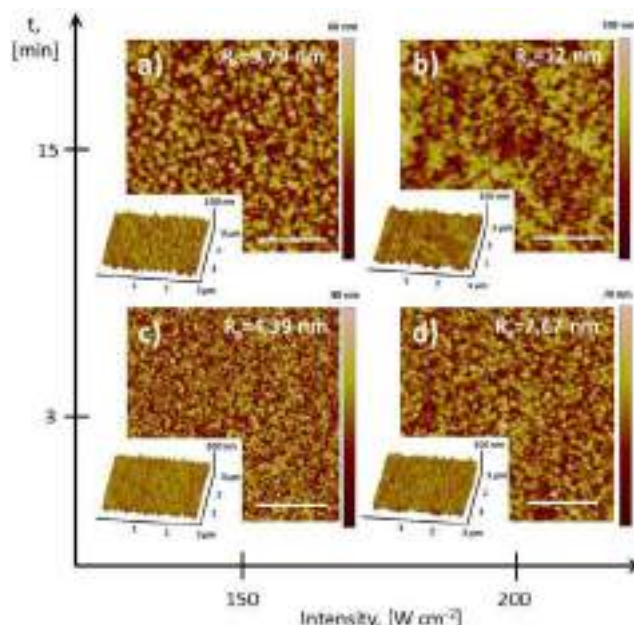
Fig. 5. AFM micrographs and 3D projections of the ultrasonically modified titanium surface at different intensities and duration: 15 min at intensity $150\ W\ cm^{-2}$ (a); 15 min at intensity $200\ W\ cm^{-2}$ (b); 3 min at intensity $150\ W\ cm^{-2}$ (c); 3 min at intensity $200\ W\ cm^{-2}$ (d). Scale bar is 1 μm.

intensities (Fig. 6). For all intensities one observes a non-monotonous behavior of roughness development with duration of HIUS treatment. The highest surface roughness 15 ± 2 nm could be achieved at highest I_2 and 10 min of treatment. Quite high surface roughness was achieved for I_1 at 5 and 10 min of treatment, 14 ± 2 nm, respectively. For all three US intensities, one can

observe the following dependence: after the first peak with the high surface roughness is achieved, the roughness first drops, but after some time it increases again, reaching the highest value of the first peak. One observes the same cyclic dependence for all three intensities; however, the peak positions vary. For instance, the curves I_1 and I_3 have analogous shapes with similar peak posi-
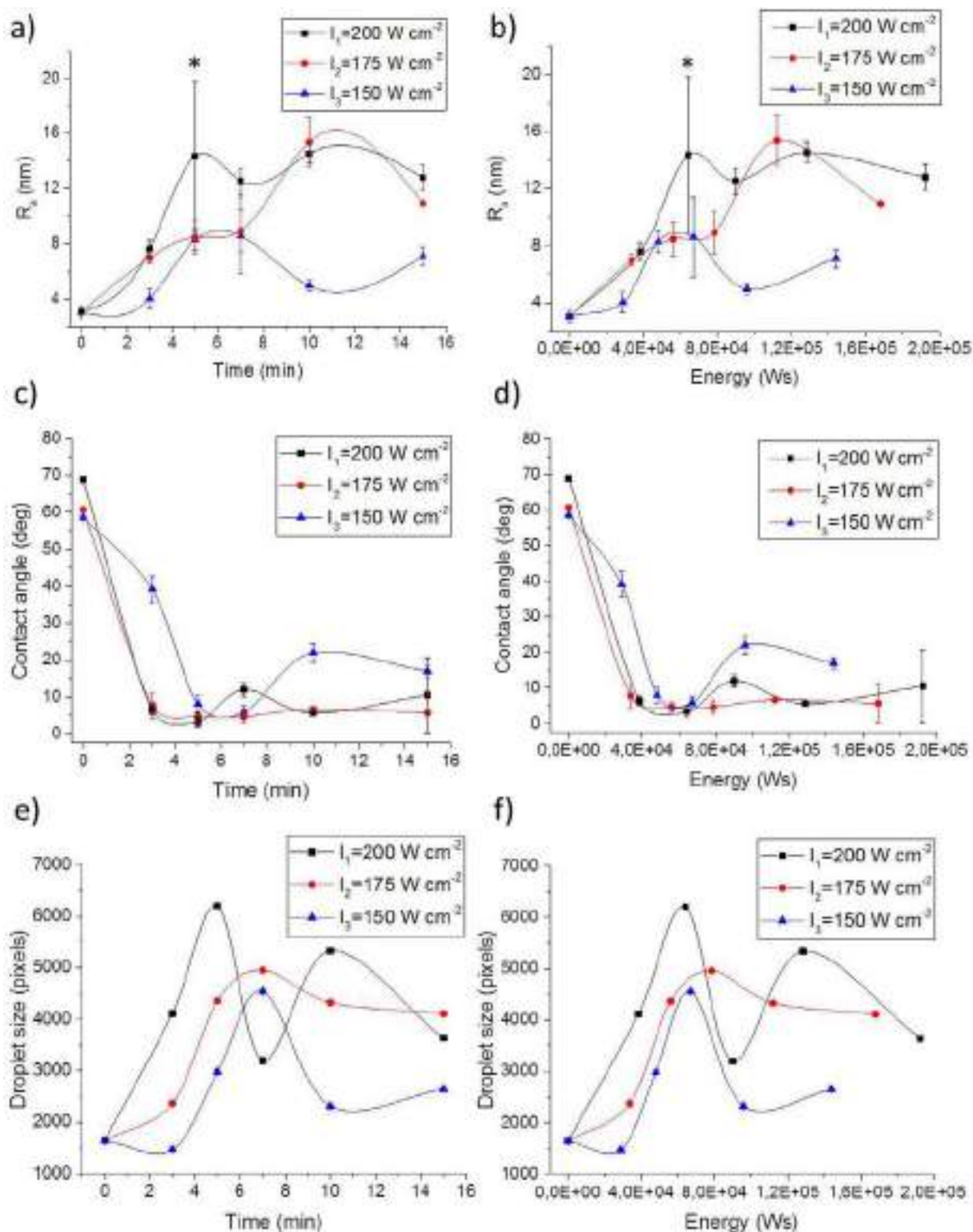
Fig. 6. Oscillations of surface roughness R_a (a, b), contact angle (c, d), and water droplet size (e, f) as a function of sonication time and energy at three ultrasound intensities: $I_1 = 200$, $I_2 = 175$, and $I_3 = 150$ W cm^{-2}. (*) Measurement is done for 10 samples.

tions; however curve I_1 looks smoother than I_2, which corresponds to smaller changes in surface roughness. The surface roughness does not monotonously increase but one observes its oscillations on the nanoscale. Two possible reasons for such oscillatory behavior can be assumed. The first one is based on purely mechanical effects, i.e. on two opposing forces: mechanical surface disruption increasing roughness and flaking off reducing the roughness. For instance, at high US intensities one can achieve high roughness at already 5 min of sonication. With further treatment, a strongly modified layer is flaking off and gets flatter, therefore, the drop in surface roughness. After that, the surface is modified again, and the roughness increases. The second explanation is based on a more complex effect, an interplay between the number of bubble collapse events and temperature effect [34] of the HIUS. The more bubble collapses takes place, the higher the roughness increases, however due to the corresponding temperature increase, the surface smoothens again. This cycle repeats. Although we use the additional NaOH treatment in order to accelerate chemical effects of HIUS over the physical ones, a local temperature variation still seems to have an impact on surface roughness, which appears as nanoscale roughness oscillations. The second explanation seems more probable, because during the flaking off one will probably obtain stronger drops and less periodic oscillations of surface roughness. We used 5 M NaOH aqueous solution with pH 13. At lower alkali concentrations pH 9 and 11, modification takes place, but at the same HIUS conditions does not provide surface roughening higher than 10 nm.

The water contact angle measurements provide evidence, that the HIUS-modified titanium surfaces exhibit extremely high hydrophilicity (θ below 10°), which may be called superhydrophilic [35]. In order to measure very low contact angles, we used a home-made system [29], where the contact angles, from the left θ_L and from the right θ_R, are continuously monitored (Fig. 7). The differences may be due to impurities and inhomogeneities of the surface chemistry and morphology. The lowest contact angle value $\theta = 3.3 \pm 1.6°$ corresponds to the peak with the highest surface roughness ($I_1 = 200$ W cm^{-2}), and this holds for all three US intensities. After that, contact angle values rise and drop again, reaching the first low value. Here, the curve I_3 shows the most significant fluctuations in contact angle with energy input, however, the contact angle values are still higher than for the higher intensities. Thus, contact angle changes depend on time and energy input non-monotonously, similar to the oscillating behavior of surface roughness (Fig. 6c, d). In addition, similar behavior was demonstrated for the changes of water droplet size in time for different US intensities (Fig. 6e, f). The following observations of water droplet size are in good agreement with changes of contact angle: (1) the fluctuations of droplet size are reversely dependent on contact angle value for all three US intensities: large water droplets correspond to small contact angles; (2) the biggest droplet size corresponds to the lowest contact angle value $\theta = 3.3 \pm 1.6°$ at $I_1 = 200$ W cm^{-2}; (3) It is known, that the contact angle is sensitive to local geometrical transformations of the solid surface. The superhydrophilicity
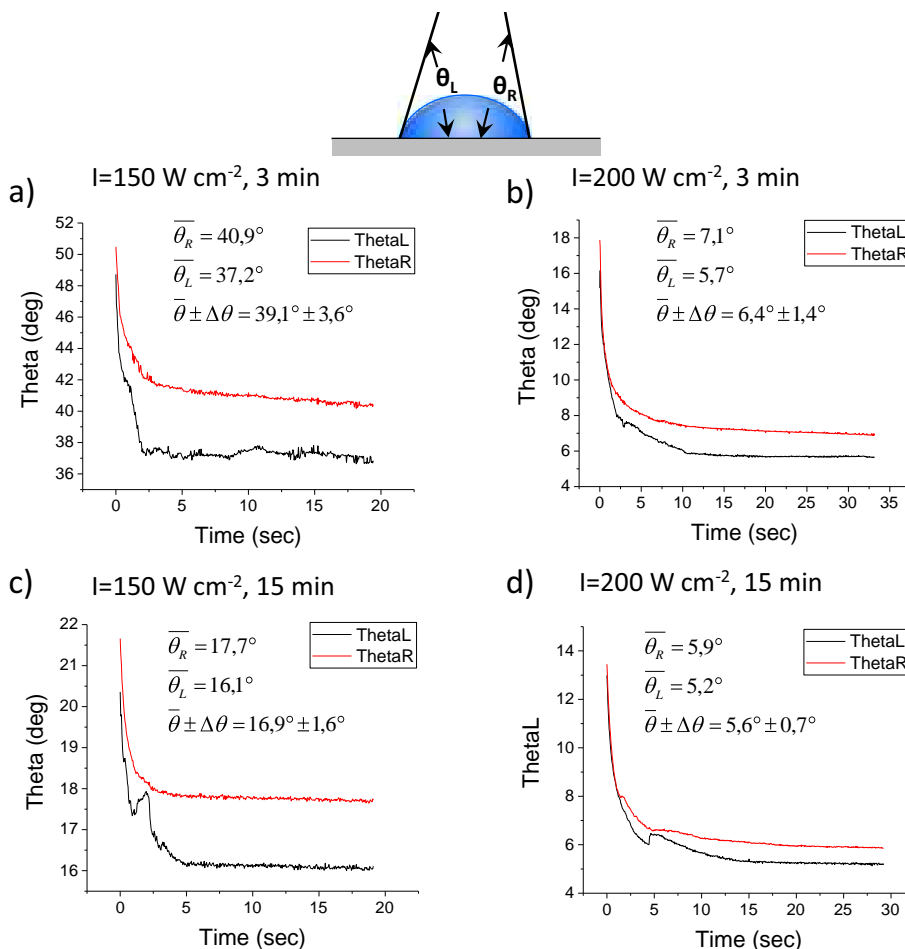
Fig. 7. Contact angle measurements. The contact angles, from the left θ_L and from the right θ_R, are continuously monitored. For the calculations, only the parallel horizontal regions were taken into account.

of the surface may be due to the nanosize features on the surface: an intrinsically hydrophobic surface becomes more hydrophobic [36], as its roughness increases, and the hydrophilicity increases with roughness for the intrinsically hydrophilic surface [37]. In our case, we deal with the intrinsically hydrophilic Ti surface due to the native TiO_2. The surface roughness of TMS surfaces does not increase continuously but changes in an oscillatory manner. The contact angle changes accordingly with nonmonotonic behavior of surface roughness. It becomes more hydrophilic with increase of surface roughness.

Nanostructured titanium has to perform well across two interfaces: between the bulk metal and the interpenetrating layer, and between the interpenetrating layer and the tissue (Fig. 8). Investigation of the physicochemical properties of the mesoporous titanium surface has demonstrated the unique achievement by HIUS treatment in NaOH. Due to its continuous transition from surface to bulk, the interpenetrating TiO_2 layer has high bonding strength to the bulk metal (Fig. 8a). In order to estimate the cytocompatibility of the produced TMS surfaces, cell culture studies with a MC3T3-E1 preosteoblast cell line were performed. Different stages of tissue formation were investigated: early stages at 24 h, 48 h, and 5 days of cell incubation on the TMS surfaces. The cell behavior was examined by confocal microscopy. At early stages (Fig. 8b), we observed quite large single cells with an easily identified nucleus, which start to spread and to form cell-cell contacts. At higher levels of proliferation (Fig. 8c), the cells form numerous cell-cell contacts, and complete coverage of the TMS surface is achieved. For the

investigation of tissue growth for longer times, cells were seeded onto the tissue engineering scaffolds with round channels of 500 μm diameter treated with HIUS. The cells formed 50–70 μm thick tissue within the microchannels after 5 days of incubation (Fig. 8d), and the kinetics of tissue growth could be quantified by measuring the projected tissue area in the microchannel (Fig. 8e) as described in [38,39]. The amount of tissue formed in the channels modified with HIUS was found to be larger than in unmodified ones. This observation demonstrates an important effect of nanostructuring on tissue growth and demonstrates that TMS can firmly integrate with the preosteoblast cell line MC3T3-E1 at different time points of tissue growth. Our results suggest that the titanium nanotopography can have a significant effect both on individual cells and tissue. The behavior of the first cell layer is important to understand and control, since we believe it to play a crucial role in the further tissue formation. As such this will be an important focus of further cell culture studies on TMS surfaces. Much research has been done on understanding 3D tissue growth in channels of different geometries. It has been shown that after cells completely cover the substrate, tissue growth, at later time points than those studied here, could be described by a model for curvature-controlled growth. This suggests that by tuning the geometry of the scaffolds for tissue engineering at multiple length scales it is not only possible to accelerate growth by large scale geometries [35], but also by controlling nano-scale topographies as demonstrated here. Further studies are needed to investigate this in more detail.
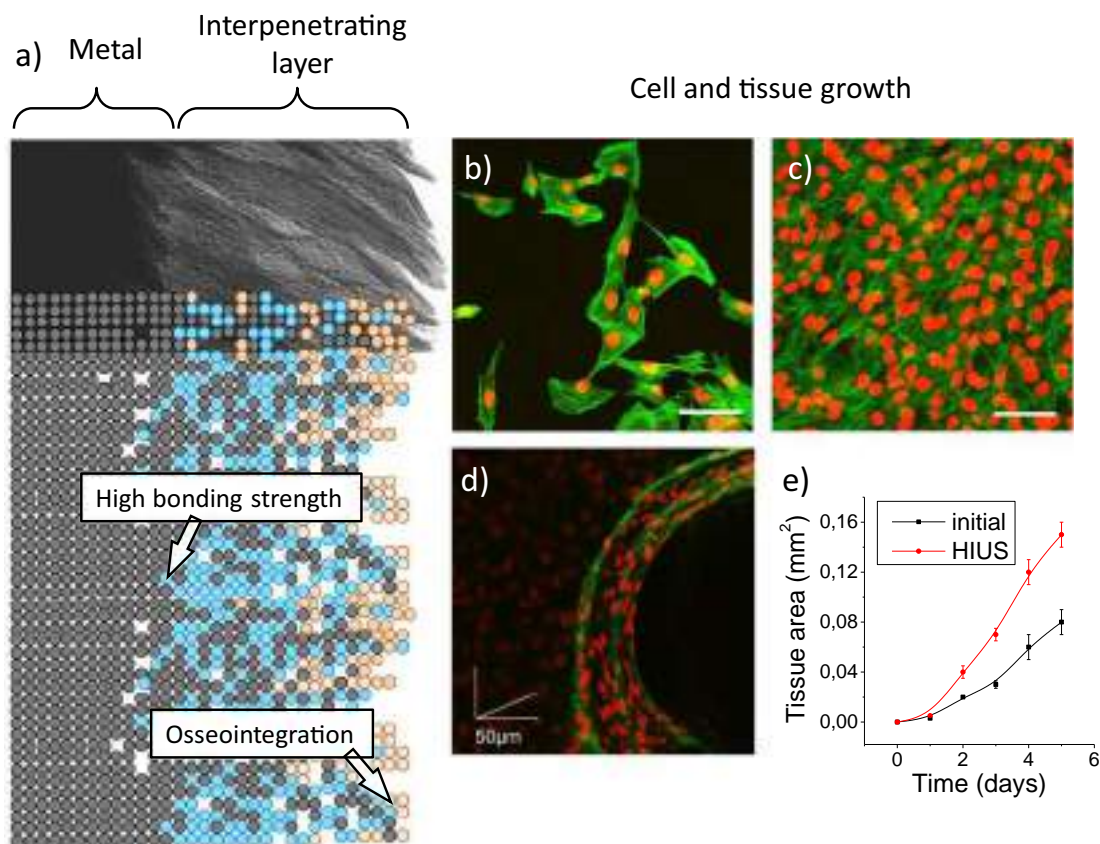
Fig. 8. Nanostructured titanium has to perform well across two interfaces: between the bulk metal and the interpenetrating layer, and between the interpenetrating layer and the tissue (a). Colors of circles correspond to the same materials as in Fig. 3. Due to its unique properties achieved with HIUS treatment in NaOH, the mesoporous titanium surface has high bonding strength to the bulk metal. It can firmly integrate with the preosteoblast cell line MC3T3-E1 at different stages of tissue formation: individual cells after 24 h of growth (b), cell layers after 48 h (c), and tissue growth in tissue engineering scaffolds after 5 days (d). Confocal microscopy images with nuclear (red) and actin (green) staining. Scale bar is 100 μm. Quantitative analysis of tissue growth in circular pores of 500 μm diameter unmodified (initial) and modified with HIUS (e). (For interpretation of the references to color in this figure legend, the reader is referred to the web version of this article.)

4. Conclusions

This work contributes to the fundamental understanding of the mechanism of acoustic cavitation at the titanium surface in combination with alkali treatment. We have shown an elaborated multi-stage process of titanium surface nanostructuring with HIUS in NaOH. By controlling the treatment parameters such as ultrasound intensity and duration of treatment, control over physical, chemical, and structural properties of the titanium surface is achieved. Conditions optimal for the formation of nanostructured TMS were found via SEM, TEM, AFM, and contact angle measurements. Sonication in alkali conditions induces changes of surface nanotopography, wettability and crystallinity of the titania surfaces. Due to the interplay between physical and chemical effects of the proposed technique, short HIUS treatment is sufficient for formation of a nanostructured titanium dioxide surface. This surface presents good cytocompatibility for MC3T3-E1 preosteoblasts, which makes them suitable for biological applications.

Acknowledgements

References

[1] F. Variola, J.B. Brunski, G. Orsini, P. Tambasco de Oliveira, R. Wazen, A. Nanci, Nanoscale surface modifications of medically relevant metals: state-of-the art and perspectives, Nanoscale 3 (2011) 335–353.
[2] T. Albrektsson, P.I. Branemark, H.A. Hansson, J. Lindstrom, Osseointegrated titanium implants – requirements for ensuring a long-lasting, direct bone-to-implant anchorage in man, Acta Orthop. Scand. 52 (1981) 155–170.
[3] M. Geetha, A.K. Singh, R. Asokamani, A.K. Gogia, Ti based biomaterials, the ultimate choice for orthopaedic implants – a review, Prog. Mater Sci. 54 (2009) 397–425.
[4] F. Variola, J. Brunski, G. Orsini, P.T. de Oliveira, R. Wazen, A. Nanci, Nanoscale surface modifications of medically-relevant metals: state-of-the art and perspectives, Nanoscale 3 (2011) 335–353.
[5] S. Bauer, P. Schmuki, K. von der Mark, J. Park, Engineering biocompatible implant surfaces: Part I: materials and surfaces, Prog. Mater Sci. 58 (2013) 261–326.
[6] K. von der Mark, J. Park, Engineering biocompatible implant surfaces: Part II: cellular recognition of biomaterial surfaces: lessons from cell–matrix interactions, Prog. Mater Sci. 58 (2013) 327–381.
[7] C. Selhuber-Unkel, T. Erdmann, M. López-García, H. Kessler, U.S. Schwarz, J.P. Spatz, Cell adhesion strength is controlled by intermolecular spacing of adhesion receptors, Biophys. J. 98 (2010) 543–551.
[8] B.S. Necula, I. Apachitei, L.E. Fratila-Apachitei, E.J. van Langelaan, J. Duszczyk, Titanium bone implants with superimposed micro/nano-scale porosity and antibacterial capability, Appl. Surf. Sci. 273 (2013) 310–314.
[9] S. Ferraris, A. Venturello, M. Miola, A. Cochis, L. Rimondini, S. Spriano, Antibacterial and bioactive nanostructured titanium surfaces for bone integration, Appl. Surf. Sci. 311 (2014) 279–291.
[10] V. Dumas, A. Rattner, L. Vico, E. Audouard, J.C. Dumas, P. Naisson, P. Bertrand, Multiscale grooved titanium processed with femtosecond laser influences mesenchymal stem cell morphology, adhesion, and matrix organization, J. Biomed. Mater. Res., Part A 100A (2012) 3108–3116.
[11] J. Banhart, Manufacture, characterisation and application of cellular metals and metal foams, Prog. Mater Sci. 46 (2001) 559–632.
[12] K.S. Suslick, Sonochemistry, Science 247 (1990) 1439–1445.
[13] S. Doktycz, K. Suslick, Interparticle collisions driven by ultrasound, Science 247 (1990) 1067–1069.
[14] B.G. De Geest, A.G. Skirtach, A.A. Mamedov, A.A. Antipov, N.A. Kotov, S.C. De Smedt, G.B. Sukhorukov, Ultrasound-triggered release from multilayered capsules, Small 3 (2007) 804–808.
[15] A.G. Skirtach, B.G. De Geest, A. Mamedov, A.A. Antipov, N.A. Kotov, G.B. Sukhorukov, Ultrasound stimulated release and catalysis using polyelectrolyte multilayer capsules, J. Mater. Chem. 17 (2007) 1050–1054.
[16] S. Nishiguchi, T. Nakamura, M. Kobayashi, H.-M. Kim, F. Miyaji, T. Kokubo, The effect of heat treatment on bone-bonding ability of alkali-treated titanium, Biomaterials 20 (1999) 491–500.
[17] E.V. Skorb, D.V. Andreeva, H. Möhwald, Generation of a porous luminescent structure through ultrasonically induced pathways of silicon modification, Angew. Chem. Int. Ed. 51 (2012) 5138–5142.
[18] J. Dulle, S. Nemeth, E.V. Skorb, T. Irrgang, J. Senker, R. Kempe, A. Fery, D.V. Andreeva, Sonochemical activation of Al/Ni hydrogenation catalyst, Adv. Funct. Mater. 22 (2012) 3128–3135.
[19] P.V. Cherepanov, I. Melnyk, E.V. Skorb, P. Fratzl, E. Zolotoyabko, N. Dubrovinskaia, L. Dubrovinsky, Y.S. Avadhut, J. Senker, L. Leppert, S. Kummel, D.V. Andreeva, The use of ultrasonic cavitation for near-surface structuring of robust and low-cost AlNi catalysts for hydrogen production, Green Chem. 17 (2015) 2745–2749.
[20] O. Baidukova, H. Mohwald, A.S. Mazheika, D.V. Sviridov, T. Palamarciuc, B. Weber, P.V. Cherepanov, D.V. Andreeva, E.V. Skorb, Sonogenerated metal-hydrogen sponges for reactive hard templating, Chem. Commun. 51 (2015) 7606–7609.
[21] E.V. Skorb, O. Baidukova, A. Goyal, A. Brotchie, D.V. Andreeva, H. Mohwald, Sononanoengineered magnesium-polypyrrole hybrid capsules with synergetic trigger release, J. Mater. Chem. 22 (2012) 13841–13848.
[22] Cavitation: A Novel Energy-efficient Technique for the Generation of Nanomaterials, Taylor & Francis group, LLC, 2014.
[23] M. Virot, T. Chave, S.I. Nikitenko, D.G. Shchukin, T. Zemb, H. Möhwald, Acoustic cavitation at the water–glass interface, J. Phys. Chem. C 114 (2010) 13083–13091.
[24] M. Virot, R. Pflieger, E.V. Skorb, J. Ravaux, T. Zemb, H. Möhwald, Crystalline silicon under acoustic cavitation: from mechanoluminescence to amorphization, J. Phys. Chem. C 116 (2012) 15493–15499.
[25] E.V. Skorb, H. Mohwald, 25th anniversary article: dynamic interfaces for responsive encapsulation systems, Adv. Mater. 25 (2013) 5029–5043.
[26] D.V. Andreeva, D.V. Sviridov, A. Masic, H. Möhwald, E.V. Skorb, Nanoengineered metal surface capsules: construction of a metal-protection system, Small 8 (2012) 820–825.
[27] K.S. Suslick, G.J. Price, Applications of ultrasound to materials chemistry, Annu. Rev. Mater. Sci. 29 (1999) 295–326.
[28] J.H. Bang, K.S. Suslick, Applications of ultrasound to the synthesis of nanostructured materials, Adv. Mater. 22 (2010) 1039–1059.
[29] S. Karpitschka, H. Riegler, Quantitative experimental study on the transition between fast and delayed coalescence of sessile droplets with different but completely miscible liquids, Langmuir 26 (2010) 11823–11829.
[30] E.V. Skorb, D. Fix, D.G. Shchukin, H. Mohwald, D.V. Sviridov, R. Mousa, N. Wanderka, J. Schaferhans, N. Pazos-Perez, A. Fery, D.V. Andreeva, Sonochemical formation of metal sponges, Nanoscale 3 (2011) 985–993.
[31] X. Liu, P. Chu, C. Ding, Surface modification of titanium, titanium alloys, and related materials for biomedical applications, Mater. Sci. Eng., R 47 (2004) 49–121.
[32] E.V. Skorb, D.G. Shchukin, H. Mohwald, D.V. Andreeva, Ultrasound-driven design of metal surface nanofoams, Nanoscale 2 (2010) 722–727.
[33] S.E. Ziemniak, M.E. Jones, K.E.S. Combs, Solubility behavior of titanium(IV) oxide in alkaline media at elevated temperatures, J. Solution Chem. 22 (1993) 601–623.
[34] P.V. Cherepanov, A. Kollath, D.V. Andreeva, Up to which temperature ultrasound can heat the particle?, Ultrason Sonochem. 26 (2015) 9–14.
[35] J. Drelich, E. Chibowski, D.D. Meng, K. Terpilowski, Hydrophilic and superhydrophilic surfaces and materials, Soft Matter 7 (2011) 9804–9828.
[36] A.B.D. Cassie, S. Baxter, Wettability of porous surfaces, Trans. Faraday Soc. 40 (1944) 546–551.
[37] R.N. Wenzel, Resistance of solid surfaces to wetting by water, Ind. Eng. Chem. 28 (1936) 988–994.
[38] C.M. Bidan, K.P. Kommareddy, M. Rumpler, P. Kollmannsberger, Y.J.M. Bréchet, P. Fratzl, J.W.C. Dunlop, How linear tension converts to curvature: geometric control of bone tissue growth, PLoS One 7 (2012) e36336.
[39] C.M. Bidan, K.P. Kommareddy, M. Rumpler, P. Kollmannsberger, P. Fratzl, J.W.C. Dunlop, Geometry as a factor for tissue growth: towards shape optimization of tissue engineering scaffolds, Adv. Healthcare Mater. 2 (2013) 186–194.

The Role of Titanium Surface Nanostructuring on Preosteoblast Morphology, Adhesion, and Migration

Yulia Zhukova, Christian Hiepen, Petra Knaus, Marc Osterland, Steffen Prohaska, John W. C. Dunlop, Peter Fratzl,* and Ekaterina V. Skorb

Surface structuring of titanium-based implants is known to modulate the behavior of adherent cells, but the influence of different nanotopographies is poorly understood. The aim is to investigate preosteoblast proliferation, adhesion, morphology, and migration on surfaces with similar surface chemistry but distinct nanotopographical features. Sonochemical treatment and anodic oxidation are employed to fabricate disordered, mesoporous titania (TMS) and ordered titania nanotubular (TNT) topographies on titanium, respectively. Morphological evaluation reveals that cells are polygonal and well-spread on TMS, but display an elongated, fibroblast-like morphology on TNT surfaces, while they are much flatter on glass. Both nanostructured surfaces impair cell adhesion, but TMS is more favorable for cell growth due to its support of cell attachment and spreading in contrast to TNT. A quantitative wound healing assay in combination with live-cell imaging reveals that cell migration on TMS surfaces has a more collective character than on other surfaces, probably due to a closer proximity between neighboring migrating cells on TMS. The results indicate distinctly different cell adhesion and migration on ordered and disordered titania nanotopographies, providing important information that can be used in optimizing titanium-based scaffold design to foster bone tissue growth and repair while allowing for the encapsulation of drugs into porous titania layer.

1. Introduction

Recent advances in material research have gained an increased knowledge on the role of the extracellular environment in tissue repair and regenerative processes.[1–3] The physical and chemical cues presented by the extracellular environment have been shown to directly impact cell behavior such as proliferation, adherence, and migration.[4] The vast majority of research is dedicated to the chemical composition of the extracellular environment and found striking impact on the differentiation potential of cells, but little is known about the impact of the extracellular environment's topography on bone progenitor proliferation, adhesion, and migration. To date, titanium and its alloys find wide application in regenerative medicine, representing clinically relevant implant materials which need further improvement for enhancement of healing and tissue regeneration.[5–7] Particularly, the speed and effectiveness with which these alloys become populated by progenitor cells, may be crucial for their efficacy in promoting repair. Besides their chemical properties, others have already proposed that the material surface topography is fundamental for this process.[8] Recently, we have shown the prospects of nanostructured titania surfaces for the development of lab-on-a-chip, light-triggered systems to guide proteins on the cell surface by dynamic oscillation of soft matter organized on titania to regulate inorganic–organic–polymeric interfaces.[9–11]

Several studies using surface structuring approaches demonstrate that cells respond to nanotopography.[12–16] This is further supported by the influence of nanoscale features on interactions between biomaterials and host tissues. For example, (1) cells grow on nanostructured extracellular matrices, (2) biological events such as signaling are orchestrated at the nanoscale level, and (3) adsorbed proteins and their aggregates are a few nanometers in dimension and their spatial patterning and deposition on surfaces influences cell biology.[17,18]

Physical cues of the extracellular space such as stiffness and topography are likely sensed by the cell's focal contact points, or focal adhesions. Selhuber-Unkel et al.[12] have shown that the spacing between gold nanopatterns on glass substrates

Y. Zhukova, Dr. J. W. C. Dunlop, Prof. P. Fratzl, Prof. E. V. Skorb
Department of Biomaterials
Max Planck Institute of Colloids and Interfaces
14476 Potsdam-Golm, Germany
E-mail: peter.fratzl@mpikg.mpg.de
Dr. C. Hiepen, Prof. P. Knaus
Institute for Chemistry and Biochemistry
Freie Universität Berlin
14195 Berlin, Germany

M. Osterland, Dr. S. Prohaska
Zuse Institute Berlin
14195 Berlin, Germany

M. Osterland
Institute for Mathematics
Freie Universität Berlin
14195 Berlin, Germany

Prof. E. V. Skorb
Laboratory of Solution Chemistry of Advanced Materials and Technologies
ITMO University
197101 St. Petersburg, Russian Federation

determines the strength of cell adhesion. These results suggest that cells sense small changes in adhesive signals and translate these into large changes in total cell strength. Oh et al.[14] showed that titania nanotube diameter can strongly alter the differentiation pathway of human mesenchymal stem cells.

Titanium is a common material used in dental and orthopaedic implants due to its inertness and high mechanical strength.[8] It is easy to integrate as an element of light-sensitive systems due to photoactivity of the titania layer.[19] A variety of surface modification strategies can be employed to titanium-based implants to enhance osseointegration.[20–23] Straightforward surface treatments of titanium and its alloys can be divided into three main groups: mechanical, chemical, and physical methods.[8,20] These methods are used either individually or in combination, and cause the formation of different nanotopographies. Major disadvantages of mechanical and physical methods include that they are expensive, time consuming, and difficult to apply for large-scale implant production.[24] By contrast, chemical treatments are attractive for large-scale manufacturing[8] because they provide uniform access of the reactive substance to all surfaces, which can be applied to multifaceted devices with complex geometries such as dental screws and cardiovascular stents. However, the majority of chemical methods modify not only topography, but also other surface features such as chemical composition,[25] wettability,[26] crystallinity,[27] and adsorption ability.[28] These surface observables can also modulate cell behavior[27,29–31] (for more information about surface modification strategies and cellular recognition of these surfaces see the review papers[32,33]) and it is difficult to distinguish which factor leads to the observed cell response.

In the studies[34,35] the nanotopography-induced osteogenic differentiation of the MC3T3-E1 cells is addressed. The corresponding analysis of the samples was performed at day 7 and day 4, respectively. The cells were also cultured in an osteogenic medium. First, in contrast to the mentioned studies, in our study we aim to investigate the effect of nanotopography alone on cell response in absence of any (bio)chemical factors. The focus of our investigation is the immediate/early response of cells just relying on the material surface topography. Therefore, the cells were cultivated in the absence of sufficient concentration of pro-osteogenic differentiation factors. Second, to understand the mechanism of the nanotopography–cells/tissue relationship, we generally propose to study cell response to nanotopography at different stages of tissue formation: starting from single cells to 3D tissue growth. For this purpose, in this study, we first provided the comprehensive investigation of the single cell response to nanotopography.

The important difference of our investigation to the study[36] is that the authors investigated the response of MC3T3-E1 cells on titanium micro-, but not nanotopography. The surface exhibited the combination of macro- (dimensions of about 10–50 µm) and microfeatures (0.5–3 µm). It has been shown that micro- and nanotopography induce very different cell responses. The scale sizing of the used materials in the mentioned study compared to the study shown here is therefore not comparable as is not the cellular response to be investigated. In contrast to microporous structuring, matrix deposition, protein absorption, and the cellular architecture at the cell–matrix interface are very different when cells are seeded on nanostructuring materials presented in this paper.

The papers of Karazisis et al.[37] and Freitas et al.[38] present the effect of Ti nanotopography on bone response by using the same method as Castro-Raucci et al.[34] and Kato et al.,[35] however applying an in vivo approach. The publication history of the articles[34,35] indicates that the studies are performed in a logical order: from in vitro to in vivo. We consider our research as a comprehensive study, investigating (i) cell response to the mesoporous titania (TMS) fabricated by the novel sonochemical treatment, and (ii) comparison between the cell responses to ordered and disordered surface nanotopography.

Moreover, in this study, high-intensity ultrasound treatment (HIUS) was used in combination with alkali-treatment to obtain controllable surface nanostructuring. This cost-effective[39] method allows for controllable modification of titanium with fast production of a mesoporous titania (TMS) layer. The major advantage of this technique is that the propagation of cavitation generates large local temperature gradients in solids, resulting in materials with compositional gradients[40] and nonequilibrium nanostructures at ambient conditions. Moreover, active OH-groups formed during the preparation procedure allow for an effective encapsulation of relevant bioactive molecules and formation of sponge-like structures.[41,42]

We have recently reported on the response of C2C12 mouse myoblast precursor cells, including their differentiation behavior, to mesoporous titania and titania nanotubes.[43] Titania nanotubes are a well-studied material,[44] produced by anodic oxidation which leads to the formation of TiO_2 nanotube arrays. We observed that the nanostructure of the material has an impact on the osteogenic differentiation, whereas it only moderately affects myogenic differentiation. Here, for the first time, we discuss cell migration characteristics of osteoblast-like MC3T3-E1 cells together with cell number, proliferation, and adhesion on titania of two different nanotopographies: disordered, mesoporous titania (TMS) and ordered titania nanotubes (TNTs).

2. Results and Discussion

2.1. Physicochemical Properties Analysis

To investigate the physicochemical properties of the titania-coated substrates, scanning electron microscopy (SEM), atomic force microscopy (AFM), and contact angle measurements were performed (**Figure 1**). The surface topography was examined using SEM. Figure 1A illustrates SEM of the titania surface nanotopographies produced by sonochemical treatment and anodic oxidation. The mesoporous titania (TMS) produced by HIUS is a disordered irregular porous TiO_2 layer. Anodization leads to the formation of TiO_2 nanotube (TNT) arrays with a regular pore diameter of ≈70 nm. As a control, either glass or untreated metal was used. A more detailed investigation of surface characteristics is shown in Kopf et al.[43] The surface roughness was quantified by AFM (Figure 1B,C). All surfaces possess nanoscale surface roughness. The arithmetic mean surface roughness (R_a) of the modified surfaces exhibited values of more than 20 nm for nanostructured surfaces and less than

ADVANCED
SCIENCE NEWS
www.advancedsciencenews.com

ADVANCED
HEALTHCARE
MATERIALS
www.advhealthmat.de
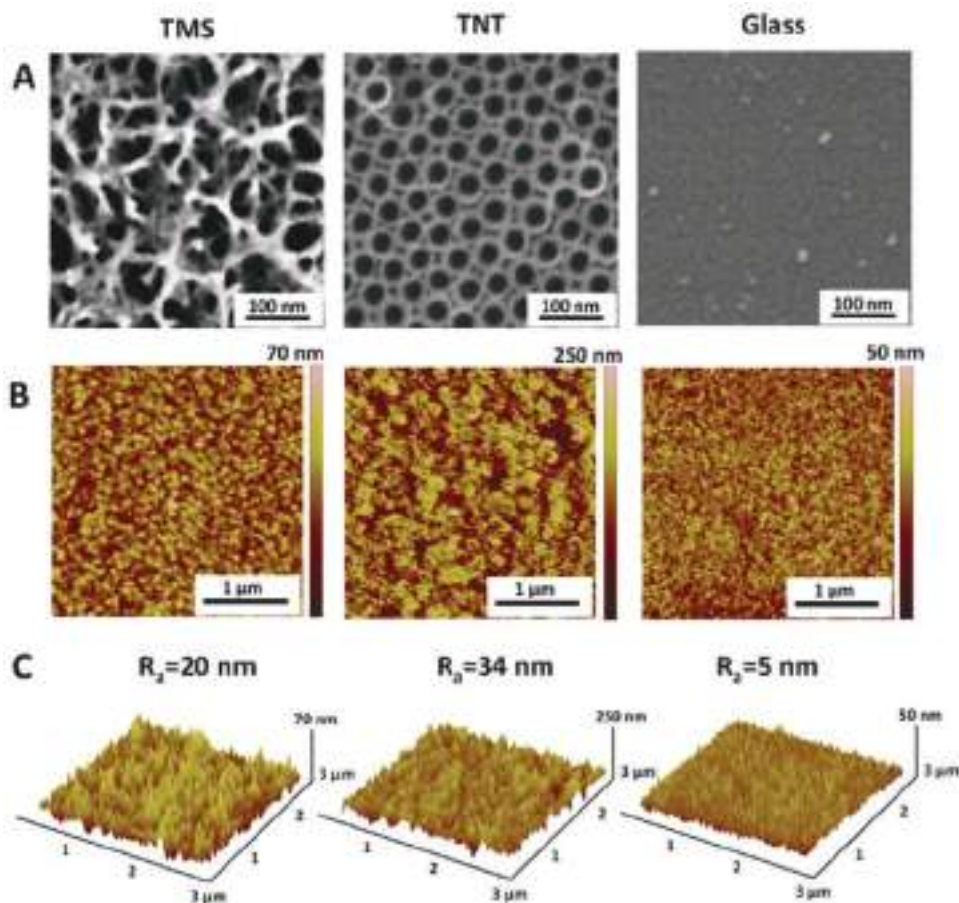
Figure 1. Physicochemical surface characterization. A) SEM images, B) AFM height images, and C) 3D roughness profiles of titania surfaces. SEM reveals disordered inhomogeneous pores of mesoporous titanium and vertically oriented pores of nanotubes with average diameter of ≈70 nm. TMS and TNT have average image roughness of ≈20 and 30 nm, respectively. The average image roughness (R_a) was calculated from images taken at three different locations on each surface.

5 nm for unmodified surfaces. The wettability of the surfaces was quantified by contact angle measurement (Figure S1, Supporting Information). All surfaces were determined to have contact angles of less than 65°, denoting hydrophilicity.[45] Both surface modifications showed very low contact angles, lower than 10°, thereby indicating their highly hydrophilic nature.

To estimate the level of nanotopography disorder, fast Fourier transform (FFT) was performed on SEM images of mesoporous and nanotubular titania surfaces (Figure S2, Supporting Information). For this purpose, the SEM images (Figure S2a,b, Supporting Information) were first binarized (Figure S2c,d, Supporting Information) and then FFT was performed twice (Figure S2e–h, Supporting Information), followed by the radial integration of the processed image. The final radial profile plot (Figure S2i, Supporting Information) depicts smooth and periodic plots for TMS and TNT, respectively. These data indicate an amorphous, disordered nature of TMS and periodic, ordered nature of TNT.

To determine the structure of titania films on the surface of nanostructured titanium, we used Raman spectroscopy. Figure S3 (Supporting Information) shows the Raman spectra of TMS and TNT surfaces heated at 450 °C. There are three bands (at 245, 449, and 612 cm^{-1}) in the spectrum of the TMS

and there are four bands (at 200, 399, 518, and 639 cm^{-1}) in the spectrum of TNT. The Raman spectra of TMS and TNT surfaces are in good agreement with the Raman spectra of rutile and anatase, respectively, available in literature.[46] Titanium dioxide occurs as two important polymorphs, the stable rutile and metastable anatase. This transition does not have a unique temperature; the reported transition temperatures vary in the range 400–1200 °C. Anatase transforms irreversibly to rutile at elevated temperatures. It is even possible to form rutile under near room temperature conditions. Since TMS surface is already partially crystalline after the HIUS treatment,[40] following temperature treatment results in transformation of anatase into rutile phase. TNT surfaces require the temperature treatment to undergo transformation from the amorphous to the crystalline anatase phase. Obtained results indicate that the rutile phase occurs in TMS surfaces whereas in TNT only an anatase modification of titanium oxide is present.

Thus, both nanostructured surfaces have comparable nanoscale surface roughness and high wettability, but different nanotopographies. Having found that the substrates are biocompatible with similar surface chemistry, we next aimed to determine the role of nanotopography in the modulation of cell behavior. Biological studies included investigation of cell

**ADVANCED
SCIENCE NEWS**
www.advancedsciencenews.com

**ADVANCED
HEALTHCARE
MATERIALS**
www.advhealthmat.de
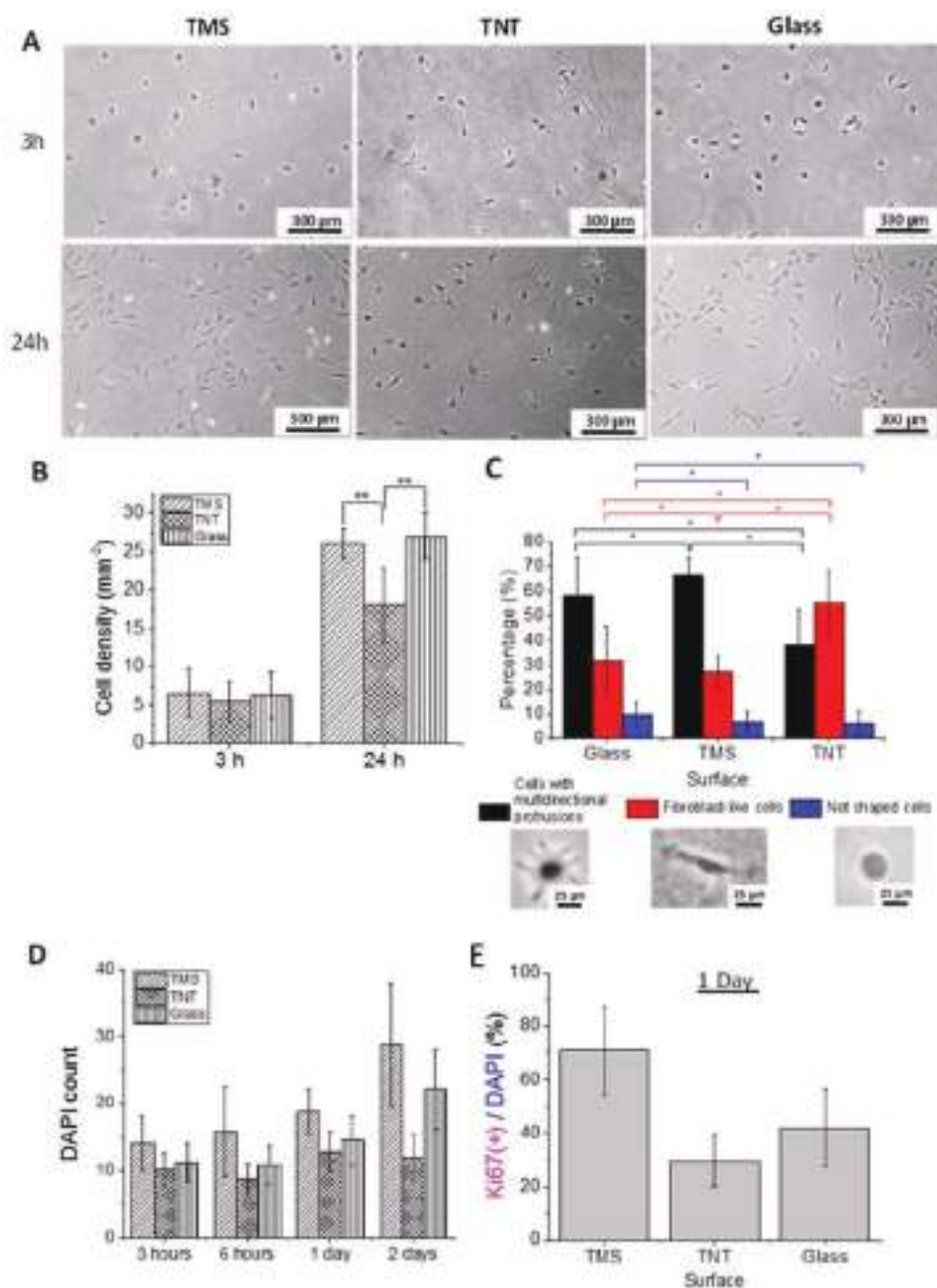
Figure 2. Cell proliferation analysis. A) Optical images of MC3T3-E1 cells after 3 and 24 h after seeding on titania surfaces. B) MC3T3-E1 cell densities on different substrates and C) analysis of MC3T3-E1 cell shape after 3 h. D,E) MC3T3-E1 cell proliferation estimated with the Ki67 assay. Error bars represent standard deviation. Three samples were tested per substrate type; three independent experiments were conducted. The Ki67 assay was performed once for all substrates in triplicates using the color deconvolution plugin of ImageJ. ** indicates $p < 0.01$; * indicates $p < 0.05$.

growth parameters such as proliferation, morphology, adhesion, and cell migration.

2.2. Cell Proliferation

To estimate MC3T3-E1 cell proliferation on surfaces, the density of adhered cells was calculated at 3 and 24 h after seeding (**Figure 2**). Figure 2A depicts that after 3 h, the seeded cells

populated TMS and glass surfaces with comparable densities, but fewer cells were present on TNT. Considering the density of cells after 3 and 24 h (Figure 2B), TNT surface slowed cell proliferation, whereas glass and TMS supported it. To validate this result by a biochemical technique, we performed Ki67 staining which indicates proliferative cells by appearance of the Ki67 protein in the nucleus of cells in G1, S, G2 or M-phase (Ki67(+)). 4′, 6-Diamidin-2-phenylindol (DAPI) counts and quantification of Ki67(+) cells are in line with the observations

ADVANCED
SCIENCE NEWS
www.advancedsciencenews.com

ADVANCED
HEALTHCARE
MATERIALS
www.advhealthmat.de

we gained by the light microscopical cell counting (Figure 2E). As previously described in Biggs et al.,[47] anchorage-dependent growth of preosteoblasts requires extracellular matrix (ECM) anchorage for efficient proliferation and differentiation. Thus, the inhibited cell proliferation could be caused by relatively weak cell adhesion to TNT, as compared to the other nanotopographies. Also, the deposition of cells endogenously produced ECM might be influenced by the hollow nature of TNT compared to TMS, which could act to trap and deposit endogenously secreted ECM proteins such as collagens and fibronectin in an inaccessible fashion for the cell to sense and adhere to. To further confirm this suggestion, we performed experiments investigating cell adhesion, described in Section 2.4.

2.3. Cell Morphology

In addition to the different cell densities, we found distinct cell morphologies on the different surfaces (Figure 2C). Three distinct cell morphologies were apparent: (1) cells with multidirectional protrusions, indicating protrusive cell behavior in all directions, (2) elongated cells with a fibroblast-like morphology displaying a distinct leading edge and retracting tail, indicating strong motile behavior, and (3) rounded cells which are attached but have not begun to spread, suggesting only mild, if any, establishment of mature focal contact points with the substratum. All three types of morphologies are seen on all substrates, but in different proportions. The majority (>50%) of cells grown on TNT are elongated; however, by contrast, cells on TMS have mainly star-like shapes (>60%) indicating the formation of actin-driven cellular processes such as lamellipodial and filopodial protrusions. On each of the three substrate types, up to 10% of cells are rounded. Taken together, the results indicate that cell density and shape at 3 h after seeding are indeed not uniform on the different substrates, thereby providing evidence of nanotopography-induced modulation of immediate-early cell attachment, spreading and formation of cellular processes. Differences in cell morphology become more pronounced with the time of cell incubation, increase of elongated cells on TNT and cells with multidirectional protrusions on TMS is seen upon incubation with substrates for 24 h.

To further verify the effect of nanotopography on cell morphology, we next performed immunocytochemical staining of the filamentous actin (F-actin) cytoskeleton. Investigation of F-actin structure and architecture further confirms the nanotopographic effects on cell shape and spreading. The fluorescence images in **Figure 3** illustrate the evolution of cell morphology over the time course of 3 h, 24 h, and 5 d after cell seeding. After 3 h (Figure 3A), adherent cells displayed a rounded or polygonal shape on glass and TMS, which is commonly described as a cobblestone-like morphology and often seen in resting bone progenitors, and a fibroblast-like shape on TNT, indicating the formation of unidirectional cellular protrusions such as lamellipodia which is required for the establishment of planar cell polarity.[48] Polarization and protrusion formation was more obvious on TNT compared to the other two substrates and is a hallmark of highly motile cells. After 24 h (Figure 3C), the adherent cells on all substrates exhibited a polygonal shape. However, cells on TNT were more elongated,

less spread along all axes of the cell body, but still possessed more cellular protrusions within the cells leading edge. Actin stress fibers tended to coalign in a parallel fashion in cells seeded on glass and TMS, whereas on TNT they aligned in the direction of cell protrusion and perpendicular to the leading edge, indicating a nonuniform F-actin alignment of the leading edge (Figure 3B). Moreover, the cell nuclei on TNT also underwent elongation, whereas the nuclei of cells on glass and TMS remained regular (Figure 3C, insets). To quantify the cell and nuclear elongation, the shape index, or circularity, of each individual cell and nucleus determining cellular (cell area factor) and nuclear elongation (nuclear area factor), respectively, was calculated using the built-in functions of the ImageJ software (Figure 3G,H). As the circularity value approaches 0, it indicates an increasingly elongated shape; the shape index of 1 indicates a perfect circle. The cell area factor of the preosteoblasts is below 0.4, indicating development of polygonal cell shape on all substrates. The nuclear area factor of preosteoblasts on TMS and glass substrates is in the range 0.7–0.9, indicating circular nuclear shape on these substrates. On TNT, the Nuclear Shape Factor is lower than on TMS and TNT and is in the range 0.5–0.65, indicating nuclear elongation. In line with the previous observations of cell morphology, we suggest a more active migratory behavior of cells populating TNT surfaces since nuclear localization and elongation follows cell spreading and protrusion formation.

To further investigate cell morphology, we next performed SEM of adherent cells (Figure S4, Supporting Information). SEM images confirmed the morphological observations of MC3T3-E1 cells cultured on substrates after 24 h. After 24 h of cell adhesion, two cell morphologies could be observed: spread (TMS) and elongated (TNT). Whereas cells on TMS display strong spreading morphology and multidirectional protrusions, cells seeded on TNT show an elongated morphology with clear unidirectional protrusion formation. The high density of the cells after 5 d in culture (Figure 3D) did not allow for accurate observation of their morphology. However, according to the calculated number of cell nuclei (Figure 3E), the cell density at this time-point followed the order: TMS > TNT. Whereas the densities of cell layers on glass and TMS were comparable, it was still possible to observe actin fibers and cell protrusions of single cells on TNT surfaces. Such low densities are presumably caused by the lower proliferation rate on TNT, as described above along with their elongated morphology. Additionally, cell height measured by confocal laser scanning microscopy after 3 h also differed between the substrates (Figure 3F), which may also contribute to cell density at later stages. The cells on glass are more flat than on nanostructured titania surfaces. Surprisingly, cells on TNT had a height comparable to the thickness on glass of ≈20 μm, while cells on TMS had the highest thickness of ≈40 μm.

The results indicate that preosteoblasts tend to have a specific morphology, height, and shape on each substrate, thereby indicating nanotopography-induced modulation of cell morphology. Notably, this observation was seen at different time points of cell adhesion: after 3 h, 24 h, and 5 d. Already after 3 h, cells cultured on glass and TMS possessed numerous multidirectional protrusions which developed homogeneously along the cell periphery. Cellular protrusions such as filopodia

ADVANCED
SCIENCE NEWS
www.advancedsciencenews.com

ADVANCED
HEALTHCARE
MATERIALS
www.advhealthmat.de
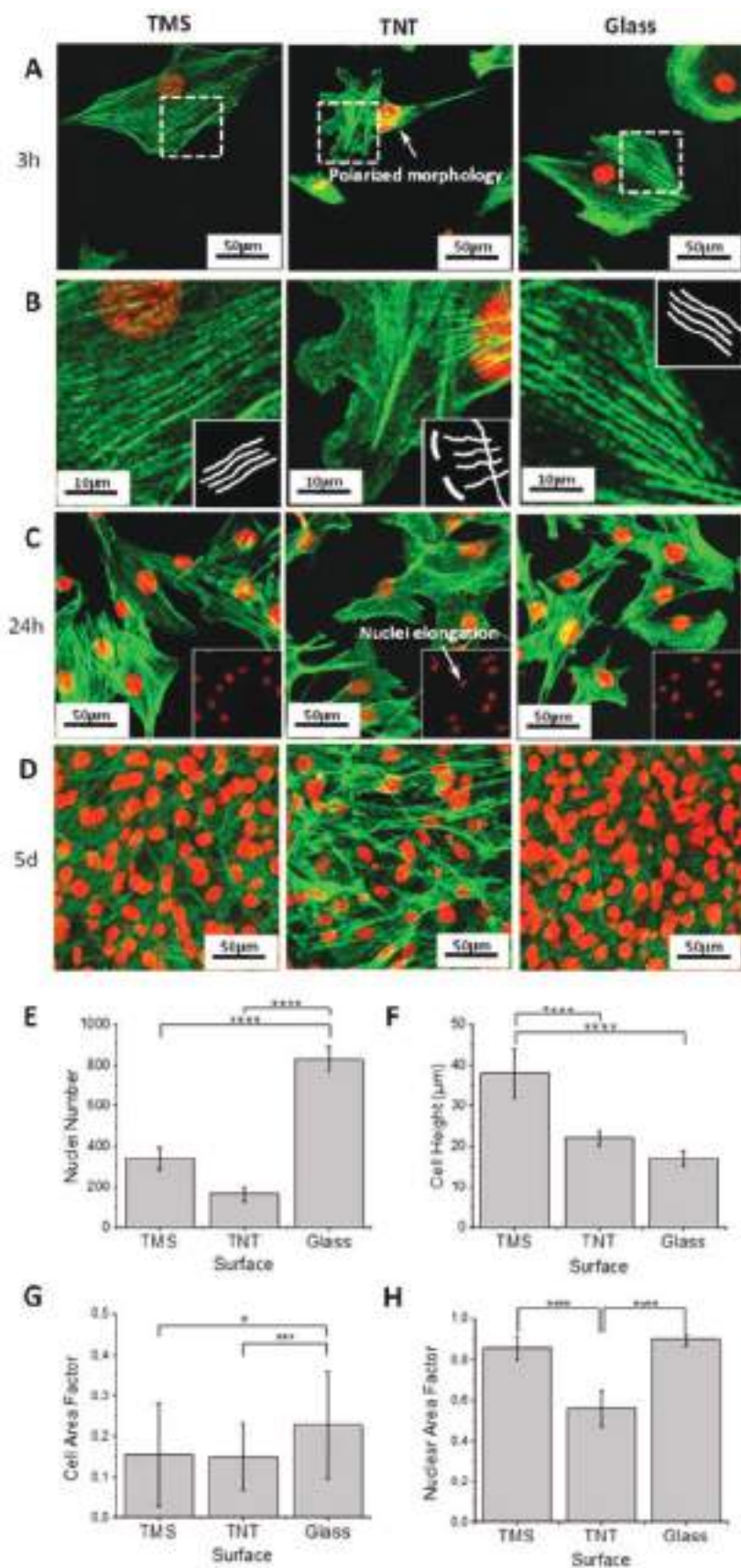
and lamellipodia are actin-rich protrusions which allow cells to probe their surface while searching for locations to make focal contacts.[16] A continuous "treadmilling-like" stabilization and destabilization of these focal contact points within cellular protrusions is a prerequisite for cellular migration.[49] Consistent with previous studies,[49] cells cultured on TNT possessed polarized morphologies, characteristic of migrating cells: a leading edge, consisting of the lamellipodium and filopodia protrusions, and a trailing edge. The fibroblast-morphology-like cell spreading on TNT surfaces and the structure of the F-actin fibers is also supporting the idea of transient adhesion formation near the leading edge and rear ends of the cells (nascent adhesion), while more mature and long lasting focal adhesion formation may appear on TMS and glass. One plausible explanation for these differences is the distribution and deposition of adsorbed proteins,[50] which can also be modulated by nanotopography. Several studies reported elongated cell morphology on TNTs of similar dimensions[48] and fibroblast-like shape on nanotextured titania produced by etching and other methods.[51–53] These cellular behaviors are considered to be related to the size of the cell–surface contact[54] and to the amount of adsorbed proteins which can be recognized by integrin transmembrane receptors. In this study, the diameter of the nanotubes was ≈70 nm, which was reported to prevent integrin clustering.[48] Such spacing provided a distribution of binding sites which was ineffective for focal contact formation and the cells had to extend their filopodia in order to find more adsorbed proteins.[55,56] In contrast to the TNT surfaces, the cells on disordered TMS substrates had relatively uniform access to adsorbed proteins due to the homogeneous localization of proteins on the surface. When anchored, filopodia converts to the flat membrane protrusions called lamellipodia.[57]

Figure 3. Cell morphology analysis. Actin (green) and cell nucleus (red) fluorescence images of MC3T3-E1 cells cultured on titania surfaces for A) 3 h, C) 24 h, and D) 5 d. B) Offsets on actin alignment. E) Number of cell nuclei calculated after 5 d of tissue growth. F) Cell thickness measured by the confocal laser scanning microscopy after 3 h of growth. G) Cell area factor and H) nuclear area factor evaluated using built-in functions of NIH ImageJ software, with a shape index of 1 representing a circle. **** indicates $p < 0.001$; *** indicates $p < 0.005$; * indicates $p < 0.05$.

ADVANCED
SCIENCE NEWS
www.advancedsciencenews.com

ADVANCED
HEALTHCARE
MATERIALS
www.advhealthmat.de

Figure 4. A) Cell adhesion analysis. Confocal microscopy images with actin (green) and vinculin (red) staining showing MC3T3-E1 cell adhesion on substrates after 3 h. B) Magnified images of focal contact points. C) Colocalization analysis of focal contact points (B) as reflected by profile plots. D) Average cell area and E) average number of vinculin adhesion plaques per cell at 3 h. Error bars represent standard deviation (±SD). Three samples were tested per substrate type; three independent experiments were conducted. * indicates $p < 0.05$.

Figure 3 shows an example of a lamellipodial cell shape developing on TNT, indicating strongly migrating cells with fewer mature focal contact points on TNT than on TMS.

2.4. Cell Adhesion

To further investigate the role of surface nanotopography in modulation of cell adhesion formation, we next aimed at characterizing the colocalization of bundled F-actin with the pan-focal adhesion marker protein vinculin. Mature and long-lasting focal adhesions with a slow turn-over are usually physically linked to large, readily visualized actomyosin bundles.[58,59] For this purpose, MC3T3-E1 cells cultured for 3 h on glass or nanostructured titanium substrates, were examined by confocal laser scanning microscopy (**Figure 4**). Figure 4A presents the images of double-stained MC3T3-E1 cells, where the green and red colors indicate F-actin fibers (stained with phalloidin Alexa488) and vinculin (stained with antivinculin antibody coupled to Alexa594), respectively.

The images of single cells in Figure 4A,B illustrate the focal contact points of MC3T3-E1 cells after 3 h of adhesion. In line with our previous observations, cells on TMS surfaces are well-spread into multiple directions; one can easily observe a large amount of actin fibers spreading in multiple directions. In contrast, cells attached to TNT are less spread and begin to form a more elongated morphology with cellular protrusions and polarization; actin stress fibers tend to align with each other in the direction of cell protrusion suggesting a motile state. Moreover, we observed a high degree of colocalization (Figure 4B,C) of dense actin bundles within the focal contact points in cells on TMS, but to a lesser extent on TNT. This colocalization of vinculin with bundles of F-actin in cells

ADVANCED
SCIENCE NEWS
www.advancedsciencenews.com

ADVANCED
HEALTHCARE
MATERIALS
www.advhealthmat.de

seeded on TMS suggests that there is more stable actin cable bundling within the focal contact points, indicating mature adhesions forming on TMS, in contrast to nascent adhesions of migrating cells on TNT.

To study cell adhesion to the substrates, various parameters were quantified such as cell area (Figure 4D) and the number of vinculin-positive plaques per cell (Figure 4E). The surface nano-topography had an influence on cell spreading, where 3 h after cell seeding, the cell-spreading area was significantly higher on TMS compared to the other surfaces (Figure 4D). TNT showed the lowest level of cell spreading. It was also evident that surface nanotopography had an influence on focal contact formation. Although the average area of one focal complex was for all surfaces in the range of $3 \pm 2 \ \mu m^2$ (data not shown), the number of vinculin-positive plaques was significantly higher on glass samples compared to TMS and TNT (Figure 4E).

Notably, although the overall number of vinculin-rich plaques per cell was rather low on both nanostructured surfaces in comparison to glass, TMS performance in cell attachment and morphology was still more favorable than TNT. A plausible explanation for this is that not only number and area of focal adhesions, but also their localization determines the strength of cell adhesion. In the case of glass and TMS, focal adhesions were localized regularly along the cell periphery, whereas on TNT cells were forming adhesion contacts only in proximity to the polarized cell protrusions. These observations are in good agreement with the estimation of cell morphology (Figure 2D), where the majority of MC3T3-E1 cells prefer to develop multidirectional protrusions on TMS (≈65%) but unidirectional protrusions on TNT (≈55%). Moreover, analysis of the colocalization of bundled F-actin (as indicated by Phalloidin-staining in green) with vinculin-rich focal contact points (red) suggests a stable accumulation of bundled F-actin with focal contact points on TMS and glass surfaces, but a rather metastable accumulation in focal contact points on TNT. It is well-known that mature and persistent cell adhesions are rich in bundled F-actin, as is the case for the TMS substrate, since the F-actin cytoskeleton couples to focal contact points only when they are stable and undergoing a slow turnover (or destabilization). By contrast, the lower amount of bundled F-actin in the focal contact points on TNT, and presumably shorter-lasting colocalization, indicates a higher turnover rate of cell adhesions, characteristic of migrating and motile cells.

The directionality of the F-actin bundles indicates different directions in cell traction forces generated on the different substrates. Here the directionality of F-actin bundles on glass and TMS is multidirectional, thereby allowing effective cell spreading. On TNT, stress fibers tend to align and orient with the length of the cell body, leading to polarization and elongation. The cytoskeletal stresses might also be directly transduced into nuclear function,[60] thereby leading to nuclei elongation on TNT.

Interestingly, compared to TMS, the glass substrate induces stronger cell attachment and a higher number of focal contacts, but weaker cell spreading. The distribution of adsorbed extracellular matrix proteins on glass seems to be different due to several reasons: surface roughness, surface area, surface geometry, and surface chemistry. Although it is still hydrophilic, glass has a significantly higher contact angle and lower surface

roughness than of the TMS. Previous studies reported that very hydrophilic substrates ($\theta < 35°$) inhibit the adsorption of serum proteins, causing lower spreading and attachment of human fibroblasts in contrast to the surfaces with moderately wettable surfaces (i.e., $\theta = 48°–62°$).[29]

Similar to our findings, multiple studies report weak cell attachment on TNT. These observations are also in line with the cell behavior observed on other ordered regular nanofeatures such as nanoposts[61] and nanopits.[62–64] The feature sizes described in these studies are in the range of 80–300 nm and higher, which is over a density threshold corresponding to a spacing of integrin-adhesive RGD ligands per unit area, which is ≈70 nm.[13,65] Some common effects of ordered nanotopographies with feature sizes exceeding 70 nm on cells include (1) reduced area of adhesion complexes, (2) increased filopodia, (3) biased orientation, and (4) constant traction forces. By contrast, increased adhesion has been reported on random nanoposts.[66] Taken together, the level of nanotopography (dis)order may have different implications for cell proliferation, morphology, and adhesion.

2.5. Cell Migration

Cellular morphology, adhesion strength, and persistence impact the dynamics of cellular motility. To further verify the effect of nanotopography on cell behavior, we asked whether it also affects cell migration. To our knowledge this is the first study to report in vitro migration of MC3T3-E1 cells on mesoporous and nanotubular titania. For this purpose, a quantitative wound healing assay using live cell microscopy was performed (**Figure 5**). Quantitative wound healing allows for measurements of the speed, dynamics, and single versus collective migratory behavior of cells populating a cell-free space on a given substrate. This mode of cellular behavior is critically important for regenerative processes in vivo, as it indicates how fast and to what degree a cell-free implant will be populated by cells contributing to the repair process.

Within 16 h of observation time, cells migrated toward the cell-free space (Figure 5A), and the overall wound closure on all three surfaces was in the range of 45%–55%. We performed a software-assisted analysis of the dynamic migratory behavior of cells on different substrates which gains insights into the dynamics of cell migration and is often applied when solely end-point measurements do not show significant differences. The trajectories of cells located within the cell-free gap are shown in Figure 5B. The analysis included dynamic investigation of mean migration speed (velocity) (Figure 5C) and mean number of neighbors (Figure 5D). The computer analysis revealed differences between the substrates in mean cellular migration speed and mean number of neighbors. The values of the mean migration speed follow the order: TNT > TMS > glass, which is inverse to the number of vinculin adhesion plaques per cell (Figure 4D). The mean speed decreases with time for all surfaces, most likely due to the decrease in the cell-free gap area. The ability of cells to migrate is a response that is coupled to cell adhesion,[65] where stronger cell adhesion coincides with a less migratory behavior displayed by the cells. Vinculin is necessary for binding cell surface integrin receptors to the ECM

ADVANCED
SCIENCE NEWS
www.advancedsciencenews.com

ADVANCED
HEALTHCARE
MATERIALS
www.advhealthmat.de
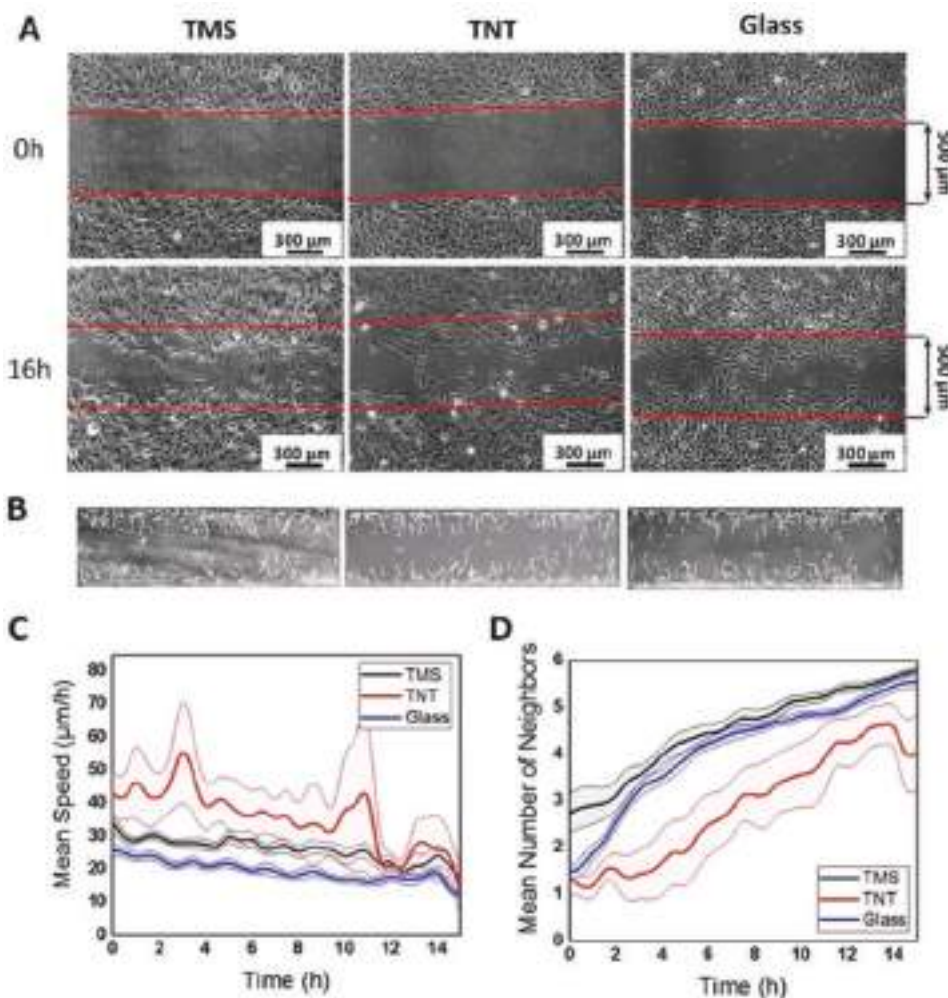
Figure 5. Cell migration analysis. A) Wound healing assay of MC3T3-E1 preosteoblast cell line on titania surfaces in presence of the proliferation-inhibiting factor Mitomycin C (10 µg mL^{-1}). α-MEM cell culture medium was supplemented with 10% FCS. Live cell imaging was monitored for 16 h. B) Cell trajectories within cell-free gap. C) Mean migration speed. Line in bold depicts the mean value, highlighted area depicts standard error of the mean (±SEM). D) Neighborhood analysis of migrating cells: the mean number of neighboring cells for each time step. Shown is the mean over three independent experiments for each substrate group (glass, TMS, TNT). A) and B) represent single experiments.

adhesion molecules, which in part controls the process of cell spreading and movement. It has been shown previously that regular nanotopography reduces cell adhesion very markedly.[66] Dalby et al.[67] showed that nanoislands caused fibroblast adhesions to be smaller and less pronounced in comparison to large dash-like adhesions on flat substrates. Moreover, such features as ruffled lamellipodial protrusions and low number of bundled long stress fibers are indicative of motile cells. It has been suggested that the structure of F-actin can serve as an indicator of more motile cells, as focal adhesion turnover (the process of forming and disassembling focal adhesions) is required for migration. Similar results were reported by Brammer et al.,[68] where small dot-like adhesions were observed on TiO$_2$ nanotubes compared to large dashed-like adhesions on flat titanium. Moreover, the cells cultured on TMS and glass here have a higher number of neighboring cells (Figure 5C) which corresponds well to the cell area (Figure 4C).

Cell migration and cell differentiation are two competing processes. Therefore, we expect the lowest alkaline phosphatase

level expression on TNT, since the cells on TNT have the strongest migratory behavior (highest migration speed), which requires more cytoskeletal transformation. We have performed the differentiation assay on early stages of MC3T3-E1 cell growth. However, we were not successful in obtaining enough RNA for qRT-PCR studies because the number of cells on surfaces at early time points was too low (Figure S5, Supporting Information). Note that in our study design, we were mostly concentrated at the investigation of single cell response to nanotopography at the early-stage of cell attachment (at 3 h). At 24 h, it is difficult to draw the (quantitative) conclusions on the nanotopography-mediated cell behavior (expressed in changes in cell adhesion and morphology) since the cell layer is to 80%–90% confluent. Moreover, we have shown the strong differences of the morphologies, developed by preosteoblasts cultured for 24 h on different substrates (Figure S4, Supporting Information).

Figure 6 depicts the cell–nanotopography interactions and corresponding effects on cell migratory behavior depending

**ADVANCED
SCIENCE NEWS**
www.advancedsciencenews.com

**ADVANCED
HEALTHCARE
MATERIALS**
www.advhealthmat.de
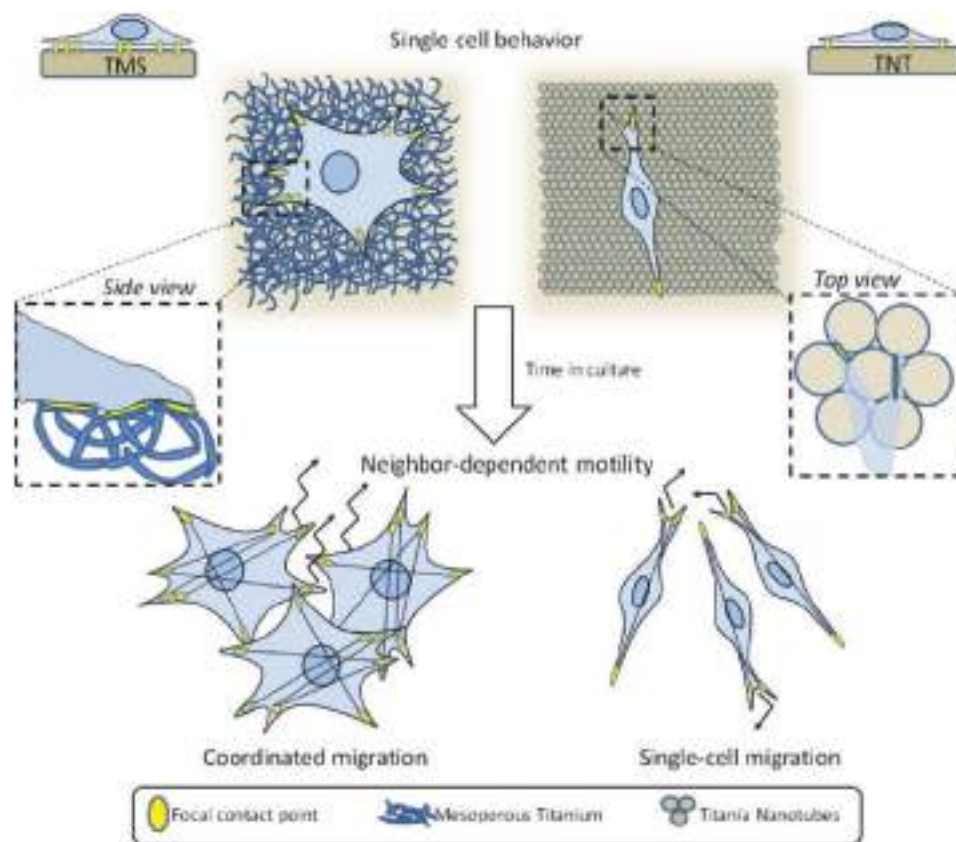
Figure 6. Cell behavior on mesoporous and nanotubular titania surfaces. Upper part depicts architecture of the cellular adhesion site formation of single MC3T3-E1 cells to TMS (left enlargement, side view) and TNT (right enlargement, top view) surfaces, respectively. Lower part depicts consequences of adhesion site architecture and corresponding cellular morphology for cell migration of neighboring cells on surfaces. Star-like cell morphology with multiple focal contact points in randomly organized cellular protrusions of cells seeded on TMS translates into a more coordinated cell migratory behavior, possibly due to a higher frequency in cell–cell interactions via cellular protrusions (left side, trajectories indicate coordinated migration). Fibroblast-like cell shape with fewer focal contact points restricted to the polarized front- and rear-ends of the cells seeded on TNT translates toward a more random single cell migratory behavior (left side), possibly due to a lower frequency of spontaneous cell–cell interaction events compared to cells seeded on TMS.

on surface (dis)order: disordered TMS compared to ordered TNT topographies. Cells cultured on TMS are larger and more spread, therefore having more opportunities to form cell–cell contacts. It was shown that cells can adopt different modes of migration, either independently as single cells, or in close proximity and therefore communicating with their neighboring cells and forming close cell–cell contacts.[69] In comparison to single cell migration (as on TNT), collective cell migration (as on TMS) is thought to support "supracellular" properties, such as collective polarization, force generation, decision making, and, eventually, complex tissue organization.

3. Conclusion

Early cell behavior critically influencing material cellularization in longer term. The effect of nanotopography on cell attachment and morphology at early stages influences the cell density at later stages, indicative of distinct cellular proliferation rates and migration speeds on the substrate. This study compares the effect of ordered (TNT) and disordered titania

(TMS) nanotopographies on early MC3T3-E1 behavior critically influencing material cellularization. We have shown here that different surface nanotopographies distinctly affect cell proliferation, morphology, adhesion, and migration. Cell morphology is affected by surface nanotopography, where cells display a polygonal cell shape and spreading on TMS surfaces and an elongated, polarized shape (with elongated cell nuclei) on TNT surfaces. Substrate nanotopography defines cell attachment, as cells can form more stable and persistent focal contact points on TMS; in contrast, focal contact point turnover is likely to be increased in cells on TNT, indicative of more motile cells. On the other hand, cells formed more vinculin-rich adhesion points on control than either nanostructured surfaces. Reduced cellular adhesions on the nanostructured surfaces may have different reasons: an unfavorable density and localization of adsorbed protein prevents integrin clustering in the case of TNT, or very low contact angles in the case of TMS. Simultaneously, the mean migration speed correlates inversely with the amount of cell adhesion, with the highest speed measured on the TNT surfaces. Mean number of neighboring cells correlates with the cell area, where cells are larger and more spread on

1601244 (10 of 13)

TMS than the elongated cells on TNT. The results of this study indicate that preosteoblasts respond differently on ordered and disordered nanotopography with altered morphology, adhesion, and migration. Future use of titanium-nanostructured surfaces in tissue applications demands an appropriate analysis of cellular function requirements, and informs biomaterial decision-making.

4. Experimental Section

Production of Nanostructured Surfaces: For the production of mesoporous titania (TMS) samples, a titanium layer (99.9%) of thickness 400 nm was deposited on glass substrates by means of electron beam physical vapor deposition method (EB-PVD). TMS were obtained by sonochemical treatment with high intensity ultrasound (HIUS) in alkali solution. The size of each substrate was ≈1 × 1 cm^2 to fit the homemade Teflon sample holder used for HIUS. Prior to sonication, the metal plates were degreased with isopropanol and rinsed with Milli-Q water (18 MΩ cm). Titanium plates were ultrasonically treated in the presence of 5 M NaOH using the ultrasonic processor UIP1000hd (Hielscher Ultrasonics GmbH, Germany) with a maximum output power of 1000 W. The apparatus was equipped with a sonotrode BS2d18 (head area 2.5 cm^2) and booster B2-2.2, magnifying the working amplitude 2.2 times. Sonication was performed at 20 kHz and a constant temperature of 333 K monitored by the thermosensor inserted into the working solution.

For the production of TNTs, a titanium layer (99.9%) of thickness 400 nm was deposited on ITO-coated glass substrates by means of the EB-PVD method. TNTs were obtained by electrochemical oxidation. For their preparation, the Ti–ITO–glass samples were anodized in an aqueous solution of ethylene glycol (2 vol% water) containing 0.75 wt% NH$_4$F. At the beginning of the anodization, the potential was linearly increased from 0 to 40 V over a period of 5 min, then the anodization was performed using the potentiostatic (40 V) mode until the total oxidation of a titanium layer on ITO.

All samples were additionally rinsed with ethanol and water and heat treated at 450 °C in the oven for at least 3 h. Bulk titanium or its alloys, although very tough, was used for modification. In the experiments with cell studies it was advantageous to prepare a nanoscale-thick Ti layer on a glass substrate rather than bulk titanium, since the optical observation of cell growth required transparent samples. After thermal treatment, the titania layer on glass was transparent enough to observe cell adhesion and growth on the surface. As a model, a 400 nm deposited layer was use on glass or on silicon for further atomic force microscopy studies.

Milli-Q water was used in all aqueous solutions. As a control, glass substrates were used.

Physicochemical Properties Analysis: The specimen surface nanotopography was inspected by SEM (Gemini Leo 1550 instrument, Leo Elektronenmikroskopie GmbH, Germany) at an operating voltage of 3 keV. Surface roughness (R_a) and 3D roughness profiles of the surfaces were obtained with AFM (Dimension, Bruker, Germany) and image analysis was performed with the Nanoscope V614r1 software. AFM measurements were carried out in air at room temperature in tapping mode with micro cantilevers OMCL-AC160TS-W (Olympus, Japan). Typical cantilever values: resonant frequency 300 kHz; spring constant 42 N m^{-1}. Atomic force images of a scan size 3 × 3 μm were made on three different locations on the same sample. Contact angles were measured using the homemade system described previously.[70] Raman measurements were performed using a confocal Raman microscope (alpha300, WITec) with a wavelength of 532 nm.

Cell Culture Model: A mouse calvarial preosteoblast cell line MC3T3-E1 was obtained from Ludwig Boltzmann Institute, Vienna, Austria. Preosteoblasts were maintained in normal culture medium α-MEM, supplemented with 10 vol% fetal calf serum (FCS), 4500 mg glucose, 0.1 vol% gentamycin, and 0.1 vol% ascorbic acid under standard culture condition (37 °C, 5% CO$_2$ in a humidified atmosphere).

Cells were passaged in total three times every 24 h by a dilution factor of 1/6. The medium was refreshed every 48 h. After reaching confluence, cells were detached from culture vessels by incubating with pronase for 3–5 min. All surfaces and scaffolds were autoclaved before cell culture experiments.

Cell Attachment: Up to 30 optical images of each sample were acquired after 3 and 24 h of growth with the phase contrast microscope (Nikon Eclipse TS100, Japan) equipped with a digital camera (Nikon Digital sight DS 2Mv). The statistical analysis of the cell attachment on different substrates was obtained using image analysis software ImageJ (version 1.47). The threshold was set between 30 and 40 (out of 255). The software automatically detects the cell outline and calculates parameters such as the number of cells per unit area (cell density [cells mm^{-2}]) and cell area per unit area of the substrate (cell coverage [%]).[71,72]

Cell Proliferation: MC3T3-E1 cells were seeded onto the biomaterial surfaces at the density of 6000 cells cm^{-2} with α-MEM medium (Invitrogen) containing 10% FCS. Cells were fixed in 4% paraformaldehyde (PFA) at the respective time points (3 h, 6 h, 1 d, and 2 d), permeabilized with 0.5% Triton-X (Sigma) in phosphate-buffered saline (PBS) for 5 min, and blocked with PBS containing 3% Normal Goat Serum (Sigma) and 2% bovine serum albumin (BSA) (Sigma) for 1 h. Cells were then washed once with TBS-T buffer. Ki67 protein was stained with primary mouse monoclonal Ki67 antibody (BD Biosciences) incubation overnight in PBS (1:100). Cells were washed three times with TBS-T, and the primary antibody was detected using a secondary antibody goat antimouse Alexa 594 (1:600) (Thermofisher). Cells were washed three times with TBS-T, and the counterstaining of nuclei was performed with DAPI (1:1000) for 5 min.

Microscopy was performed by taking five images at 40× magnification per sample. ImageJ Color deconvolution plugin was used to quantify the number of Ki67(+) nuclei normalized to the total number of DAPI positive nuclei.

Cell Morphology: Morphologies of MC3T3-E1 cells cultured on various surfaces were observed by confocal laser scanning microscopy (CLSM) and SEM. The cells were seeded onto surfaces at a density of 6000 cells cm^{-2}. Normal culture medium and standard conditions were employed. At respective time points after seeding, the cells were washed twice with PBS. To prepare samples for CLSM observation, the cells were fixed with 4% paraformaldehyde in PBS and permeabilized with buffered Triton-X100 (Sigma-Aldrich, Steinheim, Germany) for 10 min at room temperature. The scaffolds were then thoroughly washed with PBS and stained for 60–90 min with phalloidin Alexa488 (Invitrogen, Oregon, USA) (1:20) in the dark at 4 °C for cytoskeletal filamentous F-actin. Scaffolds were then thoroughly washed with PBS again and stained for nuclei with TO-PRO3 iodide (Invitrogen, Oregon, USA) (1:300) for 5 min at room temperature. The scaffolds were washed with PBS, mounted with Fluoro-Mount in an inverted position on the glass slides, and examined via confocal microscopy (Leica Microsystems, Mannheim, Germany).

To prepare samples for SEM observation, the cells were fixed twice: primary fixation with 2.5% glutaraldehyde (in PBS) for 30 min and secondary fixation with 4% PFA for 20 min. Then the cells were dehydrated using gradient ethanol solutions (25%, 50%, 75%, 90%, and 100%), each for 5 min. The treated samples were dried overnight in a desiccator, sputter-coated with gold, and observed using SEM.

Cell Adhesion: MC3T3-E1 cells were seeded onto surfaces maintaining the seeding density and culture method as described above. Cell adhesion was evaluated by immunofluorescent staining of focal contacts. At 3 h after seeding, cells were fixed with 4% paraformaldehyde in PBS, quenched for 5 min in 50 × 10^{-3} M ammonium chloride and permeabilized with buffered Triton-X-100 solution for 10 min. Specimens were then thoroughly washed with PBS and blocked in 3% BSA (in PBS) for 1 h. Afterward, the samples were incubated overnight with antivinculin antibody (Sigma V9131) (1:300 in PBS/BSA). After washing with PBS, samples were incubated with secondary goat antimouse antibody Alexa594 (Invitrogen) (1:300) for 1 h. After washing, samples were stained for 20 min with phalloidin Alexa488 (Invitrogen) (1:100).

The staining was performed at room temperature, except for the incubation with antivinculin antibody overnight at 4 °C. The stained samples were mounted with Fluoro-Mount in an inverted position on thin glass slides and examined via confocal microscopy. Imaging was conducted by using a Leica confocal laser scanning microscope (Leica Microsystems, Mannheim, Germany). The samples were excited with the argon laser line at 488 nm and 594 nm for Phalloidin Alexa488 (actin stain) and Alexa594 (focal contacts stain), respectively. The images were captured with a PL FLUOTAR objective.

Cell Migration: In order to investigate migration characteristics of MC3T3-E1 cells, a wound healing assay was performed using ibidi culture-inserts (Ibidi GmbH, Germany) according to the manufacturer's instructions. MC3T3-E1 cells were seeded to become confluent in 10 % FCS α-MEM. 1 h prior to insert removal, cells were incubated with 10 µg mL^{-1} mitomycin C to block cell proliferation. After insert removal, the wound closure was allowed to proceed and imaged by phase contrast microscopy. Pictures were taken using a 5× objective in bright field modus every 30 min for at least 16 h. Live cell imaging was performed within a heat and CO_2 controlled live cell imaging chamber (ibidi GmbH) using an automated sample table mounted on an Axiovert 200 M (Carl Zeiss, Jena, Germany) in combination with Axiovision Mark&Find tool.

The cell migration analysis was performed with an automatic algorithm originally developed for cell migration analysis in chemotaxis assays. This approach allowed for estimating migration characteristics such as mean migration speed, neighborhood analysis, and could distinguish between directed and random migration without a favored direction. In brief, the automatic tracking algorithm included two main steps: segmentation and tracking. First, the dense optical flow was computed to segment the foreground of the cells. The cell nuclei were roughly segmented by an adaptive inverse threshold, and the cell bodies were approximated from the nuclei via watershed segmentation on the foreground mask. Thus, the position and the neighborhood were computed for each cell at each time point in the time-lapse data. The neighborhood is defined here as cells with adjacent Voronoi areas. The trajectories were computed by an overlap heuristic on the nuclei mask. The analysis was restricted on cells close to the scratch area.

Gene Expression Analysis: qRT PCR cells were seeded on the different titanium surfaces and grown certain time. Cells were subsequently starved in medium with or without 30×10^{-9} M BMP2 (osteogenic differentiation). After stimulation, cells were harvested and total RNA was isolated using NucleoSpin isolation kit (Macherey&Nagel, Germany). 500 ng of RNA was subjected to reverse transcription. qRT PCR was performed using a SybrGreen-based detection system (Power SYBR Green PCR Master Mix, Life Technologies) and cDNA amplification was performed in a StepOne Plus Real Time PCR System (Life Technologies). For all used primers, amplification efficiencies were determined and mean-normalized expression ratios using hypoxanthine phosphoribosyltransferase (HPRT) as reference gene were calculated using the $2^{-\Delta\Delta C_T}$ algorithm, also known as the delta-delta-Ct (DDcT) method with efficiency correction.[43]

Image Processing: For quantification of focal contacts, confocal microscopy images were also analyzed using ImageJ 1.47 (Figure S6, Supporting Information). In all of the samples, a minimum of five individual cells were analyzed. Each image was firstly spatially calibrated and converted to grayscale 8-bit images. After that the individual cell outlines were manually traced and the threshold intensity ranges were set at 65–255 as described earlier.[70,73] Finally, the size parameters of the vinculin plaques were set between 0 and 6 µm² and number and area of the plaques were counted by the software. Up to 20 confocal planes were captured along the z-axis in order to perform 3D reconstructions and estimate the cell thickness. ImageJ 1.47 was then used to process the data and generate the 3D reconstruction. Additionally, the shape index of each individual cell or nucleus, cell area factor and nuclear area factor, respectively, determining cellular/nuclear elongation was evaluated using built-in functions of ImageJ by using the following formula

$$\text{Circularity} = 4\pi * \frac{[\text{Area of the cell}]}{[\text{Perimeter of the cell}]^2} \qquad (1)$$

with a shape index of 1 representing a circle.

The cell migration analyses were performed using Python 2.7.6 with the image processing libraries OpenCV 3.0.0 and scikit-image 0.12.3.

Statistical Analysis: Statistical significance was determined for three independent experiments (samples in triplicate for each surface type) by two-way analysis of variance (2wayANOVA) comparing the data between the substrates and the independent experiments followed by the Tukey test for means comparisons using Origin 2015. Data are expressed as mean ± standard deviation (SD). **** indicates $p < 0.001$; *** $p < 0.005$; ** $p < 0.01$; * indicates $p < 0.05$.

Supporting Information

Supporting Information is available from the Wiley Online Library or from the author.

[1] J. K. Mouw, G. Ou, V. M. Weaver, *Nat. Rev. Mol. Cell Biol.* **2014**, *15*, 771.

[2] D. Hubmacher, S. S. Apte, *Curr. Opin. Rheumatol.* **2013**, *25*, 65.

[3] F. Gattazzo, A. Urciuolo, P. Bonaldo, *Biochim. Biophys. Acta, Gen. Subj.* **2014**, *1840*, 2506.

[4] K. von der Mark, J. Park, S. Bauer, P. Schmuki, *Cell Tissue Res.* **2010**, *339*, 131.

[5] D. Karazisis, A. M. Ballo, S. Petronis, H. Agheli, L. Emanuelsson, P. Thomsen, O. Omar, *Int. J. Nanomed.* **2016**, *11*, 1367.

[6] M. Kulkarni, A. Mazare, E. Gongadze, S. Perutkova, V. Kralj-Iglic, I. Milosev, P. Schmuki, A. Iglic, M. Mozetic, *Nanotechnology* **2015**, *26*, 062002.

[7] H. N. Kim, A. Jiao, N. S. Hwang, M. S. Kim, D. H. Kang, D. H. Kim, K. Y. Suh, *Adv. Drug Delivery Rev.* **2013**, *65*, 536.

[8] Y. Zhukova, E. V. Skorb, *Adv. Healthcare Mater.* **2017**, *6*, 1600914.

[9] S. A. Ulasevich, G. Brezesinski, H. Möhwald, P. Fratzl, F. H. Schacher, S. K. Poznyak, D. V. Andreeva, E. V. Skorb, *Angew. Chem., Int. Ed.* **2016**, *55*, 13001.

[10] D. V. Andreeva, I. Melnyk, O. Baidukova, E. V. Skorb, *ChemElectroChem* **2016**, *3*, 1306.

[11] S. A. Ulasevich, N. Brezhneva, Y. Zhukova, H. Möhwald, P. Fratzl, F. H. Schacher, D. V. Sviridov, D. V. Andreeva, E. V. Skorb, *Macromol. Biosci.* **2016**, *16*, 1422.

[12] C. Selhuber-Unkel, T. Erdmann, M. López-García, H. Kessler, U. S. Schwarz, J. P. Spatz, *Biophys. J.* **2010**, *98*, 543.

[13] E. A. Cavalcanti-Adam, T. Volberg, A. Micoulet, H. Kessler, B. Geiger, J. P. Spatz, *Biophys. J.* **2007**, *92*, 2964.

[14] S. Oh, K. S. Brammer, Y. S. J. Li, D. Teng, A. J. Engler, S. Chien, S. Jin, *Proc. Natl. Acad. Sci. USA* **2009**, *106*, 2130.

[15] B. Trappmann, J. E. Gautrot, J. T. Connelly, D. G. T. Strange, Y. Li, M. L. Oyen, M. A. Cohen Stuart, H. Boehm, B. Li, V. Vogel, J. P. Spatz, F. M. Watt, W. T. S. Huck, *Nat. Mater.* **2012**, *11*, 642.

[16] E. Cukierman, R. Pankov, K. M. Yamada, *Curr. Opin. Cell Biol.* **2002**, *14*, 633.

[17] M. J. Dalby, N. Gadegaard, R. O. C. Oreffo, *Nat. Mater.* **2014**, *13*, 558.

[18] V. Schaufler, H. Czichos-Medda, V. Hirschfeld-Warnecken, S. Neubauer, F. Rechenmacher, R. Medda, H. Kessler, B. Geiger, J. P. Spatz, E. A. Cavalcanti-Adam, *Cell Adhes. Migr.* **2016**, *10*, 505.

[19] E. V. Skorb, E. A. Ustinovich, A. I. Kulak, D. V. Sviridov, *J. Photochem. Photobiol., A* **2008**, *193*, 97.

[20] E. V. Skorb, D. V. Andreeva, *Adv. Funct. Mater.* **2013**, *23*, 4483.

[21] X. Liu, P. K. Chu, C. Ding, *Mater. Sci. Eng., R* **2004**, *47*, 49.

[22] S. A. Ulasevich, S. K. Poznyak, A. I. Kulak, S. A. Karpushenkov, A. D. Lisenkov, E. V. Skorb, *RCS Adv.* **2016**, *6*, 62540.

[23] F. Variola, F. Vetrone, L. Richert, P. Jedrzejowski, J.-H. Yi, S. Zalzal, S. Clair, A. Sarkissian, D. F. Perepichka, J. D. Wuest, F. Rosei, A. Nanci, *Small* **2009**, *5*, 996.

[24] J. Banhart, *Prog. Mater. Sci.* **2001**, *46*, 559.

[25] S. A. Yavari, J. van der Stok, Y. C. Chai, R. Wauthle, Z. Tahmasebi Birgani, P. Habibovic, M. Mulier, J. Schrooten, H. Weinans, A. A. Zadpoor, *Biomaterials* **2014**, *35*, 6172.

[26] R. A. Gittens, R. Olivares-Navarrete, A. Cheng, D. M. Anderson, T. McLachlan, I. Stephan, J. Geis-Gerstorfer, K. H. Sandhage, A. G. Fedorov, F. Rupp, B. D. Boyan, R. Tannenbaum, Z. Schwartz, *Acta Biomater.* **2013**, *9*, 6268.

[27] S. Dey, M. Das, V. K. Balla, *Mater. Sci. Eng., C* **2014**, *39*, 336.

[28] C.-M. Han, H.-E. Kim, Y.-H. Koh, *Surf. Coat. Technol.* **2014**, *251*, 226.

[29] N. Faucheux, R. Schweiss, K. Lützow, C. Werner, T. Groth, *Biomaterials* **2004**, *25*, 2721.

[30] P. J. ter Brugge, J. G. Wolke, J. A. Jansen, *J. Biomed. Mater. Res.* **2002**, *60*, 70.

[31] E. Anitua, R. Prado, G. Orive, R. Tejero, *J. Biomed. Mater. Res., Part A* **2015**, *103*, 969.

[32] S. Bauer, P. Schmuki, K. von der Mark, J. Park, *Prog. Mater. Sci.* **2013**, *58*, 261.

[33] K. von der Mark, J. Park, *Prog. Mater. Sci.* **2013**, *58*, 327.

[34] L. M. S. Castro-Raucci, M. S. Francischini, L. N. Teixeira, E. P. Ferraz, H. B. Lopes, P. T. de Oliveira, M. Q. Hassan, A. L. Rosa, M. M. Beloti, *J. Cell Biochem.* **2016**, *117*, 1718.

[35] R. B. Kato, B. Roy, F. S. de Oliveira, E. P. Ferraz, P. T. de Oliveira, A. G. Kemper, M. Q. Hassan, A. L. Rosa, M. M. Beloti, *J. Cell Physiol.* **2014**, *229*, 1690.

[36] F. He, F. Zhang, G. Yang, X. Wang, S. Zhao, *Oral. Surg., Oral. Med., Oral. Pathol., Oral. Radiol. Endod.* **2010**, *110*, e13.

[37] D. Karazisis, A. M. Ballo, S. Petronis, H. Agheli, L. Emanuelsson, P. Thomsen, O. Omar, *Int. J. Nanomed.* **2016**, *11*, 1367.

[38] G. P. Freitas, H. B. Lopes, E. C. Martins-Neto, P. T. de Oliveira, M. M. Beloti, A. L. Rosa, *J. Oral. Implantol.* **2016**, *42*, 240.

[39] E. V. Skorb, H. Möhwald, *Ultrason. Sonochem.* **2016**, *29*, 589.

[40] Y. Zhukova, S. A. Ulasevich, J. W. C. Dunlop, P. Fratzl, H. Möhwald, E. V. Skorb, *Ultrason. Sonochem.* **2017**, *36*, 146.

[41] E. V. Skorb, D. G. Shchukin, H. Möhwald, D. V. Andreeva, *Nanoscale* **2010**, *2*, 722.

[42] E. V. Skorb, D. Fix, D. G. Shchukin, H. Möhwald, D. V. Sviridov, R. Mousa, N. Wanderka, J. Schaferhans, N. Pazos-Perez, A. Fery, D. V. Andreeva, *Nanoscale* **2011**, *3*, 985.

[43] J. Kopf, S. Ulasevich, O. Baidukova, Y. Zhukova, J. W. C. Dunlop, P. Fratzl, P. Rikeit, P. Knaus, S. K. Poznyak, D. V. Andreeva, E. V. Skorb, *Adv. Eng. Mater.* **2016**, *18*, 476.

[44] A. Ghicov, P. Schmuki, *Chem. Commun.* **2009**, 2791.

[45] E. A. Vogler, *Adv. Colloid Interface Sci.* **1998**, *74*, 69.

[46] D. A. H. Hanaor, Ch. S. Sorrell, *J. Mater. Sci.* **2011**, *46*, 855.

[47] M. J. Biggs, R. G. Richards, M. J. Dalby, *Nanomed-Nanotechnol. Biol. Med.* **2010**, *6*, 619.

[48] J. Park, S. Bauer, K. von der Mark, P. Schmuki, *Nano Lett.* **2007**, *7*, 1686.

[49] A. J. Ridley, M. A. Schwartz, K. Burridge, R. A. Firtel, M. H. Ginsberg, G. Borisy, J. T. Parsons, A. R. Horwitz, *Science* **2003**, *302*, 1704.

[50] C. Le Clainche, M.-F. Carlier, *Physiol. Rev.* **2008**, *88*, 489.

[51] S. D. Puckett, P. P. Lee, D. M. Ciombor, R. K. Aaron, T. J. Webster, *Acta Biomater.* **2010**, *6*, 2352.

[52] S. Lavenus, D. J. Poxson, N. Ogievetsky, J. S. Dordick, R. W. Siegel, *Biomaterials* **2015**, *55*, 96.

[53] O. Zinger, K. Anselme, A. Denzer, P. Habersetzer, M. Wieland, J. Jeanfils, P. Hardouin, D. Landolt, *Biomaterials* **2004**, *25*, 2695.

[54] J. Zhou, Y. Han, S. Lu, *Int. J. Nanomed.* **2014**, *9*, 1243.

[55] R. Zhang, H. Wu, J. Ni, C. Zhao, Y. Chen, C. Zheng, X. Zhang, *Mater. Sci. Eng., C* **2015**, *53*, 272.

[56] K. S. Brammer, S. Oh, C. J. Cobb, L. M. Bjursten, H. v. d. Heyde, S. Jin, *Acta Biomater.* **2009**, *5*, 3215.

[57] R. You, X. Li, Y. Liu, G. Liu, S. Lu, M. Li, *J. Biomed. Mater. Res., Part A* **2014**, *102*, 4206.

[58] K. A. Beningo, M. Dembo, I. Kaverina, J. V. Small, Y. Wang, *J. Cell Biol.* **2001**, *153*, 881.

[59] R. Zaidel-Bar, M. Cohen, L. Addadi, B. Geiger, *Biochem. Soc. Trans.* **2004**, *32*, 416.

[60] A. Buxboim, I. L. Ivanovska, D. E. Discher, *J. Cell Sci.* **2010**, *123*, 297.

[61] M. T. Yang, N. J. Sniadecki, C. S. Chen, *Adv. Mater.* **2007**, *19*, 3119.

[62] M. J. P. Biggs, R. G. Richards, N. Gadegaard, C. D. W. Wilkinson, M. J. Dalby, *J. Mater. Sci.: Mater. Med.* **2007**, *18*, 399.

[63] A. S. G. Curtis, N. Gadegaard, M. J. Dalby, M. O. Riehle, C. D. W. Wilkinson, G. Aitchison, *IEEE T NanoBiosci.* **2004**, *3*, 61.

[64] M. J. Dalby, N. Gadegaard, M. O. Riehle, C. D. W. Wilkinson, A. S. G. Curtis, *Int. J. Biochem. Cell Biol.* **2004**, *36*, 2005.

[65] E. A. Cavalcanti-Adam, D. Aydin, V. C. Hirschfeld-Warneken, J. P. Spatz, *HFSP J.* **2008**, *2*, 276.

[66] A. S. G. Curtis, B. Casey, J. O. Gallagher, D. Pasqui, M. A. Wood, C. D. W. Wilkinson, *Biophys. Chem.* **2001**, *94*, 275.

[67] M. J. Dalby, M. O. Riehle, H. Johnstone, S. Affrossman, A. S. G. Curtis, *Biomaterials* **2002**, *23*, 2945.

[68] K. S. Brammer, S. Oh, J. O. Gallagher, S. Jin, *Nano Lett.* **2008**, *8*, 786.

[69] P. Friedl, D. Gilmour, *Nat. Rev. Mol. Cell. Biol.* **2009**, *10*, 445.

[70] S. Karpitschka, H. Riegler, *Langmuir* **2010**, *26*, 11823.

[71] M. A. Woodruff, P. Jones, D. Farrar, D. M. Grant, C. A. Scotchford, *J. Mol. Histol.* **2007**, *38*, 491.

[72] H. Chen, W. Song, F. Zhou, Z. Wu, H. Huang, J. Zhang, Q. Lin, B. Yang, *Colloids Surf., B* **2009**, *71*, 275.

[73] M. K. Strulson, D. M. Johnson, J. A. Maurer, *Langmuir* **2012**, *28*, 4318.

1601244 (13 of 13)

Focus Article

Photomobility and photohealing of cellulose-based hybrids[(a)]

SVIATLANA A. ULASEVICH[1,2], INGA MELNYK[3], DARIA V. ANDREEVA[4], HELMUTH MÖHWALD[5]
and EKATERINA V. SKORB[1(b)]

[1] *Laboratory of Solution Chemistry of Advanced Materials and Technologies (SCAMT), ITMO University*
St. Petersburg 197101, Russian Federation
[2] *Institute of General and Inorganic Chemistry, National Academy of Sciences of Belarus - 220072 Minsk, Belarus*
[3] *Leibniz Institute of Polymer Research Dresden - Hohe Str. 6, 01069 Dresden, Germany*
[4] *Center for Soft and Living Matter, Institute of Basic Science, Ulsan National Institute of Science and Technology*
44919 Ulsan, Republic of Korea
[5] *Max Planck Institute of Colloids and Interfaces - Am Mühlenberg 1, 14424 Potsdam, Germany*

Abstract – In an effort to control the electronic and mechanical interaction between an inorganic surface and a defined polymeric coating, we present a new and easy method of a cellulose-based hybrid formation. We used Schweizer's reagent, a specific copper ammonia hydroxide-based solvent for cotton dissolution and found the optimal concentration for the formation of photosensitive uniform cellulose coating on titania, TiO_2-cellulose coating and free-standing hybrid. Photomobility, the material mobility induced by light, of a cellulose layer on a titania surface and of a TiO_2-cellulose hybrid on a silicon wafer has been studied. This can be used for photohealing, and the most promising system is the one that can be healed with light due to *in situ* activation of titania nanoparticles assembled on cellulose fibers in a hydrogel. The interfacial contact between titania particles and fiber is important for local transport of electrons and ions, thus the most promising system was obtained by *in situ* synthesis of titania nanoparticles on cellulose dispersed in Schweizer's reagent. We propose that cellulose coatings on titania surface and free-standing hybrids can be applicable for a wide range of photochemical devices: films for optics, drug delivery systems, and inks for printing of biologically relevant lab-on-chips.

Introduction. – Inorganic/organic composites are of special interest for functional and responsive materials development; while the inorganic part can lend the system high mechanical and functional stability, the organic part can provide responsive function and adaptability. Most prominent representatives for these materials are cellulose as most abundant biomaterial and TiO_2 as a well-studied inorganic material with photoelectric, catalytic and optical functions. These hybrids are studied in this paper.

Cellulose systems with a broad range of uses —for example, in composites, cosmetics and medical devices— require simple methods of preparation for combination with active nanoparticles and molecules for a stimuli-response behaviour. Cellulose is one of the most

important natural polymers, that has found a wide range of applications in industry and medicine because of its unique structural properties combined with hydrophilic nature, biocompatibility and non-toxicity [1,2]. Due to a high amount of hydroxyl groups on the fiber surface, cellulose can be easily functionalized or bio-conjugated, resulting in a rich source of new materials and platforms for diversified applications in biomedical fields such as tissue engineering and regenerative medicine or drug delivery devices [3–5]. Therefore, facile methods of cellulose processing are of high interest.

It is known [6,7] that local pH changes play an important role for drug delivery systems, dynamic regulation of adsorption/desorption of proteins [8], bacteria [9] and cells [10]. Light-pH coupling on TiO_2 surfaces was shown to be efficient for high-amplitude non-destructive manipulation of polymers deposited on semiconductor

---
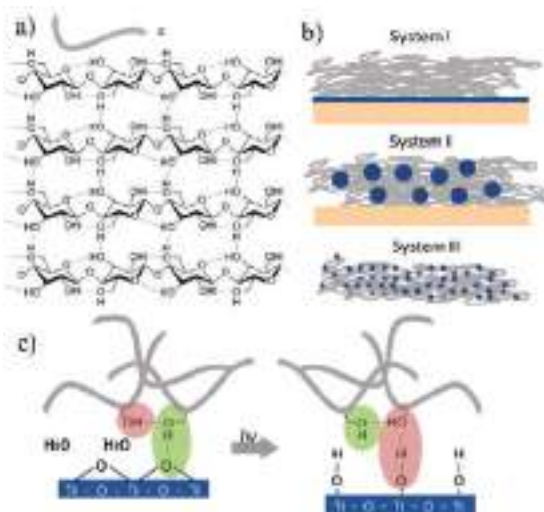
Fig. 1: (Colour online) (a) Schematic illustration of cellulose assembly with hydrogen bonds between chains (shown in (b), (c) as a grey line). (b) Three types of hybrids are in focus: cellulose assembly on TiO_2 surface (System I), assembly of cellulose with titania particles on the surface (System II), and cellulose-based free standing hydrogel with titania nanoparticles (System III). (c) Hypothesis of possible formation of hydrogen bonds at the cellulose-titania interface and their reorganization because of irradiation and change of titania surface bonds that may result in cellulose photomobility on the surface highlighted in green and red.

surfaces [10–12]. Recently we have found that nanolayers of chitosan can be used in the development of high buffering coatings to control environmental pH changes [12]. However, much of the TiO_2 function depends on the different mobility of photogenerated electrons and holes, and, therefore, the preparation of TiO_2 is expected to be very important [13]. Above all there is a fundamental difference between a surface and a nanoparticle; while charge carriers can be separated in a particle only over a maximum distance of the particle dimensions, on a surface the separation can proceed over macroscopic dimensions. Hence the following cathodic and anodic reactions can be well separated.

In this article, we suggest formation of various hybrid cellulose (fig. 1) coatings from a suitable selected solvent (Schweizer's reagent) and examine the photomobility, *i.e.*, photo-induced material mobility, and photohealing of coatings and free-standing systems.

The main question which we address here is whether cellulose layer photomobility or even cellulose hydrogel photohealing are possible due to a photoreaction on titania embedded in cellulose. Thus, on titania under supra-bandgap illumination, the illumination with energy high enough for the generation of photoholes and photoelectrons, higher than the energy of the forbidden zone (E_g), generates charges, that partly move, partly are trapped. The charge separation is converted into water splitting, and, thus, hydroxyl and proton generation are

separated [13]. This causes local pH gradients [14]. If there is a polymeric coating, this in addition may bind selectively one of the produced ions, thus modulating the pH change [12]. Altogether the interplay between the photoreaction of titania and the different mobility and the different binding capacity and responsivity of the coating lead to a responsive system with many application perspectives.

Experimental protocol. –

Materials. Sulphuric acid (1 M H_2SO_4), Cu (II) sulphate pentahydrate (purity grade $\geq$ 98%), ammonium hydroxide (28%, $\geq$ 98%), titanium(IV) butoxide ($Ti(C_4H_9O)_4$, $\geq$ 98%) were purchased from Sigma-Aldrich (Germany). Silicon (Si) wafers (100) were from CrysTech Kristalltechnologie. Pharmacy cotton wood was used as cellulose fiber precursor. TiO_2(Hombikat) nanoparticles were used as received. Millipore water (Milli-Q Plus 185) was used for preparation of aqueous solutions and sample washing.

Titania photoactive layer preparation. Si wafers with polished surface were used as substrate for titanium layers of $2\,\mu m$ thickness deposited by physical vapour deposition using a BA 510 from Fa. Balzers, Liechtenstein. Ti-covered Si wafers were fixed in a homemade sample holder for high-intensity ultrasound (HIUS) modification. The samples were sonicated for 1 min in ethanol at a sonotrode to surface distance of 5 mm. Cavitation was produced by a UIP1000hd ultrasonic device from Hielscher Ultrasound Technology equipped with a B2-1.8 booster and a BS2d22 sonotrode (head area $3.8\,cm^2$). The operating frequency was 20 kHz with a maximum intensity of $140\,W/cm^2$ and an amplitude of $106\,\mu m$. The sonication medium was cooled using an ice bath to approximately 333 K [11,12]. The advantages of HIUS preparation of active materials to achieve photoactivity can be found in all details in our previous work [11–20].

Cellulose coatings. Schweizer's reagent ($[Cu(NH_3)_4\cdot(H_2O)_2]\,(OH)_2$) was prepared by precipitating copper(II) hydroxide from an aqueous solution of copper sulphate using sodium hydroxide, then dissolving the precipitate in a solution of ammonia hydroxide. Cellulose solution was prepared by dissolving 1–50 mg of cellulose in 10 ml Schweizer's reagent. It is important for the formation of hybrid systems that additionally to cellulose other particles or molecules can be added to Schweizer's reagent. Here, in the case of the formation of a TiO_2-cellulose coating deposited on silicon we added TiO_2 particles (Hombikat) into the solution of cellulose in Schweizer's reagent. Cellulose-based coatings were obtained using spin-coating.

Spin coating was carried out under ambient conditions using a SCI spin coater (Novocontrol Technologies GmbH, Germany). A drop of the solution was placed onto the substrate rotating at 3000 rpm. One drop formed one cellulose layer. A thick cellulose layer was formed from a concentrated (up to 30 mg/ml) solution. Thin cellulose

films were obtained from a diluted solution (from 1.5 to 5 mg/ml). After deposition samples were rinsed in 0.1 M H_2SO_4 for 1 min, and then washed in Milli-Q water three times.

Cellulose free standing hybrid. For 10 ml of cellulose solution in Schweizer's reagent, $100 \, \mu L$ of $Ti(C_4H_9O)_4$ were added under vigorous stilling. Then the mixture was squeezed out of a syringe into a solution of H_2SO_4. In the time of several washings of the hybrid, it changes colour from bright blue to white. The hybrid still containing copper ions and amino groups is blue opposite to the white one that is again just a cellulose-based hybrid.

A cellulose photomobility study was conducted using atomic force microscopy (AFM). A scratch was made on the cellulose coating by tweezers. The thickness of the cellulose layer was measured before and during UV illumination using AFM. The distance between the sample and a UV-light–emitting diode (UV 365 nm LED from Thor-Lab) was 2 cm. The intensity was $5 \, mW/cm^2$.

Characterization methods. AFM measurements were performed in air at room temperature using a Nanoscope multimode AFM (Digital Instruments Inc., USA) operating in tapping mode. Typical cantilever values: resonance frequency: 300 kHz; spring constant: 42 N/m.

Infrared reflection absorption (IRRA) spectra were acquired with an IFS 66 FT-IR spectrometer (Bruker, Germany). For all measurements at 40 mN/m, p-polarized radiation was used at an angle of incidence of 70°. A total of 200 scans were acquired with a scanner velocity of 20 kHz at a resolution of $8 \, cm^{-1}$. The spectra were obtained in a range of 400–$4000 \, cm^{-1}$.

Scanning electron microscopy (SEM) was conducted with a Gemini Leo 1550 instrument (Leo Elektronenmikroskopie GmbH, Germany) at an operating voltage of 3 keV. Prior to microscopy the samples were sputtered with gold.

Transmission electron microscopy (TEM) measurements were performed on a Zeiss EM 912 Omega (Carl Zeiss AG, Germany) transmission electron microscope operated at 300 kV.

Results and discussion. – Cellulose fibers have a number of hydrogen bonds between individual chains [21] enabling facile functionalization, fig. 1(a).

Cellulose is known to be derived from D-glucose units, which condense through $\beta(1 \rightarrow 4)$-glycosidic bonds [22]. The multiple hydroxyl groups on the glucose from one chain form hydrogen bonds with oxygen atoms on the same or on a neighboring chain, holding the chains firmly together side by side and forming fibrils with high tensile strength. This makes a cellulose straight chain polymer. Due to the structural rigidity cellulose is insoluble in water and in most organic solvents [23]. Carbohydrates in aqueous alkaline solution are multiply deprotonated in the presence of tetraamine-diaquacopper dihydroxide and form chelate complexes (fig. 2). This breaks the hydrogen bonds and makes cellulose soluble.

Fig. 2: (Colour online) Cellulose (white cotton fibres) dissolution in tetraaminecopper(II) hydroxide (Schweizer's reagent) for the formation of cellulose-based hybrids.

In order to test various cellulose hybrids with induced photosensitivity, we prepared three systems: cellulose coating on TiO_2, coating of cellulose and TiO_2 nanoparticles, and free-standing cellulose-titania hybrid (fig. 1(b)).

The coatings were prepared by spin coating (fig. 3(a)). Optimization of the solution concentration is a critical issue for the formation of a uniform film [24]. Thus, a relatively high concentration of cellulose results in a viscous solution, and a spin-coated film forms from 30 mg/ml solution with different thickness over the surface (fig. 3(b)).

Variation in thickness of the coating results in different light reflection. Nevertheless, high concentrations are not appropriate for spin coating, a viscous solution may be interesting, for example, for an inkjet technology to create coloured interference layers with high accuracy without the need for high-temperature fixing. This could be useful in combination with titania nanoparticles yielding coatings with a high refractive index (ca. 2.00 over the entire visible range) when naturally dried [25]. The lack of dyes in the proposed method has good environmental prospects, because the applied systems based on a TiO_2/cellulose composite are non-toxic and biologically inert. Moreover, our work below explores in detail the principle of photosensitivity of cellulose-based hybrids and *in situ* changes of film thickness.

At lower concentration (3 mg/ml) a uniform film was formed (fig. 3(c)). After the deposition, the coating was rinsed in sulfuric solution for the removal of the copper complex and the recovery of cellulose fibers.

The nodule-like morphology of the cellulose coating formed on titania is shown in fig. 4(a),(b).

To study the photomobility of the cellulose layer we scratched the polymer layer (fig. 4(c)). Figure 4(d) shows changes of the scratch after illumination. It is seen that
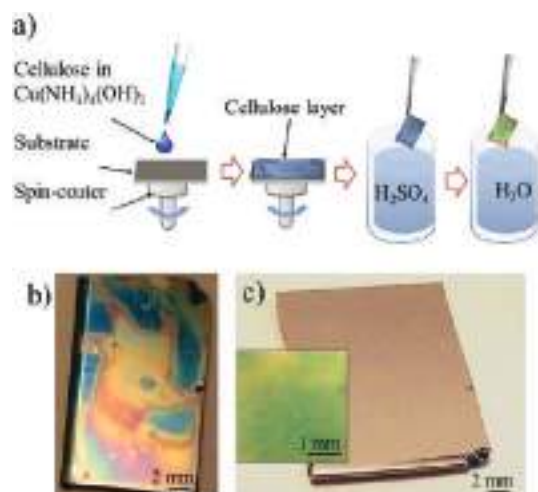
Fig. 3: (Colour online) (a) Spin-coating of Schweizer's reagent with different concentration of cellulose with or without TiO$_2$ particles on the substrate for formation of cellulose-based coatings. (b) From viscous solutions with relatively high cellulose concentration (30 mg/ml) the coatings are irregular, a different colour is attributed to a different cellulose coating thickness. (c) Uniform coating can be obtained by solution dilution (3 mg/ml). The inset obtained by different polarization shows that even thin coating affects the light polarization and the thin film has a greenish reflection.

Fig. 4: (Colour online) System I: (a), (b): AFM images showing a cellulose-based coating formed on a titania surface from 3 mg/ml solution. (c), (d): study of coating photomobility on the surface: (c) before illumination and (d) the same spot after 10 min illumination at 5 mW/cm^2, 365 nm. (e) IRRAS spectra of cellulose coating before (1) and during UV illumination (2) prove that cellulose was stable under illumination: no photodegradation is seen.

part of cellulose layer moved to the scratched side to reduce the surface energy probably due to light-induced fluidization of functional groups on the titania surface: charge separation in titania leads to a reorganization of the surface groups and water splitting, leading to a reorganization of the cellulose coating.

We see that photomobility is not due to cellulose degradation. The IRRA spectra before and after irradiation (fig. 4(e)) are identical. The IRRA spectra show the characteristic bands for cellulose and the presence of Ti-O bonds. A peak at 3650–3585 cm^{-1} can be attributed to the hydroxyl stretching vibration caused by intermolecular hydrogen bonds [26]. The broad bands at 3010–3060 cm^{-1}, 1760–1700 cm^{-1}, 1380 cm^{-1}, 1220 cm^{-1} and 970 cm^{-1} can be assigned to vibrations of carbonyl groups and composite bending vibrations of (CHO), (C–C–O), (C–O) and (C–C) of substituted glucopyranose cycles of cellulose [27–29]. The peaks at 3010–3060 cm^{-1}, 1460 cm^{-1} and 780 cm^{-1} are attributed to the C–H stretching vibration. The strong band in the region of 400–700 cm^{-1} can be assigned to the formation of Ti–O and Ti–O–Ti bonds [30].

To establish the System II we added TiO$_2$ nanoparticles into the solution of cellulose in Schweizer's reagent and spin-coated the solution with nanoparticles. The initial morphology is different for the coating with particles (fig. 5(a),(b)); however, again the analysis of the profiles of AFM images before and after irradiation (fig. 5(c),(d)) proves that the TiO$_2$ particles activate cellulose, although, in this case, to a smaller degree.

Zoomed-in AFM profiles (fig. 5(e)) from the same place before and after irradiation are different. Here the cellulose reorganized locally on the particle, but without moving drastically on the surface, in comparison, with the previous case (fig. 4) where the whole surface was covered with photoactive titania.

This can be considered in perspective if the method of hybrid formation is applicable not just for the formation of films, but also for free-standing hybrids [31], hydrogels (figs. 6,7). In this case it would not depend on the different mobility of charge carriers in titania [32]. This is the case for System III.

For the formation of hydrogels, we added a nanoparticle precursor to the Schweizer's reagent simultaneously with dispersion of cellulose fibers. Ti(C$_4$H$_9$O)$_4$ was added under vigorous stirring to *in situ* forming nanoparticles. It is known that Ti(C$_4$H$_9$O)$_4$ hydrolysis [33] results in the formation of amorphous nanoparticles. Amorphous TiO$_2$ would have less ability to degrade cellulose (less generated reactive oxygen species), but rather it would be used for its photoactivation due to the reorientation of their surface group under irradiation. We showed the possible
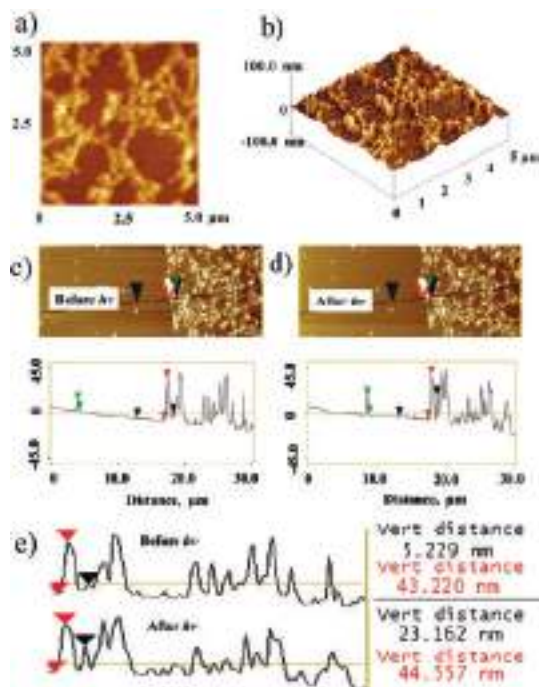
Fig. 5: (Colour online) System II: (a), (b): AFM images showing cellulose-based coating formed from a 3 mg/ml solution of cellulose that has 1 mg/ml TiO_2 (Hombikat) in solution. (c), (d): study of the change of the hybrid orientation of the surface: (c) before illumination and (d) after 10 min illumination at 5 mW/cm^2, 365 nm. (e) Zoom in (from (c) and (d)) on AFM profiles from the same line pointing more clearly to the photomobility of cellulose chains.

Fig. 6: (Colour online) Photographs of cellulose-titania hydrogels after squeezing out of a syringe Schweizer's reagent with a dissolved cellulose solution forming titania nanoparticles in the solution of H_2SO_4. The blue hybrid still contains copper ions and amino groups. After several washings of the hybrid, it changes colour from bright blue to white, which is typical for a solely cellulose-based hybrid.

photoactivation of titania amorphous films in our previous works, see for details refs. [34–36]. It can be also noted that, on the contrary to the reactions of light-heat coupling [37–39] on noble metal particles, here the heat is negligible and there is mostly light-pH (chemical reactions) coupling.

We analysed the cellulose hydrogel after washing out of Schweizer's reagent. Electron microscopy images (fig. 7(a),(b)) provide clear evidence of the formation of a fibre assembly in the hydrogel matrix. Moreover, it is seen
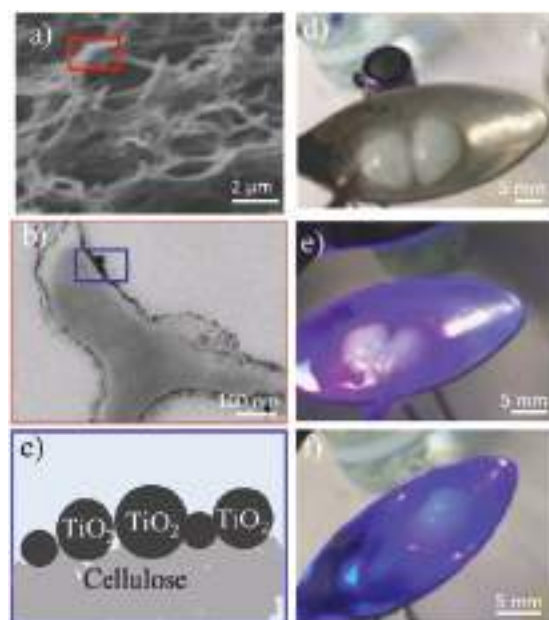
Fig. 7: (Colour online) System III: (a) SEM image of hydrogel fibers, (b) TEM image of the fiber showing the contact of polymer fibers with TiO_2 nanoparticles covering the fiber, with (c) schematic of the fiber/titania interface. (d)–(f) Light curing of cellulose/titania-based hybrid (hydrogel). Optical images of (d) composite hydrogel cut; (e), (f) light healing of the material (e) at the initial moment of irradiation, (f) after 15 min of irradiation. The red box in (a), (b) indicates higher resolution from fiber network to individual fiber. The blue box in (b), (c) shows the schematic of TiO_2 assembly along the fiber.

(fig. 7(b)) that individual fibers are covered by nanoparticles of TiO_2 maximizing, as shown in the schematic (fig. 7(c)), the interface between TiO_2 and cellulose.

We tested the behaviour of hydrogel —fiber assemblies— under irradiation. We cut one piece of hydrogel (fig. 7(d)), irradiated it and observed photohealing of the hydrogel (fig. 7(f)) due to the reorganization of alkoxy and hydroxyl groups at the TiO_2 interface that affects the mobility of polymer segments leading to the healing of the coatings.

Since there are several aspects, including light-pH coupling on TiO_2, cellulose can be followed in the presence of protons and/or electrons and the crosslinking mechanism of cotton through proton attraction is more likely. The TiO_2 under irradiation forms the pair of electron (e^-) and hole (h^+). Oxygen as a nucleophile portion of cellulose is attached to carbon with positive charge, may be activated and crosslink [40]. The mechanism through electron attack can be suggested by the oxygen radical attack to hydroxyl groups of cellulose [41].

Conclusions. – Processes at the interface of an inorganic material and an organic coating can sensitively be controlled by light, and this may contribute to their understanding. Here we concentrated on 2 widely studied systems, titania and cellulose, and show that photoinduced charge separation of titania can affect the organic

coating. It leads to material movement over microscopic dimensions and can finally be used for annealing of defects or scratches.

More specifically a facile method for the formation of optically active cellulose-based coatings is presented. Both types of hybrid coatings —cellulose on titania surface and TiO_2/cellulose on a silicon wafer— are photomobile. Here photosensitivity is due to TiO_2 photoactivation that changes its surface groups and produces charges in the coating. Free-standing hybrids of TiO_2/cellulose may recover its structure under illumination —we are able to cure the hydrogel under irradiation.

$$* * *$$

REFERENCES

[1] Ikada Y. and Hideto T., *Macromol. Rapid Commun.*, **21** (2000) 117.

[2] Khalil H. P. S. A., Tye Y. Y., Saurabh C. K., Leh C. P., Lai T. K., Chong E. W. N. and Syakir M. I., *Express Polym. Lett.*, **11** (2017) 244.

[3] Kechk S. M. and El-Kott A. F., *Natural Bacterial Biodegradable Medical Polymers: Bacterial Cellulose* (Wood Publishing, Boston) 2017, p. 458.

[4] Mohanty A. K., Misra M. and Hinrichsen G., *Macromol. Mater. Eng.*, **276** (2000) 1.

[5] Thakur V. K. and Voicu S. I., *Carbohyd. Polym.*, **146** (2016) 148.

[6] Newman M. R. and Benoit D. S. W., *Curr. Opin. Biotechnol.*, **40** (2016) 125.

[7] Senthil K. K., Manoj V. G., Vudaykiran A. and Rak B. S. F. M., *Int. J. Res. Pharm. Sci.*, **1** (2016) 454.

[8] Andreeva D. V., Melnyk I., Baidukova O. and Skorb E. V., *ChemElectroChem*, **3** (2016) 1306.

[9] Gensel J., Borke T., Pazos-Perez N., Fery A., Andreeva D. V., Betthausen E., Müller A. H. E. and Skorb E. V., *Adv. Mater.*, **24** (2012) 985.

[10] Ulasevich S. A., Brezhneva N., Zhukova Y., Möhwald H., Fratzl P., Schacher F. H., Sviridov D. V., Andreeva D. V. and Skorb E. V., *Macromol. Biosci.*, **16** (2016) 1422.

[11] Kollath A., Brezhneva N., Skorb E. V. and Andreeva D. V., *Phys. Chem. Chem. Phys.*, **19** (2017) 6286.

[12] Andreeva D. V., Kollath A., Brezhneva N., Sviridov D. V., Cafferty B. J., Möhwald H. and Skorb E. V., to be published in *Phys. Chem. Chem. Phys.* (2017), DOI: 10.1039/c7cp02618h.

[13] Maltanava H., Poznyak S. K., Andreeva D. V., Quevedo M. C., Bastos A. C., Tedim J., Ferreira M. G. S. and Skorb E. V., to be published in *ACS Appl. Mater. Interfaces* (2017), DOI: 10.1021/acsami.7b05209.

[14] Ulasevich S. A., Brezesinski G., Möhwald H., Fratzl P., Schacher F. H., Poznyak S. K., Andreeva D. V. and Skorb E. V., *Angew. Chem., Int. Ed.*, **55** (2016) 13001.

[15] Skorb E. V., Möhwald H. and Andreeva D. V., *Adv. Mater. Interfaces*, **4** (2017) 1600282.

[16] Skorb E. V. and Möhwald H., *Ultrason. Sonochem.*, **29** (2016) 589.

[17] Skorb E. V., Möhwald H. and Andreeva D. V., *Langmuir*, **32** (2016) 11072.

[18] Skorb E. V. and Möhwald H., *Adv. Mater. Interfaces*, **1** (2014) 1400237.

[19] Skorb E. V. and Andreeva D. V., *Adv. Funct. Mater.*, **23** (2013) 4483.

[20] Skorb E. V., Andreeva D. V. and Möhwald H., *Angew. Chem., Int. Ed.*, **2** (2012) 5138.

[21] Barbetta A., Fratzl P., Zemb T. and Bertinetti L., *Adv. Mater. Interfaces*, **4** (2017) 1600437.

[22] Krumm C., Pfaendtner J. and Dauenhauer P. J., *Chem. Mater.*, **28** (2016) 3108.

[23] Azizi Samir M. A. S., Alloin F. and Dufresne A., *Biomacromolecules*, **6** (2005) 612.

[24] Skorb E. V., Sviridov D. V., Möhwald H. and Shchukin D. G., *Chem. Commun.* (2009) 6041.

[25] Yakovlev A. V., Milichko V. A., Vinogradov V. V. and Vinogradov A. V., *ACS Nano*, **10** (2016) 3078.

[26] Zhang X., Chen W., Lin Z., Yao J. and Tan S., *Synth. React. Inorg. Met.-Org. Chem. J.*, **41** (2011) 997.

[27] Reichenbächer M. and Popp J., *Challenges in Molecular Structure Determination* (Springer Science & Business Media Verlag, Berlin, Heidelberg) 2012, p. 482.

[28] Krasovskii A. N., Vasil'eva I. V., Myakin S. V., Os-molovskaya N. A. and Borisova S. V., *High Energy Chem.*, **45** (2011) 390.

[29] Nelson M. L. and O'Connor R. T., *J. Appl. Polym. Sci.*, **8** (1964) 1311.

[30] Ulasevich S. A., Kulak A. I., Poznyak S. K., Karpushenkov S. A., Lisenkov A. D. and Skorb E. V., *RSC Adv.*, **6** (2016) 62540.

[31] Mamedov A. A., Kotov N. A., Prato M., Guldi D. M., Wicksted J. P. and Hirsch A., *Nat. Mater.*, **1** (2002) 190.

[32] Husemann E. and Schulz G. V., *J. Macromol. Chem.*, **1** (1943) 197.

[33] Tao Y., Pan J., Yan S., Tang B. and Longbao Zhu L., *Mater. Sci. Eng. B*, **138** (2007) 84.

[34] Skorb E. V., Antonouskaya L. I., Belyasova N. A., Shchukin D. G., Möhwald H. and Sviridov D. V., *Appl. Catal. B: Environ.*, **84** (2008) 94.

[35] Skorb E. V., Byk T. V., Sokolov V. G., Gaevskaya T. V., Sviridov D. V. and Noh C.-H., *Chem. High Energy*, **42** (2008) 127.

[36] Byk T. V., Sokolov V. G., Gaevskaya T. V., Skorb E. V., Sviridov D. V., Noh C.-H., Song K. Y., Kwon Y. N. and Cho S. H., *J. Photochem. Photobiol. A.: Chem.*, **193** (2008) 56.

[37] Skirtach A. G., Munoz J. A., Kref O., Köhler K., Piera A. A., Möhwald H., Parak W. J. and Sukhorukov G. B., *Angew. Chem., Int. Ed.*, **45** (2006) 4612.

[38] Skorb E. V., Skirtach A. G., Sviridov D. V., Shchukin D. G. and Möhwald H., *ACS Nano*, **3** (2009) 1753.

[39] Skirtach A. G., Dejugnat C., Braun D., Susha A. S., Rogach A. L., Parak W. J., Möhwald H. and Sukhorukov G. B., *Nano Lett.*, **5** (2005) 1371.

[40] Nazari A., Mantazer M., Rashidi A., Yazdanshenas M. and Moghadam M., *J. Appl. Polym. Sci.*, **117** (2010) 2740.

[41] Wang C.-C. and Chen C.-C., *Appl. Catal. A Gen.*, **293** (2005) 171.

Light-Induced Proton Pumping with a Semiconductor: Vision for Photoproton Lateral Separation and Robust Manipulation

Hanna M. Maltanava,[‡] Sergey K. Poznyak,[‡] Daria V. Andreeva,[§] Marcela C. Quevedo,[||] Alexandre C. Bastos,[||] João Tedim,[||] Mário G. S. Ferreira,[||] and Ekaterina V. Skorb*[⊥,†]

[⊥]Laboratory of Solution Chemistry of Advanced Materials and Technologies (SCAMT), ITMO University, St. Petersburg 197101, Russian Federation

[†]Department of Chemistry and Chemical Biology, Harvard University, 12 Oxford Street, Cambridge 02138, Massachusetts, United States

[‡]The Research Institute for Physical Chemical Problems, Belarusian State University, Minsk 220030, Belarus

[§]Center for Soft and Living Matter, Institute of Basic Science Ulsan, National Institute of Science and Technology, Ulsan 44919, Republic of Korea

[||]Department of Materials and Ceramic Engineering, CICECO, University of Aveiro, Aveiro 3810-193, Portugal

ABSTRACT: Energy-transfer reactions are the key for living open systems, biological chemical networking, and the development of life-inspired nanoscale machineries. It is a challenge to find simple reliable synthetic chemical networks providing a localization of the time-dependent flux of matter. In this paper, we look to photocatalytic reaction on TiO$_2$ from different angles, focusing on proton generation and introducing a reliable, minimal-reagent-consuming, stable inorganic light-promoted proton pump. Localized illumination was applied to a TiO$_2$ surface in solution for reversible spatially controlled "inorganic photoproton" isometric cycling, the lateral separation of water-splitting reactions. The proton flux is pumped during the irradiation of the surface of TiO$_2$ and dynamically maintained at the irradiated surface area in the absence of any membrane or predetermined material structure. Moreover, we spatially predetermine a transient acidic pH value on the TiO$_2$ surface in the irradiated area with the feedback-driven generation of a base as deactivator. Importantly we describe how to effectively monitor the spatial localization of the process by the in situ scanning ion-selective electrode technique (SIET) measurements for pH and the scanning vibrating electrode technique (SVET) for local photoelectrochemical studies without additional pH-sensitive dye markers. This work shows the great potential for time- and space-resolved water-splitting reactions for following the investigation of pH-stimulated processes in open systems with their flexible localization on a surface.

KEYWORDS: photocatalysis, TiO$_2$, pH gradient, nanoscale machinery, photoacid, chemical network
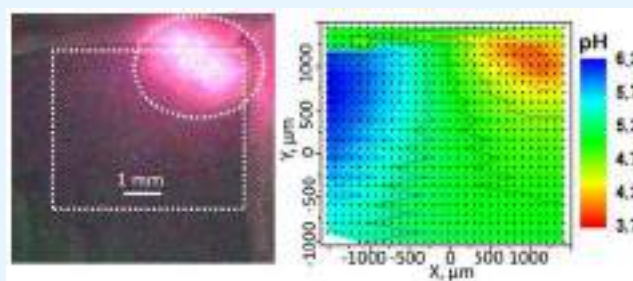
INTRODUCTION

Today, increased interest is focused on dynamic, non-equilibrium material properties varying with time: life-inspired nanoscale machinery.[1−4] It involves the needs for effective energy conversion with a focus on oscillation reactions,[5] chemical networking,[6] autocatalytic[7] and autoamplification[8] reactions, mimicking living systems,[9] using cell metabolic biomolecules,[10] and ions, e.g., proton gradients.[11] Biological systems solve such an energy-management problem by the development of unique sensory and adaptive capabilities, transport mechanisms guided with ions, proton gradients, and chemical networks.[12] It is very attractive to use light-energy conversion[13−15] for the modulation of simple, reliable chemical networking that is easy to control on the basis of existing knowledge of reliable light-sensitive materials. In many cases, it is a good variant to look for well-known processes and a sustainable system for new applications. We question if a semiconductor surface, e.g., that of TiO$_2$, has a potential as effective photoactive surface to design light-controllable networks of chemical reactions with the lateral separation of the two reactions of water splitting of a simple possible network that can be the light-assisted generation of protons from water molecules and the neutralization of H$_3$O$^+$ with OH$^-$ (Figure 1a). Robust lateral separation and understanding are the keys to deriving the system's further broad prospects.

Moreover, we have recently discussed prospects of complex material systems with pH activity[16] and introduced light−pH coupled oscillations of polymer assembly,[17] cell dynamic switching,[18] and protein recognition[19] on TiO$_2$ modified with polyelectrolytes. A vision of manipulating with spatiotemporal
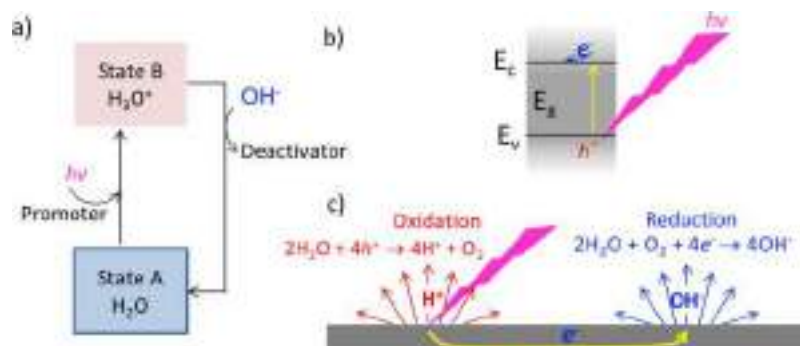
Figure 1. Suggested system for life-inspired proton pumping on a semiconductor. (a) Simplest chemical networking in focus. (b) Light induces charge separation in a nanostructured (no band-bending) semiconductor: E_c and E_v correspond to the edges of conduction and valence bands, and E_g is the forbidden zone. (c) Separation of the redox processes on semiconductor surface for the development of localized chemical networking, where the localization is determined by the position of the irradiation spot and is flexible.

processes on titania remains untouched, which motivates the present work: robust lateral separation of the two reactions of water splitting with prospects of lateral separation of the dynamic properties of pH-sensitive assemblies. The hypothesis here is that photoholes and photoelectrons may exhibit anisometric mobilities on surfaces and that the position of the photoelectrode is flexible and depends on the light focus. This may lead to a spatiotemporal separation of reduction and oxidation processes via the control of the isometry of the carrier mobility. Mechanisms for this must be elaborated.

In general, semiconductor materials have been used for artificial photosynthetic system development[20] and are also known to enable efficient solar water splitting.[21] Surprisingly, a network of chemical reactions on semiconductor surfaces for open systems is not discussed much, simultaneously having different surface- and interface-engineering strategies, such as band-structure engineering[22] and co-catalyst engineering.[23] Much is known about improving heterogeneous semiconductors in terms of charge separation and transfer, enhanced optical absorption, optimized band-gap position, lowered cost and toxicity, and improved stability.[24] Thus, when the background of formation of spatially separated reactions on TiO₂ surfaces is associated with chemical-reaction networking synergy, it is easy to further up-scale and improve the sustainability of the system.

A successful example of an application of such a spatial separation of photoreactions might be a photocatalytic lithography based on a TiO₂ layer.[25] The feasibility of the inversion of metal images obtained by the chemical deposition of metals onto nanostructured TiO₂ exposed to high radiation doses has been demonstrated,[26] and the generation of both negative and positive metallic patterns by variation of the dose was reported.[27]

Here, we focus at the beginning on macro-scale, centimeter-dimension surfaces to control the localization of different pH zones on the surface versus irradiation. Localization of chemical species may lead to a life-inspired proton pump machinery for the localization of chemical networks on the surface of TiO₂ in an open system, providing further prospects for designing far-from-equilibrium[28] and dynamic[29] oscillation gel materials,[30] stimuli-responsive drug delivery systems,[31] metastable nanoparticle assemblies,[32] and reactors to proliferate acidic and basic molecules.[7] Moreover, a thorough understanding of electron- and hole-transfer thermodynamics and kinetics will lead to elucidating the key efficiency-limiting step and designing highly efficient solar-to-fuel conversion systems.[33] In this paper, we

provide not only evidence of the possibility of spatial and temporal localization of proton pumping on semiconducting TiO₂ with light-induced water splitting but also some potential opportunities for designing an open system with localization of both H⁺ and OH⁻.

RESULTS AND DISCUSSION

Here, we concentrate on the light-promoted reaction of water protonation (Figure 1a). Under supra-bandgap irradiation of the surface of many semiconductors, e.g., TiO₂, photoholes and photoelectrons are generated (Figure 1b). In the scope of photocatalytic reactions, one can assume the possible formation of H⁺ and OH⁻ due to oxidation (ox) and reduction (red) reactions involving photogenerated charge carriers on the semiconductor surface. Surprisingly, the dynamics of the simplest reactions of the formation of proton and hydroxyl radical has not been highlighted before. Thus, our key idea is to use water splitting on a semiconductor, not focusing on the products H₂ and O₂ as usual but on reactions that provide the formation of H⁺ and OH⁻. We focus on the possibility of transforming the energy of electromagnetic irradiation into a pH gradient in time and space near the TiO₂ surface. A photocatalytically active nanostructured titanium dioxide film is the light-sensitive part of the model system. An anodized titania nanotubular layer[34] on titanium was used as the highly photoactive[17] one, wherein the dissipation of protons can be prolonged due to the porosity of the semiconductor layer that facilitates the proton detection.

A series of consecutive photocatalytic reactions leads to the development of reactive species that contribute to a pH shift. There are no data to what extent the pH can be altered laterally on semiconductor surface, e.g., TiO₂. Can the pH be changed locally from, for example, 7 to 4 during irradiation of the TiO₂ surface? Which processes are preferable in the irradiation zone: acidification or alkalinization? Does localization of H⁺ and OH⁻ correlate with localization of the irradiated area? How flexible is the localization of the process?

The inorganic surface and its nanostructuring may be involved in the reaction through process location as well as surface morphology and porosity, which are important to the prolonged effects of release of chemicals. The water oxidation reaction on TiO₂ is initiated by a nucleophilic attack of a H₂O molecule on the photogenerated hole at the O site bridging two Ti atoms, and as a result, TiO·HO−Ti (and later, TiOOH and TiOOTi) are formed.[35] During these oxygen photoevolution reactions, protons are released. At the same time, the
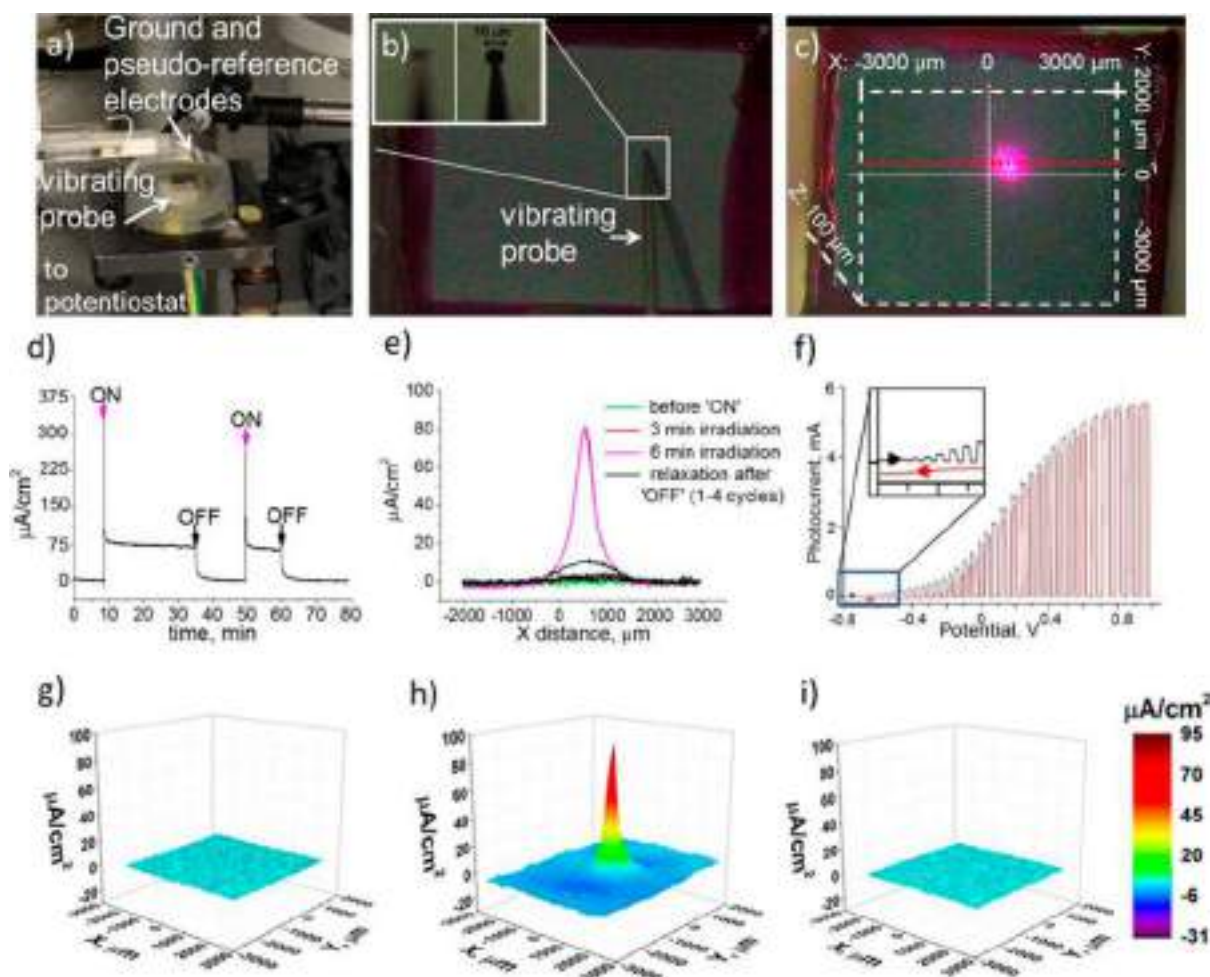
Figure 2. SVET measurements of ionic current density in electrolyte. Current density can be attributed to photocurrent. (a) Set-up of in situ scanning vibrating electrode technique (SVET) to analyze local current densities in electrolyte associated with photocurrents generated on a TiO$_2$ layer; (b) sample with vibrating probe before irradiation; and (c) sample with the position of maps (white lines), line measurements (red line), and the place of irradiation (bright spot in center of sample). (d) Ionic current density in electrolyte above the irradiated spot on a titania layer under switching on and switching off the light. (e) SVET current density measured in lines every 3 min before, during, and after irradiation. (f) Current−potential curve recorded under chopped illumination for TiO$_2$. (g−i) SVET maps (g) before irradiation, (h) during local irradiation, and (i) after irradiation (after 5 min of relaxation). The measurements were performed in 0.05 M Na$_2$SO$_4$.

photogenerated electrons reduce the surface Ti$(^{4+})$, enabling adsorption of H$_2$O, and then O$_2$ attacks it immediately to form superperoxo TiOO.[36] As a result, a hydroxide ion OH$^-$ is released. Next, TiOO is reduced to peroxo, which evolves to hydroperoxo TiOOH upon protonation. At the end, the surface is covered by hydroxyl groups. However, there are no data on the localization of processes on certain areas.

Using the scanning vibrating electrode technique (SVET) (Figure 2), we spatially resolve the in situ establishment of the ionic current density in solution induced by the photo-electrochemical processes on the surface of TiO$_2$ under local (Figure 2c) low intensity (ca. 5 mW/cm^2) light-emitting diode (LED) UV (365 nm) irradiation. It is important to discuss the efficiency of charge separation as the first light-stimulated process on TiO$_2$. SVET here is a unique tool with which to monitor the processes in situ at certain locations, which is important for following the development of photoreactions and the consecutive chemical network stability. The technique allows different modes to monitor the local ionic currents in solution associated with the photocurrent: a single spot inside the irradiation point (Figure 2d), line scan (Figure 2e), and maps of surface activity versus the irradiation spot (Figure 2g−

i) before (Figure 2g), during (Figure 2h), and after irradiation (Figure 2i). Current versus potential curves were also measured (Figure 2f).

After the turning on of illumination, the photocurrent first presents a rapid response with an initial spiking of the photocurrent, indicating a rapid filling and discharging of defect states,[37] and then a plateau for relatively constant collection from the active region is reached. In the case of two electrodes,[38] the TiO$_2$ working electrode and counter electrode, the photocurrent is caused by the separation of photogenerated electron−hole pairs within the photoelectrode: the holes move to the TiO$_2$ surface, where they are trapped or captured by reduced species in the electrolyte, while the electrons are transported to the back contact via TiO$_2$. Here, in our case, we have only one electrode, and photoelectrons are transported to adjacent non-irradiated zones.

A fast and uniform photocurrent response is clearly observed for the switch-on and -off events on SVET. A dark current is quickly achieved after irradiation is switched off. In the stationary mode, the current density line scans and current density maps associated with the photocurrent can be measured to determine the degree of localization. A dash red line of the
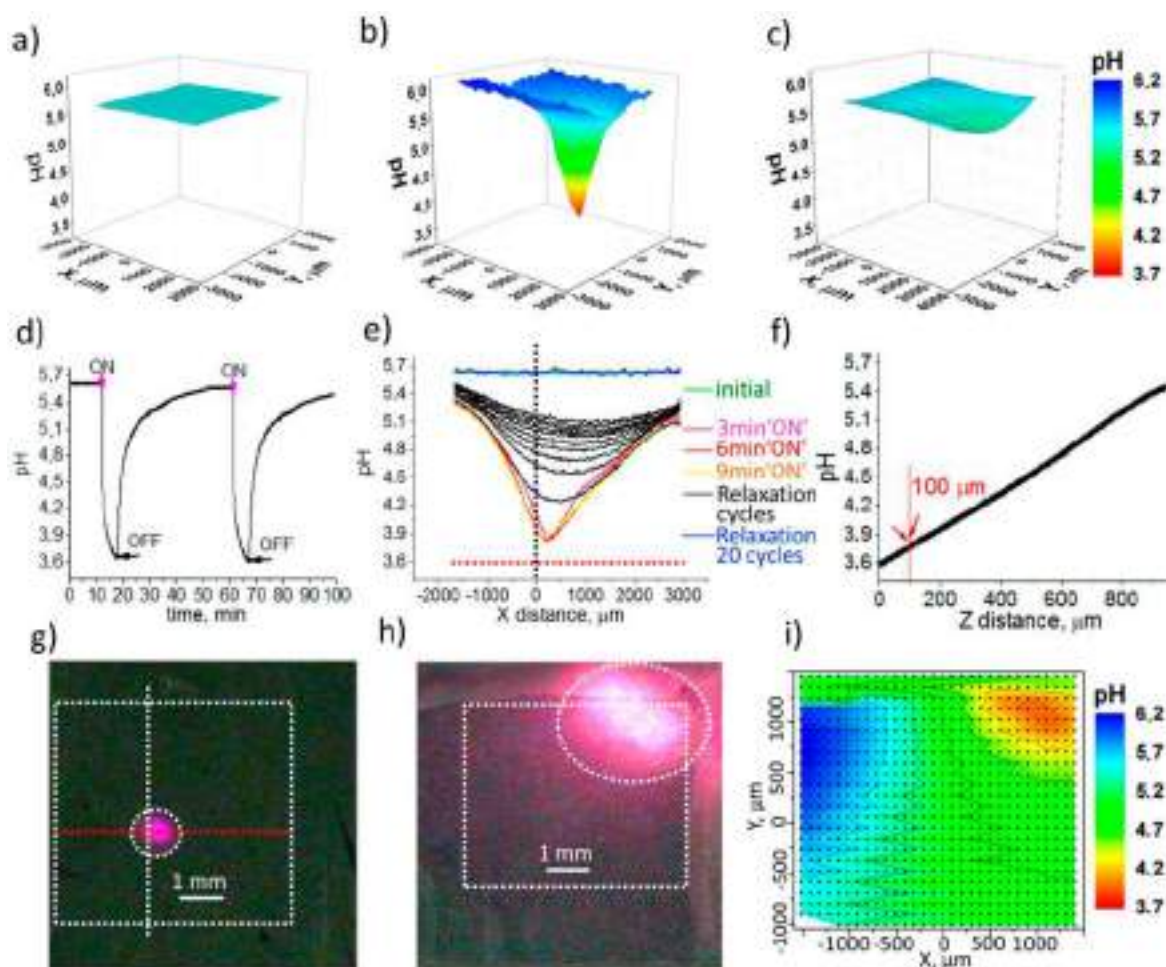
Figure 3. Light-induced flexible pH gradient and proton pumping. Maps obtained by the in situ scanning ion-selective electrode technique (SIET) to analyze local pH gradients generated on nanostructured TiO$_2$: (a) before irradiation, (b) during local irradiation, and (c) after irradiation (20 min of relaxation). (d) pH measurement inside an irradiation spot (shown in panel g) and single-spot time-evolution measurements on a titania layer after switching on and switching off the light. (e) Local pH measurements in a line (shown in panel g in red) before, during, and after irradiation (maximum coincides with the position of the irradiating spot, and the time of measurement of each line was 3 min). (f) pH in the Z direction during illumination inside the irradiated spot. (g) X−Y dashed lines shown in optical image of the surface and the location of the focused irradiation spot on TiO$_2$ described above (panels a−e) mapped in panels a−c. (h) X−Y optical image with defocused light to show the flexibility of the method to change intensity of illumination and its location and effect on the pH gradient of the surface with corresponding (i) pH map with color-pointed acidic and basic pH areas.

moving probe is indicated in Figure 2c, and the corresponding current density is shown in Figure 2e. The ionic current can be monitored versus the location of the irradiated spot. The precise value in the center under the stationary mode is 80 μA/cm^2.

After the irradiation is switched off, the current relaxation in solution is shown in lines acquired every 3 min. Within 3 min after the irradiation is switched off the current density drops to 10 μA/cm^2. Six min after the irradiation is switched off no photocurrent is detected.

Imaging and localization (Figure 2h) of the positions of hole- or electron-induced reactions across the surface relative to its irradiation spot are also measured with SVET. No currents are detected before and after irradiation (Figures 2g,i), but during irradiation, ionic currents appear in solution in response to localized surface irradiation and are positive in the irradiated points and slightly negative in the rest of the surface.

Figure 2f shows the photocurrent density versus applied bias curves under chopped illumination for the two electrode configuration (TiO$_2$ working electrode and Pt counter electrode). In comparison with the dark current, the photocurrent increases significantly with the positive scanning of the applied potential, indicating a standard n-type behavior of TiO$_2$. The on−off cycle measurements show a well-defined photoresponse after turning-on and turning-off illumination. Moreover, the value of the onset potential (Figure 2f inset) for reverse cycle is shifted to the positive direction, which can be explained by a change of the surface pH; this effect was studied in detail in situ with the scanning ion-selective electrode technique (Figure 3).

For pH modulation with light, it is important to understand how photoinitiated processes on TiO$_2$ result in the transformation of light into a pH change, including the localization of the effect. We apply SIET for mapping of the activity and migration of H$^+$ ions over the TiO$_2$ surface. SIET is one of the model unique techniques for measuring in situ change in ion concentrations very locally in space and following the processes' dynamic qualities in time. It has a big advantage for pH map monitoring because it is a unique method that allows one to measure local pH change near the surface without
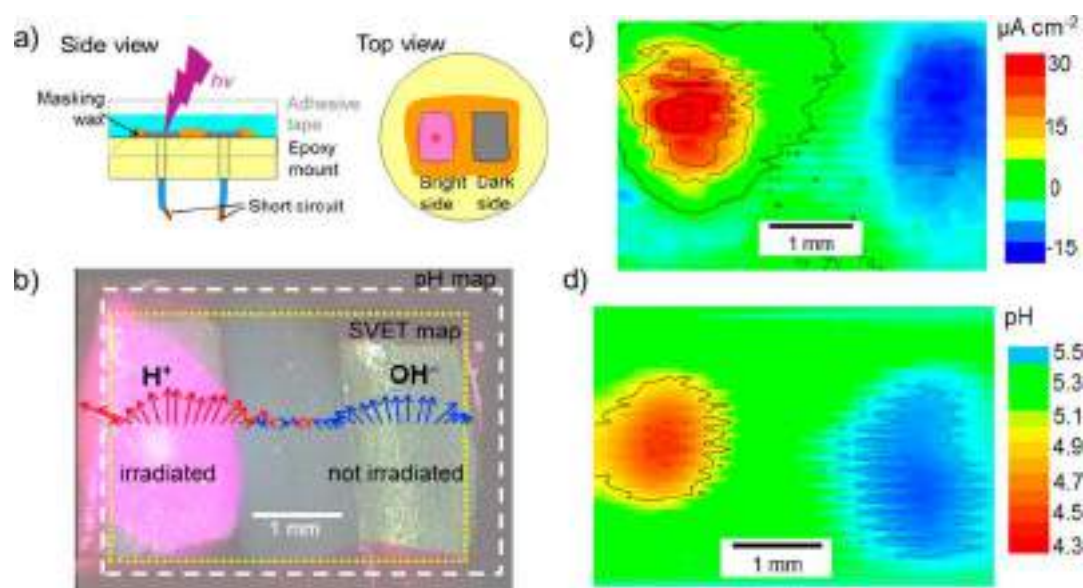
Figure 4. Prospects of chemical networking in open system. (a) Schematics of the electrochemical cell used for studying local changes in the electrolyte created by the spatial separation of light stimulated reactions on TiO$_2$. (b) Image of the cell surface with the two TiO$_2$ electrodes: one irradiated electrode with primary reaction with the photohole, production of protons, and local acidification in addition to another non-irradiated electrode with local production of hydroxide ions. The arrows are 2D vectors of the current density measured by SVET associated with the oxidation (red) and reduction (blue) reactions. The yellow dashed area corresponds to SVET map presented in panel c, and the white area indicates the pH map in panel d. (c) SVET map of the current density in solution crossing a plane parallel to the surface 100 μm above it with positive (anodic) currents in the irradiated area and negative (cathodic) currents in the non-irradiated areas. (d) SIET pH map showing local acidification in the irradiated spot and alkalization in the non-irradiated area.

any pH-sensitive dyes (markers) in the system. Dyes may themselves affect the photoreaction; here, we solved the problem. Maps of the pH are collected for pristine TiO$_2$: before illumination (Figure 3a), during illumination (Figure 3b), after switching off the irradiation, and during 40 min of relaxation (Figure 3c).

It is seen from the presented proton distribution maps that, under irradiation, as suggested in Figure 1, the reaction of the generation of protons is observed. The protons are pumped from irradiated TiO$_2$ and have a gradient over the surface. It is important to note here that an existing approach for static and localized pH gradients relies on predefined configurations of the microelectrodes.[37] However, in our case, the big advantage is that we can operate in an open system without any membranes or patterning just by changing the localization of the irradiation spot to provide a proton pump at different places and varying the intensity of illumination. To change the gradient patterns, the redesign and refabrication of photomasks, microelectrodes, and, sometimes, the chip structures themselves are required.[38] This flexibility of pH gradients is promising for the creation of life-inspired nanoscale machinery.

The other assumption may be that H$^+$ appears under UV and that OH$^-$ appears everywhere, especially at the same place as H$^+$, but that they are canceled by H$^+$. They are also produced at a longer distance but reduced quantity. We see on Figures 2h and 3b that there are some dark blue spots close to the peak. This vicinity could be explained by a limitation of the mobility of electrons, which recombine as close as possible from the UV site. It could also be explained by an attractive potential resulting from excess positive charge due to solvated H$^+$; both account for the blue spots.

The action of different photoelectrochemical reactions on the TiO$_2$ surface under UV illumination seems to be the only plausible explanation for the observed local acidification and is consistent with the mechanism proposed in Figure 1. It is seen from the SIET pH maps (Figure 3a−c) that the system effectively produces microscale pH gradients. Such engineering of pH gradients and proton pumping on TiO$_2$ can be important for various chemical and biological networks. The simplest one discussed here is the water protonation and the following system deactivation with hydroxyl ions (Figure 1). Instead of immobilized pH gradients in gels, microscale pH gradients in open systems provide new avenues for on-chip reaction networks and the identification and transfer of proteins and large molecules.

The focused single-spot measurement (Figure 3d) and line scan (Figure 3e) inside and across the irradiation spot visibly prove the effect of acidification in the irradiation spot and a slight increase of the pH in the remaining area. In comparison with SVET measurements after switching off irradiation, the relaxation time for the pH gradient is longer: 1−3 min for photocurrent versus ca. 40 min for pH gradient. Total system relaxation and return to dark characteristics is ca. 40 min (Figure 3e) for the TiO$_2$ surface used.

The relaxation time depends on morphology and characteristics of the used semiconductor surface. All above-mentioned SIET measurements were performed at 100 μm above the surface. To measure variation of the pH as a function of the distance from irradiated TiO$_2$ surface, the probe microelectrode was moved from a 2000 μm to a 0 μm distance in the Z direction. Interestingly, a linear gradient of the pH was observed in the 0−350 μm range. In the distance from 350 to approximately 1000 μm above the TiO$_2$ surface, the pH changes have shown nonlinear behavior, which can be connected with diffusion of H$^+$. The pH value above 1250 μm leveled off. In Figure 3f, the pH is plotted going from 0 to 1000 μm in the Z direction. Thus, the in situ SIET results prove that we can effectively modulate the H$^+$ activity over the

surface. Still, there remain important questions about the separation of the processes of photogeneration for H^+ and OH^- ions laterally over the TiO_2 surface.

We localized the illumination spot, and defocused (decreased the intensity of irradiation from 5 to 1 mW/cm^2) XY optical images of the surface with an illumination spot are shown in Figure 3g,h and correspond to pH maps in panels a–c and i in Figure 3, respectively. The SIET map of pH activity is shown in Figure 3i when we decrease the intensity of illumination and locate it at the edge of the measured area. We are able to see on the same surface zone the separated H^+ and OH^- activity, which was also assumed looking at Figure 3b. Several other conclusions can be suggested on the basis of SIET measurement shown in Figure 3i: the pH gradient is located in a designed way via the irradiation spot (a big advantage in comparison with nonflexible predesigned electrode pH localization[39]). It is possible to further modify the system to have a pH gradient (Figure 1), and it is worth discussing with respect to flexible surface process localization. The question is whether we can also locate the electrodes at a certain distance that have further flexibility.

We placed two TiO_2 electrodes electrically connected from the back and shined light on one of them (Figure 4). The experiment clearly indicates the distinct advantage of the combined use of photoanodes and cathodes for the microscale pH gradient profiles of both H^+ and OH^-. On the irradiated electrode, the positive current is detected versus the negative one on the non-irradiated one (Figure 4c); however, electrodes are located in the same epoxy holder and the same solution. pH maps follow the tendency of the photocurrent; there is acidification on the irradiated surface and alkalinization on the non-irradiated one (Figure 4d).

CONCLUSIONS

Light illumination of a photoconductive surface generates a conducting point that serves as a photoanode and cathode where protons and hydroxide ions are produced, leading to an increase and decrease, respectively, in the pH gradient in an open system. The flexible spatial addressability is a great advantage for open-system modulation. The spatial–temporal localization of light over photoelectrodes allows the characterization of gradient profiles without any refabrication of electrode patterns. A bimodal electrolysis enables the fine-tuning of gradient profiles and enriches the variety of available gradient patterns. Thus, the superposition of bimodal pH gradients offers a practical solution to spatially modulating pH-gradient patterns. As a corollary, this procedure also enriches the variety of available gradient patterns, which can be applied to many different experiments, such as artificially reconstructing and applying complicated biological pH gradient patterns to cells in vitro.

In this study, we introduced a novel life-inspired light-addressing method to generate microscale pH gradients and proton pumping at desired locations on a semiconductor substrate. It is always advantageous if well-studied, reliable materials can be applied to obtain new functions. Here, TiO_2 is efficient for "inorganic photoproton" cycling. Light irradiation is spatially patterned by the virtual electrodes selected by light. There are photoanode and cathode sites for H_2O electrolysis. The electrolysis at the pointed locations produces H^+ and OH^-, thus inducing pH changes. The pH imaging with in situ SIET successfully demonstrated that pH gradients were generated around the light-addressed areas. The characterization of

gradient dimensions generated by different irradiation areas and intensity proved the prominent advantage of the light-addressing technique and, in particular, the spatial flexible localization of photocathodes and photoanodes. The high degree of freedom in photoanode and photocathode location is promising for the tuning of pH gradient profiles. Another advantage of the present method is the combined use of photoanodes and photocathodes and time-controlled illumination. One can imagine a variety of gradient patterns that can be generated, for example, by multipoint surface simultaneous illumination.

EXPERIMENTAL METHODS

Titanium plates (1 mm thickness, 99.6% purity) were chemically polished in hydrofluoric acid–HNO_3 concentrated acid mixtures (1:2 in volume) to a mirror finish followed by rinsing with deionized water and drying in a stream of air. The two-step anodization was carried out in ethylene glycol with the addition of 0.75 wt % NH_4F and 2 vol % H_2O. The anodization procedure consisted of a potential ramp from 0 to 40 V (sweep rate of 200 mV s^{-1}) followed by holding of the potential constant for 1 h. The samples prepared during the first step of anodization were then ultrasonically treated in deionized water to strip off the formed TiO_2 layer and expose the underneath titanium substrate. Afterward, the titanium plate was subjected to the second anodization in the same electrolyte under the same regime to create the TiO_2 film with the more-ordered structure of vertically aligned nanopores (approximately 60 nm in diameter). Next, the resultant film was rinsed with ethanol, kept in ethanol for several hours, and dried in a stream of air.

As-prepared titania nanotubular film is amorphous. To induce its crystallization, annealing was carried out at 450 °C for 3 h in air at a heating rate of 5 °C min^{-1}. The annealed samples were then used for the SVET and SIET measurements.

SVET and SIET measurements were performed on samples glued to an epoxy support. Beeswax was utilized to insulate each sample, leaving a window of a few square millimeters exposed to the testing solution, 0.05 M Na_2SO_4. The measurements were made with a commercial system (Applicable Electronics Inc.) and the ASET software from ScienceWares. The vibrating microelectrode for SVET was an insulated Pt–Ir wire with a Pt black deposited on a spherical tip of 20 μm diameter. The probe was located 100 μm above the surface and vibrated with frequencies of 112 and 67 Hz in the directions, respectively, normal and parallel to the surface with 10 μm amplitude. The time for each SVET map (40 × 40 points) was about 15 min.

For SIET measurements, H^+-selective microelectrodes were prepared from single-barrelled borosilicate glass capillaries with an outer diameter of 1.5 mm. The P-97 Flaming/Brown Micropipette Puller, (Sutter Instruments Company) was used to shape the cone tip. The diameter of the apex of the tip was 2 μm. The capillaries were then silanized by injecting 200 μL of N,N-dimethyltrimethylsilylamine in a glass preparation chamber at 200 °C. The membrane for H^+-selective microelectrodes was composed of 6 wt % 4-nonadecylpyridine, 93 wt % 2-nitrophenyloctyl ether, and 1 wt % potassium tetrakis(4-chlorophenyl)borate. The inner reference solution contained a buffer made of 0.01 M KH_2PO_4 in 0.1 M KCl. The liquid membranes were introduced in the glass tip using an optical microscope with two 3D micromanipulators. The column length of proton sensitive probe was about 25–30 μm. A silver chlorinated wire was inserted into the internal solution as the inner reference electrode. The ion-selective microelectrodes were placed 100 μm above the monitored surface on a 30 × 30 grid (900 data points). The time of acquisition for each SIET data point was 2 s, resulting in a total scan time of about 35 min, which also includes the time for the electrode to move from point to point. In some cases, the probe was placed in a fixed position, monitoring the pH or SVET response over time. A homemade Ag/AgCl/0.1 M KCl, 0.01 M KH_2PO_4 electrode was used as an external reference electrode. The microelectrodes were mounted on the SVET–SIET system to control the position and program the

measurements. A preamplifier of 10^{15} Ω input impedance was used to measure the potential. A move−wait−measure scheme was employed for mapping above the surface.

Photoelectrochemical measurements were performed on Autolab PGSTAT 302N potentiostat in a three-electrode quartz cell equipped with a platinum counter-electrode and a saturated calomel reference electrode (SCE).

Local illumination of the TiO_2 film surface was performed using a setup equipped with UV LED (365 nm; 3 W), allowing different intensities of irradiation, e.g., 1 and 5 mW/cm², supplied by a current stabilizer and a UV light beam focusing system involving several quartz lenses.[39]

■ AUTHOR INFORMATION

Corresponding Author
*E-mail: skorb@scamt.ru.

ORCID ⓘ
Ekaterina V. Skorb: 0000-0003-0888-1693

Notes
The authors declare no competing financial interest.

■ ACKNOWLEDGMENTS

■ REFERENCES

(1) Grzybowski, B. A.; Huck, W. T. S. The Nanotechnology of Life-Inspired Systems. *Nat. Nanotechnol.* **2016**, *11*, 585−592.

(2) Chen, J. W.; Wezenberg, S. J.; Feringa, B. L. Intramolecular Transport of Small-Molecule Cargo in a Nanoscale Device Operated by Light. *Chem. Commun.* **2016**, *52*, 6765−6768.

(3) Kudernac, T.; Ruangsupapichat, N.; Parschau, M.; Macia, B.; Katsonis, N.; Harutyunyan, S. R.; Ernst, K. H.; Feringa, B. L. Electrically Driven Directional Motion of a Four-Wheeled Molecule on a Metal Surface. *Nature* **2011**, *479*, 208−211.

(4) Eelkema, R.; Pollard, M. M.; Vicario, J.; Katsonis, N.; Ramon, B. S.; Bastiaansen, C. W. M.; Broer, D. J.; Feringa, B. L. Nanomotor Rotates Microscale Objects. *Nature* **2006**, *440*, 163−163.

(5) Wong, A. S. Y.; Postma, S. G. J.; Vialshin, I. N.; Semenov, S. N.; Huck, W. T. S. Influence of Molecular Structure on the Properties of Out-of-Equilibrium Oscillating Enzymatic Reaction Networks. *J. Am. Chem. Soc.* **2015**, *137*, 12415−12420.

(6) Hermans, T. M.; Stewart, P. S.; Grzybowski, B. A. pH Oscillator Stretched in Space but Frozen in Time. *J. Phys. Chem. Lett.* **2015**, *6*, 760−766.

(7) Semenov, S. N.; Kraft, L. J.; Ainla, A.; Zhao, M.; Baghbanzadeh, M.; Campbell, V. E.; Kang, K.; Fox, J. M.; Whitesides, G. M. Autocatalytic, Bistable, Oscillatory Networks of Biologically Relevant Organic Reactions. *Nature* **2016**, *537*, 656−660.

(8) Ichimura, K. Nonlinear Organic Reactions to Proliferate Acidic and Basic Molecules and their Applications. *Chem. Rec.* **2002**, *2*, 46−55.

(9) Whitesides, G. M. Bioinspiration: Something for Everyone. *Interface Focus* **2015**, *5*, 20150031.

(10) Semenov, S. N.; Wong, A. S. Y.; van der Made, R. M.; Postma, S. G. J.; Groen, J.; van Roekel, H. W. H.; de Greef, T. F. A.; Huck, W. T. S. Rational Design of Functional and Tunable Oscillating Enzymatic Networks. *Nat. Chem.* **2015**, *7*, 160−165.

(11) Kato, M.; Zhang, J. Z.; Paul, N.; Reisner, E. Protein Film Photoelectrochemistry of the Water Oxidation Enzyme Photosystem II. *Chem. Soc. Rev.* **2014**, *43*, 6485−6497.

(12) Rivera-Chavez, F.; Baumler, A. J. The Pyromaniac Inside You: Salmonella Metabolism in the Host Gut. *Annu. Rev. Microbiol.* **2015**, *69*, 31−48.

(13) Koumura, N.; Zijlstra, R. W. J.; van Delden, R. A.; Harada, N.; Feringa, B. L. Light-Driven Monodirectional Molecular Rotor. *Nature* **1999**, *401*, 152−155.

(14) Kolesnikova, T. A.; Kohler, D.; Skirtach, A. G.; Möhwald, H. Laser-Induced Cell Detachment, Patterning, and Regrowth on Gold Nanoparticle Functionalized Surfaces. *ACS Nano* **2012**, *6*, 9585−9595.

(15) Krpetić, Ž.; Nativo, P.; Sée, V.; Prior, I. O.; Brust, M.; Volk, M. Inflicting Controlled Nonthermal Damage to Subcellular Structures by Laser-Activated Gold Nanoparticles. *Nano Lett.* **2010**, *10*, 4549−4554.

(16) Skorb, E. V.; Möhwald, H.; Andreeva, D. V. How Can One Controllably Use of Natural ΔpH in Polyelectrolyte Multilayers? *Adv. Mater. Interfaces* **2017**, *4*, 1−15.

(17) Ulasevich, S. A.; Brezesinski, G.; Möhwald, H.; Fratzl, P.; Schacher, F. H.; Poznyak, S. K.; Andreeva, D. V.; Skorb, E. V. Light-Induced Water Splitting Causes High-Amplitude Oscillation of pH-Sensitive Layer-by-Layer Assemblies on TiO_2. *Angew. Chem., Int. Ed.* **2016**, *55*, 13001−13004.

(18) Ulasevich, S. A.; Brezhneva, N.; Zhukova, Y.; Möhwald, H.; Fratzl, P.; Schacher, F. H.; Sviridov, D. V.; Andreeva, D. V.; Skorb, E. V. Switching the Stiffness of Polyelectrolyte Assembly by Light to Control Behavior of Supported Cells. *Macromol. Biosci.* **2016**, *16*, 1422−1431.

(19) Andreeva, D. V.; Melnyk, I.; Baidukova, O.; Skorb, E. V. Local pH Gradient Initiated with Light on TiO_2 for Light-Triggered Polyhistidine-Tagged Proteins Modulation. *ChemElectroChem* **2016**, *3*, 1306−1310.

(20) Skorb, E. V.; Sviridov, D. V.; Möhwald, H.; Shchukin, D. G. Light-Controllable Nanocontainer-Coatings for Corrosion Healing. *Chem. Commun.* **2009**, 6041−6043.

(21) May, M. M.; Lewerenz, H. J.; Lackner, D.; Dimroth, F.; Hannappel, T. Efficient Direct Solar-to-Hydrogen Conversion by in Situ Interface Transformation of a Tandem Structure. *Nat. Commun.* **2015**, *6*, 8286.

(22) Andreeva, D. V.; Kollath, A.; Brezhneva, N.; Sviridov, D. V.; Cafferty, B. J.; Möhwald, H.; Skorb, E. V. Using a chitosan nanolayer as an efficient pH buffer to protect pH-sensitive supramolecular assemblies. *Phys. Chem. Chem. Phys.* **2017**, DOI: 10.1039/C7CP02618H

(23) Skorb, E. V.; Antonouskaya, L. I.; Belyasova, N. A.; Shchukin, D. G.; Mohwald, H.; Sviridov, D. V. Antibacterial Activity of Thin-Film Photocatalysts based on Metal-Modified TiO_2 and TiO_2:In_2O_3 Nanocomposite. *Appl. Catal., B* **2008**, *84*, 94−99.

(24) Schneider, J.; Matsuoka, M.; Takeuchi, M.; Zhang, J. L.; Horiuchi, Y.; Anpo, M.; Bahnemann, D. W. Understanding TiO_2 Photocatalysis: Mechanisms and Materials. *Chem. Rev.* **2014**, *114*, 9919−9986.

(25) Byk, T. V.; Sokolov, V. G.; Gaevskaya, T. V.; Skorb, E. V.; Sviridov, D. V.; Noh, C. H.; Song, K. Y.; Kwon, Y. N.; Cho, S. H. Photochemical Selective Deposition of Nickel Using a TiO_2-Pd^{2+} Layer. *J. Photochem. Photobiol., A* **2008**, *193*, 56−64.

(26) Skorb, E. V.; Grützmacher, D.; Dais, C.; Guzenko, V. A.; Sokolov, V. G.; Gaevskaya, T. V.; Sviridov, D. V. Titania-Assisted Electron-Beam and Synchrotron Lithography. *Nanotechnology* **2010**, *21*, 315301.

(27) Skorb, E. V.; Sokolov, V. G.; Gaevskaya, T. V.; Sviridov, D. V. Photocatalytic Lithography with Image Inversion. *Theor. Exp. Chem.* **2009**, *45*, 40−43.

(28) Green, J. R.; Costa, A. B.; Grzybowski, B. A.; Szleifer, I. Relationship Between Dynamical Entropy and Energy Dissipation far from Thermodynamic Equilibrium. *Proc. Natl. Acad. Sci. U. S. A.* **2013**, *110*, 16339−16343.

(29) Emond, M.; Le Saux, T.; Allemand, J. F.; Pelupessy, P.; Plasson, R.; Jullien, L. Energy Propagation Through a Protometabolism Leading to the Local Emergence of Singular Stationary Concentration Profiles. *Chem. - Eur. J.* **2012**, *18*, 14375−14383.

(30) Yoshida, R.; Ueki, T. Evolution of Self-Oscillating Polymer Gels as Autonomous Polymer Systems. *NPG Asia Mater.* **2014**, *6*, e107.

(31) Skorb, E. V.; Möhwald, H. 25th Anniversary Article: Dynamic Interfaces for Responsive Encapsulation Systems. *Adv. Mater.* **2013**, *25*, 5029−5042.

(32) Jha, P. K.; Kuzovkov, V.; Grzybowski, B. A.; de la Cruz, M. O. Dynamic Self-Assembly of Photo-Switchable Nanoparticles. *Soft Matter* **2012**, *8*, 227−234.

(33) Wei, Y. K.; Su, J. Z.; Wan, X. K.; Guo, L. J.; Vayssieres, L. Spontaneous Photoelectric Field-Enhancement Effect Prompts the Low Cost Hierarchical Growth of Highly Ordered Heteronanostructures for Solar Water Splitting. *Nano Res.* **2016**, *9*, 1561−1569.

(34) Kopf, J.; Ulasevich, S.; Baidukova, O.; Zhukova, Y.; Dunlop, J. W. C.; Fratzl, P.; Rikeit, P.; Knaus, P.; Poznyak, S. K.; Andreeva, D. V.; Skorb, E. V. Ultrasonically Produced Porous Sponge Layer on Titanium to Guide Cell Behavior. *Adv. Eng. Mater.* **2016**, *18*, 476−483.

(35) Nakamura, R.; Nakato, Y. Primary Intermediates of Oxygen Photoevolution Reaction on TiO_2 (Rutile) Particles, Revealed by In Situ FTIR Absorption and Photoluminescence Measurements. *J. Am. Chem. Soc.* **2004**, *126*, 1290−1298.

(36) Nakamura, R.; Imanishi, A.; Murakoshi, K.; Nakato, Y. In Situ FTIR Studies of Primary Intermediates of Photocatalytic Reactions on Nanocrystalline TiO_2 Films in Contact with Aqueous Solutions. *J. Am. Chem. Soc.* **2003**, *125*, 7443−7450.

(37) Xiang, Q. J.; Yu, J. G.; Jaroniec, M. Enhanced Photocatalytic H_2-Production Activity of Graphene-Modified Titania Nanosheets. *Nanoscale* **2011**, *3*, 3670−3678.

(38) Suzurikawa, J.; Nakao, M.; Kanzaki, R.; Takahashi, H. Microscale pH Gradient Generation by Electrolysis on a Light-Addressable Planar Electrode. *Sens. Actuators, B* **2010**, *149*, 205−211.

(39) Fiedler, S.; Hagedorn, R.; Schnelle, T.; Richter, E.; Wagner, B.; Fuhr, G. Diffusional Electrotitration − Generation of pH Gradients over Arrays of Ultramicroelectrodes Detected by Fluorescence. *Anal. Chem.* **1995**, *67*, 820−828.

PAPER

Microbubbles trigger oscillation of crystal size in solids†

Anna Kollath,[a] Nadzeya Brezhneva,[b] Ekaterina V. Skorb[bc] and Daria V. Andreeva*[d]

An understanding of the nature and conditions of nonlinear processes in open systems is important for modulation of the microstructure of solids at a new level of complexity. We demonstrate that cavitation generated by high intensity ultrasound (HIUS) triggers nonlinear processes in microparticles and layers of titanium. We reveal a non-monotonic dependence of the size of grains in the treated solids on sonication time, and oscillation of titanium grain sizes *vs.* time of ultrasonic treatment, indicating the influence of two opposing forces: cavitation driven impact of shock heating and shear stress on surfaces. These nonlinear self-organization processes in solids promise new microstructured materials with applications among others in bio- and geosciences.

Introduction

Nonlinear modulation of microstructures concerns questions also relevant for understanding the origin of life,[1] materials science,[2] geoscience[3] and bio[4] science. Recent examples of self-organization are the formation of chiral[5] and hierarchically structured porous metal composites,[6] epitaxial strain induced transitions in layered oxides,[7] switchable infrared nanophotonic elements based on phase change materials,[8] design of autonomous motors,[9] *etc.*

However, the main question is how to establish dynamic control of useful characteristics, for example dynamic control of crystal/grain size and composition modulation in solids. A possible answer is to develop a new generation of dynamic impactors that can trigger spatiotemporal oscillations of structures and functions.

Ultrasonically triggered cavitation, which can be defined as generation, growth and violent collapse of microbubbles, is a unique but underappreciated approach for generating a strong shock impact and thus a rapid increase of temperature and pressure at a localized area (<0.02 μm).[10–12] It was demonstrated that shock waves in a cavitating suspension triggered opposite

effects, for example, melting of metal particles and formation of aggregates,[13] fragmentation of solids and disaggregation.[14]

Close to the center of a cavitation bubble, the electron temperature can reach tens of eV.[10–12] Upon bubble collapse the energy is converted into mechanical (molecular and atomic movements), thermal (random movements of atoms and molecules) and chemical energy (cleavage of chemical bonds).[15] Thus, shock impact creates highly non-equilibrium conditions for dynamic modification of liquids and solids. Here, we study the linearity of cavitation driven microstructural changes in titanium (Ti), namely changes in Ti grain sizes *vs.* time of ultrasonic treatment (sonication).

We propose that cavitation is a powerful and dynamic impactor for the modulation of solids at the atomic level. Interaction of microbubbles with surfaces can drive several forces that can lead to both grain growth and grain size reduction in solids. The main questions are: which forces drive grain growth and which forces trigger grain size reduction? What is the coupling mechanism that allows periodic switching between forces in the cavitating medium and leads to nonlinear effects in solids?

Recently, in order to elucidate the cavitation driven processes in solids we used heterogeneous AlNi alloys.[16,17] The analysis of the kinetics of crystal growth showed that the crystallite sizes of the intermetallic phases in AlNi alloys oscillate with treatment time.[16,18] These very interesting results raised questions about the physics underlying the non-monotonic changes of crystal sizes *vs.* time of cavitation impact, especially from the aspect of energy transfer in dissipative systems.[19,20] We demonstrated that propagation of cavitation generated huge temperature gradients in solids, which led to crystal growth and formation of materials with a compositional gradient.[17,21] However, what is the opposite force that might stimulate crystal size reduction and what is the coupling mechanism that provides periodic changes in the microstructure?

[a] *Physical Chemistry II, University of Bayreuth, Universitätsstraße 30, 95440 Bayreuth, Germany*

[b] *Max Planck Institute of Colloids and Interfaces, Am Mühlenberg 1, 14424 Potsdam, Germany*

[c] *Laboratory of Solution Chemistry of Advanced Materials and Technologies, ITMO University, 197101 St. Petersburg, Russian Federation*

[d] *Center for Soft and Living Matter, Institute for Basic Science, Ulsan National Institute of Science and Technology, 44919 Ulsan, Republic of Korea. E-mail: daria.baeumler@gmail.com*

In order to answer these questions we investigated microstructural and morphological changes in ultrasonically treated titanium (Ti). Ti is a relatively hard ductile material with a high melting point (1941 K).[22] It is resistant to corrosion and is a poor conductor of heat.[23,24] Thus, this material is an appropriate candidate for the investigation of cavitation induced nonlinear microstructural changes in solids. Additionally, Ti is the ninth-most abundant element in the Earth's crust (0.63 wt%) and has a broad range of biomedical, pharmaceutical and industrial applications.[25]

Here we report on the impact of cavitation on Ti using two systems: suspensions of Ti microparticles and Ti layers evaporated on a silicon substrate. In suspensions of cavitating particles energy dissipation is believed to occur *via* violent interparticle collisions.[13] If Ti layers are used, energy is transferred from a direct impact of microbubbles on the Ti surface, namely upon bubble collapse near/at the solid–liquid interface. However, the factors, namely surface roughness, composition, *etc.*, that affect energy transfer from cavitation bubbles to solids is not well understood. We followed microstructural changes in bulk Ti and on Ti surfaces, found an oscillation of Ti grain sizes *vs.* time of ultrasonic treatment and revealed the impact of cavitation driven shock heating and shear stress on grain growth and reduction cycles.

Results and discussion

The oscillation of grain sizes *vs.* sonication time in cavitating suspensions of Ti microparticles is shown in Fig. 1A. The size of grains after 3 min of treatment was nearly twice as large ($\sim$300 nm), as compared to the untreated particles ($\sim$160 nm). The observed grain growth can be explained by local heating of particles in the cavitating medium. However, after 5 min of treatment the size of the grains reduced to $\sim$200 nm and reached the initial value after 7 min of treatment. The grain size reduction might be explained by the formation of defects. As seen in Fig. 1A longer treatment led to a periodic increase and decrease in the grain size *vs.* treatment time. The interesting question is: how can cavitation trigger two opposite processes – grain growth and grain size reduction?

The observed decay in the period and intensity of oscillation allows the effect of cavitation intensity on matter to be monitored. The decay can be explained by a decrease in cavitation intensity. It is known that the intensity of continuous cavitation decreases with time due to degassing of the medium, which then leads to an increase in the nucleation barrier of the bubbles.[14,26,27] An additional source of the gas phase can accelerate recrystallization.[28] Bubbling of gas during sonication, the use of pulsed ultrasonic modes as well as gas-forming reactions in the ultrasonic medium help to avoid fading of the cavitation intensity. Thus, we see that the amplitude of crystal size oscillation depends on the intensity of cavitation, namely on the number of cavitation bubbles and, thus on the frequency of nucleation events and the number of cavitation bubbles generated by ultrasound.
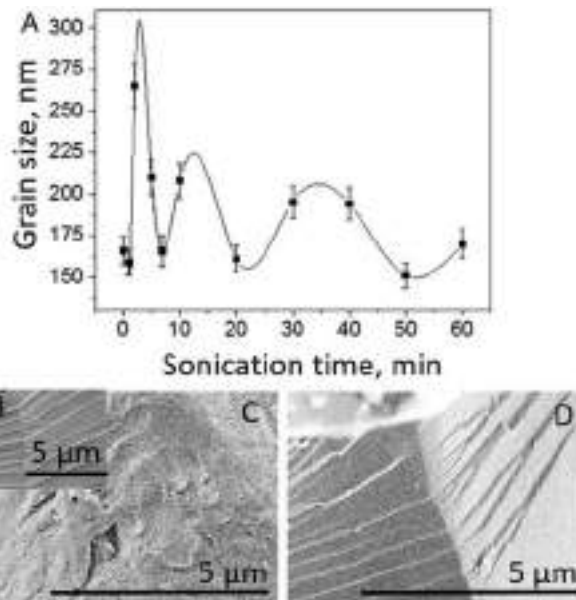
Fig. 1 Oscillation of grain size of Ti microparticles as a function of sonication time (A). Scanning electron microscopy image of the surface of the initial Ti particles (B) and after 5 (C) and 60 min (D) of HIUS modification.

On the surface of cavitated Ti microparticles (Fig. 1C) we obtained evidence of cavitation induced fractures and shear bands. It is very important that the type of crease depends on the treatment time. After 5 min of modification, we observe the formation of microdefects. However, after 60 min of modification (Fig. 1D) the surface is covered with well-defined shear bands. Thus, we can propose that the collapse of cavitation bubbles in suspensions of Ti microparticles triggers both microstructural changes in the interior of the particles and morphological changes on the surface of Ti. An interesting question is whether ultrasonic energy is transferred to solids *via* interparticle collisions or *via* bubble collapse at/near liquid–solid interfaces.

The collapse of cavitation bubbles and generation of shock stimulate very fast atomic and molecular movements at speeds comparable with the speed of sound in a liquid. In ethylene glycol, the speed of sound at 333 K is 1660 m s^{-1}.[29] However, the direct measurement of particle velocity in ethylene glycol at 10% intensity of ultrasound using optical microscopy and a high speed camera reveals that the speed of particle movement is around 1.3 m s^{-1}. Using this velocity v, the viscosity η, and the density ρ of ethylene glycol at 333 K and the diameter d of the Ti particles used ($\sim$150 μm) we can calculate the Reynolds number (Re):[30]

$$\mathrm{Re} = \frac{\rho v d}{\eta}$$

Re of a cavitating suspension of Ti particles at 10% of intensity can be up to $\sim$40. It is obvious that such extreme hydrodynamic conditions can trigger strong shear at the surfaces and, therefore, cause changes in the microstructure and morphology of the particles. However, an interesting question is whether the observed microstructural changes can be achieved, if we

This journal is © the Owner Societies 2017

Phys. Chem. Chem. Phys., 2017, **19**, 6286–6291 | 6287

avoid shear stress due to particle movements. Can the impact of bubble collapse near/at solid–liquid interfaces trigger oscillation of grain sizes on metal surfaces?

We expect that oscillation of the grain size can be achieved in the absence of particle movement, since extreme hydrodynamic conditions and turbulent flow might be due to bubble collapse and shock impact on the metal surface.

In order to prove our suggestion, we investigated the effects of cavitation bubbles on the microstructure and morphology of 2 μm Ti layers evaporated on silicon wafers. In these experiments, we monitored the impact of cavitation bubbles on the metal surface and excluded interparticle collisions.

Fig. 2 shows that the samples sonicated for 1, 5 and 10 min exhibit different surface morphologies. We observe an increase in the size of the grains on the surfaces of the samples after 5 min of treatment. The surfaces of the samples sonicated for 1 min showed the appearance of new grain boundaries. After 10 min of modification we revealed a decrease in the grain size.

Furthermore, calculation of the average size of grains on the Ti surface using TM AFM image analysis proves a non-monotonic dependence of grain size *vs.* sonication time. The grain size values are plotted in Fig. 3A. The grain size of the initial Ti surface was ~65 nm. After 1 and 10 min of sonication the crystal size was reduced to ~60 nm. However, the crystal sizes on the surfaces modified for 5 min were ~70 nm.

Monitoring of the grain size in the interior of Ti layers using XRD (Fig. 3B) also reveals a non-monotonic dependence of the grain size on sonication time in the bulk material as on the

Fig. 3 Non-monotonic dependence of the grain size on sonication time: A – the surface grain size measured by AFM; B – the interior grain size of Ti layers calculated using XRD data; C – the surface roughness of Ti.

Fig. 2 AFM images of the initial (A) and HIUS treated Ti surfaces for 1 (B), 5 (C), and 10 (D) min. The new grain boundaries, and large and small grains are highlighted.

surface of Ti layers. The initial size of the grains in untreated Ti is ~45 nm and increases to ~50 nm after 1 and 10 min of sonication and reduces to ~40 nm after 5 min of sonication. It is obvious that the observed oscillations in Ti layers are slightly beyond the error margins.

Thus, we supported this oscillatory behaviour by the analysis of the surface morphology and the crystal size distribution shown in Fig. 4 and 5. Additionally, the roughness of the sonicated surfaces was monitored using TM AFM. Fig. 3C shows that the roughness is slightly affected by cavitation. We also did not observe surface erosion and crack formation on the surface of Ti layers after 10 min treatment. Longer treatment led to delamination of the Ti layers from the Si support, and thus, is not informative for the scope of this work.

The composition of the samples was studied using Fourier-transformed infrared spectroscopy (FTIR) and X-ray photoelectron spectroscopy (XPS). The data are shown in Fig. S1 and S2 (ESI†). The surface analysis reveals the presence of

6288 | *Phys. Chem. Chem. Phys.*, 2017, **19**, 6286–6291

This journal is © the Owner Societies 2017
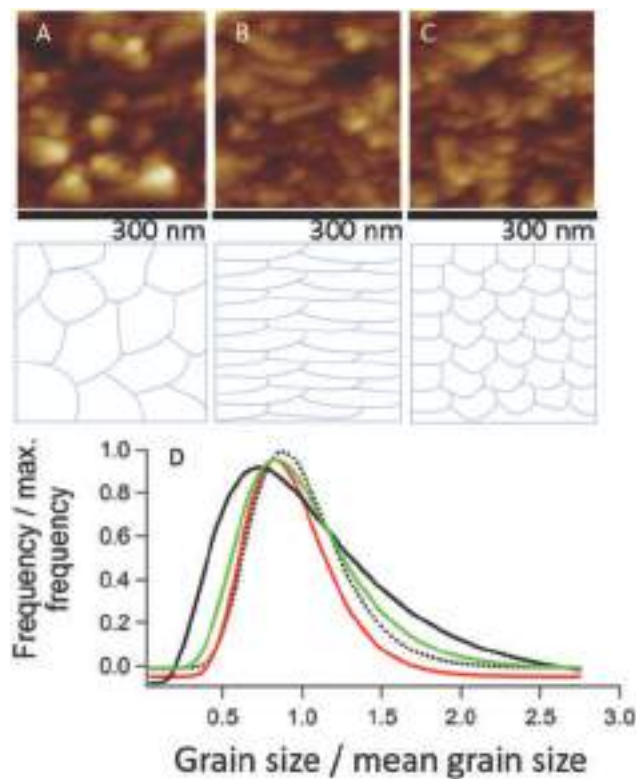
Fig. 4 AFM images and sketches illustrate dynamic morphological changes on A – initial, B – 1 min and C – 10 min HIUS treated Ti surfaces. The same z-scale as in Fig. 2 was used. D – Reduced lognormal grain size distributions of initial (dots) and HIUS treated Ti for 1 min (red), 5 min (black), and 10 min (green). Fitting parameters are shown in Table S1 (ESI†).
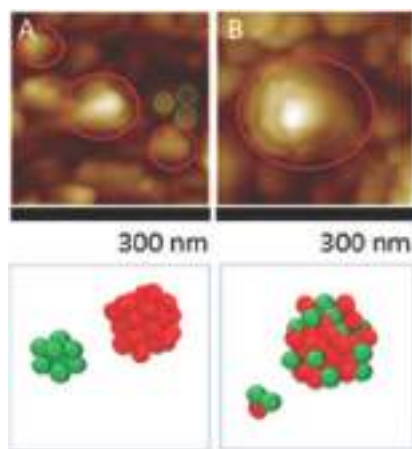
Fig. 5 AFM images illustrate the changes of grain size on A – initial and B – 5 min HIUS treated Ti surfaces. The AFM images have the same z-scale as the AFM images in Fig. 2.

titanium dioxide species. The composition of the samples did not change upon ultrasonic treatment.

It is interesting that the grain size changes on the surface and in the bulk of the Ti layers demonstrate similar non-monotonic dependence on sonication time. However, the maxima and minima are observed at different sonication times: the

maximum grain size on the surface was measured for the samples sonicated for 5 min. In contrast, the maximum grain sizes in the interior of the Ti layers were calculated for the samples sonicated for 1 and 10 min. The shift can be explained by development of gradients from the surface to the interior of solids due to the impact of cavitation bubbles on the surface.

Thus, we revealed oscillations of grain sizes in cavitating solids even in the metal layers, supporting our concept that extreme hydrodynamic conditions produced by cavitation cause repeating recrystallization cycles in solids. In this context, the next important point is establishing possible driving forces for nonlinear spatiotemporal changes in solids.

Using both Ti particles and Ti layers, we demonstrated that cavitation triggers two processes: (1) grain growth and (2) grain size reduction. Thus, we suggest that switching of grain growth and grain reduction cycles might be explained by competition of two opposing forces. It is obvious that propagation of a temperature gradient in solids is a driving force for grain growth. What is the driving force for grain size reduction?

Cavitation induced shock triggers acceleration not only of microparticles but also of molecules at solid–liquid interfaces. We can calculate the kinetic and thermal energy of $\sim$150 μm spherical Ti particles. For calculation of kinetic energy, we can use the speed of sound in ethylene glycol that is equal to 1660 m s^{-1}.[29] For calculation of thermal energy, we assume that the temperature in the cavitating system can increase up to $\sim$10 000 K.[10,13,15] The specific heat of Ti is 0.54 kJ kg^{-1} K^{-1}.[29] We see that the kinetic energy of cavitating particles is one order of magnitude larger than the thermal energy. Thus, we can assume that extreme hydrodynamic conditions have the main contribution to the modification process.

Extreme hydrodynamic conditions in the cavitating medium can introduce two forces, shock heating and shear stress on a Ti surface. Shock heating and propagation of a temperature gradient in solids leads to grain growth. Shear stress causes plastic deformations, namely the formation of new grain boundaries, that can lead to an increase in internal energy stored at grain boundaries and can be used for further crystal growth. Such mechanisms are well described and known as dynamic recrystallization.[31] However, the question is: how can the collapse of clouds of cavitation bubbles that proceeds at least every millisecond trigger oscillations with long time-scale (minutes) periodic variations?

A possible mechanism of cavitation driven dynamic recrystallization is shown in Fig. 4 and 5. Cavitation might provide oscillation between the equilibrium and non-equilibrium states of matter. This process is schematically illustrated in Fig. 4 and 5. A spatial temperature gradient is a driving force for grain growth followed by reduction in the entropy of the system, which then reaches an equilibrium state. However, cavitation induces shear stress on the surfaces, and triggers dislocations and formation of the new grain boundaries. Dislocation energy is stored at grain boundaries and the entropy of the system increases. Solids are ready for the next cycle.

As seen in Fig. 4A–C relatively isotropic grains are present on the surface of untreated Ti (Fig. 4A). Elongated grains typical of

the deformed material are seen in Fig. 4B. The anisotropic morphology is replaced by finer and almost isotropic grains (Fig. 4C) after 10 min of modification. Grain size distribution profiles shown in Fig. 4D confirm the oscillation of grain size distribution vs. treatment time. The fitting parameters of each curve in Fig. 4D are presented in Table S1 (ESI†). It is interesting that the grain size distribution for samples sonicated for 5 min is broader than the grain size distributions for samples after 1 and 10 min of treatment.

The grain size distribution for samples after 5 min of modification is a typical lognormal distribution, which can be attributed to particle coarsening due to coalescence or Ostwald ripening.[32]

A close look at the AFM images allows us to propose that the mechanism of crystal growth is Ostwald ripening. On the surface of untreated Ti (Fig. 5A) we can distinguish small grains (< 50 nm) and large grains (> 50 nm). After 5 min of treatment (Fig. 5B), the large grains became larger and the small grains became smaller. Such a mechanism of grain growth is known as Ostwald ripening[33] and is schematically illustrated in Fig. 5. It is suggested by Eberl et al.[33] that reduced lognormal plots of grain size distributions, which come close to steady-state distributions,[34,35] can describe the Ostwald ripening mechanism of grain growth. Different grain size distribution profiles for the samples after different times of modification might indicate cavitation driven temporally resolved recrystallization processes in solids.

However, the remaining questions are: what is the coupling mechanism of the two forces described here? How can we match the timescale of nucleation/collapse events of cavitation bubbles and periodicity of grain oscillations? Recently Zhang et al.[14] and Belova et al.[36] suggested that the impact of cavitation on solids in suspensions of particles depended on the nucleation events of bubbles at liquid–solid interfaces. It was demonstrated that the nucleation energy barrier drastically depended on the effective apparent contact angle of nucleation bubbles on a curved surface in contact with a liquid. Thus, we can propose that an increase in surface inhomogeneity, namely formation of new grain boundaries causes a decrease in the nucleation energy barrier. In contrast, coalescence of grains leads to a decrease in grain boundaries and, therefore, a decrease in nucleation events. Thus, our experiments provide insight into the interdependence between crystalline surfaces and cavitation bubbles and attempt to explain cavitation driven oscillations in solids. However, questions remain open for further investigations and understanding of the nonlinear dynamics of bubbles at interfaces.

Conclusions

We propose that cavitation induced shock impact on surfaces triggers nonlinear processes in solids due to two opposite forces. (1) Shock heating and propagation of a temperature gradient leads to grain growth. (2) Shear stress at liquid–solid interfaces causes dislocations and the formation of new grain boundaries and, thus, leads to a decrease in the size of grains.

Extreme hydrodynamic conditions in cavitating systems can be achieved in a wide range of heterogeneous systems. Cavitation energy can be dissipated via interparticle collisions and via bubble collapse near/at liquid–solid interfaces. It is important that this together with shock heating cavitation drives the shear stress on solids. It is possible that interdependence between crystalline surfaces and nucleation of cavitation bubbles provides coupling of two forces and leads to oscillations in solids. However, the observed discrepancy between the time-scale of periodic bubbles collapse and the oscillation of the grain size is still a remaining question.

Besides the fundamental understanding of cavitation initiated nonlinear processes for open dissipative systems, this work raises a problem of cavitation driven nonlinear processes in nature. In nature, cavitation is a common impactor of different processes related to earthquakes,[4] impact-shock synthesis of organic molecules,[1] formation of inorganic materials in fast moving magmatic melt,[37] etc. Even though we have started investigations of ultrasonically induced microstructural oscillations in solids, many questions remain for exciting research concerning cavitation triggered oscillations and self-organization in nature.

Experimental

Silicon (Si) wafers (100) with polished surfaces from CrysTech Kristralltechnologie were used as a substrate for titanium layers of 2 μm thickness deposited by physical vapour deposition using a BA 510 from Fa. Balzers, Liechtenstein. Absolute ethanol AnalR NORMAPUR from VWR Chemicals and ethylene glycol from Sigma Aldrich were used as received. Ti covered (100) Si wafers were fixed in a homemade sample holder for HIUS modification. The samples were sonicated for 1, 5, and 10 min in ethylene glycol at a sonotrode to a surface distance of 5 mm. Additionally, we sonicated suspensions of ∼150 μm Ti particles (99.5 wt%, Acros Organics) in 100 ml of ethylene glycol at a concentration of 0.05 g ml^{-1} for 0–60 min. After sonication the particles were centrifuged and washed five times with ethanol and then dried to a constant mass at 80 °C.

Cavitation was produced using a UIP1000hd ultrasonic device from Hielscher Ultrasound Technology equipped with a B2-1.8 booster and a BS2d22 sonotrode (head area 3.8 cm^2). The operating frequency was 20 kHz with a maximum intensity of 140 W cm^{-2} and an amplitude of 106 μm. The sonication medium was cooled using an ice bath to approximately 333 K. The samples modified in ethylene glycol were rinsed with ethanol after HIUS modification. The particle velocity was measured using an Axio Observer Inverted Microscope (Carl Zeiss Microscopy GmbH) equipped with a 20× objective and transmitted light bright field illumination. Recordings were done using a Phantom v1610 high speed camera with 500 000 frames per seconds.

Atomic force microscopy (AFM) was performed using a Dimension 3100 equipped with a NanoScope IV controller and a standard scanner from VEECO Instruments GmbH using tapping mode (TM). Analysis of AFM images was carried out using the programs NanoScope Analysis and ImageJ.

Surface roughness from AFM was determined using the Nanoscope Analysis program, and the crystal size was determined by taking a grain size average of three different surface areas using the program ImageJ. Therefore, crystals were divided into those with sizes larger and smaller than 50 nm. Grain size distributions were determined using the program IGOR Pro.

X-ray diffraction (XRD) was performed using a Panalytical X'Pert Pro MPD with monochromatic Cu Kα radiation, $\lambda = 1.54$ Å from $5°$ to $80°$ with 0.03 steps. Data evaluation was carried out using the program X-Pert HighScore Plus. The Ti grain size was determined using the Scherrer method (see ESI†). For the calculations we used the peak at $38.5°$ (110), which was assigned to (110) Ti (JCPDS: 00-044-1288).

Scanning Electron Microscopy (SEM) was conducted using a Gemini Leo 1550 instrument, Leo Elektronenmikroskopie GmbH, at an operating voltage of 3 keV. Samples were sputtered with gold.

X-ray photoelectron spectroscopy (XPS) analyses were carried out using M-probe apparatus (Surface Science Instruments). The source was monochromatic Al-Kα radiation (1486.6 eV).

Fourier-transformed infrared spectra were recorded using a VERTEX 70 spectrometer.

Acknowledgements

Notes and references

1 Ch. Chyba and C. Sagan, *Nature*, 1992, **355**, 125.
2 I. Lagzi, B. Kowalczyk, D. Wang and B. A. Grzybowski, *Angew. Chem., Int. Ed.*, 2010, **49**, 8616.
3 A. R. Taylor, M. A. Russell, G. M. Harper, T. F. T. Collins and C. Brownlee, *Eur. J. Phycol.*, 2007, **42**, 125.
4 F. Fusseis, K. Regenauer-Lieb, J. Liu, R. M. Hough and F. De Carlo, *Nature*, 2009, **459**, 974.
5 M. Avalos, R. Babiano, P. Cintas, J. L. Jiménez and J. C. Palacios, *Chem. Commun.*, 2000, 887.
6 J. Dulle, *et al.*, *Adv. Funct. Mater.*, 2012, **22**, 3128.
7 X.-Z. Lu and J. M. Rondinelli, *Nat. Mater.*, 2016, **15**, 951–955.
8 P. Li, X. Yang, T. W. W. Maß, J. Hanss, M. Lewin, A.-K. U. Michel, M. Wuttig and Th. Taubner, *Nat. Mater.*, 2016, **15**, 870–875.
9 Y. Wu, Z. Wu, X. Lin, Q. He and J. Li, *ACS Nano*, 2012, **12**, 10910.
10 B. P. Barber and S. J. Putterman, *Nature*, 1991, **352**, 318.
11 W. C. Moss, D. B. Clarke, J. W. White and D. A. Young, *Phys. Fluids*, 1994, **6**, 2979.
12 C. C. Wu and P. H. Roberts, *Phys. Rev. Lett.*, 1993, **22**, 3424.
13 S. J. Doktycz and K. S. Suslick, *Science*, 1990, **247**, 1067.
14 L. Zhang, V. Belova, H. Wang, W. Dong and H. Möhwald, *Chem. Mater.*, 2014, **26**, 2244.
15 J. P. Lorimer and T. J. Mason, *Chem. Soc. Rev.*, 1987, **16**, 239.
16 P. V. Cherepanov, A. Kollath and D. V. Andreeva, *Ultrason. Sonochem.*, 2015, **26**, 9.
17 P. V. Cherepanov, *et al.*, *Green Chem.*, 2015, **17**, 2745.
18 A. Kollath, P. V. Cherepanov and D. V. Andreeva, *Applied Acoustics*, 2016, **103**, 190.
19 B. V. Derjaguin, *What is friction?* AN SSSR, Moscow, Russia, 2nd edn, 1963.
20 I. Prigogine and I. Stengers, *Order out of Chaos: Man's new dialogue with nature*, Flamingo, 1984.
21 P. V. Cherepanov, I. Melnyk and D. V. Andreeva, *Ultrason. Sonochem.*, 2015, **23**, 26.
22 X. Liu, P. K. Chu and C. Ding, *Mater. Sci. Eng., R*, 2004, **47**, 49.
23 R. M. Pilliar, *Biomaterials*, 1991, **12**, 95.
24 R. Saladino, *et al.*, *Astrobiology*, 2011, **11**, 815.
25 T. Kiriyama, M. Haraguchi and R. Kuroda, *Fresenius' Z. Anal. Chem.*, 1981, **307**, 352.
26 P. R. Gogate, A. M. Wilhelm and A. B. Pandit, *Ultrason. Sonochem.*, 2003, **10**, 325.
27 M. A. Margulis, *Sonochemistry and Cavitation*, CRC Press, 1995.
28 E. V. Skorb, D. V. Andreeva and H. Mohwald, *Angew. Chem., Int. Ed.*, 2012, **51**, 5138–5142.
29 W. M. Haynes, *Handbook of Chemistry and Physics*, CRC Press, 2013.
30 G. K. Batchelor, *An Introduction to Fluid Dynamics*, Cambridge University Press, 1967.
31 M. J. Luton and C. M. Sellars, *Acta Metall.*, 1969, **17**, 1033.
32 C. G. Granqvist and R. A. Buhrman, *J. Catal.*, 1976, **42**, 477.
33 D. Eberl, *et al.*, *Science*, 1990, **248**, 474.
34 E. Fredrick, P. Walstra and K. Dewettinck, *Adv. Colloid Interface Sci.*, 2010, **153**, 30.
35 T. E. Quested and A. L. Greer, *Acta Mater.*, 2004, **52**, 3859.
36 V. Belova, D. G. Gorin, D. G. Shchukin and H. Moehwald, *Angew. Chem., Int. Ed.*, 2010, **49**, 7229.
37 E. M. Galimov, *Nature*, 1973, **243**, 389.

ADVANCED MATERIALS

Giant Incident Photon-to-Current Conversion with Photoconductivity Gain on Nanostructured Bismuth Oxysulfide Photoelectrodes under Visible-Light Illumination

Evgeny A. Bondarenko, Eugene A. Streltsov,* Mikalai V. Malashchonak,
Alexander V. Mazanik, Anatoly I. Kulak, and Ekaterina V. Skorb*

Nanostructured layered bismuth oxysulfide films synthesized by chemical bath deposition reveal a giant incident photon-to-current conversion efficiency (IPCE). This study shows that surprisingly for the cathodic photocurrent in the photoreduction process, the IPCE reaches ≈2500% in aqueous solutions containing $[Fe(CN)_6]^{3-}$. The giant IPCE is observed starting from a certain minimal oxidizer concentration ($c > 10^{-3}$ M for $[Fe(CN)_6]^{3-}$) and decreases nonlinearly with an increase of illumination intensity. Giant IPCE is determined by the decrease in resistivity of the bismuth oxysulfide film under illumination with photoconductivity gain, which provides the possibility of charge carriers from an external circuit to participate in the photoreduction process. Giant IPCE is observed not only in $[Fe(CN)_6]^{3-}$ solutions, but also in electrolytes containing other photoelectron acceptors: Fe^{3+}, I_3^-, quinone, H_2O_2. In all, solution-processed layered bismuth oxysulfide films offer large-area coverage, nontoxicity, low cost, and compatibility with a wide range of substrates. Abnormally high photoelectrochemical activity, as well as a band gap energy value favorable for efficient conversion of solar light (1.38 eV, direct optical transitions), proves the potential of bismuth oxysulfide photoelectrodes for a new generation of high-performance photoconverters.

E. A. Bondarenko, Prof. E. V. Skorb
Biomaterials
Max Planck Institute of Colloids and Interfaces
14424 Potsdam, Germany
E-mail: skorb@scamt.ru
E. A. Bondarenko, Prof. E. A. Streltsov, M. V. Malashchonak,
Prof. A. V. Mazanik
Chemistry Department
Belarusian State University
Nezalezhnastsi Av. 4, Minsk 220030, Belarus
E-mail: streltea@bsu.by
Prof. A. I. Kulak
Institute of General and Inorganic Chemistry
National Academy of Sciences of Belarus
Minsk 220072, Belarus
Prof. E. V. Skorb
Laboratory of Solution Chemistry of Advanced Materials
and Technologies (SCAMT)
ITMO University
St. Petersburg 197101, Russian Federation

In recent years, considerable research interest has been focused on the study of bismuth semiconductor compounds: vanadate $BiVO_4$,[1–5] oxyhalides BiOHal (Hal = I, Cl, Br),[6–10] sulfide Bi_2S_3,[11–15] and oxysulfides.[16–23] This is due to their attractive photocatalytic and photoelectrochemical properties, as well as the fact that bismuth is a nontoxic, inexpensive material. Moreover, as a high-Z element, bismuth demonstrates a high attenuation of X- and γ-ray quanta, making promising the development of detectors based on its semiconductor compounds.[24,25]

The first bismuth oxysulfide Bi_2O_2S reported in 1984 has the same crystalline structure as bismuth oxyhalides.[26] Both classes of compounds have a layered structure, where the $[Bi_2O_2]$ layers alternate with the layers of halogenide or sulfide anions.[26] Bi_2O_2S is a n-type semiconductor[16] and provides attractive photoelectric properties (band gap reported as 1.5[16] and 1.12 eV).[17]

Recently synthesized bismuth oxysulfide $Bi_9O_{7.5}S_6$ also has a layered structure, which consists of alternatingly packed $[Bi_2O_2]$ and $[BiS_2]$ layers held together by van der Waals interaction. The band gap energy $E_g = 1.27$ eV and direct optical transitions[18] lend this semiconductor high perspectives for solar energy applications.

The band gap energy $E_g = 0.99$ eV (direct optical transitions)[19] of layered oxysulfide Bi_2OS_2 composed of alternating $[Bi_2O_2]$ and $[BiS_2]$ layers has the lowest value among the known oxysulfides, even smaller than the band gap of bismuth sulfide ($E_g = 1.3$ eV).[20]

According to X-ray photoelectron spectroscopy (XPS), bismuth and sulfur atoms have an oxidation state of +3 and −2, respectively, in semiconductor bismuth oxysulfides considered above.[16,18] A fundamentally different situation is observed in $Bi_4O_4S_3$. It was found that $Bi_4O_4S_3$ formed by alternating $[Bi_2O_2]$, $[BiS_2]$, and $[SO_4]$ layers possesses superconductivity at temperatures less than 4.4–8.6 K.[21–23] Sulfur atoms have different oxidation states: −2 in $[BiS_2]$ layers and +6 in $[SO_4]$ ones. Oxidation states of bismuth atoms in this compound are +3 and +2.5 in $[Bi_2O_2]$ and $[Bi_2S_4]$ layers, respectively.[17] $Bi_4O_4S_3$ can be considered as one of two stable forms of $Bi_4O_4(SO_4)_{1-x}Bi_2S_4$,

where x can be equal to 0 or 0.5 corresponding to the $Bi_6O_8S_5$ and $Bi_4O_4S_3$ formula units. Elemental ratios and basic properties of the known bismuth oxysulfides, Bi_2S_3 and Bi_2O_3 are summarized in Figure S1 (Supporting Information).

The mentioned layered structure of bismuth oxysulfides suggests that variation in stacking of "building blocks" ($[Bi_2O_2]$, $[BiS_2]$, sulfur layers, etc.) can provide a possibility to synthesize new compounds. Band gap energy favorable for efficient solar energy conversion can be expected taking into account E_g values for bismuth oxide, bismuth sulfide, and known bismuth oxysulfides (Figure S1, Supporting Information).

Small diffusion length of the minority charge carriers in light absorbing material is known to be one of the limitations of photoelectrochemical energy conversion efficiency. Nanostructured photoelectrodes (arrays of nanotubes or nanorods, mesoporous films, as well as films formed by thin platelet-like crystals of nanoscale thickness) provide an attractive possibility to solve this problem. Indeed, a sufficient thickness of such nanostructured films allows efficient light harvesting, whereas a short diffusion distance for the minority carriers toward the electrolyte solution provides low recombination losses.

Photoelectrochemical and photocatalytic behavior of bismuth oxyhalides, bismuth orthovanadate, as well as bismuth sulfide Bi_2S_3 has been investigated to date in details.[1–15] The first studies of photoelectrochemical behavior of Bi_2O_2S and Bi_2O_2S/In_2O_3 heterostructure have demonstrated the possibility to utilize them as n-type semiconductors; dye-modified Bi_2O_2S/In_2O_3 is perspective as water-splitting catalyst.[16] Nevertheless, photoelectrochemistry of bismuth oxysulfides is at an early stage in general.

Previously studied oxysulfide compounds have been prepared in many cases by high-temperature solid-state synthesis. At the same time, there is a rapidly growing interest in the preparation of materials and devices for optoelectronics and solar energy harvesting using solution-based approaches due to their simplicity and low cost.[27]

In this work, chemical bath deposition (CBD) was used to produce bismuth oxysulfide films for the first time (Figure S2, Supporting Information). Surprisingly, we detected (**Figure 1**)

unique photoelectrochemical behavior of the synthesized films, not shown before for any known this material. Incident photon-to-current conversion efficiency (IPCE or Y) known as a number of electrons passing in a circuit per one incident photon reaches up to 2500% for the cathodic photocurrent.

CBD grown bismuth oxysulfide films possess a highly-developed structure formed by the randomly oriented nanoplatelets (**Figure 2**a,b). Their lateral size is of several hundreds of nanometers, whereas the thickness is remarkably smaller (tens of nanometers). The layered shape of crystallites confirmed by transmission electron microscopy (TEM, Figure 2c) provides high surface-to-volume ratio and a short path for charge carriers scavenged by electrolyte. Selected area electron diffraction (SAED, inset in Figure 2c) and high resolution TEM (Figure 2d) point to crystallinity of the prepared films with hexagonal lattice symmetry (inset in Figure 2c).

Qualitative elemental composition analysis of the synthesized films performed with XPS (Figure 2g) and energy-dispersive X-ray spectroscopy (Figure S3, Supporting Information) demonstrates the presence of Bi, S, and O. Chemical analysis (Figure S1, Supporting Information) has shown a bismuth-to-sulfur molar ratio Bi:S = 1.11:1, which is an intermediate value compared to other known bismuth oxysulfides.

XPS studies demonstrate binding energies of 159.3 and 164.6 eV for Bi $4f_{7/2}$ and $4f_{5/2}$ electrons, respectively (Figure S4, Supporting Information), which is close to values reported for Bi_2O_3 and corresponds to +3 oxidation state.[28] Peaks at 225.7 and 232.5 eV for S 2s electrons (Figure 2e) correspond to −2 and +6 oxidation states of sulfur, respectively.[29] Ion etching of the films (etching depth 10 nm) results in almost complete disappearance of the peak corresponding to the +6 oxidation state of sulfur (Figure 2f) suggesting that S^{6+} ions are formed on the surface of the film due to oxidation of S^{2-} during ambient storage. Since sulfur atoms in the films have only −2 oxidation state, the simplest formula unit can be represented as $Bi_{10}O_6S_9$, which differs from the atomic composition of all presently known bismuth oxysulfides.

The positions of lines in X-ray diffraction (XRD) patterns of the synthesized compound (Figure 2h) differ from those for any
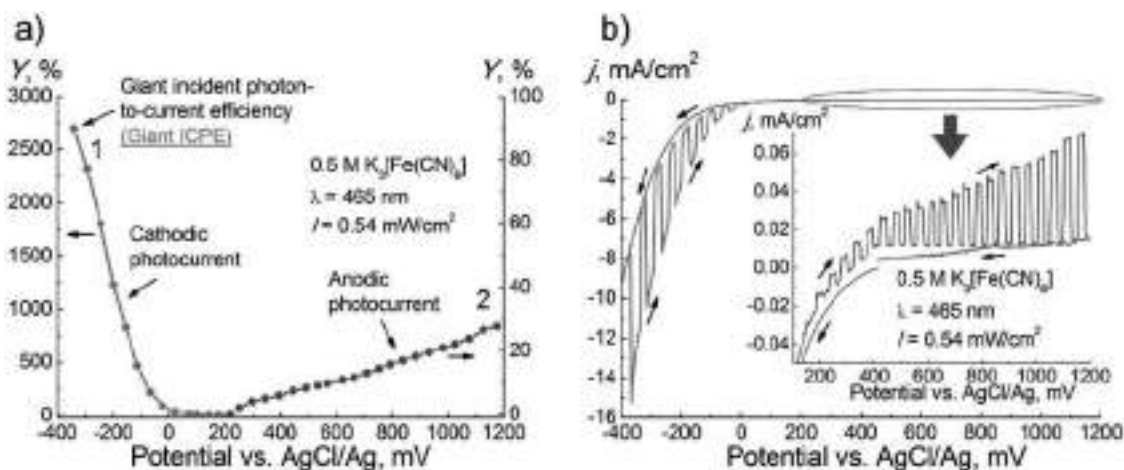
Figure 1. Photoelectrochemical behavior of bismuth oxysulfide films: a) dependence of IPCE on electrode potential for cathodic and anodic photocurrents derived from b) cyclic voltammogram with chopped illumination during anodic scan of electrode potential.
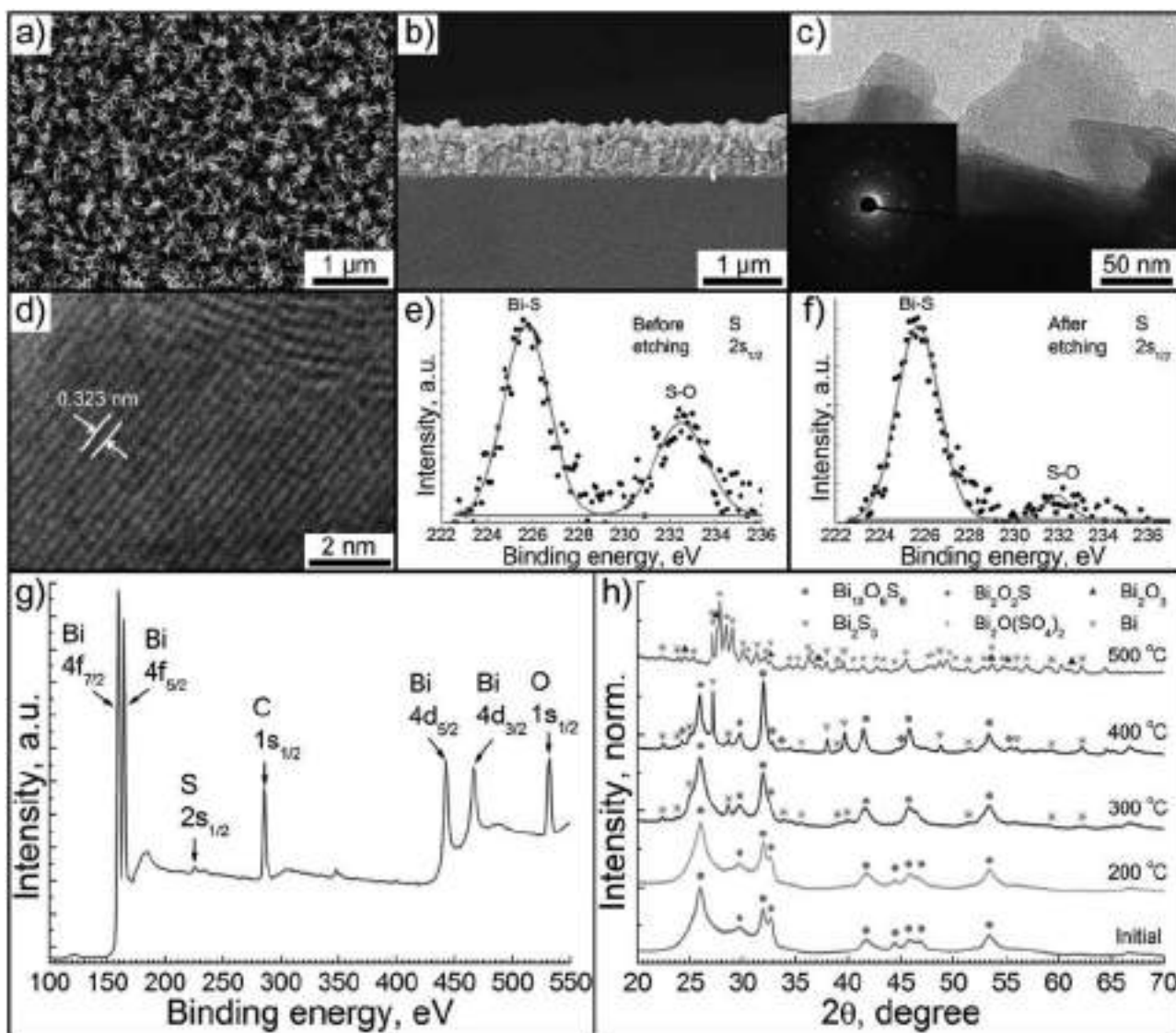
Figure 2. Structural characterization of bismuth oxysulfide: a) top-view and b) cross-sectional scanning electron microscopy (SEM) images of the film; c) transmission electron microscopy (TEM) image with selected area electron diffraction (SAED) pattern in inset; d) high-resolution transmission electron microscopy (HRTEM) image; e–g) X-ray photoelectron spectroscopy (XPS): e,f) S 2s high resolution spectra before and after surface etching; g) survey spectrum; and h) X-ray powder diffraction (XRD) of initial and heat treated samples.

oxysulfides described in the literature, which correlates with the chemical analysis results presented above. A large width of lines may originate from a high defect density in the films, a small thickness of the nanoplatelets and tensile/compressive strains due to their curvature (Figures 2a,d), which impedes a reliable identification of crystalline structure. The films were heat treated in Ar atmosphere to improve their crystallinity and to investigate thermal stability.

As seen from Figure 2h, heat treatment at 200 °C does not influence the intensity of XRD lines and their position, whereas annealing at 300 °C gives rise to formation of Bi_2S_3 crystalline phase. After annealing at 400 °C, elemental bismuth and bismuth oxysulfide Bi_2O_2S are registered along with $Bi_{10}O_6S_9$ and Bi_2S_3. Formation of Bi^0 seems to be due to Bi^{3+} reduction by S^{2-} anions. Heat treatment at 500 °C leads to the destruction

of oxysulfides and their conversion to oxide Bi_2O_3 and oxysulfate $Bi_2O(SO_4)_2$.

The thermogravimetric analysis (TGA) and differential thermal analysis (DTA) curves of bismuth oxysulfide sample from room temperature to 1000 °C under argon are shown in Figure S5 in Supporting Information. It is observed from the TGA that the weight loss (2.7 wt%) at 30–100 °C is related to the elimination of the physisorbed water, and then up to 340 °C (3.5 wt%) to the volatilization of organic residues. Sharp weight loss at 400–490 °C (6.9 wt%) can be attributed to partial loss of sulfur and solid-state transformations including a formation of new bismuth oxysulfide and sulfide phases. This observation can be confirmed by DTA that gives a broad split exothermic peak (at 469, 486 °C) corresponding to the formation of elemental bismuth and bismuth oxysulfide Bi_2O_2S (registered along

ADVANCED
SCIENCE NEWS
www.advancedsciencenews.com

ADVANCED
MATERIALS
www.advmat.de

with $Bi_{10}O_6S_9$ and Bi_2S_3) accordingly XRD data. Weight loss at 800–1000 °C is associated with oxygen and sulfur elimination from bismuth oxide, oxysulfate, and oxysulfides.

The synthesized bismuth oxysulfide films absorb visible light well (Figure S6, Supporting Information) and demonstrate cathodic photopotential revealing properties of a n-type semiconductor similar to Bi_2S_3[30] and Bi_2O_2S.[16] Both anodic and cathodic photocurrents can be generated depending on the electrode potential (Figure 1b). The most prominent property in photoelectrochemical behavior of the synthesized films is extremely high value of cathodic photocurrent in solutions containing electron acceptors (for example, $[Fe(CN)_6]^{3-}$), which corresponds to IPCE up to 2500% (Figure 1). The cathodic photocurrent increases with cathodic polarization being comparable to the dark current in the entire range of electrode potentials. It should be noted that the giant IPCE effect in 0.5 M $K_3[Fe(CN)_6]$ solution is rather stable: on the same electrode we have observed giant photocurrents in photoelectrochemical experiments periodically performed throughout the year.

The giant IPCE remains the same for films heat treated at 200 °C, but disappears after heat treatment performed at higher temperatures correlating with changes in phase composition of the films (Figure 2h).

The IPCE value for the cathodic photocurrent depends significantly on the $[Fe(CN)_6]^{3-}$ concentration in solution and exceeds 100% only for oxidizer concentration $c > 10^{-3}$ M (**Figure 3**a). The IPCE decreases with the light intensity increase (Figure 3b) demonstrating a power-like dependence of photocurrent on illumination intensity $j_{ph} \sim I^s$, with an exponent $s \approx 0.7$.

The giant IPCE is observed not only in $[Fe(CN)_6]^{3-}$ solutions, but also in electrolytes containing other photoelectron acceptors: Fe^{3+}, I_3^-, H_2O_2, quinone (Figure S7, Supporting Information). Strong concentration dependence of the photocurrent testifies that an effective capture of photoelectrons at the semiconductor/electrolyte interface is required for giant IPCE observation.

Only anodic photocurrent is observed for bismuth oxysulfide electrodes in the absence of photoelectron acceptors in the solution. The prepared bismuth oxysulfide films generate an anodic photocurrent in aqueous Na_2SO_3 solution (Figure 3c) and in solutions, which contain other acceptors of photoholes, for example, hydroquinone, Fe^{2+}, $[Fe(CN)_6]^{4-}$. Photoelectrochemical
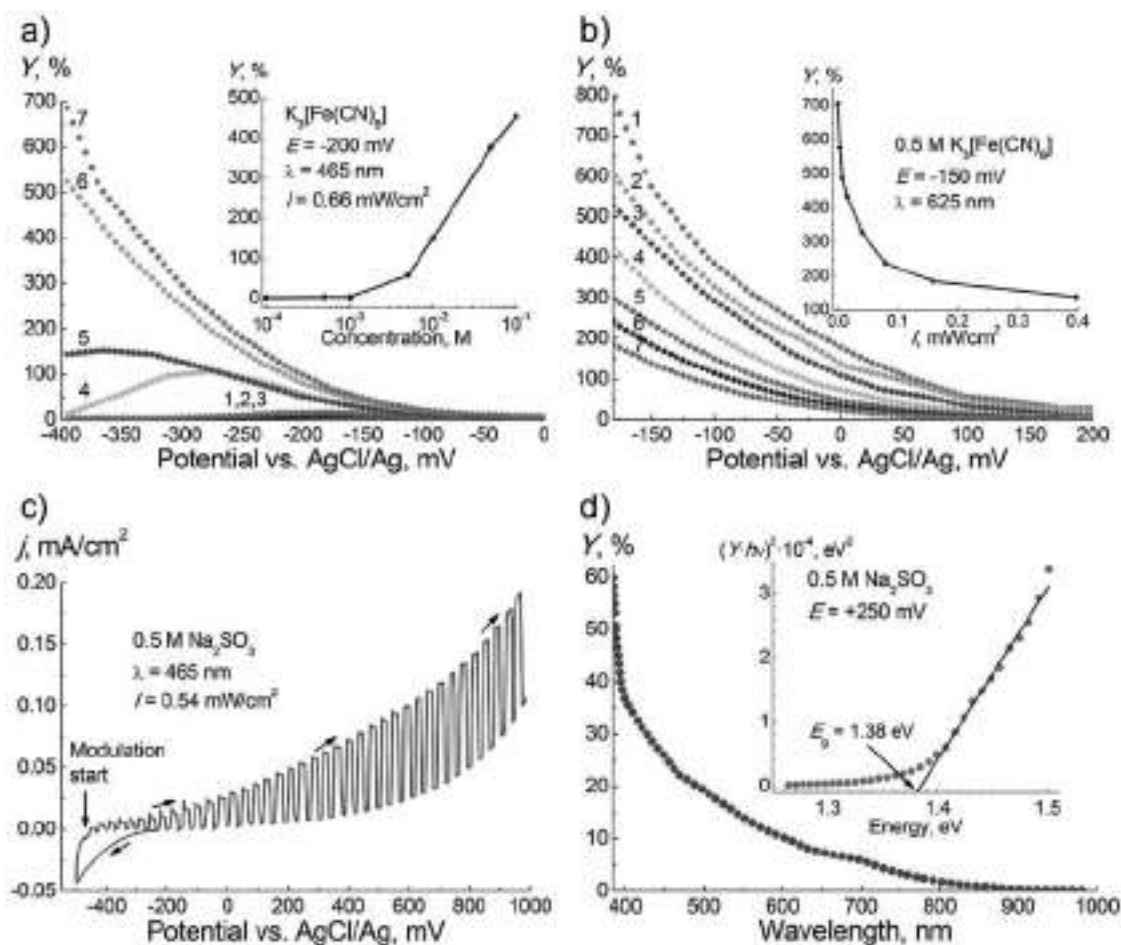
Figure 3. Photoelectrochemical behavior of bismuth oxysulfide films: a) dependence of IPCE for cathodic photocurrent on electrode potential at different concentrations of $K_3[Fe(CN)_6]$: $1–1 \times 10^{-4}$ M; $2–5 \times 10^{-4}$ M; $3–1 \times 10^{-3}$ M; $4–5 \times 10^{-3}$ M; $5–1 \times 10^{-2}$ M; $6–5 \times 10^{-2}$ M; $7–1 \times 10^{-1}$ M; b) dependence of IPCE for cathodic photocurrent on electrode potential at different illumination intensities, mW cm^{-2}: 1–0.004, 2–0.008, 3–0.016, 4–0.04, 5–0.08, 6–0.16, 7–0.40; c) cyclic voltammogram in Na_2SO_3 solution under chopped illumination during anodic scan; d) spectral dependence of IPCE for anodic photocurrent; inset: the same in the Tauc coordinates for direct optical transitions.

**ADVANCED
SCIENCE NEWS**
www.advancedsciencenews.com

**ADVANCED
MATERIALS**
www.advmat.de

activity of the bismuth oxysulfide films in anodic processes is also high: the IPCE reaches ≈40% in Na_2SO_3 solution at $\lambda = 400$ nm (Figure 3d). Extrapolation of anodic photocurrent spectra linearized in $(Y \cdot h\nu)^2 - h\nu$ coordinates (direct optical transitions) demonstrates a band gap energy of bismuth oxysulfide equal to 1.38 eV (Figure 3d, inset). It should be noted that determination of E_g from IPCE (not absorption) spectra seems to be more reliable due to minimal impact of other absorption mechanisms besides the fundamental interband transitions.

To obtain additional information about photoelectrical properties of the prepared films, solid-state measurements were also performed. A thin Au layer was sputtered on the bismuth oxysulfide film grown on FTO glass substrate. It allowed a current flow through the film in direction normal to its plane.

The $FTO/Bi_{10}O_6S_9/Au$ structure exhibits a long-time persistent photoconductivity (Figure S8, Supporting Information). We have found that the growth and decay of the conductivity after light switching-on and switching-off, respectively, are described well by stretched exponential functions

$$\sigma_{gr}(t) = \sigma_{01} + \Delta\sigma_1 \left[1 - \exp\left(-\left(\frac{t}{\tau_1}\right)^{\beta_1} \right) \right] \quad (1a)$$

$$\sigma_{dec}(t) = \sigma_{02} + \Delta\sigma_2 \exp\left(-\left(\frac{t}{\tau_2}\right)^{\beta_2} \right) \quad (1b)$$

where $\tau_1 = 1.07 \times 10^3$ s, $\tau_2 = 6.84 \times 10^3$ s, $\beta_1 = 0.71$, and $\beta_2 = 0.7$. Such long-time relaxations of conductivity are known to be inherent to highly disordered semiconductors and are determined by a wide distribution of parameters of deep charge traps within a forbidden gap.[31]

To explain the observed anomalous photoelectrochemical behavior of the prepared films, one should take into account that the electrode resistance is the primary factor limiting the current under cathodic polarization of n-type semiconductor in electrolyte with sufficiently high oxidizer concentration. In this case, the photocurrent arising under illumination is related to decrease in semiconductor resistivity (**Figure 4**) and is described by the well-known expression (the case of low absorption is considered for simplicity)[32]

$$j_{ph} = \frac{U}{l} q_e \frac{I\alpha}{h\nu} (\tau_n \mu_n + \tau_p \mu_p) \quad (2)$$
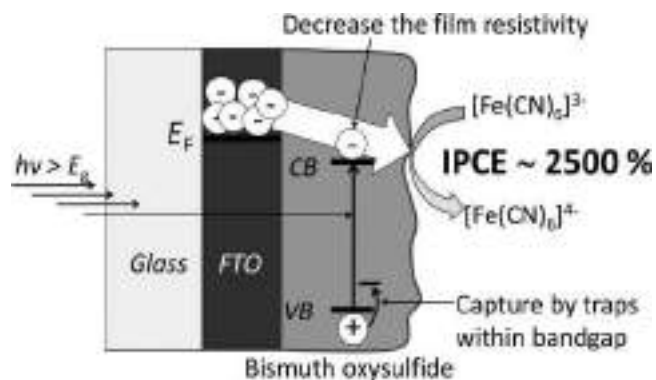
Figure 4. Sketch of giant IPCE effect.

where j_{ph} is the difference between current density under illumination and in dark (i.e., the photocurrent density), U is the voltage drop across semiconductor, l is the interprobe distance, q_e is the electron charge, I is the illumination intensity, α is the light absorption coefficient, $h\nu$ is the quantum energy, and τ_n, τ_p, μ_n, μ_p are the lifetimes and mobilities of electrons and holes, respectively.

Equation (2) demonstrates no limitations in quantum efficiency values; in other words, the number of electrons passing in the external circuit can exceed the number of incident quanta in many times (photoconductivity gain). At a moderate conductivity of the semiconductor, the main drop of electrode potential in this photoelectrochemical system occurs within the film (potential drop in the Helmholtz layer is insignificant). Increase in cathodic polarization gives rise to the growth of electric field strength in the film (multiplier U/l in Equation (2)) and, hence, to IPCE increase in agreement with experimental results (Figure 1a).

According to Equation (2), high photocurrent can be achieved in the case of a large lifetime of charge carriers. Such situation takes place in semiconductors with high density of defects, which act as traps for the carriers of particular sign and prevent their recombination with the carriers of opposite sign.[33] For example, high photoconductivity of nanocrystalline Bi_2S_3 has been explained taking into account the capture of photoholes by the traps in the forbidden gap.[11] Apparently, a similar situation occurs in the layered oxysulfide crystals. A large concentration of traps in the studied films is in a qualitative agreement with their persistent photoconductivity.

Equation (2) could also explain the observed decrease of quantum efficiency with illumination increase (Figure 3b). Indeed, the lifetime of nonequilibrium charge carriers is independent of the illumination intensity only at low excitation level (when the concentration of the photoexcited charges is much smaller compared with the equilibrium charge concentration) and decreases with the increase of excitation level. Another possible reason of IPCE decrease with the increase of optical power density can be related to the trap filling, which promotes recombination.

As is seen from Figure 3a, giant IPCE values for cathodic current cannot be achieved at low oxidizer concentrations. Therefore, the rate of the photoelectrochemical process (expressed in the terms of cathodic photocurrent density) is determined not only by the concentration of photogenerated carriers, but also, to a large extent, by parameters of the double electric layer, where discharge of electroactive species takes place. A combination of these factors determines the overvoltage of the photoelectrochemical process, which has a pronounced diffusive nature at low oxidizer concentrations.

In summary, it is discovered that the nanolayered bismuth oxysulfide films synthesized by CBD reveal unique—not shown for any known photoelectrochemical systems—properties demonstrating a giant IPCE. For cathodic photocurrent (photoreduction process), the IPCE reaches about 2500% in aqueous solutions containing electron acceptors ($[Fe(CN)_6]^{3-}$, Fe^{3+}, I_3^-, quinone, H_2O_2). A giant IPCE is observed starting from a certain minimal oxidizer concentration ($c > 10^{-3}$ M for $[Fe(CN)_6]^{3-}$) and decreases nonlinearly with the increase of illumination intensity. Giant IPCE is determined by the decrease

in resistivity of the bismuth oxysulfide film under illumination, which provides the possibility of charge carriers from external circuit to participate in the photoreduction process (Figure 4). Abnormally high photoelectrochemical activity as well as a band gap energy value favorable for efficient conversion of solar light (1.38 eV) assures that oxysulfide photoelectrodes will form the basis of a new generation of high-performance photoelectrochemical solar cells and photodetectors.

Supporting Information

Supporting Information is available from the Wiley Online Library or from the author.

Acknowledgements

Conflict of Interest

The authors declare no conflict of interest.

Keywords

[1] Z.-F. Huang, L. Pan, J.-J. Zou, X. Zhang, L. Wang, *Nanoscale* **2014**, *6*, 14044.
[2] J. Yu, A. Kudo, *Adv. Funct. Mater.* **2006**, *16*, 2163.
[3] Y. Park, K. J. McDonald, K.-S. Choi, *Chem. Soc. Rev.* **2013**, *42*, 2321.
[4] J. K. Cooper, S. Gul, F. M. Toma, L. Chen, Y.-S. Liu, J. Guo, J. W. Ager, J. Yano, I. D. Sharp, *J. Phys. Chem. C* **2015**, *119*, 2969.
[5] T. W. Kim, K.-S. Choi, *Science* **2014**, *343*, 990.
[6] S. K. Poznyak, A. I. Kulak, *Electrochim. Acta* **1990**, *35*, 1941.
[7] J. Li, Y. Yu, L. Zhang, *Nanoscale* **2014**, *6*, 8473.
[8] H. Cheng, B. Huang, Y. Dai, *Nanoscale* **2014**, *6*, 2009.
[9] D. S. Bhachu, S. J. A. Moniz, S. Sathasivam, D. O. Scanlon, A. Walsh, S. M. Bawaked, M. Mokhtar, A. Y. Obaid, I. P. Parkin, J. Tang, C. J. Carmalt, *Chem. Sci.* **2016**, *7*, 4832.
[10] M. E. Kazyrevich, M. V. Malashchonak, A. V. Mazanik, E. A. Streltsov, A. I. Kulak, C. Bhattacharya, *Electrochim. Acta* **2016**, *190*, 612.
[11] G. Konstantatos, L. Levina, J. Tang, E. H. Sargent, *Nano Lett.* **2008**, *8*, 4002.
[12] Y.-C. Lin, M.-W. Lee, *J. Electrochem. Soc.* **2014**, *161*, H1.
[13] V. Stavila, K. H. Whitmire, I. Rusakova, *Chem. Mater.* **2009**, *21*, 5456.
[14] X. S. Peng, G. W. Meng, J. Zhang, L. X. Zhao, X. F. Wang, Y. W. Wang, L. D. Zhang, *J. Phys. D: Appl. Phys.* **2001**, *34*, 3224.
[15] P. Han, A. Mihi, J. Ferre-borrull, J. Pallarés, L. F. Marsal, *J. Phys. Chem. C* **2015**, *119*, 10693.
[16] A. L. Pacquette, H. Hagiwara, T. Ishihara, A. A. Gewirth, *J. Photochem. Photobiol., A* **2014**, *277*, 27.
[17] X. Zhang, Y. Liu, G. Zhang, Y. Wang, H. Zhang, F. Huang, *ACS Appl. Mater. Interfaces* **2015**, *7*, 4442.
[18] S. Meng, X. Zhang, G. Zhang, Y. Wang, H. Zhang, F. Huang, *Inorg. Chem.* **2015**, *54*, 5768.
[19] A. Miura, Y. Mizuguchi, T. Takei, N. Kumada, E. Magome, C. Moriyoshi, Y. Kuroiwa, K. Tadanaga, *Solid State Commun.* **2016**, *227*, 19.
[20] O. Madelung, *Semiconductors: Data Handbook*, Springer-Verlag, Berlin, Germany **2004**.
[21] Y. Mizuguchi, H. Fujihisa, Y. Gotoh, K. Suzuki, H. Usui, K. Kuroki, S. Demura, Y. Takano, H. Izawa, O. Miura, *Phys. Rev. B* **2012**, *86*, 220510(R).
[22] W. A. Phelan, D. C. Wallace, K. E. Arpino, J. R. Neilson, K. J. Livi, C. R. Seabourne, A. J. Scott, T. M. McQueen, *J. Am. Chem. Soc.* **2013**, *135*, 5372.
[23] G. Liu, D. Li, S. Li, J. Wang, W. liu, Z. Zhang, *Physica C* **2015**, *510*, 27.
[24] S. Nambiar, E. K. Osei, J. T. W. Yeow, *Sci. Rep.* **2015**, *5*, 9440.
[25] A. Intaniwet, C. A. Mills, M. Shkunov, P. J. Sellin, J. L. Keddie, *Nanotechnology* **2012**, *23*, 235502.
[26] E. Koyama, I. Nakai, K. Nagashima, *Acta Crystallogr.* **1984**, *B40*, 105.
[27] S. Gaponenko, H. V. Demir, C. Seassal, U. Woggon, *Opt. Express* **2016**, *24*, A430.
[28] T. P. Debies, J. W. Rabalais, *Chem. Phys.* **1977**, *20*, 277.
[29] J. Watts, J. Wolstenholme, *An Introduction to Surface Analysis by XPS and AES*, John Wiley & Sons Ltd., Chichester, England **2008**.
[30] R. N. Bhattacharya, P. Pramanik, *J. Electrochem. Soc.* **1982**, *129*, 332.
[31] Y. Tian, C.F. Guo, J. Zhang, Q. Liu, *Phys. Chem. Chem. Phys.* **2015**, *17*, 851.
[32] R. H. Bube, *Photoconductivity of Solids*, Wiley, New York, NY **1960**.
[33] D. V. Talapin, J. S. Lee, M. V. Kovalenko, E. V. Shevchenko, *Chem. Rev.* **2010**, *110*, 389.

Check for updates

Using a chitosan nanolayer as an efficient pH buffer to protect pH-sensitive supramolecular assemblies

D. V. Andreeva, [ID] [a] A. Kollath,[b] N. Brezhneva,[cd] D. V. Sviridov,[c] B. J. Cafferty,[e] H. Möhwald[d] and E. V. Skorb [ID] *[df]

It is attractive to control the properties of macro objects and films by employing simple nanolayer composites, as in the case of nanoarchitectured Layer-by-Layer (LbL) coating. In this paper, we use chitosan as a surface-based pH buffer to protect adsorbed supramolecular fibres from pH-mediated disassembly. Protons are generated on a titania surface under illumination at 405 nm leading to an appreciable pH change on the surface. We find that supramolecular polymers that are highly sensitive to pH change will not disassemble after irradiation if a nanolayer of chitosan is present. We propose that chitosan can be used as an efficient pH-responsive protective layer for pH sensitive soft materials.

Introduction

Recently[1–3] the pH buffering activity of Layer-by-layer (LbL) assemblies of weak and strong polyelectrolytes was shown to protect metal surfaces. Local pH changes cause corrosion of metal surfaces, but binding of protons to the weak poly-electrolytes was found to inhibit the corrosion events. Thus, a nanolayer with buffering ability, resulting from the chemistry of the LbL architecture, was shown to be critical for protecting a metal surface from corrosion.

A logical continuation of that work was to use local pH changes during irradiation of semiconductor surfaces.[4–8] For example, local pH changes are generated by irradiation of TiO_2 surfaces. Light-pH coupling in TiO_2/pH sensitive LbL assemblies was shown to be efficient for high-amplitude non-destructive manipulation of soft matter deposited on the semiconductor surface.[4,5] The composite systems were promising for dynamic regulation of adsorption/desorption of proteins,[6] bacteria,[9] and preosteoblast.[5] Thus, dynamic sensors, antifouling coatings and dynamic protein separation and cleaning systems were proposed.

However, the question of proton dynamics within polyelectrolyte-based LbL assemblies remains open. It is unclear if protons are buffered effectively and if pH-sensitive soft matter can be protected against acidification of the local medium.

Here, we examine the ability of a chitosan nanolayer absorbed to a TiO_2 surface to stabilize surface-bound supramolecular assemblies against environmental pH change (Fig. 1).

[a] Center for Soft and Living Matter, Institute of basic science, Ulsan National Institute of Science and Technology, 44919 Ulsan, Republic of Korea

[b] Physical Chemistry II, University of Bayreuth, Universitätsstraße 30, 95440 Bayreuth, Germany

[c] Belarusian State University, 4 Nezavisimosti ave., 220030 Minsk, Belarus

[d] Max Planck Institute of Colloids and Interfaces, Am Mühlenberg 1, 14424 Potsdam, Germany. E-mail: skorb@pikg.mpg.de

[e] Department of Chemistry and Chemical Biology, Harvard University, 02138 Cambridge, MA, USA

[f] Laboratory of Solution Chemistry of Advanced Materials and Technologies (SCAMT) ITMO University St. Petersburg, 197101, Russian Federation

Fig. 1 Light sensitive TiO_2 layer on Si/Ti (negatively charged), positively charged layer of chitosan and negatively charged rosette-based supra-molecular polymers of coassembled triaminopyrimidine (TAP) and cyanuric acid modified with hexanoic acid (CyCo6).

This journal is © the Owner Societies 2017

Phys. Chem. Chem. Phys., 2017, **19**, 23843–23848 | 23843

Specifically, we investigate the stability of supramolecular polymers formed by triaminopyrimidine (TAP) and cyanuric acid modified with a hexanoic acid side chain (CyCo6), supramolecular polymers that are known to be extremely sensitive to pH change.[10–12]

Results and discussion

First, we formed a photoactive titania surface suitable for deposition of soft-matter. It is known that the ultraviolet irradiation of photoactive titania generates electron/hole pairs that may induce a photoreaction.[13] The titania is hydrophilic[14] and has a layer of adsorbed water.[15] Reactions with surface adsorbed water molecules can result in a possible pH change on the surface.[16] In the scope of photocatalytic reactions one can assume the possible formation of H^+ and OH^- due to oxidation (ox) and reduction (red) reactions involving photogenerated charge carriers on the semiconductor surface. That is, water splitting on a semiconductor can cause the formation of H^+ and/or OH^-. We recently studied, in detail, the process of water splitting on a titania surface[17] focusing on H^+ and OH^- (not H_2 and O_2 as usual (note, that there is no obvious gas bubbling in our system)) and we observed that this process leads to a pronounced local surface acidification of the irradiated surface and subsequent pH change. The overall pH does not change, although, a pH gradient on the surface may exist.[17] Thus the inorganic surface and its nanostructuring may be involved in the reaction through process location (Fig. 2).

The water oxidation reaction on TiO_2 is initiated by a nucleophilic attack of a H_2O molecule on the photogenerated hole at the O site bridging two Ti atoms, and as a result TiO·HO–Ti and later TiOOH and TiOOTi are formed.[18] During these oxygen photoevolution reactions protons are released. At the same time, the photogenerated electrons reduce the surface $Ti^{(4+)}$ enabling adsorption of H_2O, and then O_2 attacks it immediately to form superperoxo TiOO.[19] As a result a hydroxide ion OH^- is released. Then it is reduced to peroxo Ti(OO) which evolves to
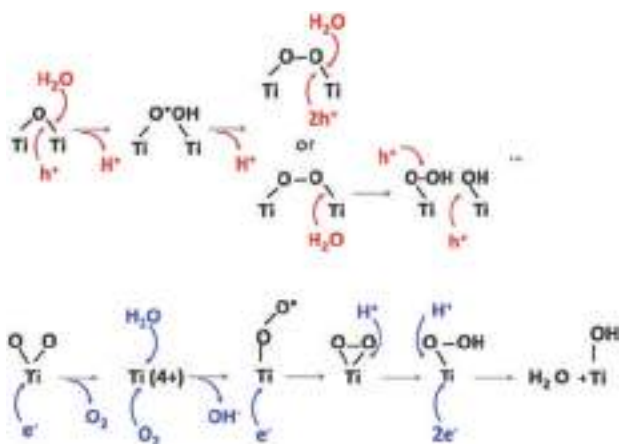
Fig. 2 Possible reorientation of titania groups and water under irradiation and reactions with photogenerated photohole (h^+) and photoelectron (e^-).
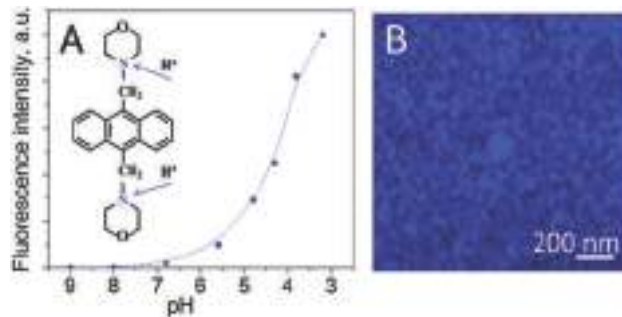
Fig. 3 (A) Calibration of fluorescent pH indicator, 4,4′-(anthracene-9,10-diyldimethanediyl)dimorpholine, that exhibits a $pK_a \sim 5.1$, and initial chemical formula showing the protonation sites; (B) confocal fluorescent images of the TiO_2 surface immediately after irradiation.

hydroperoxo TiOOH upon protonation. At the end, the surface is covered by hydroxyl groups.

This approach can also generate a high concentration of reactive oxygen species and free radicals that may cause degradation of soft matter deposited on the surface of the semiconductor.[10] In order to avoid degradation events, we produced a nanometer thick layer of TiO_2 via partial oxidation of a deposited layer of titania on silicon wafers. Morphological properties of the surface after sonochemical treatment were characterized in details in our previous work.[20] It is important here that the ultrasonically generated nanolayer of TiO_2 shows mild photoactivity under 405 nm illumination; which produces H^+ on the surface. A pH indicator shows an increase in fluorescence, seen in Fig. 3, on the surface after irradiation, corresponding to a pH that is less than 5 on irradiated surface.

We were interested in knowing how many photons are needed to release enough protons from the surface to locally change the pH from 7 to 5. If, for example, a 1 cm^2 surface of TiO_2 is irradiated in order to achieve a pH = 5 (assuming $[H^+] = 10^{-5}$ M or 6×10^{18} L^{-1} and a coating with a thickness of 50 nm, that is, $V = 5 \times 10^{-10}$ L), then the concentration of protons in the system is $[H^+] = 3 \times 10^9$ protons cm^{-2}, which is about 0.003% of the lattice sites of a typical solid (10^{15} lattice sites cm^{-2}). This means that only 0.003% of the surface atoms have to be charged to achieve pH = 5, if no losses exist. Even if we consider a low radiation intensity of 1 mW cm^{-2} = 10^{16} photons cm^{-2} s^{-1} for a quantum yield proton/photon conversion of 0.01% the photons from 1 ms irradiation would create enough protons on the TiO_2 surface to achieve LbL activation on the surface of TiO_2.

The polarization curve recorded under the chopped illumination with 405 nm laser source (shown in Fig. 4) demonstrates that the TiO_2 film has a pronounced photoactivity under the illumination, with a photocurrent onset potential of -0.6 V (vs. Ag/AgCl electrode). The observed photosensitivity in the visible range could be attributed to the optical transitions involving electronic states in the forbidden zone which result from highly defective structure inherent in titania generated via intense ultrasonic treatment.[20]

In addition to obtaining a classical I–V curve under chopped illumination we used conductive atomic force microscopy (C-AFM) to perform a local I–V study of the TiO_2 surface under

23844 | Phys. Chem. Chem. Phys., 2017, **19**, 23843–23848

This journal is © the Owner Societies 2017
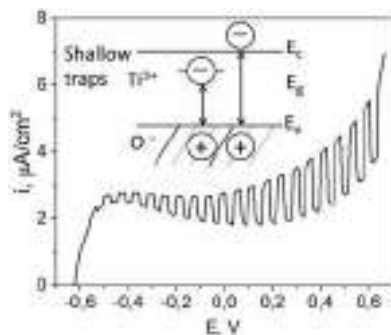
Fig. 4 Photochemical behavior of TiO$_2$. I–V curve of blank TiO$_2$ with chopped illumination. Inside schematic shows zone diagram of TiO$_2$ and suggests possible trapping in forbidden zone that may explain photo-activity during irradiation at 405 nm.
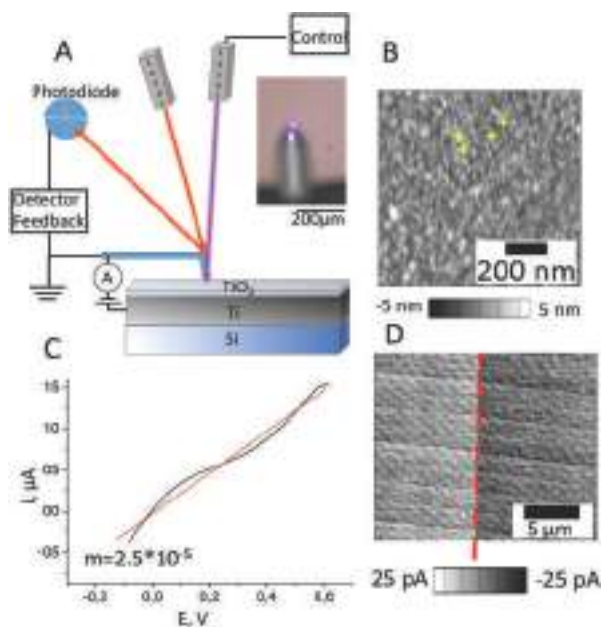
Fig. 5 (A) Atomic force microscopy (AFM) set up for a study of light stimulated processes and changes of multilayer morphology on a semi-conductor surface equipped with an additional UV-laser (inset shows the optical image of an AFM cantilever irradiated with a laser at a certain position of the light spot). (B–D) Conductive AFM (C-AFM) study of TiO$_2$ layer (B) AFM image showing in yellow certain spots that were used for I–V curve images. (C) Average current vs. voltage (I–V) curve from (B), (D) C-AFM map shows the edge between irradiated and not irradiated part of TiO$_2$ (clear edge is seen).

illumination. Fig. 5A shows the experimental set-up, there (i) we can use one extra 405 nm laser and focus it in the position of measurement, and (ii) with the use of a special metal (TiIr) tip we can study I–V in specific locations along the surface (examples are shown in yellow in Fig. 5B) and generate a current map. The C-AFM measurements were performed under ambient conditions with very sensitive current detection (from 1 pA). The C-AFM tip was used as a movable electrode to measure the I–V curves on the TiO$_2$. Fig. 5B shows an average I–V curve that, assuming a linear fit, was used to calculate a TiO$_2$ resistance of ca. 2.5×10^{-5} Ω^{-1}.

In the following we will discuss how the photoactivity of the TiO$_2$ surface and a series of photocatalytic reactions yields a local change in pH,[8] and triggers conformational changes of pH sensitive soft matter. Previously,[4] we demonstrated that the photons from 10 ms of light irradiation would create enough protons on the TiO$_2$ surface to achieve conformational changes of polyelectrolytes and LbL assemblies on the surface of TiO$_2$. It is a high priority of ours to understand how photo-initiated processes on TiO$_2$ lead to transformation of light into an appreciable pH change, including localization of the effect.

A chitosan layer with a thickness of approximately 2 nm was deposited on titania. Angle-dependent X-ray photoelectron spectroscopy (XPS) measurements (Fig. 6) were used to calculate the layer thickness (d) by measuring the positions of titanium (Ti) atoms in the bottom layer of the surface. Such a method is commonly used to calculate the thickness of self-assembled monolayer (SAM) using the position of the surface-bound sulfur atom.[21]

For these measurements, the free electron mean path exponentially decays with distance. We fixed the position of the analyzer with the lens axis 50° away from the incident beam. The take-off angle (θ) was defined as the angle between the substrate surface and the axis of the analyzer. The incident angle (γ) was defined as the angle between beam incidence and the substrate surface. We rotated the sample holder to collect the Ti2p with θ = 90° (normal emission, γ = 40°) and θ = 40° (normal emission, γ = 90°). To normalize the footprint of incident light between two different angles, the effective intensity (I_θ) is given by

$$I_\theta = I\cos(90° - \gamma) \tag{1}$$

where I is the integrated intensity of the peak. The relationship between I_θ and d can be expressed as follow:

$$I_\theta = Ie^{-d/\lambda\sin\theta} \tag{2}$$
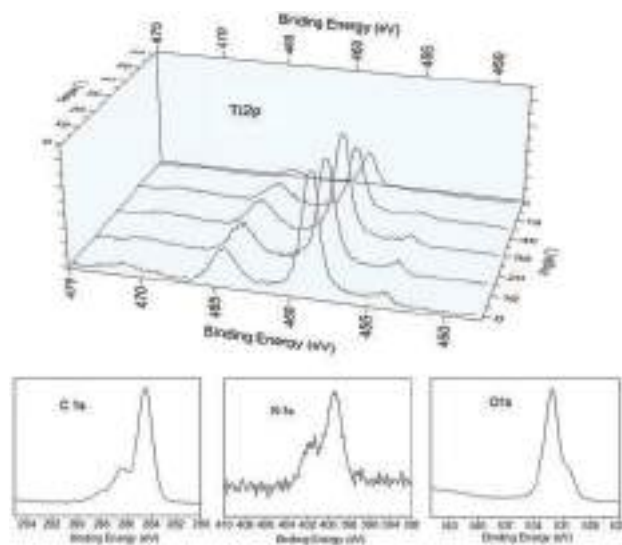
Fig. 6 Angle-dependent high resolution XPS spectrum of Ti 2P for the calculation of chitosan layer thickness and high resolution spectra of C 1s, N 1s and O 1s, proving the chitosan layer is on the surface.

Thus, I_θ ratio at 90° and 40° take-off angles can be expressed as follows:

$$\frac{I_\theta(d, 90°)}{I_\theta(d, 90°)} = \frac{e^{-d/\lambda \sin 90}}{e^{-d/\lambda \sin 40}} \qquad (3)$$

where λ is the inelastic mean free path and in our case defined as 30.5 Å. The overlayer thickness d was calculated using eqn (4):

$$d = \frac{\lambda \sin 90° \sin 40° \left[\ln\left(\frac{I_{90°}}{I_{40°}}\right)\right]}{\sin 90° - \sin 40°} \qquad (4)$$

The values of intensity I were fitted by the photoemission profiles with Voigt functions (Lorentzian (30%) and Gaussian (70%)) with Shirley plus linear background corrections.

We also examined the chitosan layer using AFM with simultaneous irradiation of the surface with 405 nm laser before (Fig. 7A and C), during (Fig. 7B and D) and after irradiation (Fig. 8).

The AFM images (Fig. 4A–D) confirm that the surface of chitosan increases in net positive charge under irradiation. For comparison, the effect of smoothing of the chitosan layer by decreasing the solution pH was observed previously by Lee *et al.*[20] and was explained to result from a change of surface

Fig. 8 AFM images showing the change of chitosan layer morphology during relaxation of the surface: in 1 min (A), and 10 min (B) after irradiation.

forces due to chitosan protonation. Here, irradiation triggers a local pH change on the semiconductor, and also may cause protonation of chitosan. It is important to note that the layer of chitosan under irradiation remains on the surface and is not detached. An explanation for the stability of the protonated nanolayer on the surface is that together with the rearrangement and structural change of chitosan chains upon protonation, ion diffusion/migration and charge regulation, chitosan forms structured hydrogen-bond networks in humid environments and a practically semicrystalline phase structure. This rigid behavior of chitosan may be a big advantage for using a chitosan nanolayer over other weak polyelectrolyte nanolayers for providing polyelectrolyte assembly stability.

We next employed pH indicators to compare photoinduced pH changes at the surface of pristine TiO_2 covered with chitosan (Fig. 7F) *vs.* bare TiO_2 (Fig. 3), to support the buffering activity of the chitosan layer. The pH indicator under irradiation didn't show any fluorescence when surfaces of TiO_2 containing a chitosan layer were analyzed, suggesting that the released protons are absorbed by chitosan molecules on the surface, effectively buffering the pH.

After the irradiation is stopped (Fig. 8), slow relaxation of the chitosan film is observed and the polymer layer reaches an equilibrium within app. 10 min. The blurriness of the AFM images can be explained due to simultaneous changes in the surface structure as a result of chitosan relaxation during acquisition.

We next examined the ability of the chitosan nanolayer to protect supramolecular structures from disassembly caused by environmental pH-change (Fig. 9). We chose TAP-CyCo6-based supramolecular polymers due to their ultrasensitive pH response.[10] Supramolecular polymers are formed in water by combining TAP and CyCo6. The monomers self-assemble into hexameric rosette structures, and hydrophobic interactions between rosettes lead to the formation of micron-length supramolecular polymers.[12] The bidirectional pH-response of this supramolecular polymer system results from the presence of an acidic monomer (Cyco6) and a basic monomer (TAP). The pH response is highly sensitive because the pK_as of the monomers are matched at 7, therefore any change in pH from neutrality will cause disassembly of the supramolecular polymers, with complete disassembly at pH below 5.5 and above 8.5.

Fig. 7 (A and B) Phase and (C and D) profile AFM scans of the titania surface at the same position (A and C) before and (B and D) 5 min after illumination with a 2 mW, 405 nm laser. (E) Schematic of proton release from a TiO_2 surface during irradiation due to photochemical reactions and chitosan layer protonation. (F) Confocal fluorescence image of the pH indicator, 4,4′-(anthracene-9,10-diyldimethanediyl)dimorpholine, during irradiation of the surface of TiO_2 covered with a chitosan layer (TiO_2@Chitosan).

23846 | *Phys. Chem. Chem. Phys.*, 2017, **19**, 23843–23848

This journal is © the Owner Societies 2017

Fig. 9   AFM images of Layer-by-Layer (LbL) deposited chitosan films on titania followed by TAP/CyCo6 deposition before (A) and after 10 min of irradiation with 9 mW intensity from a 405 nm laser (B), with the corresponding cross sections (C and D). Schematics showing TAP-CyCo6 disassembly resulting from pH-change, and (E) chitosan nanolayer as a proton sponge that affectively protects TAP-CyCo6 supramolecular polymers from disassembly (F).

We next examined if the chitosan nanolayer has enough buffering activity to protect the TAP-CyCo6 supramolecular polymers from pH-mediated disassembly caused by irradiation of the titanium surface (Fig. 6E). The supramolecular polymers were formed in water buffered with sodium phosphate at pH 6.5 and then deposited on the chitosan nanolayer. The AFM image of the surface after TAP-CyCo6 fiber deposition is shown in Fig. 6.

Next, irradiation resulted in photoreactions on the TiO_2 surface[4] leading to acidification in irradiated areas. As discussed above, in the absence of chitosan the surface pH would be expected to drop to pH 5, which would disassemble the supramolecular structures. The assemblies were, however, still observed after irradiation, even when irradiation was performed with a laser power of 9 mW for 10 min, demonstrating that chitosan nanolayer has a strong buffering capacity Fig. 6F.

Conclusions

In order to develop applications for chitosan-based materials, it will be essential to understand the efficiency of chitosan as a buffering material. Here we report that a chitosan nanolayer can be utilized as a proton sponge, thus protecting the integrity of supramolecular assemblies (even those that are highly sensitive to pH variation, such as TAP-CyCo6 assemblies) to surface-mediated pH changes. We provide further evidence here that due to the unique characteristics of chitosan chains, caused in part by

charge pairing with TiO_2 and the rigidity of the chains,[22] chitosan may strongly interact with TiO_2 and prevent penetration of protons through the chitosan nanolayer, thus protecting supramolecular assemblies associated with the nanolayer surface.

Thus we find that nanolayers of chitosan can be used in the development of surface-based material that are otherwise sensitive to environmental pH change. Particularly, for materials used in double stimuli-responsive devices that are incorporated in living systems, as chitosan exhibits pH protective properties near physiological pH. In spite of many applications of chitosan, there have been few systematic studies conducted with regard to the chitosan nanolayer buffering activity on surfaces.

Experimental

Materials

Silicon (Si) wafers (100) were from CrysTech Kristralltechnologie. Absolute ethanol AnalR NORMAPUR from VWR Chemicals was used as received. Low molecular weight chitosan, acquired from Aldrich with a molecular weight between 50 000 and 190 000 Da and a degree of deacetylation (DA) $\geq$75% was used as received for experiments. Acetic acid was purchased from EMD. Hydrochloric acid (1 M, HCl) and sodium hydroxide (1 M, NaOH) were acquired from Grüssing. Millipore water (Milli-Q Plus 185) was used for preparation of aqueous solutions and sample washing.

Titania photoactive layer preparation

Si wafers with polished surface were used as substrate for titanium layers of 2 μm thickness deposited by physical vapour deposition using a BA 510 from Fa. Balzers, Liechtenstein. Ti covered Si wafers were fixed in a homemade sample holder for high intensity ultrasound (HIUS) modification. The samples were sonicated for 1 min in ethanol at a sonotrode to surface distance of 5 mm. Cavitation was produced by a UIP1000hd ultrasonic device from Hielscher Ultrasound Technology equipped with a B2-1.8 booster and a BS2d22 sonotrode (head area 3.8 cm^2). The operating frequency was 20 kHz with a maximum intensity of 140 W cm^{-2} and an amplitude of 106 μm. The sonication medium was cooled using an ice bath to approximately 333 K.[20]

Chitosan assembly

Chitosan solution was prepared by dissolving 50 mg of chitosan in 4.95 ml of 1 wt% acetic acid to obtain 1 wt% chitosan solutions (pH $\approx$ 4). The pH of the chitosan solution was increased to pH 6.5 by addition of aqueous sodium hydroxide solution (0.1 M). Chitosan solution was deposited on the chosen substrates for 10 min by depositing drops of chitosan solution onto the substrates. Afterwards, the substrates were dried using an air pistol. The surface was washed twice.

Supramolecular assembly

For details on the synthesis of CyCo6 and TAP-CyCo6 supramolecular polymer formation and characterization see ref. 10 Briefly, supramolecular fibers were formed by combining TAP and CyCo6 at 50 mM in an aqueous solution containing 200 mM

sodium phosphate (pH 6.5). The solution was then deposited onto a substrate, which had first been prepared with chitosan. The substrate was then washed once with ice-cooled water to remove excess assemblies and phosphate buffer.

Surface characterization was performed using a Cypher S Atomic Force Microscope (AFM) from Asylum Research (Santa Barbara, California) equipped with an OTESPA-R3 Bruker cantilever with a spring constant of 26 N m^{-1} and a frequency of 300 kHz for imaging purposes. For *in situ* irradiation experiments, Asylum Research AC160TS-R3 cantilevers were used with spring constant and frequency corresponding to the OTESPA-R3 Bruker cantilever. The cantilevers were coated with Al in both cases. AFM imaging was carried out in tapping mode. Contact mode was used for conductive AFM using an ORCA cantilever holder (nA, μA) and an Asylum Research ASYELEC-01 cantilever with a spring constant of 2 N m^{-1} and a frequency of 70 kHz. The cantilevers were coated with TiIr with a tip radius of 28+/110 nm. Current–voltage curves were collected from specific surface positions in contact mode driving the sample surface from −4 to +4 V. Current maps of the surface were carried out in contact mode applying no surface bias. A blue laser with a wavelength of 405 nm incorporated into the Cypher S AFM was used as irradiation source. Irradiation power of the laser and irradiation time were varied between 2–9 mW and 1–10 min. The generally chosen laser power of 2 mW corresponds to a laser intensity of approximately 6 μW μm^{-2} given the laser diameter to be approximately 20 μm. An AFM image of the same surface position was taken after every irradiation cycle of 1 min with either the same or increasing laser power. AFM images were analyzed using the Asylum AR14 software. Current–voltage curves were analyzed using Origin Pro.

Photoelectrochemical measurements were performed using a three-electrode quartz cell using titania samples as a working electrode (WE), Pt wire as a counter electrode (CE) and Ag/AgCl (1 M KCl) as a reference electrode (RE) in 0.1 M NaOH solution. The measurements were carried out using a CompactStat potentiostat (Ivium Technologies, the Netherlands). The photo-diode with wavelength λ = 410 nm was used as a source of light and kept at a distance 5 cm away from the quartz cell.

X-ray photoelectron spectroscopy (XPS)

Measurements were performed at the X-ray photoelectron spectroscopy (XPS) measurements were performed with a Scienta ESCA-300 spectrometer. The spectra were taken using a monochromatized aluminum source Al Kα (E = 1487 eV), MX-650 VG Scienta. The base pressure in the analytical chamber was 5 × 10^{-9} mbar. The spectra acquisition was carried out in normal emission geometry with analyzer energy resolution of 0.15 eV. To probe the Ti 2p, C 1s, N 1s and O 1s, their excitation energies were used. The spectra were acquired in normal emission geometry, and the resolution was better than 0.1 eV. The spatial depth distribution of the different elements in the film, XPS spectra were taken at normal emission (90° take-off-angle) and grazing emission (10°) of the photoelectrons and compared. The uncertainty of ±2 Å takes into account the fitting errors and the angular misalignment due to sample mounting.

Notes and references

1 D. V. Andreeva, D. Fix, H. Möhwald and D. G. Shchukin, *Adv. Mater.*, 2008, **20**, 2789.
2 E. V. Skorb, D. Fix, D. V. Andreeva, H. Möhwald and D. G. Shchukin, *Adv. Funct. Mater.*, 2009, **19**, 2373.
3 D. V. Andreeva, E. V. Skorb and D. G. Shchukin, *ACS Appl. Mater. Interfaces*, 2010, **2**, 1954.
4 S. A. Ulasevich, G. Brezesinski, H. Möhwald, P. Fratzl, F. H. Schacher, S. K. Poznyak, D. V. Andreeva and E. V. Skorb, *Angew. Chem., Int. Ed.*, 2016, **55**, 13001.
5 S. A. Ulasevich, N. Brezhneva, Y. Zhukova, H. Möhwald, P. Fratzl, F. H. Schacher, D. V. Sviridov, D. V. Andreeva and E. V. Skorb, *Macromol. Biosci.*, 2016, **16**, 1422.
6 D. V. Andreeva, I. Melnyk, O. Baidukova and E. V. Skorb, *ChemElectroChem*, 2016, **3**, 1306.
7 Y. Zhukova and E. V. Skorb, *Adv. Healthcare Mater.*, 2017, **6**, 1600914.
8 E. V. Skorb, H. Möhwald and D. V. Andreeva, *Adv. Mater. Interfaces*, 2017, **4**, 1600282.
9 J. Gensel, T. Borke, N. Pazos-Perez, A. Fery, D. V. Andreeva, E. Betthausen, A. H. E. Müller and E. V. Skorb, *Adv. Mater.*, 2012, **24**, 985.
10 B. J. Cafferty, R. R. Avirah, G. B. Schustera and N. V. Hud, *Chem. Sci.*, 2014, **5**, 4681.
11 C. Li, B. J. Cafferty, S. C. Karunakaran, G. B. Schustera and N. V. Hud, *Phys. Chem. Chem. Phys.*, 2016, **18**, 20091.
12 B. J. Cafferty, I. Gállego, M. C. Chen, K. I. Farley, R. Eritja and N. V. Hud, *J. Am. Chem. Soc.*, 2013, **135**, 2447.
13 E. V. Skorb, L. I. Antonouskaya, N. A. Belyasova, D. G. Shchukin, H. Möhwald and D. V. Sviridov, *Appl. Catal., B*, 2008, **84**, 94.
14 E. V. Skorb, E. A. Ustinovich, A. I. Kulak and D. V. Sviridov, *J. Photochem. Photobiol., A*, 2008, **193**, 97.
15 Z. Zhang, K. Yao, Y. Liu, C. Jin, X. Liang, Q. Chen and L.-M. Peng, *Adv. Funct. Mater.*, 2007, **17**, 2478.
16 E. V. Skorb, D. G. Shchukin, H. Möhwald and D. V. Sviridov, *J. Mater. Chem.*, 2009, **19**, 4931.
17 H. Maltanava, S. K. Poznyak, D. V. Andreeva, M. C. Quevedo, A. C. Bastos, J. Tedim, M. G. S. Ferreira and E. V. Skorb, *ACS Appl. Mater. Interfaces*, 2017, DOI: 10.1021/acsami.7b05209.
18 R. Nakamura and Y. Nakato, *J. Am. Chem. Soc.*, 2004, **126**, 1290.
19 R. Nakamura, A. Imanishi, K. Murakoshi and Y. Nakato, *J. Am. Chem. Soc.*, 2003, **125**, 7443.
20 A. Kollath, N. Brezhneva, E. V. Skorb and D. V. Andreeva, *Phys. Chem. Chem. Phys.*, 2017, **19**, 6286.
21 O. Dannenberger, K. Weiss, H. J. Himmel, B. Jager, M. Buck and C. Woll, *Thin Solid Films*, 1997, **307**, 183.
22 D. W. Lee, C. Lim, J. N. Israelachvili and D. S. Hwang, *Langmuir*, 2013, **29**, 14222.

Photocatalytic Deposition of Hydroxyapatite onto a Titanium Dioxide Nanotubular Layer with Fine Tuning of Layer Nanoarchitecture

Sviatlana A. Ulasevich,[*,†,‡] Sergey K. Poznyak,[§] Anatoly I. Kulak,[‡] Aleksey D. Lisenkov,[‖] Maksim Starykevich,[‖] and Ekaterina V. Skorb[†]

[†]Max Planck Institute of Colloids and Interfaces, Am Mühlenberg 1, 14424 Potsdam, Germany

[‡]Institute of General and Inorganic Chemistry, National Academy of Sciences of Belarus, 220072 Minsk, Belarus

[§]Research Institute for Physical Chemical Problems, Belarusian State University, 220030 Minsk, Belarus

[‖]Department of Materials and Ceramics Engineering, Center for Research in Ceramic and Composite Materials (CICECO), University of Aveiro, 3810-193 Aveiro, Portugal

ABSTRACT: A new effective method of photocatalytic deposition of hydroxyapatite (HA) onto semiconductor substrates is proposed. A highly ordered nanotubular TiO_2 (TNT) layer formed on titanium via its anodization is chosen as the photoactive substrate. The method is based on photodecomposition of the phosphate anion precursor, triethylphosphate (TEP), on the semiconductor surface with the following reaction of formed phosphate anions with calcium cations presented in the solution. HA can be deposited only on irradiated areas, providing the possibility of photoresist-free HA patterning. It is shown that HA deposition can be controlled via pH, light intensity, and duration of the process. Energy-dispersive X-ray spectroscopy profile analysis and glow discharge optical emission spectroscopy of HA-modified TNT prove that HA deposits over the entire TNT depth. High biocompatibility of the surfaces is proven by protein adsorption and pre-osteoblast cell growth.
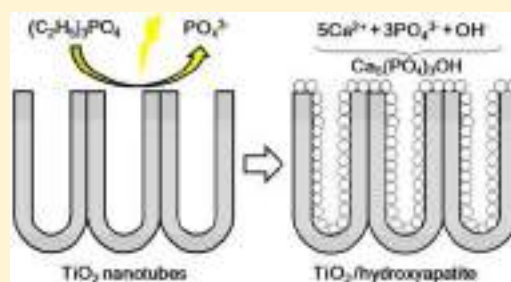
1. INTRODUCTION

Different methods are used to create hydroxyapatite (HA) coatings on bio-important substrates, such as titanium, widely applied for dental and orthopedic implants.[1−3] The plasma spraying process,[4] thermal spraying,[5] sputter coating,[6] pulsed laser deposition,[7] and chemical[8−11] and electrochemical deposition[12−17] can be mentioned. Among them, "wet" methods,[14] especially electrochemical deposition,[18] are preferable because they allow for the coating deposition onto large, irregularly shaped surfaces.[19,20]

Electrochemical deposition of HA is based on cathode electrode reactions of nitrate, peroxide, or H^+ electroreduction with a pH jump effect.[14] During these reactions, a local pH increase is created near the electrode surface, which leads to deposition of calcium phosphates on the cathode.[14−16] Generally, solutions with pH 3.5−6.0 containing low concentrations of calcium and phosphate ions are used in this method to prevent the formation of calcium phosphates in a bulk of the electrolyte. However, coatings formed from acidic solutions are brushite[17] or octacalcium phosphate[21] and not HA and contain acidic phosphate groups. Conversion of these coatings into HA coatings requires additional procedures, e.g., long-term soaking in NaOH.[17]

In the present paper, we propose a new method of photocatalytic deposition of HA onto photoactive substrates. The method is based on photodecomposition of phosphate anion precursors on the semiconductor surface. The nanotubular TiO_2 (TNT) layer is chosen as a substrate to demonstrate the method prospects because it is known to possess a high photocatalytic activity when irradiated with ultraviolet (UV) light in aqueous solutions.[22−24] TNT photoactivity can be used for the decomposition of organophosphorus compounds that are stable in alkaline solutions with the initial formation of HA and not brushite or octacalcium phosphate. In our research, we use anodic polarization for better charge separation because electrochemically assisted photocatalysis[24] is known as an effective method to increase charge separation in comparison to non-assisted photocatalysis. If charges are separated efficiently, e.g., during electrochemically assisted photocatalysis, all generated photoholes can participate in oxidation reactions. In comparison to the existing methods, electrochemically assisted photocatalytic deposition of HA looks to be similar to electrochemical deposition. Both of these methods use electrolytes, cathode and anode. However, these methods have significant differences as follows: (1) Photocatalytic deposition of HA is based on photodecomposition of organophosphorus compounds, while electrochemical deposition of HA is based on a pH jump effect.

(2) Photocatalytic deposition of HA can be conducted without polarization, while electrochemical deposition does not occur without polarization. (3) HA deposits on the anode during the photocatalytic method, while it deposits on the cathode during the electrochemical method. (4) As mentioned above, solutions for electrochemical deposition of HA are generally acidic (pH 3.5−6.0), while for photocatalytic deposition of HA, we use alkaline solutions (pH 8.0−12.0).

In addition, HA coating on TNT can result in further improvement of TNT biocompatibility, which is interesting as a result of the unique nanotubular architecture to trigger bone formation.[25] Moreover, a unique nanotubular porous architecture is prospective for surface capsule development and can be used, in the future, to build drug delivery implants.[26]

2. MATERIALS AND METHODS

2.1. Materials. Triethylphosphate (TEP, ≥99.8%), ammonium fluoride (≥99.99%, trace metals basis), calcium chloride (≥93.0%), calcium nitrate tetrahydrate (≥99.0%), ammonium nitrate (≥98%), potassium chloride (≥99.0%), NH_3 (28 wt % in H_2O, ≥99.99%), 1,2-ethanediol (anhydrous, 99.8%), and hydrogen peroxide solution (30 wt % in H_2O, ACS reagent) were supplied by Sigma-Aldrich. Titanium plates (≥99.7%) purchased from Sigma-Aldrich were used as a substrate material. Before anodic oxidation, the plates were chemically polished in a mixture (2:1 by volume of HF/HNO_3) of concentrated HF (50 wt %) and HNO_3 (65 wt %) at 80 °C for 3−5 s, thoroughly rinsed with deionized water, and then dried with nitrogen. Milli-Q water (18 MΩ cm) was used for preparing all aqueous solutions.

2.2. Preparation of TNT. Ti plates were anodized in ethylene glycol electrolyte containing 0.75 wt % NH_4F and 2 vol % H_2O to prepare the TNT layer on the Ti surface. The electrochemical anodization consisted of a voltage ramp from 0 to 40 V with a scan rate of 0.2 V s^{-1}, followed by holding at 40 V for 1 h. After the electrochemical deposition, the electrodes were rinsed with water and then dried. Then, the as-anodized samples were ultrasonically cleaned in Milli-Q water for 30 s to remove surface debris on the TNT surface. TNT layers were annealed at 450 °C for 3 h in air for TiO_2 crystallization, increasing its photocatalytic activity. Scanning electron microscopy (SEM) analysis reveals a thickness of the TNT layer of ca. 6 μm after 1 h of electrochemical oxidation.

2.3. Electrochemical and Photoelectrochemical Measurements. An electrochemical cell with a three-electrode arrangement was used for photoelectrochemical experiments. A platinum wire served as the counter electrode, and an Ag/AgCl (saturated KCl solution) electrode served as the reference electrode. Titanium plates with the grown TNT layer were used as the working electrode. The reference electrode was placed close to the working electrode using a Luggin probe capillary. The cell was provided with a quartz window for UV irradiation of the working electrode. An Autolab PGSTAT 302N potentiostat (Metrohm Autolab B.V., Netherlands) was used in these experiments. The working electrode surface was irradiated by a focused UV light beam from a high-pressure mercury lamp (250 W). Thermal radiation was filtered by a water filter equipped by high-quality quartz windows.

Prior and during photocatalytic HA deposition, an electrolyte in the cell was bubbling with Ar for 30−60 min to remove CO_2 diluted in water and to prevent carbonate HA formation.

2.3.1. X-ray Diffraction (XRD) Analysis. XRD analysis was performed using an Advance D8 diffractometer (Bruker, Germany) with Co Kα radiation. All samples were examined in the range of 2θ from 10° to 70° at a scanning speed of 1°/min and a step size of 0.03°.

2.3.2. Raman Spectra. Raman spectra were taken at room temperature using a Nanofinder high-end confocal microscope (Leica TCS SP, Germany) with a 573 nm solid-state exciting laser.

2.3.3. SEM. SEM was performed using Hitachi S4100 and Hitachi SU-70 microscopes coupled with energy-dispersive X-ray spectroscopy (EDS) for morphological characterization of the sample surface. Samples were sputtered with carbon.

2.3.4. Glow Discharge Optical Emission Spectroscopy (GDOES). GDOES depth profile analysis of the coatings was completed using a HORIBA GD-Profiler 2 operating at a pressure of 650 Pa and a power of 30 W. The anode size was of 4 mm in diameter.

2.3.5. Analysis of Free Phosphate Ions. Analysis of free phosphate ions in the electrolyte was carried out colorimetrically by a spectrophotometer Shimadzu UV 2550 with the use of the vanadium molybdenum complex.[27]

2.3.6. Biocompatibility of Stepwise HA-Modified TNT Coating. Biocompatibility of stepwise HA-modified TNT coating was demonstrated by adsorption of proteins at its surface. Mixed proteins (Alice ProteoGenix) labeled with the fluorescent dye were used as an adsorption reagent. The proteins consist of phospholyrase b, bovine serum albumin, ovalbumin, carbonic anhydrase II, soybean trypsin inhibitor A, and lysozyme, each of which was labeled with the fluorescent dye, 2-(4-amidinophenyl)-1H-indole-6-carboxamidine (DAPI). Each protein was prepared at a concentration of 7−16 mg/mL. Confocal fluorescence microscope images were analyzed after the samples were in contact with protein solution for 5 and 20 min.

2.4. Cell Culture. Murine pre-osteoblastic cells MC3T3-E1 (provided by the Ludwig Boltzmann Institute of Osteology, Vienna, Austria) were seeded with a density of 6×10^3 cells/cm^3 on the surface and cultured for 2 days in α modification of minimum essential medium (α-MEM, Sigma-Aldrich, St. Louis, MO) supplemented with 10% fetal calf serum (PAA Laboratories, Linz, Austria), 0.1% ascorbic acid (Sigma-Aldrich, St. Louis, MO), and 0.1% gentamicin (Sigma-Aldrich, Steinheim, Germany) in a humidified atmosphere with 5% CO_2 at 37 °C.

2.5. Immunofluorescent Staining. Samples with were washed with phosphate-buffered saline (PBS), fixed with 4% paraformaldehyde, and permeabilized with 0.1% Triton X-100 (Sigma-Aldrich, Steinheim, Germany) for 15 min. Then, samples were incubated for 1 h in a 1:20 solution of Alexa Fluor 488 phalloidin (Invitrogen, Eugene, OR) in the dark at 4 °C. After washing in PBS, the samples were stained for nuclei with a 1:300 solution of TO-PRO-3 iodide (Invitrogen, Eugene, OR) for 5 min.

2.6. Confocal Microscopy. Images of the cell nucleus and actin cytoskeleton cells were obtained using a confocal laser scanning microscope (Leica TCS SP, Germany). An Ar ion (488 and 514 nm) and a He−Ne laser (543 nm) were used as an excitation source.
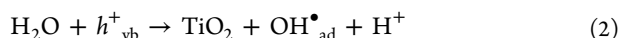
3. RESULTS AND DISCUSSION

Our method of HA photocatalytic deposition is based on photodecomposition of phosphate anion precursors on the titania surface under UV illumination and anodic polarization. Triethylphosphate (TEP) is used in the present work as the PO_4^{3-} precursor because this organic compound is highly soluble in water, non-toxic, and chemically stable in alkaline solutions and absorbs UV light weakly up to λ = 200 nm, i.e., photochemically inactive. It was shown previously[28,29] that TEP can be photocatalytically decomposed on the surface of TiO_2 particles in aqueous solutions. We use this effect to synthesize HA directly on the TiO_2 surface. During photocatalytic decomposition of TEP, phosphate ions are formed on the titania surface and can react with Ca^{2+} and OH^- ions, producing the HA film on the surface.

The mechanism of HA formation during photocatalytic deposition can be described by the following steps: (1) TiO_2 photoactivation with the formation of photoholes (h^+_{vb}) and photoelectrons (e^-_{cb}),[30]
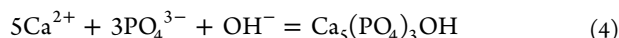
$$TiO_2 + h\nu \rightarrow h^+_{vb} + e^-_{cb} \tag{1}$$

(2) radical generation on the TiO_2 surface,

$$H_2O + h^+_{vb} \rightarrow TiO_2 + OH^\bullet_{ad} + H^+ \qquad (2)$$

(3) photodecomposition reactions,

$$TEP + OH^\bullet/h^+_{vb} \rightarrow PO_4^{3-} \qquad (3)$$

and other degraded/mineralized products,[28] and (4) interaction of phosphate anions (product of TEP decomposition) with Ca^{2+} and OH^- ions presented in the electrolyte with the formation of HA

$$5Ca^{2+} + 3PO_4^{3-} + OH^- = Ca_5(PO_4)_3OH \qquad (4)$$

The photocatalytic process on the surface of the TiO_2 electrode according to reaction 2 can lead to a local acidification of the near-surface region of the solution. This fact is confirmed by the change of the pH of the electrolyte during photocatalytic deposition of HA. When initial pH is 10.0, the resultant pH is 9.8 after 1 h of the photocatalytic deposition; the initial pH of 9.2 changes to 8.8, while the initial pH of 8.4 drops until 5.2. To smooth over this undesirable effect, we used ammonium buffer solution with pH 10.0−11.0 as a background electrolyte. High values of the pH are more preferable for HA synthesis. However, at pH values more than 12, the electrolyte becomes opaque as a result of the formation of $Ca(OH)_2$ in a bulk of the electrolyte.

Figure 1a shows typical photocurrent−potential plots measured under chopped UV illumination of the TNT
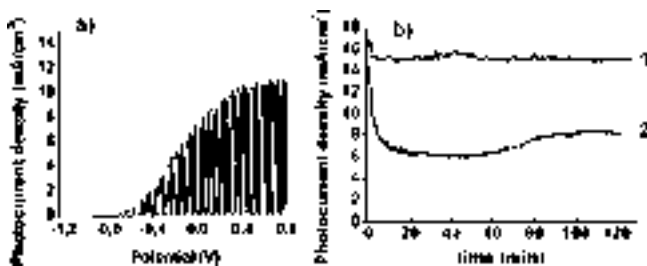
Figure 1. (a) Voltage−photocurrent dependence at +0.5 V (versus Ag/AgCl) of TNT coating in an electrolyte of 0.03 M NH_4Cl and 0.02 M TEP at pH 10 under UV irradiation. (b) Photocurrent−time dependence of TNT coating under anodic polarization at +0.5 V (versus Ag/AgCl) in an electrolyte of 0.03 M NH_4Cl and 0.02 M TEP (1) without 0.03 M $CaCl_2$ and (2) with 0.03 M $CaCl_2$ at pH 10.

electrodes in deaerated 0.03 M NH_4Cl solution with pH 10.0. The photocurrent appears at potentials from −0.8 to −0.9 V, then grows sharply with potential, and finally levels off at $E \geq 0.4$ V.

The addition of TEP to the electrolyte does not influence appreciably both the shape of the $I_{ph}-E$ curves and the photocurrent values. This effect may be concerned with the high efficiency of photohole (h^+_{vb}) and photoelectron (e^-_{vb}) separation in a bulk of the TNT electrode. However, chemical analysis showed that phosphate ions appeared in the TEP-containing electrolyte as a result of TEP photodecomposition on the TiO_2 electrode. Approximately 9×10^{-4} mol L^{-1} PO_4^{3-} ions is produced during UV illumination of 0.02 M TEP solution for 2 h. The average rate of the PO_4^{3-} ion supply in the bulk of the electrolyte is ca. 7×10^{-6} mol L^{-1} min^{-1}. This relatively slow rate of PO_4^{3-} ion generation can be explained by a complicated mechanism of TEP photodegradation, leading to a large number of products and intermediates.[28,29] Such a gradual formation of PO_4^{3-} in the electrolyte during TEP

photolysis is very preferable because HA synthesis requires a long time.[31,32]

Figure 1b presents the temporal evolution of the photo-current at a fixed potential (+0.5 V) of the TNT electrode in solution containing 0.02 M TEP and 0.03 M NH_4Cl (pH 10). After an initial insignificant drop, the photocurrent varies insignificantly with time for a long period.

The addition of Ca^{2+} ions into the electrolyte leads to about a 2 times decrease of the photocurrent for 2−10 min. This photocurrent drop can be associated with a partial blocking of the TNT surface with a growing calcium phosphate layer. There is no formation of HA in the bulk of the electrolyte.

SEM images reveal that an average inner diameter of as-prepared titania nanotubes is ca. 60 nm (Figure 2a). This
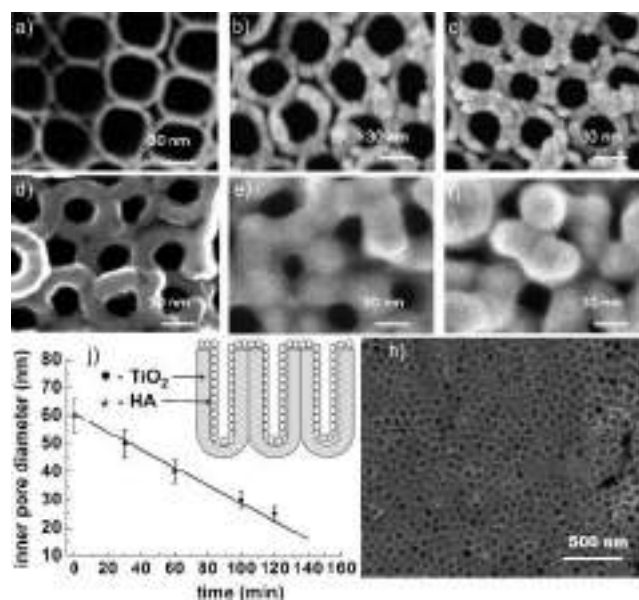
Figure 2. (a−f and h) SEM images of the TNT coating after HA photocatalytic deposition for (a) 0 min, (b) 30 min, (c) 60 min, (d) 100 min, (e and h) 120 min, and (f) 150 min. (j) Dependence of the TNT inner pore diameter upon the time of photocatalytic deposition. The inset points to the advantage of the method as a possibility to remain a unique morphology of TNT coating after HA deposition.

diameter decreases gradually during photocatalytic deposition of HA, depending upon the irradiation time (panels b−j of Figure 2). Even a 3 times decrease in the nanotube diameter remains for the unique ordered morphology of the HA-modified TNT coating. An UV irradiation longer than 120 min leads to partial closing of the pores. Figure 2h shows that HA deposits uniformly on the TNT layer and there are not uncovered areas.

The EDS analysis of the cross-section of HA-modified TNT coating shows the uniform distribution of the calcium and phosphorus elements in the thickness of the TNT nanotube layer (panels a and b of Figure 3). The EDS analysis has also revealed that the content of Ca and P elements grows by 1.3 times when increasing the time of photocatalytic deposition of HA from 1 to 2 h, indicating that the formation of HA occurs mainly during the first hour of photocatalytic deposition.

Depth profile analysis of the coatings additionally confirms the uniform distribution of Ca and P through the TNT layer (panels c and d of Figure 3). The data obtained prove that the titania nanotubes are photocatalytically covered with HA
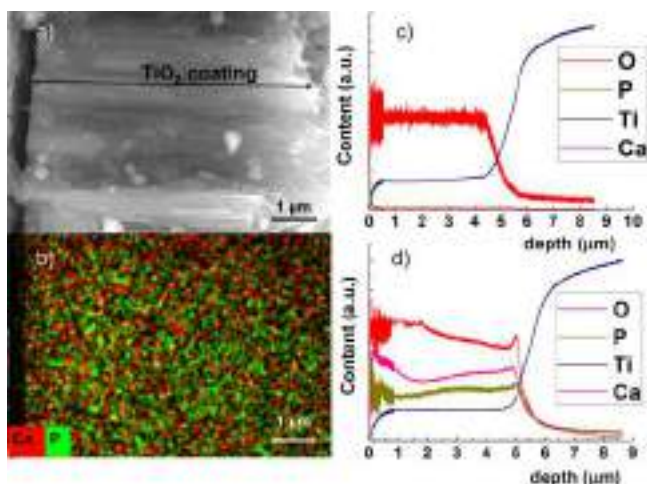
Figure 3. (a) SEM images of TNT coating with photocatalytically deposited HA (cross-section; length of the nanotubes is marked by an arrow). (b) Element distribution on the cross of TNT coating with photocatalytically deposited HA, with the image obtained by EDS analysis. Depth profile analysis of the (c) TNT coatings and (d) TNT coating with photocatalytically deposited HA.

through their whole length, as shown schematically in the inset of Figure 2j.

XRD pattern of the HA-modified TNT coating is shown in Figure 4a. It should be noted that as-deposited HA is not well-
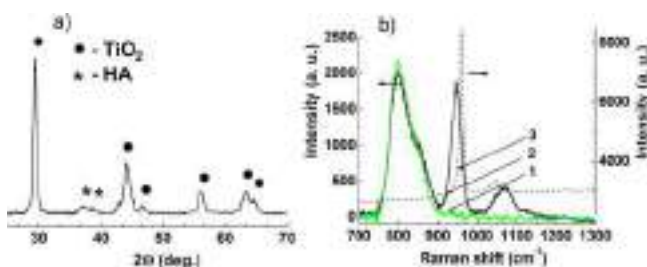
Figure 4. (a) XRD pattern of TNT nanotubes with HA deposited photocatalytically. HA-modified TNT samples were annealed at 450 °C for 3 h. (b) Raman spectra of (curve 1) TNT coating, (curve 2) photocatalytically deposited HA on TNT coating, and (curve 3) polycrystalline HA powder, as a control.

detectable in XRD spectra. Only peaks characteristic of anatase from the TNT coating are observed at 2θ: 29.4°, 44.9°, 47.0°, 55.9°, and 63.1°. After the sample was annealed, HA signals can be seen in the XRD spectrum as the crystalline phase (Figure 4a). The most intensive broad peak of HA is observed at 37−39°. Broadened peaks may indicate a small size of HA crystallites. No other phases, except TiO_2 and HA, have been detected.

Raman spectroscopy was applied for further identification. TNT has a weak signal at 800 cm^{-1} characteristic of anatase in this part of the spectrum (curve 1 of Figure 4b).[21] After photocatalytic deposition of HA, an additional band at 949 cm^{-1} and a broad band in the range of 1030−1100 cm^{-1} are seen in curve 2 of Figure 4b, which could be a superposition of two narrower bands. The Raman spectrum of polycrystalline HA as a standard is also measured and demonstrates the modes at 961, 1047, and 1074 cm^{-1} (curve 3 of Figure 4b). Thus, the additional Raman modes of the photocatalytically treated TNT electrodes can be assigned to HA. The main peak is shifted

from 961 to 949 cm^{-1} and widened. The full width at half maximum (fwhm) of this peak is 30 cm^{-1}, while the fwhm of the standard peak is 10 cm^{-1}. Its shift and broadening may be associated with the nanocrystalline structure of deposited HA.[33]

The photocatalytical deposition can be used for HA patterning using the local illumination of the TNT surface. TNT coating has been illuminated locally, with some parts remaining in the dark. HA can be formed on light-exposed areas, while not irradiated areas will be HA-free.

The biocompatibility of obtained HA−TNT coatings is demonstrated by adsorption of mixed proteins (Alice ProteoGenix) labeled with the fluorescent dye (panels a−c of Figure 5). The confocal fluorescence microscope images are
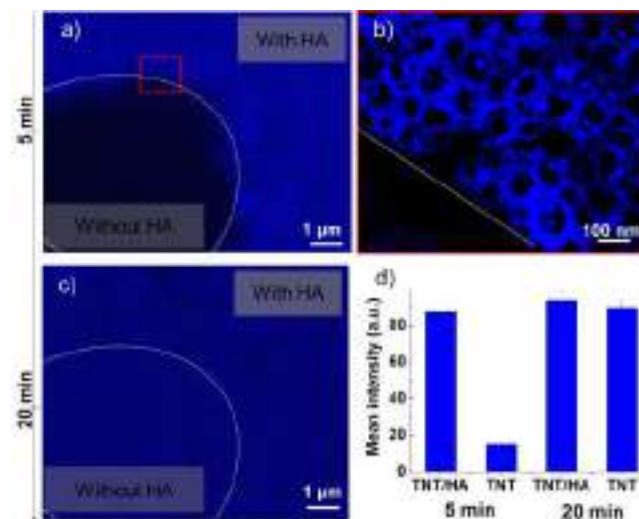
Figure 5. Confocal fluorescence microscope images of the TNT substrate with areas with (signed as TNT) and without (signed as TNT/HA) photocatalytically deposited HA: (a) after 5 min in contact with protein solution, (b) increased resolution image of panel a, and (c) after 20 min in contact with protein solution. (d) Mean fluorescence intensity of mixed proteins labeled with DAPI on the TNT substrate with areas with and without photocatalytically deposited HA. The HA side adsorbs proteins faster in comparison to the TNT side.

analyzed in different time periods after the samples are in contact with protein solution. The protein adsorption occurs faster on HA-lined TNT regions (panels a and b of Figure 5) compared to those without HA. In 5 min after contact with the protein solution, the proteins adsorb directly on the areas with HA (panels a and b of Figure 5). In comparison to HA, a neat TNT surface can also adsorb proteins but not as fast as HA. Thus, in 20 min after contact with the protein solution, the adsorption starts everywhere, on the TNT coating with and without HA (Figure 5c). Faster protein adsorption onto the HA side in comparison to TNT relies on several factors: (i) protein−material interactions, such as specific binding at the surface, non-specific binding through hydrogen bonding, and electrostatic interactions that are faster on the HA side,[34] and (ii) surface characteristics, such as energy and hydrophobicity, degree of crystallinity of HA preferable for the proteins, and ability of the charged HA surface to adsorb biological molecules containing carboxyl groups, phosphate groups, and amino groups.[34] Generally, the faster the protein adsorption, the higher the biocompatibility, which is characteristic, in our case, for the side modified with HA. Thus, a higher biocompatibility

of the surface coated with HA is expected in comparison to TNT as a result of faster protein adsorption. Indeed, cell density is significantly higher on TNT with HA coating (Figure 6).
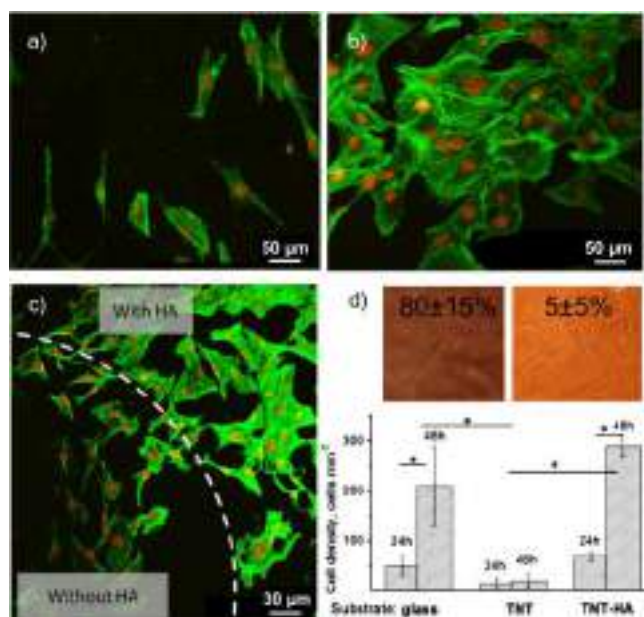
Figure 6. Pre-osteoblasts MC3T3-E1 cell growth on different substrates. Immunofluorescent analysis on cell density and morphology after 2 days of culturing on different substrates: (a) TNT, (b) TNT−HA, and (c) TNT substrate with areas with and without photocatalytically deposited HA. Cells were stained for actin using phalloidin and TO-PRO-3 iodide for nuclei. (d) Cell density on different surfaces as the culture time progressed. Insets depict cell morphologies on (left) TNT and (right) TNT−HA, pointing out the percentage of elongated cells on the corresponding substrate. Bar charts represent means ± standard deviation (SD) from three replicates each from three independent experiments. A comparison was performed by analysis of variance (ANOVA). (∗) $p < 0.05$.

The TNT surface with illuminated and non-illuminated areas, with HA and without HA, correspondingly, is examined using cell culture (Figure 6c). We observe a dramatically lower cell number on the half with a TNT surface compared to TNT−HA.

It has been demonstrated in cell culture experiments on TNT of different sizes that adhesion, proliferation, and migration of mesenchymal stem cells are optimal on ordered nanopore arrays with spacing in the range of 15−40 nm; these length scales also lead to significantly less apoptosis than on 100 nm structures.[35] As mentioned above, deposition of HA decreases the pore size from ca. 60 to 30 nm. Thus, higher biocompatibility of the surface coated with HA in comparison to TNT can also be associated with a smaller pore size.[36,37]

It is interesting that, together with a step-like gradient in cell response to nanotopology, cells also have the same tendency with respect to shape, being spindle-like on TNT [left inset of Figure 6d (ca. 80% are spindle-like)].

4. CONCLUSION

In summary, the photocatalytic deposition of HA onto a photoactive titanium dioxide nanotube layer with a remaining TNT unique nanomorphology is very promising for the formation of HA layers with a high biocompatibility. In comparison to other known methods, e.g., chemical and electrochemical methods, the proposed method is attractive as a result of the following advantages: (1) High pH of the solution favors HA formation.[31] (2) HA is formed onto TNT coating during photocatalytic deposition in a one-step procedure. Therefore, there is no need in the following hydrothermal treatment[13] or soaking in NaOH,[17] which are required in some chemical[13,36] and electrochemical[12,17,21] methods. (3) HA is deposited only on irradiated areas, providing the possibility of photoresist-free HA patterning.

■ AUTHOR INFORMATION

Corresponding Author

*E-mail: ulasevich@mpikg.mpg.de.

Notes

The authors declare no competing financial interest.

■ REFERENCES

(1) Akin, F. A.; Zreiqat, H.; Jordan, S.; Wijesundara, M. B. J.; Hanley, L. Preparation and analysis of macroporous TiO_2 films on Ti surfaces for bone−tissue implants. *J. Biomed. Mater. Res.* **2001**, *57*, 588−596.

(2) Sul, Y. Electrochemical growth behavior, surface properties, and enhanced in vivo bone response of TiO_2 nanotubes on micro-structured surfaces of blasted, screw-shaped titanium implants. *Int. J. Nanomed.* **2010**, *5*, 87.

(3) Tsuchiya, H.; Macak, J. M.; Müller, L.; Kunze, J.; Müller, J.; Greil, P.; Virtanen, S.; Schmuki, P. Hydroxyapatite growth on anodic TiO_2 nanotubes. *J. Biomed. Mater. Res., Part A* **2006**, *77A*, 534−541.

(4) De Groot, K.; Geesink, R.; Klein, C. P. A. T.; Serekian, P. Plasma sprayed coatings of hydroxylapatite. *J. Biomed. Mater. Res.* **1987**, *21*, 1375−1381.

(5) Gross, K. A.; Berndt, C. C. Thermal processing of hydroxyapatite for coating production. *J. Biomed. Mater. Res.* **1998**, *39*, 580−587.

(6) Ding, S.-J. Properties and immersion behavior of magnetron-sputtered multi-layered hydroxyapatite/titanium composite coatings. *Biomaterials* **2003**, *24*, 4233−4238.

(7) Suda, Y.; Kawasaki, H.; Ohshima, T.; Nakashima, S.; Kawazoe, S.; Toma, T. Hydroxyapatite coatings on titanium dioxide thin films prepared by pulsed laser deposition method. *Thin Solid Films* **2006**, *506−507*, 115−119.

(8) Li, P.; de Groot, K.; Kokubo, T. Bioactive $Ca_{10}(PO_4)_6(OH)_2$−TiO_2 composite coating prepared by sol-gel process. *J. Sol-Gel Sci. Technol.* **1996**, *7*, 27−34.

(9) Kodama, A.; Bauer, S.; Komatsu, A.; Asoh, H.; Ono, S.; Schmuki, P. Bioactivation of titanium surfaces using coatings of TiO_2 nanotubes rapidly pre-loaded with synthetic hydroxyapatite. *Acta Biomater.* **2009**, *5*, 2322−2330.

(10) Habibovic, P.; Barrere, F.; Blitterswijk, C. A.; Groot, K.; Layrolle, P. Biomimetic hydroxyapatite coating on metal implants. *J. Am. Ceram. Soc.* **2002**, *85*, 517−522.

(11) Sureshbabu, S.; Komath, M.; Shibli, S. M. A.; Varma, H. K. Biomimetic deposition of hydroxyapatite on titanium with help of sol-gel grown calcium pyrophosphate prelayer. *Mater. Res. Innovations* **2011**, *15*, 178−184.

(12) Han, Y.; Fu, T.; Lu, J.; Xu, K. Characterization and stability of hydroxyapatite coatings prepared by an electrodeposition and alkaline treatment process. *J. Biomed. Mater. Res.* **2001**, *54*, 96−101.

(13) Hanawa, T. Biofunctionalization of titanium for dental implant. *Jpn. Dent. Sci. Rev.* **2010**, *46*, 93−101.

(14) Duan, K.; Wang, R. Surface modifications of bone implants through wet chemistry. *J. Mater. Chem.* **2006**, *16*, 2309−2321.

(15) Wang, J.; Layrolle, P.; Stigter, M.; de Groot, K. Biomimetic and electrolytic calcium phosphate coatings on titanium alloy: Physicochemical characteristics and cell attachment. *Biomaterials* **2004**, *25*, 583−592.

(16) Wang, Y.; Tao, J.; Wang, L.; He, P. T.; Wang, T. HA coating on titanium with nanotubular anodized TiO_2 intermediate layer via electrochemical deposition. *Trans. Nonferrous Met. Soc. China* **2008**, *18*, 631−635.

(17) Sobieszczyk, S. Hydroxyapatite coatings on porous Ti and Ti alloys. *Adv. Mater. Sci.* **2010**, *10*, 19−28.

(18) Madden, J. D.; Hunter, I. W. Three-dimensional microfabrication by localized electrochemical deposition. *J. Microelectromech. Syst.* **1996**, *5*, 24−32.

(19) Redepenning, J.; Venkataraman, G.; Chen, J.; Stafford, N. Electrochemical preparation of chitosan/hydroxyapatite composite coatings on titanium substrates. *J. Biomed. Mater. Res.* **2003**, *66A*, 411−416.

(20) Shirkhanzadeh, M. Direct formation of nanophase hydroxyapatite on cathodically polarized electrodes. *J. Mater. Sci.: Mater. Med.* **1998**, *9*, 67−72.

(21) Blondeau, G.; Froelicher, M.; Froment, M.; Hugot-Le Goff, A. On the optical indices of oxide films as a function of their crystallization: Application to anodic TiO_2 (anatase). *Thin Solid Films* **1977**, *42*, 147−153.

(22) Ghicov, A.; Macak, J. M.; Tsuchiya, H.; Kunze, J.; Haeublein, V.; Frey, L.; Schmuki, P. Ion implantation and annealing for an efficient N-doping of TiO_2 nanotubes. *Nano Lett.* **2006**, *6*, 1080−1082.

(23) Mohapatra, S. K.; Misra, M.; Mahajan, V. K.; Raja, K. S. (2007). A novel method for the synthesis of titania nanotubes using sonoelectrochemical method and its application for photoelectrochemical splitting of water. *J. Catal.* **2007**, *246*, 362−369.

(24) Vinodgopal, K.; Hotchandani, S.; Kamat, P. V. Electrochemically assisted photocatalysis: Titania particulate film electrodes for photocatalytic degradation of 4-chlorophenol. *J. Phys. Chem.* **1993**, *97*, 9040−9044.

(25) von Wilmowsky, C.; Bauer, S.; Lutz, R.; Meisel, M.; Neukam, F. W.; Toyoshima, T.; Schmuki, P.; Nkenke, E.; Schlegel, K. A. In vivo evaluation of anodic TiO_2 nanotubes: An experimental study in the pig. *J. Biomed. Mater. Res., Part B* **2009**, *89B*, 165−171.

(26) Skorb, E. V.; Möhwald, H. Dynamic Interfaces for Responsive Encapsulation Systems. *Adv. Mater.* **2013**, *25*, 5029−5043.

(27) Kitson, R. E.; Mellon, M. G. Colorimetric determination of phosphorus as molybdivanadophosphoric acid. *Ind. Eng. Chem., Anal. Ed.* **1944**, *16*, 379−383.

(28) Kozlova, E. A.; Smirniotis, P. G.; Vorontsov, A. V. Comparative study on photocatalytic oxidation of four organophosphorus simulants of chemical warfare agents in aqueous suspension of titanium dioxide. *J. Photochem. Photobiol., A* **2004**, *162*, 503−511.

(29) Makie, P.; Persson, P.; Osterlund, L. Solar light degradation of trimethyl phosphate and triethyl phosphate on dry and water-precovered hematite and goethite nanoparticles. *J. Phys. Chem. C* **2012**, *116*, 14917−14929.

(30) Meunier, B.; Sorokin, A. Oxidation of pollutants catalyzed by metallophthalocyanines. *Acc. Chem. Res.* **1997**, *30*, 470−476.

(31) Narayanan, R.; Seshadri, S. K.; Kwon, T. Y.; Kim, K. H. Electrochemical nano-grained calcium phosphate coatings on Ti−6Al−4V for biomaterial applications. *Scr. Mater.* **2007**, *56*, 229−232.

(32) Onuma, K.; Ito, A. Cluster growth model for hydroxyapatite. *Chem. Mater.* **1998**, *10*, 3346−3351.

(33) Likodimos, V.; Stergiopoulos, T.; Falaras, P.; Kunze, J.; Schmuki, P. Phase composition, size, orientation, and antenna effects of self-assembled anodized titania nanotube arrays: A polarized micro-Raman investigation. *J. Phys. Chem. C* **2008**, *112*, 12687−12696.

(34) Lee, W.-H.; Loo, C.-Y.; Van, K. L.; Zavgorodniy, A. V.; Rohanizadeh, R. Modulating protein adsorption onto hydroxyapatite particles using different amino acid treatments. *J. R. Soc., Interface* **2012**, *9*, 918−927.

(35) Paramasivam, I.; Jha, H.; Liu, N.; Schmuki, P. Review of photocatalysis using self-organized TiO_2 nanotubes and other ordered oxide nanostructures. *Small* **2012**, *8*, 3073−3103.

(36) Park, J.; Bauer, S.; von der Mark, K.; Schmuki, P. Nanosize and vitality: TiO_2 nanotube diameter directs cell fate. *Nano Lett.* **2007**, *7*, 1686−1691.

(37) Cüneyt Tas, A. Synthesis of biomimetic Ca-hydroxyapatite powders at 37 °C in synthetic body fluids. *Biomaterials* **2000**, *21*, 1429−1438.

RSC Advances

Deposition of hydroxyapatite–incorporated TiO₂ coating on titanium using plasma electrolytic oxidation coupled with electrophoretic deposition

Sviatlana A. Ulasevich,*[ab] Anatoly I. Kulak,[b] Sergey K. Poznyak,[c] Sergey A. Karpushenkov,[c] Aleksey D. Lisenkov[d] and Ekaterina V. Skorb[a]

A porous hydroxyapatite (HA)–incorporated TiO₂ coating has been deposited on the titanium substrate using a plasma electrolytic oxidation coupled with electrophoretic deposition (PEO-EPD). Potassium titanium(ɪᴠ) oxalate is decomposed by micro arcs generated on the anode producing TiO₂ while HA particles have been simultaneously deposited on anode during EPD process. Hydroxyapatite and TiO₂ particles have been coagulated into roundish conglomerates with the average diameter in a range of 200–600 nm. The microstructure, as well as elemental and phase composition of the coatings have been examined by scanning electron microscopy (SEM), energy dispersive spectroscopy (EDS), glow discharge optical emission spectroscopy (GDOES), fourier transform infrared spectroscopy (FTIR) and X-ray diffraction (XRD). XRD has showed that the coatings are composed mainly of HA, rutile and anatase phases. The composition and surface morphologies are not strongly dependent on the applied voltages. The amount of HA deposited into the coating increases with increasing the applied voltage. The wear resistance of PEO-EPD coatings has been assessed using tribological tests. The bioactivity of the obtained coatings has been investigated in a simulated blood fluid.

Introduction

Titanium (Ti) and titanium alloys are frequently used as dental and orthopedic implant materials because of their excellent mechanical strength, chemical stability, and biocompatibility.[1] The biocompatibility of titanium is closely related to the properties of the surface oxide layer, in terms of its structure, morphology and composition. Thus far, a number of techniques have been developed to improve the surface properties of Ti implants such as plasma spraying, ion beam sputtering,

chemical vapor deposition, dip coating, electrophoresis and electrochemical deposition.[2–4]

Plasma electrolytic oxidation (PEO) is one of the most useful methods for surface modification because it can produce porous and firmly adherent TiO₂ films on Ti implants.[5,6] This technique is based on a combined action of electrochemical anodic oxidation, high-voltage spark and a local high-temperature treatment. The high temperature at the break-down sites and the high intensity of the electric field promote the appearance of noticeably nonequilibrium conditions and the involvement of the electrolyte components in the formation of the oxide coating. Advantages of this technique are the possibility to obtain well-adhered, firmly porous films on complex-shaped electrodes.[6,7]

Electrophoretic deposition (EPD) is another surface modification technique. It can be used to enhance the bioactivity of the surfaces by depositing of phosphate particles included in suspension toward the TiO₂ electrode surface under an applied electric field.[8,9] Advantages of this technique is short forming time, simplicity in instruments and the possibility to deposit stoichiometric, high purity coatings onto complex-shaped implants.[10–12] However, EPD technique does not provide high adhesion between the coating and substrate.[12,13]

Well-adhered coatings based on TiO₂ and biocompatible ceramic particles can be produced if EPD is combined with the PEO process (PEO-EPD).[13–20] It utilizes an electrolytic plasma to enhance the electrophoretic deposition process and improve adhesion.[13–15] This technique possesses all the advantages of wet coating methods and thus deposits the suspended particles on Ti alloy surfaces of various shapes and sizes without destroying their hydroxylated microstructure.[16–18] Furthermore, bioactive materials or antibiotics can be incorporated into the coating layer during the PEO-EPD process by tailoring the composition of the electrolyte solution.[19,20] For example, calcium and phosphate ions have been incorporated into the TiO₂ coating using an electrolyte solution containing calcium and phosphate sources.[2,5,13] More recently, well-crystallized hydroxyapatite (HA) particles together with TiO₂ coating have

*a*Max Planck Institute of Colloids and Interfaces, Am Mühlenberg 1, 14424 Potsdam, Germany

*b*Institute of General and Inorganic Chemistry of NAS of Belarus, 220072 Minsk, Belarus

*c*The Research Institute for Physical Chemical Problems of the Belarusian State University, 220030 Minsk, Belarus

*d*Department of Materials and Ceramics Engineering, CICECO, University of Aveiro, 3810-193 Aveiro, Portugal

been deposited. It has been revealed that a thin calcium phosphate layer has been directly deposited onto a plasma electrolytic oxidized Ti substrate. Calcium species have been confined to the surface regions either within the film, to a maximum depth of 18% of the film thickness, or as localized deposit on the film surface.[21,22]

Thus, it is still challenging to develop new methods that can allow the incorporation of bioactive materials, particularly in the form of crystalline phase, into the TiO_2 coating in an *in situ* manner.

In this study we suggest a new approach for uniform incorporation of HA particles into the TiO_2 coating on titanium during PEO-EPD process using an electrolyte based on potassium titanium(IV) oxalate and HA suspension. In particular, TiO_2 particles can be formed *via* the PEO process by decomposition of $K_2[TiO(C_2O_4)_2]$, while negatively charged HA particles migrate toward the Ti anode through the EPD process.

Experimental

Fabrication of HA–TiO$_2$ coatings

Plasma electrolytic oxidation coupled with electrophoretic deposition (PEO-EPD) was conducted under volt static conditions using a DC power supply with voltage and current ranges of 0–500 V and 0–3 A, respectively. The power supply provided constant voltage with an accuracy of about ±4% of the desired value. The single-compartment two-electrode electrochemical cell contained 200 mL of electrolyte. The temperature of the electrolyte was kept within a range of 25–50 °C using cold water circulating through a heat exchanger. The electrolyte was magnetically stirred to reduce temperature and concentration gradients in it.

Water–ethanol solution of 0.025 M calcium citrate $Ca_3(C_6H_5O_7)_2$, 0.025 M $K_2[TiO(C_2O_4)_2]$ and 0.006 M $Ca_{10}(PO_4)_6(OH)_2$ was prepared using commercial pure reagents and distilled water. HA suspension was synthesized from aqueous solutions of ammonium hydrophosphate and calcium chloride according the method suggested in ref. 23. The working electrode (anode) and the counter electrode were made of a titanium foil (≥99.7%). The anode area was 2 cm.[2] The cathode area was approximately 2 times larger than that of the anode. Prior to plasma electrolytic oxidation, the electrodes were chemically polished in a mixture (2 : 1 by volume of HF : HNO$_3$) of concentrated HF (50 wt%) and HNO$_3$ (65 wt%) at 80 °C for 3–5 s, rinsed with distilled water and dried with air.

Structure characterization

X-ray diffraction (XRD) analysis was performed using an Advance D8 diffractometer (Bruker, Germany) with CuKα radiation in the range of 2θ from 10° to 60° at a scanning speed of 1°/min and a step size of 0.03°. FTIR spectra were taken at room temperature using a FTIR spectrometer (MIDAC 2000, USA) in a range of 400–4000 cm^{-1}. Scanning electron microscopy (SEM) was made using Hitachi S4100 and Hitachi SU-70 microscopes equipped with an energy-dispersive X-ray spectroscope (EDS) for morphological characterization of the sample surface. Thin

layer of carbon was sputtered on the samples. Depth profiling analysis of the coatings was carried out by glow discharge optical emission spectroscopy (GDOES) using a HORIBA GD-Profiler 2 operating at a pressure of 650 Pa and a power of 30 W. The water contact angle value was measured at room temperature with an experimental angle error of ±1° using a Contact angle measuring system G10 (Kruss, Germany).

Tribological test

The dry sliding wear behavior of the PEO-EPD coatings was assessed with a Tribotec ball-on-disc oscillating tribometer. An AISI 52100 steel ball of 6 mm diameter was used as static friction partner at ambient conditions (25 ± 2 °C and 30% RH) under load in a range of 1–3 N with an oscillating amplitude of 10 mm and at a sliding velocity of 5 mm s^{-1}, for sliding distance of 12 m.

Bioactivity test

The bioactivity of the coatings was estimated by determination of the apatite formation ability in a simulated blood fluid (SBF) with ionic concentrations equal to human blood plasma. The SBF was prepared by dissolving reagent grade chemicals: KCl, NaCl, NaHCO$_3$, K$_2$HPO$_4$·3H$_2$O, MgCl$_2$·6H$_2$O, CaCl$_2$ and NaSO$_4$ according the method described by Kokubo and Takadama.[24] The pH was adjusted to 7.4 using 1 mol L^{-1} HCl and tris(hydroxymethyl)aminomethane (TRIS). The chemical composition was as follows (mmol L^{-1}): Na$^+$, 142.0; K$^+$, 5.0; Mg^{2+}, 1.0; Ca^{2+}, 2.5; Cl$^-$, 131.0; HCO$_3^-$, 5.0; HPO$_4^{2-}$, 1.0; SO$_4^{2-}$, 1.0. Plasma electrolytic coatings and Ti plate (as a reference sample) were immersed in 45 mL of the SBF solution at 37 °C for 21 days to induce apatite formation. The immersion media was updated every day. After the experiment, the samples were dried in air at room temperature and characterized using SEM.

Results and discussion

Fabrication of HA–TiO$_2$ coatings

A scheme of the experimental setup used for the PEO-EPD treatment is shown in Fig. 1a. According to preliminary results, $K_2[TiO(C_2O_4)_2]$ is decomposed by micro arcs generated on the anode, producing TiO_2 particles. The HA suspension was synthesized from alkali aqueous solutions (pH of the medium is 10.0–11.0), and HA particles in the suspension are negatively charged:[13]

$$Ca_{10}(PO_4)_6(OH)_2 + 2OH^- = Ca_{10}(PO_4)_6(O^-)_2 + 2H_2O.$$
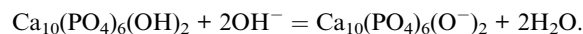
Thus, HA particles migrate towards the Ti anode and become incorporated into the TiO_2 coating, resulting in the formation of HA–incorporated TiO_2 coating on the Ti surface. Analogously to the work,[25] ethanol is added to the electrolyte in order to retard the evolution of gas at the anode and prevent the destruction of the growing coating on the titanium surface. Calcium citrate has been added to inhibit the HA transformation into tricalcium phosphate during the PEO process. Furthermore, calcium citrate promotes the formation of uniform and homogeneous
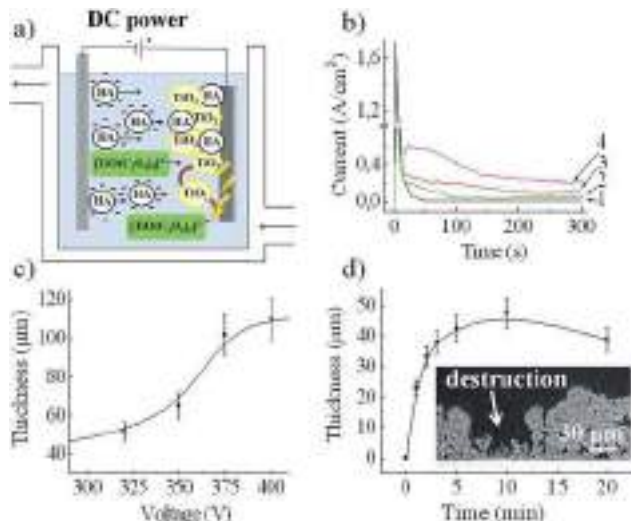
Fig. 1 (a) Scheme of the setup for PEO-EPD process. Electrodes – titanium, electrolyte: 0.025 M $K_2[TiO(C_2O_4)_2]$, 0.025 M $Ca_3(C_6H_5O_7)_2$, 0.006 M $Ca_{10}(PO_4)_6(OH)_2$; (b) current–time dependencies for PEO-EPD at 325 (1), 350 (2), 375 (3) and 400 V (4). (c) Thickness of oxide layer as a function of the applied voltage; (d) thickness of oxide layer as a function of deposition time during EPD process at 325 V. Insert shows SEM cross-sectional view of the TiO_2 layer after 20 min of PEO-EPD process.

coatings. It is visually seen that the application of the voltage higher than 320 V to the electrochemical cell results in the generation of yellow sparks. During the PEO process, the current transients are characterized by a decay of the current density from 1.6 to 0.05–0.07 A cm^{-2}, so that the higher voltage is applied, the more drastic is the current drop (Fig. 1b). Under high applied voltage ($U \geq 320$ V), within 10–150 s of the beginning of oxidation, the current density becomes almost invariable with time and the oxide film growth proceeds as a practically stationary process. At the applied voltage ranged from 320 to 400 V, an initial increase of the current changes to its further decay, which is due to the predominant passivating effect of the oxide coating formed in the interval of 25–150 s. It is clearly seen that at the PEO process, the greater is the voltage, the less is the value to which the current drops within a fixed time interval.

Uniform and smooth coatings are formed at 320 V with an average thickness of 40–45 μm (Fig. 1c). When the voltage increases up to 400 V, the thickness of the TiO_2 coating is three times larger. However, the formed coating starts to destruct due to dielectric breakdown. Thus, the optimal voltage for PEO process is 325–350 V.

The temporal evolution of the thickness during the PEO-EPD process at 320 V is shown in Fig. 1d. There is a significant increase in the thickness during the first 5 min of PEO process. Then the coating thickness becomes almost invariable with time. After 15 min of PEO process, the TiO_2 thickness begins to decrease. This may be associated with the loosening and partial destruction of the formed layer due to dielectric breakdown. This is also proved by mass decrease and SEM inspection of the coating (Fig. 1d, insert).

Morphology and composition of HA–TiO$_2$ coating

Fig. 2a shows Ti samples before and after PEO-EPD treatment in the electrolyte containing ethanol with a concentration of 20 vol%. It is evident that the PEO-EPD process leads to the formation of white or light-grey dense uniform coatings. The relative surface wettability of the coatings has been determined according to the water contact angle (Fig. 2a, insert). The wettability is found to depend on the applied voltage via PEO-EPD process. For example, the contact angle of HA–TiO$_2$ coating obtained at 325 V is 103.3° ± 5.2, while the contact angle of the coating prepared at $U \geq 350$ V is 4.3° ± 0.3. The contact angle of initial polished titanium is 70° ± 3.5. The hydrophobicity of the PEO-EPD coatings may be attributed to the formation of a hierarchical micro/nano-structure or a well-designed nanoporous structure.[26–28] The hydrophilicity could be explained by several factors: (i) changing the morphology of the PEO-EPD coatings obtained at voltage higher than 350 V and increasing its roughness and porosity.[29,30] At 400 V a bigger amount of gas released on the anode surface resulting in loosening and partial destruction of the PEO-EPD coating. (ii) When the voltage increases from 325 V to 400 V the PEO-EPD coatings become enriched with HA, which is known for its hygroscopicity[31–33] and ability to form super hydrophilic surfaces.[34–36]

Preliminary results have revealed that a highly porous uniform layer of TiO_2 forms by PEO treatment of titanium in the solution containing 0.025 M $K_2[TiO(C_2O_4)_2]$ and 0.025 M $Ca_3(C_6H_5O_7)_2$ at 320 V (Fig. 2b). The pores of the resultant coating are well separated and homogeneously distributed over the surface. The diameter of the pores varies from 0.5 to 2.5 μm. The coatings contain only Ti and O without any other elements as indicated by EDS.
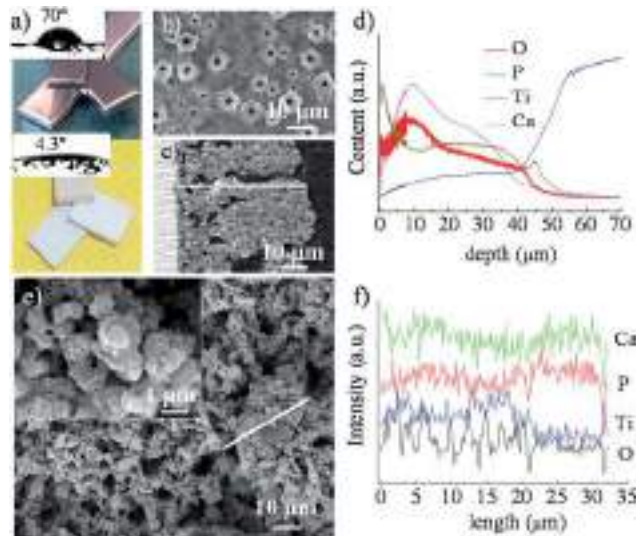
Fig. 2 (a) Images of the Ti samples before and after PEO-EPD treatment. Inserts show contact angle values; (b) SEM plan-view of the PEO treated coating; (c) SEM cross-sectional view of the PEO-EPD sample; (d) depth profile analysis of the PEO-EPD sample (element distribution on the cross of the coating was measured as shown by white line); (e) SEM plan-view images of the PEO-EPD treated samples; (f) element distribution on the plane of the PEO-EPD coating.

The PEO-EPD treatment of titanium changes drastically the morphology of the formed coatings (Fig. 2c, e and f). The coating is composed of roundish conglomerates with a size of 200–600 nm. Tiny HA and TiO_2 particles are observed on the surface, and some of the pores are clogged (Fig. 2e, insert). EDS analysis revealed the uniform distribution of Ca, P, Ti and O in a plane of the surface (Fig. 2f). The Ca/P ratio is 1.60 that is very close to the stoichiometric ratio of Ca/P in the HA (1.67).

The cross-section of the PEO-EPD coatings clearly shows the rough and porous structure of the HA–TiO_2 layer (Fig. 2c). Depth profile analysis of the PEO-EPD coatings confirms the presence of titanium and oxygen together with Ca and P in the bulk of the PEO-EPD coating (Fig. 2d). The data obtained prove that the TiO_2 and HA particles are simultaneously depositing on the Ti surface during the PEO-EPD process and coagulating into roundish conglomerates.

XRD patterns of the PEO-EPD coatings are shown in Fig. 3a. Peaks of the titanium (marked as Ti) substrate are observed on all the XRD patterns. The coatings formed by PEO of titanium in the solution containing 0.025 M $K_2[TiO(C_2O_4)_2]$ and 0.025 M $Ca_3(C_6H_5O_7)_2$ are composed of rutile (marked as R) and an equal amount of anatase (marked as A) (Fig. 3a, plot 1). The ratio of rutile/anatase content in the PEO-EPD coating does not depend on applied voltage.

After addition of HA suspension into electrolyte, peaks associated with HA (marked as HA) and tricalcium phosphate (in Fig. 3a marked as C) are detected along with rutile and anatase (Fig. 3a, curve 2). A small amount of tricalcium phosphate may be associated with a partial transformation of HA particles to tricalcium phosphate during the PEO process. It should be noted that the relative intensity of the HA peaks and the HA weight content increase with increasing the applied voltage, while the ratio of HA and TiO_2 phases changes insignificantly with the thickness increase in a range of 40–120 μm.

A FTIR spectrum of the PEO coating prepared in 0.025 M $K_2[TiO(C_2O_4)_2]$ + 0.025 M $Ca_3(C_6H_5O_7)_2$ at 320 V is shown in Fig. 3b (curve 1). The features at 3000–3750 cm^{-1} and 1300–1800 cm^{-1} in the as-deposited TiO_2 films show that there is a significant amount of water in the pores of the coating. The spectrum of the PEO-deposited TiO_2 coating exhibits a strong broad band in the region of 400–800 cm^{-1}, which can be assigned to the formation of Ti–O and Ti–O–Ti bonds. The broadening of the band related to Ti–O bond might be associated with an amorphous structure of the TiO_2 film due to incorporation of hydroxyl groups into the Ti–O bond network.[37,38] There are broad bands belonging to the OH^- and PO_4^{3-} groups of the HA in the PEO-EPD coating spectrum (curves 2 and 3, respectively). Characteristic peaks corresponding to PO_4^{3-} groups in HA (560–600 cm^{-1}, 961 cm^{-1}, 1030–1090 cm^{-1})[15,39] are visible in both spectra. The bands at 598 cm^{-1} (assigned to the deformation vibration of PO_4^{3-} ions) are shielded by broad bands of TiO_2.

Bioactivity test in SBF solution

Bioactivity of the obtained coatings is estimated by the apatite formation in SBF solution.[40–42] Fig. 4a illustrates the mass gain of the formed apatite on the PEO-EPD sample surface is in a range of 6–8%, while that on the PEO sample surface is approximately 2–3%. EDS analysis reveals an increase in the relative concentration of Ca and P in the PEO-EPD coatings after immersion in SBF for 21 days (Fig. 4b). SEM plan-view image of the PEO-EPD coatings after immersion in SBF solution for 21 days shows a thin rough apatite layer grown on the top of the coating while there is no apatite formation on the polished titanium substrate taken as a reference sample. As the amount of the formed apatite could indicate a high degree of bioactivity, the PEO-EPD coatings are expected to possess a higher bioactivity as compared with polished titanium and the PEO samples.

Tribological test

The wear rate of the PEO-EPD coating deposited at 320 V is 2.5 × 10^{-5} mm^3 N^{-1} m^{-1}, indicating a good wear resistance. It should be mentioned that the wear rate has increased from 1.9 × 10^{-4} mm^3 N^{-1} m^{-1} to 3.1 × 10^{-4} mm^3 N^{-1} m^{-1} with increasing the
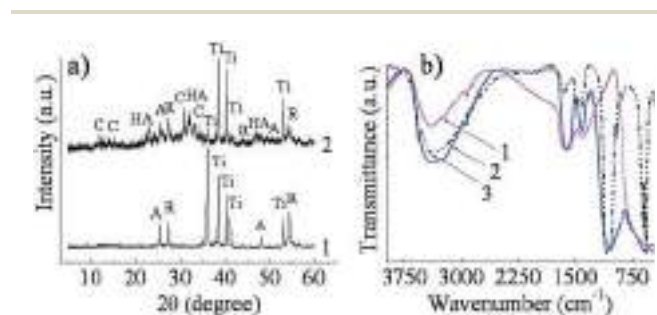
Fig. 3 XRD patterns (a) and FT-IR spectra (b) of the PEO-EPD samples obtained in the water–ethanol electrolyte containing 0.025 M $K_2TiO(C_2O_4)_2$ and 0.025 M $Ca_3(C_6H_5O_7)_2$ without (1) and with (2) 0.006 M $Ca_{10}(PO_4)_6(OH)_2$, respectively. Crystalline HA powder was used as a standard (3).
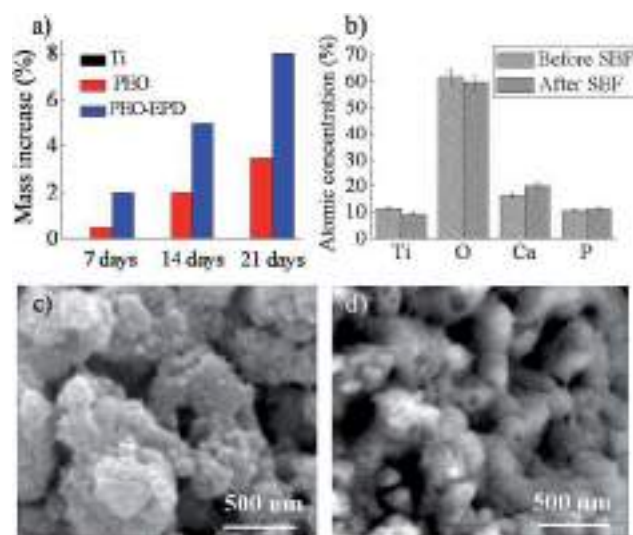
Fig. 4 Mass increase (a) and atomic concentration (b) of the PEO-EPD coatings after immersion in SBF solution for 7–21 days; SEM plan-view images of the PEO-EPD coating before (c) and after (d) their immersion in SBF solution for 21 days.

applied voltage during the PEO-EPD process. This fact may be related to an increase in the porosity and friability of the coating with increasing the applied voltage. The tribological tests have shown that the PEO-EPD coatings possess a good wear resistance. These coatings could be very prominent for biomedical applications.

Conclusions

The PEO-EPD process has been applied successfully to produce a bioactive HA–incorporated TiO_2 coating on the titanium surface in the electrolyte containing calcium citrate, potassium titanium(IV) oxalate and HA particles. The addition of ethanol to the electrolyte inhibits gaseous emission generated by the water electrolysis at the anode and allows the efficient incorporation of HA particles into the TiO_2 coating during the PEO-EPD process. The surface morphology and microstructure of the coating can be affected considerably by the applied voltage. The amount of the deposited HA can be enhanced by increasing the applied voltage. The PEO-EPD coatings induce a precipitation of apatite in SBF solution. These coatings are revealed to have a good wear resistance and could be very promising for biomedical applications.

Acknowledgements

Notes and references

1 D. M. Brunette, P. Tengvall, M. Textor and P. Thomsen, *Titanium in medicine*, Springer Verlag, Berlin, 2001.
2 L. H. Li, Y. M. Kong, H. W. Kim, Y. W. Kim, H. E. Kim, S. J. Heo and J. Y. Koak, *Biomaterials*, 2004, **25**, 2867.
3 E. V. Skorb and D. V. Andreeva, *Adv. Funct. Mater.*, 2013, **23**, 4483.
4 H. Kurzweg, R. B. Heimann and T. Troczynski, *Biomaterials*, 1998, **19**, 1507.
5 H. Ishizawa and M. Ogino, *J. Biomed. Mater. Res.*, 1995, **29**, 65.
6 A. L. Yerokin, X. Nie, A. Leyland, A. Matthews and S. J. Dowey, *Surf. Coat. Technol.*, 1999, **122**, 73.
7 Y. Han, S. H. Hong and K. Xu, *Mater. Lett.*, 2002, **56**, 744.
8 O. O. V. der Biest and L. J. Vandeperre, *Annu. Rev. Mater. Res.*, 1999, **29**, 327.
9 O. Albayrak, O. El-Atwani and S. Altintas, *Surf. Coat. Technol.*, 2008, **202**, 2482.
10 K. Grandfield, F. Sun, M. FitzPatrick, M. Cheong and I. Zhitomirsky, *Surf. Coat. Technol.*, 2009, **203**, 1481.
11 W. Jarernboon, S. Pimanpang, S. Maensiri, E. Swatsitang and V. Amornkitbamrung, *J. Alloys Compd.*, 2009, **476**, 840.
12 I. Singh, C. Kaya, M. S. P. Shaffer, B. C. Thomas and A. R. Boccaccini, *J. Mater. Sci.*, 2006, **41**, 8144.
13 X. Nie, A. Leyland and A. Matthews, *Surf. Coat. Technol.*, 2000, **125**, 407.
14 S. H. Lee, H. W. Kim, E. J. Lee, L. H. Li and H. E. Kim, *J. Biomater. Appl.*, 2006, **20**, 195.
15 Y. Bai, I. S. Park, S. J. Lee, T. S. Bae, W. Duncan, M. Swain and M. H. Lee, *Appl. Surf. Sci.*, 2011, **257**, 7010.
16 Y. Bai, K. A. Kim, I. S. Park, S. J. Lee, T. S. Bae and M. H. Lee, *Mater. Sci. Eng., B*, 2011, **176**, 1213.
17 D. Y. Kim, M. Kim, H. E. Kim, Y. H. Koh, H. W. Kim and J. H. Jang, *Acta Biomater.*, 2009, **5**, 2196.
18 L. H. Li, H. W. Kim, S. H. Lee, Y. M. Kong and H. E. Kim, *J. Biomed. Mater. Res., Part A*, 2005, **73**, 48.
19 M. S. Kim, J. J. Ryu and Y. M. Sung, *Electrochem. Commun.*, 2007, **9**, 1886.
20 J. H. Ni, Y. L. Shi, F. Y. Yan, J. Z. Chen and L. Wang, *Mater. Res. Bull.*, 2008, **43**, 45.
21 Y. Li, I. S. Lee, F. Z. Cui and S. H. Choi, *Biomaterials*, 2008, **29**, 2025.
22 E. Matykina, R. Arrabal, P. Skeldon and G. E. Thompson, *Acta Biomater.*, 2009, **5**, 1356.
23 S. A. Ulasevich, V. K. Krut'ko, O. N. Musskaya, A. I. Kulak, L. A. Lesnikovich and T. V. Safronova, *Russ. J. Appl. Chem.*, 2013, **86**, 146.
24 T. Kokubo and H. Takadama, *Biomaterials*, 2006, **27**, 2907.
25 S. Lebrette, C. Pagnoux and P. Abelard, *J. Eur. Ceram. Soc.*, 2006, **26**, 2727.
26 L. Feng, Y. Zhang, J. Xi, Y. Zhu, N. Wang, F. Xia, L. Jiang and L. Petal, *Langmuir*, 2008, **24**, 4114.
27 Y. Lai, X. Gao, H. Zhuang, J. Huang, C. Lin and L. Jiang, *Adv. Mater.*, 2009, **21**, 3799.
28 M. A. Henderson, *Langmuir*, 1996, **12**, 5093.
29 F. Rupp, L. Scheideler, D. Rehbein, D. Axmann and J. Geis-Gerstorfer, *Biomaterials*, 2004, **25**, 1429.
30 M. Lampin, R. Warocquier-Clérout, C. Legris, M. Degrange and M. F. Sigot-Luizard, *J. Biomed. Mater. Res.*, 1997, **36**, 99.
31 C. Santos, R. L. Clarke, M. Braden, F. Guitian and K. W. M. Davy, *Biomaterials*, 2002, **23**, 1897.
32 M. F. Hsieh, L. H. Perng, T. S. Chin and H. G. Perng, *Biomaterials*, 2001, **22**, 2601.
33 S. Deb, M. Braden and W. Bonfield, *Biomaterials*, 1995, **16**, 1095.
34 W. K. Yeung, G. C. Reilly, A. Matthews and A. Yerokhin, *J. Biomed. Mater. Res.*, 2013, **101**, 939.
35 N. Eliaz, S. Shmueli, I. Shur, D. Benayahu, D. Aronov and G. Rosenman, *Acta Biomater.*, 2009, **5**, 3178.
36 Y. Okabe, S. Kurihara, T. Yajima, Y. Seki, I. Nakamura and I. Takano, *Surf. Coat. Technol.*, 2005, **196**, 303.
37 M. J. Alam and D. C. Cameron, *J. Sol-Gel Sci. Technol.*, 2002, **25**, 137.
38 C. Y. Wang, H. Groenzin and M. J. Shultz, *J. Phys. Chem. B*, 2004, **108**, 265.
39 A. Ghicov, S. P. Albu, R. Hahn, D. Kim, D. T. Stergiopoulos, J. Kunze and C. A. Schiller, *J. Phys. Chem.*, 2008, **112**, 12687.
40 C. Ohtsuki, T. Kokubo and T. Yamamuro, *J. Non-Cryst. Solids*, 1992, **143**, 84.
41 T. Kokubo, H. M. Kim and M. Kawashita, *Biomaterials*, 2003, **24**, 2161.
42 T. Kokubo, *Acta Mater.*, 1998, **46**, 2519.

Macromolecular
Bioscience
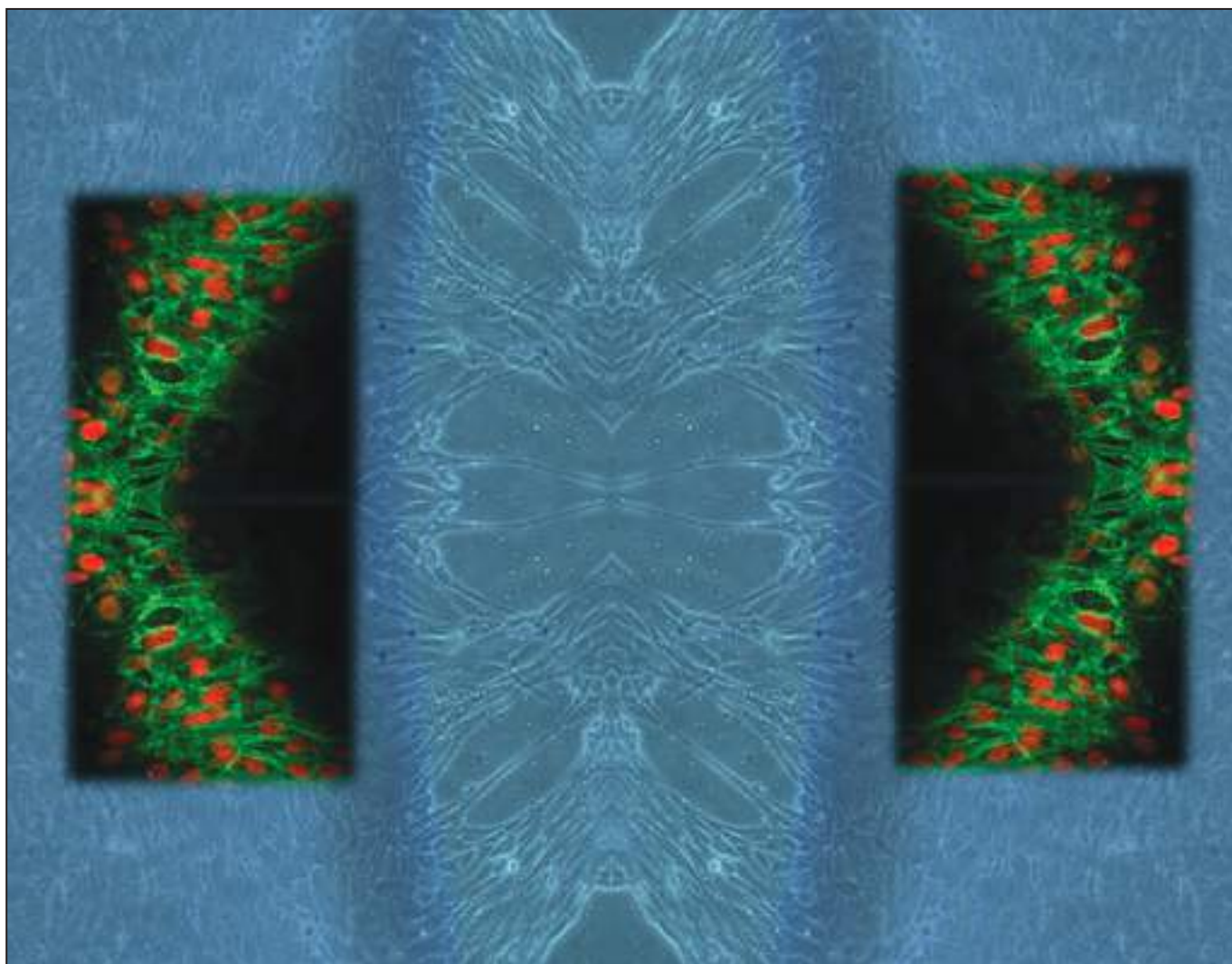
10/2016

WILEY-VCH

Switching the Stiffness of Polyelectrolyte Assembly by Light to Control Behavior of Supported Cells

Sviatlana A. Ulasevich, Nadzeya Brezhneva, Yulia Zhukova,
Helmuth Möhwald, Peter Fratzl, Felix H. Schacher, Dmitry V. Sviridov,
Daria V. Andreeva, Ekaterina V. Skorb*

Polyelectrolyte block copolymer micelles assembled thin film is switched in response to local photocatalytic reactions on titanium dioxide, resulting in a layer of variable height, stiffness in response to visible light irradiation. Preosteoblasts migrate toward stiffer side of the substrates.
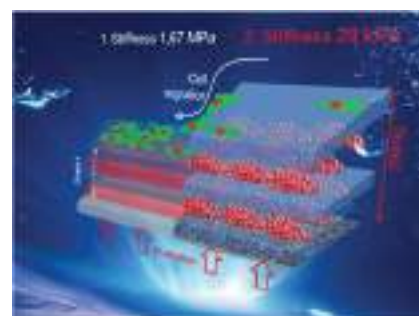
1. Introduction

Systems with a gradient in surface stiffness to control cell behavior have been extensively studied in recent years due to enormous interest in the area of biomimetic technology,[1] robotics,[2] biosensors,[3] microfluidic systems,[4] and artificial muscles.[5] The matrix stiffness alone has been implicated in regulating cellular functions, such as contraction,[6] migration,[7] proliferation,[8] and differentiation.[9] However, most materials used to control

S. A. Ulasevich, N. Brezhneva, Y. Zhukova, Prof. H. Möhwald,
Prof. P. Fratzl, Dr. E. V. Skorb
Max Planck Institute of Colloids and Interfaces
Am Mühlenberg 1, 14424 Potsdam, Germany
E-mail: skorb@mpikg.mpg.de
Dr. F. H. Schacher
Friedrich-Schiller-Universität Jena
Institut für Organische Chemie und Makromolekulare Chemie
Humboldtstr. 10, 07743 Jena, Germany
Prof. D. V. Sviridov
Chemistry Department
Belarusian State University
Leningradskaya str. 14, 220030 Minsk, Belarus
Dr. D. V. Andreeva
Physical Chemistry II
Bayreuth University
Universitätsstr. 30, 95440 Bayreuth, Germany

the behavior of supported cells are static ones, notwithstanding recent progress in dynamic stimuli-responsive materials with switchable stiffness to build up actuating materials. This has two main reasons: (1) applied stimuli for actuation affect the cell behavior negatively;[10] (2) actuating materials are toxic for cells.[11] Hence one would need a responsive system, where the environment is changed only in the support, but not around the cells attached. Here we report such a new light guided system, which is actuated under irradiation with high amplitude to guide changes of stiffness of the layer-by-layer assembled polyelectrolytes on photoactive titania surface without affecting the cellular environment.

Light is very promising as a stimulus for switching the systems due to the possibility to irradiate localized areas with fast on/off switching rates,[12] on contrary to, for example, pH- responsive control. pH- activation in most cell experiments is difficult to integrate into the process of cell seeding due to the need of mild conditions for cell cultivation.[13] Concerning the light-response only a limited number of stimuli-responsive polymers are able to undergo light initiated transitions.[14] This as well as toxic degradation products often are a drawback for experiments with cells.[15] Well-known examples are polymers with azo-groups that undergo reversible isomerization upon irradiation without photoproduct formation.[16] Unfortunately, the response on the molecular level is

relatively weak, because azobenzene molecules change their geometry from planar one to nonplanar with a decrease in the distance between the para carbon atoms only in the Angstrom range.[17] Other known examples are photocrosslinkable polymers.[18] However, such materials are difficult to be used as stimuli-responsive ones, where changes should be totally reversible. Thus, there is an urgent need to develop a strategy to actuate polymers with light for high-amplitude actuating soft matter systems: coatings, hybrids. This is achieved for the first time in this work making use of the photosensitivity of TiO_2 and the responsivity of polyelectrolytes in a composite film arrangement interacting with cells.

2. Experimental Section

2.1. Preparation of Titania Photoactive Surfaces

Glass with a vacuum deposited titanium layer (99.9%) was ultrasonically treated in 5 M NaOH (Sigma-Aldrich) at 80%-intensity with a UIP1000hd (Hielscher Ultrasonics) operated at 20 kHz with a maximal output power of 1000 W. The samples were placed into a home-made teflon holder at 1 cm distance perpendicular to the sonotrode, sonicated and washed several times without annealing. Milli-Q (18.0 MΩ cm) water was used in all aqueous solutions.

2.2. Preparation of Block Copolymer Micelles (BCM)

A linear triblock terpolymer consisted of polybutadiene (B), poly(methacrylic acid) (MAA), and quaternized poly(2-dimethylamino)ethyl methacrylate) (Dq). The triblock terpolymer $B_{800}MAA_{200}Dq_{285}$, (subscripts denoting the degrees of polymerization of the corresponding blocks, $M_n \approx 110\,000$ g mol^{-1}, *polydispersity index* = 1.10) was synthesized via sequential living anionic polymerization in tetrahydrofuran followed by polymer-analogous modifications. Details about polymerization and characterization could be found elsewhere.[19]

2.3. Layer-by-Layer (LbL) Deposition

Polyelectrolyte coating was obtained using the LbL assembly method. The LbL coatings were assembled on photoactive titanium dioxide surfaces using dip-coating in a polymer solution for 15 min. After each deposition step, the samples were washed in double distilled water and dried with a nitrogen stream. Terpolymer micelle layers were deposited from 0.45 g L^{-1} solution of micelles (VWR, AVS Titrinorm, ionic strength ≈0.05 M). The poly(acrylic acid) (PAA) sodium salt ($M_w \approx 5100$ kDa, Sigma-Aldrich) was assembled from a 2 g L^{-1} polymer solution of polyelectrolyte in a 0.5 M NaCl solution.

2.4. Characterization Methods

Scanning electron microscopy (SEM) measurements were conducted with a Gemini Leo 1550 instrument (Zeiss) at an operating voltage of 3 keV. Transmission electron microscopy (TEM) images were obtained on a Zeiss EM 912 Omega transmission electron microscope operating at 300 kV. The samples were ultramicrotomed (Leica EM FC6) and placed onto the copper grids coated with a carbon film. Infrared spectra were acquired with an IFS 66 fourier transform infrared (FT-IR) spectrometer from Bruker (Ettlingen, Germany). The infrared beam is directed through the external port of the spectrometer and is subsequently reflected by three mirrors in a rigid mount before being focused on the sample surface. A KRS-5 wire grid polarizer is placed into the optical path directly before the beam hits the sample surface. The reflected light is collected at the same angle as the angle of incidence. The light then follows an equivalent mirror path and is directed onto a narrow band mercurycadmium-telluride detector, which is cooled by liquid nitrogen. The entire experimental setup is enclosed to reduce relative humidity fluctuations. For all measurements at 40 mN/m, p-polarized radiation was used at an angle of incidence of 70°. A total of 200 scans were acquired with a scanner velocity of 20 kHz at a resolution of 8 cm^{-1}. The spectra were obtain in a range of 4000 − 400 cm^{-1}. Atomic force curves were taken with a JPK Force Robot 300 atomic force microscopy (AFM) (Nanotechnology, Germany) operating in tapping mode using C5C38 cantilevers from MIKROMASCH. The colloidal probe for atomic force microscopy was obtained by fixing glass particles (PS/Q-F-B857, Germany) with a size of 10.25 μm on a silica tip.

2.5. Photoactivity Measurements

An electrochemical cell with a three-electrode arrangement was used for photoelectrochemical experiments. A platinum wire served as the counter electrode and an Ag/AgCl (saturated KCl solution) electrode as the reference electrode. Titanium plates with grown titanium dioxide layer were used as working electrode. The reference electrode was placed close to the working electrode using a Luggin probe capillary.

2.6. Cell Culture

Murine preosteoblastic cells MC3T3-E1 (provided by the Ludwig Boltzmann Institute of Osteology, Vienna, Austria) were seeded with a density of 6×10^3 cells per cm^3 on the surface and cultured for 2 d in minimum Essential Medium Eagle (Sigma-Aldrich, St. Louis, MO) supplemented with 10% foetal calf serum (PAA laboratories, Linz, Austria), 0.1% ascorbic acid (Sigma-Aldrich, St. Louis, MO), and 0.1% gentamicin (Sigma-Aldrich, Steinheim, Germany) in a humidified atmosphere with 5% CO_2 at 37 °C. The cell density on different surface areas was monitored by bright field microscopy and documented by light micrographs. Total cell numbers were determined by manual counting of cells per image section. In total, ten image sections were analyzed for every surface type in each experiment.

2.7. Cell Migration Experiment

On the fifth day of cell seeding the "chip" was short time (10 s) irradiated from the back side and cells started their reorganization following the LbL film activated migration to the "harder" part. Cell density zone relevant calculation and corresponding imaging were done in 30 min after surface activation. Thus cells were grown on the surface 5 d. In fifth day the surface was activated by pulsed short term (10 s) irradiation from back side. The coating was fast activated. Thickness of the coating increased. In 10 min after activation the thickness was its maximum thickness and minimum stiffness. Cells started to feel the change of surface properties. Cells started to migrate into the side of higher stiffness since grown cells were preosteoblasts. Preosteoblasts liked more "harder" surface. Cells were imaged in 30 min and histogram of their surface distribution was done. Simultaneously the coating relaxed, however, due to chosen LbL composition, relaxation was very slow in comparison to activation. If coatings were fast activated and fast relaxed they could be, probably, more suitable for antifouling coatings, but not for cell growth.

2.8. Statistical Analysis

Statistic calculations were made using GraphPad Prism software (at www.graphpad.com/prism). Comparison of multiple groups was done by three way analysis of variance (ANOVA) test in the case of cell density with pairwise multiple comparison procedures by the Holm–Sidak method; and one way analysis (ANOVA) in the case of focal adhesion and gene expression. Data were normally distributed due to normality Shapiro–Wilk test. A p-value smaller than 0.05 was considered statistically significant.

3. Results and Discussion

Our system provides a novel strategy for developing a high-amplitude actuating system based on coupling light and pH to control the behavior of pH sensitive high-altitude actuating polymers not with pH, but light. The system, illustrated in Figure 1, is composed of the following blocks. The light sensitive part is a TiO_2 film (Figure 2). As pH sensitive coating we use a LbL assembled film of oppositely charged weak polyelectrolytes of BCM (positively charged layer) and PAA (negatively charged layer). We aim to prove the concept of light-pH coupled switching and thus we work with well characterized pH sensitive micelles,[19] which have shown "smart" switching under pH change. Here we demonstrate that it is possible to switch a polymer film on the surface of TiO_2 with light.

It should be noted, that pH-dependent polymers represent a class of materials with tremendous structural variety. One powerful example is "weak" polyelectrolytes,[20] where morphology and polarity strongly depend on pH. Thus such weak polyelectrolytes as BCM can show a drastic response to pH.[21] The pH-responsive behavior of the BCM can be controlled by changing the ionization degree of one of the constituting blocks; they exhibit pronounced morphological changes in response to ΔpH and can be used for multilayer formation.[19] However, the adoption of pH sensitive coatings capable to undergo reversible pH-induced swelling transitions for cell migration modulation provides a problem due to the high cell sensitivity to pH changes. We suggest using a
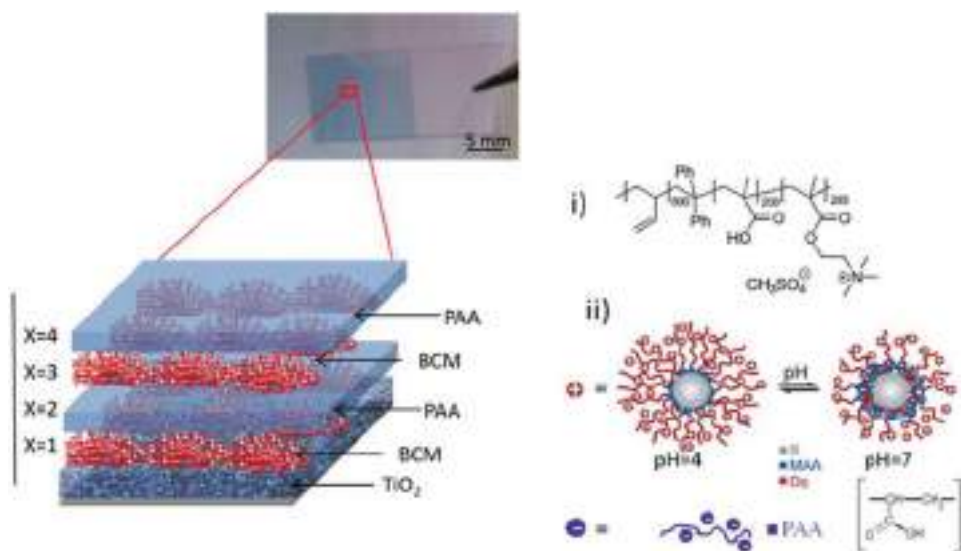
Figure 1. Schematic illustration of the fabricated multilayer system. High-amplitude switchable layer-by-layer (LbL) multilayers are built from pH sensitive positively charged block copolymer micelles (BCM) and negatively charged poly(acrylic acid) (PAA) on the surface of photoactive titania. The optical image shows a microdevice, which is a transparent substrate with a part covered with a titania layer (left) and the other half not covered with titania, but the whole surface covered with LbL, that served as a control LbL assembled coating on top of the complete surface.

www.MaterialsViews.com
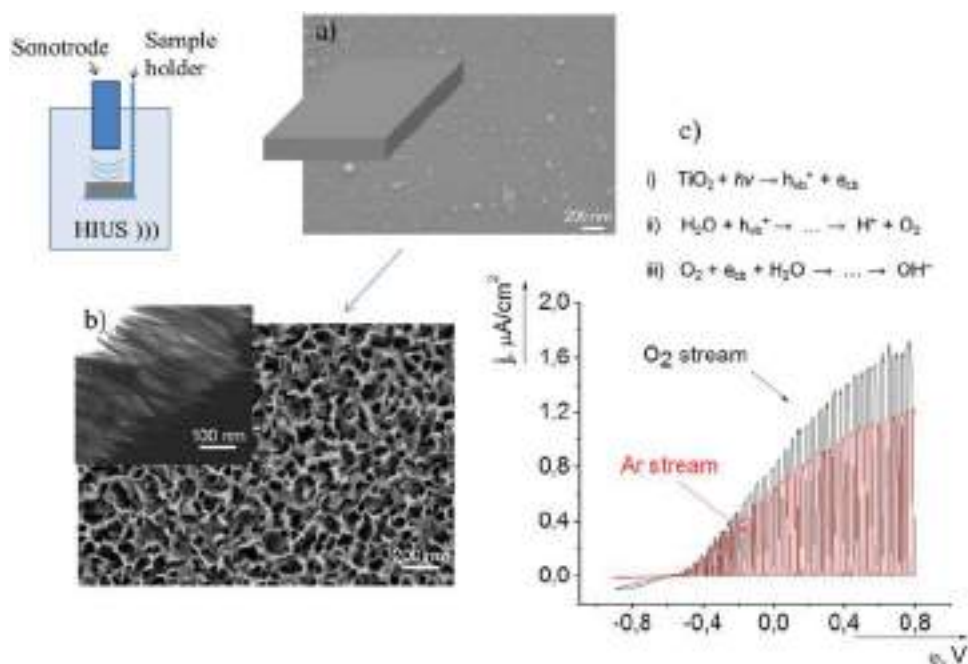
Figure 2. High intensity ultrasonication for sonochemical modification of a) initial titanium (SEM image), into b) titania based foam layer (SEM image of top view, and TEM of side view). c) Photocurrent/voltage response of a titania foam layer under Ar or O_2 bubbling in the system. Primary and secondary photocatalytic reactions on TiO_2 resulting in a local change of pH (ΔpH) of the following light-pH conversion to control pH sensitive polymer assembly: (i) light stimulated charge separation, (ii) primary reaction with a photohole with final production of protons and local surface acidification in the irradiated area, and (iii) spatially separated photoelectron reaction.

photoreaction on titania (Figure 2c) to vary the pH of the assembly locally without changing pH of cell media.

TiO$_2$ is a wide band gap semiconductor and usually activates with ultraviolet irradiation.[22] However, in our case the experiments with cells needed special precautions for titania synthesis to be able to activate it with light with wavelength $\lambda > 390$ nm. For generation of the titania film we use the nonequilibrium sonochemical treatment[23] of titanium metal to produce a titania film with additional states in its forbidden zone. Physical and chemical surface modification during ultrasonic surface treatment results in extreme local conditions for surface development allowing formation of nonequilibrium materials due to high energy localized by a sonotrode at a particular surface area.[24] There is the unique potential of locally establishing high-temperature (up to 5000 K) and high-pressure (several hundreds of bars) reactions, while the system remains macroscopically near room temperature and ambient pressure thus avoiding material recrystallization.[25] In our case, the ultrasonic technique yielding mesoporous surfaces could replace some expensive, multistage and time-consuming methods of surface engineering. A mesoporous sonogenerated foam of titanium dioxide on titanium is achieved by sonication of titanium in aqueous basic solution, the structure before and after sonochemical modification is shown in Figure 2a,b.

The resultant mesoporous titania irradiated with light $\lambda > 395$ nm exhibits photoactivity, as evidenced by

photoelectrochemical measurements (Figure 2c). It should be emphasized that the photoactivity of sonogenerated titania films appears to be shifted to the visible region as compared to crystalline TiO$_2$; this fact can be attributed to large concentration of electronic states generated in the forbidden zone of titania obtained under highly irreversible conditions of TiO$_2$ formation.

Even under mild illumination ($I_{LED(395\ nm)} < 5$ mW cm^{-2}), photoholes and photoelectrons are formed at the surface of titania. The photoproduced species are involved in different secondary reactions: while photoholes react with surface hydroxyl groups, photoelectrons can be accumulated at the surface states and scavenged by oxygen molecules. Due to high mobility of the electrons, these two processes occur at different sites of the mesoporous titania film. As a result, the photocatalytic reactions induced under local illumination are accompanied with the release of protons within the exposed area. The key idea is that if on top of a titania film a pH sensitive polymer coating is applied, the generated local ΔpH will charge and activate the polymer layer. Moreover, the oxygen presence is also a factor to regulate surface photoactivity (Figure 2c), which affects the efficiency of secondary photocatalytic reactions, including those presented in Figure 2c.

A related question on the feasibility of the process is: how many protons and photons are needed from the surface to locally change the pH from 7 to, for example, 4, on the surface? To calculate the concentration of needed

protons for activation we assume for 1 cm^2 of TiO$_2$ to achieve a pH $= 4$ or [H$^+$] $= 10^{-4}$ M or 6×10^{19} L^{-1} a coating with thickness of, e.g., 500 nm, that is, $V = 5 \times 10^{-8}$ L. The concentration of protons in the system is then [H$^+$] $= 3 \times 10^{12}$ protons per cm^2, which is about 0.3% of the lattice sites of a typical solid (10^{15} lattice sites per cm^2). This means that only 0.3% of the surface atoms have to be charged to achieve pH $= 4$, if no losses exist. Even if we consider a low

radiation intensity of 1 mW cm^{-2} $= 10^{16}$ photons per cm^2 s for a quantum yield proton/photon conversion of 0.1% the photons from 300 ms irradiation would create enough protons on the TiO$_2$ surface to achieve LbL switching on the surface of TiO$_2$.

To develop responsive surface coatings for cell experiments, we use BCM. The schematic representation of the obtained core–shell–corona micelles is shown in
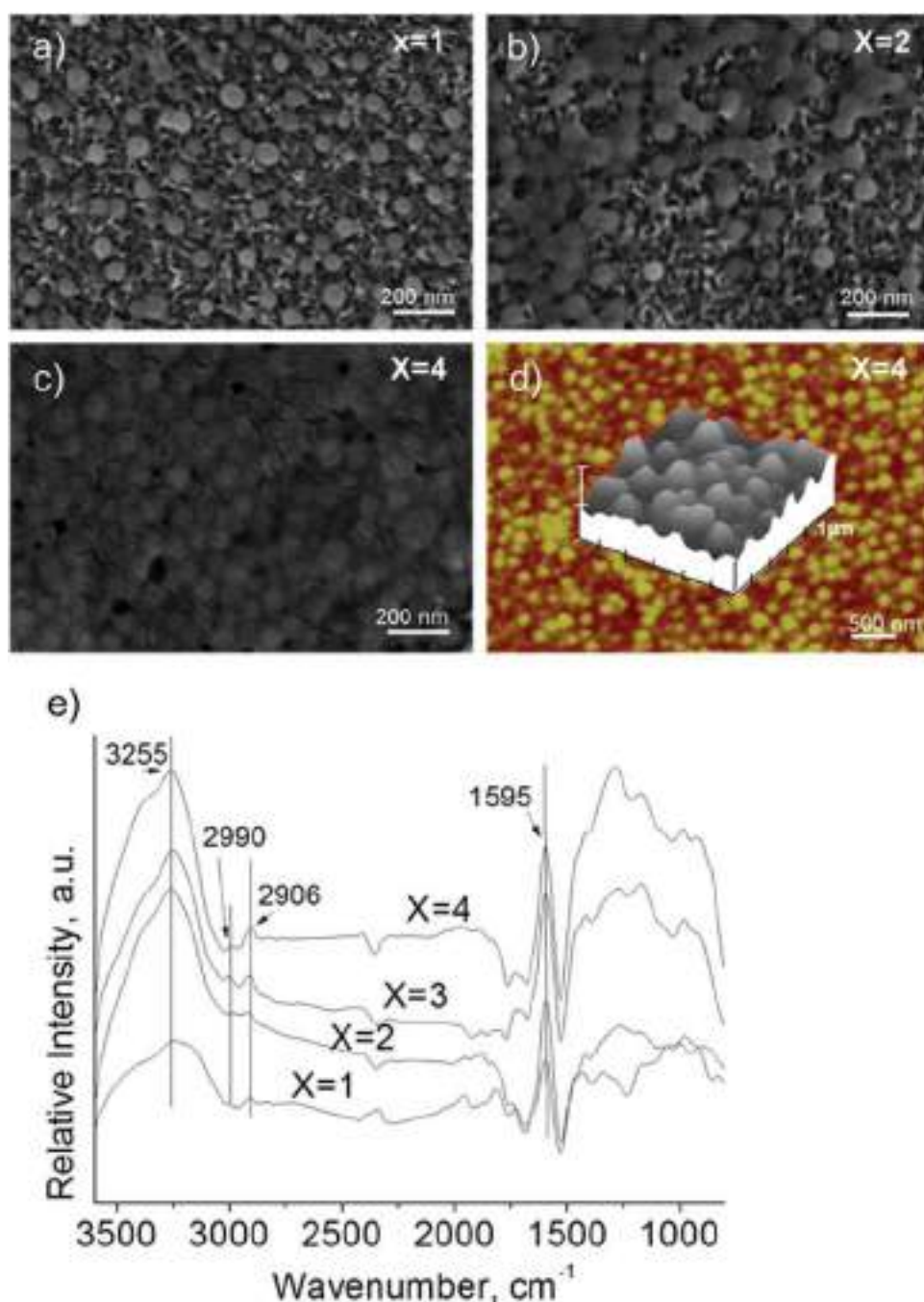
Figure 3. pH sensitive LbL assembly. a–c) SEM images of the BCM/PAA multilayer system on a sonochemically generated photoactive mesoporous TiO$_2$ sponge layer. *x* is the number of build-up steps. d) AFM image of BCM/PAA with two bilayers after four build-up steps. Inset shows 3D AFM map of 1.0 µm × 1.0 µm. e) Corresponding FT-IR spectra of each layer of the LbL assembly on a TiO$_2$ surface.

Figure 1. It is known[26] that BCM stability and reversibility of switching can be improved combining BCM with polyelectrolytes. Moreover, polymer coating assembly via LbL technique is a powerful tool to tune coating thickness and surface coverage. PAA is known as a weak polyelectrolyte which is also sensitive to pH and can be pH activated.[27] We choose it for LbL assembly of a pH sensitive coating, as it is oppositely charged compared to the micelle layer. In our case two bilayers of coating are sufficient to achieve a total coverage of the surface (Figure 3). The films are dried in a stream of nitrogen before characterization. After each deposition step and washing, the coverage is monitored and confirmed with FT-IR spectroscopy and AFM. The coating structure after each deposition step is also shown in the SEM (Figure 3a–c) images. After coating formation we check its pH sensitivity, the formed LbL assembled system can be reversibly

activated changing the pH from 7 to 4. The BCM show a rapid response to pH cycling. This is an intrinsic property of pH sensitive micelles.[21] The pH-responsive behavior of the micelles can be controlled by the ionization degree of the MAA block (pK_a, apparent ≈ 5.5). In the pH range between 7 and 4 the ionization degree, α, decreases from unity to ≈ 0. At pH 7 ($\alpha \approx 0.5$), the attraction between the negatively charged MAA and the positively charged Dq blocks induces the formation of an intramicellar interpolyelectrolyte complex (im-IPEC) shell. According to the degrees of polymerization ($DP_n(MAA) < DP_n(Dq)$), parts of the cationic Dq block remain uncomplexed forming a positively charged corona. At pH 4, the protonation of the MAA block ($\alpha \approx 0$) results in im-IPEC dissolution. As a consequence, the uncharged MAA block collapses onto the B core forming a new shell, and the length and charge density of the cationic Dq corona increase. Accordingly,
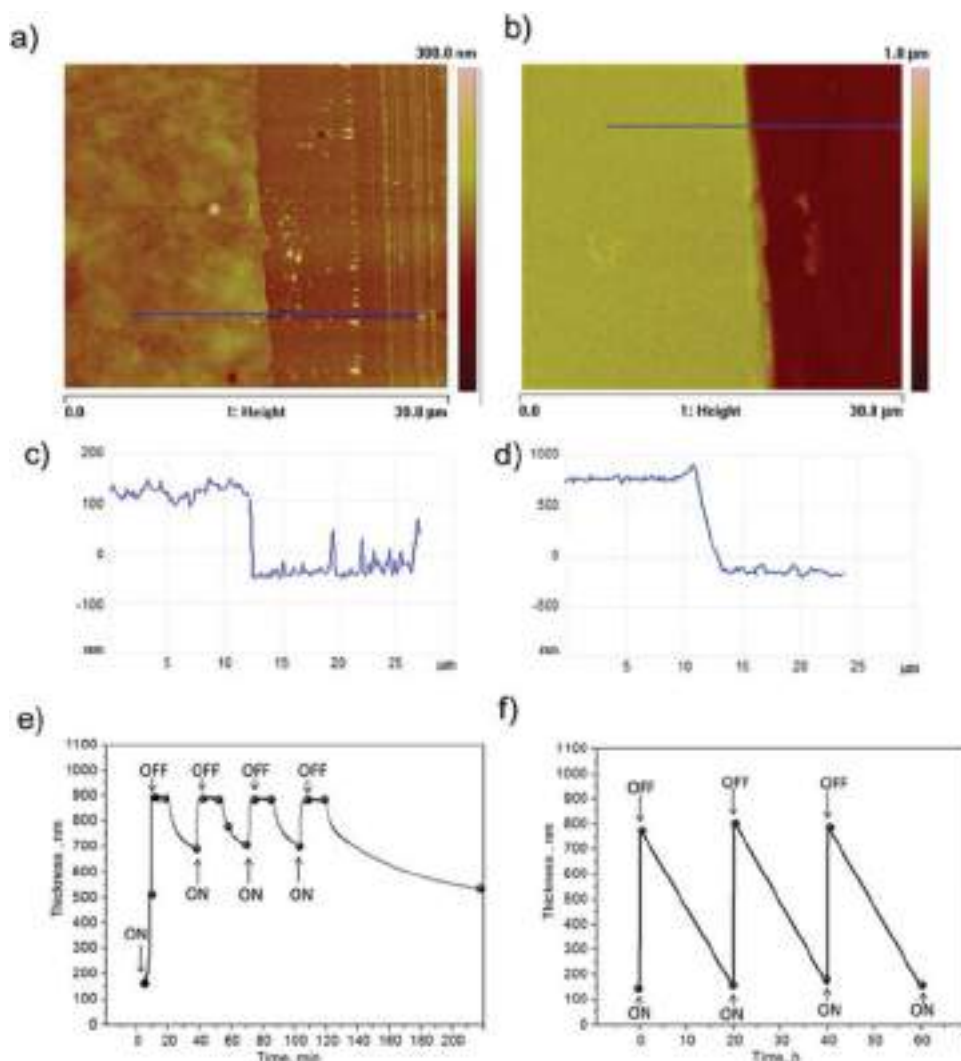
Figure 4. a,b) AFM images of scratches for thickness evaluation study with c,d) corresponding profiles of the TiO₂/BCM/PAA multilayer system (a,c) before irradiation and (b,d) after irradiation/activation. e,f) Kinetics of thickness changes on a TiO₂/BCM/PAA multilayer system in (e) minutes time scale and (f) slow (hours) relaxation to the initial state.
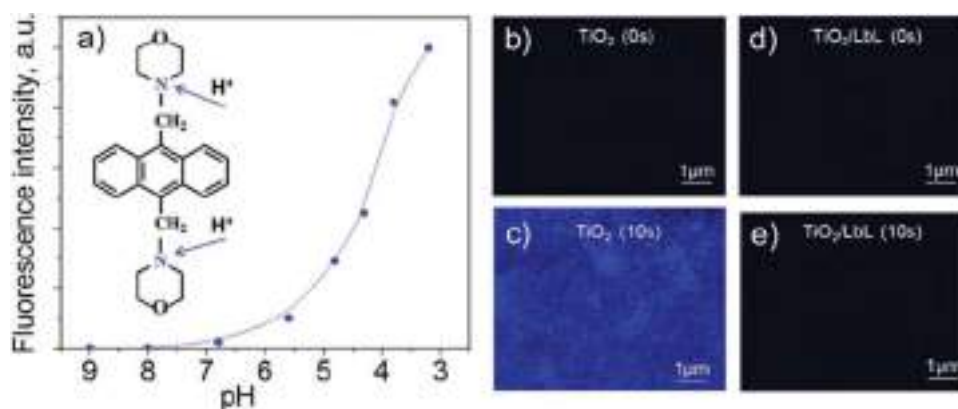
Figure 5. a) Calibration of the fluorescent pH indicator, 4,4′-(anthracene-9,10-diyldimethanediyl)dimorpholine, that exhibits a pK_a ≈5.1, and initial chemical formula to point to the protonation sites. b–e) Confocal fluorescence images of the surface of (b,c) TiO$_2$ and (d,e) TiO$_2$/LbL where the fluorescent pH dye is on top (b,d) before and (c,e) after 10 s of irradiation. Proton activity is detected on TiO$_2$, but not on TiO$_2$/LbL due to "proton sponge" polyelectrolyte activity.

the charge density of the MAA block and the dissolution or regeneration of the im-IPEC shell can be adjusted by the pH of the solution. The length and charge density of the cationic Dq corona are regulated by the shell composition and therefore can be varied by pH. Here it is a question if we can reversibly switch the LbL assembled coating with light. The power (≈5 mW cm^{-2}) and duration (less than 10 min) of irradiation are chosen not to degrade the LbL assembled coating, which was verified in control experiments.

In order to demonstrate the light induced modulation of the LbL assembly, we investigate the thickness of the LbL film on the surface of TiO$_2$ using AFM, Figure 4. By illumination for 10 min the initial coating thickness of 150 nm is increased up to a maximum thickness of 800 nm for a photoactive titania surface. Longer irradiation does not result in further change of the film thickness. Measurements of thickness versus time (Figure 4) reveal that for our system the irradiation intensity is critical. We did not vary it using short time (less than 10 min) and low light intensity (<5 mW cm^{-2}) irradiation, not to have photocatalytic degradation of LbL assembly, but local pH shift on irradiated TiO$_2$. Colloidal probe atomic force microscopy (CP AFM) measurements confirm that the LbL polymer assembly on the photoactive titania film becomes softer (ca. 28 kPa) during irradiation compared to the initial stiffness (ca. 1.67 MPa). After irradiation is switched off, the relaxation of the LbL assembled coating occurs. However, due to the complex character of the LbL assembly building blocks, e.g., BCM as one pH sensitive layer, the coating relaxation is relatively slow. The relaxation to 150 nm requires more than 20 h (Figure 4f), which characterizes the system as fast activated and slowly relaxing. Such systems are of great interest for biological applications.

Moreover, it was demonstrated,[28] that polyamines exhibit an interesting binding property that is known as "proton sponge" properties. What does it mean in our context? Protons on the pristine titania compared to the TiO$_2$/LbL surface are monitored with a pH indicator adsorbed on the surface (Figure 5). During irradiation we observed titania acidification and generation of protons on titania surface (Figure 5d). Can one use the protons to activate LbL assemblies on titania preventing H$^+$ release from the surface for cell growth? Here interesting works in connection polyelectrolytes as "proton sponges" are mentioned.[28] Polyelectrolytes as BCM can be considered as analogues to present the "proton sponge" poly(ethyleneimine) and chitosan. LbL can be activated with H$^+$, but not releasing protons yielding a whole class of pH-responsive systems for biomedical or other sensitive applications with light, while maintaining a constant, mild, bulk pH. The validity of our assumption is confirmed by Figure 5e showing that the pH on the surface of TiO$_2$ covered with BCM/PAA layers is neutral, on contrary to very acidic in the case of individual TiO$_2$.

In the bioexperiment (Figure 6) we construct our multilayers on a transparent glass substrate. The titania photoactive layer covered part of the glass slide. The other part is free of the TiO$_2$ layer. Afterward, the LbL polymer coating was built up on top to cover both sides with TiO$_2$ film and without. Cells (preosteoblast MC3T3) are cultivated on top of the surface. On the fifth day of cell growth, we performed an experiment to activate the cell migration. We irradiated the "chip", Figure 6, from the back side, TiO$_2$ adsorbs light with production of photohole and photoelectron and in the scope of photocatalytic reactions the acidification of the titania surface happens. The generated protons are immediately trapped by the BCM "proton sponge", LbL activated and changing its thickness and, stiffness resulting in cell migration over the surface. For this cell experiment it is important, that either the system is slowly or quickly relaxing, both can
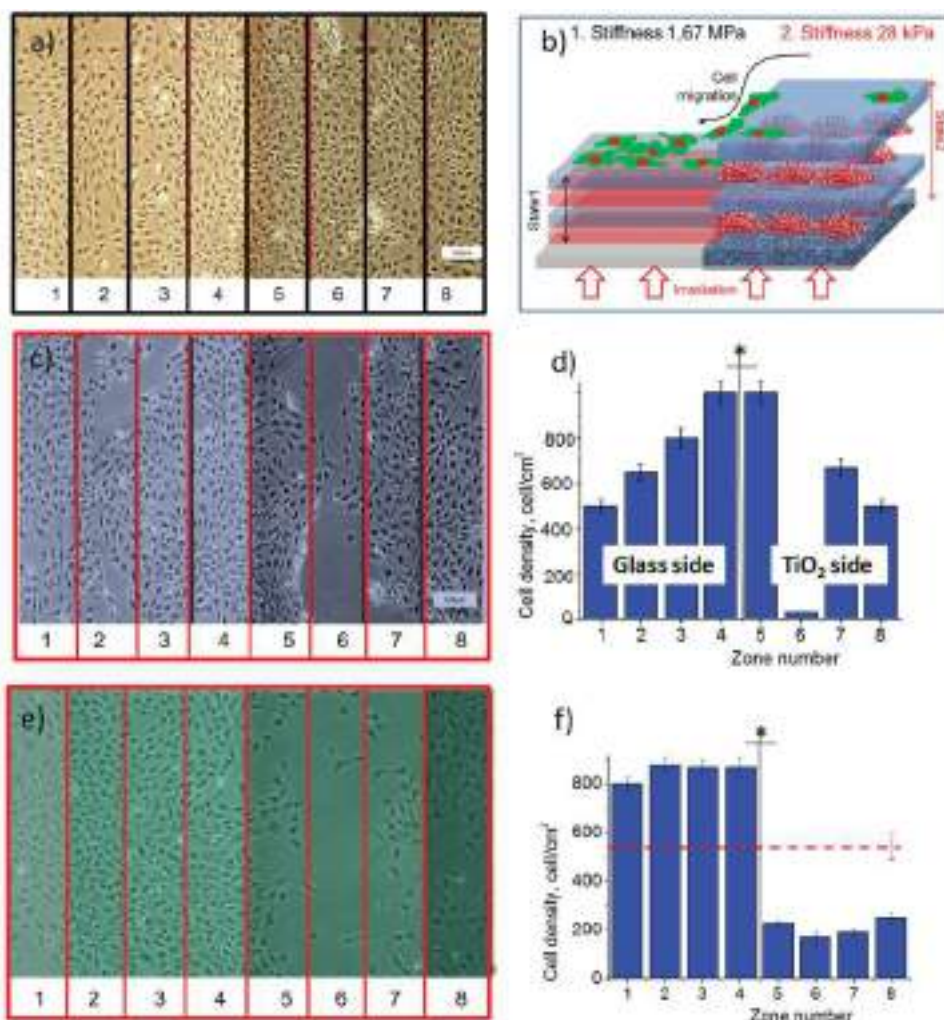
Figure 6. Bioapplication potential: cell 4D regulation on the surface. A multilayer coating designed for cell experiments was formed on glass and consists of LbL BCM/PAA two bilayer coatings either without (zones 1–4) or with (zones 5–8) a photoactive TiO$_2$ film underneath. Thus the border, where the changes are expected are between the zones 4 and 5. a) Cell (MC3T3-E1 preosteoblast) distribution over the surface after 5 d of culturing. b) Schematic of cell reorganization over the surface after irradiation. c–f) In 5 d the "chip" was short time irradiated from the back side and cells start their reorganization following the LbL film activated migration to the "harder" part (c,e) image and (d,f) cell density zone relevant calculation after irradiation of the surface after (c,d) 15 min and (e,f) 30 min of cell migration. The stiffness was measured with colloidal probe atomic force microscopy (CP AFM) and calculated with the Hertz model before and after surface film activation with light. The error bars indicate standard deviations from mean values of three biological replicates ($n = 3$). Asterisks indicate statistical significance *$p < 0.05$.

be interesting for "lab-on-chip" applications. In this paper we highlight a slowly relaxing system which activates fast (less than 10 min), however relaxation to initial 150 nm thickness is relatively slow, more than 20 h, resulting cell felt change of stiffness and reorganization.

We did several control experiments to ensure that cells migrate due to stiffness change not a pH, not light itself. Thus, cells were not sensitive to back contact side irradiation with visible light. If in the case if pristine titania cells would migrate due to surface acidification, in the case of titania covered with LbL of BCM/PAA the generated protons would be trapped in an assembly

resulting in its actuation, but not in surface proton activity. Even on low photoactive pristine titania under the used low dose of visible light irradiation (less than 10 min, less than 5 mW cm^{-2}) cells are not released from the surface due to their death, but migrate being alive. Comparing titania and TiO$_2$ covered with LbL, the explanation of migration reasons is different, being in the case of LbL assembly most probably exactly due to stiffness change.

The cells were grown on the surface for 5 d to connect with each other, so that cells can communicate translating information of the surface properties over long

distances. We did also several control experiments with individual cells (results are not shown here) indicating, that individual cells on the surface with changeable stiffness migrate, however the direction of migration is rather random, less pronounced correlation in migration of osteoblast cells to harder substrate. This is an important and interesting question to focus in future. However in the particular experiment, we chose the most appropriate time of cell seeding to highlight and prove the prospect of switching pH sensitive polymer assemblies with light using the possibility to trap protons in the polymer matrix, due to "proton sponge" activity of the used BCM, to initiate cell migration with light. The importance of the optimization of the system to particular applications should be stressed here. However millions of individual system can be imagined. This attractive and exciting idea, to module pH sensitive assemblies with light will be intensely followed in future. Here the following prospects for coculturing on such a surface can be imagined: two cell lines with different preferences for substrate stiffness can be spatially separated over the surface being controlled in time. One could imagine the prospects of such a surface for cocultures: cells growing together, which have preferences either being on harder or softer surface can be temporally separated over the surface via local swelling of high-amplitude modulated assemblies with light. In addition, there is a gradient of stiffness going from the center of an irradiated spot to horizontal and vertical (outside) direction, which can be used for understanding the processes of temporal modulation of cell migration. The magnitude can be tuned by varying intensity and duration of irradiation. The zones are located on different distance from interface between activate and nonactivated coating. The intermediate stage clearly shows that rearrangements of cells are different at different moments that can be the direction to focus in future. Next important future question is how the adherence of cells influences the coating properties. In our control experiments we confirmed that if cell deactivated they detach from the surface, however in our particular case the cells migrate to different regions without being deactivated. We are interested to use further the coating, for example, for coculture experiments, however this particular paper is proven of the prospects. There are still a lot of questions open, but it is clear that concept of using light to change pH-sensitive polymers for cell culture works and has potential for further investigation.

4. Conclusions

This work showed, that there are great prospects of conversion of energy of electromagnetic irradiation into pH gradients enabling also spatial regulation by localization of the irradiation spot onto a semiconductor titania surface. The kinetics of light-pH coupled actuation and modulation of the presented LbL architecture and the study of the relaxation process prove that such surfaces are fast switchable and slowly relaxing. We thus demonstrate that photogeneration of charges in a solid can be used to change the properties of adjacent soft matter. In this work we report on two key issues: (1) We show that by sonochemical treatment TiO_2 can be made sensitive to visible light to be able to use a light-pH coupled material to control cell migration. Quantitative analysis for the promising pH sensitive assembly of the architecture TiO_2/BCM/PAA/BCM/PAA reveals a modulation of the thickness by a factor of four and a change of elastic modulus by an order of magnitude. (2) We demonstrate that the mechanical modulus can be manipulated as much that cells respond by migrating toward the stiffer areas. The designed system to guide cells on a surface promises many applications in biosciences, fundamental cell biology, and microfluidics.

[1] D. E. Discher, P. Janmey, Y. Wang, *Science* **2005**, *310*, 1139.
[2] K. J. Kim, S. Tadokoro, in *Electroactive Polymers for Robotic Applications*, Springer, London **2007**.
[3] J. Tamayo, P. M. Kosaka, J. J. Ruz, A. San Paulo, M. Calleja, *Chem. Soc. Rev.* **2013**, *42*, 1287.
[4] L. Leng, A. McAllister, B. Zhang, M. Radisic, A. Guenther, *Adv. Mater.* **2012**, *24*, 3650.
[5] M. S. Sakar, D. Neal, T. Boudou, M. A. Borochin, Y. Li, R. Weiss, R. D. Kamm, C. S. Chen, H. H. Asada, *Lab Chip* **2012**, *12*, 4976.
[6] D. Mitrossilis, J. Fouchard, D. Pereira, F. Postic, A. Richert, M. Saint-Jean, A. Asnacios. *Proc. Natl. Acad. Sci. USA* **2010**, *107*, 16518.
[7] E. Hadjipanayi, V. Mudera, R. A. Brown, *Cell Motil. Cytoskeleton* **2009**, *66*, 121.
[8] J. P. Winer, P. A. Janmey, M. E. McCormick, M. Funaki, *Tissue Eng., Part A* **2009**, *15*, 147.
[9] A. J. Engler, S. Sen, H. L. Sweeney, D. E. Discher, *Cell* **2006**, *126*, 677.
[10] Q. Zhao, J. Heyda, J. Dzubiella, K. Täuber, J. W. C. Dunlop, J. Yuan, *Adv. Mater.* **2015**, *27*, 2913.
[11] K. Täuber, B. Lepenies, J. Yuan, *Polym. Chem.* **2015**, *6*, 4855.
[12] a) E. V. Skorb, H. Möhwald, *Adv. Mater.* **2013**, *36*, 5029; b) T. A. Kolesnikova, D. Kohler, A. G. Skirtach, H. Möhwald, *ACS Nano* **2012**, *6*, 9585; c) D. V. Volodkin, N. Madaboosi, J. Blacklock, A. G. Skirtach, H. Möhwald, *Langmuir* **2009**, *25*, 14037.
[13] D. J. Schmidt, Y. Min, P. T. Hammond, *Soft Matter* **2011**, *7*, 6637.
[14] P. Schattling, F. D. Jochum, P. Theato, *Polym. Chem.* **2014**, *5*, 25.
[15] *Generating Micro- and Nanopatterns on Polymeric Materials* (Eds: A. del Campo, E. Arzt), Wiley, Weinheim **2011**.

[16] J. Auernheimer, C. Dahmen, U. Hersel, A. Bausch, H. Kessler, *J. Am. Chem. Soc.* **2005**, *127*, 16107.

[17] F. D. Jochum, P. Theato, *Polymer* **2009**, *50*, 3079.

[18] M. Shirai, *Polym. J.* **2014**, *46*, 859.

[19] E. Betthausen, M. Drechsler, M. Förtsch, F. H. Schacher, A. H. E. Müller, *Soft Matter* **2011**, *7*, 8880.

[20] E. V. Skorb, D. V. Andreeva, *Polym. Int.* **2015**, *64*, 713.

[21] J. Gensel, T. Borke, N. Pazos- Perez, A. Fery, D. V. Andreeva, E. Betthausen, A. H. E. Müller, H. Möhwald, E. V. Skorb, *Adv. Mater.* **2012**, *24*, 985.

[22] K. Hashimoto, H. Irie, A. Fujishima, *Jpn. J. Appl. Phys.* **2005**, *44*, 8269.

[23] J. Kopf, S. A. Ulasevich, O. Baidukova, Y. Zhukova, J. W. C. Dunlop, P. Fratzl, P. Rikeit, P. Knaus, S. K. Poznyak, D. V. Andreeva, E. V. Skorb, *Adv. Eng. Mater.* **2016**, *18*, 476.

[24] E. V. Skorb, H. Möhwald, *Ultrason. Sonochem.* **2016**, *29*, 589.

[25] E. V. Skorb, D. V. Andreeva, H. Möhwald, *Angew. Chem., Int. Ed.* **2012**, *51*, 5138.

[26] J. Gensel, I. Dewald, J. Erath, E. Betthausen, A. H. E. Müller, A. Fery, *Chem. Sci.* **2013**, *4*, 325.

[27] E. V. Skorb, D. V. Andreeva, *Polym. Chem.* **2013**, *4*, 7547.

[28] a) O. Boussif, F. Lezoualc'h, M. A. Zanta, M. D. Mergny, D. Scherman, B. Demeneix, J.-P. Behr, *Proc. Natl. Acad. Sci. USA* **1995**, *92*, 7297; b) A. Akinc, M. Thomas, A. M. Klibanov, R. Lander, *J. Gene Med.* **2005**, *7*, 657; c) R. V. Benjaminsen, M. A. Mattebjerg, J. R. Henriksen, S. M. Moghimi, T. L. Andresen, *Mol. Ther.* **2013**, *21*, 149; d) I. Richard, M. Thibault, G. DeCrescenzo, M. D. Buschmann, M. Lavertu, *Biomacromolecules* **2013**, *14*, 1732.

Light-Induced Water Splitting Causes High-Amplitude Oscillation of pH-Sensitive Layer-by-Layer Assemblies on TiO₂

Sviatlana A. Ulasevich, Gerald Brezesinski, Helmuth Möhwald, Peter Fratzl, Felix H. Schacher, Sergey K. Poznyak, Daria V. Andreeva, and Ekaterina V. Skorb*

Abstract: We introduce a simple concept of a light induced pH change, followed by high amplitude manipulation of the mechanical properties of an adjacent polymer film. Irradiation of a titania surface is known to cause water splitting, and this can be used to reduce the environmental pH to pH 4. The mechanical modulus of an adjacent pH sensitive polymer film can thus be changed by more than an order of magnitude. The changes can be localized, maintained for hours and repeated without material destruction.

The use of light as an external stimulus to modulate polymer systems has great potential in biosciences, medicine, and tissue engineering, owing to the possibility to irradiate micron-sized areas with fast on/off switching rates.[1] However, only a limited number of stimuli-responsive polymers are able to undergo light-initiated transitions. Well-known examples are polymers with azo-groups that undergo reversible isomerization upon irradiation.[2] Unfortunately, the response on the molecular level is relatively weak, because azobenzene molecules change their geometry from planar to non-planar with a decrease in the distance between the *para* carbon atoms only in the Ångström range.[2] Other examples are photo-crosslinkable polymers.[3] The photo-crosslinking technique is widely used in the casting industry and in photo-resist technology and can allow for the photo patterning of pixels.[4] However, such materials are difficult to use as stimuli-responsive systems, where changes should be totally reversible. It is of importance to find a strategy to actuate

polymer systems: composites, hybrids. Light-actuating composite layer-by-layer (LbL) polyelectrolyte assemblies in most cases contain metal nanoparticles,[5–7] which couple light and temperature providing local heating and decomposition in LbL assemblies. Recently Tsukruk et al.[8] suggested using a light-initiated photochemical reaction, in which trivalent counterions, $[Co(CN)_6]^{3-}$, can be decomposed into monovalent and divalent ions, which dramatically affect the reversibly conformation and porosity of LbL films. The systems, however, are not comparable with the actuation amplitude of pH-sensitive LbL polymer films: change of thickness, stiffness. Our concept of is to couple light and pH and thereby actuate adjacent pH sensitive soft matter with light. We aimed to demonstrate the concept of nondestructive light–pH coupled switching of polymer films by activation of the pH change on titania and reversibly affecting polymer assembly (Figure 1).

[*] S. A. Ulasevich, Prof. G. Brezesinski, Prof. H. Möhwald, Prof. P. Fratzl, Dr. E. V. Skorb
Max Planck Institute of Colloids and Interfaces
Am Mühlenberg 1, 14424 Potsdam (Germany)
E-mail: skorb@mpikg.mpg.de

Prof. F. H. Schacher
Friedrich-Schiller-Universität Jena, Institut für Organische Chemie und Makromolekulare Chemie
Humboldtstrasse 10 (Germany)
Jena Center for Soft Matter (JCSM), Friedrich-Schiller-Universität Jena
Philosophenweg 7, 07743 Jena (Germany)

Dr. S. K. Poznyak
The Research Institute for Physical Chemical Problems, Belarusian State University
220030 Minsk (Belarus)

Dr. D. V. Andreeva
Center for Soft and Living Matter, Institute of basic science, Ulsan National Institute of Science and Technology
44919 Ulsan (Republic of Korea)

Supporting information for this article can be found under: http://dx.doi.org/10.1002/anie.201604359.

i) $TiO_2 + h\nu \rightarrow h_{vb}^+ + e_{cb}^-$

ii) $H_2O + h_{vb}^+ \rightarrow \ldots \rightarrow H^+ + O_2$ (inside irradiated spot)

iii) $O_2 + e_{cb}^- + H_2O \rightarrow \ldots \rightarrow OH^-$ (outside irradiated spot)

Figure 1. Surface decoration and photoinitiated light–pH reactions. Primary and secondary photocatalytic reactions on TiO₂ resulting in a local change of pH (ΔpH). The reactions are shown of i) light-stimulated charge separation, ii) primary reaction with photohole with final production of protons and local surface acidification of the irradiated area, iii) and photoelectron reaction. ΔpH will affect the dynamic layers assembled on the TiO₂ in terms of local changes in film thickness, stiffness, and permeability by regulating the time taken for the dynamic layer activation, the relaxation, and reversibility. vb = valence band, cb = conduction band.

Herein for the first time we focus on an efficient and controllable way of transforming the energy of electromagnetic irradiation into a local pH shift by using the well-established TiO₂ and, thus, into the mechanical reversible response of soft matter for high-amplitude actuation. pH-dependent polymers are a class of materials with tremendous structural variety. One example is the "weak" polyelectro-

lytes (PEs),[9] in which morphology and charge strongly depend on pH. Thus such weak polyelectrolytes as block copolymer micelles (BCM) can show a drastic response to pH.[10] The pH-responsive behavior of the block copolymer micelles can be controlled via the ionization degree of one of the constituting blocks.[11] Another class of pH dependent polymers are hydrogels.[12] They exhibit pronounced morphological changes in response to ΔpH and can also be used for multilayer formation.[13] It is important to assess, if the whole class of pH-sensitive polymers can be modulated/actuated with light, which is the focus of this study on actuating pH sensitive soft matter with light by using TiO_2 for proton pumping.

The concept is illustrated in Figure 1. We build up our system with the following blocks: the light sensitive part is a photocatalytically active nanostructured TiO_2 film. It is well established[14,15] that under supra-band gap illumination a photohole and a photoelectron are formed (Figure 1) on the surface of TiO_2. The active species formed can then take part in series of different photocatalytic reactions. Thus, the photoholes can convert the surface hydroxy groups, the photogenerated electrons can be scavenged by any scavenging agent, in most cases by oxygen. We suggest that during photocatalytic reactions both H^+ and OH^- can be generated on TiO_2. Focusing on nondestructive, temperature-independent modulation of polymers we used low power, short term irradiation and assembled LbL films on low photocatalytically active TiO_2 surfaces (Figure S1 in the Supporting Information).

For pH sensitive modulation with light, it is important to understand how photoinitiated processes on TiO_2 result in the transformation of light to a pH change, including localization of the effect. We applied the in situ scanning ion-selective microelectrode technique (SIET) with a sensitivity better than ΔpH 0.2 units for mapping of the activity and migration of H^+ ions on a TiO_2 film in aqueous solution during UV irradiation. The SIET allows measurements of the concentration of specific ions (in particular in this case, H^+ ions) at a nearly constant microdistance over the surface (Figure S2).[16] The SIET map for a TiO_2 light irradiated surface is shown in Figure 2, confirming that it is possible for TiO_2 to release protons during its irradiation. Most of the photogenerated species are used for the reactions, and we could not detect any temperature change over the surface with a sensor with sensitivity below $\Delta T = 1°$. Thus pH changes are due to the photocatalytic reaction on the TiO_2 surface, and these changes are drastic.

Figure 2b demonstrates, how the pH in the center of the irradiated spot (Figure 2a) varies upon switching on and then switching off the local UV irradiation. The duration of irradiation correlates with the pH obtained: 5 s, 1 min, and 3 min of irradiation result in pH of 5.6, 4.5, and 4 peak values, respectively. After turning off the light, the pH relaxes to the initial value over approximately 40 min. To study possible localization (Figure 2a) of proton pumping from the TiO_2 surface the 3D SIET maps are monitored (Figure 2c,d).

The pH before irradiation is about 6 all over the TiO_2 surface (Figure 2c). After starting the local surface illumination, the pH decreases significantly over the light spot
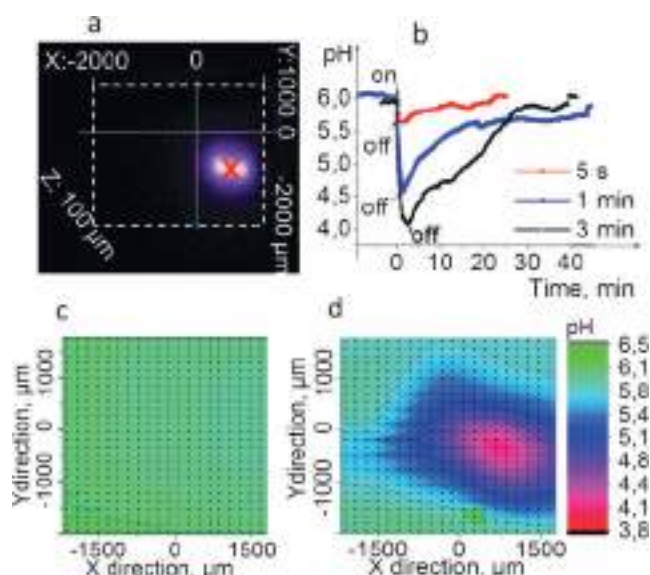
Figure 2. In situ local pH activity over a TiO_2 surface. a) Optical image of the surface during irradiation and measurements of SIET for mapping of the activity of H^+ ions over the TiO_2 film under local UV irradiation. b) Temporal evolution of the pH over the mesoporous TiO_2 film in the center of the irradiation zone (X in (a); on—illumination is switched on, off—illumination is switched off). c,d) SIET maps of proton activity c) before and d) during the exposure of certain localized areas.

(Figure 2d). In addition, there is a gradient of pH going from the center of the irradiated spot in horizontal and vertical (outside) directions. The action of different photoelectrochemical reactions (Figure 1) on the TiO_2 surface under UV illumination seems to be the only plausible explanation for the observed local acidification of the solution and confirms that TiO_2 is promising to demonstrate our concept.

The next step was the assembly of the pH-sensitive high-amplitude actuating polymer on low-photoactive TiO_2 (Figure S1). We worked with well-characterized pH-sensitive block copolymer micelles (positively charged layer, zeta-potential ca. 37 mV),[17] which had shown "smart" switching under pH change. We used a linear ABC triblock terpolymer consisting of polybutadiene (B), poly(methacrylic acid) (MAA), and quaternized poly(2-(dimethylamino)ethyl methacrylate) (Dq), BMAADq. In aqueous solution, BMAADq self-assembles into core–shell-corona micelles with a hydrophobic B core, a pH-sensitive MAA shell, and a strong cationic Dq corona. At low pH the pH sensitive MAA block is uncharged. At high pH, this block is negatively charged through the deprotonation of the carboxylic acid groups leading to intramicellar interpolyelectrolyte complex formation with the cationic corona of Dq. Hence, the composition of the micellar shell as well as the charge density of the corona can be controlled by the solution pH. A single block copolymer micelle layer is approximately 50 nm thick (Figure S3).

Recently the groups of Fery[18] and Sukhishvili[19] suggested that block copolymer micelle stability and reversibility of switching can be improved combining micelles with

polyelectrolytes via LbL assembly. Moreover the LbL assembly of block copolymer micelles (BCM) and polyelectrolytes allows coatings to have different thicknesses.[8] We LbL assembled block copolymer micelles, as the positively charged layer, and poly(acrylic acid) (PAA), as the negatively charged layer. Initially the thickness of the two bi-layers coating on $TiO_2/(BCM/PAA)_2$ was 150 nm (Figure 3a,c; Supporting Information, Figure S4). The question remains, if we could reversibly switch the LbL assemblies that are deposited on the TiO_2 surface, with light. The low power (ca. 5 mW cm^{-2}) and low duration (less than 10 min) of irradiation did not lead to degradation of the LbL assembled coating, which is verified in control experiments using Fourier transform infrared spectroscopy (FTIR; Figure S5). There are no differences in spectra detected besides a change in water content, which can be explained by a change of LbL thickness and water trapping in the LbL matrix, confirmed also with a quartz-crystal microbalance (QCM; Figure 3d).

To demonstrate the light-induced change of LbL assembly thickness and stiffness, the relaxation kinetics and process reversibility we investigated the LbL film on the surface of TiO_2 using atomic force microscopy (AFM; Figure 3). Then the illumination was switched on and changes in thickness were monitored with AFM. The thickness increased within 10 min, reaching a maximum and remaining the same the next several minutes, then starting to relax slowly, full relaxation took approximately 20 hours. Colloidal probe atomic force microscopy (CP AFM, Figure 3c(inset)) measurements confirmed that the LbL polymer assembly on the photoactive TiO_2 film became softer (ca. Young modulus 28 kPa) during irradiation compared to the initial stiffness (ca. 1.67 MPa), and the process was reversible (Figure 3c(inset)).

Interestingly our recent study proved that even short (seconds) irradiation suffices to activate the LbL assembly. QCM measurements (Figure 3d) confirmed the LbL deposition of two bilayers of (BCM/PAA) on a TiO_2 covered chip. Then we switch on the light for several seconds. It is seen that the frequency started to decrease reflecting the increase of the mass corresponding to water uptake and the LbL film thickness increased by activation as a result of H$^+$ production (shown in schematic Figure 3d).

After irradiation is switched off the relaxation of the LbL assembled coating occurs. However, owing to the complex character of the LbL assembly building blocks, for example, block copolymer micelles as one pH sensitive layer, the coating relaxation is relatively slow. The relaxation to 150 nm requires more than 20 h, which characterizes the system as fast activated and slowly relaxing. Such systems are of great interest for biological applications (see an example in the Supporting Information, Figure S6).

A related question on the feasibility of the process is: how many protons and photons are needed from the surface to locally change the pH from 7 to, for example, 4, on the surface and activate the block copolymer micelles? To calculate the concentration of protons needed for activation we assume for 1 cm^2 of TiO_2 to achieve a pH 4 or [H$^+$] = 10^{-4} M or 6×10^{19} L^{-1} a coating with thickness of, for example, 150 nm in our case, that is $V = 1.5 \times 10^{-8}$ L. The concentration of protons in the system is then [H$^+$] = 9×10^{11} protons cm^{-2}, which is about
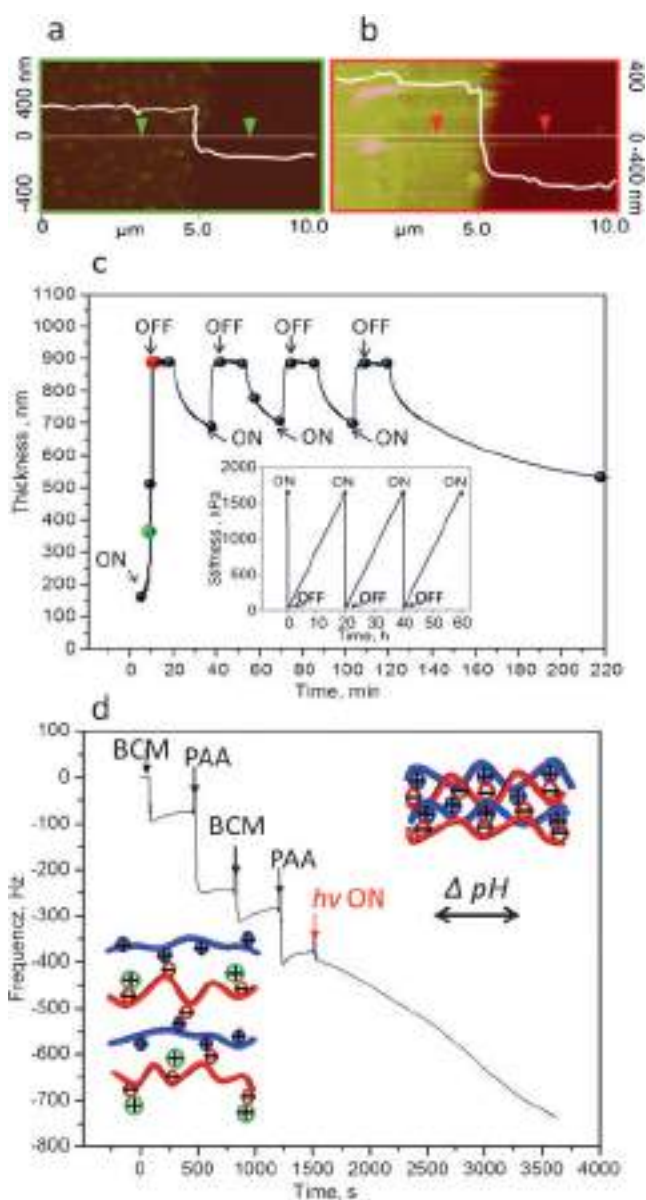
Figure 3. Light activation and relaxation of a high-amplitude switchable pH-sensitive LbL assembly on a low-photoactivity TiO_2 layer. a),b) AFM images of changes in LbL thickness during irradiation for a) 3 min; b) for 10 min; color equates to z = 0–1200 nm. c) Change of thickness and (inset) stiffness: LbL activation is significantly faster than its relaxation, cycles of light switching are marked as "ON" and "OFF", correspondingly. d) Quartz crystal microbalance measurements of LbL assembly and photoactivation by seconds-long pulse irradiation. Inset: schematic representation of the protonation of the LbL assembly and increase of its thickness.

0.1% of the lattice sites of a typical solid (10^{15} lattice sites cm^{-2}). This means that only 0.1% of the surface atoms have to be charged to achieve pH 4, if no losses exist. Even if we consider a low radiation intensity of 1 mW cm^{-2} = 10^{16} photons cm^{-2} sec^{-1} for a quantum yield proton/photon conversion of 0.1% the photons from 100 ms irradiation would create enough protons on the TiO_2 surface to achieve LbL switching on the surface of TiO_2. This also means that also less-photoactive solids could create the same effect.

We still need to answer a lot of questions, and more quantitative studies are needed. How can the photogeneration of charges in a solid be used to change the properties of adjacent soft matter with high selectivity? The question contains topics, such as photon absorption, migration, storage, carrier generation, chemical conversion into a pH gradient, lifetimes, and polymer stability. Sub-questions then are: a) the dependence on LbL architecture, b) the specificity for TiO$_2$ as a semiconductor, effectiveness of doping, duration, and intensity of irradiation.

However it is already clear that there is great potential for the conversion of energy from electromagnetic irradiation into pH gradients, thus enabling spatial regulation by localization of the irradiation spot on the semiconductor TiO$_2$ surface. Using localized in situ SIET measurements we show for the first time the possibility of efficient transformation of electromagnetic energy in the form of irradiation into a local pH shift. The LbL assembly provides an efficient structure for the fast trapping of photogenerated H$^+$ ions. The kinetics of light–pH coupled actuation and modulation show that such LbL surfaces are fast switchable and slowly relaxing. We thus demonstrate that the photogenerated charges in a solid can be used to change the properties of adjacent soft matter. Quantitative analysis for the promising pH sensitive assembly of architecture TiO$_2$/BCM/PAA/BCM/PAA reveals a modulation of the thickness by a factor of 4 and a change of elastic modulus by more than an order of magnitude. The light–pH coupled actuation of soft matter is efficient for the formation of drug delivery capsules,[7,20] self-repairing coatings, and to guide cells via local elasticity changes (Figure S6),[21] microfluidics, lab-on-chip, sensors, nano-lithography.[22]

In conclusion, we demonstrate here a simple process: irradiation of a semiconductor surface causes a charge separation, leading to water splitting and to a pH change. Unexpectedly the pH value could be reduced to pH 4, it could be localized by focusing of light, maintained over hours and effected repeatedly and reversibly.

[1] F. D. Jochum, P. Theato, *Chem. Soc. Rev.* **2013**, *42*, 7468–7483.
[2] J. Auernheimer, C. Dahmen, U. Hersel, A. Bausch, H. Kessler, *J. Am. Chem. Soc.* **2005**, *127*, 16107–16110.
[3] M. Shirai, *Polym. J.* **2014**, *46*, 859–865.
[4] *Generating Micro- and Nanopatterns on Polymeric Materials* (Eds.: A. del Campo, E. Arzt), Wiley, Weinheim, **2011**.
[5] A. G. Skirtach, P. Karageorgiev, M. F. Bedard, G. B. Sukhorukov, H. Mohwald, *J. Am. Chem. Soc.* **2008**, *130*, 11572–11573.
[6] D. V. Volodkin, N. Madaboosi, J. Blacklock, A. G. Skirtach, H. Mohwald, *Langmuir* **2009**, *25*, 14037–14043.
[7] E. V. Skorb, A. Skirtach, D. V. Sviridov, D. G. Shchukin, H. Möhwald, *ACS Nano* **2009**, *3*, 1753–1760.
[8] W. Xu, I. Choi, F. A. Plamper, C. V. Synatschke, A. H. E. Müller, V. V. Tsukruk, *ACS Nano* **2013**, *7*, 598–613.
[9] E. V. Skorb, D. V. Andreeva, *Polym. Int.* **2015**, *64*, 713–723.
[10] G. B. Webber, E. J. Wanless, S. P. Armes, Y. Tang, Y. Li, S. Biggs, *Adv. Mater.* **2004**, *16*, 1794–1798.
[11] R. Vyhnalkova, A. H. E. Müller, A. Eisenberg, *Langmuir* **2014**, *30*, 13152–13163.
[12] W. A. Petka, J. L. Harden, K. P. McGrath, D. Wirtz, D. A. Tirrell, *Science* **1998**, *281*, 389–392.
[13] M. A. Stuart, W. T. Huck, J. Genzer, M. Müller, C. Ober, M. Stamm, G. B. Sukhorukov, I. Szleifer, V. V. Tsukruk, M. Urban, F. Winnik, S. Zauscher, I. Luzinov, S. Minko, *Nat. Mater.* **2010**, *9*, 101–113.
[14] K. Hashimoto, H. Irie, A. Fujishima, *Jpn. J. Appl. Phys.* **2005**, *44*, 8269–8285.
[15] D. A. H. Hanaor, C. C. Sorrell, *J. Mater. Sci.* **2011**, *46*, 855–874.
[16] D. Fix, E. V. Skorb, D. G. Shchukin, H. Möhwald, *Meas. Sci. Technol.* **2011**, *22*, 075704.
[17] a) E. Betthausen, M. Drechsler, M. Förtsch, F. H. Schacher, A. H. E. Müller, *Soft Matter* **2011**, *7*, 8880–8891; b) A. C. Rinkenauer, A. Schallon, U. Günther, M. Wagner, E. Betthausen, U. S. Schubert, F. H. Schacher, *ACS Nano* **2013**, *7*, 9621–9631.
[18] J. Gensel, I. Dewald, J. Erath, E. Betthausen, A. H. E. Müller, A. Fery, *Chem. Sci.* **2013**, *4*, 325–334.
[19] Z. Zhu, S. A. Sukhishvili, *J. Mater. Chem.* **2012**, *22*, 7667–7671.
[20] a) E. V. Skorb, D. V. Sviridov, H. Möhwald, D. G. Shchukin, *Chem. Commun.* **2009**, 6041–6043; b) E. V. Skorb, D. G. Shchukin, H. Möhwald, D. V. Sviridov, *J. Mater. Chem.* **2009**, *19*, 4931–4937.
[21] S. A. Ulasevich, N. Brezhneva, Y. Zhukova, H. Möhwald, P. Fratzl, F. H. Schacher, D. V. Sviridov, D. V. Andreeva, E. V. Skorb, *Macromol. Biosci.* **2016**, DOI: 10.1002/mabi.201600127.
[22] E. V. Skorb, D. Grützmacher, C. Dais, V. Guzenko, V. G. Sokolov, T. V. Gaevskaya, D. V. Sviridov, *Nanotechnology* **2010**, *21*, 315301.

Ultrasonically Produced Porous Sponge Layer on Titanium to Guide Cell Behavior

By *Jessica Kopf, Svetlana Ulasevich, Olga Baidukova, Yulia Zhukova, John W. C. Dunlop, Peter Fratzl, Paul Rikeit, Petra Knaus, Sergey K. Poznyak, Daria V. Andreeva* and *Ekaterina V. Skorb**

The adhesion of cells to surfaces, as well as their proliferation, migration, and differentiation, is guided not only by chemical functionalization but also by surface nanostructuring, nanotopography.[1] Nano-patterned titanium surfaces are one example in which the scale of patterning controls the size of focal adhesions.[2] Nanoscale disorder in surface structure can be used to stimulate cell differentiation[3] or can also be used to maintain stem cell phenotypes over long times.[4] Nanoroughness modulates cells interactions and function via mechanosensing.[5] These all suggest that the careful control of surface nanostructure of such important as titanium (Ti) biomaterial[6] could be a useful tool to achieve desired cellular responses.

We first time highlight that ultrasonic treatment is able to produce surface porous sponge layer in Ti. We find it great technological advances that Ti can be also modified with high-intensity ultrasonic treatment. We really think that presenting high-intensity ultrasonic technique for Ti nanostructuring increases interest of scientists to the technique. Great advantage of our methodology is a large number of synthetic parameters which can be optimized to tune surface nanostructuring in a controllable manner. Moreover, this methodology will be very interesting in future to provide single-step hybrids and effective loading of porous structures with active chemicals. We compare our methodology with more known for bio-application anodization for surface nanostructuring.

Anodization leads to TiO$_2$ nanotube arrays covering the surface of titanium and is one of the most studied methods to develop porous surface nanotopographies with controlled pore sizes.[6] It has been demonstrated in cell culture experiments on TiO$_2$ nanotube arrays of different sizes that adhesion, proliferation, and migration of mesenchymal stem cells are optimal on ordered nano-pore arrays with spacings in the range of 15–30 nm; these length scales also lead to significantly less apoptosis than on 100 nm structures.[7,8] It should be taken into account that nanostructuring does affect cell function at many levels but in a cell specific manner, and smaller surface features (50 nm) tend to favor cell proliferation in comparison to larger features (300 nm).[9]

Anodization requires a conductive substrate, is difficult to use over large surface areas, and uses aggressive media for synthesis.[6] Recently, we have shown that ultrasonic treatments in aqueous media can produce surface porosities in various size-ranges also below 100 nm in metals such as Al or Mg.[10] Here, we demonstrate that such nanostructuring can also be effectively induced in an important biomaterial, titanium, by investigating its influence on cell behavior in comparison to the well-established electrochemical method.

To this end, we investigate the response in terms of morphology, adhesion, proliferation, and differentiation of C2C12 cells on a glass substrate and on three different titanium/TiO$_2$ surfaces: a titania mesoporous sponge layer (TMS) formed by ultrasonication, a titania nanotube layer (TNT) with comparable porosity formed by anodization, and an unmodified titanium surface (Ti) covered with a flat native oxide layer (Figure 1).

We focus on medium porosity (40–70 nm) nanostructures, which can be potentially used for surface drug delivery[11] while still allowing for cell adhesion and survival. It is seen from histogram, Figure 1, that the average pore size analyzed for TNT and TMS is the same, ca. 70 nm, however, for ordered TNT it is narrow pore size distribution and for disordered TMS the pore size distribution is broader to TNT. The critical value for TNT surface, as was shown before, are the pores more than 70 nm, critical cell fate level. To compare novel nanostructured surface of TMS with TNT, we analyze for both of the surface relatively large nanopores, 40–70 nm, to be close to fate level of TNT to see either TMS fate level is different. Indeed, our assumption, that for disordered TMS cell fate level is higher. Ultrasonication is known to produce surface modifications, including mechanical damage, through high-

[*] Dr. E. V. Skorb, S. Ulasevich, O. Baidukova, Y. Zhukova, Dr. J. W. C. Dunlop, Prof. P. Fratzl
Max Planck Institute of Colloids and Interfaces, 14424 Potsdam, Germany
E-mail: skorb@mpikg.mpg.de
Dr. J. Kopf, P. Rikeit, Prof. P. Knaus
Institute for Chemistry/Biochemistry, Freie Universität Berlin, 14195 Berlin, Germany
Dr. S. K. Poznyak
Institute for Physico-Chemical Problems of Belarusian State University, 220030 Minsk, Belarus
Dr. D. V. Andreeva
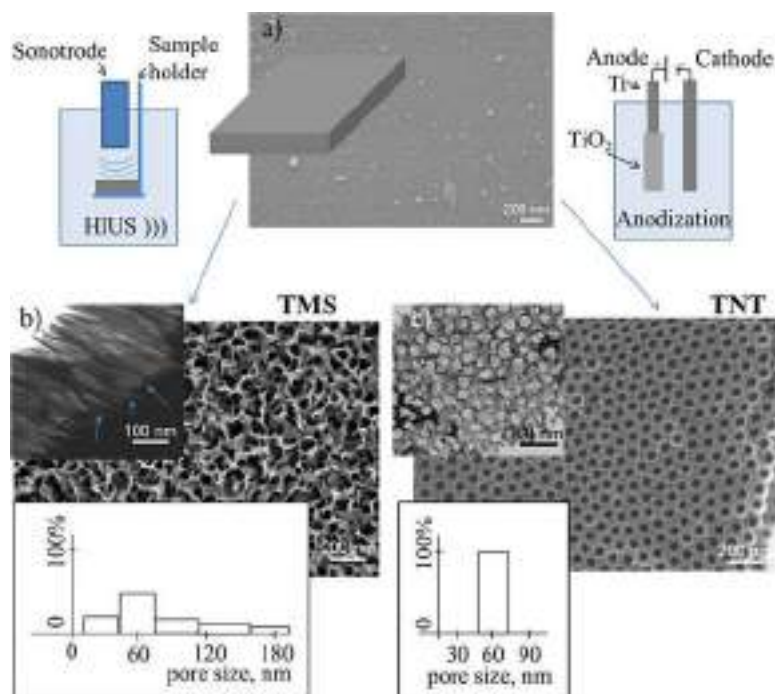*Physical Chemistry II, Bayreuth University, 95440 Bayreuth, Germany*

Fig. 1. Schematic view of the two techniques used for titanium surface nanostructuring for following nanotopography-guided cell behavior and a view of the corresponding resulting surfaces formed by modification of initial flat titanium surface (shown in (a)); SEM of the sonochemically formed under high-intensity ultrasonic treatment (HIUS) titania mesoporous sponge layer (TMS) (b) and anodized titania nanotubes layer (TNT) (c). Insets (b, c) are TEM (slice-microtome) images of a cross-section through the TMS interface, side view (b), through the TNT, top view, and histograms of pore size distribution on TMS and TNT.

anneal all three types of compared surfaces, Ti, TMS, and TNT, at 450 °C for 3 h after surface modification to remove any organic contamination and to form a surface anatase oxide layer as confirmed using Raman spectroscopy (data not shown). In the case of TNT samples, heating the samples after anodization is an important technological step[6] to crystallize the oxide layer and burn difficult to remove residual organic components, remaining in the pores. In the case of TMS, the surface is already covered with a partially crystalline oxide layer immediately after treatment, due to the high local temperature that is achieved by the high-intensity ultrasonic treatment. In our case, resulted annealed layers have peaks of just anatase. Concerning TMS layer which already has some partial crystalline before annealing, annealing at 450 °C results also in anatase structure, however, not shown in this paper, some condition of initial sonication can further result in rutile. In following, it can be in focus how surface photoactivity which is different for different crystalline modification of titania, effect cell growth under the same surface morphology.

The hydrophilicity for both treated samples (TNT and TMS) was found to be very high, upon initial wetting, with a contact angle of 5.4° ± 0.8° for TNT and 5.2° ± 0.7° for TMS; after 5 min, the contact angle was 0.0° ± 0.0° ($p = 0.05$) for both samples, compared to the initial unmodified sample where the contact angle was 80° ± 2°. Besides, the common characteristics of surface chemistry and porous topography, TMS and TNT surface have different pore orientations: semi-ordered in the case of TNT and disordered in the case of TMS focusing the present study on the difference between ordered and disordered surfaces, with straight and random sided walls. Ions presented in the solution during porous structures development can dope titania layer. It is very interesting question, effect of doped ions from electrolyte to cell behavior. In the presented case of TMS, we treated in solution of NaOH. Other solutions with different ion size and ability to go into structure of TMS can be used, e.g. LiOH, KOH. Morphology of TMS is not effected with type of cation and is similar, presented in Figure 1 for TMS. The effect for following cell growth of Li^+, Na^+, K^+ was in the statistical error, not detectable. However, not shown in this paper, different cations size results in doping of titania and drastically change photoactivity of the surface, which can be used in following to guide cell migration with different efficiency for lab-on-chip application.

Interactions between biomaterials and host tissues are controlled by nanoscale features because of the three main reasons: cells grow on nanostructured extracellular matrices; biological events (signaling, cell–substrate interactions) occur

speed liquids jets, and shockwaves generated upon the asymmetric collapse of cavitation bubbles near a surface.[12] These mechanical effects have been considered by many as negative, as they may give rise to significant erosion and abrasion, such as cavitation damage on ship propellers and artificial heart valves.[13] However, the mechano-chemical effect of cavitation has been shown to be useful for practical applications in the modification of solid surfaces (roughening, cleaning, and formation of metal sponges), using liquids as benign as water.[14]

In the case of metals, the local conditions achievable under ultrasonic treatment etch and oxidize the surfaces leading to the formation of up to 300-nm-thick sponge-like crystalline surface layers, well-adhered to the bulk metal.[10] The TMS layer produced under ultrasonic treatment on Ti, shown in Figure 1b (inset), has high adhesion to the bulk metal. The surface metal sponge covered with oxide layer is porous, has a high surface area, and is covered by active OH-groups. Furthermore, such sponges combine the beneficial properties of metals with a porous structure to give unique physical and mechanical properties such as low density, high surface-to-volume ratio, high thermal shock resistance, and high specific strength.[14] Moreover, the shape of the sonotrode can be adjusted for particular applications and allows easy modifications of large surface areas, as well as micron scale surface patterning.[15]

In order to compare the role of surface nanotopography for cell behavior only and not the effect of surface chemistry, we

at the nanometric level; adsorbed proteins and their aggregates are a few nanometers in dimension. In the paper, three biomaterial substrates (Ti, TMS, TNT) are at nanoscale different in the following morphological parameters: i) in surface roughness, ii) in pore size, and iii) in regularity of the nanopore arrangement. Each of these three parameters can critically control cell behavior. Meaningful comparisons can be drawn with studies that have used a similar surface modification technique (i.e., anodic oxidation or sonochemical modification), since although the surface roughness may be identical, but the physicochemical characteristics of the surface (wettability, surface energy, etc.) can be completely different. In our case, we have shown that TMS is unique and have higher critical fate rate in comparison with TNT, which is in focus of this paper, however, in the following the focus can be as was suggested, for example, to detailed comparison of just sonochemically formed TMS from different solutions, such as LiOH, NaOH, KOH, and CsOH. The formation of the same nanotopography can allow to go deeper into understanding the effect of ions for cell behavior on the surface as well as surface photoactivity. To move to the direction of just TMS before, it is idea to see it in comparison with well characterized and described in the literature TNT to have idea of its effect to cell. Thus, for TMS and TNT the first parameter i) surface roughness was Ra $\approx$ 30 nm which is higher to vacuum-deposited layer of titan after its thermal oxidation (Ra $\approx$ 5 nm). Critical to compare TMS and TNT are two other parameters ii) in pore size, and iii) in regularity of the nanopore arrangement. ii) Average pore size is comparable for TMS and TNT $\approx$ 70 nm, however, for TNT it is very narrow pore size distribution and for TMS it is much broader due to also the iii) parameter: regularity of the nanopore arrangement. Taking together it is expected that i) roughness effect positively to TNT and TMS in comparison with initial thermal-treated titania; ii) cells on $\geq$70 nm on TNT have been reported to be less effective in cell adhesion and proliferation, however, here we are interested in use of porosity 40–70 nm for following drug delivery and to find the system where pore size $\geq$70 nm can be fine for the cell, from this point TMS was expected to be better that TNT due to broad size distribution; iii) unregularly TMS structure in comparison with TNT should be also more preferable for the cells.

To test the surfaces, we employed C2C12 cells as a model cell line which is capable of differentiating along several lineages and is used as a model system for osteogenic and myogenic differentiation.[16] We first investigated C2C12 cell adhesion and

proliferation on different surfaces (Figure 2). Cells proliferated well on all of the surfaces, however, nanostructuring of Ti affected cell proliferation rates. For cells grown on the control titania and TMS surfaces, the cell density increased significantly with increasing culture time (Figure 2a, b, c). The density of cells in the case of TNT was much lower in comparison to glass, titania, and TMS (Figure 2d). After 24 h, C2C12 cells on the Ti and TMS surfaces had reached a density of approx. 200 cells mm^{-2}, while cells on the TNT surfaces had reached a density of only 50 cells mm^{-2} (Figure 2e, f). No significant difference in the cell density was observed between Ti and TMS, suggesting a negligible effect of irregular porosity even above 70 nm size for cell viability and growth. After 48 h of culture, cells grown on the Ti and TMS surfaces had further increased cell number to a similar extent, while hardly any proliferation for the TNT surfaces could be observed. The lower cell density on TNT surfaces might occur because the nanotubes are above 70 nm at which cell adhesion is hampered. In all, there is a highly significant difference between TNT and the other two, but not between Ti and TMS.
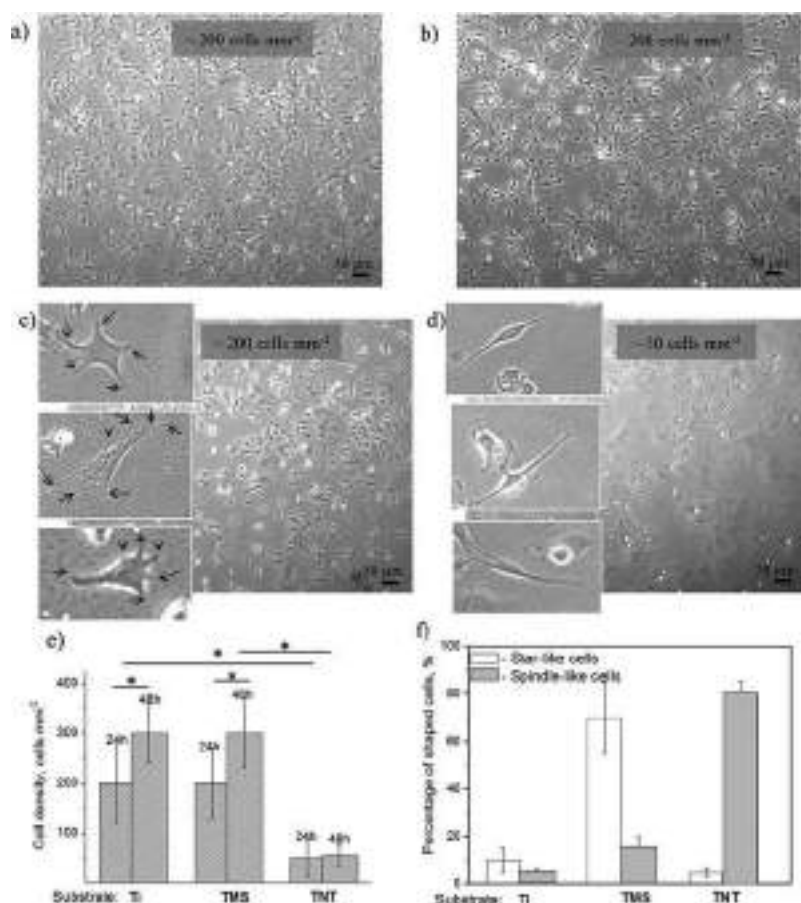
Fig. 2. The representative optical micrographs after one day of C2C12 cell growth on different substrates: glass (a), unmodified titanium (b), sonochemically formed TMS (c), and TNT nanotubes formed by anodization (d). Insets depict individual cell morphologies on different surfaces, such as "star-like" in the case of TMS and spindle-like cell morphology in the case of TNT. (e) Cell density on different surfaces as culture time prolonged. (f) Quantification of the percentage of shaped cells on different surfaces after one day of culture. Bar charts represent means $\pm$ SD from three replicates each from three independent experiments. Comparison was done by ANOVA *$p < 0.05$.

Such size effects have been demonstrated by Paramasivam et al. who investigated mesenchymal stem cells on smooth (equivalent to Ti) and 70–100 nm TNT surfaces.[7] They showed that in the case of oriented pores, a pore spacing less than 30 nm accelerated integrin clustering and focal contact formation and strongly enhances cellular activities compared to smooth surfaces.[7]

Despite these studies would suggest[7] that TNT surfaces at these larger spacings would be less preferable for cells in comparison to unmodified Ti, there is no information concerning the response of cells to disordered TMS surfaces with similar average spacing. Interestingly, our experimental results show that TMS surfaces at these length scales show no reduction in proliferation, which could mean that the mean above a certain size for cell response on disordered random-sided walls TMS is above than that for ordered straight-sided walls TNT.

Cells on different nanostructured surfaces also exhibited a distinct morphology (Figure 2f). On TMS most cells adopted a star-like morphology (shown in inset in Figure 2c), while cells grown on TNT rather exhibited an elongated spindle-like appearance (shown in inset in Figure 2d), indicating that nanotopography influences the morphology of adherent cells. The cells on the control surface were also more flattened, measured by 3D confocal microscopy. In comparison, star-like cells on TMS and spindle-like cells on TNT could be a result of the interspersed pattern of adhesion on a rough surface.

In addition to cell proliferation, we further examined focal adhesion (FA) formation and cytoskeletal structures after 24 h of C2C12 cells growth on different substrates (Figure 3). To analyze cytoskeletal structures, we performed immunofluorescent staining for actin fibers and focal adhesions using phalloidin or α-vinculin antibody, respectively. Immunofluorescent analysis of cell populations on the untreated and nanostructured substrates revealed pronounced differences in focal adhesion (FA) formation and cytoskeletal structures (Figure 3). We quantified the total vinculin area and the number of FAs, each normalized to cell area, and observed significant differences ($p < 0.05$) between untreated and nanostructured surfaces. Although TMS did not induce detectable cytotoxic effects, still fewer focal adhesions were observed and these were largely restricted to one edge of the cell membrane. The same effect was seen in the case of TNT. This can be explained through the hypothesis raised

by Paramasivam et al.[7] which suggests that vitality, proliferation, and motility of cells are critically influenced by nanoscale titania surface topography with a specific response to nanotubes with diameters between 15 and 100 nm.

In summary, FA formation of C2C12 cells as well as the total FA area per cell area was greater for the cells plated on the unmodified Ti substrate as compared to those plated on the nanostructured TMS and TNT. At the same time cells grown on TNT exhibited significantly lower proliferation rates, whereas cells on TMS and Ti showed comparable proliferation rates.

Cytoskeletal structure was also different and depended on surface nanotopography. In particular, we compared the nanotopography of titania and TMS samples (Figure 4a). For cells grown on both unmodified and nanostructured TMS, bundles of actin filaments, so-called stress fibers, could be observed. However, stress fiber formation on the control
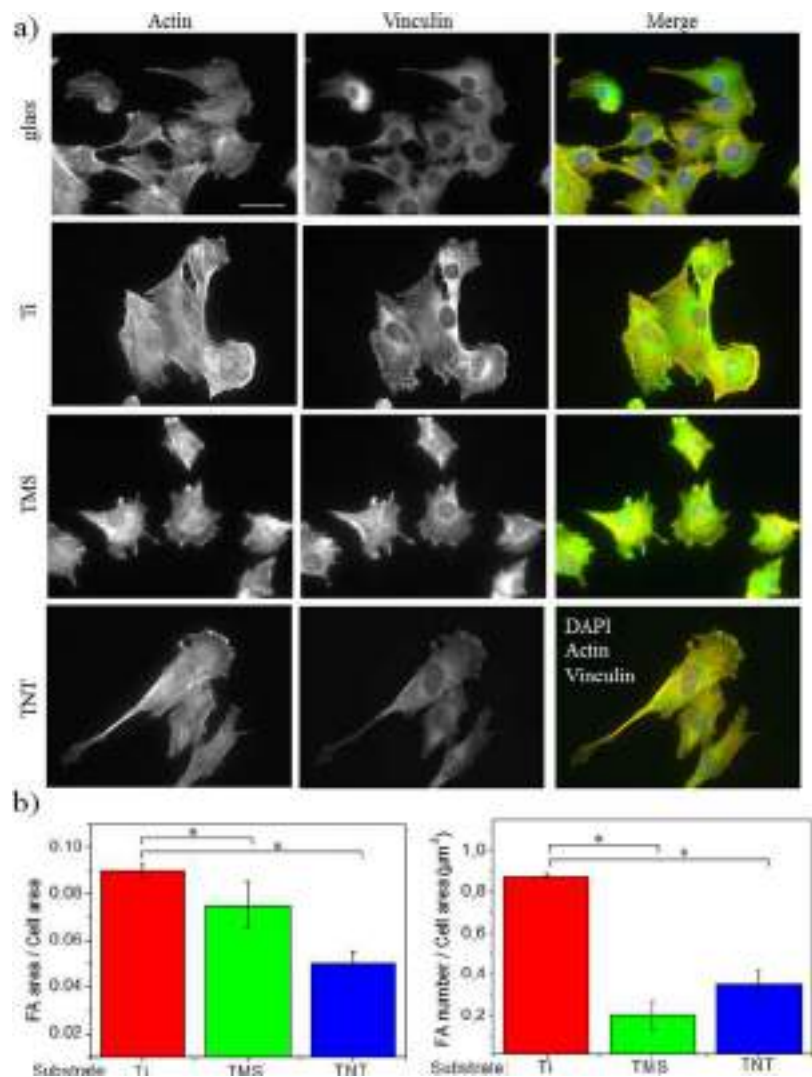
Fig. 3. Evaluation of effect of titanium nanostructuring on cell morphology and FA formation of C2C12 cells at day 1 after plating. Scale bar, 50 μm. Cells were stained for actin using phalloidin and vinculin using a specific antibody; nuclei were counterstained with DAPI. Quantitative analysis of FA formation of C2C12 cells: total FA area per cell and the number of FAs per cell area. Comparison was done by ANOVA *$p < 0.05$.

COMMUNICATION
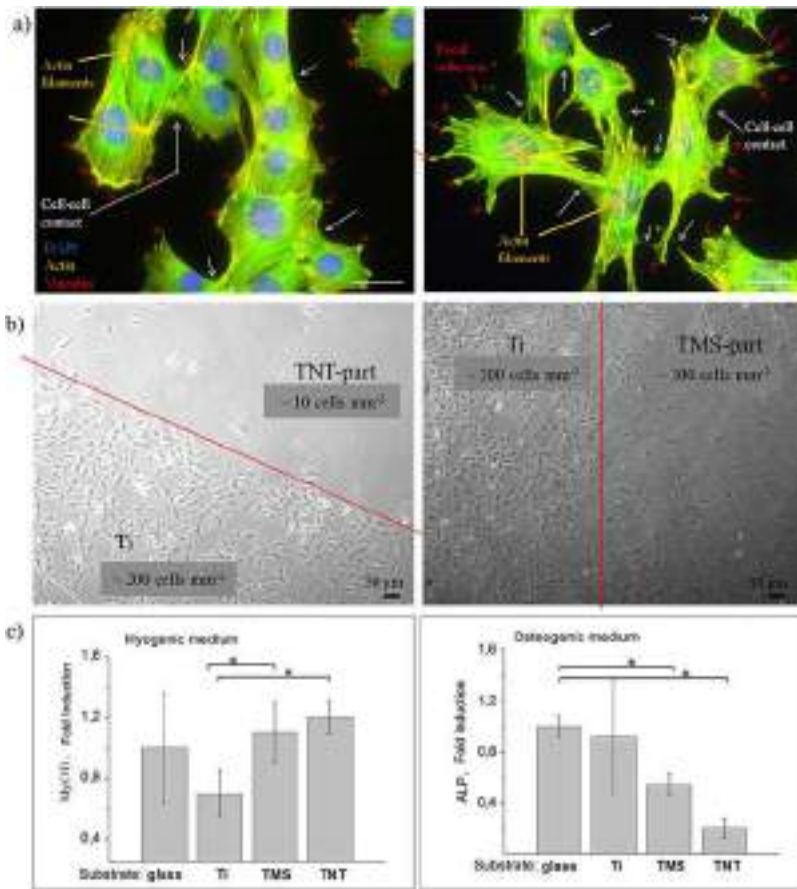
Fig. 4. (a) Immunofluorescent analysis on cell morphology on different titanium nanostructures. Cells were stained for actin using phalloidin and vinculin using a specific antibody; nuclei were counterstained with DAPI. Areas of cell–cell interactions are indicated by white arrows, focal adhesion (FA) by red arrows. Images depict morphological structures between regularly shaped cells in the case of Ti (a-left) and "star-like" shaped cells on TMS (a-right), scale bar, 50 μm. (b) Brightfield microscopic analysis of C2C12 cells grown on surfaces with a nanostructuring patterning approach. Materials exhibit two structurally different areas, one representing a titanium-nanostructured titanium surface just adjacent to an unmodified titanium surface (c) Gene expression analysis by qRT-PCR to determine C2C12 differentiation capacity on different titanium surfaces. MyoG is a myoblast-specific transcription factor whereas ALP is an enzyme, which plays a crucial role during osteogenic differentiation. The error bars indicate standard deviations from mean values of three biological replicates (n = 3). Asterisks indicate statistical significance *p < 0.05.

have a direct influence on the growing preference of cells on the same substrate, opening up bioengineering lab-on-chip possibilities. It is interesting that together with step-like gradient in cell response to nano-topology, cells also have the same tendency (see also Figure 2) with respect to shape, being spindle-like on TNT, and "star-like" on TMS the sides of the surfaces.

We further tested the ability of C2C12 cells to differentiate along two mesenchymal lineages, the myogenic and osteogenic lineages (Figure 4c). We thereby observed that the nanostructure of the material has an impact on the osteogenic differentiation while it only moderately affects myogenic differentiation. On all surfaces, C2C12 cells clearly differentiate toward the myogenic lineage, characterized by the induction of MyoD, a major myogenic transcription factor that controls the early steps of myo-genesis.[18] Conversely, during osteogenic differentiation triggered by 30 nM BMP-2, myotube formation was inhibited on all surfaces (images not shown) but osteogenic differentiation, characterized by the production of ALP was markedly different on nanostructured surfaces. Expression of alkaline phosphatase (ALP), an osteogenic marker, involved in matrix mineralization,[19] exhibited the highest expression on unmodified titanium and glass surfaces. Expression in cells differentiated on modified surfaces was much lower, showing the weakest expression on TNT surfaces. Similar trends were observed in other gene expression experiments (data not shown). However, when comparing TNT and TMS surfaces, BMP2-induced (30 nM) osteogenic differentiation was stronger on TMS than on TNT surfaces, highlighting again their potential for implant coatings and bone tissue engineering approaches. Our message is that osteogenic indeed is not too different for TNT, TMS, Ti thus one can think to use the structure for implantation, especially if additional functionality would be added, e.g., drug delivery due to porous structure. Moreover for lab-on-chip application, it is important to note that myogenic differentiations of TMS and TNT are significantly different from Ti, probably due to different initial shape of the adhered cells.

Taken together, we analyzed the prospects of ultrasonically formed mesoporous sponge layer (TMS), to guide cell behavior in comparison to flat titania and TNT, an anodized titania surface. The taking into account parameters to compare are i) surface roughness, is comparable for TNT and TMS and is higher to vacuum-deposited layer of titan after its thermal oxidation. Thus, this parameter is not one to explain the

titania was more pronounced in comparison to TMS, and fibers were longer and more uniformly distributed. Moreover, differences in cell morphology and cytoskeletal structure also affected cell–cell contacts.

Besides biological gradients, pore gradients are an attractive approach to guide cell behavior, offering a great potential for spatially controllable cell growth in implants for tissue engineering.[17] They would also be useful in the development of single-cell platforms to screen the best nanoscale architectures for the desired response of a specific cell type. Toward this aim, we also engineered surfaces nanostructured on one side, while leaving the other half surface unmodified (Figure 4b). We observed a dramatically lower cell number on the half with a TNT surface as compared to flat titania on the other half-surface (Figure 4b, left). TMS also affected cell attachment and growth (Figure 4b, right) as compared to titania. The results demonstrate that a surface that exhibits two different nanostructured areas next to each other could

COMMUNICATION

shown difference between TNT and TMS. Critical to compare TMS and TNT are two other parameters ii) pore size, and iii) in regularity of the nanopore arrangement. ii) Average pore size is comparable for TMS and TNT ≈ 70 nm, however, for TNT it is very narrow pore size distribution and for TMS it is much broader due to also the iii) parameter: regularity of the nanopore arrangement. i) The roughness effect positively to TNT and TMS in comparison with initial thermal-treated titania; ii) cells on ≥ 70 nm on TNT have less effective in cell adhesion and proliferation, however, TMS system the srytical fate size for cell is higher; iii) unregularly TMS structure in comparison with TNT can also be the factor to increase critical for cell fate pore size for higher values on TMS versus TNT and explain significantly higher proliferation on titania and the disordered TMS surface as compared to TNT. The critical value for TNT surface, as was shown before, is the pores more than 70 nm, critical cell fate level. To compare novel nanostructured surface of TMS with TNT, we analyze for both of the surface relatively large nanopores, 40–70 nm, to be close to fate level of TNT to see either TMS fate level is different. Indeed, our assumption, that for disordered TMS cell fate level is high, supported with our observation, presented in the paper. Other important point is if any novel nanostructuring methodic is suggested, one should compare it with already existing well-studied nanotopographies to go further for details of one particular methodology. Thus in our case, we present promise TMS together to, well established, TNT and in following can take attention to have careful control of just one factor, for example, sonochemical treatment for TMS in different solutions, such as LiOH, NaOH, KOH, and CsOH, under the same pH, resulting of same nano-topography, but different photoactivity; or different rough-ness of the surface formed in NaOH if take different sonication treatment time of Ti. Furthermore, nanostructure influenced the capacity of C2C12 cells to differentiate, showing that nanotopography plays also an important role during cell differentiation of other cell types, which should be consid-ered in tissue engineering strategies. In addition, a surface that exhibits two different nanostructured areas in close proximity opens opportunities to design cell culture plat-forms for controlled cell growth. The open pore structure of TMS and TNT can be loaded with chemical moieties, thus the possibility of both topographical and chemically directed cell growth and migration is attractive in future. Still, TMS surfaces allow immobilization of proteins and large molecu-lar compounds while maintaining basal osteogenic differen-tiation capacity.

1. Experimental Section

1.1. Preparation of Nanostructured Ordered and Disordered Surfaces

Glass- or ITO-coated glass substrates with a vacuum-deposited titanium layer (99.9%) were used. For TMS preparation, the Ti-glass substrates were ultrasonically treated in 5 M NaOH (Sigma–Aldrich) at 80%-intensity with an UIP1000hd (Hielscher Ultrasonics) operated at 20 kHz with a maximal output power of 1 000 W. Samples were placed into teflon home-made holder at 1 cm distance perpendicular to sonotrode. For TNT preparation, the Ti–ITO–glass samples were anodized in an aqueous solution of ethylene glycol (2 vol % water) containing 0.75 wt% NH$_4$F. At beginning of the anodizing, potential linearly increased from 0 to 40 V, than the anodizing performed at potentiostatic (40 V) mode till the total oxidation of a titanium layer on ITO. All samples were washed in ethanol and water. After washing, the structures were annealed at 450 °C in air. Milli-Q water was used in all aqueous solutions.

ITO were chosen as model substrate to have transparent surface for in situ monitoring of the cell behavior with optical microscopy to make staining and gene expression in certain moment of cell growth and to compare different cell number in time with optical microscopy. Moreover, the transparent surface to guide cell behavior is on high priority for lab-on-chip development. We did control experiments to prove that critical to guide cells is surface layer which depends on either Ti nanostructuring or nanostructuring of the layer on any enough inert substrate as, for example, Ti layer deposited in vacuum on glass, ITO surface and structured with different methods, e.g., sonochemical and electrochemical for our particular case.

1.2. Characterization Methods

Scanning electron microscopy (SEM) measurements were conducted with a Gemini Leo 1550 instrument (Zeiss) at an operation voltage of 3 keV. Transmission electron microscopy (TEM) images were obtained on a Zeiss EM 912 Omega transmission electron microscope operating at 300 kV. The samples were ultramicrotomed (Leica EM FC6) and placed onto the copper grids coated with a carbon film. Raman spectrometry of the substrates was performed using a confocal Raman microscope (alpha300, WITec) equipped with a piezoscanner. A frequency-doubled Nd:YAG laser excitation ($\lambda = 532$ nm) was used in combination with a Nikon $60\times$ objective. Contact angle was measured with an optical tensiometer Krüss G23 M.

1.3. Cell Culture

Mouse C2C12 myoblasts (ATCC CRL-1772) were used for functional assays. Cells were cultured as sub-confluent monolayers in growth medium, consisting of Dulbecco's modified Eagle's medium (DMEM) (Gibco BRL) supple-mented with 10% heat-inactivated fetal bovine serum (FBS) (Sigma), 2 mM glutamine, and 1% penicillin/streptomycin (Gibco BRL) at 37 °C and 5% CO$_2$. Cellular number and morphology on different titanium surface were monitored by bright field microscopy and documented by light micro-graphs. The distinction between differentially shaped cells was done by visual analysis. Total cell numbers were determined by manual counting of cells per image section. The total number of star- or spindle-shaped cells on each image section was counted manually by eye and normalized

to the total cell count. In total, 10 image sections were analyzed for every surface type in each experiment.

1.4. Immunofluorescent Staining

For microscopy and imaging, immunofluorescent staining was performed. At the respective time point, cells were fixed with 4% paraformaldehyde in phosphate-buffered saline, quenched for 5 min in a 50 mM ammonium chloride and permeabilized with a buffered Triton-X-100 solution for 10 min. Slides were then thoroughly washed with PBS and blocked in 3% BSA in PBS for 1 h. Subsequently, samples were incubated overnight with an anti-vinculin antibody (Sigma V9131) (1:300 in PBS/BSA). After washing with PBS, the samples were incubated with an Alexa-Fluor 488 labeled secondary goat anti-mouse antibody (Life Technologies, A-11001) (1:300) for 1 h. After washing, the samples were stained for 20 min with phalloidin Alexa-Fluor 594 (Life Technologies, A12381) (1:100) followed by incubation with DAPI (1:2 000) for 5 min. All stainings were performed at room temperature, except for the incubation with anti-vinculin antibody overnight, when the samples were left at 4 °C. The stained samples were mounted with Fluoromount-G (Southern Biotech) in inverted position on glass slides and examined via epifluorescence microscopy (Zeiss Axiovert 200M or Olympus IX inverted microscope). For presentation and calculations, the images were adjusted for brightness and color with ImageJ software (http://rsb.info.nih.gov/ij/). Confocal images that clearly showed focal adhesions were selected for analysis. RGB color images were converted to eight-bit black and white images using the image color RGB split function so that focal adhesions appeared as the black pixels. Focal adhesions were defined using Image J software by setting an intensity threshold. Image processing was identical for all cells in the different experimental groups. The number of focal adhesions per cell was counted using the analyze particles function.

1.5. Gene Expression Analysis by qRT PCR

C2C12 cells were seeded on the different titanium surfaces and grown to confluency after 6 day. Cells were subsequently starved for 3 h in DMEM without FCS supplements and stimulated for 3 days in medium containing 2% FCS (myogenic differentiation) or 2% FCS and 30 nM BMP2 (osteogenic differentiation). After stimulation, cells were harvested and total RNA was isolated using NucleoSpin isolation kit (Macherey&Nagel, Germany). 500 ng of RNA was subjected to reverse transcription. qRT PCR was performed using a SybrGreen-based detection system (Power SYBR Green PCR Master Mix, Life Technologies) and cDNA amplification was performed in a StepOne Plus Real Time PCR System (Life Technologies). For all used primers, amplification efficiencies were determined and mean-normalized expression (MNE) ratios using HPRT as reference gene were calculated using the $\Delta\Delta c_T$ method with efficiency correction.[20]

1.6. Statistical Analysis

Statistic calculations were generated using GraphPad Prism software (at www.graphpad.com/prism). Comparison of multiple groups was done three way analysis of variance (ANOVA) test in the case of cell density with pairwise multiple comparison procedures by Holm-Sidak method; and one way analysis (ANOVA) in the case of focal adhesion and gene expression. Data were normally distributed due to Normality Shapiro–Wilk test. A p-value smaller than 0.05 was considered statistically significant.

[1] M. J. Dalby, N. Gadegaard, R. O. C. Oreffo, *Nat. Mater.* **2014**, *13*, 558.

[2] T. Sjostrom, L. E. McNamara, R. M. D. Meek, M. J. Dalby, B. Su, *Adv. Healthcare Mater.* **2013**, *2*, 1285.

[3] M. J. Dalby, N. Gadegaard, R. Tare, A. Andar, M. O. Riehle, P. Herzyk, C. D. W. Wilkinson, R. O. C. Oreffo, *Nat. Mater.* **2007**, *6*, 997.

[4] R. J. McMurray, N. Gadegaard, P. M. Tsimbouri, K. V. Burgess, L. E. McNamara, R. Tare, K. Murawski, E. Kingham, R. O. Oreffo, M. J. Dalby, *Nat. Mater.* **2011**, *10*, 637.

[5] N. R. Blumenthal, O. Hermanson, B. Heimrich, V. P. Shastria, *Proc. Natl. Acad. Sci.* **2014**, *111*, 16124.

[6] E. V. Skorb, D. V. Andreeva, *Adv. Funct. Mater.* **2013**, *23*, 4483.

[7] I. Paramasivam, H. Jha, N. Liu, P. Schmuki, *Small* **2012**, *8*, 3073.

[8] J. Park, S. Bauer, K. Mark, P. Schmuki, *Nano Lett.* **2007**, *7*, 1686.

[9] A. M. Lipski, C. J. Pino, F. R. Haselton, I.-W. Chen, V. P. Shastri, *Biomaterials* **2008**, *29*, 3836.

[10] a) E. V. Skorb, D. G. Shchukin, H. Möhwald, D. V. Andreeva, *Nanoscale* **2010**, *2*, 722. b) D. V. Andreeva, D. V. Sviridov, A. Masic, H. Möhwald, E. V. Skorb, *Small* **2012**, *8*, 820. c) J. Gensel, T. Borke, N. Pazos-Pérez, A Fery, D. V. Andreeva, E. Betthausen, A. Müller, H. Möhwald, E. V. Skorb, *Adv. Mater.* **2012**, *24*, 985.

[11] a) E. V. Skorb, H. Möhwald, *Adv. Mater.* **2013**, *36*, 5029. b) E. V. Skorb, D. V. Andreeva, *Adv. Func. Mater.* **2013**, *23*, 4483. c) E. V. Skorb, H. Möhwald, *Adv. Mater. Inter.* **2014**, *1*, 1400237.

[12] L. Rayleigh, *Philos. Magaz. Ser.* **1917**, *634*, 94.

[13] G. Melan, A. Bellato, F. M. Susin, T. Bottio, V. Tarzia, V. Pengo, G. Gerosa, A. Bagno, *J. Heart Valve Dis.* **2013**, *22*, 828.

[14] a) E. V. Skorb, D. Fix, D. G. Shchukin, H. Möhwald, D. V. Sviridov, R. Mousa, N. Wanderka, J. Schäferhans, N. Pazos-Pérez, A. Fery, D. V. Andreeva, *Nanoscale* **2011**, *3*, 985. b) E. V. Skorb, H. Möhwald, T. Irrgang, A. Fery, D. V. Andreeva, *Chem. Comm.* **2010**, *46*, 7897. c)

COMMUNICATION

D. G. Shchukin, D. V. Andreeva, E. V. Skorb, H. Möhwald, in: *Supramolecular Chemistry of Hybrid Materials* (Ed: K. Rurack), Wiley-VCH, Weinheim, Germany **2010**.

[15] D. G. Shchukin, E. V. Skorb, V. Belova, H. Möhwald, *Adv. Mater.* **2011**, *23*, 1922.

[16] T. Katagiri, A. Yamaguchi, M. Komaki, E. Abe, N. Takahashi, T. Ikeda, V. Rosen, J. M. Wozney, A. Fujisawa-Sehara, T. Suda, *J. Cell Biology* **1994**, *127*, 1755.

[17] K. Kant, S. P. Low, A. Marshal, J. G. Shapter, D. Losic, *ACS Appl. Mater. Inter.* **2010**, *2*, 3447.

[18] T. L. M. Pohl, J. H. Boergermann, G. K. Schwaerzer, P. Knaus, E. A. Cavalcanti-Adam, *Acta Biomater.* **2012**, *8*, 772.

[19] T. Katagiri, A. Yamaguchi, M. Komaki, E. Abe, N. Takahashi, T. Ikeda, T. V. Rosen, J. M. Wozney, A. Fujisawa-Sehara, T. Suda, *J. Cell Biol.* **1994**, *127*, 1755.

[20] K. J. Livak, T. D. Schmittgen, *Methods* **2001**, *25*, 402.

Contents lists available at ScienceDirect

Ultrasonics Sonochemistry

journal homepage: www.elsevier.com/locate/ultson

Ultrasound-assisted synthesis of magnesium hydroxide nanoparticles from magnesium

Olga Baidukova *, Ekaterina V. Skorb

Max Planck Institute for Colloids and Interfaces, Am Mühlenberg 1, 14424 Potsdam, Germany

ABSTRACT

Acoustic cavitation in water provides special kinetic and thermodynamic conditions for chemical synthesis and nanostructuring of solids. Using cavitation phenomenon, we obtained magnesium hydroxide from pure magnesium. This approach allows magnesium hydroxide to be synthesized without the requirement of any additives and non-aqueous solvents. Variation of sonochemical parameters enabled a total transformation of the metal to nanosized brucite with distinct morphology. Special attention is given to the obtaining of platelet-shaped, nanometric and de-agglomerated powders. The products of the synthesis were characterized by transmission electron microscopy (TEM), electron diffraction (ED), scanning electron microscopy (SEM) and X-ray diffraction (XRD).

© 2016 Elsevier B.V. All rights reserved.

1. Introduction

Magnesium hydroxide (brucite) due to its specific properties has found an application in many fields. It is widely used in flame-retardant composite materials due to its ability to endothermically decompose with water release at high temperatures without production of toxic or corrosive substances [1,2], as an acidic waste neutralizer in paper industry and environmental protection field [3,4]. Besides, nanosized MgO products are commonly produced by a thermal decomposition of $Mg(OH)_2$ precursors [5,6]. The microstructure of the hydroxide, i.e. its particle size, shape and agglomeration are crucial in both applications. Among methods which are used for magnesium hydroxide synthesis are hydration of magnesium oxide [7,8], precipitation of a magnesium salt with an alkaline solution [9,10], sol–gel technique [11] and microwave-assisted synthesis [12,13]. However existing methodologies are multistep and require some other chemical presence in solution, e.g. NaOH or NH_4OH. In our case, magnesium hydroxide nanoparticles can be formed by sonochemical oxidation of magnesium in pure solutions. Special attention is given to the obtaining of platelet-shaped, nanometric and de-agglomerated powders.

Thus, in this paper we present a novel method for synthesis of nanosized magnesium hydroxide from pure magnesium by using high intensity ultrasound. The effect of ultrasound on a material

is based on acoustic cavitation: generation, growth and collapse of bubbles [14]. Acoustic waves create in liquid a cavitation field of interacting microbubbles [15]. These microbubbles are reaction sites used for chemical synthesis and nanostructuring within which free radicals and excited species are formed due to thermal cleavage of volatile solutes [16]. The interfacial region around the bubbles has unique conditions for synthesis reactions: high temperature (up to 5000 K), high pressure (about 2000 bar) and fast heating and cooling rates [14]. Moreover, collapse of microbubble enables continuous transport of chemicals to the reaction sites [17]. Ultrasound-assisted synthesis and nanostructuring of solids in water is based on physical and chemical effects, i.e. fragmentation of particles and increase of the surface area in the first case and selective etching and oxidation of the metal surface caused by formed during water sonolysis hydroxyl radicals in the second case [18–22] (Fig. 1).

2. Results and discussion

The schematic presentation of ultrasound driven formation of magnesium hydroxide structures in water is schematically shown in Fig. 2. In order to illuminate the ultrasound driven physical and chemical processes in liquid–metal system, we investigated magnesium at different sonication conditions (solvent, concentration of the metal). A mesoporous magnesium sponge-like structure with a thin magnesium hydroxide upper layer and agglomerates of magnesium hydroxide platelets covering the surface were formed by the ultrasound-assisted method at the concentration

---

* Corresponding author.
  E-mail address: baidukova@mpikg.mpg.de (O. Baidukova).
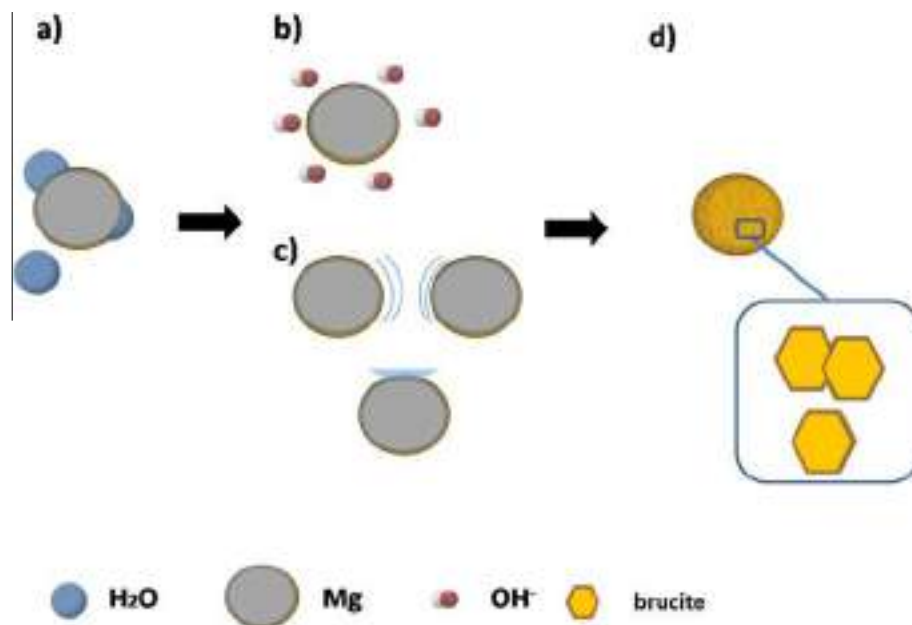
Fig. 1. Sonochemical modification of magnesium particles: (a) initial particles; (b) sonochemical effect: surface oxidation; (c) sonophysical effects: interparticle collisions and surface impinging by high velocity microjets; (d) formation of a mesoporous magnesium structure covered with brucite.
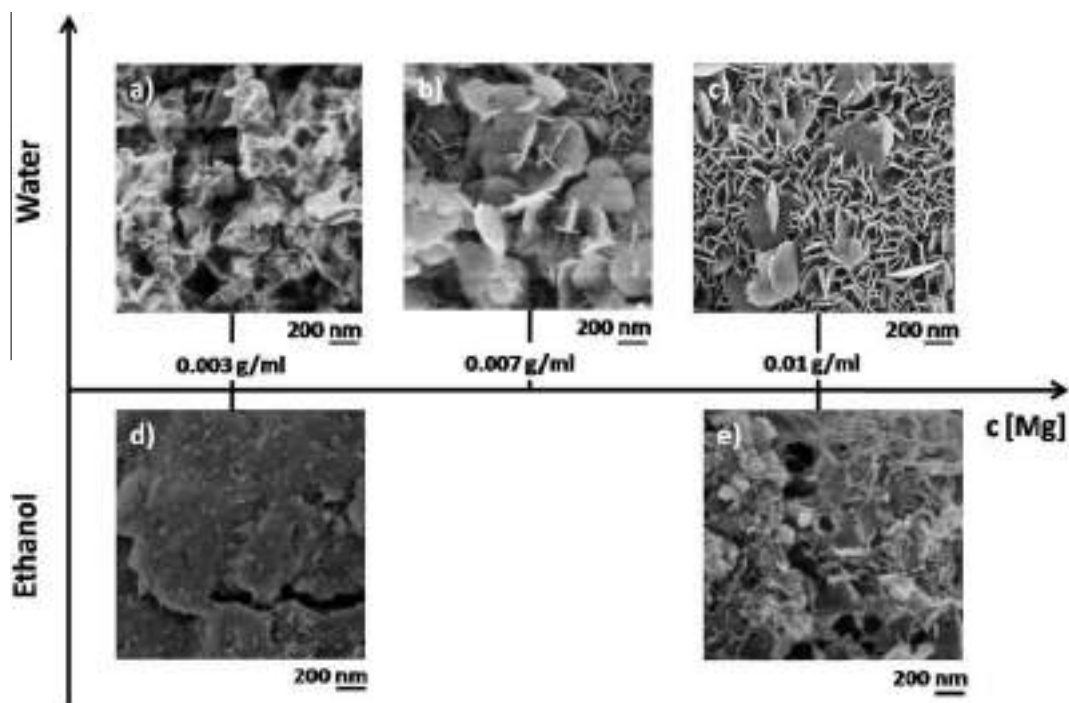
Fig. 2. The schematic presentation of the effect of acoustic cavitation on modification of magnesium particles at different concentrations and in different solvents. A mesoporous sponge-like structure with a thin brucite upper layer and brucite nanosheet-like agglomerates covering the surface were formed by ultrasound-assisted method at the concentration of aqueous magnesium solution 0.01 g/ml (c) and 0.007 g/ml (b), whereas at the lower concentration 0.003 g/ml magnesium exhibits complete transformation into brucite (a). The sonochemical treatment of magnesium in ethanol shows no presence of brucite (d, e).

of aqueous magnesium solution 0.01 g/ml (Fig. 2c) and 0.007 g/ml (Fig. 2b), whereas at the lower concentration 0.003 g/ml a complete transformation of magnesium into magnesium hydroxide was observed (Fig. 2a). In the latter case there is a sufficient amount of hydroxyl radicals per magnesium ion to achieve a quick oxidation of magnesium resulting in the indistinct morphology of the obtained magnesium hydroxide structures. In the meantime, a reduced amount of hydroxyl radicals per magnesium ion slows

down the oxidation process and allows the formation of hexagonal platelet-like magnesium hydroxide structures. The sonochemical treatment of magnesium in ethanol shows no presence of magnesium hydroxide (Fig. 2d, e).

The marked diffraction peaks in the XRD pattern of the ultrasonically treated magnesium (Fig. 3) are attributed to magnesium hydroxide of the hexagonal structure with the lattice constants $a = 3.1442$ Å and $c = 4.7770$ Å comparable to the reported data
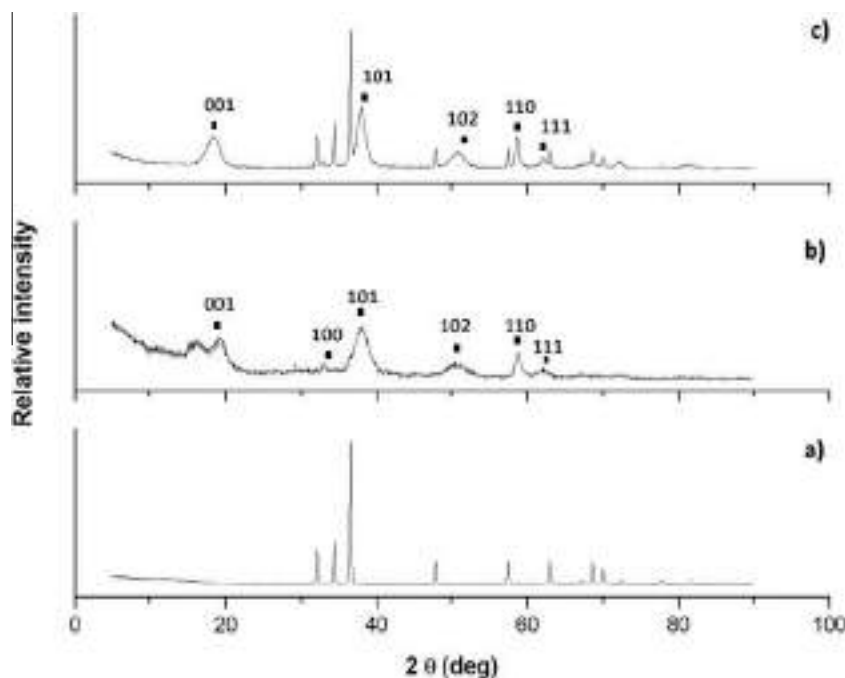
Fig. 3. XRD patterns of the initial magnesium particles (a), the magnesium particles sonochemically treated in water at the concentration 0.003 g/ml (b) and at the concentration 0.01 g/ml (c). The marked diffraction peaks are attributed to the (0 0 1), (1 0 0), (1 0 1), (1 0 2), (1 1 0) and (1 1 1) atomic planes of brucite. The broadening of the peaks indicates reduction of the grain size. The estimated crystallite size is 5.65 nm (0 0 1), 4.05 nm (1 0 1) and 3.14 nm (1 1 0) for the sample with the lower concentration of Mg (b) and 6.42 nm (0 0 1), 4.05 nm (1 0 1) and 4.88 nm (1 1 0) for the sample with the higher concentration of Mg (c).

(JCPDS 44-1482). The definite broadening of the peaks points at a small grain size of magnesium hydroxide. The crystallite size was estimated using the Debye–Scherrer formula [23] and exhibits different values, namely 5.65 nm (0 0 1), 4.05 nm (1 0 1) and 3.14 nm (1 1 0) for the sample with the higher concentration of Mg (0.01 g/ml) and 6.42 nm (0 0 1), 4.05 nm (1 0 1) and 4.88 nm (1 1 0) for the sample with the lower concentration of Mg (0.003 g/ml). This indicates that the particles are thin and plate-shaped, with layers in the (0 0 1) direction. Characteristic peaks for an Mg phase are also detected.

The TEM analysis and the electron diffraction patterns (ED) shown in Fig. 4b confirm a hexagonal lamellar structure, and diffraction peaks of (0 0 2), (1 0 0), (1 0 2) and (1 1 0) can be seen. The magnesium hydroxide structures are in a size range of 70–200 nm and about 20 nm thick, which is larger than the corresponding XRD values. This indicates that lamellar magnesium hydroxide particles are composed of much smaller crystallites. Such structure is synthesized as a result of accelerated mass transport when the sheets break, bend and otherwise distort during the cavitation.

In addition, degradation of magnesium in an aqueous solution and the subsequent formation of hexagonal platelet-like magnesium hydroxide structures were observed in the presence of chlorides (Fig. 5). Ions of chloride which are rapidly absorbed on the magnesium surface facilitate a faster degradation of magnesium compared to the anodic dissolution of magnesium in an aqueous solution without chlorides (Fig. 6) and speed up the transformation of magnesium to brucite.

Hence, the ultrasound-driven synthesis of magnesium hydroxide based on the experimental results can be described using the following three stages: (1) ultrasound-assisted formation of Mg ions and hydroxyl radicals, (2) interfacial reaction between Mg ions and hydroxyl radicals, resulting in the formation of magnesium hydroxide species and (3) growth of magnesium hydroxide structures of platelet-like morphologies.

In the beginning of the ultrasound treatment the surface of the metal starts to degrade and appeared cracks can serve as

nucleation sites for cavitation bubbles [16,17]. Simultaneously, water dissociates into hydrogen cations (H^+) and hydroxyl radicals (OH^-) due to the collapse of the cavitation bubbles [18–22,24,25] (Eq. (1)). With the increase of sonication time the area of the modification increases and the metal grains can be pulled out of the metal matrix [16,17]. A magnesium hydroxide layer is being formed gradually due to the interaction of metal ions and hydroxyl radicals [16,17] (Eq. (2)):

$$H_2O \rightarrow H^+ + OH^- \tag{1}$$

$$Mg^{2+} + 2OH^- \leftrightarrow Mg(OH)_2 \tag{2}$$

The $Mg(OH)_2$ nuclei grow individually forming hexagonal hydroxide platelets and agglomerate. Such behavior can be explained by rapid heating and cooling rates in the interfacial region around the bubbles and change of viscosity of the water phase [16,17]. With the increase of temperature, the viscosity of the water phase decreases leading to the enhanced tendency of the $Mg(OH)_2$ nuclei to collide and to aggregate [16,17]. Thus, the $Mg(OH)_2$ morphologies can be not uniform ranging from nanoparticles to nanosheets [13].

3. Conclusion

We have demonstrated a novel and simple synthetic approach for preparation of $Mg(OH)_2$ structures in water. Ultrasound irradiation constitutes a green and economical procedure for the synthesis of inorganic nanostructures without additional reagents and time consuming chemistry. The formation of magnesium hydroxide is driven by oxidation of the metal caused byproducts of water sonolysis, i.e. free radicals. This process is accompanied by interparticle collisions and surface erosion. In order to explore these effects we varied solvents and concentration of the metal in the solution. Magnesium hydroxide was obtained in deionised water via the ultrasound-assisted method, whereas the results of magnesium modification in ethanol showed no presence of magnesium
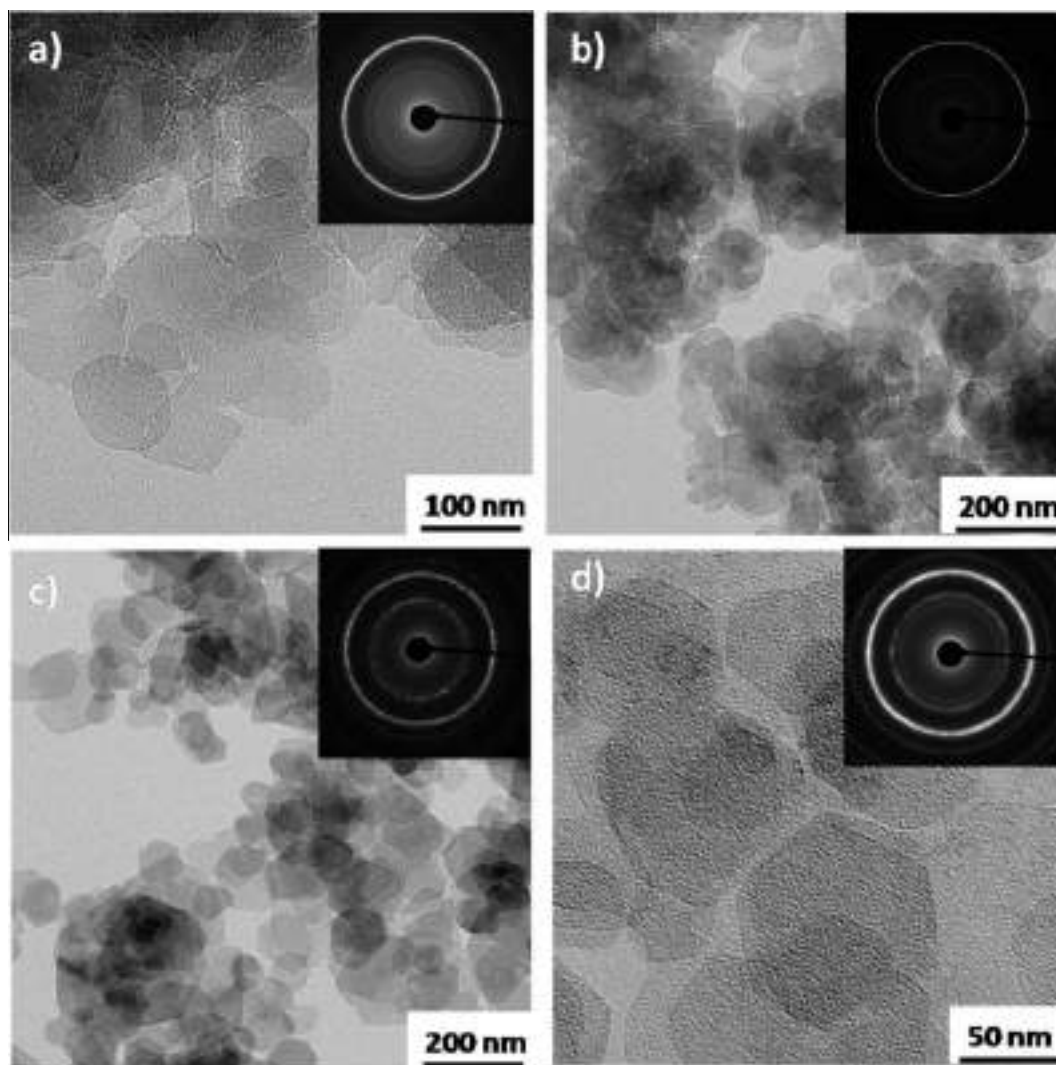
Fig. 4. TEM images of magnesium particles modified by the ultrasound-assisted method at the concentration of aqueous magnesium solution 0.003 g/ml (a), 0.007 g/ml (b), 0.01 g/ml at a lower magnification (c) and a higher magnification (d). The insets show electron diffraction (ED) of the samples. The brucite particles exhibit a hexagonal structure of 100–200 nm size and about 20 nm thickness.
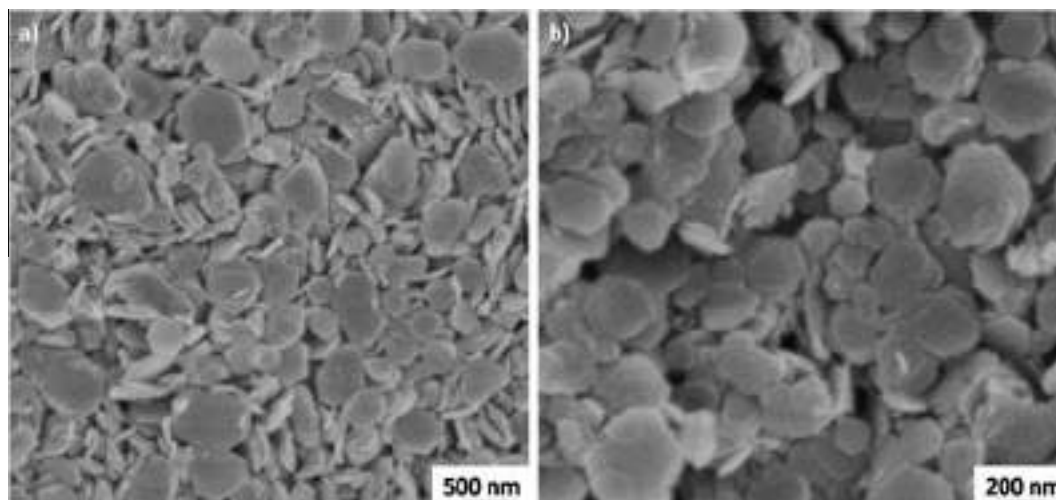

Fig. 5. SEM images of magnesium particles modified by the ultrasound-assisted method at the concentration of aqueous magnesium solution 0.01 g/ml in the presence of Cl$^-$ at a lower magnification (a) and a higher magnification (b).
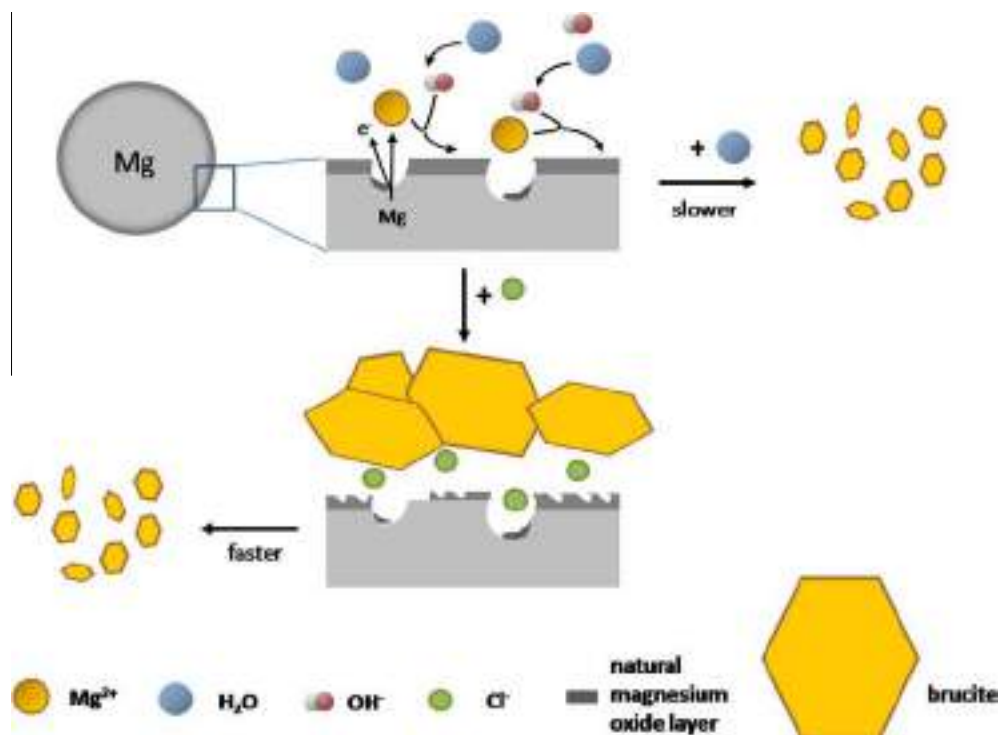
Fig. 6. Schematic presentation of how Cl⁻ can be used to facilitate a faster transformation of Mg to brucite.

hydroxide structures. A total conversion of magnesium into magnesium hydroxide was achieved at lower concentrations of magnesium in the solution. Platelets grew preferentially with an increasing magnesium concentration as well as in the presence of chloride ions.

4. Experimental Section

4.1. Mg(OH)₂ preparation

Magnesium particles (−325 mesh size, 99.8% purity) were supplied by Alfa Aesar and used as received. Magnesium powder was sonicated in Milli-Q water and ethanol at the concentrations 0.003 g/ml, 0.007 g/ml and 0.01 g/ml for 30 min. A UIP1000hd (Hielscher Ultrasonics) operated at 95% intensity and 20 kHz with a maximal output power of 1000 W. An ice bath was used to maintain the temperature of the solution at around 20 °C. After the sonication the samples were centrifuged and then dried.

Chloride salt was added to magnesium powder as we are interested in speeding up the transformation of magnesium to brucite. The sonication procedure was conducted as described above. After the sonication the samples were centrifuged and then dried. To achieve a faster transformation we suggest to use NaCl. Other chloride precursors such as iron chlorides and palladium chloride result in the formation of composites doped with iron oxide nanoparticles or palladium nanoparticles. In the presence of Cl⁻ the further brucite dissolution is possible, however it can be controlled with duration of sonochemical processes and chloride concentration.

4.2. Characterization methods

Scanning electron microscopy (SEM) measurements were conducted with a Gemini Leo 1550 instrument (Zeiss) at an operation voltage of 3 kV. Transmission electron microscopy (TEM) images and electron diffraction (ED) patterns were obtained on a Zeiss EM 912 Omega transmission electron microscope operating at 300 kV. The samples were ultramicrotomed (Leica EM FC6) and placed onto the copper grids coated with a carbon film.

Powder X-ray diffraction (XRD) patterns for phase identification were obtained with a Bruker D8 diffractometer with CuKα radiation (λ = 1.54056 Å). Data were measured over the range of 2θ = 5 to 90°, at steps of 0.05° and 1 s per a step.

References

[1] R.N. Rothon, P.R. Hornsby, Flame retardant effects of magnesium hydroxide, Polym. Degrad. Stab. 54 (1996) 383–385.
[2] A. Durin-France, L. Ferry, J.M. Lopez Cuesta, A. Crespy, Magnesium hydroxide/ zinc borate/talc composition as flame-retardants in EVA copolymer, Polym. Int. 49 (2000) 1101–1105.
[3] J.L. Booster, A.V. Sandwijk, M.A. Reuter, Conversion of magnesium fluoride to magnesium hydroxide, Miner. Eng. 16 (2003) 273–281.
[4] J.C. Kang, S.P. Schwendeman, Comparison of the effects of Mg(OH)₂ and sucrose on the stability of bovine serum albumin encapsulated in injectable poly(D,L-lactide-co-glycolide) implants, Biomaterials 23 (2002) 239–245.
[5] A. Bhargava, J.A. Alarco, I.D.R. Mackinnon, D. Page, A. Ilyushechkin, Synthesis and characterisation of nanoscale magnesium oxide powders and their application in thick films of Bi₂SrCa₂CuO₈, Mater. Lett. 34 (1998) 133–142.
[6] Y. He, J.Y. Wang, H. Deng, Q. Yin, J. Gong, Comparison of different methods to prepare MgO whiskers, Ceram. Int. 34 (2008) 1399–1403.
[7] M. Laska, J. Valtyni, P. Fellner, Influence of pH on the crystal size distribution of Mg(OH)₂ prepared by the hydration of MgO, Cryst. Res. Technol. 28 (1993) 931–936.
[8] Y. Ding, G. Zhang, H. Wu, B. Hai, L. Wang, Y. Qian, Nanoscale magnesium hydroxide and magnesium oxide powders: control over size, shape and structure via hydrothermal synthesis, Chem. Mater. 13 (2001) 435–440.
[9] C. Henrist, J.-P. Mathieu, C. Vogels, A. Rulmont, R. Cloots, Morphological study of magnesium hydroxide nanoparticles precipitated in dilute aqueous solution, J. Cryst. Growth 249 (2003) 321–330.

[10] X. Song, S. Sun, D. Zhang, J. Wang, J. Yu, Synthesis and characterisation of magnesium hydroxide by batch reaction crystallization, Front. Chem. Sci. Eng. 5 (2011) 416–421.

[11] G. Kordas, Sol–gel preparation of MgO fibers, J. Mater. Chem. 10 (2000) 1157–1160.

[12] H. Wu, M. Shao, J. Gu, X. Wei, Microwave-assisted synthesis of fibre-like Mg (OH)$_2$ nanoparticles in aqueous solution at room temperature, Mater. Lett. 58 (2004) 2166–2169.

[13] R. Al-Gaashani, S. Radiman, Y. Al-Douri, N. Tabet, A.R. Daud, Investigation of the optical properties of Mg(OH)$_2$ and MgO nanostructures obtained by microwave-assisted methods, J. Alloys Compd. 521 (2012) 71–76.

[14] K.S. Suslick, G.J. Price, Application of ultrasound to materials chemistry, Annu. Rev. Mater. Sci. 29 (1999) 295–326.

[15] L.H. Thompson, L.K. Doraiswamy, Sonochemistry: science and engineering, Ind. Eng. Chem. Res. 38 (1999) 1215–1249.

[16] D.G. Shchukin, E.V. Skorb, V. Belova, H. Möhwald, Ultrasonic cavitation at solid surfaces, Adv. Mater. 23 (2011) 1922–1934.

[17] D.G. Schukin, H. Möhwald, Sonochemical nanosynthesis at the engineered interface of a cavitation microbubble, Phys. Chem. Chem. Phys. 8 (2006) 3496–3506.

[18] E.V. Skorb, O. Baidukova, A. Goyal, A. Brotchie, D.V. Andreeva, H. Möhwald, Sononanoengineered magnesium–polypyrrole hybrid capsules with synergetic trigger release, J. Mater. Chem. 22 (2012) 13841–13848.

[19] E.V. Skorb, D. Fix, D.G. Shchukin, H. Möhwald, D.V. Sviridov, R. Mousa, N. Wanderka, J. Schäferhaus, N. Pazos-Pérez, A. Fery, D.V. Andreeva, Formation of oxide-stabilized mesoporous metal sponges by ultrasound, Nanoscale 3 (2011) 985–993.

[20] O. Baidukova, H. Möhwald, A.S. Mazheika, D.V. Sviridov, T. Palamarciuc, B. Weber, P.V. Cherepanov, D.V. Andreeva, E.V. Skorb, Sonogenerated metal-hydrogen sponges for reactive hard templating, Chem. Commun. 4 (2015) 7606–7609.

[21] N. Pazos-Pérez, T. Borke, D.V. Andreeva, R.A. Alvarez-Puebla, Silver coated aluminium microrods as highly colloidal stable SERS platforms, Nanoscale 3 (2011) 3265–3268.

[22] N. Pazos-Pérez, J. Schäferhaus, E.V. Skorb, A. Fery, D.V. Andreeva, Ultrasound driven formation of metal-supported nanocatalysts, Micropor. Mesopor. Mater. 154 (2012) 164–169.

[23] J.I. Langford, A.J.C. Wilson, Scherrer after sixty years: a survey and some new results in the determination of crystallite size, J. Appl. Cryst. 11 (1978) 102–113.

[24] K. Makino, M.M. Mossoba, P. Riesz, Chemical effects of ultrasound on aqueous solutions. Formation of hydroxyl radicals and hydrogen atoms, J. Phys. Chem. 87 (1983) 1369–1377.

[25] M. Altmaier, V. Metz, V. Neck, R. Muller, T. Fanghanel, Solid–liquid equilibria of Mg(OH)$_2$(cr) and Mg$_2$(OH)$_3$Cl·4H$_2$O(cr) in the system Mg–Na–H–OH–Cl–H$_2$O at 25°C, Geochim. Cosmochim. Acta 67 (2003) 3595–3601.

Local pH Gradient Initiated by Light on TiO$_2$ for Light-Triggered Modulation of Polyhistidine-Tagged Proteins

Daria V. Andreeva,[c] Inga Melnyk,[b] Olga Baidukova,[a] and Ekaterina V. Skorb*[a]

A new principle of photo-assisted spatial desorption of (poly)-histidine-tagged (His-Tag) proteins on a TiO$_2$ surface is suggested. A semiconductor TiO$_2$ surface is decorated by layer-by-layer (LbL) assembly of a strong polyelectrolyte, namely, polystyrene sulfonate (PSS), and nickel–nitrilotriacetic acid (NTA). The PSS/NTA multilayer architecture provides n-fold ($n \times$ NTA) binding efficiency for more precise protein recognition in comparison to existing molecular His-Tag protein recognition with one- and threefold multiplication (1$\times$NTA, 3$\times$NTA). Spatially resolved desorption of proteins is regulated by non-photodestructive short-term low-intensity light irradiation ($<$ 5 mW cm^{-2}). The local pH shift on irradiated TiO$_2$ selectively affects the pH-sensitive NTA/protein complex, but not the LbL assembly of PSS and NTA, which is stable in a broad pH range.

Immobilised proteins show much promise as the basis for fabrication of different biosensors with electrochemical, optical and capacitive readouts. To integrate the protein recognition elements into lab-on-chip devices one needs to exert remote control over adsorption and desorption of proteins.[1] In particular, the immobilisation of proteins containing short (poly)histidine affinity tags (His-Tags) plays an important role in current research. These proteins are indicators for many disorders, including liver cirrhosis, AIDS and renal disease.[2]

Specific amino acid side chains of the His-Tag sequence have a strong affinity to transition metals, for example, nickel.[3] Moreover, chelation of transition metals by nitrilotriacetic acid (NTA) offers a possibility for reversible binding of biopolymers. Protein adsorption on a surface is reversed by washing with a solution of imidazole, which coordinates to the metal ion and leads to protein release.[4] Methods that do not require extra chemicals, for example, systems that can be regulated with light, are of interest.[5]

Light is an attractive stimulus for such systems because the intensity, duration and localisation of irradiated spots can be easy controlled.[6] The NTA His-Tag can not be manipulated by light, but it is a pH-sensitive complex.[7] Herein, we propose a new method to manipulate the NTA His-Tag through coupling of two stimuli: using light to change pH.

The concept of a new generation of light-responsive molecular actuators is based on in situ conversion of electromagnetic energy to a local pH shift.[8] Thus, highly efficient and versatile dynamic recognition systems for protein detection and manipulation can be constructed by combining light- and pH-sensitive elements in one composite material. For example, UV irradiation of photosensitive TiO$_2$ initiates photochemical reactions on the TiO$_2$ surface with a local pH shift in the irradiated spot that can affect the processes of selective adsorption and desorption of proteins if protein bonding is pH-sensitive. We propose a well-defined layer-by-layer (LbL) nanonetwork in which the pH-sensitive NTA His-Tag complex is assembled with polystyrene sulfonate (PSS), whereby the electrostatic bonding NTA and PSS is not pH sensitive.

Usually, NTA is deposited on a surface by coordination to gold through thiol groups[9] and covalent bonding by silane coupling agents[10] and polymers.[11] We aimed to organise NTA by LbL assembly (Figure 1) to increase the concentration of bonded protein in comparison with silylation.

The multilayered architecture allows significant enhancement of the recognition function of the system. The multilayers are formed by electrostatic interaction of NTA complexes and negatively charged functional groups of PSS. The concentration of NTA in the LbL assemblies is regulated by the concentration of functional groups in PSS and by the number of adsorbed PSS layers and can be varied on demand. Importantly, the PSS/NTA multilayers are stable in a broad pH range, whereas interactions of His-Tag proteins with NTA are sensitive to pH shifts. Due to the special architecture of the LbL assembly, it is possible to combine in one system elements with different sensitivities to pH and thus to construct an effective protein recognition/manipulation system.

The assembly of PSS layers on a TiO$_2$ surface was performed in aqueous solution at a pH below the isoelectric point (IEP) of titanium dioxide (here the IEP was pH 6.6). The [TiOH$_2$] surface below the IEP is positively charged and ensures the interaction with the negatively charged polyelectrolyte PSS. The subsequent NTA His-Tag layers were deposited at pH 7.4 (Figure S1 of the Supporting Information). The mean surface roughness of the multilayers after each deposition step was measured by AFM. The mean surface roughness of the first PSS layer was about 9 ± 2 nm (Figure 2a).

Adsorbed NTA molecules on the substrate lead to a slight increase in the roughness to about 11 ± 2 nm (Figure 2b), which remains the same on subsequent deposition of the protein on the surface (Figure 2c). The presence of each adsorbed layer

[a] O. Baidukova, Dr. E. V. Skorb
   Max Planck Institute of Colloids and Interfaces
   Am Mühlenberg 1, 14424 Potsdam (Germany)
   E-mail: skorb@mpikg.mpg.de

[b] I. Melnyk
   Leibniz Institute of Polymer Research
   Hohestrasse 6, 01069 Dresden (Germany)

[c] Dr. D. V. Andreeva
   Center for Soft and Living Matter, Institute of Basic Science
   Ulsan National Institute of Science and Technology
   44919 Ulsan (Republic of Korea)

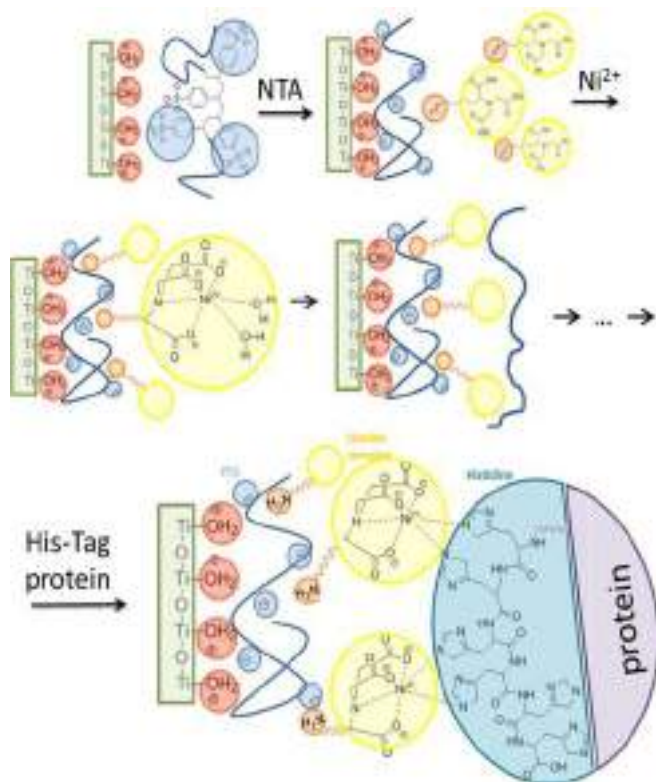   Supporting Information for this article can be found under http://dx.doi.org/10.1002/celc.201600268.

Figure 1. Schematic illustration of LbL assembly of strong polyelectrolyte PSS and pH-responsive Ni^{2+}–NTA His-Tag protein for *n*-fold recognition and manipulation of protein.
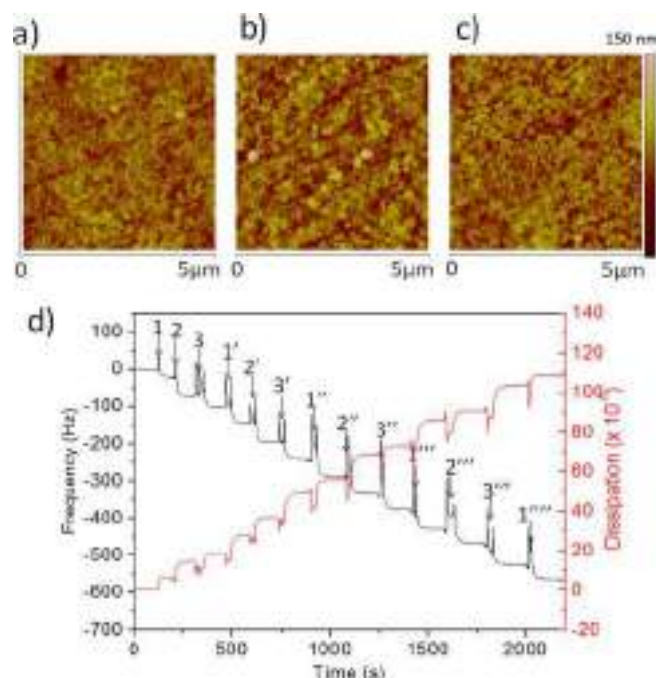

Figure 2. a–c) AFM images of TiO_2 with adsorbed layers of a) PSS, b) NTA and c) His-Tag protein. d) QCM data confirming effective assembly of a multilayered system on titania to give a final $TiO_2/(PSS/NTA/protein)_4/PSS$ structure by adsorption of 1) PSS, 2) NTA and 3) protein.

was also confirmed by contact-angle measurements. TiO_2 is strongly hydrophilic with a contact angle of less than 10°, and adsorption of PSS leads to an increase in the contact angle to 22°. After the deposition of NTA a decrease in contact angle was detected. The contact angle increases again after the protein is adsorbed. These changes confirm multilayer build-up. Multilayer formation on titania-covered quartz crystals was monitored with a quartz-crystal microbalance (QCM; Figure 2 d). The frequency and dissipation curves versus time show pronounced growth of the multilayers.

The key point of this work is the transformation of electromagnetic energy into a pH shift through photocatalytic reactions on TiO_2.[8] Many works have reported the formation of oxygen vacancies by supra-bandgap illumination of TiO_2,[12] which then release free radicals to kill bacteria[13] and decompose organic molecules.[14] In this work, we aimed to find conditions to change pH locally and reversibly and to modulate protein on the surface without its decomposition. Non-destructive low-intensity (<5 mW cm^{-2}) irradiation was used (Figure S2).

We used the scanning ion-selective electrode technique (SIET) for in situ monitoring of proton generation on TiO_2 and regulation of proton migration in the multilayers. SIET allows measurements of the concentration of specific ions[15] (here, H^+ ions) at a nearly constant microdistance (here, 100 μm) over the surface (Figure 3 a).
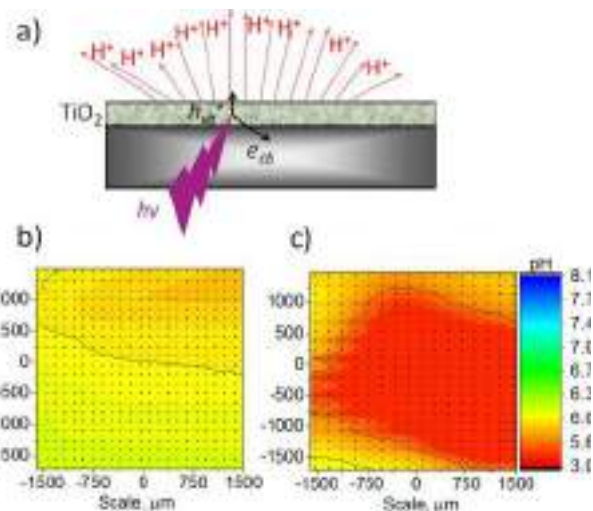
Figure 3. a) The red arrows are schematic 2D *z* vectors of the current density associated with proton formation on the irradiated titania surface. b), c) In situ SIET mapping of the activity of H^+ ions over the TiO_2 film b) before and c) under localised UV irradiation.

In photocatalytic reactions usually H^+ is discussed as a side product. For example, in water oxidation with photoholes, protons are formed on the surface ($H_2O + h^+ \rightarrow \rightarrow H^+ + O_2$) and result in a local pH shift in the irradiated zone. The SIET results prove the development of pH shift in the irradiated zone on the TiO_2 surface. The possible vectors of H^+ release from the irradiated spot, based on SIET *z* scans, are illustrated in Figure 3 a. SIET maps of the TiO_2 surface before and during irradia-

tion are shown in Figure 3b and c, respectively. The pH before irradiation is about 6 all over the titania surface (Figure 3b). After starting the local surface irradiation, the pH decreased significantly above the light spot (Figure 3c). Transition from pH 6.0 to less than pH 4 (acidic) was observed in the irradiated zone (Figure 3c). This result clearly indicates that protons are efficiently generated on the TiO_2 surface during irradiation.

Figure 4 shows how the pH changes with time on TiO_2 with LbL-organised PSS/NTA layers. For this study, the SIET pH microelectrode was located in the centre of irradiated spot and the pH was measured every 0.2 s. Figure 4 shows that when irradiation was switched on the pH immediately decreased to about 3.8. When irradiation was switched off, the pH relaxed back. Cycles of pH decrease during irradiation and increase without irradiation were repeatable.
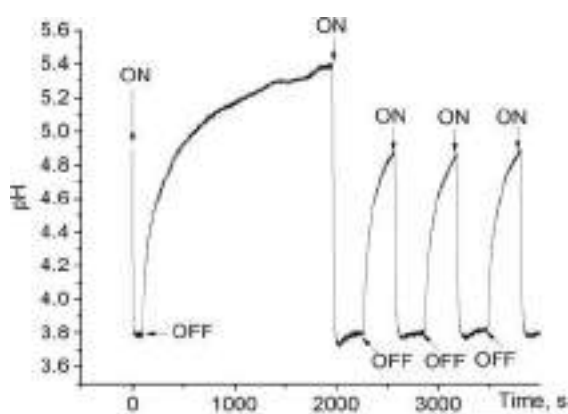
Figure 4. SIET time evolution of the activity of H^+ ions over the TiO_2/PSS/NTA surface in the centre of irradiated spot. ON and OFF indicate switching on and off of irradiation.

Next, we used the light-triggered pH shift in the multilayers for controlling electrostatic NTA–Ni^{2+}/His-Tag interactions (Figure 5). His-Tag bonding is very sensitive to the local environment. A pH value of 4 leads to dissociation of NTA–Ni^{2+}/His-Tag due to protonation of the protein. In the model chip the system modulation is monitored by QCM (Figure 5b,c) and confocal laser fluorescence microscopy (CLFM; Figure 5d,e and Figure S3).

The adsorption of each following layer resulted in a decrease in QCM frequency and thus an increase in the quantity of the adsorbed components (Figure 5b). The mass of three layers was 16 $ng\,cm^{-2}$. Immediately after short-term irradiation (1 s) even on the surface of low-photoactivity titania (photocurrent was about 1.5 $\mu A\,cm^2$), desorption of protein was detected. Protein was released and the mass decreased to 12 $ng\,cm^{-2}$. Adsorption/desorption of protein can be switched on and off several times (Figure 5b,c). CLFM was used to monitor the process of protein adsorption and light-induced protein desorption for the systems TiO_2/PSS/NTA/His-Tag protein (Figure 5d) and TiO_2/(PSS/NTA/His-Tag)$_4$/PSS (Figure 5e). Figure 5d shows that for TiO_2/PSS/NTA/His-Tag, after switching on irradiation, protein is immediately desorbed from the surface. In Figure 5e the surface of TiO_2/(PSS/NTA/His-Tag)$_4$/PSS is shown after irradi-
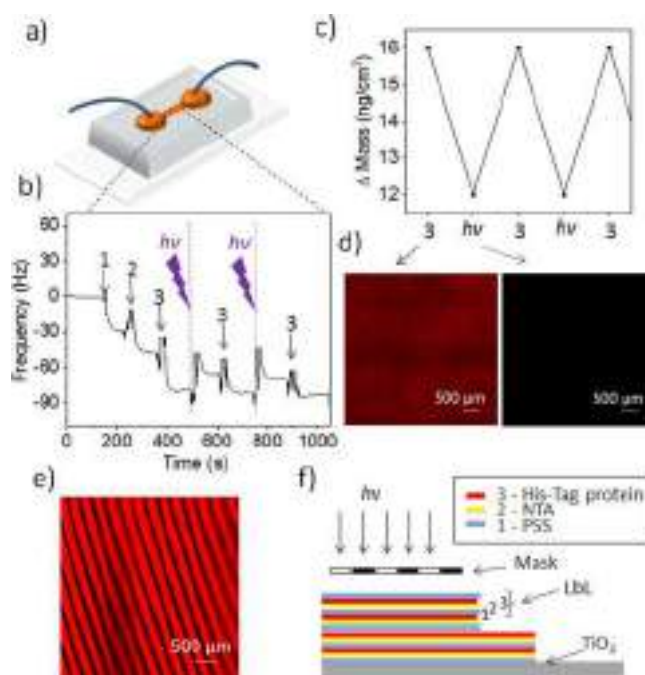
Figure 5. a) Microfluidic chamber for studying light-induced modulation/desorption of His-Tag protein on TiO_2/LbL surface. b) QCM frequency change during the adsorption of 1) PSS, 2) NTA and 3) His-Tag protein; *hv* corresponds to the short period (1 s) of irradiation and results in protein desorption. Cycles of adsorption and light-induced desorption were repeated several times and also presented as mass change (c). d), e) Confocal fluorescence images of LbL-decorated titania surfaces of two architectures: d) TiO_2/PSS/NTA/His-Tag before (left) and after (right) irradiation; e) TiO_2/(PSS/NTA/His-Tag)$_4$/PSS after irradiation through a photomask (f).

ation through a photomask. A schematic of irradiation with a photomask is shown in Figure 5f. After surface irradiation through a photomask, protein was desorbed in irradiated areas and remained on the non-irradiated surface. Careful analysis of the QCM data revealed that 1 s of irradiation releases about 98% of the protein (Figure 5b), and a further 10 s of irradiation is enough to release all protein from the surface, as was confirmed by CLFM. From a comparison of intensity it can be concluded that the multilayered system has a higher concentration of protein in the multilayers and higher relative fluorescence intensity (see also calibration of intensity versus the number of deposited layers in Figure S3). Importantly, the detached protein retained its activity, which was analysed with carbonic anhydrase quantifying esterase activity in the reaction with *p*-nitrophenyl acetate.[16] Short-term irradiation is preferable for fast pH switching and protein detection without denaturation.

In summary, our results prove that His-Tag proteins can be effectively adsorbed in an LbL assembly and released due to a local pH shift on an irradiated TiO_2 surface. Advantages of our strategy compared to existing molecular His-Tag protein recognition and manipulation are clearly evident: 1) The photochemical reaction on a semiconductor layer (here TiO_2) leads to conversion of the energy of electromagnetic irradiation to a local pH shift allowing manipulation of a dynamic pH-sensitive protein-recognition element. 2) The LbL assembly serves

as a well-defined nanonetwork for control over spatial distribution, thickness, concentration and orientation of recognition molecules. Due to electrostatic interactions in LbL assemblies, immobilisation of highly sensitive biomolecules can occur without inhibiting their activity. Furthermore, long-term mechanical and chemical stability of the recognition system can be achieved. 3) The mono-NTA (1×NTA) surface is the traditional approach for capturing His-Tag proteins but it only achieves weak binding and low selectivity of recognition elements,[15] whereas the LbL approach leads to improved binding stability and increased binding selectivity towards proteins and provides *n*-fold multiplication of recognition (*n*×NTA) elements for highly precise recognition. Various photocatalytic studies claim reactions with H$^+$ or OH$^-$ but, surprisingly, we are the first to experimentally confirm that the local pH can deviate by several pH units from the average pH when TiO$_2$ is exposed to light. Notwithstanding the existing literature on ways to desorb proteins from surfaces, our light-controllable protein desorption can find its place among existing methods. Our method is easy to control by means of the intensity, duration and localisation of irradiation. No other chemicals are needed. We maintain that light control over local pH is a promising strategy to manipulate pH-responsive polymer systems, not only for biosensing, but also for biomedical and other applications.

Experimental Section

Materials

Polystyrene sulfonate sodium salt (PSS, $M_w = 70\,000$), (3-glycidyloxy-propyl)trimethoxysilane, 4-(2-hydroxyethyl)-1-piperazineethanesulfonic acid and nickel(II) sulfate hexahydrate were purchased from Aldrich (Germany) and were used without further purification. Aminocaproic nitrilotriacetic acid (NTA, Santa Cruz Biotechnologie) was used as received. His-Tag-terminated protein (A2M recombinant human protein His-Tag from Life Technologies) was labelled by 6X His tag antibody (FITC), IgG, Rabbit, Polyclonal von GeneTex Inc. Sodium chloride (purity grade: $\geq 99.5\%$) was obtained from Fluka and used for preparation of polyelectrolyte dipping solutions. Recombinant human carbonic anhydrase III (Creative BioMart recombinant proteins, Hölzel Diagnostika Handels GmbH), muscle-specific, His-Tag, was used in experiments to detect the protein activity after desorption in a reaction with *p*-nitrophenyl acetate (Sigma-Aldrich).[16] Microscopy glass slides were used as substrates. Commercial TiO$_2$ nanoparticle powder (average particle size 20 nm) was used as received. Hepes-buffered saline (HBS) was 10 mм 4-(2-hydroxyethyl)-1-piperazineethanesulfonic acid and 150 mм NaCl in water adjusted to pH 7.4 with NaOH. 50 mм NTA, 40 mм Ni^{II} and His-Tag protein solutions were based on HBS. A dip-coating solution of TiO$_2$ was prepared by dispersion of particles in water with ultrasound for 2 min and adjusted to pH 3.

Layer-by-Layer Formation: Deposition of the First Layer

PSS was electrostatically bound to the TiO$_2$ surface. A 2 g L^{-1} PSS dipping solution was made from 50 mм NaCl in Millipore water and was adjusted to the desired pH 3 by addition of 1 м HCl. The substrates were dipped into the solution for 15 min. After the ad-

sorption step the glass slide was rinsed three times with Millipore water adjusted to pH 3.

NTA Immobilisation and Chelate-Complex Activation

The PSS-covered surface of TiO$_2$ was subsequently was modified with NTA solution in Millipore water for 1 h, followed by washing steps with HBS and water. The chelate complex was activated by addition of 40 mм NiSO$_4$ aqueous solution for 15 min and rinsing with buffer solution several times.

Histidine Adsorption

Protein (0.05 mg mL^{-1}) was immobilised on the surface by a dip-coating technique. After an adsorption time of 3 h the sample was washed in HBS three times for 5 min and dried in an argon stream. To determine binding in the absence of Ni complex, 5 mм EDTA was added to the protein solution.

SIET for Detection of Proton Photogeneration on the Surface

SIET was applied for mapping the activity of H$^+$ ions on the surface in aqueous solution under local UV irradiation. Micropotentiometric SIET allows measurements of the concentration of specific ions (here, H$^+$ ions) at a quasiconstant microdistance over an electrode surface in solution. A potentiometric cell consists of a reference electrode and an ion-selective microelectrode. The pH microelectrode was calibrated before and after each experiment by using a set of commercial buffers. The linear range of the response was 3–9; the Nernstian slope was 58 ± 2 mV dec^{-1}. Local illumination of the surface was performed by using a setup equipped with a UV LED (365 nm) supplied by a current stabiliser and a UV light-beam-focusing system involving several quartz lenses. The local activity of H$^+$ was mapped sequentially 100 μm above the surface. Map, line, and point measurements were performed similarly, and the sampling rules at each point were 0.5 s of waiting followed by 0.2 s of acquisition. The equipment used was manufactured by Applicable Electronics Inc. (USA). The pH microprobes were made in the laboratory and consisted of silanised borosilicate glass capillaries thinned to 2 μm. The tip was filled with a 30 μm column of hydrogen ionophore II cocktail A (Fluka, Ref. 95297) and the internal solution was 0.1 м KCl + 0.01 м KH$_2$PO$_4$. An Ag|AgCl wire inside the micropipette served as internal reference and a homemade silver/silver chloride electrode in 0.05 м NaCl worked as external reference. The pH microelectrode was mounted in a pre-amplifier (input resistance $> 10^{15}$ Ω), which was placed in the 3D positioning system also used for SIET. An IPA2 amplifier (input resistance $> 10^{12}$ Ω) was controlled by the ASET program to measure and record the data.

Infrared Reflection Absorption Spectroscopy (IRRAS)

IRRAS was used to monitor LbL assembly. Spectra were acquired with an IFS 66 IR spectrometer from Bruker (Ettlingen, Germany). The IR beam is directed through the external port of the spectrometer and is subsequently reflected by three mirrors in a rigid mount before being focused on the sample surface. A KRS-5 wire-grid polariser is placed in the optical path directly before the beam hits the sample surface. The reflected light is collected at the same angle as the angle of incidence. The light then follows an equivalent mirror path and is directed onto a narrow band mercury cad-

QCM with Dissipation Monitoring

QCM measurements were performed with a Q-sense E4 instrument by using an open module (Q-sense QOM 401) and a quartz crystal sensor with an electrode covered with 120 nm of titanium (QSX 310, AT cut, 5 MHz) and a negatively charged native surface TiO$_2$ layer. For the measurements a sensor was placed in a sensor chamber and 1 mM NaCl buffer was added until a stable frequency baseline was reached. Next, a positively charged polyelectrolyte solution was pipetted onto the sensor surface and the resonant frequency and dissipation were measured. When the frequency line stabilised, the polyelectrolyte solution was removed, the sensor surface was washed with 1 mM NaCl, and a reverse-charged polyelectrolyte solution was introduced. A decrease in the frequency of the crystal indicates mass accumulation due to polyelectrolyte deposition on the surface. Dissipation or energy loss is a measure of the viscoelasticity of the molecular layer on the sensor surface. The changes in mass for rigid films were calculated by using the Sauerbrey equation.[17] If the change in dissipation exceeds the critical value of 2×10^{-6}, the Sauerbrey equation must be extended to incorporate the elasticity of the deposit. Thus, soft films can be analysed by applying the Voigt model in the software QTools.[18]

Confocal Laser Scanning Microscopy

Reversible desorption of His-tagged proteins was detected with a Leica TCS SP8 confocal laser scanning microscope.

Acknowledgements

[1] G. B. Sigal, C. Bamdad, A. Barberis, J. Strominger, G. M. Whitesides, *Anal. Chem.* **1996**, *68*, 490 – 497.

[2] H. Zhu, M. Bilgin, R. Bangham, D. Hall, A. Casamayor, P. Bertone, N. Lan, R. Jansen, S. Bidlingmaier, T. Houfek, T. Mitchell, P. Miller, R. A. Dean, M. Gerstein, M. Snyder, *Science* **2001**, *293*, 2101 – 2105.

[3] E. L. Schmid, T. A. Keller, Z. Dienes, H. Vogel, *Anal. Chem.* **1997**, *69*, 1979 – 1985.

[4] Y.-C. C. Liu, N. Rieben, L. Iversen, B. S. Sorensen, J. Park, J. Nygard, K. L. Martinez, *Nanotechnology* **2010**, *21*, 245105 – 07.

[5] F. D. Jochum, P. Theato, *Chem. Soc. Rev.* **2013**, *42*, 7468 – 7483.

[6] a) E. V. Skorb, D. V. Andreeva, *Adv. Funct. Mater.* **2013**, *23*, 4483 – 4506; b) T. A. Kolesnikova, D. Kohler, A. G. Skirtach, H. Möhwald, *ACS Nano* **2012**, *6*, 9585 – 9595; c) J. J. Giner-Casares, M. Henriksen-Lacey, I. Garc, L. M. Liz-Marz, *Angew. Chem. Int. Ed.* **2016**, *55*, 974 – 978.

[7] S. Sannino, T. Anelli, M. Cortini, C. Masui, M. Degano, R. Fagioli, K. Inaba, R. Sitia, *J. Cell Sci.* **2014**, *127*, 4260 – 4269.

[8] S. A. Ulasevich, G. Brezesinski, H. Möhwald, P. Fratzl, F. H. Schacher, S. K. Poznyak, D. V. Andreeva, E. V. Skorb, *Angew. Chem. Int. Ed.* **2016**, DOI: 10.1002/anie.201604359.

[9] J. C. Love, L. A. Estroff, J. K. Kriebel, R. G. Nuzzo, G. M. Whitesides, *Chem. Rev.* **2005**, *105*, 1103 – 1169.

[10] J. Zhao, M. Milanova, M. M. C. G. Warmoeskerken, V. Dutschk, *Col. Surf. Physicochem. Engineer. Aspects.* **2012**, *413*, 273 – 279.

[11] J. E. Gautrot, W. T. S. Huck, M. Welch, M. Ramstedt, *ACS Appl. Mater. Interfaces* **2010**, *2*, 193 – 202.

[12] L. A. Miccio, M. Setvin, M. Muller, M. Abadía, I. Piquero, J. Lobo-Checa, F. Schiller, C. Rogero, M. Schmid, M. Sanchez-Portal, U. Diebold, J. E. Ortega, *Nano Lett.* **2016**, *16*, 2017 – 2022.

[13] E. V. Skorb, L. I. Antonouskaya, N. A. Belyasova, D. G. Shchukin, H. Möhwald, D. V. Sviridov, *Appl. Catal. B* **2008**, *84*, 94 – 99.

[14] E. V. Skorb, E. A. Ustinovich, A. I. Kulak, D. V. Sviridov, *J. Photochem. Photobiol. A* **2008**, *193*, 97 – 102.

[15] D. Fix, E. V. Skorb, D. G. Shchukin, H. Möhwald, *Meas. Sci. Technol.* **2011**, *22*, 075704 – 075710.

[16] J. A. Verpoorte, S. Menta, J. T. Edsall, *J. Biol. Chem.* **1967**, *242*, 4221 – 4229.

[17] G. Sauerbrey, *Z. Angew. Phys.* **1959**, *155*, 206 – 222.

[18] B. D. Vogt, E. K. Lin, W.-L. Wu, C. C. White, *J. Phys. Chem. B* **2004**, *108*, 12685 – 12690.

Highly Efficient Photodegradation of Organic Pollutants Assisted by Sonoluminescence

Anna V. Volkova[1], Silke Nemeth[2], Ekaterina V. Skorb[3] and Daria V. Andreeva*[2]

[1]Institute of Chemistry, St. Petersburg State University, St. Petersburg, Russia
[2]Physical Chemistry II, Bayreuth University, Bayreuth, Germany
[3]Max Planck Institute of Colloids and Interfaces, Potsdam, Germany

ABSTRACT

The mechanism of the photodegradation of azo dyes via ultrasonication is studied using a combination of the high-performance liquid chromatography and UV–vis spectroscopy with detailed analysis of the kinetics. Based on the kinetics studies of the sonodegradation, it was proposed that the degradation of azo dyes was a multistage process that involved: (1) the direct attack of azo bonds and phenyl rings of dyes by the sonochemically formed reactive oxygen species; (2) the activation of semiconductor particles by the light emitted during cavitation and the triggering of the photocatalytic pathways of dye degradation and (3) increase of the adsorption capacity of the semiconductor particles due to the sonomechanically induced interparticle collisions. The detailed kinetics study can help in following an effective process up-scaling. It was demonstrated that extremely short pulses of light flashes in a cavitated mixture activated the surface of photocatalysts and significantly enhanced dye degradation processes.

INTRODUCTION

Photocatalytic cleaning of wastewater is one of the environmental sanitation technologies that is very important for many aspects of daily life (1). The polluted water can contain nonbiodegradable and toxic compounds (2). Azo dyes from the textile industry are the examples of such dangerous waste (3). Since the production of the azo dyes is very cheap, this class of pollutants poses a challenge for decontamination and recovery of environment (4).

Use of ultrasound for the photocatalytic dye degradation of organic pollutants provides novel technological solutions for wastewater treatment (5–13). Installation of ultrasonic devices in pipes, pumps and tubes of water supply systems can ensure effective water sanitation in places that are not accessible for the state-of-the-art UV technology. Several works proposed use of ultrasound for the photocatalytic degradation of some organic pollutants. The studies focused on the use of ultrasound as an addition to the UV-lamp-assisted heterogeneous degradation in the presence of photocatalytic nanoparticles (5,6,12,13) and as a source of free radicals and reactive oxygen species (ROS) in the homogeneous process of the dye degradation, including the Fenton reactions (7,10). The ultrasound-assisted degradation of chlorinated hydrocarbons (8,9), phenols (9,10), drugs (11,12) and dyes (5,13) was investigated. In our work, we go beyond state-of-art in detailed analysis of processes kinetics which can result in following easy of the processes up-scaling. A complex sequence of reactions involving oxidation and reduction pathways is not fully understood, our studies suggest principal steps which are involved.

The attack of the organic molecules by the hydroxyl radicals (OH$^\bullet$) formed in a sonicated mixture causes the sonolytic degradation of organic compounds. It is shown that phenols and the pollutants containing phenyl rings are very sensitive to the ultrasound treatment. Ashokkumar *et al.* (11) revealed that the sonolytic degradation of martius yellow proceeds due to hydroxylation of aryl rings of the dye.

If the active species attack both benzene and/or naphthalene rings and azo group –N=N–, very stable dye molecules can be degraded. It was reported (14,15) that OH$^\bullet$ first attacks the azo groups of the dye molecules since the absorption energy values of the $\pi \rightarrow \pi*$ transitions in the benzene rings are much higher than those of the $n \rightarrow \pi*$ transitions in the azo groups. The decoloration of azo dye solutions due to the destruction of the long conjugated system in the dye molecules occurs very fast. However, the complete mineralization of aromatic compounds, including the intermediate products of dye decomposition is still a challenge. Here, we propose that use of ultrasound can significantly enhance the dye degradation process due to simultaneous triggering of different mechanisms of production of the active species.

Here, we report on the ultrasound-assisted decomposition of azo dyes by ROS and by activation of the surface of photocatalysts by sonoluminescence (SL). The light emission produced in the cavitated liquid is essential for the activation of the photoreaction on the surface of semiconductor particles. We propose that the SL can be a beneficial alternative to the existing UV-light-assisted methods.

Sonoluminescence is the light emission produced in a cavitated liquid using high intensity ultrasound, a spark discharge, a laser pulse, etc. (16). According to the works of Gaitan *et al.* (17), Moss *et al.* (18), Barber and Putterman (19), Hiller *et al.* (20) and Suslick *et al.* (21) published in the early nineties via cavitation acoustic energy can be converted to optical energy. It was demonstrated that the cavitation bubbles can emit a pulsed flash of light (with a broad spectral range in the visible–UV region) with the pulse widths that is <50 ps (20). The radius of

the single bubbles can grow up to 50 μm (19) and the temperature of its interior is in the range of ~10^4 K (22).

In particular applications, namely, sonochemical synthesis (23), surface nanostructuring (24–26), sonocatalysis (27), etc. sonochemistry does not operate with the single bubbles, but with the clouds of cavitating bubbles that interact with a matter. The light emitted from the clouds of bubbles is known as multibubble sonoluminescence (MBSL) (28). The effective emission temperature from the bubbles in water was measured in the range 2000–4000 K (29). The temperature inside the cavitation bubbles, the intensity and the spectrum of SL depends on solvent nature, solvent temperature and the presence of additives (incl. gases and ions) (30). A number of the publications from Suslick *et al.* (29) showed that the emission temperature within the imploding cavitation bubbles depends on both the polytropic ratio and the thermal conductivity of the bubble content. In particular, Suslick *et al.* (29) postulated that the temperature of MBSL decreases as the vapor pressure increases. The presence of the rare gases (argon, xenon) in the cavitated liquid can brighten SL.

The mechanism of the light emission in cavitated liquids is still discussed a lot. The thermal and electrical approaches are two major theories that are currently used for the explanation of SL. According to the electrical theory (Margulis *et al.* (31–33)) an electrical microdischarge can be expected in the large deformed gas-filled bubbles (such bubbles were experimentally observed). The bubble fragmentation process can be responsible for the light emission. The thermal theory of SL proposes that the high temperatures can be reached upon the cavitation collapse (34–36). Up to now, the thermal theory is verified by a number of experiments and can explain the effect of the dissolved gases and the nature of the solvents on the intensity and the spectrum of SL as well as SL in nonpolar liquids.

MBSL is followed by photons emissions and chemisonoluminescence of the OH radicals formed inside the bubbles (36,37). The radicals and the excited molecules, including the ROS are formed from solvents and additives upon the bubble collapse. Thus, in a cavitated solution several mechanisms of the dye degradation might occur: (1) the direct attack of azo dyes by the ROS generated upon the bubble collapse (homogeneous process); and (2) the SL-assisted degradation of dyes by the activation of the photoreactions on the surface of the semiconductor particles (heterogeneous process).

Here, we used titanium dioxide (TiO$_2$) particles as a photocatalyst and Direct Blue 71 (DB71) (38,39) as a substrate. The aqueous suspensions of DB71 and TiO$_2$ were sonicated at a frequency of 20 kHz and intensity of 140 W cm^{-2}. As a reference, we used silicon dioxide particles. We focused on the investigation of the kinetics of the SL-assisted degradation of DB71 at different conditions. Based on these data, we propose the mechanism of degradation of azo dyes and reveal the role of the SL in the degradation process.

MATERIALS AND METHODS

Materials. Direct Blue (DB71; C$_{40}$H$_{28}$N$_7$NaO$_{13}$S$_4$, M$_W$ = 965.94) was purchased from Aldrich (dye content 50%). DB71 is an azo dye in which the chromophore part of the molecular structure contains azo bonds and shows a strong absorbance in the visible region, while the absorbance peaks of the benzene and naphthalene rings appear in the UV region. The absorbance peaks in UV region (210 and 290 nm) and at 584 nm are, respectively, attributed to these aromatic rings and azo linkage (38,39).

Titanium (IV) butoxide (tetrabutyl titanate (Ti(OBu)$_4$) was purchased from Aldrich (reagent grade 97%), isopropyl alcohol (C$_3$H$_7$OH), acetic acid (CH$_3$COOH) and sodium chloride (NaCl) obtained from Vekton as analytical grade reagents were used for the synthesis of titanium dioxide. Hydrochloric acid (1 M HCl) and sodium hydroxide (NaOH), used to adjust the pH of solutions, were purchased from Aldrich. Ultrapure water, used to prepare the solutions, was purified by a Milli-Q water system (Millipore).

Silicon dioxide (SiO$_2$) particles (0.304 μm) were purchased from Particles GmbH and used as received.

Synthesis of TiO$_2$ particles. 12 g CH$_3$COOH was dissolved in 50 g C$_3$H$_7$OH, and then 20 g Ti(OBu)$_4$ was added with stirring. This mixture was slowly dripped into the 100 mL Milli-Q water with vigorous stirring at room temperature. The prepared dense suspension was stirred for 30 min. Then, 200 mL 1 M NaCl solution was added to the suspension for better precipitation. The precipitate was filtered, washed for several times with ultrapure water, cleaned by electrodialysis and dried at 373 K and, finally, calcinated at 773 K. Size, morphology and structure of the synthesized particles were characterized by transmission (TEM, Zeiss EM922 Omega, EFTEM operating at 200 kV), scanning (SEM, LEO 1530 FE-SEM, Zeiss) electron microscopy, dynamic light scattering (DLS, Zetasizer Nano ZS, Malvern Instruments) and powder X-ray diffractions.

Electrokinetic experiment. Electrophoretic mobility (U_{eph}) values were measured using a Zetasizer Nano ZS analyzer (Malvern Instruments) according to the M3-PALS technology in a universal capillary U-shaped cell (DTS 1060) thermostated at 293 K. Zeta-potential values of titanium dioxide particles were calculated through the Smoluchowski equation using experimental values of electrophoretic mobility in pH range 3–9.5 and at dye concentration 5 × 10^{-5} M. The pH values were adjusted by adding dilute HCl and NaOH to dye solution.

Catalytic experiment. 50 mL of DB71 solution (2.5 × 10^{-5}– 1 × 10^{-4} M) pure and containing various amounts of catalyst TiO$_2$ (0.2– 1.0 g L^{-1}) at pH 6.2 and pH 3.5 (adjusted by adding dilute HCl solution) was sonicated for 60 min with an ultrasound (US) tip (VIP1000hd; Hielscher Ultrasonics GmbH, Germany) operated at 20 kHz with a maximum output power of 1000 W ultrasonic horn BS2d22 (head area of 3.8 cm^2) and equipped with a booster B2-1.8. The maximum intensity was calculated to be 140 W cm^{-2} at a mechanical amplitude of 106 μm. pH values were controlled by pH-meter (SB70P Benchtop). The reaction temperature was kept 20°C using a homemade reaction cell.

TiO$_2$ powder was directly added to DB71 solution (the reaction mixture was continuously sonicated from the initial time of mixing) or TiO$_2$ powder was pretreated before use. TiO$_2$ powder was dispersed in 25 mL MilliQ-water or HCl solution with pH 3.5 for 10 min using US. After the pretreatment, TiO$_2$ suspensions were mixed with 25 mL of the concentrated DB71 solution and stirred. Then, the sonication was applied and the start of US treatment was taken as "zero time" for the reaction. The absorbance at "zero time" was used for the calculation of absorption values of dye molecules on TiO$_2$ surface.

The reference adsorption experiments were carried out using the stirring as a pretreatment procedure at pH = 3.5 for the 5 × 10^{-5} M DB71 solutions at different catalyst concentration. The procedure was similar to US pretreatment. After adding the catalyst suspension to the dye solution the prepared mixture was stirred in the dark for 10 min with a magnetic stirrer at 293 K to reach the adsorption–desorption equilibrium of DB71 molecules on the titania surface.

The photolytic and photocatalytic experiments were carried out using 450 W UV lamp, equipped with a 420 nm cutoff filter (λ = 380 nm). For these experiments, 10 mL of 10^{-4} M DB71 solution at pH 3.5 was taken. For photocatalytic experiment, pretreatment procedure for 10 min via stirring and TiO$_2$ concentration 1.0 g L^{-1} were used.

During the process of dye degradation under US and UV treatment, 1 mL of DB71 solution was collected. Then, these samples were centrifuged for 2–4 min to separate the suspended catalyst particles from aqueous solution. The absorbance of the dye solution samples was measured using an Agilent 8453 UV/VIS spectrophotometer with ultrapure water in the reference beam in the cuvettes with gap width 1 mm.

Absorbance measurements were carried out between 300 and 700 nm. The maximum absorbance value was determined at 584 nm. To determine dye concentration during degradation process the calibration curve was plotted. The change of the absorbance was in direct proportion to the concentration of dye solution at λ_{max} = 584 nm and therefore the ratio of current absorbance (A) to initial absorbance (A_0) were used instead of the ratio of concentrations for the characterizing of the degradation process.

Analysis of degradation products. The degradation products were analyzed by reversed-phase high-performance liquid chromatography (RP-HPLC) with fluorometric detection and high-performance liquid chromatography coupled to mass spectrometry (HPLC-MS).

The liquid chromatograph LC-20 Prominence with fluorometric detector RF-20A («Shimadzu», Japan) was used for RP-HPLC analysis. The excitation and emission wavelengths were 270 and 310 nm, correspondingly. The stationary phase was Supelco Discovery C18 column (250 mm × 4.6 mm, 5 μm), the mobile phase was water–methanol mixture (eluent A—50% MeOH + 0.1% CH₃COOH, eluent B—50% H₂O + 0.1% CH₃COOH). The flow rate was 0.5 mL min⁻¹ and the injection volume was 20 μL. The phenol, hydroquinone, resorcin, pyrocatechol, 1-naphthol and 2-naphthol were used as standards for possible products.

The HPLC-MS analysis was performed using ultra-high-resolution QTOF mass spectrometer «MaXis» (Bruker Daltonik GmbH, Germany). The scanned mass range was m/z 50–1500 and the capillary voltage was set at 4.5 kV. The column used was Zorbax SB-C18 (150 mm × 2.1 mm, diameter of sorbent particles 3.5 μm). The mobile phase was acetonitrile–water mixture (A + B, where A—H₂O + 0.1% HCOOH, B—CH₃CN + 0.1% HCOOH). We used gradient elution regime: starting condition 10% CH₃CN, after 20 min 80% CH₃CN. The injection volume was 10 μL. The spectra were recorded in positive ionization mode (negative ion mode did not show any acceptable results). These analyses were performed at the Center for chemical analysis and materials research of the St. Petersburg State University.

RESULTS AND DISCUSSION

Dye degradation in the cavitated mixture proceeds due to the multistage redox reactions in:

1 The homogeneous process—the active species produced by cavitation directly attack the dye molecules in bulk solution; and
2 The heterogeneous process—SL triggers the photocatalytic reactions on the semiconductor surface and, then, the photocatalytically formed active species attack the dye molecules.

Direct degradation of DB71 via ultrasonication (homogeneous process)

Sonolysis of aerated water due to the collapse of cavitation bubbles leads to the formation of the ROS (superoxide, hydrogen peroxide, hydroxyl radicals) (40). Some of these water cleavage reactions are listed in the Eqs. (1)–(4).

$$H_2O +))) \rightarrow H^. + HO^. \qquad (1)$$

$$HO^. + HO^. \rightarrow H_2O_2 \qquad (2)$$

$$H^. + O_2 \rightarrow HOO^. \qquad (3)$$

$$HOO^. + HOO^. \rightarrow H_2O_2 + O_2 \qquad (4)$$
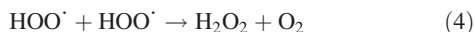
The sonolytically formed ROS directly trigger the degradation of the organic pollutants, according to the Eq. (5) (homogeneous process):

$$Dye + ROS(OH\cdot) \rightarrow oxidation\ of\ dye \qquad (5)$$

However, as seen in the kinetic curves (Fig. 1A, curve 1) DB71 is relatively stable to ultrasound treatment in the aqueous solution at neutral pH. We detected the negligible (<5% in range of experimental error) degradation of DB71 for 60 min of the irradiation of the aqueous dye solution. The slow degradation of DB71 at neutral pH in the absence of the catalyst shows that

active species cannot effectively attack the azo bonds of DB71 in bulk media.

Degradation in the presence of photocatalyst (heterogeneous process)

The heterogeneous process of the ultrasound-assisted degradation of dye provides a small enhancement of the efficiency of degradation (Fig. 1B, curve 1). The presence of TiO₂ increases the degradation of DB71 up to 10% at neutral pH.

The light activation of the photocatalyst's surface stimulates the photochemical reactions. The electron promotion from the valence band to the conduction band of TiO₂ leads to the formation of the electron–hole pairs (Eq. (6)).

$$TiO_2 + h\nu \rightarrow TiO_2(e_{CB}^- + h_{VB}^+) \qquad (6)$$
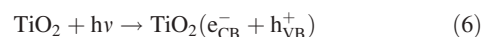
These electrons and holes can directly attack the dye molecules, causing their degradation (Eqs. (7)–(8)):

$$Dye + h_{VB}^+ \rightarrow oxidation\ of\ the\ dye \qquad (7)$$
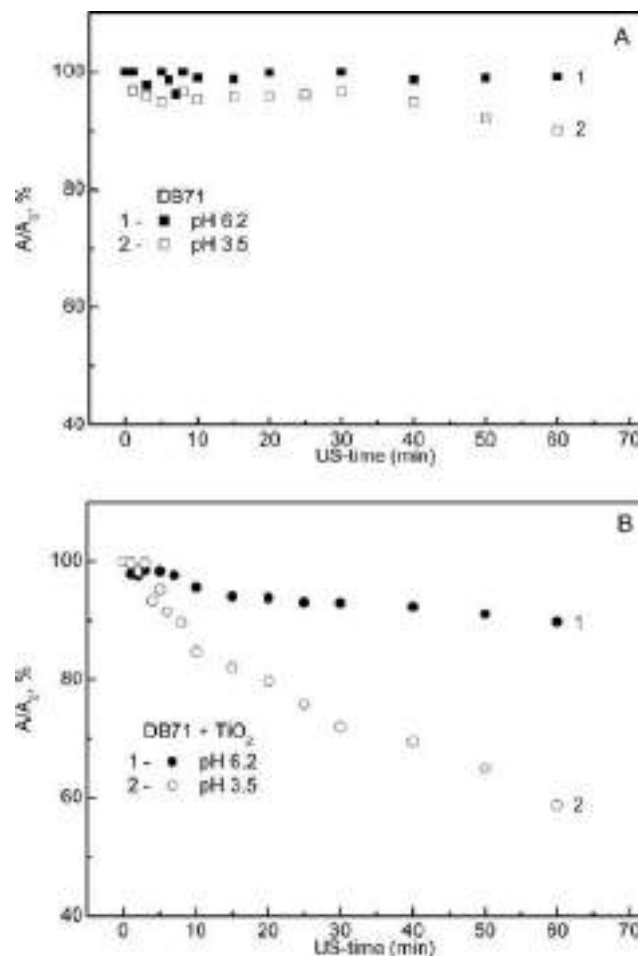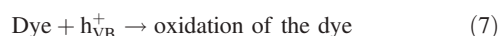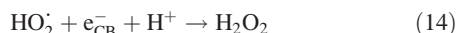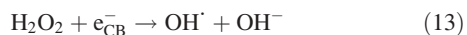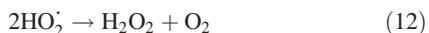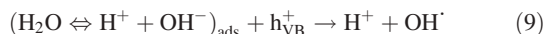

Figure 1. Degradation of DB71 in the absence (A) and in the presence (B) of catalyst ([DB71] = 5 × 10⁻⁵ M, [TiO₂] = 0.2 g L⁻¹) at pH 6.2 (curve 1) and 3.5 (curve 2).

$$\text{Dye} + e_{CB}^- \rightarrow \text{reduction of the dye} \tag{8}$$
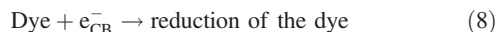
Then, the electrons and holes trigger generation of ROS on the semiconductor surface (Eqs. (9)–(14)).

$$(H_2O \Leftrightarrow H^+ + OH^-)_{ads} + h_{VB}^+ \rightarrow H^+ + OH^{\cdot} \tag{9}$$

$$O_{2(ads)} + e_{CB}^- \rightarrow O_2^{\cdot -} \tag{10}$$

$$O_2^{\cdot -} + H^+ \rightarrow HO_2^{\cdot} \tag{11}$$

$$2HO_2^{\cdot} \rightarrow H_2O_2 + O_2 \tag{12}$$

$$H_2O_2 + e_{CB}^- \rightarrow OH^{\cdot} + OH^- \tag{13}$$

$$HO_2^{\cdot} + e_{CB}^- + H^+ \rightarrow H_2O_2 \tag{14}$$

In addition, the presence of the photocatalytic particles in the reaction mixture might stimulate heterogeneous nucleation and collapse of cavitation bubbles and, thus, enhance the efficiency of the dye degradation. However, the addition of the photocatalytically inactive SiO_2 to the reaction mixture did not affect the dye degradation process.

Thus, the dye degradation in the heterogeneous process proceeds due to two mechanisms (1) SL-assisted activation of the catalyst surface; and (2) direct attack of dye molecules by the ultrasonically formed active species.

Optimization of the reaction conditions

Effect of pH. The kinetic curves 2 in Fig. 1A,B demonstrate that the efficiency of dye degradation depends on pH values of the sonicated solution for both the homogeneous process and the heterogeneous one. Decrease of the solution pH (~3.5) leads to the faster dye degradation. In the homogeneous process, the efficiency of the DB71 degradation increases up to 10%, in the heterogeneous process—up to 40%. The possible explanation of the pH-dependent degradation of dye in the homogeneous and heterogeneous processes is schematically illustrated in Fig. 2.

pKa values of the known dyes are >3.7 (41–43). At pH < 3.7, the DB71 is protonated. In the protonated molecules, the electron density is shifted to the chromophore part of the molecule, the conjugation system is destroyed (44) (Fig. 2A). Furthermore, the protonated dye molecules are relatively hydrophobic (41,45) (Fig. 2B). The hydrophobic molecules in water tend to concentrate into the interfacial region of the gas-filled cavitation bubbles (41,46–49) and, thus, became more accessible for the ultrasonically formed active species than at neutral pH. In the photocatalytic degradation of organic dye (DB71), pH values of the solution were adjusted to be 6.2 and 3.5 using hydrochloric acid. The chlorine ions exist in the reaction system. Cl^- can be oxidized to form chloride radicals, showing a high oxidative activity. To exclude the effect of chloride ions, the pH was control additionally with another acids, providing the conclusion that in our case, chloride ions do not affect the reactions, probably, due to their negligible concentration.
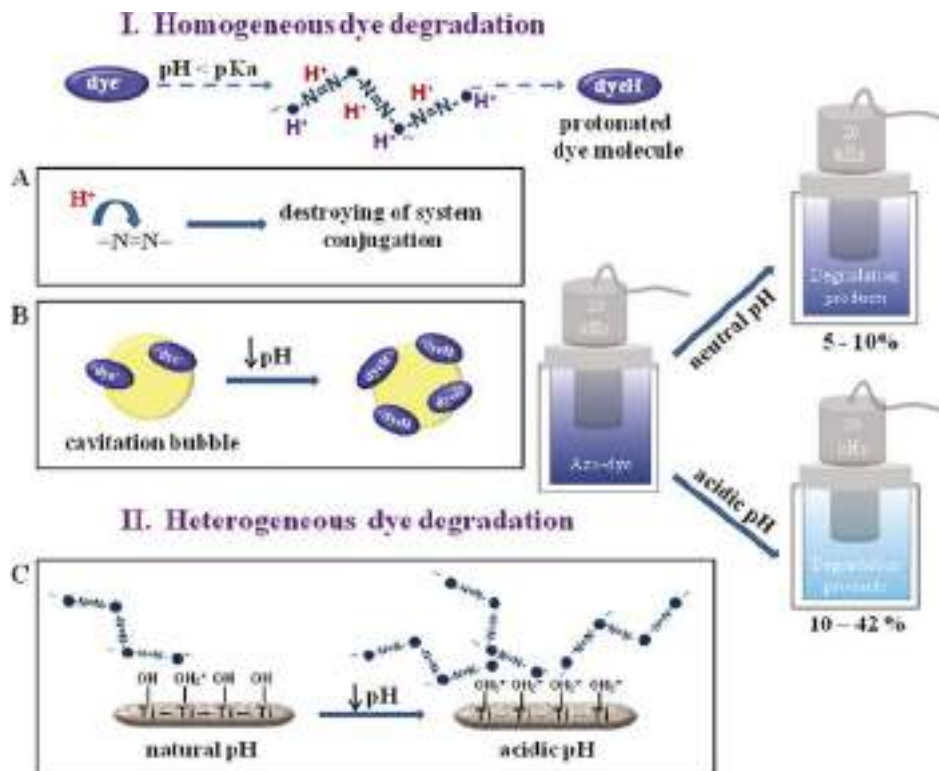
Figure 2. The pH effect on sonoluminescence (SL)-assisted photocatalytic dye degradation process in the homogeneous process of dye degradation (without photocatalyst) (I) and in the heterogeneous process (in the presence of TiO_2) (II). Effect of pH can be explained by: (A) shift of electron density in the chromophore part of DB71; (B) increase of hydrophobility of the dye molecule and its concentration in relatively hydrophobic interface of cavitation bubble; and (C) enhancement of dye adsorption on the titania surface due to electrostatic interactions.

In the heterogeneous process (Fig. 2C), adsorption of the substrate molecules on the photocatalyst surface is an important step of the dye degradation process (50). The point of zero charge (pH_{PZC}) of TiO_2 in an indifferent electrolyte (NaCl) is equal to 6.0 ± 0.2 (51). Therefore, the TiO_2 surface is positively charged in acidic medium (pH < 6.0) and negatively charged at pH >6.0. Thus, at pH ~3.5 adsorption of the negatively charged organic ions on the titania surface is more efficient than at higher pH and the heterogeneous dye degradation can be significantly enhanced.

Effect of TiO$_2$ dispersion: stirring and presonication. Intense sonication leads to dispersion of aggregated particle, cleaning of catalyst surface (52,53). We investigated the effects of sonication of the titania powder on the adsorption ability of the particles for the substrate molecules (Table 1). As a reference, we measured the adsorption capacity of the prestirred particles.

The adsorption values n_2^S — the number of dye moles adsorbed per gram of TiO_2 (mol g^{-1}), were calculated using equation ($n_2^S = \Delta C/W$), where ΔC is the difference between the initial concentration (C_0) and the equilibrium dye concentration in the aqueous phase (C), W is the titania concentration, g L^{-1}.

The observed decrease of the DB71 concentration is mostly due to the adsorption of the dye molecules on the photocatalyst surface. The presonicated particles have the higher n_2^S than the prestirred particles.

Additional activation of catalyst's surface by sonication. As seen in Table 1 in the prestirred mixtures, the adsorption value, n_2^S, does not depend on the initial catalyst concentration (W). In contrast, in the adsorption experiments with the presonicated particles, we observed the nonmonotonic dependence of n_2^S with W. We explain this effect by additional activation of the catalyst's surface due to the sonochemical formation of the ROS, e_{CB}^-, h_{VB}^+ in the TiO_2 surface during presonication.

Thus, ultrasonication of TiO_2 can mechanically disperse and clean the particles and trigger formation of ROS, e_{CB}^-, h_{VB}^+ on the TiO_2 surface, therefore, activate the catalyst's surface before use.

Effect of TiO$_2$ concentration. We monitored the effect of the catalyst concentration on the degradation rate for the presonicated TiO_2 (*TiO_2) and for the nonpretreated TiO_2. Figure 3 shows the kinetics curves A/A_0 vs sonication time (US time). Increasing of the photocatalyst's concentration enhances the dye degradation process in the presence of both *TiO_2 and TiO_2.

If the catalyst concentration is equal to 1 g L^{-1}, we observed the complete decoloration in 10 min of reaction in the presence of *TiO_2 and in 60 min in the presence of TiO_2. The faster decoloration in the presence of the presonicated photocatalyst particles is probably due to the higher dispersion and the higher activity of the presonicated photocatalyst at the beginning of the degradation process.

The detailed analysis of the kinetic curves in Fig. 3 showed that the time-dependent decreasing of the dye concentration was nonmonotonous. In 10 min of sonication, we observed the complete disappearance of the dye molecules in the liquid phase. However, in 20 min of sonication, the dye concentration in the liquid phase was increased again up to 10%. We explain this effect by the very high adsorption capacity of the ultrasonically activated particles. The dye degradation rate is much lower than its adsorption rate on the catalyst's surface. The further intense sonication of the particles leads to the partial desorption of the dye molecules that were not degraded during this time.

Effect of DB71 concentration. The initial concentration of the substrate is one of the most important factors of dye degradation for a practical application. The analysis of the kinetic curves in Fig. 4 reveals that the decrease of the initial DB71 concentration [DB71] enhances the degradation rate. Up to 20% and 70% of DB 71 were degraded after 60-min sonication at dye concentration equal to 1×10^{-4} M and 5×10^{-5} M, correspondingly. We detected almost complete decoloration after 40-min treatment at [DB71] = 2.5×10^{-5} M.

The dye adsorption on the catalyst's surface increases with increasing of the substrate concentration at the constant concentration of the catalyst according to the Langmuir isotherm. The enhanced dye adsorption should accelerate the dye degradation. However, the superfluous adsorption of the dye molecules can decrease light penetration to the catalyst's surface and, thus, slow down the e_{CB}^-/h_{VB}^+ pair formation (53).

Intermediates of DB71 degradation

Monitoring of the degradation process using a combination of reversed-phase high-performance liquid chromatography (RP-HPLC) with fluorometric detection, high-performance liquid chromatography coupled to mass spectrometry (HPLC-MS) and UV–Vis spectroscopy showed that ultrasonication causes formation of colored intermediates and colorless compounds (naphthalene and benzene derivatives) before complete mineralization. UV–Vis spectra of the degraded mixture showed the slight hypsochromic shift of the absorbance maximum of DB71 due to the presence of the colored intermediates. These intermediates can be formed by hydroxylation of aromatic rings of DB71. The detected colorless products were phenol, hydroquinone, pyrocatechol and phthalates. The detailed analysis of the intermediates and the products is given in Figure S1 and Table S1 (Supporting Information).

Kinetic of DB71 degradation

The homogeneous and heterogeneous degradation of DB71 can be described by the pseudo-first-order kinetics with respect to the concentration of the dye in the bulk solution (41,54,55):
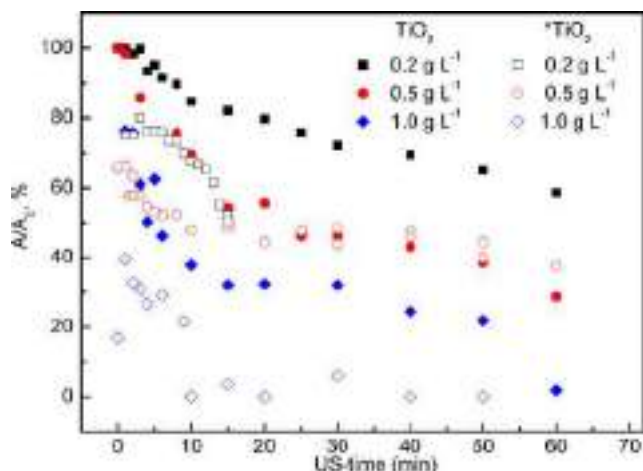
Table 1. Adsorption characteristics of TiO_2 pretreated via presonication and via prestirring at pH 3.5.

W, g L^{-1}	Presonication			Stirring		
	$C \times 10^5$, M	$\Delta C \times 10^5$, M	$n_2^S \times 10^5$, mol g^{-1}	$C \times 10^5$, M	$\Delta C \times 10^5$, M	$n_2^S \times 10^5$, mol g^{-1}
0.2	7.5	2.5	11.4	8.8	1.2	6.0
0.5	6.6	3.4	6.8	7.1	2.9	5.8
1.0	1.7	8.3	8.3	4.2	5.8	5.8

Figure 3. The effect of presonicated (*TiO$_2$) and nonpretreated (TiO$_2$) catalyst's concentration on the degradation of DB71 ([DB71] = 5 × 10^{-5} M, pH 3.5).
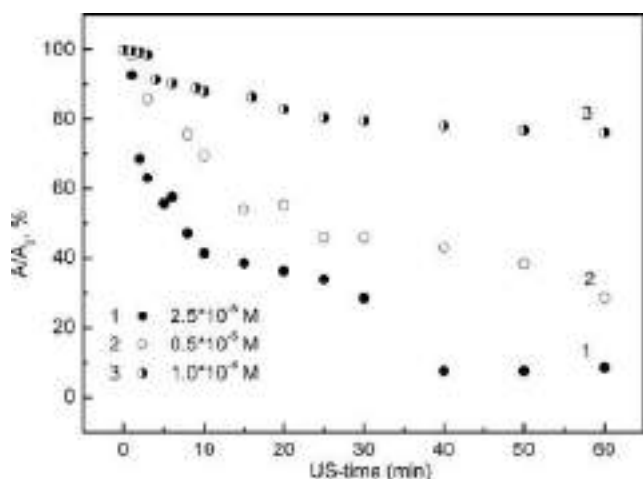

Figure 4. Effect of the initial concentration of DB71 on the degradation process ([TiO$_2$] = 0.5 g L^{-1}, pH 3.5).

$$r = -dC/dt = k_{app}C \qquad (15)$$

where r is the rate of dye degradation (M min^{-1}), t is sonication time (min), k_{app} is the apparent pseudo-first-order rate constant (min^{-1}), the initial concentration (C_0) and the equilibrium dye concentration in the aqueous phase (C). The integrated form of this equation with the boundary condition $t = 0$, $C = C_0$ can be written as:

$$\ln(C/C_0) = -k_{app}t (C \sim A, \ln(A/A_0) = -k_{app}t) \qquad (16)$$

and, therefore:

$$C = C_0 e^{-k_{app}t} (A = A_0 e^{-k_{app}t}) \qquad (17)$$

Kinetic of DB71 degradation (homogeneous process). ln A/A_0 vs US-time for the homogeneous dye degradation (Fig. 5A at 0 g L^{-1} catalyst's concentration) has a linear dependence. The value of the apparent first-order rate constant k_{app} can be deter-

mined from the slope of this plot and it is equal to 1.7 × 10^{-3} min^{-1}.

Kinetic of DB71 degradation (heterogeneous process) in the presence of nonpretreated TiO$_2$. The plots of ln A/A_0 vs US-time for the heterogeneous process at the different TiO$_2$ concentrations (Fig. 5A) and the dye concentrations (Fig. 5B) have two regions (I and II). The dye degradation in the heterogeneous process is obviously a multistage process:

Stage I—the conversion of dye to intermediates in US-time ≤12 ± 2 min; and
Stage II—the simultaneous degradation of dye and intermediates at US-time >12 ± 2 min.

The calculated apparent pseudo-first-order rate constants are shown in Table 2. k_{appI} is the apparent pseudo-first-order rate constant at the stage I (≤12 min) of the reaction. k_{appII} is the apparent pseudo-first-order rate constant at the stage II (>12 min) of the reaction.

The k_{appI} values increase with increasing of the catalyst concentration and decrease with increasing of the DB71 concentration. The Langmuir–Hinshelwood (L-H) model describes this dependence (41,54,56,57). In this model, the reaction rate is proportional to the surface coverage (θ) and the Eq. (15) can be written as:

$$r = -dC/dt = k\theta = kKC/(1 + KC) \qquad (18)$$

and, therefore,

$$k_{app} = kK/(1 + KC) \qquad (19)$$

where k is the apparent L-H rate constant (M min^{-1}), K is the Langmuir adsorption constant (M^{-1}).

Increase of the catalyst concentration results in the formation of the additional available active sites (θ) for the adsorption of dye molecules.

According to the Eq. (19), k_{app} is inversely proportional to the dye concentration, C, when the other parameters are constant, whereas the reaction rate increases with increasing the dye concentration. However, at the high concentration of the dye the degradation process can slow down due to the screening of the catalyst surface by the adsorbed dye molecules.

The L-H model is not valid for the stage II (>12 min). At the stage II, the concentration of the intermediates becomes significant. The presence of the intermediates slows down the degradation rate (41,56). The k_{appII} value does not depend on the dye and catalyst concentrations within the error of the constant calculation (±2.0 × 10^{-3} min^{-1}). Thus, if $C_0 = 1.0 × 10^{-4}$ M we observed decrease of the degradation rate due to the screening of the catalyst's surface by the adsorbed DB71 molecules.

We can write the empirical equation for the nonpretreated titania:

$$A = A_0 e^{-k_{appI}t} \text{ for the stage I } (t \le 12 \text{ min}); \text{ and}$$

$$A = (A_0 e^{-12k_{appI}}) e^{-k_{appII}t} \text{ for the stage II } (t > 12 \text{ min}).$$

Kinetic of DB71 degradation (heterogeneous process) in the presence of pretreated TiO$_2$ (TiO$_2$).* The plots of ln A/A_0 vs US-time and k_{app}^* for the presonicated titania are presented in Fig. 5C
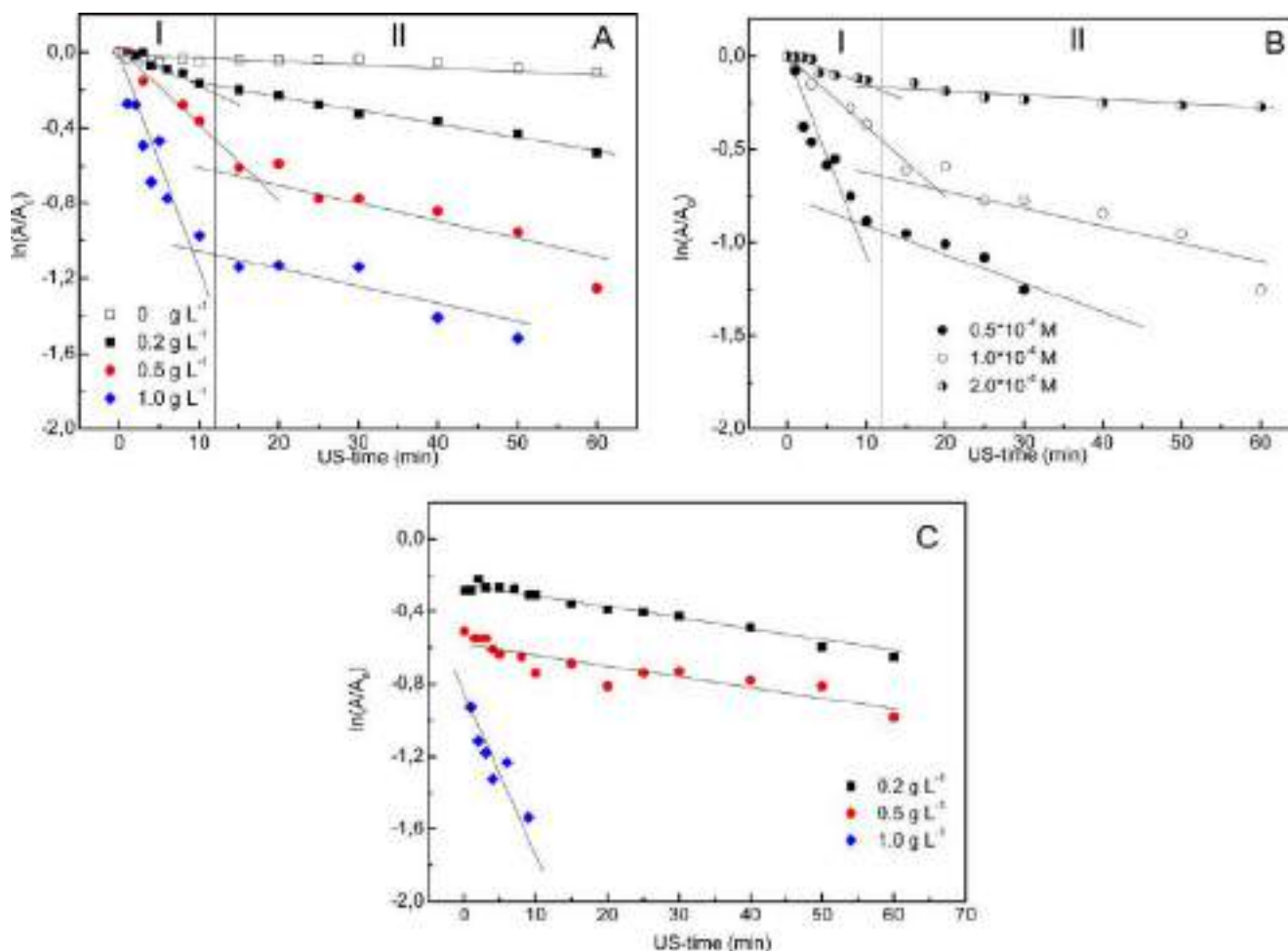
Figure 5. $\ln(A/A_0)$ *vs* sonication time plot for TiO_2 concentrations = 0, 0.2, 0.5 and 1.0 g L^{-1} at concentration of DB71 = 5 × 10^{-5} M (A); $\ln(A/A_0)$ *vs* sonication time plot for concentrations of DB71 = 2.5 × 10^{-5}, 5 × 10^{-5} and 1 × 10^{-4} M at TiO_2 concentration = 0.5 g L^{-1} (B); $\ln(A/A_0)$ *vs* sonication time plot for concentrations of the presonicated *TiO_2 = 0.2, 0.5 and 1.0 g L^{-1} at concentration of DB71 = 5 × 10^{-5} M (C).

Table 2. Kinetic constants for dye degradation process over the nonpretreated catalyst.

[DB71], M		5 × 10^{-5}		2.5 × 10^{-5}	5 × 10^{-5}	1 × 10^{-4}
[TiO_2],g L^{-1}	0.2	0.5	1.0		0.5	
k_{appI}, min^{-1}	1.8 × 10^{-2}	4.0 × 10^{-2}	1.1 × 10^{-1}	1.1 × 10^{-1}	4.0 × 10^{-2}	1.6 × 10^{-2}
k_{appII}, min^{-1}	8.0 × 10^{-3}	1.0 × 10^{-2}	1.0 × 10^{-2}	1.3 × 10^{-2}	1.0 × 10^{-2}	2.5 × 10^{-3}

and in Table 3. As we discussed above, the presonication of the aqueous titania dispersions leads to the activation of the catalyst surface by the formation of electron–hole pairs and ROS in the presonication stage. In this case, the stage I of the reaction is very fast. Due to this, we can observe the relatively slow stage II in the kinetic curves only. Furthermore, the calculated k_{app} values for the heterogeneous process (8.4 × 10^{-2} min^{-1} at the *TiO_2 concentration = 1 g L^{-1}) are significantly higher than the calculated k_{app} for the homogeneous process of dye degradation (1.7 × 10^{-3} min^{-1}).

Comparison of degradation of DB71 by the SL-assisted processes and the state-of-the-art UV-assisted method

Figure 6 shows the kinetics curves of the DB71 photocatalytic degradation triggered by the SL and the UV light. Compa-

ring the efficiency of the both processes demonstrates that the SL-assisted process is faster than the UV-assisted one. The calculated apparent constant of the UV-assisted DB71 decomposition in the presence of the pretreated via stirring 1.0 g L^{-1} of titania is 7.2 × 10^{-3} min^{-1} that is one order of magnitude lower than for the SL-assisted dye degradation in the presence of the presonicated titanium dioxide (8.4 × 10^{-2} min^{-1}; Fig. 6).

In addition to the photocatalytic reactions on the catalyst surface stimulated by light, ultrasonication of the aqueous solutions results in the bulk generation of OH radicals. These ultrasonically triggered two mechanisms of the formation of the active species can explain the higher efficiency of the sonocatalytic process of dye degradation. Moreover, the shift of absorbance maximum on the UV spectra for the UV-assisted process was not observed that might be due to the different mechanisms of the SL- and UV-assisted photocatalytic dye degradation.

Table 3. Kinetic constants for dye degradation process over the presonicated catalyst ([DB71] = 5 × 10^{-5} м).

	[*TiO$_2$], g L^{-1}		
	0.2	0.5	1.0
k_{app}^*, min^{-1}	8.0×10^{-3}	8.0×10^{-3}	8.4×10^{-2}
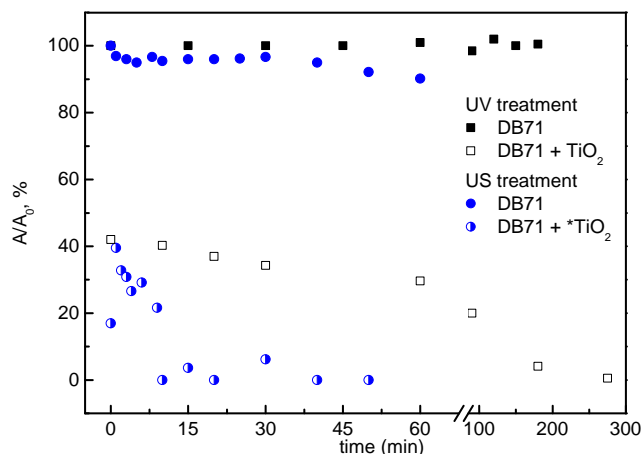
Figure 6. The degradation of DB71 ([DB71] = 5 × 10^{-5} м, [presonicated *TiO$_2$] = 1.0 g L^{-1}, pH 3.5) via ultrasonication (US treatment) and irradiation with UV lamp (UV treatment).

CONCLUSION

We demonstrated that sonodegradation of organic pollutants is a multistage process of dye decomposition that proceeds via formation of different intermediates and relies on several mechanisms of the generation of active species. Fundamentally, this research reveals that light emitted in cavitated liquid is essential for initiation of the photoreactions on the surface of the semiconductor particles. We showed that the sonochemically formed active compounds alone cause relatively slow degradation of azo dyes. The activation of the photocatalysts by SL makes the major contribution to the degradation process. Based on the kinetics studies of the sonodegradation process, it was proposed that the sonodegradation of azo dyes was a multistage process that involved: (1) the direct attack of azo bonds and phenyl rings of dyes by the sonochemically formed reactive oxygen species; (2) the activation of semiconductor particles by the light emitted during cavitation and the triggering of the photocatalytic pathways of dye degradation; and (3) increase of the adsorption capacity of the semiconductor particles due to the sonomechanically induced interparticle collisions. The detailed kinetics study can help in following an effective process up-scaling.

SUPPORTING INFORMATION

Additional Supporting Information may be found in the online version of this article:

Supporting Information is available from the Wiley Online Library at DOI: 10.1562/2006-xxxxxx.s1. or from the author.

Figure S1. RP-HPLC chromatograms with flourometric detection for samples at [DB71] = 5 × 10^{-5} м, [TiO$_2$] = 1 g L^{-1} and various sonication times: A—15 min, B—60 min (sample 1).

Figure S2. XRD pattern of the TiO$_2$ particles.

Figure S3. SEM (A) and TEM (B) images of the TiO$_2$ particles.

Figure S4. Size distribution by number of the TiO$_2$ particles.

Table S1. Molecular ions [M-H]$^+$ of some DB71 degradation products detected by HPLC-MS.

Data S1. Analysis of degradation products.

REFERENCES

1. Vandevivere, P. C., R. Bianchi and W. Verstraete (1998) Treatment and reuse of wastewater from the textile wet-processing industry: Review of emerging technologies. *J. Chem. Technol. Biotechnol.* **72**, 1–12.
2. Forgacs, E., T. Cserhati and G. Oros (2004) Removal of synthetic dyes from wastewater: A review. *Environ. Int.* **30**, 953–971.
3. Hao, O. J., H. Kim and P. C. Chiang (2000) Decolorization of wastewater. *Crit. Rev. Environ. Sci. Technol.* **30**, 449–505.
4. Defale, N., N. N. Rao, S. U. Meshram and S. R. Wate (2008) Decolorization of azo dyes and simulated dye bath wastewater using acclimatized microbial consortium biostimulation and halo tolerance. *Bioresour. Technol.* **99**, 2552–2558.
5. Berberidou, C., I. Poulios, N. P. Xekoukoulotakis and D. Mantzavinos (2007) Sonolytic, photocatalytic and sonophotocatalytic degradation of malachite green in aqueous solutions. *Appl. Catal. B* **74**, 63–72.
6. Davydov, L., E. P. Reddy, P. France and P. G. Smirniotis (2001) Sonophotocatalytic destruction of organic contaminants in aqueous systems on TiO$_2$ powders. *Appl. Catal. B* **32**, 95–105.
7. Ertugay, N. and F. N. Acar (2013) Sonocatalytic degradation of Direct Blue 71 azo dye at the presence Zero-Valent Iron (ZVI). *Desalination Water Treat.* **51**, 7570–7576.
8. Hung, H.-M. and M. R. Hoffmann (1999) Kinetics and mechanism of the sonolytic degradation of chlorinated hydrocarbons: Frequency effects. *J. Phys. Chem. A* **103**, 2734–2739.
9. Petrier, C. and A. Francony (1997) Ultrasonic waste-water treatment: Incidence of ultrasonic frequency on the rate of phenol and carbon tetrachloride degradation. *Ultrason. Sonochem.* **4**, 295–300.
10. Petrier, C., M. F. Lamy, A. Francony, A. Benahcene and B. David (1994) Sonochemical degradation of phenol in dilute aqueous solutions: Comparison of the reaction rates at 20 and 487 kHz. *J. Phys. Chem.* **98**, 10514–10520.
11. Singla, R., F. Grieser and M. Ashokkumar (2009) Sonochemical degradation of martius yellow dye in aqueous solution. *Ultrason. Sonochem.* **16**, 28–34.
12. Guyer, G. T. and N. H. Ince (2011) Degradation of diclofenac in water by homogeneous and heterogeneous sonolysis. *Ultrason. Sonochem.* **18**, 114–119.
13. Zhaia, Y., Y. Li, J. Wanga, J. Wanga, L. Yina, Y. Kongb, G. Hana and P. Fana (2013) Effective sonocatalytic degradation of organic dyes by using Er^{3+}:YAlO$_3$/TiO$_2$-SnO$_2$ under ultrasonic irradiation. *J. Mol. Catal. A, Chem.* **366**, 282–287.
14. Tunc, S., T. Gürkan and O. Duman (2012) On-line spectrophotometric method for the determination of optimum operation parameters on the decolorization of Acid Red 66 and Direct Blue 71 from aqueous solution by Fenton process. *Chem. Eng. J.* **181–182**, 431–442.
15. Sathishkumar, P., S. Anandan, P. Maruthamuthu, T. Swaminathan, M. Zhou and M. Ashokkumar (2011) Synthesis of Fe^{3+} doped TiO$_2$ photocatalysts for the visible assisted degradation of an azo dye. *Colloids Surf. A, Physicochem. Eng. Asp.* **375**, 231–236.

16. Walton, A. J. and G. T. Reynolds (1984) Sonoluminescence. *Adv. Phys.* **33**, 595–660.
17. Gaitan, D. F., L. A. Crum, C. C. Church and R. A. Roy (1992) Sonoluminescence and bubble dynamics for a single, stable cavitation bubble. *J. Acoust. Soc. Am.* **91**, 3166–3183.
18. Moss, W. C., D. B. Clarke, J. W. White and D. A. Young (1994) Hydrodynamic simulation of bubble collapse and picosecond sonoluminescence. *Phys. Fluids* **6**, 2979–2985.
19. Barber, B. P., R. A. Hiller, R. Lijfstedt, S. J. Putterman and K. R. Weninger (1997) Defining the unknowns of sonoluminescence. *Phys. Rep.* **281**, 65–143.
20. Hiller, R., S. J. Putterman and B. P. Barber (1992) Spectrum of synchronous picosecond sonoluminescence. *Phys. Rev. Lett.* **69**, 1182–1184.
21. Suslick, K. S., S. J. Doktycz and E. B. Flint (1990) On the origin of sonoluminescence and Sonochemistry. *Ultrasonics* **28**, 280–290.
22. Brenner, M. P. (2002) Single-bubble sonoluminescence. *Rev. Mod. Phys.* **74**, 425–484.
23. Xu, H., B. W. Zeiger and K. S. Suslick (2013) Sonochemical synthesis of nanomaterials. *Chem. Soc. Rev.* **42**, 2555–2567.
24. Dulle, J., S. Nemeth, E. V. Skorb and D. V. Andreeva (2012) Sono-nanostructuring of zinc-based materials. *RCS Adv.* **2**, 12460–12465.
25. Andreeva, D. (2011) High-precision nano-structuring with ultrasound: A new method of producing porous metals. *Int. J. Mater. Res.* **102**, 597–598.
26. Dulle, J., S. Nemeth, E. V. Skorb, T. Irrgang, J. Senker, R. Kempe, A. Fery and D. V. Andreeva (2012) Sonochemical activation of Al/Ni hydrogenation catalyst. *Adv. Funct. Mater.* **22**, 3128–3135.
27. Suslick, K. S., J. W. Goodale, P. F. Schubert and H. H. Wang (1983) Sonochemistry and sonocatalysis of metal-carbonyls. *J. Am. Chem. Soc.* **105**, 5781–5785.
28. Flannigan, D. J. and K. S. Suslick (2005) *Nature* **2005**, 52–55.
29. McNamara, W. B., Y. T. Didenko and K. S. Suslick (1999) Sonoluminescence temperatures during multi-bubble cavitation. *Nature* **401**, 772–775.
30. Ashokkumar, M., R. Hall, P. Mulvaney and F. Grieser (1997) Sonoluminescence from aqueous alcohol and surfactant solutions. *J. Phys. Chem. B* **101**, 10845–10850.
31. Margulis, M. A. (2000) Sonoluminescence. *Uspechi Fiz. Nauk* **170**, 263–287.
32. Margulis, M. A. and I. M. Margulis (1999) Theory of local electrification of cavitation bubbles: New approaches. *Ultrason. Sonochem.* **6**, 15–20.
33. Margulis, M. A. (1985) Investigation of electrical phenomena related to the cavitation. 2. Theory of the sonoluminescence and sound-chemical origination. *Z. Fiz. Khim.* **59**, 1497–1503.
34. Noltingk, B. E. and E. A. Neppiras (1951) Cavitation produced by ultrasonics. *Proc. Phys. Soc. London B* **63**, 674–685.
35. Neppiras, E. A. and B. E. Noltingk (1951) Cavitation produced by ultrasonics – Theoretical conditions for the onset of cavitation. *Proc. Phys. Soc. London B* **64**, 1032–1038.
36. Didenko, Y. T. and K. S. Suslick (2002) The energy efficiency of formation of photons, radicals and ions during single-bubble cavitation. *Nature* **418**, 394–397.
37. Hilgenfeldt, S., S. Grossmann and D. Lohse (1999) A simple explanation of light emission in sonoluminescence. *Nature* **398**, 402–405.
38. Saien, J. and A. R. Soleymani (2007) Degradation and mineralization of Direct Blue 71 in a circulating upflow reactor by UV/TiO$_2$ process and employing a new method in kinetic study. *J. Hazard. Mater.* **144**, 506–512.
39. Saien, J. and A. R. Soleymani (2009) Comparative investigations on nano and micro titania photocatalysts in degradation and mineralization: Use of turbidity in kinetic studies. *J. Iran. Chem. Soc.* **6**, 602–611.
40. Dharmarathne, L., M. Ashokkumar and F. Grieser (2013) On the generation of the hydrated electron during the sonolysis of aqueous solutions. *J. Phys. Chem. A* **117**, 2409–2414.
41. Ghows, N. and M. H. Entezari (2013) Kinetic investigation on sono-degradation of Reactive Black 5 with core-shell nanocrystal. *Ultrason. Sonochem.* **20**, 386–394.
42. Oliveira, H. P. (2008) Determination of pKa of dyes by electrical impedance spectroscopy. *Microchem. J.* **88**, 32–37.
43. Al-Degs, Y. S., M. I. El-Barghouthi, A. H. El-Sheikh and G. M. Walker (2008) Effect of solution pH, ionic strength, and temperature on adsorption behavior of reactive dyes on activated carbon. *Dyes Pigm.* **77**, 16–23.
44. Feng, X., S. H. Zhu and H. Hou (2006) Investigation of 207 nm UV radiation for degradation of organic dye in water. *Water SA* **32**, 43–48.
45. Okitsu, K., K. Iwasaki, Y. Yobiko, H. Bandow, R. Nishimura and Y. Maeda (2005) Sonochemical degradation of azo dyes in aqueous solution: A new heterogeneous kinetics model taking into account the local concentration of OH radicals and azo dyes. *Ultrason. Sonochem.* **12**, 255–262.
46. Sostaric, J. Z. and P. Riesz (2002) Adsorption of surfactants at the gas/solution interface of cavitation bubbles: An ultrasound intensity-independent frequency effect in sonochemistry. *J. Phys. Chem. B* **106**, 12537–12548.
47. Ashokkumar, M., P. Mulvaney and F. Grieser (1999) The effect of pH on multibubble sonoluminescence from aqueous solutions containing simple organic weak acids and bases. *J. Am. Chem. Soc.* **121**, 7355–7359.
48. Price, G. J., M. Ashokkumar, T. D. Cowan and F. Grieser (2002) Sonoluminescence quenching by organic acids in aqueous solution: pH and frequency effects. *Chem. Commun.* **16**, 1740–1741.
49. Yim, B., Y. Nagata and Y. Maeda (2002) Degradation of phthalic acid esters in aqueous solutions. Acceleration of hydrolysis by sonochemical action. *J. Phys. Chem. A* **106**, 104–107.
50. Xu, Y. and C. H. Langford (2001) UV- or visible-light-induced degradation of X3B on TiO$_2$ nanoparticles: The influence of adsorption. *Langmuir* **17**, 897–902.
51. Volkova, A. V., L. E. Ermakova, N. F. Bogdanova, E. A. Tarabukina and M. P. Sidorova (2010) Electrosurface characteristics of titanium dioxide in solutions of simple electrolytes: I. Effect of nature of counterions on adsorption and electrokinetic parameters of TiO$_2$. *Colloid J.* **72**, 743–748.
52. Mandzy, N., E. Grulke and T. Druffel (2005) Breakage of TiO$_2$ agglomerates in electrostatically stabilized aqueous dispersions. *Powder Technol.* **160**, 121–126.
53. Ghows, N. and M. H. Entezari (2011) Exceptional catalytic efficiency in mineralization of the reactive textile azo dye (RB5) by a combination of ultrasound and core-shell nanoparticles (CdS/TiO$_2$). *J. Hazard. Mater.* **195**, 132–138.
54. Yetim, T. and T. Tekin (2012) Sonophotocatalytic degradation kinetics of an azo dye amaranth. *J. Chem. Soc. Pak.* **34**, 1397–1402.
55. Zhang, K. and W. Oh (2010) Kinetic study of the visible light-induced sonophotocatalytic degradation of MB solution in the presence of Fe/TiO$_2$-MWCNT catalyst. *Bull. Korean Chem. Soc.* **31**, 1589–1595.
56. Lazar, M. A., S. Varghese and S. S. Nair (2012) Photocatalytic water treatment by titanium dioxide: Recent updates. *Catalysts* **2**, 572–601.
57. Konstantinou, I. K. and T. A. Albanis (2004) TiO$_2$-assisted photocatalytic degradation of azo dyes in aqueous solution: Kinetic and mechanistic investigations. A review. *Appl. Catal. B* **49**, 1–14.

The use of ultrasonic cavitation for near-surface structuring of robust and low-cost AlNi catalysts for hydrogen production†

P. V. Cherepanov,[a] I. Melnyk,[a] E. V. Skorb,[b] P. Fratzl,[b] E. Zolotoyabko,[c] N. Dubrovinskaia,[d] L. Dubrovinsky,[e] Y. S. Avadhut,[f] J. Senker,[f] L. Leppert,[g] S. Kümmel[g] and D. V. Andreeva*[a]

Ultrasonically induced shock waves stimulate intensive interparticle collisions in suspensions and create large local temperature gradients in AlNi particles. These trigger phase transformations at the surface rather than in the particle interior. We show that ultrasonic processing is an effective approach for developing the desired compositional gradients in nm-thick interfacial regions of metal alloys and formation of effective catalysts toward the hydrogen evolution reaction.

The hydrogen evolution reaction (HER) is an important technological process for the production of molecular hydrogen through water splitting.[1] Catalysts for the HER reversibly bind hydrogen to their surface.[2] Rapid HER kinetics was observed when utilizing expensive metal catalysts.[3–5] Recently, it was shown that near-surface and surface alloys potentially can have excellent catalytic properties for hydrogen production.[6,7] However, up to now such alloys were prepared by time and energy consuming deposition–annealing procedures using transition metals and the Pt(111) surface.[7,8] In this paper, we propose a novel and efficient ultrasound-assisted approach to the manipulation of the metal alloy surface at the atomic level. We use shock impact of billions of collapsing cavitation bubbles during ultrasonic processing for near-surface phase transformation in AlNi particles, the transformation which can hardly be achieved by conventional methods.

According to Nørskov et al.,[2] the free energy of hydrogen adsorption (ΔG_{H^*}) on a catalyst surface is a reliable descriptor of catalytic activity for a variety of compounds. The value of ΔG_{H^*} close to zero indicates that hydrogen intermediates are bound neither too strongly nor too weakly to the catalyst surface. In order to disclose which intermetallic phase in AlNi alloys could potentially be active in HER, we calculated the free energy of hydrogen adsorption for AlNi intermetallics (see the ESI† for details of our density functional theory (DFT) calculations).

Fig. 1 demonstrates that the HER can proceed nearly thermo-neutrally at the (100)-planes of Al_3Ni_2. In contrast, a value of ΔG_{H^*} for the $Al_3Ni(010)$ surface plane is more negative due to pronounced surface reconstruction upon hydrogen adsorption and, hence, this plane can be considered equally inactive as pure Ni.

The obtained results, therefore, indicate that the $Al_3Ni_2(100)$ phase in our intermetallic system is expected to be the most active for electrocatalysis. By measuring the particles'

[a]Physical Chemistry II, University of Bayreuth, DE-95440 Bayreuth, Germany.
E-mail: daria.andreeva@uni-bayreuth.de
[b]Max Planck Institute of Colloids and Interfaces, DE-14424 Potsdam, Germany
[c]Department of Materials Science and Engineering, Technion – Israel Institute of Technology, 32000 Haifa, Israel
[d]Materials Physics and Technology at Extreme Conditions, Laboratory of Crystallography, University of Bayreuth, DE-95440 Bayreuth, Germany
[e]Bayrisches Geoinstitut, University of Bayreuth, DE-95440 Bayreuth, Germany
[f]Inorganic Chemistry III, University of Bayreuth, DE-95440 Bayreuth, Germany
[g]Theoretical Physics IV, University of Bayreuth, DE-95440 Bayreuth, Germany.
E-mail: stephan.kuemmel@uni-bayreuth.de
†Electronic supplementary information (ESI) available: Samples' preparation, PXRD, NMR data, EDS analysis and temperature experiments. See DOI: 10.1039/c5gc00047e
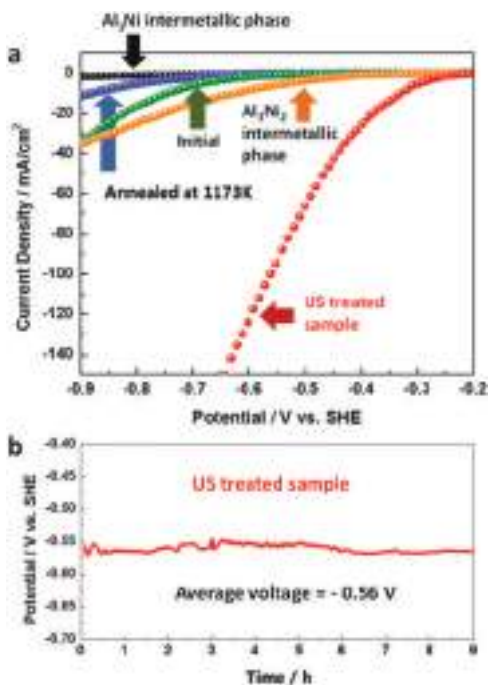
Fig. 1 Calculated free energy diagram for hydrogen evolution at a potential U = 0 relative to the standard hydrogen electrode at pH = 0. Values for Pt and Ni are taken from ref. 33. $Al_3Ni_2(100)$ shows a high potential for the hydrogen evolution reaction.

Fig. 2 HER current–potential profiles for the initial and ultrasonically modified AlNi (50 wt% Ni) alloys, bulk commercial Al_3Ni and Al_3Ni_2 phases, as well as AlNi alloy annealed at 1173 K (a). Galvanostatic HER profile for ultrasonically modified AlNi (50 wt% Ni) alloy (b).

activity in HER, we can evaluate how accessible the surface of the $Al_3Ni_2(100)$ phase is for H-adsorption.

In order to experimentally evaluate the predicted activity of the intermetallics during water splitting, we tested the functioning of bulk commercial Al_3Ni_2 and Al_3Ni compounds in HER. The HER current/potential profiles are shown in Fig. 2a.

It is well known that hydrogen production at the surface of efficient electrocatalysts must be characterized with closer to zero overpotential and high current density output. As predicted by our DFT calculations, our experimental results clearly show that the beneficial phase for water splitting is Al_3Ni_2, whereas the Al_3Ni phase binds H too strongly. However, the measured electrocatalytic characteristics of the unstructured bulk Al_3Ni_2 are not as spectacular as predicted by DFT calculations, probably due to the low accessibility of the active $Al_3Ni_2(100)$ planes for hydrogen adsorption. Therefore, the decisive question is whether it is possible to find an efficient method for structuring of the Al_3Ni_2 phase.

Recently, it has been argued that structuring of near-surface regions in metal alloys is of great importance for achieving enhanced catalytic activities of intermetallic compounds.[6] High electrocatalytic activity was observed[7,8] for structured compounds with enhanced accessibility of potentially active crystal planes. Thus, the relatively poor (higher onset overpotential and lower apparent current density values) electrocatalytic behavior of Al_3Ni_2 can be enhanced by structuring of the AlNi alloys containing the Al_3Ni_2 hexagonal phase. Upon controlled structuring of intermetallic phases in the AlNi alloy,

we do achieve preferential orientation of the (100) hexagonal crystal planes[9] at the surface and, thus, the enhancement of the Al_3Ni_2 activity toward HER.

According to the AlNi binary phase diagram[10] (Fig. S1, ESI†) and the previous work on electrocatalytic application of AlNi compounds[11–14] the best AlNi candidates for the catalyst preparation are AlNi alloys with nearly 50 wt% of Ni. The Rietveld refinement of the powder X-ray diffraction (PXRD) patterns of the investigated samples showed that this alloy is a mixture of Al (2 wt%), Al_3Ni (43 wt%), and Al_3Ni_2 (55 wt%). However, during alloy preparation from melt, the desirable clustering of Al_3Ni_2 at the surface of Al_3Ni is kinetically restricted due to the preferable nucleation of the Al_3Ni phase on the surface of the already formed Al_3Ni_2 phase. At the same time, the formation enthalpies are $\Delta H \approx -65$ kJ mol^{-1} and $\Delta H \approx -45$ kJ mol^{-1} for Al_3Ni_2 and Al_3Ni, respectively.[15] This means that the Al_3Ni_2 phase is thermodynamically more stable than the Al_3Ni phase. Indeed, according to the equilibrium phase diagram at 1124 K, the Al_3Ni phase can be transformed into the Al_3Ni_2 phase ($Al_3Ni \xrightarrow{1124 \text{ K}} Al_3Ni_2 + L_{15.3 \text{ at\% Ni}}$).[10] Thus, in principle, it should be possible to trigger the desirable phase transformation by conventional heating. However, the obtained product is not electrochemically active (Fig. 2a, blue curve), since the highly active surface planes of the (100)-type remain undeveloped. Therefore, a novel technological solution is required for dedicated near-surface phase transformations in AlNi particles.[16–18]

Technologically fast and controllable local heating of a surface can be achieved by the impact of micron-size high-energy cavitation bubbles.[19] Collapsing of cavitation bubbles that are generated in ethanol by high power ultrasound (HPUS) at 20 kHz induces shock waves and intensive turbulent flow.[20–22] In suspensions cavitation triggers intensive interparticle collisions that result in an extremely rapid local rise of the surface temperature of the sonicated particles followed by quenching down to the surrounding medium temperature of 333 K. In this paper, we investigate the HPUS-induced structuring of the intermetallic phases by using ~140 μm particles of AlNi alloys suspended in ethanol (for details see ESI†). The catalyst preparation route *via* ultrasonication is sketched in Fig. 3 and explained in the ESI,† Fig. S3.

Indeed, the HPUS treatment of AlNi particles causes remarkable modification of the morphology and surface composition in the AlNi alloys. The compositional and morphological changes are clearly visible, when comparing the energy-dispersive X-ray spectroscopy (EDS) results, the ^{27}Al solid state nuclear magnetic resonance (NMR) spectra, X-ray photoelectron spectroscopy (XPS) data and the scanning electron microscopy (SEM) images. The SEM pictures (Fig. 4b) show the surface roughening after the HPUS treatment. This surface modification is clearly revealed in comparison with the relatively smooth particle surface before the treatment (Fig. 4a). Furthermore, EDS analysis of the surface composition of the particles before and after sonication shows a mixture of phases near the surface of pristine particles (Table S2, ESI†). In contrast, after the HPUS treatment (Fig. 4c and d), EDS
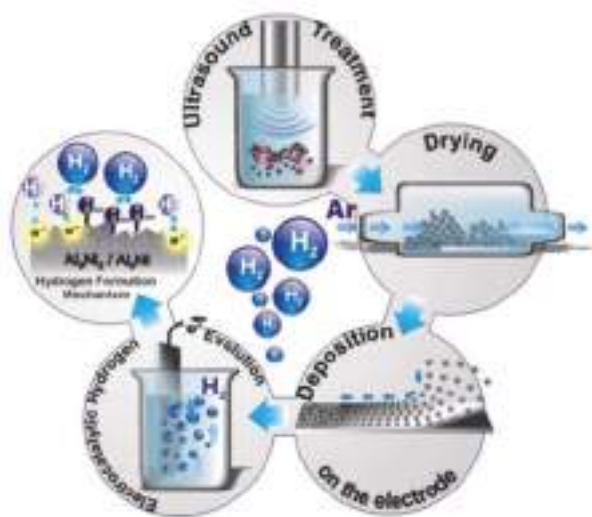
Fig. 3 Schematic illustration of the catalyst preparation procedure. First 10 wt% suspensions of alloy particles (~140 μm) are sonicated in ethanol at a frequency of 20 kHz and an intensity of 140 W cm^{-2} for 1 h. This processing results in the activation of the catalyst surface (change in the crystal structure, phase composition, and morphology). After that the modified particles are centrifuged and dried in an Ar atmosphere. The dried particles are deposited on a substrate and their electrocatalytic activity is evaluated.

Fig. 4 Scanning electron microscopy images taken from the surface of AlNi (50 wt% Ni) before (a) and after (b) ultrasonication. The inserts show selected area electron diffraction patterns, which demonstrate the tendency to form larger intermetallic crystals after the HPUS treatment. The sketches illustrate the random phase distribution in the initial AlNi particles and the preferential clustering of the Al_3Ni_2 phase upon the HPUS treatment. Energy dispersive X-ray analysis of the metal surface after ultrasonication proves the formation of Al_3Ni_2 at the surface, where aluminum to nickel ratio is 3 : 2 (c, d). ^{27}Al MAS NMR spectra (blue) of the sample sonicated in ethanol (f) as well as pristine AlNi (e) and their corresponding simulated spectra (red) are shown below, respectively. In addition, the relative intensities of each resonance are indicated (see also Table S1, ESI†). The asterisks denote spinning sidebands. X-ray photoelectron spectra of the initial (g) and modified samples (h).

detects the presence of a solitary Al_3Ni_2-phase at the surface. Additional evidence of the microstructure refinement in the alloys after the HPUS treatment is provided by selected area electron diffraction (SAED) (see inserts in Fig. 4a and b). The ultrasonically induced clustering of intermetallic phases in the modified AlNi particles is also schematically illustrated in Fig. 4a and b.

The EDS results, as well as the ^{27}Al solid state NMR spectra (Fig. 4e and f) and XPS surface analysis (Fig. 4g and h), provide clear evidence of the spatial re-distribution of the phases within metallic particles after the treatment.

The EDS results, as well as the ^{27}Al solid state NMR spectra and XPS surface analysis, provide clear evidence of the spatial re-distribution of the phases within metallic particles after the treatment. Due to the skin effect (see ESI†) the penetration depth of rf fields into conducting and magnetic materials is limited. Thus the ^{27}Al NMR spectra (Fig. 4e and f) enhance the surface content of the AlNi alloy before and after ultrasonication. Both materials exhibit five different resonances (Fig. 4e and f) which are assigned on the basis of the observed chemical shift. The main contribution arises from metallic Al (5.7/5.9 wt%), Al_3Ni (52.6/50.1 wt%), Al_3Ni_2 (40.9/43.1 wt%), and $Al(OH)_3$ (0.8/0.9 wt%) before and after sonication. While the Al as well as Al_3Ni ratios are slightly higher compared to the results of the PXRD analysis, the Al_3Ni_2 ratio is lower. This indicates a slight enrichment of Al and Al_3Ni at the surfaces of the alloy particles compared to the bulk composition. Interestingly, sonication increases the surface content of Al_3Ni_2 from 41 to 43 wt%. In parallel the percentage of Al_3Ni decreases

from 52.6 to 50.1 wt% leading to a decreased Al_3Ni/Al_3Ni_2 ratio from 1.3 to 1.15. This finding supports the hypothesis that Al_3Ni transforms slowly in Al_3Ni_2 during sonication. In contrast, the PXRD patterns showed that the sonication negligibly affected the bulk ratio of the phases in the samples. Furthermore, XPS surface analysis showed the increased concentration of Ni^0 at the surface (Fig. 4h) upon sonication of AlNi alloy particles in ethanol that also might confirm the formation of the more Ni-enriched Al_3Ni_2 phase compared to Al_3Ni that covers the unmodified surface (Fig. 4g).

The formation of the Al_3Ni_2 phase on the alloy surface is possible if cavitation bubbles can heat the surface to above 1124 K. At this temperature the catalytically inactive Al_3Ni phase is transferred into the beneficial Al_3Ni_2 phase. The spectroscopic surface analysis before and after the HPUS treatment reveals the formation of the Al_3Ni_2 phase and, thus, proves local surface heating up to ~1124 K.

The development of the ultrasonically induced temperature gradient within the particles can stimulate additional crystal growth. We analyzed the PXRD patterns (Fig. S4, ESI†) and calculated the crystallite sizes before and after the HPUS treatment using the Williamson–Hall (W–H) method[23–25] (for details, see ESI†). According to our estimations, the Al_3Ni_2 and Al_3Ni crystallites in the HPUS-treated AlNi are nearly twice as large (131 nm for Al_3Ni_2; 113 nm for Al_3Ni) as pristine particles (87 nm for Al_3Ni_2; 56 nm for Al_3Ni). By assuming diffusion-controlled crystal growth during the treatment period (1 h), we estimate the diffusion rate in the AlNi (50 wt% of Ni) to be about 2×10^{-18} m^2 s^{-1}. The reference experiments (heating the particles in an oven for 1 h at different temperatures (for details see Fig. S5, ESI†)) showed that the observed atomic diffusion proceeds at an average temperature in the particle interior that is about $T \approx 823$ K.

Surface structuring *via* ultrasonication increases the accessibility of the DFT-predicted beneficial $Al_3Ni_2(100)$ phase for H adsorption, which in turn should enhance the catalytic efficiency toward HER. In fact, we did observe outstanding improvement of the electrocatalytic properties (Fig. 2a) of AlNi particles after ultrasonication. The onset overpotential *vs.* SHE is significantly lowered to −0.25 V as compared to −0.65 V for pristine AlNi alloy particles. At the same time, the apparent current density values are strongly enhanced. For example, a drastic (more than 200-fold) increase in the current density was observed at an onset overpotential value of −0.4 V and was found to be 28.19 mA cm^{-2} (HPUS-treated) as compared to 0.13 mA cm^{-2} (initial).

Another very important parameter for evaluating the material's electrocatalytic performance is the exchange current density (i0), which reflects the intrinsic rate of electron transfer between the electrocatalyst's surface and the analyte. Therefore, we replotted the HER current/potential profiles in the Tafel coordinates and calculated i0-values for both the pristine and the HPUS-treated AlNi alloy particles. The calculated i0-value of 17.37 mA cm^{-2} for the HPUS-modified alloy particles is three orders of magnitude higher than for the untreated ones (0.016 mA cm^{-2}). All in all, our study shows that HPUS is a unique technological approach for producing the low-cost and efficient AlNi catalyst for water splitting. The ultrasonically generated AlNi catalyst is very robust and exhibits excellent stability in electrochemical use (Fig. 2b).

Conclusions

Using density functional theory, we first predicted that the Al_3Ni_2 phase is potentially effective in the hydrogen evolution reaction. However, bulk unstructured Al_3Ni_2 compounds demonstrated relatively low efficiency due to the low accessibility of the favorable (100) atomic plane. We propose structuring of AlNi alloys containing the Al_3Ni_2 phase as an efficient and low cost technological approach for enhancing the accessibility of the $Al_3Ni_2(100)$ planes that are active in hydrogen adsorption. The formation of the Al_3Ni_2 phase on the surface of AlNi

alloys is kinetically restricted, but we demonstrate that processing of the metal surface by ultrasonically generated cavitation bubbles creates large local temperature gradients in the metal particles. These stimulate the desired phase transformations at the surface rather than in the particle interior. In particular, we show that collapsing cavitation bubbles heat the surface above 1124 K, thus triggering the near-surface transformation of the catalytically inactive Al_3Ni phase into beneficial Al_3Ni_2. In the particle interior, the estimated mean temperature reaches 824 K, which is well below the phase transition temperature, but still enough for substantial solid-state diffusion and crystal growth. This simple, fast, and effective ultrasonic approach toward directed surface modification can be extended to other intermetallic systems for sustainable energy generation.

Experimental

The AlNi (50 wt% Ni) alloy was prepared by melting Al (99.99% purity grade) and nickel (99.99% purity grade) foils (purchased from Sigma-Aldrich) using a Mini ARC melting device MAM-1 (Edmund Bühler Gmbh), TIG 180 DC. The HPUS treatment of AlNi alloy particles was performed using a Hielscher UIP1000hd, (Hielscher Ultrasonics GmbH, Germany) at an operating frequency of 20 kHz. Electrochemical characterization was accomplished in a three electrode cell using a 510 V10 Potentiostat/Galvanostat in the 1 M H_2SO_4 electrolyte. PXRD accompanied by Rietveld refinement, SEM and energy-dispersive EDS and solid state ^{27}Al NMR[26] were employed to verify the phase composition of the prepared AlNi alloys. TEM was used to obtain SAED patterns. DFT calculations were performed using the Vienna ab-initio Simulation Package.[27–32] Detailed information regarding sample preparation, ultrasound treatment, characterization methods, and calculations is available in the ESI.†

Acknowledgements

Notes and references

1 A. Züttel, A. Borgschulte and L. Schlapbach, *Hydrogen as a future energy carrier*, Wiley-VCH, Weinheim, Germany, 2008.

2 E. Skulason, V. Tripkovic, M. E. Björketun, S. Gudmundsdottir, G. Karlberg, J. Rossmeisl, T. Bligaard, H. Jonsson and J. K. Nørskov, *J. Phys. Chem. C*, 2010, **114**, 18182.

3 B. Hinnemann, P. G. Moses, J. Bonde, K. P. Jorgensen, J. H. Nielsen, S. Horch, I. Chorkendorff and J. K. Nørskov, *J. Am. Chem. Soc.*, 2005, **127**, 5308.

4 T. F. Jaramillo, K. P. Jørgensen, J. Bonde, J. H. Nielsen, S. Horch and I. Chorkendorff, *Science*, 2007, **317**, 100.

5 M. S. Faber and S. Jin, *Energy Environ. Sci.*, 2014, **7**, 3519.

6 J. Greeley and M. Mavrikakis, *Nat. Mater.*, 2004, **3**, 810.

7 A. S. Bandarenka, A. S. Valera, M. Karamad, F. Calle-Vallejo, L. Bech, F. J. Perez-Alonso, J. Rossmeisl, I. E. L. Stephens and I. Cherkendorff, *Angew. Chem., Int. Ed.*, 2012, **51**, 11845.

8 J. Knudsen, A. U. Nilekar, R. T. Vang, J. Schnadt, E. D. L. Kunkes, J. A. Dumesic, M. Mavrikakis and F. Nesenbacher, *J. Am. Chem. Soc.*, 2007, **129**, 6485.

9 P. V. Cherepanov, I. Melnyk and D. V. Andreeva, *Ultrason. Sonochem.*, 2015, **23**, 26.

10 D. Batalu, G. Cosmeliata and A. Aloman, *Metal. Int.*, 2006, **11**, 36.

11 P. V. Cherepanov, M. Ashokkumar and D. V. Andreeva, *Ultrason. Sonochem.*, 2015, **23**, 142.

12 D. Miousse and A. Lasia, *J. Appl. Electrochem.*, 1995, **25**, 592.

13 P. Los, A. Rami and A. Lasia, *J. Appl. Electrochem.*, 1993, **23**, 135.

14 A. Rami and A. Lasia, *J. Appl. Electrochem.*, 1992, **22**, 376.

15 D. Shi, B. Wen, R. Melnik, S. Yao and T. Li, *J. Solid State Chem.*, 2009, **182**, 2664.

16 A. Ilbagi, P. D. Khatibi, H. Henein, R. Lengsdorf and D. M. Herlach, *J. Phys.: Conf. Ser.*, 2011, **327**, 1.

17 D. M. Herlach, *Phase transformation in multicomponent melts*, John Wiley & Sons Ltd, 2009.

18 J. Dulle, S. Nemeth, E. V. Skorb, T. Irrgang, J. Senker, R. Kempe, A. Fery and D. V. Andreeva, *Adv. Funct. Mater.*, 2012, **22**, 3128.

19 B. J. H. Bang and K. S. Suslick, *Adv. Mater.*, 2010, **22**, 1039.

20 K. S. Suslick, *Science*, 1990, **247**, 1939.

21 S. J. Doktycz and K. S. Suslick, *Science*, 1990, **247**, 1067.

22 W. B. McNamara, Y. T. Didenko and K. S. Suslick, *Nature*, 1999, **401**, 772.

23 T. Ungar, A. Revesz and A. Borbely, *J. Appl. Crystallogr.*, 1998, **31**, 554.

24 K. Venkateswarlu, A. C. Bose and N. Rameshbabu, *Physica B*, 2010, **405**, 4256.

25 A. K. Zak, W. H. A. Majid, M. E. Abrishami and R. Yousefi, *Solid State Sci.*, 2011, **13**, 251.

26 R. Bhattacharyya, B. Key, H. Chen, A. S. Best, A. F. Hollenkamp and C. P. Grey, *Nat. Mater.*, 2010, **9**, 504.

27 G. Kresse and J. Furthmüller, *Comput. Mater. Sci.*, 1990, **6**, 15.

28 G. Kresse and J. Furthmüller, *Phys. Rev. B: Condens. Matter*, 1996, **54**, 11169.

29 P. E. Blöchl, *Phys. Rev. B: Condens. Matter*, 1994, **50**, 17953.

30 J. K. Nørskov, T. Bligaard, A. Logadottir, J. R. Kitchin, J. G. Chen, S. Pandelov and U. Stimming, *J. Electrochem. Soc.*, 2005, **152**, J23.

31 H. J. Monkhorst and J. D. Pack, *Phys. Rev. B: Solid State*, 1976, **13**, 5188.

32 B. Hammer, L. B. Hansen and J. K. Nørskov, *Phys. Rev. B: Condens. Matter*, 1999, **46**, 7413.

33 J. Greeley, T. F. Jaramillo, J. Bonde, I. B. Chorkendorff and J. K. Nørskov, *Nat. Mater.*, 2006, **5**, 909.
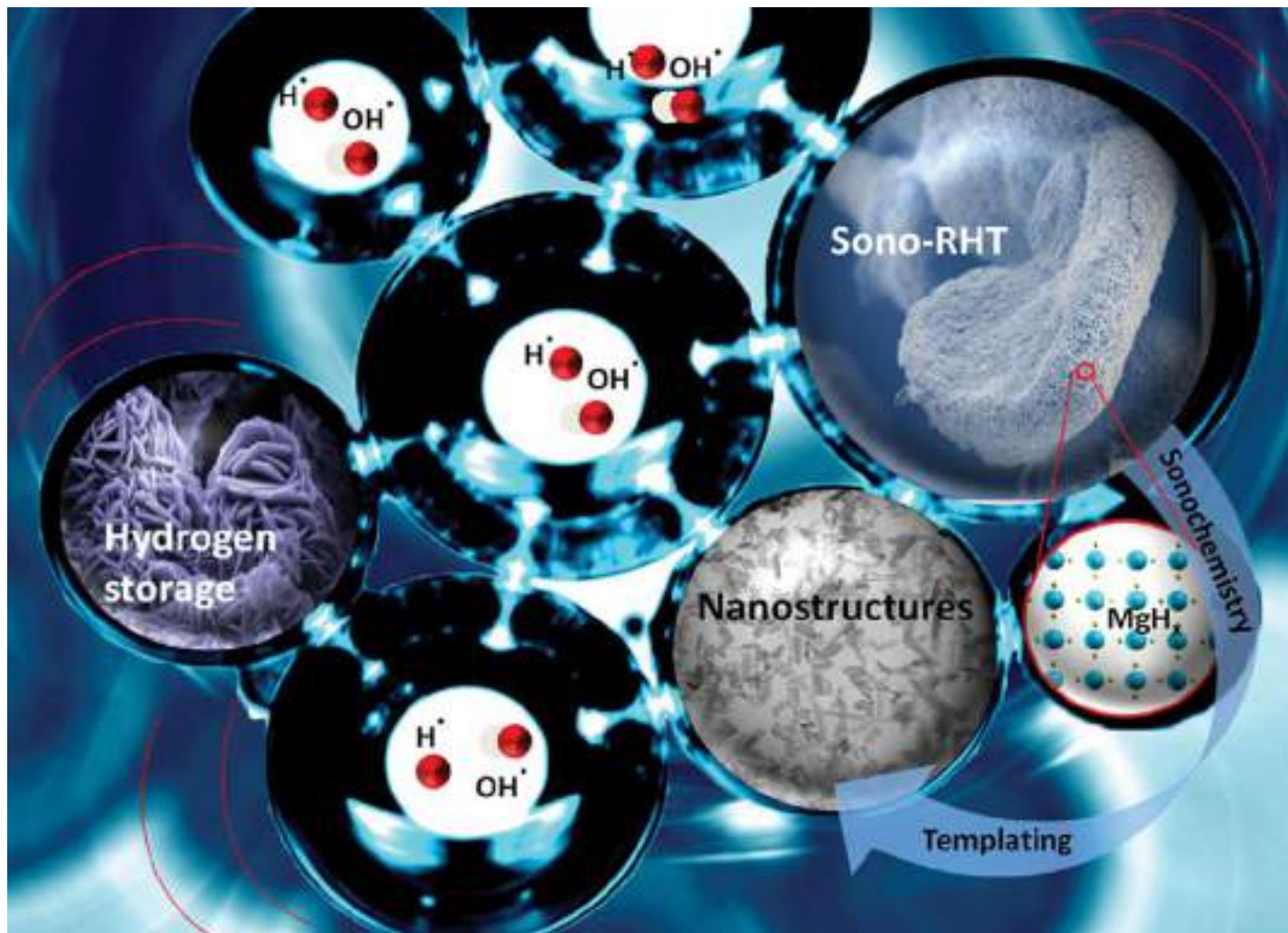
Showcasing work from Ekaterina Skorb's laboratories at the Max Planck Institute of Colloids and Interfaces, Germany, the Belarusian State University, Belarus, and the University of Bayreuth, Germany
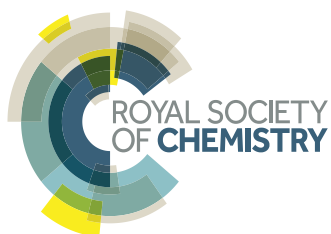
Sonogenerated metal-hydrogen sponges for reactive hard templating

Sonochemically generated microbubbles can be considered as microreactors containing free radicals and excited species. The unique conditions of such "Bubbles HARD ROCK" can be effectively used for chemical synthesis and nanostructuring of solids.

ROYAL SOCIETY
OF **CHEMISTRY**

www.rsc.org/chemcomm

ChemComm

Sonogenerated metal-hydrogen sponges for reactive hard templating†

Olga Baidukova,[a] Helmuth Möhwald,[a] Aliaksei S. Mazheika,[b] Dmitry V. Sviridov,[b] Tatiana Palamarciuc,[c] Birgit Weber,[c] Pavel V. Cherepanov,[d] Daria V. Andreeva[d] and Ekaterina V. Skorb*[ab]

We present sonogenerated magnesium-hydrogen sponges for effective reactive hard templating. Formation of differently organized nanomaterials is possible by variation of sonochemical parameters and solution composition: Fe_2O_3 nanorods or composite dendritic Fe_2O_3/Fe_3O_4 nanostructures.

Synthesis of nanostructured materials by using a reactive hard template (RHT) approach was first introduced in 2007 by Thomas et al.[1] with great advantage of omitting high temperatures or harsh reagents for removal of a template. Herein we combine both RHT and the sonochemical approaches to synthesise hierarchically structured materials and propose a novel method of template-assisted synthesis of nanostructures by using sono-chemistry (sono-RHT, Fig. 1). The sono-RHT concept, which combines the advantages of hard templating with in situ decomposition, i.e., removal of a template, is a time saving and step-reducing process.

Synthesis and nanostructuring of solids by using sonochemical methods attract fundamental and technological interest due to the unique potential of locally generated high temperature (up to 5000 K) and high pressure (several hundreds of bars) processes provided by intensive ultrasonication.[2a] The propagation of the acoustic waves in liquid generates a cavitation field consisting of a large number of interacting microbubbles.[2b] These microbubbles can be considered as microreactors containing free radicals and excited species that can be used for chemical synthesis and nanostructuring of solids.[2c] Symmetric and asymmetric micro-bubble collapses can provide constant delivery of chemicals to the reaction zone.[2d] Recently, we demonstrated that inorganic materials could adopt a variety of different morphologies upon sonication of aqueous suspensions of solid particles. For instance,

depending on sonication time, amorphous or crystalline silicon particles and quantum dots can be formed from silicon slurries.[3a] Sonochemical modification of Zn particles[3b] leads to the formation of nanocomposite particles where ZnO nanorods are attached to the metallic Zn core. Sonochemically modified Al and Mg[3c] exhibit a mesoporous inner structure and a significantly increased surface area (up to 300 m^2 g^{-1}). The mechanism of ultrasound-assisted modification of solid particles in water relies on the interplay of the sonomechanical effect – fragmentation of particles accompanied by the increase of the surface area and the sonochemical effect – the interfacial Red/Ox reactions and etching of a metal surface triggered by free radicals formed during water sonolysis. The contribution of these two sono-effects depends on physical (melting point, hardness, and crystallinity) and chemical (electrode potentials) properties of the metals. Furthermore, the sonochemical
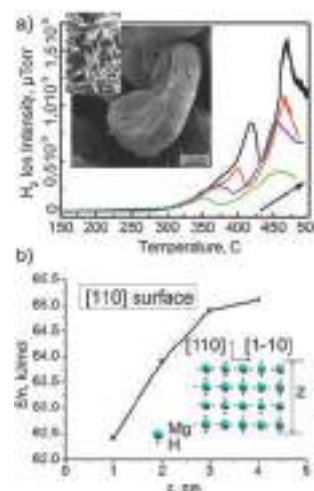

Fig. 1 (a) Temperature programmed desorption of hydrogen from the sonogenerated metal-hydrogen sponge for reactive hard templating (sono-RHT); arrows show a ramping rate increase from 5 K min^{-1} to 20 K min^{-1} with the 5 K min^{-1} step. Insets show SEM and TEM images of sono-RHT. (b) Normalized per number of Mg-atoms desorption energies of hydrogen of different thickness slabs within the DFT level.

[a] Max Planck Institute of Colloids and Interfaces, Am Mühlenberg 1, 14424 Potsdam, Germany. E-mail: skorb@mpikg.mpg.de

[b] Belarusian State University, 220030 Minsk, Belarus

[c] Inorganic Chemistry II, University of Bayreuth, Germany

[d] Physical Chemistry II, University of Bayreuth, Germany

oxidation of "reactive" metals (Al and Mg) is followed by the production of a highly concentrated reducing agent, *e.g.* hydrogen, on the metal surface.

The "reactive" Al and Mg are not only oxidized during ultrasonic treatment in water, but they also serve as effective donors of electrons that result in H_2 production. Sonochemical modification of Al and Mg leads to the simultaneous formation of mesoporous metal frameworks and generation of H_2 in the pores. Magnesium as one of the most reactive metals was used as a model reactive metal for the proof of the principles of sono-RHT. The images of Mg used as a sono-RHT are shown in Fig. 1a(insets). Sonication of aqueous suspensions of Mg leads to the formation of highly active magnesium hydrides of different compositions. The temperature programmed desorption of hydrogen (Fig. 1a) indicates the presence of hydrogen in the sonicated Mg. Moreover several adsorbed hydrogen clusters can be suggested since there are at least two peaks visible in the spectrum.

The calculated energy of hydrogen desorption is *ca.* 65.7 kJ and *ca.* 389.3 kJ. The magnesium hydrides rapidly decompose under extreme conditions during sonication in water with the production of H_2, and thus, magnesium is a promising material that can be used for the sono-RHT synthesis. The concentration of the residual hydrogen in the sonicated and dried Mg powder was calculated *ca.* 1.13 µl mg^{-1}.

Both Mg and MgH$_x$ clusters can be formed. Some of the possible geometries of MgH$_x$ were calculated recently by the density functional theory (DFT) (B97) method.[4a] Comparable to our sono-RHT are hydrogen-enriched Mg$_{15}$H$_x$ clusters, which were also taken into account. The extra hydrogen atoms are less strongly bound to the hydride structure and can therefore be released at lower temperatures. Moreover in our case we formed mesoporous sponge structures in which clusters are difficult to be aggregated. Mesoporous sponge has different nanosized units of MgH$_x$ slabs in the composition. We calculated for different thickness for MgH$_2$ crystal (100) slabs the energy of total hydrogen desorption from each single slab by DFT within the hybrid PBE0 method.[4b] It was shown that complimentary to our experimental data are slabs with thickness between 2 and 3 nm. The entire dehydrogenation of MgH$_2$ slabs, the sum of desorption energies of all H-layers, is about 65 kJ mol^{-1} for (110) with z = 3 nm (Fig. 1b). This value is very close to the experimentally obtained value. The ΔH^O_{298} of entire dehydrogenation was calculated only for the 1 nm slab (110) due to the high computational effort needed. It is 59.3 kJ mol^{-1}, whereas electronic energy is 62.3 kJ mol^{-1}. The difference of 3 kJ mol^{-1} is vanishingly small, less than the error of application of different exchange–correlation functionals. In such a way, the first peak of H_2 thermodesorption (65.7 kJ mol^{-1}) is most probably the desorption of the whole hydrogen from MgH$_2$ nanoparticles of several nm size. This is less than $\Delta_f H^O_{298}$ (MgH$_2$) −76.46 kJ mol^{-1} due to the unique morphology of MgH$_x$ used for sono-RHT and is promising fact for solid hydrogen storage.

Overall a general sono-RHT synthetic procedure of nanostructures includes the following steps: (i) sonochemical formation of the mesoporous metal RHT; (ii) ultrasound assisted loading of the RHT with chemical precursors for nanoparticle synthesis; (iii) reduction of precursors due to interaction with the sono-activated metal surface; and (iv) the RHT decomposition due to the electrochemical processes stimulated by ultrasound. Herein, we demonstrate the sono-RHT for the synthesis of hierarchically structured materials.

Magnetic nanoparticles were synthesized by reduction of Fe(II) or Fe(III) ions from the corresponding chloride (Fig. 2) or nitrate (not shown here) salts. The formation of the magnetic iron-based materials in the pores of the sono-RHT (Mg) was followed by simultaneous electrochemical degradation of the RHT triggered by sonication. The morphology and composition of magnetic nanoparticles are dependent on the used precursors. The final magnetic materials are dark brownish powders that are composed of 4/m 3 2/m Fe$_3$O$_4$ – 32/m Fe$_2$O$_3$ (Fig. S2 right and Table S1, ESI†) or 32/m Fe$_2$O$_3$ (Fig. S2 left and Table S1, ESI†). By using the sono-RHT method it is possible to control the parameters during the synthesis such as concentration of the RHT, concentration and type of precursors and solvent as well as duration and intensity of sonication, *etc.* Certain equilibrium structures can be obtained under particular preparation conditions.

The sono-RHT synthesis was performed by sonication of 1 wt% aqueous suspension of *ca.* 100 µm magnesium particles. Then aqueous solutions of iron salts (to achieve a concentration of 2 wt% in the resultant solution) were added to the suspension. The structures in Fig. S2 left (ESI†) correspond to the samples that are prepared by using a FeCl$_2$ precursor. The structures in
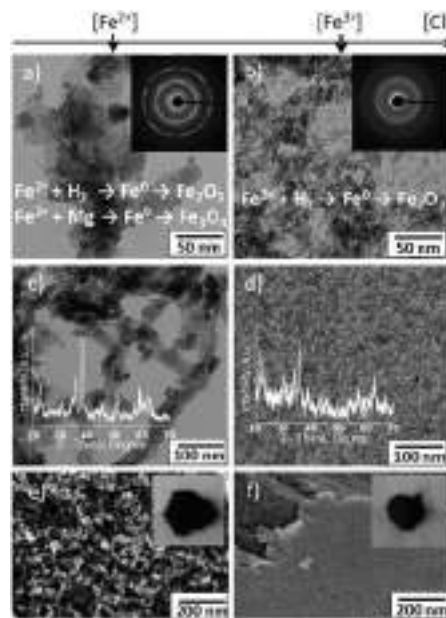

Fig. 2 Characterisation of magnetic materials formed by the sono-RHT method. (a–d) TEM images of (a, c) Fe$_3$O$_4$–Fe$_2$O$_3$ dendritic structure, insets show (a) electron diffraction (ED) of the sample, both hydrogen and magnesium are introduced as reduction agents with Fe^0 as the intermediate, (c) XRD pattern. (b, d) Fe$_2$O$_3$ magnetic rod-shaped nanoparticles, insets show (b) ED of the sample and point hydrogen as the main reduction agent with Fe^0 as the intermediate, (d) XRD pattern; (e, f) SEM images of (e) dendritic structures and (f) nanoparticles; insets show optical images of the samples.

Fig. S2 right (ESI†) correspond to the samples that are synthesized in the presence of a $FeCl_3$ precursor.

By using the same concentration of the iron salts, Cl^- concentration was higher in the presence of $FeCl_3$. Since the Cl^- anions are known as corrosive agents for Mg we expect that the degradation of the metal sono-RHT will be faster at higher chloride concentrations. Indeed, the degradation of Mg was slower in the presence of nitrate and $FeCl_2$ in comparison to the degradation of the RHT in the presence of $FeCl_3$. The rate of Mg degradation strongly affects the morphology and composition of the resultant iron-based materials. In the case of slow decomposition of the sono-RHT decomposition process, Mg^0 from the metal framework could be involved in the reduction process together with hydrogen as an additional reduction agent. This results in the formation of the iron-based dendritic porous structure on the surface of the metal surface as evidenced by TEM images (Fig. S2 left, ESI†). Since the sonication was performed in aqueous media, reduced iron nanostructures are rapidly oxidized with the formation of various iron oxides. Thus, a hierarchically structured iron based material consisting of a dendritic porous substance covered by nanoparticles was formed by using the sono-RHT method. The chemical composition of these structures will be discussed below. Shortly, the dendritic porous Fe_3O_4–Fe_2O_3 is covered by Fe_2O_3 nanoparticles.

If the reduction agent is mostly H_2, which is produced during the course of the fast decomposition of the magnesium framework (at high Cl^- concentration when $FeCl_3$ is used), rod-shaped Fe_2O_3 nanoparticles are formed (Fig. S2 right, ESI†).

The results of the magnetization measurements of the iron based nanoparticles and dendritic structures are shown in Fig. 3. All samples show a superparamagnetic behaviour. The material itself is ferromagnetic, thus the observed magnetic moment is much higher than for paramagnets and the sample does not follow the Curie law. However, there is no hysteresis because the particles are small: they change their orientation when the orientation of the external magnetic field is changed. This is observed when the particle size is smaller than the size of the Weiss areas of the ferromagnet/ferrimagnet. The temperature dependence was investigated in order to see, if the movement of the particles is blocked below a certain temperature (blocking temperature), which is not the case.

The Mössbauer spectrum (Fig. 3a) of the dendritic particles (Fig. S2 left, ESI†) can be approximated by a superposition of two doublets and two sextets (Table S1, ESI†). The values of quadrupole splitting (QS) to input A of the doublet of the outer shell and core Fe^{3+} decrease in comparison with the values measured for the nanoparticles mostly due to the size effect. (Fig. S2 left, ESI†). It is seen from Fig. 3a that in the case of the dendritic structure there is one maximum in total QS distribution due to an increase in the range of distributions of QS of each doublet, with a decrease of the value of the quadrupole splitting of iron ions from the outer shell of the nanoparticles. The spectrum and distribution of QS for the dendritic structures suggested their porous character which is also seen from electron microscopy (Fig. S2 left, ESI†). The presence of two sextets indicates a magnetic interaction between iron atoms in the dendritic structure. The parameters (Table S1, ESI†) of the
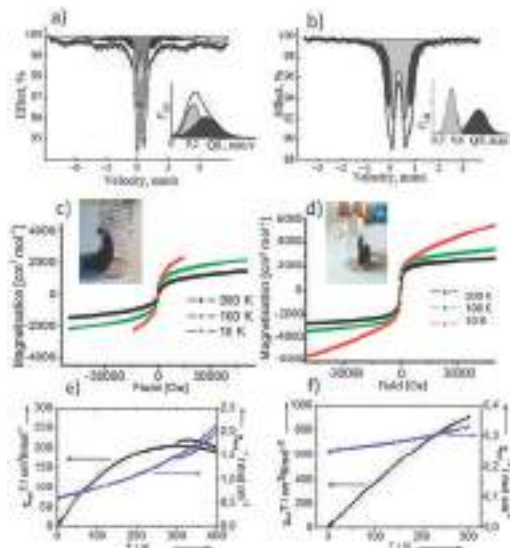

Fig. 3 Magnetic properties and structure analysis. (a, b) Mössbauer spectra (MS) of (a) dendritic particles and (b) nanoparticles. (c, d) Magnetisation at different temperatures of (c) dendritic particles and (d) nanoparticles; insets show optical images of dried powder attraction and orientation by a constant magnet in glass tubes. (e, f) χ_{mol} and $\chi_{mol} T$ vs. T plots of (e) dendritic and (f) nanoparticles in the temperature range 300–0 K.

sextets (IS) might be assigned to ferromagnetic magnetite Fe_3O_4.[5a] One of the sextets with parameters IS = 0.28 ± 0.01 mm s^{-1} and $H_{eff} = 48.0 \pm 0.02$ T corresponds to Fe^{3+} ions, which are in tetrahedral positions (A-position). Simultaneously the second sextet with parameters IS = 0.51 ± 0.01 mm s^{-1} and $H_{eff} = 44.4 \pm 0.02$ T corresponds to $Fe^{2,5+}$ ions (mixture of Fe^{3+} and Fe^{2+}), which are in an octahedron coordination (B-positions) in spinel magnetite. The stoichiometric ratio of the first to the second sextets is close to the theoretical value of 2 ($A_{(B)}/A_{[A]} \sim 2.1$).

The Mössbauer spectrum (Fig. 3b) of the nanoparticles (Fig. S2 right, ESI†) is a superposition of two doublets with approximately the same values of the isomeric shift (IS = 0.38 ± 0.02 mm s^{-1}), corresponding to iron(III) ions, and different values of quadrupole splitting (QS = 0.50 ± 0.02 mm s^{-1} and QS = 0.91 ± 0.02 mm s^{-1}). The parameters can be attributed to Fe_2O_3 in the superparamagnetic state.[5b] Thus, intermediate Fe^0 is not observed in the structure of the nanoparticles. However, the quadrupole splitting suggests the asymmetric density of the electric charge from iron ions in the core (QS = 0.91 mm s^{-1}) to the outer shell (QS = 0.50 mm s^{-1}) of the particle and justifies the assumption of an intermediate.

In order to compare the proposed sono-RHT method with a conventional method of synthesis of iron based materials we performed the synthesis with and without sonochemical irradiation of a solution of the Mg RHT and the iron(III) salt. Two types of particles and their magnetic behaviour are shown in Fig. S1 (ESI†). It is seen that particles prepared using a sono-RHT and described in the paper are different from non-magnetic particles prepared when a Mg RHT was not sonochemically irradiated.

In summary, the combination of the sonochemical approach and the RHT concept for a sono-RHT opens great prospects for the formation of a variety of nanomaterials in aqueous solutions. The structures that can be obtained are affected by the preparation conditions. The acoustic cavitation in water and the shape-defining effect of the reactive template material provide the special thermodynamic and kinetic conditions for the synthesis of nanostructures of particular morphology. The results presented here provide guidelines for the expansion of the concept towards a broad variety of chemical systems. As one of the following perspectives of the method we would like to highlight the formation of biocompatible nanostructures. Thus the hybrid inorganic–organic biocompatible structures with polypyrrole[6] can find their application in biosensors, bioactuators, and even nanorobotics.

Notes and references

1 A. Fischer, M. Antonietti and A. Thomas, *Adv. Mater.*, 2007, **19**, 264.
2 (a) K. S. Suslick, L. A. Crum and L. A. Encycl, *Acoustics*, Wiley-Interscience, N.Y., 1997; (b) L. H. Thompson and L. K. Doraiswamy, *Ind. Eng. Chem. Res.*, 1999, **38**, 1215; (c) D. G. Shchukin, E. V. Skorb, V. Belova and H. Möhwald, *Adv. Mater.*, 2011, **23**, 1922; (d) D. G. Shchukin and H. Möhwald, *Phys. Chem. Chem. Phys.*, 2006, **8**, 3496.
3 (a) E. V. Skorb, D. V. Andreeva and H. Möhwald, *Angew. Chem. Int. Ed.*, 2012, **51**, 5138; (b) J. Dulle, S. Nemeth, E. V. Skorb and D. V. Andreeva, *RCS Advances*, 2012, **2**, 12460; (c) E. V. Skorb, D. Fix, D. G. Shchukin, H. Möhwald, D. V. Sviridov, R. Mousa, N. Wanderka, J. Schöferhans, N. Pazos-Perez, A. Fery and D. V. Andreeva, *Nanoscale*, 2011, **3**, 985.
4 (a) R. W. P. Wagemans, J. H. Lenthe, P. E. Jongh, A. J. Dillen and K. P. Jong, *J. Am. Chem. Soc.*, 2005, **127**, 16675; (b) C. Adamo and V. Barone, *J. Chem. Phys.*, 1999, **110**, 6158.
5 (a) G. F. Goya, T. S. Berquo, F. C. Fonseca and M. P. Morales, *J. Appl. Phys.*, 2003, **94**, 3520; (b) R. Zboril, L. Machala, M. Mashlan, J. Tucek, R. Muller and O. Schneeweiss, *Phys. Stat. Solid.*, 2004, **1**, 3710.
6 E. V. Skorb, O. Baidukova, A. Goyal, A. Brotchie, D. V. Andreeva and H. Möhwald, *J. Mater. Chem.*, 2012, **22**, 13841.

Particle
& Particle Systems Characterization

WILEY-VCH

FULL PAPER
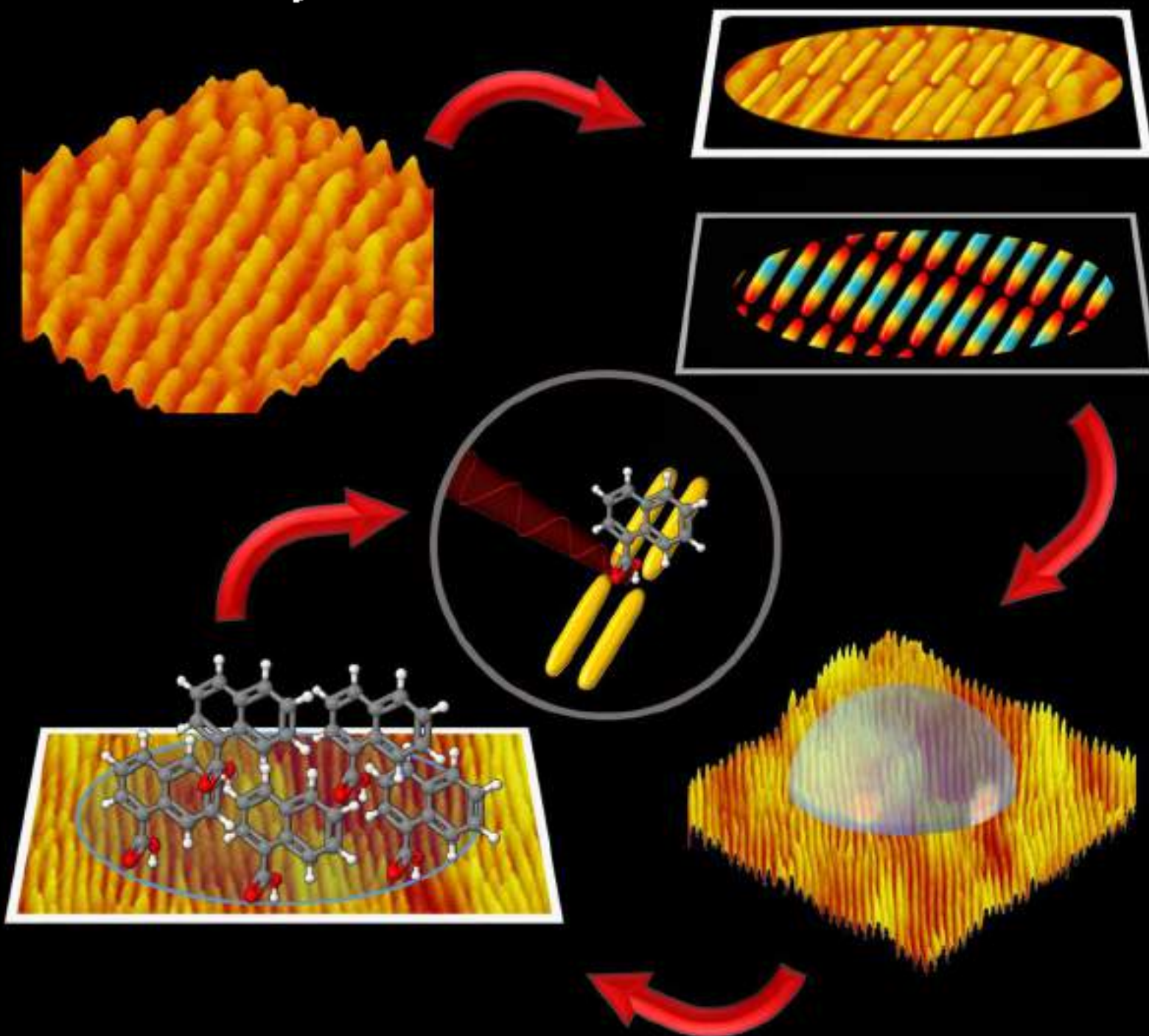
SERS Platforms of Plasmonic Hydrophobic Surfaces for Analyte Concentration: Hierarchically Assembled Gold Nanorods on Anodized Aluminum

Moritz Tebbe, Pavel Cherepanov, Ekaterina V. Skorb, Sergey K. Poznyak, Javier García de Abajo, Andreas Fery, Daria V. Andreeva, Ramon A. Alvarez Puebla, and Nicolas Pazos-Perez*

Efficient and homogeneous surface-enhanced Raman scattering (SERS) substrates are usually prepared using lithographic approaches, physical evaporation, or in situ chemical reduction. However, these approaches are time-consuming, expensive, and very difficult to upscale. Alternatively, template-assisted approaches using colloidal suspensions of preformed nanoparticles have become more popular because of their low cost, fast production, and ability to be scaled up easily. One of the limitations of these methods is the dimensions of the structured surfaces. In this context, a new method for designing low-cost, up-scalable surface patterns that match building block dimensionality based on anodization of aluminum, enabling a hierarchical organization of anisotropic nanoparticles, is presented. The proposed new technology starts with anodized aluminum oxide with regular parallel linear periodicities. To produce a highly efficient plasmonic surface, gold nanorods are assembled into parallel lines where the long axes of the Au rods are also oriented along the substrate lines, thus inducing reproducible tip-to-tip plasmonic coupling with the corresponding generation of highly active hotspots. Additionally, this advanced material presents an inherent hydrophobicity that can be exploited as a method for concentration of analytes on the surface. SERS detection is demonstrated with benzenethiol and 2-naphtoic acid.

1. Introduction

Surface-enhanced Raman scattering (SERS) is an ultrasensitive analytical technique with potential detection limits down to the single molecule, the possibility of multiplex analysis, and small sample preparation requirements.[1] SERS relies in the excitation of the vibrational fingerprint of the analytical target through the localized surface plasmon resonance (LSPR) generated by a plasmonic material, in close proximity to the analyte, upon illumination with a plasmon-frequency-tuned laser line.[2] Beside factors arising from the molecular structure of the probe under study or its interaction with the plasmonic material (chemical effects),[3] the intensity in SERS is extremely sensitive to the optical efficiency of the plasmonic enhancer, which is capable of amplifying the signal of extremely diluted targets against the inelastic optical background.

SERS can be achieved directly in solution or in thin films. Although SERS in solution (i.e., in colloidal dispersions of nanoparticles) represents a convenient way of analyzing certain samples,[4] thin films add versatility and can be prepared on fully portable optimal substrates that are used in a similar fashion as a reactive strip in field analysis.[5] A way of producing plasmonic thin films is by using physical methods such as physical evaporation on flat or patterned substrates.[6] Although this is an efficient method, it usually leads

M. Tebbe, P. Cherepanov, Prof. A. Fery, Dr. D. V. Andreeva,
Dr. N. Pazos-Perez
Physical Chemistry II
Universität Bayreuth
Universitätsstraße 30, Bayreuth, Germany
E-mail: nicolas.pazos@uni-bayreuth.de
Dr. E. V. Skorb
Max Planck Institute of Colloids and Interfaces
Wissenschaftspark Golm
Am Mühlenberg 1, Golm 14424, Germany
Dr. E. V. Skorb, Prof. S. K. Poznyak
Chemistry Department
Belarusian State University
Leningradskaya str. 14, Minsk 220030, Belarus

Prof. J. G. de Abajo, Prof. R. A. A. Puebla
ICREA, Passeig Lluís Companys 23
08010, Barcelona, Spain
Prof. J. G. de Abajo
ICFO – The Institute of Photonic Sciences
Mediterranean Technology Park
Av. Carl Friedrich Gauss 3 08860, Castelldefels - Barcelona, Spain
Prof. R. A. A. Puebla, Dr. N. Pazos-Perez
Departamento de Quimica Fisica e Inorganica
Universitat Rovira i Virgili and Centro de Tecnologia Quimica de Cataluña
Carrer de Marcel·lí Domingo s/n 43007, Tarragona, Spain
Dr. N. Pazos-Perez
Medcom Advance, Viladecans Business Park - Edificio Brasil
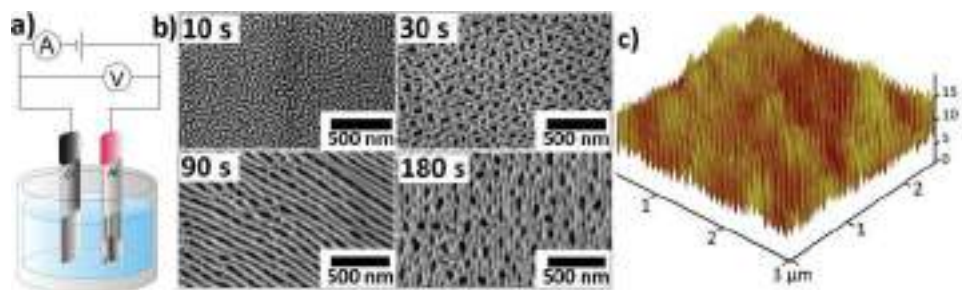Bertran i Musitu 83-85 08840, Viladecans – Barcelona, Spain

Figure 1. a) Schematic representation of the ionized aluminum oxide (AAO) substrate preparation through galvanostatic anodization. b) Time-dependent evolution of surface morphology of aluminum substrate. c) AFM image of aluminum plate anodized for 90 s.

to rather inhomogeneous films in which plasmonic coupling takes place randomly at so-called hotspots, therefore resulting in a loss of linearity of the signal with analyte concentration.[7]

In an effort to produce geometrically homogeneous substrates, well-established lithographic approaches such as e-beam, focused-ion beam or dip-pen patterning have been proposed.[8] These approaches are however time-consuming, expensive, and very difficult to upscale. Alternatively, evaporation can be also carried out on complex surfaces such as monolayers of self-assembled polymer beads with a subsequent treatment to remove the polymer (i.e., nanosphere lithography).[9] In this case, the resulting material presents homogeneous patterned features with controlled dimensions and localized surface plasmon resonances (LSPRs). However, this method leads to large nanostructured features (over hundreds of nanometers) and is rather constrained to the few obtainable shapes and dispositions.[10] Alternatively, optical thin films can be also produced by in-situ chemical reduction of metallic salts on polymers or even using colloidal suspensions of preformed nanoparticles with their posterior retention on the desired surface by self-assembly,[11] Langmuir-Blodgett[12] or layer-by-layer methodologies.[13] Both methods present a low degree of control on the position of the nanoparticles, which yields materials with similar drawbacks to those obtained by physical evaporation.

During the last years, the development of routes to organize particles down to the nanometer scale has significantly improved. Recently, our groups developed new methodologies for the fabrication of homogeneous and efficient plasmonic surfaces for SERS, including supercrystals and organized lines of particles.[14] Specifically, nanoparticle line imprinting using wrinkles as templates has some advantages over other approaches. It is easily up scalable, inexpensive, and highly efficient. The main limitation for nanoparticle assembly using template-assisted methods is the texture size of the structured surface that is employed. As for bottom-up assembly approaches, the dimensions of the structures and the building blocks have to match. This implies that the features of the template require dimensions within the nanometer scale.

Anodized aluminum[15] surfaces emerge as good alternatives to the above-mentioned methodologies. In general, these materials consist of a packed array of hexagonal columnar cells with central, cylindrical, uniformly sized holes ranging from 4 to 200 nm in diameter with inter-hole distances between 50 and 500 nm.[16] The geometrical characteristics make of these self-ordered structures a very exciting alternative material for organization of nanoparticles. Additionally, anodized aluminum

presents a natural hydrophobicity that may favor the spontaneous concentration of the target analyte onto the plasmonic surface. In this work, we suggest a new pathway to design low-cost, up-scalable surface patterns based on anodization of aluminum (Al), which match template and building block dimensionality, enabling a hierarchical organization of anisotropic nanoparticles. Moreover, the proposed new technological approach shows the unprecedented formation of a periodic linear parallel array nanostructure on the surface of anodized aluminum oxide (AAO). This structure enables the organization of Au NRs and due to its hydrophobic nature, creates a SERS substrate capable of concentrating an analyte deposited from solution increasing its sensitivity.

2. Results and Discussion

A schematic representation of the electrochemical cell for AAO formation with platinum and aluminum electrodes immersed in the electrolyte is shown in **Figure 1**a. The mechanism of pore formation in AAO is based on two processes: dissolution and growth of aluminum oxide. The diameter, length, and arrangement of the pores depend on the electrolyte used, the applied voltage, the current density, the reaction time, and the temperature.[17] Consequently, the morphology of the final AAO can be tuned by adjusting the preparation conditions. In the present work, porous AAO templates were prepared via electrochemical oxidation of aluminum in phosphoric acid solutions under galvanostatic regime. As aluminum anodization is a time-dependent process, a study of the temporal evolution of the obtained structure was carried out. Figure 1b shows SEM images of AAO revealing different structures after anodization times of 10, 30, 90, and 180 s. After 10 s, we observed formation of the hillock-like surface morphology,[18,19] followed by formation of the porous surface after 30 s. The grooved morphology reveals after 90 s of modification, finally converting into the cell-like surface morphology of the used template.

The mechanism formation of this peculiar hillock-like surface morphology can be explained in a similar way to that already described for porous AAO.[20] Briefly, upon the initiation of the anodization process, a constant current was applied and a nonconductive layer of aluminum oxide start to grow, and associated with it the anodizing voltage increases. Thus, the phosphate ions present in the working electrolyte incorporate into the AAO crystal structure. This incorporation takes place by replacing oxygen atoms on the surface of aluminum causing
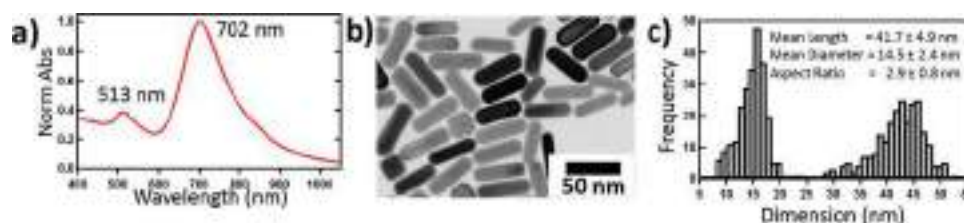
FULL PAPER

Figure 2. a) UV–vis–NIR spectrum, b) TEM image, and c) size distribution histograms of the prepared gold nanorods (GNRs).

the formation of hillocks [Figure 1b (10 s)].[18] With longer (>30 s) anodization times, a further transformation into porous AAO occurs (Figure 1b). For our purpose, the periodically grooved AAO structure (see Figure 1b, 90 s) is the most interesting one. Accordingly, the current density and anodization time were tuned in order to up scale the process for the formation of a grooved template after relatively short times. For this purpose, we adjusted the applied current density to a value of 16 mA cm^{-2}, allowing the preparation of a grooved template in 90 s. The resulting periodically grooved template exhibited a mean groove width of 36 nm (Figure 1c). Although parallel aligned pores with controllable size has been previously described,[20] the formation of periodically grooved AAO surfaces with periodicities in the nanometer regime has not been reported to the best of our knowledge. The generation of such structures could be explained by a voltage change during the anodization process. The application of a constant current implies that as the nonconductive layer of aluminum oxide grows, the resistance changes and produces a reduction in the voltage. The merging of newly formed hillocks occurs in lateral directions, forming well-pronounced corrugated morphologies of the AAO layer. Further continuation of anodization induces the formed grooves to merge with each other to reestablish a porous morphology (Figure 1b, 180 s). Consequently, the competing processes of oxide layer creation and metal dissolution[21] lead to the formation of variety of different AAO morphologies.

The linear features formed on AAO are ideal substrates on which to arrange gold nanorods (GNRs) and have those interacting in close tip-to-tip proximity. Among the plasmonic properties and applications of these particles,[22] GNRs are known to generate extremely efficient plasmon coupling when interacting tip-to-tip.[23] Therefore, we chose these particles as the plasmonic material to generate a densely populated surface of highly active hotspots. GNRs were prepared to match the size of the structures (36 nm mean groove width) by using the Murphy method,[24] with cetyltrimethylammonium bromide (CTAB) as stabilizer and Ag(I) to induce rod-like growth along the single crystalline facets of the seed particle. **Figure 2** shows GNRs of ≈42 nm in length with a thickness of ≈15 nm (aspect ratio of ≈3) exhibiting LSPRs at 513 and 702 nm, corresponding to their transversal and longitudinal modes, respectively. In order to organize the particles onto the template, a concentrated solution

of GNRs was first centrifuged to decrease the amount of free CTAB and avoid the crystallization of the surfactant in the pores, and then spin-coated onto the template (**Figure 3**a) using a suitable spin speed and concentrations of CTAB and particles. The matching of particle size and nanoscale surface topography is critical to generate macroscopic hierarchical structures of anisotropic particles by bottom-up template-assisted self-assembly. Besides, the compatible wettability of the nanostructure surface with the particle solution is responsible for successful particle organization using spin coating. The latter is a well-established method of material deposition based on centrifugal forces and evaporation of the residual solvent.[25] Upon evaporation of the solvent on the nanostructured surfaces, capillary forces drag the nanoparticles into the cavities, assembling them in a close packed arrangement because of the Rayleigh instabilities and the preceding solvent front along the alumina grooves and inside the pores.[26]

The contact angle of a drop of water on the unmodified alumina is 79°. For porous surfaces, their wettability increases as a function of pore size. The contact angle for the used substrate was measured to be 104° (Figure 3b) for a mean pore size of 36 nm (estimated by PSD analysis of the AFM images).[27] The nanostructured surface thus becomes more hydrophobic after modification, in good agreement with the modified Laplace model or the capillarity and line-tension model for AAO.[28] For spin coating, we need to provide the surfaces with
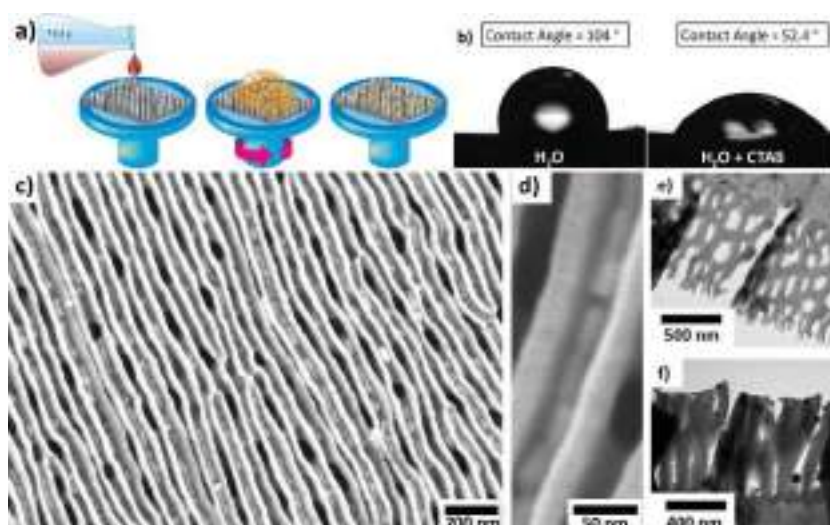

Figure 3. a) Scheme illustrating the organization of GNRs on the AAO template. b) Wettability of AAO for pure water and water solution of CTAB. c,d) SEM images of the GNRs organized onto the AAO template at different magnifications. e,f) TEM images of the microtomed template (e) before and (f) after GNRs organization.
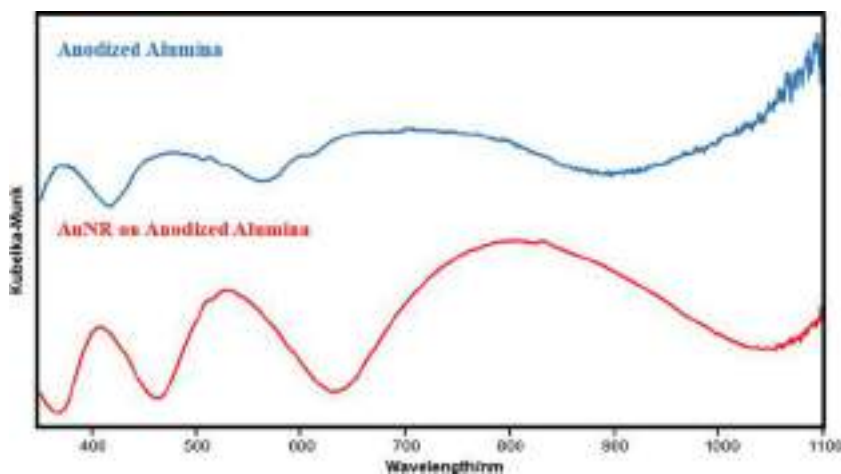
![Materials Views logo]
www.MaterialsViews.com

Particle
& Particle Systems Characterization
www.particle-journal.com

FULL PAPER

Figure 4. UV–vis–NIR reflectance spectra of the AAO template before and after the GNR organization. Both measurements were made at 60°.

adequate wettability. The aqueous suspensions of GNRs stabilized by CTAB have a surface tension of 35 mN m^{-1} (above critical micelle concentration of CTAB).[29] At the same time, the contact angle between the used solution containing CTAB and the AAO was 52.4°. Consequently, CTAB provided the enhanced wettability of the nanostructured alumina substrate. Figure 3c,d shows that GNRs are linearly aligned inside the grooves. We stress again that the observed preferential organization along the long axes of the rods (Figure 3c,d) is achieved because of the chosen sizes of the rods (42 × 15 nm) and the width of the grooves (36 nm). Furthermore, we observe the presence of darker spots within these grooves, corresponding to pores of the anodized surface. The TEM images of the ultramicrotomed surfaces before (Figure 3e) and after (Figure 3f) particle deposition reveals the presence of GNRs inside both grooves and pores.

Optical reflectance spectroscopy of the Au nanorod arrays supported in AAO matrix reveals an interference pattern with several features in the UV-Vis-NIR region (see **Figure 4**). The interferometric signals are shifted toward longer wavelengths when Au rods are present, this effect arise from a modulation of the local dielectric causing a shift in signals[30] and, can be related to a change of the effective optical thickness (product of thickness and refractive index),[31] which is attributed to a change in the refractive index of the layer medium when Au rods are present.[30,32]

Although there is a high density of AuNRs on AAO substrates that are aligned along the surface indentations, their plasmonic resonances are sensitive to variations in their geometrical dimensions, as well as to the gap distances between contiguous rods (see **Figure 5**). Additionally, these plasmons are generally expected to lie below 700 nm light wavelength (Figure 2a,b), and therefore, they cannot be directly excited neither by the 785 nm laser light nor by the emitted inelastic signal at even larger wavelengths. However, the gap geometry leads to large field enhancements near the surface even at lower photon energies due to non-resonant plasmon polarization, thus contributing to a substantial SERS enhancement, as shown in Figure 5c. The actual value of the enhancement depends on the specific

gap separations. In our samples, we expect to have a distribution of separations of the order of a few nanometers down to touching. The effect of the substrate is not contemplated in the calculations shown in Figure 5, but as already mentioned the substrate will have a strong influence on the dielectric environment and will lead to a substantial redshift of the spectra similar to the simulations shown in Figure 5a,c for rods in water compared with air. Furthermore, the tip-to-tip dimer configuration may also lead to a further red shift as depicted in Figure 5a,b. Thus, both effects will lead to a larger SERS enhancement because of a greater degree of overlap with the wavelengths of excitation of the light.

In order to test the optical efficiency of our materials for SERS, we designed an experiment involving two well-known analytes, benzenethiol (BT) and 2-naphtoic acid (NA). Furthermore, the same experiment was carried out on a commercial optical surface (Klarite) (see **Figure 6**) in order to compare the results with those obtained from a common SERS substrate. Before the analyte deposition, the plasmonic substrates were treated with oxygen plasma to eliminate residual CTAB from the plasmonic surfaces.[33] Both substrates were subsequently exposed to benzenethiol in gas phase. It is important to note that with this experimental setup the gaseous BT is adsorbed onto the entire plasmonic surfaces. Although both plasmonic substrates show clearly the vibrational pattern of BT (C–H bending at 1022 cm^{-1}, ring breathings at 1073 and 999 cm^{-1}, and ring stretching at 1570 cm^{-1}),[34] the average intensity of the obtained spectra is remarkably different, as shown in Figure 6. It is thus instructive to point out some differences between both types of samples (AAO-GNRs and Klarite). First, AAO-GNRs films provide a homogeneous signal through the entire film, which is covered with a rather homogenous density of hotspots (mainly rod ends and tip-to-tip gaps), while Klarite substrates present a high activity only in a sparse set of randomly occurring spots on the surface. The homogeneous distribution of hotspots (tip-to-tip plasmonic coupling between the rods trapped in the grooves) in our films is in clear contrast with the commercial substrate, which exhibits a characteristic random distribution of such optically high-efficient regions for evaporated films. Furthermore and importantly, our substrates provide a five-fold higher signal than provided by the best spots in the Klarite substrate.

The effect of hydrophobicity provided by the AAO-GNRs substrate after plasma cleaning of CTAB on aqueous solutions deserves further consideration. We studied it, a diluted solution of NA in water (10 μL, 10^{-5} M) was cast over both substrates and air dried. The intrinsic hydrophobicity of the alumina seems to determine the contact angle of occurring droplets in the AAO-GNRs substrates, which is similar to the one reported above (105°), with the final result of a concentration of the analyte on a small spatial region that is fully covered with plasmonic particles. In contrast, the drop contact angle in the commercial substrate was much smaller (68°), thus resulting in more diluted analyte distributions on the surface. As a consequence, although
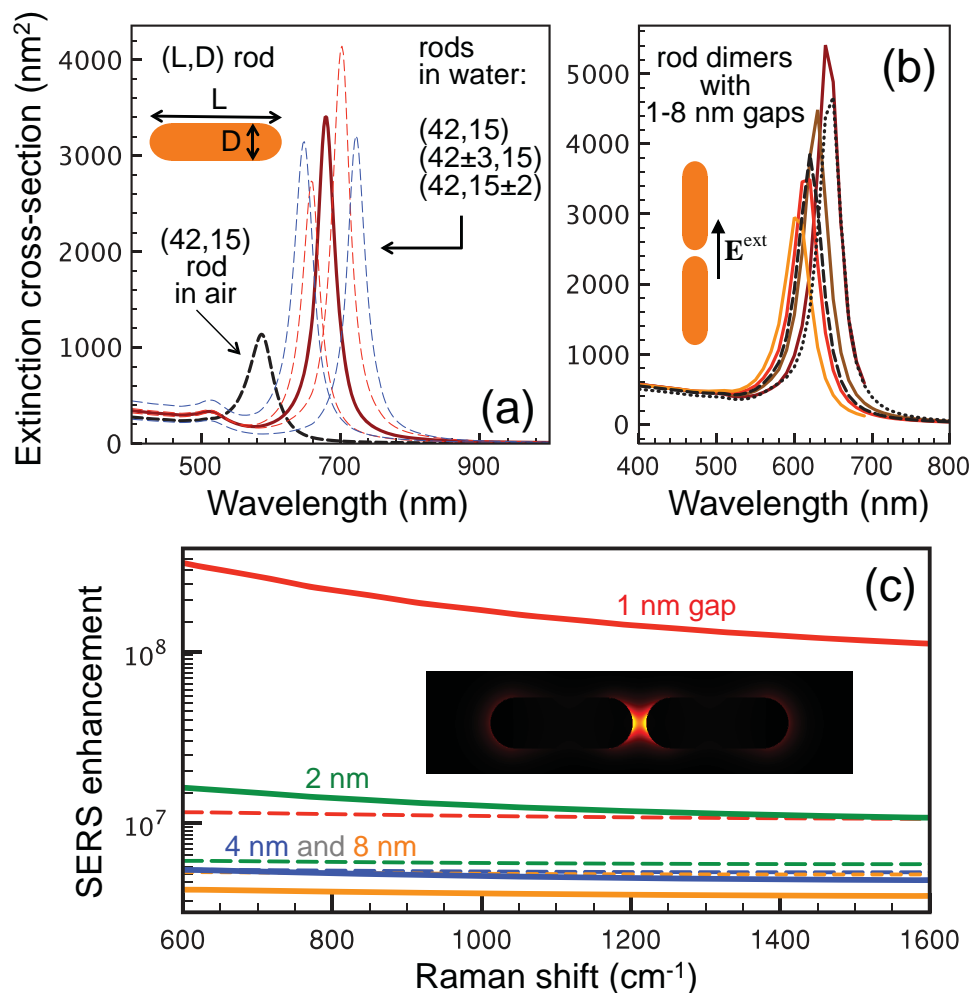
FULL PAPER

Figure 5. Optical response and SERS activity of individual and paired GNRs. a) Extinction cross-section of individual AuNRs of dimensions similar to those shown in Figure 2. The longitudinal resonance of rods in water (right curves) is considerably red-shifted with respect to airborne rods (left curves), and it is also shifted due to variations in rod dimensions, giving rise to an observed broad peak (Figure 2a). b) Optical resonance of pairs of AuNRs longitudinally aligned as observed on an AAO sample (Figure 3). A plasmon redshift accompanied by an increase in cross section is observed as the gap is narrowed down from 8 to 1 nm (solid curves). The plasmon is also sensitive to the dimensions of the rods (see dotted curve, corresponding to a (39,15)–(42,15) dimer, and dashed curve, for (42,13)–(42,15), both of them with a 2-nm gap). c) Surface-averaged SERS enhancement factors for molecules distributed 0.5 nm away from the surface of two neighboring nanorods aligned as shown in the inset of (b). The rods are assumed to be either in air (broken curves) or in water (solid curves) and illuminated with 785 nm light (a water environment might be more appropriate to describe residual humidity surrounding the rods during the SERS measurements). The enhancement is referred to the Raman signal from the same molecules away from the rods, averaged over polarizations and molecule orientations for both illumination and light collection along directions normal to the rod axes. The inset in (c) shows the near-field intensity of the gap mode in the 4-nm-gap dimer in water (linear scale saturated to 5000 times the incident field).

both surfaces show SERS activity of NA (ring stretching at 1632 and at 1388 cm^{-1}, CH bending at 1468 cm^{-1}, ring breathing at 1018 cm^{-1}, and C-H deformation at 770 cm^{-1}),[35] AAO-GNRs substrates exhibit a similar surface homogeneity to that commented above, but with an additional intensification of the SERS signal that is quantified by a 40-fold observed increase in intensity with respect to the commercial substrate.

3. Conclusion

In summary, we demonstrate a new method for the large-scale production of efficient plasmonic surfaces based on controlled

organization of gold nanorods retained on AAO surfaces. We take advantage of colloid synthesis methods to prepare particles with appropriate dimensions and we use surface chemistry to retain and align them on grooved AAO substrates. This results in an abundant distribution of hotspots originating in tip-to-tip interaction between the rods, where SERS amplification is taking place. We further exploit the physical and chemical properties of the AAO surface to design an optical sensor with the ability of concentrating trace amounts of analytes in an aqueous solution, yielding further intensification of the SERS signals. This method of preparing plasmonic substrates paves the road for the fabrication of reactive-strip optical sensors that are especially suitable for field analysis in environmental
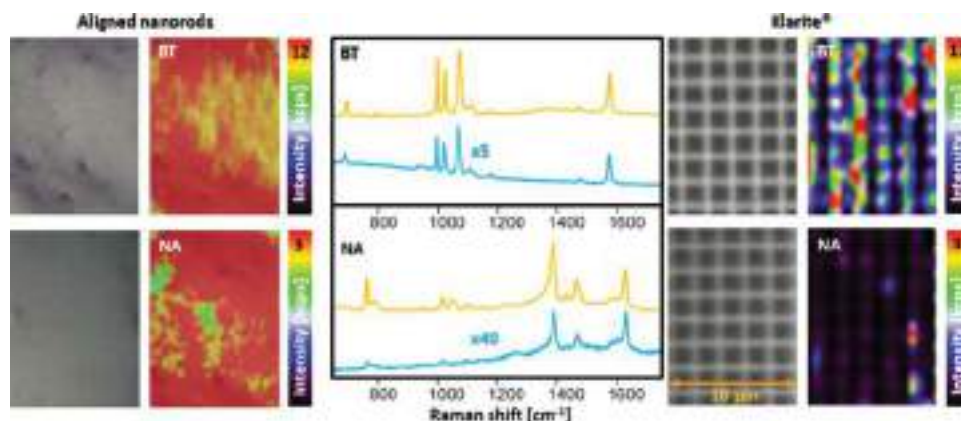
Figure 6. Optical and SERS images (left) and SERS spectra (yellow) of BT and NA in AAO-GNRs compared with the same analytes on a commercial surface Klarite (right and blue spectra).

monitoring or the design of diagnostic devices for medical applications.

4. Experimental Section

Materials: Silver nitrate (99.9999 %, AgNO$_3$), sodium borohydride (99.99 %, NaBH$_4$), gold(III) chloride trihydrate (99.9 %, HAuCl$_4$·3H$_2$O), nitric acid (32.5 %, HNO$_3$), benzenethiol, 2-naphthoic acid, and ascorbic acid (99 %) were purchased from Sigma–Aldrich (Germany). Cetyltrimethylammonium bromide (99 %, CTAB) was obtained from Merck. All reactants were used without further purification. Mili-Q water (18 MΩ cm^{-1}) was used in all aqueous solutions, and all the glassware was cleaned with aqua regia before the experiments. High-purity Al foil of 1-mm thickness (99.997 %) supplied by Sigma–Aldrich was used as a substrate for fabrication of AAO. Phosphoric acid, perchloric acid, and ethanol were also supplied by Sigma–Aldrich (Germany) and used as received.

Preparation of AAO Substrates: Al foils were cut in rectangles (7 mm × 40 mm), cleaned with acetone, and distilled water in order to remove any residuals and then dried under dry air. After cleaning, the Al foils were electrochemically polished in a 1:4 mixture solution of 65 wt% HClO$_4$ and 96 vol% ethanol. Temperature during the polishing procedure was kept under 5 °C. Mirror-finished Al foils with exposed-to-anodization area of 3 cm^2 were used as an anode in a home-made two-electrode electrochemical cell with Pt-wire electrode serving as a cathode (distance between electrodes was set to 1 cm). The anodization process was performed in galvanostatic mode under a constant current of 16 mA cm^{-2} for time periods of 10, 30, 90, and 180 s at ambient temperature. 1.0 M H$_3$PO$_4$ was used as a working electrolyte.

Preparation of Gold Nanorods: Particles of ≈42 nm length and 15 nm width were produced by adapting an established procedure reported.[24,36] Briefly, seed particles were prepared by adding 300 μL of a 0.01 M NaBH$_4$ solution in a 5-mL mixture of 0.1 M CTAB and 0.25 × 10^{-3} M HAuCl$_4$ under vigorous stirring. The solution was stirred rapidly for 2 min followed by continued slow stirring. A 200 mL of a 0.1 M CTAB solution containing 0.25 × 10^{-3} M HAuCl$_4$, 0.04 × 10^{-3} M AgNO$_3$, 1.3 mL of a 0.1 M HNO$_3$ solution to adjust the pH, and 0.35 × 10^{-3} M ascorbic acid as reducing agent were prepared. 2 mL of the prepared seeds was added to this solution after 30 min of stirring. The entire solution was mixed extensively and reaction took place at 32 °C for 24 h. The particles were cleaned and concentrated via multiple centrifugation steps at 16 000 rcf for 30 min to a final gold concentration of 5 mg mL^{-1} and 7.5 × 10^{-3} M CTAB.

Nanorod Organization: In order to organize the particles, a solution containing Au NRs was spin-coated on the aluminum substrates, which were pasted on a glass slide as support. The most critical experimental parameters to achieve a good particle organization are the CTAB and particle concentration together with the spin speed and time. These parameters were adjusted in order to achieve the best results as follow: 20 μL of the particle solution (5 mg mL^{-1} Au and 7.5 × 10^{-3} M CTAB) were spin-coated at 2000 rpm for 120 s. The substrates with the deposited nanoparticles show a red color.

Characterization: UV–vis spectroscopy (PerkinElmer, Lambda 19), UV–vis reflectance spectroscopy (Analytik Jena AG, SPECORD PLUS), transmission and scanning electron microscopy (TEM, LEO 922 EFTEM operating at 200 kV and LEO 1530 FE-SEM, Zeiss, respectively) were applied to characterize the optical response, structure, and size of the nanoparticles and their arrays. AFM images were obtained using a commercial atomic force microscope (DimensionTM 3100M equipped with a Nanoscope IIIm controller, Veeco Instruments Inc., USA) operating in tapping mode. Silicon cantilevers with a force constant of typically 35–47.2 N m^{-1} (OMCL-AC160TS, Olympus, Japan, typical frequency of 303 kHz) were utilized.

SERS Characterization: Benzenethiol was adsorbed in gas phase on the whole surface of the metallic samples by casting a drop of BT (0.1 M in ethanol) in a Petri dish where the substrate was also contained. A diluted solution of naphthoic acid (10 μL, 10^{-5} M) was cast on the plasmonic surfaces and air dried. SERS spectra were collected in backscattering geometry with a Renishaw Invia Reflex system equipped with a 2D-CCD detector and a Leica confocal microscope. The spectrograph used a high-resolution grating (1200 g cm^{-1}) with additional band pass filter optics. Excitation of the sample was carried out with a 785-nm diode laser line, with acquisition times of 200 ms and power at the sample of about 1 mW, using the Renishaw's StreamLine accessory. The laser was focused onto the sample with a 50× objective providing a spatial resolution of ca. 1 μm.

[1] a) N. J. Halas, M. Moskovits, *MRS Bull.* **2013**, *38*, 607; b) B. Sharma, M. Fernanda Cardinal, S. L. Kleinman, N. G. Greeneltch, R. R. Frontiera, M. G. Blaber, G. C. Schatz, R. P. Van Duyne, *MRS Bull.* **2013**, *38*, 615.

[2] R. A. Álvarez-Puebla, *J. Phys. Chem. Lett.* **2012**, *3*, 857.

[3] A. Otto, *J. Raman Spectrosc.* **2005**, *36*, 497.

[4] C. Andreou, M. R. Hoonejani, M. R. Barmi, M. Moskovits, C. D. Meinhart, *ACS Nano* **2013**, *7*, 7157.

[5] R. Zhang, B. B. Xu, X. Q. Liu, Y. L. Zhang, Y. Xu, Q. D. Chen, H. B. Sun, *Chem. Commun.* **2012**, *48*, 5913.

[6] W. B. Lacy, J. M. Williams, L. A. Wenzler, T. P. Beebe Jr., J. M. Harris, *Anal. Chem.* **1996**, *68*, 1003.

[7] A. Otto, *J. Raman Spectrosc.* **2006**, *37*, 937.

[8] a) N. A. Abu Hatab, J. M. Oran, M. J. Sepaniak, *ACS Nano* **2008**, *2*, 377; b) N. L. Rosi, C. A. Mirkin, *Chem. Rev.* **2005**, *105*, 1547.

[9] B. Sharma, R. R. Frontiera, A. I. Henry, E. Ringe, R. P. Van Duyne, *Mater. Today* **2012**, *15*, 16.

[10] K. Matczyszyn, J. Olesiak-Banska, *J. Nanophotonics* **2012**, *6*, 064505.

[11] L. Guerrini, E. Pazos, C. Penas, M. E. Vázquez, J. L. Mascareñas, R. A. Alvarez-Puebla, *J. Am. Chem. Soc.* **2013**, *135*, 10314.

[12] A. Tao, F. Kim, C. Hess, J. Goldberger, R. He, Y. Sun, Y. Xia, P. Yang, *Nano Lett.* **2003**, *3*, 1229.

[13] N. P. W. Pieczonka, P. J. G. Goulet, R. F. Aroca, *J. Am. Chem. Soc.* **2006**, *128*, 12626.

[14] a) M. Alba, N. Pazos-Perez, B. Vaz, P. Formentin, M. Tebbe, M. A. Correa-Duarte, P. Granero, J. Ferré-Borrull, R. Alvarez, J. Pallares, A. Fery, A. R. De Lera, L. F. Marsal, R. A. Alvarez-Puebla, *Angew. Chem. Int. Ed.* **2013**, *52*, 6459; b) N. Pazos-Pérez, W. Ni, A. Schweikart, R. A. Alvarez-Puebla, A. Fery, L. M. Liz-Marzán, *Chem. Sci.* **2010**, *1*, 174.

[15] a) H. Masuda, K. Fukuda, *Science* **1995**, *268*, 1466; b) E. V. Skorb, D. V. Andreeva, *Adv. Funct. Mater.* **2013**, *23*, 4483.

[16] K. Nielsch, J. Choi, K. Schwirn, R. B. Wehrspohn, U. Gösele, *Nano Lett.* **2002**, *2*, 677.

[17] F. Li, L. Zhang, R. M. Metzger, *Chem. Mater.* **1998**, *10*, 2470.

[18] M. Michalska-Domańska, M. Norek, W. J. Stępniowski, B. Budner, *Electrochim. Acta* **2013**, *105*, 424.

[19] P. Chaudhar, *J. Appl. Phys.* **1974**, *45*, 4339.

[20] K. Kant, S. P. Low, A. Marshal, J. G. Shapter, D. Losic, *ACS Appl. Mater. Interfaces* **2010**, *2*, 3447.

[21] K. Rana, G. Kucukayan-Dogu, E. Bengu, *Appl. Surface Sci.* **2012**, *258*, 7112.

[22] H. Chen, L. Shao, Q. Li, J. Wang, *Chem. Soc. Rev.* **2013**, *42*, 2679.

[23] a) J. Aizpurua, G. W. Bryant, L. J. Richter, F. J. García de Abajo, B. K. Kelley, T. Mallouk, *Phys. Rev. B* **2005**, *71*, 235420; b) A. Lee, A. Ahmed, D. P. dos Santos, N. Coombs, J. I. Park, R. Gordon, A. G. Brolo, E. Kumacheva, *J. Phys. Chem. C* **2012**, *116*, 5538; b) L. Wang, Y. Zhu, L. Xu, W. Chen, H. Kuang, L. Liu, A. Agarwal, C. Xu, N. A. Kotov, *Angew. Chem. Int. Ed.* **2010**, *49*, 5472.

[24] N. R. Jana, L. Gearheart, C. J. Murphy, *J. Phys. Chem. B* **2001**, *105*, 4065.

[25] a) D. E. Bornside, C. W. Macosko, L. E. Scriven, *J. Appl. Phys.* **1989**, *66*, 5185; b) P. Colson, R. Cloots, C. Henrist, *Langmuir* **2011**, *27*, 12800.

[26] a) R. Seemann, M. Brinkmann, S. Herminghaus, K. Khare, B. M. Law, S. McBride, K. Kostourou, E. Gurevich, S. Bommer, C. Herrmann, D. Michler, *J. Phys. Condes. Matter* **2011**, *23*, 184108; b) R. Seemann, M. Brinkmann, E. J. Kramer, F. F. Lange, R. Lipowsky, *Proc. Natl. Acad. Sci. USA* **2005**, *102*, 1848.

[27] a) S. Karan, B. Mallik, *Phys. Chem. Chem. Phys.* **2008**, *10*, 6751; b) C. Xu, H. Tian, C. E. Reece, M. J. Kelley, *Phys. Rev. Special Topics - Acceler. Beams* **2012**, *15*, 043502.

[28] V. Raspal, K. O. Awitor, C. Massard, E. Feschet-Chassot, R. S. P. Bokalawela, M. B. Johnson, *Langmuir* **2012**, *28*, 11064.

[29] M. T. Yatcilla, K. L. Herrington, L. L. Brasher, E. W. Kaler, S. Chiruvolu, J. A. Zasadzinski, *J. Phys. Chem.* **1996**, *100*, 5874.

[30] D. P. Lyvers, J.-M. Moon, A. V. Kildishev, V. M. Shalaev, A. Wei, *ACS Nano* **2008**, *2*, 2569.

[31] V. S.-Y. Lin, K. Motesharei, K.-P. S. Dancil, M. J. Sailor, M. R. Ghadiri, *Science* **1997**, *278*, 840.

[32] D.-K. Kim, K. Kerman, M. Saito, R. R. Sathuluri, T. Endo, S. Yamamura, Y.-S. Kwon, E. Tamiya, *Anal. Chem.* **2007**, *79*, 1855.

[33] R. A. Alvarez-Puebla, A. Agarwal, P. Manna, B. P. Khanal, P. Aldeanueva-Potel, E. Carbó-Argibay, N. Pazos-Pérez, L. Vigderman, E. R. Zubarev, N. A. Kotov, L. M. Liz-Marzán, *Proc. Natl. Acad. Sci. USA* **2011**, *108*, 8157.

[34] N. Pazos-Perez, C. S. Wagner, J. M. Romo-Herrera, L. M. Liz-Marzán, F. J. García De Abajo, A. Wittemann, A. Fery, R. A. Alvarez-Puebla, *Angew. Chem. Int. Ed.* **2012**, *51*, 12688.

[35] R. A. Alvarez-Puebla, R. F. Aroca, *Anal. Chem.* **2009**, *81*, 2280.

[36] B. Nikoobakht, M. A. El-Sayed, *Chem. Mater.* **2003**, *15*, 1957.

ice | science

Formation of polypyrrole/metal hybrid interfacial layer with self-regulation functions via ultrasonication

Ekaterina V. Skorb Dr.*
Max Planck Institute of Colloids and Interfaces, Potsdam, Germany

Chemistry Department, Belarusian State University, Minsk, Belarus

Olga Baidukova MSc
Max Planck Institute of Colloids and Interfaces, Potsdam, Germany

Olga A. Andreeva Dr.
Institute of Macromolecular Compounds Russian Academy of Science, St. Petersburg, Russia

Pavel V. Cherepanov PhD
Physical Chemistry II, Universusity of Bayreuth, Bayreuth, Germany

Daria V. Andreeva Dr.*
Physical Chemistry II, Universusity of Bayreuth, Bayreuth, Germany

The authors proposed a novel method of formation of polymer/metal hybrid interfacial layer with switchable properties by using ultrasonication. Intensive ultrasonication leads to the formation of a rough metal interface and triggers free-radical polymerization of monomers in the interfacial region of metal surface. Thus, polymer layer exhibits excellent adhesion to the bulk metal. The novel concept was demonstrated for polypyrrole/aluminum systems. Hydrophilic/hydrophobic properties and corrosion resistance also due to doping/dedoping of polypyrrole of the interfacial layers can be adjusted based on particular application. The proposed method can serve as a platform for formation of interfaces with self-regulating properties: self-healing, switchable hydrophylicity.

1. Introduction

Construction of artificial self-regulating interfaces is an emerging field of material science and biomimetic chemistry.[1–3] One of the approaches for the development of interfaces with self-regulation functions could be the formation of composite hybrid surfaces with the use of conducting polymers. In general, conducting polymers have a great potential in terms of self-regulation and self-healing due to their stimuli-responsive properties,[4–6] such as doping/dedoping. Relatively recent publications demonstrated that conducting surfaces can mimic self-healing and self-regulation ability of natural skin.[1]

Self-regulating properties occurring due to the use of conducting polymers rely on several mechanisms. Electrically conducting polymers are sensitive to gases, humidity, ions, biomolecules and so on and used for construction of sensors.[6] Conducting polymer can adsorb and release active compounds (healing agents, corrosion inhibitors, antibiotics and drugs) via doping/dedoping process that is sensitive to external stimuli (pH, ionic strength and applied potential).[7–9] It was also shown that model dyes could be loaded to/released from the systems containing polypyrrole (PPy) with response to external stimuli.[4,5,7] Conducting polymers such as PPy or polyaniline could passivate the metal substrates and,

thus, prevent their degradation in aggressive media. Kowalski and Ohtsuka[8,9] highlighted healing ability of PPy deposited on steel surface.

Application of conducting polymers for the formation of active interfaces is still a developing area of nanoengineering. Poor mechanical properties, brittleness and delamination of films formed by conducting polymers significantly restrict their application.[10] Unexpected delamination of the conducting polymer layers results in breakdown of hybrid material properties. Here, a novel approach for construction of conducting polymer/metal interfaces via ultrasonication is proposed. The great advantage of the method is the formation of surface metal sponges layer without additional surface pretreatment with possibility to integrate in the structure different substances. The intensive sonication of metal surfaces in the presence of a monomer (pyrrole) leads, at the end, to one-step formation of hybrid metal–polymer interfaces. Recently, the authors reported that metal surfaces can be nanostructured by using ultrasound.[12,13] Ultrasound-induced shock waves and microjets at liquid–solid interface lead to the chemical and mechanical etching of metal surfaces providing the formation of porous interfacial layer. At the same time, free radicals produced by ultrasonication can trigger free-radical polymerizations of monomers. Here,

---

*Corresponding author e-mail addresses: skorb@mpikg.mpg.de; daria.andreeva@uni-bayreuth.de

123

Bioinspired, Biomimetic and Nanobiomaterials
Volume 2 Issue BBN3

Formation of polypyrrole/metal hybrid
interfacial layer with self-regulation
functions via ultrasonication
Skorb, Baidukova, Andreeva, Cherepanov and
Andreeva

time-dependent ultrasound-induced formation of the polymer/ metal composites hybrids is demonstrated on a model PPy/ aluminum system. The properties and functions of aluminum and its composites and hybrid with PPy (hybrid PPy/aluminum interface formed after a longer-term sonication of surface) were studied by using infrared reflection adsorption spectroscopy (IRRAS), static and dynamic contact angle measurements, scanning electron and atomic force microcopies (SEM and AFM). Scanning vibrating electrode technique (SVET) was used for monitoring surface degradation in aggressive media also for molybdate-doping system.

2. Experimental section

2.1 Materials
Pyrrole (98%, Sigma-Aldrich, Germany) was distilled before use. Aluminum plates (99,999%, 1 mm × 10 cm × 10 cm, Sigma-Aldrich, Germany) were cut to 1 mm × 1 cm × 1 cm pieces, degreased in isopropanol and rinsed with purified water. There were no other steps of aluminum pretreatment before sonication. The lubricating fluid used for the test of 'slippery' hybrid interface was perfluorinated fluid (3M Fluorinert FC-70, Sigma-Aldrich, Germany). The testing liquid for 'slippery' hybrid interface was decane (99%, Sigma-Aldrich, Germany). Water was purified before use in a three-stage Millipore Milli-Q Plus 185 purification system and had a resistance higher than 18·2 M·cm.

2.2 Sonication of aluminum plates in the presence of pyrrole
Each plate was fixed in the home made sample holder that allows to control the sample position and the distance to the sonotrode (5 mm). The samples were sonicated in 4 wt.% of aqueous solution of pyrrole. The sonication cell was thermostated at 65°C. VIP1000hd (Hielscher, Germany) ultrasound device was operated at 20 kHz with a maximum output power of 1000-W ultrasonic horn BS2d22 (head area of 3·8 cm²) and equipped with a booster B2-1·2. The maximum intensity was calculated to be 57 W/cm² at mechanical amplitude of 81 μm.

2.3 Infrared reflection adsorption spectroscopy
IR spectra were acquired with Brucker IFS 66 FT-IR spectrometer (Ettlingen, Germany). The infrared beam was directed through the external port of the spectrometer and subsequently reflected by three mirrors in a rigid mount before being focused on the sample surface. A KRS-5 wire grid polarizer was placed into the optical path directly before the beam could hit the sample surface. The reflected light was collected at the same angle as the angle of incidence. The light then followed an equivalent mirror path and was directed onto a narrow-band mercury–cadmium–telluride detector, which was cooled by liquid nitrogen. The entire experimental setup is enclosed to reduce relative humidity fluctuations. For all measurements at 40 mN/m, p-polarized radiation was used at an incidence angle of 70°. A total of 128 scans were acquired with a scanner velocity of 20 kHz at a resolution of 8 cm⁻¹.

2.4 Microscopy studies
SEM measurements were conducted with a Gemini Leo 1550 instrument at an operation voltage of 3 keV. Samples were sputtered with gold. AFM (Molecular Force Probe 1D AFM, Asylum Co, Santa Barbara, USA) was used to study morphology and determine the roughness of aluminum sonicated without pyrrole and in the presence of pyrrole after the formation of regular PPy monolayer connected with aluminum. Before the AFM study, the metal plates were subjected to grinding and polishing.

2.5 Static and dynamic contact angle measurements
The hydrophilic/hydrophobic properties of the plates and lubricate-loaded 'slippery' nanotextured hybrid interface were studied using the Contact Angle Measurement System G10 (Krüss, Germany) at room temperature. For measuring the contact angle, the samples were dried before in the flow of nitrogen. The droplet volume for the measurement was around 5 μl, and the macroscopic droplet profile was captured through a camera equipped with an optical system for amplification of the captured images. For the contact angle hysteresis measurements, the surface was tilted with respect to the horizontal plane until the liquid droplet started to slide along the surface. The droplet profile was fitted into a spherical cap profile by special software. The accuracy of the contact angle measurements was ~0·1°.

2.6 Scanning vibrating electrode technique
SVET with the current density measurements is based on the detecting the voltage drop at the tip of a vibrating microelectrode immersed in a conductive solution. In combination with a lock-in amplifier, the signal-to-noise ratio increases dramatically, so very low currents down to μA/cm² can be measured. The SVET experiments were performed by using the equipment supplied by Applicable Electronics (Forestdale, MA, USA). For SVET, the tip of a PtIr electrode (Science Products GmbH, Germany) was electrodeposited with platinum black in a 1 vol.% lead acetate with 10 vol.% platinum chloride solution and vibrated at a frequency of 843 Hz with amplitude of 20 μm. The electrode was calibrated by positioning it above an artificial point current source. The response was about 3 V/(μA/cm²). Samples for SVET measurement were 1 × 2 cm aluminum and Ppy/aluminum plates. Areas of 2 × 2 mm² were exposed for the measurements, and other parts of the samples were covered with a Polyester 5 adhesive tape (3M Company). The anticorrosion coating of each sample was scratched to introduce a defect extending to the metal surface; the area of the defect was in the range of 0·1–0·3 mm². The sample was mounted in a homemade epoxy-resin cell. The immersion solution was 0·1-M NaCl. Scans were initiated within 5 min of immersion and were collected every 30 min for the duration of the experiment, typically 12 h. Each scan consisted of 400 data points obtained on a 20 × 20 grid, with an integration time of 1 s per point. A complete scan required 10 min. The normal or z component of the measured current density in the plane of the vibrating electrode is plotted in 3D format over the scan area, with positive and negative current densities representing anodic and cathodic regions, respectively.

Bioinspired, Biomimetic and Nanobiomaterials
Volume 2 Issue BBN3

Formation of polypyrrole/metal hybrid
interfacial layer with self-regulation
functions via ultrasonication
Skorb, Baidukova, Andreeva, Cherepanov and
Andreeva

3. Results and discussion

Modification of aluminum plates by ultrasound is schematically illustrated in Figure 1(a).

Sonication of aluminum plates in water (Figure 1, (1)) was described in detail in Ref.11–13. Shortly, ultrasound treatment of the plates in water results in the removal of initial oxide layer and formation of the ultrasonically modified layer (US-Al) consisting of metallic aluminum and aluminum hydroxides (boehmite and byerite). Formation of the aluminum hydroxide layer was confirmed by powder X-ray diffraction and ^{27}Al solid-state NMR.[11–13] The microscopic monitoring of the metal surfaces versus sonication time reveals an increase in surface roughness with the modification time. IRRA spectra (Figure 2) of the aluminum plates after ultrasound treatment show the intensive peak at 1088 cm^{-1} that can be attributed to OH groups of the aluminum hydroxide present on the surface. Due to high roughness and presence of OH groups on the surface, US-Al provides very good adhesion of deposited materials, such as, polyelectrolyte multilayers. The water contact angle measurements evidence that the ultrasound-modified surfaces exhibit higher hydrophylicity compared with the initial one.[12] Hydrophilic (water contact angle *ca.* 11°) aluminum surface formed after 30 min of sonication is shown in Figure 1(b) and 1(c), (left).

In this study, aluminum plates were modified in the presence of pyrrole in order to create a stable hybrid interfacial layer. PPy/aluminum hybrid interfaces were formed by 30-min sonication of aluminum plates in the presence of 4 wt.% aqueous solution of pyrrole (Figure 1(2), 1(b), 1(c) (right)). Time dependable sonochemical formation of the composite hybrids was monitored by using SEM, AFM and IRRA spectroscopy (Figure 2). The combination of microscopic and spectroscopic methods proves the formation of conducting polymer layer on the surface, at the beginning of the modification (up to 2 min). The baseline shift in the IRRA spectrum of the 2-min sonicated samples (Figure 2(e)) could be an indirect evidence of the conducting material presence.[14] In the beginning, moments (2–10 min of modification) of sonochemical treatment, the surface of the samples is covered by randomly distributed polymer aggregates of PPy (Figure 2(a)–2(c)). The spectra show typical bands of PPy at 1560 cm^{-1} (ν, C=C), at 1320 cm^{-1} (ν, C-N) and 1050 and 930 cm^{-1} (characteristic vibration of the pyrrole ring). However, the bands at 1700 cm^{-1} (ν, C=O) and 3270 and 1650 cm^{-1} (ν, NH and ν, C=N) correspond to overoxidized PPy. Intensities of the bands corresponded to OH groups in US-Al are increased in the spectra up to 10 min of ultrasonic treatment. During 10 min of modification, the bands of OH groups are so intensive that the characteristic bands of PPy could not be distinguished. The 30-min sonicated sample formed well adhered regular distribution over the surface and connected with aluminum hybrid PPy/aluminum layer. Thus, the formation of a rough interfacial layer due to mechanical and chemical etching of the surface triggered by cavitation occurs after a longer-term ultrasonic surface treatment (Figures 1 (right) and 2(d) and 2(e) (upper spectrum)). The IRRA spectra (Figure 2(e)) showed that the surface modified for 30 min is still covered by PPy. The SEM images

of these samples demonstrate the formation of rough surface with homogeneously distributed polymer layer repeated the morphology of US-Al. The samples prepared by 30 min of sonication inhibit excellent adhesion of the polymer layer to the bulk metal most likely due to impregnation of PPy into the aluminum hydroxide layer and formation of PPy/aluminum hybrid. The characteristic bands of OH groups decreases due to the formation of hydrophobic PPy/aluminum interface (Figure 1(b), right): the interfacial hybrid layer changes contact angle of aluminum surface significantly, from 11° to 115°.

Recently, Aizenberg *et al.*[15] introduced distinguished 'slippery' surfaces, bioinspired by *Nepenthes* pitcher plants, useful in fluid handling and transportation, optical sensing, medicine, as self-cleaning and antifouling materials. Suggested here PPy/aluminum nanotextured porous surfaces could also be used for the creation of a robust synthetic 'slippery' surface (Figure 3(a)). Thus, hybrid PPy/aluminum surface formed in 30 min after sonochemical aluminum treatment in the presence of pyrrole (Figure 1 (right)) was loaded by vacuum pumping with lubrication agent. The fluid spreads into the whole interfacial layer through capillary wicking. The overcoating can be controlled by the fluid volume given to a known surface area of the sample. 'Slippery' effect was tested with the lubricating low-surface-tension perfluorinated liquid (3M Fluorinert) that is nonvolatile and is immiscible with both aqueous and hydrocarbon phases. Decane, as model hydrocarbon liquid, was tested for repelling (Figure 3(b)). Lubricate-loaded PPy/aluminum surface exhibits decane repellency. Mobility at sliding angle *ca.* 3° of the decane drop on the surface is shown in Figure 3(b).

The self-regulating activity of the PPy/aluminum hybrid surfaces after 30-min sonication with well-adhered interfacial layer was studied by using scanning vibration electrode technique (SVET). The samples prepared by 2–10-min sonication showed delamination of the PPy layer and thus are not useful as protective systems. An excellent adhesion of the PPy layer and high corrosion resistance was observed for the 30-min sonicated samples. The SEM images show that the rough surfaces of these samples are homogeneously covered by a thin PPy layer. The roughness is comparable with the US-Al surface. The thickness of the PPy should be comparable with the thickness of the sonochemically formed aluminum hydroxide layer and is *ca.* 3–5 nm. The time monitoring of the corrosion propagation in 0·1-M NaCl of the 30-min sonicated PPy/aluminum samples reveals the suppression of the degradation process. The plates sonicated in the presence of pyrrole for 30 min (Figure 4(d)) clearly demonstrate the healing process of the defected area. The corrosion degradation rapidly propagated around the defected area in the initial aluminum plates and the hybrid PPy/aluminum samples. The anodic (Figure 4, curve 1) and cathodic (Figure 4, curve 2) activity was observed in 15 min after defect formation. The defect propagation leads to enhancing the anodic and cathodic activity in the damaged zone. The rest of the surface emits negligible ion flux indicating the absence of the corrosion processes. However, the defected zone on the PPy/aluminum hybrid surface was passivated
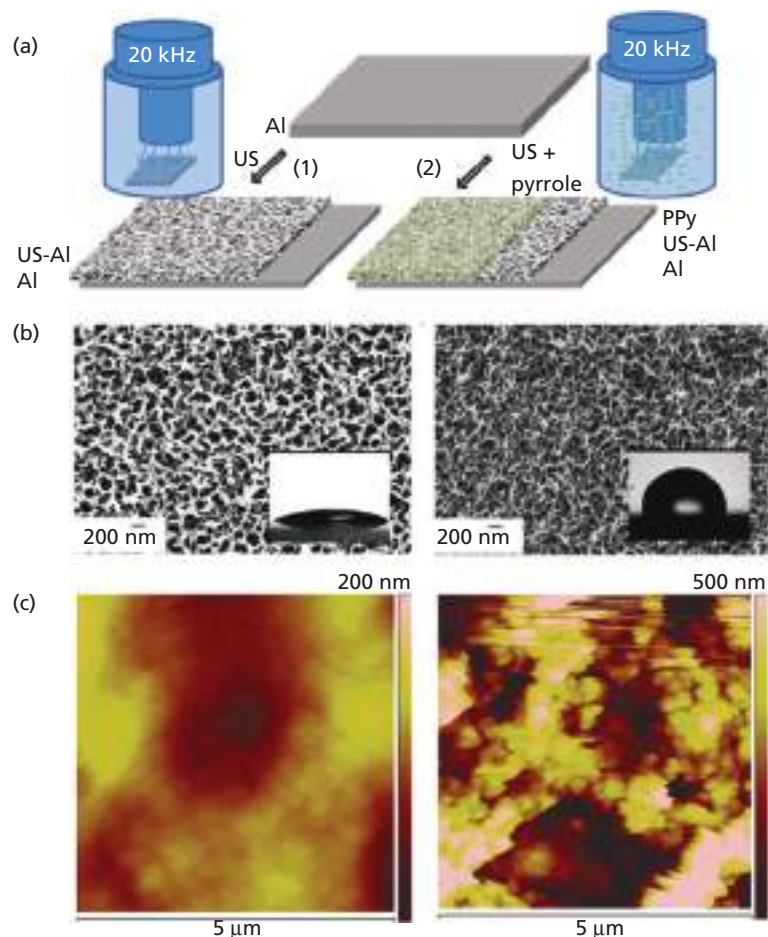
Bioinspired, Biomimetic and Nanobiomaterials
Volume 2 Issue BBN3

**Formation of polypyrrole/metal hybrid
interfacial layer with self-regulation
functions via ultrasonication**
Skorb, Baidukova, Andreeva, Cherepanov and
Andreeva

Figure 1. (a) Schematic of formation of the hybrid interfacial layers
via ultrasonication at 20 kHz: (1) aluminium plates sonicated in water
for 2, 5, 10 and 30 min as blank experiments. The material has an
ultrasonically modified layer (US-Al) on metal surface; (2) aluminium
plates sonicated in the presence of 4 wt.% solution of pyrrole in
water for 2, 5, 10 and 30 min. The material has US-Al layer and
the hybrid PPy/aluminium layer. (b) Scanning electron microscopy
and (c) atomic force microscopy images of the samples prepared
in water (left) and in the presence of pyrrole (right) after 30 min of
sonochemical treatment. The inserts in (b) are the optical photographs
of water drops on the surfaces.

in time (>4 h), and there was no propagation of the corrosion process
detected after 10 h of immersion in the aggressive solution. The
healing effect was not detected in the case of unmodified aluminium
(Figure 4(a)). An anodic and cathodic activity tends to increase
in time. Optic microphotographs (Figure 4(b) and 4(e)) prove the
different corrosion propagation in the case of hybrid surface and the
initial aluminum surface. The products of corrosion degradation can
be clearly seen in the optical microphotograph of the unmodified
aluminum (Figure 4(b)). The degradation products in the PPy/
aluminum samples are localized around the defected area and do not
distribute on the whole investigated area (Figure 4(d)). Since good

corrosion protection was revealed for the 30-min sonicated samples,
where PPy incorporated in the aluminum hydroxide layer, the
authors propose that the mechanism of anticorrosion protection of
the PPy/aluminum hybrid surface is based on the barrier properties
of the PPy. PPy enhances the resistance of the aluminum hydroxide
layer and prevents penetration of Cl$^-$ in the metal surface. Doping
of PPy with corrosion inhibitors, here molybdate ions, as shown in
schematic (Figure 4(g)) provide additional corrosion protection of
the metal surface. The corrosion inhibitors can release on demand
in corrosion pits via pH-dependant doping/dedoping process. The
barrier properties of PPy and doping/dedoping of the polymer with

126

Bioinspired, Biomimetic and Nanobiomaterials
Volume 2 Issue BBN3

Formation of polypyrrole/metal hybrid
interfacial layer with self-regulation
functions via ultrasonication
Skorb, Baidukova, Andreeva, Cherepanov and
Andreeva
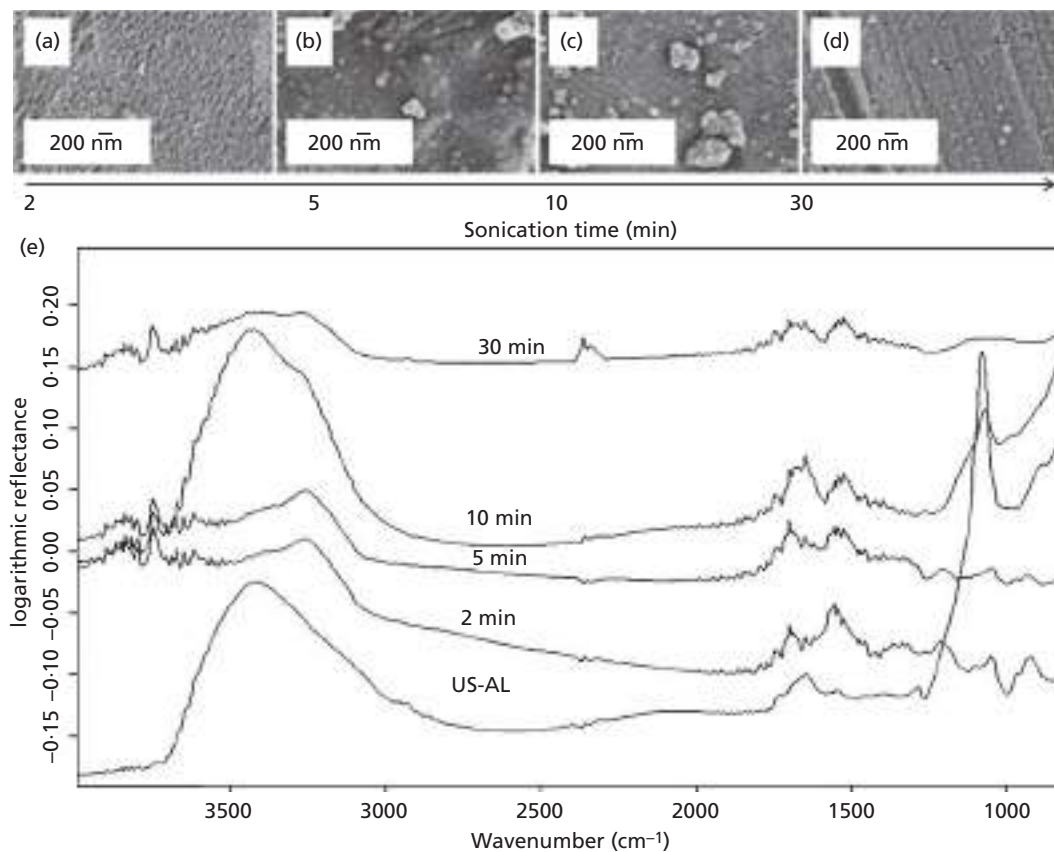
Figure 2. Scanning electron microscopy images of the PPy/aluminium samples prepared for (a) 2, (b) 5, (c) 10 and (d) 30 min of sonication. Infrared reflection adsorption spectra (e) of the same samples.
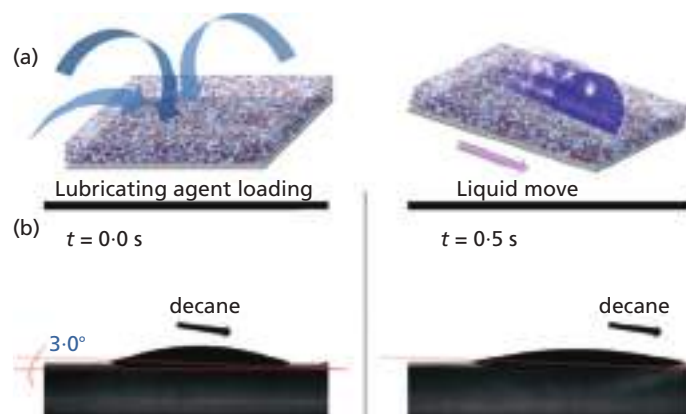
Figure 3. (a) Schematics showing the fabrication of lubricate-loaded PPy/aluminium surface (left) and decane repelling test (right). (b) Optical micrographs demonstrating the mobility of a low-surface-tension liquid hydrocarbon – decane sliding on the lubricate-loaded PPy/aluminium surface at a low angle *ca*. 3°.

Bioinspired, Biomimetic and Nanobiomaterials
Volume 2 Issue BBN3

**Formation of polypyrrole/metal hybrid
interfacial layer with self-regulation
functions via ultrasonication**
Skorb, Baidukova, Andreeva, Cherepanov and
Andreeva
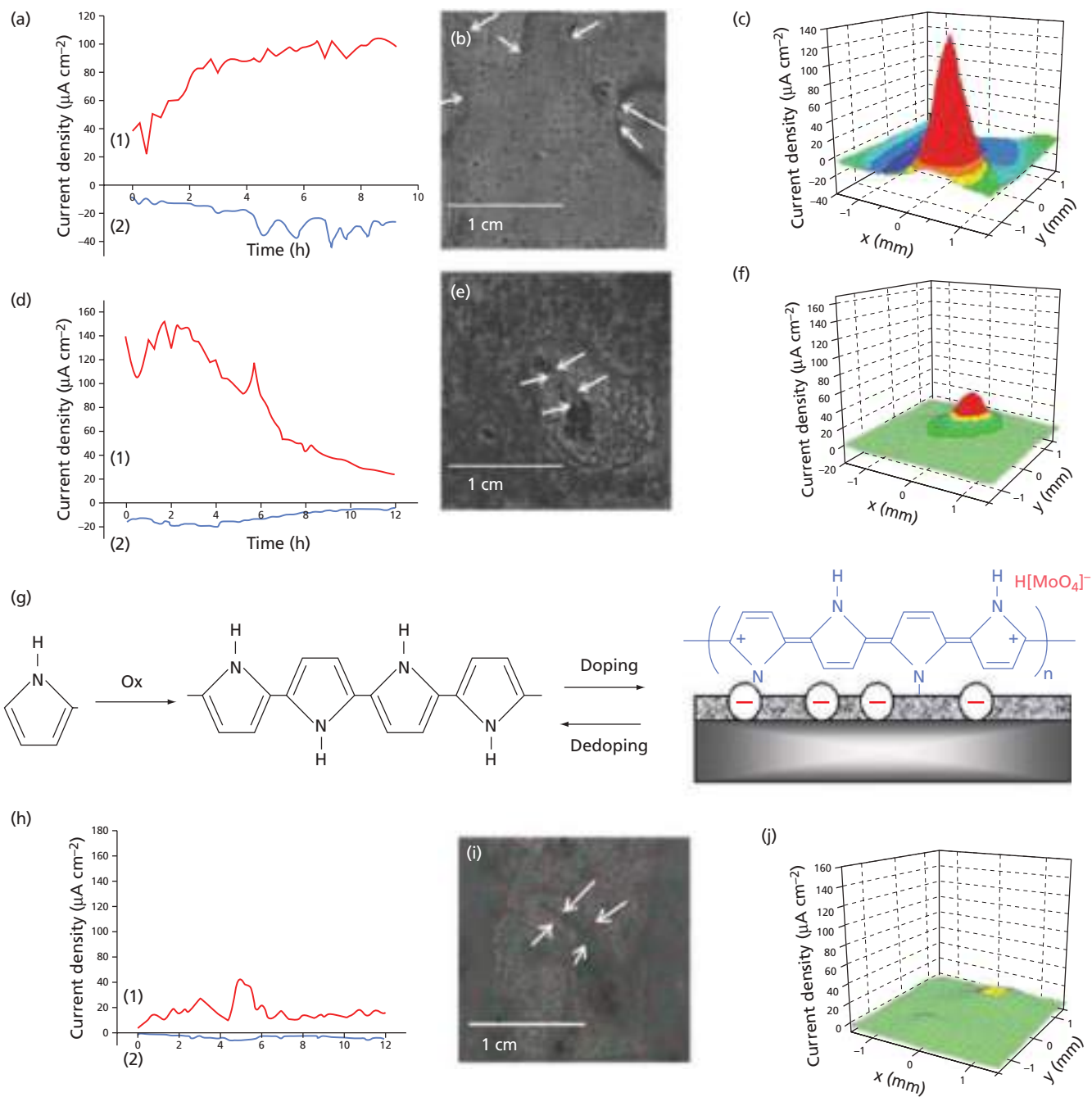
Figure 4. Time monitoring of anodic (1) and cathodic (2) current above the initial aluminium surface (a), the surface covered by PPy/aluminium hybrid layer (c) and hybrid layer doping (scheme shown in (g)) with molybdate (h) immersed in 0·1-M NaCl. (b), (e) and (i) show optical photographs and 3D current density maps of the defected areas of the same samples in 12 h after testing.

corrosion inhibitors (molybdate) were found to be the key factors in the passivation mechanism of corrosion. Moreover, prospects of pH-dependent doping/dedoping of PPy opens new opportunities for anticorrosion protection. The doped hybrid nanonetwork exhibits very high corrosion protection because of the nature and versatility of the PPy and possibility of molybdate to adsorb on corrosion pits and locally prevent corrosion propagation. The anticorrosion activity of the coating is based on the following mechanisms: (*1*)

Bioinspired, Biomimetic and Nanobiomaterials
Volume 2 Issue BBN3

Formation of polypyrrole/metal hybrid
interfacial layer with self-regulation
functions via ultrasonication
Skorb, Baidukova, Andreeva, Cherepanov and
Andreeva

PPy provides a barrier between surface and environment and (2) PPy can be effective carrier for inhibitor allowing its release on demand.

4.   Conclusion

The authors proposed a novel ultrasound-assisted concept for the formation of the conducting polymer/metal hybrid interfacial layer. The concept was demonstrated on a model PPy/aluminum systems but can be adjusted to metal surfaces applicable for biomedicine (titanium), automotive and aerospace (magnesium, steel) industries. The polypyrrole/aluminum hybrids show high potential as a component of self-regulation and biomimetic systems. The authors demonstrated that corrosion resistance of hybrid system and hydrophilic/hydrophobic properties of surfaces can be tuned via ultrasonication.

Acknowledgements

REFERENCES

1. Tee, B. C.-K.; Wang, C.; Allen, R.; Bao, Z. An electrically and mechanically self-healing composite with pressure- and flexion-sensitive properties for electronic skin applications. *Nature Nanotechnology* **2012**, *7*, 825–832.

2. White, S. R.; Sottos, N. R.; Geubelle, P. H.; Moore, J. S.; Kessler, M. R.; Sriram, S. R.; Brown, E. N.; Viswanathan, S. Autonomic healing of polymer composites. *Nature* **2001**, *409*, 794–797.

3. Burattini, S.; Greenland, B. W.; Chappell, D.; Colquhoun, H. M.; Hayes, W. Healable polymeric materials: a tutorial review. *Chemical Society Reviews* **2010**, *39*, 1973–1985.

4. Parakhonskiy, B.; Andreeva, D. V.; Möhwald, H.; Shchukin, D. Hollow polypyrrole containers with regulated uptake/release properties. *Langmuir* **2009**, *25*, 4780–4786.

5. Andreeva, D. V.; Gorin, D. A.; Shchukin, D. G.; Sukhorukov, G. B. Magnetic microcapsules with low permeable polypyrrole skin layer. *Macromolecular Rapid Communications* **2006**, *27*, 931–936.

6. Adeloju, S. B.; Wallace, G. G. Conducting polymers and the bioanalytical sciences: new tools for biomolecular communications. *Analyst* **1996**, *121*, 699–703.

7. Skorb, E. V.; Baidukova, O.; Goyal, A.; Brotchie, A.; Andreeva, D. V.; Möhwald, H. Sononanoengineered magnesium–polypyrrole hybrid capsules with synergetic trigger release. *Journal of Materials Chemistry* **2012**, *22*, 13841–13848.

8. Kowalski, D.; Ueda, M.; Ohtsuka, T. Self-healing ion-permselective conducting polymer coating. *Journal of Materials Chemistry* **2010**, *20*, 7630–7633.

9. Kowalski, D.; Ueda, M.; Ohtsuka, T. Self-healing ability of conductive polypyrrole coating with artificial defect. *ECS Transactions* **2008**, *16*, 177–182.

10. Andreeva, D. V.; Pientka, Z.; Brozová, L.; Bleha, M.; Polotskaya, G. A.; Elyashevich, G. K. Structure, transport and mechanical properties of gas-seperation membranes containing polypyrrole. *Thin Solid Films* **2002**, *406*, 54–63.

11. Skorb, E. V.; Shchukin, D. G.; Möhwald, H.; Andreeva, D. V. Sonochemical design of cerium-rich anticorrosion nanonetwork on metal surface. *Langmuir* **2010**, *26*, 16973–16979.

12. Skorb, E. V.; Shchukin, D. G.; Möhwald, H.; Andreeva, D. V. Ultrasound-driven design of metal surface nanofoams. *Nanoscale* **2010**, *2*, 722–727.

13. Andreeva, D. V.; Sviridov, D. V.; Masic, A.; Möhwald, H.; Skorb, E. V. Nanoengineered metal surface capsules: construction of a metal-protection system. *Small* **2012**, *8*, 820–825.

14. Andreeva, O. A.; Burkova, L.; Smirnov, M.; Elyashevich, G. K. Correlation between IR spectra and electric conductivity of polyethylene-polypyrrole composites. *Polymer Science Series B* **2006**, *48*, 331–334.

15. Wong, T.-S. S.; Kang, H.; Tang, S. K. Y.; Smythe, E. J.; Hatton, B. D.; Grinthal, A.; Aizenberg, J. Bioinspired self-repairing slippery surfaces with pressure-stable omniphobicity. *Nature* **2011**, *477*, 443–447.

WHAT DO YOU THINK?

To discuss this paper, please email up to 500 words to the managing editor at bbn@icepublishing.com

Your contribution will be forwarded to the author(s) for a reply and, if considered appropriate by the editor-in-chief, will be published as a discussion in a future issue of the journal.

ICE Science journals rely entirely on contributions sent in by professionals, academics and students coming from the field of materials science and engineering. Articles should be within 5000-7000 words long (short communications and opinion articles should be within 2000 words long), with adequate illustrations and references. To access our author guidelines and how to submit your paper, please refer to the journal website at www.icevirtuallibrary.com/bbn

Article

# Crystalline Silicon under Acoustic Cavitation: From Mechanoluminescence to Amorphization

Matthieu Virot,*[†,‡] Rachel Pflieger,[†] Ekaterina V. Skorb,[‡] Johann Ravaux,[†] Thomas Zemb,[†] and Helmuth Möhwald[‡]

[†]Institut de Chimie Séparative de Marcoule (ICSM), UMR 5257 CEA/CNRS/UM2/ENCSM, ICSM Site de Marcoule, BP 17171, 30207 Bagnols-sur-Cèze, France

[‡]Max Planck Institute of Colloids and Interfaces (MPIKGF), Wissenschaftspark Potsdam-Golm, Am Mühlenberg 1 OT Golm, 14476 Potsdam, Germany

Ⓢ Supporting Information

ABSTRACT: The physicochemical behavior of crystalline silicon under acoustic cavitation is investigated in water sparged with argon at low temperature (10 and 20 °C). Surprisingly, spectroscopic investigations reveal that argon (bubbling continuously through the liquid phase during experiments) can be ultrasonically excited via mechanoluminescence, i.e., emission of light caused by mechanical action on a solid. This phenomenon is highlighted for the first time on an extended solid surface using these conditions and results from an interaction between the acoustically generated bubbles and the Si surface. The concomitant physical and chemical transformations induced at the solid−liquid interface are investigated (SEM, AFM) to characterize the generated stress and defects in combination with the roughness and wettability increases (evolving from ~46° to ~4°). Phase transformations of the Si lattice are observed (Raman spectroscopy, TEM) evidencing the complex stress state induced by acoustic cavitation in the Si crystal structure. The mechanisms involved during Si sonication are discussed.
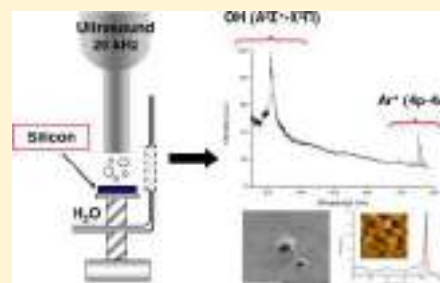
1. INTRODUCTION

With the current prospects toward development of specific materials and methodologies offering a wide control over their physical and chemical properties, ultrasound appears to be a promising tool allowing several possibilities for manipulation of surfaces at the atomic level and synthesis of new nanostructures.[1−4] Ultrasound benefits are generally attributed to the acoustic cavitation phenomenon, i.e., nucleation, growth, and rapid implosive collapse of acoustically generated microbubbles in liquids. Acoustic cavitation is able to locally generate extreme transient conditions of ~5000 K and ~1000 bar ("hot spots"), going along with formation of excited species and free radicals (e.g., via homolytic dissociation of water) and a possible light emission propagating from the UV to the near-IR, referred to as sonoluminescence.[1,2,5−7] In heterogeneous systems, acoustic cavitation goes with generation of shock waves and microjets that can affect a solid surface in view of specific applications such as cleaning, extracting, soldering, etc.[5−8] Over the past decade, scientific interest in sonication of heterogeneous systems has considerably increased and focused on various topics such as, for instance, preparation of nanoparticles,[1,2,4] catalysis,[9] preparation of porous and nanostructured materials,[2,10] nucleation processes,[11,12] sonophotoluminescence,[13] etc. In 2006, Eddingsaas and Suslick evidenced the possible triggering of mechanoluminescence (i.e., light emission caused by application of mechanical energy on a solid) during sonication of organic crystal slurries.[14−16] The high-velocity interparticle collisions created during sonication (20 kHz) of

suspensions of sucrose and resorcinol crystals in organic solvents allowed spectroscopic observation of gas discharges and crystal luminescence usually observed for triboluminescence.[14−16] This emission of light was attributed to a piezoelectrification of the newly created surfaces during fracture and was later investigated by other authors on lanthanide crystals sonicated in perfluorodecalin and undecane.[17,18]

Cavitation effects at the solid−liquid interface have not been totally deciphered yet, and an understanding of the mechanisms generated at the interface is still an important challenge. Despite the numerous investigations dealing with ultrasonic treatment of materials, the behavior of silicon under acoustic cavitation remains a topic scarcely reported in the literature. However, Si is an industrial key material that has been widely considered in microelectronic technology, integrated circuits, and optoelectronic devices.[19−21] In addition, modification of crystalline Si into amorphous silicon (a-Si) and polycrystalline silicon (poly-Si) represents a challenge of paramount importance in the development of, for instance, less expensive solar cells, image sensors, or thin film transistors.[10,21−24] Several techniques have been devoted to deposition or transformation of these Si structures, such as plasma-enhanced chemical vapor deposition,[25] electron irradiation,[26] indentation,[27−29] plasma arc processing,[30] microcutting,[31] ball milling,[32,33] etc. The few studies related to sonication of Si were principally focused on

surface cleaning[34,35] or the luminescence behavior of poly-Si and porous Si.[36−39] However, an original and environmentally friendly way of Si modification, using ultrasonic treatment in view of development of porous luminescent structures, was recently described in the literature.[10] Sonication of Si in the presence of reducing agents was found to dramatically influence the nature of luminescent centers. As such, the nonequilibrium conditions provided by acoustic cavitation phenomena appear to represent an original alternative for surface modification of Si-based materials. It is thus interesting to evaluate the potential of high-intensity ultrasound in this area aiming at controlling at the small scale the Si physicochemical properties such as wetting, porosity, morphology, optoelectronic properties, etc.

This work comes within the scope of a currently evolving domain dealing with engineered interfaces of acoustically generated cavitation bubbles for manipulation of surfaces at the small scale. This paper contributes to the understanding of the mechanisms involved at the surface of crystalline Si during acoustic cavitation (20 kHz) in aqueous solution under argon bubbling. Spectroscopic effects developed near the surface of the Si wafer during sonication are investigated. The concomitant physicochemical transformations occurring at the Si surface and within its structure are described and studied during the early stage of the erosion process. The mechanisms involved in the various highlighted phenomena are discussed.

2. EXPERIMENTAL SECTION

Materials. Crystalline silicon wafers (Prime CZ, N−As, one side polished, thickness 850 μm), with a (100) surface crystallographic orientation, were purchased from Siltronix (Archamps, France). They were cut into the appropriate diameter to fit the Teflon sample holder used for sonication experiments. Special care was taken to use smooth samples, devoid of apparent defects that could play a role during sonication. The various experiments were performed in deionized Milli-Q water (resistivity higher than 18.2 MΩ·cm at 25 °C).

Sonication and Sonoluminescence. In typical experiments, the Si samples were loaded on a homemade sample holder, allowing maintaining a controlled and reproducible distance from the ultrasonic probe.[13] This sample holder is manufactured from Teflon and allows a flat angle treatment of the Si surface. The sample is sonicated at 20 kHz using a 1 cm² titanium horn (Vibra-cell, Sonics & Materials, 750 W) mounted on top of a cylindrical reactor and fixed with a watertight Teflon ring, allowing its reproducible immersion into deionized water (250 mL). Experiments were performed at constant temperature (10 or 20 °C) using a Lauda RE 210 cryostat and measured with a thermocouple inserted into the reactor. Sonication was performed under argon bubbling (100 mL min^{-1}) through the solution 20 min before sonication and during the whole experiments. In order to ensure a maximal effect of cavitation, the tip of the probe is regularly changed.

For sonoluminescence investigations, experiments were performed using the devices described elsewhere.[13,40] Briefly, the light emitted within the reactor is collected through a quartz window and imaged onto the slit (0.1 mm) of a spectrometer (SP 2356i, Roper Scientific; gratings 300 gr/mm blz. 300 and 150 gr/mm blz. 500) coupled to a CCD camera (Spec10-100BR with UV coating, Roper Scientific) cooled with liquid nitrogen. Spectra are recorded with appropriate filters from 250 to 800 nm acquired during 300 s and corrected for background noise and quantum efficiencies of gratings and CCD.[40] The

acoustic power P_{ac} (W mL^{-1}) or ultrasonic intensity I_{ac} (W cm^{-2}) delivered to the solution was measured using the conventional thermal probe method. Sonochemical production of H_2O_2 was measured spectrophotometrically as a chemical way of cavitation control using Ti(IV) in ~2 M HNO$_3$−0.01 M [N$_2$H$_5$][NO$_3$] at λ_{max} (ε) = 410 nm (780 cm^{-1} M^{-1}).[41] Under these conditions, with an applied acoustic intensity of I_{ac} = 32 W cm^{-2}, the formation rate of H_2O_2 was measured to be ~4.2 × 10^{-1} μM min^{-1}, which is in agreement with the literature.[8]

Characterization. Different samples were studied using a scanning electron microscope (SEM, FEI QUANTA 200 ESEM FEG) coupled with energy-dispersive X-ray spectroscopy (EDX, Bruker SDD 5010). To characterize the topography of the various samples, atomic force microscopy (AFM) was applied to obtain quantitative data about the roughness, height profile, and created hole depths of the sonicated surfaces. Measurements were carried out in air at room temperature using a D3100 Nanoscope IIIa MultiMode microscope (Digital instruments/Veeco, Inc., Santa Barbara, CA) in tapping mode with silicon cantilevers (Nanoworld, Neuchâtel, Switzerland). The typical resonance frequency of the cantilevers was 285 kHz, and the spring constant was 42 N m^{-1}. In this study, recorded images possess a scan area of 40 × 40 μm². Analyses and treatments of the various images were carried out with the software provided by the manufacturer.

The surface of the different Si wafers was studied using a Raman microspectrometer (μ-Raman). The apparatus (Horiba-Jobin Yvon Aramis) is equipped with an edge filter and a He−Ne laser (λ = 633 nm). The laser beam is focused on the Si samples using a microscope (Olympus BX 41) with a ×100 magnification, resulting in a spot of about 1 μm². Spectra were collected between 100 and 1100 cm^{-1} with usual averaged measurements of 4 scans of 8 s each. The apparent contact angle of the Si wafers was investigated with deionized Milli-Q water droplets using a contact angle meter (Software DSA 1, Krüss GmbH, Hamburg, Germany). The reported contact angles are obtained from a mean average of ~10 measurements. Transmission electron microscopy (TEM) was used to investigate the structural modification and the local orientations of the Si structures using a Zeiss EM 912 Omega (Carl Zeiss AG, Germany) operating at 120 kV and equipped with an electron-diffraction unit. For analyses, samples were ultra-microtomed (Leica EM FC6) or gently broken before being deposited with ethanol on a carbon-coated copper grid.

3. RESULTS AND DISCUSSION

The 20 kHz sonication of the surface of a water-immersed silicon wafer in the presence of argon (bubbling continuously through the liquid phase) leads to spectroscopic observation of several emission lines (Figure 1). Spectra are constituted by a broad continuum superimposed with particular emission peaks. The continuum is typical for multibubble water sonoluminescence and found to be in agreement with previous investigations.[13,40] It is generally considered that the continuum results from a combination of bremsstrahlung, recombination of H and OH° species, deexcitation of water molecules, and/or OH(B$^2\Sigma^+$–A$^2\Sigma^+$) emission.[40] The intense emission lines around 310 nm are attributed to OH(A$^2\Sigma^+$−X$^2\Pi$) transitions; these excited OH° radicals result from the homolytic dissociation of water molecules inside the cavitation bubbles. The observed lines can be decomposed into several vibrational transitions, e.g., the 0−0 transition at 310 nm, the 1−0 between ~290 and 300 nm, and the 0−1 at ~340 nm.[13,40] The most
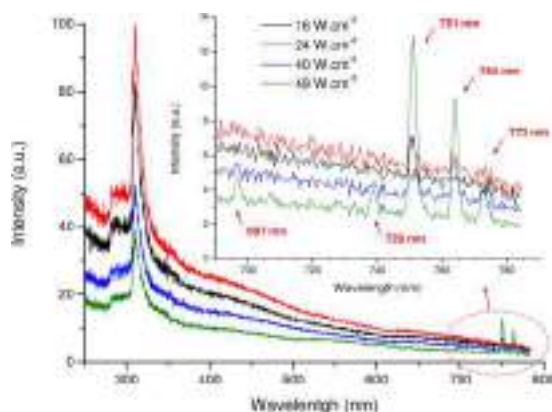
Figure 1. Normalized sonoluminescence spectra obtained during sonication of a Si wafer in H_2O using different acoustic intensities (10 ± 1 °C, Ar, ~2 mm from the sonotrode, focusing near the surface). (Inset) Magnification of the 690−790 nm region.

interesting features extend in the near-IR range, where several emission lines are observed at 697, 739, 751, 764, and 773 nm. These lines are attributed in agreement with the literature to the 4p−4s manifold transitions of the excited argon atom (Ar*).[42,43] The relevant region can also be observed in Supporting Information Figure SI.1, where the background of the different spectra was subtracted in order to appreciate the relative intensity of the main Ar* and $OH(A^2\Sigma^+-X^2\Pi)$ transitions versus the applied acoustic intensity.

According to Figure 1 and Supporting Information Figure SI.1, observation of Ar* transitions clearly depends on the applied acoustic intensity. Application of an acoustic intensity of ~16 W cm^{-2} does not permit observation of any significant Ar* line; however, a threshold intensity of 24 W cm^{-2} is observed. Thereafter, the intensity of the different Ar* lines increases almost linearly with the applied acoustic intensity, while the intensity of $OH(A^2\Sigma-X^2\Pi)$ transitions decreases (Figure 1 and Supporting Information Figure SI.1). The decrease of the $OH(A^2\Sigma-X^2\Pi)$ transitions can be explained by a modification of the geometry of the cavitation cloud of bubbles as a function of the applied acoustic intensity. It is important to mention that sonication of pure water with argon bubbling continuously in the liquid phase did not lead to Ar* observation; similarly, sonication of a silica surface in water did not permit the observation of excited species emission (except that of OH* from water sonoluminescence). Furthermore, spectra observed with Si result from optimization of the experimental parameters: sonication at a high distance from the sonotrode did not permit observation of any Ar* line; a ~2 mm probe−sample distance was necessary to obtain relevant spectra. It is important to note that the physical effects (e.g., sonication erosion) of a solid surface highly depend on the distance between the surface and the sonotrode.[8,13] An increase of this distance drops dramatically the surface-induced cavitation effects. These observations permit one to evidence the link between the sonicated solid surface and Ar* observation.

The observed Ar* excitation level (>13 eV above the ground state) most probably results from a dielectric breakdown occurring during formation of cracks in Si crystals during sonication.[14−18] Ar* emission can therefore be attributed to gas discharges. Combination of the experimental settings with the observed spectroscopic variations evidence a direct relationship with the mechanical stimuli created at the Si−water interface. In

consequence, the observed phenomenon is attributed to mechanoluminescence, i.e., light emission resulting from mechanical deformation of a solid.[44] It is important to emphasize that this mechanism of excitation differs from that recently discovered during sonication of suspensions of piezoelectric organic crystals (i.e., triboluminescence, see Introduction).[14−18] Indeed, the here-described emission of Ar* does not involve collisions with particles or piezo-electrification of the surface since we consider an extended solid surface and a centrosymmetric crystal.

The ultrasonically induced stress state at the surface of the sample was investigated using different techniques. The first observation (optical microscopy) revealed that deformation of the surface is very slow and presents a long incubation period of cavitation erosion. Higher magnification (SEM) shows that the Si wafer undergoes dramatic changes at the small scale under sonication (Figure 2). An increasing density of cracks and small pits is appearing with the duration and intensity of the acoustic cavitation. The size of the primary holes was measured using AFM and found to be about ~0.5−2 μm thick and ~30−70 nm deep. The erosion mechanism is in good agreement with previous observations on glass surfaces, although the depth of
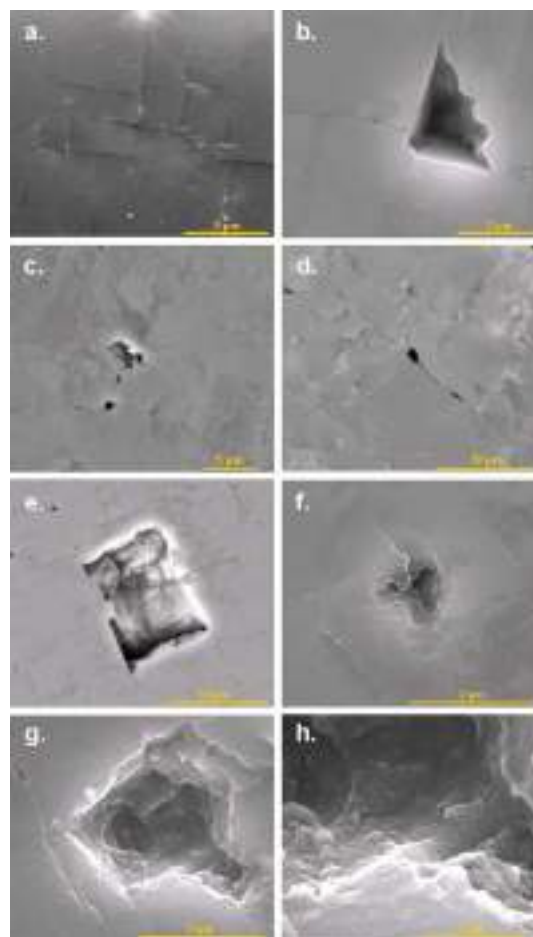

Figure 2. SEM observation of the silicon surface evidencing the crystallographic propagation of cracks and defect evolution after (a) 5 h of sonication, (b and c) 7 h of sonication, (d) 9 h of sonication, (e) 12 h of sonication, and (f−h) 15 h of sonication. Conditions: I_{ac} = 32 W cm^{-2}, Ar, 20 °C, H_2O, V = 250 mL. Note the general rectilinear geometry (a−e) and the plastic area (e−h) of some created defects suggesting a local brittle-to-ductile transition.

the holes is in comparison smaller for Si.[8] This might be the result of the hardness of the sample supposed to be stronger for Si. Prolonged sonication allows acceleration of the erosion phenomenon (an incubation period of ~4 h appears necessary), which leads to generation of secondary effects characterized by the presence of larger eroded areas (~5−10 μm) and the intersection of the cracks (Figure 2d).

The fissures were found to propagate straight and intersect with 90° angles, which is in agreement with the cubic crystal orientation of (100) Si wafers (Figures 2 and 3 and Supporting
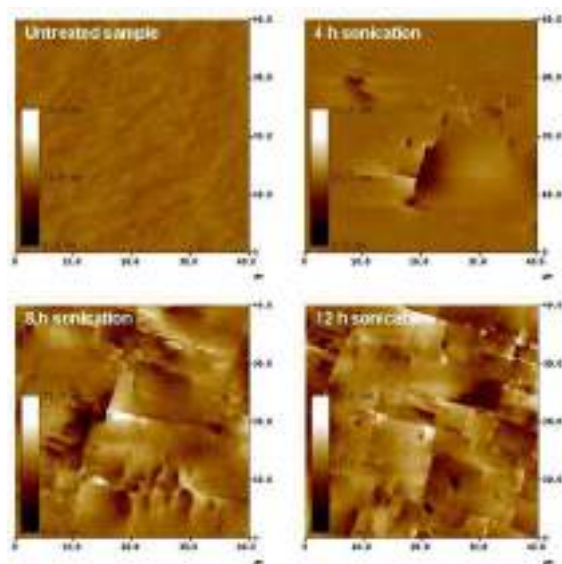
Figure 3. AFM topographic measurements of a silicon surface for different sonication times at I_{ac} = 32 W cm^{-2} (Ar, 20 °C, H$_2$O, V = 250 mL).

Information Figures SI.2 and SI.3). The observed perfect cleavages result from an interaction with the bulk material and therefore testify the extreme conditions generated by acoustic cavitation. SEM observations of the created defects suggest the coexistence of two modes of fracture at the surface of the sample. Indeed, some created defects exhibit an erosion in agreement with the brittle nature of crystalline Si at room temperature (linear cracks and defects as observed in Figure 2a−e), while other areas suggest the presence of plastically deformed areas (Figure 2e−h), evidencing a local disorder as observed in ref 36. Finally, note the presence of surface deformations which were revealed by SEM and AFM investigations (Figures 2 and 3, and Supporting Information Figure SI.3). These features are also increasing with the sonication time and intensity and characterized by height differences when considering the two sides of a crack (see the AFM scan line in Supporting Information Figure SI.2).

AFM topographic measurements allow one to monitor the morphological evolution of the sonicated Si wafer for long periods of treatment and demonstrate the relative increase of the roughness of the surface (Figure 3). The corresponding surface roughness was quantified (Figure 4) using R_a (arithmetic average of the absolute values of the surface height deviations measured from the mean plane) and R_q (root-mean-square average of height deviations taken from the mean image data plane) parameters.[8] The initial surface was found to be totally flat, devoid of defects, with a measured roughness lower than 1 nm. After 4 h of sonication, the surface reaches a
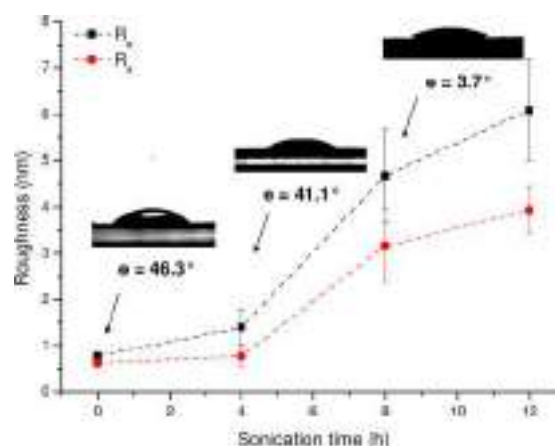
Figure 4. Measurements of the roughness and contact angle of the silicon wafer surface as a function of the sonication time (Ar, 20 °C, I_{ac} = 32 W cm^{-2}, H$_2$O, V = 250 mL).

roughness of 0.77 and 1.39 nm for R_a and R_q, respectively, while 12 h of sonication leads to a roughness around 3.9 and 6.1 nm for R_a and R_q, respectively. The roughness of the Si surface is therefore increasing with sonication time for both parameters, which is in agreement with SEM measurements. In comparison with the measurements performed on various glass and metallic surfaces in previous investigations, the erosion damage and roughness increases observed for Si are less pronounced and quite slow.[8,45] These observations emphasize the better cavitation erosion resistance of Si and confirm the long incubation period observed for Si with microscopy.

The corresponding water contact angle measured on the various samples shows an important increase of the hydrophilicity of the Si surface going from ~46° to ~4° within ~8 h of sonication (Figure 4). The contact angle is very sensitive to local physical transformations of a surface. Therefore, the created superhydrophilicity of the surface may be the result of an increase of the density of hydroxyl groups at the newly created surfaces or to an inverse lotus effect, since AFM showed an increase of roughness. The nonlinear behavior of the contact angle and roughness versus the sonication time suggests a possible concomitant contribution of both physical (roughness) and chemical (density of OH groups) phenomena.

In addition to local chemistry, the strains ultrasonically generated at the Si surface may modify the interatomic distances and lattice vibration frequencies of the crystalline structure.[32,33] μ-Raman spectroscopy appears to be a candidate of choice to investigate the mechanical stress and local atomic arrangement at the surface of the wafer. At atmospheric pressure, the untreated Si wafer exhibits a cubic diamond structure (space group $Fd3m$) characterized by a narrow Raman peak at ~521.5 cm^{-1} and corresponding to the transversal optical (TO) phonon of the crystalline c-Si (phase conventionally labeled Si−I).[27−30] This peak was found to be predominant in all of our Raman spectra and can be observed in Figure 5 (depicted in red for all spectra); it corresponds to the triply degenerated optical phonon in the center of the Brillouin zone.[27−30,46] After sonication, some spectra were found to present a broadened TO c-Si band with a measured full width at half-maximum (FWHM) up to $\Gamma_c \approx$7.1 cm^{-1} (against ~3.4 cm^{-1} for the nontreated c-Si, Figure 5a). TO peak broadening can be attributed not only to an increase in the density of defects within the crystals but also to a phonon
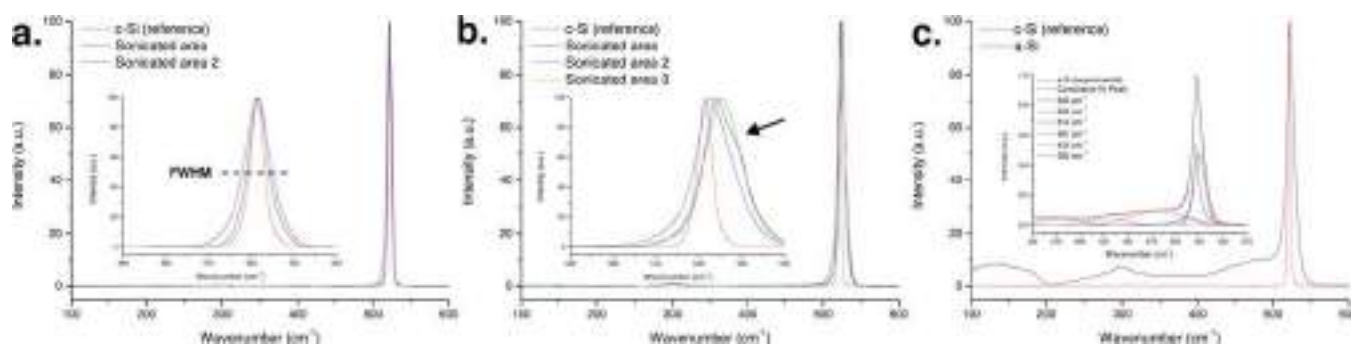
Figure 5. Raman spectra measured around localized defects after 8 h of sonication (I_{ac} = 32 W cm^{-2}, Ar, 20 °C, H$_2$O, V = 250 mL). For all spectra, the crystalline reference sample c-Si is depicted in red. Spectra characterize different features: (a) broadening of the TO c-Si peak, (b) broadening, frequency shift, and quasi-split of the TO peak, and (c) formation of an amorphous structure. Insets of a and b are magnification of the relevant zone; inset of c is a deconvolution of the amorphous spectrum between 350 and 575 nm.

confinement effect resulting from the presence of polycrystalline Si (poly-Si).[23,27−29,32,33,47] Other sonicated areas were found to present a high-frequency shift and showed the apparition of a shoulder on the TO c-Si peak (black arrow in Figure 5b). These features are representative for an anisotropic compressive stress going along with a lattice deformation and leading to removal of the degeneracy of the Raman modes.[47,48] The observed frequency shift is known to be influenced by the mechanical stress generated in the crystalline structure and reflects a discrepancy in the distribution of the bond length of the sonicated Si.[32,33]

It is generally admitted that a compressive stress results in a frequency increase of the Raman bands, whereas a tensile stress will downshift the Raman frequency.[30,47,48] In our case, the upward shift ($\Delta\omega$) of the Si peak, in comparison to the unstressed Si, confirms a compressive strain in the lattice. Assuming a uniaxial strain, the maximum resulting stress (σ) can be estimated using the following linear eq 1[49]

$$\sigma(MPa) = -434\Delta\omega(cm^{-1}) \quad (1)$$

This gives a localized residual stress of ∼1.8 GPa, which corresponds to a strain (ε) of about 1.38% according to eq 2, and considering a Young's modulus $E_{[100]}$ of ∼130 GPa.[28,49]

$$\varepsilon(\%) = \sigma/E = -0.334\Delta\omega(cm^{-1}) \quad (2)$$

The most striking features characterized with μ-Raman spectroscopy are depicted in Figure 5c. The spectrum is composed of several broad bands with a massive peak between 400 and 550 cm^{-1}. This part of the spectra was deconvoluted into several components; the best fit obtained resulted in the sum of several Gaussian peaks and one Lorentzian peak at ∼522 cm^{-1} for c-Si (insert of Figure 5c.). Note in this case that the main c-Si peak is composed of two components resulting from deformation of the lattice (other deconvolutions did not fit). According to deconvolution and in agreement with the literature, this spectrum exhibits the features of amorphous Si (a-Si) in combination with a c-Si peak at ∼522 cm^{-1} generated from the surrounding crystalline Si. a-Si shifts are located at ∼481 cm^{-1} (TO mode), ∼380 cm^{-1} (longitudinal optic, LO mode), ∼310 cm^{-1} (longitudinal acoustic, LA mode), and one broad peak around ∼100−200 cm^{-1} (transverse acoustic, TA mode).[24,27−33,46] In general, the obtained μ-Raman spectra exhibited a background asymmetry and a width increase of the TO c-Si peak that further indicate the presence of an amorphous Si phase and strengthen the highlighted discrepancies of the Si bond lengths and angles.[27] Note that the a-Si

observation is in agreement with the plastically deformed areas observed with SEM. The deconvolution spectra also show the presence of a peak at 514 cm^{-1}, which is typical for the presence of grain boundaries, or crystalline Si particles. A contribution of silica formation may also be involved during sonication processing; however, it is important to mention that its signature was not evidenced with μ-Raman, IR-TF, and X-ray reflectivity investigations. Note finally that the aging of the Si wafer in pure water during several days did not generate observable differences with the reference sample. The same remark rose when measuring after several hours in pure water on a nonactively sonicated area (e.g., side of the sample) or on a zone which was cut to fit the sample holder.

Amorphization of crystalline Si results from a structural destabilization of the Si structure and evidences a degree of atomic disorder at the surface of the sample.[32,33] This phenomenon can take place far below the melting temperature and has been reported to occur under several experimental conditions such as electron irradiation.[26] However, this phenomenon involves high energies (∼1 MeV) not reached in our study. Among the other reported methods, high-pressure investigations such as nanoindentation revealed an interesting way of amorphization through metallization of c-Si.[27−29,46] The high stress (∼9−16 GPa) provided to the crystal structure during indentation allows transformation of the cubic Si−I phase into a metastable metallic β-Sn phase (Si−II, body-centered tetragonal phase).[27−29] As a function of the pressure release, the metallic structure Si−II is able to lead to polymorphic metastable phases of crystalline Si−III (bc8, body-centered cubic structure, 8 atoms per unit cell) and Si-XII (r8, rhombohedral structure, 8 atoms per unit cell) phases but also to an amorphous Si phase (a-Si) or a mixture of both. The a-Si phase is favored during fast unloading processes, whereas the polymorphic phases are favored during slow release of pressure. Note that the deconvoluted spectra (Figure 5c) also showed a peak at ∼430 cm^{-1}, which can be attributed to bc8-type structure in accord with the literature.[27−29,32,33] The presence of the deformations (Supporting Information Figures SI.2 and SI.3) and the plastically deformed areas (Figure 2) observed with SEM, in combination with the spectroscopic observation of a-Si, and bc8 structure, suggest the possible Si amorphization through the metallic Si−II phase. It is important to emphasize that metallization of Si was reported to occur under Si compression with shock waves (evidenced with reflectivity and conductivity measurements).[50,51]

In a review devoted to the phase transformations of Si under contact, Domnich and Gogotsi concluded that Si phase transformation can be described as a deformation-induced transformation.[27−29] A thermodynamic nonequilibrium state of disorder equivalent to high-temperature amorphization may be generated during ultrasonic processing as it was, for example, reported for ball milling.[32,33] This amorphization may result from a loss of lattice stability during the cyclic compressions/decompressions of the collapsing bubbles.[27,29] It is important to emphasize that the range of pressure usually involved during these transformations is close to the pressures generated by the shock waves during sonication.[8] Acoustic cavitation is known to generate highly nonequilibrium conditions able to create transient decompression at the surface of the solid faster than what was observed by indentation. Combination of the lattice distortion with the generated compressive and shear strains induced by cavitation may therefore promote amorphization of the intervening material. Note that Si amorphization was recently reported to occur with electrosprayed nanodroplets bombarded toward a Si surface.[52]

TEM investigations confirmed the presence of a perfect diamond cubic single-crystalline structure for the nontreated sample devoid of phase transformation. Measurements carried out on the sonicated samples revealed the presence of a complex structure exhibiting complicated diffraction contrast because of the presence of a highly stressed and distorted structure (Figure 6, electron diffraction patterns inserted for
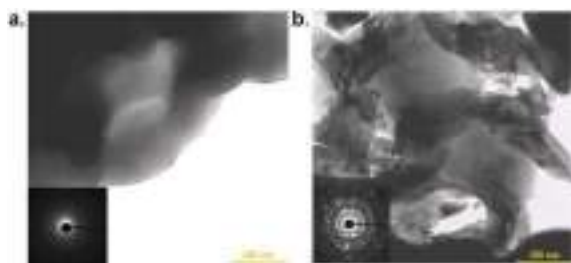
Figure 6. Bright-field TEM observation of a Si-sonicated area after 8 h of sonication (Ar, I_{ac} = 32 W cm^{-2}, 20 °C, H$_2$O, V = 250 mL) showing an amorphous Si structure (a) and a polycrystalline Si structure (b) with the corresponding electron diffraction patterns.

each image). An increase of the apparent porosity of the resulting sample can also be underlined. The corresponding electron diffractograms suggested the presence of several phases: (i) the initial crystalline structure, (ii) wide diffuse rings resulting from a randomized distribution of Si atoms within the investigated structures and corresponding to the amorphous phase a-Si, and (iii) several concentric speckle-like halo rings typical for poly-Si. Therefore, TEM measurements were found to be consistent with the μ-Raman investigations. Correlation of the various experimental results indicates the presence of mixed domains composed of crystalline, amorphous, and polycrystalline phases. The presence of a transition stage where several phases are coexisting can be assumed. The presence of Si particles can result from fragmentation of c-Si with ultrasound and their embedding in an amorphous phase (a-Si or a-SiO$_x$) but also to partial recrystallization which may occur after amorphization and during sonication due to local sample heating and the generated solid frictions during erosion. A similar behavior was reported for the ball milling treatment of crystalline Si.[32,33]

The different highlighted features evidence the complex stress state existing at the sonicated interface. According to the above observations, the mechanism of Ar excitation (Figure 1) results from the strains generated at the Si surface and in its crystalline structure. Indeed, Si phase transformation such as amorphization or metallization is known to go with a drastic change in density leading to volume expansion or contraction.[27−29,31] Therefore, these local transformations are able to fracture, deform, and dislocate the Si (sub)surface. In the mean time, the generated strains and distortions affect the electron density of states (thus affecting the thermal and electrical properties of silicon).[32,33] The introduced fractures induce a separation of the previously linked atoms responsible for a decrease of the wave function overlap across the crack. It results in creation of localized states associated with an increase of electron energy.[44] An electron hole recombination may then occur leading to the dielectric breakdown of the surrounding gas and de facto to the Ar* emission. Noteworthy, Ar* emission probably goes with Si emission usually observed around 1240 nm and between 3450 and 4965 nm.[26] Although Ar* transitions were observed, possible emission of the solid state component cannot be observed under these conditions since it occurs in a wavelength range not detected using our setup.

4. CONCLUSION

This work contributes to the understanding of the mechanism involved during cavitation at the solid−liquid interface following sonication at 20 kHz. High-power ultrasound was shown to induce interfacial changes of the physical, chemical, and structural properties of crystalline Si. Although cavitation erosion of Si involves formation of pits and cracks, its behavior under cavitation was found to be different from that observed on other materials such as glasses or metals. For the first time, ultrasound-induced mechanoluminescence is observed on an extended solid surface and a different mechanism of light emission is proposed. The gas discharge occurring at the solid−liquid interface opens new alternatives concerning monitoring of microscopic and macroscopic processes developed at the interface for medical, environmental, chemical, or engineering applications. Furthermore, spectroscopic and microscopic investigations strongly revealed the stress and dramatic transformations locally created during sonication. These properties may provide an interesting route of investigations devoted to the mechanical, electrical, and optoelectronic properties of Si (solar cells, transistors, MEMs, etc.).

■ ASSOCIATED CONTENT

Ⓢ Supporting Information

Additional spectra, AFM, and SEM pictures. This material is available free of charge via the Internet at http://pubs.acs.org.

■ AUTHOR INFORMATION

Corresponding Author

*E-mail: matthieu.virot@cea.fr.

Notes

The authors declare no competing financial interest.

■ ACKNOWLEDGMENTS

■ REFERENCES

(1) Vinodgopal, K.; Neppolian, B.; Lightcap, I. V.; Grieser, F.; Ashokkumar, M.; Kamat, P. V. *J. Phys. Chem. Lett.* **2010**, *1*, 1987−1993.

(2) Bang, J. H.; Suslick, K. S. *Adv. Mater.* **2010**, *22*, 1039−1059.

(3) Patete, J. M.; Peng, X.; Koenigsmann, C.; Xu, Y.; Karn, B.; Wong, S. S. *Green Chem.* **2011**, *13*, 482−519.

(4) Gedanken, A. *Ultrason. Sonochem.* **2004**, *11*, 47−55.

(5) Suslick, K. S.; Flannigan, D. J. *Annu. Rev. Phys. Chem.* **2008**, *59*, 659−683.

(6) Leighton, T. G. *The Acoustic Bubble*; Academic Press: London, 1994.

(7) Suslick, K. S. Sonoluminescence and Sonochemistry. In *Encyclopedia of Physical Science and Technology*, 3rd ed.; Meyers, R. A., Ed.; Academic Press: San Diego, CA, 2001.

(8) Virot, M.; Chave, T.; Nikitenko, S. I.; Shchukin, D. G.; Zemb, T.; Mohwald, H. *J. Phys. Chem. C* **2010**, *114*, 13083−13091.

(9) Török, B.; Balázsik, K.; Felföldi, K.; Bartók, M. *Ultrason. Sonochem.* **2001**, *8*, 191−200.

(10) Skorb, E. V.; Andreeva, D. V.; Möhwald, H. *Angew. Chem., Int. Ed.* **2012**, *51*, 5138−5142.

(11) Rivas, D. F.; Prosperetti, A.; Zijlstra, A. G.; Lohse, D.; Gardeniers, H. J. G. E. *Angew. Chem., Int. Ed.* **2010**, *49*, 9699−9701.

(12) Belova, V.; Gorin, D. A.; Shchukin, D. G.; Möhwald, H. *Angew. Chem., Int. Ed.* **2010**, *49*, 7129−7133.

(13) Virot, M.; Pflieger, R.; Ravaux, J.; Nikitenko, S. *J. Phys. Chem. C* **2011**, *115*, 10752−10756.

(14) Eddingsaas, N. C.; Suslick, K. S. *Nature* **2006**, *444*, 163.

(15) Eddingsaas, N. C.; Suslick, K. S. *J. Am. Chem. Soc.* **2007**, *129*, 6718−6719.

(16) Eddingsaas, N. C.; Suslick, K. S. *Phys. Rev. Lett.* **2007**, *99*, 234301.1−4.

(17) Sharipov, G. L.; Abdrakhmanov, A. M.; Tukhbatullin, A. A. *Tech. Phys. Lett.* **2009**, *35*, 452−455.

(18) Sharipov, G. L.; Tukhbatullin, A. A.; Abdrakhmanov, A. M. *Prot. Met Phys. Chem. Surf.* **2011**, *47*, 13−19.

(19) Schmidt, V.; Wittemann, J. V.; Gösele, U. *Chem. Rev.* **2010**, *110*, 361−388.

(20) Spinelli, P.; Verschuuren, M. A.; Polman, A. *Nature* **2012**, *3*, 692.

(21) Kumar, P.; Kiran, M. S. R. N. *Sci. Technol. Adv. Mater.* **2010**, *11*, 025003.1−8.

(22) Derkacs, D.; Lim, S. H.; Matheu, P.; Mar, W.; Yu, E. T. *Appl. Phys. Lett.* **2006**, *89*, 093103.1−3.

(23) Monroy, B. M.; Remolina, A.; García-Sánchez, M. F.; Ponce, A.; Picquart, M.; Santana, G. *J. Nanomater.* **2011**, 190632.1−9.

(24) Gajović, A.; Gracin, D.; Juraić, K.; Sancho-Parramon, J.; Čeh, M. *Thin Solid Films* **2009**, *517*, 5453−5458.

(25) Viera, G.; Mikikian, M.; Bertran, E.; Roca i Cabarrocas, P.; Boufendi, L. *J. Appl. Phys.* **2002**, *92*, 4684−4694.

(26) Yamasaki, J.; Takeda, S.; Tsuda, K. *Phys. Rev. B* **2002**, *65*, 115213.1−10.

(27) Domnich, V.; Gogotsi, Y. *Rev. Adv. Mater. Sci.* **2002**, *3*, 1−36.

(28) Das, C. R.; Hsu, H. C.; Dhara, S.; Bhaduri, A. K.; Raj, B.; Chen, L. C.; Chen, K. H.; Albert, S. K.; Ray, A.; Tzeng, Y. *J. Raman Spectrosc.* **2010**, *41*, 334−339.

(29) Wermelinger, T.; Spolenak, R. *J. Raman Spectrosc.* **2009**, *40*, 679−686.

(30) Stopford, J.; Allen, D.; Adrian, O.; Morshed, M.; Wittge, J.; Danilewsky, A. N.; McNally, P. J. *Microelectron. Eng.* **2011**, *88*, 64−71.

(31) Tanikella, B. V.; Somasekhar, A. H.; Sowers, A. T.; Nemanich, R. J.; Scattergood, R. O. *Appl. Phys. Lett.* **1996**, *69*, 2870−2872.

(32) Unifantowicz, P.; Vaucher, S.; Lewandowska, M.; Kurzydłowski, K. J. *J. Phys.: Condens. Matter* **2008**, *20*, 025205.1−5.

(33) Morris, M. A.; Morris, D. G. *J. Mater. Sci.* **1991**, *26*, 4687−4696.

(34) Deymier, P. A.; Khelif, A.; Djafari-Rouhani, B.; Vasseur, J. O.; Raghavan, S. *J. Appl. Phys.* **2000**, *88*, 2423−2429.

(35) Podolian, A.; Nadtochiy, A.; Kuryliuk, V.; Korotchenkov, O.; Schmid, J.; Drapalik, M.; Schlosser, V. *Sol. Energy Mater. Sol. Cells* **2011**, *95*, 765−772.

(36) El-Bahar, A.; Stolyarova, S.; Chack, A.; Weil, R.; Beserman, R.; Nemirovsky, Y. *Phys. Status Solidi* **2003**, *197*, 340−344.

(37) Kalem, S.; Yavuzcetin, O.; Altineller, C. *J. Porous Mater.* **2000**, *7*, 381−383.

(38) Kayahan, E. *Appl. Surf. Sci.* **2011**, *257*, 4311−4316.

(39) Koshka, J.; Ostapenko, S.; Ruf, T.; Zhang, J. M. *Appl. Phys. Lett.* **1996**, *69*, 2537−2539.

(40) Pflieger, R.; Brau, H.-P.; Nikitenko, S. I. *Chem.—Eur. J.* **2010**, *16*, 11801−11803.

(41) Nikitenko, S. I.; Venault, L.; Moisy, P. *Ultrason. Sonochem.* **2004**, *11*, 139−142.

(42) Suslick, K. S.; Flannigan, D. J. *Annu. Rev. Phys. Chem.* **2008**, *59*, 659−683.

(43) Bruggeman, P. D.; Schram, D. C.; Kong, M. G.; Leys, C. *Plasma Process. Polym.* **2009**, *6*, 751−762.

(44) Chandra, B. P.; Patel, R. P.; Gour, A. S.; Chandra, V. K.; Gupta, R. K. *J. Lumin.* **2003**, *104*, 35−45.

(45) Skorb, E. V.; Shchukin, D. G.; Möhwald, H.; Andreeva, D. V. *Nanoscale* **2010**, *2*, 722−727.

(46) Li, X.; Lu, J.; Yang, S. *Tribol. Int.* **2009**, *42*, 628−633.

(47) Anastassakis, E. *J. Appl. Plys* **1999**, *86*, 249−257.

(48) De Wolf, I. *Semicond. Sci. Technol.* **1996**, *11*, 139−154.

(49) Himcinschi, C.; Reiche, M.; Scholz, R.; Christiansen, S. H.; Gösele, U. *Appl. Phys. Lett.* **2007**, *90*, 231909.1−3.

(50) Zaporozhets, Y. B.; Mintsev, V. B.; Fortov, V. E. *Sov. Tech. Phys. Lett.* **1987**, *13*, 83−84.

(51) Gilev, S. D.; Trubachev, A. M. *J. Phys.: Condens. Matter* **2004**, *16*, 8139−8153.

(52) Gamero-Castaño, M.; Torrents, A.; Valdevit, L.; Zheng, J.-G. *Phys. Rev. Lett.* **2010**, *105*, 145701.1−4.

Journal of Materials Chemistry

PAPER

Sononanoengineered magnesium–polypyrrole hybrid capsules with synergetic trigger release

Ekateriva V. Skorb,*[a] Olga Baidukova,[a] Ankit Goyal,[a] Adam Brotchie,[a] Daria V. Andreeva[b] and Helmuth Möhwald[a]

This paper describes the ultrasonic-assisted preparation and characterisation of magnesium–polypyrrole hybrid capsules loaded with the organic fluorophore rhodamine 6G (Rh6G). Hybrids were prepared through sonication of magnesium and pyrrole without initiator or with Fe(III) as the polymerisation initiator in water and alcohol solutions. We studied the hybrids' morphology, ζ-potential, FTIR spectra, sonoinduced phase transformation and fluorescent properties. The properties of the obtained hybrids, as well as the dye-loading efficiency, were found to depend on the ultrasonic conditions. The fluorophore release from the free or surface sonoimmobilised capsules in aqueous solutions of different pH values and under electric current was also studied. Effective pH-responsive release, including step-wise release, was confirmed for the hybrid system. The electric current was also shown to trigger the release of hybrid capsules sonoimmobilised onto an Ni patterned ITO surface.

Introduction

Conducting polymers like polypyrrole have attracted great attention due to their conductive nature, good adhesion properties onto metal surfaces, anticorrosive nature and stability under harsh environmental conditions.[1–3] Polypyrrole (Ppy) finds vast applications in anticorrosive coatings,[1] biosensors,[4] controlled drug delivery,[5] gas sensors,[6] photovoltaic cells,[7] fuel cells,[8] artificial muscles,[9] *etc.* There are several methods for pyrrole polymerisation, for example using oxidants like ferric salts,[10] ammonium persulfate[11] or using cationic photoinitiators like iron arene salts,[12] *etc.* For biological applications, polypyrrole has advantages as it is biocompatible, stable and conductive.[13] Its conductive nature allows an applied current to be switched on and off reversibly, to facilitate the controlled delivery of drugs or release of other chemicals. In addition, due to its stability, it can protect the capsules used in controlled release systems from degradation before reaching the target site. These properties of Ppy help to overcome the present problem of achieving efficient low molecular weight active component delivery.

Various nanoparticles, such as Fe_2O_3, Ag, Pd, Au, Ti, TiO_2, V_2O_5 and C, have been used to form Ppy nanocomposites.[3,14,15] There has been to date, however, no reported study of reactive templating, for example, with calcium carbonate or, as presented in this paper, active metals (Mg). One should take into account that comparing the conductivity, magnesium has lower conductivity than noble metals such as Au or Ag. However, magnesium is very interesting as a templating material due to its biocompatibility, degradability and possible application as an *in vivo* corrosion implant.[16,17] Moreover, it was shown by us recently that magnesium (also Al, but not Au or Ag) could be effectively converted into sponges by application of ultrasound even in pure water. We have investigated several groups of metals under different sonication conditions. Magnesium chosen for this study is ideal as it is liable to undergo oxidation and its melting point is within the range achievable during ultrasonic processes (cavitation and inter-particle collisions). This simple process, free of byproducts, also enables the loading of sponges with active agents in the same process. The sponges system can be loaded with active chemicals (vitamins and drugs, corrosion inhibitors, enzymes, DNA fragments, antibodies, bone morphogenetic proteins, *etc.*). As an analogue to novel Mg sponges, a drug carrier providing time-controlled drug release on demand that is widely applied nowadays is $CaCO_3$.[18] A pH change could be used as an appropriate trigger to control release in the case of magnesium and magnesium-based hybrids. One of the great advantages of the Mg–Ppy hybrid, compared with Mg itself, is the possibility of construction of a unique encapsulation system, having porous surfaces with active component release on demand.

In the present work we describe an ultrasound-assisted method for the formation of magnesium–polypyrrole hybrid capsules with and without an initiator (Fe(III)). Ultrasound has many advantages over conventional synthesis techniques because it is

[a]*Max Planck Institute of Colloids and Interfaces, Wissenschaftspark Golm, Am Mühlenberg 1, 14476 Golm, Germany. E-mail: skorb@mpikg.mpg.de; Fax: +49 331567 9202; Tel: +49 331567 9233*
[b]*Physical Chemistry II, University of Bayreuth, Universitatstr., 30, Bayreuth, 95440, Germany*

This journal is © The Royal Society of Chemistry 2012

J. Mater. Chem., 2012, **22**, 13841–13848 | 13841

both environmentally friendly and cheap. Reactions that with other techniques would require the use of harsh reaction conditions (high temperature, high pressure and in organic solvents) can be carried out in aqueous systems under ambient conditions with ultrasound.[19–22] Not only does this allow reactions to be carried out under milder conditions but it also reduces the number of synthesis steps, permits the use of lower purity chemicals and gives higher yields.[23] Moreover, for polymerisation reactions, ultrasound can increase the reaction rate and monomer conversion percentage, compared with other techniques, largely because it enhances mass transport to the reaction site.[24] In particular, the molecular weight of Ppy in the hybrid system can depend on temperature, pressure, gas content, pH, solvent, duration and intensity of the ultrasound. Moreover, in the case of hybrid systems, of great importance is the matrix (here Mg) and its response to ultrasound as well as porosity type (pore shape and size). Despite great interest[25–27] in the prospective field of metal–polymer interactions due to the application of high-intensity ultrasound (thought to arise through cavitation-assisted processes), there is still a general lack of knowledge about such processes. A few reports have concentrated on characterisation of the chemical interactions between metals and untreated polymer surfaces, whereas some others have concentrated on plasma-treated polymer surfaces. From the studies on untreated polymer surfaces, several general observations can be made. Typically, for polymers that do not contain carbon–oxygen or carbon–nitrogen functionalities, little to no chemical interaction is observed, irrespective of the reactivity of the metal.[28] For reactive metals, such as Al, Mg, Cr, and Ni, extensive chemical interactions can occur, typically with oxygen atoms in oxygen-containing polymers.[29] For metals with moderate chemical reactivity, such as Cu, Ti and Ag, chemical interactions were found to be polymer dependent.[30] The formation of defined hybrids using the green ultrasonic method is of great interest due to their advanced functionalities (e.g., synergetic (pH and electric current) time-resolved active component release), which can be used as capsules.

Rhodamine 6G (Rh6G) is a cationic lipophilic dye, which is among the most stable organic fluorophores. It is mostly applied in laser technology, as well as having applications in fluorescent bio-imaging.[31–33] Owing to its lipophilic character, Rh6G is also known as a distinct stain for lipids and phospholipid-based polymers.[32] Systems loaded with the Rh6G fluorophore may be useful for different biological and technological applications. For example, polymer particles incorporating dyes are applicable to cell labelling,[33] sensitive diagnostic reagents,[34] flow tracing[35] and electronic inks.[36] Thus, in this work we chose Rh6G as a model to investigate novel hybrid materials formed through sonication for low molecular weight molecule storage and release on demand.

Experimental section

Materials

Magnesium particles used for the experiments were supplied by Alfa Aesar of -325 mesh size and 99.8% purity and were used as received. Pyrrole (98%, reagent grade) was supplied by Sigma Aldrich. For all experiments, water was purified before use in a three-stage Millipore Milli-Q Plus 185 purification system and

had a conductivity lower than 18.2 MΩ cm. Fe(III) (FeCl$_3$·6H$_2$O, 97% purity, Sigma Aldrich) was used as the pyrrole polymerisation initiator. Rhodamine 6G (Rh6G) was supplied by Sigma Aldrich and had a 98% dye content.

Magnesium PPy hybrid preparation

Magnesium powder was sonicated in 60 mL Milli-Q water or alcohol solution with a 20 kHz horn-type sonicator (Hielscher UIP1000hd, Germany) equipped with a booster B2-1.2, operated with a maximal output power of 1000 W. The surface area of the horn tip (Hielscher, BS2d22) was 3.8 cm^2 and sonication was performed in a thermostatted flow cell (FC100L1-1S) at 65 °C. The maximum calorimetric intensity was calculated as 57 W cm^{-2} at a mechanical amplitude of 81 μm. Samples were centrifuged after sonication and then dried after removing the extra water.

Experiments with pyrrole without initiators

Magnesium particles were sonicated in solution for 5 minutes. Pyrrole was subsequently added to achieve 5 wt% pyrrole solution and sonication was continued up to 30 minutes. The weight ratio of magnesium : pyrrole was 2 : 1.[37]

Experiments with initiators

Fe(III) was used as the initiator. The molar ratio of iron : pyrrole was 3.4 : 1. We sonicated magnesium with aqueous salt solution for 5 minutes and then pyrrole was added as described above.

R6G loading

Samples were loaded by simultaneous sonication of magnesium and Rh6G. Thus magnesium was sonicated for 5 minutes in the presence of Rh6G. Pyrrole was then added and sonicated as described above.

Capsule sonoimmobilisation

An ITO glass metal patterned surface was formed as in ref. 38–40 and placed in a home-manufactured Teflon sample holder that allowed the sample to be held at a reproducible distance from the ultrasonic horn. This sample holder allowed a flat angle treatment of the sample with a 2 cm distance between the probe and the sample. Preformed hybrid capsules (10 wt%) were added to an aqueous solution and sonicated for 5 minutes under the same conditions as above. The glass containing the sonoimmobilised hybrid capsules was then washed several times and dried in N$_2$ flow.

Characterization

A Zeta Sizer Nano ZS (Malvern Instruments, UK) was used to determine the size distribution and ζ-potential of the containers.

Microscopy

A conventional transmission electron microscope (TEM), a Zeiss EM 912 Omega (Carl Zeiss AG, Germany), equipped with an electron diffraction unit was used. It was operated at 120 kV and was employed to study the particles' morphology, crystal structure and local orientation. Scanning electron microscopy (SEM)

was performed with a Gemini Leo 1550 instrument at an operating voltage of 3 keV to study the morphology of the samples. A Leica TCS SP (Leica, Germany) confocal laser scanning microscope (CSFM) with a 100× oil immersion objective and numerical aperture of 1.4 was also used.

Infrared spectroscopy

Fourier transform infrared (FTIR) measurements were carried out with a Bruker Hyperion 2000 IR microscope equipped with a 158 IR objective and MCT detector, operated at room temperature with KBr pellets. For powdered samples the traditional infrared analysis method is the collection of a KBr pellet spectrum with an aliquot of the sample. Spectra between 400 and 4000 cm^{-1} were recorded with 2 cm^{-1} resolution in the transmission mode using a DTGS detector.

X-ray diffraction

XRD patterns for phase identification were collected using a Bruker D8 diffractometer with CuKα radiation ($\lambda_1 = 1.54053$ Å). Data were measured over the range of $2\theta = 5$ to $90°$, at steps of $0.05°$ and 1.0 s per step.

Nitrogen sorption

Nitrogen adsorption–desorption isotherms were measured at 77 K using a Quantachrome Quadrasorb adsorption instrument and the BET method was used for surface area determination.

Cavitation bubble dynamics

Bubble oscillation and collapse dynamics were investigated by measuring the intensity of scattered laser light from a spatially stable single bubble.[41] A rectangular glass resonator cell was constructed with a piezo-ceramic transducer glued to the base. Degassed water (24 mbar, 105 mL) was added to the cell, which was subsequently tuned to resonance (27 kHz) using a power amplifier (Krohn-Hite, model 7500) and function generator (Linear Krohn-Hite, model 1200A). With the acoustic pressure initially set at 0.9 bar (measured with a Dapco Industries needle hydrophone), a bubble was introduced to the solution by dropping water on the air–water surface with a syringe. The bubble forms at the acoustic pressure antinode of the cell, where it is spatially stable for several minutes. A 5 mW pen laser was aligned with the bubble and an end-on Hamamatsu photomultiplier tube was orientated at 90 degrees to the laser beam. The scattered light intensity from the oscillating bubble was then captured on a digital oscilloscope (Hameg, model HM407), which was connected to a PC. Using the same solution and experimental conditions, pyrrole was added and the experiment repeated. This procedure was then performed at a higher acoustic pressure of 1.1 bar, in order to observe the influence of the additive on sonoluminescence (emitted from the bubble in water above a threshold pressure of about 1 bar).

Release experiments

The loading efficiency was determined *via* absorption (8453 UV-visible spectrophotometer, Agilent Technologies) and

fluorescence (FluoroMax-4, HORIBA Jobin Yvon) techniques. The hybrid capsules were dispersed in water. The dispersion was stirred for a chosen time and then centrifuged. The supernatant was then filtered to remove the remaining particles. As a reference, water solutions of the respective Rh6G with known concentrations were prepared and a calibration curve was recorded. A fluorimeter (FluoroMax-4) was used to determine the release dynamics in water. A water suspension of hybrid capsules (0.02–0.05 mg mL^{-1}) was placed in a quartz cuvette. The fluorescence intensity was observed every 2 minutes and the scattering was suppressed by polarising filters in the excitation and detection beams. The optical density at the absorption bands of highest wavelength was set below 0.1 to avoid reabsorption effects. Different pH regions were analysed. Absorption was also measured after step-wise changing of the pH. The electric current-induced release from sonoimmobilised capsules was studied *in situ* in confocal fluorescence mode.

Results and discussions

There has been emerging interest in the last few decades in hierarchically ordered 3-D networks, which can be considered as carriers for active chemicals.[42–44] Green and inexpensive production of such carriers is a major focus of current research, as is their formation and well-defined organisation to achieve controllable chemical release. The application of ultrasound for metal-based sponge formation due to metal modification has been the focus of our work over the last two years.[21,23,33,45–48] We have demonstrated that these sponges may be used as carriers of active chemicals. The general concept of ultrasound-driven modification of metal microparticles (μPs) in water is as follows: the mechanism of modification of the metal structure under ultrasound irradiation is complex and involves a variety of aspects related to thermal etching and oxidation of metal surfaces. It is seen from Fig. 1 that modification of magnesium proceeds through different stages, and at the end we can achieve a total transformation of the metal to brucide (Fig. 1f).

For chemical carriers, the most important structure is one with maximal porosity, which in our case is achieved for the partially oxidised mesoporous magnesium μPs (Fig. 1b and 2). The same
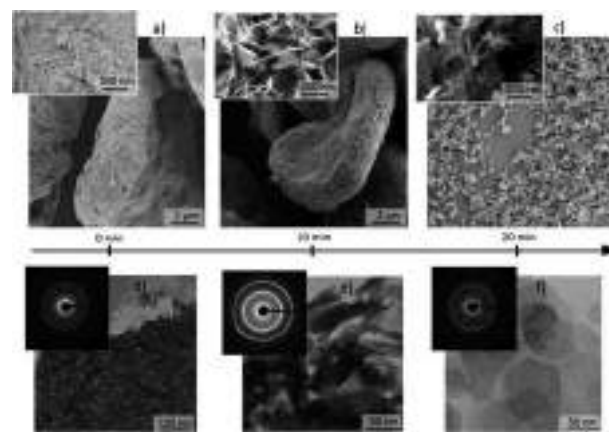

Fig. 1 Influence of sonication time on magnesium particles: (a–c) SEM and (d–f) TEM/ED images of initial, 10 minutes and 20 minutes sonicated samples.

tendency of crystalline phase sonotransformation was shown for aluminum,[21] with one possible phase being a mesoporous metal skeleton stabilised with an oxidised metal nanolayer. It was shown that the surface areas for the same sonication time for Mg and Al were 69 m² g⁻¹ and 54 m² g⁻¹, respectively. Furthermore, Mg sponges were characterised by larger pores than Al sponges: the average pore diameters were about 14 nm in the case of Mg and about 4 nm in the case of Al.[21] The modification of magnesium is faster in comparison with aluminum and, therefore, in the present study we use a shorter sonication time in comparison with that in ref. 21, trying to prevent total structure oxidation in favour of achieving higher porosity. Indeed, as is evident in Fig. 3, we achieve an even more porous structure with a surface area of 260 m² g⁻¹ and pore size of 7 nm.

Development of hybrid capsules is suggested for a system of three components: liquid (water or alcohol); solid (Mg-μPs); and a chosen additive (pyrrole) (Fig. 3).

The most pronounced effects of ultrasound on liquid–solid systems are both mechanical and chemical, attributed to symmetric and asymmetric cavitation collapse and active species formation in the reaction medium (Fig. 3). Symmetric bubble collapse in a liquid medium causes shock waves with high pressures in addition to high gas temperatures in the collapsed cavities. These high-pressure, high-temperature conditions exist for short time periods and are unique for the synthesis of complex hybrids with the reactor at ambient conditions.[19–22] Shock waves also potentially create microscopic turbulences.[49] This phenomenon increases the transfer of mass across the solid, thus increasing the intrinsic mass-transfer coefficient, as well as possibly creating or modifying existing 3-D networks, such as hybrid solid (Mg)–polymer (Ppy formed from pyrrole) interactions. Alternatively, this phenomenon may result in further and/or different 3-D ordering of the network formed. When bubble collapses occur near a solid surface that is several orders of magnitude greater in scale than the cavitation bubbles,[50] they occur asymmetrically,[51] and solvent microjets are formed perpendicular to the solid surface. These microjets have an estimated speed of 100 m s⁻¹ (ref. 19) and lead to pitting, erosion of the surface, particle breakage and collision. Moreover, this behaviour leads to an enhancement in heterogeneous reactions (secondary cavitation-assisted processes) with active species formed in the reactor. Thus, a part of the vaporised molecules from the surrounding medium can be dissociated to form radical species, such as OH and H, for water sonolysis.[52] Radicals can also form by hydrogen abstraction of some organic additives
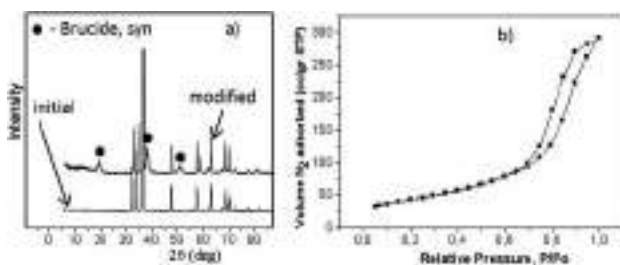
Fig. 2 (a) XRD patterns of initial (upper) and modified (lower) (10 minutes sonication) magnesium particles; (b) N₂ adsorption–desorption of modified magnesium particles.
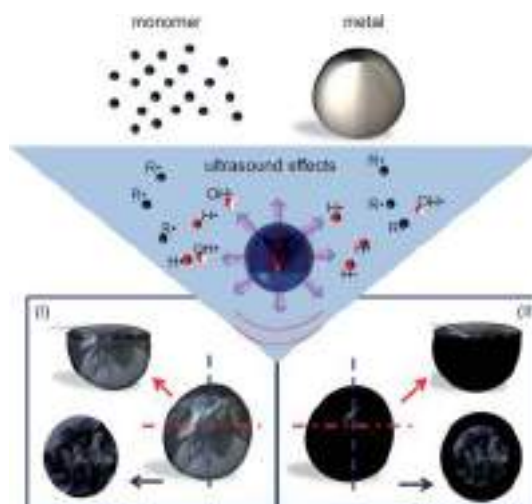
Fig. 3 Schematic representation of the research objectives and sonochemical synthesis mechanism: initial materials – monomer, metal (magnesium) μPs – upper part; possible ultrasonic effects in the reactor – physical (shock waves and liquid jets) and chemical (formation of radicals from monomer and sonolysis of the liquid vapour (here, water shown)) – middle part; and some examples of systems which could be expected after applying ultrasonic exposure: the metal and polymer could form a porous hybrid system; formation of core@shell structures such as metal and/or hybrid@polypyrrole – lower part of the scheme.

(*e.g.*, RH forms R'), either by reaction with a primary radical formed during cavitation collapse and/or by the direct pyrolysis of RH molecules during bubble collapse.[53] Recent studies[21,23,27,45–48,54] have suggested scenarios and provided prospective defined cavitation pathways for surface modifications based on the surfaces' different responses to ultrasound. The different responses result from differences in the surfaces' hydrophilic/hydrophobic properties or chemical reactivity. Thus, comparison of bubble formation on hydrophobic and hydrophilic surfaces with that in the bulk reveals a stronger response on the hydrophobic part of a patterned surface than on the hydrophilic part.[54] If a surface changes its hydrophilicity/hydrophobicity during a sonochemical process, it is clear that the sponge response to ultrasound becomes nonlinear. The presence of additives in the sonochemical reactor can also influence the cavitation process. The role of an additive can be played by monomer or polymer molecules (here pyrrole and polypyrrole, respectively). These additives accumulate at the gas–liquid interface of cavitation microbubbles and the formed 3-D network. During collapse, the center of the bubble is characterised by high temperatures and pressures, whereas the bulk liquid remains under normal conditions. A transition zone also exists between the interface and bulk liquid.[55] Molecules are present in both the transition zone and the outer liquid phase. Additives or formed species (Fig. 3) can even penetrate inside bubbles. Single-bubble sonoluminescence studies (Fig. 4) show that pyrrole present in the solution completely quenches the luminescence which means formed species are present and liable to react inside the bubble core. However, as can also be seen in Fig. 4, the presence of pyrrole at the interface does not affect the time of bubble collapse or the size of the bubble, which is related to the intensity of the scattered light.
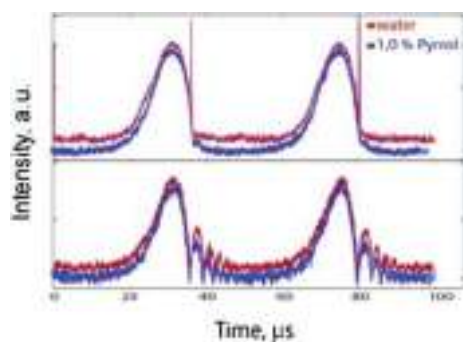
Fig. 4 Time-resolved observation of single bubble collapse in pure (upper curves, red) or pyrrole (lower curves, blue) containing solution. The sonoluminescence is superimposed on the scattered light signal at high acoustic pressure for water. In the presence of pyrrole this is completely quenched.

During the process of polymerisation the formation of long-chain molecules (polypyrrole) and the reactive species formed from them, such as long-chain radicals, takes place. The time required for the orientation of long-chain molecules at the gas–liquid interface is longer than that required for short-chain molecules and longer than the bubble lifetime.[56] The organic molecules, nanoparticles and ions near the bubble interface influence the cavitation process, which increases surface pressure, and leaves the molecules in the correct orientation and chemical state for transport and attachment to the surface.[57] Five main effects of cavitation are known for monomers and polymers: the formation of free radicals during the cavitation process,[58] polymerisation,[59] chain reorientation,[60] polymer decomposition[61] and the involvement of organics in chemical processes such as oxidation and bond breakage.[62]

Different hybrids can therefore be expected to form in our system. In particular, we found two main products (Figs. 3 and 5) depending on the solvents used: (1) interpenetrated magnesium polypyrrole (Mg–Ppy) hybrid formed in aqueous solution; (2) core@shell (Mg@Ppy) hybrid formed in alcohol solution. The presence of polypyrrole is visible in the FTIR spectra (Figs. 5e and f).[63] The peaks at 1540 and 1450 cm^{-1} can be attributed to C–N and C–C asymmetric and symmetric ring-stretching, respectively. Additionally, the peaks near 1160 and 890 cm^{-1} represent the doping state of polypyrrole, the peak at 1030 cm^{-1} is attributed to C–H deformation and N–H stretching vibrations, and the broad band at 1300 cm^{-1} is attributed to the C–H and C–N in-plane deformation vibrations, respectively. It is seen in the SEM and TEM images (Figs. 5a and c) that Mg–Ppy can still be characterised as porous with a rough surface. In alcohol solution a thicker amorphous (also see XRD pattern Fig. 5f) surface layer of polypyrrole Mg@Ppy with defined surface "flower" morphology is also observed (Figs. 5b and d). Differences in the structures formed could be due to differences in bubble collapse scenarios depending on the solution vapour pressure.[64] XRD and FTIR patterns (Fig. 5e and f) also provide evidence that oxidation in the presence of pyrrole in the solution proceeds more slowly in comparison with pure solution. Oxidation is slower since, first of all, the formed active oxygen species are involved in pyrrole polymerisation, which is apparent to the eye as a black color in solution.
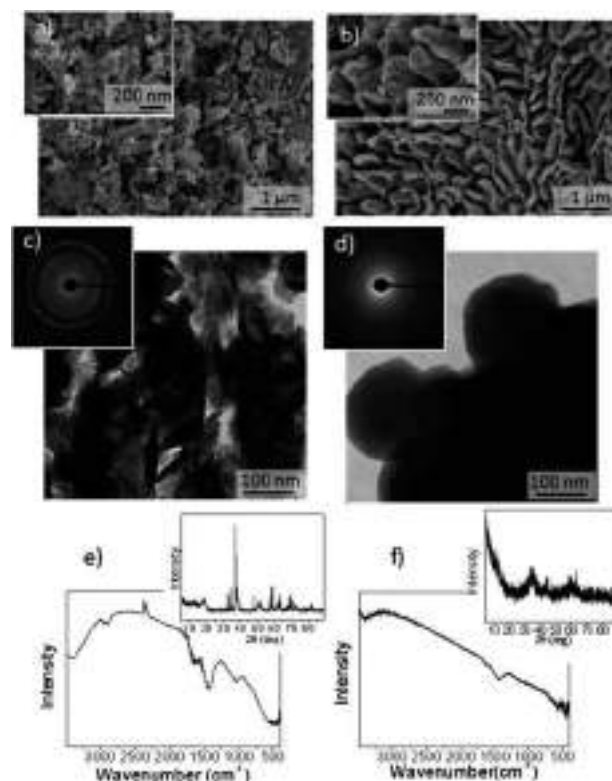
Fig. 5 (a and b) SEM images, (c and d) TEM and ED (insets) images, (e and f) FTIR spectra and XRD patterns (insets) of structures formed after sonication (30 minutes) of magnesium in (a, c and e) aqueous or (b, d and f) methanol solution containing 5 wt% of pyrrole (monomer).

The process of polymerisation can be stimulated by initiators. Here we use Fe(III) as a known effective initiator for pyrrole polymerisation. However, if Fe(III) salt is added to the reaction medium together with the monomer, polymerisation starts very fast in solution and the formation of a pronounced 3-D network is difficult to achieve. We performed short-time pre-sonication of our μ-sized magnesium particles in Fe(III) solution to achieve the formation of the first level of a 3-D network containing the initiation centers inside the 3-D network. Pyrrole solution was subsequently added as the second step in the 3-D network formation/modification. It is seen in the optical image (Fig. 6a, inset) that the resulting hybrid also exhibits the pronounced characteristic polypyrrole black color. FTIR spectra (Fig. 6c) reveal the characteristic polypyrrole bands, which are narrower in comparison with the previous case of hybrid formation without initiator. There was no evidence of interconnectivity between the formed polypyrrole (see TEM image in Fig. 6b). The polypyrrole formed is localised in the pores of magnesium. This result can be explained by taking into account the faster polymerisation with initiator and the negligible time for rearrangement of the polymer structure especially when the polymer is inside the porous magnesium and not in the solution. Such hybrids with formed polymer of lower molecular weight could potentially be used in the future for some interesting purposes, such as for the second rearrangement of the polymer structure. However, it is the interpenetrating hybrid, as for Mg–Ppy formed without initiator, that is of the greatest interest here because of its possible multi-trigger (pH and electric current flow active
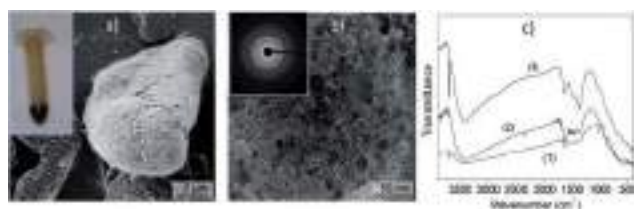
Fig. 6 (a) SEM and sample tube optical (inset) images, (b) TEM and ED (inset) images of a magnesium–polypyrrole hybrid formed after the sonication (30 minutes) of Fe(III) (initiator of polymerisation)-loaded magnesium in aqueous solution containing 5 wt% of pyrrole (monomer). (c) FTIR spectra of the hybrids formed after sonication with varying concentration of magnesium particles in solution: (1) 0.3 g mL^{-1}, (2) 0.05 g mL^{-1}, (3) 0.1 g mL^{-1}.

chemical release) capability. Before beginning our study it was assumed that magnesium would be responsible for pH-triggered release due to its chemical properties. Ppy was expected to be responsible for electrically stimulated release if the formation of a connected network through the entire hybrid could be achieved.

Here a single-step loading of Mg–Ppy hybrid carriers (capsules) with Rh6G by ultrasonic treatment of a Rh6G solution[23] (Fig. 7) was established. The multi-step loading, as reported in our previous work,[65–67] of a pre-formed magnesium 3-D network applying vacuum pump loading is possible. However, it goes without saying that a single-step process is economically preferable in materials synthesis. Using a single-step approach, we then continued sonication with pyrrole in solution for the formation of interpenetrating Mg–Ppy–Rh6G hybrids. The confocal fluorescence and SEM images of the

formed structure are shown in Fig. 7a; it is seen that Rh6G can be stored in such a hybrid. Rh6G loading contents were 0.05 g g^{-1} and 0.03 g g^{-1} in the case of Mg–Rh6G and Mg–Ppy–Rh6G, respectively. In our previous work (ref. 23) the possibility was discussed of loading due to chemisorption; however, here there was no chemisorption detected, and thus the loading is due to physical Rh6G entrapment. From the release kinetics (Fig. 7b), it can also be seen that a hybrid Mg–Ppy carrier has better long-term storage ability in comparison with magnesium loaded with Rh6G. Thus, Ppy can prevent the fast degradation of magnesium in aqueous solution as could be the case for unprotected magnesium. However, from the perspective of implant construction, both systems could be promising for drug, vitamin, antibody and protein delivery. It is also very important that the pH dramatically affects Rh6G release. The release kinetics after an hour from Mg–Ppy–Rh6G at different pH values are shown in Fig. 7c. Moreover, the step-wise release is also characteristic of such hybrids (Fig. 7d).

One of the advantages of polypyrrole is its conductive nature, a characteristic which it imparts to the hybrids presented here, namely Mg–Ppy–Rh6G. The formation of nickel patterns on ITO glass (Fig. 8b) was performed, as described in our previous work (ref. 38–40). We used the sonoimpregnation procedure (Fig. 8a) for the deposition of Mg–Ppy–Rh6G hybrids onto a nickel metal surface. In this way, the sonication of ITO glasses in the presence of loaded hybrids can result in the connection of the hybrids with nickel occurring much faster than a possible connection of the hybrid with ITO glass.[68] The melting

Fig. 7 (a) 3-D confocal microscopy reconstruction of the sononanoengineered magnesium–polypyrrole hybrid loaded with fluorophore Rhodamin 6G (Rh6G) (fluorescence mode); the inset shows the SEM image of the hybrid. (b) Time-resolved release of Rh6G from porous magnesium (Mg–Rh6G) and the hybrid capsules (Mg–Rh6G–Ppy) in aqueous solution at neutral pH. (c) Rh6G release after 60 minutes in aqueous solution at different acidic pH values. (d) Time-resolved release under initial pH = 4 and two step-wise pH changes: pH change 1 to pH = 3 and pH change 2 to pH = 1.
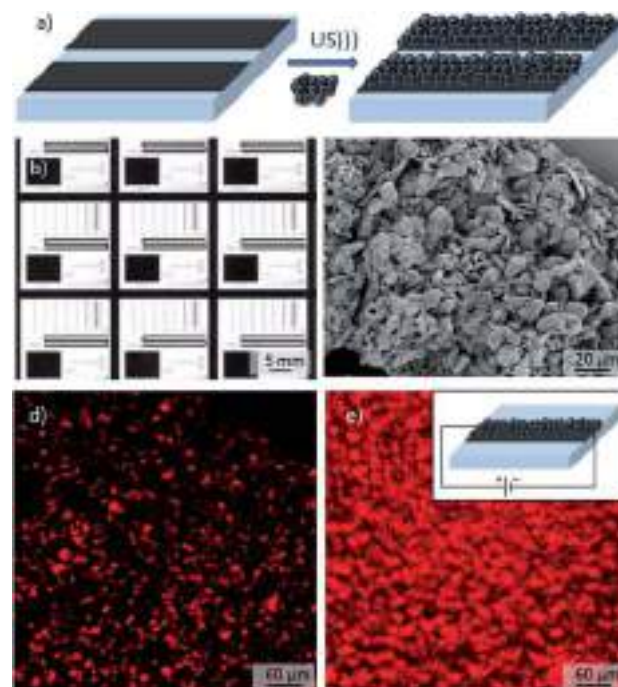

Fig. 8 (a) Schematic representation of the process of sonoimpregnation (5 minutes) of hybrid particles on a patterned surface. (b) Optical image of the initial nickel patterned ITO glass electrode. (c) SEM image of patterned sonoimpregnated surface of Rh6G-loaded hybrid. (d) Confocal microscopy image (fluorescent mode) of (c). (e) is (d) after electric current flow (shown schematically in the inset).

temperatures of the substrate (the part of the substrate with the metal patterns) and the hybrid, as well as the time of sonication, are critical parameters for this study. Since we use short-term sonication, we prevent the sonoimpregnation of the loaded hybrid into ITO glass, evident in the SEM image (Fig. 8c). The electric current in such a system as depicted schematically in Fig. 8e (inset) results in the release of Rh6G from the hybrid due to a change in polymer density. This can be seen in the confocal fluorescence images of a surface with sonoimmobilised capsules before and after electrical current (Figs. 8d and e, respectively).

Conclusions

Effective hybrid capsules with synergetic trigger release are expected to be of great interest for the next decade, since time- and space-resolved release of active chemicals (labelling fluorescent dyes, drugs, vitamins, antibodies, etc.) could provide further successful use of encapsulation systems in the construction of medical devices, corrosion termination and as surfaces for stem cell research. We presented here a solution of the problem. Thus, hybrid systems whose components are sensitive to different factors (such as Mg to pH change, and polypyrrole to electric current flow) represent ideal candidates in the design of such capsules. We have presented a sonochemical approach for the formation of such hybrids, which has great potential due to its ecologically friendly nature and amount of process steps, additives and reagents.

Acknowledgements

Notes and references

1 *Handbook of Organic Conductive Molecules and Polymers*, ed. H. S. Nalwa, John Willey & Sons, New York, 1997.
2 D. E. Tallman, G. Spinks, A. Dominis and G. G. Wallace, *J. Solid State Electrochem.*, 2002, **6**, 73.
3 E. V. Skorb and D. G. Shchukin, in *European Coatings Tech Files*, ed. G. Gehrenkemper, Vincentz Network GmbH & Co, Germany, 2010.
4 M. Gerard, A. Chaubey and B. D. Malhotra, *Biosens. Bioelectron.*, 2002, **17**, 345.
5 N. K. Guimard, N. Gomez and C. E. Schmidt, *Prog. Polym. Sci.*, 2007, **32**, 876.
6 J. Janata and M. Josowicza, *Nat. Mater.*, 2003, **2**, 19.
7 J.-D. Kwon, P.-H. Kim, J.-H. Keum and J. S. Kim, *Sol. Energy Mater. Sol. Cells*, 2004, **83**, 311.
8 R. Bashyam and P. Zelenay, *Nature*, 2006, **443**, 63.
9 T. Mirfakhrai1, J. D. W. Madden and R. H. Baughman, *Mater. Today*, 2007, **10**, 30.
10 D. V. Andreeva, D. V. N. V. Bobrova, V. K. Lavrentév, Z. Pientka, G. A. Polotskaya and G. K. Elyashevich, *Polymer Sci. A.*, 2002, **44**, 424.
11 P. Mavinakuli, S. Wei, Q. Wang, A. B. Karki, S. Dhage, Z. Wang, D. P. Young and Z. Guo, *J. Phys. Chem. C*, 2010, **114**, 3874.
12 *New Concepts in Polymer Science*, ed. V. E. Gul', Brill Academic Pub., 1996.
13 D. V. Andreeva, D. A. Gorin, D. G. Shchukin and G. B. Sukhorukov, *Macromol. Rapid Commun.*, 2006, **27**, 931.
14 P. Gomez-Romero, *Adv. Mater.*, 2001, **13**, 163.
15 A. Malinauskas, J. Malinauskiene and A. Ramanavicius, *Nanotechnology*, 2005, **16**, R51.
16 M. P. Staiger, A. M. Pietak, J. Huadmaia and G. Dias, *Biomaterials*, 2006, **27**, 1728.
17 F. Witte, V. Kaese, H. Haferkamp, E. Switzer, A. Meyer-Lindenberg, C. J. Wirth and H. Windhagen, *Biomaterials*, 2005, **26**, 3557.
18 D. V. Volodkin, R. Klitzing and H. Möhwald, *Angew. Chem., Int. Ed.*, 2010, **49**, 9258.
19 K. S. Suslick and L. A. Crum, *Encyclopedia of Acoustics*, ed. M. J. Crocker, Wiley & Sons. Inc., N.Y., 1995.
20 M. A. Margulis, in *Sonochemistry Basis*, High School, Moscow, 1984.
21 E. V. Skorb, D. Fix, D. G. Shchukin, H. Möhwald, D. V. Sviridov, R. Mousa, N. Wanderka, J. Schäferhans, N. Pazos-Pérez, A. Fery and D. V. Andreeva, *Nanoscale*, 2011, **3**, 985.
22 D. G. Shchukin, E. V. Skorb, V. Belova and H. Möhwald, *Adv. Mater.*, 2011, **23**, 1922.
23 D. V. Andreeva, D. V. Sviridov, A. Masic, H. Möhwald and E. V. Skorb, *Small*, 2012, **8**, 820.
24 F. G. Hammitt, in *Cavitation and Multiphase Flow Phenomena*, McGraw-Hill Book Co., N.Y., 1980.
25 M. Stamm, *Polymer Surfaces and Interfaces*, Springer, Berlin, 2008.
26 D. G. Shchukin, D. V. Andreeva, E. V. Skorb and H. Möhwald, in *Supramolecular Chemistry of Hybrid Materials*, ed. K. Rurack, Wiley-VCH, Germany, 2010.
27 D. V. Andreeva, E. V. Skorb and D. G. Shchukin, *ACS Appl. Mater. Interfaces*, 2010, **2**, 1954.
28 L. J. Gerenser and K. E. Goppert-Berarducci, in *Metallized Plastics, Fundamental and Applied Aspects*, ed. K. L. Mittal, Plenum Press, N.Y., 1992.
29 M. Rubinstein and R. H. Colby, *Polymer Physics*, Oxford University Press Inc., N.Y., 2003.
30 G. Ferey, Hybrid porous solids: past, present, future, *Chem. Soc. Rev.*, 2008, **37**, 191.
31 *Dye Laser Principles*, ed. F. Duarte and L. Hillman, Academic, N.Y., 1990.
32 J.-H. Wang, J. Bartlett, A. Dunn, S. Small, S. Willis, M. Driver and A. Lewis, *J. Microsc.*, 2005, **217**, 216.
33 J. Gensel, T. Borke, N. Pazos-Pérez, A. Fery, E. Betthausen, A. H. E. Müller, D. V. Andreeva, H. Möhwald and E. V. Skorb, *Adv. Mater.*, 2012, **24**, 985.
34 K. Kellar and M. Iannone, *Exp. Hematol.*, 2002, **30**, 1227.
35 G. Visscher, M. Haseldonckx, W. Flameng, M. Borgers, R. Reneman and K. Rossem, *J. Neurosci. Methods*, 2003, **122**, 149.
36 D. Yu, J. An, J. Bae, D. Jung, S. Kim, S. Ahn, S. Kang and K. Suh, *Chem. Mater.*, 2004, **16**, 4693.
37 D. V. Andreeva, Z. Pientka, L. Brozová, M. Bleha, G. A. Polotskaya and G. K. Elyashevich, *Thin Solid Films*, 2002, **406**, 54.
38 E. V. Skorb, T. V. Byk, V. G. Sokolov, T. V. Gaevskaya, D. V. Sviridov, C.-H. Noh, K. Y. Song, Y. N. Kwon and S. H. Cho, *J. Photochem. Photobiol., A*, 2008, **193**, 56.
39 E. V. Skorb, T. V. Byk, V. G. Sokolov, T. V. Gaevskaya, D. V. Sviridov and C.-H. Noh, *High Energy Chem.*, 2008, **42**, 127.
40 E. V. Skorb, T. V. Byk, V. G. Sokolov, T. V. Gaevskaya and D. V. Sviridov, *Theor. Exp. Chem.*, 2009, **45**, 40.
41 T. Matula, *Philos. Trans. R. Soc. London, Ser. A*, 1999, **357**, 225.
42 *Emerging Technologies and Techniques in Porous Media*, ed. D. B. Ingham, Springer, 2004, p. 507.
43 *Porous Media: Applications in Biological Systems and Biotechnology*, ed. K. Vafai, CRC Press, 2010, p. 599.
44 J.-R. Li, R. J. Kuppler and H.-C. Zhou, *Chem. Soc. Rev.*, 2009, **38**, 1477.
45 E. V. Skorb, H. Möhwald, T. Irrgang, A. Fery and D. V. Andreeva, *Chem. Commun.*, 2010, **46**, 7897.
46 E. V. Skorb, D. G. Shchukin, H. Möhwald and D. V. Andreeva, *Nanoscale*, 2010, **2**, 722.
47 N. Pazos-Pérez, J. Schäferhans, E. V. Skorb, A. Fery and D. V. Andreeva, *Microporous Mesoporous Mater.*, 2012, **154**, 164.
48 J. Schäferhans, S. Gómez-Quero, D. V. Andreeva and G. Rothenberg, *Chem.–Eur. J.*, 2011, **17**, 12254.
49 V. P. Skripov, E. N. Sinitsyn, P. A. Pavlov, O. V. Ermakov, G. N. Muratov, N. V. Bulanov and V. G. Baidakov, *Thermophysical Properties of Liquids in the Matastable (Superheated) State*, Gordon and Breach, N.Y., 1988.
50 E. A. Neppiras, *Phys. Rep.*, 1980, **61**, 160.
51 K. S. Suslick and G. J. Price, *Annu. Rev. Mater. Sci.*, 1999, **29**, 295.
52 J. G. Adewuyi, *Environ. Sci. Technol.*, 2005, **39**, 8557.
53 J. Z. Sostaric and P. Riesz, *J. Phys. Chem. B*, 2002, **106**, 12537.
54 V. Belova, D. A. Gorin, D. G. Shchukin and H. Möhwald, *Angew. Chem., Int. Ed.*, 2010, **49**, 7129.
55 D. G. Shchukin and H. Möhwald, *Phys. Chem. Chem. Phys.*, 2006, **8**, 3496.

56 J. Z. Sostaric and P. Riesz, *J. Am. Chem. Soc.*, 2001, **123**, 11010.
57 L. H. Thompson and L. K. Doraiswamy, *Ind. Eng. Chem. Res.*, 1999, **38**, 1215.
58 H. Endo, *J. Acoust. Soc. Am.*, 1994, **95**, 2409.
59 M. Zeng, H. N. Gao, Z. Q. Wu, L. R. Fan, T. H. Zheng and D. F. Zhou, *J. Macromol. Sci., Part A: Pure Appl. Chem.*, 2010, **47**, 1042.
60 A. V. Mohod and P. R. Gogate, *Ultrason. Sonochem.*, 2011, **18**, 727.
61 M. M. Caruso, D. A. Davis, Q. Shen, S. A. Odom, N. R. Sottos, S. R. White and J. S. Moore, *Chem. Rev.*, 2009, **109**, 5755.
62 K. Okitsu, Y. Mizukoshi, H. Bandow, T. A. Yamamoto, Y. Nagata and Y. Maeda, *J. Phys. Chem. B*, 1997, **101**, 5470.

63 M. Omastova, M. Trchova, J. Kovarova and J. Stejskal, *Synth. Met.*, 2003, **138**, 447.
64 D. J. Flannigan, S. D. Hopkins and K. S. Suslick, *J. Organomet. Chem.*, 2005, **690**, 3513.
65 E. V. Skorb, D. Fix, D. V. Andreeva, D. G. Shchukin and H. Möhwald, *Adv. Funct. Mater.*, 2009, **19**, 2373.
66 E. V. Skorb, D. G. Shchukin, H. Möhwald and D. V. Sviridov, *J. Mater. Chem.*, 2009, **19**, 4931.
67 E. V. Skorb, D. V. Sviridov, H. Möhwald and D. G. Shchukin, *Chem. Commun.*, 2009, 6041.
68 M. Virot, T. Chave, S. I. Nikitenko, D. G. Shchukin, T. Zemb and H. Möhwald, *J. Phys. Chem. C*, 2010, **114**, 13083.

Sonochemistry

Generation of a Porous Luminescent Structure Through Ultrasonically Induced Pathways of Silicon Modification**

Ekaterina V. Skorb,* Daria V. Andreeva, and Helmuth Möhwald

In heterogeneous solid–liquid systems, cavitation can induce three main effects: 1) Surface damage can occur at the liquid–solid interface through both symmetric bubble collapse, resulting in shock waves and subsequent microstreaming,[1] and asymmetric bubble collapse, resulting in surface microjets that are several orders of magnitude larger than the cavitation bubble size. For example, at 20 kHz, the maximum size of a cavitation bubble is approximately 50 μm.[2] 2) Chemical surface modification/stabilization owing to ultrasonic free-radical formation[1] can occur. 3) Fragmentation of brittle solids and an increase in their surface area can occur through high-velocity interparticle collisions in suspensions of solid species (Figure 1).[1,2]

Recently, we have demonstrated the effect of ultrasound on the phase transitions in metal particles.[3] The ultrasonication of metals has been found to cause crystal deformation, cleavage of chemical bonds, and phase transformations between amorphous and crystalline forms. These effects result in an increase in the surface area of metal systems that is stabilized by the formation of a thin oxide layer on the surface of the metal skeleton. Moreover, ultrasonic processes may cause phase segregation because of the crystallization of one of the components in metal alloys or in metal solutions.

Herein, we focus on the ultrasound-assisted modification of silicon. For applications related to optics[4a,b] or drug delivery,[4c,d] silicon suffers from an absence of intrinsic fluorescence and a lack of simple "green" modification techniques to render it suitable for such applications. In our study, we investigate the pronounced and controlled response of silicon surfaces to ultrasonic treatment, together with the formation of porous optically active silicon. This novel ultrasound-assisted method avoids the use of HF or similarly
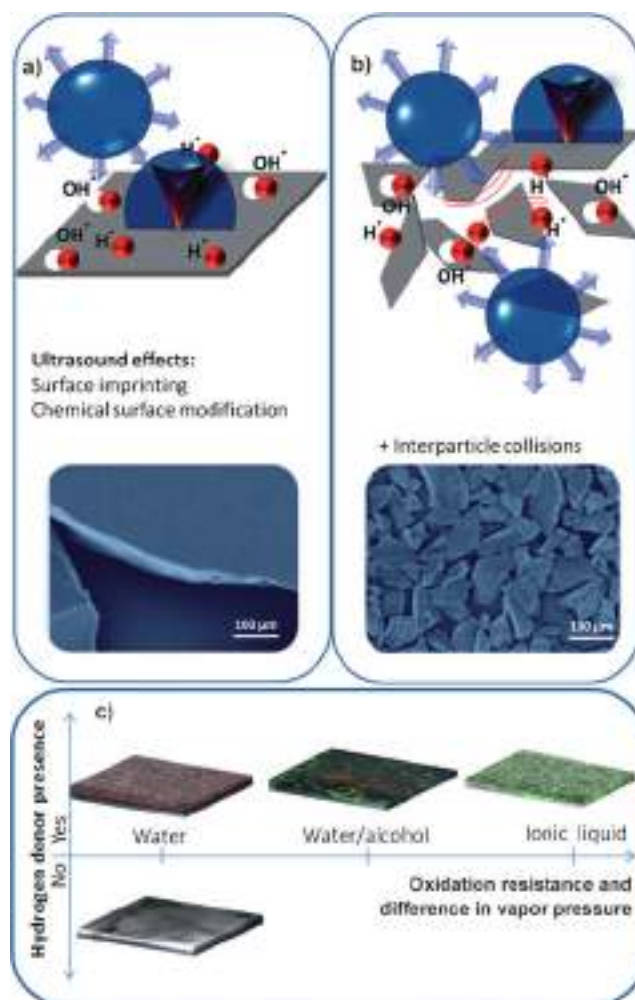
Figure 1. Ultrasonic effects (surface imprinting, interparticle collisions and chemical surface modification by free radicals) and initial SEM images of a) Si plates and b) μ-sized Si particles. c) 3D schematic reconstruction, based on μ-confocal and TEM measurements of photoluminescence and porosity change, respectively, of Si after sonication in controlled solvent conditions.

[*] Dr. E. V. Skorb, Prof. H. Möhwald
Interface Department, Max Planck Institute of Colloids and Interfaces
Am Mühlenberg 1, 14476 Potsdam (Germany)
E-mail: skorb@mpikg.mpg.de

Dr. D. V. Andreeva
Physical Chemistry II, University of Bayreuth
Universitatstrasse 30, 95440 Bayreuth (Germany)

Supporting information for this article is available on the WWW under http://dx.doi.org/10.1002/anie.201105084.

aggressive media, which are detrimental to the environment.[4]

The ultrasound-assisted modification of silicon plates, in the form of both crystalline silicon wafers and amorphous silicon deposited onto glass, and μ-sized particles is illustrated in Figure 1. In general, the interaction of cavitation bubbles with the silicon surface results in mechanical and chemical modification. The ultrasonic modification of solids is known to be controlled by various sonication conditions, including the intensity and duration of sonication, the solvent, and the

concentration and size of the sonicated species, oxidants, and reducing agents involved.[1,3,5]

The important innovation we introduce here is the addition of hydrogen donors during ultrasonication, which has dramatic influence on the process. The sonication of silicon species in water that does not contain a hydrogen donor results in the formation of an oxidized surface caused by the oxidation of the silicon by-products of water sonolysis. The samples are characterized by a slight increase in their surface roughness and the absence of photoluminescence (Figure 1c; see also the Supporting Information, Figure S1). The hydrogen donors slow the surface oxidation processes, which are brought on by free radicals formed during water sonolysis, and stabilize the porous structure through the formation of silicon-terminated bonds. In this case, Si−H bonds could be formed as an alternative to, or together with, Si−O bonds. The illustration in Figure 1c, based on a 3D reconstruction of TEM and µ-confocal measurements of the surface after high-intensity ultrasonic exposure, shows our general concept of a single-step "green" method for the construction of surfaces with different porosities. Without a reducing agent present during modification in water, neither porous nor luminescent structures were observed. However, in the presence of a reducing agent, luminescent structures with a range of porosities (25–40% in water, 60–70% in water/alcohol mixtures, and 40–50% in an ionic liquid) were detected. Furthermore, the differences in porosities correlate with differences in photoluminescence (green or red).

We used Mg or Al in water and water/alcohol mixtures, or NaBH$_4$ in an ionic liquid as the hydrogen donors. The formation of hydrogen-terminated bonds on the surface of the silicon during ultrasonication could significantly slow or prevent surface oxidation, even in a water solution, as evidenced by infrared reflection absorption spectroscopy (IRRAS; Supporting Information, Figure S2). Figures 2a–d and S2 were obtained from wafer plate samples modified in the presence of hydrogen-donor species. The formation of channel-like structures was observed in samples prepared by 5 min of sonication. We have recently demonstrated similar modification features (channel-like structures) for metals.[3] Samples modified for 20 min reveal partial surface amorphization (Figure 2b), which later converts into a completely amorphous microporous silicon structure (Figure 2c). Thus, the hydrogen-donor materials stimulate the formation of Si−H bonds, which stabilize the ultrasonically formed structures and allow for the possible formation of nanocrystalline silicon (nc-Si). The formation of Si−H bonds is also indicated by the IRRA spectra (Supporting Information, Figure S2).

The structure of the modified silicon may influence the electronic properties, charge separation, optical properties, electroadsorption, and electroreflection. For certain applications,[4] the partially hydrogenated microporous silicon with visible red photoluminescence, as shown in Figure 2d, is advantageous. In water solutions, the photoluminescent centers are submicron sized and closely packed, which protects them from agglomeration; their cooperative effect is visible in µ-confocal photoluminescence.

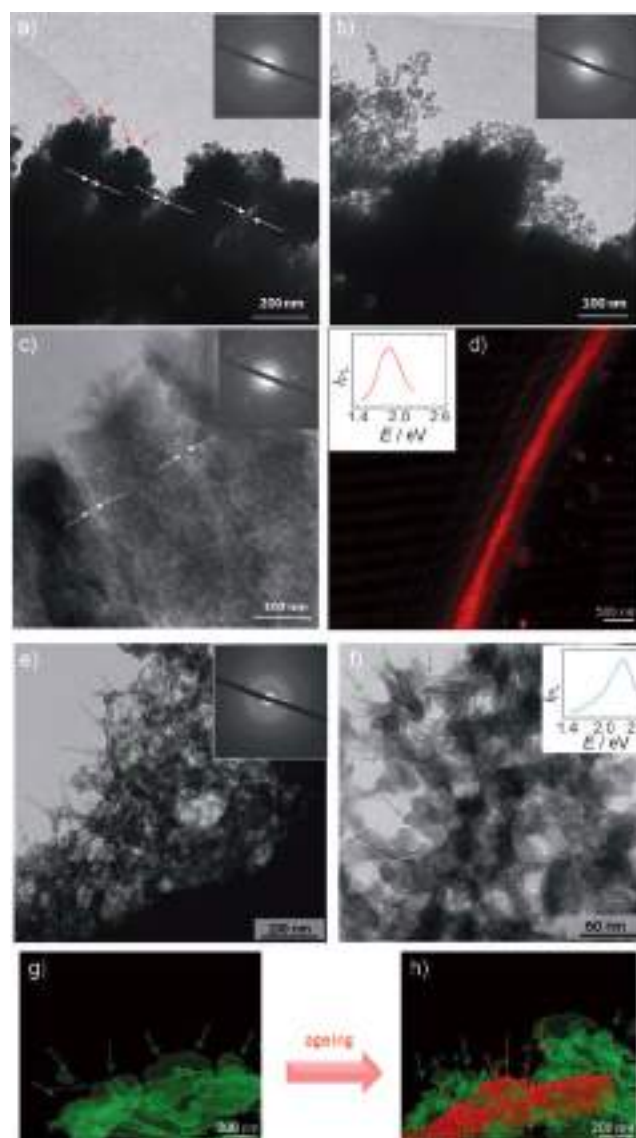Numerous models[6] can be proposed to explain the photoluminescence of the modified silicon, including quan-

Figure 2. a–c) TEM images of the surface of ultrasonically modified silicon wafers in aqueous solution in the presence of a hydrogen-donor material (Mg powder) after a) 10 min, b) 20 min, and c) 30 min of modification. Insets (a–c) show electron-diffraction (ED) patterns of the samples modified for the corresponding time. d) µ-confocal photoluminescence (PL) spectra (fluorescence mode, side view) of the silicon after 30 min of modification. Inset (d) shows the fluorescence emission spectrum of the surface. The preferable channel-like modification is shown by the white arrows. e, f) TEM images of the surface of a silicon wafer sonicated (20 kHz, 57 Wcm^{-2}) in a water/alcohol mixture (higher vapor pressure in comparison with water) in the presence of a hydrogen donor material (Mg powder) for 30 min. Insets show the corresponding ED (e) and fluorescence emission (f) spectra of the surface. g, h) µ-Confocal PL spectra (fluorescent mode, side views) of silicon after 30 min of modification (g) followed by ageing (h). The green and red arrows show side views of the PL spectra.

tum confinement, surface states, defects in the oxide, and the formation of hydrogen-terminated bonds. Radiative recombination is another possibility, but of a different nature. Radiative recombination takes place within the surface amorphous layer. Surface states that localize electrons and

holes, either separately or together, subsequently recombine radiatively. A surface defect renders one undulation nonradiative, whereas an exciton localized in a neighboring undulation recombines radiatively. Radiative recombination occurs from the Si hydride bonds. Partially oxidized Si structures containing various defects can act as radiative centers in porous Si, for example, an oxygen shallow donor or a nonbridging oxygen hole center and a Si dangling bond. In this case, the luminescence of silicon sonicated in an aqueous solution can be explained by the formation of hydrogen-terminated bonds, and/or nonterminated bonds, and/or the formation of nc-Si in the porous matrix of SiO_x.

Different solvents can stimulate various bubble-collapse scenarios.[7] The speed of the sonochemical processes and thus the production of excited species (radicals) strongly depends on the vapor pressure of the solvent. Therefore, surface oxidation by free radicals greatly depends on the nature of the solvent. In this study, we performed the sonication of silicon species in water, water-alcohol mixtures, and in ionic liquids (Figure 1). The modification of silicon in water/alcohol solutions (Figure 1) results in a decrease in the oxidizing ability; it also influences the kinetics owing to the higher vapor pressures of the solvent mixtures compared with that of water.[5b–d] Additionally, as shown in Figure 2e–h, sonication in water/alcohol mixtures leads to silicon with a higher porosity than samples sonicated in water, with porosity ranging from the micro-scale to the meso-scale. Moreover, as shown in Figure 1c and Figure 2e–h, the character of the luminescence strongly depends on the conditions of sonication. The difference in photoluminescence, red after sonication in water and initially green after sonication in a water/alcohol mixture, involves the formation of a partially oxidized Si structure containing various defects, as well as hydrogen-terminated and/or nonterminated bonds.[6]

We can change the character of the photoluminescence from green to red, for example, in samples exposed to water, by aging and partially oxidizing the silicon (Figure 2 g,h), thus going through mostly hydrogen-terminated and/or nonterminated bonds to a partially oxidized Si structure. The light emitted by a single point on the silicon surface was estimated by a 3D reconstruction of the porous μ-sized structure (Supporting Information, Figure S3). We conclude that the modification starts from the outer surface layers (Figure S3 a), as all of the fluorescent dots are located on the surface of sonochemically exposed samples. These dots are probably formed on the spots where bubble collapse occurs. Shock waves or liquid jets crashing into the surface introduce defects in the silicon and defect states. Further modification causes deeper modification of the silicon. Figure S3 b shows that the fluorescent centers are distributed both on the surface and in the matrix of porous silicon. Their emission changes from green to red because of the changes in the structures of the luminescent centers.[6]

It has been suggested that, in ionic liquids (IL), the oxidation could be avoided by simultaneous (re)crystallization, which could lead to green luminescence (Figure 1) vis-à-vis hydrogen-terminated and/or nonterminated bonds.[6] As shown in Figure 3a,b, we are making progress towards process control, which is a high priority for this nonequili-
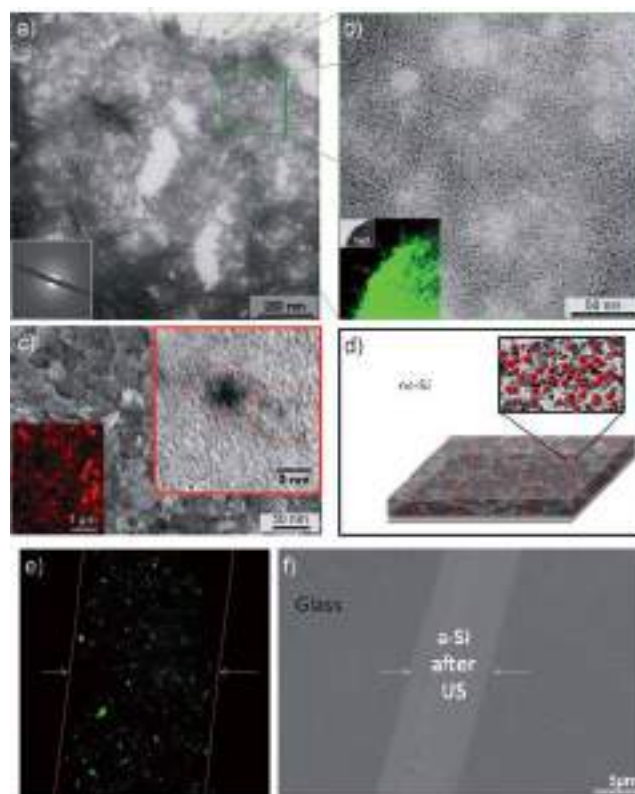

Figure 3. a,b) TEM images of the silicon surface after 30 min of sonication in 1-butyl-3-methylimidazolium chloride in the presence of a hydrogen donor material (NaBH₄). Insets show corresponding electron-diffraction (a) and μ-confocal photoluminescence (PL)(b) spectra (fluorescent and optical modes, side view). The green arrows show a side view of PL. c) SEM/HRTEM/μ-confocal PL (fluorescent mode, top view) of the a-Si on the glass after sonication. d) Illustration of the formation of nc-Si in the porous matrix. e) μ-confocal image in fluorescent mode of the a-Si patterned glass sonicated for 30 min in a water/alcohol mixture in the presence of a hydrogen donor material (Mg). The red lines and the white arrows show the pattern area. f) The corresponding SEM image.

brium process[1] using high-intensity ultrasound. In particular, applying the method in solvents with a negligible vapor pressure,[7] such as the ionic liquid 1-butyl-3-methylimidazolium chloride, allows the formation of structures with medium (40–50%) porosity, although with an irregular pore distribution (Figure 3a,b). Moreover, the formation of nc-Si in the silicon matrix is clearly visible (Figure 3b).

We also confirmed that pronounced modification of amorphous silicon (a-Si), such as silicon deposited onto glass, which is used in advanced techniques for photovoltaic devices,[8] is possible. Figure 3c,d shows that a pronounced surface roughness can be achieved with simultaneous local crystallization and red-photoluminescent nc-Si formation, as well as formation of partially oxidized Si structures containing various defects.

Because the degree of structural order in solid silicon can be locally changed while simultaneously achieving photoluminescence, the development of a technique for the modification of patterned surfaces (Figure 3e,f) with the

formation of distributed luminescent spots is possible. Patterns can be produced by ion-beam-assisted vacuum deposition, which has been used to deposit amorphous silicon onto glass through a specific mask that protects some areas from deposition, thus allowing for surface patterning.[8]

We performed an additional experiment on particles of silicon (ca. 100 µm diameter) to prove that the formation and subsequent phase transitions (crystalline–amorphous–crystalline) of nc-Si are possible without oxidation in water solution in the presence of a hydrogen donor. The µ-sized particles were modified within 35 min of sonication (Figure 4).
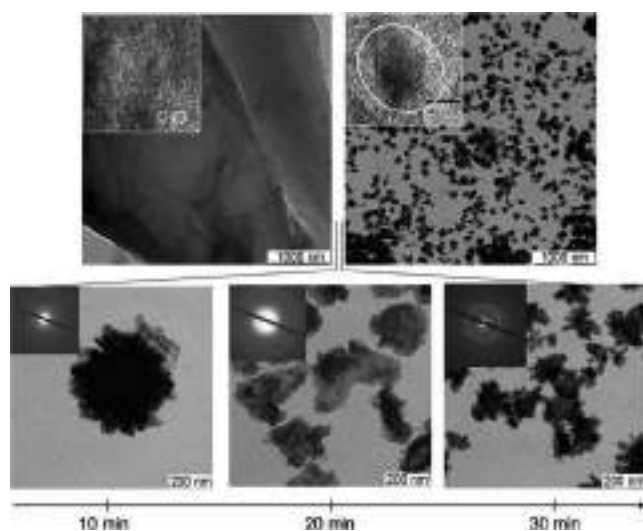
Figure 4. TEM images of µ-sized silicon particles modified by ultrasonication in aqueous solution in the presence of a hydrogen-donor material (Mg) before and after a 35 min modification (upper left and right images, respectively). The HRTEM images (upper insets) show the crystalline structure. The bottom images are the TEM/electron-diffraction images vs. modification time (10 min (left), 20 min (middle) and 30 min (right)). The observed modification kinetics are faster than those observed with plates.

The resulting particles exhibit a pronounced crystalline structure, and their size decreases to the submicron scale. The amorphization of the particles is observed within 20 min of modification. Further exposure (> 30 min) causes well-pronounced crystal growth from the amorphous phase, as well as a further size decrease (Figure 4; see also the Supporting Information, Figure S4). The observed phase transition (between crystalline and amorphous) is probably the main factor responsible for ultrasound-assisted silicon modification. The special conditions provided by high-intensity ultrasound could affect the melting and growth of the silicon crystals. The form of a solidified microstructure can be controlled by fast local heating and cooling cycles provided by cavitation. The crystal formation depends upon the difference between the rates of attachment and detachment of atoms at the interface. The rate of attachment depends on the rate of diffusion in the liquid and therefore is affected by sonication.

We have demonstrated the formation of porous silicon with unique optical properties through a "green" method of ultrasonication including: 1) the one-step formation of silicon with a purposefully variable porous structure, 2) the formation of photoluminescent centers and defect states that could be centers for charge separation, and 3) the possibility of patterned surface-selective modification. The high potential of ultrasound results from the interplay of different mechanisms (Figure 1), and the silicon modification demonstrated here relies on this interplay. Nucleation and bubble collapse affect the surface of a material. First, fast silicon oxidation could be avoided by the possible formation of structure-stabilizing bonds; in this case, by hydrogenation. Next, the solid is modified further, with pores formed deep inside. This process requires material transport over µm dimensions during the bubble collapse and following the stabilization of the material. Moreover, the kinetics of the process are highly dependent on the solvent. Thus, solvents with higher vapor pressures than water allow the porosity to be tuned while also allowing the manipulation of the oxidizing ability of the solvent. These modifications influence the nature of the luminescent centers, suggest possible silicon pathways in IL, and allow us to propose mechanisms for the modification of materials with different initial crystallinities, as well as with patterned surfaces. The findings presented here provide guidelines for the expansion of the concept towards a broad variety of systems. Thus, the possibility of ultrasonic structure formation enables the use of a "green" medium under ambient conditions in previously inaccessible areas of material science.

Experimental Section

Silicon wafers (Sigma–Aldrich), 2-propanol (Alfa Aesar), 1-butyl-3-methylimidazolium chloride (Sigma–Aldrich), magnesium powder (325 mesh, 99.8%, Alfa Aesar), and sodium borohydride (Sigma–Aldrich) were used as received. Water was purified prior to use in a three-stage Millipore Milli-Q Plus 185 purification system, and exhibited a resistivity greater than $18.2\ M\Omega\,cm^{-1}$. Silicon wafers were degreased in flowing 2-propanol and rinsed in purified water. The µ-Si particles were obtained through the milling of wafers.

Ultrasonic treatment was carried out in a thermostated reactor (65°C). The unit VIP1000hd (Hielscher, Germany) was operated at 20 kHz, with a maximal electric output of 1000 W, and equipped with an ultrasonic horn BS2d22 (head area of $3.8\ cm^{2}$) and a booster (B2-1.2).

Scanning electron microscopy (SEM) measurements were conducted with a Gemini Leo 1550 instrument at an operating voltage of 3 keV. Transmission electron microscopy (TEM) measurements were performed on a Zeiss EM 912 Omega (Carl Zeiss AG, Germany) transmission electron microscope operated at 300 kV and equipped with an electron-diffraction (ED) unit. The unit cell and symmetry of an unknown phase that has been determined from the geometry of the diffraction pattern with the proper interpretation of the intensities of spots yields the positions of atoms in the crystal. High-resolution transmission electron microscopy (HRTEM) was performed by TEM in a Philips CM30 operated at 300 kV. The samples were ultramicrotomed (Leica EM FC6) and placed onto carbon-coated copper grids.

The photoluminescence (PL) spectra were obtained at room temperature using either a pulsed-excitation nitrogen laser (337 nm) or a continuous-excitation HeCd laser (325 nm). The luminescence spectra were measured using a Jobin–Yvon H20 monochromator and a Hamamatsu TV R316 or R712 photomultiplier cooled to −20°C. The µ-confocal PL was measured by confocal laser scanning microscopy (CLSM, Leica, Germany), which is an important

method for obtaining high-fluorescence (red-green) and transmission-mode resolution images and for 3D reconstructions.

[1] a) *Chemistry with ultrasound. Critical reports on applied chemistry* (Ed.: T. J. Mason), Elsevier, Essex, **1990**; b) *Ultrasound, It's Chemical, Physical, and Biological Effects* (Ed.: K. S. Suslick), Wiley-VCH, Weinheim, **1989**; c) G. Cravotto, P. Cintas, *Angew. Chem.* **2007**, *119*, 5573–5575; *Angew. Chem. Int. Ed.* **2007**, *46*, 5476–5478; d) *Sonochemistry and Cavitation* (Ed.: M. A. Margulis), Gordon & Breach, London, **1995**; e) K. S. Suslick, G. J. Price, *Annu. Rev. Mater. Sci.* **1999**, *29*, 295–326.

[2] a) *Sonochemistry and sonoluminescense. Series C: Mathematical and Physical Science* (Eds.: L. A. Crum, T. J. Mason, J. L. Reisse, K. S. Suslick), NATO ASI Series, Kluwer Academic Publishers, Dordrecht, **1999**; b) N. A. Tsochatzidis, P. Guiraud, A. M. Wilhelm, H. Delmas, *Chem. Eng. Sci.* **2001**, *56*, 1831–1840.

[3] a) E. V. Skorb, D. Fix, D. G. Shchukin, H. Möhwald, D. V. Sviridov, R. Mousa, N. Wanderka, J. Schäferhans, N. Pazos-Pérez, A. Fery, D. V. Andreeva, *Nanoscale* **2011**, *3*, 985–993; b) E. V. Skorb, H. Möhwald, T. Irrgang, A. Fery, D. V. Andreeva, *Chem. Commun.* **2010**, *46*, 7897–7899; c) J. Gensel, T. Borke, N. Pazos Pérez, A. Fery, D. V. Andreeva, E. Betthausen, A. H. E. Müller, H. Möhwald, E. V. Skorb, *Adv. Mater.* **2012**, *24*, 985–989; d) D. V. Andreeva, D. V. Sviridov, A. Masic, H. Möhwald, E. V. Skorb, *Small* **2012**, *8*, 820–825.

[4] a) L. T. Canham, *Nature* **2000**, *408*, 411–412; b) J. D. Holmes, K. P. Johnston, R. C. Doty, B. A. Korgel, *Science* **2000**, *287*, 1471–1473; c) Y. Y. Li, F. Cunin, J. R. Link, T. Gao, R. E. Betts, S. H. Reiver, V. Chin, S. N. Bhatia, M. J. Sailor, *Science* **2003**, *299*, 2045–2047; d) C. Gurtner, A. W. Wun, M. J. Sailor, *Angew. Chem.* **1999**, *111*, 2132–2135; *Angew. Chem. Int. Ed.* **1999**, *38*, 1966–1968.

[5] a) E. V. Skorb, D. G. Shchukin, H. Möhwald, D. V. Andreeva, *Nanoscale* **2010**, *2*, 722–727; b) K. S. Suslick, J. J. Gawienowski, P. F. Schubert, H. H. Wang, *Ultrasonics* **1984**, 33–36; c) B. A. Oakley, G. Barber, T. Worden, D. Hanna, *J. Phys. Chem. Ref. Data* **2003**, *32*, 1501–1533; d) L. H. Thompson, L. K. Doraiswamy, *Ind. Eng. Chem. Res.* **1999**, *38*, 1215–1249; e) D. G. Shchukin, E. V. Skorb, V. Belova, H. Möhwald, *Adv. Mater.* **2011**, *23*, 1922–1934.

[6] a) L. Pavesi, L. D. Negro, C. Mazzoleni, G. Franzo, F. Priolo, *Nature* **2000**, *408*, 440–444; b) A. G. Cullisa, L. T. Canham, P. D. J. Calcott, *J. Appl. Phys.* **1997**, *82*, 909–965; c) M. V. Wolkin, J. Jorne, P. M. Fauchet, *Phys. Rev. Lett.* **1999**, *82*, 197–200.

[7] a) P. M. Kanthale, M. Ashokkumar, F. Grieser, *Phys. Chem. Lett. C* **2007**, *111*, 18461–18463; b) D. S. Jacob, V. Kahlenberg, K. Wurst, L. A. Solovyov, I. Felner, L. Shimon, H. E. Gottlieb, A. Gedanken, *Eur. J. Inorg. Chem.* **2005**, 522–528.

[8] C. Boehme, K. Lips in *Charge Transport in Disordered Solids with Applications in Electronics, Vol. 5* (Ed.: S. Baranovski), Wiley, Chichester, **2006**, pp. 179–219.

Ultrasound driven formation of metal-supported nanocatalysts

Nicolas Pazos-Perez [a], Jana Schäferhans [a], Ekaterina V. Skorb [b], Andreas Fery [a], Daria V. Andreeva [a,*]

[a] Physical Chemistry II, University of Bayreuth, Universitatstr. 30, D-95440 Bayreuth, Germany
[b] Max Planck Institute of Colloids and Interfaces, Am Mühlenberg 1 OT Golm, 14476 Potsdam, Germany

ARTICLE INFO

ABSTRACT

Bimetal nanocatalysts with a narrow pore size distribution and high surface area were prepared using a fast, easy and "green" method of ultrasound irradiation in water. The concept is demonstrated for the case of aluminum–gold, silver or platinum, but applicable to a large range of nanoparticles. The application as effective nanocatalysts is shown.

© 2011 Elsevier Inc. All rights reserved.

1. Introduction

The application of ultrasound to nanocomposite preparation has raised much interest in recent years [1–3]. First of all the reduction of metal salts in the presence of ultrasound has been widely used in the preparation of heterogeneous catalysts [4]. Metal nanoparticles were prepared by the sonication of a corresponding metal salt in the presence of stabilizers [5]. However, the direct sonochemical reduction of metals does not allow the control over the morphology, monodispersity, and size of the nanoparticles even in presence of stabilizers [6]. Recently, we proposed a novel up–bottom method for the ultrasound-assisted formation of multimetal composites from metal alloys particles [7]. We showed that ultrasonic processes could cause phase segregation in metal alloys, for example, aluminum/palladium (1% Pd) due to the crystallization of one of the components (Pd) of the alloy. This very promising method is, however, restricted by a number of the available metal alloy particles. Another bottom–up method of formation of composite materials by sonication is ultrasound-assisted intercalation of molecules into layered inorganic solids [8]. It was shown that high temperatures (up to 5000 K) and high pressures (hundreds of bars) together with a shock wave generated by ultrasound [9,10] could enhance the penetration of inorganic species into the interlayer spacing of solids. The sonochemical insertion of NPs into two-dimensional mesoporous alumina sheets has been demonstrated [11], where the silver NPs were spread homogeneously in the predesigned mesoporous alumina matrix. High-intensity ultrasound dramatically increases the rates of intercalation of a wide range of compounds into various layered inorganic solids, such as ZrO_2 [12] and clays [13]. The adsorption of organic or inorganic compounds between the atomic sheets of layered solids permits the systematic change of optical, electronic, and catalytic properties.

Here we propose a novel bottom–up method of formation of nanocomposites consisting of the mesoporous metal frameworks as a support and noble nanoparticles (NPs). In our previous works [14,15] we already demonstrated the successful preparation of mesoporous metal frameworks from μm-size aluminum (Al), magnesium (Mg) and zinc (Zn) particles in aqueous media by using ultrasound. The ultrasonically formed mesoporous metal frameworks exhibit relatively high surface area (up to 80 m^2/g) and narrow pore size distribution (2–4 nm). In this study ultrasound is applied to both the formation of the support frameworks and the incorporation of metal NPs. We demonstrated that the novel procedure allows an easy, fast and surfactant free approach to produce high quantities of stable bimetallic particles with a narrow pore size distribution and high surface areas. High local energy provided by ultrasound leads to formation of very stable composite materials where metal active phase is supported by another metal phase. The novel composite materials can be directly used as nanocatalyst and exhibit an enhanced catalytic rate constant.

2. Experimental

2.1. Materials and methods

Al powder (<160 μm, Roth), trisodium citrate dehydrate, silver nitrate (99.9% $AgNO_3$), tetrachloroauric acid ($HAuCl_4 \bullet 3H_2O$), hexachloroplatinate ($HPtCl_6$) and sodiumborohydryde ($NaBH_4$) were purchased from Sigma–Aldrich. All reactants were used without

further purification. Mili-Q water (18 MΩ cm^{-1}) was used in all aqueous solutions.

UV–Vis/near-IR spectroscopy (PerkinElmer, 65 Lambda 19), transmission and scanning electron microscopy (TEM, LEO 922 EF-TEM operating at 200 kV and LEO 1530 FE-SEM, Zeiss, respectively), in combination with an ultra-microtome (Ultracut E Reichert Jung, thickness 50 nm) were applied to characterize the optical response, structure, and size of the nanoparticles. Powder X-ray diffraction (PXRD) (Q–Q mode using a Stoe STADI P X-ray Transmission diffractometer: Cu Kα 1 , irradiation, room temperature, 2•Q = 5–90), inductive coupled plasma (ICP) (PerkinElmer plasma 400 with Ar plasma), the Brunauer–Emmett–Teller method [16] (BET) and the Barrett–Joyner–Halenda [17] (BJH) (Quantachrom) evaluation of the adsorption branch of the isotherm, were used to characterize the composition, surface area and pore size distribution of the samples.

2.2. Synthesis of Ag, Au and Pt nanoparticles

To an aqueous solution 2.5×10^{-4} M of sodium citrate (250 mL), the necessary volume of an aqueous metal salt solution (HAuCl$_4$, AgNO$_3$ or HPtCl$_6$) was added in order to obtain a final metal salt concentration of 2.5×10^{-4} M. The mixture was vigorously stirred meanwhile a fresh prepared ice-cold NaBH$_4$ solution (0.1 M, 7.5 mL) was quickly added [18–20]. The agitation was continued during 2 h. The bottle was left open in order to avoid overpressure during the NaBH$_4$ hydrogen release and to ensure its total decomposition.

2.3. Ultrasonication (US)

Forty milliliter of 10 wt.% suspension of aluminum particles in purified water were pre-sonicated during 30 min with an ultrasonic horn operated at 20 kHz with a maximal output power of 1000 W in an ice-cold flask (at 65 °C temperature). The maximum intensity was calculated to 57 W/cm^2 at a mechanical amplitude 81 μm (described in detail in Refs. [14,15]). Then 1 g of pre-sonicated dried (an oven at 85 °C during 24 h) Al particles was mixed with 250 mL of the noble metal nanoparticles dispersion. The mixture was sonicated 57 W/cm^2 during 5–50 min. After that the solution, comprising mesoporous Al particles filled with small noble metal nanoparticles, was centrifuged (3500 rpm, 20 min), the supernatant discarded and dried in an oven at 85 °C during 24 h.

2.4. Catalytic reaction

The electron transfer reaction between hexacyanoferrate (III) and thiosulfate was carried out by mixing potassium hexacyanoferrate (III) (150 μL, 0.1 M) and sodium thiosulfate (300 μL, 0.1 M) into 15 mL water. The mixture was magnetically stirred at room temperature meanwhile 150 mg of porous aluminum particles filled with platinum were added. Aliquots at different reaction times were investigated previous centrifugation (3000 rpm, 1 min) via UV–Vis-spectroscopy in order to follow the electron transfer reaction.

3. Results and discussion

The schematic illustration of the formation of functional nanostructures consisting of mesoporous aluminum frameworks with incorporated Au, Ag or Pt NPs is in Fig. 1. Fig. 1 illustrates the steps of the formation of Al-supported nanocatalysts. At the beginning, the 160-μm-Al particles are pre-sonicated for 30 min at 57 W/cm^2 in order to form porous metal frameworks (Fig. 1A–C). Then, the mixture of the pre-treated (sonicated) aluminum particles

(Fig. 1C) and the noble NPs (Au, Ag or Pt) synthesized as described in Refs. [18–20] was sonicated for the additional time at the same intensity (Fig. 1D). Fig. 1E demonstrates the desired metal-supported nanocatalysts consisted of mesoporous aluminum support and homogeneously distributed NPs of Au, Ag, or Pt.

In particular, the preparation procedure of metal-supported nanocatalysts begins with ultrasound-assisted pre-treatment of the support (here Al) particles. The initial 160-μm-Al particles were pre-sonicated for 30 min. As we showed previously [14,15], sonication of aluminum particles results in particle breakage (approximately 160 μm initial particles are broken into 10–20 μm shown in Fig. 2 A and B) and formation of a porous structure (TEM image, Fig. S1). The BJH and BET (Fig. 2 C and D) reveals formation of mesoporous structure with a pore size distribution between 1–4 nm and a surface area of 60 m^2/g after 30 min of sonication at 57 W/cm^2 [14]. The surface of the aluminum oxide was explored by means of nitrogen adsorption measurements, N$_2$ (77 K) (Fig. 2 C). The adsorption–desorption isotherm cannot be rigorously classified into any IUPAC group [21,22]. The initial part corresponds to type II, typical of nonporous or acroporous materials, and represents a process of unrestricted monolayer–multilayer adsorption. The observed hysteresis loop in the multilayer range, associated with capillary condensation in mesopores, is characteristic of type IV isotherms. However, it is possible to classify this isotherm as group IIb if the new classification system proposed by Rouquerol et al. [22] is considered. The hysteresis loop can be classified into type H-4, according to IUPAC classification standards [22]. This is typical of particles with narrow openings. The point of closure ($p/p_0 = 0.42$) is attributed to the surface tension of the liquid adsorbate reaching an unstable state at a specific pressure. The surface area value, obtained by applying the BET method [16] is 60 m^2/g. The BJH pore distribution [17] for adsorption of N$_2$ at 77 K (Fig. 2 D), shows a maximum at 4 nm. Based on these results, this material can be classified as mesoporous. The surface area of the initial Al particles was 0.12 m^2/g therefore; the surface area is increased by a factor of 500 after the ultrasound treatment. Thus, pre-treatment results in formation of the Al frameworks characterized by high surface area and a narrow pore size distribution. We used these frameworks for incorporation of NPs and achieve their homogeneous distribution inside of the Al frameworks.

It is very important that in our previous works [14,15] we showed that the sonication up to 120 min does not lead to complete oxidation of the metals. The ^{27}Al MAS NMR and PXRD spectra exhibit the signals and picks that were assigned to Al and aluminum oxides [15]. The high local temperature generated by acoustic cavitation has been found to cause phase transitions (amorphous ↔ crystalline) resulting in increased surface area of metal systems. Free radicals produced during cavitation oxidize the metal surface and stabilize the porous metal skeleton by formation of a thin oxide layer. Thus, the aluminum frameworks consist on porous aluminum structure covered by a thin oxide layer.

These porous metal frameworks were used for ultrasound-assisted incorporation of the metal NPs. For this propose the mixture of the Al framework particles and the noble NPs was further sonicated. The formation of nanocomposites was proved by the color test (Fig. 3 A, B, and C). Digital photographs (Fig. 3) clearly show the color changes of the aluminum frameworks after sonication in presence of the aqueous suspensions of Au, Ag and Pt NPs. The TEM image of the microtomed mesoporous bimetallic (Al–Au) particle (D) proved the homogeneous distribution of NPs within the frameworks. The perfect distribution of the monodisperse particle within the frameworks was also observed for Ag and Pt loaded samples. The linear dependence of the Au intake in Al frameworks vs. the sonication time (Fig. 3 E) allows the precise control over the amounts of noble metal NPs incorporated in the system. The
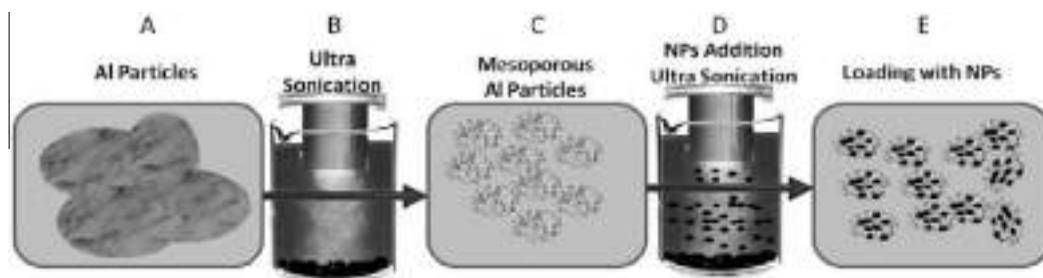
Fig. 1. Schematic illustration of the sonochemical production of aluminum-supported nanocatalysts. A – The 160-μm-Al particles; B – Pre-treatment by sonication of initial Al particles for 30 min at 57 W/cm^2; C – The porous Al frameworks; D – Sonication of the mixture of the pre-treated Al particles and the noble NPs (Au, Ag or Pt); E – The desired Al-supported nanocatalysts consisted of mesoporous aluminum support and homogeneously distributed NPs of Au, Ag or Pt.
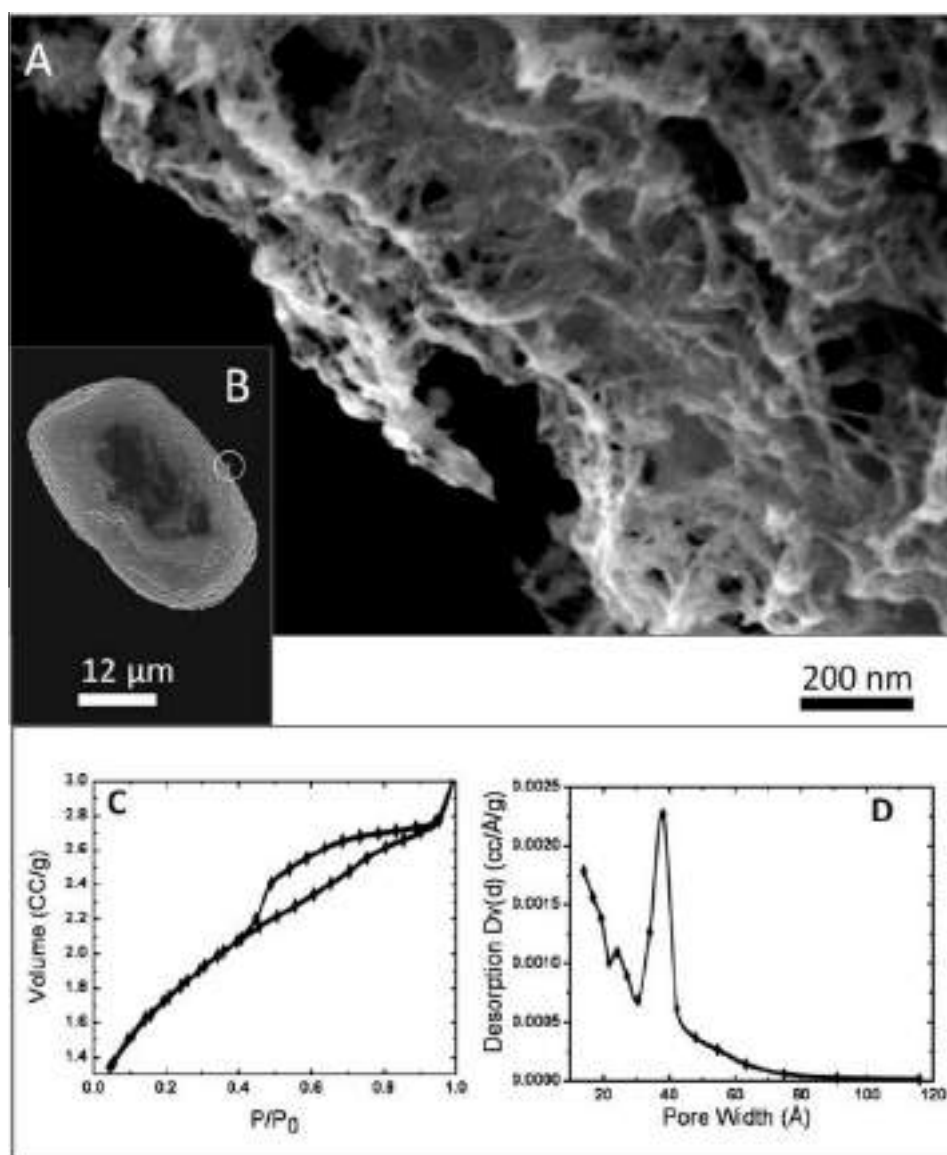

Fig. 2. Scanning electron microscopy (SEM) image of mesoporous aluminum particles after sonication (A). Low magnification SEM image of A (B). BET analysis (C) and BJH evaluation (D) of the mesoporous Al particles.

UV–Vis spectral characterization of Au and Al–Au are shown in Fig. S2, after loading the Al frameworks the intensity of the plasmonic band considerably decrease due to that the contribution to the signal comes only from the Au particles adsorbed on the Al surface, and also because of the big scattering observed due to the Al particle size. An important point concerning this procedure is the formation of a stable, surfactant free system, which could be an effective alternative to existing nanocatalyst. The ICP analysis discloses the maximal loading up to 1 wt.% of Au, 0.72 wt.% of Ag and 1 wt.% of Pt into the Al frameworks (the Ag and Pt contents were
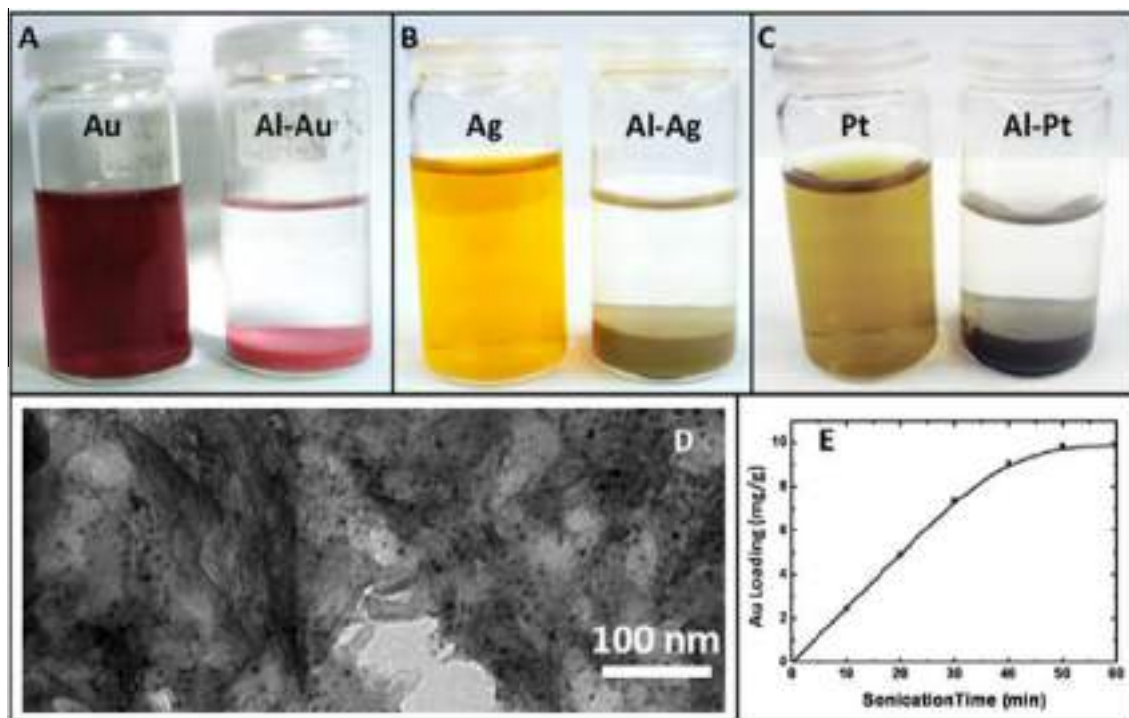
Fig. 3. Digital photographs of Au, Ag and Pt nanoparticles suspensions (A, B and C respectively) before (left) and after (right) the ultrasound-assisted loading in Al nanostructures. The particles sediment due to their incorporation into the Al particles. TEM image of microtomed mesoporous bimetallic (Al–Au) particle (D). The linear dependence of the Au intake in the Al particles vs. the sonication time. In 50 min of sonication the saturation is achieved (E).

calculated from the concentrations and volumes used). The lower Ag weight content in respect to the Au and Pt arises from the lower molecular weight of the Ag.

The structure of the NPs within the Al frameworks was analyzed by Powder X-ray Diffraction (PXRD). The PXRD analysis (Fig. 4 A) reveals the presence of crystalline NPs in the metal system. Since the PXRD method can not indicate if the NPs are located within the mesopores or deposited on the surface, the distribution of NPs within the mesoporous matrix can be proved by the TEM image of the ultramicrotomed samples (Fig. 3D). The aluminum frameworks consists on the aluminum covered by bayerite Al(OH)$_3$ and boehmite AlO(OH) oxide [23] layer. The quantity of bayerite increases during formation of the porous structure, which corresponds to the formation of the higher surface areas of the samples.

The formation of mesoporous metal composites with high surface area (the surface area for the Al–Au system achieves 110 m^2/g) and the narrow pore size distribution is proved by the analysis of the nitrogen adsorption isotherms (Fig. 4 B and C). It is interesting that the micropores (<3 nm) formed in pre-treated Al particles (Fig. S2) are blocked by the NPs. As in the case of the bare mesoporous aluminum the isotherms can be classified into the group IIb [22]. However, the hysteresis loops clearly changes to H-3 type [22]. This is typical of aggregated particles that form plates and give rise to formations such as rifts or wedges. These isotherms show unlimited adsorption within a large range. The closure of the loop is gradual and this confirms the existence of mesopores formed by parallel plates or wedge-shaped sites where desorption occurs due to capillary evaporation. The presence of narrow openings, which implies sharp desorption, can be discarded. This points towards to the retention of the nanoparticles into the initial aluminum pores while generating a new porous surface.

It is remarkable that 60 min ultrasound treatment of suspension of different metal particles results in formation of the nanocomposites with high surface area, narrow pore size distribution and homogeneous spreading of the functional centers. Ultrasound-as-

sisted formation of mesoporous bimetal structures is based on specific interactions of cavitation bubble and metal particles. In heterogeneous solid–liquid systems [24–26] cavitation could have three main effects: (1) surface damage at the liquid–solid interface by symmetric bubble collapse (shock waves and subsequent microstreaming) and (2) asymmetric bubble collapse (microjets occur at the surface several orders of magnitude larger than the cavitation bubble size, e.g. at 20 kHz the maximum size of a cavitation bubble is approximately 5 μm [27]), and interface effects are observed with solids from ca. 200 μm; 3) chemical surface modification/stabilization due to ultrasonic induced formation of free radicals [28]. Thus, the asymmetric collapse of bubble and surface imprinting by high speed microjets are observed for "large" particle. This results in the formation of the metal frameworks, namely, particle fragmentation and surface area increase. The "small" particles (here, ~4 nm particles of noble metals) are moved violently within shock waves generated by the symmetric collapse of cavitation bubbles in bulk and incorporated in porous support. Nature of the metal particles (melting point and tendency to oxidation by free radicals produced by sonication) determines the surface morphology of the particles after sonication. In our previous works [14,15,29–31] we demonstrated that the surface of Al is oxidized immediately by highly reactive radicals derived from water and oxygen (active oxygen species). On the contrary, the noble metals exhibit very low tendency to oxidation and have relatively high melting points. Due to their nature NPs are resistant to ultrasound irradiation and remain their initial properties in the ultrasonically prepared bimetal nanostructures.

3.1. Catalytic properties

As a proof of principle we performed a model catalytic reaction on Pt NPs because of their multiple catalytic applications [32]. The kinetic of the reduction of ferricyanide by thiosulfate [33] was investigated by monitoring the intensity of the hexacyanoferrate
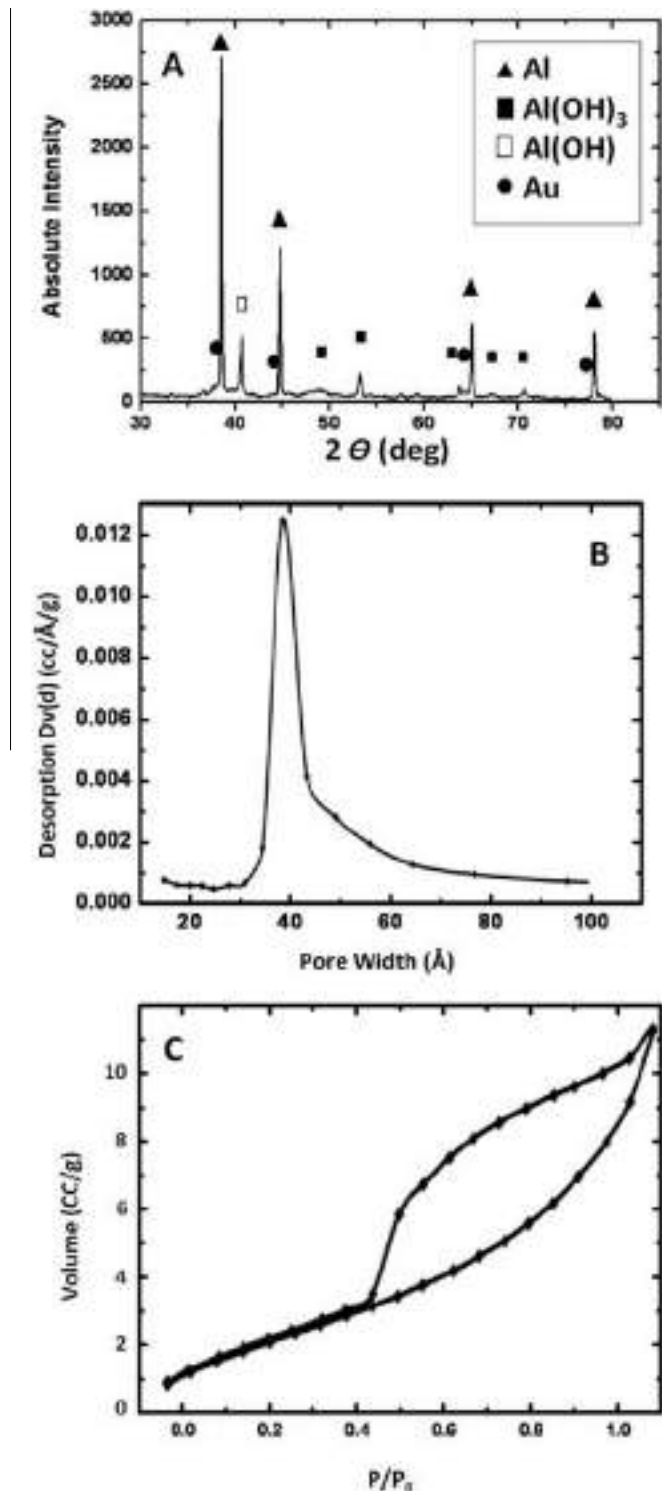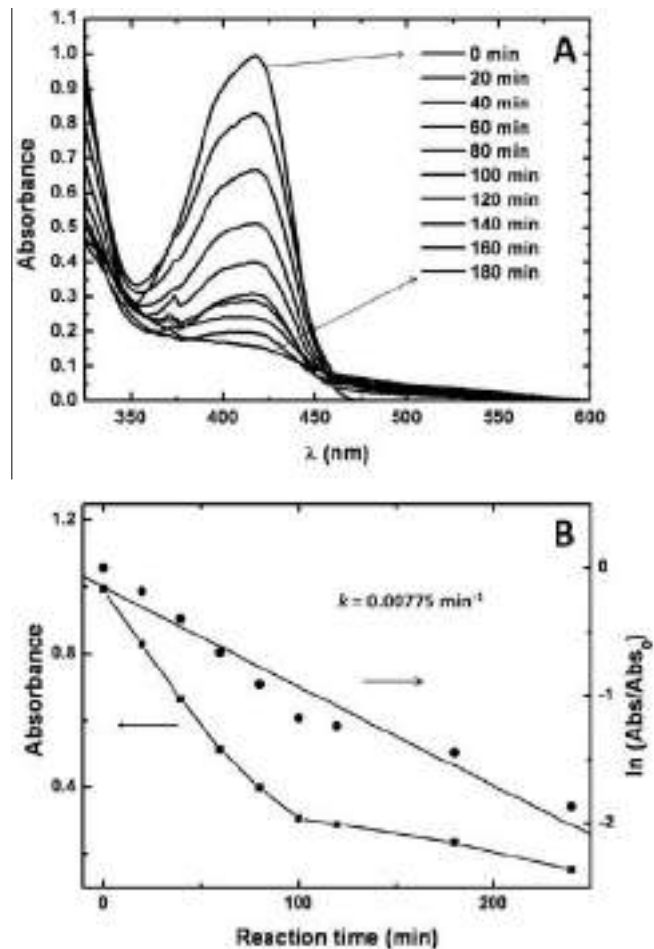
Fig. 5. Absorption spectra monitoring every 20 min the electron transfer reaction between hexacyanoferrate (III) and thiosulfate by using Al–Pt sponges with time (A). Plot showing the hexacyanoferrate (III) absorbance (concentration) as a function of the reaction time (B, squares). Relationship between the logarithmic scale of the normalized absorbance (against the absorbance at the beginning of the reaction) and the reaction time (B, circles). The calculated reaction rate constant (k) of Al–Pt nanostructures was 0.00775 min^{-1}.

Fig. 4. PXRD spectrum of Al–Au system (A). Metallic Al is marked by triangles, aluminum oxides – Squares and Au – Circles. The calculated Au content from ICP is 1 wt.%. BJH (B) and BET (C) characterization of the mesoporous Al–Au systems. Pore size distribution for all cases was determined to be ~4 nm. Surface area: 110 m^2/g.

(III) absorption peak at 420 nm as a function of time via UV–Vis absorption spectroscopy.

We can clearly see (Fig. 5 A) from the decrease of the maximum absorbance related to hexacyanoferrate (III) the >70% conversion is observed after 1.7 h at ambient conditions. As shown in Fig. 5 B, the absorbance maximum decays logarithmically with the time (black squares) indicating a first order kinetics for the hexacyanoferrate

(III) decomposition. Thus, plotting the ln(Abs) vs. the reaction time demonstrates a linear relationship. Based on this linear dependence the reaction rate constant (k) can be calculated. This reaction rate constant of Al–Pt nanostructures was calculated to 0.0077 min^{-1}, which is much higher to the value reported by Maitra et al. [34] for the same reaction using Pt nanoparticles of different sizes. This is probably due to the fact that by using ultrasound we could manipulate by smaller surfactant-free particles. Thus, higher surface area is available to the catalytic reaction. Moreover, the similar high value was obtained by El-Sayed et al. [35] (0.0076 min^{-1}) for the same reaction but with gold nanocages. However, the rate of the reported in Ref. [35] reaction was accelerated by surface plasmon resonance. Based on our experiments and the literature we can conclude that the novel catalytic system developed here exhibit high efficiency, good recyclability, easy handling and high stability.

4. Conclusions

In summary, we propose a novel concept of ultrasound driven formation of bimetal nanocatalysts. We showed that sonochemical manipulation of structure and properties of metals depends on the size and nature of metal particles. The "large" solid surfaces are

fragmented, oxidized, and pores are formed deep inside. Simultaneously, the "small" metal nanoparticles are incorporated and homogeneously distributed inside the porous matrix remaining their initial morphology, structure and properties. This novel procedure allows an easy, fast and surfactant free approach to production of high quantities of stable bimetallic particles with a narrow pore size distribution and high surface areas. The successful application as nanocatalysts demonstrated a higher rate constant for catalytic conversion than previously reported. The concept is applicable on a large range of materials providing a basis for many types of applications in chemistry, materials science and medicine where the structure and properties of metal nanocomposites can be easy controlled by ultrasound.

Acknowledgment

Appendix A. Supplementary data

Supplementary data associated with this article can be found, in the online version, at doi:10.1016/j.micromeso.2011.08.011.

References

[1] K.S. Suslick, D.J. Casadonte, Journal of the American Chemical Society 109 (1987) 3459.
[2] K.S. Suslick, R.E. Johnson, Journal of the American Chemical Society 106 (1984) 6856.
[3] J.H. Bang, K.S. Suslick, Advanced Materials 22 (2010) 1039.
[4] K. Chatakondu, M.L.H. Green, M.E. Thompson, K.S. Suslick, Chemical Communications (1987) 900.
[5] K. Okitsu, Y. Mizukoshi, H. Bandow, Y. Maeda, T. Yamamoto, Y. Nagata, Ultrasonics Sonochemistry 3 (1996) S249.
[6] W. Chen, W. Cai, Journal of Colloid and Interface Science 238 (2001) 291.
[7] D.V. Andreeva, International Journal of Materials Research 102 (2011) 597.
[8] K.S. Suslick, D.J. Casadonte, M.L.H. Green, M.E. Thompson, Ultrasonics 25 (1987) 56.
[9] H. Endo, Journal of the Acoustical Society of America 95 (1994) 2409.
[10] T.A. Weber, E. Helfland, Journal of Chemical Physics 72 (1980) 4014.
[11] S. Bhattacharyya, A. Gabashvili, N. Perkas, Journal of Physical Chemistry B 111 (2007) 11161.
[12] V. Singh, V. Sapehiyia, L.K. Goverdhan, Journal of Molecular Catalysis A: Chemical 210 (2004) 124.
[13] S. Swain, A.I. Isayev, Polymer 48 (2007) 289.
[14] E.V. Skorb, D. Fix, D.G. Shchukin, H. Möhwald, D.V. Sviridov, R. Mousa, N. Wanderka, J. Schäferhans, N. Pazos-Pérez, A. Fery, D.V. Andreeva, Nanoscale 3 (2011) 985.
[15] E.V. Skorb, H. Möhwald, T. Irrgang, A. Fery, D.V. Andreeva, Chemical Communications 46 (2010) 7897.
[16] S. Brunauer, P.H. Emmett, E.J. Teller, Journal of the American Chemical Society 60 (1938) 309.
[17] E.P. Barrett, L.G. Joyner, P.P. Halenda, Journal of the American Chemical Society 73 (1951) 373.
[18] N.R. Jana, L. Gearheart, C.J. Murphy, Journal of Physical Chemistry B 105 (2001) 4065.
[19] N.R. Jana, L. Gearheart, C.J. Murphy, Chemical Communications 6 (2001) 17.
[20] J. Zeng, J.Y. Lee, W. Zhou, Applied Catalysis, A: General 308 (2006) 99.
[21] K.S.W. Sing, D.H. Everett, R.A.W. Haul, L. Moscou, R.A. Pierotti, J. Rouquerol, T. Siemieniewska, Pure and Applied Chemistry 57 (1985) 603.
[22] F. Rouquerol, J. Rouquerol, K.S.W. Sing (Eds.), Adsorption by powders and Porous Solids, Academic Press, London, 1999.
[23] R. Schoen, C.E. Roberson, American Mineralogist 55 (1970) 43.
[24] K.S. Suslick, Science 247 (1990) 1439.
[25] J.P. Lorimer, T.J. Mason, Journal of the Chemical Society Reviews 16 (1987) 239.
[26] K.S. Suslick, G.J. Price, Annual Review of Material Science 29 (1999) 295.
[27] N.A. Tsochatzidis, P. Guiraud, A.M. Wilhelm, H. Delmas, Chemical Engineering Science 56 (2001) 1831.
[28] A. Weissler, Journal of the American Chemical Society 81 (1957) 1077.
[29] D.V. Andreeva, D. Fix, H. Mohwald, D.G. Shchukin, Advanced Materials 20 (2008) 2789.
[30] E.V. Skorb, D.G. Shchukin, H. Möhwald, D.V. Andreeva, Langmuir 26 (2010) 16973.
[31] E.V. Skorb, D.G. Shchukin, H. Möhwald, D.V. Andreeva, Nanoscale 2 (2010) 722.
[32] A.D. Taylor, M. Michel, R.C. Sekol, J.M. Kizuka, N.A. Kotov, L.T. Thompson, Advanced Functional Materials 18 (2008) 3003.
[33] R. Narayanan, M.A. El-Sayed, Journal of Physical Chemistry B 107 (2003) 12416.
[34] R.K. Sharma, P. Sharma, A. Maitra, Journal of Colloid and Interface Science 265 (2003) 134.
[35] C.W. Yen, M.A. El-Sayed, Journal of Physical Chemistry C 113 (2009) 19585.

ADVANCED MATERIALS

ACTIVE SURFACES

A cavitation-engineered 3D sponge network is presented as a kaleidoscope image in its active surface construction. The work of D. V. Andreeva, E. V. Skorb, and co-workers, presented on page 985, was inspired by the urgent need for time- and spaceresponsive biocompatible surfaces for antifouling systems, the constriction of metal implants, stem-cell research, SERS studies, etc. Adhesion of cells onto the surface is self-regulated by their metabolism. Controlled patterning and the deactivation of bacteria are also possible on these surfaces.

COMMUNICATION

Cavitation Engineered 3D Sponge Networks and Their Application in Active Surface Construction

Julia Gensel, Tina Borke, Nicolas Pazos Pérez, Andreas Fery, Daria V. Andreeva,*
Eva Betthausen, Axel H. E. Müller, Helmuth Möhwald, and Ekaterina V. Skorb*

Controlling cell positioning, adhesion, spreading, growth and migration on surfaces is of interest in fundamental cell biology,[1] tissue engineering,[2] cell-based biosensor development,[3] bio-electronics[4] and protection of biocompatible devices.[5] Various methods have been used to direct the adhesion of cells to selected areas of a substrate, including micropatterning,[6] soft lithography,[7] patterning through pores in elastomeric membranes,[8] patterning by using three-dimensional microfluidic systems,[9] laminar-flow patterning,[10] local oxidation by using microelectrodes,[11] and a spectacular method of layer-by-layer deposition.[12] One particularly versatile approach to control cell attachment and patterning is the physical or chemical adsorption of functional molecules such as extracellular matrix proteins and pH- or temperature- sensitive polymers to selected areas of a substrate.[13] The effects significantly depend on the properties and nature of the underlying substrate,[14] and substrates with complex 3-D network are of high priority.[15]

The market for joint-implant surgery, as an example of a biocompatible device, is expected to reach $17.4 billion by 2012 – an annual growth rate of more than 9 percent since 2008, when estimates pegged its value at $12.2 billion.[16] Thus, green and inexpensive methods of surface modification are in focus as well as fundamental aspects of processes which can be used for surface engineering.

Ultrasound of high intensity could provide green and fast physical and chemical surface modification due to high energy localized by a sonotrode at a particular surface area.[17] The shape of the sonotrode can be adjusted to particular applications and allows easy modification of large sample areas.[18] Acoustic cavitation offers the unique potential of locally establishing high-temperature (up to 5000K) and high-pressure (several hundreds of bars) reactions, while the system remains macroscopically near room temperature and ambient pressure.[19] Thus,

ultrasound could replace some expensive, multi-stage and time-consuming methods of surface engineering. For example, formation of fine porous metal structure with large pores (200 μm to 2 mm) needs special casting conditions or can be made by sputter deposition.[20] For formation of porous metals with pore size distribution between 2 and 50 nm (mesoporous materials) chemical[21] or electrochemical dealloying[22] of expensive noble metal containing alloys[23] has to be used. These syntheses normally employ high temperatures (e.g. >1000 °C) rendering the material chemically inert and hindering facile postchemical functionalisation. Commonly, the processes require very harsh reagents.

We suggest using ultrasonically formed metal sponges for nanoconstruction of protected biocompatible surfaces. Recently, we demonstrated that ultrasonic treatment of biocompatible metal surfaces (aluminum, magnesium, iron, and titanium) changes their morphology (roughness, porosity), chemistry (surface oxidation by the products of water sonolysis) and properties (adhesion, hydrophilic/hydrophobic etc).[17,24] Intensive etching and oxidation of metals by ultrasound leads to formation of a 200-nm-thick sponge-like surface layer well-adhered to the bulk metal. The surface metal sponge is porous, has a high surface area and is covered by active OH-groups. Such kind of surfaces can provide effective storage and release on demand of functional compounds (antiseptics, disinfectants, corrosion inhibitors, drugs etc) as well as excellent adhesion of protective coatings or cells. Furthermore, such sponges combining the beneficial properties of metals and porous structure have unique physical and mechanical properties such as low density, high surface-to-volume ratio, high thermal shock resistance, and high specific strength that are important for their application.[20–25]

Liquid motion in the vicinity of cavitation sites generates very large shear and strain gradients that are caused by the very rapid streaming of solvent molecules around the cavitation bubble and by the intense shock waves emanating upon collapse.[26] Thus, cavitation stimulates intercalation of low molecular weight compounds into the porous interior of metal sponges.[27] We applied here this effect of sonication to incorporate the antiseptic/ disinfectant, silver (Ag), into a porous Al surface. The ultrasonic assisted generation of surface Al sponges and their upload with Ag was performed in a step-wise mode at the same reactor unit (**Figure 1**).[24,27] The maximum silver concentration was estimated by EDS 0.03 wt%.

Then, ultrasonically formed sponge-like silver/aluminum (Ag/Al) surfaces as well as Ag free surfaces were used for self-assembled immobilization of pH-responsive triblock terpolymer micelles. The self-cell release surface regulation and antibacterial

Prof. H. Möhwald, Dr. E. V. Skorb
Max Planck Institute of Colloids and Interfaces
Wissenschaftspark Golm, Am Mühlenberg 1, Golm 14476, Germany
E-mail: skorb@mpikg.mpg.de
J. Gensel, T. Borke, Dr. N. P. Pérez, Prof. A. Fery, Dr. D. V. Andreeva
Physical Chemistry II
University of Bayreuth
Universitätstr., 30, Bayreuth 95440, Germany
E-mail: daria.andreeva@uni-bayreuth.de
E. Betthausen, Prof. A. H. E. Müller
Macromolecular Chemistry II
University of Bayreuth
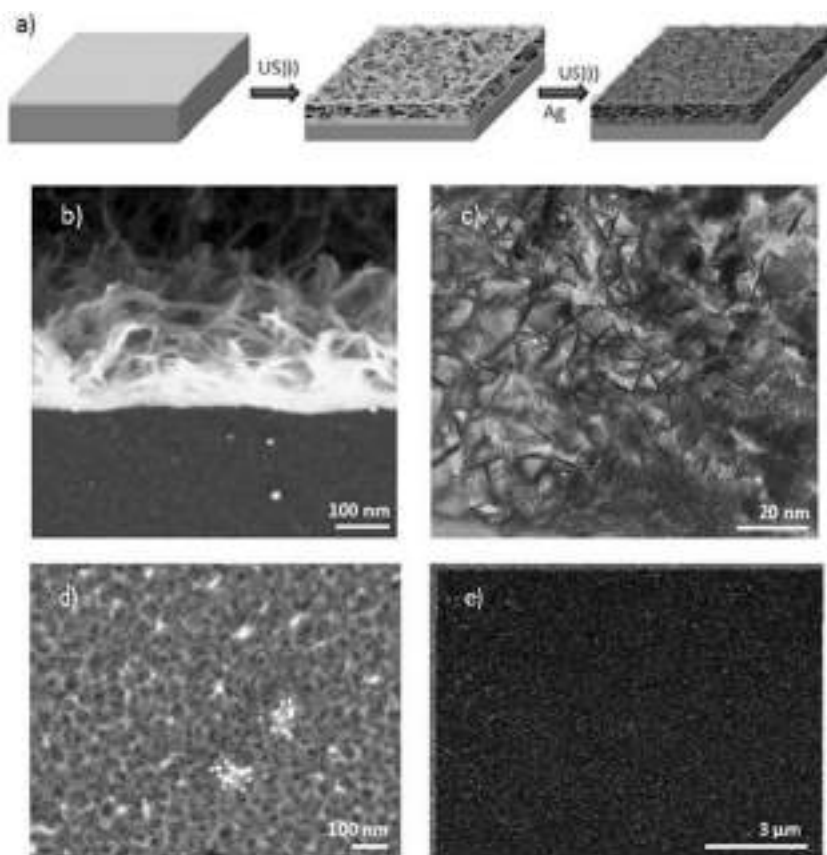Universitätstr., 30, Bayreuth 95440, Germany

Figure 1. a) Schematic reconstruction based on SEM/EDS measurements of the sonochemically formed porous aluminum layer and silver incorporation into the sponge. b) SEM (side-view) and c) TEM images of a 200-nm aluminum layer deposited on a glass substrate modified via ultrasonication (20 kHz, 57 W/cm²) in aqueous solution after a 60-s modification. d) SEM (top-view) e) EDS mapping (aluminum (dark) and silver (white)) of aluminum based sponge after ultrasonic assisted silver incorporation.

behaviour of the micelles can be controlled by the ionization degree of the MAA block ($pK_{a,apparent} \sim 5.5$). In the pH range between 7 and 4 the ionization degree, α, decreases from unity to ~0.[29] At pH 10 ($\alpha \sim 1$), the attraction between the negatively charged MAA and the positively charged Dq blocks induces the formation of an intramicellar interpolyelectrolyte complex (*im*-IPEC) shell. According to the degrees of polymerization ($DP_n(MAA) < DP_n(Dq)$), parts of the cationic Dq block remain uncomplexed forming a positively charged corona. At pH 4, the protonation of the MAA block ($\alpha \sim 0$) results in *im*-IPEC dissolution. As a consequence, the uncharged MAA block collapses onto the B core forming a new shell, and the length and charge density of the cationic Dq corona increase. Accordingly, the charge density of the MAA block and the dissolution or regeneration of the *im*-IPEC shell can be adjusted by the pH of the solution. The length and charge density of the cationic Dq corona are regulated by the shell composition and therefore can be varied by pH. This short-term response to pH changes was shown to be completely reversible within several cycling steps.[28b]

Due to the cationic nature of the Dq corona, BMAADq micelles can be immobilized on negatively charged surfaces, while their core-shell-corona structure remains intact upon adsorption to a solid support.[28b] Therefore, a negatively charged Al sponge surface was used to immobilize the triblock terpolymer micelles by a simple dip coating method. To conclude on micelle adsorption onto the aluminium sponge (Figure 2) by
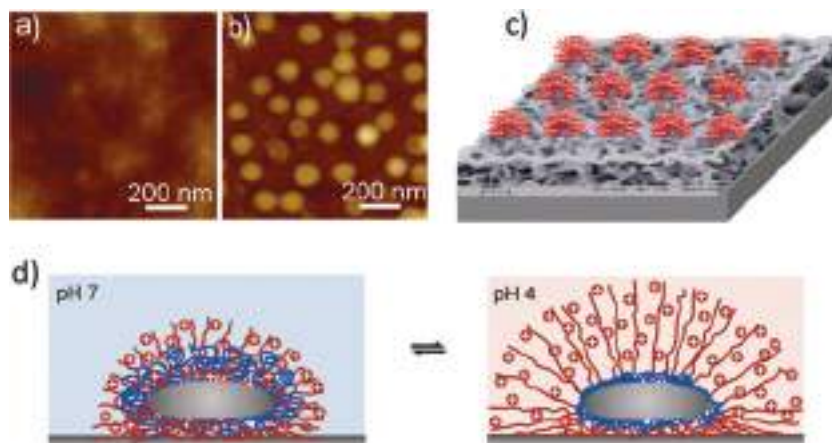
properties were tested by using *Lactoccocus. Lactis 411* bacteria as a model system. These types of bacteria produce lactic acid in their life cycle and change the pH of their environment. To develop responsive surface coatings, we used a linear ABC triblock terpolymer consisting of polybutadiene (B), poly(methacrylic acid) (MAA), and quaternized poly(2-(dimethylamino) ethyl methacrylate) (Dq), $B_{800}MAA_{200}Dq_{285,}$ (subscripts denoting the degrees of polymerization of the corresponding blocks) which was recently designed by the Müller group.[28] For simplicity, the polymer will be denoted as BMAADq throughout the manuscript. In aqueous solutions, BMAADq self-assembles into core-shell-corona micelles with a hydrophobic B core, a pH-sensitive shell and a cationic Dq corona. The schematic representation of the obtained core-shell-corona micelles is shown in **Figure 2**.

The terpolymer micelles show a rapid response to pH cycling.[28] The pH-responsive

Figure 2. Surface immobilization of pH-responsive triblock terpolymer micelles on a porous aluminum surface formed by ultrasonication: a, b) AFM images of a sponge-like Al surface before and after adsorption of BMAADq micelles, respectively (height image scale: 0–100 nm); c, d) Schematic representation of adsorbed micelles on the porous surface depicting their pH-dependent structure.
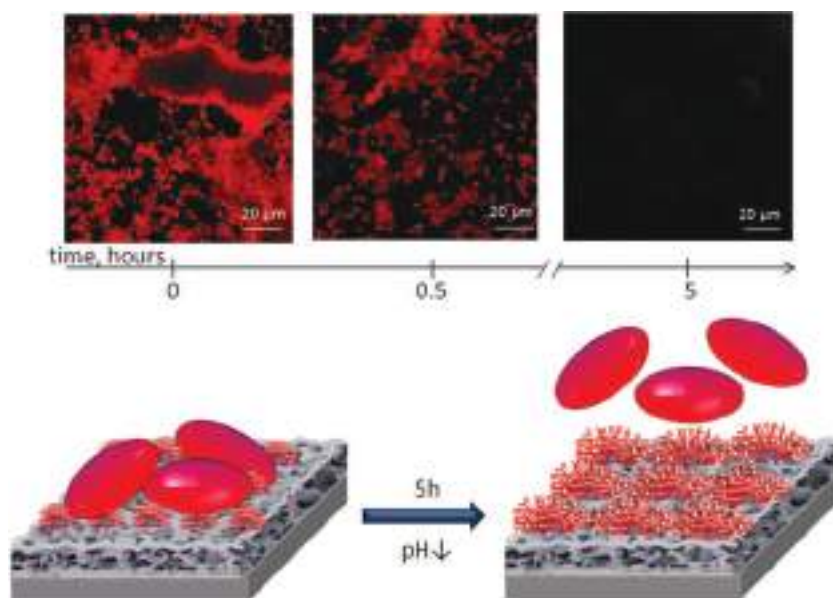
Materials
Views
www.MaterialsViews.com

ADVANCED
MATERIALS
www.advmat.de

COMMUNICATION

Figure 3. Confocal kinetic study (fluorescence mode) and schematic illustration of pH triggered self-cleaning behavior of the porous Al surface covered with micelles. As model cells *Lactococcus Lactis 411* bacteria were used.

atomic force microscopy (AFM), Figure 2b shows AFM height image of the dry micelles adsorbed from pH 10 buffer solution on an ultrasonically designed aluminum sponge as a monolayer. The surface adsorption of BMAADq micelles leads to regular arrays of particles with uniform size and spherical-cap shape. The adsorption is driven by the release of counter ions and hydration water.[30] The surface exclusion effect leads to formation of a laterally patterned monolayer of micelles, as often reported for the adsorption of charged colloidal particles.[31]

The cell adsorption on the metal/micelle surface is illustrated in the sketch (**Figure 3**, bottom). Indeed, as shown by the confocal fluorescence kinetic study (Figure 3, top), the number of adsorbed microorganisms drastic decreases already after 30 min of the experiments. After 5 hours we didn't observe any evidence of bacteria presence on the surface. This spectacular cell-cleaning surface effect is a pH-trigged desorption of the bacteria due to changes in morphology of the charged Dq corona. The lactic acid produced by *L. Lactis* loaded with Rh6G decreases the local pH of the metal/ micelle/ bacteria system together with having slightly positive charge. The decrease of the pH results in *im*-IPEC dissolution and therefore in switching of the surface properties.[28b] At pH 4 the length of the charged Dq corona increases and the adsorbed bacteria are detached from the surface and the positively charged micelles. Thus, we achieve pH-regulated self-cleaning of the metal/micelle network.

The use of ultrasound for the formation of complex structures of Ag/Al sponges serves as the basis for the development of synergetic surfaces. The novelty of this work is the design of 3D architecture surfaces with both space- and time-dependent functionality (cell attraction, pH-triggered self-cleaning, antiseptic/disinfection). The different surface functionality and reactivity can be controlled by surface patterning. The combination of adhesion control through patterning and active component containing sponge use is shown in **Figure 4**. We patterned micelle lines on the ultrasonically formed Al and Ag/ Al sponge-like surfaces. It is seen that after 5 hours of the experiment the bacteria are desorbed on the micelle patterns. Simultaneously the micelle-free porous surface provides high cell adhesion. The adsorbed bacteria are deactivated by Ag ultrasonically incorporated into the porous Al matrix in the case of the Ag/Al/micelle sponge-like surface. We cultivated the bacteria detached from the micelle patterns of porous surfaces (Figure 4d). Note that due to high initial bacteria concentration $(5 \times 10^4$ CFU/mL) the suspension was diluted by a factor of 100 to calculate the CFU/mL in the case of the silver-free surface. In the control experiment with Ag-free Al sponges we observed an intense bacteria growth. After 24 hours of incubation of the bacteria from the Ag/Al/micelle surface the 2×10^3 times decrease in survival factor from 80% to 0,05% and change of reduction
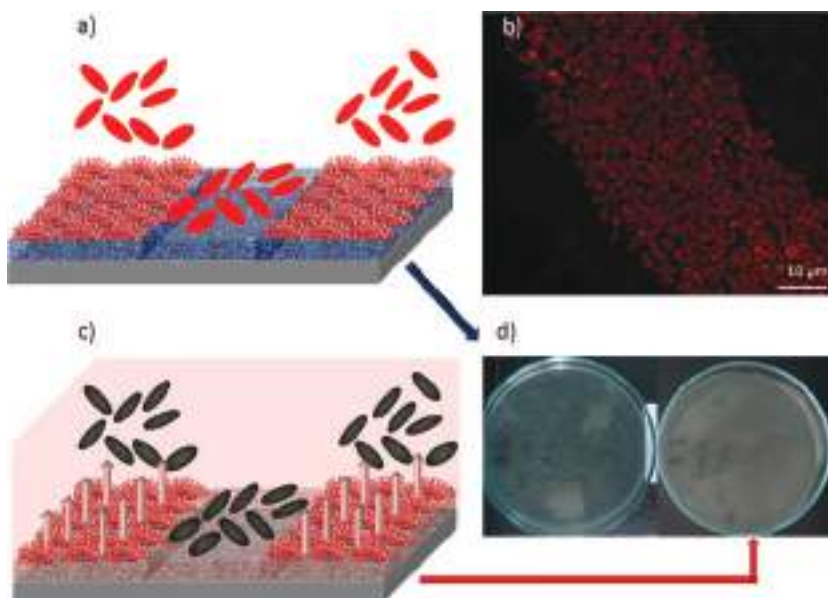

Figure 4. a, b) Controllable bacteria adsorption on porous aluminum surfaces patterned with micelles: sketch and confocal fluorescence images, correspondingly. c) Synergetic surface activity: variation of cell adhesion through patterning with micelles and self-cleaning by antiseptic/ disinfectant properties of porous Ag/Al surface. d) Petri dish of *Lactococcus Lactis 411* after 24h incubation to analyse the inactivation behaviour of the Ag/Al/micelle surface (right, 20 CFU/mL) and the control Al/ micelle surface (left, 100-times diluted, ca. 400 x 100 CFU/ mL). Initial bacteria concentration was 5×10^4 CFU/mL.

COMMUNICATION

factor from 1 to 2×10^3 was observed. The antimicrobial activity clearly indicates the antiseptic/disinfectant activity of the Ag/Al sponge surface.

In the long run, we suggest a novel concept of protection of biocompatible surfaces. We present a nice way of functionalizing a metal surface with a soft matter layer. This is not always easy to achieve and there are specific applications where one has to work on metal substrates such as anti fouling systems,[32] implants, stem cell research, SERS[33] etc. We described an effective sonochemical pathway of surface engineering providing lot of space for further optimization with an ultrasound assisted adsorption of temperature sensitive polymers in focus, some candidates are thermoresponsive poly(N-isopropylacrylamide) (PNIPAM)[34] and polyoxazolines[35] that change their morphology and reactivity in a narrow temperature region. These polymers can be extremely promising in the construction of 3-D temperature sensitive biosensors making use of the high surface area of metal sponges. For example, in our previous work on thermo-sensitive microgels,[34] we presented a switchable system, which, however, receives energy from an external source. However in our particular case it is very important that the bacteria's metabolism basically acts as a source of chemical energy to trigger the response. Here, the bacteria themselves bring in the power and trigger the response. That's actually a nice way of designing "active" coatings.

Experimental Section

Materials: The triblock terpolymer $B_{800}MAA_{200}Dq_{285}$ (subscripts denoting the degrees of polymerization of the corresponding blocks, $M_n \sim 110\ 000$ g/mol, PDI = 1.10) was synthesized via sequential living anionic polymerization in THF followed by polymer-analogous modifications. Details about polymerization and characterization can be found elsewhere. (Reference 28a and b) Silver nitrate (99.9% $AgNO_3$) was purchased from Sigma-Aldrich. All reactants were used without further purification. Milli-Q water (18.2 MΩ cm) was used in all aqueous solutions.

Preparation of mesoporous Al and Ag/Al plates: A glass substrate with an aluminum layer (thickness: 200 nm, vapor deposited, 5 mm² plate) was sonicated in 130 mL Milli-Q water for 60 s at 100% intensity with a Hielscher UIP1000hd (Germany) operated at 20 kHz with a maximal output power of 1000 W. The apparatus was equipped with a BS2d22 ultrasonic horn (head area of 3.2 cm²) and with a booster (B2-1.2). The maximum intensity was calculated to 57 W·cm⁻² at a mechanical amplitude of 81 μm. During sonication the samples were fixed in a home-made Teflon holder. The distance between Al-plate and ultrasonic horn was 1 cm. After replacing the water by 120 mL of an aqueous silver salt solution with the metal salt concentration of 2.5×10^{-5} M, the plates were sonicated at 50% intensity for additional 30 s.

Adsorption of BMAADq micelles on mesoporous metal plates: The triblock terpolymer micelles were adsorbed on freshly prepared substrates from a 0.45 g/L BMAADq in pH 10 buffer solution (AVS Titrinorm from VWR, ionic strength ~ 0.05 M) via the dip coating method. After 15 minutes the plates were rinsed with milli-Q water (18.2 MΩ cm) and dried with a stream of nitrogen.

Micelle surface patterning: Selective adsorption of micelles onto the aluminum surface was controlled by a preformed Teflon mask. In particular, after ultrasonic modification of the aluminum surface, the mask protected plate in the special holder was dip coated into the micellar solution as described before.

Characterization Methods: Atomic force microscopy (AFM) images of dried samples were taken with a Dimension 3100 equipped with a NanoScope V controller (Veeco) operating in Tapping Mode using standard Si_3N_4 cantilevers (Olympus) with a typical spring constant of ~42 N/m and a typical resonance frequency of 300 kHz (OMCL-AC160TS).

Scanning electron microscopy (SEM) measurements were conducted with a Gemini Leo 1550 instrument at an operation voltage of 3 keV. Samples were sputtered with gold. Microprobe analysis was performed using energy dispersive spectrometry (EDS) Model 6587, Pentafet Link, Oxford microanalysis group, UK.

Transmission electron microscopy (TEM) images were obtained on a Zeiss EM 912 Omega transmission electron microscope operating at 300 kV. The samples were ultramicrotomed (Leica EM FC6) and placed onto the copper grids coated with a carbon film.

Confocal Scanning Fluorescence Microscopy (CSFM). A Leica TCS SP confocal laser scanning microscope (Leica, Germany) with a 100× oil immersion objective (numerical aperture 1.4) was used.

The self-regulated bacterium adsorption properties of the samples were determined using gram-positive bacteria *Lactococcuslactis ssp. lactis 411* as the test cultures. The overnight cultures were cultivated in peptone-yeast MRS medium. Rhodamine 6G was added to the bacteria suspension to achieve a concentration of 10^{-7} M. After 30 min the bacteria were centrifuged and washed two times. Then the ultrasonically formed aluminum sponge modified with micelles was deposited on the bottom of flat sample cells, which were filled with 0.2 mL of the bacteria suspension. The adsorption equilibrium was typically attained in 5–10 min and the initial adsorption efficiency was measured with a confocal microscope. The same spot of the sample was controlled for the next six hours and imaged every 15-30 min. The standard deviations of three replicate experiments were within 7%. In the control test, in which the ultrasonic-engineered aluminum sponge was not additionally modified with micelles, no change in the bacteria adsorption was detected indicating no self-regulated bacteria release.

To evaluate the surface biocide activity, two parameters were calculated: (i) the survival ratio and (ii) the reduction factor. The survival ratio (S = C/C₀ · 100%, where C₀ is the initial number of colony-forming units (CFUs) and C the number of CFUs after desorption) provides information on the overall bactericidal efficiency of the system. The reduction factor (RF = N_c/N, where N and N_c are the numbers of CFUs remaining in suspension after contact with the silver-loaded and silver-free sponge, respectively) allows to determine the efficiency of inactivation.

[1] a) S. Raghavan, C. S. Chen, *Adv. Mater.* **2004**, *16*, 1303; b) C. S. Chen, M. Mrksich, S. Huang, G. M. Whitesides, D. E. Ingberg, *Science* **1997**, *276*, 1425; c) T. Ekblad, L. Faxlv, O. Andersson, N. Wallmark, A. Larsson, T. L. Lindahl, B. Liedberg, *Adv. Funct. Mater.* **2010**, *20*, 2396.

[2] a) J. Ziauddin, D. M. Sabatini, *Nature* **2001**, *411*, 107; b) J. El-Ali, P. K. Sorger, K. F. Jensen, *Nature* **2006**, *442*, 403; c) R. Langer, J. P. Vacanti, *Science* **1993**, *260*, 920.

[3] a) M. Veiseh, H. Zareie, M. Zhang, *Langmuir* **2002**, *18*, 6671; b) H. Kim, R. E. Cohen, P. T. Hammond, D. J. Irvine, *Adv. Funct. Mater.* **2006**, *16*, 1313; c) T. H. Park, M. L. Shuler, *Biotechnol. Prog.* **2003**, *19*, 243.

[4] a) N. Okochi, T. Okazaki, H. Hattori, *Langmuir* **2009**, *25*, 6947; b) M. Situmorang, J. J. Gooding, D. B. Hibbert, D. Barnett, *Electroanalysis* **2001**, *13*, 1469.

[5] a) I. Banerjee, R. C. Pangule, R. S. Kane, *Adv. Mater.* **2011**, *23*, 690; b) C. Y. Flores, C. Diaz, A. Rubert, G. A. Benitez, M. S. Moreno, M. A. F. L. Mele, R. C. Salvarezza, P. L. Schilardi, C. Vericat, *J. Col. Interface Sci.* **2010**, *350*, 402.

[6] a) V. A. Liu, S. N. Bhatia, *Biomedical Microdevices.* **2002**, *4*, 257; b) T. Y. Yu, C. K. Ober, *Biomacromolecules* **2003**, *4*, 1126; c) J. H. Ward, R. Bashir, N. A. Peppas, *J. Biomedical Mater. Res.* **2001**, *56*, 351.

[7] K. Y. Suh, J. Seong, A. Khademhosseini, P. E. Laibinis, R. Langer, *Biomaterials* **2004**, *25*, 557.

[8] E. Ostuni, R. S. Kane, C. S. Chen, D. E. Ingber, G. M. Whitesides, *Langmuir* **2000**, *16*, 7811.

[9] W. Tan, T. A. Desai, *Biomed. Microdevices* **2003**, *5*, 235.

[10] S. Takayama, J. C. McDonald, E. Ostuni, M. N. Liang, P. J. Kenis, R. F. Ismagilov, G. M. Whitesides, *Proc. Natl. Acad. Sci. USA* **1999**, *96*, 5545.

[11] a) M. Nishizawa, K. Takoh, T. Matsue, *Langmuir* **2002**, *18*, 3645; b) H. Kaji, K. Tsukidate, T. Matsue, M. Nishizawa, *J. Am. Chem. Soc.* **2004**, *126*, 15026.

[12] a) P. Roacha, T. Parker, N. Gadegaard, M. R. Alexander, *Surf. Sci. Reports* **2010**, *65*, 145; b) G. Decher, *Science* **1997**, *277*, 1232; c) M. Nolte, B. Schoeler, C. S. Peyratout, D. G. Kurth, A. Fery, *Adv. Mater.* **2005**, *17*, 1665; d) Y. Lvov, F. Caruso, *Anal. Chem.* **2001**, *73*, 4212; e) E. Kharlampieva, V. Kozlovskaya, S. A. Sukhishvili, *Adv. Mater.* **2009**, *21*, 3053.

[13] a) R. Singhvi, A. Kumar, G. P. Lopez, G. N. Stephanopoulos, D. I. C. Wang, G. M. Whitesides, D. E. Ingber, *Science* **1994**, *264*, 696; b) M. D. Kurkuri, C. Driever, G. Johnson, G. McFarland, H. Thissen, N. H. Voelcker, *Biomacromol.* **2009**, *10*, 1163; c) M. C. Berg, S. Y. Yang, P. T. Hammond, M. F. Rubner, *Langmuir* **2004**, *20*, 1362.

[14] a) K. Lewandowska, E. Pergament, N. Sukenik, L. A. Culp, *J. Biomed. Mater. Res.* **1992**, *26*, 1343; b) U. Hersel, C. Dahmen, H. Kessler, *Biomaterials.* **2003**, *24*, 4385; c) W. Feng, S. Zhu, K. Ishihara, J. L. Brash, *Langmuir* **2005**, *21*, 5980; d) Z. Zhang, S. Chen, Y. Chang, S. Jiang, *J. Phys. Chem. B* **2006**, *110*, 10799.

[15] a) S.-H. Lee, J. J. Moon, J. L. West, *Biomaterials* **2008**, *29*, 2962; b) K. Rechendorff, M. B. Hovgaard, M. Foss, V. P. Zhdanov, F. Besenbacher, *Langmuir* **2006**, *22*, 10885.; c) Y. Dou, K. Lin, J. Chang, *Nanoscale.* **2011**, DOI: 10.1039/c1nr10028a; d) P. Roach, D. Farrar, C. C. Perry, *J. Am. Chem. Soc.* **2006**, *128*, 3939.

[16] "The future of the Orthopedic Devices Market to 2012", Mike King, Oct. 12, **2008**, www.hipresurfacingnews.com.

[17] a) D. V. Andreeva, *Int. J. Mat. Res.* **2011**, *102*, 597; b) D. V. Andreeva, D. V. Sviridov, A. Masic, H. Möhwald, E. V. Skorb, *SMALL.* **2011**, doi:10.1002 smll.201102365; c) E. V. Skorb, D. G. Shchukin, H. Möhwald, D. V. Andreeva, *Nanoscale* **2010**, *2*, 722; d) D. V. Andreeva, D. G. Shchukin, H. Möhwald, *Adv. Mater.* **2008**, *20*, 2789; e) J. Lu, K.-H· Zum Gahr, J. Schneider, *Wear* **2008**, *265*, 1680;

[18] a) J. Schäferhans, S. Gomez-Guero, D. V. Andreeva, G. Rhotenberg, *Chem. Eur. J.* **2011**, *17*, 12254; b) Hielscher GmbH, http://www.hielscher.com/ultrasonics/industry.htm.

[19] a) L. H. Thompson, L. K. Doraiswamy, *Ind. Eng. Chem. Res.* **1999**, *38*, 1215; b) K. S. Suslick, L. A. Crum, in *Encyclopedia of Acoustics*(Ed: M. J. Crocker), Wiley & Sons. Inc., N. Y. **1995**; c) J. H. Bang, K. S. Suslick, *Adv. Mater.* **2010**, *22*, 1059.

[20] a) J. Banhart, *Prog. Mater. Sci.* **2001**, *46*, 559; b) G. J. Davies, S. J. Zhen, *J. Mater. Sci.* **1983**, *18*, 1899; c) H. Hakamada, M. Mabuchi, *Scr. Mater.* **2007**, *56*, 1003.

[21] J. Erlebacher, M. J. Aziz, A. Karma, N. Dimitrov, K. Sieradzki, *Nature* **2001**, *410*, 450.

[22] Y. Ding, J. Erlebacher, *J. Am. Chem. Soc.* **2003**, *125*, 7772.

[23] *Preparation of Solid Catalysts*,(Eds: G. Ertl, H. Knözinger), Wiley-VCH, Weinheim, Germany **1997**.

[24] a) E. V. Skorb, D. Fix, D. G. Shchukin, H. Möhwald, D. V. Sviridov, R. Mousa, N. Wanderka, J. Schäferhans, N. Pazos-Pérez, A. Fery, D. V. Andreeva, *Nanoscale* **2011**, *3*, 985; b) E. V. Skorb, H. Möhwald, T. Irrgang, A. Fery, D. V. Andreeva, *Chem. Comm.* **2010**, *46*, 7897; c) D. G. Shchukin, D.V. Andreeva, E. V. Skorb, H. Möhwald, in: *Supramolecular Chemistry of Hybrid Materials* (Ed: K. Rurack), Wiley-VCH, Weinheim, Germany **2010**.

[25] a) Y. Sugimura, J. Meyer, M. Y. He, H. Bart-Smith, J. Grenstedt, A. G. Evans, *Acta Mater.* **1997**, *45*, 5245; b) O. Mizuno, T. Matsuura, S. Nakayama, K. Harad, A. Yamakawa, *SEI Tech. Rev.* **2003**, *55*, 95.

[26] a) M. A. Margulis, Sonochemistry basis, High School, Moscow, **1984**; b) K. S. Suslick, G. J. Price, *Annu. Rev. Mater. Sci.* **1999**, *29*, 295.

[27] a) E. V. Skorb, D. G. Shchukin, D. V. Andreeva, *Langmuir* **2010**, *26*, 16973; b) D. G. Shchukin, E. V. Skorb, V. Belova, H. Möhwald, *Adv. Mater.* **2011**, *23*, 1922; c) N. Pazos-Pérez, J. Schäferhans, E. V. Skorb, A. Fery, D. V. Andreeva, *Micropor. Mesopor. Mater.* **2011**, doi:10.1016/j.micromeso.2011.08.011.

[28] a) E. Betthausen, M. Drechsler, M. Förtsch, F. H. Schacher, A. H. E. Müller, *Soft Matter* **2011**, *7*, 8880; b) J. Gensel, E. Betthausen, C. Hasenöhrl, K. Trenkenschuh, M. Hund, F. Boulmedais, P. Schaaf, A. H. E. Müller, A. Fery, *Soft Matter.* **2011**, *23*, 11144.

[29] a) H. Dautzenberg, W. Jaeger, J. Kötz, B. Philipp, C. Seidel, D. Stscherbina, in *Polyelectrolytes*, Carl Hanser Verlag, München, **1994**; b) I. Borukhov, D. Andelman, R. Borrega, M. Cloitre, L. Leibler, H. Orland, *J. Phys. Chem. B* **2000**, *104*, 11027; c) G. Battaglia, C. Fernyhough, A. J. Ryan, *Soft Matter* **2009**, *5*, 1674.

[30] a) C. B. Bucur, Z. Sui, J. B. Schlenoff, *J. Am. Chem. Soc.* **2006**, *128*, 13690; b) J. B. Schlenoff, A. H. Rmaile, C. B. Bucur, *J. Am. Chem. Soc.* **2008**, *130*, 13589; c) P. Schaaf, J. Talbot, *J. Chem. Phys.* **1989**, *91*, 4401.

[31] a) G. B. Webber, E. J. Wanless, S. P. Armes, F. L. Baines, S. Biggs, *Langmuir* **2001**, *17*, 5551; b) M. Borkovec, R. Pericet-Camara, B. P. Cahill, G. Papastavrou, *Chem. Comm.* **2007**, *266*; c) E. V. Skorb, D. Fix, D. V. Andreeva, D. G. Shchukin, H. Möhwald, *Adv. Funct. Mater.* **2009**, *19*, 2373; d) E. V. Skorb, D. G. Shchukin, H. Möhwald, D. V. Sviridov, *J. Mater. Chem.* **2009**, *19*, 4931; e) K. Sakai, E. G. Smith, G. B. Webber, M. Baker, E. J. Wanless, V. Bütün, S. P. Armes, S. Biggs, *Langmuir* **2006**, *22*, 8435.

[32] a) D. V. Andreeva, E. V. Skorb, D. G. Shchukin, *Appl. Mater. Inter.* **2010**, *2*, 1954; b) E. V. Skorb, D. V. Sviridov, H. Möhwald, D. G. Shchukin, *Chem. Comm.* **2009**, *6041*; c) E. V. Skorb, A. Skirtach, D. V. Sviridov, D. G. Shchukin, H. Möhwald, *ACS Nano* **2009**, *3*, 1753.

[33] N. Pazos-Perez, T. Borke, D. V. Andreeva, R. A. Alvarez-Puebla, *Nanoscale* **2011**, *3*, 3265.

[34] a) S. Schmidt, M. Zeiser, T. Hellweg, C. Duschl, A. Fery, H. Möhwald, *Adv. Funct. Mater.* **2010**, *20*, 3235; b) R. Álvarez-Puebla, R. Contreras-Cáceres, I. Pastoriza-Santos, J. Pérez-Juste, L. M. Liz-Marzán, *Angew. Chem. Int. Ed.* **2009**, *48*, 138.

[35] M. Meyer, M. Antonietti, H. Schlaad, *Soft. Matter.* **2007**, *3*, 430.

FULL PAPER

Sonochemical Activation of Al/Ni Hydrogenation Catalyst

Jana Dulle, Silke Nemeth, Ekaterina V. Skorb, Torsten Irrgang, Jürgen Senker, Rhett Kempe,* Andreas Fery, and Daria V. Andreeva*

This paper proposes a sonochemical approach to the nanostructuring of Al/Ni catalyst with high content of accessible Ni centers and a high reusability. The surface and bulk composition as well as pore size distribution of this catalyst are controlled synergistically by adjusting the ultrasound intensity in aqueous solution. Sonochemical activation of Al/Ni alloy leads to formation of mesoporous Al/Ni metallic based frameworks with surface area up to 125 $m^2 g^{-1}$, and regular distribution of nickel active center in the porous matrix. One of the opportunities of porous Al/Ni catalyst is that due to a time-resolved controllable formation of protective oxide layer it can be stored and handled under air in comparison to traditional Raney catalysts which need inert conditions. The Al/Ni catalyst is characterized by scanning electron microscopy (SEM), electron diffraction spectroscopy (EDS), X-ray photoelectron spectroscopy (XPS), confocal scanning fluorescence microscopy (CSFM), solid-state NMR experiments, and powder X-ray diffraction analysis (PXRD). The catalytic activity was investigated for the hydrogenation of acetophenone.

1. Introduction

In recent years attention has been devoted to nanostructured metals because of their unique properties and potential applications in a variety of fields.[1–5] Especially their use as a support material and/or active agent for heterogeneous catalyst became more important.[6–8] Approaches towards the fabrication of porous metals are based on both template-free

and template-assisted methods. Typical template-free methods are chemical or electrochemical dealloying procedures.[9] Mesoporous gold, platinum, and palladium can be formed by the dealloying process.[10] The formation of a uniform porosity after the dealloying process is possible if an alloy system is a monolithic phase because the nanoporosity is formed by a self-assembly process through surface diffusion and not by the simple dissolution of one phase from a multiphase system. For example, mesoporous gold prepared by dealloying from gold–silver alloys has disordered mesostructures, and the wide pore-size distributions of these mesostructures are not suited for the selective transport and adsorption of catalyzed species. A typical example of chemical dealloying is the preparation of "Raney nickel".[11] Raney nickel is produced when a block of a nickel-aluminum alloy is treated with concentrated sodium hydroxide. However, the dissolution of aluminum ions during the catalyst formation step could accelerate the formation of catalytically inactive surface nickel aluminate species.

The template methods are based on electroplating,[12] chemical reduction,[13] or plasma spraying[14] techniques. These methods require the use of preformed templates, such as self-assembled liquid-crystal surfactants,[15] colloidal crystals,[16] porous block copolymers,[17] or anodic porous alumina.[18] By using mesoporous silica as a template, mesoporous metals with highly ordered networks and a narrow pore-size distribution can be obtained. Because fluoric acid or sodium hydroxide is used to remove silica, the metals prepared using this method are limited to those unaffected by the dissolution agents (e.g. gold, platinum, and silver).[19] The template methods also have some disadvantages. These methods are multistage and involve a sacrificial second phase, which increases production costs because of the formation of the template and its subsequent removal, combined with the waste generation, especially when up-scaling the procedure.

Supported nickel catalysts play an important role in heterogeneous catalysis such as hydrogenation, hydrogenolysis, and partial oxidation of methane. One of the most successful methods of the activation of Al/Ni systems is the so-called Raney process, patented by the American engineer Murray Raney in 1925.[11,20] This process based on oxidation of aluminum to aluminum oxide and partial dissolution of aluminum component by using a strong base solution. However, the hydrolysis rate of alumina

J. Dulle, S. Nemeth, Prof. A. Fery, Dr. D. V. Andreeva
Chair of Physical Chemistry II
University of Bayreuth
Universitätsstr. 30, Bayreuth 95440, Germany
E-mail: daria.andreeva@uni-bayreuth.de

Dr. T. Irrgang, Prof. R. Kempe
Inorganic Chemistry II
University of Bayreuth
Universitätstr. 30, Bayreuth 95440, Germany
E-mail: kempe@uni-bayreuth.de

Dr. E. V. Skorb
Max Planck Institute of Colloids and Interfaces
Wissenschaftspark Golm
Am Mühlenberg 1, Golm 14476 Germany

Prof. J. Senker
Inorganic Chemistry III
University of Bayreuth
Universitätsstr. 30, Bayreuth 95440, Germany

www.MaterialsViews.com

ADVANCED
FUNCTIONAL
MATERIALS
www.afm-journal.de

FULL PAPER

precursor in Raney process is difficult to control. The final outcome is pyrophoric and sensitive to storage conditions.[21,22] These facts encouraged us to apply an ultrasound of high intensity (USHI) for the activation of the Al/Ni alloy, where the output is a catalytic active Al/Ni catalyst, which can be stored and handled under ambient conditions.

Recently[23–28] we have found that ultrasound treatment had dramatic effects on the morphology of aluminum particles. In particular, surface areas of the sonicated colloidal particles could be significantly increased when compared with untreated colloids. Intensive etching and oxidation of aluminum by ultrasound leads to formation of a sponge-like metal matrix stabilized by a thin metal oxide layer.[25] These metal sponges could be a perfect support for a heterogeneous catalyst. Based on the known physical and chemical effects of the high-intensity ultrasound outlined in Ref. [23–39] we expect that properties of metals such as resistance to oxidation and melting point could determine their behavior in the ultrasonic field and the final surface morphology, composition and properties of a catalyst. The dramatically different ability of the metals to respond to ultrasound irradiation can be exploited for the formation of nanoscale composites; thus, if alloy particles consisting of resistant and sponge-forming compounds are treated, a microphase separation could be expected under ultrasound irradiation. We tested this idea for the aluminum/nickel (1:1) system and generated an Al/Ni alloy catalyst stabilized by a thin oxide layer. Herein, we present the results of the catalyst characterization of the sonochemically prepared/activated Al/Ni alloy powder and its application for the hydrogenation of acetophenone as a model reaction.
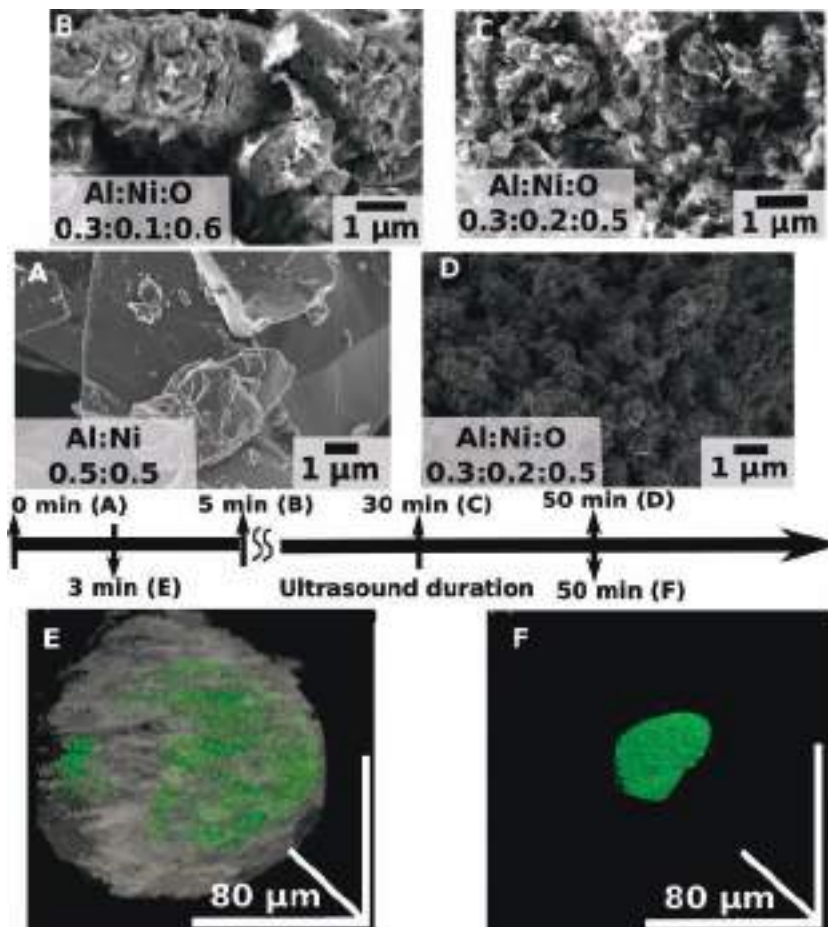

Figure 1. SEM images and the aluminum (Al), nickel (Ni) and oxygen (O) ratio measured by EDS (inserts) of Al/Ni particles: A–initial; B–after 5 min; C–30 min and D–50 min of sonication at 140 W cm^{-2}. 3D confocal microscopy reconstruction of the Al/Ni nanostructure loaded with fluorescein: (E) the alloy particle after 3 min (the reconstruction of both transmission and fluorescent mode) and (F) 50 min of sonochemicalexposure at 140 W cm^{-2}.

2. Results and Discussions

2.1. Catalyst Activation and Characterization

The sonochemical nanostructuring of metal alloys is based on microphase separation in an alloy due to different phase response to ultrasonic effects. The initial 1:1 Al/Ni alloy consists of Al_3Ni_2 and Al_3Ni intermetallides. Collapse of cavitation bubbles generated by ultrasound is followed by high local (μm^2 area) temperature (up to 5000 K) and a high heating/cooling rate. Thus, ultrasound of high intensity (USHI) provides unique conditions for metal treatment and should affect the microstructure of an alloy. Moreover, recently it was shown that aluminum could be not just oxidized itself during ultrasonic treatment in aqueous solution, but also could serve as an effective donor of reducing agent (H_2).[40] The finding is extremely important for

Al/Ni catalysts in situ activation during preparation. The catalyst activation in H_2 could be expected during the catalyst formation without the total transformation of metallic nickel to oxide. We could expect even reduction process during sonication,[40] also in the porous metal matrix. The aluminum/nickel (1:1) alloy powder was treated in a 10 wt% aqueous suspension with USHI at 140 W cm^{-2} from 30 sec to 50 min. The USHI driven interparticle collisions result in continuous breakage of 100 μm initial particles. It was shown that at surfaces several times larger than the resonance cavity size (e.g., at 20 kHz the maximum size of a cavitation bubble is approximately 5 μm)[41a] microjets of liquid can impact the solid surface.[41b] Thus, we choose 100 μm initial particles in order to maximise this effect of cavitation. The scanning electron microscopy (SEM) images show that after 50 min of sonication the particles were broken into 10–20 μm species (**Figure 1**, A–D).

The 3D reconstructions of the transmission and fluorescence images of the confocal scanning fluorescence microscopy (CSFM) of the sonicated Al/Ni particles loaded with the dye demonstrate the formation of porous inner structure. As longer sonication time of the particles as deeper the dye could
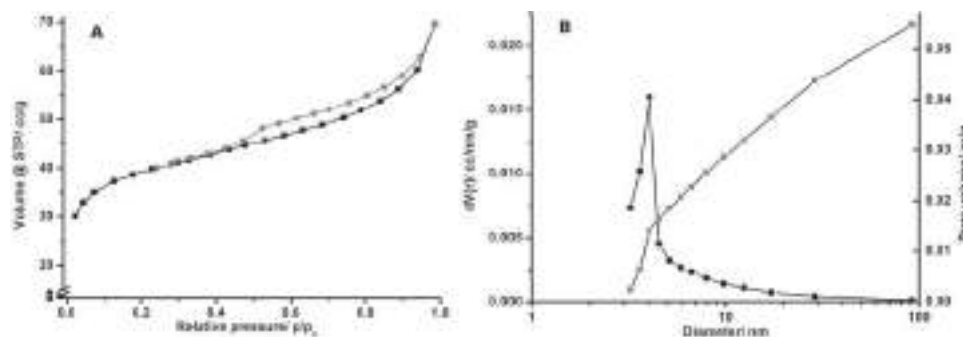
FULL PAPER

Figure 2. N_2 Adsorption (-■-)–desorption (-●-) isotherms of Al/Ni particles prepared by 50 min of sonication at 140 W cm^{-2} (A). BJH pore size distribution (-●-) and pore volume (-■-) of the same particles (B).

penetrate into the matrix of the alloy particle (Figure 1, E/F). The 50-min-sonicated samples could be completely saturated by the dye. The detailed evaluation of porous structure was made by the Barrett–Joyner–Halenda method (BJH) and the Brunauer–Emmett–Teller method (BET).[42,43] The N_2 adsorption/desorption isotherm (**Figure 2**, A) can be classified as group IIb if the new classification system proposed by Rouquerol et al.[44,45] is considered. The hysteresis loop corresponds to type H-1, according to IUPAC classification standards.[46] The pore size distribution, evaluated by BJH, proves the formation of mesopores with a pore size of about 4 nm for the Al/Ni alloy (Figure 2, B). The highest surface area according to BET was found to be 125 m^2 g^{-1} after 50 min of sonication at 140 W cm^{-2}. Initial Al/Ni alloy particles show a surface area of 0.2 m^2 g^{-1} only. We increased by a factor of 625 the surface area for our modified samples. Compared to commercial Raney nickel, which has a surface area of 50 m^2 g^{-1},[47] the sonochemically formed Al/Ni with a surface area of 125 m^2 g^{-1} exhibits a clear advantage.

In order to estimate the concentration of high-energy kinks and breaks accessible for catalysis, we analyzed the metal surface area of the Al/Ni alloys via pulse titration. For the Al/Ni material we obtained 1.14 m^2 g^{-1} metal surface of nickel, which gives a surface area per gram of nickel of 3.78 m^2 g^{-1}.

The oxidation/reduction processes during sonication were monitored by the electron diffraction spectroscopy (EDS) (Figure 1, A–D, inserts). We observed increase of oxygen concentration on metal surface which indicates oxidation process and formation of a novel metal oxide layer on the increased surface area of the porous metal matrix. The thickness of the metal oxide sonochemically generated on the surface of the modified metal was previously estimated by field ion microscopy less than 2 nm.[25]

Having in mind that the catalytic properties of a material depend on its inner structure, morphology, and composition, a closer look to the sonochemically induced changes inside Al/Ni particles has been taken. The inductively coupled plasma mass

spectrometry (ICP) method showed that the overall Al:Ni ratio in the samples did not change. For the sonicated Al/Ni alloy we determined a Ni content of 49.5% before and after ultrasonic treatment. Thus, treatment does not cause leakage of active metals from the samples.

The precise analysis of the powder X-ray diffraction (PXRD) of the sonicated Al/Ni alloy in comparison to the untreated alloy shows the formation of bayerite (Al(OH)$_3$) as a main oxidation product of the aluminum (**Figure 3**, A/C). The initial Al/Ni alloy consists mostly of intermetallic Al$_3$Ni$_2$ with an admixture of Al$_3$Ni. Upon USHI treatment, bayerite appears as the main oxidation product, while the relative concentration of Al$_3$Ni$_2$ exhibits the most pronounced decrease (the Al$_3$Ni phase remains untouched). Nickel metal is not evident in diffraction pattern. Although in an oxide form, nickel would be rather crystalline than amorphous. The absence of the characteristic patterns of NiO might be explained its low concentration in
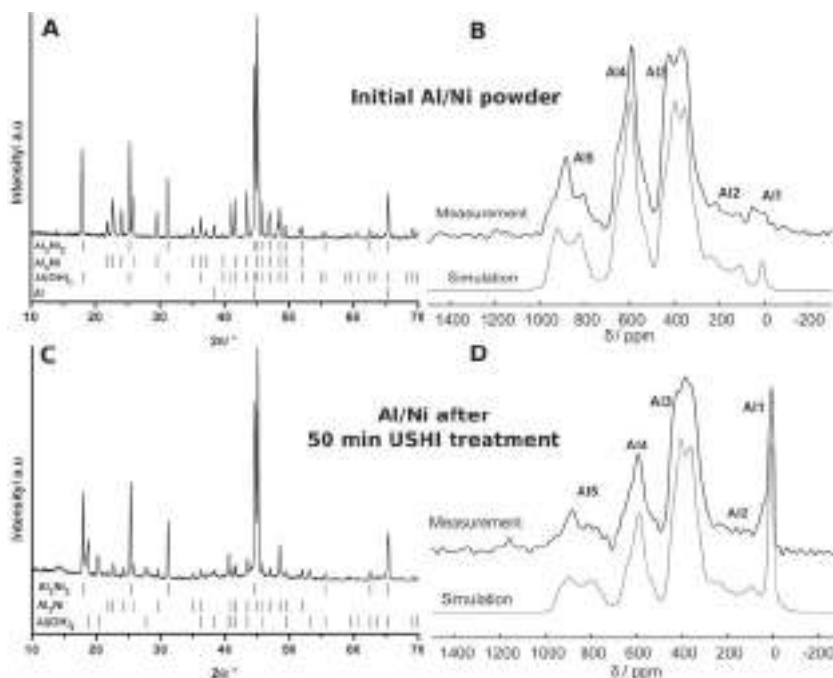

Figure 3. PXRD (left) and ^{27}Al NMR (right) of Al/Ni -alloy particles: initial (A/B) and after 50 min of sonication at 140 W cm^{-2} (C/D). 27AlNMR spectra were recorded by using [Al(H$_2$O)$_6$]$^{3+}$ as a reference. (*) indicates the spinning sidebands.

Materials
Views
www.MaterialsViews.com

ADVANCED
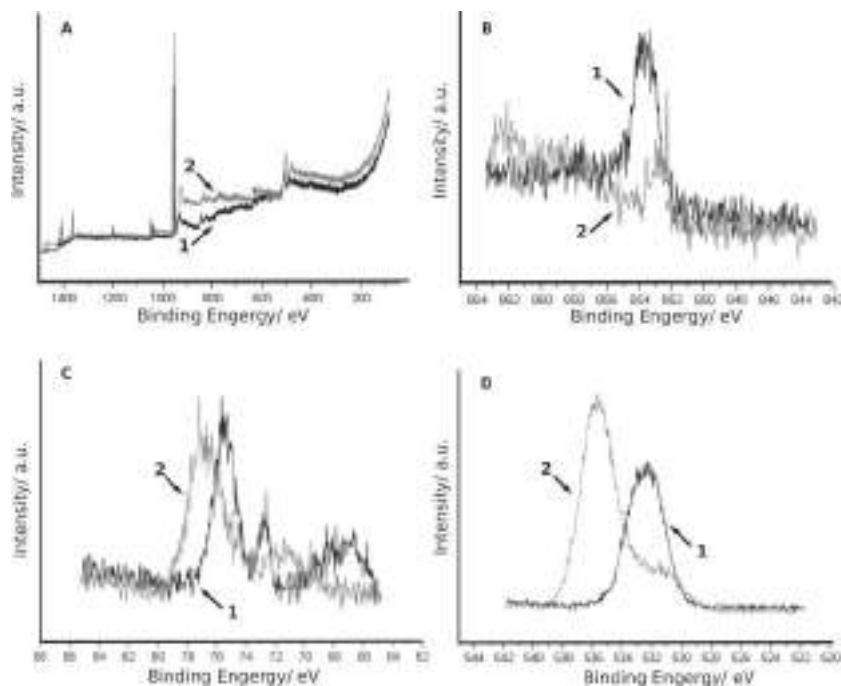FUNCTIONAL
MATERIALS
www.afm-journal.de

Figure 4. X-ray photoelectron (XPS) spectra of samples before (1) and after 50 min (2) of sonication treatment at 140 W cm^{-2} intensity. Survey spectra (A), Ni2p peaks (B), Al2p peaks (C), and O1s peaks (D).

hampered by different spin-spin relaxation times, the comparison between both data sets reveals that mainly alloy phase Al4 is affected during the sonication process.

The XPS analysis is demonstrated in **Figure 4**. The spectra were recorded before and after 50 min of ultrasonic treatment of the particles at 140 W cm^{-2}. The components at 852.3 (shown in Figure 4, B) and 854.0 can be attributed to metallic Ni and NiO.[48,49] Peaks position indicates the partial reduction of Ni during the process. After 5-min-sonication we could observe in the spectra the peaks related to the metal oxides only. However after 50-min-sonication we could distinguish the peaks of metallic nickel in the XPS patterns. The fact of formation of metallic nickel could be explained due to in situ activation of catalyst centers (Ni) during sonication. Aluminum peaks can be attributed to both phases: metallic aluminum and the oxidized aluminum. The peaks of aluminum and nickel oxides indicate partial surface oxidation (see also PXRD (Figure3)) of metals in the alloy. Thus, we can conclude that the sonochemical activation of the Ni/Al catalyst is probable due to generation of H$_2$[40] during partial oxidation of aluminum matrix. A conceptual novelty of the proposed ultrasound assisted Al/Ni activation is redox reactions controllable by sonication parameters and the material itself. The structure optimization for maximum catalytic efficiency can be done by adjustment of time and intensity of solication and catalyst composition.

By summarizing the results illustrated in Figures, we see that: (i) at the beginning stages of sonication of the alloy particles the increase of oxide phase could be attributed to partial oxidation of aluminum and nickel and the formation of porous structure with increased surface area; (ii) further sonication results in generation of metallic Ni detected by XPS due to possible reduction process[40] in porous matrix. Thus, relaying on the analytical methods we can assume that the sonochemically activated Al/Ni catalyst composed on unmodified Al/Ni skeleton with surface changed aluminum (oxidized) and catalytic active nickel centers regularly distributed in this matrix. The PXRD and ^{27}Al MAS NMR experiments could detect the oxidation of Al during sonication. Our previous works[25] on ultrasound treatment of aluminum and nickel particles demonstrate that aluminum exhibits increase of surface area and formation of porous matrix after sonication stabilized by sonogenerated aluminum oxide. Nickel particles are relatively resistant to ultrasound irradiation and slight change in surface morphology was detected. The SEM images demonstrate formation of a rough metal oxide on the surface of the modified Ni particles. Since the concentration of NiO is very low in the system we could detect it by using XPS only. Formation of a several-nm-thick metal oxide layer plays an important role in structure stabilization without negative effect to its catalytic activity. The importance of formation of metal oxide for the structure stabilization
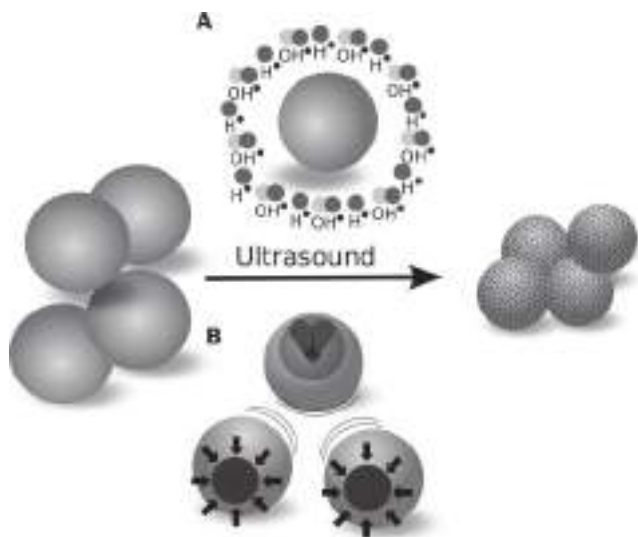
the system also due to its in situ reduction by hydrogen produced in sonogenerated pores. Nickel oxide was not detected probably due to mentioned reduction process and its negligible quantity per surface area. Nickel being amorphous also does not show pronounced peak in PXRD. Thus, beside cavitation induced oxidation process, we can expect the continuous reduction of the nickel particles due to formation of reducing agent (hydrogen).[40] We propose that ultrasound-driven activation of Al/Ni particles results in the formation of a Al/Ni mesoporous matrix stabilized by a thin oxide layer. In situ activated nickel centers by partial reduction of nickel particles are probably distributed in porous matrix (see also the TEM image in Figure S1). In order to prove this consideration we performed the detailed nuclear magnetic resonance (NMR) and X-ray photoelectron spectroscopy (XPS) analysis of the novel material.

Solid state ^{27}Al NMR experiments proved presence of metallic and oxidized aluminum species. Due to the quadrupolar interaction the ^{27}Al NMR resonances are usually broad and structured. Nevertheless, at least five different species can be distinguished. The sharp resonance at 10 ppm (Al1) appears significantly only in the spectrum of the sonicated sample, which can be assigned to aluminum oxide or hydroxide (Figure 3, B/D). All other four resonances (Al2-Al5 with $\sigma_{iso} \approx$ 300 ppm, 470 ppm, 670 ppm, and 980 ppm) are dominated by both the knight shift and the quadrupolar interaction, which demonstrates that they belong to different Al/Ni alloys with a low local symmetry for the Al sites. Details of the relevant refinement parameters are given in supporting information. The ^{27}Al MAS NMR spectra show that the metal particles are composed of the same alloy phases before and after the sonication. Although the intensities of the ^{27}Al resonances might be

Figure 5. Sonochemical modification of metal particles: (I) initial particles; (II) chemical aspect surface oxidation (A) and physical aspects (B) interparticle collisions; (III) formation of mesoporous metals.

during sonication can be proved by the addition experiments in an inert solvent. It has been suggested that in IL the oxidation could be avoided. We performed the sonication of Al/Ni alloy in ionic liquid (IL), 1-butyl-3-methylimidazolium chloride), in order to see if the similar mesoporous structure could be formed without metal oxide stabilization. The sonication in ionic liquid did not lead to formation of porous structure. There were no other crystalline phases detected. Thus, the surface oxidation has a crucial role in stabilization of the modified metal matrix and formation of porous structure. Furthermore, the sonogenerated oxide layer provides excellent stability of the catalyst during its exploitation. The sonicated Al/Ni can be stored and used at ambient conditions in comparison to Raney nickel that is pyrophoric and requires special storage conditions.[21,22]

Thus, sonochemical modification of metal particles schematically illustrated in **Figure 5** has the following effects generated by acoustic cavitation: sonochemical one - surface redox reactions by sonogenerated free radicals (A) and sonomechanical one - interparticle collisions (B). USHI induces particle breakage and increase of surface area of the material. Simultaneously depassivation of metal surface occurs due to cavitation stimulated breakage of initial oxide layer. Then the increased metal surface is stabilized by sonogenerated oxide layer. The generation of hydrogen during sonochemical oxidation of aluminum matrix plays an important role in catalyst activation. By adjustment of the sonication process we can avoid the complete material oxidation and achieve the particle reduction of nickel particles.

2.2. Catalytic Performance

The central motivation for the investigation described here is the influence of an ultrasonic treatment on morphology, texture, and performance of a composite material. In this paper,
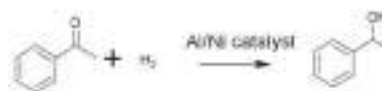
Scheme 1. Hydrogentation of acetophenone.

we tested the catalyst for the model reaction of hydrogenation of acetophenone (**Scheme 1**). As a material of interest, Al/Ni alloy powder sonicated for 50 min with maximum surface area of 125 m^2 g^{-1} was chosen. This material has previously shown its potential as catalyst.[24]

The initial Al/Ni alloy particles show no catalytic activity in the hydrogenation of acetophenone under 60 bar H$_2$-pressure and stirring at room temperature (RT) and water as a solvent. No or poor catalytic activity for commercially available and untreated Al/Ni alloys have also been reported.[50,51] On a contrary the sonochemically activated Al/Ni material demonstrates catalytic activity. It is important, that there were no side products observed during the hydrogenation of acetophenone under the used condition (RT, 60 bar of H$_2$). The catalytic experiments are summarized in **Table 1**.

The conversion of acetophenone to 1-phenylethanol was measured after 24 hours of reaction by gas chromatography (GC). The optimal conversion (>99.9%) of acetophenone was observed when 50 mg of catalyst were used (Table 1, Entry 1-2).

The pressure of the hydrogen applied during the catalytic reaction has its crucial influence on the conversion of acetophenone to 1-phenylethanol (Table 1, Entry 2-5). To avoid diffusion limitation we have chosen a pressure of 60 bar as the standard condition. It was observed that the yield of 1-phenylethanol decreases when the pressure is reduced. The maximum yield of 1-phenylethanol was observed at a hydrogen pressure of 40 bar, 5 bar hydrogen pressure gave a yield of 34%.

Using the optimal conditions of 50 mg of Al/Ni catalyst and a hydrogen pressure of 60 bar the conversion was studied based on the reaction time. Therefore, several catalytic runs were performed and stopped after a specific period of time. The complete consumption of the applied acetophenone was observed after the reaction time of 4 hours.

In addition the Al/Ni catalyst was tested under standard conditions (RT, 60 bar H$_2$, water as the solvent, 50 mg Al/Ni

Table 1. Conversion of acetophenone in dependence of H$_2$-pressure, amount of catalyst, as well as amount of substrate for a reaction time of 24 h at RT, stirring and 1 mL water as a solvent.

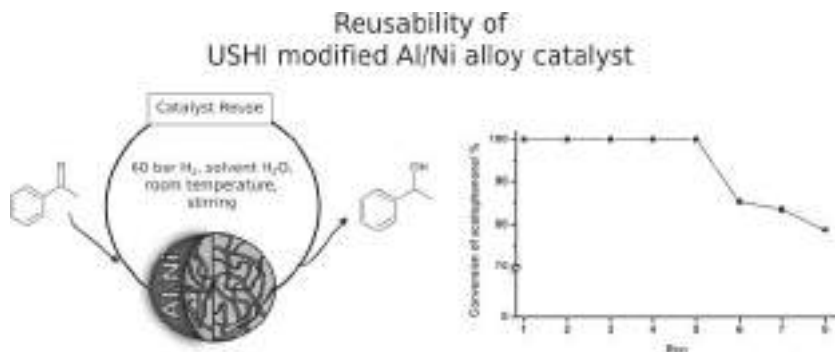| Entry	Catalyst [mg]	Acetophenone [μL]	H$_2$-pressure (bar)	Conversion of acetophenone [%]
1	25	300	60	36
2	50	300	60	> 99.9
3	50	300	5	34
4	50	300	20	79
5	50	300	40	> 99.9
6	50	500	60	> 99.9
7	50	700	60	> 99.9
8	50	900	60	> 99.9
9	50	1100	60	> 99.9

Figure 6. Reusability of Al/Ni catalyst under standard condition, namely 50 mg of USHI modified Al/Ni catalyst, 1 mL water as a solvent, reaction time 6 h at room temperature under 60 bar H_2 and stirring.

catalyst, stirring, 24 h reaction time) with higher amounts of acetophenone, namely 300 mL up to 1.1 mL (9.57 mmol). One could see that performance of the catalyst has not changed (Table 1, Entry 2 and 6-9).

To investigate the catalyst reusability, we performed catalytic reactions under the conditions described above and the reaction time of 6 hours (**Figure 6**). It was found that under these conditions the catalyst produces >99.9% 1-phenylethanol within the first five runs. After 5 runs the yield slightly decreased upon reuse, but still remained effective after 8 runs. The consumption of the acetophenone is gone down to 78% after 8 runs.

The unique morphology of our sonoactivated Al/Ni system (presence of metallic Ni and sonogenerated metal oxides) provides easy and efficient catalytic performance of the material. First of all the catalyst does not require preactivation stage before use. If the catalyst was preactivated for 24 h in a hydrogen atmosphere (solid catalyst material) no increase in catalytic activity was observed. Then, the sonoactivated Al/Ni can be a good alternative to the commercial Raney nickel. The activity of sonochemically activated Al/Ni was compared with the commercial Raney Ni catalyst. Similar activities were observed, conversion of acetophenone to 1-phenylethanol (60 bar H_2 pressure) at room temperature, for our best catalyst and commercial Raney nickel catalyst.

3. Conclusions

The sonochemical activation of Al/Ni particles results in nano-structuring of initial Al/Ni alloy and formation of an effective catalyst for the hydrogenation of acetophenone. The novel formation/activation method is based on the cavitation induced mechanochemical particle breakage and metal depassivation (breakage of initial oxide layer). The structure stabilisation is achieved by sonochemical formation of surface metal oxide layer. The self-regulated nickel reduction process (also in porous matrix of the catalyst) is responsible for formation of active centres of the catalysts. Thus, upon sonochemical activation the alloy species adopt a number of features attractive for catalytic applications: high surface area (up to 125 m^2 g^{-1}) and narrow pore size (~4 nm) distribution, presence of metallic nickel. In addition, the easy storage and handling of the metal based stabilized by thin oxide layer Al/Ni catalyst is an advantage of our

system. The ability to reuse the catalyst with little or no decrease of product yield makes the procedure of ultrasound activation for catalyst formation an attractive alternative to other preparation methods. Thus, the sono-chemically activated Al/Ni alloy could become a great alternative to known Raney nickel[20] and other heterogeneous hydrogenation catalysts. The findings presented here provide guidelines for the extension of the concept towards a broad variety of systems.

4. Experimental Section

Materials: Aluminum-nickel alloy powder (Fluka) (composition: 50 wt% aluminum and 50 wt% nickel) was used with a particle size ca. 100 μm as received. The water was purified before use in a three stage Millipore Milli-Q Plus 185 purification system and had a resistivity higher than 18.2 MΩ ·cm.

Preparation of Al/Ni catalyst: 5 g of the commercial Al/Ni alloy were dispersed in purified water (50 mL) and sonicated up to 50 min with an ultrasound tip (VIP1000hd, Hielscher Ultrasonics GmbH, Germany) operated at 20 kHz with a maximum output power of 1000 W ultrasonic horn BS2d22 (head area of 3.8 cm^2) and equipped with a booster B2-1.8. The maximum intensity was calculated to be 140 W cm^{-2} at mechanical amplitude of 106 μm. To avoid the temperature increase during sonication the experiment was performed in a thermostatic cell. After the USHI treatment, the sample was dried under vacuum with a heat gun.

Scanning electron microscopy: Scanning electron microscopy (LEO 1530 FE-SEM, Zeiss) was applied to characterize the optical response, structure, and size of the nanoparticles.

Powder X-ray diffraction: Powder X-ray diffraction (PXRD) diagrams were collected at θ–θ mode using a Stoe STADI P X-ray Transmission diffractometer: Cu Kα1, irradiation, room temperature, 2∗θ = 5–90.

^{27}Al *MAS NMR*: The ^{27}Al MAS NMR spectra were recorded at room temperature with a Bruker Avance II 300 FT NMR spectrometer operating at 78.2 MHz for ^{27}Al. The samples were loaded into 2.5 mm ZrO_2 rotors and mounted in a commercial triple resonance MAS probe (Bruker). All spectra were collected using proton broadband decoupling with a spinal64 sequence and a nutation frequency of 70 kHz. The recycle delay and spinning speed were adjusted to 1 s and 30 kHz. To eliminate not desirable signals from the probe we applied a rotor-synchronized Hahn echo sequence with a 16 step phase cycle and a nutation frequency of 50 kHz. The first and second pulse of the echo were set to 1 μs and 2 μs, respectively, to ensure that the signal intensity becomes independent from the magnitude of the quadrupolar coupling. The chemical shift of the ^{27}Al resonance is given with respect to $[Al(H_2O)_6]^{3+}$. The simulations of the MAS spectra were carried out with the program package SIMPSON.[52]

Surface area and pore size distribution: Surface area and pore size distribution based on physisorption (adsorption and desorption of gases) were measured by the BET (Brunauer-Emmett-Teller)[43] and BJH (Barrett-Joyner-Halenda)[42] method using N_2 at 77 K on a vacuum gas sorption NOVA 2000e (Quantachrome). The samples were dried under vacuum for 24 h at 300 °C.

Pulse Titration Analysis: Pulse Titration Analysis was performed by CHEMBET Pulsar TPD/TPR (Quantachrome) with hydrogen as the titration gas at a temperature of 300 K. Five hydrogen impulses were applied with a flow rate of 75 cm^3 min^{-1} at an ambient pressure of 760.00 mmHg.

Inductively Coupled Plasma (ICP): Inductively Coupled Plasma by Perkin Elmer, Plasma 400 with Argon Plasma determined the nickel content.

FULL PAPER

X-ray Photoelectron Spectroscopy (XPS): XPS spectra were acquired with a SPECS hemispherical energy analyzer (Phoibus 100) and SPECS focus 500 X-Ray monochromator using the Al Kα with energy of 1486.74 eV.

Confocal Scanning Fluorescence Microscopy (CSFM): A Leica TCS SP confocal laser scanning microscope (Leica, Germany) with a 100× oil immersion objective, numerical aperture 1.4 was used. The particles were loaded with a water-soluble fluorescent dye, Fluorescein. The pores of the particles were closed by the procedure suggested in.[53–56]

Catalytic application of the modified Al/Ni material: The hydrogenation of ketones was studied as described in Ref. [58,59]. The hydrogenation experiments were carried out using a Parr Instrument stainless steel autoclave N-MT5 300 mL equipped with heating mantle and temperature controller. Gas chromatography (GC) analyses were performed on an Agilent 6890 N Network GC System using a Lipodex E column (25 m × 0.25 mm; Machery & Nagel). We placed 0.05 g of the catalyst and 1 mL water in a glass vial. Additionally acetophenone (300 μL, 0.31 g, 2.57 mmol) was transferred via sealed Fortuna-Pipette. The filled vial was put into the autoclave. Subsequently, the autoclave was purged three times with hydrogen. The reduction was carried out at room temperature under vigorous stirring by using a continuous pressure of 60 bar of hydrogen. The experiment was stopped after the hydrogen gas was released. The reaction mixture was worked up by the addition of dodecane (584 μL, 0.44 g, 2.57 mmol) as internal standard and 2.5 mL diethyl ether. The product was extracted from the organic layer. The catalytic reactions were all carried out twice and several runs were analyzed.

Reusability: For testing the reusability of the catalyst, the reaction mixture was extracted 5 times with 2.5 mL of ether and afterwards treated in a standard ultrasound bath for 5 min. To remove the ether, the mixture was heated in 90 °C water bath for 10 minutes. After that, the Al/Ni catalyst was used again for the hydrogenation under standard conditions.

Supporting Information

Supporting Information is available from the Wiley Online Library or from the author.

Acknowledgements

[1] R. Karmhag, T. Tesfamichael, E. Wackelgard, A. Niklasson, M. Nygren, *Sol. Energy* **2000**, *68*, 329.
[2] T. Hyeon, *Chem. Commun.* **2003**, 927.
[3] K. Kim, S. C. Jeoung, J. Lee, T. Hyeon, J. I. Jin, *Macromol. Symp.* **2003**, *201*, 119.
[4] I. S. Lee, N. Lee, J. Park, B. H. Kim, Y. W. Yi, T. Kim, T. K. Kim, I. H. Lee, S. R. Paik, T. Hyeon, *J. Am. Chem. Soc.* **2006**, *128*, 10658.
[5] W. J. Tseng, C. N. Chen, *J. Mater. Sci.* **2006**, *41*, 1213.
[6] A. Houdayer, R. Schneider, D. Billaud, J. Ghanbaja, J. Lambert, *Synthetic Met.* **2005**, *151*, 165.
[7] A. Saxena, A. Kumar, S. Mozumdar, *Appl. Catal. A-Gen.* **2007**, *317*, 210.
[8] J. Banhart, *Prog. Mater. Sci.* **2001**, *46*, 559.
[9] J. Erlebacher, M. J. Aziz, A. Karma, N. Dimitrov, K. Sieradzki, *Nature* **2001**, *410*, 450.
[10] Y. Ding, J. Erlebacher, *J. Am. Chem. Soc.* **2003**, *125*, 7772.
[11] M. Raney, *USA Patent, US1563587*, **1925**.
[12] H. M. Luo, L. Sun, Y. F. Lu, Y. S. Yan, *Langmuir* **2004**, *20*, 10218.
[13] Y. Yamauchi, T. Momma, T. Yokoshima, K. Kuroda, T. Osaka, *J. Mater. Chem.* **2005**, *15*, 1987.
[14] A. Devasenapathi, H. W. Ng, C. M. S. Yu, S. W. Lim, *J. Mater. Sci.* **2005**, *40*, 5463.
[15] G. S. Attard, P. N. Bartlett, N. R. B. Coleman, J. M. Elliott, J. R. Owen, J. H. Wang, *Science* **1997**, *278*, 838.
[16] O. D. Velev, P. M. Tessier, A. M. Lenhoff, E. W. Kaler, *Nature* **1999**, *401*, 548.
[17] H. Maeda, Y. Kusunose, M. Terasaki, Y. Ito, C. Fujimoto, R. Fujii, T. Nakanishi, *Chem-Asian J* **2007**, *2*, 350.
[18] H. Masuda, K. Fukuda, *Science* **1995**, *268*, 1466.
[19] H. J. Shin, C. H. Ko, R. Ryoo, *J. Mater. Chem.* **2001**, *11*, 260.
[20] M. Raney, *Ind. Eng. Chem.* **1940**, *32*, 1199.
[21] J. Masson, P. Cividino, J. Court, *Appl. Catal. A-Gen.* **1997**, *161*, 191.
[22] P. Mars, T. V. D. Mond, J. J. Scholten, *Ind. Eng. Chem. Prod. Rd.* **1962**, *1*, 161.
[23] E. V. Skorb, D. G. Shchukin, H. Möhwald, D. V. Andreeva, *Nanoscale* **2010**, *2*, 722.
[24] E. V. Skorb, H. Möhwald, T. Irrgang, A. Fery, D. V. Andreeva, *Chem. Commun.* **2010**, *46*, 7897.
[25] E. V. Skorb, D. Fix, D. G. Shchukin, H. Möhwald, D. V. Sviridov, R. Mousa, N. Wanderka, J. Schäferhans, N. Pazos-Pérez, A. Fery, D. V. Andreeva, *Nanoscale* **2011**, *3*, 985.
[26] J. Schäferhans, S. Gomez-Quero, D. V. Andreeva, G. Rothenberg, *Chem.-Eur. J.* **2011**, *17*, 12254.
[27] N. Pazos-Perez, J. Schäferhans, E. V. Skorb, A. Fery, D. V. Andreeva, *Micropor. Mesopor. Mat.* **2012**, *154*, 164.
[28] N. Pazos-Perez, T. Borke, D. V. Andreeva, R. A. Alvarez-Puebla, *Nanoscale* **2011**, *3*, 3265.
[29] J. P. Lorimer, T. J. Mason, *Chem. Soc. Rev.* **1987**, *16*, 239.
[30] K. S. Suslick, G. J. Price, *Annu. Rev. Mater. Sci.* **1999**, *29*, 295.
[31] T. Prozorov, R. Prozorov, K. S. Suslick, *J. Am. Chem. Soc.* **2004**, *126*, 13890.
[32] J. H. Bang, K. S. Suslick, *Adv. Mater.* **2010**, *22*, 1039.
[33] G. Cravotto, P. Cintas, *Angew. Chem. Int. Edit.* **2007**, *46*, 5476.
[34] J. Lindley, T. J. Mason, *Chem. Soc. Rev.* **1987**, *16*, 275.
[35] K. S. Suslick, S. J. Doktycz, E. B. Flint, *Ultrasonics* **1990**, *28*, 280.
[36] S. J. Doktycz, K. S. Suslick, *Science* **1990**, *247*, 1067.
[37] J.-L. Luche, *Ultrason. Sonochem.* **1994**, *1*, S111.
[38] D. V. Andreeva, D. V. Sviridov, A. Masic, H. Möhwald, E. V. Skorb, *Small* **2012**, *6*, 1679.
[39] J. Gensel, T. Borke, N. Pazos-Perez, A. Fery, D. V. Andreeva, E. Betthausen, A. Müller, H. Möhwald, E. V. Skorb, *Adv. Mater.* **2012**, *24*, 985.
[40] E. V. Skorb, D. V. Andreeva, H. Möhwald, *Angew. Chem. Int. Ed.* **2012**, doi: 10.1002/anie.201105084.
[41] a) N. A. Tsochatzidis, P. Guiraud, A. M. Wilhelm, H. Delmas, *Chem. Eng Sci.* **2001**, *56*, 1831; b) G. I. Kuvshinov, N. V. Dezhkunov, V. I. Kuvshinov, P. P. Prokhorenko, *Inzh.-Fiz. Zh.* **1980**, *39*, 866.
[42] E. P. Barrett, L. G. Joyner, P. P. Halenda, *J. Am. Chem. Soc.* **1951**, *73*, 373.
[43] L. Brunauer, S. Deming, W. E. Deming, E. Teller, *J. Am. Chem. Soc.* **1940**, *62*, 1723.
[44] K. S. W. Sing, D. H. Everett, R. A. W. Haul, L. Moscou, R. A. Pierotti, J. Rouquerol, T. Siemieniewska, *Pure Appl. Chem.* **1985**, *57*, 603.
[45] F. Rouquerol, J. Rouquerol, K. S. W. Sing, *Academic Press, London* **1999**, 467.
[46] S. J. Gregg, K. S. W. Sing, *Academic Press, London* **1982**, 303.

[47] B. Zeifert, J. S. Blasquez, J. G. C. Moreno, H. A. Calderon, *Rev. Adv. Mater. Sci.* **2008**, *18*, 633.

[48] S. R. Kirumakki, B. G. Shpeizer, G. V. Sagar, K. V. R. Chary, A. Clearfield, *J. Catal.* **2006**, *242*, 319.

[49] J. Jun, M. Dhayal, J. H. Shin, Y. H. Han, N. Getoff, *Appl. Surf. Sci.* **2008**, *254*, 4557.

[50] J. Petro, L. Hegedus, I. E. Sajo, *Appl. Catal. A-Gen.* **2006**, *308*, 50.

[51] F. Alonso, P. Riente, J. A. Sirvent, M. Yus, *Appl. Catal. A-Gen.* **2010**, *378*, 42.

[52] M. Bak, J. T. Rasmussen, N. C. Nielsen, *J. Magn. Reson.* **2000**, *147*, 296.

[53] R. B. Grubbs, *J. Polym. Sci., Part A: Polym. Chem.* **2005**, *43*, 4323.

[54] E. V. Skorb, D. Fix, D. V. Andreeva, H. Möhwald, D. G. Shchukin, *Adv. Funct. Mater.* **2009**, *19*, 2373.

[55] E. V. Skorb, D. V. Sviridov, H. Möhwald, D. G. Shchukin, *Chem. Commun.* **2009**, 6041.

[56] E. V. Skorb, A. G. Skirtach, D. V. Sviridov, D. G. Shchukin, H. Möhwald, *ACS Nano* **2009**, *3*, 1753.

[57] E. V. Skorb, D. G. Shchukin, H. Möhwald, D. V. Sviridov, *J. Mater. Chem.* **2009**, *19*, 4931.

[58] Y. Mei, G. Sharma, Y. Lu, M. Ballauff, M. Drechsler, T. Irrgang, R. Kempe, *Langmuir* **2005**, *21*, 12229.

[59] G. Sharma, Y. Mei, Y. Lu, M. Ballauff, T. Irrgang, S. Proch, R. Kempe, *J. Catal.* **2007**, *246*, 10.

RSC Advances

PAPER

Sononanostructuring of zinc-based materials

Jana Dulle,[a] Silke Nemeth,[a] Ekaterina V. Skorb[b] and Daria V. Andreeva*[a]

We performed the sonochemical nanostructuring (sononanostructuring) of zinc particles, which produced a core–shell "hedgehog" zinc-based material by a "green" ultrasound method. The core–shell "hedgehogs" consist of a metallic zinc core covered by zinc oxide nanorods. Due to the "hedgehog" morphology, the novel zinc-based material exhibited increased surface area, high accessibility for substrate molecules and could be a promising component of sensors, catalysts, active feedback coatings, and photovoltaic systems. We demonstrate the results of the photocatalytic performance of the zinc-based core–shell "hedgehogs".

1. Introduction

Ultrasound (US) technology is a green chemistry tool for the direct delivery of energy in a chemical reactor. Ultrasound-assisted processes can be carried out under relatively mild conditions and do not require aggressive media or harsh chemical additives. The energy is concentrated locally inside and near cavitation bubbles.[1–5] In general, the collapse of acoustic cavitation microbubbles (frequency of 20 kHz) under the ambient conditions of the bulk solution is characterized by intensive local effects: temperature increase (up to 5000 K), pressure increase (of about 1000 atmospheres), and heating and cooling rates above 10^9 degrees per second. The sonochemical effects include the formation of radicals from solvents and the enhancement of reaction rates at ambient temperature. Thus, ultrasound can be used for fast and effective modification, fragmentation of particles, etching of metal surfaces, depassivation of metal surfaces, oxidation, and for the growth stimulation of a novel metal oxide/hydroxide interfacial layer.

Here we propose an easy ultrasound-driven method of the modification of zinc particles, so-called "sononanostructuring" of zinc particles, by using US. The novel US-assisted modification method leads to the formation of core–shell "hedgehog" zinc-based materials. Wide band-gap semiconductor materials like nanostructured zinc oxide (ZnO) are important for several applications, such as transparent semiconductors, gas sensors, solar cell windows, and photovoltaic devices.[9,10] Thus, ZnO in the form of powders,[11–15] nanoparticles,[16–19] nanoplatelets,[20] plates,[21] or thin films,[22–24] has already gained interest as a photocatalyst for the degradation of water pollutants. Photocatalytic materials have become a promising alternative

for environmental reprocessing[25] due to their ability to degrade different organic compounds in a more efficient way than other processes, *e.g.*, biodegradation techniques.[26,27] The polluted water contains toxic compounds that are persistent and not biodegradable. Dyes from the textile industry are examples of such dangerous waste. The degradation of these dyes is a serious problem worldwide.[28–32] The cleaning of the highly contaminated waste is important for the environment and human beings. With this in view, ZnO is considered as a low cost photocatalyst for photodegradation.[13,16,33–35] The high photocatalytic efficiency of ZnO is attributed to its ability to generate H_2O_2[36,37] and to the high number of active sites with high surface reactivity.

The formation of ZnO nanostructured materials varies from the sol–gel method,[38] the use of a thermal plasma reactor,[16] the chemical vapour deposition method,[39] alkali precipitation,[12] and spray pyrolysis[40] to orient the attachment of preformed ZnO nanoparticles.[41] Here, we propose an alternative approach: direct oxidation of the zinc surface by using a sonochemical approach. The ZnO nanorods form a shell attached to the metal zinc core. The novel approach is based on our previous works.[3,4,6–8] Recently, we demonstrated that mesoporous metal structures stabilized by a metal oxide layer could be formed using ultrasound. The sononanostructuring of zinc particles requires relatively mild conditions: aqueous media without any additional oxidants. Production expenses including the ultrasound equipment and energy costs of preparing the particles are rather low. The US-assisted method can be up-scaled by using different sonotrodes or a series of sonotrodes.[6] One of the advantages of the proposed sononanostructuring process is that a wide range of Zn-based materials with various morphologies and functionalities can be prepared. The photocatalytic performance was demonstrated as one of the potential applications of the sononanostructured Zn. Furthermore, the ultrasound-assisted modification was performed under different conditions in order to help understand the mechanisms of the sononanostructuring of Zn.

[a]Physical Chemistry II, University of Bayreuth Universitätsstrße, 30 95440 Bayreuth, Germany. E-mail: daria.andreeva@uni-bayreuth.de; Fax: +49 921552059; Tel: +49 921552750
[b]Max Planck Institute of Colloids and Interfaces, Am Mühlenberg 1, 14424 Potsdam, Germany. E-mail: skorb@mpikg.mpg.de; Fax: +49 331567 9202; Tel: +49 331567 9233

2. Experimental

2.1. Formation of core–shell "hedgehogs" from Zn particles

Zinc powder (Sigma Aldrich, $\geq$99%, initial size $\sim$50 µm and 4 µm) was dispersed in ultrapure MilliQ-water and sonicated for different durations with an ultrasound tip (VIP1000hd, Hielscher Ultrasonics GmbH, Germany) operated at 20 kHz with a maximum output power of 1000 W ultrasonic horn BS2d22 (head area of 3.8 cm^2) and equipped with a booster B2-1.8. The maximum intensity was calculated to be 140 W cm^{-2} at a mechanical amplitude of 106 µm. The concentration of the initial powder was varied in the range 0.01–0.1 g mL^{-1}. During treatment the sample was cooled in a thermostatic flow cell. After the treatment, the modified zinc (US-Zn) sample was dried for 24 h.

2.2. Characterisation methods

Transmission and scanning electron microscopy (TEM, Zeiss EM922 Omega, EFTEM operating at 200 kV and SEM, LEO 1530 FE-SEM, Zeiss), in combination with an ultra microtome (Ultracut E, Reichert Jung, thickness 50 nm) were applied to characterize the optical response, structure, and the size of the zinc powder.

The powder X-ray diffraction (PXRD) patterns were collected in the θ–θ mode using a Stoe STADI P X-ray transmission diffractometer: Cu-Kα_1, irradiation, room temperature, 2θ =5–90°.

The surface area is based on physisorption (adsorption and desorption of gases) and was measured by the BET (Brunauer–Emmett–Teller)[48] method using krypton at 77 K on a vacuum gas sorption Autosorb-1 and Autosorb Degasser apparatus (Quantachrom). Each sample was dried under vacuum for 24 h at 100 °C.

X-ray photoelectron spectroscopy (XPS) was acquired with a SPECS hemispherical energy analyzer (Phoibus 100) and SPECS focus 500 X-Ray monochromator using the Al-Kα with energy of 1486.74 eV.

2.3. Photocatalytic experiments

The photocatalytic activities were used for the as-prepared and filtered samples in order to separate the free ZnO nanorods formed by sonication. The core–shell Zn/ZnO particles were used for the degradation of methyl orange (MO, ACS reagent, Sigma-Aldrich) in solution in the presence of UV light.

The degradation of MO dye was estimated by evaluation of the intensity of the absorption band centred at 464 nm, as a function of the illumination time.

The initial pH of these solutions was 5.4. A 450 W UV lamp, equipped with a 420 nm cut-off filter (λ = 380 nm) was used (UV-F 400 F, Dr. Hönle, Germany) to irradiate the stirred dispersions. The sample was placed at a distance of 25 cm from the UV lamp, the average light intensity was 15 mJ cm^{-2} (measured by tesa® UV Strip – UV Scan, Dr. Hönle, Germany). 10 mg of zinc modified for different lengths of sonication time were dispersed in a 10 mL MO suspension (0.1 mM) and stirred at room temperature. Prior to irradiation, the suspensions were magnetically stirred in the dark for 30 min to reach an adsorption–desorption equilibrium. At given time intervals, 1

µL of the solution samples were collected and analysed by recording the absorption of MO from 190 nm to 800 nm using an Agilent 8453 UV/VIS spectrophotometer with ultrapure water in the reference beam. The degradation percentage was obtained as well as the rate of reaction constant k. This rate of reaction was used to compare the efficiency of the catalysts. For the reusability experiments the catalyst was washed in ultrapure water several times and dried.

The reaction with UV radiation and catalyst follows the first reaction order

$$[A]_t = [A]_0 e^{-kt} \tag{1}$$

with $[A]_t$ as the concentration at time t and $[A]_0$ as the starting concentration, with k (min^{-1}).

3. Results and discussion

3.1. Sonication of Zn particles: formation of the Zn-based core–shell "hedgehogs"

Recently we have suggested that the surface preferable orientation etching/oxidation of metal particles[4] during their ultrasound modification is an important aspect in the nanostructuring of such metals as aluminum and magnesium. In general, the ultrasound-driven modification of metals is base on cavitation induced metal depassivation (breakage of initial oxide layer), mechanochemistry (due to particle collision), and sonochemistry (structure stabilization by the sonogenerated oxide layer). Thus, the sonicated species adopts a number of features which are attractive for further applications, e.g., high surface area (more than 100 m^2 g^{-1} for aluminum-based alloys), narrow pore size distribution in the mesoscopic range. We also demonstrated that long-term (longer then 90 min) ultrasound treatment of Zn particles results in the complete conversion of Zn into Zn oxide. Our current research demonstrates that the short-term ultrasound treatment (up to 90 min) of Zn particles gives a Zn-based material with amazing variable core–shell "hedgehog" morphologies, which depend on the initial particle sizes, Zn concentration in the solution and the duration of the sononanostructuring.

The general concept of ultrasound-driven modification of zinc particles is shown in Fig. 1. During the US treatment of zinc particles the following phenomena could be observed (Fig. 1A): (I) formation of cavitation bubbles in the aqueous suspension of zinc particles; (IIa) the red/ox reactions at the interfacial regions; (IIb) interparticle collisions; (III) generation of the core–shell "hedgehog" zinc. Moreover (IV) total oxidation with total conversion to oxide structure is possible (not shown in the sketch).

Zn particles of the size $\sim$4 µm and $\sim$50 µm were used for Zn sononanostructuring. The morphology of the modified Zn-based particles was studied by using scanning and transmission electron microscopy (Fig. 2). The particles after 10 min of sonication consist of the metallic Zn core covered by ZnO nanorods. The core–shell morphology can be clearly seen in the TEM image of the cross section of the modified Zn particle (Fig. 1B). The nanorods are attached perpendicularly to the Zn core. The SEM image (Fig. 1C) shows that the nm-long rods homogeneously cover the metal surface, forming so-called "hedgehogs" from Zn particles. We explain the formation of
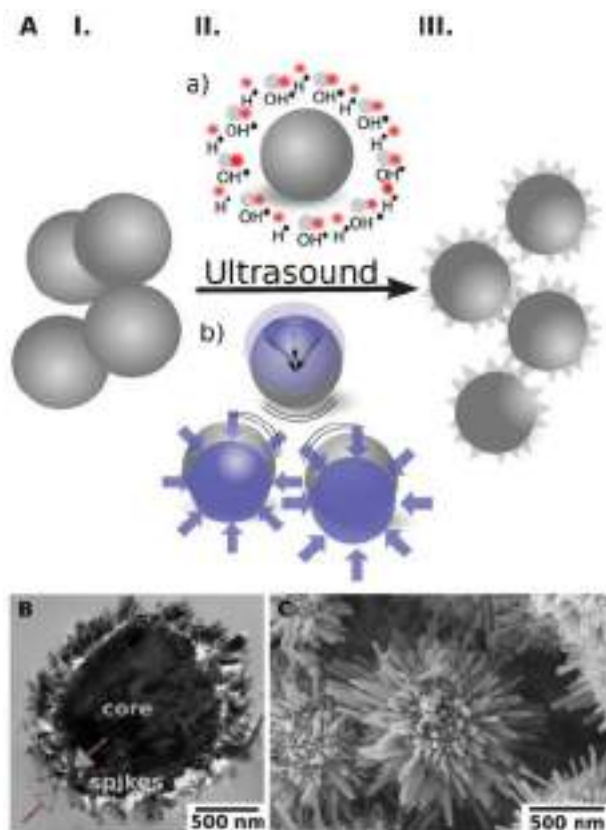
Fig. 1 A – Sonochemical modification of zinc particles: (I) initial particles; (II) (a) chemical aspect due to surface oxidation; (b) physical aspects are caused by interparticle collisions and surface impinging by high velocity microjets providing preferable directions of etching; (III) formation of "hegdehog" zinc particles. B, C – TEM (B, 10 min US) and SEM (C, 15 min US) images of the core–shell "hedgehog" structure: metal core and the oxide nanorods attached to the core after US treatment.

Fig. 2 XPS spectra of the "hedgehog" zinc particles (A) and the ZnO nanorods (C), and SEM image of the ultramicrotomed Zn/ZnO particle (B) and ZnO nanorods (D) after 15 min of US treatment.

the core–shell "hedgehog" morphology to be as a result of the oxidation of the surface of Zn particles by free radicals generated during cavitation.

3.2. Mechanism of formation of core–shell Zn-based "hedgehogs"

The formation of the core–shell Zn-based morphology was confirmed by the TEM images (Fig. 1B) and the XPS experiments (Fig. 2). The XPS spectra (Fig. 2A, C) correspond to the Zn $2p_{3/2}$. It is clearly seen that after modification, in the case of the "hedgehog" structures, there are two peaks, corresponding to the metallic core and oxidized shell. In the case of ZnO nanorods, a shift of the peak is attributed to the change of Zn^0 to Zn^{2+}.

The growth of ZnO on the zinc particles can be controlled by the duration of the sonication (Fig. 3). The ultrasound-stimulated formation of zinc oxide on the surface of the zinc particles (here, ~ 4 μm initial Zn particles) occurs after short-term sonication. 60 s US treatment leads to the appearance of 60 nm long ZnO nanorods on the Zn core (Fig. 3D). After 10 min of sononanostructuring the ZnO nanorods grow up to 160 nm and cover the entire core (Fig. 3F).
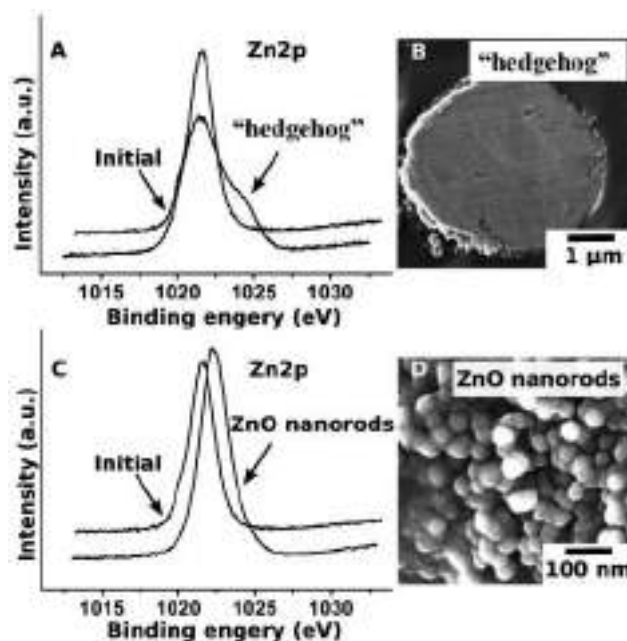
Longer treatments (>30 min) destroy the relatively long nanorods (Fig. 3G). The 160 nm nanorods are removed from the particle surface due to friction forces during interparticle collisions. Then the surface oxidation starts again. The 60 min-sonicated samples are covered by 20 nm nanorods. The PXRD patterns in Fig. 3 A–G confirm the cycle character of the ultrasound-driven modification of Zn. A 10 min ultrasonic treatment leads to the partial conversion of Zn into ZnO, which results in the "hedgehog" morphology of the particles. The PXRD pattern of the 10 min-modified samples exhibits the peaks of both the metallic Zn and ZnO. After 30 min the "hedgehog" structures lose their spikes. Two separate phases, Zn particles and ZnO nanorods, can be distinguished and separated. The PXRD pattern of the Zn after loss of the ZnO nanorod shell is shown in Fig. 3E.

The size of the initial Zn particles also affects the modification process and, therefore, the morphology of the modified systems (Fig. 4). The modification of the ~ 4 μm and ~ 50 μm particles leads to surface oxidation, growth of ZnO nanorods and their detachment. These ZnO nanorods are formed and detached in a cyclic manner. The PXRD patterns and the SEM images in Fig. 3 show that the nanorods grow, reach a maximum size, detach during sonication, and then the cycle starts again. However, the character of growth of the metal oxide depends on the particle size. The SEM images (Fig. 4) demonstrate that the ~ 50 μm particles are covered by randomly attached ZnO nanorods (Fig. 4A, C, E). The concentration of these nanorods increases with the sonication duration. The increase in ZnO concentration on the surface of the ~ 50 μm particles was confirmed by PXRD (not shown here). The ~ 4 μm Zn particles are covered by the perpendicularly attached ZnO. The surface area of the initial ~ 4 μm zinc particles is 0.4 m^2 g^{-1}. The surface area of these particles reaches 2.6 m^2 g^{-1} after 10 min of
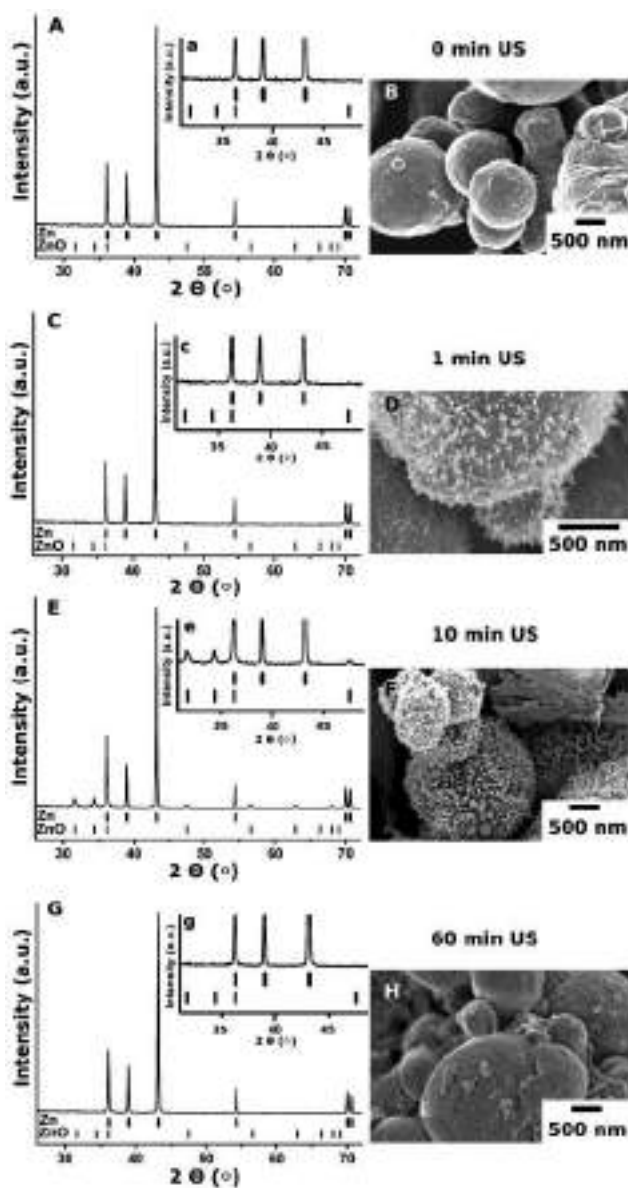
Fig. 3   PXRD patterns and SEM images of the initial zinc particles (A, B) and the particles treated for 1 min (C, D), 10 min (E, F) and 60 min (G, H) by ultrasound. The inserts (a, c, e, g) show the magnified part of the PXRD patterns with the ZnO attributed peaks.

sonication. After 30 min of US treatment, the surface of the "hedgehogs" is covered by 20 nm ZnO rods and has the surface area of 1.3 m^2 g^{-1}. The surface area of the $\sim$50 μm particles can achieve a maximum of 20 m^2 g^{-1} after 10 min of sonication due to the formation of a thick layer of randomly distributed 160 μm ZnO spikes. After 90 min of modification the surface area of the $\sim$50 μm particles is also decreased up to 12 m^2 g^{-1}, which is due to the formation of 100 nm nanorods on the metal surface. Thus, the surface area of the modified particles depends on the character of growth and distribution of the ZnO nanorods on the metal core. At the beginning of the sonication treatment (10–15 min) we observed the formation of the very interesting tubular ZnO nanorods[4] on the surface of the $\sim$50 μm particles that are probably responsible for the increased surface area of such particles. However, as we will demonstrate in the next part of this
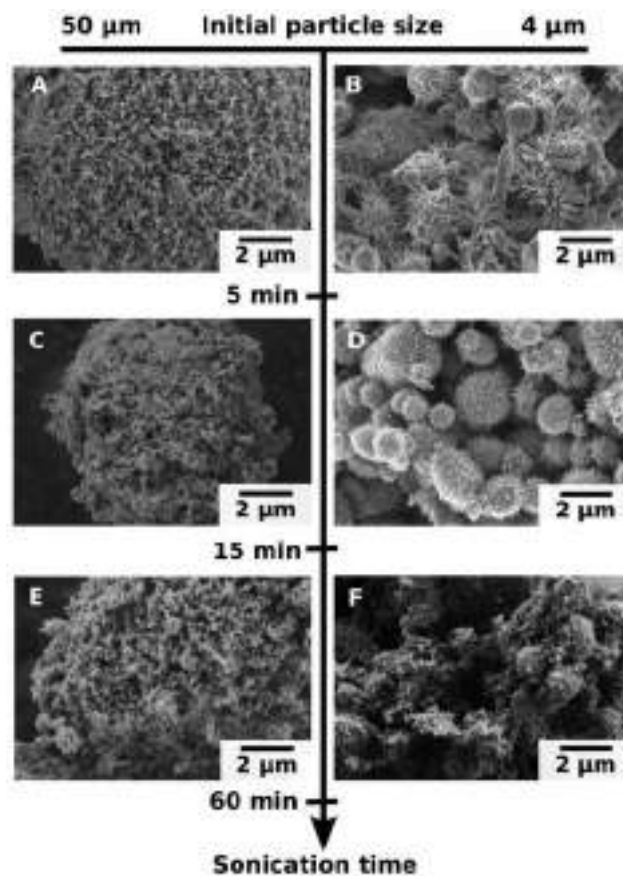

Fig. 4   SEM images of the $\sim$4 μm and $\sim$50 μm initial particle size after 5 (A, B), 15 (C, D) and 60 min (E, F) of US treatment.
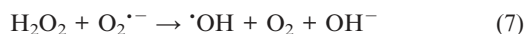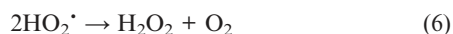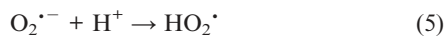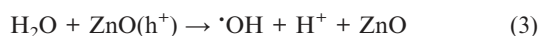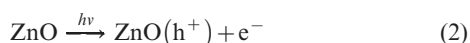
article, these nanorods do not significantly contribute to the catalytic activity of the Zn particles. It is likely that they are not accessible to the substrate molecules. The 15 min-sonicated $\sim$4 μm Zn particles (Fig. 4D) demonstrate the core–shell morphology, where the Zn core is homogeneously covered by a monolayer of ZnO nanorods. The longer sonication time (the 60 min-sonicated particles in Fig. 4F) leads to the formation of randomly distributed 100 nm ZnO nanorods, similar to the ZnO layer formed on the $\sim$50 μm particles. These particles demonstrate the highest catalytic activity which we will discuss here later.

Based on all characterizations performed above, we can summarize that the ultrasound modification of the Zn particles has a cycle character that depends on the sonication time and particle size. The free radicals generated by the ultrasound oxidize the surface, after which, the ZnO nanorods rapidly grow on the metallic core. The long nanorods are detached because of interparticle collisions in the sonicated suspensions. We could distinguish two phases: the relatively smooth Zn particles and the ZnO nanorods. When the oxidation continues and the nanorods grow again on the surface. The size of the nanorods can be controlled by the particle size and the duration of sonication. Short-term sonication (up to 90 min) leads to the formation of core–shell "hedgehogs" with an increased surface area.

3.3. Photocatalytic activity

The functionality of the sononanostructured Zn can be related to its properties as a semiconductor. When the modified zinc is

illuminated by UV light, the migration of electrons to the zinc core begins (eqn (2)), and so positive holes (h^+) are formed.[42–44] When the semiconductor is immersed in an aqueous medium, the spontaneous adsorption of water molecules in the liquid occurs. Then an electron is transferred to the acceptor molecule and the donor molecule gives an electron to the semiconductor particle. The holes generate $^{\bullet}$OH by reacting with the water molecules (eqn (3)), and the O_2 molecule accepts an electron to form the super-oxide radical $O_2^{\bullet-}$ (eqn (4)). These $O_2^{\bullet-}$ radicals act as strong oxidizing agents and they also contribute to the formation of hydrogen peroxide (eqn (5)–(8)).[45] Thus, as an example of the possible application range of the sononanostructured zinc, we tested the photocatalytic activity of the core–shell "hedgehog" in the detoxification of methyl orange (MO). The radicals formed in the presence of a semiconductor can react with the dye molecule, disrupting it in its conjugated system, which leads to the complete decomposition of the dye.[46,47]

$$ZnO \xrightarrow{h\nu} ZnO(h^+) + e^- \qquad (2)$$

$$H_2O + ZnO(h^+) \rightarrow {}^{\bullet}OH + H^+ + ZnO \qquad (3)$$

$$O_2 + e^- \rightarrow O_2^{\bullet-} \qquad (4)$$

$$O_2^{\bullet-} + H^+ \rightarrow HO_2^{\bullet} \qquad (5)$$

$$2HO_2^{\bullet} \rightarrow H_2O_2 + O_2 \qquad (6)$$

$$H_2O_2 + O_2^{\bullet-} \rightarrow {}^{\bullet}OH + O_2 + OH^- \qquad (7)$$

$${}^{\bullet}OH + dye\ (MO) \rightarrow dye\ (MO)\ mineralization \qquad (8)$$

In Fig. 5 are highlighted some results of the detoxification of MO by the core–shell "hedgehog" zinc. The dye degradation was monitored using the UV/VIS spectra. The absorption peaks, corresponding to dye, diminished and finally disappeared under irradiation, which indicates that the dye is degraded. No new absorption bands appear in either the visible or ultraviolet regions. The spectrum of MO in the visible region exhibits a band with a maximum at 464 nm. The decrease of the absorption peaks of MO at $\lambda_{max} = 464$ nm indicates a rapid degradation of the azo dye. It also indicates that the nitrogen–nitrogen double bond (–N=N–) of MO is the most active site for oxidation attack. Complete degradation of the dye was observed after 50 min using the optimized conditions. MO in the absence of the photocatalyst is stable under UV-irradiation. In the absence of photocatalyst no colour change was observed.

To optimize the ultrasound treatment of the Zn particles, we tested the catalytic activity of the US-Zn prepared over different sonication times. Fig. 5 shows the catalytic activity of the samples prepared at different concentrations of Zn in water and by using ~50 µm and ~4 µm initial Zn particles. For all samples we observed the cycle character of the reaction rate constant *vs.* sonication time.

At the beginning of modification, up to 10 min of sonication, we observed an increase in the rate constant for all samples. After 10 min of US exposure the activity decreases rapidly and
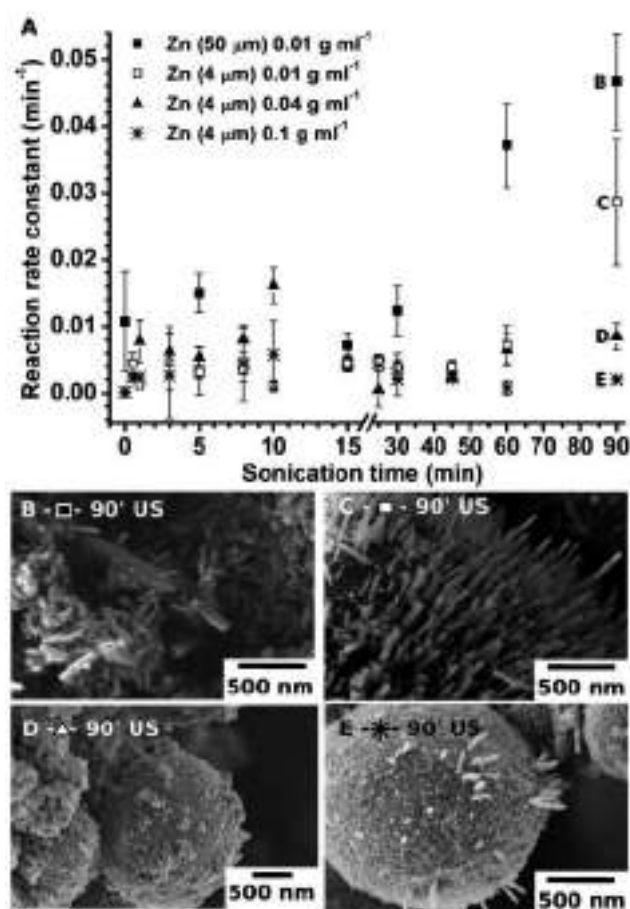

Fig. 5 The reaction rate constant k is shown to be independent of the ultrasound treatment duration. We used 10 mg of the US-Zn (A). The SEM images of the samples prepared for 90 min of sonication: 0.01 g mL^{-1} 50 µm Zn particles (B), 0.01 g mL^{-1} 4 µm particles (C), 0.04 g mL^{-1} 4 µm particles (D) and 0.1 g mL^{-1} 4 µm particles (E).

converges to a k value comparable to the untreated zinc. The observed dependence can be explained by the ultrasound-driven change of the particle morphology. During the first 10 min of modification, "hedgehogs" with increased surface areas are formed. After long exposure to US, the "hedgehogs" lose their spikes, which results in the loss of photocatalytic activity (Fig. 3).

The catalytic activity of the sononanostrustured Zn prepared at longer sonication times (up to 90 min) strongly depends on the concentration of the sonicated particles and the initial size of the Zn particles. The ~4 µm and ~50 µm zinc particles exhibit different photocatalytic activity. We observed, that 90 min US exposure leads to the highest reaction rate constant $k \sim 0.05$ min^{-1} for 10 mg of ~50 µm Zn particles, where the same amount of ~4 µm zinc particles reached $k \sim 0.03$ min^{-1}.

The fact that the modified ~4 µm and ~50 µm zinc particles exhibit different activities could be explained by the higher concentration of ZnO nanorods randomly attached to the bigger Zn core, which are more accessible to the MO molecules. The difference in the surface morphology of both samples (~4 µm and ~50 µm Zn particles) can be clearly seen in the SEM images in Fig. 5. Additionally, the surface area of the ~50 µm particles is 12 m^2 g^{-1} and 1.3 m^2 g^{-1} after 90 min-sonication. This is not the maximum surface area we could achieve for the

sononanostructured Zn. However, the 90 min-sonicated Zn-based materials exhibit the highest rate of MO conversion, which is probably due to the better accessibility of the ZnO nanorods formed in 90 min modification. The control experiments with commercial ZnO demonstrate an activity similar to US-Zn. The reaction rate constant of the commercial ZnO was estimated to be *ca.* 0.05 min^{-1}. In Fig. 5A we can also see the influence of the concentration of the sonicated particles on the rate constant. The optimal concentration of Zn particles during sononanostructuring was found 0.01 g mL^{-1}. The higher concentration of Zn particles leads to fast Zn modification but the nanorods might also be rapidly detached from the Zn core surface due to the vigorous interparticle collisions stimulated by the sonication. At the same time, the lower Zn concentration (<0.01 g mL^{-1}) leads to a reduction in the number of collision events between the particles. The particle modification became very slow and we could not achieve the "hedgehog" morphology and comparable catalytic activity.

4. Conclusions

We have shown that the sononanostructuring of zinc is an easy and green method for the production of a wide spectrum of interesting zinc-based materials with spectacular morphologies and functionalities, *i.e.*, core–shell "hedgehogs" and ZnO nanorods. By using ultrasound, the nanostrucruring of zinc can be performed in a fairly easy and cost efficient way,[7,8] avoiding aggressive media, harsh additives and oxidants. The Zn/ZnO "hedgehogs" have a Zn metallic core covered by ZnO nanorods. The form and length of these nanorods can be controlled by the sonication conditions. The "hedgehogs" demonstrate a good photocatalytic activity due to the semiconductive nature of the ZnO spikes. We do believe that the sonochemical approach to the nanostructuring of materials provides a novel methodology for the focused construction and functionalization of solids. The nanostructured semiconductor zinc-based material demonstrated here could be a promising component in the construction of a whole range of composite systems for photocatalysis, gas sensing, photovoltaic, *etc.* The metallic nature of the Zn core could be applied to the formation of corrosion protection systems.

Acknowledgements

References

1 K. S. Suslick, *Science*, 1990, **247**, 1439–1445.
2 K. S. Suslick, D. J. Casadonte, M. L. H. Green and M. E. Thompson, *Ultrasonics*, 1987, **25**, 56–59.
3 E. V. Skorb, D. G. Shchukin, H. Möhwald and D. V. Andreeva, *Nanoscale*, 2010, **2**, 722–727.
4 E. V. Skorb, D. Fix, D. G. Shchukin, H. Möhwald, D. V. Sviridov, R. Mousa, N. Wanderka, J. Schäferhans, N. Pazos-Pérez, A. Fery and D. V. Andreeva, *Nanoscale*, 2011, **3**, 985–993.
5 E. Skorb, D. Shchukin, H. Möhwald and D. Andreeva, *Langmuir*, 2010, **26**, 16973–16979.
6 D. V. Andreeva, D. V. Sviridov, A. Masic, H. Möhwald and E. V. Skorb, *Small*, 2012, **8**, 820–825.
7 N. Pazos-Perez, J. Schäferhans, E. V. Skorb, A. Fery and D. V. Andreeva, *Microporous Mesoporous Mater.*, 2012, **154**, 164–169.
8 J. Schäferhans, S. Gómez-Quero, D. V. Andreeva and G. Rothenberg, *Chem.–Eur. J.*, 2011, **17**, 12254–12256.
9 S. J. Pearton, D. P. Norton, K. Ip, Y. W. Heo and T. Steiner, *Prog. Mater. Sci.*, 2005, **50**, 293–340.
10 H. M. a. Ô. Ôzgûr, *Zinc Oxide, Fundamentals, Materials and Device Technology*, Wiley-VCH Verlag, Weinheim, 2009.
11 B. Dindar and S. Içli, *J. Photochem. Photobiol., A*, 2001, **140**, 263–268.
12 D. Li and H. Haneda, *Chemosphere*, 2003, **51**, 129–137.
13 S. K. Kansal, M. Singh and D. Sud, *J. Hazard. Mater.*, 2007, **141**, 581–590.
14 H. Fu, T. Xu, S. Zhu and Y. Zhu, *Environ. Sci. Technol.*, 2008, **42**, 8064–8069.
15 N. Daneshvar, D. Salari and A. R. Khataee, *J. Photochem. Photobiol., A*, 2004, **162**, 317–322.
16 H.-F. Lin, S.-C. Liao and S.-W. Hung, *J. Photochem. Photobiol., A*, 2005, **174**, 82–87.
17 C. Hariharan, *Appl. Catal., A*, 2006, **304**, 55–61.
18 K. G. Kanade, B. B. Kale, J.-O. Baeg, S. M. Lee, C. W. Lee, S.-J. Moon and H. Chang, *Mater. Chem. Phys.*, 2007, **102**, 98–104.
19 R. Ullah and J. Dutta, *J. Hazard. Mater.*, 2008, **156**, 194–200.
20 C. Ye, Y. Bando, G. Shen and D. Golberg, *J. Phys. Chem. B*, 2006, **110**, 15146–15151.
21 E. Yassıtepe, H. C. Yatmaz, C. Öztürk, K. Öztürk and C. Duran, *J. Photochem. Photobiol., A*, 2008, **198**, 1–6.
22 B. Pal and M. Sharon, *Mater. Chem. Phys.*, 2002, **76**, 82–87.
23 J. L. Yang, S. J. An, W. I. Park, G. C. Yi and W. Choi, *Adv. Mater.*, 2004, **16**, 1661–1664.
24 A. M. Ali, E. A. C. Emanuelsson and D. A. Patterson, *Appl. Catal., B*, 2010, **97**, 168–181.
25 M. R. Hoffmann, S. T. Martin, W. Choi and D. W. Bahnemann, *Chem. Rev.*, 1995, **95**, 69–96.
26 P. R. Gogate and A. B. Pandit, *Adv. Environ. Res.*, 2004, **8**, 501–551.
27 C. Comninellis, A. Kapalka, S. Malato, S. A. Parsons, I. Poulios and D. Mantzavinos, *J. Chem. Technol. Biotechnol.*, 2008, **83**, 769–776.
28 J. W. Tang, Z. G. Zou, J. Yin and J. H. Ye, *Chem. Phys. Lett.*, 2003, **382**, 175.
29 R. Asahi, T. Morikawa, T. Ohwaki, K. Aoki and Y. Taga, *Science*, 2001, **293**, 269.
30 X. Tao, W. Ma, T. Zhang and J. Zhao, *Angew. Chem., Int. Ed.*, 2001, **40**, 3014.
31 W. Ma, J. Li, X. Tao, J. He, Y. Xu, J. C. Yu and J. Zhao, *Angew. Chem., Int. Ed.*, 2003, **42**, 1029.
32 J. W. Tang, Z. G. Zou, J. Yin and J. H. Ye, *Angew. Chem., Int. Ed.*, 2004, **43**, 4463.
33 B. Pal and M. Sharon, *Mater. Chem. Phys.*, 2002, **76**, 82–87.
34 A. A. Aal, S. A. Mahmoud and A. K. Aboul-Gheit, *Mater. Sci. Eng., C*, 2009, **29**, 831–835.
35 E. YassItepe, H. C. Yatmaz, C. Öztürk, K. Öztürk and C. Duran, *J. Photochem. Photobiol., A*, 2008, **198**, 1–6.
36 E. R. Carraway, A. J. Hoffman and M. R. Hoffmann, *Environ. Sci. Technol.*, 1994, **28**, 786–793.
37 A. J. Hoffman, E. R. Carraway and M. R. Hoffmann, *Environ. Sci. Technol.*, 1994, **28**, 776–785.
38 S. Liao, H. Donggen, D. Yu, Y. Su and G. Yuan, *J. Photochem. Photobiol., A*, 2004, **168**, 7–13.
39 J. J. Wu and S. C. Liu, *Adv. Mater.*, 2002, **14**, 215–218.
40 M. Bizarro, *Appl. Catal., B*, 2010, **97**, 198–203.
41 C. Pacholski, A. Kornowski and H. Weller, *Angew. Chem., Int. Ed.*, 2002, **41**, 1188–1191.
42 P. V. Kamat, *Pure Appl. Chem.*, 2002, **74**, 1693–1706.
43 A. Wood, M. Giersig and P. Mulvaney, *J. Phys. Chem. B*, 2001, **105**, 8810–8815.
44 F. Han, V. S. R. Kambala, M. Srinivasan, D. Rajarathnam and R. Naidu, *Appl. Catal., A*, 2009, **359**, 25–40.
45 M. Bizarro, M. A. Tapia-Rodríguez, M. L. Ojeda, J. C. Alonso and A. Ortiz, *Appl. Surf. Sci.*, 2009, **255**, 6274–6278.
46 J. M. Herrmann, *Top. Catal.*, 2005, **34**, 49–65.
47 C. A. K. Gouvêa, F. Wypych, S. G. Moraes, N. Durán, N. Nagata and P. Peralta-Zamora, *Chemosphere*, 2000, **40**, 433–440.
48 S. Brunauer, L. S. Deming, W. E. Deming and E. Teller, *J. Am. Chem. Soc.*, 1940, **62**, 1723–1732.

small

Metal Capsules

A sonodesigned metal-based sponge can form as a surface layer on metal capsules with the possibility of multicomponent loading and time-resolved release. The capsules can be loaded with active agents, such as corrosion inhibitors, vitamins and drugs, enzymes, DNA fragments, or antibodies. The porous layer is continuous with the bulk metal allowing for excellent double-side adhesion during the construction of a feedback (anticorrosion, biocide) coating. This system could potentially be used to develop new medical therapies, such as laboratory organ/tissue growth for human transplants.

Nanoengineered Metal Surface Capsules: Construction of a Metal-Protection System
E. V. Skorb et al.

Nanoengineered Metal Surface Capsules: Construction of a Metal-Protection System

Daria V. Andreeva, Dmitry V. Sviridov, Admir Masic, Helmuth Möhwald, and Ekaterina V. Skorb*

The huge economic impact arising from the degradation of metal surfaces in a whole range of industries (e.g., the medical, pharmaceutical, food, automotive, and maritime industries) promotes the development of novel protective strategies.[1,2] The economical impact of corrosion damage only in the USA was estimated to be 276 billions US dollars per year.[2] As far as public safety and protecting of environment are concerned, effective, inexpensive, and environmentally friendly technologies for surface damage prevention are required. Here we suggest a novel method for a metal protective system based on the ultrasound treatment of metal surfaces.

Acoustic cavitation offers the unique potential for locally establishing high-temperature (up to 5000 K) and high-pressure (several hundreds of bars) reactions, while the system remains macroscopically near room temperature and ambient pressure.[3] Interactions between cavitation bubbles and solids lead to interfacial melting, plastic deformation, etching, and oxidation of the latter. Thus, ultrasound could be effectively used for surface modification and could even replace some expensive, multistage, and time-consuming methods of surface engineering.[4] The ultrasound treatment here is a fast and environmentally friendly method: the treatment is performed in aqueous solution. It can be applied to large surfaces by using a series of sonotrodes. Recently we suggested employing high-intensity focused ultrasound for the modification of metal surfaces. We demonstrated that at certain conditions ultrasound-assisted modification of metal surface leads to the formation of a 200-nm-thick mesoporous metal layer (a so-called "surface metal sponges").[5] The surface metal sponges have high surface area and strong adhesion to the bulk material. The porous matrix of the sponges can be loaded with an active compound and can be easily covered by different coatings due to the high roughness of the sonochemically modified layer. Here we use the surface metal sponges as a component of an encapsulation system for metal protection.

In general, the encapsulation system suggested here consists of the following components: the sonochemically formed surface metal sponges adhered to the bulk metal, which can be loaded with a variety of agents (corrosion inhibitors, biocides, enzymes, DNA fragments, antibodies, etc.), and a protective coating, a soft matter layer. Thus, the loaded metal sponges have the functionality of porous capsules. Compared to existing encapsulation systems,[6] the surface capsules are continuous with the bulk metal and do not need to be immobilized on the surface or incorporated into a protective coating. Furthermore, the rough surface of the metal capsules provides excellent adhesion for a protective coating. For the proof of concept of this novel surface protection method, we loaded the surface capsules with doxorubicin (antibiotic), benzotriazole (corrosion inhibitor), and 8-hydroxyquinoline (antiseptic), and we covered the capsules with a sol-gel coating.

Surface sponges can function as a system that can be used for encapsulation of active compounds (AC), as shown in **Figure 1**. The scanning electron microscopy (SEM) images show the cross-section (Figure 1b) and the surface (Figure 1c) of the sponges' layer. The pore size and volume as well as the surface composition of ultrasonically formed metal sponges has been studied in detail and previously reported.[5] The average pore diameter, ~4–7 nm, and surface area, up to 80 m^2/g, were estimated for aluminum sponges. In addition to the geometric features, the porous sponges are covered by a thin (up to 2 nm) metal oxide layer that might positively influence the upload of AC. The X-ray diffraction (XRD) patterns (Figure S1, Supporting Information (SI)) provide evidence that a thin oxide layer consists of bayerite $Al(OH)_3$ and böhmite $AlO(OH)$. The quantity of bayerite increases during the formation of the porous structure, which corresponds to the increase of the surface area of the sample. Surface –OH groups of the metal oxide layer may allow for chemisorption of AC (Figure S2, SI). Regulation of porosity, roughness and surface chemistry of metal sponges, and, therefore, the morphology and properties of the metal capsules can be achieved by varying i) the sonication time, ii) solvent, iii) and by using different metals and metal alloys.[5]

Dr. D. V. Andreeva
Physical Chemistry II
University of Bayreuth
Universitatstr. 30, 95440 Bayreuth, Germany

Prof. D. V. Sviridov
Chemistry Department
Belarusian State University
Leningradskaya str. 14, 220030 Minsk, Belarus

Dr. A. Masic, Prof. H. Möhwald, Dr. E. V. Skorb
Interface and Biomaterial Departments
Max Planck Institute of Colloids and Interfaces
Am Mühlenberg 1, 14476 Potsdam, Germany
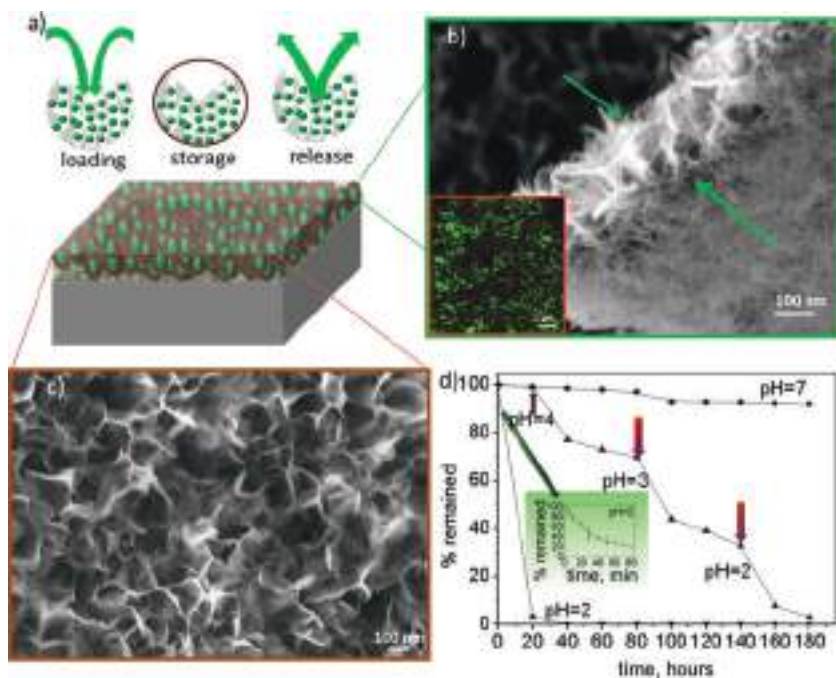E-mail: skorb@mpikg.mpg.de

Figure 1. a) Schematic illustration of upload, storage, and release of active component (upper row) and general view of capsules generated at the metal surface (below). b) SEM image of the cross-section of the aluminum sponge-like layer (indicated by arrows). Inset: the luminescent confocal image (top view) of the surface capsules loaded with doxorubicin. c) SEM image of the rough surface of the metal surface sponges. d) Doxorubicin release under different pH (inset shows time-resolved release at acid pH = 2).

than 2, the release continues due to the degradation of the metal oxide and dissolution of aluminum. Thus, the generation of a pH-responsive encapsulation system on a metal surface can be carried out in a single-step.

In the Type II system (Figure 2d), the surface sponges can be used for the construction of metal–polyelectrolyte (PE) capsules in order to store AC and to release them on demand (**Figure 3**). The pores of the metal sponges can be simply sealed by PE complexes.[9,10] The PE complexes are a universal encapsulation and carrier system and provide safe storage of the AC and can release them in response to external stimuli (pH,[9a] ionic strength,[9b] temperature,[9c] light,[9d,11] etc.). In this case, we do not need a specific interaction (chemisorptions) between the metal surface and AC. The principle involved in loading the surface capsules is the same as was suggested for mesoporous capsules.[12] The upload and release of the AC can be controlled by the formation of complexes between the AC and PE.[9] The AC/PE complex has one or two pH windows (pH regions of complex instability), which provides an easy way to manipulate upload and release. These pH windows can be adjusted by choosing the appropriate PE compositions. The formation
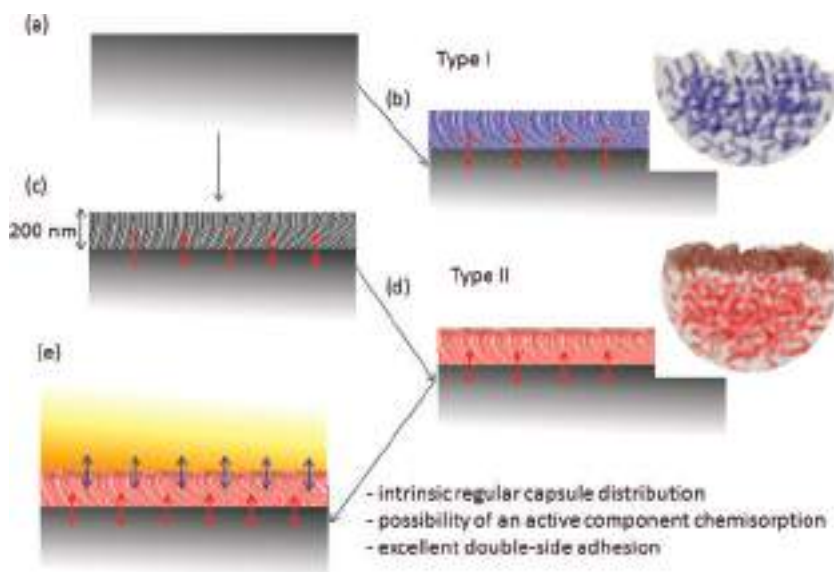
Here we propose two types of encapsulation systems based on the surface metal sponges. Both types are schematically illustrated in **Figure 2**. The simultaneous activation and modification of the metal surface and AC by ultrasound occurs in Type I. The metal capsules can be formed and loaded by ultrasound treatment of the metal surface in presence of an active component. As a model we used a fluorescent antibiotic, doxorubicin. Doxorubicin can form active radicals[3] and can be attached to an activated metal surface during sonication.[3,7] To successfully achieve formation of the surface capsules loaded with doxorubicin, the aluminum surface was sonicated in a 0.005 M aqueous solution of doxorubicin in a thermostated flow cell at 20 kHz and an intensity of 57 W/cm^2. The metal surface capsules loaded with doxorubicin[8] are shown in Figure 1b (inset). Attenuated total reflectance (ATR) IR spectra (Figure S2, SI) confirm the chemisorption of doxorubicin. The pH-dependent release from such capsules is shown in Figure 1d. At pH = 7, the encapsulation system is very stable, and a negligible release from the capsules can be detected. At pH = 2–4, we monitored the step-wise release of chemisorbed doxorubicin. At pH values lower

Figure 2. Scheme showing the formation of surface capsules on the metal surface: a) the initial metal plate, b) the single step involved in the encapsulation system of Type I, in which there is simultaneous activation of the metal surface and active component, c) the sonochemically formed layer of surface metal sponges for design of system of Type II, d) the encapsulation system of Type II, in which the surface is loaded with an active agent and protected by a polyelectrolyte complex, e) the encapsulation system of Type II, in which the surface is covered by a sol-gel coating and used for corrosion tests. The adhesion of the capsules' layer to the bulk metal is indicated with red arrows. Blue arrows indicate the high adhesion of a sol-gel coating to the rough surface of the surface capsules.
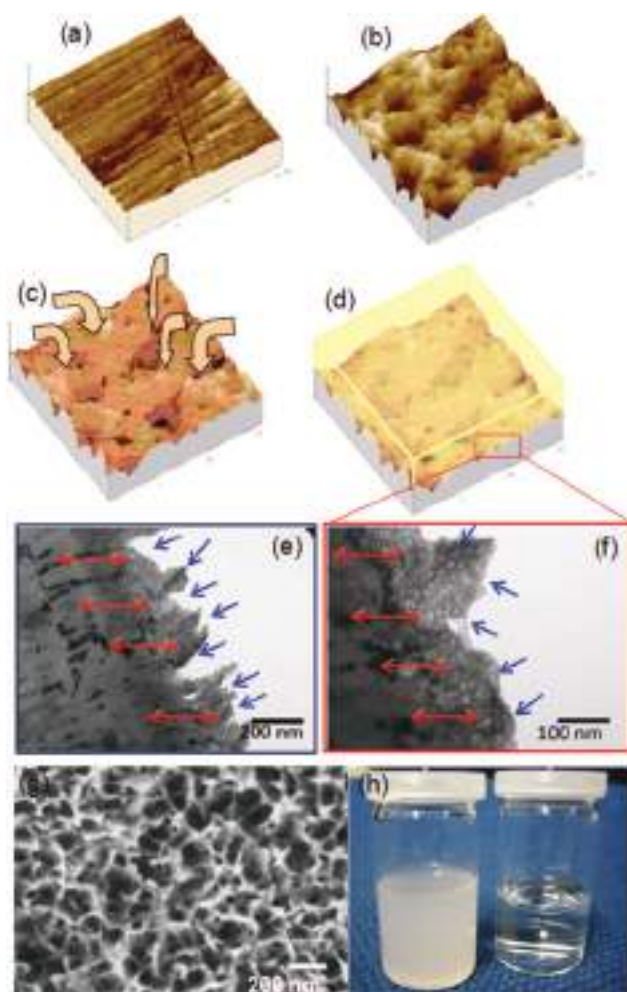
© 2012 Wiley-VCH Verlag GmbH & Co. KGaA, Weinheim

Figure 3. Schemes based on atomic force microscopy (AFM) images: a) polished aluminum before modification; b) sonochemically modified aluminum; c) aluminum loaded with surface AC, and d) covered by a polyelectrolyte complex. The surface capsule layer is protected by a polymer film. e,f) Transmission electron microscopy (TEM) images of aluminum with a surface capsule layer for AC storage (blue arrows indicate the loading direction, red arrows indicate the interface between the bulk metal and capsules' layer). g) SEM image of the sonochemically produced capsules' layer (metal sponges) loaded with 8-HQ/PSS; h) visual test of the 8-HQ/PSS complex formation at pH = 7 (turbid solution, left) and its disintegration at pH = 10 (clear solution, right).

of the surface metal capsules sealed by a AC/PE complex is shown in Figure 3a–d. Here, the ultrasonically formed 200-nm-thick metal sponge layer (Figure 3e,f) was saturated by 8-hydroxyquinoline (8-HQ) or benzotriazole (BTA) after being exposed to their solutions, and then washed and dried. The plates were then immersed for 15 min in a 2 mg/mL aqueous solution of negatively charged sodium polystyrene sulfonate (PSS). The pores were sealed due to the complexation between the AC (8-HQ or BTA) and the polyelectrolyte (PSS). The stability of the AC/PE complex was visually tested at different pH values (Figure 3h). The 8-hydroxyquinoline/ PSS complex is formed at pH = 7 (turbid solution, Figure 3a, left), and it disintegrated at pH = 10 (clear solution, Figure 3a, right).

Three different pH regions were analysed: pH > 10, pH = 7, and pH < 3. The release of the AC from the surface capsules at different pH is shown in Figure S3 in the SI. The rough metal surface even after pore sealing with the AC/PE complex (Figure 3g) provides a perfect adhesion for further coatings (for example in industrial application, primer- or pigment-containing top coatings) on the metal surface covered by surface capsules.

The high anticorrosion impact of the sonochemically modified metal surface was measured by a scanning vibrating electrode technique (SVET) (**Figure 4**). We tested the capsules loaded with BTA, a corrosion inhibitor, and covered by a sol-gel coating (Figure 2e). The local changes in pH accompanying the corrosion process leads to the disintegration of the BTA and polyelectrolyte (PSS). The inhibitor can be released from the capsules and heal the corrosion pits. When the pH returns to the initial value, the pores are closed again due to complex recovery.[10][d] The 3D SVET maps demonstrate the ionic currents above the mechanically defected surface. The sample (Figure 4b) with surface capsules loaded with a corrosion inhibitor, here BTA, exhibits very high corrosion resistance in 0.1 M NaCl. The naked aluminum surface (Figure 4a) is rapidly corroded in the same conditions.

The surface capsules loaded with 8-HQ provide long-term antiseptic activity of the metal surface. The metal surface contaminated by *E. Coli* bacteria before and after biocide release is shown in Figure 4c and d, respectively. The bacteria were visualized by the LIVE/DEAD BacLight Bacterial Viability Kits reactive. This method provides a sensitive, fluorescence-based assay for bacterial cell viability. The reagent employs two nucleic acid stains: the green-fluorescent SYTO 9 stain and the red-fluorescent propidium iodide stain. Live bacteria with intact membranes fluoresce green, while dead bacteria with damaged membranes fluoresce red. Live and dead bacteria visualization (Figure 4c,d) provides evidence of the high biocide activity of the metal surface with 8-HQ-loaded capsules.

Thus, we have presented a novel encapsulation system based on a sonochemically formed porous metal layer, which is continuous with the bulk metal. The high surface area of this layer allows the upload of active components (corrosion inhibitors, antiseptics, antibiotics, DNA fragments, etc.). We propose two types of encapsulation systems (Figure 2). According to the Type I system, the spontaneous release of loaded components from the surface capsules can be prevented through chemisorption of the AC to the porous metal capsules due to presence of –OH groups. In the Type II encapsulation system, complex formation between an AC and PE can be used. Both encapsulation systems suggested here could solve crucial problems in surface engineering and surface protection: adhesion of a protective system to the surface and release of an active compound on demand. The surface metal capsules are continuous with the bulk metal, and the capsule does not need to be immobilized on the surface or incorporated and distributed in the protective coating. The high roughness of the sonochemically modified metal surface allows excellent long-term adhesion of traditional protective coatings. This novel concept based on surface metal sponges opens prospects in metal nano-engineering and
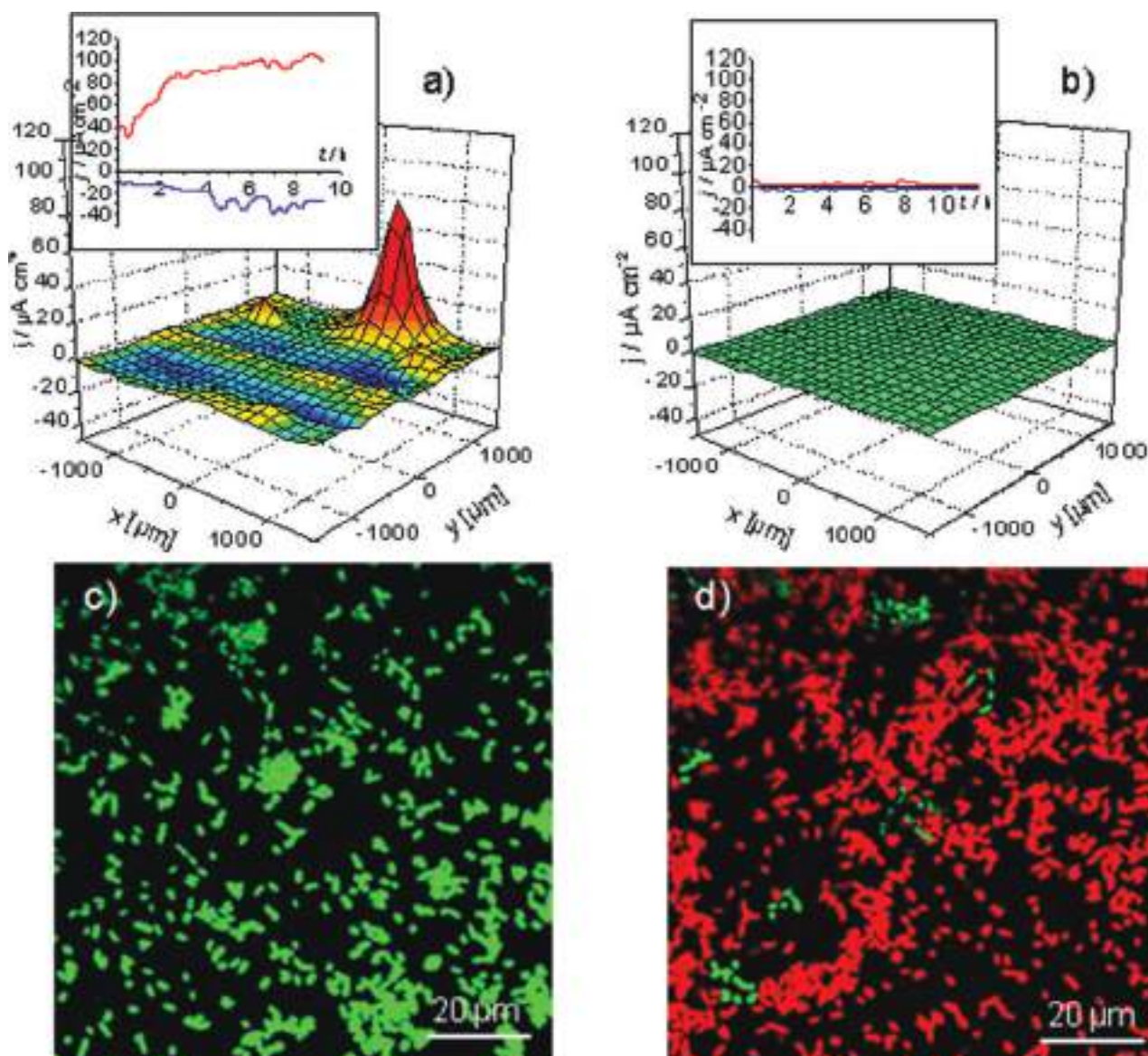
Figure 4. a,b) 3D SVET maps of the ionic currents above the defected aluminum surface area: naked (a) and covered by the surface capsules loaded with benzotriazole (b). The capsules are sealed by complexation with PSS. The measurements were performed in 0.1 M NaCl. The insets show the kinetics of anodic (red) and cathodic (blue) corrosion activity. c,d) Confocal images show the inactivation of *E. Coli* due to 8-hydroxyquinoline release from the surface capsules' layer: before release stimulation (c) and after release (d). Inactivated bacteria are red, and living bacteria are green.

surface protection as well as in encapsulation and polyelectrolyte applications.

Experimental Section

Materials: Aluminum was used as a model metal substrate, which has the ability to assist with the ultrasonic formation of surface metal sponges. For all experiments, aluminum samples of 10 mm × 20 mm were polished and degreased in isopropanol flow and rinsed in purified water. For the confocal experiments a 200 nm thick aluminum layer was deposited by evaporation to a glass substrate of the same size. Doxorubicin, 8-HQ, BTA, PSS (molecular weight, M_W = ~70 kDa), zirconium *n*-propoxide (TPOZ),

3-glycidoxypropyltrimethoxysilane (GPTMS), propanol, ethylacetoacetate, and HNO_3 were purchased from Sigma-Aldrich. The water was purified in a three-stage Millipore Milli-Q Plus 185 purification system and had a resistivity higher than 18.2 MΩ cm.

Preparation of Surface Capsules, Loading and Release Experiments, Type I: In a single step, each plate was sonicated in a 0.005 M aqueous solution of doxorubicin in a thermostated flow cell (FC100L1-1S) at 65 °C with a VIP1000hd (Hielscher, Germany) operated at 20 kHz with a maximal output power of 1000 W, ultrasonic horn BS2d22 (head area of 3.8 cm²), and equipped with a booster B2-1.2. The maximum intensity was calculated to be 57 W/cm² at a mechanical amplitude of 81 μm.

Preparation of Surface Capsules, Loading and Release Experiments, Type II: Following a general method involving serveral

steps, the aluminum plate is first sonicated as indicated for the Type I preparation. Afterwards, the samples were placed in solutions of 8-HQ or BTA within pure water; they were then pumped under vacuum for 30 min, washed, and dried. The procedure was repeated 5 times to achieve higher loading capacity.[12] Then the plates were placed for 15 min in a 2 mg/mL aqueous solution of PSS to achieve pore closure due to the complexation between the active component (AC: 8-HQ; BTA) and polyelectrolyte (PSS).

The loading of surface capsules was monitored by ATR spectra. To record ATR FT-IR spectra, an FT-IR microscope (Hyperion 2000, Bruker Optics, Germany) equipped with a liquid-nitrogen-cooled detector and connected to a Vertex 70 FT-IR spectrometer (Bruker GmbH, Germany) was used. The IR beam was focused on the sample surface through an ATR objective (Bruker Optics, Germany), which is characterized by a Ge internal reflection element with a tip of 100 μm. A total of 256 scans were co-added per sample spectrum and apodized, applying the Blackman–Harris three-term function and a zero filling-factor of 2.

The release of AC was studied in aqueous solution using UV–vis spectra at chosen time intervals. Different pH regions were analysed.

Formation of Sol-Gel Coating onto Metal Plate: For corrosion tests the plates were covered with a hybrid SiO_x/ZrO_x based film.[12] The hybrid film was obtained by a controllable sol-gel route in *n*-propanol. Two different sols were combined together, forming a final sol, which was applied on the aluminum alloy. The first sol was prepared by hydrolyzing TPOZ (70 wt% TPOZ precursor in *n*-propanol) mixed with ethylacetoacetate (1:1 volume ratio) by the addition of acidified water (pH < 1). At first, the mixture of TPOZ and ethylacetoacetate was stirred under ultrasonic agitation at room temperature for 20 min to achieve complexation of the precursor. Then, acidified water in a 1:3 molar ratio (Zr/H_2O) was added to the mixture drop by drop, and the mixture was agitated for 1 h. The second organosiloxane sol was obtained by hydrolyzing GPTMS in 2-propanol by addition of acidified water in a 1:3:2 (GPTMS/2-propanol/water) molar ratio. In the final step, the zirconia-based sol was added drop by drop to the second organosiloxane sol in a 1:2 volume ratio. The resulting sol-gel system was ultrasonically agitated for 60 min and aged for 1 h at room temperature before deposition on the aluminum alloy. The AFM estimated film thickness was ca. 1.5 μm.

Corrosion Test: SVET experiments were performed using the equipment supplied by Applicable Electronics (Forestdale, MA, USA). The immersion solution was 0.1 M NaCl. Scans were initiated within 5 min of immersion and were collected every 30 min for the duration of the experiment, typically 16 h.

Biocide Activity Study: The biocide properties of the plates with surface capsules that were loaded with 8-HQ were analyzed. A rapid epifluorescence staining method using the LIVE/DEAD Bacterial Viability Kit (BacLight) was applied to estimate both viable and total counts of bacteria on the surface of the plate with surface capsules. The plate for these experiments was glass with a 200 nm layer of aluminum loaded with 8HQ. The surface was scanned before and after 8-HQ release with a Leica TCS SP inverted confocal microscope system (Leica, Germany) equipped with a 100× and 40× oil immersion objective having a numerical aperture of 1.4 and 1.25, respectively. An Ar-ion (488 nm, 514 nm) and a He-Ne laser (543 nm) were used as excitation sources and chosen according to the fluorophore in the sample.

BacLight is composed of two nucleic-acid-binding stains: SYTO 9TM and propidium iodide. SYTO 9TM penetrates all bacterial membranes and stains the cells green, while propidium iodide only penetrates cells with damaged membranes, and the combination of the two stains produces red fluorescing cells.

Supporting Information

Supporting Information is available from the Wiley Online Library or from the author.

Acknowledgements

[1] G. H. Koch, M. P. H. Brongers, N. G. Thompson, Y. P. Virmani, J. H. Payer, www.nace.org.

[2] a) Advanced Drug Delivery, (Eds: M. M. de Villier, Y. M. Lvov), **2011**, *63*, 699; b) E. J. Anglin, L. Cheng, W. R. Freeman, M. J. Sailor, *Advanced Drug Delivery* **2008**, *60*, 1266.

[3] a) M. A. Margulis, *Sonochemistry Basis*, High School, Moscow, **1984**; b) H. Endo, *J. Acoust. Soc. Am.* **1994**, *95*, 2409; c) L. H. Thompson, L. K. Doraiswamy, *Ind. Eng. Chem. Res.* **1999**, *38*, 1215; d) K. S. Suslick, L. A. Crum, *Encyclopedia of Acoustics* (Ed: M. J. Crocker), Wiley & Sons. Inc., New York **1995**; e) T. Prozorov, R. Prozorov, K. S. Suslick, *J. Am. Chem. Soc.* **2004**, *126*, 13890; f) D. G. Shchukin, E. V. Skorb, V. Belova, H. Möhwald, *Adv. Mater.* **2011**, *23*, 1922.

[4] a) O. D. Velev, P. M. Tessier, A. M. Lenhoff, E. W. Kaler, *Nature* **1999**, *401*, 548; b) H. J. Shin, R. Ryoo, Z. Liu, O. Terasaki, *J. Am. Chem. Soc.* **2001**, *123*, 1246.

[5] a) E. V. Skorb, D. G. Shchukin, H. Möhwald, D. V. Andreeva, *Nanoscale* **2010**, *2*, 722; b) E. V. Skorb, H. Möhwald, T. Irrgang, A. Fery, D. V. Andreeva, *Chem. Comm.* **2010**, *46*, 7897; c) D. V. Andreeva, *Int. J. Mater. Res.* **2011**, *102*, 597; d) E. V. Skorb, D. G. Shchukin, H. Möhwald, D. V. Andreeva, *Langmuir.* **2010**, *26*, 16973.

[6] a) D. G. Shchukin, H. Möhwald, *Chem. Commun.* **2011**, *47*, 8730; b) D. V. Andreeva, D. G. Shchukin, *Materials Today* **2008**, *11*, 24; c) D. G. Shchukin, H. Möhwald, *SMALL* **2007**, *3*, 926; d) H. Lomas, A. P. R. Johnston, G. K. Such, Z. Zhu, K. Liang, M. P. van Koeverden, S. Alongkornchotikul, F. Caruso, *Small* **2011**, *7*, 2109.

[7] M. Stamm, *Polymer Surfaces and Interfaces*, Springer, Berlin **2008**.

[8] a) H. Wendel, E. Stanchina, J. Fridman, A. Malina, S. Ray, S. Kogan, C. Cordon-Cardo, J. Pelletier, S. Lowe, *Nature* **2004**, *428*, 332; b) N. Lomovskaya, S. L. Otten, Y. Doi-Katayama, L. Fonstein, X.-C. Liu, T. Takatsu, A. I.-Solari, S. F. F. Torti, A. L. Colombo, C. R. Hutchinson, *J. Bacteriol.* **1999**, *181*, 305.

[9] a) G. B. Suchorukov, A. L. Rogach, B. Zenli, T. Liedl, S. G. Skirtach, K. Köhler, A. A. Antipov, N. Gaponik, A. S. Suscha, M. Winterhalter, W. J. Parak, *Small* **2005**, *1*, 194; b) G. Decher, *Science* **1997**, *277*, 1232; c) Y. Lvov, F. Caruso, *Anal. Chem.* **2001**, *73*, 4212; d) J. Hiller, J. D. Mendelsohn, M. F. Rubner, *Nat. Mater* **2001**, *1*,

59; e) S. Srivastava, N. Kotov, *Acc. Chem. Res.* **2008**, *41*, 1831; f) E. Kharlampieva, V. Kozlovskaya, S. A. Sukhishvili, *Adv. Mater.* **2009**, *21*, 1.

[10] a) V. Kozlovskaya, S. A. Sukhishvili, *Macromolecules* **2006**, *39*, 5569; b) D. O. Grigoriev, K. Köhler, E. V. Skorb, D. G. Shchukin, H. Möhwald, *Soft Matter* **2009**, *5*, 1426; c) J. A. Jaber, J. B. Schlenoff, *Macromolecules* **2005**, *38*, 1300; d) E. V. Skorb, D. G. Shchukin, in *European Coatings Tech Files* (Ed: G. Gehrenkemper), Vincentz Network GmbH & Co, Germany **2010**; e) D. V. Andreeva, D. Fix, H. Möhwald, D. G. Shchukin, *Adv. Mater.* **2008**, *20*, 2789; f) D. V. Andreeva, E. V. Skorb, D. G. Shchukin, *Appl. Mater. Interfaces* **2010**, *2*, 1954.

[11] a) E. V. Skorb, A. Skirtach, D. V. Sviridov, D. G. Shchukin, H. Möhwald, *ACS Nano* **2009**, *3*, 1753; b) A. Skirtach, P. Karageorgiev, M. F. Bedard, G. B. Sukhorukov, H. Möhwald, *J. Am. Chem. Soc.* **2008**, *130*, 11572; c) A. G. Skirtach, A. M. Javier, O. Kreft, K. Köhler, A. P. Alberola, H. Möhwald, W. J. Parak, G. B. Sukhorukov, *Angew. Chem. Int. Ed.* **2006**, *118*, 4728.

[12] E. V. Skorb, D. Fix, D. V. Andreeva, H. Möhwald, D. G. Shchukin, *Adv. Funct. Mater.* **2009**, *19*, 2373.